Handbook of Aluminum

Volume 1
Physical Metallurgy and Processes

Handbook
of Aluminum

Volume 1
Physical Metallurgy and Processes

edited by

George E. Totten
G. E. Totten & Associates, Inc.
Seattle, Washington, U.S.A

D. Scott MacKenzie
Houghton International Incorporated
Valley Forge, Pennsylvania, U.S.A.

Current printing (last digit):
10 9 8 7 6 5 4 3 2 1

PRINTED IN THE UNITED STATES OF AMERICA

Preface

Although there are a limited number of reference books on aluminum metallurgy, there is a significant and continuing need for a text that also addresses the physical metallurgy of aluminum and its alloys and the processing of those alloys that will be of long-term value to metallurgical engineers and designers. In addition, a number of vitally important technologies are often covered in a cursory manner or not at all, such as quenching, property prediction, residual stresses (sources and measurement), heat treating, superplastic forming, chemical milling, and surface engineering.

We have enlisted the top researchers in the world to write in their areas of specialty and discuss critically important subjects pertaining to aluminum physical metallurgy and thermal processing of aluminum alloys. The result is an outstanding and unique text that will be an invaluable reference in the field of aluminum physical metallurgy and processing.

This is the first of two volumes on aluminum metallurgy and some of the topics include:

- Pure aluminum and its properties.
- An extensive discussion of the physical metallurgy of aluminum, including effect of alloying elements, recrystallization and grain growth, hardening, annealing, and aging.
- Sources and measurement of residual stress and distortion.
- An overview of aluminum rolling, including hot rolling, cold rolling, foil production, basic rolling mechanisms, and control of thickness and shape.
- A detailed discussion of extrusion design.
- A thorough overview of aluminum welding metallurgy and practice.

- Casting, including design, modeling, foundry practices, and a subject often not covered in aluminum metallurgy books—casting in a microgravity environment.
- Molten metal processing and the use of the Stepanov continuous casting method.
- Forging design and foundry practice.
- Sheet forming.
- An overview of equipment requirements and a detailed discussion of heat treating practices.
- An in-depth discussion of aluminum quenching.
- An overview of machining metallurgy and practices, including material property dependence, machining performance process parameters, and design.
- An extensive, detailed, and well-referenced overview of superplastic forming.
- A thorough discussion of aluminum chemical milling, including pre-mask cleaning, maskant applications, and scribing, etching, and demasking.
- Powder metallurgy including: applications, powder production, part production technologies, and other processes.

The preparation of this book was a tremendous task and we are deeply indebted to all our contributors. We would like to express special thanks to Alice Totten and Patricia MacKenzie for their assistance and patience throughout the process of putting this book together. We would also like to acknowledge The Boeing Corporation and Houghton International for their continued support.

George E. Totten
D. Scott MacKenzie

Contents

Part Two   PROCESSING OF ALUMINUM

Appendixes

Contributors

Taylan Altan, Ph.D.   Ohio State University, Columbus, Ohio, U.S.A.

A. K. Balaji, Ph.D.   The University of Utah, Salt Lake City, Utah, U.S.A.

Charles E. Bates, Ph.D., F.A.S.M.   The University of Alabama at Birmingham, Birmingham, Alabama, U.S.A.

John T. Berry, Ph.D.   Mississippi State University, Mississippi State, Mississippi, U.S.A.

Niels Bogh, B.Sc.   International Thermal Systems, Puyallup, Washington, U.S.A.

Umesh Chandra, Ph.D.   Modern Computational Technologies, Inc., Cincinnati, Ohio, U.S.A.

Rafael Colás, Ph.D.   Universidad Autónoma de Nuevo León, San Nicolás de los Garza, Mexico

Carl E. Cross, Ph.D.   The University of Montana, Butte, Montana, U.S.A.

Shuvra Das, Ph.D.   University of Detroit Mercy, Detroit, Michigan, U.S.A.

D. Eskin, Ph.D.   Netherlands Institute for Metals Research, Delft, The Netherlands

Bruce M. Griffin, B.S.M.E.T., M.S.M.E. The Boeing Company, St. Louis, Missouri, U.S.A.

Robert Howard, B.Sc. Consolidated Engineering Company, Kennesaw, Georgia, U.S.A.

I. S. Jawahir, Ph.D. University of Kentucky, Lexington, Kentucky, U.S.A.

Kai F. Karhausen, Ph.D. VAW Aluminium AG, Bonn, Germany

Laurens Katgerman, Ph.D. Netherlands Institute for Metals Research, Delft, The Netherlands

Serhat Kaya, M.Sc. Ohio State University, Columbus, Ohio, U.S.A.

Antti S. Korhonen, D.Tech. Helsinki University of Technology, Espoo, Finland

Howard A. Kuhn, Ph.D. Scienda Building Sciences, Orangeburg, South Carolina, U.S.A.

Stephen Liu, Ph.D. Colorado School of Mines, Golden, Colorado, U.S.A.

D. Scott MacKenzie, Ph.D. Houghton International Incorporated, Valley Forge, Pennsylvania, U.S.A.

Weimin Mao, Ph.D. University of Science and Technology Beijing, Beijing, China

Kazuho Miyamoto, Dr.Eng. Miyamoto Industry Co. Ltd., Tokyo, Japan

Per Thomas Moe, M.Sc.-Eng. Norwegian University of Science and Technology, Trondheim, Norway

Joseph W. Newkirk, Ph.D. University of Missouri–Rolla, Rolla, Missouri, U.S.A.

Stanislav Prochorovich Nikanorov, Dr.Sc. A.F. Ioffe Physical Technical Institute of Russian Academy of Sciences, Saint Petersburg, Russia

David L. Olson, Ph.D. Colorado School of Mines, Golden, Colorado, U.S.A.

Ryotatsu Otsuka, Dr.Eng. Showa Aluminum Corporation, Osaka, Japan

Vsevolod Vladimirovich Peller A.F. Ioffe Physical Technical Institute of Russian Academy of Sciences, Saint Petersburg, Russia

Norman Ridley, B.Sc., Ph.D., D.Sc., C.Eng., F.I.M. University of Manchester, Manchester, England

Jeffrey R. Shenefelt, Ph.D. Mississippi State University, Mississippi State, Mississippi, U.S.A.

Kichitaro Shinozaki National Institute of Advanced Industrial Science and Technology, Tsukuba, Japan

James T. Staley, Ph.D.* Alcoa Technical Center, Alcoa Center, Pennsylvania, U.S.A.

Henry W. Stoll, Ph.D. Northwestern University, Evanston, Illinois, U.S.A.

Sigurd Støren, Ph.D. Norwegian University of Science and Technology, Trondheim, Norway

Alexey Sverdlin, Ph.D. Bradley University, Peoria, Illinois, U.S.A.

Hans M. Tensi, Ph.D. Technical University of Munich, Munich, Germany

William J. Thomas, Ph.D. General Motors, Troy, Michigan, U.S.A.

Murat Tiryakioğlu, Ph.D. Robert Morris University, Moon Township, Pennsylvania, U.S.A.

George E. Totten, Ph.D., F.A.S.M. G.E. Totten & Associates, Inc., Seattle, Washington, U.S.A.

Salvador Valtierra, Ph.D. Nemak Corporation, Monterrey, Mexico

Eulogio Velasco, Ph.D. Nemak Corporation, Monterrey, Mexico

Glenn M. Webster, A.A.S. G.E. Totten & Associates, Inc., Seattle, Washington, U.S.A.

---

*Retired

1

Introduction to Aluminum

ALEXEY SVERDLIN

Bradley University, Peoria, Illinois, U.S.A.

1 INTRODUCTION AND GENERAL OVERVIEW

Aluminum is the most heavily consumed non-ferrous metal in the world, with current annual consumption at 24 million tons. About 75% of this total volume, or 18 million tons, is "primary aluminum" (that is, aluminum extracted from ore, as opposed to secondary aluminum which is derived from scrap metal processing).

The ancient Greeks and Romans used alum in medicine as an astringent, and in dyeing processes. In 1761 de Morveau proposed the name "alumine" for the base in alum. In 1807, Davy proposed the name aluminium for the metal, undiscovered at that time, and later agreed to change it to aluminum. Shortly thereafter, the name aluminium was adopted by IUPAC to confirm with the "ium" ending of most elements. Aluminium is the IUPAC spelling and therefore the international standard. Aluminium was also the accepted spelling in the United States until 1925, at which time the American Chemical Society decided to revert back to aluminum, and to this day Americans still refer to aluminium as "aluminum".

While the opportunities are growing, aluminum must continue to compete with various materials that offer lower cost or other competitive advantages. Aluminum companies must continue to innovate to provide customers with better enabling technologies and superior materials with unique properties. Aluminum manufacturers must explore new process technologies to drive down production costs and make aluminum more competitive. Over the next two decades, investment in research and technology development may likely be the most important factor in product competitiveness.

The process of primary aluminum production can be divided into three independent stages which are, as a rule, carried out at different plants. These are:

- The actual mining of the necessary raw materials (bauxite and a variety of other ores);
- The processing of the ore and preparation of aluminum oxide (alumina);
- Production of primary aluminum from alumina.

World production of primary aluminum totaled 18.056 million metric tons in 1991 [1]. In 1983, more than 70% of the world's bauxite was produced in Australia, Guinea, Jamaica, Brazil, and the former Soviet Union. Bauxite reserves in the United States are less than 1% of the world total (Table 1).

Over the decade, 1983–1993, world production increased 20.3%, and annual growth rate of more than 2.0%. The United States accounted for 22.8% of the world's 1993 production while the European Community accounted for 12.5%. The Republics of the former Soviet Union accounted for 21.0%. The others 43.6% include Asia (11.6%), Canada (10.1%), South America (9.9%), Oceania (8.5%), and Africa (3.4%). The total U.S. supply in 1991 was 8,020 thousand metric tons, with primary production representing about 51.3% of total supply, imports accounting for 17.4%, and secondary recovery representing 31.2%.

World primary aluminum production from 1981 through 1991 is shown in Fig. 1. In 1995, U.S. primary aluminum smelters produced 3.375 million metric tons of aluminum, 17.3% of the total world production of 19.442 million metric tons (Fig. 2). Production of primary aluminum in 1996 in the United States was reported to be 3.577 million metric tons, an increase of about 6% over 1995. Recycling is a critical component of the aluminum industry; in 1995, secondary refiners recovered 3.188 million metric tons of recycled aluminum, representing a little more than one-third of the total U.S. aluminum supply of 9.265 million metric tons [2].

The world aluminum industry is composed of six large integrated firms, their subsidiaries, or affiliates Alcan Aluminum Ltd, Aluminum Company of America (Alcoa), Reynolds Metals Company, Kaiser Aluminum and Chemical Corporation, Pechiney, and Swiss Aluminum Limited (Alusuisse) and about 50 smaller publicly
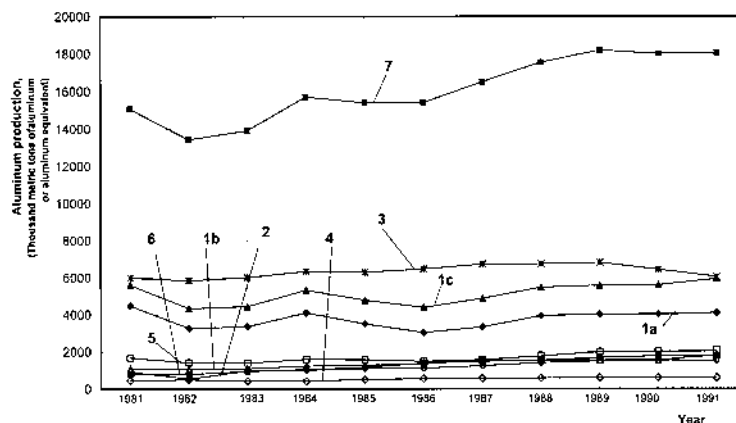
Figure 1   World primary aluminum production from 1981 through 1991: 1. North America (a – United States; b – Canada); 2. South America; 3. Europe; 4. Africa; 5. Asia; 6. Oceania; 7. World Total.

Table 1 World Primary Aluminum Production from 1981 through 1991 [1]

Country	1981	1982	1983	1984	1985	Years 1986	1987	1988	1989	1990	1991
North America	5605	4339	4444	5321	4782	4392	4883	5478	5585	5615	5951
a. United States	4489	3274	3353	4099	3500	3037	3343	3944	4030	4048	4121
b. Canada	1116	1065	1091	1222	1282	1355	1540	1534	1555	1567	1830
South America	788	795	938	1048	1153	1389	1486	1543	1692	1783	1794
Europe	5998	5838	6015	6330	6290	6471	6716	6747	6819	6445	6065
Africa	473	500	420	410	513	554	579	591	607	616	612
Asia	1682	1417	1390	1595	1568	1488	1577	1775	1995	2012	2091
Oceania	533	544	697	1001	1092	1118	1256	1414	1502	1542	1543
World Total	15079	13433	13904	15705	15398	15412	16517	17548	18200	18013	18056
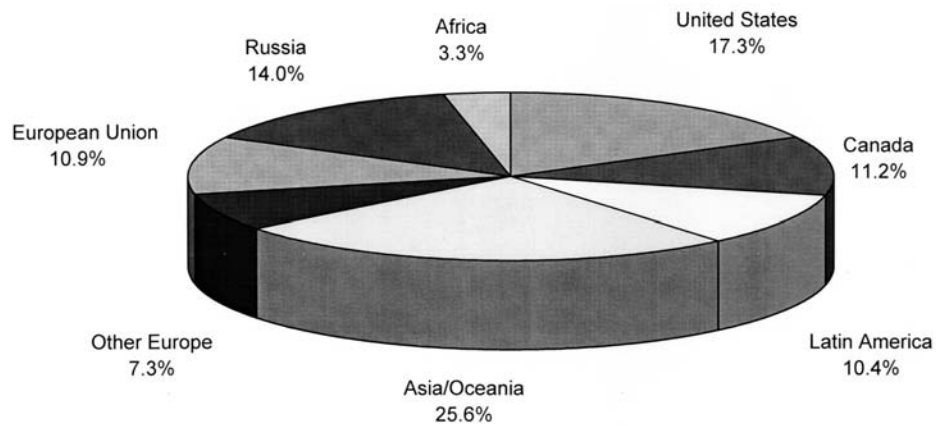
Figure 2　World primary aluminum production.
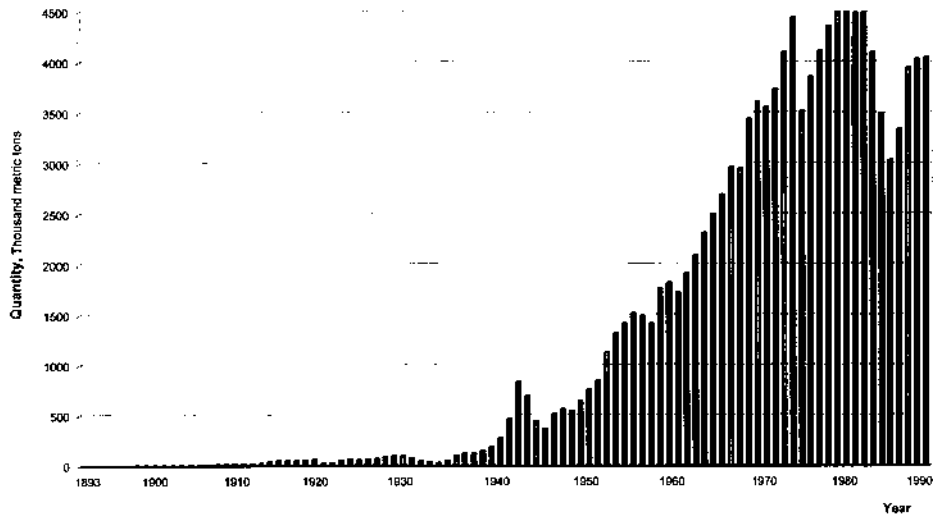
Figure 3　U.S. primary aluminum production.

owned companies, and governments of centrally planned and market economy countries that control about 40%, 25%, 35% and of world aluminum production capacity, respectively [3]. U.S. primary aluminum metal production from 1893 through 1990 is presented in Fig. 3 [4] and U.S. imports for consumption in April and 1999 year-to-date shown in Table 2 and Fig. 4. [5].

Although the United States continues to be the leading producer of primary aluminum metal in the world, its dominance in the industry has begun to wane. In 1960, the United States accounted for slightly more than 40% of the world's production. In 1990, the U.S. share of world production had decreased to 23%. Most

WORLD
TOTAL

a)
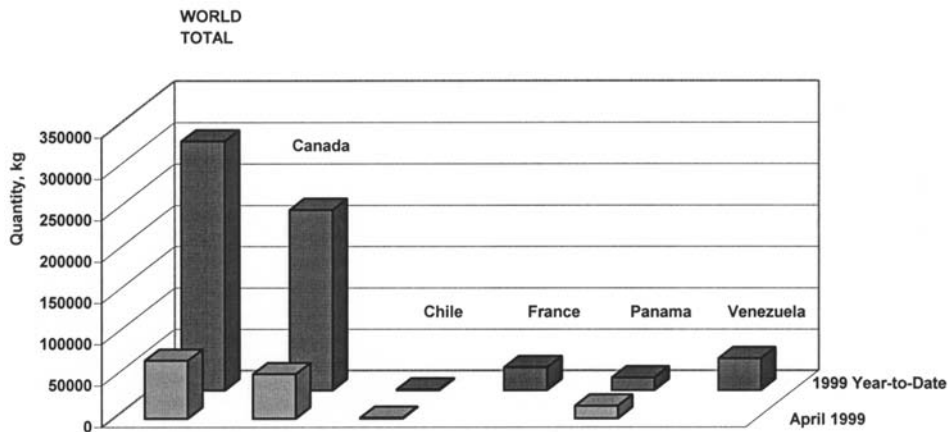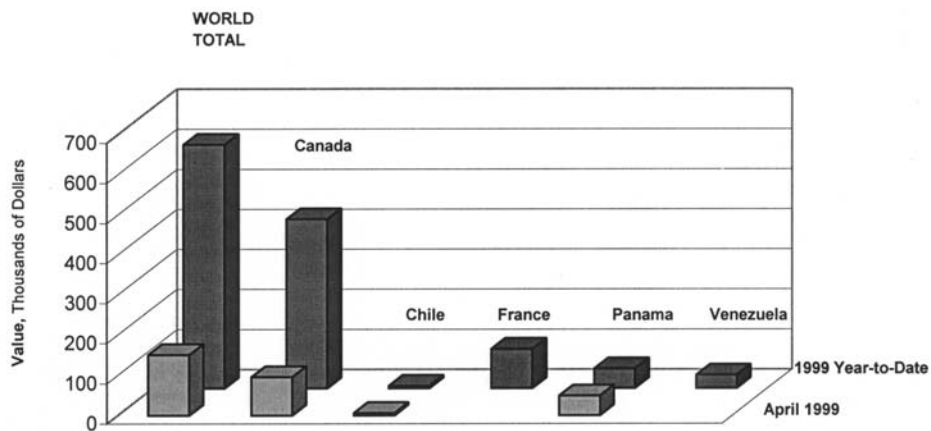
WORLD
TOTAL

b)

Figure 4 U.S. imports for consumption of aluminum: April 1999 and Year-to-Date cross-section dimension not greater than 9.5 mm in coils. (a) Quantity, in Kilograms; (b) Customs Value, in Thousands of Dollars.

of the restructuring of the world aluminum industry began in the late 1970s and continues to this day. Australia and Canada have emerged as major metal producers. Other countries entering the world market today are Brazil, China, Norway, Venezuela, and several countries in the Persian Gulf area [2].

Another factor that should be considered in analyzing the domestic aluminum industry is the growing importance of secondary aluminum to the domestic supply situation. Secondary aluminum is defined as aluminum recovered from both new and old purchased scrap. New scrap generated by fabrication of aluminum products

Table 2 U.S. Imports for Consumption of Aluminum: April 1999 and 1999 Year-to-Date (Customs Value, in Thousands of Dollars) (Units of Quantity: Kilograms)

Country	April 1999		1999 YTD	
	Quantity	Value	Quantity	Value
WORLD TOTAL	200,237,195	249,906	528,455,522	699,432
Australia	9,035,342	10,793	20,175,358	32,574
Austria	–	–	2,489	5
Bahrain	239,104	312	239,104	312
Brazil	619,451	748	3,231,529	4,353
Canada	57,287,283	73,741	200,313,608	267,738
China	–	–	8,219,905	10,966
Germany	238,594	310	274,266	1,091
France	7,190	44	39,391	736
India	1,517,506	1,839	1,792,797	2,342
Ireland	–	–	3,074	6
Japan	–	–	730	19
Mexico	2,813	4	3,630	6
Netherlands	20,504	28	21,978	31
New Zealand	12,712,597	15,572	20,158,130	26,158
Norway	–	–	18,5222	123
Russia	101,602,508	124,494	225,620,083	292,072
South Africa	–	–	7,278,263	9,080
Tajikistan	2,252,476	3,379	15,124,748	18,040
Turkey	21,000	21	21,000	21
United Arab Emirates	222,333	289	421,234	564
United Kingdom	–	–	85	6
Venezuela	14,458,494	18,332	25,495,598	33,191

may be either home scrap (sometimes called runaround scrap) or prompt industrial scrap. Home scrap is recycled within the company generating the scrap and consequently seldom enters the commercial secondary market. Prompt industrial scrap, however, is new scrap from a fabricator who does not choose to, or is not equipped to, recycle the scrap. This scrap then enters the secondary market. Old scrap is a product of obsolescence and becomes available to the secondary industry when consumer products have reached the end of their economic life and have been discarded. In 1960, 397,000 metric tons of aluminum was recovered from new and old scrap. In 1990, almost 2.4 million metric tons of aluminum was recovered from purchased scrap. More than half of this secondary aluminum was recovered from postconsumer, or old, scrap [1].

By 2000, total U.S. aluminum demand, including primary metal, old scrap, and nonmetal uses, is expected to reach about 9.3 million metric tons, equivalent to an annual rate of growth of 3.2% from the 1983 level. The forecast range of domestic aluminum demand in 2000 is 6.4–13 million tons. Rest-of-the-world aluminum demand in 2000 is expected to range from 29 to 56 million tons.

The annual production of primary metal in the United States is expected to decline to about 4 million tons per year by 2000, and the remainder of the U.S.

metal supply is expected to be obtained from other countries and the recycling of old scrap.

2 THE MAIN TYPES OF ALUMINUM ORES

In nature, aluminum does not exist as a metal because of the high chemical affinity for oxygen. Aluminum compounds, primarily the oxide in forms of various purity and hydration, are widely distributed in nature. In these forms, aluminum is the second most plentiful metallic element on Earth silicon—27.5%. It has been estimated that 8% of the Earth's crust is composed of aluminum. The elements are iron (approximately 5.0%), magnesium (approximately 2.0%), zinc and tin (0.004% each) [5–7], follow aluminum in content in the Earth's crust.

Although aluminum is one of the most abundant materials in the Earth's crust (invariably as alumina or in some other combined oxide form) any usable ore deposit must be readily amenable to benefice, so that a pure aluminum oxide can be obtained. However, physical benefice of the oxides has not been very successful. Consequently chemical processing has always been necessary to extract pure alumina from the other ingredients associated with it in the deposit. This, therefore, restricts the practical range of materials. Any chemical benefice must be based on selective removal of either the aluminum oxide or the other ingredients. However, frequently the other oxides are chemically similar, and this problem is compounded by the amphoteric behavior of aluminum which makes it extremely difficult to selectively remove the impurities (or "gangue"). Therefore benefice processes are usually based on selective dissolution of aluminum oxide. Kinetically, dissolution in strong caustic is favored. Therefore, mineralogical deposits which contain silica in structural forms that will readily dissolve in concentrated caustics, are unsatisfactory [8].

Bauxites contain hydrated forms of aluminum oxide, and are thus the most economically amenable mineralogical sources for chemical benefice to produce alumina. They occur in several different structural forms, depending on the number of molecules of water of hydration and also the crystalline form. The name "Bauxite" is derived from the village Les Baux in the south of France, where the mineral was first commercially exploited [8].

Historically, the commercial production of primary aluminum has been based almost entirely on the use of bauxite, in which aluminum occurs largely a hydrates of alumina. However, deposits containing aluminum in the other mineral forms are widespread and virtually inexhaustible. The average aluminum content of the Earth's crust has been estimated at 15.7% on an Al_2O_3 basis, and deposits containing more than 13% aluminum (25.0% Al_2O_3) are common [3].

Information on bauxite reserves and resources ranges from reports based on thorough exploration for some deposits to reports giving only a total quantity estimate based on unspecified field work for other deposits. The reserve and reserve-based estimates in Table 3 are the result of evaluating data and information obtained from many sources. Salient bauxite statistics from 1945 through 2000 presented in Fig. 5.

Major deposits of bauxite are located in countries remote from the main aluminum producing and consuming centers in North America and Europe. Most of the high grade bauxite deposits suitable for extraction of alumina occur in tropical

Table 3 World Bauxite Resources, January 1985 [3] (Million Metric Tons of Bauxite)

Region	Reserves	Reserve base*
North America and Caribbean Islands		
United States	38	40
Dominican Republic	30	45
Haiti	10	15
Jamaica	2,000	2,000
South America		
Brazil	2,250	2,300
Guyana	700	900
Suriname	575	600
Venezuela	235	240
Europe		
France	30	40
Germany	2	2
Greece	600	650
Hungary	300	300
Italy	5	5
Romania	50	50
Spain	5	5
Former Soviet Union	300	300
Yugoslavia	350	400
Africa		
Cameroon	680	800
Ghana	450	560
Guinea	5,600	5,900
Mozambique	2	2
Sierra Leone	140	160
Zimbabwe	2	2
Asia		
China	150	150
India	1,000	1,200
Indonesia	750	805
Malaysia	15	15
Pakistan	20	20
Turkey	25	30
Oceania		
Australia	4,440	4,600
Other	200	200
Total	21,000	23,000

*The reserve base includes demonstrated resources that are currently economic (reserves), marginally economic (marginal reserves), and some of those that are currently sub-economic (sub-economic resources)
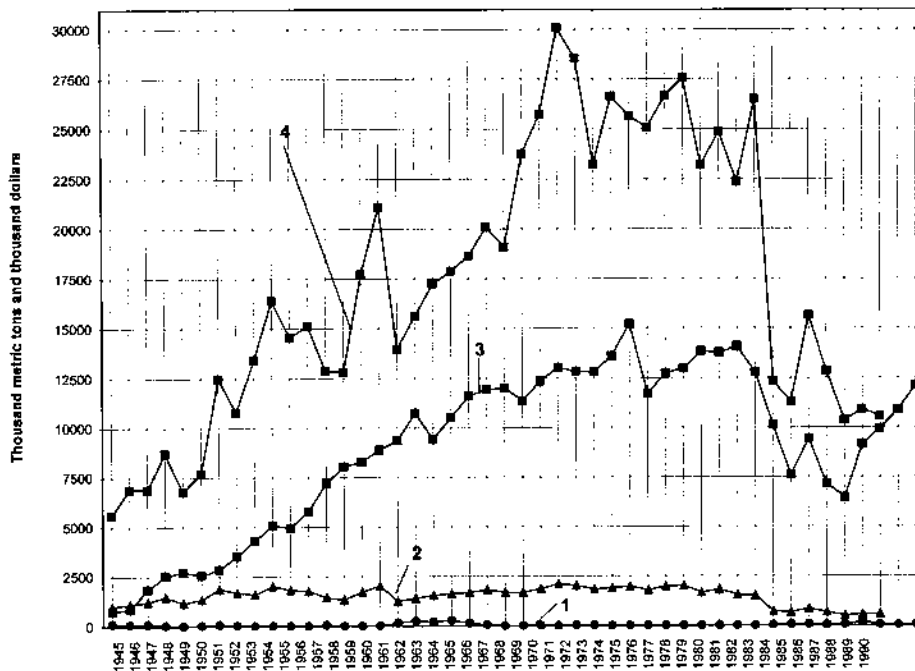
Figure 5 Salient bauxite statistics.

or semitropical regions. In all these deposits, the hydrated aluminum oxide is invariably associated with small amounts of compound of iron, silicon and titanium and trace amounts of other elements. Most of the tropical deposits are of a blanket-type which can be over 7 m thick and mined by open-cast methods. Inter-layered deposits and small pocket deposits are also found. Some of them are also amenable to open-cut mining. In physical appearance, the various bauxite deposits can differ considerably. This is due to prior weathering, basic variations In the crystalline form of the hydrated aluminum oxide, and variations in the nature of impurities associated with it [8].

Bauxite is found within 30 million-year-old weathered rock, which has broken down to leave a high proportion of aluminum bearing minerals. A combination of rainfall and organic acids caused the weathering of the dolomite and granite rocks until most of the elements are dissolved, leaving a reddish soil known as laterite which is rich in aluminum oxides and iron. The developed bauxite deposits are common throughout the world. Pure alumina (Al_2O_3) can be reduced comparatively cheaper and easier from bauxite. From alumina, the metallic aluminum can be received by electrolysis [8–12]. However, the comparative limitation of bauxite deposits and complex mining operations at many bauxite deposits have resulted the necessity of development of other types of raw materials to extract aluminum profitably.

The major deposits in central Arkansas were formed by weathering, during Eocene time, or nepheline syenite intrusive of Late Cretaceous age. The predominant aluminum oxide mineral in the bauxite is the trihydrate form, gibbsite. Some

deposits are residual on the igneous rock and clay, while others are the result of transportation and accumulation of eroded deposits. The composition of the ore mined in Arkansas varies widely within a range of 40% to 52% Al_2O_3, 7% to 17% SiO_2, and 6% to 12% Fe_2O_3.

The bauxite deposits in the coastal plain of Alabama and Georgia are found as lenses within flat-laying beds of kaoinitic clay, which are overlain by sand and clays of early Tertiary age. The grade of the bauxite is 48% to 56% Al_2O_3, 12% to 16% SiO_2, and less than 2.5% Fe_2O_3. The low iron oxide content qualifies this ore for use in refractories and chemicals [3].

In Jamaica, the bauxite deposits fill sinkholes, channels, and blanket uneven depressions in the karst surface of limestone of middle Tertiary age. Jamaican bauxite is largely gibbsitic, although mixture containing up to 20% monohydrate alumina occur. Ore grade is 45% to 49% Al_2O_3, 0.8% to 8% SiO_2, 17% to 22% Fe_2O_3, and 2.5% TiO_2. The bauxite deposits in the Dominican Republic and Haiti are similar in grade, age and genesis, and are identified as ''Jamaican type'' bauxites.

Bauxite deposits in Suriname and Guyana are scattered throughout a narrow belt extending along the contact between the Precambrian crystalline rocks of the Guyana Shield and the sedimentary beds of Tertiary or later age that form the coastal plain. The alumina mineral is gibbsite and the ore is high grade: typically 55% to 60% Al_2O_3, 2% to 5% SiO_2, and less than 3% Fe_2O_3.

In the large deposits discovered in northern Brazil since 1967, the bauxite occurs as a residual capping on dissected plateaus several hundred feet above the Amazon or other nearby rivers. The ore has developed on unconsolidated Tertiary sediments and is convert by 12–30 of kaolinitic clay. The approximate grade after washing is 55% Al_2O_3, 3.5% SiO_2, and 11% Fe_2O_3.

The Weipa bauxite deposit in Queensland, Australia, occurs in the upper portion of a flat-laying laterite that extends for more than a hundred miles along the West Coast of the Cape York Peninsula. The bauxite ranges in thickness from a few feet to 30 ft and is covered by a soil overburden 1–3 ft thick. The deposits are associated with Tertiary kaolinitic sands, from which they were probably derived. The grade of the beneficiated bauxite is 53% to 58% Al_2O_3, 4% to 7% SiO_2, and 12% Fe_2O_3.

In Guinea, the large Sangaredi bauxite deposits occurs as laterite caps on inland plateaus at elevations of 900 ft or more above sea level. Most of the bauxite is believed to have formed through weathering of schists and sand-stones of Devonian or Post-Devonia Age. Typical ore contains 57% to 60% Al_2O_3, less than 1% SiO_2, and 2% to 4% Fe_2O_3.

Many of the European bauxite deposits are associated with pockets and depressions in the karst weathering surface of Mexozoic limestone beds that have been buried, folded, and faulted subsequent to the development of the bauxite. European bauxites are composed predominantly of monohydrate alumina minerals, although some gibbsitic deposits are mined in Hungary and a few other countries [3].

Bauxites represent mountain rocks, the main component of which is aluminum oxide. Bauxite contains a large number of impurities such as silica, iron and titanium oxides, and various other elements mostly in minor or trace amounts [13]. The amount of free aluminum oxide can vary. Typical economic bauxite ores contain greater than 45% alumina, less than 12% iron oxides and less than 8% of combined silica. The bulk density of most bauxites is between 1.3 and 1.9 g/cm^3. The general

Table 4 Minerals Commonly Found in Bauxites

Minerals	Chemical composition
Gibbsite (hydragillite)	α-$Al_2O_3.3H_2O$
Bàehmite	α-$Al_2O_3.H_2O$
Diaspore	β-$Al_2O_3.H_2O$
Hematite	α-Fe_2O_3
Goethite	α-$FeOOH$
Magnetite	Fe_3O_4
Siderite	$FeCO_3$
Ilmenite	$FeTiO_3$
Anatase	TiO_2
Rutile	TiO_2
Brookite	$Al_2O_3.2SiO_2.3H_2O$
Kaolinite	$Al_2O_3.2SiO_2.2H_2O$
Quartz	SiO_2

classification of bauxite rocks based on their chemical structure can be represented in Table 4 [14–16].

In various types of ores, free aluminum oxide is presented as a trihydrate ($Al_2O_3 \cdot 3H_2O$) which is crystallized in monoclinic crystallographic system or a monohydrate ($Al_2O_3 \cdot 3H_2O$) which is crystallized in orthorhombic crystallographic system.

Silicon dioxide is the main harmful impurity in bauxites. It is present at the form of free silica or as a compound with other elements. In addition, bauxites have the iron in the various forms. Besides the main chemical elements, bauxites contain Ti, S, Li, Cu, Ag, Au, Be, Zn, Sr, Cd, Ba, Sc, rare-earth elements such as B, Ga, Ge, Zr, Sn, Hf, Pb, P, V, Nb, Bi, Cr, Mo, Mn, Co, Ni, and U.

Free moisture in crude bauxite may range from 5% to 30% [5]. In dried bauxite, most of the free moisture has been removed by heating crude bauxite in rotary drying kilns at about 600°F. Calcined bauxite is heated in the kilns to 1700–1900°F to reduce 1 ton of calcined bauxite.

Cell-grade alumina specifications and typical specifications for grades of bauxite are presented in Table 5 and 6.

The nepheline rocks are the second most important type of aluminum raw material after bauxites. These rocks contain $Na[AlSiO_4]$ mineral. The theoretical composition of nepheline is 35.7% Al_2O_3; 42.4% SiO_2; 21.9% Na_2O. There are many different types of the nepheline rocks. They are rich with potassium only or with sodium and potassium. Nephelines crystallize in the hexagonal close-packed lattice of the pyramidal class. Normally they can be found as granular and solid mountain mass (massif). As crystals nepheline is seldom found. Usually nepheline has light coloring or it is colorless. Nepheline is rather easily dissolved in mineral acids with SiO_2 forming a gel [17].

In spite of that, aluminum in nepheline also contains silicon, the significant contents of alkalis in the composition of this mineral enables the opportunity to reduce from them an aluminum oxide and produce the by-products of sodium

Table 5   Cell-Grade Alumina Specifications, in Weight-Percent

Impurity	Maximum content	Impurity	Maximum content
SiO_2	0.015	B_2O_3	0.001
Fe_2O_3	0.015	TiO_2	0.002
MnO	0.002	P_2O_5	0.001
NiO	0.005	MgO	0.002
Cr_2O_3	0.002	CaO	0.040
CuO	0.010	Na_2O	0.400
V_2O_5	0.002	K_2O	0.005
ZnO	0.010	Chloride, residual	0.050
Ga_2O_3	0.020	–	–

Table 6   Typical Specifications for Grades of Bauxite (Weight-percent, Maximum Content Unless Otherwise Specified)

Constituent	Metal grade (dried Jamaican type)	Refractory grade (calcined)	Abrasive grade (calcined)
Al_2O_3	47.0*	86.5*	83.0*
SiO	3.0	7.0	6.0
Fe_2O_3	22.0	2.5	8.0
TiO_2	3.0	3.75	3.0–4.5**
$K_2O + Na_2O$	NS	0.2	0.7
$MgO + CaO$	NS	0.3	NS
CaO	NS	NS	0.2
MgO	NS	NS	0.4
$MnO_2+Cr_2O_3+V_2O_5$	2.0	1.0	1.0
P_2O_5	1.5	NS	0.5
Loss on ignition	NS	0.5	1.0

* Minimum
** Range
NS No specification

carbonate and cement. Usually the nepheline rocks can be found as the mountain masses in combination with alkaline rocks.

Alunite is $KAl_3[SO_4]_2[OH]_6$ belongs to the group of the alkaline double sulfate of aluminum. It is also the important raw material for aluminum production. The chemical composition of this ore can vary significantly. Theoretical composition of alunite is 37.0 wt% Al_2O_3; 11.4 wt% K_2O; 38.6 wt% SO_3; 13.0 wt% H_2O. In addition to the compounds above, SiO_2, CaO and Fe_2O_3 can be present.

Alunite crystallizes in the tetragonal system. Usually it consists of small crystals with grayish, yellowish or reddish color. Due to the potassium and sulfur contents, potassium fertilizers and sulfuric acid can be extracted.

Disthene (kyanite) is a high quality raw material for electrothermal reduction of aluminum. The minerals of this group represent polymorphic modifications of

Table 7 Comparison of Bauxites [8]

Bauxite type	Gibbsite (Hydragillite)	Bàhmite	Diaspore
Composition	$Al_2O_3.3H_2O$	$Al_2O_3.3H_2O$	$Al_2O_3.3H_2O$
Maximum alumina content, wt %	65.4	85	85
Crystal system	Monoclinic	Orthorhombic	Orthorhombic
Density, g/cm^3	2.42	3.01	3.44
Temp. for rapid dehydration (°C)	150	350	450
Solubility of Al_2O_3 (g/l) in 100 g/l Na$_2$O aqueous solution at 125°C	105	45	Virtually insoluble

the substance with the chemical formula of AlOAl [SiO$_4$]. Theoretical chemical composition is 63.2% Al_2O_3 and 36.8% SiO_2.

Disthene crystallizes in the triclinic lattice. Most frequently disthene crystals have light-blue, grayish-blue, least often yellow or brown color and glassy glance. Anisotropy of hardness and coloring were noticed on disthene crystals. So on a plane (100) in a direction ‹100› hardness is equal 4.5 and along a direction ⟨010⟩ is 7.0. Coloring along the base plane is olive-green, and through lateral planes is redish-brown.

Table 7 [8] summarizes the basic differences of the three fundamental forms of bauxite which occur, namely gibbsite, bàhmite and diaspore. It is seen that the latter two are in the monohydrate form, whereas the former is a trihydrate. The two monohydrate forms give rise to different structural forms of alumina on rapid dehydration, while they also exhibit different solubilities in caustic soda. Gibbsite dissolves much more readily. In caustic soda (having a higher solubility as well as dissolving faster), but it has a lower intrinsic alumina content. The conditions for the dissolution of the alumina hydrate will vary for the different structural forms, and also depend on caustic soda concentration and temperature.

Many of the deposits currently being mined have a dominance of gibbsite (trihydrate), but they often have a significant proportion of a monohydrate crystalline form also. Therefore, the chemical processing must be a compromise between the optimum conditions for each of the two types. This is particularly so for the extensive bauxites occurring in the northern area of Australia—which is the main supplier for the present world market.

As already mentioned, the main impurities are compounds of iron, silicon and titanium. The iron compounds occur chiefly in the form of haematite (Fe_2O_3), siderite ($FeCO_3$) and goethite ($FeO·OH·nH_2O$). The silicon compounds occurs in the various structural forms of quartz as well as hydrated double salts with alumina such as kaolinite and halloycite ($Al_2O_3·2SiO_2·3H_2O$). Generally titanium occurs in, the form of rutile (TiO_2), but it can also be present in small amounts as ilmenite or anatase. The compounds of iron and titanium are insoluble in caustic solutions and therefore present no problem for the selective dissolution of the aluminum oxide. The silicon occurring as quartz does not present a serious problem either, since it has

Table 8 Typical Compositions from Different Bauxite Deposits (in Weight %) [8]

Oxides*	African Gold Coast	British Guyana	Darling Ranges (Western Australia)	Greece	Weipa (Australia)
Al_2O_3	55.2	61.1	30–35 available	60.2	57.0
SiO_2	2.0	5.0	1–2 reactive SiO_2 18–22 quartz	3.1	5.0
Fe_2O_3	11.5	1.5	20.0	21.7	7.5
TiO_2	2.1	2.5	–	3.0	2.5
Ignition loss	29.3	30.0	20.0	11.7	27.0

*Balance, minor impurities which include MgO,V_2O_5, P_2O_5, Ga_2O_3, CaO, ZrO_2, MnO, Cr_2O_3, ZnO, organic materials, etc.

only a limited solubility in the caustic soda solution used. This contrasts with the combined forms (kaolinite and halloycite) which readily c solution. The dissolution of silica leads to a reduction in the yield of the extracted alumina, and therefore the soluble desirable. Consequently the silica content is usually referred to as reactive or unreactive, depending on its tendency. Table 8 summarizes a range of compositions predominantly containing gibbsite [8].

3 REDUCTION OF ALUMINUM

Modern-day aluminum production involves two independent industrial processes for the transition from the naturally occurring aluminum oxide ores to the extracted metal (Fig. 6) [18]. The reduction of aluminum oxide to aluminum includes two main stages:

- production of an aluminum oxide (alumina) from aluminum ores. It can be done by different chemical methods.
- Production of aluminum from an aluminum oxide by electrolysis with fused sodium aluminum fluoride (Na_3AlF_6) commonly called cryolite [6,8,14,18–20].

3.1 Production of Aluminum Oxide from Bauxites

3.1.1 The Bayer Process

All commercially produced alumina from bauxite is obtained by a process patented by Karl Bayer in 1888 (German Patent 43,977). The Bayer process involves a caustic leach of the bauxite at elevated temperature and pressure, followed by separation of the resulting sodium aluminate solution and selective precipitation of the aluminum as the hydrated aluminum oxide ($Al_2O_3 \cdot 3H_2O$).

Alumina (aluminum oxide) is white powder produced from bauxite ores by treating them with caustic soda in the Bayer process (Fig. 7) [8]. The actual processing conditions such as the leach temperature, holding time, and caustic concentration, as well as the costs, are influenced by the type of bauxite to be processed.
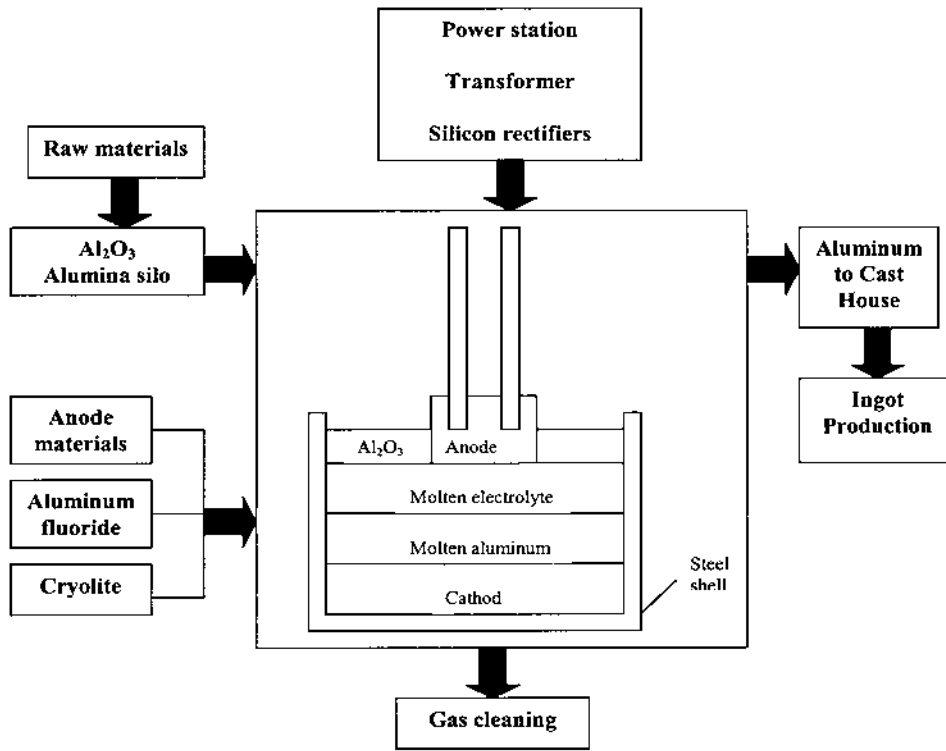
Figure 6 Flow-sheet for aluminum production from alumina.

As a result, a Bayer alumina plant is designed to treat a specific bauxite and cannot use a bauxite that is too different from the one the plant was designed to use, without major plant modifications [3].

The Bayer process is initiated by mixing crude bauxite with preheated spent leach solution. Lime is added during this initial step to control the phosphorus content and to increase the solubility of alumina. The resulting slurry, containing 40% to 50% solids, is pumped with additional caustic leach solution to pressurized digesters where high-pressure steam is used to raise the temperature. Alumina and some of the silica are dissolved during this step, soluble sodium aluminate is formed, and a complex sodium aluminum silicate is precipitated.

The technological scheme of the Bayer bauxite processing method consists of several operations. Bauxite coming from a mine is dried, and progressively crushed. Then it is placed into an autoclave with a NaOH solution at 230°C and higher than atmospheric pressures.

Digestion, in tanks 10–15 ft in diameter and up to 90 ft high, takes up to 5 hr. Leaching temperatures range form about 140°C to about 323°C, with corresponding pressures ranging from about 60 psi to over 1000 psi. The lower temperature ranges are used for bauxites in which nearly all of the available alumina is present as gibbsite. The higher temperature is needed to digest bauxite having a large percentage of bàehmite. Caustic concentration of the spent leach solution, expressed as
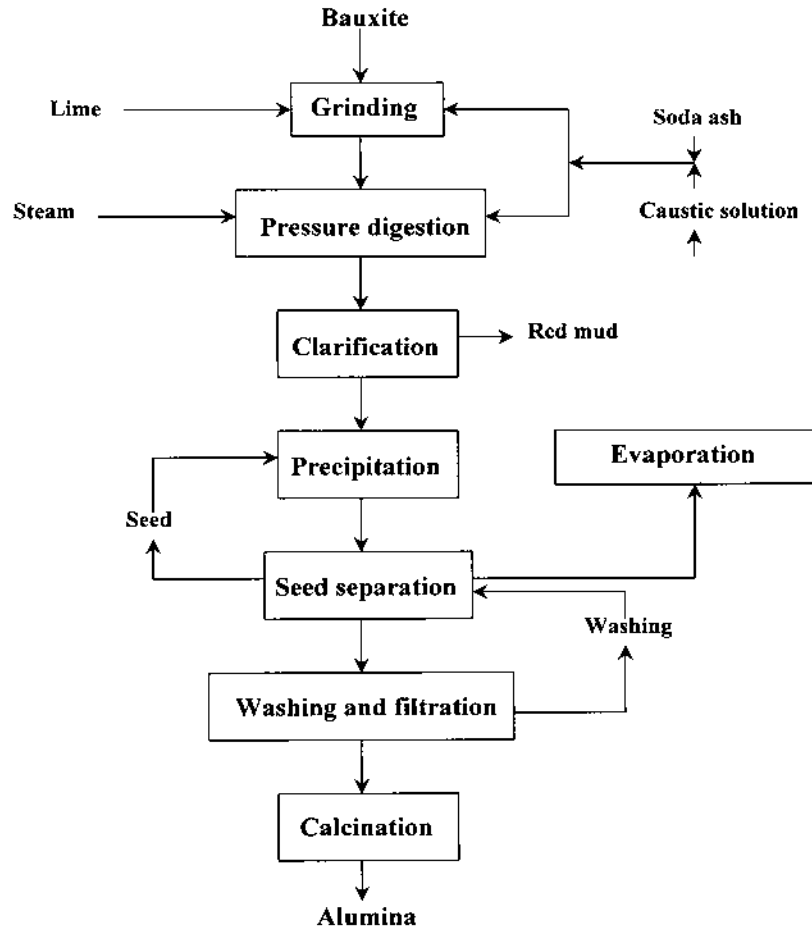
Figure 7 The flow-sheet of the Bayer process.

grams per liter of sodium carbonate (Na_2CO_3), averages about 200 g/l for gibbsitic bauxite and about 300 g/l for bauxites with a high bàehmite content.

Bauxites arrive on chemical processing without the preliminary mechanical enrichment. This process involves digesting bauxite at high temperatures with caustic soda which dissolves the alumina leaving iron oxide and silicates as waste products (red mud). This is accomplished by the following chemical reaction

$$Al(OH)_{3(sol)} + NaoH_{(liq)} \Longleftrightarrow NaAlO_{2(liq)} + H_2O$$
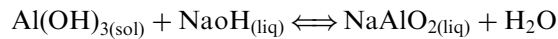
The resulting slurry of sodium aluminate solution and insoluble red mud from the digesters is cooled to atmospheric boiling temperature, and a coarse sand waste fraction is removed by gravity separators or wet cyclones. The fine solids in the red mud are then separated by decantation of the overflow in setting tanks measuring about 15 ft in depth and 50–125 ft in diameter [3].

$$2NaAlO_2 + 4H_2O \Rightarrow 2NaOH + Al_2O_3 \cdot 3H_2O$$
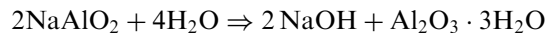
The clarified sodium aluminate liquor is cooled until it becomes supersaturated, then seeded with fine crystals of alumina trihydrate. The alumina is precipitated as the trihydrate, separated by sedimentation or filtration, and washed. The spent leach solution containing caustic soda is regenerated in the precipitation step, and together with the alumina remaining in solution, is recycled to the digesters. The filtered and washed alumina trihydrate is calcined for use in making metal.

$$Al_2O_3 \cdot 3H_2O \Rightarrow Al_2 + H_2O$$
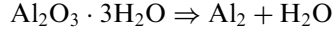
Two forms of calcined alumina are used to produce aluminum. European Bayer plants have traditionally produced a fine-grained highly calcined, floury alumina while North American Bayer plants have always produced a coarser grained, porous, sandy alumina that has not been totally calcined to the alpha alumina. The red mud contains Fe_2O_3, TiO_2, the sodium aluminosilicate, and a small quantities of other metal oxides. Because the complex represents a loss of both alumina and soda a low reactive silica content in the bauxite is desirable. The loss of soda is made up by adding caustic soda or soda ash and lime to the spent leach solution to bring it up to the appropriate caustic concentration before it is recycled.

The liquor is washed out and is separated from the red mud. The liquor is filtered and then a small amount of aluminum hydroxide is introduced and slowly mixed. As a result, aluminum oxide is precipitated, from the aluminate solution.

The precipitated trihydrate (aluminum hydroxide) is filtered and is then calcined in a rotary kiln at 1200–1300°C to remove the water of hydration and to leave the alumina in a form suitable for use in the electrolytic production of aluminum.

Invariably, the alumina prepared by the Bayer process has small amounts of impurities associated with it and typical impurity levels are summarized in Table 9 [8].

Variations in impurity levels will occur with different ore types, but the values show that a fairly high quality material is produced in the Bayer process. Some of the sodium oxide will be as sodium aluminate, and the small amounts of calcium oxide are present by virtue of the technology used to reconstitute the sodium hydroxide liquor for the extraction stage. This method is used for processing of high quality bauxites only.

Table 9.   Typical Impurities in Commercial Hydrated and Calcined Alumina [8]

Impurity	Percentage impurity Dried alumina trihydrate	Normal calcined alumina
SiO_2	0.020	0.03
Fe_2O_3	0.015	0.02
Na_2O	0.250	0.50
CaO	0.030	0.05
Loss on ignition	34.700	0.80
Moisture (free)	0.400	–

3.1.2   The Production of Alumina from Bauxites with the Higher Silicon Content

The production of alumina (aluminum oxide) from bauxites with the higher silicon content (from 8% to 15% silica) and other inclusions from aluminum raw materials is carried out by the agglomeration [14,18]. This combination process has been developed by Alcoa. In this process, the bauxite is mixed with the limestone and the sodium carbonate. The mixture agglomerates in rotary furnaces at 1200–1300°C. In the agglomeration process the sodium carbonate reacts with aluminum oxide forming the sodium aluminate:

$$Al_2O_3 + Na_2CO_3 = 2NaAlO_2 + CO_2.$$
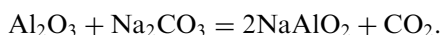
The received aluminum oxide is crushed and leached by water or a soda solution. As a result aluminum passes into a solution. The non-soluble red mud is separated from it. Then a solution free from silicon dioxide is produced by heating with a lime in an autoclave at 160°C. The silicon dioxide precipitates out as non-soluble calcium silicate (white mud). The calcium silicate is separated from the liquor by filtration. The resulting liquor precipitates aluminum hydroxide by passing carbon dioxide though the liquor:

$$2NaAlO_2 + 3H_2O + CO_2 = 2Al(OH)_3 + Na_2CO_3.$$
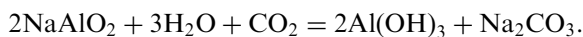
Formed aluminum hydroxide has been separated by filtration, then washed out and calcined for alumina production. Extraction alumina by an agglomeration method accounts for 90% of total alumina products. A portion of the washed alumina may be left in the trihydrate form for chemical uses or it may be further processed under controlled conditions to produce a variety of chemical alumina, such as activated or tabular alumina for uses other than metal production.

3.1.3   The Combine Method (Bayer Process with Agglomeration)

For processing high silicon content bauxites sometimes, it is expedient to apply a combination of a Bayer process with the method of agglomeration [8]. The combination of the Bayer process and agglomeration process improves the technological cycle of processing bauxite and enables the use of low quality bauxites.

In the former Soviet Union, alumina is extract from nepheline [(Na, K)AlSiO$_4$] flotation concentrates and other non-bauxitic materials containing about 30% alumina. Nepheline syenite has been mined at Belogorsk in Siberia and obtained as a byproduct of apatite recovery from syenite deposits in the Kola Peninsula.

3.1.4   Processing Method for Alumina from Nepheline

The processing method for alumina from nepheline ores consists in the agglomeration of a charge comprised of nepheline concentrate and limestone into the rotating furnaces at the temperature of 1280–1310°C [8,18]. Calcium oxide of limestone reacts with nepheline. A cake consisted of bicalcium silicate and sodium aluminate is formed. A cake is leached by the sodium-alkali-aluminate solution which sodium

and potassium aluminates pass into. Formed at the carbonization, aluminum hydroxide drops out into a deposit, and sodium carbonate and potash remain in a solution.

$$2NaAlO_2 + 3H_2O + CO_2 = 2Al(OH)_3 + Na_2CO_3.$$
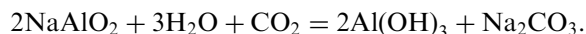
Filtered and calcined aluminum hydroxide is a final product from which pure aluminum is extracted from. The process of extraction makes about 80% of Al_2O_3.

Historically, a small tonnage of alumina has been extracted commercially in Norway from high-iron bauxites by the Pedersen process. In this process, bauxite, limestone, coke, and iron ore are smelted in an electric furnace to produce pig iron and calcium aluminate slag containing 30% to 50% alumina. The slag is leached with sodium carbonate solution, and alumina trihydrate was precipitated by carbon dioxide. During World War II, the process was also used at a Swedish plant to treat andalusite (Al_2SiO_5).

3.1.5 The Pechiney H-Plus Process

In Europe, the major development has been the process called the Pechiney H-Plus process. Developed by Pechiney in France the process consists of sulfuric acid leaching of the raw material, hydrocholric acid addition to the leach liquor and crystallization of $AlCl_3 \cdot 6H_2O$ by saturation of the leach liquor with gaseous HCl [21]. The aluminum trichlorid precipitate is purified by dissolution and reprecipitation. The final product is calcined to form alumina and to produce HCl for recycle. Successful laboratory scale development has been followed by a pilot plant operation at 15–20 tons Al_2O_3 per day scale at Marseilles. According to Cohen and Mercier [22], the alumina so produced has a higher purity than alumina produced from bauxite by the Bayer process. The process flow-sheet is shown in Fig. 8. An analysis of the potential economics of the process indicated that, with heat recovery, the total operating cost to produce alumina from coal shale would probably be 1.15–1.4 times the cost of production from bauxite at 1978 bauxite and energy prices.

3.1.6 Technology for the Recovery of Metallurgical-Grade Alumina from Coal Ash

Large quantities of coal ash are produced in the United States every year by coal-burning power-plants. In 1975, this amounted to 60 million tons, of which 42.4 million tons was boiler slag [23]. (Fly ash is the fine material that is carried out of the boiler with the stack gases and is collected by precipitators. Bottom ash is coarser material that falls through the grate, and boiler slag is the molten as that collects at the bottom of slag tap boilers.)

Fly ash, bottom ash, and boiler slag all contain significant amounts of Al_2O_3 and therefore can be considered as potential sources for the production of metallurgical-grade Al_2O_3. Typically, fly ash contains from 15% to 30% SiO_2, 50% Fe_2O_3, up to 20% Al_2O_3, with the remainder containing alkali and alkaline-earth oxides plus some unburned carbon [24]. Fly ash cannot be considered a high-grade potential source of metallurgical-grade Al_2O_3 when compared with the large reserves of kaolinitic clays (35–40% Al_2O_3) and anorthosite (25–30% Al_2O_3) [25].
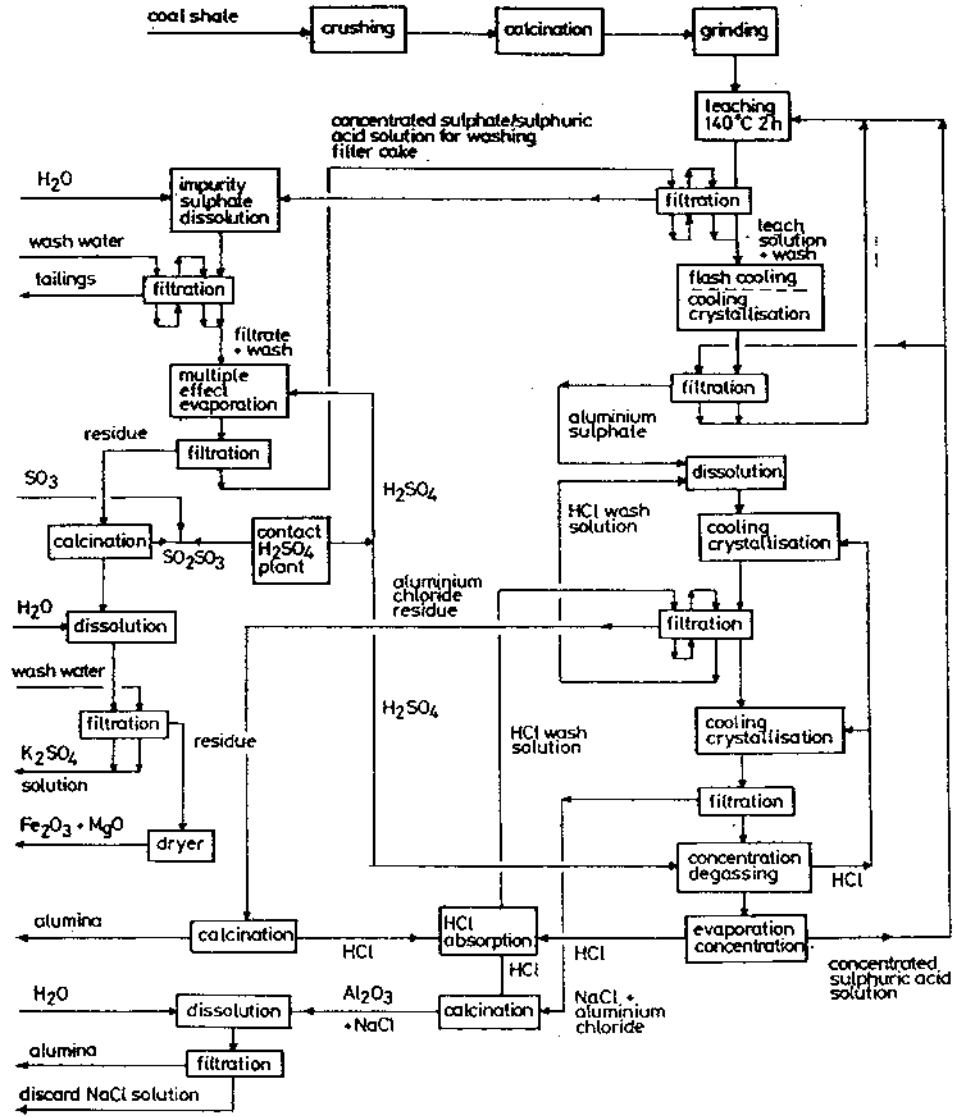
Figure 8 Flow-sheet of the Pechiney H-Plus process.

Considerable economic benefit would result if fly ash could be physically ben-eficiated to upgrade its Al_2O_3 content before being processed by extractive metallurgical technique. A form of beneficiation that has been studied is magnetic separation. Scientists in the former Soviet Union have applied this technique to the ashes from a coal-gasification plant to produce a nonmagnetic fraction con-taining greater than 30% Al_2O_3 [26].

Table 10 shows the calculated costs in the United States as of late 1976 to produce 1 ton of Al_2O_3.

Table 10 Calculated Costs in the U.S. to Produce 1 Ton of Alumina [27]

Material	Cost per ton, U.S. Dollars	Process cost, U.S. Dollars	
		Fly ash	Bauxite
Bauxite	16.00	–	41.32
Fly ash	–	–	–
Soda ash	55.00	11.55	4.12
Limestone	5.00	58.50	0.38
Lime	25.00	–	–
Starch	220.00	–	1.10
Coal	20.00	40.00	–
Oil	133.00	21.28	10.30
Steam	–	13.80	11.81
Electricity	(*)	16.50	1.08
TOTAL		167.38	70.11

*Cost of electricity was $0.015 per kilowatt-hour

Of the three general methods (alkaline-sinter process, acid-leach process, chlorination processes) examined for recovering metallurgical-grade Al_2O_3 from coal ash, sintering (lime or lime-soda) offers the most short-term potential. It has been demonstrated that Al_2O_3 can be produced by this procedure, and the incorporation of a desilication step would possibly produce a grade of Al_2O_3 acceptable to the aluminum industry. The major unresolved problem with lime sintering is economic. Coal ash is basically a low-grade source of Al_2O_3, and the reagents and operating costs to conduct a high-temperature sintering operation are high. To be economically viable, the production of Al_2O_3 from coal ash by a sintering process should be integrated with cement production.

Direct acid treatment of coal ash does not appear promising. Some form of pretreatment of the ash, such as reaction with limestone during power generation, may provide a means to improve the yield of Al_2O_3 during acid leaching.

Dry chlorination of coal ash at high temperature is interesting because of the effective conversion of the aluminum values of $AlCl_3$. Dry chlorination expensive in money and energy to decompose [27].

3.2 Production of Commercial Purity Aluminum

Primary aluminum is produced by the reduction of alumina by electrolysis in a molten bath of natural or synthetic cryolite (Na_3AlF_6), which serves as an electrolyte and a solvent for the alumina.

3.2.1 Electrolytic Reduction (Smelting)

Commercial purity aluminum is manufactured mainly by electrolysis [28–32]. The process used for the electrolytic reduction of alumina to the metal does not differ fundamentally from the original process devised in 1889 by Hêr$\ddot{U}$ult and Hall. The main change being an increase in the size of each electrolytic cell [33].
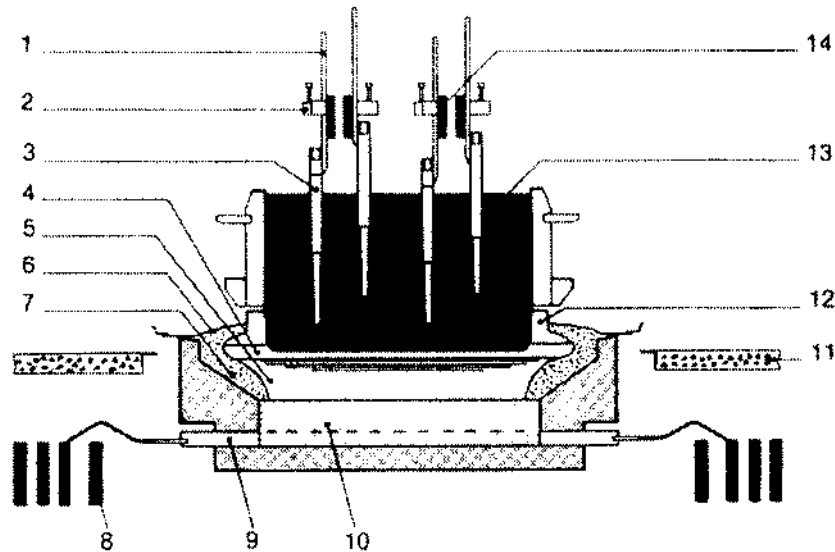
Figure 9 Schematic diagram of an electrolytic cell fitted with a "Söderberg" anode.
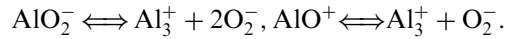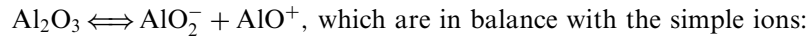
Primary aluminum production is electricity-intensive. The current U.S. average energy consumption for aluminum reduction is estimated to be 15.18 kWh/kg of aluminum. The lowest energy consumption that can be achieved today is about 13.0 kWh/kg of aluminum for a line of modern, high-amperage reduction cells. Production cells normally have current efficiencies ranging from 85% to 95%. Large, modern reduction cells operate with current efficiencies of 94–96% [34].

Figure 9 is a diagrammatic section of a multi-anode furnace from which the main points of construction can be seen. The outer casing consists of a brick-lined rectangular steel box which acts as container and support. Inside this box the cathode is constructed of baked carbon or graphite blocks, cemented together with a paste of ground coke and pitch, and of such a shape as to contain the bath of electrolyte. The electrolyte is largely molten cryolite or with additions of calcium fluoride and aluminum fluoride are made and alumina. A typical composition of this solution consists of cryolite 75–90%, alumina 2–8%, aluminum fluoride up to 10%, calcium fluoride 5%.

The anode consists either of a number (as many as twenty) or pre-baked carbon blocks dipping into the molten electrolyte, or of a single massive Sàderberg electrode. Although there are two fundamental designs of anodes used in industrial aluminum electrowinning, they are both formulated form similar materials and undergo the same type of reactions within the operating cell. For environmental reasons, there has been an increasing tendency to move to the "pre-baked" anodes, and therefore the presentation of data and discussion of reactions will be biased towards this form of anode. The Sàderberg type of electrode uses the waste heat of the furnace to bake the anode paste in situ instead of this being done as a separate operation as with the pre-baked anodes.

Electrolysis of Aluminum Oxide (Figure 9)

Aluminum oxide Al_2O_3 dissolves in molten cryolite Na_3AlF_6 at the temperature of 950–970°C [7] and break down electrochemically by discharging aluminum cations on the cathode (the molten aluminum), and the acid-containing ions (oxygen ions)—on the graphite-carbonic anode. The molten cryolite dissociate on ions Na^+ and AlF_6^{3-}:

$$Na_3Al_6 \Longleftrightarrow 3Na^+ + AlF_6^{3-} \text{ and aluminum oxide—on complex}$$
$$\text{ions } AlO_2^- \text{ and } AlO^+ :$$
$$Al_2O_3 \Longleftrightarrow AlO_2^- + AlO^+, \text{ which are in balance with the simple ions:}$$
$$AlO_2^- \Longleftrightarrow Al_3^+ + 2O_2^-, AlO^+ \Longleftrightarrow Al_3^+ + O_2^-.$$
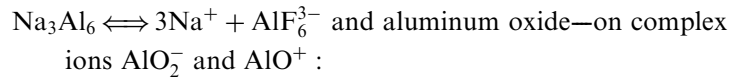
The reduction of trivalent aluminum is the predominant process occurring at the cathode:

$$Al_3^+ + 3e \rightarrow Al$$
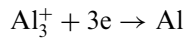
In addition the incomplete discharge of the trivalent aluminum with the formation of univalent ions can take place: $Al^{3+} + 2e \rightarrow Al^+$ and discharge univalent ions with settling of the metal:

$$Al^+ + e \rightarrow Al.$$

At the graphite anode there is the discharge of oxygen ions. The oxygen oxidizes carbon of the anode and is released as a mixture of $CO_2 + CO$.

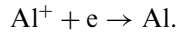The primary aluminum (raw aluminum) taken from an electrolyser contains three groups of impurities: a non-metallic (fluorine salts), such as α- and γ-aluminum oxide, aluminum carbide and aluminum nitride, and graphite particles; metallics such as iron and silicon passing from raw materials, coal materials and structural electrolyzer elements; and gaseous—mainly hydrogen formed as a result of electrolitic water dissociation.

For simultaneous aluminum purification from non-metallic impurities and hydrogen, the filtration through a fluxing filter with the adding blowing nitrogen is applied. As a result of such purification the contents of hydrogen in aluminum is reduced from 0.22 down to 0.16 cm^3 on 100 g of metal.

The most effective method of simultaneous purification of aluminum from sodium, hydrogen and non-metallic impurities, is by bubbling a gas mixture of nitrogen with 2–10% Cl through the molten metal. This method of purification permits a lower sodium content of 0.0003–0.001% at the total consumption of a gas mixture from 0.8 up to 1.5 m^3/g of the metal [32].

Future Developments in Hall–Héroult Cells

With the gains in productivity and cost reductions achieved over the past decade allowing aluminum to remain a competitive commodity metal and meet the growth in world demand of 2–3% per year, the primary aluminum industry has become complacent in searching for alternative processes. Intellectual energy has been focused on cost cutting and environmental concerns [43].

Inert anodes have been the dream of aluminum producers from the beginning, and numerous materials have been tried. But there are no really inert materials so far. In the cathode, prolonged cell life, a lower cathode voltage drop, stability over time, and more resistant sidewalls are needed. While a 1300 day life was acceptable 50 years ago, and 2000 day lives are acceptable today, cathode lives of more than 3000 days will be demanded in the future. With the rise in use of graphitic blocks to decrease the cathode voltage drop, improved abrasion resistance is a necessary challenge. One solution is a coating with TiB_2 [43].

There are significant efforts to develop transition stable wetted cathodes and nonconsumable anodes. It looks as if aspects of designs for retrofitted cells and advances in material science will be resolved in industrial tests by 2005. In 1997, the Aluminum Association and the U.S. Department of Energy joined forces to fund further the search for materials for the inert anodes. From the present perspectives, meaningful pilot bipolar cells for liquid aluminum could be in progress by 2010 at the earliest [43].

There are challenges remaining in the section and management of the lining of the reactor. Even when the pure CO evolved in this process is reconverted to electrical energy, there is twice as much CO_2 evolved as for the electrolytic process, although the unit energy is lower.

Perhaps an alternative approach in extracting aluminum in the liquid state could derive from what is being discovered about slurry electrolytes. In this method, solid aluminum, even if dendritic, could be electrodeposited on a rotating disc cathode form a low melting (540–600°C) all-fluoride electrolyte using a nonconsumable anode. The solid aluminum would be removed within the fully enclosed cell and transported to a melting furnace above 660°C where the solid aluminum and entrapped bath would be separated. In this concept, the bath is recycled to the cell, and the now-liquid aluminum processed conventionally [43].

3.2.2   The ALCOA Chloride Process

In January 1973 ALCOA [35] announced the development of a new aluminum electrolysis process. The process employs electrolysis of aluminum chloride dissolved in alkali and alkaline earth chloride melts. Among the most favorable aspects of the process are reduced electrical energy consumption ($\sim 30\%$), less pollution and more flexible operation.

The first step of the ALCOA process is the production of very pure alumina by the Bayer process. The two succeeding steps are the chlorination of alumina and the electrolysis of the dissolved molten aluminum chloride. The resulting aluminum chloride is purified by passage through a special filter before resublimation in an inert gas. The alumina is then transported to a tank where it is stored in the crystalline state. The cell used for the electrolysis consists of a steel mantle lined with a thermally insulating, non-conducting refractory material which is not corroded by the electrolyte.

The total energy consumption of the process depends on the raw materials used, e.g. bauxite versus pure alumina and petroleum coke versus carbon coke.

While the Hall–Héroult process has its fluoride emission problem, the chlorination steps in the ALCOA process may result in chlorinated hydrocarbons being formed. The economic potential for this process is strongly dependent on the cost of producing $AlCl_3$ in the chlorination step.

The advantages of the ALCOA method is compared with electrolysis of the kryolite–aluminum oxide melt (Al_2O_3 dissolved in cryolite Na_3AlF_6) are: energy saving up to 30%; an opportunity of application Al_2O_3 with the higher silicon content; substitution of cryolite by cheaper salts; reducing or completely eliminating the problem of fluorine liberation.

3.2.3 The Toth Process

This process is based on reduction of $AlCl_3$ by Mn and bears the name of its inventor Charles Toth. Since 1968 the process has been described in several patents [24] and also has received considerable publicity in the financial and engineering press. The Toth process comprises four major steps:

Step 1: at the temperature of 925°C

$$Al_2O_3 \text{ (in clay)} + 3C + 3Cl_2 = 2AlCl_3 + 3CO$$
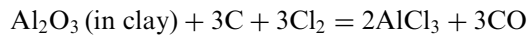
Step 2: at the temperature of 230°C

$$2AlCl_3 + 3Mn = 2Al + 3MnCl_2$$
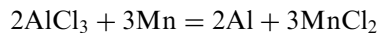
Step 3: at the temperature of 600°C

$$2MnCl_2 + O_2 = 2MnO + 2Cl_2$$
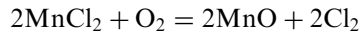
Step 4: at the temperature of 1750°C

$$MnO + C = Mn + CO$$
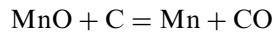
The total reduction considered being

$$2Al_2O_3 \text{ (in clay)} + 3O_2 + 12C = 4Al + 12CO$$
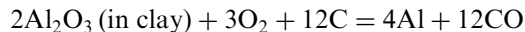
Toth process is an indirect carbothermal reduction of alumina. Several types of cheap minerals with Al_2O_3 contents as low as 30–40 wt%, for instance kaoline labradorite and bauxite, are potential raw materials.

Beside the potential use of low grade ore, the really favorable aspect of the Toth process is its presumably low demand of electrical energy, i.e. 5% of the Hall–Héroult process according to the inventor. It must be recognized, however, that the appreciable reduction in electrical energy is largely compensated by an increased carbon consumption.

A successful large-scale operation of the Toth process still remains to be demonstrated and considerable work has to be done before the final answer to its potential can be given.

3.2.4 Aluminum Extraction from Anorthosite by Leaching with Hydrochloric Acid and Fluoride

The United States is more than 90% dependent on imported bauxite as a source for aluminum, but it has vast non bauxitic aluminum resources, such as kaolinite, anorthosite, alunite, etc. To reduce this dependence, the Bureau of Mines conceived a raw materials-process technologies matrix as a means of systematically

investigating the technology options available for processing domestic aluminum resources [36]. Resources considered were clay, anorthosite, alunite, dawsonite contained in oil shale, and coal as and coal shale [25,37].

Most of the research on alumina recovery from anorthosite was concentrated on the lime-soda-sinter process [38]. Anorthosite is sintered with soda ash and limestone. Leaching, desilication, and precipitation steps are performed before alumina is recovered as the trihydrate. The lime-soda-sinter process has two major drawbacks:

- In addition to mining anorthosite, large amounts of limestone and soda ash are required.
- Sintering is performed at $1300°C$, which consumes appreciable amounts of energy.

Another method for recovering alumina from anorthosite is the melt-quench technique [39] in which a charge of anorthosite is arc melted at approximately $1650°C$ and then rapidly cooled. The resulting amorphous product is amenable to alumina extraction by acid. Because of their crystalline structure, aluminum silicates, such as anorthosite, are not readily attacked by a mineral acid unless the crystalline structure is altered. Acid in conjunction with the fluoride ion disrupts the silicate structure sufficiently so that acid leaching is effective in extracting the aluminum content.

Anorthosite is a rock composed mainly of calcium-rich plagioclase. Anorthosite resources of the United States are estimated at 599 billion tons averaging 27% Al_2O_3 [25]. Large anorthosite deposits are located in Minnesota, New York, Wyoming, and California. Chemical analysis of the anorthosite is the following: 29.3% Al_2O_3, 2.0% Fe_2O_3, 11.5% CaO, 0.15% TiO_2, 51.4% SiO_2, 5.1% Na_2O, 0.29% K_2O, 0.26% MgO.

Excellent aluminum extractions were obtained from Wyoming anorthosite by countercurrent leaching with hydrochloric acid and fluoride ion. The model (Fig. 10) schematically illustrates simulated three-stage countercurrent leaching by a series of batch tests. Fresh HCl leachant moves downwards; anorthosite ore moves to the right. The two upper rows prepare leaching acid for use in the bottom row, where ore is contacted by acid of increasing strength. Since the spent liquors from the initial first and second rows are not utilized in the stages immediately below, they are discarded. Fluoride was added to the fresh leaching acid. H_2SiF_6, Na_2SiF_6, and CaF_2 were used as sources of fluoride, and at equivalent amounts of fluoride addition no difference was noted in their effect. Retention time for each stage was 2 h, or a total leach time of 6 h.

The leaching process eliminates the energy-intensive step of high-temperature calcination. Countercurrent leaching resulted in a more efficient use of acid and fluoride than single-stage leaching. Ninety percent of the aluminum values were extracted with 95% of stichiometric HCl requirement and a F/Al ratio of 0.27. If acid concentration is increased, the fluoride addition can be decreased.

3.2.5 Alternative Methods of Production

Despite several disadvantages, the electrolytic method for the production of aluminum is still the only process practiced on an industrial scale. The main drawbacks are:
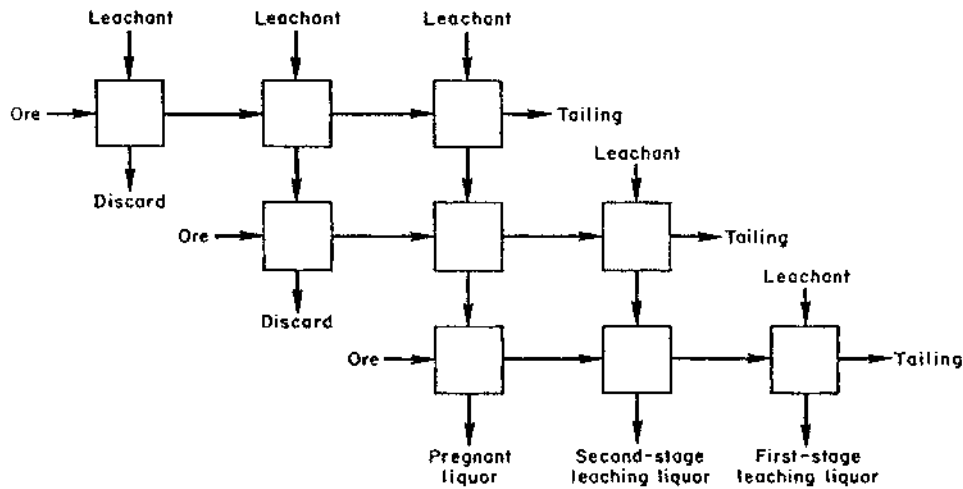
Figure 10 Diagram of simulated, three-stage countercurrent leaching.

- the very large size of the economic unit
- the employment of low voltage D.C. as a source of energy
- the additional capital investment in the alumina factories

Continued efforts have been made to devise a process that would be free from these problems, and recently a certain amount of progress has been made. It is comparatively simple to reduce crude bauxite in an electric furnace with carbon, but the result is an alloy of aluminum with iron and silicon, which must be purified. Two methods are available: in one the aluminum is dissolved in a suitable solvent, e.g. Zn, Mg, or Hg, the impurities filtered off, and the solvent recovered by distillation, in the other, which has been operated on a pilot scale in Canada, the aluminum is volatilized as a sub-halide. The Al-Fe-Si alloy is treated with aluminum chloride at $1000–1200°C$ at atmospheric pressure. The resulting sub-chloride, $AlCl$, is passed to a condenser where the aluminum is deposited according to the reaction:

$$3AlCl \Longleftrightarrow 2Al + AlCl_3$$
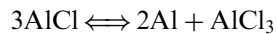
The aluminum chloride is recycled.

Another method which has reached pilot plant stage in France depends on the reduction of pure alumina with carbon, and instead of capturing the aluminum vapor in another metal and so obtaining an alloy, the vapor is captured, and re-oxidation prevented, with aluminum carbide. The two reactions:

$$Al_2O_3 + 3C = 2Al + 3CO$$

and

$$2Al_2O_3 + 9C = C_3Al_4 + 6CO$$
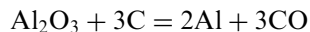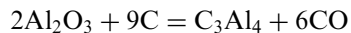
proceed simultaneously, and under the right conditions at 2400°C an alloy of aluminum and the carbide is obtained which may contain as much as 80% aluminum. This, on cooling, deposits the carbide, which can be separated by fluxing with fused chlorides. The carbide is recycled.

None of these methods saves energy in comparison to the electrolytic method, but they do open up the possibility of working smaller units, with lower capital investment.

4   PRODUCTION OF SUPER PURITY ALUMINUM (REFINEMENT)

The production of superpurity aluminum, 99.99+% purity, requires special procedures, such as a continuous electrorefining of commercially pure aluminum in a Hoopes cell.

The electrolitic refinement of aluminum carries out by the three-layer method [7,19,40]. For this purpose there are three layers available into the electrolizer (Fig. 11). The bottom layer serves as the anode. It represents a refined (purified) aluminum alloy with copper. Copper is introduced to increase the density of a layer. An average density layer is the molten electrolyte. Its density is less than the density of an anode alloy and higher than one of purified (cathode) aluminum which is above an electrolyte (a molten top layer).

At anode dissolution more electropositive impurities than aluminum such as Fe, Si, Ti, Cu, and other, remain in an anode alloy. Aluminum is dissolved only at the anode. It goes into electrolyte in the form of metal ions Al^{3+}:

$$Al - 3e \rightarrow Al^{3+}$$
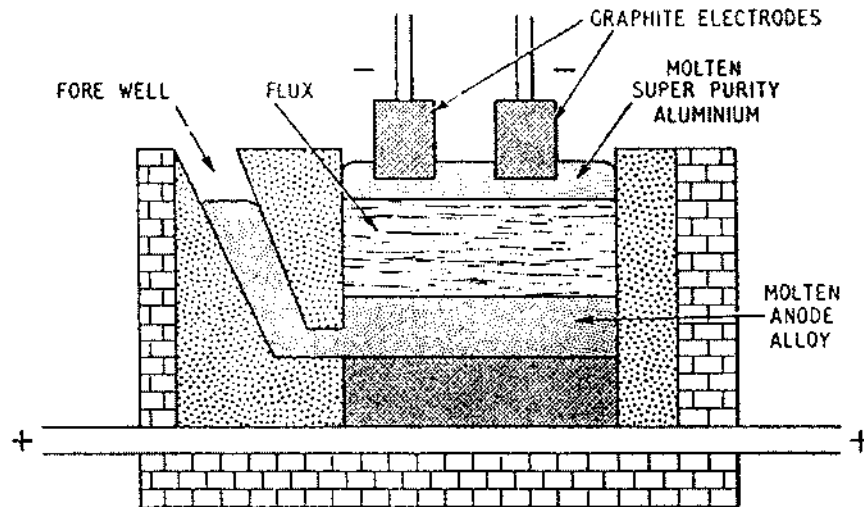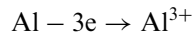
Figure 11   Super-purity refining furnace.

During the electrolysis, ions of aluminum are transferred to the cathode:

$$Al^{3+} + 3e \rightarrow Al.$$
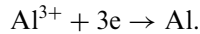
As a result, a layer of the molten purified aluminum is accumulated on the cathode.

More electronegative impurities than aluminum such as Ba, Na, Mg, Ca can be dissolved electrochemically on the anode. These ions report to the electrolyte. Because of the small amount of electronegative impurities in the raw aluminum they have not accumulated to a great extent in the electrolyte. The discharge of these ions on the cathode does not practically occur because their electrode potential is more electronegative than aluminum.

The fluoride–chlorine electrolyte is more common for this process The chemical composition of it is 55–60% $BaCl_2$, 35–40% AlF_4 + NaF and up to 4.0% NaCl. Mole ratio NaF/Al_3 is 1.5–2.0; The melting point of the electrolyte is 720–730°C. The temperature of the electrolysis is approximately 800°C. The electrolyte density is 2.7 g/cm³.

The anode alloy is prepared from the primary aluminum and pure copper (99.90–99.95% Cu) which is introduced into the metal in quantity of 30–40% [7]. The density of a liquid anode alloy of such composition is 3.0–3.5 g/cm³. Density of pure molten cathode aluminum is 2.3 g/cm³. Purity of aluminum refined by the three-layer method is 99.95%. Purity is determined based on the quantity of five main impurities such as Fe, Si, Cu, Zn, Ti.

On evidence derived from [6] refined aluminum has the following composition: Fe – 0.0005–0.002%; Si – 0.002–0.005%; Cu – 0.0005–0.002%; Zn – 0.0005–0.002%; Mg – traces; Al – other. Refined aluminum usually processes into a semi-finished product of the specified above composition or alloyed by magnesium.

4.1 Production Extreme Purity Aluminum

4.1.1 Zone Melting

The principle of zone melting consists of repeated passing of a melted zone along an aluminum ingot [7]. The impurities decreasing the melting point aluminum at the zone melting are concentrated in the molten zone and are transferred to the end as an ingot. These impurities are Ga, Sn, Be, Sb, Ca, Th, Fe, Co, Ni, Ce, Te, Ba, Pt, Au, Bi, Pb, Cd, In, Na, Mg, Cu, Si, Ge, Zn. The impurities increasing the melting point are concentrated in a solid (initial) part of an ingot. These impurities are Nb, Ta, Cr, Ti, Mo, V. The impurities such as Mn and Sc do not change the melting temperature of aluminum and are not removed at the zone melting.

Aluminum has significant chemical activity. Therefore, zone melting should be carried out in a vacuum or in an atmosphere of inert gas (argon or helium). During the zone melting in a vacuum, extreme purity of aluminum can be achieved because some impurities "volatilize." Typical elements that volatilize are Mg, Zn, Cd, alkaline and alkaline-earth metals.

By zone melting with several consecutive cycles, it is possible to achieve very pure aluminum [41]. The initial material of each new cycle is the purest part of an ingot received at the previous cycle. The purity of received aluminum is determined based on the difference of the main impurities such as Si, Fe, Mg, Mn, Ti, Cu, Cr, Zn, Na, V making up more than 99.9999%.

Another method of achieving extreme purity aluminum is refined electrolysis of pure or commercial pure aluminum [6]. Complex aluminorganic aluminum compounds are applied as the electrolyte. Electrolysis does at $100°C$ between solid aluminum electrodes. The composition of electrolyte can differ. For example, in [42], electrolysis of 50% solution of $NaF \times 2Al(C_2H_5)_3$ in toluene is applied. Using this method, the metal purity of 99.999–99.9999% can be achieved.

REFERENCES

1. J. R. Devis, Ed. *Aluminum and Aluminum Alloys*, ASM International, 1993.
2. *Aluminum Industry Technology Roadmap*, May 1997, The Aluminum Association, Inc., in conjunction with the U.S. Department of Energy. A report.
3. F. X. McCawley and L. H. Baumgardner, "Aluminum", *Mineral Facts and Problems*, 1985 Edition, United States Department of the Interior.
4. http://minerals.usgs.gov/minerals/pubs/commodity/aluminum/stat/tb12.txt.
5. *Aluminium properties, physical metallurgy and phase diagrams*. American Society for Metals, Metals Park, Ohio, 1967, p. 530.
6. *Aluminium-Tashcenbuch*, Aluminium-verlag GMBH, Dusseldorf, 1974, p. 663.
7. I.N. Fridlyander, *Physical Metallurgy of Aluminium and Its Alloys*, Moscow, 1983, p. 287 (in Russian).
8. K. Grjotheim and B. J. Welch, *Aluminum Smelter Technology, A Pure and Applied Approach*, Aluminium-Verlag GMBH, Düsseldorf, 1997.
9. A. S. Russell, "Developments in Aluminum Smelting, Alum. and Suppl." June 1981, 57(6), pp. 105–109.
10. A. I. Belyaev, M. B. Rapoport, and L. A. Firsanova, *Electrometallurgia Aluminia*, Moscow-Leningrad, 1938 (in Russian).
11. V. P. Mashovets, *Electrometallurgia Aluminia*, Moscow, 1953 (in Russian).
12. J. D. Edwards, F. C. Frary, and Z. Jeffries, New York and London, 1930.
13. F. Schmid, "Geology of Recent/Potential Bauxite Producing Areas in Sierra Leone and in the People's Revolutionary Republic of Guinea (West Africa)," *Bauxite-Proceedings of the 1984 Bauxite Symposium*, Los Angeles, CA, February 27–March 1, 1984, pp. 486–499.
14. "Industry Requirements to Ores Quality," *Aluminum, Handbook for Geologists*, Moscow, 1962, p. 60 (in Russian).
15. Yu. K., Goretskiy, "Trends in Bauxites Distribution and Conditions of Their Formation, Bauxite and Their Mineralogy," Genesis, Academy of Science of the USSR, 1958 (in Russian).
16. A. P. Vinogradov, "Trends in Elements Distribution in Earth Crust, GeoKhimia," No. 1, Academy of Science of the USSR, 1956 (in Russian).
17. V. Smirnov, "Alumina Production in Russia Part I: Historical Background," JOM, 1996, 48(8), pp. 24–26.
18. A. I. Lainer, *Aluminum Oxide Production*, Moscow, Metallurgiszdat, 1961 (in Russian).
19. V. A. Mazel, *Aluminum Oxide Production*, Moscow, Metallurgiszdat, 1955 (in Russian).
20. Prof. D. Altenpohl, *Aluminum Viewed from Within, An Introduction into the Metallurgy of Aluminum Fabrication*, 1st Edn, Aluminium-Verlag GMBH, Düsseldorf, 1982.

21. D. S. Flett, "Aluminum from indigenous resources: present position in Aluminum and its future patterns of use in Great Britain," ASM, 1982.
22. J. Cohen and H. Mercier, "Recovery of alumina from non-bauxitic aluminum-bearing raw materials," AIME Annual Meeting, Las Vegas, 1976.
23. J. A. Eisele and D. J. Bauer, "Evaluation Technology for the Recovery of Metallurgical-grade Alumina from Coal Ash," U.S. Department of the Interior, Bureau of Mines, 1979.
24. D. C. Cavin, W. A. Klemn, and G. Burnet, "Analytical Methods for Characterization of Fly Ash," Proc. Iowa Acad. Sci., 1974, 81(3).
25. U.S. Bureau of Mines, *Potential Sources of Aluminum*, BuMines IC 8335, 1967, p. 148.
26. S. A. "Ash as a Source of Iron Production," Nauch. Tr. Mosk. Gorn. Inst, 1959, 27, pp. 137–43; In *Chem. Abst.*, 1961, 55, 1632h.
27. F. A. Peters, Private Communication, 1977. Available for consultation from J. A., Eisele, and D. J. Bauer, Bureau of Mines, Reno Metallurgy Research Center, Reno, Nev.
28. R. Zimmerman, and K. Gunter, *Metallurgy and Materials Science*, Handbook, Metallurgiszdat, Moscow, 1982, p. 480 (in Russian).
29. A. I. Belyaev, *Metallurgy of Light Non-Ferrous Alloys*, Metallurgia, Moscow, 1970, p. 366 (in Russian).
30. World Metal Statistics, 1981, 7, p. 36.
31. Yu. V., Baimakov, and M. M. Vetukov, *Electrolisis of Metaled Salts*, Metallurgia, Moscow, 1966, p. 560 (in Russian).
32. Yu. I., Barsukov, A. M. Voroshenkov, et al. In: *Scientific Research and Experience of Design in Metallurgy of Light Metals*, Metallurgia, Moscow, 1981, pp. 110–116 (in Russian).
33. P. C. Varley, *The Technology of Aluminum and Its Alloys*, CRC Press, 1970.
34. Nolan Richards, "Strategies for Decreasing the Unit Energy and Environmental Impact of Hall–Heroult Cells," Light Metals, 1994.
35. K. Grjotheim, C. Krohn, and H. A. Øye, Aluminum, 1975, 8(4).
36. P. R. Bremner, J. A. Eisele, and D. J. Bauer, "Aluminum Extraction from Anorthosite by Leaching with Hydrochloric acid and Fluoride," Report of investigations, United States Department of the Interior, Bureau of Mines, 8694, 1982.
37. "Mineral Facts and Problems," Bulletin 671, 1980, p. 17.
38. R. A. Brown, F. J. Cservenyak, R. G. Anderberg, H. J. Kandiner, and F. J. Frattali, "Recovery of Alumina From Wyoming Anorthosite by the Lime-Soda-Sinter Process," BuMines RI 4132, 1947, p. 127.
39. H. Leitch, H. Iverson, and J. B. Clemmer, "Extraction of Alumina by Leaching Metled and Quenched Anorthosite in Sulfuric Acid," BuMines RI 6744, 1965, p. 32.
40. A. A. Kostukov, I. T. Kil, V. P. Nikiforov, et al., *Non-Ferrous Alloys Handbook, Aluminum Production*, Metallurgia, Moscow, 1971, p. 560 (in Russian).
41. S. E. Maraev, Yu. I., Belyakov, et al., "Casting and Machining of Aluminum and Its Alloys," Transactions of VAMI, 1979, 105, pp. 76–85 (in Russian).
42. *Metal*, 1973, 3, pp. 203–211.
43. H. A. Øye, N. Mason, R. D. Peterson, N. E. Richards, E. L. Rooy, F. J. Stevens McFadden, and R. D. Zabreznik, "Aluminum: Approaching the New Millennium," JOM, February, 1999, pp. 29–42.

2

Properties of Pure Aluminum

ALEXEY SVERDLIN

Bradley University, Peoria, Illinois, U.S.A.

1 INTRODUCTION

Aluminum's unique properties – its light weight, high strength, and resistance to corrosion – make it an ideal material for use in conventional and novel applications. Aluminum has become increasingly important in the production of automobiles and trucks, packaging of food and beverages, construction of buildings, transmission of electricity, development of transportation infrastructures, production of defense and aerospace equipment, manufacture of machinery and tools, and production of durable consumer products. As demand for more technologically complex and ecologically sustainable products increases, opportunities for aluminum will continue to expand [1].

Aluminum is the third most abundant element in the Earth's crust. Aluminum is the chemical element of the 3rd group in the periodic table of the elements. The atomic number of aluminum is 13, values for the atomic weight are 26.9815 based on 12C, and 26.98974 based on ^{16}O [2]. Aluminum has a silver-white color. It does not have any natural isotopes. Its artificial isotopes are radioactive isotopes – ^{26}Al and ^{26}Al. The isotope ^{26}Al has a half-life of 10^6 years and isotope ^{27}Al is stable and consists of 14 neutrons and 13 protons. Table 1 lists the properties and characteristics of some isotopes found in aluminum.

The nuclear properties of aluminum are of practical interest. The naturally occurring isotope Al^{27} has a cross section for thermal neutrons of 0.21 barn (1 barn $= 10^{-24}cm^2$). This low cross section combined with the short half-life of the radioactive product from the irradiation of aluminum an especially attractive material for use within nuclear reactors. In the early nuclear reactors, aluminum was used almost exclusively for protective sheaths around uranium fuel elements and as tube and fittings for conducting coolant through the pile.

Table 1 Isotopes of Aluminum [3]

Isotope	Half-life	Particles absorbed	Type of decay	Energy of radiation, ev*	Some typical modes of formation
Al^{23}	0.13 sec	–	–	–	–
Al^{24}	2.7 sec	Neutron	$\beta+$	~8.5	Mg^{24} (p, n)
			γ	1.38–7.1	–
Al^{25}	7.5 sec	Neutron	$\beta+$	3.2	Mg^{25} (p, n)
Al^{26m}	7.0 sec	Neutron	$\beta+$	3.2	Mg^{25} (d, n)
Al^{26}	10^6 years	Neutron	ec (**)	–	Mg^{25} (d, n)
			β	1.16	Mg^{26} (p, n)
			γ	1.83, 1.14	Al^{27} (n, 2n)
Al^{27}	100% abundance, stable	–	–	–	–
Al^{28}	144 sec	2 protons	$\beta-$	2.86	Al^{27} (n, γ)
		1 proton	γ	1.78, 1.27	Al^{27} (n, γ)
Al^{29}	396 sec	Proton	$\beta-$	2.5, 1.4	Al (α, 2p)
		Proton	γ	1.28, 2.43	Mg (α, p)

* Electron-volts
** Electron capture

Aluminum may possess a coordination number for oxygen of either 4 or 6. The process of recrystallization of aluminum oxide is normally slow. Thus, there are a great many crystal structures for aluminum oxide. The corundum structure has only 6 coordinate Al in hexagonal crystals. It can probably be viewed as a distorted hexagonal closest packed structure of oxide ions, with some of the octahedral holes occupied by Al^{3+} ions. Beta alumina has spinal structure with extra cation vacancies to bring the stoichiometry to M_2O_3 from the ideal spinal formula of MM_2O_4.

2 GRADES OF ALUMINUM

Depending on amount of impurities, aluminum is classified into extreme purity aluminum and commercial purity aluminum (primary aluminum).

In Russia there are four grades of extreme purity metal with the content of aluminum no less than 99.996%; 99.99%; 99.97%, 99.93%, other elements present are iron, silicon, copper [4]. The chemical composition of primary aluminum is presented in Table 2 (Russian Standard GOST 11069–74) [4].

Table 3 shows nomenclature for the various degrees of purity of aluminum accepted in the USA [5]. Aluminum exceeding 99.99% in purity, produced by the Hoopes [6] electrolytic process, was first available early in 1920. In 1925, Edwards [7] reported some of the physical and mechanical properties of this grade of aluminum. Taylor, Willey, Smith, and Edwards [8] published a paper in 1938 that gave several properties for 99.996% Al that was produced in France by a modified Hoopes process.

Table 2 Russian Classification of Aluminum

Grade	Al, %	Impurities, %, not more than						Total of controlled impurities
		Fe	Si	Cu	Zn	Ti	Others	
Extreme purity aluminum								
A999	99.9999	–	–	–	–	–	–	0.001
Super purity aluminum								
A995	99.995	0.0015	0.0015	0.001	0.001	0.001	0.001	0.005
A99	99.99	0.003	0.003	0.003	0.003	0.002	0.001	0.010
A97	99.97	0.015	0.015	0.005	0.004	0.002	0.002	0.030
A95	99.95	0.030	0.030	0.005	0.002	0.005	0.005	0.050
Commercial aluminum								
A85	99.85	0.08	0.06	0.01	0.02	0.010	0.02	0.15
A8	99.80	0.12	0.10	0.01	0.04	0.020	0.02	0.20
A7	99.70	0.16	0.16	0.01	0.04	0.020	0.02	0.30
A7E	99.70	0.20	0.08	0.01	0.04	0.010	0.02	0.30
A6	99.60	0.25	0.20	0.01	0.06	0.030	0.03	0.40
A5	99.50	0.30	0.30	0.02	0.06	0.030	0.03	0.50
A5E	99.50	0.35	0.12	0.02	0.04	0.015	0.02	0.50
A0	99.0	0.50	0.50	0.02	0.08	0.030	0.03	1.00

Table 3 The Various Degrees of Purity of Pure Aluminum (the USA Standard) [5]

Aluminum, %	Designation
99.5000 to 99.7900	Commercial purity
99.8000 to 99.9490	High purity
99.9500 to 99.9959	Super purity
99.9960 to 99.9990	Extreme purity
> 99.9990	Ultra purity

Based on ISO standards the classification of aluminum is shown in the Table 4 [9].

The chemical composition of the extreme purity and primary aluminum according to the DIN1712 is shown in Table 5 [4].

Table 6 lists the AA wrought alloys that are covered by standards as used in Great Britain, Germany, France, Japan, Russia, and in the Recommendations of the International Organization for Standardization (ISO). The list includes only those alloys that are essentially in agreement composition-wise with the composition of the AA alloy. Standards are subject to change and the actual issue of the specification or standard currently in effect should be consulted for full information.

Table 4 Classification of Aluminum Based on International Standard (ISO)

Purity of aluminum	Designation
Extreme purity	A199.99R; A199.95R; A199.9R; A199.8; A199.7
Commercial purity	A199.8; A199.7; A199.5
For electrical industry (wires)	A199.4; A199.0; A198 E-Al
Extreme purity	A199.99R; A199.95R; A199.9R; A199.8; A199.7; A199.5
Commercial purity	E-Al*
For electrical industry (wires)	E-Al**

* Electrical conductivity in annealing condition is more than 35.7 μOhm $\times$ mm^{-2}
** Electrical conductivity in annealing condition is more than 35.4 μOhm $\times$ mm^{-2}

Table 5 The Chemical Composition of the Aluminum of Different Grades (the German Standard)

Grade	Number	Allowable impurities						
		Total	Including					
			Si	Fe	Ti	Cu	Zn	Others
A 199.99R	3.0400	0.01	0.060	0.005	0.002	0.003	0.005	0.001
A 199.99R	3.0300	0.10	0.050	0.035	0.006	0.005	0.040	0.003
A 199.8H	3.0280	0.20	0.150	0.15	0.030	0.010	0.060	0.010
A 199.7H	3.0270	0.30	0.200	0.25	0.030	0.010	0.060	0.010
A 199.5H	3.0250	0.50	0.300	0.40	0.030	0.020	0.070	0.030
A 199.0H	3.0200	1.00	0.500	0.06	0.030	0.020	0.080	0.030

3 PHYSICAL PROPERTIES

The properties of aluminum depend to some extent on purity. This may vary from the ordinary aluminum of commercial purity to super-purity aluminum. For special purposes, aluminum may be further purified by zone refining to give a purity of about 99.99995%. Aluminum is well known for its low density, 2.7 g/cm^3, high reflectivity and high electrical and thermal conductivity. It is very resistant to atmospheric corrosion, due to instantaneous formation of an adherent oxide film, which protects the metal against further attack. The more important physical properties are shown in Table 7, which also indicates how these properties are affected by purity [11]. It will be seen that the main effects of purity are upon electrical resistivity (the electrical resistance offered by a material to the flow of current, times the cross-sectional area of current flow and per unit length of current path; the reciprocal of the conductivity) and thermal conductivity.

Table 6 International Cross References on Aluminum [10]

USA AA	UK BS	Germany DIN	France NF	International ISO	Japan JIS	Russia GOST
1050	–	–	–	–	A 1050	–
1050A	1B	A 199.5	A5	Al 99.5	–	–
1060	–	–	–	Al 99.6	A 1060	A6
1065	–	–	–	–	–	–
1070	–	–	–	–	A 1070	A7
1070A	–	A 199.7	A7	Al 99.7	–	–
1080	–	–	–	–	A 1080	–
1080A	A8	A 199.8	A8	Al 99.8(A)	–	–
1085	–	–	–	–	A 1085	–
1090	–	–	–	–	A 1N90	–
1098	–	A 199.98R	–	–	–	–
1100	A45	–	A45	Al 99.0 Cu	A 1100; A 1N00	–
1185	–	–	–	–	A 1185	A85
1199	–	–	–	–	–	A99
1200	A4	A 199	A4	Al 99.0	A 1200	A0
1230	–	–	–	Al 99.3	A 1N30	–
1250	–	–	–	–	–	–
1350	–	–	–	E-Al 99.5	–	A5E
1350A	–	E-Al	–	–	–	–
1370	–	–	A-U6MT	–	–	–

Table 7 Physical Properties of Aluminum (after P. C. Varley)

| Property	Purity, %				
	99.999	99.990	99.800	99.500	99.000
Melting point, °C		660.2	–	–	657.0
Boiling point, °C		2480	–	–	–
Latent heat of fusion, cal/g		94.6	–	–	93.0
Specific heat at 100°C, cal/g		0.2226	–	–	0.2297
Density at 20°C, g/cm^3	2.7	2.7	2.71	2.71	
Electrical resistivity, $\mu\Omega$-cm at 20°C	2.63	2.68	2.74	2.8	2.87
Temperature coefficient of resistivity		0.0042	0.0042	0.0041	0.0040
Coefficient of thermal expansion $\times 10^6$ (20–100°C)		23.86	23.5	23.5	23.5
Thermal conductivity, e.g. units at 100°C		0.57	0.56	0.55	0.54
Reflectivity (total), %		90	89	86	–
Modulus of elasticity, lb/in$^2 \times 10^{-6}$		9.9	–	–	10.0
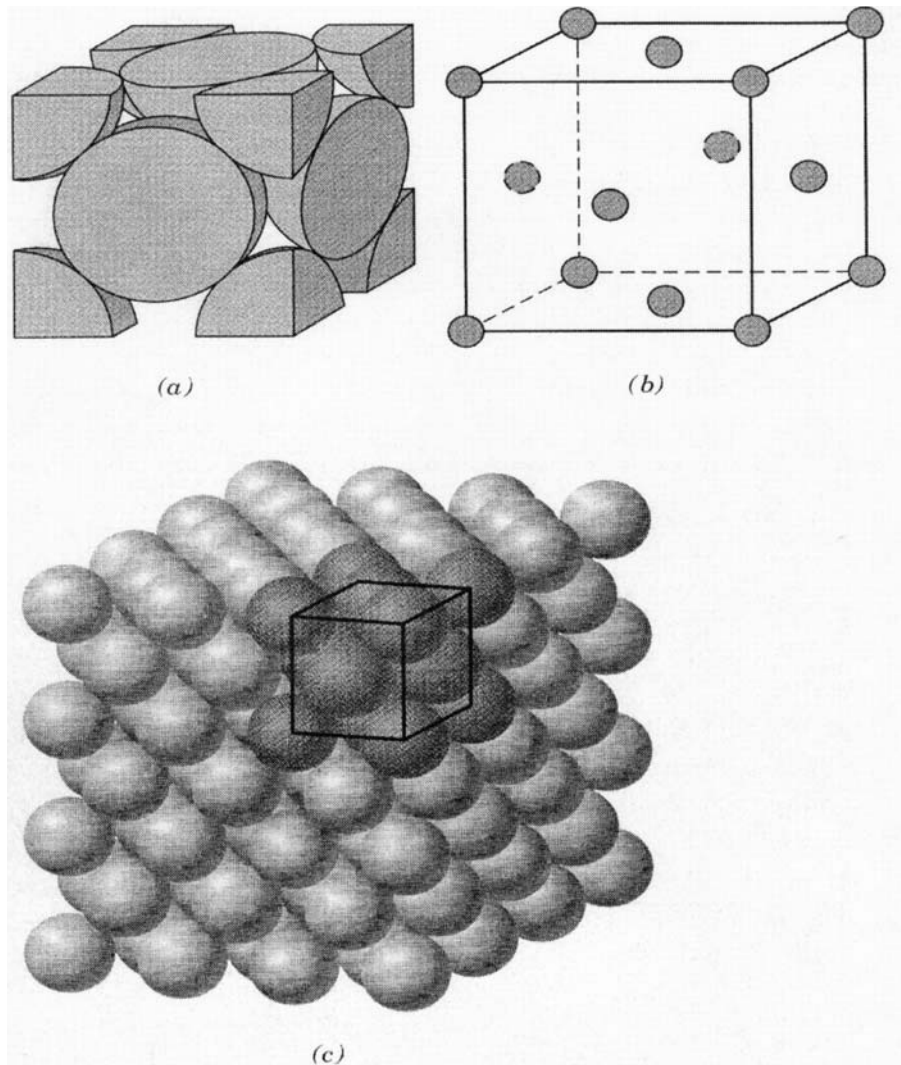
Figure 1   The crystal structure of aluminum – the face-centered cubic crystal structure: (a) a hard sphere unit cell representation, (b) a reduced-sphere unit cell, and (c) an aggregated of many atoms [85,86].

3.1   CRYSTAL STRUCTURE AND ATOMIC RADIUS

Aluminum has the face-centered cubic crystal structure over the whole temperature range up to the melting point with the coordination number 12 (each atom had the same number of nearest-neighbor or touching atoms) (Fig. 1) [12]. This crystal structure is the most packed cubic lattice. The closest distance between two atoms in the aluminum structure is 2.863Δ. The atomic packing factor is 0.74. The accepted lattice constant of aluminum crystal structure a is 4.0414Δ at room temperature [13]. The lattice is stable at the temperatures from 4K up to a melting point of 933K [14]. Measurements of 99.99% Al (corrected for refraction) by Figgins et al. [15] give

$a = 4.04963\Delta$ at 25°C (standard deviation 0.00002Δ) agreeing very well with the results of Straumanis [16]

Atomic radius of aluminum determined as half of the distance between the nearest-neighbors in a crystal structure of a pure element is equal to 1.43Δ [17–19]. There is the metallic bonding in aluminum crystal structure. The atomic weight of aluminum is 26.9815 (on carbon ^{12}C) and 26.98974 (on oxygen ^{16}O) [20].

The equilibrium interatomic distance at metallic bonding corresponds to strong overlapping of the external electron shells. Therefore, the atomic radius is equal approximately to the orbital radius of external shells.

The ionic radii describe more precisely the interatomic distance. The ionic radius of aluminum is 0.53Δ that is calculated based on the distribution of the density of electrons [19]. The interatomic distance in the aluminum crystal structure can be described by a system of atomic-ionic radii. This distance is defined by an orbital radius of a free atom and equals 1.23Δ.

3.2 Defects of a Crystal Lattice

Vacancies are the simplest point defects in a crystal lattice. It is a normally occupied lattice site from which an atom or ion is missing. The ability of a crystal to keep point defects, formed in one way or another depends on their mobility in a crystal.

One way that determines the vacancy concentration, is the measurement of the length of a specimen and the period of a lattice during heating to a given temperature: $Gv = 3 \, (\Delta L/L - \Delta a/a)$, where $\Delta L/L$-change in length of a specimen at some instant, $\Delta a/a$-change in the period of a lattice at the same instant. The equilibrium concentration of vacancies in pure aluminum at the temperature close to the melting point using this formula is 9.4×10^4 [21,22]. The energy of formation ($Å_f$) and migration ($Å_M$) vacancies and also the energy of activation for self-diffusion (E_{sd}) of vacancies in aluminum are shown in Table 8 [21]:

The equilibrium concentration of vacancies at any temperature can be determined by the formula: $n = e^{-Es/KT}$. The vacancies will make an impact on electrical resistivity of the metal. The most sensitive to their presence is electrical resistivity. For aluminum the value of electrical resistivity caused by vacancies and interstitial atoms is 3.4 $\mu\Omega \times \text{cm/at}\%$ [23,24].

Supersaturation of the metal by vacancies will make an impact on its mechanical properties. The critical shear stress for the quenched crystals of aluminum is approximately five times higher than for annealed crystals. Dislocations are the linear crystalline defects around which there is atomic misalignment. Plastic deformation corresponds to the motion of dislocations in response to an applied shear stress. Edge, screw, and mixed dislocations are possible [22–24].

Slip occurs on the most densely packed crystallographic planes and, in those planes, along directions having the greatest atomic packing (the slip plane is the crystallographic plane along which the dislocation line). For metals with FCC crystal structure including aluminum, the slip directions are ⟨110⟩-type because the shortest vector of a lattice is equal 1/2 of the direction ⟨110⟩. For this crystal structure, the slip planes are {111}-type. The magnitude and direction of the lattice distortion associated with a dislocation is expressed in terms of a Burger vector. The splitting width of a dislocation is determined by the packing defect energy

Table 8   Energy of Formation, Migration and Self-Diffusion of
Vacancies in Aluminum

Defect	E_f, eV	E_m, eV	E_{sd}, eV
V_1	0.76	0.65	1.4
V_2	$E_b = 0.17$	0.50	–

V_1 = single vacancy (a vacancy which has no other vacancy in its nearest proximity);
V_2 = two-vacancy (a pair of two vacancies lying close to one another);
$Å_b$ – the bonding energy of two-vacancies

Table 9   The Relationship Between the Critical Stress and the Shear Modulus for Aluminum

Reaction	300 k	900 K
The complete dislocation; homogeneous nucleation	7.0	4.6
Nucleation on the surface dislocation jog*	4.6	2.6
The partial dislocations; homogeneous nucleation	8.5	5.8
Nucleation on the surface dislocation jog	6.0	4.8

* (an offset in the dislocation line, resulting from the intersection of two dislocations, or a step created in the
dislocation line when a dislocation moves from one slip plane to another)

between the atoms. The greater the packing defect energy, the less the partial
dislocations are diverged. For aluminum this value is very high and equals 135
ergs/cm^{-2} [22].

Several slip systems may exist for a particular crystal structure. The number of
independent slip systems represents the different possible combinations of slip planes
and directions. For aluminum with FCC crystal structure, there are 12 slip systems:
four unique {111} planes and, within each plane, three independent ⟨110⟩ directions.

The critical stress σ required for noticeable rate of the dislocation nucleus for-
mation can be represented by the relationship σ/G, where G is the shear modulus.
Table 9 shows this relationship for aluminum.

3.3   Density

The theoretical density of aluminum calculated on the translation period of the
lattice (the minimum distance over which a unit cell must be successively translated
in any of the directions peculiar to a given crystal system, in order to create a crystal
lattice) is equal 2.69872 g/cm^3 [25]. Perryman [26] has found that density of alumi-
num is 2.6984 ± 3 g/cm^3 at 20°C as the mean of 12 determinations. The experimental
values of for a polycrystalline material are in the limits from 2.6966 to 2.6988 g/cm^3
and for monocrystals are on 0.34% is higher. The density of the molten aluminum
with purity 99.996% is shown in Fig. 2 [27].

The density the solid and molten aluminum is reduced in accordance with
increasing of its purity [4,28]. Figure 3 shows value of density of aluminum
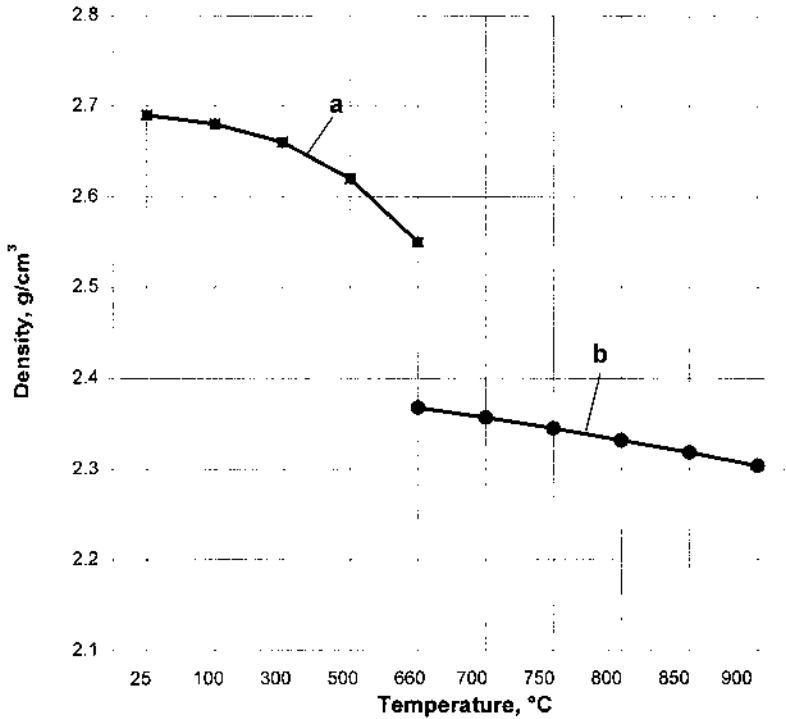depending on purity and the temperature.

Figure 2 Density values of the molten aluminum, 99.996% purity. (a) solid, (b) liquid.

3.4 Thermal Expansion

Taylor and others in [29] studied the elevated-temperature thermal expansion of 99.996 Al. Table 10 shows the average expansion coefficients obtained by four different researchers. Figure 4 presents low-temperature thermal expansion. Figure 5 shows the instantaneous temperature coefficients of linear expansion from absolute zero to 500°C. Figure 6 represents the average coefficients of thermal expansion for pure aluminum received by Willey who developed three equations that are useful in calculating linear expansion over three temperature ranges [30]:

$$L_t(-60 \text{ to } 100°C) = L_0[1 + C(22.17t + 0.012t^2)10^{-6}] \tag{1}$$

$$L_t(0 \text{ to } -200°C) = L_0[1 + C(21.57t + 0.00443t^2 - 0.000124t^3)10^{-6}] \tag{2}$$

$$L_t(0 \text{ to } 500°C) = L_0[1 + C(22.34t + 0.00997t^2)10^{-6}] \tag{3}$$

Where L_0 is length at 0°F, L_t is length at temperature t, °F, within the range indicated, and C is alloy constant that equal to 1.0 for pure aluminum.

3.5 Thermal Conductivity

Aluminum, having excellent electrical conductivity, is also a good conductor of heat. Electrical conductivity of metals, as well as thermal conductivity, is governed by
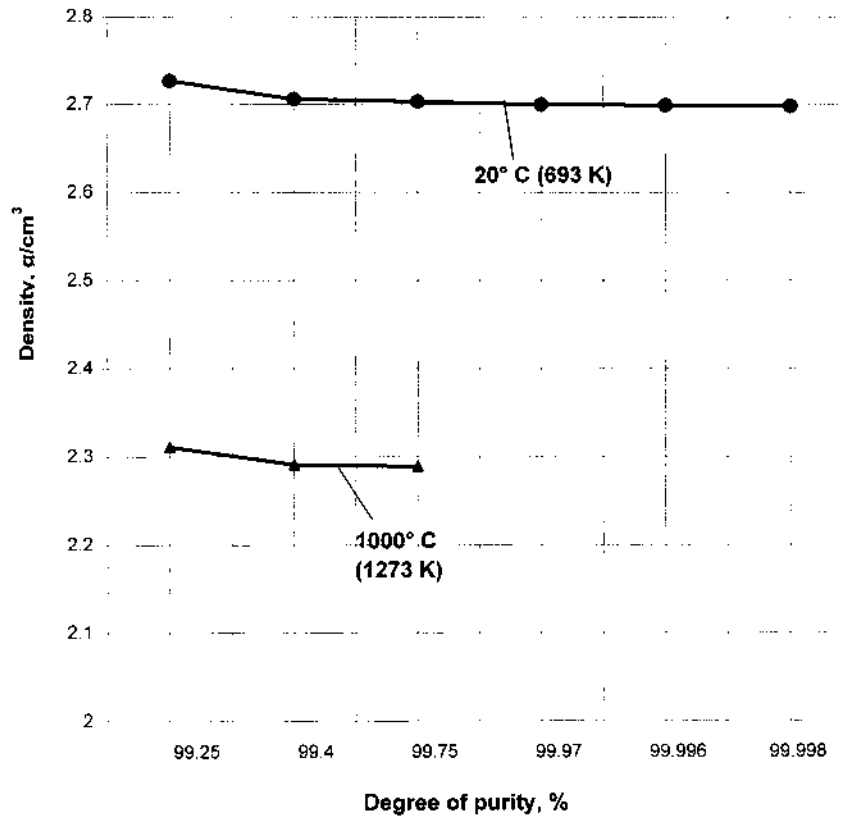
Figure 3 Density values of aluminum depending on purity and the temperature.

Table 10 Average Coefficient of Thermal Expansion of Aluminum

Aluminum purity, %	Coefficient of thermal expansion, micro-cm/cm/°C			
	20–100°C	20–200°C	20–300°C	20–400°C
99.997 (31)	23.9	24.3	25.3	26.5
99.996 (32)	23.9	24.6	25.4	26.5
99.952 (33)	23.4	24.5	25.5	–
99.996 (30)	23.6	24.6	25.5	26.5

behavior valence (external) electrons. On data [29], thermal conductivity of aluminum at room temperature (293K) is 50 cal/cm^2/sec/cm/°C.

Figure 7 shows the low-temperature thermal conductivity of a single crystal of 99.996 Al. Some values for the thermal conductivity of aluminum from 20°C (68°F) to the melting point of 660°C (1220°F) have been reported. The best data is obtained by calculating the thermal conductivity from room-temperature electrical-conductivity data, using one of these equations:
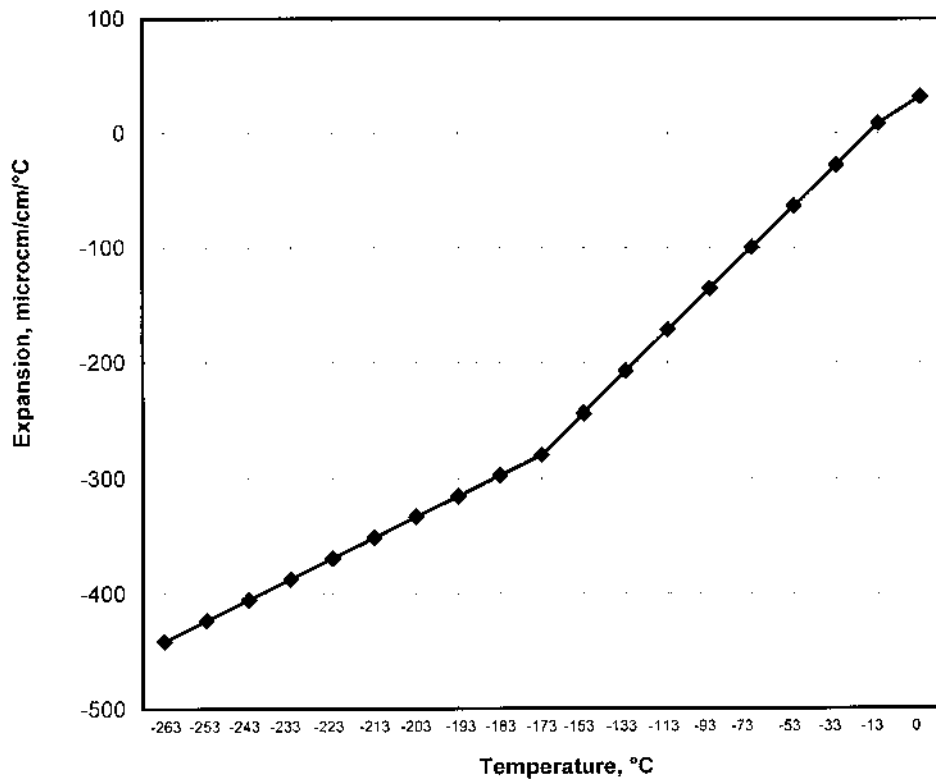
Figure 4 Low-temperature linear coefficient of expansion of aluminum [34].

Thermal conductivity values for pure aluminum calculated from the following equations:

$$K = 4.65\lambda T \times 10^{-9} + 0.05 \qquad [36]$$

$$K = 5.02\lambda T \times 10^{-9} + 0.03 \qquad [37]$$

$$K = 5.3\lambda T \times 10^{-9} + 0.025 \qquad [38]$$

$$K = 4.9\lambda T \times 10^{-9} + 1.2T \times 10^{-4} \qquad [39]$$

Thermal conductivity values for pure aluminum calculated from each of these equations are shown in Table 11.

Figure 8 (top) shows the thermal conductivity from 0 to 900°C; (bottom) from 0 to −273°C [35].

However, thermal conductivity is not completely dependent on the behavior of electrons. Inasmuch as the thermal energy of a crystal, above all the energy of the atom vibration near to their equilibrium interstitial positions of a lattice, the energy can be spread from a point to a point at the expense of interaction of atoms with each other. The vibrations of a lattice are described by sound waves
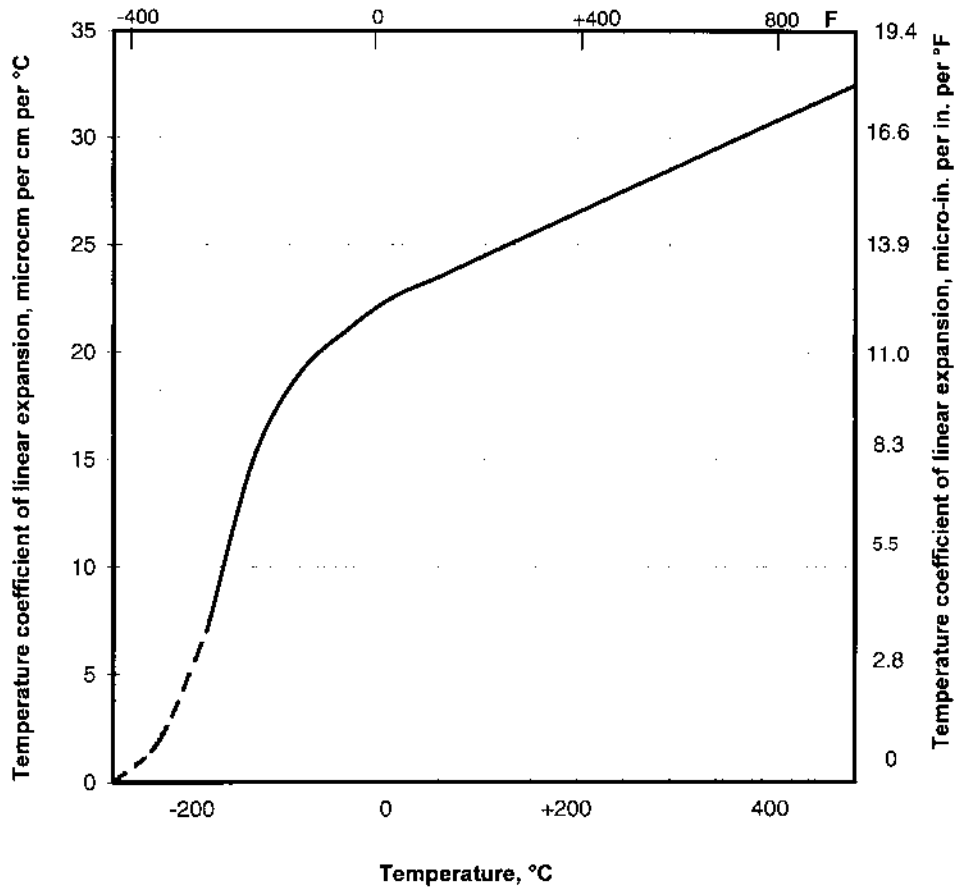
Figure 5   Expansion characteristics of extreme-purity aluminum [11].

propagation, named phonons [18]. According to this definition the total thermal conductivity k_t is the sum of the two contributions, or

$$k = k_p + k_e$$

where k_p and k_e represent the lattice vibration and electron thermal conductivity, respectively. For metals having good thermal conductivity at room temperature k_t is 10–100 cal/cm^2/sec/cm/°C. In metals electron thermal conductivity prevails and the value k_f is close to 1.

The thermal conductivity k is impossible to consider as a linear function of the temperature [18]. The results of experiments [36,39] show it clearly. For aluminum the value k in the interval of temperatures from 120 to 700K changes less than on 50%, whereas the electrical conductivity in the same interval of temperatures changes on 1300%.

At elevated temperatures the aluminum thermal conductivity depends on purity of the metal and increases with the higher purity. For commercial aluminum (99.49% and 99.70% Al) the thermal conductivity at 200° is 209 and 222 Bt/m-K,
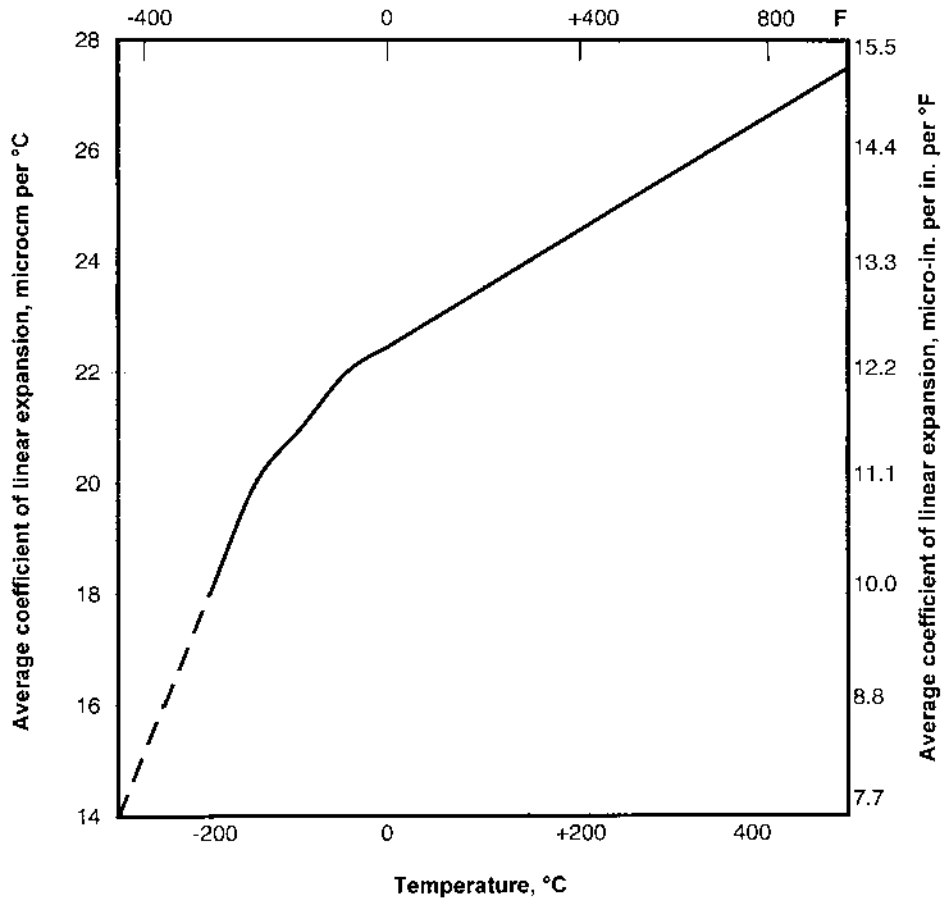
Figure 6   Average coefficient of linear expansion of extreme-purity aluminum from 20°C to temperature t [11].

respectively. For electrolytic refined aluminum with purity 99.9% at 190°C thermal conductivity increases up to 343 Bt/m-K. The impurities, such as Cu, Mg, and Mn in aluminum reduce the thermal conductivity. For example, the addition of 2% Mn reduces the thermal conductivity from 209 to 126 Bt/m-K [40].

At the temperatures >100K, the true thermal conductivity of completely annealed aluminum with the extreme purity (99.99%) is not sensitive to the degree of purity. At elevated temperatures, sensitivity to purity of a material, controllable by electrical resistivity, is displayed [41].

3.6   Debye Temperature

Debye temperature is the temperature, characteristic for a given substance, at which the whole spectrum of frequencies of atomic vibrations in the crystal lattice becomes narrowed close to its upper limit. The thermal atomic vibrations of the lattice are
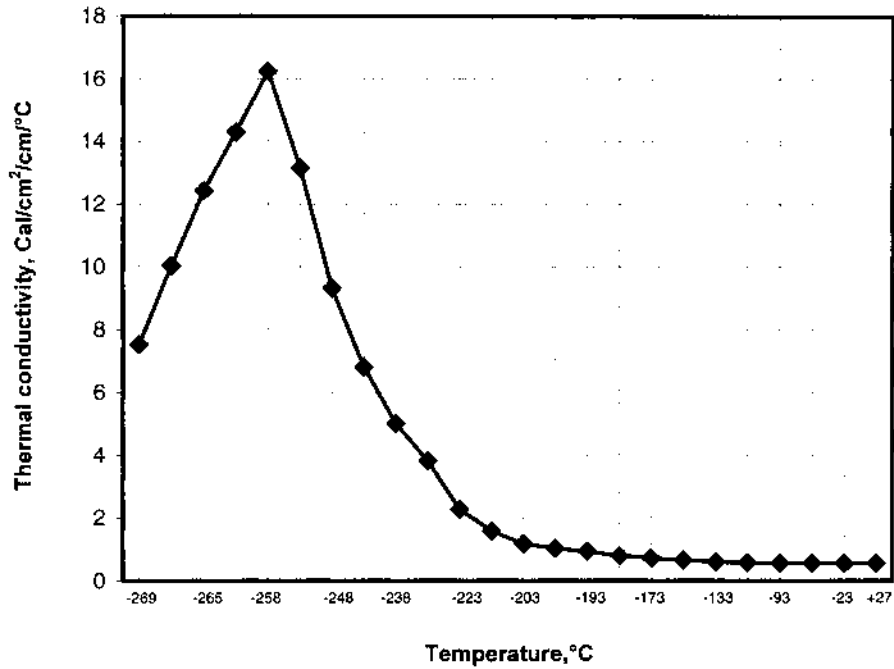
Figure 7   Thermal conductivity of 99.996 aluminum at low-temperature [35].

Table 11   Thermal Conductivity of Pure Aluminum

Temperature, °C	Cal/cm²/sec/cm/°C				
	Equation [36]	Equation [37]	Equation [38]	Equation [39]	Average
25	0.57	0.59	0.62	0.59	0.59
100	0.54	0.56	0.59	0.56	0.56
200	0.52	0.54	0.56	0.55	0.54
400	0.50	0.52	0.54	0.55	0.53
600	0.49	0.50	0.52	0.56	0.52

qualitatively defined in two temperature areas, determined by a ratio between the energy of thermal vibrations of atom and the bonding energy between atoms in a solid state.

In the first area for temporary intervals $t < 10^{-13}$ sec the lattice is not a periodic structure. The atoms are shifted about their equilibrium position. However, for $t \gg 10^{-}$ sec a balance of atoms positions occurs. Periodicity of a lattice is displayed. It reflects the periodicity of balance arrangement of the separate atoms.

At low temperatures the bonding energy of atoms is so great in comparison with the energy of vibrations that an atom at the displacement from the balance position in some direction entraps the adjacent atoms in the same direction. There is the coordinated displacement of atoms [18,42].
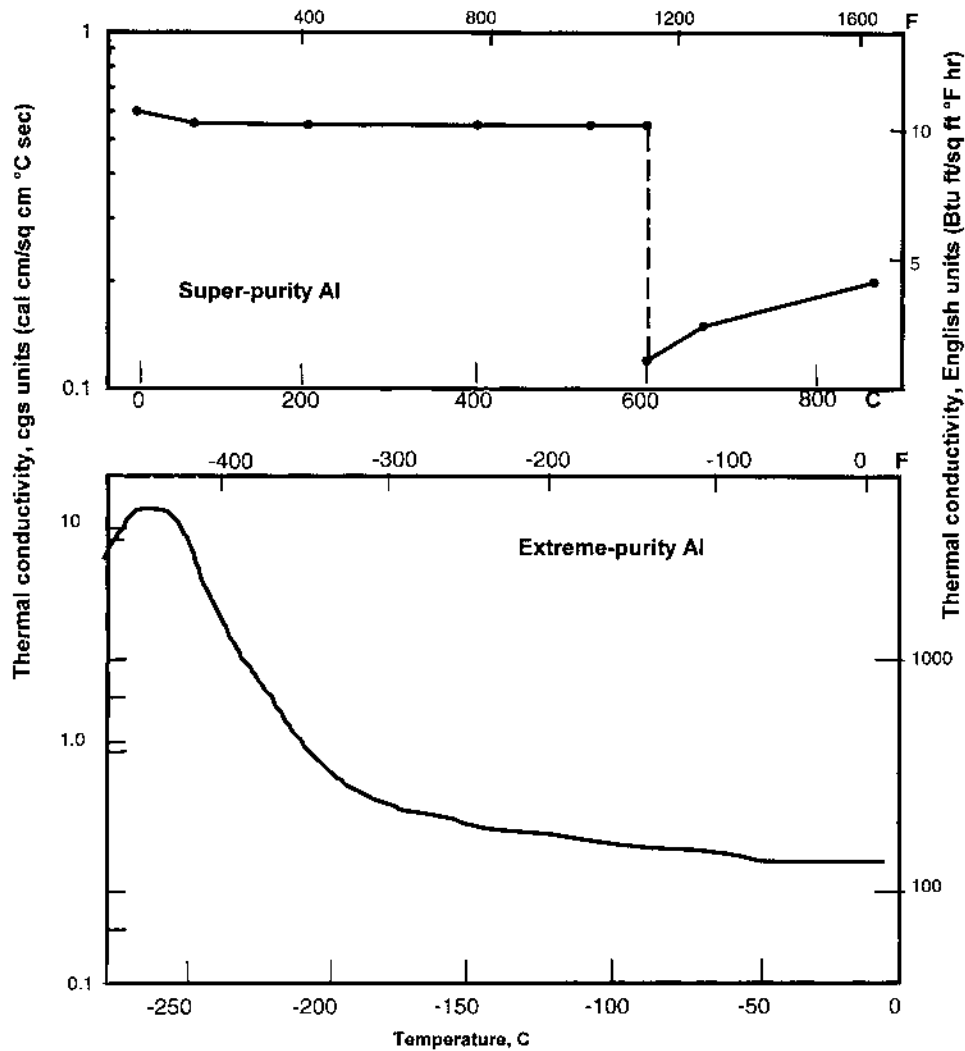
Figure 8 Thermal conductivity of super-purity aluminum from 0 to 900°C (top). Thermal conductivity of extreme-purity aluminum from 0 to −273°C (bottom).

Debye temperature defines the temperature at which it is necessary to carry out annealing of a monocrystal for residual stress removal. Annealing at a temperature close to $T_m > T_D$ does not improve but worsens a crystal lattice as it results in occurrence of vacancies, interstitial atoms, etc.

Annealing at the temperatures $T_m < T_D$ thermal vibrations cannot not remove residual stresses of a lattice. For pure aluminum this temperature is 375K [18].

3.7 Magnetic Susceptibility

The magnetic permeability of a substance is given by $\mu = 1 + 4\pi K$, where K is the magnetic susceptibility. If the susceptibility is positive, the material is "para-
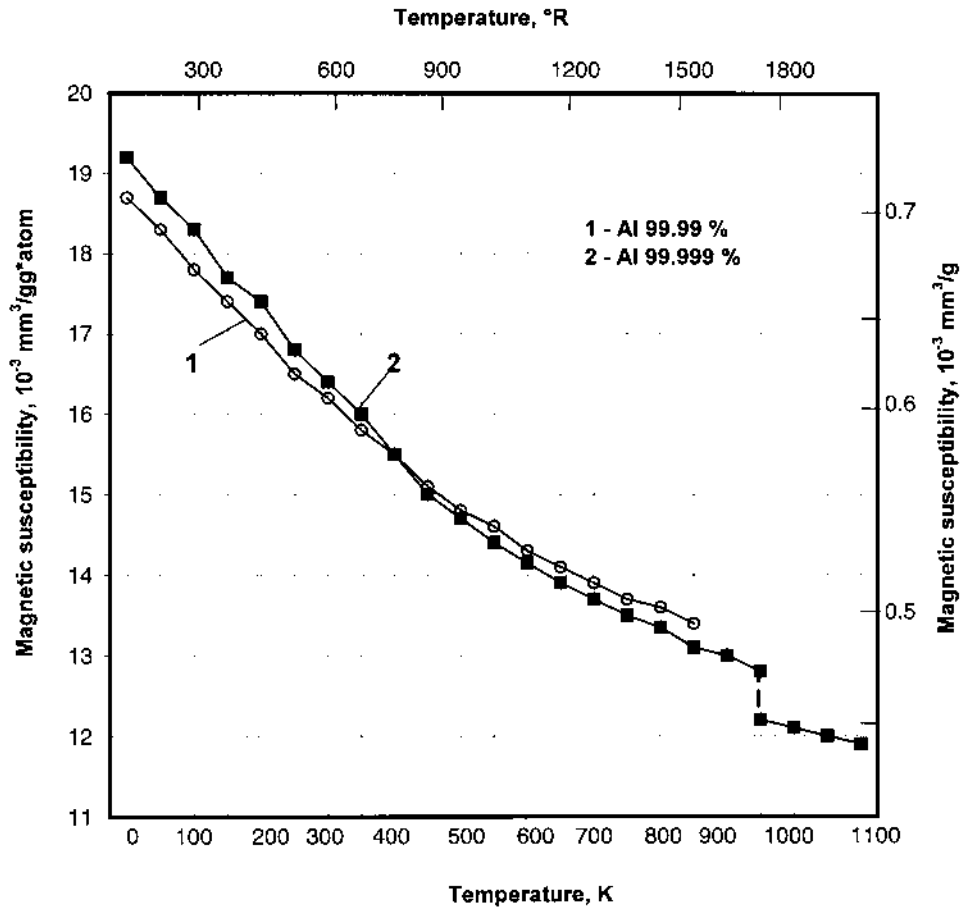
Figure 9   Magnetic susceptibility of aluminum as a function of temperature and purity [43].

magnetic" and the permeability is greater than unity. Paramagnetism is a property characterizing materials that have a permanent magnetic moment. Because aluminum has an odd number of valence electrons (3), it is paramagnetic. Its magnetic susceptibility depends on the temperature [43]. Figure 9 shows the dependence of magnetic susceptibility on the temperature and purity of [43].

Sleepy [44] showed that for unalloyed aluminum containing small amounts of impurities, the effect of strain sensitivity on magnetic susceptibility is negligible (99.999% $Al - 0.6276 \times 10^{-6}$ per gram; 99.99% $Al - 0.6267 \times 10^{-6}$ per gram). Alloying of aluminum with the small additives Fe, Mn increases its magnetic susceptibility slightly. An introduction of other alloying elements decreases this tendency to its reduction [25]. The deformation also promotes decreasing of magnetic susceptibility: at 50% deformation of aluminum this characteristic has decreased on 5–15%.[25,43,45,46].
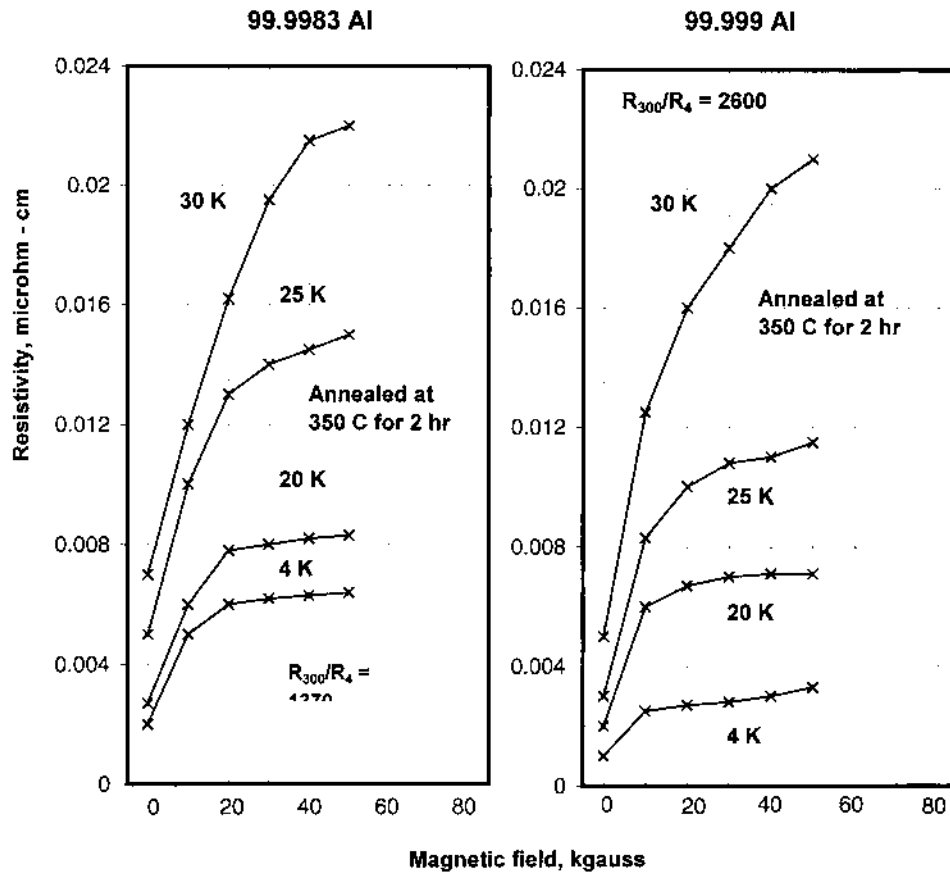
Figure 10   Transverse magnetoresistance curves for 99.983 and 99.999 Al. Sample size was 40 in long, 0.004 in thick, and 0.25 in wide [47].

3.8   Transverse Magneto-Resistance

Because refrigeration of the conductor of an electromagnet can result in over-all power savings through reduction in the resistivity of the conductor, data on the magneto-resistance are necessary. The use of aluminum in a high-field magnet is advantageous because its magneto-resistance tends to saturate at a low value. Figure 10 [47] shows the magneto-resistance of 99.9983 and 99.999 Al. These data indicate that the magneto-resistance of both aluminum specimens at 20K approaches saturation at approximately 20 kgauss.

3.9   Electrical Properties

Electrical resistance can be measured by the resistance-ratio test. This test is a very sensitive qualitative method of measuring purity of 99.999% and higher. The resistance of electrons through a sample of high-purity metal, particularly at low temperatures, is extremely sensitive to the amount of trace elements present in the sample.
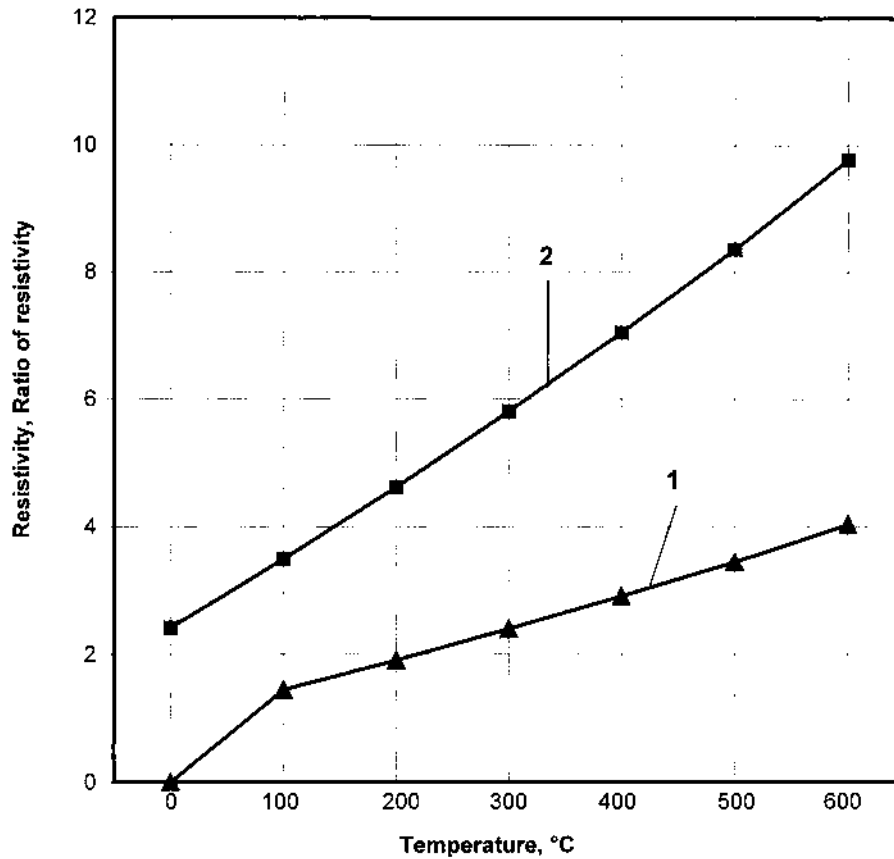
Figure 11   Elevated-temperature resistivity of aluminum [50]. (1) Ratio of resistivity at t to reistivity at 0°C; (2) Resistivity calculated from Pocharsky's rations, mW-cm.

      Gauthier [48] showed that a volume conductivity for 99.997 Al of 65.45% (a resistivity of 2.6434 $\mu\Omega$-cm) at 20°C. Taylor's results of the volume resistivity are 2.6548 $\mu\Omega$-cm (the volume conductivity is 64.94%) [32] for 99.996 Al at the same temperature. Babilon [49] determined that the volume resistivity of 99.993 Al is 2.6484 $\mu\Omega$-cm (the volume conductivity is 65.1%)

      Willey [8] determined that Matthiessen's law holds for high-purity aluminum from 0 to 300°C, and the term 0.0115 $\mu\Omega$-cm-cm/°C may be used to determine the resistivity of pure aluminum over this temperature range. Pochapshky confirmed that statement with his results (Fig. 13) [50].

      The results of the resistivity of molten aluminum are presented in Fig. 12 [51] and Fig. 13 shows the resistivity from 0 to 1200°C.

      As the purity of aluminum increases, the electrical resistivity at low temperature decreases. At the boiling point of liquid helium, 4.2K, very small changes in metal purity cause large changes in resistivity, contrary to the elevated temperature behavior (Fig. 14) [52].
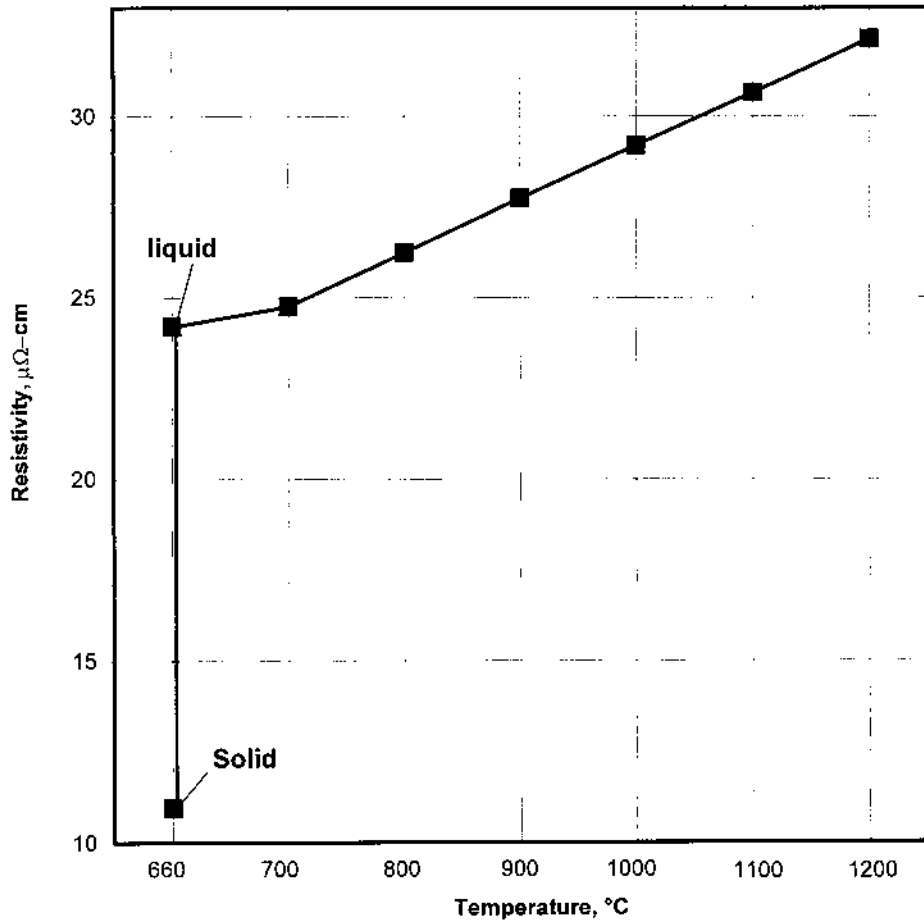
Figure 12   Resistivity of molten 99.99 aluminum [16,49].

Aluminum exhibits superconductivity near absolute zero. Although values for the superconducting transition temperature for 1.14–1.97K have been reported, data or Satterhwaite [53] show the best value for the transition temperature to be 1.187K.

3.10   Electrical Conductivity

Aluminum, relating to the trivalent metals, is a good conductor. The electron's behavior in aluminum is similar to the behavior of free electrons. Electrical resistivity of extreme purity aluminum (99.990%) at room temperature is 2.65498×10^{-8} Ωm or 64.94% of electrical resistivity annealed copper based on the international standard [24,41].

The grain size affects slightly on electrical resistivity of aluminum but its electrical conductivity after strain hardening in a direction of deformation grows by 0.5–1.0% [32].

Figure 13 Electrical resistivity of extreme-purity aluminum from 0 to 1200°C [16, 49].

Electrical conductivity of aluminum strongly depends on a nature and quantity of impurities present. According to I. N. Fridlyander [4] impurities having increasingly negative influence on electrical conductivity can be arranged in the following order: Cr, V, Mn, Ti, Mg, Ag, Cu, Zn, Si, Fe, Ni.
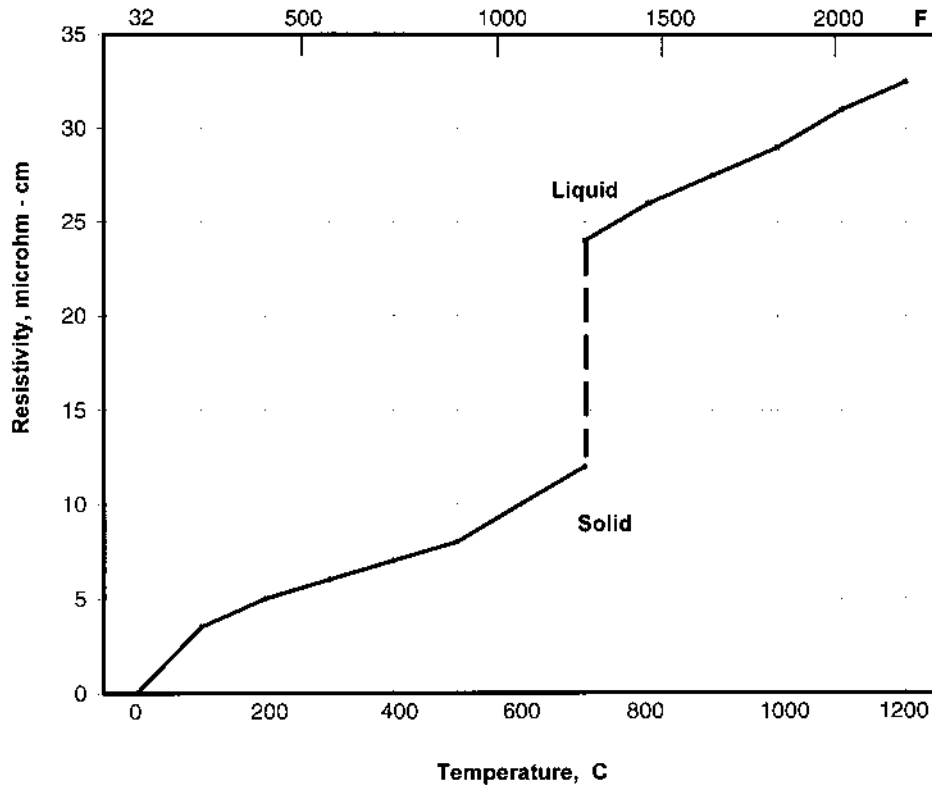
The main impurities in aluminum are Si, Fe, Cu, Zn, and Ti. At the contents of Si up to 0.006% the value the ratio Fe/Si (from 0.8 up to 3.8) affects slightly the electrical resistivity. But the increasing of the Si content up to 0.15–0.16% will change the picture. This ratio will affect drastically. Table 12 shows the character of this influence.

Impurities such as Cr, V, Mn, Ti influence most negatively on electrical resistivity of aluminum. Therefore in aluminum, intended for an electrical industry, the total amount of $Cr + V + Mn + Ti$ should not exceed 0.015% and even 0.01% with the content of silicon accordingly 0.12 and 0.16%.

The specific electrical resistance of aluminum of commercial purity increases 164% at the transition from a solid condition into liquid: $\rho_s = 1.65 \times 10^{-8}$ Ωm; $\rho_l = 27.1 \times 10^{-8}$ Ωm (Figures 13 and 14). For 99.99% purity aluminum $\rho_s = 10.8 \times 10^{-8}$ Ωm; $\rho_l = 26.6 \times 10^{-8}$ Ωm. At temperatures close to the absolute zero aluminum has superconductivity[25].
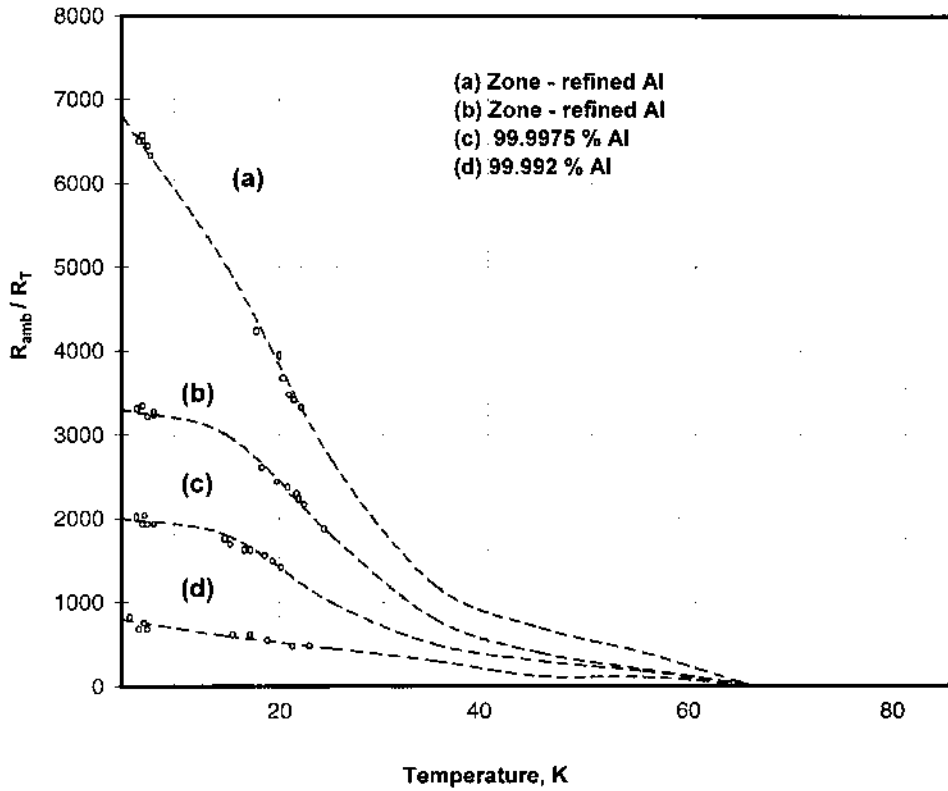
Figure 14 Electrical conductivity R_{amb}/R_t of aluminum of various degree of purity, as indicated, annealed for days at 400°C [50].

Table 12 Influence of the Fe/Si Ratio on Electrical Resistivity of Aluminum [54]

Content, %				ρ, $\mu\Omega$-m	σ, Mcm/m	ρ, $\mu\Omega$-m	σ, Mcm/m
Al	Fe	Si	Fe/Si	cold-worked		annealed	
99.657	0.16	0.15	1.07	0.02812	35.56	0.02767	36.14
99.578	0.23	0.16	1.44	0.02816	35.51	0.02771	36.09
99.515	0.30	0.15	2.00	0.02822	35.43	0.02778	35.99
99.374	0.43	0.16	2.68	0.02829	35.39	0.02783	35.93
99.235	0.57	0.16	3.56	0.02838	35.24	0.02788	35.86
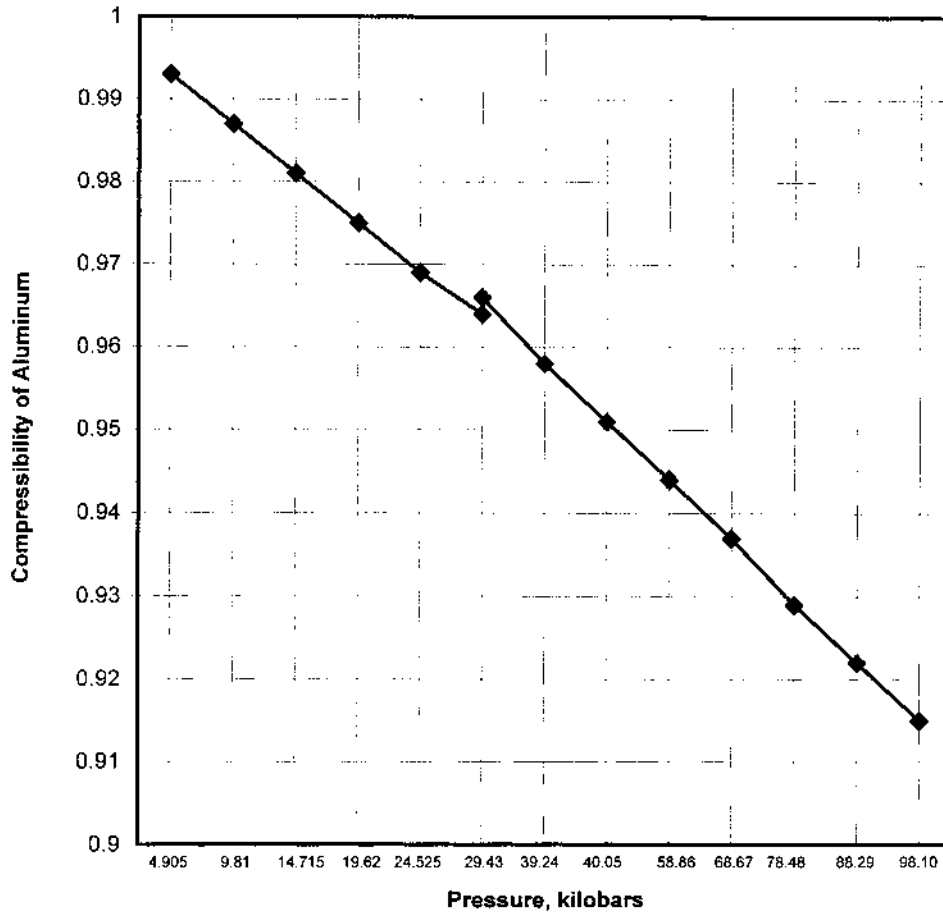
Figure 15 Compressibility of aluminum [57].

3.11 Compressibility

Using a reflected light technique, Doran, Fowles, and Peterson measured the compressibility of aluminum at pressures between 10 and 130 kilobars. Their results (Fig. 15) showed the good agreement with the data received by Bridgman [55,56].

Results of Doran and et al. that are presented in Fig. 16 [57] found an excellent correlation with other researchers.

3.12 Optical Properties

The optical properties of a metal are characterized by the index of refraction, n, and the extinction coefficient, k. Scientists from the United States Army Engineering Research and Development Laboratory and the U.S. Naval Research Laboratory determined the optical properties of evaporated aluminum films. Their results are presented in Tables 12, 13 and Fig. 17.
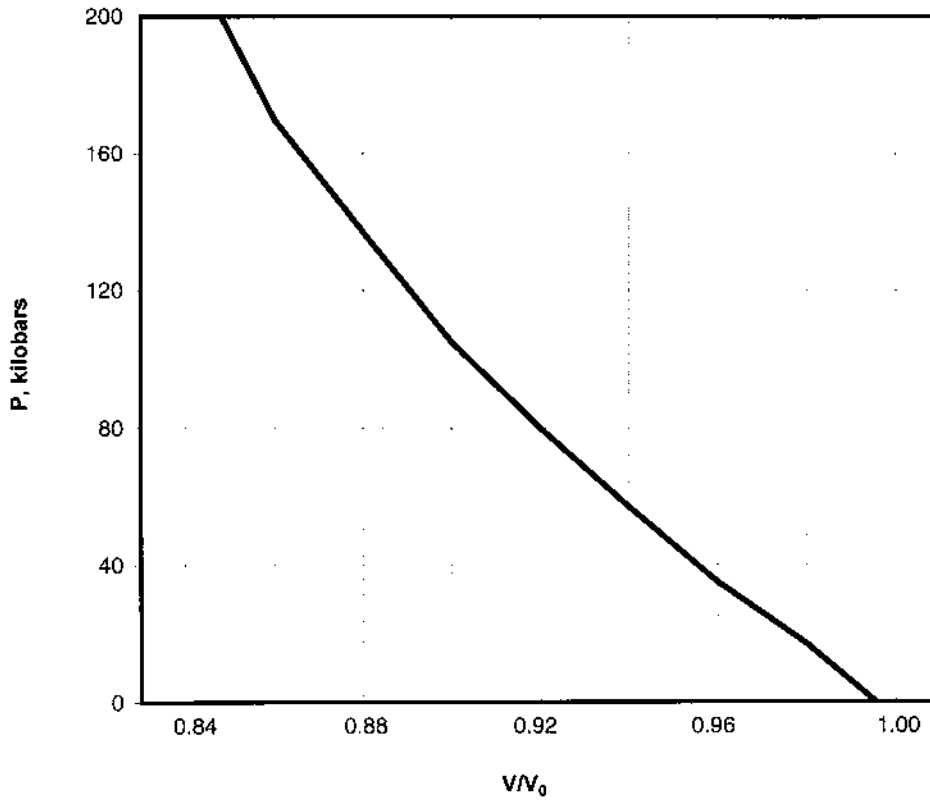
Figure 16 Pressure-compression points for aluminum [57].

Table 13 Reflectance and Emissivity of Aluminum with Various Surface Treatments [61]

Surface Treatment	Reflectance, %	Emissivity, % at 9.3 μ
R5 bright dip	90	3
Black paint	5	95
White paint	90	92
Black anodic coatings	5	95
Clear anodic coatings	80	35–65

3.12.1 Spectral Reflectance

The reflectivity of smooth aluminum surfaces to light is more than 90% for wavelengths from 0.9 to 12 μm [25]. At wavelengths below 0.2 μm, at which wavelength the reflectivity of smooth aluminum surfaces are about 70%. Bennett, Silver, and Ashley [60] investigated the reflectance of 99.999 Al. Their results are presented in Figs. 18 and 19.

Highest reflectivity is obtained by vapor deposition, which can produce very smooth surfaces. Vapor-deposited films require a minimum thickness of about
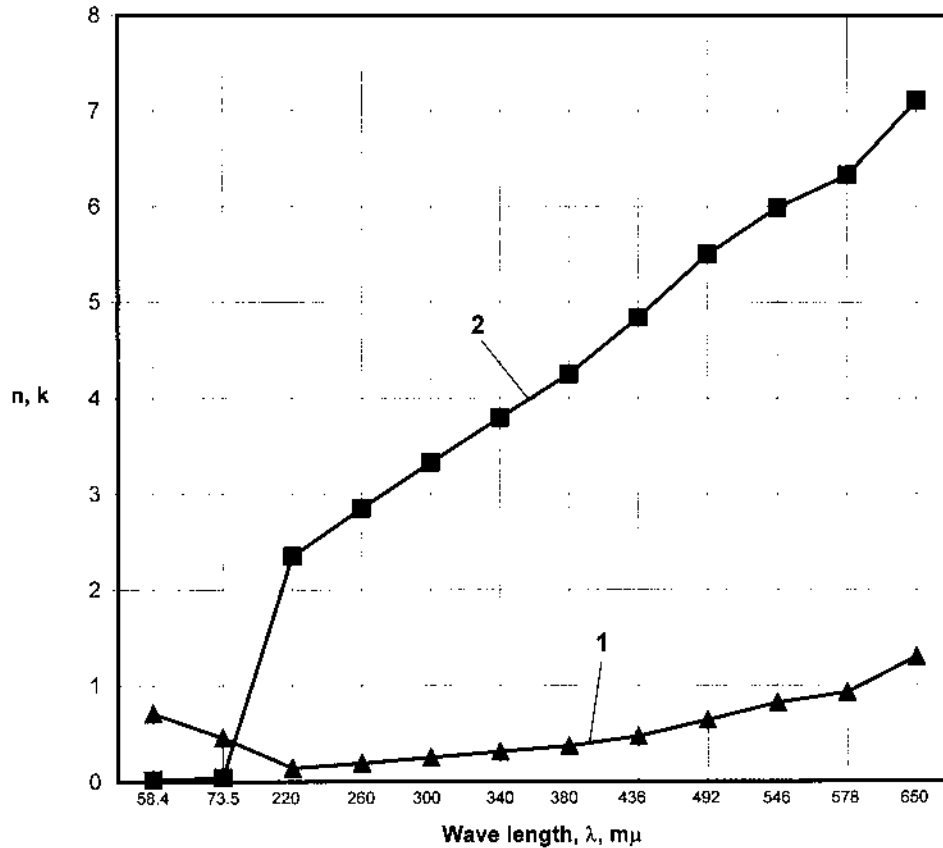
Figure 17 Optical properties of vacuum-deposited aluminum (10^{-5} to 10^{-6} mm Hg pressure) [58,59]. (1) Index of refraction, n; (2) Extinction coefficient, k.

10^{-5} cm for maximum reflection. The reflecting poser of an aluminum surface decreases with roughness. A sandblasted aluminum surface may exhibit only 15–25% of the reflectivity of a polished surface of metal of the same composition. Figure 19 [46] presents the normal spectral reflectance for various pure aluminum surfaces from brightened aluminum to aluminum having a clear oxide coating. Although most clear anodic coatings a few tenths of a mil thick reduce the reflectance of 99.99 Al only to 80%, they have much greater effect on the emissivity, depending upon the electrolyte in which the anodic coating is formed.

Emissivity of polished aluminum at room temperature is only several percent of that of a blackbody [25]. Rough finishes may raise the emissivity to about 20–30%. Emissivity increases with temperature to reach values of 15–20% for the liquid state. Figure 9 shows the relation between oxide film thickness and emissivity at 100°F for anodized films formed in different electrolyses [61].

The emissivity of aluminum at 4K ($-452°F$) and 76K ($-322.6°F$) is 1.1% and 1.8% respectively. Goldsmith, Waterman and Hirschhorn [62] showed that alumi-
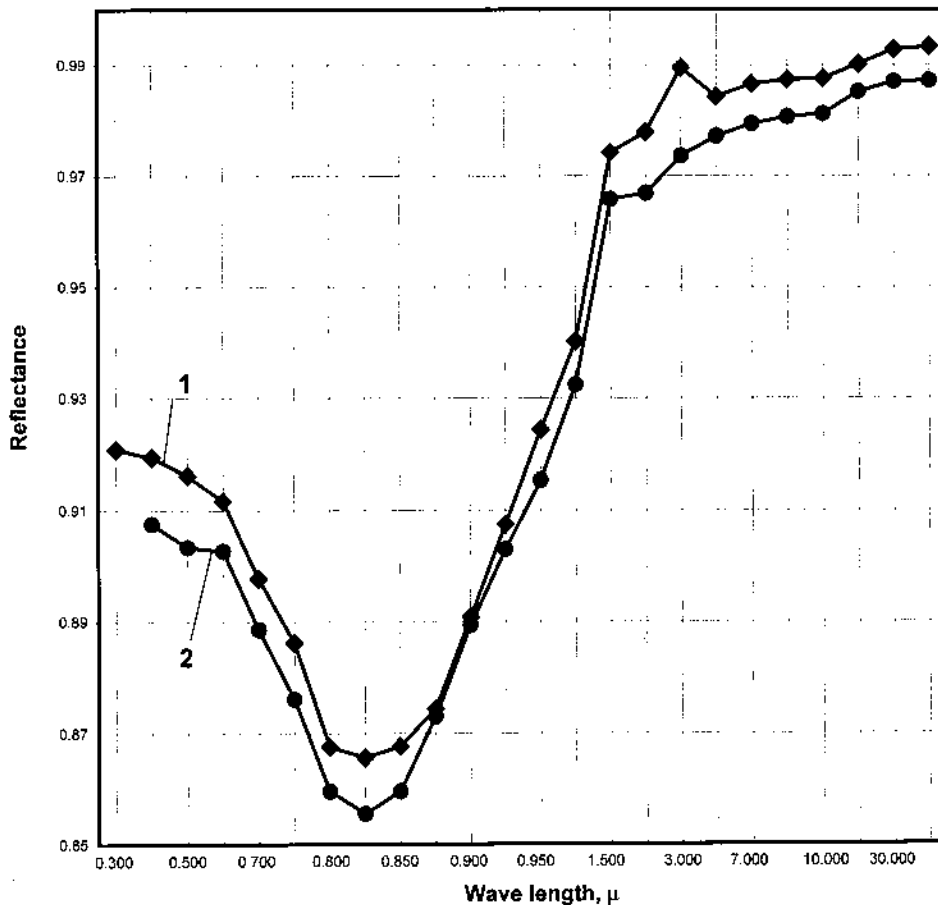
Figure 18 Reflectance of freshly prepared and aged vacuum-deposited films (10^{-9} to 10^{-10} mm Hg vacuum). (1) Ultra-high vacuum; (2) High vacuum and aged.

num heated to 600°C might have emissivity as low as 6%. Moeller and Miething [63] showed that the emissivity of molten aluminum to be 12% at 700°C and 17% at 1000°C.

3.13 Solidification and Melting

Solidification of liquid aluminum begins at 660.37°C [25]. The process of solidification of the liquid metal usually begins at separate points. In a volume of the metal they located chaotically. The arrangement of atoms in the small volumes of the melt is similar to their arrangement in a crystal lattice [17]. In particular, the coordination numbers of the first sphere are found. The essential distinction lies in the fact that the mobility of atoms in a liquid state much more than in solid one. In a molten metal there are the separate areas both with smaller, and with larger coordination numbers. In a certain moment there are the areas with the coordination number similar to a solid crystal. In aluminum this number is equal to 12. The stab-
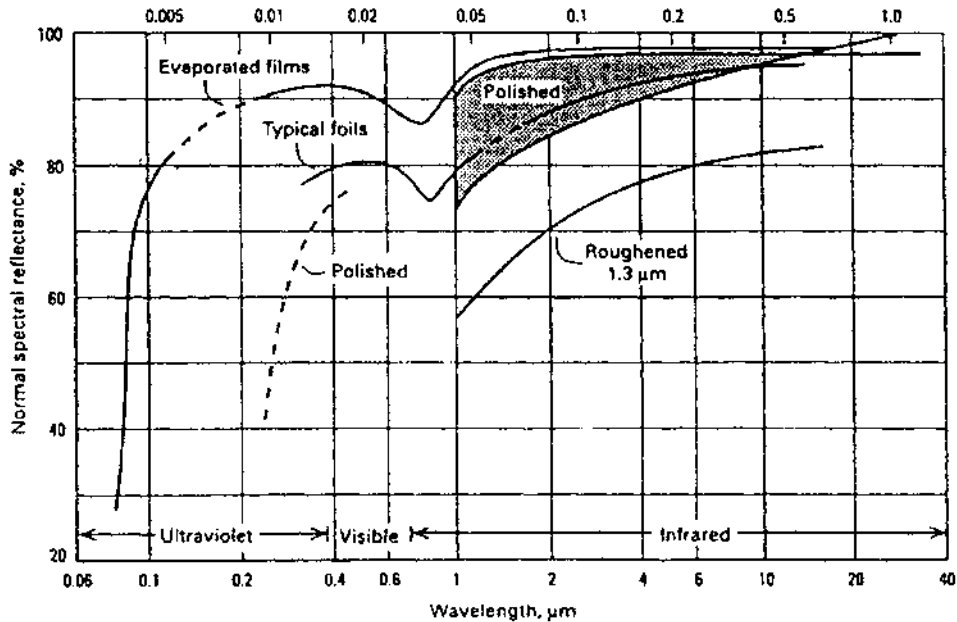
Figure 19 Spectral reflectance of aluminum [41].

Table 14 The Coordination Numbers in the Melt and the Crystal of Aluminum at the Temperature of 700°C

The interatomic distance d and the coordination number k			
Liquid state		Crystal	
The first area d, Δ	k	The first area d, Δ	k
2.96	10–11	2.86	12

ility of such an area depends on their size. Under certain conditions they can become a nucleus of crystallization. In other words, if the size of a nucleus is less than the critical radius r_k, there will occur its spontaneous disintegration. If the size of a nucleus is larger than r_k growth will take place. The value of r_k, at which nucleus is growing, should be about 10 atomic diameters. Aluminum has an atomic diameter is 2.86Δ so the size of a nucleus should be equal or exceed the value 2.86Δ [17]. Table 14 shows the coordination numbers in the melt and the crystal of aluminum [17].

Melting of aluminum with purity of 99.996% occurs at the temperature of 933.4°C [18]. At the melting point there is a step change of many properties of the metal such as density, electrical resistivity, deformability, and others (Table 15).

Above the melting temperature the crystal lattice can remain ''mechanically'' stable. In aluminum an interval overheating (stability of a lattice) is up to 5°C. The melting point depends on purity of aluminum [4,64]. Table 16 shows the relationship between the purity of aluminum and its melting point.

Table 15 Relative Changes of Volume, Entropy, Electrical Resistivity at Melting Point

Metal	$\Delta V/V_{sol}$	$\Delta S/R$	ρ_{lio}/ρ_{sol}
Aluminum (Al)	5.4	1.1	1.9

Table 16 Relationship Between the Purity of Aluminum and its Melting Point

Degree of purity, %	99.2	99.5
The melting point, °C	657	658
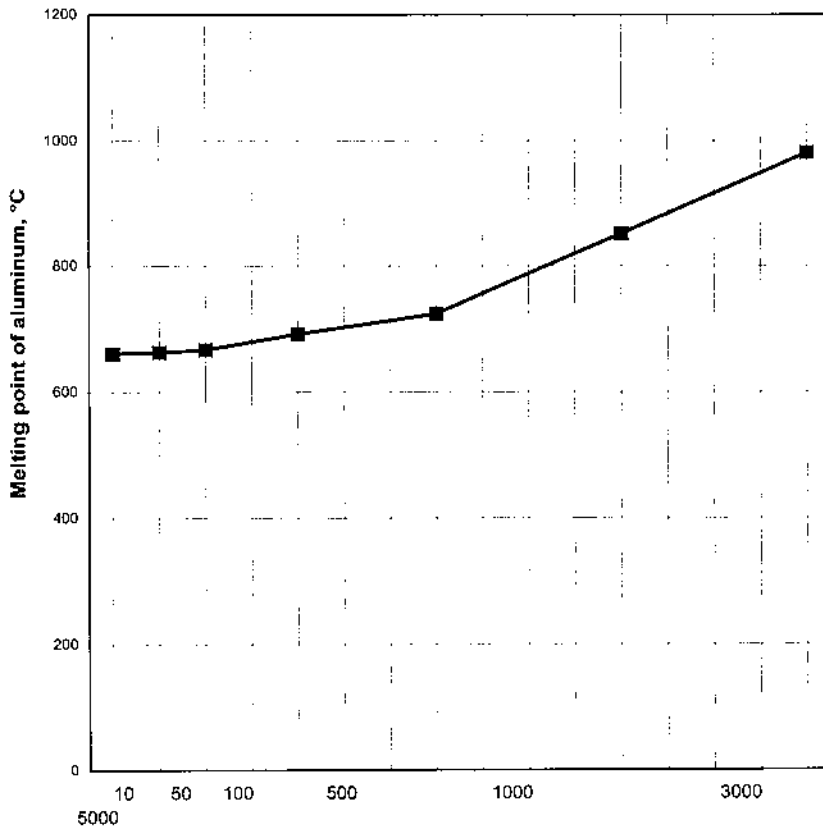
Figure 20 Relationship between the melting point of aluminum and the applied pressure.

The specific heat of melting for pure aluminum is 2.56 ± 0.05 kkal×mol (397 J×g^{-1}) [65]. The melting temperature grows with increasing of pressure. Figure 20 represents the change of the melting temperature at normal pressure depending on applied pressure. It is expressed by a derivative of dT_{mp} with respect to dP, 10^{-2}°C/MPa ($dT_{mp}\ dP = 6.41$ [66].

(a)

(b)
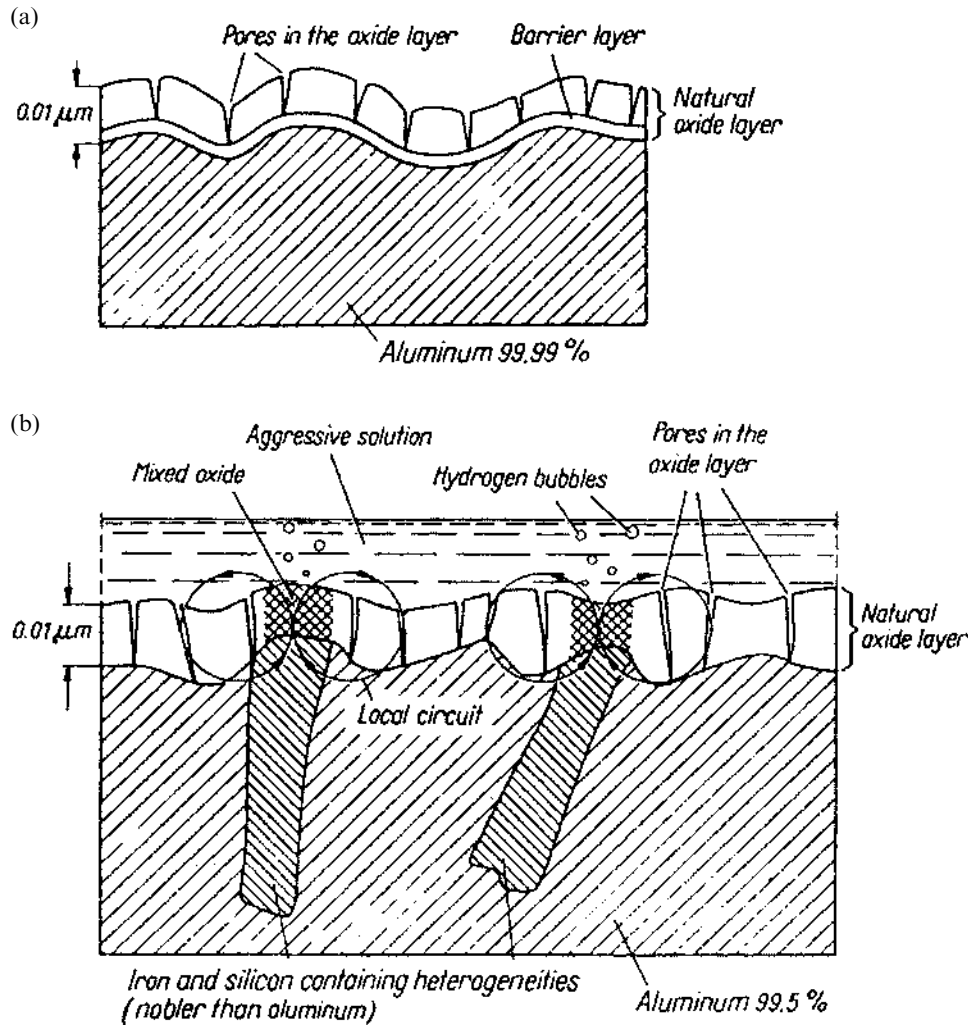
Figure 21 (a) Natural oxide layer on super purity aluminum; (b) Corrosion of 99.5% aluminum covered with a natural oxide layer, in an aggressive solution.

4 CORROSION PROPERTIES

Corrosion is one of the main reasons for failure of the engineering materials in service. Pure aluminum resists corrosion better than commercial one. That is why it is used for cladding alloys. Aluminum has a resistance to corrosion in some common environments, including the ambient atmosphere. It has been associated with the presence a continuous oxide film on its surface [67]. The standard electrode potential of aluminum is less than the majority of aluminum alloys. Therefore protecting aluminum by forming a protecting cathodic layer. In air at the room temperature this film on a surface of aluminum will be formed in 10^{-4} sec [68]. This film prevents further deterioration of the metal. Its thickness in usual conditions is 5–20 nm. The molecule volume of the oxide is almost in 1.3 times more than vol-

ume of aluminum participating in the oxidation reaction. The thickness of a film is increased in presence the water vapor. At the elevated temperatures the film has the complex structure.

A role of a protective film on a surface of aluminum reflects specifity of its behavior but do not explain its interaction with various environments (Figs. 21 and 22) [69]. Aluminum and its alloys are sensitive to various kinds of local corrosion under the stressed and unstressed conditions.

The following are lists of chemicals where there is considerable resistance to corrosion (Table 17) and where aluminum has poor corrosion resistance (Table 18) [70].

The standard electrode potential of aluminum (value of the equilibrium reversible potential at activity of ions of aluminum equal 1.0) is 1.663 V with respect

Table 17 Aluminum Has Good Resistance Toward these Chemicals

Acetic acid	Chlorides of Sodium, Potassium and Magnesium	Milk Products	Sulfites
Acetone	Detergents	Molasses	Sulfur
Acetylene	Emulsifier	Naphtha and Naphthalene	Sulfur Dioxide both dry and wet
Alum	Essential Oils	Nitric Acid Strong	Tannic acid Dilute
Ammonia	Fatty acids	Oxalic acid	Tartaric acid
Ammonium Chloride	Fluorine (Dry)	Phenol	Vegetable Oils
Aniline and its compounds	Fruit juices	Seawater	Vinegar
Brine (Saturated)	Glycerin	Silicic acid	Water
Calcium Chloride	Hydrocyanic acid	Sodium Silicate	Yeast
Carbon Disulfide	Lactic acids	Starch	
Carbonic acid	Maleic acid	Sugar, Syrups, etc.	
Chlorine (Dry)	Meat juice	Sulfates of Sodium, Potassium and Magnesium	

Table 18 Aluminum Cannot Resist Action of the Following Chemicals

Calcium Hypochlorite	Fluorine (Wet)	Mercuric Chloride	Sodium Sulphite
Caustic Soda	Hydrochloric acid	Nickel Salts	Sulfur Trioxide
Caustic Potash	Hydrobromic acid	Nitric acid dilute	Sulfuric acid
Chlorine (Wet)	Hydrofluoric acid	Phosphoric acid	Zinc Chloride
Copper Salts	Hydrogen Peroxide	Sodium Hypochloride	

to the normal hydrogen electrode [68,71]. Therefore, in "the order of voltage" aluminum is located in more negative area than Cu, Cr, and Fe. This metal is increasingly active.

From the diagram it is worth noting that aluminum having rather negative values of electrode potential should not be destroyed in water, i.e. it is in the field of immunity in the form of a neutral material. However, as a result of reduction of water there is a process of increasing of alkalinity of the electrolyte. This shifts into the area of solubility aluminate-ions in water [72].

Dissolving of compact aluminum in sour solutions proceeds on reaction

$$Al \Longleftrightarrow Al^3 + 3e$$

According to this reaction equilibrium electrode potential [35]:

$$\varphi_p = -1.663 + 0.0197$$

Electrode potentials of allocation of hydrogen and oxygen

$$\varphi_{o2} = 1.23 - 0,059\text{pH} + 0.0147\lg P_O,$$

$$\varphi_{H2} = -0.059\text{pH} - 0.0295\lg P_H$$

Aluminum electrodes are highly irreversible in aqueous solutions containing aluminum ions [3]. Measured potentials of aluminum in highly basic solutions, such as aqueous sodium hydroxide, are anodic to those measured in acid solutions, as would be predicted by the Nernst equation. Figure 22 [73] illustrates the solution potential of 99.999 Al in a 4% NaCl solution as pH varies from 1 to 11.

Table 19 shows that the potential of high-purity aluminum varies considerably in different types of electrolytes, as does that of several other pure metals. In most electrolytes, aluminum is cathodic to magnesium and zinc and anodic to iron and copper [5].

The transition from area of solubility of trivalent ions of aluminum into passive area according to the diagram of electrochemical balance corresponds to formation of aluminum oxide from a liquid phase. At normal conditions in water at temperature not higher than 60°C amorphous hydrated aluminum oxide $Al(OH)_3$ will be formed on a surface in passive area [68]. At the same temperatures crystal trihydrate of aluminum bayerite-oxide with a monoclinic lattice will be formed. According to [74] under normal conditions the aluminum oxide film is formed. The first layer with the thickness no more than 10 nm consists of the amorphous aluminum oxide. The second layer is composite and consists of bayerite and bemite with an orthorhombic crystal lattice. The thickness of a layer depends on the character of environment and the duration of endurance. At temperatures 60–80°C and high a monohydrate oxide-boehmite will be formed on the surface of aluminum.

The most stable form of oxide is hydrargillite (gibbsite), which is trihydrate as well as bayerite but has the different crystal lattice. Hydrargillite (gibbsite) will not be practically formed on a surface of aluminum. As at elevated temperatures on the surface of aluminum boehmite is formed so it is possible to consider that
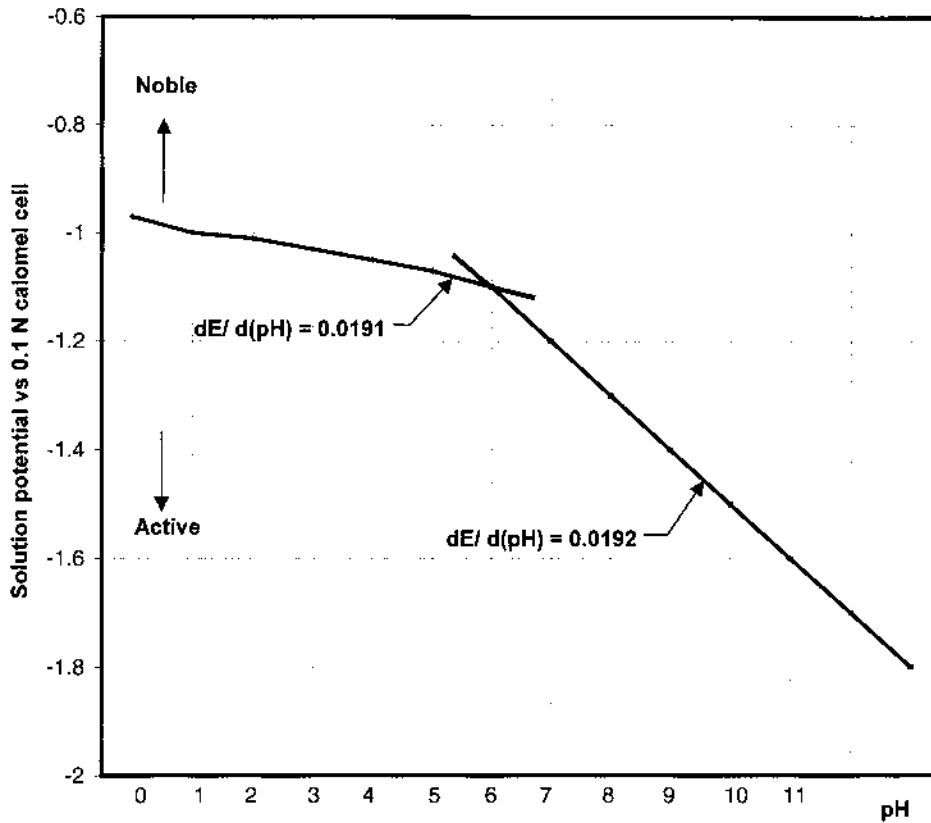
Figure 22   Solution potential at room temperature with changing pH, of extreme-purity aluminum in 4% NaCl solution [53].

Table 19   Potentials of Metals in Several Solutions [73]

Solution	Potential, 0.1N calomel scale				
	Mg	Al	Zn	Fe	Cu
1M NaCl	-1.72	-0.86	-1.15	-0.72	-0.35
1M Na_2SO_4	-1.75	-0.50	-1.19	-0.76	-0.14
1M Na_2CrO_4	-0.96	-0.71	-0.67	-0.16	-0.13
1M HCl	-1.63	-0.80	-1.14	-0.66	-0.20
1M HNO_3	-1.49	-0.49	-1.06	-0.58	-0.12
1M NaOH	-1.47	-1.50	-1.51	-0.22	-0.35
1M NH_4OH	-1.43	-0.80	-1.50	-0.18	-0.53

the corrosion resistance in real water environments will be characterized by the diagram constructed for boehmite. The formation of oxide from the state occurs according to the reaction:

$$2Al^{3+} + 4H_2O = Al_2O_3 \times H_2O + 6H^+$$
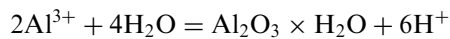
The formula calculated for this reaction can be presented as:

$$pH = 2.67 - 0.33 \lg a^+_{Al3}$$

From the formula it is apparent that at activity $a_{Al3}{}^+ = 1$ pH value is 2.67. At this pH, a transition into the passive region occurs. At decreasing activity, the boundary of absolute value of hydrogen electrode grows. For the normal atmospheric conditions it is possible to accept activity close to 10^{-6}.

Solution of boehmite in alkaline area is defined by the reaction:

$$Al_2O_3 \times H_2O + (H_2O) \Leftrightarrow 2AlO_2^- + 2H^+2H^+ + (H_2O)$$

The arrangement of the boundary ordinates on the diagram determined by the equation:

$$pH = 12.3 - \lg a^-_{ALO2}$$

The meanings of the hydrogen parameter will depend on the activity:

$$pH = 12.3 \text{ at } a_{AlO2}- = 1 \text{ and } pH = 6.3 \text{ at } a_{AlO2} = 10^{-6}$$
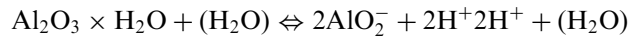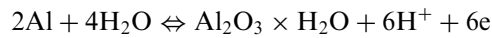
In passive area boehmite can be formed by the direct oxidation of compact aluminum:

$$2Al + 4H_2O \Leftrightarrow Al_2O_3 \times H_2O + 6H^+ + 6e$$

In alkaline environments aluminum as well as oxides are dissolved with formation of aluminate-ions:

$$Al + 2H_2O \Leftrightarrow AlO^{2-} + 4H^+ + 3e$$

The calculated equation: $\Omega = -1.26 + 0.0197 \lg a^-_{AlO2} - 0.0788 \text{ pH}$.

It defines an arrangement of a series of inclines on the diagram at various values of aluminate-ions activity. These inclines divide areas of insolubility and solubility of aluminates. On the diagram there is the vertical line at $pH = 5.07$. It is a border of existence Al^{3+} and AlO^{2-}. The location of this line on the diagram is calculated from the conditions of the floating balance:

$$Al^{3+} + 2H_2O \Leftrightarrow AlO^{2-} + 4H^+$$

$$\lg [AlO_2^-]/[Al^{3+}] = -20.30 + 4\,pH$$

The diagrams of electrochemical balance establish the corrosion conditions of aluminum and its alloys in the plain water environments. They can be used at development of the optimum parameters for some processes.

There is the opportunity of "disruption" the oxide film on a surface of aluminum. It is associated with the formation in a barrier layer of narrow channels with increased ionic conductivity [72]. It is achieved at a certain energy level of a surface. The absorption of certain anions, first of all halide anions, lowers the level of energy necessary for displaying of this effect.

Increased corrosion or disruption of the oxide film a consequence of introduction into a film of certain elements at alloying of the metal [75]. For example, the introduction of tin into a film increases it ionic conductivity. It increases the rate of solution of aluminum.

Pitting is the most common form of very localized corrosion attack in aluminum in which small pits or holes form. The disruption of the oxide film causes this form of corrosion. Thus the significant part of a surface is in a passive condition. The formation of the pits themselves is strongly accelerated by the addition of oxidizers. It especially occurs in solutions containing chloride and phosphate ions. the oxidizers exert the greater influence in acid environments than in alkaline. The most effective oxidizers are hydrogen peroxide and free chlorine (chlorinade water or calcium hypochlorite and to a smaller degree are sodium chlorate and nitric acid). In the formed pit, dissolution of the metal occurs intensively. The meaning of corrosion potential depends on purity of the metal. The literature indicates [72] that the probability of occurrence of corrosion pits decreases on aluminum with purity of 99.99%.

The corrosion resistance of electrolytic purified (refined) aluminum (99.99% Al) in 3–15 times is higher than for commercial purity aluminum. The corrosion rate of aluminum of various purity characterized by weight losses or volume of hydrogen escaping from the surface unit in 5% HCl solution is shown in Fig. 23.
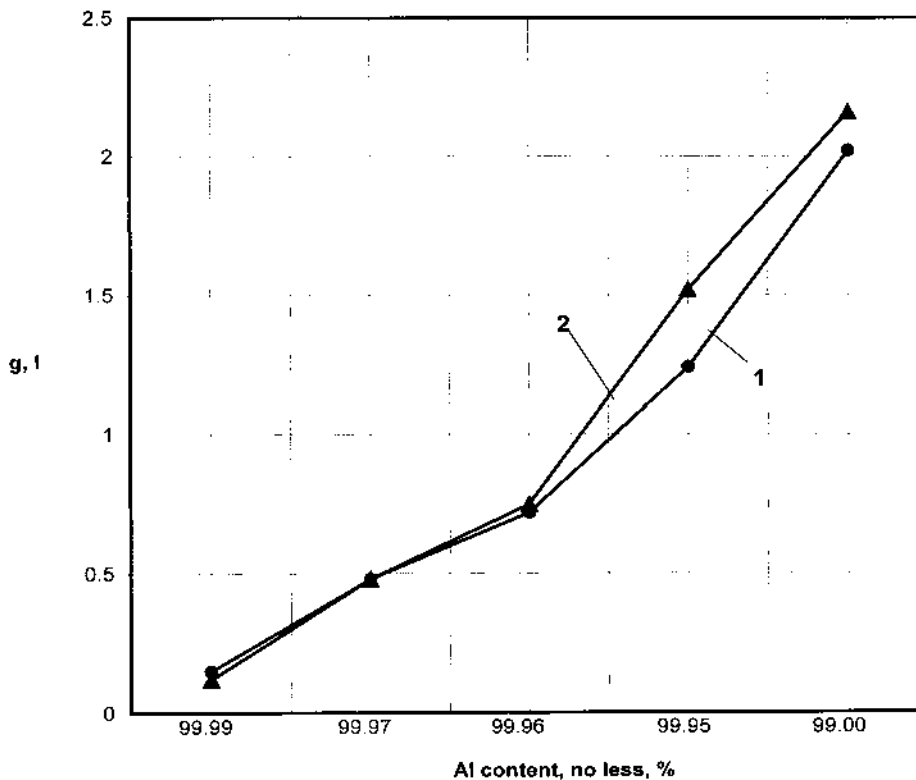

Figure 23   Weight losses and the hydrogen content in aluminum of various purity. (1) Mass loss, g, m^2*h; (2) Hydrogen content, I, m^2*h.

For aluminum with purity 99.99% and higher the rate of corrosion mainly depends on the copper content. So an aluminum sheet (copper content higher than 2×10^{-3}%), with thickness of 1.5 mm, in 20% HCl acid during 1 week corroded completely through; in the same conditions aluminum with $0.9 - 3 \times 10^{-4}$%Cu completely corroded through after two weeks only. The corrosion resistance of aluminum decreases with the Fe content. Aluminum with the Fe content no more than 0.003% corrodes with the rate of 0.10–0.157g/(m$^2 \times$h).

Titanium does not have appreciable influence to corrosion resistance of aluminum in 5% HCl solution. Beryllium (Be) in amount of 0.05–0.5% reduces slightly corrosion resistance of aluminum of commercial purity. At addition of 0.14–0.19% Nb reduces the corrosion resistance considerably.

The small additives of Gallium and Rhenium negatively influence on corrosion resistance. For aluminum A7 containing 0.5% Ga, the rate of corrosion reaches 120 g/m$^2 \times$ h). For aluminum containing 0.3% Re the rate is 250 g/m$^2 \times$h) [4].

Aluminum is not resistant to corrosion in many mineral acids, except for acids with strong oxidizing properties. But the action of such acids depends on their concentration: diluted HNO_3 is rather aggressive environment for aluminum, but after achievement of the concentration of 80% the rate of solution does not exceed 0.1 mm/year [76]. The acid at concentration more than 98% is not active in relation to aluminum. In diluted H_2SO_4 (from 1% up to 20%) all grades aluminum including high purity, have low resistance to corrosion even at room temperature.

Hydrogen halide acids react with aluminum and they are not used in contact with aluminum and its alloys. In organic acids the aluminum is destroyed very slowly, with the exception of formic acid, oxalic acid and some chlorine-containing acids. Glacial acetic acid does not have an appreciable effect on aluminum but the rate of corrosion grows at low concentrations.

The alkalis are usually aggressive in relation to aluminum. At the same time aluminum is resistant to ammonium hydroxide even at pH13. Such salts as chromates, bichromates, silicate, and borates have appreciable inhibiting action and can be used for the protection of aluminum against corrosion in water systems with a closed cycle.

Aluminum has very high resistance in relation to concentrated hydrogen peroxide. It is characterized by good resistance to many organic compounds including acetaldehyde, formaldehyde, and tetrachloride glycerin and also has good resistance to petroleum products [76,77].

5 MECHANICAL PROPERTIES

The mechanical properties of aluminum depend not only upon purity and applied heat treatment. The influence of purity is shown in Fig. 24 [11]. Figure 25 shows the effect of purity on strength and hardness of unalloyed aluminum and Fig. 26 typical tensile properties of alloy 1199 (99.9 wt% Al).

The elastic properties for extremely pure aluminum are: E = 69–72 GPa, G = 25–26.5 GPa, v = 0.31 [54]. Figures 27–29 show mechanical properties of aluminum at various temperatures and applied cold work.

Figure 30 shows relationship between mechanical properties of commercial aluminum and cold work applied. (E = 70–72.5 G; = 27–28 GPa; (v = 0.31–0.33 (for thin clad sheets E = 68.5–70 GPa) [78].
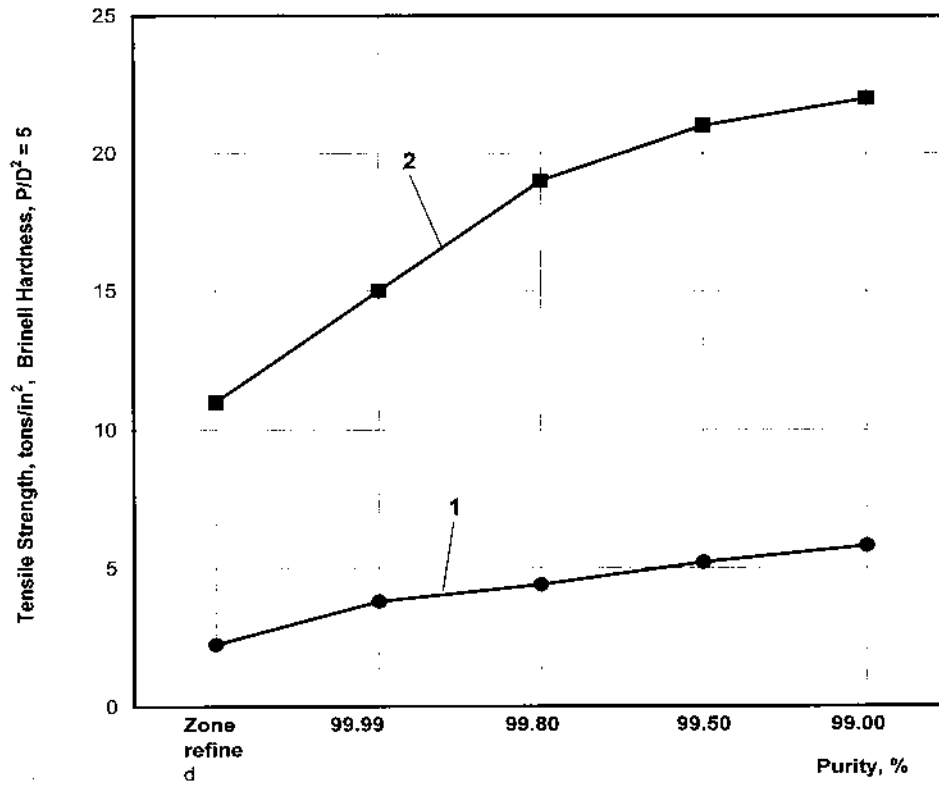
Figure 24 Mechanical properties of annealed aluminum of various purities [11]. (1) Tensile strength, t/in^2; (2) Brinell hardness.
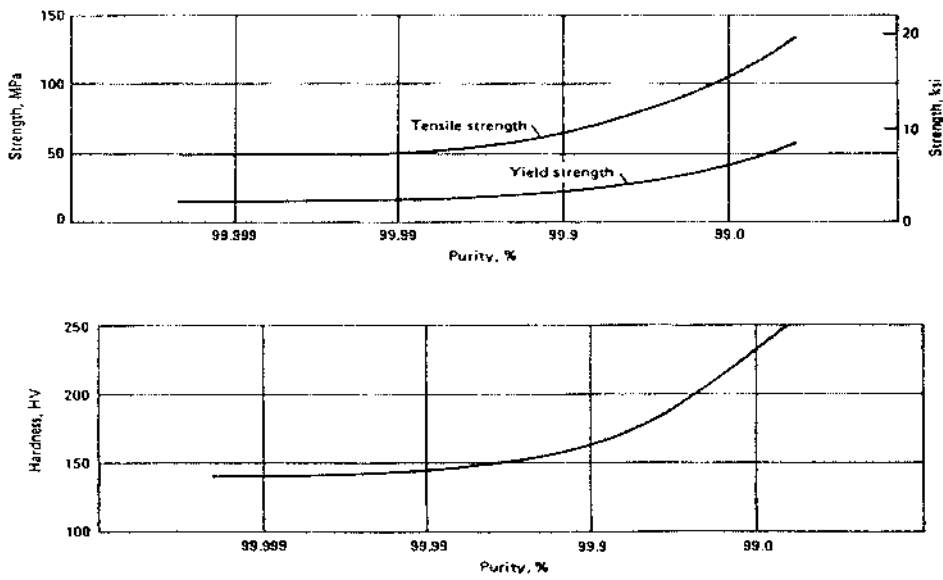
Figure 25 Effect of purity on strength and hardness of unalloyed aluminum.
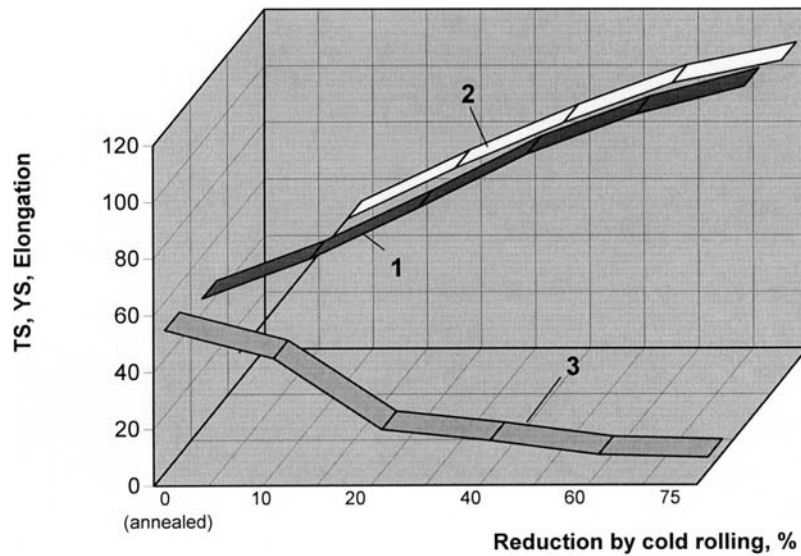
Figure 26 Typical tensile properties of 1199 aluminum: (1) Tensile strength (TS), MPa; (2) Yield strength (YS), MPa; (3) Elongation, %.
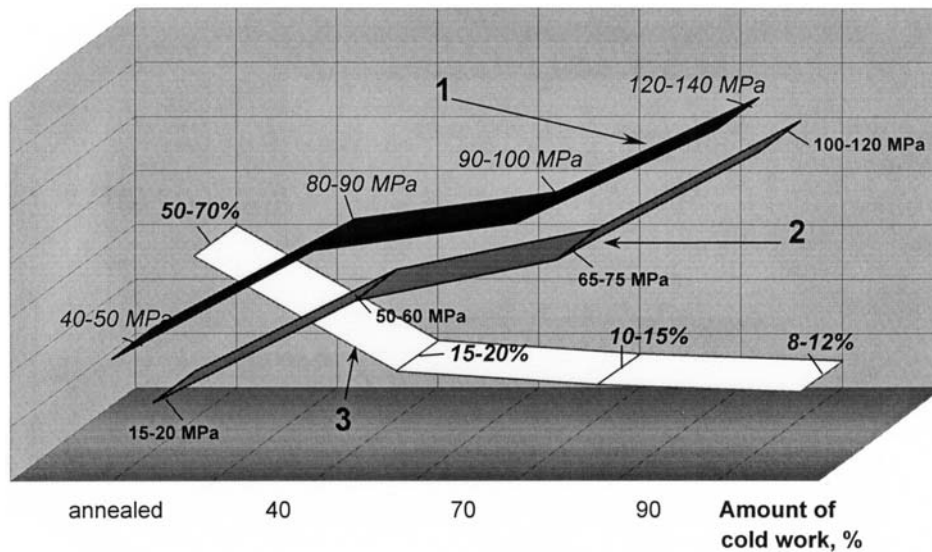
Figure 27 Mechanical properties of aluminum (99.50%) depending on cold work [41]. (1) Tensile strength, MPa; (2) Yield strength, MPa; (3) Elongation, %.

The mechanical properties of pure aluminum, as well as other metals, depend on the temperature of the test. Mechanical properties such as resistance to plastic deformation (tensile strength, yield strength), resistance to the penetration (hardness), as well as impact are the most sensitive to the temperature. The elastic
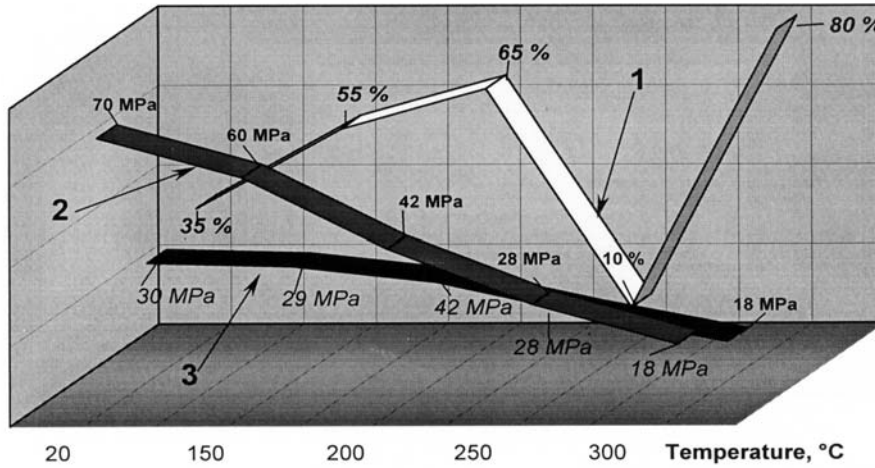
Figure 28 Mechanical properties of aluminum (99.50%) at elevated temperatures. [41]. (1) Tensile strength, MPa; (2) Yield strength, MPa; (3) Elongation, %.
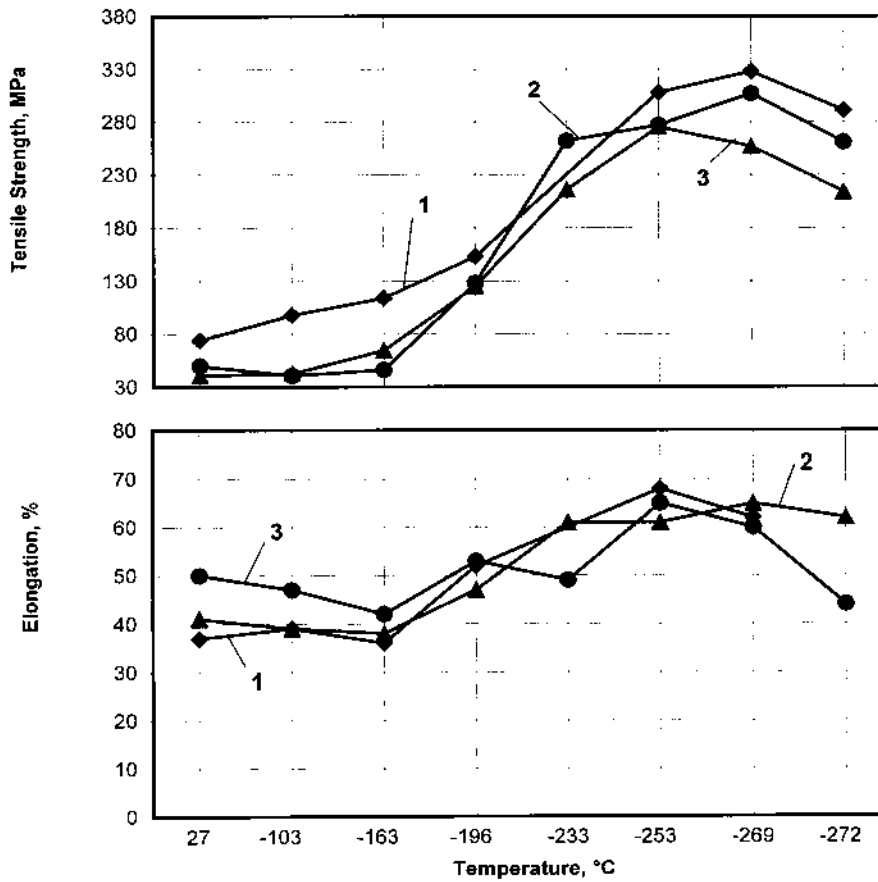
Figure 29 Mechanical properties of different degree of purity aluminum at various temperatures: (1) Purity 99.5%; (2) Purity 99.99%; (3) Purity 99.997%.
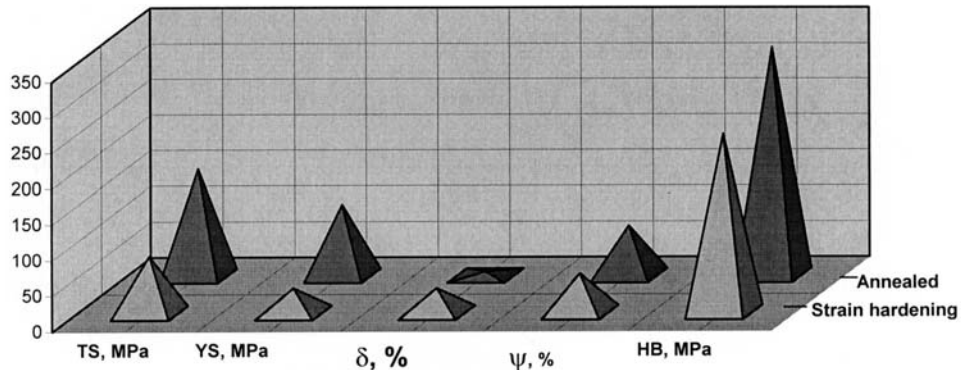
Figure 30 Mechanical properties of commercially aluminum (rods, sheets) for different heat treatment condition (annealed, strain hardening).
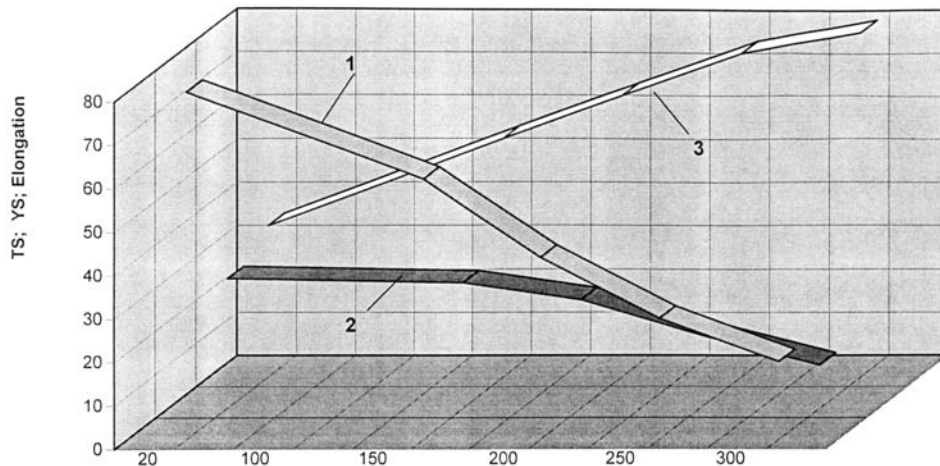
Figure 31 Mechanical properties of annealed aluminum of 99.3% purity at elevated temperatures [78,79]. (1) Tensile strength, MPa; (2) Yield strength, MPa; (3) Elongation, %.

properties of metals and alloys change with the temperature in a smaller degree. The mechanical properties of aluminum at low temperatures and elevated temperatures are shown in Fig. 29 and 31.

Pure aluminum is a non-heat-treatable alloy. There are the various grades of pure aluminum in which the strength is developed largely by strain hardening from the basic annealed temper. A high grade of pure aluminum that became available early in this century was utilized for electrical conductors. This wrought material is known as EC (electrical conductor) metal, has a minimum aluminum content of 99.45%. Pure aluminum of this grade is also used for foil and is designated 1145 alloy. The various grades of pure aluminum used commercially have distinctly higher strength in the annealed condition, and stable properties are developed in the various strain-hardened tempers (Table 20).

Hardness of aluminum as function of purity is shown in Fig. 32.

Table 20   Typical Mechanical Properties of Commercially Pure Aluminum

Alloy	Temper	TS, psi	YS*, psi	%EL, in 2 in.	HB,**	Shear strength, psi	Fatigue limit***
1199	O	6500	1500	50	–	–	–
	H18	17000	16000	5	–	–	–
1180	O	9000	3000	45	–	–	–
	H18	18000	17000	5	–	–	–
1060	O	10000	4000	43	19	7000	3000
	H14	14000	13000	12	26	9000	5000
	H18	19000	18000	6	35	11000	6500
EC	O	12000	4000	23****	–	8000	–
	H14	16000	14000	–	–	10000	–
	H19	27000	24000	2.5****	–	15000	–
1145	O	11000	5000	40	–	8000	–
	H18	21000	17000	5	–	12000	–
1100	O	13000	5000	35	23	9000	5000
	H14	18000	17000	9	32	11000	7000
	H18	24000	22000	5	44	13000	9000

*Yield strength, 0.2% offset, **500-kg load, 10-mm ball, 30 sec, *** Based on 5000 million cycles using an R.R. Moore-type rotating-beam machine, **** Elongation in 10 in.
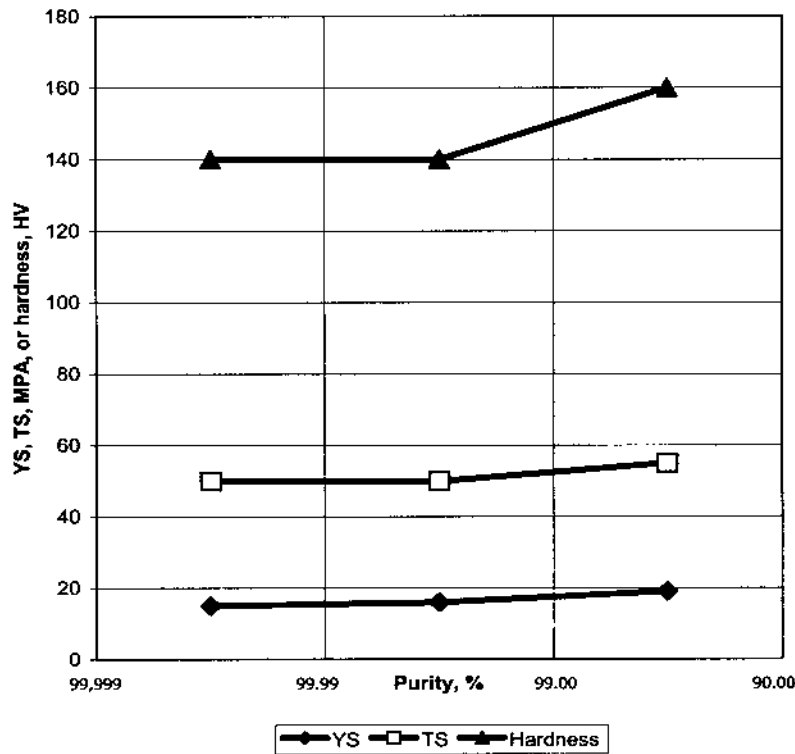
Figure 32   Hardness and strength of aluminum as functions or purity.

Fatigue is a form of failure that occurs in structures subjected to dynamic and fluctuating stresses. There is a limiting stress level called the fatigue limit. The fatigue limit is the maximum stress amplitude level below which a material can endure an essentially infinite number of stress cycles and not fail. Most nonferrous alloys such as aluminum, copper, magnesium, do not have a fatigue limit, in that the S–N curve continues its downward trend at increasingly greater N values (where S is stress amplitude and N is the number of cycles to fatigue failure).

The fatigue behaviors may be classified into two domains. One is associated with relatively high loads that produce not only elastic strain but also some plastic strain during each cycle. Consequently, fatigue lives are relatively short; this domain is termed low-cycle fatigue (frequency $f = 0.1$–5 hertz) and occurs at less than about $N = 10^4$–10^5 cycles. For lower stress levels wherein deformations are totally elastic, longer lives result. This is called high-cycle fatigue (frequency $f = 20$–50 hertz) inasmuch as relatively large numbers of cycles are required to produce fatigue failure $N = 10^7$ cycles [79].

Damage or fatigue failure at high-cycle area occurs basically at elastic and in low-cycle area at elastic-plastic deformation. The endurance characteristics depend on the shape and size of a specimen but also types and frequency of loading. Resistance to fatigue decreases with increasing load frequency and increasing the absolute sizes of a specimen. The endurance of metals depends on a surface finish. It has been observed that fatigue life is especially sensitive to the condition and configuration of the component surface. Improving the surface finish by polishing will enhance fatigue life significantly. Like all other metals, when subjected to repeated loading aluminum alloys will fail by fatigue at a lower stress than they can withstand when loaded statically. For a rough estimation of the endurance limits for aluminum is possible to use the following ratio: an endurance limit at tension-compression ($\sigma_{-1}^t = (0.85$–$0.95)\sigma_{-1}$; at torsion $\tau_{-1} = (0.55$–$0.65) \sigma_{-1}$. The endurance limit of commercial purity aluminum at axial (tension-compression), (flexural) bending loading on the basis of 2×10^7 cycles depends on preliminary heat treating. Table 21 shows the results of this test [78].

5.1   The Failure Characteristics

Unlike steel specimens, the impact test with a notch for aluminum and its alloys does not have a great deal of importance because aluminum and its alloys do not have a sharp ductile-to-brittle transition temperature. Aluminum having FCC crystal structure remain ductile even at extremely low temperatures [4];

Table 21   Results of Fatigue Test of Commercial Purity Aluminum

Semi-product, heat treatment	σ_b, MPa	σ_{-1}, MPa
Sheet, annealed	80	35
Sheet, strain hardening	150	50

To determine the characteristics of failure of aluminum and its alloys at different conditions. The test can be applied. The determined energy of crack propagation is the total energy required for the crack propagation referring to the final cross-sectional area of a specimen. Compared to the meanings of impact tests, the cracking energy is the best combination of toughness with ductility that characterized the resistance of a material to the crack propagation in a field of the elastic deformation. The tear test can be applied to aluminum and its alloys despite their high ductility.

The specifics of the crack initiation at the failure of aluminum of the grade A99 containing no more than 0.01% of an impurity is described in [80]. The failure of the majority of pure metals under tension is preceded by the necking. The voids occur which link and form the crack. These cracks result the specimen's failure. The characteristics of pure aluminum are the necking process, which is not followed by the porosity formation. The cracks are initiated and propagate in the planes of intensive deformation.

At the room temperature crack are not observed in pure aluminum until close to specimen failure. The irregularity the crystal orientation of in polycrystalline aluminum creates inhomogenity of the deformation. Increasing the temperature up to 300°C does not show the micro crack initiation up to the deformation of 50–70%. At the elevated temperatures a deformation proceeds also non-uniformly: alongside with the areas having local tension deformation of about 7–8% are observed areas with compression up to 5–8%.

At 20°C areas with increased and lowered local deformation are not rearranged. These areas are the centers of the sensitivity to damage. Rearrangement occurs at elevated temperatures above 300°C.

In this case the centers of the sensitivity to damage will be formed at the later stage of deformation. So, at the temperature of 300°C the localization of deformation in the separate micro centers is found out at $\varepsilon > 10$–15%, whereas at 20°C $\varepsilon < 1$–2%. Therefore, at room temperature the centers of failure will be formed at initial stages of deformation at elevated temperatures, but at later stages (deformation more than 10–15%). Submicroscopic cracks initiate inside grains at location of crossing slop planes. The average deformation at which their initiation begins grows with increase of the temperature. In all investigated cases, the failure is transcrystalline.

6 HYDROGEN SOLUBILITY IN ALUMINUM

With nitrogen aluminum creates an aluminum nitrate AIN at 700°C. The reaction is very intensive at 830°C. Aluminum nitrite hydrolyzes easily in the presence of water in the following reaction.

$$AlN + 3H_2O \Rightarrow Al(OH)_3 + NH_3$$
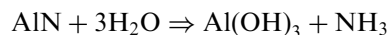
But hydrogen is the only gas to be soluble in both solid and molten aluminum. Ransley and Neufeld [81], Opie and Grant [82], and Eichenauer, Hattenbach, and Pebler [83] developed equations to determine the solubility of hydrogen in

molten aluminum (Fig. 33). Table 22 compares the results of those calculations.

$$\text{Log } S = 2.796 - (2760/T) \,(\text{molten aluminum}) \qquad [81]$$
$$\text{Log } S = 0.788 - (2080/T) \,(\text{solid aluminum}) \qquad [81]$$
$$\text{Log } S = 2.620 - (2550/T) \,(\text{molten aluminum}) \qquad [82]$$
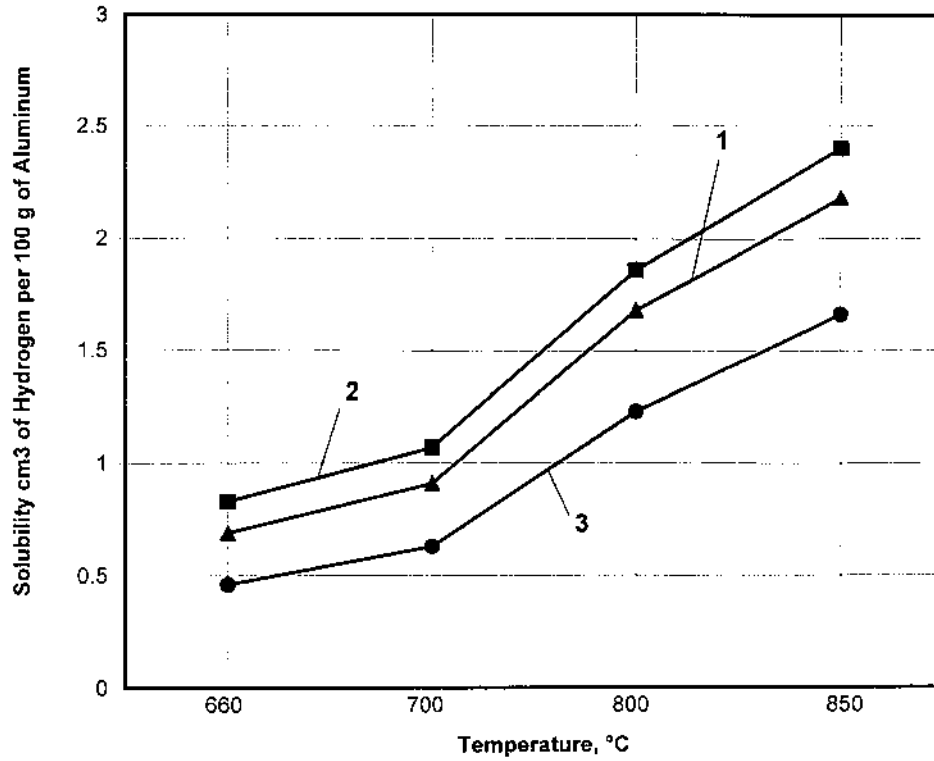
Figure 33   Solubility of Hydrogen in molten aluminum with 1 atm of hydrogen over the melt [81–83]: (1) [81]; (2) [82]; (3) [83].

Table 22   Chemical Composition Limits of Wrought Aluminum Alloys

AA Designation	Si	Fe	Cu	Mn	Mg	Zn	Ti	Others	Aluminum, min
EC	–	–	–	–	–	–	–	–	99.45
1050	0.25	0.40	0.05	0.05	0.05	0.05	0.03	0.03	99.50
1060	0.25	0.35	0.05	0.03	0.03	0.05	0.03	0.03	99.60
1100	1.0 Si + Fe		0.05–0.20	0.05	–	–	–	0.05	99.00
1145	0.55 Si + Fe		0.05	0.05	–	–	–	0.03	99.45
1175	0.15 Si + Fe		0.10	–	–	–	–	0.02	99.75
1230	0.70 Si + Fe		0.10	0.05	–	0.10	–	0.05	99.30
1235	0.65 Si + Fe		0.05	–	–	–	–	0.05	99.35
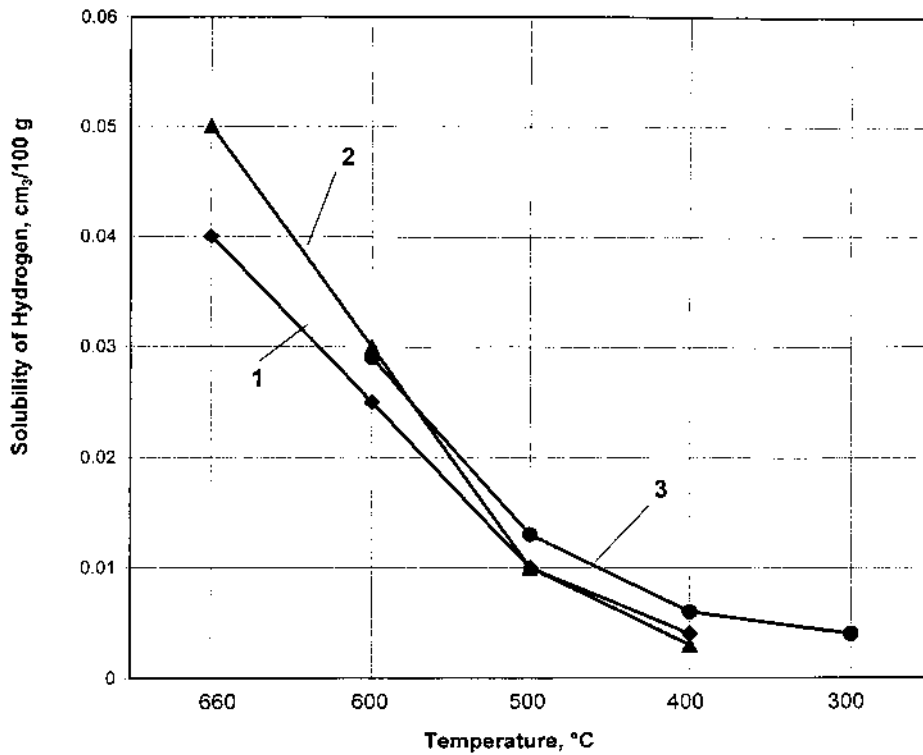
Figure 34   The solubility of hydrogen in solid aluminum [54,81,83]: (1) [81]; (2) [83]; (3) [54].

$$\text{Log S} = 2.969 - (3086/T) \, (\text{molten aluminum}) \qquad [83]$$
$$\text{Log S} = 1.961 - (3042/T) \, (\text{solid aluminum}) \qquad [83]$$

where S is the solubility of hydrogen in cm^3 per 100 g of metal and T is temperature in K.

Figure 34 shows the solubility of hydrogen in solid aluminum. During melting, hydrogen can be introduced into molten aluminum from the following sources: from gas entrapped on the oxide film of the solid before melting, from reaction of aluminum with moisture that is in the atmosphere over the melt, or from reaction with moisture in the refractory containing the melt.

7   TYPICAL CHARACTERISTICS AND APPLICATIONS

The first wrought aluminum alloy has been produced in the USA in 1888. This alloy was designated as 1100 alloy. The various grades of pure metal were utilized directly as wrought products for specific applications in the early development of the industry. For instance the alloy EC (electrical conductor) had a minimum aluminum content of 99.45%. 1145 aluminum alloys is used for foil production. Chemical composition of some aluminum alloys is shown in Table 22 [84] and typical characteristics and applications in Table 23 [5]

Table 23 Standard Products Chart for Super and Commercial Purity Aluminum

Alloy	Sheet	Plate	Foil	Drawn tubing	Extruded shapes	Bar	Wire	Rod	Rivets	Forgings	Impacts
1199	–	–	X	–	–	X	X	X	–	–	X
1180	–	–	X	–	–	–	–	–	–	–	–
1060	X	X	–	X	X	–	X	–	–	–	–
EC	X	X	–	X	X	X	X	X	–	–	–
1145	X	–	X	–	–	–	–	–	–	–	–
1100	X	X	X	X	X	X	X	X	X	X	X

An important application of pure aluminum is as cladding, to improve resistance to corrosion of heat treatable alloys or to improve finishing characteristics of non-heat-treatable alloys.

REFERENCES

1. International Bulletin 14b, International Union of Pure and Applied Chemistry, 1961.
2. J. E. Lewis, National Academy of Sciences, Nuclear Science Series 3032, 1961, p. 3.
3. Aluminum Properties, Physical Metallurgy and Phase Diagrams, American Society for Metals, Metals Park, Ohio, 1967, p. 530.
4. I. N. Fridlyander, *Physical Metallurgy of Aluminum and Its Alloys*, Moscow, 1983, p. 287 (in Russian).
5. J. L. Brandt, "Properties of Pure Aluminum, Aluminum," Vol. 1, Properties, Physical Metallurgy and Phase Diagrams, ASM, 1967, p. 2.
6. F. C. Frary, "The Electrolytic Refining of Aluminum," Trans. Am. Electrochem. Soc., 1925, 47, pp. 275–286.
7. J. D. Edwards, "The Properties of Pure Aluminum," Trans. Am. Electrochem. Soc., 1925, 47, 275, 47, pp. 287–300.
8. L. A. Willey, Alcoa Research Laboratories, 1940.
9. A. I. Lainer, *Aluminum Oxide Production*, Metallurgiszdat, Moscow, 1961 (in Russian).
10. "The Metals Red Book," Nonferrous Metals, Vol. 2, CASTI Publishing Inc., 1998.
11. P. C. Varley, *The Technology of Aluminum and Its Alloys*, CRC Press, International Scientific Series, London, 1970.
12. W. Witt, Z. Naturforsch. A, 1967, 22A, 92.
13. W. B. Pearson, *A Handbook of Lattice Spacing and Structures of Metals and Alloys*, Pergamon Press, 1958.
14. A. H. Kottrell, *Structure of Metals and Alloys*, 1959, p. 288.
15. B. F. Figgins, G. O. Jones, and D. P. Riley, Phil. Mag, 1956, 1(8), pp. 747.
16. M. E. Straumanis, J. Appl. Phys. 1949, 20, pp. 726.
17. G. Schulze, *Metallophysik*, Academic-Verlag, Berlin, 1967, p. 501.
18. C. Wert and R. Thomson, *Physics of Solids*, McGraw-Hill Company, 1964. p. 588.
19. *Modern Crystallography*, Vol. 2, Crystal Structure, Moscow, Nauka, 1979, p. 358 (in Russian).
20. R. S. Dalzymple, Corrosion, 1959, 12, 602.
21. A. Kelly and G. W. Groves, *Crystallography and Crystal Defects*, London, 1970, p. 501.
22. I. I. Novikov, *Defects of the Crystal Structure of Metals*, Moscow, Metallurgia, 1983, p. 230.
23. G. Hurt and I. Lote *Theory of Dislocations*, 1972, p. 599.
24. E. Hetch, *Aluminum, Properties and Physical Metallurgy*, Handbook, 1989, p. 421.
25. L. F. Mondolfo, *Aluminum Alloys: Structure and Properties*. Butterworths, Boston, 1976, p. 17.
26. E. C. W. Perryman, 1955 (private communication).
27. E. Gebhardt, M. Becker, and A. Dorner, Z. Metallk, 1953, 44, 44, pp. 573–575.
28. K. Smith, *Metals*, Handbook, 5th Edn, 1980, p. 446.
29. C. S. Taylor, L. A. Willey, D. W. Smith, and J. D. Edwards, The Properties of High-Purity Aluminum, Metals & Alloys, Vol. 9, 1938, pp. 189–192.
30. L. A. Willey, Alcoa Research Laboratories, 1957.
31. F. C. Nix and D. McNair, Phys. Rev., 1941, 60, pp. 597–605.
32. Kostukov A. A., Kil I. T., Nikiforov V. P. et al. *Non-Ferrous Alloys Handbook, Aluminum Production*, Moscow, Metallurgia, 1971, p. 560 (in Russian).
33. P. Hidnert and H. S. Krider, J. Res. Natl. Bur. Stand., 1952, 48, pp. 209–220.

34. V. J. Johnson, Wright Air Development Center, TDR–60–56, Part II, October 1960, p. 1.132.
35. R. A. Andrews, R. T. Webber, and P. A. Spohr, Phys. Rev., 1951, 84, pp. 994–996.
36. C. S. Smith and E. W. Palmer, Trans. AIME, 1935, 117, pp. 225–245.
37. L. W. Kempf and C. S. Taylor, Trans. AIME, 1937, 124, pp. 287–299.
38. R. W. Powell and M. J. Hickman, Metallurgia, 1944, 41, pp. 15–20.
39. W. Bungardt and R. Kollenbach, Z. Metallk, 1951, 42, pp. 82–91.
40. S. Caplan and G. Chanin, "Critical-field Study of Superconducting Aluminum," Phys. Rev., 1965, 138(5), pp. 1428–1433.
41. Y. S. Touloukian and C. Y. Ho, *Properties of Aluminum and Aluminum Alloys*. Thermophysical properties. Research Center, Purdue University, West Lafayette, IN, Report 21, 1973, pp. 518–519.
42. N. B. Brandt and S. M. Chudinov, *Electron Structure of Metals*, Moscow, Moscow University, 1973, p. 330.
43. H. Borchers and W. Hepp, "Magnetic Studies of Aluminum Alloys without Ferromagnetic Phases," Zeitschrift fuer Metallkunde, 1969, 60(9), pp. 722–729.
44. W. C. Sleepy, Alcoa Research Laboratories, 1963.
45. W. Kestemich, H. Ullmaier, and W. Schilling, "The Influence of Fermi Surface and Defect Structure on the Low Field Galvanomagnetic Properties of Al," J. Phys. F. Metal Physics, 1976, 6(10), pp. 1867–1883.
46. C. Papastaikoudis, D. Papadimitropoulos, and E. Rocofyllou, "Low-Field Hall Coefficient R°_H of Dilute Al-3d Alloys at 4.2K," Phys. Rev. B, Solid State, 1980, 22(6), pp. 2070–2076.
47. J. R. Purcell and R. B. Jacobs, *Cryogenics*, 1963, 3, pp. 109–110.
48. G. G. Gauthier, "The Conductivity of Super Purity Aluminum: the Influence of Small Metallic Additions," J. Inst. Metals, 1936, 59, pp. 129–150.
49. C. F. Babilon, Alcoa Research Laboratories, 1960.
50. T. E. Pochapsky, Act. Met., 1953, 1, pp. 747–751.
51. A. Roll and H. Motz, Z. Metallk, 1957, 48, pp. 272–280.
52. Ultra High Purity Metals, American Society for Metals, Metal Park, Ohio, 1962, p. 150.
53. C. B. Satterhwaite, "Thermal Conductivity of Normal and Superconducting Aluminum," Phus. Rev., 1962, 125, pp. 873–876.
54. M. E. Drits., P. B. Budberg, N. T. Kuznetsov, A. M. Drits, and V. M. Panovko, Properties of elements, Vol. 1, Metallurgy, Magazine "Non-Ferrous Alloys", 1997, pp. 432.
55. P. W. Bridgman, "Linear Compressions to 30,000 Kg/cm^2, Including Relatively Incompressible Substances," Proc. Am. Acad. Arts Sci., 1949, 77, pp. 187–234.
56. P. W. Bridgman, "Compressions of 39 Substances to 100,000 Kg/cm^2, Including Relatively Incompressible, Proc. Am. Acad. Arts Sci., 1948, 76, pp. 55–70.
57. D. G. Doran, G. R. Fowles, and G. A. Peterson, Phys. Rev. Letters, 1958, 1, pp. 402–404.
58. G. Hass and J. E. Waylonis, J. Opt. Soc. Am., 1961, 51, pp. 719–722.
59. R. P. Madden, L. R. Canfield, and G. Hass, J. Opt. Soc. Am., 1963, 53, pp. 620–625.
60. H. E. Bennett, M. Silver, and E. J. Ashley, J. Opt. Soc. Am., 1963, 53, pp. 1089–1095.
61. A. L. Sopp, Jr. and J. L. Brandt, Alcoa Research Laboratories, 1963.
62. A. Goldsmith, T. E. Waterman and H. J. Hirschhorn, Wright Air Develop Div. Tech. Rept. 1958, Vol. I, P.I–A–Z, pp. 58–476.
63. M. Moeller and H. Miething, Radiation Emission of Molten Aluminum, Giesserei-Z., 1924, 21, pp. 444–446.
64. D. D. Wagan, W. H. Evans, and V. B. Parkez, "Selected Values of Chemical Thermodinamic Properties. National Bureau of Standards," Technical Notes No. 270, Washington, USA, 1969.

65. D. R. Stull and H. Prohet, JANAF Thermomechanical Tables, 2nd edn, U.S. Dept. of Commerce Washington, D.C., 1971.
66. C. Babb, Rew. Mod. Phys., 1973, 35, pp. 400–412.
67. W. H. Ailor, et al., "A Review of Aluminum Corrosion in Tap Waters," J. Hydronautics, 1969, 3, pp. 105–115.
68. V. S. Sinyavski, V. D. Valkov and V. D. Kalinin, "Corrosion and Metal Protection of Aluminum Alloys," Moscow, Metallurgia, 1986, p. 368.
69. D. Altenpohl, *Aluminum Viewed from Within*, 1st Edn, Aluminum-Verlag GMBH, Dusseldorf, 1982.
70. D. S. Naudu, *Engineering Materials and Their Testing*, Part II, Non-Ferrous Metals and Their Alloys, Asia Publishing House, New York, 1966.
71. N. D. Tomashev, *Theory of Corrosion and Metal Protection of Metals*, Academy of Science of the USSR, Moscow, 1960, p. 480.
72. M. Pourbaics, *Atlas d'equilibes electrochemiques*, Granthier-Villards, Paris, 1963, p. 420.
73. R. H. Brown, Alcoa Research Laboratories, 1945.
74. G. A. Genrig and M. H. Peterson, Corrosion, 1981, 37(4).
75. D. S. Keir, M. I. Pryor, and P. S. Sherry, J. Eletrochem. Soc., 1967, 114(8), p. 777.
76. M. B. Altman, G. N. Andreev, Yu. B. Arbuzov, et al., *Application of Aluminum Alloys*, Metallurgia, Moscow, 1985, p. 313.
77. V. F. Henely, *Anodic Oxidation of Aluminum and Its Alloys*, Pergamon Press., 1982, p. 156.
78. F. I. Kvasov and I. N. Fridlyander, 2nd Edn, *Commercial Aluminum Alloys*, Handbook, Metallurgia, Moscow, 1984.
79. I. S. Grigoriev, *Physical Values*, Handbook, Meilihova E. Z., Atomizdat, 1991, p. 1132.
80. M. E. Drits, A. M. Korolkov, Yu. P. Gook, et al., *Failure of Aluminum Alloys under Tension*, Nauka, Moscow, 1973, p. 215.
81. C. E. Ransley and H. Neufeld, "The Solubility of Hydrogen in Liquid and Solid Aluminum," J. Inst. Metals, 1947/1948, 74, pp. 599–620.
82. W. R. Opie and N. J. Grant, "Hydrogen Solubility in Aluminum and Some Aluminum Alloys," Trans. AIME, 1950, 188, pp. 1237–1241.
83. W. Eichenauer, K. Hattenbach, and Z. Pebler, "The Solubility of Hydrogen in solid and Liquid Aluminum," Z. Metallk, 1961, 52, pp. 682–684.
84. *Aluminum Standards and Data*, 2nd Edn, December 1969, The Aluminum Association.
85. W. G. Moffatt, G. W. Pearsall, and J. Wulff, *The Structure and Properties of Materials*, Vol. 1, Structure, John Wiley and Son, New York, 1964, p. 51.
86. W. D. Callister, *Materials Science and Engineering: Introduction*, 5th Edn, John Wiley and Son, New York, 2000.
87. C. C. Gidwell and C. L. Hogan, "Thermal Conductivity of Aluminum: The Influence of Small Metallic Additions," J. Inst. Metals, 1936, 59, pp. 129–150.

3

Physical Metallurgy and the Effect of Alloying Additions in Aluminum Alloys

MURAT TIRYAKIOĞLU
Robert Morris University, Moon Township, Pennsylvania, U.S.A.

JAMES T. STALEY*
Alcoa Technical Center, Alcoa Center, Pennsylvania, U.S.A.

1 PHYSICAL METALLURGY OF ALUMINUM ALLOYS

1.1 Introduction

Aluminum, like all pure metals, has a low strength, and cannot be readily used in applications where resistance to deformation and fracture is essential. Therefore other elements are added to aluminum, primarily to improve strength. Typical tensile strengths range from 45 MPa (6.5 ksi) for 1199-O sheet to almost 700 MPa (100 ksi) for 7055-T77 extruded products. The low density combined with high strength have made aluminum alloys attractive in applications where specific strength (strength-to-density ratio) is a major design consideration. For structural use, the strongest alloy which meets minimum requirements for other properties such as corrosion resistance, ductility, toughness, etc., is usually selected if it is cost effective. Hence, composition is first selected for strength.

The properties of aluminum alloys depend on a complex interaction of chemical composition and microstructural features developed during solidification, thermal treatments, and (for wrought products) deformation processing. Although pure aluminum is very resistant to corrosion because of the presence of a film of

---

* Retired.

aluminum oxide, corrosion resistance generally decreases with increasing alloy content, so tempers have been developed to improve the corrosion resistance of the highly alloyed materials.

Although the low strength of pure aluminum limits its usefulness, aluminum has a theoretical shear strength of between 0.9 and 2.62 GPa [1,2], depending on whether the displacement of atoms follow a straight or a zig zag path. The significant difference between the strengths of commercial alloys and theoretical strength is due to the presence of lattice defects, mainly dislocations. Therefore all strengthening mechanisms in commercial alloys are aimed at limiting the movement of dislocations.

1.2   Lattice Defects and Strengthening Mechanisms in Aluminum

1.2.1   Point Defects

If an aluminum atom is removed from the lattice, a *vacancy* is formed. A vacancy contracts the site diameter by approximately 20%. If an atom is replaced in an interstitial position, a so-called *Frenkel* defect is formed. Since the diameter of an aluminum atom is 2.86 Å, and that of the interstices is 1.17 Å, there are very few Frenkel defects in aluminum alloys [3]. Vacancies favor the progress of diffusion at free surfaces or dislocations. Because vacancies have strain energy (due to contraction) as well as surface energy, they are attracted to regions of strain in the lattice, e.g. to solute atoms of different size from solvent atoms, and dislocations. Point defects are illustrated in Fig. 1 [4].

1.2.2   Dislocations

Dislocations are line defects in crystals, and contribute to the deformation of the crystal by getting activated at a much lower stress than required to deform a perfect
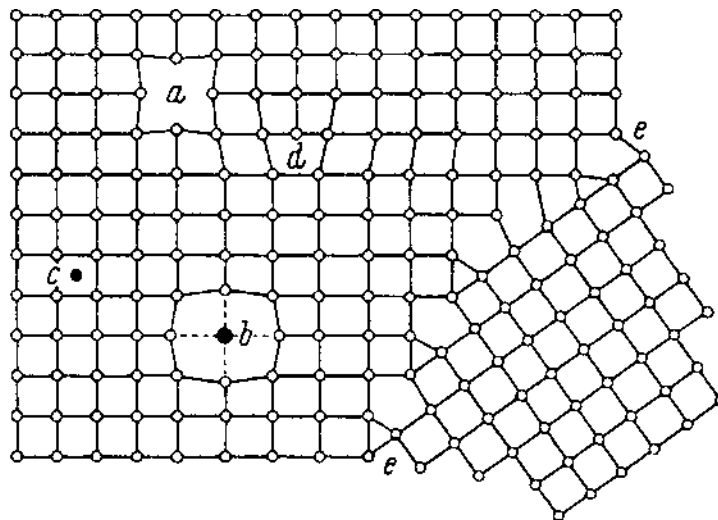

Figure 1   Lattice defects in crystals [4]: (a) vacancy; (b) solute atom; (c) interstitial; (d) dislocation; and (e) grain boundary. (Courtesy of TMS and the Aluminum Association).
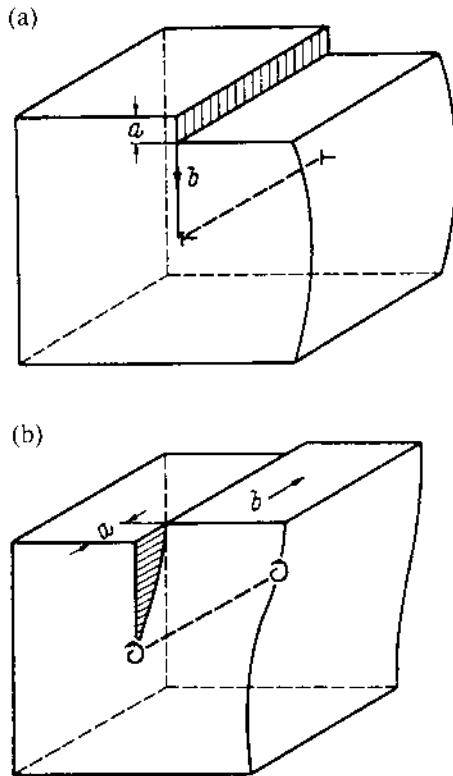
(a)

(b)

Figure 2 Two distinct dislocation types [4]; (a) edge; and (b) screw. Generally all dislocations have screw and edge components. (Courtesy of TMS and the Aluminum Association).

crystal. There are essentially two types of dislocations; edge and screw. An edge dislocation can be interpreted as an extra half-plane of atoms in the lattice, as depicted in Fig. 2(a) A screw dislocation is harder to visualize, and cannot be interpreted as an extra plane of atoms. A screw dislocation is depicted in Fig. 2(b). In general, almost all dislocations have edge and screw components. A dislocation is characterized by the magnitude and direction of the slip movement associated with it, which is called the Burgers vector, b, and the difference in the amount of slip across the dislocation line is constant. The magnitude of Burgers vector in aluminum is 0.286 nm. Further discussion on dislocations can be found in classical references, such as 5–7.

An important difference between the motion of a screw dislocation and that of an edge dislocation is due to the cylindrical symmetry of a screw dislocation about its axis. To a screw dislocation all the directions around its axis look the same, and therefore, the motion of the screw dislocation is not restricted to a single slip plane, as in the case of a gliding edge dislocation. The process whereby a screw dislocation glides into another slip plane having a slip direction in common with the original slip plane is called *cross-slip*.

The glide motion of an edge dislocation is restricted, since it can only glide in that slip plane which contains both the dislocation line and its Burgers vector.
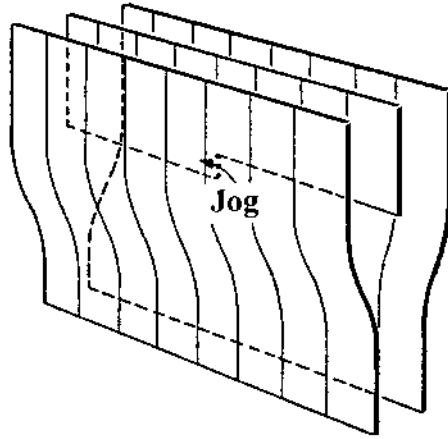
Figure 3 A jog in a dislocation.

However, movement of the dislocation line in a direction normal to the slip plane can occur under certain conditions. If vacancies diffuse to the dislocation line, it climbs up and the extra half-plane will shorten. This process is called *dislocation climb*, and requires mass transport by diffusion. However, since the vacancies will not arrive at the dislocation at the same instant, or uniformly, the dislocation climbs one atom at a time. Moreover, the dislocation will not lie in a particular slip plane, but instead some sections will lie in one plane and other sections in parallel neighboring planes. Where the dislocation jumps from one plane to another is known as a *jog*, which can be interpreted as a short length of dislocation not lying in the same slip plane as the main dislocation but having the same Burgers vector, as depicted in Fig. 3.

A jog in an edge dislocation will not impede the motion of the dislocation in its slip plane since it can generally glide with the main dislocation line. A jog in a screw dislocation is merely a small piece of edge dislocation, and can move in two ways; (i) it may move sideways along the screw dislocation and attach itself to an edge component of the dislocation line; or (ii) may be dragged along with the screw dislocation. This second process requires the jog to climb, and creates a row of point defects. Such a movement is difficult but necessary to give the dislocation sufficient mobility [8].

1.2.3 Stacking Faults

In face-centered cubic (fcc) metals like aluminum, dislocations are unstable, and split into partial dislocations by creating a faulted region between the two partials, as shown in Fig. 4, to lower the elastic energy of the crystal. In aluminum, the atoms on the atomic planes on either side of the fault plane find themselves surrounded by near neighbor atoms in hexagonal close packing (hcp) environment. The equilibrium distance between the dislocation pairs is expressed by [5],

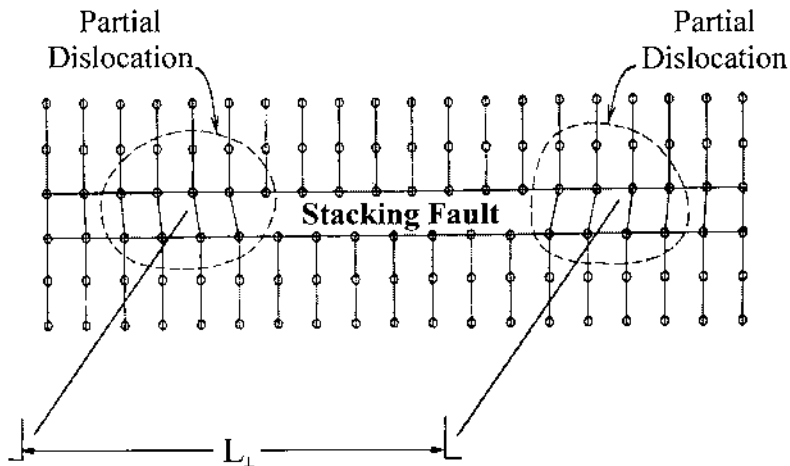$$L_\perp = \frac{G_{Al} b^2}{2\pi\gamma} \tag{1}$$

Figure 4 Stacking fault in an fcc crystal created when dislocations become unstable and split into two partial dislocations. Atoms on both sides of the fault find themselves in an hcp environment. [Source Ref. 9].

G_{Al} is 23 GPa [1], and aluminum has a high stacking fault energy ($\gamma_{Al} = 200$ mJ/m^2 [1,8]. $L_\perp$ is only about 1 to 2 atoms diameters in aluminum [8] so that dislocations are relatively unextended. However alloying additions decrease stacking fault energy of aluminum [10], and consequently increase $L_\perp$. Also the width of the stacking fault may differ from $L_\perp$ for a particular alloy concentration because of applied or internal stresses [11]. If dislocations are piled up against an obstacle, their width may be considerably reduced. $L_\perp$ is also important to the phenomenon of cross-slip in which a dislocation changes from one slip plane to another intersecting slip plane. For glide to occur, the glide plane must contain both the Burgers vector and the line of dislocation, and consequently, for cross slip to take place, a dislocation must be in an exact screw orientation. In aluminum, where the dislocations are relatively unextended, frequent occurrence of cross-slip is expected.

Faulted dislocation loops are observed in high purity aluminum (99.9999%) [12]. These loops form by the collapse of vacancy discs onto a closed-packed plane, and are called *Frank sessile dislocation loops*. These loops are metastable, and readily transform to prismatic loops under small external stresses. An extensive discussion on stacking faults is provided in Reference 10.

1.2.4. Grain Boundaries

Most metals in commercial use are polycrystalline, i.e. the mass as a whole is made up of a large number of small interlocking crystals, or grains. Each grain is joined to its neighbors at all points on its surface by a grain boundary, the shape of which generally bears no relation to the internal symmetry of the crystal, as depicted in Fig. 1. The packing of the atoms in the boundaries is almost as compact as that within the grains themselves. The thickness of grain boundaries in aluminum is about 4 Å [13]. The orientations of the crystal axes in the different grains are often distributed randomly, so that most of the grain boundaries are large angle boundaries, separating grains which are some 20 degrees or more apart in orientation. In many

cases, however, the orientations are grouped closely about a mean value; this is called a *local orientation*. The relationship of orientation of grain with respect to the external surfaces of the material is called *texture*.

1.2.5 Sources of Dislocations

Dislocations in aluminum alloys may be generated as a result of (i) quenching stresses, which mainly arise from the retention of an excess concentration of vacancies [14,15]; (ii) cold work, or (iii) misfit stresses created during the nucleation of a phase.

The equilibrium concentration of vacancies at a particular temperature is given by;

$$c_v = e^{\frac{-E_f}{q^T}} \tag{2}$$

The equilibrium concentration of vacancies in pure aluminum as a function of temperature is given in Fig. 5. Assuming that all vacancies at the equilibrium concentration at an elevated temperature, T_2, are retained at the end of a quench to cool aluminum to a lower temperature, T_1, the consequent chemical stress is given by [8];

$$\sigma_c = \frac{E_f}{b^3}\left[1 - \frac{T_1}{T_2}\right] \tag{3}$$

For aluminum, E_f is about 0.7 eV so that quenching from 900K to 300K produces a chemical stress of about 3 GPa. This stress is extremely high, several times the theoretical yield stress of aluminum, and must be relieved in some way. Migration of vacancies to grain boundaries and dislocations will naturally occur, but vacancies form additional vacancy sinks by the spontaneous nucleation of dislocation loops.
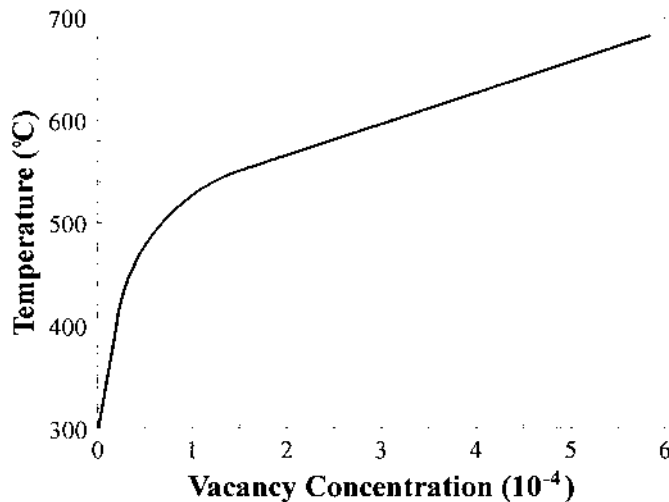

Figure 5 Equilibrium concentration of vacancies as a function of temperature [Source Ref. 8].

High supersaturation of vacancies favor the formation of dislocation loops [14,16,17], which originate from the collapse of discs of vacancies [15,18]. The average number of loops can be as high as 10^{15} cm^{-3}, with the density of dislocations in loops about 10^{10} cm^{-2} [17]. Lower supersaturations lead to the formation of dislocation spirals which result from the climb of screw dislocations by the absorption of vacancies [18]. Alloying additions may have a strong effect on whether vacancies condense into loops or spirals. Elements with high binding energies with vacancies, such as Li and Si, retard the formation of loops and helices.

In general, mobile dislocations are produced in metals by nucleation, multiplication or unpinning during cold work. Stress concentrations appreciably reduce the value of external stress required to nucleate dislocations. Regions that favor the nucleation of dislocations include surface irregularities, inclusions and grain boundaries. Dislocations are emitted from grain boundaries after only small deformations, and jogs on screw dislocations are important in multiplication [8].

Dislocations may multiply in number when dislocation sources within the crystal are active. The operation of one of these sources, a Frank–Read source [19], is shown in Fig. 6(a). A Frank–Read source in an Al-4 wt%Cu alloy [20] is shown in Fig. 6(b). The dislocation rings are symmetrically arranged about the source, but since they are inclined at an angle to the foil, only a part of the second and third ring lies in the thickness of the foil. After their production by the source, these rings have acquired vacancies, and formed complex helices, which have been dissociated under the action of stress, into a screw dislocation and adjacent series of loops.

Figure 6(c) shows a perfect example of a Bardeen–Herring climb source, observed in an Al-3.5 wt%Mg alloy [21]. In this case, the concentric loops have been produced by climb rather than slip. The multiplication mechanism is similar to Frank–Read source, but because screw dislocations climb into helices, only edge dislocations can act as a source dislocation by expanding in the climb plane, as the extra half plane of atoms is removed by the condensation of vacancies introduced by quenching.

When a crystal is deformed nonuniformly, slip requires that dislocations be generated if all parts of the crystal are to deform in a compatible way. These dislocations are called *geometrically necessary dislocations* [22], and there exist geometric relationships between the deformation and the number of dislocations needed to accommodate it with minimum internal stress. Dislocations are not geometrically necessary in the uniform deformation, such as simple tension, of a pure single crystal. Nevertheless dislocations do accumulate, causing the crystal characteristic work hardening (to be explained in the section ''Dislocation–Dislocation Interactions''). There is no simple geometric argument to predict the density of these dislocations. Since their accumulation is probably a result of chance encounters in the crystal, they are called *statistically stored dislocations* [23].

Dislocations can also be generated as a result of misfit stresses created upon the nucleation and growth of second phase particles, especially dispersoids and precipitates. Whether dislocations will be generated is determined by the nature of the particle-matrix interface [23]. Nucleation of new dislocations form a coherent interface between the second phase particle and the matrix is extremely difficult. In case of incoherent or weak interfaces, nucleation of dislocations is relatively easy, requiring a stress of G/100, which decreases as particles grow. It is estimated [24]

(a)
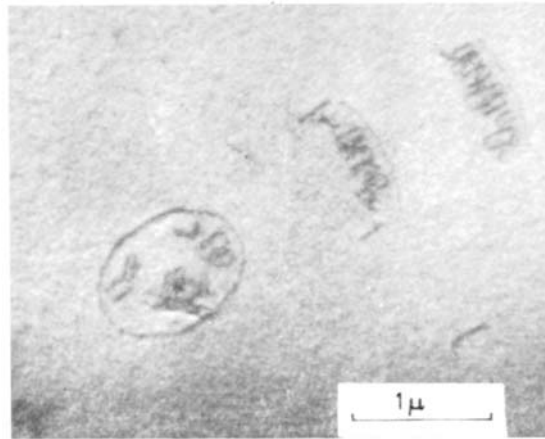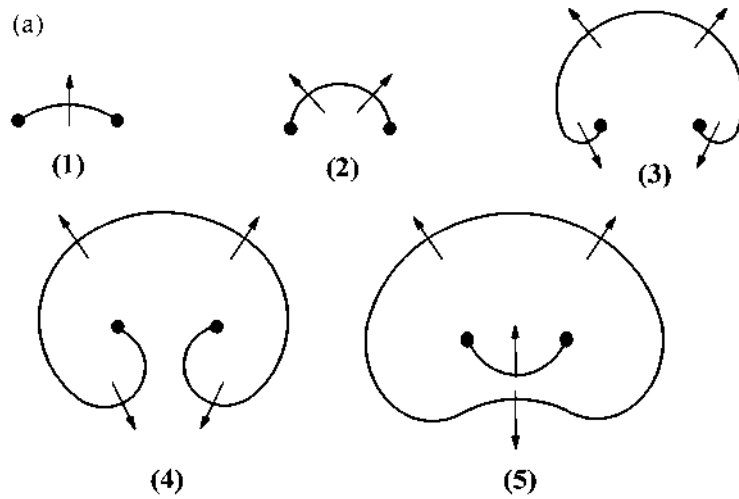
(b)

Figure 6 Dislocation sources in aluminum. The Frank–Read source generates additional dislocations when a dislocation line is pinned by two obstacles and bow under applied stress (a). If the stress is large enough, the bowed parts of the dislocation extend far enough to contact, leaving dislocation loops behind. A Frank–Read source in an Al-4 wt% Cu alloys is shown in (b) [20].

that the critical value of ε, where precipitates lose coherency, and misfit stresses result in formation of new dislocation loops, is 5%. Some of these dislocations glide along the precipitate-matrix interface to become a misfit dislocation, while others creep into the matrix, and become lattice dislocations [25]. As the precipitated particles grow, more and more dislocations are generated [26].

1.2.6   Dislocations and Strengthening Mechanisms

Useful strength can be defined as the resistance of a material against plastic deformation and against formation and growth of cracks. Therefore a strengthening
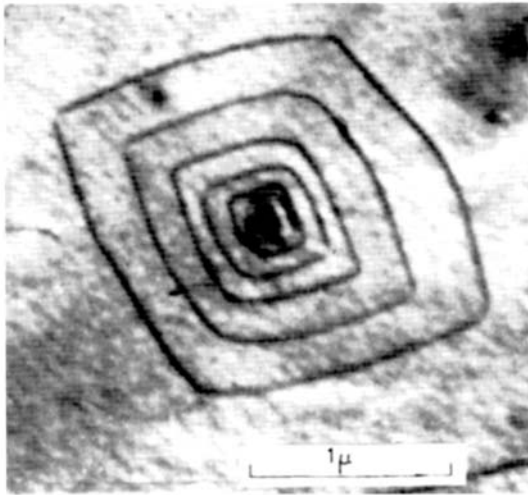
(c)

Figure 6 Dislocation sources in aluminum. (c) A Bardeen–Herring climb source, observed in an Al-3.5 wt% Mg alloy [21]. (Micrographs are courtesy of Prof. R. E. Smallman, The University of Birmingham, United Kingdom).

mechanism should simultaneously contribute to both aspects of strength, or increase one without impairing the other. Resistance to plastic deformation will be discussed in this section. The formation and growth of cracks will be addressed in ''Mechanical Behavior of Aluminum Alloys'' section in this chapter.

The yield stress is defined as the stress at which dislocations travel significant distances in the material, causing macroscopic deformation to take place. In a single crystal, the stress at which dislocations glide freely is called the critical resolved shear stress (CRSS). In a polycrystal, the yield stress, YS (or σ_y), is related to the CRSS by the Taylor Factor, M (~ 3), which accounts for the fact that not all grains have favorably oriented slip planes and that material continuity must be preserved. The yield stress is related to the grain size and texture of the material through the parameter M. For a single phase alloy, if the value of M is known for a particular grain structure, then the yield strength is fully determined by the CRSS of the single crystal [27]. CRSS of crystals containing particles, however, may be higher or lower than predicted by the Taylor Factor depending on the morphology, size and habit plane of particles.

CRSS for aluminum is 0.79 MPa [9], which is lower than the theoretical shear strength of aluminum by several orders of magnitude. Therefore the movement of dislocations has to be limited or delayed through various strengthening mechanisms before aluminum can be used in commercial applications where resistance to deformation is necessary. Strengthening will result whenever a dislocation encounters an irregularity within a crystal lattice. Hence large particles, small particles, foreign atoms, or the interaction of dislocations with other lattice defects will all result in strengthening, either because a dislocation is repelled by particles

or atoms, so that it must do more work to reach them, or because it is attracted to them and making it difficult to pull away. For more details, the reader is advised to refer to milestone reviews provided in Refs 1 and 28.

Dislocation–Vacancy Interaction

As indicated above, a vacancy contracts the site diameter by about 20%. This local strain interacts with dislocations, resulting in increased resistance to shear stress. In aluminum single crystals, tensile properties are significantly affected by cooling conditions from elevated temperatures, as depicted in Fig. 7(a). Note in Fig. 7(a) that there is a tremendous increase in yield stress of the aluminum single crystal when it is quenched rather than furnace cooled. The reason for the difference in the two tensile curves is a result of the condensation of vacancies on existing dislocations, which create jogs, and therefore, increase the friction between the matrix and the dislocation during glide [29]. A dislocation should possess, in thermal equilibrium, a certain number of jogs [29]. This number decreases exponentially with decreasing temperature so that, by quenching with sufficient cooling rate from a high temperature, it may be possible to retain quenched-in jogs on dislocations, which would then provide a frictional force resisting the glide motion of dislocations at room temperature. Also excess vacancies, retained during the quench, migrate at room temperature to dislocations, where they form atmospheres or jogs, or clusters together to form voids, or rings of sessile dislocations [29]. The magnitude of increase in CRSS depends on the temperature from which aluminum is cooled, as depicted in Fig. 7(b), indicating that the more vacancies are quenched in, the higher the increment in CRSS.

Dislocation–Solute Atom Interaction

An alloying element going into solid solution always strengthens the solvent metal. In dilute solutions the amount of strengthening is generally proportional to the solute concentrations, and if more than one solute is present, their effects are usually additive. The strengthening produced by a given element in aluminum depends primarily on the difference in size between the solute and the solvent [30–32]. However when the size difference is small (e.g. Zn or Ag in aluminum), electrostatic interaction due to valence difference between the solute atom and the matrix becomes important [32,33]. Valence difference represents the change in the number of electrons contributed to the metallic bond. The effect of alloying elements in aluminum is most pronounced at lower concentrations and become less effective for the higher percentages of alloying elements.

Dislocation movements are not greatly hindered by a random array of solute atoms on the solvent lattice. However solute atoms tend to collect preferentially at the dislocations, when the stress fields created by the solute atoms are combined with those of dislocations. The tendency for solute atoms to segregate to dislocations will be stronger, the greater the misfit between the solute and the solvent atoms. Solute atoms also segregate into the stacking faults between dislocations to lower their elastic energy. Because the energy of the fault is lowered by such segregation, energy must then be supplied to move a dislocation from the region where equilibrium was obtained, since this motion restores the energy of the fault to its normal value for the given total solute concentration. In this way a dislocation may be pinned [34]. This is called *Suzuki locking*.
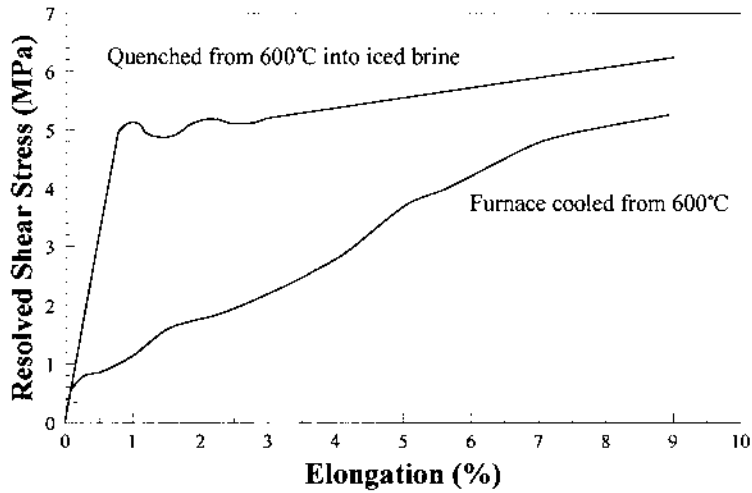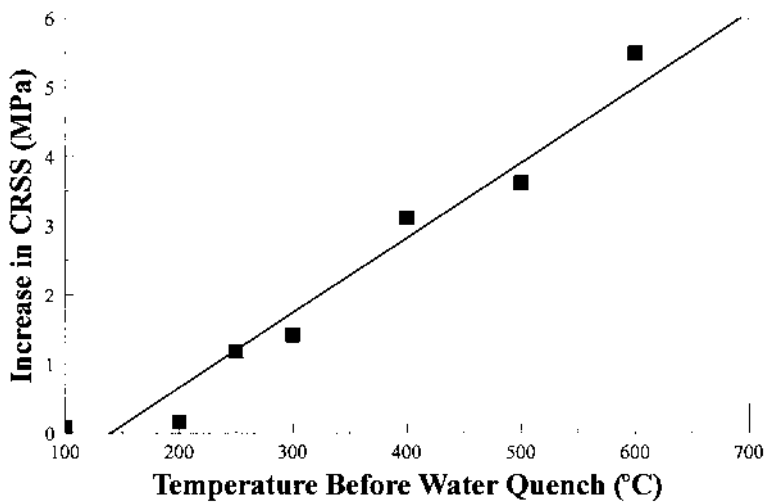
Figure 7 Tensile curves (a) of quenched and furnace cooled aluminum single crystals indicate that segregation of vacancies to dislocations is, at least partially, responsible for the increase in CRSS [Source Ref. 29]. This is supported by the dependence of CRSS on temperature before quenching (b) [Source Ref. 29].

The locking of a dislocation by a solute atmosphere results in a significant increase in the stress necessary for the start of dislocation movement. This strengthening mechanism is called *solid solution strengthening*. In order to produce solid solution strengthening, the element added must have appreciable solubility at the annealing temperature, must remain in solution after a slow cool from the anneal, and in non-heat treatable alloys, must not react with other elements to form

Table 1 Maximum Solid Solubility and Different Methods of Expressing Size Differences Between Solute Atoms and Aluminum Found in Literature

Solute Element	Max. Solid Solubility (at.%)	$(r_3\text{-}r_{Al})/r_{Al}$ [¥] (×100)	Volume Size Factor [‡] (%)	$(r_3\text{-}r_{Al})/r_{Al}$ * (×100)	Volumetric Change [†] (%)
Ag	23.8	+0.46	0[§]		
Co	<0.01	−12.64		−12.7	
Cr	0.40	−5.36		−10.1	
Cu	2.48	−5.35	−18.9	−10.8	−37
Fe	0.025	−5.92		−11.4	
Ge	2.30	+0.53	+13.4		+23
Li	13.9	+4.20	+3.2		
Mg	16.26	+5.92	+32.2		+30
Mn	0.90	−5.64	−51.2	−9.5	
Ni	0.023	−13.21		−12.7	
Si	1.59	−1.89	−12.5		
Zn	66.4	−3.15	−5.9	−3.2	−1

[¥]: calculated using the data on difference in atomic radii of element and aluminum, listed in Ref. 35; [‡]Ref. 36; *: Ref. 32; [†]Ref. 5; [§]: estimated to be 0 following the results of Ref. 33.

insoluble particles. Maximum solid solubility of some elements is given in Table 1. Of all elements, Zn has the highest solid solubility in aluminum. Ag, Mg, and Li have solid solubilities greater than 10 at%. Solid solution strengthening becomes less effective at higher temperatures where diffusion becomes more rapid.

Although it is well established that atomic size differences between the atoms of the solute and the solvent result in strengthening, there is not a common method to quantify the atomic size difference between aluminum and other alloying elements. The differences between atomic radii gives only qualitative information, since the size difference usually results in a redistribution of solvent atoms around the solute. A list of data on atomic size differences in aluminum alloys provided in the literature is given in Table 1. Note in Table 1 that different measures used to quantify atomic size difference yield different results, and the only thing in common is the sign of the measures for a particular element.

The increase in Vickers hardness of several aluminum alloys has been expressed by [32];

$$\Delta H_{\mathrm{v}} = K\left(\left|\frac{r_3 - r_{Al}}{r_{Al}}\right| f_{\mathrm{s}}\right)^{1.33} \tag{4}$$

following the strengthening model given in Ref. 5, although a linear relationship between size difference and increase in Vickers hardness has also been observed [3]. Cr, Mn, Cu, Zr increase the hardness of aluminum according to Eq. (4), while Fe, Co and Ni harden the matrix to a greater extent than predicted by Eq. (4) [32,37]. This is due to the clustering tendency of Fe, Co, and Ni in aluminum. In another study [38], Ni and Sn were found to form clusters in as-quenched condition with sizes ranging from 25 to 50 Å. Zn also forms clusters [15].
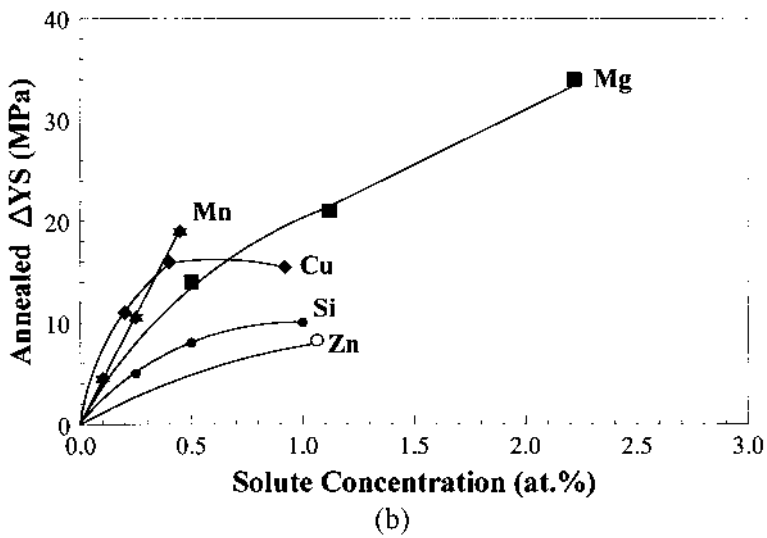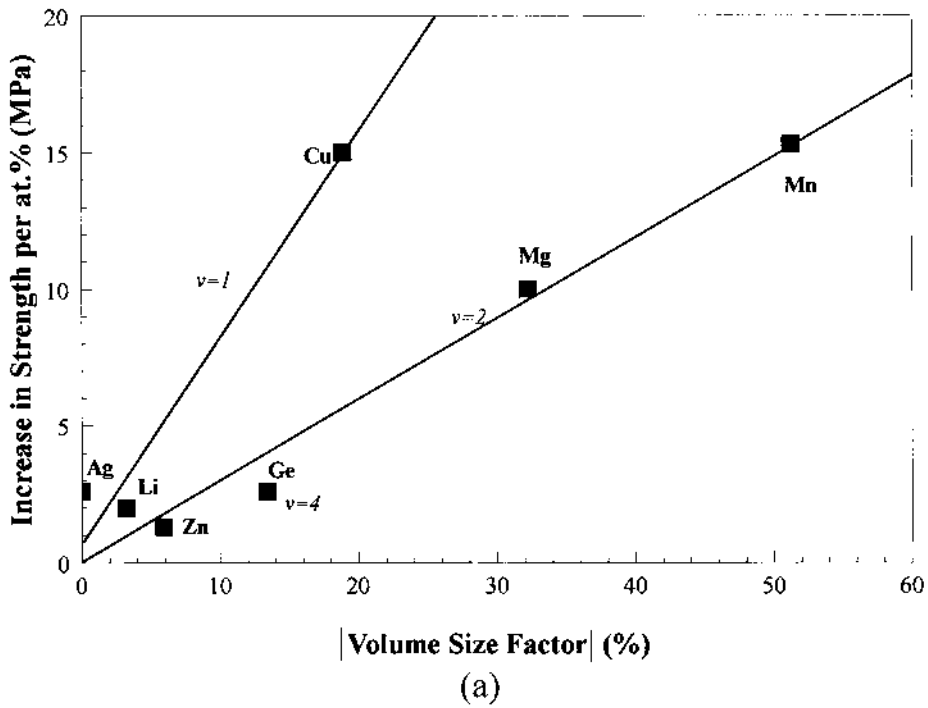
Figure 8 (a) Results of Ref. 30 replotted using the absolute values of volume size factors for various elements listed in Table 1. Increment in yield strength is determined by volume size factor, as well as the number of valence electrons in the solute atoms. The effect of various elements and their concentration on yield strength as a function of (b) atomic percent solute [Source Ref. 39].
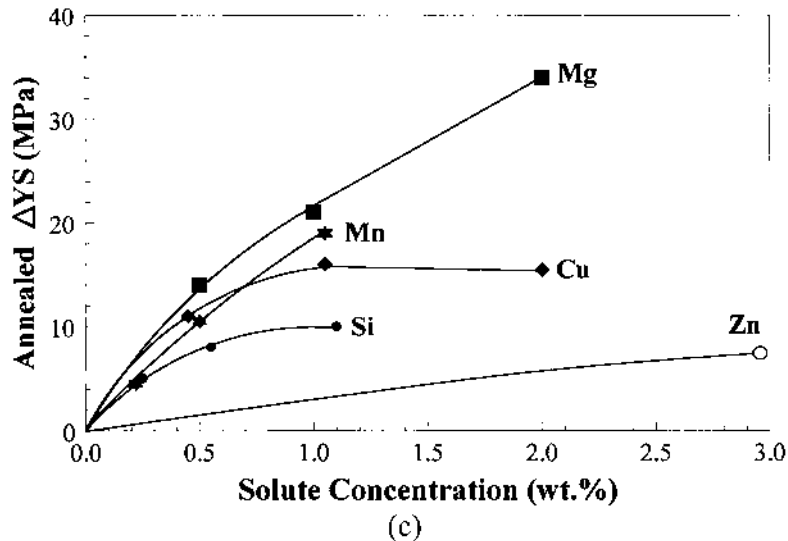
Figure 8 (c) weight percent solute. Although Cu is the most effective solute element on an atomic basis, Mg gives most increase in yield strength on a weight basis.

When results of Ref. 30 for various elements versus volume size factors listed in Table 1 are plotted, relationships presented in Fig. 8(a) are obtained. Note in Fig. 8(a) that elements with same number of valence electrons lie on the same line, and the line for elements with two valence electrons go through the origin, despite the fact that aluminum has three valence electrons. These results are in excellent agreement with the findings of Ref. 33, with the exception of Ge which lies close to the line for $v = 2$. This, however, is not unexpected, since the valence difference between Al and Ge is the same as that between Al and all elements with two valence electrons.

Figure 8(b) and 8(c) [39] show the increase in yield strength upon the addition of alloying elements on an atomic and weight % basis, respectively. Note in Fig. 8(b) and (c) that all elements initially increase strength, but the effect of concentration is not linear, and not all elements are equally effective. On an atomic basis, Mn and Cu are the most effective strengtheners at levels of 0.5 at% or less. However, Mn usually precipitates as a dispersoid during ingot preheating and hot processing so only 0.2–0.3 wt% Mn (0.1–0.15 at%) will be in solution in Al-Mn based 3XXX alloys. Cu additions to non-heat treatable alloys are commonly held to about 0.3 wt% (0.1 at%) to avoid possible formation of Al-Cu-Fe constituents, grain boundary precipitates or precipitation hardening effects. Therefore only modest solution strengthening can be achieved with Mn and Cu. Mg, though not as effective as Mn or Cu on an atomic basis, is very effective on a weight basis, and has the added advantage that it is highly soluble in Al. Some 5XXX sheet and plate (used in the O-temper) relies mainly on Mg in solution (up to 6 wt%) for strength, in which annealed yield strengths of up to 175 MPa (25 ksi) are achievable. The amount of Mg that can be retained in solution in commercial alloys is affected by the presence of other elements, mainly Cu and Si, which react with Mg during cooling

to form either Al-Cu-Mg or Mg-Si phases, thus lowering the solute content of the matrix. Zn is highly soluble in Al but is least efficient in strengthening [39]. Nevertheless Zn is present in some non-heat treatable alloys at levels of approximately 1 wt% to adjust solution potential. In ternary alloys of Al-Mg-Si, Al-Cu-Mg, and Al-Zn-Mg, the solution strengthening effect of the elements is enhanced when they work in combination; their strengthening is greater than predicted by the sum of the individual components.

Solute atoms also affect the Modulus of Elasticity (E) in aluminum alloys. Dislocations anchored to lattice sites can add to the elastic lattice distortion produced by an externally applied stress, and result in significantly lower E than in the absence of dislocations [3]. Since the mobility of dislocations is reduced by solute atoms, the mobile dislocations are anchored, resulting in an increase in E. Si, Cu and Li increase E by 8.5, 4.4 and 1.5%/at% in solution respectively [3].

Dislocation–Dislocation Interactions

Distortion around a dislocation line creates a strain field, which influences the behavior of other dislocations in the crystal. A positive edge dislocation attracts a negative edge dislocation lying on the same slip so that their respective strain fields should cancel. Moreover, the dislocations in a crystal will interact with each other to take up positions of minimum energy to reduce the total strain energy of the lattice. Hence the number of dislocations within the lattice affects the nature of deformation significantly.

DISLOCATIONS AS OBSTACLES. Not all dislocations get activated during deformation. *Sessile* dislocations cannot glide in the usual manner, and can act as obstacles to the glide motion of glissile dislocations. The simplest of these is the Frank sessile dislocation loop, which has been mentioned previously. Although these dislocation loops are metastable in pure aluminum, the addition of an alloying element to aluminum may alter the stability of a Frank sessile dislocation loop. Frank sessile dislocation loops are shown in Fig. 9 [40], which shows prismatic and sessile loops (A) in the same field of an Al-3.5 wt% Mg alloy. The fringe contrast inside the loops marked A indicates that the dislocation line surrounds a stacking fault. In this alloy, the stability of the fault may be attributed to the local clustering of solute atoms which presumably lowers the stacking fault energy, or locks the defect by a Suzuki mechanism [8].

Another common obstacle is that formed between extended dislocations on intersecting {111} slip planes. Three partial edge dislocations can react to form a Lomer–Cottrell sessile dislocation, with a stacking fault wedge. They can be generated by a dislocation reaction between two suitable chosen extended dislocations on intersecting {111} planes [11]. If a group of glissile dislocations is piled up against a Lomer-Cottrell dislocation, the width of the stacking fault wedge may be reduced. If this reduction is sufficiently large, the Lomer–Cottrell dislocation may collapse by becoming a glissile dislocation and gliding away. The stress acting on the leading dislocation of a pile-up of N dislocations is found by [11];

$$\tau_p = N\tau_r \tag{5}$$

If the number of dislocations in a pile-up and the applied stress acting on these dislocations are large enough, it is possible to bring the two partial dislocations of an extended screw dislocation completely together, making it easier for these
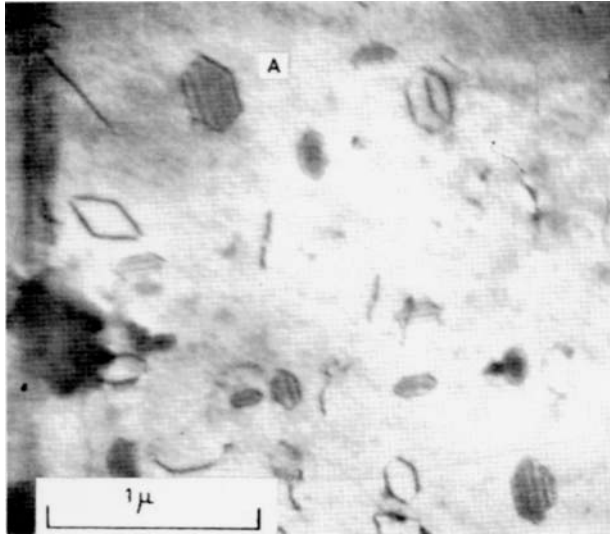
Figure 9 Frank sessile dislocation loops in an Al-3.5 wt% Mg alloy [40]. (Courtesy of Prof. R.E. Smallman, The University of Birmingham, United Kingdom).

dislocations to cross-slip [11]. In the case of screw dislocations piled up against a Lomer–Cottrell dislocation under increasing stress, the screw dislocations leave the pile-up by cross slip before the sessile dislocation collapses.

Dislocations that penetrate the glide plane more or less perpendicularly also contribute to the flow stress. These dislocations are called the *dislocation forest*. Depending on whether the dislocations that cut across one another are of the edge or screw type, the result may be the creation of a line of vacancies in the lattice.

DEFORMATION AND STRAIN HARDENING.   Deformation of metals occurs primarily by the motion of existing dislocations, and by the creation of new dislocations through mechanisms such as the Frank–Read source. Dislocation glide occurs on intersecting slip planes within the grain, and with mutual interference with slip planes from adjacent grains. For this gliding motion to start, the applied shear stress must be large enough to overcome the opposing action of the stress fields of the dislocations surrounding a moving (glissile) dislocation. The main contribution comes from dislocations which are roughly parallel to the glissile dislocation, and have the same Burgers vector. If these dislocations are distributed in a random pattern, and if the density per unit area is ρ_D, the increase in yield stress in given by [11,41];

$$\Delta\sigma_y = M\alpha Gb\sqrt{\rho_D} \tag{6}$$

where, α is a constant of the order 0.2–0.3, and its exact value depends on alloy composition.

During deformation, the dislocation density, ρ_D, increases when dislocation generation and multiplication occur faster than annihilation by dynamic recovery. The increase in dislocation density with increasing deformation in an Al-Li-Cu alloy

Figure 10 The increase in dislocation density with increasing deformation in an Al-Li-Cu alloy using data provided in Ref. 42.

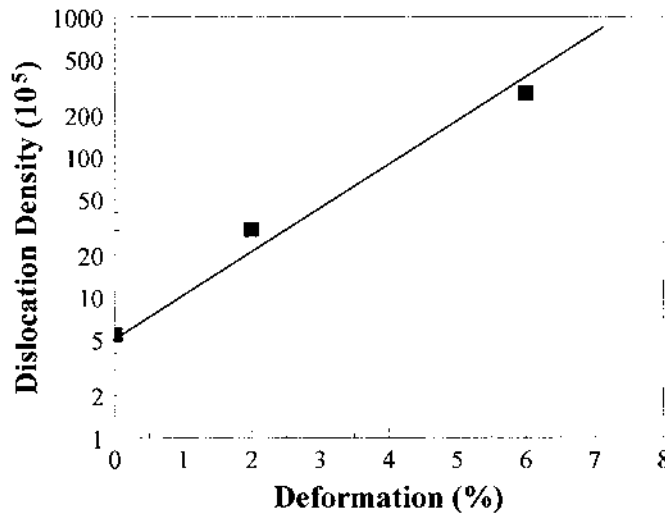is shown in Fig. 10. With deformation, dislocation tangles are formed, which decrease the mean slip distance, and result in increased strength. Therefore, the interactions of dislocations cause further deformation to become more difficult thus strengthening the metal through *strain hardening*. The initial strain hardening in pure aluminum is close to $G/20$, which represents the maximum value expected from dislocation storage [41]. The strain hardening decreases linearly with the stress, the rate of this decrease being slower when the deformation temperature is lowered.

The increase in strength with increasing dislocation density with deformation is used as a basis for certain deformation processes to obtain a given set of properties in a wrought product. The strengthening of a metal through these deformation processes is called *work hardening*, which is the principal means by which non-heat treatable alloys are strengthened. The most common means of work hardening in non-heat treatable aluminum alloys is by cold rolling of sheet and foil.

A part of the energy expended in deformation is stored in the deformed metal structure as dislocations and dislocation substructures. This energy acts as a thermodynamic driving force which tends to return the metal to its undeformed state if the temperature is raised sufficiently for the required reactions to occur at an appreciable rate. Thus as the temperature is raised, recovery and recrystallization return the metal to the fully annealed state. Therefore, work hardening is a suitable strengthening mechanism only for service conditions where the metal will never be heated to the point that softening will lower the strength below the design level.

In quenched aluminum foils given small amount of plastic deformation at room temperature, the dislocation loops combine with moving dislocations to form irregular, kinked dislocation lines [8]. Moreover, all loops are removed after only 5% reduction in thickness by cold-rolling, and as the amount of cold work is increased, the tangle of jogged dislocation lines gradually changes to a network of well-defined subgrains. The high flow stress observed in the stress-strain curve

for quenched aluminum in Fig. 7(a) can be qualitatively understood on this basis because the first dislocation to move appreciable distances become heavily jogged almost immediately by combination with loops [8].

THE EFFECT OF ALLOYING ADDITIONS ON STRAIN HARDENING. Solute atoms can have a dramatic effect upon the work and strain hardening behavior of Al. Solutes can enhance strain hardening through several possible mechanisms [43]; (i) precipitation during deformation; (ii) increasing the rate of dislocation multiplication; and (iii) reducing the rate of recovery. Precipitation was found [44] to play an important role in the strain aging behavior of Al-3 wt%Mg alloys. High rate of strain hardening in Al-Mg alloys has also been suggested [45] to be due to an increased rate of dislocation multiplication, and reduced rate of recovery. Evidence for the influence of solutes on recovery is based on the nature of the substructures in deformed material. Aluminum, because of its high stacking fault energy, undergoes extensive dynamic recovery during deformation, resulting in an as-formed microstructure of well-defined cells or subgrains. The substructure and texture formed at high temperatures in alloys closely resemble those formed in pure metals at low temperatures where recovery is slow. Hence the addition of solutes has the same effect as lowering the temperature, i.e. it slows down recovery processes [45]. Since the effect of dynamic recovery in lowering work-hardening rate is detrimental to formability [46], it is of great importance to suppress dynamic recovery in alloys designed for high formability.

From a practical viewpoint, the strain hardening response of materials which have the same tensile elongation can be expressed as the difference between the ultimate strength (UTS) and yield stress obtained in a tensile test. Figure 11 [39] shows the difference between UTS and YS for the alloys shown in Fig. 8(b) and (c). Figure 11 indicates that Cu is the most efficient in promoting strain hardening of Al, and continues to be effective even at levels where its effect on solution strengthening levels off (Fig. 8). Si also follows this same trend, although to a lesser extent than Cu. Mg shows good strain hardening potential while Zn has little effect on tensile strain hardening. In an early study [33] on the strain hardening behavior of binary alloys, it was found that the tensile stress-strain curves for alloys with different solutes could be made to coincide by comparing "equivalent" solute concentrations. Of the solutes tested, Cu is the most efficient in promoting strain hardening. The overall effect of solute elements can be expressed in terms of K, a term which represents the copper equivalent for 1 at% of various solute elements [33]. K is a function of the change in lattice parameter of the aluminum matrix upon alloying additions, and the difference in valence between solute and aluminum. The values of K reported are listed in Table 2. Following Table 2, for instance, a 1.0 at% Mg alloy would have a similar tensile strain hardening behavior to a 0.37 at% Cu alloy.

Another way of representing the work hardening behavior is in terms of the strain-hardening exponent, n, used in stress-strain relationship, defined by Hollomon [48];

$$\sigma_t = k \epsilon^n \tag{7}$$

k and n values for several commercial aluminum alloys are given in Table 3. Research at Alcoa laboratories [49] showed that the yield strength during cold rolling can be related to the true rolling strain ($\epsilon = \ln (T_i/T_f)$) following the above
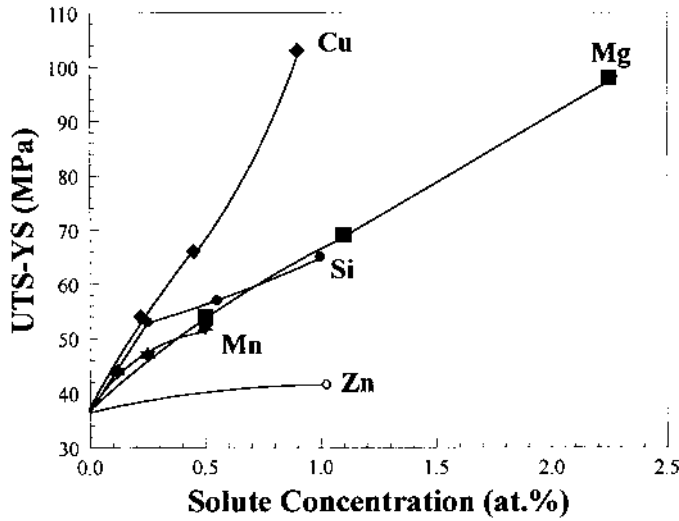
Figure 11 The difference between the ultimate strength (UTS) and yield strength obtained in a tensile test for various alloying additions in aluminum [Source Ref. 39].

Table 2 K Parameter Showing Cu Equivalent for 1 at% of Various Solute Elements, and Corresponding Doherty Solute Work Hardening Parameters

Element	K[†]	H (GPa)[‡]
Cu	1.00	3.38 ± 0.20
Ge	0.64	
Si		1.56 ± 0.05
Mg	0.37	1.52 ± 0.14
Mn		1.03 ± 0.17
Cd	0.33	
Ag	0.15	
Zn	0.071	0.27

[†]: Ref. 33; [‡] Ref. 47.

mentioned Hollomon equation;

$$YS = k\, \epsilon^n \tag{8}$$

Figure 12 shows the YS versus true rolling strain for several binary alloys. In rolling, as in tensile straining, all elements are not equally effective in promoting work hardening, and higher solute levels results in enhanced hardening.

The effect of the solute atoms on work hardening can also be expressed by comparing k values in Eq. (8) (YS after a true rolling strain of 1 (63% cold roll)) of aluminum and the alloy [47]. The Doherty solute work hardening parameter,

Table 3 Strain Hardening Parameters for Various
Commercial Alloys

Alloy	n	k (MPa)
1100 – O	0.242	146
3003 – O	0.242	188
6061 – O	0.209	224
5052 – O	0.198	281
5454 – O	0.189	340
5086 – O	0.193	368
5456 – O	0.178	479
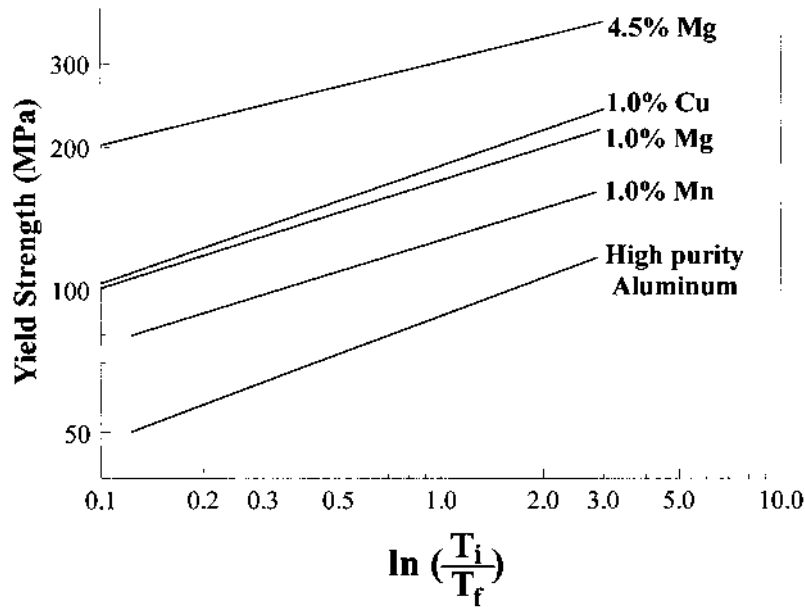
Figure 12 YS versus true rolling strain curves for several binary alloys [Source Ref. 39].

H, can then be expressed as;

$$H \text{ (solute)} = \frac{k_{alloy} - d_{Al}}{(\text{at. fraction solute})^{\frac{2}{3}}} \tag{9}$$

Within acceptable limits of scatter, each solute element can be characterized by an H parameter. The higher the H parameter, the more efficient the alloying additions in promoting work hardening during cold rolling. A list of H values for several elements are given in Table 2. It is evident in Table 2 that Cu is very effective in promoting work hardening during cold rolling. On per atom basis, Cu is the most efficient element of those shown in Table 2 in inhibiting dynamic recovery and promoting dislocation storage during cold rolling. Mg and Si are less effective than Cu, but still provide good enhancement of work hardening. Zn has little effect

on work hardening. In ternary alloy systems, Al-Mg-Si, Al-Zn-Mg and Al-Cu-Mg, work hardening is greater than the effect predicted by simply summing the effect of individual solutes.

Dislocation-Grain Boundary and -Substructure Interaction

A dislocation which reaches a grain boundary cannot continue its slip motion into another grain because of the difference between orientation of the slip planes and directions between two neighboring grains. Hence grain boundaries serve as obstacles to the movement of dislocations, which pile up near the boundaries. Therefore with decreasing grain size, less distance can be traveled by a glissile dislocation before reaching a grain boundary, resulting in higher strength. This strengthening mechanism is called *grain size hardening*. Strengthening due to grain size effects can be described by the Hall–Petch equation;

$$\sigma_{\mathrm{y}} = \sigma_{\mathrm{f}} + k_{\mathrm{l}} d^{-m} \tag{10}$$

The exponent, m, is $1/2$ for grain size hardening. Frictional stress, σ_{f}, and k_{l} are affected by alloy content, grain size uniformity and shape as well as crystallographic texture. σ_{f} is 10 MPa for pure aluminum [50], and increases with increasing alloy content. Since grain size is not a major factor in increasing strength in commercial alloys, k_{l} is relatively low for Al alloys (0.065 MPam $^{-1/2}$ for pure aluminum [31] and 0.1–0.2 MPam$^{-1/2}$ for many aluminum alloys [2]). It is the experience of one of the authors (JTS) that grain boundaries and subgrains do not provide significant strengthening in heat treatable alloys. However strength of unrecrystallized material is higher when a strong texture is formed, particularly in extruded products. This texture strengthening is lost when the material recrystallizes. Nevertheless grain size effects do become significant when the alloy is underaged, and consequently precipitates are sheared by glissible dislocations [51], and also in nonheat-treatable Al-Mg alloys [52].

Aluminum disfavors localized slip due to its extremely high stacking fault energy [53]. However when precipitates smaller than a critical size are present in the alloy, localized slip is observed, since the precipitates can be readily sheared by glissile dislocations. Consequently grain size effects become important to minimize the detrimental effect of localized slip. The yield strength of recrystallized 7475 alloy as a function of temper and grain size is shown in Fig. 13. Note in Fig. 13 that the sensitivity of yield strength to grain size is much lower when the alloy is overaged than when it is underaged. The combined effect of heat treatment and grain size effects has also been reported for Al-Mg-Si alloys [54,55].

Even though a reduction in grain size may increase strength in some cases, extremely fine grain sizes are undesirable for formability and fracture toughness. During forming operations, grain boundaries can act as sinks for dislocations, and lead to a loss in strain hardening capacity and uniform elongation [56]. During fracture, an extremely fine grain size reduces the fracture toughness by decreasing crack tortuosity [53].

The high stacking fault energy of aluminum and consequent development of well-defined subgrains during deformation make it responsive to *substructure hardening*, which also follows Eq. (10). The exponent m in Eq. (10) varies between $1/2$ and 1 in substructure hardening. The substructures produced at low homologous temperatures are usually called *cells*, and have walls consisting of tangled dis-
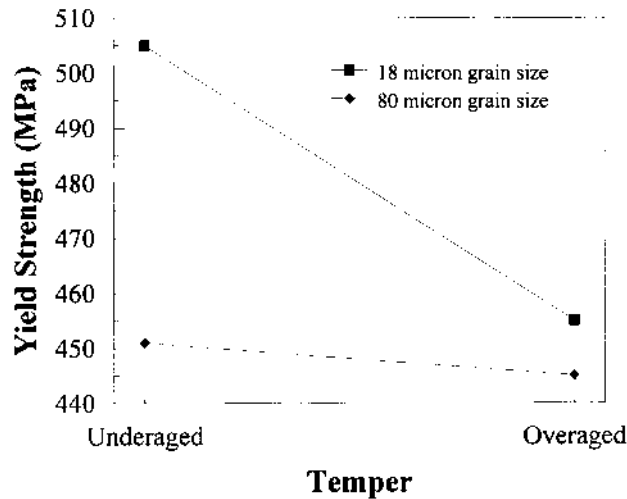
Figure 13 The yield strength of recrystallized 7475 alloy as a function of temper and grain size, using data provided in Ref. 51.

locations, whereas the substructures produced at higher temperatures are referred to as *subgrains*, and have narrow, well-defined walls. The value of *m* varies from 1 to 1/2 as recovery proceeds or as cells approach subgrains, and this trend is probably related to the impenetrable character of subgrain boundaries [57,58]. The subgrains formed during hot working are more effective for substructure strengthening, $m \approx 1/2$, than the cells produced during low temperature deformation, $m \approx 1$.

A series of wrought aluminum alloys (some of the 8XXX series) have been developed with a very fine grain strcuture stabilized by a nearly uniform dispersion of fine particles. The tensile properties of these alloys have a stronger grain size dependence ($m \approx 1$) than observed in coarser grained materials [59]. The strong grain size hardening effect is, unfortunately, accompanied by a loss of further hardening ability during tensile deformation; the small mean free path of dislocations, which is limited by the grain size, results in less dislocation–dislocation interaction. At very small grain sizes (~ 1 μm), this lack of work-hardenability can severely limit tensile ductility at room temperature.

Dislocation-Particle Interactions

Hard, minority-phase particles inhibit the movement of dislocations, and therefore, increase strength. If these particles are non-deformable, the strengthening mechanism is called *dispersion strengthening*. However if strengthening is due to the presence of coherent precipitates which are capable of being sheared by dislocations, then the mechanism is called either *precipitation hardening* or *age hardening*. Dispersion strengthening in aluminum alloy products is provided by dispersoids, which form by solid state precipitation, either during ingot preheating or during the thermal heat treatment of cast shapes. Dispersoids are composed of slow diffusing elements, which are soluble in molten aluminum but which have limited solubility in solid aluminum. Mn, Cr, and Zr are typical dispersoid forming elements. Unlike

the precipitates which confer precipitation hardening, dispersoids are virtually impossible to dissolve completely. More discussion about dispersoids and precipitates is provided later in this chapter.

AGE HARDENING. Precipitates form during aging, at either an ambient or elevated temperature, in alloy systems which have a sloping solvus line, i.e. decreasing solid solubility with decreasing temperature. Details regarding precipitation during aging will be discussed later in this chapter.

Depending on the size, spacing, and degree of coherency, precipitate particles are either sheared, or looped and bypassed by the dislocations during plastic deformation. Small particles which are coherent or partially coherent with the matrix are sheared by moving dislocations. Consequently the strengthening mechanisms associated with the presence of particles are reduced. This results, successively, in a local decrease in resistance to further dislocation motion, concentration of slip, and destruction of the strengthening agents. Sheared precipitates and localized slip in an Al-8.1 at% Li, are shown in Fig. 14 (a) and (b). Coherent δ' (Al$_3$Li) are sheared by glissile dislocations in Fig. 14, and slip is localized, as shown with arrows. For this cutting mechanism, increase in strength due to the interaction of a glissile dislocation with the particle can be represented by;

$$\Delta \sigma_{\mathrm{y}} = c f^m r_{\mathrm{P}}^q \tag{11}$$

The exponents m and q are always positive, usually around 0.5, and strength increases with both volume fraction and particle size. The relationship between precipitate radius (r_{P}) and CRSS in an Al-Li alloy is shown in Fig. 15. As particles grow, coherency strains build up, and are finally released when the particles become incoherent, e.g. during the transformation from the transition phase to the equilibrium phase, as depicted in Fig. 16. At this stage, dislocations are created at the interface between the precipitate and the matrix as a result of the misfit stresses. The loss of coherency is accompanied with a change in particle-dislocation interaction from one of shearing, to that of dislocation looping or by-passing, Fig. 17. This results in a significant increase in resistance to dislocation motion, and this strengthening mechanism is referred to as *Orowan Strengthening (or looping)*. Strengthening is obtained due to formation of dislocation loops around the precipitates that have attained a critical size, and therefore can no longer be sheared by glissile dislocations. This also increases the strain hardening rate. A graphical explanation of Orowan looping for a pure edge dislocation is given in Fig. 18 [61]. In Fig. 18(a), the dislocation has been held up by a set of particles intersecting the slip plane. As the applied stress rises, the screw components of the dislocation, formed when the dislocation took up the shape shown in *a*, cross slip, as shown in *b*. These screw components are of opposite sign on each side of a single particle. Consequently they attract each other, as in *c*, and annihilate each other, as depicted in *d*. The process leaves a prismatic loop around each particle and corresponding prismatic jogs in the dislocation line. Any dislocation with an edge component behaves in a similar way. After maximum strength is obtained, strength is related to precipitate size, following the equation [62];

$$\Delta \sigma_{\mathrm{y}} = \beta r_{\mathrm{P}}^{-1} f^{0.5} \tag{12}$$

It has been shown [63] recently that f in Eq. (12) is not constant since the solute

(a)

(b)
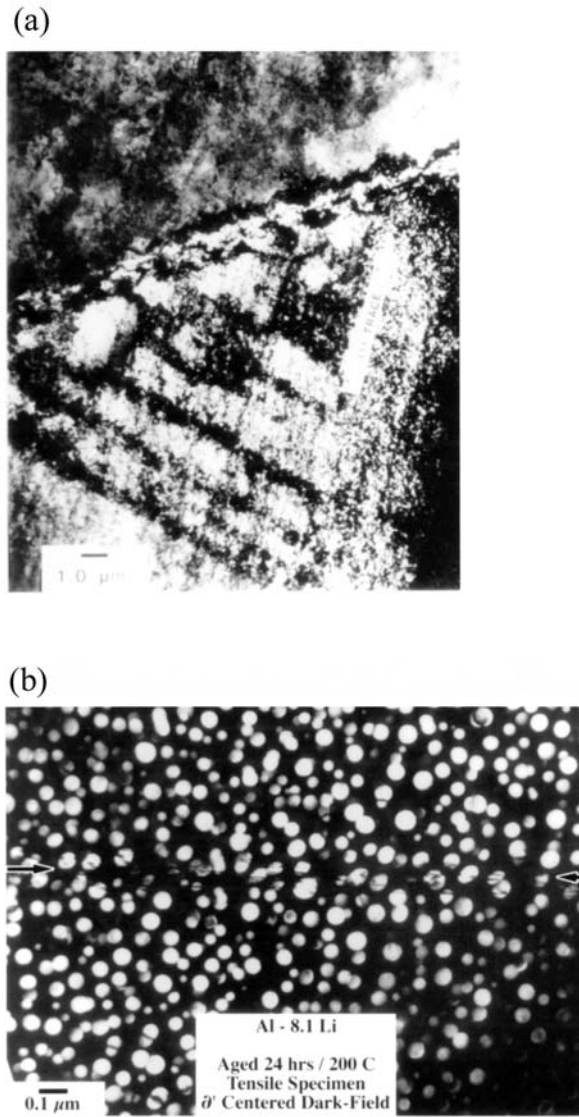
Figure 14 Deformation structure near the fracture surface of an Al-2 wt% Li alloy. (a) Strain localization in the vicinity of grain boundary; (b) Sheared Al₃Li precipitates within slip band. (Courtesy of Prof. E. A. Starke, Jr., University of Virginia).

concentration of solute in the matrix phase changes as the dispersion coarsens. A more detailed discussion on this subject is provided in Ref. 63. The critical diameter at which the transition occurs for a noncoherent particle with a different crystal structure is given by [53,64,65];

$$(D_p)_{s \to b} = \frac{4\pi b C \, G_{Al}}{G_{particle}} \tag{13}$$
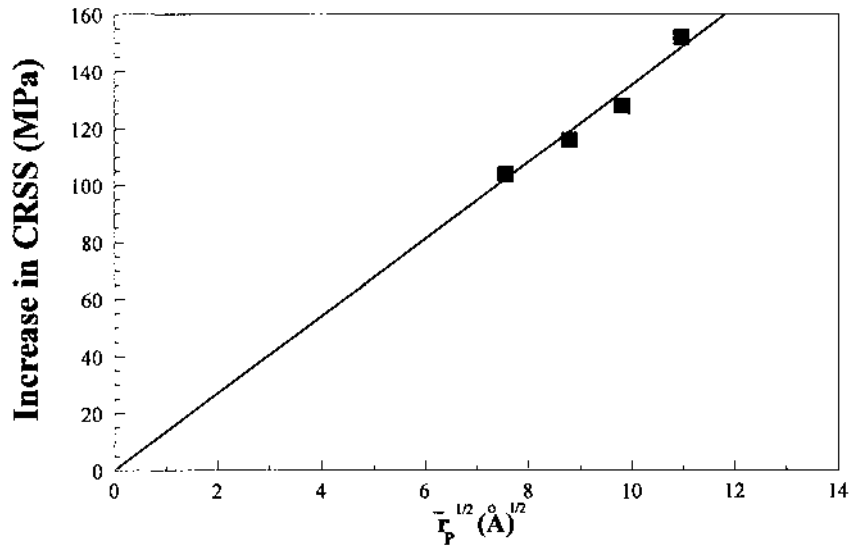
Figure 15 The relationship between precipitate radius (r_p) and CRSS in an Al-Li alloy. Data provided in Ref. 60.
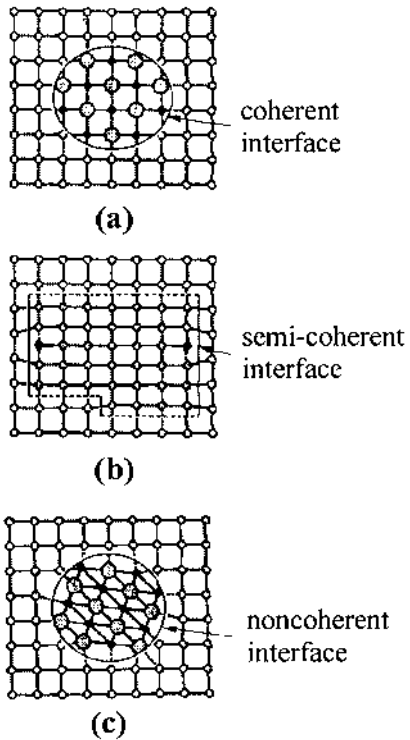
Figure 16 Structural relations between matrix and precipitate [Source Ref. 53]. (a) Coherent, stress-free, ordered particle (δ'-Al$_3$Li); (b) partially coherent precipitate (θ', Cu$_2$Al; β', Mg$_2$Si); (c) noncoherent precipitate (θ, Cu$_2$Al; Si).
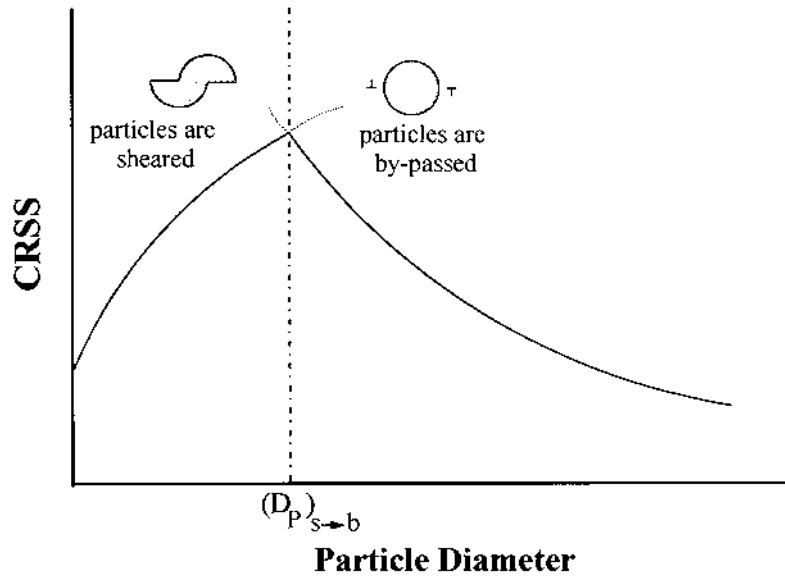
Figure 17 Change in CRSS as a function of precipitate size. Maximum strength is obtained where the dislocation-precipitate interaction changes from shearing to by-passing (looping).
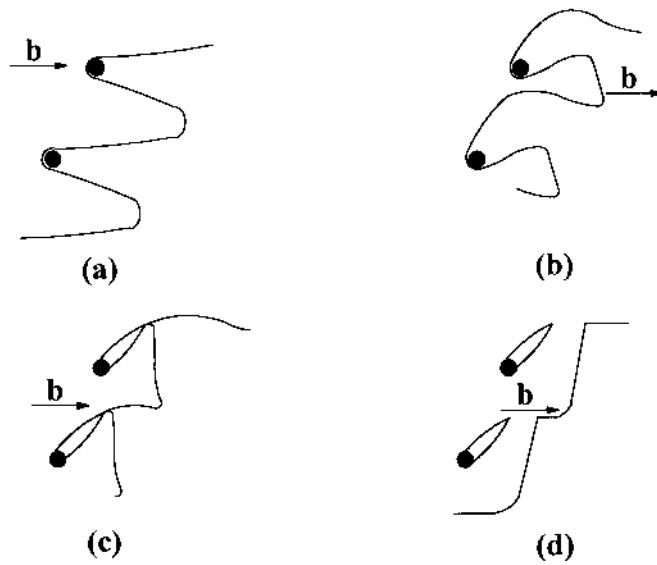
Figure 18 A graphical explanation of Orowan looping for a pure edge dislocation.

for an ordered, coherent, stress-free particle [53];

$$(D_p)_{s \to b} = \frac{G_{Al} b^2}{\gamma_{APB}} \tag{14}$$

Table 4 A List of Calculated and Experimental Critical Precipitate Sizes in Aluminum Alloys

Particles	$(D_p)_{s \to b}$	Comments	Reference
Diamond (Ge)	0.2		66
Si, FeAl$_3$, CuAl$_2$	0.5–5		66
Zn	15		66
δ'(Al$_3$Li)	50	Passage of single dislocations	66
	> 500	Dislocation pairs	66
T$_1$	0.8†		65
S$'$	2		65
η'	6‡		67

†: critical plate thickness; ‡: experimental finding.

C is a dimensionless parameter determined by the shape of the particle [66], and is close to unity for spherical particles. A list of estimated critical particle diameters in aluminum alloys is presented in Table 4. $(D_p)_{s \to b}$ represents the maximum effective diameter of a precipitate. For more discussion on the calculation of the critical particle diameter, see Ref. 65.

The transition in dislocation–particle interaction from shearing to by-passing tends to increase work hardening rate with strain due to the formation of a dislocation forest [68], and homogenizes deformation, which usually results in an improvement of ductility and stress–corrosion resistance, but usually a decrease in fracture toughness and fatigue crack propagation resistance [69].

The increase in CRSS due to Orowan looping, ΔCRSS$_{Ol}$, can also be represented to include the effect of particle spacing, λ, by [70];

$$\Delta \text{CRSS}_{Ol} = \frac{2GB}{4\pi\sqrt{1-v}} \frac{1}{\lambda} \ln\left(\frac{D_p}{r_0}\right) \qquad (15)$$

Maximum hardening is expected when the spacing between particles is equal to the limiting radius of curvature of glissile dislocations, i.e. about 50 atomic spacings or 10 nm [71].

GP ZONES AND INTERMEDIATE PRECIPITATES. The strength of an age hardened alloy depends on the ability of the precipitates to resist the movement of dislocations during deformation. Individual GP zones have only a slight effect in this regard, because they are readily sheared by glissile dislocations; the stress required to shear GP zones is an order of magnitude less than that necessary to force dislocation loops between precipitate particles [72]. Nevertheless the presence of GP zones normally delays the activation of dislocations due to their high volume fraction, and therefore causes a large increase in yield strength.

Misfit between GP zones and the aluminum matrix determines the shape of GP zones. Because of the small difference in volume between equal numbers of aluminum alloys and of clusters of aluminum, zinc and magnesium atoms, aluminum alloys containing zinc and magnesium develop zones which maintain an approximately spherical morphology during natural aging and in the initial stages of arti-

ficial aging. In contrast, clusters of aluminum, copper, and magnesium atoms occupy a smaller volume than equal numbers of aluminum atoms. Consequently Al-Cu-Mg alloys, such as 2024, develop platelike zones surrounded by an elastic strain field.

Once GP zones are sheared, dislocations may continue to pass through the same particles, and deformation then tends to become localized on the active slip planes so that intense slip bands develop. Consequently dislocations pile up at grain boundaries and a microstructure which may lead to an increased tendency for intergranular fracture, develops.

Intermediate precipitates usually resist shearing by dislocations, and they are more stable at elevated temperatures. However, when they are widely spaced, they can usually be by-passed by moving dislocations. The greatest impedance to dislocation motion, and hence greatest potential for strengthening occurs when an alloy contains precipitates that are large enough to resist shearing by dislocations, and yet are too finely spaced (interparticle distance ~ 10 nm) to be by-passed [73]. This is, however, difficult to achieve in practical aluminum alloys, and maximum response to hardening is usually observed when the microstructure contains a combination of large, closely spaced, shearable GP zones and more widely spaced intermediate precipitates.

Applied and residual stresses may change the stability of a phase, and may move the solvus line either into the single-phase or two-phase region. Consequently, externally applied stresses and internal stresses associated with second phase particles can affect both nucleation and growth of precipitates and subsequently their coarsening behavior. If precipitation occurs preferentially on certain habit planes due to the applied stresses, an anisotropy of strength properties may result.

THE EFFECT OF PRECIPITATE SHAPE. The particles may form in a variety of shapes (e.g. spheres, discs, and rods), depending on the misfit between particle and the matrix, and the interfacial energy. The shape that occurs generally minimizes the total energy associated with the formation of the particle. For instance, when the atomic misfit is very small, spherical particles are formed. However when the atomic misfit is large, the particles generally assume the shape of discs or rods to minimize the strain energy [69]. Although atomic misfit is a potent strengthener, it adversely affects ductility, and enhances precipitate coarsening rate at elevated temperatures [68].

The effect of particle shape on λ and D_p in Eq. (15) for aluminum is given in Table 5. λ varies with the shape, orientation and distribution of the particles. For a given volume fraction and number density of precipitates per unit volume, ΔCRSS produced by $\{111\}_\alpha$ plates is invariably larger than that produced by $\{100\}_\alpha$ plates, and for both precipitate orientations, ΔCRSS increases with an increase in plate aspect ratio [70]. When the aspect ratio of the plates exceeds a critical value, the $\{111\}_\alpha$ or $\{100\}_\alpha$ plates both form an essentially closed, continuous network. Provided that the plates resist shearing by glissile dislocations, the dislocations generated within the tetrahedral or cubic volumes cannot escape, and in the limit, the theoretical ΔCRSS is infinitely large. In practice, however, accumulation of dislocations will lead to local stress concentrations exceeding the yield strength of precipitates, and result in precipitate shearing. Also plate shaped precipitates formed on the $\{111\}_\alpha$ and $\{100\}_\alpha$ planes are more effective in reducing λ than rod shaped precipitates formed in $\langle 100 \rangle_\alpha$ directions. Plate shaped precipitates provide a much more effective barrier to glissile dislocations than either rod-shaped

Table 5 The Effect of Precipitate Shape and Orientation on Orowan Strengthening (*Source*: Refs 70 and 74)

Shape and Orientation	λ	D_p
Randomly Oriented Spheres	$0.538 D_s \left(\dfrac{2\pi}{3f}\right)^{0.5} - \dfrac{\pi D_s}{4}$	D_s
Randomly Oriented Plates	$\dfrac{D_{PL}}{C} \left(1 - \dfrac{\pi TC}{2D_{PL}}\right); C = \left(\dfrac{f D_{PL}}{T}\right)^{0.5} + \left(\dfrac{2}{\pi} - \dfrac{\pi T}{2D_{PL}}\right)\dfrac{f D_{PL}}{T}$	$1.414 D_R$
Randomly Oriented Rods	$D_R \left(\dfrac{\pi}{2f}\right)^{0.5} - D_R$	$1.414 D_R$
$\{100\}_\alpha$ Plates	$0.931 \left(\dfrac{0.306 \pi D_{PL} T}{f}\right)^{0.5} - \dfrac{\pi D_{PL}}{8} - 1.061 T$	$1.225 T$
$\{111\}_\alpha$ Plates	$0.931 \left(\dfrac{0.265 \pi D_{PL} T}{f}\right)^{0.5} - \dfrac{\pi D_{PL}}{8} - 0.919 T$	$1.061 T$
$\langle 100 \rangle_\alpha$ Rods	$1.075 D_R \left(\dfrac{0.433 \pi}{f}\right)^{0.5} - 1.316 D_R$	$1.316 D_R$

or spherical precipitates. For $\langle 100 \rangle_\alpha$ precipitate rods that are resistant to shearing, the Orowan increment in CRSS is invariably larger than that produced by spherical precipitates.

PRECIPITATE SIZE DISTRIBUTION. In a precipitation hardened alloy, not all precipitates have the same size, i.e. there exists a distribution of precipitate sizes, and hence a distribution of obstacle strengths. Even in monodisperse spherical particles, the obstacle strength distribution still exists since these particles will be cut at various cross-sections [75]. Since the value of the CRSS depends more strongly on the precipitate size after by-passing begins than before, peak strength will occur almost immediately after the largest of the precipitates reaches $(D_p)_{a \rightarrow b}$ not when the average sized precipitate reaches $(D_p)_{s \rightarrow b}$. The amount of strengthening provided by the precipitates is most closely related to the average precipitate size. Consequently, the maximum achievable strength increases as the precipitate size distribution narrows. As illustrated in Fig. 19, when the largest precipitates reach $(D_p)_{s \rightarrow b}$ the average precipitate diameter of a narrow distribution is greater than the average diameter for a broad distribution. The strength of the narrow distribution is correspondingly higher [27,76]. Thus CRSS at peak strength is maximized if all precipitates are the same size. In addition, $(D_p)_{s \rightarrow b}$ is not constant for a particular alloy system, and changes with precipitate spacing, i.e. total volume fraction of precipitates [76].

In aluminum alloys, which are strengthened by metastable precipitates, isothermal aging can produce microstructures containing more than one type of precipitate, each of which can strengthen the matrix by a separate mechanism. The distribution of obstacle strengths under these circumstances will generally
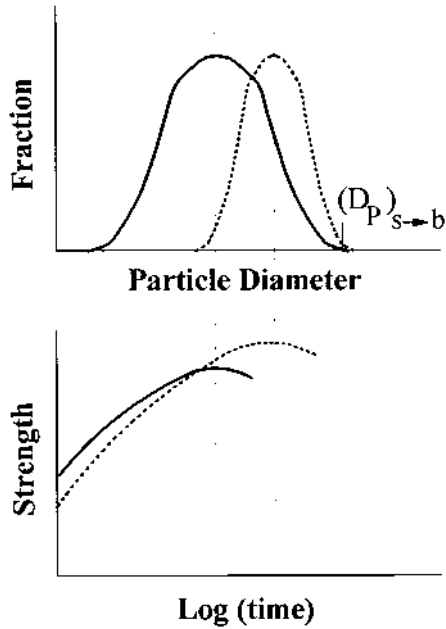
Figure 19   The effect of precipitate size distribution on aging curve. Peak strength occurs almost immediately after the largest of the precipitates reaches $(D_p)_{s \to b}$. The amount of strengthening provided by the precipitates is, however, most closely related to the average precipitate size.

be far broader than that due to the presence of a single type of precipitate [75]. Also some commercial alloys are subjected to dual aging treatments, which can produce polymodal particle size distributions.

PRECIPITATION HARDENING MECHANISMS OTHER THAN OROWAN LOOPING.   Precipitation strengthening can also be due to: (i) chemical strengthening; (ii) stacking-fault strengthening; (iii) modulus strengthening; (iv) coherency strengthening; and (v) order strengthening. In many alloy systems, two or more of these mechanisms are operative simultaneously. For a more detailed discussion of these mechanisms, reader is advised to refer to the excellent review provided in Ref. 75.

The passage of a dislocation through the precipitate creates two ledges of a new precipitate-matrix interface of specific energy, γ_s. Therefore the resultant increase in strength can be written as [72];

$$\Delta \text{CRSS}_c = \left(\frac{6\gamma_s^3 bf}{pi\Gamma} \right)^{\frac{1}{2}} (r_p)^{-1} \tag{16}$$

Chemical strengthening is effective only when the precipitates are small. Chemical strengthening has been suggested [77] as the hardening mechanism in the Al-Zn system, although this can only be valid for short aging times; strength is inversely dependent on the particle size, and requires an increasing particle volume fraction to provide strengthening.
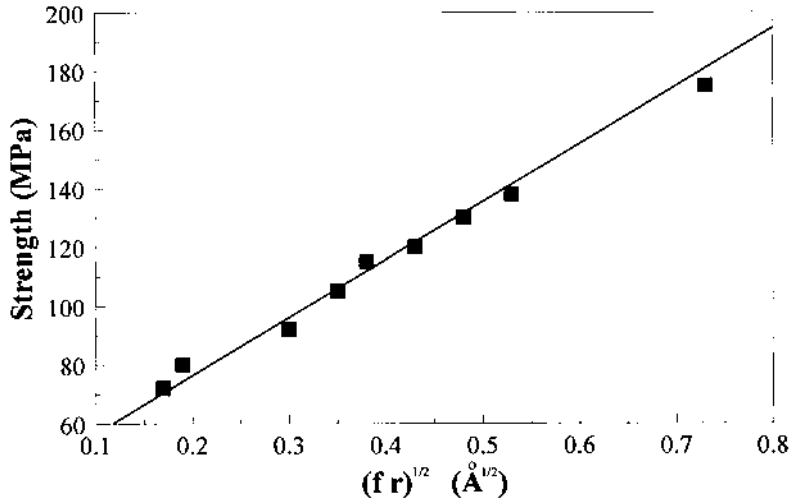
Figure 20 Stacking fault strengthening in an Al-Zn-Mg alloy (Source Ref. 79). The slope of the line indicates a γ of 350 mJ/m^2 for GP zones.

When the stacking fault energies of the precipitate and matrix phases differ, the motion of the dislocations will be impeded because the separation of the partial dislocations varies depending upon the phase in which the dislocations reside. The increase in CRSS of underaged alloys due to stacking fault strengthening varies as [78];

$$\Delta \mathrm{CRSS}_{\mathrm{sf}} = \Delta \gamma^{15} \left(\frac{3\pi^2 f\, r_{\mathrm{p}}}{32\,\Gamma\,b^2} \right)^{0.5} \tag{17}$$

The strengthening in Al-Ag alloys is explained by stacking fault strengthening [78], which is also responsible for strengthening due to GP zones in Al-Zn-Mg alloys [79]. This relationship is depicted in Fig. 20 for an Al-Zn-Mg alloy. The slope of the line in Fig. 20 indicates a γ of 350 mJ/m^2 for GP zones.

The energy of a dislocation is a function of the shear modulus of the lattice in which it resides. As a dislocation moves from the matrix into a particle of different shear modulus, there is a change in the dislocation energy, and hence, an interaction force between the dislocation and the particle. Therefore, modulus strengthening is due to the difference in elastic moduli of the matrix and the precipitate. For small particle sizes, the increase in CRSS can be explained by [80];

$$\Delta \mathrm{CRSS}_{\mathrm{m}} = 0.9(r_p f)^{0.5} \frac{\Gamma}{b} \left(\frac{\Delta G}{G} \right)^{1.5} \left[2b\, \ln \left(\frac{2r_{\mathrm{p}}}{f^{0.5} b} \right) \right]^{-1.5} \tag{18}$$

Strengthening due to GP zones in Al-Zn-Mg alloys has also been attributed [80] to modulus strengthening, but peak aged strengths benefit from an additional hardening due to Orowan strengthening. In another study on Al-Zn-Mg alloys [81], strength was found to be change linearly with $(fr_P)^{0.5}$, but slope was dependent on aging
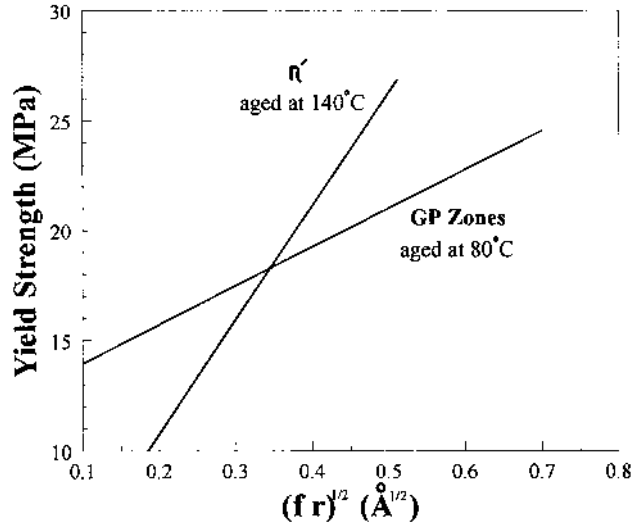
Figure 21 Modulus strengthening in Al-Zn-Mg alloys (Source Ref. 81). Aged strength changes linearly with $(f\,r_P)^{0.5}$, but slope is dependent on aging temperature. At the lower temperatures, the particles should be primarily GP zones, while at higher aging temperatures, the η' (MgZn$_2$) should be dominant.

temperature, as depicted in Fig. 21. At the lower temperatures, the particles are expected to be primarily GP zones, while at higher aging temperatures, the η' (MgZn$_2$) is expected to be dominant. There is also significant modulus strengthening in Al-Li alloys [30]. In those alloys, where aging is accompanied by a significant change in the volume fraction of particles and overaging is still accompanied by particle shear, modulus strengthening could be very important [82]. In aluminum alloys, Al-Zn-Mg, Al-Cu and Al-Cu-Mg are such systems. Unfortunately, the moduli of precipitate phases are largely unknown, and can be estimated only indirectly, making comparison between experiment and theory difficult.

The strengthening of alloys by misfitting coherent precipitates occurs as a result of the interaction between the stress fields of the precipitates and the dislocation. The increase in CRSS due to coherency strengthening is given by [28];

$$\Delta\mathrm{CRSS_{co}} = 1.2 f^{0.5}\left(\frac{\Gamma^3\,G\,\epsilon}{b^3\,r_\mathrm{p}^3}\right)^{0.25} \tag{19}$$

where

$$\epsilon = \left(\frac{a_p - a_\mathrm{Al}}{a_\mathrm{Al}}\right)\left[1 + \frac{2G(1 - 2v_\mathrm{p})}{G_p\,(1 + v_\mathrm{p})}\right] \tag{20}$$

Coherency strengthening can be expected to contribute to strength development in alloys, where coherent particles are tetragonally distorted and non-spherical, such as in Al-Cu alloys. It has recently been suggested that precipitate-dislocation inter-

action in Al-Zn-Mg and Al-Zn alloys is governed by coherency strengthening [83]. However, limited information is available in the literature on coherency strengthening in aluminum alloys.

Strengthening by ordered precipitates occurs when a matrix dislocation shears an ordered precipitate and creates an antiphase boundary (APB) on the slip plane of the precipitate phase. The APB energy per unit area on the slip plane, γ_{APB}, represents the force per unit length opposing the motion of the dislocation as it penetrates the particle. It is a characteristic of alloys strengthened by ordered precipitates that dislocations travel in groups, the number of dislocations in the group being determined by the number required to restore perfect order in the precipitate. The increase in CRSS is given by [75];

$$\Delta \text{CRSS}_o = \left(\frac{3\pi^2\, \gamma_{APB}^3 f\, r_p}{128\, b^2\, \Gamma}\right)^{0.5} \tag{21}$$

Order strengthening can account for the strengthening in Al-Li alloys, where the strengthening phase is ordered Al_3Li (δ') phase. Although in binary Al-Li alloys, strengthening was found [30] to be due to combined effect of modulus hardening and order strengthening, strengthening due to δ' phase in two Al-Li-Cu alloys has been found [84] to follow Eq. (21). Also order strengthening was suggested [85] to be the strengthening mechanism in Al-Mg-Si alloys with rod shaped β' precipitates.

1.2.7   Combination of Strengthening Mechanisms

In commercial alloys, usually more than one strengthening mechanism is in effect. For instance, the matrix is rarely pure, but contains solute atoms which are themselves obstacles to glide of dislocations. Other strengthening mechanisms, such as grain size effects, may also play a role in the strength of the alloy. Also some alloys contain more than one precipitate type, and each will make its own contribution to the strength of the alloy.

The total strength of an alloy can be considered as the sum of several components;

$$\sigma_\tau = \sigma_f + \Sigma\, \Delta\sigma_i \tag{22}$$

$\Delta\sigma_i$ representing the strength contribution of distinct strengthening mechanisms. As mentioned previously, σ_f is 10 MPa for pure Al. When several precipitate phases are present, their combined contribution can be found following a general superposition equation [75,84];

$$\Delta\sigma_p^q = \Delta\sigma_{p1}^q + \Delta\sigma_{p2}^q + \Delta\sigma_{p3}^q + \cdots\cdots \tag{23}$$

Although q in Eq. (23) is usually assumed to be 2, experimental findings are best represented when q is 1.5 [84]. An excellent example of the use of Eqs (22) and (23) has been provided in Ref. 82, using an Al-2.5 wt% Li-1.2 wt% Cu-0.7 wt% Mg-0.1 wt% Zr alloy. The contributions of alloying additions to strength are shown in Fig. 22. The Al-Li component of the alloy precipitates the ordered δ' phase, which provides order hardening. The Al-Cu-Mg component of the alloy precipitates S phase (Al_2CuMg), which could give stacking fault, modulus or coherency strengthening.
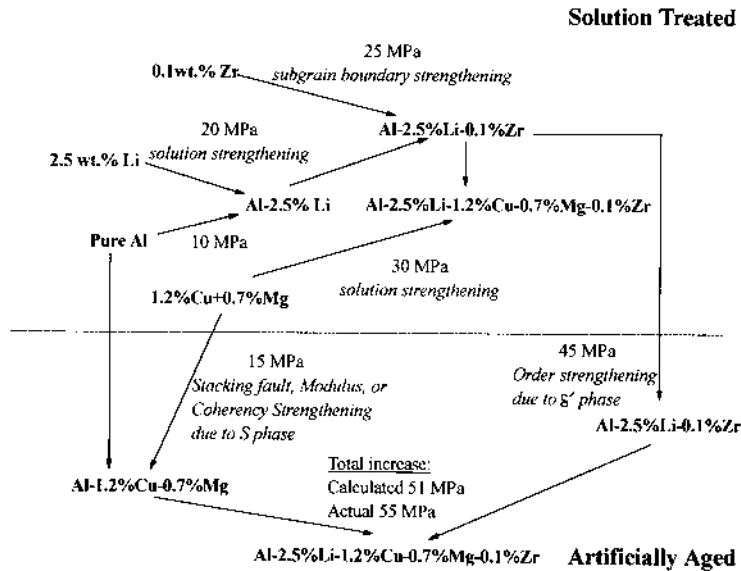
Figure 22 Contributions of alloying elements to the strength of an Al-2.5 wt% Li-1.2 wt% Cu-0.7 wt% Mg-0.1 wt% Zr alloy in solution treated and artificially aged condition.

Zr addition gives rise to the precipitation of Al_3Zr dispersoids, which may not provide significant dispersion strengthening (due to its low volume fraction). However Al_3Zr dispersoids prevents recrystallization [86], and consequently, give extensive grain boundary and subgrain boundary strengthening. The Al-2.5 wt% Li binary alloy has a solution treated strength of 30 MPa, but Zr addition increases strength to 55 MPa. With Cu and Mg additions, solution treated strength increases to 85 MPa. Hence the grain size contribution is 25 MPa (55–30), the solution strengthening due to lithium is 20 MPa (30–10), and strengthening due to combined addition of Mg and Cu is 30 MPa (85–55). Peak aged strength of Zr containing Al-Li alloy is 100 MPa, so that $\Delta\sigma_{\delta'}$ is 45 MPa (100–55). The increase in strength of an Al-1.2 wt% Cu-0.6 wt% Mg alloy after aging ($\Delta\sigma_s$) is 15 MPa. Therefore a combined strengthening on aging of $(45^{1.5} + 15^{1.5})^{1/1.5} = 51$ MPa, which is in agreement with experimental findings (55 MPa after 24 hr at 190°C).

2 THE EFFECT OF ALLOYING ELEMENTS ON PROPERTIES OF ALUMINUM ALLOYS

Alloying elements affect properties of aluminum alloys in a variety of ways. If hard, nonductile particles of a second phase are formed, strong barriers are produced. Edge dislocations are repelled by such particles and screw dislocations have difficulty in bypassing them. Even in solid-solution alloys, the ease with which screw dislocations may cross-slip is markedly affected, contributing to solid solution strengthening. The presence of particles, which constitute strong barriers to dislo-

cation movement, affects work hardening rates as well. When particles of a second phase are present, the slopes of the stress-strain curves are markedly increased.

2.1 The Use of Equilibrium Phase Diagrams

Although few products are sold and used in their equilibrium condition, equilibrium phase diagrams are an essential tool in understanding effects of composition and both solidification and solid state thermal processing on microstructure. For aluminum alloys, phase diagrams are used to determine solidification and melting temperatures, the solidification path, and the equilibrium phases that form and their dissolution temperatures. In addition to determining appropriate temperatures for casting and thermal treatments, phase diagrams are used to determine the maximum levels for ancillary element additions of certain elements to prevent the crystallization of coarse primary particles.

 The most important liquid–solid transformations for aluminum alloys are the eutectic and the peritectic. The Al-Cu system contains a typical eutectic reaction at 548°C, Fig. 23. During solidification of hypoeutectic alloys (those containing less
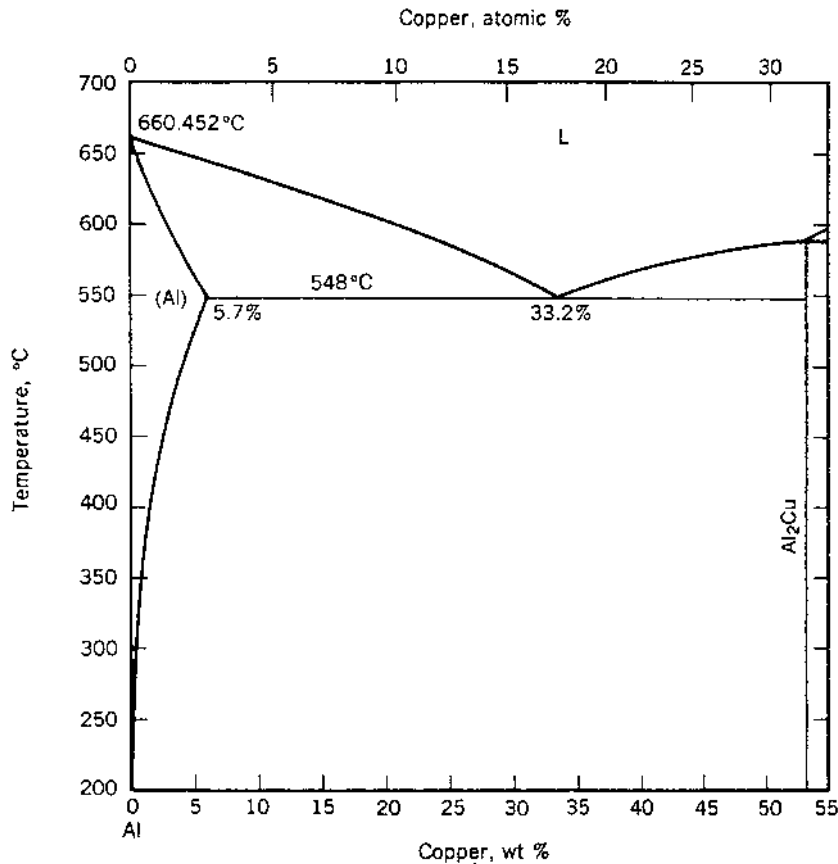
Figure 23 Al-rich corner of Al-Cu phase diagram. Drawn by Dr. Joanne Murray. (Courtesy of Alcoa).

Chromium, atomic %
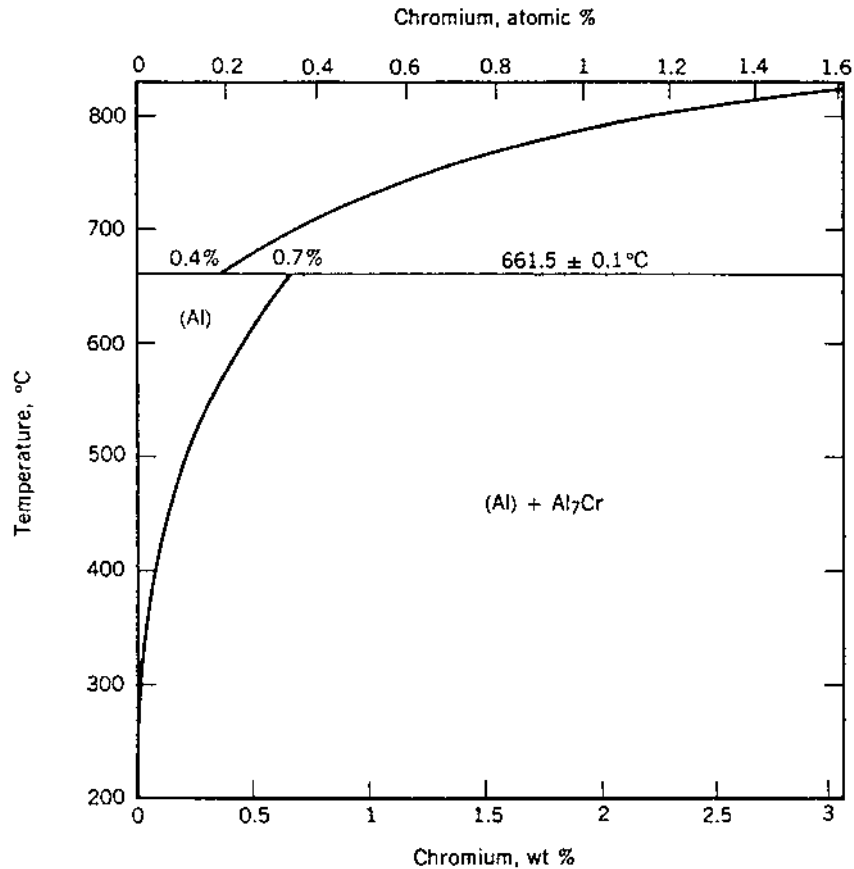
Figure 24   Al-Cr phase diagram. Drawn by Dr. Joanne Murray. (Courtesy of Alcoa).

than the eutectic composition, 33.2% Cu), an aluminum rich phase (α-aluminum) forms initially. When the temperature falls to the eutectic temperature, the remaining liquid separates into α-aluminum and an intermetallic compound, Al_2Cu. The Al-Cr system exhibits a typical peritectic reaction at 661°C, Fig. 24. During solidification of alloys containing more than the peritectic composition, 0.41% Cr, but less than 0.77, maximum solid solubility, an intermetallic compound, Al_7Cr, forms first. When the temperature falls to the peritectic temperature, the remaining liquid along with the Al_7Cr transforms to α-aluminum under equilibrium conditions. Under commercial solidification conditions, however, the primary particles of Al_7Cr would not have the opportunity to transform to α-aluminum, so they would be retained in the solid.

Virtually all aluminum alloys contain some Fe which is an impurity remaining after refining bauxite and smelting. The phase diagram presented in Fig. 25 predicts that during solidification of an Al-Fe alloy containing a few tenths of a percent of iron, most of the iron remains in the liquid phase until a eutectic of solid solution plus Al_3Fe intermetallic constituent particles having a monoclinic crystal structure freezes. Depending on solidification rate and on the presence of other elements such

Iron, atomic %
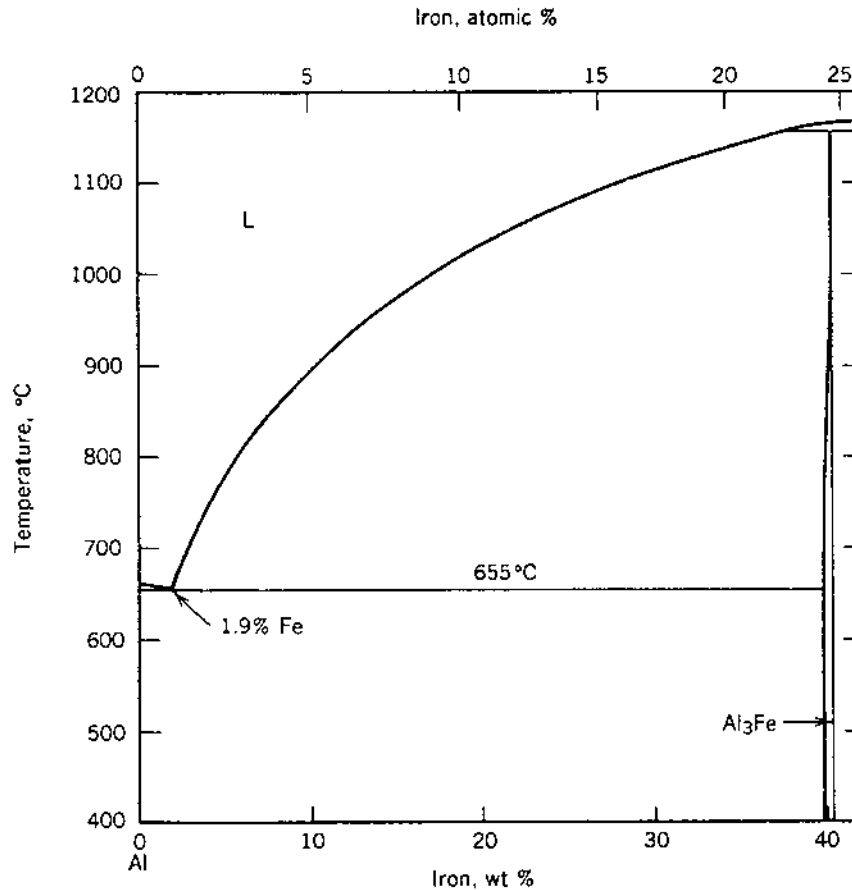
Figure 25 Al-rich corner of Al-Fe phase diagram. Drawn by Dr. Joanne Murray. (Courtesy of Alcoa).

as Mn, constituent particles of the metastable orthorhombic Al_6Fe phase may form instead of the equilibrium Al_3Fe. The maximum solid solubility of iron in aluminum is 0.05%.

2.2 Microstructural Features Not Inferred from Alloy-Temper Designations

The alloy designation system defines the alloy content, and the temper designation system identifies many of the thermal and mechanical processes which control the microstructure and, hence, the bulk properties of aluminum alloy products. Nevertheless, many metallurgical features are not specified by these systems. The features include non-metallic inclusions, porosity, second phase particles, grain and dislocation structure, and crystallographic texture.

2.2.1   Inclusions (Oxides)

These are typically oxides of aluminum, Al_2O_3 and magnesium, MgO, and the mixed oxide, spinel, $MgAl_2O_4$. Oxides that originate in the crucible and find their way into the aluminum part are called "old" oxides, whereas those that form during filling of the ingot or castings are called "young" oxides. Old oxides are much thicker than the young, can be easily distinguished by microscopy and x-ray analysis. Filtration of the molten metal is used to control old oxides, which can give rise to problems ranging from pinholes in foil to reduced fatigue life in structural wrought products and castings.

Young oxide films are primarily introduced into aluminum parts as a result of turbulence at the fluid surface, which occurs when flow velocity exceeds a critical value (0.5 m/sec for aluminum alloys) [87]. When this limit is exceeded, the oxides on the flowing surface fold over the outer dry, nonwetting surfaces, and are incorporated into the casting, resulting in an oxide film defect; since there is no bonding between the folded oxide layers, these oxide defects are essentially cracks. A young oxide film covering over aluminum dendrites is shown in Fig. 26. Grain boundaries are one of the expected locations for double oxide films because growing dendrites cannot cross these films because of the entrained layer of air. A second likely location is on or in many intermetallic compounds. This is because those that precipitate as a result of peritectic reactions at temperatures above the general freezing point of the alloy have been clearly demonstrated to deposit on oxide films floating in the alloy [88].

Oxide film defects significantly affect the reliability of parts: (i) bending strength of aluminum castings is reduced by as much as 90% when the critical velocity is exceeded [87]. This is depicted in Fig. 27, which shows that the bending

Figure 26   A young oxide film in an Al casting alloy lying on dendrite tips. (Courtesy of Prof. J. Campbell, The University of Birmingham, United Kingdom).
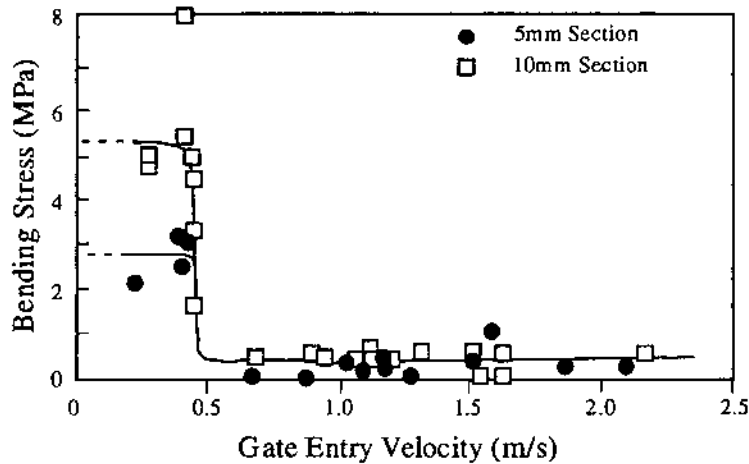
Figure 27 Bending strength as a function of gate velocity in Al castings [Source Ref. 87]. When gate velocity exceeds 0.5 m/sec, result is a decrease in bending strength by an order of magnitude.

strength of turbulently filled castings is only 10% of that of quiescently filled castings. (ii) The scatter in mechanical properties, which is mainly due to the formation of oxide defects, is greatly affected by how the molten metal fills the mold cavity, especially in the early stages of filling [89]. (iii) Oxide defects can be as small as 10^{-6} m in width, with film thickness as low as 10^{-8} m [89]. Therefore the sensitivity of current non-destructive inspection techniques is not adequate to detect all entrained oxides [90]. (iv) The harmful effect of oxide defects might become even more pronounced by heat treating the aluminum part to the peak aged condition (T6), subsequently increasing strength at the expense of ductility [90]. (v) It is estimated [91] that 80% of scrap in aluminum castings is the result of oxide cracks created during mold-filling. (vi) The presence of oxide film defects decrease fatigue life of aluminum components by several orders of magnitude [92]. The contribution of oxides to failure will be discussed later in this chapter.

2.2.2 Porosity

Porosity reduces ductility and increases susceptibility to the initiation of fatigue cracks. An SEM micrograph of such crack-initiating porosity is presented in Fig. 28. Porosity may arise from either shrinkage during solidification or from hydrogen in solution in the metal. Hydrogen pores are usually spherical whereas shrinkage porosity is more elongated, and consequently affect mechanical properties more adversely than the hydrogen pores. Hydrogen control during solidification is extremely important because of the 10-fold decrease in the solubility of hydrogen in aluminum as it solidifies. Hydrogen induced porosity can also occur in solid aluminum products when they are heated to high temperatures in humid environments.

Real time x-ray radiography has shown [93] that the overriding factor in generation of porosity is surface turbulence during filling; oxides entrained into the aluminum bulk provide heterogeneous nucleation sites for hydrogen. Therefore
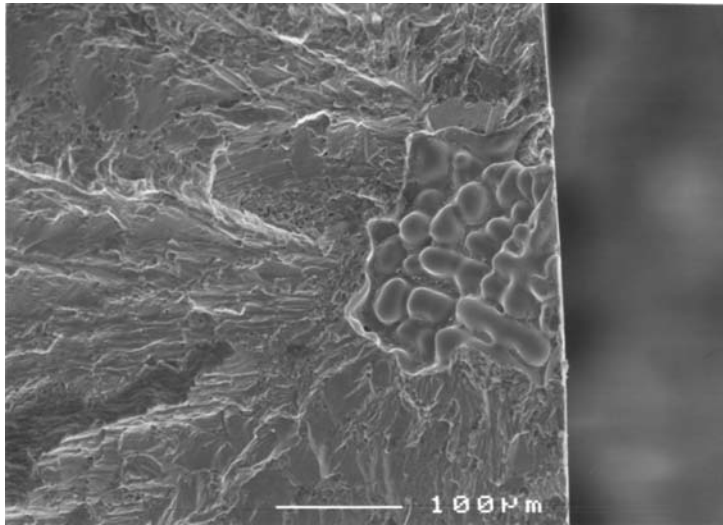
Figure 28 Porosity that served as a fatigue crack initiator in Al-Si casting alloys. (Courtesy of Dr. O. Wang, Worcester Polytechnic Institute).

it is now suggested [93] that a double requirement be made for the content of dissolved gas in the melt to be high, but the gas porosity level to be low. This will ensure that the damaging but undetectable oxide film defects are effectively labeled, and made plainly visible on x-ray radiographs and polished sections by the precipitation of dissolved gas.

        Provided that the porosity content is low enough, most of the porosity can be closed by thermal mechanical treatments. Isostatic pressure can be used to close the pores in castings, and conventional forging and extrusion are effective in healing ingot porosity. In aluminum castings, for the isostatic pressure processing to give best results, the density of oxide film defects in the casting has to be at a minimum [90]. Porosity in thick rolled products is particularly difficult to close because tensile stresses may arise during rolling of thick plate. With additional rolling to thinner plate and sheet, the pores eventually heal.

2.2.3   Second Phase Particles

These are divided into four classes based on their mode of formation and their ability to be dissolved: primary particles, constituents, dispersoids, and precipitates.

Primary Particles
These particles form when some phase other than aluminum solid solution separates first from the melt. Primary silicon particles, as presented in Fig. 29, form in castings when hypereutectic Al-Si alloys solidify by eutectic decomposition. Ductility decreases with increasing size of the silicon particles, so control is important. The coarse, faceted primary Si particles are refined to spherulitic using additives containing phosphorous. In certain casting alloys and 8XXX wrought alloys, primary Fe-bearing constituents can form if the alloying content is such that the alloy
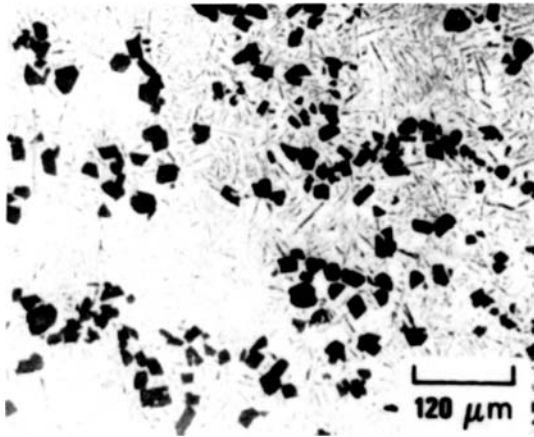
Figure 29 Primary Si particles in hypereutectic Al-Si alloys. (Courtesy of Prof. J. E. Gruzleski, McGill University, Canada).
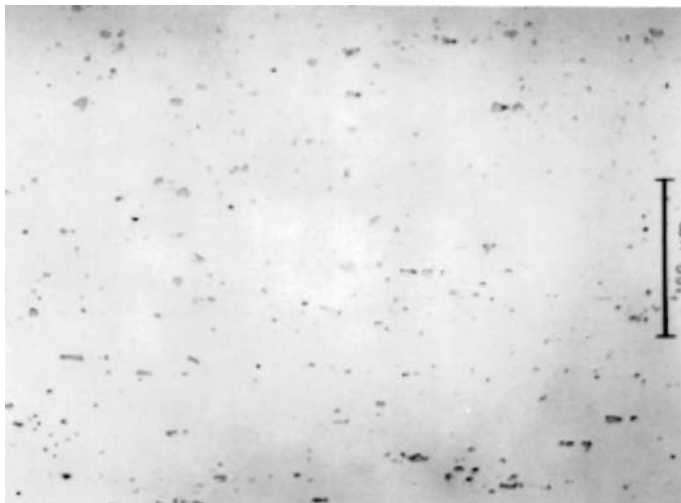
Figure 30 Constituent particles in alloy 2024 sheet. Reprinted from Ref. 95. (Courtesy of Alcoa).

is hypereutectic. In wrought alloys, macroscopically large, undesirable primary particles of Al_7Cr, Al_3Ti, or Al_3Zr may form by a peritectic reaction, if chemical composition is not closely controlled.

Constituents

These are intermetallic compounds which form by eutectic reaction during solidification, or essentially pure silicon which forms during solidification of hypoeutectic Al-Si alloys. Constituent particles in alloy 2024 sheet are shown in Fig. 30. One class, the insoluble constituents, are composed of either iron or silicon

plus another alloying element. They may include aluminum as one of the components [94,95] (e.g. Al_7Cu_2Fe). The volume fraction of insoluble constituents after preheating cannot be modified by dissolution because of the low solubility of constituent phases. Depending on the iron level and the temperature of thermal processing, however, Al-Fe particles may transform from one phase to another. Although silicon has appreciable solubility in aluminum, its solubility is decreased by alloying elements, particularly magnesium. Consequently, while soluble in some alloys, Mg_2Si is virtually insoluble in alloys such as 7075.

The size and size distribution of insoluble particles which do not undergo a phase transformation are controlled by the rate of ingot solidification, the chemical composition, and the extent and nature of bulk deformation. Particle size decreases as solidification rate increases, as iron and/or silicon content decreases, and as the amount of deformation increases [94,95]. The diameter of constituents depends on solidification rate and thermal–mechanical history, but is usually from 1 to $30\mu m$. In hypoeutectic 3XX.0 and 4XX.0 castings, modification by elements such as strontium significantly refines the flake structure of the silicon particles to a finer fibrous morphology.

Intermetallic constituent particles which do not contain iron may be highly soluble or sparsely soluble depending on the solute content of the alloy. For example, the composition of alloy 2024 is broad enough that fully solution heat treated products may contain (i) both Al_2Cu and Al_2CuMg particles; (ii) either Al_2Cu or Al_2CuMg particles; or (iii) none of these particles. Also Al_2CuMg can readily be dissolved in 7075, but it is more difficult to dissolve in 7050. Moreover, Mg_2Si particles, which are insoluble in 7075, are highly soluble in 6013.

One purpose of the process referred to as ingot preheating or homogenization is to dissolve the lacy network of soluble constituents. In as-cast ingot, the particles may either be equilibrium or metastable phases. During ingot preheating, the equilibrium phase particles may grow by precipitation of atoms from a supersaturated solution while the metastable phase particles may transform to equilibrium phase particles. During fabrication of the ingot, the insoluble particles along with any undissolved soluble particles can be broken into smaller pieces and aligned parallel to the major axis of working.

Constituent particles have a noncoherent interface with the matrix, and are too coarse to interfere with the movement of dislocations or grain boundaries. Consequently they provide no strength increase. One exception may be Al-Fe-Si alloys; in an unpublished study [49] on Al-0.05 wt% Si-Fe alloys, where Fe content ranged from 0.15 to 1.17 wt%, the yield strength of the annealed alloy was found to increase by approximately 7 MPa/vol% constituent. Constituent particles may serve as sites for particle stimulated nucleation of recrystallization.

Constituents are generally detrimental to the fatigue resistance and fracture toughness of high-strength alloy products [96]. These particles fracture at relatively low plastic strains (25–50% of constituent particles are cracked after 7% plastic strain in uniaxial tension [31]) and provide low energy sites for the initiation and growth of cracks. Constituents are tolerated in commercial alloys because their elimination would necessitate a significant cost increase [94]. In high toughness aluminum alloys such as 7475 or 2124, the iron and silicon levels are deliberately controlled at low levels. Al_7Cu_2Fe is the predominant constituent observed in Al-Cu-Li alloys. Despite the harmful effects of constituents in high-strength alloys,

Table 6 Constituents in Some Wrought and Cast Aluminum Alloys

Alloy	Observed Constituent Phases
1350	$Al_{12}Fe_3Si$, Al_6Fe
2014	$Al_4CuMgSi_4$, $Al_{12}(Fe,Mn)_3Si$
2X24	Al_7Cu_2Fe, $Al_{12}(Fe,Mn)_3Si$, Al_2CuMg, Al_2Cu, $Al_6(Fe,Cu)$
2X19	Al_7Cu_2Fe, $Al_{12}(Fe, Mn)_3Si$, Al_2Cu
2090	Al_7Cu_2Fe
2091	Al_7Cu_2Fe, Al_3Fe, $Al_{12}Fe_3Si$
2095	Al_7Cu_2Fe, Al_2CuLi, Al_6CuLi_3
3XXX	$Al_6(Fe,Mn)$, $Al_{12}(Fe,Mn)_3Si$
5083	Mg_2Si, $Al_{12}(Fe,Mn)_3Si$, Al_7Cr
6013	$Al_{12}(Fe,Mn)_3Si$
6061	Mg_2Si, $Al_{12}(Fe,Mn)_3Si$
7X75	Al_7Cu_2Fe, $Al_{12}(Fe,Mn)_3Si$, $Al_6(Fe,Mn)$, Mg_2Si, SiO_2[†] $Al_{23}CuFe_4$[†]
7X50	Al_7Cu_2Fe, Mg_2Si, Al_2CuMg
7055	Al_7Cu_2Fe, Mg_2Si
7079	$Al_6(Fe,Mn,Cu)$, Mg_2Si
8090	Al_3Fe
319	Si, Al_5FeSi, $Al_{15}(Fe,Mn)_3Si$
A357	Si, $Al_8FeMg_3Si_6$, Al_5FeSi

[†]: Ref. 97.

the ability of alloy 3004-H19 to make commercially successful beverage relies on careful control of size, volume fraction, and distribution of $Al_{12}(Fe,Mn)Si$ constituent particles.

Phases which have been observed to be insoluble and sparsely soluble constituent particles in products of some aluminum alloys are presented in Table 6. Higher purity versions may not have all of the insoluble constituents present.

Dispersoids

Aluminum combines readily with the transition metals, chromium, manganese, and zirconium to form intermetallic phases with little or no solubility in the aluminum matrix. Because of their slow diffusivity in aluminum, these alloying additions form very small precipitates, less than 1 micron in size, either during solidification or ingot preheat. This fine distribution of precipitates, called dispersoids, delays or prevents static recrystallization during processing, and because they are strung out in the working direction (a process called mechanical fibering), they aid in retaining the elongated or pancake shaped grains that develop during working. Dispersoids have dual, but contradictory roles; they suppress recrystallization or limit the movement of grains, favoring the transgranular mode of fracture associated with the highest energy absorption, but also nucleate microvoids by decohesion at the matrix interface, leading to the formation of void sheets between larger voids [98]. Consequently, careful control of dispersoids is important. Dispersoids found in several commercial alloys, and pinning of a grain boundary by dispersoids, are shown in Fig. 31.
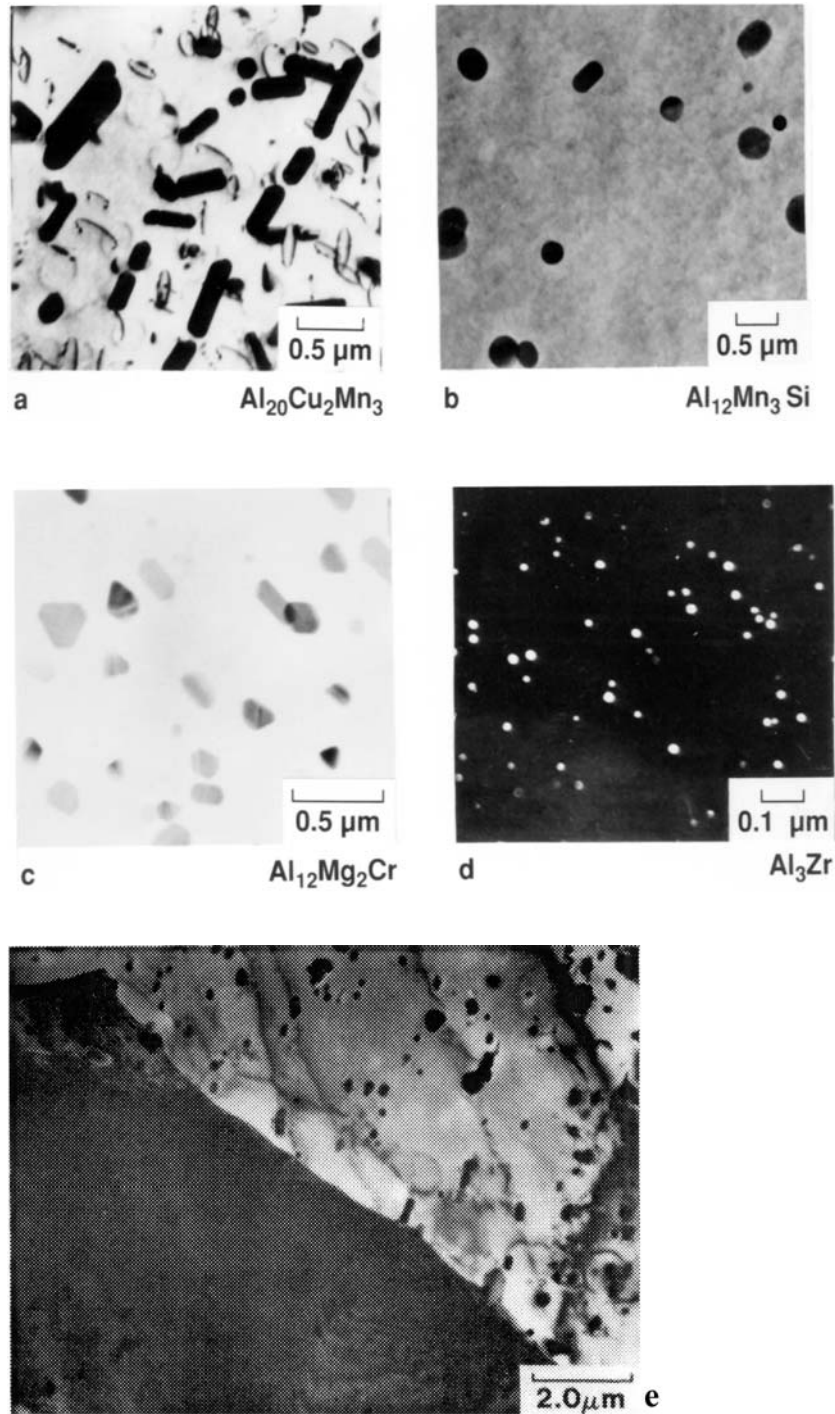
Figure 31 Dispersoids in alloys (a) 2024; (b) 6013; (c) 7075; (d) 7050; and (e) 3004. Dispersoids pin grain boundaries during the recrystallization as shown in (e). Reprinted from Ref. 95. (Courtesy of Alcoa).

Table 7 Dispersoids in Aluminum Alloys

Alloy	Dispersoid
2X24	$Al_{20}Cu_2Mn_3$
5083	$Al_{11}Cr2$, $Al_6(Fe,Mn)$
6013	$Al_{12}Mn_3Si$
7046	Al_3Zr
7X75	$Al_{12}Mg_2Cr$
7X50	Al_3Zr
7055	Al_3Zr
2090	Al_3Zr
2091	Al_3Zr
2095	Al_3Zr
8090	Al_3Zr
3003	$Al_{12}(Mn,Fe)_3Si$, $Al_6(Mn,Fe)$

The effectiveness of a particular dispersoid in controlling the grain structure depends on its size, spacing, and coherency. Small particles (normally less than 0.4 μm in diameter) retard discontinuous recrystallization by pining subgrain boundaries and preventing subgrain coalescence. Small, closely spaced particles have the greatest effect in retarding recrystallization. Coherent dispersoids (e.g. Al_3Zr) are more effective than the incoherent dispersoids (e.g. $Al_{12}Mg_2Cr$ and $Al_{20}Mn_3Cu_2$) in inhibiting boundary migration, because the dispersoid-matrix interface must either change from coherent to semicoherent or incoherent as the boundary passes the dispersoid, or alternatively, dissolve and reprecipitate after the boundary passes through its local. Both processes require considerable energy. Incoherent dispersoids giving high interfacial energies tend to be located at the grain boundaries, and are effective initiators of failure due to cavitation under creep loading at high temperatures [99]. A number of casting alloys, and some wrought alloys, contain elements which can form either constituents or dispersoids depending on the solidification rate. Dispersoids found in some aluminum alloys are listed in Table 7. Note in Table 7 that the most common dispersoid in high strength aluminum alloys is Al_3Zr (β'). Alloying additions of less than 0.18 wt% Zr, result in approximately spherical β', as shown in Fig. 31(d), due to its low misfit with the Al matrix ($\sim 0.6\%$ [100]). β' can be coherent, or semi coherent depending on process history [101].

Precipitates
These particles can form during any thermal operation below the solvus. In properly solution heat-treated products, all precipitates dissolve during the solution heat treatment operation. Depending on quench rate and alloy, precipitates may form during the quench from the solution heat treatment temperature at grain and subgrain boundaries and at particle-matrix interfaces. These coarse precipitates do not contribute to age hardening, and may serve to reduce properties such as ductility and fracture toughness. After the quench, Guinier–Preston (GP) zones form at ambient temperature (natural aging). These are agglomerates of atoms of the major solute elements with a diffuse, coherent boundary between the GP zone and the matrix. During elevated temperature precipitation heat treatments (artificial

aging) GP zones may either nucleate metastable precipitates, or they may dissolve, and metastable precipitates nucleate separately. Cold working subsequent to quenching introduces dislocations which may serve to nucleate metastable or equilibrium precipitates. With prolonged artificial aging, equilibrium precipitates may form. Coarse equilibrium precipitates form during annealing treatments of heat-treatable alloy products, O temper. They also form during most thermal-mechanical treatments prior to solution heat treatment, and during a slow quench from solution treatment temperature.

PRECIPITATE MORPHOLOGY.   High tensile yield strength is frequently associated with alloys containing intrinsically strong, plate shaped precipitates with $\{111\}_\alpha$ and $\{100\}_\alpha$ plates and large aspect ratios [70]. The high tensile strengths observed in Al-Cu-Li (2090) and Al-Cu-Li-Mg-Ag (2095) alloys may be attributed to a uniform distribution of T1 precipitate plates of high aspect ratio (70:1) formed on $\{111\}_\alpha$ planes. Also an Al-Cu-Mg-Ag alloy, hardened with thin plates of Ω phase on the $\{111\}_\alpha$ planes, with an aspect ration of 30:1, may develop high values of tensile yield strength. Furthermore, the well-known high strength of Al-Zn-Mg-Cu alloys is associated with the combined effect of number density and aspect ratio of plates of the phase η', which also form on the $\{111\}_\alpha$ planes [70]. The matrix strengthening precipitates in some aluminum alloys are presented in Table 8. Note that T1 in Al-Cu-Li alloys is an equilibrium phase, and so is an exception to the generality that equilibrium precipitates do not appear until overaging begins.

QUENCH SENSITIVITY.   All heat treatable, high-strength aluminum alloy products progressively lose their ability to develop the maximum strength attainable with a particular aging treatment as rate of cooling from the solution treatment temperature decreases. This quench sensitivity is attributed to loss of solute by precipitation during the quench as coarse, heterogeneously nucleated particles of the equilibrium phase and to loss of vacancies to sinks. Quench sensitivity is higher in the more concentrated alloys, and enhanced in alloys containing incoherent particles whose

Table 8   Major Precipitates Observed in Some Aluminum Alloys

Alloy–Temper	Major Precipitates
2X24-T3, T4	G-P zones
2X24-T6, T8	$S' =$ precursor to S, Al_2CuMg
2X19-T8	$\theta' =$ precursor to θ, Al_2Cu
6013-T6	$Q = Al_5Cu_2Mg_8Si_6$
7X75-T6	$\eta' =$ precursor to η, $MgZn_2$ or $Mg(Zn,Cu,Al)_2$
7X75-T76	$\eta'; \eta$
7X75-T73	η
7050-T76	η'
7050-T74	η
7150-T6	η'
7150-T77	$\eta'; \eta$
7055-T77	$\eta'; \eta$
2090-T8	$T_1 = Al_2CuLi; \delta' = Al_3Li$
2095-T6, T8	$T_1; \theta'$
2091-T3	$\delta'; T_1$
8090-T8, T7	$\delta'; S'$
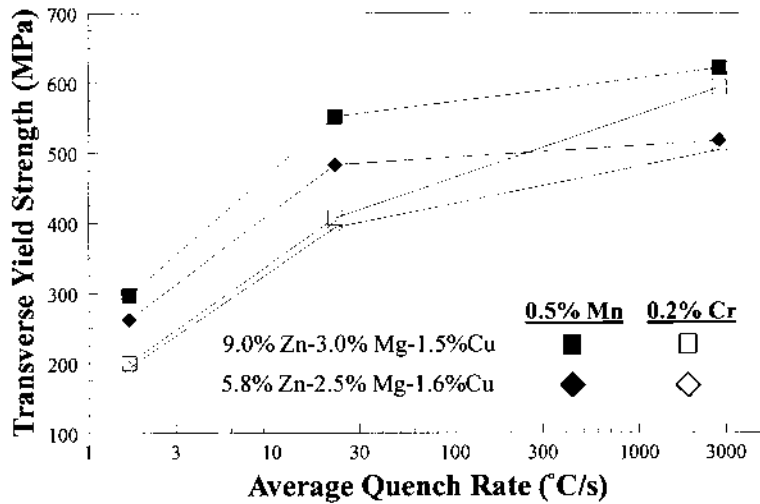
Figure 32 Effect of dispersoid type and solute level on quench sensitivity of 7XXX-T6 sheet as a function of cooling rate calculated between 400°C and 290°C.

interfaces serve as nucleation sites for heterogeneous precipitation for precipitates. The effect of dispersoid type on quench sensitivity is depicted in Fig. 32, which shows yield strength as a function of average cooling rate (400–290°C) and dispersoid type ($Al_{12}Mg_2Cr$ vs. $Al_{20}Cu_2Mn_3$) in Al-Zn-Mg-Cu alloy sheet in a T6 temper [95]. The effect of dispersoid type on strength quench sensitivity in 7XXX alloy products is attributed to their relative abilities to nucleate η at elevated temperatures. In 2X24 alloys, $Al_{20}Cu_3Mn_2$ dispersoids nucleate dislocations at the particle-matrix interface during the quench. These dislocations serve as nucleation sites for subsequent precipitation. Consequently, alloys that contain Cr and Mn as dispersoid-forming elements are more quench-sensitive (Cr containing dispersoid causing the greatest increase in quench sensitivity [71]) than those that contain Zr, which forms a coherent dispersoid. Nucleation is difficult on coherent interfaces, so the newer alloys are less quench sensitive.

Aging practice can also affect quench sensitivity. For production reasons, the practice that provides the target properties in the shortest controllable time is preferred, and most aging treatments are developed using this criterion. The material used to develop the aging practice is usually quenched at a high rate, and such material can develop high strength with short aging times at relatively high aging temperatures. Neither aging at lower temperatures nor preceding the high temperature aging treatment by one at a lower temperature has any significant effect on strength of the rapidly quenched material. When products of the same alloy are quenched at a low rate, however, strength can be substantially affected by such modifications in the aging practice. This behavior is schematically described in Fig. 33 [95]. The decrease in strength of slowly quenched material aged by the standard practice is attributed to a loss of solute atoms and to vacancy depletion. The portion of the strength decrease attributable to vacancy depletion is the amount that can be regained by lower temperature aging treatments, i.e. the difference between the
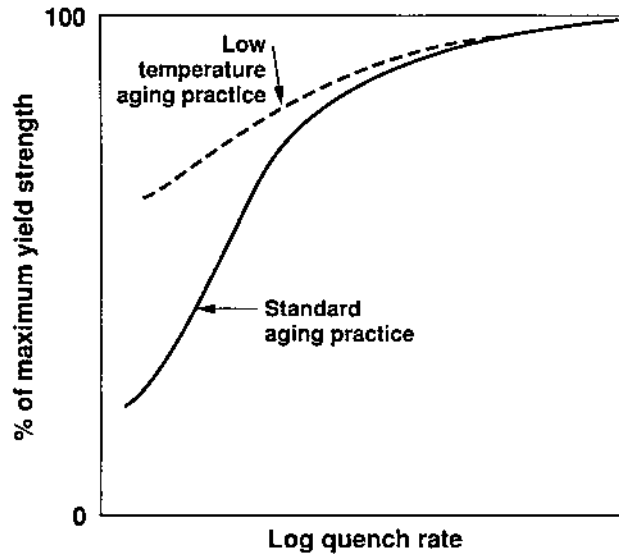
Figure 33   A schematic illustration of the effect of aging treatment on quench sensitivity of a high strength aluminum alloy product.

two curves in Fig. 33. This behavior is believed to occur because vacancy depletion by slow quenching lowers the temperature below which homogeneous nucleation is possible, T_v, Fig. 34. When the aging temperature is below T_v, the precipitates are coarser, and more widely spaced than those produced at high aging temperatures below T_v. Consequently, preceding the standard aging treatment by an aging step at a temperature below T_v can improve the precipitate distribution and increase strength of material quenched at a low rate. The effects of quench path on the ability to develop strength are discussed in Chapter 9.

HETEROGENEOUS NUCLEATION OF PRECIPITATES AND PRECIPITATE FREE ZONES. Homogeneous nucleation of the equilibrium phase is normally very difficult because of high interfacial energy. This barrier can be overcome by (i) a precipitation sequence that involves several metastable phases having lower interfacial energy, e.g. GP zones; or (ii) heterogeneous nucleation at defects which accommodate the precipitate. In defect-aided nucleation, sites are not determined by statistical fluctuations, but by the type, density, and distribution of effective defects [64]. Vacancy-aided nucleation comes closest to homogeneous nucleation; it may produce very fine particles if small vacancy clusters, rather than dislocation loops, determine the sites. The high rate of nucleation and growth of precipitates in aluminum alloys at aging temperatures is attributed to retention of vacancies which are in equilibrium at the solution temperature. Due to vacancies, GP zone formation at low temperatures occurs at a rate many orders of magnitude greater than that expected from diffusion at high temperatures (e.g. 10^7 times the anticipated rate in Al-Cu alloys [15]).

In nucleation at dislocations and grain boundaries, the precipitate distribution depends on the distribution of nonequilibrium defects. Slow cooling allows some vacancies to be lost at sinks and precipitates to nucleate at grain boundaries.
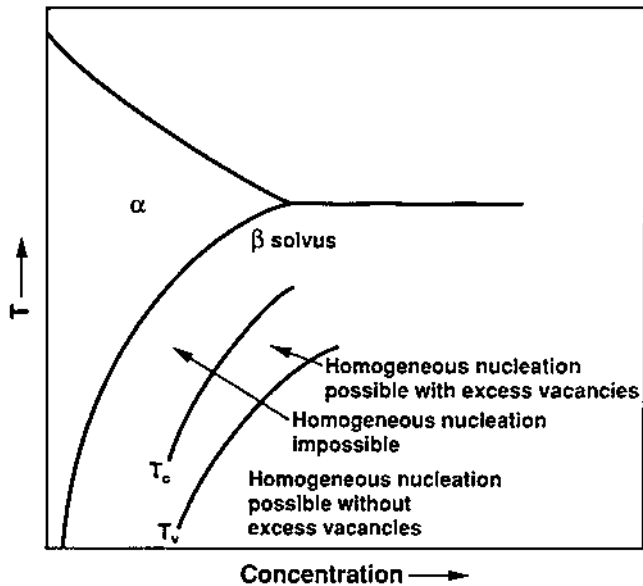
Figure 34 A schematic illustration of the effect of vacancies on possibility of homogeneous nucleation. Increasing quench rate moves T_v closer to T_c.

Dislocations split into two partial dislocations, which form a stacking fault with an hcp structure, and this may result in the segregation of the solute to the fault. A precipitate may nucleate at the stacking fault if this phase and the fault have the same crystal structure [15]. An example is the hexagonal γ' phase in aluminum-silver alloys [102]. Silver in solid solution reduces the stacking fault energy of aluminum significantly. Consequently Frank sessile dislocations, which contain a stacking fault within, are stable immediately after quenching. Also helical dislocations introduced during quenching degenerate on aging into long, narrow stacking faults as a result of localized silver enrichment. The stacking faults then act as nuclei for γ' phase.

The nucleation and growth of precipitates at dislocations is usually most evident when the degree of supersaturation or undercooling is low, or when the dislocation density is high. Under certain circumstances, however, a relatively low initial density of dislocations may have an unexpectedly large effect on the overall decomposition process, through the ability to instigate repeated nucleation.

The formation of precipitate free zones (PFZ) is usually due to solute and vacancy depletion in the environment of grain boundaries. A PFZ in an Al-Zn-Mg alloy is presented in Fig. 35, which shows η' precipitates in the matrix and η precipitates at the grain boundary. PFZs also occur around coarse dispersoids [103,104], which may act as heterogeneous nucleation sites for precipitates during a slow quench. PFZs usually get narrower for higher solution treatment temperatures and faster quenching rates, both of which increase the excess vacancy content. When the PFZ is mainly a result of a depletion in vacancies, low temperature aging is sometimes effective in decreasing the PFZ width by supporting nucleation.
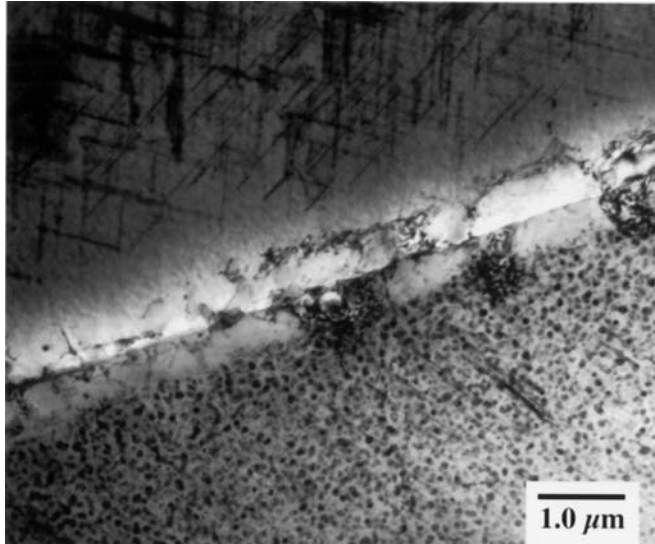
Figure 35 Precipitate-free zones in an Al-Zn-Mg alloy. (Courtesy of Prof. E. A. Starke, Jr., University of Virginia).

For example, an aging temperature of 93°C eliminates PFZs in an Al-Zn-Mg-Cu alloy even when cooled very slowly (2°C/sec) from solution treatment temperature [104]. PFZs in 2XXX and some 8XXX alloys can be eliminated by dislocation-aided nucleation provided by cold work prior to aging [64].

2.2.4 Grain Structure

The grain size of aluminum alloy ingots and castings is typically controlled by the introduction of inoculants which form intermetallic compounds containing Ti and/or B. During deformation processing, the grain structure becomes modified. Most aluminum alloy products undergo dynamic recovery during hot working. Static recrystallization may occur between or following rolling passes; alloys containing high amounts of Mg (lowers the stacking fault energy) may recrystallize dynamically during deformation processing. During deformation, the crystal lattice of the aluminum matrix rotates at its interfaces between constituent and coarse precipitate particles. These high energy sites serve to nucleate recrystallization. This process is termed particle stimulated nucleation (PSN), and is an important mechanism in the recrystallization process of aluminum. The particle size which will serve as a nucleus decreases as deformation temperature decreases and strain rate increase. Dispersoid particles retard the movement of high angle grain boundaries. Consequently, hot worked structures are resistant to recrystallization and often retain the dynamically recovered subgrain structure in the interiors of elongated cast grain boundaries. In heat treated products containing a sufficient quantity of dispersoids, the unrecrystallized structure of hot worked plate, forgings and extrusions may be retained after solution heat treatment. Degree of recrystallization of hot worked products has an effect on fracture toughness. Recrystallized products develop lower toughness than do products which are either partially or completely recrystallized.

This behavior is attributed to precipitation on the recrystallized high angle grain boundaries during the quench. These grain boundary precipitates, along with the PFZs which accompany them, increase the tendency for low energy intergranular fracture. Products such as sheet, rods, and tubing which are cold rolled almost invariably recrystallize during solution heat treatment or annealing to O temper. It was mentioned above that grain size is not a major factor in increasing strength in commercial alloys. Several measures of formability are influenced by grain size, however, so grain size is controlled for this reason. One particular use of grain size control is to produce stable, fine grains, < 10 micrometers, which help develop superplastic behavior in aluminum alloy sheet.

2.2.5 Crystallographic Texture

Cast aluminum ingots and shapes generally have a random crystallographic texture. With deformation, certain preferred crystallographic orientations develop. For flat rolled products and extrusions having a high aspect ratio of width to thickness, the deformation texture is similar to that in pure face centered cubic metals. The predominant textures are $\{110\}[112]$, $\{123\}[634]$, and $\{112\}[111]$. In extruded or drawn rod or bar, the texture is a dual fiber texture in which almost all grains are aligned so that the grain directions are either [001] or [111]. During recrystallization, a high concentration of grains in the $\{001\}[100]$ (cube) or $\{011\}[100]$ (Goss) orientations may develop, especially in high purity alloys. In alloys with substantial volume fractions of constituent phases, PSN of recrystallization will tend to promote a more random texture.

Control of crystallographic texture is particularly important for nonheat-treatable sheet which will be deep drawn by customers. If texture is not random (and it rarely is), ears will form during the drawing process. In processing nonheat-treatable alloy products such as 3004-H19 can sheet, earing is controlled by balancing the cube texture developed during annealing with the deformation textures producing by rolling to the final temper. In heat-treatable alloys, texture has the most potent effect on the properties of extrusions which have a strong dual fiber texture. Strengthening by this process is so potent that the longitudinal yield strengths of extruded products exhibiting this texture are about 70 MPa (10 ksi) higher than strength in the transverse direction. If this texture is lost by recrystallization, strength in the longitudinal direction decreases to that in the transverse directions.

2.3 Mechanical Behavior of Aluminum Alloys

Parts fail usually due to improper design of the component (e.g. at sharp radii in the part), due to environmental effects (due to corrosion), or mechanically by the initiation of cracks from their most serious defects. Provided that the part has been properly designed and environmental effects are taken into consideration, material's performance can be improved, if the defects contributing to mechanical failure are eliminated. Hence, strength and durability are then limited by the next most serious family of defects. When each family of defect has been removed, the material will fail from metallurgical features, such as the large intermetallic compounds or other brittle phases which might be present. Finally, if these in turn are removed, we have
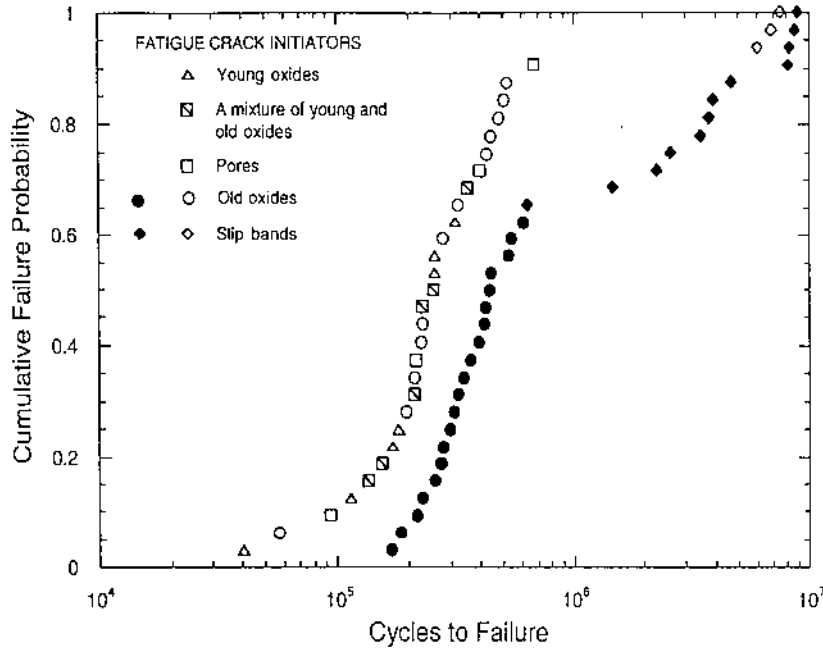
Figure 36 Correlation between fatigue crack initiators and fatigue life distributions for turbulently filled (open symbols) and quiescently filled (solid symbols) aluminum castings. (Reprinted from Ref. 92). (Courtesy of Prof. J. Campbell, The University of Birmingham, United Kingdom).

the ultimate resistance to failure as dictated by the metallurgy of the alloy, i.e. resistance to slip, grain size, etc. Hence there is a hierarchy of defects and microstructural features, which determine the mechanical behavior of alloys.

To understand the causes of failure in most manufactured components, it is essential to identify those features which might have direct precedence in the hierarchy. Such a hierarchy is clearly seen in the fatigue life versus probability of failure plot in Al-Si-Mg alloy castings, presented in Fig. 36 [92]. Note in Fig. 36 that, failure due to different crack initiators have distinctive slopes. There is an ultimate curve somewhere in the vicinity of the four points with the highest fatigue life. Therefore the majority of the fatigue failures are approximately a factor of 100 lower than what could be obtained in a defect-free material. Oxide films seem to be at the top of the hierarchy of defects, followed by porosity, although, of course, it is to be noted that these two defect types are often practically indistinguishable because the porosity is sometimes merely the local divergence of an enfolded oxide film. Reducing the size of shrinkage defects in cast alloys will increase the fatigue life, but only up to the stage at which initiation from persistent slip bands on the surface becomes operative [105]. In wrought alloys, microporosity and constituent particles affect fatigue resistance most [106]. In other words, microporosity and constituents were found to reside at the top of the hierarchy.
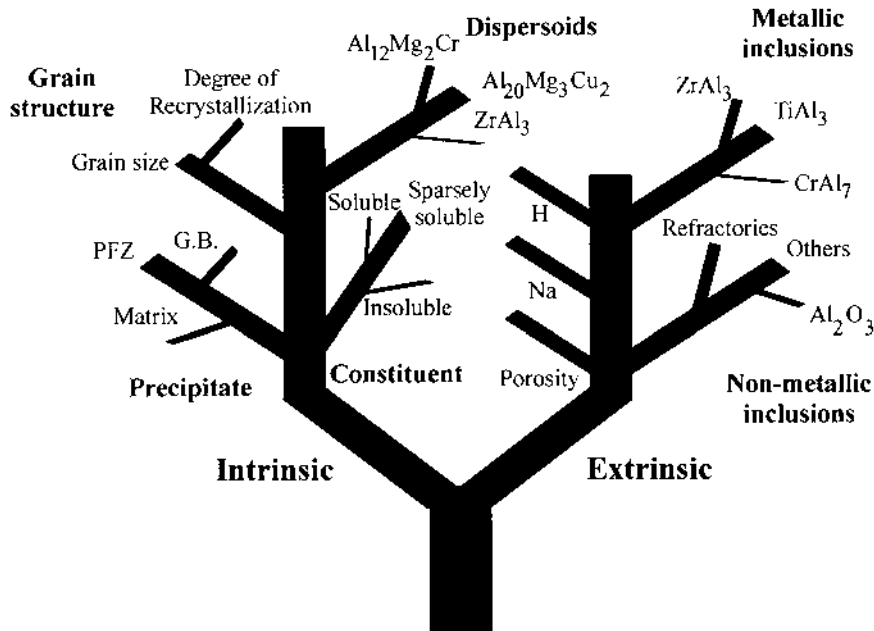
Figure 37 Staley's Toughness Tree (Source Ref. 107). Toughness is determined by a combination of intrinsic and extrinsic factors.

Effects of metallurgical features on fracture toughness, however, are not hierarchical. Staley's Toughness Tree [107], which shows intrinsic and extrinsic factors affecting the toughness of aluminum alloys, is presented in Fig. 37. This figure is an effective tool for classifying the contribution of microstructural features to toughness. The metallic and nonmetallic inclusions on the right-hand-side are treated as extrinsic effects, because they are considered to be extraneous to the features imposed by the physical metallurgy of the material. On the other hand, the features on the left of the tree are not defects but are features of the microstructure of the alloy. They can be controlled by the composition and by both solidification and deformation processing. The distribution of microstructural features as well as their volume fraction are significant in both initiating damage, as in the case of void nucleation at hard particles strongly bonded to the matrix, and in defining the distribution of voids and microcracks [108]. The distribution determines the strains and the overall damage levels, at which a critical size of defect can develop, and result in fracture.

2.3.1 Mechanisms of Fracture

The gliding motion of dislocations can lead to homogeneous or a highly localized distribution of strain. Localization can be transcrystalline and intercrystalline (crossing or along grain boundaries). Fracture is usually easier when strain localization at both locations occurs. Transcrystalline localization is favored by a high level of CRSS due to shearable obstacles. Shearing leads to a reduction

of their cross-section, and therefore to a local reduction of the resistance to the motion of n additional dislocations, unless they pile up at an obstacle like a grain boundary. Slip weakens the initial slip planes, and slip will continue on these preferred planes until the back stress due to dislocation pile-ups restores the original strength on the particular planes. The number of dislocations, N, that pass on a typical plane from the time deformation begins until local slip ends can be used as an indicator of slip localization [109]. N increases with increasing volume fraction and size of shearable particles, and increasing grain size [53]. If the pile-up stress, τ_p, exceeds the crack nucleation stress at the grain boundary, intergranular fracture starts. This type of strain localization does not have a significant effect on the yield strength [110], but generally has a deleterious effect on the toughness. Intense slip bands can act as stress concentrations across grain boundaries, leading to premature intergranular failure or premature transgranular failure in the coarse slip bands [65].

When fracture is transgranular, precipitate type (underaging versus overaging) has little effect on the combination of strength and toughness that is developed; lower-strength tempers provide higher toughness. Quenching or aging treatments that increase the amount of intergranular fracture, however, decrease toughness with no effect on strength or tensile elongation [111,112].

Increasing the degree of aging from the underaged up to peak-strength condition always leads to a monotonic decrease in fracture toughness [113]. Overaging beyond the peak-aged condition can, however, lead either to a significant restoration of the toughness, to small recovery, no recovery, or even a decrease in toughness. Restoration of toughness is observed in materials in which matrix microstructure dominates fracture, and small or no recovery, and, particularly, a loss in toughness, is observed in materials in which grain boundary microstructures dominate. The type of behavior depends upon the alloy composition. In general, 2XXX and 7XXX alloys tend to show the behavior indicated in Fig. 38(a), while Al-Li alloys with high Li contents tend to show the behavior of Fig. 38(b). Fracture toughness is strongly affected by the extent of precipitation on grain boundaries.

Intercrystalline localization at room temperature is intensified by both the extent of precipitation on grain boundaries and the PFZs. Effects of precipitation on grain boundaries on fracture toughness is shown in Fig. 39 for two experimental aluminum alloys [114,115], which show full intercrystalline fracture. The higher the strength of the material, the higher the tendency to intensify intercrystalline slip because the difference in the yield stress between the interior and the PFZ progressively increases (up to ~ 600 MPa) [53]. Hence fracture takes place by localized yielding in PFZ.

Aluminum alloys which exhibit the highest fracture toughness at a particular strength level are designed and fabricated to minimize strain localization. They generally display ductile fracture associated with crack nucleation at intermetallic constituent particles followed by void nucleation and coalescence at dispersoid particles as discussed in the following section.

2.3.2   Void and Crack Formation

The most critical stage in controlling fracture toughness of high-strength aluminum alloy products is in controlling the initiation of voids [116]. Most models of void initiation involving particles rely on the premise that the particles offer interfaces that decohere or fracture internally due to deformation-induced internal stresses
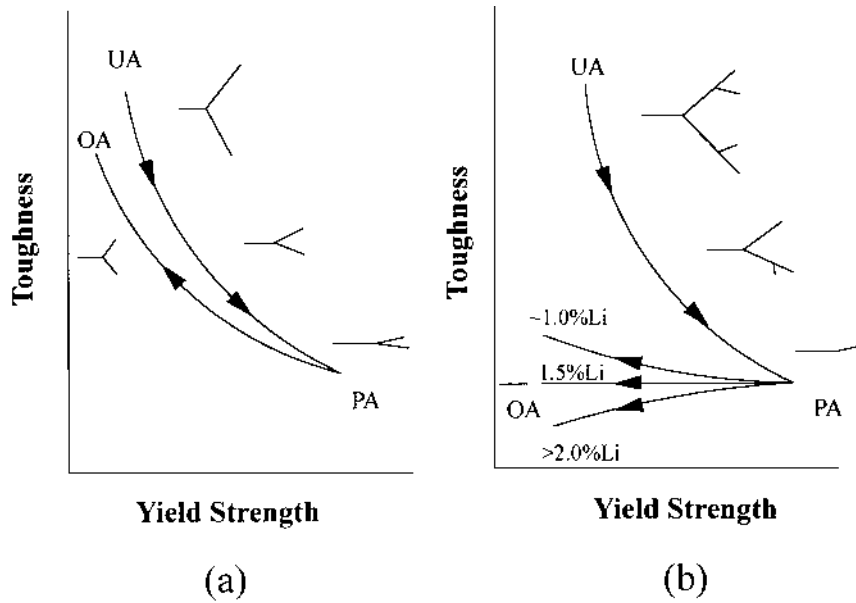
Figure 38 Toughness-strength relationships and accompanying crack formation as a function of temper. (a) less pronounced toughness variation from underaged → peak aged → overaged; and (b) significant variation in toughness from underaged → peak aged → overaged condition.
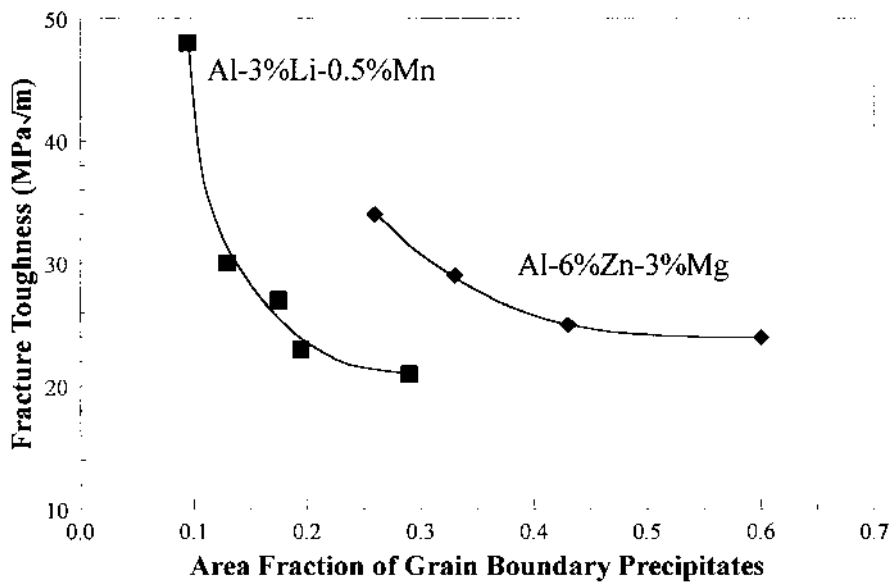
Figure 39 Variation in fracture toughness with area fraction of grain boundary precipitates, at constant matrix yield strength, using data for Al-3 wt% Li-0.5 wt% Mn from Ref. 114, and Al-6 wt% Zn-3 wt% Mg from Ref. 115.

arising from the differences in deformation resistance between matrix and particle. However, bonding strength between the matrix and the particle is a very important factor in determining void nucleation [117]. In alloys containing strongly bonded particles, the yield stress is normally only a fraction of the cohesive strength between the particle and matrix. Consequently, some plastic deformation is necessary to concentrate stress on the interface or inside the particles. With decreasing particle size, tendency for void nucleation at the interface can be reduced. Very small particles cannot nucleate a cavity since the elastic strain energy stored around them is not sufficient for producing the surface energy of the cavity.

Constituents, dispersoids and precipitates all influence fracture toughness, fatigue-crack growth at intermediate and high level of stress intensity under constant-amplitude loading, and fatigue-crack growth under spectrum loading [118]. Constituents produce incipient cracks when they either fracture or separate from the matrix under stress. These incipient cracks reduce the energy to propagate a crack, thus decreasing both fracture toughness and resistance to growth of fatigue cracks. Constituents affect fatigue-crack initiation at low stress levels, even though they may not fracture or separate from the matrix. Constituents increase the local stress, which increases the probability of introducing coarse, persistent slip bands.

The size of second phase particles affects average crack advance per cycle. This is illustrated in Fig. 40, which shows incremental crack advance relative to the size of constituents, dispersoids and precipitates in constant amplitude crack growth tests of Al-Zn-Mg Cu alloy sheet [111]. High volume of constituents may improve resistance
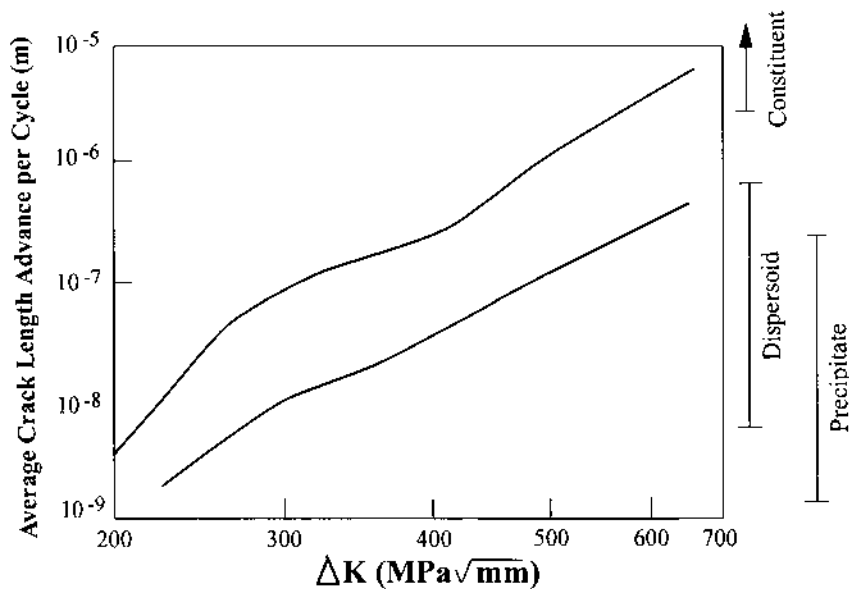
Figure 40   The effect of second phase particles on average crack advance per cycle (Source Ref. 111).
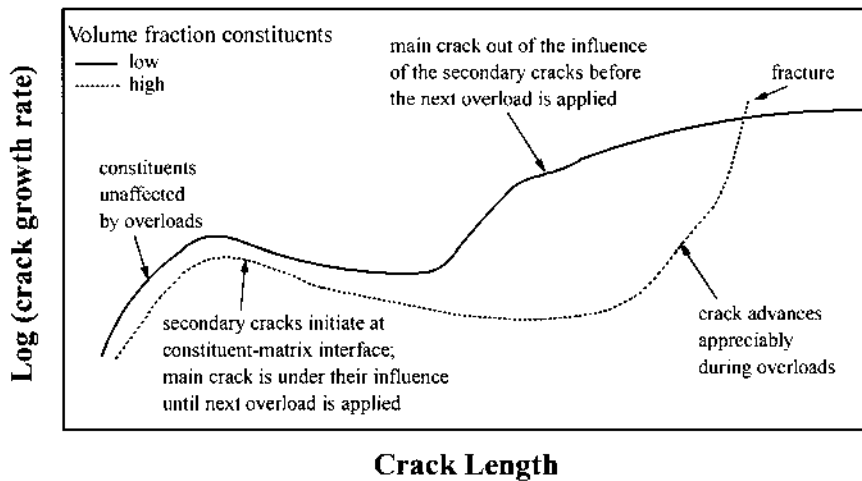
Figure 41 The effect of volume fraction of constituent on crack growth rate as a function of crack length.

to fatigue crack growth under particular conditions of variable amplitude loading where large tensile overloads are applied. The effect of volume fraction of constituent on crack growth rate as a function of crack length is schematically presented in Fig. 41. Secondary cracks nucleated at constituent-matrix interface are higher in number in the high constituent alloy, and delay the growth of the primary crack, until it finally comes out of the influence of the secondary cracks.

Dispersoid particles decrease the energy to propagate a crack by initiating microvoids, which coalesce and link the incipient cracks formed at constituents. Hence they can influence fracture toughness, fatigue-crack growth. Precipitates (as in Al-Zn-Mg-Cu alloys) affect toughness by their effects on strength and fracture mode. Toughness and high-strain amplitude fatigue life generally increase as strength decreases, by either underaging or overaging, and are higher when the fracture mode is transgranular. On the other hand, increasing strength increases fatigue life at low strain amplitudes. With low levels of cold work and with underaged and peak-aged tempers, the toughness and resistance to fatigue-crack growth of Al-Cu-Mg-Mn alloys increase as strength increases. High levels of cold work in naturally aged tempers provide superior combinations of strength and resistance to fatigue-crack growth, however, in overaged tempers provide inferior combinations of strength, toughness and resistance to fatigue-crack growth. In Al-Li alloys, the high volume fraction of coherent, ordered Al_3Li precipitates increases both the elastic modulus and the resistance to fatigue-crack growth at intermediate levels of stress intensity. However the presence of these precipitates substantially increase the planarity of slip. This results in alloys with low fracture toughness, low fatigue-crack growth resistance at high levels of stress intensity, and short fatigue life at high plastic strain.

2.4   Major Alloy Systems

2.4.1   Al-Fe-Si Alloys

Fe is the most common impurity found in Al. It has a high solubility in molten Al but in solid Al, the maximum solubility of Fe is very low; approximately 0.05%, as depicted in Fig. 25. Therefore any Fe beyond solubility limit forms constituents at grain and cell boundaries. The Al-Fe phase diagram in Fig. 25 predicts that the Fe will be present in the form of the Al_3Fe constituent, but in most commercial solidification processes of 1XXX alloys, metastable phases Al_6Fe or Al_mFe are observed [59,119]. A high temperature preheating (16 hr at 607°C) of binary Al-Fe ingot produces Al_3Fe constituents, and a lower temperature preheating (16 hr at 482°C) results in the formation of Al_6Fe constituents. When Si is present, $Al_{12}Fe_3Si$ (α-phase) or $Al_9Fe_2Si_2$ (β-phase) may be found in the 1XXX alloy sheet [59]. These Al-Fe and Al-Fe-Si intermetallics constitute an important part of the microstructure, and can affect the material behavior during subsequent fabrication processes. As mentioned previously, constituent content increases strength about 7 MPa/vol%, Fig. 42. The increase in strength is observed with increasing constituent content, regardless of temper and intermetallic type.
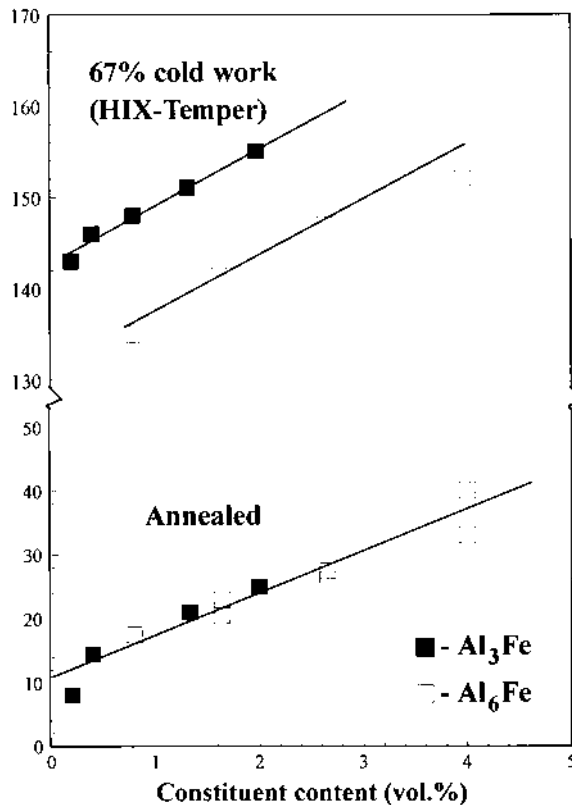
Figure 42   Yield strength versus volume fraction constituent (Al_3Fe or Al_6Fe) for Al-0.05 wt% Si-x Fe series of 1XXX alloys. (Source Ref. 39).

The formability of Al-Fe alloys may be influenced by the size and distribution of constituents [120]; coarse Al_3Fe constituents crack and produce notches that reduce formability and fatigue resistance. Finely dispersed Al_6Fe particles, on the other hand, do not have the deleterious effect on formability. However, the role of Al-Fe constituents in controlling recrystallization and texture (discussed previously) will have an indirect but critical impact on formability in 1XXX sheet and foil products. Therefore it is essential to control the formation and the content of these phases, especially in dilute alloys. This can be achieved by controlling the cooling rate during solidification, or by modification of the alloy content to enhance the stability of a desired phase. Solidification front velocity affects the type of the Al-Fe constituent in alloys with 4.6–6.1 wt% Fe [119]. At front velocities below 0.5 mm/sec, Al_3Fe is the dominant constituent, and at higher velocities, the dominant constituent phase becomes Al_6Fe. The presence of Si increases the stability of Al_3Fe with respect to increase in solidification front velocity. An addition of 0.75 wt% Mg further enhances the stability of Al_3Fe [119]. On the other hand, rare earth addition, such as Ce and La were found [121] to eliminate the formation of Al_3Fe.

1XXX alloys are strengthened by cold work, which increases the dislocation density of the alloys, and promotes the accumulation of dislocations in cellular structures. The lattice strain is lower in alloys with high Fe content, which indicates that the additional volume fraction of Fe-bearing constituents promotes particle-induced dynamic recovery for rolling to very high strains [59]. This effect can also be seen in Fig. 43, which shows the dislocation structure in alloy 1145-H19. The cold rolling of Al-Fe alloys promotes the accumulation of dislocations in cellular structures.

The initial flow stress of alloy 1145 is quite low, and work-hardening is sustained to quite high strains [122]. At low strains, the microstructure shows the development of dislocation tangles particularly in the vicinity of grain boundaries. With increasing strain, the tangles develop into well-defined cell walls. The cells are
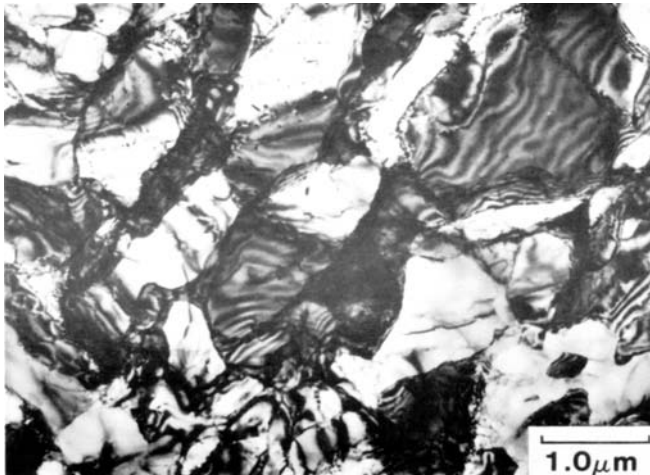
Figure 43 Transmission electron micrograph illustrating the dislocation structure in alloy 1145–H19 foil. Reprinted from Ref. 39. (Courtesy of Alcoa).
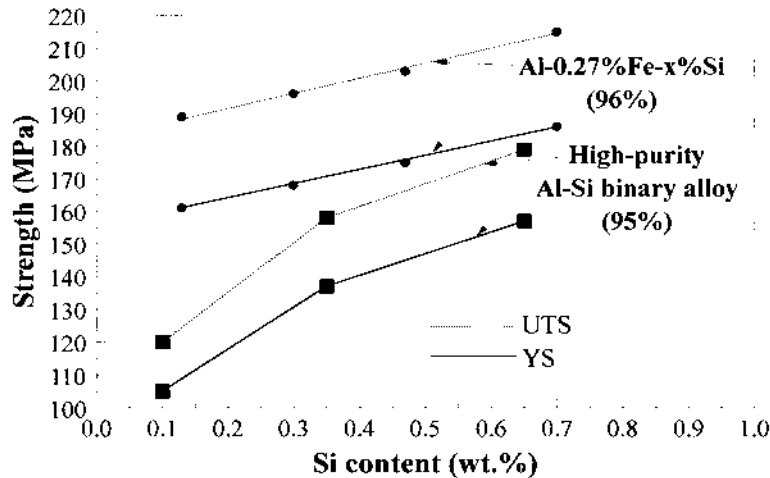
Figure 44   Strength versus Si content for Al-0.27 wt% Fe-x Si and high purity Al-Si binary alloys after cold-rolling. (Source Ref. 39).

essentially equiaxial near the grain boundaries but may be elongated in the grain interiors where the number of operating slip systems may be less than the five required to maintain compatibility at the grain boundaries.

The dislocation cells become smaller with increasing strain, but appear to reach a limiting size of a little less than one micron at a true strain of around 0.15. Additional plastic strain leads to a gradual increase in the misorientation across the cell walls and there is a gradual sharpening of the walls indicative of the relaxation of the dislocation structure into a more stable arrangement.

The strength of Al-Fe-Si alloys increases with increasing Si content, Fig. 44. Si in solution increases the extent of strain hardening; Si atoms impede dynamic recovery during cold work and promote strain hardening via dislocation multiplication [59]. This effect is illustrated in Fig. 45, which compares the dislocation structures of pure Al and Al-1.0 wt% Si after 90% cold-reduction by rolling.

The Fe content in solid solution prior to annealing affects the onset of recrystallization; increasing Fe in solid solution increases the temperature at which recrystallization starts [59], Fig. 46. This retardation of recrystallization is caused by the precipitation of fine Al-Fe particles during the anneal. Si has a similar effect on recrystallization; when Si precipitates prior to or during annealing, fine Al-Fe-Si or Si particles impede early stages of recrystallization within the deformation zones. This leads to a reduction in the number of deformation zones that can otherwise serve as effective nuclei for new grains.

With increasing amounts of Fe and Si out of solution as constituent particles during deformation processing, the volume fraction of particles having a size that can nucleate recrystallized grains increases. An example of effect of Fe additions on achieving fine grain sizes in 1XXX alloy sheet is illustrated in Fig. 47.

2.4.2   Al-Cu and Al-Cu-Mg Alloys

Copper is added to aluminum mainly to increase strength. As the Cu content increases, there is a continuous increase in hardness, but strength, and especially
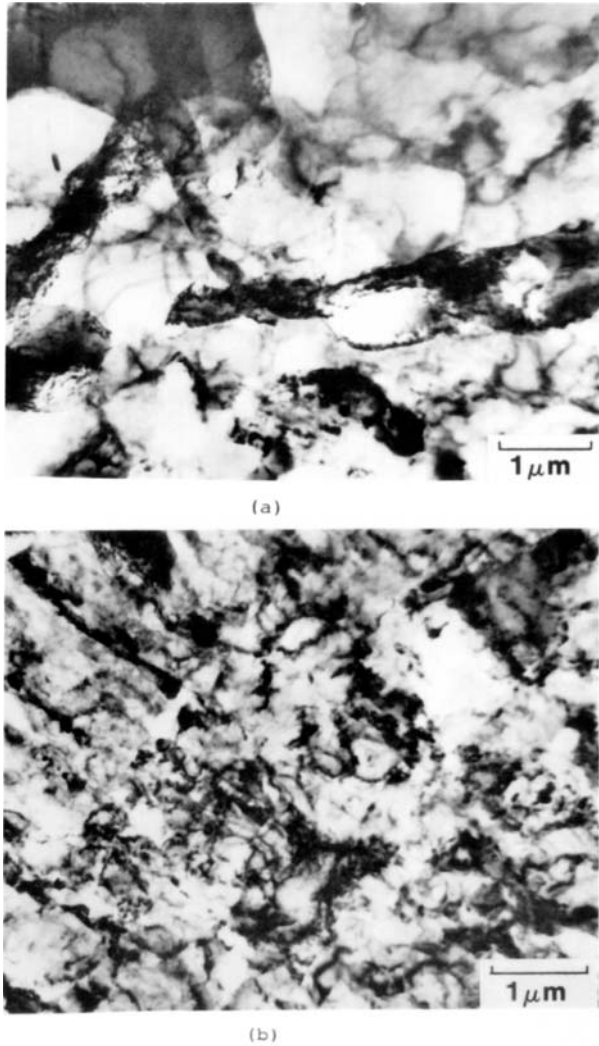
Figure 45 Transmission electron micrographs comparing the dislocation structures of (a) pure Al; and (b) Al-1.0 wt% Si after 90% reduction by rolling. Reprinted from Ref. 39. (Courtesy of Alcoa).

ductility, depend on how the Cu is distributed. During aging of Al-Cu alloys, Cu atoms cluster into two dimensional disc-shaped GP zones, usually 30–50 Å in diameter [69], on the $\{100\}_\alpha$ matrix planes. Above 100°C, three dimensional zones are formed. The maximum temperature at which GP zones are stable is relatively low [123]. If a quenched Al-Cu alloy is heated above 190°C, the GP zones redissolve in the aluminum matrix. Equilibrium and metastable equilibrium solvi are given in Ref. 124. Precipitation follows the sequence;

GP zones $\rightarrow$ θ'' (sometimes referred to as GP$_2$) $\rightarrow$ $\theta' \rightarrow \theta$
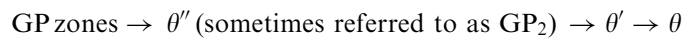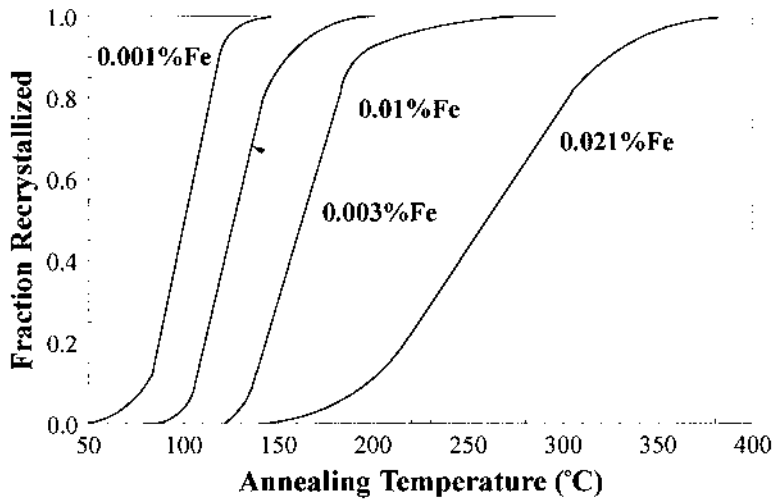
Figure 46 The effect of Fe in solid solution on recrystallization of high purity lXXX sheet. Reprinted from Ref. 39. (Courtesy of Alcoa).
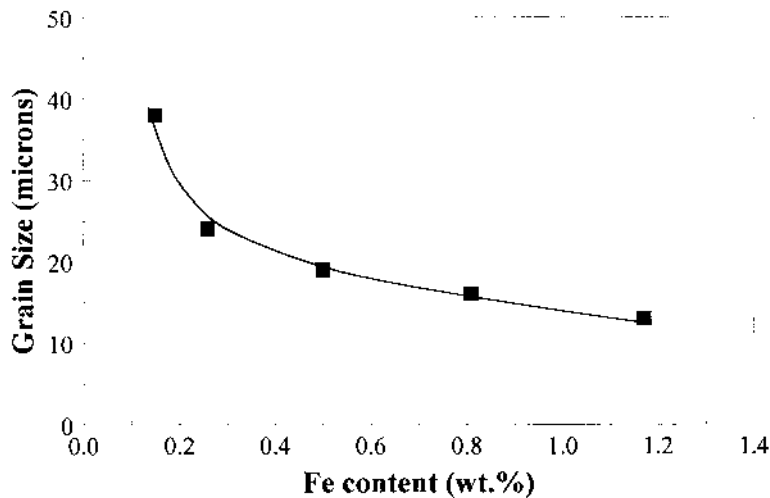
Figure 47 The effect of Fe additions on annealed grain size of Al-Fe-0.05 wt% Si. Data are given in Ref. 39.

Micrographs of precipitating phases are presented in Fig. 48 [125]. GP zones are several layers thick with compositions varying from 25 to 45 at% Cu [126]. θ'' precipitates have nearly the same composition as the GP zones, but consist of Al-rich layers separated by Cu-rich layers [126]. Depending on the aging time and the temperature, θ'' may transform into the transition phase θ', which has the same chemical composition as the equilibrium phase, θ (Al$_2$Cu). However θ' has a tetragonal structure, and is only partially coherent with the matrix. θ' particles
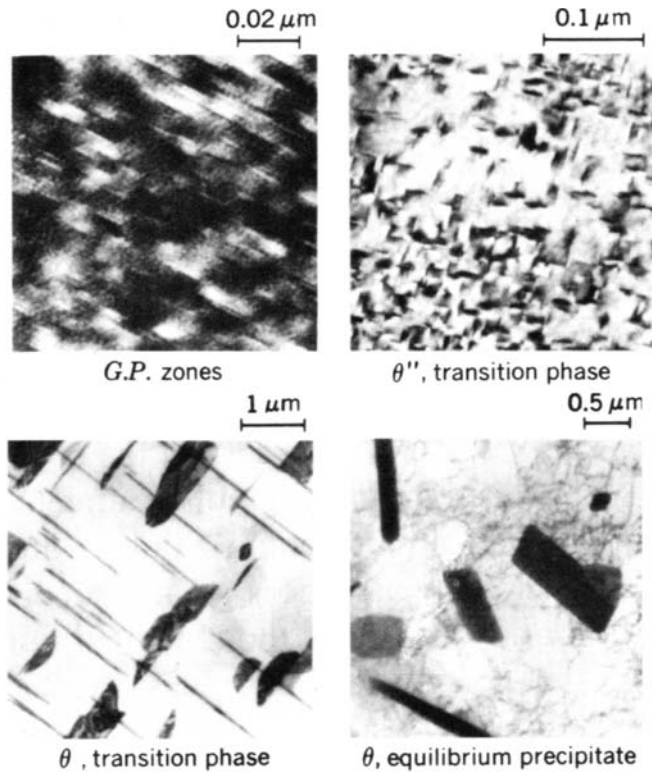
Figure 48 Transmission electron micrographs of (a) GP zones; (b) θ' phase; and (c) θ'' phase in Al-Cu alloys [125].

nucleate heterogeneously at the θ''/Al matrix interface or nearby at a defect and dissolving the θ'' precipitate by attracting the Cu [127], as shown in Fig. 49(a). θ' is fully coherent with the matrix along the broad faces, and often nucleates on dislocations. Therefore the distribution of θ' is heterogenous, and reflects the distribution of dislocations [69]. The $\theta' \rightarrow \theta$ transformation is a gradual process, and θ' particles are present even at advanced stages of θ precipitation [128]. The θ precipitation stage is separate and distinct from the θ' stage. θ may nucleate at θ'/matrix interface [127], as seen in Fig. 49(b). The growth of θ involves the concurrent dissolution of θ' particles, with solute supplied to θ particles along dislocation [128]. Extended aging delay may result in the nucleation and rapid growth of θ' and/or θ precipitates during subsequent artificial aging, resulting in lower properties [129].

Aging curves for an Al-4 wt% Cu alloy, solution treated at 550°C and water quenched to 20°C are shown in Fig. 50 [130]. Note in Fig. 50 that peak hardness and time required to reach peak hardness is a function of aging temperature. Precipitation at higher temperatures occurs more rapidly, so that peak hardness is obtained at shorter times as aging temperature increases. However, the degree of supersaturation also decreases with increasing temperature, resulting in decreasing magnitudes of peak hardness.
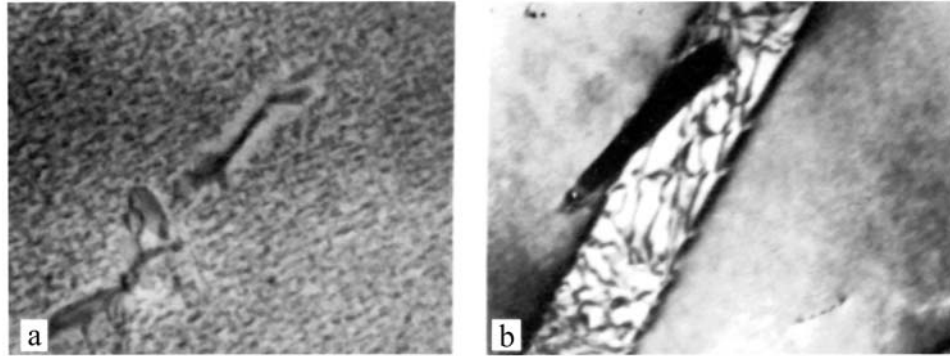
Figure 49 The heterogeneous nucleation of (a) θ' particles at the θ''/Al matrix interface; and (b) θ particles at the θ'/Al matrix interface. (Courtesy of Prof. E. Hornbogen, University of Ruhr, Germany).
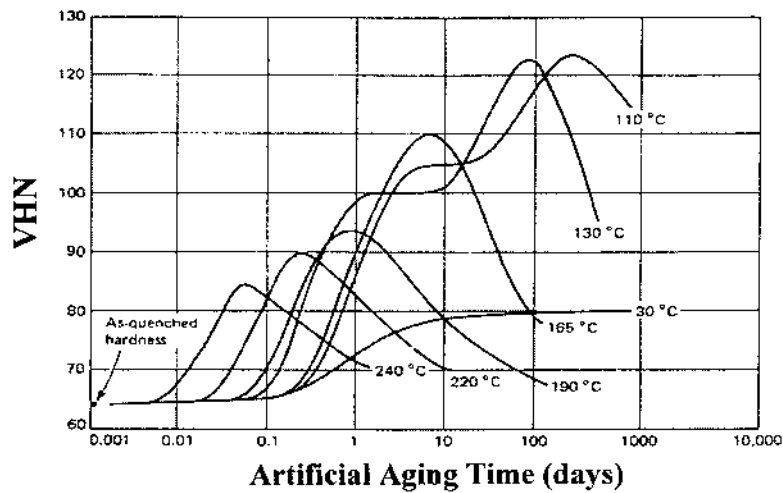
Figure 50 Aging curves of an Al-4 wt% Cu alloy (Source Ref. 130). Peak hardness and time to reach peak hardness is strongly affected by aging temperature.

In binary Al-Cu alloys, the orientation of θ'' and θ' is affected by the applied stress (can be either external or residual), which affects the nucleation, but not subsequent growth [131,132]. This effect is shown in Fig. 51. Tensile stress applied in the [001] direction favors the formation of GP zones and θ' parallel to the [001] axis, while the compressive stress results in the preferential formation of GP zones and θ' perpendicular to the stress axis [131]. This is explained by the minimization of the strain energy of GP zones and θ' plates associated with nucleation; the misfit strain of GP zones in the direction parallel to the disc plane is larger than that in the perpendicular direction [131], and θ' particles have a misfit of about -4.5% with the Al-matrix, and tend to nucleate to cancel this misfit. The stress orienting effect is determined in the early stages of precipitation, where GP zones are
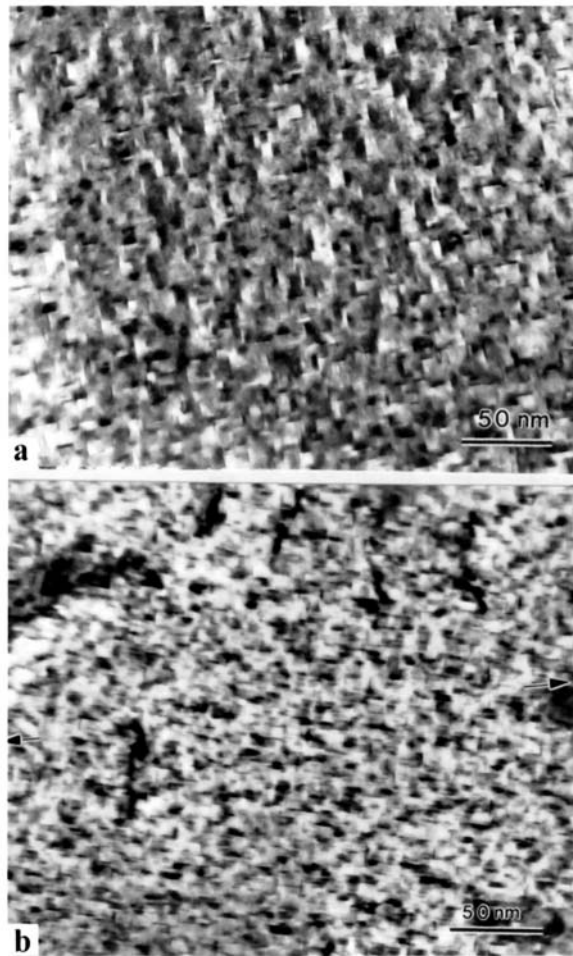
Figure 51 Microstructure of an Al-5 wt% Cu alloy (a) in stress-free state; and (b) when a tensile stress of 69.5 MPa is applied. θ'' precipitates, which are randomly distributed in stress-free state, align themselves preferentially with the stress axis. (Courtesy of Prof. E. A. Starke, Jr., University of Virginia).

preferentially formed under the stress below the critical temperature. There is a critical temperature [131,133] and a critical stress [132] for θ'' and θ' to align with the applied stress. The critical temperature is between 180°C and 190°C [131,133]; if the alloy is aged at a temperature above the critical temperature, θ' is formed directly and the precipitation is not affected by an applied stress. The applied stress should be in excess of the critical stress for the alignment of precipitates. The critical stress is temperature dependent, and was found [132] to be approximately 19 MPa at 160°C. Ω precipitates, which have a misfit of -9.3%, were also found [132] to align with the applied stress. The critical stress for Ω precipitates is between 120 and 140 MPa at 160°C.
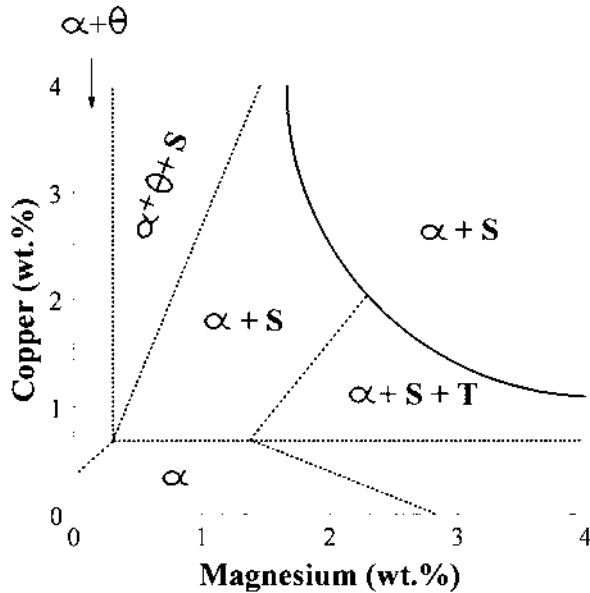
Figure 52 Phase fields in Al-Cu-Mg alloys as a function of Cu and Mg content.

The addition of Mg to Al-Cu alloys enhances both the magnitude and rate of natural aging [57,69]. This enhancement probably results from the complex interactions between Mg atoms in solution and vacancies [64]. The identity of the strengthening precipitates in individual alloys is determined by the weight ratio of Cu:Mg. Phase fields as a function of Cu and Mg content is shown in Fig. 52. There is generally a significant increase in the hardness achievable with increasing Mg content and Cu:Mg ratio.

In Al-Cu-Mg alloys with low Cu:Mg ratios (< 1), the as-quenched alloy contains a uniform dispersion of dislocation loops, and independent clusters of Cu and Mg [134]. Shortly after the start of aging (at 150°C), dislocation loops become unstable, rapidly coarsen and grow into helical dislocation lines, and Cu-Mg co-clusters form [134]. In Al-Cu-Mg alloys with higher Cu:Mg ratios, loops are stable for prolonged times at temperatures around 180°C. At high Mg concentrations, S′ and S phases (Al_2CuMg) are observed. The formation of Cu-Mg co-clusters, which preceeds that of GP zones and S phase, is linked to the rapid hardening reaction. Further aging results in the formation of rod-like GP zones. The transition phase, S′, has the same chemical composition and a crystal structure very similar to the equilibrium S phase. The S′ precipitates normally nucleate on dislocations, and grow as laths on $\{210\}_\alpha$ planes along $\langle 100 \rangle_\alpha$ directions. These processes occur during the second stage of hardening. The S′ phase grows gradually at the expense of the GP zones and peak hardness is associated with the formation of independently nucleated S phase. The precipitation follows the sequence:

$$SSSS \rightarrow \text{pre-precipitate stage} \rightarrow \text{GP zones} + S' \rightarrow S$$
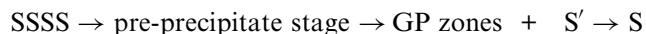
Most alloy development has focused on alloys with Cu:Mg weight ratios≥1.5:1, which fall within the $(\alpha + S)$ and $(\alpha + \theta + S)$ phase fields in Fig. 52. There is a significant hardness achievable with an increase in Mg content, and with increasing Cu:Mg ratios in excess of approximately 6.5:1 $(\alpha + \theta + S$ alloys), the precipitation processes are similar to those in binary Al-Cu alloys, accompanied with those specific to the ternary system [135].

Trace additions of Ag promote greater response to age hardening in all aluminum alloys containing Mg [135]. Ag additions have little or no effect on the precipitation of the θ' phase in either Al-Cu or Al-Cu-Mg alloys [135]. However Ag additions may result in the formation of new precipitates, the exact nature of which depends on the Cu:Mg ratio. Small additions of Ag (~ 0.1 at%) to Al-Cu-Mg ternary alloys with a low Cu:Mg ratio, such that they lie in the $(\alpha + S + T)$ field in Fig. 52, result in fine, stable precipitates of a Z-phase [136], with two distinct orientations. At higher Cu:Mg ratios, such that the alloy composition lies in the $(\alpha + S)$ field in Fig. 52, a fine, uniform precipitation of $\{111\}_\alpha$ X phase [137], is observed instead of the S′ or S phases, which results in enhanced response to age hardening [138]. The composition of the X′-phase is 20–25 at% Cu, 15–25 at% Mg and 50–65 at% Al [139]. Recent findings [140] indicate that up to 5 at% Ag is contained in the X′-phase, probably as a result of Mg-Ag co-clusters detected at the early stages of precipitation. In alloys with high Cu:Mg ratios, Ag promotes formation of Ω, that forms as finely dispersed plates on the $\{111\}_\alpha$ planes [141], which partially or completely replaces the above mentioned precipitation sequence in Al-Cu based systems [132]. The orientation of Ω is presented in Fig. 53.

When Si and Ge are added to Al-Cu-Mg alloys, independent clustering of Cu, Mg, Si and Ge were observed [142] in the as-quenched microstructure. Mg and Ge form co-clusters shortly after the start of artificial aging, which lead to the formation of GP zones. Si is also associated with these zones. These GP zones are con-
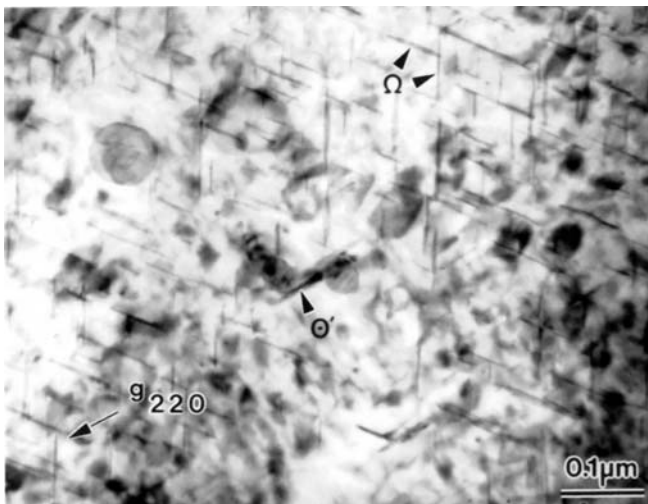
Figure 53 The orientation of the Ω precipitate ([110]α) in Al-Cu-Mg-Ag alloys. (Courtesy of Prof. E. A. Starke, Jr., University of Virginia).

sumed by the precipitation of the more stable θ' and by the gradual formation of rod-shaped Cu-Mg rich precipitates. Si is segregated to these zones, and Ge is associated with the larger zones. Mg and Si were found [142] to be associated with some θ' precipitates.

Discs of vacancies retained during quenching collapse to form dislocation loops with high densities in Al-Cu-Mg alloys [143,144]. These loops disappear when Ag is added to the alloy [144,145]. The high binding energy between Ag atoms and vacancies is most probably responsible for this change in lattice defect distribution. Consequently vacancies aggregate and condense in the supersaturated solid solution [144]. Si additions accelerate the interaction of solute atoms, by increasing the free vacancy content of the alloy [140]. In the as-quenched condition, independent clusters of Cu, Mg and Ag form. Immediately after the start of artificial aging, co-clustering of Ag and Mg atoms occurs. Cu then migrates to the sites of these co-clusters, and extremely small precipitates containing Ag, Mg and Cu atoms form. These precipitates are the precursors of the Ω [143–145] and X$'$ [140] phases. Ω co-exists with minor fractions of precipitates such as θ'' and and θ', which form on the $\{100\}_\alpha$ planes in binary Al-Cu alloys. Ω is also the predominant strengthening phase in the commercial 201, which is the strongest of all aluminum casting alloys [135,146]. This phase shows high stability up to 200°C [147], and shows high resistance to creep [148–150]. However prolonged aging at 250°C results in the replacement of Ω with θ [147].

Trace additions of Cd, In or Sn increase the strength and hardness of artificially aged Al-Cu alloys by promoting nucleation of a finer, more uniform dispersion of θ' [130,151]. Additions of In to Al-Cu-Mg alloys result in the nucleation of In-bearing precipitates early during artificial aging, which act as heterogeneous nucleation sites for θ' and S precipitates, and significantly accelerate the aging process [152]. Cd, In, and Sn retard the formation of GP zones, as ternary trace modified alloys are observed to age-harden more slowly than the binary alloys at room temperature. At elevated aging temperatures, the microalloying additions favor the formation of fine-scale θ' phase at the expense of GP zones and θ''. Trace additions of Cd (~ 0.1 at%) have the same effect in Al-Cu-Mg alloys with high Cu:Mg ratios as in binary Al-Cu alloys [138].

Somewhat larger additions of Li has the same effect as trace additions of Sn, Cd and In on Al-Cu and Al-Cu-Mg alloys [135,153]. Small additions of Li (1.0–1.5%) to Al-Cu-Mg-Ag alloys stimulates a greater age-hardening response than observed in the quaternary alloy. Li additions progressively increase hardness and time required to achieve maximum hardness (See Al-Li, Al-Cu-Li Alloys section in this chapter for more discussion). Li has a high binding energy with vacancies, and consequently inhibits their condensation into dislocation loops or helices [154]. However, the strong lithium/vacancy interaction slows the kinetics of the homogeneous precipitation of S. Trace additions of Ge to Al-Cu-Mg alloys encourage θ' nucleation [155]. Mg interacts strongly in solid solution with both Ge and Si, and quaternary Al-Cu-Mg-Ge alloys exhibit a much stronger age-hardening response than simple ternary Al-Cu-Mg alloys of similar composition. Si additions also increase response to age hardening in Al-Cu-Mg alloys, and therefore commercial alloys contain some minor additions of Si. The addition of Si to alloys with a Cu:Mg ratio of approximately 2 improves mechanical properties significantly, by promoting a refined distribution of the S phase (Al_2CuMg) [156]. In the presence of small

concentrations of Si and/or Ge, Ag has much less effect on the age hardening response in Al-Cu-Mg-Ag alloys. The presence of Si and Ge favor the formation of the rod-like zones during the early stages of aging, exhausting the supply of Mg and thus preventing the formation of the Ω phase that is characteristic of the quaternary alloy [135]. The $\langle 100 \rangle_\alpha$ lath-like precipitates in turn promote a fine distribution of θ' plates [156]. The additions of Si to an Al-4.0 wt% Cu-0.3 wt% Mg alloy have been found [156] to enhance response to age hardening, and for Si contents 0.3–0.7 wt%, maximum hardness (after artificial aging at 200°C) exceeds that obtained by a 0.4 wt% Ag addition. Si additions promote a fine, dense and uniform distribution precipitation of $\{100\}_\alpha$ plates of θ' and $\langle 100 \rangle_\alpha$ laths of Q phase [156] (See Al-Mg-Si-Cu alloys section in this chapter for more discussion on the Q phase). Minor additions of Si (0.15–0.50 wt%) suppress the formation of Ω phase in an Al-4.5 wt% Cu-0.3 wt% Mg-0.7 wt% Ag, without adversely affecting mechanical properties [157]. Sn additions significantly affect the decomposition of Al-Cu alloys [158]. Artificial aging is accelerated while natural aging is retarded.

Si increases feedability and resistance to hot cracking during casting. Fe reduces hot cracking in Al-Cu alloys, but both Fe and Si can form constituent phases (e.g. Al_7Cu_2Fe and Mg_2Si) which reduce fracture toughness. Improvements in both fracture toughness and ductility of 2XXX alloys can be obtained by reducing the levels of Fe and Si impurities as well as that of Cu, all of which favor formation of large, brittle compounds in the cast materials [71]. Si, however, is an intentional alloying element in the Al-Cu-Mg alloy 2014 because of its effect on increasing strength. Effects of Si will be discussed in more detail in the Al-Cu-Mg-Si section.

Iron may also be an alloying element in Al-Cu alloys. About 1% each of Fe and Ni are present in equal amounts in 2618, the alloy used on the SST.

Manganese is added to most commercial Al-Cu alloys. It was present along with Cu and Mg in the first precipitation hardenable alloy discovered by Wilm. It forms $Al_{20}Cu_2Mn_3$ dispersoid particles which provide some dispersion strengthening, and also serve to nucleate precipitates during aging on dislocations which emanate from the particle matrix interface during quenching.

The addition of Zr reportedly raises the tensile strength [159]. Zirconium was added to alloy 2219 to enhance strength at elevated temperatures.

Pb and Bi have been added to Al-Cu alloys to form discrete particles in the microstructure, and assist with chip formation [160], but recent health concerns have led manufacturers to investigate other elements such as Sn for Pb.

Response to age hardening is enhanced by cold work prior to artificial aging (T8 temper) and the yield strength can be increased by as much as 35% compared to the T6 temper [71]. Enhanced hardening is observed in alloys based on the Al-Cu, Al-Cu-Mg and Al-Cu-Li systems in which each of the primary intermediate strengthening precipitates nucleates with difficulty. In these alloys, the dislocations introduced during cold work provide preferred heterogeneous nucleation sites [161,162]. As a result, the hardness and tensile strengths of Al-Cu alloys are increased. In 2XXX alloys strengthened by θ', S', or T1, attainable strength increases significantly because dislocations serve to nucleate these metastable precipitates, and promote the development of finer, more closely spaced particles. Because of this strong effect, alloys 2219 (θ'), 2024 (S'), and 2090 (T1) are used almost exclusively in T3 and/or T8 tempers. Deformation at elevated temperatures prior to artificial aging also improves tensile properties of Al-Cu-Mg ternary alloys, due to the sub-

a
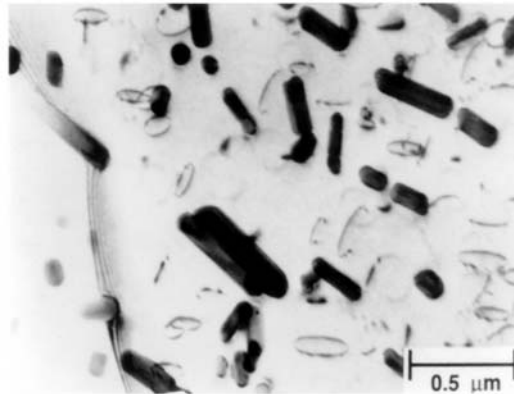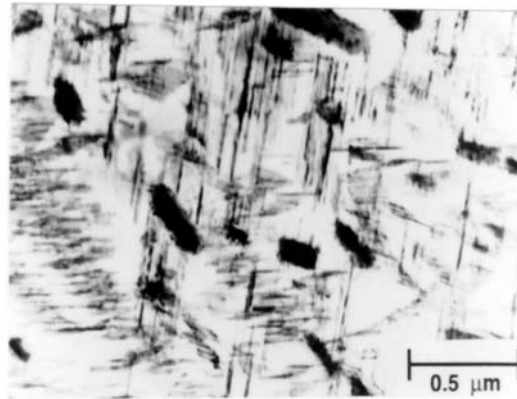
b
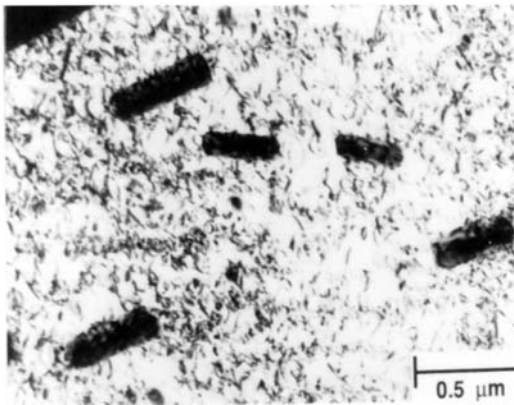
c

Figure 54 The effect of cold work and heat treatment on precipitate dispersion in alloy 2024 sheet. (a) no cold work (T4); (b) no cold work (T6); (c) 1% cold work (T31); (d) 1% cold work (T81); (e) 6% cold work (T36); and (f) 6% cold work (T86). Reprinted from Ref. 95. (Courtesy of Alcoa).
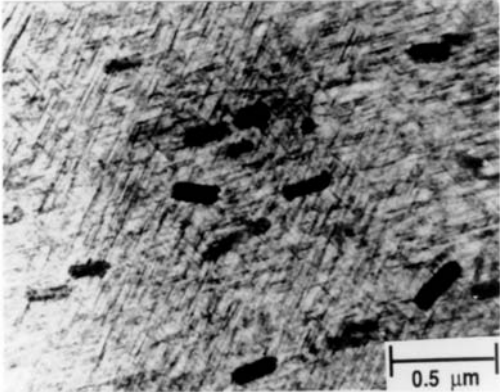
d
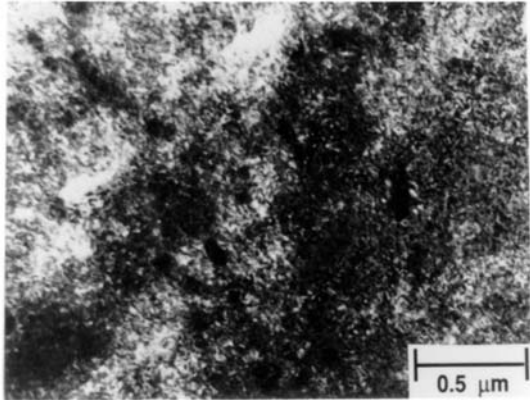
e
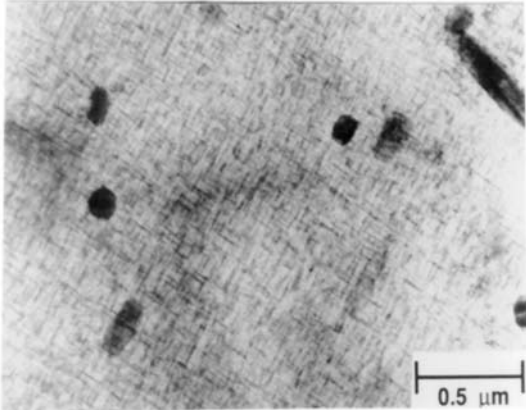
f

Figure 54   *Continued.*

sequent more homogeneous precipitation of strengthening phases [162]. The effect of cold work and temper on the microstructure of 2024 sheet is presented in Fig. 54 [95]. In 2XXX alloys strengthened by S′, θ′ or T1, attainable strength increases significantly because dislocations serve to nucleate these metastable precipitates and promote the development of finer, more closely spaced particles. The dislocation density is low in 2024-T4 sheet, and it increases with increasing cold work from 1% in the T31 temper to 6% in the T36 temper. When the T4, T31, and T36 products are artificially aged at 175°C to the T6, T81, and T86 tempers, respectively, the size and spacing of the metastable S′ precipitates decreases appreciably with increasing amount of cold work, Fig. 54. Comparison of microstructures of alloy 2219 and alloy 2519 plate illustrates a positive synergistic effect of adding small amounts of Mg and cold working on precipitate dispersion in alloys strengthened by θ′, Fig. 55 [95]. The effect of change in microstructure on tensile properties is presented in Fig. 55(e). The combined effect of adding Mg and cold working is to increase strength by 190 MPa instead of the 150 MPa attributable to their effects considered separately. In presence of trace elements, the very fine dispersion of θ′ present in undeformed alloys is replaced by a comparatively coarser distribution. Hence properties are reduced [135]. Ag containing Al-Cu-Mg alloys do not to respond to cold work prior to artificial aging [163], nor does the Al-Cu-Mg-Si alloy 2014.

2.4.3 Al-Li and Al-Cu-Li Alloys

Lithium is one of the relatively few elements that has high solubility in aluminum with a maximum value of approximately 4 wt% (16 at%) at 610°C, Fig. 56. This is significant because, for each 1% addition, the density of an aluminum alloy is reduced by 3%, accompanied by a 6% increase in elastic modulus [141]. The effect of Li content on tensile properties in Al-Li binary alloys is shown in Fig. 57. The effect of increasing Li content in both T4 and T6 tempers is to increase UTS and YS and decrease elongation.

Many of the metallurgical characteristics of Al-Li alloy products are attributed to a high volume fraction of ordered Al_3Li, δ′, precipitates, as presented previously in Fig. 14. These spherical particles are sheared by pairs of dislocations; the first dislocation disrupts the order, which is restored by the following one (although it has been suggested [84] that the trailing dislocations avoid δ′ particles). This behavior serves to localize deformation as bands on particular slip planes. Although strain localization is detrimental to tensile properties, it results in superior crack growth performance under cyclic loading conditions; the concentration of slip forces the advancing crack to follow a particular set of slip bands in a grain. When a grain boundary is reached, the crack must abruptly change direction as it grows. Above a critical size, δ′ particles are by-passed by Orowan strengthening mechanism or double cross-slip. In binary alloys, Υ_{APB} is approximately 150 mJ/m^2, and $(D_p)_{s \to b}$ is 34 nm [164].

Nucleation of fine δ′ ($\sim$20 Å in diameter [164]) is almost inevitable during the quench in alloys containing more than 7 at% Li [101] ($\sim$1.9 wt% Li). Lowering the Li content below this limit (1.9 wt%) lessens grain boundary precipitation and consequently increase elongation [165]. Due to the low misfit of δ′ in Al matrix (-0.08±0.02% [166]), and its low interfacial energy ($\sim$14 mJ/m^2), δ′ forms by homogeneous nucleation. The morphology of δ′ is almost invariably spherical and the distribution is homogeneous and insensitive to variations in pre-aging thermal
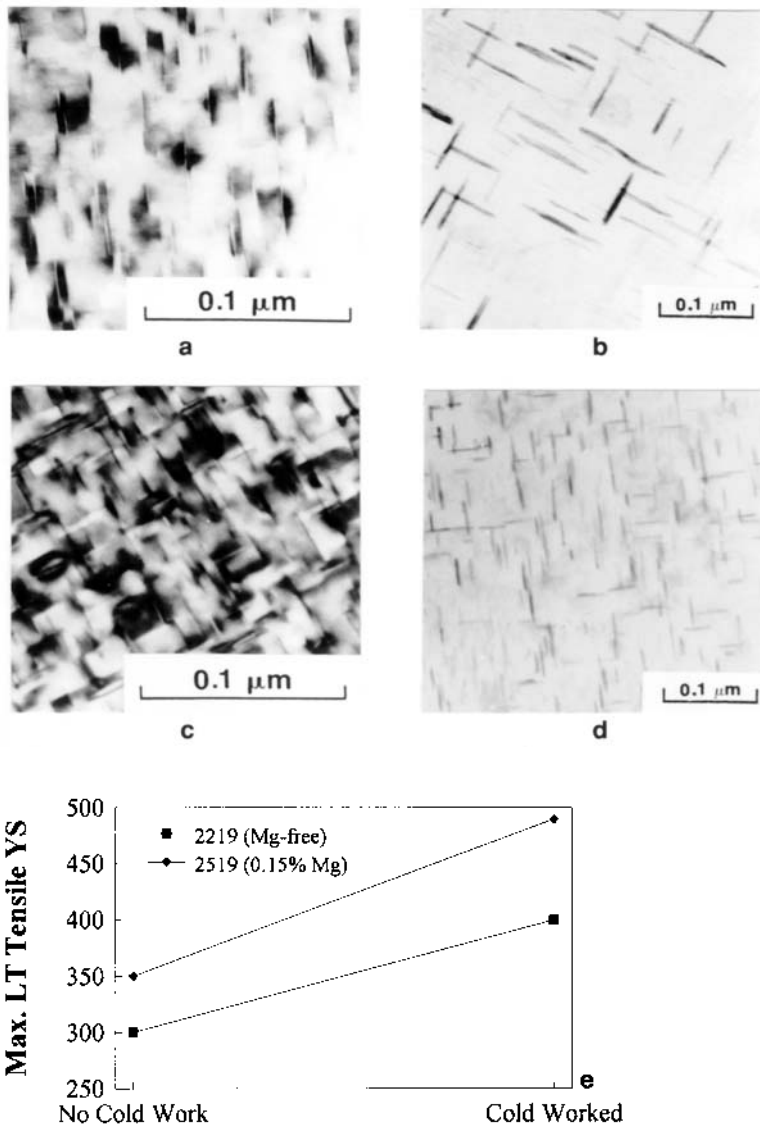
Figure 55 The effects of 0 (a and c) versus 20% cold work (b and d) on precipitate dispersion in alloy 2219 (a and b, no Mg) and 2519 (c and d, 0.15 wt% Mg), and the consequent changes in mechanical properties (e). Micrographs reprinted from Ref. 95. (Courtesy of Alcoa).

history. However, when the heat treatment temperature is low (within 40°C of the solvus), δ' nucleates and grows on dislocations [101,167], preferentially at the compressive side of edge dislocations [167]. The shape of δ' that precipitates on dislocations has been described as disc-like [101] and kidney-bean shaped [168]. The growth of δ' on dislocations is associated with the climb of the dislocation toward the tension side [168]. δ nucleates heterogeneously due to the large misfit

Lithium, atomic %
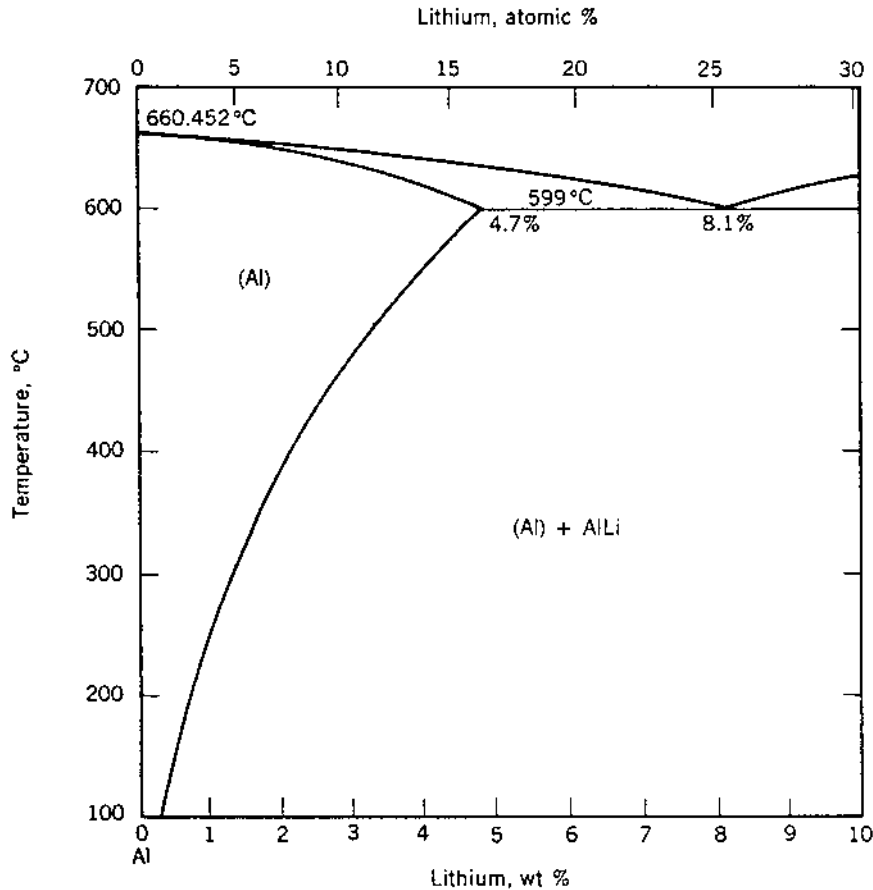
Figure 56   Al-rich end of Al-Li phase. Drawn by Dr. Joanne Murray. (Courtesy of Alcoa).

between δ and Al [101], generates a high density of mismatch dislocations, and cause dissolution of surrounding δ' in an Al-10.7 at% Li alloy [166]. δ forms initially at grain boundaries where it generates δ' PFZs, and within the matrix.

In overaged alloys, wide PFZs and coarse grain boundary precipitates can act as preferential deformation sites [169]. The dislocation pile-ups on the slip bands concentrate the stress on grain boundaries which may contain equilibrium precipitates, and promote intergranular fracture and low fracture toughness. Grain size effects become important in these instances since slip distance can be reduced by reducing the grain size. Hence stress concentration is reduced at grain boundaries due to reduced number of dislocation in the pile-ups. Consequently, early crack nucleation is prevented so that the fracture mode can be changed from a low energy intergranular to a high energy transgranular mode [169].

Strain localization of Al-Li binary alloys can be reduced, and even eliminated by alloying additions. For instance, ternary additions of 0.2 wt% Ge increase the solid solubility of Li in aluminum, and result in the precipitation of rod-shaped Ge particles approximately 15–20 nm in length at peak hardness [170]. The ger-
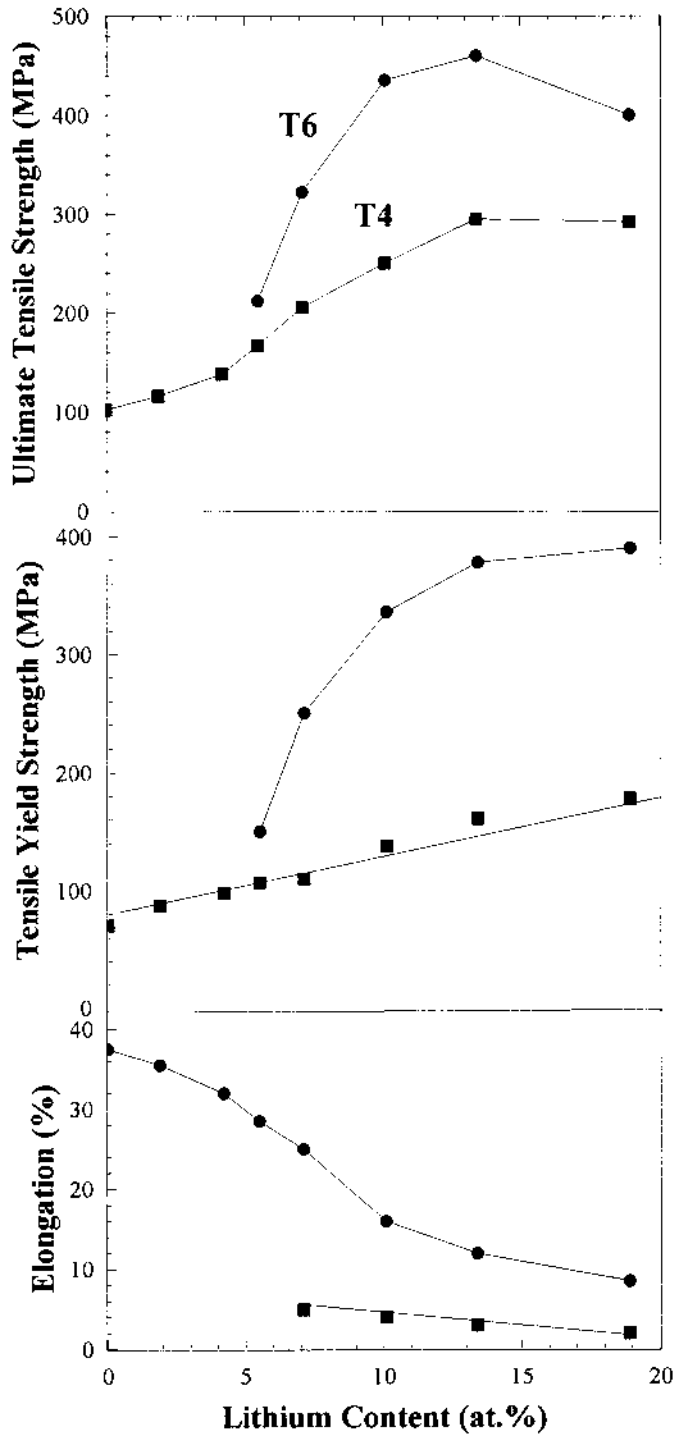
Figure 57 The effect of Li content on tensile properties in Al-Li binary alloys. Data are provided in Ref. 30.
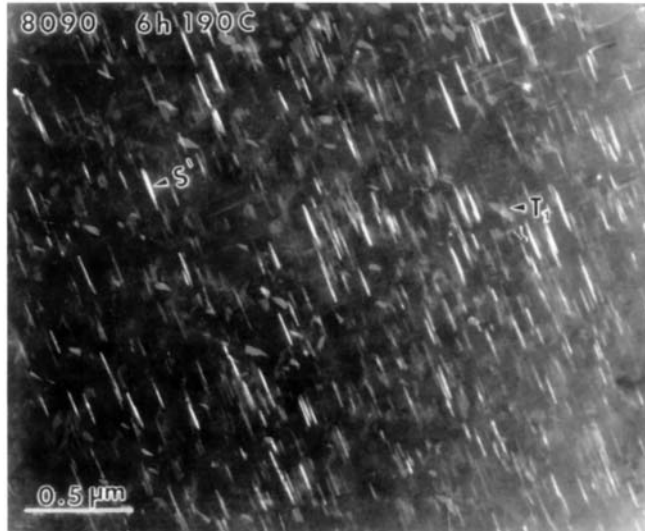
Figure 58 S′ and T1 precipitates in 8090 alloy. (Courtesy of Prof. E. A. Starke, Jr., University of Virginia).

manium particles effectively disperse dislocation slip, providing a homogeneous distribution of stresses during deformation. Despite the effectiveness of Ge in dispersing slip, commercial alloys containing Li rely mainly on Cu and Mg additions to minimize strain localization.

Additions of Cu and Mg lower the solubility of Li in Al, and cause precipitation of other phases Al_2CuLi (T1) and Al_2CuMg (S′) which provide more effective barriers to dislocations and promote more homogeneous deformation [141]. S′ and T1 precipitates are primary strengthening phases in 8090 alloy, as seen in Fig. 58, after 6 h of artificial aging at 190°C. When Al_2CuLi precipitates on $\{100\}_\alpha$ planes rather than along the $\{111\}_\alpha$, they are referred to as T2 phase [171], which is primarily responsible for the creation of PFZs around grain boundaries in Al-Li-Cu alloys [110]. Cu additions also decrease the grain size, which result in a decrease in the length of dislocation pile-up and the dislocation density in PFZs [169], changing the fracture mechanism from intergranular to transgranular. Cu additions also decrease $(D_p)_{s\rightarrow b}$ from 34 nm to 18 nm [164]. This is possibly due to an increase in the stacking fault energy of the alloy after the Cu addition, which makes the shearing of δ′ more difficult. The δ′ precipitates are by-passed in Al-2.7 wt% Li-1.9 wt% Cu alloys only after 2 h of artificial aging at 190°C [164].

The exact nature of the phase equilibria of the quaternary Al-Li-Cu-Mg alloys depends on the relative concentrations of all three alloying elements [64]. For instance, in alloys with a Cu:Li ratio of 2–3, T1 growth is accomplished by the accretion of Li from the solid solution [101]. However for lower Cu:Li ratios, e.g. 3:2, T1 can grow at the expense of δ′. If T1 nucleates homogeneously from prior GP zones, the alloy has low strength but high ductility, whereas the heterogeneous nucleation of T1 phase on dislocations results in considerable loss in both strength

and ductility [172]. In high strength Al-Cu-Li alloys, such as 2095, the high Cu:Li ratio produces a high volume fraction of T1 without δ', in addition to both S' and θ'.

Mg additions to Al-Cu-Li alloys increase the density of dislocation loops in the as-quenched microstructure, favoring the nucleation of T1 plates [173,174]. 0.5 wt% Mg additions may increase the T6 yield strength of Al-Cu-Li alloys by as much as 30%, resulting from the precipitation of fine θ'' and GP zones in the early stages of aging, and T1 phase with a high aspect ratio in the latter stages of aging. Larger Mg additions (0.5–1.0 wt%) to a high Cu alloy suppress the formation of θ', and introduce the S' phase. Since S' contains no Li, δ' precipitation is markedly influenced by the Mg addition. Unless magnesium levels exceed 2 wt% or aging treatments are extended, Al_2MgLi is absent in the age-hardened microstructure [154]. In general, for alloys containing approximately 4.5 wt% Cu and 1 wt% Li, δ' is suppressed.

Zr, when in solution, slows the coarsening rate of δ' by a factor of ten at 250°C [99]. Al_3Zr dispersoids create dislocation loops around them upon nucleation [153,175,176]. These dislocation loops, which are glissile and can be multiple around the β' dispersoid [175], serve as heterogeneous nucleation sites for δ' precipitates [153,154,175], as well as S' and θ' phases in an Al-Li-Cu-Mg-Zr (8091) alloy [100,175]. Also PFZs around β' particles were observed in an Al-Li-Cu-Zr alloy [100].

Trace additions of indium increase the T6 yield strength of Al-Cu-Li alloys by as much as 25% [173,174]. In affects precipitation by increasing the thickness of the $\{100\}_\alpha$ plates during the early stages of aging and later by promoting more homogeneous precipitation of T1. The increase in strength is due to the increase of the thickness of the $\{100\}_\alpha$ precipitates, indicating a shift from θ'' to θ', and accelerating the transition from particle shearing to by-passing. In additions do not affect aging or strength in the presence of Mg [173,174].

Cd additions to Al-Cu-Li alloys is effective in nucleating θ' [177], as in Al-Cu binary alloys. The effect of 0.28 wt% Cd and 2% stretch on precipitation of θ' in an Al-4.5 wt% Cu-1.2 wt% Li alloy is shown in Fig. 59. Precipitate distribution in peak-aged, Cd-free alloy (M1) is shown in Fig. 59(a). Stretching prior to aging results in enhanced precipitate dispersion in this alloy, Fig. 59(b). In the Cd-added alloy (M2), precipitate dispersion is also enhanced, even in the unstretched condition, Fig. 59(c). Stretching results in minor enhancement in dispersion of θ', Fig. 59(d). Cd is, therefore, more effective in nucleating θ' than a 2% stretch prior to aging. In addition, M2-T6 has a yield stress 14% higher than that of M1-T651. M2 also ages at a faster rate, reaches maximum hardness sooner, and obtains a higher maximum hardness than M1.

Deformation in Al-Li-Cu prior to aging results in improvements in strength and toughness [42]. The T1 phase forms with some difficulty in ternary Al-Cu-Li alloys during conventional isothermal aging treatments and, when possible, it is common in commercial practice for such alloys to be deformed plastically before aging (T8 temper) to induce increased heterogeneous nucleation of the T1 plates and a more uniform precipitate distribution. The maximum strength is achieved by a tensile plastic deformation of 3–6% [135]. Nucleation of the T1 phase is apparently stimulated strongly by an increase in the dislocation density although the T1 plates are coherent with the aluminum matrix and have only a small misfit strain
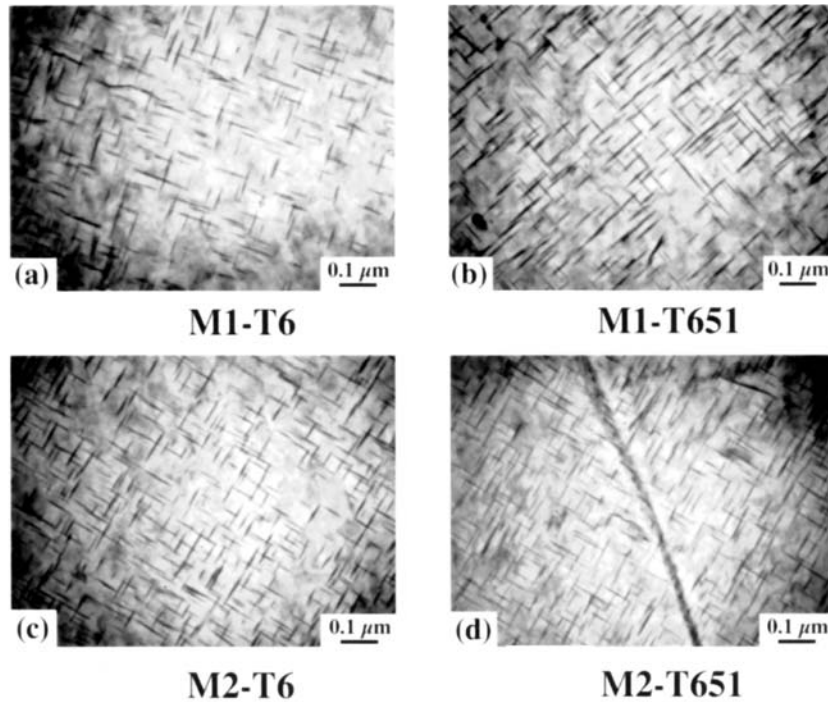
Figure 59   The effect of Cd additions and cold work on the microstructure of an Al-4.5 wt%
Cu-1.2 wt% Li alloy. (a) M1-T6; (b) M1-T651; (c) M2-T6; (d) M2-T651. (Courtesy of Prof. E.
A. Starke, Jr., University of Virginia).

($\sim 0.12\%$) [135]. Precipitation at grain boundaries is reduced as the amount of
stretching is increased [42]. The role of the trace additions of Mg and Ag in Al-Li-Cu
alloys stimulate the formation of the T1 phase, and thus eliminate the need for the
deformation step that is common in the processing of ternary Al-Li-Cu alloys.
The resulting alloys have a substantial strength advantage over ternary Al-Li-Cu
alloys and Al-Cu-Mg-Ag alloys [135].

Toughness of Al-Cu-Li alloys is affected significantly by the concentrations of
Cu and Li. Aging of alloys with high Li/Cu ratio (≥ 0.8) beyond the peak strength
does not improve the fracture toughness of the alloys even though the yield strength
falls significantly on overaging [113]. Limited recovery of toughness on overaging is
observed in alloys with a high Li content, in which grain boundary fracture occurs
from voids initiated around grain boundary precipitates. A low Li/Cu ratio ensures
that the volume fracture of slip dispersing Al-Cu-Li precipitates is larger than that
of δ' [178]. In underaged, high-Li content alloys, in which the amount of grain
boundary precipitates is limited, mixed mode (transgranular and intergranular)
fractures occur often with the types of crack branching illustrated schematically
in Fig. 38. Transgranular fracture in alloys with low Li/Cu ratio can be enhanced
by adding Zr and hot rolling to maintain an unrecrystallized structure, and preceding
artificial aging by a large amount of cold work to refine precipitate size both in the
matrix and the boundaries [178].

Al-Li-(Cu) alloys can fail in several modes [179,180]: (i) ductile, microvoid coalescence, with the voids nucleated at precipitates (δ' or S) at grain or subgrain boundaries or the Fe-bearing constituent; or (ii) brittle, intergranular separation with no associated plastic deformation. The segregation of alkali metal impurities, such as Na and K, contributes to this embrittlement [141]. Na and K react preferentially with Li when this element is present [181] above a critical amount, resulting in intergranular brittle "islands". The failure mode depends on temper, orientation of the tensile axis within the plate, and test temperature [179,182,183]. Additional fracture processes are explained in Ref. 180.

2.4.4   Al-Mn Alloys

The phase diagram for Al-Mn system is given in Fig. 60, which shows that the eutectic Al-MnAl$_6$ is at approximately 1.9 wt% Mn and 930K (657°C). Mn produces a modest solid-solution strengthening, but is more effective in promoting work hardening during cold-rolling. Mn content in commercial Al-Mn alloys is often less than 1.25 wt%, although as much as 1.82 wt% is soluble in Al. The 1.25 wt% limit is
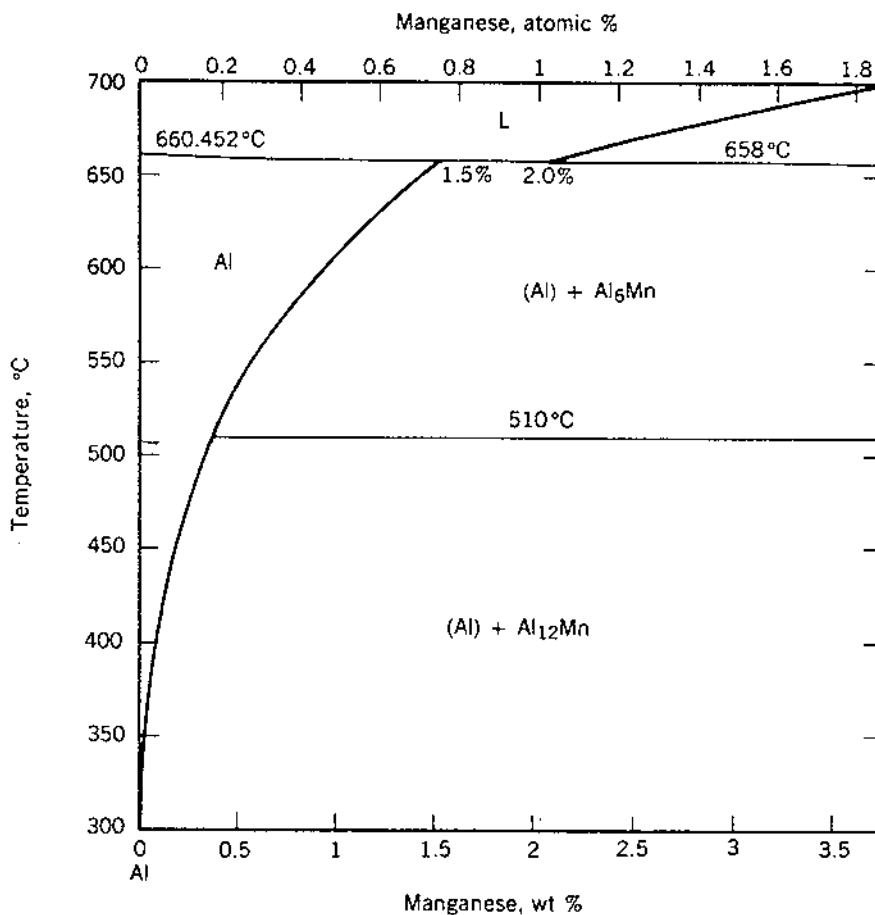
Figure 60   Al-Mn phase diagram. Drawn by Dr. Joanne Murray. (Courtesy of Alcoa).

imposed because Fe decreases the solubility of Mn, and therefore increases the probability of forming large primary particles of $Al_6(Mn,Fe)$, which can have a negative effect on ductility [64,184]. All 3XXX alloys contain controlled amounts of Fe and Si that play a vital role in the phase reactions and microstructural development [59]. During solidification, substantial amounts of Mn are retained in solution in the aluminum matrix. Typical as-cast 3003 ingot contains 0.7–0.9 wt% Mn in solution; the remainder is present as Al-Mn-Fe and Al-Mn-Fe-Si constituent particles. During homogenization, $Al_{12}(Mn,Fe)_3Si$ or $Al_6(Mn,Fe)$ dispersoid particles precipitate from the supersaturated matrix. If the Si content is less than 0.07 wt%, the dispersoid phase is usually $Al_6(Mn,Fe)$. The size of the dispersoid particles depends on the thermal conditions used for the homogenization, but are typically less than 1 μm in diameter. Microstructure of alloy 3004 after various stages of processing is presented in Fig. 61, which shows the progressive increase in microstructural homogeneity during processing to sheet. Constituents and dispersoid are shown (a) in a homogenized 500 mm thick ingot; (b) after hot rolling to 47 mm slab; and (c) after rolling to 0.33 mm sheet.

Figure 62 shows the yield and ultimate tensile strengths of binary Al-Mn alloys for two tempers, in which the Mn has been retained in solution by a high temperature anneal and a rapid quench [59]. Note in Fig. 62 that annealed yield strength increases approximately 21 MPa and ultimate tensile strength about 42 MPa per wt% Mn in solution. The H19 yield strength only increases about 35 MPa per wt% Mn. Mg, on the other hand, raises the H19 yield strength by 70–85 MPa per 1 wt%. Hence Mn is not as effective in promoting work hardening as Mg. Thus many commercial 3XXX alloys contain Mg and/or small Cu additions to achieve higher strength.

The kinetics of the Mn precipitation reaction can be markedly affected by alloy composition [59]. Si accelerates the precipitation of Mn, and results in a denser distribution of $Al_{12}(Mn,Fe)_3Si$ and reduces the Mn retained in solution after homogenization. If sufficient Si is present some or all of the $Al_6(Mn,Fe)$ phase present after casting transforms to the $Al_{12}(Mn,Fe)_3Si$ [59,185]. Additionally, increasing the Fe/Mn ratio may promote the formation of the alternative $Al_{13}(Fe,Mn)_4$ phase in as- cast alloys [185].

In deformed binary Al-Mn alloys, cell formation follows the initial increase in dislocation density, regardless whether Mn is retained in solution or is present as a dispersoid. With increased rolling, the subgrain structure becomes more well-defined and the subgrain size decreases. The subgrain interiors tend to be relatively free of dislocations. When Mg is added for strengthening, the tendency toward cell formation is reduced and the dislocation density of the alloy increases with increasing Mg content. The effect of Mg additions to Al-Mn alloys on substructure is presented in Fig. 63. Mg-bearing alloy (3004) has a finer substructure with an overall higher dislocation content, and hence, a higher strength.

2.4.5 Al-Mg Alloys

Mg forms a complicated system with Al, as depicted in Fig. 64. At the aluminum end, there is a eutectic, liquid$\rightarrow$Al$+$ Mg_5Al_8 at 35 wt% Mg. Mg decreases the density of Al; density decreases linearly by approximately 0.5% for every 1 wt% Mg in solid solution [120].
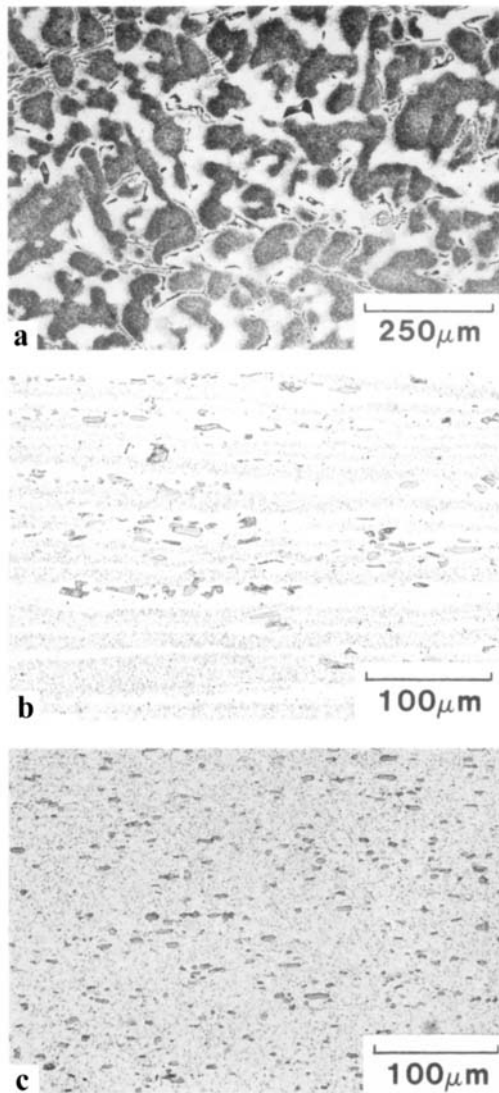
Figure 61 Optical micrograph of alloy 3004 after (a) preheating; (b) hot rolling; and (c) cold rolling. Reprinted from Ref. 39. (Courtesy of Alcoa).

Mg has a very high solid solubility in aluminum (up to 14.9 wt% at 450°C). Its solubility decreases to approximately 1.7 wt% at room temperature, but the rate of decomposition of the supersaturated solid solution is very low [9]. In commercial alloys, essentially all of the Mg can be retained in solution without the need for extraordinary quenching procedures. Binary Al-Mg alloys show an abnormally small response to aging; precipitation may occur, but no hardening is observed until the Mg content exceeds 5%. In cold worked alloys, rod-shaped precipitates of Al_3Mg_2 (β phase) are nucleated on dislocations [15], but have no significant strength-
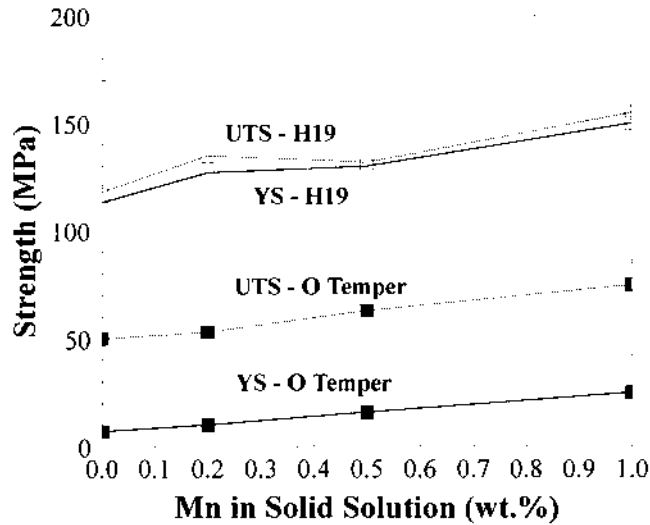
Figure 62   The effect of Mn in solution on strength of annealed and fully hardened sheet. (Source Ref. 39).

ening effect. However, in alloys with Mg content higher than 4%, cold work may result in precipitation at grain boundaries [186]. No wrought 5XXX alloys exploit precipitation hardening to obtain higher levels of strength. Casting alloys with a high Mg content can exhibit some degree of age hardening behavior when subjected to the right thermal conditions [57]. The nucleation and growth of the β phase on grain boundaries in certain Al-Mg (> 3%Mg) alloys at ambient temperatures reduce ductility and resistance to stress-corrosion cracking [15].

The strength of 5XXX series alloys in the O temper is controlled primarily by a combination of solid solution hardening from the Mg atoms and grain size strengthening. Mg in solution imparts a limited solution hardening effect for annealed alloys. Figure 65 illustrates the effect of Mg in solution on the tensile properties of annealed high purity Al sheet. Both yield strength and ultimate tensile strength increase with increasing Mg content while elongation drops sharply with even small Mg additions. Similar behavior with increasing Mg content is observed in tensile properties of commercial alloys. On an atomic basis, Mg is more efficient in strengthening in concentrations less than 1 at% than in more concentrated alloys. At Mg levels < 1 at%, the incremental increase in yield strength is proportional to (at% Mg)$^{2/3}$, whereas in the more concentrated alloys, this increase is proportional to (at% Mg)$^{1/3}$. Hence the solid solution strengthening effect of Mg differs from dilute to concentrated alloys [59].

Mg content in commercial 5XXX alloys ranges from 0.5 to about 6 wt%. Alloys with low Mg contents are used where formability or surface finishing are critical. The good formability of the Al-Mg alloys is attributable to the high strain hardening rate, which is maintained to the high forming strains achieved with these alloys. Higher Mg alloys are used in structural applications where strength, fracture and fatigue resistance, and weldability are important. Some of the casting alloys
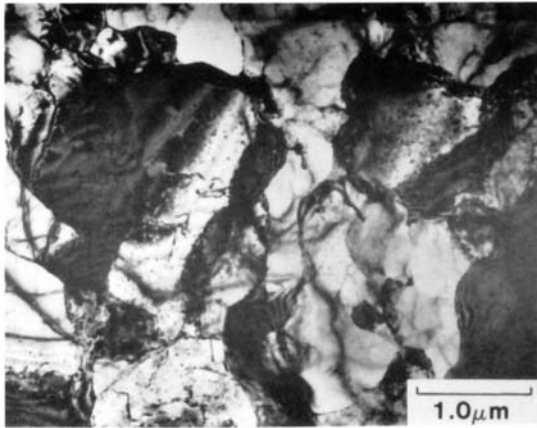
(a)
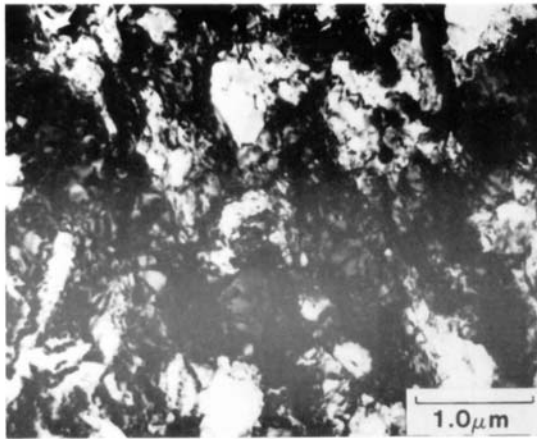
(b)

Figure 63 Dislocation and subgrain structure of (a) alloy 3003 (1 wt% Mn); and (b) alloy 3004 (1 wt% Mn, 1 wt% Mg) after 90% cold-rolling. Mg addition reduces the extent of dynamic recovery that occurs during rolling. Reprinted from Ref. 39. (Courtesy of Alcoa).

have extremely high Mg (up to 12%) and a good combination of castability and strength [120]. Wrought alloys containing more than 5 wt% Mg are produced in special tempers designed to improve their susceptibility to stress-corrosion.

Many investigators have tried ternary additions to Al-Mg alloys to increase strength. The addition of 0.3 wt% Sc increases the yield strength of an Al-5.25 wt% Mg alloy by more than 100% to 365 MPa by stimulating age hardening [187]. Strength in Al-4 wt% Mg-Sc alloys increase with increasing Sc content up to 1 wt% Sc, primarily due to the precipitation of coherent, ordered, spherical Al_3Sc precipitates [187]. Small additions of Ag may stimulate age-hardening in alloys containing 5% and down to as little as 1% Mg [15]. However Ag additions do not affect
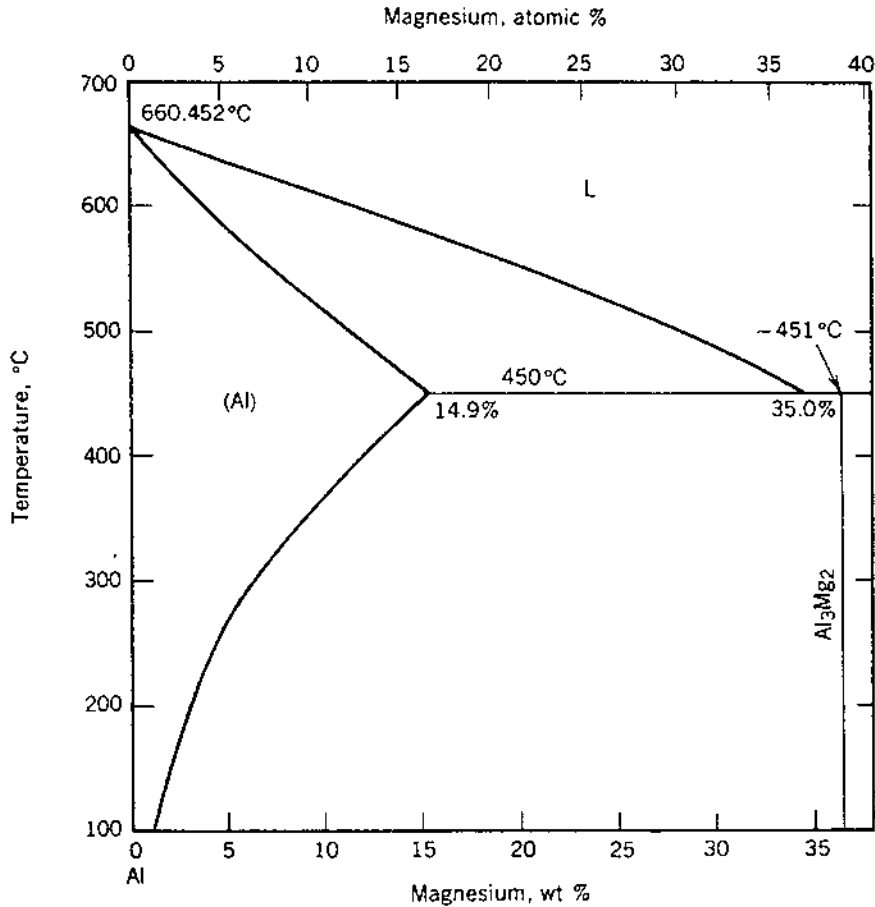
Figure 64   Al-Mg phase diagram. Drawn by Dr. Joanne Murray. (Courtesy of Alcoa).

the age-hardening response in presence of Sc [187]. Cu additions to Al-7 wt% Mg alloys induce response to age hardening, but result in severe solute segregation problems [188]. Zn additions to Al-Mg alloys can result in strengthening through the precipitation of a T-phase ($Al_2Mg_3Zn_3$).

In 5XXX series of Al-Mg alloys, strength is developed through mainly work hardening, and solution strengthening, and to a lesser extent by grain size effects. The high purity Al-Mg binary alloys show a more rapid rise in tensile strength than in yield strength, indicating that Mg is promoting work hardening, Fig. 65. The addition of Mg to pure aluminum results in a decrease in the strain hardening exponent n, but an increase in k, Fig. 66. With increasing Mg content, n remains constant, but k continues to increase, indicating that Mg increases the rate of strain hardening. As mentioned previously, Mg raises the H19 yield strength by 70–85 MPa per 1 wt%. This effect of Mg on work hardening is microstructurally related to its effect on development and retention of lattice strain. The microstructure of deformed Al shows evidence of mutual dislocation annihilation and extensive dislocation rearrangement into cells and subgrains. As Mg is added to Al, the
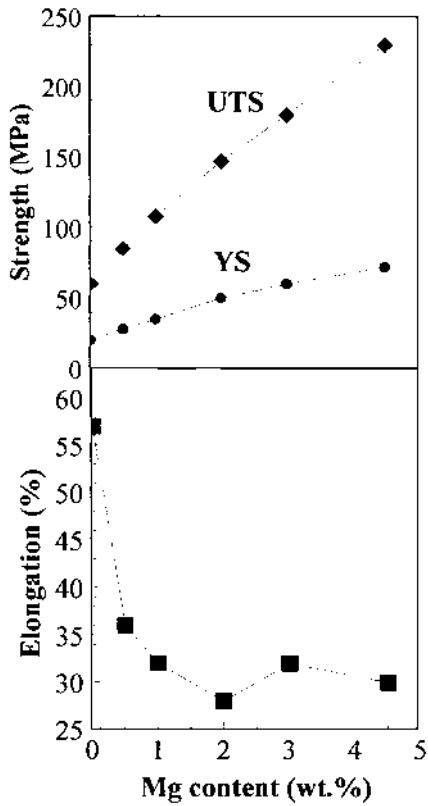
Figure 65 The effect of Mg in solution on tensile properties of annealed Al-Mg binary alloys. (Source Ref. 59).
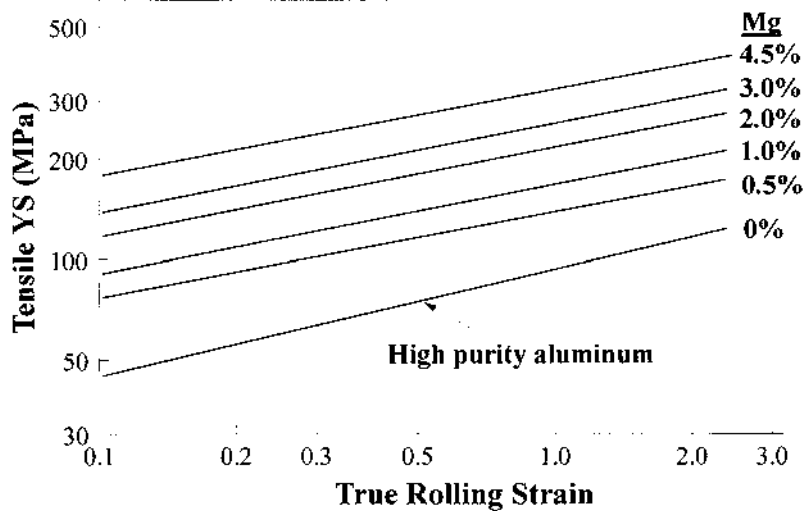
Figure 66 Strain hardening response of high-purity Al and Al-Mg alloys during cold rolling, following Eq. 8. (Source Ref. 39).
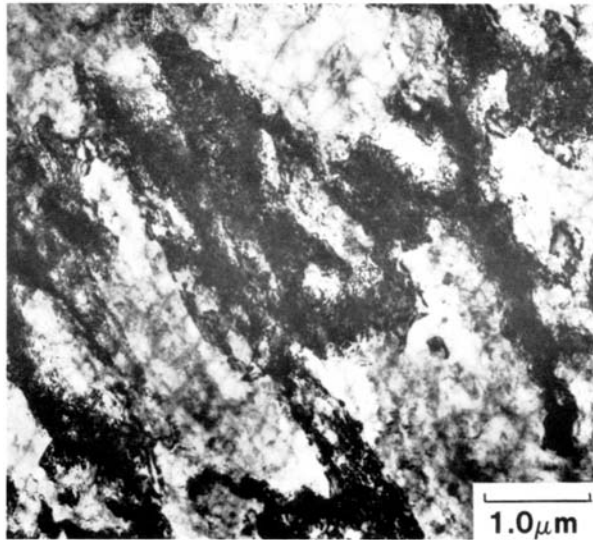
Figure 67 TEM micrograph showing the dense, entangled dislocation structure present in fully hardened (H19) 5182 alloy (4.5 wt% Mg, 0.35 wt% Mn). Reprinted from Ref. 39. (Courtesy of Alcoa).

amount of retained lattice strain after deformation increases. Higher Mg contents result in a more rapid increase in lattice strain and higher amounts of retained strain for a given amount of deformation. Therefore the tendency for dynamic recovery and dislocation rearrangement into lower energy configurations is reduced, with an increase in the dislocation content of the alloy and a more uniform dislocation distribution [59]. This can be seen by comparing Fig. 67 with Fig. 43. These figures show the H19 dislocation structure found in alloys 5182 and 1145, respectively. While 1145 shows clear evidence of subgrain formation, alloy 5182 shows little evidence of dynamic recovery with the retention of a dense uniform dislocation network. Thus, by suppressing recovery, Mg increases both the dislocation multiplication and storage rates leading to increased strength [59]. The effect of Mg content on annealed grain size is shown in Fig. 68, which shows that increasing the Mg content to 3.5% results in progressively finer annealed grain sizes in a series of high purity Al-Mg binary alloys, cold-rolled 89% prior to annealing [189].

The combination of Mg in solution and cold working is extremely effective in achieving high strength. However alloys with high Mg content may be susceptible to intergranular corrosion or stress-corrosion cracking, and are notoriously hard to fabricate during hot and cold working. Therefore to increase strength, other solid solution elements are added to Al-Mg alloys. A requirement for such an addition will be that the element provides additional work hardening but will not chemically interact with Mg and remove it from solid solution. Mn is often added to 5XXX alloys to further strengthen the alloy at lower Mg levels. Relatively small additions of Mn to a 3.5% Mg binary can be more efficient in promoting strengthening than further Mg additions. The Mn addition may also decrease recrystallized grain size, depending upon process conditions. Mn is retained in solution in these alloys so that results
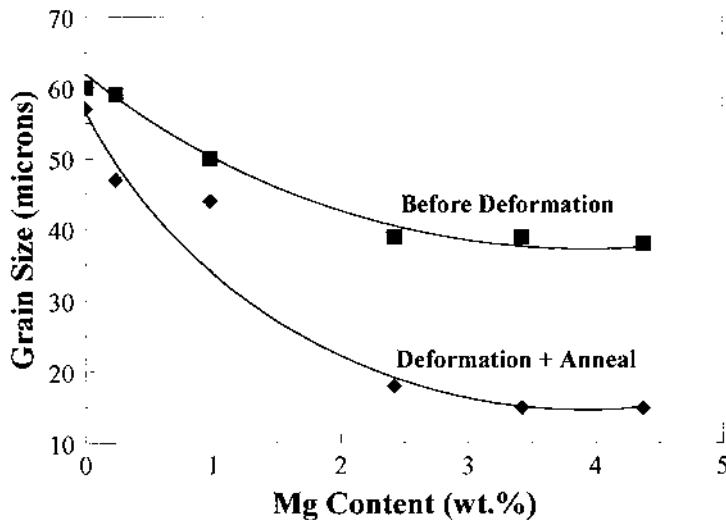
Figure 68 The effect of Mg content on annealed grain size in a series of high purity Al-Mg binary alloys. All alloys contained 0.05% Fe, 0.05% Cu, 0.04%Si, 0.01%Ti. Data obtained from Ref. 185.

are attributable to solution effects. At higher levels, the Mn precipitates as Al_6Mn dispersoids, which retard recrystallization, and hence greatly enhance the rate of work hardening. In Al-Mg-Mn alloys, the optimum dispersion of Al_6Mn occurs at a Mg content of 4.5 wt% and a Mn content of 2 wt% [190]. Al_6Mn dispersoids also alter the failure mechanism from necking to cavitation [191]. The combination of 0.2 wt% Zr and 1.6 wt% Mn has shown good results in superplastic forming operations due to fine grain sizes with the additional Mn and the fine Al_3Zr dispersoids [192].

Grain size makes a larger contribution to strength in 5XXX alloys than in most other aluminum alloys. The typical k value (Eq. (7) for Mg-free alloys is 0.15 or less, as compared to greater than 0.2 in the Al-Mg alloys [52]. 5754 has a k of 0.22 and a σ_f of 42.5 MPa, whereas 518 has a k of 0.30 and a σ_f of 57.6 MPa [52]. The difference in the Petch parameters in two alloys is most probably due to the higher Mg content of 5182. The frictional stress, σ_f, reflects any solution hardening due to Mg, and can be expressed as a function of Mg concentration [52];

$$\sigma_f = 15.5 \ (\text{wt}\% \ \text{Mg}) \tag{24}$$

σ_f and k are also influenced by the grain size uniformity and shape as well as the crystallographic texture. These microstructural variables are, in turn, influenced by the dispersoid content in the alloy (i.e. the Mn content) and processing parameters such as the extent of cold work and the final annealing treatment.

The constituent phases in 5XXX alloys can be of various types depending upon the specific composition [59]. Due to the very low solubility of Mg_2Si in aluminum at high Mg contents, it is often present in the microstructure as a major constituent phase. Since the presence of Mg_2Si has a deleterious effect on ductility, fracture

resistance, and most types of forming behavior, the Si content is usually tightly controlled in commercial 5XXX alloys [120]. As with the 3XXX alloys, the presence of Fe, Mn, and Si are also present as $Al_{12}(Fe,Mn)_3Si$, $Al_6(Fe,Mn)$, or Al_3Fe. Commercial alloys can contain up to 1 wt% Mn. When Mn precipitates as a dispersoid during preheating, the $Al_6(Mn,Fe)$ phase is favored since the Si is consumed by Mg_2Si. Cr is often added for corrosion protection, and has a very low solubility in Al. During solidification and preheating, ternary compounds of Al, Mn, and Cr can form in alloys containing both Cr and Mn. In wrought sheet products, Cr is often present as the E phase ($Al_{12}Mg_2Cr$) as a result of precipitation during the preheat. However, Cr may be retained in solution due to its low diffusivity in Al or precipitated as binary Al-Cr phase, depending upon exact alloy composition and process conditions.

During annealing, alloys with higher Mg content lose proportionately more of their strength through recovery than do lower Mg alloys [59], which lose more of their strength through recrystallization, as shown in Fig. 69(a). Figure 69(b) shows that for alloys partially annealed back to the same strength level from the fully hard condition, the higher Mg alloy will have the higher elongation because of the greater extent of recovery. Increasing Mg and decreasing annealing temperature decrease the size of the recovered subgrains, resulting in higher retained strength. Other elements present in solution will exert an influence on the recovery behavior, but Mg, because of its strong influence on dislocation mobility, is dominant.

The thickness of the oxide layer on the surface of Mg containing molten Al alloys is much thicker than that of pure Al [193]. Therefore, Be and Li have been used to reduce the oxidation of Mg at high temperature especially in the liquid state [120]. Be was also found [194] to spheroidize Fe-bearing phases, and hence increase crack resistance, in Al-7 wt% Mg-3 wt% Zn alloy. Machinability is improved with increasing Mg content [195], and by Li [195] or Pb additions [120]. Additions of Cr, Zr, and Ti reduce deep drawing properties [57]. Improvements in drawability can be obtained by controlling the crystallographic texture during processing since the correct texture gives the proper orientation of slip systems to resist thinning in the thickness direction [57]. Mn, Cu, and Cr increase strength at the expense of ductility, especially in Mg alloys, but these additions are found in many of the commercial high Mg alloys as well.

2.4.6 Al-Si and Al-Mg$_2$Si Alloys (Al-Mg-Si, Al-Si-Mg)

The Al-Si binary system is shown in Fig. 70, and the effect of Si content on tensile yield strength in binary Al-Si alloys is shown in Fig. 71. In binary Al-Si alloys, Si forms very small, coherent [197] clusters in solid solution, the nature of which depends on Si content [198]; in hypoeutectic and eutectic alloys, Si atoms associate with Al atoms as Al-Si clusters, whereas in hypereutectic alloys, they are present as Si-Si clusters. The condensation of excess vacancies into dislocation loops aids the nucleation of Si clusters [199,200]. Si precipitates with a diamond structure, without intermediate stages from these clusters. The new phase forms as rods or triangular plates on several planes of the aluminum matrix [155]. Nuclei are very small, and vacancies play an important role during the transformation from the coherent clusters to a noncoherent particle, which occurs at a cluster diameter less than 2 nm. Since Si precipitates cannot be sheared by dislocations, dislocations pile up at each Si precipitate during plastic deformation [201], resulting in the strengthening of each slip plane and slip dispersion. The precipitation of Si becomes easier
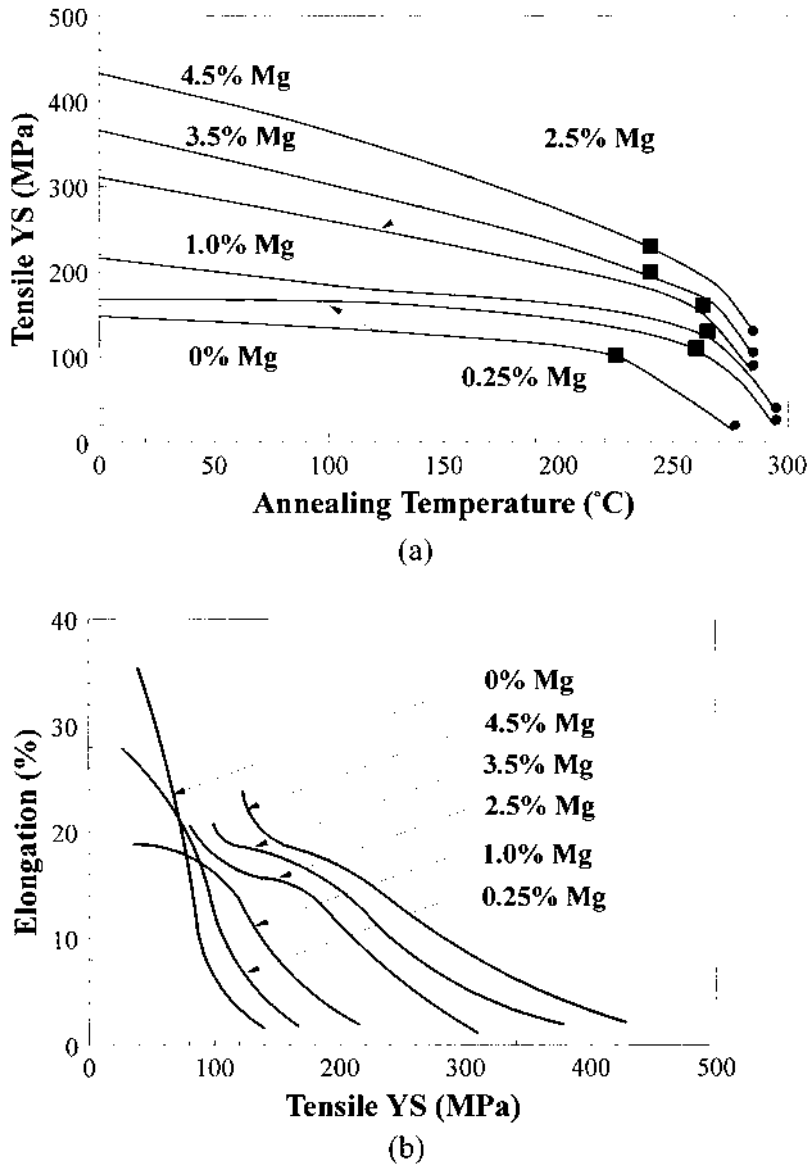
Figure 69 (a) Partial anneal curves for a series of binary Al-Mg alloys cold-rolled 70% and annealed for 2 h at the annealing temperature; and (b) recovery of elongation with decreasing strength for the partially annealed alloys shown in (a). (Source Ref 59).

with Ge additions [202]. Because the level of strength attainable by Si alone is low, and Ge additions are expensive, no precipitation hardenable Al-Si or Al-Si-Ge alloys have been commercialized. Al-Si alloys, however, are used as brazing sheet and as welding rod.

Mg is often added to Al-Si alloys to form the pseudo-binary Al-Mg_2Si (Mg:Si= 1.73) for strengthening by the formation of Mg_2Si precipitates. In alloys, with a large
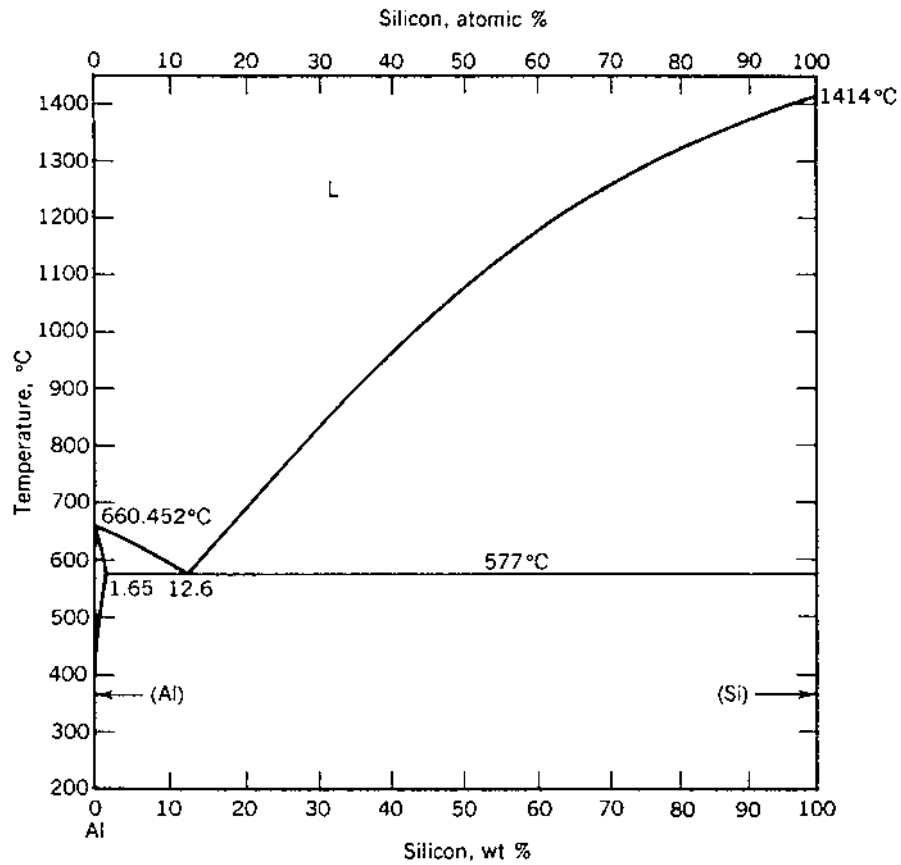
Figure 70   Al-Si phase diagram. Drawn by Dr. Joanne Murray. (Courtesy of Alcoa).
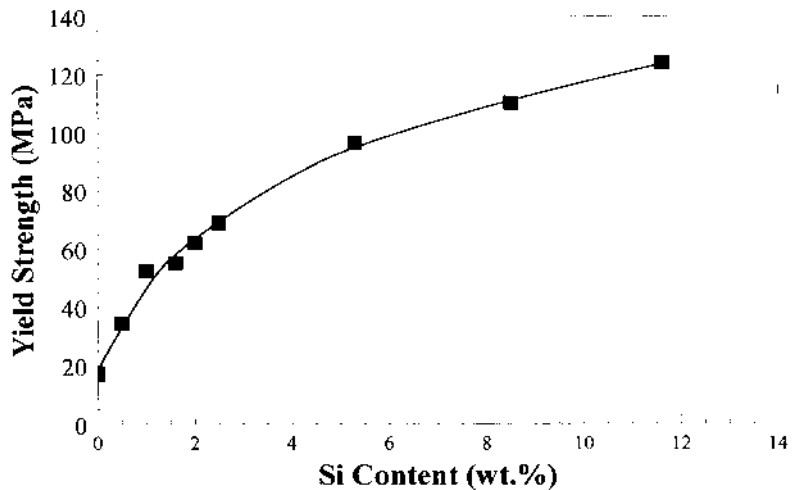
Figure 71   The effect of Si content on tensile yield strength of Al-Si binary alloys. Data obtained from Ref. 196.
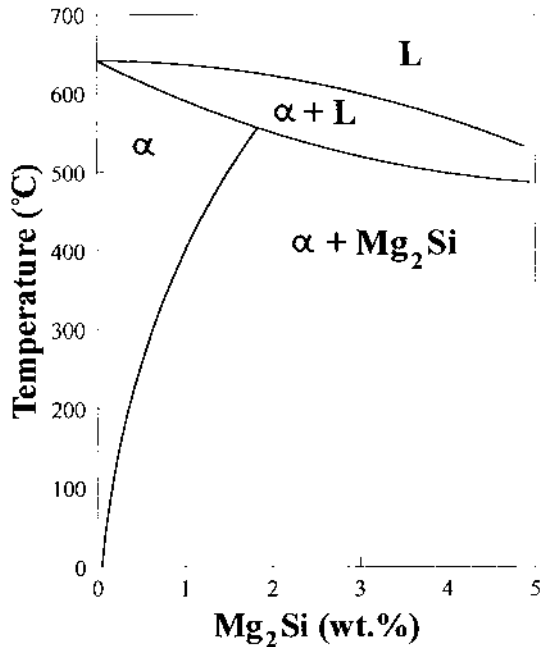
Figure 72 Pseudo-binary Al-Mg$_2$Si phase diagram.

excess of Si, Mg$_2$Si content can be found by [203];

$$\% \text{ Mg}_2\text{Si} = 1.578 \times \% \text{ Mg} \tag{25}$$

The pseudo-binary system, which is presented in Fig. 72, has a eutectic at 595°C and a maximum solid solubility of 1.85 wt% Mg$_2$Si. Si available for Mg$_2$Si formation is affected by the presence of Mn and Fe in the alloy, and is expressed by [204];

$$\text{Si (available for Mg}_2\text{Si)} = \text{wt}\% \text{ Si} - \frac{1}{4}(\text{wt}\% \text{ Fe} + \text{wt}\% \text{ Mn}) \tag{26}$$

Most commercial aluminum alloy extrusions are produced in the Al-Mg-Si alloy (6XXX series). They may be divided into three groups [71,184]. Alloys in the first and second group have balanced amounts of Mg and Si. In the first group, they add up to between 0.8% and 1.2%. These alloys, typified by 6063, can be readily extruded and can be air quenched at the extrusion press, eliminating the need for a separate solution treatment operation. The alloys in the second group contain Mg plus Si in excess of 1.4%. Consequently, they develop higher strength on aging. Because they are more quench sensitive, the products are usually either quenched in water after extrusion or separately solution treated and water quenched as separate operations. About 0.25 wt% Cu is added to Al-1.0 wt% Mg-0.6 wt% Si alloys (6061) to improve mechanical properties (The physical metallurgy of the Al-Mg-Si-Cu alloys will be discussed in a later section). The alloys in the third group contain Si in excess of that needed to form Mg$_2$Si and the presence of this excess Si promotes an additional response to age hardening by both refining the size of
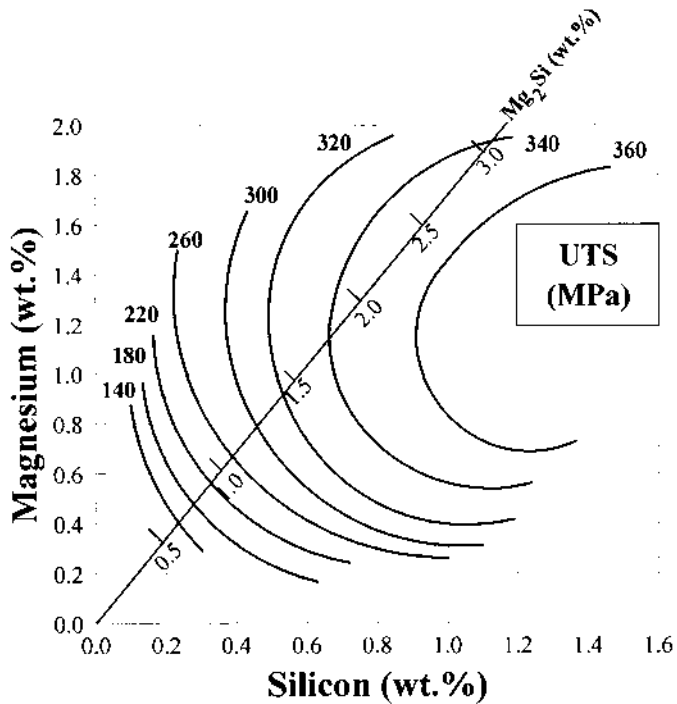
Figure 73 The effect of Mg and Si contents on the ultimate tensile strength of Al-Mg₂Si alloys (Source Refs 205 and 206).

the Mg₂Si particles and precipitating as Si. The effect of Mg and Si contents on the ultimate tensile strength of Al-Mg₂Si alloys is given [205,206] in Fig. 73. Si may also reduce ductility and cause intergranular embrittlement, which is attributed in part to the tendency of Si to segregate to the grain boundaries. The presence of Cr and Mn counter this effect by promoting fine grain size and inhibiting recrystallization during solution treatment.

Al-Si-Mg alloys (5–20 wt% Si) are the most widely used aluminum casting alloys because of their excellent casting properties. Expansion of silicon constituent phase during solidification partially compensates for the contraction of aluminum, and thus diminishes tendency toward shrinkage and hot tearing. Si likewise reduces the coefficient of expansion of the alloy [207]. However the size, shape and orientation of Si particles determine the fracture behavior of casting alloys [208]. The microstructure of an Al-7 wt% Si casting alloy is presented in Fig. 74, which shows Al-Si eutectic among white Al dendrites. Addition of 0.1 wt% Mg decreases the Si eutectic temperature by 10°C [209]. The tensile properties of Al-Si-Mg casting alloys were found [210] to be interrelated which can be expressed as;

$$\sigma_Y = a \, \sigma_{UTS} - b \, \log(\% \text{ elongation}) - c$$

For Al-10 wt% Si-Mg castings, a, b, and c are 1.02, 44, and 31 consecutively. For Al-7 wt% Si-Mg alloys, a, b, and c are 1.0, 60 and 13 consecutively. Yield strength
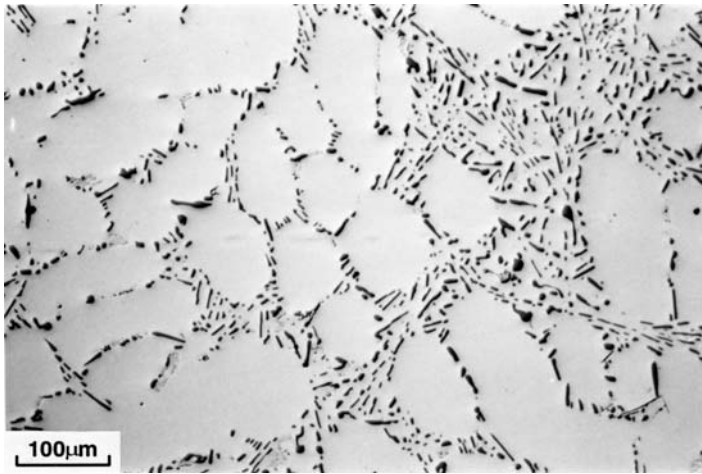
Figure 74 Microstructure of an Al-7 wt% Si-0.35 wt% Mg alloy. (Courtesy of Dr. Q. Wang, Worcester Polytechnic Institute).
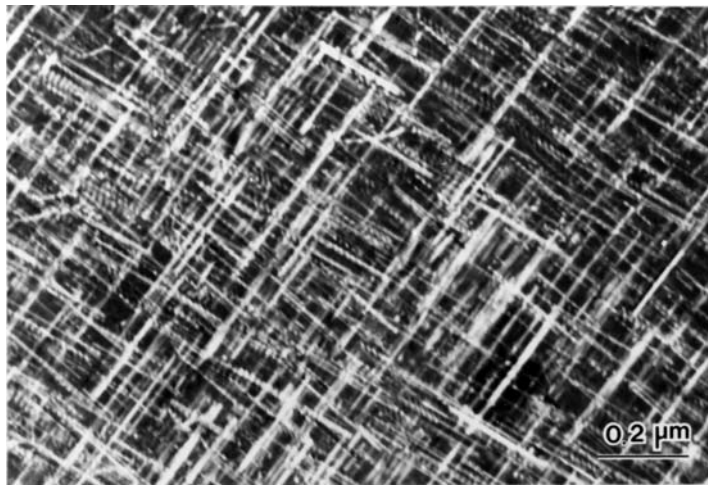
Figure 75 Rod shaped precipitates in Al-Mg$_2$Si alloys. (Courtesy of A. Sachdev, General Motors Corp.).

in cast alloys is not affected by porosity, whereas UTS and elongation decrease sharply with increasing pore area [211,212].

Al-Mg$_2$Si alloys are normally aged at about 170°C and the complete precipitation process is among the most complex of all age hardenable aluminum alloys. The precipitation sequence has been subject to significant discussion and research [197,213–224] and the latest findings indicate the sequence, SSSS $\rightarrow$ independent clusters of Mg and Si, co-clusters of Si and Mg $\rightarrow$ GP zones $\rightarrow$ Si rich phase $\rightarrow$ β'' $\rightarrow$ β' $\rightarrow$ β (Mg$_2$Si). Figure 75 shows the rod-shaped precipitates (β') in Al-Mg-Si alloys.

The first stage of precipitation involves two distinct clustering reactions [221,222]. Mg clusters were found [222] in the as quenched state of an Al-0.65 wt% Mg-0.72 wt% Si alloy. The Si clusters form extremely rapidly after quenching [199], within the first minute of artificial aging at 200°C [197], and affect subsequent stages of precipitation. Excess Si reduces the solubility of Mg_2Si, enhances the rate of precipitation, and increases the density of GP zones. GP zones are fine plates having a thickness of one atomic layer, i.e. 2.5 nm, and a length of about 30 nm [225], and are formed randomly in the matrix and also heterogeneously on matrix dislocations [226,227]. GP zones consist of alternating arrangement of the columns of Mg and Si atoms along the $\langle 100 \rangle_\alpha$ direction, with a chemical composition of Mg:Si = 1 [225]. These zones are only partially coherent, in contrast to the completely coherent GP zones, which are a common feature of most age-hardening aluminum alloys. GP zones can exist over a wide temperature range (up to 260°C [218]), and their stability is very high.

Several GP zones aggregate with increasing aging time to form needles and exhibit a complicated morphology [225]. The GP zones and the β'' precipitates are coherent along $\langle 100 \rangle_\alpha$ directions with needle-like shape. The chemical composition of β'' phase is Si:Al:Mg = 6:3:1 [223]. The formation of the GP zones and the β'' precipitates are parallel and competitive processes [197]. The results of differential scanning calorimetry on 6061 alloy indicated that transition from GP zones to β'' proceeds without the dissolution of GP zones [224]. The β' transition phase is rod-shaped and also lies $\langle 100 \rangle_\alpha$ direction [69]. The equilibrium phase, β-Mg_2Si, is in non-coherent platelets, and makes little contribution to the strength of Al-Mg-Si alloys.

The GP zones and the β'' precipitates are easily sheared by dislocations due to their coherency with the matrix and small size [201], which produces strain localization. Intense slip bands in an Al-Mg-Si alloys formed due to the presence of shearable precipitates are illustrated in Fig. 76. The presence of dispersoids
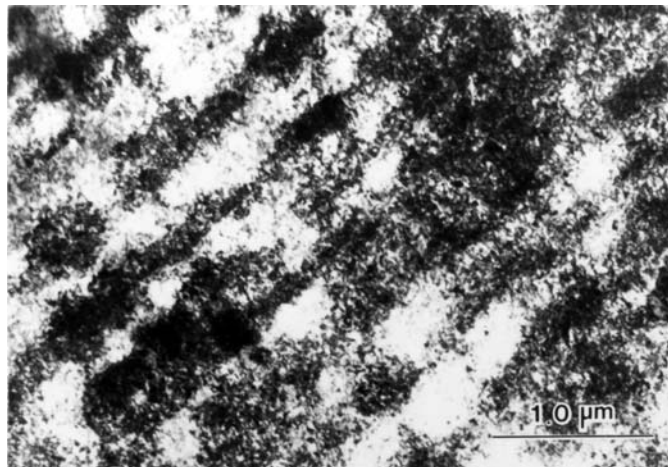
Figure 76 Transmission electron micrograph showing intense slip bands in an Al-Mg-Si alloy aged to produce shearable precipitates. (Courtesy of A Sachdev, General Motors Corp.).

Figure 77 Dark field TEM of β' precipitates following 4% tensile strain. (Courtesy of A Sachdev, General Motors Corp.).

homogenizes the slip distribution in underaged alloys [228]. Therefore, local strain concentrations at grain boundaries, and consequent intergranular fracture are reduced. β' precipitates cannot be sheared by dislocations, and increase strength by Orowan looping. This is shown in Fig. 77. The fringes on the rod-shaped precipitates are loops left behind during dislocation by-pass.

When β' nucleates on dislocations, dislocation motion accompanies precipitation [229]. There is a strain field associated with the β'' particles, which gets gradually relieved as the transformation progresses. When dislocations are available for precipitation, β'' and β' may nucleate on any given dislocation in an orientation perpendicular to the Burgers vector [227], so that the misfit between the needle and the matrix is partially relieved during the nucleation and early stages of growth of the needle. This configuration allows the dislocations to climb uniformly on the $\{100\}_\alpha$ plane normal to b, in the $\langle 001 \rangle_\alpha$ direction, providing vacancies. The dislocation/precipitate relationship is then determined by the relative rates of climb and of particle growth [229].

The effect of the aging delay (the time spent by the alloy at room temperature between quenching and artificial aging) on properties after artificial aging depends on the Mg_2Si content [71,203,204,230], excess Si concentration, [230], quench rate [231], the temperature during the aging delay [203,204,214,219,226,232,233], the duration of the aging delay [203,204,214,219,226,233,234], heating rate to artificial aging temperature [204], as well as the temperature and duration of artificial aging [204,215,226,230,235,236]. The effect of 24 hr of aging delay on the change in the ultimate tensile strength of Al-Mg-Si alloy extrusions as a function of Mg and Si contents for wrought alloys is given [205,206] in Fig. 78.

The occurrence of heterogeneous precipitation on dislocations indicates that solute supersaturation is not high in the alloy. Hence at low concentrations of Mg and Si (lower than 0.9 at% Mg_2Si), heterogeneous precipitation on aging immediately after quenching can be expected [230]. At high concentrations of Mg and
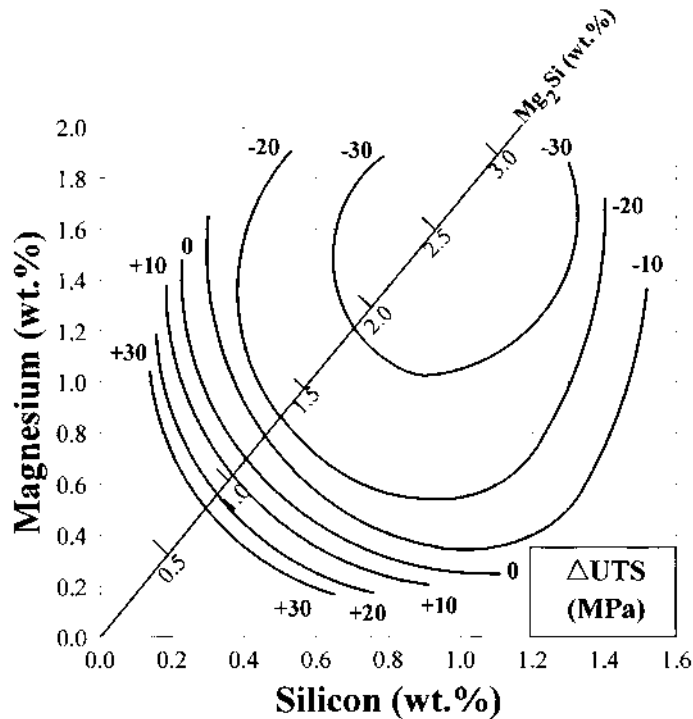
Figure 78 The effect of 24 h of aging delay (preaging at room temperature) on the tensile strength of Al-Mg-Si extrusions as a function of Mg and Si contents (Source Refs 205 and 206).

Si (higher than 1.1 at% Mg_2Si), precipitation is homogeneous when the alloy is aged immediately after quenching. The effect of aging delay is partially determined by whether nucleation is homogeneous or heterogeneous.

In alloys containing more than 1.1 at% Mg_2Si, many small clusters are formed during aging delay at ambient temperature. However, being smaller than 10 Å in size, these clusters are able to make only a modest contribution to the mechanical properties of the alloy [215,230]. When the aging temperature is raised, the clusters cannot grow easily because of the decrease of solute atoms in the matrix. Subsequently, only a small number of clusters grow at the expense of others, forming a coarser precipitate structure. If the alloys is artificially aged without any aging delay, the number of clusters formed at the beginning is much smaller, so that a large proportion of solute atoms are still in solution. During artificial aging, some of these clusters will be able to absorb the excess solute, and grow to a suitable size to improve the mechanical properties; this is associated with a finer precipitate structure. On the other hand, in alloys containing less than 0.9 at% Mg_2Si, aging delay at room temperature causes the refining of the final aged structure, since the clusters may act as nuclei of the precipitates [230]. Also heterogeneous precipitation on dislocations at low Mg_2Si levels may also be attributed to the artificial aging temperatures being higher than the critical temperature above which GP zones do not form [204]. The critical temperature, T_v is a function of Mg_2Si content and is

expressed by;

$$T_v(°C) = 111 + 71(\text{wt\% Mg}_2\text{Si}) \qquad (28)$$

During the room temperature aging delay, the zone formation takes place on finely distributed Si precipitates. If the duration of aging delay is short, then a relatively large concentration of alloying elements remain in solid solution. During the subsequent high temperature (above 70°C) aging, there is practically no new nucleation, and therefore, the further clustering takes place on the zones formed during the aging delay. In the case of short aging delays, a fine distribution and a large enough size of particles will successively develop with increasing aging time. On the other hand, in such a case the Mg concentration will increase quickly in the zones. With increasing aging delay, the number of zones increases and the solute concentration decreases. As a result of this fact, either the suitable size or the critical Mg concentration can be reached only after a much longer time during artificial aging [203,231], because it needs the resolution of some zones, the process of which is much slowed down by the strong binding between the Mg and Si atoms. With increasing aging delay, the stability of the zones increases, which leads to the increase of the time necessary to dissolve them. In such a case, the growth of the zones at a higher temperature proceeds without a reduction in their density. This fact is very significant, and can be explained as being due to the progressive establishment of a more stable internal structure of the zones during aging delay [215].

The addition of small amounts of Cu (e.g. 0.25 wt%) may lessen the adverse effects of delays at room temperature by reducing the onset and rate of natural aging [226], and/or promoting an increased response to artificial aging [230]. At the same time Cu, Ag, Be, Cd and Zn were found [230] to have an adverse effect on hardness upon natural aging during the aging delay, possibly due to the increase in solid supersaturation. A short preaging treatment at a higher temperature than that of artificial aging, dissolves the GP zones formed during the aging delay [220,230,232,233,236] which may adversely affect the properties after artificial aging. Also an artificial aging temperature of 200°C was found [236] to eliminate the adverse effect of aging delay for an Al-7 wt% Si-0.4 wt% Mg casting alloy. In addition, a two step artificial aging treatment, consisting of 0.5 hr at 160°C immediately after quenching, followed by natural aging (aging delay) and a final artificial aging of 16 hr at 160°C, was found [226] to eliminate the adverse effects of aging delay in an Al-1.2 wt% Mg$_2$Si alloy. This is attributed to the large number of stable clusters, which grow during the first artificial aging step, and do not dissolve during storage at room temperature.

Mn additions results in the formation of insoluble Al$_{10}$Mn$_2$Si particles, which decrease Si content in the matrix [230]. Consequently response to artificial aging is reduced, which is associated with a coarser precipitate structure due to the decrease in Mg$_2$Si content. On the other hand, the negative effect of aging delay is decreased by the addition of Mn, particularly when the alloy are quenched slowly (15°C/min), because of the decrease in solid supersaturation. Cr, Zr, V and Fe have similar effects [230].

The quench sensitivity of 1 wt% Mg$_2$Si alloys with different alloying additions, and some 6XXX series alloys is given [231] in Fig. 79(a) and (b), respectively. Difference in yield strength is due to the cooling rates of specimens in still air and cold water (0.65 and >1000°C/sec, respectively). Alloys with Mn and Cr show the

(a)

(b)
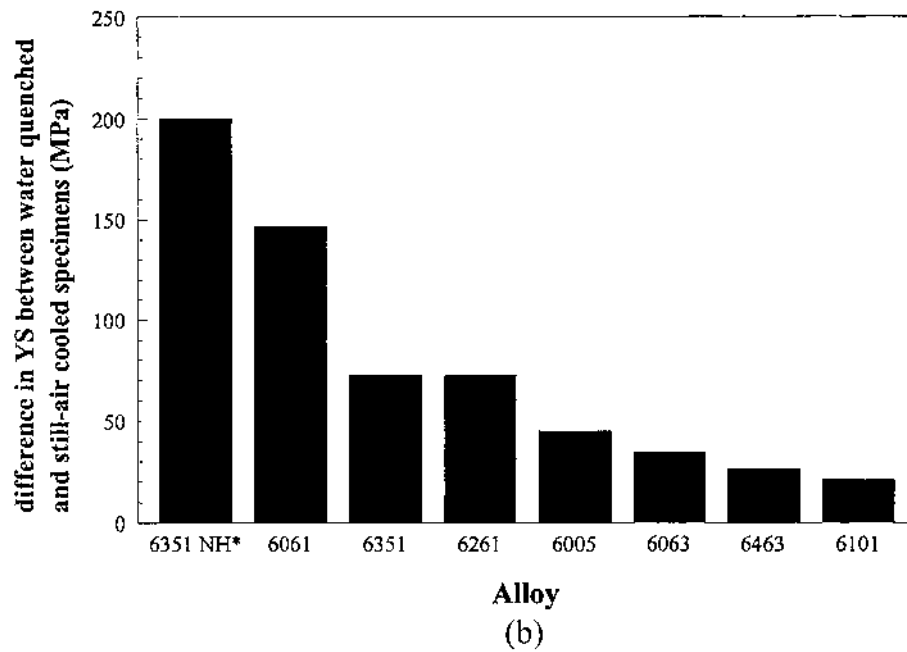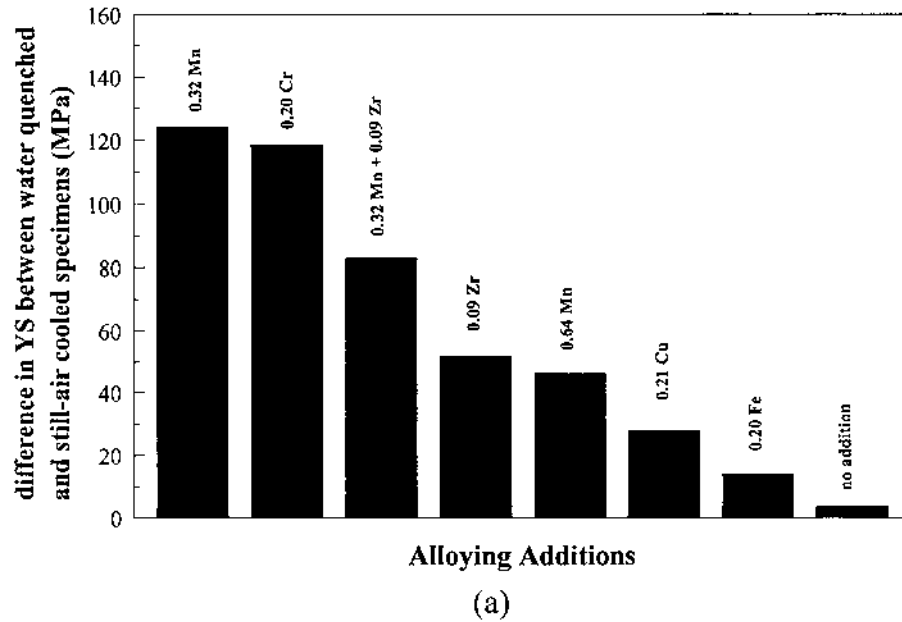
Figure 79   The difference in yield strength between water quenched and still air cooled specimens of (a) Al-1 wt% Mg$_2$Si; and (b) some commercial alloys. Data presented in Ref. 343.

highest quench sensitivity, due to formation of Mn- and Cr-bearing dispersoids which provide heterogeneous nucleation sites for β''. Figure 79(b) also shows the importance of ingot homogenization on quench sensitivity, of 6351 in particular. Homogenized samples are less sensitive to cooling rate during the quench.

During the aging of Al-Mg_2Si alloy, a transition from a fast to slow reaction takes place, indicating that there is a pronounced interaction between vacancies and GP zones [215,226,230]. As vacancies arrive at GP zones, they become blocked there, and will be eliminated from the matrix for a long time. Accordingly, a rapid transition is expected from a high to a low rate of reaction. During the fast reaction, the GP zones form at a rate governed by the concentration of excess vacancies (a rate which will rapidly decline as the zones grow). Finally a state of equilibrium between the vacancies arriving at the zones and those leaving will be established. From that moment, the reaction will continue more slowly. This phenomenon occurs for aging temperatures below $80°C$ [215]. Only when the temperature is relatively high ($>120°C$) is it possible for a tiny concentration of thermal vacancies to be present, so that the zones can grow.

Temper affects the width of PFZs formed in Al-Mg_2Si alloys. Underaged Al-Mg_2Si alloys have narrower PFZs than the overaged alloys [228]. Additionally overaged alloys also contain more grain boundary precipitates, which are mainly Si [218]. This results in lower fracture stresses and fracture strains in the overaged materials.

During the artificial aging of cast Al-7 wt% Si-0.4 wt% Mg alloys, there exists an interval where strength remains essentially constant near its peak value, but elongation increases [234,237]. Also peak strength and minimum ductility do not coincide in these alloys [237]. Modification of the Si eutectic by Na decreases age hardening rate due to the formation of ternary compounds of Na, Al and Si [234].

Impurities and alloying additions affect properties of wrought and cast Al-Mg-Si alloys. Fe has a mild strengthening effect up to 0.8–0.9 wt% and may be added to die cast alloys to minimize soldering to the die but with a loss of ductility. When Mn is added to the high Fe alloys, some increase in toughness may result. Mn, Cr, Ti, Zr all slightly harden the alloys. Zr forms fine spherical Al_3Zr dispersoids, the formation of which is strongly enhanced by excess Si [238]. Sr is added to Al-Si-Mg casting alloys to modify the Si eutectic, and to wrought alloys to modify the AlFeSi intermetallic constituents. In these alloys, Sr promotes the formation of more desirable Chinese-script α-Al_8Fe_2Si instead of plate-like β-Al_5FeS, which creates significant misfit strain in the aluminum matrix [239]. These large Fe-bearing intermetallics may also block feeding paths in casting alloys, and consequently result in porosity [240]. Good modification by Sr additions suppresses the formation of these large constituents, and help feeding [241]. Since α-Al_8Fe_2Si contains less Si, Sr additions result in more excess Si available for Mg_2Si precipitation [242]. Consequently, β'' precipitates are denser and finer in Sr containing alloys, resulting in higher strength. Sr however retards the growth of β' and inhibits the formation of the equilibrium β-phase during artificial aging by decreasing the Si diffusion rate at the Al matrix-Mg_2Si interface, and, therefore increasing resistance to overaging [242]. The formation of a Chinese-script constituent instead of β-Al_5FeSi is also favored by small additions of Mn or Cr [209,243]. Mn additions results in the formation of α-$Al_{15}(Mn,Fe)_3Si_2$, which is virtually insoluble in Al matrix [244]. Mn additions also increase resistance to recrystallization in 6XXX alloys [245]. The
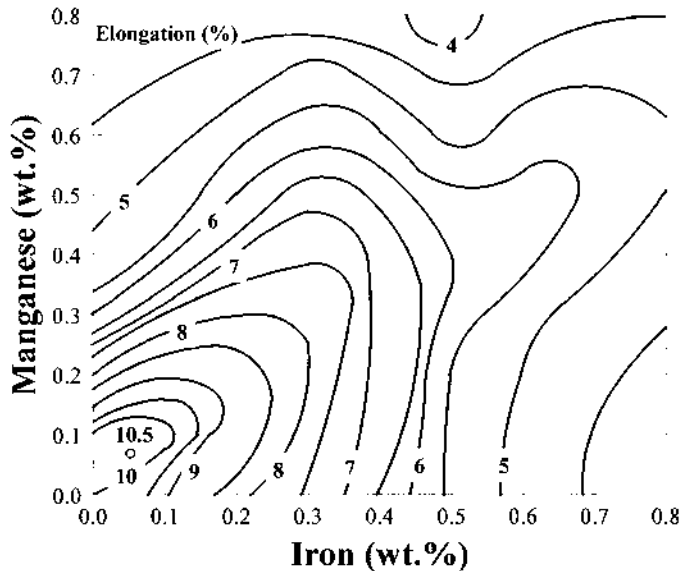
Figure 80 The effect of Mn and Fe concentrations on elongation in an Al-12 wt% Si alloy (Source Ref. 147).

effect of Fe and Mn contents on the elongation in Al-12 wt% Si alloy castings is given [246] in Fig. 80. Trace additions of Be alters the morphology of β-Al$_5$FeSi into a new phase (Al$_8$BeSiFe$_2$) with Chinese-script morphology [247,248]. Addition of 0.1 wt% Be to an Al-0.75 wt% Mg-0.5 wt% Si alloy significantly increases the hardening rate and the maximum hardness level of the alloy following solution and aging treatments [249]. This is due to a significant increase in the density of precipitate particles. The addition of 0.2 wt% Ca to the same alloy has the opposite effect of Be, i.e. decreasing the hardening rate and the maximum hardness level, as well as decreasing the density of precipitate particles.

Deformation of the solution treated Al-Mg$_2$Si alloys prior to artificial aging usually changes properties only slightly [161], due to the relatively easy precipitation of GP zones. Nevertheless misfit in precipitates is relieved by the presence of dislocations, which reduces the precipitation temperatures of phases [220], accelerates artificial aging [220,250,251], and change the effect of natural aging during aging delay on the properties after artificial aging [250]. Since Si nucleates heterogeneously on dislocations, a higher response to deformation prior to artificial aging can be expected when the alloy has excess Si.

2.4.7 Al-Mg-Si-Cu

When Cu is added to 6XXX series of Al-Mg-Si or Si added to the 2XXX series or cast Al-Cu-Mg alloys (e.g. casting alloy 320), the Al-Mg-Si-Cu family of alloys is formed with varied properties and applications. The aging response in such alloys often appears to be quite complex, due to the occurrence of many intermediate phases.

The underlying common feature in all these alloys is the occurrence of the Q phase, which has been previously designated as W, h-AlCuMgSi and λ. An excellent review is provided in Ref. 252.

The Q phase exists as a quaternary phase, and is ubiquitous as an equilibrium phase at most of the compositions in the Al-Mg-Si-Cu alloys. The Q phase cannot coexist with the S or T phases commonly observed in the Al-Cu-Mg system, or with the Al_8Mg_5 (β) phase in the Al-Mg system [252]. In addition, as mentioned previously, Si additions to an Al-Cu-Mg-Ag alloys results in the precipitation of Q′ phase, which in turn, prevents the nucleation of Ω phase, that is the characteristic of Al-Cu-Mg-Ag alloy [156]. Q′ also promotes a finer distribution of θ′.

Unlike β″ to β′ transition which involves a transition to a crystallographically new phase, the lath shaped precursor phase of Q maintains the same crystal structure and even morphology from peak age through the overaged condition. Only its size increases [213,252,253]. The exact composition of the Q phase is unknown, but has been stated as $Al_4Cu_2Mg_8Si_7$ [254], $Al_5Cu_2Mg_8Si_6$ [255] and $Al_4CuMg_5Si_4$ [120]. When Q forms from the liquid, it forms in a complex honeycomb morphology of micron size, as shown in the SEM secondary electron image for a 2014 sample in Fig. 81(a) [252]. Optically the structure appears as heavily networked as shown in Fig. 81(b) [252]. Sometimes, Q has Mg_2Si phase interspersed within its interstices as shown by the black dots in the 2017 sample in Fig. 81(c). The as-cast Q phase morphology changes with long thermal exposure during homogenization, and the Q phase may also precipitate in the solid state during high temperature anneals. In these cases, it often forms as round or oval particles at the grain boundaries [256]. Q′ has a lath morphology and the orientation relationship has the long axis parallel to $\langle 100 \rangle$ and $\{150\}$ habit planes of the matrix. Since both Q′ and β′ have their long dimensions parallel to the $\langle 100 \rangle$ directions of the aluminum matrix, Q′ can easily be mistaken for β′. The lath morphology distinguishes Q′ from the needle shaped β′.

Because of the shape and habit plane of the Q′ precipitate, it has a total of 12 variants within the aluminum matrix [252]. A moving dislocation, therefore, sees a different configuration of strain fields and precipitate morphologies in front of it. This may be one of the causes of the increase in strength of the Al-Mg-Si alloys with Cu additions [252]. Also for many commercial alloy compositions, the relative amount of Q′ phase is expected to be higher than the other strengthening phases. This follows from the fact that equilibrium phase calculations show Q as the dominant phase present at all these compositions, and the lath phase (i.e. Q′) increases in amount with aging compared to other phases [213,216]. Thus the overall volume fraction of Q′ may be much higher than either β′ or θ′. Also, the Q′ precipitates have very fine sizes, most likely even finer than β′. Hence, the combinations of high volume fraction, fine size and morphological advantage puts Q′ as a likely dominant strengthening phase in Al-Mg-Si-Cu alloys [252].

Most commercial compositions in the ternary Al-Mg-Si alloys, at normal aging temperatures, occur in a ternary phase field consisting of the equilibrium phases; primary aluminum, β and (Si). When Cu is added, the coexisting phase fields expand into three tetrahedron composition spaces. Inside each of these, there exists a four phase equilibrium consisting of the two common phases, namely Al, and the quaternary intermediate phase (Q), and two of the other three phases, namely θ, β and Si. This is schematically shown in Fig. 82 [252]. When Si is added to the

(a)

(b)

(c)
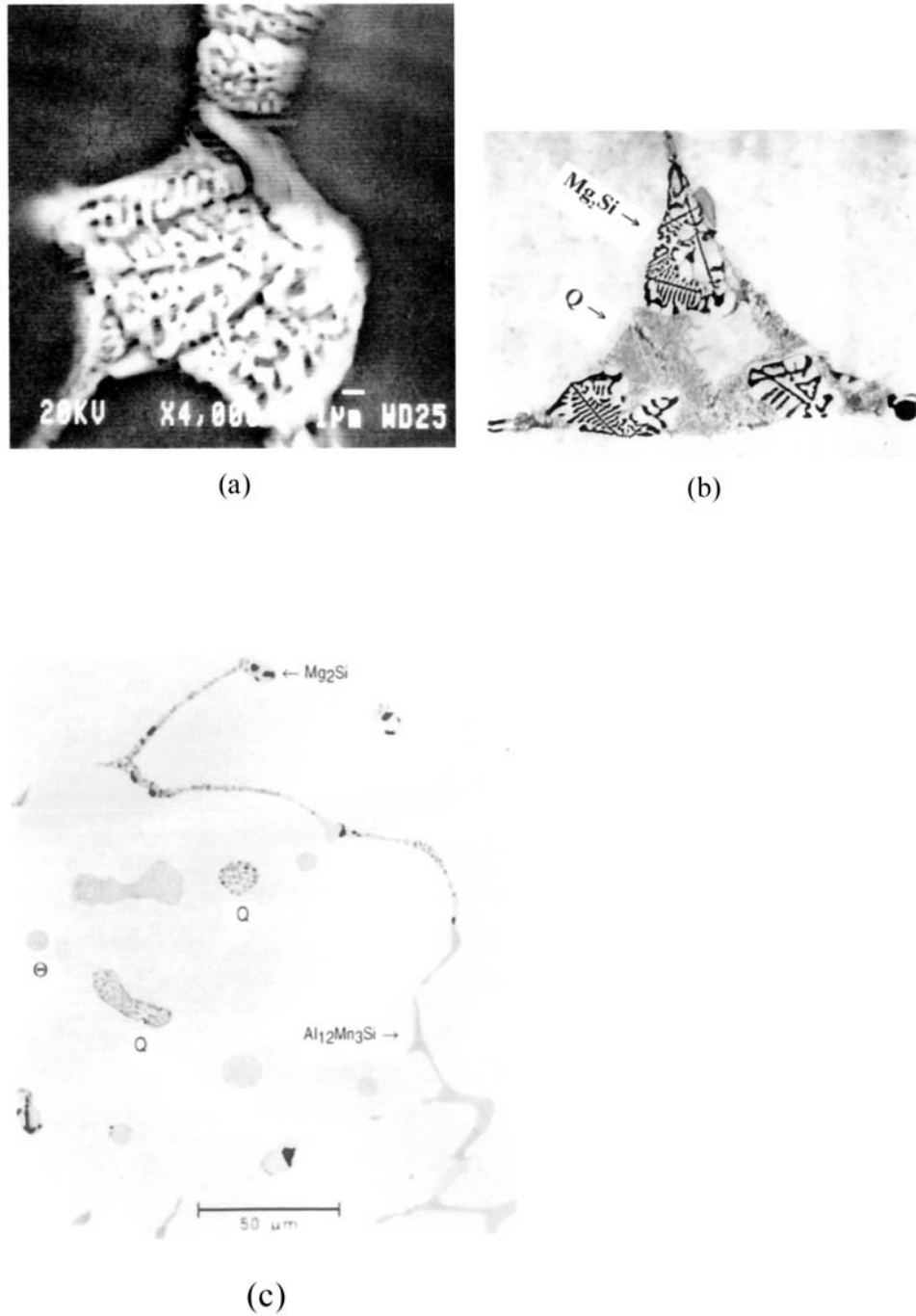
Figure 81 The structure of Q phase in (a) 2014 alloy, showing the honeycomb structure; (b) an ingot sample with Mg:Si > 1, showing the Q phase with an intertwined structure; and (c) 2017 alloy showing dark Mg_2Si particles interspersed inside the Q phase. Reprinted from Ref. 252. (Courtesy of Alcoa).
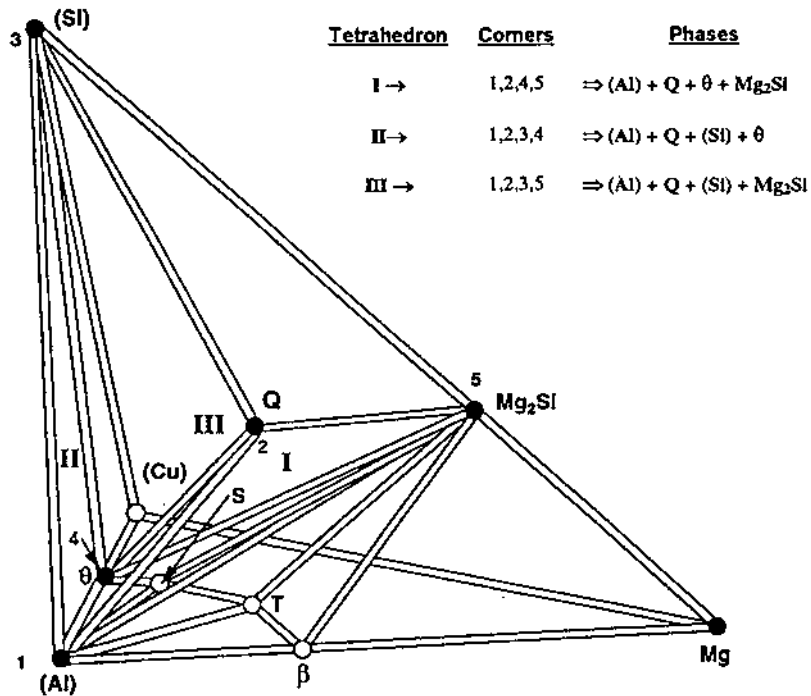
Figure 82 Line diagram of stable equilibrium phase fields in Al-Mg-Si-Cu system at normal aging temperatures. Reprinted from Ref. 252. (Courtesy of Alcoa).

Al-Cu-Mg alloys, the three-phase field, consisting of Al, θ and S, expands into the tetrahedron consisting of (Al), θ, S and β phases at low Si content. At higher Si contents, a switch over occurs to the tetrahedron in which Q replaces S, and the tetrahedron consists of the phases (Al), θ, β and Q, similar to those present when Cu is added to 6XXX alloys. This switch over to the tetrahedron phase fields containing S to the tetrahedron containing Q accounts for the abrupt change in phase combinations that have been observed in the past above certain Si levels in Al-Cu-Mg alloys [257]. Each tetrahedron being associated with specific phase combinations also shares the particular engineering properties identified with different alloys. The distribution of some of the common commercial alloys in the three tetrahedron phase fields is listed in Table 9. Although only Cu additions to Al-Mg-Si will be discussed hereafter, equivalent phase relations and property results can also be expected with Si additions to Al-Cu-Mg.

When the Mg:Si ratio is greater than about 1, the compositions lie, at normal aging temperatures, in Tetrahedron I having the coexisting phases, (Al), Q, θ and β. When Mg:Si is less than 1, the compositions correspondingly occupy Tetrahedron II having the coexisting phases, (Al), Q, θ and (Si). Tetrahedron III composition field is occupied when the Cu level is low. This level of Cu varies with the Mg and Si, and is generally less than 0.2–0.5%. A clearer view of the tetrahedral phase fields is shown in a schematic projection of the (Al) corner of the tetrahedron onto the Q corner of the tetrahedron whereby the tetrahedrons are projected in

Table 9   The Distribution of Some of the Common Commercial Alloys in the Three
Tetrahedron Phase Fields (*Source*: Ref. 252)

Tetrahedron			Composition		
I	II	III	Mg	Si	Cu
2017			0.40–0.8	0.2–0.8	3.50–4.5
2036			0.30–0.6	0.5	2.20–3.0
6061		6061	0.8–1.2	0.4–0.8	0.15–0.4
6013			0.8–1.2	0.6–1.0	0.60–1.1
	2014		0.20–0.8	0.5–1.2	3.90–5.0
	2008		0.25–0.5	0.5–0.8	0.7–1.1
	6111		0.50–1.0	0.7–1.1	0.50–0.9
	6009	6009	0.40–0.8	0.6–1.0	0.15–0.6
		6016	0.25–0.6	0.9–1.3	0.2
		6022	0.45–0.7	0.8–1.5	0.01–0.11
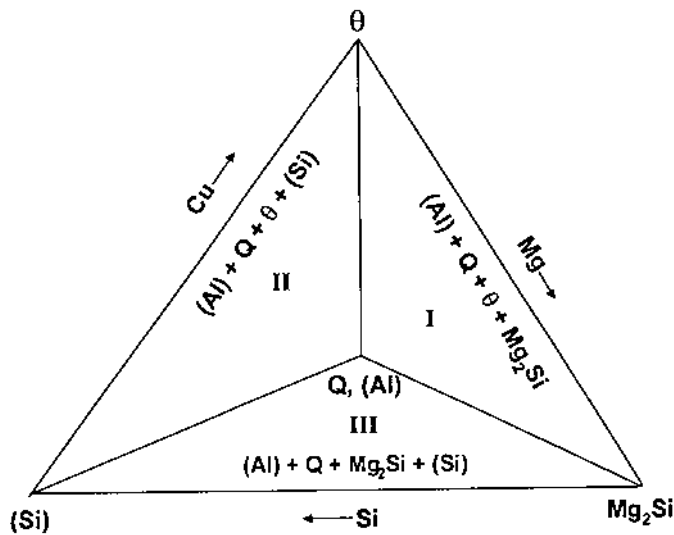
Figure 83   Al-Mg-Si-Cu alloys grouped by phase field occupancy on a pseudo-projection of
four-phase field tetrahedron. Reprinted from Ref. 252. (Courtesy of Alcoa).

two dimensions as triangular fields, as shown in Fig. 83. In the Al-Mg-Si alloys, a
Mg/Si ratio of 1.73 (corresponding to the 2:1 stoichiometry of Mg_2Si) is assumed
for the formation of β, and for the calculation of excess Si required to form the
(Si) phase. Recent studies [216] however showed that for the metastable precursor
phases, the appropriate composition ratio should be more like 1:1. In the
Al-Mg-Si-Cu system, the Mg/Si ratio defining the tetrahedron boundary is also close
to 1:1 [252]. Thus all the excess Si compositions, only those having Mg/Si < 1,
belong to the Tetrahedron II phase field. In other words, the stabilization of (Si)
in preference to Mg_2Si requires higher Si in the quaternary alloy than assumed
in the ternary alloy.

In both Tetrahedron I and II, Cu has the strongest (positive) effect on the amount of θ and much less on the amount of other coexisting phases. Increasing Si strongly increases Q in Tetrahedron I, and (Si) in Tetrahedron II. Increasing Mg increases Mg_2Si in Tetrahedron I and Q in Tetrahedron II. Although the addition of Cu to Al-Mg-Si alloys introduces the Q phase, it also be discussed hereafter, equivalent phase relations and property results can also be expected with Si additions to Al-Cu-Mg.

Figure 84 shows how specific alterations, often in terms of Mg:Si ratio, can change alloy types. The composition alterations change the alloy type from one tetrahedron phase field to another, or even to a three phase or two phase field paralleling a shift to a ternary composition. It may be noted that the switch from Tetrahedron I to II occurs with a decrease of Mg or an increase of Si or their combinations. The reverse composition relations hold for a switch from Tetrahedron II to I.

The tetrahedron phase fields refer to the equilibrium phases. They do not predict all the metastable phases that may occur during artificial aging. Irrespective of the composition fields, the metastable β'' is the dominant intermediate phase present in both the Al-Mg-Si and the Al-Mg-Si Cu alloys in the early stages of aging. The β'' phase is needle shaped with the long axis along $\langle 100 \rangle$ of the matrix. After peak aging of the Al-Mg-Si-Cu alloys, some of the needle shaped β'' precipitates are replaced by rod shaped phase β' and other are replaced by lath shaped precipitates. The lath shaped precipitate was originally observed [253] in 6061 alloy, and was called B'. The distinct lath morphology was confirmed [213,216] to be associated with the precursor of Q phase. This phase grows at the expense of β'', and in overaged tempers it completely replaces β'', when the Cu addition is 1.0 wt% [213]. Table 10 provides a brief review of the literature in terms of the phases identified during the artificial aging of Al-Mg-Si-Cu alloys [252].

Large increases in strength can be obtained on adding Cu to Al-Mg-Si alloys, accompanied by considerable refinement in the precipitate structure. Although the increase in strength has been ascribed [259] to finer and more numerous β' precipitates, they are more likely to be the Q phase precursors [252].

2.4.8 Al-Zn-Mg Alloys

Alloys based on the Al-Zn-Mg system have the highest response to age hardening of all aluminum alloys. These 7XXX alloys have lower densities than Al-Cu based alloys, and their high specific strength combined with recent advances in improving their resistance to stress corrosion cracking (SCC), fracture toughness, and resistance to exfoliation corrosion have allowed alloys based on this system to remain the choice for compressively loaded structure for aircraft. The high strength alloys are also used for sporting goods. Other, lower strength weldable alloys compete with Al-Mg-Si alloys for use in construction and ground transportation applications.

Mg addition greatly reduces the low temperature solubility of Zn in Al [261]. Spherical GP zones are formed after quenching and during aging from room temperature up to approximately 162°C. The zones at the start are mainly Zn clusters, and Mg diffuses to them with the help of vacancies [262] to form GP zones with an average Zn:Mg ratio of 4:1 [263]. Resistivity and strength data for 7075-W and 7050-W indicate that GP zones nucleate during the first day of natural aging, and then grow with no change in aging kinetics between one day and several years
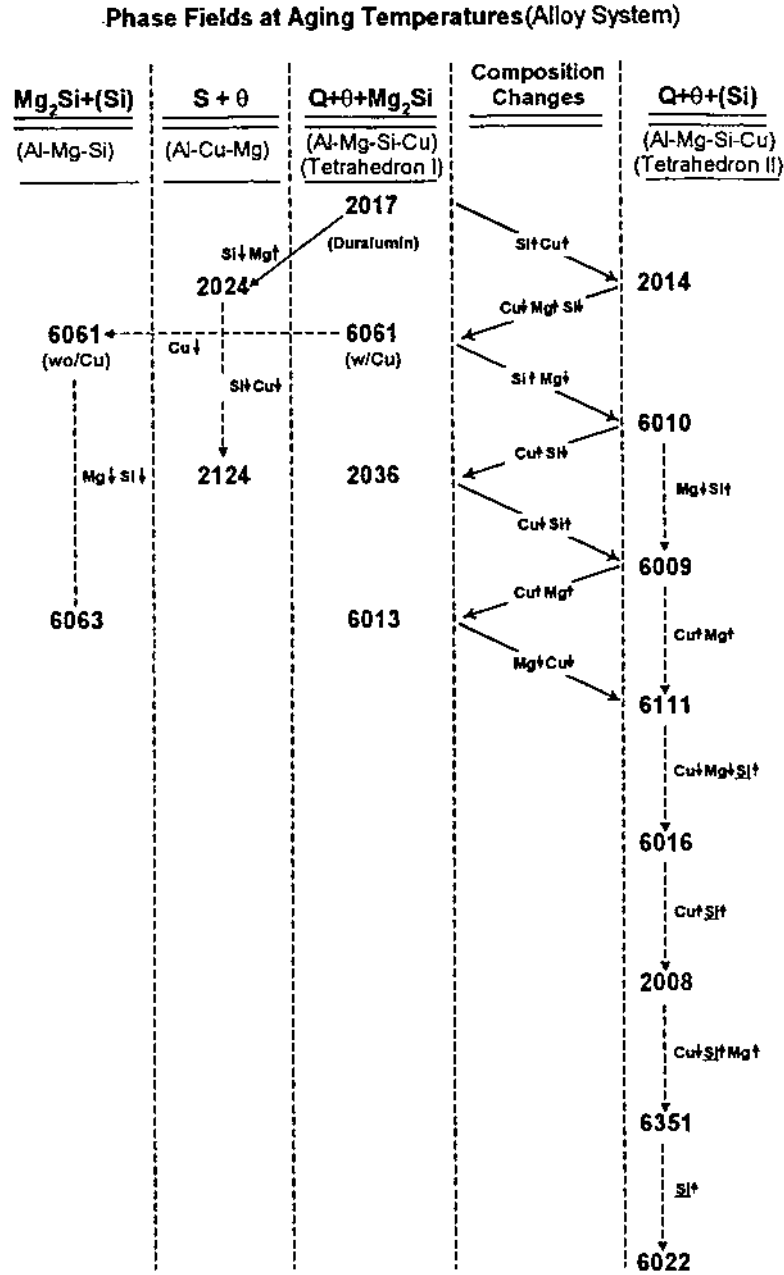
Figure 84 Commercial Al-Mg-Si-Cu alloys grouped in different phase fields. The shift of the phase fields with composition changes from one alloy to another is shown by the arrows. The alloys are arranged vertically down in each column in the chronological order of their development. Reprinted from Ref. 252. (Courtesy of Alcoa).

Table 10 Phases Identified During the Artificial Aging of Al − Mg − Si − Cu Alloys

Mg	Si	Cu	Metastable Phase(s)	Stable Phase Tetrahedron	Reference
1.0	0.6	0.3	B′, β′	I	253
0.9	0.25	2.0	β′,S′, X′	I	257
0.9	0.48	2.0	Q′, θ′, X′	I	257
0.8	0.79	0.18	B′, β′	III	216
0.87	0.65	1.0	L, β′	I	213
1.0	0.58	0.52	β′; "Rectengular"	I	258
0.6	0.8	0.3,0.6	β′; Θ′	II	259
0.53	0.87	4.3	λ′; Θ′	II	260

[95], Fig. 85. These results are consistent with the theory that the yield strength of 7XXX-W products is proportional to the size of GP zones. Extended warm aging of alloys with high Zn:Mg ratios produces the transition precipitate η', the precursor of the equilibrium $Mg(Zn,Cu,Al)_2$, η phase. Figure 86 shows η' precipitates in the matrix and η at grain boundaries in 7075-T735. For low Zn:Mg ratios, T phase $((Al,Zn)_{49}Mg_{32})$ may form [69,135]. Typical values of tensile strength achievable in this system are superimposed on the ternary phase diagram in Fig. 87. Thin dashed lines represent ultimate tensile strength and the thin solid lines represent the tensile yield strength as a function of composition.

It is widely recognized that the precipitation sequence in Al-Zn-Mg-(Cu) alloys can take many forms depending on conditions of quenching and aging. The phases formed depend more on the temperature of aging than the position of the alloy in the phase diagram. An extensive review of the phases formed is given in Ref. 264. Because of the great importance of precipitate size and distribution, maximum strengths are achieved in the commercially important peak aged T6 and overaged T7 tempers when the following sequence is observed [104]:

$$SSSS \rightarrow GP \text{ zones} \rightarrow \eta' \rightarrow \eta$$
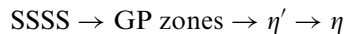
where the assumption is that each metastable decomposition product in someway generates nuclei for the subsequent stage. GP zones are coherent, whereas η' is semicoherent and η is incoherent [118]. Both GP zones and η' are sheared by dislocations, and the energy to shear η' is about twice that required to shear GP zones [82]. η' and η can form directly during quenching and aging by heterogeneous nucleation. Since η' is semicoherent, it can nucleate and grow directly on dislocations and subgrain boundaries. Likewise, η can nucleate and grow directly on grain boundaries and other incoherent boundaries such as those that exist between the matrix and $Al_{12}Mg_2Cr$ dispersoids. Stacking fault energy of η' precipitates is reported as 350 [79] to 370 mJ/m^2 [67]. In an Al-Zn-Mg-Cu alloy (7050), σ_f, α, and β were found [67] to be 150 MPa, 3.8×10^7 MPa m$^{-0.5}$, and 6.7 MPa m, respectively. $(D_p)_{s \rightarrow b}$ is 6 nm at an f of 0.038.

There exists a strong interdependence between quenching and aging treatments of Al-Zn-Mg-Cu alloys [104,265]. This interaction is more or less dominated by the
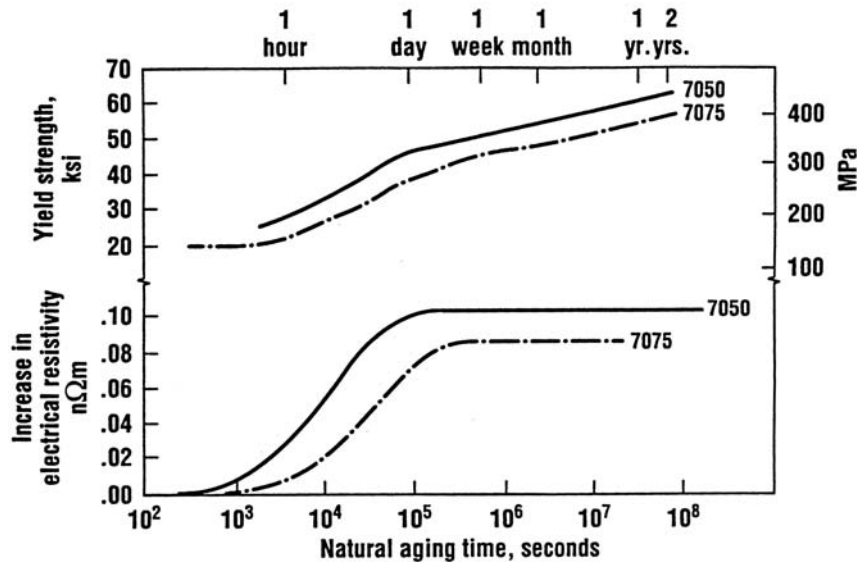
Figure 85   The effects of natural aging time on strength and resistivity of alloys 7075 and 7050 sheet. Reprinted from Ref. 95. (Courtesy of Alcoa).
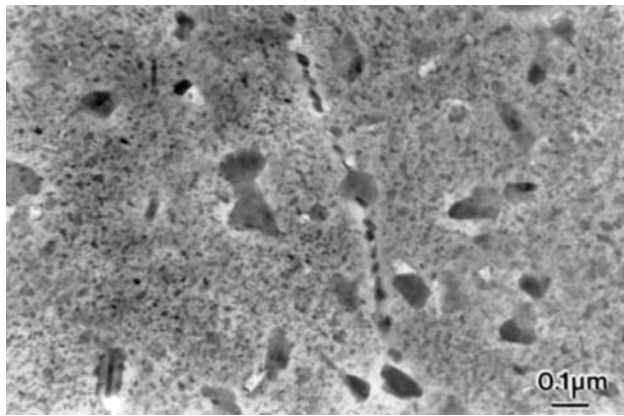
Figure 86 η' precipitates in matrix and η precipitates on grain boundaries in 7075–T735. (Courtesy of Prof. E. A. Starke, Jr., University of Virginia).

influence of quench rate on nucleation and stability of GP zones. Both volume fraction of GP zones and their size are greater for more rapidly quenched samples after a particular amount of natural aging. Because GP zones nucleate homogeneously, precipitate density is high and spacing is small. This in turn promotes a favorable distribution of η' as the degree of precipitation is advanced during artificial aging. At the lower temperatures, the formation of the GP zones is spontaneous, but on aging above a critical temperature, there emerges an apparent
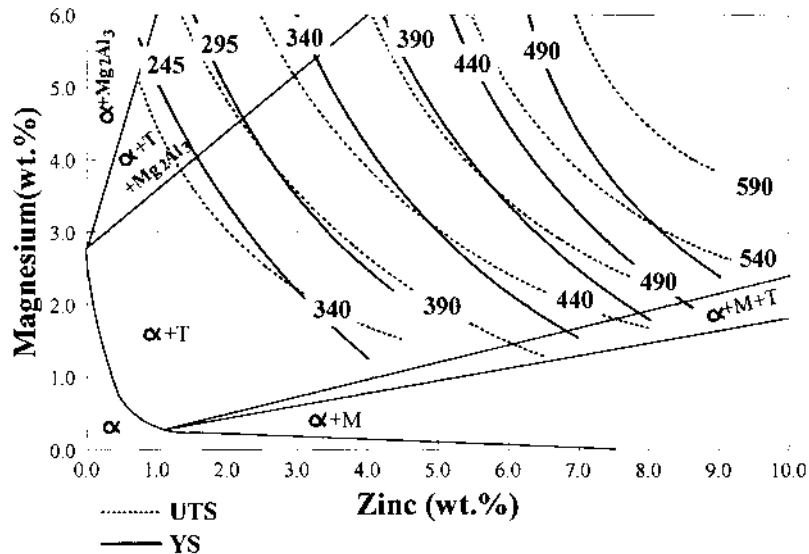
Figure 87 Al-Zn-Mg ternary phase diagram and the typical values of tensile strength achievable in this alloy system (Source Ref. 272).

barrier to nucleation, resulting in a heterogeneous precipitation of GP zones on lattice defects, particularly on dislocation loops, which vary in size from about 700 Å to about 1500 Å in diameter in Al-Zn binary alloys [266]. This critical temperature for spontaneous GP zone formation varies with alloy composition, and lies typically between 90°C and 180°C [135]. If for some reason GP zones become unstable during the early stages of artificial aging and dissolve, η' (or η) heterogeneously nucleates directly (misfit $\sim 7\%$ [118]) in much coarser distribution, resulting in degraded strengths. Aging delay produces a narrow, stable GP zone size distribution, which remains stable upon final artificial aging [267]. Because the GP zones that form during low temperature aging of Al-Zn-Mg and Al-Zn-Mg-Cu alloys have very low coherency strains [267], deformation prior to aging has little or no effect on the precipitation behavior [69,118,161,268]. The introduction of heterogeneous sites can even reduce strength by altering the relative amounts of the different precipitates (GP zones, η' and η), the relative proportions of which determine strength [118]. Depending on the aging treatment, the net effect can be lower strength [95,118]. For instance, strength of hot worked alloy 7075 products is virtually unaffected by introducing dislocations during the mechanical stress relief following quenching when they are aged 24 hr at 121°C (T6 temper). In contrast, strengths of similar material overaged at temperatures of about 150°C or higher (T7 temper) are progressively reduced as the magnitude of the deformation introduced after quenching is increased [118]. This is due to a coarse distribution of η precipitates which provide lower strength than those nucleated at GP zones [95].

Copper additions above 0.25 wt% increase the strength of Al-Zn-Mg alloys [64,69,267], but the main reason for this addition is to provide improved resistance to stress-corrosion cracking [160] and to stimulate the precipitation throughout

the matrix, and thereby reducing the size of PFZ [118]. Additions above about 1.5 wt% significantly increase resistance to stress-corrosion cracking even in the critical short-transverse direction [269]. Concentrations up to 1 wt% do not change the basic precipitation mechanism, and in this range, add a component of solid solution hardening. When in excess of 1 wt%, Cu precipitates during aging, decreases the coherency of the precipitate when aged to peak strength [69], and increases the temperature of GP zone formation [270]. In quaternary Al-Zn-Mg-Cu alloys, the phases $MgZn_2$ and AlMgCu form an isomorphous series, with Al and Cu substituting for Zn in $MgZn_2$. The phase in the region near $MgZn_2$ is often designated $Mg(Zn,Cu,Al)_2$. Copper affects the precipitation reactions. Early work showed effects during the early stages of hardening [271]. Once the first stage of hardening is completed, the Cu-bearing quaternary alloy were reported to age-harden in the same way as the equivalent ternary alloys [135]. Later work, which led to the development of 7050, however, showed strong effects of Cu contents above about 2 wt% on aging response during the high-temperature (above about 150°C) stage of aging to T7-type tempers. The substitution of Cu and Al for Zn in eta phase during aging above this temperature significantly improves resistance to stress-corrosion cracking (even in short-transverse direction) and to exfoliation corrosion. This high-temperature aging reduces strength, but subsequent aging at lower temperatures increases strength [272].

The addition of Cu to Al-Zn-Mg alloys progressively reduces their weldability. The sum, [Zn] + [Mg] + [Cu], controls strength and formability [120], but resistance to SCC and exfoliation corrosion depends strongly on the levels and ratios of these elements. The effect of three alloying additions on yield strength developed in freshly quenched (W), and peak strength (T6) is depicted in Fig. 88 [273]. The increase in W temper is due to solution strengthening, whereas in T6 temper, is due to age hardening, which is much more effective in increasing strength than solutes.

The addition of Ag to Al-Zn-Mg alloys can stimulate an enhanced response to age hardening in a manner similar to its effects in Al-Cu-Mg alloys [271,274]. Figure 89 [274] represents the Al-rich corner of the Al-Zn-Mg phase diagram and shows contours representing constant increments in hardness that may be achieved with the addition of 0.5 wt% Ag. Figure 89 shows that the response of Al-Zn-Mg alloys to Ag additions is not controlled by the position of the alloy in the phase diagram. The maximum hardening response occurs when Ag is added to compositions for which the product [Zn]×[Mg]=8.5 (wt%) [274]. Ag stimulates a finer and more uniform nucleation of η'. This is due to an interaction between vacancies, Mg and Ag atoms. It is suggested [275] that Ag reduces the size of the stable GP zones. Ag additions, however, are not practical in commercial 7075 alloy, because mill heating rates are low enough to allow stable GP zones to form before precipitation temperature is reached [275,276]. In addition, Ag containing alloys develop lower strengths than Ag-free alloys with 0.2 wt% Cr or 0.35 wt% Mn, when the quench rate is not high. This quench sensitivity may be due to the high level of interaction of Ag atoms with vacancies [275]. Quench sensitivity of some commercial and experimental alloys is presented in Fig. 90.

In weldable alloys, solidification cracking susceptibility increases with increasing Cu and Cr contents, and decreases with increasing Mn and Zr contents [277]. Effects of Fe and Si impurities depend on the alloy. In the weldable alloys, Fe and Si combine with Al during a eutectic reaction to form Al-Fe-Si constituent
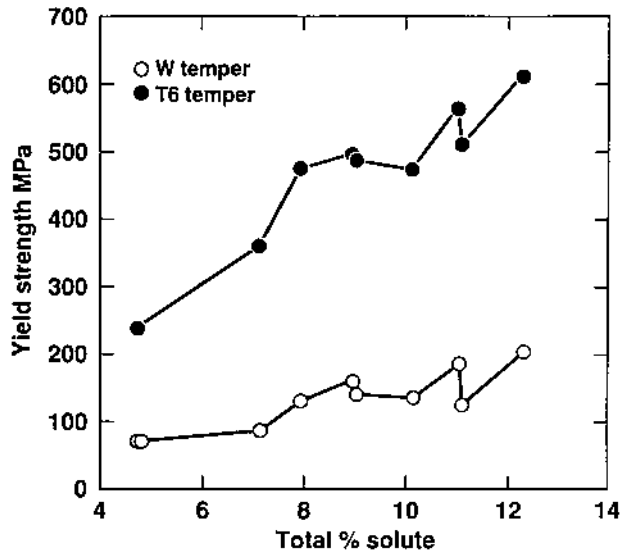
Figure 88 The effect of three alloying additions on yield strength developed in freshly quenched (W), and peak strength (T6). Reprinted from Ref. 95. (Courtesy of Alcoa).
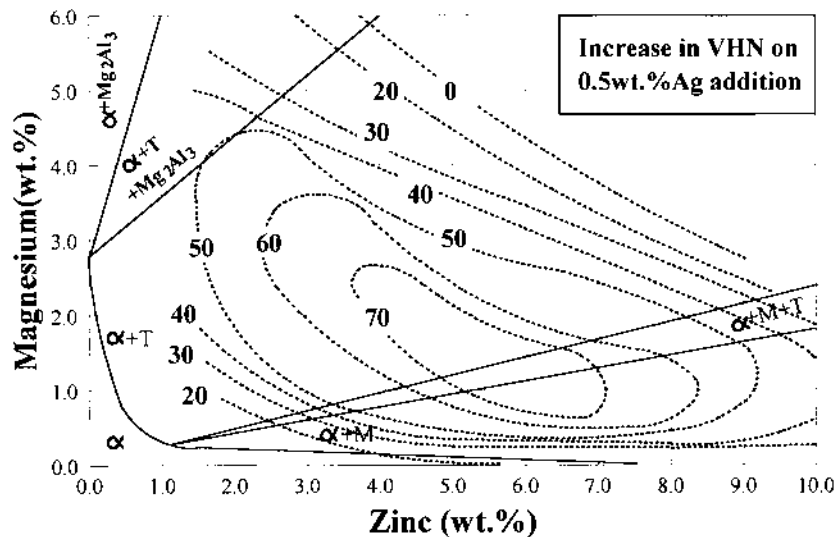
Figure 89 The increase in hardness that can be achieved by 0.5 wt% Ag additions superimposed on the ternary phase diagram (Source Ref. 272).

particles. In 7XXX alloys containing Cu, however, all of the Fe resides in the intermetallic phase Al_7Cu_2Fe. There is virtually no effect of Fe on strength since Cu is not the major strengthening addition in 7XXX alloys [64]. However increasing Fe content causes a decrease in fracture toughness. Si results in the formation of
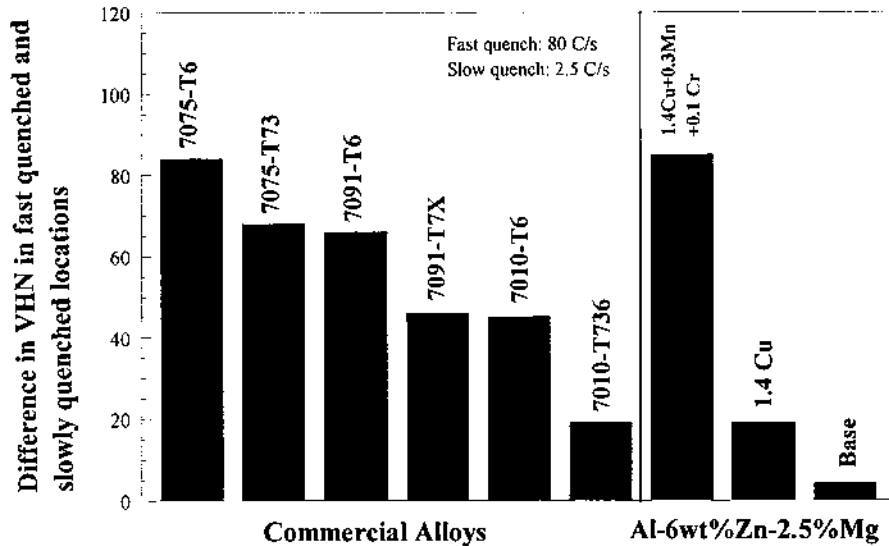
Figure 90 Quench sensitivity of some commercial and experimental alloys, expressed in terms of difference in Vicker's Hardness Number (VHN) between the fast-quenched and slowly-quenched locations. Data obtained from Ref. 103.

Mg_2Si constituent phases. The combined effect of Fe and Si on the toughness of 7050 alloy is given [107] in Fig. 91. Formation of Mg_2Si removes Mg from solid solution and thus lowers the amount of Mg available for precipitation of the strengthening phase, $Mg(Zn,Cu,Al)_2$. Therefore, when reducing Si levels to increase fracture toughness, Mg levels must also be reduced to avoid a strength increase and an associated drop in toughness. The constituent particles formed by Fe and Si can stimulate quench sensitivity and can magnify the effects produced by dispersoid forming additions when these are present [278] as discussed in the following section.

Dispersoid forming elements are added to all commercial Al-Zn-Mg-(Cu) alloys. They improve resistance to stress-corrosion cracking in the longitudinal and long-transverse directions by precipitating as dispersoids which control the degree of recrystallization and modify the grain structure by Zener drag. In alloys containing less than about 2% Mg, Cr precipitates as Al_7Cr, but forms $Al_{12}Mg_2Cr$, (E phase), dispersoids in alloys with higher Mg. This noncoherent dispersoid increases the quench sensitivity in 7XXX alloys, particularly those containing Cu by nucleating η phase at the dispersoid-matrix interface during the quench. Manganese has also been added, usually in conjunction with Cr, to form dispersoids in 7XXX alloys. It forms $AlMn_6$ in Cu-free alloys and $Al_{20}Cu_2Mn_3$ in Al-Zn-Mg-Cu alloys. Both of these dispersoids are larger than E phase particles and are not as effective in controlling the degree of recrystallization and the shape of recrystallized grains. Zr is the most effective alloying addition for inhibition recrystallization. Zirconium forms a coherent Al_3Zr dispersoid approximately 20 nm in diameter which minimizes quench sensitivity [69,279].

Depending on particle size and the nature of the particle-matrix interface, dispersoids play a significant role in the fracture process. The strength-toughness
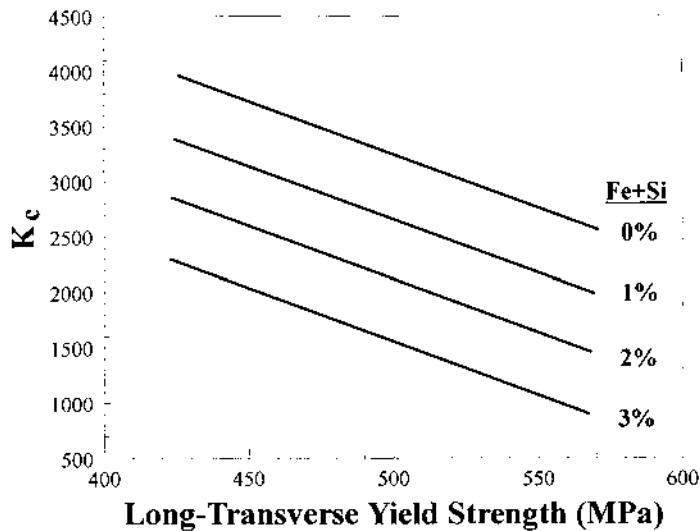
Figure 91   The combined effect of Fe and Si on the toughness of 7050 alloy (Source Ref. 107).

(represented by propagation energy) relationships in Fig. 92 were determined [107] for 7075 variants containing different dispersoid forming elements. Since Zr particles are smaller and coherent with the matrix, they tend not to participate in the fracture process. Fracture resistance is maximized by reducing the volume fraction of constituent particles, and relying on Zr additions for grain structure control. The presence of incoherent Mn-bearing dispersoids not only decreases toughness significantly, as depicted in Fig. 92, but also accelerates crack propagation under cyclic loads [280]. Aging times and temperatures should be chosen to minimize grain boundary precipitation, since fracture toughness decreases with increasing area fraction of grain boundary precipitates for Al-Zn-Mg alloys. The fracture toughness of 7XXX alloys also decrease with an increase in the extent of recrystallization. The fracture path (in plain-strain fracture toughness) of 7050 alloy specimens is a function of the degree of recrystallization, specimen orientation, and aging conditions [281].

In Al-Zn-Mg alloys, easy motion of dislocations within the PFZs along grain boundaries leads to a large local strain hardening. The cracking properties of these alloys have been explained [282] by the large internal stresses appearing at grain boundaries where dislocation bands are formed in the aged alloy. These dislocation bands are formed when moving dislocations cut through dispersely distributed precipitates.

Cr improves resistance to stress-corrosion cracking, but forms a noncoherent dispersoid ($Al_{12}Mg_2Cr$) which increases the quench sensitivity of Al-Zn-Mg alloys. Zr is the most effective alloying addition for inhibiting recrystallization. Zr forms a coherent dispersoid which minimizes quench sensitivity [279]. V has a greater effect on the quench sensitivity of Al-Zn-Mg alloys than Cr and Mn [278]. The effect of Zr
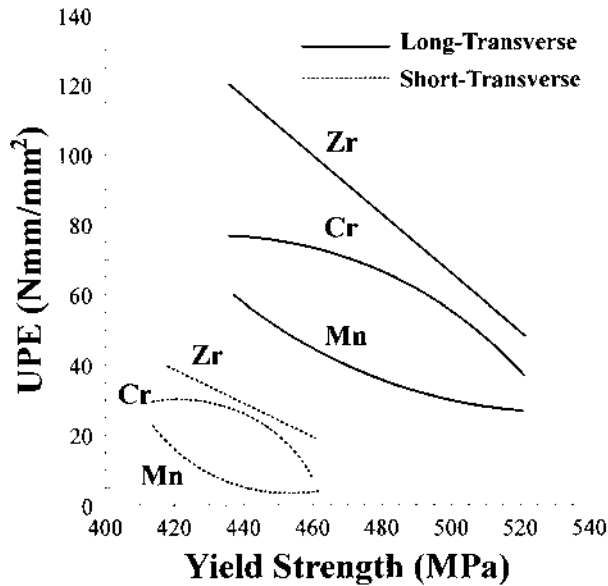
Figure 92 The strength-toughness relationship for 7075 variants containing different dispersoid forming elements (Source Ref. 107).

on quench sensitivity is the less than V, Cr and Mn. Commercial impurities, such as Fe and Si, alone can stimulate quench sensitivity, and can magnify the effects produced by minor alloying additions when these are present [278]. For a given minor alloying addition and impurity level, alloys with lower solute supersaturations exhibit lower quench sensitivity. Alloys with high Zn:Mg ratios allow solute supersaturation to be reduced without sacrificing age-hardening capacity [278].

Additions of Sc result in formation of coherent Al_3Sc dispersoids, which retard recrystallization [283–285] by increasing the recrystallization temperature to above 600°C [285]. Despite their coherency, Al_3Sc dispersoids cause significant lattice strain due to high coherency mismatch. As a result, dislocation motion is blocked and grain growth is impeded. When Sc is present in the alloy together with Zr, the synergism between these two elements is particularly effective in inhibiting recrystallization through the formation of extremely fine, thermally stable $Al_3(Sc_{l-x}Zr_x)$ particles [285]. These particles have also been found [283] to impede the initiation of fatigue cracks.

Acknowledgments

Nomenclature

a:	lattice parameter
b:	Burger's vector
e_s:	shear strain
G:	shear modulus of aluminum
v:	Poisson's ratio
R:	radius of an atomic site
ε:	atomic size difference between aluminum and the solute atom
K:	a constant
G_p:	shear modulus of solute atom
λ:	the effective inter-particle spacing
λ_G:	geometric slip distance
D_p:	the mean planar diameter of the particles
r_o:	the core radius of the dislocations
c:	an alloy constant that depends on the particular strengthening mechanism
f:	the volume fraction
r_d:	the particle radius
σ_y:	yield strength
σ_f:	frictional stress
σ_t:	true stress
d:	grain/substructure size
k_l:	a constant that characterizes the difficulty of transmitting slip across the boundary for a given alloy system.
U:	specific surface energy of GP zones
Γ:	line tension of dislocations
ρ_{GD}:	density of geometrically necessary dislocations
ρ_D:	dislocation density
ε:	true strain
$L_\perp$:	equilibrium separation of dislocations
γ:	stacking fault energy of aluminum
E_f:	energy of formation
T:	temperature
q:	Boltzmann constant
τ_p:	stress acting on a pile-up of dislocations
M:	Taylor's factor (~ 3)
$(D_p)_{s \rightarrow b}$:	critical precipitate diameter at which precipitates can no longer be sheared by dislocations
γ_{APB}:	anti-phase boundary energy

REFERENCES

1. A. Kelly and N. H. MacMillan. *Strong Solids*. Clarendon Press, Oxford, 1986.
2. J. D. Embury. "Strengthening Mechanisms in Al Alloys: An Overview of Natural Limits and Engineering Possibilities," Mat. Sci. Forum., 1996, 217–222, pp. 57–70.
3. M. Van Lancker. *Metallurgy of Aluminium Alloys*. John Wiley & Sons Inc., New York, 1967.

4. D. Altenpohl. *Aluminum: Technology, Applications, and Environment, A Profile of a Modern Metal 6th Edn*. TMS and the Aluminum Association, 1998.

5. I. Friedel. *Dislocations*. Pergamon Press, Oxford, 1964.

6. H. G. Van Buren. *Imperfections in Crystals*. Interscience Publishers, New York, 1960.

7. A. H. Cottrell. *Dislocations and Plastic Dlow in Crystals*. Clarendon Press, Oxford, 1953.

8. R. M. Smallman. *Modern Physical Metallurgy*. Butterworths, London, 1963.

9. J. D. Verhoeven. *Fundamentals of Physical Metallurgy*. John Wiley & Sons, New York, 1975.

10. J. W. Christian and P. R. Swann. "Stacking Faults in Metals and Alloys," in *Alloying Behavior and Effects in Concentrated Solid Solutions* (T. B. Massalski, ed.), 1965, pp. 105–269.

11. A. Seeger. "The Mechanism of Glide and Work-Hardening in Face-Centered Cubic and Hexagonal Close-Packed Metals," in *Dislocations and Mechanical Properties of Crystals*. John Wiley & Sons, New York, 1956, pp. 243–329.

12. R. M. J. Cotterill and R. L. Segall. "The Effect of Quenching History, Quenching Temperature and Trace Impurities on Vacancy Clusters in Aluminium and Gold." Phil. Mag., 1963, 8, pp. 1105.

13. A. H. Cottrell. *Theoretical Structural Metallurgy*. Edward Arnold Ltd, London, 1955.

14. G. Das. Influence of Quenching Conditions on Vacancy Loops in Aluminum. MSc Thesis. University of California Berkeley, 1964.

15. I. J. Polmear. "Nucleation from Super-Saturated Solid Solutions." J. Aust. Inst. Met., 1966, 11, pp. 246–257.

16. R. W. Sparks. A Study of the Quench Hardening of an Aluminum-0.3 Atomic Percent Magnesium Alloy. MS Thesis, University of Delaware, 1970.

17. P. B. Hirsch, J. Silcox, R. E. Smallman, and K. H. Westmacott. "Dislocation Loops in Quenched Aluminium." Phil. Mag., 1958, 8, pp. 897–908.

18. A. H. Cottrell. "Point Defects and the Mechanical Properties of Metals and Alloys at Low Temperatures," in *Vacancies and Other Point Defects in Metals and Alloys*, The Institute of Metals, 1958, pp. 1–39.

19. F. C. Frank and W. T. Read, Jr. "Multiplication Process for Slow Moving Dislocations." Phys. Rev., 1950, 79, pp. 722–723.

20. K. H. Westmacott, B. Hull, R. S. Barnes, and R. E. Smallman. "Dislocation Sources in Quenched Aluminium-Based Alloys." Phil. Mag., 1959, 4, pp. 1089.

21. K. H. Westmacott, R. S. Barnes, and R. E. Smallman. "The Observation of a Diclocation 'Climb' Source." Phil. Mag., 1962, 7, pp. 1585–1596.

22. A. H. Cottrell. *Mechanical Properties of Matter*. John Wiley and Sons, 1964.

23. M. F. Ashby. "The Deformation of Plastically Non-Homogeneous Alloys," in *Strengthening Methods in Crystals* (A Kelly and R. B. Nicholson, eds.), John Wiley and Sons, 1971, pp. 137–192.

24. D. A. Porter and K. E. Easterling. *Phase Transformations in Metals and Alloys*. Van Nostrand Reinhold, New York, 1981.

25. J. K. Lee. "Dynamic Interaction between a Coherent Precipitate and an Edge Dislocation." Metall. Mater. Tran. A, 1998, 29A, pp. 2039–2048.

26. E. R. Parker. "Strain Hardening." In: *The Strengthening of Metals*, Ed. D. Peckner, Reinhold Publishing Co., New York, 1964, pp. 77–92.

27. J. Glazer and J. W. Morris, Jr. "Theory of Strengthening by Ordered Precipitates," in *Aluminum Alloys – Physical and Mechanical Properties* (E. A. Starke, Jr. and T. H. Sanders, Jr., eds.), West Midlands, EMAS, 1986, 2, pp. 783–796.

28. L. M. Brown, and R. K. Ham. "Dislocation-Particle Interactions," in *Strengthening Methods in Crystals* (A. Kelly and R. B. Nicholson, eds.), John Wiley and Sons, 1971, pp. 9–135.

29. R. Maddin and A. H. Cottrell. Quench Hardening in Aluminium Single Crystals. Phil. Mag., 1955, 46, pp. 735–743.

30. B. Noble, S. J. Harris, and K. Dinsdale. "Yield Characteristics of Aluminium-Lithium Alloys." Metal. Sci., 1982, 16, pp. 425–430.

31. J. D. Embury, D. J. Lloyd, and T. R. Ramachandran. "Strengthening Mechanisms in Aluminum Alloys," in *Treatise on Materials Science and Technology*, Academic Press, 1989, 31, pp. 579–601.

32. A. Fontaine. "Clustering Effects in Splat-Cooled Al-Transition Metal Alloys," in *Rapidly Quenched Metals* (N. J. Grant and B. C. Giessen, eds.), 1976, 1, pp. 163–167.

33. J. E. Dorn, P. Pietrokowsky, and T. E. Tietz. "The Effect on the Plastic Properties of Aluminum Alloys." Trans. AIME, J. Metals, 1950, 188, pp. 933–943.

34. H. Suzuki. "The Yield Strength of Binary Alloys." In: *Dislocations and Mechanical Properties of Crystals*. John Wiley & Sons, New York, 1956, pp. 361–389.

35. J. E. Hatch. *Aluminum: Properties and Physical Metallurgy*, Metals Park, OH, American Society for Metals, 1984.

36. H. W. King. "Atomic Volume and Size Correlations in Solid Solutions," in *Alloying Behavior and Effects in Concentrated Solid Solutions* (T. B. Massalski, ed.), 1965, pp. 85–104.

37. E. Sahin and H. Jones. "Extended Solid Solubility, Grain Refinement and Age Hardening in Al-1 to 13 wt% Zr Rapidly Quenched from the Melt." In: *Rapidly Quenched Metals III*. (B Cantor, ed.), The Metals Society, 1978, 1, pp. 138–146.

38. A. Bonefačić, M. Kerenović, A. Kirin, and D. Kunstelj. "Segregation of Solutes in Al-Ni and Al-Sn Alloys and its Influence on their Mechanical Properties." J. Mater. Sci., 1975, 10, pp. 243–251.

39. R. E. Sanders, Jr., S. F. Baumann, and H. C. Stumpf. "Non-Heat-Treatable Aluminum Alloys." In: *Aluminum Alloys – Physical and Mechanical Properties*. Eds. E. A. Starke, Jr, T. H. Sanders, Jr. West Midlands: EMAS, 1986, 3, pp. 1441–1484.

40. K. H. Westmacott, Hull, R. S. Barnes, and R. E. Smallman. "Vacancy Trapping in Quenched Aluminium Alloys." Phil. Mag., 1961, 6, pp. 929–935.

41. A. Deschamps, L. Le Sinq, Y. Br³chet, J. D. Embury, and M. Niewczas. "Anomalous Strain Hardening Behaviour of a Supersaturated Al-Zn-Mg Alloy." Mater. Sci. Eng., 1997, A234–236, pp. 477–480.

42. R. J. Rioja, P. E. Bretz, R. R. Sawtell, W. H. Hunt, and E. A. Ludwiczak. "Precipitation Reactions, Strength and Toughness of Al-Li-Cu Alloys," in *Aluminum Alloys – Physical and Mechanical Properties* (E. A. Starke, Jr. and T. H. Sanders, Jr., eds.), West Midlands: EMAS, 1986, 3, pp. 1781–1797.

43. C. G. Schmidt and A. K. Miller. "The Effect of Solutes on the Strength and Strain hardening Behavior of Alloys." Acta. Metall., 1982, 30, pp. 615–625.

44. A. R. C. Westwood and T. Broom. "Strain-Ageing of Aluminum-Magnesium Alloys at Temperatures between 208° and 369°K." Acta. Metall., 1957, 5, pp. 249.

45. J. G. Morris. "Dynamic Strain Aging in Aluminum Alloys." Mater. Sci. Eng., 1974, 13, pp. 101–108.

46. J. T. Al-Haidary, and N. J. Petch, "E. R. De Los Rios." Phil. Mag. A, 1983, 47, pp. 869–890.

47. R. D. Doherty. Unpublished research at Alcoa Laboratories, 1983–1985.

48. J. H. Hollomon. "Tensile Deformation." Trans. AIME, 1945, 162, pp. 268–290.

49. H. C. Stumpf. Unpublished research at Alcoa Laboratories, 1965–1971.

50. N. Hansen. "The Effect of Grain Size and Strain on the Tensile Flow Stress of Aluminum at Room Temperature." Acta. Metall., 1977, 25, pp. 863–869.

51. R. D. Carter, E. W. Lee, E. A. Starke, Jr., and C. J. Beevers. "The Effect of Microstructure and Environment on Fatigue Crack Closure of 7475 Aluminum Alloy." Metall. Trans. A, 1984, 15A, pp. 555–563.

52. G. B. Burger, A. K. Gupta, P. W. Jeffrey, and D. J. Lloyd. "Microstructural Control of Aluminum Sheet Used in Automotive Applications." Mater. Characterization, 1995, 35, pp. 23–39.

53. E. Hornbogen and E. A. Starke, Jr. "Theory Assisted Design of High Strength Low Alloy Aluminum." Acta. Metall. Mater., 1993, 41, pp. 1–16.

54. J. D. Embury. "Basic Microstructural Aspects of Aluminum Alloys and Their Influence on Fracture Behaviour." AGARD Conference Proceedings No. 185: Specialists Meeting on Allay Design for Fatigue and Fracture Resistance, Brussels, Belgium, 13–19 Apr 1975, pp. 1.1–1.13.

55. J. D. Evensen, N. Ryum, and J. D. Embury. "The Intergranular Fracture of Al-Mg-Si Alloys." Mater. Sci. Eng., 1975, 18, pp. 221–229.

56. D. J. Lloyd. "Deformation of Fine-Grained Aluminium Alloys." Metals. Sci., 1980, 14, pp. 193–198.

57. E. A. Starke, Jr. "Aluminium Alloys of the 70s: Scientific Solutions to Engineering Problems." An Invited Review. Mat. Sci. Eng., 1977, 29, pp. 99–115.

58. F. R. N. Nabarro. "Work Hardening of Face Centered Cubic Single Crystals," in *Strength of Metals and Alloys* (ICSMA 7), 1985, 3, pp. 1667–1700.

59. R. E. Sanders, Jr., S. F. Baumann, and H. C. Stumpf. "Wrought Non-Heat Treatable Aluminum Alloys." In: *Treatise on Materials Science and Technology*, Academic Press, 1989, 31, pp. 65–105.

60. Y. Brechet, P. Guyot, and F. Louchet. "Modelling Tensile Curves at Constant Strain Rate for Hardening by Shearable Precipitates: Application to Al-2.5% Li," in *Aluminum Alloys – Physical and Mechanical Properties* (E. A. Starke, Jr. and T. H. Sanders, Jr., eds.), EMAS, West Midlands, 1986, 2, pp. 951–962.

61. M. F. Ashby and G. C. Smith. "Direct Electron Microscopy of Thin Foils of Internally Oxidized Dilute Copper Alloys." Phil. Mag., 1960, 5, pp. 298–301.

62. H. R. Shercliff, Ø Grong, O. R. Myhr, and M. F. Ashby. "Process Modelling Applied to Age Hardening Aluminium Alloys." Proceedings of the Third International Conference on Aluminium Alloys, pp. 357–369, pp. 22–26 June 1992.

63. A. J. Ardell. "Temporal Behavior of the Number Density of Particles During Ostwald Ripening." Mater. Sci. Eng., 1997, A238, pp. 108–120.

64. C. P. Blankenship, Jr., E. A. Starke, Jr., and E. Hornbogen. "Microstructure and Properties of Aluminum Alloys," in *Microstructure and Properties of Materials* (J. C. M. Li, ed.), World Scientific, 1996.

65. C. P. Blankenship, Jr., E. Hornbogen, and E. A. Starke, Jr. "Predicting Slip Behavior in Alloys Containing Shearable and Strong Particles." Mat. Sci. Eng., 1993, A169, pp. 33–41.

66. E. Hornbogen. "Review: A Systematic Description of Microstructure." J. Mater. Sci., 1986, 21, pp. 3737–3747.

67. L. Cottignies and P. Guyot. "Precipitation Kinetics and Strengthening in AlMgZnCu Alloys." Mat. Sci. Forum, 1996, 217–222, pp. 1263–1268.

68. T. Balakrishna Bhat, and V. S. Arunchalam. "Strengthening Mechanisms in Alloys." In: *Alloy Design*. (S. Ranganathan, V. S. Arunchalam, and R. W. Cahn, eds.), Indian Academy of Sciences, 1981, pp. 23–44.

69. E. A. Starke, Jr. "Heat-Treatable Aluminum Alloys," in *Treatise on Materials Science and Technology*, Academic Press, 1989, 31, pp. 35–63.

70. J. F. Nie, B. C. Muddle, and I. J. Polmear. "The Effect of Precipitate Shape and Orientation on Dispersion Strengthening in High Strength Aluminium Alloys." Mat. Sci. Forum., 1996, 217–222, pp. 1257–1262.

71. I. J. Polmear. *Light Alloys*. 3rd Edn. Halsted Press, London, 1996.

72. A. Kelly and M. E. Fine. "The Strength of an Alloy Containing Zones." Acta. Metall., 1957, 5, pp. 365–367.

73. I. J. Polmear. "Role of Age Hardening in Modern Aluminium Alloys." Proceedings of the 3rd International Conference on Aluminium Alloys. 22–26 June 1992. pp. 371–384.
74. P. M. Kelly. "The Effect of Particle Shape on Dispersion Hardening." Scrip. Metall., 1972, 6, pp. 647–656.
75. A. J. Ardell. "Precipitation Hardening." Metall. Trans. A., 1985, 16A, pp. 2131–2165.
76. J Glazer, and JW Morris, Jr. "The Effect of the Precipitate size Distribution on the Aging Curve of Order Hardening Alloys." Acta. Metall., 1988, 36, pp. 907–915.
77. S. D. Harkness and J. J. Hren. "An Investigation of Strengthening by Spherical Coherent GP Zones." Metall. Trans., 1970, 1A, pp. 43–49.
78. V. Gerold and K. Hartmann. "Theoretical and Experimental Investigations on Stacking Fault Strengthening." Trans. Jap. Inst. Met., 1968, 9(supplement), pp. 509–513.
79. I. Kovacs, J. Lendvai, T. Ungar, T. Turmezey, and G. Groma. "The Properties of an AlZnMg Alloy Deformation Strengthened by Guinier-Preston Zones." Acta. Metall., 1977, 25, pp. 673–680.
80. A. Melander and P. A. Persson. "The Strength of a Precipitation Hardened AlZnMg Alloy." Acta. Metall., 1978, 26, pp. 267.
81. T. Ung²r, J. Lendvai, I. Kovacs, G. Groma, and F. Kovacs-Csetenyi. "Quantitative Investigation of the Reversion Process of GP Zones in an Al-Zn-Mg Alloy." Z. Metallk. 1976, 67, pp. 683.
82. D. J. Lloyd. "Precipitation Hardening," in *Strength of Metals and Alloys* (ICSMA 7), 1985, 3, pp. 1745–1778.
83. V. Gerold. In: *Structure and Structure Development of Al-Zn Alloys*. Ed. H. Loffler. Berlin, Akademie Verlag, 1995, pp. 156.
84. J. C. Huang and A. J. Ardell. "Strengthening Mechanisms in Two Al-Li-Cu Alloys." In: *Aluminium Technology '86*. Ed. T. Sheppard, London, The Institute of Metals, 1986, pp. 434–441.
85. A. K. Sachdev. "Correlating Strain Hardening and Strain Rate Sensitivity to Deformed Substructure in Aged Al-Mg-Si Alloy," in *Aluminum Alloys – Physical and Mechanical Properties* (E. A. Starke, Jr. and T. H. Sanders, Jr., eds.), EMAS, West Midlands, 1986, 2, pp. 813–826.
86. N. Ryum. "Precipitation and Recrystallization in an Al-0.5 wt% Zr Alloy." Acta. Metall., 1969, 17, pp. 269–278.
87. J. Runyoro, S. M. A. Boutorabi, and J. Campbell. "Critical Gate Velocities for Film-Forming Casting Alloys: A Basis for Process Specification." AFS Tran., 1992, pp. 225–234.
88. N. D. G. Mountford, and R. Calvert. "Precipitation Effects in Liquid Aluminium Alloys: Experiments with a Pulsed Ultrasonic Technique." J. Inst. Metals., 1959–1960, 88, pp. 121–127.
89. N. R. Green and J. Campbell. "Influence of Oxide Film Filling Defects on the Strength of Al-7Si-Mg Alloy Castings." AFS Tran., 1994, pp. 341–347.
90. M. Tiryakioglu, J. Campbell, and N. R. Green. "Review of Reliable Processes for Aluminium Aerospace Castings." AFS Tran., 1996, pp. 1069–1078.
91. J. Campbell. "Invisible Macrodefects in Castings." Presented at 3rd European Conference on Advanced Materials and Processes (EUROMAT), Paris, 8–10 June 1993.
92. C. Nyahumwa, N. R. Green, and J. Campbell. "The Concept of the Fatigue Potential of Cast Alloys," in *Advances in Aluminum Casting Technology* (M Tiryakioglu and J Campbell, eds.), Metals Park, ASM International, 1998.
93. J. Campbell. "The Ten Casting Rules: Guidelines for the Reliable Production of Reliable Castings: A Draft Process Specification," in *Advances in Aluminum Casting Technology* (M Tiryakioglu and J. Campbell, eds.), ASM International, 1998.

94. J. T. Staley. "Modeling Quenching of Precipitation Strenghtened Alloys: Application to an Aluminum-Copper Lithium Alloy." PhD Dissertation, Drexel University, 1989.

95. J. T. Staley. "Metallurgical Aspects Affecting Strength of Heat Treatable Alloy Products Used in the Aerospace Industry." Proceedings of the Third International Conference on Aluminum Alloys, Trondheim, Norway, June 1992, pp. 107–143.

96. J. T. Staley. "Microstructure and Toughness of High-Strength Aluminum Alloys," in *Properties Related to Fracture Toughness*. ASTM STP, 605, 1975, pp. 71–103.

97. M. Gao, C. R. Feng, and R. P. Wei. "An Analytical Electron Microscopy Study of Constitutent Particles in Commercial 7075-T6 and 2024-T3 Alloys." Metall. Mater. Trans. A, 1998, 29A, pp. 1145–1151.

98. J. G. Kaufman. "Design of Aluminum Alloys for High Toughness and High Fatigue Strength." AGARD Conference Proceedings No. 185: Specialists Meeting on Allay Design for Fatigue and Fracture Resistance, Brussels, Belgium, 13–19 April 1975, pp. 2.1–1.26.

99. M. E. Fine. "Stability and Coarsening of Dispersoids in Aluminium Alloys," in *Dispersion Strengthened Aluminum Alloys* (Y-W Kim and W. M. Griffith, eds.), TMS, 1988, pp. 103–121.

100. M. H. Tosten and P. R. Howell. "The Early Stages of Aging in an Al-3% Cu-2%Li-0, 12%Zr Alloy," in *Aluminum Alloys – Physical and Mechanical Properties* (E. A. Starke, Jr. and T. H. Sanders, Jr., eds.), EMAS, West Midlands, 1986, 2, pp. 727–741.

101. D. B. Williams and P. R. Howell. "The Microstructure of Aluminum-Lithium Base Alloys." In: *Treatise on Materials Science and Technology*, Academic Press, 1989, 31, pp. 365–388.

102. R. B. Nicholson and J. Nutting. "The Metallography of Precipitation in an Al-16%Ag Alloy." Acta. Metall., 1961, 9, pp. 332–343.

103. H. J. Kolkman, W. G. J.'t Hart, and L. Schra. "Quench Sensitivity of Airframe Aluminium Alloys." Proceedings of the Conference on Strength of Metals and Alloys, vol 2. Finland, August 1988, pp. 597–602.

104. R. R. Sawtell and J. T. Staley. "Interactions between Quenching and Aging in Alloy 7075." Aluminium, 1983, 59, pp. 127–133.

105. M. J. Couper, A. E. Neeson, and J. R. Griffiths. "Casting Defects and Fatigue Behavior of an Aluminium Casting Alloy." Fatigue Fract. Engng. Mater. Struct., 1990, 13, pp. 213–227.

106. J. R. Brockenbrough, R. J. Bucci, A. J. Hinkle, P. E. Magnusen, and S. M. Miyasoto. "Role of Microstructure on the Fatigue Durability of Aluminum Aircraft Alloys." 1993 Year End Report. ONR Contract No. N00014–91-C-0128. ALCOA, 1993.

107. J. T. Staley. "Microstructure and Toughness of High Strength Alloys." Presented at ASTM Symposium on Properties Related to Toughness, Montreal, Canada, 22–27 June, 1975.

108. J. D. Embury and G. Burger. "The Influence of Microstructure on Toughness." In: *Strength of Metals and Alloys* (ICSMA 7), 1985, 3, pp. 1893–1915.

109. J. M. Duva, M. A. Daeubler, E. A. Starke, Jr., and G. Luetjering. "Large Shearable Particles Lead to Coarse Slip in Particle Reinforced Alloys." Acta. Metall., 1988, 36, pp. 585–589.

110. W. A. Cassada, G. J. Shiflet, and E. A. Starke, Jr. "Characterization of Two Grain Boundary Precipitates in Al-Li-Cu Alloys with Electron Micro-Diffraction," in *Aluminum Alloys – Physical and Mechanical Properties* (E. A. Starke, Jr. and T. H. Sanders, Jr., eds.), EMAS, West Midlands, 1986, 2, pp. 695–710.

111. J. T. Staley. "How Microstructure Affects Fatigue and Fracture of Aluminium Alloys." Proceedings of the Tenth Symposium on Naval Structural Mechanics: Fracture Mechanics, Washington DC. 11–13 September 1978, pp. 671–684.

112. J. T. Staley. "Influence of Microstructure on Fatigue and Fracture of Aluminium

Alloys.'' Aluminium. 1979, 55, pp. 277–281.

113. A. K. Vasudevan, R. D. Doherty, and S. Suresh. "Fracture and Fatigue Characteristics in Aluminum Alloys." In: *Treatise on Materials Science and Technology*, Academic Press, 1989, 31, pp. 445–462.

114. A. K. Vasudevan and R. D. Doherty. "Grain Boundary Ductile Fracture in Precipitation Hardened Aluminum Alloys." Acta Metall., 1987, 35, pp. 1193–1219.

115. P. N. T. Unwin and G. C. Smith. "The Microstructure and Mechanical Properties of Al-6% Zn-3% Mg." J. Inst. Metals., 1969, 97, pp. 299–310.

116. R. H. Van Stone, T. B. Cox, J. R. Low, and J. A. Psioda. "Microstructural Aspects of Fracture by Dimpled Rupture." Int. Metal. Rev., 1985, 30, pp. 157–179.

117. A. S. Argon, J. Im, and R. Safoglu. "Cavity Formation from Inclusions in Ductile Fracture." Metall. Trans. A, 1975, 6A, pp. 825–837.

118. T. H. Sanders, Jr. and J. T. Staley. "Review of Fatigue and Fracture Research on High Strength Aluminum Alloys." Proceedings of Conference on Fatigue and Microstructure, St. Louis, MO, 14–15 October 1978, pp. 467–522.

119. I. Todd and H. Jones. "The Effect of Cumulative Alloying Additions on Intermetallic Phase Selection in Alloys Based on Al-0.5 wt% Fe." Materials Science Forum, 1996, pp. 217–222, 201–206.

120. L. F. Mondolfo. "Aluminum Alloys: Structure and Properties." Butterworths, London, 1976.

121. F. Pan, D. V. Edmonds, X. Yang, S. Zhou, and P. Ding. "Effect of Rare Earth Additions on the As-Cast Microstructure and Intermetallic Compounds in Commercial Purity Aluminum." In: *Advances in Production and Fabrication of Light Metals and Metal Matrix Composites*, 1992, pp. 361–370.

122. B. A. Parker, "Formability and Microstructure," in *Treatise on Materials Science and Technology*, Academic Press, 1989, 31, pp. 539–562.

123. P. G. Shewmon. *Transformations in Metals*. McGraw-Hill, New York, 1969.

124. R. H. Beton and E. C. Rollason. "Hardness Reversion of Dilute Aluminium-Copper and Aluminium-Copper-Magnesium Alloys." I. Inst. Metals., 1957, 86, pp. 77.

125. A. G. Guy. *Introduction to Materials Science*. McGraw Hill, New York, 1972.

126. K. Hono, T. Hashizume, Y. Hasegawa, T. Satoh, K. Hirano, and T. Sakurai. "An Atom Probe Field Microscopic Study of GP Zones in Al-Cu Alloys," in *Aluminum Alloys – Physical and Mechanical Properties* (E. A. Starke, Jr. and T. H. Sanders, Jr., eds.), EMAS, West Midlands, 1986, 1, pp. 635–645.

127. P. Haasen. *Physical Metallurgy*. Cambridge University Press, Cambridge, 1978.

128. J. Karov and W. V. Youdelis. "Growth Kinetics of θ'- and θ-phases in Al-3Cu Alloy." Mat. Sci. Tech., 1986, 2, pp. 1183–1188.

129. L. J. Swartzendruber, W. J. Boettinger, L. K. Ives, S. R. Coriell, and R. Mehrabian. "Relationship Between Process Variables, Microstructure and NDE of a Precipitation Hardened Aluminum Alloy," Proceedings of the Nondestructive Evaluation of Microstructure Characterization and Reliable Strategies, 1981, pp. 253–271.

130. N. J. H. Holroyd, A. K. Vasudevan, and L. Christodoulou. "Stress Corrosion of High-Strength Aluminum Alloys." In: *Treatise on Materials Science and Technology*, Academic Press, 1989, 31, pp. 463–483.

131. T. Eto, A. Sato, and T. Mori. "Stress-Oriented Precipitation of G. P. Zones and θ' in an Al-Cu Alloy." Acta. Metall., 1978, 26, pp. 499–508.

132. B. Skrotzki, G. J. Shiflet, and E. A. Starke, Jr. "On the Effects of Stress on Nucleation and Growth of Precipitates in an Al-Cu-Mg-Ag Alloy," Met. Mat. Tran. A, 1996, 27A, pp. 3431–3444.

133. T. Eto, A. Sato, and T. Mori. Acta Metall., 1978, 26, pp. 499–508.

134. S. P. Ringer, K. Hono, I. J. Polmear, and T. Sakurai. "Precipitation Processes During the Early Stages of Ageing in Al-Cu-Mg Alloys." App. Surf. Sci., 1996, 94/95, pp. 253–260.

135. B. C. Muddle, S. P. Ringer, and I. J. Polmear. "High Strength Microalloyed Aluminium Alloys," in *Advanced Materials '93, VI/Frontiers in Materials Science and Engineering* (S. Somiya et al. eds.), 1994, pp. 999–1023.

136. H. D. Chopra, B. C. Muddle, and I. J. Polmear. "The Structure of Primary Strengthening Precipitates in an Al-1.5 wt% Cu-4.0 wt% Mg-0.5 wt% Ag Alloy." Phil. Mag. Let., 1996, 73, pp. 351–357.

137. H. D. Chopra, L. J. Liu, B. C. Muddle, and I. J. Polmear. "The Structure of Metastable $\{111\}_\alpha$ Precipitates in an Al-2 5 wt% Cu-1.5 wt% Mg-0.5 wt% Ag Alloy." Phil. Mg. Let., 1995, 71, pp. 319–324.

138. S. R. Arumalla and I. J. Polmear. "Fatigue and Creep Behaviour of Aged Alloys Based on Al-4% Cu-0.3% Mg," in *Strength of Metals and Alloys* (ICSMA 7), 1985, 1, pp. 453–458.

139. S. P. Ringer, I. J. Polmear, and T. Sakurai. "Effect of Additions of Si and Ag to Ternary Al-Cu-Mg Alloys in the $\alpha + S$ Phase Field." Mat. Sci. Eng., 1996, A217/218, pp. 273–276.

140. S. P. Ringer, T. Sakurai, and I. J. Polmear. "Origins of Hardening in Aged Al-Cu-Mg-Ag Alloys" Acta Mater., 1997, 45, pp. 3731–3744.

141. I. J. Polmear. "Advanced Light Alloys," in *New Horizons for Materials* (P. Vincenzini, ed.), Techna. Srl, 1995, pp. 33–44.

142. S. P. Ringer, S. P. Swenser, B. C. Muddle, I. J. Polmear, and T. Sakurai. "APFIM/TEM Observations of a High Strength – Creep Resistant Al-Cu-Mg-Si-Ge Alloy," Mat. Sci. Forum, 1996, 217–222, pp. 689–694.

143. K. Hono, T. Sakurai, and I. J. Polmear. "Pre-Precipitate Clustering in an Al-Cu-Mg-Ag Alloy." Scrip. Met. Mat., 1994, 30, pp. 695–700.

144. K. Hono, T. Sakurai, and I. J. Polmear. "Pre-Precipitate Clustering in Aged Aluminium Alloys." Mat. Sci. Forum, 1995, 189–190, pp. 249–254.

145. S. P. Ringer, K. Hono, I. J. Polmear, and T. Sakurai. "The Effect of Ag and Mg Additions on Precipitation in Al-Cu-(Li) Alloys: Atom Probe/Transmission Electron Microscopy Observations." In: Proceedings of an International Conference on Solid-to-Solid Phase Transformations in Inorganic Materials PTM'94, The Minerals, Metals & Materials Society, July 17–22, 1994, pp. 165–170.

146. I. J. Polmear. "Development of an Experimental Wrought Aluminium Alloy for Use at Elevated Temperatures," in *Aluminum Alloys – Physical and Mechanical Properties* (E. A. Starke, Jr. and T. H. Sanders, Jr., eds.), EMAS, West Midlands, 1986, 1, pp. 661–674.

147. S. P. Ringer, W. Yeung, B. C. Muddle, and I. J. Polmear. "Precipitate Stability in Al-Cu-Mg-Ag Alloys Aged at High Temperatures." Acta. Metall. Mater., 1994, 42, pp. 1715–1725.

148. B. Skrotzki, H. Hargarter, and E. A. Starke, Jr. "Microstructural Stability under Creep Conditions of Two Al-Cu-Mg-Ag Alloys." Mat. Sci. Forum, 1996, 217–222, pp. 1245–1250.

149. I. J. Polmear. "Design and Evaluation of Creep Resistant Al-Cu-Mg-Ag Alloys." Proceedings of IMMA Conference, 1996, 1, pp. 9–12.

150. I. J. Polmear, G. Pons, H. Octor, C. Sanchez, A. Morton, W. Borbidge, and S. Rogers. "After Concorde: Evaluation of an Al-Cu-Mg-Ag Alloy for Use in the Proposed European SST." Mat. Sci. Forum, 1996, 217–222, pp. 1759–1764.

151. J. M. Silcock, T. J. Heal, and H. K. Hardy. "Structural Ageing Characteristics of Binary Aluminium-Copper Alloys." J. Inst. Metals, 1953–1954, 82, pp. 239–248.

152. A. K. Mukhopadhyay, K. S. Prasad, and C. R. Chakravorty. "Precipitation in an Al-Cu-Mg Alloy Containing Trace Addition of In." Mat. Sci. Forum, 1996, 217–222, pp. 753–758.

153. L. I. Kaygorodova, R. R. Romanova, YaV. Zhingel, A. M. Drits, and V. A. Rasso. "Features of Natural Ageing of An Aluminium-Lithium Alloy with High Copper Content." Phys. Met. Metall., 1991, 71, pp. 164–170.

154. P. J. Gregson and H. M. Flower. "Phase Transformations in Al-Li-Cu-Mg-Zr Alloys," in *Aluminium Technology '86*. (T. Sheppard, ed.), The Institute of Metals, London, 1986, pp. 423–428.

155. E. Hornbogen, A. K. Mukhopadhyay, and E. A. Starke, Jr. "Precipitation Hardening of Al-(Si,Ge) Alloys." Scr. Met. et Mat., 1992, 27, pp. 733–738.

156. X. Gao, J. F. Nie, and B. C. Muddle. "Effects of Si Additions on the Precipitation Hardening Response in Al-Cu-Mg(-Ag) Alloys." Mat. Sci. Forum, 1996, 217–222, pp. 1251–1256.

157. S. Abis, P. Mengucci, and G. Riontino. "Effects of Si Additions in the Precipitation Hardening of An Al-Cu-Mg-Ag Alloy." Proceedings of the Third International Conference on Aluminium Alloys, 1992, pp. 231–236.

158. C. W. Bartges and J. S. Lin. "Effect of Sn Additions on GP Zone Formation in Al-Cu Alloys." Scr. Met. Mat., 1993, 28, pp. 1283–1286.

159. G. E. Spangler, R. F. Ashton, and D. S. Thompson. "Advances in Aircraft Alloy Technology and Fabrication Practice," in Aluminum Transformation Technology-1981, 1981, pp. 483–519.

160. J. T. Staley. "History of Wrought-Aluminum-Alloy Development," in *Treatise on Materials Science and Technology*, Academic Press, 1989, 31, pp. 3–31.

161. S. P. Ringer, B. C. Muddle, and I. J. Polmear. "Effects of Cold Work on Precipitation in Al-Cu-Mg-(Ag) and Al-Cu-Li-(Mg-Ag) Alloys." Metall. Mater. Trans., 1995, 26A, pp. 1659–1671.

162. S. G. Mazzini. "Influence of Deformation Before Artificial Aging on Properties of Al-Cu-Mg Aluminum Alloy." Scrip. Metall. Mater., 1994, 31, pp. 1127–1130.

163. W. A. Cassada and M. F. Bartholomeusz. "The Effect of Cu and Mg Content on Mechanical Properties of Al-Cu-Mg Alloys with and without Ag Additions." Mat. Sci. Forum, 1996, 217–222, pp. 1765–1770.

164. P. Sainfort, and P. Guyot. "Dislocation-Precipitate Interactions in Al-Li Binary and Al-Li-Cu Ternary Alloys" in *Strength of Metals and Alloys* (ICSMA 7), 1985, 1, pp. 441–445.

165. V. G. Davydov, L. B. Ber, and V. N. Ananiev. "Phase Transformations and Heat Treatment Regimes of Commercial Aluminum Alloys." Mat. Sci. Forum, 1996, 217–222, pp. 859–864.

166. D. B. Williams and J. W. Edington. The precipitation of δ' (Al$_3$Li) in Dilute Aluminium-Lithium Alloys, 1975, 9, pp. 529–532.

167. Z. M. Wang and G. J. Shiflet. "Heterogeneous Nucleation of δ' on Dislocations in a Dilute Aluminum-Lithium Alloy." Metall. Mater. Trans., 1996, 27A, pp. 1599.

168. Z. M. Wang, and G. J. Shiflet. "Growth of δ' on Dislocations in a Dilute Al-Li Alloy." Metall. Mater. Trans. A, 1998, 29A, pp. 2073–2085.

169. A. O. Kujore. "The Effect of Alloy Composition on the Deformation Behavior and Tensile Properties of Al-3Li-X Alloys." PhD Dissertation, Georgia Institute of Technology, 1983.

170. W. A. Cassada, G. J. Shiflet, and E. A. Starke, Jr. "The Effect of Germanium on the Precipitation and Deformation Behavior of Al-2Li Alloys." Acta. Metall., 1986, 34, pp. 367–378.

171. R. J. Rioja and E. A. Ludwiczak. "Identification of Metastable Phases in an Al-Li-Cu alloy (2090)." Proceedings of the Third International Al-Li Conference. Oxford, England 8–11, July 1985, pp. 471.

172. J. E. O'Neal and K. K. Sankaran. "Precipitation in Al-Li-Cu Alloys." Proc. Thirty-Ninth Annual EMSA Meeting, 1981, pp. 44–45.

173. M. D. Schuler. "Intergranular Corrosion of Aluminum." MSc Thesis, University of Southern California, 1968.

174. D. L. Gilmore and E. A. Starke, Jr. "Trace Element Effects on Precipitation Processes and Mechanical Properties in an Al-Cu-Li Alloy." Metall. Tran. A, 1997, 28A, pp. 1399–1415.

175. C. N. J. Tite, P. J. Gregson, and P. D. Pitcher. "Further Precipitation Reactions Associated with β' (Al_3Zr) Particles in Al-Li-Cu-Mg-Zr Alloys." Scrip. Metall., 1988, 22, pp. 1005–1010.

176. P. D. Pitcher. "Aging of Forged Aluminum-Lithium 8091 Alloy." Scrip. Metall., 1988, 22, pp. 1301–1305.

177. W. X. Feng, F. S. Lin, and E. A. Starke, Jr. "The Effect of Minor Alloying Elements on the Mechanical Properties of Al-Cu-Li Alloys." Metall. Trans. A, 1984, 15A, pp. 1209–1220.

178. J. T. Staley and R. D. Doherty. "Quench Sensitivity of an Al-Cu-Li Alloy Plate." Proceedings of the Fifth Aluminum-Lithium Conference, Williamsburg, V. A. 27–31, March 1989, 1, pp. 345–354.

179. D. Dew-Hughes, E. Creed, and W. S. Miller. "Grain Boundary Failure in an Al-Li Alloy." Mat. Sci. Tech., 1988, 4, pp. 106–112.

180. W. E. Quist and G. H. Narayanan. "Aluminum-Lithium Alloys," in *Treatise on Materials Science and Technology*, Academic Press, 1989, 31, pp. 219–254.

181. I. J. Polmear. "Recent Developments in Light Alloys." Mat. Tran. JIM., 1996, 37, pp. 12–31.

182. V. S. Sandler, L. N. Leshchiner, and T. P. Fedorenko. "Effect of Aging Conditions on the Nature of Fracture in the 1441 Alloy of the Al-Cu-Mg-Li System." Metal Science and Heat Treatment, 1993, pp. 229–231.

183. W. S. Miller, M. P. Thomas, D. J. Lloyd, and D. Creber. "Deformation and Fracture in Al-Li Base Alloys," Mat. Sci. Tech., 1986, 2, pp. 1210–1213.

184. P. C. Varley. *The Technology of Aluminium and Its Alloys*. Newnes-Butterworths, London, 1971.

185. H. Cama, J. Worth, P. V. Evans, A. Bosland, and J. M. Brown. "Intermetallic Phase Selection and Transformation in Aluminium 3XXX Alloys." Proceedings of the 4th Decennial International Conference on Solidification Processing, Sheffield, July 1997, pp. 555–558.

186. M. D. Schuler. "Intergranular Corrosion of Aluminum." MSc Thesis, University of Southern California, 1968.

187. B. A. Parker, Z. F. Zhou, and P. Nolle. "The Effect of Small Additions of Scandium on the Properties of Aluminium Alloys." J. Mat. Sci., 1995, 30, pp. 452–458.

188. Y. L. Liu, and S. B. Kang. "Effect of Copper Addition and Heat Treatment on Segregation Behavior of Al-7Mg-Cu Alloys." Mat. Sci. Tech., 1996, 12, pp. 628–634.

189. J. T. Staley and J. K. McBride. Unpublished research at Alcoa, 1965.

190. N. Nishi, S. Kami, Y. Takahashi, H. Komoto, and J. G. Conley. "The Mechanical Properties of Al-Ni-Mg and Al-Mn-Mg Die Casting Alloys," in *Dispersion Strengthened Aluminum Alloys* (Y-W. Kim and W. M. Griffith, eds.), TMS, 1988, pp. 451–464.

191. E. M. Taleff, G. A. Henshall, T. G. Nieh, D. R. Lesuer, and J. Wadsworth. "Warm Temperature Tensile Ductility in Al-Mg Alloys." Metall. Mater. Trans A, 1998, 29A, pp. 1081–1091.

192. C. A. Lavender, J. S. Vetrano, M. T. Smith, S. M. Bruemmer, and C. H. Hamilton. "Development of Superplasticity in 5083 Aluminum with Additions of Mn and Zr." Mat. Sci. Forum, 1994, 170–172, pp. 279–286.

193. R. W. Smith and L. Clapham. "Influence of Lithium on Cast Al-Si Eutectic Alloys." In: *Reduction and Casting of Aluminum*. (C. Bickert, ed.), Pergamon Press, New York, 1988, pp. 257.

194. V. S. Zolotorevskii. "Modern Cast Aluminum Alloys." Metal Science and Heat Treatment, 1994, pp. 382–388.

195. M. A. Savas and S. Altintas. "A Comparative Investigation of the Mechanical Properties and Machinability in Al-Mg Cast Alloys," in *Advances in Aluminum Casting Technology* (M. Tiryakioglu and J. Campbell, eds.), ASM International, 1998.

196. E. Erginer. "The Strengthening of Aluminum due to its Cast Microstructure Modified by Silicon." PhD Dissertation, Brown University, 1969.

197. I. Dutta and S. M. Allen. "A Calorimetric Study of Precipitation in Commercial Aluminium Alloy 6061." J. Mater. Sci. Let., 1991, 10, pp. 323–326.

198. S. K. Bose and R. Kumar. "Rapid Solidification of Al-Mg-Si Alloys from the Liquid State," in *Rapidly Quenched Metals* (N. J. Grant and B. C. Giessen, eds.), 1976, 1, 169–177.

199. E. Ozawa and H. Kimura. "Behavior of Excess Vacancies during the Nucleation of Precipitates in Aluminum-Silicon Alloys." Mater. Sci. Eng., 1971, 8, pp. 327–335.

200. D. L. Zhang. "Preccipitation of Excess Silicon During Heat Treatment of Cast Al-7 wt% Si-0.4 wt% Mg Alloy." Mat. Sci. Forum, 1996, 217–222, pp. 771–776.

201. L. Zhen and S. B. Kang. "Deformation and Fracture Behavior of Two Al-Mg-Si Alloys." Metall. Mater. Trans., 1997, 28A, pp. 1489–1497.

202. E. Hornbogen, A. K. Mukhopadhyay, and E. A. Starke, Jr. "Nucleation of the Diamond Phase in Aluminium Solid Solutions." J. Mat. Sci., 1993, 28, pp. 3670–3674.

203. P. R. Austen and H. M. Williamson. "The Effects of Non-Standard Ageing Treatments on the Fracture Properties of Al-Mg-7 wt% Si Alloys." J. Austral. Inst. Met., Mar., 1975, 20, pp. 39–43.

204. R. C. Dorward. "Preaging Effects in Al-Mg-Si Alloys Containing 0.6 to 0.9 Pct Mg$_2$Si." Metall. Trans., 1973, 4, 507–512.

205. J. Langerweger. "Influence of Heat Treatment Practice on Extrudability and Properties of AlMgSi Alloy Sections," in *Aluminium Technology '86* (T. Sheppard, ed.), London, The Institute of Metals, 1986, pp. 216–222.

206. J. Langerweger. "Influence of Heat Treatment Practice on the Extrudability and on the Properties of Al-Mg-Si." Proceedings of the Second Arab Aluminum Conference, 1985, 1, pp. 1–10.

207. J. Charbonnier, J. J. Perrier, and R. Portalier. "Recent Developments in Aluminum-Silicon Alloys Having Guaranteed Structures of Properties." AFS Int. Cast. Met. J. Dec., 1978, pp. 17–26.

208. F. T. Lee, J. F. Major, and F. H. Samuel. "Effect of Silicon Particles on the Fatigue Growth Characteristics of Al-12 Wt Pct Si-0.35 Wt Pct Mg-(0 to 0.02) Wt Pct Sr Casting Alloys." Metall. Mater. Trans. A, 1995, 26A, pp. 1553–1570.

209. L. A. Narayanan, F. H. Samuel, and J. E. Gruzleski. "Crystallization Behavior of Iron-Containing Intermetallic Compounds in 319 Aluminum Alloy." Metall. Mater. Trans. A., 25A, pp. 1761–1773.

210. M. Drouzy, S. Jacob, and M. Richard. "Interpretation of Tensile Results by Means of Quality Index and Probable Yield Strength." AFS Int. Cast. Met. J. June 1980, pp. 43–50.

211. M. K. Surappa, E. Blank, and J. C. Jaquet. "Effect of Macro-Porosity on the Strength and Ductility of Cast Al-7 Si-0.3 Mg Alloy." Scripta. Metall., 1986, 20, pp. 1281–1286.

212. A. Herrera and V. Kondic. "Effect of Porosity on Tensile Properties of Two Al-Si Alloys." British Foundryman, pp. 460–465.

213. L. Sagalowicz, G. Hug, D. Bechet, P. Sainfort, and G. Lapasset. "A Study of the Structural Precipitation in the Al-Mg-Si-Cu System." Proceedings of the 4th International Conference on Aluminum Alloys (ICAA4), 1994, pp. 644–651.

214. I. Kovacs, J. Lendvai, and E. Nagy. "The Mechanism of Clustering in Supersaturated Solid Solutions of Al-Mg_2Si Alloys." Acta Metall., 20, pp. 975–983.

215. C. Panseri, and T. Frederighi. "A Resistometric Study of Preprecipitation in an Aluminium-1.4 % Mg_2Si Alloy." J. Inst. Met., 1996, 94, pp. 99–107.

216. G. A. Edwards, G. L. Dunlop, and M. J. Couper. "Fine-Scale Precipitation in Al Alloy 6061." Proceedings of the 4th International Conference on Aluminum Alloys (ICAA4), 1994, pp. 628–635.

217. S. Ceresara, E. Di Russo, P. Fiorini, and A. Giarda. "Effect of Si Excess on the Ageing Behaviour of Al-Mg2 Si 0.8% Alloy." Mat. Sci. Eng., 1969/1970, 5, pp. 220–227.

218. G. Thomas. "The Ageing Characteristics of Aluminium Alloys: Electron-Transmission Studies of Al-Mg-Si Alloys." J. Inst. Met., 1961/1962, 90, pp. 57–63.

219. I. Kovacs, J. Lendvai, and E. Nagy. "The Mechanism of Clustering in Supersaturated Solid Solutions of Al-Mg_2Si Alloys." Acta Metall., 1972, 20, pp. 975–983.

220. S. B. Kang, L. Zhen, H. W. Kim, and S. T. Lee. "Effect of Cold Rolling and Aging Treatment on Mechanical Property and Precipitation Behavior in a Al-Mg-Si Alloy." Mater. Sci. Forum, 1996, 217–222, pp. 827–832.

221. A. K. Gupta and D. J. Lloyd. "The Precipitation in a Superpurity Al-Mg-Si Alloy." Proceedings of the 3rd International Conference on Aluminum Alloys, 1992, pp. 21–25.

222. M. Murayama, K. Hono, M. Saga and M. Kikuchi. "Atom Probe Studies on the Early Stages of Precipitation in Al-Mg-Si Alloys." Mater. Sci. Eng., 1998, A250, pp. 127–132.

223. K. Matsuda, T. Naoi, K. Fujii, Y. Uetani, T. Sato, A. Kamio and S. Ikeno. "Crystal Structure of the β'' phase in al Al-1.0 Mass% Mg_2Si-0.4 Mass% Si Alloy." Mater. Sci. Eng., 1999, A262, pp. 232–237.

224. G. A. Edwards, K. Stiller, G. L. Dunlop and M. J. Couper. "The Precipitation Sequence in Al-Mg-Si Alloys." Acta Mater., 1998, 46, pp. 3893–3904.

225. K. Matsuda, H. Gamada, K. Fujii, Y. Uetani, T. Sato, A. Kamio, and S. Ikeno. "High Resolution Electron Microscopy on the Structure of Guinier Preston Zones in an Al-1.6 Mass Pct Mg_2Si Alloy." Metall. Mater. Trans. A, 1998, 29A, pp. 1161–1168.

226. D. W. Pashley, J. W. Rhodes, and A. Sendorek. "Delayed Ageing in Aluminium-Magnesium-Silicon Alloys: Effect on Structure and Mechanical Properties." J. Inst. Metals, 1966, 94, pp. 41–49.

227. M. H. Jacobs. "The Structure of the Metastable Precipitates Formed during Ageing of an Al-Mg-Si Alloy." Phil. Mag., 1972, 26, pp. 1–13.

228. A. K. Busby, L. Edwards, and J. W. Martin. "Effect of Aging and Dispersoid Content on Tensile Properties of Al-0.6 Mg-1Si Alloys." Mater. Sci. Tech., 1986, 2, pp. 363–367.

229. P. A. Beaven, A. P. Davidson, and E. P. Butler. "Precipitation on Dislocations in Al-Mg-Si: Mechanisms and Kinetics." Proceedings of International Conference on Solid to Solid Phase Transformations, 1982, pp. 661–665.

230. Y. Baba and A. Takashima. "Influence of Composition on the Two-Stage Aging of Al-Mg-Si Alloys." Trans. Jap. Inst. Metals, 1969, 10, pp. 196–204.

231. I. T. Taylor. "The Relationship between Cooling Rate and Age-Hardening Characteristics of a Number of Aluminium-Magnesium-Silicide Alloys." Canadian Metall. Quar., 1973, 12, pp. 93–103.

232. H. Uchida and H. Yoshida. "Improvement in Paint Bake Response of an Al-Mg-Si Alloy by Reversion," in Aluminium and Magnesium for Atomotive Applications, (J. D. Bryant, ed.), The Mineral, Metals & Materials Society, 1996, pp. 97–104.

233. H. Nakamura. "Effects of Pre-Aging on Age Hardening of an Al-1.6% Mg2Si Alloy at 165°C." Keikinzoku (Light Metals), 1973, 23, pp. 389–392.

234. S. Shivkumar, C. Keller, and D. Apelian. "Aging Behavior in Cast Al-Si-Mg Alloys." AFS Trans., 1990, pp. 905–911.

235. S. A. Court, H. D. Dudgeon, and R. A. Ricks. "Improved Performance in Al-Mg-Si (6XXX) Extruded, Structural Alloys Through Microstructural Control." Proceedings of the 4th International Conference on Aluminum Alloys (ICAA4), 1994, pp. 404–411.

236. S. Murali, Y. Arunkumar, P. V. J. Chetty, K. S. Raman, and K. S. S. Murthy. "The Effect of Preaging on the Delayed Aging of Al-7Si-0.3Mg." JOM., Feb. 1997, 49, pp. 29–33.

237. T. Din and J. Campbell. "High Strength Aerospace Aluminum Casting Alloys: A Comparative Study." Mat. Sci. Tech., 1996, 12, pp. 644–650.

238. T. Sato, A. Kamio, and G. W. Lorimer. "Effects of Si and Ti Additions on the Nucleation and Phase Stability of the L12-Type Al3Zr Phase in Al-Zr Alloys." Mat. Sci. Forum, 1996, 217–222, pp. 895–900.

239. M. H. Mulazimoglu, A. Zaluska, J. E. Gruzleski, and F. Paray. "Electron Microscope Study of Al-Fe-Si Intermetallics in 6201 Aluminum Alloy." Met. Mat. Tran. A, 1996, 27A, pp. 929–936.

240. S. Shivkumar, L. Wang, and D. Apelian. "Molten Metal Processing of Advanced Cast Aluminum Alloys." JOM, 1991, pp. 26–32.

241. G. K. Sigworth. "Determining Grain Size and Eutectic Modification in Aluminum Alloy Castings." Modern Casting., 1987, 77, pp. 23–25.

242. M. H. Mulazimoglu, A. Zaluska, F. Paray, and J. E. Gruzleski. "The Effect of Strontium on the Mg2Si Precipitation Process in 6201 Aluminum Alloy." Met. Mat. Tran., A, 1997, 28A, pp. 1289–1296.

243. L. A. Narayanan, F. H. Samuel, and J. E. Gruzleski. "Dissolution of Iron Intermetallics in Al-Si Alloys through Nonequilibrium Heat Treatment." Met. Mat. Tran. A, 1995, 26A, pp. 2161–2174.

244. A. M. Samuel, J. Gauthier, and F. H. Samuel. "Microstructural Aspects of the Dissolution and Melting of Al2Cu Phase in Al-Si Alloys During Solution Heat Treatment." Met. Mat. Tran. A, 1996, 27A, pp. 1785–1798.

245. R. A. Jeniski, Jr., B. Thanaboonsombut, and T. H. Sanders, Jr. "The Effect of Iron and Manganese on the Recrystallization Behavior of Hot-Rolled and Solution Heat Treated Aluminum Alloy 6013." Met. Mat. Tran. A, 1996, 27A, pp. 19–27.

246. U. Heilscher, H. Arbenz, and H. Dieckmann. "Eigenschaften Eisenarmer Aluminium-Silicium-Gußleigerungen." Giesserei., 1966, 5, pp. 125–133.

247. S. Murali, A. Trivedi, K. S. Shamanna, and K. S. S. Murthy. "Effect of Iron and Combined Iron and Beryllium Additions on the Fracture Toughness and Microstructures of Squeeze-Cast Al-7Si-0.3Mg Alloy." J. Mat. Eng. Per., 1996, 5, pp. 462–468.

248. S. Murali, K. S. Raman, and K. S. S. Murthy. "Al-7 Si-0.3 Mg Cast Alloy: Formation and Crystal Structure of β-FeSiAl$_5$ and (Be-Fe)-BeSiFe$_2$Al$_8$ Phases." Mat. Sci. Forum, 1996, pp. 207–212, 217–222.

249. T. Xiao and W. V. Youdelis. "Effect of Beryllium and Calcium on Aging Behaviour of Al-0.75Mg-0.5Si Alloy." Mat. Sci. Tech., 1989, 5, pp. 991–994.

250. A. Latkowski and M. Bronicki. "Hardness and Electric Resistance after Thermo-Mechanical Treatment of the AlMgSi Alloys." Aluminium, 1991, 67, pp. 796–797.

251. O. R. Myhr, H. R. Shercliff, and T. Furu. "The Influence of Hot-Working and Ageing on Notched-Strength and Ductility of Aluminium Alloy AA6082." Mat. Sci. Forum, 1996, pp. 217–222, 1221–1226.

252. D. J. Chakrabarti, B. Cheong, and D. E. Laughlin. "Precipitation in Al-Mg-Si-Cu Alloys and the Role of the Q Phase and Its Precursors." Presented at the Fall Meeting of TMS, San Antonio, TX, February 1998.

253. S. D. Dumolt, D. E. Laughlin, and J. C. Williams. "Formation of a Modified β' Phase in Aluminum Alloy 6061." Scripta. Metall., 1984, 18, pp. 1347–1350.

254. L. Arnberg and B. Aurivillius. "The Crystal Structure of $Al_x Cu_2 Mg_{12-x}$ Si_7 (h-AlCuMgSi)." Acta Chem. Scandinavica A. 1980, 34A, pp. 1–5.

255. G. Phragmen. "On the Phases Occupying in Alloys of Aluminum with Copper, Magnesium, Manganese, Iron, and Silicon." J. Inst. Metals, 1950, 77, pp. 489–552.

256. A. K. Gupta, A. K. Jena, and M. C. Chaturvedi. "Insoluble Phases in Al-1.52Cu-0.75Mg Alloys Containing Silicon." Mater. Sci. Tech., 1987, 3, pp. 1012–1018.

257. H. Suzuki, I Araki, M. Kanno, and K. Ito. "Effects of Si Addition on the Aging Behavior of Al-2% Cu-0.9% Mg Alloy." J. Japn. Inst. Metals, 1977, 27, pp. 239–245, (Japanese).

258. M. Tamizifar and G. W. Lorimer. "The Effect of Copper on the Aging Response of an Aluminum-Magnesium-Silicon Alloy." The Third International Conference on Aluminum Alloys, 1992, 1, pp. 220–225.

259. T. Sakurai and T. Eto. "Effect of Cu Addition on the Mechanical Properties of Al-Mg-Si Alloys." Proceedings of the Third International Conference on Aluminium Alloys, 1992, pp. 208–213.

260. B. Dubost, J. Bouvaist, and M. Reboul. "Prevention of Intercrystalline Corrosion and Stress Corrosion on Alloy 2214 through 'High-Low' Precipitation Aging." The First International Conference on Aluminum Alloys, 1986, 2, pp. 1109–1123.

261. I. J. Polmear. "The Ageing Characteristics of Ternary Aluminium-Zinc-Magnesium Alloys." J. Inst. Metals., 1957–1958, 86, pp. 113–121.

262. A. M. El Sheikh. "Precipitation Hardening and Substructure Features in Al-Zn-Mg Alloys." In: *Strength of Metals and Alloys* (ICSMA 7), 1985, 1, pp. 483–488.

263. J. Lendvai. "Precipitation and Strengthening in Aluminium Alloys." Mat. Sci. Forum, 1996, 217–222, pp. 43–56.

264. L. F. Mondolfo. "Structure of the Aluminium:Magnesium:Zinc Alloys." Metall. Rev., 153, 1971, pp. 95–124.

265. A. Deschamps, and Y. Brechet. "Influence of Quench and Heating Rates on the Ageing Response of an Al-Zn-Mg-(Zr) Alloy." Mat. Sci. Eng., 1998, A251, pp. 200–207.

266. J. T. Grider. "Quenching Defects in Aluminum Plus Ten Atomic Per Cent Zinc." MSc Thesis. University of Missouri-Rolla, 1971.

267. J. T. Healey. "Guinier-Preston Zone Evolution in 7075 Aluminum." PhD Dissertation. University of Florida, 1976.

268. E. Ülvan. "Physical Metallurgy and Heat Treatment of Wrought Aluminum Alloys," in *Physical Metallurgy and Heat Treatment of Non-Ferrous Metals and Alloys.* Johannesburg, South African Institute of Foundrymen, 1988.

269. J. T. Staley and W. Haupin. "Aluminum and Aluminum Alloys," in *Encyclopedia of Chemical Technology*. 4th Edn. 1992, 2, pp. 184–251.

270. N. Q. Chinh, Zs. Kov²cs, L. Reich, F. Sz³kely, J. Illy, and J. Lendvai. "Precipitation and Work Hardening in High strength AlZnMg(Cu,Zr) Alloys." Mater. Sci. Forum, 1996, 217–222, pp. 1293–1298.

271. I. J. Polmear. "The Ageing Characteristics of Complex Al-Zn-Mg Alloys." J. Inst. Metals, 1960, 89, pp. 51–59.

272. J. T. Staley, R. J. Rioja, R. K. Wyss, and J. Liu. "Processing to Improve High Strength Aluminum Alloy Products." Presented at the Ninth International Conference on Production Research, Cincinnati, OH August 1987, pp. 17–20.

273. H. O. Bailey and D. A. Lukasak. Unpublished research at Alcoa, 1991.

274. J. T. Vietz, K. R. Sargant, and I. J. Polmear. "The Influence of Small Additions of Silver on the Ageing of Aluminium Alloys: Further Observations on Al-Zn-Mg Alloys." J. Inst. Metals, 1963–64, 92, pp. 327–333.

275. J. T. Staley, R. H. Brown, and R. Schmidt. "Heat Treating Characteristics of High Strength Al-Zn-Mg-Cu Alloys With and Without Silver Additions." Metall. Trans., 1972, 3, pp. 191–199.

276. J. T. Staley. "Investigation to Improve the Stress-Corrosion Resistance of Aluminum Aircraft Alloys through Alloy Additions and Specialized Heat Treatment." Final Report, Naval Air Systems Command Contract N00019–68-C-0146, Alcoa Research Laboratories, 1969.

277. H. T. Kim, S. W. Nam, and S. H. Hwang. "Study on the Solidification Cracking Behavior of High Strength Aluminum Alloy Welds: Effects of Alloying Elements and Solidification Behaviours." 1996, 31, pp. 2859–2864.

278. H. A. Holl. "Development of High Strength Al-Zn-Mg-Cu Alloys with Reduced Quench Sensitivity." Metallurgy Note 59, Melbourne: Department of Supply, Australian Defence Scientific Service, 1968.

279. J. E. Vruggink. "Quenching Rate Effects on Mechanical Properties of Heat-Treatable Aluminum Alloys." Presented at the Fall Meeting of TMS, Detroit, MI, October 1968.

280. M. Harrison, and J. W. Martin. "Effect of Dispersoids on Fatigue Crack Propagation in Al-Zn-Mg Alloys," in *Strength of Metals and Alloys* (ICSMA 7), 1985, 2, pp. 1261–1266.

281. N. U. Deshpande, A. M. Gokhale, D. K. Denzer, and J. Liu. "Relationship between Fracture Toughness, Fracture Path, and Microstructure of 7050 Aluminum Alloy: Part II. Multiple Micromechanisms-Based Fracture Toughness Model." Metall. Mater. Trans. A, 1998, 29A, pp. 1191–1202.

282. N. Ryum. "Influence of a Precipitate-Free Zone on the Mechanical Properties of an Al-Mg-Zn Alloy." Acta Metall., 1968, 16, pp. 327–332.

283. V. V. Zakharov and T. D. Rostova. "High-Resource High-Strength Aluminum Alloys." Metal Science and Heat Treatment, 1996, 37, pp. 203–207.

284. V. V. Zakharov. "Industrial Aluminum Alloys with Scandium Additive." Metal Science and Heat Treatment. 1996, 37, pp. 283–285.

285. L. S. Kramer, W. T. Tack, and M. T. Fernandes. "Scandium in Aluminum Alloys." Adv. Mater. Proc., Oct 1997, 152, pp. 23–24.

4

Recrystallization and Grain Growth

WEIMIN MAO

University of Science and Technology Beijing, Beijing, China

1 INTRODUCTION

The human history of using metals can be traced back to tenth millennium BC, during which people in the Middle East could fabricate natural copper and use it [1]. In the seventh millennium BC people in Anatolia could possibly produce lead and copper [2]. Towards the end of the fourth millennium BC the people knew already that natural copper could be hardened by cold-working and softened by annealing [3], therefore the recrystallization treatment should be one of the oldest physical metallurgical processes used by human being. The concept of ''recrystallization'' appeared in 19th century [4] and the corresponding theories have been intensively investigated since then.

The recrystallization will appear in all reheating processes of aluminum alloys which have been hot or cold deformed. All heating processes of aluminum poly-crystalline alloys would induce grain growth. The recrystallization and grain growth will change the chemical, physical and mechanical properties of the alloys. Therefore the corresponding heat treatments have been widely applied in the production of aluminum alloys, such as hot rolling, thermomechanical working, recrystallization annealing, grain growth heating, aging etc.

At the beginning of this chapter the basic formation mechanisms and characteristics of deformation microstructure, as well as the defect structure in aluminum alloys are briefly reviewed. Starting from the deformed state the recovery and primary recrystallization processes including formation of recrystallization texture during annealing are introduced. Then the process of dynamic recrystallization is discussed. At the end of the chapter the processes of normal grain growth as well as anomalous grain growth, i.e. the secondary recrystallization are reviewed.

2   STRUCTURE OF DEFORMED ALUMINUM

2.1   Crystallographic Deformation Process

Aluminum is a crystalline material with rather high stacking fault energy [5] (SFE, $250\,mJ/m^2$), so its plastic deformation is carried out mainly by dislocation slips in the lattice structure. Under the critical resolved shear stress (CRSS, 7.9×10^5 N/m^2) [6] on a definite crystallographic plane (slip plane) the dislocation slip will start in a way shown in Fig. 1, in which the unit translation vector **b** in slip direction of atoms is called Burgers vector. A slip system consists of a slip plane and a slip direction, however, in aluminum and its alloys the slip plane is the $\{111\}$ plane and the slip direction is the $\langle 110 \rangle$ direction.

Different slip systems on several slip planes are very often activated simultaneously during cold deformation, which results in a multi-slip of dislocations. The deformation induced density increase of vacancies, dislocations and grain boundaries act as obstacles to further movement of dislocations and lead to work hardening of deformed aluminum.

2.2   Deformation Microstructure

Cold deformation can result in the shape change of grains in polycrystalline aluminum, and the grains could be elongated along the external drawing stress. Figure 2 gives the shape change of grains in a commercially pure aluminum
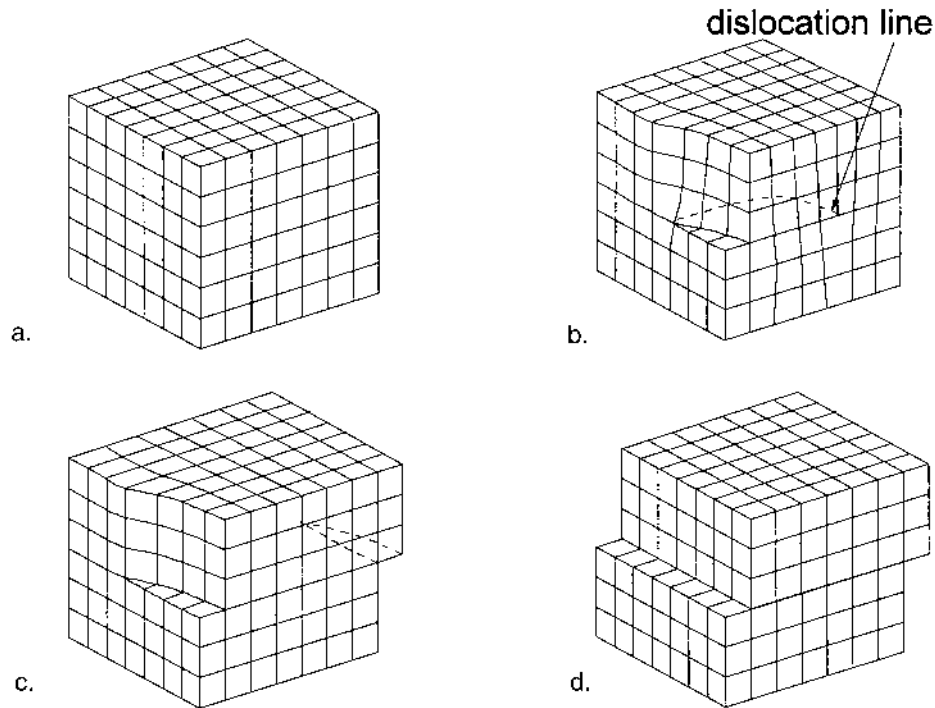
Figure 1   Fundamental process of dislocation slip in crystallographic lattice (a, b, c, d).
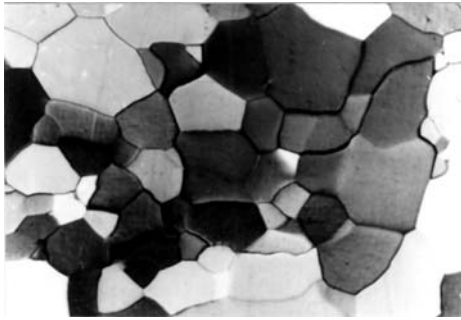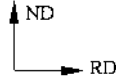
(a)

(b)
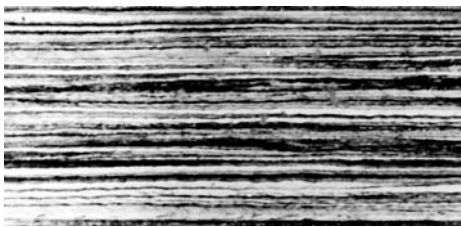
(c)

Figure 2   Cold rolling structure in a commercially pure aluminum (99.9%Al) $\vert\frac{100\,\mu\mathrm{m}}{}\vert$, (a) 0% reduction; (b) 45% reduction; (c) 95% reduction.

(99.9% Al) during cold rolling. It can be seen that the grains are elongated in the rolling direction. An important microstructure characteristic is the cell structure which can be observed using transmission electron microscopy [7]. Figure 3 shows the cell structure of a 80% rolled Al-1.3 wt% Mn alloy sheet [8]. The dislocation density is very low within the cells but very high in the cell walls. Generally the cell size is 1–3 μm or less, and the orientation differences between adjoining cells are less than 2°. The cells will become more elongated if the deformation degree increases.

Figure 3 Cell structure of 86% cold rolled Al-1.3 wt% Mn alloy sheet ⊢— 1 μm —⊣. (Courtesy of Dr. P. Yang, from Ref. 8.)

2.3 Defects Induced by Deformation and the Stored Energy

Certain crystal defects exist always in aluminum lattice even in an undeformed stable state. The defects include point defects (vacancies, interstitial atoms, substitutional atoms), one-dimensional defects (dislocations), two-dimensional defects (boundaries, stacking fault, etc.) and three-dimensional defects (particles of second phase, impurities, etc.). These defects will act as obstacles to dislocation movement.

During deformation the moving dislocations intersect with other dislocations, and lead to the increase of vacancy density mostly from the non-conservative motion of jogs on dislocations [9]. Considering the changes of deformation microstructure, e.g. shown in Fig. 2, the length of grain boundaries are also increased in deformed matrix. However, the most important defect increase after deformation should be the dislocation multiplication. When a piece of aluminum is plastically deformed, a large amount of external work is expended. Most of the work is transformed into the form of heat energy, but a small fraction of it will remain in the deformed matrix as stored energy, of which about 80–90% will be the energy due to the generation of dislocations [6]. The portion of stored energy induced by vacancies is so small that it could be actually neglected, and the most sub-boundaries induced by deformation consist of special dislocation configurations which contribute to the increase of dislocation density.

The dislocation density ρ and the stored energy increases with increasing degree of deformation. It is estimated that the dislocation density in aluminum is $10^{10}/m^2$ in the annealed state [10] and $10^{15}/m^2$ in a heavily deformed state [5],

(cf. Section 3 of this chapter, dislocation energy per unit volume could be estimated at 0.5 ρGb^2, where G is about 2.5×10^{10} N/m^2 and b is 3.5×10^{-10}m for aluminum) therefore the corresponding energy should be roughly 20 J/m^3 and 2×10^6 J/m^3 respectively. So the stored energy in heavy deformed aluminum is about 2×10^6J/m^3.

The impurity atoms in aluminum lattice increase the stored energy at a given strain, since they hinder the normal dislocation motion and thereby result in an additional dislocation multiplication. The dislocation multiplication is also enhanced by decreasing initial grain size, i.e. more boundaries, or by particles of second phase. These defects act as obstacles to dislocation movement.

2.4   Deformation Texture

Grain orientation will be rotated relative to the external stress axes during plastic deformation. If a drawing force **F** acts on an aluminum single crystal and leads to activation of a slip system (Fig. 4(a)), there will be a moment $\mathbf{M} = \mathbf{F} \cdot \times$ acting on the deformed crystal (Fig. 4(b)). The orientation of the crystal will remain unchanged after the dislocation slips to certain extent. The applied moment will result in a rotation of the crystal into a stable state shown in Fig. 4(c), after which the crystal orientation has been changed. The similar orientation change could also appear in the compression deformation of an aluminum single crystal (Fig. 5).

If the deformation and the corresponding orientation rotation proceed further, other slip systems can also be activated, which will influence the rotation path of the crystal orientation. But the orientation change will become less and less obvious if the crystal has been deformed heavily, i.e. the crystal orientation has approached the final stable position. The orientation changes in a polycrystalline aluminum
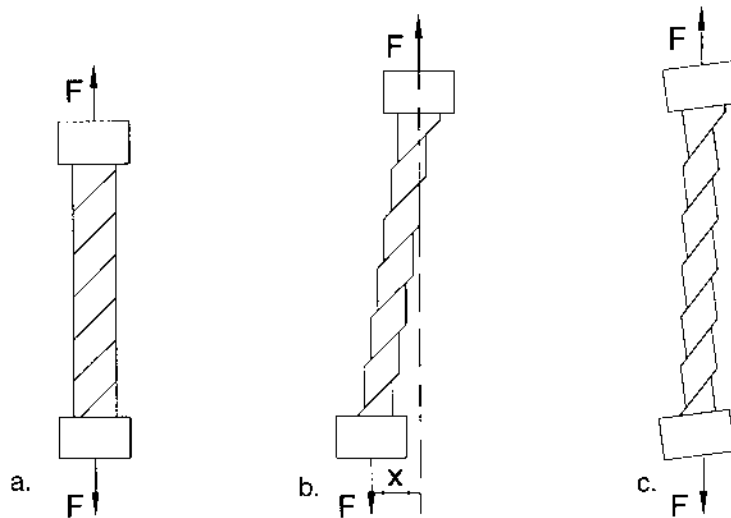
Figure 4   Rotation of an aluminum single crystal during tensile test (a, b, c).
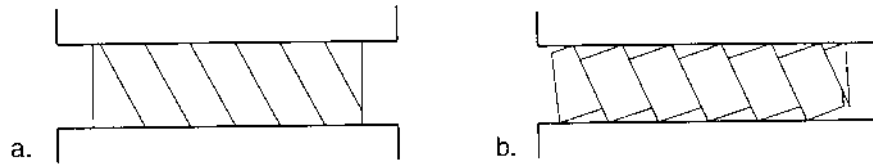
Figure 5   Rotation of an aluminum single crystal during compression test (a, b).
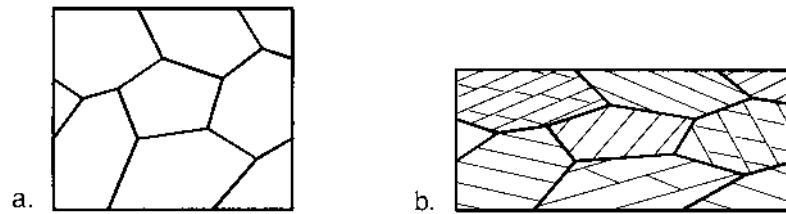
Figure 6   Deformation process of a polycrystal (a, b).

are more complicated. Figure 6 gives schematically a compressing or rolling process of a polycrystal. The grain orientations have different rotation behaviors, but they will rotate towards one or several final stable orientation positions after heavy deformation, and therefore a deformation texture will be formed, i.e. the grain orientations have a preferred distribution. The most important characteristic of texture is that the orientation distribution of a polycrystal has apparently deviated from the random distribution.

The wire drawing texture in aluminum is $\langle 111 \rangle$ fiber texture [11], and the rolling textures are $\{112\}\langle 111 \rangle$, $\{011\}\langle 211 \rangle$ and $\{123\}\langle 634 \rangle$ [12]. The shear deformation, e.g. torsion deformation [13] or inhomogeneous rolling [14] produces $\{001\}\langle 110 \rangle$ and $\{111\}$ fiber texture.

3   RECOVERY

3.1   Recovery Phenomena

Because of the high stored energy the deformed aluminum is in an unstable state. But at very low temperature the deformed state remains unchanged, since the defect structure is still mechanically stable. On annealing the stored energy induced by heavy deformation is progressively released due to the thermodynamic activation process.

For the first annealing stage at relatively low temperature or for short time the dislocation density is drastically reduced from $10^{15}/m^2$ down to $1.5 \times 10^{14}/m^2$ [5], but the basic deformed microstructure is retained, and therefore this stage is called recovery. The stored energy released during the recovery annealing of deformed aluminum should be entirely caused by dislocation rearrangement and reduction, since vacancies produced by deformation have migrated out of the lattice structure at room temperature [15].

At the beginning of annealing the recovery process starts immediately, i.e. no incubation period. There is no migration of high angle boundaries during recovery. After recovery the deformation texture remains, the electrical resistivity is slightly decreased [16] and 40% of the hardness induced by work hardening could be recovered for deformed pure aluminum [17].

3.2 Dislocation Mechanism of Recovery

The dislocation mechanism of recovery is based on the interactions of the long range stress fields between dislocations. The shear stress field of an edge dislocation, for instance, is [18]

$$\tau_{xy} = \frac{Gb}{2\pi(1-v)} \frac{x(x^2-y^2)}{(x^2+y^2)^2} = \frac{Gb}{2\pi(1-v)r}\cos\theta\cos2\theta \tag{1}$$

where G is the shear modulus, b is length of Burgers vector, v is Poisson's ratio, r is the distance to the dislocation inducing the stress field. The angle θ is defined in Fig. 7.

If there is another parallel edge dislocation at position (x, y), of which the length of Burgers vector is also b (Fig. 7), the interaction force F should be

$$F = \tau_{xy} \cdot b = \frac{Gb^2}{2\pi r(1-v)}\cos\theta\cos2\theta \tag{2}$$

If the two edge dislocations of same sign are parallel mutually on the same slip plane ($\theta = 0$), then $F > 0$ is valid and the two dislocations are tend to repel each other. In the reversed case the dislocations of opposite sign will attract, combine and finally annihilate each other (Fig. 8(a)). When the two edge dislocations of opposite sign are parallel mutually on separated but rather close slip planes (Fig. 8(b)), then the two dislocations will also attract each other until the angle θ reaches $\pi/4$ or $3\pi/4$ according to Eq. (2). They can not combine and annihilate each other directly. However there will be a row of vacancies or interstitial atoms formed between
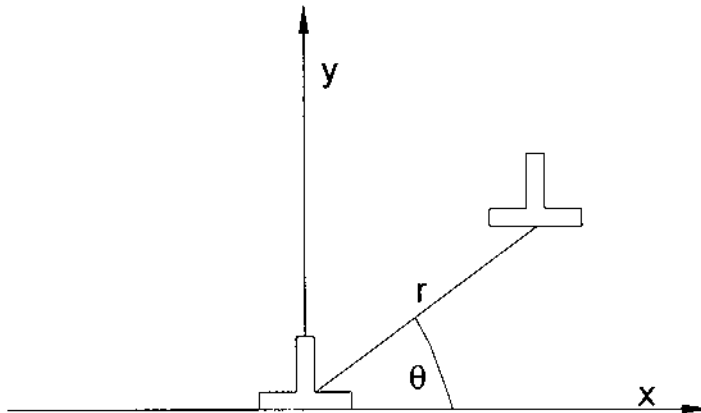
Figure 7 Interaction between edge dislocations.
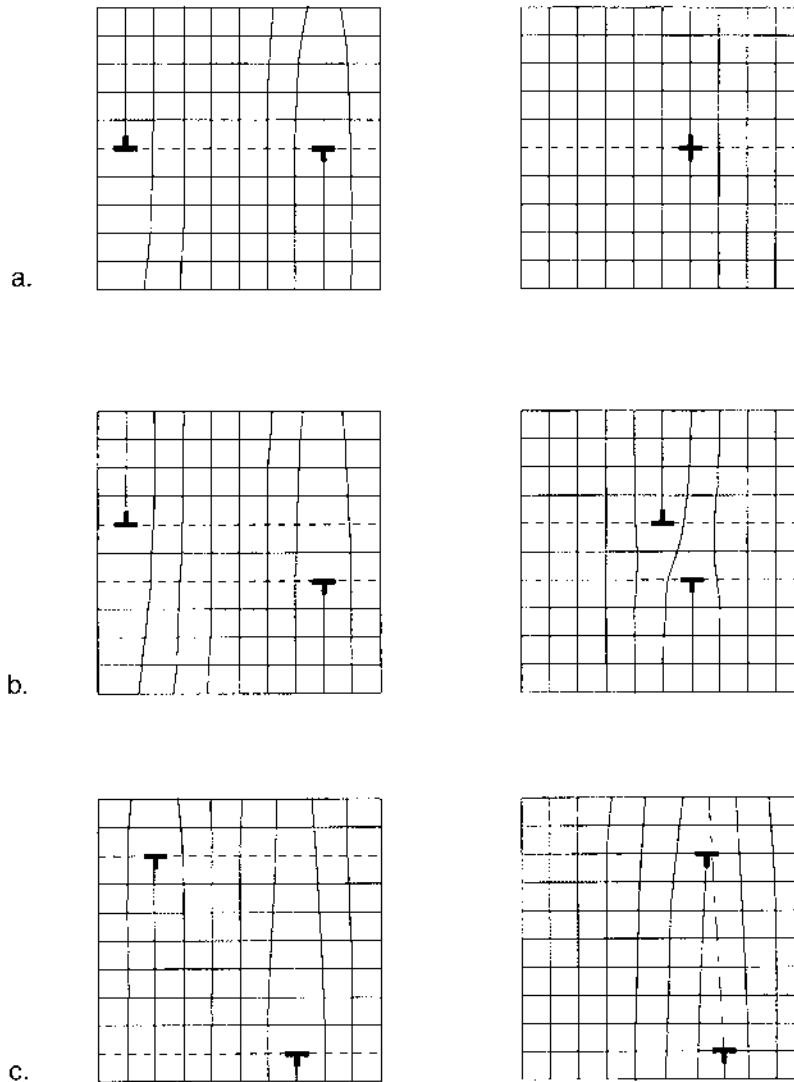
Figure 8 Migration of edge dislocations with parallel Burgers vectors. (a) unlike dislocation on the same slip plane; (b) unlike dislocations on separated slip planes; (c) like dislocations on separated slip planes.

the two dislocations, which will approach each other step by step by means of diffusion of vacancies and interstitial atoms, i.e. the climb of edge dislocation, and finally annihilate each other completely. In the case that the two edge dislocations of same sign locate on separated slip planes (Fig. 8(c)) $F < 0$ will be valid according to Eq. (2) when the value of θ is between $\pi/4$ and $3\pi/4$. The two dislocations will attract each other and keep θ at $\pi/2$, where the $F = 0$ and the dislocation structure becomes stable. A low angle boundary (Fig. 8(c),

Figure 9 Polygonization process (a, b).

dot-and-dash line) will be formed if more edge dislocations are periodically arranged in this way. With increasing dislocation number and decreasing dislocation distance in the boundary the low angle boundary could become a high angle boundary.

Similar recovery process for screw dislocations will also occur [18]. The interaction force F between screw dislocations has radial symmetry

$$F = \frac{Gb^2}{2\pi r} \tag{3}$$

The force between parallel screw dislocations of opposite sign is attractive, and that of same sign is repulsive.

After the dislocation reconfiguration mentioned above the dislocation density is drastically reduced, and the dislocation structure is in a low energy state. During the recovery the low angle boundary will absorb more and more dislocations. In some special cases a high angle boundary could also be formed by a very strong recovery process.

3.3   Polygonization

After cold deformation dislocations have piled up on slip planes (Fig. 9(a)). The stress fields from the dislocation pileups will result in torsion of the lattice. The evaluation of dislocation configuration during recovery, e.g. like that shown in Fig. 8(c), leads to formation of several low angle boundaries (Fig. 9(b)). The low angle boundaries divide a deformed grain into several pieces or sub-grains, in which there will be no torsion. The formation process of the recovered sub-grains surrounded by low angle boundaries is called polygonization. Because of the combination effects between the dislocations in the low angle boundaries, the stress fields of the dislocations do not have a long range area.

On the other hand the cell structure formed in cold deformation could also be transformed into the sub-grain structure, during which the cells are coarsened, the cell walls are thinned and sharpened due to the regulation of dislocations, and the dislocation density within the cells decreases further.

3.4   Recovery Kinetics

Concerning the dislocation mechanism the recovery annealing can be described by a second order kinetics [19]

$$\frac{\mathrm{d}\rho}{\mathrm{d}t} = -k\rho^2 \tag{4}$$

where ρ is dislocation density during annealing, t is annealing time, k is a constant depending on annealing temperature. In the integrated form Eq. (4) can be expressed

$$\rho = \frac{1}{kt + \frac{1}{\rho_0}} \tag{5}$$

where ρ_o is dislocation density before annealing. Compared with ρ the initial dislocation density ρ_0 is much higher [5] and the $1/\rho_0$ could be therefore neglected. In this case the equation can be transformed into

$$\frac{\mathrm{d}\rho}{\mathrm{d}t} = -\frac{1}{kt^2} \tag{6}$$

The kinetics were confirmed in zone-refined aluminum containing 0.0068 at% Cu [20].

4   PRIMARY RECRYSTALLIZATION

4.1   Concept of Primary Recrystallization

The unstable state due to the high defect density of deformed aluminum could result in a recrystallization process at elevated temperature, during which the dislocation density will be reduced down to an equilibrium value (e.g. $10^{10}/m^2$ [10]). Therefore the driving force for the recrystallization is the stored energy. Even after a recovery annealing, in which the stored energy is drastically reduced, the remained dislocation density (e.g. $1.5 \times 10^{14}/m^2$ [5]) is still high enough to drive the recrystallization process.

Recrystallization is a process, in which a new microstructure with relative equilibrium defect density is formed. The recrystallization includes nucleation and growth of new grains, in which the new grains grow until they touch each other and the deformed matrix with high defect density is completely or essentially replaced by the new grains. In most cases the grain growth during recrystallization is associated with migration of high angle boundaries.

The recrystallization does not include the process that large grains swallow small grains, of which both have low defect density. So the recrystallization mentioned here is called primary recrystallization, of which the word "primary" is often omitted.

In principle there is no fixed recrystallization temperature and the recrystallization of deformed aluminum could appear at any temperature above 0K. But it would take too much time, e.g. several years, to complete the recrystallization at lower temperature, and makes no sense for the industrial purpose. For example, the recrystallization in deformed aluminum with high purity could be completed at 150°C for 50 sec, but that in deformed Al-0.01 at% Fe alloy would need more than 10 billion years at 150°C to complete the recrystallization [21]. So the Al-0.01 at% Fe could practically not be recrystallized at 150°C. The impurity of aluminum is also an important effect factor on practical recrystallization temperature. The commercially pure aluminum, for instance, can be recrystallized at 200–300°C, but the zone refined pure aluminum could be recrystallized even at room temperature.

4.2 Nucleation

Nucleation is a thermal activation process, which is rather complicated and appears in the local area of a few hundreds or thousands of aluminum atoms. It is commonly very difficult to catch and observe the initial stage of nucleation, therefore many details of nucleation process are not clear so far.

According to the classic homogeneous nucleation theory [22] the change of free energy ΔF due to the formation of a spherical recrystallization nucleus consists of the decreasing of stored energy F_s and the area increasing of boundary with the energy γ between nucleus and deformed matrix. If the radius of the spherical nucleus is R, then the ΔF could be written as

$$\Delta F = -\frac{4}{3}\pi R^3 F_s + 4\pi R^2 \gamma \tag{7}$$

ΔF will reach maximum when $d\Delta F/dR$ is equal to zero, and the critical radius of the nucleus R_c can be obtained

$$R_o = \frac{2\gamma}{F_s} \tag{8}$$

The nucleus could grow freely when the condition $R > R_c$ is satisfied. Dislocation energy could be estimated at 0.5 Gb^2, where G is about 2.5×10^{10} N/m^2 [23] and b is 3.5×10^{-10}m for aluminum. Considering that the dominant part of stored energy F_s in deformed aluminum consists of dislocation density (10^{15}/m^2), F_s could be therefore calculated as 1.53×10^6 J/m^3. The boundary energy of 99.99% Al is about 0.6–1.9 J/m^2 [23], so according to Eq. (8) the R_c is roughly around 1–3 μm, which approaches the size order of deformation cells. Figure 10 gives the calculated relation
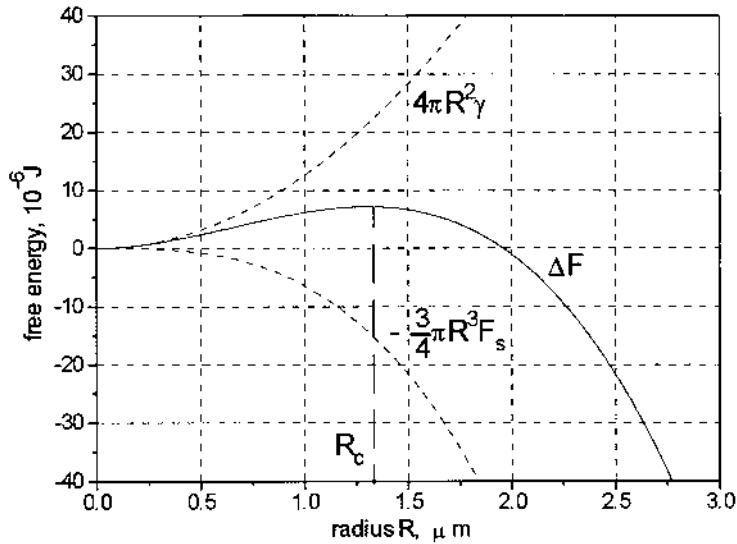
Figure 10 The calculated relation between free energy ΔF and nucleus radius R.
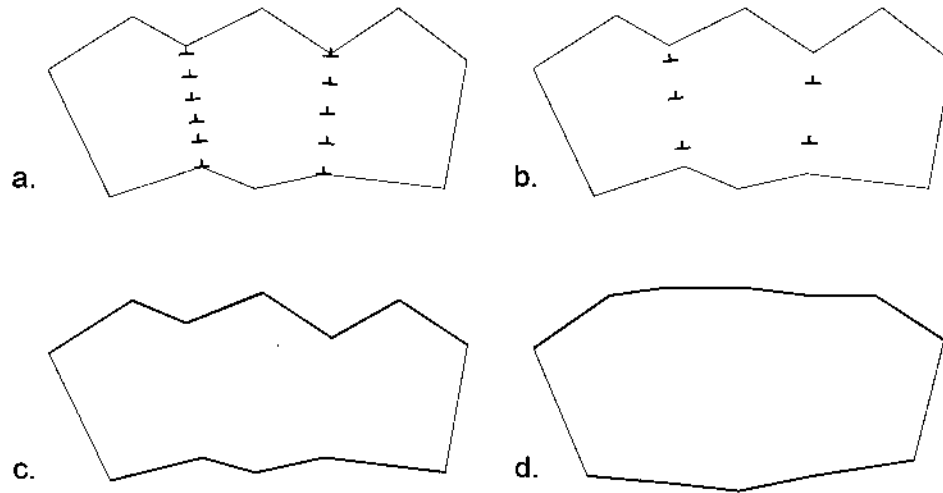
Figure 11   Schematic representation of subgrain coalescence (a, b, c, d).

exhibited by Eq. (7) for aluminum using the data mentioned above. Actually the dislocation is always inhomogeneously distributed in the deformed matrix, the R_c should be much smaller in the area with higher dislocation concentration.

In the classic nucleation theory the important point for aluminum and its alloys is that the nuclei must reach a critical size in order to grow freely. It should be indicated that the critical size for recrystallization nuclei is not identical to that in general phase transformation, i.e. the critical size could be quite different in deformed matrix concerning the local dislocation density around the nuclei.

In many cases the sizes of cells existing in the deformed matrix are smaller than the critical size and the cells are surrounded by the low angle boundaries, which are not very mobile because of their stable dislocation configuration. Therefore the cells could not grow freely. In the initial stage of recrystallization annealing a subgrain coalescence process [19] could produce a large subgrain greater than the critical size by polygonization and climbing of dislocation. Figure 11 gives a schematic representation of subgrain coalescence. At appropriate temperature the edge dislocations will climb out, and the cells become a large subgrain, during which the cells have to slightly change their orientations in order to be combined into one grain. After several steps of the coalescence the subgrain become larger than the critical size and the boundaries shown in Fig. 11(c) and (d) in thick line could be transformed progressively into mobile high angle boundaries.

In same cases the difference of dislocation densities between two sides of a high angle boundary is very distinct because, e.g. the strain is rather inhomogeneously distributed among the differently oriented initial grains at low deformation degree. Sometimes inhomogeneous recovery in the heavy deformed matrix could also lead to fairly different reduction of dislocation densities among the grains due to their different initial orientations followed by different deformation experiences and therefore different dislocation configurations. Generally the high angle boundary is very mobile and the different dislocation densities could induce a boundary migration in the direction of high dislocation density, which is called "strain induced

(a)

(b)

Figure 12 Heterogeneous nucleation. (a) on grain boundary in forged Al-0.01 wt% Ti alloy $\underset{\longmapsto 2\,\mu m \longmapsto}{}$; (b) around second phase particles in rolled Al-1.3 wt% Mn alloy [8]. (Fig. 12(b) courtesy of Dr. P. Yang, Ref. 8.)

boundary migration'' (SIBM) and was observed in 20% compressed high purity aluminum (99.99%) [24]. The subgrain behind the high angle boundary on the side of lower dislocation density could be therefore enlarged to a size over R_c and grow up as a recrystallization nucleus.

According to Eq. (8) it is known that R_c will be decreased when the dislocation density, i.e. the stored energy becomes higher. During cold deformation dislocations will pile up around obstacles like grain boundaries, particles of second phase etc, where the dislocation density is obviously higher than the average value, and therefore the positions around grain boundaries and second phase particles will become preferred places for nucleation [25,26]. That is the heterogeneous nucleation and relative smaller subgrains could already grow freely. The nucleation preferably along the grain boundaries was observed in high purity Al-0.008 wt% Cu alloy [25]. Figure 12 exhibits the observed nuclei formed on grain boundary in forged Al-0.01 wt% Ti alloy (Fig. 12(a)) or around the second phase particles in rolled Al-1.3 wt% Mn alloy (Fig. 12(b)) [8].

4.3 Grain Boundary Migration

After nucleation the nuclei will grow into deformed matrix by migration of high angle boundaries, which is a thermal activation process and is strongly dependent on recrystallization temperature.

The atoms near grain boundaries will jump from one grain to an other by means of overcoming the barrier energy Q_a during the thermal activation. But straight boundaries will not move if the grains are not deformed and in a stable state, since the atom jumps are equalized in mutual directions and lead to a dynamic equilibrium. In the case of growth of a recrystallization nucleus the atom jumps will become quite different. Because of the stored energy F_s the atoms in deformed matrix are in higher energy state, and the energy increase per atom F_{sa} is

$$F_{\mathrm{sa}} = F_s \frac{a^3}{4} = F_3 \frac{b^3}{3\sqrt{3}} \tag{9}$$

So the barrier energy for an atom to jump in the direction from nucleus to deformed matrix is $Q_a + F_{sa}$ and in the reversed direction is Q_a-F_{sa} respectively, which results in a boundary migration.

The migration velocity V of the boundaries can be calculated as

$$V = b\upsilon c_v \left[\exp\left(-\frac{Q_\mathrm{a} - F_\mathrm{sa}}{kT}\right) - \exp\left(-\frac{Q_\mathrm{a} + F_\mathrm{sa}}{kT}\right) \right] \tag{10}$$

where b is the length of Burger's vector representing the distance of atom jumps, υ is vibration frequency of atoms (about $10^{13}/\sec$ [10,27]), k is the Boltzmann constant, c_v is the vacancy density (about 10^{-5} at 700K and 10^{-4} at 800K [23]). The Q_a is about 4.5×10^4 J/m [28], i.e. 7.47×10^{-20} J/atom.

According to Eq. (10) the calculation of the average migration velocity at 700K is about 0.08 μm/sec for heavy deformed aluminum and is about 0.01 μm/sec for deformed and recovered aluminum. At 800K the velocity, according to the calculation, is about 1.85 μm/sec and 0.28 μm/sec respectively. If the dislocation density in deformed matrix is $10^{16}/m^2$ instead of $10^{15}/m^2$, then the velocity is about 0.8 μm/sec. The calculation results approach the order of practically observed velocity in aluminum. One of the important points of the calculations mentioned here is to observe the influences of temperature and dislocation density on the boundary migration.

An other form of Eq. (10) is

$$V = b\upsilon c_v \exp\left(-\frac{Q_\mathrm{a}}{kT}\right)\left[\exp\left(\frac{F_\mathrm{sa}}{kT}\right) - \exp\left(-\frac{F_\mathrm{sa}}{kT}\right) \right] \tag{11}$$

Because the value of F_{sa}/kT here is very small the equation could be simplified in first approximation of power expansion as

$$V = b\upsilon c_v \exp\left(-\frac{Q_\mathrm{a}}{kT}\right)\left[1 + \frac{F_\mathrm{sa}}{kT} - 1 + \frac{F_\mathrm{sa}}{kT} \right]$$

$$= 2b\upsilon c_v \frac{F_\mathrm{sa}}{kT}\exp\left(-\frac{Q_\mathrm{a}}{kT}\right) \tag{12}$$

It is obvious that Eq. (12) does not consider the influence of solute atoms, particles of second phase and orientation difference between nuclei and deformed matrix.

The grain boundaries provide sites with lower potential energy for impurity or alloy atoms, which will tend to adhere to the moving boundaries. Therefore the boundaries have to overcome additionally the migration resistance induced by the adherence effect of solute atoms, and the migration will slow down if the content c of solute atoms increases. The migration velocity v was found to be inversely proportional to Cu content in aluminum [29].

Because of the low potential energy an atmosphere of solute atoms could be formed around boundaries, i.e. the concentration of solute atoms in grain boundaries is higher than the average value, in which the solute atoms would be dragged along by the moving boundaries that keep the atmosphere around them. Only when the migration velocity of boundaries driven by, e.g. higher stored energy become greater, and the solute atoms could not accompany the boundary migration, then the boundaries would migrate freely, similar to the case in pure aluminum [30].

The average distance of atom jumps from one grain to an other depends on the orientation difference of the two grains, and therefore the barrier energy Q_a could be also quite different, which will influence the velocity of boundary migration. Figure 13 gives an example of calculated jumping distance for aluminum, in which the orientation difference of two grains is characterized by a rotation of certain angle θ around a common $\langle 111 \rangle$ axis [31]. So it was found that a boundary would have very high migration velocity if two neighboring grains on two sides of a boundary have a special orientation relationship [32]. For aluminum the velocity reaches a maximum value when the orientation relationship between the deformed matrix and growing grains is characterized by a rotation of about 40° around one of their common $\langle 111 \rangle$ axis [31,32].
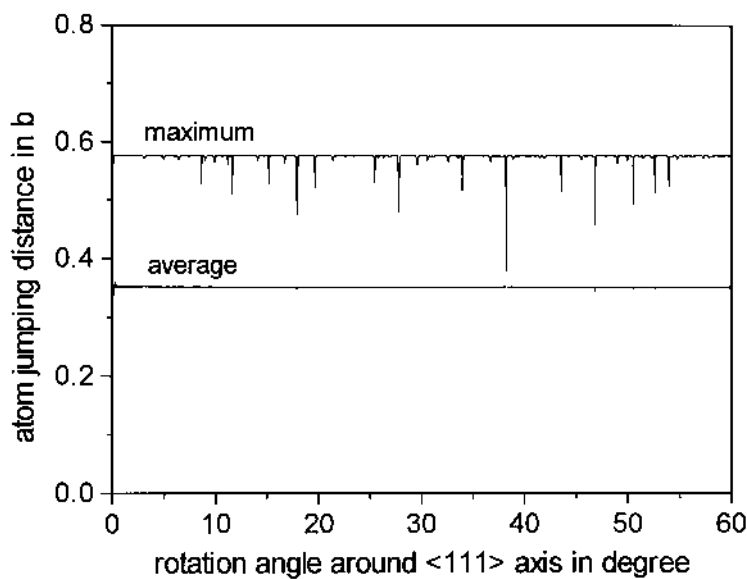
Figure 13 Calculated jumping distance for aluminum. (From Ref. 31.)

The orientation difference and solute atoms could mutually influence the migration velocity. In the case of two neighboring grains having certain orientation relationship, where a coincidence lattice with low reciprocal density (Σ value) forms, the solute atoms to the boundary would be obviously reduced because of the special atom arrangement of the boundary, and result in a low barrier energy Q_a as well as high boundary mobility. Fridman et al. [33] observed, for example, that the migration velocity of high angle boundaries in pure aluminum with 99.99995 at% Al is very high and independent on the orientation difference. The migration velocity is reduced obviously when the purity is down to 99.9992 at% Al, but is hardly decreased at several points where the orientations of concerned two grains form a special coincidence lattice with low Σ value [33].

Commonly the particles of second phase will hinder the boundary migration during recrystallization. But if the existence of particles induce a drastic heterogeneous nucleation the recrystallization process will be accelerated, which was observed in aluminum alloys containing particles of Al_2Cu or Al_3Fe [34].

4.4   Recrystallization Kinetics

The primary recrystallization consists of nucleation and grain growth, therefore the nucleation rate N and the migration velocity V will determine the recrystallization process and the final recrystallization grain size.

The N and v are defined as

$$N = \frac{\frac{dn}{dt}}{1 - x} \tag{13}$$

$$V = \frac{dR}{dt} \tag{14}$$

where x is the volume fraction of recrystallized matrix, t is annealing time, R is the radius of recrystallization grain and n is the number of newly formed nuclei per unit volume. According to Eq. (13) N is the number of newly formed nuclei per unit time and per unit volume of retained deformation matrix.

Observing the recrystallization process started from time point $\tau > 0$, a newly formed spherical nucleus at τ will grow up to a time point $t > \tau$, by which the increase in recrystallized volume V_τ is

$$V_\tau = \frac{4}{3}\pi v^3 (t - \tau)^3 \tag{15}$$

where the velocity V is considered to be a constant. According to Eq. (13) the dn at τ could be expressed as

$$dn_\tau = N(1 - x)d\tau \tag{16}$$

The nuclei formed at any τ in the interval between 0 and t will contribute to the volume increasement dx as

$$dx = V_\tau dn_\tau$$
$$= \frac{4}{3}\pi N v^3 (t - \tau)^3 (1 - x)d\tau \tag{17}$$

which could be transformed into a format of definite integral

$$\int_0^x \frac{dx}{1 - x} = \int_0^t -\frac{4}{3}\pi N v^3 (t - \tau)^3 \, d\tau \tag{18}$$

and therefore the fraction of recrystallized volume x could be obtained as

$$x = 1 - \exp(-\frac{1}{3}\pi N v^3 t^4) \tag{19}$$

which is called Johnson–Mehl equation [35]. It can be seen in Eq. (19) that the recrystallized volume x changes from 0 to 1 while the annealing time runs from 0 to infinity, which could be qualitatively confirmed by the recrystallization annealing at 300°C of a 95% rolled high purity (99.998 wt% Al) aluminum sheet (Fig. 14) [36]. In most cases the v and N are not constants during the recrystallization of aluminum [37], but the deduction process described above could still give us an important impression about the kinetics of the primary recrystallization.

Define t_c as

$$t_c = \left(\frac{3}{\pi N v^3}\right)^{\frac{1}{4}} \tag{20}$$
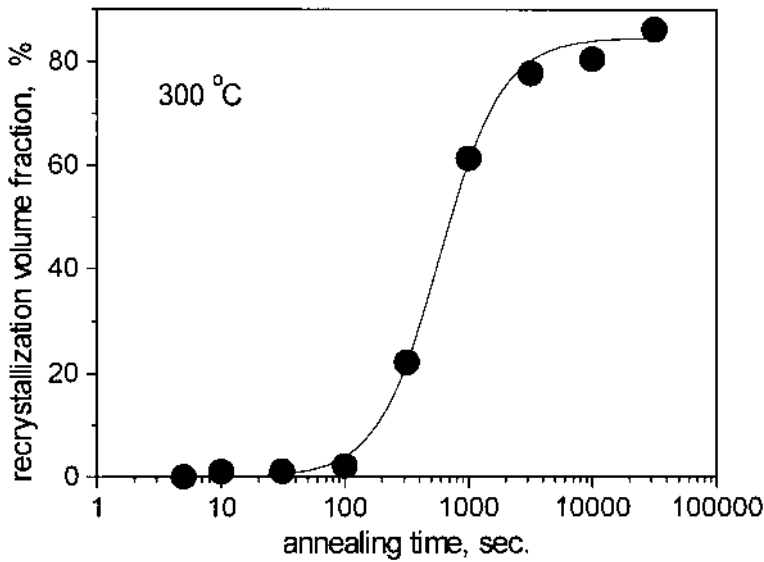
Figure 14 Recrystallized volume of a 95% rolled high purity (99.998 wt% Al) aluminum.

then Eq. (19) can be written as

$$x = 1 - \exp\left[-\left(\frac{t}{t_c}\right)^4\right] \tag{21}$$

If t is equal to t_c then about 63% of the deformed matrix has been recrystallized. It could be estimated that the recrystallization grains have been in contact with each other at t_c and the recrystallization grain size is roughly fixed. So considering Eq. (20) the recrystallization grain size d, i.e. the diameter of a primary recrystallization grain can be calculated as

$$d = 2R = 2\int_0^{t_c} vdt = 2vt_c = 2\left(\frac{2v}{\pi N}\right)^{\frac{1}{4}} \tag{22}$$

and t_c is the characteristic recrystallization time. It is should be noticed that the grain size of primary recrystallization is mainly determined by the ratio of v/N according to Eq. (22) from which the grain size d will be increased by increasing v or decreased by increasing N respectively.

Anderson and Mehl [37] have investigated the nucleation rate N and migration velocity v during the recrystallization annealing of elongated pure aluminum. They found that the ratio v/N is increased with increasing tensile deformation or with arising annealing temperature, which would result in refined grain size after the primary recrystallization.

4.5   Recrystallization in situ (Continuous Recrystallization)

After primary recrystallization not only the deformed structure has been eliminated but the orientation distribution of deformed matrix has also disappeared completely. Therefore the process is called discontinuous recrystallization.

During annealing of deformed aluminum there could be another recrystallization process, in which the deformation structure is eliminated in a quite different way. When aluminum has experienced a special range of deformation degree and the migration of boundaries is obstructed drastically, e.g. by precipitates, only a extremely strong recovery process could appear, in which high angle boundaries would be slowly formed by gradual subgrain coalescence. In this case an entirely new structure with very low defect density is formed though there will be no migration of the high boundaries. In order to differ from the normal recrystallization this recrystallization process is called recrystallization in situ or continuous recrystallization. The important characteristic of continuous recrystallization is that the grain orientations in deformed matrix are not changed essentially during annealing [38].

Figure 15(a) shows the deformation structure of commercially pure aluminum (99.9 wt% Al) which has been forged 25% in two mutually vertical directions. The original grain boundaries before deformation can be observed. After annealing at 350°C for about 40 min the continuous recrystallization is completed, in which the newly formed grains are still in the area of original grains (Fig. 15(b), left part). The deformed structure has been transformed into new grains by a very strong recovery while the orientations of deformation grains remain. Obvious boundary

(a)
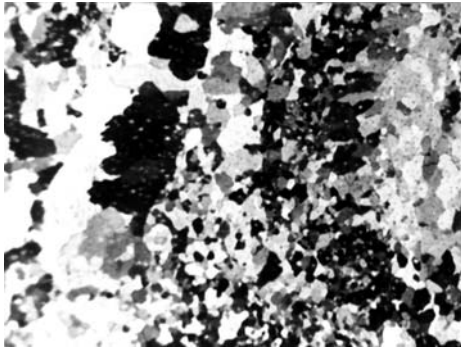
(b)

Figure 15 Microstructure showing continuous recrystallization in aluminum $\underset{\longmapsto}{\overset{200\,\mu m}{\longmapsto}}$, (a) forged; (b) annealed.

migration over original grain boundaries was not observed since the precipitates containing the common impurity atoms like iron, silicon etc. were accumulated on the original boundaries and obstruct the boundary migration during annealing.

Ito et al. [39] have investigated the recrystallization behaviors of high-purity aluminum-iron alloys. They found that the continuous recrystallization would appear obviously around 400°C when the content of iron exceeds 0.01 wt% because there will be many precipitates of FeAl$_3$ on the boundaries.

5 RECRYSTALLIZATION TEXTURE

Texture is a significant characteristic of polycrystalline aluminum and accompanies almost all kinds of physical metallurgical processes. A {100} fiber texture in aluminum ingots, for instance, is established very often [40] because of the oriented heat conduction and corresponding growth selection of grains during solidification. Different textures are surely formed after hot or cold deformation as well as annealing. Therefore a piece of polycrystalline aluminum without texture could be hardly

found. Many aluminum alloys are used in annealed state and it is important to reveal the formation mechanisms of recrystallization texture, by which the induced anisotropy has significant influence on many useful properties.

5.1   Pole Figure Determination

Pole figure is a conventional method to describe texture in aluminum and is obtained by means of measuring diffraction data of polycrystals, for which commonly the x-ray diffraction technique [41] or neutron diffraction technique [42] are used. Figure 16 demonstrates schematically the structure of a x-ray texture goniometer, on which the pole figures of aluminum samples are measured using reflection technique.

According to Bragg-law used for the pole figure measurement [11] there is:

$$2d_{hkl}\sin\theta = n\lambda \tag{23}$$

where λ is the wavelength, d_{hkl} is the distance constant of certain {hkl} lattice plane, θ is the Bragg angle and n should be one for the first order reflection. If an incident beam initiated by x-ray tube and certain {hkl} lattice plane of a sample are so located that the corresponding angle θ between them is obtained according Eq. (23), then the diffraction intensity can be recorded in direction 2θ by a detector (Fig. 16). During
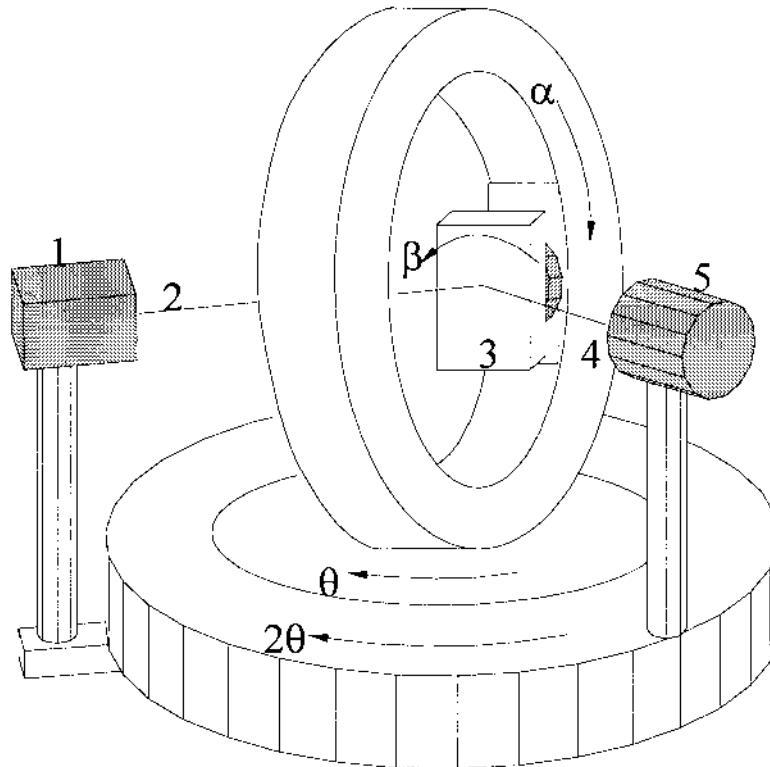
Figure 16   Structure of a x-ray texture goniometer, (1) X-ray tube; (2) incident beam; (3) sample; (4) reflection beam; (5) detector.
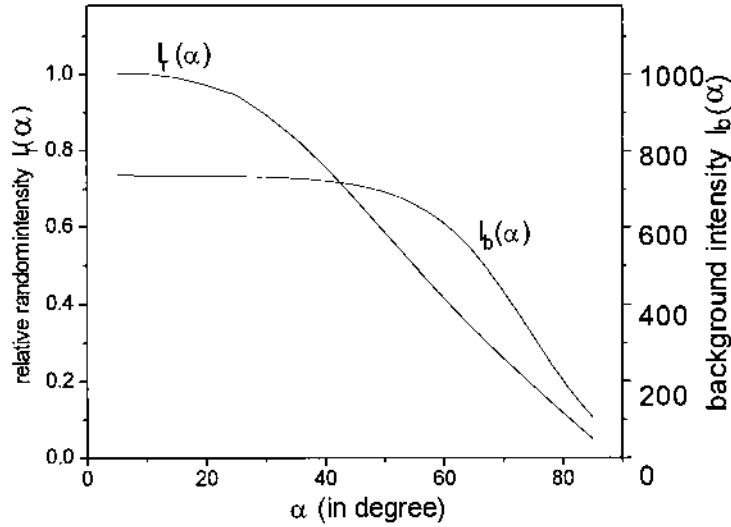
Figure 17 $I_r(\alpha)$ and $I_b(\alpha)$ of an aluminum powder sample.

the measurement the rotation angle $\alpha(0\text{-}\pi/2)$ and $\beta(0\text{-}\pi)$ should be so changed that the intensity $I(\alpha,\beta)$ in all sample directions can be obtained (Fig. 16). For an aluminum powder sample with random texture the intensity I_p should be a function of angle α, i.e. $I_p(\alpha)$. Because of the geometrical structure of the goniometer the $I_p(\alpha)$ is decreased with increasing α and is independent on β. On the other hand a part of the measured intensity belongs to the background $I_b(\alpha)$ [41], and should be reduced from the $I_p(\alpha,\beta)$. Figure 17 gives the changes of the $I_r(\alpha)$ and $I_b(\alpha)$ data taken from an aluminum powder sample, where the relative random intensity $I_r(\alpha)$ is:

$$I_r(\alpha) = \frac{I_p(\alpha) - I_b(\alpha)}{I_p(0^o)} \tag{24}$$

representing the relative changes of $I_p(\alpha)$.

Therefore the measured pole figure data $P_{hkl}(\alpha,\beta)$ should be expressed as:

$$P_{hkl}(\alpha,\beta) = \frac{I(\alpha,\beta) - I_b(\alpha)}{I_r(\alpha)} \frac{1}{N} \tag{25}$$

where N is the normalized factor and can be deduced by

$$\frac{1}{2\pi} \int\limits_{\alpha=0}^{\pi/2} \int\limits_{\beta=0}^{2\pi} p_{hkl}(\alpha,\beta) \sin\alpha \, d\alpha \, d\beta = \frac{1}{2\pi} \sum_{\alpha=0(\Delta\alpha)}^{\pi/2} \sum_{\beta=0(\Delta\beta)}^{2\pi} p_{hkl}(\alpha,\beta) \sin\alpha \Delta\alpha \Delta\beta \equiv 1 \tag{26}$$

where $\Delta\alpha$ and $\Delta\beta$ are the measuring steps.
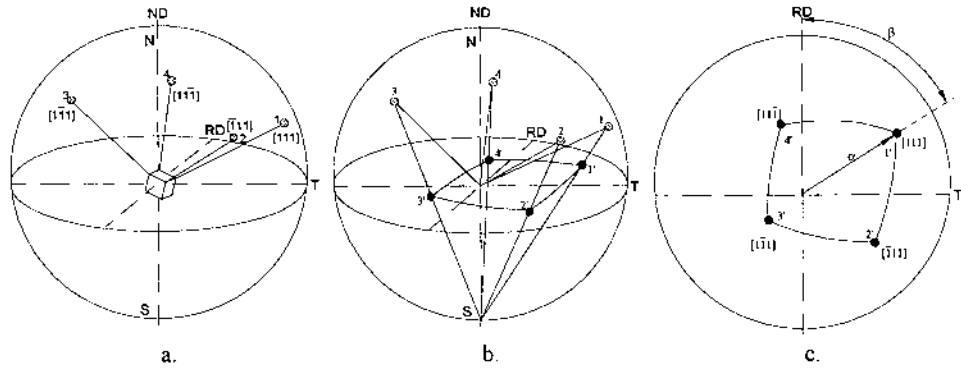
Figure 18   Stereographic {111} projection of a grain (a, b, c).

5.2   Description of Recrystallization Texture

Figure 18 shows the stereographic {111} projection of a grain at the center of a unit sphere [43], in which a coordinate system relative to rolling specimen is taken as an example.

The coordinate position in the pole figure (Fig. 18(c)) can be expressed as (α, β) according to the geometry of spheres. Figure 19 gives the measured {200} and {111} pole figures of a recrystallized pure aluminum sheet, of which the measured data have been corrected according to Eqs (25) and (26).

Generally a pole figure gives the information about stereographic density distribution $P_{hkl}(\alpha, \beta)$ of corresponding {hkl} planes, which could be expressed as series expansion of spherical harmonics [44]

$$p_{\text{hkl}}(\alpha, \beta) = \sum_{1=0}^{\infty} \sum_{n=-1}^{1} F_{1(\text{hkl})}^{n} K_{1}^{n}(\alpha, \beta) \qquad (0 \le \alpha \le \pi, 0 \le \beta \le 2\pi) \qquad (27)$$

where $K_{1}^{n}(\alpha, \beta)$ is the known spherical harmonics and F_{1}^{n} is a group of constants.
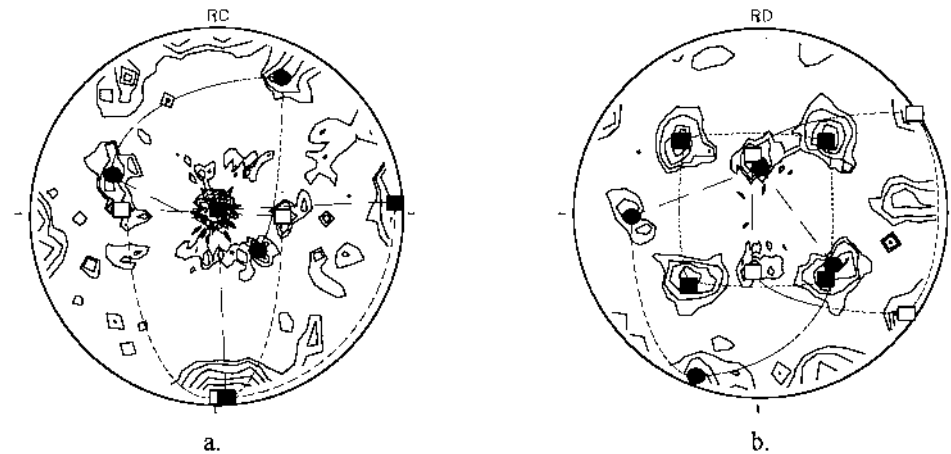
Figure 19   Pole figures of a recrystallized pure aluminum sheet, ■ Cube {001}⟨100⟩, ● R {124}⟨211⟩, □ Goss {011}⟨100⟩, (a) {200}; (b) {111}.
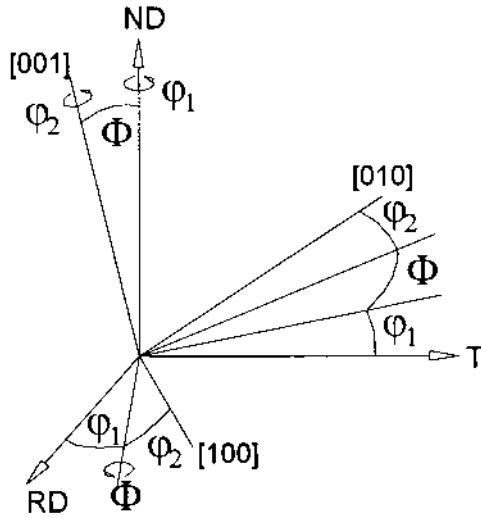
Figure 20 Definition of Euler angles.

An orientation has three independent parameters, therefore Bunge [44] defines three rotation angles, i.e. φ_1, Φ and φ_2 showing in Fig. 20 to describe grain orientation, for example, in the coordinate system relative to rolling specimen, where the grain orientation could be obtained by individual φ_1, Φ and φ_2 rotations of crystalline coordinate in the specimen coordinate. Hence a Euler space [44] can be established with three mutually perpendicular axes of φ_1, Φ and φ_2 which are called Euler angles. The miller index $\{hkl\}$ $\langle uvw \rangle$ are often used to express an orientation in rolling samples, and the relationship of miller index and Euler angles can be described as

$$
\begin{bmatrix}
\cos\varphi_1\cos\varphi_2 - \sin\varphi_1\sin\varphi_2\cos\Phi & \sin\varphi_1\cos\varphi_2 + \cos\varphi_1\sin\varphi_2\cos\Phi & \sin\varphi_2\sin\Phi \\
-\cos\varphi_1\sin\varphi_2 - \sin\varphi_1\cos\varphi_2\cos\Phi & -\sin\varphi_1\sin\varphi_2 + \cos\varphi_1\cos\varphi_2\cos\Phi & \cos\varphi_2\sin\Phi \\
\sin\varphi_1\sin\Phi & -\cos\varphi_1\sin\Phi & \cos\Phi
\end{bmatrix}
$$

$$
= \begin{bmatrix}
u & kw - lv & h \\
v & lu - hw & k \\
w & hv - ku & l
\end{bmatrix}
\tag{28}
$$

Table 1 gives some important texture components frequently observed in aluminum alloys. Using the Euler space the texture of polycrystalline materials can be obviously better represented by the orientation distribution function (ODF) $f(\varphi_1, \Phi, \varphi_2)$ like

$$
f(\varphi_1, \Phi, \varphi_2) = \sum_{l=0}^{\infty} \sum_{m=-1}^{1} \sum_{n=-1}^{1} C_1^{mn} T_1^{mn}(\varphi_1, \Phi, \varphi_2)
\tag{29}
$$

$$
(0 \le \varphi_1 \le 2\pi, 0 \le \Phi \le \pi, 0 \le \varphi_2 \le 2\pi)
$$

Table 1   Important Texture Components in Aluminum Alloys

Component name	{hkl} ⟨uvw⟩	$\varphi_1, \Phi, \varphi_2$
cube	{001}⟨100⟩	0°, 0°, 0°
rotated cube	{001}⟨110⟩	45°, 0°, 0°
copper	{112}⟨112⟩	90°, 35°, 45°
brass	{011}⟨211⟩	35°, 45°, 0°
Goss	{011}⟨100⟩	0°, 45°, 0°
S	{123}⟨634⟩	59°, 37°, 63°
R	{124}⟨211⟩	57°, 29°, 63°
–	{111}⟨112⟩	90°, 55°, 45°

where T_1^{mn} (φ_1, Φ, φ_2) is the known generalized spherical harmonics and C_1^{mn} is a group of constants. According to the mathematical relation between Eqs (29) and (27) the following equation can be obtained [44]

$$F_{1(\text{hkl})}^n = \frac{4\pi}{2l+1} \sum_{m=-1}^{1} C_1^{mn} K_1^{*m}(\alpha_{\text{hkl}}^*, \beta_{\text{hkl}}^*) \tag{30}$$

where K_1^{*m} (α_{hkl}^*, β_{hkl}^*) is the known conjugate complex function of $K_1^m(\alpha,\beta)$, and (α_{hkl}^*, β_{hkl}^*) are the spherical polar coordinates of direction ⟨hkl⟩ with respect to the crystalline coordinate system according to the geometry of spheres.

An ODF can be obtained by several sets of measured pole figure data p_{hkl} (α,β) and the calculation using Eqs (27), (30) and (29) [44], which can be represented as density distributions on different φ_2 sections. Figure 21 gives an example of ODF section analysis for the recrystallization texture in 95% rolled and annealed high purity aluminum. Commonly a recrystallization texture consists of several texture components, of which the volume fraction and the scattering width [45] can be also calculated according to the ODF. Because of the symmetry existed in the aluminum polycrystalline the Euler space is commonly reduced down to $0 \leq \varphi_1$, Φ, $\varphi_2 \leq \pi/2$ (Fig. 21).

5.3   Formation of Recrystallization Texture

The two basic processes of recrystallization, i.e. the nucleation and the following grain growth which will contribute to the recrystallization texture, have to be considered for the interpretation of texture formation.

One of the most prevailing interpretations for the formation of recrystallization texture is the theory of oriented nucleation proposed by Dillamore and Katoh [46]. During deformation the grain orientations will rotate along certain orientation lines from unstable divergent zone in the Euler space towards several symmetrical stable convergent zones. Between the symmetrical orientation variants transition bands consisting of continually neighboring subgrains will be formed over the original unstable orientation. Around the original orientation and several points in the orientation lines, where the orientation gradient is often rather high, the subgrains will be surrounded frequently by the very mobile high angle boundaries after the polygonization and several steps of subgrain coalescence during annealing.
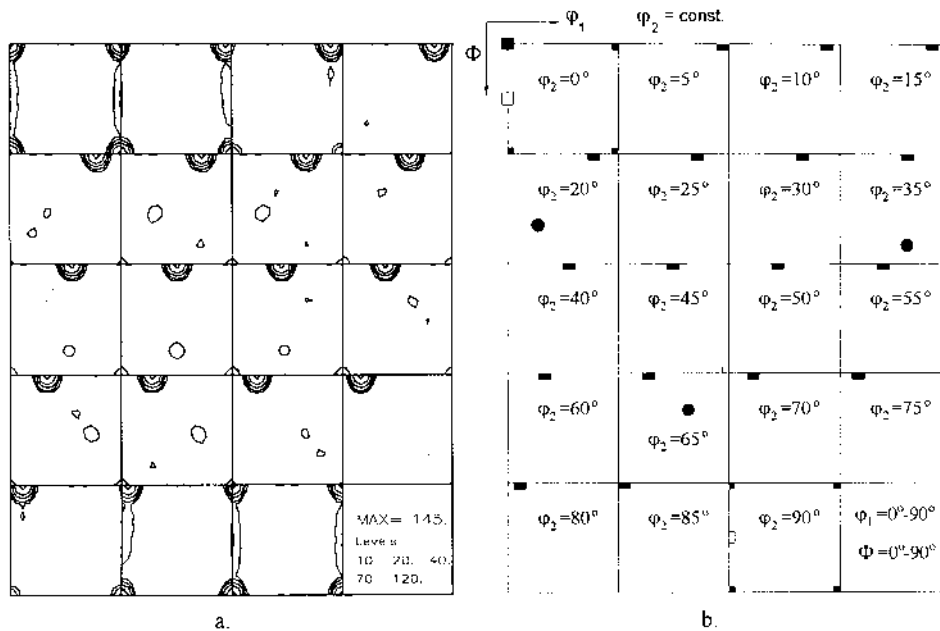
Figure 21 ODF analysis of recrystallized pure aluminum sheet (a, b), ■ {001}⟨100⟩, ●
{124}⟨211⟩, □ {011}⟨100⟩.

The enlarged subgrains can grow up as nuclei rapidly, and their orientations will
determine the final recrystallization texture. The theory could explain, for example
the formation of cube texture {001}⟨100⟩ and R texture {124} ⟨211⟩ in annealed
aluminum sheets.

An other important interpretation for the formation of recrystallization
texture is the theory of growth selection proposed mainly by Lücke [47]. The theory
is based on the direct statistic measurements of the boundary migration rate in
growth selection experiments in several hundreds of deformed single aluminum
crystals [32]. It was found, that a boundary between the deformed matrix and
growing grains in aluminum would have very high migration velocity if the
orientation relationship of the two neighboring grains is characterized by a rotation
of about 40° around one of their common ⟨111⟩ axis [32] because of the special
atomic structure in the boundaries [31]. The orientation relationship is often called
briefly 40° ⟨111⟩. The theory could also explain the formation of cube texture {001}
⟨100⟩ and R texture {124}⟨211⟩ in annealed aluminum sheets.

The common texture components of rolled and annealed pure aluminum sheets
are the cube texture {001}⟨100⟩, R texture {124}⟨211⟩ and sometimes also the Goss
texture {011} ⟨100⟩ (Figs 19 and 21). Conventional impurity atoms have obvious
influence on the recrystallization texture components [39]. The impurity atoms will
generally reduce the cube texture but increase the R texture, especially when they
precipitate during the recrystallization annealing. If the precipitation temperature
is avoided the volume of cube texture will be increased, and therefore the annealing
temperature is very important for the texture formation [39].
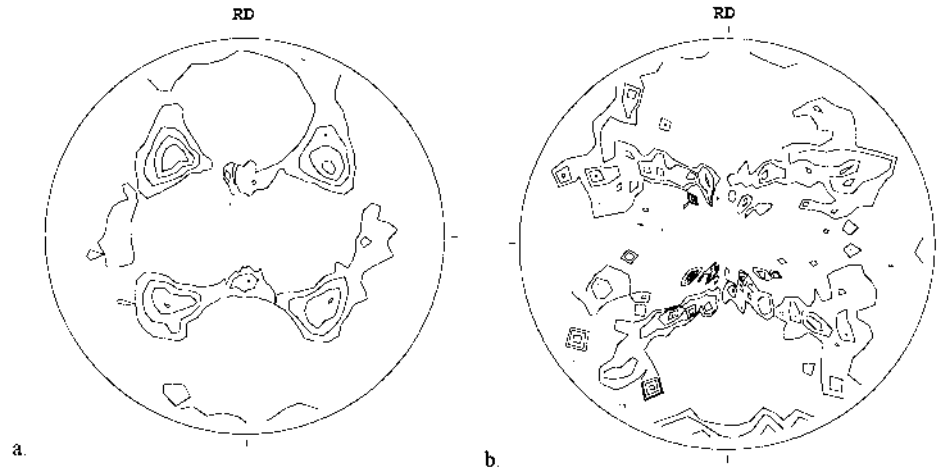
Figure 22 {111} pole figures of 95% rolled aluminum after primary recrystallization, (density levels: 2, 4, 7, 11, 16). (a) 240°C, 600 sec and 300°C, 3162 sec (Max = 14.5); (b) 300°C, 316 sec (Max = 20.2).

Due to the strong reduction of stored energy the recovery annealing prior to primary recrystallization will change the annealing time and the texture composition. Figure 22 gives an example showing the influence of recovery annealing prior to primary recrystallization on the final primary recrystallization texture. Ninety-five percent rolled pure aluminum sheet (99.998 wt% Al) is annealed at 240°C for 600 sec and then at 300°C for 3162 sec, after which strong cube texture and R texture have been obtained (Fig. 22(a)). The 240°C annealing here is only a recovery treatment and the recrystallization does not occur. But the texture components become multivariate if the sheet is directly annealed at 300°C without recovery treatment (Fig. 22(b)). The analysis of texture components for the two annealing processes is listed in Table 2, in which the clear effect of recovery treatment can be observed. The recovery treatment has obviously reduced the recrystallization driving force so that the primary recrystallization could be carried out slowly, during which

Table 2 Texture Components of 95% Rolled and 300°C Annealed Pure Aluminum

Annealing	Texture component	Volume fraction
240°C, 600 sec	{001}⟨100⟩	54%
300°C, 3162 sec	{124}⟨211⟩	26%
no recovery annealing	{001}⟨100⟩	12%
300°C, 316 sec	{011}⟨611⟩	8%
	{013}⟨100⟩	6%
	{149}⟨511⟩	15%
	{225}⟨554⟩	8%
	{239}⟨311⟩	10%
	{269}⟨354⟩	23%

some specially oriented subgrains or nuclei could grow up more rapidly [32,46] and dominant the formation of recrystallization texture, i.e. the cube and R texture. But if the high stored energy is not obviously reduced by the recovery treatment before primary recrystallization the recrystallization becomes a rash process, in which many differently oriented subgrains or nuclei have the possibility to grow up rapidly due to the high driving force, and therefore leads to the multivariate recrystallization texture.

5.4 Recrystallization Controlled by Oriented Nucleation

According to the prediction of Dillamore and Katoh [46] the orientation $\{001\}\langle 100 \rangle$ in aluminum rolling sheet is located in the divergent zone, and the $\{011\}\langle 211 \rangle$ is located in the convergent zone. During rolling deformation the grains oriented around $\{001\}\langle 001 \rangle$ will rotate at first towards the $\{011\}\langle 100 \rangle$ in two directions. Then the orientations move towards the two variants of $\{001\}\langle 211 \rangle$, i.e. the $(011)[2\bar{1}1]$ and $(011)[21\bar{1}]$. The paths of orientation changes are demonstrated by the vector lines in the $\varphi_2 = 0°$ section of the ODF (Fig. 23(a)), which shows the orientation chains of the subgrains including the $\{001\}\langle 100 \rangle$ and $\{011\}\langle 100 \rangle$ in the transition bands mentioned by Dillamore and Katoh [46].
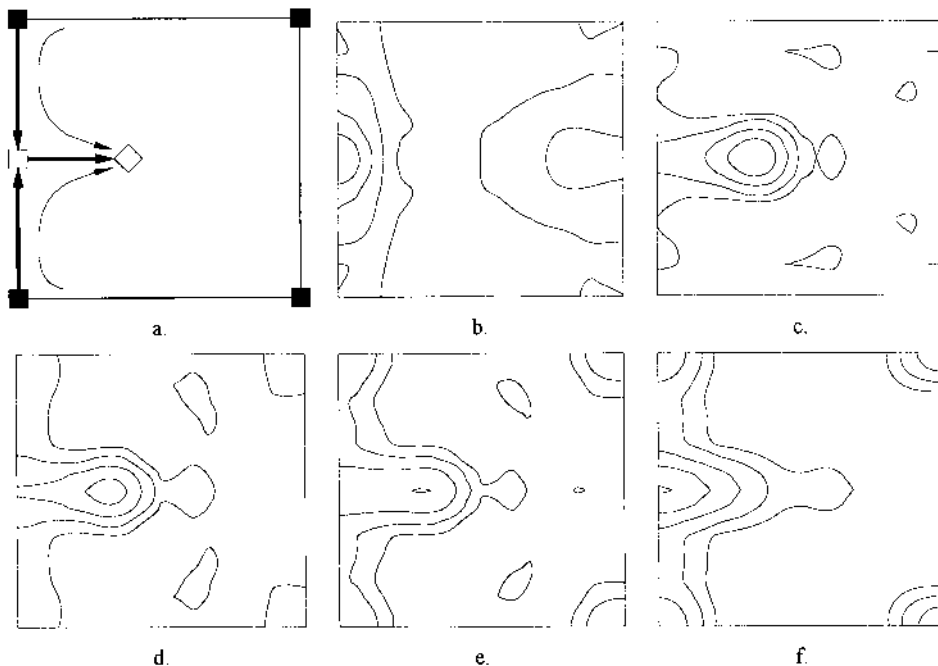
Figure 23 The texture evaluation during rolling and annealing in an Al-0.01%Ti alloy sheet (ODF $\varphi_2 = 0°$ section, density levels: 1, 3, 7, 13, 21.), ■ $\{001\}\langle 100 \rangle$, □ $\{011\}\langle 100 \rangle$, ◇ $\{011\}\langle 211 \rangle$. (a) trace of transition bands; (b) initials state (max = 20.4); (c) 95% rolled (max = 20.5); (d) 300°C 5.27 min (max = 16.9); (e) 300°C 16.7 min (max = 13.4); (f) 300°C 1093 min (max = 22.1).

It is obvious that the formation of the transition bands depends on the initial distribution of grain orientations, i.e. the initial texture. Figure 23(b) gives the initial texture of an Al-0.01 wt% Ti alloy sheet [48], in which a strong $\{011\}\langle100\rangle$ texture and certain density distribution around $\{001\}\langle100\rangle$ are observed. After 95% rolling reduction the grain orientations have moved to the $\{001\}\langle211\rangle$ (Fig. 23(c)) and the trace of the transition bands can still be observed. During annealing at 300°C the transition bands are generally strengthened (Fig. 23(d)—(f)) which indicates the recrystallization process is controlled by the oriented nucleation in the transition bands. However the main texture components after the recrystallization are the $\{011\}\langle100\rangle$ and $\{001\}\langle100\rangle$ (Fig. 23(f)).

The cube orientation $\{001\}\langle100\rangle$ has certain meta-stability during rolling deformation and some of its subgrains could survive even after heavy rolling [49], which results in the formation of cube texture in the following annealing (Fig. 23(f)). The strong Goss texture $\{011\}\langle100\rangle$ after annealing (Fig. 23(f)) is obviously induced by the strong initial Goss texture (Fig. 23(b)) and the corresponding higher nucleation possibility in the transition bands.

Titanium atoms in the aluminum alloy should be in the form of $TiAl_3$ and precipitated at initial boundaries before rolling deformation. In this case the grains could hardly grow over the initial boundaries during annealing. The oriented nucleation process in the areas of original boundaries could be carried out without interruption [48], and show the strong effect on the final recrystallization texture.

5.5   Recrystallization Controlled by Growth Selection

It is assumed according to the observation of Ibe et al. [32], that there should be differently oriented nuclei formed during annealing. But the cube and R texture would be dominant in the annealed rolling sheet, since both the orientations have an orientation relation of $40° \langle111\rangle$ to the S texture $\{123\}\langle634\rangle$ which is the main rolling texture in aluminum and its alloys.

Figure 24(a) gives the $\{111\}$ pole figure of a 95% rolled pure aluminum sheet (99.998 wt% Al) [50], which shows more than 60% S texture. At the initial stage of annealing the nuclei form in the deformation transition bands while the matrix is not changed apparently. Figure 24(b) shows that the orientations of the nuclei are located in the transition bands between cube and S orientation [50] and the density is increased in the corresponding positions in the $\{111\}$ pole figure, while the main rolling texture remains unchanged. With increasing annealing time the growth rate of the nuclei is quite different. Figure 24(e) gives the optical structure of 316 sec annealed sheet. In the deformation matrix the size of newly formed grains is very different. Using a $\{100\}$ plane etching technique the individual grain orientations could be determined [50]. The results indicate that all the huge grains have the cube or R orientation. The corresponding pole figure (Fig. 24(c)) shows also the strong density increasement around cube and R orientation in the transition bands (by reference to Fig. 19(b)). Because of the high purity of the sheet the growth competition among the nuclei is rather freely without strong obstructs induced by the impurity atoms. Figure 24(e) demonstrates the obvious advantage of the grains oriented around cube and R orientation in the growth competition due to the special boundary structure [31], and finally the cube and R texture become dominant in the annealed sheet (Fig. 24(d)).
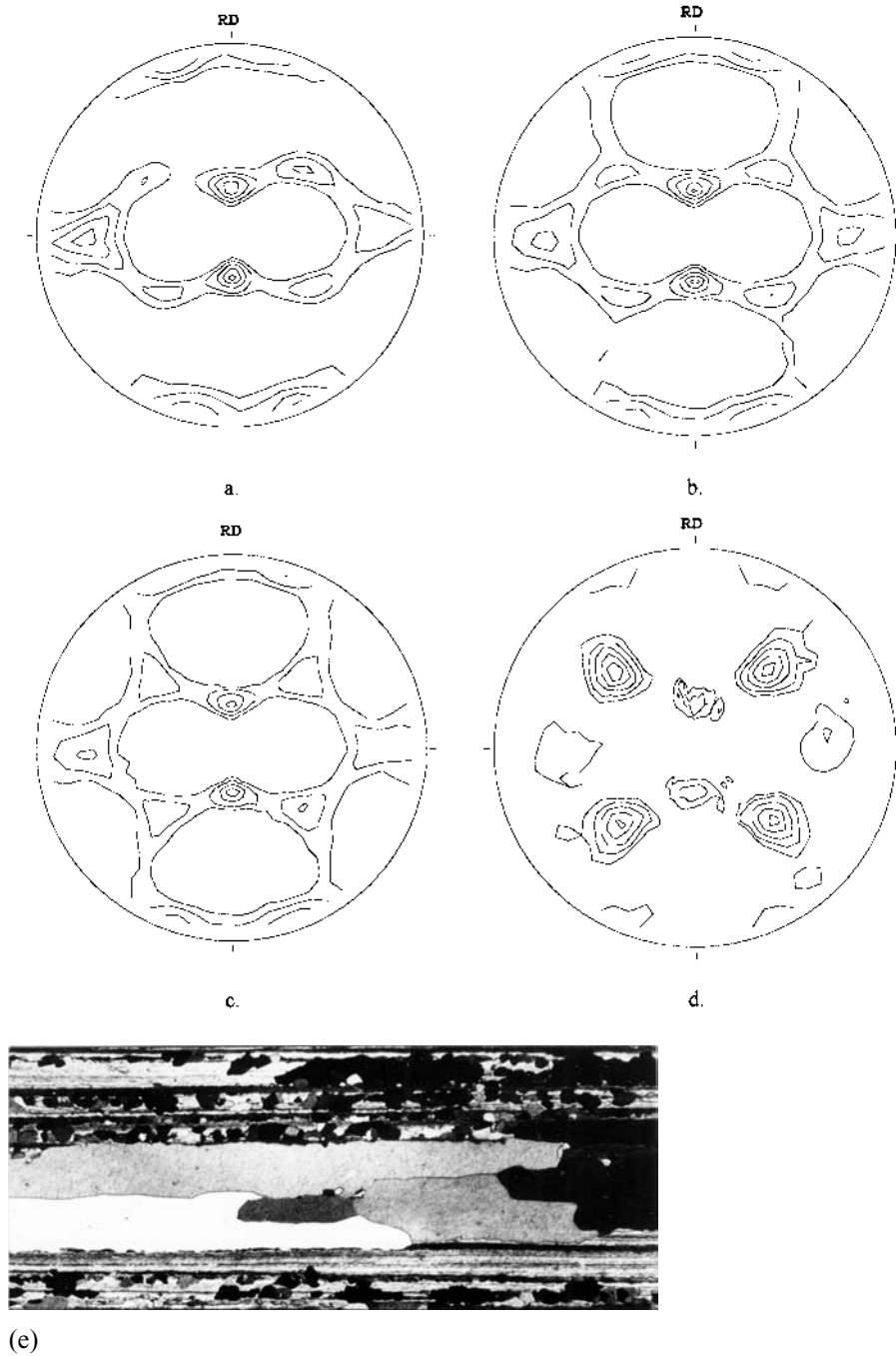
Figure 24 {111} pole figures and microstructure of 95% rolled and 300°C annealed pure aluminum sheet (99.998 wt% Al, density levels: 1, 2, 4, 7, 10), (a) 95% rolled (max = 11.0); (b) 100 sec annealed (max = 11.6); (c) 316 sec annealed (max = 9.4); (d) 31620 sec annealed (max = 12.8); (e) microstructure of *c* $\underset{\longrightarrow \text{RD}}{\overset{\uparrow \text{ND}}{\left|\right.}}$ $\underset{100\,\mu m}{\longmapsto\!\!\!\longmapsto}$. (From Ref. 10.)

6 DYNAMIC RECOVERY AND DYNAMIC RECRYSTALLIZATION

6.1 Dynamic Recovery

Because of the work hardening effect the flow stress for plastic deformation will be increased with increasing strain. It is known that the work hardening is associated with the dislocation density in deformed aluminum alloys. The rate of dislocation multiplication and therefore the work hardening rate at high strain are commonly reduced by certain softening mechanism, of which the softening effect is defined as dynamic recovery. Sometimes the work hardening effect in aluminum could be fully compensated by the softening effect of the dynamic recovery which can be strengthened at elevated deformation temperature, and the flow stress will reach its maximal value.

The mechanism of dynamic recovery is generally similar to that of the normal recovery, i.e. static recovery. The dislocation density will be reduced because of the cross-slip of screw dislocations as well as the climb of edge dislocations. For many fcc metals the perfect dislocations will dissociate on their {111} slip planes into two partial dislocations, between which a stacking fault is created [51]. The dissociation width depends on the stacking fault energy of the alloys, and for aluminum and its alloys the dissociation width is generally very small due to their very high stacking fault energy. For the cross-slip and the climb the dissociated two partial dislocations must first recombine into a perfect dislocation over a certain length by thermal activation, which depends strongly on the deformation temperature. The necessary activation energy of the dynamic recovery is inversely proportional to the stacking fault energy. The polygonization process of static recovery could also appear in the dynamic recovery.

6.2 Dynamic Recrystallization

With increasing deformation temperature the tendency for a recrystallization process arises continuously out of the increasing thermal activation. If the temperature and the strain are high enough the corresponding recrystallization could really appear during deformation, which is defined as dynamic recrystallization. The strong softening effect of the dynamic recrystallization induced by the elimination of large numbers of dislocations by the migration of high angle boundaries will lead to a drop in flow stress after it has reached a maximum. Comparing with the dynamic recrystallization the primary recrystallization is a static recrystallization. But the word "static" is commonly omitted.

The behavior of dynamic recrystallization is expressed very often in a flow stress curve against strain. Two typical flow stress curves in hot deformed metals could be observed. One shows a single peak in flow stress and the other shows multiple peaks frequently with decreasing amplitude against the strain. Figure 25 demonstrates schematically the two curves, between which a transition could appear, e.g. the cyclic peak curve could be transformed into single peak curve as the strain rate is increased or the deformation temperature is decreased [52].

The recrystallization during hot deformation is based on a similar way shown in Fig. 14. The first recrystallization period will start if the strain ε reaches a critical value ε_c [53], where the stored energy is high enough. The stored energy in the corresponding recrystallized grains will increase immediately because of the continuous
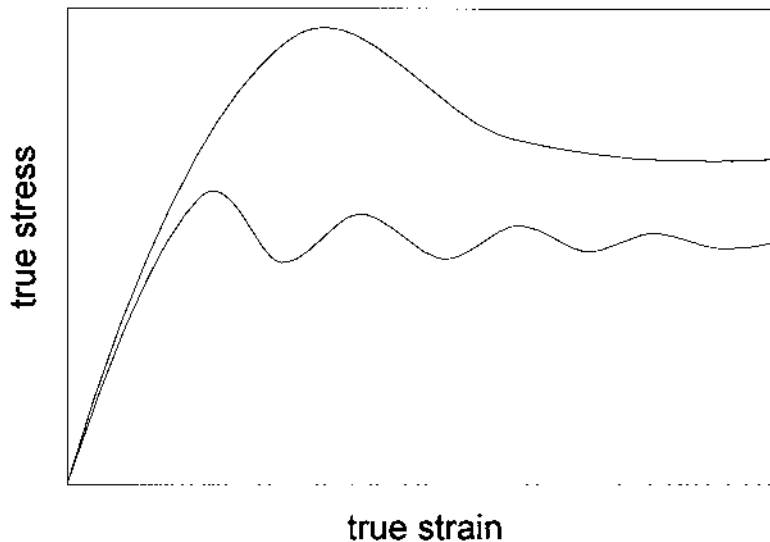
Figure 25 Typical flow stress curves of dynamic recrystallization.

deformation process, and the next recrystallization period will start if the ε_c in the recrystallized grains of last recrystallization period is reached again. Therefore the dynamic recrystallization is consisted of a series of recrystallization periods [53].

In the case of high deformation temperature or low strain rate, a great part of deformed matrix in the last recrystallization period has recrystallized before the next recrystallization period starts, therefore a multiple peak curve with relative low stress level would be obtained (Fig. 25).

In the case of low deformation temperature or high strain rate, the great part of deformed matrix in the last recrystallization period has not recrystallized before the next recrystallization period starts already. The hardening and softening effects in different recrystallization periods during hot deformation will overlap and be integrated, so that a single peak curve with relative high stress level would be obtained (Fig. 25). At very high strain a balance between hardening effect and softening effect could be reached and the stress would become rather constant. But the flow stress at high strain could also arise when the strain rate is increased continuously, e.g. in the case of hot compression with constant compression speed [54–57].

6.3 Hot Deformation Behavior in Pure Aluminum and Aluminum Alloys

Many commercial aluminum alloys will experience hot deformation at elevated temperature. Figure 26(a) gives the microstructure of a hot rolled (522–294°C) Al-0.0035 wt% Cu alloy, which shows a typical deformation structure. The recrystallization structure was obtained only after an additional annealing of the hot band (Fig. 26(b)).

For a long time many people believe that pure aluminum did not undergo dynamic recrystallization [58,59], since aluminum is noted for the very strong effect of simultaneous dynamic recovery during hot deformation. Due to the very high
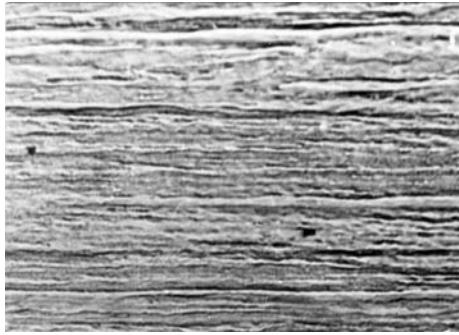
(a)
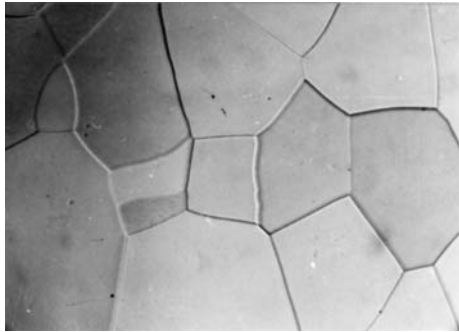
(b)

Figure 26 Microstructure of Al-0.0035 wt% Cu alloy $\underset{\longmapsto}{\overset{100\,\mu m}{\longmapsto}}$. (a) hot rolled; (b) hot rolled and annealed.

stacking fault energy the dislocation density in deformed aluminum would be reduced drastically by the dynamic recovery at elevated temperature. In this case the dynamic recrystallization could not start because of clearly decreased driving force, though recrystallized structure was observed after following cooling or annealing, which should be introduced by a static recrystallization process, i.e. a primary recrystallization process [59].

It is clear that the stored energy after a heavy recovery in hot deformation is still high enough for a recrystallization process, and the static recrystallization could always appear during cooling or annealing afterwards [58–60]. But under the condition of drastically reduced stored energy the extended incubation period becomes so long that the recrystallization can not really start during hot deformation. Yamagata found in his compression experiments that only under very low deformation speed (0.06 mm/min or 1 mm/min) the typical mechanical behavior of dynamic recrystallization could be observed in single crystal and polycrystal aluminum with high purity (≥99.999 wt% Al) [54–56], where the incubation period could be exceeded during hot deformation. However if the purity is reduced, e.g.
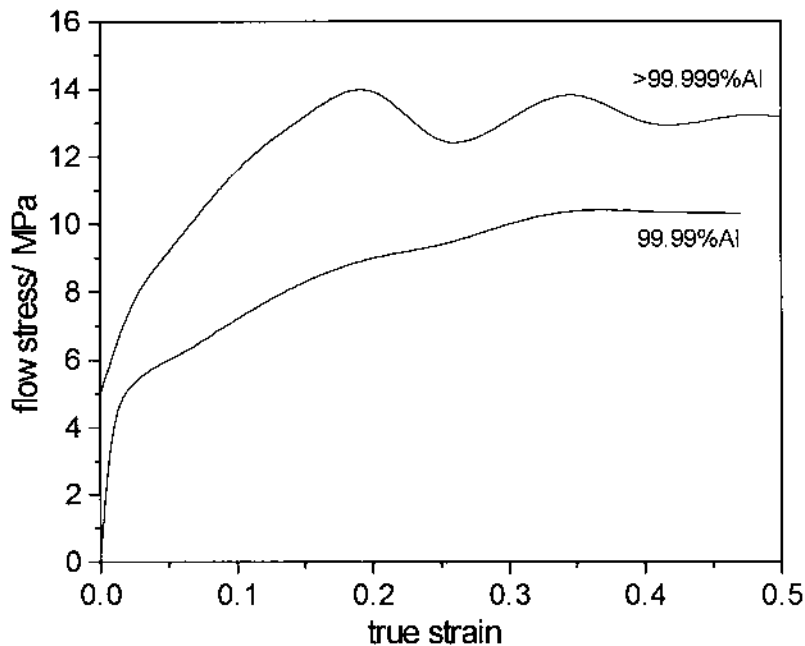
Figure 27 Mechanical behavior of hot compressed polycrystal pure aluminum (according to Yamagata [54,57]).

down to 99.99 wt% Al, the dynamic recrystallization could not observed any more [57]. It seems that the impurity atoms in pure aluminum would inhibit the migration of high angle boundaries of dynamic recrystallization and prolong the incubation period further.

Figure 27 gives schematically the mechanical behavior of hot compressed poly-crystalline aluminum with the purity of > 99.999 wt% Al and 99.99 wt% Al respectively, which was observed by Yamagata [54,57]. The aluminum with the purity of > 99.999 wt% Al (containing Cu: 0.5, Fe: < 1, Si: 1, Mg: 1 and Ag: < 2, all in ppm) was compressed at 341°C under a speed of 1 mm/min [54], and the aluminum with the purity of 99.99 wt% Al (containing Cu: 10, Fe: 36 and Si: 26, all in ppm) was compressed at 310°C under a speed of 0.06 mm/min [57]. A clear dynamic recrystallization behavior was observed in high purity aluminum, but was not when the purity is reduced down to 99.99 wt% Al [57]. The relatively high flow stress level of the high purity aluminum was induced by the higher com-pression speed.

Blade has ever investigated the effects of common impurity atoms on the recrystallization behavior after hot deformation [60]. Based on a super-purity alumi-num the addition of Fe, Si and Cu would influence the volume fraction of recrystallization after 50% hot rolling and 30 sec delay before quenching. It can be seen in Figure 28 [60] that Fe will inhibit clearly the static recrystallization pro-cess, which should also occur during dynamic recrystallization.

For the aluminum alloys the alloyed elements or increasing impurity atoms will preferentially accumulate around the dislocations induced by hot deformation, and reduced therefore the stacking fault energy. In this case the dynamic recovery could
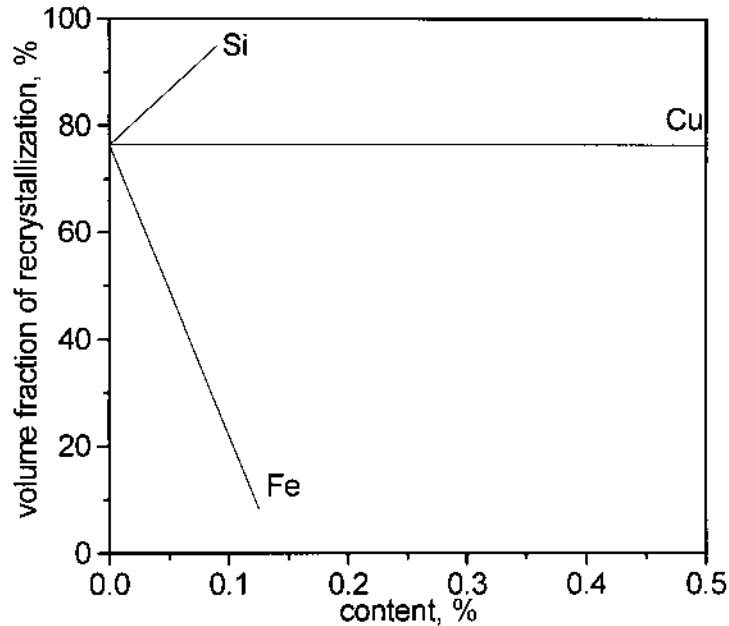
Figure 28 Effect of impurity atoms in super-purity aluminum on the static recrystallization after hot rolling (entry and exit temperature for the hot rolling was 500°C and 390°C respectively, according to Blade [60]).

not reduce so much stored energy like that appeared in high purity aluminum, and the dynamic recrystallization will start during hot deformation [61]. Figure 29 demonstrates schematically the mechanical behavior in Al-Mg alloy system during 50% hot compression [59], in which the tendency for dynamic recrystallization increases with increasing magnesium addition in solid solution. The similar behavior was also observed in Al-Mn and Al-Mg-Mn alloy systems as well as in commercial purity aluminum (99.5 wt% Al) [62].

7 NORMAL GRAIN GROWTH

7.1 Concept of Normal Grain Growth

Normal grain growth or continuous grain growth is defined as the homogeneous increase of average grain size in polycrystalline aluminum during annealing, of which the word "normal" or "continuous" is sometimes omitted. Figure 30 gives the observed evaluation of grain size during annealing of an Al-3 wt%Mg alloy [63]. The normal grain growth can be a process following primary recrystallization, or occur in an initially undeformed material. In fact, the grain growth will appear in almost all annealing processes.

The normal grain growth is carried out essentially by the migration of high angle boundaries, which differs from the subgrain coalescence process discussed in Section 3 of this chapter (Fig. 11). During the normal grain growth curved boundaries migrate frequently towards the centers of curvature, therefore the relative large
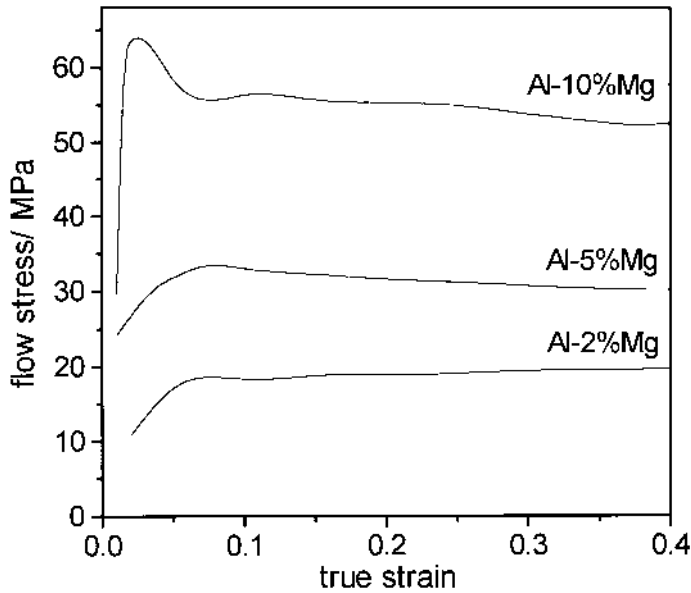
Figure 29 Flow stress curves of hot compressed Al-Mg alloys at 0.9 T_m (T_m: melting point, according to Gardner and Grimes [59]).

grains will grow up by means of consuming the small neighboring grains [64]. But the growing grains could be consumed either if they have touched a larger grain. The migration rate of high angle boundaries, i.e. the consumption rate of the small neighboring grains becomes more rapidly just as the small grains are about to disappear (see Eqs. (32) and (33)). In two-dimensional structure observed in single phase aluminum alloys the grain boundary angles tend frequently towards 120° when they meet each other (Fig. 30).

7.2 Driving Force for Normal Grain Growth

It can be seen in Fig. 30 that the total grain boundary area per unit volume decreases during the grain growth. Therefore the decrease of boundary energy is the driving force for the normal grain growth. The total grain boundary energy per unit volume F_b could be estimated as

$$F_b = \frac{\dfrac{4\pi R^2 \gamma}{2}}{\dfrac{4}{3}\pi R^3} = \frac{3\gamma}{2R} \tag{31}$$

which is shown in Fig. 31 where the average radius of spherical grains is R and the boundary energy γ of pure aluminum should be roughly 1.0 J/m^2 [23].

So according Eq. (31) the decrease of total grain boundary energy per unit volume will be, e.g. about 1.5×10^4 J/m^3 if the average radius of spherical grains increases from 50 μm to 100 μm.
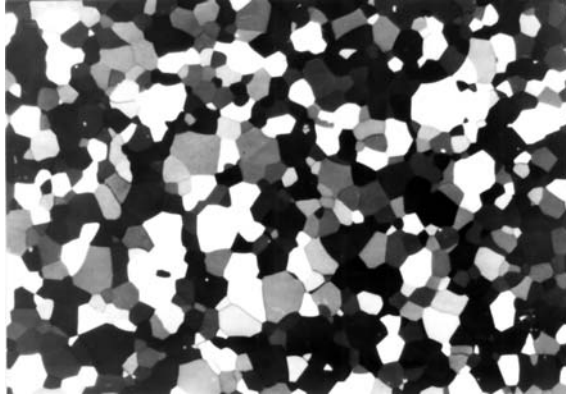
(a)
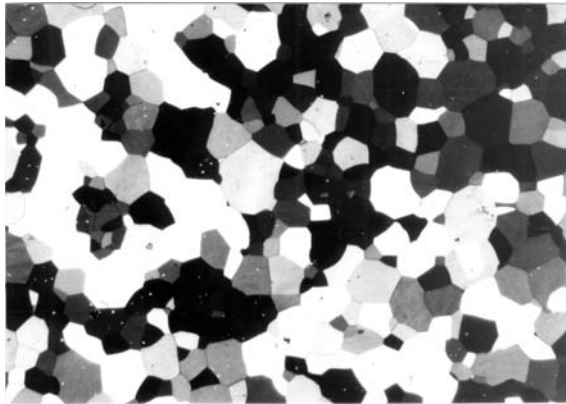
(b)
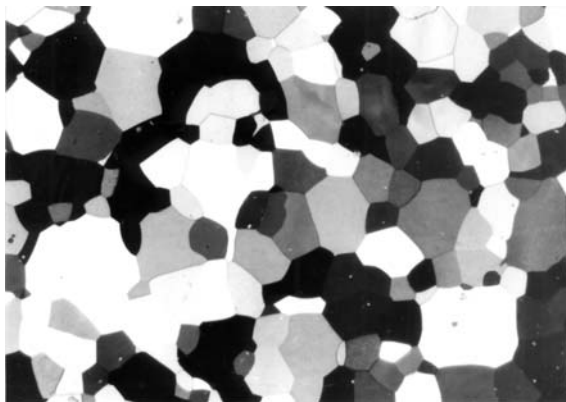
(c)

Figure 30 Microstructure of 95% rolled and 500°C annealed Al-3 wt% Mg alloy [63] $\underset{\longmapsto\!\!\!\longmapsto}{^{200\,\mu m}}$. (a) 40 sec; (b) 80 sec; (c) 160 sec. (Courtesy of Dr. X. Zhao.)
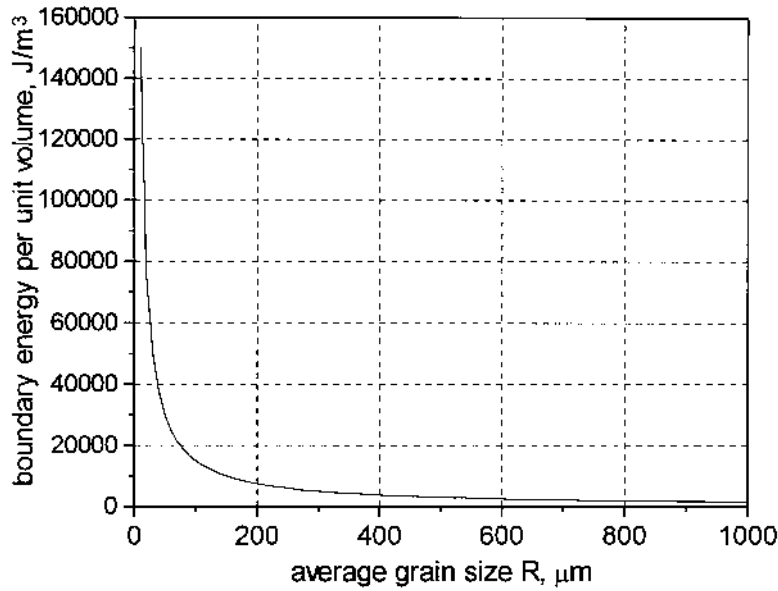
Figure 31 Calculated relationship between average grain size and boundary energy per unit volume.

7.3 Kinetics of Normal Grain Growth

The boundary tension ΔP which induces the migration of curved boundaries towards the curvature centers can be expressed as

$$\Delta P = \frac{2\gamma}{R} \tag{32}$$

where the R is the curvature radius representing the grain size. If the size of a shrinking grain is R_s while its neighboring grain with size R is growing (Fig. 32), the boundary migration velocity v can be written as

$$v = -\frac{dR_s}{dt} \tag{33}$$

which is proportional to the boundary tension ΔP. Comparing Eqs (32) and (33) the relation of grain size R_s and annealing time t can be statistically deduced as

$$R_s^2 = R_{s0}^2 - C\gamma t \tag{34}$$

where R_{s0} is the initial size of the shrinking grain at $t = 0$ and C is a constant concerning annealing temperature. Correspondingly the following equation

$$R^2 = R_0^2 + C\gamma t \tag{35}$$
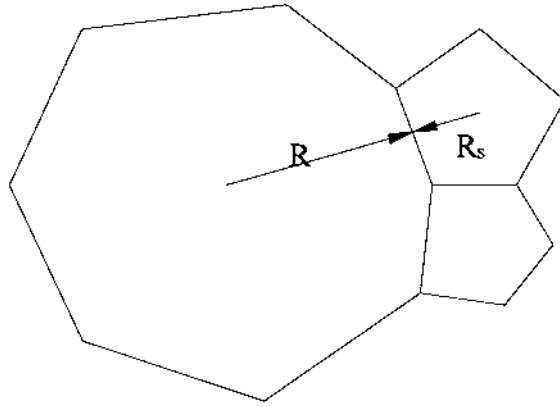
Figure 32 Grain growth driven by the boundary energy.

can be obtained for the growing grain on the assumption that the large grain grows homogeneously in all directions. Equation (35) could roughly express the increase of average grain size while the annealing proceeds, i.e. the average grain size R is proportional to $\sqrt{t}$.

Figure 33 demonstrates the evaluation of grain size distribution during annealing of a 95% rolled Al-3 wt% Mg alloy [63] (cf. Fig. 30), in which the increase of grain size during annealing is observed. In many cases the size of the largest grains is 3–4 times of the average size.

7.4 Obstructs of Normal Grain Growth

It has been mentioned in Sec. 3 of this chapter that impurity atoms will reduce the boundary migration velocity. It was observed that increasing the impurity content of copper in zone-refined aluminum from 4.3 to 258 (at.) ppm drops clearly the grain boundary velocity [29].

Lücke and Detert [65] have established an atomistic theory to explain the impurity effect. The impurity atoms in solid solution tend often to segregate to grain boundaries due to interaction between impurity atoms and grain boundaries that are the energy sinks for impurity atoms. Therefore the grain boundary impurity concentration c_B can be expressed as

$$c_B = c \exp(-\frac{Q_B}{kT}) \tag{36}$$

where c is bulk impurity concentration and Q_B is interaction energy between impurity atom and grain boundary. If impurity atoms are attracted to the boundaries the interaction energy Q_B will be negative.

Supposing that a grain boundary starts to pull away from the impurity atoms, there will be a drag force created by the impurity atoms which compel the boundary to carry them along and obstruct the normal grain growth.

Concerning Eq. (36) the segregation of impurity atoms in grain boundaries is reduced when the interaction energy Q_B is very low or annealing temperature T is very high. In this case the boundary migration is rather free like that in pure
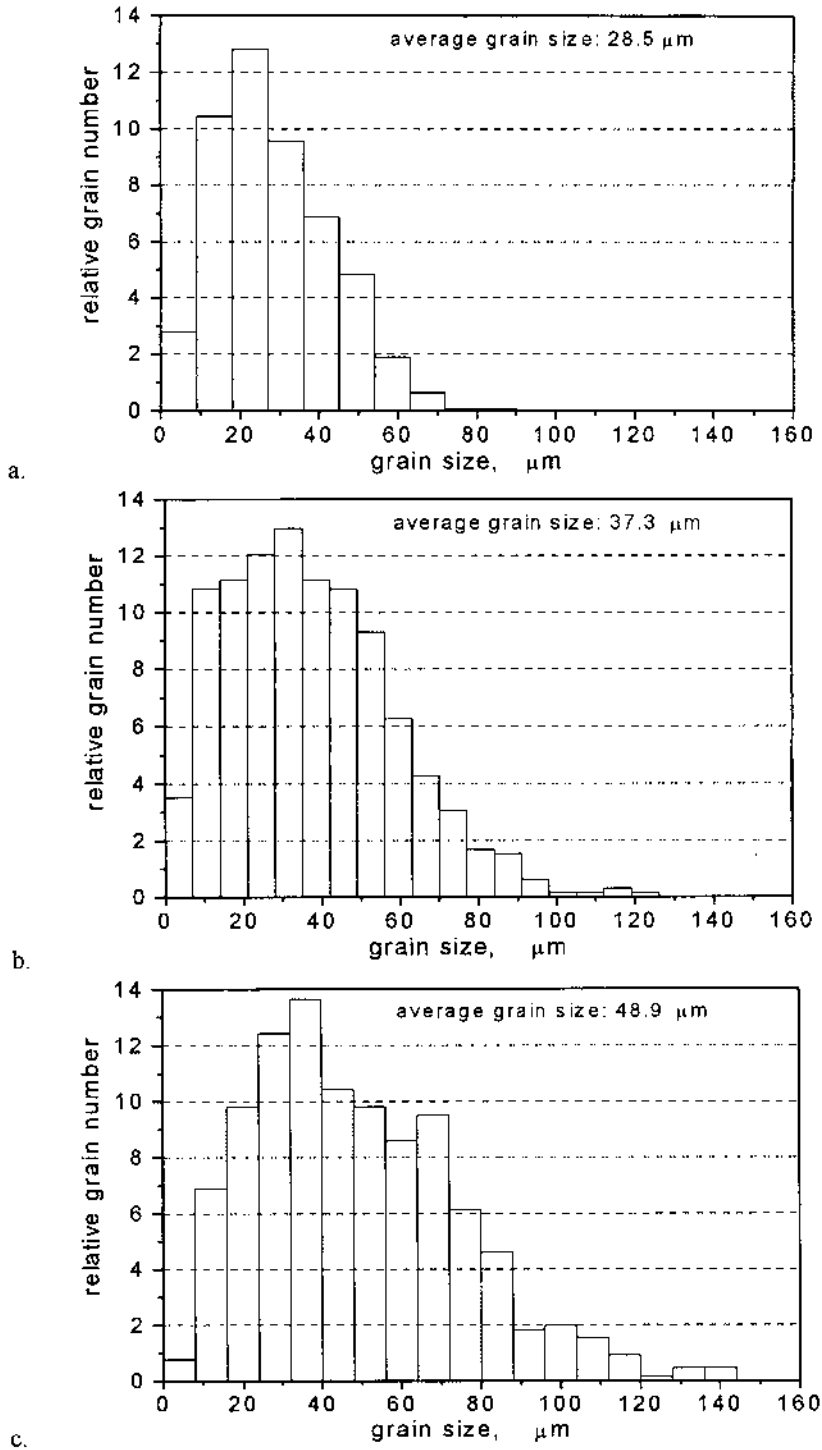
Figure 33 Grain size distribution of 95% rolled and 500°C annealed Al-3 wt% Mg alloy [63]. (a) 40 sec; (b) 80 sec; (c) 160 sec. (Courtesy of Dr. X. Zhao).

aluminum. On the other hand, the grain boundaries can also migrate freely if the driving force (Eq. (31)) is high enough to induce a very rapid boundary migration so that the impurity atoms can not be dragged along any more [65].

When a boundary is moving over second phase particles there will be a restraining force acting on the moving boundary, which is called Zener force [66] P_z and can be expressed as

$$P_z = \frac{3f\gamma}{2r} \tag{37}$$

where r is radius of second phase particles, f is the volume fraction of the second phase and γ is the grain boundary energy. According to Eq. (32) the boundary tension ΔP which drives grain growth is reduced with increasing average grain size R. If the ΔP in an aluminum alloy containing second phase particles is reduced down to a level of corresponding P_z, i.e. $\Delta P = P_z$, then the grains will stop growing. In this case a stable average grain size R_c can be estimated using Eqs (32) and (37), i.e.

$$R_c = \frac{2\gamma}{P_z} = \frac{4r}{3f} \tag{38}$$

Equation (38) indicates that the grain size in an aluminum alloy containing second phase particles could only be increased to a limited value R_c during annealing, which is influenced by particle radius and volume fraction of the second phase.

8   ANOMALOUS GRAIN GROWTH (SECONDARY RECRYSTALLIZATION)

8.1   Phenomenon of Anomalous Grain Growth

In some cases the normal growth of most grains are obstructed during annealing and only very few grains could grow anomalously. This process is the anomalous grain growth or discontinuous grain growth. The few growing grains are called here secondary grains, the most obstructed and then consumed grains are called matrix, and therefore the process is also called secondary recrystallization. Figure 34 gives an example of the anomalous grain growth in Al-3 wt% Mg alloy [63].

The phenomenon that the normal growth of most grains are obstructed could be induced by second phase particles, textures or sample surfaces.

8.2   Anomalous Grain Growth Induced by Second Phase Particles

To insure the fine grain structure and the corresponding mechanical properties the second phase particles are often designed and treated to precipitate in many aluminum alloys, and concerning Eq. (37) and (38) the particles can obstruct the grain growth. During the normal grain growth the large size grains have high potential to grow and the small size grains have high potential to shrink. During high temperature annealing the second phase particles could grow, coalesce themselves or be resolved in the matrix, i.e. the r value in Eq. (37) is increased, which will reduce the restraining force. In this case the boundaries of very large and very small grains could overcome the obstruction and migrate. In other words the large grains would overcome the obstruction and grow up when their sizes are large than certain upper limit, and the small grains would also overcome the obstruction and shrink when
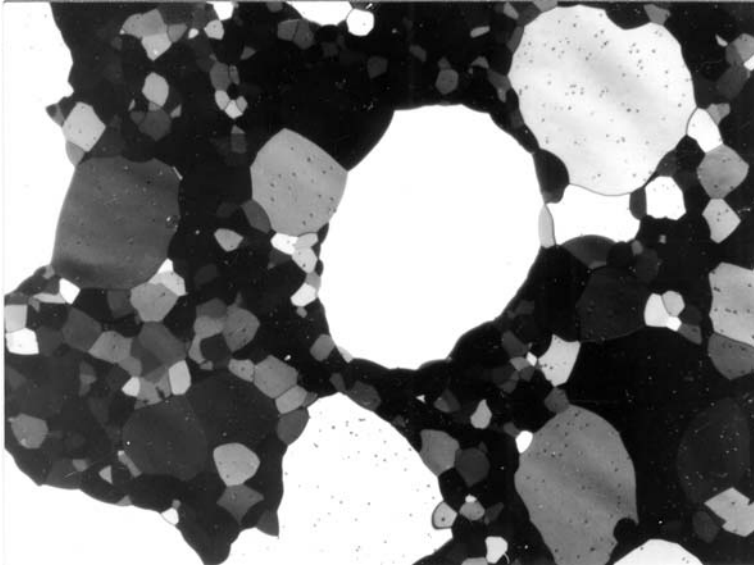
Figure 34 Microstructure of 95% rolled 300°C 10 min and 500°C 160 sec annealed Al-3 wt% Mg alloy [63] $\underset{\text{200 }\mu\text{m}}{\longmapsto}$, (Courtesy of Dr. X. Zhao.)

their sizes are smaller than certain low limit. Because of the obstruction of second phase particles the increase of average grain size, i.e. the grain size of the matrix becomes very slow or even come to a stop during annealing while few large grains over the upper limit could continuously grow, which will result in an anomalous grain growth.

8.3 Anomalous Grain Growth Induced by Texture

In many annealed aluminum alloys there is often a very strong single texture component in company with same other weak texture components. In this case a grain oriented in the strong texture component neighbors frequently with the grains oriented in the same texture component, and therefore the boundaries between them are low angle boundaries that are not very mobile. So the grains of the strong texture component could hardly grow. At same time grains oriented in the weak texture component neighbor also frequently with the grains oriented in the strong texture component, and reversely the boundaries between them are generally very mobile high angle boundaries. These grains oriented in weak texture components will disappear very fast if their sizes are very small, but they can grow rapidly as secondary grains and result in an anomalous grain growth when their sizes are larger than the grains oriented in the strong texture component.

Eichelkraut has observed the anomalous grain growth induced by texture in a 95% rolled Al-1 wt% Mn alloy [67–69]. The primary recrystallization of 95% cold rolled alloy sheet was completed after annealing at 620°C for 1 sec and a very strong cube {001}⟨100⟩ texture component is formed, of which the volume fraction is about 87%. During the following annealing two periods of anomalous grain growth or secondary recrystallization have appeared (Fig. 35) [67–69]. In the first period
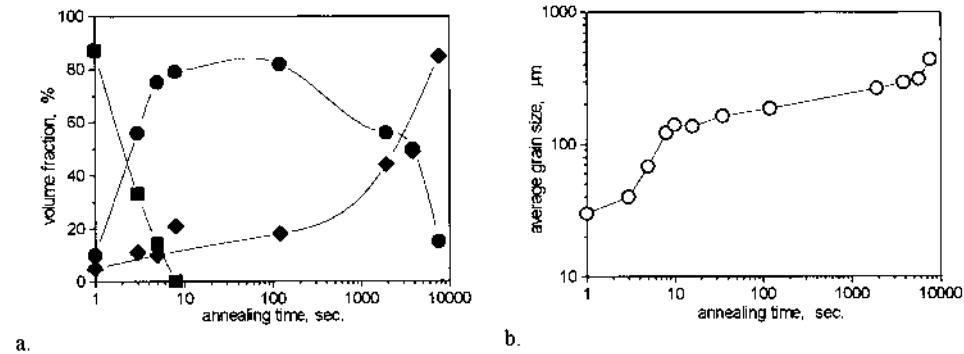
Figure 35   Texture and grain size evaluation of 95% rolled Al-1 wt% Mn alloy during annealing at 620°C [67] (■ $\{001\}\langle100\rangle$, ● $\{011\}\langle133\rangle$, ◆ $\{001\}\langle320\rangle$), (a) texture components; (b) average grain size. (Courtesy of Dr. H. Eichelkraut.)

the texture component $\{011\}\langle133\rangle$ has replaced the cube texture, and in the second period the texture component $\{001\}\langle320\rangle$ has replaced the $\{011\}\langle133\rangle$ (Fig. 35(a)). Simultaneously the growing rate of average grain size shows two corresponding steps of rapid increase (Fig. 35(b)).

Zhao et al. have investigated the anomalous grain growth induced by texture in a 95% rolled Al-3 wt% Mg alloy in more detail [63, 70–72]. The primary recrystallization is completed during annealing at 300°C for 200 sec, after which the rolling texture component $\{011\}\langle211\rangle$, $\{112\}\langle111\rangle$ (Fig. 36(b)) as well as $\{123\}\langle634\rangle$ have disappeared and a strong cube texture $\{001\}\langle100\rangle$ and a very weak R texture $\{124\}\langle211\rangle$ near $\{112\}\langle312\rangle$ are formed (Fig. 36(c)). When the alloy sheet is heated at 400°C for 20 sec after annealing at 300°C for 600 sec, the cube texture is strengthened further and the orientation density reaches 119.9 (Fig. 36(d)). With increasing annealing time the cube texture is consumed and disappears, and the texture component $\{112\}\langle312\rangle$ and $\{001\}\langle490\rangle$ appear and are strengthened (Fig. 36(e) and (f)) after the secondary recrystallization is completed.

Figure 37 demonstrates the corresponding evaluation of texture components and average grain size [63]. It is clear that the anomalous grain growth is a process in which the texture components $\{112\}\langle312\rangle$ and $\{001\}\langle490\rangle$ replace the strong cube texture in the way discussed above. After 1000 sec at 400°C the survived grains oriented around $\{112\}\langle312\rangle$ and $\{001\}\langle490\rangle$, of which the number has been consumed by cube texture (Fig. 37(a)), should have relative large size and then grow in the cube grains while the cube grains can not grow quickly because of the frequent low angle boundaries.

Observing the evaluation of average grain size in Fig. 37(b) it can be seen that in primary stage of annealing at 400°C before 3000 sec the average size of all grains is roughly identical to the average size of cube grains. The few large grains oriented around $\{112\}\langle312\rangle$ and $\{001\}\langle490\rangle$ do not distinctly influence the average size of all grains. In the following annealing stage large number of cube grains are consumed drastically by the very large grains oriented around $\{112\}\langle312\rangle$ and $\{001\}\langle490\rangle$, so that their average size is reached rapidly by the average size of all grains, after which the cube grains have disappeared and the anomalous grain growth is completed.
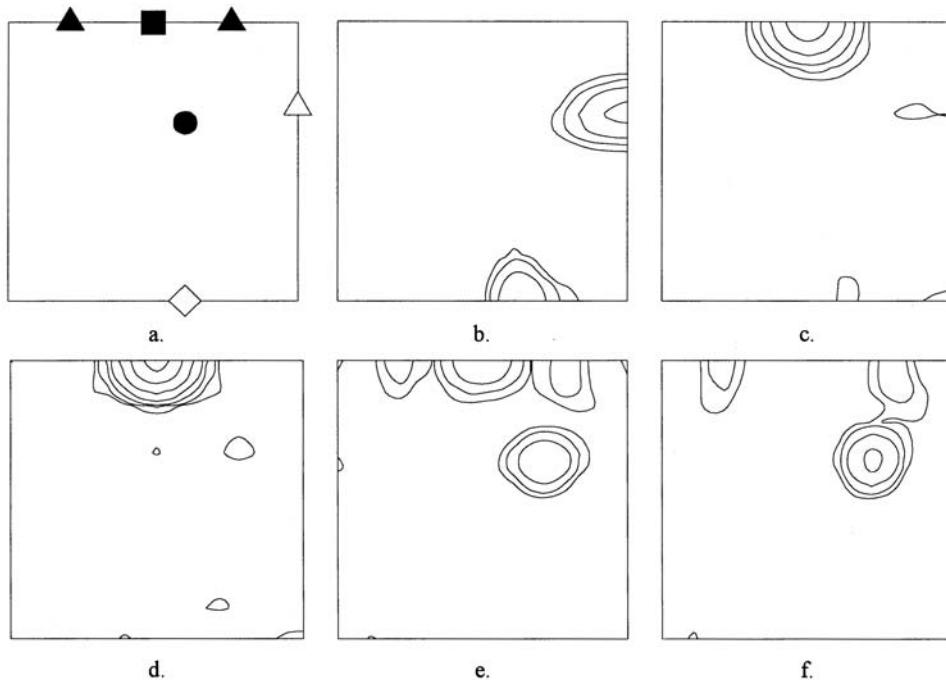
Figure 36 Evaluation of orientation distribution in $\varphi_2 = 45°$ section for the 95% rolled Al-3 wt% Mg alloy during annealing [63] (density levels: 2, 4, 8, 16, 32, 64, 99), (■ {001}⟨100⟩; ▲ {001}⟨490⟩; ● {112}⟨312⟩; ◇ {011}⟨211⟩; △ {112}⟨111⟩), (a) orientation positions in $\varphi_2 = 45°$ section; (b) 300°C, 0 sec (95% rolled) max = 19.6; (c) 300°C, 200 sec max = 46.1; (d) 300°C, 600 sec 400°C, 20 sec max = 119.9; (e) 300°C, 600, sec 400°C, 3500 sec max = 16.0; (f) 300°C, 600 sec 400°C, 4800 sec max = 18.5. (Courtesy of Dr. X. Zhao.)
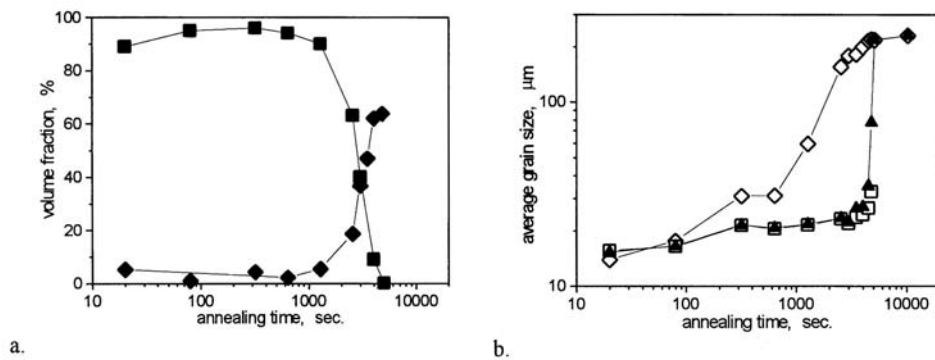
Figure 37 Texture and grain size evaluation of 95% rolled Al-3 wt% Mg alloy during annealing at 400°C after annealing at 300°C for 600 sec [63]. (a) texture components, ■ {001}⟨100⟩; ◆ {112}⟨132⟩ and {001}⟨490⟩; (b) average grain size, □ for grains oriented around {001}⟨100⟩, ◇ for grains oriented around {112}⟨132⟩ and {001}⟨490⟩, ▲ for all grains. (Courtesy of Dr. X. Zhao.)
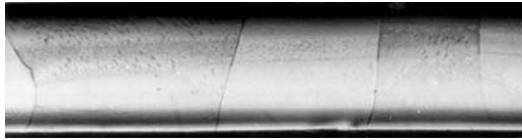
(a)
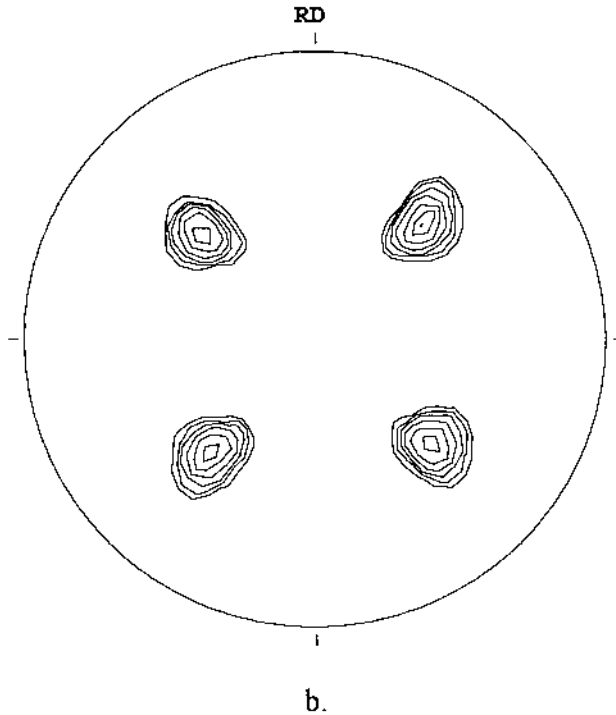
b.

Figure 38 Result of surface induced anomalous grain growth in high purity aluminum, (a) microstructure ⊢——40 μm——⊣; (b) {111} pole figure (max = 30.8, levels: 1, 2, 4, 8, 14, 22, 30).

8.4 Anomalous Grain Growth Induced by Surface

When aluminum alloys are very thin and the ratio between surface area and grain boundary area is relatively high the decrease of surface energy could control the process of grain growth and induce an anomalous grain growth. In this case only the grains could grow up, of which their surface' energy is very low, and other grains with rather high surface energy will be consumed. It could be imaged that this anomalous grain growth will lead to a strong texture. Figure 38 gives an example of thin (less than 0.1 mm) high purity aluminum foil (> 99.99%Al), in which the grain thickness is identical to the foil thickness after final annealing (Fig. 38(a)) and the a very strong cube texture is formed (Fig. 38(b)) which indicates that the surface energy of {001} planes in the annealing atmosphere is the lowest.

9   SUMMARY

Aluminum is a fcc metal with high stacking fault energy, of which the dislocation density multiplied by cold deformation will be clearly reduced in the recovery process during annealing or heating. The recrystallization in aluminum and its alloys is commonly a process including nucleation and growth of new grains, of which the driving force in deformed matrix is the energy stored in the lattice defects consisting mainly of dislocations. Both of the homogeneous nucleation as well as the heterogeneous nucleation on grain boundaries and around second phase particles are possible. The grain growth rate are influence by the purity, impurity atoms, temperature, precipitates, boundary misorientations etc. Textures will be formed after the primary recrystallization. The dynamic recrystallization during hot deformation could only appear in the aluminum alloys easily, in which the stacking fault energy and therefore the recovery effect are drastically reduced by the alloyed elements or impurity atoms. The grains in annealed aluminum and its alloys will grow normally or anomalously during heating process, of which the basic driving force is the grain boundary energy. The anomalous grain growth induced by texture or surface will produce very sharp textures. The corresponding mechanisms of the processes mentioned in this chapter including recovery, primary recrystallization, dynamic recrystallization, normal grain growth as well as anomalous grain growth have been discussed.

REFERENCES

1. P. Knauth, *The Metalsmiths*, Time-Life Books, Niederland, 1974, pp. 30–54.
2. B. Gille, *The History of Techniques*, Gordon and Breach Science Publishers, 1986, 1, pp. 1246–1307.
3. E. Marcorini, *The History of Science and Technology*, Facts On File, New York, 1988, 1, pp. 1–15.
4. J. Czochralski, "Geschichtlicher Beitrag zur Frage der Rekristallisation," Z. Metallkde, 1927, 10; pp. 316–320.
5. E. Hornbogen and H. Warlimont, *Metallkunde*. Springer-Verlag, Berlin, 1991, pp. 60–62.
6. J. D. Verhoeven, *Fundamentals of Physical Metallurgy*, John Wiley & Sons Inc., New York, 1975, pp. 60–74, and 325–329.
7. P. R. Swann, "Dislocation Arrangements in Face-Centered Cubic Metals and Alloys," in: *Electron Microscopy and Strength of Crystals*, (G. Thomas, and J. Washburn, ed.), Interscience Publishers, New York, 1963, pp. 131–181.
8. P. Yang, "Nucleation Mechanism and Recrystallization Textures in a Pure Al-1.3%Mn alloy." PhD dissertation, RWTH Aachen, FRG, 1996.
9. J. D. Eshelby, "Point Defects," in: *The Physics of Metals*. (2. Defects), (P. B. Hirsch, ed.), Cambridge University Press, London, 1975, pp. 1–7.
10. G. Gottstein, "Metalkundliche Grundlagen, Ursachen und Erscheinungsformen der Rekristallisation," in: *Rekristallisation metallischer Werkstoffe*, (G. Gottstein, ed.), DGM-Informationsgesellshaft, Oberursel, 1984, pp. 13–37.
11. G. Wassermann and J. Grewen, *Texturen metallischer Werkstoffe*. Springer-Verlage, Berlin, 1962, pp. 148–161 and 19–22.
12. W. Mao, "Rolling Texture Development in Aluminum" Chin. J. Met. Sci. Technol. 1991, 7; pp. 101–112.
13. W. Truszkowski, J. Krol, and B. Major, "Inhomogeneity of Rolling Texture in fcc Metals," Metall. Trans. 1980, 11A, pp. 749–758.

14. W. Mao. "Texture in Inhomogeneously Rolled Aluminum Sheet," Transactions NFsoc, 1992, 2, pp. 98–103.

15. R. W. Cahn, "Recovery and Recrystallization," in: *Physical Metallurgy*. 3rd Edn, (R. W. Cahn, and P. Haasen, eds.), North-Holland Physics. Publishing, Amsterdam, 1983, pp. 1593–1611.

16. K. Holm and E. Hornbogen, "Annealing of Supersaturated and Deformed A1-0.042 wt% Fe solid solution," J. Mater. Sci. 1970, 5, pp. 655–662.

17. K. Lücke and R. Rixen, "Rekristallisation und Korngröße," Z. Metallkde. 1968, 59, pp. 321–333.

18. D. Hull, *Introduction to Dislocation*, 2nd Edn., Pergamon Press, Oxford, 1975, pp. 87–90.

19. H. Hu. "Recovery, Recrystallization and Grain Growth," in: *Metallurgical Treatises*, (J. K. Tien, and J. F. Elliott, eds.), Metallurgical Society of AIME, New York, 1981, pp. 385–407.

20. R. A. Vandermeer and P. Gordon. "The Influence of Recovery on Recrystallization of Aluminum," in: *Recovery and Recrystallization of Metals*, (L Himmel, ed.), Interscience Publishers, New York, 1963, pp. 211–238.

21. C. Därmann, "Rekristallisation Homogener Legierungen," in: *Rekristallisation metallischer Werkstoffe*, (G. Gottstein, ed.), DGM-Informationsgesellshaft, Oberursel, 1984, pp. 99–124.

22. C. N. R. Rao and K. J. Rao. *Phase Transformation in Solids*. McGraw-Hill Inc., London, 1978, pp. 83–85.

23. L. F. Mondolfo, *Aluminum Alloys: Structure and Properties*, Butterworths, London, 1976, pp. 68–95 and 11–55.

24. S. P. Bellier and R. D. Doherty, "The Structure of Deformed Aluminum and its Recrystallization-Investigations with Transmission Kossel Diffraction," Acta Metall. 1977, 25, pp. 521–538.

25. R. A. Vandermeer, and P. Gordon. "Edge-Nucleated, Growth Controlled Recrystallization in Aluminum," Trans. Met. Soc. AIME, 1959, 215, pp. 577–588.

26. O. Engler, P. Yang, and X. Kong. "On the Formation of Recrystallization Textures in Binary A1-1.3% Mn Investigated by Means of Local Texture Analysis," Acta Metall. 1996, 44, pp. 3349–3369.

27. A. Seeger and H. Mehrer, "Analysis of Self-Diffusion and Equilibrium Measurements," in: *Vacancies and Interstitials in Metals*, (A. Seeger, D. Schumacher, W. Schilling, and J. Diehl, eds.), American Elservier Publishing Co., New York, 1970, pp. 1–54.

28. J. S. Kirkaldy, *Diffusion in the Condensed State*. The Institute of Metals, London, 1987, pp. 81–83.

29. P. Gorden and R. A. Vandermeer, "Grain-Boundary Migration," *Recrystallization, Grain Growth and Texture*, ASM Metals Park, Ohio, 1966, pp. 205–266.

30. K. Lücke, R. Rixen, and F. W. Rosenbaum, "On the Theory of Grain Boundary Motion," in: *The Nature and Behavior of Grain Boundaries*, (H. Hu, ed.), Plenum Press, New York, 1972, pp. 245–283.

31. W. Mao, "Model for Rapidly Moving Boundaries." Science in China 1992, 35, pp. 336–343.

32. G. Ibe, W. Dietz, A. C. Fraker, and K. Lücke, "Vorzugsorientierungen bei der Rekristallisation gedehnter Einkristalle aus Reinst-Aluminium," Z. Metallkde 1970, 61, pp. 498–507.

33. E. M. Fridman, C. V. Kopezky, and L. S. Shvindlerman, "Effects of Orientation and Concentration Factors on Migration of Individual Grain Boundaries in Aluminum," Z. Metallkde 1975, 66, pp. 533–539.

34. E. Hornbogen and U. Köster, ''Recrystallization of Two Phase Alloys,'' in: *Recrystallization of Metalic Materials*, (F. Hassber, ed.), Dr. Riederer Verlag, Stuttgart, 1978, pp. 215–255.
35. W. A. Johnson, and R. F. Mehl, ''Reaction Kinetics in Processes of Nucleation and Growth,'' Trans. AIME 1939, 135, pp. 416–458.
36. W. Mao, ''Texturentwicklungen in Reinem Aluminium,'' PhD dissertation, RWTH Aachen, FRG, 1988.
37. W. A. Anderson and R. F. Mehl. ''Recrystallization of Aluminum in Terms of the Rate of Nucleation and the Rate of Growth,'' Trans. AIME 1945, 161, pp. 140–172.
38. W. Mao. ''Influence of Rolling Reductions on Recrystallization Texture in Commercially Pure AI,'' Chin. J. Met. Sci. Technol. 1990, 6, pp. 257–262.
39. K. Ito, R. Musick, and K. Lücke, ''The Influence of Iron Content and Annealing Temperature on the Recrystallization Textures of High-Purity Aluminum-Iron Alloys,'' Acta. Metall. 1983, 31, pp. 2137–2147.
40. J. Hirsch, E. Nes, and K. Lücke, ''Rolling and Recrystallization Textures in Directionally Solidified Aluminum,'' Acta Metall. 1987, 35, pp. 427–438.
41. M. Humbert, ''Intensity Corrections, Resolving Power and Statistical Relevance in Pole Figure Measurements,'' in: *Experimental Techniques of Texture Analysis*, (H. J. Bunge, ed.), DGM-Informationsgesellschaft, Oberursel, 1986, pp. 29–50.
42. P. I. Welch, ''Neutron Diffraction Texture Analysis,'' in: *Experimental Techniques of Texture Analysis*, (H. J. Bunge, ed.), DGM-Informationsgesellschaft, Oberursel, 1986, pp. 183–207.
43. A. H. Windle, *A First Course in Crystallography*, G. Bell and Sons Ltd., London, 1977, pp. 88–97.
44. H. J. Bunge, ''General Outline and Series Expansion Method,'' in: *Quantitative Texture Analysis*, (H. J. Bunge, and C. Esling, ed.), DGM-Informationsgesellshaft, Oberursel, 1986, pp. 1–72.
45. K. Lücke, J. Pospiech, K. H. Virnich, and J. Jura, ''On the Problem of the Reproduction of the True Orientation Distribution from Pole Figures,'' Acta Metall. 1981, 29, pp. 167–185.
46. I. L. Dillamore and H. Katoh, ''The Mechanisms of Recrystallization in Cubic Metals with Particular Reference to their Orientation Dependence,'' Metal Science, 1974, 8, pp. 73–83.
47. K. Lücke, ''The Formation of Recrystallization Textures in Metals and Alloys,'' Proceedings of 7th International Conference on Textures of Materials, Noordwijkerhoud, 1984, pp. 195–210.
48. W. Mao, ''Recrystallization Mechanism of Cold Rolled A1 Sheet Containing Ti,'' Chinese Science Bulletin, 1992, 37, pp. 1479–1482.
49. A. A. Ridha and W. B. Hutchinson, ''Recrystallization Mechanisms and the Origin of Cube Texture in Copper,'' Acta Metall. 1982, 30, pp. 1929–1939.
50. W. Mao, J. Hirsch, and K. Lücke, ''Influence of the Cube Starting Texture on Rolling and Recrystallization Texture Development,'' Proceedings of 8th International Conference on Textures of Materials, Pennsyvania, 1988, pp. 613–618.
51. P. Haasen, *Physical Metallurgy*, Cambridge University Press, London, 1978, pp. 265–302.
52. T. Sakai and J. J. Jonas, ''Dynamic Recrystallization: Mechanical and Microstructural Considerations,'' Acta Metall. 1984, 32, pp. 189–209.
53. M. J. Luton and C. M. Sellars, ''Dynamic Recrystallization in Nickel and Nickel-Iron Alloys During High Temperature Deformation,'' Acta Metall. 1969, 17, pp. 1033–1043.
54. H. Yamagata ''Multipeak Stress Oscillations of Five-Nine-Purity Aluminum During a Hot Compression Test,'' Scr. Met. Mat. 1992, 27, pp. 201–203.

55. H. Yamagata, "Dynamic Recrystallization of Single-Crystalline Aluminium During Compression Tests," Scr. Met. Mat. 1992, 27, pp. 727–732.
56. H. Yamagata, "In situ Observation of Dynamic Recrystallization in Five-Nine Aluminum by a Transmission Laue Method," Scr. Met. Mat. 1994, 30, pp. 411–416.
57. H. Yamagata, "Dynamic Recrystallization and Dynamic Recovery in Pure Aluminum at 583 K," Acta Metall. Mater. 1995, 43, pp. 723–729.
58. H. J. McQueen, W. Blum, S. Straub, and M. E. Kassner, "Dynamic Grain Growth, a Restoration Mechanism in 99.999 Al," Scr. Met. Mat. 1993, 28, pp. 1299–1304.
59. K. J. Gardner and R. Grimes, "Recrystallization During Hot Deformation of Aluminum Alloys," Metal Science 1979, 13, pp. 216–222.
60. J. C. Blade, "Recrystallization in Hot Rolling of Dilute Aluminum Alloys," Metal Science 1979, 13, pp. 206–210.
61. S. P. Belyayev, V. A. Likhachev, M. M. Myshlyayev, and O. N. Seb'kov, "Dynamic Recrystallization of Aluminum," The Physics of Metals and Metallography 1981, 52, pp. 143–152.
62. W. Lehnert, G. Drossel, O. Liesenberg, W. Huppatz, M. Paul, S. Friedrich, and C. Kammer, *Aluminium-Taschenbuch*. 15. Auflage. Band 2. Aluminum-Verlag GmbH, Düsseldorf, 1996, pp. 38–42.
63. X. Zhao, "A Study on the Grain Size Distribution and Texture Controlled Grain Growth in Cold Rolled Sheet Metals," PhD dissertation, Zhejiang University, China, 1990.
64. P. Cotterill and F. R. Mould. *Recrystallization and Grain Growth in Metals*. Surrey University Press, London, 1976, pp. 271–274.
65. K. Lücke, and K. Detert, "A Quantitative Theory of Grain-Boundary Motion and Recrystallization in Metals in the Presence of Impurities," Acta Metall. 1957, 5, pp. 628–637.
66. F. J. Humphreys, "Recrystallization Mechanisms in Two-Phase Alloys," Metal Science 1979, 13, pp. 136–145.
67. H. Eichelkraut, "Theoritische und experimentelle Untersuchungen zum Kornwachstum in Metallen in Gegenwart von Texturen und Partikeln," PhD dissertation, RWTH Aachen, FRG, 1988.
68. G. Abbruzzese, K. Lücke, and E. Eichelkraut. "Grain Growth in the Presence of Textures, Theoretical Approach Comparison to Experiments," Proceedings of 8th International Conference on Textures of Materials, Pennsyvania, 1988, pp. 693–704.
69. H. Eichelkraut, G. Abbruzzese, and K. Lücke, "A Theory of Texture Controlled Grain Growth-II, Numerical and Analytical Treatment of Grain Growth in the Presence of Two Texture Components," Acta Metall. 1988, 36, pp. 55–68.
70. X. Zhao, "The Effect of Texture on Grain Growth," Textures and Microstructures 1993, 21, pp. 147–159.
71. I. Heckelmann, X. Zhao, K. Lücke, and G. Abbruzee, "Texture Development During Grain Growth," Textures and Microstructures 1991, 14–18, pp. 769–774.
72. X. Zhao, "Grain Growth and Texture Development of Al-3%Mg Alloy During Annealing," J. Zhejiang University (Natural Science) 1994, 28, pp. 268–272.

5

Hardening, Annealing, and Aging

LAURENS KATGERMAN and D. ESKIN

Netherlands Institute for Metals Research, Delft, The Netherlands

Aluminum alloys are largely divided into two groups: casting alloys and wrought alloys. For casting alloys, the final product is formed directly without any plastic deformation. By application of special foundry techniques, complex geometries can be formed in near-net shape. Aluminum casting alloys are not considered in this chapter although some general principles of aging and precipitation hardening are also applicable.

For aluminum wrought alloys the products are formed by hot and cold deformation of (semi) continuously cast half-products. Typical deformation processes involved are hot and cold rolling, drawing, forging and extrusion.

The strength of aluminum wrought products can be improved in two different ways:

- cold deformation
- alloying

During cold deformation, crystal defects are generated leading to improved strength properties.

Alloying elements are usually added to aluminum to increase strength. By alloying the strength of aluminum alloys increases by three separate mechanisms:

- Solid-solution hardening. Alloying elements dissolve completely in the aluminum matrix to form a solid solution. The local distortion of the aluminum lattice obstructs dislocation motion leading to increased strength.
- Dispersion hardening. The alloying elements form very fine insoluble dispersion of intermetallic phases. Transition elements typically are added to achieve this effect.
- Precipitation hardening (age-hardening). Alloying elements are brought in solid solution at high temperatures and quenched to room temperature. At intermediate temperatures below 200°C very fine particles are pre-

Table 1   Temper Designations for Aluminum Alloys

Temper	Description
F	As-fabricated
O	Annealed or recrystallized
H	Work hardened; The H is followed by 2 digits
W	Solution heat treated
T	Thermally treated; The T is always followed by 1 or more digits

cipitated from the supersaturated solid solution (SSSS) resulting in substantial increases in strength. The applied thermal treatment is also called aging. Aluminium-Copper is the classic example for precipitation hardening.

Wrought aluminum alloys that obtain their strength through a combination of precipitation and deformation are called heat-treatable. The other alloys obtain their strength through cold deformation and are classified as nonheat-treatable or also as work hardening alloys. The different tempers for these alloys are indicated with a specific code following the AA alloy designation (Table 1). In general heat-treatable alloys receive a T-temper while work hardening alloys are given H-tempers. The general effect of these tempers on alloys strength is given in Fig. 1.

1   HARDENING MECHANISMS

In general, the strength of aluminum alloys can be increased by several methods:

- Solid-solution hardening
- Grain-size strengthening
- Work or strain hardening
- Precipitation hardening (aging)
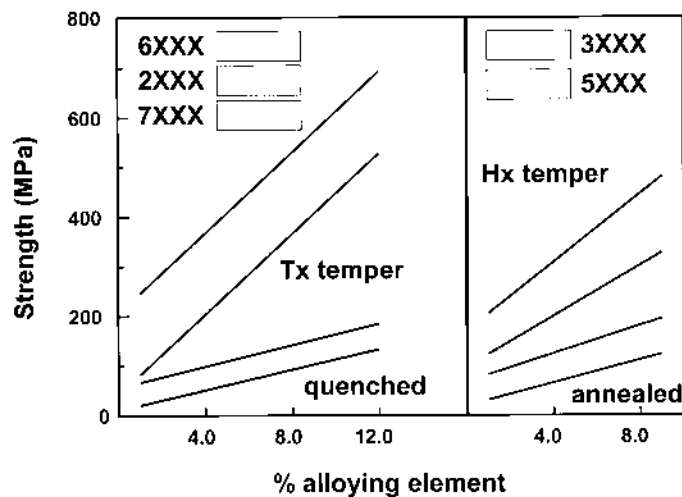
Figure 1   Effect of composition and temper on strength of commercial aluminum alloys.

1.1 Solid-Solution Hardening

Solid-solution hardening involves an increase in tensile strength and yield stress produced by alloying elements in solid solution. The elements in solution produce elastic distortions in the parent lattice thereby acting as a barrier to dislocation movements. Although most elements can alloy with aluminum, comparatively few elements have sufficient solid solubility to give a substantial solution hardening effect.

Strengthening from solute atoms arises either from differences in atomic size between the solute and solvent atoms or from differences in elastic modulus [1]. The size effects can be considered in terms of the different atomic volumes of aluminum (Ω_A) and solute atoms (Ω_S) expressed as:

$$\frac{\Omega_S - \Omega_A}{\Omega_A} \tag{1}$$

Figure 2 clearly indicates that the size effect is the dominant source of solute-strengthening in aluminum alloys [2]. The combination of solubility and size effect makes Cu and Mg the prominent solutes for solid-solution hardening. On a weight basis Mg is more effective than Cu (although on an atomic basis Cu is more potent). Figure 3 illustrates the effect of Mg in solid solution on the strength of binary Al-Mg alloys [3]. Both yield strength and ultimate tensile strength increase with increasing Mg level while elongation drops sharply with even small Mg additions. The more rapid rise of UTS compared to YS is explained by the additional effect of Mg on work hardening. Solutes also introduce other effects such as dynamic strain aging resulting in serrated yielding in Al-Mg alloys.

The effect of Mg in solid solution on commercial nonheat-treatable alloys is given in Fig. 4.
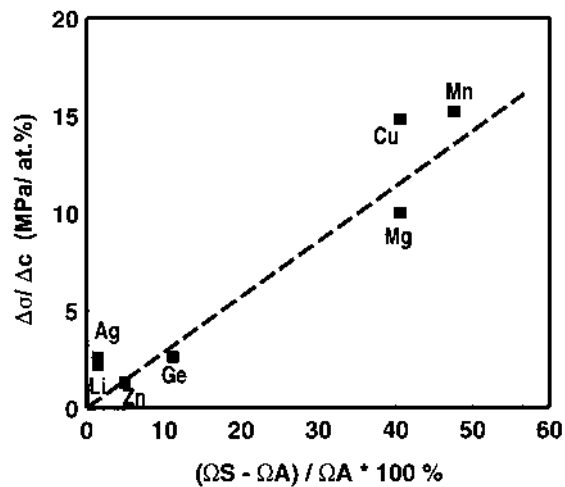
Figure 2 Strengthening due to atomic size effects [2].
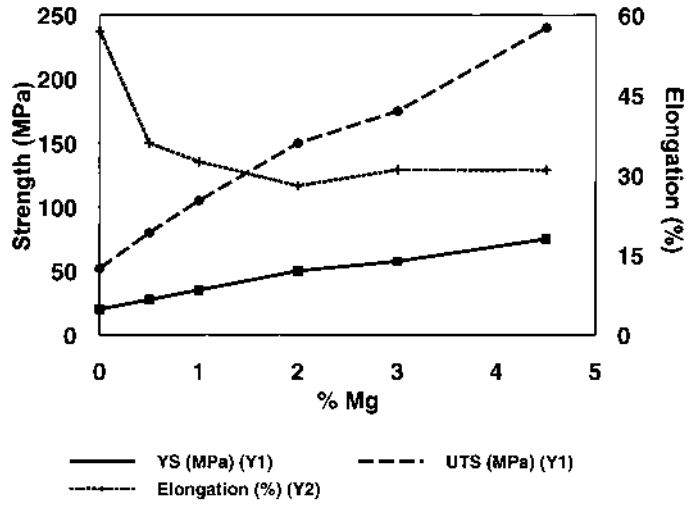
Figure 3   Effect of Mg in solution on tensile properties of annealed Al-Mg binary alloys. (From Ref. 3.)
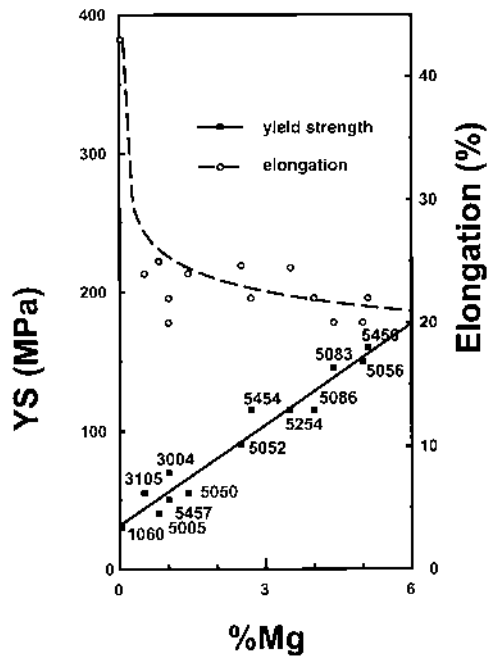
Figure 4   Effect of Mg on tensile properties of nonheat-treatable commercial aluminum alloys. (From Ref. 8.)

1.2 Grain-Size Strengthening

The effect of grain size on alloy strength is commonly expressed by the well-known Hall–Petch equation [4]:

$$\sigma_y = \sigma_o + kd^{-\frac{1}{2}} \tag{2}$$

where σ_y is the yield stress of the alloy, σ_o the frictional stress, d the average grain size and k a constant that characterizes the difficulty of transmitting slip across the grain boundary for a given alloy system. Because the value of k is approximately five times smaller than ferrous alloys the grain-size effect in aluminum alloys is not very strong. However considerable strengthening can be achieved at very fine grain sizes, because it has been demonstrated that the Hall–Petch relationship remains operative [5].

1.3 Work-Hardening

Properties of metals are changed by cold working. For most metals tensile strength, yield strength and hardness increase at the expense of ductility and formability. Work hardening is used extensively to strengthen nonheat-treatable alloys. In addition work hardening increases the strength achieved through solid-solution and dispersion hardening. The typical strain hardening tempers of nonheat-treatable alloys are given in Table 2.

The effect of work hardening is clearly shown in Table 3, where we can see a sharp increase in mechanical properties with increasing amount of cold work, while the elongation decreases significantly.

1.4 Precipitation Hardening

The heat treatment including quenching and aging is the most widely used way to improve strength properties of aluminum alloys. The quenching should be understood as the fixation of the high-temperature state of the alloy at lower temperatures. In other words, this procedure produces the supersaturated (in alloying elements) aluminum solid solution. It is noteworthy that the supersaturation can be achieved during casting, upon cooling an ingot or semifinished item in air, or as a result

Table 2 Temper Designations for Strain-Hardened Alloys

F	As-fabricated. No control over the amount of strain hardening; no mechanical property limits.
O	Annealed, recrystallized. Temper with the lowest strength and greatest ductility.
H1	Strain hardened.
H2	Strain hardened and partially annealed.
H3	Strain hardened and stabilized.
H112	Strain hardened during fabrication. No special control over amount of strain hardening, but requires mechanical testing and meets minimum mechanical properties.
H321	Strain hardened during fabrication. Amount of strain hardening controlled during hot and cold working.
H116	Special strain hardened, corrosion resistant temper for aluminum magnesium alloys.

Table 3 Tensile Properties of Aluminum Sheet

Alloy-Temper	UTS (MPa)	YS (MPa)	Elongation (%)
1100-O	75	25	30
1100-H14	110	95	5
1100-H18	150	—	4
5052-O	170	65	19
5052-H34	235	180	6
5052-H38	270	220	4

of rapid cooling after special annealing. The aging is a term covering the processes of precipitation hardening which can occur at room temperature (natural aging) or at higher temperatures requiring special heating (artificial aging). In late stages of aging, softening may occur. This is due to the change of structure and distribution of former hardening phases.

The effect of precipitation hardening (or aging) is determined by several parameters listed below.

- The chemical composition of a supersaturated solid solution. This composition is controlled by the initial temperature at which the solid solution is formed and by the cooling rate enabling the fixation of the high-temperature composition at lower temperatures. It should be mentioned that the composition of the supersaturated solid solution and the composition of the alloy are, generally, different. It becomes obvious if you look at a phase diagram of any multicomponent system. Take, for example, casting alloys of the Al-Si system. These alloys usually contain 5–18% Si. However, the concentration of silicon in a supersaturated solid solution is determined by the solubility of silicon at the eutectic temperature and will not exceed 1.65% Si. The content of main alloying elements in the supersaturated solid solution can be dramatically decreased in the presence of other additives and impurities. These additives can bind important elements (e.g. Cu, Mg, and Si) in insoluble phases and, thereby exclude them from the process of aging. Some small additions, however, may favorably affect the internal structure.
- The phase composition of aging products formed upon decomposition of the supersaturated solid solution. Mainly, these products are meta-stable phases in a form of coherent and semicoherent precipitates. The phase composition of these precipitates is, generally, different from that predicted by the equilibrium phase diagram. The precipitation usually starts with the segregation of the solute atoms in some crystallographic planes of the matrix. Then, these preprecipitates (or zones) acquire their own crystal lattice, first similar to that of the matrix. Their structure and composition gradually changes, approaching the structure and composition of the equilibrium phase. The vivid example of these changes is the precipitation of Mg_2Si in Al-Mg-Si alloys, which is discussed further in 2.4. Only for simple alloying systems, where only one phase can precipitate, this phase

is a meta-stable modification of the relevant equilibrium phase, e.g. in Al-Si and Al-Cu systems.

- The kinetics of precipitation. This parameter is very important, especially in multi-phase systems. The sequence of phase precipitation depends on temperature and phase properties. Obviously, the temperature provides the thermodynamic stimulus for the decomposition of a supersaturated solid solution. Depending of the annealing temperature a specific metastable phase may precipitate. At low temperatures, it is usually zones or coherent precipitates. At higher temperatures, it may be semicoherent metastable phase or the equilibrium phase. In the case of competitive precipitation of several phases, the advantage goes to the phases with a simple structure, formed by faster diffusing elements. This sequence controls the continuous depletion of the solid solution with respect to the elements incorporated in precipitated phases. Accordingly, the kinetics of precipitation can determine the phase composition.

- Temperature and time. These technological parameters affect all previously mentioned phenomena and are extremely important. The combination of time-temperature conditions is called the aging mode.

- The properties of precipitated phases. These properties greatly determine the hardening effect and include the type of bonding with the matrix, the shape, the composition, and the time-temperature stability. Generally, semicoherent precipitates are more efficient for hardening than coherent particles. However, it is true only under similar conditions: the same size and precipitation density. The finer the precipitates and the larger the precipitation density, the higher the strength of the aged alloy. On the other hand, the fracture toughness and other service characteristics are usually better for the solid-solution state (after quenching) or in the stage of zone precipitation. It should be also noted that the structure with metastable phases is thermally unstable. Therefore, the creep resistance of aluminum alloys is higher in the overaged state, when more stable phases are formed.

The basic temper designations for heat-treatable alloys are given in Table 4. Solution heat treatment is performed by heating cast or wrought products to a temperature usually 5°C below the solidus. In the case of cast products, two-step homogenization is applied, the first step being some degrees below nonequilibrium solidus. The duration of solutionizing is chosen to be sufficient to dissolve all nonequilibrium phase constituents, allowing the maximum of alloying elements to enter the solid solution. Rapid cooling is frequently used to preserve the high-temperature composition of the solid solution at lower temperatures (quenching).

Age hardening of aluminum-copper-magnesium alloys (Duralumin) was discovered by Alfred Wilm in 1906. The basic requirement for an alloy to be susceptible to age hardening is a decrease in solid solubility of one or more alloying elements with decreasing temperature. The major alloying elements that meet these requirements are copper, lithium, magnesium and zinc. The thermal treatment for age hardening normally involves a solution treatment at high temperature followed by a rapid quench to room temperature to form a supersaturated solid solution (SSSS) and a controlled decomposition at intermediate temperatures. The complete decompo-

Table 4 Temper Designations for Heat-treatable Aluminum Alloys

O	Annealed.
F	As fabricated.
W	Solution heat treatment: spontaneous natural aging after solution treatment
T1	Cooled after high-temperature processing and naturally aged to substantially stable condition.
T2	Cooled after high-temperature processing, cold worked and naturally aged to substantially stable condition.
T3	Solution heat-treated, cold worked and naturally aged to substantially stable condition.
T4	Solution heat treated and naturally aged to a substantially stable condition.
T5	Cooled after high-temperature processing and artificially aged.
T6	Solution heat-treated and artificially aged, usually to the maximum strength.
T7	Solution heat-treated and stabilized or overaged.
T8	Solution heat-treated, cold worked and artificially aged.
T9	Solution heat-treated, artificially aged and cold worked.
T10	Cooled after high-temperature processing, cold worked and artificially aged.

sition of the SSSS is a complex process, which may involve several stages including metastable phases. In the initial stages coherent Guinier-Preston zones are formed, named after the two researchers who independently detected these phases from streaks in x-ray diffraction patterns [6,7].

The thermal treatment for aging of aluminum alloys is a three-stage process:

- Solution treatment: dissolution of constituents and intermetallics.
- Quenching: to maintain the supersatured solution of alloying elements and excess vacancies.
- Aging: precipitation of intermediate phases at room temperature (natural aging) or at elevated temperature (artificial aging).

1.4.1 Solution Heat Treatment

To realize precipitation hardening it is necessary to create a solid solution in which a maximum of alloying elements is in solution. The minimum solution temperature is determined by alloy composition (e.g. the solvus position and eutectic temperature). Exceeding the eutectic temperature can lead to incipient melting of eutectic phases which is detrimental for mechanical properties. A too-low solution temperature can have a significant effect on final properties (Table 5).

1.4.2 Quenching

Quenching is the critical step during a precipitation treatment. During quenching the supersaturated solid solution as well as the excess vacancies need to be maintained. Solute precipitating on grain boundaries and vacancies migrating to interfaces and grain boundaries do not contribute to the aging process. In general the higher the quench rate the better combinations of strength and toughness are achieved. Also stress corrosion and corrosion resistance are better for high quench rates. Only Cu free 7XXX alloys form an exception to this general trend. The disadvantages

Table 5 Effect of Solution Temperature on Mechanical Properties After Aging

Solution temperature (°C)	UTS (MPa)	Yield Strength (MPa)
6061-T6		
493	301	272
504	316	288
516	333	305
527	348	315
2024-T4		
488	419	255
491	422	259
493	433	269
496	441	271

of a high quench rate are residual stresses and distortion of the quenched product. Consequently the maximum quench rate depends largely on the dimensions of the product. The quench rate can be controlled by proper selection of the quenching medium and temperature.

1.4.3 Precipitation from Solid Solution

The general condition for precipitation of supersaturated solid solutions requires a fine dispersion of precipitates during aging. The aging temperature needs to be below the equilibrium solvus line as well as below the GP solvus line (Fig. 5). The presence of excess vacancies promotes diffusion and the formation of zones is substantially faster than under equilibrium conditions. During precipitation first clusters of solute atoms are formed followed by the formation of metastable precipitates. The strengthening mechanism is caused by the coherent precipitates of solute atoms.
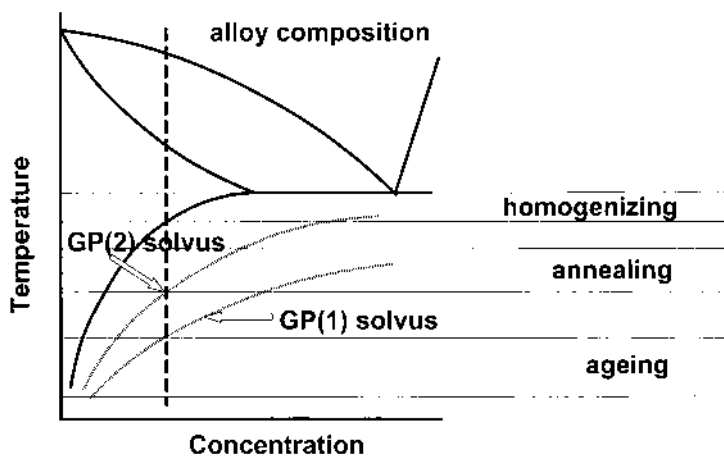
Figure 5 Temperature ranges for heat treatment and relevant solvus lines for binary aluminum alloys.
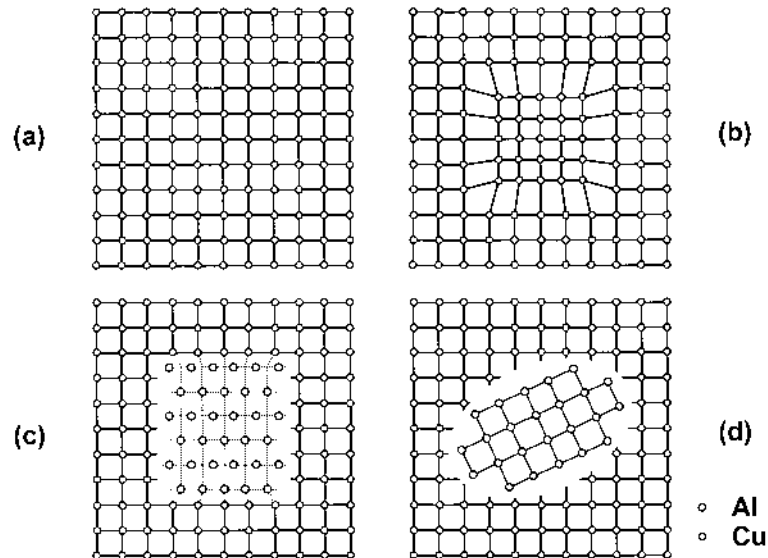
Figure 6 Schematic of different stages during precipitation of aluminum alloys; (a) solid solution; (b) coherent GP zone; (c) semicoherent precipitate; (d) incoherent equilibrium precipitate.

The difference in size between the aluminum and solute atoms causes elastic stresses in the aluminum matrix. These stress fields inhibit and hinder dislocation movement resulting in higher strength values. Size, form and distribution of GP zones is strongly alloy dependent. Spherical GP zones are formed if the difference in size between aluminum and solute is small (e.g. Al-Zn alloys). For large differences as in the Al-Cu system the zones are plate-like. Typical size for GP zones is 1–5 nm. GP zones are more like local variations in concentration than a separate phase. They are fully coherent with the matrix. The subsequent metastable phases formed during precipitation are semicoherent. A metastable precipitate has its own crystal structure and only along specific crystallographic directions is coherency maintained. The final structure in a precipitation sequence consists of coarse equilibrium precipitates with a marginal effect on strength properties. The different stages during precipitation are illustrated in Fig. 6.

The increase in strength during natural aging is continuous or becomes stable. During artificial aging strength and hardness go to a maximum value and decrease after that. The decrease in strength after extended aging times or at high aging temperatures is called *over aging*. The change in strength during precipitation is given in Fig. 7 as a function of time and aging temperature.

The major effects can be summarised as follows:

- The kinetics of hardening can be retarded or suppressed by decreasing aging temperature.
- Maximum strength decreases with increasing aging temperature.
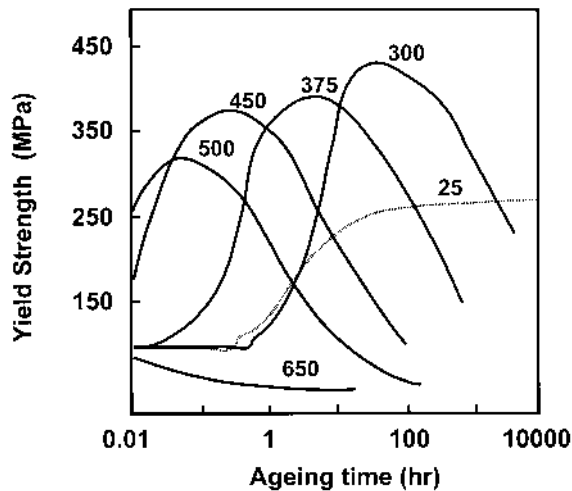
Figure 7 Isothermal aging curves for AA2014. (From Ref. 9.)

2 AGING OF COMMERCIAL ALUMINUM ALLOYS

In this part of the Chapter, we will consider main features of precipitation hardening for major groups of commercial alloys. The sequence of consideration will be as follows: the chemical composition, phase composition, phase properties, kinetics of precipitation, aging modes, and achieved mechanical properties [8–10]. Some additional numbers may be added to the designation of the basic tempers as already described in Table 4. These additional tempers are given in Table 6 [10].

2.1 Structure of Supersaturated Solid Solutions and Nucleation of Precipitates

The quenching results in the supersaturation of an aluminum solid solution in alloying elements. However, the supersaturation with respect to vacancies occurs simultaneously. This process is known as "quenching of vacancies." The supersaturation in vacancies may dramatically affect the defect structure of the supersaturated solid solution and the early stages of its decomposition.

Excess vacancies form prismatic dislocation loops in diluted aluminum alloys, whereas, in heavily alloyed solid solutions, helicoid dislocations. The latter are the result of interaction between quenched vacancies and screw dislocations. These structure features can be easily observed in a transmission electron microscope. Alloying with elements forming atom-vacancy complexes increase the number of helicoids and hamper the formation of prismatic loops. The presence of dislocations in the structure of the supersaturated solid solution, generally, facilitates the precipitation of semicoherent phases, because dislocations provide free surface for a semicoherent boundary and, thus decrease the energy of its formation (Table 7). For example, the semicoherent S′ (Al_2CuMg) phase in Al-Cu-Mg alloys tend to precipitate on dislocation loops.

Table 6 Additional Tempers for Heat-treatable Aluminum Alloys

Temper	Description
Tx51	Stress relieved by stretching. Applies to plate, extruded shapes and drawn tubes stretched up to 3% after solution heat treatment or cooling from an elevated temperature fabricating process; these products receive no further straightening.
	Tx510 Products with no further straightening.
	Tx511 Products with minor straightening after stretching to comply with standard tolerances.
Tx52	Stress relieved by compression. Products are stress relieved up to 5% by compression after solution heat treatment or cooling from an elevated temperature fabricating process.
Tx53	Stress relieved by combined stretching and compressing. Applies to die forgings that are stress relieved in the finish die.

Designations for products heat treated from O or F tempers to demonstrate response to heat treatment:

T42	Solution heat treated from O or F temper and naturally aged to a substantially stable condition.
T62	Solution heat treated from O or F temper and artificially aged.

Table 7 The Correlation Between the Type of Precipitates and the Place of their Formation

Interface type	Grain boundary (G)	Dislocation (D)	Vacancy (V)	Homogeneous nucleation (H)
Coherent (C)	$G_C \rightarrow$	$D_C \rightarrow$	$V_C \rightarrow$	$\leftarrow H_C$
		$\downarrow$	$\downarrow$	$\uparrow$
Semicoherent (SC)	$G_{SC} \rightarrow$	D_{SC}	$\leftarrow V_{SC}$	$\leftarrow H_{SC}$
	$\downarrow$			
Incoherent (IC)		$\uparrow$	$\uparrow$	$\uparrow$
	G_{IC}	D_{IC}	$\leftarrow V_{IC}$	$\leftarrow H_{IC}$

The decomposition starts with the formation of submicroscopic regions enriched in alloying elements, these regions having the same structure as the matrix. This stage is called the zone stage, as the Guinier–Preston zones are formed. During this early period of precipitation, the electrical resistivity of the quenched alloy increases in two steps. In the first stage, the resistivity changes very rapidly during first minutes (so-called rapid reaction). After that the resistivity grows very slowly (slow reaction). The first stage is interpreted in terms of segregation of solute atoms on specific crystal planes. These zones are very small and uniformly distributed in the volume. It is believed that this process occurs very rapidly, perhaps by a spinodal mechanism, by fluctuations without nuclei formation [11,12].

Let us consider in more detail the difference between ''nucleation and growth'' and ''spinodal'' mechanisms of decomposition [13]. In the case of nucleation and

growth, the decomposition is initiated by the formation of energetically stable solute-rich clusters (hetero phase nuclei). Only thermal composition fluctuations with sufficiently large compositional amplitudes can lower the free energy of the system and hence can lead to the formation of stable nuclei. The formation of these nuclei by this mechanism requires a nucleation barrier to be overcome and is characterized by an incubation period. Upon spinodal decomposition, the nonequilibrium solid solution is unstable with respect to the formation of spatially extended thermal composition fluctuations with small amplitudes. Hence, the decomposition is initiated by the spontaneous formation and subsequent growth of coherent composition fluctuations. This type of decomposition occurs without incubation period and is typical of, for example, Al-Zn and Al-Zn-Mg alloys. In the case of spinodal decomposition, the concentration profile of solute in the matrix looks like a wave with gradually increasing amplitude.

It was established by numerous studies that the actual room-temperature diffusion of solute atoms upon the segregation proceeds at rates several orders of magnitude higher than the normal diffusion at the same temperature [14]. The most adopted explanation is that the diffusion rate is determined by the vacancy concentration equilibrium at the quenching temperature. This also explains the fact that the cooling rate affects essentially the kinetics of precipitation. However, the question remains: why is the vacancy concentration retained anomalously high during a considerable time, despite numerous sinks?

The possible explanation is that zones are able to absorb and evolve vacancies, acting like a pump [15]. Part of vacancies is inevitably lost in sinks, and the diffusion rate gradually decreases remaining, however, higher than normal.

Hence, in the early stages of decomposition (so-called zone stage), pre-precipitates or clusters are formed within the matrix crystal lattice. These processes are very important upon natural aging. The zones are precipitates with the completely isomorphic to the matrix structure. Evidently, elastic stresses and strains arise around these preprecipitates due to local expansion or shrinkage of the matrix crystal lattice. These stress fields interact with dislocations, slow down their movement and, thereby, harden the alloy. There are also other mechanisms of hardening described earlier in this Chapter.

Main strengthening is associated with coherent and semicoherent precipitates that create large elastic distortions at interfaces with the matrix. Nevertheless, what is the interface? Nowadays, the interface is considered as the interface surface proper and the transition regions determining stresses both in the matrix and in the precipitate. The formation of coherent or semicoherent phase is caused by the considerably lower surface energy for such precipitates as compared with the more stable phases. For example, the surface energy of the coherent θ'' (Al_2Cu) phase is three times lower than that for the semicoherent θ' phase [16]. Upon growth of particles, the coherency is being lost, first along some directions and then at the entire boundary.

Another very important problem is: where do precipitates tend to nucleate? Unlike zones that usually precipitate homogeneously or onto vacancy clusters, the metastable phases may form in various places. This process is usually controlled by crystal defects. Table 7 shows the dependence between the type of precipitates and the place of its formation [17]. The arrows show the direction of decreasing energy for precipitation.

One can see that coherent phase are predominantly nucleate homogeneously, if their formation does not create large strains. In the case when the specific volume of the zone or the new phase is larger than that of the matrix, the coherent phase will nucleate at vacancy clusters. Semicoherent precipitates tend to form at dislocations, which ease the formation of the semicoherent boundaries. In addition, incoherent particles nucleate at grain boundaries.

2.2   Aging in Commercial Al-Cu Alloys

The Al-Cu system is the classics of aging theory and is well studied. At the same time, this system is a base for the entire family of commercial alloys: wrought (Duralumin, 2XXX series) and casting (2XX.0 series). Alongside copper, these alloys may contain magnesium, silicon and transition metals. The magnesium- and silicon-containing materials will be considered below. However, there are a few commercial alloys where copper is the main alloying component, which determines the phase composition and aging phenomena. Some of the alloys are listed in Table 8. It should be noted that simple Al-Cu alloys are not widely used nowadays and are more and more replaced with Al-Cu-Mg wrought alloys or Al-Si-Cu-Mg casting alloys.

The composition of the supersaturated solid solution can be more or less reliably predicted from the equilibrium phase diagram of the Al-Cu or systems that are more complex. Castings or deformed products from alloys of this group are usually water quenched from high temperatures. These temperatures are chosen to be about 5°C below the equilibrium solidus.

The decomposition of a supersaturated Al-Cu solid solution results in the formation of the following phases: θ'', θ', and θ' (Al_2Cu). These phases are, respectively, coherent, semicoherent and incoherent (stable). Before the precipitation of the θ'' phase, the Guinier–Preston zones (GPZ) are formed in the aluminum solid solution. It is well adopted that the composition of all these phases is close to the stoichiometry of the Al_2Cu phase. The information on the crystal structure and orientation relationships for phases typical of the Al-Cu system are given in Table 9 [18].

Upon natural aging, the precipitation starts from the formation of GPZ. The density of their precipitation is 10^{17}–10^{18} cm^{-3} at a size of up to 5 nm and a spacing of 2.5–4 nm [19]. The coherent phase succeeds the zones, being formed either homogeneously in the matrix or onto the zones. The θ'' precipitates appear as disks

Table 8   Chemical Compositions of Some Commercial Al-Cu Alloys

Alloy	Cu, %	Other elements, %
295.0	4.5	1.1Si
224.0	5.0	0.35Mn; 0.1V; 0.2Zr
213.0	7.0	2Si
2025	4.4	0.8Mn; 0.8Si
2011	5.5	0.4Bi; 0.4Pb
2219	6.3	0.3Mn; 0.1V; 0.18Zr; 0.06Ti

Table 9 Crystal Structure and Orientation Relationships for Al-Cu Phases

Phase	Crystal structure	Lattice parameters, nm		Orientation relationship
		a	c	
θ''	Tetragonal	0.404	0.768	$(001)_p \parallel (001)_{A1}$; $[100]_p \parallel [100]_{A1}$
θ'	Tetragonal	0.404	0.580	$(001)_p \parallel (001)_{A1}$; $[100]_p \parallel [100]_{A1}$
θ	Tetragonal	0.6066	0.4874	—

or thin plates in $\{100\}$ matrix planes. The typical size of coherent particles ranges from 10 to 100 nm with a spacing from 20 to 100 nm [17]. These two types of precipitates assure hardening upon natural aging.

The phase composition of alloys aged at higher temperatures (artificial aging) depends on time-temperature conditions. Each metastable phase has its own metastable solvus and forms only under it. If the temperature of annealing is higher than the metastable solvus of, say, the θ'' phase, then this phase will never be formed and the decomposition will start immediately with the formation of the semicoherent θ' phase. On the other hand, under suitable temperature conditions the coherent phase can precipitate first and then will be substituted by the θ' phase. The considerably high temperature of artificial aging (170–200°C) provides sufficient thermodynamical stimulus for the successive formation of the entire series of phases, from GPZ to the equilibrium Al_2Cu phase. The particles of the θ' phase usually precipitate onto dislocations (decorating them) and then replace θ'' particles in the matrix as they are losing coherency. The size of semicoherent particles is 10–60 nm at a precipitation density of 10^{11}–10^{12} cm^{-3} [17].

It is worth noting that semicoherent particles demonstrate higher strengthening ability than coherent precipitates. This is because several hardening mechanisms can simultaneously act. Therefore, Al-Cu alloys artificially aged to the stage of θ' precipitation may be much harder than those reinforced only by coherent particles of the close size and precipitation density.

Incoherent particles of Al_2Cu phase have virtually no effect on the strength because of their large size, low precipitation density, and absence of stress fields around.

Small additions of some elements can affect the internal structure of aged Al-Cu alloys. It is known that Cd, In, Sn, Mg, Li, Be, Mg + Ge, and Mg + Si slow down the formation of GP zones and facilitate the substitution of the θ'' phase for the θ' phase [18, 20, 21]. The latter precipitates as very fine plate and efficiently hardens the alloy. Cadmium is known to accelerate copper diffusion in solid aluminum [22]. Beryllium deteriorates hardening upon natural aging [23]. Transition metals such as Zr, Ti and Mn form dispersoids that provide nucleation sites for relatively large θ' particles and thus decrease the aging effect [24].

Table 10 and Table 11 show typical temper modes and mechanical properties of some Al-Cu alloys.

2.3 Aging in Commercial Al-Cu-Mg Alloys

The development of Duralumin results in the design of alloys containing, alongside copper, magnesium. This enlarges the possibilities of hardening, now with two

Table 10   Temper Modes for Some Commercial Al-Cu Alloys

Alloy	Solution treatment	Aging
295.0	515°C, 12 hr	155°C, 3–6 hr (T6)
2025	515°C (T4)	170°C, 10 hr (T6)
2011	525°C (T3)	160°C, 14 hr (T8)
2219	535°C (T31)	175°C, 18 hr (T8)
		190°C, 18–26 hr (T8, T6)

Table 11   Typical Mechanical Properties for Some Al-Cu Alloys

Alloy	*UTS*, MPa	*YS*, MPa	*El*, %
295.0 T6	250	165	5.0
224.0 T7	380–420	276–330	10.0–4.0
213.0 F	165	103	15
2025 T6	400	255	19
2011 T3/T8	380/405	295/310	15/12
2219 O/T62	175/415	75/290	18/10

Table 12   Chemical Composition of Some Commercial Al-Cu-Mg Alloys

Alloy	Cu, %	Mg, %	Other elements,%
242.0	4.0	1.5	2.0Ni
201.0	4.6	0.35	0.7Ag; 0.35Mn
222	10.0	0.25	
2036	2.6	0.45	0.25Mn
AK4-1 (Russian)	2.3	1.5	1.2Ni; 1.2Fe
2218	4.0	1.5	
2014	4.4	0.5	0.8Mg; 0.8Mn
2024-2224	4.4	1.5	0.6Mn

phases, Al_2Cu and Al_2CuMg (*S*). Either phase or both may precipitate with respect to the composition of the supersaturated solid solution. The formation and features of the Al_2Cu-based phases were discussed earlier. However, it is noteworthy to mention that magnesium being in the solid solution (up to 0.4%) efficiently refines θ' particles and increases their precipitation density, thus improving hardening [21, 25]. It is supposed that magnesium increases the binding energy between solute atoms and vacancies, facilitates the formation of immobile stable complexes, and thus slows down diffusion. These complexes then serve as nuclei for the θ' phase. Alongside improved strength, the creep resistance is also increased due to a higher thermal stability of θ' particles.

   The chemical compositions of some commercial alloys are given in Table 12. The composition of the solid solution after quenching from about 500–505°C is close to that of the alloy.

Table 13 Crystal Structure and Orientation Relationships for Al-Cu-Mg Phases

Phase	Crystal structure	Lattice parameters, nm			Orientation relationship
		a	b	c	
S''	Orthorhombic	0.400–0.405	0.905–0.925	0.718–0.724	$(100)_p \parallel (210)_{Al}$; $[010]_p \parallel [120]_{Al}$
S'	or monoclinic				$(011)_p \parallel (031)_{Al}$; $[100]_p \parallel [100]_{Al}$
S	Orthorhombic	0.400–0.404	0.923–0.925	0.714–0.717	$(121)_p \parallel (001)_{Al}$; $[11\bar{3}]_p \parallel [100]_{Al}$
					$(011)_p \parallel (001)_{Al}$; $[100]_p \parallel [100]_{Al}$
					$(110)_p \parallel (001)_{Al}$; $[1\bar{1}3]_p \parallel [100]_{Al}$
					$(010)_p \parallel (100)_{Al}$; $[100]_p \parallel [021]_{Al}$
	Orthorhombic	0.401	0.935	0.715	—

The decomposition of Al-Cu-Mg alloys (Cu : Mg > 2 at.%) starts with the segregation of copper and magnesium atoms in $\{100\}_{Al}$ and $\{210\}_{Al}$ planes [18]. These clusters are called Guinier–Preston–Bagaryatsky zones (GPBZ).

The sequence of precipitation of quasi-binary Al-Al$_2$CuMg alloys is as follows: GPBZ, coherent S'' phase, semicoherent S' phase, and stable S phase. The crystal structures of these phases are shown in Table 13 [18,25–28].

The structure of all S-phase modifications are very close, therefore some authors consider them as a one structure differently distorted due to coherent or semicoherent junction with the matrix [26,29]. The orientation relationships for GPBZ and S'' precipitates slightly deviate (by 4–5°) from the ideal OR given in Table 9. The transition from one modification to another occurs continuously upon aging, the crystal lattice being rotated and sheared. In the case when S'' and S' particles grow freely, they form typical conglomerates of thin elongated laths, frequently decorating dislocation loops. These particles are aligned with the ⟨100⟩ matrix lattice direction and have the $(210)_{Al}$ and $(110)_{Al}$ habitus. After nucleation, S precipitates rapidly grow filling the entire solid solution volume with agglomerates.

When the alloying level is low (1.5% Cu and 0.7% Mg), the S' phase forms rods in the ⟨100⟩$_{Al}$ direction and $\{100\}_{Al}$ planes [28].

In alloys with the S phase as the main hardener, the strengthening occurs in two distinct stages separated by a plateau, which may last for many hours [30]. The first stage of hardening, contributing about 70% to the total strength, is attributed to the (Cu, Mg) cluster formation. These clusters are precursors of GPBZ and S'' phase, which precipitation occurs in the second stage of hardening. The S' and S phases are formed onto dislocation loops during the stage of a plateau.

In the alloys with an excess of copper (with respect to the stoichiometry of the S phase), the Al$_2$Cu phase is formed additionally. Mondolfo [18] concludes that the latter phase plays the major role in hardening alloys with the ratio Cu : Mg = 8. On decreasing the ratio to 4, both phases participate in strengthening. Moreover, the S phase dominates in the range of Cu : Mg ratio from 4 to 1.5. On further decreasing the ratio, the Al$_6$CuMg$_4$ phase has to precipitate. However, there are only few data on such alloys.

It should be noted that GPB zones are more thermally stable than GP zones. According to Silcock [25] in an alloy with Cu : Mg = 7, the maximum hardness is achieved by the combination of phases: θ' and S'' (at 130°C and 165°C) and S'', S' and θ' (at 190°C). The coherent S'' phase can be retained at considerably high
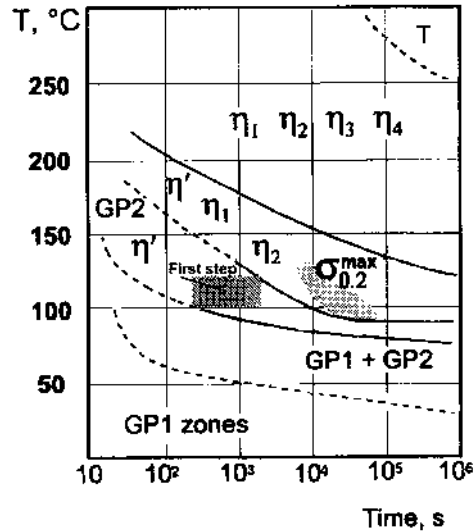
Figure 8 Time-temperature diagram for aging of a 2024-type alloy.

temperatures. We can conclude that the Al_2Cu phase acts more efficiently at low aging temperatures (below 165°C), whereas the role of the Al_2CuMg phase becomes dominant at higher temperatures.

The TTT diagram for aging of a 2024-type alloy is given in Fig. 8. [31]. This diagram shows the phase composition and hardening effect in time-temperature axes.

The presence of silicon impurity in commercial Al-Cu-Mg alloys may change essentially the phase composition and precipitation sequence of aging products, thereby affecting the mechanical properties. These phenomena will be considered below in the section about Al-Cu-Mg-Si alloys. The addition of silver in Al-Cu-Mg alloys can considerably improve properties after aging and increase thermal stability of structure and properties due to the change of phase composition. The decomposition of alloys, containing more magnesium than copper and small additions of silver, occurs with the formation of a so-called X' phase in addition to the S phase [30]. The X' phase has a hexagonal structure and is very close in composition to the S phase, except small content of Ag (5 at.%).

In the alloys with high Cu:Mg ratio, a new phase conventionally designated as Ω is formed instead of the θ' phase. This phase has a tetragonal structure with lattice parameters $a = 0.6066$ nm and $c = 0.496$ nm or an orthorhombic structure with $a = 0.496$ nm, $b = 0.859$ nm and $c = 0.848$ nm. The precipitates of the Ω phase appear as fine plates, the (Ag, Mg) clusters and GP zones earlier formed on $\{111\}_{Al}$ planes continuously transforming to the Ω phase. As distinct from GP zones, which are depleted of copper and enriched in magnesium and silver, the Ω phase has the copper concentration close to that in the Al_2Cu phase, magnesium and silver being evolved to the interface with the matrix [32]. Even small impurities of silicon (0.15%) completely suppress the formation of the Ω phase.

In addition to the Ω phase, the so-called σ phase may be formed in Al-Cu-Mg-Ag alloys (3–4% Cu, 0.45% Mg, 0.4% Ag), especially in composite

Table 14 Temper Modes for Some Al-Cu-Mg Alloys

Alloy	Solution treatment	Aging
242.0	515°C, 5–12 hr	205–230°C, 3–5 hr (T61)
201.0	490–510°C, 2 hr + 525–530°C, 14–20hr	155°C, 20 hr (T6)
222.0	510°C, 12 hr	155°C, 11 hr (T6)
2036	500°C (T4)	
AK4-1	525–535°C	190°C, 9–14 hr (T6)
2014	500°C (T4)	160°C, 18 hr (T6)
2024–2224	495–510°C	190°C, 9–12 hr

Table 15 Typical Mechanical Properties of Some Al-Cu-Mg Alloys

Alloy	UTS, MPa	YS, MPa	El, %
242.0 O/T61	185/325	125/290	1.0/0.5
201.0 T4/T6	365/485	215/435	20/7
222 O/T62	185/420	140/330	1.0/4.0
AK4-1 T6	430	340	8.0
2218 T61	440	370	10
2014 O/T6	185/485	95/415	18/13
2024 O/T62	185/440	75/345	22/5

materials [33]. This phase has a composition of $Al_5Cu_6Mg_2$ and a cubic structure with $a = 0.831$ nm. It should be noted that, according to the phase diagram, the $Al_5Cu_6Mg_2$ phase cannot be in equilibrium with aluminum. The only possibility of its appearance is the strongly metastable state of an alloy and the effect of silver (as a stabilizer of this phase). The σ phase has a simple cube-on-cube orientation relationship with the aluminum matrix. It precipitates as the semicoherent phase with a high solvus (above 700°C), which makes it quite stable at high temperatures, above 200°C. On decreasing the Cu:Mg ratio from 10 to 7, the precipitation of the σ phase begins to dominate over the formation of the Ω phase. Although these phases may coexist with each other and with metastable modifications of θ and S phases. In any case, silver addition improves the thermal stability of Al-Cu-Mg alloys and, nowadays, there are several Ag-containing alloys intended for use in airspace industry.

Typical temper modes and mechanical properties of Al-Cu-Mg alloys are listed in Table 14 and Table 15.

2.4 Aging in Commercial Al-Mg-Si Alloys

Very different in structure, properties and destination alloys belong to this system. There are casting alloys containing 4–18% Si and 0.15–1% Mg and there are very widely used extrudable alloys of the 6XXX series, containing 0.5–1.5% Si and 0.5–1.5% Mg with various ratios. The compositions of some commercial alloys are given in Table 16.

Table 16   Chemical Compositions of Some Commercial Al-Mg-Si Alloys

Alloy	Mg, %	Si, %	Other elements, %
356.0	0.35	7.0	—
369.0	0.35	11.5	—
360.0	0.50	9.5	—
357.0	0.55	7.0	—
6151	0.6	0.9	0.25Cr
6063	0.7	0.4	—
6061	1.0	0.6	0.28Mn
6053	1.2	0.7	0.25Cr

It is very important to note that the aging effect and properties are very much dependent on the ratio between magnesium and silicon in the supersaturated solid solution. The excess of silicon (with respect to the stoichiometry of the Mg_2Si phase) can considerably change the kinetics of precipitation and the phase composition.

The decomposition of the supersaturated solid solution results in precipitation of the β (Mg_2Si) phase and free Si (in the alloys with its excess). The coherent β'' phase is an efficient hardener and participates in processes of natural and artificial aging. In the stage of softening, it gives place to the semicoherent β' phase, which is considerably stable. The decomposition starts directly with the formation of β' particles at temperatures above 300°C, and the sole equilibrium β phase precipitates upon annealing above 400°C [34].

The transformation between Mg_2Si modifications is a subject of discussion. Really, there is no reliable explanation how the monoclinic phase can transform to hexagonal or orthorhombic and then to the cubic equilibrium phase. Moreover, the development of high-resolution electron microscopy gave rise to new discoveries. It was found that, unlike all other known metastable phases in aluminum alloys, the semicoherent phase might have several modifications. The cause of this unique phenomenon is still unclear. Maybe it is due to the uniqueness of the Mg_2Si phase proper. This phase is composed of metal and semiconductor, which have to determine its unusual behavior.

The composition of metastable phases, i.e. Mg:Si ratio, is different from that of Mg_2Si (Mg:Si = 2 at.%). The Mg:Si ratio continuously increases in the series GPZ, β'', β', β. In other words, metastable phases are enriched in silicon. The structures and orientation relationships of phases typical of Al-Mg-Si alloys are listed in Table 17 [18,35–40].

The maximum strength is achieved in alloys with an excess of silicon and in the stage of β'' precipitation. There is no unanimous opinion on the reasons of that. It is more or less adopted that the silicon-vacancy complexes acts as nucleation sites for the coherent phase.

The nonequilibrium solid solution of magnesium and silicon in aluminum decomposes even at room temperature. In the balanced alloys or in the alloys with Mg:Si ratio above 1.73 wt% the decomposition proceeds in the following steps: the formation of needle-like zones along the $\langle 100 \rangle_{Al}$ crystal direction; the ordering of their structure and the formation of β'' needles; the transition from β'' needles

Table 17 Crystal Structure and Orientation Relationships for Phases in Al-Mg-Si Alloys

Phase	Crystal structure	Lattice parameter, nm			Orientation relationship
		a	b	c	
β''	Monoclinic	0.616	0.616	0.710	$(101)_p \,\|(001)_{A1};\ [10\bar{1}]_p \,\|[010]_{A1}$
				$\gamma = 82°$	
		0.77	0.67	0.203	$(001)_p \,\|(001)_{A1};\ [100]_p \,\|[310]_{A1}$
				$\gamma = 75°$	
β'	Hexagonal	0.705		0.405	$(001)_p \,\|(100)_{A1};\ [100]_p \,\|[011]_{A1}$
	Hexagonal	0.405		0.67	$(\bar{1}\bar{1}0)_p \,\|(001)_{A1};\ [2\bar{2}1]_p \,\|[100]_{A1}$
	Hexagonal	0.407		0.405	
	Hexagonal	1.04		0.405	$(001)_p \,\|(001)_{A1};\ [1\bar{2}0]_p \,\|[100]_{A1}$
	Hexagonal	0.705		1.215	
	Orthorhombic	0.684	0.793	0.405	
	Orthorhombic	0.672	0.787	0.405	
β	Cubic	0.639 or 0.6351			$(001)_p \,\|(001)_{A1};\ [100]_p \,\|[100]_{A1}$
Si	Cubic	0.543			$(0\bar{2}2)_p \,\|(100)_{A1};\ [111]_p \,\|[010]_{A1}$

to β' rods; and the formation of the equilibrium β phase as plates or cubes [41]. During artificial aging of dilute Al-Mg-Si alloys ($Mg_2Si < 0.8\%$) the coherent β'' phase nucleates onto zones. In this case, the internal structure formed upon preliminary natural aging provides the conditions for the formation of very fine, uniformly distributed β'' precipitates.

The transition between metastable modifications is likely to occur separately. In other words, coherent precipitates dissolve, semicoherent particles are formed at dislocations, and the coherent phase may precipitate on dislocations or grain boundaries. However, there is an opinion that these transformations occur by the diffusionless, shear mechanism (like martensite) [14]. It should be noted that during high temperature annealing (at 300–350°C) the β' and equilibrium β phases may coexist for a long time, large precipitates with the structure of β' being almost incoherent [34].

Zones are precipitated very intensively, the precipitation density being 3×10^{15} mm^{-3} and the size, 6×20–100 nm. The coherent phase has the same precipitation density with the size somewhat larger, 5×16–200 nm [42]. The zone stage lasts from 5 h to 8 min at 150–200°C, respectively, while the transition to the β' phase requires 200 to 8 h in the same temperature range [43].

Solute copper accelerates the precipitation of the β'' phase, refines its particles by three times and promotes the homogeneous distribution of precipitates [44]. This effect can be observed at copper concentrations lower than 2%.

Alloys with an excess of silicon has one major difference from alloys with Mg:Si ratio lower than 1.73 wt%. In these alloys, free silicon precipitates and affects the entire situation. Let us consider briefly the precipitation of silicon from the supersaturated solid solution.

The Al-Si system has all necessary features enabling one to expect precipitation hardening. However, no hardening occurs during precipitation of silicon from the supersaturated solid solution. Silicon atoms segregate on vacancy clusters or free silicon nucleates on dislocation loops very rapidly after quenching. Due to the large difference in lattice parameters between silicon and aluminum, the precipitates almost immediately loose coherency. In the temperature range from 150°C to 250°C, the complete precipitation of silicon takes 17 h to 30 min, respectively [45,46]. Silicon particles appear in the structure as prisms, rods or plates. Their size and interparticle spacing is considerably larger than those required for hardening effects. Solute copper may affect the precipitation of silicon, refining its particles [17]. Hence, silicon does not directly participate in strengthening.

However, its effect on the sequence of precipitation and the variation in the composition of the supersaturated solid solution is very important. Silicon accelerates the formation and increases the precipitation density of spherical (Al, Mg, Si) zones. These zones act like nuclei for the coherent β'' phase. Recently, it has been found that the Mg:Si ratio in the semicoherent phase β' phase is lower in the alloys with an excess of silicon, as compared with balanced alloys (1.21 and 1.75 at.%, respectively).

From the analysis of numerous literature data, we can conclude that the sequence of precipitation in Al-Mg$_2$Si-Si alloys is as follows (in parentheses the temperature range according to DSC analysis [45]:

- Formation of magnesium and silicon segregates in the matrix crystal lattice (below 100°C).
- Nucleation of needle-like zones onto these segregates (200–250°C).
- Nucleation of free silicon with rapidly lost coherency. The (Al, Mg, Si) zones remain unchanged (240–320°C).
- Formation of the coherent β'' phase onto (Al, Mg, Si) zones (below 450°C).
- Formation of the semicoherent β' phase (below 450°C).
- Formation of the equilibrium β phase (above 400°C).

The delay between quenching and artificial aging in Al-Mg$_2$Si-Si alloys decreases the hardening effect. However, small copper additions can minimize this effect. Cadmium, indium, and lead also diminish this effect, but only upon aging at temperatures below 160–170°C.

Some Al-Mg-Si alloys contain Sb, Pb or Sn that are added either to modify the Al-Si eutectics or to improve machinability of alloys. These elements can considerably worsen the mechanical properties, binding part of magnesium in insoluble, brittle particles of the Mg$_2X$ type. In this case, the efficient concentration of magnesium in the supersaturated solid solution is decreased.

Temper modes and mechanical properties of some Al-Mg-Si alloys are given in Table 18 and Table 19.

2.5   Aging in Commercial Al-Cu-Mg-Si Alloys

The Al-Cu-Mg-Si system provides a base for several groups of commercial wrought and casting alloys: Duralumin (2024 with silicon impurity), forging alloys (2014), and high-strength and heat-resistant Al-Si alloys. The compositions of some alloys are given in Table 20.

Table 18 Temper Modes for Some Al-Mg-Si Alloys

Alloy	Solution treatment	Aging
356.0	540°C, 12 hr	155°C, 3–5 hr (T6)
357.0	540°C, 8–12 hr	175°C, 6 hr or 155°C, 10–12 hr
6151	515°C (T4)	170°C, 10 hr (T6)
6063	520°C (T4)	175°C, 8 hr (T6)
6061	530°C (T4)	160°C, 18 hr or 170°C, 8 hr (T6)
6053	520°C (T4)	170°C, 10 hr (T6)

Table 19 Typical Mechanical Properties of Some Al-Mg-Si Alloys

Alloy	*UTS*, MPa	*YS*, MPa	*El*, %
356.0 F/T6	164/262	124/185	6.0/5.0
360.0 F	325	170	3.0
357.0 F/T6	172/345	90/296	5.0/2.0
6151 T6	330	295	17
6063 O/T6	90/240	50/215	20/12
6061 O/T6	125/310	55/275	25/12
6053 O/T6	110/255	55/220	35/13

Table 20 Chemical Compositions of Some Commercial Al-Cu-Mg-Si Alloys

Alloy	Cu, %	Mg, %	Si, %	Other elements, %
324.0	0.50	0.55	7.5	—
336.0	1.0	1.0	12.0	2.5Ni
355.0	1.25	0.50	5.0	—
332.0	3.0	1.0	9.5	—
A319.0	3.5	0.3	6.0	—
333.0	3.5	0.3	9.0	—
238	10.0	0.25	4.0	—
4032	0.9	1.0	12.2	0.9Ni
AK6 (Russian)	2.2	0.6	0.95	0.6Mn
2618	2.3	1.6	0.18	1.1Fe; 1.0Ni; 0.07Ti
2014	4.4	0.5	0.8	0.8Mn
AK8 (Russian)	4.5	0.6	0.9	0.7Mn

On one hand, the phase composition of these alloys is extensively studied for many years. On the other hand, usually the decomposition phenomena in such alloys are considered separately for either alloy or alloy groups, which results in contradictory results when comparing different compositional ranges. The main problem is that the phase composition of these alloys is very complex and can hardly be predicted using the equilibrium phase diagram. Several phases can precipitate solely or in combination depending on the proportion and concentration of alloying elements.

The decomposition of multicomponent supersaturated solid solutions is a very important problem of modern physical metallurgy. It is likely that the final structure formed in an alloy after decomposition is determined by the composition of a supersaturated solid solution and the sequence of phase precipitation or, in other words, by kinetics. It is clear that this structure, in turn, determines the mechanical properties.

The phase composition of wrought alloys is more or less known. Depending on the Cu:Mg and Mg:Si ratios the phase composition in the stage of maximum hardening varies from S' to $S' + \theta'$ then to $\theta' + \beta''$ and, finally, to $\theta' + \beta'' + Si$. There is controversial information on the phase composition of alloys, containing 2–4% Cu and magnesium and silicon in the Mg:Si ratio less than unity (excess of silicon). According to the equilibrium phase diagram, there should be the cubic quaternary Q ($Al_4CuMg_5Si_4$) phase instead of Mg_2Si. The Q phase has a complex cubic structure with $a = 1.263$ nm [18] or a hexagonal structure with $a = 1.04$ nm and $c = 0.405$ nm [47]). Some authors report that they have observed "precursors" of the Q phase in the stage of hardening [48,49]. The main argument is that these precipitates giving the electron diffraction pattern very close to that of the β'' (or β') phase contain copper. For example, Yao et al. [50] have found in Al-Mg-Si-Cu alloys air-cooled from solutionizing temperature the so-called B' phase with lattice parameters similar to those of the β' phase ($a = b = 1.05$ nm and $c = 0.405$ nm), but containing copper. Note that the suggested structure of the B' phase is similar to that of the Q phase [47]. However, the same phase is observed in copper-free alloys. This may attest for the possible dissolution of copper in a Mg_2Si-based phase. Recently, Cayron and Buffat [51] reported that the structure of the B' (or β'_C) phase could be easily transformed to the structure of the Q phase by substituting silicon atoms for copper. Of course, there should be the Q phase in these alloys, at least in the equilibrium state. However, the question remains opened when it will form, during hardening in the temperature range from 150°C to 250°C, or later after dissolution of hardening β'' precipitates, or only at higher temperatures.

The mutual effects of alloying elements are very strong. Copper and excess silicon refine β'' precipitates; magnesium facilitates the formation of the θ' phase instead of θ'' but with very close distribution and size parameters [42,52,53].

The most complicated is the analysis of casting Al-Si alloys in which the composition of the supersaturated solid solution and the composition of the alloy are completely different and determined by the limit solubilities and the solution treatment mode. The maximum solubilities of copper, magnesium and silicon in Si-rich alloys are 4.0%, 0.3% and 0.77%, respectively [18]. It has been shown that silicon-containing phases precipitate only upon artificial aging, whereas the hardening at room temperature is determined by GP and GPB zones [54].

The examination of the entire compositional range of supersaturated solid solutions in Al-Cu-Mg-Si alloys may help to understand the problem. This was done for alloys containing 4% Cu and aged at 170°C for 20 hr [36].

The results of these investigations are given in Fig. 9. We can see that the composition of the supersaturated solid solution affects dramatically the phase composition of aging products. Depending on the Mg:Si ratio, Duralumin (2024 type) fall into the phase regions (Al) + S', (Al) + S' + $''$ or (Al) + $'' + \beta''$; forgeable alloys of the 2014 type fall into the phase region (Al) + $'' + \beta''$; and heat-treatable silumins have the phase composition (Al) + $'' + \beta'' + Si$. The change of the phase composition
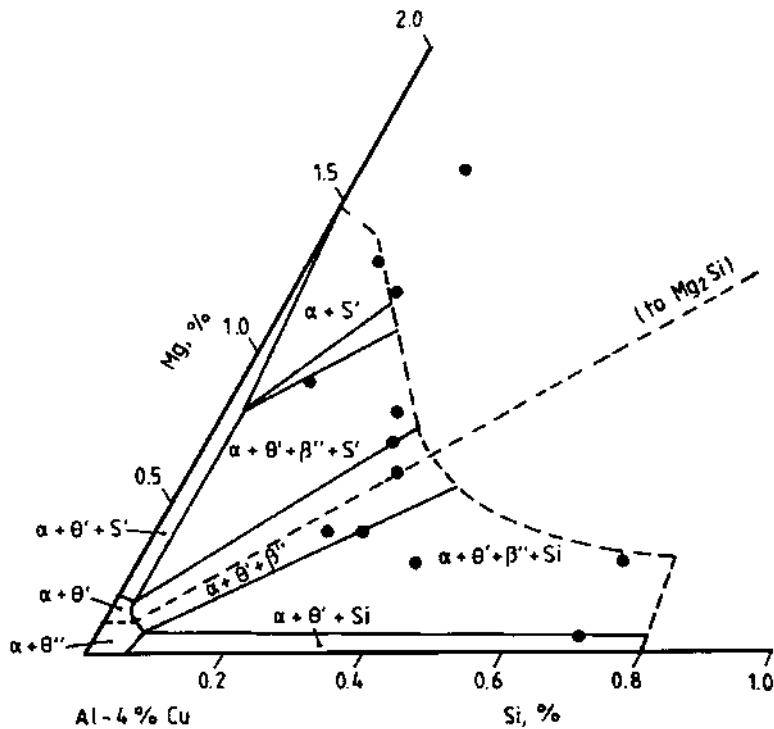
Figure 9 Phase field distribution in Al-4% Cu-Mg-Si alloys aged at 170°C for 20 hr.

is accompanied by the essential change in the internal structure. The structure composed by '' and β'' precipitates is much finer than that containing S' phase.

When discussing these results, we have to mention the following:

- The metastable phase composition in the range of 2XXX series alloys corresponds with their equilibrium phase composition according to the phase diagram.
- The phase composition of alloys with an excess of silicon differs from that according to the equilibrium phase diagram.
- According to the equilibrium phase diagram, all casting Al-Si alloys with magnesium and copper have to contain the quaternary Q phase.

The difference between the equilibrium and metastable phase composition can be explained in terms of precipitation kinetics. The decomposition occurs in the following sequence: clusters and zones (Mg, Si) and (Al, Cu); Si; β''; and ''. In such a scheme of precipitation, the supersaturated solid solution gradually depletes of Si, Mg and Cu due to the formation of binary phases, and there is no material left to form the Q phase. The precipitation of other phases with simple composition is thermodynamically more favorable. So, the β'' phase precipitates instead of the Q phase. Later, the coherent phase can transfer to the semicoherent variant of β' or B', and finally to the equilibrium Q phase.

The change of phase composition affects the aging response and mechanical properties of alloys. It has been shown that the maximum hardening effect and

Table 21 Effect of Silicon on the Phase Composition and Mechanical Properties of Aged (170°C, 20 hr) Extruded Plates from 2224-type Alloys

Alloy	2224 alloy	2224 alloy with 0.6% Si
Aging products	S'', S' and traces of θ'	β'' and θ'
UTS, MPa	535	520
YS, MPa	365	415
El, %	13.5	14.0
Low-cycle fatigue, kc	72	75
Fatigue endurance, kc	324	906
Fatigue crack propagation rate, μm/cycle ($\Delta K = 19$ MPa m$^{1/2}$)	3	7
Fracture toughness, MPa m$^{1/2}$	50.3	50.3

the highest strength refers to the phase composition with hardening phases β'' and $''$. This is an unusual result. Previously, the S' phase was considered as the most efficient hardener in the alloys of this system. The results given in Table 21 demonstrate that the introduction of Si in the stoichiometric ratio with Mg in high-purity Duralumin increases the yield strength and fatigue endurance with other vital properties preserved [36]. This is due to the dramatically changed the phase composition and internal structure. The same is true for casting alloys.

It should be noted that usually silicon is considered as a harmful impurity in wrought and casting aluminum alloys. This element really decreases ductility and fracture toughness of solid-solution type alloys. This is mainly due to the formation of intermetallics with iron impurity. However, being introduced in nearly stoichiometric ratio with magnesium (Mg:Si = 1.73 wt%) in alloys pure with respect to iron, silicon changes the phase composition of aging products and improves characteristics of the alloy.

Impurities and small additions can considerably affect the hardening effect of Al-Cu-Mg-Si alloys, mainly due to the binding of main alloying elements in insoluble particles and to the decreasing content of copper and magnesium in the supersaturated solid solution. It has been found that iron, nickel and cobalt reduce the copper concentration in the supersaturated solid solution from 4 to 2.5–3.5%. Antimony and lithium lower the magnesium content. These effects are illustrated in Table 22 [55]. Note that mutual alloying with iron and manganese restores the composition of the solid solution and the tensile properties.

Typical temper modes and mechanical properties of some commercial Al-Cu-Mg-Si alloys are shown in Table 23 and Table 24.

2.6 Aging in Commercial Al-Zn-Mg-(Cu) Alloys

The compositions within the Al-Zn-Mg-(Cu) system form important series of commercial materials. The quaternary alloys yield the highest strength for commercial aluminum wrought (7XXX series) and casting (7XX.0 series) alloys. The chemical compositions of some alloys are given in Table 25.

Table 22 Effect of Additional Alloying on the Composition of the Supersaturated Solid Solution and Tensile Properties after Aging of Cast Al-Cu-Mg-Si Alloys

Alloy composition, wt%			Composition of supersaturated solid solution, wt%			Additional phases	UTS, MPa	YS, MPa	El, %
Cu	Mg	Si	Cu	Mg	Si				
4.5	0.3	6.0	4.1	0.25	0.65		440	385	3.5
+0.5 Co			3	0.3	0.61	(AlCoCuFe)	355	325	1.5
+0.3 Sb			3.7	0.1	0.64	Mg$_2$Sb	405	330	3
4.5	1.2	0.63	4	0.61	0.29		450	442	1.1
+0.8 Fe			3.1	0.56	0.32	(AlCuFe), (AlCuFeSi)	366	365	0.4
+0.8 Fe+0.8 Mn			4.2	0.55	0.24	(AlFeMnSi)	416	415	1

Table 23   Temper Modes for Some Al-Cu-Mg-Si Alloys

Alloy	Solution treatment	Aging
336	515°C, 8 hr	205°C, 7–9 hr (T65)
355.0	525°C, 4–12 hr	155°C, 5–5 hr (T6)
		170°C, 14–18 hr (T62)
332.0	—	205°C, 7–9 hr (T5)
A319.0	505°C, 12 hr	155°C, 2–5 hr (T6)
333.0	505°C, 6–12 hr	155°C, 2–5 hr (T6)
4032	510°C (T4)	170°C, 10 hr (T6)
AK6	505–525°C	20°C, > 96 hr
		160–170°C, 10–15 hr (T6)
2618	530°C (T4)	200°C, 20 hr (T6)

Table 24   Typical Mechanical Properties of Some Al-Cu-Mg-Si Alloys

Alloy	*UTS*, MPa	*YS*, MPa	*El*, %
324.0 F/T62	205/310	130/270	2.5/3.0
336.0 T65	325	295	0.5
355.0 F/T6/T61	160/240/270	85/170/240	3.0/3.0/1.0
332.0 T5	250	195	1
A319.0 F/T6	185/250	125/165	2.0/2.0
333.0 F/T6	235/290	130/205	2.0/1.5
238.0 F	210	165	1.5
4032 T6	380	315	9
AK6 T6	420	330	13
AK8 T6	490	420	10
2618 T61	440	370	10
2014 O/T6	185/485	95/415	18/13

Table 25   Chemical Compositions of Some Commercial Al-Zn-Mg-(Cu) Alloys

Alloy	Zn, %	Mg, %	Cu, %	Other elements, %
513.0	1.8	4.0	—	
363.0	3.8	0.3	3.0	5.25Si; 0.25Sn; 0.25Pb
707.0	4.25	2.1	< 0.20	0.5Mn; 0.3Cr
711.0	6.5	0.35	0.5	1Fe
771.0	7.0	0.9	—	0.13Cr
7005	4.5	1.4	—	0.14Zr; 0.03Ti; 0.45Mn; 0.13Cr
1911 (Russian)	4.1	1.9	—	0.35Mn; 0.13Zr
7075–7475	5.6	2.2–2.5	1.6	0.23Cr
7050	6.2	2.2	2.3	0.12Zr
7178	6.8	2.7	2.0	0.23Cr
7001	7.4	3.0	2.1	0.26Cr
7049	7.7	2.4	1.6	0.16Cr

The solid solution range in these alloys are very wide and almost all zinc, magnesium and copper can be introduced into the supersaturated solid solution during quenching. It is worth to note that the supersaturated solid solution in copper-free Al-Zn-Mg alloys can be obtained even during rather slow cooling, in air.

First, we consider the Al-Zn-Mg system. This alloying system is well studied, although there are still disputes about the origination of GP zones and the meta-stable phase composition. The following phases are formed during aging: GP zones (MgZn); η'; η (MgZn$_2$); T'; and T (Al$_2$Mg$_3$Zn$_3$ or (AlZn)$_{49}$Mg$_{32}$). As Mg:Zn ratio ranges from 2:5 to 1:7, the precipitation sequence goes through zones and coherent precipitates to the η phase. At Mg:Zn $= 0.5$–6, the decomposition finishes with the formation of the T phase [18]. Two types of GB zones are distinguished in Al-Zn-Mg alloys: GP1 are formed during natural aging and GP2 (or vacancy-rich clusters) originate during quenching and are likely to be precursors for the η' phase. The metastable η' phase forms in the compositional range much wider than the (Al) $+ \eta$ region on the equilibrium phase diagram, covering part of the (Al) $+ T$ phase field. The very important feature of this system is that the η phase may have a series of orientation relationships, typical of the aging mode and the alloy composition. This specific feature is reflected in the designation of η precipitates with a subindex. The η_i phases precipitate in the temperature range from 100°C to 200°C and can nucleate either on η' particles or independently. The data on the crystal structure and orientation relationships of possible phases in Al-Zn-Mg alloys are shown in Table 26 [18,56].

The addition of up to 1% copper to Al-Zn-Mg alloys does not affect significantly the precipitation mechanism. Copper remains mainly in the solid solution, not forming own phases. Higher copper content contributes to hardening either

Table 26 Crystal Structure and Orientation Relationships of Phases in Al-Zn-Mg Alloys

Phase	Crystal structure	Lattice parameter, nm		Orientation relationship
		a	c	
η' (R)	Hexagonal	0.496	0.702	$(001)_p \parallel (110)_{A1}$; $(100)_p \parallel (001)_{A1}$
η'_2 (R$_2$)		0.496	0.554	
η_1	Hexagonal	0.515–0.523	0.848–0.862	$(001)_p \parallel (110)_{A1}$; $(100)_p \parallel (001)_{A1}$
η_2				$(001)_p \parallel (1\bar{1}\bar{1})_{A1}$; $(100)_p \parallel (110)_{A1}$
η_3				$(001)_p \parallel (1\bar{1}\bar{1})_{A1}$; $(110)_p \parallel (110)_{A1}$
η_4				$(001)_p \parallel (110)_{A1}$; $(\bar{1}20)_p \parallel (1\bar{1}\bar{1})_{A1}$
η_5				$(302)_p \parallel (110)_{A1}$; $(\bar{1}20)_p \parallel (1\bar{1}\bar{1})_{A1}$
η_6				$(201)_p \parallel (1\bar{1}2)_{A1}$; $(1\bar{2}0)_p \parallel (1\bar{1}\bar{1})_{A1}$
η_7				$(104)_p \parallel (110)_{A1}$; $(\bar{1}20)_p \parallel (1\bar{1}\bar{1})_{A1}$
η_8				$(001)_p \parallel (31\bar{1})_{A1}$; $(\bar{1}20)_p \parallel (1\bar{1}2)_{A1}$
η_9				$(001)_p \parallel (110)_{A1}$; $(120)_p \parallel (001)_{A1}$
η_{10}				$(001)_p \parallel (1\bar{1}\bar{1})_{A1}$; $(110)_p \parallel (1\bar{3}4)_{A1}$
η_{11}				$(001)_p \parallel (110)_{A1}$; $(100)_p \parallel (0\bar{1}\bar{1})_{A1}$
T'	Cubic	1.42–1.44 1.39	-2.75	$(100)_p \parallel (111)_{A1}$; $[010]_p \parallel [11\bar{2}]_{A1}$
	Hexagonal			
T	Cubic	1.416–1.429	—	$(100)_p \parallel (112)_{A1}$; $[001]_p \parallel [1\bar{1}0]_{A1}$

by increasing the stability of GPZ (copper atoms enter the zones) or by altering the composition of η phase during aging above $150°C$, or by the formation of the S' (Al_2CuMg) phase [57]. Aksenov et al. [57] also showed that the addition of 1–2% Cu to Al-Zn-Mg alloys increases the metastable solvus of the hardening η'_2 phase and therefore contributes to additional hardening by improving the stability of this phase. According to Mondolfo [18], the main constituents of alloys containing 5–8% Zn, 23% Mg and up to 1.5% Cu are the $MgZn_2$-$AlCuMg$ and $Al_2Mg_3Zn_3$-Al_6CuMg_4 phases, which form series of solid solutions between isomorphic phases from Al-Mg-Zn and Al-Cu-Mg systems.

The properties of Al-Zn-Mg-Cu alloys are much dependent on the total concentration of alloying elements. If the overall content of Zn, Mg and Cu exceeds 9%, the alloys exhibit the highest strength at expense of corrosion resistance, weldability and toughness. In the range of alloying concentration from 6% to 8%, the balanced complex of properties can be achieved. In addition, at the concentration range from 5% to 6%, the fabricability becomes paramount and stress-corrosion susceptibility vanishes.

The natural aging of Al-Zn-Mg-(Cu) alloys occurs very efficiently and continues for years. Due to this instability in properties, these alloys are seldom used in the RT-aged condition (W temper). Stable properties, higher strengths and fracture toughness, and improved corrosion resistance are obtained after various modes of artificial aging. In difference from Al-Cu-Mg-(Si) and Al-Mg-Si alloys aged typically in the range from $160°C$ to $190°C$, the Al-Zn-Mg-(Cu) alloys receive higher properties upon annealing in the temperature range from $115°C$ to $130°C$.

The maximum strengthening is associated with precipitation of coherent GP zones and the semicoherent η' phase. The solvus temperature of GP zone formation increases with magnesium and zinc concentrations. The zones are very small (2–3.5 nm) and spherical in shape, whereas the η' phase forms round- or plate-shaped particles. The GP zones nucleate homogeneously in the matrix and gradually transform to either η or T phases with respect to the Mg:Zn ratio. The η phase precipitates in various shapes such as plates, rods and laths, depending on the orientation relationship [56]. Crystal defects such as dislocations, small- and large-angle boundaries represent sites for the preferential formation of semicoherent or incoherent particles. On aging at temperatures above the solvus of GPZ or during slow cooling upon quenching, the precipitation of these not hardening phases occurs and decreases the final strength of the alloy. Hence, the right choice of the quenching rate and the aging temperature is very important for receiving necessary properties.

A time-temperature diagram showing the phase composition of aging products in a 7075-type alloy is given in Fig. 10 [31].

The most widely used aging mode for Al-Zn-Mg-(Cu) alloys is a two-step aging. The aim of the first step ($100–110°C$) is to grow up GP zones that are stable at higher temperatures and provide sites for the formation of meta-stable hardening phases. During the second step ($150–160°C$) the alloy acquires desirable properties. There are several purposes of the two-stage aging: (i) to diminish the harmful effect of intermediate natural aging (or delay between quenching and artificial aging); (ii) to reduce the overall treatment time; and (iii) to improve corrosion resistance.

High-strength Al-Zn-Mg-Cu alloys are very sensitive to stress corrosion, which limits their application. The susceptibility to stress corrosion is due to inhomo-
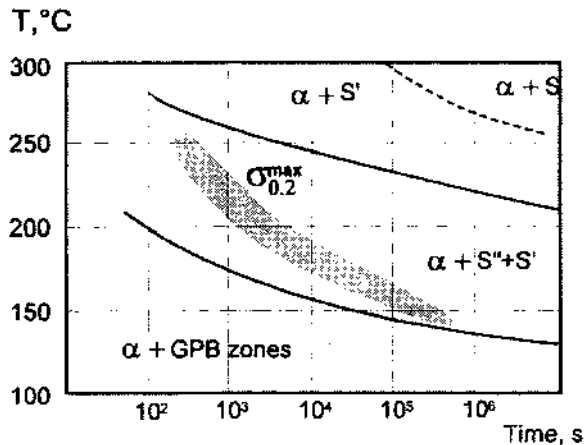
Figure 10 Time-temperature diagram for aging of a 7075-type alloy.

geneous precipitation of semicoherent and incoherent phases and due to the formation of so-called precipitation-free zones near grain boundaries. The nucleation of GP zones is much dependable on the efficient vacancy concentration in the supersaturated solid solution. As the grain boundaries provide good vacancy sinks, the nearby regions can be depleted of vacancies or solute atoms, or remain supersaturated without decomposition [18]. Special heat treatment modes were designed to improve the stress-corrosion resistance of these alloys. These tempers are based on the fact that overaging may decrease the selective corrosion at grain boundaries. The practice is to use either two-step aging (100–120°C, 1–24 hr and 160–175°C) or one-step aging at 160–175°C but with well-controlled heating rate. In both cases the aim is to produce numerous GPZ stable at higher temperatures, and then transform them to homogeneously distributed intermediate and stable phases upon overaging.

Additions of transition metals also are aimed on the improving corrosion resistance due to the redistribution of precipitates, grain refinement and hardening the precipitation-free zones.

The temper modes and mechanical properties of some commercial Al-Zn-Mg-(Cu) alloys are listed in Table 27 and Table 28.

2.7 Aging in Commercial Al-Li Alloys

Alloys containing lithium attract more and more attention during recent two decades. These alloys have several advantages: low weight, high rigidity, excellent fatigue and cryogenic toughness. Most of these materials are wrought and heat treatable. Main application is airspace industry. Each 1% Li within the limit solubility decreases the density of an alloy by 3% and increases the Young modulus by 5%. There are several groups of alloys with lithium: Al-Cu-Li; Al-Mg-Li; and Al-Cu-Mg-Li. Binary Al-Li alloys have not found any commercial application,

Table 27 Temper Modes for Some Al-Zn-Mg-(Cu) Alloys

Alloy	Solution treatment	Aging	Comments
707	530°C, 4–16 hr	175°C, 4–10 hr (T7)	
711.0	—	20°C, 21 day (T1)	
771.0	590°C, 6 hr°	130°C, 3 hr (T6)	Cooling in air after solutionizing
7005	400°C	20°C, 82 hr or 100–110°C, 8 hr + 145–155°C, 16 hr	Press quenched
7075	480°C (W)	120°C, 24 hr (T6) or 95°C, 4 hr + 157°C, 8 hr	Rapid cooling upon quenching and rapid heating to aging temperatures
7475	480°C (W)	120°C, 3 hr + 160°C, 3 hr	Rapid cooling upon quenching and rapid heating to aging temperatures
7050	475°C (W)	120°C, 3 hr + 165°C, 1 hr (T61) or 100°C, 8 hr + 165°C, 24–26 hr (T7351)	Rapid cooling upon quenching
7178	470°C (W)	120°C, 24 hr (T6)	Rapid cooling upon quenching
7001	465°C (W)	120°C, 24 hr (T6)	Rapid cooling upon quenching
7049	470°C (W)	20°C, 48 hr + 120°C, 24 hr + 165°C, 10–16 hr (T73)	Rapid cooling upon quenching

Table 28 Mechanical Properties of Some Al-Zn-Mg-(Cu) Alloys

Alloy	UTS, MPa	YS, MPa	El, %
513.0 F	186	110	7.0
707.0 F	255	207	1.0
711.0 F	240	125	8.0
771.0 F/T6	305/330	250/260	3.0/9.0
7005 O/W/T6	195/345/350	80/205/290	11.5/30/42
7075 O/T6	230/570	105/505	17/11
7475 T7351	505	435	14
7050 T7651	550	490	11
7178 O/T6	230/605	105/540	15/10
7001 O/T6	255/675	150/625	14/9.0
7049 T73	540	475	10

however the precipitation phenomena in these alloys is worth considering in order to better understand the aging of more complex materials. Some alloy compositions are given in Table 6.29.

The decomposition of the Al-Li supersaturated solid solution occurs with the homogeneous formation of the ordered δ' (Al₃Li) phase which later gives place to the equilibrium AlLi phase [58]. At usual concentrations of Li (1.5–2.5%), the solvus of the intermediate phase is about 150–250°C. The very fine, spherical precipitates or clusters of Al₃Li are formed during quenching, and the artificial aging results only in their growth. The rapid lithium diffusion along dislocation lines, grain

Table 29 Compositions of Some Aluminum Alloy Containing Lithium

Alloy	Li, %	Cu, %	Mg, %	Other elements, %
Weldalite049	1.3	5.4	0.4	0.4Ag; 0.14Zr
1420 (Russian)	2.0	—	5.5	0.09–0.15Zr
1421 (Russian)	2.0	—	5.0	0.2Mn; 0.2Sc; 0.15Zr
VAD23 (Russian)	0.9–1.4	4.5–5.8	—	0.4–0.8Mn, 0.1–0.25Cd
2091 (USA)	1.7–2.3	1.8–2.5	1.1–1.9	0.04–0.16Zr
CP276 (French)	1.9–2.6	2.5–3.3	0.2–0.8	0.04–0.16Zr
2090 (USA)	1.9–2.6	2.4–3.0	0.05–0.25	0.08–0.15
8090 (European)	2.2–2.7	1.0–1.6	0.6–1.3	0.04–0.16Zr

Table 30 Crystal Structure and Orientation Relationships of Phases Formed in Al-Li Alloys

Phase	Crystal structure	Lattice parameter, nm		Orientation relationship
		a	c	
δ'	Cubic	0.401	—	$(001)_p \parallel (001)_{A1}$; $[100]_p \parallel [100]_{A1}$
δ	Cubic	0.6356–0.638	—	$(100)_p \parallel (110)_{A1}$; $[011]_p \parallel [1\bar{1}1]_{A1}$
T_1 (Al_2CuLi)	Hexagonal	0.497	0.935	$(001)_p \parallel (111)_{A1}$; $(100)_p \parallel (\bar{1}\bar{1}0)_{A1}$; $(110)_p \parallel (2\bar{1}\bar{1})_{A1}$
T_2 (Al_6CuLi_3)	Icosahedral			
T_B ($Al_{7.5}Cu_4Li$)	Cubic	0.583	—	$[100]_p \parallel [110]_{A1}$; $[001]_p \parallel [001]_{A1}$
R (Al_5CuLi_3)	Cubic	1.3914 or 1.403	—	$[100]_p \parallel [\bar{1}\bar{1}1]_{A1}$; $[010]_p \parallel [\bar{1}01]_{A1}$; $[001]_p \parallel [\bar{1}\bar{1}\bar{2}]_{A1}$
Al_2LiMg	Cubic	2.031	—	$(\bar{1}10)_p \parallel (\bar{1}10)_{A1}$; $[110]_p \parallel [111]_{A1}$

boundaries and interfaces with dispersoids causes the formation of precipitation-free zones and discontinuous precipitation of δ. On further aging the coherent δ' phase transforms to the semicoherent and, finally, incoherent δ' (AlLi) phase. The latter appears as plates and frequently forms onto grain boundaries. It is likely that the AlLi phase nucleates and grows independently of its precursor.

The crystal structure and orientation relationships of phases formed in various Al-Li alloys are given in Table 30 [18,58,59].

Al-Li alloys are unique with respect to microstructures formed during aging. The δ' phase once precipitated retains its coherency even after long aging times. Additionally, long aging of Al-Cu-Li alloys at temperatures above 190°C produces grain-boundary precipitates of the icosahedral phase, which is quite unusual for common processing procedures. The behavior of the δ' phase is very similar to that of the Al_3Sc phase [60].

However, the precipitation-free zones and grain-boundary precipitates along-side homogeneously distributed coherent particles inside grain determine the limi-

tation of Al-Li alloys—fast crack propagation and uneven dislocation slip with relevant stress accumulation and cracking.

In commercial alloys, the dislocation slip is homogenized and the precipitation-free zones are reduced by introducing dispersoids (e.g. Al_3Zr) and semicoherent/incoherent precipitates such as T_x, θ (Al_2Cu) and S' (Al_2CuMg).

Magnesium and copper are the most widely used additions to Al-Li alloys. They improve strength by solid solution and precipitation hardening and minimize the formation of precipitation-free zones, thereby increasing fatigue endurance and fracture toughness. Zirconium stabilizes substructure, preventing the development of recrystallization. In addition, the introduction of transition metals, such as Zr and Sc, considerably slows down the lithium diffusion and the coarsening of δ' particles [61]. Moreover, the presence in the structure of coherent or semicoherent Al_3Zr and Al_3Sc particles provides places for preferential nucleation of the δ' phase. The latter forms so-called composite particles with the core of Al_3TM and the envelope of Al_3Li.

The precipitation sequence in Al-Li-Mg alloys is: supersaturated solid solution, δ (Al_3Li); Al_2LiMg. The only effect of magnesium at early stages of decomposition is the reduced solid solubility of lithium. Therefore, the precipitation density of δ' increases. Later, magnesium and lithium form the ternary compound. The latter is incoherent and nucleates on grain boundaries or dislocation networks during quenching or overaging.

In the Al-Li-Cu alloys, the decomposition occurs as follows; supersaturated solid solution, GPZ, Al_2Cu (θ'', θ', θ) or Al_3Li (δ') and, finally, T_1 (Al_2CuLi). Instead of T_1, other T_x phases (see 60) can be formed depending on the Cu:Li ratio. On decreasing this ratio, the equilibrium phase composition changes from θ to T_B, T_1, T_2 and, finally, to AlLi. On overaging, the R phase forms in addition to T_B and T_2 phases [59]. Generally, copper accelerates the decomposition and hardening in Al-Li alloys. The hexagonal T_1 phase appears in structure as hexagonal-shaped plates. With respect to the supersaturation, T_1 nucleates either on GPZ or at dislocations.

During precipitation in an Al-2.7% Li-1.9% Cu alloy, plates of the T_1 phase rapidly fill the entire volume of the grain dividing it into cells filled, in turn, with δ' particles [62]. As a result of this structure formation, the yield strength of the alloy increases and the deformation becomes more uniform. However, the latter effect may be much less pronounced if there are regions free of T_1 particles.

Huang and Ardell [63] demonstrated that the equilibrium phase diagram cannot predict the phase composition after aging. They studied two alloy, containing, respectively, 2.3% Li; 2.85% Cu and 2.90% Li; 0.99% Cu. Both alloys contained also 0.12% Zr. According to the equilibrium phase diagram, the first alloy has to contain T_1 and T_2 phases whereas the second one, δ and T_2. However, the TEM study revealed that both alloys contained after aging δ' and T_1, and the first alloy in addition, θ'. The latter phase frequently serves as a substrate for δ'. The θ' phase is observed up to the peak hardness range, afterwards its dissolves giving place to the T_1 phase.

Figure 11 demonstrates a time-temperature diagram for phase distribution and hardening of a 1450 (Al-Li-Cu-Zr) Russian alloy. Alloying with both magnesium and copper makes the phase composition and precipitation sequence more complex [59]. In addition to δ' and T_x phases, the S' (Al_2CuMg) and R (Al_5CuLi_3) phases
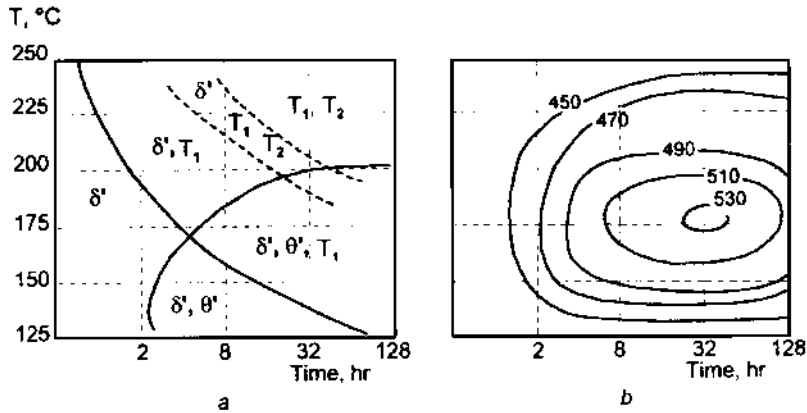
Figure 11 Time-temperature diagram for aging of a 1450 (Al-Li-Cu-Zr) alloy (a); and corresponding distribution of yield strength values (b).

Table 31 Temper Modes for Some Al-Li Alloys*

Alloy	Solution treatment	Aging
1420	450°C	170°C, 8–24 hr (T6) or 120°C, 12–18 hr (T7)
VAD23	520°C	160°C, 10 hr (T6)
2091	530°C (T3)	120°C, 24 hr (T84)
CP276	540°C (T3)	190°C, 12–15 hr (T6)
2090	540°C (T3)	165°C, 24 hr (T83)
8090	530°C (T3)	190°C, 12 hr (T6)

*Stretching or cold working after quenching and before aging is obligatory

precipitate, contributing to further improved hardening. The S' particles decorate subboundaries and prevent or delay the development of dynamic recovery, thus improving high-temperature stability of the alloy up to 250°C.

Typical temper modes and mechanical properties of some Al-Li-based alloys are given in Table 31 and Table 32.

3 PRECIPITATION PHENOMENA IN ALUMINUM ALLOYS WITH TRANSITION METALS

The main peculiar feature of transition metals (TM) in aluminum alloys is the formation of supersaturated solid solutions during solidification. The higher the cooling rate, the larger the solubility of TM in solid aluminum. The supersaturated solutions obtained in this way are characterized with much higher stability than ordinary supersaturated solid solutions formed by copper, magnesium, zinc, silicon, and lithium upon quenching. The temperature of decomposition for Al-TM solid solutions is between 250°C and 650°C, depending on the transition metal.

Table 32   Mechanical Properties of Some Al-Li Alloys

Alloy	*UTS*, MPa	*YS*, MPa	*El*, %	Other properties*
Weldalite049 T6	720	680	3.5	
1420* T6 (extruded bars)	505	380	8.0	
1421* T6 (extruded bars)	530	465	5.5	
VAD23 T6	580–660	540–600	5.0–9.0	
2091* T651 (sheet)	480	430	12	$E = 78.8$ GPa
CP276* T6 (extruded bars)	640	590	5.0	$K_{IC} = 39$ MPa$\sqrt{}$m; $E = 90.2$ GPa
2090 O/T83	215/530	195/517	11/3.0	$K_{IC} = 38.5$ MPa$\sqrt{}$m; $E = 78.5$ GPa
8090* T6 (extruded bars)	555	445	7.0	$K_{IC} = 37$ MPa$\sqrt{}$m; $E = 81.2$ MPa

*Experimental results [60,64–66]

Table 33   Effect of Cooling Rate on the Composition of Al-based Solid Solution

V_c, K/s	Mn, %	Cr, %	Zr, %	V, %	Ti, %	Sc, %
10^{-1}	1.82	0.82	0.28	0.37	0.28	0.4
10^1	2.5	0.4	0.1	0.1	0.1	0.4
10^2	2.8	0.7–1.0	0.15–0.17	0.25	0.2	0.5
10^3	3.0–5.0	1.5–3.5	0.5–0.7	1.3	0.4–1.0	1.1
10^4	5.0–7.0	2.0–5.7	0.9–1.7	—	1.4	—
10^5	6.1–10.0	5.35–5.7	1.2–2.0	1.3	—	3.2
10^6	8.6–14.0	5.8–7.75	2.5–2.8	2.6	3.7–5.0	—

Modern ingot and casting metallurgy operates with cooling rates of 10–100 K/sec. At such cooling rates, the aluminum solid solution can be saturated with TM up to the equilibrium limit solid solubility in eutectic systems or to the equilibrium concentration of TM in the liquid phase in peritectic systems.

The use of rapid solidification techniques, such as atomization, splat cooling and melt spinning, can increase the cooling rate up to 10^7 K/sec and enrich the solid solution to much larger extent. Table 33 and Table 34 demonstrate the supersaturation degree, phase composition and hardening effect of some Al-TM binary alloys [60]. The high structural and phase stability of Al-TM alloys makes these alloys promising for commercial use. This stability is connected mainly with very low diffusion rates of these elements in solid aluminum and sometimes with good structural match between crystal lattices of TM aluminides and aluminum (a cubic structure with $a = 0.404$ nm).

In binary systems, transition metals react with liquid aluminum either by eutectic (Mn, Fe, Sc, Ni) or peritectic (Cr, V, Zr, Ti, Mo) reactions. The type of the phase diagram determines some differences in the alloy behavior. The formation of a supersaturated solid solution in peritectic systems requires deeper undercooling,

Table 34 Parameters of Binary Al-TM Alloys and Effect of Precipitation Hardening

System	Phase	Crystal structure	Limit solubility (C), at %	Temperature of decomposition, °C	Effect of precipitation hardening, $\Delta H/C$ [at. %]
Al-Mn	Al_6Mn	Orthorhombic: $a = 0.6498$ nm; $b = 0.7552$ nm; $c = 0.8870$ nm Cubic (meta stable $Al_{12}Mn$): $a = 0.747$ nm	0.88	300–350	10
Al-Cr	Al_7Cr	Orthorhombic: $a = 2.48$ nm; $b = 2.47$ nm; $c = 3.02$ nm,	0.41	450–500	51
Al-Zr	Al_3Zr	Tetragonal: $a = 0.4006$ nm; $c = 1.727$ nm Cubic (meta stable): $a = 0.407$ nm	0.093	400–450	154
Al-V	$Al_{11}V$	Cubic: $a = 1.4586$	0.21	500–550	31
Al-Ti	Al_3Ti	Tetragonal: $a = 0.3848$ nm; $c = 0.8596$	0.17		—
Al-Sc	Al_3Sc	Cubic: $a = 0.4104$ nm	0.28	250–350	208

which is evidenced by the existence of a threshold cooling rate, about 10^2 K/sec. On the contrary, the supersaturation in eutectic systems increases continuously with undercooling (or cooling rate). The decomposition in alloys of eutectic systems occurs at lower temperatures and proceeds more rapidly than in peritectic-type alloys. The diffusion coefficients of elements forming eutectic systems with aluminum are by an order of magnitude higher than those of peritectic systems.

It should be also noted that the dendritic segregation formed upon solidification in Al-TM alloys cannot be easily eliminated by homogenization. This is obviously due to low diffusion rates of transition metals, which range from 10^{-14} to 10^{-12} cm^3/sec at 500°C.

There are several mechanisms, by which transition metals act in aluminum alloys. These are grain refinement of the as-cast structure, slowing down or preventing the recrystallization of deformed alloys (structural hardening), and precipitation hardening. The first two mechanisms are widely used in commercial aluminum alloys, which frequently contain small additions of Ti, Mn, Zr, and Cr. The third mechanism is less used. There are several causes of this. Firstly, there are only a few transition metals that form coherent or semicoherent precipitates during decomposition of the supersaturated solid solution. Actually, there are only zirconium and scandium (see Table 34). Secondly, the temperature ranges of precipitation hardening in commercial wrought alloys (150–200°C) and in Al-TM alloys (250–450°C) are very different. Therefore, one has to choose which mechanism of hardening is preferable, by usual hardening phases considered previously in this Chapter or by aluminides of transition metals.

The challenge is to use the precipitation hardening with Al-TM phases in nonheat-treatable aluminum alloys, e.g. Al-Mg. This way was applied to the development of Al-Mg-Zr-Sc alloys and gave excellent results [60]. All mechanisms of

transition metals in aluminum alloys are due to the formation of considerably fine aluminides either during solidification or during annealing. Mostly, the aluminides formed upon solidification have an ability to refine grains, serving as nucleation sites for aluminum solid solution. Lamikhov and Samsonov [67] showed that the refining ability of transition metals added to 99.99% pure Al decreases from Sc to Ni in Period IV and from Zr to Mo in Period V. The incompleteness of the *d*-shell and the crystal structure of aluminides are likely the most important parameters determining the refining effect.

The hindering of recrystallization processes occurs by pinning-down small-angle boundaries and dislocations by fine, not necessarily coherent, aluminide particles (dispersoids). These particles are usually formed during high-temperature decomposition, e.g. during solution treatment (which is homogenization for main alloying elements and heterogenization for transition metals). Yelagin [68] analyzed the effects of transition metals on recrystallization of aluminum and its alloys. Binary alloys were cast, annealed at 500°C, hot rolled at 420–450°C, annealed at 450°C, and cold rolled. Table 35 demonstrates the maximum increments of recrystallization temperatures upon addition of TM. The analysis of the data shows that (i) the recrystallization temperature in binary alloys of aluminum with Period IV TM increases after a certain threshold concentration which is close to the limit solubility of TM at a temperature of solution treatment; (ii) in the case of Period V TM, the recrystallization temperature increases even with very small additions; and (iii) some TM cause pronounced maxima of the recrystallization temperature against the concentration, these maxima being correlated with the limit solubility of TM in aluminum.

Transition metal acts as an efficient antirecrystallizer agent under the following conditions: incomplete $3d$ electron shell with minimum electrons; large difference in atomic radii with aluminum; formation of supersaturated solid solution upon solidification; and the decomposition of this solid solution with precipitation of thermally stable fine dispersoids.

Let us briefly consider the effects of some commonly used transition metals in aluminum alloys.

Table 35 Maximum Increments of the Temperatures of Recrystallization Onset (t_r^s,) and Finish (t_r^f) in Al-TM Alloys

Element	Atomic radius, nm	C, at%	Δt_r^s, K	Δt_r^f, K
Sc*	0.16	0.20	120	320
Ti	0.145	0.25	5	180
V	0.136	0.21	15	15
Cr	0.128	0.35	45	30
Mn	0.131	0.77	30	25
Fe	0.137	0.04	65	35
Ni	0.124	0.04	− 10	5
Zr	0.16	0.09	105	240
Nb	0.147	0.12	35	35
Mo	0.14	0.12	70	45

Chromium is a usual addition to Al-Mg, Al-Mg-Si and Al-Mg-Zn alloys. It is used to control grain structure in wrought products by delaying or preventing recrystallization during heating or hot working. The formed substructure is favorable for stress-corrosion resistance and fracture toughness. However, when a hardening phase tends to precipitate onto Cr-containing dispersoids, the quench sensitivity may increase.

Iron is usually considered as a harmful impurity in aluminum alloys. Nevertheless, its addition along with manganese in 8XXX series alloys produces good combination of strength and ductility at room temperature and helps to retain strength at elevated temperatures. This is due to the fine grain size stabilized by dispersed iron-rich precipitates. In order to prevent the depletion of the solid solution of copper and magnesium in 2XXX series alloys, iron is combined with manganese or nickel. In this case, the amount of insoluble phases containing copper, magnesium, silicon and iron is essentially decreased, being replaced by AlFeMnSi and AlFeNi compounds.

Manganese is a very typical addition in many commercial aluminum alloys. Manganese has the highest solid solubility among TM in aluminum and can provide solid solution hardening as well. However, the most important is the structural hardening due to the decomposition of Al-Mn supersaturated solid solution. Alloys of the Al-Cu-Mg system usually contain 0.5–0.8% Mn, which simultaneously improves strength and ductility of extruded products. Manganese (up to 1.25%) is a main alloying element in 3XXX alloys used for can production. Its purpose is to allow high deformation degrees and to prevent grain growth. These effects are due to the slowing down recrystallization and considerably uniform distribution of manganese precipitates throughout the grain volume. At the same time, manganese precipitates increase the quench sensitivity of heat treatable aluminum alloys. Manganese is also the cheapest addition in aluminum.

Scandium is a new element in aluminum alloys. The interest to this element is increasing during recent decade thanks to the unique combination of properties in Al-Sc alloys [60]. All valuable features of scandium in aluminum are due to the formation of the Al_3Sc phase either during solidification or upon decomposition of the supersaturated solid solution. The vital feature of this phase is a cubic structure with the lattice parameter only slightly different from that of aluminum (0.4104 nm and 0.404 nm, respectively). This is the best match in all known equilibrium phases. The antirecrystallizing effect of scandium is very high and can be used in almost all commercial aluminum alloys. However, the precipitation hardening, which is very efficient in Al-Sc alloys (Table 36), can be successfully applied only to nonheat-treatable alloys, such as Al-Mg and Al-Mn alloys.

It should be noted that scandium is quite expensive, therefore its concentration should be as low as possible. It was found out that the mutual introduction of Sc and Zr allows one to decrease the amount of scandium to 0.15–0.2% and even improve mechanical properties, service characteristics, and thermal stability. The reason is in the formation of two coherent cubic phases with close crystal structures (equilibrium Al_3Sc and metastable cubic Al_3Zr). These phases together precipitate in the temperature range 300–400°C, which is between effective temperature ranges of binary Al-Sc and Al-Zr alloys, and produce higher strength than in binary alloys. The advantage of ternary alloys becomes more pronounced at higher annealing temperatures and on longer exposures [69]. The decomposition occurs by the formation

Table 36   Hardening Effects Upon Aging of Different Aluminum Alloys

Alloy composition, wt%	C_Σ, at%	f, vol.	ΔYS_{max}, MPa	$\Delta YS_{max}/C_\Sigma$
1Mg; 0.6Si; 0.25Cu	1.77	1.65	140	79
4Cu; 1.5Mg	3.41	6.80	260	76.2
4.5Zn; 1.8Mg	3.95	2.72	230	58.2
5Zn; 2.3Mg; 1.7Cu	5.99	4.62	290	48.4
6Cu	2.5	7.5	140	56.0
5.5Mg; 2.8Li	0.99	3.98	190	190.9
4.2Cu; 0.6Mg; 1Si	3.49	6.51	270	77.3
0.5Sc	0.12	0.48	120	1000

of coherent spherical Al_3Sc and Al_3Zr precipitates, latter being finer than former. On increasing the temperature of annealing, Al_3Zr particles grow slowly retaining coherency and harden the matrix, whereas Al_3Sc precipitates coarsen, loose coherency and pin-down dislocations. In the temperature range from 350°C to 450°C and on soaking times up to 200 hr, the size of Al_3Zr particles ranges from 5 to 11 nm and that of Al_3Sc, from 25 to 35 nm. The alloying of aluminum alloys with Sc and Zr is the mainstream in physical metallurgy of these alloys.

Zirconium proper is a very important addition to structural aluminum alloys. The main role of this element is to slow down or prevent the development of recrystallization and, thereby, improve strength and service characteristics of wrought products. The supersaturated solid solution of Zr in aluminum formed upon solidification decomposes during solution treatment and hot deformation with the formation of fine dispersoids of the metastable cubic Al_3Zr phase. These precipitates very efficiently pin down dislocations and small-angle boundaries, promoting the formation of polygonized or very fine-grained recrystallized structure in deformed products. Such structure not only increases mechanical properties, but also decreases the anisotropy of properties and stress-corrosion susceptibility. Additions of zirconium (as well as Sc) to Al-Li alloys assure a more homogeneous distribution of hardening phases, especially Al_3Li, and reduce the precipitate-free zones near grain boundaries. This effect is because cubic Al_3Zr acts like a substrate for the precipitating Al_3Li phase. As a result rather evenly distributed composite particles are formed, increasing the strength and toughness of an alloy.

Let us consider in more detail two groups of commercial alloys. First group includes Al-Mn alloys and represents up to now the only one series of commercial wrought aluminum alloys containing solely transition metals. Second group consists of Al-Mg-Sc alloys and vividly shows the possibility of precipitation hardening with the aid of transition metals.

3.1   Commercial Al-Mn Alloys

Commercial Al-Mn alloys are among oldest aluminum materials. The first alloy known today as 3003 was introduced in 1906. In the end of 1920s a 3004 alloy appears. Amazingly but these alloys are still in use without major changes in com-

Table 37 Chemical Compositions, Temper Modes and Mechanical Properties of Commercial Al-Mn Alloys[#]

Alloy	Mn, %	Mg, %	Annealing	UTS, MPa	YS, MPa	El, %
3003	1.0–1.5	—	400–600°C	110*/150**	42/145	35/12
3004	1.0–1.5	0.8–1.3	415°C	180*/240***	70/200	22/11
3105	0.2–0.8	0.2–0.8	345°C	115*/170**	55/150	24/5

[#] All Al-Mn alloys contain up to 0.25% Cu, 0.70% Fe, and 0.3–0.6% as impurities.
* Annealed (O).
** Worked H14.
*** Worked H34.

position. This proves the value of manganese as an important alloying element. Table 37 shows the compositions, treatment modes and properties of commercial Al-Mn alloys.

The strength of the 3003 alloy is essentially higher than that of commercially pure aluminum, and the 3004 alloy is even considerably stronger. The dispersion and structural hardening with manganese aluminides is in a base of the structure and properties of these alloys. Besides, the solid-solution hardening of magnesium is employed in the 3004 alloy.

Manganese easily forms supersaturated solid solution in aluminum upon ingot casting ($V_c < 10^2$ K/sec). This solid solution decomposes at temperatures above 325°C with precipitation of fine Al_6Mn or more complex (AlFeMn) and (AlFeMnSi) dispersoids. There is no real precipitation hardening. However, these dispersoids efficiently hinder grain growth upon recrystallization and provide for the formation of fine-grained structure in sheets and other deformed products. High iron and silicon content and small amounts of copper and magnesium also tend to refine the grain size [18]. Iron is also very important in these alloys from the viewpoint of texture. It prevents the formation of earing upon deep drawing due to the control of texture [9].

All these alloys possess high corrosion resistance, weldability, excellent machinability and good resistance to grain growth. The tensile properties considerably increase with decreasing temperature and, on the other hand, retain sufficient level up to 200°C. They are used in production of general-purpose structures, chemical-resistant and food-compatible equipment, and packaging. The 3004 alloy is the main material for beverage cans.

3.2 Commercial Al-Mg-Sc Alloys

Conventional commercial Al-Mg alloys (5XXX series) are distinguished for their excellent corrosion resistance, weldability and machinability. They contain up to 6% Mg. Despite high solubility of magnesium in aluminum and the fact that this solubility decreases with temperature, there is no hardening associated with precipitation of the Al_3Mg_2 phase. The particles of this phase are formed mainly on grain boundaries, being incoherent and polycrystalline. The main hardening mechanism in these alloys is solid-solution hardening by magnesium retained in the solid solution. Usually Al-Mg alloys are used in annealed or strain-hardened states.

To improve strength and prevent grain growth upon recrystallization, commercial Al-Mg alloys contain small additions of manganese, chromium and titanium. The drawback of these alloys is low strength, especially yield strength. The strongest Al-Mg alloys exhibit the yield strength only as high as 150 MPa in the annealed state and up to 420 MPa after severe working [9].

To overcome this limitation, a few commercial Al-Mg alloys containing scandium and zirconium were developed in 1970s–1980s in Russia [60].

The alloying of aluminum with magnesium increases its lattice parameter and decreases the dimensional misfit between Al_3Sc and the matrix to 0.54% in an Al-6.5% Mg alloys. As a result, the coherency of Al_3Sc remains stable to higher temperatures (450°C) and on longer exposures (up to 10 hr), assuring a higher thermal stability of Al-Mg-Sc alloys. The recrystallization starts in an Al-6.5%Mg-0.2% Sc alloy at about 400°C and never finishes up to the liquidus temperature. The studies performed [60,70,71] confirmed that fine coherent Al_3Sc precipitates formed during aging of Al-Mg-Sc alloys at 300-350°C increase the starting recrystallization temperature by 50–175°C and make the complete recrystallization impossible. Additions of zirconium further improve mechanical properties and thermal stability of structure and allow a lower concentration of scandium. The formed structure makes these alloys naturally superplastic, allowing elongation up to 700 % at 450–470°C [72].

Several mechanisms of hardening are employed in Al-Mg-Sc alloys: grain refinement during casting, precipitation hardening during annealing, and structural hardening by preventing dynamic and static recrystallization. In addition, the solid-solution hardening with magnesium acts in these alloys just in the same manner as in Al-Mg alloys. Annealing of ingots before deformation should be performed in the temperature range from 250°C to 350°C. In this case, the decomposition of a supersaturated solid solution of scandium and zirconium occurs with the formation of fine spherical coherent precipitates of Al_3Sc and Al_3Zr 40–300 nm in size. These particles greatly contribute to the strength by precipitation and structural hardening. Commercial Al-Mg alloys containing 2–6% Mg and 0.1–0.6% Sc form a 157X series of Russian Alloys. Hot- and cold-worked semifinished products from these alloys are used in worked and annealed states for the structures of ships and airspace vehicles. All these alloys possess high corrosion resistance, perfect weldability, good properties at room and cryogenic temperatures, sufficient strength, and natural superplasticity.

A 1570 alloy contains 5–6% Mg and small additions of Sc, Zr, and Mn [73] and is the strongest of the known commercial Al-Mg alloys. The stronger the working, the higher the strength. After annealing at 320°C for 1 hr, rolled sheets, forgings and extruded shapes from this alloy exhibit the following tensile properties: $UTS = 380$–440 MPa; $YS = 250$–340 MPa, and $El = 16$–20%. By comparison, the strength of a 1570 alloy is 100 MPa higher than that of commercial Sc-free Al-Mg alloys.

The structure formed in hot rolled and annealed plates from a 1570 alloy demonstrates nonrecrystallized grains ($150 \times 50 \times 20$ μm in size); equiaxed subgrains (5 μm in size), Al_6Mn dispersoids (0.4 μm in size) at grain boundaries, and coherent Al_3Sc and Al_3Zr precipitates (less than 20 nm in size) inside subgrains [74]. These structural features are responsible for the properties of commercial products from Al-Mg-Sc alloys.

However, the acting mechanisms of hardening determine a disadvantage of these alloys. The maximum strength is achieved during annealing (aging) prior to deformation, which makes the working more difficult and does not permit use of intermediate anneals without the loss of strength.

The commercial Al-Mg-Sc alloys are valuable and indispensable in applications where one needs the combination of light weight, sufficient strength at room and cryogenic temperatures, excellent corrosion resistance and weldability.

REFERENCES

1. R. L. Fleischer, Acta Met. 1963, 11, p. 203.
2. F. W. Noble, S. J. Harris, and K. Dinsdale, Met. Sci., 16, p. 425.
3. R. E. Sanders, S. F. Baumann, and H. C. Stumpf, *Aluminium Alloys—Contemporary Research and Applications* (A. K. Vasudevan and R. D. Doherty, eds.), 1989, pp. 65–104.
4. E. O. Hall, Proc. Phys. Soc., London, 1951, B64, p. 747.
5. J. D. Embury, D. J. Lloyd, and T. R. Ramachandran, *Aluminium Alloys—Contemporary Research and Applications*, (A. K. Vasudevan and R. D. Doherty, eds.), 1989, pp. 579–601.
6. A. Guinier, Nature, 1938, 142, p. 569.
7. G. D. Preston, Nature, 1938, 142, p. 570.
8. J. R. Davis (ed.), Aluminium and Aluminium Alloys, ASM Specialty Handbook, ASM Int., 1993.
9. J. E. Hatch (ed.), Aluminium: Properties and Physical Metallurgy, Metals Park, ASM, 1984.
10. H. Chandler (ed.), Heat Treater's Guide. Practices and Procedures for Nonferrous Alloys, ASM Int., 1996.
11. A. Naudon, J. Delafond, A. Junqua, and J. Mimault, J. Appl. Crystallogr., 1978, 11(5), pp. 569–572.
12. F. Cuisiat, P. Duval, and R. Graf, Scr. Metall., 1984, 18(10), pp. 1051–1056.
13. R. Wagner and R. Kampmann, in *Materials Science and Technology*, (R.W. Cahn, P. Haasen, and E. J. Kramer, eds.), Vol. 5, Phase Transformations in Materials, Ch. 4, VCH, Weinheim, pp. 212–303.
14. A. Kelly and R. B. Nicholson, ''Precipitation Hardening,'' in *Progr. Mater. Sci.,* Vol. 10, 1963, Pergamon Press, Oxford, pp. 149–391.
15. T. Federigi and G. Thomas, Philos. Mag., 1962, 7(73), pp. 127–131.
16. J. D. Boyd and R. B. Nicholson, Acta. Metall., 1971, 19(12), pp. 1379–1391.
17. J. W. Martin, *Micromechanisms in Particle-Hardened Alloys*, 1980, Cambridge University Press, Cambridge.
18. L. F. Mondolfo, *Aluminium Alloys: Structure and Properties*, 1976, Butterworths, London.
19. A. J. Perry, Acta Metall., 1966, 14(3), pp. 305–312.
20. H. K. Hardy, J. Inst. Met., 1951–52, 80(5), pp. 483–492.
21. W. K. Armitage, J. Inst. Met., 1970, 98(2), pp. 46–51.
22. G. B. Stroganov, in *Legirovanie i obrabotka legkikh splavov* (Alloying and Processing of Light Alloys), 1981, Nauka, Moscow, pp. 172–178.
23. J. B. Nuyten, Scr. Metall., 1969, 3(9), pp. 645–648.
24. Y. Baba, Trans. Jpn. Inst. Met., 1969, 10(3), pp. 188–195.
25. J. M. Silcock, J. Inst. Met., 1960–61, 89, pp. 203–210.
26. A. A. Alekseev, L. B. Ber, L. G. Klimovich, and O. S. Korobov, Phys. Met. Metalloved, 1978, 46(3), pp. 548–556.

27. A. A. Alekseev and L. B. Ber, in *Legirovanie i obrabotka legkikh splavov* (Alloying and Processing of Light Alloys), 1981, Nauka, Moscow, pp. 178–189.
28. A. K. Gupta, P. Gaunt, and M. C. Chatuverdi, Philos. Mag. A, 1987, 55(3), pp. 375–387.
29. A. A. Alekseev, L. B. Ber, S. G. Pavlenko, L. G. Klimovich, Fiz. Met. Metalloved., 1982, 53(4), pp. 772–779.
30. S. P. Ringer, T. Sakurai, and I. J. Polmear, Acta Mater., 1997, 45(9), pp. 3731–3744.
31. V. G. Davydov, L. B. Ber, and V. N. Ananiev, Mater. Sci. Forum, 1996, 317–222(2), pp. 859–864.
32. L. Reich, M. Murayama, and K. Hono, Acta Mater., 1998, 46(17), pp. 6053–6062.
33. Q. Li and F. E. Wawner, J. Mater. Sci., 1997, 30(20), pp. 5263–5370.
34. D. G. Eskin, V. Massardier, and P. Merle, J. Mater. Sci., 1999, 34(4), pp. 811–820.
35. R. P. Wahi and M. von Heimendahl, Phis. Status Solidi (A), 1974, 24(2), pp. 607–612.
36. D. G. Eskin, Z. Metallkde., 1992, 83(10), pp. 762–765.
37. K. Matsuda, S. Tada, S. Ikeno, and A. Kamio, Proc. 4th Int. Conf. On Aluminium Alloys: Their Physical and Mechanical Properties, Atlanta, 1994, GIT, pt. 1, pp. 598–604.
38. K. Matsuda, S. Ikeno, T. Sato, and A. Kamio, Mater. Sci. Forum, 1996a, 217–222, pp. 707–712.
39. K. Matsuda, S. Ikeno, T. Sato, and A. Kamio, Scr. Mater., 1996b, 34(11), p. 1797.
40. K. Matsuda T. Naoi, K. Fuji, Y. Uetani, T. Sato, A. Kamio, S. Ikeno, Mater. Sci. Eng. A, 1999, 262(1-2), pp. 232–237.
41. T. V. Schegoleva, Fiz. Met. Metalloved., 1968, 25(2), pp. 246–254.
42. R. E. Mould and D. E. Mapother, Phys. Rev., 1962, 125(1), pp. 33–43.
43. G. B., Stroganov, V. A. Rotenberg, and G. B. Gershman, *Splavy alyuminiya s kremniem* (Alloys of Aluminium with Silicon), 1977, Metallurgiya, Moscow.
44. D. W. Evans and J. Aucote, Proc. 3rd Int. Alum. Extrusion Technol. Seminar, Atlanta, 1984, Vol. 1, pp. 53–62.
45. M. Kanno, H. Suzuki, and Y. Shiraishi, J. Jpn. Inst. Light Met., 1978, 28(11), pp. 553–557.
46. H. Suzuki, M. Kanno, G. Itoh, K. Itoi, J. Jpn. Inst. Met., 1982, 46(1), pp. 78–84.
47. P. Villars and L. D. Calvert, *Pearson's Handbook on Crystallographic Data for Intermetallic Phases*, Vol. 1 2nd edn., 1991, ASM, Metals Park.
48. M. J. Starink, V. M. F. Abeels, and P. Van Mourik, Mater. Sci. Eng. A., 1993, 163(1), pp. 115–125.
49. D. J. Chakrabarti, B.-K. Cheong, and D. E. Laughlin, *Proc. Automotive Alloys II*, San Antonio, Feb. 1998, TMS/AIME, Warendale, pp. 27–44.
50. J.-Y., Yao, G. E. Edwards, and D. A. Graham, Mater.Sci. Forum, 1996, 217–222(2), pp. 777–782.
51. C. Cayron and P. A. Buffat, in *Proc. ICAA'7*, Charlottesville, 2000, Mat. Sci. Forum, 2000, 331–337, pp. 1001–1006.
52. R. P. Wahi and M. von Heimendahl, Aluminium, 1972, 48(10), pp. 673–675.
53. V. Willing, M. von Heimendahl, and W. Wischnack, Z. Metallkde., 1975, 66(3), pp. 127–131.
54. D. A. Petrov, *Voprosy Teorii Splavov Alyuminiya* (Problems of Theory of Aluminium Alloys), Metallurgizdat, Moscow.
55. D. G. Eskin, Z. Metallkde, 86(1), pp. 60–63.
56. P. Degischer, W. Lacom, A.-M. Zahra, and C. Y. Zahra, (1980) Z. Metallkde., 1980, 72(4), pp. 231–238.
57. A. A. Aksenov, V. S. Zolotorevskii, G. M. Kuznetsov, and A. N. Kiselev, in *Metallovedenie i obrabotka tsvetnykh metallov* (Physical Metallurgy and Processing of Non-Ferrous Metals), 1992, Nauka, Moscow, pp. 171–180.

58. T. H. Sanders, Jr. and E. A. Starke, Jr, Proc. Second Int. Conf. Aluminium-Lithium Alloys II, Monterey (Cal.), April 1983, 1984, Metall. Soc. AIME, Warrendale, London, pp. 1–15.
59. Y. S. Lee, J. Mater. Sci. Lett., 1998, 17, pp. 1161–1164.
60. L. S. Toropova, D. G. Eskin, M. L. Kharakterova, and T. V. Dobatkina, *Advanced Aluminium Alloys Containing Scandium: Structure and Properties*, 1998, Gordon and Breach, Amsterdam.
61. Y. Miura, K. Horikawa, K. Yamada, and M. Nakayama, Proc. 4th Int. Conf. On Aluminium Alloys: Their Physical and Mechanical Properties, Vol. 2, 1994, GIT, Atlanta, pp. 161–168.
62. O. Sainfort and P. Guyot, Proc. 3rd Int. Conf. Aluminium-Lithium Alloys III, Oxford, July 1985, 1986, The Institute of Metals, London, pp. 420–426.
63. G. C. Huang and A. J. Ardell, Proc. 3rd Int. Conf. Aluminium-Lithium Alloys III, Oxford, July 1985, 1986, The Institute of Metals, London, pp. 455–470.
64. M. E. Drits, L. S. Toropova, and G. L. Nagornychnykh, Izv. Vyssch. Uchebn. Zaved., Tsvetn. Metall., 1983, 3, pp. 111–112.
65. P. E. Bretz and R. R. Sawtell, Proc. 3rd Int. Conf. Aluminium-Lithium Alloys III, Oxford, July 1985, 1986, The Institute of Metals, London, pp. 47–56.
66. P. Meyer and B. Dubost, Proc. 3rd Int. Conf. Aluminium-Lithium Alloys III, Oxford, July 1985, 1986, The Institute of Metals, London, pp. 37–46.
67. L. K. Lamikhov and G. V. Samsonov, Tsvetn. Met., 1964, 8, pp. 79–82.
68. V. I. Yelagin, *Legirovanie deformiruemykh alyuminievykh splavov perekhodnymi metallami* (Alloying of Wrought Aluminium Alloys with Transition Metals), 1975, Metallurgiya, Moscow.
69. M. E. Drits, L. S. Toropova, and Yu.G. Bykov, in *Metallovedenie, liy'e I obrabotka legkikh splavov* (Metals science, casting, and Processing of Light Alloys), 1986, Metallurgiya, Moscow, pp. 189–195.
70. J. Royset and N. Ryum, Proc. 4th Int. Conf. On Aluminium Alloys: Their Physical and Mechanical Properties, Atlanta, 1994, pt. 1, GIT, pp. 194–201.
71. Y. Miura, K. Horikawa, K. Yamada, and M. Nakayama, Proc. 4th Int. Conf. On Aluminium Alloys: Their Physical and Mechanical Properties, Vol. 2, 1994, GIT, Atlanta, pp. 161–168.
72. A. A. Alalykin, I. I. Novikov, V. K. Portnoy, and V. I. Pavlov, in Proc. 2nd Int. Conf. On Aluminium Alloys: Their Physical and Mechanical Properties, Beijing, 1990, Int. Academic Publ., pp. 403-407.
73. Yu. A. Filatov, V. I. Yelagin, and V. V. Zakharov, in Abstr. Int. Conf. On Scandium and Prospects of Its Use, 1994, Moscow, p. 18.
74. O. Roder, O. Schauerte, G. Lutjering, and A. Gysler, Mater. Sci. Forum, 1996, 217–222(3), pp. 1835–1840.

6

Residual Stress and Distortion

SHUVRA DAS

University of Detroit Mercy, Detroit, Michigan, U.S.A.

UMESH CHANDRA

Modern Computational Technologies, Inc., Cincinnati, Ohio, U.S.A.

1   INTRODUCTION*

Residual stresses are defined as those stresses which exist in an elastic body when all external loads are removed. All residual stress systems are self-equilibrating: that is the resultant forces and the moment that they produce are zero. Classically, residual stresses have been categorized into three types according to the length scale over which they act. "Type I" stresses act over distances measured in millimeters and are often referred to as macroscopic. Stresses that act over lengths of microstructure (typically 1–100 micrometers) are called "Type II" stresses. This can occur between different phases or between embedded particles. And stresses that exist at an atomic scale and vary over individual grains are described as "Type III." Type III stresses are equilibrated over a small part of the grain. Types II and III are often collectively referred to as microstrain effects while Type I is called macrostrain effect.

Residual stresses are most commonly associated with metalworking processes [2–5], and may be induced during forging, sheet metal forming, welding, heat treatment, composites manufacturing, and during most other manufacturing processes. Many of the effects of residual stresses are detrimental in nature. For example, tensile residual stresses on the outer surface of a component subjected to fatigue loading leads to premature failure of products, elastic strain recovery

---

* This chapter is an update of an earlier work by U. Chandra [1]. The present update is primarily due to S. Das.

(springback) of sheet metal parts lead to undesired dimensional changes, "hot-tearing" in castings increase rejection and scrap, residual stresses in metal-matrix composites lead to failure at the interface between the matrix and reinforcement, part distortion or dimensional instability associated with welding permanently deforms the parent material, and presence of residual stresses may accelerate stress-corrosion cracking. Residual stresses have a few beneficial applications. For example, shot peening is used to induce compressive residual stress on the surface of components to increase their fatigue life.

Quite often, permanent distortions or deformations in the part accompany residual stresses. Distortions in individual components may lead to a lot of difficulty during assembly of products. For example, in aerospace and automobile industries the final product is assembled from a large number of smaller parts. Even small amounts of distortion in each individual member may require additional force to be applied during assembly which may lead to severe distortion and residual stress in the final product. Thus, distortions in smaller components have the potential of generating a domino effect leading to the damage of the final product.

Distortions and residual stresses are outcomes of manufacturing processes and cannot be completely avoided. Proper understanding of the process of stress formation, however, can lead to reduction of residual stress through process planning, and/or stress relaxation in products through one or more of the many methods available. A logical way to control residual stresses and distortions in a product consists of the following steps: (1) understanding the fundamental sources of their generation; (2) identification of critical parameters associated with the particular process which created the residual stresses; (3) understanding the relative significance of each one of these parameters; and (4) experimentation with the most significant parameters until a suitable combination is obtained which results in the desired outcome. If, in spite of the best efforts to control them, the residual stress in a product is higher than acceptable, the only recourse left is the use of one of the various techniques of stress relief or the inducement of a stress pattern more favorable than the original.

Most manufacturing processes are complex combinations of heat transfer, mechanical deformation, and metallurgical changes. Thus, understanding the origins of residual stresses require a good understanding of the above three aspects and their complex interaction. With the exception of a few idealized cases, analytical solution for residual stresses is impossible. Thus, common approaches taken are experimental trials on the shop floor, and numerical modeling. Trials on the shop floor have been the traditional approach to understanding residual stress and its effects. While a few such trials are inadequate for generating enough information, extensive experimentation is costly and time consuming. As a result, for practical purposes, this approach by itself helps in developing more of a general, qualitative understanding rather than a comprehensive and quantitative one. Over the last few decades, numerical modeling of manufacturing processes has become very popular. Attempts have been made to model many of the well-known manufacturing processes. While the finite element method is the most commonly used technique in these models, finite difference and control volume methods are also used, especially where fluid-flow is involved. The main advantage of computer models is their cost-effectiveness. Prior to making even the first prototype, processes can be studied in great detail through modeling. The effect of process parameters on desired out-

comes can be checked, and the process parameters can even be optimized before making the first part. While modeling has a lot of advantages, all computer models are approximations of the real-world and their outputs are dependent on the quality of approximation and the accuracy of input parameters, such as material properties. It is perhaps a judicious approach to use a combination of modeling and experimentation to study residual stress and distortion.

The following section discusses some fundamental sources of residual stresses and distortions related to the various manufacturing processes reviewed in this article. This is followed by a summary of the mathematics which forms the basis for the development of appropriate computer software. Then, some commonly used techniques of measuring residual stresses, including the hole drilling method and the x-ray diffraction method, are summarized. All of these sections are quite general in the sense that the discussion is applicable to most engineering materials. In subsequent sections, residual stresses and distortions associated with different manufacturing processes are discussed. This discussion is limited to the most common manufacturing processes used for aluminum processing, namely sheet metal forming, casting, welding, heat treatment, and metal matrix composite manufacturing. The control of residual stresses in a few selected manufacturing processes is also discussed. Some thoughts about the simulation of commonly used stress relief methods are included, as well.

Historically, processing of steel has received a lot more attention than aluminum processing. As a result, the phenomena of residual stress and distortion in steel is better documented and the corresponding data base is quite well established. Similar information for aluminum alloys is usually non-existent. While the basic mechanism of residual stress formation and associated part distortion remains the same for aluminum, significant differences arise due to difference in material properties and metallurgy. For example, Young's modulus of aluminum is about one-third that of steel, coefficient of thermal expansion is almost twice that of steel, thermal conductivity is about five times that of steel, and the yield stress of certain aluminum alloys could be as low as 25% of that of some steels. All of these factors and many others determine the difference in behavior of aluminum as compared to steel. In this article, attempts have been made to highlight the effect of all these differences on the residual stress and distortion patterns encountered in aluminum products.

2   FUNDAMENTAL SOURCES OF RESIDUAL STRESSES

In manufacturing processes, residual stresses are caused by a combination of some or all of the following fundamental sources: (1) unequal plastic deformation in different portions of the product due to mechanical loads or constraints; (2) unequal plastic deformation due to thermal loads; (3) volumetric changes and transformation plasticity during solid state phase transformation; and (4) a mismatch in the coefficients of thermal expansion. The mechanics related to these sources is explained in the remainder of this section. Also, an interesting concept related to the effect of material removal (e.g. a casting mold, a forging die or the material removed during machining) on the magnitude and distribution of residual stresses in the workpiece is discussed.
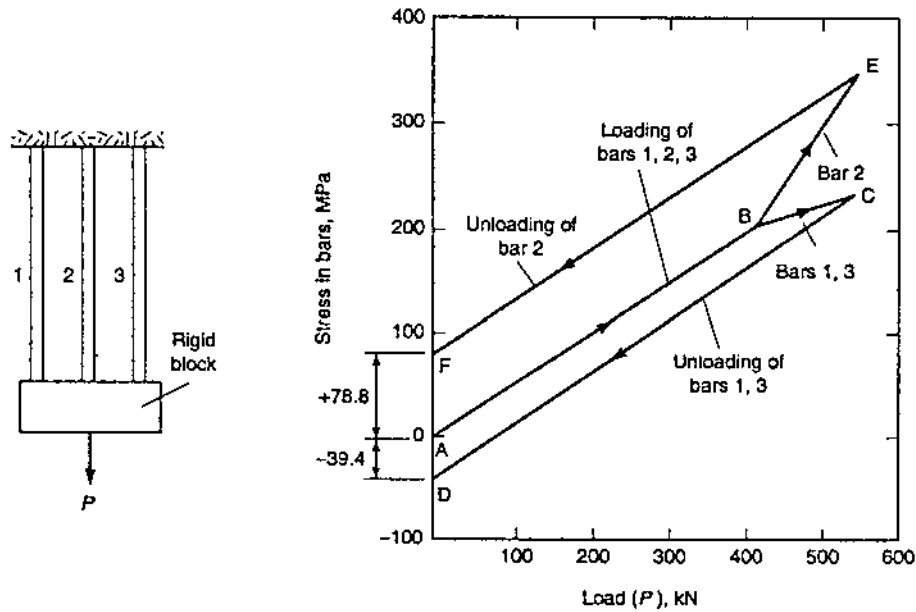
Figure 1   Residual stresses caused by mechanical loads in an assembly of three bars. (From Ref. 6.)

2.1   Mechanical Loads

In order to understand the generation of residual stresses due to mechanical loads, consider the example shown in Fig. 1, adopted from [6]. It consists of an assembly of three bars, each 254 mm (10 in.) long with a cross-section of 25.4 mm (1 in.) square. The bars are spaced 25.4 mm (1 in.) apart, center to center. The two outer bars are made of the same material with an elastic modulus of 206.84 GPa (30,000 ksi), yield strength of 206.84 MPa (30 ksi), and plastic modulus of 41.37 GPa (6,000 ksi). The middle bar has a higher yield strength of 413.7 MPa (60 ksi) but the same elastic and plastic modulii as the two outer bars. The upper ends of the three bars are fixed and not allowed to move in any degree of freedom; their lower ends are tied to a rigid but a weightless block. Also, the assembly carries a load P in the center, as shown in the figure.

Now consider two different loading histories. In the first case, the load P is gradually increased from zero to 400.3 kN (90 kips), and then brought back to zero. When P is 400.3 kN (90 kips), each bar shares 133.45 kN (30 kips) and the stress in none of them exceeds its yield strength. On unloading, the original zero stress state in each bar is restored, and no residual stresses are introduced.

In the second case, P is increased from zero to 533.8 kN (120 kips) and then brought back to zero. The entire history of stresses in the three bars is shown in Fig. 1(b). When P exceeds 400.3 kN (90 kips), the two outer bars deform plastically and due to reduced modulus begin to share less load. The stress in the two outer bars follow the path ABCD, whereas that in the middle bar follows the path ABEF. It can be seen that when P is again zero (unloading), the stresses in the three bars

do not go back to zero. Instead, the middle bar has a residual tensile stress of 78.8 MPa (11.43 ksi), and each of the two outer bars have residual compressive stress of 39.4 MPa (5.71 ksi). Since there is no external load on the assembly, the residual stresses in the three bars are in self-equilibrium. A comparison of the two loading histories indicates that the presence of unequal plastic deformation in the three bars is responsible for the generation of residual stresses. By the same token, mechanical residual stresses occur in any component when the distribution of plastic deformation in the material is inhomogeneous, such as the surface deformation in shot peening operation.

2.2   Thermal Loads

A similar three bar model explaining the generation of residual stresses due to unequal plastic deformation caused by thermal loads is discussed by Masubuchi [7], presumably adopted from [8]. In this model, three carbon-steel bars of equal length and cross-sectional area are connected to two rigid blocks at their ends. The middle bar is heated to 593°C (1100°F) and then cooled to room temperature while the two outer bars are kept at room temperature. Some of the details are not clearly explained in [7], but the problem is very similar to the previous example. It is obvious that when the temperature in the middle bar is raised, the requirements of compatibility and equilibrium require that a compressive stress be generated in the middle bar and tensile stresses in the two outer bars; the stress in each of the two outer bars being half of that in the middle bar. If the temperature in the middle bar is so high that its stress exceeds yield but in the two outer bars the stresses are still below yield, residual stresses will occur in the three bars when the temperature of the middle bar is brought back to room (i.e. on unloading). Similarly, if the stresses in all the three bars exceed yield but by different amount, residual stresses will still occur when the temperature of the middle bar is brought back to room. Indeed, this case is very similar to that of a cylinder immersed vertically in a quenchant where, during the initial stages of quenching, the temperature in the outer layer is lower than the inner core.

2.3   Solid State Transformation

In quenching, welding and casting processes, while cooling, many metals undergo one or more solid state transformations. These transformations are accompanied by a release of latent heat, a change in dimension (volume) and a pseudo-plasticity effect (transformation plasticity). All of these affect the state of residual stresses in the part. The release of latent heat during solid state transformation is similar to that released during liquid to solid transformation, albeit of a smaller amount. Usually, in most analyses this latent heat release is ignored. The change in volume (dimension) however, has a significant effect.

In aluminum alloys, significant time-dependent dimensional changes can be attributed to the metallurgical structure changes from solution, precipitation and transformation (metastable to equilibrium precipitate changes) of soluble alloy phases. The dimensional change due to phase transformation is dependent on the alloy phases present. For example, binary systems like Al-Cu, Al-Si, Al-Mg, exhibit the largest changes while those based on ternary systems, such as Al-Cu-Mg and Al-Si-Mg, because of the off-setting effects of multiple solutes and formation

of different precipitating phases, generally undergo lower dimensional changes [9,10]. The reason for this dimension change is that the substitutional solid solution-forming elements that are major alloying components of aluminum alloys exhibit limited, temperature dependent solubility in the solid state and either expand or contract the atomic lattice, depending on their atomic sizes relative to that of the solvent aluminum atoms. Figure 2 shows the effect of precipitation on unit linear
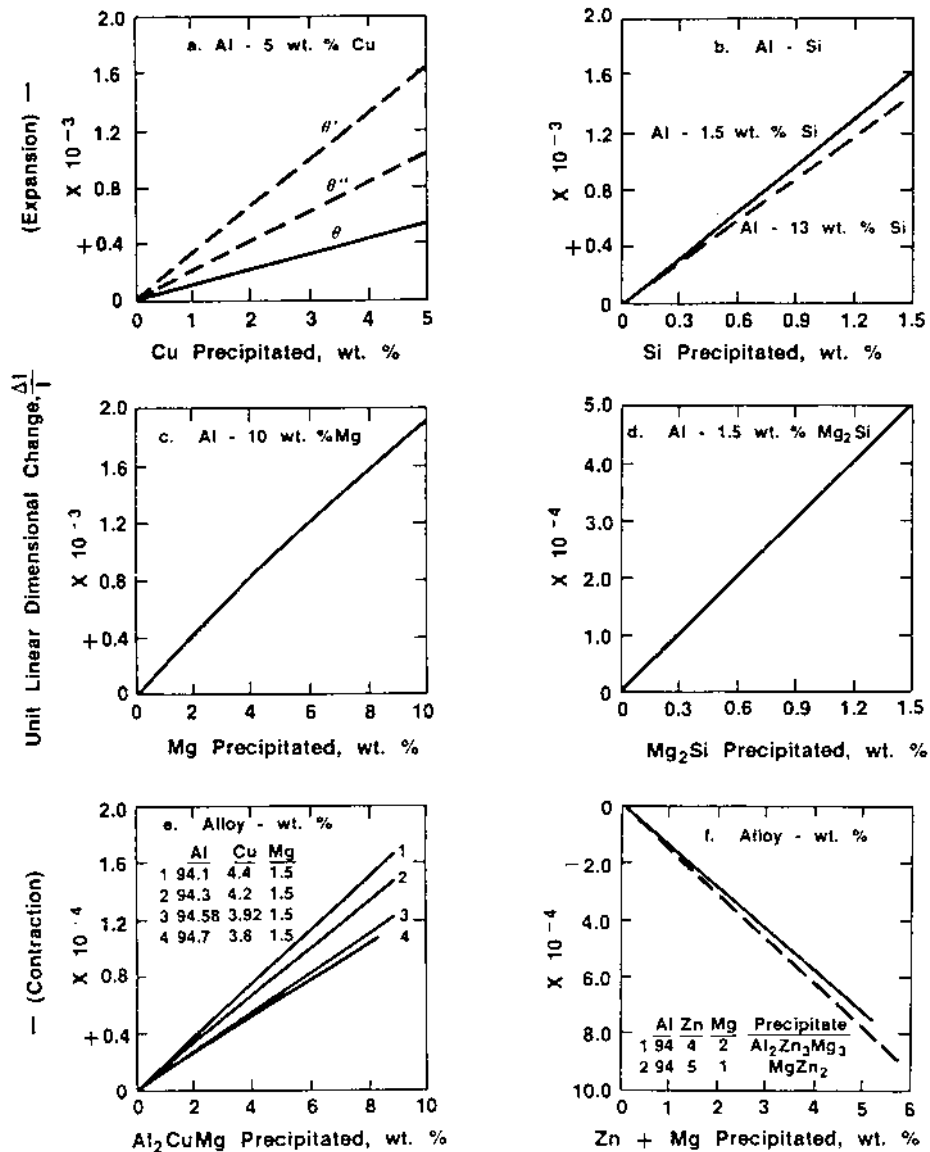

Figure 2 Effect of precipitation on dimensional changes in various aluminum alloys. (From Ref. 9.)
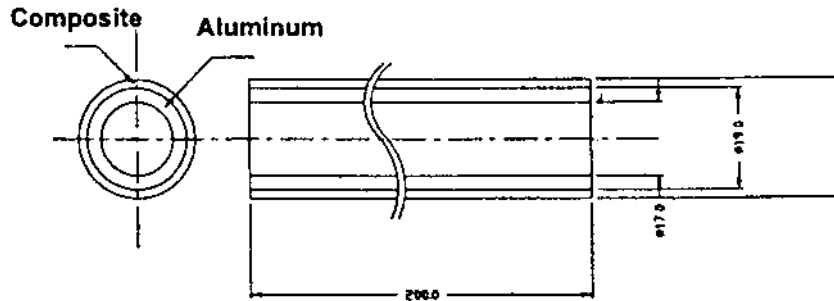
Figure 3 Co-cured aluminum and composite shaft. (From Ref. 13.)

dimensional changes for various binary and ternary alloys based on specific volume calculations [9,10]. This change in linear dimensions when combined with even very low stress can result in residual plastic strains. Two widely accepted mechanisms for transformation plasticity are due to Greenwood and Johnson [11], and Magee [12]. According to the former, the difference in volume between two coexisting phases in the presence of an external load generates microscopic plasticity in the weaker phase. This, in turn, leads to macroscopic plastic flow, even if the external load is insufficient to cause plasticity on its own.

2.4 Mismatch of Thermal Expansion Coefficient

Thermal stresses introduced due to the mismatch of thermal expansion coefficient can be easily followed from the following example [13]. Figure 3 shows a composite shaft consisting of an aluminum inner shaft and a composite outer shell. These are co-cured from a temperature of 120°C down to ambient conditions. Since the cure of the composite part of the hybrid shaft initiates at 120°C, the aluminum tube expands as the cure temperature rises until 120°C without constraint by the composite part. After co-curing the composite part to the aluminum tube, the hybrid shaft is cooled down to the room temperature of 20°C. In this particular case, the coefficient of thermal expansion of the composite shaft was negligible ($-0.9 \times$ 10E-6/C) in comparison to that of the aluminum shaft ($23 \times$ 10E-6). As a result, tensile stress in the axial direction occurs in the aluminum shaft and compressive stress in the axial direction occurs in the composite. This occurrence can be shown through simple analysis. The force equilibrium for the two shafts can be written as:

$$A_a \sigma_a + A_c \sigma_c = 0$$

where A represents the cross-sectional area σ represents normal stress. The subscripts a and c are used for aluminum and composites, respectively.

The condition of equal axial strain of the two materials is written as follows:

$$\frac{\sigma_a}{E_a} + \alpha_a \Delta T = \frac{\sigma_c}{E_c} + \alpha_c \Delta T$$

where E stands for Young's Modulus, α stands for coefficient of thermal expansion, and ΔT stands for temperature change. From the two equations, the thermal residual stresses in the composite and the aluminum can be written as:

$$\sigma_a = -(\alpha_a - \alpha_c)\Delta T \frac{E_c E_a A_c}{E_c A_c + E_c A_a}$$

and

$$\sigma_a = (\alpha_a - \alpha_c)\Delta T \frac{E_c E_a A_a}{E_c A_c + E_a A_a}$$

respectively. In this particular case, residual stress in aluminum was 58.96 MPa and the same in the composite was -183.29 MPa.

2.5   Material Removal

A fact which is often overlooked in discussing residual stresses due to various manufacturing processes is the effect of material removal on the state of stresses in the product. Consider, for example, that a casting mold has to be finally broken and removed, or that a forging die has to be retracted. Likewise, in making a machined part some of the material has to be removed. All of these operations change the state of stress in the part. In order to fully understand this concept, we consider an example discussed in [6].

The example entails an assembly of two concentric springs of slightly different lengths, l_i and l_o, as shown in Fig. 4(a); the subscripts i and o refer to inner and outer springs, respectively. The bottom ends of the two springs are fixed. Then, the upper ends are tied to a rigid block which is free to move only in the vertical direction. The two springs adopt a compromise length, l, which is in between l_i and l_o, as shown in Fig. 4(b). As a result, the two springs develop equal and opposite forces; compressive in the longer inner spring and tensile in the outer shorter spring. The assembly of the two springs may be viewed as analogous to the assembly of a cast part and its mold, or to the assembly of the forged part and the die, or to a machined part before some portion of it is removed. Then, the removal of the outer spring becomes analogous to removal of material during machining [6,14], of the casting mold [15–18], or of the forging die [19]. We consider two cases. In the first case, the stresses in both springs are assumed to be within their elastic limits. When the outer spring is removed, the force acting on it is transferred to the inner spring in order to satisfy equilibrium and the inner spring returns to its original length. In the second case, we assume that the inner spring has undergone a certain amount of plastic deformation. When the outer spring is removed the inner spring does not return to its original length, l_i. In either case, since the two springs and, hence, the forces are concentric the residual stress in the inner spring becomes zero when the outer spring is removed.

Although only one of the three examples discussed in [6] is presented here, important conclusions drawn from all three examples are quite relevant: (a) when the material removal is symmetric with respect to the stress distribution the residual stresses in the remainder of the assembly or part are very small or even zero; (b) when
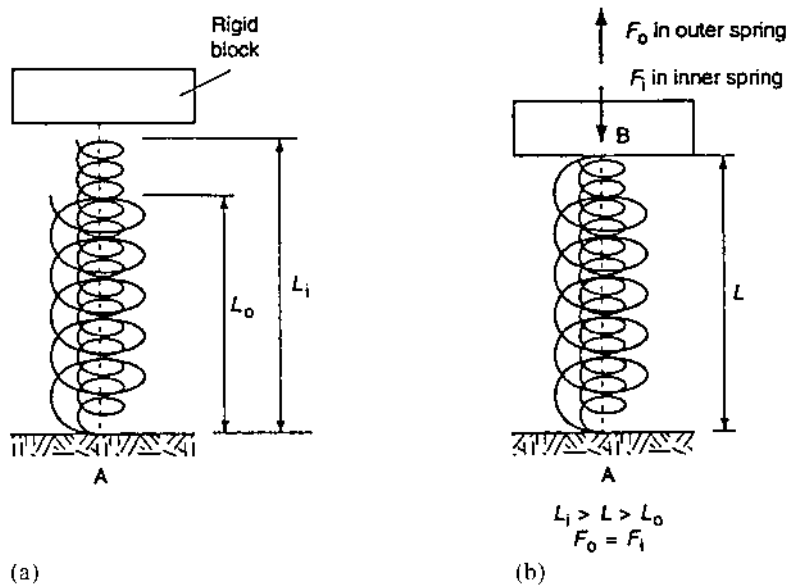
Figure 4 Residual stresses in an assembly of two springs with unequal initial lengths (a, b). (From Ref. 6.)

the material removal is not symmetric with respect to the stress distribution the residual stresses in the remainder of the assembly or part are not necessarily small; and (c) material removal may result in an increase in stresses at some locations of the assembly or the part.

3 COMPUTER PREDICTION OF RESIDUAL STRESSES

In recent years, the finite element method has become the pre-eminent method for computer prediction of residual stresses due to various manufacturing processes. A transient, nonlinear, thermo-mechanical analysis software is generally employed for the purpose. Some of the mathematics which forms the basis of such software is common for all manufacturing processes. Such common mathematics is summarized in this section. But, since every process is unique, some mathematical requirements are, in turn, dependent upon the process. Also, for the simulation of certain processes a sequential thermal mechanical analysis is adequate, whereas for others a coupled analysis may be preferred or even essential. Such subtleties will be pointed out later when individual processes are discussed.

Ignoring convection, the following conduction heat transfer equation is solved with appropriate initial and boundary conditions:

$$\nabla \cdot (k \nabla T) + Q_c = \rho C_p \frac{\partial T}{\partial t}$$

where T is the temperature at an arbitrary location in the workpiece at time t; k is the thermal conductivity of the material; Q_c is the rate of heat generated per unit volume; ρ is the density; C_p is the specific heat and ∇ is the differential operator; all material properties are assumed to vary with temperature. The initial and boundary conditions are process dependent. Details of converting the above equation into its finite element form and of numerical solution are available in a number of technical papers and textbooks and are not repeated here.

The transient temperatures computed above are used as loading for the subsequent transient stress/displacement analysis. The finite element representation of the structural equations are generally referred to as the force-displacement formulation. Forces (tractions) and displacements are treated as primary variables. Stresses on the other hand are secondary variables and are calculated from derivatives of displacements and material properties. As a result, displacement data across the whole field needs to be calculated before stress results can be found. Like in the physical world, in the numerical world as well stresses and displacements are closely related and all residual stress calculation is accompanied by distortion calculations as well.

Using the incremental theory, the total strain increment $\{\Delta\varepsilon\}$ at time t can be divided into various components:

$$\{\Delta\epsilon\} = \{\Delta\epsilon^e\} + \{\Delta\epsilon^t\} + \{\Delta\epsilon^p\} + \{\Delta\epsilon^{cr}\} + \{\Delta\epsilon^v\} + \{\Delta\epsilon^{tr}\}$$

where superscripts e, t, p, cr, v, and tr refer to elastic, thermal, plastic, creep, volumetric change and transformation plasticity components, respectively. The first three strain terms are needed in the simulation of every manufacturing process discussed here, whereas the use of other three terms is dependent upon the process and will be pointed out as appropriate. Also, mathematical details for the first four strain terms are discussed in most standard references, whereas the details for the last two terms are discussed often in the context of the simulation of quenching and welding processes [11,20]. In the finite element approximation these strain increments are converted to displacement increments at different points. The term Q_c in the heat transfer equation accounts for the release of latent heat during liquid to solid or solid state phase transformation and the heat of plastic deformation, e.g. in forging and other bulk deformation processes. The latter, leads to a coupling between the thermal and mechanical analyses.

At present, no computer software or code is capable of predicting residual stresses caused by all manufacturing processes. However, several general purpose finite element codes are capable of predicting these stresses to a reasonable degree of accuracy for at least some of the manufacturing processes. In addition, some codes permit customized enhancements leading to more reliable results for a specific process. As will be discussed in subsequent sections, when relatively simple geometries are involved, these available codes are capable of predicting residual stresses due to casting, forging, and quenching to a reasonable degree of accuracy. Similarly, they can predict residual stresses due to welding when only a few passes are involved. But, further improvements may be needed when the geometry of a workpiece is complex, or when a weld with a number of passes is involved.

4 MEASUREMENT OF RESIDUAL STRESSES

It is generally not possible to measure residual stresses in a product during its manufacture; instead, they are measured after the manufacturing process is complete. Smith et al. [21] has divided the residual stress measurement methods into two broad categories: mechanical and physical. The mechanical category includes the stress relaxation methods of layer removal, cutting, hole drilling and trepanning, whereas the physical category includes x-ray diffraction (XRD), neutron diffraction, acoustic and magnetic. The layer removal technique as originally proposed by Mesnager and Sachs is only applicable to simple geometries such as a cylinder with no variation along its axis or circumference, or to a plate with no variation along its length or width. Thus, whereas it could be used to measure quench induced residual stresses in a cylinder or a plate, it is not suitable for measuring complex stress patterns such as those due to welding. The layer removal and cutting techniques, however, have been applied to pipe welds in combination with conventional strain gages and XRD measurements. The general procedure for layer removal methods is (a) creation of a new stress state by machining or layer removal; (b) detection of the local change in stress by measuring the strain or displacement; and (c) calculation of the residual stress as a function of the strain measured using the elastic theory (analytical approach or finite element calculations).

Hole drilling and trepanning techniques can be used in situations where the stress variation is non-uniform, but they are generally restricted to stress levels of one-third of the material yield strength. Also, the two techniques can be unreliable in areas of steep stress gradients, and require extreme care while drilling a hole or ring in terms of its alignment as well as the heat and stress generation during drilling [22]. For such reasons, and others, these two techniques have found little application in the measurement of weld-induced residual stresses.

Of the methods in the physical category, x-ray diffraction (XRD) is probably the most widely used method; the neutron diffraction method is relatively new. These two methods measure changes in the lattice of the crystals and from these measurements the components of strains and stress are computed. The x-ray diffraction (XRD) technique has undergone many improvements in recent years. With the development of small portable x-ray diffractometers the technique can be used for on site measurement of residual stresses. It should be noted, however, that this technique is capable of measuring strains in only a shallow layer (approximately 0.0005 in. thick) at the specimen surface. To measure sub-surface residual stresses in a workpiece, thin layers of material are successively removed and XRD measurements are made at each exposed layer. For reasons discussed in Section 2.5, the measurements at an inner layer should be corrected to account for the material removed in all the previous layers. Reference [23] gives analytical expressions for such corrections in case of simple geometries and stress distributions. For more complex cases, it still remains difficult to accurately determine sub-surface residual stresses.

Because of limitations in most measurement methods it is often a good idea to combine different techniques of measurement or combine measurement techniques with numerical tools to obtain all the necessary information. For example, for quality assurance purposes, many times hole drilling and XRD methods are used to calibrate other techniques such as ultrasonic and magnetic methods. And the later

Table 1   Comparison of Different Residual Stress Measurement Techniques [24].

Method	Holedrilling	Deflection	Sectioning	X-Ray	Neutron Diff.	Ultrasonics	Magnetic
Type of stress analyzed	First kind	First kind	First kind	I & II or III	I & II	I & II & III	I & II & III
Minimum analysis zone	$0.5\ mm^2$	$1000\ mm^2$	$100\ mm^2$	$0.5\ mm^2$	$4\ mm^3$	$0.1\text{–}30\ mm^2$	$1\text{–}100\ mm^2$
Minimum depth analysis	$20\ \mu m$	$20\ \mu m$	1–2 mm	$2\text{–}30\ \mu m$	1 mm	$15\text{–}300\ \mu m$	$100\ \mu m$
Measuring time for first point	40 min	30 min	40 min	20 min	2 hr	2–4 mins	Instantly
Measuring time for stress field	2 hr	8 hr	5–200 hr	8 hr	1 week	20 min	10 min
Equipment cost ($)	10–50 k	1 k	15 k	100–200 k	few100 mil.	40–200 k	10–60 k
Multi-phase material analysis	Mean stress in all phase	Mean stress in all phase	Stresses in each phase	Stresses in each phase	Mean stress in all phase	Mean stress in all phase	Mean stress in all phase
Problem for large grain size	No	No	No	Yes	No	Yes	Yes
Aluminum alloy	Yes	Yes	Yes	grain size problem	Yes	Yes	No
Composite	Yes	No	No	Crystalline matrix only	Crystalline matrix only	Difficult	Ferromagnetic matrix
Welded structure	Yes	No	Yes	Yes	Yes	Yes	Yes
Machined parts	Yes	Yes	No	Yes	No	Yes	Yes
Surface hardened parts	Yes	Yes	Difficult	Yes	Yes	Yes	Yes
Heat treated parts	Difficult for thin parts	Yes	No	Yes	No	Difficult for surface stress	Yes

two methods (which are faster) are used on production line parts. A nice tabulated summary that compares all the experimental techniques in available in literature [24] and is partially reproduced here as Table 1. This table is very useful for someone who is trying to choose the right measurement technique for a specific case.

5 RESIDUAL STRESSES AND DISTORTIONS DUE TO VARIOUS MANUFACTURING PROCESSES

5.1 Heat Treatment

Heat treatment to increase the strength of aluminum alloys is a three step process: (a) solution heat treatment; (b) quenching; and (c) age hardening. Not all aluminum alloys are heat treatable. The 2xxx, 6xxx and 7xxx wrought alloys and 2xx.0, 3xx.0, and 7xx.0 series casting alloys are heat treatable. Most of the heat treatable alloys contain combinations of magnesium with one or more of the elements copper, silicon, and zinc.

Solution heat treatment consists of soaking the alloy at a temperature sufficiently long enough to achieve a nearly homogenous solid solution. Residual stress development and distortion is not generally associated with this stage of the heat treatment process. In order to preserve the solid solution formed the alloy is quickly cooled (quenched) to a lower temperature to impart the desired metallurgical and mechanical properties. The need to be ''quickly cooled'' varies from alloy to alloy. For example, 7075 alloy requires a drastic quench to retain the solute atoms in solid solution and is known to be the most sensitive alloy to cooling rate; whereas, alloy 6063 requires the slowest cooling rate and is the least sensitive alloy [25]. Most of the time the cooling rates have to be well controlled so that it fits a certain window. Slow cooling rates may lead to formation of undesired phases and very fast cooling rates may lead to severe levels of residual stresses and distortions. Effectiveness of quenchants is determined through a factor called quench severity factor. It is the ratio of the coefficient of heat transfer between the quenchant and the part surface, and two times the thermal conductivity of the metallic part. This factor controls the cooling rate of the part during quenching. Cold water, the most effective quenchant, can be used to achieve cooling rates as high as 200°C/sec (400°F/sec) at the midplane of a 25 mm (1 in.) thick aluminum alloy plate [26]. Cooling rates can be lowered through the use of hot water, by reducing the velocity of quenchant around the part and through the use of polymer quenchants, such as polyalkaline glycol. The heat removal characteristic of a quenchant is known to be affected by a number of factors including the size, shape and orientation of the workpiece (even for simple shapes such as plates and cylinders, the heat removal is different at the bottom, top and side surfaces); the use of trays and fixtures to hold the workpiece in the quenchant; composition of the quenchant; size of the pool and its stirring, etc [27–29].

Quenching is the one heat treatment process that is universally associated with the formation of residual stress and distortion. It is well known that residual stresses are a result of differential thermal expansion and contraction during non-uniform cooling of parts and solid state phase transformations. For example, during quenching of thick sections when the still warm central section contracts it pulls in the cold outer shell. This results in residual stresses throughout the part.

Thermally induced residual stress magnitude increases with section size. Phase transformation stresses will increase in proportion to the amount of newly precipitating phases and the difference between their coefficients of linear expansion and the alpha-solid solution. The resulting distribution of residual stresses in quenched parts is usually desirable since compressive stresses are located on the outer surfaces and tensile stresses are in the interior. This distribution pattern helps to deter fatigue failure and stress corrosion cracking. However, machining of quenched parts, especially non-symmetrical machining (with respect to the stress distribution pattern) may lead to severe distortion. Positioning of parts during heating and quenching have significant effect on the ultimate distortion of the part. Non-uniform heating and cooling of parts may lead to distortion and higher residual stresses. For example, sheet metal parts warp if heating and cooling of the parts are not uniform. Thus, extreme care is needed to maintain uniformity of heat transfer when parts are loaded in the furnace and subsequently, when they are dipped in the quench bath.

Several techniques are used in industry to correct the above mentioned problems. Residual stress levels may be reduced by reducing the cooling rate. Slower quenchants like boiling water are used for this purpose. Figure 5 [26] shows the effect of slower quenchants on alloy 6151. A second approach is to alter the processing sequence so that the part is rough machined close to its final dimensions, and then quenched and fine machined. This approach reduces the part thickness and thus the level of residual stresses induced in the part. Post-quenching treatments for stress distortion reduction is a third approach. Straightening of parts after distortion is an expensive but sometimes necessary means to control distortion. Press straightening, roll straightening and straightening through stretching are some of the well known methods used in practice [27]. While mechanical stretching can reduce residual
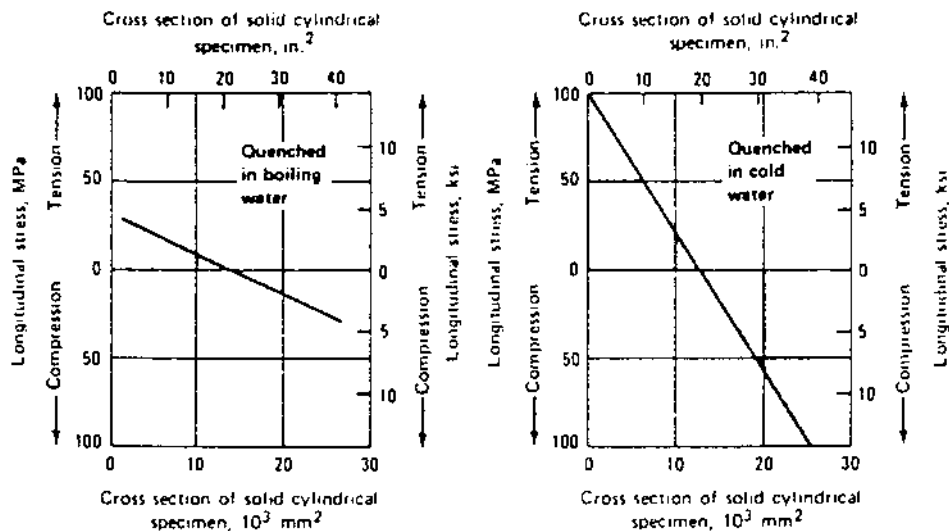
Figure 5 Effect on quenching rate (from 540°C) on residual stresses in solid cylinders of 6151 alloy. (From Ref. 26.)

stresses along with distortions, other techniques like precipitation heat treatment and uphill quench are also used. The degree of relaxation through precipitation heat treatment is dependent on the time, temperature of treatment and the alloy composition [30]. Up-hill quench is exactly opposite to the quenching process itself. In this approach the temperature of the part is lowered to a sub-zero temperature ($-195°$C) and then rapidly heated through a blast of steam [26]. It has been recorded that stress reduction as high as 83% has been achieved through this technique [26].

In the past, using trial-and-error, shop floor personnel have come up with some interesting strategies to control the residual stresses (and warpage), e.g. air delay or an intentional delay while transporting the workpiece from the heating furnace to the quenchant, and time quenching or performing the quenching operation in two steps. In the first step, the part is quenched in a medium such as salt bath until the part has cooled below the nose of time-temperature transformation curve, followed by quenching in second medium such as air to slow the cooling rate. Obviously, perfecting the quenching operation by trial-and-error can be an extremely time consuming task.

At first glance, computer simulation of the quenching process may appear to be simple. It involves an uncoupled transient nonlinear small deformation thermo-mechanical analysis as outlined in Section 3, with due consideration to solid state transformation effects [10,31]. Some researchers have also included the creep effect. However, the major difficulty lies in a lack of knowledge of the heat removal characteristic of various quenchants, which is mathematically represented as the convective heat transfer coefficient at the outer boundary of the workpiece. This difficulty has been overcome by one of two approaches. Through the solution of inverse problems researchers were able to calculate the convective heat transfer coefficient at different locations on the part by tracking the temperature history in the part interior during quenching [32,33]. A second and less accurate method is to approximate the part surface heat transfer coefficient through the use of relationships that are available for different common surface configurations such as vertical and horizontal flat plate, etc [34]. Other difficulties arise due to the lack of thermophysical and mechanical properties of the workpiece material at elevated temperatures. Still, at least in the U.S., major aircraft engines manufacturers and their forging vendors have been using computer simulation to control quench related cracking and residual stresses for some time. One such example involving a turbine disk is discussed in Ref. [35]. The reported work was performed without the benefit of a sophisticated simulation software which accounts for solid state transformation effects. For proprietary reasons, few such cases are published in the open literature.

Case Study: Quenching of an Aluminum Impeller

This is a summary of a case study reported in [35]. Figure 6 shows the picture of an aluminum impeller used in turbomachinery. After forging the impellers were heated to $530°$C and quenched in boiling water. The material used for this product was Al 2618 (Al, Cu 2-2.6%, Mg 1.2–1.8%, Ni 0.9–1.4%, Fe 0.9–1.4%, Si 0.2%, Ti 0.1%). Figure 7 shows typical distortion pattern that arise during quenching. The procedure followed in the analysis of this process is described below.
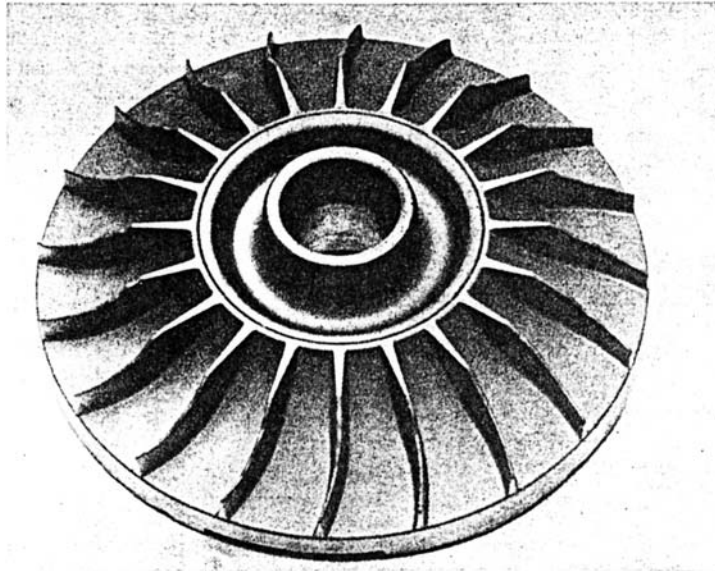
Figure 6   Forged turbocharger impeller. (From Ref. 35.)
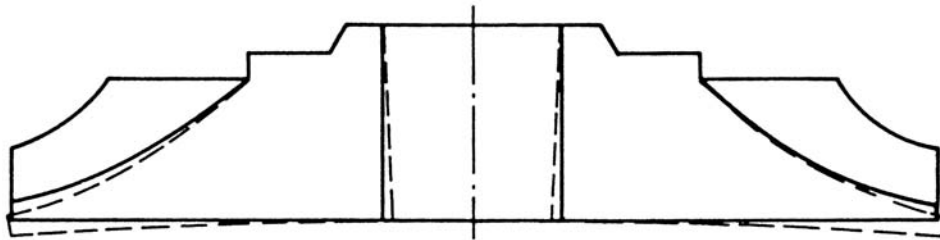
Figure 7   Typical distortion pattern in impeller due to quenching. (From Ref. 35.)

Using thermocouples in test parts cooling curves for quenching in boiling water were developed at different locations in the part. Since this alloy does not undergo significant dimensional change due to phase transformation during quenching it was assumed that only macro-residual stresses were induced. Figure 2 [9] confirms that the length change is really negligible in ternary alloys like this. Although the geometry of the problem was not fully axisymmetric (due to the existence of the fins) it was assumed to be axisymmetric for two reasons: for large number of fins and their regular distributions, actual distortion pattern was observed to be axisymmetric; and the more critical areas during later operation were near the central bore which was more-or-less an axisymmetric region. FEM codes ADINAT and ADINA were used for thermal and residual stress calculations, respectively. Temperature dependent thermal and structural properties were used. For the transient thermal analysis, all nodes in the axisymmetric model were assumed to be at the initial temperature of 530°C. After many trials, it was deter-
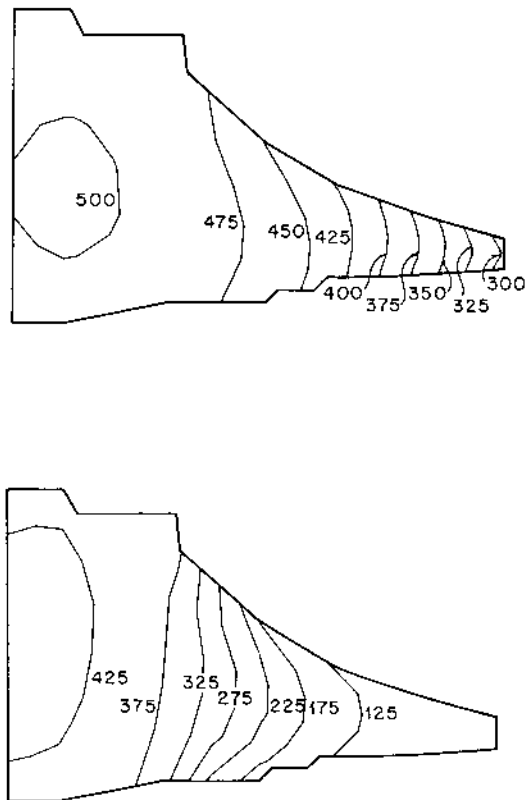
Figure 8 Calculated temperature distribution 15 and 30 sec after immersion. (From Ref. 35.)

mined that standard values for a downward facing flat surface may be used to approximate the surface heat transfer coefficient. To reach this conclusion the measured cooling curves were compared with simulated curves from thermal analyses with different surface heat transfer coefficient distributions. Figure 8 shows temperature contours 15 and 30 sec after immersion. For residual stress calculations, an elastic-plastic analysis was performed using the infinitesimal plasticity theory. Creep effects were ignored. Figure 9 shows the tangential residual stress distribution. Stress values were experimentally determined by making cuts around strain gages fixed at different locations in the part. Figure 10 shows comparisons of calculated and measured residual stresses at different locations in the bore. Figure 11 shows a similar comparison for different locations on the upper and the lower surfaces.

From this effort some conclusions could be drawn. Results obtained with "reasonable" data show that computational techniques can produce results that are in good agreement with reality. However, the output is only as good as the input data. For example, for thermal analysis accurate representation of convective heat transfer coefficient is very important. This is also the parameter that is very difficult to measure accurately. Many processing factors influence this and the best way to determine this is to use the solution of inverse problems [32,33]. For stress cal-
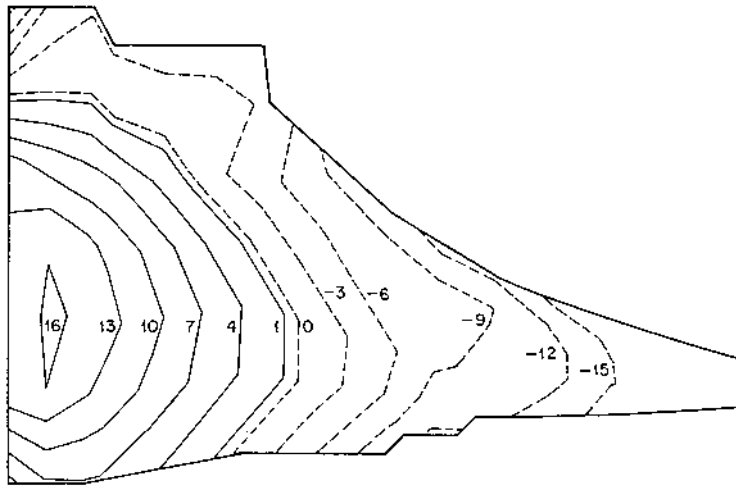
Figure 9 Calculated tangential residual stress distribution (in N/mm²). (From Ref. 35.)
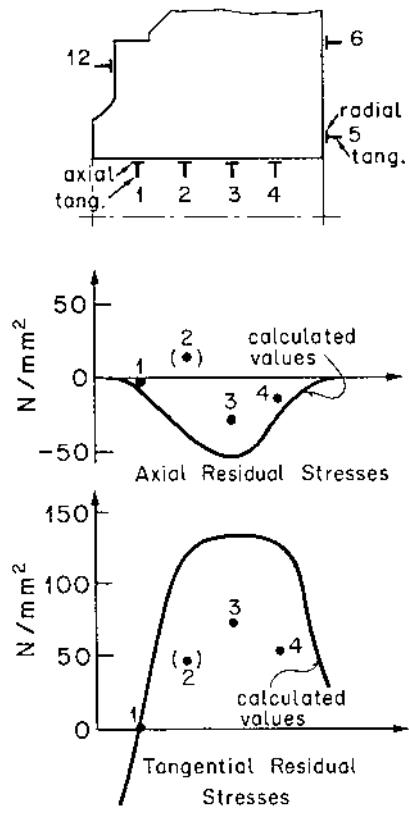
Figure 10 Calculated and measured residual stresses in the bore. (From Ref. 35.)
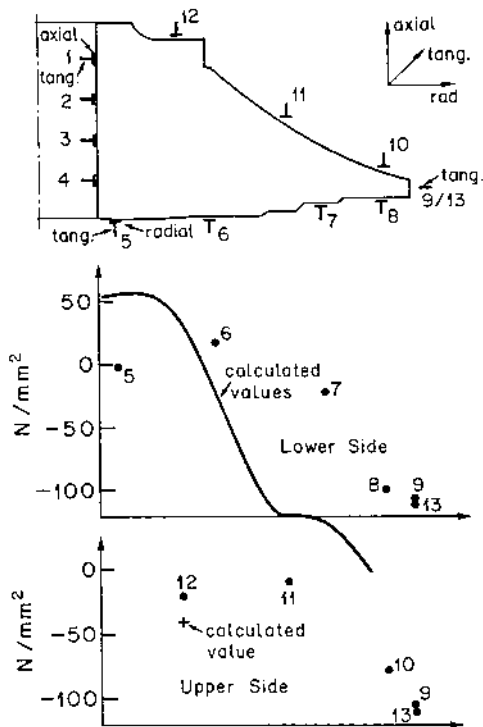
Figure 11 Calculated and measured residual stresses in the upper and lower surfaces. (From Ref. 35.)

culations the most difficult data to obtain is the flow stress and work hardening rate at different temperatures. For Al 2618, the material is in a stable state above 400°C and below 150°C. In between these temperatures it is in a transient state and the above mentioned property curves had to be approximated.

5.2 Welding

Most welding processes can be characterized as heating from a moving heat source that results in melting of the base metal, and subsequent solidification of base metal and added filler material. Most of the heat supplied by the arc to the base material is conducted away by the base material resulting in uneven expansion and contraction in area surrounding the weld. This non-uniform expansion and contraction and the accompanying plastic deformation are the primary sources of residual stresses and distortions in welded joints. During the cooling process, solid state phase transformations occur in the fusion and heat affected zones. Solid state phase transformations are quite often accompanied by volume change and transformation plasticity and these contribute to the final residual stress magnitude as well. The residual stress distribution in welded joints depends upon a number of process and design parameters such as the heat input, speed of the welding arc, material

properties, preheat, thickness of the welded part, groove geometry, and weld schedule. The following general statements about welding residual stresses are true irrespective of material, welding process, and design detail [36].

   (a) High multi-axial residual stresses occur in the fusion and heat affected zones of the welded joint.
   (b) The maximum residual stresses generally reach the yield limit or even higher (if strain hardening is present). However, lower values are possible if transformation stresses are present.
   (c) The residual stresses may vary significantly from point to point in the fusion one and the heat affected zone.
   (d) Residual stress distribution may also vary significantly from part surface to the interior.
   (e) Substrate geometry can significantly affect residual stress distribution; e.g. stress patterns in flat plates are quite different from those in pipe welds [37,38].
   (f) Considerable differences exist between the stress patterns from single- and multi-pass welds [39,40].

Distortions in welded joints are a result of the residual stresses induced and in general can be categorized into the following types [36]: (a) In-plane distortion, e.g. longitudinal or transverse shrinkage of the welded plate; (b) Distortion perpendicular to the plane of the welded component, e.g. plane or axisymmetrical angular shrinkage of welded plates; (c) Bending distortion; and (d) Twisting distortion. In the assembly of large structures, distortion in welded subassemblies can cause serious mismatch in final assembly, and force fit of mismatched sections introduces more difficulties. Many of these problems can be minimized by adjusting dimensions, welding procedures, and welding sequences to anticipate the direction and magnitude of possible distortion.

Distortion control is possible through the control of several parameters. In general these parameters fall within two broad categories: design related variables and process related variables. Important control strategies that depend on design practices include choosing plates with appropriate thickness, reducing stiffener spacing, using a bevel T-stiffener web, optimizing assembly sequencing, properly applying jigs and fixtures, etc. Strategies that involve control of welding parameters include reducing fillet welds, using high speed welding, using a low heat input process, using intermittent welds, and balancing heat about the plate's neutral axis in butt joint welding.

Even though welding processes for aluminum have made significant progress [41–44], there is a perception in industry that aluminum is difficult to weld relative to steel. For example, airplane structures (where alloys Al 2024 and 7075 are used extensively) use thousands of riveted joints but hardly any welded joint at all. Eighty to ninety percent of metals welded are steels whereas, aluminum only comprises a majority of the remaining 10–20%. Specifically, aluminum and steel differ in their response because (1) the welding process is affected by their different physical and chemical properties; and (2) the welded properties are influenced by their metallurgical differences. Most of the residual stress and distortion work related to welding focuses on steels. Although the main principles of stress formation remains the same for aluminum there are subtle differences due to the fact that
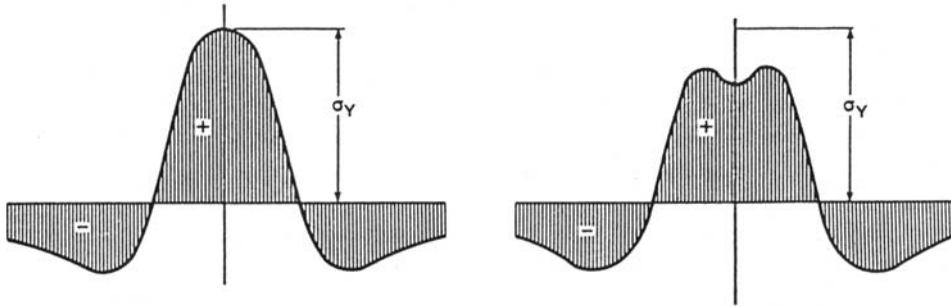
Figure 12 Typical longitudinal residual stresses in mild steel and aluminum due to welding. (From Ref. 36.)

material properties of aluminum alloys are significantly different from those of steel. Figure 12 shows a comparison of weld-longitudinal stress profile for mild steel and aluminum alloy [36] and the following discussion summarizes the effect of material property differences [36].

As far as residual stress and distortion is concerned, the thermophysical properties of aluminum alloys have a significant impact on the final results. Table 2 shows a list of relevant thermophysical properties for several alloys. These data will be used for a comparative assessment of aluminum and steels. Temperature dependency is ignored for this assessment. Increase in melting temperature increases residual stress and distortion. As far as the influence of melting temperature goes, aluminum is more suitable for welding than steels. Thermal diffusivity (the ratio of conductivity to the product of density and specific heat) affects residual stress and distortion positively. This means small thermal conductivity and large density and specific heat will be ideal. Considering only thermal diffusivity aluminum is less suitable for welding than the steel alloys.

Increase in the coefficient of thermal expansion increases residual stresses and distortions and vice versa. The actual influence of this property is somewhat curtailed by the phase transformation effects. Since the thermal expansion coefficient of aluminum is almost twice as that of steels, aluminum is significantly less suitable for welding than steel. Elastic modulus influences residual stresses positively and deformations negatively, i.e. increase in elastic modulus increases residual stresses and decreases deformation. As a result, aluminum will have lower stresses but higher deformations. Influence of yield strength is quite similar to that of elastic modulus, i.e. its increase will increase residual stress but will decrease distortion. Thus, aluminum alloys would be lower in residual stresses and higher in deformation than steels.

The above mentioned property influences on welding residual stress and distortion can all be summarized in the form of two non-dimensional numbers called welding suitability indices for residual stress and distortion [36]. They are written as follows:

$$\lambda_\sigma = \frac{T_m^* a^* \alpha^* E^* K_{Ic}}{T_m a \alpha E K_{Ic}^*}$$

$$\lambda_\epsilon = \frac{T^* a^* \alpha^* E^* \sigma_Y}{T_m a \alpha E \sigma_Y^*}$$

Table 2 Comparison of Weld Suitability Factors for Steel and Aluminum [36].

Base Metal	Melting Point (C)	Diffusivity (m²/sec) × 10 E(-6)	Thermal expansion (1/C)	Elastic Modulus GPa	Yield Point MPa	Fracture Toughness (N/mm$^{3/2}$)	Weld Suitability (stress)	(dist.)
low-alloy steel	1520	7.5–9.5	11E(-6)	210	200–700	>800	1	1
High-alloy steel	1400	5–7.5	16E(-6)	200	250–550	>800	1.07	0.86
Aluminum	600	75–100	24E(-6)	65	80–280	>600	0.28	0.01

where T_m is the melting point, a is thermal diffusivity, α is thermal expansion coefficient, E is modulus of elasticity, σ_y is the yield stress, and K_{Ic} is the fracture toughness for mode I cracking. The properties with asterisk are for the reference material (low-alloy steel). Table 2 lists these factor values for aluminum. It is clear from the data that aluminum alloys on average appear less suitable (than steel) for welding as far as residual stress and distortion is concerned.

Welding engineers have long used trial-and-error to obtain a suitable combination of these parameters in order to control the residual stresses. The role of computer simulation in the prediction of residual stresses in weldments is the subject of a recent review [16]. Major elements of computer simulation of the process are: (a) mathematical representation of the heat input from the welding source; (b) a transient thermal analysis; and (c) a transient stress/displacement analysis; the flow of molten metal and thermal convection in the weld pool are generally ignored. Following Rosenthal [45], a semi-steady state approach is often used, although some attempts at full three-dimensional analysis have also been made. As mentioned earlier, it is now possible to account for volumetric change and transformation plasticity effects [10,11]. Due to the short time periods involved, creep is usually ignored. In the case of a single pass weld or a weld with few passes (e.g. 4 or 5), it is now possible to predict residual stresses with reasonable accuracy [39]. But, as the number of passes increases (e.g. 20 or 30), it becomes computationally intractable to model each pass [40]. The scheme of lumping several passes into one layer has been employed with some success [40]. In addition to excessive computation time, other major difficulties with the simulation of a multi-pass weld are: (a) the numerical errors tend to accumulate with each pass; and (b) the changes in metallurgical and mechanical properties of material in previously deposited layers during deposition of a subsequent layer are difficult to quantify and to account for in the finite element analysis. The technique of lumping several layers together aggravates these problems.

A very interesting effort related to in-process control and reduction of residual stresses and distortions in weldments is being pursued by Masubuchi and co-workers at M.I.T. [46,47]. The effort aims at moving beyond mere analysis of residual stresses and distortions to aggressively controlling and reducing them. To accomplish this objective, the effort is subdivided into the development of the following three primary capabilities: (1) prediction; (2) sensing; and (3) control. For prediction purposes, a series of computer programs have been developed, including simple but fast one-dimensional programs which analyze only the most important stress component, i.e. the one parallel to the weld line. Sensing capability refers to a set of devices including, (a) a laser interferometer to measure minute amount of distortions; (b) a laser vision system to measure large amount of distortions; and (c) a mechanical system to measure radii of curvature. Finally, to control the residual stresses, various techniques including changes in heating pattern and application of additional forces have been attempted. References [45,48] provide further examples of the application of this methodology in reduction of residual stresses in weldments in high-strength steels and girth-welded pipes.
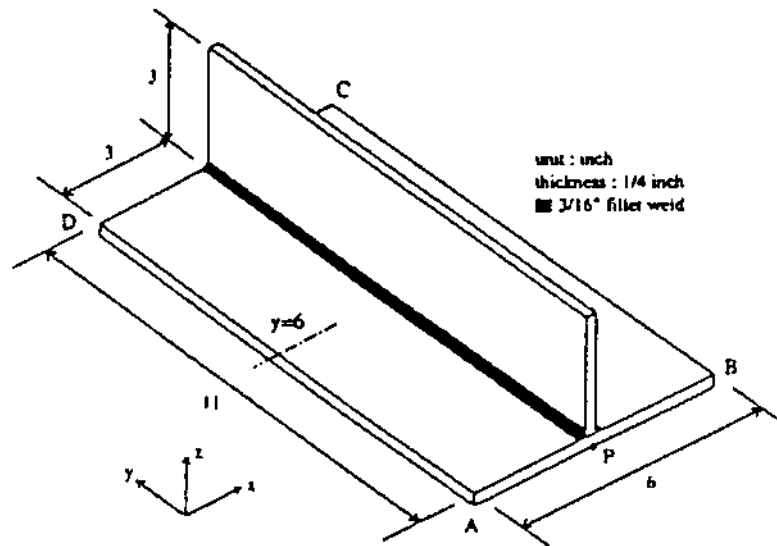
Figure 13 Stiffened aluminum panel for residual stress characterization. (From Ref. 42.)

Case Study: Welding Distortion of a Thin-Plate Panel Structure

In this work [42] the effect of process parameters, weld schedule, and joint design were studied for thin-walled aluminum panel structures. Both numerical and experimental techniques were used in this study. Several types of distortions like buckling, bending and warping were examined in this work. For the purpose of brevity, only a part of the work will be described here.

To examine the angular bending phenomenon numerical analysis and experimental investigation was conducted on an Al-5454-H34 T-joint specimen. Figure 13 shows a picture of the set-up. The gas metal are welding process was used with A5556 welding wire (1.6 mm diameter). The welding conditions were 200–220 A, 24 V, 53.3 cm/min welding speed. The right hand joint was welding first and after complete cooling to the room temperature the left hand joint was welded. Figure 14 shows a comparison of the experimental and numerical results for the final bending of the plate.

Figure 15 shows a set-up used to study the effect of weld sequence on the final distorted shape of the panel. Figure 16 shows the four different weld sequences that were used in this study. Number 1 deposits welds from inner panels outward, No. 2 lays welds from outer panels inward, and No. 3 and No. 4 are similar to Nos. 1 and 2 respectively with some added requirements. Sequence 3 searches for the joint with highest restraint to deposit the next weld as the assembly process progresses and No. 4 lays the next weld at the least restrained joint. Figure 17 compares the distortion of the panels at four different cross-sections from the four welding sequences. The global distortion of the panel in all cases show a downward movement and tilting toward the unsupported corner due to structural weight. The panel warps about the middle longitudinal stiffener. Sequences 2 and 4 result in greater angular bending curvatures than the other two sequences. The angular

Angular Bending at Y = 6 inch
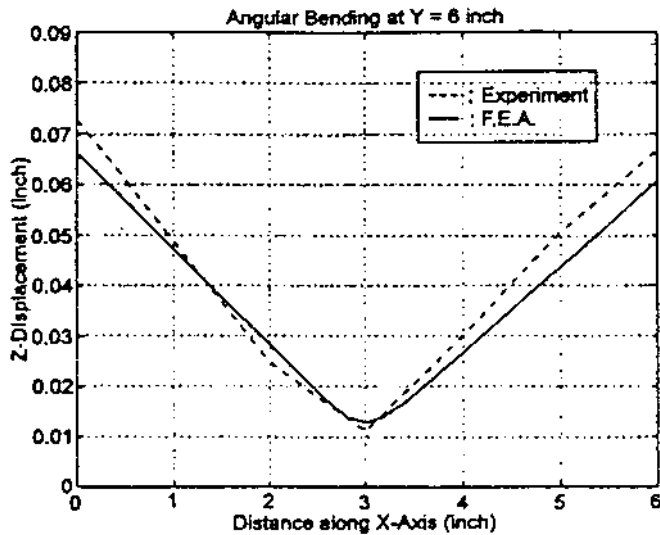
Figure 14 Angular distortion on the back side of T-flange: simulated and measured. (From Ref. 42.)
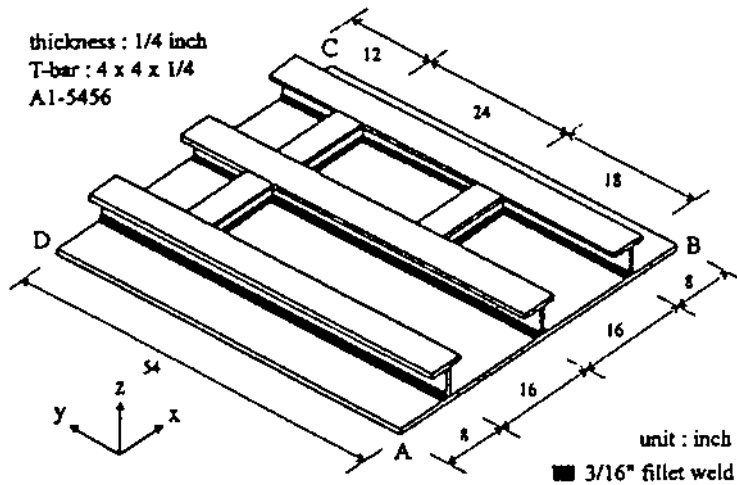
Figure 15 Aluminum panel for study of welding sequence effect on distortion. (From Ref. 42.)

distortions of the skin plate from sequences 1 and 3 are similar in magnitude and shape. It appears that the sequence that follows the most restrained joint for depositing the next weld during assembly results in smaller angular distortion in the skin plate. Of the four sequences, sequence No. 3 is the best in terms of minimizing distortion.
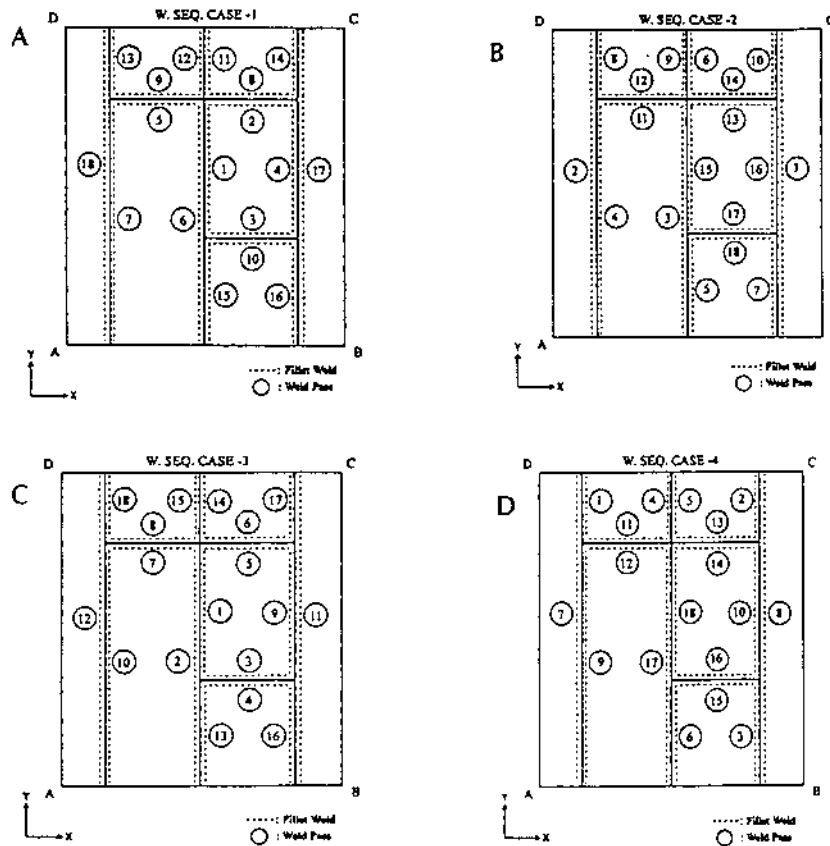
Figure 16 Welding sequences for angular distortion of aluminum panel structure. (A) Welding sequence 1, (B) welding sequence 2, (C) welding sequence 3, and (D) welding sequence 4.

5.3 Sheet Forming Processes

Sheet metal forming processes are used extensively in the automotive industry and the aerospace industry for making body panels. They can be divided into two main categories; (a) those requiring only local deformation such as piercing, blanking, v-bending, air-bending, etc; and (b) those requiring deformation spread over extensive area of the sheet such as, drawing, pure stretching, reverse drawing, etc. In addition, a third category, stamping refers to shallow parts that are blanked out of sheet metal with only minor forming operations done on them.

Technical data on forming from steel sheets is quite well established. Similar information about aluminum is not easily available. However, most of the technology for forming of steel can be altered and used with aluminum if careful attention is paid to the effect of property differences of the two materials. For example, when using aluminum deep drawn parts, essentially higher component tolerances must be taken into account because of lower E-modulus of aluminum alloys. Coefficient of thermal expansion of aluminum is almost twice as high as that
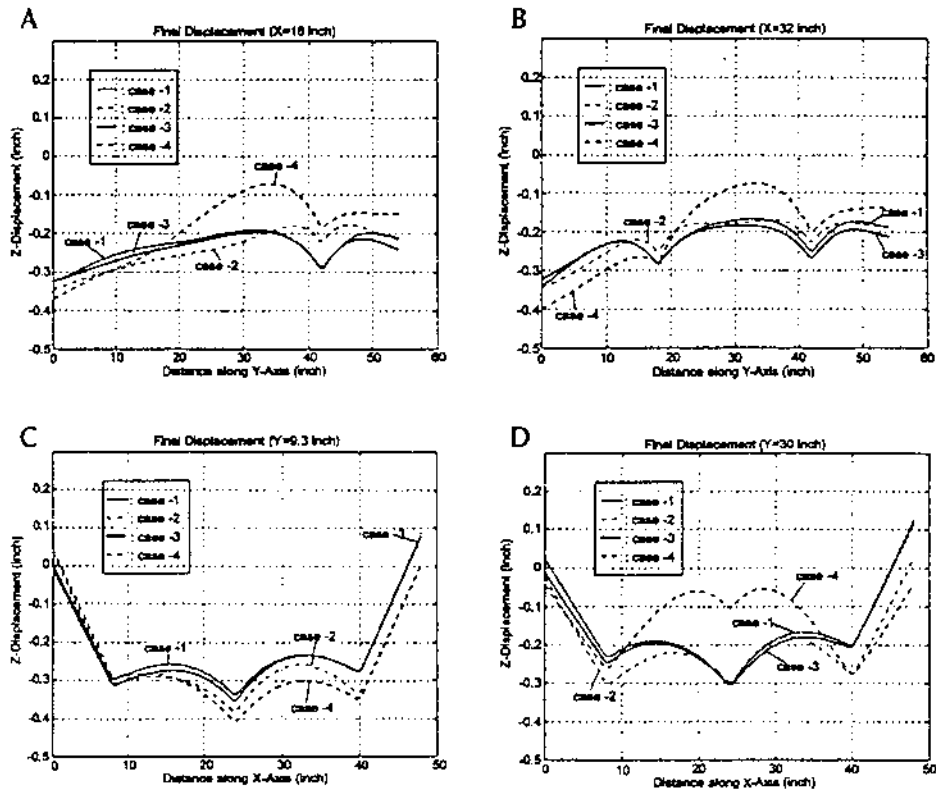
Figure 17 Distortion displacements at four cross-sections of the panel from four welding sequences. (A) At x = 40.6 cm, (B) at x = 81.3 cm, (C) at y = 23.6 cm, and (D) at y = 76.2 cm. (From Ref. 42.)

of steel. As a result, joints between separate sheet-metal parts have to be designed appropriately to account for higher expansion and contraction. Reference [49] shows that not accounting properly for thermal expansion lead to problems during the assembly of roof mountings and engine hood assembly for Porsches.

Distortion, more than residual stress, is a critical parameter for product effectiveness in sheet forming of aluminum. Several types of distortion defects are common. The most important ones are wrinkling, springback, earing and warping. Wrinkling is a form of buckling that occurs due to lack of sufficient hold-down forces and is common in many drawing processes. Wrinkling in flanges occur in partially drawn products when the blakholder forces are not large enough. Improper clearances between punch and die can cause wrinkling in the drawn part. Clearances between punch and die are typically equal to the metal thickness plus about 10% per side for drawing aluminum alloys of low or intermediate strength. An additional 5–10% clearance may be needed for higher strength alloys and harder tempers [26]. Excessive clearance may result in wrinkling of the sidewalls of the drawn shell. Insufficient clearance burnishes the sidewalls and increases the force required for drawing.

Springback or partial return to the original shape upon removal of the bending forces, occurs in most bending operations and is the most common form of distortion observed in sheet-metal forming. Spring-back may be corrected by overbending, by bottoming or setting. Bottoming or setting is accomplished by striking the metal severely at the area containing the radius so as to obtain localized flow. Bottoming is sometimes accomplished by placing a bead on the apex of the punch so as to concentrate the plastic deformation at the bead.

Springback correction by overbending (the most commonly used method) complicates tool design in that the die must be designed to ensure the correct degree of over-bending. In order to do that one needs to have an accurate estimate of the amount of spring-back a-priori. The amount of springback depends on the yield strength and thickness of the materials and on the bend radius. Springback allowance, or degree of overbending required increases with increasing yield strength and bend radius, but it varies inversely with stock thickness. Table 3 lists overbending required for 2024-O, 7075-O, and 2024-T3 alloys [26]. The yield strength of the first two alloys is a minimum of 76 MPa and that of 2024-T3 is 345 MPa. The effects of yield strength, bend radius and stock thickness is clear from the data.

Along with other factors, the degree of anisotropy introduced due to rolling or crystallographic textures affect springback [50] as well. Figure 18 shows the effect of bend angle on the degree of spring back for an Al-Li alloy at three different orientations with the rolling direction [50]. Actual degree of springback is known to fluctuate with faults of fabrication in the rolling mills. If one considers the

Table 3   Springback Allowances for 90 Degree Bends [26].

Sheet Thickness (mm)	Spring back allowance, in degrees for bend radius (mm) of:							
	2.4	3.2	4.8	6.4	7.9	9.5	11.1	12.7
2024-O and 7075-O								
0.51	3	4	5.5	7.5	8.5	9	9.5	12
0.64	2.75	3.75	5.5	6.5	8	8.25	8.75	10.75
0.81	2.25	3	4.75	6	6.75	7	7.5	9.5
1.02	2	3	4	5	6	6.25	6.75	8.75
1.29	2	2.5	3.5	4	5	5.25	5.75	7.5
1.63	1.5	2	2.75	3.75	4.5	5	5.5	6.75
2.06	1	1.5	2	2.5	3.25	3.5	4	4.75
2.39	N/A	N/A	1.75	2.5	3	3.25	3.75	4.5
3.18	N/A	N/A	1.5	2	2.25	2.75	3	3.75
2024-T3								
0.51	10	12	15.5	19	22.5	24	27.25	33.5
0.64	8.75	10.5	14	16.75	17.75	21	23	28.5
0.81	7.75	8.75	12	14.5	16.75	17.75	19.25	24
1.02	7.25	8.25	10.75	12.75	14.5	15.25	17	20.5
1.29	N/A	N/A	9	10.5	12.25	13	14.5	16.75
1.63	N/A	N/A	8	9.75	11.25	12	12.75	15
2.06	N/A	N/A	N/A	N/A	9.5	10.5	11.25	13
2.39	N/A	N/A	N/A	N/A	8.75	9.75	10.5	12
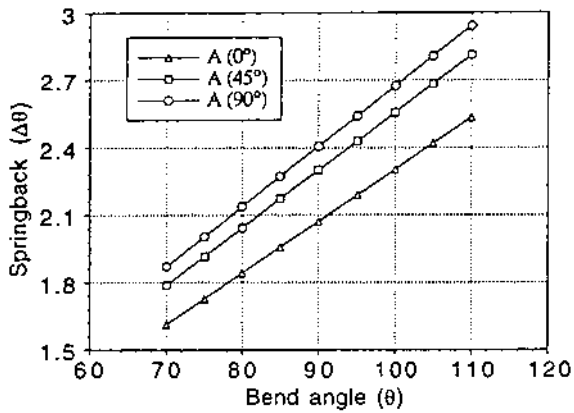
Figure 18 Effect of bend angle on calculated springback for recrystalized 8090 alloy (A) testing at 0, 45 and 90 degrees from rolling direction of sheet. (From Ref. 50.)
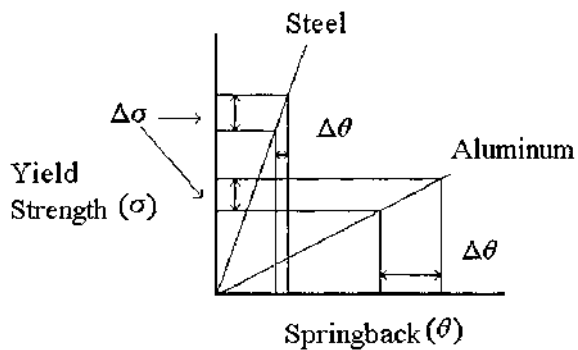
Figure 19 Influence of Young's Modulus and yield strength on springback. (From Ref. 49.)

spring-back after an idealized bending process in which the strain hardening, internal stress ratios and sheet thickness are ignored (Fig. 19), then it is found that for the same absolute faults of fabrication at the rolling mills the spring-back fluctuations for steel sheet, amounts to only one-third of the aluminum value [49]. This indicates that for rolling aluminum alloys the semifabricator needs to reduce fluctuations in the fabrication process. The designer on the other hand needs to be aware of the effects on tolerances that these fluctuations will have.

Springback in bending processes has been well studied. Nadai [51] studied bending of a beam from elementary theory and Hill [52] completed a general theory and solution for bending under plane strain. Although the analytical expression for spring-back is well established for simple sheet metal bending operation [53], for complicated shapes elastic-plastic finite element analysis has to be used to determine spring-back [50,54–60]. In recent years, many researchers have used the finite element method to study springback during the sheet metal forming process. It is important to note, however, spring-back is an elastic recovery process, and it cannot be calculated using an ideal plastic material model [55]. An elastic-plastic or

elastic-viscoplastic model is necessary [55]. Metal forming operations involve large deformations occurring over a small time period. In order to capture all the events in a numerical model one has to use very small time steps. As a result implicit codes (which are in general slower than explicit codes) take an enormous amount of time to solve these problems. Analysts have had more success with explicit codes in solving metal forming problems. Table 4 shows a comparison of some of the commercial forming simulation codes used in industry [61].

Another distortion problem that is commonly encountered is called earing. This is encountered mostly in deep-drawing processes. As a result of earing the top edges of drawn cups are not completely even. The edges along the perimeter of the cup are wavy, consisting of crests and valleys. These projections are called ears. Four ears are quite common, but occasionally two, six or even eight may be found. Earing is due to planar anisotropy and correlates well with the angular position of the coefficient of anisotropy (r-value). At angular positions of low r values, more thickening occurs, so that the wall heights are lower. At positions of high r, the walls are thinner and higher.

Warping is caused by nonuniformity of stress distribution in the drawing of rectangular or irregular shapes. This effect increases with increased size of the part. Changes can sometimes be made in dimensional details of the drawing tools to eliminate these defects without the need for extra forming operations.

Case Study: Use of Active Binder Force Control in Springback Reduction

In this example [57], the authors used numerical and experimental techniques to: (a) determine the effects of restraining force (binder force) on the springback phenomena in a stamping operation of aluminum sheets; (b) develop a strategy to control the binder force during the forming operation so that a robust repeatable stretch history could be achieved; and (c) implement the above strategy. The material chosen for experimentation and simulation was Al 2008 blanks, 210 mm long, 46 mm wide, and 1.06 mm thick and it was assumed to be isotropic elastic-plastic and Von Mises' yield criterion and isotropic hardening were used to determine deformation.

A FE model of the sheet and the tooling was developed and the simulation was performed using ABAQUS [62]. Figure 20 shows the FE model. Using constant binder forces analyses were performed for different binder forces and Fig. 21 shows a comparison of the springback results. It is clear that the degree of springback decreases with the increase in binder force. Actual forming experiments were carried out and the degree of springback measured for different binder forces. Figure 22 shows comparisons of experimental and numerical data.

Since it was clear that the degree of springback decreases with the increase in binder forces, the effects of variable binder force on springback were specially studied. This time the load on the binder was very low at the beginning. This allows the draw-in process and minimizes the maximum final strain in comparison to constant high binder force situations. After the part is partially formed under low binder force conditions, a simultaneous stretch is applied by increasing the binder force in order to produce plastic stretch. Figures 23(a) and 23(b) show the variable binder force and the corresponding springback values respectively. Different variable binder force distributions were tried and the best results were obtained if the force was increased from 4 kN to 32 kN when the punch stroke was at about 65% of

Table 4 Comparison of Sheet-Metal Forming Simulation Codes [61].

Solution Strategy		Dynamic Explicit	Static explicit	Static Implicit	Large step method	One step method
Formulation FE Codes		Incremental Method LS-DYNA3D PAM-STAMP OPTRIS	ITAS3D	MTLFRM	AUTO FORM	SIMEX ISOPUNCH A F ONE STEP FAST FORM3D
Company Using Codes		All	Nissan Nippon Steel	Ford	Benz Volvo Ford Chrysler Nissan Sollac	Renault Benz Volvo Sollac National Steel
Processes Simulated	deformation due to sheet weight	Oca	All	All	Some	—
	binder wrapping	Some	All	All	All	—
	deep drawing	All	All	All	All	All
	spring back	Oca	Oca	Some	Oca	—
Defects Predicted	wrinkle	S	S	S	P	P
	thickness/tearing	S	S	S	S	S(P)
	surface defects	I	I	I	I	I
	springback related defects	P(I)	P	S	P(I)	I

All = In all cases, Some = In some cases, Oca = Occasionally, S = Satisfactorily Predicted, P = Possible to Simulate but poor Results, I = Impossible to Simulate.
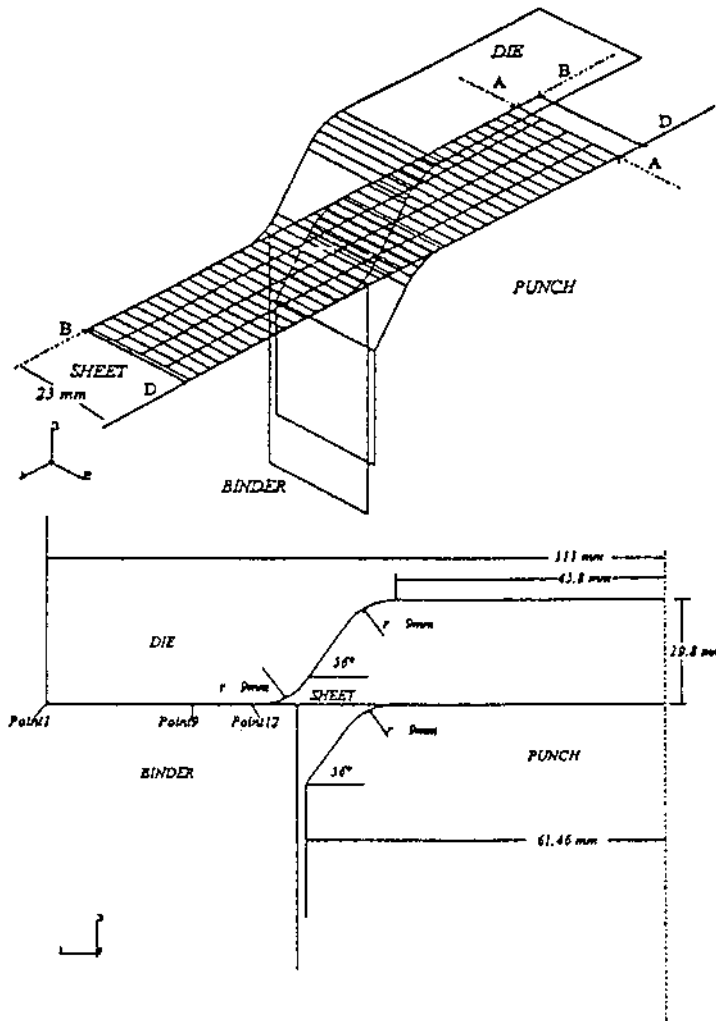
Figure 20   FE model of the tooling and un-deformed blank. (From Ref. 57.)
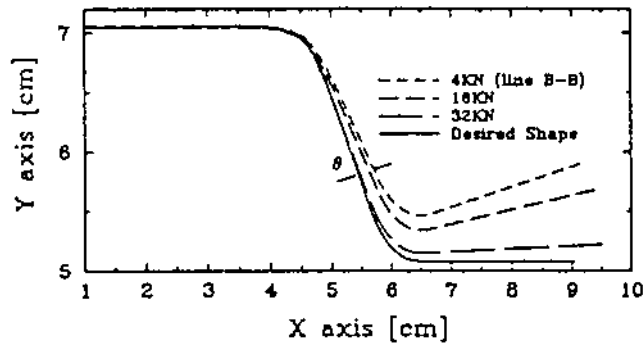
Figure 21   Comparison of springback for various constant binder forces. (From Ref. 57.)
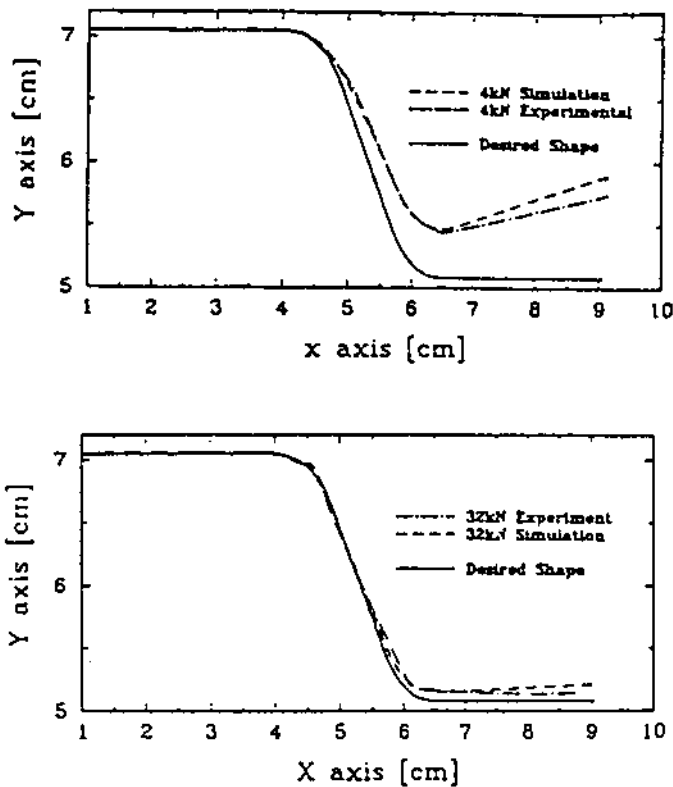
Figure 22 Springback data comparison for constant force case: simulation and experimental results. (From Ref. 57.)

the total stroke. This provides the smallest spring back (1.14 degrees versus 1.336 degrees for the constant force of 32 kN), and dramatically decreases the maximum strain incurred by the sheet (maximum principle of 0.087 vs 0.125 for the constant force of 32 kN).

5.4 Casting

Similar to products made by other manufacturing processes, castings are also prone to residual stresses and distortions. But, very little of this subject has been discussed in the literature. Foundries are reluctant to acknowledge the presence of such problems with their products or to share their in-house recipe to minimize them. A review of the transactions of the American Foundrymen's Society, most early textbooks on casting, and the ASM Handbook on Casting [63]; see below for reference numbers] provides little insight on the subject. In a recent book, Campbell [64] has presented a summary of the experimental study on residual stresses in simple shapes conducted by Dodd in 1950 [65]. The conclusions of these experiments could have been more economically and easily arrived at by using the basic concepts fully discussed in Ref. [4], and summarized earlier in Section 2 of this chapter.
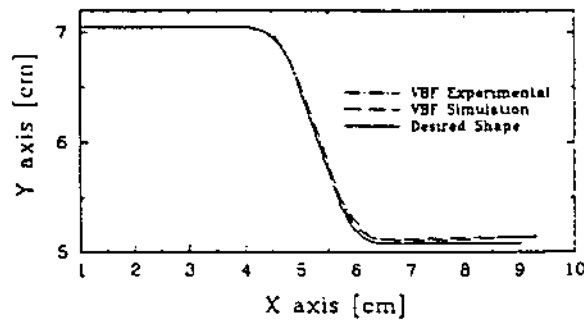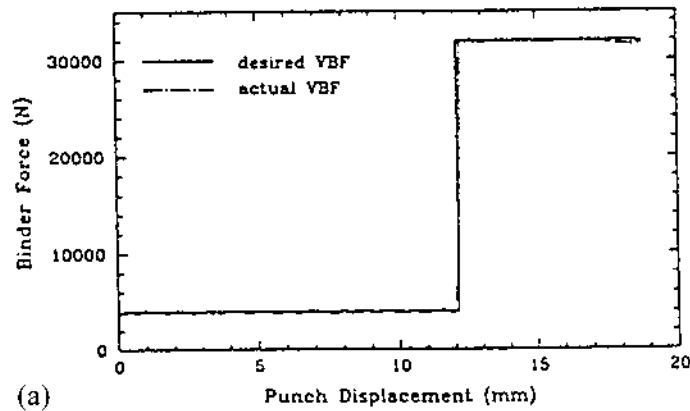
Figure 23 (a) Variable binder force and (b) corresponding spring back data. (From Ref. 57.)

Earlier attempts at mathematical prediction of residual stresses and distortions in castings were too simplistic and of little practical merit [66,67]. Due to the inherent complexity of the casting process, its finite element based computer simulation is now generally favored [68–73]. As discussed by Chandra [4,16], computer prediction of residual stresses and distortions in castings requires a coupled, transient, nonlinear thermo-mechanical analysis software with further ability to account for the following: (1) latent heat release during liquid to solid transformation; (2) transfer of heat and forces at the mold-metal interface; (3) constitutive model for the cast metal in the liquid, mushy and solid state including creep at elevated temperatures; (4) constitutive model for the mold (e.g. sand, metal or ceramic); (5) solid state transformation; (6) enclosure radiation at the mold surface to model the investment casting process; (7) mold withdrawal to model directional solidification; and (8) mold (material) removal.

Computer simulation of simple sand mold castings by Chandra and co-workers indicates that [17,18]: (1) for an accurate prediction of transient and residual stresses,

it is important to consider creep at elevated temperature (just below the solidus); creep is also found to make the stress distribution more uniform; (2) just prior to mold removal, the stresses in the casting can be extremely high, but after the mold removal they become small (owing to the springback discussed earlier), except in the area of stress concentration; and (3) a small variation in mold rigidity does not have any noticeable effect on residual stresses. The residual stresses after the mold removal will not necessarily be small if the casting is complex and the mold-removal is asymmetric with respect to the stress distribution. The conclusion regarding the effect of mold rigidity is in agreement with Dodd's aforementioned experiments with greensand molds with variable water content [65].

The application of finite element based computer simulation methodology to predict residual stresses and distortions in castings is still in the evolution stage. But, it is now possible to study the effect of the various process and design parameters on the residual stresses and distortions in complex castings, e.g. superheat, mold stiffness and design, design of gating and risers, and the design of the part itself. Also, residual stresses due to different casting practices such as sand mold, permanent mold, investment casting, etc, can be determined. As the manufacturers and end users of cast products become more aware of the status and benefits of the computer simulation methodology, it can be expected to play a very important role in controlling residual stresses and distortions in complex industrial castings. The biggest limiting factor in the use of simulation is the lack of thermophysical and mechanical properties data for the cast metal and the mold materials.

5.5 Metal-Matrix Composites (MMC)

Aluminum is a commonly used material in metal-matrix composites. Al/SiC, Al/Graphite, Al/Boron, Al/Al$_2$O$_3$ are all well known aluminum matrix composite systems. These composite materials are used to make products such as automotive disk brake rotors, pistons, upper control arms, etc. Residual stresses are inherent in metal-matrix (as well as organic-matrix and ceramic) composites. Stresses that are the result of differences in thermal expansion coefficients are frequently dominant. Sometimes, phase transformations (during quenching, welding, etc) can result in additional micro-residual stresses as well. In addition, small amounts of plastic deformation can significantly alter the residual stress state produced during fabrication. The magnitude and the nature of the residual stresses significantly affect the mechanical properties of metal-matrix composites. For example, tensile residual stresses present within the MMCs before the application of external load, may initiate some of the early damages [74].

Many traditional manufacturing processes like casting, extrusion, powder consolidation and some non-traditional processes like semi-solid forming, squeeze casting and diffusion bonding, etc, are used in manufacturing composites. Processing temperatures on metal-matrix composites are usually several hundred degrees above ambient. Cooling, thus results in thermal residual stresses due to large temperature gradients within the part and due to mismatch of thermal expansion coefficients between the matrix and the fibers. While the temperature gradients can be reduced by slow cooling, the expansion coefficient mis-match cannot be avoided. For example, the thermal expansion coefficient for aluminum (matrix) is $25 \times 10E(-6)/K$ and that of SiC (reinforcement) is $4 \times 10E(-6)/K$. Thus, on cooling, the larger con-

traction of the matrix in comparison to the reinforcement leads to tensile stresses in the matrix and compressive stresses in the reinforcement. In continuous fiber or aligned whisker composites, the anisotropic shape of the reinforcement induces larger axial than transverse residual stresses. Studies about residual stresses in many metal-matrix systems can be found in literature, for example: Al/SiC [75], Al/Graphite [76,77], Al/B [78], Al/Al$_2$O$_3$ [79]. Also, all aspects of metal matrix composites, including residual stresses, are discussed extensively in [80].

In designing metal-matrix composites, it is usually not possible to exploit the strength of the reinforcement without incurring some plastic deformation in the matrix. During mechanical deformation, the presence of hard reinforcement particles promotes heterogeneous plastic deformation in the matrix. This results in residual stresses after the load has been removed. Alternatively, plastic deformation from thermal cycling can reduce residual stresses present at room temperature. For example, cooling to cryogenic temperatures produces plastic flow in the matrix of an Al/graphite composite. On returning to room temperature, the original residual stress are reduced by 30% [80]. These effects are more pronounced in Al/B composite. Sometimes the plastic deformation on cooling can be great enough for the initial matrix tensile stress to become compressive at sufficiently low temperatures [80]. In practice, separating the origin of residual stresses is quite difficult and studies of plastic deformation must be accompanied by numerical calculations.

The numerical methods used (primarily, FEM) most often are based on the classical continuum mechanics with the mis-match of properties accounted for. Unit cell models are very commonly used in composite analyses, especially for two dimensional approximations of continuous fiber composites. Figure 24 shows examples of some of the unit cells used in practice [80] to determine the influence of reinforcement cross-section shape on the residual stress itself. The unit cell approach works quite well for continuous fiber composites. It is expected though that with the increase of computing power it will soon be possible to realistically compute three-dimensional distributions for problems that require three-dimensional analyses.
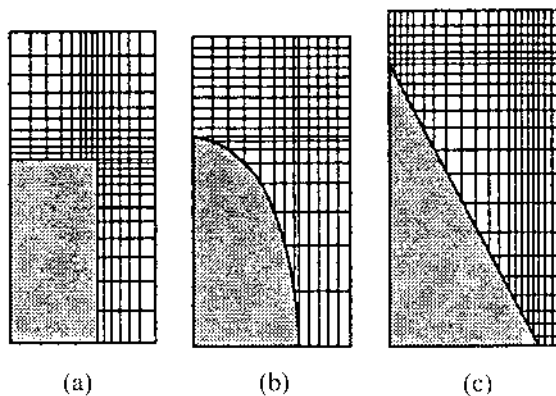
Figure 24   FE mesh for (a) cylindrical, (b) ellipsoidal, and (c) conical reinforcements. (From Ref. 57.)

Case Study: Residual Stresses in Cast SiC/Al Composites

Thermal residual stresses developed during casting of Al/SiC composites were studied as a function of cooling rate and volume fraction of fibers [74]. Thermo-elastoplastic FEM analysis was used for the study. Phase change of the matrix and temperature dependency of material properties were accounted for. Figure 25 shows a schematic of the casting set-up that was studied. The corresponding finite element mesh for a 20% by vol. of reinforcement is shown in Fig. 26. The matrix and fibers are modeled using 356 four-noded plane strain temperature displacement elements per section. The circular regions represent the matrix. The angle θ was measured from the x axis in the counter-clockwise direction to represent the direction in the matrix. Following are some of the features of this case study.

In order to study the residual stress formation mechanism first a thermal analysis was performed using the mesh shown. The thermal history data was then used to perform a residual stress analysis. Results show that the matrix undergoes significant plastic deformation during cooling from liquidus to room temperature. The residual stress was maximum at the fiber-matrix interface and reduced as the distance from the interface increased. Figure 27 shows the equivalent stress
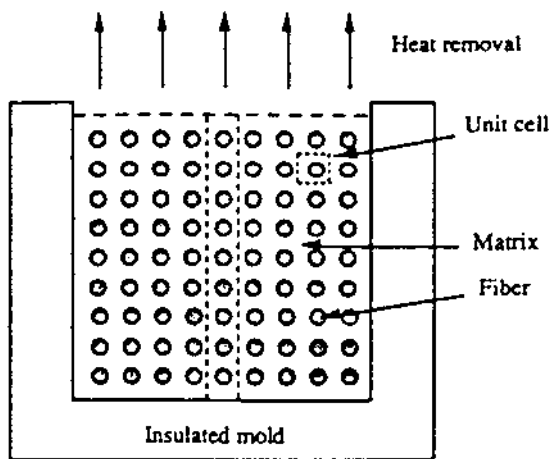
Figure 25 Casting setup used to model fiber-reinforced composite. (From Ref. 74.)
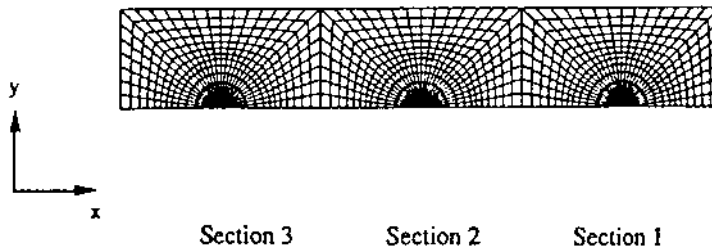
Figure 26 FE model for composites reinforced with fibers. (From Ref. 74.)

around the SiC fiber in the elastoplastic matrix. Figure 28 shows how the residual stress decreased as the distance from the interface increased. The matrix undergoes significant plastic deformation during cooling from the liquidus temperature to room temperature.

In order to study the effect of residual stress on mechanical behaviour composites with and without residual stresses, specimens were subjected to a transverse tensile mechanical loading. Composites consisting of 10, 20, and 30% by vol. of fibers were used in this study. The results showed that the modulus of elasticity was lowered due to the presence of residual stresses. This was due to the plastic deformation already present in the composite. The yield stress of composites, however, were raised due to the presence of residual stresses.
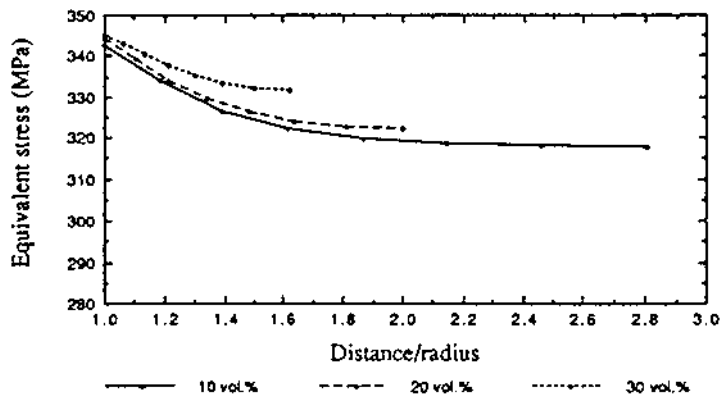
Figure 27   Equivalent stresses around the SiC fiber in the matrix subjected to a uniform temperature change. (From Ref. 74.)
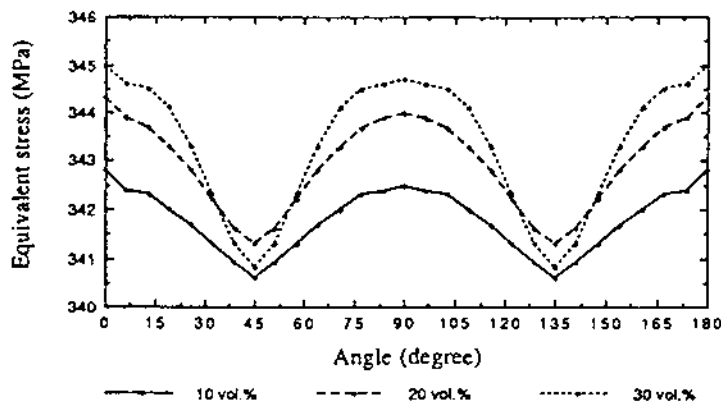
Figure 28   Equivalent stresses in the matrix as a function of distance from the interface: along 0, 90 and 180 degrees directions and along the 45 and 135 degree directions. (From Ref. 74.)

5.6 Stress Corrosion Cracking (SCC)

In corrosive environments existence of residual stresses, especially tensile residual stresses, can accelerate the corrosion processes in aluminum alloys leading to cracks in the component. As a simple thumb rule it can be said that surfaces residual stress that is tensile increases the chance of stress corrosion cracking and conversely compressive surface residual stress decreases the chance of SCC. This is why shot peening is sometimes used to help inhibit SCC. SCC in aluminum is dependent on the direction of application of stress as well. For example, for flat rolled products (sheet and plate), this situation occurs when (residual) stress is in the short transverse direction (normal to the rolling plane) and crack growth occurs in the rolling plane [26]. For forgings and extrusions, the grain patterns are much more complex, but maximum susceptibility occurs when stress is applied normal to the two principal grain flow directions, with crack growth occurring in the plane of metal flow [26].

It is known that alloys that contain appreciable amounts of soluble elements such as copper, magnesium, silicon, and zinc, are susceptible to SCC [26]. Stress-corrosion cracking in aluminum alloys is mainly intergranular in nature. This requires the grain boundaries to be anodic with respect to the rest of the microstructure so that corrosion propagates along these boundaries. For example, in 2xxx alloys the solute-depleted regions are the most anodic and in 5xxx alloys, the $Mg_2 Al_3$ precipitate along the boundaries is the most anodic. Thick sections of 2xxx alloys in naturally aged T3 and T4 tempers are susceptible to SCC, while thin sections are not. This difference is due to the quenching rate difference of thinner and thicker sections [26]. For the 5xxx series, susceptibility to SCC is low for lower magnesium content (i.e. $< 3\%$). If the magnesium content is higher than 3% the chances of $Mg_2 Al_3$ precipitating is higher which increases the susceptibility to SCC. 6xxx alloys are not susceptible to SCC at all. For 7xxx alloys, although the occurrence of SCC is low for highest strength tempers, parts that are machined from forgings and tempered parts that are thick have been found to be quite susceptible to SCC. Stress corrosion cracking is a very specialized topic and will not be dealt with in any more detail in this chapter. For information, references such as [26] should be consulted.

6 STRESS RELIEF AND DISTORTION CONTROL

The basic premise of a stress relief method is to produce rearrangement of atoms or molecules from their momentary equilibrium position (higher residual stress state) to more stable positions associated with lower potential energy or stress state. These methods can be classified into three broad categories: thermal, mechanical and chemical ([4], p. 134). The following remarks are concerned with the methods in the first two categories.

Thermal stress relief methods include annealing, aging, reheat treatment (e.g. post-weld heat treatment), and others. In general, a stress relief operation involves heating the part to a certain temperature, holding at the elevated temperature for a specified length of time, followed by cooling to room temperature. Primary reduction in residual stresses takes place during the holding period due to creep

and relaxation. In aluminum alloys, precipitation heat treatments are quite commonly used for stress relief. The degree of relaxation of stresses is primarily dependent upon the temperature of the precipitation treatment and alloy composition. In general, the precipitation treatments used to obtain the T6-type tempers provide only modest reduction in stresses, ranging from about 10–35%. To achieve a substantial reduction, heat treatment to the T7 temperature level is required. This, however, is accompanied by substantial reduction in strength. Uphill quenching (as described earlier) is another thermal residual stress relief method that is used for both quenched parts and metal matrix composites. Computer simulation of a thermal stress relief method generally entails a thermal-elastic-plastic-creep analysis of the part. A simple one-dimensional computer analysis of residual stresses in thin plates along with experimental verification is discussed by Agapakis and Masubuchi [81]. Josefson, on the other hand, has presented more sophisticated thermal-elastic-plastic-creep simulations of the annealing of single pass and multi-pass girth-butt welds in pipes [82,83].

A number of sub-categories of mechanical stress relief methods are listed in [4]. Out of these, methods such as stretching, upsetting, bending and straightening, etc, are common. Mechanical stress relief works somewhat in the following fashion. Assume that a metal strip has tensile residual stresses equal to the yield strength in its outer layers and compressive stress equal to the yield strength in its central layers. If this metal is stretched, the outer layers will flow plastically, the stresses will increase slowly in this region according to the hardening characteristics of the metal. The metal in the inner layers deform elastically, and the stresses increase rapidly according to Hooke's law. If now the stretching is stopped the stresses reduce uniformly across the specimen width. The final stress pattern that the metal retains consists of a reduced level of tensile stress on the outer surface and a reduced level of compression at the center. Typical levels of stretching deformation used for aluminum alloys range from 1% to 3%. FEA simulation of these methods do not pose much difficulty. However methods such as shot peening (a frequently used stress relief method) is likely to be difficult to simulate; and to the best of our knowledge, no attempt has yet been made to do so. The obvious reason is that, whereas it should be possible to model a single impact, modeling multiple impacts will be difficult, just as modeling multi-pass welding.

In recent years, the method of vibratory stress relief (especially in the subresonant region) has received considerable attention [84,85]. The basic premise of this method is that the presence of residual stresses in a part changes (increases) its natural resonant frequency. When the part is subjected to vibrations below its new frequency, the metal absorbs energy. During this process, the stresses redistribute gradually and the resonant frequency shifts back to the point corresponding to a residual stress free (or almost free) state. The process does not change the metallurgical or mechanical properties of the material. The technique has been found successful in relieving residual stresses induced by thermal processes such as welding and casting but not those induced by cold working. It has also been applied to reduce residual stresses in parts prior to machining in order to minimize distortions. It has been found particularly beneficial in low and medium carbon steels, stainless steels, aluminum alloys, but not in copper alloys. In view of the fact that the technique is much simpler, quicker and inexpensive than the thermal relief methods, it merits further study.

7 SUMMARY

Residual stresses are by-products of manufacturing and have the potential for causing premature failures. These failures could be cracks or fracture, degraded material properties, or undesired distortions. This article explains some of the fundamental causes which are common to the generation of these stresses in almost all manufacturing processes. It also identifies the various parameters which influence the magnitude and distribution of residual stresses in aluminum parts due to processes such as casting, quenching, sheet-metal forming, welding, and composites manufacturing. Attempt is made to include a lot of details in each case through the discussion of relevant case studies. Control and minimization of residual stresses and distortion are discussed in the context of different manufacturing processes. The article discusses the application of both the trial-and-error approach and the computer prediction approach for the determination of residual stress and distortion; with an emphasis on computer simulation. Most importantly, it points out several practical issues which require careful attention in order for the computer simulation technique to provide meaningful answers to the manufacturing engineers.

REFERENCES

1. U. Chandra, "Control of Residual Stresses," ASM Handbook, Vol. 20, Material Selection and Design, G. E. Dieter (Vol. chair), ASM International, Materials Park, OH 1997, pp. 811–819.
2. E. Heyn, "Internal Strains in Cold Wrought Metals, and Some Troubles Caused Thereby," Institute of Metals, 1914, 12, pp. 1–37.
3. E. Orowan, "Classification and Nomenclature of Internal Stresses," in Proceedings of Symposium on Internal Stresses, Institute of Metals, 1948, pp. 47–59.
4. W. M. Baldwin, *Residual Stresses in Metals*, Edgar Marburg Lecture, American Society for Testing Materials, 1949.
5. R. G. Treuting, J. J. Lynch, H. B. Wishart, and D. G. Richards, *Residual Stress Measurements*, American Society of Metals, Cleveland, OH, 1952.
6. U. Chandra, "Validation of Finite Element Codes for Prediction of Machining Distortions in Forgings," Commun. Num. Methods Eng., 1993, 9, pp. 463–473.
7. K. Masubuchi, *Analysis of Welded Structures*, Pergamon Press, New York, 1980, pp. 94–96.
8. W. M. Wilson and C. C. Hao, "Residual Stresses in Welded Structures," The Welding Journal, 1974, 26(5, Res. Suppl.), pp. 295s–320s.
9. H. Y. Hunsicker, "Dimensional Changes in Heat treating Aluminum Alloys," Metall. Trans. A, May 1980, 11A, pp. 759–773.
10. J. E. Hatch, *Aluminum: Properties and Physical Metallurgy*, ASM, Metal Park, OH, 1984.
11. G. W. Greenwood, and R. H. Johnson, "The Deformation of Metals Under Small Stresses During Phase Transformation," Proceedings of the Royal Society, 1965, 283, pp. 403–422.
12. C. L. Maggee, *Transformation Kinetics, Microplasticity and Aging of Martensite in FE31 Ni*, Ph.D. Thesis, Carnegie Institute of Technology, Pittsburgh, PA.
13. D. H. Cho, and D. G. Lee, "Manufacturing of Co-Cured Composite Aluminum Shafts, with Compression during CO-Curing Operation to reduce Residual Thermal Stresses," J. Comp. Mater., 1998, 32(12), pp. 1221–1241.

14. U. Chandra, S. Rachakonda, and S. Chandrasekharan, "Total Quality Management of Forged Products Through Finite Element Simulation," in *Proceedings of 3rd International SAMPE Metals and Metals Processing Conference*, Vol. 3, (F. H. Froes, W. Wallace, R. A. Cull, and S. Strucholt, eds.), SAMPE International Business Office, Covina, CA, 1992, pp. M379–393.

15. U. Chandra, "Computer Prediction of Hot Tears, Hot Cracks, Residual Stresses and Distortions in Precision Castings: Basic Concepts and Approach," in Proceedings of Light Metals (J. Evans, ed.), TMS, Warrendale, PA, 1995, pp. 1107–1117.

16. U. Chandra, "Computer Simulation of Manufacturing Processes – Casting and Welding," Comp. Model. Simul. Eng., 1996, 1, pp. 127–174.

17. U. Chandra, R. Thomas, and S. Cheng, "Shrinkage, Residual Stresses, and Distortions in Castings," Comp. Model. Simul. Eng., 1996, 1, pp. 369–383.

18. A. Ahmed, and U. Chandra, "Prediction of Hot Tears, Residual Stresses and Distortions in Castings Including the Effect of Creep," to be published.

19. U. Chandra, S. Chandrasekharan, and R. Thomas, "Finite Element Analysis of the Thread Rolling Process," Reports, Concurrent Technologies Corporation, submitted to Knolls Atomic Power Lab, Schenectady, NY, 1995.

20. J. M. Bergheau, and J. B. Leblond, "Coupling Between Heat Flow, Metallurgy and Stress-Strain Computations in Steels: The Approach Developed in the Computer Code SYSWELD for Welding or Quenching," in Proceedings of the Conference on Modeling of Casting, Welding and Advanced Solidification Processes V (M. Rappaz, M. R. Ozgu, and K. W. Mahin, eds.), TMS, Warrendale, PA, 1991, pp. 203–210.

21. D. J. Smith, G. A. Webster, and P. J. Webster, *Measurement of Residual Stress and the Effects of Prior Deformation Using the Neutron Diffraction Technique*, The Welding Institute, Cambridge, UK, 1987.

22. C. O. Ruud, "A Review of Nondestructive Methods for Residual Stress Measurement," J. Metals, 1981, 33(7), pp. 35–40.

23. M. E. Hilley, J. A. Larson, C. F. Jatczak, and R. E. Ricklefs (eds.), *Residual Stress Measurement by X-Ray Diffraction – SAE J784a*, Society of Automotive Engineers, Inc., Warrendale, PA, 1971.

24. J. Lu, *Handbook of Measurement of Residual Stresses*, The Fairmont Press, Lilburn, GA, 1996.

25. J. F. Shackelford, *Introduction to Materials Science for Engineers*, Prentice-Hall, New Jersey 1992.

26. J. R. Davis (ed.), *ASM Speciality Handbook: Aluminum and Aluminum Alloys*, ASM International, Materials Park, OH, 1993, pp. 290–327.

27. H. E. Boyer, and P. R. Cary, *Quenching and Control of Distortion*, ASM International, Metal Park, OH, 1988, p. 11.

28. T. V. Rajan, C. P. Sharma, and A. Sharma, *Heat Treatment – Principles and Techniques*, Prentice-Hall of India Private Ltd, 1988.

29. S. Segerberg, and J. Bodin, "Variation in the Heat Transfer Coefficient Around Components of Different Shapes During Quenching," in Proceedings of the First International Conference on Quenching and Control of Distortions, (G. E. Totten, ed.), ASM International, Metal Park, OH, 1992, pp. 165–170.

30. I. F. Kolobnev, *Heat Treatment of Aluminum Alloys*, Isreal program for Scientific Translations, Jerusalem, 1963.

31. S. Das, G. Upadhya, and U. Chandra, "Prediction of Macro- and Micro-Residual Stress in Quenching Using Phase Transformation Kinetics," in Proceedings of the First International Conference on Quenching and Control of Distortions (G. E. Totten, ed.), ASM International, Metal Park, OH, 1992, pp. 229–234.

32. S. Das, and A. J. Paul, "Determination of Interfical Heat Transfer Coefficients in Casting and Quenching Using a Solution Technique for Inverse Problems Based on the Boundary Element Method," Metall. Trans. B, Dec. 1993, 24B, pp. 1077–1086.

33. J. V. Beck, B. Blackwell, and C. R. St. Clair, *Inverse Heat Conduction: Ill-Posed Problems*, John Wiley and Sons, New York, NY, 1985.

34. R. A. Wallis, N. M. Bhathena, P. R. Bhowal, and E. L. Raymond, "Application of Process Modelling to Heat Treatment of Superalloys," Industrial Heating, 1988, pp. 30–33.

35. C. R. Boer, et al., *Process Modeling of Metal Forming and Thermomechanical Treatment*, Springer-Verlag, Berlin, 1986, pp. 380–400.

36. D. Radaj, *Heat Effects of Welding: Temperature Field, Residual Stress, Distortion*, Springer-Verlag Berlin, 1992.

37. E. F. Rybicki, P. A. McGuire, E. Merrick, and J. Wert, "The Effect of Pipe Thickness on Residual Stresses Due to Girth Welds," ASME J. Pressure Vessel Tech., 1982, 104, pp. 204–209.

38. U. Chandra, "Determination of Residual Stresses due to Girth-Butt Welds in Pipes," ASME J. Pressure Vessel Tech., 1985, 107, pp. 178–184.

39. S. Das, G. Upadhya, U. Chandra, M. J. Kleinosky, and M. L. Tims, "Finite Element Modeling of Single-Pass GMA Weldment," *Modeling of Casting, Welding and Advanced Solidification Processes VI*, (T. S. Piwonka, V. Voller, and L. Katgerman, eds.), TMS, Palm Coast, FL, March 21–23, 1993, p. 593.

40. S. Das. D. K. Moyer, M. L. Tims, G. Upadhya, and M. J. Kleinosky, "Modeling Heat Transfer, Microstructure Development, Transformation Plasticity and Residual Stresses in GMA Multi-Pass Butt Welds," presented at International Conference on Modeling and Control of Joining Processes, Miami, Fl, Dec. 1993, pp. 8–10.

41. O. R. Myhr, et al., "Modeling of Microstructure Evolution, Residual Stresses and Distortions in 6082-T6 Aluminum Weldments," Welding J., July 1998, 77, pp. 286s–292s.

42. C. L. Tsai, S. C. Park, and W. T. Cheng, "Welding Distortion of a Thin-Plate Panel Structure," Welding J., May 1999, 78, pp. 156s–165s.

43. M. Hval, et al., "Numerical Modeling of Ductile Fracture Behavior in Aluminum Weldments," Welding J., May 1998, 77, pp. 208s–217s.

44. P. Dong, J. K. Hong, P. Rogers, "Analysis of Residual Stresses in Al-Li Repair Welds and Mitigation Techniques," Welding J., November 1998, 77, pp. 439s–445s.

45. D. Rosenthal, "The Theory of Moving Sources of Heat and Its Application to Metal Treatments," Trans. ASME, Nov. 1946, pp. 849–866.

46. K. Masubuchi, "In-Process Control and Reduction of Residual Stresses and Distortion in Weldments," in Proceedings of Practical Applications of Residual Stress Technology, (C. O. Ruud, ed.), ASM International, Materials Park, OH, 1991, pp. 95–101.

47. K. Masubuchi, "Research Activities Examine Residual Stresses and Distortion in Welded Structures," Welding J., Dec. 1991, pp. 41–47.

48. R. M. Chrenko, "Residual Stress Studies of Austenitic and Ferritic Steels," Conference on Residual Stresses in Welded Construction and Their Effects, London, Nov. 1977.

49. U. Steuer, H. P. Bauerle, and K. Lupfert, "Experiences with Aluminum Components in the Porche 928 Car Body," *Aluminum and Automobile*: Lectures held on an International Symposium Organized by the Aluminum-Zentrale, Aluminum-Verlag, Dusseldorf, Germany, 1981.

50. X-Hu Zeng, "Anisotropic Spring-back in Various Aluminum-Lithium Sheet Alloys," Scand. J. Metall., 1995, 24, pp. 39–47.

51. A. Nadai, *Flow and Fracture of Solids*, McGraw-Hill, New York, 1950.

52. R. Hill, *The Mathematical Theory of Plasticity*, Oxford University Press, Oxford, UK, 1950.

53. W. M. Hosford, and R. M. Cadell, *Metal Forming*, Prentice-Hall, Engelwood Cliffs, NJ, pp. 250–252.

54. C. H. Toh, ''A Simplified Three-Dimensional Finite Element Method for the Analysis of Sheet Metal Forming,'' Manufacturing Technology review, NAMRC 16 Proc., NAMRI/SME, 1988, pp. 119–124.

55. A. Chandra, ''Agenerallized Finite Element Analysis of Sheet Metal Forming With an Elasto-Viscoplastic Material Model,'' J. Eng. Ind., Feb. 1986, 108, pp. 9–15.

56. I-N. Chou, and C. Hung, ''Three-Dimensional Finite Element Analysis of Sheet-Metal Bending With Complex Die Geometry,'' J. Eng. Mater. Tech. Aug., 1997, 119, pp. 324–331.

57. M. Sunseri, J. Cao, A. P. Karafillis, and M. C. Boyce, ''Accommodation of Springback Error in Channel Forming Using Active Binder Force Control: Numerical Simulations and Experiments,'' J. Eng. Mater. Tech., July 1996, 118, pp. 426–435.

58. Z. Kampus, and K. Kuzman, ''Experimental and Numerical (FEM) Analysis of Deep Drawing of Relatively Thick Sheet Metal,'' J. Mater. Process. Tech., 1992, 34, pp. 133–140.

59. M. Geiger, and A. Sprenger, ''Controlled Bending of Aluminum Extrusions,'' CIRP Annals, 1998, 47(1), pp. 197–202.

60. Z. Tan, B. Persson, and C. Magnusson, ''An Empiric Model for Controlling Springback in V-die Bending of Sheet Metals,'' J. Mater. Process. Tech., 1992, 34, pp. 449–455.

61. A. Makinouchi, C. Teodosiu, and T. Nakagawa, ''Advance in FEM Simulation and its Related Technologies in Sheet Metal Forming,'' CIRP Annals, 1997, 47(2), pp. 641–649.

62. ABAQUS, Hibbett, Karlsson, Sorensen, Inc., Pawtuckett, RI.

63. D. M. Stefanescu (Vol. Chair), *Metals Handbook: Casting, Volume 15*, 9th Edn, ASM International, Metals Park, OH, 1988.

64. J. Campbell, *Casting*, Butterworth Heinmann, Oxford, UK, 1991.

65. R. A. Dodd, W. A. Pollard, and J. W. Meier, ''Hot Tearing of Magnesium Casting Alloys,'' AFS Trans., 1957, 65, pp. 100–117.

66. J. H. Weiner, and B. A. Boley, ''Elasto-plastic Thermal Stresses in a Solidifying Body,'' J. Mech. Phys. Solids, 1963, 11, pp. 145–154.

67. O. Richmond, and R. H. Tien, ''Theory of Thermal Stresses and Air Gap Formation During the Early Stages of Solidification in a Rectangular Mold,'' J. Mech. Phys. Solids, 1971, 19, pp. 273–284.

68. R. W. Lewis, and P. M. Roberts, ''Finite Element Simulation of Solidification Problems,'' App. Sci. Res., 1987, 44, pp. 61–92.

69. A. L. Purvis, E. K-. Asibu, Jr., and R. D. Pehlke, ''Modeling Thermal Stresses During Solidification,'' *Modeling of Casting Welding and Advanced Solidification Processes – VI* (T. S. Piwonka, V. Voller, and L. Katgerman, eds.), Palm Coast, FL, March 21–26, 1993, pp. 601–608.

70. B. G. Thomas, ''Stress Modeling of Casting Processes: An Overview,'' *Modeling of Casting Welding and Advanced Solidification Processes – VI*, (T. S. Piwonka, V. Voller, and L. Katgerman, eds.), Palm Coast, FL, March 21–26, 1993, pp. 519–534.

71. J. A. Dantzig, ''Thermal Stress Development in Metal Casting Processes,'' Metall. Sci. Tech., 1989, 7(3), pp. 133–178.

72. E. Onate, D. Celentano, R. Codina, S. Oller, and O. Soto, ''Finite Element Models for Analysis of Mould Filling and Solidification in Casting,'' *Modeling of Casting Welding and Advanced Solidification Processes – VII*, (M. Cross, and J. Campbell, eds.), TMS, Warrendale, PA, 1995, pp. 189–196.

73. P. Chow, C. Bailey, M. Cross, and K. Pericleous, ''Integrated Numerical Modeling of the Complete Casting Process,'' *Modeling of Casting Welding and Advanced Solidification Processes – VII*, (M. Cross, and J. Campbell, eds.), TMS, Warrendale, PA, 1995, pp. 213–222.

74. S. Ho, and A. Saigal, "Thermal Residual Stresses and Mechanical Behavior of Cast SiC/Al Composites," Mater. Sci. Eng., 1994, A 183, pp. 39–47.

75. T. Lorentzen, and A. P. Clarke, "Thermomechanically Induced Residual Strains in Al/SiCp Metal-Matrix Composites," Comp. Sci. Tech., 1998, 58, pp. 345–353.

76. P. Predecki, and C. S. Barett, Proceedings of the twenty-eighth Sagamore Army Materials Research Conference (E. Kula, and V. Weiss, eds.), Plenum Press, New York, pp. 409–424.

77. S.-D. Tsai, D. Mahulikar, H. L. Marcus, et al., Mater. Sci. Eng., 1981, 47, pp. 145–149.

78. T. R. Stepanova, "Dependence of Residual Stresses in Boron-Aluminum on Structural Features of the Material and Preliminary Thermomechanical Treatment," Mech. Comp. Mater., 1990, 26, pp. 319–323.

79. M. Guagliano, "A Numerical model to Investigate the Role of Residual Stresses on the Mechanical Behavior of Al/Al2O3 Particulate Composites," J. Mater. Eng. Perform., April 1998, 7(2), pp. 183–189.

80. S. Suresh, A. Mortensen, A Needleman, *Fundamentals of Metal Metrix Compostes*, Butterworth-Heinmann, Stoneham, MA, 1993.

81. J. E. Agapakis, and K. Masubuchi, "Analytical Modeling of Thermal Stress Relieving in Stainless and High Strength Steel Weldments," Weld. Res., Suppl. 1984, pp. 187s–196s.

82. B. L. Josefson, "Residual Stresses and Their Redistribution During Annealing of a Girth-Butt Welded Thin-Walled Pipe," ASME J. Pressure Vessel Tech., 1982, 104, pp. 245–250.

83. B. L. Josefson, "Stress Redistribution During Annealing of a Multi-Pass Butt-Welded Pipe," ASME J. Pressure Vessel Tech., 1983, 105, pp. 165–170.

84. R. A. Claxton, "Vibratory Stress Relieving – Its Advantages and Limitations as and Alternative to Thermal Treatments," Heat Treatment of Metals, 1974, pp. 131–137.

85. A. G. Hebel, Jr., "Subresonant Vibrations Relieve Residual Stress," Metal Progress, Nov. 1985, pp. 51–55.

7

Rolling of Aluminum

KAI F. KARHAUSEN

VAW Aluminium AG, Bonn, Germany

ANTTI S. KORHONEN

Helsinki University of Technology, Espoo, Finland

1   INTRODUCTION

Rolling is a basic process for producing strip and sheet. Due to small product thickness, the demanded tight tolerance and quality requirements such shapes are difficult to produce directly by casting. In addition to producing the required shape, deformation by rolling ensures that the microstructure of the product is adjusted for further processing. The typical dendritic or coarse cellular as cast microstructure is effectively modified by hot rolling. Recrystallization processes lead to a complete re-organization of microstructure. This improvement of micro-structure and mechanical properties is also important for manufacturing thicker products such as plates. Compressive deformation by rolling may even close existing pores or voids. In addition, the development of texture during hot and cold rolling plays a significant role in establishing the final properties of aluminum sheet. These processes will be discussed in detail in this chapter.

The use of aluminum has increased in many applications [1,2]. Its light weight is an obvious advantage and it has gained interest, e.g. in attempts to save energy by developing light weight constructions. Aluminum alloys offer adaptable tensile strength levels between 60 and 530 MPa, good castability and formability, good chemical resistance, versatile possibilities of surface treatments and high electrical as well as thermal conductivity. Optimum alloys can be found for a variety of applications in transportation, structural components, packaging, electronics and for machine components. In addition to the supply for various applications in the expanding transportation market, the traditional usage of rolled aluminum sheet

and plate material is in can body and can top stock, food and medical packaging, closure caps, thin foil, fin stock for air conditioners, brazing sheet for heat exchangers, decorative panels and lithographic sheet.

From a historical perspective the dominant material in rolling is steel, which accounts for the largest quantity in the world's metal rolling production. The advances in the rolling of steel strip and sheet [3,4] therefore often found their way into the rolling of aluminum as well. In the case of aluminum one difference is that thinner sheets and foils make up a more significant portion of the product palette. The rolling of thin gauges presents some basic difficulties, which will be discussed in detail. Excluding the striking metallurgical differences between aluminum and steel, lower hot rolling temperatures for aluminum, which are about one half of that for steel, and differing frictional conditions, the basic rolling technology for both steel and aluminum is based on the same general mechanical principles. Some features of modern aluminum rolling mills are first briefly reviewed and the basic mechanics of rolling are discussed.

2   HOT ROLLING OF ALUMINUM

Figure 1 shows some basic casting and hot rolling mill configurations for aluminum strip production. The basic difference in the type of production method depends on the required production capacity. Due to the lighter weight of aluminum, the production capacities of aluminum mills are usually lower than those for steel. The choice of mill depends on the product spectrum and the capacity requirements. Single stand mills, where multi-pass rolling is performed in reversing manner is usually used for roughing passes as well as for finish rolling. Tandem mills, where several stands are in line, are used for the finish hot rolling passes. An alternative to the tandem mill can be the Steckel-type mill, in which reversing rolling is performed from coil to coil. A traditional hot reversing roughing mill and hot tandem finishing mill production system becomes economical for steel if the annual production exceeds 0.5 million tons; and with an increased number of furnaces, roughing mill and finishing mill stands annual production can easily be extended up to several millions of tons. An alternative in the case of steel is thin slab casting technology, which can be employed to replace the traditional reversing roughing mill, if the surface quality is not critical and the production spectrum is not wide.

One producer of rolling mills for both steel and aluminum [5] recommends that more than 600,000 tons per year (see Fig. 1.5) can be obtained with the classical hot reversing roughing and tandem finishing mill concept for rolling aluminium strip. A single stand reversing hot mill alone is capable of a production of up to 160,000 tons per year.

The reversing roughing mill combined with a Steckel-type reversing hot or warm finishing mill is recommended for smaller amounts of production. It offers the advantage of producing small batches on a "just-in-time" basis, which is not economical in tandem mills. It should be mentioned, however, that for some products this concept may lead to severe problems in mechanical properties due to the longitudinal variation of texture and microstructure.

For still smaller amounts of production thin slab casting or thin strip casting may be considered. The twin roll caster may be used in low-capacity plants for casting mainly soft alloys down to a nominal minimum strip thickness of 6 mm.

1.1 – Strip Casting-Rolling
Production Capacity < 10.000 tpy

Strip Caster

1.2 – Thin Slab Casting – Hot Tandem Finishing
Production Capacity < 120.000 tpy

Hot Tandem Finishing Mill

Thin Slab Caster

1.3 – Hot Reversing Roughing/Finishing
Production Capacity < 150.000 tpy

Hot Reversing Roughing/
Finishing Mill

Ingot Scalping

**1.4 – Hot Reversing Roughing Mill –
Reversing Warm Finishing Mill**
Production Capacity
< 250.000 tpy

Reversing Warm
Finishing Mill

Ingot Scalping

Hot Reversing
Roughing Mill

**1.5 – Hot Reversing Roughing Mill –
Tandem Finishing Mill**
Production Capacity
< 600.000 tpy

Hot Tandem
Finishing Mill

Hot Reversing
Roughing Mill

Ingot Scalping

Figure 1 Hot strip casting and rolling mills for aluminum alloys. (From Ref. 5.)

A belt-type caster followed by tandem hot rolling can be employed for a full range of alloys including the 1100, 3000 and 5000 series. The caster produces alloys in the thickness region of 16–20 mm and after the tandem finishing mill, a thickness down to 2 mm or 3 mm is obtained.

In aluminum rolling the requirements for dimensional accuracy and flatness have been increasing steadily. For this reason various control techniques have been developed where the shape of the roll gap is influenced by the geometrical and thermal crown of the rolls as well as by the application of torques to influence bending. Systems which deserve special attention are those based on variable crowns and lateral shifting of work rolls, such as CVC (Continuously Variable Crown), UPC (Universal Profile Control) or HVC (Horizontal Vertical Crown), usually applied with additional roll bending [6–8]. For an even finer adjustment of shape, selective spray cooling is applied to the work rolls. Combinations of these methods offer shape control within a broad range. The CVC concept has become popular both in new mills and in revamping older installations. The world's largest aluminum-processing plant of Alunorf, Germany (a joint venture of VAW and Alcan), with an annual production capacity of 1.4 million tons of hot strip and 900,000 tons of cold strip has been reported to employ CVC in its newest hot and cold strip mills [9].

Hot working is defined as a forming operation in the range above 0.6 times the melting temperature of the metal, which in the case of aluminum is above 300°C. As compared to cold working, forming in this region is assisted by dislocation climb, cross slip and activation of additional slip systems. Strain hardening, which in cold working causes high pressures, is reduced considerably by dynamic recovery, resulting in the formation of polygonized dislocation arrays of lower energy. Further softening is induced by static recovery (annihilation and rearrangement of dislocations) and recrystallization (nucleation and growth of new grains) during interstand times or upon subsequent annealing. These factors lead to considerably lower flow stresses which, apart from lowering the necessary energy for rolling and lowering the pressure on the roll-set, enhance the formability of the material by reducing stress concentrations which initiate failure. Thus, high reductions above 50% can be accomplished. A compact overview on the current understanding of the structural influences in hot rolling is given by McQueen [10].

During hot rolling, aluminum alloys undergo significant changes in microstructure and texture, which determine the product quality. Thus, tight control of metallurgical changes is required in order to ensure a cost-efficient production of high-quality sheet material. All major aluminum rolling mills employ thermomechanical processing-routes in which the rolling operation is not only employed to achieve the desired reduction, but to accomplish well-defined metallurgical properties. Consequently, hot rolling procedures for aluminum alloys differ considerably from the steel rolling practice.

The development of the most important metallurgical features during a typical processing route of Al-Mg-Mn alloys is depicted in Fig. 2 [26]. The conventional processing route of hot rolled sheet today starts with a DC (Direct Chill) casting operation [1]. As the overall efficiency of the processing route is to a large degree determined by batch size, it is usual to aim for the largest ingots that can be processed in the hot mill. Modern machines can handle drop weights exceeding 100 tons. The resulting low cooling rates lead to coarse precipitates and segregations. The most
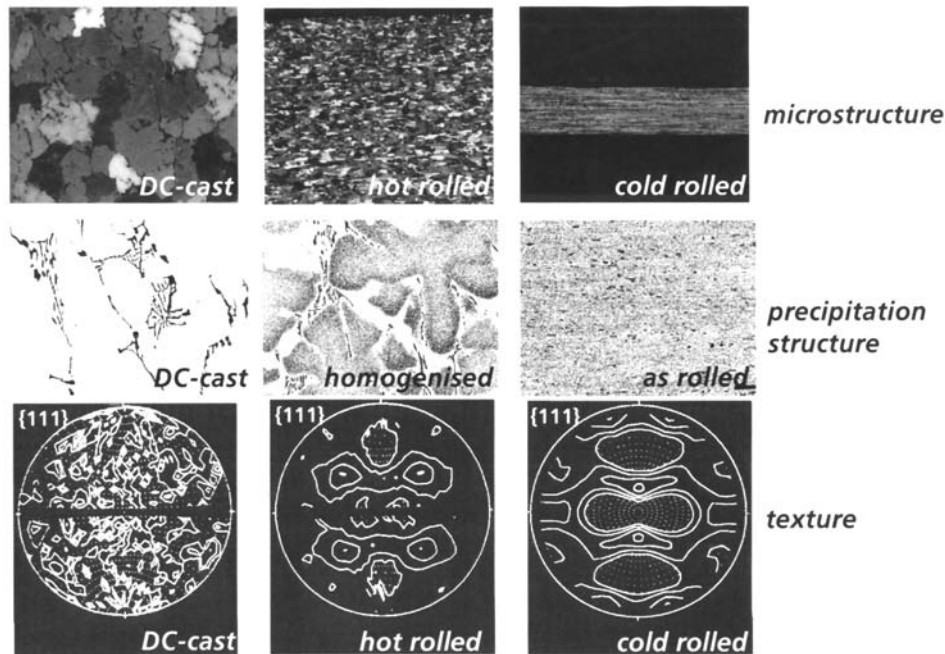
Figure 2 Evolution of grain structure, precipitation structure and texture in sheet production of Al-Mg-Mn alloys. (From Ref. 26.)

dominant features of the cast ingot are the cell size, as well as type, size and distribution of constituent particles and eutectic precipitates.

Furthermore, the highly heterogeneous cooling rates from the DC casting impose variations in microstructure throughout the slab. Due to grain refinement, a close to random texture is usually observed (Fig. 2(a)). Surface segregations may be removed by a subsequent scalping operation. Even 100% of the production may be scalped before rolling to ensure good quality of the products. Subsequently follows an ingot homogenization treatment, during which internal stresses are relieved, elements in supersaturated solid solution (Fe, Mn, Si, Cr, etc.) are precipitated, microsegregations are leveled to some extent by long range diffusion and primary phases are transformed. When the alloy is held at high temperature for a sufficient time, precipitates coarsen. It has been shown for alloy AA3003 [11], that the mean dispersoid size can be varied between 0.03 and 0.17 μm with a concurrent variation in dispersoid density between 740 and $11\mu m^{-3}$ for low and high temperature annealing respectively. As the dispersoid size strongly affects recrystallization during and after hot rolling, it needs to be controlled by optimum heat treatment conditions. From homogenization the slab is usually cooled down to hot rolling temperature. This leads to a further reduction of elements in solid solution and a growth of coarser secondary particles. The microstructural state of the slab before hot rolling significantly influences most final properties of a number of product groups.

The hot rolling operation is performed at the highest possible temperature to lower flow stress in order to reduce loads and to achieve high reductions. An upper

temperature limit is imposed by the need for controlling recrystallization and precipitation, dependent on the alloy, as well as by the occurrence of pick-up. During conventional rolling, the coarse as cast structure changes to a deformed and recrystallized structure having considerably finer grain size. Coarse primary precipitates are crushed and become distributed more evenly. Decreasing temperatures during rolling and an increase in vacancy concentration in the lattice due to deformation lead to a further precipitation of secondary phases.

   With regard to microstructure, hot rolling can be seen as a succession of deformation and annealing steps. The most dominant metallurgical features are recrystallization and the development of preferred crystal orientations (texture). Both processes are interrelated and influenced by ongoing precipitation. Recrystallization is particularly determined by the alloy system and the processing conditions. In high-purity aluminum, the grain boundary mobility is high and the material already shows rapid recrystallization during processing (dynamic recrystallization). However, in customary industrial alloys, dynamic recrystallization may be observed only at extremely high temperatures, where the effect is mainly caused by local bulging of grain boundaries and not by nucleation and growth. For these materials, recrystallization typically takes place during inter-stand times or after rolling at elevated temperatures (post-dynamic or static recrystallization). In commercially pure alloys such as AA1050, typically used for packaging foil or lithographic sheet, elements with low solubility, like Fe and Si, interact with the grain boundaries and efficiently obstruct recrystallization when present as finely dispersed precipitates. The presence of Mn and Cr causes the same effect unless the elements are already bound in coarse particles. Within the Al-Mg-Mn alloy system, used in considerable amounts for beverage cans or automotive components, recrystallization covers a broad range within the scope of industrial conditions and thus can be influenced to a large degree by the choice of rolling parameters. Figure 3 gives an example of the recrystallization spectrum of alloy AA5182 [12]. In industrial practice, the recrystallized structure can be obtained in a separate annealing treatment, but more sophisticated technologies utilize self-annealing on the coil from the rolling heat.

   Grain size and especially texture development are determined by recrystallization, which in turn govern the properties of products delivered in hot rolled condition as well as those of subsequently cold rolled sheets. Cold rolled products particularly, such as can body stock, require a distinctive cube texture in the hot rolled condition in order to reduce earing upon the drawing operations of the can manufacturer. The formation and evolution of cube components has received much attention of researchers and industry [13–15]. During hot rolling with little inter-stand recrystallization, the cube nuclei are formed at the expense of rolling texture components, and they can grow upon subsequent annealing. A coarse size and large inter-particle spacing are desired to enhance recrystallization during coiling. On the other hand, this may cause inter-stand recrystallization leading to the formation of large cube bands which deform unfavorably in subsequent passes. To restrain inter-stand recrystallization, the rolling temperature can be lowered, or the rolling speed can be increased. In this situation another restriction is introduced by the occurrence of particle-stimulated nucleation (PSN). The transition range from cube texture to the random PSN texture is depicted in Fig. 4 for alloy AA3104 with a given constitution before rolling [16]. In addition, the
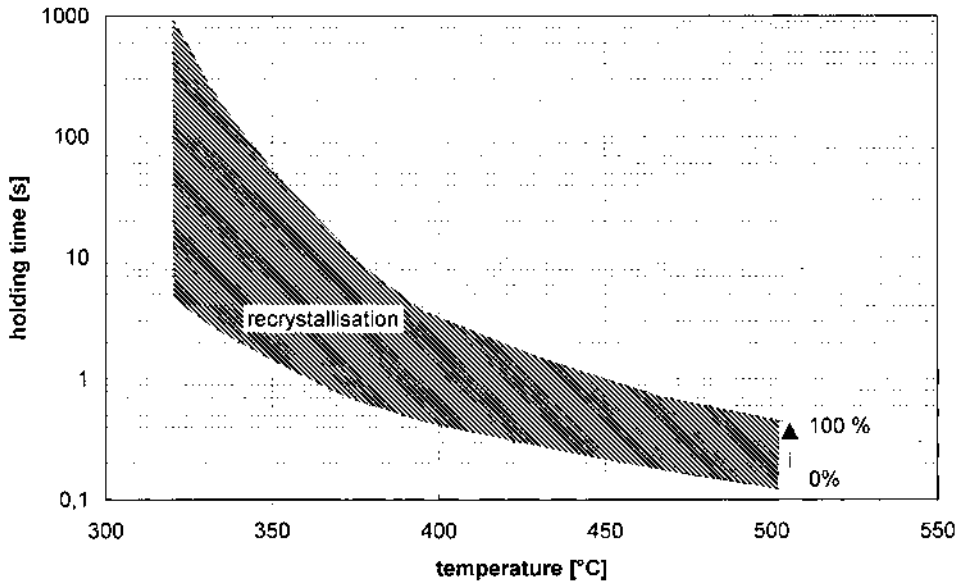
Figure 3 Spectrum of recrystallization for alloy AA5182. (From Ref. 12.)
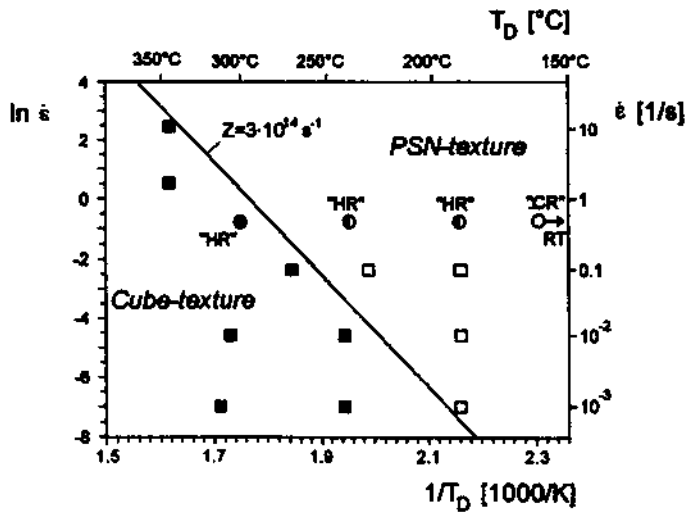
Figure 4 Cube vs PSN texture dependent on forming conditions for alloy AA3104. (From Ref. 16.)

importance of size and distribution of coarse constituent particles (Fig. 5) emphasizes the need for understanding the development of microstructure throughout the whole process chain [18].

Hot rolling is the dominant process in the production chain of aluminum strips and sheets inducing microstructural heterogeneities in the end product. It is obvious,
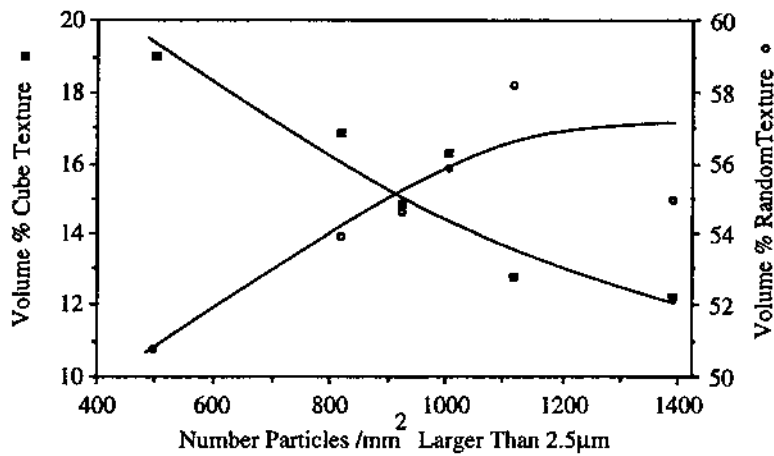
Figure 5 Cube vs PSN texture dependent on the state of precipitation for alloy AA3104. (From Ref. 17.)

that discontinuous rolling on a reversing mill causes heterogeneities along the rolling direction. The delay time between head and tail continuously increases, so that for some passes the slab may partially recrystallize if no precautions are taken. Furthermore, especially in the roughing passes, the deformation is characterized by large gradients in strain rate and temperature in strip thickness. Heterogeneities in width may become severe, when operating at low speeds and if the mill is not equipped with selective cooling systems.

From the above it can be deduced that tight metallurgical constraints are imposed on the hot rolling schedule and processing parameters have to be controlled within narrow windows. The discussed mechanisms are governed by the initial state of the ingot (alloy composition, state of microstructure, constitution-size- and distribution of precipitates and elements in solid solution) in combination with the applied hot rolling and annealing conditions (temperature-time history, strain path, strain rates and tooling boundary conditions). The layout and optimization of such complex interacting systems can only be performed if the microstructure can be quantified at all processing stages. Thus, predictive models are essential for this task and are subject of major research efforts in the aluminum industry.

Figure 6 documents an application in which the computed fraction of inter-stand recrystallization in a tandem hot finishing mill and the percentage of cube texture and earing are correlated [12], the results of which are used for pass optimization in order to reduce earing in the end-user-product.

In comparison to steel industry, where modeling techniques for multi-pass hot rolling have a long tradition and are well advanced [e.g. 19–22], the modeling of aluminum alloys is at a considerably earlier stage. In steel, the influence of texture on recrystallization is usually neglected, and the only material parameters that need to be considered in the austenitic regime are grain size and work-hardening and -softening kinetics. The kinetics of static recrystallization are usually assumed to
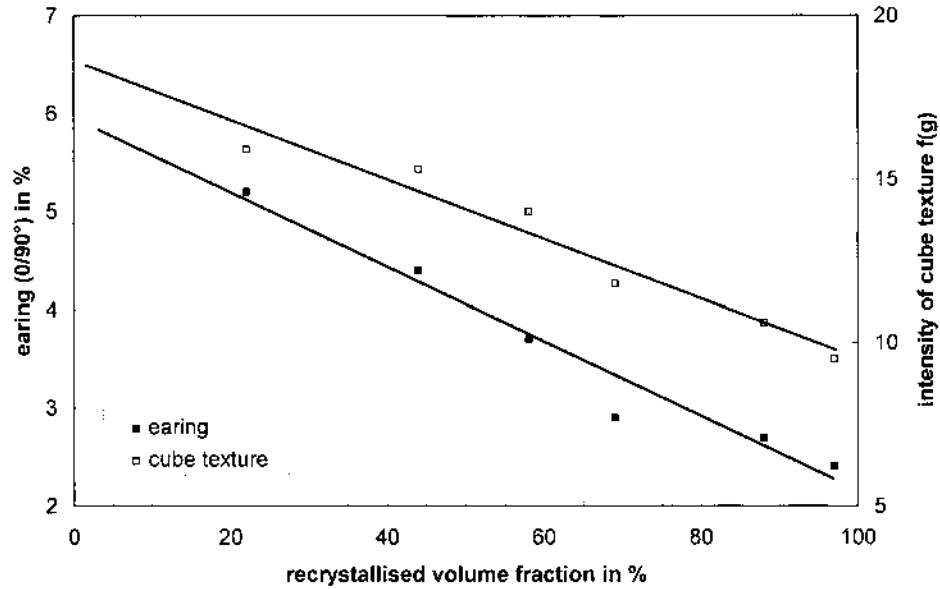
Figure 6 0/90° earing and cube intensity vs computed fraction of interstand recrystallization after the first pass of a three stand hot mill for alloy AA5182. (From Ref. 12.)

follow an Avrami equation of the following form:

$$X = 1 - \exp\left(-C\left(\frac{t}{t_{0.5}}\right)^{k}\right) \tag{1}$$

X is the recrystallised volume fraction after an annealing time t, and C and k are constants. The characteristic time needed for 50% recrystallisation $t_{0.5}$ is usually expressed in terms of an empirical formulation such as

$$t_{0.5} = a \times \varepsilon^{-b} \times d_0^c \times Z^{-d} \quad \exp\left(\frac{Q_{\text{res}}}{RT}\right), \tag{2}$$

where a–d are constants, Q_{rex} is the activation energy for recrystallization, d_{o} is the initial grain size and R is the universal gas constant. Z is the Zener–Hollomon-Parameter which can be understood as a temperature compensated strain rate which characterizes the forming conditions during rolling. It is calculated as

$$Z = \varepsilon \times \exp\left(\frac{Q_{\text{def}}}{RT}\right), \tag{3}$$

where Q_{def} is the apparent activation energy for deformation. In a similar manner empirical formulations for the recrystallized grain size d_{rex} have been developed

in forms such as

$$d_{\text{rex}} = e \times d_0^f \times \varepsilon^{-g} \tag{4}$$

Again, e–g are empirical constants.

Attempts to apply similar sets of equations to Al alloys may be successful in limited cases, but generally turn out to be difficult. For example, Sellars [23] reported that microstructures calculated by these equations appear unrealistic, as too large grain sizes were predicted. It is concluded, that in modeling multi-pass hot rolling of Al alloys some unresolved questions exist, and it appears, that more fundamental descriptions of the evolution of microstructure are required than for steels. It is of particular importance to account for particle precipitation and dissolution and to identify the nature of different possible nucleation sites for recrystallization.

The development of such models is subject to current research and advances have been made to incorporate physically based characterization of potential nucleation sites for recrystallization and their respective efficiency under various deformation conditions [24,25]. In such way also the evolution of recrystallization texture is incorporated.

3   COLD ROLLING OF ALUMINUM

The applications of cold rolled aluminum strip have traditionally been in the beverage can, food packaging, building construction and automobile industries. Trends include rolling of wider strips up to 2000 mm and reducing the gage from 0.35 mm and 0.30 mm down to 0.25 mm. Reduced thickness gage and shape tolerances have also been predicted [5]. Figure 7 represents various types of cold rolling mills offered by one producer [5]. The selection of mill depends on the required throughput, alloy, temper and material finish requirements.

The most conventional approach would be to start with either 6-high or 4-high heavy-gage cold strip mills (2.1 or 2.2 in Fig. 7). They are said to offer the flexibility to cover the complete range of alloys over a wide gage range from 14 to 0.3 mm. The capacities of these mills can reach up to 100,000 tons per year.

If still higher throughput is required, a continuous cold rolling line that utilizes a two- or three-stand tandem mill is recommended. They can be used for large-scale production of a limited range of products. The capacity of such a line would be about 300,000 tons per year. Tandem mills for the rolling of steel strip usually contain more stands depending on the amount of production. Often the cold rolling mills for steel strip may contain up to six stands. The last stand may even be a 6-high mill.

Light-gage strip mills are used for further processing after the heavy-gage mill. They may be either 6-high or 4-high design. They may be used to roll gages down to 0.02 mm. In particular, the 6-high type mill with shifting of intermediate rolls can be utilized for foil-roughing applications. The capacities are of the order of 30,000 tons per year. Finally for special applications such as polish rolling of bright-finish material, a two-high mill (2.4) with limited reductions at low throughput speeds may be used.
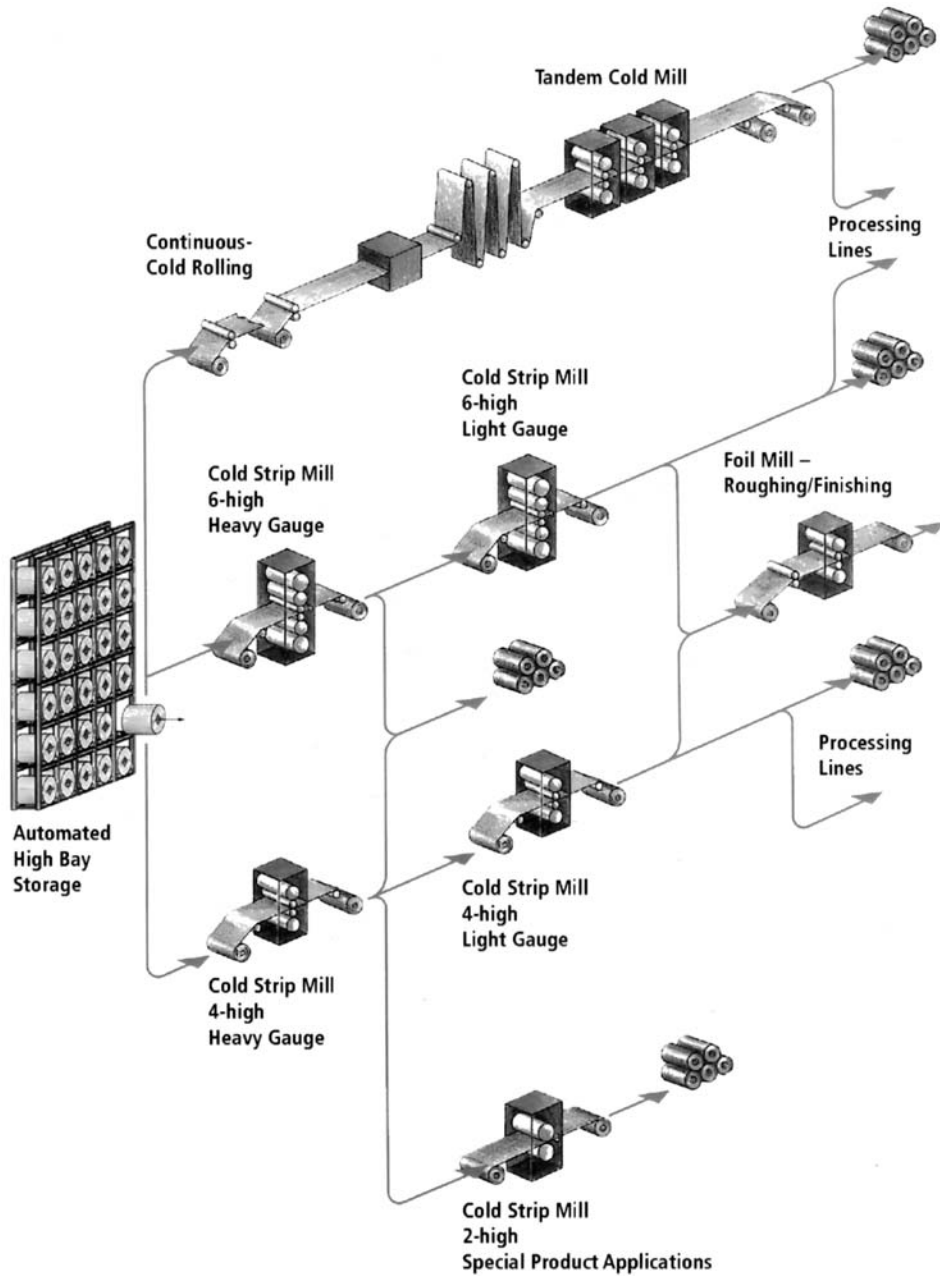
Figure 7 Cold rolling mills for aluminum alloys. (From Ref. 5.)

Further processing to aluminum foil may finally be done in special 4-high mills. The trend in industry has been towards thinner gages and their market share has been increasing. High-quality process control is required for rolling speeds exceeding 1000 m/min. Up to speeds of 1500 m/min, 4-row cylindrical roller bearings and 2-row

axial roller bearings are being used. If the rolling speeds exceed 1500 m/min, oil film bearings are used instead [5].

As the specific rolling pressure increases towards thin gages, roll flattening and roll bending increase. Special attention has to be paid to the strip edges, as roll flattening decreases gradually from the loaded centre of the roll towards the lesser loaded segments of the roll outside the strip. In addition, an unfavorable thermal crown develops, which gains significance with thinner gages. Counter bending of the rolls proves to be ineffective since the strip is embedded in the rolls. As a consequence the so-called "edge drop" problem is frequently encountered, leading to tight edges, which in turn may cause quarter buckles or edge tearing. Accordingly, a major concern in cold rolling is to relieve the local pressure on the edges without affecting general flatness or shape. Various advanced control technologies have been developed for this purpose, such as zone cooling of the rolls, inflatable backup rolls or utilization of 6-high mills with lateral shifting of intermediate rolls.

In the cold working regime (below 100°C), dislocation climb and cross slip are very much restricted. The material undergoes considerable strain hardening where fracture usually occurs before a steady state is reached. A defined strain is applied during cold rolling to achieve the desired product strength by strain hardening, and to produce a plane sheet with well-defined and sometimes structured surfaces. An additional change in microstructure is caused by further crushing and alignment of constituent particles.

The strength of non-heat-treatable Al-Mg (Mn, Cu) alloys of the AA3xxx or AA5xxx groups is based on solid solution hardening and, to a lesser degree, on dispersoids. For these alloys, strain hardening during cold rolling may increase the strength to above 400 MPa. However, the strong interaction of Mg with dislocations may lead to problems with peak stress and serrated flow curves (Portevin–Le Châtelier effect) and resulting Lüders line formation. Measures can be taken to avoid this effect, but they generally result in a loss in strength. For this reason, age-hardenable alloys (AA2xxx, AA6xxx) are often utilized for panel applications, such as car bodies, where homogeneous surfaces are dominant product characteristics. The strength of these alloys is based on precipitation hardening, which is obtained after a solution treatment and subsequent ageing. In any case, the microstructural and textural characteristics of the hot rolled band determine the achievable product quality after cold rolling and heat treatments to a large extent [26].

The control of preferred grain orientations (texture) deserves special attention during the cold rolling of all alloy groups. The texture determines the anisotropy of various sheet properties that are of crucial importance to most subsequent processing operations. For can body applications, anisotropy is usually expressed by the percentage earing level of a drawn cup. Another quality measure is the r-value, which defines the ratio of strain in sheet width to sheet thickness in uniaxial deformation. Strong texture variations result in r-value differences that cause thickness irregularities in any deep drawing operation.

For non-heat-treatable alloys, the cold rolling passes and annealing conditions need to be designed in order to meet the requirements on both strength and texture. The texture development during cold rolling is shown in Fig. 8 for alloys AA3104 and AA5182 [27]. The partially recrystallized hot rolled band will show the typical rolling texture (ß-fibre) that leads to 0/45° earing. The dominant cube texture
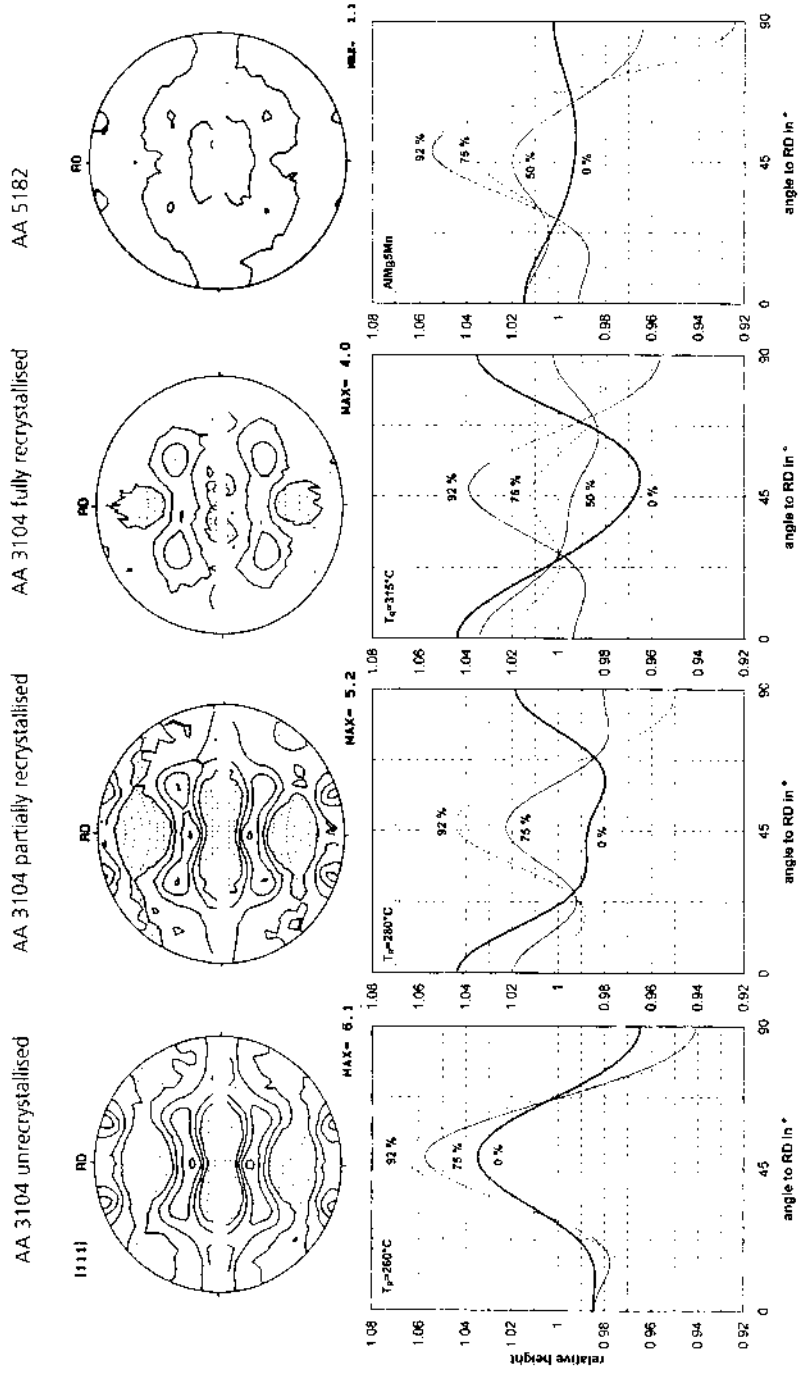
Figure 8 Evolution of texture and earing in sheet production of Al-Mg-Mn alloys. (From Ref. 27.)

components, as present in the fully recrystallized hot rolled band, will result in 0/90° earing, while the RD-rotated cube texture component produces additional ears at 0/180°. Six-ear or eight-ear cup profiles reflect the intensity of different texture components. Subsequent cold rolling and eventual intermediate annealing procedures, which are adjusted to the condition of the hot rolled band, can be performed in such a way, that anisotropy is balanced, while at the same time work-hardening attains the desired strength level. The development of earing from the correspondent different initial textures and for varying cold reductions is shown in the lower part of Fig. 8.

4   BASIC MECHANICS OF ROLLING

Although fast modern computers now allow even three-dimensional numerical simulation of forming processes such as rolling, the simple slab method is still exploited by industry, e.g. for rolling load calculation.

The equilibrium of forces in the horizontal direction requires that

$$(\sigma + d\sigma)(h + dh) - \sigma h = 2pRd\varphi \sin\varphi \pm 2\,\mu p\,Rd\varphi \cos\varphi. \tag{5}$$

The sign before the last term depends on the position of the slab within the roll bite. From entry up to the neutral plane the rolled material flows slower than the rolls rotate and the material is therefore drawn in by the frictional forces. After the neutral plane the velocity of the material exceeds the rotational speed of the rolls and the direction of the frictional forces therefore changes.

The classical theories of rolling have been discussed in numerous books [3,4,28–33] and a detailed discussion is therefore not necessary here.

Considering the forces acting on a cross-hatched slab of rolled material, as shown in Fig. 9, leads to the so-called von Kármán–Siebel equation, which forms the basis of the calculation of the rolling load.
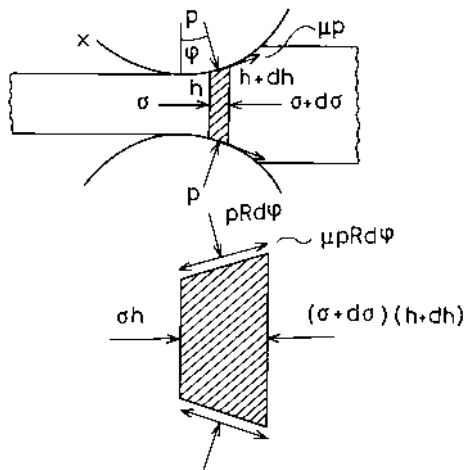
Figure 9   Stresses and forces acting on a slab of rolled material.

The zones from entry to the neutral plane and from the neutral plane to exit are called backward and forward slip zones, respectively.

Omitting the second order differentials in Eq. (5) and rearranging leads to the von Kármán–Siebel equation

$$\frac{d(\sigma h)}{d\varphi} = 2pR(\sin\varphi \pm \cos\varphi). \tag{6}$$

This equation is, however, rather difficult to solve and various simplifications have been proposed since the 1920s to facilitate its solution both in hot and cold rolling. Today, due to the increased use of computers, these solutions lose their importance, since the differential Eq.(5) can now be solved numerically without any further simplifications.

4.1 Hot Rolling

There are some characteristic features of hot rolling, that may be used to derive a simplified equation for rolling load calculation. It should be noted that what is presented here, is done only to illustrate the principle. For the actual calculations the original references given in previously mentioned works [3,4,28–31] should be consulted.

The friction in hot rolling is usually high. Even the adherence of the material to the rolls may take place. This is called sticking friction. There is very little generally available information on the coefficient of friction in hot rolling of aluminium.

Generally the coefficients in hot rolling are considered to be high. Often the values cited are about $\mu = 0.3$ or 0.4 or even more.

Pietrzyk and Leonard [29] discuss some previous work on friction in hot rolling of aluminum. They report the values given by Geleji [34,35].

$$\mu = 1.05 - 0.0005T - 0.056v, \text{ for steel rolls}$$
$$\mu = 0.94 - 0.0005T - 0.056v, \text{ for cast iron rolls}$$
$$\mu = 0.82 - 0.0005T - 0.056v, \text{ for ground steel or cast iron rolls.}$$

In applying Geleji's formulae, temperature should be in °C and v is the rolling speed in m / sec. Actually these type of temperature corrected empirical formulae were originally developed for steel by Eklund and Siebel [28]. Geleji later added the correction factor for rolling speed.

Geleji [35] also gives some numerical values for the coefficient of friction in hot rolling of aluminum. According to him in hot rolling of 99.5% Al alloy with slight oil lubrication μ varies from 0.47 to 0.60 depending on the reduction and thickness. For hot rolling of Duralumin with emulsion based lubricant he gives three values for $\mu = 0.3$, 0.43 and 0.6 depending on thickness and reduction.

If no lubricant is used severe sticking of the aluminum to the rolls may result [29,32]. Local breaking of the oxide film on the surface may expose islands, where metal adheres to the rolls. Suitable coolants such as fortified mineral oil emulsions may be used to prevent further problems, even if a coating of aluminum on the rolls tends to form. Detached fragments may become embedded in the rolled product and cause problems. Insufficient lubrication may even cause the slab to wrap around the rolls into a tightly adherent band [29,32]. Ensuring effective contaminant-free
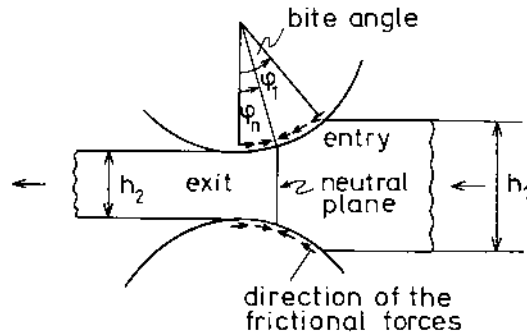
Figure 10   Frictional forces within the roll gap.

lubrication in hot rolling of aluminum is very important. Filtration and prevention of contamination, e.g. with bearing oils is required to prevent premature change of the coolant emulsions [32].

Since rolling loads in hot rolling are usually lower than in cold rolling, flattening of the rolls may be disregarded in simplified load calculation.

When rolling thicker slabs, spreading may cause problems. For relatively thin and wide strip the assumption of plane strain, i.e. no spreading, may be used for simplicity.

Various solutions have been derived, e.g. by Orowan (1946), Sims (1954) and Alexander and Ford (1955).

Since the contact length is usually small, it may be assumed in Fig. 10 that $\sin\varphi \approx \varphi$ and $\cos\varphi \approx 1$. If sticking friction is assumed, it means that

$$\mu p = k, \tag{7}$$

where k is the shear strength of the rolled material. After making these simplifications into Eq. (6) it takes the form

$$\frac{d(\sigma h)}{d\varphi} = 2R(p\varphi \pm k). \tag{8}$$

The roll pressure distribution $p = p(\varphi)$ may then be solved from this equation by assuming that the normal stresses σ and p are bound by the condition

$$p - \sigma = \frac{\pi}{4} \times 2k, \tag{9}$$

After substituting p to replace σ, Eq. (8) may be solved for p. Rolling load is then obtained by integrating

$$P = R \int_{0}^{\varphi 1} p\,d\varphi,, \tag{10}$$
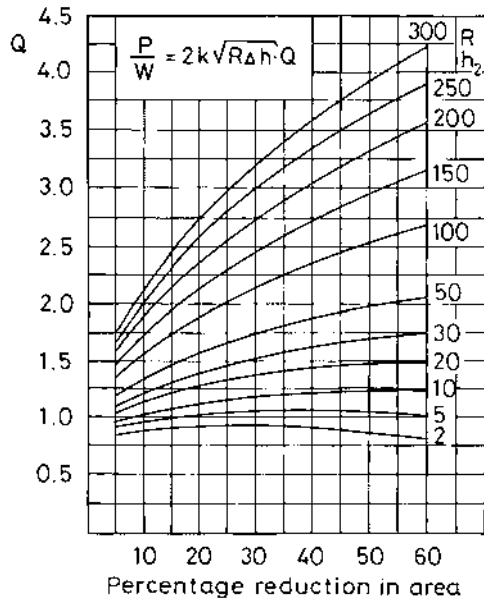
Figure 11 Larke's values of the Sims function Q. (From Ref. 31.)

where p is the rolling load per unit width. A simplified formula to calculate the load was developed by Sims (see, e.g. Ref. 31 for details). According to Sims, the load is obtained from

$$P = 2k\sqrt{R\Delta h} \times Q, \tag{11}$$

where Q can be obtained from the nomogram developed by Sims. The nomogram is shown in Fig. 11. The correction coefficient Q is a function of the relation of roll radius to exit thickness and percentage reduction defined by

$$r = \frac{\Delta h}{h_1} \times 100\% = \frac{h_1 - h_2}{h_1} \times 100\%. \tag{12}$$

It may be noted that $\sqrt{R\Delta h}$ represents approximately the contact length in rolling. Q includes the extra load due to friction. If compared to frictionless compression between flat plates, which would correspond to $Q = 1$, the loads in actual hot rolling may be considerably higher—up to even four times.

4.2 Cold Rolling of Aluminium

Cold rolling differs from hot rolling in that the rolling loads are usually higher, which may lead to considerable roll flattening. With smaller reductions and thinner strip, the elastic deformation of the strip may no longer be ignored. Elastic zones both at exit and entry may have to be considered.

Generally, lubrication can be considered as a key factor for cold rolling of aluminum. The coefficient of friction in cold rolling is usually much lower than in hot rolling. The magnitude depends of course on the type of lubrication that
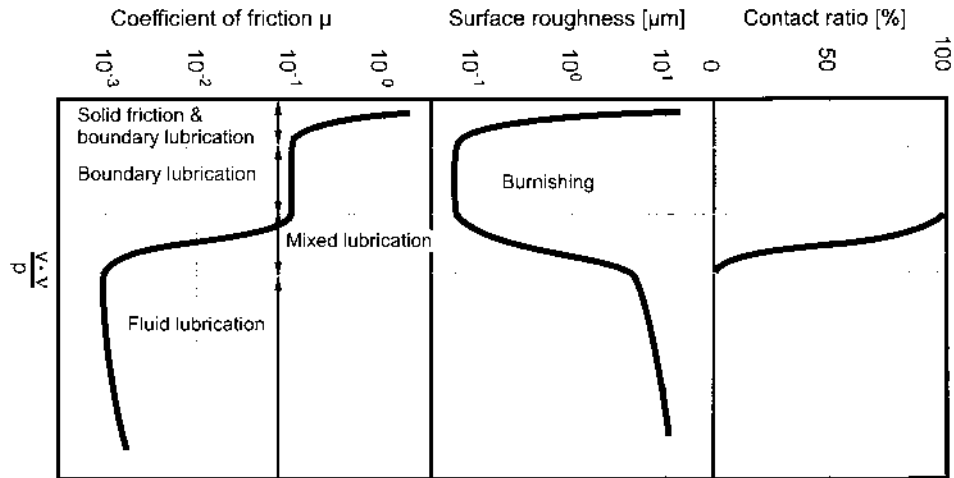
Figure 12 Characteristics of friction in cold rolling.

is used. The lowest values may be less than 20% of those in hot rolling. The successful cold rolling of aluminum requires a carefully balanced amount of friction. On the one hand, low friction levels reduce loads, prevent welding, and secure a more homogeneous deformation, which increases workability and minimizes residual stresses. Furthermore, a continuous lubricant film acts as a protective shield to reduce wear. On the other hand, a certain amount of friction is required to ensure a stable controllable rolling situation and to avoid surface defects related to skidding. A well-known defect, directly related to unstable friction, is the so-called "herringbone defect."

Lubrication is to a large degree governed by lubricant viscosity v, rolling speed v and surface pressure p. The dependencies are represented by the well-known Stribeck curve (Fig. 12). Usually, a mixed lubrication regime is aimed at, in which hydrodynamic pockets are interspersed with boundary lubricated zones. This is important for rolling efficiency and especially for the surface finish. The extent of lubricant pockets and areas of boundary lubrication determine the surface appearance [36].

The most common lubricants in cold rolling of aluminum are mineral oils of low viscosity, in which the oil film is strengthened by boundary additives. Emulsions are increasingly being used for sheet rolling [32]. Heating during rolling or subsequent annealing may result in brown or black stains, which is a major problem associated with lubricants. For foil rolling, paraffin (kerosene) is used in purified form, but staining during subsequent annealing can still be a serious problem [32].

In conventional cold rolling theories, it is usually assumed that the coefficient of friction is small and constant and that the bite angle is small, which leads to assumptions $\sin\varphi = \varphi$ and $\cos\varphi = 1$. After making these assumptions, the von Kármán–Siebel equation (Eq. (6)) takes the form

$$\frac{d(\sigma h)}{d\varphi} = 2pR'\left(\varphi \pm \mu\right), \tag{13}$$

where R' is the deformed roll radius. To solve this equation σ may be eliminated from the yield condition by assuming that both σ and p are principal stresses. Thus

$$p - \sigma = 2k = \frac{2}{\sqrt{3}}\bar{\sigma}, \tag{14}$$

where $\bar{\sigma}$ is the effective stress or yield stress in uniaxial tension.

After eliminating σ in Eq. (13) by using Eq. (14), rearranging, ignoring a small term $[(s/2k)\text{-}1]$, putting $h = h_2 + R'\ \varphi^2$ and integrating one obtains

$$p = C \times 2k\frac{h}{R'}e^{\pm\mu H}, \tag{15}$$

where $H = 2\ \sqrt{R'/h_2}$ arctan $[\sqrt{R'/h_2} \cdot \varphi]$ and C is an integration constant which can be solved from the boundary conditions.

If there are front or back tensions affecting, the yield condition (14) gives as boundary conditions

$$\begin{cases} p = p_1 = 2k_1 - t_1, \text{when } \varphi = \varphi\,(\text{entry}) \\ p = p_2 = 2k_1 - t_2, \text{when } \varphi = 0\ \ (\text{exit}) \end{cases} \tag{16}$$

where t_1 and t_2 are back and front tension, respectively and k_1 and k_2 are the corresponding yield stresses in pure shear.

By substituting the boundary condition from Eqs. (16)–(15) and solving C one finally obtains at the exit side

$$p^+ = \frac{2kh}{h_2}\left(1 - \frac{t_2}{2k_2}\right)e^{\mu H} \tag{17a}$$

and on the entry side

$$p^- = \frac{2kh}{h_1}\left(1 - \frac{t_1}{2k_1}\right)e^{\mu(H_1 - H)}. \tag{17b}$$

Rolling force per unit width can now be solved by integrating

$$P = R'\left(\int_0^{\varphi,'} p + d\varphi + \int_{\varphi_n}^{\varphi_1} p - d\varphi\right), \tag{18}$$

where φ_n is the angle at the neutral point.

Various modifications of the solution of the von Kármán–Siebel equation for cold rolling have been presented by different authors. Some of the pressure distributions obtained from various solutions have been compared in Fig. 13.
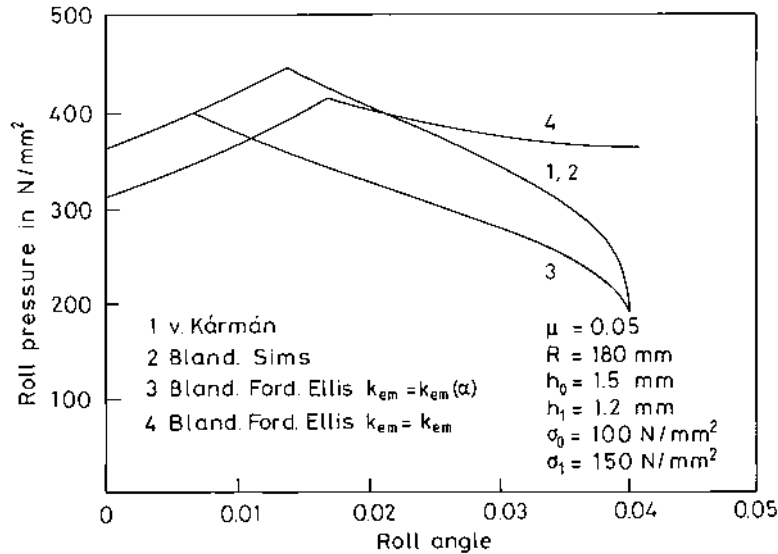
Figure 13 Roll pressure as a function of roll angle calculated by four different methods. From the dissertation of Teusch. (From Ref. 37.)

The deformed roll radius R' is usually solved from the equation by Hitchcock [38]

$$R' = R\left[1 + \frac{16(1 - v^2)}{\pi E} \times \frac{P}{b\Delta h}\right], \tag{19}$$

where R is the undeformed roll radius, E and v are Hooke's modulus and the Poisson ratio for the rolls, P is the roll force, b is the width of the strip and Δh is the draft (change of thickness).

In Hitchcock's formula the pressure on the rolls is assumed to be elliptically distributed along the arc of contact. The contour of the deformed rolls then remains circular. This assumption only holds for passes of sufficient strip thickness and reduction. When the entry strip thickness decreases, rolling loads increase and consequently roll flattening increases. A theoretical limit is reached, when both the rolls and the strip deform only elastically and no further plastic reduction can be attained. Thereby, a minimum accessible gage is defined under the assumption of roll flattening as described above. Nevertheless, rolling practice shows, that passes well below this limit can still be rolled, and measured loads appear to be considerably lower than the calculated ones. Löffler and Kramer [28] state that with a roll diameter of, e.g. 300 mm, exit thicknesses of below 13 μm can be processed.

4.3 Rolling of Aluminium Foils

The application of conventional rolling theories, as described above, fails when the exit thickness falls below 100–70 μm [28]. The reason for this is, that the contour of the deformed rolls is assumed to remain circular with an enlarged radius. As a consequence of the assumption, that plane cross sections remain plane, continuous
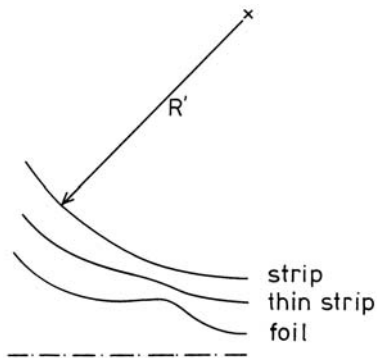
Figure 14 Change of roll contour as strip thickness decreases. (From Ref. 28.)

plastic reduction occurs through the roll bite. Relative slip between work rolls and strip occurs along the entire arc of contact except for the neutral point, where the shear direction is reversed. In terms of the Coulomb friction law it follows, that limiting friction prevails throughout the roll gap, and predicted loads are unrealistically high.

It was already shown by Orowan in 1943 that the deformed roll contour does not remain circular when thin strips are rolled. The development of roll flattening with decreasing strip thickness is illustrated schematically in Fig. 14. This contour development could also be verified experimentally [39]. To account for such effects, the complexity of rolling models increases drastically as elastic strip deformation has to be considered and roll pressure and elastic roll deformation equations need to be solved simultaneously. Specific rolling models [40–43] and finite element methods [44] have been developed and successfully applied to foil rolling and temper rolling processes. The strip is generally divided into two elastic zones before and after the roll gap, and two distinct plastic zones that are separated by a central zone, where the material remains rigid and is transported without plastic reduction (Fig. 15).
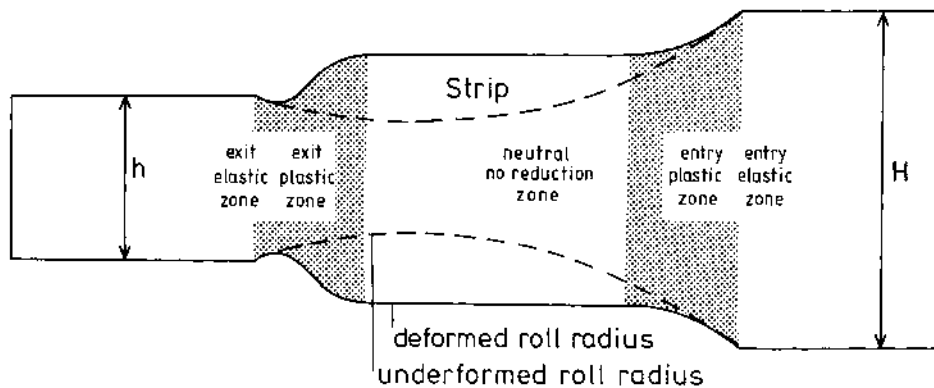
Figure 15 Deformation zones in foil rolling. (From Ref. 45.)

Haeseling et al. [40] calculated stress distributions and compared strip and foil rolling. Their results are shown in Fig. 16. It can be seen that, while in strip rolling a typical friction hill-type pressure distribution is obtained, in rolling of foils a Herzian distribution prevails. In addition to the Herzian distribution a peak on the exit side

(a)

Pass: 99.5% Aluminium 2000 mm × 700 μm ⟶ 300 μm
Yield stress: 105 N/mm^2 = const.   Roll separating force: 3050 kN

(b)

Pass: 99.5% Aluminium 2000 mm × 33 μm ⟶ 14.5 μm
Yield stress: 125 N/mm^2= const.
Roll separating force: 6250 kN incl. roll kissing
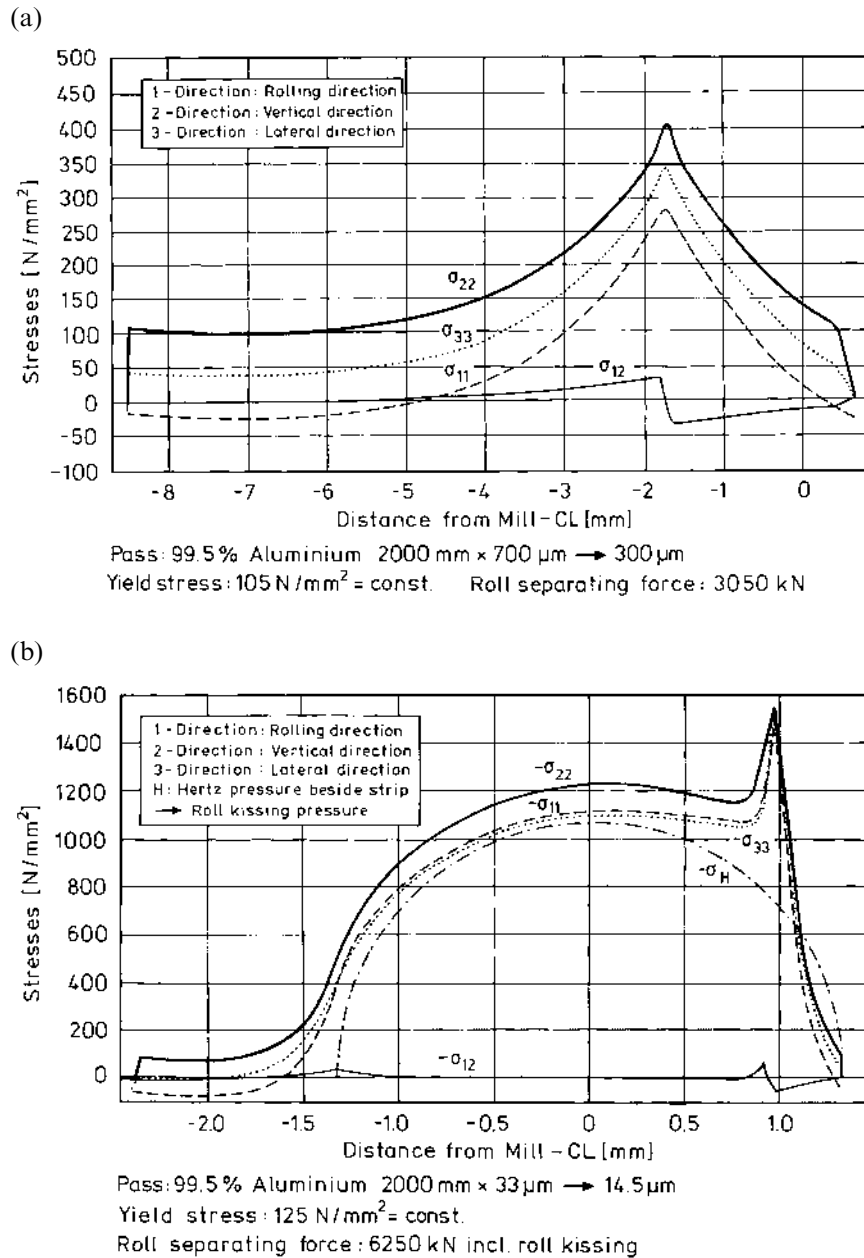
Figure 16 (a) Calculated friction hill-type distribution of stresses in strip rolling; and (b) calculated distribution of stresses in foil rolling. (From Ref. 40.)

appears. This peak resembles the one observed in bearings operating under elastohydrodynamic lubrication conditions.

The tribological aspects gain importance with decreasing gages, as the ratio of contact surface to deformed volume increases. A brief overview on the importance of lubrication in foil rolling is given in [46]. The oils are exposed to high thermal loads, high pressures and high shear rates and the complex interactions in the roll gap, responsible for the shear stresses in foil rolling are not yet fully understood. Of utmost importance is the amount of oil being entrained into the roll gap, which determines the frictional conditions and thereby the possible reduction of the pass as well as the surface quality of the product. Basically three mechanisms supply the roll bite with oil, which are depicted in (Fig. 17).

1. *Hydrodynamic entrainment*: In the wedge between roll and strip hydrostatic pressure builds up in the oil which is dependent on velocities, gap geometry and rheologic behaviour of the oil. The oil film thickness at the point, where the oil pressure reaches the yield point of the strip, is entrained into the roll gap.
2. *Surface roughness*: Additional oil is entrapped in valleys of the surface roughness of roll and strip, independently of speed.
3. *Adhesive layers*: Due to physisorption and chemisorption, boundary layers develop, which principally depend on temperature and the properties of oil, roll and strip.

In foil rolling, the combination of high speeds and the over-supply of oil leads to an hydrodynamics lubrication regime at the inlet of the roll gap. Here the aluminum is separated from the roll by a continuous oil layer. During deformation the oil film thickness is reduced and metallic contact occurs. Thereby, a mixed lubrication regime is usually reached. Due to its technological importance, especially for rolling in thin dimensions, a number of works are dedicated to formulate suitable friction models in the mixed lubrication regime [e.g. 47–50], but still a number of open questions remains.
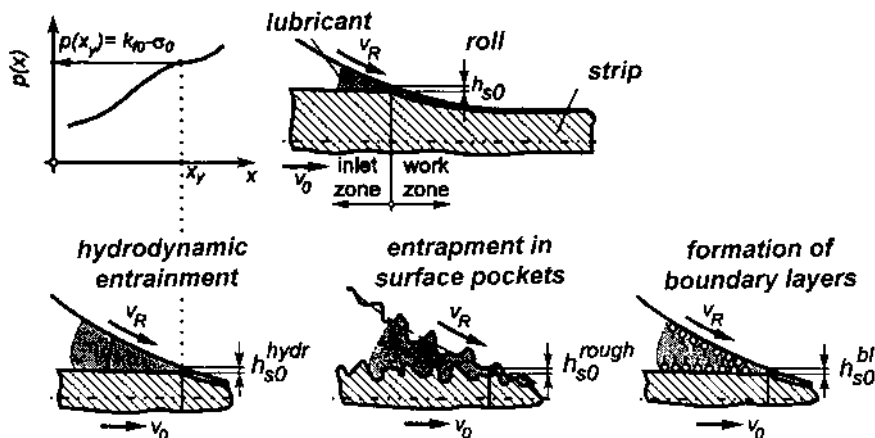
Figure 17 Mechanisms of oil entrainment during cold- and foil-rolling.

5   CONTROL OF THICKNESS AND SHAPE

Customers of rolling mills require increasingly dimensionally accurate products. Great efforts have been spent on ensuring that flat rolled products possess the correct dimensions, flatness and shape. Sophisticated control systems have been developed for this purpose and it is an area where rolling mill operators and suppliers of the required technology compete. Although there exist standards describing dimensional tolerances of flat rolled products, these often lag behind the development of technology and customers may even specify the thickness as some fraction of what is defined in the standards. Modern unmanned production methods require consistently good dimensional accuracy and shape for flat rolled products in order to avoid disturbances or breaks in production. In addition, accurate dimensional control may give savings in product weight. This may produce further savings in, e.g. maximizing the pay load and reducing energy costs in transportation.

The elastic spring of the mill stand changes the exiting strip thickness from the value of the roll gap setting. Variations in friction, front and back tension, thickness, flow stress and temperature may all lead to changes in thickness as illustrated schematically in Fig. 18.

Due to coiling of the strip, some deviation in flatness results [51]. However, more serious is a non-uniform deformation in the transverse direction and the result-
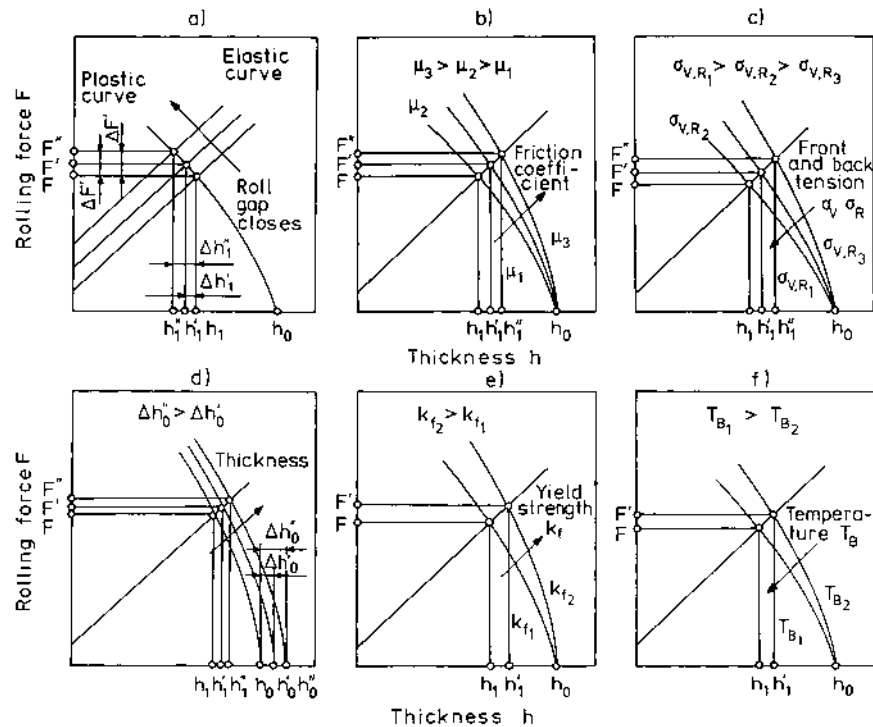
Figure 18   Schematic representation of changing (a) roll gap setting; (b) friction; (c) front or back tension; (d) strip thickness; (e) flow stress; and (f) temperature on the final thickness of the rolled strip. (From Ref. 30.)
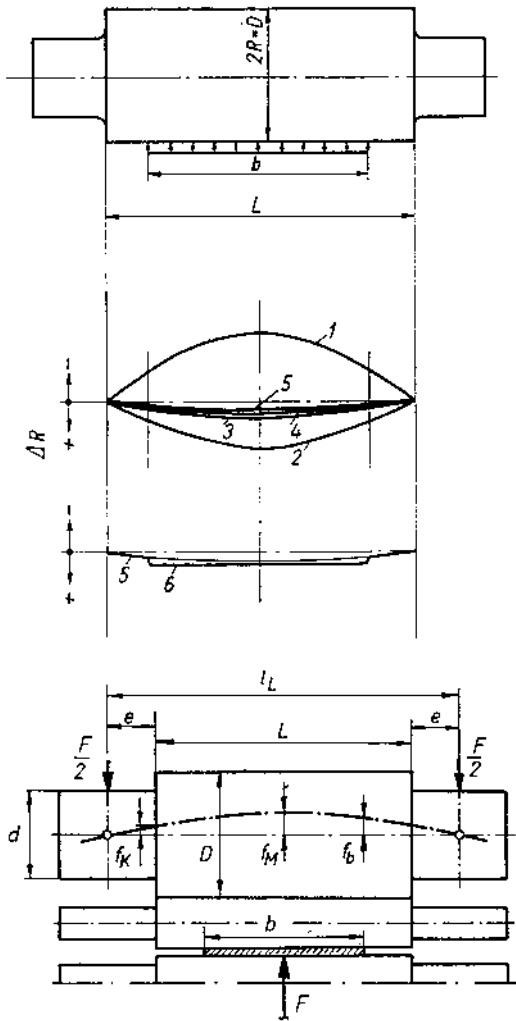
Figure 19 Effects of various factors on roll crown (1. elastic deformation of the roll due uniformly distributed load; 2. ground roll barrel; 3. thermal expansion; 4. effect of non-zero crown of the entering strip; 5. real roll crown of a new roll; 6. effect of roll wear on crown). (From Ref. 30.)

ing shape defects. An attempt to reduce the thickness of the rolled material results in bending of the rolls (Fig. 19). This leads to a thicker centre in relation to the edges.

Based on Fig. 20 strip profile or crown is defined as a thickness difference [1]

$$C_r = h_m - h_r. \tag{20}$$

Too high reductions of the strip edges may result in buckling close to the edges. To describe the waviness a concept called percentage steepness is defined as [3,51]

$$S_p = \frac{h}{l} \times 100[\%], \tag{21}$$
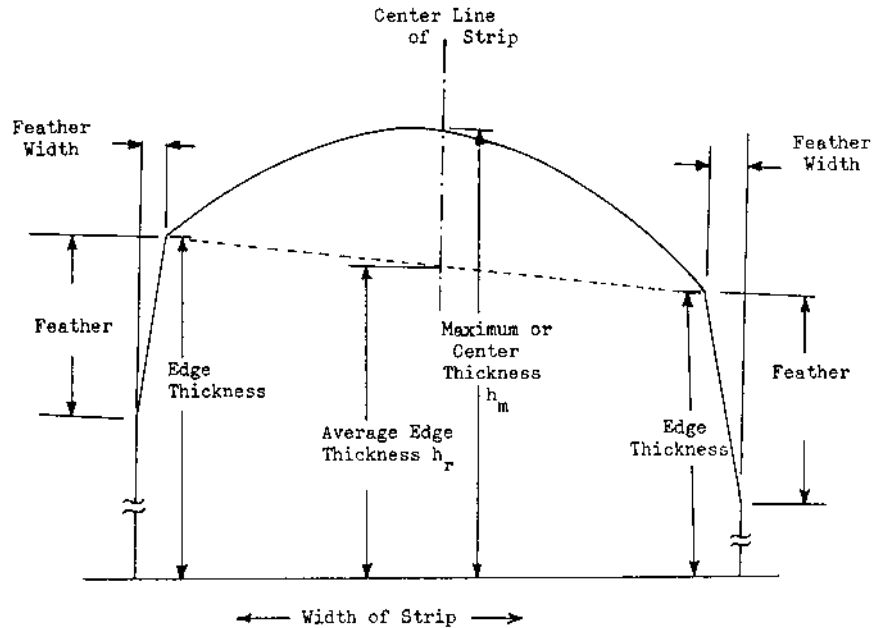
Figure 20 A sketch to illustrate the strip crown. (From Ref. 52.)

where l is the wavelength and h is the amplitude. Yet another measure of flatness is the I value, defined as relative elongation multiplied by 10^5

$$I = \frac{\Delta l}{l} \times 10^5. \tag{22}$$

Assuming that buckles are sinusoidal, it can be shown, that the I unit and steepness are interrelated. The I unit is also related to stress in the strip according to the equation

$$I = \frac{\Delta \sigma}{E} \times 10^5. \tag{23}$$

Since controlling of the shape is important, great efforts have been put to developing various techniques. A more detailed review has been made, e.g. by Ginzburg [3]. A brief summary is given in Fig. 21 [53], which represents five techniques including continuously variable crown (CVC), double-chock bending, use of six-high mill, variable crown using internally pressurized rolls and axially crossed rolls. Yet another important technique is the selective cooling of rolls.

To improve productivity and product quality, automatic shape control (ASC) and gage control (AGC) systems are employed. Figure 22 represents an example of a six-high mill used for cold rolling of aluminum strip [5,54]. In this example strip tension is measured and the required correction is provided by bending, shifting and cooling of the rolls.

VARIOUS CROWN AND SHAPE CONTROL FACILITIES

CVC

double chock bending

variable crown

crossed rolls

6Hi mill
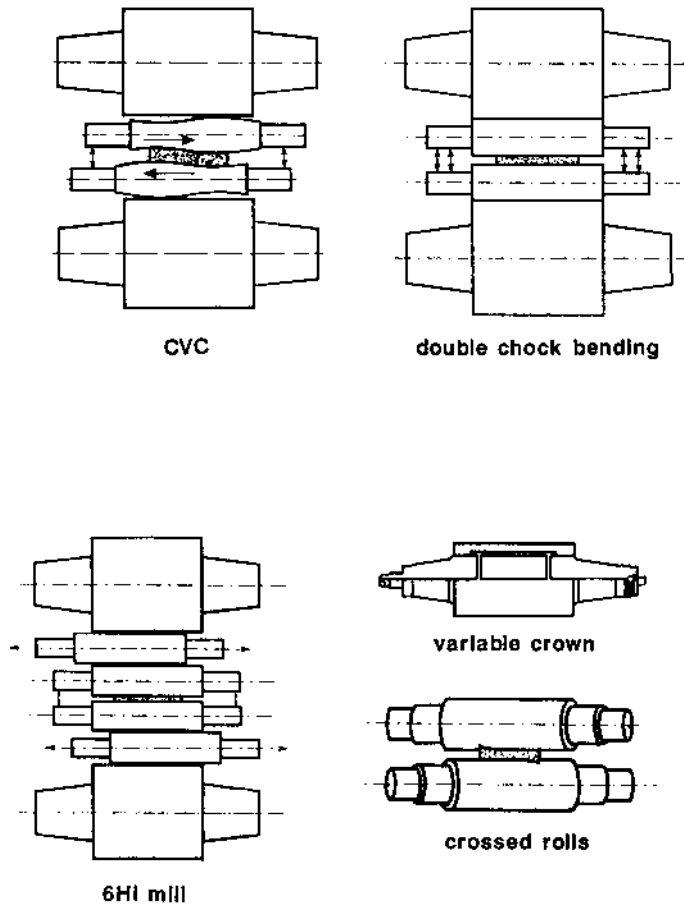
Figure 21 Some crown and shape control techniques. (From Ref. 53.)

To optimize the rolling process, various computer models are being used both on-line and off-line. Models are required for the elastic spring of the mill stand, rolling force and friction, thermal effects and roll wear in order to be able to predict the shape of the strip.

An effective mathematical model can determine the roll gap profiles of the individual stands and activate the adjusting systems to present them in real time as a function of individual operating parameters. The schematic principle of such an on-line model is shown in Fig. 23.

In addition to on-line models, off-time models can be used to calculate the strip profiles. The requirements for an effective process model are especially demanding for aluminum hot strip mills since the thermal crown of the work roll is subject to relatively large changes. The crown usually grows from strip to strip. In addition
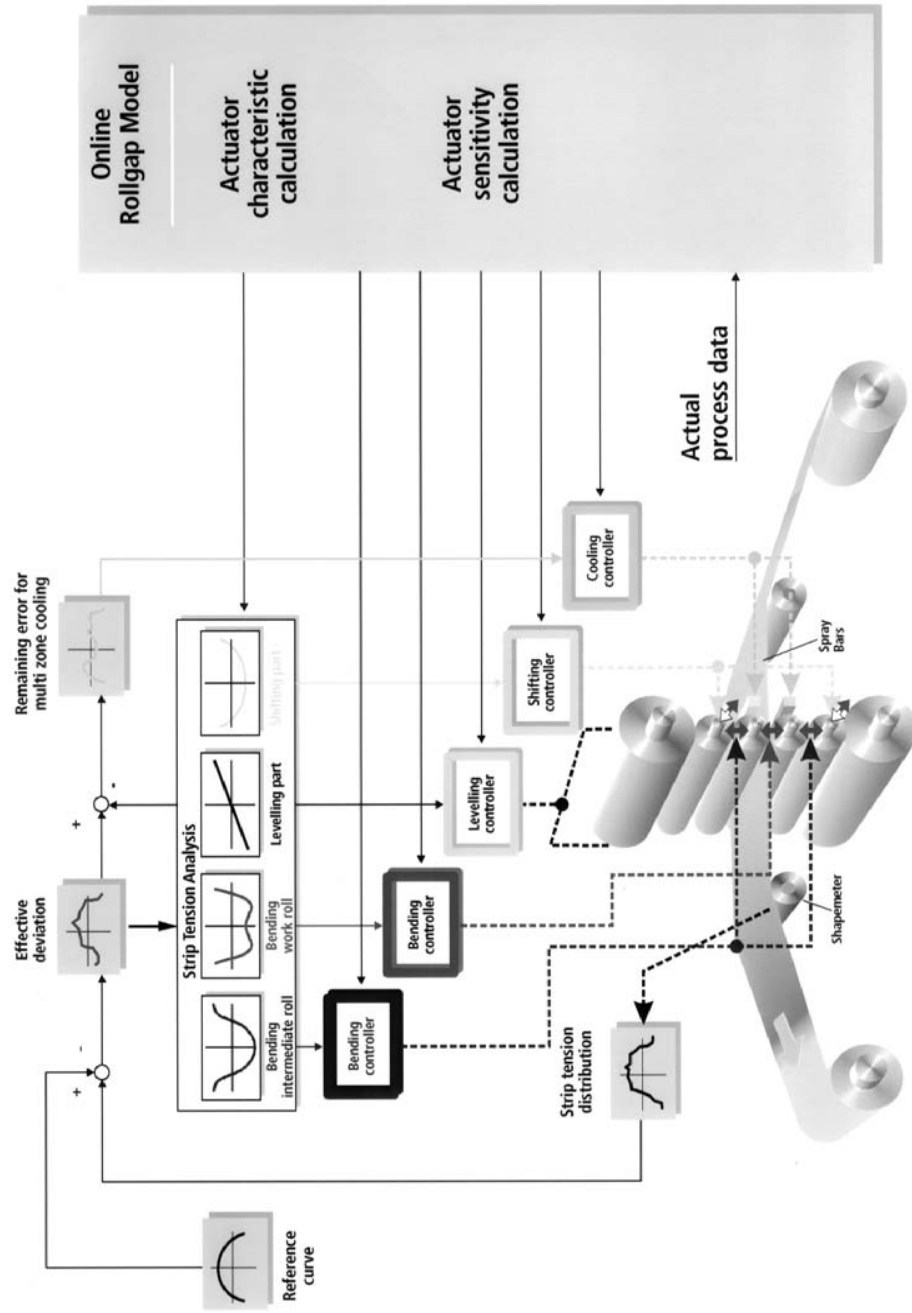
Figure 22 Schematic layout of automatic gage and shape control system for a six-high cold strip mill. (From Ref. 5.)
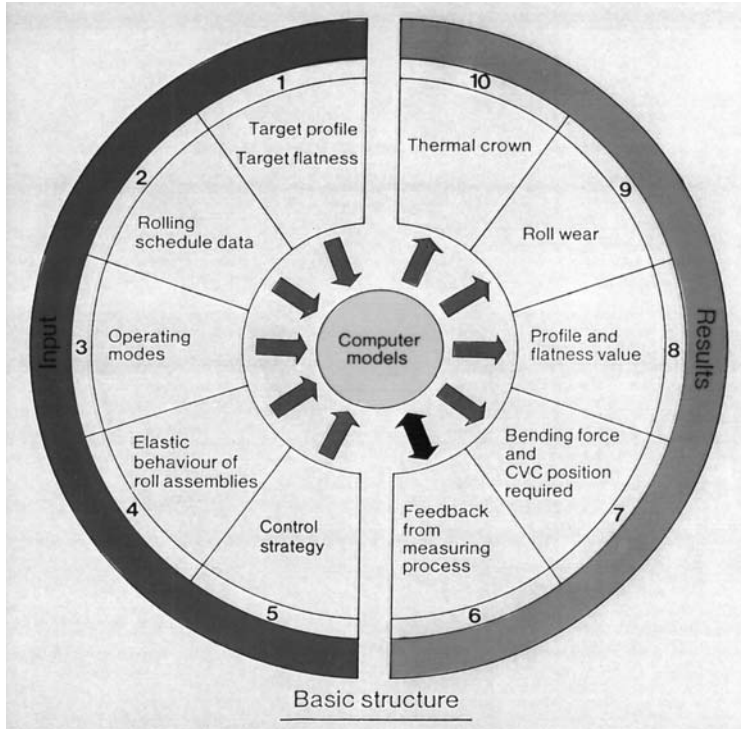
Figure 23 A schematic view of an on-line model for profile and flatness control. (From Ref. 6.)
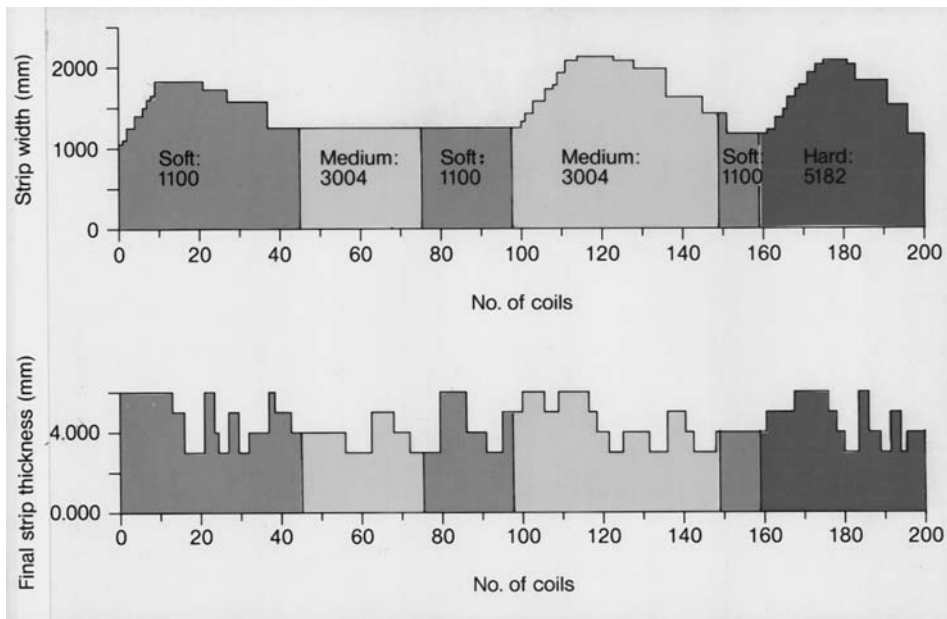
Figure 24 An assumed schedule used for simulating hot strip rolling. (From Ref. 6.)
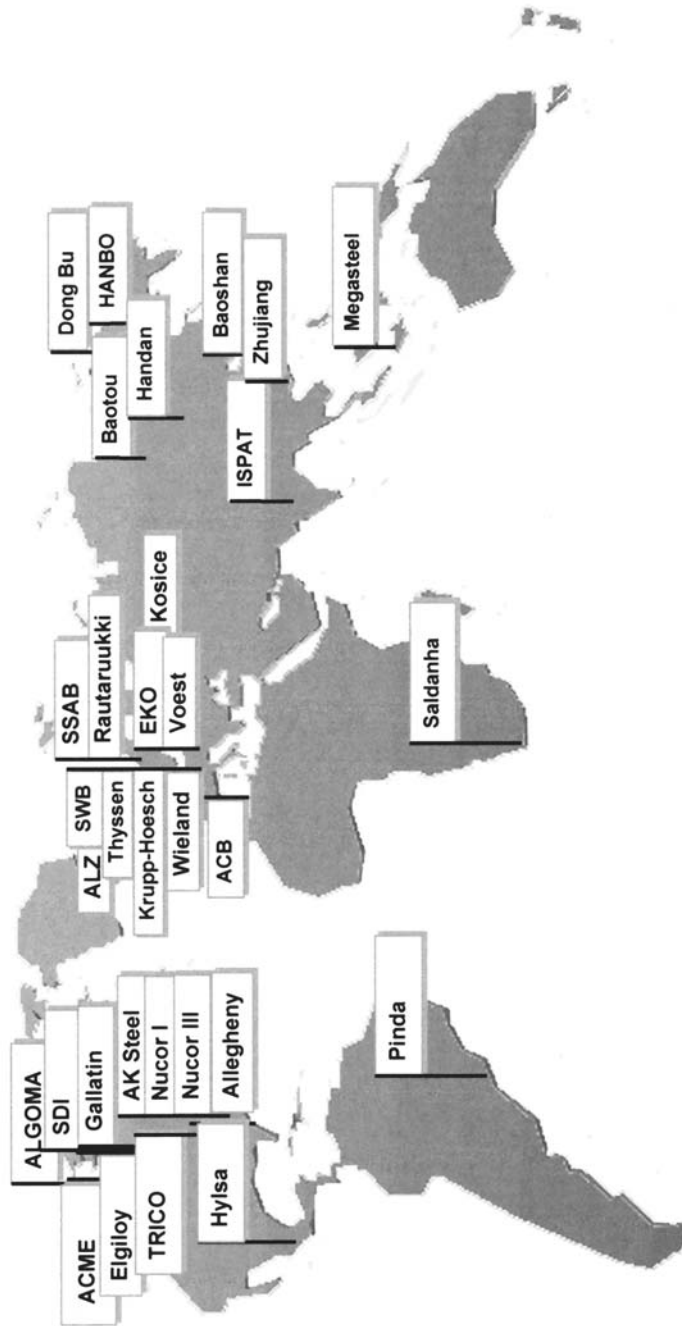
Figure 25 Rolling mills applying artificial neural networks for process control. Major neural mill automation systems by Siemens AG (implemented or under progress). (From Ref. 55.)

the varying rolling forces from strip to strip and from the head- to the tail-end causes additional variation in the roll gap profile. Figure 24 shows an assumed schedule that was used in an off-line model to simulate hot strip rolling [6].

As evident from the foregoing, the control of shape, tolerance and flatness is an critical issue in rolling mills. Further development may be expected in new kinds of models and computational techniques that do not suffer from the limitations of traditional physical or mechanical models.

One such relatively new development when it comes to rolling is neural networks. They are especially suited to applications where there is a lot of data available, but the processes are not yet accessible to physical simulation. Rolling of metals is one such area. Provided that sufficient measurement data is available, an artificial neural network can be taught and it can learn the dependencies hidden in the vast amount of data.

The application of neural networks is rather new in rolling and applications are just beginning to emerge. Despite this, there are already a number of rolling mills, where neural networks are being used for process control, as illustrated in Fig. 25 [55].

The best results of artificial neural networks are probably obtained when they are combined with other existing physical or statistical models [56–58]. Yet another areas where artificial neural networks have been successfully applied is in the prediction of the mechanical properties and controlling of the annealing process.

A rather recent development in the application of neural networks in rolling is the self-organizing maps, or Kohonen maps. They have been successfully applied to control many other processes, e.g. in the paper industry, but results in rolling are just beginning to appear.

REFERENCES

1. D. Altenpohl, *Aluminium Viewed from Within*, 1st edn, Aluminium-Verlag, Düsseldorf, 1982.
2. *Aluminium, Properties and Physical Metallurgy* (John E. Hatch, ed.), ASM, Metals Park, OH, 1984.
3. V. B. Ginsburg, *Steel-Rolling Technology*, Marcel Dekker, 1989.
4. W. L. Roberts, *Flat Processing of Steel*, Marcel Dekker, 1989.
5. H. R. Barnes, L. Niemeyer, R. Finck, and P. Huck, *Technological Advances in Aluminium Rolling*, Product Information of Mannesmann Demag AG, Hüttentechnik, MDS Walzwerkstechnik, 1992.
6. W. Rohde, D. Rosenthal, and J. Seidel, "Hot strip mills for aluminium: control concepts and mathematical models for high product quality," presented at the 7th Int. Conf. on Aluminium Sheet and Plate, Nashville, Tennessee, USA, June 23–26, 1992. SMS Technical Report, Rolling Mills.
7. R.-M. Guo, Iron and Steel Engineer, 1988, 65(12), p. 45.
8. E. Kersting and H. Teichert, Proc. 4th Int. Steel Rolling Conf., Deauville, France, 1987, 1, p. A.19.1.
9. H.-J. Wortberg, K. Eckelsbach, and K. Klamma, Alunorf—ein richtungsweisendes Walzkonzept für Aluminiumband, Aluminium 1995, 71(5), p. 546.
10. H. J. McQueen, JOM, June 1998, p. 28.
11. T. Doko, S. Asami, and K. Yagi, Trans. JIM 1988, 38, p. 386.

12. J. Hirsch, K. F. Karhausen, and R. Kopp, Proc. 4th Int. Conf. on Aluminium Alloys, Atlanta, USA, 1994, p. 476.
13. H. Weiland and J. Hirsch, Textures and Microstructures 1991, 14/18, p. 645.
14. C. Maurice and J. Driver, Acta Met. 1993, 41, p. 1653.
15. O. Daaland et al., Proc. 3rd Int. Conf. on Aluminium Alloys, Trondheim, Norway, 1992, p. 297.
16. O. Engler, B. Mülders, and J. Hirsch, Zeitschrift für Metallkunde 1996, 87(6), p. 454.
17. R. K. Bolinbroke, and G. J. Marshall, Material Science Forum 1993, 113/115, p. 685.
18. G. J. Marshall, Proc. 5th Int. Conf. on Aluminium Alloys, Grenoble, France, 1996, Part 1, p. 19.
19. C. M. Sellars and J. A. Whiteman, Met. Sci. 1979, 13, p. 187.
20. P. Choquet, B. de Lamberterie, C. Perdic, and H. Biausser, Proc. 4th Int. Steel Rolling Conf., Deauville, France, 1987, 1, p. B.5.1.
21. W. Roberts, A. Sandberg, T. Siwecki, and T. Werlefors, HSLA steels: Technology and applications, ASM, Metals Park, OH, 1984, p. 67.
22. T. Senuma and H. Yada, Proc. 7th Risø Int. Symp. on Metallurgy and Materials Science, Roskilde, Denmark, 1986, p. 547.
23. C. M. Sellars, Mater. Sci. Tchnol., 1990, 6, p. 1072.
24. H. E. Vatne, K. Marthinsen, R. Ørsund, and E. Nes, Metall. Mater. Trans. 1996, 27A, P. 4133.
25. O. Engler and H. E. Vatne, JOM, June 1998, p. 23.
26. J. Hirsch, Proc. of THERMEC'97, Australia (T. Chandara and T. Sakai, eds.), TMS-Warrendale, PA, 1997, p. 1083.
27. J. Hirsch, P. Wagner, and H. Schmiedel, Proc. of the 5th Int. Conf. on Aluminium Alloys, Grenoble, France, 1995, Part 1, p. 641.
28. L. J. Löffler and A. Kramer, "Der Walzspalt des Aluminiumfolienwalzens," in *Walzen von Flachprodukten* (P. Ossenbühl and H. Jung, eds.), DGM Informationsgesellschaft, 1994, p. 27.
29. M. Pietrzyk and J. G. Lenard, *Thermal-Mechanical Modeling of the Flat Rolling Process*, Springer Verlag, 1991.
30. K. Weber, *Grundlagen des Band-Walzens*, VEB Verlag, 1973.
31. E. C. Larke, *Rolling of Strip, Sheet and Plate*, 2nd edn, Chapman and Hall, London, 1967.
32. G. W. Rowe, *Principles of Industrial Metalworking Processes*, Edward Arnold, 1977, p. 241.
33. H. Ford and J. M. Alexander, *Advanced Mechanics of Materials*, 2nd edn, Ellis Horwood Ltd, 1977.
34. A. Geleji, *Walzwerks- und schmiedemaschinen*, zweite Auflage, VEB Verlag Technik, Berlin, 1961.
35. A. Geleji, *Bildsame Formgebung der Metalle*, Akademie Verlag, 1967, p. 595.
36. N. Kawai and K. Dohda, *Advanced Technology of Plasticity*, Vol. I, 1984, p. 145.
37. H. Teutsch, "Ein mathematisches Modell mit numerischem und analytischem Ansatz zur Berechnung der Profilform beim kaltwalzen von Band," Dr. rer. nat. Thesis, RWTH Aachen, 1984.
38. J. H. Hitchcock, Report of ASME Research Committee on Roll Neck Bearings, 1935.
39. A. Kramer, "Untersuchungen zum Kaltwalzen von dünnem Band und Folie nach dem Verfahren der Ähnlichkeitstheorie," Dr.-Ing. Thesis, RWTH Aachen, 1994.
40. G. Haeseling, H. G. Hartung, S. Kastner, and A. Kramer, "New Foil Rolling Theories and their importance in Industrial Practice," in Proc. of the 2nd Int. Conf. on Modeling of Metal Rolling Processes (J. H. Beynon, P. Ingham, H. Teichert and K. Waterson, eds.), The Institute of Materials, 1996, p. 224.

41. N. A. Fleck, K. L. Johnson, M. E. Mear, and L. C. Zhang, J. of Eng. Manufacture, 1992, 206, p. 119.
42. C. Luo and H. Keife, J. of Mat. Proc. Tech. 1998, 74, p. 158.
43. S. A. Domanti, W. J. Edwards, and P. T. Thomas, AISE Annual Convention, Cleveland, USA, 1994.
44. P. Gratacos, C. Montmittonet, C. Fromholz, and J. L. Chenot, Int. J. Mech. Sci, 1992, 34(3), p. 195.
45. C. A. Fryer, M. S. Lubomirski, and P. J. Reeve, "Application of a non-circular are roll force model for light reductions and thin gauge products," in *Modeling of Metal Rolling Processes* (J. H. Beynon, P. Ingham, H. Teichert and K. Waterson, eds.), The Institute of Materials, 1996, p. 465.
46. G. K. Cheng, Lubr. Eng. 1983, 39(2), p. 87.
47. Y. H. Tsao and L. B. Sargent, ASLE Trans 1977, 20(1), p. 55.
48. S. Sheu, "Mixed librication in bulk metal forming processes," PhD thesis, Evanston, Illinois, Northwestern University, 1985
49. W. R. D. Wilson, Proc. Trans. ASME, J. Eng. Mat. Techn. 1991, 113(1), p. 60
50. H. Yamamoto, M. Ataka, and K. Nakajima, Proc. 6th Int. Congr. on Tribology (EUROTRIB'93), 1993, p. 180.
51. W. von Asten, and H. Schmiedel, "Planheitsmessung von dünnen Aluminiumbändern," in *Walzen von Flachprodukten* (H. Galla and H. Jung, eds.), DGM Informations-Gesellschaft Verlag, 1987, p. 195.
52. W. L. Roberts, *Hot Rolling of Steel*, Marcel Dekker, 1983.
53. G. Dolle, "Development of rolling techniques for flat products," in Proc. 4th Int. Steel Rolling Conference, Deauville, France, IRSID, 1987, 1, p. 1.1.
54. J. Kaulen, H. Teichert, P. Kern, and M. Steffens, "Optimierung eines 6-hig UC Aluminium-Kaltwalzgerüstes mit Hilfe eines geeigneten Walzpaltmodells," in *Walzen von Flachprodukten* (P. Ossenbühl and H. Jung, eds.) DGM Informationsgesellschaft Verlag, 1994, p. 141.
55. M. Jansen, E. Broese, B. Feldkeller, O. Gramckow, T. Poppe, M. Schlang, and G. Soergel, "Application of neural networks to process control in steel industry," *IFAC Symposium on Automation in Mining, Mineral and Metal Processing* (J. Heidepriem, ed.), Pergamon, Elsevier, New York, 1998, p. 193.
56. J. Larkiola and A. S. Korhonen, "Application of neural networks in rolling of steel (Invited lecture), IPMM'97," Proc. of the Australasia-Pacific Forum on Intelligent Processing & Manufacturing of Materials, (T. Chandra, S. R. Leclair, J. A. Meech, B. Verma, M. Smith, and B. Balachandran, eds.), Watson and Ferguson Co., Brisbane, 1997, 1, P. 324.
57. J. Larkiola, "Dimensional Ranges and Rolling Efficiency in a Tandem Cold Rolling Mill," Doctor of Technology Thesis, Helsinki University of Technology, 1997.
58. P. Myllykoski, "On using artificial neural networks to predict process and quality parameters in steel strip production," Doctor of Technology Thesis, Helsinki University of Technology, 1997.

8

Extrusion

SIGURD STØREN and PER THOMAS MOE

Norwegian University of Science and Technology, Trondheim, Norway

1 INTRODUCTION

This chapter is devoted to extrusion of aluminum alloys and divided into three main sections. Section 2 covers the basic parameters of extrusion needed for designing an aluminum section and a die, for understanding the processing steps, and for optimizing productivity, cost and product quality. A specific section shape is used to illustrate the interaction between these parameters. Section 3 is focused on the commercial applications aspects of extruded sections, life cycle aspects, alloy selection and section design guidelines. Section 4 covers the extrusion process in some detail, focusing on the basics of quantitative modeling of metal flow in the container and through the die. In the final section, some of the outstanding research challenges in the theory of extrusion of thin walled aluminum sections are discussed: (1) 3D-modeling of thin-walled extrusion; (2) the bearing channel friction in interaction with die deflections and section surface formation; (3) stability of flow; and (4) limits of extrudability.

The intention is that the chapter should give the reader an overview of the practical aspects of extrusion as well as an understanding of the present state of the theoretical work and some challenges in this branch of metal forming science and technology. However, the study of extrusion as a process is both relatively complex and multidiciplinary, and this chapter can hardly give the answer to all problems that may be encountered. Thus, before making detailed section design and alloy decisions, the reader is advised to contact an extrusion plant. Even though theoretical and experimental work has managed to explain a number of relevant phenomena, the quality of an extruded profile and naturally also of a complete product based on extrusions is still mainly dependent on the experience of personnel close

to or at the extrusion plant. One may also confer with more general works on extrusion [1,2].

2 BASIC PARAMETERS OF EXTRUSION

2.1 The Process

The most common method for producing aluminum profiles is that of direct extrusion (Fig. 1). Here, the ram is moving into the container at one end, and pushes the billet through the opening of the die at the other end. The temperature of the deforming aluminum alloy is in the range of 450–600°C during the process cycle. In contrast to the extrusion of steel, aluminum extrusion is taking place in absence of any lubrication of the die. Hence, the material sticks to the container and the die, giving a highly inhomogeneous flow with large degree of visco-plastic shear flow (See Sec. 4). The material far a way from the wall is flowing easier than that closer to it, with the surface of the billet remaining in the container. The billet and the container are normally circular cylindrical, but can in special cases be rectangular with rounded corners.

A special feature in extrusion of aluminum alloys is the production of hollow sections (Fig. 2). In this case the metal flows into the opening between the die and the mandrel. The mandrel is kept in position by bridges. The billet material is forced, by the movement of the ram, into the portholes in the bridge die, called the feeder ports. Under the bridges, adjoining metal streams meet and are forgewelded together in the weld chamber, before flowing through the bearing channel, i.e. the opening between the die and the mandrel.

Besides direct extrusion, two other special extrusion methods are used, indirect extrusion, and continuous extrusion, the Conform method [3]. In indirect extrusion (Fig. 3) the die is pushed into the container, where as the extrudate is flowing in opposite direction through the hollow stem. In the continuous extrusion (Fig. 4) a continuous feedstock is fed into a groove in a rotating wheel. Pressure is built
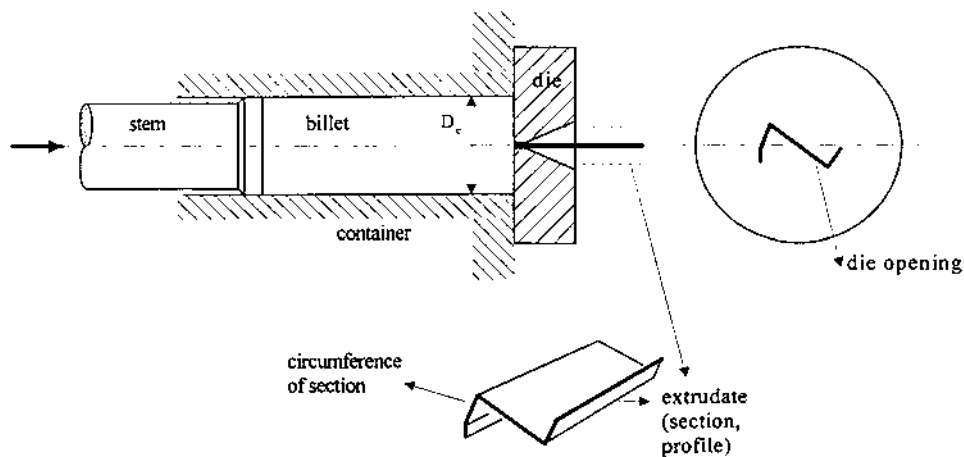
Figure 1 Direct extrusion of an open section.
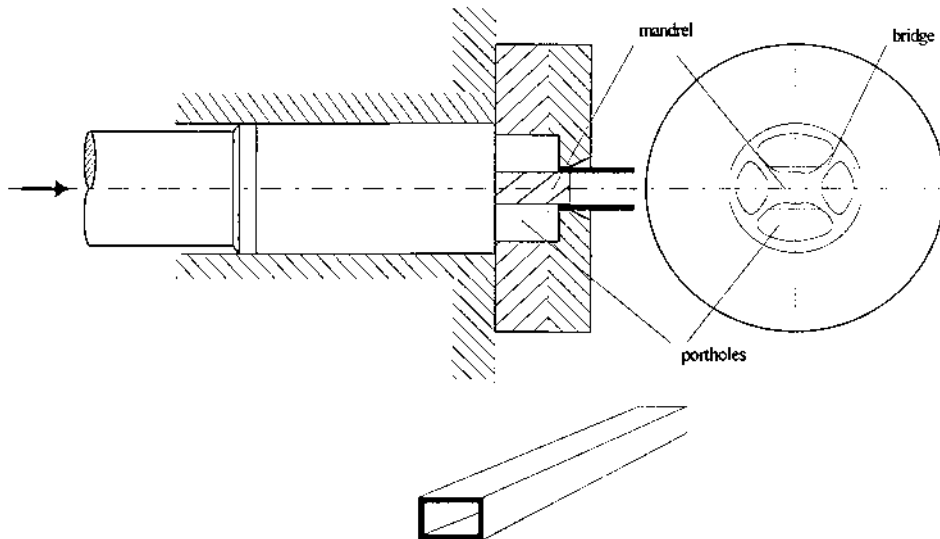
Figure 2 Direct extrusion of a hollow section.
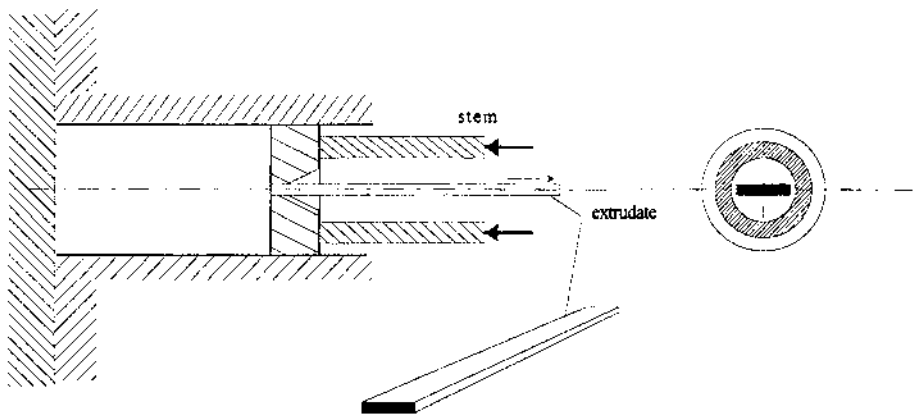
Figure 3 Indirect extrusion.

up by friction between the groove walls and the feedstock in the gap between the wheel groove, the feeder plate and the abutment. The metal is then forced to the die opening in a continuous flow. Both open and hollow sections can be produced.

Extrusion in rectangular containers, indirect extrusion and continuous extrusion are used for special products in limited quantities. Therefore, in the rest of this chapter the direct extrusion of open and hollow sections are dealt with.

The main parameters of the billet, the container and the extruded section are (Fig. 1):

- Diameter of the container: D_c [m]
- Cross section area of the container: $A_{\text{container}} = A_c = \dfrac{\pi}{4} D_c^2 \, [m^2]$
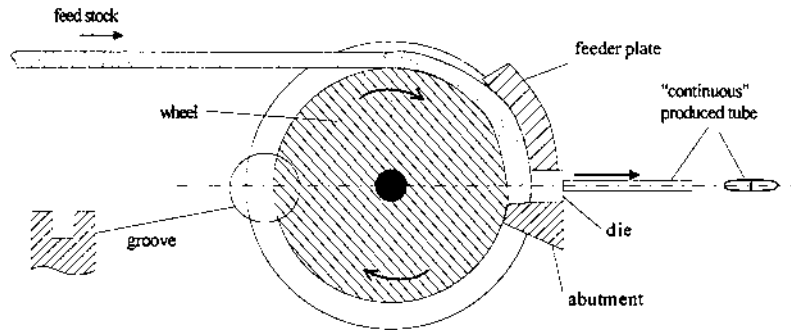
Figure 4 Continuous extrusion.

- Billet weight: $W_{\mathrm{b}} = \rho\,\dfrac{\pi}{4}D_{\mathrm{b}}^2 L_{\mathrm{b}}\,[\mathrm{kg}]$
- Billet diameter $D_{\mathrm{b}}\,[\mathrm{m}]$
- Billet length $L_{\mathrm{b}}\,[\mathrm{m}]$
- Density of aluminum: $\rho = 2700\,[\mathrm{kg/m^3}]$
- The circumscribed diameter of the section: $d\,[\mathrm{m}]$
- Section thickness: $t\,[\mathrm{m}]$
- Cross sectional area of the section: $A_{\mathrm{section}} = A_{\mathrm{s}}\,[\mathrm{m^2}]$
- Weight of section per meter length: $w_{\mathrm{s}} = A_{\mathrm{s}}\rho\,[\mathrm{kg/m}]$
- Reduction ratio: $R = \dfrac{A_{\mathrm{c}}}{A_{\mathrm{s}}}$

The most common values for the diameter of the container are 0.178 m and 0.208 m. The billet diameter is usually 5–10 mm less than the container diameter, allowing the billet to enter the container easily. The circumscribed diameter of the profile is usually less than 0.9 times the diameter of the container, but specially designed dies with a so-called expansion chamber may actually allow for $d > D_{\mathrm{c}}$. The section thickness often varies over the cross section of the profile. The reduction ratio is normally in the range of 20–80. If R is very high ($R > 70$) and the section is of a proper shape, the die is usually designed with more than one die opening (Fig. 5). In this case, the reduction ratio is:

$$R = \frac{A_{\mathrm{c}}}{A_{\mathrm{s}}n} \qquad\qquad (n = \text{number of die openings})$$

When an extrusion press cycle is carried out (see Sec. 4 for details), a small part of the billet is left in the container, the *discard* (Fig. 6). The length of the discard is normally around 10–20 mm.

- Discard length: L_{d}
- Discard weight: $W_{\mathrm{d}} = \rho\dfrac{\pi}{4}D_{\mathrm{c}}^2 L_{\mathrm{d}}\,[\mathrm{kg}]$
- The weight of the extruded section: $W_{\mathrm{s}} = W_{\mathrm{b}} - W_{\mathrm{d}}\,[\mathrm{kg}]$
- Length of the extruded section: $L_{\mathrm{s}} = \dfrac{W_{\mathrm{s}}}{w_{\mathrm{s}}}\,[\mathrm{m}]$
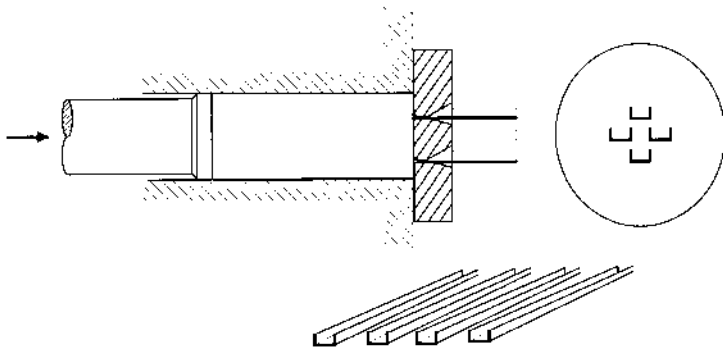
Figure 5   A multihole die.
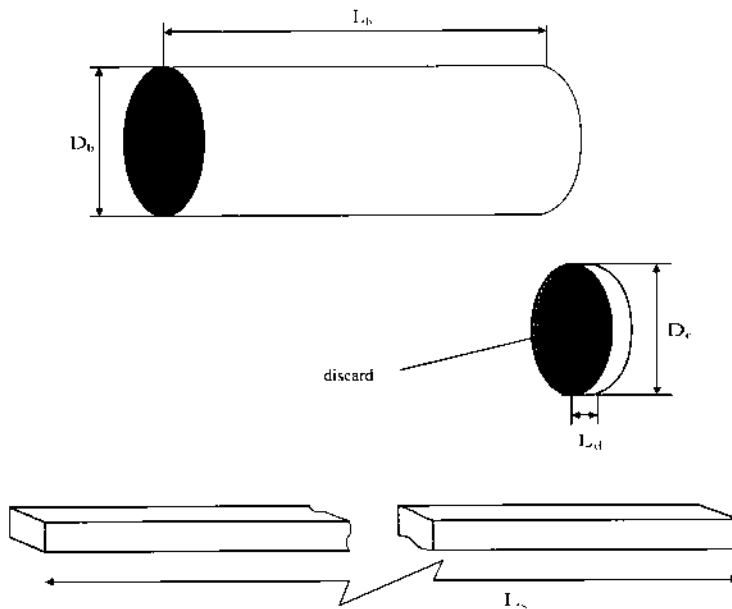
Figure 6   Billet, discard, and the extruded section.

2.2 The Die

The tooling package is to perform the deformation of the aluminum and must naturally withstand very large forces. Tools are generally made of high strength steels such as H11 and H13, and surface in direct contact with the flowing material is hardened through nitriding prior to any use. Furthermore, the complete tooling package will be comprised of a great number of parts which all are meant to support the die when pressure is applied by the stem. The complete tooling package will be

designed differently for the extrusion of hollow or open profiles. In any case, however, a bolster will be situated directly behind the die and provide the main support. The die and bolster will then be placed in a horseshoe clamp, which is firmly attached to the press structure.

In the case of extrusion of open sections one die design does not differ significantly from another although the bolster may provide varying degrees of support. Various die designs have, however, been developed for the extrusion of hollow profiles. The names of the most commonly used die types are porthole, spider and bridge, and for the extrusion of 6XXX-alloys porthole dies have traditionally been most popular, partly due to the ease with which they can be cleaned after extrusion.

The design of a porthole die is displayed in Fig. 7. The outer contour of the section is formed by the die plate (Fig. 7(a)). The tongue will be less stiff and weaker than the rest of the plate because it supports the pressure from the deforming material on the tongue only along one edge. The inner circumference of the section is formed by the mandrel (Fig. 7(b). The mandrel is an integrated part of the porthole
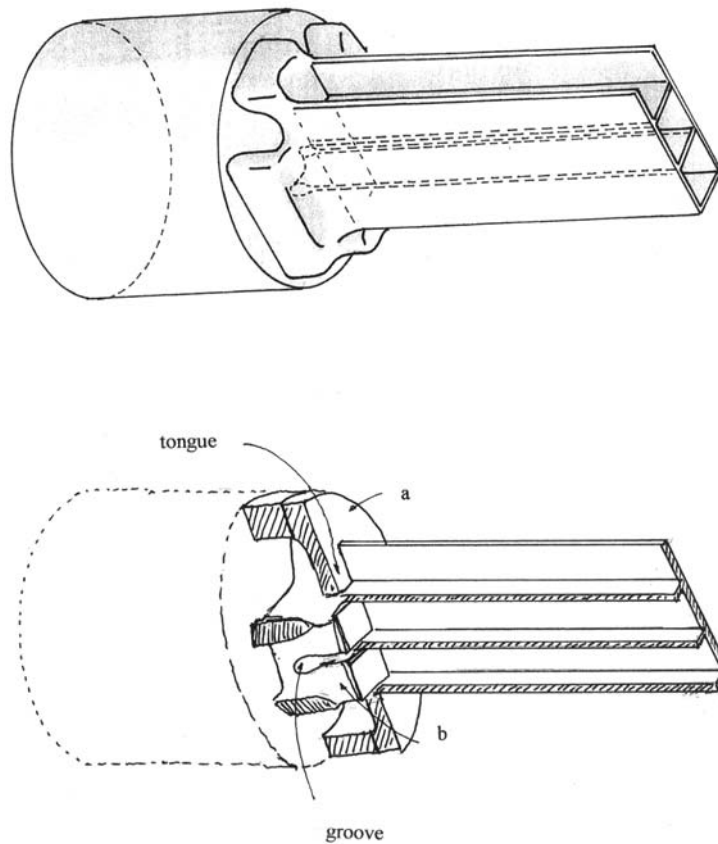
Figure 7   Billet, die, and extruded section in the process of extrusion.

die, connected to the rest of the die by webs, or bridges. In the mandrel a groove is machined out. This groove enables the internal rib in the hollow section to be formed.

The deforming alloy is flowing over the bridges and down into the feeder ports. Under each bridge, in the weld chamber, the two neighboring metal streams are forge-welded together. In this process the temperature of the material will not exceed that of melting, but welding will take place due to high pressures and diffusion rates. The alloy is also flowing into the groove in the mandrel from two sides, and in the center of the groove the two streams of metal are forge-welded, before the material flows into the bearing channel. All such welds are denoted seam welds. If pressures are not high enough in the weld zones, insufficient welding will take place. Furthermore, if material flows in an uncontrolled manner, one will not be able to predict the exact position of the weld. All these phenomena are highly unwanted and, hence, detailed studies of such can be found in the literature [4].

When designing mandrels one has to keep the following in mind:

- The stiffness and strength of the bridges should be optimized. The feeder ports should at the same time be as large as possible in order to reduce the load on the mandrel and allow for higher extrusion speed. This will, however, result in a weak bridge construction with unwanted flexibility and an increased risk of die deflection.
- Controlled flow out of the bearing channel should be sought. The die and the bearing channel should be designed so that the section leaves the bearings at a uniform speed and without generating excessive tensile or compressive stresses. Of special importance is the control of metal flow and die welding of the inner rib, because this cannot be inspected from outside during the press cycle.
- The surface of the section should be homogeneous and leave the die without streaks and stripes at the highest acceptable speed.

Clearly, there is a complex, but a very fascinating design-optimizing challenge here. Today, die design competence exists mainly as practical knowledge by highly skilled die designers, die producers and die correctors in the die shops. As will be pointed out in Secs. 4 and 5, however, the development of 3D computer simulation of hot extrusion processes is approaching such a level of precision that it can be used as a tool for die design. It must, however, be done in close cooperation with skilled and experienced die specialists.

2.3 The Manufacturing System

Satisfactory control of the material flow may be viewed as the key element in a successful production of aluminum profiles. In this context the last assertion has two alternative interpretations, and both are in fact equally correct. In order to produce extrusions with the desired quality at an optimum pace, one has to establish some sort of an understanding of the mechanisms of plastic flow of material in the container and die. However, if an enterprise is to succeed economically in the extrusion business, it is as important that it masters the logistics, that is the control of the material flow in and around the production facilities. The extrusion process is carried out in an extrusion plant, which often has a lay out similar to
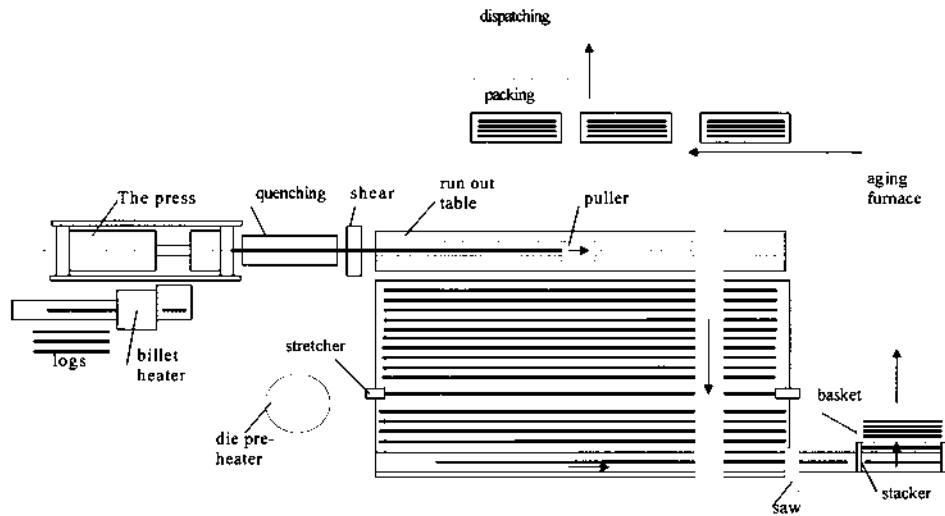
Figure 8   Layout of an extrusion plant.

that presented in Fig. 8. Although heat treatment in general is the most time consuming part of the production system, other process steps may in fact constitute the actual bottlenecks. The pressing of profiles is one such as it is non-continuous, and as considerable time is spent on changing dies, reloading new material into the container and performing maintenance tasks. Procedures are made even more complicated as new production orders for profiles often may necessitate several trial runs on the press. If the material is not transported effectively, down times may easily be long, and the most important parameter of all, productivity, will, consequently, be low.

As is seen on Fig. 8 the extrusion process is comprised of a great number of steps. One of the most important, however, is the production of raw material for the process, and this usually does not take place in the plant. Feed stock for the process is logs, normally in lengths of 6–7 m. They are supplied from the cast house of primary aluminum smelter or a secondary (recycled) aluminum cast house. The logs are produced as visualized in Fig. 9.

The liquid metal at temperature above 700°C is cleaned, added alloying elements and grain refiner before entering the casting table. By passing the casting molds with direct water cooling, the liquid aluminum alloy solidifies into a log. After casting, the log is homogenized in a temperature cycle that secures the best possible extrudability by establishing a homogeneous distribution of alloying elements and by dissolving phases with low melting points, typically Mg_2Si [5,6]. The logs are then transported to the extrusion plant.

In the plant a number of distinct processing steps takes place (Fig. 8). The logs are first taken one by one from the log stacker and transported to the induction heater. Here, a certain temperature profile is imposed on the log, and it is then cut into billets of a prescribed weight. In some plants the logs are cut prior to any heating.
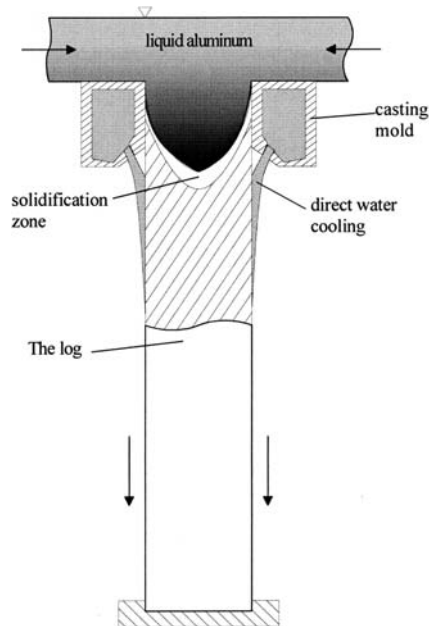
Figure 9 Direct chilling casting (DC-casting) of logs.

The billet is then loaded into the extrusion press, where the ram pushes it into the container. The end of the billet surface in contact with the ram, has been given a coating so that it does not stick to the *dummy block* between the ram and the billet. Because the billet has smaller diameter than the container bore, it is given an upsetting in order to fill the container. In this phase there is a risk of entrapping air in the container, and, thus, the ram stops after upsetting, unloads, and moves a small distance backwards to let the possible entrapment leave. This is called the *burb cycle*.

Thereafter, the extrusion process commences. The ram pushes the billet through the die opening. The load capacity of the press with a container diameter of 0.178 m is normally 16 MN, which corresponds to a specific pressure of 643 MPa. If the container diameter is 0.208 m, the load capacity is normally 22 MN and the specific pressure 647 MPa. The temperature of the billet prior to extrusion is in the range 450–470°C. In the induction heater, the billet may have been given varying temperature along its length in order to compensate for the heat generation caused by the shearing along the container walls when it is pushed through the container (see also Sec. 4). This is called *tapering*, and the highest temperature is usually in the front end of the billet. The temperature of the section leaving the die is in the range of 550–600°C. The taper should be given in such a way that the run out temperature is constant as this will result in minimum variation of dimensions and properties during the press cycle.

As the section front leaves the die, it is gripped by a *puller*, which guides the section out on the *run out table*. The profile is then quenched and further cooled down when moving sideways along the table. The lengths of the profiles upon leaving

the die may be from 20 to 50 m, depending on the length of the billet and the reduction ratio. Normally, a number of charges (billets) are performed with the same die in a production set up. In this case, one may weld the profile from the new charge directly to the one produced in the foregoing charge, creating a so-called *charge weld*. This procedure simplifies production, but necessitates cutting of the profile during extrusion. On the cooling table the section is given a plastic deformation of 0.5–2% elongation in order to eliminate internal stresses due to uneven cooling over the cross section of the profile and straighten up possible bends and twists before going into the cutting saw. The extruded section is finally cut into prescribed lengths, normally 6 m. The process of cutting may vary somewhat from one plant to another.

The cut sections are stacked in bins and transported through the aging oven where they spend 3–6 hr at temperature in the range of 170–190°C. After aging the sections are inspected and packed before they are delivered to the customer for further fabrication and surface treatment, followed by joining and assembling into the finished component or product.

With a generic aluminum section (Fig. 10) some important features and characteristics of die design and productivity for aluminum extrusions will be demonstrated.

An order of 200 sections à 6 m of alloy AA6060 (Al-MgSi0.5) shall be produced in a 16 MN press with container diameter of 0.178 m and run out table length 42 m. The following typical process parameters can be calculated and controlled:

- The cross sectional area of the container is:

$$A_c = \frac{\pi}{4} 0.178^2 = 24.9 \times 10^{-3} \,[\text{m}^2]$$

- The cross sectional area of the extruded section is

$$A_s = 0.084 \times 0.02 - 2 \times 0.028 \times 0.016 + (0.003^2 - \pi \times 0.0015^2)$$
$$\frac{10}{4} = 0.437 \times 10^{-3} \,[\text{m}^2]$$

- The reduction ratio can, thus, be calculated to:

$$R = \frac{A_c}{A_s} = \frac{24.885}{0.437} = 57$$
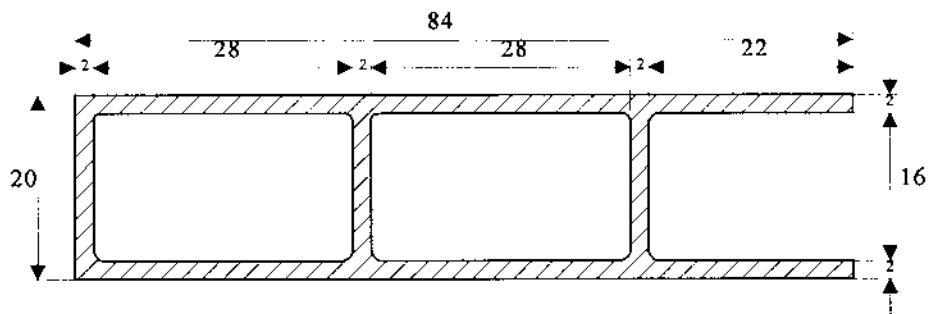
Figure 10   A "generic" extruded aluminum section.

This is a reduction ratio within the acceptable range for a one hole die.

- The circumscribed diameter of the section is:

$$d = \sqrt{0.02^2 + 0.084^2} = 0.086\,[\text{m}]$$

This is well bellow the maximum recommended diameter of $0.9 \times 0.178 = 0.16[\text{m}]$

- Special features of the section shape that should be noticed, are a hollow rectangular section with constant wall thickness, an outer tongue and an inner rib. Furthermore, the profile is symmetric about the horizontal axis.

2.4 Productivity and Cost

A number of aspects are important to consider for a customer who is to choose between the many different suppliers of aluminum profiles. As a great number of sections ought to and have to be designed and manufactured for only one product type, customer service stands out as particularly important. Furthermore, the supplier must of course be able to deliver the section requested within an agreed time limit and to the specified quality. If the profile geometry is fairly complicated or a very high strength alloy is chosen, some suppliers may fall out of the race, but for most profiles one may not be able to differ on these grounds alone. And in the end, thus, all usually comes down to money. The basic parameters in the extrusion business are the prices per meter or per kg extruded section. These measures are dependent on the choice of alloy and the geometry of the section, and one has to contact different suppliers in order to determine exact prices. These should not differ too much since there is an active market mechanism working. This mechanism will, however, also pressure the suppliers to continuously seek to increase productivity and cut costs. It is in the creative negotiations between the customer and the supplier that the right price is agreed upon as a consequence of a section design with the right balance between requirements for functionality and the cost efficiency in the extrusion plant. Important parameters that determine the productivity and cost of the extruded section are:

- Length produced per press cycle
- Length of end cuts that have to be scrapped
- Number of cut lengths per billet
- The discard weight per billet
- Number of billets produced, i.e. gross weight delivered to the press
- Net weight ordered
- The dead cycle, i.e. the time between each press cycle
- The ram speed
- The acceleration time, i.e. the time to reach the full ram speed
- Time for die change
- The price of billet delivered at the press
- Die cost
- Production cost
- Unpredicted press stop

● Unpredicted quality scrap, i.e. the number of sections produced, which are not conforming with the required quality.

The production cost may be measured as cost per minute extrusion time spent. This measure contains all direct costs and man-hour costs in the plant, divided by the estimated availability of the press in minutes.

The following example is meant to illustrate a typical calculation of the cost per meter and cost per kg extruded profile. The calculations are meant to refer to the section in Fig. 10, and data from the example of the previous section is used.

● The gross material mass (weight) is first calculated.

The sections are cut to lengths of 6 m, of which 6 may be produced from each billet. In addition the first and the last meter of the total section is assumed to be of inferior quality and therefore scrapped. The total section length produced in the press cycle is then:

$$6 \cdot 6 + 2 = 38 \, [\text{m}]$$

The mass per meter section can be calculated from the cross-section area and the density:

$$0.437 \times 10^{-3} \times 2700 = 1.18 \, [\text{kg/m}]$$

The previously calculated data can be used to find the run out mass per billet:

$$1.18 \times 38 = 44.84 \, [\text{kg}]$$

The length of the billet is chosen so that the discard length is 0.02 m. As the container diameter is 0.178 m, the mass of the discard is:

$$\pi \times (0.178/2)^2 \times 0.02 \times 2700 = 1.34 \, [\text{kg}]$$

The total mass of each billet may be calculated to be:

$$44.84 + 1.34 = 46.18 [\text{m}]$$

In order to compensate for possible quality scrap of 6%, 12 more lengths than ordered are produced. The total number of cut lengths are then 212, and the corresponding number of billets is:

$$212/6 = 35.3$$

Hence, 36 billets must be ordered and the gross material mass will consequently be:

$$36 \times 44.18 = 1614 \, [\text{kg}]$$

● The net mass of the sections delivered to the customer is, however, only:

$$200 \times 6 \times 1.18 = 1416 \, [\text{kg}]$$

● The yield, which is the gross mass of the material divided by the delivered mass is then

$$\frac{1416}{1614} = 0.877 = 87.7 \, [\%]$$

- The total production time should then be calculated.

  The run out speed of the press for this particular alloy and geometry is found to be 36 m/min or 0.6 m/sec. The additional time spent pr charge on reaching the desired run out speed, the acceleration time, is found to be 7 sec. Since the length of the billet (38 m) is known, the total time of a press cycle can be calculated to be:

  $$38/0.6 + 7 = 70 \, [\text{sec}]$$

  The dead cycle time then has to be assessed. The time spent on cutting of the discard after extrusion, inserting a new billet and performing the burb cycle is found to be 15 sec. If one expects no additional unexpected stops, one only has to add the time spent on changing the die prior to extrusion. For this particular press this is found to be 180 sec. The total production time without any unpredicted stops and delays is then:

  $$(70 + 15)36 + 180 = 3240 \, [\text{sec}] = 54 \, [\text{min}] = 0.9 \, [\text{hr}]$$

- The productivity is viewed as the net mass delivered divided by the total extrusion time and can optimistically be calculated to be:

  $$1416/0.9 = 1573 \, [\text{kg/hr}]$$

- Finally a calculation of cost has to be performed.

  The material cost of the billet is set to 1.5 US\$/kg. Production cost is in this example found to be 50 US\$/min and the die cost for the order is US\$ 2000. The total cost respectively without and with the die cost is then:

  $$1.5 \times 1614 + 50 \times 54 = 5121 \, [\text{US\$}] \qquad 5121 + 2000 = 7121 \, [\text{US\$}]$$

  The corresponding costs pr m section delivered can be calculated:

  $$5121/1200 = 4.27 \, [\text{US\$/m}] \qquad 7121/1200 = 5.93 \, [\text{US\$/m}]$$

  Finally, the cost pr kg delivered section is:

  $$5121/1416 = 3.62 \, [\text{US\$/kg}] \qquad 7121/1416 = 5.03 \, [\text{US\$/kg}]$$

  The same die can often be used in several production orders. If all die cost is placed on the first order, one can produce the next orders without any die cost. Maintenance cost of the die is included in the production costs.

2.5 Measures of Section Quality

2.5.1 Process Variability

The aluminum extrusion process is unique in the sense that it offers the possibility to produce almost ready to use profiles of high quality and with large functional freedom at a relatively low cost. The product quality, which in the very end will be judged by the product's ability to satisfy customer demands, relies heavily on the restrictions imposed on design by the process itself. Purely geometrical considerations indicate that profile dimensions necessarily will be limited by the press capacity and size, and it is known that material flow also puts restrictions on both wall thickness and changes in such. However, product quality is probably to the

largest extent affected by the mere variability in chemical composition, microstructure, geometrical dimensions, mechanical properties and surface finish over the length and width of the profile. Such variations are connected to the transient nature of the extrusion process and the difficulties to establish a system of measurement and control of important parameters during the press cycle. Changes in temperature, deformation history and material composition of the extruded profile will be encountered both during the course of a press cycle and from one billet to another. Furthermore, both production parameters and dies have to be changed in order to extrude different aluminum alloys due to the fact that both their metallurgical and thermomechanical properties may differ considerably. If attention is not paid to controlling the material flow in the factory, the production of profiles with uneven and thereby also inferior properties will ultimately lead to either the distribution of products of poor quality or to low productivity due to excessive scrapping. Therefore, most producers of aluminum profiles stress the use of house-keeping and have established routines for production of profiles of different alloys based on experience. However, in order to make proper use of such routines sufficiently reliable and consistent, measurements of production parameters such as temperatures and pressures have to be obtained. This task is not easily performed due to the noise inherent in the process.

2.5.2 Dimensional Variability

In order to make a direct assembly of extruded profiles possible, the characteristic dimensions of the product such as straightness, thickness, height, width, length and angles have to be made within sufficiently narrow tolerances. Dimensional variability is to a certain extent always existent and often in the order 0.25 mm on thin-walled profiles. Open or partly open profiles tend to experience larger variation than closed ones, whose die construction is more robust. Based on experience with when the process can be expected to be under control, tolerance on wall thickness is often set to be around 10% of the nominal measure. Measurement of profile dimensions is usually implemented as a standard procedure at extrusion plants.

Table 1 which is taken from the German standard DIN 17615, gives an indication of within which tolerances the open profile in Fig. 11(a) can be delivered. Thickness variations may be caused by the changing deflection and temperature of the die during a press cycle. Another cause of thickness variations is wear. In the case of large production series, dies are often bought from die manufacturers with too narrow bearing surfaces as to compensate for future wear. Furthermore, dies are also produced within certain tolerances, although somewhat narrower than those of the profiles. As a result of both these factors, die changes may cause variation in profile geometry. A last reason for variation in wall thickness is the deformation of dies through fracture when extruding hollow profiles. This is caused by uneven loading, which very often is a result of flow imbalance and is most common when extruding alloys of higher flow resistance such as for instance the 7XXX-series. Fracture need not always immediately be fatal, and the presence of a crack may very well lead to a gradual reduction of the die strength and increasing deviation from nominal thickness. The presence of a crack combined with flow imbalance will also often result in thickness variations along a wall.

Table 1 Tolerances on Section Thickness after DIN 17 615

Measure of thickness, s, from [mm]:	Measure of thickness to [mm]:	Allowed deviation [mm]:
–	1.5	± 0.15
1.5	3	± 0.20
3	6	± 0.25
6	10	± 0.30
10	15	± 0.40
15	20	± 0.50
20	30	± 0.60
30	40	± 0.70

Variation in height and width of the profile may be due to variation in manufactured die dimensions or wear. However, larger deviations will be measured if profile walls are curved. In this case, tolerances are set with regard to the maximum curvature that can be accepted. The curving of profile walls is often a result of varying flow velocity across the profile, which again is due to variation in wall thickness and friction conditions in different parts of the outlet of the die. Table 2 shows tolerances with regard to curvature of walls in the profile given in Fig. 11(b).

Prior to stretching operations profiles very often have a certain curvature, a warping, in the direction of extrusion (Fig. 11(c). This is often also a result of variations in flow velocity in the profile, but can be caused by the uneven cooling rates of walls with different thickness. DIN 17615 gives tolerances on the deviation from straightness as a function of length as given in Table 3 and Fig. 11(c). Flow imbalance may also lead to twisting of the profile along the extrusion direction. Fig. 11(d) and Table 4 show that this deformation is often measured as a distance, v, which can be taken to be a function of both the length and the width of the profile.

Even though the height, width and thickness of a profile may be within tolerances, assembly may be hindered by deviations in angular measures as shown in Fig. 11(e). Direct measurement of angles on the profile is most easily done with the help of electronic equipment, but is relatively time consuming in comparison with simpler mechanical methods. DIN 17615 proposes the use of the length w as a measure of angular deviation and this can be taken as a function of the profile width as seen in Table 5.

2.5.3 Variability in Surface Properties

High surface quality is usually obtainable when extruding aluminum profiles, and the combination of a very even surface, outstanding optical properties and large corrosion resistance makes the use of aluminum preferable to for instance steel in many applications. However, surface quality is extremely dependent on die design, billet quality and extrusion practices in general, and a series of surface defects may develop if proper attention is not paid to controlling the process [7]. Given the excessive noise in extrusion equipment, it is not always possible to sort out the causes for defects, and very often several different error mechanisms may be operating simultaneously.
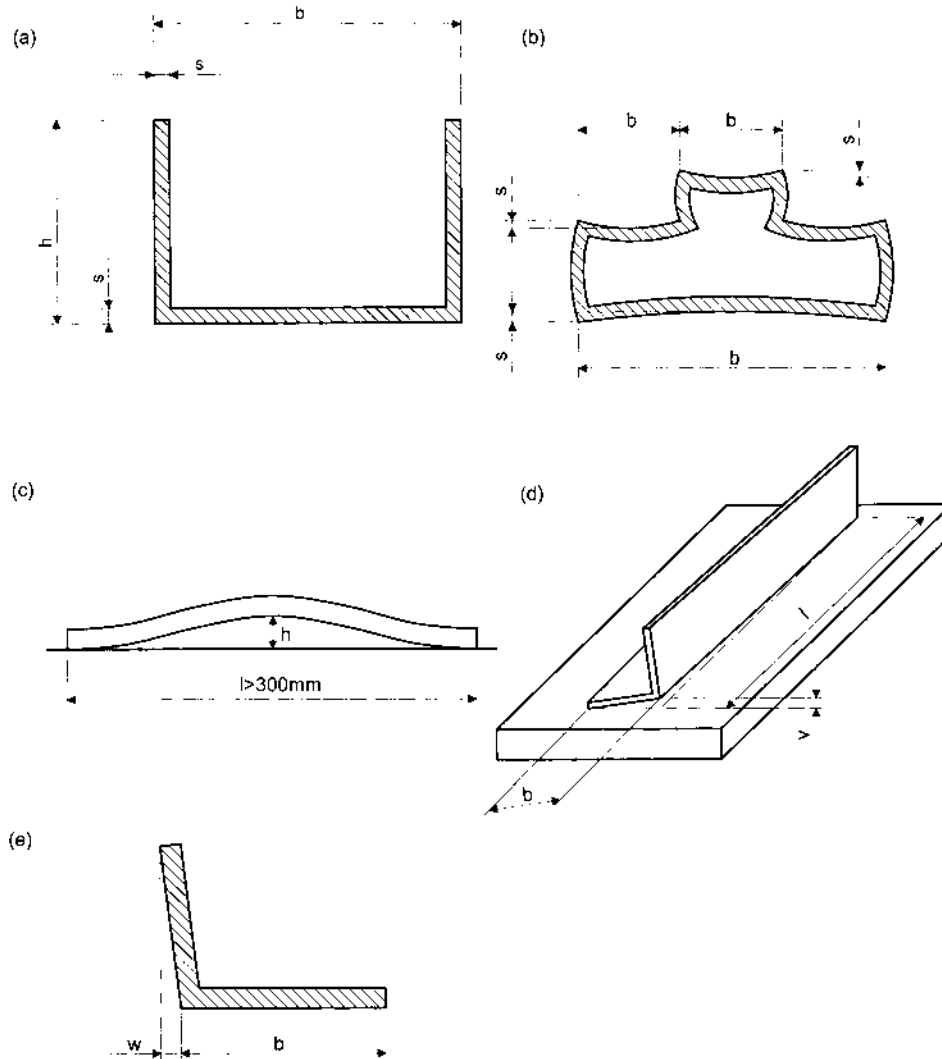
Figure 11   Measures of geometrical deviation: (a) Wall thickness; (b) Curvature of walls;
(c) Profile warping; (d) Profile twisting; (e) Angular deviation.

Corrosion properties are related to the content of different alloying elements, in particular Cu, and are therefore mostly dependent on the properties of the billet. However, by extruding with the wrong parameters changes in chemical composition, grain sizes and surface roughness may be unfavorable to corrosion properties.

Die lines and pick ups are common surface defects shown in Fig. 12(a) and (b) and give an indication that the profile surface is formed in the presence of hard and uneven attributes or particles in or around the bearing channel. Rough and worn out dies or abrupt changes in bearing lengths may be the cause, but it may just as well be that oxide build-ups behind bearings or hard particles from the billet cause the defects. In the first case dies should either be polished and nitrided

Table 2 Tolerances on Transversal Curvature after DIN 17 615

Measures of width of wall, b, from [mm]:	Measures of width of wall, b, [mm]:	Tolerance on straightness, e, [mm]
–	40	0.20
40	60	0.30
60	90	0.40
90	120	0.45
120	150	0.55
150	180	0.65
180	210	0.70
210	240	0.75
240	270	0.80
270	300	0.90

Table 3 Tolerances on Longitudinal Curvature on Profile after DIN 17 615

Length to 1 [mm]	1000	2000	3000	4000	5000	6000	Above
Tolerance h [mm]	0.7	1.3	1.8	2.2	2.6	3.0	3.5

Table 4 Tolerances on Profile Twisting after DIN 17 615 (all measures in mm)

Width, b From:	To:	Length, l 0–1000	1000–2000	2000–3000	3000–4000	4000–5000	5000–6000
–	25	1.0	1.5	1.5	2.0	2.0	2.0
25	50	1.0	1.2	1.5	1.8	2.0	2.0
50	75	1.0	1.2	1.2	1.5	2.0	2.0
75	100	1.0	1.2	1.5	2.0	2.2	2.5
100	125	1.0	1.5	1.8	2.2	2.5	3.0
125	150	1.2	1.5	1.8	2.2	2.5	3.0
150	200	1.5	1.8	2.2	2.6	3.0	3.5
200	300	1.8	2.5	3.0	3.5	4.0	4.5

Table 5 Tolerances on Deviation from Straightness of Angles

Width, b, from [mm]:	Width, b, to [mm]:	Tolerance deformation, w
–	40	0.3
40	100	0.6
100	300	0.8
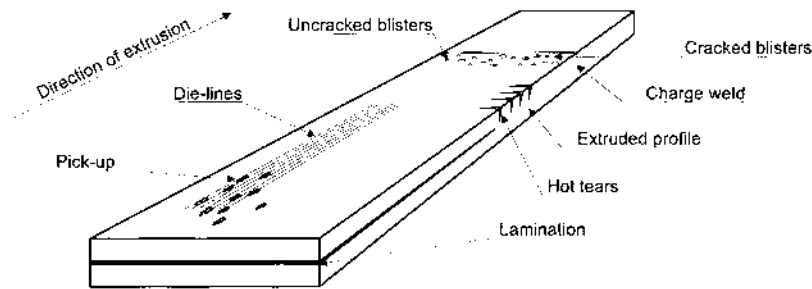
Figure 12 Visualization of various surface defects.
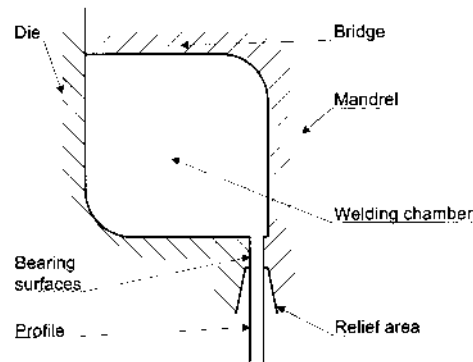
Figure 13 Detail from a porthole die: An area of relief may be found behind the bearings.

[8,9] or scrapped. Oxide build-ups behind bearings are often the result of a too small relief area (Fig. 13), and this phenomenon can be reduced by either increasing the relief or the use of nitrogen shrouding behind the bearings in order to avoid the oxidation. Hard particles in the extruded sections often originate from oxidized and even dirty material on the billet surface even when performing direct extrusion. Inflow of material from billet surface will take place if the container temperature is too high, causing a low yield resistance and easy flow of surface material [10]. Inflow to the bearing channel may also take place if a too large profile is extruded or the container is misaligned so that surface material may flow directly out of the bearing channel. Hard particles may also exist in the interior of the billet if it is not properly homogenized, or, in the case of 6061 and 6063 alloys, the iron content is high so that AlFeSi particles are formed. As to complicate matters further, research has shown that the presence of die lines will be heavily dependent on the size of the bearing angles when defects are caused by AlFeSi particles.

The profile surface may contain blisters as shown in Fig. 12(c), which may be inclusions of air, oxides or even oil. Such blisters degrade surface appearance and mechanical properties, and when the profile is cooled, blisters may also crack, creating a distinct sound and causing open holes in the profile surface. They may be a result of inflow of material from the surface of the billet or inclusions that are already contained in the interior of the billet prior to extrusion. However,

blisters containing air, are often caused by air trapped in the container due to too fast upsetting or air trapped in hollow porthole dies prior to extrusion. Hence, they may very often be found close to the forward part of the profile or charge welds. When extruding light metals, lubricants are not used. Contamination of oil must therefore be avoided. Lamination is also a result of contamination and should be avoided in order to preserve both mechanical strength and in some cases also appearance. This phenomenon may be a result of inflow of oxidized and contaminated material from the surface or from the charge weld.

Sometimes, when studying an extruded aluminum profile, areas of different shades of gray color may be detected. This surface defect is called structural streaking and is a result of varying reflective properties across the surface. While streaking seldom will be a reason for scrapping the material, efforts are often made to extrude under conditions that give even optical properties. This is especially the case if surface treatments such as etching and/or anodizing are to be employed since these processes tend to accentuate streaking. Streaking is a result of variations in grain size and grain orientation of the finished product, and three somewhat different types have been identified. These are streaks caused by variations in bearing surfaces, variation in temperature, amount of hot work and recrystallization. However, as streaking in general is a result of the whole thermo-mechanical and metallurgical treatment of the material, it is not always possible to differ between the different types. So-called bearing streaks are often due to uneven bearing surfaces, having created depressions in the profile surface. Hence, light is reflected in different planes and streaks are only visible when viewed from specific directions. A type of combined bearing and grain size streaking is caused by sudden shifts in bearing lengths due to varying profile thickness. Apart from leading to problems connected to filling, such a die design will give abrupt changes in grain sizes and orientations and also reflective properties over short distances in the profile. Furthermore, as the amount of heating is varying, the temperatures and the degree of recrystallization may also be expected to be changing. Oxide streaks can be recognized as dark streaking areas of varying width and intensity on etched or anodized parts. The presence of such streaks is linked to the inflow of oxidized material from the billet surface to the bearing channel. Oxide streaks will be avoided if inflow is hindered. In general, structural streaking will be less of a problem if material in all parts of the profile cross-section undergoes much of the same thermo-mechanical loading. Furthermore, experience has shown that a minimum degree of choke on bearings should be sought in order to reduce variation in reflective properties.

Cracking or tearing of the extruded profile is experienced when process control is lacking. If the temperature of the extruded metal on the bearings is too high as a result of preheating of billet or high extrusion rate, partial melting of Mg_2Si particles will take place [11]. Thus, cracking of profile surface or so-called hot tearing may be the result. If cracks develop in the die or pick-ups are created through insufficient clearance behind bearings, edges may be torn.

Surface quality is often also reduced through scratches and gouges asserted in material handling processes on the run-out table, lift-overs, walking beams, saw tables or in stations for packaging and stacking. Efforts must be made so that profiles are not damaged in transport. Great emphasis has been laid on establishing best practice in handling materials and on securing that equipment used can cause mini-

mal damage. However, due to the large variability in profile geometry and the great demands on material handling, many operations must be performed manually at high costs.

3 APPLICATIONS, ALLOY SELECTION AND DESIGN CONSIDERATIONS

By developing products out of materials found in nature mankind has managed to differentiate itself from the animals. The fact that historians have tended to denote periods by the names of the materials found in the tools and other equipment of the times, indicates that one assesses the use of materials to be of prime importance to human life. Today, one recognizes the stone, bronze and iron age, but not surprisingly, when dealing with the present, the determination of the material with the greatest importance turns out to be harder. Some emphasize that relatively new materials such as plastics are omnipresent and have brought enormous changes to human life over the last decades while others maintain that the increasing use of computers marks the entrance to the silicon age. However, the fact still remains that iron in the form of steel even today by far is the most favored material for most applications. The strongest contender of the metals is aluminum, but as for volumes produced, steel is about 20 times larger. So, in spite of the several industrial revolutions that have taken place in last century, it may still be claimed that the contemporary period is the one that was allegedly introduced by the Hittite development of iron around 1300 BC [12].

3.1 Product Development

Innovative thinking is maybe the one most important virtue of a designer, but if ideas are to be transformed to innovations, proper use of knowledge of and experience with both design principles, processes and materials is mandatory. In fact, modern product developers often stress that focus must not be placed on the mere functional properties of the product and the ability of the product to satisfy consumer's demands, but also on the chain of processes from raw material to components, joining, surface treatment and assembly. Obviously, a quality product will not only be satisfactory to the user, but also to the producer in that it creates possibility to generate a surplus.

Three aspects are of equally great importance when creating a new component that is to satisfy the user's notion of quality. In Fig. 14 product development is given as a combination of function, production and material. The functional side is linked to the transforming of new concepts of for instance physical or structural origin to products that are of lasting value to the user. The goal for the production system is to establish processes and routines so that new products can be manufactured within calculated costs and time limits. When developing a new product one should attempt to make use of possibilities offered by manufacturing systems to forward functionality rather than letting the system impose restrictions or additional cost. Obviously, when having decided on a concept, the most optimal production process should always be sought. However, one should also bear in mind that manufacturing processes automatically offer new degrees of functionality to the product. Therefore, the alternative candidates of production methods should be evaluated at a very early stage in the design process.
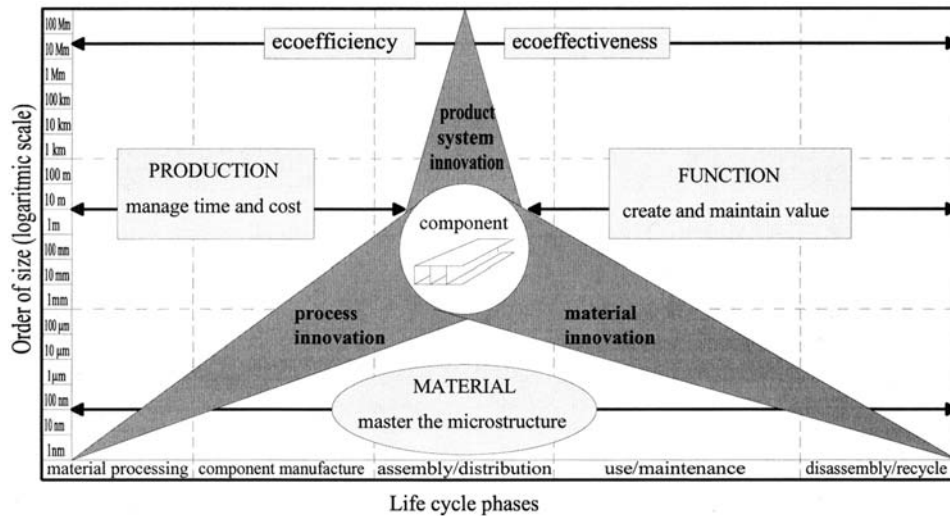
Figure 14 The Life-Cycle-View (LCV) of a component.

Another fundamental aspect of product development is the use of materials. Traditional use of materials is limited to choosing on the basis of only certain tabulated data such as yield limit or tensile strength and, in some cases, corrosion properties, and often due to limited knowledge of alternative materials, steel is the most favored material for most constructional applications. However, materials should not only be chosen, but also designed so that both functional demands are satisfied and so that production is simplified. For a long time, more advanced users of materials, such as the aircraft industry, have realized that optimal solutions only can be reached by making use of the whole specter of new materials and by obtaining knowledge about and manipulating the microstructure. In this way, the design process has been brought all the way down to atomic level, thus spanning more than ten orders of magnitude (Fig. 14). Over the last decade it has become apparent that thorough knowledge of material properties is prerequisite in almost all design work and that the traditional practice neither is in accordance with customers demands nor international standards.

As shown in Fig. 14 product innovation is taking place in parallel to innovation connected to the properties of process and material. New or improved materials or processes will increase possibilities to create products with new functions or improve older products. As shown, a large number of fields of research will in one way or another contribute to the development of new and better products. As the possibility to improve products increases, so does consumer demands to quality. While factories earlier could produce and sell enormous numbers of standardized goods with often inferior quality, today's consumers demand products with which they can identify themselves, and which are virtually perfect. An example of enterprises which meet such demands each day are of course those of the automotive industry.

Furthermore, one has over the last couple of decades witnessed an increasing consciousness of environmental protection and sustainability, and in the very recent years, this emphasis has not only focused attention to cleaner production, health and

safety within the individual production plant, but also on the product life cycle and loop closing of products, components and materials. A consequence of the interest in including industrial ecology and ecodesign into industrial practice is that important new concepts and methods are under development [13]. They are Life Cycle Assessment (LCA), Life Cycle Cost (LCC), eco-efficiency and eco-effectiveness. It is not possible to go into these concepts here, but the combined ecologic and economic life cycle performance of products and processes will probably be among the more important features of successful products and processes in the years ahead. Thus, it seems natural that the designer must think more in terms of establishing life cycle systems than isolated products. Innovations for exploiting the life cycle merits of aluminum alloys should be the hallmark of aluminum components and structures. Figure 14 shows a Life Cycle View (LCV) of a component, placed in a life cycle time scale (abscissa) and an order of size scale (ordinate). Here the interactions between the details and the whole are visualized, so that critical success parameters can be identified more easily. Very often one sees that successful products are a result of combined innovations of process, material, product and production.

In the UNEP-manual [14] van Hamel has designed a so-called "Ecodesign Strategy Wheel" (ESW) as a tool to formulate strategies for improvements of economic and ecological performance of products, processes and practice, both in a short term and in a long term perspective, Fig. 15. An existing product is used as a present time reference of improvement (improved eco-efficiency) and a scenario of a possible future sustainable society as the goal to strive for (measure of eco-effectiveness). It may be useful to see the connection between the Figs. 14 and 15. The Life Cycle View (LCV) can be transformed into the Ecodesign Strategy Wheel (ESW) by bending the LCV into a cylinder and view it from above, Fig. 16.

As can clearly be seen, the work of the product developer is both getting increasingly difficult and challenging, and greater demands are placed on his or her ability to master all aspects of the product development process. Innovative thinking and a well documented understanding of customer's needs will of course still be at the center of attention, but the model discussed may be an important tool when establishing an integrated method of product development, which in any way is bound to take function, production and material aspects into account.

Table 6 gives an overview of extrusion based systems and components and the generic alloy selection for the different applications areas. With a generic alloy selection here one understands an alloy, generally used for the specific application, which will be available in most markets and with properties best documented. It should then be the alloy first selected by the designer, and only be changed if special combinations of properties, not found in the generic alloys, is needed. It is then important to contact potential suppliers of the section to ensure that the alternative alloy is available to acceptable price and with properties documented. A short description of some typical products in these main application areas are given below. It is recommended, however, to actively collect information brochures and inspiration material from aluminum producers, extrusion plants and final product manufacturers as basis for understanding the rich diversity of design solutions based on extruded aluminum rods, tube and sections that is possible [15].

@ New Concept Development directed towards sustainability
Dematerialisation
Sheared use of the product
Integration of functions
Functional optimization of product (components)

PRODUCT SYSTEM LEVEL

7. Optimization of end-of-life system
Reuse of prduct
Remanufacturing/refurbising
Recycling of materials
Safer incineration

6. Optimization of initial lifetime
Reliability and durability
Easier maintenance and repair
Modular product structure
Classic design
Strong product-user relation

PRODUCT COMPONENT LEVEL

1. Selection of low-impact materials
Cleaner materials
Renewable materials
Lower energy content materials
Recycled materials
Recyclable materials

2. Reduction of materials usage
Reduction in weigth
Reduction in transport volume

5. Reduction of impact during use
Lower energy consumption
Cleaner energy source
Fewer consumables neede
Cleaner consumables
Now waste of energy and/or consumables

3. Optimization of production techniques
Alternative production techniques
Fewer production steps
Lower/cleaner energy consumption
Less production waste
Fewer/cleaner production consumables

PRODUCT STRUCTURE LEVEL

4. Optimization of distribution system
Less/cleaner/reusable packaging
Energy-efficient transport mode
Energy-efficient ligistics

(a) Existing product

(b) Short term strategy for improved ecoefficiency

(c) Longt term strategy for improved ecoeffectiveness

Figure 15 The Ecodesign Strategy Wheel (ESW) with (a) reference product profile; (b) Short term development strategy; (c) Long term development strategy.

3.2 Designing with Aluminum Sections

Even though one may find that the ideal material to be used for a product is aluminum and that manufacturing should take place in the form of extrusion of profiles, there is still great freedom with regard to the functions that the product could fulfil [16]. Aluminum profiles are used in a number of applications, and the following five groups may be identified:

- Buildings, architecture and furniture
- Structural
- Transport
- Heat exchangers and electrical conductors
- Durables and Mechatronics
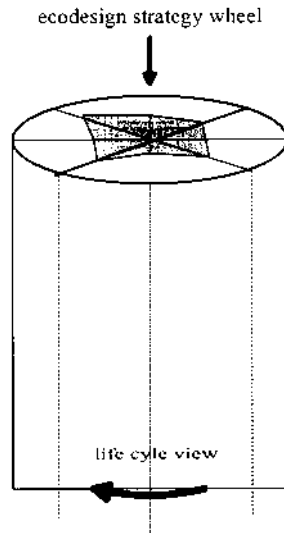
Figure 16 Two aspects of life cycle thinking.

A short listing of some typical products in these main application areas is given in Table 6. Although profiles are produced as long beams, and thus, originally only contain variations in two dimensions, forming or cutting processes may be used to modify the product so that parts with variations in all three directions may be obtained. Furthermore, as a large number of alloys with a specter of properties have been developed, the choice of aluminum puts very few limitations on design. It is recommended to actively collect information brochures and inspiration material from aluminum producers, extrusion plants and final product manufacturers as basis for understanding the rich diversity of design solutions based on extruded aluminum rods, tube and sections that is possible.

Aluminum is at the present undoubtedly one of the most popular engineering materials. Its popularity is mirrored by the fact that the metal, in terms of volumes produced, is second only to steel and as large as all other non-ferrous metals combined even though it was first introduced only about 100 years ago. The reason for the material's enormous success lies in its thermal, mechanical and electrical properties, or in short in its microstructure. Aluminum is light, but some of its alloys are able to compete with comparable steel alloys in terms of both yield limit and tensile strength. At the same time much less effort is needed in hot forming of aluminum than of steel with the same yield limit at room temperature. This is due to the fact that aluminum has a rather low melting point and that hardening processes, such as aging, are taking place. Furthermore, even though Young's modulus of aluminum is only 1/3 of the modulus of steel, aluminum beams can be stiffer than steel beams of the same weight due to the fact that aluminum is lighter than steel. The ratio of Young's modulus to weight is about the same for the two materials, but such a comparison is unfair to aluminum because the lower density offers the opportunity to place material at farther from the neutral axis, thus creating larger momentum. Aluminum is also a very efficient conductor of both heat and electricity. Because an undamaged and untreated surface reflects almost 90% of vis-

Table 6 Applications of Extruded Aluminum Rod, Tube and Sections

Main Process	Systems components	Generic alloys	Selected applications				
			Building architectual furniture	Welded structural	Transport	Heat exchangers electrical conductors	Durables mechatronics
HOT EXTRUSION OF ALUMINUM	Systems of sections	AA6060 AA6063	windows and doors shelves shower cabinets		utility vehicles	conductors cables multiport tubes	housingss
	Structural sections	AA6082 AA6061	building structures scaffolding	bridges	utility vehicles		ladders stairs
	Bended and locally formed sections	AA6060 AA6063 AA6082	furniture ship windows frames	space frames	bumpers seating spaceframe	bended tubing in heat exchangers	
*ROD	Components manufactured by shearing, drilling, milling, etc	AA6060 AA6063	hinges building elements			cooling elements	tooling hosing multifunctional components
*OPEN SECTION	Cold drawn tubes	AA3103			radiators air conditioning systems fuel lines	air conditioning systems heating equipment	
*TUBE	Coldforged components from rod, tube and section	AA6351			steering column		
*HOLLOW SECTION	Hot forged components from rod	AA7075			air craft components		

ible incoming light, aluminum exposed to direct illumination will be extremely resistant to heating. This makes the material useful for structural purposes. If, however, aluminum attains higher temperatures elongation will be larger although thermal stresses will be smaller, a result of aluminum's higher thermal coefficient of elongation but lower elastic modulus. One of the appealing characteristics of many aluminum alloys is a high corrosion resistance.

Over the last 30 years questions have been raised as to whether the production of aluminum is in accordance with the principles of a sustainable development and related thinking. The major concern has been that although aluminum is the most common metal on earth, so called high-grade deposits of bauxite are to a certain extent limited. Another objection has been related to the large amounts of energy needed to produce primary aluminum. The aluminum industry has responded by developing LCAs and by modifying and improving the Bayer process so that it accepts bauxite that was formerly assessed as low-grade. However, it turns out that recycling of aluminum is a result of market mechanisms and the properties of aluminum and not of state legislation as is the case for plastic materials and to a certain extent steel [17]. The fact that a much larger amount of energy is needed to produce primary aluminum from raw material than secondary metal through remelting, makes efforts invested in recycling highly profitable. One is today talking about an aluminum bank, which exchanges metal with the market by selling finished products and buying scrap. A closed loop has long ago been established. At present, about 30% of the material going into new components is of secondary kind. The driving force in the material bank is of course energy, usually supplied by hydroelectric power plants. Had it not been for human interference aluminum in the form of pure metal would be non-existent in nature as the spontaneous process of oxidation through the times have degraded all material, leaving only Al_2O_3. Large amounts of energy are needed to extract metal from its oxide. Hence, aluminum metal might be looked upon as an energy investment. As questions are raised regarding the soundness of using energy producing metal one has to assess the alternatives, that is merely comparing energy investments. Much smaller energy investments are done when producing steel, but one might say that the oxide layer of aluminum represents a more secure bank than steel does. However, by employing light metals in, for instance, the transport sector one can obtain reductions in fuel consumption, which is the equivalent of being paid back on the initial energy investment. In structural applications the payback on the energy investment can not so easily be detected, but if the need for maintenance or use of materials can be reduced, energy is eventually saved. This analysis should be an integrated part of the LCA and product development process, and the designer should always ask whether energy can be gained by applying aluminum in a construction. In the aircraft industry a conclusion on this question was reached, if not formally, but at least intuitively, already in the 1920 by the construction of the world's first aluminum aircraft Ju-7. Today, airframes consist about 70–80% by weight of aluminum, of which a large part is in the form of profiles. In other parts of the transport industry demands for lightweight have until recently not been that strict, but as environmental issues are pressed and competition is increasing both with regard to prices and velocity, new materials and concepts are brought forward. Examples of just this are the employment of aluminum in high-speed

trains such as the French TGV duplex, the German Maglev system and the Japanese superconducting Maglev system. Changes are even taking place within shipping, which traditionally has been viewed as a notoriously conservative enterprise. Passenger transport have already for some time been carried out by aluminum-intensive fast ferries, and so-called high speed surface effect ships for transport of goods are also under development. As aluminum frames are being employed to a greater extent in both buses and commercial vehicles, the next breakthrough is expected to take place in the automotive industry. However, even though LCAs are performed in this industry, consumers still tend to look more at the initial cost than costs related to use. Hence, the lightweight solutions are not sought as vigorously as in the other branches of transport industry. New cars contain about 70 kg of aluminum parts, and smaller production series of more expensive cars have been made with so-called space-frames of aluminum. Such frames comprise the structural elements of the car.

In connection with material forming, one should notice that aluminum is unique in the sense that it can be extruded to a beam with a cross section of almost any form, open or hollow. Due to the large forces that are generated when extruding steel, geometrical forms must be kept simple and only smaller reductions in sizes of cross sections can be obtained. Another light metal, of which some use has been made in for instance the automotive industry, magnesium, is less extrudable due to its hexagonal close packed structure.

A world of new opportunities with regard to functionality and form arises when designing with aluminum profiles. In all there are very few limitations to the forms that can be produced by extrusion of aluminum, the largest problem being that variations in geometrical features are only two-dimensional in nature. However, beams may be given different lengths and profiles can also be altered by the processes of bending and hydroforming. Therefore, fully three-dimensional structures as the space-frame of a car or a window frame may be designed. The case in the following chapter gives an example of a simpler but successful design that managed not only to satisfy the original demands imposed on functionality, but also to incorporate other useful functions. This is a result of the freedom that aluminum, as a light metal, and extrusion, as a versatile process, offer. The most serious restrictions encountered in the design process, are caused by designer's experience with steel constructions. Steel products comparable to extruded profiles are manufactured in standardized forms and dimensions, and a steel design will often be an assembly of a series of such parts. Machining operations must be applied in order to impose modifications. Even though aluminum profiles of standard shapes are sold, it is usually better to think in terms of new profile designs better suited for the application. Extrusion tools are relatively cheap to produce. The prices of open dies can be expected to range from $1000 to $2000 while hollow dies will be more expensive, from $1500 to $4000. Tools for complicated profiles will naturally be manufactured at higher costs.

However, if profiles can be made so that machining, welding and assembly operations can be avoided, investments in dies may be worthwhile even for smaller production series. Hence, the development of tailor-made products may prove to be cheaper than mass production of standardized products with simple shape. This fact indicates that the extrusion process is well adapted to consumer's demands and their notion of quality.
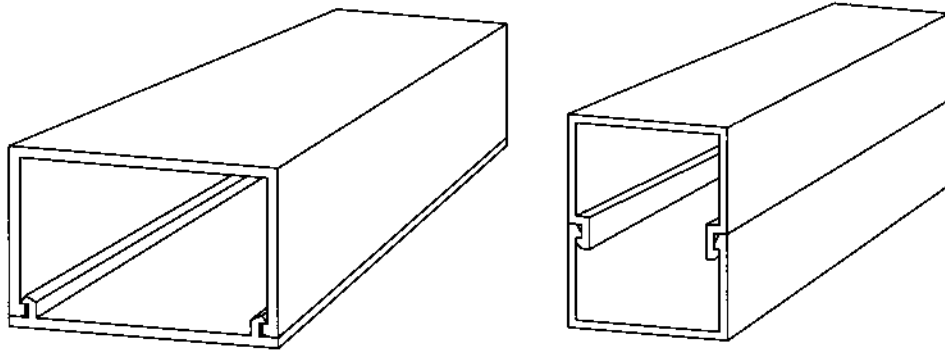
Figure 17 Joining of sections by the use of snap solutions.

As for functions that can be integrated in a profile, limitations are only imposed by the human imagination. An example of a function that is in common use is the locking mechanisms, which simplifies assembly and reduces the number of parts needed in the design. Generally, such a solution also reduces the cost of the product and is often necessary to secure competitiveness. Figure 17 displays examples of various locking devices. The basis for all these is aluminum relatively low modulus of elasticity.

Cast and extruded aluminum parts complement each other in most applications, but if both processing methods can be used to produce a part, extruded products are usually preferred. Tools needed for casting operations are more expensive than dies, and the production rates of the two processes are not comparable. This indicates that wherever possible, solutions including profiles should be sought. Another reason for choosing profiles to cast products is that wrought alloys usually have better mechanical properties than cast alloys. This is partly due to defects created during casting and partly to the fact that cast alloys contains large amounts of silicon and copper, which cause a heterogeneous structure with brittle secondary faces. In general cast alloys have lower elongation and strength, especially in fatigue. The progress in improving casting alloys and controlling the casting process in the recent years, however, has been impressive, both for aluminum and magnesium alloys, as well as for steel. The designer should therefore take care to make process selection based on the present state of the art.

Alloy development is the subject of continuous research. By systematically varying the content of different alloying elements improvements in properties such as tensile strength, ductility, fracture strength, fatigue strength, corrosion resistance and formability are sought. At present about 350 wrought alloys are commercially available, but not all of these are interesting from a designer's point of view. While the aluminum industry must continuously seek alloys with improved properties, the designer should concentrate on a group of so-called generic alloys. On Table 6 an overview of extrusion based systems, components and the generic alloy selection for the different applications areas is given. A generic alloy selection is taken to be an alloy, which is generally used for the specific application, is available in most markets and has properties that can be expected to be thoroughly documented. It should be the alloy preferred by the designer, and the choice should only be changed if special

combinations of properties, not found in the generic alloys, are needed. It is important to contact potential suppliers of the section to ensure that the alternative alloy is available to acceptable price and with properties documented. When choosing particular alloys one must also remember that an alloy, which is optimal with regard to all properties, does not exist. Alloys with high yield and tensile strengths are usually harder to extrude, thus resulting in lower production rates (Fig. 18), higher prices and limitations on product geometry. Thin-walled sections of high strength material are for instance not extruded easily. Some alloys are also in possession of relatively low corrosion resistance even though mechanical strength may be high. The group of generic alloys should contain elements that can be used for most applications.

Profiles containing precipitation hardening alloys are relatively easily formed, but gain high strength after heat treatment. This explains why about 80% of all extruded products are made of the 6XXX-series of alloys. Members of this group can gain from medium to high strengths. High extrusion speeds and very high productivity can be obtained when extruding the alloys with medium strength. 6XXX-alloys are generally relatively corrosion resistant, but this property is both dependent on the chemical composition and the thermal treatment the material has undergone. While the alloy 6060 contains limited amounts of magnesium and silicon and is of only medium strength, tensile strength the high alloy metal 6082 has a tensile strength of about 340 MPa at room temperature in the T6-condition.

For sections that are not carrying loads the 6XXX-series is the natural choice. In such cases even the 3XXX and 1XXX may be applied as these alloys are in possession of superior corrosion and conduction properties. If a product is designed to carry loads, different 6XXX-alloys may still represent alternatives, but one should
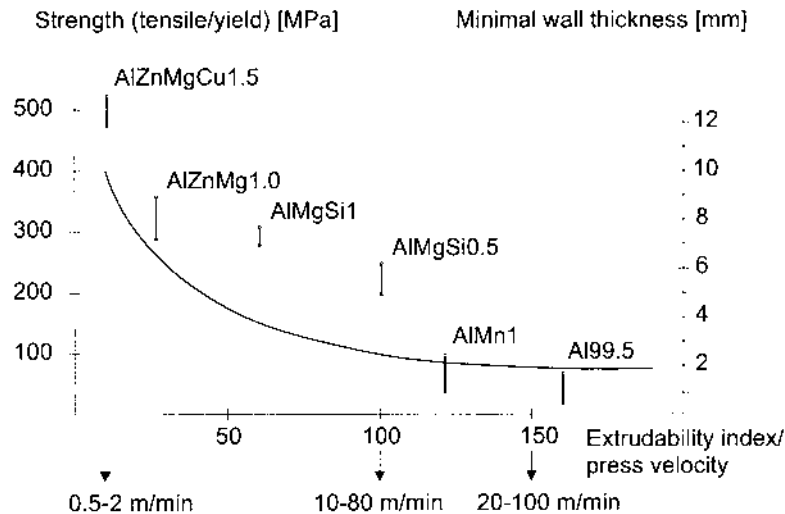
Figure 18 Relation between material strength, minimum wall thickness and extrudability/press velocity. The results apply only to a section with a specific geometry, but similar curves may be established for all profiles.

always evaluate whether it is profitable to reduce weight by using alloys of higher strength. It has been found that both in structural applications and in many areas of transport designing with the 6XXX-series is most rational due to the low cost of extrusion. In some branches of transportation such as aviation and of course space flight the use of material with the highest strengths is mandatory. Production costs connected to extrusion will be substantial, but by decreasing weight or increasing the load capacity these expenses are soon covered.

The strengthening mechanism of the 7XXX-series is also precipitation hardening, and as for load capacity and strength these alloys represent the next step on the ladder. In aerospace construction 7075 is a preferred alloy. The automotive industry has also made use of several of the 7XXX-alloys. However, the fact that dies will experience more wear and that extrusion rates will be lower for higher strength metals applies also to this group and is limiting its usefulness in most applications. The low extrusion rates will not only be a result of the material's higher flow resistance, but also of a somewhat lower melting point of some phases. Besides, if the quench rate after extrusion is low, corrosion resistance will generally be unsatisfactory. Larger contents of copper are causing the high strength/low extrudability as well as the degraded corrosion properties.

The 2XXX-series has traditionally also been used in aerospace construction and shows extremely good damage tolerance. It has both high fracture toughness and high resistance to fatigue crack propagation. As the 2XXX-alloys contain much copper, they tend to show low corrosion resistance. Important alloys are the 2X24 [18] and the 2X19. The 2020 and 2090 alloys are so-called lithium alloys. For every weight percent of lithium added, the elastic modulus of the material is increased by 6% and the density lowered 3%. Hence, very stiff and light aluminum constructions can be developed by the application of lithium alloys. Use has been made of such materials both in fighter aircraft and space shuttles, but only to a limited extent in commercial aircraft. Another important property of the 2XXX-series is that high strength can be obtained at relatively high temperatures. This, however, complicates extrusion, and products made of 2XXX-alloys are today mainly manufactured in other forming processes.

3.3 Limitations on Section Design

Even though one should focus on possibilities when designing with extruded profiles, one is sooner or later bound to encounter the limitations that the process imposes. Evidently these limits are dependent on both the process equipment and practice and on the choice of material. If the process is not properly controlled or the design and choice of material is not in accordance with the choice of process, poor product quality will unavoidably be the final result. In the last part of the second section of this chapter some of the symptoms of low product quality were discussed, and their cause has and will be further discussed. Suppliers of extruded profiles have established general design rules, which can be used to secure that a design is in harmony with the process. Some of these are general in character, while other are referring to specific dimensions and are necessarily dependent both on material and process equipment. However, apart from restrictions on the size of the largest sections produced, there are seldom any absolute limitations. Very few profiles may prove to be impossible to manufacture, but there is always the danger that

the quality or the price of the product may be unsatisfactory to the consumer. In order to develop a quality product, the designer must try reach production friendly solutions through discussions with experienced people at an extrusion plant.

If full freedom in designing a functional product is to be obtained, no limitations should be placed on form. However, as will be understood from a study of flow patterns, a key word in relation to the process of extrusion is symmetry. Asymmetric profiles cause flow imbalance and necessitate complicated die design. Flow velocity in the cross-section must be controlled, and this often leads to low extrusion rates. Furthermore, as dies may experience uneven loading, there is an increased danger of fracture and unstable tools, especially when extruding higher strength alloys. Asymmetric profiles may also cause thermal gradients in both die and profile during cooling. Hence, not all parts of the profile will be given the same thermomechanical treatment, and the result of this is a loss of control with metallurgical processes in a product with large variation in both microstructure and properties. A last problem connected to asymmetric profiles is that possible bending and stretching operations may be more complicated to perform. Examples of deviations from symmetry are given in Fig. 19. The mass distribution over the profile cross section should not be uneven. Large ratios between the thickest and thinnest walls in a profile may also be difficult to handle, and large eccentric hollows also cause an unwanted flow pattern.

Naturally strict limitations exist with regard to the size of the profile, and specific numerical values must be sought from the producer. If the profile has a too large circumference circle diameter, that is the smallest circle surrounding the profile, problems connected to inflow of material from the billet surface may arise. Furthermore, extrusion of large profiles is often synonymous with very open die designs, which usually are weakly supported, and in the case of hollow profiles, larger forces on the mandrel of the die are generated. The result will be larger dimensional variations and also poorer surface quality due to either die lines or streaking. On the other hand profiles with too small dimensions give larger press ratios. In this case the press may not be able to supply the needed force to generate the profile. The solution is then often to press several strands simultaneously in order to increase productivity (Fig. 5).

Simplicity is another key word in almost all areas of production. This certainly also applies to the extrusion process even though its largest virtue maybe the complex profiles it offers. Both hollow profiles and profiles with large tongues tend to increase the complexity of the production, and thus should in fact be avoided if possible. Dies, which are made for such profiles, are more complex and necessarily also more expensive. However, the largest problem is that they tend to generate larger forces due to the restrictions they impose on flow, and that at the same time their weaker design gives them a lower load capacity. Die breakage and large deflections are usually the results. Dimensional variability and poor surface quality can usually be expected in such cases. The solution may often be that tongues are made with smaller length to width ratios so that they can be properly supported and that hollow profiles are made as two open sections, which later can be assembled.

A lot of special forms and features are usually included in the extruded profile so that the product is able to perform a large number of functions. However, the addition of even small attributes may lead to large changes in both productivity and product quality, and one should always assess whether a feature is necessary

Long thin detail in a hollow   Long thin part of a profile   Tongue

Excentric hollow

Thin internal wall

Uneven distribution   Interior detail   Sudden step in   Sharp
of material   without a purpose   wall thickness   corners
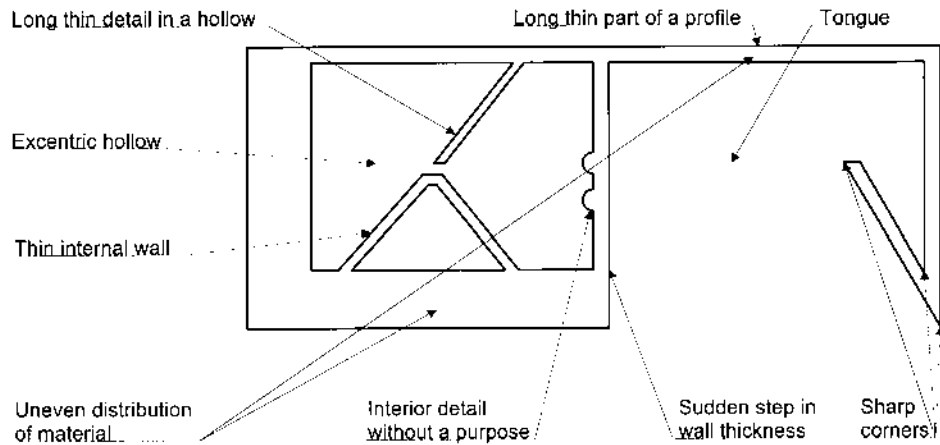
Figure 19   An extruded profile with a complex geometry.

and whether it could be made in a more process friendly manner. Examples of features that are difficult to handle are:

- Sharp corners may in some cases cause incomplete filling and in others tearing (Fig. 19). Besides, crack initiation and growth usually takes place in the parts of the die where sharp angles exist. Hence corners should always be rounded. The smallest radiuses that should be used are around 0.4–1.0 mm. Only for special purposes may a radius of 0.2 mm be applied.
- Sudden steps in wall thickness and thus also the bearing lengths of the die should be avoided (Fig. 19). Two related types of flow problems will be the result of such changes. On the one hand, complete filling of the sharp corners around steps in wall thickness will be hard to perform if bearings are not carefully designed. On the other hand, streaking may be the result of microstructural differences caused by the abrupt change in the conditions of deformation and cooling from areas of large to small thickness. The solution to this problem is a gradual change from thicker to thinner regions. If this proves impossible, the streaking can be made less appalling simply by constructing a notch that may mark a natural border between thicker and thinner regions. However, this does nothing to decrease the problems connected to varying mechanical properties, and may in turn cause a larger flow resistance.
- At a certain point extrusion of thin-walled parts will always represent a problem. For such parts friction forces are high, and flow speed is hard to control. The result may be incomplete filling of some parts of the cross-section and of course a need for greater extrusion force. If internal walls are too thin (Fig. 19), complete filling is even harder to obtain, and pressures in the welding chamber may not be sufficiently high to secure a proper weld. Weak or non-existent seam welds are both disastrous to profile quality and hard to detect. Hence, internal thin walls should be avoided. Often it may be better to use larger wall thickness to secure filling

even though material cost increases. Another problem with internal walls is that the whole die concept becomes weaker and that there is a greater danger of die breakage.

- Details generally cause problems connected to flow balance and friction heating, and as a result, production rates are limited (Fig. 19). Furthermore, tearing of the surface and incomplete filling may be additional problems. Details that do not fill any functional purpose should therefore not be added to a profile. Obviously, one should try to design details sufficiently thick and not to long. At the same time corners must be rounded. One also ought to bear in mind that internal details are usually more problematic than external.

Apart from these limitations on form connected to the process, there are a lot of others that are related to the use of the product. One such may for instance be that corrosion should be prevented by avoiding geometry that can lead to the gathering of water in the profile. Whereas designers who are not accustomed to working with aluminum profiles, easily may overlook one of the many restrictions imposed by both process and material aspects, the experienced ones will develop a product which integrates most of the aspects previously mentioned. However, to all designers, the establishment of a method of design that systematically incorporates the treatment of all aspects of importance, is a necessity when applying aluminum for constructional purposes.

3.4 Case: Helicopter Landing Deck on Offshore Platform

Usually aluminum profiles are most competitive in applications where they must be designed to fulfil many functions at the same time. Helicopter decks on offshore platforms is such an application. On platforms, such as the tension leg platform, Snorre, in the North Sea, weight aspects are often critical. Furthermore, the corrosion properties of the material must be outstanding, as weather conditions are often very harsh. Originally, helicopter decks were made out of steel plates that were welded together and supported by traditional steel beams, but the solution was by far optimal. The construction has gradually been modified, and the aluminum deck in use today is about 60% lighter than the original one. By using profiles, large design flexibility has also been obtained, and many more functions have been implemented in the construction. It was expected that the surface construction of the helicopter deck should perform the following functions:

- Carry structural loads
- Carry concentrated loads
- Carry torsion loads
- Be simple to assemble
- Prevent slipping
- Lead away petrol and rain water
- Allow circulation of air in order to prevent crevice corrosion
- Lead fire extinguisher fluid
- Lead deicing cables

Demands were that the helicopter deck had to be designed so that it could easily be fitted to the platform, and that it was constructed in accordance with regulations and standards. Evaluation criteria would be related to the weight and the strength of the construction and to corrosion properties. Furthermore, as almost always, the product had to be evaluated on the basis of life cycle cost.

The original steel construction did not have the desired functionality, but it was able to carry the specified loads. Hence, when the first modifications in aluminum were made, the design was not altered but dimensions were changed to suit the properties of aluminum better. Of course modifications to dimensions can be done in a number of ways. If the length of the rung is kept constant the thickness of the profile may be increased about three times, resulting in a profile of the same weight and only marginally increased stiffness. A simple calculation can be made to show the effect of a uniform thickening of the whole profile. The geometry is shown in Fig. 20. The moment of inertia can be calculated to be:

$$I_x = \frac{1}{12}((8h_1^3 + 12h_1^2h_2 + 6h_1h_2^2) \times w_1 - h_2^3w_2) \tag{1}$$

For the steel beam both h_1 and w_2 can be set to t, and h_2 and w_1 to l. This gives a moment of inertia equal to:

$$I_x^S = \frac{1}{12}(5tl^3 + 12t^2l^2 + 8t^3l) \tag{2}$$

Since the density of aluminum is about $1/3$ that of steel the dimensions h_1 and w_2 may
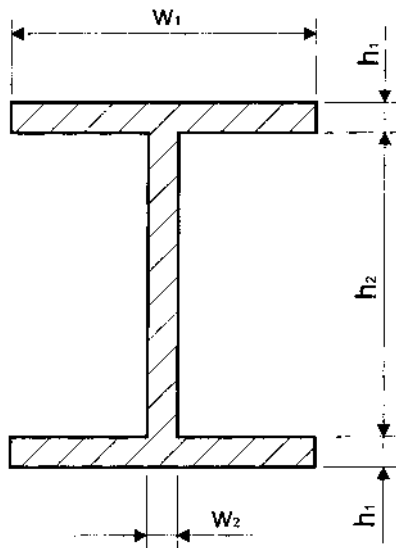
Figure 20 Simple I-beam originally in use in helicopter decks and manufactured through the processes of rolling and welding.

be set to $3t$. This gives a moment of inertia of:

$$I_x^A = \frac{1}{12}(15tl^3 + 108t^2l^2 + 216t^3l) \tag{3}$$

The stiffnesses that are obtained for steel and aluminum are respectively:

$$W_x^S = \frac{E}{12}(15tl^3 + 36t^2l^2 + 24t^3l) \tag{4}$$

$$W_x^A = \frac{E}{12}(15tl^3 + 108t^2l^2 + 216t^3l) \tag{5}$$

E represents the elastic modulus of aluminum. Since l is much greater than t the first term will be dominant, and it can be seen that no large gains can be achieved by using aluminum in this way. However, a much larger increase in stiffness can be obtained if the rungs are made slimmer and taller and the flanges are designed thicker. If for instance h_2 and b_1 are set to $3l$ while the thickness of both flanges, and if the rungs keep the thickness t, the profile can gain a stiffness of:

$$W_x^A = \frac{E}{12}(135tl^3 + 108t^2l^2 + 24t^3l) \tag{6}$$

Clearly, by intelligent design bending stiffness may be increased enormously. However, the calculations just made are extreme cases. Problems would arise if the last cross-section were to be used, both because the flanges could not carry the possible concentrated forces and because rotations due to torsion of such a section would be large. The torsion momentum would depend on the thickness of the section in the third power. The torsion stiffness of the original steel section will be about one third of that of the extreme aluminum section. The aluminum profile, however, will be more severely loaded due to the long flanges and rungs. The optimal cross section of the type given in Fig. 20 could be reached by maximizing both bending and torsion stiffness with respect to the different measures. Such an analysis reveals that the use of aluminum profiles generally is preferable to the use of steel. However, when constructing with profiles even larger gains in torsion stiffness can be made by applying hollow profiles. By turning to extruded profiles much freedom in functionality can be obtained, and a positive side effect of this is that the profile may be given such a form that all the desired functions mentioned above can be fulfilled. Different stages in the development process are shown in Fig. 21. The same figure shows the aluminum profile which is currently in use in platform decks in the North Sea.

4   THE EXTRUSION PROCESS

4.1   Describing the Conditions of Flow

Traditionally, advances in extrusion technology have come as a result of experimenting. In fact, as the process has until recently been viewed as too complex to be understood in its entirety, the key to success in the extrusion business has been the establishment of a system of best practice based on experience gained through
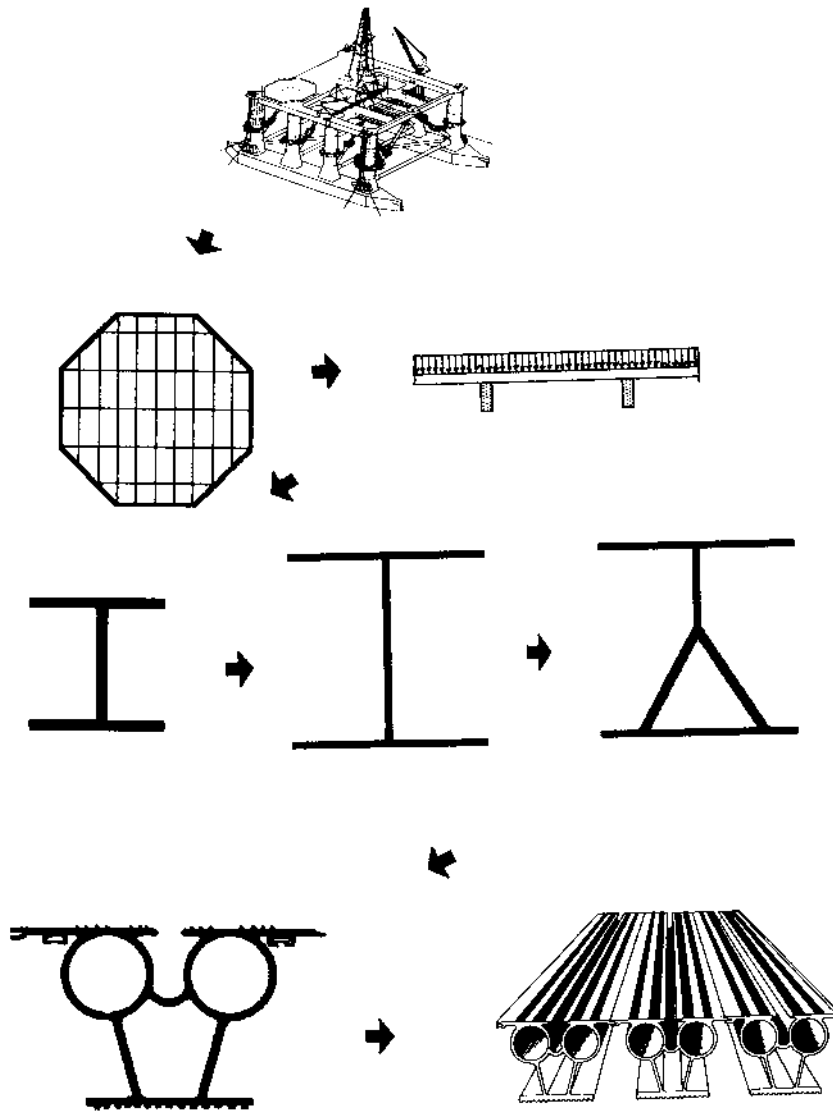
Figure 21   The profile development process and the profile in use today.

trial and error. Experiments are still expected to be an important element in establishing knowledge of fundamental aspects, and due to the large amount of noise in data received from extrusion presses, one can hardly expect to avoid errors, from which insight should be gained. However, the impetus for discovering and improving methods for predicting results a priori is large. Experiments are usually expensive and time-consuming, and practices such as die correction, which even to this day to a large extent is based on the experience of the workman, will most probably neither satisfy demands to productivity nor quality in terms of for instance dimensional variability. Hence, research is today focused on the development of

mathematical methods that are able to describe and thereby also predict both the macroscopic and microscopic changes taking place during deformation. In this way the manufacture of dies and the control of process parameters can be performed in such a manner that profiles will be produced within the narrowest tolerances and to a low cost. As extrusion is a process taking place in the presence of large deformations and at relatively high temperatures an establishment of such a mathematical fundament is both a complicated and to a large extent a multidisciplinary task. A unified approach must link knowledge of metallurgical processes at high temperatures and strain rates with the continuum theories of rheology [19] or plasticity. Furthermore, as analytical results can hardly be obtained, the development of effective numerical procedures will be of greatest importance. Naturally, a thorough understanding and experience with all aspects of the process will also be a prerequisite for establishing a model.

4.1.1 Experimental Studies of Flow

Hot extrusion of aluminum is performed at temperatures from about $450°C$ to something above $600°C$, depending on the melting point of the alloy. At these temperatures the material has a relatively low resistance against dislocation movement, and shear deformation will therefore be initiated when the extrusion force reaches a certain limit. The material then starts flowing out of the die and will permanently change shape. If homogenous deformation had taken place, the longitudinal logarithmic strain would be equal to In (R). Strains of magnitude $\varepsilon_z = 4$ are therefore not unusual as profiles quite commonly are extruded with reduction ratios of 50 and above. In fact, strains may locally be much larger than this value as the deformation during extrusion is extremely inhomogeneous due to extensive shearing. During extrusion aluminum has the characteristics of a viscoplastic fluid, which start to flow when the stress reaches the yield limit, and the extrusion process itself will in principle be a forced unsteady flow through a reduction. Macroscopically, the flow field will be characterized by the local velocities, temperatures and stresses, for which values can be measured at the boundary between aluminum and container/die.

The velocity field describes the particle velocities at all points in the container and bearing channel and, therefore, also the flow at all times. The rates of strain and rotation of particles may be of larger interest in the study of changes to microstructure during extrusion, but these quantities can be derived directly from the velocity field. However, due to the high pressure and temperature in the container, flow rates are extremely difficult to measure. Conventional flow meters are generally not constructed for the relevant conditions. Furthermore, the velocity field may be expected to be relatively complex and inhomogeneous, especially if complicated profiles are extruded. A few measuring points at the boundary would therefore not reveal all the characteristics of the flow. Only when the material leaves the die, can particle velocities be measured directly and easily. The flow velocity ought then to be approximately uniform across the profile cross-section, directed normal to the opening and of a magnitude equal to the reduction rate times the velocity of the stem.

As hot aluminum behaves viscoplastically, the material will stop flowing when the extrusion force is relaxed so that stresses fall below yield. This property is important because information about the total deformation of the material will be saved in its structure after extrusion. This is not the case for perfect fluids such as for instance

water, for which the measurement of total strains is of both minimal interest and impossible as the material deforms also when forces are removed. In order to establish the deformation history during extrusion, one performs a number of tests which may be interrupted at various stroke lengths. This will provide information on the total deformation at different stages. If the velocity of the stem is known, the approximate flow rate and strain rate at each point may also be calculated. There are a number of variations of this technique, which bears the name viscoplasticity. Model materials such as wax, clay, plasticine or even lead have earlier been used extensively when simulating extrusion of aluminum [20]. The billets are first parted, and a rectangular grid is applied on the surfaces of each half. The two parts are thereafter extruded together, and the distortion of the grid is in the end studied. The changes in geometry can be used directly to calculate strains and rotations. The use of model material is advantageous in that extrusion can be performed with a low force and that both the equipment and the model material are relatively cheap. There are, however, also a number of short-comings connected to such a use. It is always difficult to be certain that the material models the aluminum correctly, especially since temperature effects, which are totally neglected when using model materials, are known to be of large importance to the flow characteristics of aluminum. Furthermore, model materials are also susceptible to plastic deformation during post-extrusion treatment.

The interest in model materials has over the last years fallen, as modeling of extrusion process has increasingly become the realm of finite element programs. However, the method described above may also be applied to the extrusion of aluminum as shown in Fig. 22. The unmodified version of the technique works well for reduction ratios up to about 3, but at this point the material is so deformed that the grid may be erased locally, especially in shear zones. Valberg [21–24] has developed an alternative method, which can be applied when extruding at much larger ratios. Some alloys of aluminum share mechanical properties even though their composition may differ. This is the case for a number of AlMgSi and AlCu alloys, the
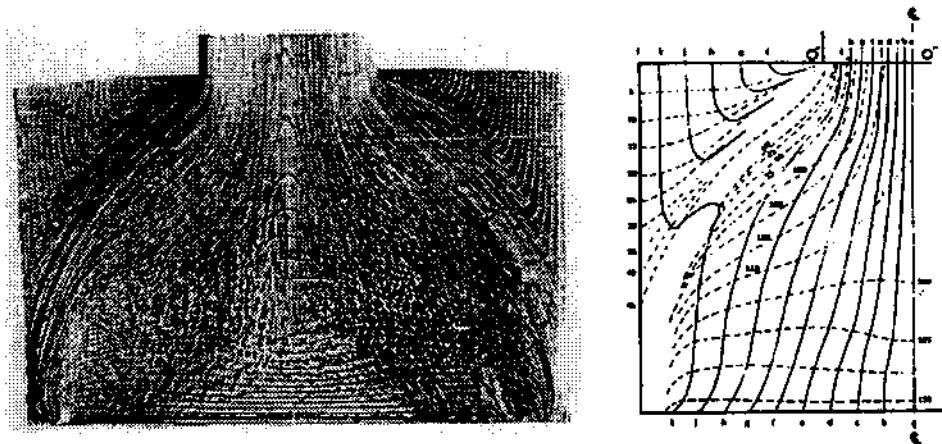
Figure 22   The split billet technique applied on the extrusion of aluminum. The partial extrusion of a billet at a reduction ratio of about $R=2$ is shown.

first group remaining gray, the second turning black when etched. Thus, the AlCu alloy may therefore work as a so-called indicator or marker material. By drilling evenly separated longitudinal and transversal holes in different parts of a plane of symmetry and inserting pins of indicator material, a grid is formed (Fig. 23). A certain portion of the billet is then extruded, and the aluminum is carefully removed from the container and die. By splitting the billet and profile along the axis of symmetry, grinding and etching, the deformation of the material is made visible (Fig. 24). A grid pattern may then be reproduced. By this technique metal flow may be investigated up to logarithmic strains of about $\varepsilon = 10$.

The marker material technique has been applied in the study of porthole die extrusion [25], two-hole die extrusion [26], flow adjacent to bearing walls [27,28] and with a 3D-version [29] also in the study of more general flow patterns. However, the most easily analyzable results are provided by simple axisymmetric extrusion, which also has been the standard test case for earlier techniques. General theory connected to direct extrusion describes four categories of flow in the container (Fig. 25(a)). These differ due to varying degrees of friction between metal flow and container walls. Only flow type B is of interest in the study of aluminum extrusion, the reason being that the other types either underestimate the influence of friction or assume inhomogeneous material behavior. After in depth study of flow patterns during both direct and indirect extrusion, Valberg [30] has proposed two new general flow patterns more in accordance with observations, flow types A_1 and B_1. Figure 25(b) shows a typical grid on a partially extruded billet at various stroke lengths.
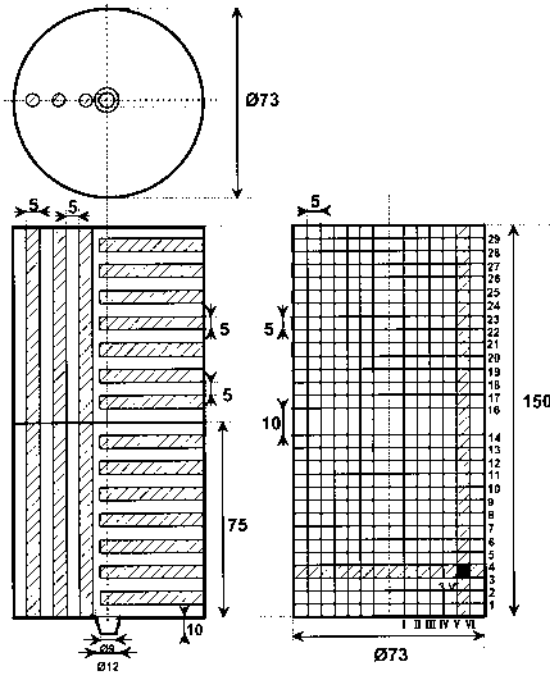
Figure 23   The preparation of gridded billets in accordance with Valberg's technique.
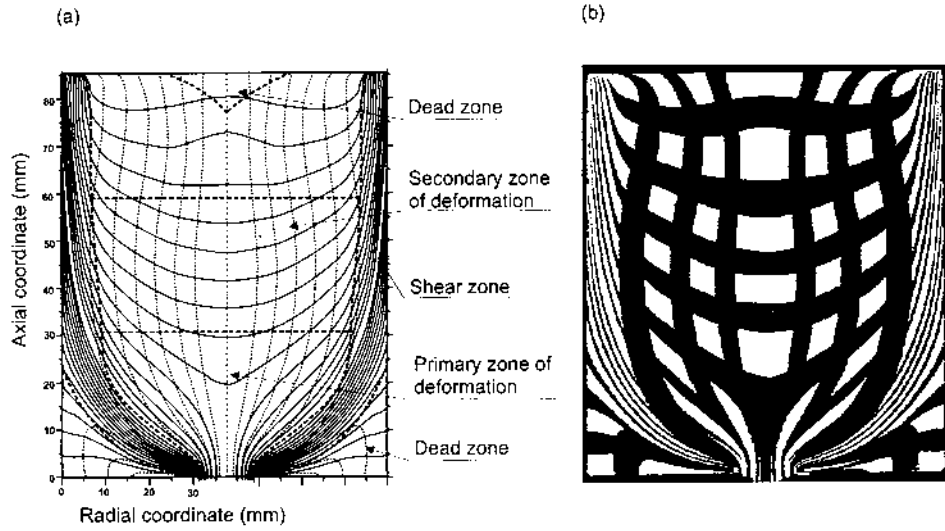
Figure 24 Determination pattern in a partially extruded billet. (a) Reconstructed deformation field; (b) The original patterns on the partially extruded billet.
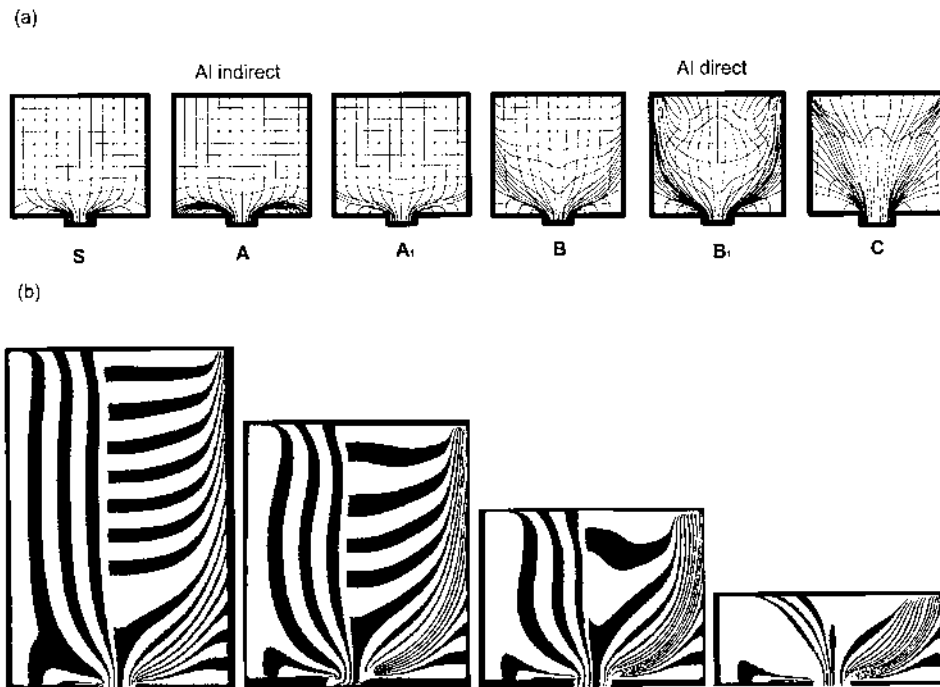
Figure 25 (a) Classes of flow patterns during axisymmetric extrusion according to Pearson, Dürrschnabel and Valberg; (b) Experimentally determined flow pattern for direct extrusion of aluminum at various stroke lengths.

When studying such grids one must bear in mind that the extrusion process is transient in its nature and that the deformation paths will change during extrusion. Whereas the initial deformation may be relatively homogeneous, deformation will in later periods be characterized by localized shearing. In the very end the direction of flow will even change as the material starts flowing in the radial direction towards the die opening. Figure 24(b) represents material flow at an early part of an intermediate period of almost steady state and reveals that the flow pattern will be strongly influenced by shearing towards the container walls. Hence, deformation can be viewed as inhomogeneous, and a number of distinct regions may be identified. The one closest to both the centerline and die opening is called the primary zone of deformation, and in this the material necessarily has to undergo relatively large deformations as it enters the bearing channel. In the secondary zone of deformation only a relatively small distortion of the grid may be observed, and friction between the stem and the aluminum will in fact even prevent deformation in the uppermost part, creating a zone of minimal deformation, a dead zone [31]. The zone of intense shear will stretch from the die opening and to the stem. This deformation mode is caused by the condition of full sticking of material particles to the container wall. In the corner close to the die surface the sticking condition will immobilize the material, and another dead zone, bordering to the area of shear, will be formed.

   Experiments reveal that the flow pattern in the container will actually depend on temperature conditions. If the container is relatively hot, the material in the outer part of the billet will be more mobile due to lower material resistance to flow. As a result the aluminum may no longer stick perfectly to the container wall and inflow of surface material may either take place along the surface of the stem or directly through the shear zone and into the die opening. This is an unwanted effect since the surface material usually contains impurities and defects caused by rough handling of billets or inverse segregation. The flow pattern will also change due to geometrical variations. A small reduction ratio will for instance yield a smaller dead zone close to the die, and the result may also then be that material flows directly from the billet surface and out into the die opening.

   A study of the deformed grid in the profile after a complete extrusion charge reveals that extruded products are far from homogeneous with respect to the deformation undergone. Figure 26 is a representation of such a grid where the longitudinal axis is scaled down. The first material leaving the die opening will have undergone a relatively small degree of deformation, but as extrusion proceeds, the material in the profile will have been deformed while passing through at least a part of the primary deformation zone. Region 2 is characterized by a grid that is very homogeneous, indicating that material particles originally coming from the secondary deformation zone have undergone almost the same deformation history. Hence, when extruding this material the process will resemble one of steady state. Region 3, however, is constituted of the material that was hindered from deforming by the stem during the extrusion charge, and the degree of deformation can therefore be expected to be much smaller. A layer of heavily shear deformed material will exist closest to the profile surface [32]. The growth of this layer towards the end of the profile indicate that the shear zone in the billet gradually will flow out of the container as the stem is brought closer to the die. In order to find how the container is emptied during extrusion, Valberg has developed so-called emptying-diagrams. These consist of lines, on which all particles will need the same
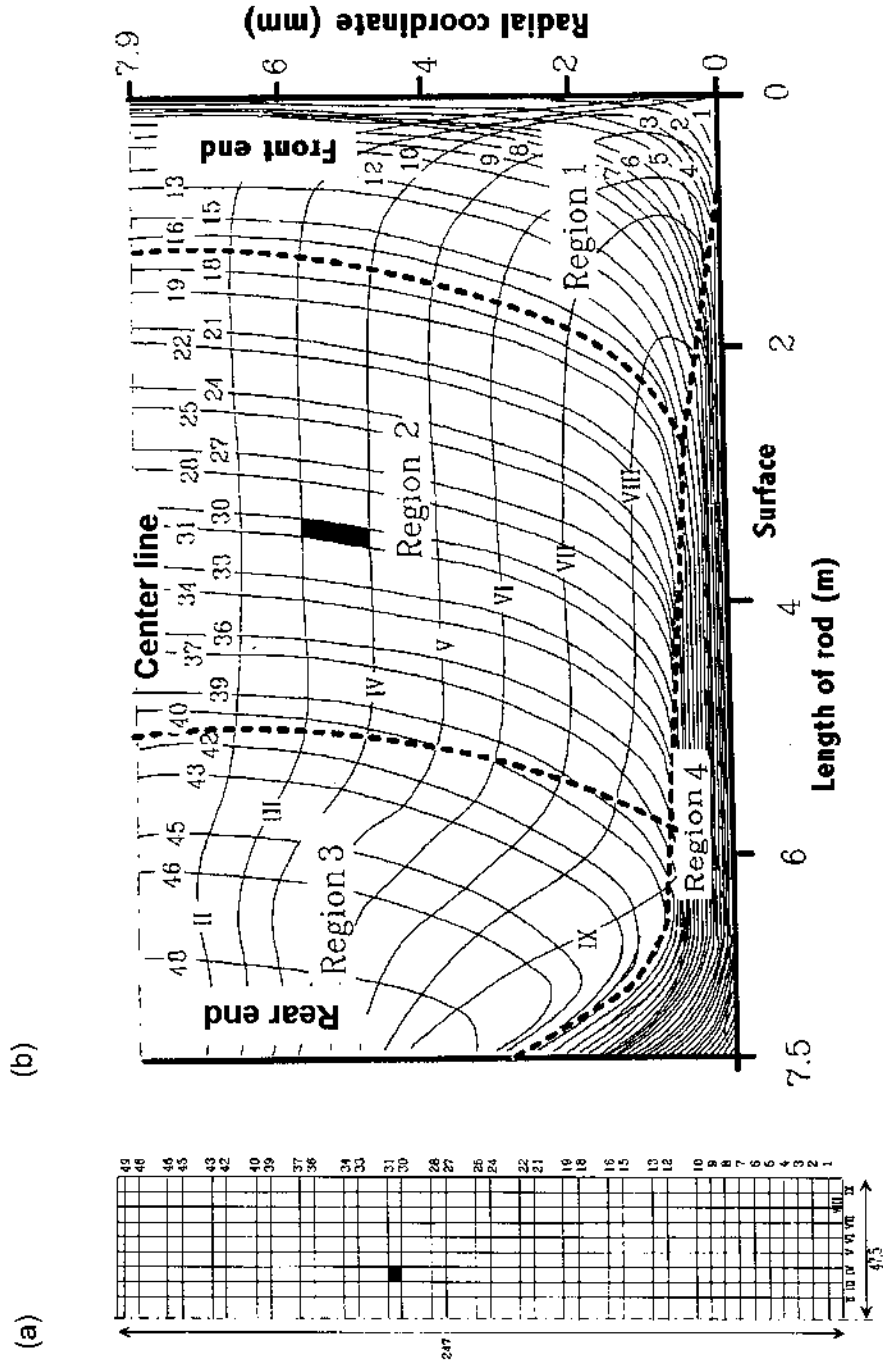
Figure 26 (a) Original grid on an axisymmetric billet; (b) Deformed grid on an axisymmetric profile (Valberg-plot). The longitudinal axis is scaled down.
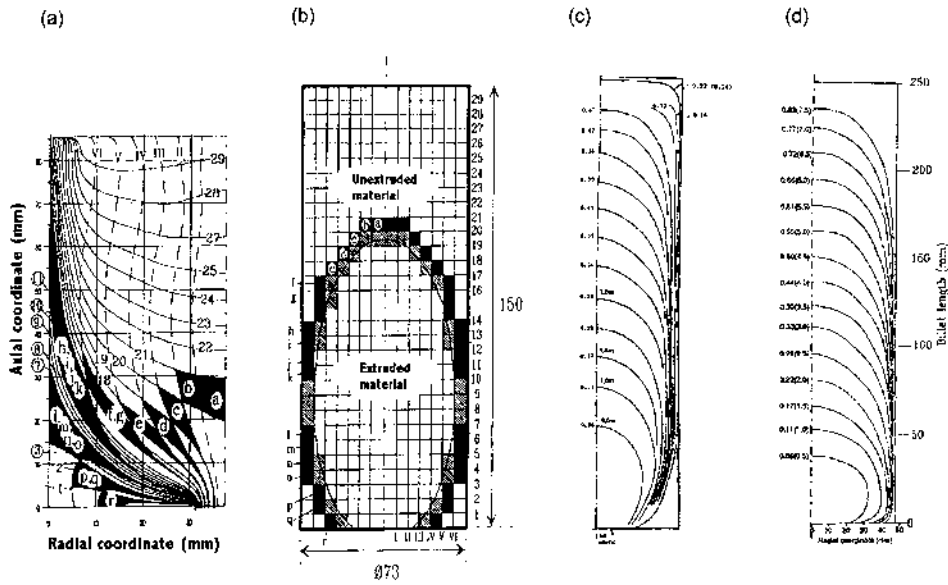
Figure 27 Emptying diagrams for axisymmetric extrusion. (a) and (b) Determination of one iso-residence-time curve; (c) and (d) Complete diagrams for respectively direct and indirect extrusion.

amount of time to reach the exit. Hence, the lines are denoted iso-residence-time lines. They are constructed by placing a grid over the extruded profile, finding the crossing points with the deformed grid of the marking material and then tracing these points back to the corresponding undeformed grid in the billet. In Fig. 27(c), a number of such lines are shown. As expected, the bulk of the dead zone close to the die will not flow into the die opening until the very end of the charge. During the whole extrusion process, however, parts of the shear zone will be transported out into the profile, and the dead zone will gradually be reduced in size. Figure 27(a) and (b) also reveals that the surface layer of the profile will be generated from the material in the shear zone of the billet.

The observation that the size of the dead zone varies during an extrusion charge is extremely important to the understanding of the extrusion process as a whole. Energetically the process of extrusion through flat dies seem favorable to that through tapered dies, as the metal is allowed to find the most optimal flow path by varying the inclination of the shear zone through the charge. However, as the flow pattern is unsteady, the properties of the product will necessarily also vary along its length. One of the objectives with using feeders such as that shown in Fig. 28, is to stabilize the conditions at the inlet to the bearing channel. In this way deformation paths for particles in the back and in the front of the billet will be more equal. Other reasons for applying feeders, however, are usually viewed as more important. As the metal in the feeder is not removed when the butt of the billet is cut, one may weld metal from two charges together and almost extrude continuously. The advantage of applying a feeder is then that production rates will be increased. The drawback is that the charge weld formed most probably will con-
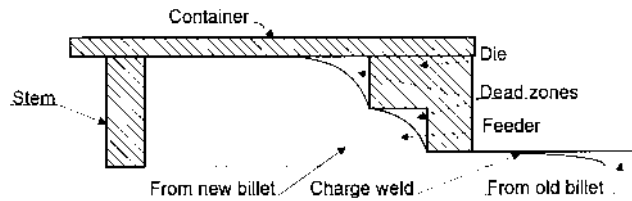
Figure 28   A schematic example of direct extrusion with a feeder.

tain inclusions of oxides and therefore have inferior mechanical and corrosion properties. As charge welds under the influence of varying material velocity over the profile cross section will become a parabolic line extending often many meters along the its length, low weld quality may lead to extensive scrapping.

4.1.2 Temperature and Metallurgy

Variations in temperatures during extrusion seem to influence flow behavior in a number of ways. As indicated, flow patterns may be changed considerably by rendering the temperature distribution in the container. Furthermore, it is known that the extrusion pressure may be lowered if either the temperature of the billet or the velocity of the stem is increased, and that there are certain limitations, since the material starts melting or cracking if it leaves the die with a too high temperature. The observations indicate that there is a strong coupling between what would be regarded as thermal and mechanical effects [33]. In order to describe the temperature field during extrusion, a system for measuring temperature at surface between the flowing alloy and tooling has been developed by Lefstad [34,35]. The method has its limitations since it does not reveal the complete temperature field, but it is well suited for studying the temperature of the flowing metal on the bearing surfaces close to the outlet. Due to frictional forces the temperature can be expected to be highest in this part of the flow.

   In principle, all the effects witnessed on a macroscopic level could be explained with an atomistic perspective. The close coupling between the temperature field and the mechanical forces are simply due to the exchange of kinetic and potential energy of the atoms. Today some phenomena such as frictional behavior and dislocation movement are explained partly with such a perspective [36], but no complete atomistic description of the extrusion process can be found in literature. There are presently no ways of performing satisfactory measurements on flow, and the modeling methods are not able to handle the complexity of the problem. Hence, simplifications are sought. As will be explained in the next section, modeling is today primarily performed with the thermo-mechanical continuum theory. This is, however, merely a mathematical tool, which can be used to quantify states of deformation and pressures, and it will not reveal any new fundamental mechanisms. The problems of extrusion, related to speed limits, flow resistance, evolution of microstructure, stability of flow, surface quality and so forth are generally of metallurgical and micro-structural origins. Furthermore, since the flow- and temperature fields are influenced by the flow-resistance of the hot metal, which is strongly dependent on the alloy constituents, microstructure and metallurgical state

of the deforming material, there is a strong interaction between flow, temperature and micro-structural evolution. If the continuum theory shall be able to model and quantify such phenomena properly, one must be able to relate the parameters of the model to the thermodynamics and kinetics of the material. An example of such is the description of recrystallization, of whose degree is influenced by such factors as temperature, time and deformation [37,38]. When extruded under similar conditions, different alloys need not experience the same amount of recrystallization. If quantitative description of the degree of deformation is to be given by a continuum model, the rate of recrystallization must be related to the values of deformation provided by a mathematical calculation as well as the constitution of the alloy. In the present state of the art of extrusion technology, the continuum description of thin-walled extrusion has not yet reached the point where the metallurgical phenomena can be explained quantitatively based on the continuum-mechanical description of the flow- and temperature field.

An important fact that is often forgotten is that the complete thermo-mechanical history of the material should be known if one is to assess the microstructure. Focus should not only be placed on the mere extrusion charge, but on all the process steps. A study of the influence of Mg_2Si particles on the maximal allowed extrusion speed gives an example of this [39,40]. The example applies probably to most 6XXX-alloys and in fact also to some of the 7XXX-series. The billet is prepared for extrusion after casting by homogenizing, controlled cooling after homogenizing and preheating before extrusion. Based on the chemical constituents of the alloy (Fig. 29(a)), given here for an AA6060-alloy (also showing AA6082 for comparison) with equilibrium-diagram (Fig. 29(b)), the initial temperature distribution in the billet at the starting point of extrusion should be such that the magnesium and silicon are completely in solid solution before the alloy leaves the die. At the same time the extrusion speed should be selected in order to give shortest possible press-cycle time without causing overheating or unacceptable risk for production stops and/or quality problems. If there is eutectic left with melting point at 585°C (Fig. 29(d)), then this will be the maximum temperature without overheating. Otherwise, the solidus line will give the upper temperature limit. Clearly, by preparing the billet in an optimal manner, high gains in productivity can be achieved.

Studies of microstructure in profiles often reveal a relatively large degree of inhomogenity over the cross-section. This applies to the size and form of crystals and to the dislocation density. Mechanical testing usually give results in accordance with such observations. As Valberg's experiments explain, this is to be expected because the deformation of the material during extrusion is extremely inhomogeneous, and the same will naturally also be the case for the temperature history. In the early studies of microstructure evolution during extrusion insufficient attention was paid to these facts, and very often only average values of deformation and temperature were assessed. In this way the limits of the extrusion process can hardly be studied and the variability of the process only poorly understood. Figure 29 also explains the importance of knowing the exact temperature-, strain- and strain rate-history for each particle in the deforming alloy and especially for those that undergoe the largest strains. The largest differences will be experienced when the material particles enter the bearing channel. Here, the material close to the die will be exposed to shear strain rates up to about 10,000 [1/sec], whereas
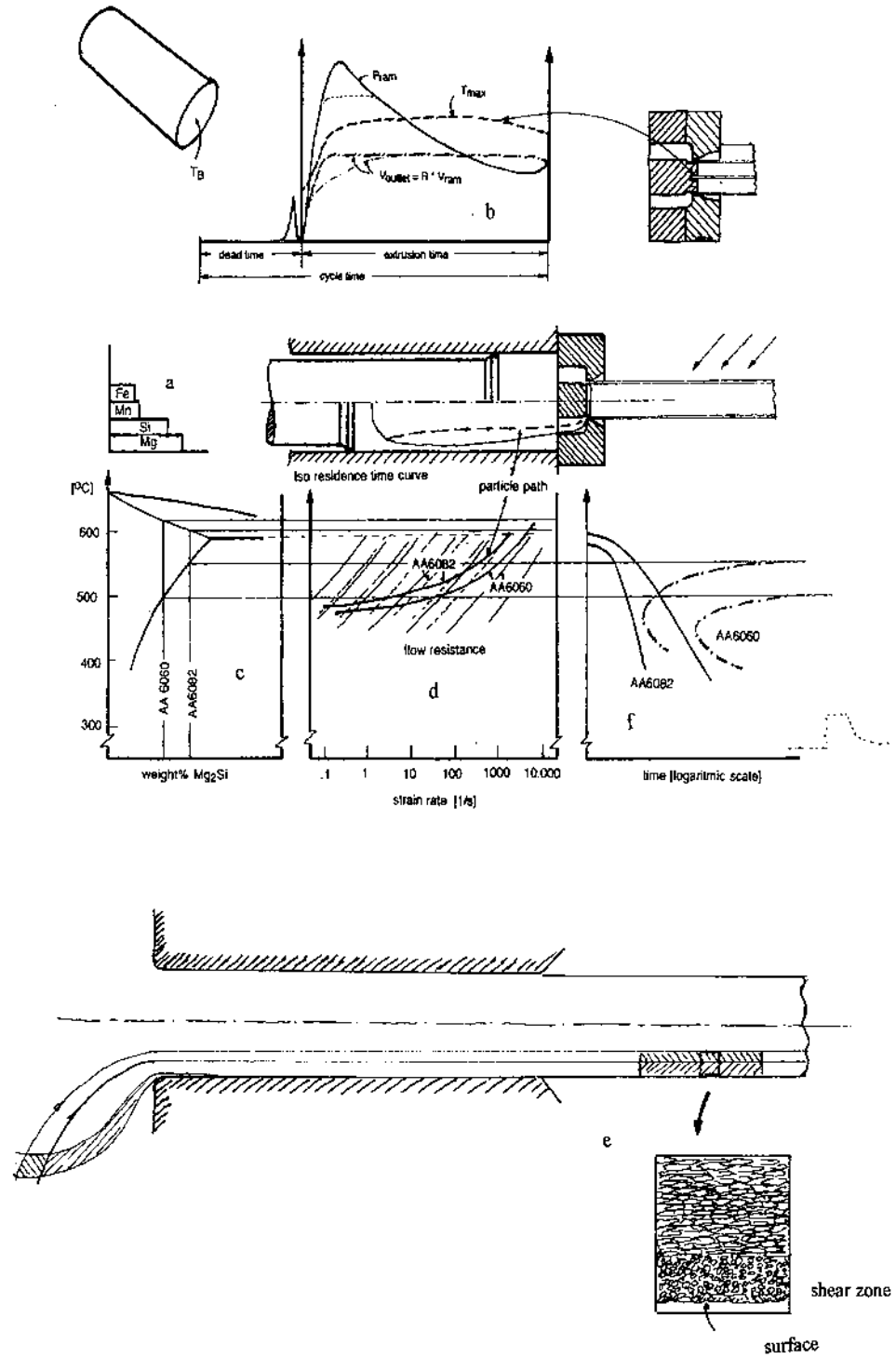
Figure 29 Relation between metallurgy and process parameters.

the strain rate in the center of the bearing channel is in the range of 0.1 [1/sec]. As shown on the micrograph Fig. 29(e), there is a considerable degree of variation in microstructure in an extruded section. Partial recrystallization over the cross section may here also occur, and this gives rise to unsatisfactory large variability of properties and surface appearance. Since every material element in the billet goes through different strain rate-, temperature- and strain-histories as shown on Fig. 29(d), it is important that the alloy is not very sensitive to these variations with respect to flow resistance and final microstructure after extrusion and quenching and aging (Fig. 29(f)).

4.2 Predicting the Conditions of Flow

4.2.1 Mathematical Approaches

The traditional method of treating macroscopic problems within both solid and fluid mechanics has since the 18th century been through the principles of continuum mechanics [41]. The fundamental equations obtained within the frames of this perspective are those of motion and conservation of heat, expressed incrementally. Furthermore, the assumption is that processes on a microscopic scale will average out so that the material properties will be continuous functions in space except in the case of discrete discontinuities. Material behavior will, however, be determined by processes taking place at levels from atomic to grain-size. In mechanics, constitutive equations can be utilized to characterize the relationship between measures such as deformation and stress. Purely elastic atomic lattice deformation may be represented by Hooke's law, which is a linear relationship between stress and strain. As elastic behavior generates no permanent deformations and in a thermodynamic sense may be looked upon as ideally reversible, it may also mathematically be characterized by functions of states. From a computational point of view this makes the material model attractive [42]. Deformations taking place during extrusion, however, contain only a minor and in fact in many cases a negligible elastic component. As the profile is generated from a billet, the material has to undergo permanent deformation. On a microscopic scale this deformation is caused by the sliding of dislocations through the grains [43]. As long as force is applied, energy will be dissipated, and therefore the process is thermodynamically irreversible. Consequently, the material behavior should be presented mathematically by history dependent functionals [44]. A further complication is that plastic material behavior usually can be taken to be non-linear. Hence, a theory of plasticity is bound to be of another dimension of complexity compared to purely elastic theory.

4.2.2 Different Perspectives

As extrusion basically is a non-steady flow problem, principles of fluid mechanics may be applied to evaluate both deformation and stresses. The viscosity will in this case be a function of the strain rate. As the material will not flow below a certain yield limit, a constitutive model such as that of Bingham may be appropriate if the necessary corrections are made for temperature effects on yield stress. The fluid mechanical or rheological approach, which addresses strain rates or time increments of strain, is favorable for many reasons.

Firstly, stresses generated through plastic deformation at high temperatures are found to be almost independent of the total strain, but extremely dependent on the strain rate. Secondly, flow is viewed in an Eulerian sense, by which is meant that components of flow velocity and stress are related to spatial coordinates, and that deformation is assessed in an incremental manner, the reference state at all times being that of the last time step.

Hence, an Eulerian formulation of the constitutive relation will therefore never violate the principle of material objectivity, which states that the constitutive relation should be independent of the choice of reference frame [45]. A rotation of the element should for instance not cause changes in stresses as long as the strains are held constant. Incremental deformations will to a close approximation always be in accordance with this principle.

Another favorable aspect with an Eulerian description is that computer code can be made very efficient due to the fact that velocities and stresses can be evaluated in a mesh that does not deform. However, as the Eulerian approach only assesses increments, information about each particle's total stress/strain history is lost, and elastic deformation can only with some difficulty be described. When evaluating the flow pattern, elastic strains are generally small, and it can be assumed that they only are of minor influence. However, elastic stresses may be of importance for instance to the surface quality of the product as friction in the bearing channel is affected by pressure due to elastic strains. A last problem connected to the Eulerian description in connection to extrusion is that the extruded profile is free to move as a rigid body in any direction as it leaves the bearing channel. Furthermore, deformation is then not plastic, and the movement will not be confined within certain limits, but should be calculated for the rigid body from the laws of motion. Furthermore, the boundary conditions of traction caused by a puller may not easily be described in the Eulerian system.

The Lagrangian description has traditionally been most popular when describing the movement and deformation of a rigid body. This approach assesses deformation of particles in relation to a fixed reference state in space, thus making use of so-called material coordinates. This view is favorable in that the total strain history is kept, and therefore that both elastic and plastic deformation may be included in calculations. Furthermore, an arbitrary movement of particles in space can be described when boundary conditions are given. This makes it possible to predict deformations also when the material moves out of the bearing channel. A problem is, however, that deformation and rotations tend to be large during extrusion. A Lagrangian description of finite deformation is not automatically in accordance with the principle of objectivity, the cause being that the material derivative of stress is not an objective measure even though stress is. Again this is a minor problem when evaluating only plastic strains as it is done on an incremental basis. However, when adding elastic deformation components the principle of material objectivity satisfied only by making use of an alternative material derivative of stress that compensates for any rotations of particles. In plasticity theory the Jaumann derivative is in common use. An analytical treatment of finite elasto-plastic deformation is by no means trivial. Lagrangian numerical calculations, however, are widely performed, and these make use of an element net that moves and deforms with the material particles. Calculation times tend to be higher for Lagrangian codes than for Eulerian even in the case when elastic deformations are disregarded, the

reason being that meshes have to be regenerated during simulations due to large distortions and loss of numerical accuracy. A promising method for evaluation of the state of deformation during extrusion seems to be the combination of the two descriptions in an Arbitrary Lagrangian–Eulerian (ALE) code.

4.2.3 Plasticity and Extrusion

Whereas the theory of rheology is focused on solving problems where stresses are given as functions of temperature and strain rates, the classical theory of plasticity was originally established to handle isothermal solid state problems where the stress after having exceeded the yield point, still was a function of strain [46–48]. An example of such a problem is that of the low-temperature uniaxial tensile test where a plot of true stress to true strain will usually give a monotonically increasing curve. Plastic deformation can be assumed to be initiated when the yield limit is reached. An increase in yield stress as a result of further deformation is called hardening. Several simplified material models have been established so that calculations can be made easier. When applying a perfectly plastic model it is assumed that plastic deformations are dominating and that the material does not strain harden. An elastic/plastic model can be utilized when the elastic strain component is of a certain value (Fig. 30). Strain hardening models such as that of Ramberg and Osgood also simplify matters in that hardening behavior is characterized by one parameter, the hardening exponent.

In principle, one is not to expect that the material shows any strain hardening behavior during extrusion. Such is traditionally connected to the pile up of dislocations, but at characteristic temperatures from 450°C to 600°C recovery and recrystallization mechanisms will contribute to the reduction of dislocation tangles during deformation. At a given stress, continuous deformation should therefore be possible. However, the strain rate will be of importance to the yield stress as the rates of creation and destruction of dislocation tangles will determine the equilibrium dislocation density. As for temperatures, the yield stress may be expected to follow the same Arrhenius relationship as metallurgical processes generally
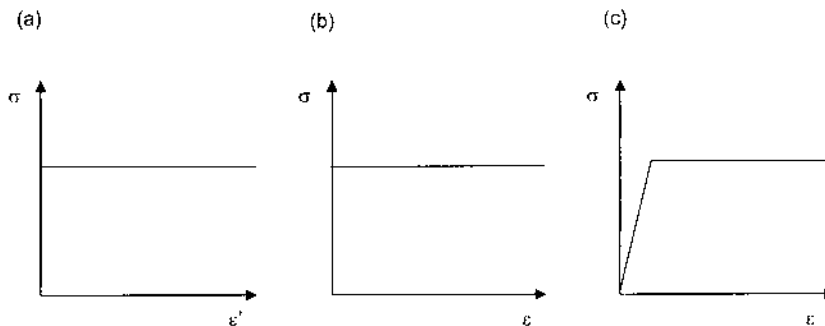
Figure 30 Simple constitutive relations: (a) Bingham fluid without strain rate hardening; (b) Rigid plastic material without strain hardening; (c) Elastic plastic material without strain rate hardening.

do. Hence, the yield stress can generally be expressed as a function:

$$\bar{\sigma} = f(\bar{\epsilon}, \dot{\bar{\epsilon}}, T) \tag{7}$$

The equation is given in terms of equivalent stress and plastic strain:

$$\bar{\sigma} = \sqrt{\frac{3}{2}(s_{ij}s_{ij})} = \sqrt{\frac{3}{2}[(\sigma_x - \sigma_o)^2 + (\sigma_y - \sigma_o)^2 + (\sigma_x - \sigma_o)^2 + 2\tau_{xy} + 2\tau_{yz} + 2\tau_{zx}]}$$
$$= \frac{1}{\sqrt{2}}\sqrt{(\sigma_x - \sigma_y)^2 + (\sigma_y - \sigma_z)^2 + (\sigma_z - \sigma_x)^2 + 6\tau_{xy} + 6\tau_{yz} + 6\tau_{zx}}$$

$$\tag{8}$$

$$\dot{\bar{\epsilon}} = \sqrt{\frac{2}{3}(\dot{\epsilon}_{ij}\dot{\epsilon}_{ij})} = \sqrt{\frac{1}{3}(2\dot{\epsilon}_x^2 + 2\dot{\epsilon}_y^2 + 2\dot{\epsilon}_x^2 + \dot{\gamma}_{xy}^2 + (\dot{\gamma}_{yz}^2 + \dot{\gamma}_{zx}^2)} \tag{9}$$

The equivalent measures of stress and strain are of interest when the state of stress is multiaxial. It can be shown that dissipation in general can be given as $\dot{\omega} = \sigma_{ij}\dot{\epsilon}_{ij} = \bar{\sigma}\dot{\bar{\epsilon}}$, and for a purely tensile test the equivalent stresses and strains will reduce to σ_z and ϵ_z. In simulation of extrusion extensive use is made of the Norton–Hoff relation:

$$\bar{\sigma} = K\bar{\epsilon}^n\dot{\bar{\epsilon}}^m e^{\frac{\beta}{T}} \tag{10}$$

where $n = 0$ can be used to remove any strain dependence. n and m are material constants. β is a parameter often set equal to the Q/R where Q is the activation energy and R is the universal gas constant. Another frequently used relation in the study of extrusion is that of Zener and Hollomon [49] which is given by:

$$\bar{\sigma} = \frac{1}{\alpha}\arcsin h\left(\frac{Z}{A}\right) = \frac{1}{\alpha}\arcsin h\left(\frac{\dot{\bar{\epsilon}} \times e^{\frac{Q}{RT}}}{A}\right) \tag{11}$$

In this case the yield stress is taken to be independent of the total strain. α and A are parameters which can be applied in curve fitting. Experiments indicate that the Zener–Hollomon relation may be satisfactory both when performing torsion tests on aluminum and during extrusion. Improvements to this material law have, however, been suggested. The main difference between torsion testing and extrusion is that the former assumes steady state while the strain rates may vary considerably in the later.

Typical stress-strain curves obtained through torsion, compression or tension tests at temperatures around that of extrusion are shown in Fig. 31. As changes in strain rates and temperatures tend to influence yield stress more than the total strain, rheological modelling seems preferable to modelling through plasticity theory. However, if a perfectly plastic or a plastic material model with low strain hardening is adopted, effects of strain rate and temperature can be implemented by calculating the yield stress on the basis of relations such as Norton–Hoff or Zener–Hollomon. The important point is that a deformation mechanism based on dislocation glide is one of shear and, hence, should be modelled macroscopically as one that relates increments of strains to the deviatoric stress state. Both theories
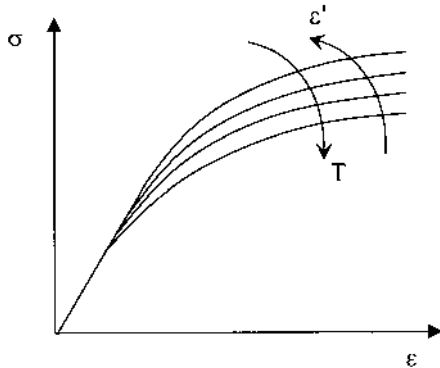
Figure 31 More general stress-strain curves' dependence on temperature and strain rates.

of rheology and plasticity have this perspective and have for a long time been widely used to describe the extrusion process. Early analytical and semi-analytical work has, however, not managed to solve the complex problem of extrusion in its entirety. Rheological approaches have been based on simple material models and have only assessed very simplified flow fields. Techniques related to plasticity theory have traditionally been popular when calculating very rough estimates of for instance the necessary extrusion force. By applying the so-called slip line theory one has been able to find closed form solutions for particle paths and stress states for simple geometries, but material models are generally limited to perfectly plastic, and temperature effects and material anisotropy have been neglected. However, modern numerical programs offer the user the possibility to implement constitutive models based on microstructural considerations and are able to perform coupled thermomechanical analysis for complex geometries. The last being of greatest importance due to the large variation in temperature in the container and bearing channel. Furthermore, by obtaining the temperature and strain history of the individual particles numerical programs should be able to describe changes in microstructure and the consequences of these. Both continuum plasticity theory and rheology are the building bricks for such programs.

4.2.4 Yield Criteria

For tensile tests yielding is initiated when the axial stress component reaches the yield limit, $F(\sigma_z) = 0$. In the general case it can be expected that all components of stress have an influence on the point of yielding, and in a six-dimensional space a yield surface $F(\sigma_{ij}) = 0$ may be defined. The assumption is made that deformation is purely elastic in the case where $F(\sigma_{ij}) < 0$. In classical plasticity theory one then usually resorts to two simplifications. The first is that the material is isotropic, thus implying that the yield surface is determined only by the principle stresses, $F(\sigma_1, \sigma_2, \sigma_3) = 0$, and therefore also the stress invariants, $F(J_1, J_2, J_3) = 0$. The second is that the hydrostatic pressure has no effect on yielding. Then the yield criterion can be written in terms of the deviatoric invariants:

$$F(J_2', J_3') = 0 \tag{12}$$

where

$$J_1' = s_{ij} = 0 \qquad J_2' = \frac{1}{2} s_{ij} s_{ij} \qquad J_3' = \det(s_{ij})$$

and S_{ij} is the deviatoric stress, $S_{ij} = \sigma_{ij} - \sigma_o \delta_{ij}$. σ_o is the hydrostatic stress. The assumptions made are more or less applicable to most engineering materials. However, alternative anisotropic yield criterions have been developed so that materials with strong anisotropy can be handled.

When applying the assumptions of isotropy graphical representation of the yield criterion can be made in the 3 dimensional $\sigma_1, \sigma_2, \sigma_3$-space. By assuming that hydrostatic pressures do not influence yielding, one is able to reduce the yield surface to a yield locus in the deviatoric plane, which is defined by the normal $(\sigma_1, \sigma_2, \sigma_3) = (1,1,1)$. If it is assumed that the material is isotrpic and that yielding will take place at the same stress level both in tension and compression, the yield locus must be symmetric about the six axes defined by the projections of the σ_1, σ_2 and σ_3-axes into the deviatoric plane. The last assumption is, however, not always correct due to the Bauschinger effect, which will be explained later.

The most commonly applied yield criteria are those of von Mises and Tresca. The von Mises criterion assumes that F only is a function of the second invariant of deviatoric stress. For many materials, experiments often indicate that yielding only to a very limited extent is dependent on the third invariant and thus confirms the hypothesis of von Mises. Mathematically the representation is:

$$J_2' - K_M^2 = \frac{1}{6}\left[(\sigma_1 - \sigma_2)^2 + (\sigma_2 - \sigma_3)^2 + (\sigma_3 - \sigma_1)^2\right] - k_M^2 = 0 \tag{13}$$

Hence, the von Mises criterion has the nice property that it appears as a circle in the deviatoric plane. Furthermore, the second invariant of deviatoric stress is simply the square of the expression for equivalent stress. This indicates that the von Mises criterion bases the criterion of yielding on the deformation energy absorbed by the material. The natural alternative to this is the Tresca criterion, which states that yielding will take place when the maximum shear stress reaches a critical value. This may be expressed as:

$$\tau_{max} = \max\left[\frac{1}{2}\mid \sigma_1 - \sigma_2 \mid, \frac{1}{2}\mid \sigma_2 - \sigma_3 \mid, \frac{1}{2}\mid \sigma_3 - \sigma_1 \mid\right] = k_T \tag{14}$$

The yield locus will in this case be a hexagon in the deviatoric plane. Also the Tresca criterion may be expressed in terms of the second and third invariants. In Fig. 32 both the von Mises and the Tresca yield loci are presented. Which one of the criteria that are the most conservative depends on the choice of κ_M and κ_T. If it is assumed that yielding first is taking place at a characteristic yield stress for pure tension, σ_Y, one would expect that:

$$k_M = \frac{\sigma_y}{\sqrt{3}} \qquad k_T = \frac{\sigma_y}{2} \tag{15}$$
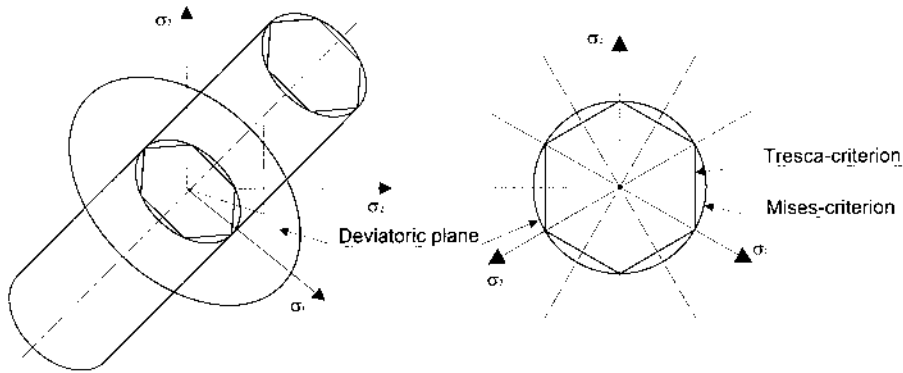
Figure 32 The yield surface, the yield locus and the deviatoric plane.

The result is that the locus of the von Mises criterion will circumscribe that of Tresca. However, if it shear stress is the reference for yielding then both are given as $\kappa_M = \kappa_T = \tau_Y$. In this case the Tresca criterion is the least conservative except in the point of maximal shear.

An interesting property of the yield locus is that singular points may exist, such as the case for the Tresca criterion. The singularity should from a macroscopic perspective be explained as a result of the sudden change of plane of maximum shear stress when loading from one state of stress to another. Consequently, the plane of shear deformation is also changed. However, the Tresca yield locus can also be explained on the basis of knowledge about glide systems in fcc-crystals. As a simplification, a state of plane stress is assumed. In this case shear deformation through dislocation movement may take place in three separate groups of planes (Fig. 33). The principal stresses are directed along the axes of the coordinate system. The same
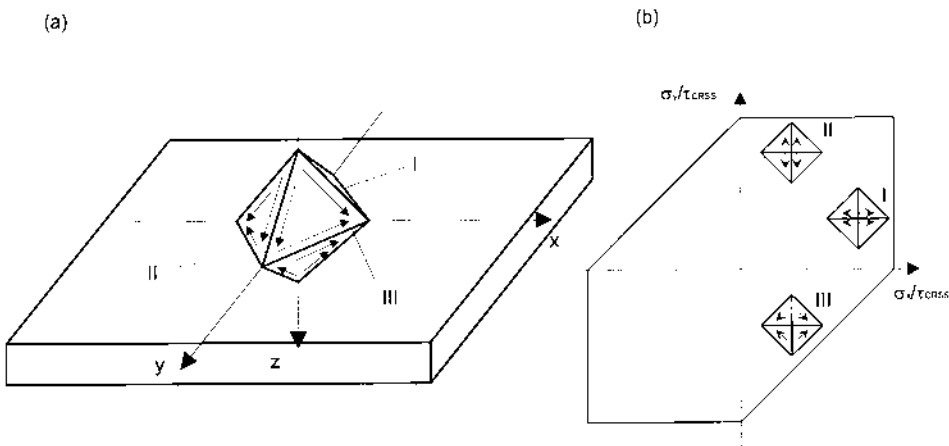
Figure 33 (a) An ideal (1 0 0)[1 0 0] texture; (b) The yield locus for ideal (1 0 0)[1 0 0] texture material.

axes also define the (1 0 0) [1 0 0] texture of the fcc-lattice, which is taken to be homogeneous, so that all the grains have oriented the {1 0 0} plane normal to the x-direction. If it is assumed that deformation is only taking place on the glide plane with the largest shear stress, the ratios of the stresses $\sigma_x : \sigma_y : \sigma_z$ will determine the deformation of the grains. If σ_x is the largest stress and $\sigma_z = 0$ the smallest, one can expect that the first glide system will be operative. Subsequently, if σ_y is the largest stress and $\sigma_z = 0$ the smallest, deformation will be of the second type. The last alternative is that σ_x and σ_y are the extreme principal stresses in which case the third modus of deformation is relevant. With the help of Schmid's law a yield locus can be constructed in the $\sigma_x \sigma_y$-plane. Figure 33 shows that such an analysis renders the Tresca yield locus. The singular points are the results of a limited amount of glide systems. While single crystal materials might follow a yield criterion such as that of Tresca, most materials contain grains with all sorts of orientations and glide systems. In this case deformation will take place in a series of directions yielding a number of straight lines defining a yield locus that resembles that of von Mises. A locus without singularities is often denoted regular.

4.2.5   Strain Hardening and Plastic Flow

Material behavior at stresses above the yield limit will depend on both the hardening behavior and boundary conditions. Whereas flow of a perfectly plastic material will be completely restricted by outer constraints, deformation of a strain hardening material can only take place if the stresses are increased gradually. Furthermore, in order to calculate deformations a constitutive relation between stresses and strains has to be established. An interesting observation in relation to the preceding determination of the yield locus on the basis of microplasticity, is that any increment of plastic strain will be in a direction normal to the yield surface. Thus, an indication is given that both stresses and strains can be determined if the form of the yield surface is known during deformation.

A uniaxial tensile test can be performed to determine the increase of yield strength during plastic deformation. However, as such a test alone is not able to describe the form of the yield surface during triaxial loading, firm knowledge of changes caused by yielding are even harder to obtain. The most attractive hardening principle mathematically is the isotropic (Fig. 34(a)). When applying this principle it is assumed that plastic deformation causes the yield surface to expand uniformly. Hence, upon yielding the expression:

$$F(J_2', J_3', \bar{\sigma}) = f(J_2', J_3') - \bar{\sigma} = 0 \tag{16}$$

applies. The equivalent stress is taken to be a function either of the energy spent during plastic deformation or the total plastic strain. These are denoted the work hardening and the strain hardening hypothesis respectively. Such functions can be obtained through tensile and compressive testing. The main problem with an assumption of isotropic hardening is that it is not in accordance with the Bauschinger effect, which can be witnessed during cyclic loading. After the material has been deformed plastically in tension, yielding will take place at lower compressive stresses than that of the expected yield point in compression. Kinematic hardening rules describe a movement of the yield surface in space so that the ratio of the yield limits in different directions is altered. A mathematical expression that can be used to
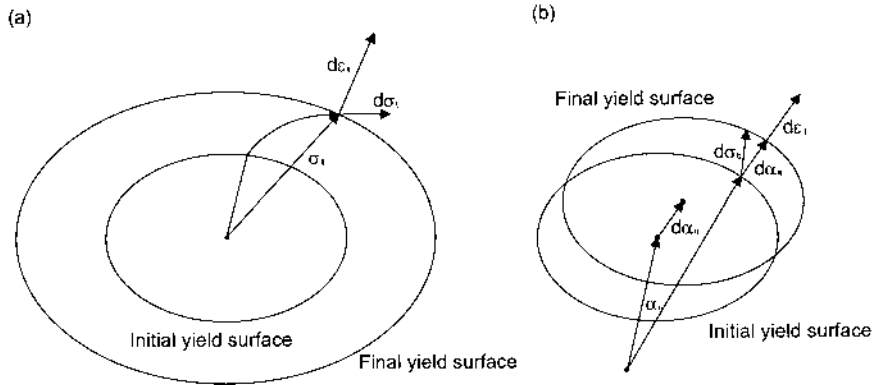
Figure 34 Strain hardening rules: (a) Isotropic; (b) Kinematical.

describe such a behavior is:

$$F(s_{ij}, \alpha_{ij}) = f(s_{ij} - \alpha_{ij}) - k = 0 \tag{17}$$

where α_{ij} describes the movement of the yield surface and is known as the back ratio. κ will for a strict kinematic rule be a constant. However, newer models often let both α_{ij} and κ vary so that the proposed law can be better fitted to data.

In the mathematical treatment of plastic strains generated by loading it is rational to define a plastic potential, g, which is to set the ratios of the plastic strain increments. One can expect that this function, as the yield function, originally is one of all stress components. If such a relation is known, the plastic stresses can be derived from the mere definition of a potential function, namely that the increment of strain shall be normal to the potential surface:

$$d\varepsilon_{ij}^p = \frac{\partial g}{\partial \sigma_{ij}} d\lambda \tag{18}$$

$d\lambda$ is simply a constant. The previous microplastical considerations have shown that the yield surface at least in the case of yield by the Tresca criterion also can be expected to be a potential surface. If g is set equal to f, the associated flow rule is adopted. Such an assumption can in most cases be expected to yield satisfactory results because many of the characteristics of g are equal to those of f. Whereas the assumption that yielding is unaffected by hydrostatic stress limits the evaluation of yield to the deviatoric plane, a choice of an incompressible material model leads to the conclusion that the hydrostatic stress line in a $\sigma_1\sigma_2\sigma_3$-system nowhere can be perpendicular to a potential surface. Hence, a potential surface will be fully described by its locus in the deviatoric plane. As plastic deformation is one of shear, an assumption about incompressibility leads only to marginal errors. Mathematically such a relation is written:

$$d\varepsilon_x^p + d\varepsilon_y^p + d\varepsilon_x^p = \begin{bmatrix} 1 \\ 1 \\ 1 \end{bmatrix} \left[(d\varepsilon_1^p \quad d\varepsilon_2^p \quad d\varepsilon_3^p \right] = 0 \tag{19}$$

In the $\sigma_1\sigma_2\sigma_3$-system an incremental change in strain will generate the stress component $2G(d\varepsilon_1{}^p, d\varepsilon_2{}^p, d\varepsilon_3{}^p)$, where G is a constant of proportionality. It can be observed that this component has a direction perpendicular to the line $(\sigma_1,\sigma_2,\sigma_3)=(1,1,1)$ and therefore lies in the deviatoric plane. The locus described in such a plane by a potential surface, also has to be symmetrical with respect to the stress axes due to assumptions of isotropy and independence of sign reversals. When one discusses states of stresses and the corresponding increment of strains, the incompressibility assumption allows one to view these states as vectors in the deviatoric plane (Fig. 35).

Drucker has proved that unless the material shows strain softening behavior such as that of for instance soils and rocks, the flow rule will be associated and the normality rule will hold. Drucker then has defined a stabile material as one for which the inequality:

$$W = \int_{C_\sigma} \Delta\sigma_{ij}d\varepsilon_{ij} = \int_{C_\sigma} (\sigma_{ij} - \sigma_{ij}^o)d\varepsilon_{ij} \geq 0 \tag{20}$$

holds during a complete load cycle where the original stress state, σ^o, may or may not be one of yielding. A material on which an external agency does positive work during an elastic-plastic stress cycle is considered strain hardening. As the inequality will not be satisfied if the material is strain softening, the postulate is often referred to as Drucker's strain hardening postulate. To a close approximation the net plastic work done over the loading part of the cycle can be expressed as:

$$(\sigma_{ij} - \sigma_{ij}^o)d\varepsilon_{ij}^p + \frac{1}{2}d\sigma_{ij}d\varepsilon_{ij}^p > 0 \tag{21}$$

Drucker's first and second postulate follows from this inequality. If it is assumed that the original state of stress is one of yielding, the first term cancels. In accordance with the inequality, the first postulate states that the plastic work done by an external agency during the application of additional stress is positive for a work hardening and zero for a non-hardening material. If the last part of the postulate is to be true, vectors representing the increments of stress and plastic strain have to be perpendicular. In a non-hardening material loading is assumed
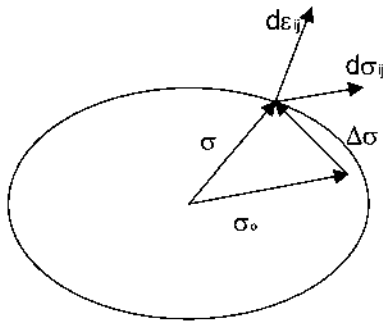
Figure 35   The yield locus in relation to Drucker's hardening postulates.

to be neutral, that is all load paths are tangential to the yield surface. Therefore the increment of strain is directed normally to it, thus resulting in the normality law. If the material is hardening, it must be assumed that the increment of stress is a linear combination of a plastic and an elastic part, and that the last is directed tangentially to the yield surface. As the elastic part of the stress increment does no irreversible work, the increment of plastic strain is also in this case directed normal to the yield surface.

Drucker's second postulate is connected to the first part of the inequality above and states that the net work done by an external agency during a cycle of addition and removal of stresses is non-negative. If it is assumed that the original state of stress is not one of yielding, the last term in the inequality can be neglected. The result is:

$$(\sigma_{ij} - \sigma_{ij}^o)d\varepsilon_{ij}^p > 0 \tag{22}$$

This inequality also bears the name the maximum work theorem. From Drucker's second postulate it can be seen that the angle between the vectors $\boldsymbol{\sigma}$-$\boldsymbol{\sigma}^o$ and $\boldsymbol{\varepsilon}^p$ can not be obtuse. Hence, as the vector $\boldsymbol{\varepsilon}^p$ is always normal to the yield surface and $\boldsymbol{\sigma}^o$ is located inside the yield surface, this surface has to be convex at all points.

If it is assumed that yielding is initiated according to the von Mises criterion and that the flow rule is associative, the plastic strains can be calculated to be:

$$d\varepsilon_{ij}^p = \frac{\partial f}{\partial \sigma_{ij}}d\lambda = \frac{3}{2\sigma}(\sigma_{ij} - \sigma_{ij}^o\delta_{ij})d\lambda = \frac{3s_{ij}}{2\sigma}d\lambda \tag{23}$$

This rule can also be written in the form:

$$\frac{d\varepsilon_x^p}{s_x} = \frac{d\varepsilon_y^p}{s_y} = \frac{d\varepsilon_x^p}{s_x} = \frac{d\gamma_{xy}^p}{\tau_{xy}} = \frac{d\gamma_{yz}^p}{\tau_{yz}} = \frac{d\gamma_{xz}^p}{\tau_{xz}} = d\lambda \tag{24}$$

indicating that the increments of strain are proportional to the deviatoric stress components. If the material is assumed to be rigid/plastic, the names of Lévy and von Mises are connected to the equations. If the material model also contains an elastic strain component the above relations are those of Prandtl and Reuss.

The constant of proportionality $d\lambda$ is expected to be related to the increment of equivalent strain, the reason being that the increment of plastic strain is determined by the strain hardening behavior of the material. By applying the measures of equivalent stress and strain one can relate the hardening behavior of a uniaxial test to that of the multiaxial actual load case. From the definition of equivalent stress and strain it is known that:

$$\dot{\omega} = \overline{\sigma}\dot{\overline{\varepsilon}} = \sigma_{ij}\dot{\varepsilon}_{ij} = s_{ij}\dot{\varepsilon}_{ij} \tag{25}$$

If only plastic components of strain are evaluated, the flow rule can be applied in order to eliminate the increment or in this case the material derivative of plastic strain:

$$\overline{\sigma}\dot{\overline{\varepsilon}} = s_{ij}\left(\frac{3}{2\overline{\sigma}}s_{ij}\right)\dot{\lambda} = \overline{\sigma}^2\frac{\dot{\lambda}}{\overline{\sigma}} = \overline{\sigma}\dot{\lambda} \tag{26}$$

This gives the result $\dot{\lambda} = \dot{\bar{\varepsilon}}$ or $d\lambda = d\bar{\varepsilon}$ and a final flow rule of the form:

$$d\varepsilon_{ij}^p = \frac{3d\bar{\varepsilon}^p}{2\bar{\sigma}}(\sigma_{ij} - \sigma_{ij}^0\delta_{ij}) = \frac{3d\bar{\varepsilon}^p}{2\bar{\sigma}}s_{ij} \tag{27}$$

The total strain increment will generally be the sum of both an elastic and a plastic part. The elastic component can be obtained by the use of Hooke's law on an incremental form, and from this equation it can be seen that the ratio of the components of elastic strain will be determined by the increment of stress and not the full deviatoric stress as the case is for the plastic component. A particular formulation of stress-strain relationship developed by Hencky assumes that also the ratios of plastic strains are given by those of deviatoric stress. This can only be expected to hold if the loading is proportional, that is, if the stress components experience a proportional increase during loading. As initially indicated the load path is generally history dependent and must be calculated incrementally.

4.2.6 The Uniqueness Theorem

The Lévy–Mises equations reveal both the strengths and the weaknesses connected to the description of extrusion through the theory of plasticity. Deformation is described as one that is initiated by deviatoric stresses and the components of deformation will be determined by their ratio. This is in accordance with the notion that plastic deformation is connected to the glide of dislocations. However, the material is expected to experience strain hardening defined by a curve relating the equivalent stress and strain. At the relevant temperatures little hardening is experienced and, therefore, the derivative of a stress-strain curve will be almost zero. This means that it is not possible to calculate the total strain from the stress alone. Thus, the stress state in the material during extrusion will not be determined by the strain, but by geometry of the tooling and by temperatures and strain rates.

An important property that applies to hardening and non-hardening materials alike is that the state of stress is unique when certain tractions, T_j, and velocities, v_j, are defined on separate parts, S_F and S_v, of the boundary. The proof of this is as follows for a non-hardening material strains. One may assume that two consistent solutions, $(\boldsymbol{\sigma}, \boldsymbol{v})$ and $(\boldsymbol{\sigma}^o, \boldsymbol{v}^o)$, for the stress and associated velocity distribution, that corresponds to the same boundary conditions, exist. The principle of virtual work is then applied to the differences in the field quantities over the volume of interest:

$$\int (T_j - T_j^o)(v_j - v_j^o)dS = \int (\sigma_{ij} - \sigma_{ij}^o)(\dot{\varepsilon}_{ij} - \dot{\varepsilon}_{ij}^o)dV + \int (k - \tau^o)[v]dS_D$$
$$+ \int (k - \tau)[v^o]dS_D^o \tag{28}$$

The two last terms are connected to the virtual energy dissipated due to velocity discontinuities [v] and [v^o] on surfaces S and S^o in the volumes with the solutions $(\boldsymbol{\sigma}, \boldsymbol{v})$ and $(\boldsymbol{\sigma}^o, \boldsymbol{v}^o)$ respectively. k is the shear stress on the surfaces of discontinuity, and it is known that neither τ nor τ^o may be larger than k. Hence, the two last integrals on the right hand side will yield solutions greater or equal to zero. The integral on the left side must be equal to zero since it is assumed that the same bound-

ary conditions are applied in the two cases. The maximum work inequality gives:

$$(\sigma_{ij} - \sigma_{ij}^o)(\dot{\varepsilon}_{ij} - \dot{\varepsilon}_{ij}^o) = (\sigma_{ij} - \sigma_{ij}^o)\dot{\varepsilon}_{ij} + (\sigma_{ij}^o - \sigma_{ij})\dot{\varepsilon}_{ij}^o \geq 0 \tag{29}$$

It follows that both terms on the right hand side are positive and that they must separately vanish. This can only take place if $\boldsymbol{\sigma} = \boldsymbol{\sigma}^o$. The two states of stress are equal. In the case of extrusion the value of the yield strength will not be a constant but a function of temperature and strain rate and therefore of spatial coordinates. The above analysis, however, seems to apply also in this case because the volume of material can always be made so small that spatial variations can be overlooked.

In relation to extrusion the uniqueness theorem states that if the load on the tools can be determined uniquely one may in theory also expect to find a unique stress distribution in the flowing metal. However, the matters are complicated by the fact that in reality boundary conditions on the tools are not prescribed but determined by a friction rule. Tresca friction and assumption of full sticking will not cause any problems as it is characterized by a tangential shear stress with a value of yield, but some simplifications have to be made so that the uniqueness theorem may hold also for Coloumb friction.

The determination of the unique state of stress constitutes no small problem even though such a state is known to exist. In the early parts of the development of the theory of plasticity the extrusion process represented a natural test case for analytical work. Therefore, several solutions based on larger and smaller simplifications have been developed. Usually one assumes the material model to be perfectly plastic, and the yield stress to be independent of both strain rate and temperature. The geometry is taken to be either plane or axially symmetric. A state of plane strain corresponds to the extrusion of an infinitely thick plate while axial symmetry only yields cylinders.

4.2.7 Upper and Lower Bound Solutions

The plasticity theory has the advantage that it facilitates a simple procedure for calculation of an upper and a lower estimate for the boundary forces needed to cause plastic deformation. Such estimates can be obtained for a range of material models and in the presence of both small and large deformation. If it is assumed that the yield behavior is perfectly plastic the simplest estimates can be reached. In order to obtain a lower bound on applied forces one assumes a stress field, $\boldsymbol{\sigma}^o$ that satisfies the equilibrium equations and boundary conditions without violating the yield condition. As the stresses need not be in accordance with a constitutive relation, such a field will generally not be the actual and is instead denoted statically admissible. The actual stress and associated strain is σ and ε. The principle of virtual work can in this case be written as:

$$\int (T_j - T_j^o)v_j dS = \int (\sigma_{ij} - \sigma_{ij}^o)\dot{\varepsilon}_{ij} dV + \int (k - \tau^o)[v]dS_D \tag{30}$$

where S_D are the surfaces of velocity discontinuity for the actual solution, and k is the shear yield stress. $[v]$ is the actual velocity discontinuity. As the admissible shear stress on the actual discontinuity, τ^o, will not be larger than k, the last integral on the right hand side is not negative. The first integral is non-negative by the maximum work inequality. In this case the traction caused by the actual stresses and

statically admissible ones need not be the same. If the velocity normal to the boundaries where forces are prescribed, S_F, are assumed to be zero, the following will hold on the rest of the boundary, S_v:

$$\int T_j v_j dS_v \geq \int T_j^o v_j dS_v = \int l_i \sigma_{ij}^o v_j dS_v \tag{31}$$

The lower bound theorem, thus, states that the rate of work done by actual surface tractions on S_v is greater than or equal to that done by surface tractions in a statically admissible stress field. If the v_j is uniform on S_v, one will find that the load of the statically admissible field will give a lower bound to the actual one. The principle can be directly applied in extrusion. The velocities normal to the container wall and the die will be zero. S_v can be assumed to consist of two parts, the surface between the billet and the stem and surface defined by the die opening. The tractions on the last part of the surface can be assumed to be approximately zero. Hence, as the velocity on the surface of the stem is uniform, an analysis will yield a lower estimate of the extrusion force at a certain time during extrusion.

Figure 36(a) gives an example of a statically admissible flow field. The extrusion is assumed to be frictionless. Lines of stress discontinuity are drawn. The normal stress components to such lines as well as the shear stress have to be continuous if equilibrium is to be achieved. The normal component of stress along the line, however, may differ from one side of the discontinuity to the other as shown in Fig. 37. In Fig. 36(b) the Mohr circles for all the stress states are drawn. Two interesting observations can be made. Firstly, the yield criterion will nowhere be violated, and secondly, a stress discontinuity only amounts to a rotation of the Mohr circle about a vertical line going through the point (σ, τ). Geometrical considerations limit the use of the proposed field to cases where the reduction ratio is equal to or larger than three. The necessary pressure applied to the billet in order to cause yielding has been calculated to be $p = 5k(R - 1)/R$, where k is the shear yield stress.
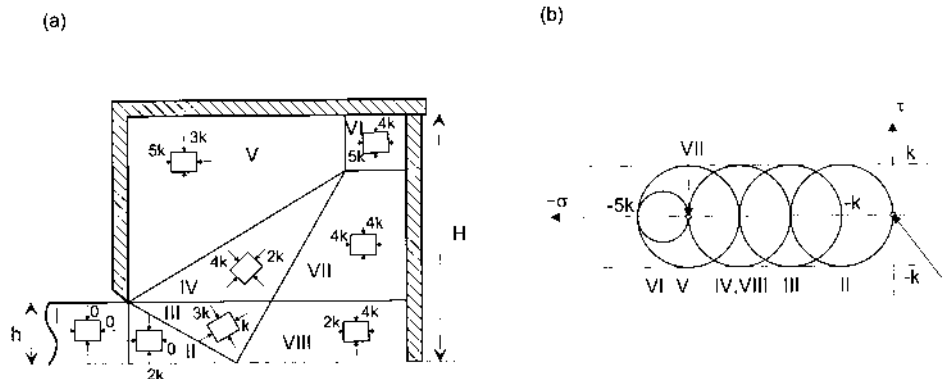
Figure 36 (a) Statically admissible stress field during extrusion; (b) The corresponding states of stress in a Mohr-diagram.
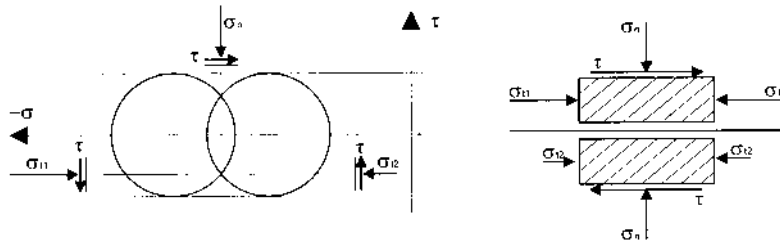
Figure 37   Possible stress discontinuity in the deforming material.

In order to obtain an upper estimate on the extrusion force the upper bound theorem is applied. One can assume that v^o is a continuous velocity field satisfying the incompressibility condition. Then the material derivative of ε^o may be calculated and the corresponding stress σ^o is finally obtained from the normality rule. The actual strain rate is denoted σ. The virtual work principle can be used to obtain the following relation:

$$\int T_j v_j^o dS = \int \sigma_{ij}\dot{\varepsilon}_{ij}^o dV + \int \tau[v^o]dS_D^o \tag{32}$$

The assumed velocity field may contain surfaces of discontinuity $[v^o]$. It is known that the actual shear stress, τ, on the virtual surface of discontinuity can not be larger than k. By the maximum work inequality, $\sigma_{ij}\dot{\varepsilon}_{ij}^o \leq \sigma_{ij}^o\dot{\varepsilon}_{ij}^o$ as σ^o is on the yield surface while σ may either be inside or on. If the virtual velocity field, v^o, is regarded to be kinematically admissible, it also satisfies the boundary conditions on the part of the surface where the velocity is prescribed, S_v. The last equation is then rendered, resulting in the inequality:

$$\int T_j v_j^o dS_v \leq \int \sigma_{ij}^o\varepsilon_{ij}^o dV + \int k[v^o]dS_D^o - \int T_j v_j^o dS_F = \int T_j^o v_j^o dS_v \tag{33}$$

The upper boundary theorem, thus, states that the rate of work done by the unknown surface tractions on S_v is less than or equal to the rate of internal energy dissipated in any kinematically admissible velocity field. The last equation to the right of the inequality sign may be used to obtain an expression for an upper limit on the extrusion force applied. This limit is denoted T_j^o.

In Fig. 38(a) a kinematically admissible flow field for axisymmetric extrusion analog to that proposed by Avitzur [50–52] is shown. The material is assumed to flow like rigid body with speed of the stem, v_0, in the leftmost part of the container. At the surface where the material enters the deformation zone there is a discontinuity in velocity of $v = v_0\cos\theta$ tangential to surface marking the inlet to the primary deformation zone (Fig. 38(b)). Then the material velocity increases according to the relation $v = v_0(r_0/r)^2\cos\theta$. In the end of the zone a new discontinuity is encountered. In the dead zone surrounding the deformation zone the material is assumed to be rigid. The velocity field described is kinematically admissible, but it need not be the actual field. The experiments performed by Valberg and presented

earlier, show that the dead zone will communicate with the flow and that no absolute velocity discontinuity will exist between the flow and the dead zone. Instead the flow velocity is expected to gradually decrease towards the container wall. At all times a boundary layer will exist along the whole container wall and one can not expect the leftmost zone to be perfectly rigid. Furthermore, the form of the velocity field will change as the stem is brought closer to the die. In the limiting case, the material will flow in a radial direction towards the bearing channel and the whole dead zone will disappear. As extrusion proves to be a transient process, the solution obtained will only be applicable at a certain stage. However, as long as all the relevant effects are taken into consideration, the proposed velocity field will produce an upper bound on the force needed to initiate deformation. Better upper bounds may be found in literature [53–56], but for these calculations may be more complicated.

According to the last equation and Fig. 38(a) the work that the stem does on the metal has to compensate for the dissipation of energy in the deformation zone, on the surfaces of velocity discontinuity and in connection with shearing of material on the discontinuity close to the dead zone. In addition, the extrusion force has to be increased due to friction in the container and on the yield surface. Fortunately, in an upper boundary analysis each effect can be treated separately. The force needed to deform the material in the two velocity discontinuities can be shown to be equal. The change in velocity over the first discontinuity is according to Fig. 38(b) $[v] = v_0 \sin\theta$. Integration has then to be performed over the whole surface of discontinuity, which is assumed to spherical:

$$F_D \cdot v_o = 2 \int_A k[v]dA = \int_o^\alpha kv_o \sin\theta \times 2\pi R^2 \sin\theta d\theta = 2k \times \pi r_o^2 \left(\frac{\alpha}{\sin^2\alpha} - \cot\alpha\right) \times v_o$$

$$(34)$$

As v_0 appears on both sides and can be dropped, an expression for the force F_D is obtained.
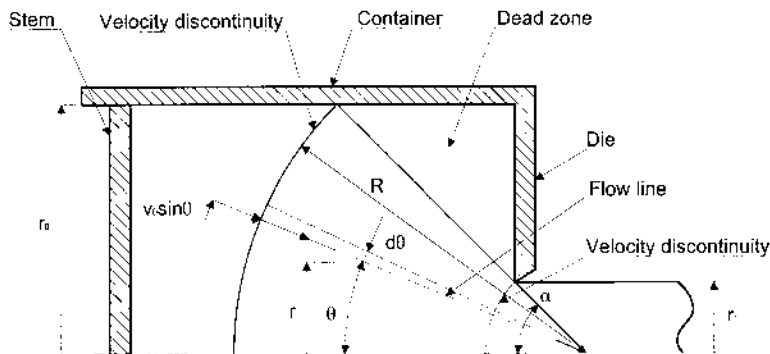
Figure 38 Kinematically admissible flow field similar to that proposed by Avitzur.

An expression for the force F_F caused by the friction between the dead zone and the flowing material can be obtained if the third term on the right side of the upper bound inequality is integrated over a conical surface:

$$
F_F v_o = \int\limits_{A_2} \tau_j v_j dA = k \int\limits_{A_2} v_o \left(\frac{r_o}{r}\right)^2 \cos \alpha \, dA = k v_o r_o^2 \cos \alpha \int\limits_{\frac{r_1}{\sin\alpha}}^{\frac{r_0}{\sin\alpha}} \frac{1}{r^2} 2\pi r \sin \alpha \, dr
$$

$$
= \pi r_o^2 \sin \alpha \cos \alpha \, \mathrm{ln}\left(\frac{r_o}{r_1}\right)^2 \times v_o \tag{35}
$$

Again an expression for the force is obtained by dropping the term v_0, which appears on both sides of the equality.

The force needed to deform the material in the primary deformation zone can be estimated by using the first term on the right hand side of the upper bound inequality. Given the velocity field v, the components of strain may be expressed as:

$$
\dot{\varepsilon}_r = -2\dot{\varepsilon}_\theta = -2\dot{\varepsilon}_\varphi = -2v_0 \frac{r_0^2}{r^3} \cos \theta \quad \dot{\varepsilon}_{r\theta} = -\frac{1}{2} v_0 \frac{r_0^2}{r^3} \sin \theta \quad \dot{\varepsilon}_{r\varphi} = \dot{\varepsilon}_{\theta\varphi} = 0 \tag{36}
$$

The equivalent strain rate is expressed in the same way in the $r\theta\varphi$-coordinate system as in one of xyz, and as a result the equivalent strain will be given as $(v_0/3^{1/2})(r_0{}^2/r^3)$ $(11\cos^2\theta\text{-}1)$. A calculation of the given conical volume integral then results in the following expression:

$$
F_v v_o = \int\limits_V \bar{\sigma} \dot{\bar{\varepsilon}} dV = \bar{\sigma} \int\limits_{r_1}^{r_0} \int\limits_0^\alpha \dot{\bar{\varepsilon}} \times 2\pi r \times r d\theta \, dr = \frac{\bar{\sigma}}{\sqrt{3}} \pi r_0^2
$$

$$
\int\limits_0^\alpha \sin \theta \sqrt{11\cos^2 \theta + 1} \mathrm{d}\theta \, \mathrm{ln}\left(\frac{r_0}{r_1}\right)^2 v_0 \tag{37}
$$

As expected all components of force are dependent on the yield stress given in terms of shear or equivalent stress. Furthermore, the angle α, which defines the dead zone, also has an influence on the extrusion force. Most importantly, however, the expressions indicate that the force is a function of the reduction ratio. If all terms are added and the reduction ratio, R, is the only parameter of interest the force equation may be written:

$$
F = a + b \, \ln R \tag{38}
$$

Experiments confirm this relationship for various metals over a range of extrusion speeds. The equation may also be expected to hold for various profile geometries, but more complex profiles will generally necessitate a higher extrusion force than simpler ones with the same R-ratio since the friction surface to total volume ratio can be expected to be larger [57,58]. Therefore, the constants a and b will be dependent on profile geometry. The value of a and F will also vary over the press cycle as shown in Fig. 39. In the case of direct extrusion the largest variations are due to the fact that both the surface area and friction force between
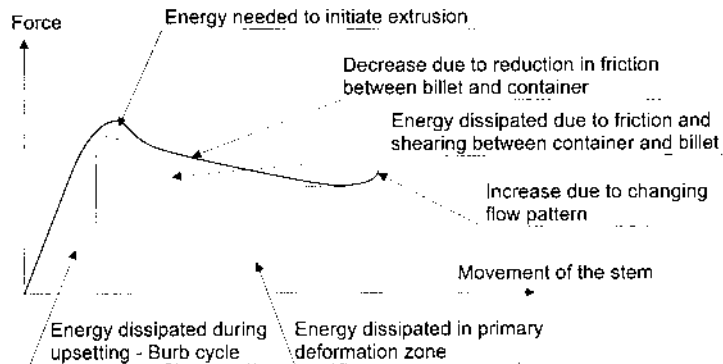
Figure 39   General relation between extrusion force and stroke length.

billet and container decrease over time. However, other variations may be expected as the movement of the stem alters the geometry of the flow field. In the last phase of the extrusion charge, the press force will experience a sharp increase as the material from the dead zone moves towards the bearing channel. Another reason for variations in press force is an increase or a decrease in yield stress caused by variations in strain rates or temperatures. The degree of hardening will be highest in the last part of the charge as the metal then experiences very high strain rates. A high degree of plastic deformation causes dissipation of energy and potentially also temperature variations in time and space. If the billet is not properly preheated, temperatures particularly in the central deformation zone, close to the container wall and in the bearing channel will increase gradually, resulting in lower flow resistance.

4.2.8   Slip Line Theory

As shown, the calculation of an upper and a lower boundary estimate may be carried out relatively effortlessly, but such estimates only yield a certain indication of one parameter of interest, the extrusion force. Whereas the lower boundary estimate reveals nothing in connection to the velocity field, the upper boundary calculation gives no indication of the stresses present in the flowing metal. Furthermore, the proposed velocity and stress fields are only kinematically and statically admissible respectively, and will only in the limiting case be equal to the actual fields. An exact solution has only for a few problems been indicated by the equivalence of the upper and lower bounds. Generally, a principle of maximizing or minimizing of energy can not be expected to yield the exact solution since the proposed form of the field can not be expected to be correct in the very beginning. Therefore, the most interesting parameters to the quality of the finished products such as temperature, strain and strain rate history of individual material elements can not be obtained through the presented limit analysis.

The theory of slip line fields assumes that either a state of plane strain or axial symmetry exists. Furthermore, when elastic strains are neglected, calculations may be made for hardening as well as non-hardening materials. An assumption of a constant yield stress, however, leads to the simplest results. The method will at least provide an estimate of both the stress and velocity field. The slip line method is also one that is based on an initial proposal of a kinematically admissible velocity

field. However, by combining the kinematical evaluation with the use of equilibrium equations, constitutive relations and stress boundary conditions, the proposed field will yield stresses that are in equilibrium and actually also satisfy boundary conditions. However, one is not guaranteed that the stresses in the assumed rigid region do not violate the yield condition and that they are in equilibrium. Therefore, a proposed slip line field may be viewed as an upper bound, which in the limit will be an exact solution. But, as this solution is obtained in a more rigorous manner through a relatively systematic procedure of the slip line theory than through a standard upper bound analysis, a firmer knowledge of the strain and strain rate history for a particle can be gained. Furthermore, by obtaining knowledge of the flow line of the material, one will also be able to calculate adiabatic changes in temperature.

If it is assumed that the material responds perfectly plastic to loading, the constitutive relation will be that of Lévy and von Mises. Plane strain is assumed and the z-direction is taken to be perpendicular to the plane. Since the material is incompressible, the coordinate strain increments, $d\varepsilon_x$ and $d\varepsilon_y$ will be equal in magnitude but opposite in sign. Hence, the deformation will be one of pure shear. As $d\varepsilon_z$ is set to zero, the Lévy–Mises equation for the z-direction can be applied in order to obtain:

$$\sigma_z = \frac{1}{2}(\sigma_x + \sigma_y) \tag{39}$$

Equation (39) shows that the largest and smallest stresses at all times may be found in the xy-plane, which is in accordance with the fact that deformation is one of shear in this plane. Furthermore, the stress σ_z is equal to the hydrostatic stress. Since extrusion is a process in which the hydrostatic stress may assumed to be negative, the negative sign convention is applied, $p = -\sigma_z$. If it is assumed that the material follows the von Mises criterion for yielding, the last equation can be applied in 13. The result is:

$$(\sigma_x - \sigma_y)^2 + 4\tau_{xy}^2 = 4k^2 \tag{40}$$

where k is the shear yield stress. It can be observed that if relations for the normal stress, σ, and the shear stress, τ, on a surface with an inclination of ϕ to the x-axis is calculated, squared and added the Mohr circle emerges as:

$$\left(\sigma - \frac{1}{2}(\sigma_x + \sigma_y)\right)^2 + \tau^2 = \frac{1}{4}(\sigma_x - \sigma_y)^2 + \tau_{xy} \tag{41}$$

Hence, in a Mohr-diagram all stress states in the plastic region will be described as circles with radiuses of magnitude k. From the typical Mohr-circle in Fig. 40(b) it can be seen that the state of stress at each point in the material can be described merely by the hydrostatic pressure, p, and the orientation, ϕ, of the plane with the largest shear stress:

$$\sigma_x = -p - k\sin 2\phi \qquad \sigma_y = -p + k\sin 2\phi \qquad \tau_{xy} = k\cos 2\phi \tag{42}$$

A new coordinate system $\alpha\beta$ can then be defined so that the shear stress has its maximum value along the axes α and β. A convention is then that the line of action of the algebraically greatest principal stress makes a counterclockwise angle of

(a)   (b)
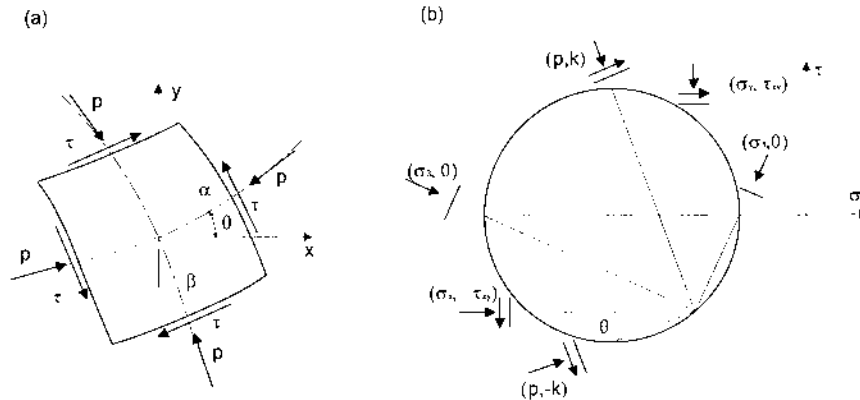
Figure 40   (a) The slip lines in relation to the cartesian coordinate system; (b) State of stress in a material particle.

$\pi/4$ with the α-direction (Fig. 40). As the plane of greatest shear changes from point to point in the material, the coordinate system will have to be curved. However, the α- and β-lines will still be orthogonal at each point. Since the deformation is expected to be one of shear, the α- and β-lines are called slip lines or shearlines.

As the deformation is assumed to be quasi-static and body forces are neglected, the equations of equilibrium reduce to:

$$\frac{\partial \sigma_x}{\partial x} + \frac{\partial \tau_{xy}}{\partial y} = 0 \qquad \frac{\partial \tau_{xy}}{\partial x} + \frac{\partial \sigma_y}{\partial y} = 0 \tag{43}$$

These are the differential equations that have to be solved if the state of stress in the material during extrusion is to be obtained. In order to reduce the number of unknowns, σ_x, σ_y and τ_{xy} are substituted with p and ϕ in accordance with Eqs. (42):

$$\frac{\partial p}{\partial x} + 2k\left(\cos 2\phi \frac{\partial \phi}{\partial x} + \sin 2\phi \frac{\partial \phi}{\partial y}\right) = 0 \qquad \frac{\partial p}{\partial y} + 2k\left(\sin 2\phi \frac{\partial \phi}{\partial x} - \cos 2\phi \frac{\partial \phi}{\partial y}\right) = 0 \tag{44}$$

The Eqs. (44) may be described as hyperbolic. In such a case, solutions for p and ϕ can be obtained in parts of the xy-plane merely by solving a simplified version of the equations of interest along certain curves that cross a line, along which a boundary condition is prescribed. The lines of interest are called characteristics and are defined as curves in the xy-plane, across which the derivatives of p and ϕ may be discontinuous. It turns out that for this problem there are two distinct and perpendicular characteristics going through each point, having slopes $\tan\phi$ and $-\cot\phi$ to the x-axis. Thus, in the slip line analysis, the α- and β-lines are actually the characteristics of interest. If the state of stress is given at a certain boundary, it will also be uniquely defined in all points of the xy-plane which share both its characteristics with the boundary line (Fig. 41(a)). Thus, some peculiarities exist. It turns out the state of stress will not be influenced by conditions on other parts of the boundary of the material. Furthermore, by the definition of characteristics,
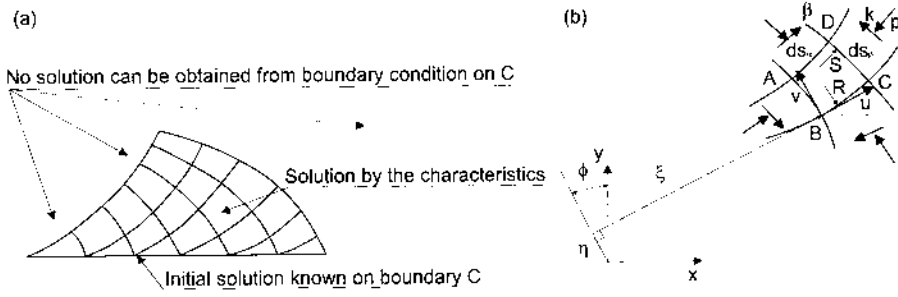
Figure 41 (a) Area with uniquely defined slip line solution; (b) Mikhlin-coordinates, ξ, $\bar{x}$ and η, $\bar{y}$ in relation to slip line grid.

the state of stress or any other field may change abruptly when crossing the α- or β-lines. These observations, however, are actually in accordance with the understanding of plastic deformation.

The velocity distribution in the flowing metal may be calculated only if isotropy and incompressibility is assumed:

$$\frac{2\dot{\gamma}_{xy}}{\dot{\varepsilon}_x - \dot{\varepsilon}_y} = \frac{\tau_{xy}}{\sigma_x - \sigma_y} \qquad \frac{\partial v_x}{\partial x} + \frac{\partial v_y}{\partial y} = 0 \tag{45}$$

By introducing the Eqs. (42) in the isotropy condition, a, the following relation may be obtained:

$$\cos 2\phi \frac{\partial v_x}{\partial x} + \sin 2\phi \frac{\partial v_x}{\partial y} + \sin 2\phi \frac{\partial v_y}{\partial x} - \cos 2\phi \frac{\partial v_y}{\partial y} = 0 \tag{46}$$

The velocity equations are also hyperbolic, and the characteristics of stress and strain are found to coincide at all points due to isotropy. Thus, the characteristic directions are those of both maximum shear stress and strain.

Both equations of stress and of velocity should be solved in the coordinate system defined by the slip lines. If it is assumed that the x and y directions at a particular point are oriented along the tangents to the α- and β-lines, the angle ϕ may be set to zero, rendering Eqs. (44):

$$\frac{\partial p}{\partial x} + 2k \frac{\partial \phi}{\partial x} = 0 \qquad \frac{\partial p}{\partial y} - 2k \frac{\partial \phi}{\partial y} = 0 \tag{47}$$

Since the original point chosen was arbitrary, the relations will hold at any point. If the Eqs. (47) are integrated along α- and β-lines respectively, the relation between the hydrostatic pressure p and the orientation, ϕ, of the slip line field relative to a rigid x-axis is:

Constant along an α-line: Constant along a β-line:

$$p + 2k\phi = C_1 \qquad\qquad p - 2k\phi - C_2 \tag{48}$$

These are the Hencky equations, which simply represent equilibrium along a slip line. It can be observed that the hydrostatic pressure will not change along a straight line. Generally p will vary along a curved line, the result being that the center of the Mohr-circle is translated along the σ-axis.

If the velocity equations are viewed in a coordinate system with axes tangential to the slip lines, the rate of extension vanishes along the slip lines:

$$\left(\frac{\partial v_x}{\partial x}\right)_{\phi=0} = \left(\frac{\partial v_y}{\partial y}\right)_{\phi=0} = 0 \tag{49}$$

If u and v are the velocity components along the slip lines, the velocity components along the x- and y- coordinate axes can generally be expressed as:

$$v_x = u\cos\phi = v\sin\phi \qquad v_y = u\sin\phi + v\cos\phi \tag{50}$$

By substituting Eq. (50) into (49) and setting $\phi = 0$, differential relations along the slip lines are obtained:

Along an α-line: Along a β-line:

$$du - vd\phi = 0 \qquad dv + ud\phi = 0 \tag{51}$$

These are the Geiringer equations [59]. Even though incompressibility is assumed, the velocity component tangential to a slip line may change. Such a variation is introduced by the curving of the slip lines. A constant tangential velocity along a slip line can be expected if the slip line is straight or if the velocity component normal to the slip line is zero. The last is the case for curved slip lines marking the boundary between flowing metal and dead zones.

Velocity discontinuities can be expected to be present when the hyperbolic equations are solved. Since mass has to be conserved the velocity component normal to a line of discontinuity can not alter when passing it. The tangential component, however, may change (Fig. 41(b)). Hence, the discontinuity line may be looked upon as one alone which the rate of shear is infinite. The discontinuity line will then also be a slip line. Along such a line the change in tangential velocity will be constant.

Two theorems that are of practical interest when a slip line field is to be drawn are Hencky's first and second theorem. These follow directly from the Hencky equations. The first states that the following relations can be taken to hold for the values of ϕ and p in the point A, B, C and D on the Fig. 41(b):

$$\phi_C - \phi_D = \phi_A - \phi_B \quad p_C - p_D = p_A - p_B \tag{52}$$

Thus, when going from one slip line to another in the same family the angle turned and the pressure change will always be the same.

Hencky's second theorem is based on the first and states that the curvature of lines of the other family decreases in proportion to the distance travelled along a slip line. If R and S are the curvatures along the α- and β-lines respectively and s_α and s_β the corresponding coordinates, the theorem yields:

$$\frac{\partial R}{\partial s_\beta} = -1 \frac{\partial S}{\partial s_\alpha} = -1 \qquad \Rightarrow$$

Along an α-line: Along a β-line:

$$dS + Rd\phi = 0 \qquad dR - Sd\phi = 0 \tag{53}$$

The last is a result of the mere definition of curvature. As can be seen, the curvature will decrease steadily as one moves to the concave side of the slip line. If the plastic zone extends sufficiently far, the radius of curvature finally vanishes. Discontinuities may, however, exist. The differential Eqs. (53) are of the same form as (51). Furthermore, by moving along the slip lines, the Mikhlin coordinates shown in Fig. 41(b), will change according to an equation of the same form:

Along an α-line: Along a β-line:

$$d\bar{y} + \bar{x}d\phi = 0 \qquad d\bar{x} - \bar{y}d\phi = 0 \tag{54}$$

The equations of the slip line theory can either be solved analytically, numerically or graphically. Complete analytical solutions are available for only a few problems. An example that will be provided is the process of frictionless plane strain extrusion at $R = 3$. If an area is determined uniquely by the stress boundary conditions, however, the pressures and slip line directions at a point (m,n) can be determined directly from known values at neighboring points by the Hencky equations:

$$p(m, n) = p(m, n - 1) + p(m - 1, n) - p(m - 1, n - 1) \tag{55}$$

$$\phi(m, n) = \phi(m, n - 1) + \phi(m - 1, n) - \phi(m - 1, n - 1) \tag{56}$$

The velocity field and the geometry of the slip line field have to be calculated with the help of Eqs. (51), (53) and (54) within the area that is defined uniquely by the boundary solutions. If the slip-lines are curved at all points a closed form solution may be obtained by combining each pair of equations to the equation of telegraphy:

$$\frac{\partial^2 f}{\partial\alpha\partial\beta} = f \tag{57}$$

f may in this case be either the velocities, curvatures or Mikhlin variables. α and β are the coordinates along the slip lines and are related to ϕ as $\phi = \phi_{\mathrm{o}} - \alpha + \beta$ where ϕ_{o} is a reference. Depending on the curvatures of the slip lines, a solution giving the form of the field and the velocities will be provided by either the modified Bessel function of the first kind or the Bessel function of first kind:

$$f(\alpha, \beta) = \sum_{n=0}^{\infty}[\alpha_n f_n(\alpha, \beta) + c_n f_{n+1}(\beta, \alpha)] \qquad f_n(\alpha, \beta) = \left(\frac{\alpha}{\beta}\right)^{n/2} I_n\left(2\sqrt{\alpha\beta}\right) \tag{58}$$

$$f(\alpha, \beta) = \sum_{n=0}^{\infty}[\alpha_n g_n(\alpha, \beta) + c_n g_{n+1}(\beta, \alpha)] \qquad g_n(\alpha, \beta) = \left(\frac{\alpha}{\beta}\right)^{n/2} J_n\left(2\sqrt{\alpha\beta}\right) \tag{59}$$

The constants will then be determined from the boundary conditions.

As the analytical solution may be hard to perform, the geometry of the slip line field may be calculated numerically by the discretisation of the Eqs. (54). A constant angular distance in both α- and β- direction is chosen. The values of the Mikhlin coordinates in a point (m,n) are then calculated as those in neighboring points (m,n − 1) and (m − 1,n) are already known.

$$\bar{x}(m, n) - \bar{x}(m, n - 1) = \frac{1}{2}[\bar{y}(m, n) + \bar{y}(m, n - 1)]\mu\Delta\phi \tag{60}$$

$$\bar{y}(m, n) - \bar{y}(m - 1, n) = -\frac{1}{2}[\bar{x}(m, n) + \bar{x}(m - 1, n)]\lambda\Delta\phi \tag{60}$$

μ and λ are either -1 or 1 depending on whether $\Delta\phi$ decreases or increases when going from the neighboring points. The velocity field can be found in the same manner.

A complete geometrical slip line solution is provided by Prager's method [60] (Fig. 42). As three aspects are of interest, the stress state, the velocity distribution and the geometry of the slip line field, it seems natural to generate three geometrical representations, the stress plane, the hodograph and the physical plane. The stress plane consists of a number of Mohr's circles, representing the state of stress at all points in the material. As the material is assumed to yield, all states provide circles with the same radius, k. The position of the pole will then be of primary interest since it will characterize the state of stress. When one moves along a curved slip line, the stresses are observed to change and consequently also the position of the pole. Lines showing its movement can then be drawn in the stress plane. The lines corresponding to the movement along an α- and β-lines are the cycloids that would be generated if the Mohr-circle had rolled without slipping on the lines $\tau = k$ and $\tau = -k$. More importantly it can be shown that their form corresponds to the form of the slip lines in the physical plane.

The hodograph is simply a representation of the velocity vectors at each point in the physical plane. The vectors are constructed from the same point so that the changes in velocity between two points will be given by the vector drawn between the their arrow heads. An important property is that while the slope of the α-line is
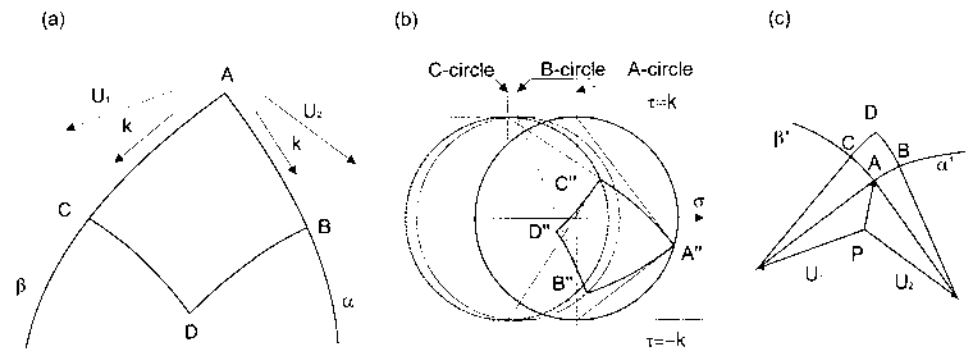
Figure 42   Slip line solution by Prager's method: (a) The physical plane; (b) The stress plane; (c) The hodograph.

$\tan\phi$, the relation dv_y/dv_x will be $-\cot\phi$ along the line. Hence, the vector giving the change in velocity at a point will be directed normal to the slip lines. This is in accordance with the fact that no elongation will be expected along the slip lines.

4.2.9 Frictionless Extrusion with $R = 3$

A simple analytical slip line solution may be obtained if it is assumed that extrusion of $R = 3$ with no friction forces along the container wall and die is performed as shown in Fig. 43(a). The problem is regarded as one of steady state. A velocity is prescribed for the piston. Other boundary conditions are assumed to be expressed in terms of stress. Neither a bearing channel nor a puller is included in the analysis. Therefore the material will be free from tractions at the die opening, $\sigma_x = 0$ and $\tau_{xy} = 0$. It may then be seen that some kind of discontinuity must exist since equilibrium does not allow the stress component along the x-axis to be zero for the material close to the die. The solution is the construction of a fan field since this allows an abrupt change in the hydrostatic pressure along a given line.

If it is assumed that the state of stress in zone I is one of yielding, it can be determined uniquely by the boundary conditions. The Mohr circle reveals that the stress component $\sigma_y = -2k$. As a result the lines of maximum shear must be inclined at an angle of $\pi/4$ and $-\pi/4$ to the x-axis. Hencky's first theorem indicate that both the angle ϕ and the hydrostatic stress, $p = k$, will be uniform in zone I, and therefore it will have the form of a triangle with straight edges.

In zone II the α-lines are taken to be radial and β-lines tangential. As the radial lines are straight, the hydrostatic pressure can be expected to be uniform along these lines. A singularity will then exist at the point where the radial lines run together, the presence of a sharp edge being the cause. Along the β-lines the expression $p - 2k\phi$ is constant. If ϕ is chosen to be $-\pi/4$ at the boundary between zone I and zone II where $p = k$, the pressure along an arbitrary β-line will be $p = k + k\pi/2 + 2k\phi$. The boundary to zone III will be a straight line at $\phi = \pi/4$. The reason is that the characteristics also in this region must be straight and inclined at an angle $\pi/4$ and $-\pi/4$ due to the boundary condition $\tau_{xy} = 0$ at the die. Hence, the hydrostatic pressure increases from k to $k(1 + \pi)$ from region I to III. This corresponds to a movement of the center of the Mohr circle a distance $k\pi$ to the left. The coordinate stresses in region III may then be calculated to be:

$$\sigma_x = -p - k\sin 2\phi = -k(1 + \pi) - k\sin 2\frac{\pi}{4} = -2k\left(1 + \frac{\pi}{2}\right) \tag{62}$$

$$\sigma_y = -p + k\sin 2\phi = -k(1 + \pi) + k\sin 2\frac{\pi}{4} = -k\pi \tag{63}$$

$\tau_{xy} = 0$ in accordance with the boundary condition and Hencky's first theorem. These results can also be obtained graphically through Fig. 43(c). The stress component σ_x *constitutes the pressure experienced by the die.*

The velocity field may then be calculated. The material to the left of the plastic zone is assumed to be rigid and is therefore expected to move with the same velocity, V, as the stem. Since the incompressibility condition can be expected to hold, the velocity of the extruded profile will be $R \times V$. The straight characteristics of region I indicate a uniform velocity of the same magnitude in the x-direction. In region III the material must flow along the die surface. Since the characteristics are straight
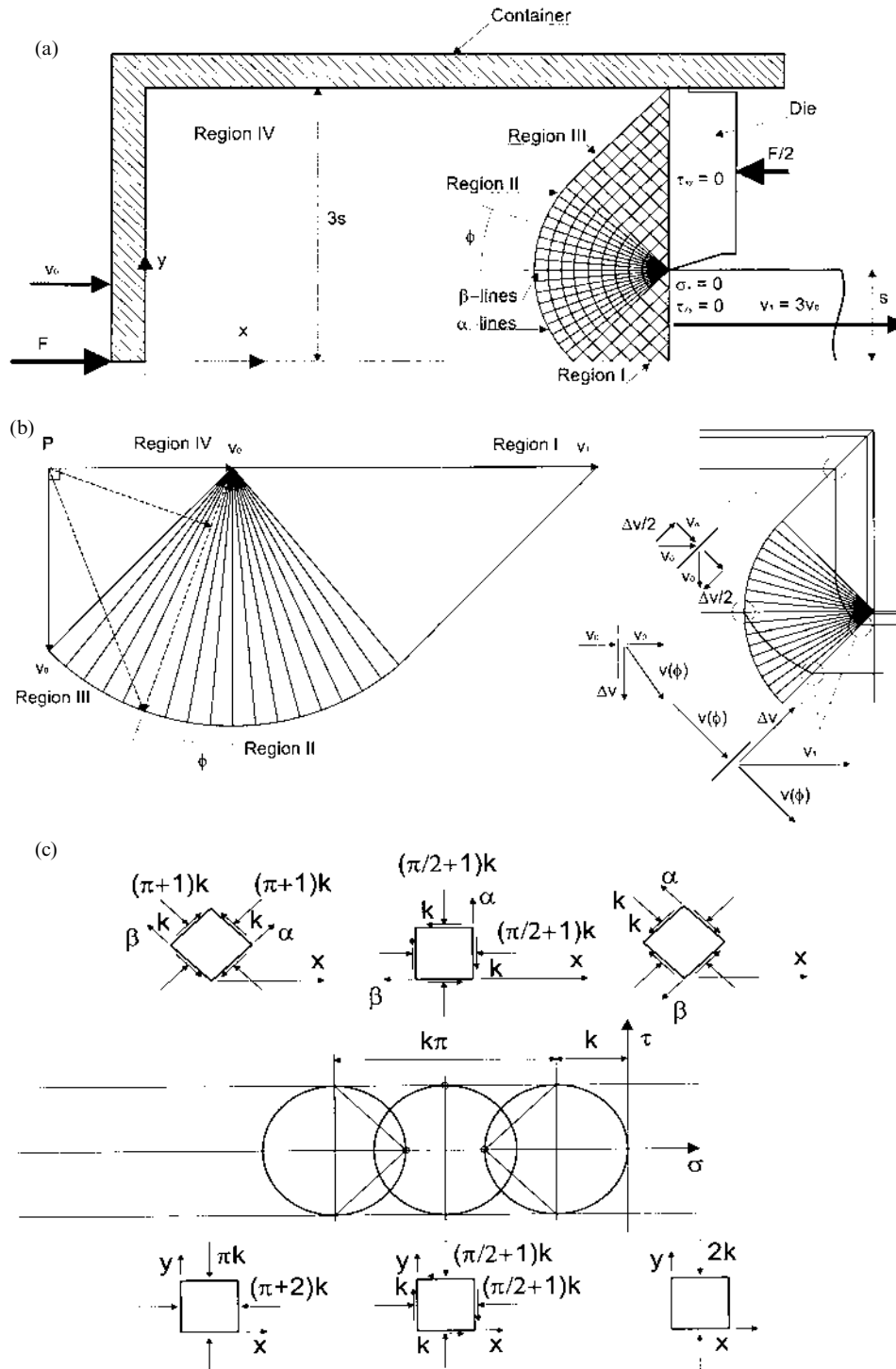
Figure 43   Slip line solution for indirect extrusion at $R = 3$. (a) Geometry and slip line grid; (b) The hodograph (velocity field) and the flow lines; (c) The state of stress.

also in this region, one must expect that the velocity is uniform. The line that separates region III from the rest of the container, must then be a velocity discontinuity. As expected, this is also a slip line. The change in flow velocity will be directed tangentially to the discontinuity line and be $\sqrt{2}V$ (Fig. 43(b)). As can be seen, the flow velocity in region III will also be V.

The remaining question is then how velocity changes take place in the fan. The simplest way to answer this is by constructing the hodograph (See Fig. 50(b). The velocity vectors representing region I, III and IV are drawn first. The vector representing the discontinuity between the regions III and IV is then added, confirming assumptions made earlier. One should notice, however, that the magnitude of a velocity discontinuity is constant along a characteristic. Therefore, the velocity discontinuity at each point along the outer β-characteristic may be drawn as a radial line with a length $\sqrt{2}V$ starting from the end of velocity vector of region IV. The circle sector generated in the hodograph will span the same angle, $\pi/2$, as the sector in the physical plane. Thus, there must also be a velocity discontinuity of the same magnitude on the border between the fan and region I. As expected, the geometry of the hodograph resembles that of the characteristics in the physical plane.

The main objective with using the slip line theory is to obtain a simple mathematical description of the flow paths and deformation history. The uniform flow velocity in regions I, II and IV may easily be described by constant components in the x and y direction. In order to obtain expressions for the velocity in region II one has to apply the Geiringer equations. In polar coordinates the criterion of no elongation along stream lines may be written as:

$$\dot{\varepsilon}_{\mathrm{r}} = \frac{\partial v_{\mathrm{r}}}{\partial r} = 0 \qquad \dot{\varepsilon}_{\phi} = \frac{\partial v_{\phi}}{r\partial\phi} + \frac{v_{\mathrm{r}}}{r} = 0 \tag{64}$$

The first equation confirms that the radial velocity only will be function of the angle ϕ. As no radial discontinuity in velocity can be allowed for a material particle going from the outer field and into the fan, v_{r} must be cosine function which yields $-V$ for $\phi = 0$. The second of Eq. (64) may then be solved with the boundary condition $v_{\phi}(\pi/4) = -\sqrt{2}V$. The velocity components in the fan are then:

$$v_{\mathrm{r}} = -V\cos\phi \qquad v_{\phi} = V\sin\phi - \sqrt{2}V \tag{65}$$

The shear strain rate and equivalent strain rate may be calculated from the above expressions:

$$\dot{\gamma}_{\mathrm{r}\phi} = \frac{1}{r}\frac{\partial v_{\mathrm{r}}}{\partial\phi} + \frac{\partial v_{\phi}}{\partial r} - \frac{v_{\phi}}{r} = \sqrt{2}\frac{V}{r} \qquad \dot{\bar{\varepsilon}} = \frac{\dot{\gamma}_{\mathrm{r}\phi}}{\sqrt{3}} = \sqrt{\frac{2}{3}}\frac{V}{r} \tag{66}$$

By the help of the definition of radial and tangential velocity, the flowline through the fan for a particle starting at (r_0, ϕ_0) on the boundary may be calculated:

$$\frac{v_{\mathrm{r}}}{v_{\phi}} = \frac{dr}{rd\phi} = \frac{-V\cos\phi}{V\sin\phi - \sqrt{2}V} = \frac{\dfrac{1}{\sqrt{2}}\cos\phi}{1 - \dfrac{1}{\sqrt{2}}\sin\phi} \tag{67}$$

Integration and use of the of the known starting point (r_0, ϕ_0) at an edge of the fan provides the equation for the flowline:

$$r = r_\mathrm{o} \frac{\sqrt{2} - \sin \phi_\mathrm{o}}{\sqrt{2} - \sin \phi} \tag{68}$$

Some of the possible flowlines are shown in Fig. 43(b). If such a line enters fan at r_0 on the characteristic $\phi = \pi/4$, the ratio r/r_0 will be independent of the value of r_0. This is due to the lack of variation in particle velocity along an α-characteristic. As a result, all such flowlines in the fan have the same form. By inserting data one finds that $r < r_0$ for all ϕ except when $r = r_0 = 0$. This is accordance with the fact that the material is compressed during extrusion.

The study of deformation of rectangular grid patterns constructed on the billet proves valuable as it opens for a comparison of the experimental and analytical results. Furthermore, emptying diagrams, which can be derived numerically, may also provide information about the origin of material particles in the profile. Thus, at least qualitative data on the deformation of material particles and the danger of inferior surface quality due to the inflow of particles from the billet surface, may be obtained through the use of slip line theory. If one is to relate the position of a particle in the billet to that in the extruded profile, one has to calculate both the coordinates of the path-line and time spent on travelling along the line. As material particles in all but the fan region are expected to run along straight lines with a prescribed velocity, most of the necessary calculations are trivial. In the fan, Eq. (68) describes the flowlines. The corresponding expression for the time needed for a particle to travel from one point on the flowline to another, must be derived from the definition of tangential velocity, $v\backslash phi = r \, d\phi/\mathrm{dt}$. An integration then results in:

$$
\begin{aligned}
t &= \int_{\phi_0}^{\phi} \frac{r}{v_\phi} d\phi = -\frac{r_0}{V}(\sqrt{2} - \sin \phi_0) \int_{\phi_0}^{\phi} \frac{d\phi}{(\sqrt{2} - \sin \phi)^2} \\
&= \frac{r_0}{V}(\sqrt{2} - \sin \phi_0) \left[\frac{\cos \phi}{\sqrt{2} - \sin \phi} - 2\sqrt{2} \arctan\left(\sqrt{2} \tan \frac{\phi}{2} - 1\right) \right]_{\phi_0}^{\phi}
\end{aligned} \tag{69}
$$

where ϕ_0 and ϕ are the angles marking respectively the start- and the endpoints of the flowline. In order to calculate the time spent on going through the whole fan, one must set $\phi = -\pi/4$ and (r_0, ϕ_0) either equal to ($r_0 < R$, $-\pi/4$) or (R, $-\pi/4 < \phi_0 < \pi/4$) depending on the boundary section of the fan crossed.

Figure 44(a) reveals the geometry of the calculation model. The deformation of a straight line starting at $x = 2L$ is then studied by calculating the time taken for a particle to flow from the line to various points and then drawing iso-time curves. In the region denoted IV, the material will move uniformly and the line will remain straight until a part of it touches the fan. The material in the fan will then accelerate, and due to the geometry of the fan field a part of the line at a short distance from the centerline will move forward relative to line segments both on the left and the right side. Particles on the centerline will experience a sudden increase in velocity when entering region I. However, it turns out that some particles that have been accel-

erated through the fan on the average will move the fastest, and, thus, constitute the most forward part of the iso-time curve in the profile. The particles close to the container walls will be delayed due to the long distance they have to travel. Since zero friction conditions are assumed, however, material from the container surface will eventually reach the profile surface and potentially cause poor surface quality. Dead zones will not be present. The last observation is confirmed by Fig. 44(b), which is the emptying diagram for the model used. The diagram is obtained by calculating the time each particle in the container will need to reach the die opening of container. Iso-residence-time curves are then drawn. The two diagrams presented essentially give the same description of the extrusion process.

If it is assumed that extrusion is performed with a high flow rate, heat transfer will mainly be convective and the temperature of a particle will at any point be proportional to the amount of heat received. Conditions are then assumed to be adiabatic. As a material is deformed, the energy spent on deforming it will either be stored in the microstructure through a high dislocation density or dissipated as heat. In the case of cold working the first part will not amount to more than about 5%. As both work hardening and recovery/recrystallization take place during extrusion the dislocation density does not necessarily increase and therefore the part of the energy stored in the microstructure may be neglected. As a result one may roughly state that the increase in thermal energy of a particle will be equivalent to the heat provided by dissipation:

$$pc\dot{T} = \alpha_{ij}\dot{\varepsilon}_{ij} = \overline{\sigma}\dot{\overline{\varepsilon}} \tag{70}$$
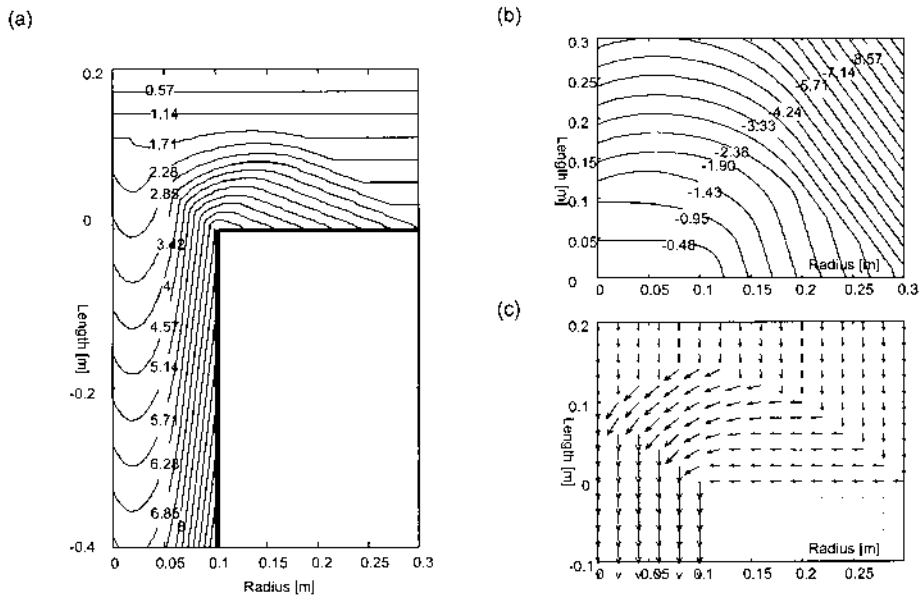
Figure 44 Material deformation in extrusion with $R = 3$ and $v_0 = 0.05$ m/sec. All times in seconds. (a) The deformation of a line which is straight at $x = 2$ L $= 0.2$ m and $t = 0$ s; (b) The emptying diagram; (c) Velocity vectors.

where ρ is the density and c the heat capacity. The temperature will increase through the fan and when crossing a velocity discontinuity. In the areas where the material moves with a uniform velocity, no strain rates are expected and therefore no increase in temperature either. An analytic expression for the rise in temperature through the fan is obtained by performing an integration of Eq. (70) with respect to the time spent on travelling from one point, (r_0, ϕ_0), to another, (r, ϕ). Equation 66 is an expression for the equivalent strain, and Eqs. (68) and (69) must be applied as they describe the path followed and relate the time increment to an increment in the angle, ϕ. If k is taken to be constant, an expression for the difference between the temperatures at two points in the fan is:

$$
\begin{aligned}
T - T_0 &= \int_{t_0}^{t} \frac{\bar{\sigma}}{\rho c} \dot{\bar{\varepsilon}} dt = \sqrt{\frac{2}{3}} \frac{\bar{\sigma}}{\rho c} \int_{t_0}^{t} \frac{V}{r} dt = \sqrt{\frac{2}{3}} \frac{\bar{\sigma}}{\rho c} \int_{\phi_0}^{\phi} \frac{1 - \sqrt{2}\sin\phi}{\sqrt{2} - \sin\phi} \\
&- 2 \frac{\sec^2\phi(\sqrt{2} - \sin\phi)}{1 + \left(\sqrt{2}\tan\frac{\phi}{2} - 1\right)^2} dt
\end{aligned}
\tag{71}
$$

If $\bar{\sigma} = \sqrt{3}k$ and integration is performed the result is:

$$
T - T_0 = 2\sqrt{2} \frac{k}{\rho c} \left(\arctan\left(\sqrt{2}\tan\frac{\phi_0}{2} - 1 \right) - \arctan\left(\sqrt{2}\tan\frac{\phi}{2} - 1 \right) \right)
\tag{72}
$$

The adiabatic temperature change through the fan is only dependent on the point where the material enters and on the total angle turned. In other words, an increment of temperature change will only depend on the increment of change in angle. The material that enters the fan at the angle $\phi = \pi/4$ will experience a temperature rise that is independent of r_0, and, therefore, the material closest to the surface will leave with a uniform temperature. Even though the value of the strain rate goes to infinity for small radiuses, temperature changes will be limited as the time spent in the fan approaches zero. If, however a material particle enters the fan at an angle $\phi_0 < \pi/4$, the increase in temperature through the fan will be smaller, and the material in the center of the profile can be expected to be colder than that on the surface.

Velocity discontinuities represent areas of concentrated shear. If it is assumed that the discontinuity has a certain thickness, δ, the strain rate experienced by a particle going through a discontinuity will be $\dot{\gamma} = \Delta v/\delta$ where Δv is the sudden change in velocity tangentially to the discontinuity. The time spent on passing the discontinuity will be $\Delta t = \delta/v_n$ where v_n is the component of the velocity normal to the discontinuity line. The total straining of a material particle going through the discontinuity will then be $\gamma = \dot{\gamma} \cdot \Delta t = \Delta v/v_n$. On the discontinuity between region III and IV v_n can be expressed as:

$$
\Delta\gamma = \frac{\Delta v}{v_n} = \frac{V\sqrt{2}}{V\sqrt{2}} = 2
\tag{73}
$$
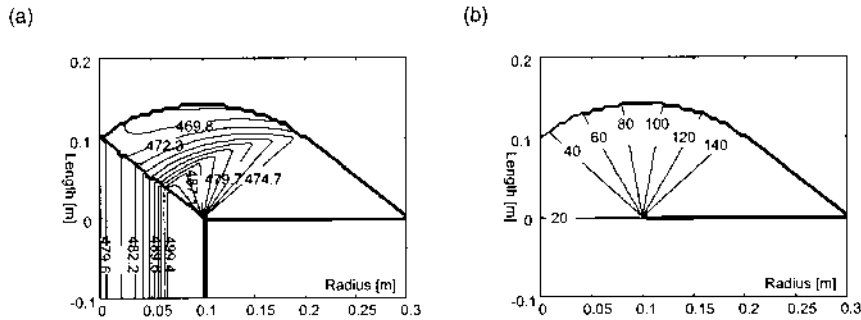
Figure 45 (a) Temperatures given under adiabatic conditions with billet preheated to 450°C; (b) Hydrostatic pressure during extrusion [MPa].

In the same way the discontinuities between the regions I and II and II and IV can be shown to give the total strain of respectively $2/3$ and $\sqrt{2}/cos\phi$. The rise in temperature due to a number of velocity discontinuities can be calculated to be:

$$\Delta T = \frac{k\Sigma\Delta\gamma}{\rho c} \tag{74}$$

If it is assumed that the billet originally has a uniform temperature of 450°C, the adiabatic temperature at a certain point may be calculated simply by adding the contributions from all areas of shear the particle at the point has passed. The result is shown in Fig. 45(a). In reality, both friction at the container wall and at bearing surfaces will contribute to even higher temperatures close to the surface of the profile. The adiabatic assumption may also often prove to be not entirely correct, and as a result, the temperatures at least in the profile leaving the container may be lower and more uniform than expected.

4.2.10 Alternative Slip Line Fields

The motivation for choosing a case with an R-ratio of 3 and frictionless conditions is mathematical simplicity and not the model's coherence with reality. Extrusion usually takes place at R-ratios that can be many tenfolds larger than 3, and due to the presence of friction, the velocity fields differ significantly from the one proposed. However, as the extrusion process traditionally has been a popular test case for the application of theory, a large number of analytical and semi-analytical slip line solutions have been found. Books on the classical slip line theory [61,62] present quite a few problems with different assumptions connected to friction and reductions.

Figure 46 gives an example of a slip line field in the case where there is sticking friction between the flowing metal and the tooling. If the friction model is to be that of Tresca, the shear stress between the container wall and the flowing metal is equal to the shear yield stress of the metal. As this is also the maximum shear stress possible, the slip lines that interfere with the walls have to be either normal or tangential to it except at singularities. The slip lines of both families also have
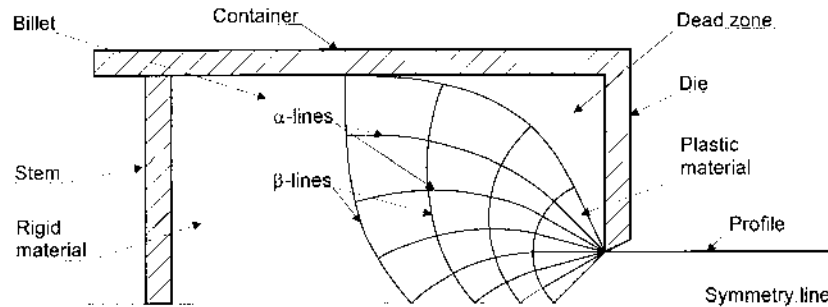
Figure 46 Slip line field for the direct extrusion of aluminum under the assumption of full sticking at the walls of the container and the die.

to meet the center axis at an angle of $\pi/4$ due to the symmetry condition. The slip line field may then be calculated both analytically and numerically as earlier described.

When applying numerical methods the slip lines in the grid should be separated by a constant increment of the angle, $\Delta\phi$. The geometry of the container, particularly the R-ratio, will uniquely determine the angle between the outermost radial lines of the fan. If R reaches about 12.5, the analysis breaks down as the upper radial line then is tangential to the surface of the die. When the slip line field is determined, the stresses follow directly from Hencky's equations. The coordinates in a xy-system may be calculated by starting at the fan and working outwards under the assumption that the line segment between two nodes is approximately straight.

In order to obtain the velocity field, the boundary conditions have to be determined. The material to the right of the slip line field is assumed to move uniformly at the pace of the piston. This can be used to calculate the velocity components along the velocity field in the rightmost part of the slip line field. In the dead zone the material velocity is expected to be zero, and velocity components normal to the closest slip line vanish. Consequently the velocity tangential to this slip line is constant and equal to the velocity of the piston, which then also is the magnitude of the velocity discontinuity along the line. A last boundary equation is that the components of velocity along the symmetry line must be equal as it is a flowline. In order to obtain a numerical solution to the problem a discrete form of the Geiringer equations have to be applied. The values of the components of velocity in a node are then found from the corresponding values in the neighboring nodes. By a method of trial and error, the velocity components at all points on the symmetry lines are varied until all boundary conditions are satisfied simultaneously.

4.2.11 The Slab Method Applied in the Study of Friction on Bearing Surfaces

The strip or slab method, which is a part of the elementary plasticity theory, is based on a simplified view of the state of stress in the material. Usually only conditions of plane strain are considered. The work piece is directed along an axis, say the x-axis, and then divided into a number of infinitesimally thin strips, each with a thickness dx. These are studied individually. In order to make this division worthwhile one has to neglect all other velocity components than that along the x-axis. At

the same time one assumes that the principal directions of stress and strain are along the coordinate axes. Differential relations describing both the velocity field and the stress field may then be obtained simply by asserting that the equations of conservation of volume and motion in x-direction have to be satisfied. The relation between different components of stress is obtained through the Tresca yield criterion.

The slab method has been applied on a range of problems connected to materials forming, such as drawing, rolling, forging and extrusion. The results obtained are usually the forming forces, which strictly must be taken to be lower bounds as the method is based on equilibrium considerations. However, the slab methods will at best only give a simplified view of the stresses and deformation in the metal and at worst provide totally erroneous results. This is especially the case when the slab method is applied in the study of the relatively complex flow in the container during extrusion, as the assumption regarding the principal directions of stress need not be correct. Another problem is that the slab method does not accept large changes in geometry along the x-axis because the analysis then will be inconsistent. The extrusion force may be calculated to be in accordance with the relation $F = a + b\,\mathrm{In}(R)$ also with the slab method, but one must be aware of the fact that the method of calculation only guarantees the result in case of small values of the reduction ratio.

In relation to the extrusion process, the slab method may probably most effectively be applied in the study of the pressure build-up through the bearing channel. Usually, analytical solutions neglect the presence of such a channel all together, but in practical extrusion bearing surfaces of zero length are neither possible nor desirable. The pressure build-up caused by the friction between the flowing material and the bearing surfaces may actually be utilized to control the flow and therefore also the profile quality. The aim will then always be that the velocity in the cross-section of the profile leaving the die should be as uniform as possible and that no internal stresses should be generated. The general rule is that a material particle will flow in the direction of the lowest pressure gradient. If the material flows to fast over a certain part of the cross section as a result of low flow resistance, one must attempt to force the material flow in other directions by increasing the length of the bearing channel and thereby also the total friction force. As less material then is expected to enter the region, the flow speed is reduced and hopefully made more equal to that of neighboring parts of the cross section.

When bearing channels are not properly adjusted, as often is the case in connection with complex die geometry, the result will be unbalanced and uncontrolled flow, but not necessarily totally unusable products. If the material flows faster in parts of the cross-section, the profile can be expected to bend as its leaves the die. If velocity gradients perpendicular to the flow direction also exist during further extrusion, the profile walls may buckle or twist in areas with too great speed and experience thinning or even tearing where the velocity is to low. However, as more of the profile is extruded the material will usually leave the die at an almost uniform speed. This is due to the fact that velocity gradients will cause shear stresses, which in the next turn will contribute to the reduction of such gradients. The result is that residual compressive stresses can be found in the parts of the profile that experienced the largest flow velocity in the bearing channel. Tensile stresses will be generated in slow flowing parts so that a force equilibrium eventually will exist. This self-stabilizing effect is present in a number of metal forming processes and explains

why relatively satisfactory product quality can be obtained without total process control. However, complete reliance on such an effect is not desirable since the control of flow velocity in products with variable wall thickness and especially in thin-walled section is inefficient. Furthermore, residual stresses have to be properly removed by a stretching operation. This is particularly important if further operations such as for instance bending are to be performed on the profile.

The lengths of the bearing surfaces may be from a couple of millimeters to about a centimeter, and the surface area constitutes only a very small percentage of the total area of interaction between the flowing metal and the die. Furthermore, short bearing surfaces are generally preferred as they generate less friction and therefore reduce the need for a large extrusion force. However, even relatively short bearing lengths generate large increases in the needed extrusion pressure. And most importantly, the interaction between the flowing metal and the bearing surfaces is maybe the most complex and variable element of the extrusion process and, thus, can be expected to be of prime importance to product quality. As will be explained in the next section, the study of interaction between flow stability, die deflection and friction in the bearing channel is one of the most interesting fields of research.

A simple slab analysis will be performed in order to calculate a rough mean value for the pressure rise through the bearing channel due to the presence of friction. As will be explained later, one may assume that the flowing material sticks to the bearing surface over the first 4 mm and that the shear stress in the sticking region is constant and equal to the shear yield stress k. The friction close to the outlet will be of Coulomb type, and it is assumed that the shear stress in the slipping region decreases linearly from the slip point and towards the outlet. The last assumption is probably only correct if the normal stress to the bearing also can be expected to decrease towards the opening. The bearing surfaces are taken to be parallel at all points. Usually, bearing surfaces are either converging or diverging and are said to be designed with respectively a choke or a release. The establishment of the position of the slip point where material starts gliding along the bearings and a surface may be said to be created, represents the main problem. Even though experiments have confirmed the presence of such a point, and its position has been determined for various choke angles, bearing lengths, alloys and extrusion rates, no rigorous method of estimation this parameter has yet been developed. Hence, when performing both analytical and numerical calculations, assumptions are usually made regarding the position of the transition region. This introduces an uncertainty into the analysis. In the following slab calculations (Fig. 47) the friction against the bearings will be described by the equations:

$$
\begin{aligned}
0 < x < 4 \,[\text{mm}]: \qquad & \tau = 30 \qquad [\text{MPa}] \\
4 < x < 8 \,[\text{mm}]: \qquad & \tau = 55 - \frac{25}{4}x \quad [\text{MPa}]
\end{aligned}
\tag{75}
$$

The slip point is, thus, assumed to be at $x = 4$ mm, and the shear stress at the opening is set to 5 MPa. Finally, the principal stress directions are chosen to be parallel to the coordinate directions. This is actually only correct near the x-axis, along which the coordinate shear stresses may be expected to vanish due to symmetry. Close to the bearing surfaces the presence of the boundary condition makes it evident that the assumption regarding principal directions must be

(a)

(b)   (c)
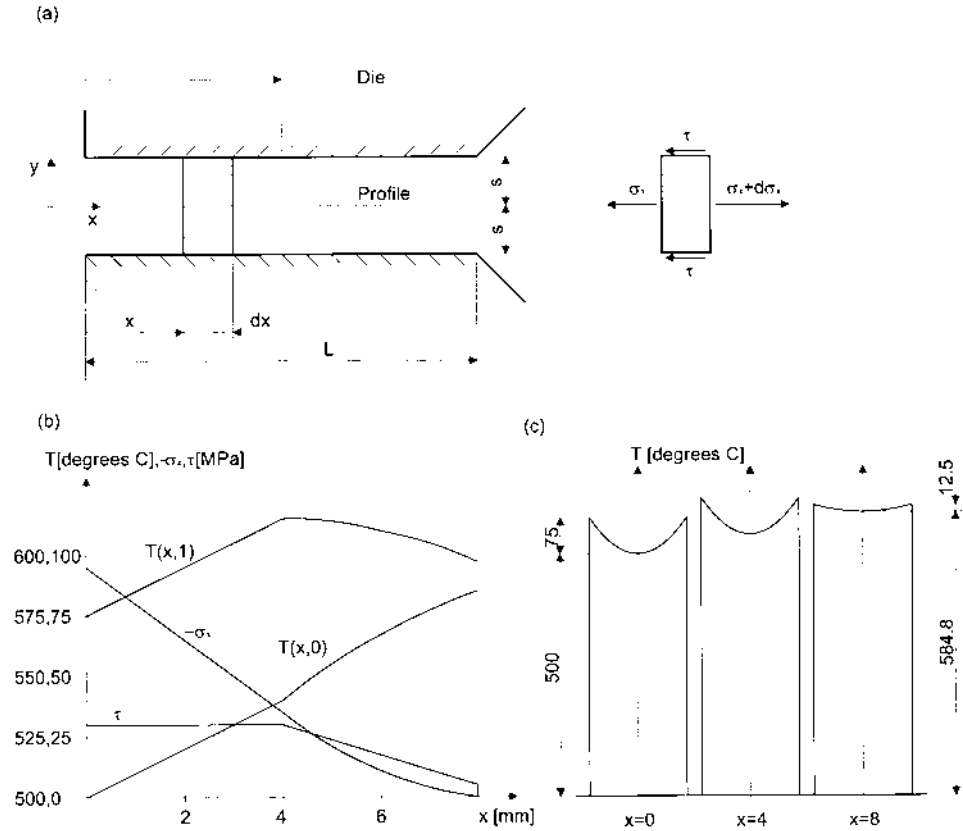
Figure 47 Slab model of the material flow in the bearing channel. (a) The geometry of the model; (b) Variation in stresses and temperatures throughout the bearing channel ($L = 8$ mm); (c) Development of the temperature field in the bearing channel.

incorrect. However, if it is assumed that the inconsistencies may be neglected, a force equilibrium will yield a differential equation for the x-component of stress:

$$\left(\sigma_x + \frac{d\sigma x}{dx}dx\right) \times 2s - \sigma_x \times 2s - 2\tau \times dx = 0 \qquad d\sigma_x = \frac{\tau}{s}dx \tag{76}$$

Integration from $x = 8$ to $x = 0$ mm then provides the stress along the bearing channel. First, the integration is performed from $x = L = 8$ mm to $x = x_s = 4$ mm with the assumption that $\sigma_x(L) = 0$. Then, $\sigma_x(x_s) = -70$ MPa is found and the data is used in the integration from $x = x_s$ to $x = 0$. The result is:

$$0 < x < 4\,[\text{mm}]: \qquad \sigma_x(x) = \sigma_x(x_s) - \int_x^{x_s} 30d\xi = -190 + 30x$$

$$4 < x < 8\,[\text{mm}]: \qquad \sigma_{\text{x}}(x) = \sigma_{\text{x}}(L) - \int\limits_{\text{x}}^{L}\left(55 - \frac{25}{4}\xi\right)d\xi = -\frac{25}{8}x^2 + 55x - 240$$

(77)

From the criterion of full sticking and the above equations it may be seen that the stress component normal to the bearing surface will decrease linearly in the sticking region, which is in accordance with the assumptions made. At the inlet to the bearing channel the x-component of normal stress is then calculated to be -190 MPa. This result may be used as a rough estimate in a slip line analysis.

The slab method may also yield a rough estimate of the temperature increase through the bearing channel. The y-axis is assumed to be directed normal to the bearing surfaces. As heat will be generated on the surface between the flowing metal and the die it is natural to expect that the temperatures of greatest magnitude may be found in this area. At the same time, the temperature will increase steadily towards the outlet of the bearing channel. A simple approximate temperature field can be assumed to satisfy the relation:

$$T = T_{\text{s}} + \Delta T\left(\frac{y}{s}\right)^2$$

(78)

where 2s is the width of the bearing channel, and the parameters T_{s} and ΔT are only dependent on x. It is then assumed that all heat generated on the boundary between the die and profile will contribute to an increased temperature in the profile and that heat conduction only will take place in the y-direction. Thus,

$$q_{\text{y}} = -\lambda\left(\frac{dT}{dy}\right)_{\text{y=s}} = \frac{2\lambda\Delta T}{s} = -\tau v \qquad \Delta T = \frac{v \times s}{2\lambda}\tau$$

(79)

where v is the extrusion speed and τ is the shear stress on the boundary. ΔT will then be a function of τ and therefore also x. In this example the following material parameters are used: $v = 1\,\text{m/sec}$, $\lambda = 200\,\text{W/mK}$, $\rho = 2700\,\text{kg/m}^3$ and $c = 1100\,\text{W/mK}$. For $x < 4$ mm ΔT will be constant and equal to the original value of 75°C since the shear stress is constant. From $x = 4$ to $x = 8$ mm the value of ΔT will decrease linearly to 12.5°C at the outlet due to decreasing τ. Since the heat generation connected to friction will be spent on increasing the temperature, T_{s} must be expected change along x. As ΔT will not be altered for $x < 4$ mm, all heat added will contribute to the increase of T_{s}. The heat balance for an element is then:

$$-q_y\,dx\,dt = \rho\,c\,dT_{\text{s}}\,s\,dx \qquad T_{\text{s}}(x) = \frac{q_{\text{y}}\,x}{\rho\,c\,s\,v} = \frac{\tau\,x}{\rho\,c\,s} = 10.1x$$

(80)

x is given in millimeters. As only changes in temperatures are to be assessed, $T_{\text{s}}(0)$ is set to 0, and the value of T_{s} at $x = 4$ mm can be calculated to be 40.4°C. A similar equation may be derived from the heat balance in the case where ΔT varies along x:

$$-q_y\,dx\,dt = \rho\,c\left(dT_{\text{s}} + \frac{1}{3}d\Delta T\right)s\,dx$$

(81)

The term $1/3$ is due to the parabolic ΔT-distribution. Integration and substitution of $q = -\tau v$ then yield:

$$T_s(x) = T_s(x_s) + \frac{1}{3}\Delta T(x_s) - \frac{1}{3}\Delta T(x) + \frac{1}{\rho\, c\, s}\int\limits_{x_s}^{x}\tau(\xi)d\xi \tag{82}$$

In the present example a closed form solution can be reached if the functions $\Delta T(x)$ and $\tau(x)$ are inserted. x is to be given in millimeters.

$$T_s(x) = -37.67 + 23.73x - 1.05x^2 \tag{83}$$

The temperature in the middle of the profile at the outlet ($x = 8$ mm) may thereafter be calculated to be approximately $84.8°$C. As expected the temperature in the mid-section of the profile has risen through the bearing channel, but the transversal temperature gradients are reduced due to the decreasing amount of dissipation through friction in the slipping zone. If x and y still are taken to be in millimeters, the total temperature function may be written:

$$T(x, y) = 10.1x + 75y^2$$
$$T(x, y) = -37.67 + 23.73x - 1.05x^2 + 2.5\left(55 - \frac{25}{4}x\right)y^2 \tag{84}$$

The curves for $T(x, 0)$ and $T(x, 1)$ are given in Fig. 47. Here, it is assumed that $T_s(0) = 500°$C and not 0.

4.2.12 Numerical Analysis

A complete analytical description of the extrusion process is of interest since it simplifies parameter studies, and since numerical results can easily be obtained and therefore also applied in on-line process control. However, such solutions are rarely found for more complex geometries with multiaxial stress and strain-states, and will only under the simplifying assumption of adiabatic conditions yield a proper estimate on both the strain rate and temperature history. Today, it seems as the most satisfactory alternative or complement to closed form solutions has been provided by the finite element method (FEM) [63–65].

A FEM solution for a plastically deforming material is, however, nothing but an upper bound solution, as the method utilizes the calculation of work done on the volume of the elements during a virtual deformation. The main difference between a numerical and an analytical approach is that fewer elements usually are applied in the later, and therefore, that the corresponding kinematically admissible velocity field provides a higher upper bound. If one assumes that the material model and boundary conditions give an accurate description of reality, a numerical method will in the very limit of infinitesimal elements both yield a solution which is correct and continuous. Such is evidently inachievable as the number of elements and therefore also the computation time would be infinite. Presently, the numerical codes for axisymmetric and plane strain solutions work satisfactorily, and some approaches have been made in order to solve problems of the full three dimensions.

Undoubtedly, the finite element method constitutes a valuable tool when one is to simulate both continuum thermomechanical and metallurgical aspects of the extrusion process [66,67]. The approach, however, has to be indirect as the FEM method does not address problem at micromechanical level. Firstly, constitutive relations such as that of Zener–Hollomon may be determined experimentally, and one should therefore theoretically be able to predict material behavior with the help of the principles of metallurgy. Furthermore, material anisotropy may be determined from metallurgical studies, and such information may in theory, even though still not in practice, be implemented in a numerical code. Shorter routines for calculation of changes in the microstructure of the material after and during extrusion may also be added to the FEM-program. The elongation, shearing and rotation of grains can then be calculated through a Taylor-analysis [68], and although the theoretical fundament of this approach is far from flawless, experiments tend to give results in fair accordance with calculations. By obtaining information about stain, strain rate and temperature history of each particle one should also be able to assess the degree of recrystallization and changes in dislocation density.

Numerical modeling of extrusion also has other advantages to analytical calculations. Since conduction of heat may be simulated, one need not limit the analysis to one of large extrusion rates and adiabatic conditions [69]. Furthermore, the equilibrium and energy equations may be solved simultaneously, the result being that one manages to capture the strong two-way thermo-mechanical coupling inherent in the equations. Whereas simpler calculations may be performed so that the temperature field is affected by mechanical dissipation, one will hardly be able to model the temperature's influence on the constitutive relation. Consequently information on the softening effect on material during extrusion is lost in analytical calculations. One may, however, argue that calculations with one way coupling and a perfectly plastic material model will give results not far away from those provided by a more complete model. The reason for this is that larger strain rates and the higher temperature caused by increased dissipation, affect the shear yield stress in opposite directions. Furthermore, as shear deformation preferentially takes place on planes with the lowest shear resistance, there is some kind of a self-regulating mechanism, which establishes a state of quasi-equilibrium between the deformation and temperature field at all times. Even though it has not been proven, one may expect that the shear stress on the planes of deformation will approximately be a constant, a yield stress.

Numerical simulations are also advantageous in that they have the potential for capturing the thermo-mechanical interaction between the flowing metal and the tooling. Until now only two aspects of this coupling have been properly exploited, the description of friction on the bearings and on the container wall and the description of heat conduction between the tools and the aluminum. A solution of the complete heat conduction problem can only be found if the geometry of the stem, die and container is prescribed, the mode of heat exchange between the flow and the tools is determined and the temperature field is calculated by FEM. Various FEM-packages perform this calculation in a satisfying manner. Few numerical codes, however, provide solutions for deformation of and stresses in the die, container and stem, and since most programs only manage to describe plane or axisymmetric geometry, the solutions that exist, yield insufficient information for

use for instance in the construction of dies [70]. Full thermo-mechanical description of this coupling for three dimensional geometry would be valuable since it would increase the understanding of how the deformation of the die influences aspects of profile quality such as dimension and surface finish, and since it could be used as a tool for designing new dies and profiles. A study of such is today hindered by the extremely long calculation times for three dimensional codes and incomplete understanding of friction phenomena especially in the bearing channel.

$$\rho \left[\frac{\partial ui}{\partial t} + (u_j - u_{oj}) \frac{\partial u_i}{\partial x_j} \right] = \frac{\partial \sigma_{ij}}{\partial x_j} \tag{85}$$

$$\rho c \left[\frac{\partial T}{\partial t} + (u_i - u_{0i}) \frac{\partial T}{\partial x_i} \right] = -\frac{\partial q_i}{\partial x_i} + s_{ij}\dot{\varepsilon}_{ij} \tag{86}$$

Equations (85) and (86) are respectively the equations of motion and energy. ρ is the density of the material, $\mathbf{u}_0$ is simply a reference velocity. The total stresses σ_{ij} is composed of a deviatoric and a hydrostatic part, s_{ij} and $-p\delta_{ij}$ respectively. Equation (85) reveals that a numerical procedure takes the acceleration terms into account. This stands in sharp contrast to analytical solutions, which usually assume stead-state conditions. Such an assumption is, however, only satisfactory in the mid-part of the extrusion charge. The extrusion process is transient in nature, and especially in the first and last parts of the extrusion run will a steady state assumption lead to numerical errors of some magnitude.

The description of the problem is, however, not complete as the constitutive relations are not defined. The usual assumption is that conduction is determined by Fourier's law, and a Zener–Hollomon relation may be applied in the mechanical equation. The last defines only a relation between shear stresses and strains, and the last equation of interest is that of incompressibility. Elastic effects may also be simulated, but as earlier explained calculations then tend to be more complicated.

An element formulation may then be reached by multiplying Eq. (85) by a virtual velocity, (86) by a virtual temperature and the incompressibility equation by a virtual pressure, applying the constitutive relations and then integrating over the complete volume of the element. A system of equations which yields the change in velocity, pressure and temperature over a time increment is then reached. If the temperature and velocity fields are to be solved simultaneously, calculation times may be very high. Instead equations of temperatures and velocities/pressures are often uncoupled and calculated separately by an iterative technique. The reference list provides an example of a system of equations for one element, which is solved in the numerical program ALMA2π [71]:

$$\begin{bmatrix} \mathbf{k}_{uu} & \mathbf{k}_{up} \\ \mathbf{k}_{up}^T & \mathbf{0} \end{bmatrix} \begin{bmatrix} \Delta\mathbf{u} \\ \Delta p \end{bmatrix} = \begin{bmatrix} \mathbf{s}_{nod} \\ \mathbf{0} \end{bmatrix} - \begin{bmatrix} \mathbf{s}_{sig} + \mathbf{s}_{acc} \\ \mathbf{s}_{ine} \end{bmatrix} \tag{87}$$

$$\mathbf{m}\Delta\dot{\mathbf{T}} + (\mathbf{k}_{con} + \mathbf{k}_{dif})\Delta\mathbf{T} = \mathbf{S}_{nod} - \mathbf{m}\dot{\mathbf{T}} - (\mathbf{k}_{con} + \mathbf{k}_{dif})\mathbf{T} + \mathbf{S}_{heat} \tag{88}$$

The different $\mathbf{k}$s represent "stiffness" matrices and the $\mathbf{S}$s are the "loads". In the energy Eq. (88) the temperature state of the last time step as well as the dissipative heat will be the loads. Besides the traditional loads on the nodes, the acceleration term will be regarded as a load in the mechanical Eq. (87).

A number codes, which can be utilized in the study of extrusion, has been developed. Some of these programs are made with somewhat more general perspectives, but function quite well in the study of extrusion although they are not ideally suited. One such is the program FIDAP, which is addressing more general fluid mechanical problems with an Eulerian perspective, and others are programs such as Forge2, Autoforge and Deform, which are Lagrangian programs meant to handle various problems in the field of materials forming. The main weakness of all these codes is that they originally were not meant to handle the special geometry of the extrusion process. Problems arise when material is entering the bearing channel and undergoes extreme deformation. In Lagrangian programs elements are severely deformed and will not yield proper results unless remeshing is performed continuously. In Eulerian codes a constant velocity at the outlet can not be specified, and therefore one will not be able to simulate the self-stabilizing effect which usually takes place in the bearing channel. Special programs, which handle most case-sensitive aspects, have been developed. One such is ALMA2π, which has been developed at SINTEF/Norwegian University of Science and Technology supported by Hydro Aluminium.

Experiments performed with the split-billet technique indicate that material deformation during extrusion is localized to very narrow shear zones as the one extending from the outlet of the container towards and along the container wall. This is typical for plastic deformation as the underlying equations in the case of constant yield shear strength will be hyperbolic and in fact allow distinct velocity discontinuities. Infinitely large spatial changes in velocity can, however, not be found for results provided by FEM, as the underlying equations are no longer hyperbolic, and as the solution itself is not given as a continuous function in space. A perfectly plastic material behavior for the whole billet is in fact impossible to simulate with methods known today, as the stiffness matrix will be singular and the velocity field indeterminate. Furthermore, if the material shows very low strain rate hardening, calculation times tend to be very long because a great number of iterations are needed to determine the states of deformation and stress. If sufficiently small elements are applied and the strain and strain-rate hardening exponents in a Norton–Hoff relation are taken to be sufficiently low, however, results in satisfactory accordance with as well analytical as experimental result can be obtained. Figure 48 provides a comparison of a deformed network found experimentally and numerically. When studying the figure, one should remember that flow in the container is more easily simulated than that in the bearing channel, and that numerical results need not be that satisfactory in regions with large strain rates.

5   RESEARCH TOPICS

The use of aluminum sections in buildings, architecture, furniture, transport, electronic equipment, heat exchangers, and in mechanical design generally, is well established. The thin-walled complex, multifunctional shape, with its low cost dies, with its availability, flexibility in shape, ease of fabrication and attractive surface, has made it a favorite for the creative designer. Many successful products have been created. Still there are considerable innovative potentials in exploiting the extrusion technology, its downstream processes and the aluminum alloys. Particular challenges are within the following areas:
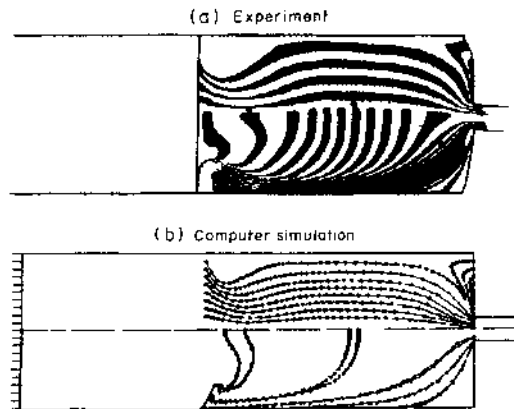
Figure 48 Comparison of numerically calculated (a) and experimentally found flow field; (b) for a reduction ratio of about 6 and under the assumption of full sticking at walls.

- Reducing the variability of dimensions, shape, properties and surface appearances without cost increase.
- Reducing wall thickness with narrow tolerances and increasing the strength of a section at reduced cost.
- Combining generally available sections to large sections by stir welding, instead of using large presses for large sections with limited availability and high cost.
- Combining extrusion, bending and hydroforming for cost-effective production of complex three-dimensional shapes with narrow tolerances and properties.

As will and has been shown in this chapter, the hot extrusion process is characterized by:

- A strong interaction between mechanical, thermal and metallurgical parameters during a press cycle.
- A continuous and transient variation of temperature distribution and metal flow field in container and die during the press cycle. Each material element goes through a different thermo-mechanical history.
- Sharp gradients in strain rate and temperature, both spatial and temporal, when the deforming material flows into and through the bearing channel.
- An interaction between the displacements of the bearing channel walls, bearing channel friction, formation of the section surface and the stability of flow.
- An absence of adequate in line sensors, predictors and actuators for controlling the variations in dimensions and shape of the extruded sections.
- An absence of analytical models of the extrusion process being able to "catch" the basic feature of thin walled extrusion; the self-stabilization of the process.

- An absence of 3D numerical codes that are at a stage of development where studies of the self-stabilization phenomenon can be studied.

Some selected research topics will be discussed that now seems ripe for "attack". These topics are considered as fundamental, pre-competitive problems, that will form the base for the scientific theory of thin-walled extrusion. According to Støren [72], by the theory of extrusion we understand a theory that is able to make predictions about:

- The flow pattern, the distribution of temperature and stresses and the evolution of microstructure of the deforming material in the container and the through the whole process.
- The properties of the extruded, heat treated and fabricated section as function of chemical composition, initial microstructure, shape of the section and the parameters of the processes that the section passes trough from raw material to finished product.
- The sensitivity to variations in the die and section design and processing history on the material properties, surface, dimensional tolerances and optimal processing speed with a specified shape, alloy and production set up.

As pointed out by Bishop [73] already in 1957 one has to apply the continuum thermo-mechanics of extrusion to quantify phenomena that are primarily of metallurgical origin, such as speed limit phenomena, flow resistance, the evolution of microstructure and the properties of the extruded section. A fully coupled theory of mechanical, thermal and metallurgical parameters has therefore to be developed. This, then may give the basis for the synthesis of alloy development, process-innovation and production optimization that is needed to release the potential of extrusion-based components and products with respect to the improvements in quality properties, economic efficiency and ecological effectiveness (Figs. 14 and 15). In the following, a possible "research strategy" to achieve this is outlined.

5.1 Numerical 3D Simulation and Laboratory Extrusion Experiment Validation

The development of software for 3D thermo-elasto-viscoplastic flow of metals in interaction with thermo-elastic deflections of the tooling and the die is now approaching a level of precision and speed that the basic problem of the thin-walled extrusion process can be attacked [74], namely the phenomena of self-stabilization. With self-stabilization one understands the ability of the process to react to variations in the flow-, temperature- and the flowstress-field of the material approaching the bearing channel in such a way that the variation in dimension, shape, microstructure and surface-properties are kept within the required limits during a press cycle. In order to study this basic phenomenon in a systematic and quantitative way, the following set of systematic experiments is proposed performed (Fig. 49):

- Thin strip extrusion
- Thin-walled tube extrusion
- Rectangular hollow thin walled section
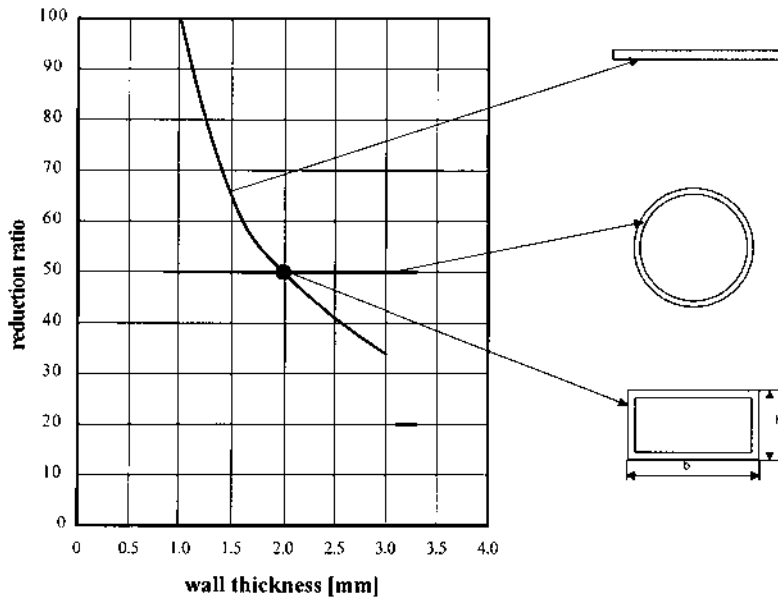
Figure 49 Generic sections for 3D modeling.

For the thin strip the width is kept constant, whereas the thickness is gradually reduced, giving an increase in reduction ratio, until instability in the form of buckling of the section is reached. In the tube, the reduction ratio is kept constant, whereas the tube diameter is increased and the wall thickness is decreased until the limit of satisfactory extruded section is reached. In the rectangular hollow section, the cross sectional area of the mandrel and the thickness of the section are kept constant, whereas the width/height-ratio is increased until the limit of satisfactory extruded section is reached. In the numerical simulation of these processes one will see that bearing channel phenomena will have major influence of the simulation results.

5.2 Die Deflections, Friction and Surface Formation in the Bearing Channel

A proper understanding of the interaction between the aluminum and the bearing surfaces has been viewed as a key to controlling dimensional variability and surface quality of the extruded profiles, and intensive research has over the last few years been undertaken in this field [75]. Most of the interest has been connected to the study of choked dies as only these are of commercial interest. If the die is designed with a release, friction forces will naturally be lower. However, the surface quality will usually be unsatisfactory since tearing, die lines or streaking may be caused by pick up deposited directly behind the main area of contact between die and the extruded metal.

Due to the existence of friction forces and a non-linear material model, the flow through the bearing channel is a plug flow driven by the change in pressure from the inlet to the outlet. However, since the bearings are relatively narrow, a steady state can hardly be obtained. As a result, the velocity profile may be expected to change

almost continuously through the bearing channel. In the inlet, velocity components normal to the bearings will exist as the material flow enters the channel from the container. At the outlet the velocity field ought to be uniform.

Figure 50 shows some of the phenomena observed in an experimental set up of extrusion of a thin strip with a split die, advised by Abtahi [76–78] and further studied by Tverlid [79] and Aukrust et al. [80]. In the inlet to the bearing channel, the flowing material is sticking to the die due to high contact pressures. By this one understands that there will be no relative velocity between particles on the boundary between the metal and the tool and, therefore, no distinct surface of the extruded metal either. The shear stress will be given by the constitutive equation of the deforming metal and may be relatively high due to high strain rates, 1000 to 10,000 [1/sec]. As the pressure normal to the bearing surface decreases towards the outlet, however, one is to expect that the sticking friction at a certain point, the slip point, must be replaced by sliding. The sliding friction is regarded to be of Coulomb type since there only will be partial contact between deforming material and the bearings and the magnitude of shear stress is found to be dependent on the pressure normal to the bearing surface. Over a relative short distance denoted
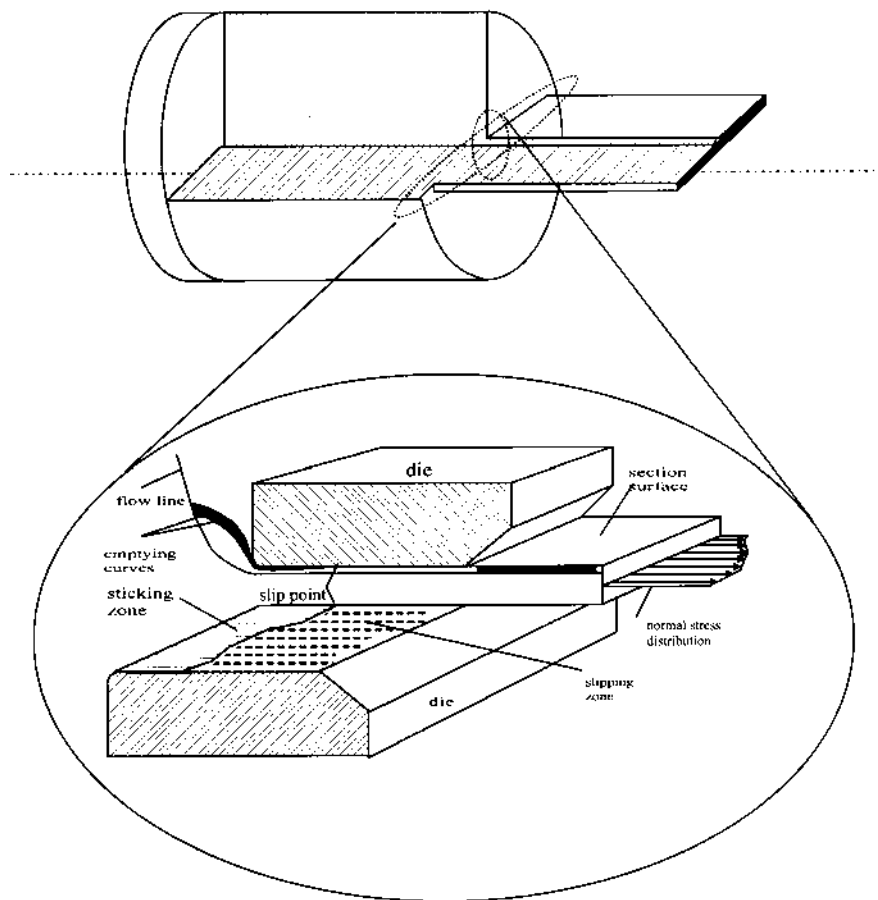
Figure 50 Bearing channel friction and stability of flow.

the transition region the slipping speed is increased from zero to full outlet extrusion speed. A positive gradient in the slipping speed means that new surface is forming. In the same region material particles will also move in a direction normal to the bearings. The position of the slip point will be determined partly by the normal stresses in the end of the bearing channel, the angle of choke, which affects the pressure build-up, and the inlet radius to the bearing channel. Only in the limiting case of very large angles should one expect the slip point to be close to the outlet.

The surface structure and topology of an extruded section is created and modified in the transition and slipping regions. Furthermore, the presence of a layer of oxidized metal is thought to be importance to both the friction conditions and surface generation. While such a layer is broken up and removed from the sticking region of the bearing surfaces, it remains attached to the bearings and simplifies gliding in the region of slipping. In the case of extrusion with the 6XXX-series of alloys, it has been found that micro die lines present on the profile surface can be related to hard particles existing in the adhesive layer of the slipping region. The regions of slip and stick may easily be identified on the bearings of a die after extrusion as a relatively thick adhesive or oxidized layer is a witness of the presence of the former. Between the areas of slipping and sticking, a transition region of a certain length is also found to exist.

During the press cycle, the forces on the die and the temperature distribution in the die, will vary, giving variations in die deflections. This then, dependent on the tooling and die design, may cause variations in the choke angle and the bearing channel opening during a press cycle. These parameters, the normal stress at the outlet, and the deflection of the bearing surfaces of the die, influence the friction and the local reduction ratio, and thus the pressure build up in the bearing channel. Physical understanding and quantification of these effects, constitute a major scientific challenge to the study of thin walled, dry friction, hot extrusion of aluminum.

5.3 The Stability of Flow

When the material in some parts of a thin section tends to flow faster than the rest of the section, compressive stresses is set up in those parts and tensile stresses in others (Fig. 50). The variations in normal stresses over the cross section of the extruded profile leaving the bearing channel, will influence the position of the slip point. Under the influence of compressive stresses the slip point moves towards the outlet, and a higher friction and thus also a higher pressure build-up in the bearing channel is experienced. Tensile stresses have the opposite effect. The slip point is moved away from the outlet, and friction is reduced in the bearing channel, causing a reduced pressure build up in the inlet. This conclusion can be drawn directly from the simple slab analysis in the previous chapter. The change in pressure distribution, depending of the material response to stress variations, will promote a more balanced outlet flow.

If the change in outlet normal stress distribution causes buckling in the compressive region or thinning and even cracking in the tensile stress region, or if the pressure build-up in the inlet to the bearing channel cause redistribution of loads on the die that give die defections that acts against the self-stabilization effect or gives unacceptable variations in section thickness, then the limits of extrudability is reached.

From this description it is clear that a detailed thermo-mechanical quantitative model of these effects is critical if a successful 3D-computer codes describing the extrusion process are to be developed. Detailed physical models of material response, of the conditions in the bearing channel, of surface formation and of stick-slip mechanisms cover several levels of magnitude, from atomistic to continuum level.

5.4 Alloy Development, Process Innovations and the Limits of Extrudability

Based on the progress of 3D-simulation and experimental validation of flow in thin-walled extrusion, combined with the

- Computation of the tool and die deflection
- Detailed quantitative description of the response of the alloy with respect to microstructural evolution and flow resistance
- Understanding and modeling of the bearing channel friction and surface formation phenomena
- Prediction of the limits of self-stabilization of flow

the limits of extrudability can be studied in a systematic and quantitative way. Combined with the knowledge and creativity of the experienced extrusion metallurgist, production and die experts as well as the product designers, this new scientific based knowledge of extrusion will give way to alloy systems based on recycled aluminum, new innovative principles of die, tooling and press design, section handling and down stream processes with quality properties, economic efficiency and ecological effectiveness that mark the sustainable products of tomorrow.

REFERENCES

1. K. Laue and H. Stenger, *Extrusion: Process, Machinery, Tooling*, American Society for Metals, Metals Park, OH, 1981.
2. L. Bello, "Die corrections for changing flow characteristics," in Proc. 2nd Int. Al. Extr. Techn. Sem., Chicago, Illinois, 1980, pp. 89–115.
3. J. R. Dawson, "Development of Conform Technology for the Manufacture of Multi-Port Tube," in Proc. 6th Int. Al. Extr. Techn. Sem., Chicago, Illinois, 1996, Vol. II, pp. 435–439.
4. H. Valberg, "Extrusion Welding in Porthole Die Extrusion," in Proc. 6th Int. Al. Extr. Techn. Sem., Chicago, Illinois, 1996, Vol. II, pp. 213–224.
5. O. Reiso et al., "The Effect of Cooling Rate After Homogenization and Billet Preheating Practice on Extrudability," in Proc. 6th Int. Al. Extr. Techn. Sem., Chicago, Illinois, 1996, Vol. I, pp. 1–10.
6. O. Reiso et al., "The Effect of Cooling Rate After Homogenization and Billet Preheating Practice on Extrudability," in Proc. 6th Int. Al. Extr. Techn. Sem., Chicago, Illinois, 1996, Vol. I, pp. 141–148.
7. N. C. Parson et al., "Surface Defects on 6XXX Alloy Extrusions," in Proc. 6th Int. Al. Extr. Techn. Sem., Chicago, Illinois, 1996, Vol. I, pp. 57–67.
8. G. E. Totten and M. A. H. Howes, *Steel Heat Treatment Handbook*, Marcel Dekker, 1997, pp. 692–715.

9. D. Pye, ''A Review of Surface Modification Techniques for Pre-Heat-Treated H 13 Extrusion Dies and Emerging Technologies,'' in Proc. 6th Int. Al. Extr. Techn. Sem., Chicago, Illinois, 1996, Vol. II, pp. 197–200.

10. L. Hanssen, P. Lindviksmoen, and S. Rystad, ''Effect of Blend and Extrusion Parameters on Material Flow,'' in Proc. 6th Int. Al. Extr. Techn. Sem., Chicago, Illinois, 1996, Vol. II, pp. 83–87.

11. M. Lefstad and O. Reiso, ''Metallurgical Speed Limitations During the Extrusion of AlMgSi-Alloys,'' in Proc. 6th Int. Al. Extr. Techn. Sem., Chicago, Illinois, 1996, Vol. I, pp. 11–21.

12. *Encyclopedia Britannica* 15th edn, Micropaedia, Vol. 5, p. 951 (Hittite), Chicago, 1992.

13. T. E. Graedel and B. R. Allenby, *Industrial Ecology*, Prentice-Hall, Englewood Cliffs, N.J., 1995.

14. H. Brezet and C. van Hemel, ''Ecodesign: A Promising Approach to Sustainable Production and Consumption,'' Modul B: Optimization of the End-of-Life System, United Nations Environment Programme, Paris, 1997.

15. *Alulib – A Source of Inspiration*, Interactive CD-rom. (www.alulib.com). Skanaluminium. Oslo 1997.

16. J. G. Bralla et al., *Handbook of Product Design for Manufacturing*, Ch. 3.1, Metal Extrusions McGraw-Hill, New York, 1986.

17. D. G. Altenpohl, *Aluminum: Technology, Applications, and Environment*, 6th edn, The Minerals, Metals and Materials Society, 1998.

18. C. Yao and K. B. Mueller, ''Metal Flow and Temperature Developed During Direct Extrusion of AA2024,'' in Proc. 6th Int. Al. Extr. Techn. Sem., Chicago, Illinois, 1996, Vol. II, pp. 141–146.

19. H. A. Barnes, J. F. Hutton and K. Walters, *An Introduction to Rheology*, Elsevier, Amsterdam, 1989.

20. K. Lange et al., *Handbook of Metal Forming*, McGraw-Hill, New York, 1985.

21. H. Valberg, ''Metal Flow in Direct Axisymmetric Extrusion,'' in Proc. Int. Conf. Dev. Form. Techn., Lisbon, Portugal, 1990, Vol. 2, pp. 1.11–1.38.

22. H. Valberg, ''Metal Flow in the Direct Axisymmetric Extrusion of Aluminium,'' J. Mat. Proc. Techn., 1992, 31, pp. 39–55.

23. H. Valberg and R. A. Groenseth, ''Metal Flow in Direct, Indirect and Porthole Die Extrusion,'' in Proc. 5th Int. Al. Extr. Techn. Sem., Chicago, Illinois, 1992, Vol. I, pp. 337–357.

24. H. Valberg, ''Forming of Metals by Forging, Rolling, Extrusion, Drawing and Sheet-metalforming, Department of machine design and materials technology,'' The Norwegian University of Science and Technology, 7491 Trondheim, Norway, unpublished work (in Norwegian), pp. 125–134.

25. H. Valberg and R. A. Groenseth, ''Deformation and Metal Flow when Extruding Hollow Aluminium Profiles,'' The 2nd East-West Symp. Mat. Proc., 1991, also published in: Int. J. Mat. Prod. Techn., 1993, 8, 1, pp. 1–22.

26. H. Valberg, F. P. Coenen and R. Kopp, ''Metal Flow in Two-Hole Extrusion,'' in Proc. 6th Int. Al. Extr. Techn. Sem., Chicago, Illinois, 1996, Vol. II, pp. 113–124.

27. H. Valberg and T. Malvik, ''An Experimental Investigation of the Material Flow inside the Bearing Channel in Aluminium Extrusion,'' Int. J. Mat. Prod. Techn., 9, 1994, 4/5/6, pp. 428–463.

28. H. Valberg and T. Malvik, ''Metal Flow in Die Channels of Extrusion,'' in Proc. 6th Int. Al. Extr. Techn. Sem., Chicago, Illinois, 1996, Vol. II, pp. 17–28.

29. H. Valberg, A. W. Hansen and R. Kovacs, ''Deformation in Hot Extrusion investigated by means of a 3-D Grid Pattern Technique,'' in Proc. 4th Int. Conf. Techn. Plasticity, Beijing, China, 1993, Vol. I, pp. 637–645.

30. H. Valberg, "A Modified Classification System for Metal Flow Adapted to Unlubricated Hot Extrusion of Aluminum and Aluminum Alloys," in Proc. 6th Int. Al. Extr. Techn. Sem., Chicago, Illinois, 1996, Vol. II, pp. 95–100.

31. J. Kialka and W. Z. Misiolek, "Studies of Dead Metal Zone Formation in Aluminum Extrusion," in Proc. 6th Int. Al. Extr. Techn. Sem., Chicago, Illinois, 1996, Vol. II, pp. 107–111.

32. H. Valberg, "The profile surface formation during the extrusion of metals," Doctoral Thesis NTH, 1988.

33. P. K. Saha, "Influence of Plastic Strain and Strain Rate on Temperature Rise in Aluminum Extrusion," in Proc. 6th Int. Al. Extr. Techn. Sem., Chicago, Illinois, 1996, Vol. I, pp. 355–359.

34. M. Lefstad, "Metallurgical Speed Limitations in Extrusion of AlMgSi-alloys," Doctoral Thesis, University of Trondheim, 1993.

35. A. W. Hansen and H. Valberg, "Accurate Measurements Inside the Tool in Hot Working of Metals," in Proc. 6th Int. Al. Extr. Techn. Sem., Chicago, Illinois, 1996, Vol. II, pp. 11–15.

36. G. E. Dieter, *Mechanical Metallurgy*, McGraw-Hill, New York, 1986.

37. W. Hufnagel et al., *Aluminium Taschenbuch*, Aluminium-Verlag, Dusseldorf, 1983, pp. 266–296.

38. T. Sheppard, "Development of Structure, Recrystallization Kinetics and Prediction of Recrystallized Layer Thickness in Some Al-alloys," in Proc. 6th Int. Al. Extr. Techn. Sem., Chicago, Illinois, 1996, Vol. I, pp. 163–170.

39. A. Jackson and T. Sheppard, "Observations on Production and Limit Diagrams for the Extrusion Process," in Proc. 6th Int. Al. Extr. Techn. Sem., Chicago, Illinois, 1996, Vol. I, pp. 209–216.

40. M. Lefstad and O. Reiso, "Metallurgical Speed Limitations During the Extrusion of AlMgSi-Alloys," in Proc. 6th Int. Al. Extr. Sem., Chicago, Illinois, 1996, Vol. I, pp. 11–21.

41. L. E. Malvern, *Introduction to the Mechanics of a Continuous Medium*, Prentice-Hall, New Jersey, 1969.

42. S. P. Timoshenko and J. N. Goodier, *Theory of Elasticity*, 3rd edn. McGraw-Hill, New York, 1970.

43. W. Yang and W. B. Lee, *Mesoplasticity and its Applications*, Springer Verlag, 1993.

44. J. Lemaitre and J. L. Chaboche, *Mechanics of Solid Materials*, Cambridge University Press, 1990.

45. A. S. Khan and S. Huang, *Continuum Theory of Plasticity*, John Wiley and Sons, New York, 1995.

46. J. Chakrabarty, *Theory of Plasticity*, McGraw-Hill, New York, 1987.

47. R. Hill, *The Mathematical Theory of Plasticity*, Claredon Press, Oxford, 1950.

48. B. A. Druyanov and R. I. Nepershin, *Problems of Technological Plasticity*, Elsevier, Amsterdam, 1994.

49. C. Zener and J. H. Hollomon, "Effect of Strain Rate upon Plastic Flow of Steels," J. Appl. Phys. 1944, Vol. 15, p. 22.

50. B. Avitzur, *Metal Forming: Process and Analysis*. McGraw-Hill, New York, 1968.

51. B. Avitzur and W. Pachla, "The Upper Bound Approach to Plane Strain Problems Using Linear and Rotational Velocity Fields-Part I: Basic Concepts," J. Eng. Ind., Nov. 1986, 108, pp. 295–306.

52. B. Avitzur and W. Pachla, "The Upper Bound Approach to Plane Strain Problems Using Linear and Rotational Velocity Fields-Part I: Applications," J. Eng. Ind., Nov. 1986, 108, pp. 307–316.

53. G. Grasmo, "Friction and Flow Behaviour in Aluminium Extrusion," Doctoral Thesis 1995:37 NTH, 1995.

54. Z. Jia et al., "Application of Upper Bound Element Technique (UBET) for Aluminium Extrusion," in Proc. 6th Int. Al. Extr. Techn. Sem., Chicago, Illinois, 1996, Vol. II, pp. 247–252.
55. B. Tibbets and J. Wen, "Control Framework and Deformation Modeling of Extrusion Processes: An Upper Bound Approach," in Proc. 6th Int. Al. Extr. Techn. Sem., Chicago, Illinois, 1996, Vol. I, pp. 375–385.
56. T. Kakinoki, K. Katoh and M. Kiuchi, "Application of Upper Bound Method to Extrusion Die Design," in Proc. 6th Int. Al. Extr. Techn. Sem., Chicago, Illinois, 1996, Vol. II, pp. 5–9.
57. R. Akeret, "Influence of Cross-Sectional Shape and Die-Design in the extrusion of Aluminium-Part I-Processes in the Deformation Zone," Aluminium English, 1983, 59(9), pp. 276–280.
58. R. Akeret, "Influence of Shape and Die Design on Metal Flow, Extrusion Load and Speed," in Proc. Extr.-Sci. Tech. Dev., Deutsche Gesellschaft fur Metallkunde E. V., Obenwisel, 1981, pp. 191–204.
59. H. Geiringer, "Fundéments mathématiques de la théorie des corps plastiques isotrops," Mémorial des Sciences Mathématiques, 1937, p. 86.
60. W. Prager, "A geometrical discussion of the slip line field in plane plastic flow," Transactions of the Royal Institute of Technology, Stockholm, Sweden, No. 65, 1953.
61. W. Johnson, R. Sowerby and J. B. Haddow, *Plane-Strain Slip-line Fields: Theory and Bibliography*. Edward Arnold, London, 1970.
62. W. Johnson, R. Sowerby and R. D. Venter, *Plane Slip Line Fields for Metal Deformation Processes*, Pergamon Press, Oxford, 1982.
63. R. D. Cook, D. S. Malkhus, and M. E. Plesha, *Concepts and Applications of Finite Element Analysis*, 3rd edn. John Wiley and Sons, New York, 1989.
64. O. C. Zienkiewicz and R. L. Taylor, *The Finite Element Method*, 4th edn, Vol. 1, McGraw-Hill, London, 1991.
65. O. C. Zienkiewicz and R. L. Taylor, *The Finite Element Method*, 4th edn, Vol. 2, McGraw-Hill, London, 1991.
66. R. Kopp, "Zur Simulation Strangpressens," Symposium Strangpressen, Garmisch-Partenkirchen, Germany, 1997, pp. 69–83.
67. J. Kusiak et al., "Application of the Finite-Element Technique to the Simulation of the Aluminium Extrusion Process," in Proc. 6th Int. Al. Extr. Sem., Chicago, Illinois, 1996, Vol. I, pp. 361–367.
68. T. Furu, K. Pedersen, and S. Abtahi, "Microstructurally Based Modeling Applied to Cold Extrusion of Aluminum," in Proc. 6th Int. Al. Extr. Techn. Sem., Chicago, Illinois, 1996, Vol. I, pp. 341–347.
69. K. Holthe and S. Tjøtta, "The Heat Balance During Multiple Press Cycles," in Proc. 6th Int. Al. Extr. Techn. Sem., Chicago, Illinois, 1996, Vol. I, pp. 387–392.
70. I. Skauvik et al., "Numerical Simulation in Extrusion Die Design," in Proc. 6th Int. Al. Extr. Sem., Chicago, Illinois, 1996, Vol. II, pp. 79–82.
71. K. Holthe, S. Støren, and L. Hansen, "Numerical simulation of the aluminium extrusion process in a series of press cycles," in Proc. 4th Int. Conf. Num. Meth. Ind. Form. Proc., Valbonne, France, 1992, pp. 611–618.
72. S. Støren, "The Theory of Extrusion – Advances and Challenges," Int. J. Mech. Sci. 1993, 35(12), pp. 1007–1020.
73. J. F. W. Bishop, Metall. Rev., 1957, 2, p. 361.
74. S. Støren and G. Grasmo, "High Velocity Extrusion of Thin-Walled Aluminium Sections," in Proc. 5th Int. Al. Extr. Techn. Sem., Chicago, Illinois, 1992, pp. 353–357.
75. R. Akeret, "Influence of Cross-Sectional Shape and Die-Design in the extrusion of Aluminium-Part II-Friction in the Die land," 1983, 59(10), pp. 355–360.

76. S. Abtahi, "Friction and Interface Reactions on the Die Land in Thin-walled Extrusion," Doctoral Thesis 1995:42 NTH, 1995.
77. S. Abtahi, T. Welo, and S. Støren, "Interface Mechanisms on the Bearing Surface in Extrusion," in Proc. 6th Int. Al. Extr. Techn. Sem., Chicago, Illinois, 1996, Vol. II, pp. 125–131.
78. T. Welo, S. Abtahi, and I. Skauvik, "An Experimental and Numerical Investigation of the Thermo-Mechanical Conditions on the Bearing Surface of Extrusion Dies," in Proc. 6th Int. Al. Extr. Techn. Sem., Chicago, Illinois, 1996, Vol. II, pp. 101–106.
79. S. Tverlid, "Modelling of Friction in the Bearing Channel of Dies for Extrusion of Aluminium Sections," Doctoral Thesis 1997:147 NTH, 1997.
80. T. Aukrust et al., "Texture and Grain Structure in Aluminium Sections," in Proc. 6th Int. Al. Extr. Techn. Sem., Chicago, Illinois, 1996, Vol. I, pp. 171–177.

9

Aluminum Welding

CARL E. CROSS

The University of Montana, Butte, Montana, U.S.A.

DAVID L. OLSON and STEPHEN LIU

Colorado School of Mines, Golden, Colorado, U.S.A.

1 INTRODUCTION

Aluminum welding metallurgy and the processes used to weld and join aluminum have advanced significantly over the past 10–20 years. Many aspects of aluminum welding that were once considered limiting, oxide removal for example, are now much better accommodated. It is generally accepted that extra care must be taken in joint preparation and in the quality of consumables (shielding gas and filler metal), however, new techniques have been developed and commercialized to help achieve this goal.

Aluminum weld metal is unique with regard to most ferrous alloys in that there are no solid-state phase transformations upon cool down. Thus, its microstructure is determined by solidification alone. In addition, aluminum is particularly susceptible to the formation of solidification defects: porosity and hot cracking. Modeling of weld solidification has made it easier to understand the effect of process parameters and alloy composition on microstructure, thus allowing for the avoidance of defects.

Aluminum welds are also unique in that the weld metal and heat-affected zones are normally the weakest parts of the joint. The concept of weld over-matching, while common to ferrous weldments, is not applicable to aluminum. For this reason, weld strength efficiencies for aluminum weldments are normally on the order of 50% or lower. Models for precipitate coarsening and dissolution in the heat-affected zone now allow for the prediction and optimization of mechanical behavior. Also, development of new filler alloys hold promise for improved joint efficiencies.

In this chapter, all of the major topics pertinent to aluminum welding are addressed. These topics include the weld thermal experience and weld zones,

solidification, porosity, hot cracking, heat-affected zone, mechanical properties, corrosion, and welding processes. Modern models, theories and concepts are presented regarding each of these topics, with reference given to the most recent or pertinent research.

2   WELD ZONES AND THE THERMAL EXPERIENCE

Most joining processes involve localized heating of the base material (forging, extrusion, plate, sheet, or casting) and sometimes involve the addition of a filler metal (wire, rod, or pre-placed shim). In order to achieve a metallurgical joint, sufficient heat must be applied to melt the base metal and the filler metal (in the case of welding) or just the filler metal (in the case of brazing). This heat can be supplied from a plasma arc, an electron beam, a laser beam, a gas torch, or by frictional means. For all of these localized heat sources, the highest temperature reached in the base material occurs at a location closest to the heat source.

In the case of arc welding, a molten weld pool forms beneath the arc. This liquid pool becomes superheated 100–200 degrees above the liquidus temperature of the alloy, directly under the arc. Heat is distributed throughout the weld pool by means of liquid convection, with flow rates on the order of meters per second. The primary driving force for convection is the Lorentz Force, resulting from the flow of current, causing molten metal to flow inward and downward towards the bottom of the weld pool. Buoyancy, arc pressure and surface tension forces can also influence fluid flow, but normally to a lesser extent.

2.1   Weld Zones

The different zones of a weldment are defined in the schematic of Fig. 1. The dividing boundary between fused and non-fused base metal is called the *fusion boundary*. The fusion boundary is sometimes referred to as a *fusion line*, particularly when interpreting weld cross-sections in two dimensions. The fusion boundary represents the liquidus isotherm for the base metal alloy. All material lying within the fusion boundary has been completely fused into the liquid state and, upon solidification, is called weld metal. Its composition is a hybrid mixture of filler metal and base metal alloys, as controlled by the amount of dilution of each respective alloy.

Just inside the fusion boundary is the unmixed zone (UMZ), a narrow and diffuse region in the weld pool which is not influenced by the rapid connective mixing of the weld pool.

Its composition is the same or nearly the same as that of the base metal, since little or no mixing with the filler metal occurs in this zone. In the case of autogenous welding, or when the filler metal alloy is the same as the base metal alloy, the UMZ will have the same composition as the weld metal.

Outside of the fusion boundary is the heat affected zone (HAZ), where the base metal microstructure has been influenced in some manner by the thermal experience. These changes in microstructure can include recovery, recrystallization, grain growth, and precipitation reactions (e.g. dissolution, coarsening and re-precipitation) depending upon the location in the HAZ, the severity of heating (i.e. peak temperature and time at temperature), and the alloy in question.
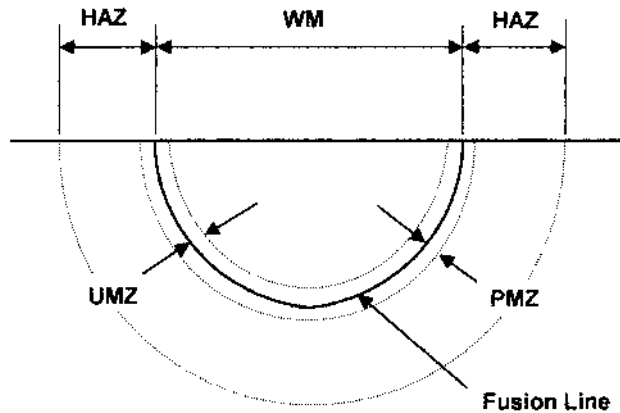
Figure 1 Transverse weld cross-section depicting important weld zones: Heat Affected Zone (HAZ), UnMixed Zone (UMZ), and Partially Melted Zone (PMZ).

Just outside the fusion line lies the partially melted zone (PMZ), a region in the HAZ where the peak temperature has exceeded the equilibrium solidus or the eutectic temperature for the corresponding eutectic constituents present. Melting in this region involves both equilibrium melting and non-equilibrium melting (i.e. constitutional liquation) of eutectic constituents occurring along grain boundaries.

2.2 Thermal Experience

Analytical equations describing the conductive heat flow in welding, based upon a point heat source moving on top of an infinitely large plate, are often useful in understanding weld behavior. For example, the equation defining the steady-state weld isotherm (temperature T) for 3-dimensional heat flow is given as [1]:

$$T = T_o + (Q/2\pi Kr) \exp\left[(v/2\alpha)(\xi - r)\right] \tag{1}$$

where
$T_o =$ preheat temperature
$Q =$ power input (ηIV)
$K =$ thermal conductivity
$v =$ velocity of heat source (dx/dt)
$\alpha =$ thermal diffusivity ($K/\rho C_p$)
$\xi =$ lineal distance behind heat source (in negative x direction)
$r =$ radial distance from point source
$\eta =$ arc efficiency
$I =$ welding current
$V =$ welding voltage
$x =$ axis along welding direction
$t =$ time
$\rho =$ density
$C_p =$ specific heat

Table 1 Comparison of Thermal Properties [2]

Metal	K (W/mm°C)	α (mm^2/sec)	ρCp (J/mm^3°C)
Steel	0.04	8	0.005
Titanium	0.03	10	0.003
Aluminum	0.23	85	0.003

The fusion boundary can be roughly defined by this equation, setting the temperature (T) equal to the liquidus temperature (note that the weld pool shape is also influenced by convective heat flow, not included in this equation). The term ($v/2\alpha$) controls the shape of the weld pool: low values result in a spherical shape, whereas high values result in a teardrop shape. The characteristic high thermal diffusivity of aluminum (see Table 1), results in aluminum weld pools being more spherical in shape compared with either steel or titanium when welded at the same travel speed.

Two factors of great importance in understanding microstructural damage experienced in the HAZ are peak temperature and cooling rate. Both of these factors can be derived from Eq. (1). The equation for peak temperature (T_p) at the plate surface, expressed as a function of distance from the weld centerline (y), is given as follows [3]:

$$T_p = T_o + (Q/\pi Ke)(v/2\alpha)/[(v/2\alpha)^2 y^2 + 2] \tag{2}$$

Also, the cooling rate (dT/dt) experienced at a particular temperature (T) is given as [3]:

$$dT/dt = -(2\pi K v/Q)(T - T_o)^2 \tag{3}$$

It should be noted that the cooling rate is inversely proportional to the power ($Q = \eta IV$), which is also sometimes expressed in term of welding heat input ($H = \eta IV/v$):

$$dT/dt = C_1 v/Q = C_1/H \tag{4}$$

Thus, high heat input results in a higher peak temperature at a given distance from the weld center. It also results in slower cooling rates at any given temperature. When welding at constant heat input, the peak temperature reached decreases in a continuous manner with increasing distance (y) from the fusion line. The cooling rate also decreases as the temperature drops. This behavior is summarized in Fig. 2 where temperature profiles, representing different distances from the fusion line, are compared.
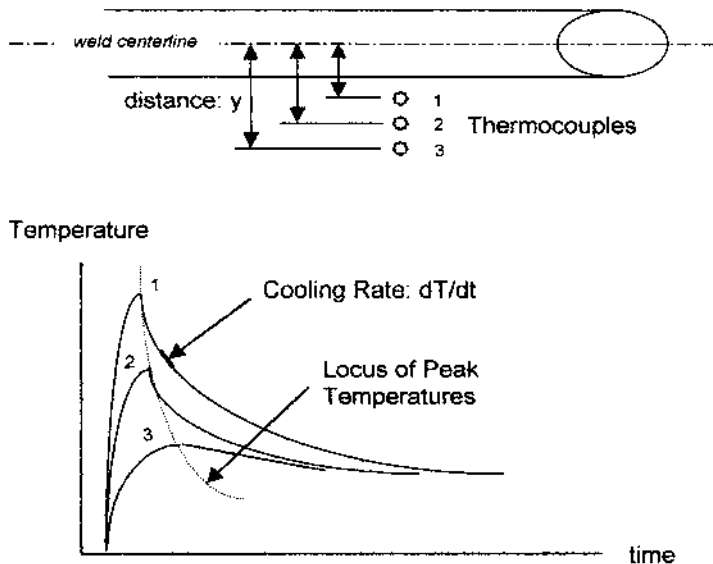
Figure 2 Weld thermal profiles for three different thermocouples spaced at increasing distance from the weld centerline.

For the case of through-thickness welding (i.e. 2-dimensional heat flow) on a plate of thickness (h), the following equations for peak temperature and cooling rate should be used [3]:

$$T = T_o + Q(2h)^{-1}(\pi K \rho C_p v r)^{-1/2} \exp[(v/2\alpha)(\xi - r)] \tag{5}$$

$$T_p = T_o + Q/[(2Khy)(v/2\alpha)(2\pi e)^{1/2}] \tag{6}$$

$$dT/dt = -2\pi K \rho C_p h^2 (H)^{-2} (T - T_o)^3 \tag{7}$$

It should be noted that for thinner plates (smaller h), the peak temperature will be higher for a given distance from the weld center and the cooling rate will be slower.

When using analytical equations for 2- and 3-dimensional heat flow predictions, the arc efficiency and thermal properties at elevated temperature are not readily available. Arc efficiency can vary from 40% to 95%, depending upon the welding process and conditions. Thus, some form of calibration is normally needed, such as welding on a plate with implanted thermocouples. Care should also be taken that these equations only be applied under steady-state conditions. Aluminum alloys will tend to have much larger transient regions, at weld start and stop, than do ferrous alloys.

3 WELD SOLIDIFICATION

Melting is the key to bridging together (i.e. fusing) two separate pieces of metal. However, the solidification which follows is important to the integrity of the joint,

determining weld metal microstructure and occurrence of defects. Two key solidification parameters that determine solidification microstructure are growth rate (R) and temperature gradient (G). Welding process parameters can influence these solidification parameters in a variety of different ways. The relationship between welding parameters, solidification parameters and weld metal microstructure will be discussed in detail in this section. Although the formation of solidification defects can sometimes be related to welding parameters, they are more often tied to alloy content and impurities as will be discussed in following sections.

3.1   Grain and Sub-Grain Structure

Weld metal solidification occurs within a bounded region (or "mushy zone") which trails the moving weld pool, as shown in Fig. 3. The upper boundary of this region is defined by the weld pool (or liquidus temperature), while the lower boundary is defined by the lowest melting eutectic temperature. Within this mushy zone, solidification takes place in the form of grains and sub-grains (i.e. cells, columnar dendrites or dendrites). Each grain is a single crystal having a unique orientation. Each sub-grain within a grain assumes this same crystallographic orientation, with the axis of each dendrite aligned in a $\langle 100 \rangle$ direction.

Morphologies for the different types of sub-grains are shown schematically in Fig. 4. The particular type of sub-grain that forms depends upon the amount of undercooling present. Low undercooling favors cell formation where as high undercooling favors dendrite formation. At very high undercooling, nucleation will occur ahead of the solid/liquid interface resulting in equiaxed dendrites and grain refinement.
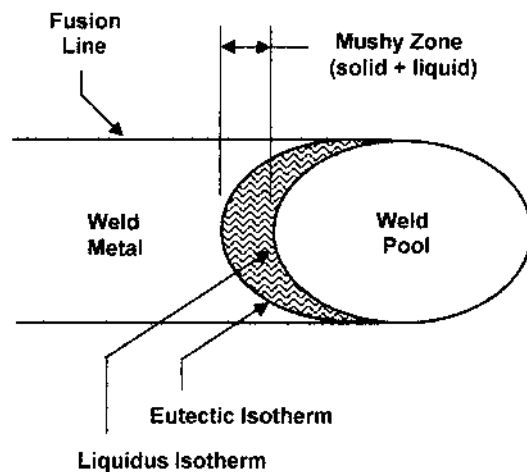
Figure 3   Top view of weld showing two-phase (liquid + solid) mushy zone which trails behind the weld pool.

Figure 4 text labels: Cellular, Cellular Dendritic, Dendritic, Equiaxed Dendritic, Undercooling
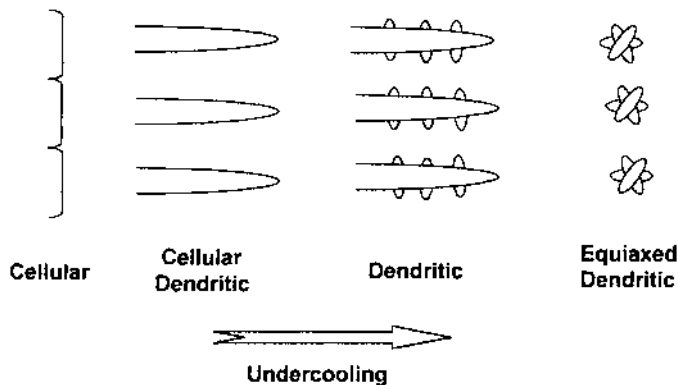
Figure 4 Different forms of solidification sub-structure dependent upon the extent of undercooling.

An equation for solidification undercooling (ΔT), generated as a result of solute partitioning and curvature, is given as follows: [4]:

$$\Delta T = DG/R + AR^{1/2} \tag{8}$$

where D is liquid diffusivity and A is a material constant. It is noted that high undercooling can occur at either very low growth rates (first term) or at very high growth rates (second term). The first term can normally be neglected except for very low growth rates ($< 0.3\,\text{mm/sec}$) experienced along the fusion boundary.

Weld metal grains tend to nucleate off of base metal grains, assuming their same size and crystallographic orientation (i.e. epitaxial nucleation). Once nucleated, weld metal grains will grow normal to the weld pool interface to minimize grain boundary surface area and, hence, grain boundary energy. For this reason, the shape of the weld pool determines the shape of the weld metal grains. As shown in Fig. 5, a teardrop shaped weld pool will yield straight columnar grains, where as a circular shaped pool will yield curved columnar grains.

Each grain can be taken to consist of a packet of sub-grains (cells or dendrites), all oriented in the same direction. From Fig. 6 it is seen that grains will grow at a velocity (R_g) related to the weld travel speed (v) and the grain orientation angle (ϕ).

$$R_g = v\cos\phi \tag{9}$$

Thus, grains along the fusion boundary grow at low velocities approaching zero (i.e. $\phi \to 90°$) and grains at the weld center grow at velocities approaching the weld travel speed (i.e. $\phi \to 0°$).

3.2 Preferred Orientation

Dendrites tend to grow in a particular crystallographic direction, with their long axis aligned in a $\langle 100 \rangle$ cube direction. If the dendrites within a grain are growing in the same direction as the grain itself, the growth rate of the dendrites will be the same as that of the grain. This orientation is preferred, because the dendrite growth rate
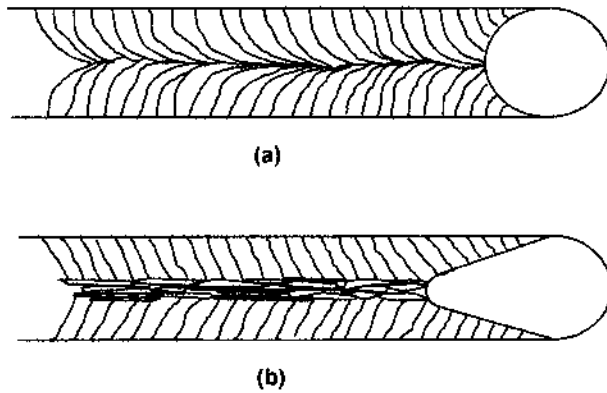
Figure 5 Top view of two welds comparing grain structure for (a) circular weld pool; and (b) tear-drop weld pool.
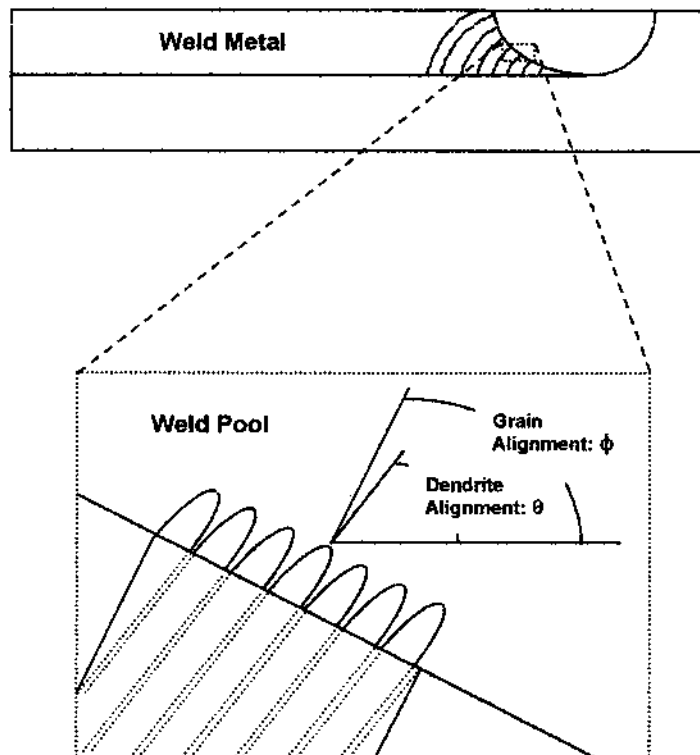
Figure 6 Longitudinal cross-section of weld showing close-up of fusion line and orientation angles for grains (ϕ) and dendrites (θ).

and solidification undercooling are minimized. If the dendrites are growing at some angle different from that of the grain, they must do so at higher growth rates and higher undercoolings (recall Eq. (8)). The relationship between solidification growth rate (R), grain orientation (ϕ), dendrite orientation (θ), and weld travel speed (v) is given as [5]:

$$R = v \cos \phi / \cos (\phi - \theta) \tag{10}$$

Those grains with dendrites having the preferred orientation will tend to overgrow, by means of lateral movement, other adjacent grains. This process, referred to as competitive grain growth, tends to result in a few large columnar grains dominating the weld metal. These columnar grains can nucleate and grow from one weld pass to another, sometimes extending the full depth of a multi-pass joint. In some instances, when the dendrite misalignment and corresponding undercooling is high enough, a nucleation event may occur producing a new grain with a random crystal orientation.

Because of the competitive growth and re-nucleation mechanisms, most grains observed in the weld metal have dendrites with a preferred or near-preferred orientation. Thus, the solidification growth rate is nearly the same as the grain velocity (i.e. $R \approx R_g$). This means that solidification growth rate approaches zero at the fusion boundary, and it approaches the weld travel speed near the weld center. For this reason, it is not uncommon to observe a change in sub-grain morphology from cells near the fusion boundary, to dendrites or equiaxed dendrites at the weld center.

3.3 Dendrite Spacing

The spacing between primary dendrites (ψ) for a particular alloy has been shown to be proportional to the inverse square root of cooling rate, where cooling rate is equivalent to RG [6]:

$$\Psi = K_1 (dT/dt)^{-1/2} = K_1 (RG)^{-1/2} \tag{11}$$

where K_1 is a material constant.

Since cooling rate is inversely proportional to heat input (recall Eqs. (3) and (7)), the following relationships are appropriate utilizing Eq. (11) [7,8]:

$$\Psi = K_2 H^{1/2} \quad , \text{for 3-dimensional heat flow} \tag{12}$$

$$\text{and} \quad \Psi = K_3 H \quad , \text{for 2-dimensional heat flow} \tag{13}$$

In welding, where the cooling rate is on the order of 100°C/sec, the dendrite spacing is found to be around 10 μm. This value can vary by several microns depending upon the heat input and alloy composition. High heat input corresponds to slow cooling rates and coarser dendrite spacing. Since weld metal grain size is on the order of 100 μm, each grain will contain roughly ten dendrites. These values can be compared to castings, which cool around 10°C/sec and have dendrite spacings on the order of 100 μm.

3.4 Microsegregation

Most alloying additions to aluminum result in the partitioning of solute atoms into the liquid between the dendrites and the eventual formation of a eutectic. As the interdendritic liquid becomes enriched in solute and approaches the eutectic composition, a eutectic is formed at the base of the dendrites. The eutectic second phase compound is most often discontinuous, growing in an uncoupled manner. However, a few alloying elements are peritectic formers and will partition to solid rather than the liquid. Table 2 lists the binary and ternary reactions formed with aluminum pertinent to the welding of commercial alloys.

For the binary alloying elements found in the standard commercial filler alloys 2319, 5356, and 4043 (i.e. Cu, Mg, Si), it is observed that they all form simple eutectics. It is also observed that some transition elements (e.g. Fe, Sc and Mn) tend to form high melting eutectics, while others (e.g. Zr, Ti and V) tend to form high temperature peritectics. The ternary alloy systems, originating from the dilution of common base metal alloys, can form different eutectics depending upon the composition of the weld metal and, hence, the filler alloy used. Magnesium has the effect of lowering the melting temperature. The Al-Mg binary system and the Al-Mg-Cu, Al-Mg-Zn, and Al-Mg-Si ternary systems containing high Mg, all form low melting temperature eutectics.

The tendency for a given alloying element to partition can be ascertained by its partition coefficient (k). An average value for this coefficient can be found by taking the ratio of the slope of the liquidus line to the slope of the solidus line on a binary phase diagram. Values close to unity indicate little partitioning, whereas values

Table 2 Solidification Reactions Important to the Welding of Commercial Wrought Aluminum Alloys (Data from Ref. 9)

Alloy System	Reaction	Temp ($°C$)	Compound	
Al-Cu	E	547	$CuAl_2$	
Al-Mg	E	450	Mg_5Al_8	
Al-Si	E	577	Si	
Al-Sc	E	655	$ScAl_3$	
Al-Fe	E	655	$FeAl_3$	
Al-Mn	E	657	$MnAl_6$	
Al-Zr	P	660	$ZrAl_3$	
Al-Ti	P	665	$TiAl_3$	
Al-V	P	661	VAl_{10}	
Al-Mg-Cu	E	518	$CuMgAl_2$	
		507	$CuMgAl_2 + CuAl_2$	(high Cu)
		449	$CuMg_4Al_6 + Mg_5Al_8$	(high Mg)
Al-Mg-Zn	E	489	$Mg_3Zn_3Al_2$	
		475	$Mg_3Zn_3Al_2 + MgZn_2$	(high Zn)
		447	$Mg_3Zn_3Al_2 + Mg_5Al_8$	(high Mg)
Al-Mg-Si	E	595	Mg_2Si	
		555	$Mg_2Si + Si$	(high Si)
		449	$Mg_2Si + Mg_5Al_8$	(high Mg)

E: Eutectic   P: Peritectic

Table 3 Comparison of Partition Coefficients (k) and Quantity of Eutectic per Eq. (14) (Data from Ref. 9)

Alloy System	k	C_E (wt%)	C_o (wt%)	$(C_o/C_E)^{1/(l-k)}$ (wt%)
Al-Cu	0.17	33	1	1.48
Al-Mg	0.43	35	1	0.20
Al-Si	0.14	12	1	5.56
Al-Sc	0.52	0.6	0.1	2.39
Al-Fe	0.022	1.8	0.1	5.21
Al-Mn	0.95	1.9	0.1	10^{-24}

much less than one indicate extensive partitioning. In addition, the weight fraction of eutectic generated (f) can be approximated using the Scheil Equation [10]:

$$f = (C_o/C_E)^{1/(1-k)} \tag{14}$$

where C_o is the alloy composition and C_E is the eutectic composition. Values for partition coefficient and weight fraction are compared in Table 3 for binary systems important to aluminum welding.

For most cases, Cu, Mg, and Si elemental compositions will vary from 1 to 4 wt%. For purposes of comparison, a value of 1 wt% was chosen for C_o in Table 3. It should be noted that Mg generates very small quantities of eutectic, whereas Si generates large quantities of eutectic. In the case of the transition elements, a value of 0.1 was chosen for C_o, because this value is the normal concentration level found for these elements in commercial alloys. It is observed that Fe, a common impurity element in aluminum, generates large quantities of eutectic. For this reason, Fe can have a profound effect on solidification, blocking the flow of interdendritic fluid to feed shrinkage [11]. Mn, however, sometimes added for solid solution strengthening, generates essentially no eutectic at this solute level. The role of Sc, as a grain refiner, will be discussed in another section.

3.5 Macrosegregation

Unlike in castings, where gravity fed solutal flow during solidification can lead to large differences in composition from top to bottom, the average composition throughout a weld bead is normally quite uniform. This uniformity is due to the rigorous stirring action in the weld pool and the limited solidification time relative to castings. However, there are two notable exceptions to this norm. When using a filler alloy that differs significantly from the base metal (e.g. using alloy 4043 filler to weld alloy 2219), the unmixed zone (UMZ) at the periphery of the fusion boundary will be different in composition to the weld center. Also, the phenomenon of banding can result in large, repetitive variations in composition, observed as continuous bands that extend across the width of the weld metal as shown in Fig. 7.

Banding originates as the result of non-continuous advancement of the weld pool [12]. Even when the welding torch advances in a smooth and continuous manner and the welding current is held constant, the weld pool may oscillate. These
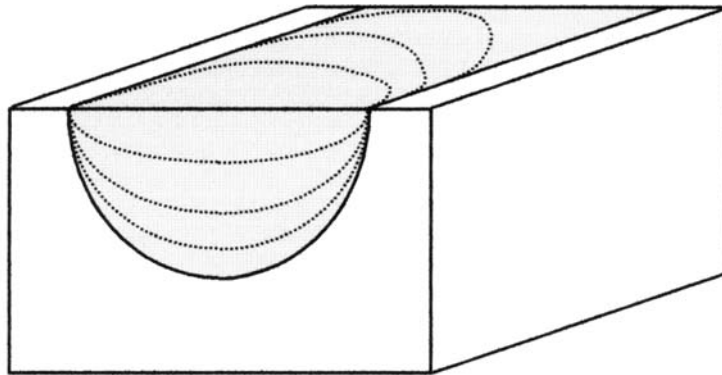
Figure 7 Transverse cross-section and top view of weld showing a form of macrosegregation known as banding.

oscillations arise due to small fluctuations in current or voltage that are remnant from the modulated 60 Hz AC power source, or from natural harmonics associated with the liquid pool itself. When the welding current or voltage are intentionally pulsed, this practice likewise serves to oscillate the weld pool. As the pool oscillates, the solidification growth rate (R) will decrease and increase accordingly, in some cases actually becoming negative (i.e. remelting).

These periodic variations in velocity serve to disrupt the diffusion profile of solute ahead of a growing interface, as suggested in Fig. 8. Rapid increases in growth rate will trap this solute, resulting in higher than normal solute levels in the solid. A sudden drop in growth rate will, likewise, result in lower than normal solute levels in the solid. The extra undercooling associated with either very high or very low growth rates (recall Eq. (8)) can also cause grain refinement, a side effect often observed with banding.
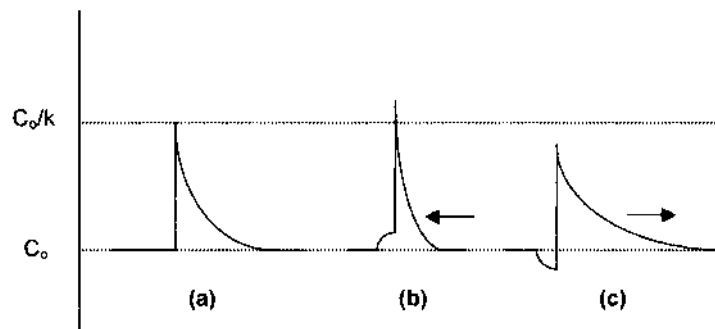
Figure 8 Solute concentration profile ahead of moving solid/liquid (S/L) interface for different conditions of (a) steady-state; (b) rapid increase in growth rate; and (c) rapid decrease in growth rate. At the S/L interface, the ratio of solute in the solid to the solute in the liquid remains constant.

3.6 Grain Refinement

Achieving fine grains uniformly throughout the weld metal is considered desirable from the standpoint of improved ductility, toughness and resistance to hot cracking (a solidification defect discussed in the next section). Conditions favorable for grain refinement include high undercooling plus the presence of a suitable substrate upon which to nucleate new grains.

Substrates most suitable for nucleation sites should be similar in crystal structure and atomic spacing to aluminum. The closer the substrate is to meeting these conditions, the less undercooling will be necessary to initiate a nucleation event. Thus, grain refinement can occur with either high undercooling and a poor substrate or low undercooling and a potent substrate.

In the case of aluminum, the high temperature peritectic reaction with either Ti or Zr is often utilized for grain refinement because it results in the ideal substrate for nucleation [13]:

$$L + TiAl_3 = Al\,(substrate), 665°C \tag{15}$$

$$L + ZrAl_3 = Al\,(substrate), 660°C \tag{16}$$

Particles of $TiAl_3$ or $ZrAl_3$ are often intentionally added to welding filler alloys for purposes of grain refinement (roughly 0.15 wt% Ti or Zr). When the filler alloy is fused into the weld pool, these particles become liberated and make their way to the solidification front. Here the peritectic reaction coats these particles with a layer of solid aluminum providing an ideal substrate. If the particles completely melt on their journey through the superheated weld pool, they cannot participate in grain refinement (a phenomenon referred to as fading). The gas-metal arc welding process (GMAW) is particularly troublesome in this regard, where molten drops from the filler wire must first pass directly through the welding arc, increasing the chances for particle dissolution.

Boron, when added together with Ti, improves the nucleating efficiency although the exact role that boron plays is not entirely understood. Boron is often present in filler alloys, but it is added at such low levels (< 0.03 wt% B) that it need not be listed in composition tables. One theory [14] proposes that boron forms a protective boride (TiB_2) coating on the $TiAl_3$ particles, helping to slow down dissolution. This coating would have the effect of increasing the chances that a $TiAl_3$ particle may reach the solidification interface intact.

In recent developments [15], Scandium has also been found to produce grain refinement, but only when added at high levels (> 0.50 wt% Sc, i.e. hypereutectic). The $ScAl_3$ pro-eutectic compound apparently serves as a potent nucleating substrate, because of a closely matched lattice spacing to aluminum. Smaller amounts of Sc can also result in grain refinement if Zr is present (e.g. 0.20 wt% Sc + 0.15 wt% Zr). It is believed that Zr can replace Sc in the $(Sc, Zr)Al_3$ compound, requiring less Sc to be used to get primary crystals for grain refinement [16].

Two regions in the weld metal where you are most likely to find grain refinement is along the weld center and at the weld fusion boundary. At the weld center, the grains become aligned in the direction of torch travel (i.e. grain orientation angle $\phi = 0°$) yielding the highest growth rates (recall Eq. (10)). These

high growth rates result in high undercooling and a higher likelihood for grain nucleation (recall second term in Eq. (8)). A region of equiaxed grains at the weld center is commonly observed in aluminum weldments [17].

Along the fusion boundary, where the growth rate approaches zero ($\phi = 90°$), there is also high undercooling as demonstrated in Ref. 18 (recall first term in Eq.(8)). The existence of equiaxed grains at the fusion boundary, although less common, has been observed for some base metal alloys containing Zr (e.g. alloys 2195 and 7108). The occurrence of these fine grains has, in some cases, been associated with poor mechanical properties [19].

For these alloys, Zr has been added to the base metal as a dispersoid former to prevent recrystallization during high temperature forming operations and heat treatment. It has been shown that $ZrAl_3$ dispersoids are picked up from the base metal during melting and become free in the unmixed zone (UMZ) to nucleate new grains according to the peritectic reaction in Eq. (16) [20]. Those particles swept into the turbulent weld pool will more likely become dissolved. Hence, nucleation events are concentrated along the fusion boundary.

4   POROSITY

At the high temperatures experienced by the arc welding processes the weld pool can approach the boiling temperature of aluminum at the pool surface. Aluminum experiences two orders of magnitude change in hydrogen solubility on cooling from the initial high temperature to the on set of solidification [21–23]. The sensitivity of aluminum to hydrogen is not so much associated with the difference of gas solubility in the liquid and solid at the melting temperature, but rather with the particular conditions of the temperature existing in an arc melted weld pool [24]. The hydrogen is dissolved in the aluminum in accordance with the high temperature equilibrium, and rapid stirring of the pool by electromagnetic forces causes the whole pool to attain a high gas content corresponding to the high temperature at the surface.

Aluminum weld pools can hold hydrogen contents up to seventy times the melting point solubility [25,26]. This effect is very pronounced for aluminum, where the temperature of the region under the arc is greatly superheated and where the weld pool can become supersaturated to such an extent that gas pores will form without the aid of solidification. During the rapid cooling of a typical aluminum weld there is insufficient time for the hydrogen to transport to the liquid surface and escape from the weld pool [27]. The result is the formation of pores in the weld deposit [28–34].

4.1   Thermodynamic Requirement

The requirement to form a pore is that the sum of the partial pressure of soluble gases, P_g, must exceed the sum of the following pressure terms [29,35–37]:

$$P_g > P_a + P_h + P_b \tag{17}$$

where P_a is the pressure of the ambient atmosphere, P_h is the hydrostatic pressure, and P_b is the capillary contribution to the pressure due to the curvature of the pore. The magnitude of these terms must be considered. Typically P_a will be one atm, P_h is neglected and P_b is given by the following equation:

$$P_b = 2\gamma/r \tag{18}$$

where γ is the surface tension between the molten metal and the gas in the pore, and r is the radius of pore curvature. There are situations, such as with the use of pressure inert gas metal arc, PIGMA, welding where the P_a term becomes significant.

4.2 Homogeneous Nucleation

The desire for a pore to form is insufficient to achieve porosity, for pore formation must also encounter and overcome the kinetic activation energy barrier, such as nucleation [38–40]. There is a critical pore radius r_c for which, when it is exceeded, the pore will homogeneously nucleate and grow spontaneously to unlimited dimensions. An expression for this critical radius has been developed for the formation of a single-gas-phase pore, and is given by:

$$r_c \geq \frac{2\gamma V \phi}{kT \ln(P_g/P_o)} \tag{19}$$

where V is the atomic volume of the gas phase, P_g/P_o is the degree of supersaturation of the metastable gas phase, ϕ is the correction factor for a heterogeneous medium, P_o is the equilibrium pressure for the single gas phase, k is the Boltzmann constant, and T is the temperature (in degrees Kelvin). Consequently, the formation of a gas nucleus is only possible at a definite supersaturation ($P_g/P_o > 1$).

A Boltzmann probability distribution expression is used to define the rate of nucleation, I. The exponential describes probability of overcoming the nucleation activation energy barrier from a solution absent of non-wettable interfaces:

$$I = A \exp\left(-\frac{4}{3}\pi \frac{r_c^2 \gamma}{kT}\right) \tag{20}$$

where A is a constant approaching Avogadro's number.

Substituting Eq. (19) for r_c into Eq (20), the following rate expression results for nucleation of a single-gas-phase pore:

$$I = A \exp\left(-\frac{16\pi\gamma^3 V^2}{3kT\chi^2}\right) \tag{21}$$

where $\chi = kT \ln(P_g/P_o)$.

Assuming the liquid metal has a surface tension of 1500 dynes/cm, and a temperature of 2000 K, the probability of homogeneous nucleation of gas bubbles in liquid metal of a typical weld pool volume is very small, if not negligible. A more likely situation is that of heterogeneous nucleation where solid/liquid interfaces become lower energy barrier sites for nucleation. Heterogeneous nucleation can be achieved by less gas volume than experienced by homogeneous nucleation.

4.3 Heterogeneous Nucleation

Equation (17) can be modified to achieve a better fit for the heterogeneous nucleation of gas pores. The following modification has been proposed [37–39]:

$$P_g = P_a + h\rho + \beta\gamma(1 + \cos\theta) \tag{22}$$

where h is the height of the liquid metal column, ρ is the density of the liquid metal, θ is the contact angle between the gas and the substrate, and β is a coefficient which empirically relates liquid-metal adhesion to the substrate. This adhesion is considered to hinder heterogeneous nucleation of a gas phase on the substrate. The second term, $h\rho$, was referred to in Eq. (17) as P_h. Equation (22) also accounts for the influence of the radius of curvature of the pores through the last term.

The critical radius for heterogeneous nucleation, r_c, is given as follows:

$$r_{c(het)} = r_c f(\theta) \tag{23}$$

where

$$f(\theta) = \left(\frac{2 + 2\cos\theta + \sin^2\theta\cos\theta}{4}\right)^{1/3} \tag{24}$$

For the complete wetting case where $\theta = 0$ and $f(\theta) = 1$, the equation assumes the form given by Eq. (19) (see Fig. 9(a)).

Pores of gas are commonly formed on the surfaces of solid non-metallic inclusions which are present in the weld pool. In this case the nucleus will have a lens shape because of poor wetting of the solid non-metallics by the liquid metal (see Fig. 9(b)). With complete non-wetting ($\theta = 180°$), $f(\theta)$ is zero. In this case the probability of formation of stable gas-phase nuclei as θ approaches $180°$ is high. Note that with heterogeneous nucleation a large critical radius of curvature can result with a minimal volume of gas. Therefore, the surfaces of dendrites and precipitated crystals, which are well wetted by the liquid metal and which can potentially form contact angles close to zero, create high capillary resistance, which inhibits the formation of gas nuclei.
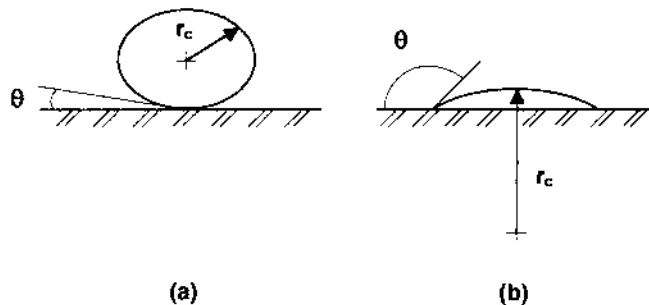
Figure 9 Different wetting conditions for the nucleation of gas pores, where (a) the liquid wets the substrate; and (b) the gas wets the substrate. Condition (b) favors heterogeneous nucleation, achieving a critical radius (r_c) with less gas volume.

4.4 Sources of Porosity

The effect of supersaturation of hydrogen has been found to be the major cause of porosity. The entrapment of various gases, the cooling rate of the weld pool and erratic wire feed have all been identified as additional sources. There are many ways in which gas can enter the weld pool, including entrapped shielding gas, air, the product of violent arc action or dissolved hydrogen.

One source of weld contamination by hydrogen can be traced to the existence of hydrogen-forming compounds, including oil, drawing compounds and shop grease [41]. The pores in an aluminum weld are often the result of pyrolysis of organic contaminations. Graphite has been applied on the faying edges of specimens to promote the reaction of carbon with the oxide film, and pores did not form. These results suggest that carbon in organic compound is not responsible for pore formation, but hydrogen or water are a source of porosity. A pre-welding vacuum heat-treatment of aluminum parts prior to welding to reduce hydrogen sources, and thus porosity, has been suggested.

Nearly all porosity in aluminum alloys is due to hydrogen formed by the reaction of water vapor with the molten aluminum. The effect of moisture on the formation of aluminum weld metal pores has been studied and showed that the addition of dry hydrogen to the argon cover gas does not increase the pore concentration. However, the addition of water vapor to the argon caused rapid pore formation in the weld metal. The moisture content of the air around the arc was reported to be less important than that of the cover gas. Porosity has been related to the shielding gas dew point. A dew point threshold for porosity of approximately $-40°C$ has been reported. Dew points above $-40°C$ promote porosity.

4.5 Hydrogen Partitioning

Besides the solubility issue, the equilibrium partition ratio, which describes the hydrogen content at the traveling solid/liquid interface, is instrumental in maintaining sufficient high-localized hydrogen contents in welds that have been made to minimize hydrogen pickup [39,42]. With an equilibrium partition ratio of 0.05 hydrogen will be rejected at the solid/liquid interface, which can achieve extremely high hydrogen concentration in the interdendritic region during solidification.

The content of the dissolved gas lies in the range between its solubility in the solid and liquid metal, i.e. $S_s < C_0 \leq S_l$. The process of pore formation depends to a large extent on the redistribution of dissolved gas in the liquid metal ahead of the solidification front.

The gas concentration ahead of the solidification front, $C(x)$, is given by:

$$C(x) = \left[1 + \frac{1-k'}{k'}\exp\left(\frac{-Rx}{D}\right) \right] \tag{25}$$

where x is the distance into the liquid from the solidification front, k' is the equilibrium partition ratio equal to S_s/S_l, R is the rate of solidification and D is the diffusion coefficient of the gaseous element in the liquid. The maximum gas content is observed at the solidification front and it is equal to C_0/k'.

4.6 Growth Kinetics

The size, morphology, and distribution of pores are primarily affected by the solidification rate. To achieve large spherical pores requires relatively slow travel speeds and/or high heat input resulting in a slow solidification rate. The slow solidification rate results in wide spacing between cellular-dendritic arms of the growing solid phase, which allows for heterogeneous pore nucleation at the solid/liquid interface and for detachment from this interface.

The size of spherical pores is directly influenced by mechanical entrapment of pores to achieve even larger pores. The pore sizes are also dependent on the level of hydrogen supersaturation and the time to solidify. The larger pores have a greater bouyancy and tend to escape from the weld pool, especially at slower solidification rates where the interdendritic spaces are wide [28]. The influence of welding process parameters is directly related to the issue of time to solidify and to the electrode to work spacing which influences the atmospheric hydrogen pick up. The influence of welding variables on porosity has been reported for gas metal arc aluminum welds [43].

The growth kinetics of pores in liquid metal is related to the following factors: (i) inertia of liquid metal; (ii) surface tension and isobaric gas pressure; (iii) gas content of the metal; and (iv) pressure of the welding arc.

The rate of travel of the walls of the expanding gas cavity, dr/dt, from pore radius r_0 to r_1 is approximated by the following equation:

$$\frac{dr}{dt} = \frac{2}{3}\frac{(P_g - P_a - P_{arc} - P_h - P_b)(r_1 - r_0) - 2\gamma}{\eta} \tag{26}$$

where P_{arc} is the pressure from the arc on the weld pool, η is the coefficient of viscosity, r_0 is the initial radius, and r_1 is the final radius of the pore. The radius or size of the pore will depend on the time during which the metal is in the molten state. This behavior is controlled by the heat input as established by the welding conditions [42–44]. This model does not consider the influence of a number of factors, especially the diffusion in liquid metal.

The smaller pores, spherical and angular pores, are primarily formed in the tightly spaced cellular-dendritic structures. At very fast welding rates small intercellular pores cannot form since the rate of formation is less than rate of the advancing cells. At intermediate welding rates where pore formation occurs with little growth, the interdendritic pores may not be able to detach from the solid/liquid interface but still extend with mechanical entrapment in the direction of solidification resulting in a wormhole porosity. Wormhole pores are normally not observed in aluminum welds.

Porosity is often distributed in the banding zones in aluminum welds [28]. The banding zones are the result of a change in the solute concentration, in this case its hydrogen, due to a change in solidification rate which is inherent to the fluctuations common to the welding process. Such banding zones are present in nearly all weld deposited by gas tungsten arc and gas metal arc aluminum welds.

The pore concentration, pore distribution in the weld and its size distribution are directly related to two competing processes. When solidification times are long, the hydrogen pores can escape the weld pool resulting in a low pore concentration, but when the solidification time is reduced, the pore concentration will first increase
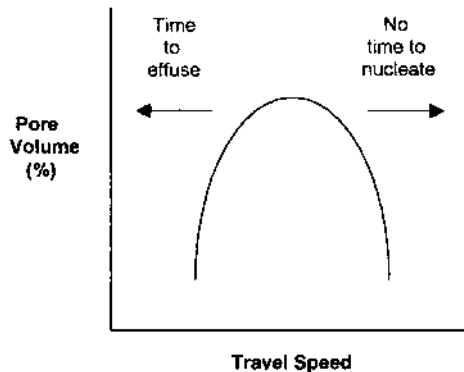
Figure 10 Schematic diagram demonstrating how amount of weld metal porosity can vary with welding travel speed resulting in peak susceptibility.

due to entrapment and then decrease due to insufficient time to nucleate and grow a pore. This behavior is demonstrated in Fig. 10, where the quantity of porosity is shown to be a function of weld travel speed.

In order to minimize porosity, the welding process parameters can be altered after knowing which side of this maximum the process lies. If to the left of this maximum, one must change the welding parameters to even slower solidification rates. If to right of the maximum, one must change the welding parameters to further increase the solidification rate. Increasing the travel speed allows for this modification without much interference with the electric energy generation of the welding arc.

4.7 Effect on Mechanical Properties

The influence of porosity on aluminum weld metal mechanical properties has been reported by a number of investigators [30,31,45,46]. There is a combination of pore size and distribution of porosity which is critical to the degrading of the tensile strength and ductility. The tensile elongation of aluminum alloy welds was found to drop immediately as the porosity level is increased. Weld tensile ductility was reported to be reduced by as much as 50% from its highest level with porosity of about 4 vol%. The tensile strength was found to be very tolerant to some porosity. The yield strength was only slightly reduced by porosity levels up to about 4 vol%. The loss in aluminum weld metal transverse tensile strength and fatigue life was found proportional to the loss of sound metal area in the plane of the expected fracture. Recently the correlation between interdendritic pore formation and the susceptibility to hot cracking has been reported [47–49].

5 HOT CRACKING

Hot cracking is a term used by welding engineers to identify a crack defect that forms during weld metal solidification. It is similar in nature to the cracking found in castings known as hot tearing. Mechanistically, it involves the tearing apart of liquid films due to stresses and strains arising from solidification shrinkage and thermal

contraction. These liquid films and corresponding hot cracks occur primarily along grain boundaries, but they can also be found interdendritically. In either event, the surface of hot cracks are characteristically smooth and undulating, without any of faceting or dimpling characteristic of wrought alloy fractures. Hot cracks are normally located along the weld centerline, either at the weld crown or root.

5.1   Mechanism

Liquid films associated with hot cracking are typically related to the formation of low melting eutectics. When there is a large difference between the liquidus of an alloy and its lowest melting eutectic, the corresponding large solidification range can subject the liquid film to more shrinkage. Plus, it becomes more difficult to feed shrinkage over large distances. As solidification is completed at the base of the dendrites and shrinkage is culminated, the ability to feed this shrinkage with interdendritic liquid becomes critical.

One model [50] proposes that hot cracking may occur whenever the rate of grain separation (i.e. shrinkage) exceeds the rate of liquid back filling (i.e. feeding). When this happens, the pressure in the interdendritic liquid drops and may even become negative (i.e. unstable) for a short moment of time. With a negative pressure in the liquid, tearing may initiate either on oxide inclusions (i.e. decohesion, [51]) or as a result of cavitation [47].

It should be noted that the interdendritic pressure drop is also conducive to pore nucleation (recall Eq. (17)). Which of these defects happens to form first, hot crack or pore, will be determined by kinetics (i.e. the rate of pressure drop). Once nucleated, a hot crack will often grow in a continuous manner, trailing behind the weld pool.

5.2   Mechanical Aspect

There is also a mechanical aspect to the hot cracking problem. The tensile and compressive cells which form around a moving weld pool interact with their surroundings to produce both inward and outward movement of material behind the traveling weld pool [52]. These strain cells are influenced by the degree of restraint (i.e. fixturing, component size and shape, etc.), weld heat input, and welding speed. If this strain becomes positive in the region undergoing solidification, it will combine with the solidification shrinkage strain to promote hot cracking. If this strain becomes negative within this region, then hot cracking can be avoided.

5.3   Effect of Grain Morphology

Because hot cracks nucleate and grow along grain boundaries, it follows that grain size and shape can have a strong influence on cracking susceptibility. Small grain size is normally considered beneficial for avoiding crack initiation. The weld induced strain will be distributed more evenly over a greater number of grain boundary films, thus resulting in a smaller strain per film. In terms of crack propagation, however, small grains may sometimes provide for easier crack growth once initiated, particularly when compared against large grains with high curvature.

It is preferable to have grains with a high degree of curvature, such as those grains obtained with a spherical shaped weld pool (Fig. 5(a)). In this condition, any crack that nucleates at the weld center, will automatically grow out of the field of maximum strain. In situations where the welding speed is high and a tear-drop shaped weld pool is formed, a continuous grain boundary tends to form along the weld centerline, aligned for easy crack propagation (Fig. 5(b)).

5.4 Peak Susceptibility

When the hot cracking susceptibility of an aluminum alloy is compared in terms of solute content, a peak in susceptibility is commonly observed. For example, this peak susceptibility behavior is shown in Fig. 11 for several binary alloys. Here, the hot cracking susceptibility is expressed in terms of the total (accumulated) crack length generated in a Varestraint weldability test [53].

At low solute levels, it can be argued that the crack susceptibility is low because a dendritic network has not yet been fully developed. Also, the amount of eutectic liquid generated will be low, which means that there will be thin liquid films having greater resistance to tearing. At high solute levels, however, there becomes large amounts of interdendritic liquid available for feeding of shrinkage. Solute levels, intermediate to these two extremes, result in the peak in susceptibility.
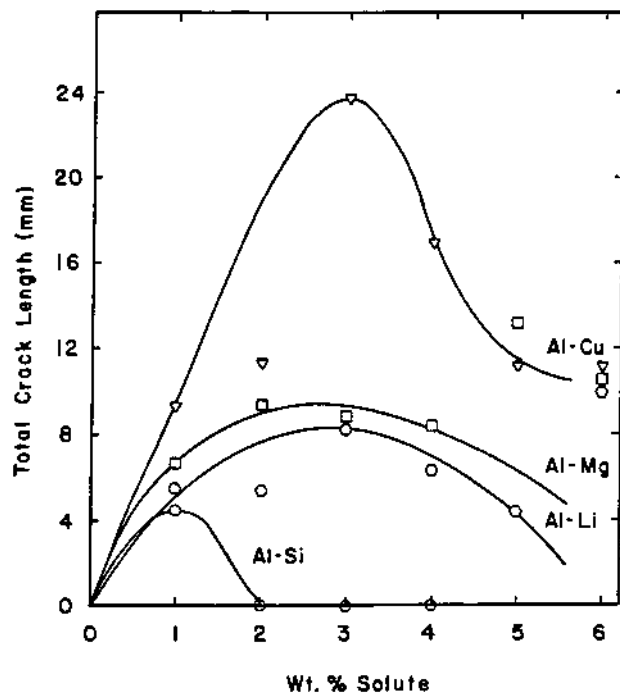
Figure 11 Experimental results from Varestraint Test showing four different aluminum binary alloys exhibiting peak hot cracking susceptibility behavior. (From Ref. 53.)

From Fig. 11 it should be noted that Si generates the least amount of cracking. This result is believed to be due to the large quantity of eutectic available for back filling (recall Table 3). For this reason, Al-Si filler alloys (e.g. 4043, 4047) are often used for joining crack sensitive alloys. Mg, even though it has a large solidification range (Table 2), generates very small amounts of eutectic which provides resistance to hot cracking. Al-Mg filler alloys are common (e.g. 5183, 5356) and Al-Mg base metal alloys (e.g. 5083) are considered to be readily weldable at high Mg content (≥ 4 wt%).

When considering the behavior of commercial alloys consisting of multi-component alloy systems, there appears to be a strong influence on hot cracking susceptibility by the Al-Cu-Mg eutectic. This behavior is suggested in Fig. 12 which shows castability (hot tearing) data for Al-Mg-Cu ternary alloys [54], superimposed with modern commercial alloys [55]. This figure shows peak susceptibility behavior in three dimensions, with contour lines representing the total crack length generated in a cast ring test.

Binary alloys such as 5083 (high Mg) or 2219 (high Cu) are considered to have good weldability and are located at the base of the peak. Aerospace alloys such as 7075 and 2024, located closer to the peak, are considered unweldable. The weldability of any of the alloys shown can be improved by dilution with either a high Mg or a high Cu filler alloy, shifting the weld metal composition away from the peak. Similar cracking diagrams exist for Al-Mg-Si and Al-Mg-Zn alloys and can be used to predict weldability and dilution effects in a similar manner [56].
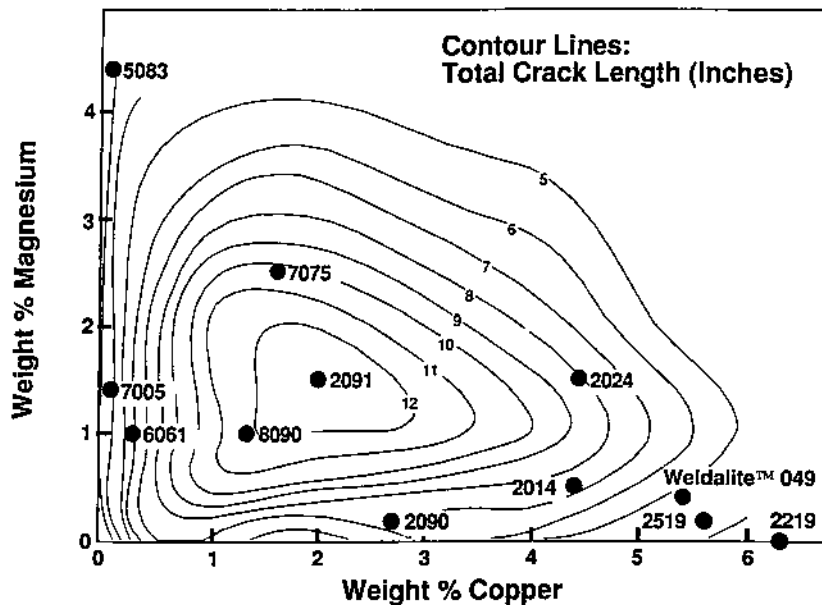
Figure 12   Modern commercial alloys are superimposed upon Ring Casting Data [54] demonstrating effect of weld dilution and composition on hot cracking susceptibility [55]. Lines represent iso-crack length and culminate in a peak susceptibility in 3-dimensional space.
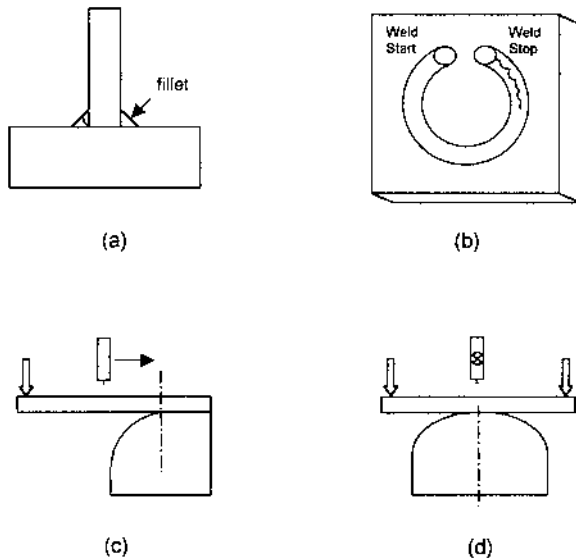
Figure 13 Comparison of hot crack weldability tests for plate and extrusions: (a) Inverted T-Test; (b) Circular Patch Test; (c) Varestraint Test; and (d) Trans-Varestraint Test.

5.5 Weldability Testing

Numerous weldability tests have been developed to evaluate hot cracking susceptibility. Included among the more common tests for plate and extrusions are the Inverted T-Test, Patch Test, Varestraint Test, and Trans-Varestraint Test. Also, for sheet material, there is the Houldcroft Test and the Sigmajig Test. In each of these tests, there are conditions of either high restraint (intrinsic type test) or imposed strain (extrinsic type test) which help to promote the formation of hot cracks. Alloys are rated in terms of the extend of cracking, often expressed as the total length of cracks generated. Such tests are useful in making relative comparisons, but cannot be used to predict cracking under normal welding conditions. Weldability tests are described below and are compared in Fig. 13 and 14 for plate metal and sheet metal, respectively.

5.5.1 Inverted T-Test [57]

This test involves making small fillet welds on both sides of a T-joint, with one of the members being large in cross section. After having welded one side and nearly completing the next, the degree of restrain increases to the point where cracking begins as the weld is completed. The total length of crack is taken as a measure of crack sensitivity.

5.5.2 Circular Patch Test [58]

This is a popular weldability test due to its simplicity and easy of execution. It involves making a weld on a flat plate in the form of a circle. As the weld nears the end of the circular loop, it begins to experience the shrinkage strains associated
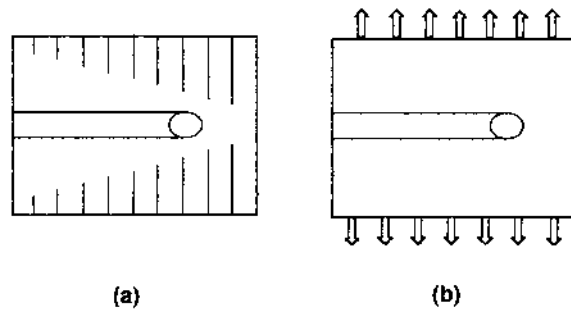
Figure 14   Comparison of hot crack weldability tests for thin sheet: (a) Houldcroft Test; and (b) Sigmajig Test.

with the initial portion of the weld loop. Thus, at some point around the loop, cracking will initiate at the centerline and trail the weld pool till weld completion. The total length of crack is taken as a measure of crack sensitivity.

5.5.3 Varestraint Test [59]

In this test, a strain of known magnitude is applied to a weld coupon during the welding process. This is accomplished by bending the coupon over a mandrel, with a known radius of curvature, at a very high strain rate. Bending is initiated as soon as the weld torch passes the point of tangency where the coupon meets the mandrel. The arc is not extinguished and the torch does not stop until well beyond this point. The strain can be varied by varying the radius of curvature and assumes values that are normally between 0.25% and 2%. Note that the strain is applied along the direction of welding. A pattern of cracks is formed at the location where the strain is applied, with numerous cracks radiating outward from the weld pool. The total length of cracks, for a particular applied strain, is taken as a measure of crack sensitivity.

5.5.4 Trans-Varestraint Test [60]

Similar to the Varestraint Test, this test involves the rapid application of a known strain to a weld coupon during welding. Again, the strain is fixed by the radius of the mandrel. However, in this case the strain is applied normal to the welding direction, which more closely mimics real life conditions. Normally only a few (1–3) centerline cracks are formed, the total length of which is taken as measure of crack sensitivity.

5.5.5 Houldcroft Test [61]

A weld is initiated at the very edge of a sheet having pre-cut, through-thickness slots. These slots are arranged normal to the welding direction, are evenly spaced, and become progressively longer in length with distance from the weld start. A crack is initiated immediately at the weld start and grows behind the weld pool until the degree of restraint becomes significantly diminished (from the longer slots). The over-all length of crack is taken to be a measure of crack sensitivity.

5.5.6 Sigmajig Test [62]

In this test, a coupon consisting of a sheet of material is clamped at its outer edges and uniformly stressed normal to the welding direction prior to and during welding. A weld is made down the center of the coupon. This test is repeated at different stress levels until cracking is initiated. The critical stress to initiate cracking is taken as a measure of crack sensitivity.

5.6 Comparison of Commercial Alloys

Weldability test results for several different commercial alloys, using three different testing methods, are compared in this section. Results from the inverted tee-test, used by Dudas and Collings [55, 63], are summarized in Fig. 15. Here it is observed that certain alloys considered to be unweldable when welded autogenously (i.e. alloys 6061, 7005, and 2014) all generate high crack length values. The total crack length can be significantly reduced, however, by using an appropriate filler alloy (e.g. 4043 or 5356) thereby making these alloys weldable. Weldable alloys 5083 and 2219 generate much lower crack levels (compared to autogenous 6061, 7005, or 2014 welds), crack length values that can be reduced even further by using an appropriate filler alloy.

Results from a Trans-Varestraint weldability test study [64] are shown in Fig. 16. In this study, filler alloys were used for all tests. Similar to Fig. 15, alloy 2219 is found to be the most weldable. Alloy 2519, which is similar to 2219 but with 0.5 Mg
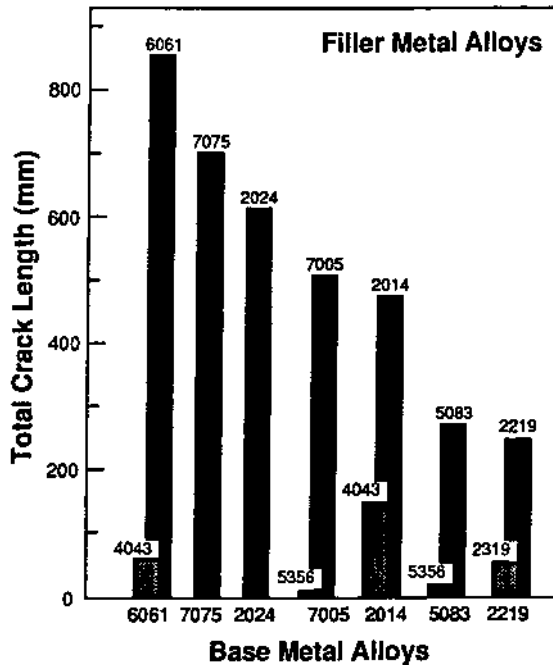
Figure 15 Experimental results from Inverted T-Test comparing hot cracking susceptibility for various alloys. (From Refs. 55,63.)
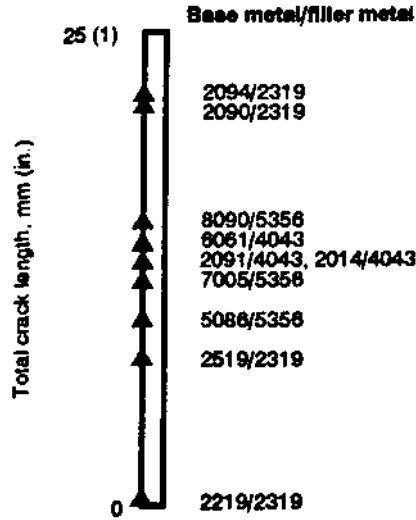
Figure 16 Experimental results from Trans-Varestraint Test comparing hot cracking susceptibility for various alloys. (From Ref. 64.)
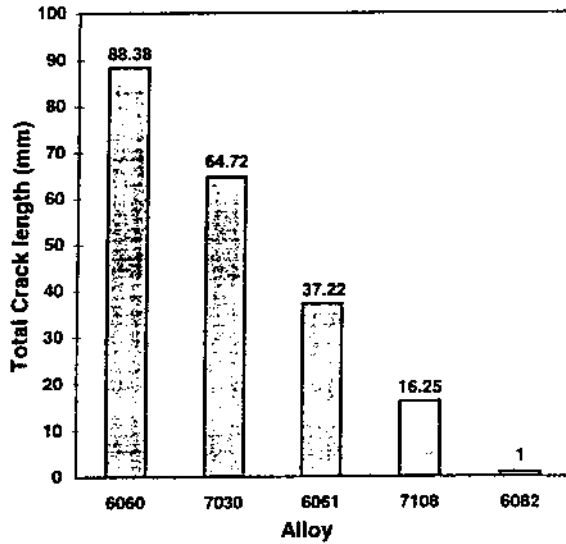
Figure 17 Experimental results from Circular Patch Test comparing hot cracking susceptibility for various alloys. (From Ref. 16.)

added, is less weldable than 2219. Alloys 6061, 2014, and 7005 have about the same weldability, but are less weldable than 2219, 2519, and 5086. The least weldable alloys are the Al-Cu-Li-Mg alloys 2094 and 2090.

Results from a Circular Patch Test [16] are shown in Fig. 17, where all of the tests performed involved autogenous welding. Alloys 6060, 7030, and 6061 are gen-

erally considered unweldable (without a filler). Alloys 7108 and 6082, however, can be readily welded, particularly when using a filler. This trend is reflected in the total crack length ranking of these alloys.

6 HEAT AFFECTED ZONE

The Heat Affected Zone (HAZ) consists of base material lying outside the fusion boundary that has been modified by the weld thermal experience. Modifications to the base metal microstructure in the HAZ can include recovery, recrystallization and grain growth, partial melting, and precipitation reactions. The occurrence of any one of these modifications normally results in a drop in strength and a decrease in joint efficiency. Damage to the HAZ is often monitored using a hardness traverse across the welded joint.

6.1 Recovery, Recrystallization and Grain Growth

Material that lies ahead of the moving weld pool will experience heat from the welding torch even before melting begins. For material that lies outside the fusion zone, wrought grains are exposed to elevated (sub-liquidus) temperatures for periods of several seconds. Providing there is sufficient cold work in the base metal, this thermal cycle will result in recovery, recrystallization and grain growth. This normally results in large, equiaxed grains along the fusion boundary from which weld metal grains will eventually nucleate (i.e. epitaxial nucleation).

In alloys that depend upon cold work for strength (e.g. 5083-H38), the recrystallization process accounts for a majority of strength loss in the weldment. For precipitation hardened alloys, however, this may contribute only slightly to the over-all strength loss. Alloys containing grain pinning dispersoids will be less susceptible to this problem. For example, alloys containing zirconium dispersoids (e.g. 7108 and 6082) will have less recrystallization and grain growth than zirconium free alloys (e.g. 7030 and 6060).

6.2 Partial Melting

There is a region adjacent to the fusion boundary in the HAZ where the peak temperature resides between the liquidus and solidus of the base metal. It is here where equilibrium super-solidus melting can occur. The thickness of this region is normally less than one grain diameter. However, when there are eutectic constituent particles present at grain boundaries, it is also possible to get sub-solidus melting. This occurs as a result of constitutional liquation and can extend the melting range down to the eutectic temperature of the constituent particles.

The mechanism of constitutional liquation involves the dissolution of constituent particles and the formation of a concentration gradient into the precipitate free zone [65]. If, within this established concentration gradient, the eutectic composition is reached and the eutectic temperature is exceeded, then melting will occur. The liquid thus formed will tend to wet the grain boundary. This same problem, when encountered in the high temperature processing of alloys, is often referred to as "hot shortness." Recent modeling work [66] has shown that liquation can be avoided if the heating rate is sufficiently slow, such that the constituent particle becomes completely dissolved prior to reaching the eutectic temperature.

Liquation, by itself, is not overly detrimental to mechanical properties. However, if sufficient tensile strain is present in this region at the same time the grains are liquated, then the liquid films may rupture and form liquation cracks. There appears to be an association here with the choice of filler alloy selected and the ability to load the grains [67,68]. If the solidus temperature of the weld metal is close to the base metal (e.g. 5356 filler and 6061 base metal), then there is a high likelyhood for cracking. If the solidus temperature of the weld metal is much lower than the base metal (e.g. 4043 filler and 6061 base metal), cracking can be avoided.

Liquation cracks (also called micro-fissures or grain boundary openings-GBO) can potentially impair the fatigue life and fracture toughness of a joint. This defect is a common problem when welding 6xxx and 7xxx alloys, particularly those alloys with large recrystallized grains (e.g. 7030 and 6060). Since liquation cracks are generally too small to be resolved with radiography, they often go undetected unless observed in weld cross-sections using optical metallography.

6.3   Precipitation Reactions

When welding heat treatable alloys, the HAZ can suffer significant loss of strength derived from precipitation hardening. This strength loss is due to precipitation reactions involving dissolution or coarsening. Considerable insight has been gained from recent modeling work [69–72], coupling heat flow with dissolution and liquation mechanisms. When considering precipitation reactions, it is useful to divide the HAZ into two regions, near and far, as discussed below.

In the near HAZ, where the peak temperature exceeds the solvus temperature, there is complete dissolution of hardening precipitates. In 6xxx and 7xxx alloy systems, where the hardening precipitates are β'' (Mg_2Si) and η' ($MgZn_2$) respectively, the dissolved solute in the near HAZ remains in solution upon weld cool down. This dissolution results in very low as-welded strength. Post weld natural aging, however, allows for fine precipitate formation and the partial recovery of strength. This aging response is particularly strong for 7xxx alloys which can regain half of their strength loss after aging thirty days at room temperature. In the case of 2xxx alloys, where θ' ($CuAl_2$) is a hardening precipitate, there is a re-precipitation of θ' upon weld cool down, with a preference for nucleation at grain boundaries and the formation of precipitate free zones [69].

In the far HAZ, where the peak temperature does not exceed the solvus temperature, there can exist conditions of either partial dissolution of precipitates or precipitate coarsening. The extent of dissolution or coarsening will vary as a function of peak temperature and, hence, distance from the fusion boundary. Myhr et al. [70] have successfully modeled the alloy 6082 HAZ using a dissolution model predicting the hardness profile as shown in Fig. 18. Because so much solute goes into solution, the near HAZ can respond to post weld aging as suggested in this figure. The far HAZ, however, remains unresponsive to aging. Martukanitz [71,72], on the other hand, has modeled the alloy 2219 HAZ based upon a precipitate coarsening model, assuming that large precipitates grow at the expense of the dissolution of small precipitates. In this case, no part of the HAZ responds to post-weld aging, because there is no excess solute in solution.
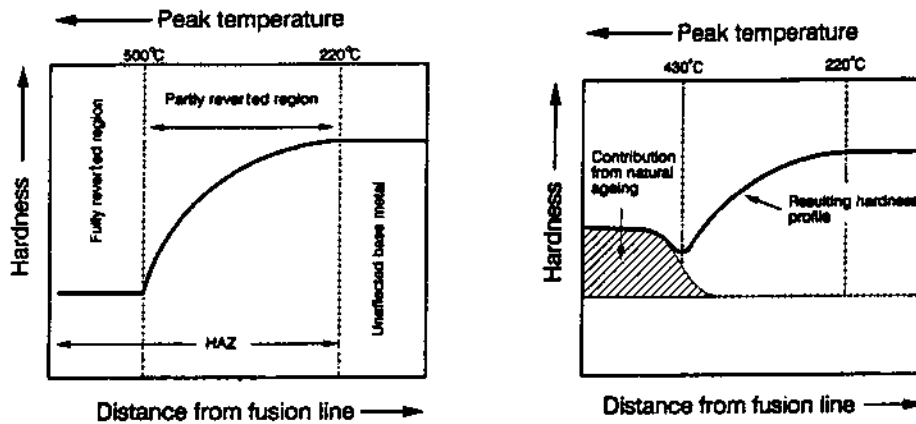
Figure 18 Schematic diagrams depicting HAZ hardness profiles for Alloy 6082-T6 (a) immediately following welding; and (b) after room temperature aging. (From Ref. 70.)

7 MECHANICAL PROPERTIES OF WELDED JOINTS

Aluminum weldments have the unique distinction of possessing very low joint efficiencies, yielding at stresses that are 35–65% of the base metal strength. This severely restricts the designer's ability to make full use of the attractive strength-to-weight properties of many modern aluminum alloys. Aerospace users have traditionally worked around this problem by making welded panels thicker at the weld joint, but not without major cost penalties to panel fabrication. Often large volumes of plate material must be removed by machining or chemical milling in regions away from the joint to maintain weight savings.

7.1 Condition of Testing

When a weldment is loaded in tension, transverse to the weld, there exists a state of iso-stress in each of the weld zones (assuming a uniform cross-section). Under these conditions, yielding will occur in the zone with the lowest yield strength. Likewise, failure will occur in the zone with the lowest tensile strength, analogous to a chain failing at its weakest link. However, when a weld is evaluated in a bend test, there exists a state of iso-strain in each of the weld zones. In this case, failure will occur in the zone having the lowest ductility. For aluminum, the zone of lowest ductility is usually the weld metal due to its coarse solidification structure.

In many cases of tensile or bend testing of weldments, failure actually initiates in a zone due to the presence of a defect, irrespective of its strength or ductility. For this reason, it becomes important to know the quality of the weld when trying to analyze weld properties. If reinforcement and undercuts are machined away and radiography is used to screen tensile bars free from defects, the relative strength of the respective zones can be determined without bias. In some instances, it is useful to machine test specimens entirely from the weld metal or HAZ in order to isolate mechanical properties. HAZ microstructures can be simulated in test coupons using programable electrical resistance heating devices (e.g. a gleeble machine). Likewise, weld metal microstructures can be simulated using chill castings.

Critical to the interpretation of aluminum weld ductility data, obtained from a cross-weld tensile specimen, is an understanding that most of the strain accumulated in the specimen occurs over a narrow band in the weld metal and HAZ. This narrow band may only comprise about 10–15 mm of a 25 mm or 50 mm gage length. This behavior is contrary to what normally occurs in a tensile test of a homogeneous material, where strain is uniform over the entire gage length until the onset of necking. It follows that the weld ductility calculated for a 25 mm gage specimen will be significantly higher (roughly twice) than the ductility calculated for a 50 mm gage specimen. It becomes particularly important, therefore, to state a gage length whenever reporting weld ductility data.

7.2 Zones of Weakness

The global strength of a weldment is influenced by the mechanical properties of each of its different weld zones: base metal, HAZ, and weld metal. Each zone is comprised of a unique wrought or cast microstructure, and likewise exhibits a unique response to mechanical loading within the weldment. The HAZ itself consists of a continuous gradient of microstructures and hardnesses (recall Fig. 18), each differential portion of which has its own unique mechanical properties.

In most aluminum weldments, the weld metal is the weakest zone. A notable exception to this is welded 6xxx alloys, where the HAZ is the weakest zone. The presence of excessive weld metal reinforcement (i.e. over-bead and under-bead) will also tend to shift failure into the HAZ. Thus, when attempting to analyze weld tensile data, it is important to know whether or not the reinforcement has been removed prior to testing.

Weld fracture often initiates near the fusion boundary and is sometimes associated with undercut at the weld toe (over-bead or under-bead). Undercut can serve as an effective stress riser, particularly when forming a sharp notch. Other weld defects may also provide fracture initiation sites, including oxide inclusions, hot cracks, porosity in the weld metal, and liquation cracks in the HAZ. Porosity, when distributed uniformly as spherical pores, is not considered to be an effective stress riser, but it does reduce the load bearing area of the joint.

Coarse grained structures in the HAZ, adjacent to the fusion line, are also inherently weak. In the case of 2xxx alloys, cracks initiate in the near-HAZ where coarse grain boundary precipitates are formed. The mechanism for this cracking involves the concentration of slip in the precipitate-free zones next to the coarse precipitates. Once initiated, however, these cracks tend to grow into the weld metal. The tendency for cracks to grow into the weld metal can be related to the nature of the columnar weld metal grains. Long columnar grains, extending from one weld pass to another, provide a continuous crack path for easy propagation.

7.3 Hardness Traverses

A hardness traverse is a series of hardness measurements made across a weldment, in a line, perpendicular to the welding direction. Made on the top surface of the weld or on a weld cross-section, a hardness traverse is a useful tool to help identify the weak zones of a weld. It also helps to define the extent of damage in the HAZ, something that will vary with weld parameters and welding processes. High power density pro-
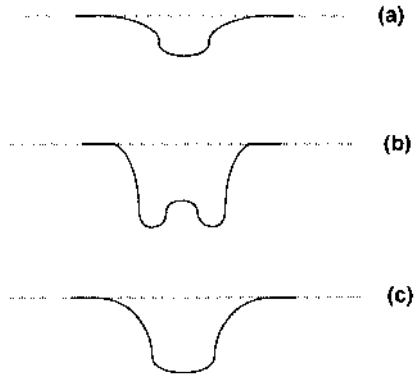
Figure 19 Schematic diagram showing characteristic hardness traverse across weldment in (a) 5xxx; (b) 6xxx; and (c) 7xxx alloys.

cesses, such as electron beam or laser, will produce a much narrower HAZ than will arc welds. Each alloy system, however, will tend to display a particular hardness traverse behavior as suggested in Fig. 19.

Low to medium strength Al-Mg (5xxx series) alloys, Fig. 19(a), achieve their strength primarily from solid solution hardening and cold work. When welded, the strength from cold work is lost in the HAZ, but the solid solution strengthening remains. Because these alloys do not acquire strength from precipitation hardening, they are immune to the problems normally associated with dissolution or coarsening. Thus, the strength loss from welding is minimized.

Medium strength Al-Mg-Si (6xxx series) and Al-Mg-Zn (7xxx series) alloys, Fig. 19(b) and (c), depend primarily upon precipitation hardening for strength. Welding results in the dissolution of precipitates and weakening in the HAZ. While both alloy types will experience some post-weld aging in the weld metal and HAZ (more so for the 7xxx alloys), the 6xxx alloys remain weakest in the HAZ. Because the 7xxx welds are weakest in the weld metal, significant efforts have been expended to develop new filler alloys capable of achieving higher weld metal strengths [73–75].

7.4   Selection of Filler Alloys

Considering the many different types of base metal alloys that have been developed, there are relatively few filler alloys available from which to choose. In Table 4 are listed the commonly used and readily available filler alloys, together with some less common and less available alloys. The 1100 filler is used exclusively for low solute alloys. Its use results in low strength, high ductility welds. However, it may also cause hot cracking if used to weld high solute alloys.

The 2319 filler is very specialized, having been developed specifically for welding alloy 2219. It has the same copper content as alloy 2219 (6 wt% Cu), but also contains some grain refiners (Ti, Zr, and V). This filler alloy has since been successfully used to weld alloy 2519 (a high strength version of 2219) as well as several new Al-Cu-Li-Mg alloys.

Table 4 Nominal Compositions for Common Filler Alloys Used to Weld Aluminum.

Filler Alloy	Si	Mg	Zn	Cu	Mn	Cr	Fe	Ti	Zr	V
1100	(a)	–	0.10	0.20	0.05	–	(a)	–	–	–
2319	0.20	0.02	0.10	*6.3*	*0.30*	–	0.30	*0.15*	*0.18*	*0.09*
4043	*5.25*	0.05	0.10	0.30	0.05	–	0.80	0.20	–	–
5356	0.25	*5.00*	0.10	0.10	*0.12*	*0.12*	0.40	*0.13*	–	–
5183	0.40	*4.80*	0.25	0.10	0.75	0.10	0.40	0.15	–	–
5556	0.25	*5.00*	0.25	0.10	0.75	*0.12*	0.40	*0.12*	–	–
5039†	0.10	*3.80*	*2.80*	0.03	*0.40*	*0.15*	*0.40*	0.10	–	–
5180†	0.35	*4.00*	*2.20*	0.10	*0.50*	*0.10*	–	0.13	0.15	–

(a) Si + Fe = 1.0.

Values in wt%, maximum and mid-range (italic). Data from Ref. 76, unless noted † from Ref. 77.

Alloy 4043 (5 wt% Si) is the most universal of all the fillers and is capable of welding all other aluminum alloys, although its use is not recommended for welding high Mg alloys or parts to be anodized. Compared to 5xxx fillers, it does not produce joints that are as strong or ductile. However, it does exhibit excellent weldability, which is useful when welding crack sensitive alloys (e.g. 2014 and 6061). A brazing alloy 4047 (12 wt% Si eutectic) is sometimes used to weld particularly difficult alloys.

The 5xxx fillers are the most commonly used (e.g. 5356, 5183, and 5556), with alloy 5356 being the most common alloy. These alloys all contain around 5 wt% Mg. Fillers 5183 and 5556 have higher levels of trace elements Zn and Mn. There are also special fillers containing high levels of Zn (e.g. 5039 and 5180) for improved strength. 5xxx fillers are often the cause of porosity, originating from surface contamination of the wire.

7.5 Comparison of Tensile Properties

The cross-weld tensile properties of numerous different aluminum weldments are compared in Table 5. The non-heat treatable alloys (1100, 3003, and 5083) are at the top of the table, and the heat treatable alloys (2xxx, 6xxx, and 7xxx) are at the bottom. Joint efficiency is taken to be the ratio of weldment-to-base metal yield strengths. The only aluminum alloy that demonstrates 100% efficiency in the welded condition is the fully annealed alloy 1100–0 (commercially pure), with all other alloy efficiencies varying between 33% and 65%.

The 3003-H18 alloy weldment demonstrates very low efficiency (33%) because its primary source of strength (i.e. cold work) is lost in the HAZ and weld metal. The 5083–H321 alloy weldment demonstrates relatively high efficiency (64%) because, even though its cold work is lost, solid solution strengthening is maintained. 5xxx series alloys are popular for use in welded construction because of this efficiency and because of their exceptionally good weldability.

The 6xxx alloy weldments have the lowest strengths and efficiencies among the heat treatable alloys. The use of a 5xxx filler improves slightly the strength of these alloys, even though failure still occurs in the HAZ. However, the use of 4043 is often preferred for reasons of weldability, providing better resistance to hot cracking and

Table 5 Transverse Tensile Properties of Gas-Metal Arc Welded Aluminum Alloys Comparing Yield Strength (YS) and Elongation (E) in a 5 cm Gage

Base Metal Properties			Weldment Properties				
Base Metal	YS (MPa)	E (%)	Filler Metal	YS (MPa)	E (%)	Efficiency (%)	Ref.
1100–0	34	35	1100	41	23	121	78
3003-H18	186	4	1100	62	15	33	78
5083-H321	228	16	5356	145	16	64	78
2219-T81	352	10	2319	179	3	51	78
2014-T4	290	22	4043	138	4	48	78
2519-T87	448	12	2319	203	5	45	79
6061-T6	276	12	4043	124	8	45	78
			5356	138	11	50	78
6063-T6	214	12	4043	83	8	39	78
6082.26-T6	290	13	5183	135	9	47	80
7005-T63	317	12	5556	207	10	65	78
7039-T64	379	13	5356	148	10	39	77
			5183	182	10	48	77
			5180	203	12	54	77
			5039	210	10	55	77
7108.70-T6	360	10	5183	196	5	54	80
7108.70-T79	320	11	5183	195	6	61	80

liquation cracking. The 7xxx alloys give the best overall performance in strength and efficiency, primarily due to their active response to post weld natural aging. The use of specialty filler alloys 5180 and 5039 are observed to give a boost in strength.

8 CORROSION

Aluminum welds do not behave as wrought metal and exhibit their own corrosion behavior. Welds exhibit special microstructural features that need to be recognized and understood to predict acceptable corrosion service life of welded structures [81–83]. Welds inherently possess compositional and microstructural heterogeneities which can be classified depending on dimensional scale. On the largest scale, a weld consists of a transition from wrought base metal through a heat affected zone and into the solidified weld metal. The resulting variation in the corrosion potential from the fusion to the base material for an aluminum alloy is illustrated in Fig. 20. Depending upon the alloy system in question, the differences in corrosion potential between the HAZ and parent material can lead to selective corrosion.
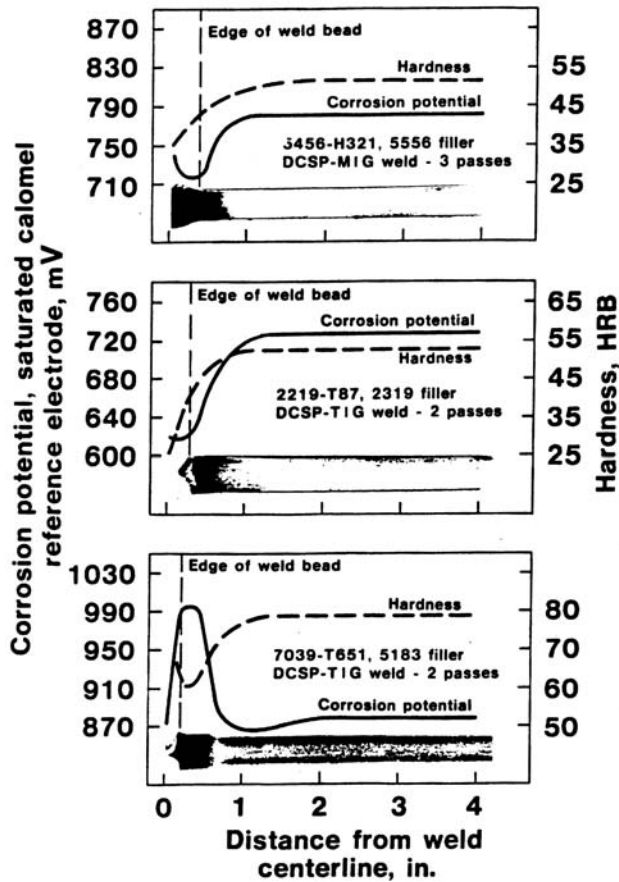
Figure 20   Effect of the heat of welding on hardness and corrosion potential for three different alloys (From Ref. 84.)

Besides the galvanic corrosion due to potential differences between the fusion zone and base metal compositions, the fusion zone itself offers a microscopic galvanic effect due to microcompositional segregation resulting from solidification [85,86]. This microsegregation results in compositional gradients of both major and trace elements on the scale of a few microns within individual weld beads. The heat affected zone is characterized by the fact that every position relative to the fusion line has experienced a unique and different thermal profile resulting in each position having its own microstructural features and corrosion susceptibility. Gradients on a similar scale exist within the solidified multi-pass weld metal due to bead-to-bead variations in thermal experience.

Aluminum weldments can experience most of the classical forms of corrosion but they particularly susceptible to those forms affected by variations in microstructure and composition. Specifically galvanic, pitting, stress, and intergranular corrosion [87].

8.1 Galvanic (Two-metal) Corrosion

Variation in electrochemical potential between the aluminum alloys to be joined and the filler metal can result in the classical galvanic attack where the more anodic material adjacent to the boundary between the different materials is subject to attack. The damage decreases as the distance to this boundary increases and there is a dependence on the ratio of the cathode to anode areas.

There are a number of common weld deposit/base metal combinations that are known to form galvanic couples. For most aluminum alloys, the weld metal and the heat-affected zone become more noble relative to the base metal. Certain aluminum alloys form narrow anodic region in the heat-affected zone and are prone to localized attack. Alloys 7005 and 7039 are particularly susceptible to this problem [85,86].

8.2 Intergranular Corrosion

The mechanism for intergranular corrosion involves the establishment of local galvanic cells between micro-constituents present at grain boundaries. A comparison is made in Table 6 between the relative corrosion potentials for common constituents found a grain boundaries. In the case of 2xxx alloys, $CuAl_2$ grain boundary precipitates are found to be cathodic relative to their adjacent, low copper, precipitate free zones (PFZs). Thus, when exposed to an electrolyte, the PFZs will preferentially corrode. In the HAZ of welds made on 2xxx alloys, the formation of coarse $CuAl_2$ precipitates at grain boundaries is to be expected. These alloys typically display poor corrosion resistance.

In the case of 5xxx or 7xxx alloys, the grain boundary precipitates will be, respectively, Mg_2Al_3 or $MgZn_2$. Both of these precipitates are observed to be anodic relative to their adjacent PFZs. Thus, when exposed to an electrolyte, the grain boundary precipitates will corrode. The danger to the alloy then depends upon whether or not the grain boundary precipitates are continuous. If continuous, the material is referred to as ''sensitized'' and the grain boundaries will be susceptible to attack. 5xxx alloys that have been welded are normally not in a sensitized condition. However, 7xxx alloys that have experienced HAZ liquation are particularly susceptible to this problem. The effect of this is demonstrated by the spike in corrosion potential for alloy 7039 in Fig. 20.

Table 6 Electrode Potentials of Aluminum Constituents [88]

	Potential (volts)*
Mg_2Al_3	−1.24
$MgZn_2$	−1.05
99.95 Al	−0.85
$CuAl_2$	−0.73
$FeAl_3$	−0.56
Si	−0.26

*0.1N calomel scale, 53 g/l NaCl + 3 g/l H_2O_2 at 25°C

8.3 Pitting

Pitting is a form of localized attack caused by a break down in the thin passive oxide film that protects the material from the corrosive environment. Pits are the result of a concentration cell established by a variation in solution composition in contact with the alloy material. Such compositional variations result when the solution associated with a surface irregularity is different from that of the bulk solution composition. Pitting has a delay time prior to nucleation and growth and its nucleation is very site selective depending upon the microstructure. Pitting occurs when the material/solution combination achieves a potential that exceeds a critical value, the pitting potential. Once a pit has formed it will act as an anode supported by relatively large adjacent cathodic surface. Pits are often initiated at specific microstructural features in the weld deposit [87]. The pit becomes deeper at an accelerated growth rate. Weld metal has a higher probability of being locally attacked because of microsegregation in the dendritic structure.

In many aluminum alloys that experience precipitation of a second phase, especially due to the thermal experience of welding, have produced significant compositional gradients in the alloy matrix adjacent to the precipitate due to diffusion control during the precipitate growth. The adjacent region is often depleted in a specific alloy addition that is important in maintaining a passive film, thus subjecting this narrow anodic region to very localized galvanic attack being driven by relatively large surrounding cathodic regions resulting in pit initiation and growth. This behavior is commonly experienced from welding in precipitation strengthened alloys, resulting in first pitting in the heat affected zone and then often resulting in the initiation of stress corrosion cracking from bottom of these pits.

8.4 Stress Corrosion Cracking

Aluminum weldments can be susceptible to stress corrosion cracking when experiencing specific environmental conditions. Stress corrosion cracking requires the proper combination of corrosive media, susceptible microstructure and tensile stress. Stress corrosion cracks have an anodic crack tip and often leave apparent corrosion products along the fracture. Cracking is often characterized by crack branching and usually has a delay time prior to crack initiation with initiation often occurring at corrosion pits. A weld, with its various heterogeneous microstructural features, becomes an excellent candidate for stress corrosion cracking.

The thermal experience of welding is often very localized which results in strains that can cause distortion and residual stresses. Welds are often loaded in tension due to residual stress to a level approaching the yield strength of the base metal. Welding parameters influence the amount and distribution of residual stress since the extent of the stressed region and the amount of distortion is directly proportional to the size of the weld deposit which is directly related to the heat input. These residual stresses can be important in the generation and propagation of environmentally enhanced cracking.

It is known that post-weld heat treatment can reduce the tendency for stress corrosion cracking by redistributing the localized load and reducing the magnitude of the residual tensile stress available to induce stress corrosion cracking. In a recent study, post-solidification heat treatments were shown to also modify the local composition gradients that significantly altered the susceptibility of the solidified microstructure to stress corrosion cracking [89].

Corrosion can be minimized in aluminum weldments by the following practices [90]: (i) Selection of materials and welding consumables which reduce macro-and micro compositional differences; (ii) Selection of proper cleaning process can reduce defects that are often sites for corrosion attack; (iii) Promotion of deposits that have relatively flat beads with low profiles; (iv) Production of complete penetration; (v) Selection of post weld heat treatment to reduce corrosion susceptibility; (vi) Utilization of coating and passivation treatments; and (vii) Avoidance of forming crevices.

9 WELDING AND JOINING PROCESSES

Pure aluminum and most aluminum alloys can be welded by gas tungsten arc welding (GTAW), gas metal arc welding (GMAW), plasma arc welding (PAW), electron beam welding (EBW), resistance spot welding (RSW), and friction welding (FW). Fine wires can be welded by ultrasonic welding (UW). It is also possible to join aluminum alloys by brazing, soldering and diffusion welding.

Less commonly, welding of aluminum alloys can also be done using shielded metal arc welding (SMAW), laser beam welding (LBW), electroslag (ESW) and electrogas (EGW) welding, and projection welding (PW).

9.1 General Considerations

In general, aluminum is not more difficult to weld than other metals and alloys; it is just different, which may require some special attention. For example, its higher thermal and electrical conductivity require greater weld input. In fact, aluminum welding typically requires three times the current needed for low C-steel in weld cycles 1/10 as long. Joint surface cleaning is far more critical than in steel welding, often requiring mechanical abrasion or chemical etching to remove thick oxide layers. Joint preparation can be done by a cutting operation, such as sawing, chipping, machining, or plasma arc cutting. Welding polarity can also be adjusted to fracture and remove the tenacious oxide layer. Joint surfaces should also be cleaned of dirt and grease.

Because of its high reactivity with both oxygen and nitrogen, a protective atmosphere is needed to protect the molten weld pool. Because of the softness of aluminum and its alloys, improper wire brush cleaning or grinding is not recommended, due to greater possibility of embedded contaminants. Only stainless steel brushes should be used and they should be designated for exclusive use on aluminum to avoid contamination. Time between cleaning and welding should be minimal, or the surfaces should be re-cleaned. Brushing may be required between weld passes.

To minimize risk of porosity in welds, wet or damp parts should not be welded. If the ambient temperature is below 32°F (0°C), a heated shelter type structure should be used and the joint area must be preheated.

9.2   Aluminum Oxide – The Protective Skin

When fresh aluminum metal is exposed to air, Al_2O_3 immediately forms (to about 15 Å Thick). In cool and dry environment, the layer stabilizes at about 25–50 Å. In hot, humid, or anodizing conditions, the layer can grow to 25,000–50,000 Å. The "self-healing" oxide layer regenerates itself when scratched. Al_2O_3 is responsible for the corrosion resistance of aluminum. Al_2O_3 is electrically non-conductive which causes arc instability. It has very high melting point (2066°C) and may contribute to cold lap type defects. Al_2O_3 is hygroscopic and exists mostly in the hydrated form. Besides the weld joint area, the oxide may also need to be removed from the ground contact point.

9.3   Surface Preparation – Oxide Removal

Surface cleanliness is essential to the success of welding aluminum alloys. In particular, the adherent surface oxide must be removed for stable welding and quality weldments. As a minimum requirement, wire brushing using stainless steel brushes is highly recommended. Vigorous brushing of the weld joint will expose fresh metal and promote arc stability. In addition, the oxide must be removed from the ground contact point to provide good electrical contact and thus, arc stability. Machining is sometimes performed to remove the oxide layer. Caution should be exercised regarding coolant, which is generally a source of contaminants. Most often, machining is done dry to avoid contamination. Grit blasting is another method used for oxide removal. Because of the softness of the metal and the possibility of embedding contaminants, the blasting is done using dry ice. Solid CO_2 particles later vaporize leaving no contamination behind.

In addition to mechanical abrasion, thick oxide layers can also be removed by chemical etching. Both acid and alkaline solutions, e.g. nitric acid (HNO_3) and sodium hydroxide (NaOH), are used for this purpose. As an example, parts are immersed in 50% nitric acid aqueous solution at room temperature for 15 min to remove the oxide layer. The parts are then rinsed in cold water, followed by hot water, to remove the residual acid solution such that corrosion does not continue. It is most critical that the parts be dried thoroughly to avoid hydrogen pickup during welding. A combination of alkaline and acid solutions will give excellent results as well. The parts are first immersed in a 5% NaOH aqueous solution heated to approximately 70°C for about 1 min. After rinsing in cold water thoroughly, the parts are then immersed in concentrated nitric acid at room temperature for approximately 30 sec. Again, cold and hot water rinse and drying follow. This method is most effective in removing thick, adherent oxide layers.

Finally, cathodic cleaning is also used to rid aluminum plates of their oxides. This is essentially the gas tungsten arc (GTA) process with the part attached to the negative pole. This process relies on the stream of positive ions that bombard the part surface and crack the oxide layer. The cracked oxide particles are removed

in the arc plasma. Similar principle is used when welding aluminum alloys using AC welding. Half of the welding cycle will be DCEP providing the oxide cleaning action.

In addition to oxide removal, the joint must be degreased immediately prior to welding. This is normally accomplished by wiping the joint with methanol, ethanol, or in extreme cases, acetone. This operation will remove oils left from finger prints and from other sources of contamination that may potentially provide hydrogen to the weld and result in porosity.

9.4 Gas-Tungsten Arc Welding

9.4.1 Power Supplies

Most thin section GTAW of aluminum alloys is done with alternating current (AC) because it provides a combination of ease of arc control, arc cleaning action, and current-carrying capacity without electrode overheating. However, when high penetration is required, direct current with negative electrode polarity (DCEN) is preferred, using helium as a cover gas.

9.4.2 AC Arc Instability

Aluminum is not as effective an electron emitter as is tungsten in AC welding. Reduced current flow may result during the electrode positive half cycle (particularly if the oxide layer is thick or the travel speed is high). The difference in current flow tends to rectify the AC current and overheat the transformer. As a result, cooling of the power source is thus needed. Quite often, battery bias is also used to compensate and balance the current flow.

9.4.3 Effect of Electrode Tip Shape

A balled tip and a pure tungsten electrode is commonly used for AC welding, because of its greater arc stability and wear resistance. It is made by striking an arc with the electrode positive configuration and increasing the current until the tip begins to melt and forms a ball of the proper diameter – about the diameter of the electrode.

A sharp tip and a zirconia-tungsten electrode is preferred in DCEN welding. Welding with DCEN requires extra care in joint preparation, because of the absence of cleaning from the electrode positive cycle experienced with AC welding.

9.5 Gas-Metal Arc Welding

9.5.1 Power Supplies

Most aluminum alloys can be welded using GMAW. This is normally accomplished in the DCEP mode using either constant voltage (CV) or constant power (CP) machines. The CP (i.e. "drooper") machines are preferred for their good arc stability with a recommended slope of 1 volt per 5–10 amperes.

9.5.2 Effect of Contact Tip

Contact tip is critical in obtaining stable arc in aluminum welding. A smooth inner surface is required so that the wire does not bind to the contact tip. Additionally, the wire should enter with a slight cast to assure a consistent point of contact. The contacts tips are generally long, about 100 mm, because longer tips will result

in multiple points of contact, minimizing arcing and rough spots within the tip. Note that the longer contact tip is not for preheating as in steel welding, because aluminum wires do not require preheat. To cope with burnback, half-section tips can be used.

9.6 Effect of Shielding Gas in Arc Welding

Both argon and helium are used in GTAW and GMAW of aluminum alloys. Helium exhibits higher ionization potential and hotter arc temperature than does argon. Therefore, a helium arc will also have higher arc voltage and provide greater heat input. Helium is preferred for welding thick sections ($> 2\,mm$).

Argon, on the other hand, has lower ionization potential and larger atomic radius. Since the atoms are larger, they diffuse more slowly and can displace air more effectively from the weld zone, in the flat position. The larger atomic radius makes argon more effective in sputtering cleaning of oxide layer on the joint surface. Argon shielding also results in better arc stability.

A helium-argon mixture (50–75 vol% He) provides an ideal combination characterized by superior metal flow and wetting, good arc stability and minimum spatter. These gas mixtures also tolerate wider ranges of arc current, arc voltage, and travel speed without resulting in increased weld porosity.

The gases used must be welding grade (at least 99.99% purity). The dew point of these gases should be kept below $-76°F$ ($-60°C$) to minimize moisture and hydrogen pickup. For aluminum welding, pre- and post-flow must be considered, usually by automatic sequencing by the welding equipment. Pre-flow has the function of purging the gas lines and post-flow protects the hot work and tungsten electrodes (in GTAW).

9.6.1 Inert Gas Backing

It is not common to use backside shielding when welding aluminum. However, when welding with full penetration, the backside of the weld may experience excessive oxidation if not protected in some manner. If underbead oxidation occurs, it is common to observe cold laps at the edge of the weld root face. In most cases, the use of a backing material (ceramic or metallic) will help to minimize this oxidation. In extreme cases, backside shielding should be used. Welding grade argon is typically used as the backing gas, even if helium is being used as the main shielding gas.

9.7 Filler Metal Selection Criteria and Guidelines

Filler metal selection is based on factors such as weld hot cracking susceptibility, HAZ cracking (liquation cracking) susceptibility, required weld strength and ductility, corrosion resistance, service at high temperatures, weld metal fluidity and melting point, color match with base metal, and GMAW wire feedability.

There are numerous filler alloys to select from (recall Table 4) in order to meet the various different criteria outlined above. Some of the intricacies of this selection were discussed in the previous sections on hot cracking, liquation cracking, and mechanical properties. However, for general use, most aluminum welding can be accomplished reasonably well using one of three different fillers (1100, 4043, or 5356). These filler alloys are also the ones that are most readily available commercially. The proper selection among this group of fillers is summarized in Table 7.

Table 7 Base Metal-Filler Metal Matching in Aluminum Alloying Welding

Base Metal welded to Base Metal	7005	6061 6063 6351	5454 5154A	5086 5083	5052	5005 5050A	3004 Alclad 3004	1100 3003 1200
1100								
1200								
3003	5356	4043	4043	5356	4043	4043	4043	1100
3004								
Alclad 3004	5356	4043	5356	5356	5356	4043	4043	
5005								
5050A	5356	4043	5356	5356	4043	4043		
5052	5356	5356	5356	5356	5356			
5083								
5086	5356	5356	5356	5356				
5154A								
5454	5356	5356	5356					
6061								
6063								
6351	5356	4043						
7005	5356							

9.7.1 Wire Feeding

One of the common practical problems that welding professionals face in GMAW of aluminum alloys is filler metal feedability. This problem is particularly true for the softer alloys (e.g. 1100). Even though push feed systems can be used to deliver the filler metal, a push-pull system is always preferred to more smoothly deliver the filler wire to the arc. The multiple rollers can control the wire feed speed, lessen the tension on the wire, and minimize wire breakage and bird-nesting.

9.7.2 Care and Storage of Filler Metal

To avoid welding problems, always choose "Fresh" welding filler metal. Always check for contamination such as oil, dust, deposit from industrial fume, etc. Critical components of the wire drive system, e.g. drive rolls, guides and liners, and must also be checked for contamination. Spools of aluminum filler metals must be covered, even during use. While not in use, filler metals should be stored in bags with proper desiccant.

9.8 Pre- and Post-Weld Heat Treatment

It is not common, nor is it recommendable, to use preheat or postheat in aluminum welding. Such heat treatment is only performed under very special circumstances for very specific reasons. For example, preheat can be used to dry off moisture from parts prior to welding. It may also help limit weld distortion and permit higher welding speeds.

Some practical guideline regarding conditions that may require preheating are:

1. Never weld Al alloys when the temperature of the metal is below the dew point of the surrounding atmosphere.
2. Never weld outdoors in the early morning.
3. Never weld in a mist or fog, or when the temperature is below freezing.

In the case of postheat, certain age hardenable alloys (e.g. 6xxx and 7xxx) will respond to post weld heat treatment to achieve a small boost in strength. However, this strength gain is normally accompanied by a very large (and unacceptable) drop in ductility. The range of temperatures must be carefully controlled. For example, Alloy 6061 in the heat-treated condition should not be heated above 300–350°F (149–177°C) for periods longer than 30–40 min. A good rule-of-thumb is not to heat above 250°F (121°C) and not to hold longer than 30 min. For non-heat-treatable alloys, heating can be detrimental. Sensitization is known to occur in 5xxx series alloys when heated to 150°F (65°C). Heating can result in loss of mechanical properties of work hardened alloys because of recovery and recrystallization.

9.9 Special Concerns in Arc Welding

9.9.1 Defects

The primary difficulty in welding aluminum alloys is the susceptibility to hot cracking (i.e. solidification cracking). This is particularly true for the age hardenable alloys. Porosity is another major concern that occurs particularly in 5xxx and 6xxx series alloys. Liquation cracking is also a serious problem for certain 6xxx and 7xxx alloys.

9.9.2 Strength Loss

Loss of mechanical properties because of welding thermal cycle is also important. Other difficulties such as weld distortion and loss of corrosion resistance (such as those found in high Mg 5xxx series alloys) are considered secondary difficulties.

9.9.3 Soot Removal

Particularly when gas metal arc welding the 5xxx series alloys, or using 5xxx series filler metals, a sooty deposit generally occurs around the weld. This material is composed primarily of magnesium oxide, MgO. The deposit can be easily wiped off if done immediately. If left on for a prolonged period, e.g. a few hours, wire brushing may be required.

9.9.4 Health

Aluminum and its oxides are non-toxic, but care should be taken to provide adequate ventilation to protect against the ingestion of excessive amounts of particulates. The major constituent of the fume is aluminum oxide. Other minor components are particles containing for example aluminum-copper, aluminum-magnesium, depending on the filler alloy used. As a result of the higher current required for welding aluminum alloys and the highly reflective aluminum surface, arc burns are frequently reported.

9.10 Resistance Welding

Spot and seam welding are the two most used resistance welding processes for aluminum sheet and small parts [91–96]. Resistance spot welding [97] is defined as a process in which faying surfaces are joined in one or more spots by the heat generated by the resistance to the flow of electric current through the work piece that are held together under force by electrodes. The contacting surface representing a local high resistance is ohmically heated with single or multiple current pulses. The electrode force is maintained while the weld metal rapidly cools and solidifies.

Resistance seam welding [98] is defined as a process in which heat generated by the resistance to the electric current in the work metal is combined with pressure to produce a welded seam. The resulting seam weld consists of a series of spot welds. Resistance seam welding offers gas and liquid tight points and a high-speed production process. Aluminum and aluminum alloys can be lap seam welded but not mash seam welded, where work metal is compressed at the joint to reduce joint thickness, due to the narrow plastic range of aluminum alloys (about 95–205°C)

Resistance welding processes fuse parts by the heat generated from the flow of current through a resistance for a given time. The machine needs to have adequate capacity to provide the current necessary for the gauge of material to be welded. The current should be adjustable in amplitude as well as time and impulses. The current can be cyclical or direct current and from a single phase or poly-phase power source. The time of current flow often is adjustable in one cycle steps. The number of cycles range from one to thirty cycles. The applied pressure and holding should be adjustable for 1–99 cycles. The tip force should be able to be adjusted to meet the requirement for a specific thickness. The electrodes best suited for aluminum fabrication are the copper–cadmium alloy class I.

Resistance spots welds should be used in shear loading. The shear strength is a function of alloy composition, section thickness, weld spacing and set up and welding parameter scheduling. Spot welds in tension may have strengths that vary from 20–90% of their shear strength. When tensile and combined loads are to be used, testing is required to verify that the joint strength can fulfill the service condition.

All aluminum alloys, both non heat treatable and heat treatable, are suitable for resistance welding [99–103]. Aluminum and aluminum alloys have high thermal and electrical conductivity (Table 8) and to make a spot weld a high welding current and relatively short welding time are needed. Pure aluminum has the highest electrical conductivity and thus will require a greater energy input for a given weld. Shrinkage cracks in aluminum weld metal are mainly critical to the copper-bearing alloys (2017, 2024 and 7075). The alloys 2014, 3003, 5050 and 6061 show less shrinkage. The chromium-bearing alloys (5052 and 6053) may develop porosity, depending on temper.

A spot weld consists of a central oval core which has a granular or equiaxed zone [102]. Surrounding this oval core zone is another zone made up of a columnar dendritic grain structure. These two zones make up the weld nugget and they are both cast structures. Outside the columnar zone there is a layer of material that has been altered by the thermal experience.

The hardness of an alloy, and thus the temper, is one variable influencing weldability. In general, alloys in the softer tempers are much more susceptible

Table 8   Melting Ranges, Electrical and Thermal Conductivities, and Resistance
Weldability of Common Aluminum Alloys (From Ref. 104)

Alloy and temper	Melting Range (°C)	Electrical Conductivity, %IACS (a)	Relative thermal Conductivity, % (b)	Resistance Weldability (c)
Non-heat-treatable wrought aluminum alloys				
1350-H19	646–657	62	60	ST
1060-H18	646–657	61	57	ST
1100-H18	643–657	57	55	RW
3003-H18	643–654	40	39	RW
3004-H38	629–652	42	42	RW
5005-H38	632–652	52	51	RW
5050-H38	627–652	50	49	RW
5052-H38	593–649	35	35	RW
5083-H321	574–638	29	30	RW
5086-H34	584–640	31	32	RW
5154-H38	593–643	32	32	RW
5182-O	574–640	31	31	RW
5454-H34	602–646	34	34	RW
5456-H321	571–638	29	30	RW
Heat-treatable wrought aluminum alloys				
2014-T6	510–638	40	39	ST
2024-T361	501–638	30	31	ST
2036-T4	554–638	41	40	RW
2219-T37	543–643	28	29	ST
6009-T4	560–649	44	43	RW
6010-T4	585–649	39	38	RW
6061-T6	593–649	43	43	RW
6063-T6	615–654	53	51	RW
6101-T6	615–652	57	55	RW
7075-T6	447–638	33	33	ST
Aluminum casting alloys				
413.0-F	574–582	31	32	LW
443.0-F	574–632	37	37	RW
308.0-F	521–613	37	37	ST
238.0-F	507–599	25	26	LW
513.0-F	579–638	34	34	ST
520.0-T4	449–604	21	22	NR
333.0-T6	516–585	29	30	ST
C355.0-T61	546–621	39	38	ST
356.0-T6	557–613	39	38	ST
712-F	604–643	40	39	RW

Wrought and casting alloys are identified by Aluminum Association designations.
(a) International Annealed Copper Standard, volume basis at 20°C (68°F). For comparison, copper alloy
102 (oxygen-free copper) is 101% and low-carbon (1010) steel about 14%.(b) Based on copper alloy 102
as 100%, which has a thermal conductivity of 391 W/m · K (226 Btu/ft · h · °F) at 20°C (68°F). Low-carbon
steel has a thermal conductivity of about 13% on this relative scale. (c) RW, readily weldable; ST, weldable in
most applications but may require special techniques for specific applications; LW, limited weldability
and usually requires special techniques; NR, welding not recommended

to excessive indentation and sheet separation and to low or inconsistent weld strength. Greater deformation under the welding force causes an increase in the contact area and variations in the distribution of current and pressure. Welding of aluminum alloys in the annealed condition or in the softer tempers is not recommended without special controls.

High-strength alloys, such as alloys 2024 and 7075, are easy to resistance weld, but may require applications of a forge pressure, because they are more susceptible to cracking and porosity than the lower-strength alloys. Aluminum clad alloys can also be resistance welded.

To minimize the likelihood of cracking or porosity in the weld, careful control of the electrode force is necessary. If the force is applied too soon, the welding current may be insufficient due to a premature loss of contact resistance. Thus, correct initiation of the force relative to the current is essential.

The narrow plastic range between softening and melting means that welding forces, time, and current need to be closely controlled. For consistent weld quality, it is essential that the tenacious surface oxide films are removed by mechanical or chemical techniques prior to welding.

9.10.1 Surface Preparation

A primary consideration in spot or seam welding is associated with the cleanness of its surface. Any type of impurity on the faying surfaces is incorporated in the weld, causing oxides and blowholes. Gas shielding may be required to maximize joint quality.

For critical applications, a 2–6 min immersion in a room temperature solution of a nitric-hydrofluoric acid ($120\,g/l$ of 68% NHO_3, $2\,g/l$ of 48% HF and $2\,g/l$ of a wetting agent) is an acceptable practice. The immersion practice schedules involve (after degreasing, if necessary) 30 sec cold running-water rinse, 10 sec in hot water ($60–71°C$) and an air blast dry.

9.10.2 Classifications

Spot welding is characterized into four classifications that are based on the function of spot welding [92]. Class I is for applications that require high integrity and are used in highly critical locations. Class II is for sheet metal surfaces that must be free from surface markings or imperfections after metal finishing to the extent the spot welds are not usually apparent after painting. Class II welding should not exceed ten percent tip indentation. Class III is for sheet metal surfaces which may be visible but are not exposed external surfaces. Their welds have structural requirements and may be painted or not painted. A twenty percent indentation is acceptable in Class I and III welds.

Class IV welding is for applications where no structural strength is required and does not have surface indentation requirements. Nugget penetration range of 20–80% is acceptable. Size and weld spacing for spot welds depend on the thickness of the metal being formed. Excessive force is characterized by extreme indentation, sheet separation, work distortion, unsymmetrical welds and the need for higher current.

Class I welding does not allow any surface cracks. Visible surface cracks should not be present in over ten percent of the Class II welds and twenty percent for Class III welds. The 10–20% should not be consecutive. Surface cracks are permitted

in Class IV welds provided the crack length does not exceed 50% of the weld nugget diameter. Surface cracks in the parent metal around the weld or extending from the weld into the parent metal should not be permitted. Expulsion, which is caused by insufficient forces, is not permitted in Class I welds but permitted in Class II, III and IV welds. Lack of fusion within the weld should not be permitted in any weld class.

9.11 High Energy Beam Welding

Both electron beam and laser beam can be used to weld aluminum alloys. Because of low power and heat input of laser beam welding (LBW) and electron beam welding (EBW), only a small volume of metal will be affected by overaging or annealing as a result of the welding thermal cycle. Thus, HAZ degradation is not expected to be severe. However, the highly localized mechanical property mismatch between the HAZ and the base metal can be detrimental because of the local deformation, particularly in structural components. The high power density, however, may lead to loss of strengthening elements such as Mg and Zn in the weld metal. For example, the hardness of a 6061 alloy weld may be affected by Mg vaporization. Subsequent heat treatments to the T6 condition will not be able to produce strengths to the base metal level because of the lower content of the alloying element to precipitation strengthen. The loss of Mg is important to the 5xxx and 6xxx series while the loss of Zn is important to the 7xxx series alloys.

In the case of LBW, the major difficulty is actually the low laser beam-material coupling in the 1.06 (Nd:YAG laser) to $10.6 \, \mu$m (CO_2 laser) range wavelength. Polished aluminum surfaces typically reflect over 90% of the laser energy. Many methods such as mechanical or chemical roughening, deposition of absorptive paints or coatings, anodization and dyeing the aluminum surface have been developed, with different degree of success, to improve the absorptivity of laser energy. Once melting is initiated, however, the formation of a vapor plume helps to achieve more efficient coupling.

In the case of EBW, welding can be performed in high vacuum ($ < 10^{-3}$ Torr), medium vacuum (10^{-3} to 25 Torr) or in atmosphere with helium shielding. Most aluminum alloys can be processed, but cracking may occur in 2xxx, 6xxx, and 7xxx series alloys. The addition of filler metal may prevent weld cracking.

Despite some of the difficulties mentioned in the earlier paragraphs, both LBW and EBW are used in the aerospace and automotive industries.

9.12 Solid-State Joining Processes

All of the standard solid-state (i.e. non-fusion) joining processes can be used to join aluminum alloys to themselves and to dissimilar metals. These processes include: ultrasonic welding, friction welding, explosive welding, and diffusion welding. Using high frequency (ultrasonic) vibration in *ultrasonic welding*, work pieces can be joined by holding them together under low pressure. Because of the low energy input involved, only thin gage materials can be joined using this technique. Most aluminum alloys can be ultrasonically welded with minimum surface preparation such as degreasing and oxide removal. Their chemical composition and temper conditions affect only slightly the weldability.

9.12.1 Friction Welding

Friction welding involves the joining of two parts by physically rotating one part relative to the other under pressure such that frictional forces and heat are generated, thus resulting in the plastic flow of material and mechanical interlocking. This is a popular way of making dissimilar metal joints.

9.12.2 Explosive Welding

Explosive welding is particularly useful in the joining of aluminum alloys to other metals in the lap configuration. The shock wave produced by the detonation of the explosives creates a high velocity jet at the faying surfaces. With the salient jet, a layer of the surface, including oxides, is removed while the two "stripped" parts are driven together to establish a high quality bond. Joint preparation includes cleaning of the faying surfaces within a specified time before welding.

9.12.3 Diffusion Welding

As its name indicates, diffusion welding relies on the atomic diffusion which is a function of time and temperature. Typically a long process, the faying surfaces must be well prepared in terms of dimension and flatness so that intimate contact can occur. Too thick a surface oxide layer can be a problem because of the excessive long time for its dissolution. An interlayer of another metal such as silver and copper is often inserted between the two parts to promote bonding. Because of the long processing time and possibility of reaction with oxygen and nitrogen, diffusion welding is done in vacuum or in atmospheres of high purity inert gas.

9.13 Special Joining Processes

Two specialized joining processes, developed especially for aluminum, have gained widespread interest in recent years and have proven capable of producing exceptionally high quality joints in an economical and efficient manner. These joining processes include the *Variable Polarity Plasma Arc* process (VPPA) and the *Friction Stir Welding* process (FSW).

The VPPA process [105, 106] incorporates new advancements in power supplies now capable of providing rapid polarity switching from electrode positive (EP) to electrode negative (EN). It is now also possible to set the EN and EP times independently so as to favor either good penetration (EN) or good cleaning action (EP). Typical settings utilize a 19 millisec EN cycle followed by a 4 millisec EP cycle. This corresponds to a switching frequency of 77 Hz. When this power supply is combined with a plasma arc welding process, used in a keyhole mode of operation in the vertical-up position, this becomes a viable method for joining 5–25 mm thick plate in a single pass.

The FSW process [107] is basically a form of friction welding, but without having to rotate the parts to be joined. Instead, a cylindrical tool, spinning at high velocity, is passed along the weld joint thereby causing metal from one plate to flow into the other plate. The cylindrical tool consists of a shoulder and a pin. The shoulder rides on the top of the plate, exerting pressure and preventing extrusion of metal out of the joint. The pin resides inside the metal and serves to generate frictional forces that cause the metal to flow in a circular motion. These frictional forces also generate heat, which serves to make the metal plastic. Because of the

large forces generated, this process requires rigid fixturing and hold-down clamps. It is best suited for long and straight joints in plate of moderate thickness. It has significant advantages over arc welding, resulting in negligible residual stress and a reduced loss of strength. All of the problems associated with liquation and solidification are avoided.

REFERENCES

1. D. Rosenthal, ''Mathematical Theory of Heat Distribution during Welding and Cutting,'' Weld. J., 1941, 20, pp. 220s–234s.
2. Ø. Grong, ''Metallurgical Modelling of Welding,'' Inst. of Metals Pub., London, 1997, p. 3.
3. C. M. Adams, Jr., ''Cooling Rates and Peak Temperatures in Fusion Welds,'' Weld. J., 1958, 37, pp. 210s–215s.
4. M. H. Burden and J. D. Hunt, ''Cellular and Dendritic Growth II,'' J. Crystal Growth, 1974, 22, pp. 109–116.
5. W. F. Savage and R. H. Hrubec, ''Synthesis of Weld Solidification using Crystalline Organic Materials,'' Weld. J., 1972, 51, pp. 260s–271s.
6. P. E. Brown and C. M. Adams, Jr., ''Rapidly Solidified Alloy Structures,'' Trans. AFS, 1961, 69, pp. 879–891.
7. P. E. Brown and C. M. Adams, Jr., ''Fusion Zone Structures and Properties in Aluminum Alloys,'' Weld. Journal, 1960, 39, pp. 520s–524s.
8. R. A. Jarman and M. F. Jordan, ''Relationship between Heat Input and Dendrite Structure of Full-Penetration Weld Beads in a Commercial Al-Cu Alloy,'' J. Inst. Metals, 1970, 98, pp. 55–57.
9. L. F. Mondolfo, *Auminum Alloys: Structure and Properties*, Butterworths Pub. 1979.
10. M. Flemings, *Solidification Processing*, 1974, McGraw Hill Pub., p. 142.
11. J. E. Eklund, ''On the Effects of Impurities on the Solidification and Casting of Aluminium Alloys,'' PhD Thesis, Helsinki Univ. of Technology, 1991.
12. A. T. D'Annessa, ''Characteristic Redistribution of Solute in Fusion Welding,'' Weld. J., 1966, 45, pp. 569s–576s.
13. F. A. Crossley and L. F. Mondolfo, ''Mechanism of Grain Refinement in Aluminum Alloys,'' J. Metals, 1951, 191, pp. 1143–1148.
14. L. Arnberg, L. Backerud, and H. Klang, ''Evidence of Metastable Phase in Al-Ti-B System,'' Metals Tech., 1982, 9, pp. 14–17.
15. A. F. Norman, P. B. Prangnell, and R. S. McEwen, ''The Solidification Behaviour of Dilute Aluminium-Scandium Alloys,'' Acta Materialia, 1998, 46, pp. 5715–5732.
16. M. G. Mousavi, C. E. Cross, and Ø. Grong, ''Effect of Scandium and Titanium-Boron on Grain Refinement and Hot Cracking of Aluminium Alloy 7108,'' to be published in Sci. Tech. Weld. Joining, 1999.
17. S. Kou and Y. Le, ''Welding Parameters and the Grain Structure of Weld Metal – A Thermodynamic Consideration,'' Met. Trans., 1988, 19A, pp. 1075–1082.
18. C. E. Cross, Ø. Grong, and M. G. Mousavi, ''A Model for Equiaxed Grain Formation along the Weld Metal Fusion Line,'' Scripta Materialia, 1999, 40, pp. 1139–1144.
19. C. E. Cross, L. W. Loechel, and G. F. Braun, ''Weldalite™ 049 Weld Development for Aerospace Tankage,'' Proc. 6th Int. Al-Li Conf., Deutsche Gesellschaft fur Materialkunde, 1991, pp. 1165–1170.
20. A. Gutierrez and J. C. Lippold, ''A Proposed Mechanism for Equiaxed Grain Formation along the Fusion Boundary in Aluminum-Copper-Lithium Alloys,'' Weld. J., 1998, 77, pp. 123s–132s.

21. W. R. Opie and N. J. Grant, "Hydrogen Solubility in Aluminum and Some Aluminum Alloys," Trans. AIME, 1950, 188(10), pp. 1237–1241.

22. C. Ransley and J. Neufeld, "The Solubility of Hydrogen in Liquid and Solid Aluminum," J. Inst. Metals, 1948, 74, p. 599.

23. R. A. Woods, "Porosity and Hydrogen Absorption in Aluminum Welds," Weld. J., 1974, 53(3), pp. 97s–108s.

24. D. G. Howden, "An Up-to-Date Look at Porosity Formation in Aluminum Weldments," Weld. J., 1971, 50(2), pp. 112–114.

25. P. D. Hess, "Measuring Hydrogen in Aluminum Alloys," J. Metals, 1973, (10), pp. 46–50.

26. D. E. J. Talbot, "Effects of Hydrogen in Aluminum, Magnesium, Copper and their Alloys," Int. Met. Rev., 1975, 20, pp. 166–184.

27. G. K. Sigworth and T. A. Engh, "Chemical and Kinetics Factors Related to Hydrogen Removal from Aluminum," Met. Trans., 1982, 13B, pp. 447–459.

28. J. H. Devletian and W. E. Wood, *Factors Affecting Porosity in Aluminum Welds: A Review*, Welding Research Council Bulletin 290, WRC, New York, NY, December, 1983.

29. R. E. Trevisan, D. D. Schwemmer, and D. L. Olson, "The Fundamental of Weld Metal Pore Formation," *Welding: Theory and Practice*, Chap. 3, 1990, Elsevier Science Pub.

30. R. F. Ashton, R. P. Wesley, and C. R. Dixon, "The Effect of Porosity of 5086–H116 Aluminum Alloy Welds," Weld. J., 1975, 54, pp. 95s–98s.

31. R. J. Shore and R. B. McCauley, "Effect of Porosity on High Strength Aluminum 7039," Weld. J., 1970, 49(7), pp. 311s–321s.

32. Z. P. Saperstein, G. R. Prescott, and E. W. Monroe, "Porosity in Aluminum Welds," Weld. J., 1964, 43(10), pp. 443s–453s.

33. R. P. Martukanitz and P. R. Michnuk, "Sources of Porosity in Gas Metal Arc Welding of Aluminum," in *Trends in Welding Research*, ASM Int., Materials Park, OH, 1982, pp. 315–330.

34. F. R. Collins, "Porosity in Aluminum-Alloy Welds," Weld. J., 1958, 38(6), pp. 589–593.

35. G. D. Nikiforov, S. A. Trusov and S. A. Silanteva, "The Redistribution of Hydrogen during Solidification of Aluminum," Svar. Proiz., 1980, 9, pp. 34–37.

36. M. Uda and S. Ohno, "Porosity Formation in Weld Metal-I. Effect of Hydrogen on Porosity Formation in Pure Aluminum at Non-arc Melting," Trans. Nat. Res. Inst. Metals, 1974, 16(2), pp. 67–74.

37. L. S. Sapiro, "A New Equation for Evaluating the Condition of Generation of Gas Phase and Porosity in Metal," Svar. Proizvod, 1973, 20(1), p. 14.

38. G. D. Nikiforov and V. V. Redchits, "The Mechanism of Nucleation of Gas Bubbles in the Weld Pool in the Welding of Active Metals," Svar. Proizvod, 1977, 24(8), p. 53.

39. I. K. Pokhodnga and L. I. Demchenk, "Numerical Research in the Growth of a Gas Bubble during the Solidification of Metal Weld Pool," Avtom. Svarka, 1977, 30(11), p. 8.

40. G. D. Nikiforov and A. Makhortova, "The Mode of Formation of Pores in Welding Aluminum and its Alloys," Svar. Proizvoid, 1961, 7(3), p. 5.

41. R. C. Andrew, "Sources of Hydrogen Porosity in Aluminum Alloy Welds," Aust. Weld. Res., 1975, 4(2), pp. 1–19.

42. I. K. Pokhodnga, L. I. Demchemko, V. F. Shelopakov, V. N. Denchenko and V. M. Abdulakh, "On the Mechanism of Formation of Pores in Welded Joint," Avtom. Svarka, 1978, 31(6).

43. R. C. Andrew and G. A. Chadwick, "Influence of Welding Variables on Porosity in Aluminum Alloy MIG Welds," Australian Weld. Res., 1975, 4(2–4).

44. A. I. Gorshkov, "Kinetics of the Growth of Gas Bubble in the Molten Pool and the Formation of Pores in the Weld Metal in the Welding of Titanium," Svar. Proizvod, 1975, 22(6), p. 54.
45. R. C. Andrew and J. Waring, "Effect of Porosity on Transverse Weld Fatigue Behavior," Welding Journal, 1974, 53(2), pp. 85s–90s.
46. J. F. Rudy and E. J. Rupert, "Effects of Porosity on Mechanical Properties of Aluminum Welds," Weld. J., 1970, 49(7), pp. 322s–336s.
47. C. E. Cross, D. L. Olson, and G. R. Edwards, "The Role of Porosity in Initiating Weld Metal Hot Cracks," *Proc. Int. Conf. on Modeling and Control of Joining Processes*, AWS, Miami, FL, 1993, pp. 549–557.
48. B. Dixon, "Initiation and Growth of Weld Solidification Cracks," *Proc. Solidification Processing*, Sheffield, Inst. Metals, London, 1987, pp. 350–352.
49. M. Holt, D. L. Olson, and C. E. Cross, "Interfacial Tension Driven Fluid Flow Model for Hot Cracking," Scripta Metallurgica et Materialia, 1992, 26, pp. 1119–1124.
50. U. Feurer, "Influences of Alloy Composition and Solidification Conditions on Dendrite Arm Spacing, Feeding and Hot Tearing Properties of Aluminum Alloys," *Proc. Int. Sym. Quality Control of Eng. Alloys*, Delft, 1977, pp. 131–145.
51. J. Campbell, *Castings*, 1991, Butterworth-Heinemann Pub., p. 224.
52. R. A. Chihoski, "The Character of Stress Fields Around a Weld Arc Moving on an Aluminum Sheet," Weld. J., 1972, 51, pp. 9s–18s.
53. C. E. Cross and D. L. Olson, "Hot Tearing Model to Assess Aluminum Weldability," Conf. Proc. Aluminum Alloys: Their Phys. and Mech. Prop., Univ. Virginia, 1986, pp. 1869–1875.
54. W. I. Pumphrey and D. C. Moore, "Cracking During and After Solidification in some Aluminum-Copper-Magnesium Alloys of High Purity," J. Inst. Metals, 1948, 73, pp. 425–438.
55. C. E. Cross, L. S. Kramer, W. T. Tack, and L. W. Loechel, "Aluminum Weldability and Hot Tearing Theory," in *Weldability of Materials*, 1990, ASM Int. Pub., pp. 275–282.
56. M. G. Mousavi, C. E. Cross, Ø. Grong and M. Hval, "Controlling Weld Metal Dilution for Optimized Weld Performance in Aluminum," Sci. Tech. Weld. Joining, 1997, 2, pp. 275–278.
57. J. Dowd, "Weld Cracking of Aluminum Alloys," Weld. J., 1952, 31, pp. 448s–456s.
58. T. W. Nelson, J. C. Lippold, W. Lin, and W. A. Baeslack III, "Evaluation of the Circular Patch Test for Assessing Weld Solidification Cracking, Part 1 – Development of a Test Method," Weld. J., 1997, 76, pp. 110s–119s.
59. W. F. Savage and C. D. Lundin, "The Varestraint Test," Weld. J., 1965, pp. 433s–442s.
60. T. Senda, F. Matsuda and G. Takano, "Studies on Solidification Crack Susceptibility for Weld Metals with Trans-Varestraint Test," J. Japan Weld. Soc., 1973, 42, pp. 48–56.
61. P. T. Houldcroft, "A Simple Cracking Test for Use with Argon-ARc Welding," British Weld. J., 1955, 2, pp. 471–475.
62. G. M. Goodwin, "Development of a New Hot-Cracking Test: The Sigmajig," Weld. J., 1987, 66, pp. 33s–38s.
63. J. H. Dudas and F. R. Collins, "Preventing Weld Cracks in High-Strength Aluminum Alloys," Weld. J., 1966, 45, pp. 241s–249s.
64. C. E. Cross and W. T. Tack, "Selection and Weldability of Aluminum-Lithium Alloys," in *ASM Handbook Vol. 6: Welding, Brazing and Soldering*, 1993, ASM Int., Materials Park, OH, pp. 549–553.
65. J. J. Pepe and W. F. Savage, "Effects of Constitutional Liquation in 18-Ni Maraging Steel Weldments," Weld. J., 1967, 46, pp. 411s–422s.
66. B. I. Bjørneklett, Ø. Frigaard, Ø. Grong, O. R. Myhr, and O. T. Midling, "Modelling of Local Melting During Friction Stir Welding of Al-Zn-Mg Alloys," *Proc. Int. Conf. Aluminum Alloys-6*, Vol. 3, 1998, Japan Inst. Light Metals, pp. 1531–1536.

67. N. F. Gittos and M. H. Scott, "Heat Affected Zone Cracking of Al-Mg-Si Alloys," Welding Journal, 1981, 60, pp. 95s–103s.

68. M. Katoh and H. W. Kerr, "Investigation of Heat-Affected Zone Cracking of GMA Welds of Al-Mg-Si Alloys using the Varestraint Test," Weld. J., 1987, 66, pp. 360s–368s.

69. S. D. Dumolt, D. E. Laughlin, and J. C. Williams, "The Effect of Welding on the Microstructure of the Age Hardening Aluminum Alloy 2219," *Proc. Int. Aluminum Welding Conf.*, 1982, Welding Research Council, pp. 115–134.

70. O. R. Mhyr and Ø. Grong, "Process Modelling Applied to 6082-T6 Aluminum Weldments-I. Reaction Kinetics," Acta Materialia, 1991, 39, pp. 2693–2702.

71. R. P. Martukanitz, "Modeling of the Heat Affected Zone of Aluminum Arc Welds," *Conf. Proc. Advances in Welding Science and Technology*, 1986, ASM Int. Pub., pp. 193–210.

72. R. P. Martukanitz, "Microstructure Evolution within the Heat Affected Zone of Al-Cu and Al-Cu-Li Alloys," PhD Thesis, Penn. State Univ., 1998.

73. F. E. Gibbs, "Development of Filler Metals for Welding Al-Zn-Mg Alloy 7039," Weld. J., 1966, 45, pp. 445s–453s.

74. K. Nakata, Y. Miyanaga, F. Matsuda, K. Tsudamoto, and K. Arai, "New 7% Mg Welding Electrode for Crackless Welding of Al-Zn-Mg (7N01) High Strength Aluminum Alloy," Trans. JWRI, 1980, 9(2), pp. 205–216.

75. C. E. Cross and Ø. Grong, "Microstructure and Mechanical Properties of Simulated Al-Mg-Zn Weld Metal Modified with Sc and Zr," *Proc. Int. Conf. Aluminum Alloys-6*, 1998, Japan Inst. Light Metals, pp. 1441–1446.

76. Handbook, "Aluminum Standards and Data," Aluminum Association, Washington, D.C., 1984.

77. I. B. Robinson and F. R. Baysinger, "Welding Aluminum Alloy 7039," Weld. J., 1966, 45(10), pp. 433s–444s.

78. Handbook, *Welding Kaiser Aluminum*, Kaiser Aluminum, Oakland, CA, 1978.

79. R. A. Gentry and F. G. Armao, "Weldability of Aluminum Alloy 2519–T87," Report No. 52-90-14, Alcoa Technical Center, PA, 1990.

80. A. O. Kluken and B. Bjørneklett, "A Study of Mechanical Properties for Aluminium GMA Weldments," Weld. J., 1997, 76(2), pp. 39–44.

81. R. G. Buchheit, Jr., J. P. Moran, and G. E. Stoner, "Localized Corrosion Behavior of Alloy 2090-The Role of Microstructural Heterogeneity," Corrosion, 1990, 46(8), pp. 610–617.

82. O. I. Stekov et al. "Method of Evaluating the Influence of Non-Uniformity of Welded joint Properties on Corrosion," Svar. Proiz, 1972, 19(9), pp. 34–36.

83. R. G. Buchheit, Jr., J. P. Moran and G. E. Stoner, "Localized Corrosion Behavior of Alloy 2090. The Role of Microstructural Heterogeneity," Corrosion, 1990, 46(8), pp. 610–617.

84. J. E. Hatch, (ed.), *Aluminum Properties and Physical Metallurgy*, 1984, ASM Pub., p. 284.

85. A. Wahid, D. L. Olson, D. K. Matlock, and C. E. Cross, "Corrosion of Weldments," *ASM Handbook*, Vol. 6, 10th edn., Welding, Brazing and Soldering, 1993, ASM Int. Pub., pp. 1065–1069.

86. K. F. Krysiak, "Corrosion of Weldments," *ASM Handbook*, Vol. 13, 9th edn., Corrosion, 1987, ASM Int. Pub., pp. 344–368.

87. D. E. Davies, J. P. Dennison, and M. L. Mehta, "Evidence of Intergranular Corrosion in a High Purity Aluminum-Zinc-Magnesium Alloy in Unstressed Condition," *Proc. U.R. Evans Int. Conf. on Localized Corrosion*, 1971, Williamsburg, NACE, Horriton, TX.

88. K. R. Van Horn, (ed.), *Aluminum*, Vol. I, Properties, Physical Metallurgy and Phase Diagrams, 1967, ASM Pub., p. 212.
89. G. L. Berry, Jr, D. L. Olson and D. K. Matlock, "Influence of Microcompositional Gradients on Stress Corrosion Crack Propagation," Mat. Eng. Sci, 1991, A148, pp. 1–6.
90. F. C. Brautigan, "Welding Practices that Minimize Corrosion," Chem. Eng., 1977, 17(1), pp. 145–147.
91. Reynolds Aluminum, *Resistance Welding Aluminum*, 1963, Reynolds Metals Co. Pub., Richmond, VA, pp. 1–27.
92. A. W. M. Bosman, "Resistance Welding Aluminum and its Alloys: A State of the Art Review," IIW Doc. XII-1432-96, 1996, AWS, Miami, FL, pp. 1–10.
93. RWMA, *Resistance Welding Manual*, 4th edn, 1991, RWMA, Philadelphia, PA.
94. P. B. Dickerson and B. Irving, "Welding Aluminum: It is not as Difficult as It Sounds," Weld. J., 1992, 71(4), pp. 45–50.
95. Aluminum Association, "Tentative Guide to Automotive Resistance Spot Welding of Aluminum," Report T10, The Aluminum Association Inc., New York, NY, 1973.
96. F. R. Hoch, et al, "Aluminum Alloys," *AWS Welding Handbook*, Vol. 4, 1982, pp. 362–369.
97. N. T. Williams, "Resistance Spot Welding," *ASM Handbook*, Vol. 6, Welding, Brazing and Soldering, 1993, ASM Int. Pub., pp. 228–229.
98. M. J. Karagoulis, "Resistance Seam Welding," *ASM Handbook*, Vol. 6, Welding, Brazing and Soldering, 1993, ASM Int. Pub., pp. 238–245.
99. C. A. Roest and D. D. Rager, "Resistance Welding Parameters Profile for Welding of Aluminum," Weld. J., 1974, 53, pp. 529–536.
100. D. Aidun and D. Bennett, "Effect of Resistance Welding Variables on the Strength of Spot Welded 6061-T6 Aluminum Alloy," Weld. J., 1985, 64, pp. 15–26.
101. S. M. Darwish and M. S. Soliman, "Variables of Spot Welding Commercial Aluminum Sheets having Different Thickness," Int. J. Material and Product Tech., 1994, 9(4/5/6), pp. 394–402.
102. American Welding Society, "Recommended Practices for Resistance Welding," ANSI/AWS Doc. C.1.1: 199, 1999, AWS, Miami, FL.
103. J. Matsumoto and J. R. Lian, "Resistance Spot Welding of Aluminum Alloy," Welding in the World, 1994, 34, p. 407.
104. "Procedure Development and Process Considerations for Resistance Welding", ASM Handbook, Vol. 6, Welding, Brazing and Soldering, 1993, ASM Int. Pub., p. 848.
105. A. C. Nunes, Jr., E. O. Bayless, Jr., C. S. Jones, III, P. M. Munafo, A. P. Biddle, and W. A. Wilson, "Variable Polarity Plasma Arc Welding on the Space Shuttle External Tank," Weld. J., 1984, 63(9), pp. 27–35.
106. M. Tomsic and S. Barhorst, "Keyhole Plasma Arc Welding of Aluminum with Variable Polarity Power," Weld. J., 1984, 63(2), pp. 25–32.
107. C. J. Dawes and W. M. Thomas, "Friction Stir Process Welds in Aluminum Alloys," Weld. J., 1996, 75(3), pp. 41–45.

10

Casting Design

HENRY W. STOLL

Northwestern University, Evanston, Illinois, U.S.A.

1   INTRODUCTION

As manufactures seek to reduce weight and cost of products, aluminum alloy casting has emerged as an ''optimal'' material and manufacturing process choice in many situations. This is because aluminum casting offers the important advantage of being able to produce lightweight, highly complex functional shapes quickly and easily. Cost is reduced because numerous parts and complex construction and processing steps typically associated with built up structures and weldments can be replaced by a single cast part. Weight is reduced because the lightweight aluminum alloy can be located where it is needed and because sections can be thinner since load does not transfer across part interfaces, i.e. through fasteners or welds. To harvest these advantages, there are certain desirable goals that the aluminum casting designer should strive for.

1. **Maximize Functionality**: The engineer should design as much function as possible into the casting while also ensuring that the casting will successfully withstand the service requirements for which it is intended. This means that a single cast part may take the place of many individual separate parts, eliminating assembly operations, reducing weight, and frequently improving the overall structural integrity. For example, the numerous separate parts (formed sheet metal components plus rivets and other hardware) in a built-up aircraft access door can be replaced by a single monolithic aluminum casting.
2. **Optimize Manufacturing Characteristics**: In casting, the part being produced and the tooling used to produce the part interact in complex ways, which effect the quality, cost, and lead-time of the casting. Because of these complex interactions, part geometry not only determines the functionality

and structural integrity of the casting, it also determines the mold con-
struction, mold filling and material solidification processes involved in
producing the casting. These processes in turn affect cycle time, casting
quality, and material properties such as yield strength, ultimate strength,
and fatigue resistance. Casting geometry must therefore be determined
based on both functional and processing requirements. Casting
manufacturability is optimized by considering the foundry, tooling,
and secondary processing (e.g. machining, heat treating, etc.) needs early
in the design process, before design decisions become fixed and therefore
difficult and costly to change.

3. **Minimize Material Usage**: The minimum volume of metal that will satisfy
the structural, functional, appearance and manufacturability requirements
of the application is usually the best choice. Metal casting offers two
unique and very desirable design advantages that facilitate material
minimization: (1) metal mass can be located exactly where it is needed;
and (2) complex, three-dimensional geometry is readily created.

To achieve these goals, it is essential that the aluminum casting designer have a
good working knowledge of the following subjects.

- The advantages and limitations of the various casting processes used for
  producing aluminum castings.
- Types of geometry related casting defects, there causes, and methods of
  prevention.
- The service and casting characteristics of aluminum alloys and their suit-
  ability for each of the various casting processes.
- Thermal processing of aluminum castings (e.g. heat treating, welding) and
  its effect on production and service performance of the casting.
- Pattern, permanent mold, and die casting die construction and operation.
- Sources of casting cost and design considerations that drive these costs.
- Sources of machining cost and design considerations that drive these costs.
- Mechanical properties of cast aluminum alloys.
- Structural design principles and practices.
- Concurrent engineering methods and practices.

This chapter discusses the issues and practices associated with aluminum
casting design. The focus is on aluminum casting design in general including both
expendable molds (e.g. sand casting, investment casting, etc.) and permanent molds
(e.g. die casting).

2 CASTING PROCESSES

Casting is a manufacturing process in which molten metal alloy is poured or other-
wise caused to flow into a shape that approaches that of the finished component.
In creating the casting, the melt is conducted to the cavity in a highly controlled
manner using a system of channels, reservoirs, and other flow elements, which
we will collectively refer to as the *rigging system*. The shape is provided by the *mold*,
which is, in essence, a cavity having the negative shape of the component and sized to
compensate for dimensional changes (shrink) that occur as the alloy solidifies and

cools to room temperature. The mold may be expendable or permanent. An *expendable mold* is used only once and is typically broken into pieces to free the solidified casting. A *permanent mold*, on the other hand, is intended to be reused over and over again and is designed to release the solidified casting by opening and closing. In this section, we briefly overview the various casting processes to provide the background needed to discuss casting design. See Chapter 15 for a more in-depth discussion of casting process details.

2.1 Rigging System

In most casting processes, the rigging system performs two major functions: (1) fill the mold cavity with molten metal; and (2) feed additional molten metal to the casting to compensate for shrinkage that occurs as the casting solidifies. The typical rigging system is made up of a variety of different elements or features that allow it to perform these functions (Fig. 1).

The filling function is performed by the *running system*, which includes the pouring cup, sprue, runners, in-gates, and other channeling and flow control elements. For example, in the sand casting process, molten alloy is poured into the *pouring cup*, which is a receptacle sized and shaped to accommodate the stream of metal and smooth its flow. The *sprue* transports the metal to one or more *runners*, which in turn distribute the metal to the cavity. Typically the sprue is conical in shape to help minimize or reduce turbulence and mixing of air with the metal flow. The runners generally have large cross-sections and are often shaped to streamline and slow down the flow and deliver it to various regions of the mold cavity with a uniform flow rate. The runners are connected to the cavity by *gates* that control the flow of metal into the cavity. Typically, gates have reduced cross-sections to control the metal flow and to allow easy separation of the rigging system from the solidified casting. A *well* at the base of the sprue may also be provided to retain
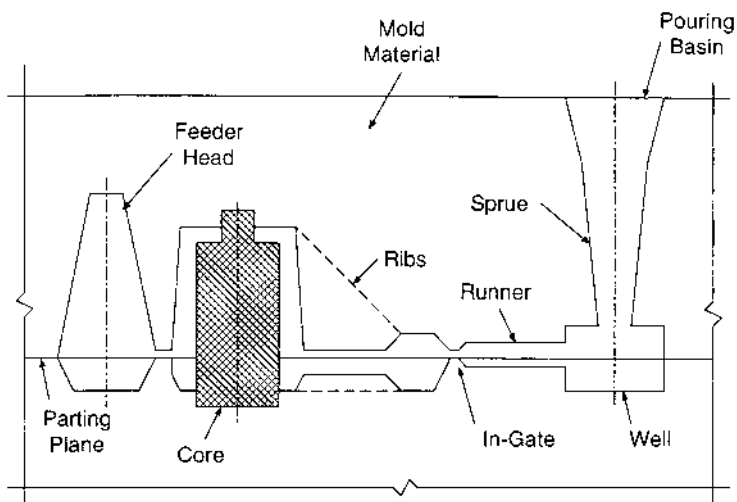
Figure 1 Typical rigging system elements.

contaminants such as refractory materials that may have been washed off the mold walls during pouring as well as non-metallic compounds formed by the molten metal reacting with air.

The *feeding system* helps avoid flaws such as porosity and shrinkage cavities by locating feeders at one or more locations around the casting (Fig. 1). *Feeders* (also called *risers* or *feeder heads*) are reservoirs of molten metal that continue to supply the casting with metal until it is completely solidified. Feeders are typically located at "chunky" regions of the casting that are likely to require additional metal supply as they solidify. In addition to feeders, detail casting geometry can help eliminate casting defects as discussed throughout this chapter.

2.2 Expendable Mold Casting Processes

Expendable mold casting includes a variety of casting processes such as sand casting, shell molding, vacuum molding, the lost foam process, and investment casting. In all of these processes, the expendable mold is prepared by consolidating a refractory material (sand or other refractory powder or slurry) around a *pattern* that defines the shape of the mold cavity (Fig. 2). Typically, the pattern will also define the shape of the rigging system, although, in some specialized cases, the runners and gates may be manually added during molding. The processes differ in that, in some cases the pattern is reusable and in others, it is expendable.

Sand casting, shell molding, vacuum molding, and other similar casting processes employ reusable patterns. To be *reusable*, the pattern is typically made of a material that is durable enough to permit repeated consolidation of the refractory and is shaped to allow withdrawal from the consolidated refractory mold. To allow withdrawal of the pattern from the mold, a *parting plane* is selected that conveniently divides the cavity into two or more parts. Surfaces that are perpendicular to the parting plane are sloped (i.e. have *draft*) to facilitate easy pattern removal. In addition, the pattern dimensions are increased (*shrinkage allowance*) to compensate for shrinkage that occurs as the solidified casting cools to room temperature.

Since the reusable pattern imprint forms the cavity, the pattern creates the external shape of the cast part. Internal features such as recesses, internal cavities, holes, and other undercuts are formed by cores. A *core* is a full-scale model (modified by the shrinkage allowance) of the internal feature that is typically made of sand
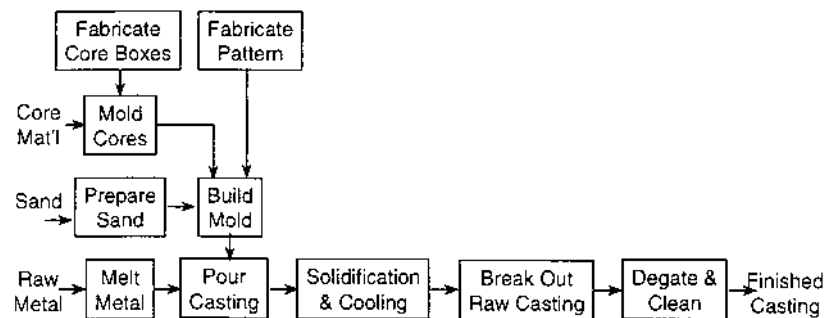
Figure 2 Steps in the production of a sand casting.

formed into the desired shape by a *core box*. The cores are placed in the mold cavity after the pattern is withdrawn and are supported by *core prints* (nesting holes provided by the pattern), and also by *chaplets* (metal supports that ultimately melt into the casting) in some cases, that allow the molten metal to flow between the core and the mold wall. In some cases, cores may also be necessary to produce a desired "zero" draft external surface, depending on the parting line selected.

Casting processes, such as the lost foam process and investment casting process, employ expendable patterns. An *expendable* pattern is typically destroyed as part of the casting process. In the *lost foam process* (also called the expanded polystyrene casting process, the lost pattern process, and evaporative foam process), for example, the pattern is made of polystyrene foam that vaporizes when the molten metal is poured into the mold. The polystyrene pattern typically includes the rigging system and may also contain internal cores (if needed), thus eliminating the need to fabricate and place individual cores in the mold. Also, since the pattern itself becomes the cavity, considerations of draft and parting plane can be ignored. The pattern can be made in a variety of ways depending on the quantity of castings to be made. For one-of-a-kind castings, the foam may be manually cut and assembled to form the pattern. For large production volumes, on the other hand, an automated molding operation can be utilized.

In *investment casting*, a pattern made of wax is coated with a refractory material to make the mold. The wax is then melted out of the mold prior to pouring the molten metal. Investment casting is capable of very intricate shapes, close dimensional control ($\pm$ 0.076 mm), good surface finish, and is a net shape process since no subsequent machining is normally required. Because the pattern is expendable, there is no need to remove the pattern so cores and draft are not needed, and the only limitation on shape is that the ceramic shell must be removable after the casting has solidified. The disposable wax patterns are readily produced in large quantities by injection molding into metal dies. Note that, in this case, some draft may be necessary to permit removal of the wax pattern from the metal die.

2.3 Permanent Mold Casting Processes

In *permanent mold casting*, the mold is made of metal (usually steel or cast iron) and is designed to open and close at the parting plane. The cavity and rigging system are machined into the mold halves to provide accurate dimensions and good surface finish. A prime requirement of permanent mold casting is that the solidified casting be readily removed from the mold cavity. This requires generous draft on surfaces that are perpendicular to the parting plane. In addition, cored features such as undercuts and transverse holes must not prevent opening of the mold and/or ejection of the solidified casting. When the cavity is filled under gravity or low pressure feed, sand cores may be placed in the permanent mold to produce desired interior features while still allowing the mold to open and close and the part to be readily ejected. This approach is often referred to as *semipermanent mold casting*. In high production applications and/or when filling pressure is high, more costly and complicated moveable metal cores must be used. Also, in more mechanized applications, *ejector pins* are necessary to remove the solidified casting from the mold.

A variety of different permanent mold casting processes are used. *Gravity-fed permanent mold casting* is similar to expendable mold casting processes such as sand casting except the mold is made of an appropriate permanent material. In *low pressure permanent mold casting*, the mold is located directly above the melting or holding furnace and metal is fed by air pressure into the mold cavity. In *die casting*, metal is forced into the mold cavity under moderate to high pressures. In the *cold-chamber die casting process* typically used for aluminum alloys, molten metal sufficient for one shot is transferred into the shot chamber and then injected by a plunger into the mold cavity.

2.4 Finishing Processes

Finishing processes are required to clean the solidified casting and prepare it for use in its intended application. For example, the rigging system (e.g. gates, runners, risers, sprue, etc.) must be removed by either breaking off (brittle materials) or sawing and grinding (more ductile materials). Remnants of the gate as well as flash must then be removed in additional trimming operations. Inspection is another important finishing process. If defects are found in the finished casting, they can often be repaired by welding.

After the casting has been cleaned and inspected, it may be further processed in a variety of ways. These operations, which are often referred to as secondary processing, might include stress relieving, heat treating, hot isostatic pressing (HIP), welding, machining, joining, painting, and plating. The final surface finish of most aluminum castings usually falls into one of three broad categories: as cast, mechanically finished, and/or chemically finished. The as cast surface finish of aluminum castings is often good enough for use without further treatment in many applications. In other applications, the appearance or quality of the surface finish can be enhanced by mechanical or chemical treatments. The most common mechanical finishing methods include abrasive blasting, ball burnishing, wire brushing, tumbling, and buffing.

Surface appearance and corrosion resistance may be further enhanced by chemical conversion coatings (e.g. Alodine or Irridite processes) or by anodizing. Chemical conversion processes enhance appearance by imparting a translucent color ranging from gold to a gray-green, but these coatings are not very durable or wear resistant. In the anodizing process, an anodic coating of aluminum oxide is applied to the aluminum casting by an electrochemical process similar to electroplating. Anodized finishes are more durable and wear resistant, but also reveal casting defects such as pinhole porosity and dross inclusions, so closely controlled foundry conditions and precise alloy composition is essential.

3 CASTING PROCESS SELECTION

The selection of a particular casting process to produce a specific part is governed by a variety of factors and considerations. Paramount among these is the geometric configuration and design features of the casting, which essentially determine the feasibility of the different processes. When more than one casting process option is feasible, the choice will then usually depend on size (weight), production quantity,

cost targets, and budget constraints. Also, depending on the application, functional requirements such as soundness, pressure tightness, mechanical properties, and so forth may strongly affect the process selection.

Tolerance capability is typically better for permanent mold casting processes because the metal mold is usually more accurate. Also, the metal mold (often combined with higher pressure and therefore better thermal contact) extracts heat faster, which produces better mechanical properties due to increased solidification rates and the finer microstructure that results. Operator skill also tends to be less for permanent mold processes since these processes are usually more mechanized. Expendable mold processes such as sand casting, on the other hand, are capable of producing complex external and internal shapes and are also suitable for relatively small production quantities. Also, expendable mold casting processes tend to have less porosity defects provided that good casting technique is used.

Unit cost is highly dependent on production quantity because tooling cost (patterns, molds, etc.) must be distributed over the number of castings shipped. Typically, expendable mold casting involves more manual labor and worker skill and is better suited for lower production quantities. For low production quantities, the casting process involving the least tooling investment will typically result in the lowest unit cost. However, unit cost is often high for low production quantities because of the additional manual labor involved. With higher production quantities, unit cost decreases since tooling cost is amortized over the higher number of parts and more mechanization of the process can be justified. Permanent mold processes such as die casting, however, typically require very high production quantities to offset the very high initial tooling investment required.

4 DESIGN RELATED CASTING DEFECTS

Casting defects occur for many reasons. Some are foundry or process related. For example, common sand casting defects include sand blow, pinholes, sand wash, scabs, penetration, mold shift, core shift, and mold crack. Others are common to casting processes in general and result because of undesirable interactions that occur between the casting geometry, alloy, and process. We refer to these as *design related casting defects* because they involve the casting geometry and can often be avoided by appropriate casting and rigging system design.

4.1 Porosity

Porosity is a casting defect that typically appears as a network of small voids distributed in various regions of the casting. If the porosity can be seen by the naked eye during radiographic inspection, it is referred to as *macroporosity* while porosity that requires magnification to be seen is referred to as *microporosity*. Porosity in cast aluminum is caused by gas bubbles that get trapped in the solidifying alloy (*gas porosity*) and by voids that form between dendrites due to solidification shrinkage effects (*shrinkage porosity*). Gas bubbles are caused by hydrogen that precipitates out as the molten metal solidifies due to the dramatic change in solubility and by air that is entrained during high velocity flow of the molten metal during filling of the mold cavity. Shrinkage pores develop when the interdendritic flow of molten metal becomes blocked. The size of shrinkage porosity often depends

on solidification rate since dendrites are larger with slower solidification. Such pores can also be enlarged by trapped gas. Gas pores are usually fairly spherical in shape while shrinkage pores typically have more irregular and elongated shapes.

Macroscopic porosity degrades both static and dynamic properties of the casting by reducing cross sectional area and by acting as internal stress risers and crack initiation sites. In addition, macroporosity can detract from functionality and/or appearance if it occurs on a critical surface or if machining or other finishing operations expose it. Also, porosity can be a potential problem if pressure tightness is a concern.

4.2   Shrinkage Cavity

A *shrinkage cavity* is a large irregularly shaped void in the solidified casting. This defect occurs when the supply of molten metal feeding a region of the casting is either depleted or is unable to flow sufficiently to compensate for solidification shrinkage of the alloy. Such defects typically occur in *hot spots* which are regions of the casting that cool more slowly than surrounding regions and are therefore cut off from a supply of molten metal.

4.3   Misruns

The term *misrun* is used to describe situations where a region of the mold cavity is not completely filled with metal. Misruns usually occur because the molten metal solidifies prematurely or is too thick or viscous to flow into a particular feature or region of the casting. For this reason, geometry related misruns usually occur in mold cavity cross sections that are too thin.

4.4   Cold Shuts

As molten metal fills the mold cavity, the liquid flow often divides into two or more streams as it flows around cores and other obstacles. *Cold shuts* occur when the portions of the metal flow rejoin but fail to fuse completely. Lack of fusion usually results because of premature freezing. Oxidation of the flow surfaces can also prevent complete fusion.

4.5   Hot Tears

A *hot tear* is a separation of the metal that appears as a tear or crack. Hot tearing occurs when the mold prevents the casting from contracting naturally as it solidifies and cools. Unyielding mold walls that constrain contraction of the cooling casting induce tensile stress in the casting. Tearing or cracking then occurs in regions where the tensile stress exceeds the strength of the solidifying material. Avoiding hot tearing is complicated by the fact that the solidifying alloy gains strength as it cools.

4.6   Warping and Distortion

Stress develops when thinner, less massive regions cool faster and therefore become stronger and more rigid than adjacent regions that are more massive and therefore slower cooling. This stress causes deformation that is "frozen in" as *residual stress* when the whole casting gains sufficient rigidity. Residual stress may cause warping

and other undesirable distortions of the cooled casting. Also, subsequent machining of the casting or other processing can relieve these stresses resulting in additional warping.

4.7 Metallurgical Defects

Metallurgical defects include inclusions of non-metallic particles, oxide films, and secondary phases that form during solidification. *Inclusions* are insoluble non-metal aggregates that are suspended in the liquid aluminum. They may form during solidification or before solidification begins. Also, in some expendable mold processes, they may also be washed off of the mold wall and/or introduced in other ways during the casting process. Inclusions act as stress concentration points and reduce dynamic properties. They can also be detrimental during machining by causing excessive tool wear and breakage as well as unacceptable surface defects.

Oxide films, which form on the surface of the molten metal as it flows through the rigging system and fills the mold cavity, are similar to inclusions and are of particular concern in aluminum casting. If the film folds over on itself as a result of turbulent flow or "waterfalling," the effects can be particularly damaging. *Waterfalling* occurs when molten metal falls to a lower level during mold filling.

Secondary inclusions or *second phases* can form as the primary alloy phase starts to freeze causing the remaining liquid to progressively concentrate in various solutes. Like inclusions and oxide films, second phases act as stress raisers and can nucleate cracks if they have the proper size and shape.

4.8 Mechanical Property Variation

Mechanical properties such as yield and ultimate strength of the casting alloy may vary with location in the casting. This scatter in property values is often due to variation in solidification rate that occurs in different regions of the casting. For example, "chunky" regions of the casting will cool more slowly than thin, less massive regions. Regions that cool more slowly typically have courser grain structure and therefore less strength than regions that cool more quickly and therefore have finer grain structure. Also, for long freezing range alloys (i.e. alloys whose constituent components solidify at significantly different temperatures), microsegregation of the alloy composition may occur which can also result in variation of mechanical properties. Another source of variation is the presence of casting defects such as porosity.

Uncertainties in casting strength can be of great concern in the design of safety-critical castings such as those used in automotive suspension components and in aerospace applications. In industries such as aerospace, these uncertainties are accounted for by using both statistical design allowables and a casting factor [1]. The static strengths of alloys that can be used in airframes are given in [2] and are based on rigorous statistical analysis of strength testing data. The *casting factor* is used to increase the margin of safety:

$$S_D = P/CF \tag{1}$$

where S_D is the design strength, P is the design allowable, and CF is the casting factor. The value of the casting factor to be used in a particular casting design is determined by part criticality and inspection to be made on the casting. In addition to x-ray, penetrant and visual inspections, requirements may include periodic destructive testing and testing sample coupons. Inspection requirements become increasingly strict with decreasing casting factor. For example, the smallest casting factor that can be used in the design of a critical part is 1.25. Use of this CF value requires 100% visual, magnetic/penetrant and x-ray inspection of all castings plus destructive testing of three castings. A comprehensive discussion of casting factors is given in [3].

5   GEOMETRY/MATERIAL/PROCESS INTERACTIONS

Design related casting defects are caused by undesirable interactions that occur between the casting geometry (including the rigging system), the alloy, and the casting process. Understanding how casting geometry, the material in both its liquid and solid phases, and the casting process interact provides the insight needed to specify the best casting geometry from a function, form, and fabrication point of view. In the following, we explore several geometry/material/process interactions that are pivotal to good casting design. Many of the terms and discussion are based on [4]. For a more in-depth discussion of these topics, the reader is referred to this reference.

5.1   Fluid Life

Fluid life or *fluidity* refers to the ability of the molten alloy to fill the mold cavity, flow through thin narrow channels to form thin walls and sections, and conform to fine surface detail. In addition to temperature of the molten metal, fluid life also depends on chemical, metallurgical, and surface tension factors. Therefore, the fluid life of each alloy is different. For example, aluminum 356 is considered to have excellent fluid life whereas the fluid life of aluminum 206 is only fair to good. Misruns and related casting defects can be avoided by proper consideration of the fluid life of the particular casting alloy to be used. Fluid life determines the minimum wall thickness and maximum length of a thin section. It also determines the fineness of cosmetic detail that is possible. Hence, knowing that an alloy has limited fluid life suggests that the part should have softer shapes (i.e. generous radii, etc.), larger lettering, finer detail in the bottom portion of the mold, coarser detail in the upper portions of the mold, more taper leading to thin sections, and so forth.

5.2   Solidification Shrinkage

Shrinkage occurs in three distinct stages: liquid shrinkage, liquid-to-solid shrinkage, and solid shrinkage. *Liquid shrinkage* is the contraction of the liquid before solidification. *Liquid-to-solid shrinkage* or *solidification shrinkage* is the shrinkage that occurs as the disconnected atoms and molecules of the molten metal form into the crystals of atoms and chemical compounds that constitute the solid metal. *Solid shrinkage* is the shrinkage that occurs as the solid metal casting cools to ambient temperature. Although liquid shrinkage is important to the metal caster, it is

not an important design consideration. Solidification shrinkage and solid shrinkage, on the other hand, are extremely important and must be carefully considered during casting design.

Different alloys have differing amounts of liquid-to-solid shrinkage (e.g. aluminum 356 has little shrinkage tendency while aluminum 520 has a large shrinkage tendency). Most importantly, there are three different types of solidification shrinkage: directional, eutectic, and equiaxed [4]. In alloys that solidify directionally, solidification moves along predictable pathways determined by the casting geometry and thermal gradients in the mold. For example, solidification will typically begin at the mold wall and move perpendicularly toward the center of the part. This is called *progressive* solidification. Solidification will also begin in cooler regions where the mold surface area to metal volume ratio is large and travel toward the hotter regions of the casting. This is called *directional* solidification. The key is to configure the part geometry so that directional solidification can occur before progressive solidification shuts off the source of liquid metal supply (the riser). Without proper pathway geometry (e.g. risering and tapering), voids (shrinkage cavities) or pores due to isolated internal shrinkage can result.

In eutectic-type solidification, the liquid metal cools and then solidifies very quickly all over. This behavior minimizes internal shrinkage and the need for risers and makes this type of alloy the most forgiving of the three. Eutectic-type materials that have very little solidification shrinkage often require no risering at all. As discussed previously, *risers* are reservoirs of molten metal that continue to supply the casting with metal until it is completely solidified. The key geometric concern for eutectic-type solidifying alloys like aluminum 356 which have small but appreciable solidification shrinkage is to ensure that the avenue of liquid metal supply stays open and functioning all the way to final solidification.

In addition to solidifying both progressively and directionally from the mold walls, alloys that exhibit an equiaxed solidification behavior also begin to solidify throughout the liquid, forming "mushy" regions consisting of equiaxed islands of solid. These equiaxed islands can block the avenues of liquid metal supply making these alloys difficult to feed. One way to mitigate this effect is to decrease the length of the mushy zone by increasing the thermal gradient (e.g. increase the solidification rate by adding chills, etc). Alternatively, the casting can be designed to have small thermal gradients. In this approach, thermal mass is spread out and distributed uniformly throughout the casting. This causes the shrinkage to be distributed as microscopic pores throughout the volume of the casting. In both approaches, the effect on mechanical properties is greatly minimized by the small size, rounded shape, and uniform dispersion that result.

Pure aluminum and short freezing range alloys that have a high percentage of aluminum will typically exhibit directional solidification behavior whereas eutectic alloys such as aluminum-silicon (11.6% Si) exhibit the desirable eutectic-type solidification. Long freezing range aluminum alloys, on the other hand, are more likely to exhibit equiaxed-type solidification.

5.3 Solid Shrinkage

Solid shrinkage is often called "pattern maker's shrink" because the tooling must be properly sized so that the part will shrink to the desired final size and shape upon

cooling. Solid shrinkage is critical for two important reasons. First, the shrinkage must be predicted and then built into the patterns/dies and corebox dimensions. If this is not done correctly, then the tooling will need to be modified iteratively to achieve an acceptable production casting. This adds time and cost to the design cycle and introduces quality risk in the final product. Second, as the casting cools, it may not be able to shrink uniformly because some regions are stiffer than others. This can result in undesirable residual stresses and/or undesirable distortion and warpage. Creating casting geometry that makes shrinkage predictable and that avoids residual stress and warping is therefore highly desirable.

5.4 Slag/Dross Formation

Slag is typically composed of liquid nonmetallic compounds (usually fluxed refractories), products of alloying, and products of oxidation in air. *Dross* refers to non-metallic compounds produced primarily by the molten metal reacting with air. Aluminum alloys are quite sensitive to slag/dross formation and are therefore more likely to contain non-metallic inclusions. In addition to process and quality control techniques, part geometry can be used to dramatically reduce the likelihood of non-metallic inclusions. For example, because slag/dross are buoyant in aluminum, the probability of having an inclusion in a critical machined surface can be reduced by designing the part so that these surfaces are located in the lower portion of the mold. Similarly, the rigging system can be designed to control the amount of oxidation that occurs due to turbulent flow and entrained air and to avoid waterfalling.

5.5 Fluid Flow

Another key geometry/process interaction involves the flow of molten metal into the mold cavity. As mentioned previously, turbulent flow through gates and other channels can effect the amount of oxidation and consequent dross formation that occurs. Another consideration is the force generated by the molten metal as it flows into the mold cavity and the turbulence of the flow in the cavity since both of these effects can displace cores and erode mold walls, especially sharp edges and high detail features. Steep thermal gradients can also arise due to fluid flow. If the flow separates to pass around cores and other features and the joins together again, weld lines (cold shuts), non-metallic inclusions, and other flaws can occur due to cooling and oxidation of the flow front. In order to minimize undesirable effects of fluid flow, the casting must be poured slowly. Unfortunately, this gives the molten metal more time to oxidize and increases process cycle time. Undesirable interactions due to fluid flow effects can often be reduced or eliminated by designing the casting geometry and rigging as a system.

5.6 Heat Transfer Considerations

The geometry must also be selected with an understanding of the heat transfer conditions involved. If the geometry is such that the heat cannot escape, a hot spot is likely to occur. For example, narrow peninsulas or tight corners of mold material surrounded by molten metal will get hot very quickly and as a result, solidification of the molten metal in these regions will be slower than surrounding regions. This

creates the possibility of ''hot tears'' or ''shrinkage pulls'' because the hotter material will have less tensile strength and is therefore less able to resist internal forces that develop due to solidification and solid shrinkage. Shrinkage cavities can also form because liquid metal supply paths close off before the material in the region of the hot spot is fully solidified.

Just the opposite situation occurs when sharp corners or narrow peninsulas of molten metal are surrounded by mold material. In these cases, the molten metal cools and solidifies very quickly. This is generally a desirable situation. However, if cooling is too rapid, it can cause cold cracking due to stressing of the solidified skin or thin region by solidification shrinkage occurring at a slower rate in more massive adjacent regions. Also, difficult to machine or undesirable material properties may result from to rapid cooling of some alloys.

5.7   Geometry/Alloy Interactions

It is important to note that each aluminum alloy has its own unique set of casting characteristics. In most cases, it is the combination of material properties possessed by a particular alloy that determines the most desirable casting geometry. For example, aluminum 356 has excellent fluid life, and more eutectic type than directional type solidification. This combinations of properties makes this alloy well suited for precision casting and permits fine detail and thin walls everywhere. However, although still relatively small, solidification shrinkage is significant enough to warrant consideration especially with respect to risering, section size, and feeding pathways.

Aluminum 514 is at the opposite end of the spectrum. This alloy has relatively poor fluid life and large, directional type solidification shrinkage. This combination of material properties makes 514 less casting friendly. As a result, careful attention to casting geometry is essential. Because of its poor fluid life, fine detail and thin sections are difficult. Most importantly, because of its large solidification shrinkage, feeding of the casting is a great concern. Risers need to be large and the geometry must be carefully designed to ensure proper feeding of the casting. Also, because of its unfavorable combination of properties, aluminum 514 requires softer shapes (i.e. large radii, rounded shape, large lettering, no sharp detail) compared to casting friendly materials such as aluminum 356.

Aluminum alloys, such as 356, exhibit good casting characteristics largely because of their relatively high silicon content. High silicon content is, in fact, the main difference between widely used aluminum casting alloys and other aluminum casting alloys. The addition of silicon reduces the solidification temperature range and produces more eutectic type solidification. This improves castability by increasing fluid life and feeding and reducing hot tearing. Aluminum alloys having lower silicon contents (e.g. almost all of the alloys in the 2xx.x, 5xx.x, 7xx.x, and 8xx.x groups), on the other hand, exhibit much less friendly casting characteristics. Hence, geometry/material interactions for these alloys must be carefully considered during the early stages of design if sound castings that transition quickly into production is to be obtained.

6   ALLOY SELECTION

Alloy selection is a pivotal determination that must be made early in the casting design. In many respects, alloy selection is just as important as the structural design of the casting since a good structural design may give unsatisfactory service if it is cast from an unsuitable alloy. As discussed in the previous sections, it is essential that the designer not only consider physical and mechanical properties when selecting a casting alloy, but also the casting process and foundry characteristics and how these are likely to interact with the detail geometry of the casting. Hence, alloy selection should be based on all of the following considerations.

- The ability of the alloy to meet service and code requirements.
- The suitability of the alloy for the casting process.
- The size and complexity of the casting configuration.
- The minimum section thickness required.
- Heat treatment considerations. Will heat treatment be required? Or, can a self-aging or non-heat treatable alloy be used?

It is the designer's responsibility to select the alloy that will best satisfy these requirements. In most situations, some intelligent compromise must be made since it is unlikely that any one alloy will be able to satisfy all requirements equally well. However, with a good understanding of the needs of the design, together with knowledge of how the detail casting geometry, casting process, and alloy interact, it is possible to design the casting so that all demands are effectively balanced. Achieving this balance is the goal of good casting design.

7   THERMAL POST-PROCESSING

Aluminum castings may be further processed thermally after casting to improve mechanical properties and correct defects.

7.1   Heat Treatment

Heat treatment is used to modify or change the alloy structure and mechanical properties and is typically specified to provide one or more of the following benefits.

- Improved mechanical properties
- Internal stress relief
- Improved dimensional stability
- Improved machinability
- Improved corrosion resistance

In general, no one single time and temperature cycle will produce all of these beneficial effects, so, as with alloy selection, some intelligent compromise may be necessary.

An aluminum alloy whose tensile strength is improved by thermal treatment is said to be *heat treatable*. Generally, alloys containing significant amounts of copper or magnesium are heat treatable. Alloys for which thermal treatment has no effect on tensile strength are termed *non-heat treatable*. However, even though heat treatment does not improve strength in these alloys, it can be used to improve other properties. In those alloys that are heat treatable, essentially two types of heat treatment are

possible: *solution heat treatment* and *precipitation hardening* (also referred to as *aging*). In non-heat treatable alloys, the heat treatment processes used are *annealing* and *stress relieving*.

In *solution heat treatment*, the casting is heated rapidly and uniformly to a temperature as close to the melting point of the eutectic as possible (typically 800–1000°F). The casting is held (soaked) at this temperature for a specified number of hours and then quenched in hot water. *Quenching* is the rapid reduction in temperature of the casting to roughly 180°F. A uniform rate of quenching is required to prevent the development of localized areas of thermal stress and distortion. If straightening of the casting due to quench distortion is necessary, it should be performed as close as possible to the time of quenching (within 24 h or less) since the casting will typically gain strength as it ages, even at room temperature. In some cases, this completes the heat treatment. However, for the majority of castings that have been solution heat-treated, additional aging or precipitation hardening is required.

Aging or precipitation hardening is the part of the thermal treatment that actually increases the strength of the alloy under the influence of heat. The strengthening process, which is referred to as *artificial aging*, is carried out by heating the casting to some intermediate temperature (usually 300–500°F) and soaking it for a period of time (2 h to three weeks depending on temper). It is important for the designer to know that some aluminum alloys will age naturally (*natural aging*) at room temperature without the application of heat. Natural aging in service can result in a loss of ductility and dimensional stability. Also, some aluminum casting alloys can overage (*overaging*) if held to long at an elevated temperature resulting in a loss of tensile strength combined with an increase in ductility and dimensional stability. This is one of the reasons why the temperature of the service environment is an important consideration in aluminum casting alloy selection.

There are several basic thermal treatments or tempers applied to castings. These are summarized as follows. See Chaps 2 and 5 for a more in-depth discussion of heat treatment.

- F-Temper: as cast condition with no special control of thermal conditions in the process.
- O-Temper: annealed condition. Applied to castings that have been heat treated to improve dimensional stability or ductility.
- T4-Temper: solution heat-treated, quenched, and naturally aged.
- T5-Temper: cooled from an elevated temperature and artificially aged. This temper improves mechanical properties and dimensional stability, especially for castings intended for high temperature service environments.
- T6-Temper: solution heat-treated, quenched, and artificially aged. This heat treatment develops optimum mechanical properties and good ductility and dimensional stability.
- T7-Temper: solution heat-treated, quenched, and overaged. Overaging improves the dimensional stability of the casting, but is accompanied by some reduction in tensile properties.

The most desirable mechanical properties are obtained by use of both solution and aging treatment (T6 and T7). However, the feasibility of this thermal processing depends on the casting size and configuration, so it is important to plan on this processing in the design stage.

7.2 Hot Isostatic Pressing (HIP)

In some applications where fatigue failure and/or pressure tightness is a concern, it is desirable to have essentially 100% of theoretical density. In *hot isostatic pressing*, the casting is placed in a pressure vessel (autoclave) and an inert gas (e.g. argon) is introduced. The gas is then heated to increase its pressure and to put pressure on the casting. The heat also softens the casting allowing internal voids to collapse under the pressure. If the HIPing is performed properly, no residual voids will remain in the material except for surface connected porosity. This type of porosity cannot normally be healed by HIPing and must be weld repaired. Also, if the porosity is relatively large, HIP will form small dimples on the surface of the casting that may also require weld repair. Because HIPing is a thermal process (as well as a pressure process), it can modify the microstructure and hence the casting properties if not carefully planned and performed. HIP treatment is relatively inexpensive and has made it possible to use alloys that do not solidify pore free (e.g. long freezing range equiaxed alloys) in fatigue-critical and other high-integrity applications.

7.3 Weld Repair

Weld repair is a common practice for filling surface connected porosity, post-HIP surface depressions, and other defects such as cold shuts. In general, a casting may not be welded without permission of the customer. Therefore, to simplify weld repair, the designer should clearly specify the maximum size, number and location of possible defects that could be repaired by welding. Most importantly, areas where welding is not allowed should be clearly specified. It is also very important for the designer to fully understand how the welded area will influence mechanical properties such as fatigue resistance and ultimate strength. Repair welding should be performed prior to any heat treatment and final non-destructive testing.

8   TOOLING CONSIDERATIONS

In casting, tooling is used to create the mold cavity and cores and to hold the whole package together so that molten metal can flow and solidify to form the cast part. The tooling differs considerably however, between permanent and expendable mold casting. In permanent mold casting processes, the tooling consists of a steel or cast iron mold (or die) and moving and non-moving steel cores. In expendable mold casting, tooling is used to shape the cavity (pattern) or to form the pattern (investment casting). Tooling is also used to mold cores that are placed in the cavity to form undercuts and internal features.

Tooling is also similar in many respects. In all cases (both expendable mold and permanent mold), the mold is divided into two halves so that the final casting, core, or pattern can be withdrawn (Fig 3). When the mold halves close, the core and cavity, or two cavities meet, producing the air space into which the molten aluminum alloy flows (Fig. 3(a)). From the inside, the mating junction between the mold halves appears as a line. This line also appears on the casting and is called the *parting line* or *parting plane*. Similarly, all surfaces that are perpendicular to the parting plane must be tapered in the direction of mold opening so that the solidified casting, core, or pattern can be withdrawn easily from the mold. This taper, which is commonly referred to as *draft*, allows the molded part to break free by creating a clearance

Parallel Draft

Draft Angle

Upper Mold Half

Parting Plane

Casting

Draft

Draft

Mold Cavity

Lower Mold Half

(a) Mold Closed   (b) Mold Open   (c) Draft on Cast Part
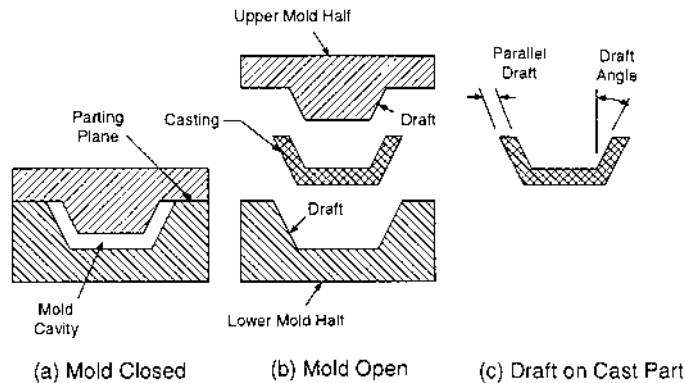
Figure 3 The mold is divided into two halves so that the final casting, core, or pattern can be withdrawn. (a) The mating junction between the mold halves defines the parting plane; (b) Draft provides ejection clearance upon mold half separation; (c) With draft, walls and other features cannot be exactly perpendicular to the parting plane.

as soon as the pattern starts to be withdrawn or the mold starts to open (Fig. 3(b)). Any feature that prevents the mold from opening or the pattern from being withdrawn is referred to as an *undercut*. In permanent molds that are mechanized, *side action* (camming) is used to move a core so that the mold can open and/or the part ejected (Fig. 4). In expendable molds and semi-permanent casting processes, manually placed sand cores are used. In all cases, cores are expensive and introduce complexity and quality risk into the process.

Detail geometry of the cast part determines, to a large extent, cost of the tooling as well as time and effort required to design and construct the tooling. In the following, we explore how casting geometry impacts tooling design and construction for several major casting processes.

8.1 Tooling for Sand Casting

Tooling for sand casting processes can be made in many different ways depending on the detail geometry of the part and on cost, quality, and lead-time requirements. Major decisions include the fabrication method, material, and tooling approach to be used. Traditionally, patterns and core boxes have been manually fabricated from handcrafted prototypes of clay, wood, plastic or other materials. This time consuming process can now be performed using CNC machining processes to generate the tooling by removing material from a starting workpiece (subtractive process) or by using one or more FFFF (Fast Free Form Fabrication) processes to generate the tooling by building it up one layer at a time (additive process).

FFFF methods can be used in a variety of different ways to facilitate the rapid fabrication of foundry tooling for different casting processes (Fig. 5). Layered Object Manufacturing (LOM) and StereoLithography are typical of the several FFFF processes that are commonly used for rapid tooling. In the LOM process (Fig. 6), the part or tool is built-up by laser cutting sheets of paper in the shape of the part cross-section and stacking and gluing the sheets together to form the three-dimensional part. In StereoLithography, the layers are created by using a laser
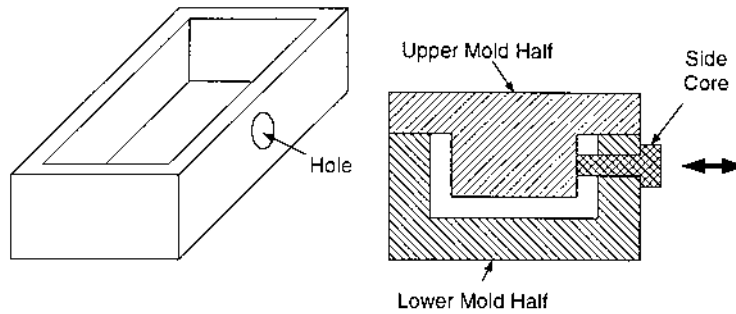
Figure 4   In die-casting and mechanized permanent mold casting, undercuts that prevent mold opening require core slides.
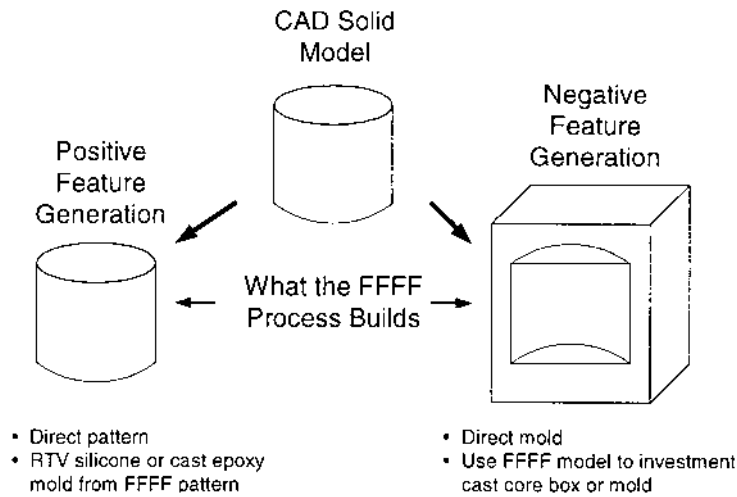
Figure 5   Using FFFF processes to fabricate foundry tooling for casting presents a myriad of possibilities.

to selectively photo cure a special kind of resin, called a *photopolymer*, that has the property of turning solid under the influence of certain wavelengths of light. For the shape of each slice to be known, FFFF processes must be computer controlled using a CAD solid model representation of the part geometry. FFFF methods can greatly reduce tooling lead-time and cost, however it may also introduce additional error. For example, the LOM process requires tessellation of the solid model and smoothing and sealing of the finished tooling (Fig. 6). See [5] for further discussion of rapid tooling methods.

With the addition of rapid tooling as a pattern fabrication method, there are three basic categories of fabrication methods to consider: manual, FFFF, and CNC machining. Each of these categories has a range of choices. For example, there are several FFFF processes that might be used depending on the capability of the particular pattern shop involved. In addition to patterns, core fabrication must also be considered. Cores can be fabricated directly or molded using a core box.
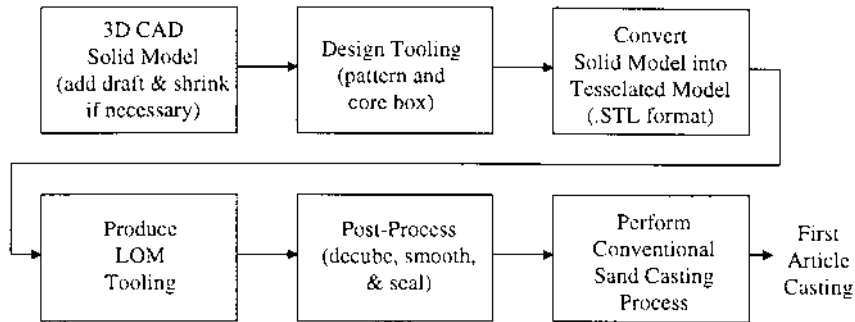
Figure 6 LOM based rapid tooling process for sand casting.

Typically, a core box would be used when higher production quantities are required. Like patterns, either the core itself or the core box can be fabricated using manual, CNC machining, or FFFF methods.

Sand casting tools can generally be fabricated from a large variety of different materials. Frequently used materials for reusable patterns include mahogany or other wood, urethane plastics, synthetic materials, metals and FFFF materials. Mahogany and other woods are particularly well suited for manual fabrication because they are easy to work with. Urethane plastic offers high quality and strength. Synthetic materials such as renboard are popular because of their durability and machineability. Metals (mainly aluminum and steel) are used when long tool life is a concern. FFFF materials range from polymer, paper, nylon, ABS plastic, wax, etc. depending on the particular FFFF processes used.

The *tooling approach* relates to the way the mold cavity is created. Commonly used tooling approaches include single or loose patterns, gated patterns, match-plate (mounted) patterns, and cope and drag (top and bottom) patterns. A *loose pattern* is essentially a model of the cast part that incorporates the allowances and core prints necessary for producing the casting. Such patterns are generally made of wood, but can also be made of metal, plaster, plastic, wax, or any other suitable material. Relatively few castings are typically made from any one loose pattern since hand molding is practiced and the casting production is slow and costly. The parting surface may be hand formed and gating systems are hand-cut in the sand. Drawing the pattern from the sand, after rapping it to loosen it from the sand, is also done by hand. As a result, dimensional accuracy of the casting can vary from casting to casting and is generally not very good. Loose patterns are best suited for producing prototype castings. *Gated loose patterns* are an improvement on ungated loose patterns. The rigging system is included as a part of the pattern to eliminate hand-cutting of these features. This type of pattern can produce small quantities of castings with a more rapid molding cycle.

In a *match-plate pattern*, the cope and drag portions of the pattern are mounted on opposite sides of a wood or metal plate conforming to the parting line. Rigging systems are almost always attached to the plate. Match-plate patterns are typically used with some type of molding machine and are capable of producing large quantities of small castings. This type of pattern has improved dimensional accuracy and higher production rates compared to loose patterns.

In the *cope and drag* tooling approach, cope and drag portions of the pattern are mounted on separate plates. This greatly increases the production rate by allowing the cope and drag halves of the mold to be made separately on different molding machines. Separate cope and drag plates are costly, however. Also, cost is increased because the separate pattern plates require accurate alignment of the two mold halves by means of guide and locating pins and bushings in flasks.

In practice, each tool build approach has its own set of advantages and disadvantages. Generally, the dimensional accuracy, tool life, and production rate increase as the selected tooling approach moves from loose patterns to cope and drag plates. But tooling fabrication time and cost also increase. Hence, the tooling approach selected will generally depend on the production volume required in addition to dimensional accuracy and lead-time.

Cost, lead time, and quality (e.g. tolerances) of sand casting tooling depends on the fabrication method, tool material, and tooling approach selected. These decisions, in turn, depend to a great extent on the detail casting geometry involved. Often, minor geometry decisions can inadvertently eliminate low cost and/or time efficient options from consideration. When possible, the designer should work closely with the foundry and tool builder early in the casting design process to insure that detail geometry decisions do not unnecessarily constrain tooling choices.

8.2   Tooling for Investment Casting

Investment casting offers tremendous design freedom. Complex shapes that would be too costly to machine can be produced quickly and economically as investment castings. From a design perspective, it is important to remember that the pattern for investment casting is injection molded. The designer should therefore observe good design for injection molding practices. These include well-located, straight parting line, generous draft, avoidance of undercuts, and the use of generous fillets and radii wherever possible. The molds for making the wax patterns can be fabricated in a variety of ways such as those discussed for sand casting. Therefore, as in sand casting, the designer should strive to avoid making geometry decisions that constrain tooling options unnecessarily.

8.3   Tooling for Permanent Mold Casting

Permanent casting molds are generally made of cast iron and are frequently coated with a layer of sodium silicate and clay or other insulating material. The molds are typically preheated to 150–200°C prior to pouring. Auxiliary water cooling or radiation pins may be used to cool heavy sections. Proper venting of the mold cavity is essential to avoid misruns. Only simple part geometry is suitable for permanent mold casting. If complicated coring is necessary, then semi-permanent molds that use sand cores should be used. Draft and parting line selection are also key design considerations.

8.4   Tooling for Die Casting

Die casting involves the high pressure injection of molten metal into a split metal die. Tooling for die casting is very complicated and therefore costly, even for simple shapes. Very high metal injection pressures (up to 69 MPa) must be withstood

for many thousands of cycles. Large dies are commonly cooled by channeling water behind heavier sections and through cores. The solidified part is ejected after the die opens by ejector pins that bear on the casting face. Following the molding process, the casting is trimmed using a hardened steel trimming die shaped to match the cast shape. Trimming typically involves the removal of in-gates, gates to overflow pads, parting line flash, and flash in cored holes and openings. The following general considerations are important in creating detail geometry of the die cast parts.

1. **Coring:** Undercuts that prevent die opening and/or part ejection require core slides (Fig. 4). This adds cost and complexity to the die and can increase cycle time for the process.
2. **Draft:** Draft is required to get the part out of the die and off of cores. Therefore, walls and other details cannot be perpendicular to the parting line unless expensive core slides are used (Fig. 3).
3. **Part Ejection:** After a part has been cast, it must be removed from the die. Typically, the part is mechanically ejected by ejector pins or by more costly options such as ejector sleeves or rings. Ejector pin location can be critical and should be carefully chosen to avoid stress concentration, poor appearance (ejector pins can leave unsightly marks on the part), and distortion of the part. Also, ejection is facilitated by generous draft, which decreases ejection force and helps avoid ejection problems.
4. **Die Modification:** In die casting, air and die lubricants often become entrained and trapped in the solidified casting due to the high injection velocities and solidification rates employed. This results in microporosity and uncertain mechanical properties that may not be predictable beforehand. When this is the case, it may be necessary to modify the die after it has been hardened. Ribs and other similar features can be incorporated into an existing hardened die by using electrical-discharge-machining techniques. When the use of ribs to strengthen the casting is a consideration and mechanical properties are uncertain, it may be better to under design initially, test sample castings, then add strength if necessary by removal of die steel until the optimum combination of mechanical properties and casting material conservation is achieved. This is preferable to over designing and having to lighten the die casting later by welding the die, which is a costly and life-limiting procedure. It should be noted that "test and fix" approaches should be avoided where possible by observing good casting design practices, computer simulation and an effective concurrent engineering design process.
5. **Concurrent Engineering:** After being machined, the dies must be hardened by heat treating, which makes subsequent alterations difficult. Therefore, the die caster should be involved early in the design process and agreement with the die caster on the producibility of the finalized best design should be obtained before the die is designed and fabricated.

9 DESIGN RELATED COST DRIVERS

The cost of a casting is determined by its size, configuration, and detail geometry. Size and configuration are usually dictated by the functionality and service require-

ments of the part. Given these requirements, the casting designer must specify suitable detail geometry that satisfies these requirements at the lowest possible cost. *Design related cost drivers* are detail geometry design decisions that strongly effect the cost to design, tool, and produce the casting. Important design related cost drivers for casting include the following:

- Parting line
- Amount of draft
- Number and complexity of undercuts
- Number, size and complexity of separate cores
- Section shape (e.g. junctions, ribs and webs, holes and pockets, bosses and pads)
- Casting tolerance
- Trimming
- Secondary processing (e.g. machining, heat treating, surface treatment, etc.)

The major sources of cost for most casting processes include tool cost, material cost, and production cost. Unit cost for a casting is given by the following expression:

$$\text{Cost/Part} = \frac{C_\text{T}}{N} + V\,C_M + \frac{C_\text{H} t_\text{cycle}}{Y} + \frac{C_\text{D}}{N} \tag{2}$$

where C_T = total non-recurring tooling cost ($)

C_M = material cost ($/in^3)

C_H = machine cost including labor and recurring tooling expenses ($/hr)

C_D = total development cost ($)

N = lifetime number of good castings made using the tooling

V = total material volume including rigging system (in^3)

t_cycle = cycle time to cast, trim, and finish one casting (hr)

Y = process yield (usable parts/N)

It is important to note that Eq. (2) is very comprehensive in that it includes all the costs associated with each cost source. Tooling cost for sand casting, for example, would include the cost of the pattern and core boxes, the cost of trimming dies or other finishing tools, the cost of machining fixtures, and so forth. Similarly, cycle time includes all of the cycle times associated with making the casting. For sand casting, this includes the cycle time for forming the mold cavity, molding the cores and placing them in the mold cavity, readying the mold for pouring and pouring the casting, cooling and breaking it out, trimming the rigging system, performing finishing and inspection operations, and setting-up and finish machining the casting. Cycle time also includes material handling time and other non-value-added time. Likewise, the machine cost and process yield corresponding to each cycle time is used in the production cost calculation. Finally, it should be noted that development cost includes all of the engineering cost associated with designing and testing the casting including design revisions and tooling changes.

Equation (2) clearly indicates what should be done ''by design'' to reduce cost:

- Design to minimize tooling cost
- Design to minimize material cost
- Design to minimize cycle time
- Design to maximize process yield
- Design to minimize development cost.

Achieving these objectives requires an understanding of how the design related cost drivers influence total cost. How each design related cost driver effects cost is discussed as follows.

Parting Line. The parting line establishes many aspects of both the part geometry and the process. The parting line choice effects the length, width, and depth of the mold halves which essentially establishes the pattern size and shape and the complexity and cost of the mold. In die casting and other pressure fed casting processes, the projected area established by the parting plane determines the clamping force required and therefore the size of the casting machine. This in turn effects tooling cost, machine cost, and to a lesser extent cycle time. To minimize part cost, the parting line should be selected very early in the design process. The goal should be a parting line that keeps tool complexity to a minimum. A planar parting line is preferable to a non-planer parting line. Also, when possible, a parting line that places the whole part in one mold half can greatly reduce tool cost and alignment and registration requirements across the parting line are avoided. The parting line can also be an important constraint if FFFF or CNC pattern building methods are being considered.

Draft. Generous draft is highly desirable for low part cost. Minimal draft, especially when combined with deep draws, increase tool cost because tooling surfaces become more critical and special surface treatments may be necessary. This increases cycle time and tooling cost. Minimal draft increases cycle time in permanent mold casting because the casting must be stronger and therefore cooler before it can be reliably ejected. It also increases cycle time in expendable mold casting because more care must be exercised in withdrawing patterns and so forth. Yield may also be adversely effected when difficult part ejection or pattern withdrawal results in damaged parts or molds. A difficulty that is commonly encountered when applying draft to a part is the creation of unacceptably heavy walls. One remedy is to use parallel draft which allows the wall sections to be kept uniform (Fig. 3(c)).

Undercuts. Anything that can be done to avoid undercuts or reduce their complexity will reduce tooling cost and development time. In die casting, undercuts require moving cores, which greatly increases tooling cost. Moving cores can also increase cycle time since the cores must move before the mold can open and/or the part can be ejected. The best way to avoid undercuts is to select the parting line wisely. In addition, it is often possible to design so undercuts can be created using simple tooling without the need for expensive side actions (Fig. 7).

Separate Cores. In sand casting and permanent mold casting, separate cores must be placed in the mold cavity before each part is cast to produce internal features. Expendable cores must be molded using core boxes which increases cost and cycle time. The designer should therefore strive to eliminate separate cores whenever possible. This is especially true for long, thin, and small cores, which can cause core and casting scrap. As always, judgment is required however, since
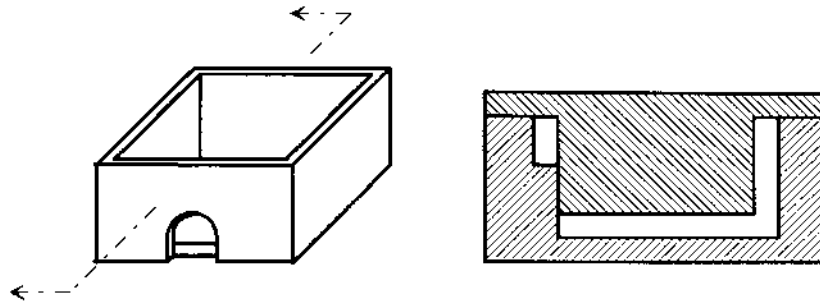
Figure 7   In some situations, a hole or depression in the side wall of a part can be cast without the need for side action cores.

coring may be desirable if it makes it possible to provide sections of uniform thickness or helps to minimize machining.

   Section Thickness. Castings are composed of various geometrical features that integrate together to define the overall shape and functionality of the casting. Each section feature, such as walls, junctions, ribs and webs, holes and pockets, bosses and pads, and so forth, involves a wall or section thickness. Hence, just about every aspect of the casting appearance, functionality, quality, and manufacturability relates to, affects or will be influenced by the section thickness selected for individual casting features. From a cost standpoint, it is safe to say that section thickness impacts all of the cost sources in one way or another. The most obvious is material cost since section thickness directly effects the material volume of the casting with less volume, and therefore less material, being more desirable. Also, less material results in faster cooling and potentially shorter cycle times. At the same time, thinner sections require longer fluid life, more injection pressure, and/or time to fill the mold. If the section is too thin, yield may be adversely effected because flow is restricted and the part will not fill out properly (e.g. misruns). Also, in die casting, high injection pressure can result in flash or highly stressed parts. In addition, thinner sections can require more mold detail and closer core/cavity alignment and fit which will increase tooling cost. Thick sections, on the other hand, cool slower, shrink more, and have more risk for sink marks and shrink cavities. They also are more difficult to feed and are therefore more likely to contain porosity. This is especially true for long freezing range equiaxed-type alloys. Hence, in addition to increasing material cost, unnecessarily thick sections can also decrease yield and increase cycle time.

   Shrinkage occurs as the molten alloy cools in the mold cavity to form the solidified casting. Since thin sections cool and contract more rapidly than thick sections, stress can be induced when thick sections that are adjacent to thin sections constrain shrinkage of the thin section. As a result, the thin sections may tear to relieve the stress, or they may deform plastically without tearing. If they do not tear, warpage and shape distortion can occur when the casting is removed from the mold. Varying section thickness, therefore, introduces a quality risk that can be avoided by employing a uniform wall thickness everywhere in the casting. By

using a uniform wall thickness, thermal mass, and therefore shrinkage, is the same everywhere.

Tolerance. Tight dimensional and form tolerance specifications increase tooling cost and reduce cycle time and yield. This is because there are many hard to control factors associated with casting processes. For example, in sand casting, equipment, metal, and sand can vary from lot to lot and foundry to foundry. Metal temperature, cooling time, and cooling conditions can vary. This, together with slight differences in core placement, mold hardness, shrinkage, internal stress, and so forth, introduce additional hard to control part to part variation. In addition, tight tolerances require more precise tooling, close process control, and often 100% gaging with resulting scrap. Therefore, whenever possible, component tolerances should be relaxed as much as possible. Also, where possible, the part should be designed so that critical dimensions do not cross the parting line to minimize positional accuracy required between mold halves.

Trimming. After the solidified casting has cooled to room temperature, the rigging system together with any flash and remaining gate and riser material must be removed. This is a time consuming (especially if performed manually) and costly (especially if trimming dies and other tooling is used) process. The rigging system also adds material cost and material handling cost. The need for trimming can be reduced by designing the casting so that a minimal number of risers and gates are needed and by designing so that the gate and riser contacts can be located in non-critical easy to access areas. Also, locating gate and riser contacts so they don't interfere with machining fixture targets will reduce trimming time, the cost of the fixture, and possibly machining cycle time because the fixturing will be easier and more consistent.

Secondary Processing. Many castings are heat-treated, finish machined, anodized, plated, painted, stress relieved, and so forth after casting. It is important that requirements and constraints imposed by secondary processing be considered early in the casting design. Often, the most effective way to do this is to involve experts in these processes early in the design before irreversible design decisions have been made.

10 CASTING DESIGN GUIDELINES

Casting design involves the specification of the overall configuration (i.e. overall shape and arrangement of features) of the casting as well as the detail geometry of the various features that comprise it. The goal of casting design is twofold: (1) satisfy the functionality and service requirements of the application; and (2) specify a casting configuration and detail design that results in low cost, high inherent quality, and short lead time. Both of these goals must be achieved if the casting is to be successful. Key design consideration include:

- What casting design will maximize economy and ease of the chosen process?
- What casting design will maximize the strength of the casting?
- What casting design will minimize the weight of the casting?
- What casting design will minimize stress in the mold and avoid tearing and cracking during solidification?

- What casting design will best facilitate proper positioning of gates, risers, and chills to insure soundness of the casting?
- What casting design will best establish and control solidification?
- What casting design will best facilitate secondary processing such as heat treatment and machining?

Specifying the best overall configuration, geometrical layout of features, and detail dimensions and tolerances that balances these considerations is the essence of casting design. This section presents a variety of guidelines for casting design that are based on a broad synthesis of the many aspects of casting design discussed in the previous sections. The guidelines are generally applicable to all alloys and casting processes. However, when applying the guidelines, the designer must consider particular geometry/alloy/process interactions that may be unique to a given alloy and process combination. In some instances, these interactions may dictate geometry decisions that differ appreciably from the guidelines presented here.

Use a Concurrent Engineering Approach. Finding the most appropriate balance between the many considerations that influence casting design requires close collaboration between the design engineer and the foundry. It is therefore strongly recommended that, as a minimum, the designer (or buyer) consult with the foundry and tooling engineer before developing the final design. Preferably, a concurrent engineering approach such as that discussed in Sec. 11 is recommended.

Design for Strength and Stiffness. The strength and stiffness of the casting will be maximized by locating material where it is needed while avoiding unnecessary bulk and weight (Figs 8 and 9). For example, if the casting is subjected to bending, then ideally the section modulus ($z = I/c$) at each section should be adjusted so that deflection is within specification and the maximum stress is equal to the allowable design strength of the chosen alloy. In general, configuration designs that utilize continuously varying section geometry to take full advantage of material properties are preferred since these configurations tend to minimize weight and also fully leverage the advantages of the casting process. This practice, which is often referred to as *shape optimization*, has been greatly facilitated by the development of powerful engineering workstations and solid modeling software that significantly enhances
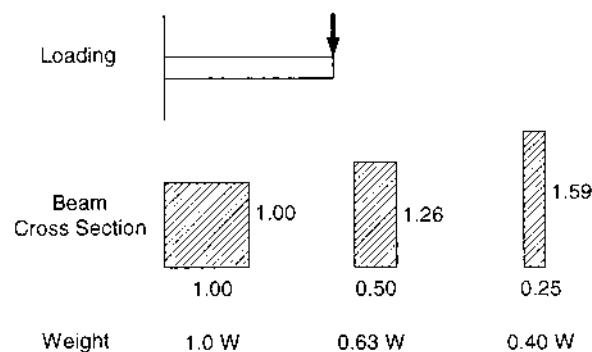
Figure 8 Weight comparison for beam cross sections having equal deflections. Note that W equals the weight of the beam having the 1×1 cross section and that the length and loading for each beam is identical.

$$I_{XX} = I \qquad I_{XX} = 0.948\,I \qquad I_{XX} = 0.478\,I \qquad I_{XX} = 0.412\,I$$
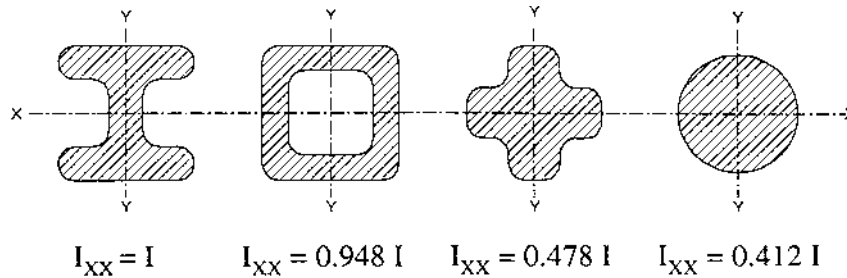
Figure 9 The area moment of inertia (I) of the four beam cross sections shown illustrate the importance of metal distribution on the load carrying capacity of a beam. All four sections have the same area and weight, and all except the round shape have the same width and height. Also, $I_{XX} = I_{YY}$ for all four cross sections. Note that the cross and round sections have only about 50% of the rigidity of the I-beam and the heavy concentration of metal in the central area of these sections makes them more susceptible to shrinkage cavities.

the engineer's ability to visualize complex three-dimensional geometry and to analyze stress levels and deflections of complex three-dimensional shapes. As has been discussed previously, an assortment of defects including variation in mechanical properties may occur as the result of hard to control factors that influence the casting process. The use of experimental methods (e.g. photo-elastic, brittle coatings, etc.) to help verify the design of more complexly shaped castings, especially those that involve load or deflection critical applications is generally recommended.

Minimize Casting Weight. Minimizing the weight of the casting minimizes material cost. It also helps to reduce the cost of material handling during production of the casting as well as during subsequent machining and assembly. In addition, lighter weight castings reduce energy costs throughout their life cycle. Weight of the casting can be reduced by (1) designing the casting for strength and deflection as discussed previously; and (2) by utilizing a minimum uniform wall thickness everywhere in the casting. Typical minimum wall thickness for investment casting, premium sand casting, and conventional sand casting are 1.5 ± 0.15 mm, 1.8 ± 0.4 mm, and 2.5 ± 0.5 mm, respectively [6]. There are a variety of design approaches that facilitate the use of thinner walls. For example, the use of ribs enables the foundry to produce thinner walls (Fig. 10). Similarly, increasing section depth allows the use of thinner walls (Fig. 8).

Use Casting Process Simulation. In *casting process simulation*, comprehensive modeling of the intended production process is performed in order to determine the size and shape of sprues, runners, gates, and risers. A variety of software for performing this type of simulation is available. In addition, methodologies have been developed to understand and predict the size and location of process related defects (microporosity, etc.). Using these methodologies, the rigging system design can be varied in the foundry system simulation to evaluate how defect size and location are to be controlled and/or eliminated. Using computer simulation early in the design process can greatly reduce the amount of "guess work" involved in specifying cost effective and functionally acceptable casting geometry. Computer based casting process simulation offers two important advantages: (1) design iterations and "what-if" analysis are much easier to perform; and (2) the "physics" engine under-
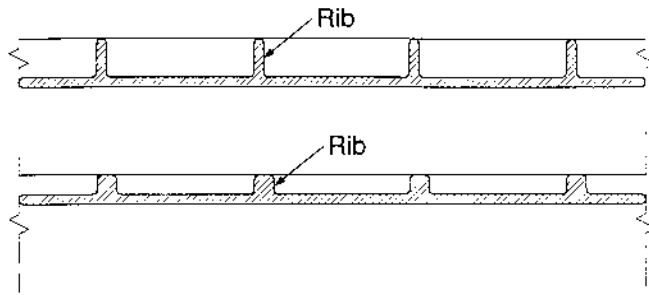
Figure 10   Depending on design considerations, ribs may be cast in many different configurations as illustrated by the two examples shown here [6].

lying the simulation software provides a consistent and predictable science base for casting design. This allows the casting geometry and rigging system to be specified and optimized as a coordinated system. Most importantly, it allows evaluation of the overall design before tools are cut and the design is irreversibly committed to hardware. When used properly, the result is a substantial reduction in design time and tooling iterations. It is extremely important to note however, that the use of casting process simulation software is not, in itself, a viable substitute for early input of experienced tooling and foundry engineers. Rather, it is a very powerful tool that helps leverage and assist the concurrent engineering approach.

   Design for Casting Soundness. Hot spots, which cause shrinkage defects and hot tears, result when the casting geometry interacts in undesirable ways with the solidification process. To avoid hot spots, the geometrical layout of the casting must insure an ample supply of molten metal to feed shrinkage throughout the solidification of the casting. The following guidelines represent preferred practice for most casting design situations. However, it is extremely important that the designer also considers specific interactions and implications that are unique to the particular combination of alloy and casting process being used.

1.   **Design for uniform wall thickness.** Shrinkage cavities will form in heavy sections that are fed by light sections because the light section will freeze and cut off the supply of molten metal. When heavy sections cannot be avoided, then risers or other costly foundry remedies such as chilling must often be used. A far preferable approach is to avoid heavy sections by designing the casting to have a uniform wall thickness (Fig. 11). In addition to helping to prevent hot spots, uniform wall thickness also helps prevent undesirable residual stress and warping of the casting. Most importantly, uniform wall design tends to minimize casting weight.
2.   **Taper or flare sections toward risers.** Tapering the geometry toward the source of molten metal helps direct and control the solidification front so that it progresses from the cooler region into the hotter region thereby insuring an ample supply of molten metal at all times. This practice is of particular importance for alloys that tend to solidify directionally.

Feasible   Preferred
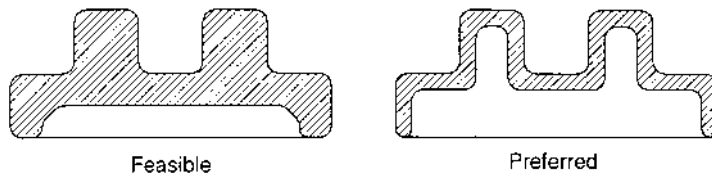
Figure 11 Component redesigned to reduce section thickness and provide a more uniform wall thickness, eliminating hot spots and shrinkage effects, reducing component weight, and reducing production cycle time (thin sections cool faster).

High Stress   Hot Spot

Radius Too Small   Radius Too Large
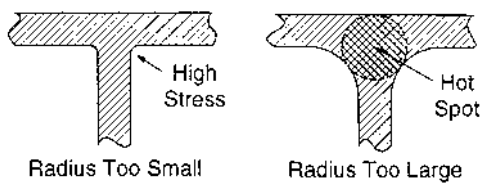
Figure 12 Avoid both too small and too large radii at the intersection of sections.

3. **Avoid isolated hot spots and sharp internal corners.** As a general principle, the corners of all intersections and junctions should have fillet radii. The size of the fillet radii used must often strike a balance between stress concentration and the possibility of a hot spot (Fig. 12). If the corner is too sharp (i.e. the fillet radius is to small), the flow of molten metal during filling will be inhibited and high stress concentration due to the small fillet radius can cause cracking during cooling or use of the casting. Conversely, if the fillet radius is made too large, isolated hot spots can occur because the metal mass at the intersection will be larger than the features that are joined. The casting designer should therefore specify corner radii that are neither too large or too small to insure that both of these undesirable effects are avoided (Figs 13 and 14). Often the best choice will depend on the particular alloy. For example, alloys that exhibit little solidification shrinkage are typically not sensitive to junction design [4].

Design to Avoid Hot Tears and Distortion. As the casting solidifies and cools, it shrinks. If the mold walls and/or cores inhibit or constrain this shrinkage, internal stress will develop (Fig. 15). This can result in hot tearing or cracking if the stress exceeds the strength of the alloy or the stress may be "frozen in" as residual stress causing distortion and warpage of the casting when it is removed from the mold and/or when it is machined. Similar effects will occur if different sections of the casting cool at different rates or if the distribution of metal is asymmetric (Fig. 16). The best way to avoid hot tears and distortion is to avoid asymmetrical distributions of metal and to use a uniform wall thickness everywhere. When this is not possible, transitions to different section thickness should be carefully designed so that the degree of constraint imposed on the solidifying casting is minimized (Fig. 17).

Equal Walls   Unequal Walls

Acceptable   Acceptable

Preferred   Preferred

(a) "L" Junctions

Preferred   Preferred

(b) "T" Junctions

Preferred   Preferred

(c) 90° Intersection
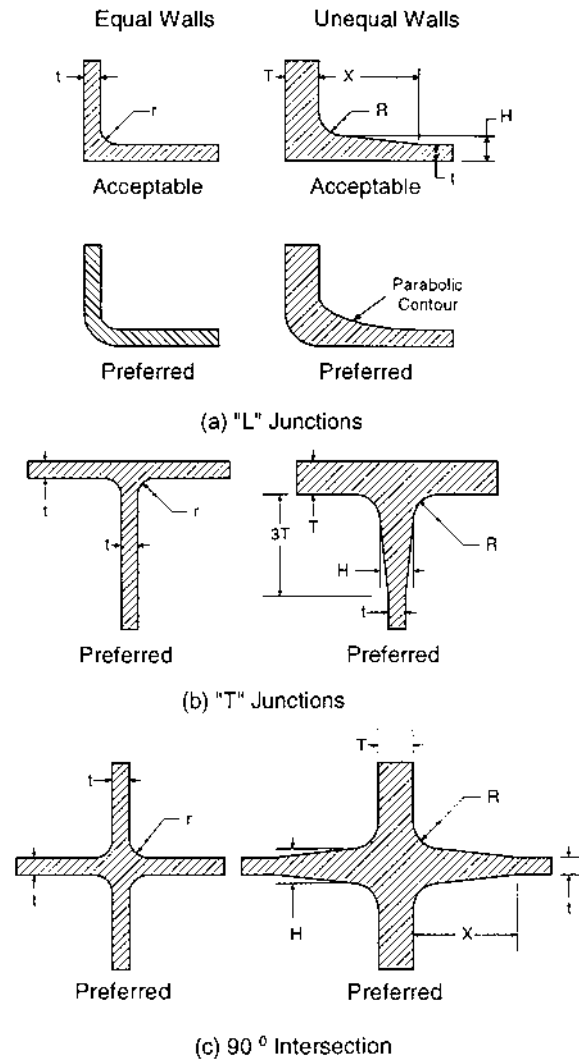
Figure 13 Detail junction design. Recommended values for r, R, H, and X typically fall in the following ranges: $0.5t \leq r \leq t$, $0.3T \leq R \leq 0.5(t + T)$, $0.3T \leq H \leq 0.5(t + T)$, and $3T \leq X \leq 4T$. The actual best values to use ultimately depend on requirements of the application and on the particular alloy and casting process being used.

Design for Metal Flow. Misruns and cold shuts occur when the molten metal solidifies prematurely in cross-sections that are too long and narrow or that are too thin. Minimum section thickness for castings are a function of the alloy composition, size, and configuration of the part. A casting is designed for metal flow by properly considering the fluid life of the alloy. Alloys having poor or fair fluid life require thicker sections than those having good to excellent fluid life.
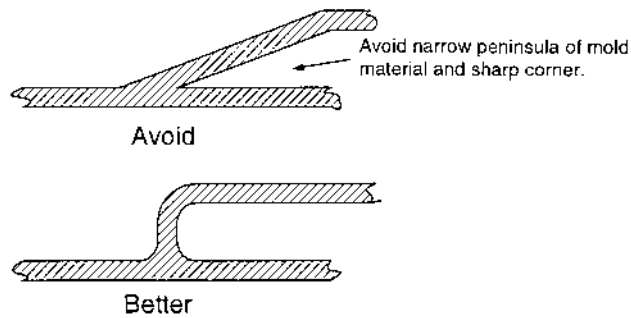
Figure 14 Avoid narrow peninsulas of mold material and sharp internal corners to avoid hot tears and cracking.

Avoid
In-line ribs may cause
cracks and distortion.

Better
Staggered ribs reduce
danger of cracks and distortion.
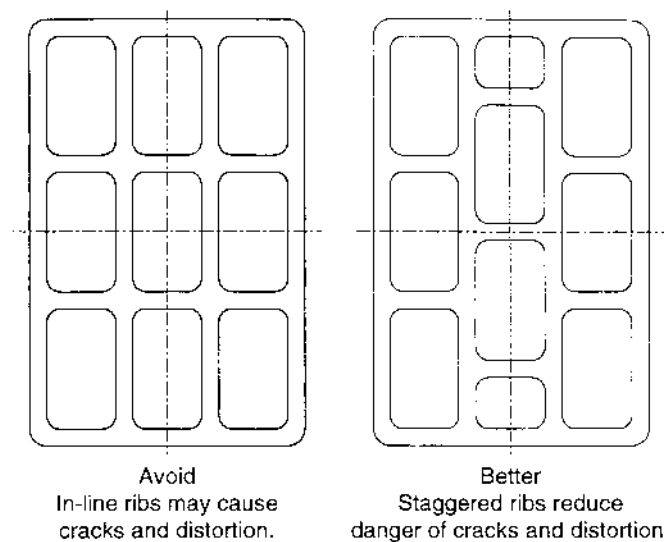
Figure 15 Staggered ribs reduce distortion caused by thermal contraction, reduce metal mass in local areas, and minimize the possibility of hot spots.

Design for Low Foundry Tooling Cost. The number of foundry tools and the number of operations required to make each piece of foundry tooling are directly determined by the casting design. Similarly, the number of operations required to make the molds and cores and assemble them for casting is determined by the casting design (Fig. 18). Therefore, every opportunity should be taken to minimize casting complexity and promote ease of fabrication while the design is in the very early stages of development, when conceptual maneuverability is wide and the design is easily changed.

Design for Heat Treatment. Guidelines for achieving a heat-treatment friendly casting design include the following:
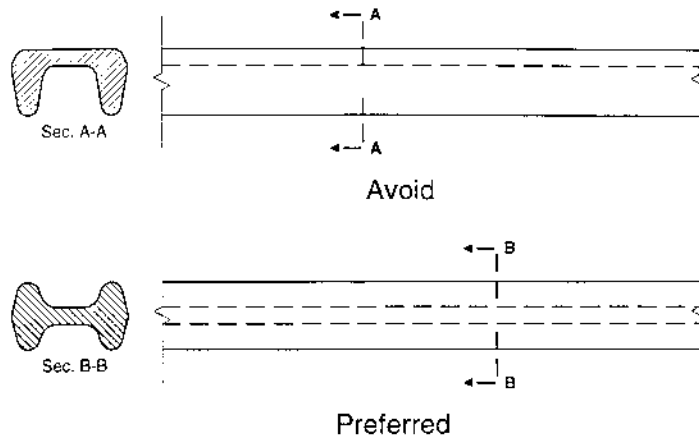
Figure 16 Avoid asymmetrical distribution of metal since this can cause distortion, especially in long castings.
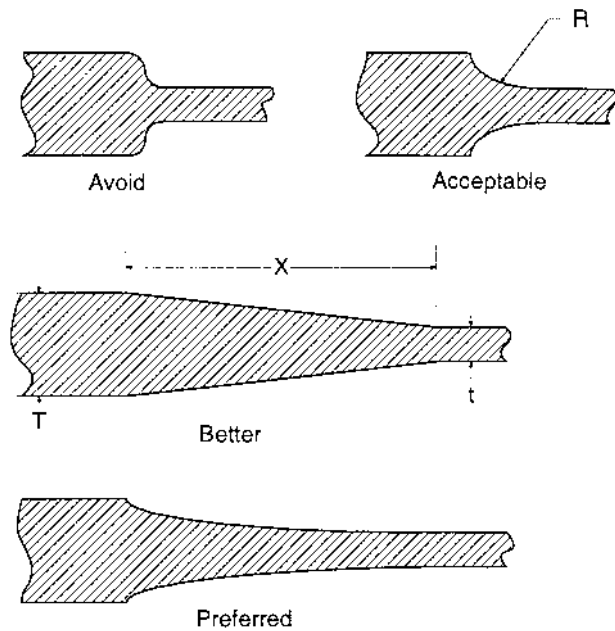
Figure 17 If a heavy section is unavoidable, transition to thinner sections should be blended over a significant length, preferably by using a smooth parabolic arc. Recommended values for R and X are: $0.3T \leq R \leq 0.5(t + T)$ and $3T \leq X \leq 4T$. The designer should consider the characteristics of the alloy and casting process as well ad the requirements of the application to select the best value.
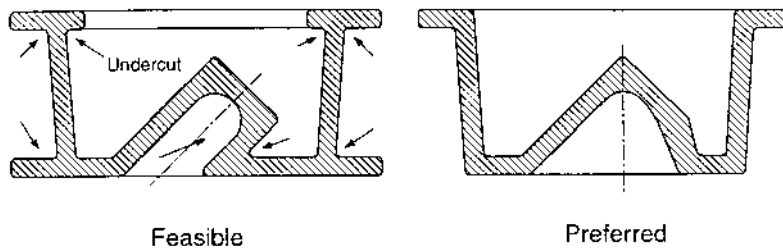
Figure 18 External and internal undercuts can be readily cast, but such features require sand cores, loose pieces, collapsible cores, moving cores, or complex parting planes. Using any of these increases tooling and production costs. Whenever possible, no cores or simple cores with core pull direction normal to the parting plane is preferred.

- Provide flat surfaces of ample size to support the casting in the furnace. Avoid large thin walls and irregular contours that have no flat surfaces. Castings that are difficult to support will distort during the high temperature treatment.
- Avoid large areas of relatively thin and unsupported walls, as these are likely to sag out of shape or position.
- Avoid relatively long and thin shapes, especially those with unequal walls and unsymmetrical metal distribution (Fig. 16). Such shapes will require supporting racks to prevent bending and can also warp during quenching. Although straightening operations may correct this, straightening is costly and may cause small hard-to-find cracks.
- Avoid sudden and drastic variations in wall thickness. Such features can introduce severe residual stress as well as wide variation in mechanical properties (Fig. 17).
- Avoid casting configurations that might prevent almost simultaneous contact of the quenching medium with all surfaces of the casting. A rapid and uniform quench is necessary to insure good and uniform mechanical properties and to reduce residual stress.
- Avoid large, hard to handle shapes that are not easily transferred rapidly and safely to the quenching tank. Quenching needs to take place within 30 sec after the casting is removed from the furnace to achieve optimum results.

When these guidelines cannot be followed, the designer is advised to consider the selection of an alloy that is suitable for lower temperature aging-only heat treatment or an alloy that is self-aging. This avoids the limitations associated with the T4 cycle as well as the expense of this cycle.

Design for Machining. Suggested guidelines for ease of machining include the following [7]:

- Reduce the volume of material to be removed.
  - Minimize the size of surfaces to be machined.
  - When possible, minimize machining allowances. Small surface size and less accuracy require less machining allowance.
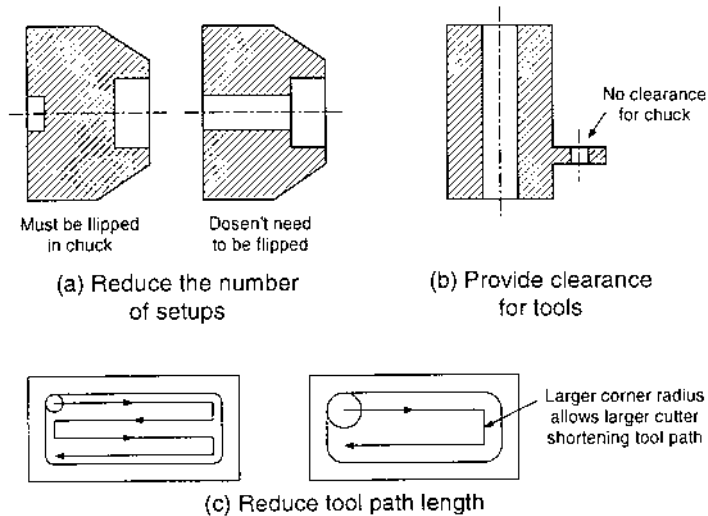
Figure 19 Approaches for simplifying the machining of a casting. (From Ref. 7.)

- When possible, specify alloys and heat treatments that result in good machinability.
- Avoid tight tolerances.
- Avoid excessively smooth surfaces.
- Drive toward a minimum number of machining setups and operations.
    - Design the casting so that all machining is performed on orthogonal and/or parallel surfaces (e.g. design so that all drilled holes are orthogonal to a machined surface).
    - Design so that all processing in one direction can be completed before moving to the next.
    - Minimize the number of machining directions (Fig. 19(a)).
- Insure access to surfaces that are to be machined.
- Provide clearance for tools (Fig. 19(b))
- Specify features such as fillet radii that allow shorter tool path lengths (Fig. 19(c))
- Use standardized features; avoid non-standard features whenever possible. For example, use only one standard fillet radius and one standard thread size.
- Avoid sharp angles, edges, and corners as these features typically cool faster resulting in harder to machine material properties.

11 CONCURRENT ENGINEERING

Casting design is the first step in the multi-step process that is required to introduce a new casting into production (Fig. 20). All of the steps that follow the initial casting design are dependent on and often constrained by the casting geometry that is specified in this first, and most important step. Ideally, the casting geometry should afford the foundry and toolmaker the greatest possible latitude to seek rigging system and
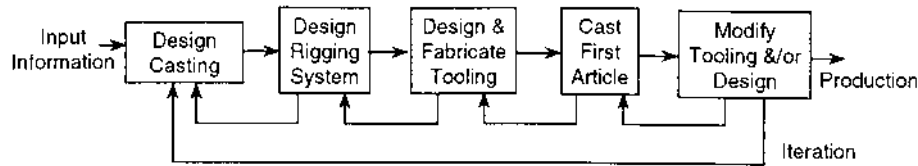
Figure 20   Casting development process.

tooling approaches that maximize the soundness and quality of the casting for the least possible cost and in the shortest possible lead time. It is therefore essential that the requirements of the "downstream" steps be properly considered in the casting design. *Concurrent engineering* is the term used to describe design processes in which all "stakeholders" including foundry, tooling, and secondary processing interests are represented from the beginning.

The concurrent engineering approach is needed in casting design because the process of designing a casting is iterative. The problem of design is typically formulated in terms of functional requirements and constraints that must be satisfied. Functional requirements relate to the functions the part must provide while constraints relate to the form (shape, size, surface finish, precision, etc.) and processing (parting line, draft, section thickness, etc.) requirements that constrain the geometry that can be selected. Based on the problem formulation, an initial design is created. This design is then evaluated and modified *iteratively* until an acceptable design is achieved. Typically, the redesign is guided by the design information, insight, and understanding that is developed in the evaluation step. To be acceptable, the design must satisfy all functional requirements and constraints.

When the casting development process is examined, it is seen that the iterative process is essentially repeated at least two and perhaps several times (Fig. 20). First the design engineer goes through the iterative design process to specify the casting geometry. This geometry is then passed on to the casting engineer who repeats the iterative design process to specify the rigging system and apply pattern maker shrink to the casting dimensions. Problems discovered during rigging system design can generate additional iterations if casting geometry changes are required. Additional iterations to the casting geometry and rigging system design may also be required during tool fabrication and preparation for production of the first article. Finally, iterative changes to the tooling and perhaps the casting and rigging system geometry may be necessary to "tweak" the design to meet production requirements.

Excessive design iterations can adversely impact the casting design in two important ways. First, design iterations significantly increase design cost and time. Second, design iterations, especially those performed late in the process, can lead to suboptimal design. The result is a casting that falls short of cost, weight, and performance targets.

11.1   Improvement Strategies

Concurrent engineering seeks to improve the casting design process by implementing the following strategies. The goal of these strategies is to shorten the design cycle and help ensure that the best possible casting design is created.

1. Develop a thorough understanding of all customer needs including downstream processing constraints before beginning the design.
2. Design the casting geometry and casting process as a coordinated system by integrating casting geometry and rigging system design into one concurrent process. Consider geometry, material, and process interactions and design related cost drivers from the beginning as part of the process.
3. Focus on creating an acceptable initial design. By spending the time "up-front" to create the best possible initial design, a large number of lengthy analyze-redesign iterations are avoided. The evaluation phase should confirm the design rather than create it.

11.2   Structured Team Approach

One way to implement concurrent engineering in casting design is to use a structured team approach. In a *structured team approach*, the casting design is performed using a multi-disciplinary team and a structured design methodology. The goal is to have all required product and process knowledge available when the key early design decisions are being made. In a structured design methodology, the overall problem of design is broken down into a series of sequential, easier to perform steps that proceed from the general to the specific. Excessive iteration and long design times are avoided by performing each step in a thorough and disciplined manner. In general, each step in the process can be further subdivided into steps to create a hierarchy of structured methodologies.

To illustrate the structured team approach, consider the simple methodology shown schematically in Fig. 21. This approach, which is derived from the general discussion of structured team approach presented in [7], recognizes that not all members of the team can be available for designing the casting on a continuous basis. Team meetings are therefore scheduled at which all salient aspects of the design are reviewed and discussed. The outcome of each meeting is a set of action steps to be implemented by individual team members. In this way, all team members are kept informed and participate in the design decision making process. At the same time, the actual detail work of creating the design is delegated to specific team members according to the skills and knowledge required. Each step of the methodology is briefly discussed as follows:

Step 1: Form Team. This is the pivotal first step in the methodology. A typical team might include a design engineer, a casting engineer, a tooling design engineer, and perhaps one or more specialists who are familiar with casting process simulation software, finite element analysis, fracture mechanics, non-destructive evaluation (NDE) techniques, and so forth. In addition, it is important that the end customer, the foundry that is to make the casting, and others concerned with secondary processing that is to be "farmed out" be properly represented on the team. This not only helps ensure that all customer and processing needs are appropriately considered, it also makes it possible to rapidly negotiate changes to the design specification when necessary, and to quickly assess cost consequences of design decisions.

Meeting 1: Clarify the Design Problem. Clarifying the problem consists of developing a general understanding of the cost, performance, and manufacturing goals and constraints of the design. A typical agenda for this meeting might include the following:
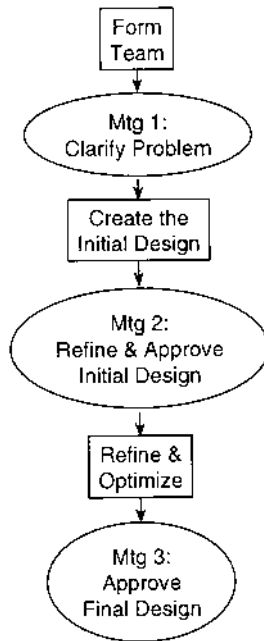
Figure 21 Simple structured team approach. (From Ref. 7.)

1. Review product background
2. Customer requirements and design objectives
3. Expected annual production volumes and target costs
4. Geometry concepts and alternatives
5. Material and processing options
6. Foundry and secondary processing locations
7. Potential geometry/material/process interactions
8. Develop a preliminary configuration design
9. Make assignments to team members to create the initial design.

Step 2: Create the Initial Design. The initial design establishes the detail layout of the casting geometry. It includes the configuration and parametric design of the part together with the rigging design required to fill the mold cavity and feed the solidifying casting. Configuration design involves the determination of what features such as walls, holes, ribs, etc. will be present and how these features will be connected to provide the desired form, fit, function, and manufacturability (e.g. parting line, coring, and draft for low tooling cost, short cycle time, and minimal trimming and secondary processing). Parametric design involves the determination of dimensions, tolerances, and exact material specifications needed to meet durability, stiffness, and/or natural frequency targets. As discussed previously, rigging design involves the location and sizing of the sprues, runners, gates, and risers.

Meeting 2: Refine and Approve the Initial Design. The goal of this meeting is to react as a team to the initial design and to make any adjustments or modifications deemed necessary by general consensus of the team. This is the time when all design

and processing issues should be discussed and resolved. If there are significant impediments to the design as proposed, these should be resolved before proceeding to Step 3.

Step 3: Refine and Optimize the Design. Once the team is confident that the initial casting geometry and rigging design is the best solution possible, the effort required to optimize details of the casting geometry and rigging system by computer analysis can be justified. The goal of this step is therefore to computer model the design and iteratively improve it until all aspects have been appropriately optimized. The amount of effort expended on this step will depend on how important it is to optimize the casting. For example, if weight and/or material cost is critical, extensive effort to minimize the amount of material used can be justified. Similarly, if safety is an important issue, comprehensive analysis to ensure acceptable fatigue life and reliable detection of flaws can be justified. The key to this step is to start with a casting geometry that is close to the optimum. This will minimize the time, analysis effort, and number of iterations required to converge to the optimum design.

Meeting 3: Approve the Final Design. The result of Step 3 will be a fully specified casting design including the detailed casting geometry, parting plane, draft, coring, riser locations and sizes, and rigging system design. In addition, the finished part design including machining, heat treating, and so forth will be fully specified. The purpose of Meeting 3 is to formally review the finished design as a team and approve the design for release to manufacturing. When the structured team approach is performed properly, the final design will almost always be approved. However, if the team decides that the design is not ready to be released, then appropriate action plans for correcting design deficiencies must be developed and implemented. One or more follow-on meetings may then be required before the design is released.

11.3 Barriers

Although simple in concept, concurrent engineering can be difficult to implement because of long standing casting procurement practices employed by many firms. These practices, such as the requirement that a competitive bidding process be used to select the foundry, often present a major barrier to an effective concurrent engineering casting design process because they force separation between casting design and the foundry. Finding creative ways to eliminate or overcome this unnatural separation is essential for the effective design of castings that meet cost, quality, and performance targets and that also transition into production in a timely and cost-efficient manner.

REFERENCES

1. M. Tiryakioglu, J. Campbell, and N. Green, "Review of Reliable Processes for Aluminum Aerospace Castings." Transactions of the American Foundrymen's Society. Vol. 103 Paper 96–158, 1996, pp. 1069–1078.
2. Military Handbook 5F: Metallic Materials and Elements for Aerospace Vehicle Structure. Department of Defense. November 1990.
3. D. McLellan. "Understanding Casting Factors in Aircraft Components." Modern Casting, October 1994, pp. 21–24.

4. *Tool and Manufacturing Engineers Handbook*, Vol. 6, 4th ed. Design for Manufacturability. (Ramon Bakerjian, Ed.), Society of Manufacturing Engineers, Dearborn, Michigan; 1992. Chap. 12, pp. 74–88.
5. M. Burns, *Automated Fabrication*, PTR Prentice Hall, Englewood Cliffs, NJ; 1993.
6. Dietmar Mietrach, (ed.), *AGARD Handbook on Advanced Casting*, AGARDograph No. 299. North Atlantic Treaty Organization Advisory Group for Aerospace Research and Development, 1991, pp. 14–16.
7. H. Stoll, *Product Design Methods and Practices*. Chap. 8, Marcel Dekker, New York, 1999.

11

Modeling of the Filling, Solidification, and Cooling of Shaped Aluminum Castings

JOHN T. BERRY and JEFFREY R. SHENEFELT

Mississippi State University, Mississippi State, Mississippi, U.S.A.

1 INTRODUCTION

That the digital computer has had a major impact on design and process engineering in the last 30 years is undeniable. Although finite difference and finite element based computational methods, as applied to stress analysis related problems, were becoming well established by the late nineteen sixties, the modeling of the solidification process had only just begun.

Currently, aided by burgeoning computational power, one is now able to model numerous aspects associated with the production of shaped castings including,

- Casting Filling
- Solidification and Cooling
- Microstructural Evolution
- Residual Stress Pattern Formation
- Heat Treatment,

together with some aspects of predicting mechanical behavior.

This chapter summarizes some of the salient aspects of heat transfer and fluid flow related modeling such as,

- Early developments
- Thermophysical data and boundary conditions
- Geometric description and discretization
- Computational techniques for solidification and filling

- Validation of contemporary casting models
- Guidelines for rigging design
- Criteria and techniques for assessment of modeling output

2   EARLY DEVELOPMENTS

The potential for computational methods as a design tool in solidification processing first became apparent during the 1940s, when under the sponsorship of the American Foundrymen's Society's Heat Transfer Committee, Paschkis and his co-workers studied the freezing of simply shaped castings using the analog computer (see Ref. 1). However, the basic impracticality of manipulating complex banks of resistors and capacitors, together with numerous manual switches, did not seize the imagination of the foundry engineer at that time. The advent of the digital computer in the 1960s changed this by facilitating the modeling of shaped casting solidification.

Fursund [2] in Denmark is acknowledged as the first individual to apply this tool to shaped casting problems. In 1962 he studied the diffusion of heat into foundry sand and its effect on the surface finish of steel castings. Soon after this work was published, the first large-scale application, again to steel casting, was made by Henzel and Keverian of G.E. [3]. In 1965 their study of solidification patterns in large steel castings appeared.

A long term investigation then commenced sponsored by AFS, again guided by their Heat Transfer Committee and conducted by Pehlke's group at the University of Michigan. An important monograph describing this early research was published through AFS in 1976 [4]. The computational technique used was the finite difference method, as was the case in many of the early studies.

During the period from 1973 to 1984, further Scandinavian contributions (Davies and co-workers, in Norway [5–7] included some of the first simulations of the freezing of aluminum alloy castings in sand and permanent molds (gravity die casting). However, the first applications of the digital computer to truly commercial aluminum castings (i.e. castings in production, where the computer was in use as a diagnostic tool) were included in the proceedings of the first Conference on the Modeling of Casting and Welding Processes (1980). Riegger of Tecumseh Products Company and Grant of Ford Motor Company described the use of the computer in the process design of die castings and low-pressure permanent mold castings, respectively [8,9].

Both of these contributions are noteworthy for their discussion of the thermophysical properties and boundary conditions associated with the casting and melting media. Additionally, both discuss cycling effects on mold temperature. Finally, both studies indicated how shrinkage defects can be relocated or eliminated with the aid of the then current computational techniques. Figures 1 and 2 show results and casting geometries associated with the solidification patterns of a simple single cylinder engine block and a brake drum, respectively.

Recognition of the complexity of the thermal contract occurring between the casting and metallic molds was reported on earlier by Tillman and Berry in 1972 [10]. An early discussion of thermal contact related issues is contained in Ref. 11. Current developments in this area will be discussed as part of the following section of this chapter. A more complete picture of the general history of computer applications in shaped casting may be found elsewhere [12].
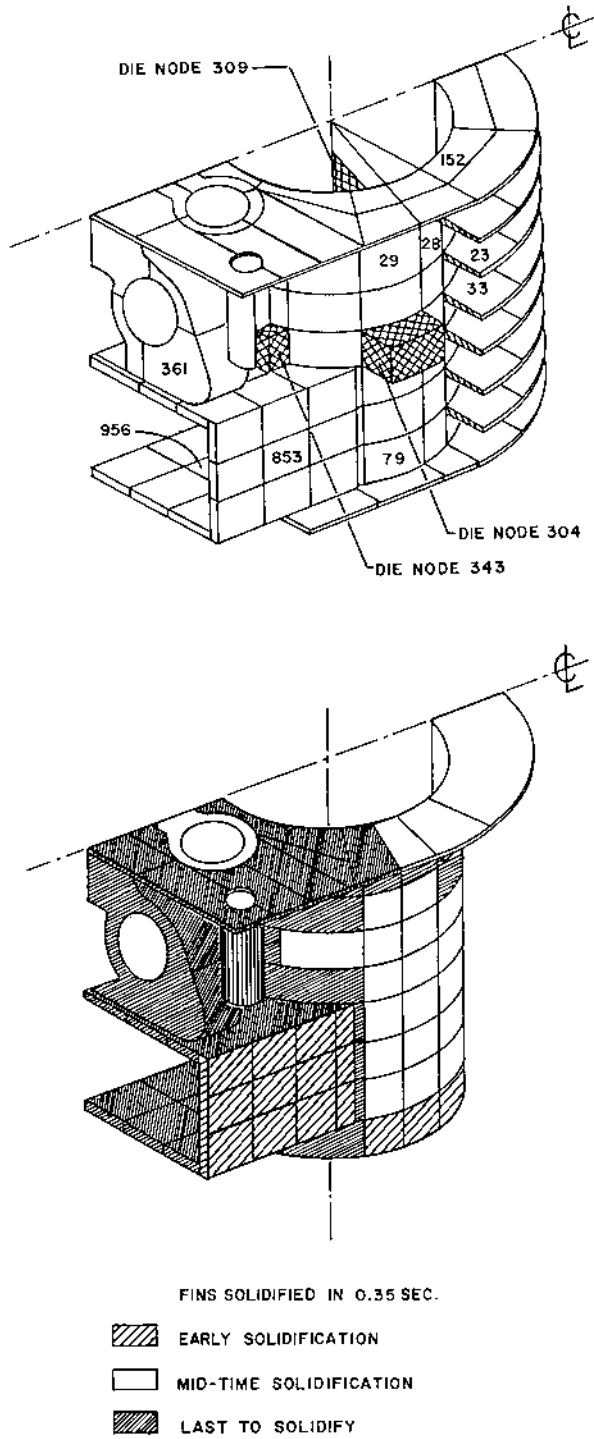
Figure 1 (Top) basic configuration of cylinder block casting (die-cast in alloy 380). (Bottom) the solidification sequence predicted. (From Ref. 8.)
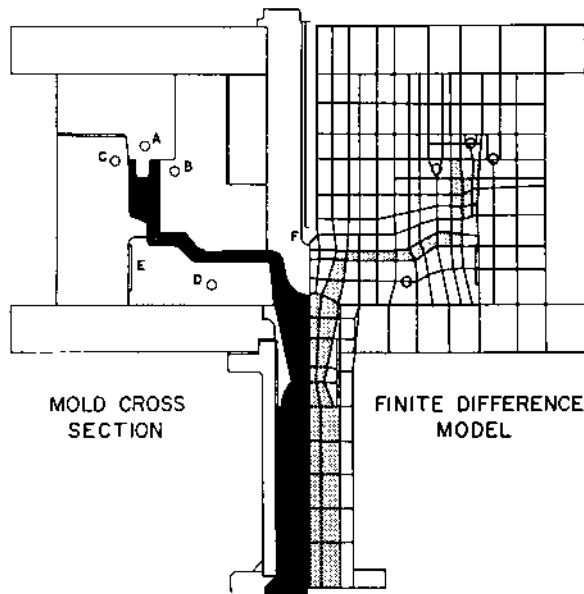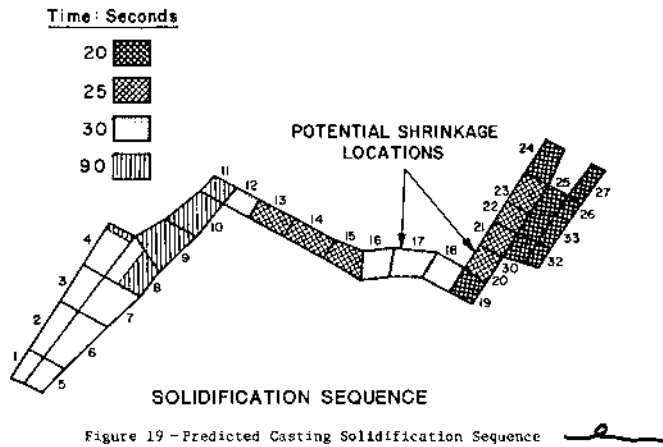
Figure 2 (Top) the discretization of the low-pressure permanent mold and casting together with thermocouple locations. (Bottom) potential shrinkage locations deduced from the solidification sequence and subsequent validated by sectioning. The casting concerned is a brake drum in alloy A355. (From. Ref. 9.)

The subsequent-growth of interest in the computer modeling of casting, especially over the last decade, has resulted in a number of highly successful modeling codes being developed, brought to market and being employed in progressive foundries across the world. A review of commercial programs available in the United States in May 1999 was published in the magazine Modern Casting. The article listed eight such codes, most of which are capable of simulating both

filling and solidification, and in some cases microstructural evolution and residual stress and/or distortion patterns [13]. A number of these modelers also contain their own databases of thermophysical properties and appropriate boundary conditions.

3 THERMOPHYSICAL DATA AND BOUNDARY CONDITIONS

As was pointed out, several early publications [6,8–10] recognized the problems associated with the lack of data capable of describing both thermal properties and boundary conditions. In particular, the selection of heat transfer coefficient data associated with mold-metal, mold-mold, and mold-external environment type contacts can become a critical issue.

Although the very early analog computer based simulations had assumed perfect thermal contact, as was true in all previous mathematical models of sand casting, the pioneer work of Pehlke et al. made clear that even the contact in such cases as sand casting is imperfect. The series of papers from this group examining both metal/mold gap formation and heat transfer coefficient estimation for a variety of contacts is still highly relevant [14–17]. A recent publication of Griffiths [18] contains a valuable review of early experiments together the results of more contemporary work.

Thermal contact with metallic chills, which is also germane to the problems associated with metallic molds, where a gap between the solidifying metal and the mold leads to a serious thermal discontinuity, has attracted much attention since the work of Pehlke et al. Figure 3 contains data obtained by Griffiths [18] for Al-7%
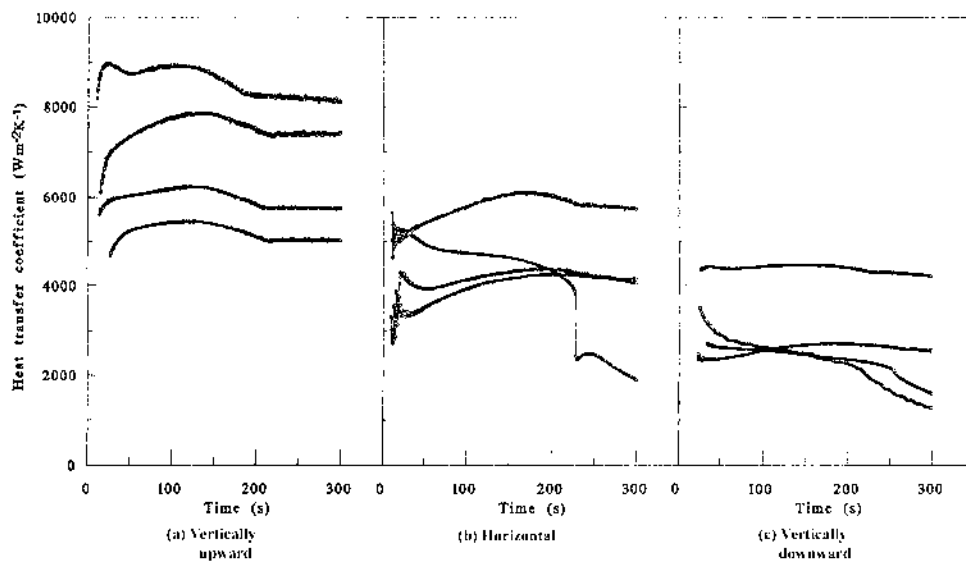
Figure 3   The effect of orientation in the heat transfer coefficient-elapsed time pattern for contact between Al-7% Si and a metallic chill. (From Ref. 18.)
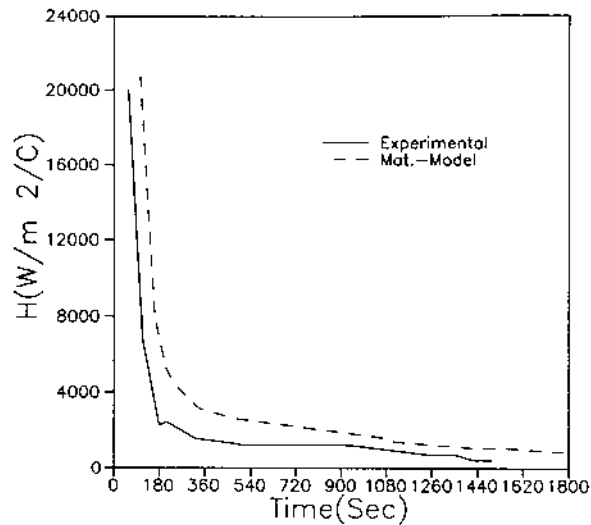
Figure 4 Temporal variation of heat transfer coefficient at metal-sand mold interface as modeled and as calculated from thermocouple measurements. Alloy is Aluminum-12% Si eutectic. (From Ref. 20.)

Si in contact with a metallic chill in various orientations. This work shows clearly how contact is affected by gravity. This research also confirms the difficulty which some workers have experienced in obtaining good reproducibility, which will be discussed later.

Thermal contact in sand and investment castings has also attracted attention in the open literature [11,17,19–26]. The determination of heat transfer coefficient (h_c) related data undertaken by Shahverdi et al. [20] for Al-12% silicon eutectic alloy cast in a sand mold is an example (Fig. 4). Again the strong dependence on elapsed time will be seen as the casting solidifies and shrinks away from the mold. Basically similar trends will be seen in Fig. 3 and 4, both of which show the marked temporal variation.

Shenefelt [27] has examined the effects of the methods employed to analyze thermocouple data gathered in such determinations using inverse methods to determine h_c. His conclusions indicate that serious uncertainties may well occur during this procedure.

In order to determine the heat flux entering a mold or the contact conductance between the mold and the solidifying material, one must use caution because large errors may occur because three sets of data are never fully known. First, inverse methods are highly susceptible to small levels of noise in temperature data. The noise contained in temperature data is never systematic and therefore filtering must be employed to calculate heat flux and thermal contact conductance. If the filtering procedure is not done properly, important data may be lost using the inverse procedure. Second, the exact location of a thermocouple(s) is never known with complete accuracy and since the inverse model is highly sensitive to thermocouple location further uncertainty arises. If the uncertainty in thermocouple location
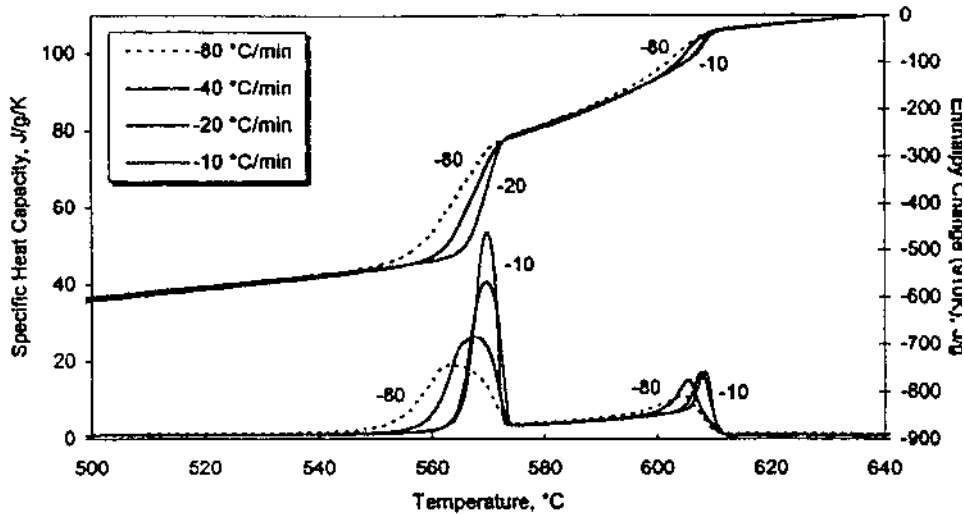
Figure 5 The measured specific heat capacity and enthalpy of the aluminum alloy LM25 as a function of temperature at various cooling rates. (From Ref. 30.)

is high (0.5 mm) the uncertainty in heat flux or contact conductance may be high enough to render the calculated data unusable. Third, most mold material properties are functions of temperature and are not clearly defined. Thus, if these properties are highly dependent on temperature and a linear simplification is employed in the inverse procedure, uncertainties in the results will occur because of the linear modeling procedure. However, it is important to note that inverse methods are much more sensitive to noise and accuracy of thermocouple location than when a linear simplification is used to model a non-linear physical situation [28,29].

At the time of writing (1999), the provision of a thermophysical data base for common casting and molding media concerning for example:

- Thermal conductivity
- Specific heat
- Density
- Latent heat
- Viscosity,

although still incomplete, has at last attracted the attention of a number of major laboratories. In particular the work currently in progress at the UK's National Physical Laboratory (NPL) represents such an effort. Figure 5 shows the variation of specific heat with temperature for an Aluminum-7% Si-Mg alloy as obtained by this group [30].

Prior to this recent resurgence of interest, the 1982 compilation of thermal properties provided by the University of Michigan Team of Pehlke et al. had remained the most reliable database for some 15 years [31].

4   GEOMETRIC DESCRIPTION AND DISCRETIZATION

Before any simulation of the pouring and solidification of a shaped casting can be undertaken, the basic geometry of the casting, its rigging (i.e. risers and gating system) as well mold detail must be accurately described. This will include the incorporation of draft, filleting, chamfering, and radii, since such detail affect both fluid flow and solidification.

A partial history of developments to 1988, which is to be found elsewhere [12] describes progress through simple wire-frame, boundary representation to truly three-dimensional constructive solid geometry based routines. Currently, many of the available commercial modelers contain at least a simple form of geometric representation. However, most are also capable of accepting files from popular computer aided design (CAD) packages.

Modeling packages can be broken into two main categories: finite difference and finite element. Finite difference modeling packages divide the area or volume of interest into smaller sub areas or volumes typically employing a structured grid. Structured grids contain ordered smaller areas (typically squares/rectangles or triangles) or volumes and therefore require many smaller units to model complex shapes. In many finite difference packages only one grid size or spacing arrangement may be employed. Therefore, if one must employ small volumes to obtain the required level or discretization in one particular area, this level of discretization must be employed throughout the entire model. This often results in finite difference models being very large and time consuming to run. Finite element packages have the ability to divide the area or volume of interest into sub areas or volumes employing an unstructured grid. An unstructured grid does not contain any extended order per se, but allows complex shapes to be modeled with fewer sub volumes than finite difference models because the element sizes are not fixed. This permits finite element packages to divide the area or volume up into sub areas or volumes using an adaptive or grid that can change fineness depending on location, resulting in a more numerically efficient model.

At the present time both finite difference and finite element schemes are in use in commercially available modeling packages.

5   VALIDATION OF CONTEMPORARY CASTING MODELS

The proof of the success of any model, whether analytical or numerical, hinges on the comparison of the model results with those of experiment.

Where only heat transfer during solidification is of interest, the validating medium will be the output of thermocouples placed in the mold or in the casting, although the latter becomes difficult physically if a monolithic metallic mold is involved.

Clearly the thermocouples employed should have a minimum thermal mass to promote both rapid response and to prevent disturbance of the thermal fields involved. Also they should enter the casting parallel to the expected isotherms to minimize conduction along the thermocouple wires.

The problem of determining temperature-time profile at the periphery of the solidifying casting was satisfactorily dealt with many years ago by Atterton and Houseman [32] by the use of an open ended thermocouple (no bead). Bare wires
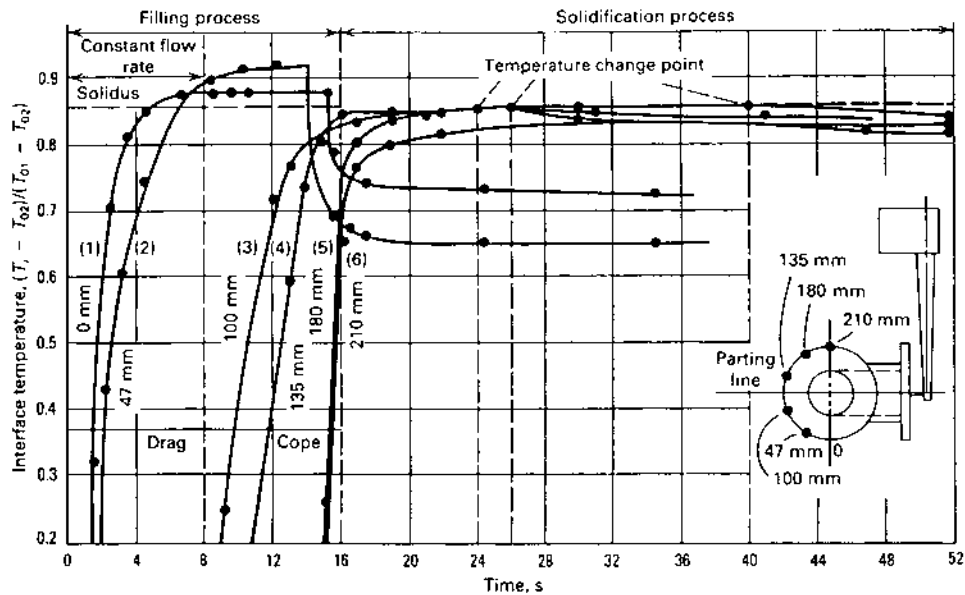
Figure 6   Mold/casting interface temperature variation at different locations during filling and solidification of a small valve body. (From Ref. 33.)

protruding from the mold are connected by the incoming molten metal and thereby the skin temperature recorded.

Temperature fields during the filling of the molten metal are equally difficult to obtain. Desai [33] appears to be one of the few investigators examining this particular problem. Although the work was conducted with a cast iron the same trends would be expected with a cast aluminum alloy. (Note the temperature at the mold-metal interface is shown in non-dimensional form, Fig. 6).

Similarly, validation of the flow patterns predicted by current code handling coupled fluid flow and heat transfer presents problems. Such information is of cardinal importance in aluminum castings where the inadvertent incorporation of the tenacious but brittle solid oxide films into the mold cavity has serious consequences. This effect has been researched in considerable depth by Campbell and his co-workers [34] at Birmingham University in the UK. Mechanical tests performed as samples of a sand-cast aluminum-7% silicon alloy indicated that liquid metal entry speeds greater than 0.5 m/sec invariably lead to oxide incorporation and thus poor mechanical behavior. (This will be discussed later.)

The Birmingham team followed up this work with carefully conceived real-time x-ray studies of molten aluminum entering a bottom-gated, vertically-parted sand-cast plate. Figure 7 shows the basic configuration of the subject casting [35], while Fig. 8(a) and (b) shows the results of a simulation which closely approximated the experimental observations. The simulation was undertaken by Ohnaka and Zhu of Osaka University [36].
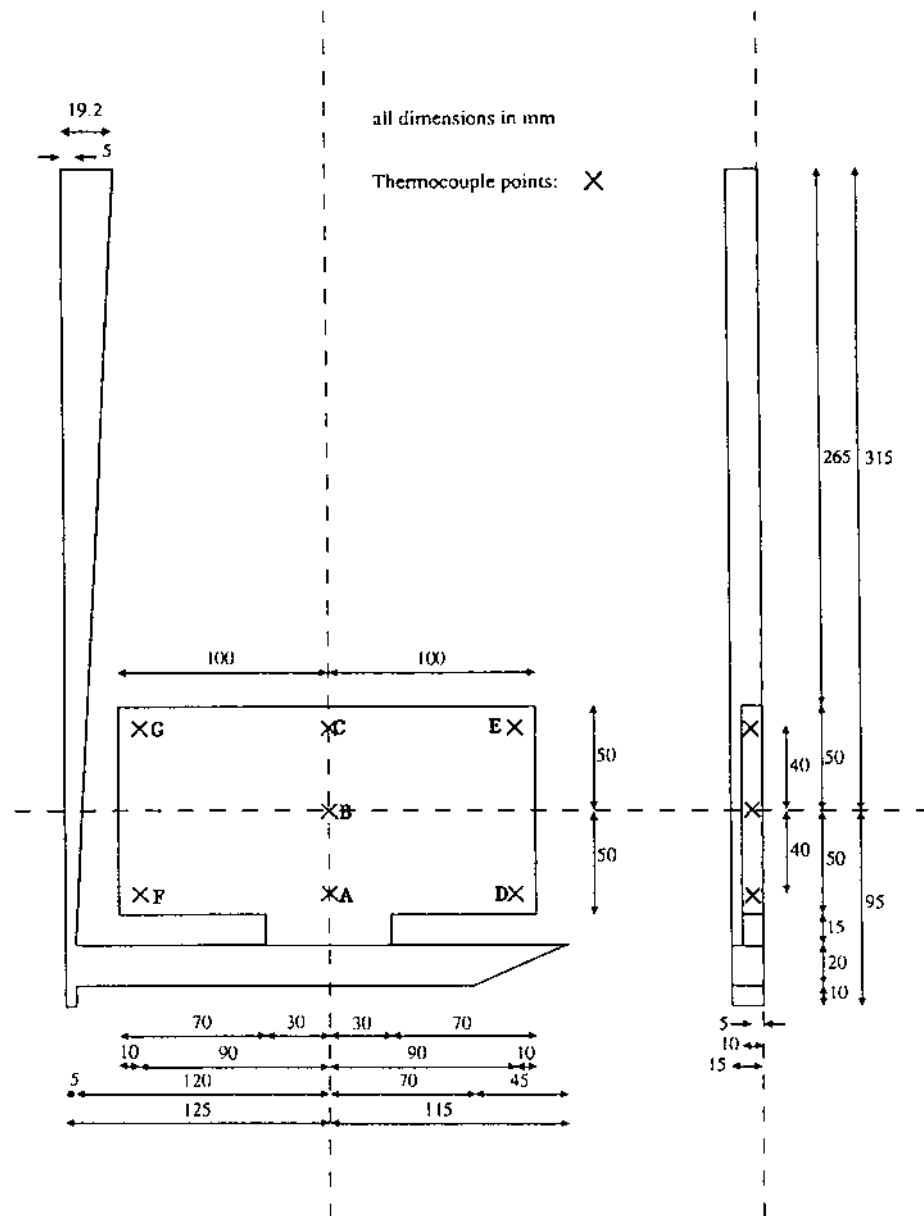
Figure 7 Configuration of vertically cast plate simulated in Fig. 8. (From Ref. 40.)

6 GUIDELINES FOR RIGGING DESIGN

In spite of the growing number of foundries applying computer modeling to assist in solving gating, filling, and feeding system related problems, surprisingly little progress has been made in building quantitative guidelines or even expert systems capable of designing such features.
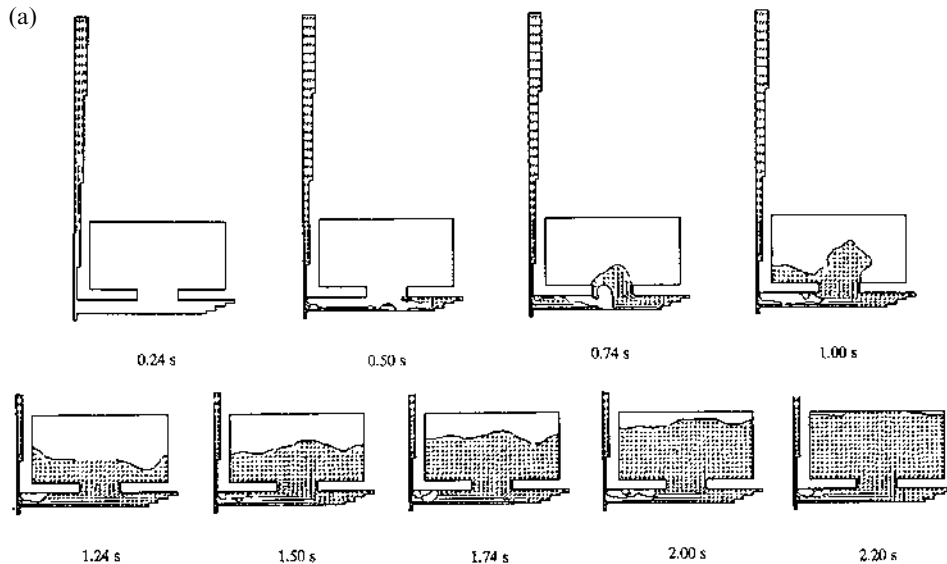
(a)

Figure 8 Results of coupled fluid flow/heat transfer simulation of vertically cast plate (99.999% pure aluminum in resin-bonded sand as performed by Ohnaka and Zhu. (a) flow sequence.

For the most part, guidelines provided by empirical information have been used by many foundry engineers in designing gating systems. This information has been drawn mainly from the recommendations of experimental work on aluminum alloys conducted at the Battelle Memorial Institute in the early 1950s [37], which resulted in recommended gating area ratios and other aspects of such systems. A scholarly review of this and previous work was conducted by Ruddle soon after the appearance of the Battelle work [38].

However, the more recent the work at Birmingham University correlating the speed of entry of the metal stream into the mold cavity proper with mechanical integrity of samples taken from the casting, has resulted in the establishment of the new criterion mentioned earlier. Runyaro et al. [34] stated that critical entry velocities exist for oxide-film forming alloys (for aluminum base approximately 0.5 m/sec).

Velocities above this value will incorporate oxide films into the molten metal stream resulting in porosity and weak interfaces and hence poor mechanical performance.

The principle of the well-known Cosworth Process, where metal is pumped in quiescently from the bottom of the mold, is an example of a technique which overcomes this difficulty of inadvertent oxide incorporation through quiescent metal entry into the mold. After filling the mold is then inverted to enhance feeding. The Rover process involves a similar approach, however the mold is not inverted after pouring. The technology of the electromagnetic pumping systems involved have been discussed by Gouwens [39].

As a result of the studies at Birmingham, Campbell has presented a new set of guidelines consisting of ten basic process design rules [40] concerning:
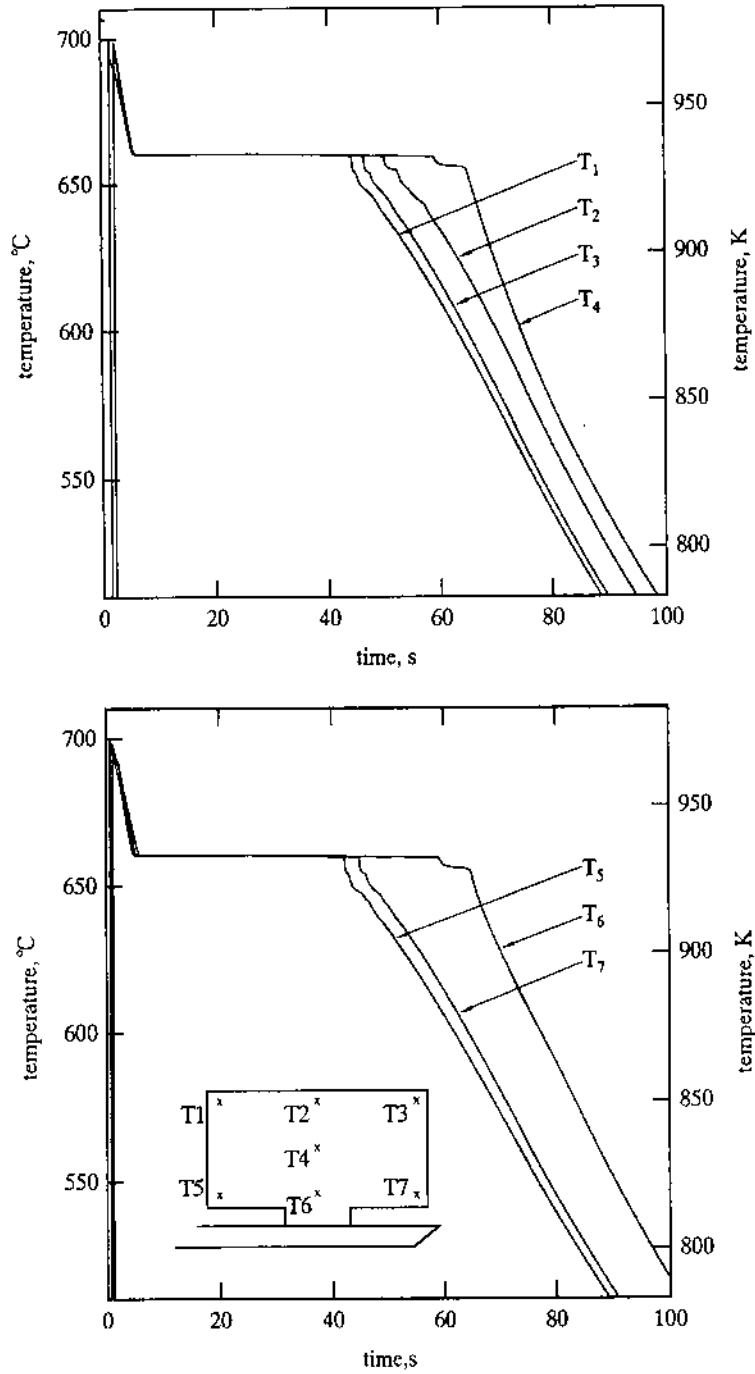
Figure 8 Results of coupled fluid flow/heat transfer simulation of vertically cast plate (99.999%) pure aluminum in resin-bonded sand as performed by Ohnaka and Zhu. Temperature-time data, both as predicted.

- A good quality melt
- The minimization of liquid front damage in pouring and filling
- The elimination of liquid front stops
- The avoidance of bubble damage
- The avoidance of core blows
- The prevention of shrinkage damage
- The minimization of uncontrolled convention
- The minimization of segregation
- The avoidance of residual stress
- The provision of agreed location points for assessment of dimensional accuracy and facilitation of machining operations

The rules do not contain specific (i.e. quantitative) recommendations regarding feeder placement and dimensioning, however.

The topic of riser design has been discussed recently by Tiryakioglu and Berry [41]. The questions of both placement and dimensioning of risers are discussed. An alternative to the well-known Chvorinov rule which relates solidification time to volume/surface area (casting modulus) is proposed incorporating volume only and a shape factor. Each thermal center in the casting must be treated as a potential source of shrinkage and a riser dimensioned to preclude this shrinkage. The paper also reviews the estimation of feeding range in connection with feeder placement.

Many foundry engineers still follow the recommendations of Jacob and Drouzy [42] who advocated from their experiments with both Al-7% Si and Al-5% Cu alloys that feeder moduli and volumes obey the following: rules:

$$\left(\frac{V}{A}\right)_{\text{feeder}} \geq 1.5\left(\frac{V}{A}\right)_{\text{casting}}$$
$$V_{\text{feeder}} \geq 0.5 V_{\text{casting}}$$

where V and A are volume and area, respectively.

7   CRITERIA AND TECHNIQUES FOR ASSESSMENT OF MODELING OUTPUT

A second stage in rigging design involves interrogation of the predictions of the computer model of the casting plus rigging design provided by the previously discussed guidelines, or from prior experience.

A case in point concerns the avoidance of unacceptable levels of dispersed porosity in cast aluminum alloys. This interrogation involves examining local values of certain criteria functions involving solidus velocity, temperature gradient at the freezing front, or cooling rate. Taylor et al. have conducted a critical evaluation of such criteria [43].

After examining the experimental work of Lee et al. [44] for Al-7 Si-Mg a number of conclusions were drawn concerning the effectiveness of criteria functions. Although they did not fully account for the variation of dispersed porosity, they did provide a general guide. A popular criterion, that of Niyama et al. [45] relates local temperature gradation at the freezing front (G) to local cooling rate (R) using

the expression:

$$\frac{G}{\sqrt{R}}$$

Taylor et al. re-derived all the commonly used criteria and indicated how they could be written in terms of two parameters, either G, or V_s, the local values of the temperature gradient and the velocity of the solidus front respectively, or both. Analysis of the data of Kao et al. [46] correlates the dependence of experimentally determined percentage porosity upon the modified form of the Niyama criterion computed as:

$$\frac{V_S}{G}$$

and initial hydrogen content of the melt in Al-7 Si-Mg, (Fig. 9). Using such partly experimental, partly computed data, acceptable levels of dispersed porosity can be expected.

8   CONCLUSIONS

Although many heat transfer and fluid flow aspects involved in the modeling of aluminum casting, especially in the stages of filling, solidification and cooling are reasonably well understood, there are still a number of factors which limit the extent to which such modeling is applied in the metal casting industry.

Among these factors are:

1. Provision of accurate thermophysical data and appropriate boundary conditions, as they apply to the casting and modeling media.
2. Reduction in person hours and computer time in describing and discretizing geometry of casting and rigging.
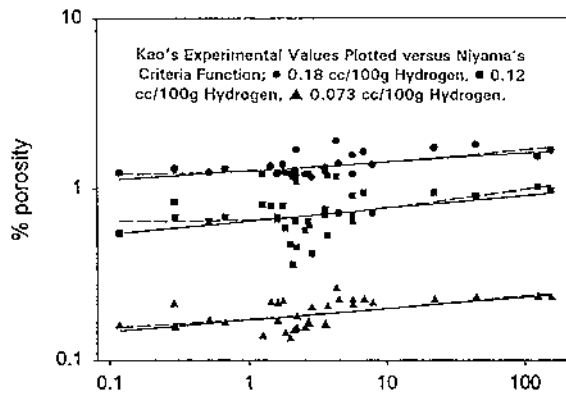
Figure 9   Illustrating use of criteria functions in the prediction of dispersed porosity in aluminum-7% Si-Mg poured with different hydrogen contents. Dotted lines represent log-quadratic relation, solid line represents power law. (From Ref. 43.)

3. Provision of adequate rigging design guidelines, preferably in the form of expert systems.

At the same time the extension of modeling techniques to the prediction of microstructural evolution, casting distortion and associated residual stress, for example, show a most encouraging trend and indicate the potential power likely to be made available in the near future.

REFERENCES

1. V. Paschkis, Transactions American Foundrymen's Society, Collected papers on analog simulation of solidification, 1945–1965, listed in Ref. 4 below.
2. K. Fursund, "Das Eindringen von Stahl in Formsand Einfluss den Oberflachenreaktion und Temperatur," Giesserei Tech. Beih., 1962, 14, pp. 51–61.
3. J. Henzel and J. Keverian, "Comparison of Calculated and Measured Solidification Patterns in a Variety of Casting," AFS Cast Metals Res. J., 1965, 1, pp. 19–30.
4. R. D. Pehlke, R. D. Marrone, and J. O. Wilkes, *Computer Simulation of Solidification*, American Foundrymen's Society, 1976.
5. V. de L. Davies, S. Stokke, and O. Westby, "Numerical Computation of Heat and Temperature Distribution in Casting," British Foundryman, 1973, 66, pp. 305–313.
6. V. de L. Davies, "Heat Transfer in Gravity Die Castings," British Foundryman, 1980, 73, pp. 331–334.
7. V. de L. Davies, "Modeling Solidification Processes and Computer Aided Design of Castings," *Proceedings of the Centennial Celebrations*, 1984, Univ. of Sheffield, pp. 101–113.
8. O. Riegger, in *Modeling of Casting and Welding Processes*, 1981, (D. Apelian and H. Brody, eds.), AIME, pp. 39–72.
9. J. Grant, in *Modeling of Casting and Welding Processes*, 1981, (D. Apelian and H. Brody, eds.), AIME, pp. 19–37.
10. E. Tillman and J. T. Berry, "Effect of Thermal Contact Resistance on the Rate of Solidification of Long Freezing Range Alloys," AFS Cast Metals Res. J., 1972, 8, pp. 1–6.
11. J. T. Berry, "The Role of the Metal/Mold Interface in Net Shape Aluminum Casting," in *Casting of Near Net Shape Products*, 1988, (Y. Sahni, J. E. Battles et al. eds.), TMS, Warrendale, PA, pp. 41–50.
12. J. T. Berry and R. D. Pehlke, "Modeling of Solidification Heat Transfer," in ASM Metals Handbook, 1988, 15, pp. 858–866.
13. T. Midea and D. Schmidt, "1999 Casting Simulation Software Survey," Modern Casting, May 1999, 89, pp. 47–51.
14. R. Ho, D. Kao, and R. D. Pehlke, "Metal-Mold Interfacial Heat Transfer," Metall. Trans., B, September 1995, 16B, pp. 595–594.
15. R. Ho, D. Kao, and R. D. Pehlke, "Mechanisms of Heat Transfer at a Metal-Mold Interface," AFS Trans., 1984, 61, pp. 587–598.
16. R. Ho, D. Kao, and R. D. Pehlke, "Transient Methods for Determination of Metal-Mold Interfacial Heat Transfer," AFS Trans., 1983, 80, pp. 689–698.
17. R. Ho, D. Kao, and R. D. Pehlke, "Determination of Metal-Mold Interfacial Heat Transfer and Simulation of Solidification of an Aluminum-13% Silicon Casting," AFS Transa., 1988, 91, pp. 129–136.
18. W. D. Griffiths, "The Heat Transfer Coefficient during the Unidirectional Solidification of the Al-Si Alloy Casting," Metall. Trans., 1999, 30B, pp. 473–482.

19. H. Huang, J. L. Hill, V. K. Suri, and J. T. Berry, in *Modeling of Casting, Welding and Advanced Solidification Processes V*, 1991, (R. Rappaz, M. Ozsu and K. W. Mahin, eds.), TMS, pp. 65–70.

20. H. R. Shahverdi, F. Farhadi, A. Karimitahari, P. Davami, and K. Asgari, "A Mathematical Model for Air-Gap Formation at the Mold-Metal Interface, etc.," Cast Metals, 1994, 6, pp. 231–236.

21. J. C. Hwang, H. T. Chuang, S. Jong, and W. S. Hwang, Trans. Amer. Foundrymen's Soc., 1994, 102, pp. 877–883.

22. Woodbury, Keith A., Chen, Yuhu, Ke, Quanpeng, Determination of Interfacial Heat Fluxes During Casting of Aluminum in Resin-Bonded Sand Molds, Paper Number HTD-324, *Proceedings of 1998 IMECE*, American Society of Mechanical Engineers, November 1998.

23. H. Huang and J. T. Berry, in *Collected Papers in Heat Transfer*, Vol. 1, 1988, ASME, pp. 93–99.

24. T. S. Piwonka and J. T. Berry, "Heat Transfer at the Mold Metal Interface in Investment Castings," 41st Ann. Technical Meeting: Investment Casting Institute, 1993.

25. J. T. Anderson, D. T. Gethim, and R. W. Lewis, "Experimental Investigation and Numerical Simulation in Investment Casting," Int. J. Cast Metals Res., 1997, 9, pp. 285–293.

26. D. O. Mahoney and D. J. Browne, "Study of the Variation of Heat Transfer Coefficients in Aluminum Investment Casting," in *Modeling of Casting, Welding and Advanced Solidification Processes, VIII*, 1998, (B. Thomas and C. Beckermann, eds.), TMS, pp. 1031–1032.

27. J. R. Shenefelt, "Heat Flux and Thermal Contact Conductance Determination Employing Inverse Heat Conduction Using Model Reduction Through Matrix Transform," Ph.D. Dissertation, May 1999, Mechanical Engineering, Mississippi State University.

28. J. V. Beck, B. Blackwell, and C. St. Clair, *Inverse Heat Conduction: Ill-posed Problems*, 1985, John Wiley, New York.

29. D. M. Trujillo and H. R. Busby, *Practical Inverse Analysis In Engineering*, 1997, CRC Press, New York.

30. P. N. Quested, K. C. Mills, R. F. Brooks, A. P. Day, R. Taylor, and H. Szelagowski, in *Solidification Processing '97*, University of Sheffield, UK, 1997, pp. 143–146.

31. R. D. Pehlke, A. Jeyarajan, and H. Wada, "Summary of Thermal Properties for Casting Alloys and Mold Materials," University of Michigan, 1982.

32. D. V. Atterton and D. Houseman, Nature, May 1953, 171, pp. 980–981.

33. P. V. Desai and K. V. Pagalthivarthi, in *ASM Metals Handbook*, Vol. 15, 1988, pp. 877–882.

34. J. Runyoro, S. M. A. Boutorabi, and J. Campbell, "Critical Gate Velocities for Film-Forming Casting Alloys," Trans. Amer. Foundryen's Soc., 1992, 100, pp. 225–234.

35. B. Sirrell, M. Holiday, and J. Campbell, in *Modeling of Casting and Welding and Advanced Solidification Processes VII*, 1995, (M. Cross and J. Campbell, eds.), TMS, pp. 915–933.

36. I. Ohnaka and J. D. Zhu, in *Modeling of Casting and Welding and Advanced Solidification Processes VII*, 1995, (M. Cross and J. Campbell, eds.), TMS, pp. 971–974.

37. K. Grube and L. W. Eastwood, Trans. Amer. Foundrymen's Soc., 1949, 57, p. 76.

38. R. W. Ruddle, *The Running and Gating of Sand Castings*, Institute of Metals, London, 1956.

39. P. R. Gouwens and L. A. Gouwens, "Controlled Pouring For Aluminum Casting Production," presented at 4th AFS International Conference on Molten Aluminum Processing, Orlando, FL, November 1995.

40. J. Campbell, "The Ten Casting Rules: Guidelines for the Reliable Production of Reliable Castings: A Draft Process Specification," in *Advances in Aluminum Casting Technology*, 1998, (M. Tiryakioglu and J. Campbell, eds.), ASM, pp. 3–19.

41. M. Tiryakioglu and J. T. Berry, "The Use of Riser Design Recommendations and Criteria Functions for the Efficient Feeding of Aluminum Castings," to be presented at AFS Conference on Filling, Gating, and Feeding of Aluminum Castings, Oct. 1999, Nashville, TN.

42. S. Jacob and M. Drouzy, "A Contribution A L'etude du Masselottage des Alliages d'Aluminum Coules en Sable," Fonderie, Dec. 1970, pp. 395–406.

43. R. P. Taylor, J. T. Berry, and R. A. Overfelt, "A Parallel Deivation and Comparison of Feeding Resistance Porosity Criteria Functions for Castings," in *Proceedings ASME National Heat Tranf. Conf.*, 1996 HTD, 323, pp. 69–77.

44. Y. W. Lee, E. Chong, and C. F. Chieu, "Pore Formation in Solidification," Metall. Mater. Trans., 1990, 21B, pp. 715–722.

45. E. Niyama, T. Uchida, M. Morikau, and S. Saito, "A Method of Shrinkage Prediction and its Application to Steel Casting Practice," AFS Cast Metals Res. J., 1982, 7, pp. 52–63.

46. S. T. Kao, E. Chong, and L. C. Chan, "Effect of Hydrogen Content on the Soundness of A356 Plate Castings," Presented at the American Foundrymen's Society 99th Casting Congress, April 1996, Kansas City, MO.

12

Castings

RAFAEL COLÁS

Universidad Autónoma de Nuevo León, San Nicolas de los Garza, Mexico

EULOGIO VELASCO and SALVADOR VALTIERRA

Nemak Corporation, Monterrey, Mexico

1 INTRODUCTION

Metal casting is reported to be a prehistoric event that appears, on the archeological records, after evidence of earlier metalworking. It is assumed that the earliest castings were made from native metals and alloys at least 10,000 years ago. Among the first metals to be cast by humankind are copper, gold, tin, lead and silver, whereas aluminum is one of the newest.

Aluminum is affected by several elements; some of them will improve its properties, allowing in some cases for heat treating, but others will be detrimental. A comprehensive account of the different effects can be found elsewhere [1], and here only a brief summary will be provided.

- Antimony contributes to the modification of the eutectic aluminum-silicon aggregate into lamellar form; the degree of modification depends on the absence of phosphorus and cooling rate. Antimony can react with strontium or calcium to form coarse intermetallics which affect both fluidity and the eutectic structure. Another detrimental effect of antimony is related to its potential toxicity.
- Beryllium addition of a few parts per million are effective to reduce oxidation losses. This element affects the morphology of iron-containing particles, with the corresponding improvement in strength or ductility. Beryllium oxide is very toxic and its compounds are listed as carcinogens, therefore special precautions have to be taken during melting and handling while liquid and its dross.

- Boron combines with other metals to form borides, such as AlB_2 and TiB_2. Titanium boride forms stable nucleation sites for active grain refining particles in molten aluminum.
- Calcium is a weak eutectic modifier agent, but it is scarcely used due to the increase of hydrogen solubility which is often responsible for casting porosity.
- Chromium additions are made in low concentrations to suppress grain growth in alloys susceptible to this phenomenon. The compound $CrAl_7$ is accounted for grain growth suppression due to its low solubility. Chromium improves corrosion resistance in some alloys.
- Copper is employed to increase strength and hardness in heat treatable alloys, this element exhibits detrimental effects like reduction in general corrosion resistance, to hot tearing and in castability.
- Iron improves hot tear resistance and reduces the tendency for die sticking or soldering in die casting. Increment in iron content reduces, however, ductility and machinability. Iron forms a series of insoluble compounds which affect the properties of a casting.
- Magnesium contributes to the increase in hardness and strength in aluminum-silicon alloys since Mg_2Si solubiliy is temperature dependent.
- Manganese is considered to be an impurity in castings and is controlled to a minimum level. It combines with iron to form insoluble phases.
- Nickel is used in combination with copper to enhance high temperature properties.
- Phosphorus is considered to be an impurity in castings due to the reduction of effectiveness of commonly employed modifiers, sodium and strontium, although it contributes to the reduction of primary silicon particles in hypoeutectic Al-Si alloys.
- Silicon increases casting characteristics of aluminum, it improves fluidity, hot tear resistance and feeding behavior. The optimum amount of silicon depends on the casting process. For slow cooling rate processes (sand or investment), the range is 5–7%, for permanent mold 7–9% and 8–12% for die casting.
- Sodium modifies the aluminum-silicon eutectic. It readily reacts with phosphorus reducing both the modification effectiveness and the size of primary silicon phases.
- Strontium is used to modify the aluminum-silicon eutectic at very low addition levels (0.008–0.04%). Higher additions are associated with the increase in porosity.
- Tin is effective in reducing friction and it is employed in bearing applications.
- Titanium is extensively used to refine grain size in aluminum castings. It is commonly employed in combination with boron.
- Zinc is added to aluminum in some alloys due to the excellent response to age hardening.

The variety of effects from different elements arises the need for grouping the different alloys. The Aluminum Association of America has designed a series of families of alloys:

- 1xx.x: Unalloyed compositions.
- 2xx.x: Alloys containing copper as their major alloying element.
- 3xx.x: Aluminum-silicon alloys also containing magnesium or copper.
- 4xx.x: Binary aluminum-silicon alloys.
- 5xx.x: Alloys containing magnesium as the major alloying element.
- 6xx.x: Unused.
- 7xx.x: Aluminum alloys containing zinc as the major alloying elements. It is common to find additions of copper, magnesium, chromium or manganese.
- 8xx.x: Aluminum alloys containing tin as major alloying element.
- 9xx.x: Unused.

Of these series, the most commonly employed is the 3xx.x due to the increase in fluidity encountered by the addition of silicon, and to the age hardening response achieved by addition of copper or magnesium. Cast pieces made from series 2xx.x 3xx.x and 7xx.x can be subjected to heat treatment, whereas the others are not.

2   MOLTEN METAL PROCESSES

Melting of commercial casting aluminum alloys require a series of steps other than melting and alloying. Molten aluminum alloys have to be protected from oxidation by fluxing and pumping, whereas their microstructure and mechanical properties, can be improved by degassing, grain refining, modification and filtration [2,3]. Some of these processes will be described in this section, leaving aspects related to grain refining and modification to the following section, where solidification phenomena are presented.

2.1   Fluxing

The term fluxing is used in the industrial practice to refer to the additives and techniques employed to purify, cover, clean, protect, deoxidize and refine a molten metal bath. Oxides and other nonmetallic inclusions can be formed in molten aluminum and they might be able to incorporate and downgrade an otherwise healthy casting. These inclusions can be originated from dirty tools, sand and other molding debris, sludge, lubricant and liquid residues, as well as from oxidation of alloying elements of the base metal.

Fluxing the melt facilitates the separation and agglomeration of undesirable particles from the liquid alloy. This process is temperature dependent, and it should be carried out at temperatures high enough to enhance chemical reactions and to facilitate physical separation of the molten alloy and the slag.

The compounds employed in fluxes should be able to comply to the following characteristics:

- They should form low-melting high-fluidity mixtures at the working temperature,
- They should decompose to generate anions capable to react with impurities in the melt, which will separate from it due to differences in density.
- They should be able to agglomerate the undesirable products and facilitate their removal by mechanical or any other physical means.

Table 1   Characteristics of Compounds Used as Fluxes for Aluminum Alloys [4]

Compound	Chemical formula	Density (g/m³) solid	liquid	Melting point (C)	Boiling point (C)
Aluminum chloride	$AlCl_3$	2.440	1.31	190	182.7*
Aluminum fluoride	AlF_3	3.070	—	1040	—
Borax	$Na_2B_4O_7$	2.367	—	741	1575
Calcium chloride	$CaCl_2$	2.412	2.06	772	1600
Calcium fluoride	CaF_2	3.180	—	1360	—
Carnalite	$MgCl_2KCl$	1.600	1.50	487	—
Zinc chloride	$ZnCl_2$	2.910	—	262	732
Zinc fluoride	ZnF_2	4.840	—	872	—
Cryolite	$3NaFAlF_3$	2.970	—	1000	—
Lithium chloride	$LiCl$	2.086	1.50	613	1353
Lithium fluoride	LiF	2.295	1.80	870	1676
Magnesium chloride	$MgCl_2$	2.325	—	712	1412
Magnesium fluoride	MgF_2	3.000	—	1396	2239
Potassium chloride	KCl	1.984	1.53	776	1500*
Potassium fluoride	KF	2.480	8.80	880	1500
Potassium borate	$K_2B_2O_4$	—	—	880	—
Potassium sulfate	K_2SO_4	2.662	—	1076	—
Potassium carbonate	K_2CO_3	2.290	—	891	—
Calcium chloride	$CaCl$	2.165	1.55	801	1413
Calcium fluoride	CaF	2.790	1.91	980	1700

* Sublimes at indicated temperature.

Table 1 [4] lists some of the compounds available for fluxing aluminum alloys.

Different types of fluxes are employed in the foundry industry depending on their function. Among them the principal are: cover, cleaning, drossing and refining fluxes.

- Cover fluxes are designed to be used in small furnaces to provide a physical barrier to oxidation of the melt and clean scrap, foundry returns or ingots being charged. These fluxes should be able to melt on the molten surface and wet the charge. Some fluorides and chlorides are designed to be used in furnaces and small crucibles. These fluxes are cost effective in oxidizing conditions, particularly in alloys with high levels of Mg.
- Cleaning fluxes are higher in chloride salts (70–75%) to facilitate wetting of oxide inclusions for easier separation from the melt and keep the walls and crucibles free of build-up.
- Drossing fluxes are designed to promote separation of aluminum oxide (Al_2O_3) from the dross layer formed on top of the surface of the molten alloy, since sludge, liquid and molten metal are usually mixed in this layer. These fluxes are designed to react with the alumina in the dross and recover the metal [5]. They contain compounds, usually fluorides, capable to react

exothermally, thus increasing in a local manner temperature and fluidity of the flux. The salts wet and dissolve thin oxide films according to the reaction:

$$6\,Na_2SiF_6 + 2Al_2O_3 \rightarrow 4\,Na_3AlF_6 + 3\,SiO_2 + 3\,SiF_4 \tag{1}$$
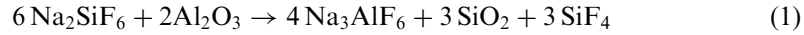
- These fluoride salts can only dissolve the very thin coat of alumina formed on top of the melt, massive Al_2O_3 particles can only be reduced by electrolytic means.
- Refining fluxes contain compounds that break down at the working temperature and are thermodynamically favorable to react with undesirable metallic elements in the base metal. Chlorine in fluxes reacts with alcaline metals to form compounds that can be removed by skimming.

2.2 Degassing

Aluminum and its alloys are very susceptible to hydrogen absorption in the molten state due to its high temperature solubility [6,7], Fig. 1, and the affinity of aluminum for oxygen. The principal source for hydrogen comes from humidity of the atmosphere in contact with the liquid metal, which reacts with aluminum:

$$3\,H_2O_{(v)} + 2\,Al \rightarrow 3\,H_{Al} + Al_2O_3 \tag{2}$$

various aluminum alloys have different sensitivities to hydrogen absorption and ensuing gas porosity if removal is not accomplished. Increment of copper and silicon reduces hydrogen solubility, whereas magnesium increases it [6], Table 2. Since the solubility of hydrogen is significantly higher in the liquid state as compared with the solid, there will be enrichment in the liquid during solidification. If it is assumed no solid diffusion and complete liquid diffusion occurs during casting, at the
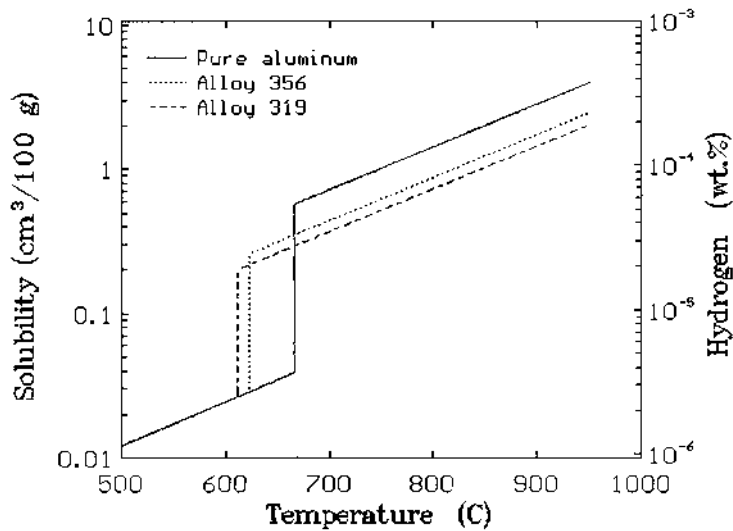
Figure 1 Solubility of hydrogen in aluminum at one atmosphere. (From Refs. 2,6,7.)

Table 2 Solubility of Hydrogen in Aluminum and its Alloys at 750°C [6]

Alloy	Hydrogen solubility (ppm)
Pure aluminum	1.20
Al-7Si-0.3 Mg	0.81
Al-4.5 Cu	0.88
Al-6Si-3.5 Cu	0.67
Al-4Mg-2Si	1.15

end of solidification there will be a large increase in hydrogen concentration in the piece. Therefore, even when the hydrogen content is below the solubility for the bulk liquid during solidification, concentration in the liquid will increase, and the solubility limit might be exceeded, resulting in a porous part.

Various thermodynamic and kinetic factors control hydrogen removal from molten aluminum. Gas removal is easier at lower temperatures and higher concentrations. Hydrogen is removed by [8]:

- Hydrogen transport in the melt to the vicinity of an inert gas bubble by convection and diffusion.
- Diffusivity transport through the thin boundary layer surrounding the bubble.
- Chemical adsorption onto and subsequent desorption from the bubble surface.
- Diffusion of hydrogen as a gas inside the bubble.
- Escape of hydrogen from the melt surface or at the refractory walls.

Consequently, hydrogen removal will depend on mass transfer coefficients. It was found that purging efficiency depends on the bubble size [9], Fig. 2. The use of porous plugs helps improve the rate by providing small bubbles, but they generally coalesce in the bath, reducing the beneficial effect. The use of an impeller with a porous plug improves the rate further by dispersing the bubbles.

It has been found that the addition of chlorine or freon [10,11] improves the rate in some cases. It is thought that the removal rate is not only due to the increase of the mass transfer coefficient, but also to combination of the halogen with hydrogen:

$$2 H_{Al} + Cl_2 \rightarrow 2 HCl \tag{3}$$

which is thermodynamically favorable in some circumstances.

When the hydrogen in molten aluminum cannot be thoroughly expelled from the casting product as it solidifies, porosity defects will result. Porosity can be very fine, widely dispersed, or localized in those areas of the casting that are the last to solidify if the entrapped gas concentration is relatively low. Hydrogen microporosity may not be harmful except when pressure tightness is sought after. On the other hand, some gas porosity defects can be fairly large and they might appear as cracks or blowholes.
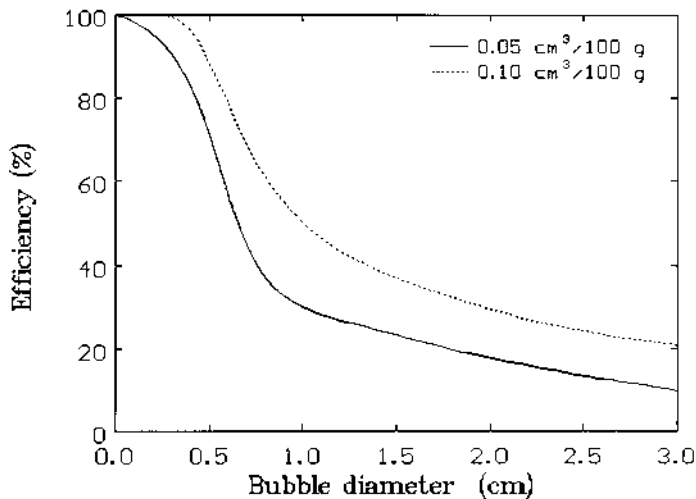
Figure 2 Hydrogen removal as a function of bubble size at two purging flows. (From Ref. 9.)

True gas porosity and shrinkage porosity should be differentiated. The former one is due to the presence of trapped gas and they appear as round holes upon metallographic examination. The latter is due to inadequate feeding during solidification and it is more irregular in shape than gas porosity [12]. Porosity defects result in the reduction of mechanical properties in aluminum alloys [13], Fig. 3.

2.3 Melt Refining

Some impurities present in aluminum can be eliminated in the molten bath; among them are the alkali metals. Of these metals, lithium, sodium and calcium are impurities from primary aluminum production that have to be removed to assure casting integrity. In some cases lithium can be associated with melting aeronautical scrap. Magnesium is another metal that can be eliminated in the melt and it is normally introduced in the scrap, since several commercial alloys contain magnesium, and they constitute a significant proportion of the scrap market available for recycling.

Removal of these impurities can be readily done in the molten alloy by introduction of chlorine or fluorine, as their reactions with these particular elements is more thermodynamically favorable than that with aluminum [14], Fig. 4. This is done in industry by addition of compounds (like AlF_3) or by bubbling gaseous chlorine.

2.4 Pumping and Filtering

Molten metals have traditionally been transferred from the furnace to the mold or casting device in ladles which are filled by gravity. Nowadays it is possible to transfer the molten metal with mechanical pumping systems [15,16] that offer several advantages over the traditional means.
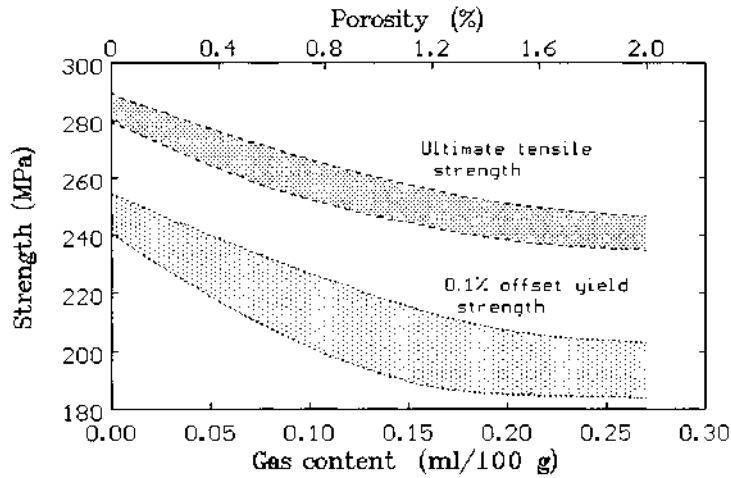
Figure 3   Tensile properties as a function of gas content in an aluminum alloy A356. (From Ref. 13.)
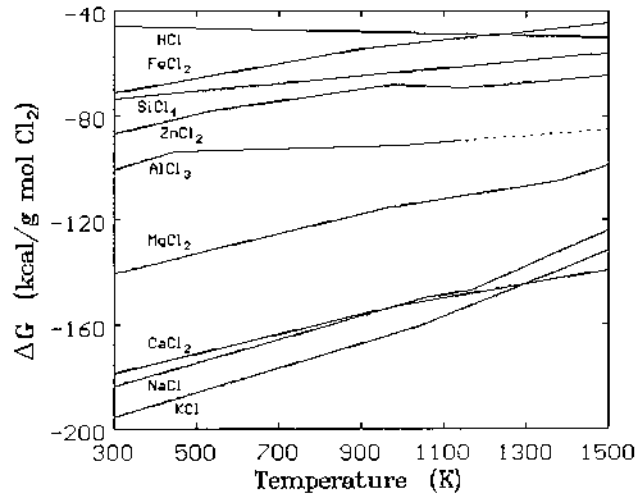
Figure 4   Thermodynamics of metal chloride formation. (From Ref. 14.)

A pumping system allows for high volumes of metal to be transferred in short periods of times, with the resulting increase of productivity. It is also possible to take advantage of this reduction in transportation and holding times, since the metal can be heated up to lower temperatures, which translates into reductions in costs (energy), and in diminishing the risk for trapping hydrogen [6,7]. Quality of the cast is also enhanced as the pump drags liquid from the bottom of holding reservoirs, avoiding trapping dross or slag.

Another modern development made to increase quality in foundries is that of filtering, especially with the tendency that aluminum has to oxidize. The filtration

process consists in passing the molten metal through a porous device (filter) in which inclusions contained in the flowing metal are trapped or captured. The filter itself should be made of a material which does not react with the alloy, and must resist thermal and mechanical stresses without breaking.

Filtration is carried out by different mechanisms. Large particles (greater than 30 μm) are trapped on the surface of the filter, and, as they agglomerate, aid filtering other inclusions during subsequent flow. Smaller particles are trapped as the liquid flows through a very tortuous path within the filter itself. The path provides for the increase in probability for a particle to detach from the liquid and attach to the wall of the filtering medium. Particles brought into contact with the filter will be retained by gravity, friction or by chemical or electrostatic bonds [3].

Filtration efficiency is affected by several factors. In general filtration is enhanced when the flow rate is reduced, or when the length (depth) of filtration increases, as the probability for a particle to attach to the filter increases.

3 SOLIDIFICATION OF ALUMINUM ALLOYS

Is not very common to produce cast pieces from series 1xx.x since they are soft and their fluidity is poor [2]. Addition of other elements, especially silicon, increases the filling capacity of aluminum alloys and allows for the obtention of complex shapes. Solidification proceeds through a series of mechanisms, which can be used to control the properties of the piece.

3.1 Nucleation and Growth

Transition from the liquid to solid occurs by nucleation and growth [2,17–19], in classical theory nucleation theory [2,17,19] the radius of an spherical stable embryo (r^*) is given by:

$$r^* = \frac{2\gamma_{sl} T_m}{L \Delta T} \tag{4}$$

where γ_{sl} is the solid–liquid interfacial free energy, L is the latent heat of transformation per unit volume, ΔT is the undercooling and T_m is the melting temperature. The critical energy of activation (ΔG^*) for an embryo of radius r^* is given by:

$$\Delta G^* = \frac{16}{3} \pi \frac{\gamma_{sl}^3 T_m^2}{L^2 \Delta T^2} \tag{5}$$

a comprehensive picture of the variation of the ΔG^* with different parameters is given elsewhere [20]. Homogeneous nucleation is only possible for high undercooling (on the order of 0.25 T_m [21]). However, any surface, such as cavities, walls or solid particles, may catalyze nucleation at a much smaller undercooling and with fewer atoms required to form the nucleus, following the phenomenon known as heterogeneous nucleation.

Once the nuclei are stable they will start to grow at a rate controlled by the atomic movility across the solid–liquid interface, and by mass and heat transfer. Solidification implies that at a given time more atoms move from the liquid side of the interface to the solid one that in the other direction. Growth also implies
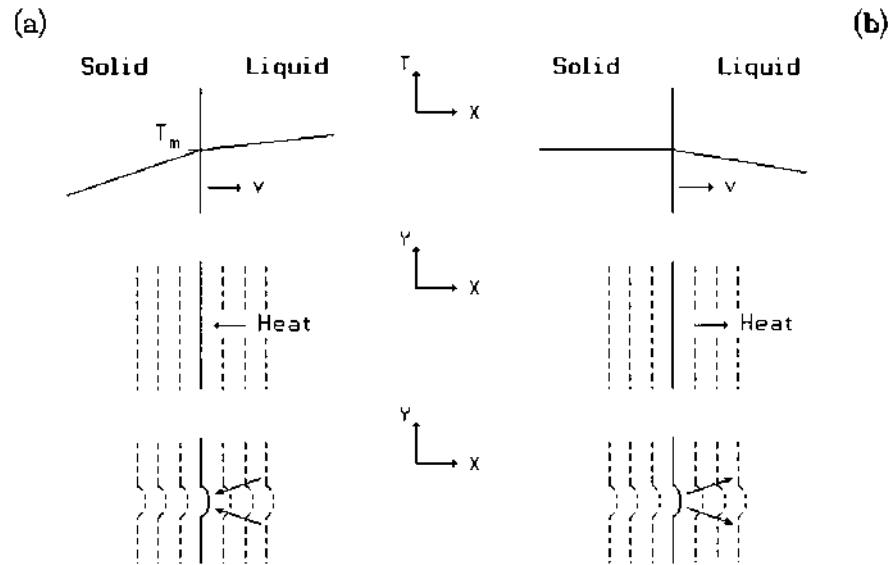
Figure 5 Advance of a solid interface; (a) normal temperature gradient; (b) inverted temperature gradient in the liquid.

that the interface keeps moving and increasing in size in such a way that solidification will only proceed if the temperature of the interface is below the melting one (T_m), due to the necessity to compensate the interfacial free energy (γ_{sl}) and the latent heat of solidification (L).

Pure metals solidify as fast as the latent heat of solidification is removed from the interface. Two cases can be considered, one in which the heat is extracted through the solid, Fig. 5(a), and in which the temperature of the liquid is above that of the interface. The advancing interface remains plane and perpendicular to the temperature gradient. If one part of the interface moves ahead of the rest it would enter hotter liquid and will slow down. Figure 5(b) shows the liquid with an inverted temperature gradient, a condition which is met in a casting when the heat is extracted slowly through the surface of the metal into the mold; solidification begins, after undercooling, at the surface and, since the region of the solid–liquid interface warms up due to the release of the latent heat, this interface advances into colder liquid ahead. Under these conditions if a small part of the interface runs on ahead of the rest, bulging out, this region moves into colder liquid and so runs on ahead still faster. The planar growth is now unstable and spikes will grow out from it into the liquid. Similarly, other arms may branch out sideways from the primary ones forming dendrites. These dendrites grow in preferred crystallographic directions, in cubic metals (like aluminum) they grow in the directions of the cube edges of the crystal cell $\langle 100 \rangle$ [22].

Addition of silicon to aluminum results in solidification of an eutectic aggregate [23], Fig. 6. The eutectic structures are characterized by the simultaneous growth of two or more phases from the liquid, it is possible to find different morphologies, they will be lamellar when the volume fraction of each phase is nearly
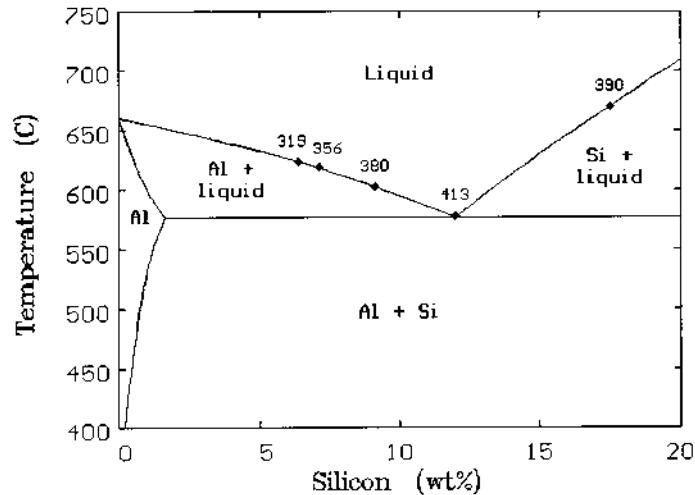
Figure 6 Section of the aluminum-silicon equilibrium phase diagram showing typical compositions of some alloys. (From Ref. 24.)

the same or if the interface of a minor constituent is faceted (when its growth is along well defined cristallographic planes, as in the case of silicon [24]). The structure will have a fibrous aspect when one phase is present in a small volume fraction [25].

3.2 Microstructural Control

A series of parameters can be employed to describe the metallurgical microstructure of aluminum castings. Separation between dendritic arms is affected by the solidification or freezing rate, distribution and aspect of the eutectic aggregate, as well as grain size, can be controlled by addition of elements or compounds and by the cooling rate. Size and distribution of intermetallic phases is much more complex, since care has to be taken on impurities content and concentration as well as other solidification conditions.

3.2.1 Dendritic Arm Spacing

Solidification of commercial alloys proceeds by formation of dendrites from the liquid. This is especially the case in hypoeutectic aluminum-silicon alloys, in which the dendrites will be of primary aluminum. Distance or separation between the different dendritic arms is normally measured on the secondary branches, rather than on the primary ones, and, for a given composition, it is controlled exclusively by the solidification rate [26–31], Fig. 7. Figure 8 shows the difference in size obtained by cooling an A319 alloy at two different rates. Microstructural examination can be used to obtain information related to the rate or time involved during solidification at different places within a complex cast by reference to data obtained in controlled unidirectionally solidified trials.

Engineering castings can be improved by optimization of the dendritic arm spacing (DAS), since both mechanical [26–37], Fig. 9, and physical properties [38,39], Fig. 10, are enhanced when this parameter diminishes.
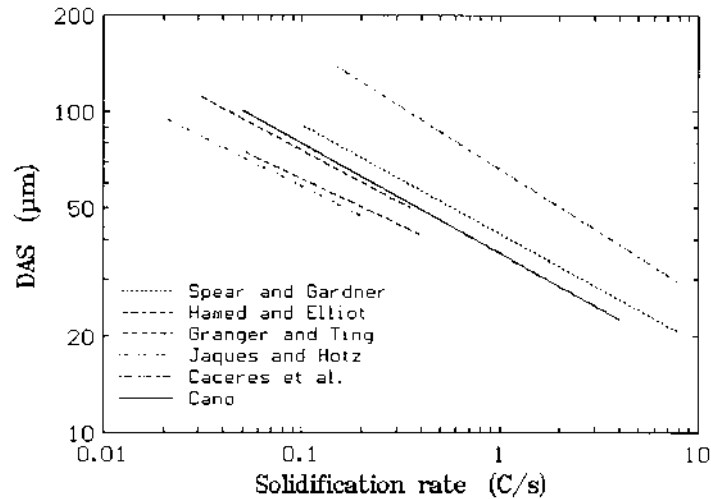
Figure 7   Secondary dendritic arm spacing (DAS) as a function of solidification rate. (From Refs. 26–31.)

3.2.2   Grain Structure

A small equiaxed grain size structure is sought-after in aluminum alloy castings because it improves resistance to hot tearing and mass feeding, at the same time that most mechanical properties and surface finish characteristics are improved. Another advantage of small equiaxed grain structure over large columnar ones is that of homogeneity, which results in less segregation and better response to heat treatment. A more homogeneous structure has defects, such as porosity and intermetallics more uniformly distributed and therefore less harmful.

Increment in the resistance to hot tearing with reduction in grain size is attributed to decrease in the coherency temperature [40]; combination of a large volume fraction of eutectic liquid and low coherency temperature in aluminum-silicon alloys results that material containing at least 5% of silicon exhibits a low crack tendency [41]. Mass feeding and reduced shrinkage porosity are thought to be associated with grain refining, although there is not enough evidence for it [42]. There is evidence [43] that in aluminum-silicon alloys as the grain is refined, porosity due to hydrogen is reduced.

Reduction of grain size is achieved by increasing the nucleation efficiency of primary aluminum embryos. This can be done by increasing the cooling rate (which will also help to improve the properties as the DAS is reduced) or by mechanical agitation to detach dendrite arms, but in practice, addition of chemical aggregates is used to provide the necessary nuclei.

In most casting processes the metal solidifies as soon as it touches the walls of the mold, and, due to the high nucleation rate encountered in this region, a layer of small equiaxial grains is formed, Fig. 11. This layer finishes when nucleation is stopped by the increase in temperature produced by the release of the latent heat of solidification (*L*). Some of the originally equiaxed grains will be able to grow nevertheless, forming a layer of big columnar grains, which contribute in the
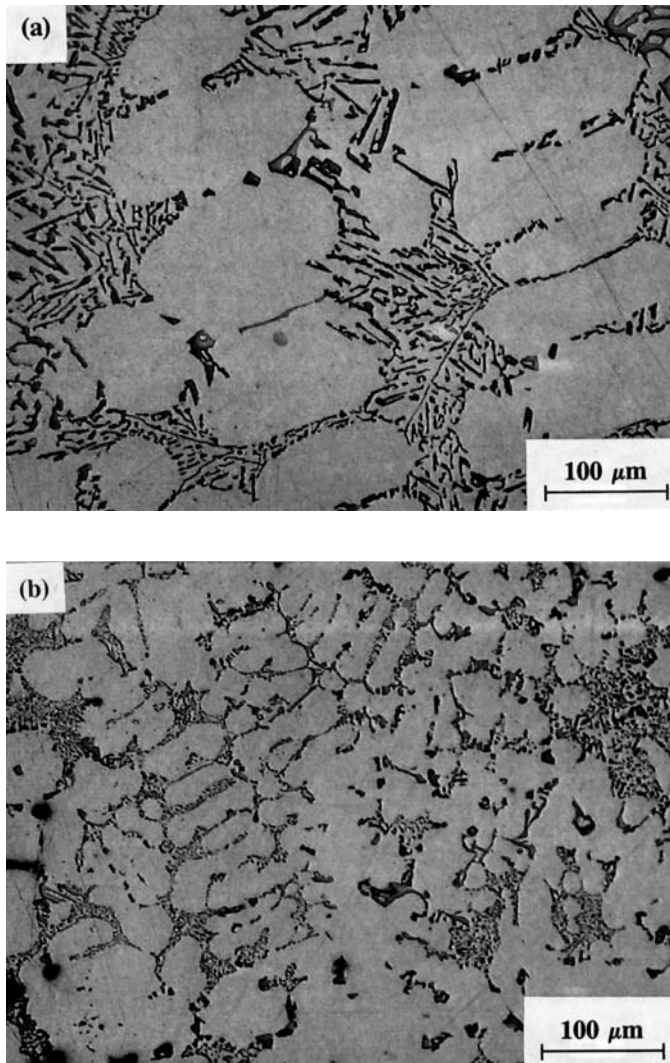
Figure 8 Micrographs of dendrites obtained from samples solidified at low (a); and high (b) rates.

reduction of mechanical properties in the piece. This columnar region ends when the temperature gradients change and nucleation of new grains takes place. Addition of particles which are able to nucleate with low undercoolings (below 1°C), such as the intermetallics $Al_{15}(Fe,Mn)_3Si_2$, can be formed in front of the columnar grains and they will promote formation of new aluminum grains [43].

Optimum grain refining can be obtained when a surface is provided at, or just above, the liquidus temperature of the alloy. Such conditions are met with the addition of Al_3Ti particles contained within a master alloy [43]. Titanium is soluble in liquid aluminum, Fig. 12, and it is required to have at least 0.15% Ti in the alloy to provide for the peritectic reaction and grain refining effectiveness. Industry is
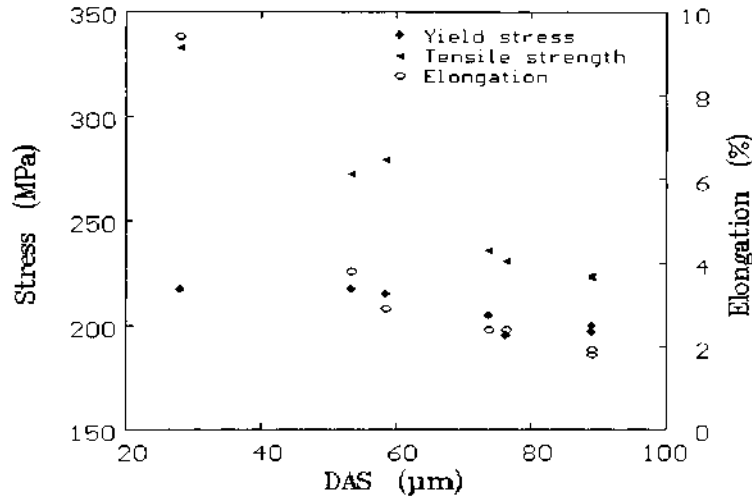
Figure 9 Mechanical properties of a C355-T6 alloy as a function of DAS. (From Ref. 35.)
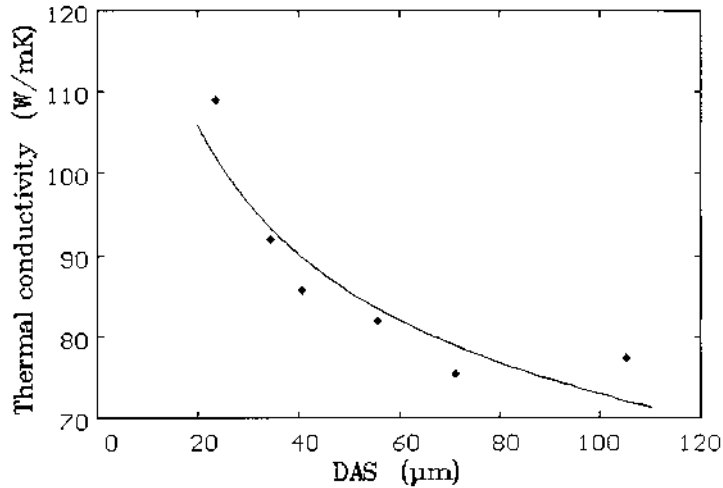
Figure 10 Thermal conductivity in a A319 alloy as a function of DAS. (From Ref. 38.)

moving down to the use of titanium-boron master alloys in which the titanium ranges from 3% to 10% and a Ti:B ratio of 3:50 provides for soluble Al_3Ti and insoluble $(Ti,Al)B_2$ particles in an aluminum matrix, Fig. 13. Since these master alloys are effective at significant contents in Ti (0.01–0.03% in the cast alloy), it has been suggested that the predominant role in nucleation is taken by the boride particles [44].

3.2.3 Modification

The term modification is referred in foundry industry to the morphological changes that take place in the aluminum-silicon eutectic aggregate [45]. This process can
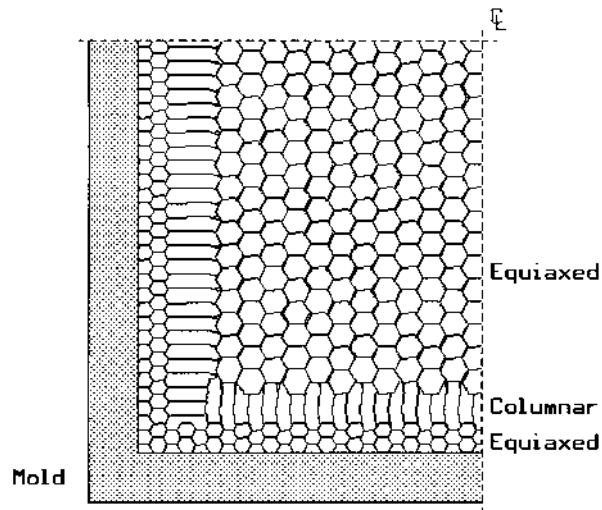
Figure 11 Typical grain variation observed in castings.
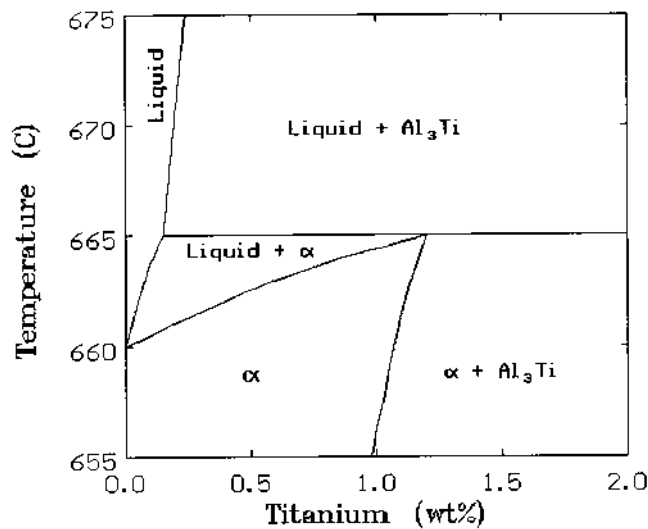
Figure 12 Section of the aluminum-titanium equilibrium phase diagram.

be conducted either in hypo or hypereutectic alloys by addition of different elements or by increasing the solidification rate. Modification changes the sharp needle aspect commonly encountered in untreated alloys, Fig. 14(a), to a fibrous, coral like aspect, Fig. 14(b).

Elements from groups Ia and IIa, as well as some rare earths, can be employed as modifiers, among them sodium and strontium are preferred due to their strong effect at low addition levels. Experimental results show that the degree of modification, for a given alloy, depends on the amount of Sr added, as well as
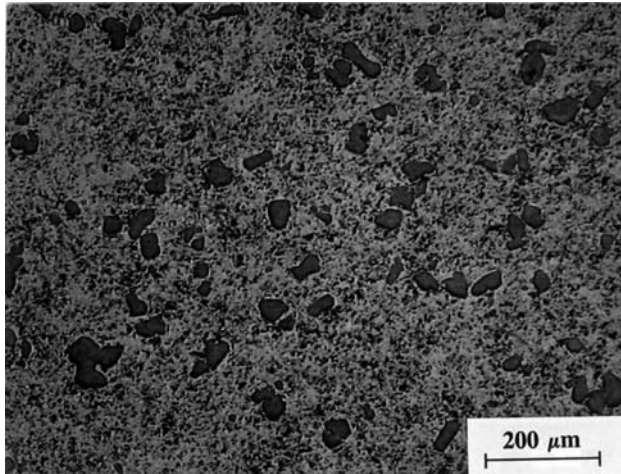
Figure 13   Microstructure of a titanium-boron master alloy.

the time evolved between addition and casting. Figure 15 shows such behaviour taking as reference the lowest temperature recorded as the eutectic reaction takes place [43].

Crossley and Mondolfo [46] have proposed a physical model based on the assumption that in unmodified casts silicon grows at a faster rate than aluminum, resulting in sharp acicular particles, addition of sodium or any other modifier agent hinders growth of silicon and promotes that of aluminum as its surface tension is reduced. Shamsuzzoha et al. [47] proposed that growth of silicon occurs in a ledge-wise manner, in such a way that its {111} planes encroach along the ⟨112⟩ directions. During slow cooling twinning is frequent, and promotes a small angular distortion along the twinning planes, which is responsible for branching. When the solidification rate is increased, silicon atoms do not have time enough to accommodate in the ledges, promoting a twinning at a higher rate, which implies the increase in distortion and branching. Shu-Zu and Hellawel [48] have proposed a mechanism based in the enrichment of the modifying atoms at the silicon–liquid interface, in such a way that this absorption will distort the ledges and promote twinning and branching.

3.2.4   Porosity

Porosity in aluminum cast alloys is associated either with the presence of hydrogen (trapped while liquid and expelled as the metal solidifies, due to its drop in solubility, Fig. 1), or to the volumetric contraction occurring as the liquid metal freezes [2]. Porosity in a casting is irregular due to the combination of the above mentioned factors, however, it is possible to determine the origin of certain pores, based on their distribution and morphological aspects [2].

Big macroscopic shrinkage cavities are normally assumed to be due to contraction and are associated to faulty feeding designs, and to the inability to allow liquid metal to flow into already solidified regions. A molten alloy will exhibit three different contraction stages, Fig. 16 [2]. The first one (liquid) does not have a dramatic effect in castings, and it is normally noticed only as a reduction in height
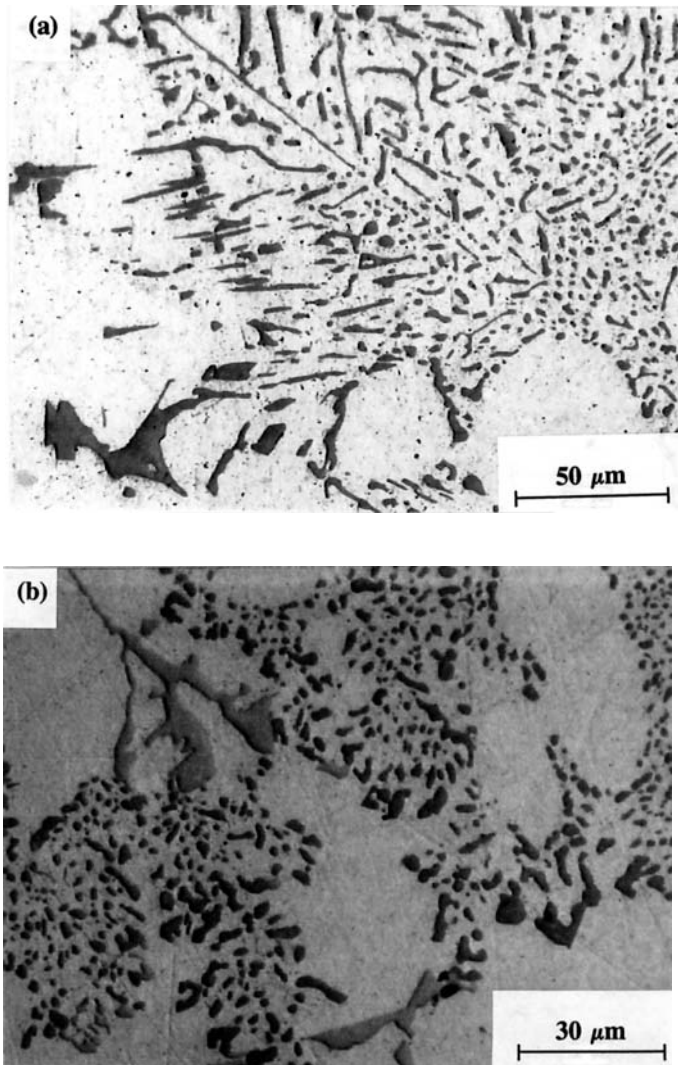
Figure 14 Typical eutectic structures found in unmodified (a); and modified (b) aluminum-silicon alloys.

of the liquid held in the feeder. Contraction during solidification (second stage) is cause of most problems, and it is due to the change from a random open liquid structure into a more compact solid one. Figure 17 shows how shrinkage cavities can be formed when casting with a faulty feeding design. In this figure, it is assumed that the mobility of the liquid–solid interphase is the same in all directions (t_1), but as time increases (t_2), the faulty design will allow contact between moving interphases, which will result in liquid metal being isolated from the feeder; once this liquid solidifies, it will leave behind a series of cavities.

As was mentioned above, the decrease of solubility of hydrogen is thought to be responsible for most small gaseous pores in aluminum castings. A series of models
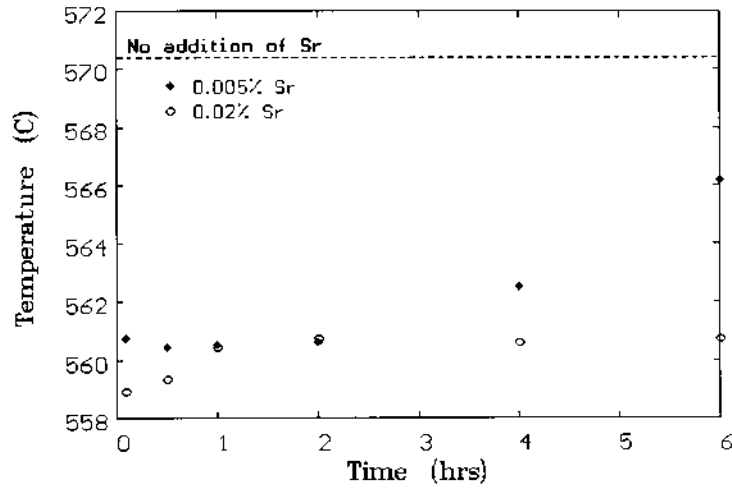
Figure 15 Changes in the eutectic temperature as a function of time elapsed since addition of strontium in a A356 alloy. (From Ref. 43.)
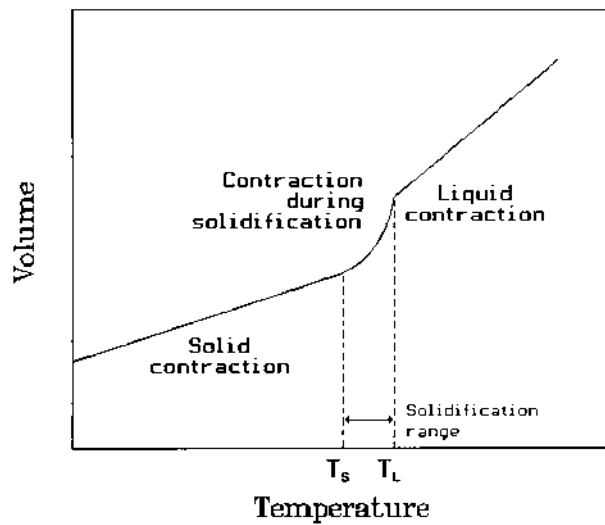
Figure 16 Contraction due to different phenomena. (From Ref. 2.)

[49–52] have been developed to explain the formation of these pores based on nucleation and growth mechanisms, models that require different geometrical consideration and the knowledge of difficult to measure parameters like surface tension and supersaturation pressure.

3.2.5 Intermetallics

The most common intermetallic phases found in aluminum castings are related to contamination with iron, which has a limited solubility in liquid aluminum [23].

Feeder
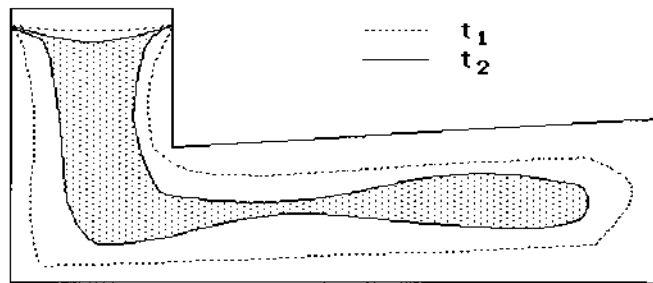
Figure 17 Formation of shrinkage cavities due to missdesign of the feeding system.

100 μm
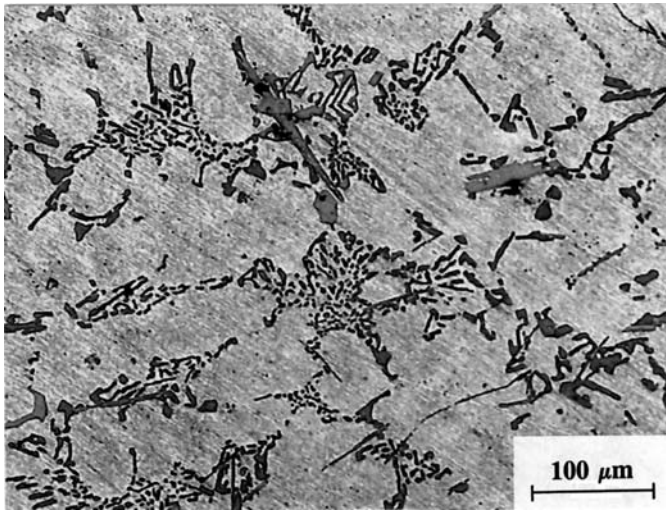
Figure 18 Intermetallic β-Al$_5$FeSi.

Of these intermetallic phases, the β-Al$_5$FeSi is the most detrimental to mechanical properties [53,54], due to its needle shape microstructure, Fig. 18, and its low coherency with the aluminum matrix [55]. Addition of manganese transform these intermetallics into the less deleterious α-Al$_{15}$(Fe, Mn)$_3$Si$_2$ phase, which due to its aspect, Fig. 19, is commonly referred as chinese script. A drawback of addition of manganese is the increment in both hardness and quantity of intermetallic particles for a given iron content, in such a way that the positive effect of manganese on the modification of the intermetallic morphology to increase the resistance to crack propagation is offset by the increased brittleness and volume of the α particles [56].

Intermetallic phases can be formed in aluminum castings at high temperatures, before the aluminum dendrites are formed, concurrent with the solidification of the alloy, or they can form complex eutectic phases which solidify at temperatures as low as 480°C [43,53–60]. A short summary of the intermetallic phases encountered in Al-Si alloys is presented in Table 3.
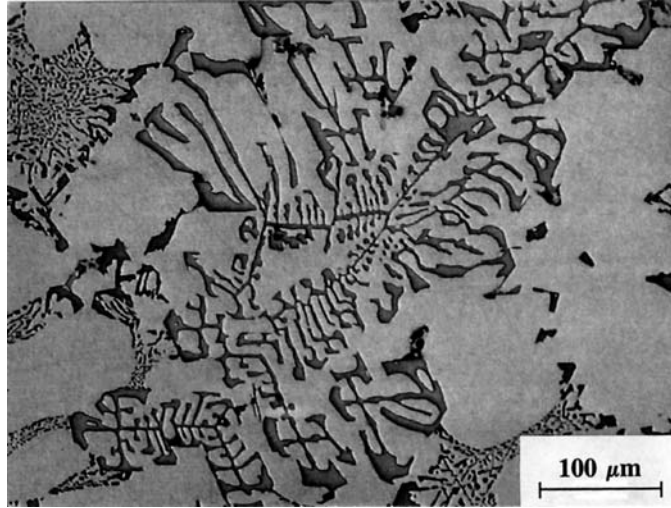
Figure 19 Intermetallic α-Al_{15} $(Fe,Mn)_3Si_2$.

Two factors are known to control the morphology and nature of the intermetallics found in cast alloys, and they are the solidification rate and the chemical composition [53–60]. The solidification rate exerts a direct impact on the kinetics and amount of iron rich phases present in the microstructure. Low cooling rates favor the formation of β needles, which are formed in well defined crystallographic planes, whereas higher rates tends to favor the Chinese script type [59], experimental results [57] show that the transition between β and α phases takes place at slower rates as the amount of iron is reduced. Several authors [53–60] have shown that the elements that control the transition from β to α depends on the amount of Fe, Mn and Cr, as the former increases β formation will be promoted, while Mn and Cr contribute to the stabilization of α particles.

A series of guidelines can be mentioned to reduce the detrimental effects of iron intermetallics:

- maintain low iron levels;
- maintain a Mn/Fe ratio higher than 0.5,
- increase the rate of solidification, and
- reduce the degree of eutectic modification.

Table 3 Intermetallic Phases in Al-Si alloys

Reaction	Phases
Pre-dendritic	$Al_{15}(Fe,Mn)_3Si_2$
Post-dendritic	$Al_{15}(Fe,Mn)_3Si_2$-Al_5FeSi
Eutectic	Al_5FeSi-Mg_2Si
Post-eutectic	$Al_5Mg_8Cu_2Si_6$-$CuAl_2$

3.3 Thermal Analysis

When a material undergoes a phase transformation, some of its characteristics (properties and structure) may change discontinuously. Most common transformations, such as boiling, melting and allotropic structural changes, are called first order transformation since the first derivative of the free energy (G) becomes discontinuous at the transformation temperature (T_t):

$$S = -\frac{dG}{dT} \tag{6}$$

where S and T are the entropy and temperature. Since

$$G = H - TS \tag{7}$$

where H is the enthalpy, H must also be discontinuous at T_t in order for both G to be continuous and S discontinuous, Fig. 20. [61]. The discontinuity in H is referred to as the latent heat of transformation, and it is this heat which will be absorbed or released during a transformation that is detected by thermal analysis.

The oldest type of thermal analysis is that of recording the changes in temperature that occurs while heating or cooling a material, which can be obtained by placing a thermocouple within the piece to be studied [62]. Figure 21 shows the sort of changes which are expected as a pure metal and a couple of alloys during their cooling and heating. The horizontal plateau observed in the pure metal and the eutectic is due to the latent heat of transformation, which has to be provided, when heating, or extracted, while cooling, in order to achieve full transformation. Both alloys show changes in slope in their cooling and heating curves as they pass through the binary phase region. It is worth noticing that the sharp changes identified as ideal, are not normally observed in most conditions due to factors such as the thermal inertia of the thermocouple, segregation, agitation, etc. This limi-
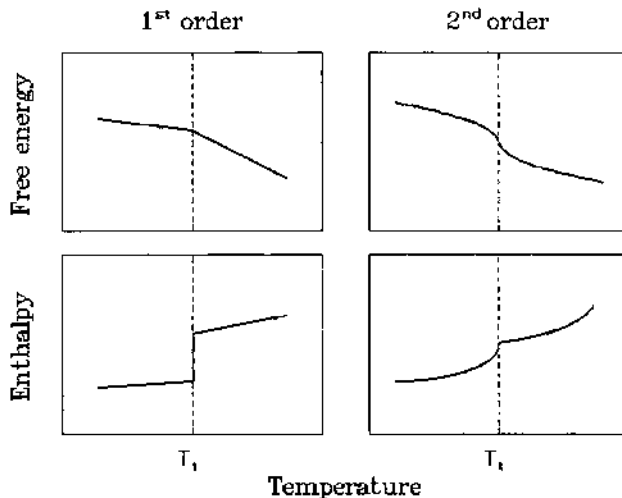
Figure 20   Temperature dependence of the free energy and enthalpy of a material as it goes through a first or second order phase transformation.
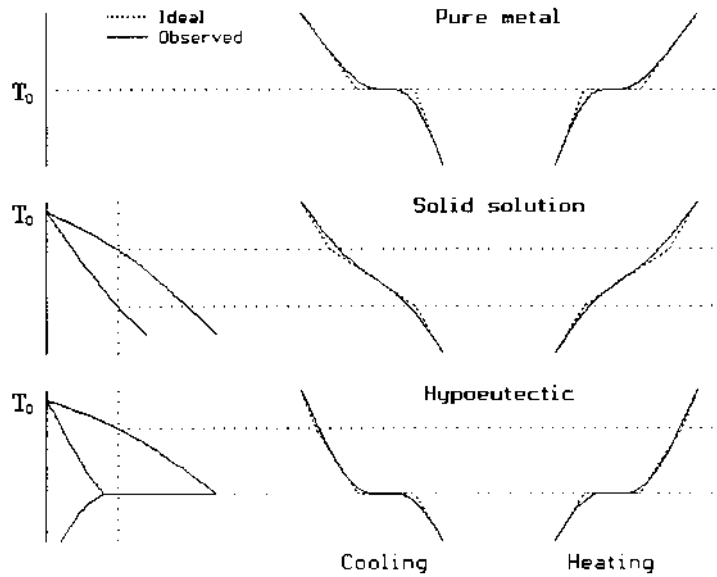
Figure 21 Ideal and observed curves obtained while cooling and heating a pure metal and a couple of alloys.
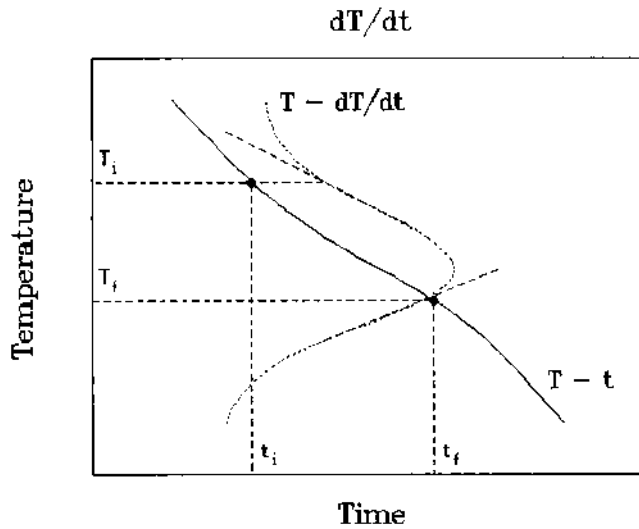
Figure 22 Schematic diagram of the cooling curve and its derivative (**dT/dt**), showing the points at which a given transformation starts and ends.

tation is overcome with the use of the derivative (dT/dt) of the heating or cooling cuves, as the points at which the transformations start and end are magnified [43,59,62], Fig. 22.

Commercial Al-Si alloys are treated as if they were made only of either primary aluminum or silicon, and the eutectic aggregate, see Fig. 6, although this is far from
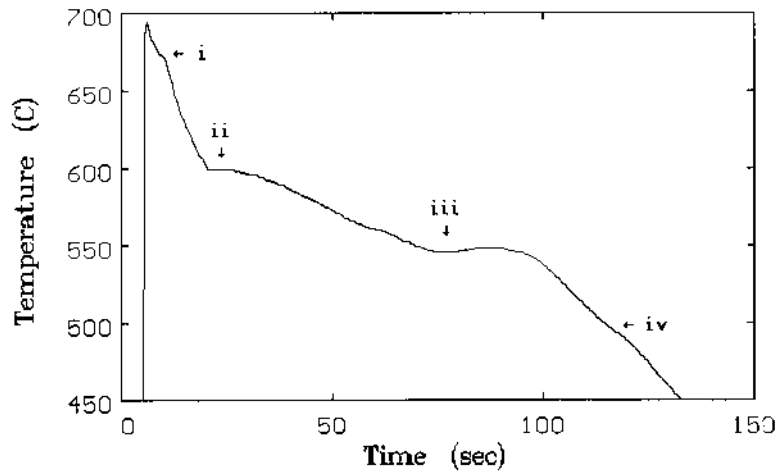
Figure 23 Solidification curve of a modified and refined type 319 alloy.
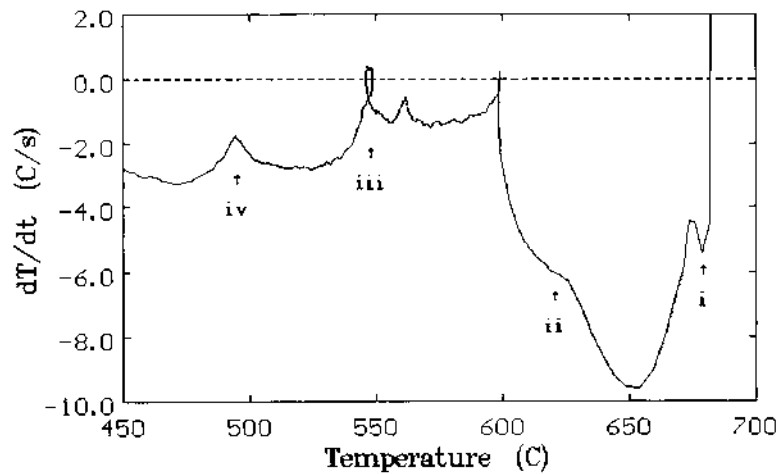
Figure 24 *dT/dt* as a function of temperature of the curve shown in Fig. 23.

true. Figure 23 shows the cooling curve recorded during solidification of a type 319 alloy to which titanium and strontium were added, respectively, to refine their grain structure and modify the eutectic aggregate. Four different reactions were detected by plotting *dT/dt* as a function of temperature, Fig. 24, and they are:

i. Peritectic precipitation of Al_3Ti.
ii. Formation of primary aluminum dendrites.
iii. Eutectic Al + Si reaction.
iv. Solidification of complex eutectic of the type $Al_5Mg_8Cu_2Si_6 - CuAl_2$.
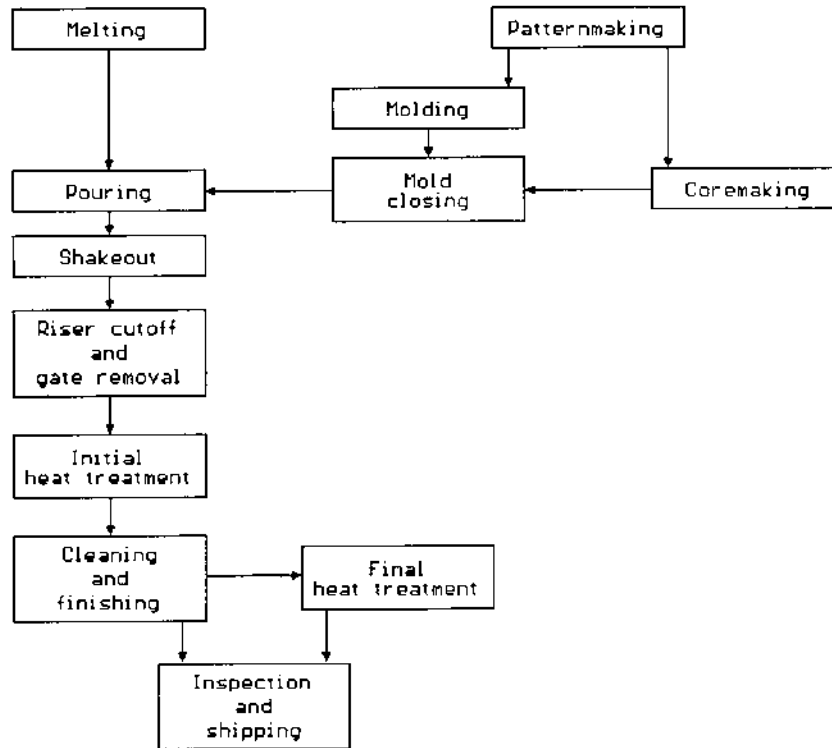
Figure 25   Simplified flow diagram of the basic operations for producing a sand casting. (From Ref. 63.)

4   CASTING PROCESSES

As was mentioned before, casting has existed since prehistoric times and a wide variety of molding and casting methods and processes have been developed over the time. Figure 25 [63] shows a simplified flow diagram of the basic operations for producing a sand casting. The right hand side of the diagram starts with patternmaking, which refers to all the operations, methods and techniques required to produce a sound quality model and are described elsewhere [64].

The molds are made by pressing the sand, bonded either with resin or clay, to the pattern, internal passageways within the casting are formed by the use of cores, which are made of sand and a binder which provide the strength to withstand the flow of molten metal. Casting production begins with melting the metal, see previous sections, which is tapped into a ladle for pouring in the mold cavity, where it is allowed to solidify within the space defined by mold and cores. After it has solidified, the casting is taken out of the mold, the risers and gates are removed, and the piece is heat treated, cleaned and inspected before it is send to the costumer.

Foundry processes can be classified based on whether the molds are permanent or expendable, subclassifications arise from the type of compound used as binder, or from the nature of the pattern (whether or not they are expandable). Table 4 [65] enlists a series of processes commonly encountered in foundries.

Table 4 Classification of Foundry Processes Based on Mold Type [65]

Expandable mold processes		
Permanent patterns	Expendable patterns	Permanent mold processes
Clay/water bonds	Foamed patterns	High and low pressure
Heat-cured resin binder	Wax patterns	die castings
Cold box resin binder		Permanent mold
No-bake resin binder		Centrifugal casting
Silicate and phosphate		Squeeze casting
bonds		
Plaster bonds		
No bond		

4.1 Sand Casting

Sand casting is one of the most versatile processes, it provides tremendous freedom of design in terms of size, shape and product quality. Different types of sands, such as silica, zirconia, olivine or chromite, are used in casting, although the most common in aluminum are silica and zircon.

Foundry silica sands are composed almost entirely of quartz, SiO_2. Some impurities may be present, such as ilmenite $FeO\text{-}TiO_2$, magnetite, FeO_3O_4, or the ferrous orthosilicate, $(Mg,Fe_2)SiO_4$, known as olivine. Silica sand is used primarily because it is inexpensive and readily available, although the crystallographic reactions that quartz undergoes on heating might produce a series of defects in the casting. The first change in volume takes place at $573°C$ is due to the displacive transformation of quartz α to quartz β, and involves an expansion of around 1.6%. Quartz β undergoes the reconstructive transformation to tridymite at temperatures above $867°C$, which contracts around 0.3%. At temperatures above $1470°C$ tridymite transforms into cristobalite [66].

Zirconia sands are constituted of zirconium silicate $(ZrSiO_4)$, which is highly refractory and exhibits excellent foundry characteristics, such as low thermal expansion, high thermal conductivity and bulk density and low reactivity with molten metal [67].

The size, distribution and shape of sand grains are important in controlling the quality of the mold. It should be realized that grain shape contributes to the amount of sand surface area, whereas size distribution controls the permeability of the mold. As the sand surface increases, the amount of bonding material must increase to achieve the desired mechanical properties, and a change in surface area, due to change in sand shape, will result in the change of the amount of binder required. Round grains have a low surface-area-to-volume ratio and are preferred for making cores because they require the least amount of binder. Angular sands have the greatest surface area and require more aggregates. According to the American Foundrymen's Society, approximately 90% of all castings produced in the United States are produced by sand molding [68].

4.1.1 Bonded Sand Processes

These processes are characterized by the addition of inorganic materials which bond the sand and include green sand molding, dry sand molding, skin dried molds, etc.

The term green sand refers to the sand molds which have been activated by the addition of water to clay-bonded sand. The clays more commonly employed in aluminum castings are bentonites and fireclays.

Bentonites are forms of an hydrated aluminum silicate (montmorillonite) which is capable of expanding as water is absorbed or contracting as it dries. There are two variants of this clay, in the first one, some aluminum atoms are replaced by sodium, which gives the clay a net negative charge and increases its activity and its ability to absorb water, whereas in the second type some of the aluminum atoms are replaced by calcium. Bentonites confer a high degree of plasticity to the sand and, as they contract when drying, they contribute in reducing the effects caused by the transformations that take place in silica. Fireclay consists essentially of kaolinite, an hydrous aluminum silicate; it is highly refractory but has low plasticity, and it is preferred in large castings [67].

When molten metal is poured into a sand mold gases, produced by the thermal decomposition of binders and any other additives employed, result. If the permeability of the mold is not sufficient to allow the escape of these fumes, pressure will increase within the mold, impeding the flow of metal or damaging its walls. But these gases are not always a disadvantage, because the gas pressure prevent metal penetration into the sand, therefore, a balance between mold permeability and the amount of fumes generated must be achieved and maintained. Permeability is controlled by the amount, size and distribution of the voids dispersed among densely packed sand grains, thus sand from a mixture of sieves is commonly recommended.

Another phenomenon which takes place when molten metal is introduced in the mold cavity is that of heat transfer from the liquid to the adjacent sand grains, causing their expansion, and, since it is required that each grain expands freely to avoid damaging the mold wall, these grains should not be densely compacted [69].

4.1.2   Resin Binder Processes

Foundries employ a variety of methods and techniques to produce cast metal parts. Molds can be made of sand or be of a permanent metal type, but in either case, when an internal conduct or passageway has to be made a core has to be used. These cores are the most fragile part of the mold assembly and are normally produced by sand bonded with an organic resin. A wide variety of resin binder processes are available, and they can be classified in the following categories [70]:

- No-bake binder systems.
- Heat-cured binder systems.
- Cold box binder systems.

In the no-bake and cold box processes, the binder is cured at room temperature, whereas in the shell molding and hot box processes, heat contributes to the polymerization reaction.

In all cases the sand is coated with two reactants that form a resin upon the application of heat or a chemical catalyst. The resin converts into a solid plastic that coats the sand so it holds its shape during pouring, an important characteristic of these systems is that the plastic degrades when liquid metal touches the cores, which allows for their rapid disgregation during shaking or further processing.

4.1.3 Unbonded Sand Processes

Casting processes in which the sand does not carry any binding material are alternatives to conventional green sand molding. Of them, the one that is taking more importance in casting aluminum parts is that of lost foam. This process dates from the early '50s and consists in the use of a polystyrene foam pattern imbedded in green sand. The pattern is left within the mold while pouring to be decomposed by the action of the heat from the molten metal, which then replaces the pattern and duplicates its surface [71].

Early lost foam was limited to rough castings because the foam material available was coarse, had to be hand fabricated, and the packed sand would not allow the escape of fumes caused by the decomposing foam, which resulted in porous pieces. Quality was enhanced by replacing green sand by unbounded sand, held in place by the pattern, which allowed rapid escape of gases. Another advantage of this method is that of reducing the time cycle of the unbounded sand, as it does not have any binder, it only has to cool down to room temperature before being used in another mold.

There are some disadvantages that affect this method, among them is the distortion to which the foam pattern can be subjected to when the sand is poured into the container or is being packed. Porosity is also a concern, since the foam and the glues employed to hold the full assembly vaporize, some of the fumes might not be able to escape, and they will be incorporated as pores within the piece. Another point of concern is the mechanical properties of the piece, due to the slow cooling caused by the low heat transfer rate between the metal–sand interface, and the thermal inertia resulting from the mass of sand used in molding.

4.1.4 Sand Reclamation

The economics of a foundry rely on sand reclamation to reduce the costs associated with new sand and those related to landfill use, as well as the problems associated with environmental control of undesirable contaminants in discarded sand. Other operational advantages results from sand reclamation, one of them is the ability to select the best sand for the casting process, in addition, the use of reclaimed sand reduces the number of variables that must be controlled, and provides consistency over a period of time.

Sand reclamation starts with the removal of foreign materials, such as metal spills, slag and paper, and the disintegration of lumps of sand. The organic and inorganic binders are removed either by scrubbing or by thermal methods, clay is normally removed as fines. The sand is brought up to specifications by the addition of new sand, clay and any other type of additives. Sand reclamation systems must be selected, taking in mind their cost, specifications of the sand, system capacity, compatibility with the molding and pouring systems and with the type of cores being used.

4.2 Permanent Mold Casting

Permanent mold casting is sometimes referred to as gravity die casting, a metal mold is usually made of two or more parts which open and close during operation. Cores can be made of removable metal pieces or, when complexity increases, of sand, in the later case this process is sometimes referred to as semipermanent mold casting.

This process is suitable for high-volume production of castings with fairly uniform wall thickness and intricate internal coring. The process can be used to produce complex castings, but quantities should be high enough to justify the cost of metallic molds. Compared to sand molding, permanent mold casting permits the production of more uniform parts, with closer dimensional tolerances, superior surface finish and improved mechanical properties. It should be mentioned that this process has a series of limitations, among them are the high tooling costs, which implies a high production volume to make it profitable. Some shapes might not be suitable to cast in a permanent mold due to parting line location, undercuts or difficulties in removing the piece from the mold. Coatings are required to protect the mold from attack by the molten metal [72].

A simple permanent mold may consist of only two pieces arranged in a book or similar type of style. The mold cavity when the halves are closed determines the shape of the casting. Metal fills the cavity by means of gates, sprues and runners; risers are added to assure proper filling as the piece solidifies and contracts. The cavity should be vented to allow air to escape. Gating systems for permanent molds are less flexible than those for sand molds, and are nearly always located in parting planes. Gating must supply metal fast enough to fill all sections of the casting with minimal turbulence, otherwise excess of oxide may form endangering the quality of the part. Molds for aluminum alloys are poured in the vertical position to allow for rapid displacement of air (venting). Special care has to be taken when designing the gating system, in most cases, the last metal that enters the cavity is the hottest, and if it remains towards the bottom of the mold, it will interfere with gravity feeding and progressive solidification, and will produce castings with shrinkage porosity.

Coatings are applied to mold surfaces to serve as a barrier between the molten metal and the mold before a skin of solid metal is formed. These coatings perform different functions, among them are: to prevent premature freezing of the metal; to control the rate and direction of solidification; to reduce the thermal shock and fatigue of the mold; and to vent air trapped in the mold cavity. Mold coatings can behave as insulating or lubricating layers, the former ones are based on ceramic formulations, whereas the later ones usually contains graphite in a suitable carrier.

One of the most important parameters to control is the mold temperature, because if it is too high, excessive flash will develop, castings might be too weak to extract undamaged and their mechanical properties and surface finish may be impaired. When the temperature is too low, cold shuts and misruns will be likely to occur, feeding will be inhibited (which generally results in shrinkage defects), hot tears and sticking of the casting to the mold will be increased. In many operations molds are preheated either by direct flame or by placing hot castings on them. Molds designed for pieces requiring high mechanical properties are normally cooled by the use of either forced air or water.

4.3   Die Casting

All the processes described in the previous sections use gravity as driving force for filling the different types of cavities. When liquid metal is pushed into a cavity, either by a ram, gas or a pump, the process is called die casting, and this can take either at high or low pressure.
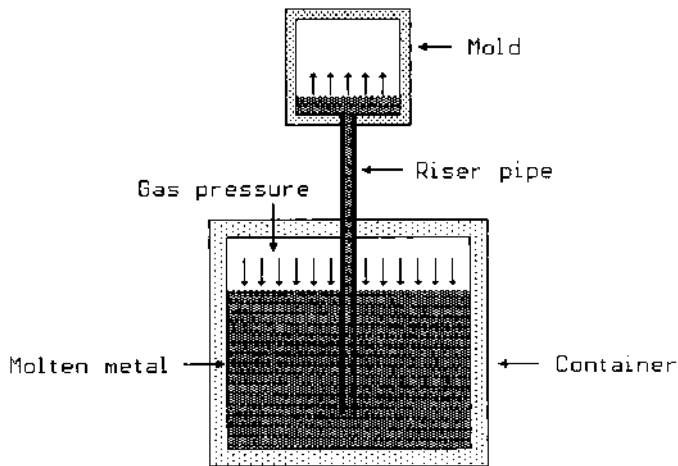
Figure 26   Schematic diagram of the low pressure process.

4.3.1   Low Pressure Die Casting

In this process liquid metal, held in a pressure tight holding furnace, fills the mold cavity by means of a riser pipe when the top surface of the vessel is pressurized, Fig. 26. After the metal fills the die, it commences to solidify, with the solidification front progressively moving from the extremities of the mold back towards the riser tube, once the front reaches the top of the pipe, the pressure on the vessel is released and the remaining liquid metal falls into the container.

Low pressure die casting is a process very similar to that of permanent mold casting in the sense that the liquid metal enters the die at a relatively low velocity and, ideally, maintains a non-turbulent flow while filling the cavity, but since there is less control of cavity fill and a greater tendency to entrain air in the metal under gravity pouring conditions, the low pressure process should provide higher quality pieces. Another difference between both processes is product yield, the runners and risers in gravity permanent mold casting can amount to 50% of the mass, whereas the yield in low pressure die casting is claimed to be as high as 95% [73].

Because the cavity fills at a slow velocity, the dies are normally coated with a thin layer of a ceramic base material to reduce the rate of heat transfer to the metallic mold. This layer also prevents molten metal attack of the die. Complex sand cores can also be used in low pressure die casting, in contrast with high pressure die casting, where sand cores tend to disintegrate when subjected to the high injection speed.

The everyday competition for lower weights in automotive industry has made some foundries to cast pieces such as road wheels and cylinder heads by low pressure. This process is also being considered for the production of high integrity castings for suspension, steering and braking applications [73].

Traditional low pressure die casting uses permanent metallic molds; in some cases, like road wheels production, no sand cores are used, however, when cylinder heads or engine blocks are cast, the sand cores are required. Recent developments in the production of engine blocks has changed the material from which the molds

Table 5 Operating Parameters for Low and High Pressure Die Casting [73]

Parameter	Low pressure	High pressure
Cavity fill time	3–30 sec	50–200 msec
Metal pressure	30–100 kPa	10–60 MPa
Gate velocity	0.1–0.6 m/sec	20–60 m/sec
Die temperature	300–450°C	120–260°C
Solidification time	30–300 sec	1–10 sec
Casting-mold heat transfer coefficient	0.2–2 kW/m^2°C	20–90 kW/m^2°C
Cycle time	5–10 min	20–120 sec

are made, the best known version is that developed by Cosworth [74], in which the mold is made from zirconia sand and it is filled by means of an electromagnetic pump, an alternative to this method is the Improved Low-Pressure Process (ILP) [75], which uses silica sand and fills the mold by the more traditional way of increasing gas pressure, see Fig. 26.

4.3.2 High Pressure Die Casting

High pressure die casting is characterized by the high speed at which the molten metal is injected within the mold cavity. Due to the very high kinetic energy of the liquid metal, no sand cores are normally used, since the impact will disintegrate them. This high kinetic energy is the cause that the machines used to produce die cast parts are rated by the closing pressure that they can exert on the dies, rather than on the capacity or weight of their castings, another limitation of this process is the need to pay for the metallic permanent mods, which translates into high volume and productivity [76].

   The metal flow in this process is turbulent and much metal will be injected as finely divided droplets which, if the heat transfer rate during solidification is low, may be the cause for porosity. This process is limited to produce small parts, in part due to the need to achieve a high transfer rate and in part due to the high closing pressure that the dies should withstand when big pieces are cast. This process is optimum to produce thin walls (of less than 0.5 mm thick) in high volumes, moreover, several small pieces can be cast together to increase productivity.

   The predominant type of die casting for aluminum alloys is that of cold chamber, which consists in a small reservoir (held at a temperature of 160–260°C) in which molten aluminum, taken from a holding furnace, is placed. Once this is done, a ram injects the metal into the cavity. The mold opens once the pieces are solid, the interior of the mold is inspected (in some cases a coating may be employed), and the die closes for the next cycle. Table 5 [73] resumes the differences between low and high pressure die casting of aluminum alloys.

5   HEAT TREATING

The broadest meaning of heat treating comprises all thermal practices intended to modify the metallurgical structure of products in order to control their physical and mechanical characteristics and accomplish specific engineering criteria, but,

in aluminum industry, the term heat treating is often used to describe the procedures and practices required to achieve maximum strength or hardness in a suitable alloy. Normal practice involves a sequence of solution heat treating, rapid cooling (quenching) and precipitation hardening (aging). Proper alloying and temper selection allows for the achievement of different features, among them [1]:

- Improve machinability.
- Achieve the mechanical properties associated with a particular condition.
- Stabilization of mechanical and physical properties.
- Ensure dimensional stability under service conditions.
- Relieve residual stresses induced by different manufacturing operations.

The Aluminum Association has standardized the definitions and nomenclature applicable to thermal practice and maintains a registry of standard practices and designations for industry, of them, the ones applicable to castings are:

O: annealed (thermal stress relieved).
T4: solution heat treated and quenched.
T5: artificially aged.
T6: solution heat treated, quenched and artificially aged.
T7: solution heat treated, quenched and stabilized (overaged).
T8: cold reduced before aging to improve compressive yield strength.

5.1 Principles of Heat Treating

Although most metals will alloy with aluminum, few of them have sufficient solid solution to serve as addition. Of the most commonly used elements, only Zn, Mg, Cu and Si have significant solubilities, Table 6. The versatility of alloying and heat treatment is manifest in the fact that it is possible to increase the yield strength of high purity aluminum by as much as 40 times [76].

The basic requirement for an alloy to be amenable for age-hardening is a decrease in solid solubility with decreasing temperature of one or more of the alloying elements. Such condition is met by different alloying combinations, of them, the most important in castings are Al-Cu, Al-Mg-Si or Al-Zn-Mg, as an example, a section of the Al-Cu phase diagram is shown in Fig. 27.

Age-hardening is produced by the formation of a series of precipitated particles which form from a supersaturated solid solution [76,77], Table 7. The complete decomposition of the solution is usually complex and may involve several stages. Early stages of decomposition involve clustering of the alloying elements to form one or two atoms layers of what are called Guinier–Preston (GP) zones. These zones retain the structure of the matrix and are coherent with it. Their formation requires movements of atoms over short distances so they are very finely dispersed in the matrix.

The intermediate precipitates are normally much larger in size than GP zones and they are only partly coherent with the matrix. They have a composition and crystal structure close to that of the equilibrium phase. These intermediate precipitates are, in some alloys, nucleated from, or at the site of the GP zones. Formation of the final equilibrium precipitates involves complete loss of coherency with the parent lattice and, because they tend to be coarsely dispersed, softening of the alloy results.

Table 6   Solid Solution of Selected Elements in Aluminum [77]

Element	Temperature (°C)	Maximum solubility (wt%)	(at%)
Ag	566	55.6	13.8
Cu	548	5.65	2.40
Cr	661	0.77	0.40
Fe	655	0.05	0.025
Mg	450	17.4	18.5
Mn	658	1.82	0.90
Si	577	1.65	1.59
Ti	665	1.30	0.74
Zn	443	70.0	28.8

5.2   Heat Treating of Cast Alloys

Heat treating of industrial casting alloys differs to that carried out in wrought alloys due to the presence of complex eutectic phases. For instance, thermal analysis obtained during solidification of a 319 alloy, Figs. 23 and 24, show the presence of a complex $Al_5Mg_8Cu_2Si_6$-$CuAl_2$ eutectic that solidifies below 500°C. If full hardening by aging of this alloy is intended, the material should be heated above 490°C to dissolve the 3.6 wt% Cu it contains, Fig. 27, and at this temperatures, any temperature variation within the furnace may endanger the surface quality of the piece, due to melting of this complex eutectic. Unfortunately, decrease in solubilization temperature results in reduction of mechanical properties, Fig. 28.

Another factor that affects heat treating is the time required to put in solution coarse microstructures resulting from slow solidification rate processes. In general,
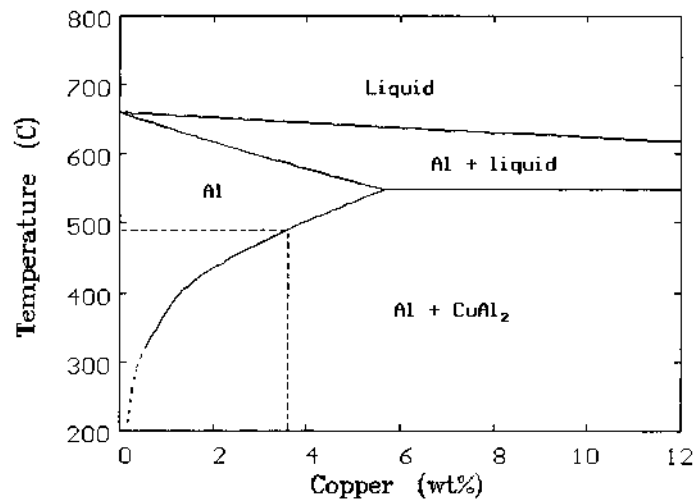
Figure 27   Section of the aluminum-copper equilibrium phase diagram.

Table 7 Precipitation Processes in Aluminum Alloys [77,78]

Alloy	Precipitates	Remarks
Al-Cu	GP zones	Probably single layers of copper atoms on $\{100\}_\alpha$
	θ''	Coherent, probably two layers of copper atoms separated by three layers of aluminium atoms. May nucleate at GP zones
	θ' tetragonal Al_2Cu	Semi-coherent plates nucleated at dislocation on $\{100\}_\alpha$
	θ body centred tetragonal Al_2 Cu	Incoherent equilibrium phase. May nucleate at surface of θ'
Al-Mg-Si	Clusters of Mg and Si atoms. GP zones?	GP zones solvus occurs at temperatures that are normally higher than the aging temperature
	β'' monoclinic	Coherent needles along $\langle 100 \rangle_\alpha$
	β' hexagonal Mg_2Si	Semi-coherent rods. May form from β''
	B' hexagonal Mg_2Si	Semi-coherent laths. Lie along $\langle 100 \rangle_\alpha$. Forms with β' Favoured by high Si: Mg ratios.
	β face centred cubic Mg_2Si	Platelets on $\{100\}_\alpha$ May transform directly from β'
Al-Zn-Mg	GP zones	Possibility of two types of zones
	η' hexagonal $MgZn_2$	May form from GP zones in alloys with Zn: Mg $> 3:1$
	η hexagonal $MgZn_2$	Forms from η'. May have one of nine orientation relationships with matrix
	T' hexagonal $Mg_{32}(Al,Zn)_{49}$	Semi-coherent. May form instead of η in alloys with high Mg: Zn ratios
	T' cubic Mg_{32} $(Al,Zn)_{49}$	May form from η if aging above 190°C, or from T' in alloys with Mg:Zn ratios
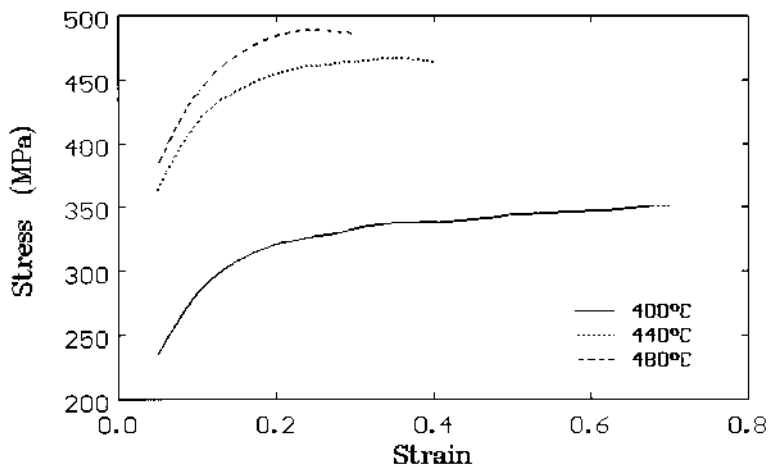
Figure 28 Stress-strain curves obtained in compression of **T4** samples from a 319 alloy solubilized at three different temperatures.

it is found that the time required to achieve solution is progressively shorter for investment, sand and permanent mold casting, but thin-walled sand castings produced with extensive chills can display finer microstructures than those obtained in heavy-section permanent mold parts.

Rapid cooling or quenching from solution should be taken special care, as it is desirable to keep in solution as much of the alloying elements as possible, but in parts in which transition from thick to thin sections is abrupt distortion will be found [78], and the cooling rate should be reduced to avoid it. Most commercial quenching is accomplished in water near the boiling point, but there is a tendency to increase the use of polymers emulsions in room temperature water [78,79]. Figure 29 [80] can be used to predict whether or not an aluminum casting may be subjected to dangerous high stresses or not as a result of the cooling rate experienced during quenching, and the distance to which heat should diffuse to obtain an uniform quench, i.e. the cooling rate should be reduced with the increase of size and mass of the heat treated pieces.

Experimental trials should be conducted to find a critical cooling rate, above which no increase of hardness is found to occur. Such a case for a 319 alloy is shown in Fig. 30, where the maximum value of hardness in samples aged at 160°C are plotted as a function of the average cooling rate detected in the 400–480°C range, and, as it can be seen, this critical rate results to be around 10°C/sec, which coincides with results obtained in wrought alloys [81,82].

Aging of aluminum alloys can be followed by conducting hardness tests in samples left at given temperatures for different times, Fig. 31. Most aluminum alloys age-harden naturally to some extent after quenching. The extent of change is highly alloy dependent, for instance, alloys A356 and C355 age within 48 hr, with insignificant changes thereafter, whereas alloy 520 hardens over a period of years [1].
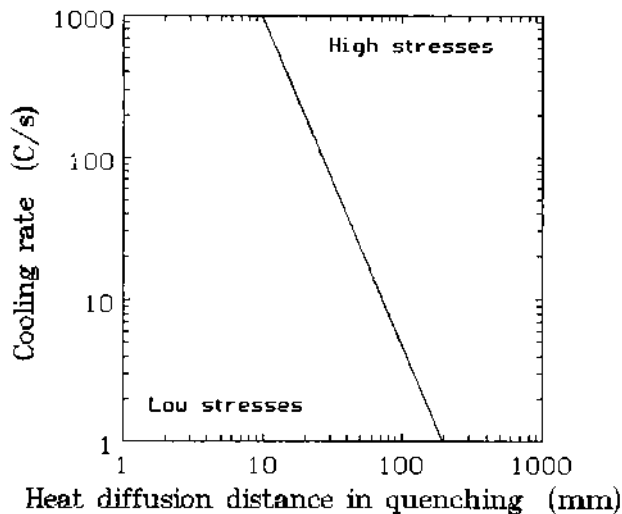
Figure 29 Threshold for the development of dangerous high stresses in aluminum castings as a function of the cooling rate and the distance for heat diffusion. (From Ref. 80.)
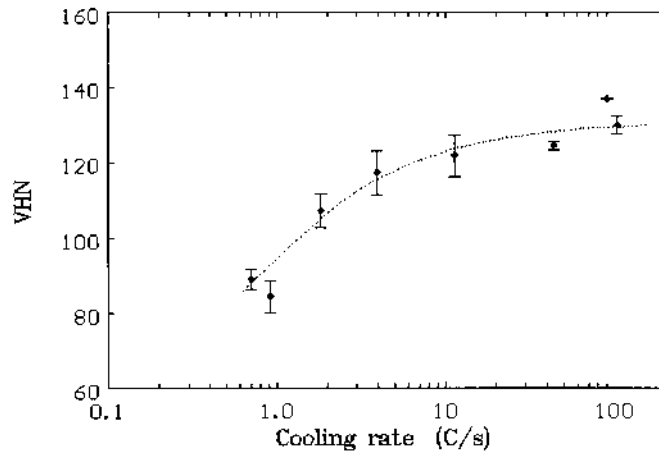
Figure 30 Variation of the **T6** hardness achieved in a 319 alloy as a function of the cooling rate averaged in the 400–480°C range.
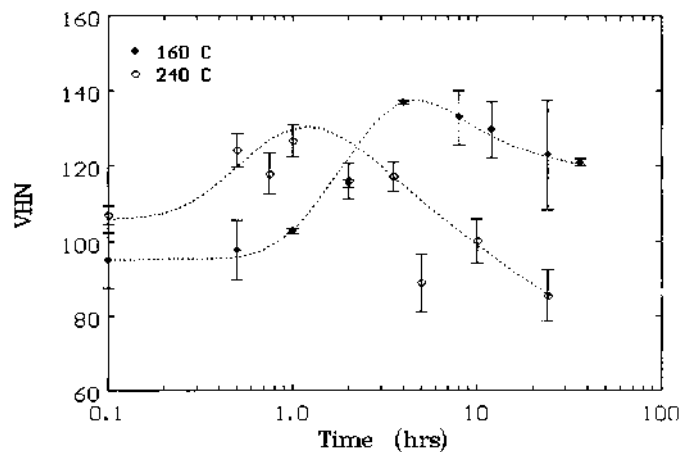
Figure 31 Aging at 160°C of a 319 alloy solubilized at 480°C for 6 hr.

The process of aging can be accelerated by increasing the temperature, but the maximum hardness which can be obtained will be reduced with the increase of temperature, as coarser and more dispersed precipitates will be formed [76,77].

The stabilization (**T7**) treatment can have some advantages over the **T6**, among them is the reduction in residual stresses which is achieved as stabilization is conducted at higher temperatures (220–240°C) than **T6** (150–180°C) [1]. Furthermore, the overaged treatment results in increased stability and performance when service involves exposure at elevated temperatures and to thermal fatigue [83].

5.3 Effects on Microstructure

Solubilization of precipitated phases is not the only microstructure feature which change as the casting alloys are heat treated. It is known that the morphology
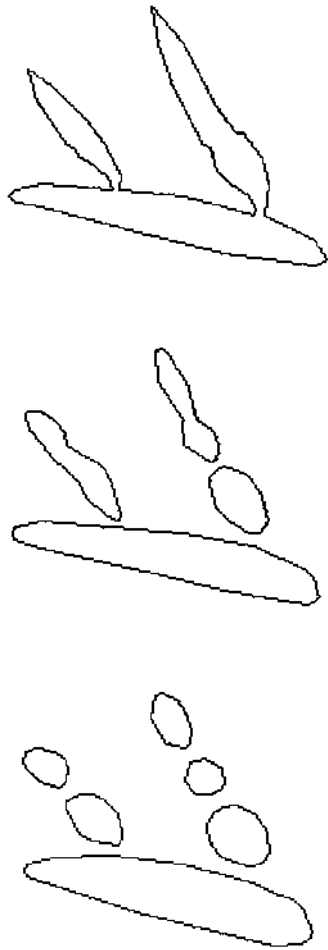
Figure 32 Spheroidization of Si platelets during solubilization.

of intermetallic phases change when the alloy is treated at high temperature for long periods of time [53,84]. Their results indicate that the morphology of β-phase platelets changes through concurrent fragmentation and dissolution at the plate tips, whereas α phase does not undergo any change. They conclude that temperature is more critical than time, once a minimum solution time is exceeded, and an optimum temperature of 535°C is quoted [84]. This temperature might be to high for an alloy containing any amount of the complex $Al_5Mg_8Cu_2Si_6$-$CuAl_2$ eutectic, see Figs. 23 and 24, and will be susceptible to an increase in porosity [53].

Solubilization contributes to modification of the Al-Si eutectic [45,48,85,86], as the sharp platelets of Si will be broken and rounded, Fig. 32, yielding to an increase in their roundness, Fig. 33, and in the mean free path between them [87], Fig. 34, which will contribute to improve physical [37,87,88] and mechanical [1,2,45–48,85,86] properties, but some troubles might arise during machining if the morphology of the silicon phase is fully rounded during heat treatment.
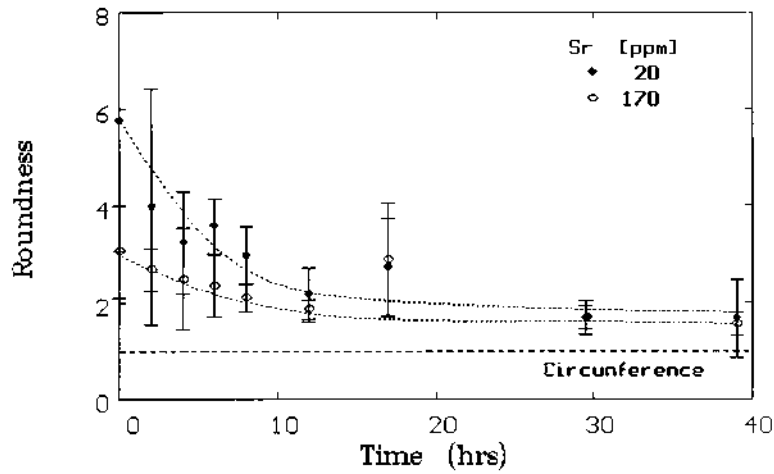
Figure 33 Change in roundness of silicon particles with time.
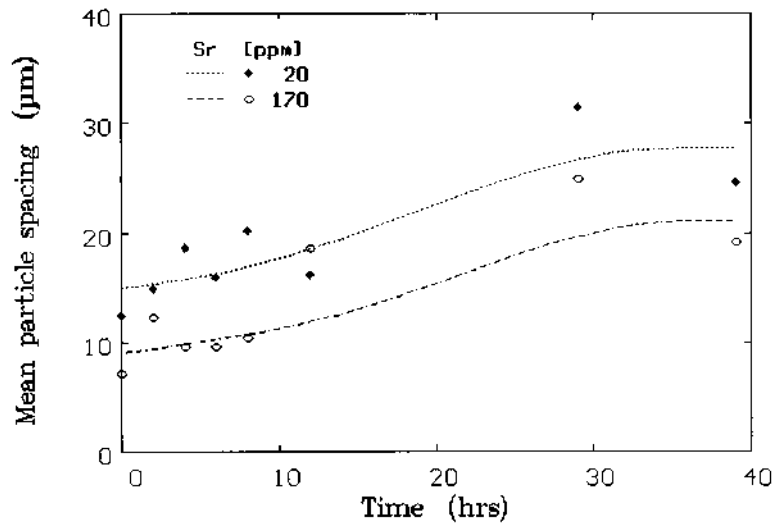
Figure 34 Change in mean particle spacing between silicon platelets with time.

6 COMPUTER MODELING

Development of computer code to predict the behavior of a metal as it is poured in a mold has matured from an academic problem, in the early '60s and '70s, to a useful tool for the operating foundryman on the shop floor. Continuous improvement in hardware in terms of speed and cost have made this task easier, but there are still some limitations related to casting complexity, and to the amount of time involved in the numerous computations required to simulate the flow, cooling and solidification of a complex casting shape.

Modeling and simulation of a problem is based on the possibility of braking it into its components parts, which will be small enough to be understood in sufficient detail. The aspects of the different parts can then be researched in an individual way, and when sufficient understanding of these has emerged, and integrated model of the whole problem is build upon this new knowledge. The capability to reproduce the behavior of such a model will depend on how finely the mechanisms of the individual components are understood, however, the advantage of this type of models is that they can now be modified, improved or scaled without loss of accuracy. Nowadays it is possible to simulate the casting process by solving the momentum, energy and continuity equations to obtain the local velocities and temperatures of the metal as it flows in a mold. Several authors [88–97] have pointed out the applications of solidification modeling as well as its limitations and potentials.

6.1 Modeling Heat Flow

Evaluation of the heat flowing from the liquid metal into the mold has been from the beginning one of the most important tasks in the simulation of castings. Two major techniques, which are the finite difference method (FDM) and the finite element method (FEM) are commonly employed to solve heat transfer problems [89,92–96]. Both of them approximate the solution of differential equations of the initial-value or boundary type, which in the case of two-dimensional conduction is given by:

$$\frac{\partial T}{\partial t} = \frac{\partial(\alpha\,\partial T)}{\partial x^2} + \frac{\partial(\alpha\,\partial T)}{\partial y^2} + Q \tag{8}$$

where T is the temperature, t the time, α the temperature dependent thermal diffusivity of the material, x and y are the spatial coordinates and Q represents the change in temperature in the material due to phase transformation, which, in the case of solidification, is given by [92]:

$$Q = L\frac{\partial X}{\partial t} \tag{9}$$

where X is the solid fraction and L is the latent heat.

The FDM divides the solution domain into many smaller regions called cells and, the governing differential equation is converted into one in differences [98] which is applied at the centre of each cell. Figure 35 shows the case in which a body is divided into a number (m) of cells to solve the two-dimensional heat flow. Two schemes can be employed to evaluate the gradients within the body by transforming Eq. (8). The first one calculates the temperatures at the centre of a cell at the end of a given cycle of computation as a function of the temperatures of the surrounding cells at the beginning of the iteration, such changes are calculated by:

$$\frac{T_a^* - T_a}{\Delta t} = \alpha\left[\frac{T_b - 2\,T_a + T_c}{(\delta\,x)^2} + \frac{T_d - 2\,T_a + T_e}{(\delta\,y)^2}\right] \tag{10}$$
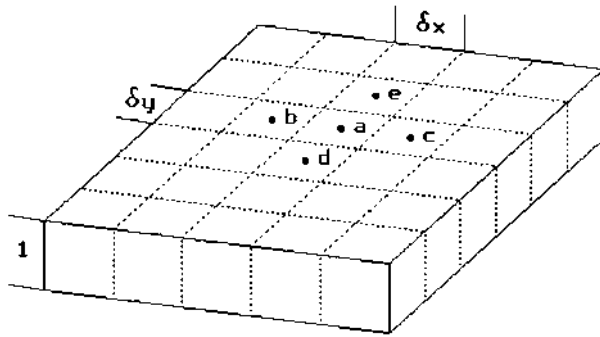
Figure 35 Division of a piece to calculate two-dimensional heat flow.

where Δt, δx and δy replace the differential terms ∂t, ∂x, ∂y, T_a, T_b, T_c, T_d and T_e, are the temperatures at the centre of cells a, b, c, d and e, at the start of the iteration, T_a^* represents the temperature at the centre of cell a after Δt has elapsed: α is evaluated at T_a.

The second scheme calculates the temperature at the end of the iteration as a function of the temperatures at the end of the cycle of their surrounding neighbors:

$$\frac{T_a^* - T_a}{\Delta t} = \alpha \left[\frac{T_b^* - 2\, T_a^* + T_c^*}{(\delta\, x)^2} + \frac{T_d^* - 2\, T_a^* + T_e^*}{(\delta\, y)^2} \right] \tag{11}$$

The former one is known as the explicit formulation and has the advantage of being faster and easier to employ, the second one, implicit, requires that all the local equations are collected to form a system of algebraic equations, that also include the boundary conditions, in terms of the unknown variables. The values of these variables are found by solving this matrix system. One limitation of FDM is that curved boundaries cannot be adequately represented, and the software has then to use very small cells, which increase their number, and the time involved in the simulation of a single cast.

The finite element method employs subdivision of the solution domain into regions of different elements of more convenient shapes (such as triangles and quadrangles) that are connected at their nodes. The method uses approximation theory to evaluate the behavior in each element and the action of the differential equations are approximated by their values at the nodes. The differential equations are transformed into finite element equations with the use of the variational principle or the weighted residual methods [99]. The local equations are collected to form a global system of ordinary differential or algebraic equations (incorporating the boundary conditions). FEM has the advantage over FDM that non-linear problems involving heterogeneous materials can be addressed. Curved and moving boundaries can also be modeled with FEM.

6.2 Fluid Flow Modeling

For industries where different shapes occur frequently, and for large components where the fill-time is an important part of the solidification time, the thermal response of a mold or die is important to the thermal field of the liquid metal, and on its solidification and production of defects. Two different cases can be considered, the first one in which very slow filling occurs and flow is nearly laminar and thermal conduction is dominant, and the more usual case where the effects due to turbulence should be taken into account.

Fluid flow modeling might be the only way to know what is going within the mold, since it is difficult to make direct observations inside them, because the metal and mold are opaque, the temperature is high and the conditions are far from stationary. Moreover, modeling can give information about velocity and pressure gradients within the molten metal, which cannot be obtained by direct observation.

When direction of flow is dictated by geometry, as in the case of flow in sprues, runners and gates, the computational techniques more employed are those based on energy balance, whereas modeling flow in open cavities requires the solution of the Navier–Stokes equation by the momentum balance method [90,91,95].

Fluid flow within a cavity during filling is transient, the amount and location of liquid changes rapidly with time, and the location of the free surface should be an integral part of the calculations. Most of the software developed to account for the location of the free surface are based on the Mark and Cell algorithm [90,91,93,95]. This method divides the system into a number of cells, and sets a series of imaginary markers (or fluid function values) are introduced to represent the location of the fluid at any instant. The velocity field of the fluid is calculated and the markers are moved (or the fluid function is updated) to separate the regions considered to be filled by the liquid from those empty. The procedure is repeated from the beginning, when the cavity is empty, until it is filled. Figure 36 shows an example of such when the boundary is delimited by fluid function values.

6.3 Microstructural Evolution

Casting is the unusual manufacturing process in which modeling activities are well developed at different scales for the multiple physical mechanisms and processes involved: nucleation, dendritic growth, liquid flow through semi-solid dendrites, latent heat evolution, etc., although not all the mechanisms are as well developed in all alloys [92,94,96].

Shaped casting thus provides an excellent illustration of a manufacturing process where modeling has produced a very wide variety of scientific and industrial tools. Casting has to couple macroscopic modeling of geometric shapes with micro-models of materials processes. For a shaped piece, its morphology itself is a property of interest only at sizes above 1 mm, whereas growth of nuclei involve phenomena at atomic scales [92,94,96,100–102].

6.3.1 Nucleation

Nucleation modeling depends on the alloy and the casting procedure, if the nucleation potential of the alloy cannot be controlled within a small range then no model will be of much help. If nucleating agents are added the availability of nucleating sites will depend only on the distribution and movement of these particles
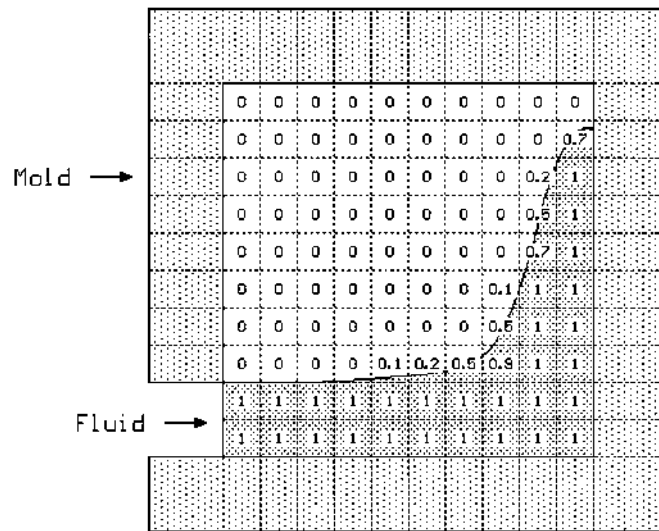
Figure 36 Positioning of the liquid boundary obtained with the fluid flow function (0 = full, 1 = empty).

and not on any stochastic process [96]. Only recently have modeling algorithms been developed to predict the probability of individual nucleation colonies, so an overall behavior can be deduced from modeling such events [100].

6.3.2 Growth Models

Modeling growth of individual microstructural features involve different scales, a grain is an order of magnitude larger than the primary dendritic spacing, which is also an order of magnitude larger than the secondary arm spacing. Modeling of the shape of dendrites has been conducted at scales of less than 10 μm and reproduces stable and unstable behavior and the transition between cellular and dendritic growth patterns [103,104], which has been incorporated into a physical-based dendrite model [100].

Growth models are required to obtain more sophisticated transport solidification models which are based on experimental data or in simple solid-fraction latent heat models. A series of attempts have been made to predict grain formation and growth since the original work by Scheil [105]. A particular problem when modeling growth is that of impingement, since a dendrite, grain or colony will be able to enlarge as long as it does not touches another growing structure.

6.3.3 Defect Prediction

Shaped castings commonly contains fluids, so the most important defects are those which can lead to leaks, either by loss of strength of directly through pores or pits near the surface. It is common practice to predict porosity based on the criterion

proposed by Niyama et al. [106]:

$$N = \frac{G}{R^{0.5}} \tag{12}$$

where N is an index which will indicate the occurrence of porosity when a critical value is exceeded, G is the maximum thermal gradient computed between a cell or element (depending if FDM or FEM is employed) and its neighbors, and R the cooling rate at the cell or element, it should be mentioned that both R and G are those at the solidus temperature. A disadvantage of such criterion is that porosity can only be determined in the piece after the simulation has finished, and not during modeling, which might affect the results since porosity will affect heat transfer in the volume surrounding it.

6.4   Interfacial Effects

As liquid metal is poured into a mold, it will establish intimate contact with the walls, where heterogeneous nucleation will be promoted, and the solid microstructure will start to develop. Heat transfer to the mold will not only be controlled by the thermophysical properties of the material from which the mold is made, but also by the type of coating or paint used to protect the wall and avoid adhesion between the liquid alloy and the mold.

The heat transfer conditions during solidification are complex because the boundary conditions change with time. As the metal solidifies, it shrinks, forming an air gap at the interface, which reduces the heat transfer rate [107–110], but also, solidification proceeds through a series of reactions which result in different microstructures, each of them with different properties, for instance, it is known that thermal conductivity is higher for solid aluminum than liquid [111].

Figure 37 [110] plots the heat transfer coefficients, as a function of time and temperature, which were found in a series of experimental trials carried out with an hypoeutectic Al-Si alloy cast on top of a steel plate, which was protected by either of two different paints (ceramic and graphite), and was cooled at its bottom either with water or air. The values recommended by a developer of computer code [112] are included for comparison.

The variation of the heat transfer coefficient shown in Fig. 37 can be rationalized in terms of the diagram shown in Fig. 38. The low heat transfer rates found at the early period of solidification can be due to the lower conductivity of the liquid as compared with the solid (a). The transfer rate will be increased as the dendritic network develops (b), because nucleation occurs at the interface and, as the individual dendrites grow and develop the secondary branches, the transfer rate will be enhanced. The decrease in the heat transfer coefficient as the eutectic starts to form (c) might be due to shrinkage of the solid crust, the establishment of a layer of lower thermal conductivity (since thermal conductivity of Si is lower than that of the A1), or by the heat evolution produced by this reaction. Once the interfacial layer has fully developed, the transfer rate will decrease as the gap generated by the shrinkage grows (d).
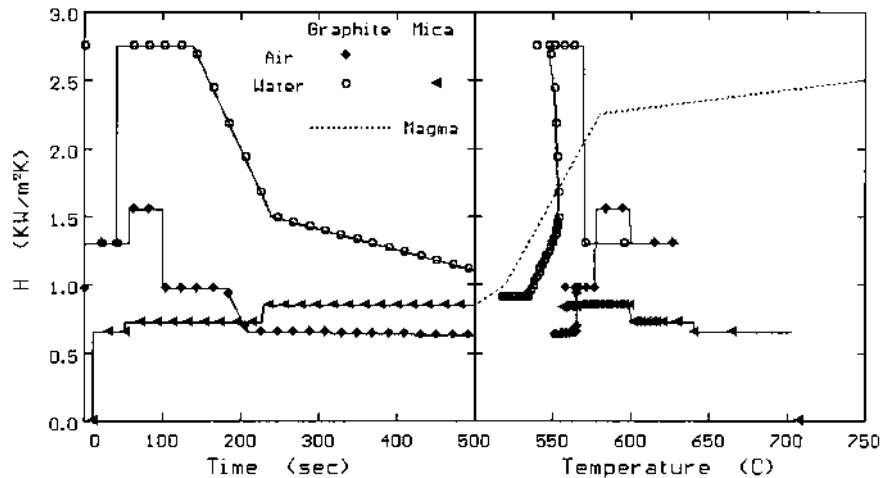
Figure 37 Heat transfer coefficients at different interfaces found when casting an aluminum alloy on top of a metal mold. (From Ref. 110. Data from Ref. 112 is added for comparison.)

6.5 A Simulation System

A casting simulation system should consist of three distinct components:

- Pre-processing.
- Processing.
- Post-processing.

The first step to simulate casting is the simplification of the physical phenomena by realistic assumptions and basic observations. This step is conducted during pre-processing by taking a solid model of the piece to be simulated, the model is then divided into small pieces (cells or elements) of appropriate shape. The thermophysical properties of the liquid, as well as of those other materials forming part of the mold are set, this can be done by a series of tables in which the temperature dependence of the variable is interpolated, or by the introduction of different parametric equations. The boundary conditions can also be set in the same way, see Fig. 37. The time required in the simulation can be shortened in pieces in which a symmetry plane is found. Figure 39 shows, as an example, the numerous small cells into which a cylinder head should be divided to simulate its casting.

Processing implies the solution of the different set of equations employed to model the casting problem. A comprehensive model should account for fluid flow and heat transfer during filling the mold, fluid flow, heat and mass transfer during solidification, as well as the thermal and mechanical stresses developed during cooling. These macro-scale phenomena should be coupled with micro-scale mechanisms (nucleation, growth, segregation, etc.) to obtain sensible results.

Post-processing in mathematical modeling and computer simulation is normally referred to the activities involved in assembling the data produced during processing in order to visualize the process, an example of such is shown in Fig. 40,
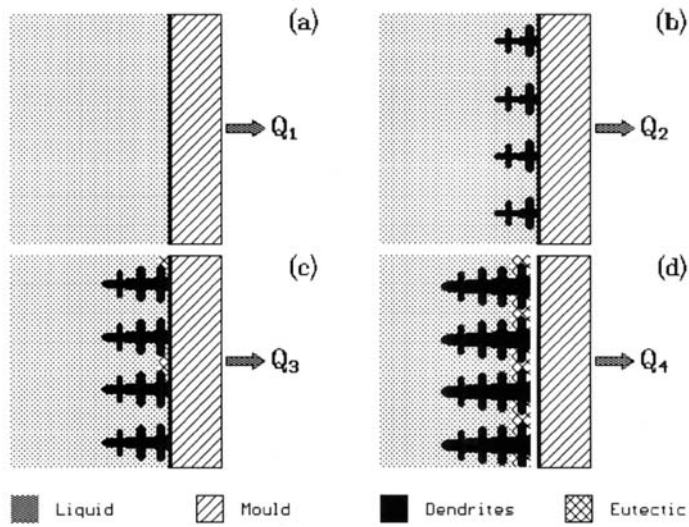
Figure 38 Solidification mechanisms which affect the heat transfer rate to the mold.
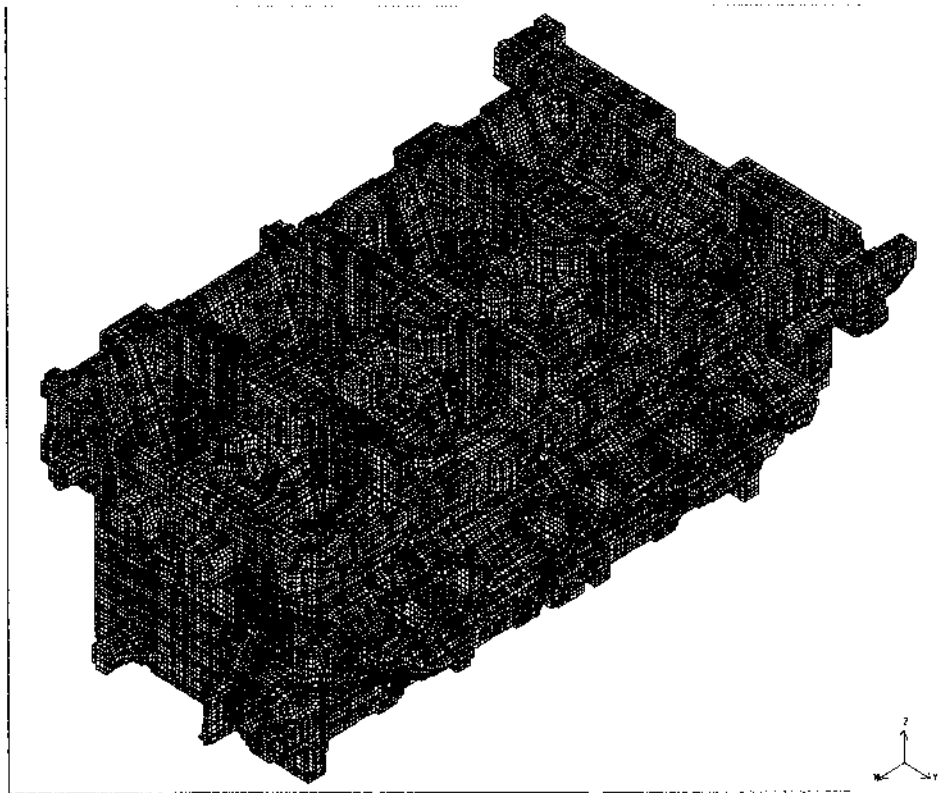
Figure 39 Example of the numerous cells required to simulate a cylinder head.
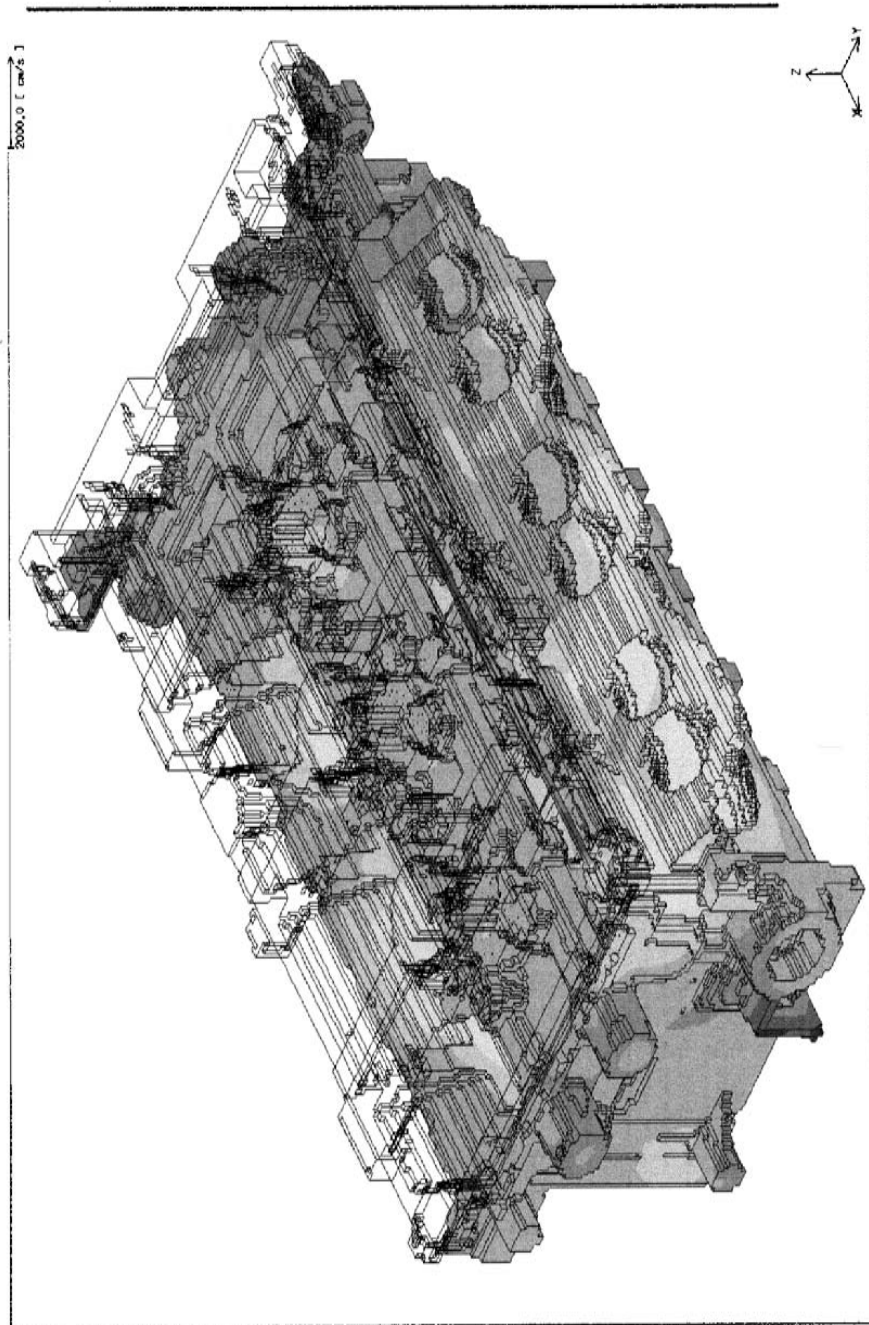
Figure 40 Thermal field computed during solidification of the piece shown in Fig. 39.

in which the thermal field obtained during solidification of the piece shown in Fig. 39 are plotted.

7 NOVEL PROCESSES

Continuous development of castings in order to obtain better properties and reduce processing costs and times has resulted in different non-traditional processes, among them, the most important are semisolid or slurry processing and particle reinforced casts.

7.1 Semisolid Processing

Metals are traditionally processed either in liquid or solid state. Processing metals while there are a mixture of solid particles dispersed in liquid is a relatively new technology which is experiencing a rapid growth [113,114]. Processing of materials in semisolid state offers distinct advantages over similar net-shaping methods. These benefits arise from the rheologic properties of the material which lie between those of a pure liquid and a pure solid. Two distinctive names are given to the process depending on whether the material is injected into a die (thixocasting) or shaped between closed dies (thixoforming), Fig. 41.

The raw material in these processes is melted and allowed to cool and solidify while its structure is altered by mechanical or electromagnetic means. The process at this stage is called rheocasting since the melt is rheologically manipulated during the liquid–solid transformation. The parts being prepared in this way are then reheated to a temperature in the mushy region and processed into complex shapes.

Semisolid processing offers several advantages over liquid metal processes, among them are the reduction in porosity as the liquid fraction to solidify is just a fraction, the heat to extract from a piece is less, which allows for higher productivity and shorter cycles, the semisolid metal has a higher viscosity than the
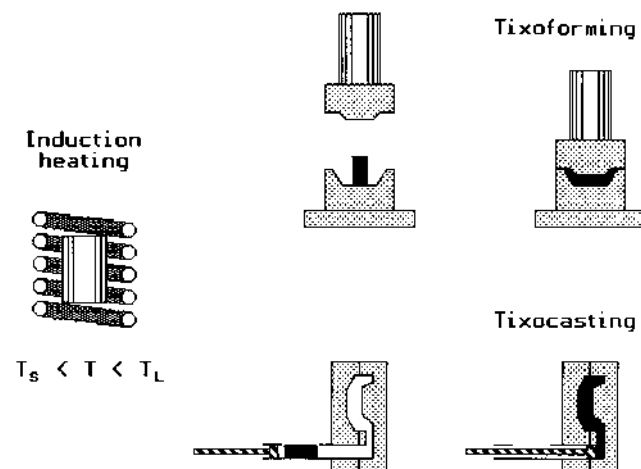
Figure 41 Schematic diagrams of the thixocasting and thixoforming processes.

liquid, which allows for filling the die cavity in a non-turbulent fashion, minimizing the potential for entrapping air. These characteristics allow for production of pressure tight and structural components employed in the automotive industry [115].

7.2 Particle Reinforced Castings

Castings reinforced by particles are special formulations of one or more materials in liquid metal in which tailored properties are achieved by systematic combination of different constituents. Modern reinforced castings differ from traditional processes in the sense that any volume, shape or size of reinforcement can be introduced into the material [116,117], Table 8.

A basic requirement for processing these materials is the intimate contact and bonding between the reinforced particles and the molten alloy. This is achieved by mixing the dispersoids into the melt or by pressure infiltration of molten alloys into preforms of a ceramic phase. Due to the poor wetability of most ceramics by molten metals, intimate contact between particles and alloy can be promoted by using external forces. Various mixing techniques have been developed to introduce the dispersoids in the melt, among the most used are: addition of particles to a vigorously agitated bath, gun injection of particles in the melt, additions of powders to ultrasonically or electromagnetically stirred alloy, and centrifugal dispersion of particles in a melt.

Aluminum alloys have been used as matrix materials in a wide variety of composites containing graphite and ceramic particles, glass microspheres and ceramic fibers [117]. The microstructures of these aluminum-silicon hypoeutectic alloys, Fig. 42, show that the primary aluminum dendrites avoid the added particles (graphite and silicon carbide in this case), and they grow by rejecting solute into the melt, while the ceramic particles will restrict diffusion and fluid flow. Primary silicon and the eutectic aggregate, in the other hand, will tend to concentrate on the particle surface [116].

Table 8 Dispersoid Used in Cast Aluminum Alloys [116,117]

Dispersoid	Dispersoid size (μm)	Amount of dispersoid (%)
Graphite flakes	20–60	0.9–1
Graphite granules	15–100	1–8
Alumina particles	3–200	3–30
Silicon carbide particles	16–120	3–20
Silicon carbide whiskers	5–10	10
Mica	40–180	3–10
Silica	5–53	5
Zircon	40	0–30
Magnesia	40	10
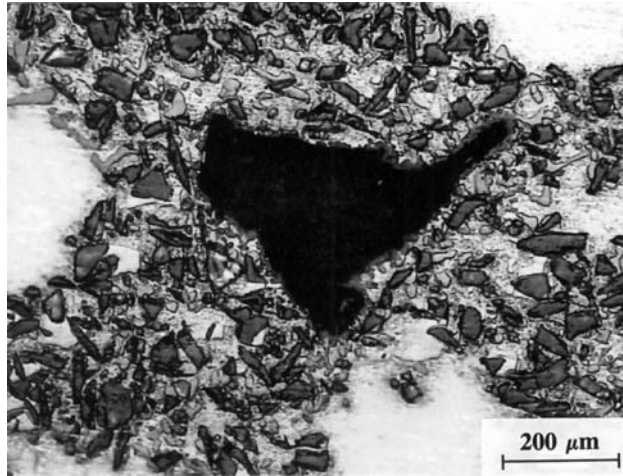
Figure 42   Micrograph of an Al-Si hypoeutectic alloy to which graphite and silicon carbide particles were added.

ACKNOWLEDGMENTS

REFERENCES

1.   E. L. Rooy, "Casting," *ASM Handbook*, Vol. 15, ASM, Materials Park, 1988, 743.
2.   J. Campbell, *Castings*, Butterworth-Heinemann Ltd, Oxford, 1991.
3.   D. V. Neff, "Casting," *ASM Handbook*, Vol. 15, ASM, Materials Park, 1988, 445.
4.   I. A. Abreu, AFS Int. Cast Met. J., 1977, p. 57.
5.   L. P. Semersky and W. F. Joseph, Die Cast. Eng., 1978, p. 22.
6.   W. R. Opie and W. J. Grant, Trans. AIME, 1950, 188, p. 1234.
7.   C. E. Ramsley and H. Neufeld, J. Inst. Met., 1947–48, 74, p. 559.
8.   G. K. Sigworth, ASF Trans., 1987, 95, p. 73.
9.   G. K. Sigworth and T. A. Engh, Metall. Trans. B, 1982, 13B, p. 447.
10.   J. Botor, Metal. Odlev, 1980, 6, p. 21.
11.   J. Botor, Aluminum, 1980, 56, p. 519.
12.   J. L. Jorstad, Int. Molten Aluminum Conf. Proc., AFS, 1986, p. 285.
13.   R. K. Owens, H. W. Antes, and R. E. Edelman, ASF Trans., 1957, 65, p. 424.
14.   B. L. Tiwari, *Light Metals*, TMS, 1982, 889.
15.   D. V. Neff, ASF Trans., 1987, 95, p. 273.
16.   D. V. Neff, *Light Metals*, TMS, 1987, 805.
17.   D. A. Porter and K. E. Easterling, *Phase Transformations in Metals and Alloys*, Van Nostrand Reinhold, 1984.
18.   H. Biloni and W. J. Boettinger, *Physical Metallurgy*, 4th edn, (R. W. Cahn and P. Haasen, eds.), North Holland, Amsterdam, 1996, 669.
19.   J. H. Perepzko, "Casting," *ASM Handbook*, Vol. 15, ASM, Materials Park, 1988, 101.
20.   W. Kurz and D. J. Fisher, Int. Met. Rev., 1979, 24, p. 177.

21. J. H. Hollomon and D. Turnbull, *Progress in Met. Phys.*, Vol. 4, Interscience, 1953, p. 333.
22. B. Chalmers, *Principles of Solidification*, Wiley, 1964.
23. *ASM Handbook*, Vol. 3, Alloy Phase Diagrams, ASM, Materials Park, 1992, p. 2.52.
24. K. Jackson, *Solidification*, ASM, Metals Park, 1971, p. 121.
25. P. Magnin and W. Kurz, "Casting," *ASM Handbook*, Vol. 15, ASM, Materials Park, 1988, p. 119.
26. R. E. Spear and G. R. Gardner, ASF Trans., 1963, 71, p. 209.
27. D. A. Granger and E. Ting, *Structures in Directionally Solidified Aluminum Foundry Alloy A356*, (D. M. Stefanescu, G. J. Abbaschian, and R. J. Bayuzick, eds.), TMS, 1988.
28. J. C. Jaquet and W. Hotz, Cast Metals, 1992, 4, p. 200.
29. Q. S. Hamed and R. Elliot, Cast Metals, 1993, 6, p. 36.
30. C. H. Cáceres, C. J. Davidson, and J. R. Griffiths, Mater. Sci. Engng., 1995, A197, p. 171.
31. S. Cano, M. Eng. (Mat.) Thesis, Universidad Autónoma de Nuevo León, 1996.
32. G. Bracale, ASF Trans., 1962, 70, p. 228.
33. J. T. Berry, ASF Trans., 1970, 78, p. 421.
34. O. Vorre, J. E. Evensen and T. B. Petersen, ASF Trans., 1985, 92, p. 459.
35. E. W. Miguelucci, ASF Trans., 1986, 93, p. 913.
36. K. Radhakrishna and S. Seshan, ASF Trans., 1992, 100, p. 667.
37. C. Huitrón, S. Valtierra, J. F. Mojica, E. Valdez, and R. Colás, *Heat Treating*, (D. L. Milam, D. A. Poteet, G. D. Pfaffmann, V. Rudnev, A. Muehlbauer, and W. B. Albert, (eds.), ASM International, 1997, p. 237.
38. C. Vázquez-López, A. Calderón, M. E. Rodríguez, E. Velasco, S. Cano, R. Colás, and S. Valtierra, Journal of Materials Research, 2000, 15, p. 85.
39. M. C. Flemings and S. Metz, ASF Trans., 1970, 78, p. 453.
40. S. Oya, T. Fujii, M. Ortaki, and S. Baba, J. Jpn. Inst. Light Met., 1984, 34, p. 511.
41. G. K. Sigworth, Int. Molten Aluminum Conf. Proc., AFS, 1986, p. 75.
42. Q. T. Fang, P. N. Anyalebechi, R. J. O'Malley, and D. A. Granger, *Proc. 3rd Int. Solidification Conf.*, Inst. Met., London, 1987.
43. L. Bäckerud, E. Król, and J. Tamminen, "Wrought Alloys", *Solidification Characteristics of Aluminum Alloys*, Vol. 1, Skanaluminium, 1987.
44. G. K. Sigworth and M. M. Guzowski, AFS Trans., 1985, 93, p. 907.
45. J. E. Gruzleski and B. M. Closset, *The Treatment of Liquid-Aluminum Alloys*, AFS, 1990.
46. F. A. Crossley and L. F. Mondolfo, Trans. AIME, 1951, 191, p. 1143.
47. M. Shamsuzzoha, L. M. Hogan, and J. T. Berry, AFS Trans., 1993, 101, p. 999.
48. Shu-Zu Lu and A. Hellawel, *Solidification Processing 1987*, Inst. Met., London, 1987, p. 131.
49. J. Campbell, *The Solidification of Metals*, The Iron and Steel Institute, London, 1967, p. 18.
50. K. Kubo and R. D. Pehlke, Metall. Trans. B, 1985, 16B, p. 359.
51. S. Srivkumar and D. Apelian, *Materials Processing in the Computer Age*, TMS, 1991, p. 389.
52. X. G. Chen and S. Engler, *98th Casting Congress*, AFS, 1994.
53. L. A. Narayan, F. H. Samuel, and J. E. Gruzlezki, Metall. Mat. Trans. A, 1995, 26A, p. 2161.
54. S. Murali, K. S. Raman, and K. S. S. Murthy, Mat. Sc. Eng., A, 1995, 190A, p. 165.
55. L. F. Mondolfo, *Manganese in Aluminum Alloys*, The Manganese Centre, Neuilly sur Seine, 1990.
56. P. Jonason, AFS Trans., 1992, 100, p. 601.
57. J. Iglessis, C. Frantz, and M. Gantois, Mém. Sc. Rev. Métallurgie, 1977, 73, p. 237.

58. S. Yaneva, N. Stoichev, Z. Kamenova, and S. Budurov, Z. Metallkunde, 1984, 75, p. 395.
59. L. Bäckerud, G. Chai, and J. Tamminen, "Foundry Alloys", *Solidification Character-istics of Aluminum Alloys*, Vol. 2, AFS/Skanaluminium, 1990
60. A. M. Samuel, P. Oullet, F. H. Samuel, and H. W. Doty, AFS Trans., 1997, 105, p. 951.
61. R. D. Shull, *Thermal Analysis in Metallurgy*, (R. D. Shull and A. Joshi, eds.), TMS, 1992, p. 95.
62. K. W. Andrews, *Physical Metallurgy, Techniques and Applications*, Vol. 1, Allen and Unwin, London, 1973.
63. P. F. Wieser (ed.), *Steel Castings Handbook*, 5th edn, Steel Founders Society of America, 1980.
64. R. C. Voigt, "Casting," *ASM Handbook*, Vol. 15, ASM, Materials Park, 1988, p. 189.
65. T. S. Piwonka, "Casting," *ASM Handbook*, Vol. 15, ASM, Materials Park, 1988, p. 203.
66. W. D. Kingery, H. K. Bowen, and D. R., Uhlmann, *Introduction to Ceramics*, 2nd edn, J. Wiley and Sons, New York, 1976.
67. T. S. Piwonka, "Casting," *ASM Handbook*, Vol. 15, ASM, Materials Park, 1988, p. 208.
68. E. J. Sikora, AFS Trans., 1978, 86, p. 65.
69. P. O'Meara, L. E. Wile, J. J. Archibald, R. L. Smith, and T. S. Piwonka, "Casting," *ASM Handbook*, Vol. 15, ASM, Materials Park, 1988, p. 222.
70. J. J. Archibald and R. L. Smith, "Casting," *ASM Handbook*, Vol. 15, ASM, Materials Park, 1988, p. 214.
71. M. Patz and T. S. Piwonka, "Casting," *ASM Handbook*, Vol. 15, ASM, Materials Park, 1988, p. 230.
72. C. E. West and T. E. Grubach, "Casting," *ASM Handbook*, Vol. 15, ASM, Materials Park, 1988, p. 285.
73. R. J. Esdaile, T. T. Nguyen, G. R. de Looze, and M. T. Murray, *1st Int. Non-Ferrous Processing and Technology Conf.*, (T. Bains and D. S. MacKenzie, eds.), ASM International, 1997, p. 213.
74. R. A. Smith and P. S. A. Wilkins, AFS Trans., 1986, 94, p. 785.
75. A. Hetke and R. B. Gundlach, AFS Trans., 1994, 102, p. 367.
76. L. J. D. Sully, "Casting," *ASM Handbook*, Vol. 15, ASM, Materials Park, 1988, p. 286.
77. I. J. Polmear, "Light Alloys," *Metallurgy of the Light Metals*, 3rd edn, Arnold, 1995.
78. J. W. Martin, *Micromechanisms in Particle-Hardened Alloys*, Cambridge University Press, 1980.
79. D. Irani, P. Olson, S. Shivkumar, and M. Tiryakioğlu, *Heat Treating*, (D. L. Milam, D. A. Poteet, G. D. Pfaffmann, V. Rudnev, A. Muehlbauer, and W. B. Albert, eds.), ASM International, 1997, p. 257.
80. M. Tiryakioğlu, J. Campbell, and N. Green, *1st Int. Non-Ferrous Processing and Tech-nology Conf.*, (T. Bains, and D. S. MacKenzie, eds.), ASM International, 1997, p. 509.
81. G. E. Totten, G. M. Webster, and C. E. Bates, *Heat Treating*, (D. L. Milam, D. A. Poteet, G. D. Pfaffmann, V. Rudnev, A. Muehlbauer, and W. B. Albert, eds.), ASM International, 1997, p. 247.
82. J. L. Cavazos, E. Hidalgo, R. Colás, and A. Salinas, *1st Int. Non-Ferrous Processing and Technology Conf.*, (T. Bains and D. S. MacKenzie, eds.), ASM International, 1997, p. 209.
83. E. Velasco, R. Colás, S. Valtierra, and J. F. Mojica, Int. J. Fatigue, 1995, 17, p. 399.
84. J. Gauthier, F. H. Samuel, and H. Liu, *Proc. Symp. Light Metals Processing and Applications*, (C. Bickert, M. Bouchard, G. Davies, E. Ghali, and E. Jiran, eds.), Canadian Institute of Mining, Metallurgy and Petroleum, 1993, p. 283.
85. J. Gauthier, P. R. Louchez, and F. H. Samuel, Cast Met., 1996, 8, p. 91.

86. P. Y. Zhu, Q. Y. Liu, and T. X. Hou, AFS Trans., 1985, 95, p. 609.
87. E. Velasco, S. Valtierra, J. F. Mojica, and R. Colás, *Advances in Aluminum Casting Technology*, (M. Tiryakioğlu and J. Campbell, eds.), ASM International, 1998, p. 127.
88. V. Páramo, R. Colás, C. Huitrón, E. Velasco, S. Valtierra, and J. F. Mojica, *1st Int. Automotive Heat Treatment Conf.*, (R. Colás, K. Funatani, and C. A. Stickels, eds.), ASM International, 1999, p. 367.
89. J. T. Berry and R. D. Pehlke, "Casting," *ASM Handbook*, Vol. 15, ASM, Materials Park, 1988, p. 858.
90. W.-S. Hwang and R. A. Stoehr, "Casting," *ASM Handbook*, Vol. 15, ASM, Materials Park, 1988, p. 867.
91. P. V. Desai and K. V. Pagalthivarthi, "Casting," *ASM Handbook*, Vol. 15, ASM, Materials Park, 1988, p. 877.
92. M. Rappaz and D. M. Stefanescu, "Casting," *ASM Handbook*, Vol. 15, ASM, Materials Park, 1988, p. 883.
93. K. S. Kannan, K. Madhusudana, R. Venkataramani, N. Ganesh, and O. Prabhakar, Ind. J. Techn., 1990, 28, p. 460.
94. J. Campbell, Mater. Sci. Techn., 1991, 7, p. 885.
95. O. Prabhakar, Bull. Mater. Sci., 1993, 16, p. 543.
96. P. M. Sargent, H. Shercliff, and R. L. Wood, *Modelling Materials Processing*, Cambridge University, 1993.
97. S. Guleyupoglu, S. Sundarraj, and M. Gungor, *Advances in Aluminum Casting Technology*, (M. Tiryakioğlu and J. Campbell, eds.), ASM International, 1998, p. 55.
98. R. L. Burden and J. D. Faires, *Numerical Analysis*, PWS, Boston, 1985.
99. K. H. Huebner, E. A. Thornton, and T. G. Byrom, *The Finite Element Method for Engineers*, John Wiley and Sons, Inc., New York, 1995.
100. M. Rappaz and Ch.-A. Gandin, Acta Metall. Mater., 1993, 41, p. 345.
101. S. P. Marsh and M. E. Glicksman, *Modeling of Casting and Welding and Advanced Solidification Processes VI*, (T. S. Piwonka, ed.), TMS, 1993, p. 55.
102. D. M. Stefanescu, *Modeling of Casting and Welding and Advanced Solidification Processes VI*, T. S. Piwonka (ed.), TMS, 1993, p. 3.
103. J. D. Hunt, Acta Metall. Mater., 1990, 38, p. 411.
104. J. D. Hunt, Acta Metall. Mater., 1991, 39, p. 2117.
105. E. Scheil, Arch. Eisenhut., 1935, 12, p. 565.
106. E. Niyama, T. Uchida, M. Morikawa, and S. Saito, AFS Intl. Cast Met. J., September 1982, p. 52.
107. K. Ho and R. D. Pehlke, Metall. Trans. B, 1985, 16B, p. 585.
108. D. Argo, R. A. L. Drew and J. E. Gruzleski, AFS Trans., 1987, 95, p. 455.
109. F. Chiesa, AFS Trans., 1990, 98, p. 193.
110. E. Velasco, J. Talamantes, S. Cano, S. Valtierra, J. F. Mojica and R. Colás, Metall. Mater. Trans., 1999, 30B, p. 773.
111. R. W. Powell, C. Y. Ho and P. E. Liley, J. Phys. Chem. Ref. Data, 1972, 1, p. 279.
112. *Magmasoft User's Guide*, Magma Foundry Technologies, Inc., Arlington Heights, Il.
113. M. P. Kenney, J. A. Courtois, R. D. Evans, G. M. Farrior, C. P. Kyonka, A. A. Koch, and K. P. Young, "Casting," *ASM Handbook*, Vol. 15, ASM, Materials Park, 1988, p. 327.
114. D. H. Kirkwood, Int. Mat. Rev., 1994, 39, p. 173.
115. C. Kyonka, L. Griffin, C. Hoskins, and S. Cevrvorst, *1st Int. Non-Ferrous Processing and Technology Conf.*, (T. Bains and D. S. MacKenzie, eds.), ASM International, 1997, p. 355.
116. P. K. Rohatgi, R. Asthana, and S. Das, Int. Met. Rev., 1986, 31, p. 115.
117. P. Rohatgi, "Casting," *ASM Handbook*, Vol. 15, ASM, Materials Park, 1988, p. 840.

13

Molten Metal Processing

RYOTATSU OTSUKA

Showa Aluminum Corporation, Sakai-shi, Osaka, Japan

1 INTRODUCTION

Virgin molten aluminum produced by Hall–Heroult process contains Fe, Si, Zn, Ga, Na as major impurity elements, Ti, V, Mn, Cu, Mg, B as minor one and Al_2O_3, Al_4C_3, VB et al. as inclusions. Na is usually removed by Cl_2 gas or $N_2 + Cl_2$ gas fluxion into virgin molten aluminum in smelter-based cast house because a few ppm Na in Al-Mg alloy induces cracking during hot working. The primary aluminum produced by smelter is usually about 99.50–99.85% pure, and a small amount of 99.85–99.96% pure aluminum can be produced from a few electrolysis cells operated carefully. Primary aluminum can be refined to 99.990–99.998% purity by three layer electrolysis process in a fused salt mixture. Three layer electrolysis and Na removal treatment are both smelter-based molten aluminum processing. Pure aluminum of 99.99% is mostly utilized as foil material for capacitors. Recently, several segregation (fractional solidification) methods which are superior on cost performance of purification process, have been developed and 99.98–99.996% pure aluminum purified by those solidification processing has come to be utilized for capacitor instead of three layer electrolysis aluminum. Ultra purity aluminum over 99.9990% can be made by zone-melting. Molten primary aluminum for electronic wire is treated by B addition for the purpose of Ti and V removal because Ti and V in solid solution remarkably reduces the electroconductivity of aluminum. Aluminum is very reactive and the chemical reaction between aluminum and water vapor generates hydrogen gas at high temperature. This is the source of hydrogen dissolved into aluminum. Hydrogen solubility in aluminum is determined by an equilibrium relationship between hydrogen concentration in aluminum and hydrogen gas partial pressure in ambient atmosphere. Hydrogen solubility in solid aluminum is far smaller than in liquid aluminum. Therefore, excess dissolved hydrogen in molten

aluminum over solid solubility forms hydrogen gas pores during solidification, or is frozen into super saturated hydrogen solid solution. Excess hydrogen frozen into solid solution heterogeneously precipitates to make gas pores during some heat treatment of cast product. These gas pores impair the strength, ductility and the cutting surface quality of cast product. This is the reason why the melt treatment to remove hydrogen gas is necessary at cast house. The removal of inclusions at cast house is also necessary to assure the quality of aluminum products because inclusions impair the mechanical property and cutting surface quality of the material. Many ways of the melt treatment to remove hydrogen gas and inclusions in aluminum have been developed. Particularly, the development of the process of inert gas dispersion into molten aluminum by a rotating nozzle (Union Carbide is the first developer in 1976) innovated the current way to remove gas and inclusion in the cast house of the aluminum industry, because of its high efficiency, low cost performance and environmental improvement. Filtration method of molten aluminum for inclusion removal has been available from long ago. The technological innovation in this area is due to the development of the new material for filtration such as foamed ceramics and bonded particle media, and the improvement of the reliability of filtration with the development of a quantitative analyzing method for inclusions. The above-mentioned processes of molten aluminum have the same purpose of "Refining." Grain refining is another type of solidification processing by which fine grain size after solidification can be obtained. Fine grain size is necessary to avoid solidification cracking. Modification treatment by a small amount of Na or Sr addition to Al-Si foundry alloy is necessary to obtain fine eutectic micro structure as solidified. Such a micro alloying effect to cast structure is also observed in intermetallic phases(Al_xFe_y) appearance of commercial pure aluminum for anodized panels. As mentioned before, several types of molten metal processing such as segregation, grain refining, modification and micro alloying may not be defined as molten metal processing but as solidification processing. So, the author here focuses on the melt treatment for refining such as hydrogen removal, inclusions removal and alkali elements removal from molten aluminum. Molten metal processing plays a very important role in the aluminum industry and the development of new process technology has made a great impact on the cost performance and the quality assurance of aluminum products.

2   REMOVAL OF DISSOLVED HYDROGEN FROM MOLTEN ALUMINUM

2.1   The Source of Dissolved Hydrogen in Molten Aluminum

Only one element of dissolved gas component in aluminum is hydrogen. Hydrogen in molten aluminum (H) has an equilibrium relationship with hydrogen gas in ambient atmosphere.

$$H = \frac{1}{2} H_2(gas) \tag{1}$$

Equilibrium constant (K_H) of eqn (1) is

$$K_H = \frac{p_{H_2}^{\frac{1}{2}}}{f_H[\% \, H]} \tag{2}$$
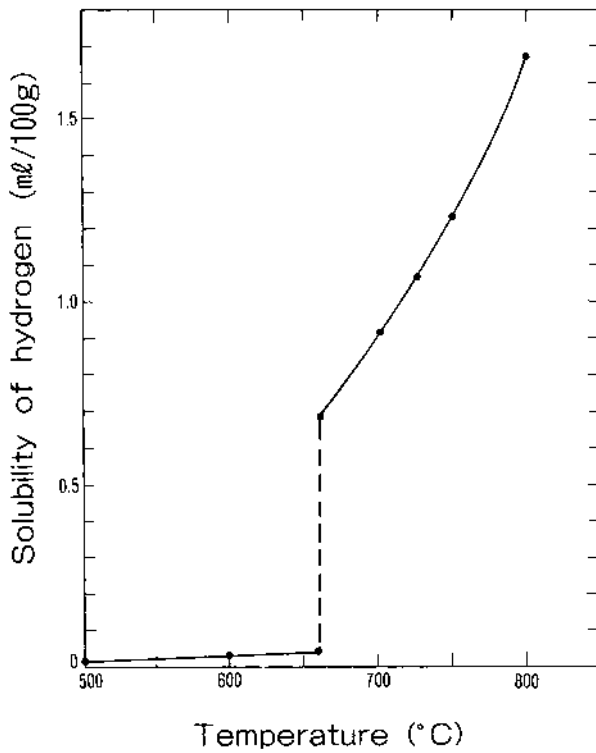
Figure 1   Solubility of hydrogen at 1 atm in 99.9985% pure aluminum. (From Ref. 1.)

where f_H is the activity coefficient of hydrogen in aluminum, $[\%H]$ is the hydrogen concentration in aluminum and P_{H2} is the partial pressure of hydrogen gas in the atmosphere. Figure 1 [1] shows the equilibrium hydrogen concentration in pure aluminum with hydrogen gas of 1 bar. (It means the solubility of hydrogen into aluminum under the atmosphere of hydrogen gas partial pressure of 1 atm.) Aluminum reacts with water vapor at high temperature and generates hydrogen gas.

$$3H_2O\,(g) + 2Al = Al_2O_3 + 3H_2\,(g) \tag{3}$$

This hydrogen gas is the source of hydrogen in aluminum. In the cast house of aluminum industry they often in humid hot season experience more troubles on cast quality for the dissolved hydrogen in the melt. This is due to the chemical reaction [Eq. (3)] between water vapor of higher partial pressure in ambient atmosphere of humid hot season and molten aluminum. TA Engh [2] proposed the numerical model of hydrogen pick-up from water vapor and he suggests the hydrogen concentration in molten aluminum which is kept for long time under the atmosphere of a constant water vapor pressure (p_{H2O}) should attain to the calculated value. In this model (Fig. 2), at the interface between molten aluminum and atmosphere, Engh looks at various steps involved as follows. Water vapor diffuses through the boundary layer to be adsorbed at the metal surface, the adsorbed molecules reacts with aluminum [Eq. (3)], hydrogen molecules are desorbed from the surface,
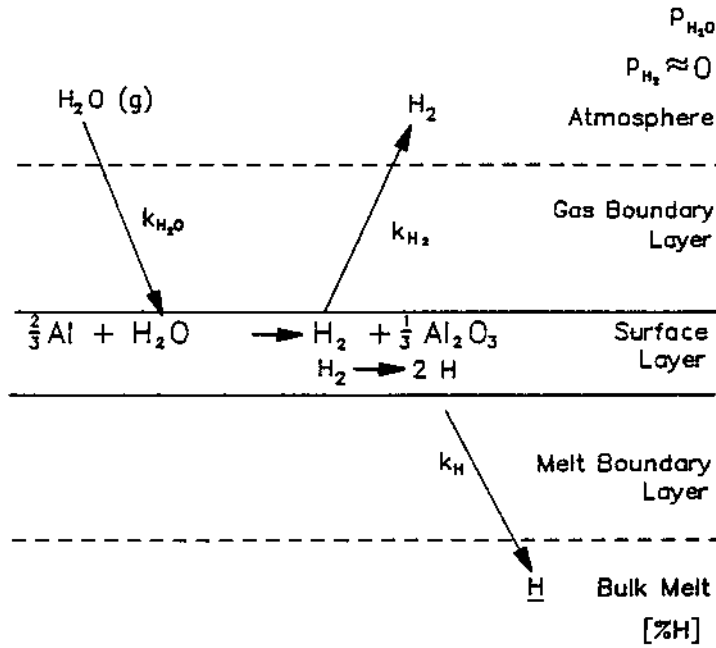
Figure 2 The mechanisms for hydrogen dissolution into the molten aluminum from moisture in the atmosphere. (From Ref. 2.)

hydrogen molecules diffuse back out of the boundary layer, hydrogen molecules dissociate and form atomic hydrogen on the surface, hydrogen atoms diffuse through the metal boundary layer. By mathematical analysis of each steps using mass transfer coefficients k at gas-melt interface and the equilibrium constant for Eq. (3) in the surface layer, the partial pressure of hydrogen gas (p_{H_2}) at the interface is given by

$$p_{H_2} = \frac{k_{H_2O}}{k_{H_2}} p_{H_2O} \tag{4}$$

where k_{H2O}, k_{H2} are mass transfer coefficients for H_2O, H_2 in gas and p_{H2O} is the partial pressure of H_2O in the atmosphere. Therefore, the hydrogen concentration in molten aluminum ($[\%H]_l$) which is kept under the atmosphere of P_{H2O} for long time is calculated from Eq. (2).

$$[\%H]_l = \frac{1}{f_H K_H} \sqrt{\frac{k_{H_2O} p_{H_2O}}{k_{H_2}}} \tag{5}$$

The mass transfer coefficients k_{H_2O} and k_{H_2} can be shown to be proportional to the square root of the diffusion coefficients in air, D_{H_2O} and D_{H_2}. Therefore,

$$[\%H]_l \approx \frac{1}{f_H K_H} \sqrt{p_{H_2O} \sqrt{\frac{D_{H_2O}}{D_{H_2}}}} \tag{6}$$

The diffusion coefficients in air are $D_{H_2O}=0.239$ cm^2/sec at 8°C and $D_{H_2}=0.634$ cm^2/sec at 0°C [3]. As a first approximation it is assumed that their ratio do not change significantly with temperature. So, we can obtain Eq. (7).

$$[\%H]_l \approx \frac{0.783}{K_H} \sqrt{p_{H_2O}} \tag{7}$$

There are few papers [4–6] which deal with the experimental result of the hydrogen concentration dependence on P_{H_2O}. Otsuka (6) made an experiment to determine the hydrogen pick up of the molten pure aluminum from the water vapor of P_{H_2O} in the ambient atmosphere. Figure 3 shows the experimental apparatus which can keep the molten metal in the atmosphere of a constant partial pressure of the water vapor. The water vapor partial pressure P_{H_2O} was controlled by blowing the dry gas (air or inert gas) of which the dew point is below -60°C through the molecular sieves (in the case of dry air) or the humidified gas through the pure water into the stainless steel box, and the value of P_{H_2O} above the melt surface was determined by the measurement of the dew point of the gas blew out of near the melt surface in the box. The temperature of the melts were controlled to 675±5°C, 700±5°C or 750±5°C. The molten aluminum of 99.99% pure in the high purity alumina crucible (inner dia 80 mm, height 170 mm) was held in stationary state or stirred state by the rotating graphite impeller (dia. 45 mm, height 30 mm) at 530 rpm. The hydrogen concentrations of the molten aluminum before and after the treatments were measured by the nitrogen fusion method (I THAC-2002 manufactured by ADAMEL LHOMARGY was used.) for the carefully machined cylindrical samples from the ingots solidified into the Ransley's mould. Figure 4 shows the experimental result of the hydrogen concentration change in the molten pure aluminum which was held at 700°C in the dry air atmosphere with 1.7×10^{-4} atm of p_{H_2O} (p_{H_2O} in the usual air in Japan is about 1.5×10^{-3}–3.0×10^{-2} atm). The hydrogen concentration of the stationary melt slowly decreases, and after long time holding more than 300 min it looks like to attain a constant value which may be same as the equilibrium value of hydrogen concentration ($0.07_{ml/100g} \fallingdotseq 0.07_{p.p.m.}$) which had been attained after about 50 min holding while stirring the melt by rotating impeller. Figure 5 shows the time dependence of the hydrogen concentration in the stirred molten aluminum under the air atmospheres containing various amounts of water vapor. The hydrogen concentration of molten aluminum attains to the equilibrium value depending on P_{H_2O} irrespective of whether the initial hydrogen concentration is lower or higher than the equilibrium one. The relationships between P_{H_2O} and the attained equilibrium hydrogen concentration ($[H_e]_{ml/100g}$) at 675°C, 700°C and 750°C are nearly linear on log–log scale when P_{H_2O} is below 1.7×10^{-2} atm as shown in Fig. 6. The correlative equations calculated are as follows.
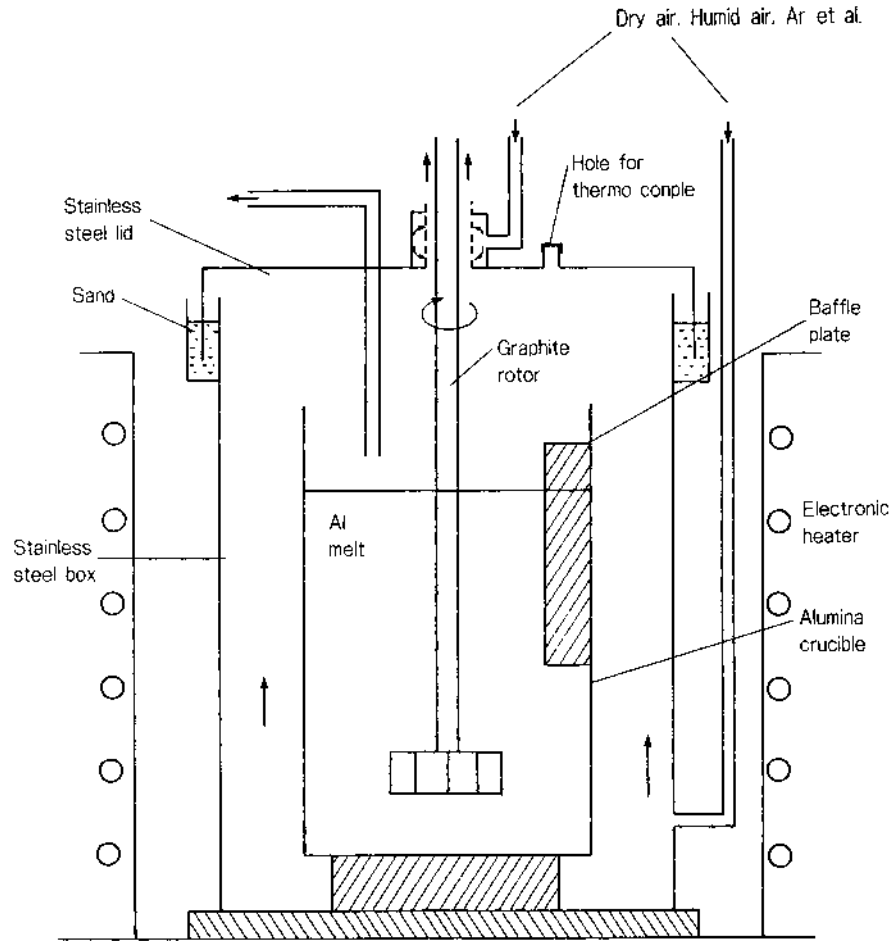
Figure 3 The experimental apparatus for the investigation of hydrogen dissolution into the molten aluminum in the high purity alumina crucible (inner dia. 80 mm, inner height 170 mm) from moisture in the atmosphere. (From Ref. 6.)

At 675°C

$$[H_e] = 3.17 p_{H_2O}{}^{0.470} \tag{8}$$

At 700°C

$$[H_e] = 3.49 p_{H_2O}{}^{0.453} \tag{9}$$

At 750°C

$$[H_e] = 3.16 p_{H_2O}{}^{0.387} \tag{10}$$

Figure 7 shows the linear relationship between log $[H_e]$ and $1000/T$ (T is the temperature of melt) at the constant value of P_{H_2O}. The activation energy of hydrogen
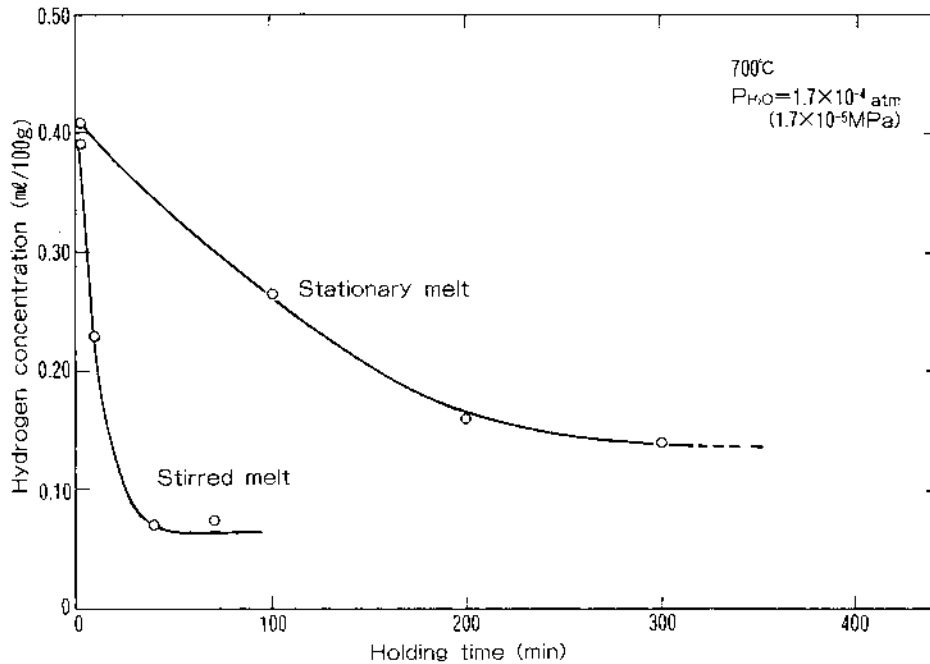
Figure 4 Hydrogen concentration change in molten 99.99% Al at 700°C under the dry air atmosphere of $P_{H_2O} = 1.7 \times 10^{-4}$ atm. (From Ref. 6.)

solution from water vapor was calculated to be 38806 cal/mol, 30977 cal/mol and 19467 cal/mol on each case of 1.0×10^{-2}, 10^{-3} and 10^{-4} atm of P_{H_2O}. They are in rough agreement with the activation energy of hydrogen solution from hydrogen gas, 28258 cal/mol [7]. These experimental result suggests the pick up of hydrogen from water vapor may occur by the model proposed by Engh and it is limited by slow mass transfer of hydrogen in molten aluminum to the surface, although these experimental values of the equilibrium hydrogen concentration is lager than the calculated value by Eq. (7). It is supposed the oxide film of molten aluminum surface may affect the hydrogen pick up of molten aluminum, because the equilibrium hydrogen concentration with P_{H_2O} in inert gas atmosphere of N_2 or Ar is lower than in air atmosphere and it is attained earlier than in air atmosphere as shown in Fig. 8.

2.2 The Principle of Hydrogen Removal from Molten Aluminum

The removal of hydrogen from molten aluminum is based on the equilibrium relationship between the hydrogen in molten aluminum and the hydrogen partial pressure in ambient atmosphere as Eq. (2). That is

$$[\%H] = \frac{K_H}{f_H} \sqrt{p_{H_2}}$$
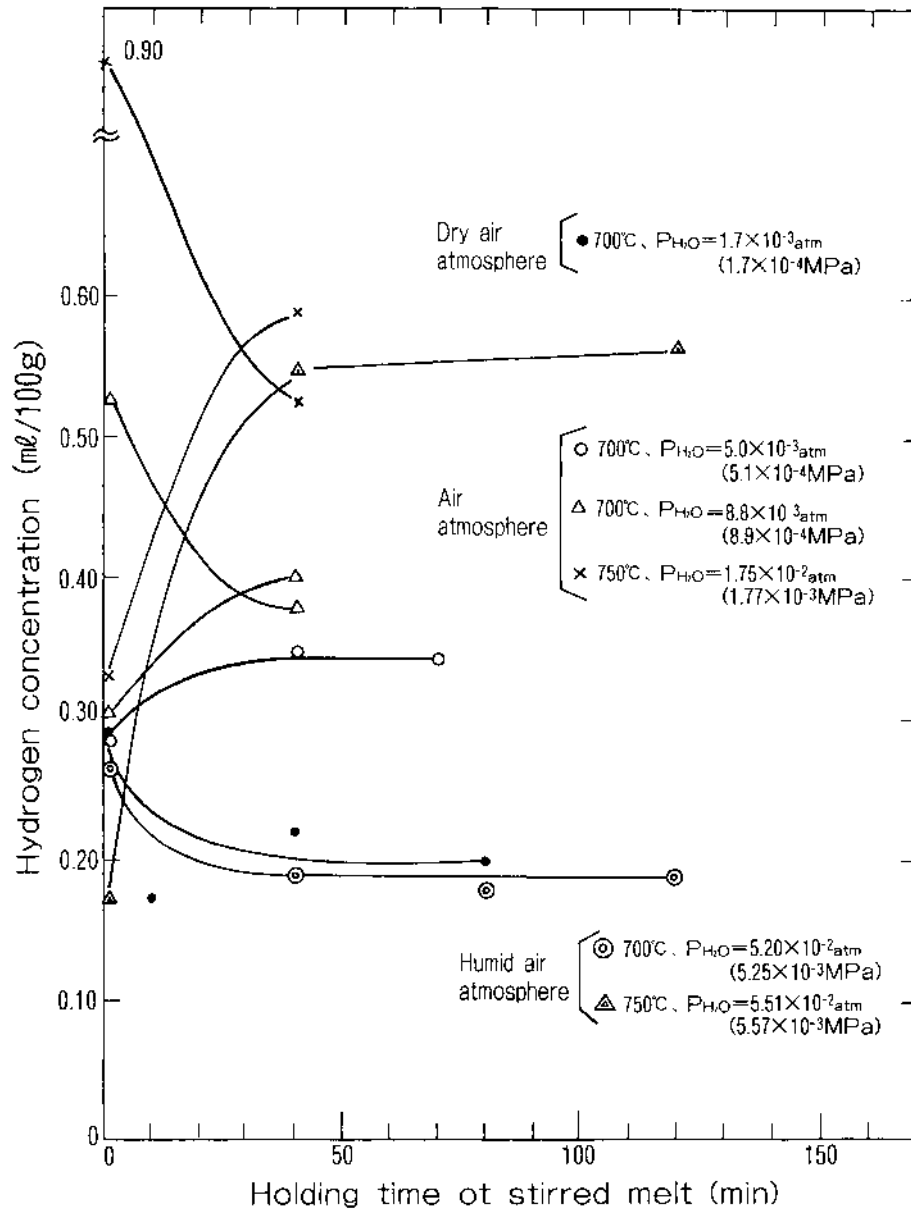
Figure 5 The time dependence of hydrogen concentration in stirred melt of 99.99% Al under the air atmospheres containing various amounts of water vapor. (From Ref. 6.)

It means that when the molten aluminum is kept under the inert gas atmosphere, in the vacuum in both of which $P_{H_2} = 0$ is formed, or injected inert gas bubbles which have no hydrogen gas ($P_{H2} = 0$) before the injection, the hydrogen in the molten aluminum diffuses to the melt surface and transfers to the gas or the vacuum. The activity coefficient of hydrogen f_H ($f_H = 1$ for pure aluminum) may change with alloying elements such as Si, Cu, and Mg. Therefore, the solubility
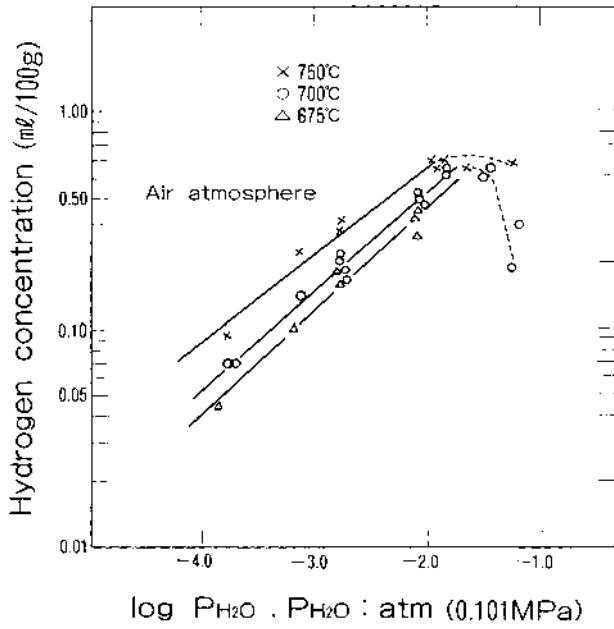
Figure 6 The relationships between $\log[H]_e$ and $\log P_{H_2O}$. (From Ref. 6.)
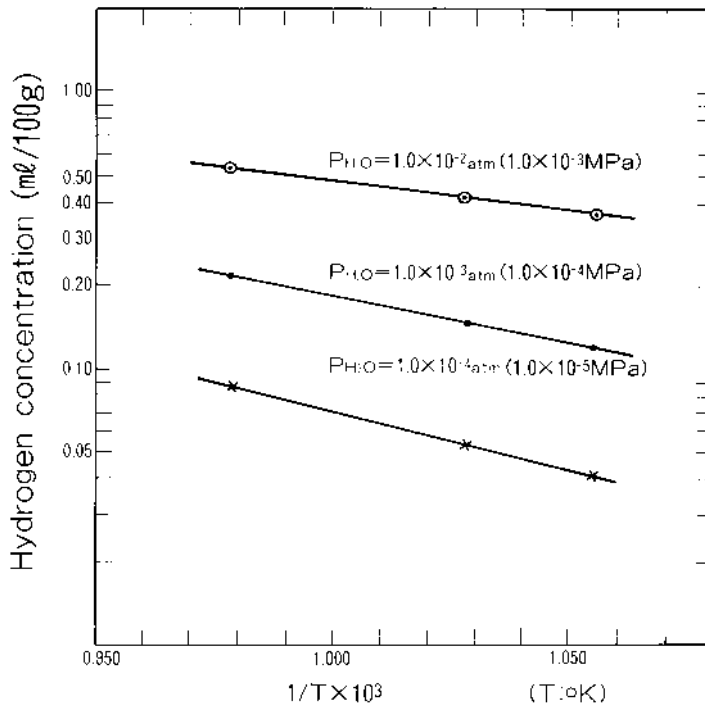
Figure 7 The relationships between $\log[H]_e$ and $1000/T$. (From Ref. 6.)
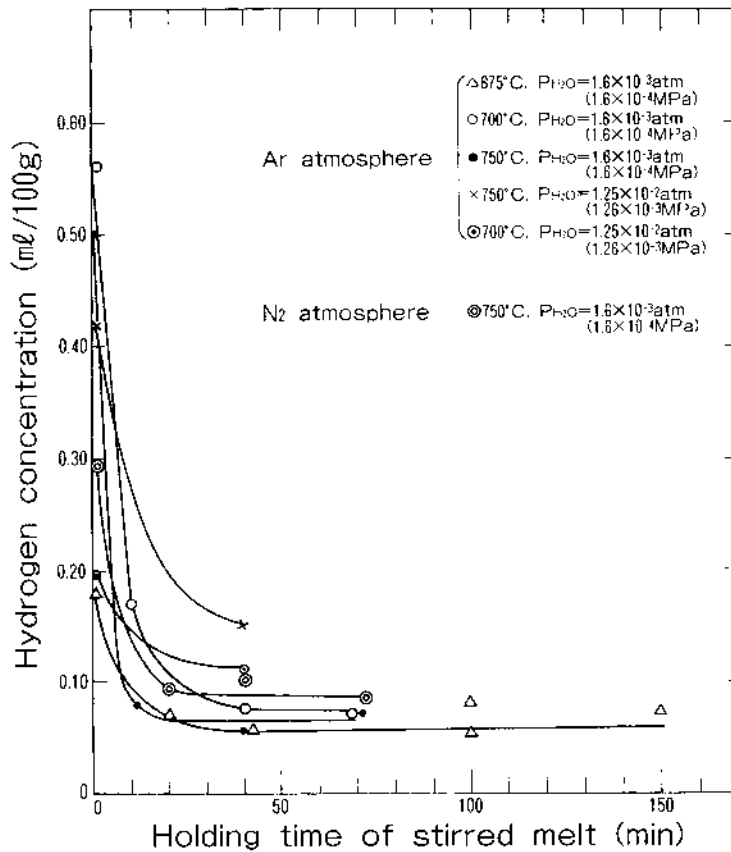
Figure 8 The time dependence of hydrogen concentration in stirred melt of 99.99% Al under the inert gas atmospheres containing various amounts of water vapor.

of hydrogen in pure aluminum may be different from aluminum alloy and the easiness of hydrogen removal will depend on alloy species. The value of f_H for an alloy can be estimated by the calculation using interaction coefficients in liquid Al-H-i alloys [8,9]. Table 1 shows the calculated f_H of several molten alloys [10]. As shown in Eq. (7) or Eqs. (8), (9) and (10), it is also very important for the hydrogen removal that the hydrogen pick up from water vapor should be avoided. Then, in the molten metal processing for hydrogen removal, the water vapor partial pressure in the atmosphere, the purge gas and the crucible material must be as small as possible.

2.3   The Molten Metal Processing for Hydrogen Removal

The current worldwide technology for hydrogen removal from molten aluminum is the inert gas purging method by rotating nozzle. In the history of aluminum industry, Cl_2 or $Cl_2 + N_2$ gas purging by lance pipe was the usual way for hydrogen removal. It is clear from the thermodynamic calculation of the Gibbs energy change of the chemical reaction between Cl_2 and H in the melt that Cl_2 gas does not react with

Table 1 Calculated Values of Hydrogen Activity Coefficient (f_H) in Molten Aluminum Alloys

Alloy	f_H
Pure Al	1.00
AA No. 6063 (Al-0.6% Mg-0.4% Si)	1.01
AA No. 3003 (Al-1.2% Mn-0.2% Si)	1.21
JIS AC7A (Al-5.0% Mg-0.4% Mn)	0.94
JIS AC8C (Al-11% Si-2.9% Cu-1.2% Mg)	2.03
AA No. 5052 (Al-2.5% Mg-0.2% Cr)	0.94
AA No. 6061 (Al-1.0% Mg-0.6% Si-0.2% Cu)	1.03
AA No. 1100 (Al-0.55% Fe-0.13% Si)	1.04
AA No. 2017 (Al-3.8% Cu-0.7% Mg-0.5% Si-0.7% Mn)	1.46

Source: Ref. 10.

H in molten aluminum to give HCl (gas) but reacts with molten aluminum to give AlCl$_3$ (gas above 183°C). They might have thought Cl$_2$ gas purging is effective for hydrogen removal due to HCl formation, but the mechanism of hydrogen removal is only due to hydrogen diffusing out of molten aluminum into AlCl$_3$ gas bubbles, similarly as in the case of inert gas purging into molten aluminum. However, it should be noticed the size of gas bubbles in molten aluminum from lance pipe is smaller in the case of Cl$_2$ gas purging in comparison with inert gas purging, and it may be due to the reduction of gas–metal surface tension in the case of AlCl$_3$ gas and the high heat of formation of AlCl$_3$ gas [11].

As described later, Cl$_2$ gas is effective on the removal of Na and oxide inclusion from molten aluminum. However, because of air pollution by Cl$_2$, N$_2$ gas purging for hydrogen removal was investigated instead of Cl$_2$ and gas purging by porous plug to give fine gas bubbles into molten aluminum was tried for the improvement of hydrogen removal efficiency. The efficiency of hydrogen removal by the inert gas purging have been drastically improved since the first inert gas dispersion process into molten aluminum by spinning nozzle (SNIF) had been developed in 1976 [11]. The gas dispersion into molten aluminum by SNIF is schematically shown in Fig. 9. The gas injection apparatus (U.S.Pat. 3743263, 1973) of SNIF is comprised of a stationary sleeve and a vaned rotor. The shaft driving an impeller is surrounded by a stationary sleeve. The lower part of the sleeve is expanded into a stator head which is partly slotted at regular intervals. Metal penetration is prevented by the pressure of the sparging gas. This gas enters the molten aluminum through a clearance between stator and impeller (rotor). The small gas bubbles (1–10 mm) produced by shear and collision with the vanes of the rotor are uniformly dispersed in the entire body of the metal. The efficiency of degassing depends on the inert gas–metal interfacial area and the inert gas–metal contact time. The minimum inert gas consumption which means maximum efficiency can be approached by providing a high specific interfacial area (surface to volume ratio) and sufficiently long contact time. SNIF can disperse far smaller sizes and larger numbers of bubbles than porous plugs, and the inert gas atmosphere of a positive pressure relative to the ambient pressure in the closed chamber prevents the infusion of water vapor into the chamber. Figure 10 shows the apparatus of SNIF for in-line refining which is located
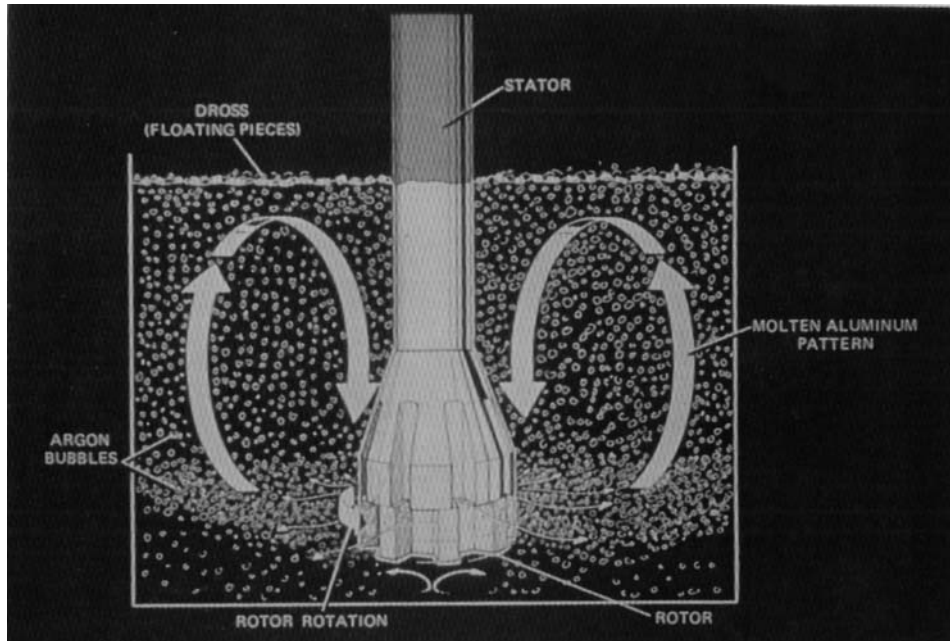
Figure 9 Ar gas bubbles dispersion into molten aluminum by SNIF rotor. (From Szekely, 1976.)
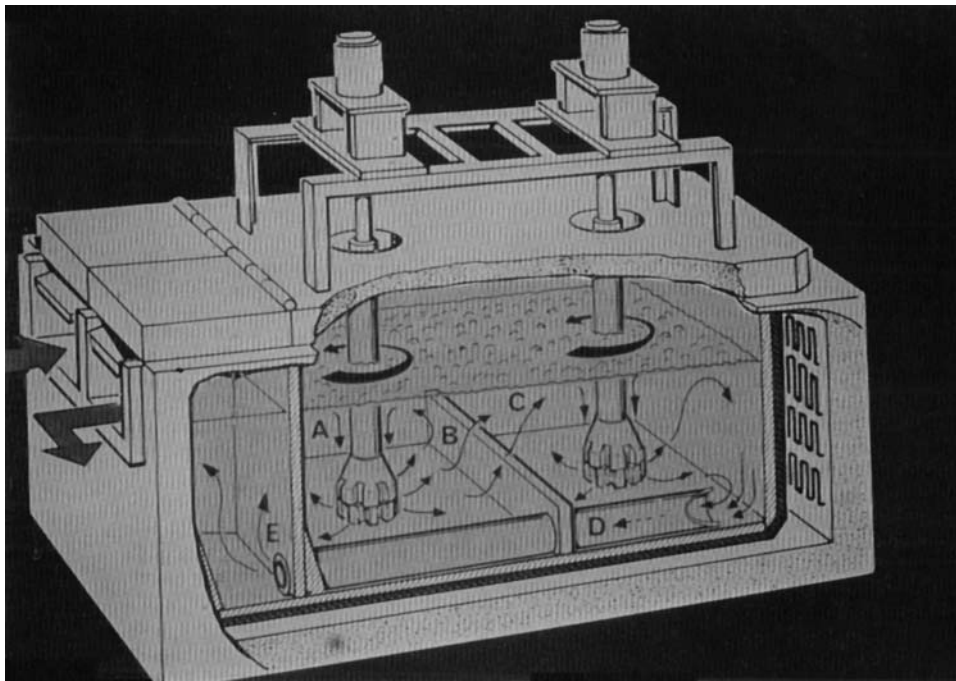
Figure 10 SNIF in-line apparatus. (From Szekely, 1976.)
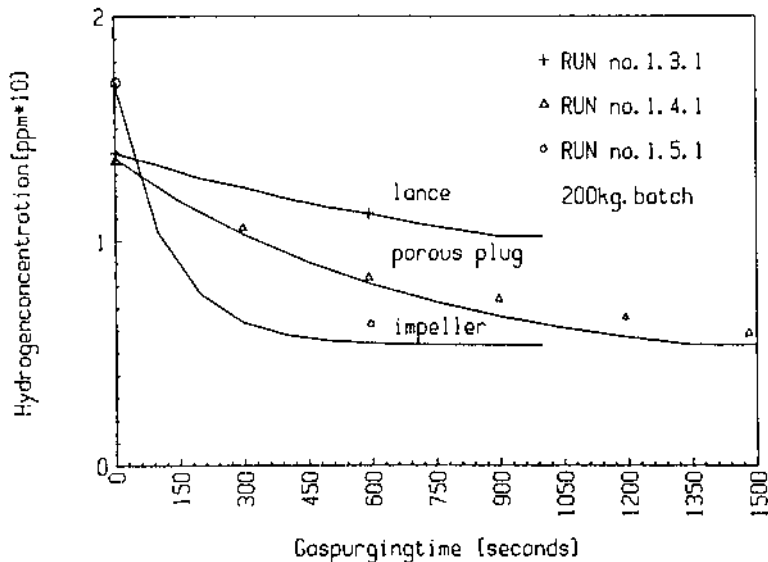
Figure 11 Hydrogen removal by gas purging with lance, porous plug and impeller in 200 kg melt of Al-7% Si-0.5% Mg for the same gas flow (6 l/min). (From Ref. 12.)

between holding furnace and casting station in the cast house of aluminum rolling company. Sigworth and Engh [8] presented a mathematical analysis of the kinetics of hydrogen removal by inert gas purging. Engh and Pedersen [12], and Engh [13] presented a model of hydrogen removal from molten aluminum by gas purging which includes hydrogen pick up from humidity (water vapor) above the melt. That is, Reduction of content of hydrogen in batch (not in-line) = Hydrogen transferred to bubbles + Hydrogen transferred to atmosphere at bath surface. The theory (calculated result) was compared with the experimental result of the hydrogen removal for Al-7%Si-0.5% Mg in a 200 kg furnace using lance, porous plug and spinning nozzle (SNIF). It is shown in Fig. 11. Figure 12 shows the calculated curves of hydrogen removal by spinning nozzle with different melt surface conditions of hydrogen pick up. The surface completely exposed to air picks up hydrogen from water vapor as was given in Sec. 2.1. When the atmosphere above the melt is covered with a lid, there should be little or no hydrogen pick-up from the air. When the surface is blown by inert gas, $[\%H]_l \approx 0$ (see Eq. 5). Those calculated curves suggest SNIF can decrease the hydrogen concentration in molten aluminum to be below 0.01 ppm (0.011 ml/100 g), however, actually, the hydrogen concentration can not be decreased below 0.05 ppm.

Usually it is very difficult to remove moisture perfectly from the atmosphere in the chamber because of the difficulty for perfect sealing (preventing air penetration) and the difficulty for the removal of the moisture adhered physically or chemically to the material of the chamber or the crucible. In the case of SNIF the inlet of molten aluminum is not sealed and a little amount of air can enter into the chamber even if a positive pressure of inert gas atmosphere is effective to prevent air infusion from the ambient atmosphere (see Fig. 10). That is the reason why the actual result differs from the calculated result. SNIF can also remove solid particles from molten metal
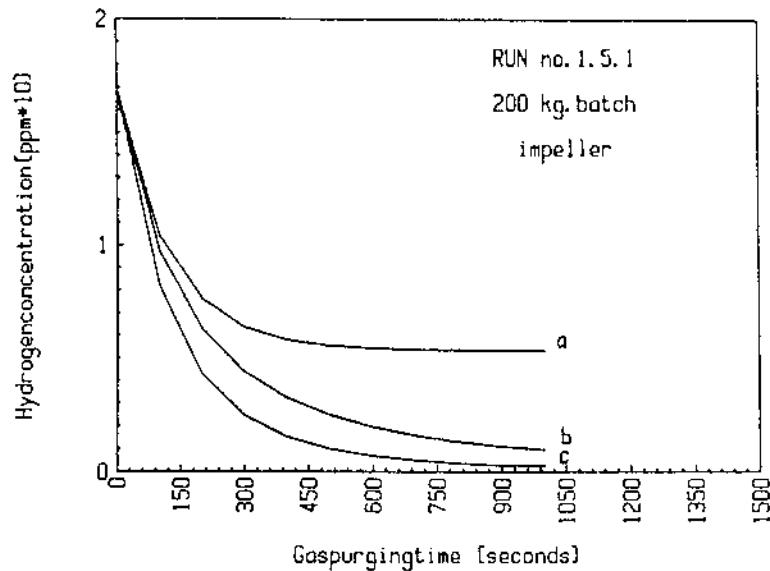
Figure 12 Calculated curves for hydrogen removal with. (a) surface completely exposed against air; (b) a lid; (c) blowing inert gas on the surface (combined with a lid). (From Ref. 12.)

by flotation [11] as described later and it was the innovative refining process for molten aluminum. However, it is a sophisticated and big apparatus (big holding capacity of molten metal in the reactor is necessary for in-line melt treatment.) which is suitable for the refining of a large amount of one species of molten alloy without changing the species of molten alloy in the chamber. Therefore, SNIF was installed mainly in the cast house for a large amount of can body sheet alloy (AA No. 3004) which should be enough refined to remove gas and inclusion in order to obtain high ductility in sheet-forming (drawing). After SNIF, Pechiney and Showa have developed new refining processes by rotating gas injector, AlPur (Fr. Patent no. 8116735) and GBF (U.S. Patent 4611790, 1986). The rotor and the treatment box of AlPur are shown in Fig. 13. AlPur in-line process has a tilting device for emptying the box in order to be easy for the change of molten metal refined and simple system for cleaning by dross removal (to open the lid).

   The degassing efficiency of AlPur in-line process ($[\% \ H]_{inlet} - [\%H]_{outlet}/ [\%H]_{inlet}$) depends on inert gas (gas injected) flow rate and rotating speed (100–250 rpm) of gas injector as shown in Fig. 14 [14]. In inert gas dispersion process the real efficiency of gas removal should be evaluated both by the reduction rate and the attainable minimum hydrogen content under the atmosphere which has p_{H_2O} of water vapor partial pressure above the melt surface. GBF which is a molten metal processing under the air atmosphere has been developed by studying chemical engineering for effective chemical reaction between gas and liquid. Figure 15 shows dispersed bubbles around rotating cylinder when N_2 gas is injected into near the center of bottom surface of rotating cylinder in the water (Jap. Pat. 529603). Large spherical cap bubbles circulate and ascend around the rotating cylinder, and near
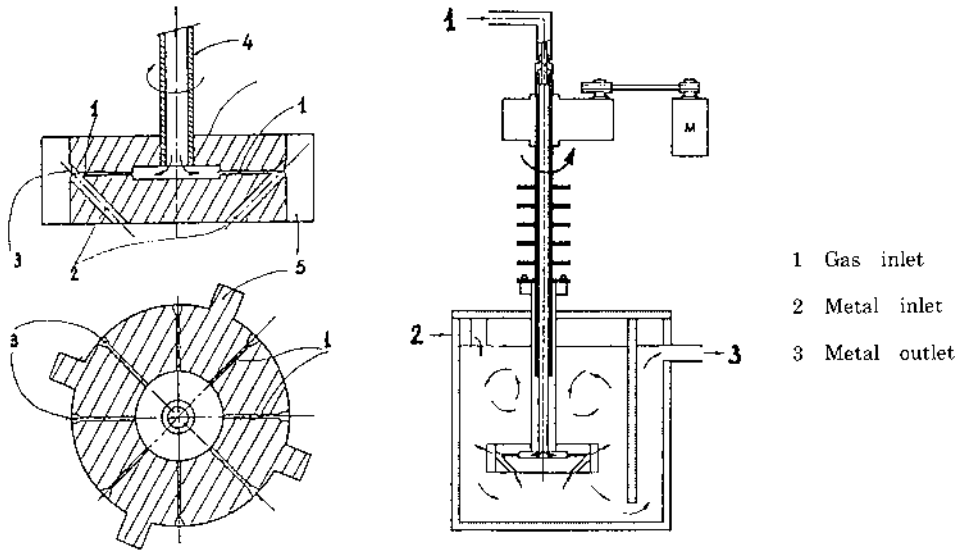
Figure 13 AlPur rotary mixer and treatment boxes. (From Ref. 14.)
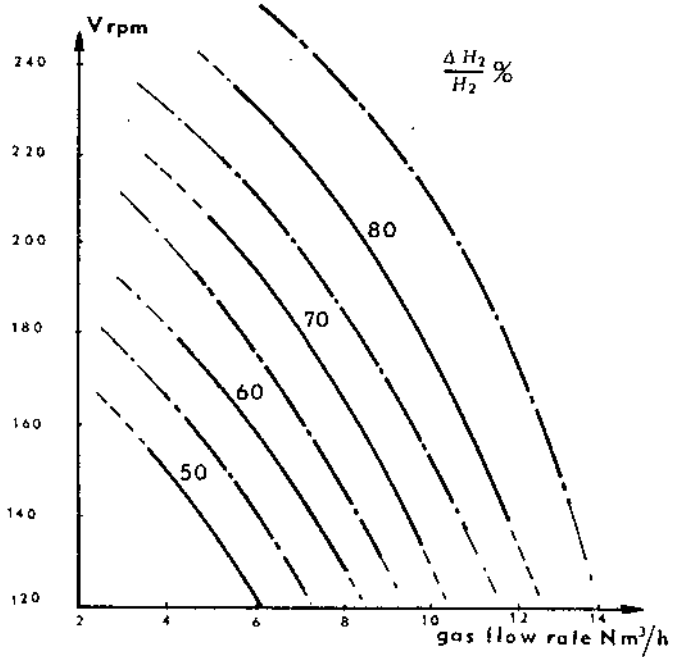
Figure 14 Degassing efficiency curves by AlPur rotary mixer; dependence on inert gas flow rate and rotating speed. (From Ref. 14.)
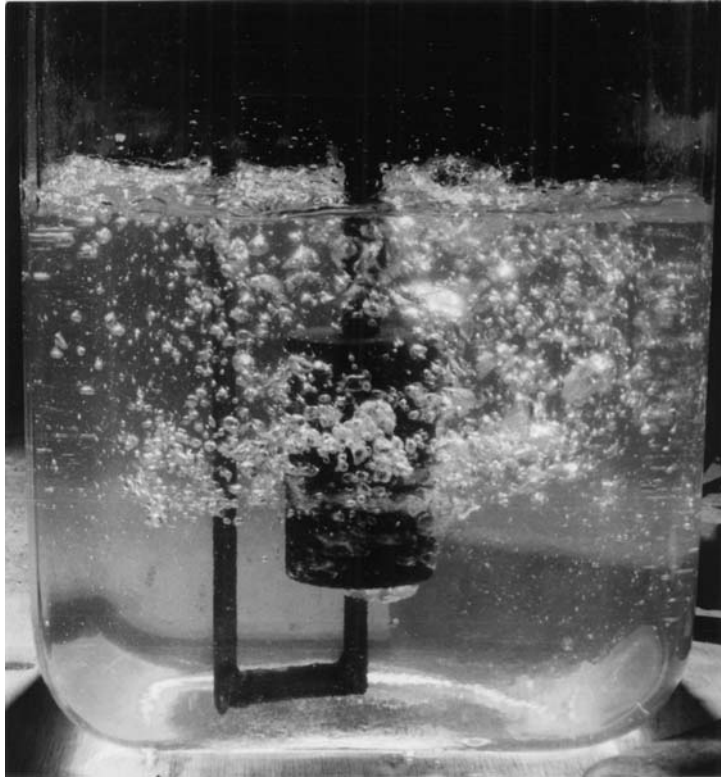
Figure 15 N$_2$ gas bubbles dispersion in water by rotating cylinder (diameter = 50 mm, height = 80 mm, rotating speed = 1000 rpm). (From Ref. 10.)

the half height of the cylinder they look to be finely dispersed centrifugally after being sucked to the cylinder surface. Water flow pattern around the rotating cylinder as shown in Fig. 16 looks to be same as typical flow pattern in baffled tank with turbine positioned on center [15]. It is revealed that bubbles on water flow is finely torn off by a vigorous turbulent flow toward centrifugal direction near the half height of the cylinder surface where down and upward flow collide with. It was found small height and large radius of cylinder, positioned near bottom was effective for more fine dispersion of bubbles, and a practical rotor (Jap. Pat. 1375860) as shown in Fig. 17 has been developed after many trials of various disk-like rotors. Figure 18 shows dispersed bubbles in the water by GBF rotating injector. Bubble size is small (1–4 mm dia.) and bubble dispersion is uniform throughout the water. Assuming bubble size in molten aluminum is nearly twice in water as Engh et al. [12] described, the size of dispersed bubbles into the melt by GBF may be about 2–8 mm diameter.

Baffle plate shown in Fig. 17 suppresses circulative flow and vortex around rotating shaft to form upward flow near baffle. Baffle plate is effective for mixing of the melt and the flotation of inclusion by forced upward flow as described later. Figure 19 shows the hydrogen removal result from molten Al-7% Si-0.3% Mg by GBF under the air atmosphere in which P_{H_2O} is 1.0×10^{-2}–1.5×10^{-2} atm (500
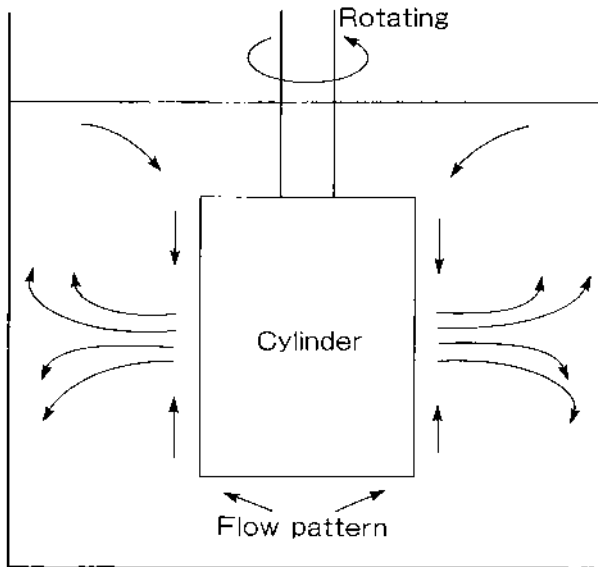
Figure 16 Flow pattern of water by rotating cylinder. (From Ref. 10.)
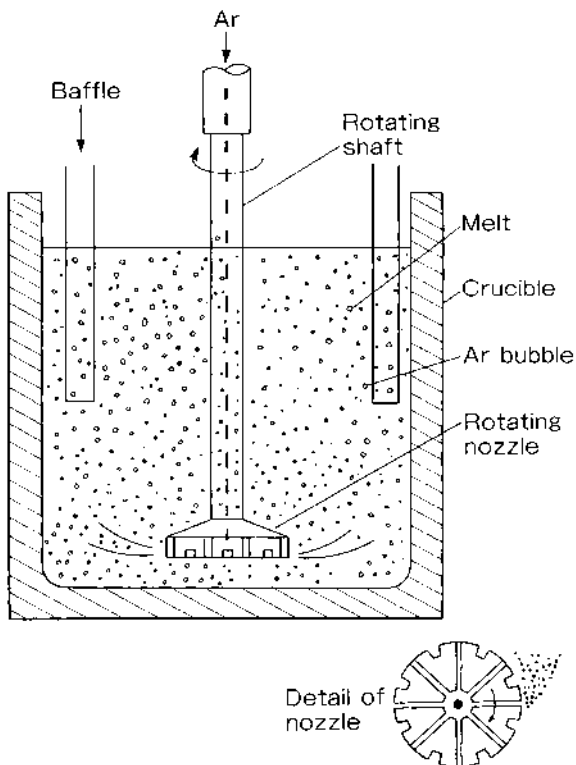
Figure 17 Schematic diagram of GBF method. (From Ref. 10.)
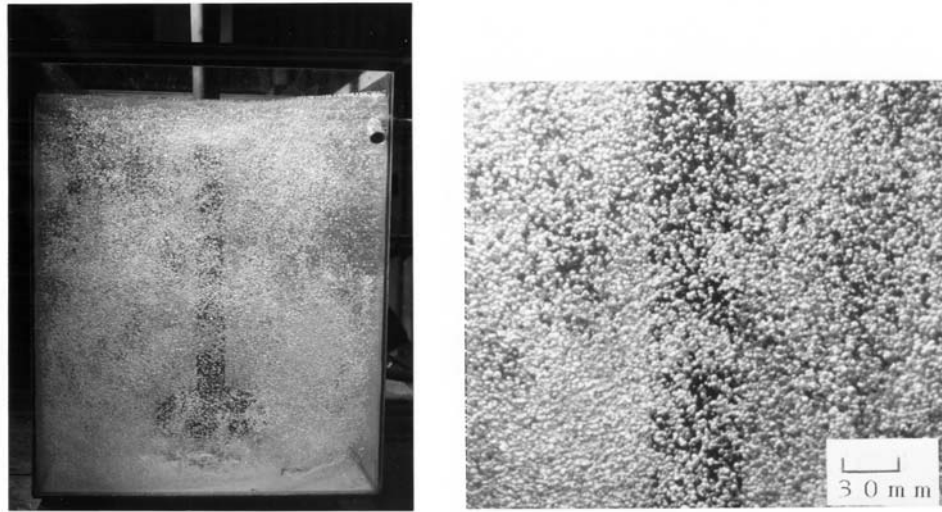
Figure 18 Ar gas bubbles dispersion into water by rotating GBF nozzle. (From Ref. 10.)
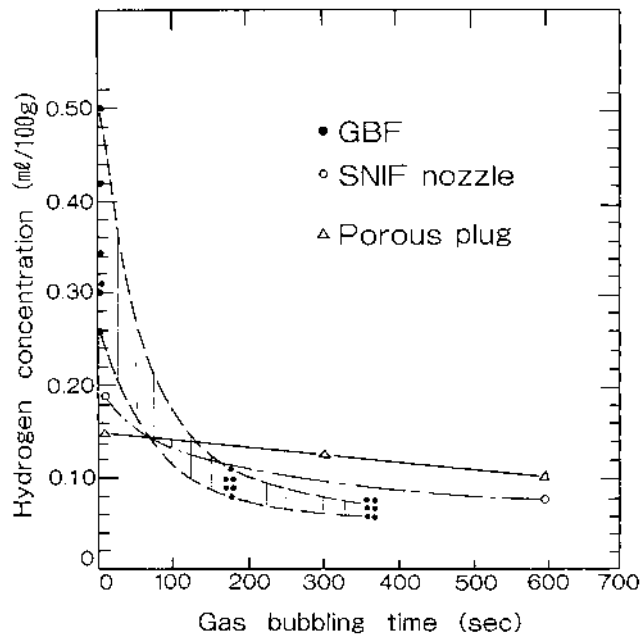
Figure 19 Hydrogen removal from molten Al-7% Si-0.3% Mg alloy by GBF treatment and hydrogen removal from Al-7% Si-0.5% Mg by SNIF nozzle or porous plug. (From Refs. 10 and 12.)
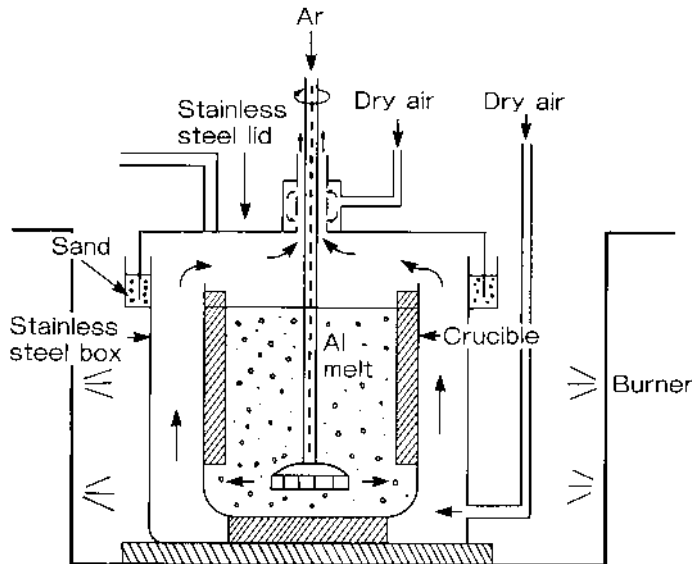
Figure 20 Experimental apparatus for GBF melt treatment in conditioned atmosphere of optional partial pressure of water vapor (P_{H_2O}). (From Ref. 10.)

kg of molten metal, 20 l/min of Ar flow rate). The result by SNIF nozzle and porous plug in Fig. 11 was also shown in Fig. 19 for the comparison of hydrogen removal effect, although Ar flow ratio is 0.4 l/min per kg molten metal (GBF) and 0.3 l/min per kg molten metal (SNIF). The influence of p_{H_2O} in the ambient air atmosphere to the hydrogen removal by GBF was examined by the experimental apparatus as shown in Fig. 20. The value p_{H_2O} in the box of the apparatus was controlled by the flow rate of the dry air of which the dew point was below $-60°C$ through the molecular sieves. The result for 99.99% Al is shown in Fig. 21. On the production of 99.99% Al foil for capacitor, hydrogen gas pores (Fig. 22) in casted slab after homogenization heat treatment at 600°C may be the origin for the cracking during hot rolling. Such pores in high purity aluminum ingot are formed by the annihilation of micro porosities (which may involve hydrogen gas) and the precipitation of excess hydrogen over the solubility (0.03 ml/100 g at 600°C [1]) at the grain boundary which may disappear or rearrange by recrystallization during homogenization heat treatment. It is known by our experience that the hydrogen content which does not induce hot cracking should be below 0.10 ml/100 g. Therefore, the hydrogen removal from 99.99% Al by GBF must be done under the dry air atmosphere of dew point below $-6°C$ ($p_{H_2O} < 3.8×10^{-3}$ atm). Hydrogen removal result for several alloys by GBF under near the same air atmosphere of p_{H_2O} is shown in Fig. 23 (AC7A and AC8C by Japan Industrial Standard are the casting alloys of Al-5.0% Mg-0.4% Mn and Al-11% Si-2.9% Cu-1.2% Mg, and 3003 by AA No. is Al-1.2% Mn-0.2% Si-0.1% Cu.) and in Fig. 24 (5052, 6061, 1100 and 2017 by AA No. are Al-2.5% Mg-0.2% Cr, Al-1.0% Mg-0.6% Si-0.2% Cu, Al-0.55% Fe and Al-3.8% Cu-0.7% Mg-0.5% Si-0.7% Mn.) The attainable hydrogen reduction level of each alloy by GBF seems to depend on the activity coefficient of hydrogen in molten
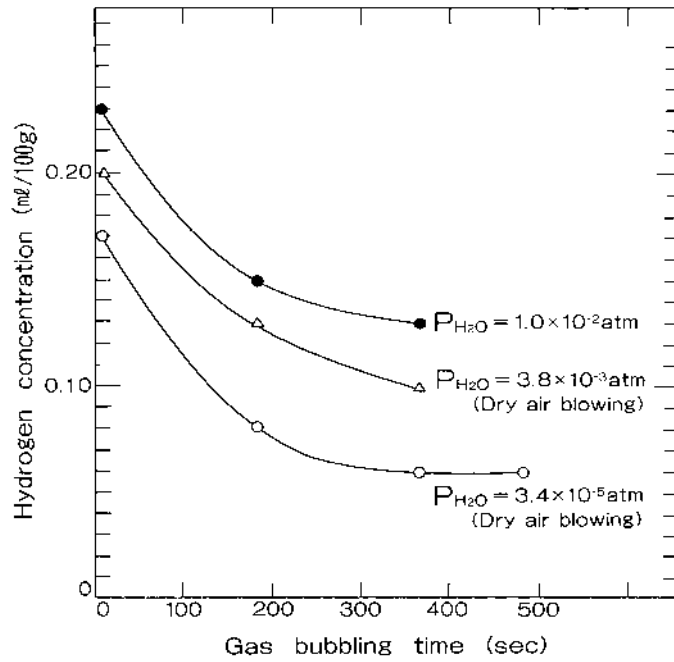
Figure 21 Hydrogen removal from molten 99.99% Al by GBF treatment in the several air atmospheres of different water vapor partial pressures (P_{H_2O}). (From Ref. 10.)
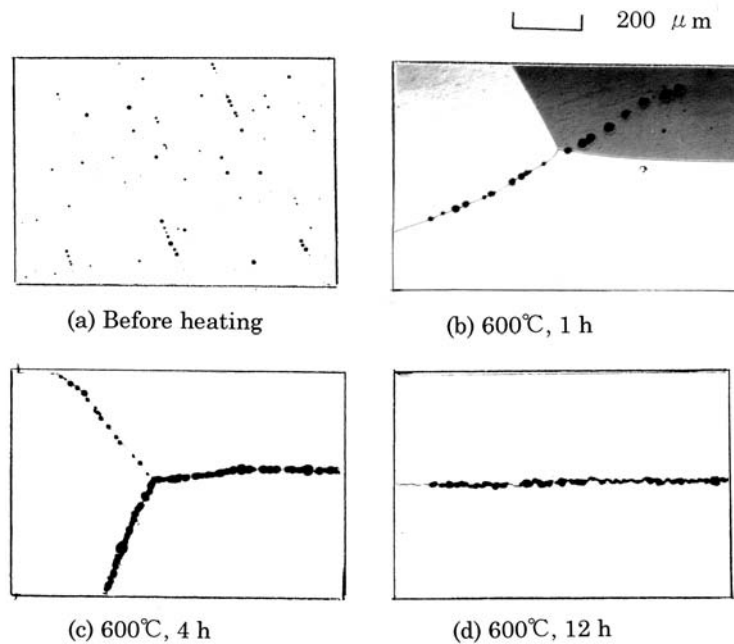
Figure 22 Development of hydrogen gas porosity in 99.99% Al ingot by homogenization heat treatment in air atmosphere of $P_{H_2O} = 3 \times 10^{-2}$atm. (a) before heating; (b) 600°C, 1 h; (c) 600°C, 4 h; (d) 600°C, 12 h.
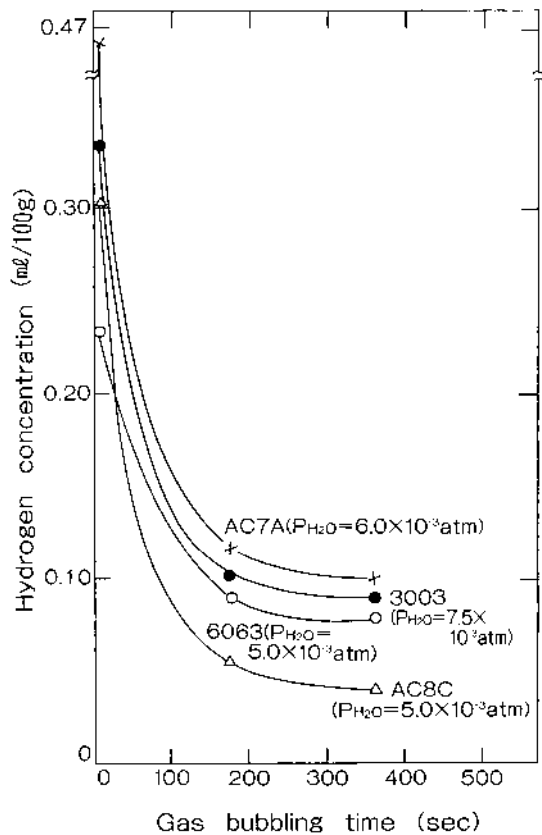
Figure 23 Hydrogen removal from molten Al alloys by GBF treatment in air atmosphere of $P_{H_2O} = 5.0 \times 10^{-3}$ to 7.5×10^{-3} atm. (From Ref. 10.)

aluminum alloy which was estimated as shown in Table 1 in Sec. 2.2 (Fig. 25). One of the unexpected results by hydrogen removal by GBF in-line treatment revealed the surface improvement of AA No. 6063 alloy billet by semi-continuous casting as shown in Fig. 26. It should be noticed from this figure that such a smooth cast surface could be obtained by the removal of hydrogen and inclusions from molten aluminum and not obtained only by inclusions removal by RMF filtration described in Sec. 3.3.3.3. Several inert gas purging methods by rotating a nozzle other than SNIF, AIPur and GBF have been developed [16–18].

3 REMOVAL OF INCLUSIONS FROM MOLTEN ALUMINUM

3.1 Inclusions in Molten Aluminum

Typical inclusions in molten aluminum are shown in Table 2. The source of inclusions is from Hall–Heroult cells of smelters and melting–casting process in all of aluminum industry. Inclusions mean solid particles in melt which are nonmetallic compound such as oxide, carbide and salt (strictly, some salts are liquid sphere in molten aluminum, for example, the melting point of $MgCl_2$ is 712°C), and
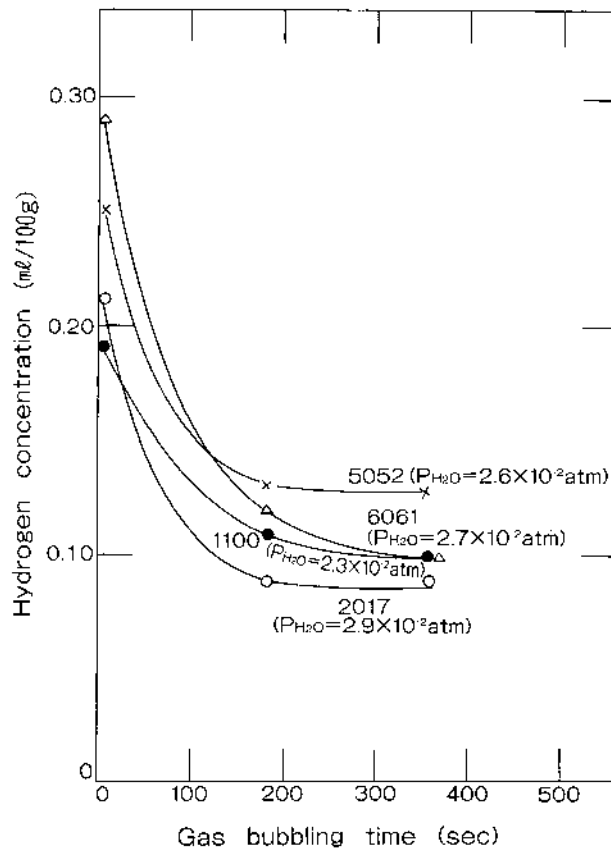
Figure 24   Hydrogen removal from molten Al alloys by GBF treatment in air atmosphere of $P_{H_2O} = 2.3 \times 10^{-2}$ to 2.9×10^{-2} atm. (From Ref. 10.)

intermetallic compound of high melting point such as TiB_2. Concentration of inclusions in aluminum usually is below 1 ppm except Al_4C_3 from Hall–Heroult cell and TiB_2 from grain refiner addition. The detrimental effect of inclusions to the properties of aluminum products appears generally on the size beyond 30 microns. Recently the rigorous drawing and ironing of 3004 alloy sheet for the thin wall can body and the high grade polishing surface for computer memory disks request the removal of smaller inclusions. In the case of very thin foil of few microns, inclusions below 10 micrometers in size may be the origin of pin hole defects. Figure 27 shows microscopic photographs of typical inclusions found in a molten aluminum alloy.

3.2   The Principle of Inclusion Removal from Molten Aluminum

3.2.1   Floatation

The floatation of solid particles from molten aluminum by the dispersed gas bubbles of SNIF process was investigated on theoretical fluid dynamics by A.G. Szekely [11]. Two mechanisms of floatation, i.e. inertial impaction and peripheral interception,
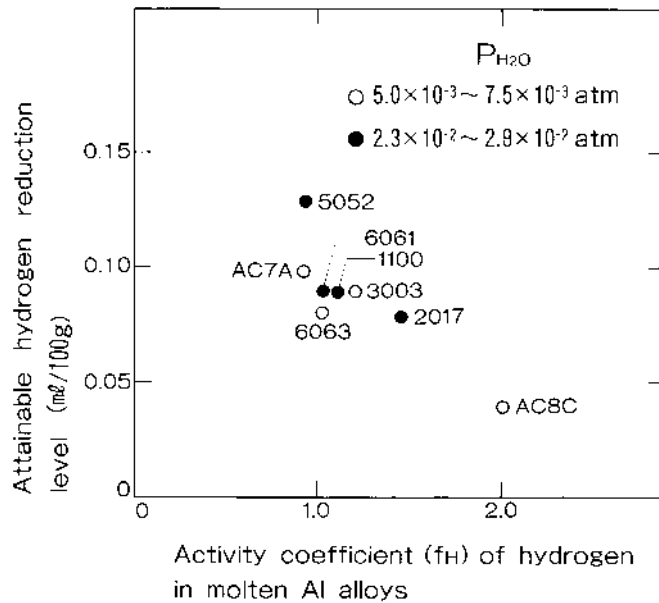
Figure 25 Relationship between activity coefficient (f_H) of hydrogen in molten Al alloys and attainable hydrogen reduction level by GBF treatment. (From Ref. 10.)

After GBF   After RMF (filtration)
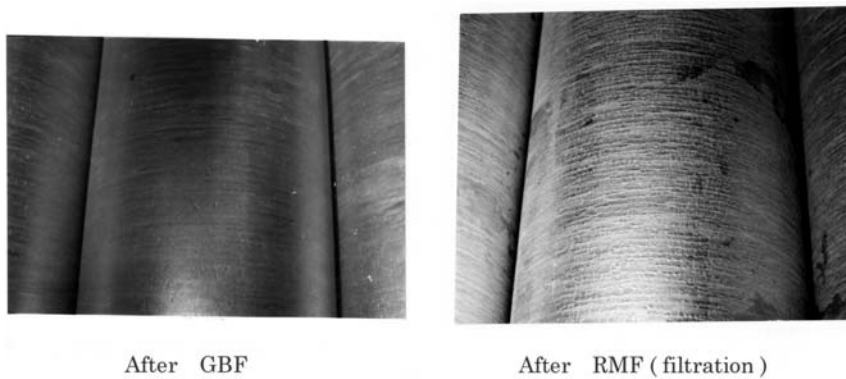
Figure 26 Cast surface improvement of AA No. 6063 alloy billet by GBF treatment.

were proposed. Inertial impaction on gas bubbles is shown in Fig. 28. The stream lines of the fluid are diverted by the sphere irrespective of whether the body is stagnant and the fluid medium is flowing or the medium is stagnant and the body is moving. The curved streamlines (shown by the thin lines on the sketch) prevent the frontal collision of small particles with the sphere. Large particles can, however, establish their own paths by inertia which are distinct from the stream lines of the fluid. The possible paths of such large particles are illustrated by the dashed lines. The interception of the path of a large particle by the sphere is still not

Table 2 Inclusions in Aluminum

Particle type	Particle phase and source	Particle shape	Size (dia.) range (microns)
Oxides	Al_2O_3 from oxidation of melt surface	films or group of films	10–1000
	Al_2O_3 from undissolved Alumina	polygonal particles	10–20
	Al_2MgO_4 from oxidation of melt surface	truncated pyramidical particles	0.1–5
		thick films or lumps	1–100
	MgO from oxidation of melt surface or alloying additions	polygonal particles	0.2–1
		films consisting of particles	10–1000
	Refractory brick (Al,Si,O)	lumps or particles	10–500
Carbides	Al_4C_3 from Hall–Heroult cell	rectangular or hexagonal discs	0.5–25
Borides	TiB_2, VB from Hall–Heroult cell	rectangular or hexagonal discs	1
	TiB_2 from grain refiner	discs	1–3
		clusters of discs	1–50
Salts	Cryolite (Na_3AlF_6) from Hall–Heroult cell	spheres	10–20
	Mg/Al chlorides from Cl_2 gas fluxing or dross fluxing		
	Na/K chlorides from dross fluxing		

Source: Refs. 19 and 20.

Figure 27 Inclusions observed in AA No. 6063 alloy melt before refining processing. Molten metal sample was filtrated through porous carbon plate and filtrated inclusions were analyzed by XMA. (a) gray small particles; Ti-B compound, black fine particles; Al_4C_3, black film; Al_2O_3; (b) cluster of fine particles; MgO including Al_2MgO_4, black particles; Al_4C_3.
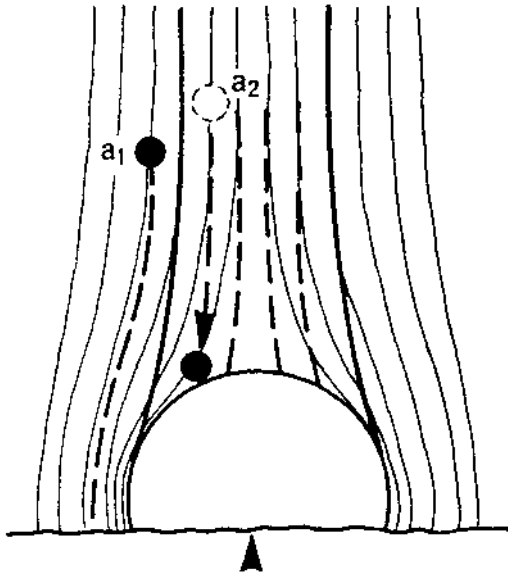
Figure 28   Inertial impaction of particles on gas bubbles. (From Ref. 11.)

guaranteed, but only those particles which are present originally in the fluid bounded by the heavy lines have chance to contact the spherical body (where the mass and velocity of particles a_1 and a_2 may be equal for example).

The number of these particles related to the total number of particles enclosed in a liquid column which has a diameter equal to the diameter of the sphere defines a contact efficiency which can be calculated if the velocity distribution and the trajectories of the particles are known. The size of the smallest particles which can be collected by inertial impaction on gas bubbles was calculated for oxide particles suspended in molten aluminum based on theoretical fluid dynamics. This calculation leads to the conclusion that all particles larger than about 80 μm can be collected from molten aluminum by inertial impaction on gas bubbles if the size of the bubbles is in the 1–10 mm range.

Small particles which are completely entrained by the stream lines of the fluid due to their small masses have a poor chance of colliding with rising gas bubbles. However, those particles can establish contact with the bubbles which are brought within a touching distance to the bubble around its equator by the streamlines of the liquid (Fig. 29). Peripheral interception is the second mechanism for flotation. The efficiency of such a peripheral contact between a gas bubble and solid particles was approximated by the simple geometric argument considering a hypothetical bubble column of $r^2\pi$ base containing n_0 number of particles at uniform distribution. Only those particles of radius a which are carried into the equatorial ring of $2a$ width of the bubble can skirt the bubble. In a decrease of the particle concentration of $\Delta n_0 = n_0 - n_0/x$, the decrease of the particle concentration due to peripheral interception by gas bubbles is expressed by Eq. (11) for gas sparging rate G m^3/kg.

$$x = \exp{(54 \times 10^4\, G \times a/r^2)} \tag{11}$$
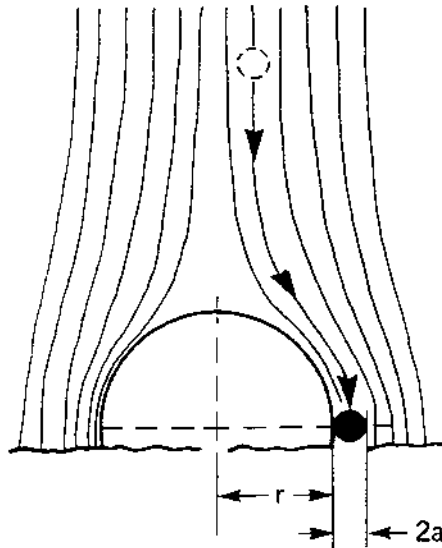
Figure 29 Peripheral interception of particles by gas bubbles. (From Ref. 11.)
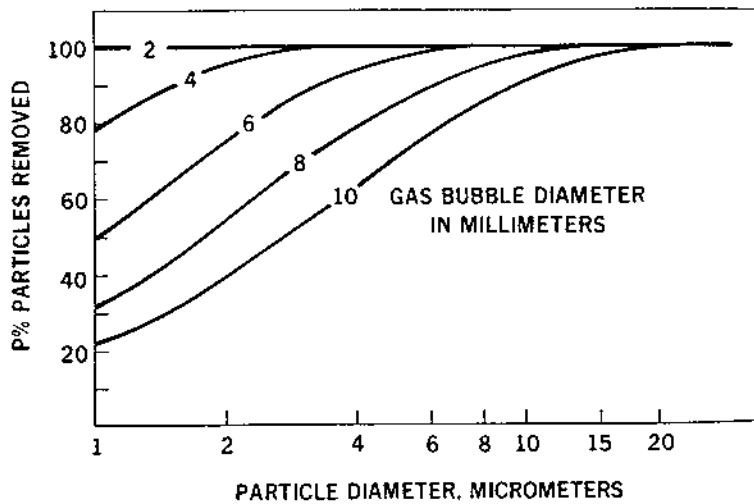
Figure 30 Flotation of particles at a gas sparging rate of 7.8 × 10 - 4 m³/kg as calculated from Eq. (10). (From Ref. 11.)

or for typical gas sparging rate (7.8×10^{-4} m³/kg) in the SNIF process

$$x = \exp(12 \times a/r^2) \tag{12}$$

The solution of this equation for 1–10 mm gas bubbles is shown in Fig. 30. From this figure it is important to produce gas bubbles as small as possible to assure

a satisfactory removal of particles from the micrometer range and is nearly imposs-ible to remove inclusions of sub micron size by 2–10 mm bubble. Szekely presented also the theory of agglomeration and the agglomeration of solid particles in molten aluminum in the SNIF process for the removal of sub micron size inclusions. Small solid particles suspended in a liquid move in a random, chaotic fashion as a result of the Brownian movement. If the size of the particles is in the micrometer and smaller range the collision of the particles inevitably leads to their coagulation due to the high specific surface energies of such small particles. This is thermal agglomeration. It is shown that the frequency of collision of particles in a given liquid is a single valued function of the temperature. In case the movement of the particles is enhanced by turbulent energy, the frequency of collision and the resulting coagulation rate of the particles can be significantly higher than due to thermal energy alone. This is turbulent agglomeration. The chaotic movement of the particles is sensitive to the scale of the turbulent eddies in which the movement of the particles is truly erratic. Large scale eddies have no significant effect on the collision of small particles and such eddies only stir the suspension, keeping the distribution of the particles uniform in the liquid. With diminishing eddies a certain scale is reached where the acceleration of the fluid in the eddies is at a maximum. The scale of such eddies is called the inner scale of turbulence. Below this critical scale, the kinetic energy of turbulence is gradually converted into heat due to the viscous resistance of the fluid. If particles are present in the fluid, the force exerted by the high acceleration present in such critical eddies pushes the particles randomly around causing them to collide with each other. The movement of the particles can be related under this condition to the volumetric dissipation rate of turbulent energy ε which is independent of the scale of motion and is a charac-teristic constant for a given flow. The constant of turbulent coagulation is shown to be proportional to $\sqrt{\varepsilon}$. This is applicable to particles not larger than about 10 μm since the inner scale of turbulence is of the order of 10–100 μm in vigorously stirred liquid. The volumetric dissipation rate of energy ε can be calculated from macroscopic parameters, such as from the size and speed of an impeller creating the macroscopic turbulence, or from the power utilized in the SNIF process for stirring a given melt volume. By the ratio of the calculated constants of turbulent and Brownian coagulation it is shown that particles less than about 0.1 μm agglom-erate predominantly due to their Brownian movement, while particles larger than that agglomerate faster by turbulence at the typical power inputs in the SNIF process. Experimental result of thermal and turbulent agglomeration of solid particles in molten aluminum has not yet been presented, but agglomeration of 10 μm SiC and Al_2O_3 in electromagnetically stirred molten aluminum was presented [21]. In this study, most of the initial 10 μm particles disappeared from the melt to form clusters in less than 1 minute and no cluster bigger than 100 μm was observed.

3.2.2 Settling

Inclusions heavier than the melt may sink and inclusions lighter than the melt may float up in the melt. Heavy inclusions in stagnant molten aluminum accumulate as a slurry in the lower part of the melt while light inclusions collect near the melt surface to form dross with oxide film. The term "settling" is used both when particles sink or float up. The fundamental equation governing "settling" of small particles in

a melt is the drag force on the particle sphere by Stokes Law. Drag force D on a particle sphere of radius r in homogeneous flow of velocity V is

$$D = C_D(\rho V^2 /2)(\pi r^2)$$

where C_D is empirical friction factor and ρ is the density of the particle. When Reynolds number $R(R = rV\rho/\mu)$ is so small that viscous force on a particle far exceed inertial forces, $D = 6\pi\mu Vr$ and $C_D = 12/R$ where μ is viscosity. If we assume the particle settles at constant terminal velocity (V_∞) in the melt, the difference between gravity and buoyancy force on the particle balances.

$$\Delta\rho g(4\pi r^3/3) = 6\pi\mu V_\infty r$$

So

$$V_\infty = \frac{\Delta\rho g r^2}{18\mu} \tag{13}$$

3.2.3 Filtration

The mechanism of molten aluminum filtration for the removal of inclusions involves cake mode filtration and deep bed filtration [22–24].

3.2.3.1 *Cake Filtration*

A rudimentary example of cake mode filtration is the fiberglass screen of trough sock or spout sock used for the removal of large inclusions. Reticulated ceramic foam plates and consolidated rigid media are commercial examples of cake mode filters (and also of depth mode filters as described later). Particles larger in size than the filter pores are strained on the surface of the filter medium. Through the depth of the filter medium particles are also trapped wherever a flow channel is smaller than the particle. As a layer of separated particles is deposited, the effective opening diameter is progressively decreased. Smaller diameter inclusion particles can now be captured in subsequent layers of separated solids, thus forming a cake. A thick layer of particles accumulates above the filter medium with little or no penetration into the internal pore structure. The resulting filter cake leads to high filtration pressure (high pressure drop) and a limited filter capacity.

3.2.3.2 *Depth Filtration*

Typical examples of depth filtration are deep bed filters such as Alcoa 94 [25] Alcoa 469 [26] and tubular cartridge filter comprised of rigid media [27]. On the case of depth filtration, particles are deposited through the depth of the filter medium, even though they are much smaller in size than the filter pore flow channels. Capture process in depth filtration involves two steps which are the transfer of inclusion from the bulk metal to the surface layer of the filter substrate and the adhesion of inclusion at a retention site on the filter substrate. Transfer processes are classified as follows [23,24].

Sedimentation or floatation; if the inclusions have a density different from that of liquid, they can be transported to the filter media away from fluid line by gravity or buoyancy. Inertia; owing to their apparent weight, inclusions can not follow the same trajectory as that of the fluid. When the direction of the fluid flow changes

suddenly, inclusions can deviate from the fluid flow path and be transported to the filter media. Hydrodynamic effects; owing to non-uniform velocity profile of fluid flow and non-spherical shape of inclusions, they may be moved laterally to the filter media by hydrodynamic effects. Direct interception; even with exactly the same density as the fluid, owing to their size, particles would not be able to follow the smallest tortuosities of the fluid flow line and they may collide directly with the filter media. Effects of turbulence; in turbulent flow, particles may be carried to the filter media. For the adhesion of inclusions on the substrate of filter, several forces can be exerted as follows. Fluid pressure; the pressure of the flowing fluid may hold the inclusions at the site of filter surface where they have been transferred. Friction; inclusions can be held at the site of filter surface by friction. Physico-chemical; physical or chemical adhesion by Van der Waals force or chemical bonding may hold the inclusions at the site of filter surface in molten aluminum.

3.3 The Molten Metal Processing for Inclusions Removal

3.3.1 Floatation Method by Gas Purging

Several results of inclusion removal by SNIF were reported. The removal of oxides was investigated by refining the melt with a higher inclusion content [28]. Size distribution of oxide inclusions observed by light microscopy analysis revealed that inclusions larger than 50 μm in cross section were removed, as shown in Fig. 31.
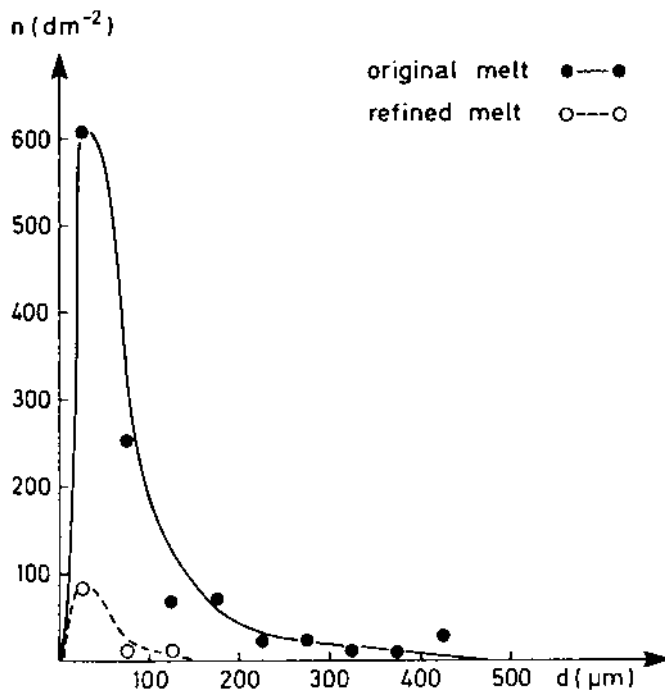
Figure 31   Size distribution (by number) of sedimented oxides in samples from the original melt and the melt refined by SNIF. The analysis was performed by the centrifugation method, and the diameter d is the maximum diameter of the oxide films. (From Ref. 28.)

The removal of borides was also measured and the result revealed that none or very little of the borides were removed by SNIF. TiB_2 in Al-Ti-B grain refining master alloy for controlling the as-cast grain size acts as nucleant and it has good wetting to molten aluminum. So TiB_2 is difficult to be separated from molten aluminum by gas purging. It should be noticed we can add Al-Ti-B master alloy into the molten aluminum before the melt treatment by gas purging such as SNIF, AlPur and GBF, but we can not do that before the filtration which is able to remove TiB_2 particles. An evaluation of a SNIF unit for inclusion removal in mass production lines revealed that inclusion removal efficiency depended on incoming inclusions concentration and Cl_2 mixing in purging gas might be effective as shown in Fig. 32 [29]. We have observed that the gas purging of Cl_2 or inert gas/Cl_2 mixtures by rotary nozzle forms less quantity of dross on the melt surface than in the case of inert gas purging. Furthermore, the dross is dry. That is different from wet dross in the case of inert gas purging. Where dry dross means more separated inclusions (mainly oxides) agglomeration from molten metal than in the case of wet dross. The mechanism of such a phenomena is not well known although the large heat of $AlCl_3$ formation may relate to it. Recently, SNIF SHEER system [30] incorporated changes to the chambers and the nozzles which increased the efficiency of the system (See Fig. 33).

A rib was added to the bottom of the chamber and it was useful to stabilize and equalize the metal flow pattern within the chamber. The action of the rib is supposed to be similar to one of the baffle plate of GBF process. It was demonstrated the
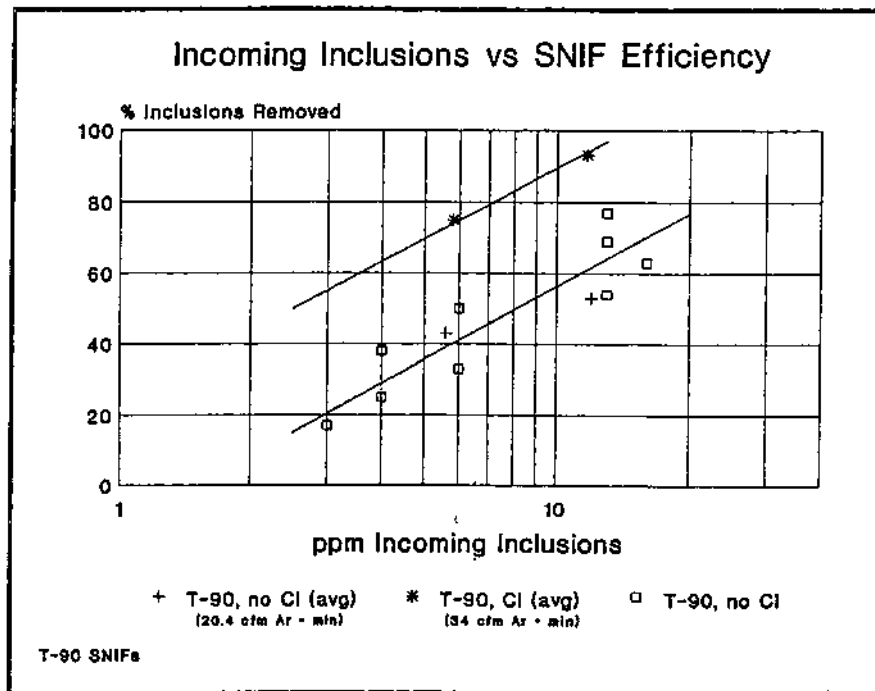
Figure 32   Incoming inclusions versus SNIF efficiency. (From Ref. 29.)
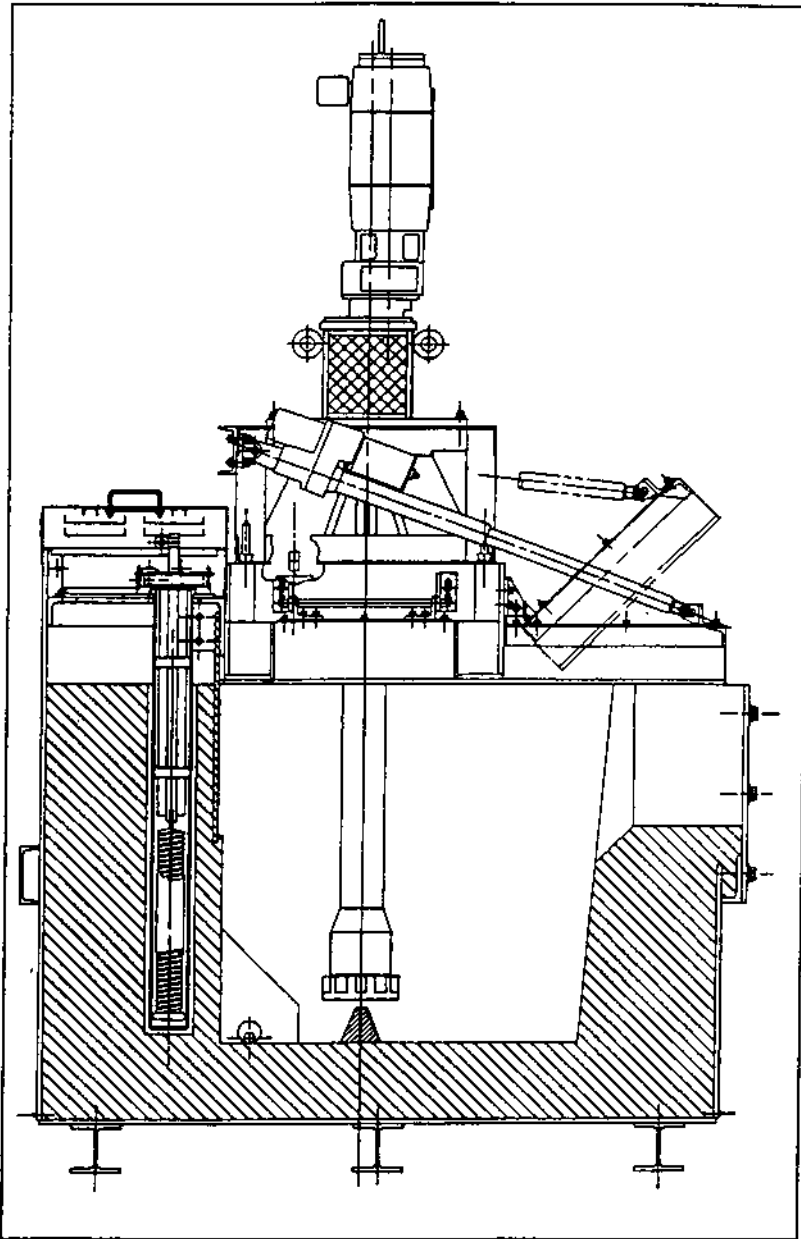
Figure 33 Cross-section of a SNIF SHEER R-140 system. (From Ref. 30.)

SHEER system removed 20% more hydrogen with 22% less process gas in comparison with current SNIF system. However, differences in inclusion removal could not be detected because of the large variability in the inclusion measurements. The high efficiency of inclusions removal by GBF may be supported by forced upward flow of molten metal by both the actions of rotating impeller and baffle

plate. Actually, it was revealed the dross (the agglomeration of inclusions such as oxide film etc. and molten metal) floatation on the melt surface by the gas dispersion from the rotating injector of GBF was drastically accelerated by the baffle plate. Several results for inclusion removal by floatation were presented for GBF. The most apparent result for the large inclusions removal from AA No. 5056 alloy melt by 3 min. of GBF treatment was presented by the inspection of stainless wire cloth (500 μm dia. pore) after being dipped into and moved in molten metal as shown in Fig. 34 [31,32]. In this figure, the convex surface of metal film shows the presence of inclusion. The inside of these convex sections were microscopically observed and it was revealed that oxide inclusions were not wetted by molten metal. In Fig. 35, the evaluation of GBF for the removal of aluminum oxide inclusions (aluminum oxide particles of 10–30 μm dia. were added by about 1 vol% into molten pure aluminum and the melt was treated for 10 min by GBF) is presented by the microscopic observation of the sample filtrated by porous carbon of 50–100 μm in pore size [33]. Showa Aluminum (Japan) produces foil including high purity foil (99.99% Al) for capacitor, sheet of AA No. 1000 series and 5052 alloy, and extrusion of almost all species of alloys. 8 in-line GBF units were installed between the holding furnaces and the casting stations in all the cast shops of Showa. The effect of both hydrogen and inclusion removal by GBF revealed notable yield improvement of foil, sheet and extrusion by the decrease of the number of defects such as pin hole, scratch like stringer, and blister etc.

3.3.2 Settling

Although it has long been recognized the holding time (that is to say killing time) after Cl_2 gas fluxing into molten aluminum is necessary for inclusions to be settled out, its quantitative study was not possible until several methods of quantitative analysis for inclusions such as PoDFA [34] and LiMCA [35] had been developed. A result of settling measured by PoDFA and LiMCA revealed the settling curve could be represented by the simple exponential decay function as shown in Fig. 36 [36]. Molten primary aluminum for electric wire is treated by B addition and stirring the melt for the purpose of the removal of Ti and V. The chemical reaction between (Ti, V) and B in molten aluminum forms high melting point intermetallic compound, TiB_2 and VB_2. TiB_2 and VB_2 agglomerates to form (Ti V) B_2 particles. By the settling of (Ti V) B_2 particles as shown in Fig. 37 [35], Ti and V in molten aluminum could be removed.

3.3.3 Filtration

3.3.3.1 *Ceramic Foam Filtration-CFF*
Ceramic foam plate (2 in thickness, 7–23 in square) is produced by using a polymeric foam precursor which is immersed in a ceramic slurry, squeezed to remove any excess and is then fired. Three- and two-dimensional images of the ceramic foam is as shown in Fig. 38 [37]. A rough characterization of the structure of the ceramic foam is given by the number of pores per inch (ppi) and commercial filter grades are 10–50 ppi. The grade of 10 ppi has 3800 μm of minimum cell size and 5100 μm of maximum cell size. The grade of 50 ppi has 1000–1150 μm of cell size. Industrial in-line application of ceramic foam filters is as shown in Fig. 39. The LiMCA II inclusion concentration data (total detected inclusion counts > 15 μm in size) for a typical cast run of

(a)

500 μ m meshes   200 μ m meshes

(b)
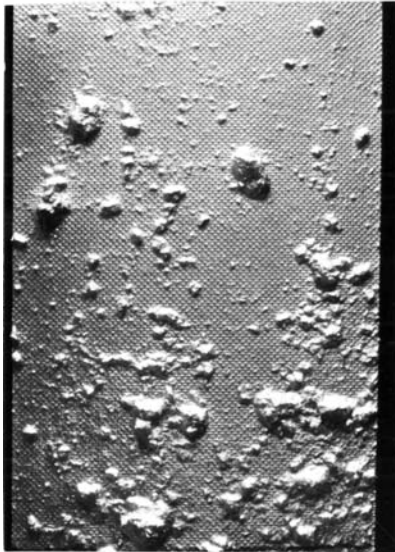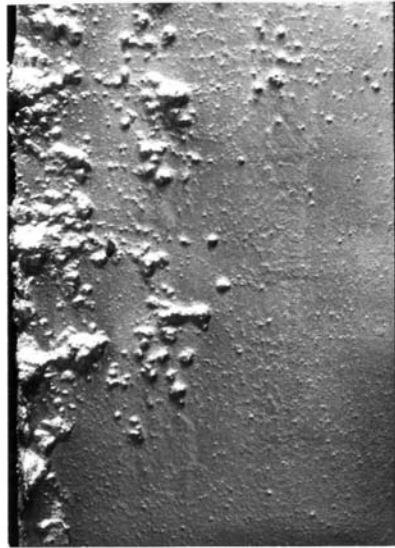
500 μ m meshes   200 μ m meshes

Figure 34 Inclusion inspection of stainless wire cloth (500 μm dia. and 200 μ m dia.) after being dipped into and moved in molten metal. (a) original melt of A A No. 5056; (b) after 6 min of GBF treatment.

(a) Original melt   (b) After GBF treatment
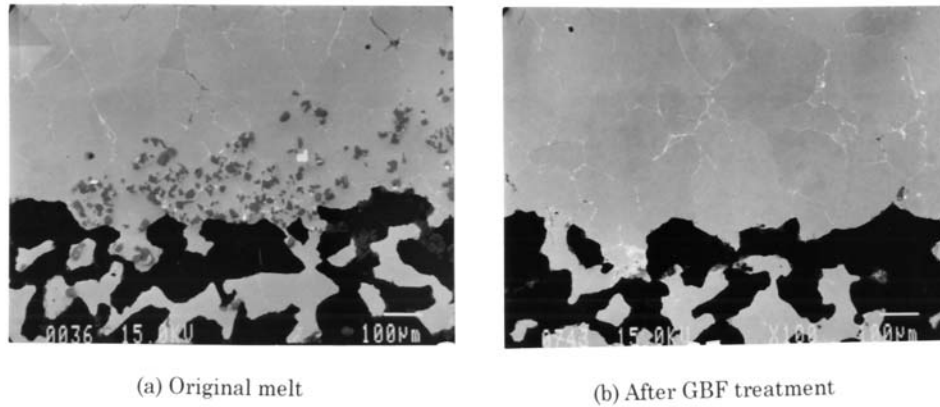
Figure 35 Microscopic observation of alumina inclusions in AA No. 1100 melt by the sample filtrated by porous carbon. (a) original melt; (b) after GBF treatment. (From Ref. 33.)
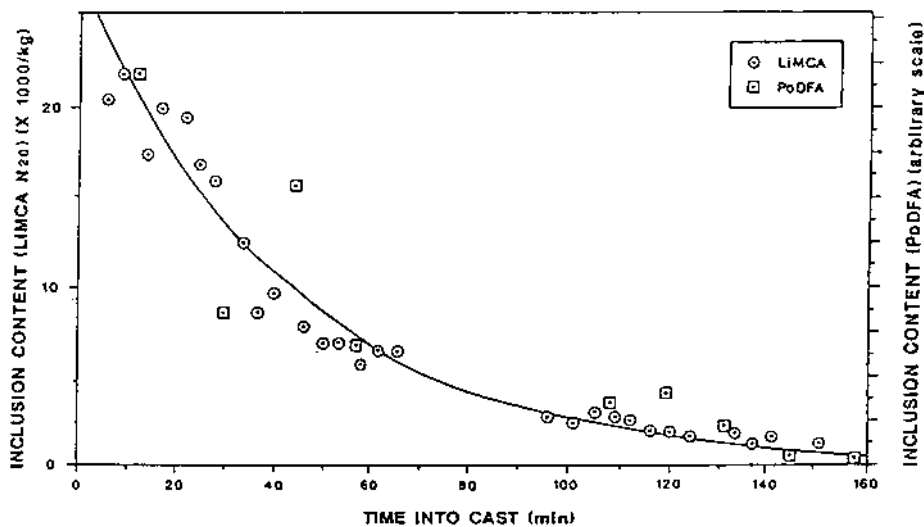
Figure 36 Effect of settling on inclusions concentration as measured by PoDFA and LiMCA. (From Ref. 36.)

AA No. 1050 at a flow rate of 167 kg/min with a 15–50 ppi ceramic foam filter was demonstrated as shown in Fig. 40 [39]. And also it was revealed the mean filtration efficiency for the fine pore CFF (50 ppi) had increased to 76% from 69% for the coarser pore CFF (30 ppi). Cake filtration takes place on the surface of filter medium in the case of inclusion diameters which are of the same order of size or larger than the holes in the filter medium such as oxide film. Depth filtration was also observed within the foamed filter medium on its internal surface as shown in Fig. 41 [38,39]. On the other hand, Fig. 42 reveals the release of inclusions from ceramic foam filter (30 ppi) during casting, and such a release has occurred for no specific reasons [40]. Although the filtration efficiency of ceramic foam filter depends on the operation
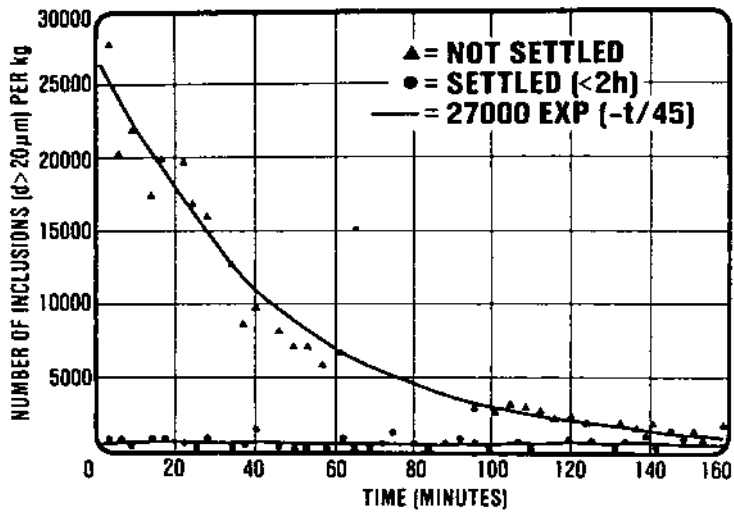
Figure 37 The settling of (TiV)B$_2$ particles from conductivity grade aluminum melts following boron additions to a holding furnace. (From Ref. 35.)
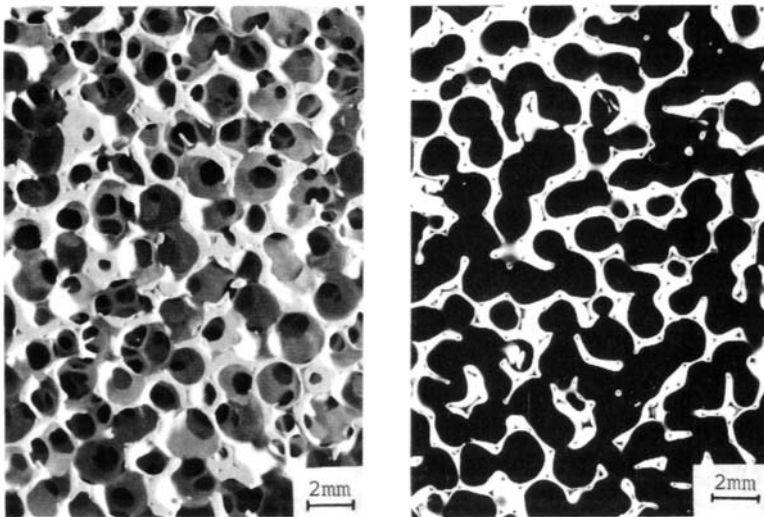
Figure 38 Three- and two-dimensional images of the ceramic foam. (From Ref. 37.)

condition such as filter cell size, metal flow rate and inclusions concentration before filtration, generally, 30 ppi ceramic foam filter can only be considered as a prefilter for critical products such as can body alloy [40].

3.3.3.2 Deep Bed Filtration-DBF

An example of deep bed filtration apparatus (Alcoa 94 process) is as shown in Fig. 43. It is strictly a packed bed tabular alumina filter. The size of the filter bed depends
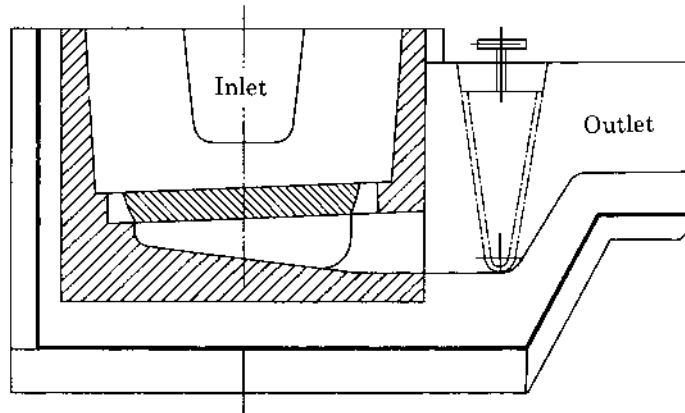
Figure 39 CFF filter box. (From FOSECO)
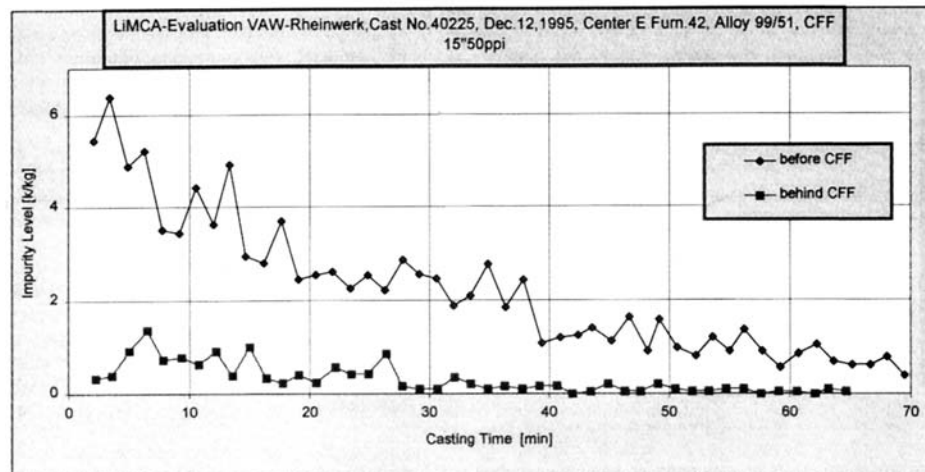
Figure 40 LiMCA II inclusion concentration data for 15–50 in ppi CFF. (From Ref. 39.)

on metal flow rate. The life of such a filter is 5000 t for unfluxed low-grade scrap, and up to 25,000 t for prefluxed metal. The packed bed filter was improved to extend the life and remove hydrogen gas by diffused argon being passed countercurrently through the melt (Alcoa 181 process-U.S. Patents 2963558 and Alcoa 469 process-U.S. Patent 2863558). Deep bed filters exhibit inclusion release at start of cast and very stable filtration performance afterwards as shown in Fig. 44 [40]. Deep bed filters that are maintained in operation for several thousands tons are much more stable due to their larger surface and volume of filtration. Nevertheless, as demonstrated in Fig. 44, deep bed filters present a release of inclusions at start of casts for a short period of time during the increase of the metal flow rate from zero to the nominal casting flow rate.

(a) └──┘ 500 μm

(b) └──┘ 50 μm
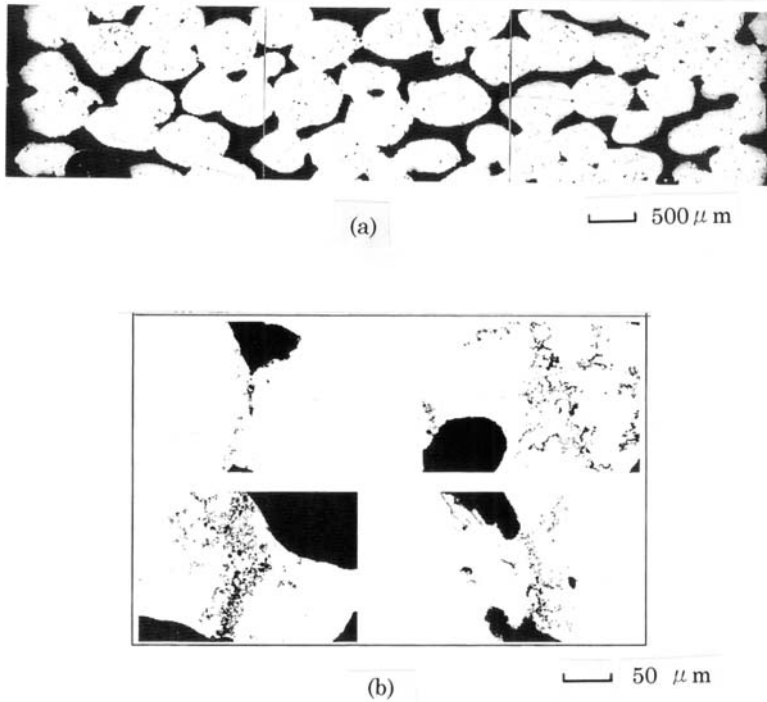
Figure 41 Cross-section through a drained 50 ppi CFF (metal flow direction is from left to right), (a) and inclusion agglomerates found within a drained 50 ppi CFF, (b). (From Ref. 39.)
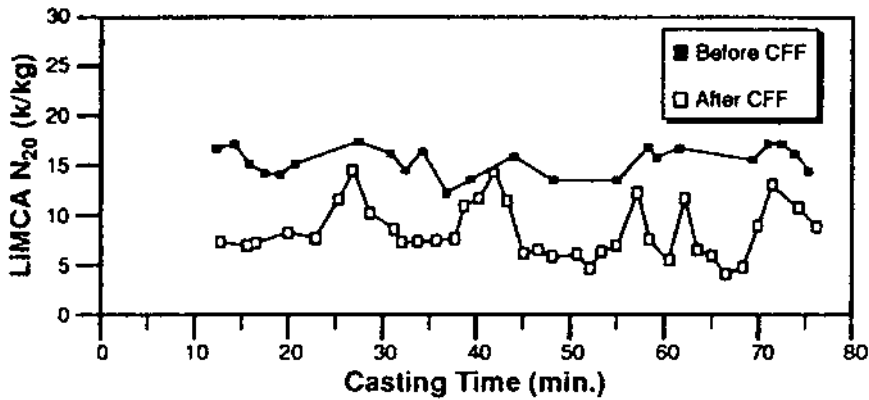
Figure 42 Release of inclusions from CFF (30 ppi) during casting. (From Ref. 40.)

3.3.3.3 Rigid Porous Media Tube Filter-RMF

RMF is utilized in the form of the cartridge filter and it was the earliest applications of the bonded particle filter media (alumina, corundum or silicon carbide). The bonded particle filter structure consists of an aggregate of mineral grain bonded with a ceramic/glass composition resistant to molten aluminum. The microstructure
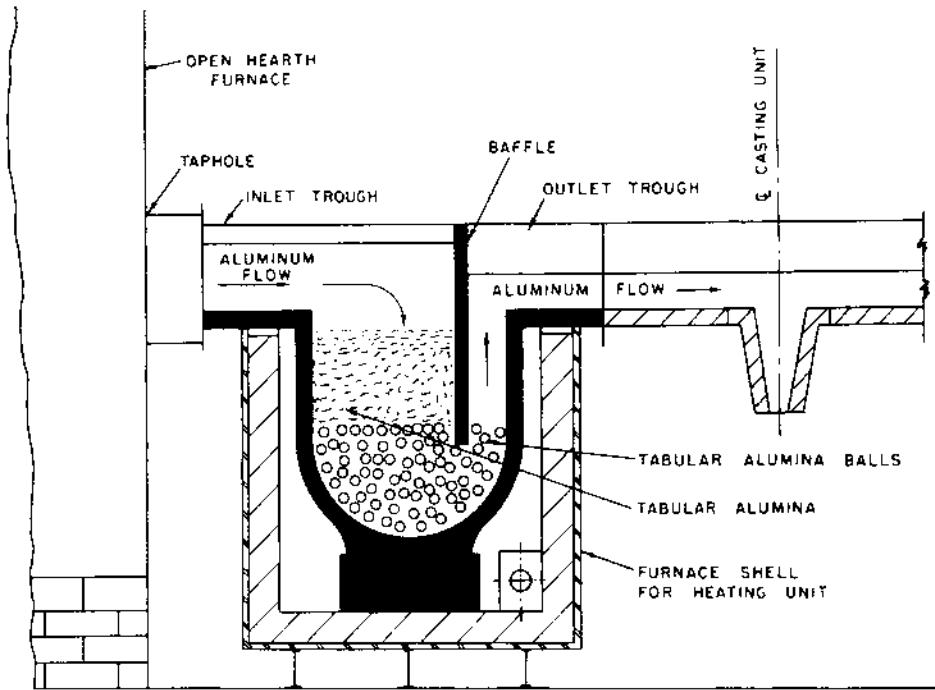
Figure 43   An example of deep bed filtration (Alcoa 94). (From Ref. 25.)
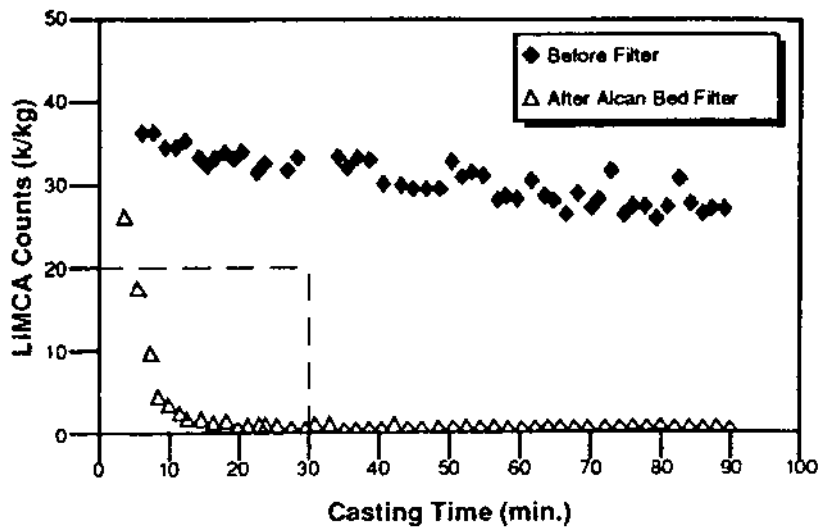
Figure 44   Inclusion concentrations measured during casting before and after filtration with Alcan bed filter. (From Ref. 40.)
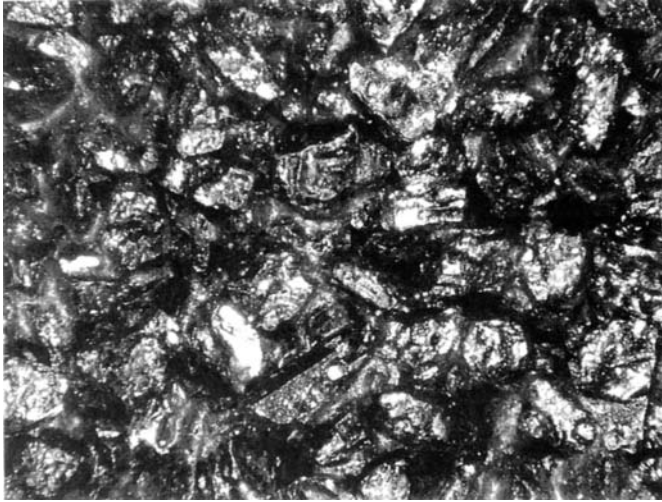
Figure 45 Microstructure of bonded particle filter, 20 grit SiC. (From Ref. 41.)

of a bonded particle filter (Fig. 45) differs considerably from ceramic foams [41]. The porosity of a BPF (Bonded particle filter) is related to a repetitive face centered close packed cubic structure, which yields a void space result 38–42%, roughly half that for a ceramic foam filter. RMF by TKR (Japan) has three grades of average pore diameter which are 760 μm (HAA), 450 μm (HC) and 340 μm (HE) [42]. Bonded particle tube cartridge filter is generally utilized as shown in Fig. 46 [43]. Filtration efficiency of RMF medium grade was studied by both theoretical and simulation method in comparison with those of DBF and CFF, and the result was as shown in Fig. 47 [44]. The investigation of the filtration efficiency of MCF (Metaullics tube cartridge filter) revealed MCF was more effective than CFF of 30 ppi or 50 ppi [39].

4   REMOVAL OF ALKALI AND ALKALINE EARTH METALS FROM MOLTEN ALUMINUM

It is known that a couple of ppm of Na in Al-Mg alloy causes cracking during hot rolling. The removal of alkali metals such as Na and Li in molten aluminum alloy which is alloyed primary aluminum from electrolytic cell with alloying metal is generally implemented by furnace chlorine fluxing in the smelters. The chlorine fluxing in the holding furnace is also for the purpose of the removal of inclusions in the melt. The melt from the holding furnace is in-line treated by SNIF, GBF et al. before the casting at the cast station. The efficiency improvement of alkali removal by chlorine gas purging in the holding furnace of the smelter-based casting system can be attained by the chemical engineering methods which increase the efficiency of chemical reaction between gas and liquid. The methods involve melt stirring, gas dispersion through the melt and fine gas bubbles dispersion into the melt [45–48]. Stevens and Yu studied the reaction rate controlling mechanisms in the stirred tank reactor of Alcoa 622 unit (Fig 48) in which a gaseous mixture of argon and chlorine was dispersed through the aluminum melt [45].
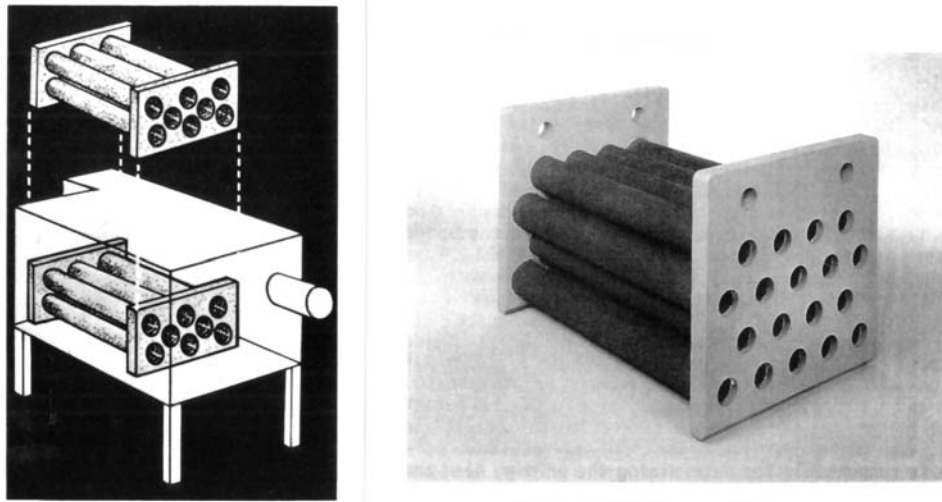
Figure 46   RMF cartridge filter. (From Refs. 41 and 43.)
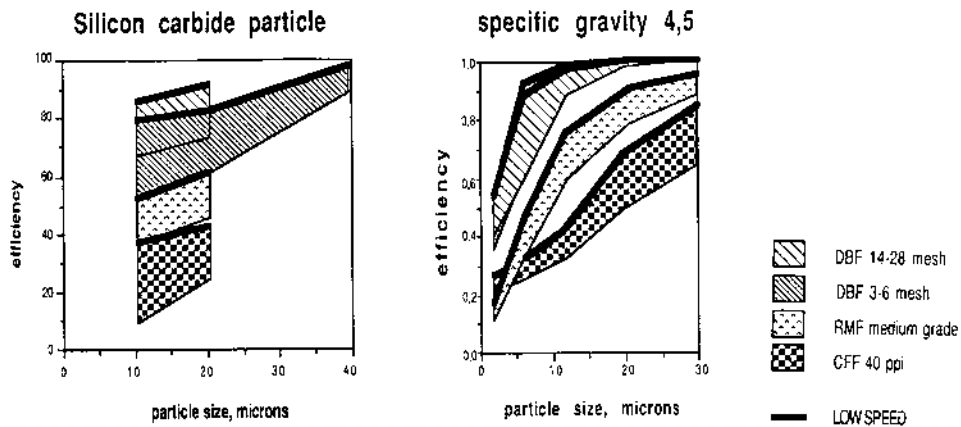
Figure 47   Comparison of (left) experimentally-determined and (right) computed values of initial efficiency for dense particles in filtering. (From Ref. 44.)

The rotor used in the reactor was a standard 305 mm diameter Alcoa 622 process rotor. The reactor contained approximately 998 kg of molten aluminum to which a known amount of calcium was added and which was maintained at a temperature of 732°C.

After examining a wide range of experimental batch reactor data, a conclusion was reached that two different reaction rate equations were required. Figure 49 shows some typical experimental data which illustrate this point. When Ca concentration is greater than 0.006%, chlorine transport to the surface of the bubble controls the rate of reaction. Thus, reaction rate is independent of Ca concentration, and a zero order reaction is observed. However, when Ca concentration is
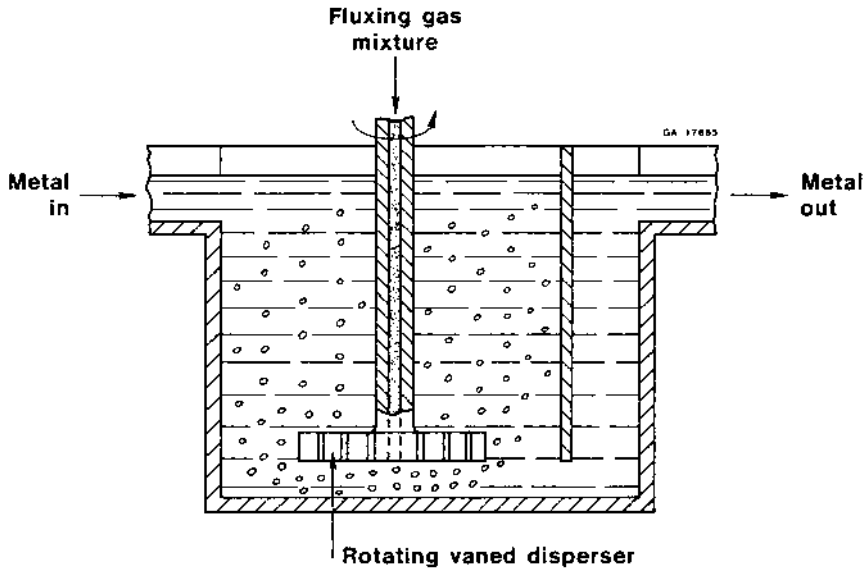
Figure 48 Alcoa 622 process. (From Ref. 45.)
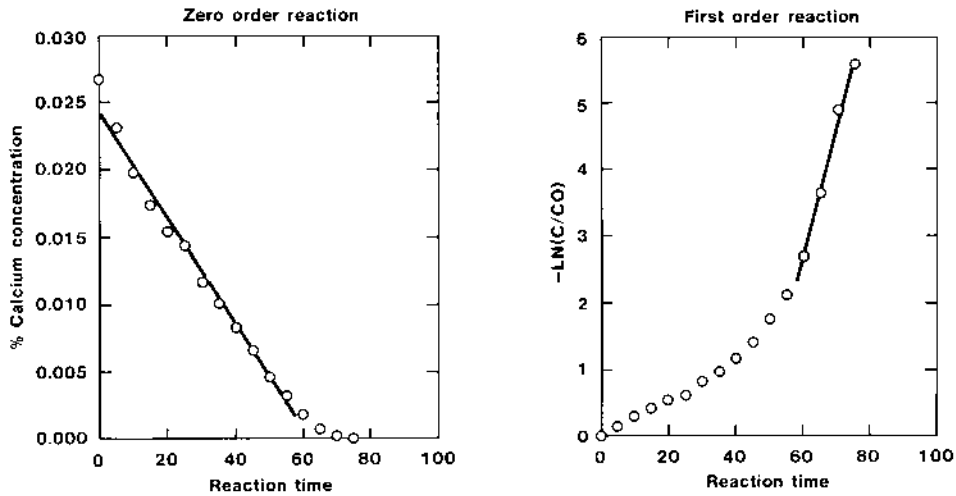
Figure 49 Typical experimental data which illustrate two different reaction rate equations, where C_0 is the initial concentration of Ca. (From Ref. 45.)

less than or equal to 0.006%, the transport of calcium through the melt to the surface of the bubble controls the rate of reaction. A first order reaction is observed. Chlorine gas in N_2/Cl_2 mixtures is employed during furnace fluxing in amounts that exceed the theoretical requirements due to inefficiency of static lance fluxing and furnace geometry. Celik and Doutre [46] investigated the effect of chlorine concentration on the rate of alkali/alkaline earth metals removal and tests were conducted
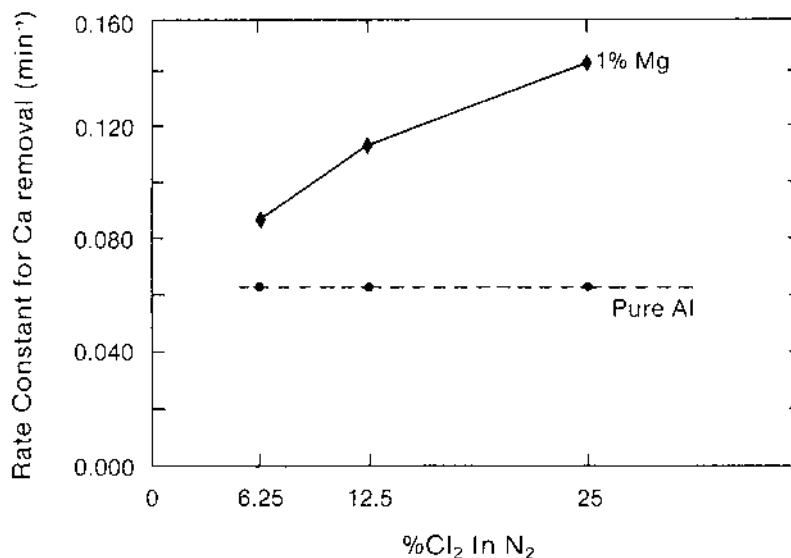
Figure 50 First order rate constant for calcium removal vs chlorine concentration. (From Ref. 46.)

in a 0.75 t furnace in which the removal rate at low levels of impurities (< 50 ppm) were determined as a function of gas flow rate and composition, metal composition (0%, 1% and 5% Mg) in the presence and absence of mechanical stirring, with and without bubble shear. This investigation revealed under all conditions examined, the removal rates followed first order rate kinetics indicating that mass transfer (diffusion) in the liquid phase was the rate determining step. Figure 50 compares the first order rate constants for the removal of calcium from pure metal and from an alloy containing 1% magnesium. Calcium was chosen as representative of the alkali/alkaline earth metal because Ca is of concern in both the smelter and remelt systems and Ca is less volatile than Na or Li making the manipulation of Ca levels more reproducible. It is clear that the removal rates are higher from alloys containing Mg than pure Al. It is also apparent from the figure that the rate of Ca removal from the pure Al was independent of the chlorine concentration in the fluxing gas at all concentrations tested, whereas, in the presence of Mg a strong dependency upon the chlorine concentration was observed. Figure 51 provides an explanation for these observations.

During these experiments the melt was fluxed for a short period of time in order to establish the calcium removal rates following which the chlorine supply was interrupted and calcium levels determined at intervals for the remainder of the experiment. The discontinuities in the slopes occurred at the time at which the chlorine supply was turned off.

In the case of the pure Al, the rate constant for calcium removal fell immediately to a very low value. On the other hand in the 1% Mg-Al alloy the removal continued to take place. Celik et al. explained these effects are due to the formation of molten $MgCl_2$ (m.p. 714°C) droplets during fluxing which range in size upwards to 100 μm. Being both small and relatively dense, these droplets can persist in
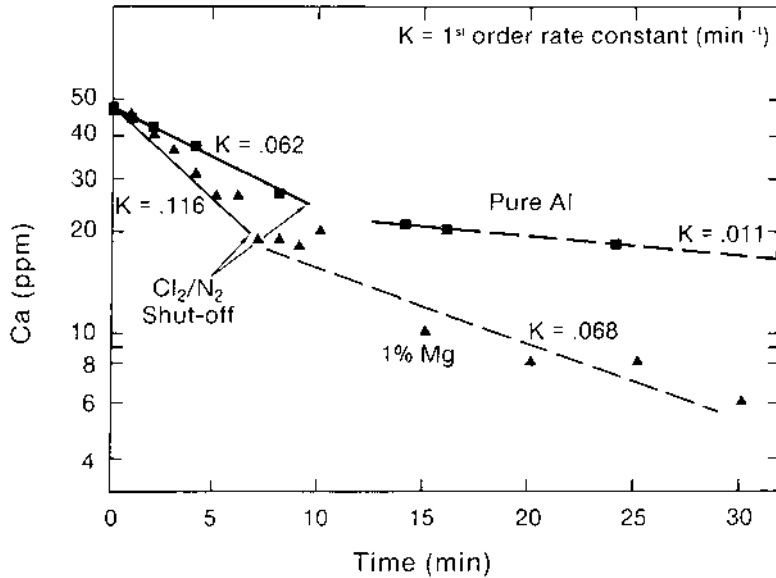
Figure 51 Demonstration of the persistence of Ca removal from an alloy containing 1% Mg after the cessation of chlorine addition. (From Ref. 46.)

the melt for some time before being eliminated by floating out or adsorption onto the furnace walls or dross layer. During their existence, these droplets can react substitutionally with Na, Li and Ca to form low melting point mixed chloride droplets which can be very difficult to remove from the melt, particularly during in-line chlorine fluxing. It is the reason why the in-line chlorine fluxing for alloys containing Mg by rotary injector should not be substituted for the furnace fluxing. Figure 52 compares the rates of removal of Ca from 5% Mg-Al alloy under the following conditions: lance injection only, lance injection and mechanical stirring (remote from the point of gas injection) and gas injection via a rotary impeller [45]. It should be noticed that the increase in the rate of impurity removal observed while using a rotary impeller to inject and disperse gas is due not only to the increase in the gas-liquid contact area but also to improved bulk metal circulation within the furnace. Figure 53 shows the experimental result of alkali and alkaline earth metals removal from molten Al-1% Mn-1% Mg by Ar + 5 vol% Cl$_2$ fluxing with GBF rotor (see the schematic diagram of GBF method in Fig. 17). Metallic sodium violently reacts with oxygen in the air and burns above the melting point (97.8°C). It may be due to the preferential oxidization of Na to form Na$_2$O$_2$ in gas at the surface of molten aluminum that we find the reduction of Na concentration after the simple melting operation. Kaestner et al. [49] showed that by inert gas purging, about 92% of Na content was removed from the melt by evaporation from the surface and only 8% was carried out of the melt by the purge gas bubbles. Figure 54 shows the experimental result which reveals the difference of Na removal rate from molten Al-5% Mg alloy between Ar gas purging and Ar + Cl$_2$ gas purging all of which were implemented by GBF method. It is clear that Ar gas purging without Cl$_2$ is also effective to reduce Na concentration which is above 50 ppm in molten Al-5%
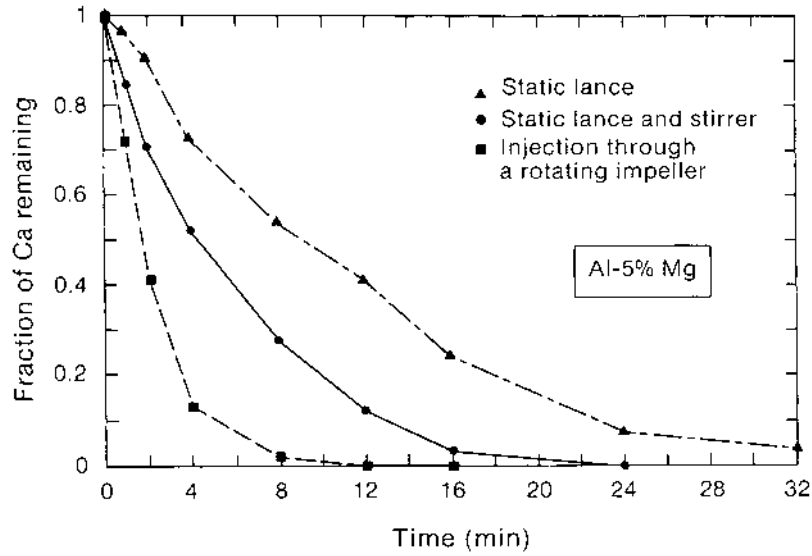
Figure 52   Demonstration of the increase in the rate of calcium removal by enhanced metal circulation and bubble dispersion in 5% Mg-Al alloy with 6% Cl_2/94% N_2. (From Ref. 46.)
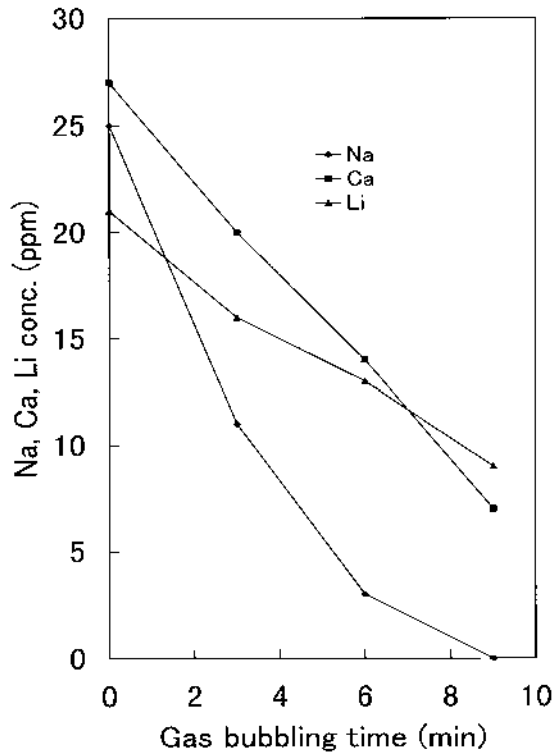
Figure 53   Na, Li, Ca removal from molten AA No. 3004 alloy by GBF with 5% Cl_2/95% Ar.
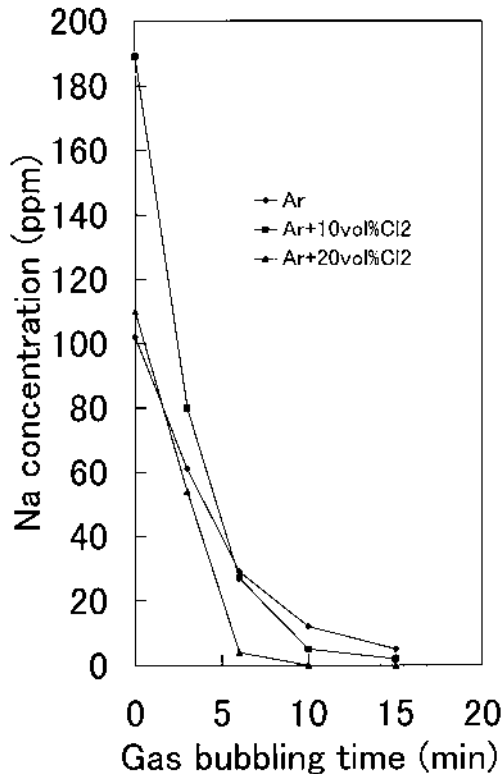
Figure 54 Na removal from molten 5% Mg-Al alloy by GBF with Ar, 10% Cl_2/90% Ar, 20% Cl_2/80% Ar.

Mg alloy to the concentration of a couple of decades ppm as well as $Ar + Cl_2$ gas purging. This result suggests Na removal by gas purging is almost by the oxidation and evaporation of Na from the melt surface while Na in the melt is above the approximated concentration of 50 ppm. Furthermore, the result of Fig. 54 reveals $Ar + Cl_2$ gas purging is necessary to reduce Na concentration to below 1 ppm.

5 THE IMPROVEMENT OF FURNACE FLUXING FROM THE ENVIRONMENTAL VIEW POINT

Although the installation of in-line facilities of molten metal processing has improved significantly molten metal quality, furnace fluxing remains to be necessary for higher aluminum quality because in-line processings remove impurities such as alkaline elements, hydrogen and inclusions in a proportional manner to the quality of inlet molten metal. The furnace fluxing consists usually of injecting chlorine gas or a gaseous mixture of nitrogen and chlorine through stationary lances. When chlorine is injected into molten aluminum, it reacts to form gaseous $AlCl_3$. Upon exposure to the atmosphere, $AlCl_3$ reacts with moisture (H_2O gas) to form Al_2O_3 and HCl. The Al_2O_3 powder thus formed is responsible for the white "fog" observed during fluxing. In the presence of Mg, chlorine will react preferentially to form

$MgCl_2$ which is liquid at the temperatures normally occurring during fluxing. At high temperatures, $MgCl_2$ can also hydrolyze to produce MgO and HCl [46]. The time available for chlorine to react is limited by the residence time of the injected gas bubbles in the melt, thus free chlorine can also be present in the off-gases. Such a gaseous and particulate emissions from furnace fluxing of aluminum alloys must be reduced to meet ever more stringent environmental emission constraints. The emissions generated during fluxing were experimentally determined as a function of gas flow rate, gas and metal composition and degree of bubble dispersion [46]. It was found that the reaction between Cl_2 and pure aluminum proceeds virtually to completion ($AlCl_3 > 98\%$ conversion) when the fluxing gas is introduced through a static lance 20 in beneath the melt surface. In the presence of magnesium, 50–90% conversion to $MgCl_2$ occurred, lowering the total amount of chlorine emitted ($AlCl_3 + Cl_2$). In Mg-containing alloys, the proportion of free chlorine emitted increased at higher chlorine concentrations, and the reason was considered to be the rapid formation of a barrier layer of $MgCl_2$ which slowed the reaction between gaseous chlorine and Al or Mg. Increasing the gas/liquid interfacial area by such an injector as rotor type nozzle led to a substantial decrease in emissions from Mg-containing alloys due to increased efficiency of conversion of Cl_2 to $MgCl_2$.

These results are summarized in Table 3. On the other hand, the effectiveness of chlorine in furnace fluxing on inclusion removal from Mg-free and Mg-containing alloys was also systematically evaluated and (apart from the generation of salt inclusions in Mg-containing alloys) no measurable differences in either the rate or extent of inclusion removal were observed. Furthermore, it was found that the prolonged cleansing effect of Cl_2 fluxing, even after the Cl_2 injection, in Al-Mg alloys occurs due to the secondary removal mechanism of residual chlorides in the furnace. Those results by Celik and Doutre suggest $MgCl_2$ salt may be a possible replacement for chlorine gas in furnace fluxing. Actually, salt addition and salt injection as alternatives to chlorine fluxing was studied in order to reduce gaseous and particulate emissions resulting from furnace fluxing of aluminum alloys [50].

For a long time, the addition of salts to the surface of molten aluminum bath has been available for the purpose of dross conditioning and furnace cleaning. In this case, the flux (salts mixture) usually contains chlorides, to provide a low melting point, fluorides to favor dross dewetting and metal coalescence and, exothermic agents such as sulfates, nitrates or carbonates. These fluxes on the bath

Table 3 Relative Emissions as a Function of Metal Composition and Fluxing Practice

Emission Metal	Injector	Free Cl_2 (%)	$Cl(-)$ (%)	Fraction emitted (%)	$MgCl_2$ estimated (%)
Pure	Lance	1	99	100	–
1% Mg	Lance	7	41	48	52
5% Mg	Lance	4	22	26	74
5% Mg In-line unit	Rotor	1	4	5	95

Source: Ref. 46.

surface can not clean the bulk of the furnace, nor are they able to remove alkalies, owing to their chemistry. $MgCl_2$ based salts can achieve significant alkali reductions and it remove fluorinated compounds from the salt chemistry because $MgCl_2$ is also aggressive towards oxide films. In order to improve the treatment of the bulk of the melt, flux injectors into metal bath have been developed [51]. Figure 55 shows an example of salt injection equipment. The feeder consists of a tank and a plate feeder. The feeder is fully automatic and gives a very accurate feeding rate. It is also equipped with an anticlogging device. It is based on fluidized transport. However, to run such systems efficiently, further modifications to the flux chemistry are required [50]. The melting point of the salt mixture, powder grain sizes and $MgCl_2$ hygroscopic tendencies must all be controlled to achieve safe, blockage-free injection. Once these parameters were under control, plant trials, performed in an 80 tonne smelter cast house furnace, produced encouraging emission reduction level. However, metallurgical efficiencies were unsatisfactory, due to the lack of dispersal and stirring associated with lance injection.

In particular, dross remained wet. The result reveals that the injection of flux below the metal surface requires some sort of metal stirring in order to distribute the flux adequately in the furnace and achieve treatment of both the bulk of the metal bath and the dross layer. Table 4, 5 and 6 present results generated under
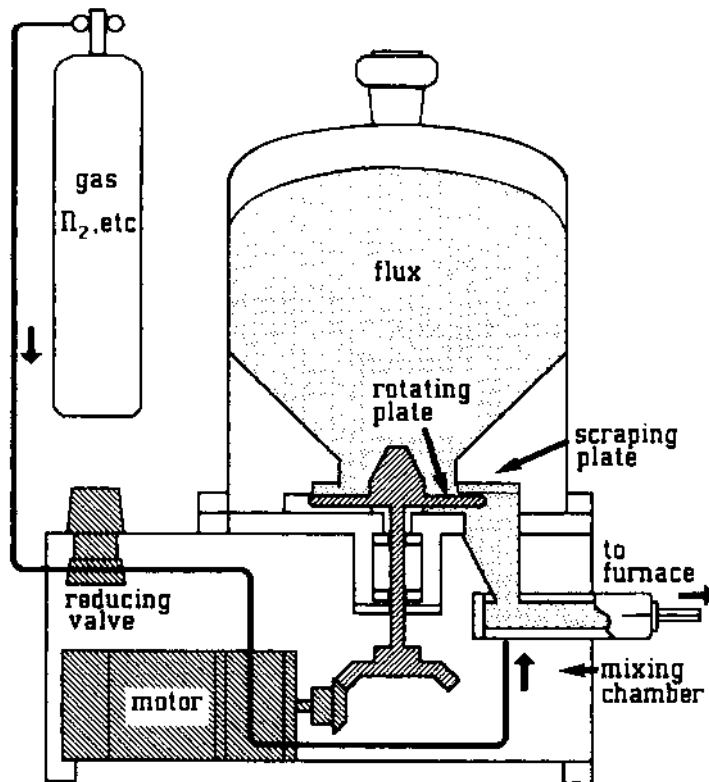
Figure 55 An outline of a plate feeder such as the Feslente feeder. (From Ref. 51.)

Table 4 Calcium Removal Rates for Low Mg Alloys ($< 1\%$) for Various Fluxing Practices

Fluxing practice	Time (min.)	Conc. Added (kg/t)	Removal rate (min^{-1})
(20% Cl_2/80% N_2)			
2 lances	45	0.24	0.032
Single lance			
+	45	0.12	0.041
AJS			
Rotor	30	0.20	0.099
($MgCl_2$ based flux)			
Salt Injection and Stirring	–	0.50	0.086

Source: Ref. 50.

Table 5 Metal Cleanliness Performances of Salt Injection and Stirring at Furnace Outlet

	PoDFA (mm^2/kg)	
Fluxing practice	1XXX	3XXX
Chlorine injection using lances	0.091	0.034
SALT		
Surface addition	0.262	N/A
Injection & Stirring	0.081	0.037

Source: Ref. 50.

Table 6 Reduction of Emissions Obtained by the Use of Salt Injection and Stirring

Fluxing Practice	Environmental Results (Arbitrary units*)					
	1XXX			3XXX		
	HCl	Cl_2	Dust	HCl	Cl_2	Dust
Chlorine injection using lances	100	5.4	63.1	29.1	11.9	17.1
SALT						
Surface addition	0.6	0.8	N/A	N/A	N/A	N/A
Injection and stirring	8.9	0.2	4.4	18.1**	0.1	1.3

*All values relative to HCl level for lance injection.
Source: Ref. 50.

full production conditions using a specially developed flux injection system based on the salt flux chemistry/injection/stirring principles (Rotary Flux Injection of industrial versions published in 1998 [52] was originated from here), in comparison with results of chlorine injection (AJS in Table 4 means Alcan Jet Stirrer [53]). As shown in Table 4 and 5, injection and stirring of solid flux below the metal surface produces alkali removal rates and metal cleanliness levels equivalent to, or better than, those of standard lance chlorine fluxing. Emissions of HCl, Cl_2 and particulates by the use of salt injection and stirring were reduced by factors of 10–25, compared with standard chlorine fluxing as shown on Table 6. One aspect that should be paid particular attention was the possible entrainment of liquified salt residue into the product. These residues can have detrimental effects on some critical products. An analytical procedure of salt residue was developed based on a metallographic examination of a solidified metal disk, and results revealed the solid flux injection technique accompanied by bath stirring resulted in entrained liquid chloride levels slightly higher than those of chlorine gas fluxing.

They also indicated inside in-line "degasser" units where the high specific energy available generates, in situ, chlorides in much larger quantities than those generated in the furnace. The finely divided droplets of liquid chlorides are easily entrained and are difficult to separate from the melt. Recently, a new type of flux which is more environmentally efficient has been developed (Y. Ohno of FOSECO, personal communication, 1998). The flux (PROMAG) which consists of KCl and $MgCl_2$ is flaky crushed powder of fused salts mixture and it has low melting point of $480°C$. PROMAG is introduced to the melt via an argon gas mixture and is mechanically stirred. In Europe, it has been used to effectively remove inclusions from recycled scrap used in the production of thin sheet and foil. Although it was demonstrated that salt injection and stirring method was possible to be an alternative with emission reductions to the use of chlorine gas fluxing, it is a fact that there remain several technological subjects to be solved.

REFFERENCES

1. C. E. Ransley and H. Neufeld. "The solubility of hydrogen in liquid and solid aluminum." J. Inst. Metals 1947/1948, 74, pp. 599–620.
2. T. A. Engh and P. Bakke. "Removal of hydrogen from molten aluminum." *Aluminum Melt Treatment and Casting, Theory and Practice* 1991, (Nilmani, ed.), Williams Center, University Melbourne, Australia, pp. 5:1–5:23.
3. R. C. Weast. *CRC Handbook of Chemistry and Physics*. 64th Edn, 1983–1984, CRC Press, pp. F-46.
4. C. E. Ransley and D. E. J. Talbot. "Wasserstoff-Porositat in Metallen unter besonderer Berucksichtigung des Aluminiums und seiner Legierungen." Z. Metallkunde 1955, 46, pp. 328–337.
5. M. Imabayashi. "Stationary concentration of hydrogen in molten aluminum." J. Japan. Inst. Light Metals 1972, 22, pp. 120–127.
6. R. Otsuka and S. Tanimoto. "Hydrogen concentration dependence of molten pure aluminum on water vapor pressure of ambient atmosphere." *Science and Engineering of Light Metals*, RASELM-'91, Japan. Inst. Light Metals, 1991, pp. 1023–1028.
7. W. Eichenauer, K. Hattenbach, and A. Pehler. "Die Loslichkeit von Wasserstoff in festem und flussigem Aluminium." Z. Metallkunde 1961, 52, pp. 682–684.

8. G. K. Sigworth and T. A. Engh. "Chemical and kinetic factors related to hydrogen removal from aluminum." Metal Trans 1982, 13B, pp. 447–460.

9. T. A. Engh. *Principles of Metal Refining*. 1992, Oxford University Press, pp. 58–61.

10. R. Otsuka, S. Tanimoto, K. Toyoda, and M. Sakaguchi. "Hydrogen removal from molten aluminum by inert gas bubbling." J. Japan. Inst. Light Metals 1990, 40, pp. 290–297.

11. A. G. Szekely. "The Removal of solid particles from molten aluminum in the Spinning Nozzle Inert Floatation process." Met. Trans 1976, 7B, pp. 259–270.

12. T. A. Engh and T. Pedersen. "Removal of hydrogen from molten aluminum by gas purging. Light Metals." Metal. Soc. AIME, 1984, pp. 1329–1344.

13. T. A. Engh. *Principles of Metal Refining*. 1992, Oxford University Press, pp. 197–207.

14. J. M. H. Hicter. "AlPur® refining process." Light Metals, Metal Soc. AIME, 1983, pp. 1005–1022.

15. R. H. Perry and C. H. Chilton, *Chemical Engineers Handbook*, McGraw-Hill Chemical Engineering Series, 1973, pp. 19–6.

16. G. P. Walker, T. A. Zeliznack, and S. R. Sibley. "Practical degassing with the R. D. U." Light Metals. Metal Soc. AIME, 1989, pp. 777–782.

17. T. Pedersen. "Refining efficiency on hydrogen, alkaline metals and inclusions in the hydro metal refining system." Light Metals. Metal Soc. AIME, 1991, pp. 1063–1067.

18. J. G. Stevens and H. Yu. "A computer model investigation of the effects of operation parameters on the hydrogen removal rate in the Alcoa 622 process." Light Metals. Metal Soc. AIME, 1992, pp. 1023–1029.

19. C. J. Simensen and G. Berg. "A survey of inclusions in aluminum." Aluminium 1980, 56 pp. 335–340.

20. J. F. Granfield. "Sources of inclusions and the defects they generate." *Aluminum Melt Refining and Alloying, Theory and Practice* 1989, (Nilmani, ed.), Williams Laboratory, University Melbourne, Australia, pp. K-1–K-6.

21. L. Marechal, N. E.-Kaddah, and P. Y. Menet. "Influence of convection on agglomeration and removal of non-metallic inclusions in molten aluminum." Light Metals, Metal Soc, AIME, 1993, pp. 907–913.

22. C. E. Eckert and R. E. Miller. "Molten aluminum filtration: Fundamentals and models." Light Metals, Metal Soc. AIME, 1984, pp. 1281–1304.

23. R. Guthrie. "General principles of melt treatment." *Aluminum Melt Refining and Alloying, Theory and Practice* (Nilmani, ed.), Williams Laboratory, University Melbourne, Australia, 1989, pp. B-1–B-19.

24. F. Frisvold and T. A. Engh. "Fundamentals of filtration." *Aluminum Melt Treatment and Alloying, Theory and Practice* (Nilmani, ed.), Williams Center, University Melbourne, Australia, 1989, pp. 23:1–23:23.

25. K. J. Brondyke and P. D. HESS. "Filtering and fluxing processes for aluminum alloys." Trans. Met. Soc. AIME, 1964, 230, pp. 1553–1556.

26. L. C. Blayden and K. J. Brondyke. "In-line treatment of molten aluminum." Light Metals, Metal Soc. AIME, 1973, pp. 493–504.

27. M. C. Mangalick. "Operation of a rigid porous media filter for liquid aluminum." Light Metal Age, 1973, Feb, pp. 5–8.

28. C. H. R. J. Simensen. "The effect of melt refining upon inclusions in aluminum." Met. Trans., 1982, 13B, pp. 31–34.

29. W. C. Eister and W. R. Krumme. "An evaluation of a SNIF unit as an inclusion removal and degassing device." Light Metals, Metal Soc. AIME, 1991, pp. 1171–1177.

30. J. E. Buehler and R. A. Frank. "Startup and evaluation of the first SNIF SHEER® SYSTEM at Kaiser Aluminum, Trentwood works." Light Metals, Metal Soc. AIME, 1993, p. 923.

31. Y. Ohno and D. T. Hampton. "The GBF rotary system for total aluminum refining." Light Metals, Metal Soc. AIME, 1993, pp. 915–921.

32. R. Otsuka. "Melting and melt refining of aluminum." J. Japan. Inst. Light Metals, 1989, 39, pp. 466–476.

33. R. Otsuka. "Melting and melt treatment of aluminum." J. Japan. Inst. Light Metals, 1994, 44, pp. 461–471.

34. D. Douttre, B. Gariepy, J. P. Martin, and G. Dube. "Aluminum cleanliness monitoring: methods and applications in process development and quality control." Light Metals, Metal Soc. AIME, 1985, pp. 1179–1195.

35. R. I. L. Guthrie and D. A. Doutre. "On-line measurements of inclusions in liquid melts." *Proceedings of International Seminar on Refining and Alloying of Liquid Aluminium and Ferro-alloys* (TA Engh, S Lyng and HA Oye, eds.), The Norwegian Institute of Technology, Trondheim, 1985, pp. 147–163.

36. J.-P. Martin and R. I. L. Guthrie. "Settling of inclusions in casting furnaces." *Aluminum Melt Treatment and Casting, Theory and Practice* (Nilmani, ed.), Williams Center, University of Melbourne, Australia, 1991, pp. 21:1–21:24.

37. L. J. Gauckler and M. M. Waeber. "Industrial application of open pore ceramic foam for molten metal filtration." Light Metals, Metal Soc. AIME, 1985, pp. 1261–1283.

38. P. Netter and C. Conti. "Efficiency of industrial filters for molten metal treatment Evaluation of a filtration process model." Light Metals, Metal Soc. AIME, 1986, pp. 847–860.

39. N. J. Keegan, W. Schneider, H. P. Krugg, and V. Dopp. "Evaluation of the efficiency of ceramic foam and bonded particle cartridge filtration systems." Light Metals, Metal Soc. AIME, 1997, pp. 973–982.

40. C. Dupuis and R. Dumont. "The impact of LiMCA technology on the optimization of metal cleanliness." Light Metals, Metal Soc. AIME, 1993, pp. 997–1002.

41. D. J. Eichenmiller, R. S. Hendeson, and D. V. Neff. "Rigid media filtration – New understanding and possibilities with bonded particle filters." Light Metals, Metal Soc. AIME, 1994, pp. 1007–1016.

42. K. Kakimoto, E. Takahasi, Y. Shiraishi, T. Yoshida, and O. Yagishita. "Filtration of molten aluminum." Light Metals, Metal Soc. AIME, 1993, pp. 1021–1028.

43. D. V. Neff and E. P. Stankiewictz. "The multicast® filtration system." Light Metals, Metal Soc. AIME, 1986, pp. 821–836.

44. J. P. Desmoulins, H. d'Hont, J. M. Hicter, and P. Netter. "Efficiency and reliability in aluminum filtering." *Aluminum Melt Treatment and Casting, Theory and Practice* (Nilmani, ed.), Williams Center, University of Melbourne, Australia, 1991, pp. 22:1–22:21.

45. J. G. Stevens and H. Yu. "A computer model of a stirred tank reactor in trace alkalline elements removal from aluminum melt – the Alcoa 622 process." Light metals, Metal Soc. AIME, 1986, pp. 837–845.

46. C. Celik and D. Doutre. "Theoretical and experimental investigation of furnace chlorine fluxing." Light Metals, Metal Soc. AIME, 1989, pp. 793–800.

47. B. Kulunk and R. Guthrie. "On the kinetics of removal of sodium from aluminum and aluminum-magnesium alloys." Light Metals, Metal Soc. AIME, 1992, pp. 963–975.

48. C. J. Simensen and M. Nilmani. "A computer model for alkali removal from molten aluminum." Light Metals, Metal Soc. AIME, 1996, pp. 995–1000.

49. S. Kaestner, J. Krueger, and F. Patak. "Refining of Virgin Aluminum by Scavenging Gas Treatment", Raffinationsverfahren Metall. Int. Symp. 1983, pp. 36–53.

50. G. Beland, C. Dupuis, and J.-P. Martin. "Improving fluxing of aluminium alloys." Light Metals, Metal Soc. AIME, 1995, pp. 1189–1195.
51. T. Pedersen and E. Myrbostad. "Refining and alloying of aluminium by injection." Light Metals, Metal Soc. AIME, 1986, pp. 759–765.
52. G. Beland, C. Dupuis, and G. Riverin. "Rotary flux injection: chlorine-free technique for furnace preparation." Light Metals, Metal Soc. AIME, 1998, pp. 843–847.
53. M.-A. Thibault, F. Tremblay, and J.-C. Pomerleau. "Molten metal stirring: the Alcan Jet Stirrer." Light Metals, Metal Soc. AIME, 1991, pp. 1005–1011.

14

Shaping by Pulling from the Melt

STANISLAV PROCHOROVICH NIKANOROV and
VSEVOLOD VLADIMIROVICH PELLER

A. F. Ioffe Physical Technical Institute of Russian Academy of Sciences,
Saint Petersburg, Russia

1   THE ESSENCE OF THE STEPANOV METHOD

Advanced casting is the continuous one. Different arrangement of the process was put forward [1]. In 1843 Laing suggested uninterrupted casting of metal into the water crystallizer copying the tube shape and pulling out from it the pipe billet solidifying from a surface by means of special rollers. Bessemer (1858) developed continuous process of obtaining a metal foil or a sheet by casting into the gap between rotating rollers. Later a great deal of variations of the equipment for the continuous casting was developed, but all of them could be classified with these two ideas. The first group of equipment includes casting when metal solidifying from its surface moves relative to a crystallizer. In that case the friction forces between the crystallizer and the solidifying surface induce the casting stresses. Casting with mobile crystallizers belongs to the second group of the processes. The mobile crystallizers move together with casting melt and billet solidifying from its surface. Rather rigid skin is created on the surface of the billet. Tensile stresses due to relative moving of solidifying surface of a metal and a crystallizer are absent here. But the difference of the thermal extension of a material of the crystallizer and of aluminum and the incompatibility of the local thermal expansion in the next areas of the growing article induce the thermal stresses in it. In the both groups of the techniques there is the continuous casting into crystallizer.

Brines (1902) communicated about obtaining metal tubes and bars directly from a melt without any crystallizer. Billet was produced by freezing a metal on the end of the bar lifted slowly from liquid metal and blown by cooling air. Shaper in that case was absent. Frozen bar was shaped by rollers. Internal surface of frozen tube was smoothed by special mandrel rod. In 1917 Czochralski [2] used a similar

way to grow single crystal ingots. In 1922 Gomperz [3] and in 1928 Kapitza [4] drew a wire and thin rods from a melt of various metals through a hole in the mica plate positioned on a surface of molten material.

In 1938 Stepanov suggested a new technological principle for shaping of solids [1]. According to that, a shape of material is created in liquid melted state so that the solidifying metal has no contact with the walls of a crucible and the shaper. A column of the liquid is pulled up from the melt by means of a rod with a seed crystal through a hole or slot in the refractory plate resting on a surface of the melted metal.

The refractory plate with the hole or the slot was called the shaper. Continuous pulling of the liquid column and simultaneous crystallizing of it on a constant height takes place. Distinctive criterion of the Stepanov method is that the process of shaping and crystallizing are divided in space. That is why, in that technique, the solidifying molten metal has no contact with the walls of crucible. This circumstances gives two consequences. Firstly, the shape of crystallizing product depends not only on a geometry of the shaper but on the surface tension and the specific gravity of the melt, the character of coupling of the liquid metal with the shaper, pulling rate and the temperature field in the growing product [5]. Therefore the hole or the slot in the shaper is not copying die as in the case of casting under pressure. This gives the possibility of growing products of a complex shape. At the same time, for good results, it is necessary to understand the nature of the capillary shaping in view of the fact that thermal effects influence the stability of the process. Nevertheless, it is known that the stability of pulled crystal products using the Stepanov method is higher compared with the Czochralski method. Secondly, there is the fact that the solidifying metal does not touch the surrounding walls. The growing of metal products is free from stresses arising from a difference of the thermal expansion of the crystallizer and the solidifying product. There are only the residual stresses due to incompatible local thermal strains which occurs during growing in connection with a difference of temperature of the next areas of a solidifying article. But it is possible to decrease them by special arrangement of the thermal field in the growing article. These reasons create an advantage of the Stepanov method as compared to the other methods of continuous casting. This advantage is very important for obtaining Al products of complex shape cross-section [6].

2   THE THEORY OF THE CAPILLARY SHAPING

In the first investigations Stepanov with co-workers grew various shaped products by means of the shapers nonwettable by melt. But as long ago as 1966 it was demonstrated that it was possible to carry the process with wettable shaper (see [1,7]).

For nonwettable shapers a lift of a melt was due to excess pressure in the liquid material. When a shaper was wetted by the melt, the latter lifted along the shaper by means of capillary forces. In 1971 the EFG-method (Edge-defined Film-fed Growth) was suggested [8]. This variation of the Stepanov method differed by the design of a shaper and a condition of fixing a melt on the shaper. Then, a number of techniques for the growth of shaped single crystals were developed, which were also variations of the Stepanov method [5].

Different variations of the Stepanov method are shown in Fig. 1. In the case of variations A and C, fixing of coupling places of the liquid material and internal vertical surface of the shaping hole takes place due to a constancy of the wetting angle Θ (for wetting condition). At variation B the melt catches on the shaper along the hole perimeter, and in D along outer shaper perimeter. A lift of the melt through the shaping hole is due to the capillary forces or excess pressure in the melt.

Growing of aluminum products is realized by variation A or B. If excess pressure in the melt is low, the bottom of the melt column is inside the shaper hole. The liquid surface together with vertical wall makes the angle Θ equal to the wetting angle. The diameter of the liquid column is shorter then the hole diameter (variation B). Therefore the diameter of the product can be both shorter or longer then the hole diameter. Variation of the boundary condition can be caused by a sharp change of the pulling rate. The boundary condition depends also on material of the shaper. If one replaces a cast iron shaper with a zirconium diborid one, a change in the catching condition for the wetting will take place because the wetting angle of cast iron by aluminum melt is much more that of zirconium diborid.

Shaping of crystal products in liquid state by means of the capillary forces is possible only with a stable shape of a meniscus and a constant height of the liquid–solid interface. Conditions can be found from analysis of the meniscus shape and heat conditions of the growth [9,10].

Equilibrium liquid shape is determined by the Laplace capillary equation:

$$(\gamma/R_1) + (\gamma/R_2) + \rho g z = \rho g h \tag{1}$$
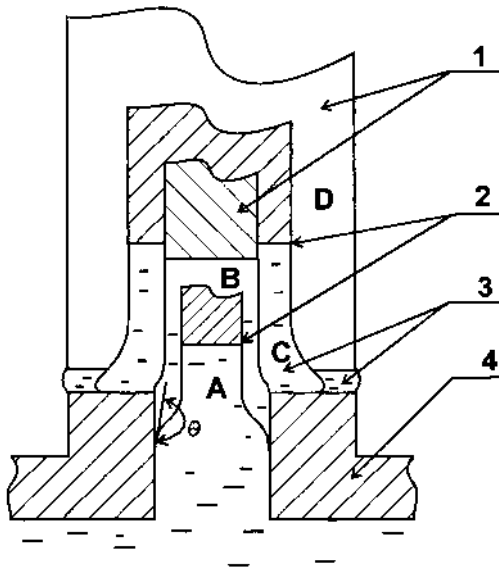
Figure 1 Variations of the Stepanov method. (1) crystal; (2) liquid–solid interface; (3) molten metal; (4) shaper.
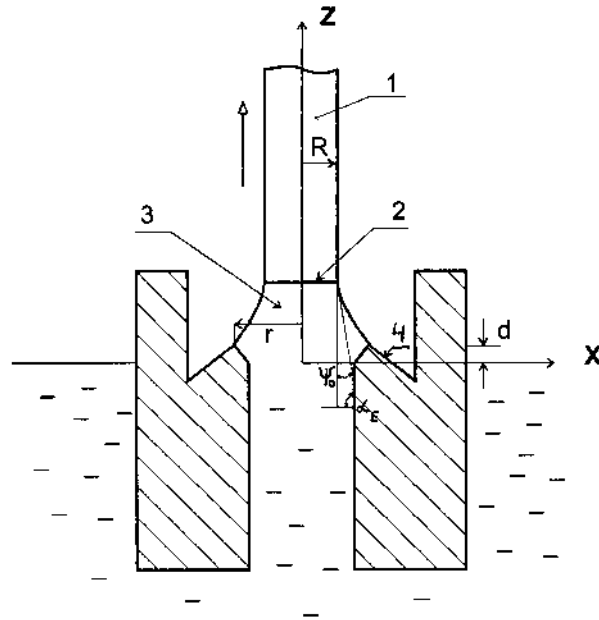
Figure 2 Growing rod. (1) crystal; (2) liquid–solid interface; (3) meniscus of a melt; (4) shaper. $\Psi_0 =$ growth angle; $\alpha_E = (\pi/2) - \Psi_O$. $\delta\alpha_E > 0$ is condition of narrowing, $\delta\alpha_E < 0$ is condition of expansion.

Here R_1 and R_2 are main radii of the curvature of liquid surface, g is the gravity acceleration, γ is the surface tension, ρ is the density, h is the height of the solid–liquid surface above the melt level.

In the case of the linkage of the liquid on the shaper edge (see Fig. 2), the boundary condition will be the following:

$$Z\mid_r = d \qquad (2)$$

Here d is the distance along axis Z from the edge of the shaper to the flat surface of the liquid. d determines the pressure in the liquid, moreover $d < 0$ for the positive excess pressure.

During the pulling of a crystal rod from the melt the angle between the crystal surface and the tangent to the melt surface at the liquid–solid interface, has a definite value Ψ_0 for a given crystallizing material. If the angle between the horizontal and the tangent to the melt surface at the interface is $\alpha_e = (\pi/2) - \psi_0$, the crystal rod grows with a constant cross-section [9]. Therefore the boundary condition on the bottom of meniscus is:

$$(dZ/dr\mid_{r=R(t)} = -tg\,\alpha_e \qquad (3)$$

In [10] the analysis of the Eq. (1) with the corresponding boundary conditions was performed for growth of crystals with different simple cross-section shapes and determined a character of the profile curves of the meniscus. In particular the results of numeral decisions for the growth of rod with round cross-section were

obtained for different diameters of the shaping hole and for pressure $d = 0.5/2r$ and 0. The limited heights of the liquid columns as a function of radius $h(R)$, profile curves and a pressure are given in Fig. 3 in units of the capillary constant $a = (2\gamma/\rho g)^{1/2}$.

It is possible to consider more complex crystal products as a combination of its simple pieces (rods, plates, tubes).

In particular, stability of the growth of the crystal rod depends on the deviation rate of the radius of its cross-section $\delta\dot{R}$ and on the deviation rate of the height of the liquid–solid interface $\delta\dot{h}$ from their equilibrium values

$$\delta\dot{R} = A_{RR}\delta R + A_{Rh}\delta h$$
$$\delta\dot{h} = A_{hr}\delta R + A_{hh}\delta h$$

(4)
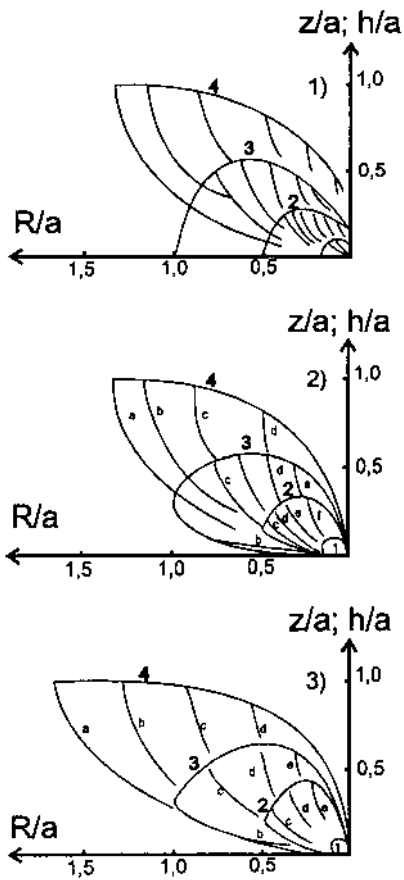
Figure 3 The regions of stable profile curves for one main radius equal to ∞. Surplus pressure: (1) $d = 0$; (2) $d = 0.25/r$; (3) $d = 0.5/r$. Border curves (1–4) and some limited profile curves (a, b, c, d, e, f) for different radii of shapers r: (1) 0.1; (2) 0.5; (3) 1.0; (4) 5.0

For the system to be stable it is necessary:

$$A_{RR} + A_{Rh} < 0, \quad A_{RR}A_{hh} - A_{Rh}A_{hR} > 0 \tag{5}$$

The coefficients A_{RR} and A_{Rh} can be found from the capillary equation for the growing crystal of the given shape and sizes when r, d, v are known and there are defined boundary conditions:

$$\begin{aligned} A_{RR} &= -v\,(\delta\alpha_e/\delta R_0) \\ A_{Rh} &= -v\,(\delta\alpha_e/\delta h_0) \end{aligned} \tag{6}$$

Here $v =$ the growth rate, index 0 corresponds to the equilibrium radius and the equilibrium height of the interface.

In the case of constant h, the stability of system is given only by the capillary effects:

$$\delta\dot{R} = A_{RR}\delta R \tag{7}$$

When $A_{RR} < 0$ process will be stable. If R increases, the change of Ψ_0 returns the crystal to undisturbed state. When h changes, R changes too. But for $A_{RR} < 0$ the change Ψ will lead to a new stable state with some changed value of R. In [9,10] it was shown that the shaper gives the capillary stability. For example, the growth of a cylindrical rod for the condition of the linkage will be stable when $R/r > \frac{1}{2}$. That condition of the capillary stability is an advantage of the Stepanov method in compared with the Czochralski one.

The sign of thermal coefficients A_{hR} and A_{hh} can be found from the decision of the non-stationary heat condition problem. The one-dimensional equation of heat conduction has the following form:

$$(1/\chi_i)\,(\delta T_i/\delta t) = \delta^2 T_i/\delta Z^2) - (v/\chi_i)\,(\delta T_i/\delta Z) - (2\mu_i/\lambda_i R)\,(T_i - T_c) \tag{8}$$

Here $i = 1, 2$ for a melt and a crystal respectively, Z is the coordinate along the growth direction, χ_i is the thermal conductivity, μ_i is the heat emission coefficient, λ is the heat conductivity, T_c is the temperature of the environment.

The boundary conditions at the bottom of the meniscus: $T_1 = T_m$ (a temperature of the melt), at the liquid–solid interface: $T_2 = T_0$ (the crystallization temperature).

At the top end of crystalline product of the length l various boundary conditions may be defined:

$$T_2\,|_{z\to\infty} = T_c, \quad T_2\,|_{Z=1} = T_c, \quad \delta T_2/\delta Z\,|_{Z=1} = 0.$$

At the interface the heat flow balance takes place:

$$-\lambda_2\,(\delta^2 T_2/\delta Z^2)\,|_{z=h} + \lambda_1\,(\delta T_1/\delta Z)\,|_{z=h} = L\,\rho\,(v - \delta h/\delta t), \tag{9}$$

here h is the coordinate of interface, L is the heat fusion.

It was shown [10] that $A_{hh} < 0$, and $A_{Rh} > 0$, $A_{Rh} < 0$ and A_{RR} may have different signs. In such systems there are thermal stability ($A_{hh} < 0$) and mutual stabilization ($A_{Rh}A_{hR} < 0$). When $A_{RR} < 0$ the system will be stable. When the

capillary stability is absent, the system can be stable since there is mutual stabilization. But in that case it is necessary to analyze actual values of the coefficients.

The consideration of the stability of the growth of different shaped crystals (rods, plates, tubes) [10] and of experiments results in the following conclusions:

(a) growing shaped crystalline products with constant cross-section by the Stepanov method is easy when the relation between the crystal and shaper sizes is $(R/r_0) > \frac{1}{2}$.

(b) There is the development of self-stabilization shaped crystal growth by the Stepanov method during forced-cooling of a local region of product.

(c) There is the development of self-stabilization for increasing pulling rates.

It was shown also that pulling of aluminum tubes is a more stable process when the diameter increases. Besides the excess pressure makes process further more stable.

Experimental tests confirmed the theory for a number of materials growing in an inert medium or vacuum. But for aluminum products growing in the air experimental values of limited stable heights of the meniscus lift were higher than theoretical calculations. In [11] it was determined that the oxide film on the surface of the liquid column of aluminum alloys increases the effective capillary constant. This increase develops with the curvature of meniscus. Thus the oxide film makes the height of the melt column higher, increases the stability of growing, and gives the possibility of pulling thin products and narrow channels in aluminum products (down to 0.5 mm).

3 EQUIPMENT

To realize possibilities of the Stepanov method, special installations and instrumentation are necessary. The installations are developed in order to obtain a large assortment of products. But each shaper is intended for growing only one type profile or some similar types.

3.1 Installations

The Stepanov method gives the possibility of pulling out a product from its melt continuously. But installation can work both continuously and semicontinuously [6]. Interruption of growing is connected with limited height of rooms and features of installations placed in them. In addition the semicontinuous installations are used for products of large-size cross-section, for the stiff material which is difficult to pack in the reception device during pulling from a melt. The use of semicontinuous installations facilitates the problem with a constant level of the liquid–solid interface and mechanical perturbation in an area of shaping during prolonged time. The type of installation, its size, electric power of melting furnace and other characteristics are conditioned by properties of melting material and requirements to a shape, size and mechanical properties of growing product. A number of experimental and

experimental-industrial installations of continuous and semicontinuous processing were developed at Ioffe Physico-Technical Institute of the Russian Academy of Sciences, St. Petersburg.

(A) Installation of semicontinuous acting consists of 7 principal parts:

1. All main elements of the installation with the exception of a furnace and control desk are positioned on a bed.
2. Pulling device gives a translation of the pulling rod with a seed of crystallization. For example, the mechanism can consist of a guide with moving carriage, steel line with a block, and winding roller with electric drive and reducer.
3. Mobile table is a support of a shaper. Keeping of constant level of melt comparatively the shaper attains by vertical translation of the table during expenditure of the melt in crucible, by means of electric motor and reducer.
4. There is the moving resistance furnace to melt and to keep constant temperature of a metal.
5. Air cooling system with a compressor provides forced cooling and crystallization of product pulled out of a melt.
6. Water cooling system reduces temperature of the installation near the melt.
7. Control desk has start-control apparatus. It has also control, measuring and indicating instrumentation. Particularly, there is direct electric drive of a pulling device and of mobile table.

Developed installations can be classified according to maximal sizes of products:

1. Installations with chamotte-graphite crucible of 70 kg aluminum melt. They give the possibility of growing products of the following cross-sections: for flat profiles up to 0.24 m; for bulk profiles inscribing into circle up to 0.15 m. Maximal length of the profiles ranges from 2 to 3 m. Nominal power of furnace is 20 kVA. Input power of the installation during the work is 7 kVA. One of the installations, ASP-1, is shown in Fig. 4.
2. Installation ASP-3 for obtaining of profiles of 3–4 m in length with a cross-section up to 0.65 m for flat profiles and up to 0.5 m diameter for bulk profiles inscribing into a circle. These installations can work with cast iron crucibles and in some cases with chamotte-graphite ones. The drive moving a seed along a vertical direction is made in the form of two carriages (two pairs of guides) with transverse balk divided by a hinge [12].
3. Installation of very large sizes with a cast iron flat crucible was also used to produce profiles of 1 m width.

Besides, some improved installations were developed for experimental and industrial production of profiles from 4.5 to 6 m in length. In those installations, an increase of the stiffness of their parts and stability of mechanism work, of standardization level, and the number of interchangeable components was provided. Thermal efficiency of the furnace was increased. Metal guides could be made, both totally and complicated, to increase a length of profiles.
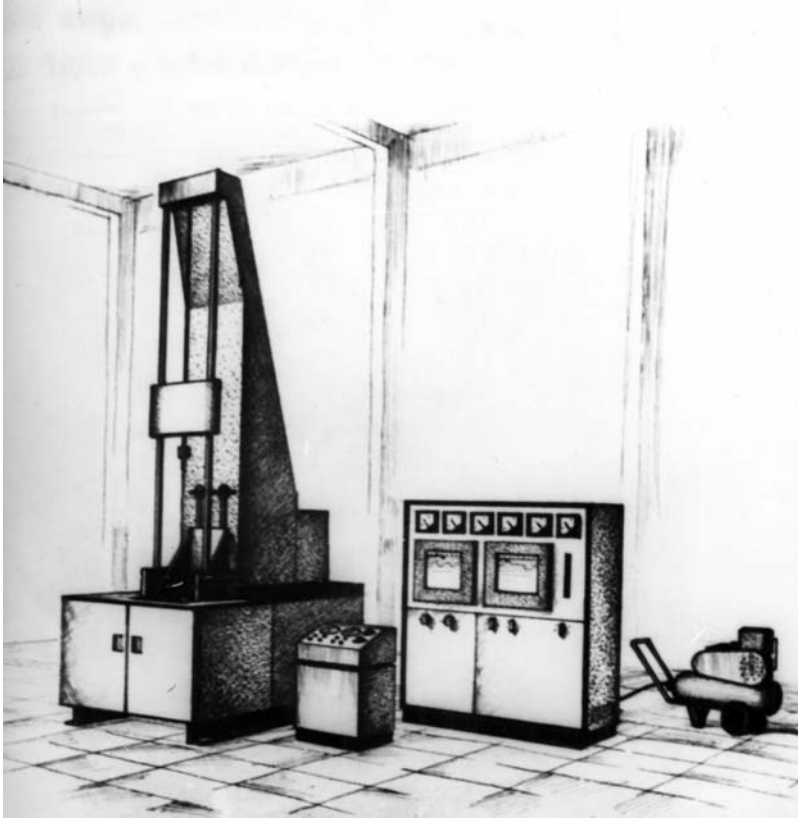
Figure 4 Installation of semicontinuous acting.

(B) Installations of continuous acting have a merit in comparison with semicontinuous one. It is possible to pull up a product of very large length, minimize operations of seeding, and reduce expenditures of raw materials and energy capacity per unit of product. But organizing the working of the continuous installations has some difficulties. First, the pulling device must give interrupted motion of product. Continuous supplement of a crucible by a melt must take place. It is necessary to have a device of interrupted extraction of a ready product. Roll systems transporting pulled products must be constructed so they do not induce any mechanical perturbations in a melt near liquid–solid interface. For suppression of some waves in a melt it is possible to use dampers or stopping devices. The system of continuous replenishment of a melt into a crucible was used. A double-chamber crucible with connecting channels was employed. Molten metal in an accessory is supplied by melting an aluminum band. Continuous reception of aluminum products was carried out by way of winding on a roller of a large diameter. In the case of complex shapes or for stiff products, the reception was accomplished in pieces. Products were cut periodically and removed by a special device during continuous pulling out [6].

3.2   Instrumentation

It is necessary to have interchangeable instrumentation for an installation to grow specific products with specific shape and sizes. It can be used to pull profiles of one kind or different kinds but having similar configuration. The instrumentation is shaping device, removable crucible and some others.

The shaping device is intended to fulfil a number of the following functions. It enables the capillary shaping of the column of a melt. It maintains a constant level of liquid–solid interface during the growth to make a profile of invariable cross-sections. It gives mechanical tie to the pulling device and growing product.

The shaping device consists of a shaper, cooler, seed holder, seed, frame and other details. Construction of the shaping device is to satisfy some additional demands [13]. It makes it possible to control temperature characteristics of crystallization and cooling together with the system of automatic control. Its design is to allow us to observe the shaping zone, have necessary stiffness and good thermal insulation from cooler up to 700–750°C. It must have simple construction and be light. Its low cost is very important for the efficiency of the Stepanov method. From the viewpoint of casting processes, shaping device is a new type of crystallizer, contactless one.

(a) A shaper has a key role to obtain predetermined cross-section of growing aluminum product. It is the holder of molten metal meniscus. Besides its profile hole limits the area of the melt where a product is growing from. The temperature of the melt near liquid–solid interface and the pressure in the melt depend on shaper construction [6]. The sizes of product cross-section depend not only on sizes of shaper hole but also on growing process (thermal regime, pressure in the melt). It is necessary to take into account the change of sizes of product due to capillary shaping, thermal expansion and the change of volume at phase transformation of aluminum. A shaper is to be undistorted up to 750–800°C and also after sharp changes of temperature in that temperature range. It is not to dissolve into molten aluminum. The shaper of small size product without internal hollows is a plate with a slot. The shaper of profile with internal hollows is made composite because it is to have details shaping the hollows into the growing product. At the same time, construction of the shaper is to be simple and stiff, so as to resist distortion due to the difference of temperature in upper and lower parts of it. It is necessary that holders have some freedom for thermal deformation. The height of the rods limiting the internal hollow should be shorter than twice their diameters.

The scheme of the shaper of a smooth wall tube is shown in Fig. 5. The shaper (Fig. 5-1) consists of the carcass, outer ring inset (I-2) and internal inset (I-3). A melt is shaped by filling the slot between the insets [6]. A shaper can be made from metal, ceramics and other materials. As a rule, cast iron of different trademarks is used for shapers working in aluminum melt. It is not wetted by molten aluminum alloys.

(b) The cooler is the receiver-distributor of air (gas or steam). It intensifies cooling of a growing product resulting in increased pulling rate [6]. Cooling air is to be distributed uniformly along the pulled profile perimeter to have the flat liquid–solid interface. It is necessary to keep in mind here, the influence of shaper on the form of the interface. But the cooler is more universal. It is possible to use the same cooler to grow different simple profiles but one type, for example, near
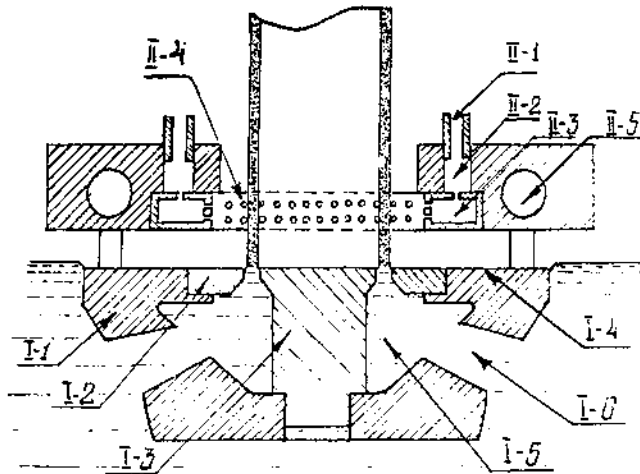
Figure 5 Shaping device of smooth wall tubes. I. Shaper; I-1 body; I–2 outside ring inset; I–3 internal inset; I–4 surface of the heat shield; I–5 work volume of the shaper; I–6 channels of feeding a melt. II. Cooler; II–1 feeding air into cooler; II–2 receiving chamber; II–3 distributing chamber; II–4 holes of jet blowing; II–5 channels for cooling by water.

sizes tubes. Fig. 5-3 shows the scheme of cooler for obtaining smooth wall tubes. The air (II-I) fed through some insets passes the in taking (II-2) and then the distributing chamber (II-3).

The best distribution of air pressure along the cooler perimeter is due to the collector and jet blowing through the hole (II-4). The cooler is cooled in turn by means of water. Localization of the insets causes some nonuniformity of the pressure along the cooler counter. The outputs of the distributing chamber can be slots in a body or nuzzles on it. In that case it takes place wide-band so called slotted blowing. Such blowing is used to cool simple profile similar ribbons or circle tubes. For cooling complicated profiles outputs of the chamber are holes. Jet blowing is used as a rule to cool profiles with different wall thicknesses. This blowing is more efficient in relation to air expenditure per weight unit of a product. To intensify blowing on thick-walled parts of profile two- and many-row disposition of holes is used as well as the decrease of spacing among them. However, one must keep in a mind that intensification of jet blowing can cause mechanical deformation of growing products and precautions are to be taken to counteract this process. When the product cross-section shape and consequently design of holes at cooler are complicated, it is sound practice to sectionalize the distribution chamber and set into air input the calibrated plugs with holes. Coolers for complicated profiles make it possible to blow up not only outside but internal parts of pulled product.

In some cases, some parts of the products produced by the Stepanov method have irregular thickness. It is connected with asymmetry of heat field induced by thermal fluctuations. In those cases a dosed injection of refrigerant, to separate pieces of the crystallizing product surface, is used to compensate for the thermal fluctuations near the crystallization zone [14].

(c) First of all, accessories of the shaping device are a seed and its holder. They provide extracting first portion of a melt and coupling pulling device and growing product. The seed is bent in the form of the slot with help of a mandrel or by bending means, and is fixed at the holder. Seed materials are copper, nickel or other metals and alloys wetted by the melt. The accessories are also the frame to tie shaper and cooler, seed rod, water and air tubes and others.

(d) Unification of shaping devices increases efficiency of production by the Stepanov technique [13]. In practice the unification of both constitution of assemblies, blocks, details and their sizes takes place. Unificated blocks, details connecting mechanisms and systems of installation with main parts of shaping device are widely used at an assembly.

For the unification, it is advisable to classify the profiles obtained by the Stepanov method. In particular, the unification of shaping devices at fabrication of profiles for solar power energetic was made on the basis of classification of the products into groups according to their shape (square, rectangular, circle etc) and sizes. Twenty different profiles were divided into six groups. Then six modes of shaper bodies were developed. Each of them gives the possibility to produce from one to nine kinds of profiles by means of special interchangeable insertion pieces. Only five modes of cooler bodies were necessary to make all profiles mentioned above.

Apart from the shaping device there are other kinds of instrumentation. Thus a continuous acting installation is a complex of interchangeable pulling rollers and dampers. They can differ for individual groups of profiles with similar shape and sizes. Crucibles of different sizes are also interchangeable.

It is possible to use chamotte-graphite, chamotte-graphite-silica carbide, cast iron and other crucibles.

4   TECHNOLOGICAL PARAMETERS

Capillary effects allow to obtain profiled aluminum products with cross-sections of different shape. Directional heat removal and flat liquid–solid interface make easier drawing out of dissolved gases. The product has high density. Liquations and shrink holes are absent. Dense oxide film creating on aluminum in air makes it possible to carry processing without protected atmosphere. Simplicity of measuring melt temperature, growth rate and temperature gradient in product permits optimum control conditions of crystallizing. However, success in realizing the objective results from the large amount of effort in supporting technological regimes.

The basic parameters of the process is the following: (1) melt temperature; (2) pulling rate; (3) height of free melt surface above its surface into shaper (excess pressure in the melt); (4) intensity of cooling [6]. The first three parameters can be measured directly, the fourth one is evaluated indirectly on expenditure, temperature and humidity of air. The temperature of aluminum melt is measured and regulated by means of a chromelalumel thermocouple. The melt level in relation to shaper is monitored by a special servosystem. Such systems allows one to keep a constant melt level by means of an automatic regulating drive on the mobile table. Measurement of the melt level in a crucible allows to organize the portion supplement of crucible by aluminum.

Cooling intensity of a crystallized product is controlled by means of measuring air expenditure with a rotameter. It is possible to control both the whole of the cooler and its sections. Automatic control of cooling is preferable, but in that case it is necessary to regulate all the parameters above. Velocity of pulling carriage with product is measured with tachogenerator or voltmeter connected to an armature circuit of a shunt pulling electric motor of independent excitation. High stability took place with electric drive based on direct-current motor with the exciting of permanent magnets. Such a system can use a traditional frequency transformer-rectifier device. It is best to use a inverter with nontransformer output.

Automatization of all the control by computer can be rigid when the parameters mentioned above are supported with some accuracy. Flexible system controls constancy of profile geometric sizes by means of regulation of one or a few parameters via a feedback circuit.

5   THERMAL CONDITIONS OF THE PROCESS

Thermal conditions play the main role in the process of obtaining profile aluminum products [15]. The rate of the process depends on the rate of crystallization. The latter is determined by the rate of removal of latent heat of crystallization. That is why regulation of the heat removal through crystallizing product gives the possibility of running the rate of pulling, shape, structure and properties of the product. Stability of the process depends on the temperature distribution in crystallizing product and thermal field in a melt near liquid–solid interface [6].

Heat exchange is determined by heat flows from crucible walls to a melt, out of the melt to the interface and through it, by latent heat of crystallization, heat flow along the pulled product and flows from and to walls of different parts of an installation. These heat flows are interconnected and influence each other. Stability of the pulling process is established by heat equilibrium in crystallization zone.

5.1 The Condition of Shaping

    A. The Stepanov method has merit in comparison with traditional casting methods. There is more constant thermal condition of process because a growing product has direct thermal bond with the bulk of liquid molten metal.

    B. The main role in regulation of heat flows and thermal field plays heat technological zone. It consists of a crucible with a melt, a furnace with heaters, a shaper, a coolers and heat shields in some cases. The zone is to give [6,15] a horizontal flat thermal field near the shaping hole and above it, assigned vertical temperature gradient in a melt and crystallizing product and overheat of all melt bulk to avoid spontaneous crystallization. The heat zone determines stability and reproducibility of thermal condition.

    C. Heat scheme of the process and temperature distribution are shown in Fig. 6. At the liquid–solid interface the heat flow balance takes place:

$$Q_1 = Q_2 + L\rho v, \tag{10}$$
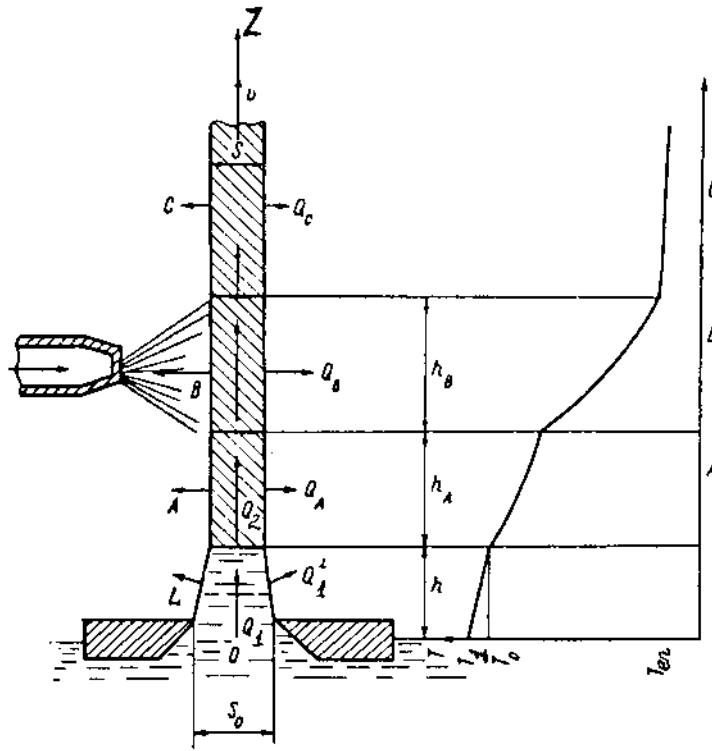
Figure 6   Heat scheme. Left part is cooling device. L = liquid piece of article; A = buffer zone; B = cooled zone; C = part cooled by free convection; T_{en}, T_o, T_1 are the temperature of medium, crystallization and melt, respecively; Q = heat flow; h = height of zone and part; S_0 = width of shaping hole, S = thickness of product. Arrows show heat flows.

where Q is heat flow, i = 1,2 for a melt and crystal, respectively, and

$$L\rho v = \lambda_1 G_1 - \lambda_2 G_2. \tag{11}$$

Here G_i is the temperature gradient.

In (10) and (11) the heat flow connected with the movement of growing product is not considered because its value in both phases is the same and the temperature break is absent. Heat of crystallization is removed only by means of a heat conductivity that is due to high temperature gradient. The height of the liquid column of aluminum above a shaper is small (0.5–5 mm). Therefore it is possible to neglect heat flow through its side surface. Heat flows Q_A, Q_B and Q_C remove a heat of crystallization and allow to cool the product.

D. (a) In the case of pulling the product of alloys there is a crystallization zone between liquid and solid states of crystallizing material. Temperatures of its bottom and top correspond to liquidus and solidus of the alloy, respectively. The length of the zone depends on the thermal regime of

pulling [6]. In the case of Al and Al-based alloys, an oxide film exists on the surface of a liquid column. It leads to more intensive cooling of the liquid zone.

(b) The thermal conditions of the process were investigated for a pulled aluminum rod of 20 mm diameter with length up to 2 m. The results of the investigations [16] of temperature distribution in a melt, crystallizing zone and near it are shown in Fig 7(a).

The cooling rate of the metal in zones is determined by equation:

$$v_c = (T_b - T_e)/t \tag{12}$$

Here T_b and T_e are the temperature in the beginning and the end of the zone. Results of determination of the cooling rate are given in Table 1. The length of the crystallized part of the rod and radial crystallizing rate as a function of time are given in Fig. 7(b). It is seen from Fig. 7(a) that the solidification of metal takes place in the zone of air injection III. Then the cooling rate reaches (Table 1) maximum value (0.75–0.85°C/sec). Fig-
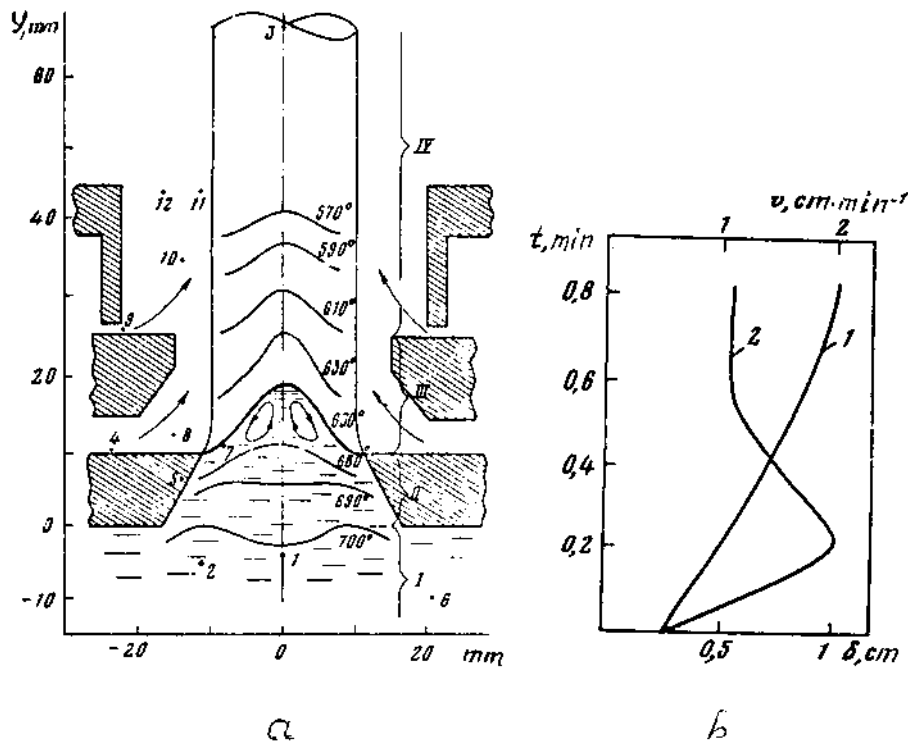
Figure 7 Heat conditions of the growth of 20 mm diameter aluminum rod. (a) Isotherms at crystallization zone: 1–12 numbers of thermocouples (1–3 thermocouples moving together with pulled crystal, the rest are fixed), I–IV cooled zones. Arrows show cooling air flows. (b) Dependence of the length δ of crystallized part of the rod (1) and the rate of radial growth v on time of motion of the rod t (2).

Table 1   Cooling Rate of Metal in Zones, $°C/s^{-1}$

Number of thermocouple in Fig. 9(a)	Zone I	Zone II	Zone III	Zone IV	Zone V
1	0.06	0	0.75	0.37	0.09
2	0.04	0.04	0.85	0.35	0.09

ure 7(b) shows that crystallization of the rod over all cross-section occurs during 0.8 min and maximal rate (2 cm/min) corresponds to the time 0.2 min from the onset of crystallization. If rather a higher coefficient of heat transfer and linear temperature distribution in oxide film is taken into account, then it is clear that the cooling rate in zone III and the solidification rate are high, $0.85°C/sec$ and 1.5 cm/min, respectively. They are close to those for continuous casting.

(c) Very important practical meaning has the heat transfer coefficient of product, α. There are some calculations of α by means of empirical equation [6]. Thus, in the case of natural cooling by free convection α is about $11.6–35 \, Wm^{-2}°C^{-1}$. This coefficient changes with temperature very slowly in the range $400–700°C$. Therefore it is possible to use the Newton's law $Q = \alpha T$. In stationary regime of crystallization for operating pulling rates the air cooling removes at least the latent heat of crystallization. Ceasing the process at the moment of detaching the blowing proves it. It gives the possibility to calculate α in the zone of frontal blowing [17]:

$$\alpha = (\rho \, L \, v / \Delta T)(F_1 / F_2) \tag{13}$$

Here ΔT is the difference between the temperature of crystallization and of environment, F_1 is the cross-section area of pulled profile, F_2 is the blowing surface. It is possible to calculate α according to (13) for F_1 is approximately equal to the area of shaping slot that is for the low crystallization interface. In the case of the high interface, the share of heat removed by blowing from liquid zone of pulled product is great. This results in too low a value α. Equation (13) may be used to calculate α only for samples without internal hollows. For tubes pulled with forced air cooling of outside surface α may be calculated by the following equation [17]:

$$\alpha = [(\rho \, v \, L / \Delta T) F_1 / F_2] - \alpha_1 (F_4 / F_2)(\Delta T_1 / \Delta T) \tag{14}$$

where α_1 is the coefficient of heat transfer for free convective heat exchange in internal part of the tube, F_4 is the internal surface of tube conforming the zone of blowing on the outside, ΔT_1 is the difference of the temperature of crystallization and of medium within the tube. The value of α decreases when the distance between air holes and cooling surface increases.

In [18] the hypothesis on presence of an ''instant'' regular regime in blown zone for variable α is put forward. Within this connection the value α calculated by means of (13) and (14) is the effective coefficient of heat transfer, α_{eff} (α in the zone of effective cooling). The zone of the most intensive cooling is, as a rule, higher than the interface. The height of the cooling zone above shaper and blowing intensity are selected so as to except perturbation of liquid zone under air flow. Under cooling zone, the heat removal by free convection [6] takes place mainly.

(d) The main role at shaping structure of pulled material belongs to the cooling rate in crystallization range, so called crystallization index [19]:

$$\chi_{Cr} = \Delta T_{Cr}/\Delta t_{Cr} = v\, G_{Cr}, \tag{15}$$

where ΔT_{Cr} is the temperature range of crystallization, Δt_{Cr} is the time of passing by the profile through the crystallization range, G_{Cr} is the temperature gradient in the crystallization range.

The crystallization rate influences more efficiently on metal capacity (the weight of length unit). It is proportional to the thermal capacity and depends on geometry and sizes of pulled product [6,20]. It is possible to take G_{Cr} equal to $(T_1 - T_0)/h$, where T_1 is the temperature of the melt and T_0 is the crystallization temperature, h is the height of liquid column [21].

E. It is worth taking into consideration the results of some technological observations. Note that the rotation of the pulled product and liquid column in opposite directions increases an intensity of heat exchange. At the same time it leads to a break of the oxide film from an edge of a shaper [14,22]. Uniform growth of all products (Al-1% Mn tube with outside ribs) depends on the distribution of cooling air. The places of freezing correspond to places of maximum blowing. The height of crystallization interface increases deep from outside wall. The difference of the height is equal to 0.3–0.5 mm for the tube with a 3 mm wall.

5.2   Temperature Field at the Crystallization Interface

A. The most influence on character of crystallization has the thermal field near the growth interface. In the case of crystallization of aluminum it is necessary to consider the liquid column of the melt above shaper, the interface and solid. For some alloys it is necessary to inspect the crystallization zone. The crystallization zone and liquid column together are called the transient zone.

B. The length of liquid column of aluminum alloys is about 0.5–5.0 mm. The length of the transient zone, L, has the following sizes for different alloys. Ribbons of Al-2% Mg-0.4% Mn alloy with temperature range of crystallization $\Delta T_{Cr} = 25°C$ have L equal to 2–4 mm. Ribbons of Al-6% Zn-2.2% Mg-1.7% Cu-0.4% Mn-0.2% Cr alloy with $\Delta T_{Cr} = 161°C$ have L equal to 15–40 mm (in the case of free convection about 35–70 mm). L is equal to 5–110 mm for 29 mm diameter circle tubes of the same alloy in the case of external cooling only.

C. Graphical analysis shows exponential character of the temperature distribution in liquid zone [23]:

$$T_L = T_1 - \Delta T_{TR} \exp(k_1 Z), \tag{16}$$

where T_L is the temperature of liquid column above shaper; $\Delta T_{TR} = T_1 - T_2$, k_1 is coefficient. Decision using of the Newton's and Fourier's equations gives the following temperature distribution along Z:

$$T_L = T_1 - \Delta T_{TR} \exp(\alpha Z/\lambda_1) \tag{17}$$

Here λ_1 is the thermal conductivity of liquid phase. It is seen from comparison of (16) and (17) that coefficient $k_1 = \alpha/\lambda_1$. It is the relative transfer coefficient.

Experimental investigation shows that temperature gradient at the interface $G_{int} = G_1 = G_2$, where subscrits 1 and 2 correspond to liquid and solid phases near the interface. Then, on the basis of the thermal equilibrium equation it is possible to receive the following equation of temperature gradient at the growth interface [23]:

$$G_{in} = v\rho_1(L + C_1 \Delta T_{TR})/(\lambda_2 - \lambda_1) \tag{18}$$

where C_1 is the thermal capacity of the liquid phase. The difference between values of G_{int} calculated according to (18) and measured is smaller than 5% [23].

Investigation of the pulling process of a 29 mm diameter tube of based aluminum alloy, so called duralumin (Al-4% Cu-1.5% Mg-0.6% Mn), with the temperature of liquidus $T_L = 638°C$ and temperature of solidus $T_S = 502°C$ gave the following result [23].

Temperature of the melt near to the shaper bottom was equal to that in a crucible, about 670–680°C. The change of temperature of the melt begins since 15 mm depth to the top of a shaper. On the top of the shaper the melt has a temperature approximately 20°C lower (650–660°C). G_1 enhances from 0 to 2–3°C/mm. In the liquid column above the shaper the gradient increases to 4.5–5.5°C/mm and temperature lowers to liquidus temperature.

5.3 Temperature Distribution in Solids for Forced Blowing

The character of the change of temperature gradient is similar to the change of cooling rate along the length of pulled product [6]. Experimental curves of the change of temperature and of its gradient for 29 mm diameter duralumin tubes are shown in Fig. 8. The tube, after passing the crystallization zone, is cooled by free convection. It is seen that the temperature of the product above crystallization zone reduces smoothly, the temperature gradient decreases monotonically [23].

5.4 Influence of the Shaper

A. The shaper not only forms pulled product cross-section but is a thermoregulator. It influences temperature distribution in the melt both at a crucible and near the growth interface [6]. It is connected differently
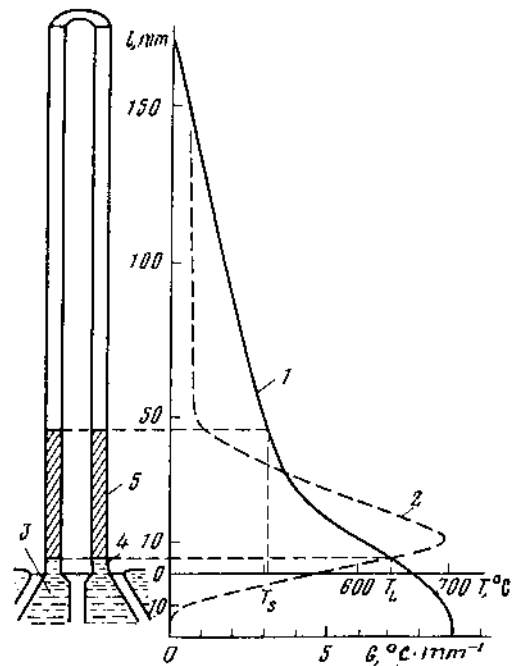
Figure 8   The change of temperature (1) and its gradient (2) in work volume of shaper, liquid zone and pulled product: (3) work volume; (4) liquid zone; (5) zone of crystallization. T_S is the temperature of solidus, T_L is the temperature of liquidus.

to its thermophysical properties from that of crystallizing melt. The influence of the shaper is most noticeable in the case of intensive blowing of pulled product when part of the air flow is deflected to the shaper. Convection heat transfer from it increases and the shaper cools off. The upper open surface of the shaper is cooled most intensively. [24]. This decreases the overheat of a melt in the work space of the shaper. The work space is a volume inside a shaper. The melt within it is continuously supplemented from a crucible during the pulling process.

B. The intensity of cooling of the work space by a shaper can be quality characterized by the value $W = F_c/F_h$, where F_h is the surface of the work space of a shaper which is heated by a melt, F_C is the open cooling surface of a shaper. They are determined by projection of the real areas on horizontal plane on the level of the work volume bottom [24]. The overheat is removed through a shaper body and a liquid zone. There are a few types of shapers of different W (see Table 2). A very hot shaper has minimum W, a very cold one has the most W. Every shaper allows to pull a product with certain minimum overheat of a melt. This minimum overheat is smaller when the value of W is lower [24]. It is worth noting that there are also shapers with W ranging between the above.

Characterization of shapers by W can be used to project constructions of shapers for different profiles. Very often different insets in shaper are used to grow products of different cross-sections. These insets with different W allow to control

Table 2 Classification of Shapers on Heat Remoal

Type	Design philosophy
Very hot, $W < 0.5$	Shaping slot is in the plate reached by a molten metal both inside slot and outside the plate. Cooled area of the plate is smaller than the projection of area of internal side surface of the slot on horizontal plane.
Moderately hot, $W = 0.2$–2.0	Shaping slot is limited at the top by plane insertion along its perimetr. Its cooled area is larger then projection of area of internal side surface of the slot on horizontal plane.
Very cool, $W > 2$	Shaping slot is limited inside and internal walls reached by a melt. Cooled surface is large.

the growth of oxide film on the surface of a pulled product in its liquid zone. The insets can be used as parts of the shaper to pull the product of complex cross-section with walls of different thicknesses, branching, bend and closed counters. The insets give both required heat removal, flat isotherms of heat field for profile of different thickness walls and easy filling of shaper slot with melt. Right choice of a shaper with necessary W also gives possibility to suppress the growth of parasitic dendrites on a product surface.

Heat characteristics of shapers can be quantitative [23,25]. They are based on Eqs. (16) and (17) which show exponential distribution of temperature along the growth axis. The value of index of the exponent is established by geometric sizes of shaper (depth, width) and heat properties of a product. It gives the possibility of classifying shapers by G and overheat $(T_1 - T_L)$ which determines the structure of product and productivity of process.

5.5 Cooling of Product

The pulling of a shaped product is possible without forced cooling in the case of natural free convection. But forced cooling enlarges productivity and makes better structure and mechanical properties of products. A number of investigations was performed to intensify cooling of growing profiles.

(a) More effective cooling takes place in the case of additional cooling zone above basic zone. Cooling in two zones gives the possibility of increased intensity of cooling and avoids displacement of the liquid column. This results in the increase of crystallization and pulling rate. It is especially important in the case of alloys with a wide temperature range of crystallization. Additional cooling zone influences structure by means of degeneration of secondary axes of dendrites [26].

(b) Water–air mix cooling of duralumin tubes increased the temperature gradient by about 25–30% and the cooling rate in crystallization zone in comparison to two-zone cooling at the same pulling rate [27].

(c) It is necessary to use internal cooling together with external for pulling of monolithic products with hollows along them (with internal dividing walls) and of closed profiles with internal parts it is necessary to use internal

cooling together with external. Two-side cooling in the some cases is useful to obtain rather simple profiles, for example, smooth tubes. Then the growth interface is more flat over thickness, the threshold of hydrodynamic stability of melt column enlarges, the geometry and structure of product is more constant over its length [14].

6 PHYSICAL CHEMISTRY OF PROCESS

1. Interaction of alloy components and impurities with aluminum and between them is similar to that for other techniques using molten based aluminum alloys. It depends on the chemical composition of the alloy, its components and impurities, their distribution coefficients. This interaction is determined by phase diagram. The kind of alloys used is also important (primary, secondary or scrap of certain composition).

2. Aluminum has rather high chemical activity. Therefore molten Al-based alloys interact with gases in the furnace and refractory materials of installation. It results in many elements and compounds going into a melt. There are H, O, C, N and metal elements or their compounds in the melt. This influences process stability as well as structure and properties of profiles. There are some distinctions of the Stepanov method in the interaction from other casting processes [28].

(a) The atmosphere in resistance furnace is the air with some moisture content. As a result, oxide film develops on a product surface. The interaction of molten aluminum with water vapor gives hydrogen which dissolves in the melt. Nitrides also arise. They can go into growing product. The oxide film produces the resistance of further oxidation of Al and of absorption of hydrogen. This resistance depends on alloy composition. Particularly the oxide film of Al-Mg alloys has some porosity and its resistance effect is rather weak.

(b) It is very important to take into account the interaction of molten alloys with a crucible and a shaper. There is long-term contact between them. Aluminosilicate refractory crucibles (chamotte and other) interact with molten aluminum reducing silica to silicon. In addition, refractory material of the crucible is impregnated by the melt along cracks. In this situation the crucible can be destroyed due to a difference in the thermal expansion coefficients. Such effects can be lowered by the use of a chamotte-graphite crucible because of its smaller chemical activity concerning molten aluminum. But it is necessary to bear in mind the rather strong oxidation of a graphite. It should be noted that the influence of alloying elements on the process of the reducion of SiO_2. This takes place when T_1 increases.

Very often a cast iron crucible and shaper are used. In this case it needs to account of gradual solution Fe into molten aluminum. Carbon of cast iron decreases slightly the solution. To decrease corrosion in a melt, special refractory and chemically stable paints are used [12,28]. But this problem is not settled totally. Magnesite and silicon carbide are also promising refractory materials.

(c) A great influence of the parameters of growing process (T_1, v, G and others) on the interaction of a melt with surrounding materials is to take into account.

3. Purification of a melt can be carried out by the same methods as for other aluminum technologies: settling, fluxing, filtration and others [28]. Some of them were tested and used for the Stepanov method. It is advisable to make the purification before inflow of a melt into the work crucible. In any case, it should be made before the shaping zone. The method of refinement is chosen with regard to required properties of growing profiles.

4. It is well known that the composition of crystallized solid differs from that of liquid due to different solubility components and impurities in both phases [29]. In the case of normal crystallization of melt column with the flat interface the impurity concentration can be given by the following equation [29]:

$$C_L = C_0 + C_0[(1 - k_{eff})/k_{eff}] \exp(-Rx/D) \tag{19}$$

Here C_L is the concentration of the impurity in the liquid on the depth x from the liquid–solid interface, C_0 is the initial impurity concentration in a melt, k_{eff} is the coefficient of effective distribution of the impurity which changes from 0 to 1 depending on crystalization conditions, R is the velocity of interface moving, D is the diffusion coefficient in the liquid.

The exponential decrease of impurity concentration with the increase of distance from the interface follows from (19). k_{eff} in the case of Al-based alloys is usually smaller 1. This results in a small increase of impurity in crystal during its pulling.

The Stepanov method has many common features with normal crystallization. Particularly in that in both cases the whole material is melted. There is only one interface. At the same time there are some distinctive features, which can create other distribution of impurities in diffusion layer and change k_{eff}. Thus the growth rate of Al profiles by the Stepanov techniques usually ranges from 30 to 150 mm$\times$min^{-1} and higher. Mixing melt is usually absent. There is a local zone of crystallization. Therefore the impurities are forced out into small volume of the melt column. Molten aluminum in a semicontinuous process of pulling is supplemented or changed after spending about 10–15% of bulk in the crucible. These peculiarities give stable impurity concentration in the transient diffusion layer. This results in constant chemical composition over the length of the growing product. It was confirmed in a number of researches [6]. This point was investigated in more detail in the Stepanov method in the case of Mg-based alloys [30]. For these alloys, the character of an impurity distribution is similar to Al-based alloys (close density, melt points and identical components of alloy and impurities). It was shown that the increase of the concentration of impurities over the length of products is insignificant: for Fe to 0.001–0.002%, Cu to 0.0001–0.0013%, Si to 0.001%.

7   QUALITY CHARACTERISTICS AND PROPERTIES

Quality characteristics of pulled products are geometric sizes, the state of a surface, a structure, mechanical, physical and chemical properties. It is very important that both of those characteristics remain constant over the whole volume of one product

and over the group of products. Demands on quality depend on specific profile application.

7.1 Geometry of Profiles

1. The notion of the geometry includes both the sizes of a product and the perfection of its shape. Usually, the accuracy of sizes of cross-section along different directions and of wall thickness is examined. In the case of a lengthy profile, the flexure along its length is important. The shape and size of the longitudinal section are taken into consideration for a profile which has a curvature along its length.

2. Demands on the geometry are variable for different applications. Thus all products grown by the Stepanov technique meet requirements to the geometry of heat exchangers to the full. For a number of applications as construction materials it is necessary to use profiles with rather tough demands on their geometry. In this case the profiles can be used both as grown and after mechanical treatment. But in some cases, for instance for wave guides, the demands on geometry are strong to such an extent that the Stepanov method is not expedient.

3. Geometry of products depends on accuracy and stability of shaping and pulling devices as well as on technological factors. There are empirical dependences of cross-section sizes of some profiles. Thus the radius of rod cross-section r can be predicted [31]:

$$r = r_0 - 0.018\,(1 - 0.1h)\,h^3 \tag{20}$$

Here r_0 is the radius of shaping hole, h is the height of the shaper. By analogy one may find the thickness of a ribbon S:

$$S = S_0 - 0.018\,(1 - 0.1\,h^3) \tag{21}$$

where S_0 is the thickness of shaping slot.

4. It is necessary to take into account the change of linear sizes of cross-section at solidification of melt column: $\varepsilon = (1_0 - 1)/1$, where 1 is the linear size of product cross-section and 1_0 is the linear size of shaping hole (in the case of casting that is linear size of an element in a cast shape). ε takes into account the change of a size both due to crystallization and owing to capillary shaping. The Stepanov method differs strongly from conventional casting in ε value. ε ranges from 0.8% to 2.5% depending on outline of cross-section, presence of connecting strips and alloy [12].

5. The dispersion of sizes of different profiles grown by the Stepanov technique was studied in many works [6,12,13,31,32]. The scatter of geometric sizes was measured for smooth circle and rectangular tubes, ribbons, rods, multichannel panels, tubes in a plate, box-like shapes, double-walled tubes with connecting strips, other very complex shapes of cross-section of various dimensions. The scatter of sizes of the majority of products of different shapes over their group amounts to $\pm 1\%$ for cross-section and $\pm 10\%$ for wall thickness. Curvature of the product (flexure) per length unit length is smaller than 0.5–1.0 mm/m. In the case of profiles of small cross-section (5–20 mm) and thickness of wall smaller than 1.2–1.5 mm, the size of straggling increases only slightly. The values mentioned above are in accord to that of pressed profiles.

Open elements of profiles, for example edges of plates or ribs, tend to more variability of sizes as against closed counters. Thus the scatter of sizes of cross-section of tubes with two ribs along them amounts up to 2.5%. But circle openings on the ends of slots shaping such ribs can make them thinner and some decrease of a deviation from rated value will take place. Note that some angular rounding off is observed in product grown by capillary shaping. The deviation of internal sizes of closed profiles is, as a rule, smaller in comparison with outer ones [31]. Changes of geometric sizes are maximum at the finish stage of the process when starting and transition regimes are important.

In [12] and [32] it was shown that the difference of wall thickness can be reduced to 6% for the shaper with a stable unchanged shaping hole. Mixing a melt also increases the constancy of wall thickness over the cross-section and the length of the product [14]. Control of constancy of wall thickness was realized for groups of tubes with two outside ribs grown by means of continuous and semicontinuous processes. Their weight per unit length and geometric sizes were measured over all their length. Deviations from standard were lower than the values mentioned above. The constancy of thickness along the length of tubes was higher for the continuous process.

7.2   The Surface Quality

1. Relief of surface, its structure and physical-chemical properties influence the strength, the friction coefficient, optic properties, the heat exchange and the corrosion resistance [6]. Therefore the surface quality determines the product applications.

2. The quality of surface for the Stepanov method is higher than for casting. Surface pores and shrinkage cavities are absent. It is connected with shaping molten material without any contact with crucible. The exterior view of product depends on alloy and its oxide film.

3. The surface is characterized, its micro- and macrorelief [6,33]. Roughness of the product surfaces was measured by feeling with a needle, with optic microscope, and by interference method with a interferometer [33]. The height of roughness determined by the needle was smaller than 14 μm, like pressed profiles. Optic microscope and interferometer saw higher smoothness. But microrelief does not show full characteristics of the surface quality. A surface can have some waviness with different spacing. The estimation of roughness in millimeters showed the highest class of smoothness.

In the case of the centimeter scale, the class of smoothness approached the highest, but single products fell beyond it [6,33]. Measurements with a universal instrumental microscope on smooth circle tubes revealed waviness with an amplitude up to 0.05 mm (in isolated cases up to 0.1 mm) and wavelength ranging from 20 to 40 mm.

7.3   Structure of Products

1. The structure depends on many factors. Among them there are chemical composition of alloy, characteristics of the regime of pulling out, heat parameters of crystallization. This results in different structure types of Al-based alloy profiles grown by the Stepanov method and possibility to control structure during process.

2. Similar to continuous casting the most typical structure of products grown by the Stepanov method is dendritic. Different structure zones of products (columnar, fanshaped, equiaxial) are created by cellular, twin and equiaxial dendrites, respectively. The structure is determined by morphological stability of dendrites of definite type.

The columnar macrostructure consists of large lengthened grains with developed cellular substructure [34]. The size of grains and cells depends on the alloy, geometry of profiles and conditions of growing. Thus, 2 mm thick ribbons of technical-grade Al pulled out at a rate ranging from 3 to 10 m/hr and at overheat from 20°C to 75°C had the grain length ranging from 50 to 500 mm and transverse sizes of grain from 0.1 to 40 mm. The macrostructure did not change when the content of Fe and Si increased, but the grain sizes decreased [6]. The columnar structure of technical-grade Al tubes with diameter ranging from 3.6 to 5.0 mm and wall thickness from 0.2 to 0.8 mm formed at temperatures ranging from 715°C to 730°C and the rate of pulling out from 6 to 8 m/hr. The grains had the length of 8–16 mm and width of 1.5–3.5 mm.

Misorientation angle changed from 2° to 4° [21]. The boundaries of impurity substructure are parallel with the long axis of the columnar grains oriented along $\langle 100 \rangle$. In two-side blowing of a ribbon, the grains nucleated on both surfaces of it under some angle (usually up to 10–12°). They developed deep into a melt up until they touched each other. In the central part of the ribbon it is possible to expose the liquating boundary of conjugation of these two systems of columnar crystals. In the case of blowing from one side, the nucleation went from this one. The grain grew under some angle in the direction of pulling out and throughout the product thickness [34].

The Al-1% Mn ribbons of thickness ranging from 0.3 to 4 mm and width from 40 to 100 mm maintained the columnar structure from the onset of the process. Its grains were extended along the direction of pulling out. The grain sizes depended on the regime of pulling out. Thus, the increase of v from 5.5 m/hr to 13.5 m/hr results in a decrease of grains from 20×3 mm^2 to 6×1 mm^2 at temperature 680°C. The decrease of grain size was particularly connected with thinning down the ribbon. When the temperature lowered from 715°C to 665°C at v equal to 6.5 m/hr, grain dimensions became 2×1 mm^2 against 15×2 mm^2. Precipitates of MnAl$_6$ phase in the form of chains extended along the ribbon were seen in longitudinal and transverse cuts of the microstructure [35]. The macrostructure of Al-(0.8–1.6)% Mg tubes obtained at a rate of 9.5 m/hr and a temperature of 700°C was columnar in the first stage of process. Microstructure was β-phase of Al-Mg$_8$ in the form of broken chains between dendritic axes [6].

The columnar structure was typical at pulling out of 2.9 mm diameter tubes of duralumin (Al-1% Cu-1.5% Mg-0.6% Mn) at temperature 680°C and rate of 3.4 m/hr and higher (G$_L$ ranged from 10°C to 12°C/mm, G$_S$ changed from 1°C to 2°C/mm). It was formed by cellular dendrites with long trunks extended along the side surface of the tube [36]. X-ray investigations showed (100) grain texture in the tube cross-section and crystallographic direction $\langle 100 \rangle$ coincides with the axis of pulling out.

Misorientation angle of the texture was 1–5°. At rate of 3.4 m/hr, macrograins amount to 2–2.5 mm. Every grain in a longitudinal cut was formed by a family of parallel primary trunks of cellular dendrites (Fig. 9(a)). In a transverse cut, the grain
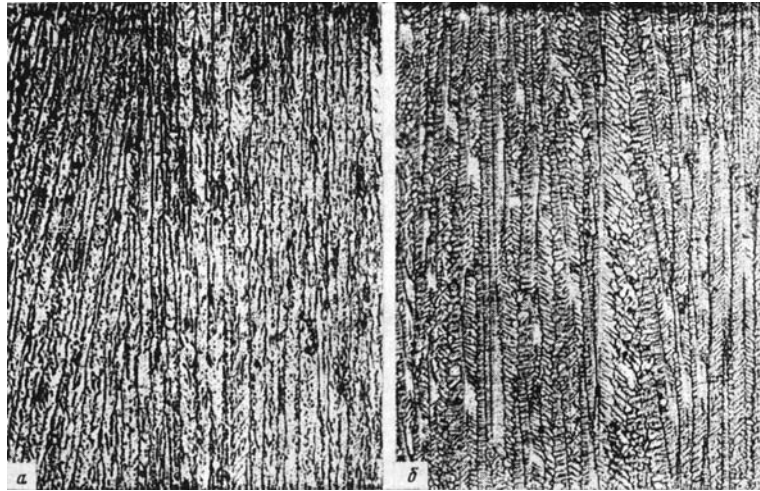
Figure 9 The structure of material of duralumin tubes (longitudinal section) for ''very hot'' shaper at temperature of the melt of 680°C and $v = 5.7$ cm/min (5^X): (a) one zone cooling (8.2 m^3/h); (b) two-zone cooling (in upper – 8.2 m^3/hr, in lower – 6.2 m^3/hr).

consists of a group of 45 μm equiaxial dendritic cells. Along dendritic cell boundaries, the eutectic interlayers arrange. They consist of α solid solution and 5 μm thick intermetallic compound Al$_2$Cu. The increase of rate of pulling out up to 3.9 m/hr leads to forming the structure like the one shown in Fig. 9(a). But unlike this structure, the dispersed cellular grains are shorter. The size of the dendritic cells in a transverse cut is about 30 μm and it changes from 120 to 200 μm in the longitudinal one [36]. During this experiment the growing rate was increased from 3.9 m/hr to 4.2 m/hr and temperature gradient of liquidus and solidus came to 12–18°C/mm and 10°C/mm, respectively. This was made by means of additional blowing through the upper zone together with the lower blowing zone. In spite of the increase of a mean temperature gradient in the crystallization zone, the product structure was columnar.

Fibrous structure is formed like the columnar one by cellular dendrites. It develops at the same rate but at a higher temperature of a melt. In the case of technical-grade Al, this structure has the length of grains ranging from 4 to 50 mm. The grains are twisted in a spiral. Misorientation angle ranges from 6° to 12° [21]. Fibrous structure in 29 mm diameter duralumin tubes develops at high overheat and large rate of pulling out. The melt temperature was higher than 700°C and the rate was more than 3.8 m/hr [37].

The forming of fibrous structure increases due to shortening of concentration supercooling zone in comparison with columnar structure. The grains are lengthened from 5 to 10 mm along the direction of pulling out and twisted slightly. They have cellular structure. In a longitudinal cut, the cells are jointed in irregular shape hexagons, their length ranging from 200 to 300 μm and width of about 40 μm. They become shorter and more equiaxial when the rate increases [37].

The fan structure formed at pulling out of Al-1% Mn ribbon in normal conditions. There are colonies of some decades of fan-shaped diverged crystals. These

crystals are flat twin dendrites (from 100 to 200 μm in thickness) developing into twinning (111) plate with orientation of primary trunks from $\langle 110 \rangle$ to $\langle 112 \rangle$ [6].

Fan structure was observed in Al-(0.8–1.6)% Mg rod of closed rectangular cross-section after pulling out a piece of the length ranging from 0.5 to 1.0 m with columnar structure [6]. Probably, this transition occurs when the impurity concentration at the crystalization interface and the concentration supercooling attain some limit. This explanation is supported by growing pure Al with a small quantity of impurities. In this case, only columnar structure forms over all the length of product. The transition takes place when the Fe content increases. Microstructure is characterized by Al_5Mg_8 β-phase in the form of broken chains between dendritic axes.

Fan structure forms in 29 mm diameter duralumin tubes at rather moderate overheat of a melt (the temperature of the melt amounts to 660–680°C) at rate ranging from 2.1 to 3.8 m/hr [36,37]. It consists of dendrites of twin structures in the form of long lamellae along direction of pulling out (Fig. 9(b)). Metallographic and x-ray investigations show that cuts of twinning plates by side surface of product are parallel to twin boundaries. The space between them changes from 0.5 to 0.15 mm when a rate increases. The growth of twin dendrites creating families of fan-shaped structure goes with the development of $\langle 100 \rangle$ secondary branches. These branches form dispersed internal grain substructure with a dendritic cell size about 44 μm (Fig. 9(b)). Twin boundaries are depleted in alloying components Cu, Mg, Mn. Liquation typical to systems with $k < 1$ in the range of secondary branches and in interdendritic spacing.

Cu concentrations amount to about 2.3% at a twin boundary, approximately 3.4% at secondary dendritic branches and about 7% for interdendritic spacing [37].

The change of one-zone for two-zone blowing with decrease of efficiency of lower zone at the same rate of about 3.9 m/hr results in the transition of a columnar structure to the fan structure shown in Fig. 9(b). The fan structure is also typical at the rate of 4 m/hr for two-zone water-air blowing [36,37].

Equiaxial structure is observed at a very small overheat of a melt. Besides this structure appears when the temperature gradient is negative for special shaper construction and in the case of pulling out at water cooling through upper zone [6,37].

3. The structure of tubes grown rotating the melt column in the shaping hole in relation to pulled product was investigated. In this situation the melt is mixed. The tubes obtained at a pulled rate of 2.9 m/hr and rotating with 0.1 rpm had a columnar structure like to the one shown in Fig. 9(a). Cell sizes were about 65 μm. The increase of the rotation rate up to 0.4 rpm led to the decrease of macrograins formed by cellular dendrites from 1.5 to 1.0 mm, the orientation factor decreased. Decreased v at the same rate of 0.4 rpm did not change the structure type, but the cells coarsened (up to 85 μm) [36].

The structure of profiles obtained by a special shaper was also studied. This shaper did not plunge into a melt. It made only a counter of its linkage with liquid melt column. Such shapers had smaller heat removal. At two-zone blowing and a rate higher than 2.6 m/hr, the twin dendrites grew stable. They were similar to the ones shown in Fig. 9(a). At a smaller rate the twin structure observed was like to one shown in Fig. 9(b). When the rate decreased from 2.4 to 2.2 m/hr at unchanged intensity of blowing, the structure coarsened. Cells increased from 45 to 60 μm. These observations show that a special shaper has heat removal smaller than the "very hot" one with W≤0.5. It decreases the zone of thermal and concen-

tration supercooling. More cold shaper is to lead to the transition of twin dendrites to the cellular ones [36].

4. Quantitative estimation of structure can be made by means of stereoscopic optic metallography. Quantity of inclusions (structure elements) in a unit of area (for Al-1% Mn twisted rib tubes) or quantity of intersections of unit length of a secant by the inclusions (for duralumin twisted smooth tubes) were calculated [14]. Microstructure of duralumin twisted tubes and ones without rotating is shown in Fig. 10. The linear orientation extent of the inclusions α_L in samples was determined [38,39]:

$$\text{for Al} - 1\% \text{ Mn alloy } \alpha_L = (X_\perp - X_{II})/(X_\perp + X_{II}), \tag{22}$$

$$\text{for duralumin } \alpha'_L = (m_\perp - m_{II})/m_\perp. \tag{23}$$

Here $X_\perp$ and X_{II} are the mean numbers of the inclusions per 1 mm^2 in transverse and longitudinal sections, respectively, $m_\perp$ and m_{II} are the mean numbers of inclusion intersections of 1 mm secant lying on longitudinal slide normally and parallel to the growing direction. These results are shown in Table 3. It is possible to draw some conclusions.

1. For tube part of an Al-1% Mn product the linear orientation extent α_L is not changed with rotation. Rotation diminishes the number of inclusions per 1 mm^2 of both slides twice. Microstructure coarsens. Probably, the rotation rate was small to reduce the microstructure.
2. Twisted Al-1% Mn ribs have α_L lower than the tube part. But the number of inclusions per 1 mm^2 is more than for the tube part. Such changes can be induced by a specific two-side blowing of the ribs and more effective mixing of a melt in the zones of their forming. It was shown also that microstructure keeps its orientation parallel to heat removal. It coincides with the direction of pulling out.
3. In the case of duralumin tubes the rotation coarsens microstructure. It is seen from comparison between Fig. 10(b) and 10(a) and from the decrease of $m_\perp$ since rotating. Probably the reasons are the same as for Al-1% Mn
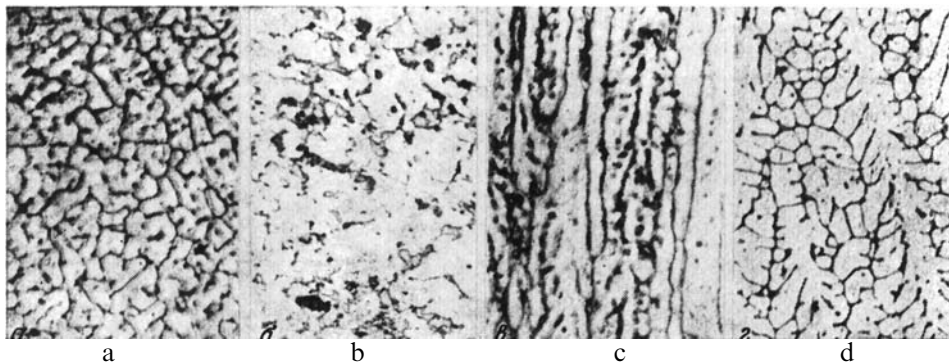
Figure 10   Microstructure of duralumin tubes grown with rotating (b, d) and without it (a,c): a, b are transverse sections, c, d are longitudinal ones; (100^X).

Table 3 Parameters of Microstructure of Tubes for Different Rotation Rate n, rpm

Parameters	Al-1% Mn tube with 3 ribs			Duralumin smooth tube	
		tube	ribs	tube	
	$n=0$	$n=0.34$	$n=0.34$	$n=0$	$n=0.42$
$X_\perp$, 10^3 per 1 mm^2	15.0 ± 1.0	$8,4\pm0.5$	11.1 ± 0.6		
X_{II}, 10^3 per 1 mm^2	2.3 ± 0.2	1.2 ± 0.5	2.4 ± 0.1		
$m_\perp$, mm^{-1}				23.9 ± 0.6	18.6 ± 0.5
m_{II}, mm^{-1}				10.0 ± 0.6	12.4 ± 0.5
α_L (α'_L)	0.73 ± 0.07	0.74 ± 0.07	0.58 ± 0.05	0.58 ± 0.04	0.33 ± 0.02

Note: Diameter of the tubes is 30 mm, pulling rate is 48 mm/min.

alloy. But the rotation induces the decrease of α'_L and the length of elements of microstructure on a longitudinal slide (Fig. 10(d) in comparison with 10(b)). This can result from a change of outer form of inclusions and formation of additional dendritic branches which is significant for a multicomponent alloy with a wide temperature range of crystallization [14].

Mechanical behavior of a grown product depends on dispersity of structure. It is determined by the specific area of interfaces of an individual alloy. Dendritic interfaces should be considered for Al-based alloys. They are much more developed than boundaries between grains and blocks. It was shown that the mean number of dendritic cells N in a unit area of a slide can be given as follows [40]:

$$N = k S_n v \tag{24}$$

Here S_n is the relative thickness. $S_n = F/P$, where F is the area of cross-section and P is its perimeter. The production vS_n characterizes productivity of the growing process. It gives the volume of a metal crystallizing per the unit time from a unit of perimeter of the shaping hole. The mean area of the cell cross-section is

$$f = 1/(kvS_n) \tag{25}$$

N as a function of vS_n is shown in Fig. 11 for different rods and ribbons of Al-1% Mn alloy (line 1) and 29 mm diameter tubes of duralumin (line 2). The coefficient k equals to 0.225×10^8 sec/cm^4 in the case of rods and ribbon and 0.0862×10^8 sec/cm^4 for duralumin tubes. The empirical dependences (24) and (26) give the possibility to control the dispersion of microstructure by v for a given relative thickness of product [40].
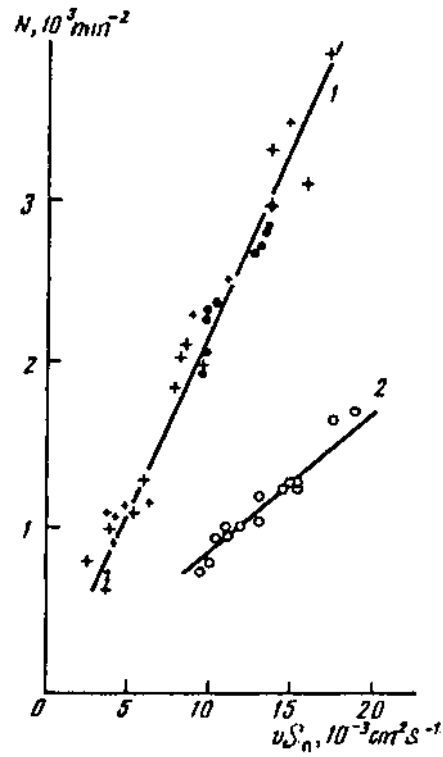
Figure 11 Dependence of dispersion N of structure on physical productivity v × S$_N$: (1) Al-Mn alloy cylindrical rod and ribbon; (2) duralumin tube.

7.4 Defects of Surface and Structure

(1) Defects of surface can arise [6] when the technological regime is wrong. Such defects are chinks caused by fusion of product wall, local freezing or eroded points of a profile. In this case it is necessary to correct faults of the regime.

(2) Contamination of a melt in seeding due to scale or other alien solid particles as well as splashing out of the melt on a surface of a shaper can induce longitudinal channel, slot or floating. They are created very often in the case of bad quality seed, seed kept too long in a melt, or displacement of a seed due to poor alignment. It is necessary to remove these faults.

(3) Some waviness, transverse struck, shears, brakes can be due to defects of installation (irregularity of moving pulling device, oscillations and others). It is necessary to improve mechanisms of the installation [6].

(4) Strong blowing can also create defects of a surface. The way of elimination of such defects is clear.

(5) Oxide film can deflect the liquid zone of product pulled out. This results in furrows, cakes and other distortions of shape. This takes place when the melt temperature is low as well as in the case of small rate of pulling out.

It is necessary to use effective purifying of a melt and other technological procedures.

(6) Irregularity of shrinkage of product during solidification induces deformation and cracks (so called "hot cracks"). It can be created by incompatibilities of local thermal deformations. It is necessary to select optimal temperature distribution along a pulled production. The increase of "hot strength" of alloys takes place when the Fe content is higher than Si content.

Defects in the form of swell, excrescences of different length or stitching structure are sometimes observed on a surface of profiles with fan structure of some alloys. Such defects were found on Al-1% Mn and Al-13% Zn ribbons. They formed when a twin plane of colonial crystals and the product surface lay at angle $\alpha > 30$–$45°$. Long excrescence (some centimeters) in the form of a drop increasing height and width grew at $\alpha = 53$–$56°$. Short excrescence about 1 mm in size were observed for $\alpha = 74$–$77°$. Stitching structure of periodically equiaxial defects about 1 mm took place for $\alpha = 80°$. They can be removed. It is necessary to use the seed with optimum structure, to increase temperature gradient in the liquid zone to lower the interface, to decrease a turbulence of cooling air flow [41].

In the case of alloys with a wide temperature range of crystallization (Al-3.5% Mg-0.5% Mn, Al-6% Zn-2.3% Mg-1.7% Ca-0.4% Mn-0.15% Ge, duralumin and some others), there are surface defects in the form of narrow ridges along the product, so-called tubercle-type defects [6,33]. These defects have different microstructure in relation to that of product [22]. It has been found that the reason for the nucleation of parasitic dendritic grains is the oxide film. The growth of a dendrite begins from oxide film where the concentration supercooling is available. The horizontal growing dendrite turns step by step with a melt flow and squeezes out a border of the oxide film. The growth and the turn of the dendrite will go until it is captured by crystallizing product. It was demonstrated that the growth of such defects can be suppressed by the increasing temperature gradient in liquid. It is recommended to use "very hot" shapers. In this case oxide film in the liquid zone does not created. Any tubercle-type defects were not observed [22].

Thus the Stepanov method makes it possibile to grow the products of rather high quality, which can be use in engineering, without treatment of its surface [6].

7.5 Properties of Products

7.5.1 Mechanical Properties

1. There is considerable information available on the mechanical behavior of both wrought and case aluminum alloy materials produced by the Stepanov technique [6].

Testing of 0.5 – 2.0 mm thick ribbons of technical grade Al alloys [42] showed that the tensile strength σ_B increased but specific elongation δ decreased with increasing Fe and Si content as shown in Table 4. Transverse samples with low impurity concentrations exhibit greater plasticity. When the impurity content increased, δ decreased sharply and became half as large as that of the longitudinal samples. The yield stress $\sigma_{0.2}$ increased with increasing impurity content. The addition of 0.1–0.2% of a Ti impurity resulted in a transition from columnar to dendritic struc-

Table 4 Influence of impurities (in wt%) and orientation on mechanical characteristics of Al ribbons

| Impurity content | | Orientation | σ_B, MPa mean | | $\delta\%$ | |
Fe	Si	of samples	value	range	mean	σ_t, MPa
0.1	0.02	II	40	38–42	35	22
		⊥	40	38–44	52	–
0.14	0.17	II	55	54–57	22	–
		⊥	53	51–56	35	31
0.29	0.32	II	69	69–70	22	41
		⊥	57	52–61	12	–
0.87	0.32	II	89	81–94	19	46
		⊥	81	73–92	8	–

Note: II = longitudinal orientation, ⊥ = transverse orientation.

Table 5 Mechanical Properties of Al Ribbons of Columnar and Dendritic Structure

| Orientation of | σ_B, MPa | | $\delta\%$ | |
samples	Columnar	Dendritic	Columnar	Dendriric
II	70	78	23	43
⊥	42	75	20	24

Note: II = longitudinal orientation; ⊥ = transverse orientation.

ture and an increase in δ_B as shown in Table 5. It is evident that this effect was due to the structural transition because the Ti impurity exhibited an insignificant increase in strength when no structural transition was observed [42]

In the case of technical grade Al tubes with a diameter from 3.6–5.0 mm and wall thicknesses ranging from 0.2 to 0.8mm, an increase of blowing intensity at a constant pulling rate led to an increase of σ_B [21]. Thermal strengthening decreased the slip rate six times (in the case of pressed samples, it was decreased by only three times). Mechanical properties of as-grown Al rods were compared with those of cast samples. Pulled samples had $\sigma_B = 56$ MPa, cast ones had 50 MPa, their torsion strength was 50 MPa and 42 MPa, respectively.

The main information on the strength of pulled products was obtained for Al-1% Mn alloy. It was connected both with high technological effectiveness of the growth of profiles by the Stepanov technique and with the possibility of wide application. Ribbons with the strength σ_B of 0.3–4 mm thick depended on impurities, regime of growth and structure and changed from 110 to 190 MPa, δ ranged from 6% to 31% [35]. The ribbons had $\delta = 13$–24% for a dendritic structure and $\delta = 8$–13% for a columnar one at a constant σ_B.

This was probably connected with different disposition of the MnAl$_6$ phase. An increase of Fe and Si content gave significant increase of σ_B. Probably, it is explained by an increase of a MnAl$_6$ amount due to a decrease of Mn solubility in Al.

Mechanical properties of Al-1% Mn profiles were investigated in more detail with tubes of rectangular cross-section of 203×102 mm^2 and wall thickness of 3

mm with internal ribs and without them [32]. The results of a great number of measurements treated statistically were as follows: σ_B ranged from 120 to 130 MPa, δ changed from 7% to 29%, the specific narrowing ψ was 16–32%, Young's modulus $E = (7.28$–$7.34) \times 10^4$ MPa, elastic limit $\sigma_{0.05}$ was 12–30 MPa, yield stress $\sigma_{0.2}$ ranged from 36.5 to 39.1 MPa, real tensile resistance changed from 150 to 185 MPa, impact viscosity α_k from 38 to 62 J$\times$cm^{-2}. Most parameters are close to the ones of pressed profiles in an annealing state. There is high homogeneity of σ_B, E and other values, but δ and ψ changed in a wide range. They had rather low values in the beginning pieces of samples, where impurity content was higher (in particular, Cu from a seed). It was revealed that material was so viscous that its fracture had plastic character.

Bending tests did not produce any cracks up to a bending angle of 180°. It is known that the Stepanov method lower values of $\sigma_{0.2}$ may exibit a favorable effect for $\sigma_B/\sigma_{0.2}$ ratios ranging from 3 to 3.5. It is also known that for $(\sigma_B/\sigma_{0.2}) \geq 1.4$, a material is strain hardened when under cyclic loading [43]. Since the $\sigma_B/\sigma_{0.2}$ ratio for materials produced by the Stepanov method vary from 3 to 3.5, this indicates that during production by the Stepanov method materials will undergo strain hardening at the beginning of the operational cycle.

In the case of hollow profiles with outside ribs, σ_B was higher and reached 130–150 MPa, δ amounted to 30%.

Al-Mg alloy profiles were studied for varying content of Mg. Thus Al-(0.8–1.6)% Mg rectangular tubes of 32×50 mm^2 cross-section with wall thickness of 0.45 mm had $\sigma_B \approx 160$ MPa [6]. δ for columnar structure ranged from 7% to 14% along longitudinal direction and from 10% to 12% along transverse one. For dendritic structure, $\delta = 20$–35% along pulling direction and 13–24% along transverse direction. Thus mechanical characteristics of the samples with dendritic structure approach to those of pressed samples in an annealing state. (After cold-working their σ_B increases but plasticity lowers 3–4 times.) Pulled fashing tubes of Al-3.5% Mg -0.4% Mn with a columnar structure had σ_B ranging from 225 to 245 MPa and mean δ equal to 15% [6].

High strength system Al-Zn-Mg-Cu was studied mainly with 29 mm diameter tubes of Al-6% Zn-2.3% Mg-1.7% Cu-0.4% Mn-0.15% Cr alloy. The tubes went through a heat treatment for strengthening. After annealing and artificial aging, σ_B increased by about 30% and achieved 460–480 MPa what is close to that of pressed profiles [6].

Testing of 29 mm diameter duralumin tubes shows an influence of the blowing regime on the strength. It was determined that at one-zone blowing $\sigma_B = 250$ MPa, $\delta = 3$–4%, at two-zone one $\sigma_B = 290$ MPa, $\delta = 8$–9% [37].

The investigation of behavior of cast alloys was performed with Al-(10–13)% Si, which is hermetic Silumin. Bands pulled out of the melt had $\sigma_B = 205$ MPa, $\delta = 11\%$.

In the case of sand casting $\sigma_B = 147$ MPa, $\delta = 4\%$, for chill-cast $\sigma_B = 156$ MPa, $\delta = 2\%$ [6]. It is seen that the pulled products have the highest characteristics. It is well known that Si does not form with Al any strengthening compounds. Therefore high σ_B and δ can be explained only by the specific technology which causes a rise of density, a decrease of gas porosity and other.

2. The dependence of mechanical properties of pulled bands on their structure and parameters of their growth was investigated [40]. The bands were pulled out of a molten Al-Mn alloy at four rates of pulling and air blowing. The dependences
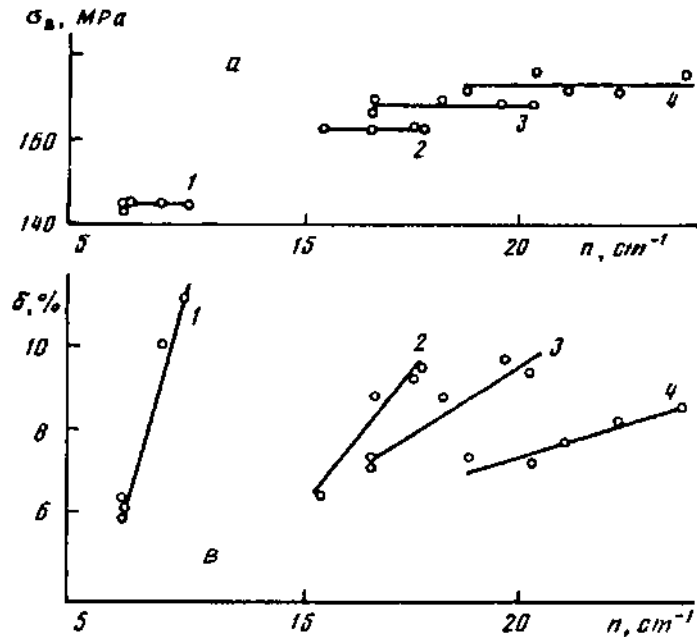
Figure 12 Strength δ_B (a) and specific elongation δ (b) of Al-Mg ribbons on number of grains along the width of sample n for four pulling regimes 1–4.

of σ_B and δ on the number of grains along the width of sample n are shown in Fig. 12. It is seen that δ increases when the mean size of grains decreases for a certain regime of pulling out. But σ_B does not depend on n. For more productive regime (higher dispersion of a microstructure), δ depends on n being weaker. This is connected with simultaneous effect of n and N, concentration of cells in the cut of grain (dispersion) on δ, but this effect acts in contrary directions. This results in unchanged mean δ for different regimes when the productivity of process changes about 5 times. σ_B does not depend on n and changes by jumps with N. The dependences of mean σ_B, microhardness H, n and δ on N are presented in Fig. 13. One can see an increase of N and n at the same time. But δ does not change practically. Mean value σ_B increases when N enlarges. The effect of grain structure of grain on σ_B is supported indirectly by the dependence of H on N because H is measured within the grain. If σ_B was determined by grain boundaries, then H would be constant at changing N. This takes place in relatively pure metals but not in alloys. These experiments showed unambiguously that the strength of products pulled out of a molten Al-Mg alloy is controlled by the dispersion of microstructure. It follows from (24) that, changing v or reducing the thickness of product S_n, we can control both the dispersion of a structure and the strength. The higher the productivity of the process the higher is H and σ_B of pulled product [40].

    3. Thus mechanical characteristics of the profiles pulled out of the melt satisfy requirements of many applications. There are the ways to enlarge the strength of profiles if it is necessary [44]. This can be made using higher strength alloys and thermal treatment of pulled products. Moreover the Stepanov method allows
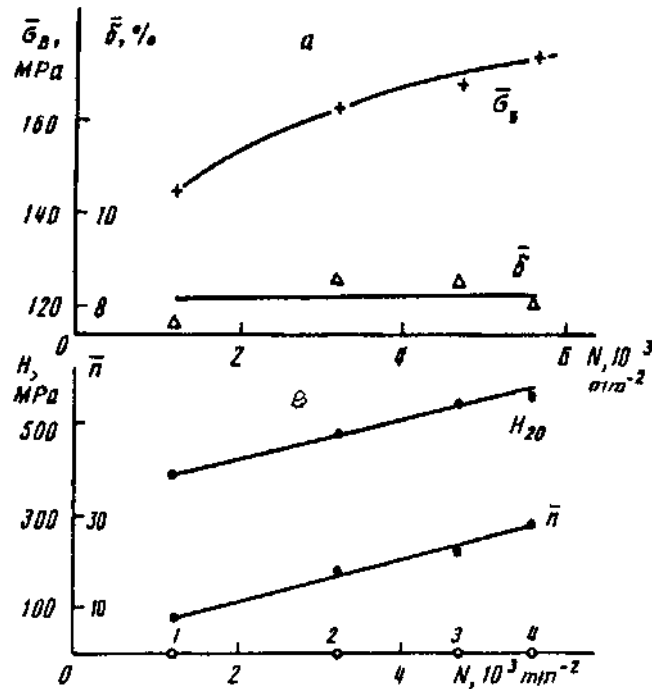
Figure 13 Dependences of σ_B and δ (a), of microhardness H and number of grains along width n (b) of Al-Mn ribbons on dispersity of structure N.

one to obtain profiles of special construction as well as profiles with increased thickness of walls in the places where this is necessary according to conditions of loading. It is also possible to strengthen the profiles covering with special layers or reinforcing by high strength fibers during their growth.

7.5.2 Physical and Chemical Properties

Pulled profiles have higher physical (density, damping capacity) [44] and chemical properties in comparison with products obtained by other methods.

Corrosion tests were performed with the profiles pulled from molten Al-Mn, Al-Mg-Mn, duralumin, technical-grade Al, Al-Si alloys. The tests were carried with NaCl solution, water of the Caspian Sea and a tap water [45,46]. In all cases pitting took place. It occurred mainly along pulling direction. The corrosion rate was higher for technical-grade Al than for Al-Mn, Al-Mg-Mg [45]. Probably, it is connected with special features of their structure. Pitting does not depend on a profile shape in contrast to the profiles obtained by deformation methods. It seems that internal stresses in pulled profiles are less. The tests showed that the stratifying corrosion was absent in profiles pulled from molten technical-grade Al and Al-Mn unlike pressed samples. As a rule, more intensive pitting occurs on an internal surface of tubes. It appears that the oxide film protecting from corrosion is less dense

and thinner on an internal surface than on the outer one. The film grows without forced air blowing.

Duralumin profiles have the highest rate of corrosion. Probably intermetalic compound $CuAl_2$ is a cathode. The Al-(10–13)% Si alloy has the most resistance to corrosion. Corrosion of this alloy is uniform. The alloy is practically free from pitting. It is seldom that a pitting takes place but it is not deep. Probably it is connected with absence of intermetalic compounds in Al-Si alloy [46].

Resistance to corrosion can be increased by covering with special decorative layers. Pulled profiles have no need in a preliminary mechanical treatment before the covering. It was shown also that pulled Al-Mn profiles were well anodized and nickel-plated [6].

8   COMPARISON WITH ALTERNATIVE METHODS

The Stepanov method (SM) was compared with the continuous cast (CC) and the deformation technology (DT) based on extrusion. Conventional cast is not considered because its worse quality and economical characteristics [44,47].

1. In SM the thermal process conditions are less variable than those for continuous casting in which a metal is subjected to hydrodynamic forces. The SM is single-pass which is a significant advantage over the multioperational DT process. In addition, SM installations are simpler and easier to automate.
2. CC can be used for casting alloys only. DT gives the possibility to work with deformable (wrought) alloys only. In the case of SM both casting and deformable alloys are suitable.
3. SM gives possibility to use a raw alloy up to 85–90%. This is significantly higher than for DT. Environment recovery for SM is also higher because single-run process.
4. Overall sizes of profiles obtained by SM are close to those sizes for DT. Flat profiles can have a width up to 70–100 cm, bulk profiles have a diameter of cross-section up to 50 cm. The length of pulled profiles ranges from 2 to 5 m. There are possibilities to enlarge these dimensions.

   Allowance for sizes of cross-section for SM is smaller in comparison with DT after extrusion and somewhat higher after all operations.

   Thickness of wall for SM can be significantly smaller in comparison with CC. Minimum thickness (0.3–0.5 mm) is also smaller in compare with DT for hard alloys. Maximum thickness of wall for SM is significant lower than for DT.
5. Quality of surface is higher than for CC. In the case of SM a roughness ranges from 1 to 10 μm. It is larger for CC and also for profiles after extrusion. DT gives high quality of a surface only after mechanical treatment. Defects of a surface for SM are less significant than for CC.

The structure of profiles obtained by DT is fine-grained. In the case of SM, there are columnar and dendritic structures. In a peculiar temperature regime or in the presence of modifiers, SM gives the microstructure similar to equiaxial.

The density of products obtained by SM is the highest. This is grounds for a homogeneity of properties over all bulk of a profile.

6. SM has facilities for additional purifying of a metal in the liquid state and for simultaneous control of geometry, structure and properties during growing. SM is more effective in comparison with DT in response to electrical power and amortization expenditures. It has facilities to change the shape of the profile, to repair installation, to produce and change instrumentation.

SM is used now for a small-scale production only. That is why its specific expenditures of labor are some what higher than for DT. They can be leveled if a broad-scale production will be managed.

7. Very important characteristics of the technology is a productivity of the process and of equipment. It depends on a pulling rate for SM and an extrusion rate for DT. The extrusion rate ranges from 5 to 2000 m/hr. The pulling rate for SM ranges from 1 to 20 m/hr. But it is necessary to account for a number of features of DT. DT uses many operations, expensive equipment, large rooms for large-sized installations. It decreases the difference of productivity of the two technologies. The difference decreases significantly for hard alloys, complex shapes and large cross-sections.

Besides, there is a possibility to enlarge the productivity of SM. It is necessary to organize a simultaneous growth of several profiles from one crucible and an increase of a pulling rate by means of more effective cooling methods.

8. SM as well as DT give the possibility to obtain profiles of various shapes including very complex ones. Some of them can be made by only one from the technologies mentioned above. Thick-walled profiles are included in an assortment of DT. They are not the purpose of SM. The latter can be used to grow many complex profiles and among them thin-walled ones. It is possible to grow polyhedral tubes; tubes with outer and inside ribs, elements, partitions, channels; products with many longitudinal hollows; tubes with bent channels, connecting strips, ribs; products with curvilinear longitudinal axis; twisted products; tubes with twisted ribs; other products of very complex shapes. Some of these products are shown in Fig. 14. Such profiles can not be obtained by CC. A number of them can not be made by DT also. Thus thin-walled profiles and a number of large-scale ones, in particular of hard, brittle alloys, products with curvilinear longitudinal axis and some other can be obtained only by SM. Thus SM has its various assortment, a part of which is not doubled the production of other methods.

An approximate estimation shows that cost prices of profiles obtained by SM and DT are close to each other. There is the following trend: the cost price of small-scale products with rather simple cross-section is lower for DT. The cost price of large-scale ones with complex cross-section is less for SM.

This consideration shows well future of SM and its application field.

Figure 14 Some shaped products pulled by the Stepanov method.

9   APPLICATION

It is possible to use the shaped products by three ways. They can be used in another method of manufacturing as billets, for example, in continuous casting to be constituent of the total metallurgical production. In the second place, they can be used as a semifinished product. At last, the shaped products can be used as grown. There are the following promising applications of pulled products.

1. Thin-walled articles with a large developed surface can be used as effective heat exchangers for a solar energy technology, for instrument making (semiconductor devices, devices for all means of transportation), for heaters and coolers of various appointments.
2. Blades for wind-operated power plant, for ventilators, as screw propellers and others.
3. Constructions of civil engineering.
4. Thin-walled bodies of different devices.
5. Sport inventory.
6. Consumer goods.
7. Packing.
8. Hothouses.
9. Tubes with outer or internal ribs of different application.
10. Printing type.

10   SHAPED COMPOSITES

The Stepanov method gives the possibility to make both a composite material and shaped composite constructions [47,48].

1. The Stepanov method was used to grow eutectic composites of Al-CuAl$_2$ with a lamellar structure and Al-Al$_3$Ni with a fibrous structure (Al$_3$Ni fibers). It is possible to pull from the melt the shaped product of an eutectic composite with a bond of its components close to ideal. But shortcomings of the processing are a low velocity and some defects of a structure.

2. The product pulled from the melt can be reinforced during its growth by continuous fibers, bands, complex half-finished articles. But it was necessary to obtain strong adhesion of components, maximum keeping qualities of raw materials, desired distribution of a reinforcement [48]. A process was developed for production of composites reinforced by boron fibers without and with heat-resistant covers of B$_4$C, BN, SiC. The fibers were distributed both over all the cross-section and locally. Profiles of rather small cross-section of various shapes were pulled up to 2 m length. Fiber filling was about 50% of the volume. Boron fibers kept their original strength. σ_B of such composites was about 800 MPa. It is equal to the strength of B-Al composites obtained by a liquid-phase method and approaches to that for solid-phase methods [49,50].

The process was developed for obtaining of flexible heaters in an Al cover [47]. Such a heater consists of Ni-Cr wires in SiO$_2$ insulation covered with Al. Experimental batches showed the possibility to increase work temperature up to 240–250°C and to use them for fire and explosion hazard works. Besides, investigations were performed on obtaining bimetal profiles. These profiles had an internal steel band and an outer Al cover. In this case, it was possible to grow the lamellar composite with well adhesion between layers and their anticorrosive protection.

REFERENCES

1. P. I. Antonov, L. M. Zatulovskii, A. S. Kostygov, D. I. Levinson, S. P. Nikanorov, V. V. Peller, V. A. Tatarchenko, and V. S. Yuferev. *Obtaining shaped single crystals and articles by Stepanov's technique* 1981, Nauka, Leningrad, USSR, pp. 8–22 (in Russian).

2. I. Czochralski. "Ein neus Verfahren zur Messung der Krystallisationsgeschwindigkeit des Metalle." Zeitschr. für Phys. Chemie, 1917, 92, 219.

3. E. V. Gomperz. "Untersuchungen an Einkristalldrachten," Zeitschr. für Phys. 1922, 8, p. 184.

4. P. Kapitza. "The study of the specific resistance of bismuth crystals and its change in strong magnetic fields and some allied problems." Proc. Royal Soc. London, ser. A, 1928, 119, p. 358.

5. P. I. Antonov, L. M. Zatulovskii, A. S. Kostygov, D. I. Levinson, S. P. Nikanorov, V. V. Peller, V. A. Tatarchenko, and V. S. Yuferev. *Obtaining shaped single crystals and articles by Stepanov's technique*, 1981, Nauka, Leningrad, USSR, pp. 22–64 (in Russian).

6. P. I. Antonov, L. M. Zatulovskii, A. S. Kostygov, D. I. Levinson, S. P. Nikanorov, V. V. Peller, V. A. Tatarchenko, and V. S. Yuferev. *Obtaining shaped single crystals and articles by Stepanov's technique*. 1981, Nauka, Leningrad, USSR, pp. 182–218 (in Russian).

7. P. I. Antonov and S. P. Nikanorov, "Physical problems in crystal growth by Stepanov method." J. Cryst. Growth, 1980, 50, p. 3.

8. H. E. La Belle and A. I. Mlavsky. "Growth of controlled profile crystals from the melt. Part 2." Mat. Res. Bull., 1971, 6, p. 581.

9. V. A. Tatarchenko and E. A. Brener. "Crystallization stability during capillary shaping." J. Cryst. Growth, 1980, 50, p. 33.

10. V. A. Tatarchenko. "Shaped crystal growth." in *Handbook of Crystal Growth*. (D. T. J. Hurle, ed), 1994, B, North-Holland, Amsterdam-London-New York-Tokyo, Vol. 2, pp. 1011–1111.

11. V. A. Tatarchenko and B. N. Korchunov, "Influence of oxide film on capillary effects," Izv. Akad. Nauk., ser.fiz., 1973, 37, p. 2295 (Bull. Acad. Sci. USSR, Phys. ser.)

12. B. N. Korchunov, V. V. Peller, A. S. Kostygov, A. S. Kholodkov, O. V. Yakovlev, and A. G. Kazakevich, "Obtaining large-size shaped products of Al based alloys by installation of semicontinuous acting." Izv. Akad. Nauk, ser.fiz., 1994, 58, pp. 182–190, (Bull. Acad. Sci. USSR, Phys. ser.).

13. A. S. Kostygov, B. N. Korchunov, V. V. Peller, G. G. Kholodkov, and O. V. Yakovlev, "Construction of shaping devices: physico-technical aspects and unification." Izv. Akad. Nauk, Ser. fiz., 1994, 58, pp. 162–167, (Bull. Acad. Sci., Phys. ser.).

14. B. N. Korchunov, A. S. Kostygov, V. V. Peller, G. G. Khohlov, and V. N. Osipov. "Influence of heat and mass exchange on geometry and structure of grown Al based alloy products," Izv. Akad. Nauk, Ser. fiz., 1988, 52, pp. 2045–2053, (Bull. Acad. Sci., Phys. ser.).

15. Yu. M. Shashkov, *Growing Single Crystals by Pulling Method*, 1982, Metallurgiay, Moscow, pp. 20–61, (in Russian).

16. P. I. Vyatkin, V. V. Peller, A. D. Stolbova, A. S. Kostygov, and B. N. Korchunov. "Some peculiarities of crystallization of Mg and Al based alloys products from the melt by Stepanov's technique." Bull. Acad. Sci. USSR, Phys. ser. 1980, 44, pp. 105–108.

17. A. S. Kostygov, V. A. Tatarchenko, and A. V. Stepanov. "Convective cooling samples obtained from the melt by Stepanov's technique." Izv. Akad. Nauk SSSR, Ser. fiz. 1972, 36, pp. 481–485, (Bull. Acad. Sci. USSR).

18. V. M. Golod and V. Yu. Fedorov. "Numeral modeling of heat regimes of process obtaining products from the melt by Stepanov's technique." Bull. Acad. Sci. USSR, Phys. ser. 1980, 44, pp. 113–115.

19. A. B. Michael and M. B. Bever. "Soldification of Al-rich Al-Cu alloys." J. Met. 1954, 6, pp. 47–56.

20. A. S. Kostygov and V. A. Tatarchenko. "Investigation of heat regime of crystallization and its influence on structure of Al alloy samples." Izv. Akad. Nauk SSSR, Ser. fiz. 1973, 37, pp. 2315–2318, (Bull. Acad. Sci. USSR, Phys. ser.).

21. V. A. Tatarchenko, G. V. Vladimirova, and A. V. Stepanov. "Structure and properties of Al products obtained from the melt by Stepanov's technique." Izv. Akad. Nauk SSSR, ser. fiz. 1971, 35, pp. 449–503, (Bull. Acad. Sci. USSR, Phys. ser.).

22. A. S. Kostygov, B. N. Korchunov, and G. G. Khohlov. "Suppression of dendrite growth creating tubercle roughness on the surface of articles grown from the melt by Stepanov's technique." Bull. Acad. Sci. USSR, Phys. ser. 1980, 44, pp. 149–152.

23. A. S. Kostygov, B. N. Korchunov, and G. G. Khohlov. "Investigation of heat regime of crystallization of aluminum alloy D16 tubes." Bull. Acad. Sci. USSR, Phys. ser. 1980, 44, pp. 100–104.

24. A. S. Kostygov, B. N. Korchunov, and G. G. Khohlov. "Classification of shapers for obtaining aluminum alloy profiles in connection with heat removel out of the melt." Bull. Acad. Sci. USSR, Phys. ser. 1980, 44, pp. 89–92.

25. V. Yu. Fedorov and P. I. Antonov. "Calculating and empirical determination of shaper thermal characteristics and choice of its construction." Izv. Akad. Nauk, Ser. fiz. 1994 58, pp. 12–18, (Bull. Acad. Sci., Phys. ser.).

26. A. S. Kostygov, B. N. Korchunov, V. Yu. Fedorov, and G. G. Khohlov. "Application of two-zone forced cooling in obtaining aluminum alloy tubes by Stepanov's technique." *Proceedings of the 9th Conference on the Preparing of Shaped Crystals and Parts by the Stepanov Method and Their Application in the Economy*, 1982, Ioffe Phys. Techn. Inst. Acad. Sci. of SSSR, Leningrad, pp. 304–308 (in Russian).

27. A. S. Kostygov, B. N. Korchunov, V. Yu. Fedorovof, and G. G. Khohlov. "Application of water-air cooling at preparing aluminum alloy tubes by Stepanov's technique." *Proceedings of the Conference on the Preparing of Shaped Crystals and Parts by the Stepanov Method and their Application in the Economy*, 1986, Ioffe Phys. Techn. Inst. Acad. Sci. of SSSR, Leningrad, pp. 298–302 (in Russian).

28. A. D. Andreev, V. B. Gogin, and G. S. Makarov. *Highly Productive Melting of Aluminum Alloys*, 1980, Metallurgiya, Moscow, pp. 5–52.

29. V. A. Tiller. "Segregation of dissolved impurities at solidifying ingot," in *Liquid Metals and Their Solidifying*, 1962, (G. L. Pozdnyakova, ed.), GNTI, Moscow, pp. 409–434 (in Russian).

30. P. M. Achunov, B. L. Baskin, M. A. Vorobyev, I. P. Vyatkin, V. I. Ivanov, B. K. Kardashev, B. N. Korchunov, A. B. Lebedev, V. V. Peller, and Yu. A. Fadin. "Investigation of structure and mechanical properties of Mg based alloys in crystallization by Stepanov's technique." Izv. Akad. Nauk SSSR, Ser. fiz. 1983, 47, pp. 1438–1451, (Bull. Acad. Sci. USSR, Phys. ser.).

31. V. M. Goldfarb, A. V. Donskoy, and A. V. Stepanov. "Some problems of shaping in preparing products from the melt," in: *Problems of Crystallization and Solid State Physics*, 1965, (G. A. Ivanov, ed.) LGPI, Leningrad, Vol. 265, pp. 61–74 (in Russian).

32. I. N. Artem'eva, Yu. S. Plishkin, V. A. Sedov, V. V. Peller, A. S. Kostygov, and B. N. Korchunov. "Physico-mechanical properties of shaped products of aluminum alloy AlMn," Bull. Acad. Sci. USSR, Phys. ser. 1976, 40, pp. 1369–1375.

33. B. N. Korchunov and A. S. Kostygov. "Quality of surface of aluminum alloy samples prepared from the melt by Stepanov's technique." Izv. Akad. Nauk SSSR, Ser. fiz. 1973, 37, pp. 2319–2321 (Bull. Acad. Sci. USSR, Phys. ser.).

34. V. O. Esin, I. G. Brodova, V. A. Tatarchenko, and A. V. Stepanov. "Peculiarities of defect structure of aluminum products grown from the melt by Stepanov's technique." Izv. Akad. Nauk SSSR, Ser. fiz. 1971, 35, pp. 504–510 (Bull. Acad. Sci. USSR, Phys. ser.).

35. V. M. Goldfarb, A. V. Donskoi, and A. V. Stepanov. "Investigation of process preparing Al-Mn ribbon from the melt," in *Problems of Crystallization and Solid State Physics* 1965, (G. A. Ivanov, ed.), LGPI Leningrad, Vol. 265, pp. 50–60 (in Russian).

36. I. G. Brodova, V. O. Esin, B. N. Korchunov, A. S. Kostygov, V. N. Osipov, V. V. Peller, I. V. Polenz, V. Yu. Fedorov, and G. G. Khohlov. "Structure of aluminum alloy tubes prepared by different variations of Stepanov's technique." Bull. Acad. Sci. USSR, Phys. ser. 1988, 52, pp. 2038–2041.

37. I. G. Brodova, I. A. Borisova, A. S. Kostygov, B. N. Korchunov, V. V. Peller, and G. G. Khohlov. "Structure of aluminum alloy D-16 articles prepared by Stepanov's technique," Izv. Akad. Nauk SSSR, Ser. fiz. 1985, 49, pp. 2435–2438 (Bull. Acad. Sci. USSR, Phys. ser.).

38. S. A. Saltikov. *Stereometric Metallography*, 1970, Metallurgiya, Moscow, pp. 232–243 (in Russian).

39. S. A. Saltikov. *Stereometric Metallography*, 1970, Metallurgiya, Moscow, pp. 136–231 (in Russian).

40. V. Yu. Fedorov. "Dependence of structure dispersion and mechanical properties of Al-Mn alloy product grown by Stepanov's technique on productivity of the process," Izv. Akad. Nauk SSSR, Ser. fiz. 1994, 58, pp. 148–157 (Bull. Acad. Sci. USSR, Phys. ser.).

41. V. O. Esin, I. G. Brodova, V. A. Tatarchenko, and A. V. Stepanov. "Peculiarities of structure of Al-Mn flat band grown from the melt by Stepanov's technique," Izv. Akad. Nauk SSSR, Ser. fiz. 1972, 36, pp. 588–594 (Bull. Acad. Sci USSR, Phys. ser.).

42. V. M. Goldfarb, A. V. Donskoi, F. M. Dyagilev, A. S. Kostygov, and A. V. Stepanov. "Structure and properties of Al and Cu based alloy products prepared in directed crystallization" in *Casting Properties of Metals and Alloys*, 1967, Nauka, Moscow, pp. 143–147 (in Russian).

43. V. S. Zolotarevski. *Mechanical Properties of Metals*, 1983, Metallurgiya, Moscow, pp. 298–338 (in Russian).

44. V. V. Peller. "Preparing shaped products of Al and Mg based alloys by Stepanov's technique in comparison with another methods." Izv. Akad. Nauk, Ser. fiz. 1994, 58, pp. 176–181 (Bull. Russian Acad. Sci., Phys. ser.).

45. A. H. Bairamov, V. V. Peller, A. S. Kostigov, B. N. Korchunov, S. M. Tagieva, and S. M. Mamedova. "Investigation of corrosion and electrochemical behavior of aluminum alloys for products prepared by Stepanov's technique." *Proceedings of the Conference on the Preparing of Shaped Crystals and parts by the Stepanov method and their application in the Economy*, 1986, Ioffe Phys. Techn. Inst. Acad. Sci. of SSSR, Leningrad, pp. 335–340 (in Russian).

46. A. H. Bairamov, V. V. Peller, S. M. Tagieva, A. S. Kostygov, B. N. Korchunov, Z. B. Sultanova, and S. G. Bektashi. "Corrosion behavior of aluminum alloys in products prepared by Stepanov's technique." *Proceedings of the Conference on the Preparing of Shaped Crystals and Parts by the Stepanov Method and their Application in the Economy*, 1989, Ioffe Phys. Techn. Inst. Acad. Sci. of SSSR, Leningrad, pp. 265–270 (in Russian).

47. P. I. Antonov, L. M. Zatulovskii, A. S. Kostygov, D. I. Levinson, S. P. Nikanorov, V. V. Peller, V. A. Tatarchenko, and V. S. Yuferev. *Obtaining Shaped Single Crystals and Articles by Stepanov's Technique*, 1981, Nauka, Leningrad, USSR, pp. 218–252 (in Russian).

48. S. P. Nikanorov and V. V. Peller. "Peculiarities and perspective of shaped composites prepared on the basis of Stepanov's technique," in *Kinetics of Deformation and Fracture of Composites*, 1983, (S. P. Nikanorov, A. M. Leksovski, eds), Ioffe Physico-Technical Inst. of Acad. Sci. USSR, Leningrad, pp. 133–148.

49. R. M. Akhunov, B. L. Baskin, V. V. Peller, Yu. A. Fadin, and G. G. Khokhlov. "Strength characteristics of shaped boron-aluminum composites," Izv. Akad. Nauk SSSR, Ser. fiz. 1972, 49, pp. 2447–2456 (Bull. Acad. Sci. USSR, Phys. ser.).

50. G. G. Khokhlov, V. V. Peller, and Yu. A. Fadin. "Structure of matrix and conserved strength of boron fibers in shaped boron-aluminum composite products prepared by Stepanov's technique," Bull. Acad. Sci. USSR, Phys. ser. 1988, 52, pp. 2061–2067.

15

Low-g Crystallization for High-Tech Castings

HANS M. TENSI

Technical University of Munich, Munich, Germany

1 INTRODUCTION

More than 350 years ago an artist illustrated the desire of mankind to explore the universe through space exploration (Fig. 1) [1]. This required the scientist to leave the world with which he was familiar to learn many new and unimaginable, miraculous and possibly even frightening things but which would also provide the potential to impart wisdom and a better understanding of the intimate world.

This was the situation, when man first started travelling into space in 1961. In the beginning the primary emphasis was to develop technology to take the cosmonauts and the astronauts into space and bring them back to earth safely. However, even during these early stages of space exploration, scientists began to demand the opportunity to conduct experiments to obtain a new or better understanding of physical, chemical and biological events occurring under the microgravity conditions of space. The objective of this work was to obtain sufficient knowledge to control fundamental properties in such a way to permit the development of new processes and/or "new materials." Of course, nobody really expected this work to lead to the addition of new elements to the Periodic Table.

For example, an important objective of material science in space is the investigation of the influence of space-conditions on the crystallization of metallic microstructures. Although castings have been used since prehistoric times, the knowledge of how to influence these microstructures and their correlation with mechanical properties is not well understood even today [2]. Improvements of the quality of AlSi-castings could not have been realized without the fundamental knowledge gained by so-called μg-experiments or only with a much greater number of empirical experiments under the much greater gravity conditions present on earth.

Figure 1 "The Doubter", wood-block printing from an unknown artist 1520–1530. (From Ref. 1.)

Experiments in the space are called μg-experiments, because the "1 g" acceleration on earth is not exactly reduced to zero while orbiting the earth over a distance of about 300 km; a residual acceleration of about 10^{-3} to 10^{-4} × "1 g" is caused by atmosphere friction and movements of the space shuttle while being maneuvered.

One of the first applications of μg-experiments was to develop safety castings for aerospace applications and microgravity conditions. This led to the subsequent development of the first commercial car to be constructed completely from aluminum, the "AUDI A8" shown in Fig. 2. In this chapter, the development of μg-crystallization of aluminum alloy castings will be discussed.

2 APPLICATION OF FUNDAMENTAL SCIENTIFIC KNOWLEDGE FOR INDUSTRIAL PROCESS DEVELOPMENT

The influence of crystallization conditions and alloying elements on casting morphology are not known because the mechanisms of formation casting morphologies is largely unknown. Quality improvement of castings requires a detailed answer to the following questions:

1. Which crystallization parameters and which chemical additions to the casting alloy composition influence on the mechanical properties?
2. Can the influence of these parameters on mechanical properties be quantified?
3. Is there an additional effect of these parameters on the mechanical attributes, and very importantly, what limitations must be considered for the different parameters?
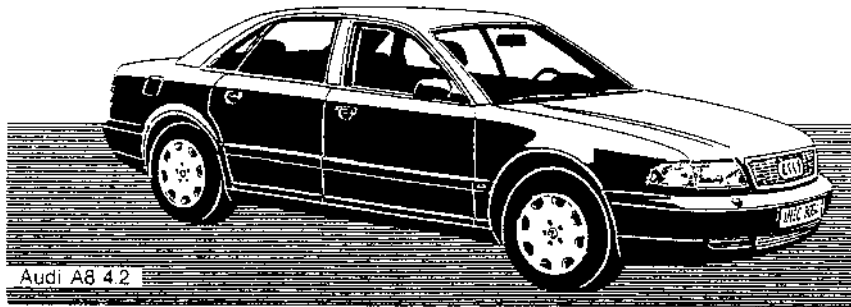
Figure 2 AUDI A8; the pressure die castings in the "space frame" structure of this car have to meet extreme qualitative safety demands. (Courtesy of AUDI AG, Ingolstadt, Germany.)
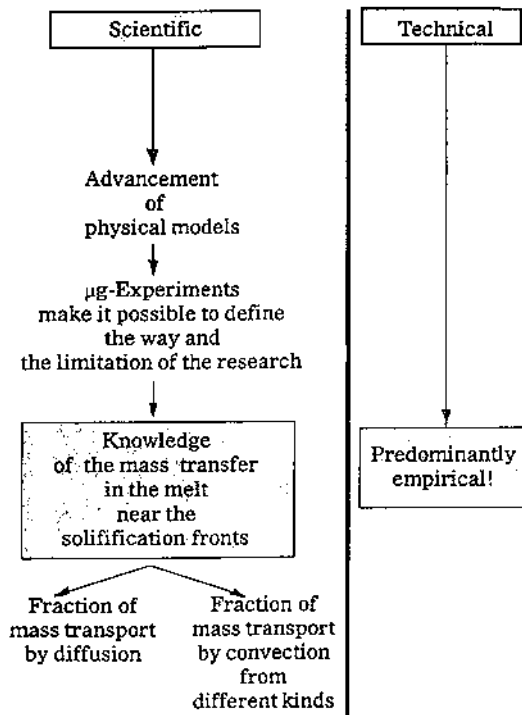
Figure 3 Present situation in developing high strength castings in the technical and scientific line.

One illustration of this is the mass transport during crystallization. Figure 3 visualizes this problem with the development of high-strength castings. However, this problem only be resolved with the use of μg-experiments to determine how mass transport in the melt in the vicinity of the solidification front is influenced by diffusion **and** by convection. For this work, the kinetics of the crystallization process must be explored by comparison of 1 g-experiments and μg-experiments, under identical crystallization parameters such as velocity of the solidification front

and the temperature gradient preceeding it. In space, convection caused by gravity is eliminated; only the so-called microconvection in the vicinity of the solidification front and the effect of diffusion are active for the mass transport. Under 1 g conditions, the influence of diffusion on the crystallization effects is superimposed by the influence of different kinds of convective mass transport.

Returning to the question of the specific material structure parameter influence on the mechanical properties: Many metallographic structures exist in the cast material which are visible with an optical microscope (OM). Submicroscopic structures are only visible under conditions of very high magnifications (over 10^3) and using specially prepared probes. This research can be performed using electron microscopes such as transmission (TEM) and scanning electronic microscopes (SEM). Quantitative determination of these structures must be carefully carried out and is to be related with the most important mechanical values like ultimate strength (R_m), yield strength (R_p) and the fracture strain (A_g). With the knowledge of the influence of crystallization parameters on material structures and their corresponding influence on mechanical strength, mechanical behavior at different positions in a cast part can be defined from the local different crystallization parameters in addition to localized different material structures! This is illustrated schematically in Fig. 4.

An important additional effect is provided by the type of macroscopic solidification occurring within the part. It is important to distinguish between the conventional solidification (so-called undirectional crystallization) and the nor-
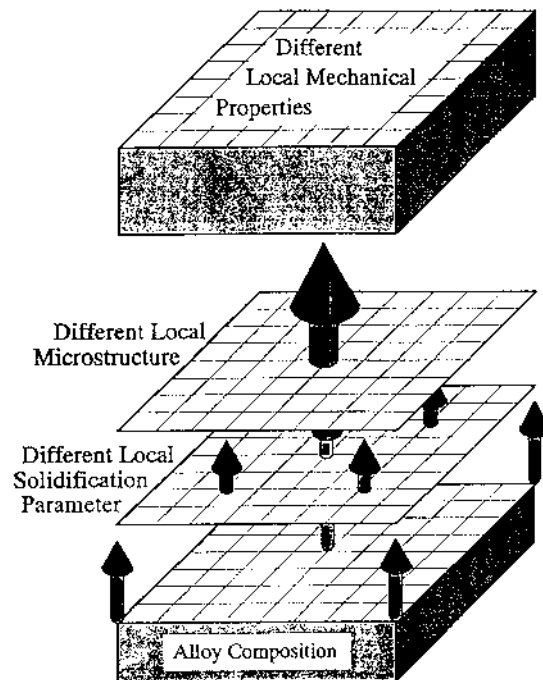
Figure 4   Local different interaction of crystallization, microstructure and mechanical properties having a defined alloy composition (schematical).
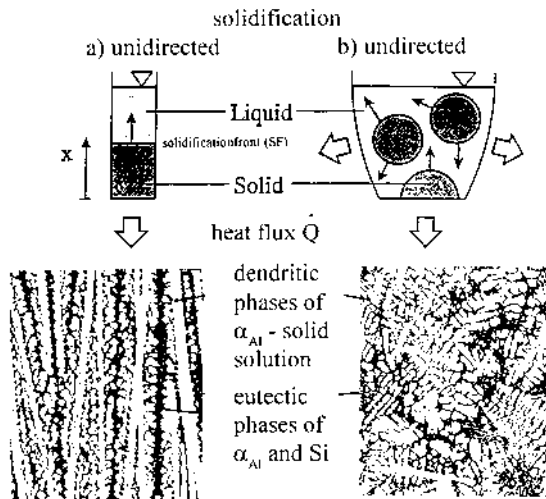
Figure 5 Metallographic structures of an unidirectionally (a) and undirectionally (b) crystallized AlSi 7-alloy with the local solidification times $t_f = 333$ sec (a) and 280 sec (b); the schematic figures show the different geometry and growth direction of the solidification fronts. (From Ref. 2.)

mal solidification (unidirectional solidification). Figure 5(A) and (B) illustrates the OM structures of an un- and unidirectional solidified AlSi-alloy with 7 wt% Silicon, exhibiting nearly the same physical solidification parameters (local solidification time $t_L = 333$ sec for unidirectionally (A) and $t_L = 280$ sec for undirectionally (B) crystallized AlSi). The different macroscopic crystallization processes are also shown: For unidirectional solidification, only one solidification front runs through the melt; for undirectional solidification, a number of nuclei are created from which the solidification fronts are moving through the melt toward each other. Of course, if the morphology of the metallographic structures influences the mechanical behavior of cast materials, the straightening of structures will also influence it! The main influence by the type of macroscopic solidification is provided on the "endurance fatigue life." Further, the unavoidable presence of "micro shrink holes" in the conventional cast parts exhibits a disadvantageous effect on mechanical properties. Figure 6 is an SEM picture of a shrink hole in cast AlSi 7 alloy; this "micro shrink hole" illustrates the sharp notches, which increase the localized mechanical stresses.

To characterize the crystallization parameters, having an unidirectional solidifying melt, the velocity V_{SF} [m/sec] of the solidification front (SF) and the temperature gradient G_{SF} [K/sec] in the melt in front of the SF must be precisely measured. The magnitude of these two parameters on the crystallized metallographic structures is illustrated by three examples in Fig. 7. One condition is with special crystallization parameters, low values of V_{SF} and high values of G_{SF}, where only one solidification front with a solidified volume consisting of one phase. A so-called single crystal (Fig. 7(A)) is obtained. Increasing V_{SF} and/or decreasing G_{SF} produces a cellular structure of the solidification front and the crystallized volume
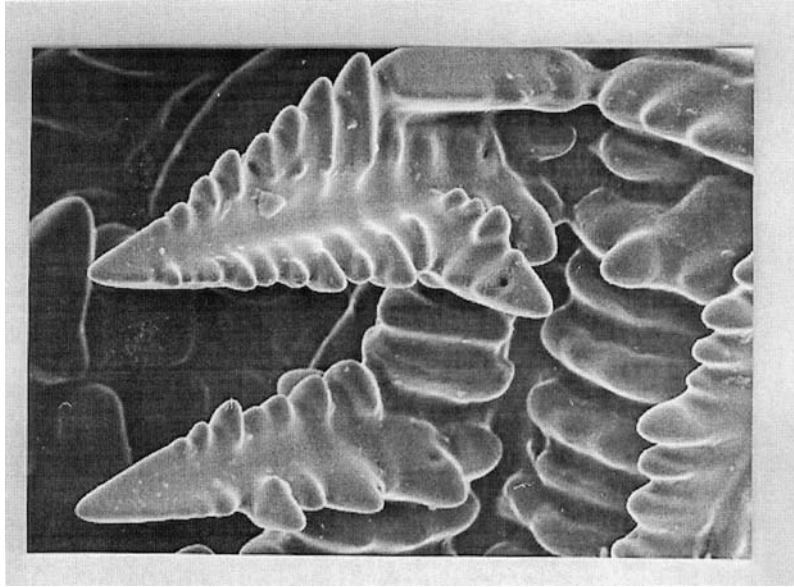
Figure 6   Wall of a shrink hole with dendrites in cast AlSi-alloy (SEM picture; ca. 1500×).

changes to a cellular morphology as shown in Fig. (B). Further increasing V_{SF} produces a dendritic solidification front and the mostly existing dendritic structures with eutectics in technical cast volumes is observed as illustrated in Fig. 7(C). Additional experiments to be described subsequently, were performed under μg-conditions in the space with the pure alloy AlCu 0.3 (0.3 wt% Copper) to determine the effect of mass transport in the melt in the vicinity of the solidification front; see Fig. 3? Of course, these solidification parameters can not be defined during an undirectional solidification! Therefore the so-called ''local solidification time'' t_1 [sec] is measured. During the time t_1 the temperature drops down from the liquidus temperature T_L [°C] of the alloy up to their eutectical temperature T_E [°C]. Between these temperature limits, the solidification of the melt runs out completely with the (linearized) cooling velocity T [K/sec]. The t_1 time can be measured easily by a so-called thermo-analysis. To compare the crystallized volumes of un- and unidirectionally solidified cast materials with their different crystallization parameters, the following relations are helpful:

$$t_1 = (T_L - T_E)/T \tag{1}$$
$$T = G_{EF} \times v_{SF} \tag{2}$$

and from (1) and (2) using the fact that $(T_L - T_E)$ is constant for a defined alloy follows:

$$t_1 = \text{const} \, (G_{EF} \times v_{SF})^{-1}$$
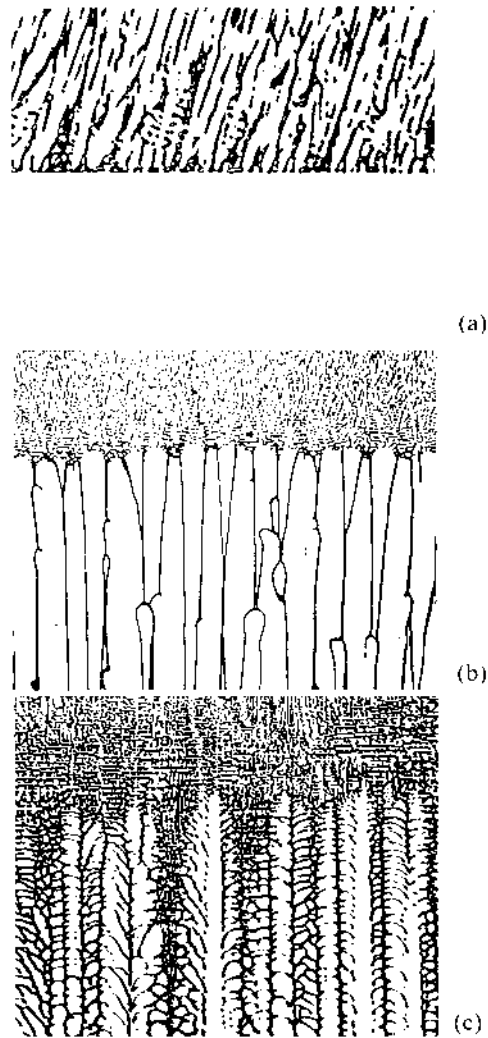
Figure 7 Metallographic longitudinal microsections of three unidirectionally solidified probes of the same AlCu0.3 alloy. In each case: above quenched liquid, below unidirectionally solidified volume under 1 g conditions [3]; (a) smooth SF: $V_{SF} = 0.51$ mm/min; $G_{SF} = 11.2$ K/mm (M = 73:1); (b) cellular SF: $V_{SF} = 0.73$ mm/min; $G_{SF} = 9.2$ K/mm (M = 37:1); (c) dendritic SF: $V_{SF} = 2.2$ mm/min; $G_{SF} = 6.4$ K/mm (M = 76:1).

Figures 8 and 9 illustrates examples of the morphology of the so-called dendrites and the eutectic volume between them. The dendrites crystallize first from the melt and consist mainly from α-Aluminum-phases with a very low content of alloying elements. Their geometry is given by the crystallographic structure (face centered cubic–ffc) and their morphology by the crystallization parameters. Figure 8 illustrates the (primary) dendrite spacing "e" and the (secondary) dendrite arm spacing
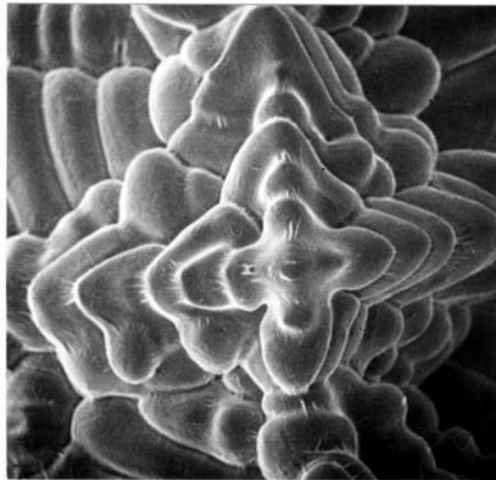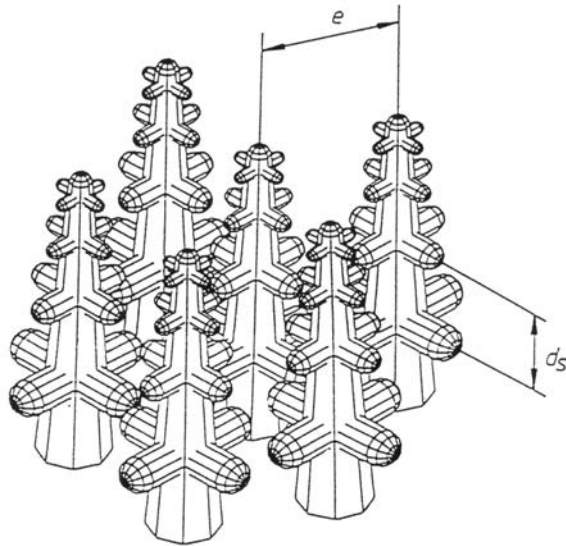
Figure 8 Schematic view of the dendritic structural characteristics in the stage of unidirectional solidification.

"d_s". Of course, the determination of "e" is only possible having unidirectional solidified cast materials. As will be shown later, "e" and "d_s" are influenced by the solidification parameters **and** by the μg-conditions.

Experimental and theoretical research has shown that there exists a strong influence of the crystallization velocity T on the values "e" and "d_s" which are determined from Eq. (3) and (4):

$$e = \text{const} \times T^{-0.5} \tag{3}$$
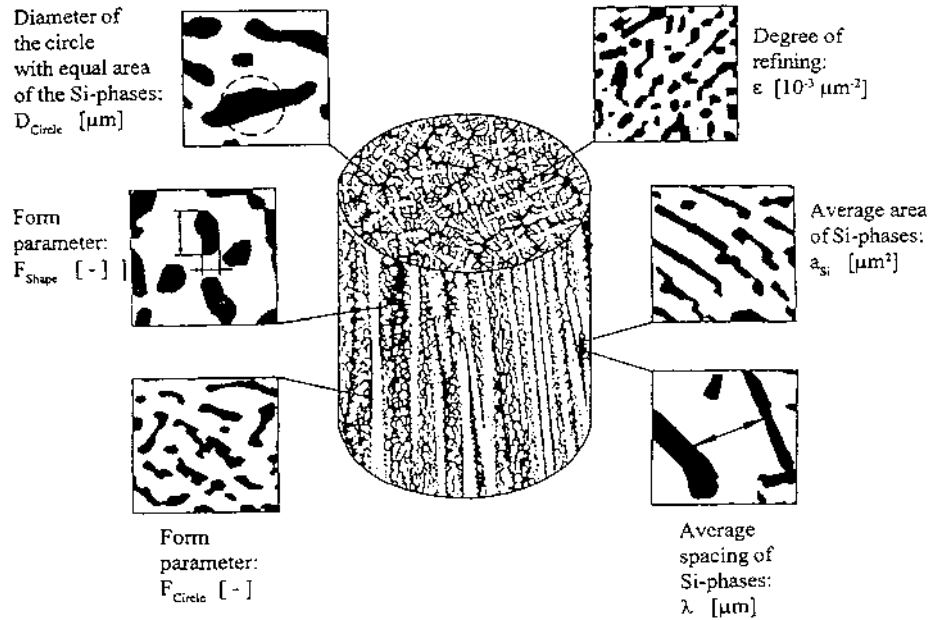
Figure 9 Schematic view of the interdendritic eutectic structural characteristics.

where T = dT/dt [K/sec] in the temperature region between start and end of solidification;

  V_{SF} = velocity of the solidification front [m/sec],

  G_{SF} = temperature gradient in front of the solidification front [K/mm],

and

$$d_s = B \times (M \times t_f)^{0.3...0.4} \tag{4}$$

where t_l = Local coarsening time [sec]; this is the time during which the dendrites are surrounded by liquid phases. The coarsening proceeds by minimizing the total energy.

  B = a constant geometric factor 4.36 ... 5.5

  M = a material factor to be calculated from the physical and metallurgical values of the melt:

$$M = \{2 \times \sigma \times D_L \ln(c_E/c_0)\}/\{\Delta H \times (1 - K_0) \times m_L \times (c_E - c_0)\};$$

where σ = surface tension [N/m],

  D_L = diffusion coefficient [cm^2/sec],

  c_E and c_0 = alloying concentration (here silicon) at the eutectic point and the initial concentration,

  ΔH = heat of fusion,

  K_0 = distribution coefficient,

  m_L = gradient of the liquidus line.

Using these equation, M calculated for AlSi 7 is 16.3×10^{-12} [cm^3/sec].

The evaluation of the eutectic morphologies are shown in Fig. 9. The details of the eutectic (having different magnifications) explain the evaluated morphology values like "Silicon content of eutectic", "volume fraction of eutectic", "degree of refining ε", "median section a_{Si}" and "shape factor F_{shape}" of cut Silicon phases and the "average eutectic spacing λ". Because the "average eutectic spacing λ" (the free path of the so-called dislocations in the α-Al-phases) has a dominant influence on the mechanical values, only λ will be used here. Influence of the cooling rate T ($= V_{SF} \times G_{SF}$) on the λ-values is given in Eq. (5).

$$\lambda = \text{const} \times (V_{SF} \times G_{SF})^{-n} \tag{5}$$

where $= 0.5$ for AlSi 7 (measured values for n from 0.44 to 0.62 for technical AlSi-alloys with Silicon contents in the range between 5 and 11 wt%)

The magnitude of the influence of these microscopic structures by the solidification parameters is illustrated in Fig. 10 where the dependance of "e" and "d_s", of T for six alloys based on the basic (pure) AlSi 7, beginning with "A357" and with 5 modification of additional alloying elements. In the area of lower T-values (between 40 to about 300 [K/sec]), where the influence is strong, alloying elements exhibit no effect. An additional comparison is provided by two pure binary AlSi alloys (AlSi 7 and AlSi 11) and the corresponding pure ternary alloys with different additions with Magnesia and Antimony. Figure 11 show the comparable diagrams where the influence of the distance from the eutectic Silicon concentration is clear!

Although there is no influence of alloying elements on dendrite morphology, the effect of alloying elements and cooling rate T on the eutecticum morphology is given in Fig. 12 for 1.0 wt% Copper added to a A357 alloy and for AlSi7Mg (corresponding to A357). Micrographs of the eutectic areas for different T-values (or put into words other for different wall thicknesses of the casting) show the change of the geometric structures of the Silicon phases. For example the change of the median section of a_{Si} is evaluated here. By the addition of copper to A357 in the area of low T-values (or high wall thickness), the a_{Si}-values are higher in the range of $40 < T < 200$ [K/min].

The isolated influence of the microstructures "d_s" and "λ" on the mechanical value R_m is exemplarily illustrated in Fig. 13. In both cases, the tensile strength increases with decreasing "d_s" and decreasing "λ". The following half-empirical relation between the mechanical value R_m and the morphology values d_s and λ was found for hypoeutectic AlSi alloys:

$$R_m(C_o, d_s, \lambda) = K_{Conc.}(C_o) + K_{Dendr.}(C_o) \times d_s^{-0.5} + K_{Eut.} \times \lambda^{-0.5} \tag{6}$$

where R_m = tensile strength (calculated); C_o = Si-concentration; d_s = dendrite arm spacing (secondary dendrite arm spacing); λ = eutectic spacing of Si-phases; $K_{conc.}$ = a constant, depending on Si-concentration (for 7 wt% $< C_o < 11$ wt% $K_{conc.} = 65$); $K_{Dendr.}$ = a constant, depending on Si-concentration (for 7 wt% $< C_o < 11$ wt% $K_{Dendr.} = 500$); $K_{eut.} = 115$.
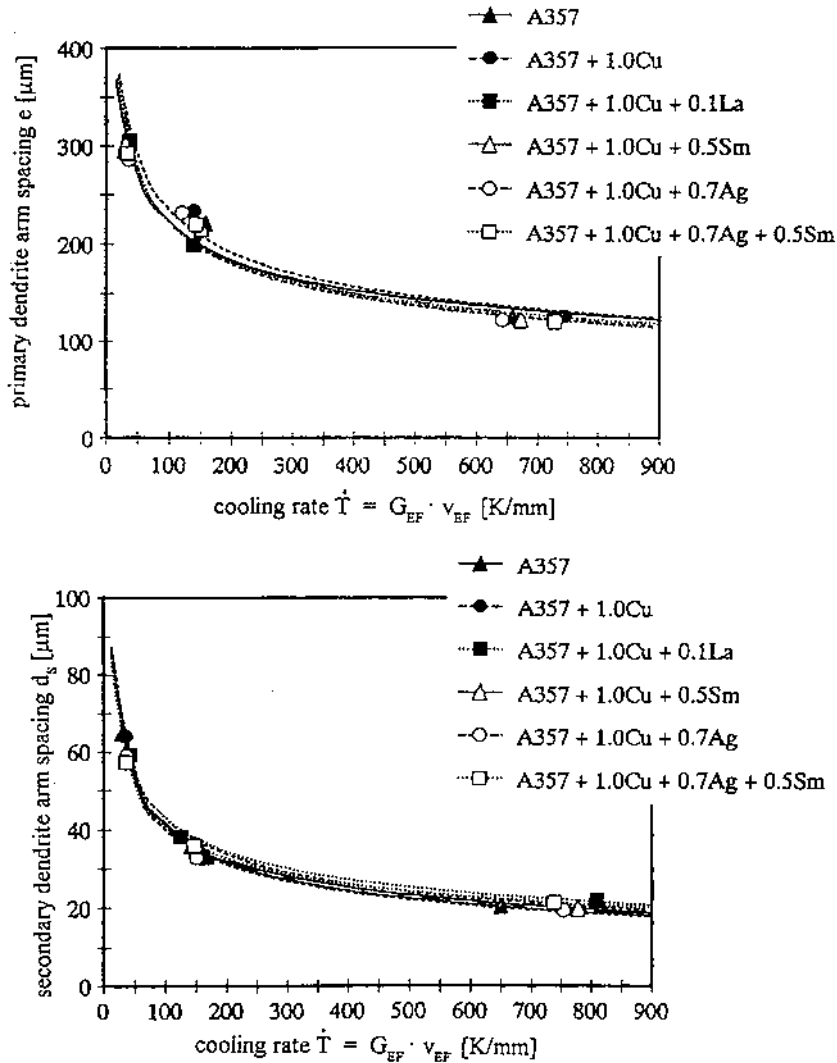
Figure 10 Influence of cooling rate T = G × v on the primary and secondary dendrite spacings for 6 technical alloys with constant Si-contents.

Of course the relationship between the OM-morphology and the the mechanical values works correctly only without the effect of age-hardening of the α-Al-phases (the α-phases of the dendrite volume and in the eutectic mixture). This means that pure AlSi-alloys with 7 and 11 wt% Silicon contents and the corresponding AlSi alloys with different Magnesium and Antimony additions (in overaged stage) show an excellent relation between measured R_m-values and the calculated R_m-values, using the OM-structures, which can be evaluated quantitatively. An example is given in Fig. 14.

The interaction of the alloying composition, the crystallization parameters, the OM- and SEM-microstructures without and with heat treatment, with the mechan-
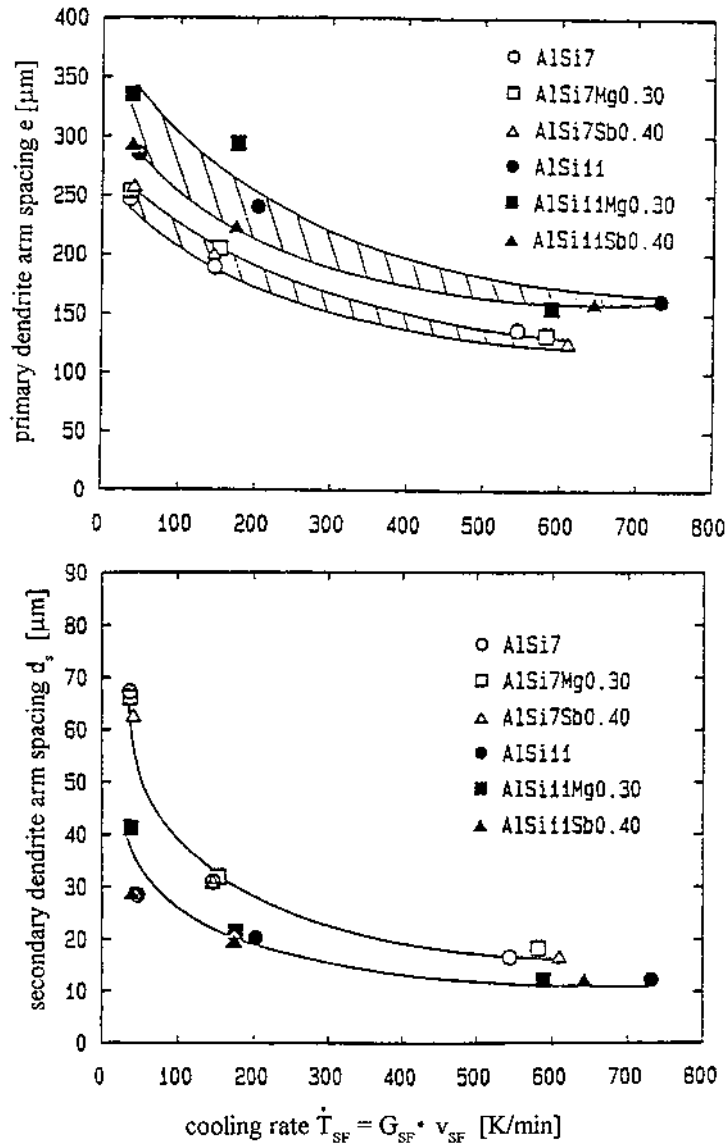
Figure 11 Influence of cooling rate T = G × v on the primary "e" and secondary "d$_s$" dendrite spacings for 6 pure binary and ternary alloys with two Si-contents.

ical behavior of the cast material are shown in Fig. 15. These are the steps used for improving the commercial A357 alloy for a cast parts for Airbus and the AUDI A8. It should be noted here that the cooling down of the cast volume after finishing the solidification must be taken into account as a heat treatment, which is difficult to characterize because of the local differences in the temperature-time-run. All heat treatments influence the morphology of the Silicon phases in the eutectic volume and the solution as well as the precipitation of alloying elements in all α -Al-phases; but the values "e" and "d$_s$" of the dendrites remain unchanged!
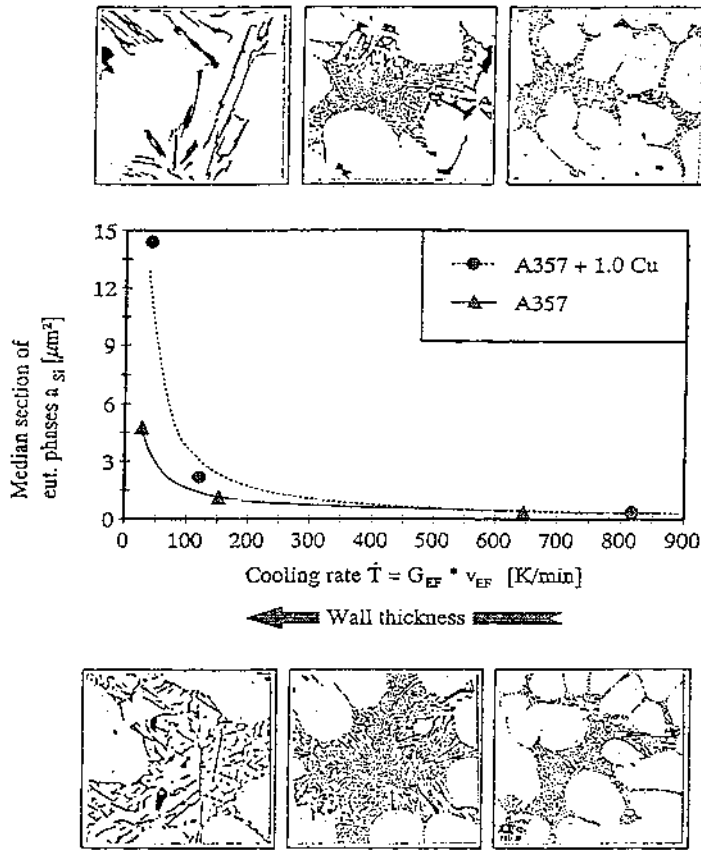
Figure 12 Eutectic microstructure influenced by the cooling rate T (or put into other words by the wall thickness of the castings.)
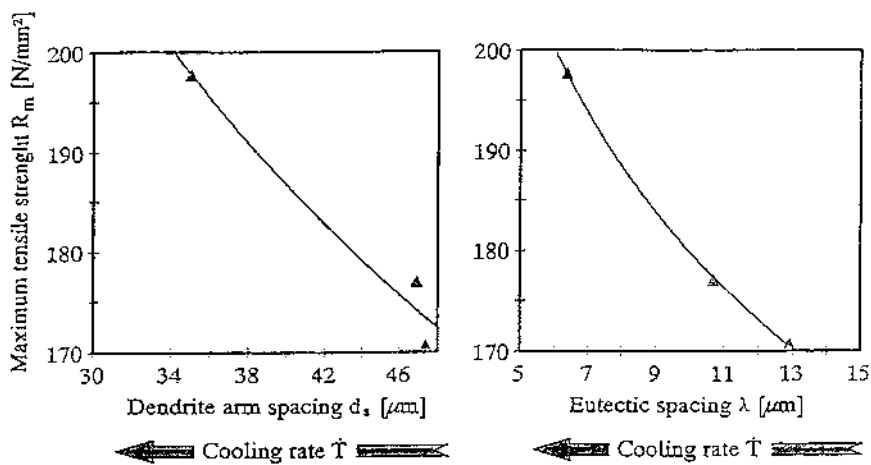
Figure 13 Examples for the relation between the microstructural parameters "d_s" and "λ" and the mechanical property R_m.
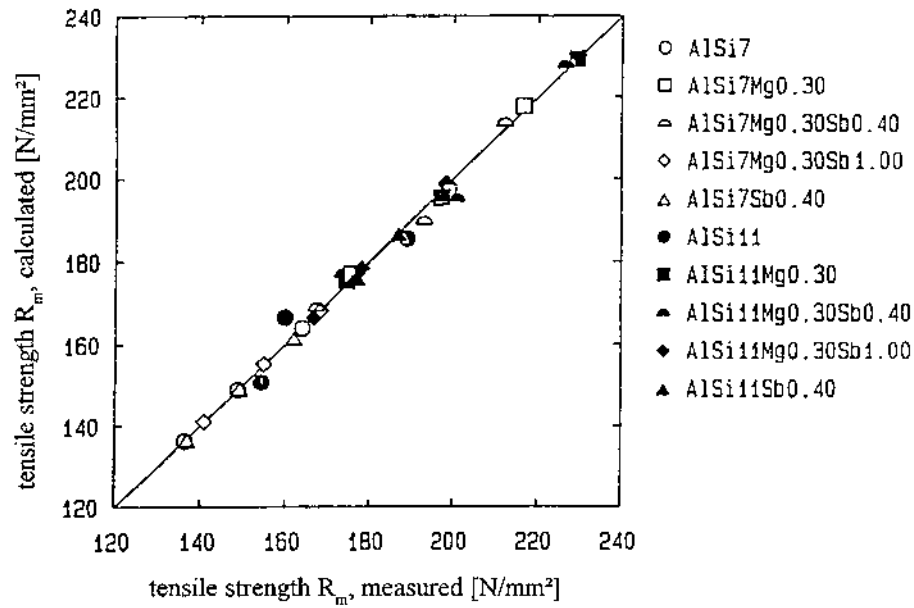
Figure 14 Relationship between the measured tensile strength R_m and, using the OM structures, calculated tensile strength R_m of unidirectionally crystallized two pure binary and eight ternary AlSi-alloys with different wt% of Si [7, 11], Sb [0.0, 0.4, 1.0] and Mg [0.0, 0.3].
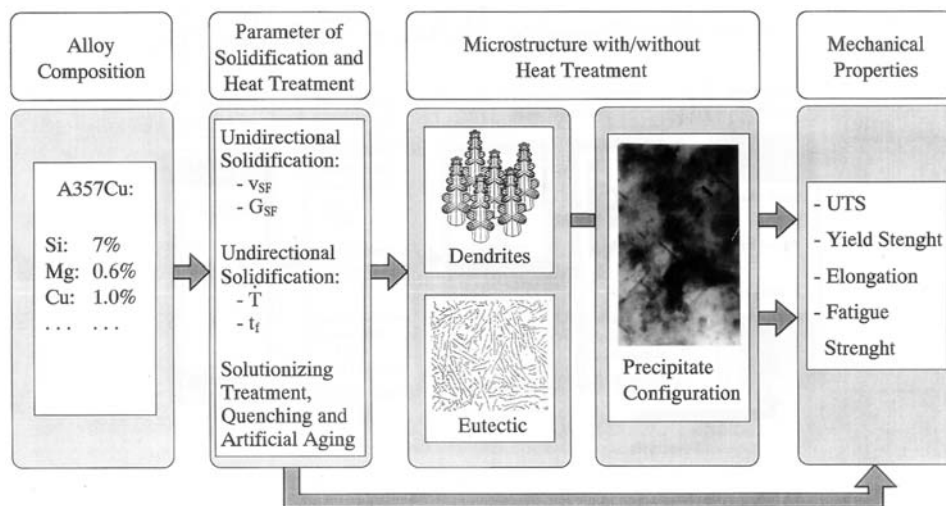
Figure 15 Interaction of alloy composition, crystallization parameters, OM- and SEM-microstructures with and without heat treatment with the mechanical values of cast parts.

3 ADDITIONAL KNOWLEDGE FROM THE μg-EXPERIMENTS IN SPACE

It has been shown that dendrite morphology and the eutectic phases are influenced strongly by the crystallization parameters. The best way to obtain precise correlations is to perform unidirectional crystallization experiments. The crystallization parameters "velocity of the solidification front" V_{EF} and the "temperature gradient at this front" G_{EF} can be measured with high precision (Lit). An additional experimental variation (important to get much more information out of one experiment!) is the sudden stopping of this solidification front by quenching the residual melt volume. This provides much more additional information from a single experiment. Figure 16 shows the different modes of operation of the experimental equipment "GFQ" (**G**radient **F**urnace with **Q**uenching **D**evices) in the space shuttle: Fig. 16A illustrates the GFQ during unidirectional crystallizing the melt; the cylindric crucible containing the melt is fixed and the combination "furnace" (Q_{in}) and cooler (Q_{out}) are running with the velocity $V_{Furnace}$ along the probe. The solidification front SF is running "up" (in space there is no up and down!) with V_{SF}. In Fig. 16(B), having enough solidified material for testing, the residual melt is quenched (Q_{quench}) by spray water from the cooler, which was pneumatic removed quickly at the position of the residual melt. The details of the quenched SF is explained in Fig. 16(C): A section diameter of the stopped SF shows the unidirectional solidified and undirectional quenched volume as well as center of the probe with the thermocouples (here four pieces) which were used to calculate V_{SF} and G_{SF} (lit).
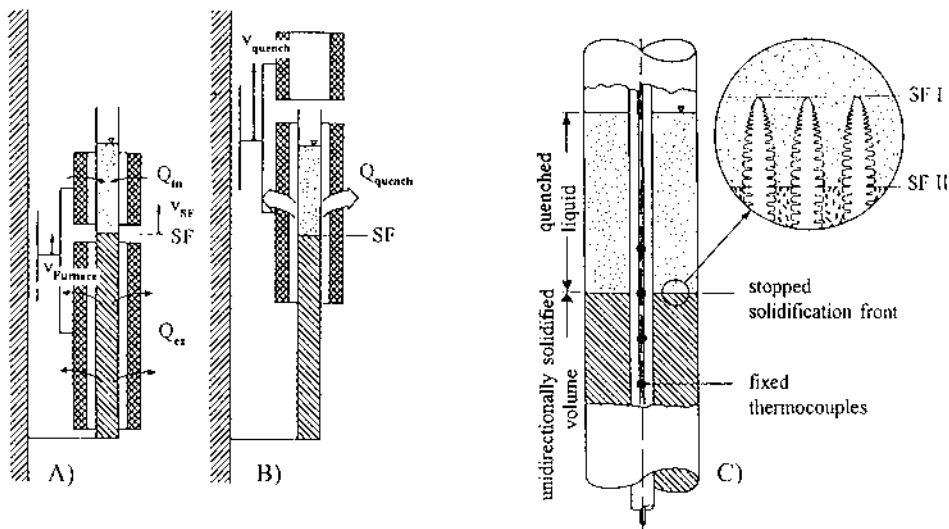
Figure 16 Gradient Furnace with Quenching Devices (GFQ) schematic in the stage of unidirectional solidification (A) and during quenching the residual melt and freezing the solidification with front (B) (see also Fig. 7). (C) shows schematically a longitudinal section through the unidirectionally solidifying probe in the area of SF's position with the central points of temperature measurements and a magnification of the solidification front during dendritic solidification with the two SFs.

With sufficient magnification of this SF, it is seen that it consists of two SFs! At SF I is the position of the top of the dendrites and at SF II the interdendritic volume crystallized with eutectic morphology (consisting of α-Al-phases and Si-phases). In the interval between SF I and SF II, the dendrite-arms are coarsening to their final size at the point of SF II. Because every position Δx in this range is equal to a defined coarsening time t_c (to be calculated with V_{SF}), with one experiment the coarsening of dendrites (this means the increasing of value d_s) for different solidification experiments can be determined according Eq. (7).

$$t_C = \Delta x / v_{SF} \; [s] \tag{7}$$

where $\Delta x =$ distance from the top of the dendrites (i.e.: I SF)

Microgravity experiments were used to address the following questions:

1. Is there an influence of μg-conditions on the distribution of alloying elements in front of a planar SF in comparison to the situation on earth (i.e. 1 g-conditions)?

    If yes, the information on the role diffusion and convection on the mass transport in relation to material structure is obtained.

2. Are there any differences in the dendrite morphology and eutectic morphology under μg-conditions?

    If yes, a correlation between mechanical properties and metallographic morphology is possible which will permit the establishment of the necessary criteria to optimize alloy composition and solidification parameters for a specific application.

To address these questions, experiments were conducted with pure AlCu and AlSi alloys in the D1- and D2-Spacelab-Missions in 1985 and 1991 and the FOTON 10- and 11-Missions in 1996 and 1997.

The first knowledge which was to be gained was the influence of material transport at the SF. Figure 17 A shows that the metallographic section diameter through an unidirectional solidified AlCu0.3 alloy in the area of the quenched SF (the central channel with the thermocouples is on the upper line, the limitation to the crucible at the lower line). The unidirectionally solidified phase has no OM-visible structure, because the solidified volume is a single crystal. The quenched melt shows the morphology of rapid crystallized volume.

Crystallization experiments with the identical parameter V_{SF} and G_{SF} were performed under 1 g- and μg-conditions (see Fig. 17(B)). By microanalysis, the distribution of Cu in the crystallization direction was determined: At the point of the SF, the discontinuous increase in concentration is related to the distribution coefficient K_0 which describes the difference in solubility of Cu in the solid and liquid phases of Al. The most important information is the changing in width δ of the so-called concentration amount in front of the SF. Figure 17(B) shows the value of δ is much higher under μg-condition than under 1 g (9 mm in comparison to 3 mm).

Using the theoretical relationship between the concentration gradient and the "mass transport coefficient" $D^{integral}$, containing the mass transport by diffusion as well as by convection, the course of $D^{integral}$ (ξ) in front of the SF under μg shows

a strong decrease from about 4.5×10^{-5} to 0.8×10^{-5} cm^2/sec. This is the opposite of what is observed under 1 g-conditions. D$^{\text{integral}}$ under 1 g originally exhibits at a greater distance from the SF a higher value than under μg (6.0×10^{-5} cm^2/sec) and the slope at the SF is only 5.5×10^{-5} cm^2/sec as shown in Fig. 17(C). These super-elevations of D$^{\text{integral}}$ are caused by the gravity-driven convection in the melt on earth. It is a well known fact that the convection in liquid take the greater part of the mass transport in liquid. For the formation of structures during solidification of alloys, the integral mass transport in the vicinity of the SF is very important because of the necessity for decomposition within this part of the melt to obtain a synchronous growth of different phases for example like α-Al-phases and Si-phases in an AlSi alloy.

Figure 18 shows the calculated distribution of Silicon in the melt in the vicinity of the eutectic solidification front (II. SF). In a large distance of the top of the dendrites (I. SF) holds. grad $C_{\text{Si}} = 0$ beginning with the primary crystallization of the α-phases, grad C_{Si} becomes $\neq 0$. In the interdendritic melt in front of the II. SF growth an axial as well as a lateral concentration gradient ($\delta C_{\text{Si}}/\delta z \neq 0$ and $\delta C_{\text{Si}}/\delta y \neq 0$), indicating that there is both an axial and a lateral mass transport.
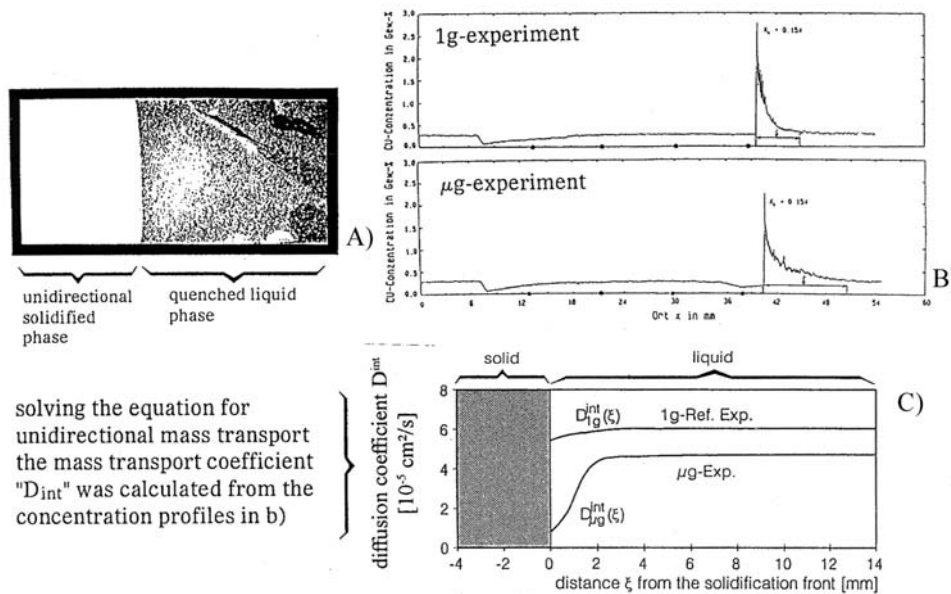
Figure 17 Experimental results from the unidirectional solidification of a pure AlCu 0.3 alloy during the D1-Mission in 1985: (A) metallographic longitudinal section in the area of a planar SF (see also Fig. 7) with the structure of the rapidly quenched residual melt in front of the SF; (B) Micro-analysis of the Cu content behind (unidirectionally crystallized) and in front of the SF in two probes; the above under earth conditions and the lower under μ g conditions crystallized under the same solidification parameters V$_{\text{SF}}$ and G$_{\text{SF}}$ (so-called reference exp.); the important difference is the amount of Cu concentration in front of the SF! (C) From (B) calculated the integral mass transport coefficients D$^{\text{int}}_{1g}$ (ξ) and D$^{\text{int}}$\mug (ξ) in front of the SF.
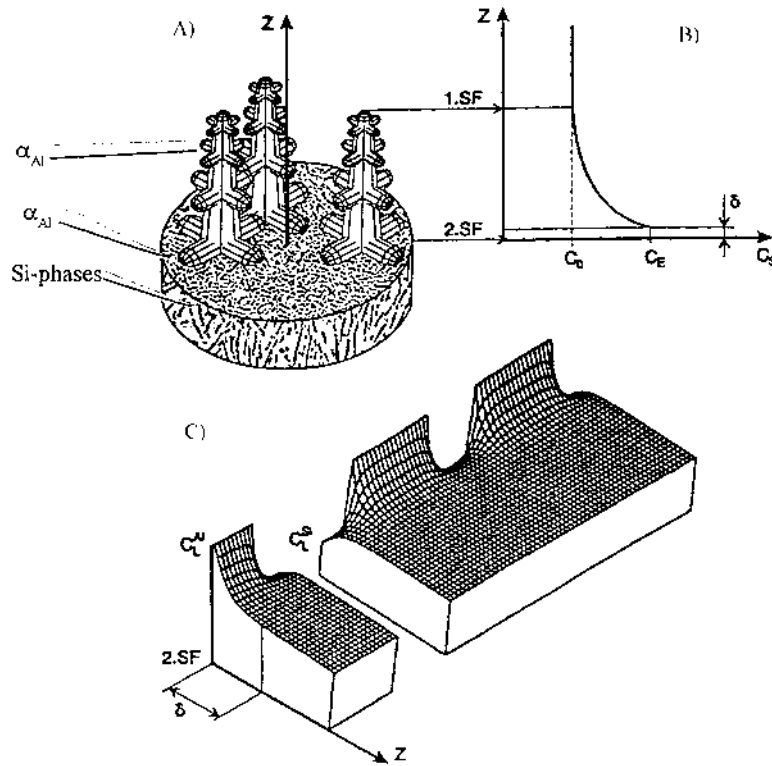
Figure 18 Unidirectional solidification of AlSi alloy with the distribution of the alloying element Si in the Al-melt in front of the I and II Solidification front (semi-schematic). (A) Growth of dendrites and the eutecticum; the residual melt between the dendrites and in front of the I. SF is removed; (B) Alloying element distribution $C_{si}(Z)$ in the residual melt between the dendrites and in front of the I SF; (C) Three dimensional alloying element distribution $C_{si}(z; x)$ in front of the II SF (eutectic solidification front) with axial and lateral concentration gradients within the so-called "diffusion boundary layer" δ , corresponding to the α - and Si-phases of the eutecticum.

Only by these mass fluxes, the extreme differences of Si-concentration in the α-phases and Si-phases of the eutectic volume can be created. Of course the high concentration gradients in the vicinity of the II. SF will be influenced strongly by every change of convection in the melt.

In the case where the macrocrystallization parameters (v_{SF} and G_{SF}) are the same under μg- and 1 g-conditions, the distances of such decompositions becomes higher by the increased value of $D^{integral}$, influenced of buoyancy driven convection (1 g-conditions). This should have an influence on the eutectic crystallization as well as on the coarsening of dendrites, because both processes depend on the mass transport at the vicinity of the SFs.

From the D1-mission, the influence of μg-conditions on the growth and the coarsening of dendrites in a pure AlSi 7 alloy was determined: Fig. 19 shows the longitudinal and transversal metallographic sections in a probe crystallized under

(A)

(B)
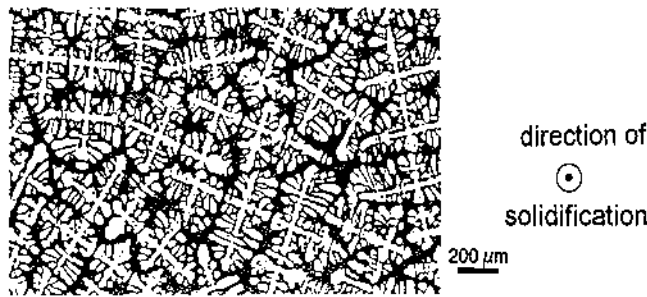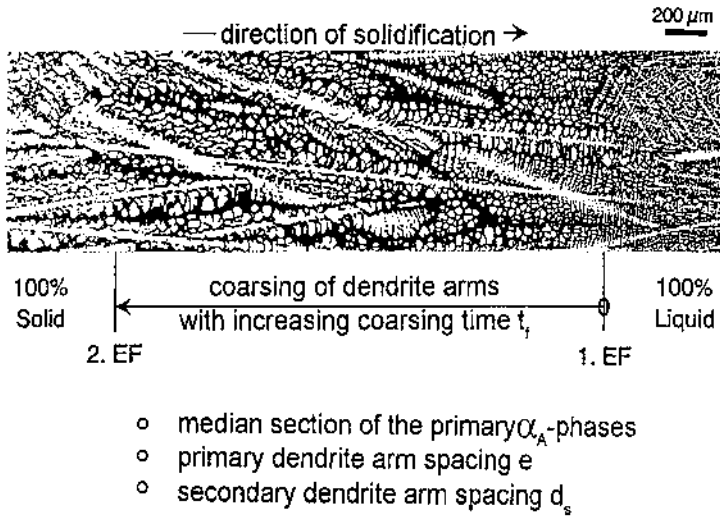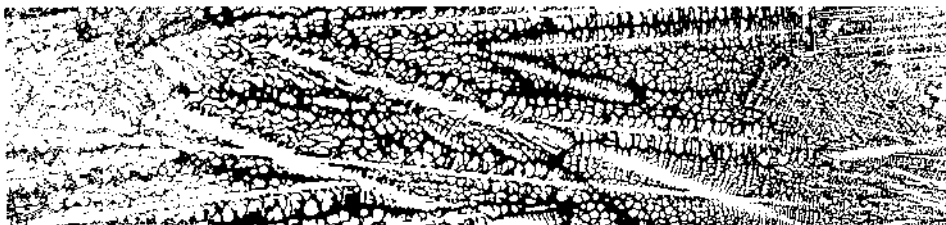
Figure 19 Under μg conditions (D1-Spacelab-Mission) unidirectional solidified pure AlSi 7 alloy. (A) Metallographic longitudinal microsections in the area of the two SF of the probe; indicated are the positions of I and II SF and the area of coarsening of the dendrites between (the volume of solid phases increases from 0% at I SF up to 100% at II SF); at the left side: 100% unidirectionally solidified volume, at the right side: 100% quenched melt; (B) Metallographic cross microsection in the area between I and II SF; the stem of the dendrites are cut, between the dendrites the quenched interdendritical residual melt (black).

μg with the parameter $V_{SF} = 5.2$ [mm/min] and $G_{SF} = 15.9$ [K/mm]. The longitudinal metallographic section corresponds to the schematic picture of the SF in Fig. 16. The positions of SF I and SF II are marked as well as the region, in which the distance d_s of the second dendrite arms growth up (coarsens). At different points in this region (this means at different coarsening times t_c), the distances d_s of dendrites were measured at different levels of newly produced metallographic planes (so-called "step-metallography"). These values were correlated with the coarsening times t_c. Additionally the primary distance "e" of the dendrites was evaluated on the transversal sections and correlated with the solidification parameters V_{SF} and G_{SF}, corresponding with the dendrite growth model of HUNDT [lit]

A summary of the dendrite arm coarsening of only two experiments under μg- and 1 g-conditions with nearly the same crystallization parameter are presented in Fig. 20: As expected, the d_s values increase with growing coarsening times t_c. Because of a better recognizability in the two identical diagrams, the metallographic determined values d_s of the μg-probe are marked in the upper, and the corresponding values of the 1 g-probe are marked in the lower diagram. For all t_c values, the μg-material shows lower values. These differences decrease with higher V_{SF} values, because of an increasing of the so-called micro-convection in the area of SF I and SF II. As already shown in Fig. 13(A), mechanical strength increases with lower d_s values. Therefore, for this defined alloy, up to a coarsening time of 25 sec below the μg-slope, a so-called unattainable area of the spacings d_s can be defined. When developing a high strength material, this μg-line shows that better d_s values and in consequence better mechanical values, can not be achieved (see also Eq. (4))!
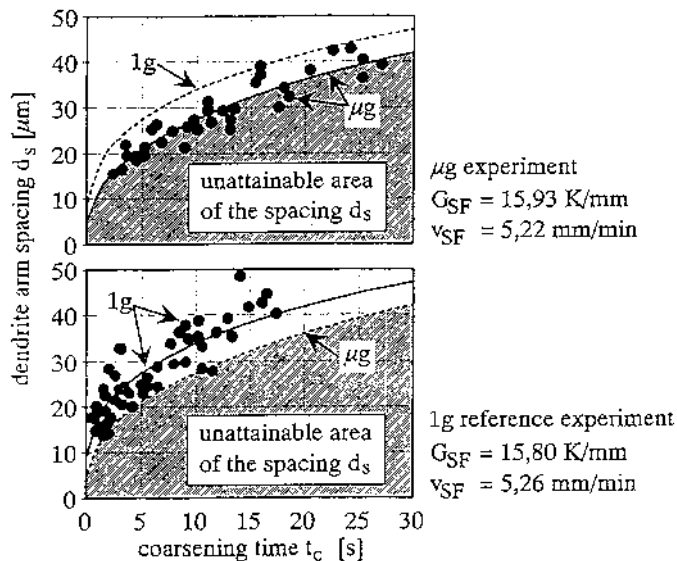
Figure 20 Dendrite arm spacing d_s in dependence of the coarsening time t_c of unidirectional solidified pure AlSi 7 alloy under 1 g-(reference) and μg-conditions (during the D1-Spacelab-Mission); the crystallization parameters are nearly the same.

To explain the dendrite coarsening, the mass transport in the vicinity of dendritic surface is examined using Eqs. (4), (8) and (9). The material constant "M" contains among other material values the (atomar) diffusion coefficient D_L in liquid. Because the integral mass transport $D^{integral}$ influences the coarsening, different components of the $D^{integral}$ must be considered. If, besides the atomar D_L, a micro-convection in the vicinity of dendrite surface is active (which would be created by the negative volume jump ΔV during the phase transition from liquid to solid), an additional mass transport by the coefficient $D_{\Delta V}$ is possible. This kind of micro-convection is also called "advection" because of the flux in direction to the solid phases. Having additional buoyancy driven convection (mostly called macro-convection), there is a further component in $D^{integral}$, described by the coefficient D_{conv}. With these assumptions, the $D^{integral}$ we get for μg-conditions is:

$$D^{integral} = D_1^{atom} + D_{\Delta V} \tag{8a}$$

and for 1 g-conditions the term

$$D^{integral} = D_1^{atom} + D_{\Delta V} + D_{conv} \tag{8b}$$

Because all other terms in "M" of Eq. (4) are constant, an integral M_{int} for μg conditions:

$$M_{int} = M_{atom} + M_{\Delta v} \tag{9a}$$

and 1 g conditions:

$$M_{int} = M_{atom} + M_{\Delta v} + M_{conv} \tag{9b}$$

is valid.

The measured values M_{int} for AlSi 7 alloy, processed during the D1- and D2-missions together with the calculated value M_{atom} (using the atomar diffusion coefficient D_1^{atom}) permit the determination of $M_{\Delta V}$ for different crystallization velocities V_{SF} under μg-conditions (see Fig. 21(A)) and further to determine the variation of M_{conv}, using the measured (constant) M_{int} under 1 g-conditions (see Fig. 20(B)). The values for $M_{\Delta V}$ are only dependant from the alloy and the crystallization parameters v_{SF} and G_{SF} (not from the buoyancy forces).

There is also an influence of the eutectic structures on the mechanical behavior. The influence of gravitational accelerated convection can be recognized under μg too.

Figure 22 provides an example of crystallization experiments conducted during the FOTON-missions. The pure near-eutectic AlSi 11 alloy was solidified under μg- and 1 g-conditions with a nearly constant temperature gradient G_{SF} (about 15 [K/mm]) and three groups of v_{SF}-velocities about 0.5, 1.0 and 1.9 [mm/min]. The metallographic pictures show the parts of the interdendritic eutecticum (without the bordering dendritic α-phases). It is obvious that with increasing v_{SF} the microstructures of the eutectica becomes more filigreed and additional that in comparison with the structures of the μg-probes the Si phases of the 1 g-probe are much rougher. Because of the strong differences in strength and ductility of the α-Al-phases and the Si-phases, this change in eutectic morphology influences the mechanical behavior also (Eq. (6)). In the following example (Fig. 23), the eutectic

μg   1g
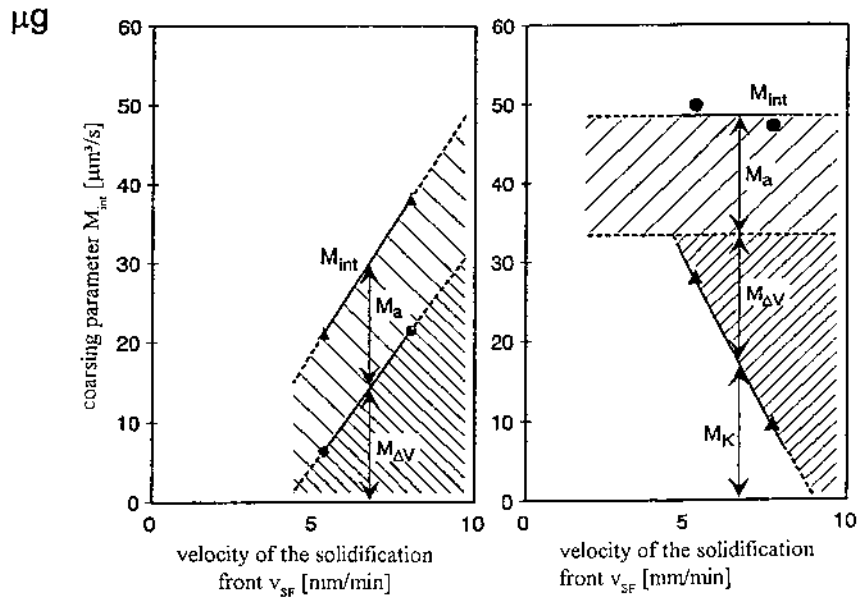
Figure 21 Influence of the solidification front velocity V_{SF} on the integral and the partial coarsening parameters M (see Eq. (7) under μg- and 1 g-conditions).

$v_{SF} = 0.4$ mm/min $v_{SF} = 0.9$ mm/min $v_{SF} = 1.9$ mm/min
$G_{SF} = 15.5$ K/mm $G_{SF} = 14.9$ K/mm $G_{SF} = 14.8$ K/mm

$v_{SF} = 0.5$ mm/min $v_{SF} = 1.1$ mm/min $v_{SF} = 1.8$ mm/min
$G_{SF} = 16.3$ K/mm $G_{SF} = 15.9$ K/mm $G_{SF} = 15.7$ K/mm
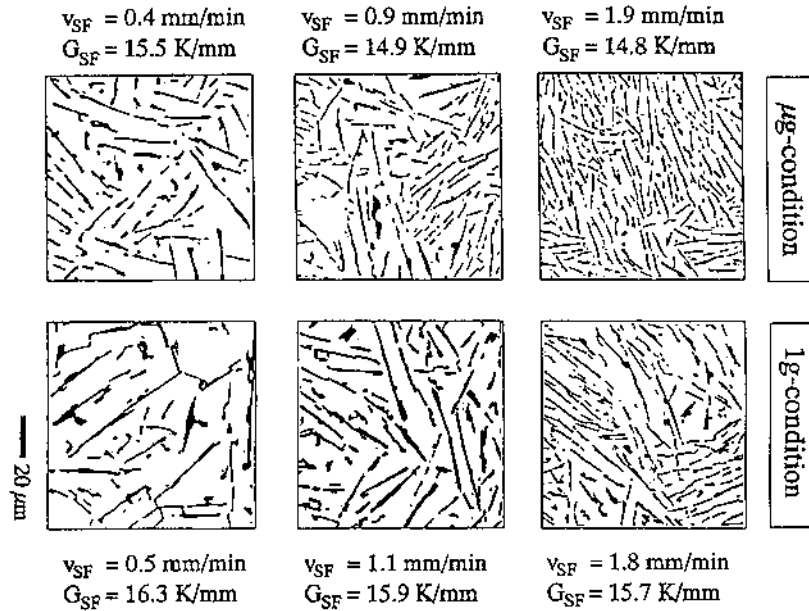
Figure 22 Influence of μg- and 1 g-conditions on the morphology of the eutecticum of the near hypoeutectic AlSi 11alloy, crystallized with three velocities V_{SF} and uniform temperature gradient G_{SF} in front of the SF; to be compared the 1 g-reference experiments to the assigned μg-experiments
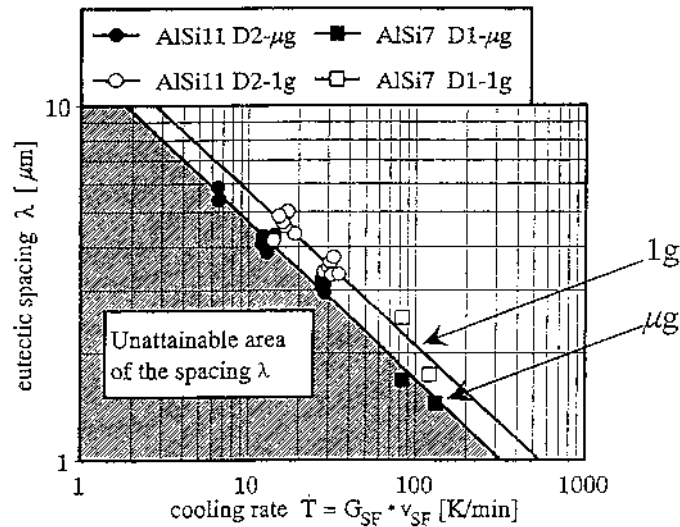
Figure 23 Influence of the cooling rate T on the morphology of a hypo- and near-eutectic AlSi alloys (here on the eutectic spacing λ), unidirectionally crystallized under μg- and 1 g-conditions in a double logarithmic scale (results from D1- and D2-Spacelab Mission). The values of λ grown under μg are smaller than under earth conditions for all crystallization parameters. The area beneath the graph for the μg-results from the boundary of the unattainable area of λ; this means that, using such alloys and the tested crystallization velocities, no smaller λ values can be obtained and that aiming at high mechanical values no better results can be reached!

spacings λ between the Si-phases were evaluated from the pure AlSi 7- and AlSi 11-probes, which were processed during the SPACELAB- and FOTON-missions. In the diagram, the correlation of the spacings λ with the cooling rate T (between T_L and T_E) of the different alloys are presented in an double logarithmic scale. The absence of buoyancy-driven convection under μg-conditions for all crystallization parameters also creates a reduction of the interdendritic eutectic spacings λ. From these results, the absolute minimum of the spacing λ is also defined by the "unattainable area" in this diagram. Therefore, these results show that the maxima of the mechanical values which can be achieved be minimizing the λ spacing in eutectic volume is restricted by the line of μg.

An additional example of the impact of gravity driven convection on the eutectic morphology is illustrated by the influence of cooling velocity T in a wide range (2 [K/min] < T < 720 [K/min]) during solidification on the spacing λ in unidirectional solidified AlSi 11 probes, described in Fig. 24: The hypo-eutectic alloy should create, according to the Al-Si-equilibrium diagram, a dendritic and a eutectic crystallization! As to be seen from the graph λ (T) is interrupted at a cooling velocity T of about 10 [K/min]. An explanation is given by the change of the eutectic volume f_{EU} [%] in dependence of T: At the same value for the cooling velocity, the value of f_{EU} jumps from 100% to a value of about 90%. This means that, having T < 10 [K/min], the volume crystallizes only in an eutectic modus and, under T > 10 [K/min], an additional dendritic volume crystallizes beginning with about 10%
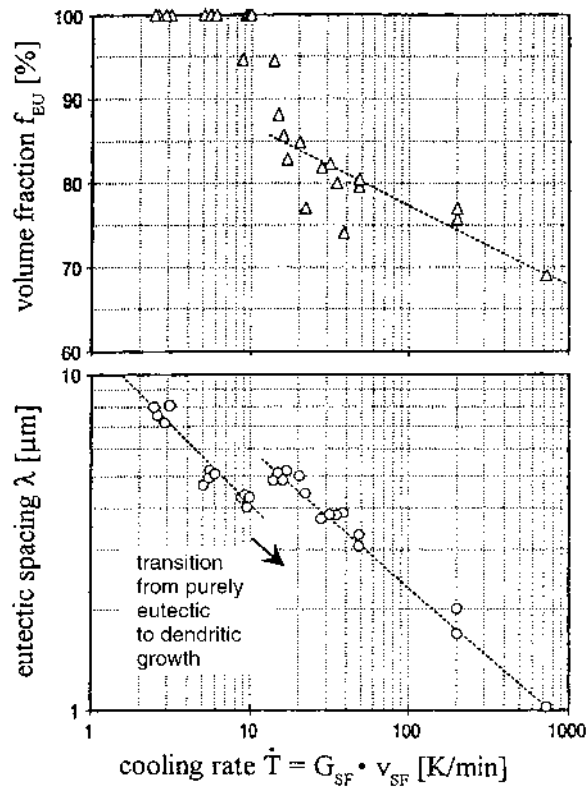
Figure 24 Influence of cooling rate T on the eutectic spacing λ of an unidirectionally crystallized AlSi 11 alloy; the discontinuity of the graph at T = 10 K/min is caused by the transition from a pure eutectic crystallization of the AlSi11 alloy to an eutectic and a dendritic crystallization. This is documented by the upper diagram with the change of "volume fraction" of eutectic f_{EU} from 100% to about 85% at the same cooling rate.

and showing a linear increase (in the double logarithmic scale!) up to a value of 30 vol%. Further experimental and theoretical work (Lit) shows that the buoyancy-driven convection in the melt will be suppressed by the dendrites behind the SF I with decreasing primary dendrite arm spacings "e"!

But with increasing solidification velocity, microscopic convection rises. As a first approximation, it can be assumed, that the sum of convection remains constant. An additional convection term occurs in the melt between SF I and SF II: The increasing volume of the dendrites behind their tips causes a so-called micro--convection. The change of liquid into solid volume produces a negative volume change ΔV causing an additional intensive convection. This ΔV-convection increases the integral mass transport coefficient "D^{int}" in liquid. Therefore the spacing λ increases with appearing of the dendrites. The value of λ is useful as a scale for the quantity of "$D^{integral}$". Figure 25 shows the change of "$D^{integral}$" in dependance on the cooling velocity T for the solidification of the AlSi 11 alloy. Because the atomar diffusion coefficient D_L^{atom} is a material constant and only influenced by the temperature, the "$D^{integral}$" is related to D_L^{atomar} in the ordinate of this diagram.
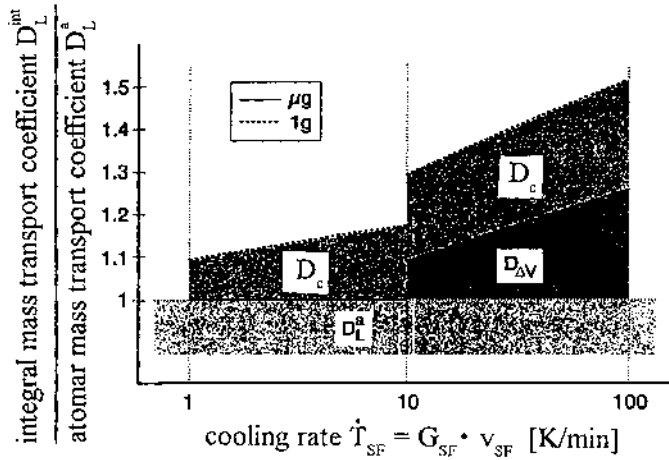
Figure 25 Ratio of the integral mass transport coefficient $D^{integr.}{}_L$ and the atomic mass transport coefficient $D^{atom.}{}_L$ (the real diffusion coefficient) depending on the cooling rate T for μg- and 1 g-conditions. Under μg the values of $D^{integr.}{}_L$ are influenced up to T < 10 K/min only by the (constant) real diffusion coefficient $D^{atom.}{}_L$, having T > 10 K/min an increasing mass transport from the volume jump $D_{\Delta V}$ enlarges the $D^{integr.}{}_L$-values. Under 1 g condition these values becomes superimposed additionally over the whole range of T by an increasing mass transport $D_{conv.}$ from the buoyancy forces.

The sum of "$D^{integral}$" consists with the change of the cooling rate T of a constant value of $D_L{}^{atom}$, an increasing mass convective transport D_{conv} by buoyancy driven convection and, passing the threshold of T = 10 [K/min], the additional mass transport $D_{\Delta V}$ by the micro-convection from the volume change ΔV.

Another important point is the geometry of the silicon phases: Figure 26 shows that the growth of the Silicon phases during eutectic crystallization is different. A lamellar geometry (a), a mostly angular geometry (b), and an angular geometry with primary Si phases (c) is shown. The dependence of all these structures on the Si-concentration and the velocity of crystallization v_{SF} is shown in Fig. 27 (Lit Lit). The different details of the Si-geometry occur in one eutectic area, which means that local differences in Si-concentration and/or v_{SF} during the eutectic solidification may exist. An important result of our μg-experiments is the absence of any influences from μg- or 1 g-conditions on these geometries of the Si-phases.

To illustrate the influence of the Si-concentration during eutectic solidification, the quenched solidification front of two AlSi alloys with 12.4 and 13.2 w% Silicon are provided in Fig. 28: The unidirectional solidified volume without any heat treatment (direct behind the quenched SF) clearly shows the change of more plate-like to complex regular geometry.

The subtle details of these structures to explain the crystallization kinetic and to calculate the mechanical material behavior rely on a two-dimensional information! This poverty in information should be explained by a comparison of two- and tree-dimensionally metallographic structures of a modified A357 alloy with different stages of heat treatments (Fig. 29): The two-dimensional OM pictures
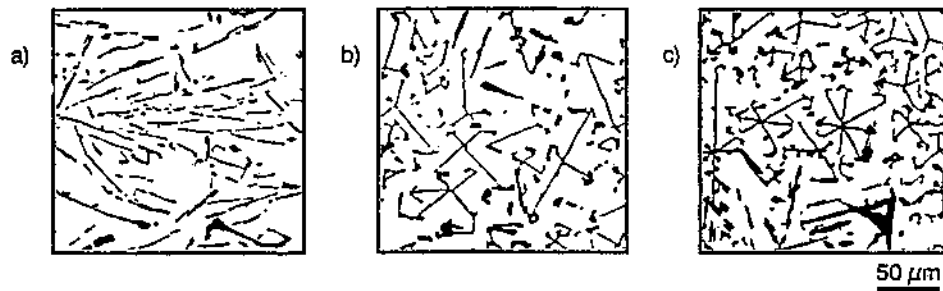
Figure 26 Influence of the Si content in near eutectic AlSi alloys (a) AlSi11.2, (b) AlSi13.2, and (c) AlSi13.8 on the morphology of the Si-phases; (a) lamellar Silicon with cellular/dendritic α_{Al}-phases; (b) mostly angular Silicon; (c) angular with additional primary Silicon; there is no influence of μg on these Silicon-morphologies!

show the intimate structures beginning with the stage "as cast" and with two solutionizing times. As already mentioned, a change of the dendrites does not occur, but the morphology of the eutectic Si-phases becomes a more spherical morphology with increasing heat treatment time. A comparison of these structures with the tree-dimension pictures, taken by an SEM, after a so-called "deep-etching" (the α-Al-phases are removed at the metallographic plane) shows that Si-balls of the OM picture (Fig. 29(B)) in reality are cylindric volumes and that a visual comparison to the SEM is possible only after a heating time 50 hr of the visual impression seems to be given only after a heating time of 50 hr (see Fig. 28(C)). This inaccurate comparison results in a so-called unsharpness in explaining the correlation of structures and mechanical behavior. To overcome these difficulties an important tool has been missing until now: the quantitative structure determination from tree-dimensional metallographic pictures.

4   DEVELOPING OF HIGH STRENGTH CASTINGS USING RESULTS FROM μg-EXPERIMENTS

The first example describes a so-called corner fitting for the plane "AIRBUS". Until now, this part was milled with differences in the wall thickness from wrought high strength Al alloy sheets. After modifying the alloy, optimizing the crystallization parameters according (Figs. 15 and 3) and using a kind of unidirectional crystallization (so-called SOPHIA process; Lit) this part was cast with the demanded local mechanical values (Fig. 30). The important condition was to guarantee a minimum of R_m and $R_{p0.2}$ as well as a maximum of fracture elongation A_5 for all wall thicknesses (it means different cooling rates T) of the corner fitting.

The microgravity experiments have shown which limiting values like dendrite arm spacing d_s and which minimal sizes of the eutectic phases, for example the average spacing λ of the Si-phases, can be achieved under utmost conditions. The objective of this work was to obtain an extensive range of the given technical possibilities to optimize (about 80% to 90%) the microscopical structures only with one parameter. Only then, any of the remaining parameters should be changed. These parameters include: chemical additions to the alloying elements, crystallization
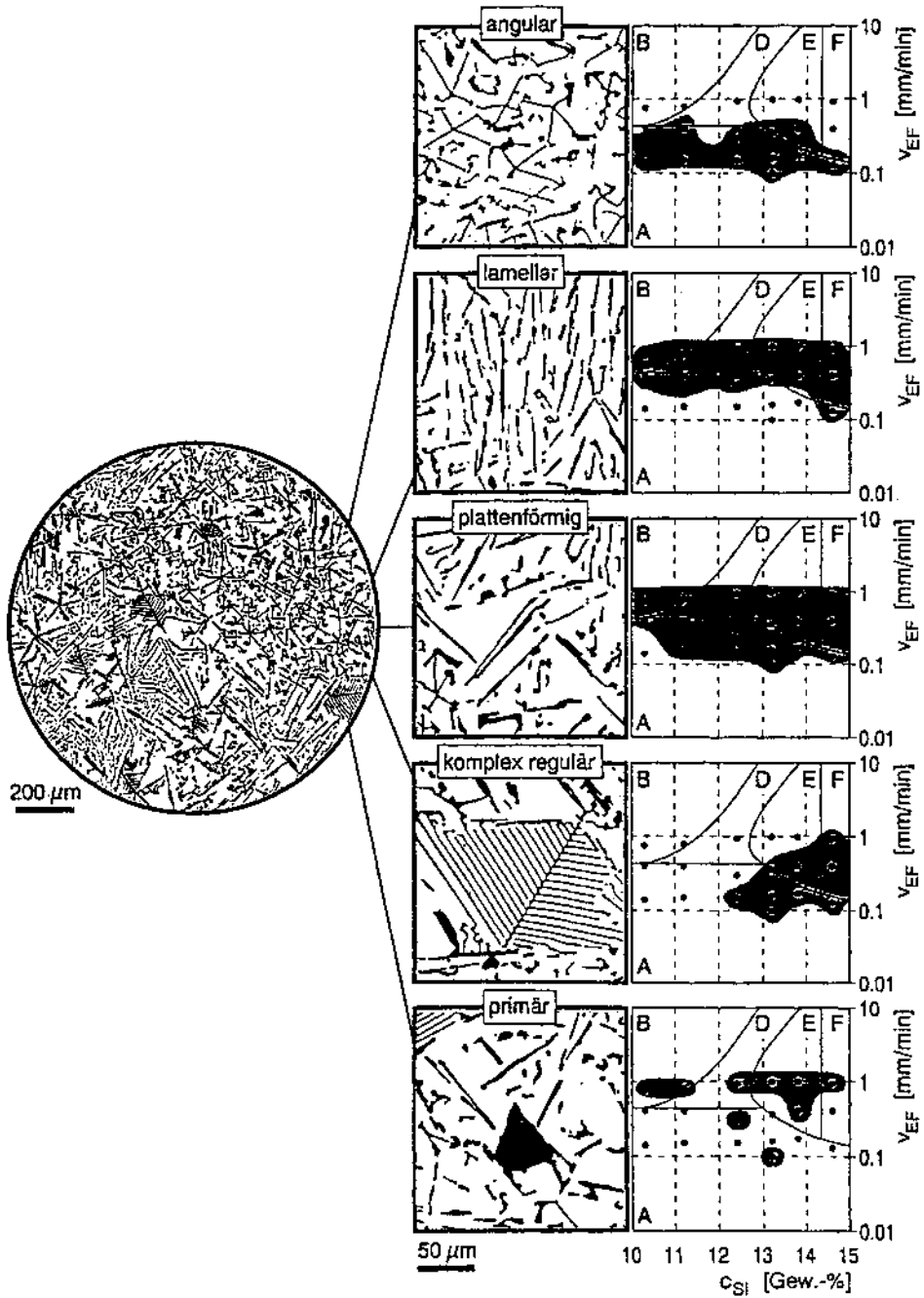
Figure 27 Definition of the different Silicon-morphologies "angular", "lamellar", "plate-like" "complex regular" and "primary" of near eutectic AlSi alloys (AlSi 10.3; AlSi 11.2; AlSi 12.4; AlSi 13.2 and AlSi 14.6) defined from one eutectic volume and corresponding with the above defined alloys and combined with the $C_{Si}(v_{SF})$-diagrams after R. Elliott (the dots in the diagrams characterize our solidification experiments).

AlSi 12.4
with predominant
angular
Si-structures
behind the
quenched SF
$v_{SF} = 0.17$ mm/min,
$G_{SF} = 10.1$ K/mm

100 µm

AlSi 13.2
with predominant
complex regular
superlattice
of the Si-phases
behind the
quenched SF
$v_{SF} = 0.13$ mm/min,
$G_{SF} = 10.3$ K/mm

100 µm
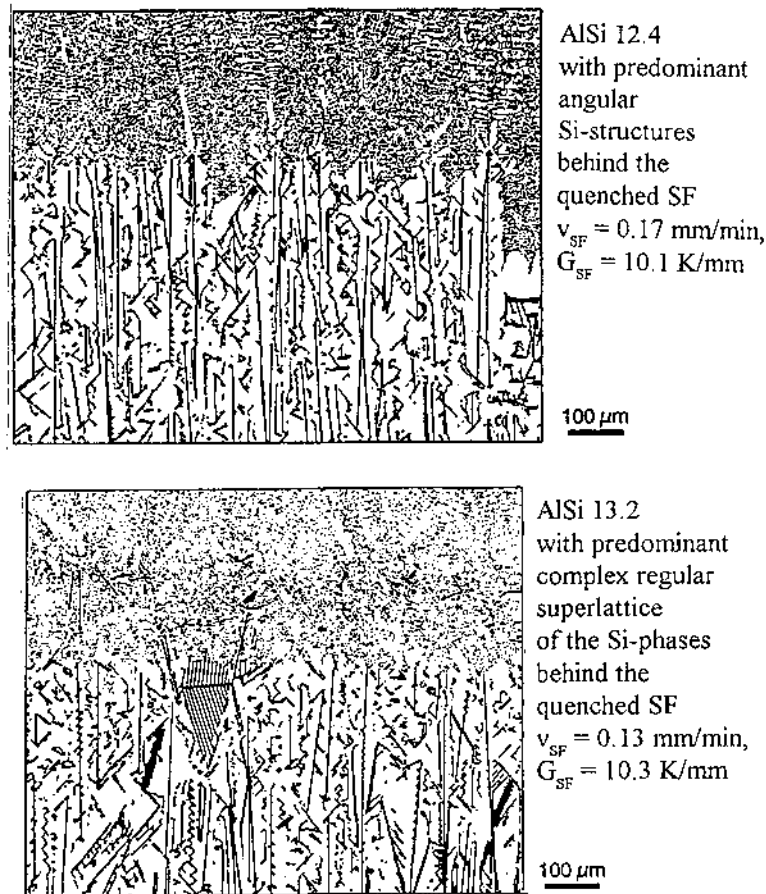
Figure 28 Example of quenched solidification front in unidirectionally crystallized AlSi 12.4 alloy ($v_{EF} = 0.17$ mm/min, $G_{EF} = 10.7$ K/min) with more angular Si-structures and AlSi 13.2 ($v_{EF} = 0.13$ mm/min, $G_{EF} = 10.3$ K/min) with more complex regular Si-structures behind the quenched SF.

parameters like v_{SF}, G_{SF} and convection conditions in liquid ahead of the solidification front, and consideration of the macroscopic conditions of the casting processes like "VAKURAL" or "SOPHIA". For the same cast part (with an equal area of wall thickness) the crystallization velocities increase using the "SOPHIA"-process (this causes low e, d_s and λ -values).

The choice of unidirectional solidification also avoids shrink holes and pores. Figure 31 shows the area of the SOPHIA process in the function $d_s(T)$. Conventionally cast parts contain the higher d_s-values. The comparison of conventional with "SOPHIA" castings shows (for all wall thicknesses in the "corner fitting" from 2 until 12 mm) together with the optimized A357 alloy composition and the optimized heat treatment, the best mechanical values R_m, R_p and A_5 for "SOPHIA" (Fig. 32).
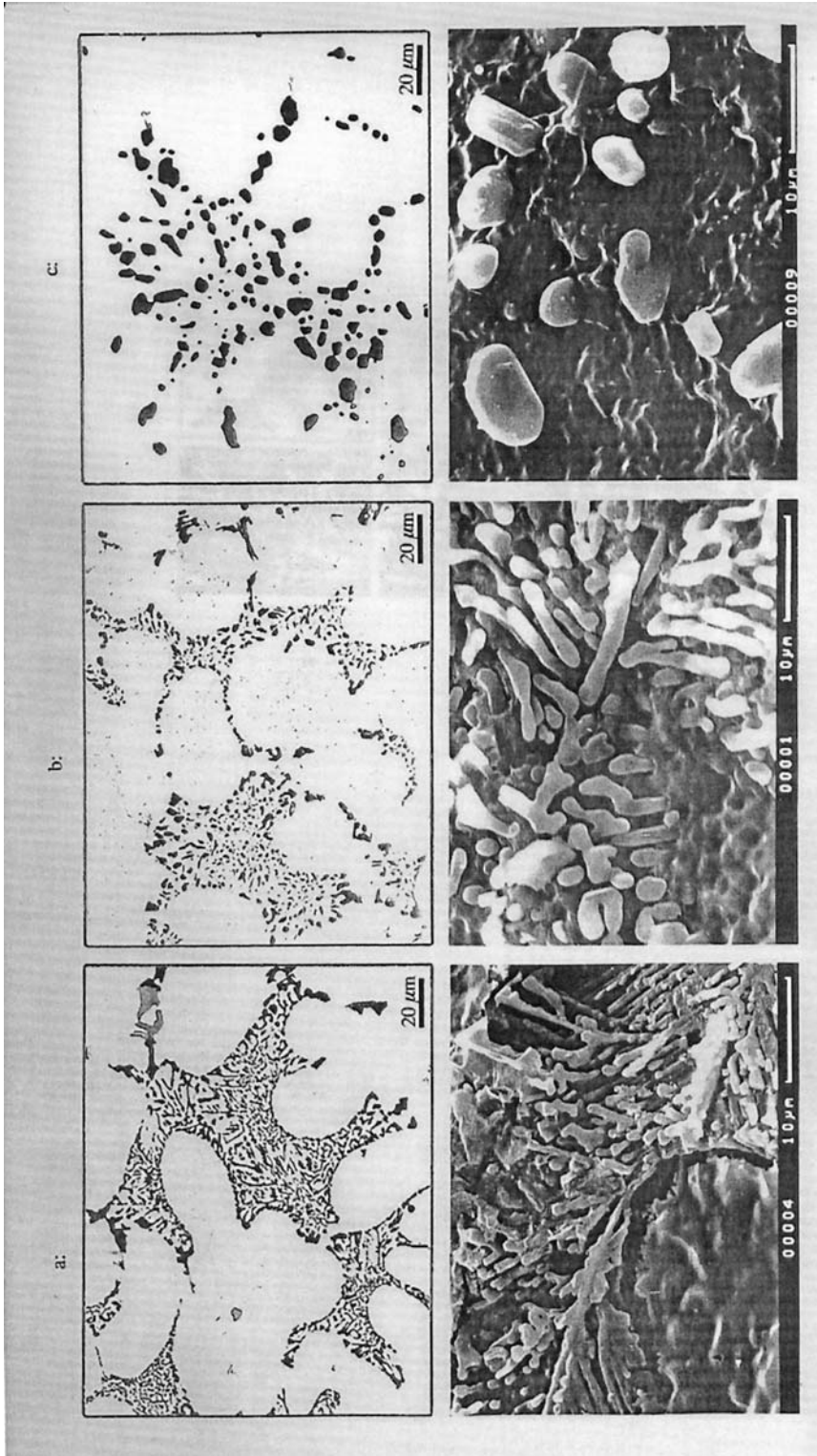
Figure 29 Comparison of the metallographic structures of a technical AlSi 7 alloy (modified A357 with 1% Cu), as cast and heat treated, in two and three dimensional view (OM- and REM-pitures). (a) as cast; (b) heat treated at 535°C over 1 hr; (c) heat treated at 535°C over 50 hr.
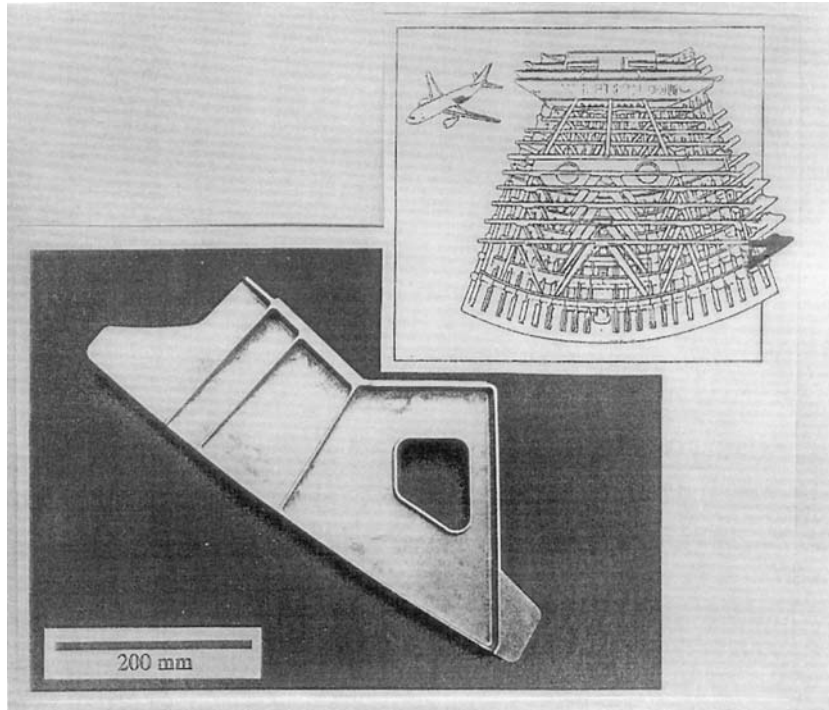
Figure 30   Example of a casting for the AIRBUS (so-called ''corner fitting'') with its position in the construction
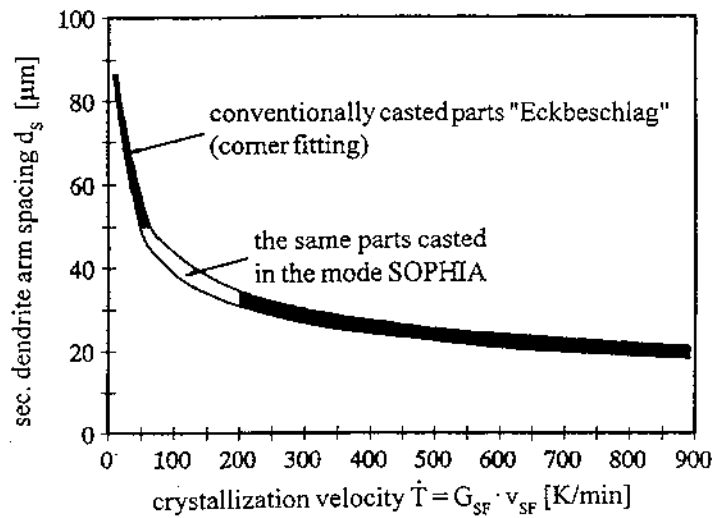
Figure 31   Dendrite arm spacing d_s influenced by the crystallization velocity T in a modified A357 alloy. The parts were cast as ''corner fitting'' using different conventional (undirectional) methods as well as using the special casting method ''SOPHIA''; as to be seen crystallization velocities from about 50 to 200 K/sec (this means for wall thicknesses from 2 to 12 mm) the values for d_s are here the best using ''SOPHIA''.
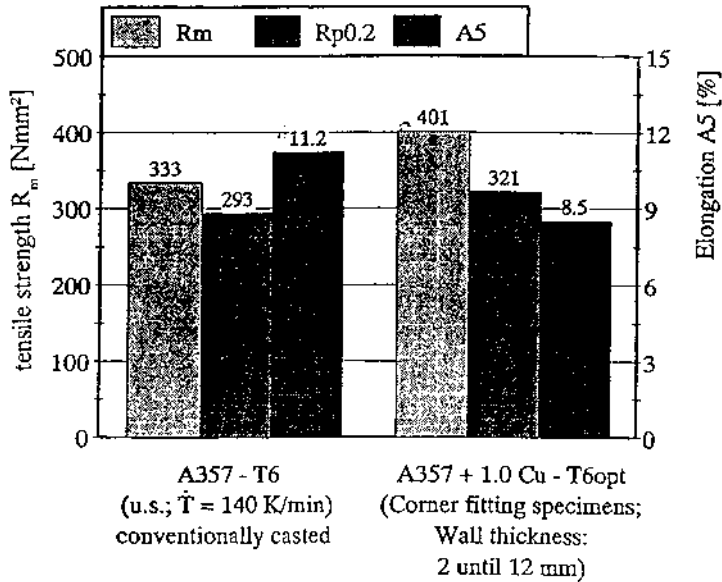
Figure 32 Comparison of the main mechanical values taken from parts of the "corner fittings" with different wall thickness using conventionally A357 alloy with conventional casting and heat treatments with the values from "corner fittings" produced using the modified A357 alloy, the casting method "SOPHIA" and a modified heat treatment T6opt.

The "flap track" "SOPHIA" casting for the AIRBUS, cast with the conventional A357 alloy and with conventional heat treating, has larger metallurgical structures (for example d_s and λ) but shows over the wall thickness from about 8 to 50 mm lower, but also well-balanced mechanical values, caused by the casting method (Fig. 33).

In the aircraft industry, the so-called "Quality Index" "Q" was created to get an useful combination of the two important mechanical values tensile strength R_m and fracture strain A_5 for materials (Eq. (8)).

$$Q = R_m + 150 \log (A_5) \tag{8}$$

Figure 34 shows the Q value of SOPHIA castings and especially the optimized SOPHIA castings using μg-results in the diagram R_m as a function of A_5. The diagonal lines describe the course of constant Q values. The highest Q value represents the most useful quality for airplanes.

An example from the automotive technique is the optimization of the mechanical properties of a VACURAL die cast part with an alloy AlSi10 Mg0.30. Figure 35 shows the AUDI A8 "space frame" with the pressure die castings "corner fitting" for the connection of the extruded shapes. For these complex parts with a large area of wall thickness, the undirectional casting with strong convection was selected and the morphologies of the eutectic and dendrite volume were minimized.
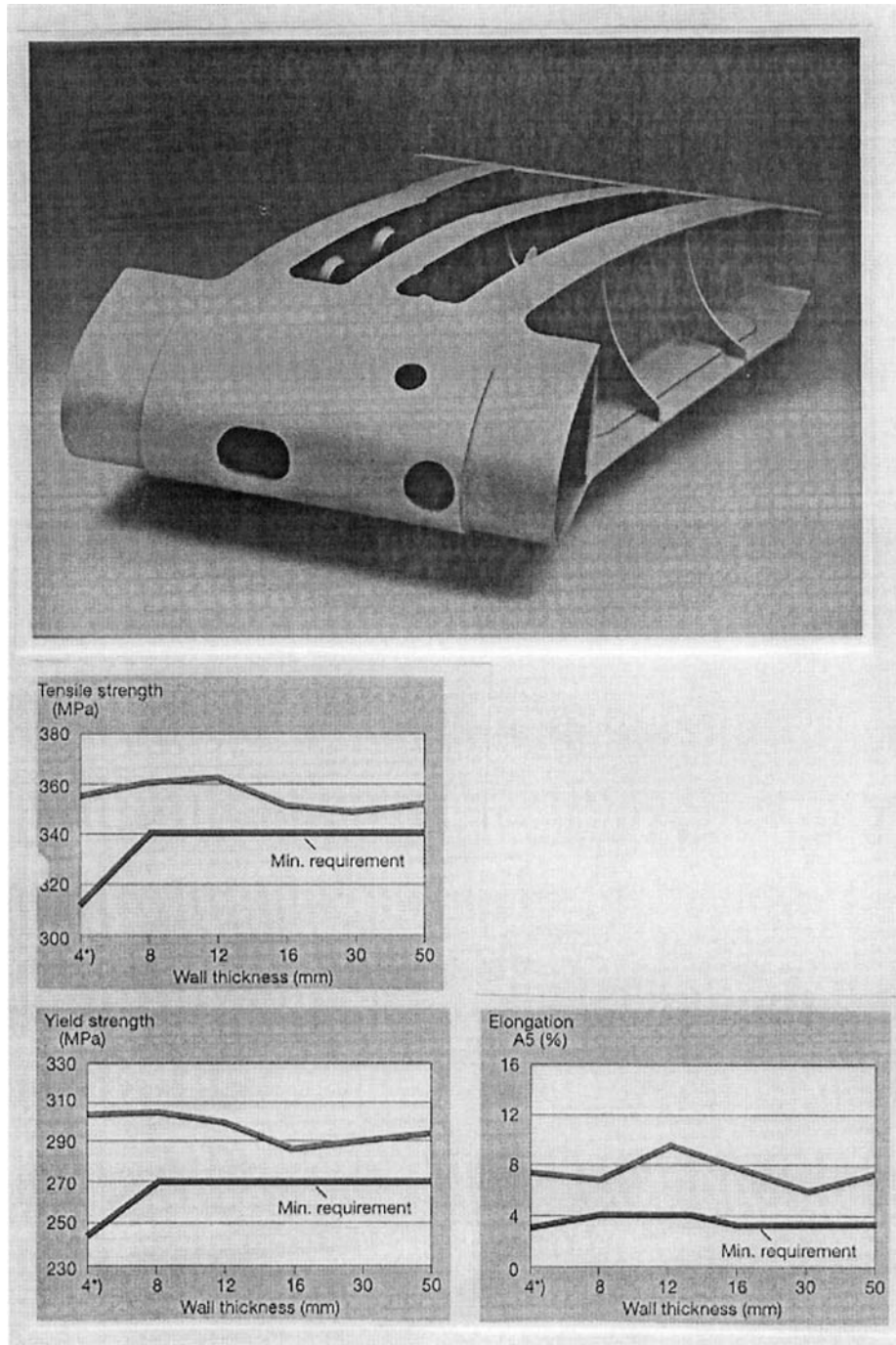
Figure 33   "Flap Track Casting" for the AIRBUS using conventionally A357 alloy and the "SOPHIA" method (max length 850 mm, wall thickness from 4 to 50 mm); the graphs below show the dependant of tensile strength, yield strength and elongation from the wall thickness (here unknown correlation with the crystallization velocities). (From Ref. 14.)
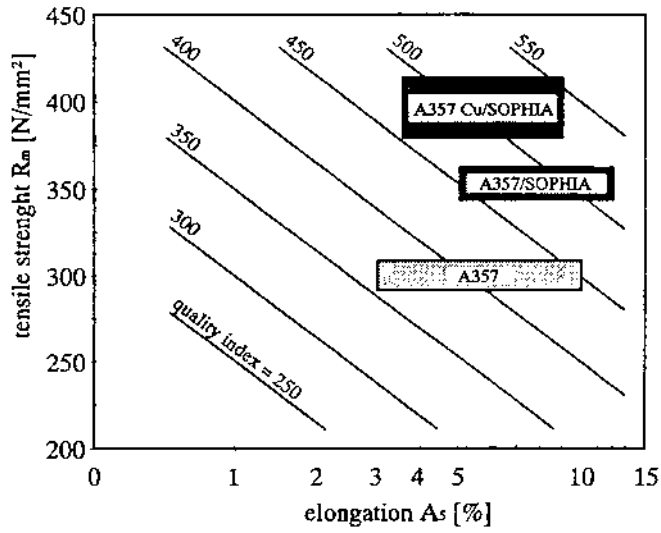
Figure 34 Classifying of different castings in the "Quality Index Q" diagram. This kind of presentation gives, for the air industry, a useful combination of the values R_m and A_5; the best qualified materials show the highest Q-value.
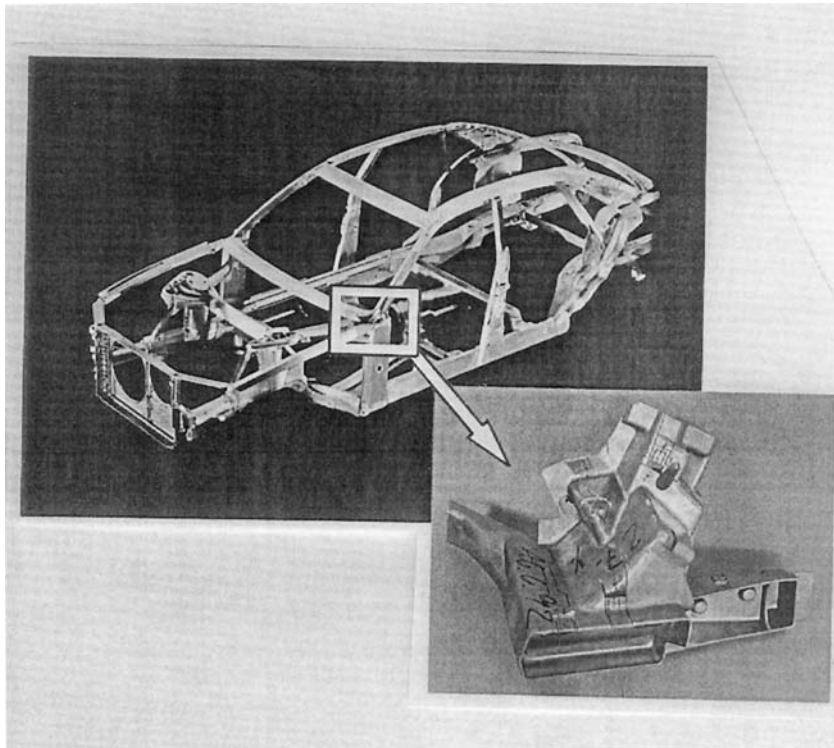
Figure 35 An example of the automotive technique is the "space frame" of the "AUDI A8" with the cast "corner fitting" (below).

The following procedures were conducted: Solidification experiments (unidirectional!) with the original die cast parts to correlate microstructural parameters and mechanical behavior. These experimental results permitted the identification of an optimum alloy composition and optimal crystallization parameters, to yield useful mechanical properties which were then used to develop the conditions of VACURAL die casting process. The castings in the space frame must meet extreme quality safety demands with high rates of R_m and R_p as well as a fracture strain A_5 which must be high as possible in each location of the casting. In case of a crash, enough deformation energy must be adsorbed by the deformation of these castings.

Figure 36 A shows the dendrite arm spacing d_s depending on the cooling rate during crystallization in detail. Two AlSi-alloys were unidirectionally crystallized and the alloy with the higher Si-content additionally VAKURAL-cast. The functions $d_s(T)$ are nearly the same. Since there is the demand for different wall thickness (i.e. "modoli"), a sufficient small d_s value also in thick zones of the cast part can be generated by a precise choice of combination of the alloying elements together with the control of the cooling- and convection-conditions (here VAKURAL). The calculated cooling velocities T for all areas of the "corner fitting" show values between 600 and 4000 K/sec. The important sector of the dendrite arm spacings d_s from about 7 to 10 μm from Fig. 36(A) is correlated with the mechanical values R_m, R_p and A_5 in Fig. 36(B). To get high enough ductility values, the d_s values were created to be < 9 μm by crystallization velocity and convection.

An integrated scheme for the development of optimized castings is provided in Fig. 37. The initial step is determining all structural parameters of the cast part which must be optimized. Secondly, the corresponding crystallization parameters must be determined. After improvement of the microstructures and comparison with the results of μg-experiments the adaption of the optimized parameters is performed to obtain optimized castings.

5 SUMMARY

The heaviest deficit in developing high strength castings is the implementation of scientific knowledge. The enlarged know-how about the mass transport during crystallization by the results from μg-experiments gives the possibility to recognize the limits in influencing the microstructures as well as the separated influence of the crystallization velocity and the macroconvection ahead the solidification front. The areas of unattainable metallographic values, for example the dendrite arm spacings d_s and the eutectic spacing λ, are the limit for getting optimized structures for a defined alloy. Because of the strong effect of the metallographic structures on the mechanical behavior of materials, this is essential for all technical castings. From this it is possible to optimize all parameters for castings, like the alloying elements, the crystallization parameters (including the convection), the macroscopic kind of (industrial) processing the crystallization and, finally, the heat treatment of the cast parts adapted to the microstructures.
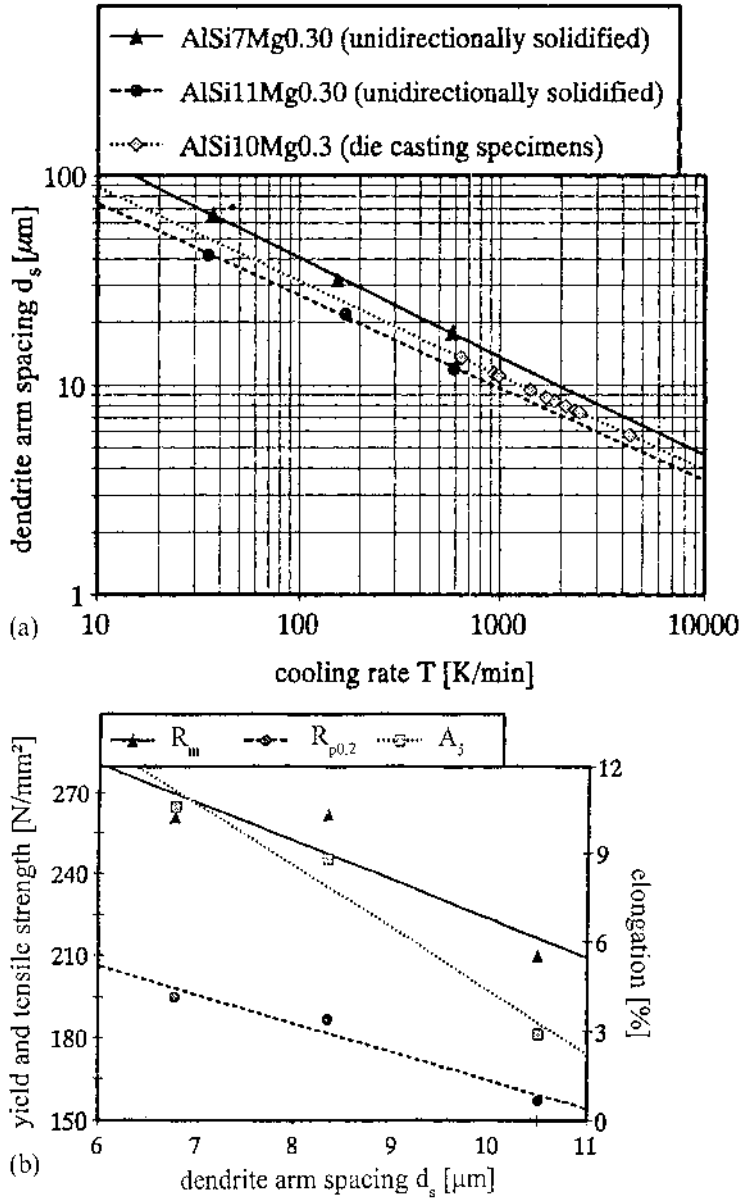
Figure 36 The corner fittings of the AUDI A8 should have well-defined mechanical values; changing the alloy and testing the dendrite arm spacings d_s under unidirectional solidification with cooling rates T according to the VACURAL die casting the optimal conditions were found; (a) Correlations d_s(T) for different AlSi alloys unidirectional and VAKURAL crystallized; (b) Correlations R_m(d_s), R_p(d_s) and A_5 (d_s) of the alloy AlSi10 Mg 0.3.
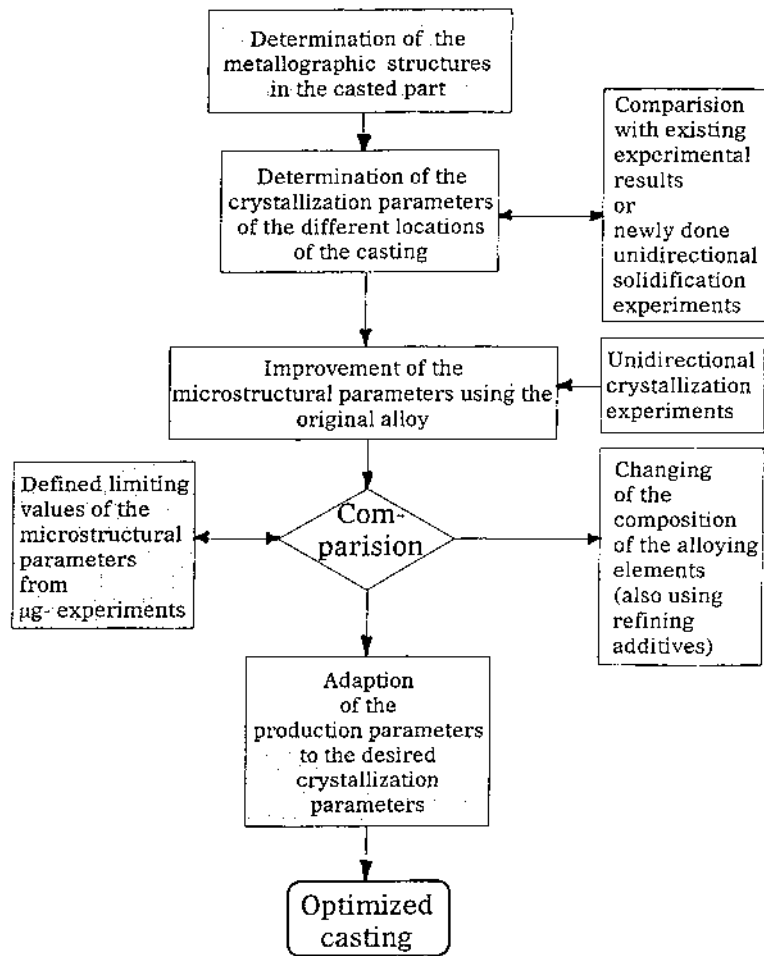
Figure 37 Scheme of the scientific development of "high tech castings" using results from μg-experiments.

Examples from the automotive and aviation industry have been provided which illustrate the value of μg crystallization studies in industrial process optimization.

LITERATURE

Basic results are from doctoral theses of my former scientific assistants; all doctoral theses: Dr.-Ing. Dissertation, Fakultät für Maschinenwesen der Technischen Universität München, FATUM.

Dieter Froschhammer, "Untersuchungen vor bewegten Erstarrungsfronten", 123 pages, 1975.

Günther Doemens, "Experimentell und theoretische Untersuchungen bei der Kristallisation legierter Metalle", 139 pages, 1973.

Heinrich Fuchs, "Dendritenmorphologie", 127 pages, 1982.

Justus Joachim, Schmidt, "Bedeutung der Konvektion für den Stofftransport in erstarrenden Metallschmelzen und ihre Auswirkung auf die Kristallisation", 224 pages, 1986.

Paul F. Harmathy, "Stofftransport vor Erstarrungsfronten", 179 pages, 1983.

Peter Peck, "Gefügemorphologie und Festigkeitseigenschaften binärer Aluminium-Silizium-Legierungen", 164 pages, 1987.

Carlo Mackrodt, "Einfluß von Veredelung und Erstarrung auf das Gefüge von AlSi-Legierungen", 130 pages, 1990.

Raimund Rösch, "Eutektikum des Aluminium-Silizium", 154 pages, 1994.

Johann Högerl, "Beeinflussung der Gefügemorphologie und der mechanischen Eigenschaften von AlSi7Mg-Legierungen", 142 pages, 1996. Fortschritt-Berichte VDI; Reihe 5: Grund-und Werkstoffe, Nr. 457, ISBN 3-18-345705-9, Düsseldorf.

Thomas Mack, "Dendritische und eutektische Kristallisation unter Mikrogravitation", 111 pages, 1998.

Fortschritt-Berichte VDI, Reihe 5: Grund-und Werkstoffe, Nr. 532, Düsseldorf ISBN 3-18-345705-9.

Paul Seibold, "Konvektion bei dendritischer und eutektischer Erstarrung", 102 pages, 1998. Typoskript-Edition HIERONIMUS, München, ISBN 3–89791–206–6, 1999.

REFERENCES

1. "The Doubter", wood-block printing from an unknown artist 1520–1530: (without more specification) in *Verstehen und Gestalten* , R. Hirschauer, R. Oldenbourg, 1997, Verlag, München, 152 pages, ISBN3-486-05223-3.

2. H. M. Tensi, R. Rösch, and C. Mackrodt, "Wechselwirkung von Erstarrungsbedingungen, Mikrogefüge und Festigkeitswerte bei gerichtet erstarrten Gusslegierungen" Schriftreihe PRAXIS-FORUM, Aluminium, 1993, pp. 98–125.

3. H. M., Tensi, H. Fuchs, P. F. Harmathy, and J. J. Schmidt, "Normalkristallisation mit Abschrecken der Restschmelze unter Weltraumbedingungen –" "Teil I: Ausgeführte Kristallisationsanlagen;" "Teil II: Experimentelle Möglichkeiten der Versuchseinrichtungen," Aluminium 1984, 60(7), pp. 614–622.

4. H. M. Tensi, R. Rösch, C. Xu, and S. Spaic, "Influence of Solidification Conditions, Heat Treatment and Strontium on the Microstructure and Strength Properties of an Industrial AlSi Cast Alloy," Aluminium 1993, 69(7), pp. 634–641.

5. H. M. Tensi and J. Högerl, "Metallographische Gefügeuntersuchungen zur Qualitätssicherung von AlSi-Gussbauteilen", Metall, 1994, 48(10), pp. 776–781.

6. H. M. Tensi, J. Högerl, T. Mack, and R. Rösch, "Quality Improvement of Castings for Cars and Airplanes by Solidification Experiments under Low Gravity," Low G 1994, 5(3), pp. 8–11.

7. H. M. Tensi and P. Pek, "Einfluß der Erstarrungsparameter auf Festigkeitswerte gerichtet erstarrter AlSi-Legierungen" Aluminium 1986, 62(10), pp. 746–750.

8. H. M. Tensi and P. Pek, "Gefügekenngrößen bei gerichtet erstarrten AlSi-Legierungen," Aluminium 1986, 62(8), pp. 577–583.

9. S. Spaic, R. Rösch, and H. M. Tensi, "Untersuchungen zur Kristallstruktur der eutektischen Erstarrungsfront einer Alsil l-Legierung," Z. Metallkde, 1993, 84(10), pp. 776–781.

10. H. M. Tensi and C. Mackrodt, "Possibility of Investigating the Crystallization Parameters during Unidirectional Solidification," Appl. Microgravity Tech. 1989, II(2), pp. 68–74.

11. H. M. Tensi and R. Rösch, "EUSO-D2-Experiment: Unidirectional Solidification with Quenching of AlSi11 Alloy," *Proc. 8th European Symp. on Materials and Fluid Sciences in Microgravity*, 1992, Brussels, Belgium, pp. 629–633, ESA SP-333 (Aug. 1992).

12. R. Rösch and H. M. Tensi, ''Interdendritic Eutectic Solidification of AlSi7.0 Alloy und Microgravity,'' Metall. Trans. B, 1993, 24B, pp. 208–212.
13. H. M. Tensi, ''Influence of Microgravity and the Morphology of the Directionally solidified,'' – Metall. Trans. A, 1988, 19A, pp. 2681–2686.
14. J. Gabriel, konstruieren+gießen 1996, 21, pp. 4–10.

16

Designing for Aluminum Forging

HOWARD A. KUHN

Scienda Building Sciences, Orangeburg, South Carolina, U.S.A.

1 OVERVIEW

In the design of aluminum forgings, as with any product, the designer must specify the material and process (based on desired properties) and the geometric details (shape, dimensions, and tolerances) such that the component will meet performance requirements. From a concurrent engineering perspective, the product design decisions should exploit the flexibility offered by the process, but not exceed its limitations. While manufacturing the product to meet the designers specifications is the job of the production engineer, collaboration between designers and producers can avoid design features that are difficult or impossible to form, thus saving rework and redesign efforts, and reducing the time to product realization.

Almost without exception, forgings are specified when critical mechanical load transmission requirements are to be met. Aluminum alloy forgings are primarily used for structural parts on aircraft and land vehicles, but other applications include housings, casings, and linkages for a wide variety of mechanical systems. Forging produces parts of high integrity because the process sequences refines and homogenizes the metallurgical structure, eliminating material defects that cause premature failure and assuring that the material strength is at its peak level. The cost of producing forgings, however, is high because of the high skill level and time required for craftsmen to produce forging dies. While forgings constitute a small percentage of the total aluminum usage, their low numbers are outweighed by their importance in critical load transmission applications.

1.1 Material Aspects

Each material process leading up to, and including, the final forging step contributes to establishment of the final metallurgical structure of the material, thereby

determining its final in-use properties. Feedstock for forging operations are produced by casting liquid metal or by consolidating powder into ingots or billets. Large dendritic grain structures, porosity, and segregation characterize the microstructure of typical castings, and an oxide network (from the surfaces of the original powders) characterizes consolidated powders. Primary working processes, such as hot rolling, extrusion, or open die forging, break up the dendrites and close up the porosity in cast ingots, and break up and distribute the oxide network in consolidated powders. Additional hot working continues to refine the microstructure.

A common characteristic of hot working processes is grain flow, or alignment of inclusions and second phase particles in the direction of metal flow, or elongation. In rolling or extrusion, of course, the grain flow is in the longitudinal direction of the rolled or extruded shape. In the forging of complex shapes, however, the grain flow will be multi-directional, following the movement of metal in the elongated directions of each geometric feature. This alignment of inclusions and second phase particles has a strengthening effect in the direction of alignment, but is accompanied by a reduction of ductility in the direction transverse to the fiber orientation. Designers can use this effect to advantage by aligning the grain flow in the direction in which the part will experience the greatest stresses during use.

To achieve the highest level of mechanical properties in aluminum forgings, heat-treatable aluminum alloys are normally specified (2000, 6000, and 7000 series). These alloys are strengthened slightly during forging as the hot working reduces the grain size and, to a small extent, carries out precipitation hardening at the hot working temperatures. Optimum mechanical properties of the part are developed subsequently through heat treatment. In this post-forging operation, the materials are solution heat treated at a temperature just below the solidus, then water quenched and artificially aged above room temperature for several hours.

Distortions of the part geometry may occur during heat treatment because of non-uniform cooling. This is largely due to adjoining geometric features that have different area to mass ratios. Whenever possible, the designer can minimize distortions due to heat treatment by avoiding designs that lead to non-uniform cooling.

1.2 Geometric Aspects

Forging of aluminum alloys is particularly applicable to producing precise, intricate shapes with good surface finish. The alloys are very ductile at hot working temperatures, and they do not develop scale during heating. In addition, the forging temperature is relatively low so the dies can be heated to nearly the same temperature as the workpiece, which prevents cooling of the workpiece and facilitates flow of metal into small cavities in the die.

However, there are limitations to the geometric complexity that can be obtained. During the forging process, force applied to the material by the forging equipment generates pressure that forces metal to flow into intricate cavities of the die. Long, thin die cavities require high pressure to force the material into them. If excessive pressures are required, the total forging load may exceed the capacity of the forging equipment. In addition, localized stresses in the die due to high pressure in the die cavities may become large enough to cause overloading failure of the die, fatigue cracking due to repeated loading, and rapid die wear in high metal flow regions. An additional limitation to shape complexity is the possibility of defect

formation in the material during forging. In particular, as the material flows around small corner radii on the die (the result of small fillet radii in the part) or undergoes very large expansion of a free surface, laps and cracks may occur.

1.3 Cost Aspects

The cost of aluminum forgings depends strongly on the quantity of parts to be produced, shape complexity of the part, and the amount of machining required to reach the finished shape, dimensions, and tolerances. *Blocker-type*, *conventional*, *high definition*, and *precision* are the classifications, respectively, of forgings that are progressively closer to the final part geometries. Blocker-type forgings, which are only a rough approximation of the desired part shape, are produced with inexpensive, simple shape dies, but they require extensive machining to reach the final shape. In contrast, precision forgings use very expensive, complex dies, but they require little, if any, machining to reach the final part dimensions. Blocker-type forgings are economical for parts in small quantities, and precision forgings are economical for producing large quantities of parts over which the high die costs can be amortized.

Process and equipment limitations also affect forging cost. Aluminum alloy billets are heated somewhat below their solidus temperature before forging because the heat generated during forging deformation causes a temperature rise in the material. If the initial billet temperature plus the temperature rise during forging exceeds the solidus, incipient melting of the material occurs, leading to severe cracking. This effect is particularly pertinent in high-speed forging, such as on a mechanical press or forging hammer, because the heat generated has little time to diffuse into the dies. This reduces the complexity of the shapes that can be produced on high-speed forging equipment, and potentially increases the amount of machining required. Thus, increasing the production rate by using a high speed forging operation also reduces the shape complexity that can be obtained and may increase the amount of machining required to reach the final shape.

1.4 Current Trends and Future Developments

While the majority of aluminum forgings are made from heat treatable alloys produced by ingot metallurgy, advanced alloys have been developed for specific property improvements. The aluminum-lithium series, for example, provides high strength and increased elastic modulus with reduced density. Premium strength alloys have also been developed by consolidating rapidly-solidified powders into forging stock. These alloys are particularly resistant to corrosion. Aluminum alloy matrix composites, reinforced with silicon carbide particulate or whiskers, provide improved strength over conventional aluminum alloys. All of these advanced alloys can be forged, requiring nearly the same forging pressure as conventional alloys, but some are less workable and prone to cracking during forging. In addition, forging of sintered aluminum powder preforms has recently become a commercial reality. The low workability of composites and powder preforms present new challenges to defect-free forging of aluminum parts.

Advances in the solidification science of aluminum have resulted in castings with reduced segregation and porosity, leading to improved properties. As a result, direct casting of complex shapes is a threat to the dominance of forgings for critical

load transmission applications. In addition, the semi-solid forming process, based on thixotropic material technology, may further erode the markets for forgings. Semi-solid processes form billets heated to a mushy state (between its solidus and liquidus) in forging or die casting equipment. The resulting material has virtually no porosity and a fine microstructure, so it can compete with forgings on the basis of structural integrity. Parts formed by semi-solid processes, however, do not have the strengthening effect of grain flow that is a feature of solid state forming. High-speed machining of complex shapes directly from heavy rolled plates is an additional threat to expanded use of forgings. Reduced set up time, machine tools of greater rigidity, precision computerized controls, and new cutting tool materials have made high speed machining a viable contender for producing complex shapes that are ordinarily made by forging.

The major deterrent to more widespread use of forging is the high cost and long lead time for the design and production of tooling. For this purpose, computer technology (CAD/CAM) is being used to expedite the design and manufacture of tooling. In addition, process simulations by finite-element modeling and physical modeling are being used increasingly by forging shops for the development of optimized process parameters, including tooling designs. This practice reduces the trial-and-error efforts required to produce successful forgings. Furthermore, rapid prototyping methods are being refined to produce tooling directly from CAD solid model files. This approach is being introduced to plastic injection molding and die casting, first, because of the lower pressures involved. One major advantage of the use of rapid tooling approaches is that internal cooling channels can be fabricated into the tooling, conforming to the part shape, and leading to much more uniform heating or cooling of the part. Collectively, these technologies will reduce the time and cost of producing forging tooling, and will alter drastically the way forging design and production is carried out in the next decade.

1.5   Rationale

To understand the design flexibility and limitations of aluminum forgings, we will review the current forging methods and materials, as well as the mechanics of metal flow during forging. These considerations will then lead to an understanding of the design guidelines for aluminum forgings.

2   FORGING PROCESS

2.1   Forging Methods

Blocker-type, *conventional*, and *high definition* approaches to forging (also known, collectively, as impression die forging) are very similar in that the tooling consists of an upper and lower die containing the negative impression of the part to be produced. A blocker-type forging, Fig. 1, produces only a rough approximation of the final part shape and dimensions, with large corner and fillet radii, generous taper (draft) angles, and a large envelope of excess metal around the part to be produced. These geometric features facilitate metal flow into the die cavities, and assure easy removal of the forged part from the dies. Considerable machining is required (as much as 90% of the material volume is removed) to obtain the final part shape and dimensions. Conventional and high definition forgings have pro-
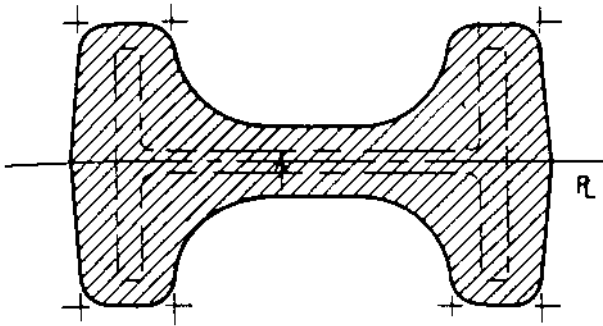
Figure 1   Blocker forging.
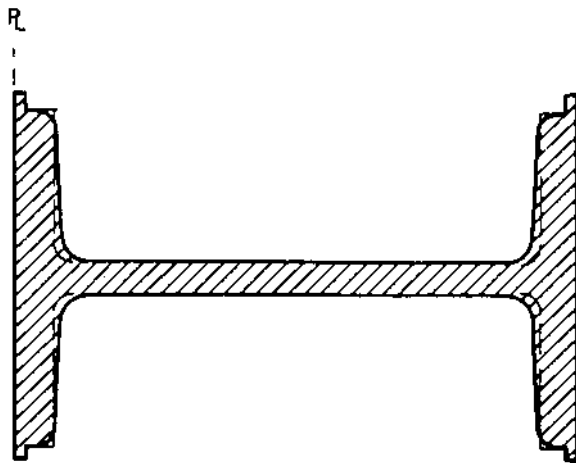
Figure 2   Precision forging.

gressively smaller machining envelopes, smaller draft angles, and smaller radii, but still require machining all over to reach the final part shape. *Precision* forging, Fig. 2, on the other hand, uses segmented tooling in a trap die concept to form the part to net, or near-net, shape requiring little or no machining. Little if any draft angles are used because the die segments separate readily from the part.

Frequently, blocker forgings are used as preforms for conventional, high definition, and precision forgings. This distributes the billet material into a shape for easier flow in the more detailed die, but at the expensive of an additional die set and process step. Open die forging methods, such as fullering, gathering, and edging, are also used to redistribute material from a simple billet or bar shape into a preform that facilitates forging of the final shape without defects.

Impression forging dies are placed in a hydraulic press, mechanical press, screw press, or forging hammer (in order of increasing forging speed, respectively) which moves the dies together and applies force to the billet. These forces compress the material between the dies, forcing the material to deform plastically and flow

into the recesses of the die, Fig. 3(a). During forging, the material flows laterally, upward and/or downward into ribs and bosses, and then through a flashland. A flash gutter, Fig. 3(b) is provided around the periphery of the part impression to allow for the escape of excess metal and to produce back pressure that helps force metal into the die details. The flash is then trimmed off to give the final forged shape. The plane between the closed dies along which the flash forms is called the parting line; location of the parting line is an important design parameter since it affects the metal flow and pattern of microstructure in the part.

Billets for forging have a fiber, or grain flow pattern, along the axial direction due to elongation of inclusions and second phase particles during hot working by rolling or extrusion. Subsequent forging deformation realigns this fiber structure along the longitudinal dimensions of the die cavities (ribs and webs) of the forging, as shown in Fig. 3(c). These inclusions and second phase particles have a strengthening effect in the same way that fibers and particulate in metal matrix composites reinforce the material in the direction of their alignment. As a result, the strength of material in the length direction of ribs and webs is greater than the strength transverse to the ribs. Similarly, the flow of metal around the corner radii of the

(a)

(b)
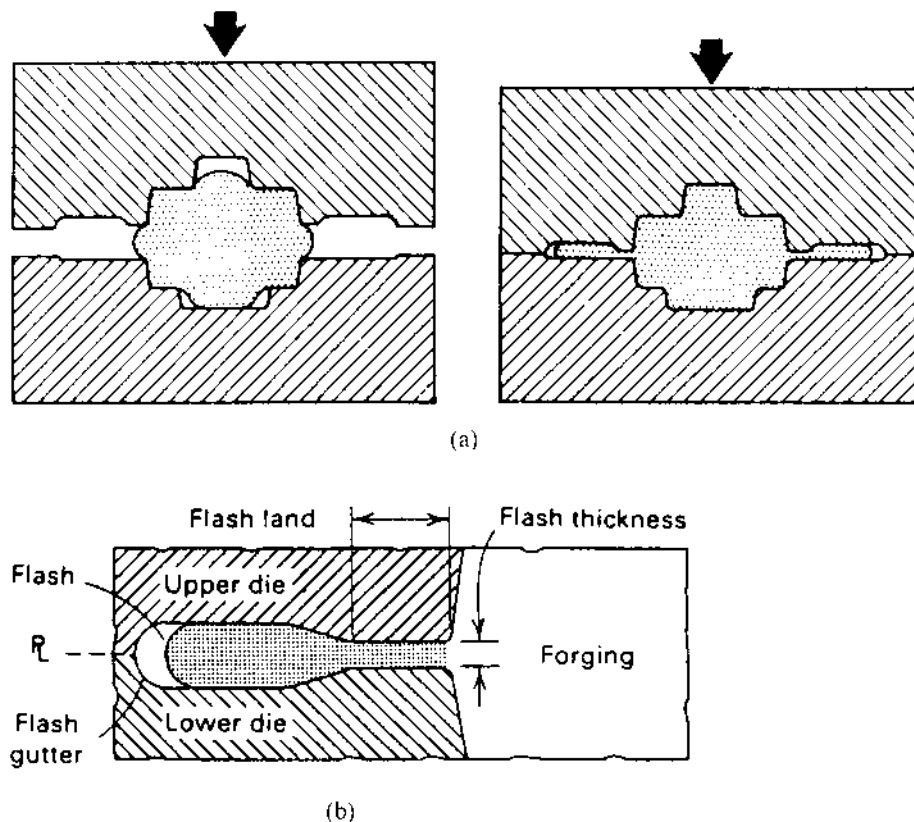
Figure 3   (a) Metal flow and formation of flash in a conventional flash gutter in impression dies; (b) Flash details.

(c)

METAL FLOW LINES

GRAIN STRUCTURE
IS RUPTURED
AT THE PARTING
LINE
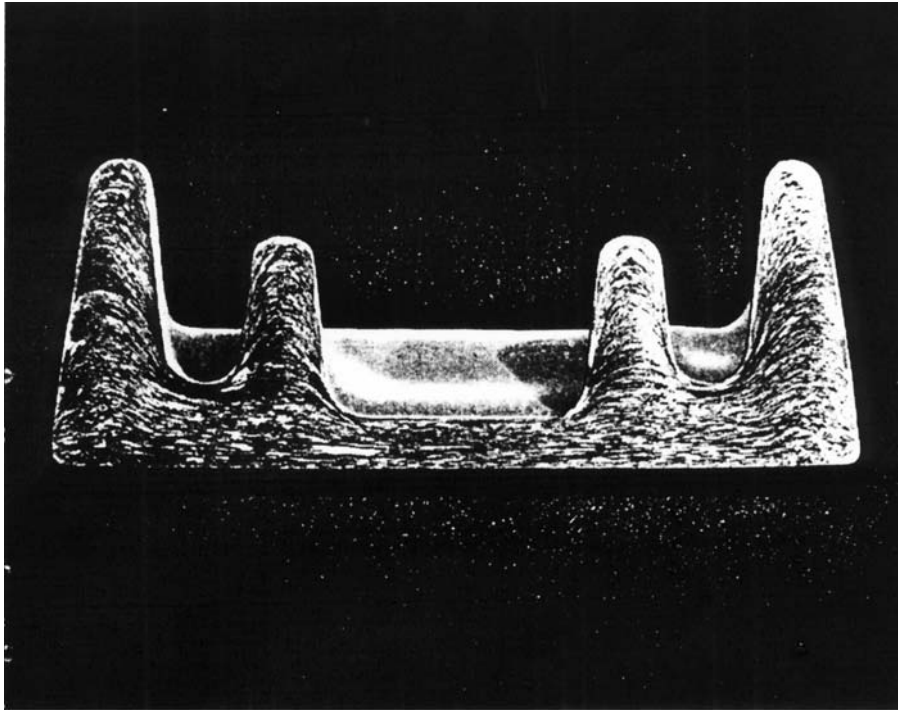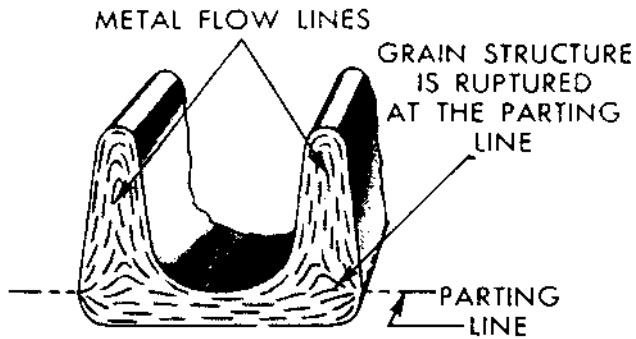
PARTING
LINE

(d)

Figure 3 (c) Section of a forging showing grain flow in the directions of metal flow; (d) Exposure of grain flow to the sheared surface by flash removal along the parting line.

die (fillet radii in the part) strengthens the corner regions of the part. Through proper design, grain flow can be oriented along the directions that will experience the greatest stress in the part during use.

Unfortunately, grain flow also occurs as material flows into the flash, Fig. 3(c), and trimming the flash may expose a plane of weakness in the material caused by the tight packing of inclusions and second phases within the narrow gap of the flashland.
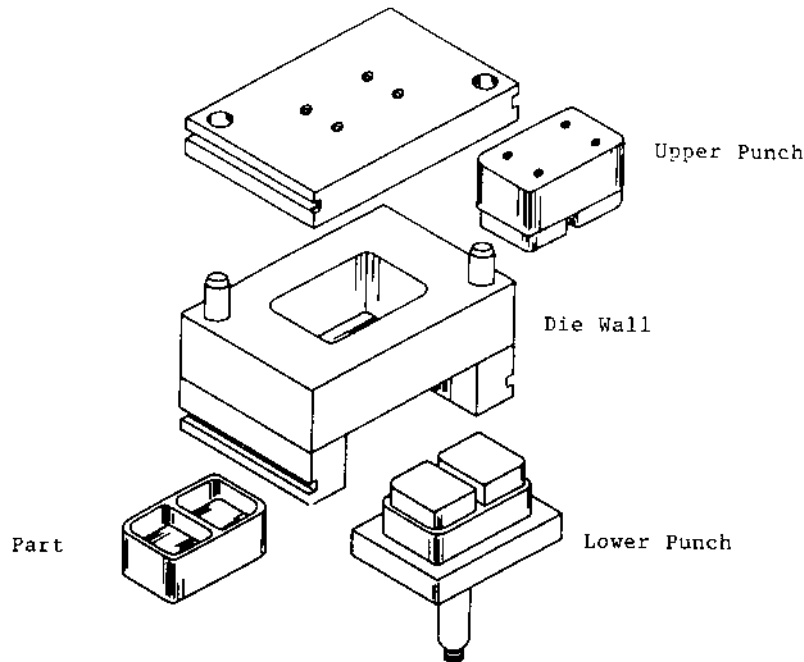
Figure 4   Through-die design for precision forging.

This plane of weakness around the periphery of the part may be a source of cracking if significant residual stresses are generated during subsequent heat treatment. Corrosion may also start along this plane of weakness when the part is placed in service or storage. Therefore, the parting line, and flash land, should not be located so that the exposed plane of weakness will be in a critical stress bearing location of the part, as in Fig. 3(d).

In contrast to impression die forging, precision forging uses a trap die tool set made of die segments assembled within a yoke or die holder, Figs 4 and 5, to produce a forging that is very close to the finished part shape and dimensions. Material flows along the web and into the ribs, as in impression die forging, but any excess material flows into thin flash zones at the top and bottom of the ribs, Fig. 2, rather than along the vertical surfaces, Fig. 1. Not only is the flash much smaller in precision forging, but any plane of weakness is at the tips of the ribs, rather than along the side of the part, and has little effect on material integrity.

Figure 4 shows a "through die" precision forging tool set. Note that the forged part is trapped within upper and lower punches and the die sidewall. The upper and lower punches form the part details and the die wall forms the outer vertical surfaces. The lower punch also serves to eject the forged part from the die. For more complicated shapes, a "wrap die" concept, Fig. 5, is used in which the die wall segments rotate outward as the part and die set are pushed upward out of the yoke after forging, or the die segments can easily be removed by hand from the forged part. This approach enables easy removal of the part from the die, which in turn eliminates the need for draft angles on the vertical surfaces. In addition, the wrap die concept allows for production of parts with undercuts, such as Fig. 6.[1,2].
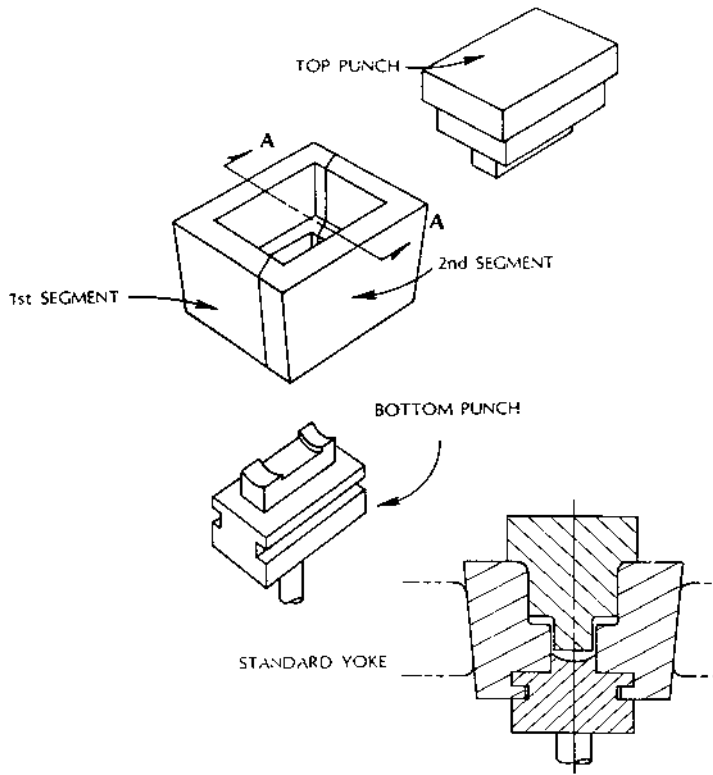
Figure 5 "Wrap die" for precision forgings.
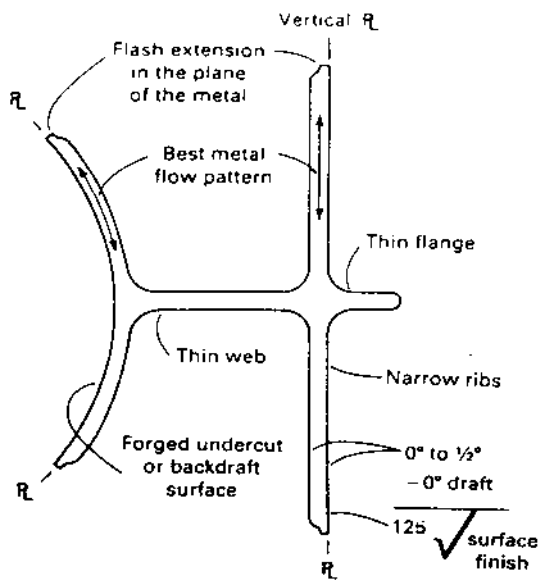
Figure 6 A precision forging showing the formation of undercuts.

Clearly the tooling cost for blocker-type impression die forging is less (by a factor of three to five) than the cost for segmented precision forging dies. This cost can be offset by the reduced cost of machining for precision forgings, making precision forging economical for large quantities by amoritizing the tooling cost.

2.2 Materials

Aluminum forgings are most commonly made of the heat treatable alloys, 2000, 6000, and 7000 series, whose composition and in-use heat treated properties are described elsewhere in this volume. For analysis of forging these alloys, however, we need to understand their mechanical properties at the temperatures and strain rates occurring in forging processes. Such data can be obtained in specialized test facilities that control the deformation stroke to give the desired strain rate, and provide a controlled heating environment around the test specimen to give the desired temperature uniformly throughout the specimen [3]. Compression testing with low friction is normally used in this type of equipment to determine flow stress curves. Compression testing with friction, as well as bend tests, are used to determine the fracture behavior.

Flow stress curves for three examples of these alloy series, AA 6061, AA 2014, and AA 7075, are shown in Figs 7–12 [4]. This reference also provides as-formed microstructures, and the flow stress data can be downloaded over the Internet for use in finite element models. Figures 7–9 show the significant effect of temperature on the flow stress; decreasing the forging temperature by 100°C more than doubles the flow stress, while increasing the forging temperature by 100°C decreases the flow stress by approximately one-half. Therefore, selection of the forging temperature has a critical effect on the ease of flow of materials, and the resulting precision and detail that can be formed in the forged part. The use of high preheat temperatures for forging, however, risks the development of hot shortness (sever

AA 6061   Strain rate 0.1/s
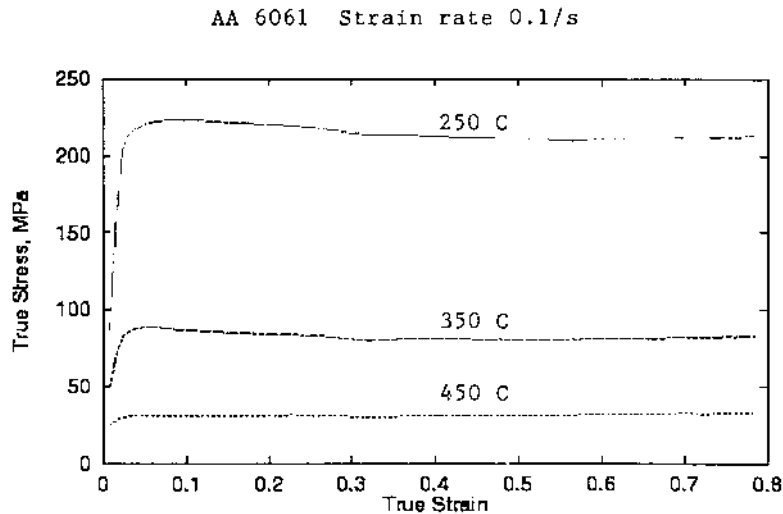
Figure 7   Flow stress curves.

AA 2014   Strain rate 0.1/s
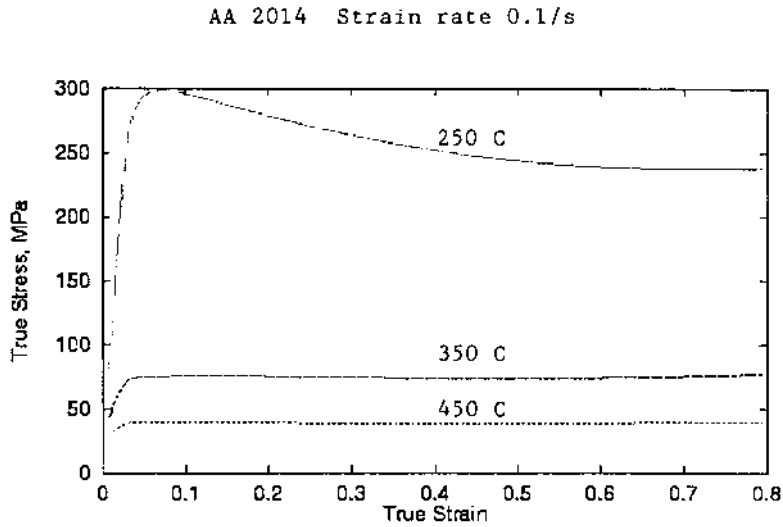
Figure 8 Flow stress curves.

AA 7075   Strain rate 0.1/s
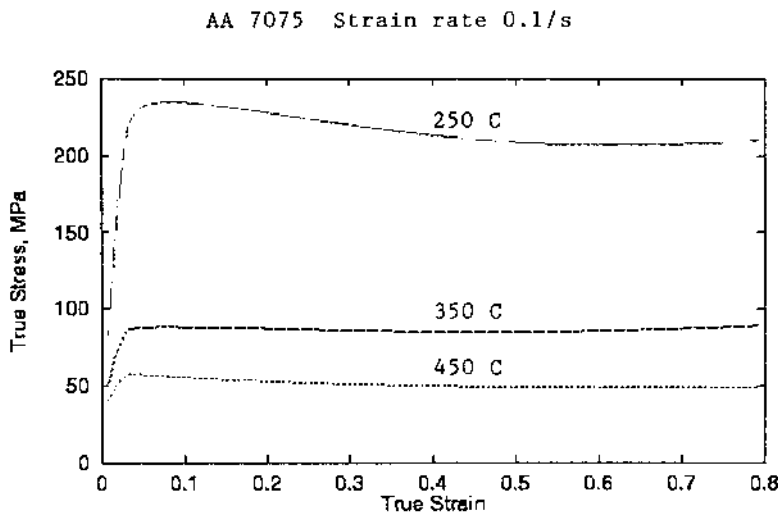
Figure 9 Flow stress curves.

cracking) due to incipient melting. The temperature rise due to deformation heating added to the billet preheat temperature may reach the solidus and melt low temperature phases in the material. This possibility is greatest in mechanical and hammer forging because the heat generated by deformation has little time to dissipate, essentially giving rise to adiabatic heating.

The flow stress of aluminum alloys is also affected significantly by strain rate, as shown in Figs 10–12. At the typical forging temperature of 350°C, increasing the strain rate from 0.1 per sec to 20 per sec increases the flow stress by one-half,

AA 6061   Temperature 350 C
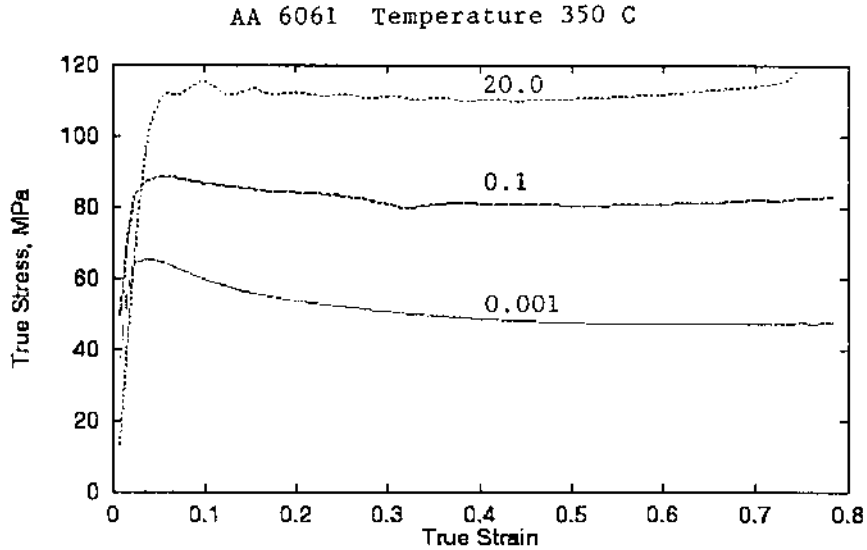
Figure 10   Flow stress curves.

AA 2014   Temperature 350 C
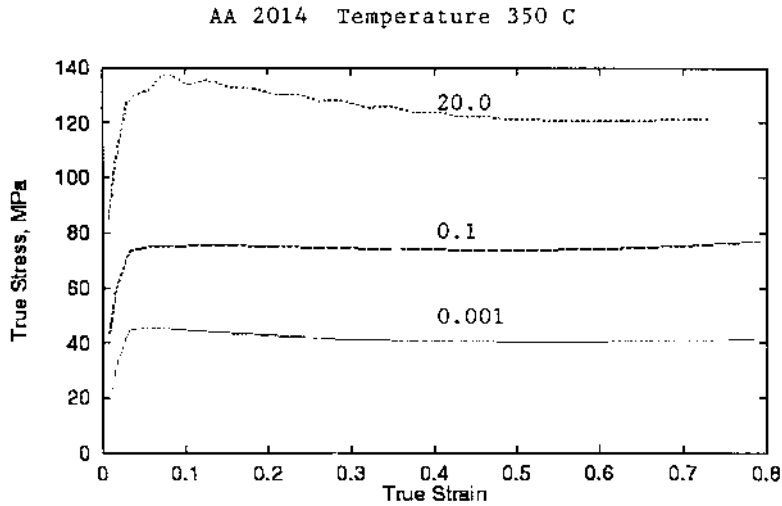
Figure 11   Flow stress curves.

while decreasing the strain rate to 0.001 per sec approximately halves the flow stress. A strain rate of 0.1 per sec is typical of hydraulic presses while the strain rate of 20 per sec is typical of mechanical presses, and the strain rate of 0.001 per sec occurs during creep forming. The low flow stress at the strain rates of hydraulic pressing enables finer details in forged parts than can be obtained in mechanical presses or hammers.

Since the forging temperature for aluminum alloys is relatively low, dies for forging aluminum (typically, a hot working grade of tool steel is used) can be heated to the forging temperature without seriously deteriorating then die material or die

AA 7075 Temperature 350 C
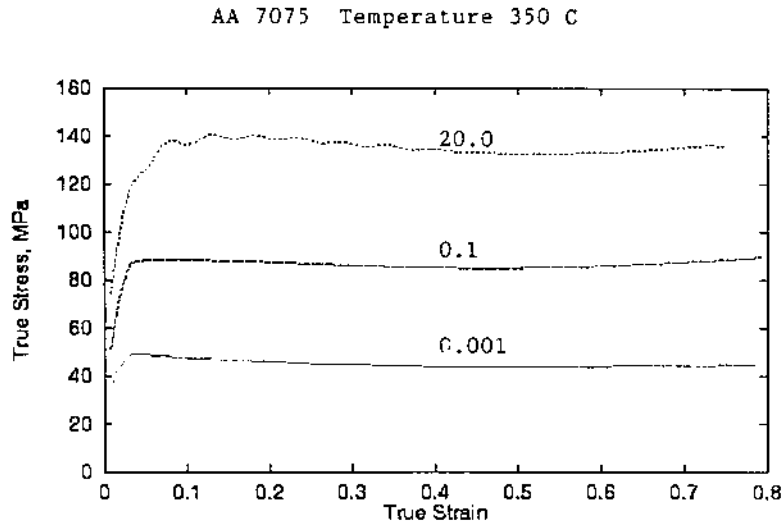
Figure 12 Flow stress curves.

surfaces. This factor further facilitates metal flow by eliminating cooling of the workpiece, so that fine detail can be developed in the forging, particularly in hydraulic presses.

Generally, the conventional alloys described above are very ductile at the forging temperatures and do not crack, even under large deformations, during forging. The advanced alloys, e.g. aluminum-lithium alloys, metal matrix composites, and consolidated rapidly solidified powders, however, may have limited ductility at forging temperatures, even though their flow stresses are similar to the conventional alloys. To evaluate the ductility of the advanced alloys for forging applications, a workability test has been used, as shown in Fig. 13. Compression of cylindrical specimens of the material generates circumferential tensile stresses and axial compressive stresses, Fig. 13(a), similar to those occurring in localized regions of a forging. Measurement of the surface strains during compression testing, Fig. 13(b), leads to a workability diagram for the material, such as Fig. 13(c), which can be used to determine the likelihood of cracking during an actual forging. This workability approach can also be used to evaluate changes in process parameters to prevent cracking.[5].

2.3 Deformation Process Mechanics

Figure 14 shows again the two extremes in producing the same part by forging: a blocker-type forging in Fig. 14(a), which has relatively large web and rib dimensions, draft angles, and radii, and requires considerable machining of material to reach the final required dimensions (shown by the dotted lines); and Fig. 14(b), which shows a precision forging approach to the same part, with little or no machining required to reach the final dimensions. The forging loads and tool design for these cases are
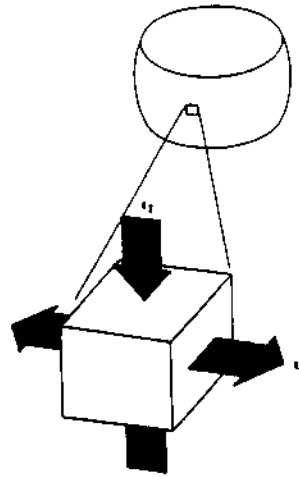
(a)
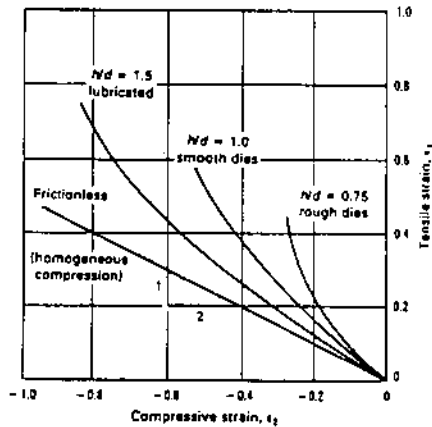
(b)
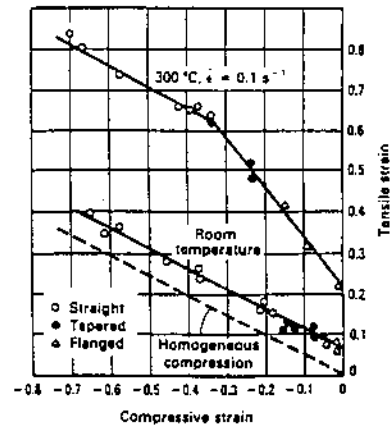
(c)

Figure 13   Workability testing: (a) upset test; (b) strains on the surface of the test specimen; (c) strains at fracture for AA 2024 at room temperature and hot working temperature.

considerably different. The forging load for precision forgings is higher than blocker forgings, and the cost of tooling for precision forged parts is considerably higher than blocker forged parts.

To understand these differences and their implications for design with forgings, we will consider the mechanics of metal flow in the rib-web type aluminum forgings shown in Fig. 14. A wide variety of shapes can be produced by forging, but the geometric features of this type of forging are representative, and will illustrate the main features of metal flow and pressures during forging. The slab method
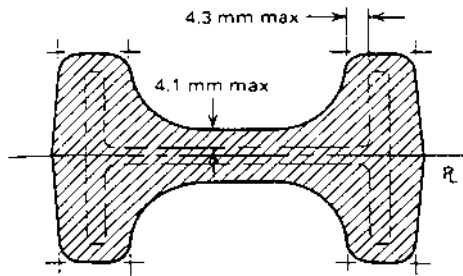
(a)
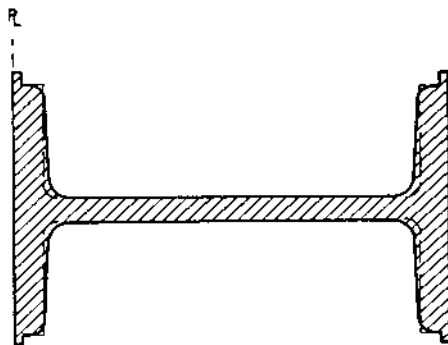
(b)

Figure 14   Blocker (a) and precision forging (b).

of analysis will be used; although it involves several approximations, it provides physical insight to the forging process and involves only simple calculations. This method of analysis is described in several references [6–8].

Generally, the forging billet is first contacted by the web sections of the die. As the billet undergoes compression, material flows laterally then vertically into the ribs. We will examine metal flow in the web and ribs separately, and then combine the results. The total load is made up of the pressure to form the web plus the pressure to form the ribs.

First, focusing on the lateral flow of metal in the web section, Fig. 15(a), we can consider the behavior of a typical vertical element of material having height t (the web thickness) and width dx as it moves to the right (positive x-direction) with the metal flow. Vertical pressure p acts on the element as the upper and lower dies press on the billet. Since the element is moving to the right, away from the centerline, friction at the die contact surfaces will act to the left on the element, opposing the relative motion. In metalworking processes, friction is most accurately represented as $f = mk$, where k is the shear yield strength of the workpiece material, and m is a friction factor that ranges from 0.0 for perfect lubrication to 1.0 for perfect sticking of the workpiece material to the die. The shear yield strength k is equal to 0.577 S, where S is the flow stress of the material [6].

With the friction forces acting to the left on the top and bottom surfaces of the element shown in Fig. 15(a), there must be an internal horizontal force acting to the right on the element to maintain equilibrium. (Even though the element is moving, its acceleration is negligible, so static equilibrium is maintained, i.e., the sum of the forces in the x-direction equals zero.) An internal pressure, designated q, acts in the x-direction on the vertical faces, differing by a differential amount dq on each side of the element.

(a)

(b)
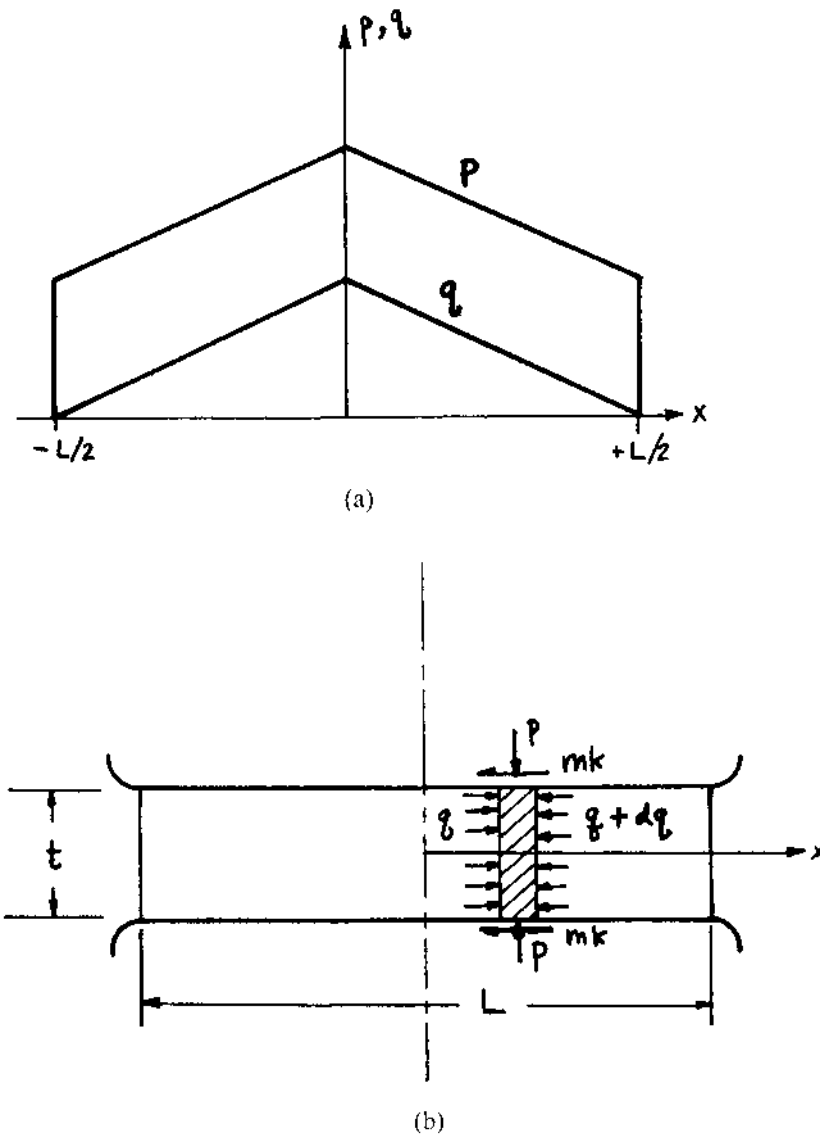
Figure 15   (a) Element of material in the web section during forging; (b) Schematic pressure distributions in the web.

Applying horizontal equilibrium to the element,

$$qt - (q + dq)t - 2mk\,dx = 0$$
$$t\,dq - 2mk\,dx = 0 \qquad\qquad (1)$$
$$dq = -2mk/t\,dx$$

As the billet spreads to the edges of the web section of the die, the ends are free from stress, so $q = 0$ at $x = L/2$. Applying this boundary condition to Eq.(1),

$$q - 0 = -(2mk/t)\,(x - L/2)$$

or $\qquad\qquad\qquad\qquad\qquad\qquad\qquad\qquad\qquad\qquad\qquad$ (2)

$$q = mk\,(L/t)\,(1 - 2x/L)$$

This distribution of internal pressure q, shown in Fig. 15(b), has a peak value at the centerline and is symmetric about $x = 0$ because material to the left of the centerline flows to the left, and is a mirror image of the element shown in Fig. 15(a).

Since the element of material in Fig. 15(a) is undergoing plastic deformation, the stresses acting on the element must satisfy the yield criterion [6],

$$p - q = 1.15\,S = 2k$$

where S is the flow stress of the material. Then the pressure on the die in the web region is

$$p = 1.15\,S + q = 1.15\,S\,[1 + (m/2)(L/t)(1 - 2x/L)] \qquad\qquad (3)$$

which is also plotted in Fig. 15(b). The peak pressure at the centerline is $1.15S\,[1 + (m/2)(L/t)]$.

Even though the web is flat and the compressive deformation is the same at any point along the web, the pressure distribution acting between the die and material is actually non-uniform, reaching a peak value at the center. Note that the pressure at any point along the web increases with increasing web length to thickness ratio L/t, friction m, and flow stress S.

If we take $m = 0.3$, a typical value for aluminum forging, $L/t = 3$ for the blocker-type forging, and $S = 100$ MPa (approximately, for convenience) from Fig. 7 (AA 6061 at 350°C, 0.1 per sec strain rate), Eq. (3) gives the peak pressure in the web as 167 MPa. For a precision forging having $L/t = 9$ (web thickness is one-third of the blocker web thickness), the peak pressure will be 270 MPa, or 60% higher than the blocker-type forging.

Figure 15 and Eq. (3) show that friction is the major constraint to metal flow in the web section, and its influence increases as the web thickness decreases. The effect of this frictional constraint can be reduced, to some extent, by tapering the web section, as shown in Fig. 16. Again examining a vertical element of material moving to the right in the web region, pressure from the die now has a component of force acting outward in the positive x-direction, counteracting the friction force acting
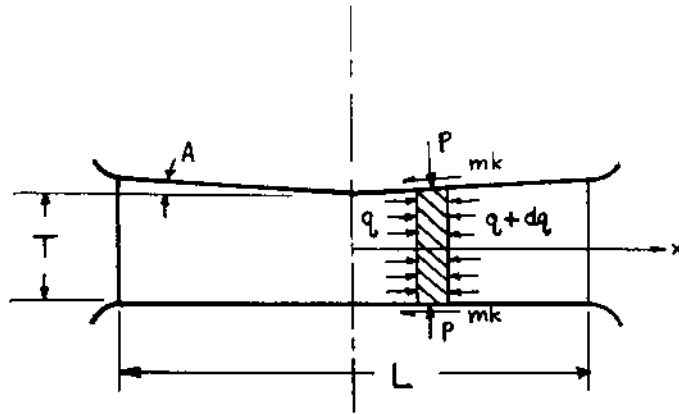
Figure 16 Element of material in a tapered web section.

inward. Equilibrium of the element in Fig. 16 gives

$$qt + p\,dt - 2\,mk\,dx - (q + dq)(t + dt) = 0$$
$$p\,dt - q\,dt - 2\,km\,dx - t\,dq = 0$$
$$dq = [(p - q)\,dt - 2\,mk\,dx]/t$$

If we again take $p\text{-}q = 2k = 1.15S$,

$$dq = 1.15\,S\,(dt/dx - m)\,dx/t \qquad\qquad (4)$$

If the taper is represented by $t = T + (\tan A)x$, where T is the web thickness at the center $(x = 0)$ and A is the taper angle, then $dt/dx = \tan A = A'$. Substituting these into Eq. (4).

$$dq = 1.15\,S\,(A' - m)\,dx/(T + A'x)$$

The boundary condition $q = 0$ at $x = L/2$ applies again, giving

$$q - 0 = 1.15\,S\,(A' - m)\,(1/A')\,[\ln(T + A'x)/\ln(T + A'L/2)]$$
$$q = 1.15\,S\,(m/A' - 1)\,\ln[(T + A'L/2)/(T + A'x)]$$

At $x = 0$, the horizontal pressure is

$$q = 1.15\,S\,(m/A' - 1)\,\ln[1 + (A'/2)(L/T)]$$

and the peak die pressure is $p = 1.15\,S + q$, or

$$p = 1.15\,S\,\{1 + (m/A' - 1)\,\ln[1 + (A'/2)(L/T)]\} \qquad\qquad (5)$$

Using Eq.(5), for a taper angle of 1°c, and all other conditions remaining the same, the peak pressure for the blocker forging $(L/T = 3)$ is 163 MPa, a reduction of only 2.4% compared to 167 MPa pressure for the flat web. A 3° taper angle reduces

the peak pressure by 6.6%. However, for the precision forging ($L/T=9$), Eq.(5) gives a peak pressure of 256 MPa for 1° taper, and 230 MPa for 3° degree taper, which are 5% and 15% less, respectively, than the 270 MPa pressure for a flat web.

Focusing now on the flow of metal into the ribs, the pressure required to force material into a rib cavity must overcome friction as well as the taper on the rib. Consider a horizontal element of material in the rib having width w and thickness dz, Fig. 17, as it moves upward (positive z-direction) with metal flow into the rib. Pressure p acts on each end of the element in contact with the die in the rib section. If there is no draft angle on the rib, the pressure p will act horizontally, but if the rib has a draft angle, a component of the pressure p will act downward in the vertical direction. Friction will also act downward on the ends of the element since the element is moving upward. Because of the friction forces and vertical components of the pressure from the die, the internal pressure q will differ by a differential amount dq on each side to maintain vertical equilibrium of the element. Applying equilibrium in the z-direction,

$$qw - (q + dq)(w + dw) + p\,dw - 2mk\,dz = 0$$
$$q\,dw - w\,dq + p\,dw - 2mk\,dz = 0$$
$$(p - q)\,dw - 2mk\,dz = w\,dq$$
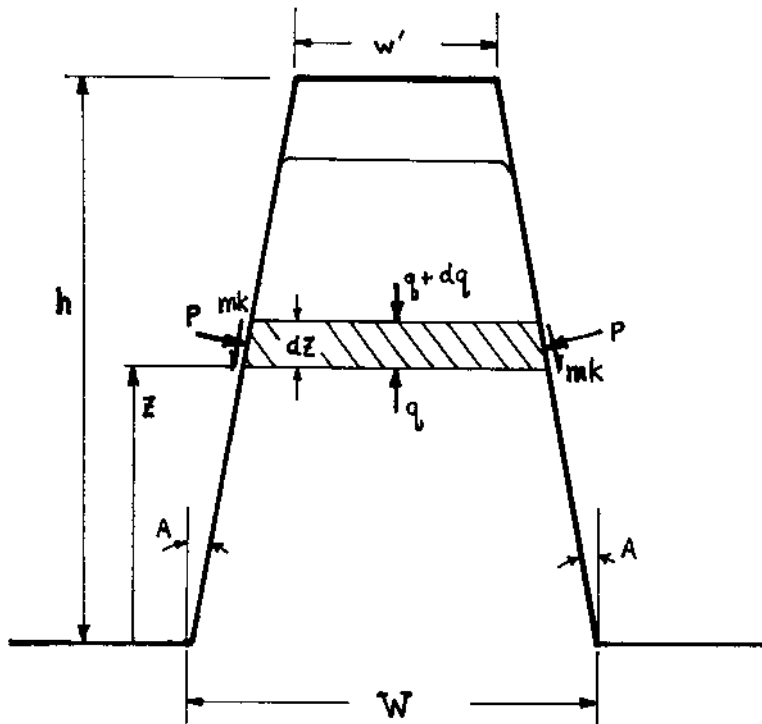
Figure 17   Element of material in the rib during forging.

Since the element is undergoing plastic deformation, the pressure difference must satisfy the yield criterion, $p - q = 2k = 1.15\,S$, giving

$$dq = 1.15\,S\,(dw/dz - 2m)\,dz/w \tag{6}$$

Also, the draft angle A on each side of the rib gives the variation of width of the element $w = W - 2(\tan A)z = W - 2A'z$, where W is the thickness of the rib at its base, $z = 0$.

Then Eq. (6) gives

$$dq = -1.15\,S\,(2A' + m)\,dz/(W - 2A'z)$$

Since the pressure q is zero at the top of the rib, $z = h$, this boundary condition gives

$$q - 0 = -1.15\,S\,(m/W)\,(z - h) \qquad\qquad \text{for } A = 0$$

and

$$q - 0 = -1.15\,S\,(2A' + m)/2A'\ln[(W - 2A'z)/(W - 2A'h)] \qquad \text{for } A > 0$$

In final form,

$$q = 1.15\,S\,m(h/W)\,(1 - z/h) \qquad\qquad [A = 0]$$

and

$$q = 1.15\,S\,(1 + m/2A')\,\ln\{[1 - 2A'(h/W)(z/h)]/[1 - 2A'(h/W)]\} \qquad [A > 0]$$

The pressure distribution for this case, Fig. 18, shows a nearly linear decrease in q from the bottom to the top of the rib (linear decrease if the draft angle $A = 0$).

At the base of the rib, $z = 0$, the pressure required to fill the rib is

$$q = 1.15\,S\,m(h/W) \qquad\qquad ([A = 0]\,(7a)$$

and

$$q = 1.15\,s\,(1 + m/2A')\,\ln[1 - 2A'(h/W)] \qquad\qquad [A > 0]\,(7b)$$

Taking $m = 0.3$ and a typical blocker-type forging rib, $h/W = 1.0$, Eqs. (7a) and (7b) give the following results for rib forming pressure for no draft and for draft angles of $1°$, $3°$ and $5°$:

A(°)	Rib Pressure (MPa) $(h = W)$
0	34.5
1	39.2
3	49.1
5	59.9

For a precision forging, with $h/W = 3$, and all other conditions remaining the same, the rib forming pressure becomes
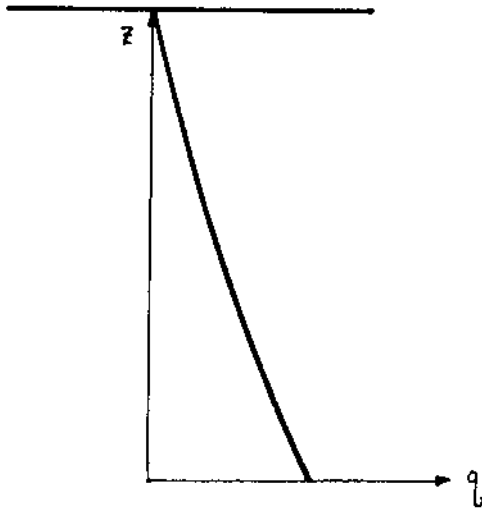
Figure 18 Pressure distribution along the length of the rib.

A(°)	Rib Pressure (MPa) ($h = 3W$)
0	103
1	121
3	167
5	213

Note that forming thinner ribs (decreasing W by a factor of 3) at least triples the rib forming pressure, and the multiplying factor increases with increasing draft angle. Also, use of a 5° draft angle rather than no draft angle approximately doubles the rib forming pressure. This is the opposite effect of the taper angle in the web, Eq. (5), where the pressure component due to the taper angle in the web counteracts the effect of friction, while in the rib the pressure component due to the taper angle augments the effect of friction.

As metal flows to the end of the rib, an additional pressure is required to completely fill the corner radii of the rib. Near the corners, a cylindrical state of stress occurs, Fig. 19, which can be treated by an equilibrium analysis similar to that for the rib and web. In this case, the material has nearly filled the corner and the unfilled region is defined by an arc of radius R.

The equilibrium analysis examines a quarter circular arc element moving into the corner at a distance r from the corner. The element is acted on by pressure from the die surfaces perpendicular to the corner. Friction also acts on the ends of the element in the direction opposing flow into the corner. These forces lead to a differential in radial pressure dq across the thickness of the arc element.

Applying equilibrium in the radial direction (origin at the intersection of the rib end and side surfaces), pressure q acting over the quarter circle arc gives a total force of $q\,r\sqrt{2}$ acting at 45° between the two corner surfaces and away from the origin. The
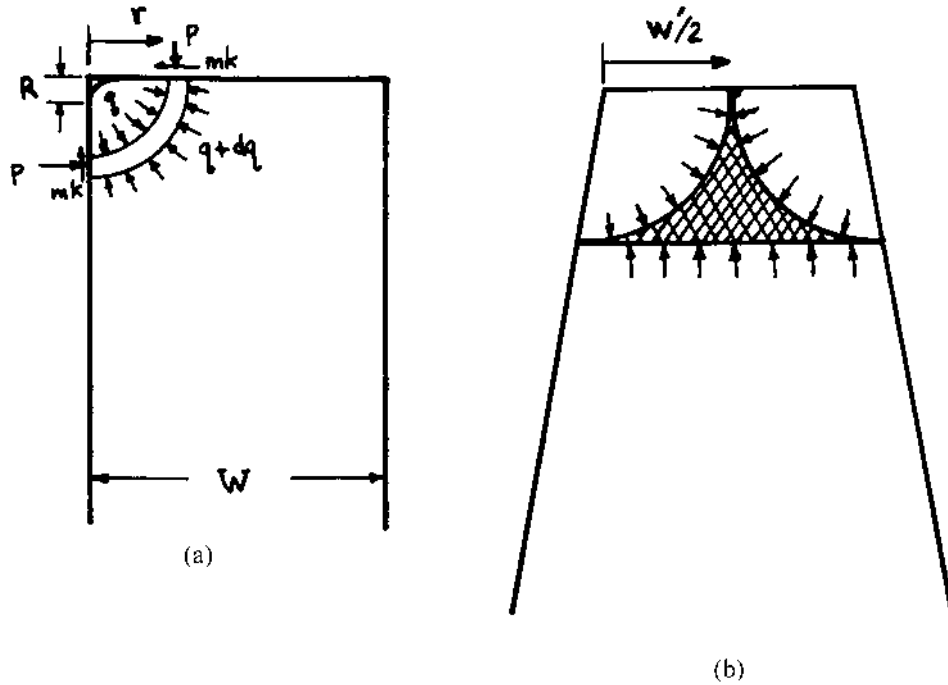
Figure 19   (a) An element of material flowing into a corner of the rib; (b) Transition from the corner cylindrical stress state to the rib linear slab stress state.

pressure $q + dq$ similarly gives a total force of $(q + dq)(r + dr) \sqrt{2}$ acting in the opposite direction. The pressure and friction forces act over the element thickness dr and their components in the 45° direction are $2(p + mk) \sqrt{2}$. The square root factors appear in all terms, canceling out, and leaving

$$q\, r - (q + dq)(r + dr) + p\, dr + mk\, dr = 0$$

or

$$dq = [mk + (p - q)]dr/r$$

Again, from the yield criterion, p - $q = 1.15\ S = 2k$, giving

$$dq = 1.15\, S\, (1 + m/2)\, dr/r$$

At $r = R$, the free surface radius, the radial pressure $q = 0$, then

$$q - 0 = 1.15\, S\, (1 + m/2)(\ln r - \ln R)$$

or

$$q = 1.15\, S\, (1 + m/2)[\ln(r/R)] \tag{8}$$

As shown in Eq. (8), in the limit, the pressure required to form a corner of zero radius ($R = 0$) is infinite. Even small corners will require very high pressures for complete filling.

Transition from the cylindrical pressure state in the corners to the linear slab stress state in the rib occurs in a transition zone, Fig. 19(b), defined by $r = w'/2$, where w' is the width of the rib at the end. Then, to calculate the pressure required to fill a corner, take $r = w'/2$ in Eq. (8). Using $m = 0.3$, $S = 100$ MPa, $w' = 12$ mm, 12 mm, and a corner radius of 1.6 mm, the pressure required to fill the corner is 175 MPa. For a corner radius of 3.2 mm, the required pressure drops to 83 MPa. Note that the corner filling pressure is the same order of magnitude as the pressure required to fill the entire rib.

The pressures required to form the die corners, ribs, and webs are additive, as shown in Fig. 20. Starting with the pressure required to fill the corner, this serves as the boundary condition for pressure in the rib. That is, taking $q1$ from Eq. (8) as the pressure needed to fill the corner, the pressure for forming the rib is $q1$ plus the calculation for rib forming (Eq. (7)), giving the total pressure $q2$ at the base of the rib. Similarly, this pressure serves as the boundary condition for the pressure in the web. In this case, from Fig. 20, the transition around the die corner involves applying the yield criterion at the junction between the rib and web. That is, $q3$ at the end of the web equals the pressure at the base of the rib, $q2$, plus 1.15 S. Then the internal pressure distribution q in the web is given by Eq. (2) plus $q3$, and the pressure distribution on the die in the web region is given by Eq. (3),
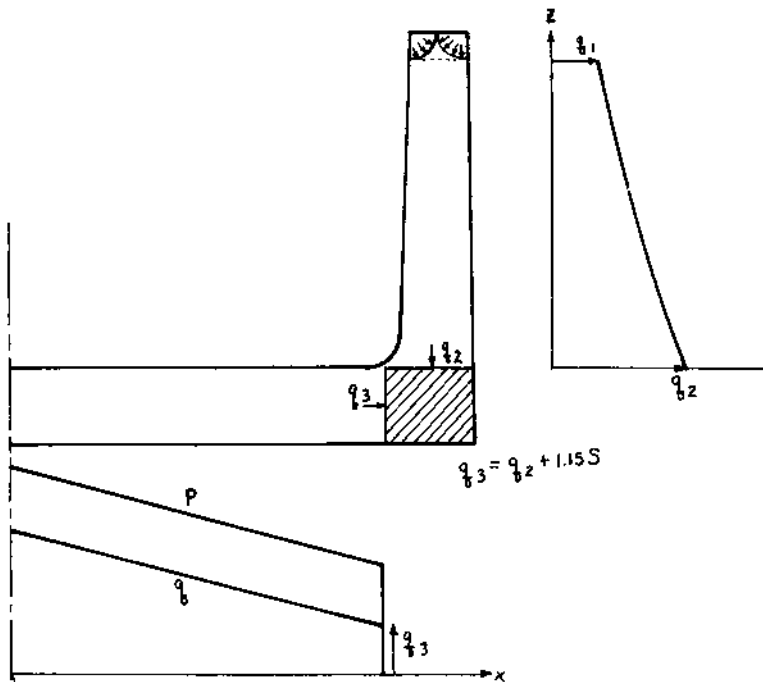
Figure 20 Accumulation of pressure: q_1 from corner filling, q_2 from rib forming, q_3 from the junction between the rib and web, and finally P due to lateral flow in the web.

modified to include $q3$. The total peak die pressure on the web at $x = 0$ (for the case of no draft angles) is then

$$p = 1.15\,S\,[1 + (m/2)(L/t) + m(h/w) + (1 + m/2)\,\ln(w'/2R)] \qquad (9)$$

where the three non-unit terms in square brackets represent the contributions to pressure from the web, rib, and corner, respectively. The pressure on the die in the web region increases substantially as the die corner radii R at the top of the ribs decrease, as the rib height h increases and the rib thickness W decreases, as well as when the web thickness t, itself, decreases. Calculation of the total forging load can be obtained by integrating the pressure distribution on the web section and the cross-sections of the ribs. The effects of web and rib angles can be included by replacing $(m/2)\,(L/2)$ by $(m/A' - 1)\,\text{In}\,[1 + (A'/2)(L/T)]$ from Eq. (5) and replacing $m(h/W)$ by Eq. (7b).

Another important aspect of metal flow during aluminum forging requires a more localized view of metal flow around a corner of the die, such as the radius between the rib and the web. If the die corner radius is too small, metal flow around the corner separates from the die. When the material reaches the top of the rib, it folds over on itself and causes a lap, as described in the sequence of Fig. 21. This phenomenon occurs only for relatively thick ribs having sufficient space for the material to fold over. Thin ribs, as in precision forging, prevent this type of defect.
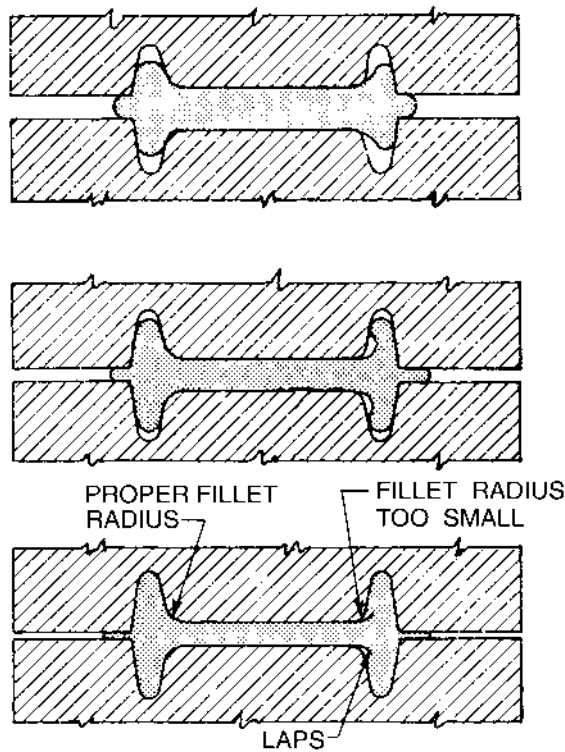
Figure 21   Illustration of the influence of die corner radius on the formation of laps.

Very high shear stresses generated during flow around such corners may cause periodic cracking in the surface material as it is extruded into the rib region, as shown in Fig. 22. For the conventional heat treatable alloys such as the 2000, 6000, and 7000 series as well as aluminum-lithium and consolidated powders, such defects are not very likely. However, in the metal matrix composites and powder alloys, cracking of this form is very prevalent. Paradoxically, cracking around the fillet radii in these hard to work alloys is less likely to occur in thin ribs than in thicker ribs because the higher pressure required to form thin ribs prevents the ductile fracture mechanism from occurring at the base of the rib. Cracking is also possible at the top of the rib in hard to form alloys, as shown in Fig. 22, because friction along the rib surfaces pulls tensile stresses on the top free surface.

Finally the influence of forging design on die stresses must be taken into account. For example, in a blocker-type forging, Fig. 14(a), pressures from the workpiece acting on the rib surfaces of the die produce a wedge effect that tends to expand the rib thickness, causing tensile stress concentration at the top of the rib cavity. However, the large radii in a blocker-type die will minimize such stress concentrations. In contrast, high definition forgins and conventional forgings have thinner ribs, which lead to sharper radii at the top of the ribs; they also have larger pressures acting on the rib sections of the die, as described by Eq. (7). This combination of circumstances leads to high stresses in the die and a greater likelihood of cracks (or die checking) in the die corners, as shown in Fig. 23. Die cracking
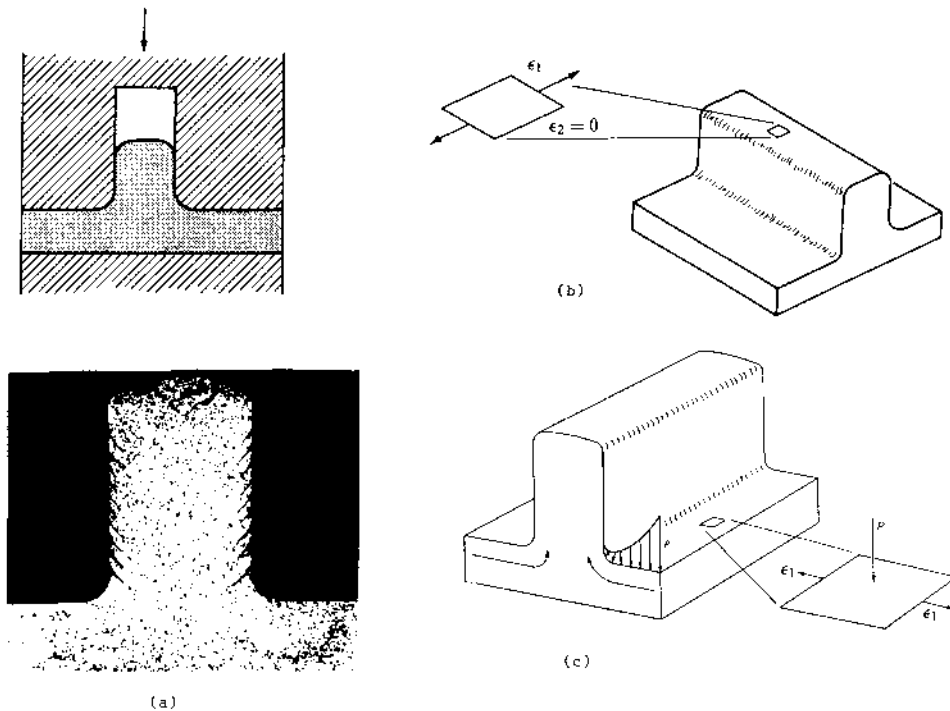
Figure 22 Fracture during rib-web forging of a hard to work alloy: (a) cracking at the top surface and at the corner radius; (b) strain state at the top of the rib; (c) strain and pressure at the corner radius.

IMPRESSION FOR ROUND-EDGED RIB

IMPRESSION FOR FLAT-EDGED RIB

DIE SECTIONS

A FULL RADIUS
GIVES MAXIMUM
DIE LIFE AND
EASE OF FILLING

SMALL RADII

DIE CHECKING TENDS
TO DEVELOP AT
SHARP CORNERS
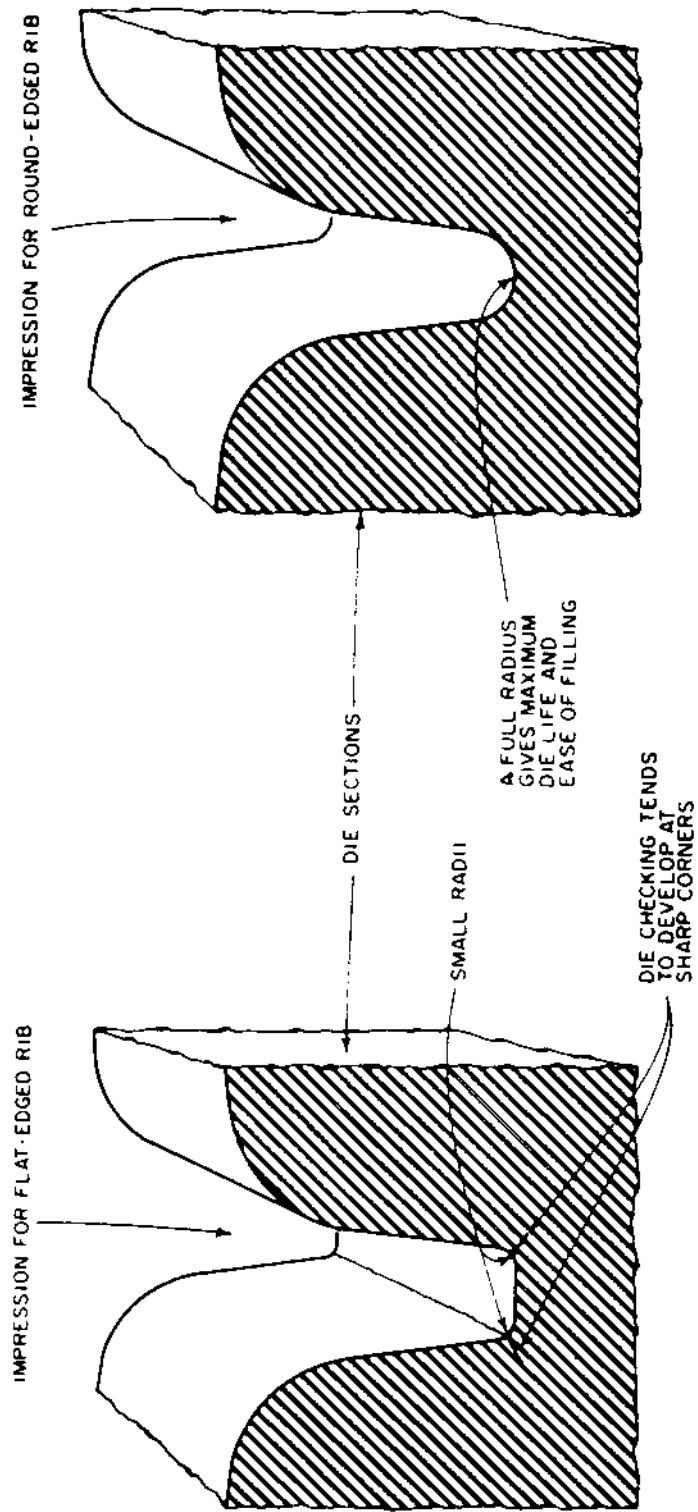
Figure 23 Influence of die fillet radius on cracking of the die (die checking).

of this type does not exist in precision forging, Fig. 14(b), because the die segments meet at the tops of the ribs to allow for a parting line and flash, so tensile stresses do not occur in the rib corners.

Die wear is an additional problem that is affected by forging design. Small fillet radii on the forged parts require small corner radii on the die, which are susceptible to high wear if they are in an area where high die pressures and high metal flow rates occur. The localized generation of heat due to high deformation is augmented by the generation of heat due to friction at the corner, which raises the temperature of the die corner and further aggravates the conditions for wear. This set of circumstances is particularly apt to occur at the corner radius joining a web and rib, especially if the rib thickness is small. The major result of these effects is reduced die life and/or increasing frequency of die reconditioning to maintain the forging dimensions within tolerance.

Insight into metal flow, defects, pressures and die stresses during forging can also be obtained through modern, high speed computing using large deformation, nonlinear finite element codes, such as ALPID, DEFORM, and ABAQUS. Figures 24 and 25 are examples of the deformation patterns predicted by such codes for a rib-web shape in precision forging and in impression die forging [9]. Such simulations use extensive computer time and are primarily useful at the present time for troubleshooting specific design problems, rather than as a general forging design tool. As computer hardware advances continue and numerical methods further reduce computational time, it is expected that computer simulations will be used iteratively to optimize forging and die designs. In the meantime, simple analyses such as Eqs. (1)–(9), empirical workability approaches such as Ref. 5, and experience-based rules of thumb are used for forging design.

3 FORGED PART DESIGN

The quantitative and qualitative results given in the previous section control the design of parts for aluminum alloy forging. Specifically, taper (draft) angles, fillet and corner radii, rib heights, and rib and web thicknesses are limited by the forging method, tooling concepts and cost constraints. In addition, selection of the forging orientation and parting line affect the grain flow, ease of forging, and cost.

3.1 Parting Line

The line of separation of the dies is called the parting line, Figs 1, 2 and 3(a), and establishing the location and shape of the parting line is the first step in forging design. The decisions on choosing the parting line are different for impression die forging and precision forging. Obviously, to separate impression dies and allow removal of the forged part, the forging can have no undercuts, such as in Fig. 6. For precision forging, the dies are made for easy removal of the part after the die segments are removed from the die holder or yoke, Figs 4 and 5. In this case, the parting line will be vertical (Fig. 2).

In impression die forging, the parting line should encompass the largest cross-section of the part. Spreading metal laterally is easier than forcing material into tall ribs, as seen from Eqs. (4) and (7). The part shown in Fig. 26, then should be forged with the orientation shown on the left because the rib heights are lower
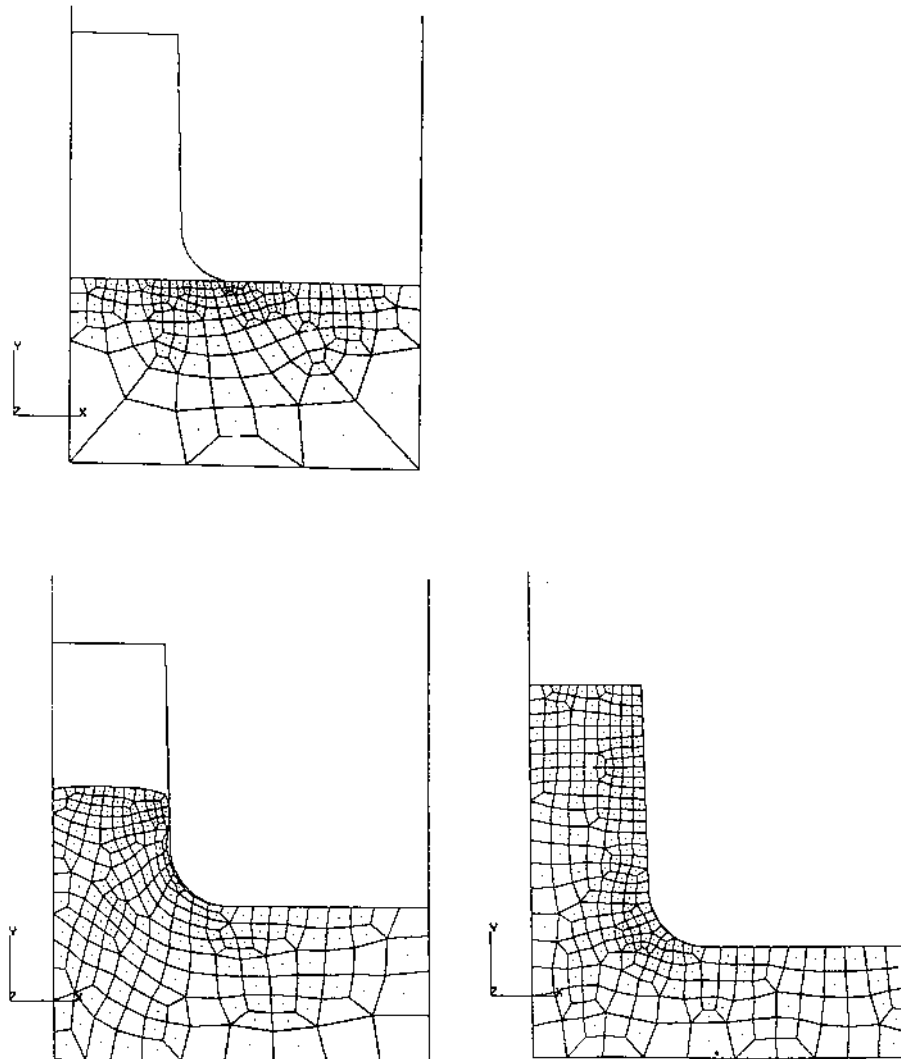
Figure 24 Simulation of a rib web shape in precision forging.

and has the largest cross-section of the two options. If the forged part can be designed with one side flat, as in Fig. 27, the parting line is at the top and die manufacture is simplified because only one impression die needs to be machined.

Parting line selection also affects the grain flow in the part. With the parting line at mid-height of a rib, Fig. 3(d), the grain flow exits into the flash along a vertical surface, and the plane of weakness may be in a critical area regarding the loads to be transmitted by the finished part. Thus, the parting line and flash should be located at the extreme ends of the ribs, i.e. at the junction with the web, or at the tips of the ribs. In precision forging, the vertical parting lines, Fig. 2, assure that the flash always exits the tips of the ribs, causing no plane of weakness at a critical location.
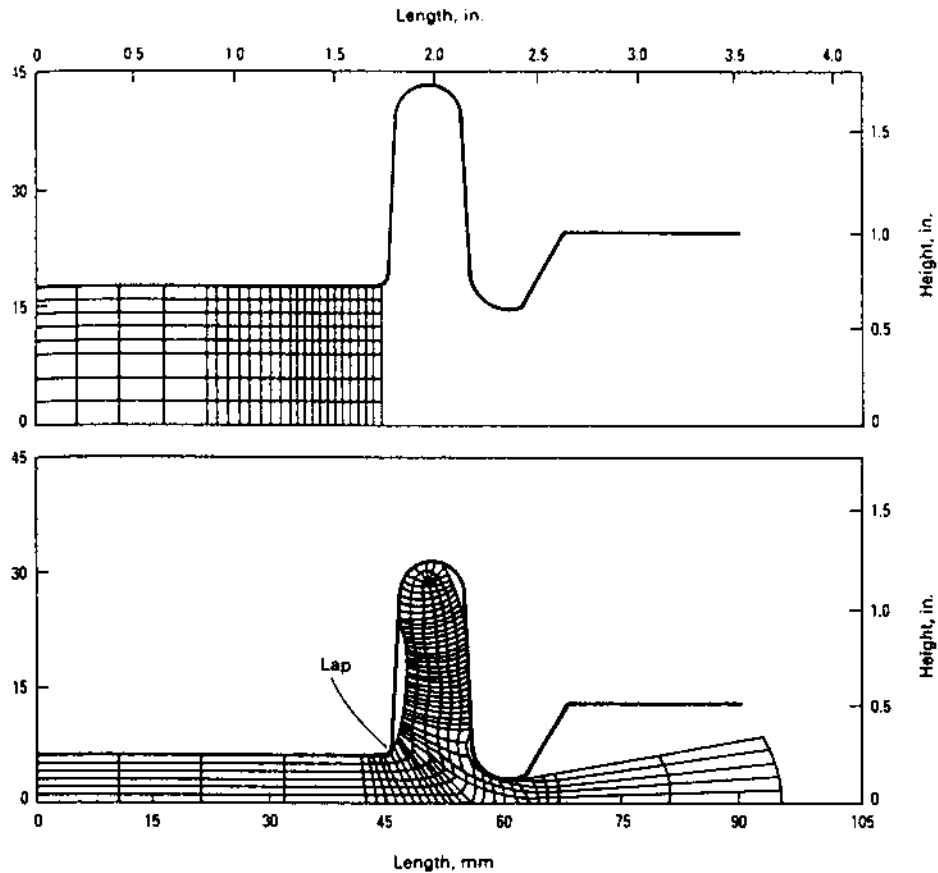
Figure 25 Simulation of a rib-web shape in impression die forging.

Planes of symmetry allow easy centering of the part along the axis of force of the forging equipment, which avoids side thrust on the dies. If the forging equipment has sufficient capacity, a plane of symmetry can be enforced by forging two non-symmetric parts as one part with a common face acting as the plane of symmetry. Then the two parts can be separated by sawing or shearing operations.

3.2 Fillets and Corners

Sharp fillet radii in the parts (small corner radii in the dies) lead to a number of problems, including laps (Fig. 21), cracks (Fig. 22), and excessive die wear. The first two defects are avoided in precision die forging because the rib sections are thin, but at the sacrifice of the high cost of precision tooling. Suggested minimum fillet radii between webs and ribs for small rib heights on blocker-type forgings is 0.50 in. and for precision forgings 0.125 in. For rib heights beyond 1 in., these part fillet radii should be increased by 0.50 in. for blockers and 0.125 in. for precision forgings, per inch of flange height. When forging hard to work alloys, these radii should be doubled.
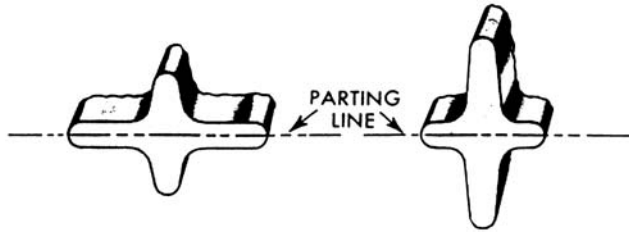
Figure 26   This section should be forged with the orientation shown on the left.
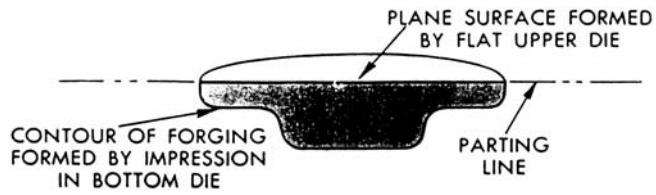
Figure 27   Forging with one flat side.
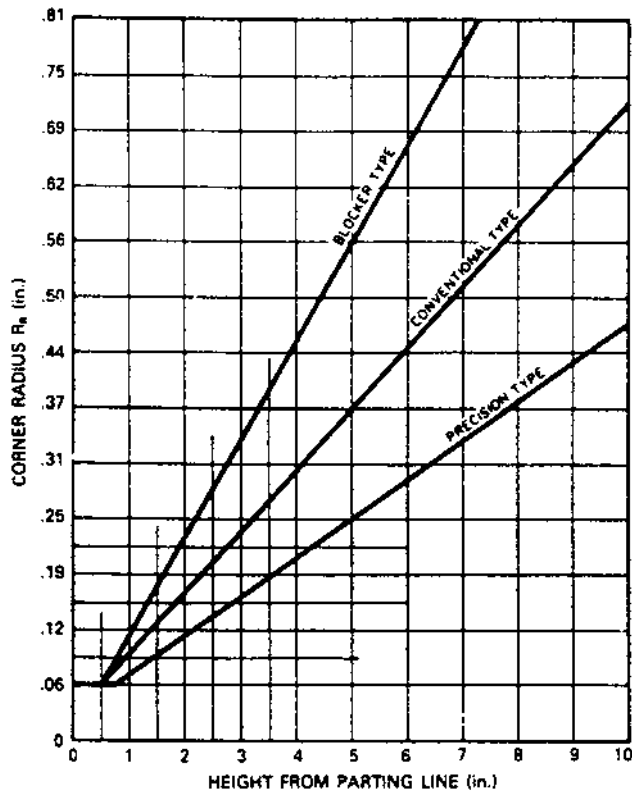
Figure 28   Recommended corner radius limits for aluminum alloy forgings.

Corner radii on forgings (fillet radii on the dies) should also be generous to allow for easy filling of the rib corners (Eq. (8)) and to minimize stress concentrations at the fillet radii of the die during forging, shown in Fig. 23. Suggested corner radii are given in Fig. 28 for impression dies. The suggested minimum radius is 1/16 in. for small distances from the parting line, and then increases linearly with increasing height.

3.3 Web Thickness

As shown by Eq. (9), thin webs and ribs cause the forging pressure to become very large. If the maximum forging pressure on the die is taken as 1400 MPa, a typical limit for hot working die steels, the limiting part dimensions can be estimated from Eq. (9) Figure 29 shows a nomogram for such limits in the form of web thickness versus plan area of the forging. As shown in Fig. 16 and Eq. (5), supplying a taper on the web, Fig. 30, reduces the peak forging pressure and facilitates metal flow from the web to the ribs.
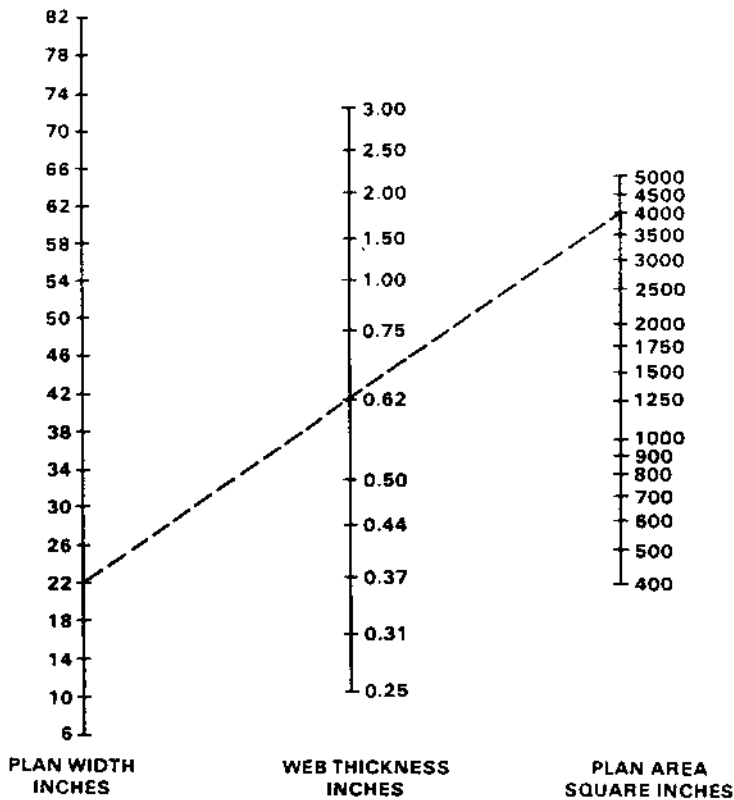
Figure 29 Nomogram for web thickness limits.

A TAPERED WEB
AIDS METAL FLOW
TO RIBS
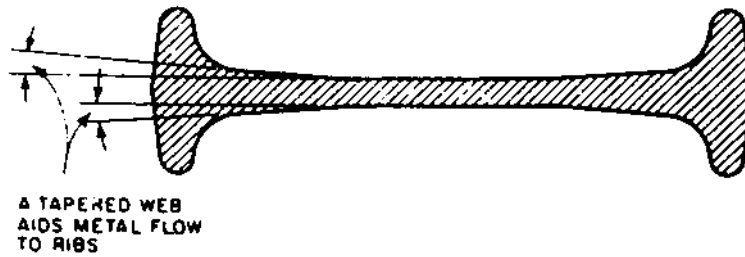
Figure 30 Tapered web facilitates metal flow to the ribs and reduces the forging pressure.
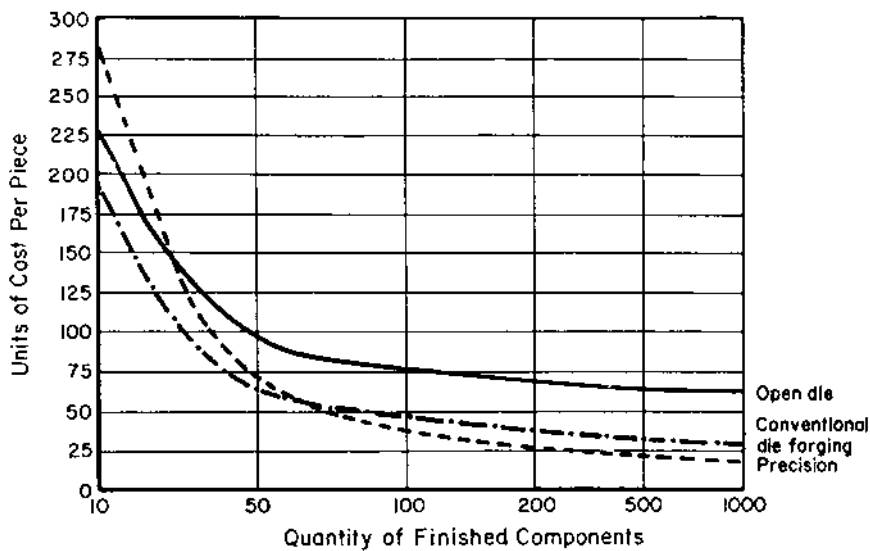
Figure 31 Example comparison of forging costs as a function of number of parts.

3.4 Rib Height

As shown in Fig. 17 and Eq. (7), long, thin ribs require considerable forming pressure. Typically, the rib height-to-width ratio limits for blocker-type forgings is 5, for conventional forgings the limit is 15, and for precision forging the limit is 23. Draft angles are typically 10°, 3° and 1°, respectively.

3.5 Cost

For rib-web type forgings typically used in airframe structures, the total cost per piece for blocker-type forgings, conventional forgings, and precision forgings are shown in Fig. 31. With precision forgings, while the tooling cost is high the per piece cost drops rapidly with increasing production quantity because the tooling cost is amortized over each part and little machining is required. With blocker-type forgings although the initial tooling cost is low, machining cost remains high. Conventional forgings are an alternative for small quantities; typically between 50 and 100 pro-

duction quantity, a crossover occurs whereby precision forgings become cheaper than conventional forgings on a per part basis. Of course, precision forgings are primarily carried out on hydraulic presses where the production rate is, at best, tens per hour so precision forging is applicable primarily for parts requiring limited annual quantities. Mechanical presses, on the other hand, which are capable of production on the order of thousands per hour, are necessary if large annual quantities are required. In this case precision forging to net shape without machining is not feasible. Therefore, the tooling approach and tooling costs will vary depending on the quantity of parts required as well as the dimensional tolerances and dimensions required.

REFERENCES

1. T. G. Byrer, S. L. Semiatin, and D. C. Vollmer (eds.), *Forging Handbook*, 1985 Forging Industry Association Cleveland, pp. 223–224.
2. ASM International, *Metals Handbook*, Vol. 14, 1988, Forming and Forging, 9th Edn, Metals Park, Ohio, p. 252.
3. G. Fitzsimons, H. A. Kuhn, and V. Ishwar, "Deformation and Fracture Testing for Hot Working Processes," Journal of Metals, May 1981, pp. 11–17.
4. National Center for Excellence in Metalworking, Atlas of Formability, www.ncemt.ctc.com/ekb/atlekb/
5. C. L. Downey and H. A. Kuhn, "Application of a Forming Limit Criterion to Design of Preforms for Powder Forging", J. Eng. Mater. Tech. Trans ASME, 1975, 97H, pp. 121–127.
6. E. G. Thomsen, C. T. Yang, and S. Kobayashi, *Mechanics of Plastic Deformation in Metal Processing*, 1965, The Macmillan Co., New York, pp. 230–234, 341–354.
7. E. M. Mielnik, *Metalworking Science and Engineering*, 1991, McGraw-Hill, New York, pp. 556–559.
8. G. E. Dieter, *Mechanical Metallurgy*, 2nd Edn, 1976, McGraw-Hill, New York, pp. 561–571.
9. ASM International, *Metals Handbook*, Vol. 14, 1988, Forming and Forging, 9th Edn, Metals Park, Ohio, pp. 428–433.
10. T. Altan, et al., *Forging Equipment, Materials, and Practices*, 1973, Metals and Ceramics Information Center, Columbus, Ohio, p. 350.

17

Forging

KICHITARO SHINOZAKI

National Institute of Advanced Industrial Science and Technology, Tsukuba, Japan

KAZUHO MIYAMOTO

Miyamoto Industry Co. Ltd., Tokyo, Japan

1   INTRODUCTION

Since 1950 parts of cameras, bicycles, and tubes have been manufactured from aluminum as it is a light metal. After 1960, aluminum was applied for automobile parts because of its high strength to weight ratio. For examples, piston for racing motorcycles were forged from 4032 alloy at 400°C and valve lifter for sports cars were forged at room temperature. Fishing reels have been forged, since 1970, at room temperature and forged pistons for racing motor cars since around 1980 [1]. The amount of aluminum which was forged has increased since around 1970 after forging of aluminum wheels started. If we could find a much stronger aluminum alloy to be forged, for example by increasing the silicon content, aluminum application to the motor car industry could be accelerated. Forging can be defined as the forming process of the bulky blank which is put on the lower die to receive compressive force from the upper die and plastic metal flow is initiated to fill the die cavity constructed by the upper and lower dies. Or the forming process of billet which is put in a container will receive compressive force from a punch and plastic metal flow is initiated to flow out from the die orifice.

When upper and/or lower dies have flat surfaces, the process is called compressive or upsetting process. This is the simplest forging operation. As a blank or billet which suffers a big compressive force during forging operation, so forged products will have a much sounder structural quality. Even if the blank or billet contains some small voids insides, they will be closed during the forging operation which is done under high compressive stress. Upsetting strain can be expressed

by engineering strain e defined by

$$e = (h_0 - h)/h \tag{1}$$

or logarithmic strain ε defined by

$$\varepsilon = \ln(h_0/h) \tag{2}$$

h_0 and h denote the heights of the billet before and after upsetting (Fig. 1). Logarithmic strain is superior to express large strain, and is often used for forging operations, because material receives a large strain by forging operation. During small strain less than 0.1, engineering strain e is nearly equal to logarithmic strain ε.

The relation between true stress (flow stress) and logarithmic strain during upsetting is shown in Fig. 2. for annealed pure aluminum (99.7% Al, 18HV). Cylindrical aluminum billet was upset in a sub-press to keep the top and bottom surfaces of a billet parallel. The upsetting test was done on a hydraulic material testing machine at room temperature. The re-shape upsetting method [2] was applied to keep the billet's height/diameter ratio between 1.5 and 0.5 during upsetting. When the h/d ratio is more than 1.5, sometimes billet will show buckling and when the h/d ratio is less than 0.5, the effect of frictional force between die and billet to flow stress will not be possible to neglect.

Generally speaking many forged products have strain between 2 and 4, so it will be easily understood that the forged product will have higher strength than the original material because of work hardening when forging has been done at room temperature. Flow stress is linked directly to each individual material components and testing conditions such as strain rate and temperature. If we do not know the flow stress–strain curve for the individual given materials, hardness could be helpful. Flow stress and hardness have very good mutual co-relations. When there is friction between the die and the block during the upset of a rectangular parallelpiped, the distortion of the top surface of the block cannot be neglected. The top view after upsetting can not be similar to the original rectangle, but more deformation along the shorter side will be observed (Fig. 3). Forged products could
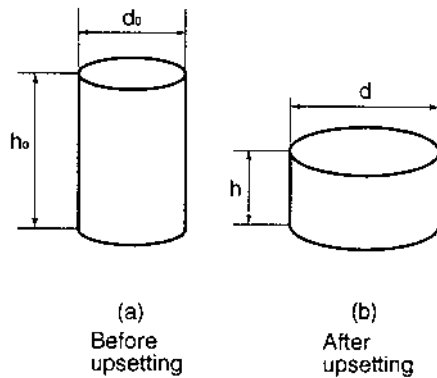
Figure 1   Dimensions of test piece of upsetting test, friction free.
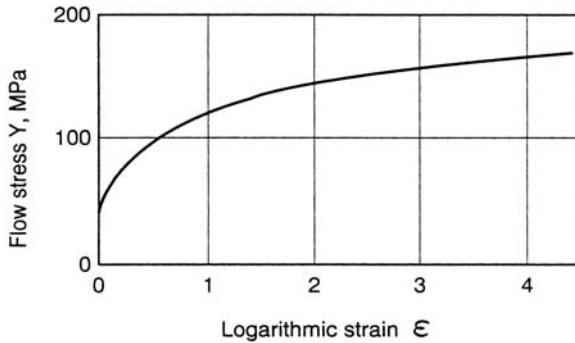
Figure 2   Flow stress versus logarithmic strain curve of pure aluminum.

---- Before upsetting
——— After upsetting
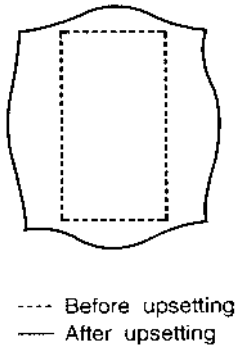
Figure 3   Top view of rectangular parallele piped test piece of upsetting test, accompanied interfacial frictional force between tool and billet.

be complex shapes in one piece with continuous fiber flow and smooth surface. Forging process could be the process which brings near net shape products with high productivity. Higher attention should be paid to not damaging aluminum forging products during and after the process.

2   BASIC FORGING OPERATIONS

Forward extrusion of rod [Fig. 4(a)], backward extrusion of can [Fig. 4(b)], simultaneous extrusion of can and can [Fig. 4(c)], can and rod or rod and rod and die forging [Fig. 4(d)] are recognized as typical basic aluminum forging operations. Actual forging will be done as combinations of them.

2.1   Forward Extrusion of Rod

Forward extrusion of rod is carried out as follows; billet which is kept in container [Fig. 4(a) 4], is forced by punch [Fig. 4(a) 1] to squeeze out from die orifice to form thinner rod. Reduction in area r is defined as

$$r = ((d_0{}^2 - d_1{}^2)/d_0^2) \times 100\% \tag{3}$$
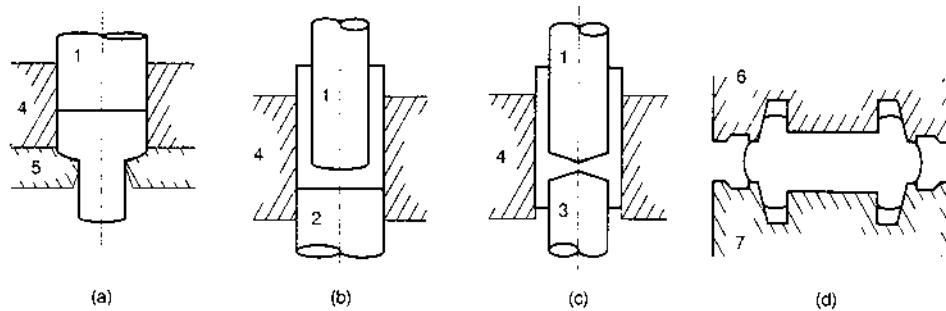
Figure 4   Basic forging operations, 1. Punch, 2. Backup punch, 3. Counter punch, 4. Container, 5. Die, 6. Upper die, 7. Lower die. (a) Forward extrusion of rod; (b) Backward extrusion of can; (c) Simultaneous extrusion of double cans; (d) Die forging.
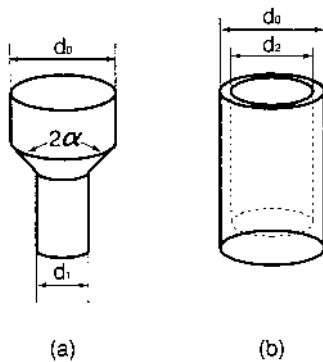
Figure 5   Dimensions of extruded products, d_0. Billet's diameter, d_1. extruded rod's diameter, d_2. Extruding punch's diameter. (a) Extruded rod; (b) Extruded can.

Reduction in area can express the percentage magnitude of deformation of extrusion.

Herewith d_0 and d_1 denote diameters of billet and extruded rod [Fig. 5(a)]. A maximum peak of extruding force is observed at an early stage of punch displacement on the punch force versus displacement diagram [Fig. 6(a)]. After showing maximum peak of extruding force, it goes down gradually along with the punch displacement decreasing billet length and causing the decrease of frictional force between billet wall and container. Extruding pressure is affected by billet material, billet temperature, reduction in area, die angle 2α, frictional force on billet surfaces, extruding speed etc.

2.2   Backward Extrusion of Can

Backward extrusion of can is carried out as extruded material goes backward through the gap between container [Fig. 4(b) 4] and punch [Fig. 4(b) 1] as the punch is coming down into the billet supported by a container and counterpunch [Fig. 4(b),
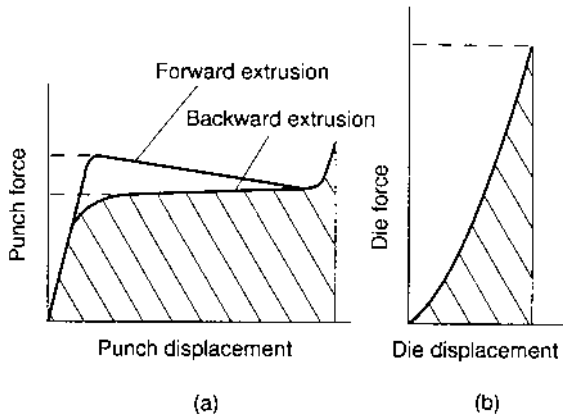
Figure 6 Punch or die force displacement diagram. (a) Extrusion of rod and can; (b) Die forging.

2]. Reduction in area r is defined as

$$r = (d_2{}^2/d_0{}^2) \times 100\%. \tag{4}$$

Herewith d_0 and d_2 denote diameters of container and punch which coincide with the diameters of outer and inner diameters of can [Fig. 5(b)]. Punch force keeps rather flat in punch force and displacement diagram because increase of frictional force on a can's wall is not so serious. However it will be almost impossible to supply additional lubricant on punch top surface during operation from outside, so it is difficult to manufacture deep cans because of a shortage of lubricant on the punch surface. It is important to protect the punch from sitting in an eccentric position or buckling to manufacture deep cans. To manufacture very thin wall can, where the reduction in area is large, or to manufacture very thick wall can, where the reduction in area is small, a higher punch pressure is needed. For medium reduction in area $r = 40$–60% approximately, punch pressure takes minimum. At the end of punch displacement, punch force will increase suddenly [Fig. 6(a)] where billet length becomes short. For forging very short billets or flat plates, higher force is needed to withstand frictional force.

2.3 Simultaneous Extrusion

Extrusion with plural die orifices is called simultaneous extrusion. Control of the length of extruded parts is made by a suitable selection of sequence or die design. For the extrusion with two orifices, if they are extremely different in reduction in area, one extrusion is done in advance and almost no extrusion is made from the other orifice. To get suitable metal flow, sometimes a counter punch is fitted at the end of the extruded part to stop partial excess metal flow. To divide a deformation process into two or three stages is another method of getting sound metal flow. In the case of their being similar in reduction in area, the extruded part's length is adjustable by changing the die or punch design slightly.

2.4   Die Forging

The process of filling up the die cavity, which is constructed with upper and lower dies and coincides with the shape of the product, is called die forging [Fig. 4(d)]. Die forces increase with the die displacement [Fig. 6(b)] slowly at the beginning where the die is not filled yet and severely at the end where most of the die cavity is filled up and some redundant metal will be hanging out of the die cavity. We have to stop the die movement before the die pressure exceeds its proof stress to prevent die breakage. Filling up the die cavity soundly with material, suitable selection of billet shape is important. Height/diameter ratio of cylindrical billet, trimming of corner edge, giving small recess or taper to the end surfaces of the billet, are effective factors to be considered on the billet. Die design will be made by selecting suitable values of roundness of die corner edge, length of die land, die orifice angle, etc.

2.5   Alloys Used in Forging

Metal flow of forging is due to the ductility of material used. Soft material causes low stress on the die. So, ductility and low flow stress are essential characteristics of forging material. Characteristics of the material are directly related to the individual material's components, crystalline structure, temperature, strain, strain rate and so on. Table 1 shows characteristic mechanical properties at room temperature, a convenient reference. In the case of cold forging, heat treatment of the billet is done before and during forging operation to arrange crystalline structure to increase or recover ductility. In the case of hot forging, billet is heated up during the forging operation to promise higher ductility and low flow stress of the material.

2.6   Examples of Forged Products

Cold forged products are shown in Figs 7–11. Hot forged products are shown in Figs 12–16. Figure 7 is of a connector of a railroad car, cold forged by Miyamoto Industry Co. from A7001. Formerly it was cast. To get higher strength parts, manufacturing technology was changed from cast to forging. Figure 8 is the housing of a hammer, cold forged by Miyamoto Industry Co. from A7001. Figure 9 is a part of an air conditioner for a motor car, cold forged by Miyamoto Industry Co. from A3003. Formerly two pieces were welded. To get higher reliability part welding was ceased. Backward extrusion of deep hole requires knowledge of the shape of the punch. Figure 10 is the housing of a maker pen, cold forged by Miyamoto Industry Co. from A1070. Process explanation is given later. Figure 11 is a hub for a spindle motor, cold forged by Miyamoto Industry Co. from A6061. Precision forging is needed to get a machining allowance of less than 0.15 mm. There are frequent model changes. Process explanation is given later. Figure 12 is part of an air conditioner, hot forged by Nichidai Co. from A1–10% Si. Counter punch was fitted to the end of the extruded part to get the same length of extruded parts. Figure 13 is piston-like, hot forged experimentally by Kubota Co. Figure 14 is a wheel for a truck, hot forged by Kobe Steel Co. from A6061. Wheels are occasionally forged or cast. Figure 15 is an automotive suspension, hot forged by Kobe Steel Co. from A7075. To understand suitable blank shape and forging temperature, simulation

Table 1 Characteristic Mechanical Properties at Room Temperature and Examples of Applications

Material	Tensile strength MPa	Proof strength MPa	Elongation %	Brinell hardness HB$_{(10/500)}$	Characteristics and examples of application
1070-O	70	30	43	19	Excellent electrical and thermal conductivity
-H18	130	125	6	35	Excellent in formability, weldability and
-H24	100	90	12	26	corrosion resistance
1100 -O	90	35	35	23	Excellent in formability, weldability and
-H12	110	105	12	28	corrosion resistance
-H14	125	118	9	32	Heat exchanger parts
-H16	145	140	6	38	Memory drum for computer
-H18	165	150	5	44	
2011 -T3	380	295	15	95	Good cutting workability
-T8	405	310	12	100	Optical appliance parts
2014 -O	185	95	17	45	High strength and forgeability and ductility
-T4	425	290	19	105	Aircraft parts, Motor car parts
-T6	485	415	12	135	
2017 -O	180	70	21	45	Aircraft, motor car and bicycle parts
-T4	425	275	21	105	High pressure cylinders for aqualungs
2024 -O	185	75	20	47	Higher in strength than 2017 and excellent
-T3	485	345	18	120	in machinability
-T4	470	325	20	120	
-T81	485	450	7	128	
-T86	515	490	5	135	
3003 -O	110	40	30	28	A little higher in strength than 1100 and
-H12	130	125	10	35	excellent in formability, weldability and
-H14	150	145	8	40	corrosion resistance
-H16	178	170	5	47	Heat exchanger parts
-H18	200	185	4	55	

Table 1   Continued

Material	Tensile strength MPa	Proof strength MPa	Elongation %	Brinell hardness HB$_{(10/500)}$	Characteristics and examples of application
5052 -O	194	90	25	47	Excellent in corrosion resistance, formability and weldability
-H32	230	195	12	60	Rivets, Machine parts
-H34	261	215	10	68	
-H36	275	240	8	73	
-H38	290	255	7	77	
5056 -O	290	151	32	65	Excellent in corrosion resistance, cutting workability and anodic oxidation processibility
-H18	435	405	9	105	Optical instruments
-H38	415	345	14	100	Telecomunication apparatus
6061 -O	125	55	25	30	Excellent in ductility, toughness and corrosion resistance
-T4	240	145	22	65	Motor car wheel
-T6	310	275	12	96	Rotor for physics and chemistry
6063 -O	90	50	–	25	Good surface processibility
-T1	150	90	20	42	Heat exchanger parts
-T5	185	145	12	60	
-T6	240	215	12	73	
7075 -O	230	105	16	60	Highest strength
-T6	570	505	11	150	Aircraft parts, Motor car parts
-T73	505	435	–	140	

(a)

(b)
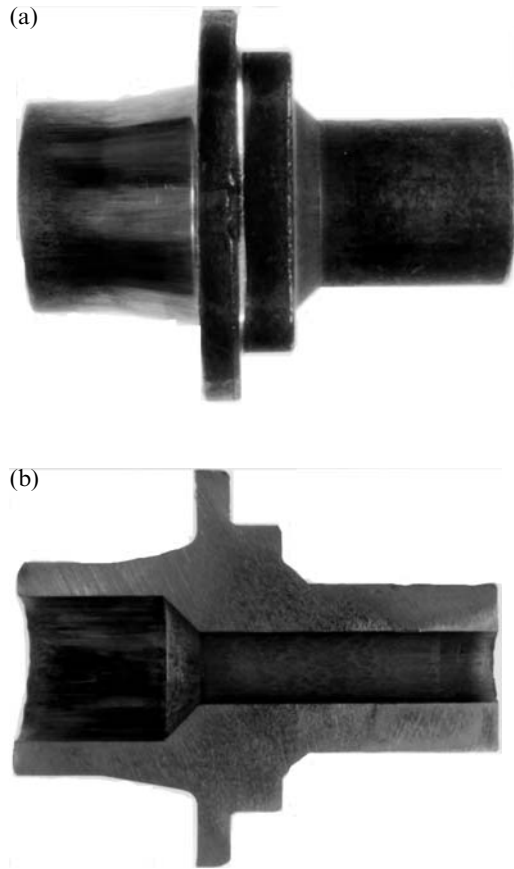
Figure 7 Connector (A7001) of railroad car forged by Miyamoto Industry Co.
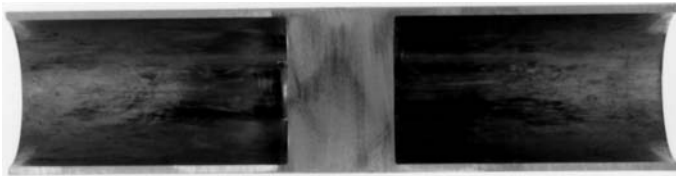
Figure 8 Housing (A7001) of hammer forged by Miyamoto Industry Co.
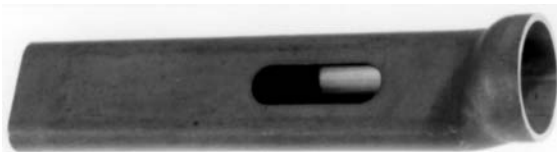
Figure 9 Part of air conditioner (A3003) of motor car forged by Miyamoto Industry Co.
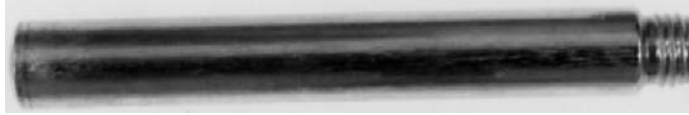
Figure 10   Housing (A1070) of maker pen forged by Miyamoto Industry Co.

Figure 11   Hub (A6061) of spindle motor forged by Miyamoto Industry Co.
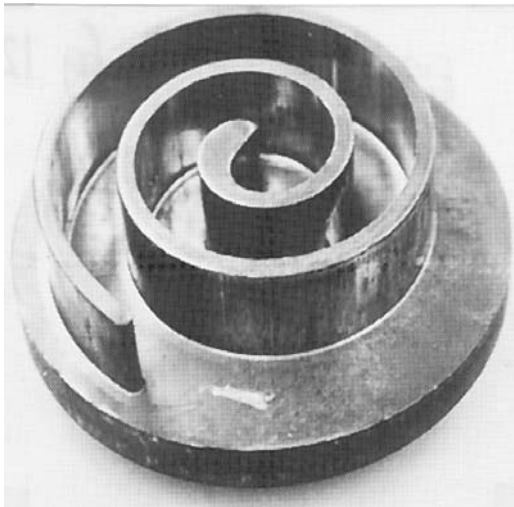
Figure 12   Part of air conditioner (A1-10% Si) forged by Nichidai Co.
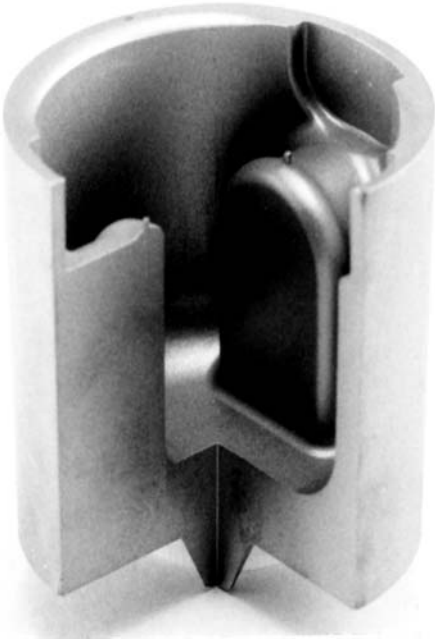
Figure 13 Piston (A1-12% Si) for motor car forged by Kubota.

Figure 14 Wheel (A6061) for truck forged by Kobe Steel Co.
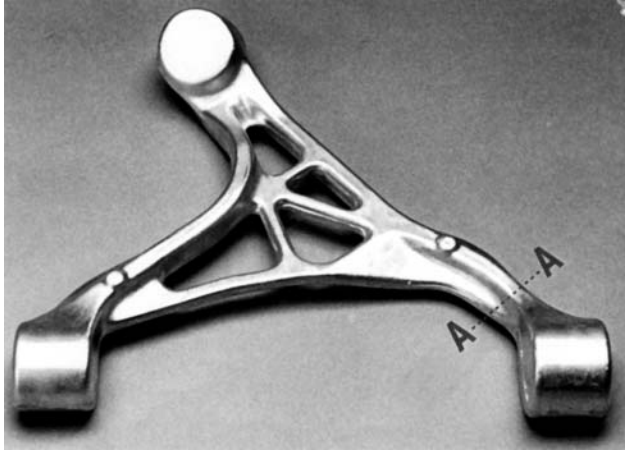
Figure 15   Automotive suspension part (A6000) forged by Kobe Steel Co.
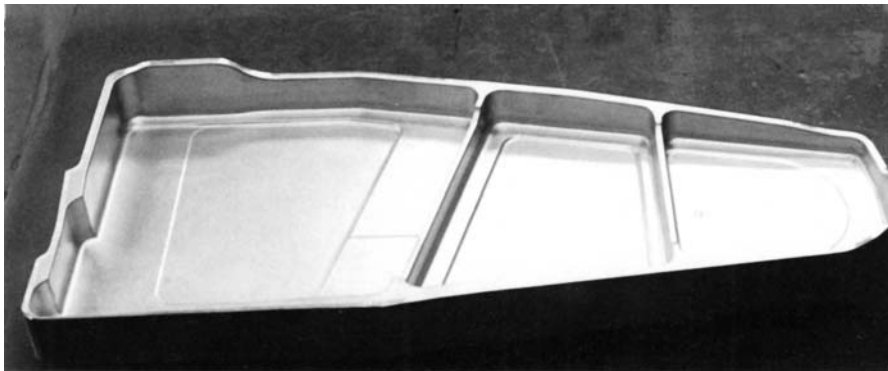
Figure 16   Part of aircraft (A7075) forged by Kobe Steel Co.

analysis by FEM was made. Figure 16 is a part for an aircraft, hot forged by Kobe Steel Co. from A7075. Its mass and x, y, z dimensions are 2.0 kg and 566 mm, 236 mm, 49 mm respectively.

3   DESIGN

3.1   Estimation of Forging Pressure

The flow stress Y of the material is able to define as a flow stress p for friction free upsetting. Analyzed result by elementary slab method for upsetting pressure p considering frictional force acting on the end surface of the billet is

$$p = Y \left(1 + \frac{\mu d}{3h} \right) \tag{5}$$

Herewith μ, d and h denote Coulomb's frictional coefficient, diameter of billet and height of the billet respectively. In some occasional cases, it is confirmed that $\mu = 0.03$–0.05 for well lubricated surfaces of cold forging products. It is easy to understand that in case of $\mu = 0$, p coincides with Y, then

$$p = Y \tag{6}$$

In the case of upsetting of thin plate under the condition of μ is not zero, as the ratio of d/h becomes larger, so higher pressure will be needed to cope with frictional force which comes from terms of $\mu d/(3h)$. Former equation can be rewritten in the form of

$$p = cY \tag{7}$$

or

$$p/Y = c \tag{8}$$

c is called constrain factor indicating how much forging pressure will be needed based of flow stress Y. c is determined by the product's shape and is independent from characteristics of individual materials.

Specific rod and can extruding pressure p/Y, analyzed by upper bound approach, are shown in Fig. 17 [3]. Solid and dotted lines correspond to specific pressure for forward extrusion of rod and backward extrusion of can respectively. Two lines are for frictional conditions of friction free and sticking. For a certain
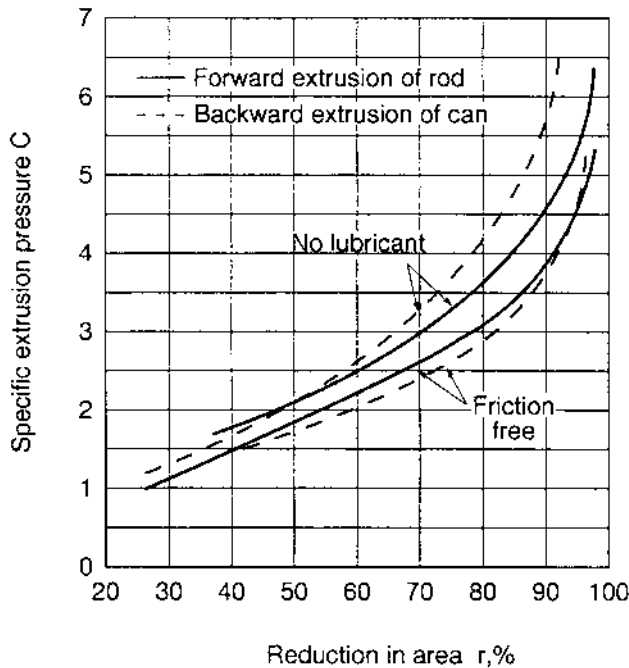
Figure 17 Relations between theoretically analyzed specific extrusion pressure and reduction in area (From Ref. 3.)

lubrication condition, specific extrusion pressure will be read from the position on Fig. 17 between solid and dotted lines depending on lubrication condition on the reduction in area of horizontal axis of the figure. Actual forged products have complicated shapes as shown in Figs 7–16. Specific pressure for complicated shape products, we have to calculate them individually. However it is possible to refer the results for similar shapes which are published in a great amount of technical reports and books [4–10].

After knowing the value of c, we have to estimate Y to be multiplied. For steady state motion problem of sheet drawing, R. Hill [11] had proven that if there is no frictional forces on die surfaces, the mean plastic work per unit volume is equal to the drawing stress p. Now for a non-hardening material, obeying the Levy–Mises yield criterion, the work per unit volume is equal to $Y \int d\varepsilon$, where $\int d\varepsilon$ is equivalent strain. We can therefore define a mean equivalent strain for sheet drawing equal to p/Y. Let us assume that this can be extend to the forging problems. Now it can be said that equivalent strain is equal to p/Y and p/Y is equal to c. Using flow stress and strain curve, say Fig. 2 for pure aluminum, mean flow stress Ym can be calculated as $\int_0^c \frac{Yd\varepsilon}{c}$. The result of the multiplication c and Ym is theoretically estimated pressure p. For any ductile materials, this method can be applied if we know individual flow stress–strain curves. For further study of non-steady state motion problems, equivalent strain is defined as [12].

$$\int d\varepsilon = \int\limits_{h_2}^{h_1} \frac{p}{Y} \cdot \frac{dh}{h} \tag{9}$$

and it was confirmed that this equation promises good estimation of equivalent strain [13].

3.2 Defects

3.2.1 Underfill and OverLap of the Skin

It is desirable to fill up the die cavity perfectly with material without underfill. But sometimes underfill is observed from the reasons of unsuitable billet shape, trapped air at die corner, excess lubricant on billet surface and so on. By choosing an appropriate billet shape, underfill defect can be averted. Appropriate billet shape can be designed by trial and error. Recently computer simulations were applied to predict appropriate billet shapes. If it is difficult to avert a defect by choosing appropriate billet shape, we have to add one more forging operation. Fig. 18 is an example of velocity distribution during the forging operation of a hub spindle motor (Fig. 11) estimated by FEM programme. It is helpful to predict underfill or overlap of the material during deformation.

3.2.2 Dead Metal and Skin Inclusion

Sometimes some part of the material is apart from the major part of the material and is split in two, along with the process going on and left from deformation. The split part is called dead metal. Dead metal is observed, for example, in the die corners, Fig. 19(a), or concave place, Fig. 19(b). If die or punch displacement is not big, dead metal does not build up but skin inclusion is observed initiating dead metal.
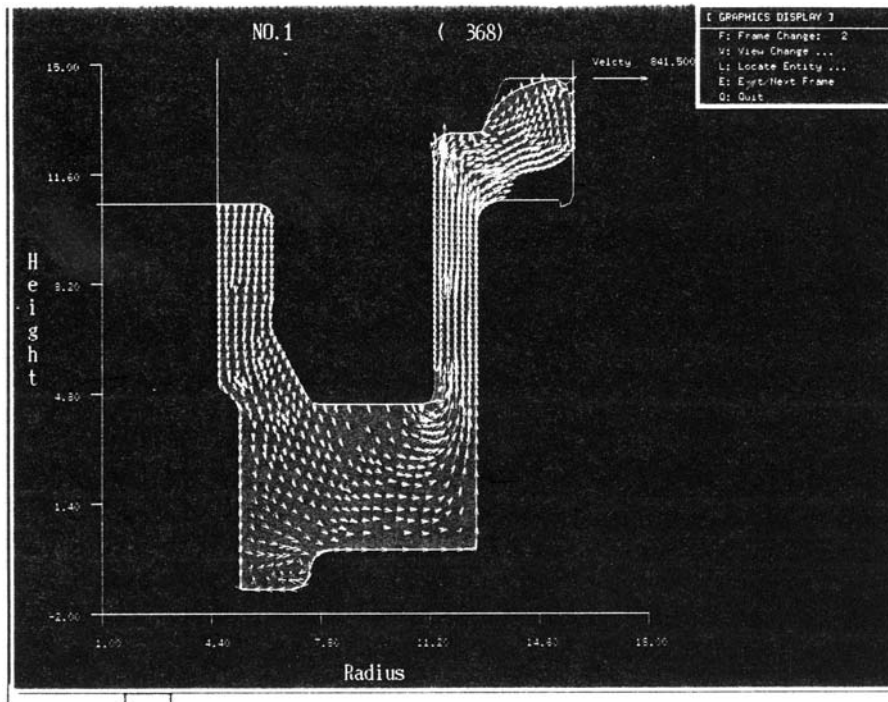
Figure 18 Analyzed velocity distribution for forging of video drum.

Dead metal and skin inclusion are initiated by too much velocity discontinuities in the deformation zone and less ductility of the material. Preparation of roundness on die corner edge or giving moderate change of die profiles are helpful to bring smaller value of velocity discontinuity, and consequently are effective methods to avoid dead metal or skin inclusion.

3.2.3 Cracking

If ductility of the material is not enough, cracking will occur at the place where large shearing or tensile stress is acting. Those stresses are initiated by velocity discontinuity during plastic metal flow and/or stresses suffered from outside. Criteria of cracking can be expressed as a function of strain and mean stress. Sometimes counter pressure is added to deformation region to prevent cracking by means of a higher mean stress. For example, in the case of rod extrusion [Fig. 4(a) and Fig 19(c)], internal compressive and tensile stresses are acting at the outer and central portions of the extruded rod. If impact extrusion is made, body force of the extruded part is pulling the deforming zone. As a result, tensile stress is increased at the central portion of the rod, and cracking is sometimes observed. The crack observed at the central portion of the rod is called a Cheveron crack [Fig. 19(c)]. We know some examples of preventing Cheveron cracks by reducing the extruding speed to reduce tensile stress on the central portion of the rod which was caused by body force. Heating up the material is effective to improve ductility. Annealing heat treatment before and during cold forging operations aims to increase ductility of the material.

3.2.4 Contraction

It is natural to think that metal flow which occurs during forging operation must be the way of minimum energy dissipation rate. For this reason, at the end of forging operation, where billet length became short, some part of metal surfaces comes apart from the die surface and makes contractions where it has kept contact with die surface beforehand. Contraction [6,7] can be seen on the central portion of the billet end surface [Fig. 19(d)] for rod extrusion, on the corner of billet bottom [Fig. 19(e)] for backward extrusion of can, or the central wall surface of billet for combined extrusion of can and can [Fig. 19(f)]. The way of getting rid of contractions is to keep billet length long, to give a larger corner radius on the punch or die to allow a wider deformation zone, or to fit a counter punch to the end of the extruded parts to give pressure to restrict the natural energy minimum metal flow.
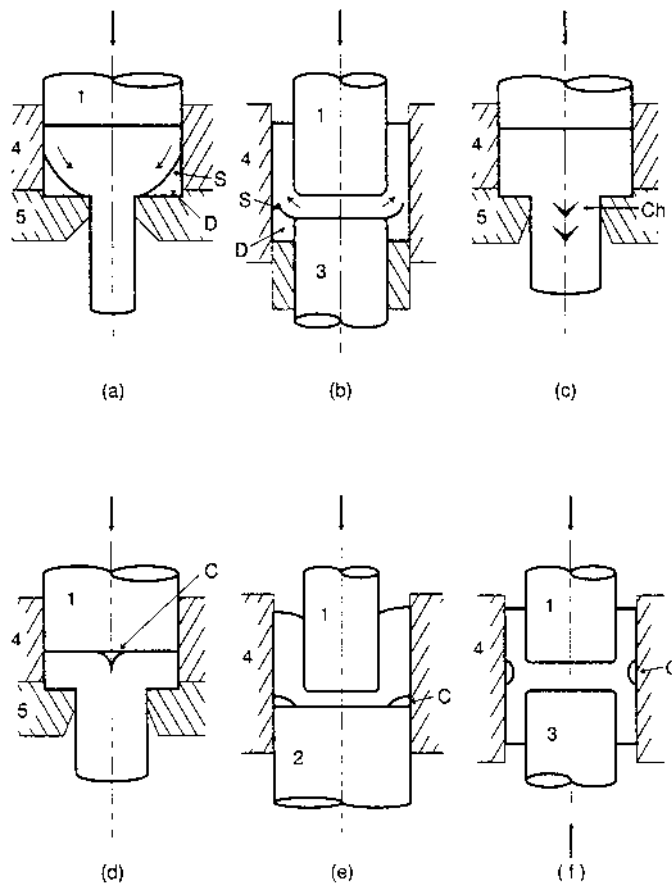
Figure 19 Forging defects, 1. Punch, 2. Backup punch, 3. Counter punch, 4. Container, 5. Die, D. Dead metal, S. Skin, C. Contraction. (a) Dead metal; (b) Skin inclusion; (c) Sheveron crack; (d), (e), (f) Contraction.

3.2.5 Grain Growth

Grain growth is observed at the heat treated place of a certain amount of strain. Forged parts have a variety of strain, so the possibility of grain growth during heat treatment is high. Large grain is poor in mechanical properties. To get a fine anodic oxidation process, uniformly distributed small size grain of 30 μm in diameter is desirable.

3.2.6 Orange Peel

Too much lubricant causes orange peel appearance on the surface of the forged products and loses smooth and bright surface.

3.3 Forging Temperature

The temperature of the materials to be forged is determined by the shape and size of the products, ductility and strength of the materials etc. Generally speaking, hot forging is applied to brittle- or high-strength materials or complex shaped products. Recommended forging temperature is shown in Table 2.

Sometimes the die is heated up during hot forging operations to get little drop in billet temperature when billet is mounted on the die. An approximate pre-heating temperature will be 80% of the billet's temperature or 50°C lower than the billet temperature [14]. Ninety percent of the energy used for forging will dissipate as heat. The heat elevates the forged product's temperature and sometimes the temperature of the forged product is higher than the billet's temperature. On the other hand, billet temperature is decreased because of the heat sink from billet to die when billet is mounted on the die. Higher materials temperature brings low flow stress and more ductility, but initiates grain growth of the material. Lower material's temperature brings little or no oxidation and precision dimension but brings higher flow stress and less ductility which initiates cracking of die and/or products. For some alloys, flow stress and ductility are very sensitive to the temperature. So, selection of forging temperature should be made carefully. Figure 20 shows the temperature distribution on A-A cross sectional area of automotive suspension parts, Fig. 15, to be produced by hot forging. To obtain precision data of flow stress for the material at high

Table 2 Forging Temperature

Materials	Forging temperature (°C)
1070	315–405
1100	315–405
2014	420–460
2017	420–470
2024	420–470
3003	315–405
5052	425–470
5056	300–500
6061	300–500
6063	350–450
7075	350–450
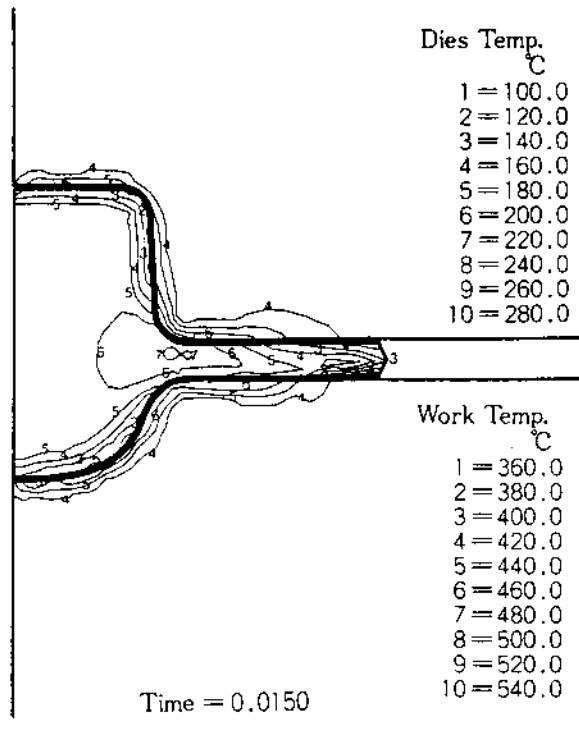
Figure 20   Temperature distribution estimated by FEM for hot die forging of automotive suspension, Fig. 19. (From Ref. 15.)

temperature and strain rate, upsetting test on press machine creating high strain rate was carried out. Using the results, the FEM analysis was done [15]. Checking analytical results of temperature distribution, forging temperature was determined. Exactly speaking similarity law is not able to be true to the problem of three dimensional hot forging deformation problem. The temperature of a small blank changes very quickly. Different lubricants have to be selected by temperature. Warm forging between 150°C and 200°C is applied for the purpose of reducing viscosity of the lubricant to get smaller frictional resistance by warming up the lubricant.

3.4   Application of Counter Punch

Heat radiation part used on a personal computer, Fig. 21, bottom, is obtained by the forward extrusion accompanied by a counter punch. Counter punch is fitted against extruding rods and supported by a hydraulic cylinder of 300 kPa. Better product, Fig. 21 bottom, which have almost the same length of extruded rods compared to the product extruded without counter punch, Fig. 21 top. Product of Fig. 12 was extruded with counter punch of 40–50 kN. Scatter of height of fin was less than 0.5 mm. A product which extruded without a counter punch, has 20 mm difference in height of extruded fin.
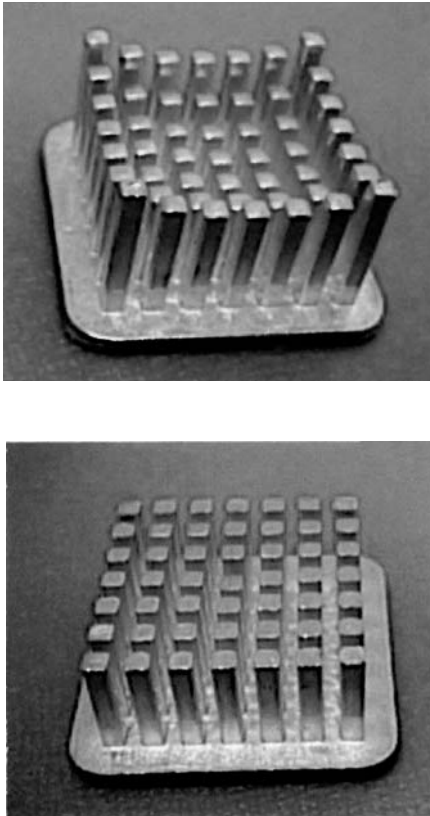
Figure 21 Heat sink (A1070) forged by Miyamoto Industry Co.

4   FORGING PROCESS

In most cases, shape, dimensions and material of the product to be forged are determined by the customer. Process design is done to forge it without defects.

4.1   Backward Extrusion of Housing of Maker Pen

A blank was pierced from thick sheet metal of pure aluminum A1050. The process is as follows: Piercing of blank → Lubricating → backward extrusion of tube at room temperature → trimming and rolling of tube end → degreasing → drying → pre--painting → drying → painting → drying → over coating → drying → inspection → finishing.

Blank (Fig. 22, top) has a recess of 0.5 mm deep on one end surface and curved surface on the other end. Zinc stearate is used as a lubricant. Extruded product is shown in Fig. 22 bottom. To get exactly the same length of tube after trimming, the extruded tube must have the same temperature. Tool set up is shown in Fig. 23. Punch 1 and die insert 3 are made from high speed tool steel M2= SKH51 of hardness of 62 HRC and 58 HRC respectively. Container 4 is made from
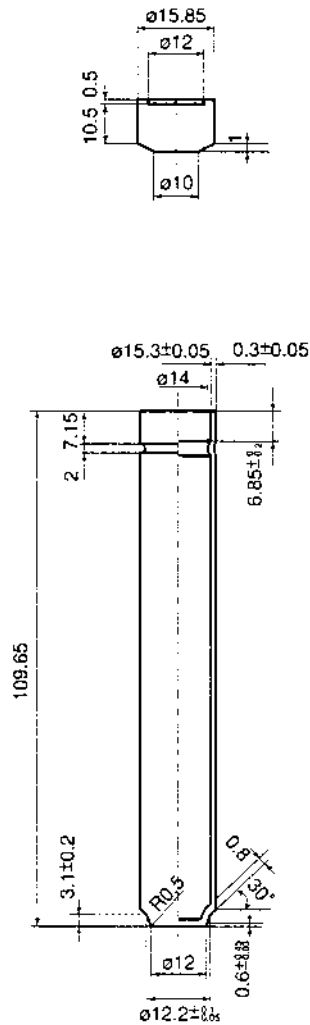
Figure 22 Housing of maker pen. Top: Billet, Bottom: Drawing of housing.

cemented carbide. The punch can be used 2 million times. Thickness of the tube bottom is 3.1 mm. To forge a thinner bottom tube, less than 3.1 mm, the die life was short. Five pieces of tube can be produced per minute.

4.2   Cold Forging of Video Drum

Aluminum alloy A2218 was selected as a material for a video drum, because of its high strength, good cutting property and good fitting characteristics with tape material. Cast aluminum bar is used as it is cheaper than rolled bar. Process is as follows: Cast bar → peeling → cutting → annealing (410°C × 1.5 hr, cooling until 260°C at the rate of 25°C/hr) → lubricating, zinc stearate → mass sorting
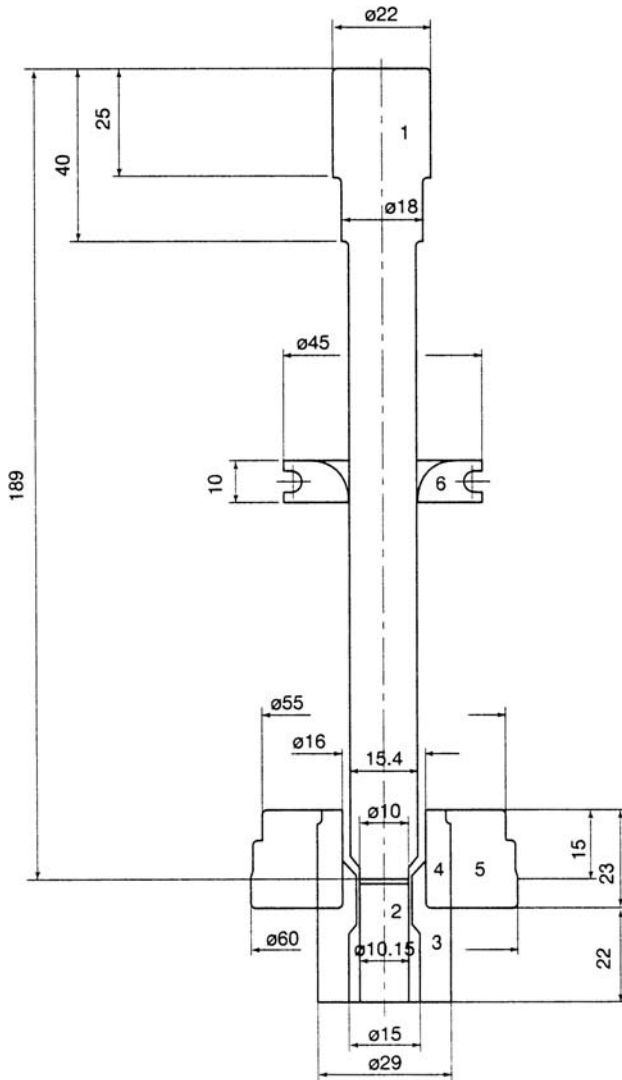
Figure 23 Tool set up for backward extrusion of maker pen housing (Fig. 22), Miyamoto Industry Co. 1. Punch, M2 = SKH51, 62 HRC; 2. Buck-up punch, H13 = SKD61, 53 HRC; 3. Die insert, M2 = SKH51, 58 HRC; 4. Container, Cemented carbide; 5. Shrink ring, H13 = SKD61; 6. Stripper.

$\rightarrow$ piercing of hole of 13.5 mm diameter, Fig. 24 $\rightarrow$ annealing $\rightarrow$ lubricating $\rightarrow$ cold forging on knuckle joint type mechanical press $\rightarrow$ heat treatment (T4:510°C×1.5 hr and T6:170°C × 8 hr minimum) $\rightarrow$ cleaning.

   Pierced blanks (Fig. 24) are sorted by mass into five classes. Sorted blanks of 70 ± 0.25 g are used as materials for Fig. 25. Tool set up is shown in Fig. 26. Punch 1 and 2 and punch cover 3 are made from alloy tool H13 = SKD61 with hardness of 53 HRC. Die insert 4, ejector 6, and shrink rings 9 and 10 are made from alloy
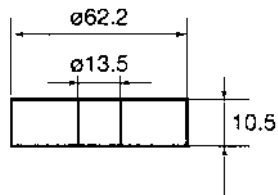
Figure 24 Billet for video drum.
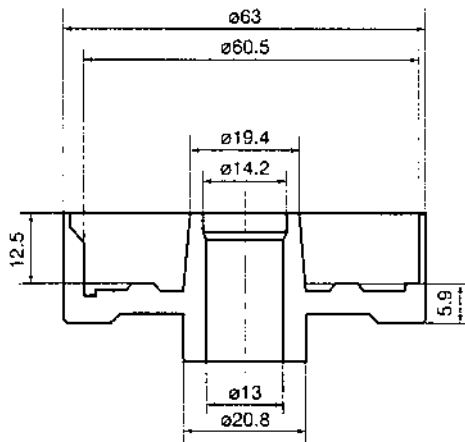
Figure 25 Drawing of video drum.

tool steel D2 = SKD11 with hardness of 55 HRC. Tool can be used about 50,000 shots.

4.3 Cold Forging of a Hub for a Personal Computer

Figure 27 bottom is a drawing of a spindle motor hub for a personal computer to be forged. Forging process is as follows: Extruded bar → drawing → cutting → annealing → lubricating → sorting by mass → cold forging on crank press, capacity of 100 t → piercing, Fig. 27 top → annealing → lubricating → cold forging on knuckle joint press, capacity of 150 t → heat treatment T6 → cleaning.

Material A2011–0 is select as is high strength and cut easily. Blank is sorted by mass. Depending on hub size blank's mass is between 12–15 g, but blank's mass scatter is less than ±0.05 g. Tool set up is shown in Fig. 28. Punch 1 is made from alloy tool steel H11 = SKD11. Die 4 and 5 is made from high speed tool steel M2 = SKH51. Punch can be used 50,000 shot. Five thousand hubs were forged per month. To get near net shape forged product (Figure 27 bottom), it is important to get suitable pre-forged product's shape (Fig. 27 top). Model is changed frequently, and each time, suitable pre-forged shapes have to be designed by experience or computer simulation as soon as possible.
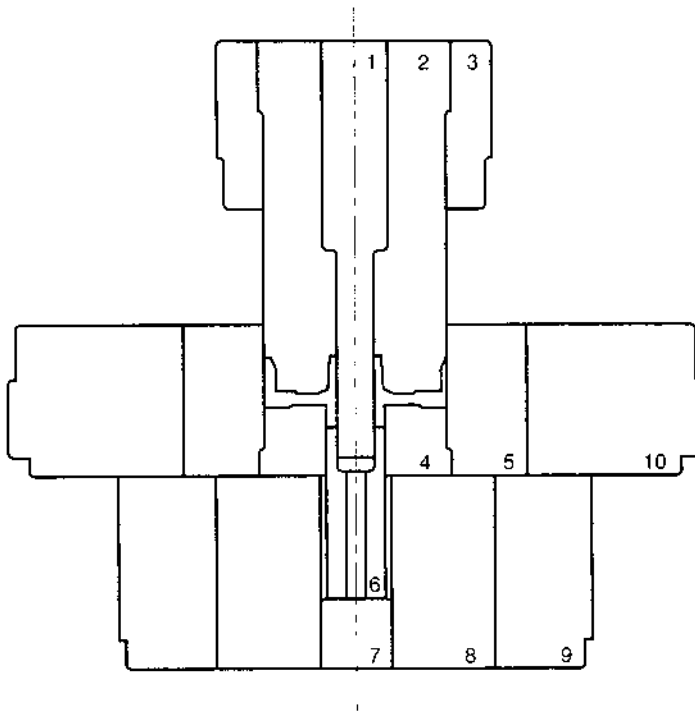
Figure 26 Tool set up for die forging of video drum, Miyamoto Industry Co. 1. Punch, H13 = SKD61, 53 HRC; 2. Punch, H13 = SKD61, 53 HRC; 3. Punch cover, H13 = SKD61, SKD61, 53 HRC; 4. Die insert, D2 = SKD11, 55 HRC; 5. Die, H13 = SKD61, 50 HRC; 6. Ejector, D2 = SKD11, 55 HRC; 7. Pressure pad, M2 = SKH51, 55 HRC; 8. Pressure pad, H13 = SKD61, 53 HRC; 9. Pressure pad cover, D2 = SKD11, 55 HRC; 10. Shrink ring, D2 = SKD11, 55 HRC.

5 PRESS

Mechanical press, hydraulic press or special purpose press are used for aluminum forging. After selecting the type of press machine, then press capacity, length of ram stroke, and automatic operating methods are checked. Productivity is dependent on the number of ram strokes per minute.

5.1 Mechanical Press

Crank press is popular as a mechanical press. It has simple mechanism but has high productivity and is convenient for multipurpose usage. As mechanism is simple, machine trouble is infrequent and automatic operation is easy. Crank press is used for both cold and hot forging. Especially in the case of hot forging, shorter contact time between hot forging material and die is desirable to escape warmup of die temperature. To keep die temperature low is good for die material because the strength of die material is poor at elevated temperature.
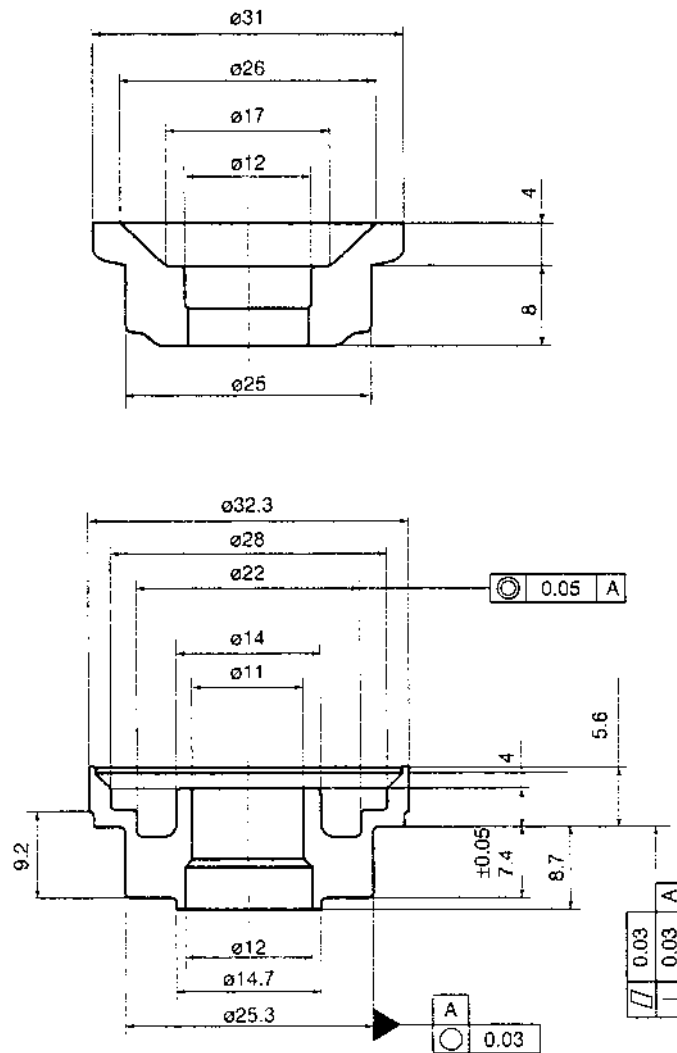
Figure 27   Drawing of hub for personal computer. Top: Pre-forming; Bottom: Drawing for forging.

5.2 Link Press

Link press, Fig. 29, enables large force at the end of ram stroke, near bottom dead center, compared to a crank press. In the case of cold forging, it is said that pushing forging material time a little bit longer to the die at the end of the ram stroke is good to get near net shape product. If contact time is longer, the die profile will be copied to material better. Hub shown in Fig. 11 was forged on a link press at room temperature.
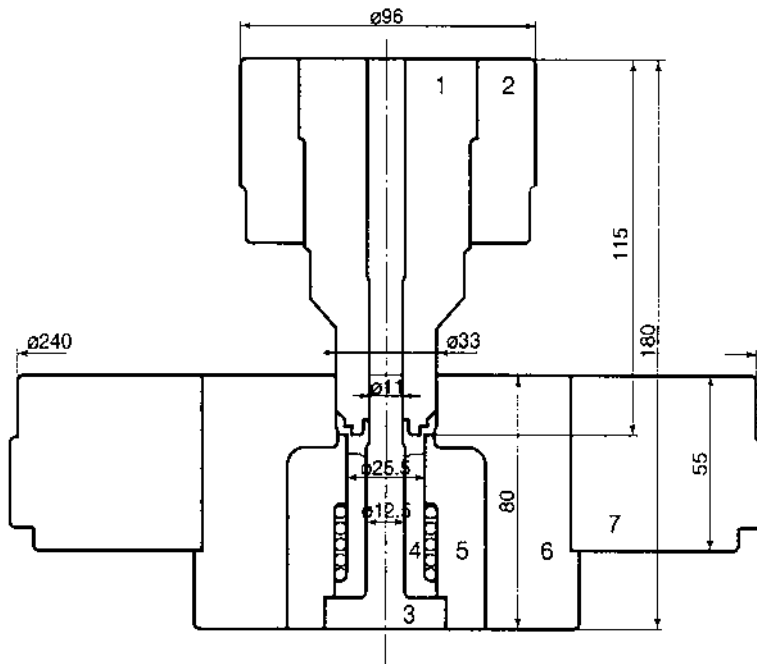
Figure 28 Tool set up for cold forging of hub of personal computer, Miyamoto Industry Co. 1. Punch, H11 = SKD6; 4,5. Die, M2 = SKH51; 6. Container, D2 = SKD11.

5.3 Hydraulic Press

Hydraulic press is large in capacity, long in ram stroke movement and easy in ram speed control. Hydraulic press is best to control die movements.

5.4 Special Purpose Press Machine

For mass production, such as the housing of a maker pen, Fig. 10, special purpose press machine is used to manufacture it automatically.

Ductility of aluminum alloy is sensitive to strain rate sometimes, so a press that has easily changed speeds is recommended for aluminum forging.

6 CONCLUSION

A trial experimental engine piston-like product is shown in Fig. 13 made from A1–13% Si. A1–13% Si powder of 400 μm diameter is produced by a spinning water atomization process. Powder is compacted to blank and sintered. Hot forging was done at 793K with graphite as a lubricant. The drum for a video is cold forged experimentally using an extruded rod of aluminium powder of A1–19.8% Si-2.0% Cu-0.9% Mg. Tensile strength, elongation and hardness of forged drum are 402 MPa, 2.7% and 79.5 HRB respectively.

Figure 29 Link press produced by Komatsu Ltd.

If precision forging technology makes it possible to manufacture higher strength aluminum alloys, the application of aluminum to automotive or other industries will be accelerated.

REFERENCES

1. K. Miyamoto, "History and practice of aluminum cold die forging," Light metals, 1993, 43(12), pp. 664–671.
2. H. Kudo, K. Sato, and I. Sawano, "Cold forgeability test of mild steel and forging force." J. Japan Soc. Tech. Plasticity, 1965, 6 (56) pp. 499–511.
3. H. Kudo, "Some analytical and experimental studies of axi symmetrical cold forging and extrusion – 1," Int. J. Mech. Sci. 2, pp. 102–127.
4. H. Kudo, *Study on Forging and Extrusion Procrsses*, Part 1 Analysis on Plane Strain Problems, 1958, Koken Syuho, (1), pp. 37–96.

5.   H. Kudo, *Study on Forging and Extrusion Processes*, Part 2 Experiment on Plane Strain Problems, 1958, Koken Syuho, 1, (2) pp. 131–150.

6.   H. Kudo, *Study on Forging and Extrusion Processes*, Part 3 Analysis on Axisymmetrical Problems, 1959, Koken Syuho, 3(3) pp. 212–246.

7.   H. Kudo, *Study on Forging and Extrusion Processes*, Part 4 Experiment on Axisymmetrical Problems, 1959, Koken Syuho, 3(4) pp. 247–299.

8.   H. Kudo, *Theory of Plasticity*, 1968, Morikita Syuppan.

9.   The Japan Society of Technology of Plasticity. *Forging Technology*, 1995, Corona pub.

10.   K. Shinozaki, ''Study on composite process cold extrusion on a multi-ram press,'' Report of Mechanical Engineering Laboratory, No. 148, 1989.

11.   R. Hill, *The Mathematical Theory of Plasticity*, Oxford Engineering Science Series, 1950, p. 172.

12.   H. Kudo, *Theory of Plasticity*, Morikita Syuppan, 1968, p. 139.

13.   K. Shinozaki, ''Preliminary study on closed die forging,'' Report of Royal Institute of Technology, Stockholm, Metal Forming, 1974.

14.   T. Matsushita, ''Temperature selection in forging operation,'' J. Japan Soc. Tech. Plasticity, 1999, 40(466) pp. 1049–1054.

15.   N. Nakamura, O. Tsuda, M. Nakao, and S. Toshima, ''Thermo rigid plastic coupled simulation of hot high speed forging of Al alloy,'' Technical report of Kobe Steel, 1994, 44(1) pp. 43–46.

18

Sheet Forming of Aluminum Alloys

WILLIAM J. THOMAS

General Motors, Troy, Michigan, U.S.A.

TAYLAN ALTAN and SERHAT KAYA

Ohio State University, Columbus, Ohio, U.S.A.

1 INTRODUCTION

Metal forming includes a large number of manufacturing processes producing industrial and military components and consumer goods. In metal forming processes, the change in shape of the processed workpiece is not accompanied by an extensive amount of metal removal [29]. Forming processes are frequently used together with other operations, (such as machining, grinding, and heat treating), in order to complete the transformation from raw material to finished parts. Forming as well as machining have been at the core of modern mass production because they primarily involve metal flow and do not depend on long term metallurgical rate processes [31].

In metal forming processes, an initially simple metal part—a billet or sheet blank—is formed by plastic deformation. Stress applied to plastically deform the metal is largely compressive in bulk forming and tensile/compressive in sheet forming, but shear stress is also applied in some processes such as blanking and shearing.

Desirable properties for forming usually include low yield strength and high ductility. These properties are affected by temperature. When the work temperature is raised, ductility is increased and yield strength decreased. The effect of temperature gives rise to distinctions between cold, warm, and hot working [15]. For example, the yield stress of a metal increases with increasing strain during cold forming. In hot forming, however, it increases when strain or deformation rate increases. Friction is another factor affecting performance in metal forming.

Complex geometries can be obtained equally well by hot or cold forming. Of course, tool stresses and machine loads are relatively lower in hot forming than cold

forming due to lower yield strength of the deforming material at elevated temperatures.

Forming processes are especially attractive in cases where:

- the part geometry is not very complex and the production volumes are high, so that tooling costs per unit product can be kept low (e.g. automotive application); or
- the part properties and metallurgical integrity are extremely important (e.g. load carrying air craft and jet engine and turbine components) [4].

The design, analysis and optimization of forming processes require (a) engineering knowledge regarding metal flow, stresses and heat transfer as well as (b) technological information related to lubrication, heating and cooling techniques, material handling, die design and forming equipment [4].

2 FORMING PROCESSES

Bending (Fig. 1), which is the most common type of deformation, occurs in almost all forming operations. Bending can also be the principal operation, such as flanging (bending over a radius) or hemming (flattening the sheet to join two sheets of metal).

Stretching (Fig. 2) is caused by tensile stresses in excess of the yield stress. These stresses typically produce biaxial strains in the plane of the sheet.

Drawing (Fig. 3) is the operation where sheet metal undergoes elongation in one direction and compression in the perpendicular direction. Many forming operations involve substantial drawing.

Coining is the compression of the metal between two die surfaces to impart some feature. Though most often applied to sheet-like workpieces, coining is fundamentally a bulk forming process because of the stress modes involved [13].
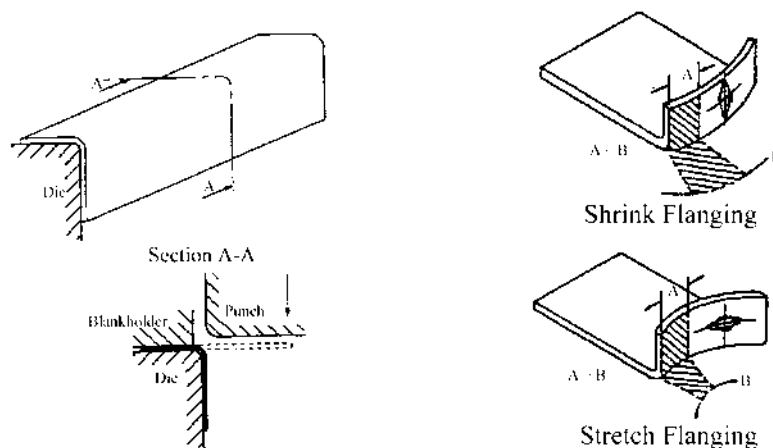
Figure 1   Bending and flanging of sheet metal. (From Ref. 27.)
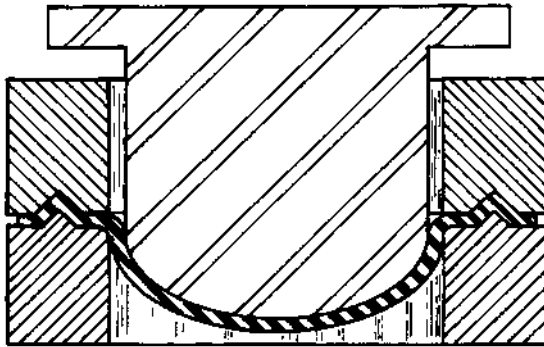
Figure 2   A section of a stretch die for a dome shaped part (From Ref. 45.)
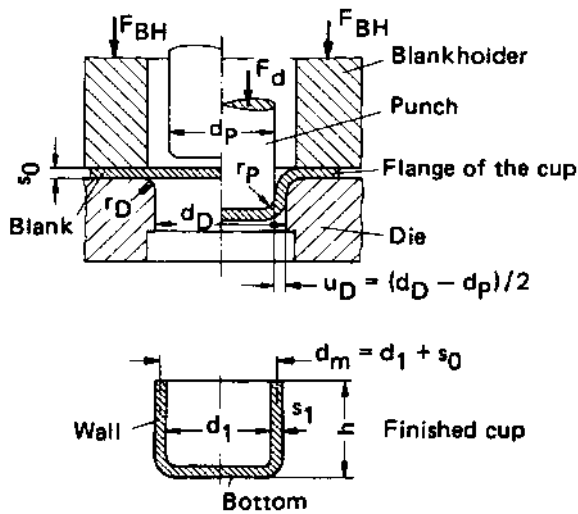
Figure 3   Deep drawing tool for a simple axisymmetric cup. (From Ref. 27.)

2.1 Bending

Bending operations are among the most common in sheet forming. Bending may occur along a straight line or along a profile (Fig. 1). Material on the outer radius of the bend is subjected to tensile stresses while material at the inner surface of the bend radius is subject to compression. In most cases, friction plays a relatively small role in the bending process.

2.2 Stretch Forming

Figure 2 illustrates a stretch forming operation to produce a dome shaped part. The edges of the blank are securely clamped with a lockbead, preventing the material outside this region from being deformed. Both the width and length dimension of the metal are changed. This type of forming is known as biaxial stretching.

Stretch forming is a very common operation. The forming of automotive, appliance, and aircraft panels are typical applications. Usually, 3–10% strain is required to obtain the mechanical properties needed for proper stiffness. Like deep cup drawing, stretch forming involving severe deformation depends on good material properties, proper lubrication of the punch, and correct die design. To obtain the necessary amount of stretch to achieve desired part stiffness, it is important to maintain adequate blank holder force to prevent metal slippage through the lockbead.

Stretch forming process failure is characterized by excessive localized thinning or necking, often leading to fracture. In general, surface roughness of both the die and material should be minimized. Especially in the boundary and mixed film lubrication regimes, roughness may result in scoring part fracture. In operations involving severe deformation, where frictional forces contribute to localized thinning and failure, lubrication is quite important [27].

Plane strain stretching is a special case of stretch forming. Under plane strain forming, the material is only elongated in one axis; there is no minor strain. This is significant because, from the forming limit diagram, it is known that this represents the condition under which failure occurs at the lowest forming depth.

2.3 Deep Drawing

Deep drawing is one of the most commonly used sheet metal forming operations (Fig. 3). It can be defined as a process in which a blank or workpiece, usually held by a blank holder, is forced into or through a die, by means of a punch. Hollow components are formed in which the thickness is essentially the same as that of the original material [27]. It differs from stretch forming in that the periphery of the blank is not fixed and is allowed to flow.

The force necessary for a deep drawing process is applied to the cup bottom by means of a punch while the actual deformation forces occur in the flange of the cup. The force is then distributed as a stress in the sheet material formed over the punch radius. This causes high tensile stresses in the cup walls. Usually, the bottom corner of the cup is the most critical area where fracture may occur, because of low work hardening. Since material is allowed to flow into the deformation region, deep drawing is generally capable of forming deeper cups than possible with normal stretching operations.

The basic components of a typical deep drawing tooling are shown in Fig. 3. The sheet metal blank with diameter d_0 is placed over a die opening with a profile radius of r_D. The blank is clamped by means of a blank holder. A punch with a diameter of d_P and a profile radius r_P moves downward and pushes the blank into the die cavity, thus forming the desired geometry of the workpiece. Cylindrical or prismatic cups, with or without a flange, can be produced with this process. The blank is forced into the die cavity against the restraining force generated either through a blank holder and/or by drawbeads. This restraining force controls the deformation (strain level and material draw in) in the entire blank [23]. The final shape can be any geometry varying from a simple axisymmetric cup to a very complex auto body panel.

The force requirement of the punch for the drawing process is limited by failure of the material in the cup wall. As this limit is approached, the metal thins excessively

in a localized area, usually near the punch radius. Many complex interactions occur during the cup drawing process. Actual force required depends on the draw ratio (blank diameter to punch diameter ratio) and the flow stress of the material. The significant independent variables in deep drawing are [23,41]:

- Material properties
- Ratio of blank diameter to punch diameter
- Shape and size of the blank
- Clearance between the punch and the die
- Punch and die corner radii
- Friction and lubrication at the punch, die, and workpiece interfaces
- Punch and blank holder velocities, and
- Blank holder technology.

2.4 Coining

By definition, sheet metal forming operations aim to deform a flat workpiece in two dimensions without intentionally creating changes in thickness. While strains do, of course, occur in the thickness direction during the previously mentioned forming operations, they are not the objective of the process. Since the intention of coining is to deform the sheet in the thickness direction, coining is technically a bulk forming or forging operation.

In coining, a punch and die contacts the workpiece on opposite sides and applies sufficient force to impart plastic deformation to the workpiece. A change in the thickness is effected, transferring the geometry of the tools to the workpiece. The name of the process is derived, of course, from its application to make coins. It is sometimes used in sheet metal stamping to emboss logos, or surface features. Also, in bending operations, the radius of the bend is sometimes coined to minimize springback.

3 PRODUCT AND PROCESS DESIGN FOR ALUMINUM

3.1 Product Design Considerations

Care must be taken in the design of aluminum products especially if the product was historically designed using steel. One of the first considerations to be taken into account is the fact that aluminum has one third the Young's modulus of steel. Thus the final product stiffness will be reduced unless the product design is accommodated. Two possibilities are to increase the ribbing used in the product and to increase the part thickness. The stiffness of the final product tends to increase in proportion to the square of the thickness. Also, ribs tend to increase stiffness in proportion to the increase in section moment of inertia.

The reduction of Young's modulus will also correlate into a proportional increase in the wrinkling, oil canning, and surface distortion tendency. Flange wrinkling can typically be controlled by the use of a blank holder, but wrinkling/oil canning/distortions in the product or addendum region can be difficult to control. Increasing material thickness can improve these issues, but the best method is to increase the geometry in the problem area by introducing features such as gainers, drawbars (see Fig. 42), ribs, or embosses. There will also be a proportional increase

in springback due to the reduction of Young's modulus. This can be offset by overcrowning the die geometry or by increasing the stretch in the final part which will be discussed in the next section.

Decreases in overall elongation and normal anisotropy are also typical in aluminum alloys. Bendability of aluminum may be an issue for many alloys as well. Part designers should be aware of minimum bend radii of the aluminum alloy to be used. If minimum bend radii are not available from the material supplier, Fig. 4 may be used. Figure 4 is a graph of minimum bend radius versus tensile reduction of area. If the reduction of area from a tensile test is known, an approximate minimum radius to thickness ratio may be obtained from this graph. If minimum bend radii are not obeyed in the part design then cracking may be observed in the final part as shown in Fig. 5. Hemming is also associated with bendability. If the material

The graph shows the equation $\frac{R}{T} = (60/r) - 1$
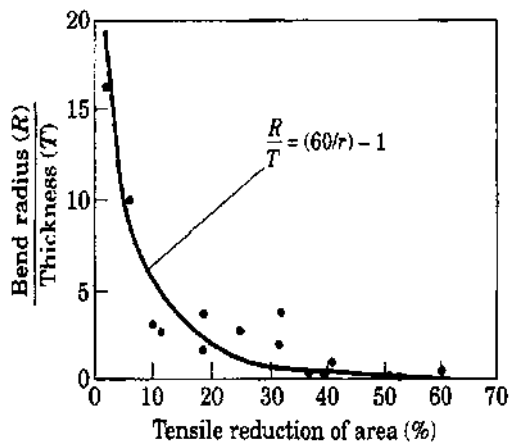
Figure 4 Minimum bend radius to thickness ratio versus tensile reduction of area.
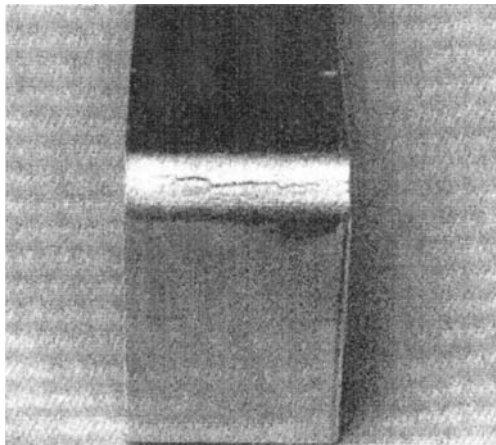
Figure 5 Cracking due to violation of minimum bend radius.
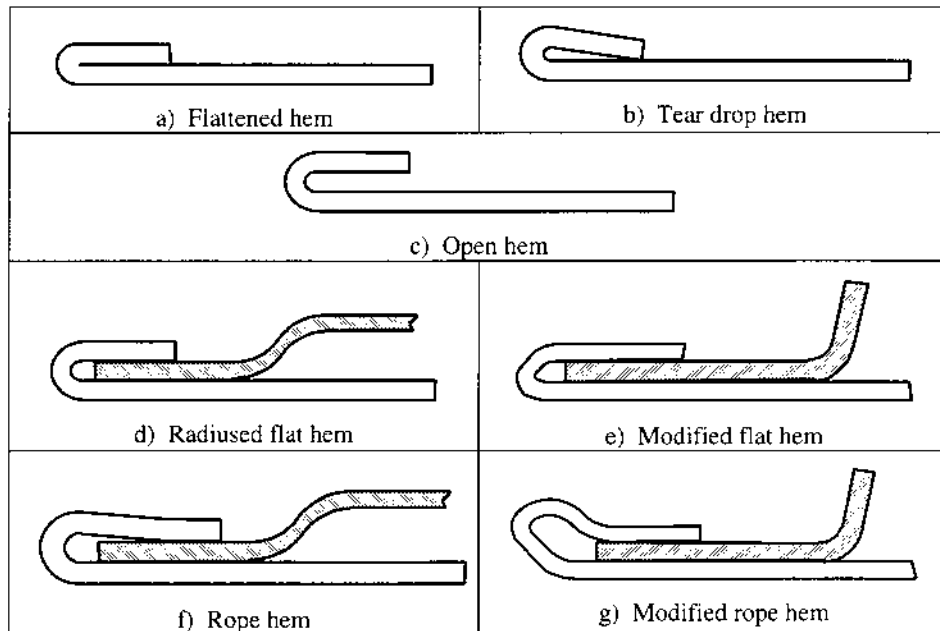
Figure 6 Alternative hem designs for aluminum.

cannot be bent to a zero radius then the hem design must reflect this. Figure 6 illustrates alternative hem designs for cases when flat hems cannot be used.

The reduction of formability of aluminum must also be taken into consideration for the drawing and stretching of deep recesses. A corresponding decrease in the depth of the recess may be needed to accommodate the formability of the aluminum.

3.2 Die and Process Design Considerations

Die and process design must be also carefully considered in order to deal with the formability window of aluminum. Table 1 list the recommended values for punch and die radii for aluminum and steel. To ensure good product quality, the process must be optimized to ensure at least 2% minimum stretch throughout the part. This minimum value of strain is confirmed by Figs. 7 and 8. Figure 7 shows that at strains less that 2%, springback is greatly increased. Likewise, Fig. 8 shows that 2% strain is required to ensure good dent resistance properties. Both graphs show that springback and dent resistance levels off at around 2% stretch.

The decrease in formability of aluminum can also be offset through the use of advanced die and process design and though the use of advanced technology. The clever use of advanced addendum design has been used successfully to widen the formability margins so that complicated geometries may be formed from aluminum [9]. The addendum is defined as the portion of the die between the die radius and the trim line. The most typical addendum feature is the drawwall which is used to connect the binder surface to the part geometry. Other addendum features include the use of gainers and drawbars. The downside to increasing the addendum regions is

Table 1 Recommended Die and Punch Radii

Material	Reference	Die, r_d	Punch, r_p
Aluminum	[5]	(4–6) t	(4–10) t
Aluminum	[27]	(5–10)t	(8–10) t
Steel	[6]	10 t	5 t
Aluminum	[6]	(–)	(4 to 8) t
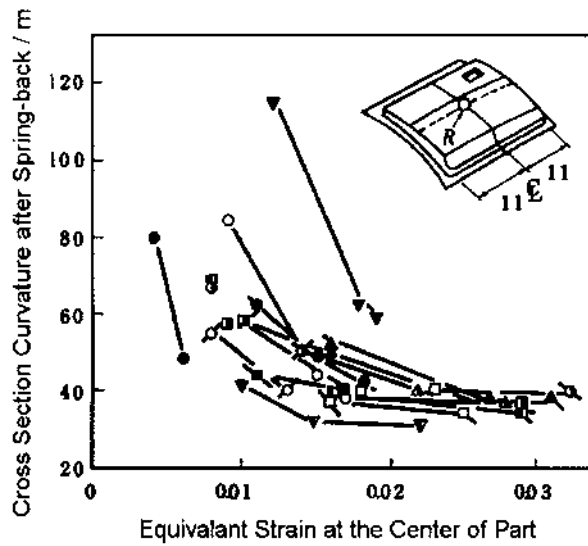
Figure 7 Effect of strain versus springback. (From Ref. 53.)
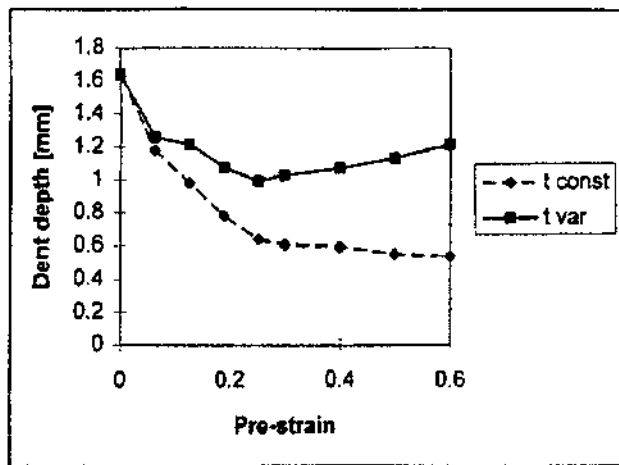
Figure 8 Effect of strain versus dent resistance. (From Ref. 49.)

that addendum is typically engineered scrap and thus this method tends to increase scrap realized per part.

The use of advanced technologies such as blank holder force control, hydroforming, and warm forming may also be use to increase the formability window of aluminum alloys. The cost associated with this solution is the capital investment of the presses and equipment needed to use these process. A description of the processes can be found in Secs 6.1–6.3.

4 VARIABLES OF THE FORMING PROCESS

The physical phenomena describing a forming operation are difficult to express quantitatively. For a given material, shape, and structure the surface transformations occurring in the plastic deformation zone are controlled by the equipment, tooling, and workpiece/tool interface. The metal flow, the friction at the tool/material interface, and the relationship between process conditions are difficult to predict and analyze. Therefore, thorough knowledge of complex interactions between the process components and the workpiece material is important for effective process design. The relationship between major process components and key technologies which enable the correct design and operation of sheet metal forming processes illustrates the hierarchical structure of the flow of knowledge from key technologies to unit processes through the five major process components.

Often, in producing discrete parts, several forming operations (e.g. preforming) are required to transform the initial ''simple'' geometry into a ''complex'' geometry, without causing material failure and degradation of material properties. Consequently, one of the most significant objectives of any method of analysis is to assist the forming engineer in the design of optimal forming sequence. For a given operation, such design essentially consists of the following steps:

   (a) predicting metal flow by establishing the geometric relationships such as shape, velocities, strain rates, and strains, between the deformed and undeformed part;
   (b) establishing the formability limits, i.e. determining whether it is possible to form the part without failure such as fracture and wrinkling;
   (c) selecting the equipment and tooling designs based on the prediction of the forces necessary to perform the forming operation.

For the understanding and design of sheet metal forming operations, it is useful to consider these processes as a system and classify them in a systematic way [4].

4.1 Sheet Metal Forming as a System

A sheet metal forming system is composed of all the input variables such as the blank (geometry and material), the tooling (geometry and material), the conditions at the tool/material interface, the mechanics of plastic deformation, the equipment used, the characteristic of the final product and finally the plant environment where the process is being conducted [4]. The application of the system approach to sheet metal forming, for example, is illustrated in Fig. 9 as applied to deep drawing.

The ''systems approach'' in sheet metal forming allows study of the input/output relationships and the effects of process variables on product quality
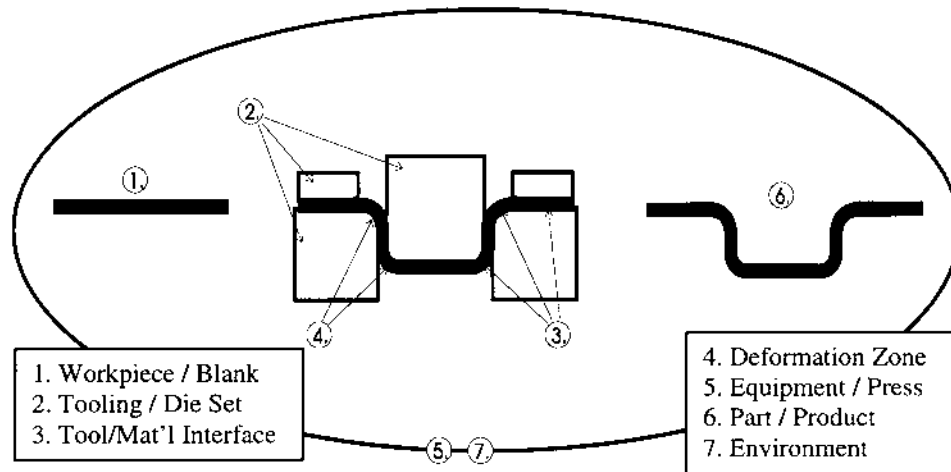
Figure 9   Sheet forming as a system.

and process economics. To obtain the desired shape and properties in the product, the metal flow should be well understood and controlled. The direction of flow, the magnitude of deformation, and the temperature involved greatly influence the properties of formed products. Process variables affecting the metal flow are given in Table 2 [4]. Also, the effect of variables on such product quality issues as fracture tendency, wrinkling tendency, and springback are shown in Table 3.

4.2   Material Characterization

In analyzing, simulating, and optimizing a sheet metal forming process for a given material, the most important variables are the initial conditions (e.g. composition, temperature, history, and prestrain), the flow stress of the deforming material under various strain and strain rates, the workability in various directions (i.e. anisotropy), and the surface conditions. Reliable estimation of tool stresses and the equipment loading, as well as prediction of metal flow and elimination of forming defects depend on the accurate determination of the flow properties of the starting material [15].

The constitutive equations [Eq. (1)] for sheet materials are usually determined based on load versus elongation data obtained from tensile tests. For a given microstructure and material flow direction, the flow stress, $\bar{\sigma}$, is expressed as a function of strain, $\bar{\varepsilon}$; strain rate, $\dot{\bar{\varepsilon}}$; and temperature, T:

$$\bar{\sigma} = f(\bar{\varepsilon}, \dot{\bar{\varepsilon}}, T) \tag{1}$$

4.3   Tooling and Equipment

Design and manufacturing of tooling are essential factors in determining the performance of deformation processes. The key to successful deformation processing is tool design which has been based, to a very large extent, on experience. Original multi-function tool designs are developed for near net shaping of complex parts.

Table 2 Significant Variables in a Deformation Process

Sheet material and blank
- Flow stress as a function of strain, strain rate, temperature and microstructure (constitutive equation)
- Formability as a function of strain, strain rate, temperature and microstructure (forming limit curves)
- Surface texture
- Thermal/physical properties (density, melting point, specific heat, thermal conductivity and expansions, resistance to corrosion and oxidation)
- Initial conditions (composition, temperature, history/prestrain)
- Plastic anisotropy
- Blank size, location, and thickness

Equipment used
- Speed/production rate
- Force/energy capabilities
- Rigidity and accuracy Tooling

Tooling
- Geometry of tools
- Binder forces
- Surface conditions
- Material/heat treatment/hardness
- Temperature

Condition at tool/material interface
- Lubricant type and temperature
- Insulation and cooling characteristics of the interface layer
- Lubricity and frictional shear stress
- Characteristics related to lubricant application and removal

Deformation Zone
- Deformation mechanics and model used for analysis
- Metal flow, velocities, strain (Kinematic), strain rate
- Stresses (variation during deformation)
- Temperatures (heat generation and transfer)

Product
- Geometry
- Dimensional accuracy/tolerances
- Surface finish
- Microstructure, metallurgical and mechanical properties

Environment
- Available man power
- Air, noise and wastewater pollution
- Plant and production facilities and control

Source: Ref. 4.

Table 3 Effect of Process Parameters on Product Quality

	Input	Fracture Tendency	Wrinkling	Springback
Blank Holder Force (BHF)	⇑	⇑	⇓	⇓
Blank Size	⇓	⇓	⇓	⇓
Sheet/Binder Friction ($\mu_{s/b}$)	⇑	⇑	⇓	⇓
Sheet/Punch Friction ($\mu_{s/b}$)	⇑	⇓	⇓	?
Thickness Homogeneity (Δt)	⇓	⇑	⇑	⇑
Nominal Thickness (t)	⇑	?	⇓	⇓
Normal Anisotrophy ($\bar{r}$)	⇑	⇓	⇓	⇑
Planar Anisotropy (Δr)	⇑	⇓	⇑	⇑
Strength Coefficient (K)	⇑	?	?	⇑
Strain Hardening Exponent (n)	⇑	⇓	?	?

To design and fabricate process tooling, computer aided engineering and computer aided manufacturing are used [15].

The productivity and reliability of equipment used for deformation processes are also very important factors, in determining the practical application of a given process. The stroke rates of the forming presses determine the production rate. Therefore, they are continuously increasing. The use of sensors for process monitoring and control continues to increase as well because it improves and maintains part quality.

Variations in tooling performance are caused by changes in setup and from continuous wear through normal usage. Sensors can also be used to continuously monitor the condition of the tooling, improving part quality as well as the production rates. This is achieved by greatly reducing unscheduled breakdowns of expensive production equipment and increasing the tool life [15].

The selection of a machine for a given process is influenced by the time, accuracy and load/energy characteristic of that machine. Optimum equipment selection requires consideration of the entire forming system, including lot size, conditions at the plant, environmental effects and maintenance requirements, as well as the requirements of the specific part and process under consideration.

The tooling variables include (a) design and geometry; (b) surface finish; (c) stiffness; and (d) mechanical and thermal properties under processing conditions [4].

4.4 Friction and Lubrication at the Tool/Workpiece Interface

Knowledge of friction and heat transfer at the tool/material interface should be expressed quantitatively in order to develop an adequate design for the process. The mehanics of interface friction are very complex. One way expressing friction quantitatively is through a friction coefficient, μ, or a friction shear factor, m. Thus the frictional shear stress, τ, is

$$\tau = \sigma_n \mu \tag{2}$$

or

$$\tau = m\bar{\sigma}/\sqrt{3} \tag{3}$$

where Δ_n or p is the normal stress or pressure at the interface, $\bar{\sigma}$ is the flow stress of deforming material and f is the friction factor ($f = m/\sqrt{3}$). For small values of pressure, which is usually the case in sheet forming, friction force increases with increasing pressure. In this case, friction conditions are best characterized by Coulomb's law [Eq. (2)]. With increasing pressure, friction force can not increase indefinitely. It approaches a finite value for very high pressures. At this time, sticking friction conditions occur when:

$$\mu p \geq k \tag{4}$$

where k is shear strength of the material, equal to $2\,\bar{\sigma}/\sqrt{4}$, according to Von Mises criterion of plastic flow. This condition occurs often in bulk forming operations where $p \gg k$. At this high pressure, since there is no relative motion between tool and the workpiece at the interface, the coefficient of friction, μ, becomes

meaningless. In this case, the friction factor, m, [Eq. (3)] is used to model friction conditions.

Recent studies in forming mechanics indicate that Eq. (3) represents the frictional shear stress in metal forming adequately and offers advantages in evaluating friction and in performing stress and load calculations. There are various methods of evaluating friction, i.e. estimating the value of μ or m. Tests most commonly used are the stretch-draw tests for sheet metal forming [4].

4.5   Deformation Zone and Mechanics of Deformation

When material is deformed plastically, metal flow is influenced mainly by (a) tool geometry; (b) friction conditions; (c) characteristics of input material; and (d) thermal conditions existing in the deformation zone [4]. Detailed understanding of metal flow enables the prediction of the quality and properties of the formed product and the force and energy requirement of the process. This leads to high quality products with minimum trial and error by optimizing the tool design and process conditions. The mechanics of deformation (i.e. the metal flow, strains, strain rates, and stresses), can be investigated using appropriate methods of analysis such as finite element, finite difference, slab method or upper bound [4].

4.6   Product Geometry and Properties

The two main characteristics of a deformed product are its geometry (e.g. dimensions, tolerances, thickness distribution and surface finish) and its mechanical properties. As in all manufactured parts, the design of the deformed part—that is the consideration of ease of deformation process during the design stage—determines the magnitude of the effort necessary for process and tool development. For example geometric features that satisfy various functional requirements such as stiffness and strength could be evaluated regarding their formability.

Product geometry and its mechanical properties are influenced by process variables. For example the process conditions (temperature, strain, and strain rate) has an effect on final product properties by determining the microstructural variations taking place during deformation. Therefore, the relationship between mechanical properties and microstructure of the final product and the quantitative effect of process conditions and heat treatment schedules on microstructural variations must be considered in a realistic systems approach [4].

4.7   Safety and Environmental Factors

Safety and environmental effects are important matters in forming process. The importance of safety increases with increasing machine speeds and forces. Adverse environmental effects of lubrication, cooling and heating fluids, noise, smoke and waste material must be considered in process development, and efforts should be made to minimize or eliminate adverse environmental effects [31].

5 MATERIAL PROPERTIES AND FRICTION IN STAMPING

5.1 Effect of Material Properties

Material can be the most influential part of the sheet metal forming. Specifically, the properties of the material, such as flow stress and anisotropy, can determine the quality of the part and its forming limits. A typical stress-strain curve determines the stress versus strain relationship of a sheet material. The standard curve is created from a simple tensile test. Figure 10 (top) gives the flow stress curve for a typical sheet material while Fig. 10 (bottom) gives the flow stress curves for 6111 aluminum and various steels.
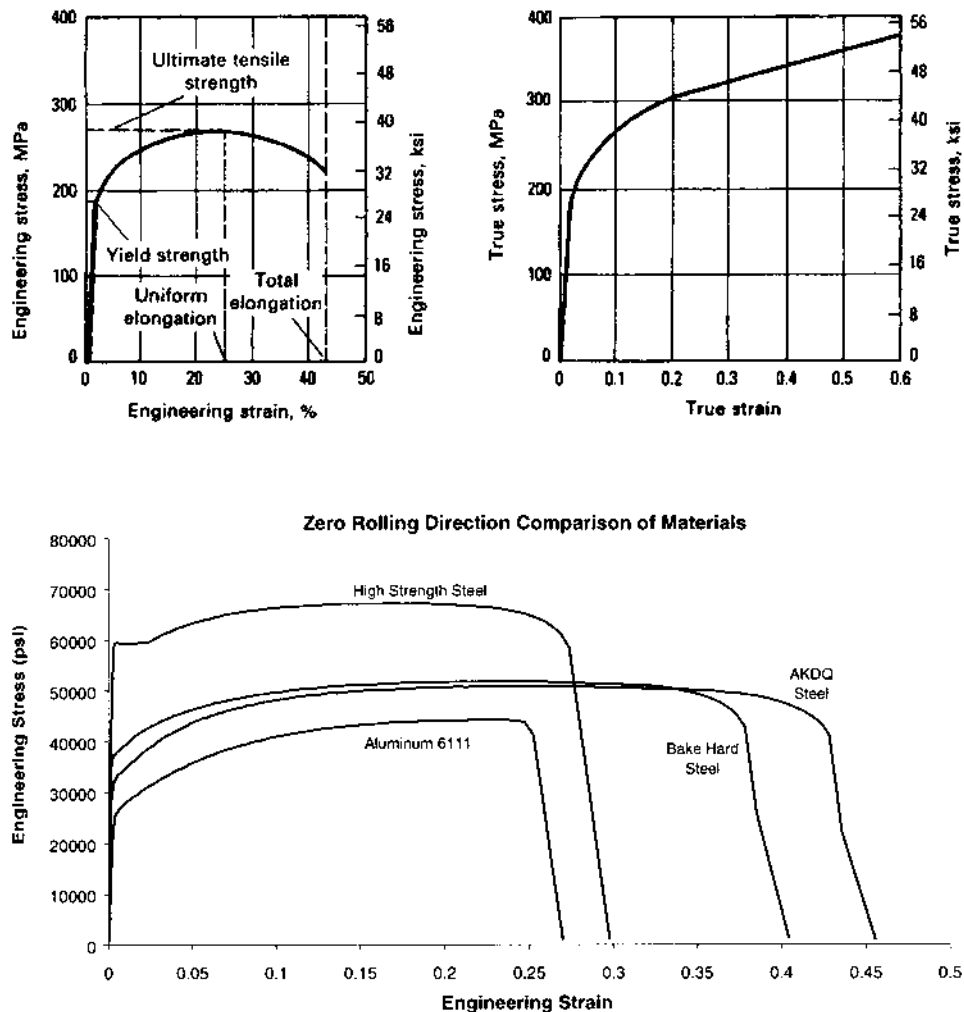
Figure 10   Material properties obtained from the tensile tests.

5.2.1 Strain Hardening

The strain hardening exponent plays a very crucial role in sheet metal forming. The strain hardening exponent is also referred to as the n-value. It is the exponent in the equation $\sigma=K\varepsilon^n$, which approximates the relationship between stress and strain in the plastic region. The n-value can be measured by calculating the slope of the log true stress/log true strain curve.

In a tensile test, the n-value is numerically equivalent to true uniform strain [50]. Therefore, the larger the n-value the more elongation can occur before necking. Thus the n-value is a measure of a material's resistance to necking. For this reason, n-value is a good measure of the stretchability of a material [50]. During stretching, a material with a large n-value will have a more uniform strain pattern than a material with a low n-value. Lower n-valued materials will localize strains and fracture earlier than higher n-valued materials. Hecker has shown that limiting depths of hemispherical cup tests can be related to n-value [18].

The n-value also has an effect on the uniformity of strain in a material with nonuniformly distributed thickness. Hosford and Caddell has shown that in a dimensionally inhomogeneous specimen, n-value plays a significant role in distributing the strains. The relationship of n-value and drawability is ambiguous. A higher n-value strengthens the cup wall, but it also strengthens the flange so more force is needed to deform it. Higher n-values improves drawing indirectly by increasing cup wall strength which allows higher blank holder forces to be used. Therefore, the n-value can be correlated to decreased wrinkling in drawing [46].

5.2.2 Anisotropy

Plastic anisotropy is a crucial factor in sheet forming. Plastic anisotropy is the concept that materials have preferred strain directions. Roll forged materials, such as sheet, exhibit this phenomenon due to the packing of grains in the thickness direction and the elongation of grains in the rolling direction. The r-value is a measure of plastic anisotropy in sheet materials and is defined as the ratio of width strain to thickness strain.

$$r = \frac{\varepsilon_{\text{width}}}{\varepsilon_{\text{thickness}}} \tag{5}$$

The r-value also varies as a function of the angle from the rolling direction. For the sake of simplification, an average or normal plastic anisotropy, r_{avg}, is defined:

$$r_{\text{avg}} = \frac{r_0 + 2r_{45} + r_{90}}{4} \tag{6}$$

where r_{45} is the r-value at $45°$ from the rolling direction, etc. The planar variation of the r-value is distinctly seen in a drawn cup. The top of the wall will form "ears" as shown in Fig. 11. Essentially the material elongates and thins more along the ears. The planar plastic anisotropy, Δr, is a measure of earing tendency and is defined as follows.

$$\Delta r = \frac{r_0 - 2r_{45} + r_{90}}{2} \tag{7}$$
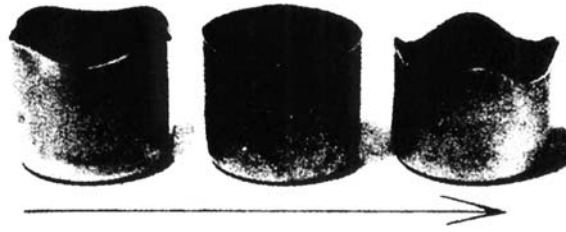
Figure 11 Earing in cup drawing. (From Ref. 21.)
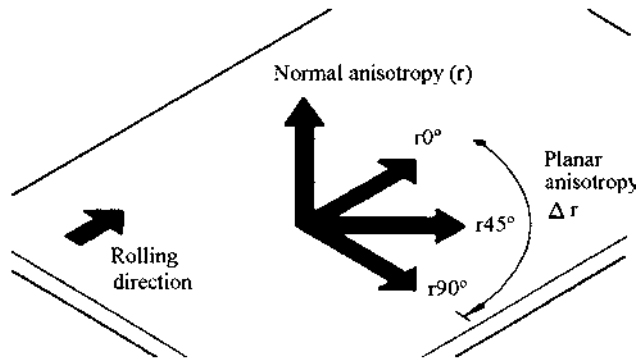
Figure 12 The *r*-values in a sheet material. (From Ref. 50.)

Figure 12 pictorially depicts the various *r*-value measurements and Table 4 provides r_{avg} and Δr values for several aluminum alloys and other selected sheet materials.

The average plastic anisotropy, r_{avg}, is a good measure of the drawability of a material. In cup drawing the majority of the deformation occurs in the flange of the cup. Higher r_{avg} values not only increases planar flow in the flange, but it decreases thinning in the cup wall and delays the onset of necking. Therefore, higher r_{avg} increases the depth of draw [38].

Under certain assumptions, the limiting draw ratio or LDR can be analytically related to the r_{avg} value. The LDR is defined as the maximum blank to punch diameter that can be successfully cup drawn in one operation. The equation to calculate LDR is [21]:

$$\ln(LDR) = \eta\sqrt{\frac{(r_{avg} + 1)}{2}} \tag{8}$$

where η represents an efficiency factor which varies with lubrication, blank holder force, material thickness, and die radius. Typical η values range from 0.74 to 0.79 [21].

Planar plastic anisotropy, Δr, has a minor but important effect on drawability. The higher the Δr the more earing occurs. Earing typically must be trimmed, therefore, an increase in Δr increases trimming and decreases the total depth of draw [21]. The *r*-value also affects wrinkling behavior. In general, high r_{avg} and low Δr

Table 4 Material Properties for Selected Sheet Metals

Material	Young's Modulus 10^6 psi (MPa)	Yield Strength ksi (MPa)	Tensile Strength ksi (MPa)	Uniform Elongation %	Total Elongation %	Strain hardening Exponent n	Average Strain Ratio r_{avg}	Planar Anisotropy r	Strain Rate Sensitivity m
Aluminum Killed Drawing Quality Steel	30 (207)	28 (193)	43 (296)	24	43	0.22	1.8	0.7	0.013
Interstitial Free Steel	30 (207)	24 (165)	46 (317)	25	45	0.23	1.9	0.5	0.015
Rimmed Steel	30 (207)	31 (214)	44 (303)	22	42	0.2	1.1	0.4	0.012
High Strength Low Alloy Steel	30 (207)	50 (345)	65 (448)	20	31	0.18	1.2	0.2	0.007
Dual Phase Steel	30 (207)	60 (414)	90 (621)	14	20	0.16	1.0	0.1	0.008
301 Stainless Steel	28 (193)	40 (276)	100 (690)	58	60	0.48	1.0	0.0	0.012
409 Stainless Steel	30 (207)	38 (262)	68 (469)	23	30	0.2	1.2	0.1	0.012
3003-O Aluminum	10 (69)	7 (48)	16 (110)	23	33	0.24	0.6	0.2	0.005
6009-T4 Aluminum	10 (69)	19 (131)	34 (234)	21	26	0.23	0.6	0.1	0.002
70–30 Brass	16 (110)	16 (110)	48 (331)	54	61	0.56	0.9	0.2	0.001

Source: Ref. 46.

values decrease the amount of wrinkling in the flange of straight walled cups and the walls of tapered cups [46]. It has been shown that the r-value has very little effect on the stretchability of a material [8].

Since the r-value varies in the plane of the sheet, blank orientation becomes an important factor in sheet forming. For example, in rectangular drawing rectangular blanks are typically used. Rectangular blanks are typically blanked side by side along a coil of steel to reduce scrap. For steel, this orients the low r-value directions (45° from rolling direction) in the corners of the rectangular shell. In rectangular forming, the critical forming regions occur in the corners of the shell which resemble cup drawing. Since high r-values increase cup drawing it is desirable to orient the high r-value directions (0° and 90° from rolling direction) along the corners of the shell. Rectangular blanks that are cut at 45° from the rolling direction orient the high r-value directions along the corners of the rectangular shell and thus improve the depth of draw [19].

5.2   Effect of Friction and Lubrication

Friction is a critical parameter of almost every manufacturing process. It appears everywhere, where two components are in contact directly or with an intermediate medium under exterior load. In contrast to material parameters such as tensile and compressive strengthening, friction is a result of a cooperation of all friction partners of a process. Hence, this can only be described as a value within an exactly defined tribological system. Generally, this system consists of a soil material, counter material, intermediate material and a surrounding medium with an exterior load. Therefore, it is necessary to consider not only the material properties, but also the load. This is especially the case for processes with nonuniform behavior. In these cases, the tribological conditions do not change only from location to location, but also during the process.

The interface between the sheet and the tooling is very important in the forming process. Friction forces resist the movement or flow of the material. Traction forces occur from the interaction of lubrication, contact force, and surface topography. Sliding contact from drawing can cause pressure welding of the sheet onto the die. Extreme pressure welding can cause the blank holder force to increase in an nonuniform fashion, causing fracture. Another way that friction influences the system is by preventing stretching of the sheet which contacts the punch. Some stretching on the top of the punch should occur to avoid elastic recovery of the material.

The variables which affect friction are many. Effects on friction can be observed as a function of:

- sliding distance/velocity
- normal force/pressure
- workpiece/tool material (hardness, surface finish, composition)
- lubricant (viscosity, composition) [13,22].

5.3   Evaluation of Formability and Friction

5.3.1   Formability

There are formability problems typically associated with each forming operation. Depending on the specific operation, different defects may occur. The major prob-

lems in sheet metal forming operations are fracturing, buckling and wrinkling, shape distortion, and undesirable surface textures. Selected defects are briefly explained below:

Fracturing (Fig. 13): occurs when a sheet metal blank is subjected forces that exceed the failure limits of the material under the given conditions.

Buckling and wrinkling (Fig. 13): In a typical stamping operation, the punch contacts the blank, stretches it, and starts to pull it through the blank holder ring. The edges of the sheet are pulled into the regions with progressively smaller perimeters. This is the reason for the compressive stresses in the circumferential direction. Buckling occurs when these stresses reach a critical level, characteristic of the material and its thickness. If the blank holder pressure is not sufficient, buckling may form waves known as wrinkles.

Shape distortion occurs when the residual stresses on the outer surfaces are different from those on the inner surfaces. When these stresses are not compensated by the geometry of the part, relaxation will cause a change in the part shape known as shape distortion.

Stretcher Strain Markings (Fig. 14): Under certain conditions during the stretching or other forming operations of some metals, especially aluminum-magnesium alloys and some low carbon steels, visible localized yielding, called stretcher strain markings, occur. They are extremely undesirable because of their negative influence on the surface quality of the
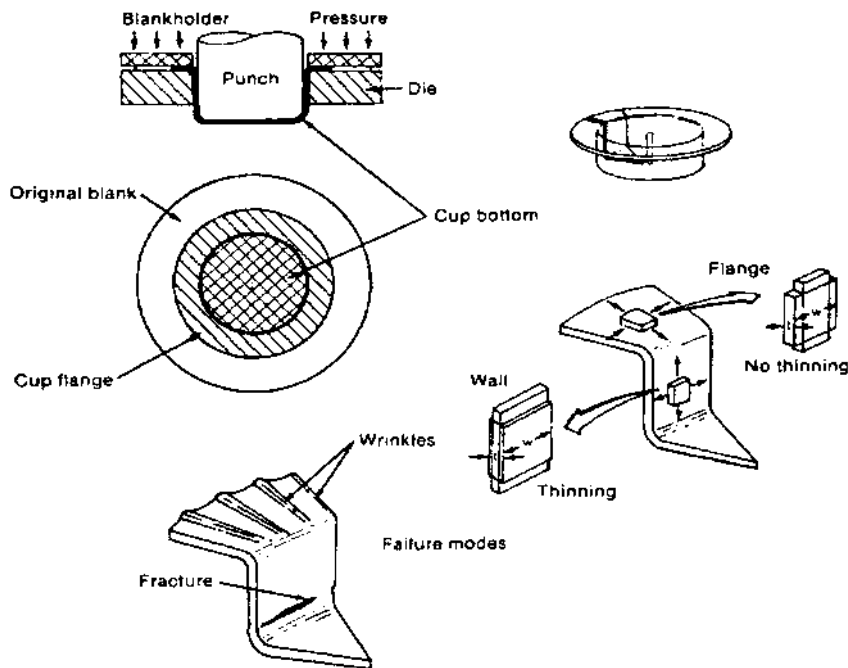
Figure 13 Forming defects associated with stretching and drawing. (Dieter, 1984)

parts. This highly visible phenomenon can not usually be concealed by painting. Therefore, these sheets cannot, for example, be used as outer auto body panels.

Two types of stretcher strains are observed. The first is called Type A ludering and is evidenced by irregular striations on the surface of the sheet (Fig. 14(a)). The tensile test of a Type A ludering shows that discontinuous stretching of the material is observed at the yield point [Fig. 14(b)]. Type B ludering consists of regular striations on the surface [Fig. 14(c)] and discontinuous stretching in the plastic region of a tensile test [Fig. 14(d)].

> *Orange Peel* (Fig. 15) is another surface defect associated with forming. Orange peel consists of a rough surface appearance typically caused by the variation of flow stress properties of the various grains contained in the material. The most convenient way to reduce orange peel is to decrease the grain size of the material [21].

It is important to recognize and understand which defects are associated with a given process and their effects on the finished workpiece. Not all failures are purely functional. Some defects, such as stretcher strains, may not affect the functionality of the part but may make the part unusable due to aesthetic considerations.

In order to test formability, we must first define it. Since most tests are only able to apply a limited variety of forming conditions to a specimen, the test is typically only able to measure formability under those conditions. This being the case, for practical application it is desirable to choose a test that best represents the critical region of forming in the stamping application. In general, formability tests may be categorized into one of several groups:

> *Standardized Tests*: Typically a laboratory setup aimed at repeatably creating or identifying a specific stress state. Often the test procedure has been well established, widely accepted, and formalized with specific guidelines including parameters such as sample size.
> *Cup Tests*: Though often standardized, the cup tests and their variants represent the majority of available formability tests, in part because they represent practical forming conditions.
> *Simulative Tests*: These tests are typically used to evaluate formability characteristics in some specific forming case. The test is usually not standardized, and often has a limited applicability.
> *Specialty Tests*: These tests are designed to test some aspect of formability for a specific process or application.

5.3.2 Standardized Tests: Tensile Tests

Because of their simplicity and broad applicability to forming processes, uniaxial tensile tests are probably the most commonly used sheet metal formability tests [44]. A specimen which has accurately parallel sides over the gage length is used in the tests (Fig. 16). The specimen is locked at each end, and stretched until it fractures. The tensile test procedures are described in ASTM E 646. The loads and the extension are measured by means of a load cell and extensometer.

The results which can be obtained directly from tensile tests are as follows:
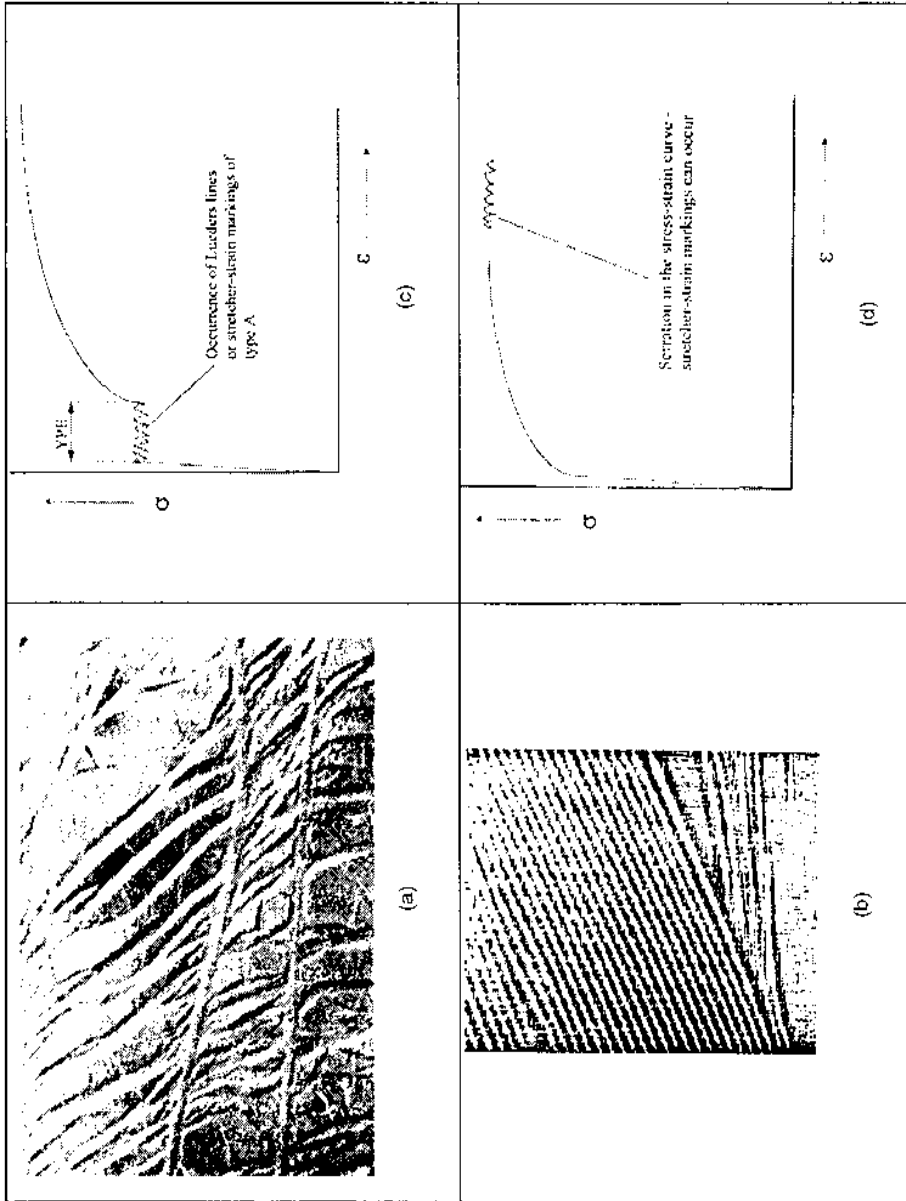
Figure 14 Various stretcher strain phenomena.
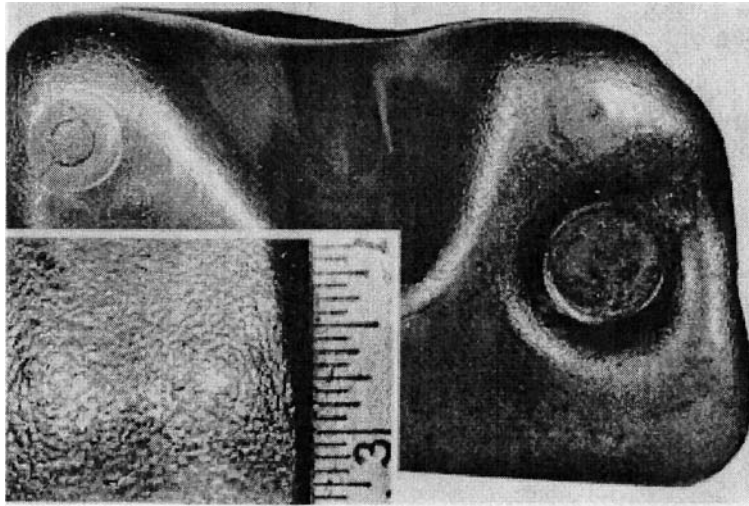
Figure 15   Orange peel. (From Ref. 21.)
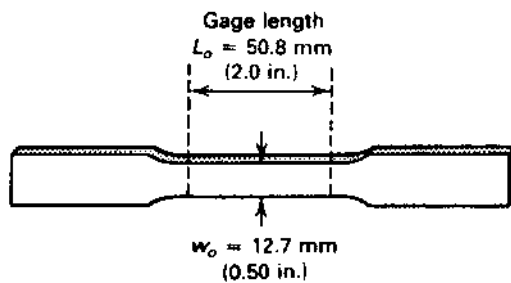
Figure 16   Tensile test specimen.

- engineering stress σ_e (load/original cross section)
- engineering strain e (elongation/original length)
- true stress σ (load/instantaneous cross section)
- true strain, ε (natural logarithm of strained length/original length).

From these values, the following parameters are calculated:

- n-value [strain hardening exponent in $\bar{\sigma} = K(\bar{\varepsilon} + \bar{\varepsilon}_0)^n$]: The slope of a graph of the logarithm of the true stress versus logarithm of the true strain in the region of uniform elongation.
- Young's modulus: The initial slope of the stress-strain curve in the elastic region.
- 0.2% Offset Yield strength: The stress at which the stress-strain curve deviates in elongation from the initial slope by 0.2%.
- Ultimate tensile strength: The maximum engineering stress that the specimen can withstand.

- *K*-value: The strength coefficient which is the true stress at a true strain of unity.
- *r*-value: The ratio of the width strain to thickness strain in the plastic region.

In addition to the above properties, by measuring the width of the specimen during the test by means of extensometers, the plastic strain ratio, *r*, can also be determined [7]. The mechanical properties of the materials tend to assume a directionality during production. That is why determining the anisotropy value is often important when material properties are being investigated.

5.3.3 Biaxial Stretch Tests

In the hydraulic bulge test (Fig. 17), in order to deform the sheet metal sample which is clamped between circular or elliptical die rings, hydraulic pressure is applied on one side. During the test the edge of the sample is prevented from slipping by a lockbead placed in the die rings. The stresses and strains in the center region can be determined from the curvature and extension of the formed specimen and the pressure of the fluid. The extension and the curvature are measured by means of a spherometer and an extensometer that are in direct contact with the dome.

5.3.4 Bending Tests

A variety of bending tests are available for use in evaluating materials. ASTM specifies some general guidelines for bending tests, but the exact method by which the bending must be applied is not regulated, (ASTM E290–92). A vise and insert setup for testing bend specimens is shown in Fig. 18.

5.3.5 Friction Testing

The friction in the tooling/workpiece interface affects the forming limits of sheet metal processes as significantly as the material properties and other process variables. In efforts to model friction phenomena correctly, several tests have been developed. The two most popular friction tests developed for sheet metal applications are the Nine drawbead test (Fig. 19) and the Duncan punch friction test (Fig. 20). Many researchers have used these test designs and tooling configurations for the basis of investigation on the effect of friction in sheet forming.
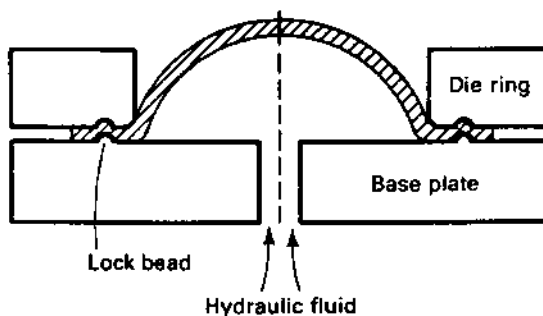
Figure 17 Hydraulic bulge test.
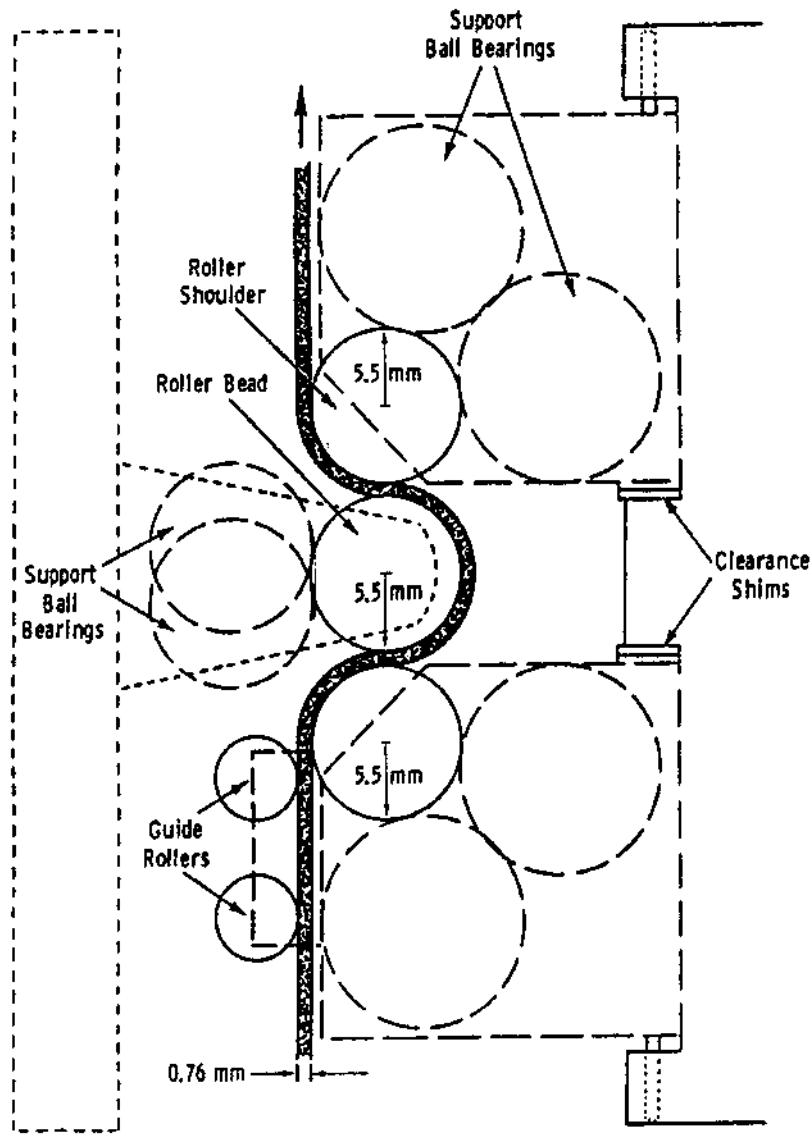
Figure 18 ASTM bend test.

In Nine's drawbead test, a strip of material is pulled through a set of rollers which force the strip to bend with and without friction (rollers are either free to roll or not, Fig. 19). The pulling loads are measured and used to estimate the friction condition in bending under tension conditions. In Duncan's test configuration, a strip of material is bent into a u-shape then stretched using rollers with or without friction (again, the rollers are either free to roll or locked, Fig. 20) The deformations loads are measured and used to calculate the friction under bending and stretching.
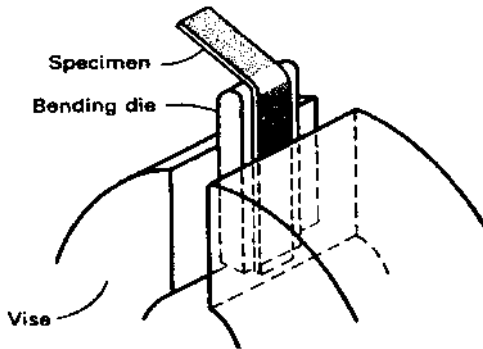
Figure 19 Nine's drawbead friction tester. (From Ref. 46.)
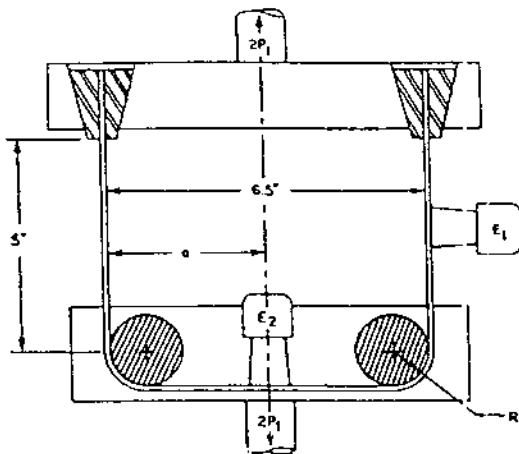
Figure 20 Duncan's friction test set. (From Ref. 12.)

6 ADVANCED TECHNIQUES TO IMPROVE FORMABILITY OF ALUMINUM ALLOYS

6.1 Blank Holder Force Control

Blank holder force (BHF) is used to suppress wrinkling and to control material flow in deep drawing processes. Two problems arise in the conventional application of blank holder force. First, a constant blank holder force is typically applied throughout the forming stroke even though the drawing ratio decreases as the flange is drawn in as shown in Fig. 21.

Second, a uniform blank holder force pattern is typically applied to the blank even though this may not be the optimal pattern. Compressive forces in the flange not only restrain material flow, but cause the material to thicken. The thickened areas are subject to high blank holder force (BHF) concentrations during the drawing process which further restrains material flow as shown in Fig. 22. To improve the effect of blank holder force, individually controlled nitrogen or hydraulic
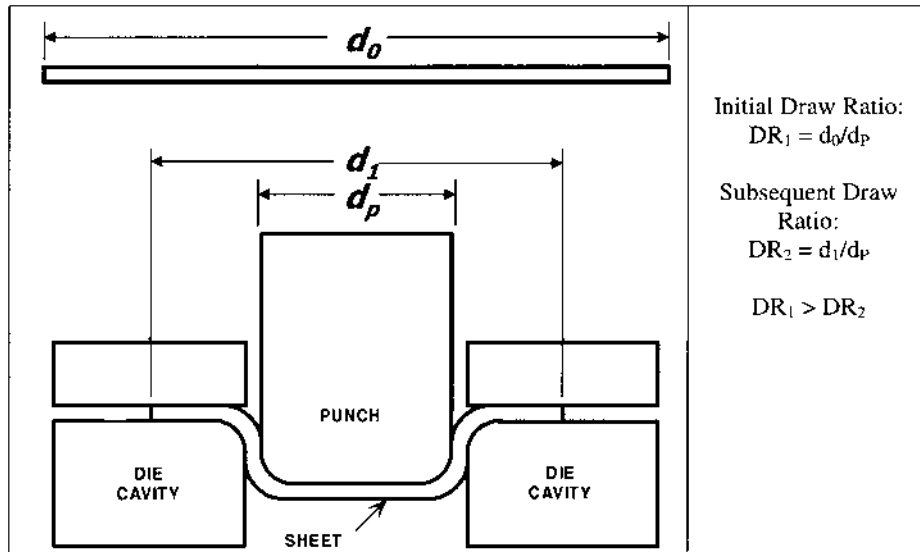
Figure 21   Reduction of draw ratio during the drawing process.
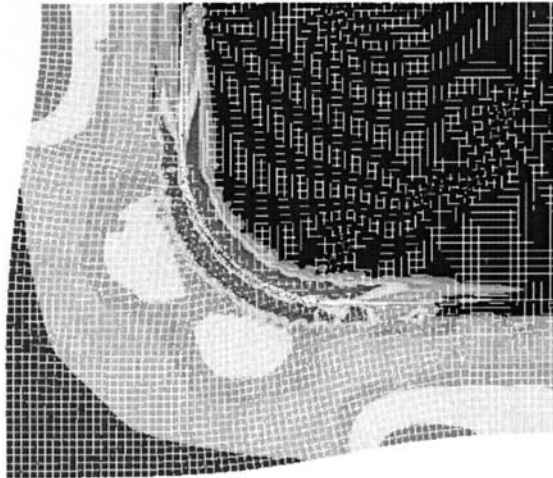
Figure 22   Predicted pressure concentrations on a rectangular pan due to thickening.

cylinders are used to apply the blank holder force. This method is demonstrated in the schematic shown in Fig. 23. Material flow can be locally controlled with this method throughout the stroke of the press [1].

How is Time Variable BHF Typically Applied?
In double action mechanical presses, BHF is applied with a position setting of the outer ram. Typically the BHF is not even known unless a loadcell is installed.
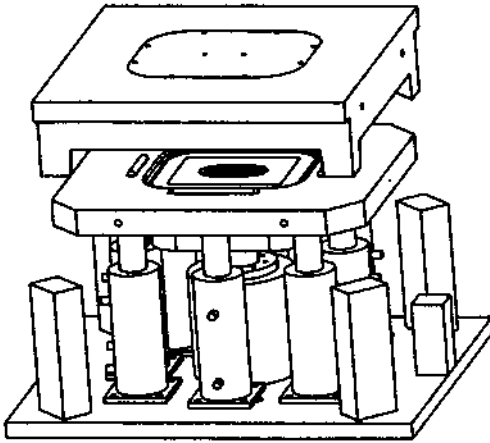
Figure 23 Blank holder force control using hydraulic cylinders in a rectangular tool.

The BHF tends to vary with the action of the mechanical linkage. In air or nitrogen cushions, the BHF typically increases with ram stroke due to the compression of the gas. In a hydraulic cushion, the BHF is typically constant throughout the ram stroke. Each of these BHF profiles are not desirable as was shown previously.

How Is Location Variable BHF Typically Applied?
Experienced tryout personnel grind the die surface or shim the tooling sections or cushion pins to vary the local BHF. Using a system, such as the one shown in Fig. 23, can clearly improve the application of BHF when compared to grinding and shimming.

Blank Holder Force Control Strategies
There have been many proposals and investigations on how to vary the BHF as a function of press stroke and position around the binder. A reasonable time varying BHF control strategy which has been shown to improve on constant BHF is to vary the BHF from the fracture limit to wrinkling limit of the BHF as shown in Fig. 24(b). Another empirical method for location variable BHF which improves on the uniform BHF is to distribute the BHF in proportion to the length to width ratio of the die cavity as shown in Fig. 24(d).

6.2 Warm Forming

Warm forming by definition is the forming of material at a temperature between cold forming and hot forming. Typically hot forming is exhibited by temperatures just below the melting temperature of the material while cold forming is conducted at room temperature. Warm forming requires less energy, insulation, technology and logistics than hot forming and thus is an attractive process for difficult to form parts.

By increasing the temperature of the aluminum sheet material, many advantages in terms of formability can be obtained. As shown in Fig. 25, the flow stress of the material tends to decrease as temperature increases. Thus forming loads tend
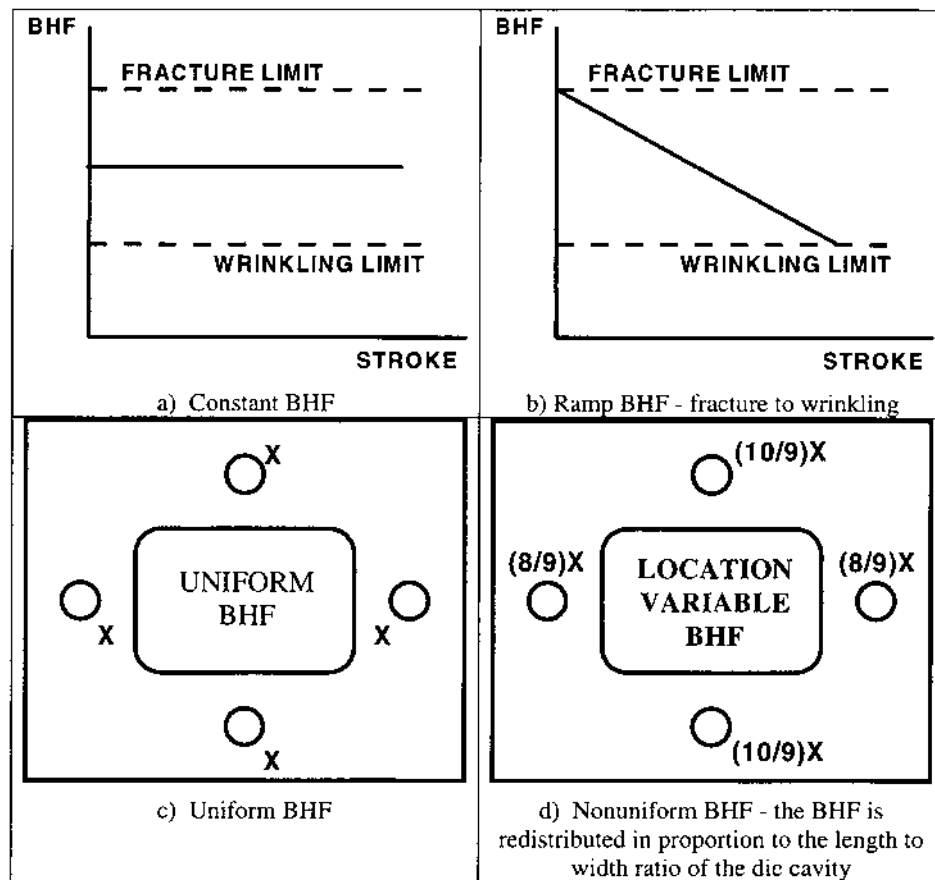
Figure 24 BHF control strategies.

to decrease. Further investigations have shown that increasing material temperatures tends to increase strain rate hardening, decrease ludering, and increase the forming limit curve [20]. This increase of material formability can be useful for deep recesses or complicated geometries. Warm forming requires an investment in equipment. An oven is needed to heat the incoming material and heater cores must be implemented into the tooling as shown in Fig. 26. Insulation must also be used to maintain die temperature efficiently.

6.3 Hydroforming

The formability of a material may also be increased using hydroforming. A schematic of the hydroforming process is shown in Fig. 27. The cost of the tooling is greatly reduced since only one die half is needed. The replacement of tool contact with fluid contact improves the process by decreasing friction on the material. The material thus deforms more uniformly and greater levels of deformation
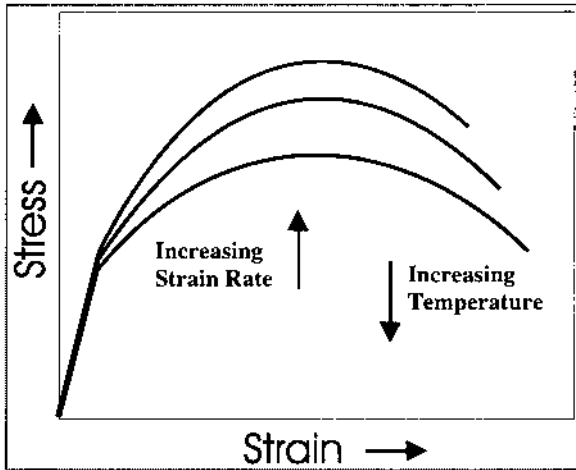
Figure 25 Effect of material temperature and strain rate on flow stress.
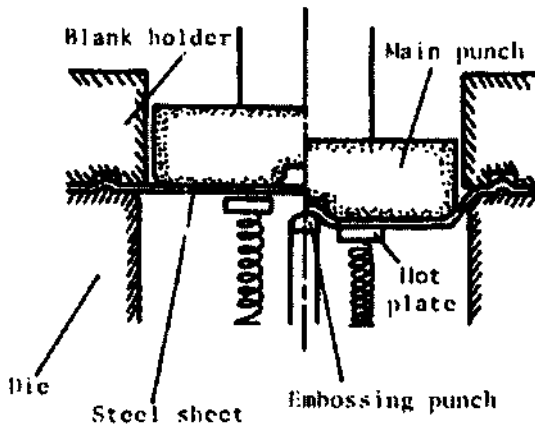
Figure 26 Warm forming tooling. (From Ref. 17.)
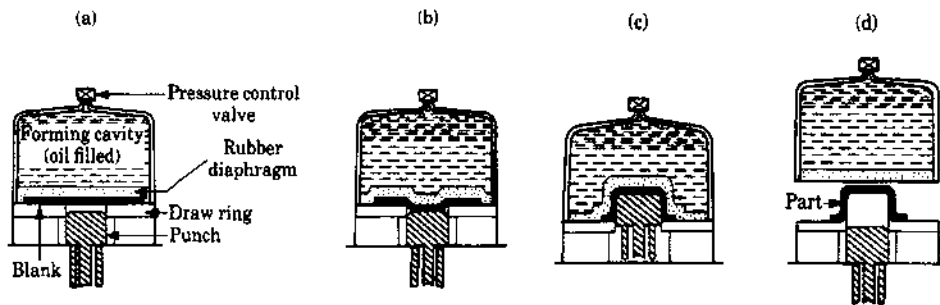
Figure 27 Hydroforming process. (From Ref. 4.)
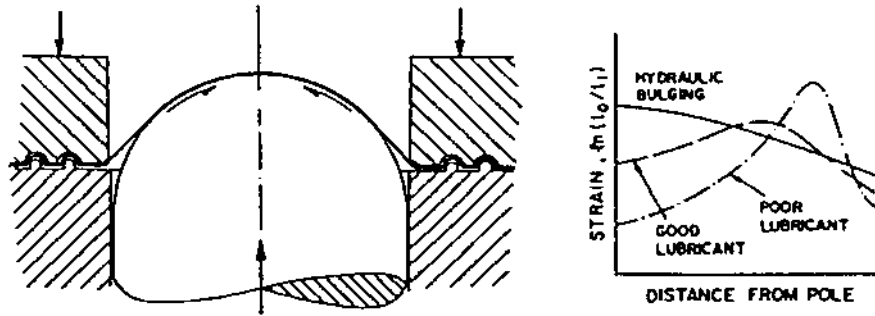
Figure 28   Strain distribution for hydroforming and deep drawing. (From Ref. 36.)
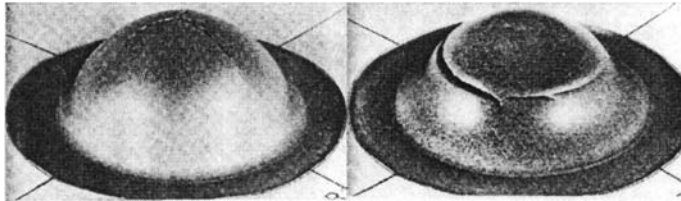
Figure 29   Fracture geometry for (left) deep drawing and (right) hydroforming. (From Ref. 51.)

may be achieved before failure. Figure 28 illustrates the difference in strain distribution for hydroforming versus deep drawing and Fig. 29 shows the differences in failure.

Another promising hydroforming technology is active hydroforming. This process is laid out in Fig. 30. Essentially, the blank is clamped, preformed and then formed. The preforming stage provide a uniform high strain to be placed on the sheet thereby improving such part characteristics as stiffness and dent resistance.

6.4   Application of Computer Simulations in Part and Process Design

The use of finite element analysis (FEA) in practice has increased in favour throughout the 1990s. Nevertheless, complete implementation of FEA has not been achieved. Simulation has been shown to not only predicted process conditions accurately in the laboratory (see Sec. 7.1) but on the shop floor as well (see Sec. 7.2).

The most common use of FE simulation in industry is to estimate the formability of the process and to determine the most optimal process conditions. The elimination of splitting and wrinkling via BHF and drawbeads is not the only possible use. The prediction of gravity/binder wrap conditions, impact line movement, surface distortions, trimming/piercing, springback, optimal blank shape, and BHF trajectory/pattern may also be achieved.
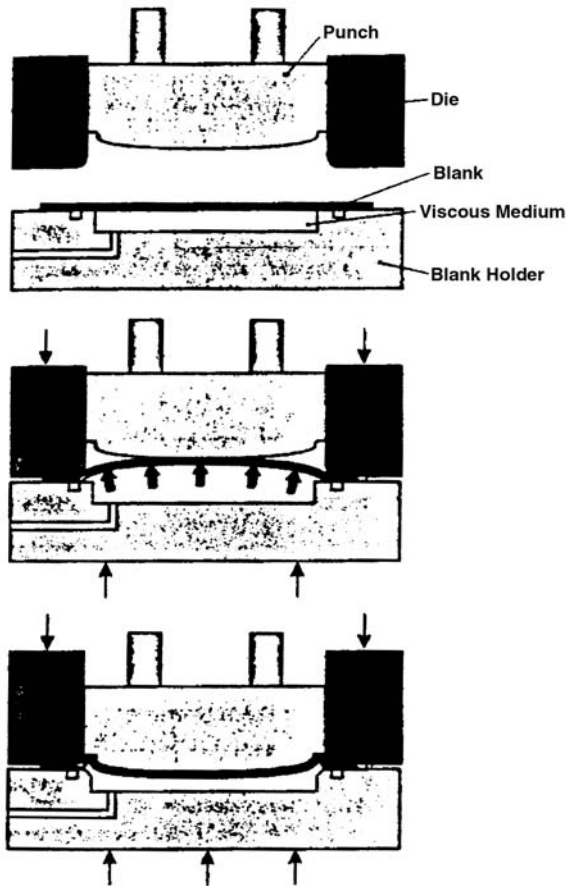
Figure 30 Active hydroforming. (From Ref. 37.)

Further, FE simulation may be used to estimate the manufacturability of product designs. A proposed outline of the design process for stampings using computer simulations is shown in Fig. 31. In this figure, the part design phase does not end after computer aided design. The initial product design is immediately simulated on the computer to estimate formability, feedback loop is introduced in case redesign is required. The optimization of part designs using FE simulation will save time later in the process. Without the use of FE simulation during the part design phase, the die and process design phase may be fraught with the task of developing a good process from a bad part design.

7 APPLICATIONS

7.1 Deep Drawing

In order to investigate BHF control, a rectangular cavity tooling was designed at the Engineering Research Center for Net Shape Manufacturing (ERC/NSM) in
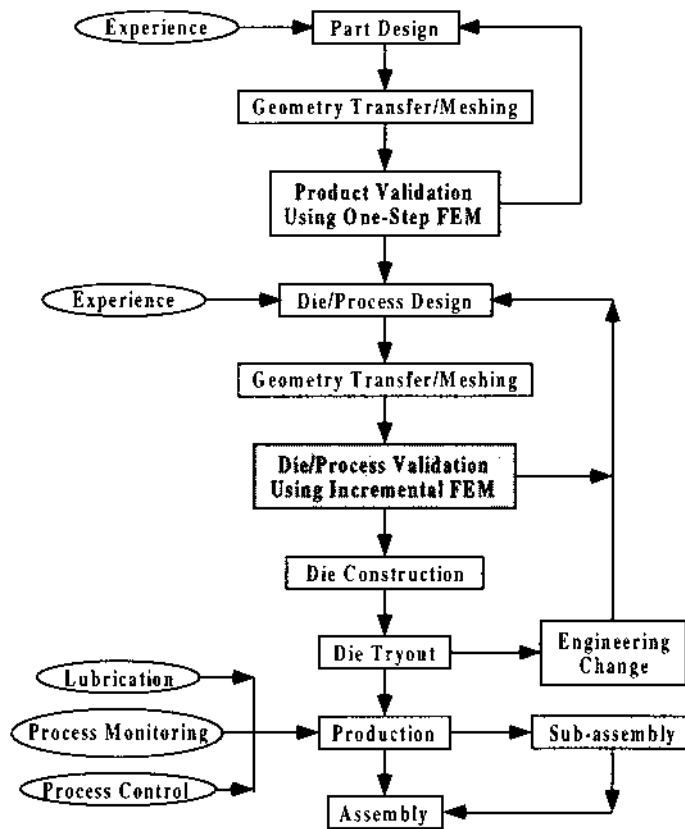
Figure 31   Proposed design process for stampings using FE simulation.

Columbus, Ohio. A schematic of the design is shown in Fig. 32, and a solid model is shown in Fig. 23. Some features of the tooling are listed in Table 5. The tooling has multiple punches including flat, singly curved, and two leveled (oil pan). The binder includes four locations for insertable drawbeads of three different heights.

Laboratory experiments were conducted with the rectangular tooling and the flat punch to investigate BHF control. A 160 ton hydraulic Minster press was used to impart the forming force and eight nitrogen cylinders were used to impart the BHF. The process parameters are shown in Table 6. The material and blank geometries are shown in Fig. 33. Two BHF patterns were studied: uniform and nonuniform. These patterns are shown in Fig. 34. Essentially, the uniform BHF pattern consists of each nitrogen cylinder imparting 5.2 ton (41.6 ton total). The nonuniform pattern consists of the corner cylinders set to 4.4 ton each and the side cylinders set to 6.0 ton each.

The reasoning behind the nonuniform BHF pattern has to do with the material flow pattern shown in Fig. 22. Typically the corners do not draw in and fracture occurs in the wall near the corners. The sides tend to draw greatly which may cause shape problems or even structural integrity problems such as oil canning (elastic instability). Thus, the nonuniform pattern reduces the BHF in the corners to increase
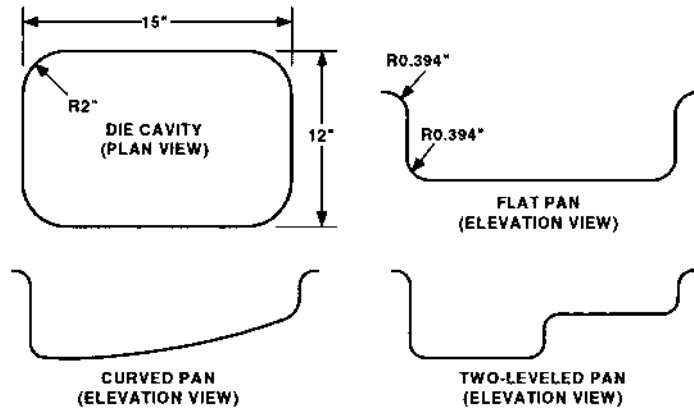
Figure 32 Rectangular cavity tooling design.

Table 5 Rectangular Cavity Tooling

Die Cavity	$12'' \times 15''$ Rectangle
	$(304.8 \times 381$ mm$)$
Punch Nose Radius	$0.394''$ (10 mm)
Die Lip Radius	$0.394''$ (10 mm)
Punch Corner Rad.	$2''$ (50.8 mm)
Punch/Die Clear.	$0.076''$ (1.9 mm)

Table 6 Process Parameters for BHF Control Experiments

Two Blank Holder	1. Uniform BHF pattern (41.6 t)
Force Patterns	2. Nonuniform BHF pattern (41.6 t)
Four Blank Types	1. Rectangular Aluminum (0.040"×20"×23")
	2. Oval Aluminum (0.040"×19.25"×22.25")
	3. Rectangular AKDQ steel (0.030"×20"×23")
	4. Chamfered AKDQ steel (0.030"×20"×23" with 2.25" chamfer)
Two Draw Depths	1. 2" Draw (50.8 mm)
	2. 3.5" Draw (88.9 mm)
Punch Speed	3.5 in/sec (90 mm/sec)

drawability and increases the BHF in the sides to improve part quality. The results of the experiments are shown in Fig. 35. These pictures show each material and blank geometry drawn under both BHF patterns. Fracture depths were increased up to 25% using this BHF control technique without any reduction of part quality. Wrinkling measurements were used to estimate part quality.

A finite element method (FEM) model of the rectangular tool was developed to investigate BHF control. In this model, the punch and die were discretized with rigid shell elements and the sheet was meshed with elastic-plastic shells. The blank holder
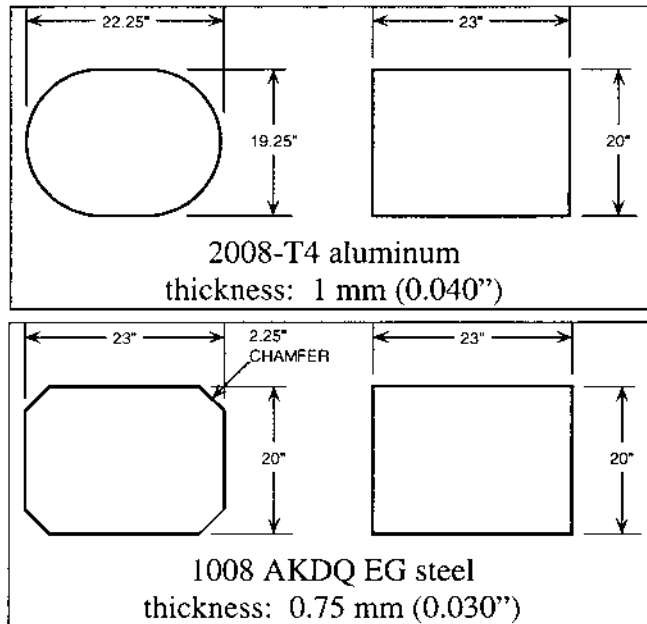
Figure 33 Blank shapes.
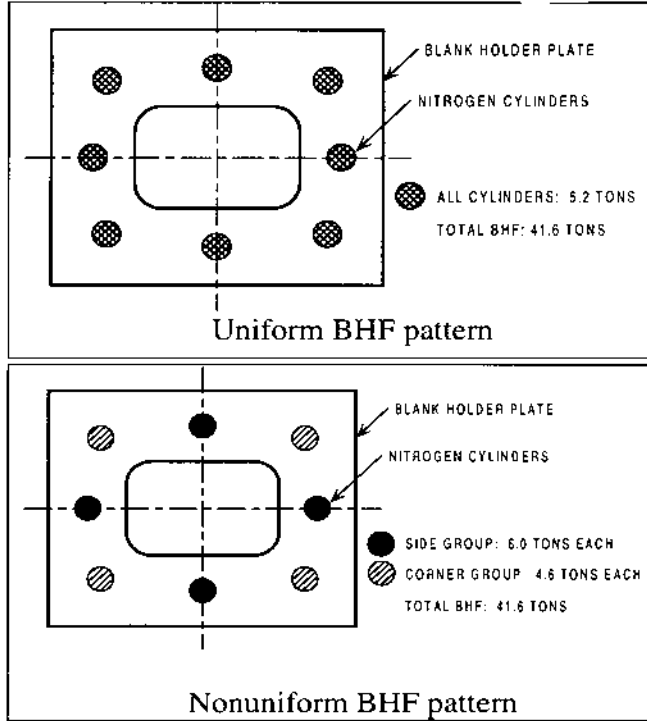
Figure 34 Experimental BHF patterns.
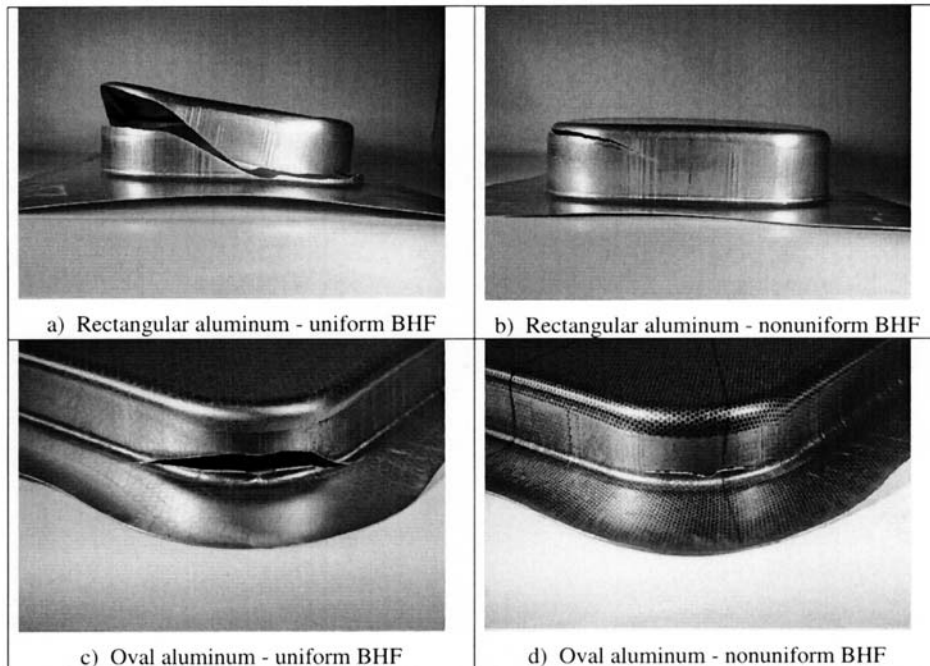
Figure 35 Effect of location variable BHF control on rectangular pan drawing.

was meshed with elastic brick elements so that the effects of nonuniform BHF patterns could be included. The meshed FEM model is shown in Fig. 36. In Fig. 37, the pressure patterns caused by the contact between the nitrogen cylinders and blank holder can be seen for both BHF patterns. This model can be used to find the optimal spatial BHF patterns and time trajectories.

Comparisons were made between experiments and simulations. Figure 38 shows comparisons between punch force measurements and predictions. A coefficient of friction of 0.075 was shown to give the best comparison (5% maximum error). Figure 39 shows strain comparisons made along the diagonal section shown. Good agreement was found for the same coefficient of friction (5% maximum error).

7.2 Stamping of Automotive Panels

This section will discuss the results of a rear deck lid simulation Two materials were simulated and forming in soft tool tryouts, 1004 AKDQ steel and 6111-T4 aluminum. The material properties are listed in Table 7. The process conditions used in the simulations are listed in Table 8. The panel geometry was symmetrical, so only half of the tooling was simulated.

The geometry for a rear deck lid draw die was obtained in IGES format and imported into I-DEAS, so that it could be cleaned up and meshed. A coarse mesh was initially defined, so that adaptive mesh refinement could later be used in regions
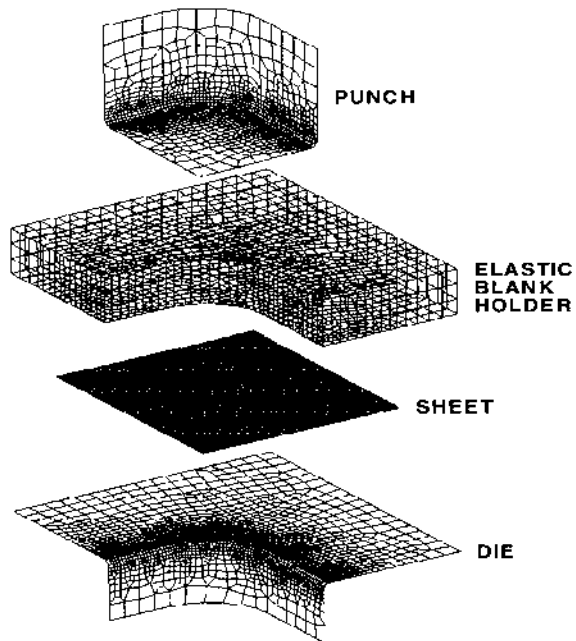
Figure 36 FEM model of the rectangular tool with elastic blank holder.
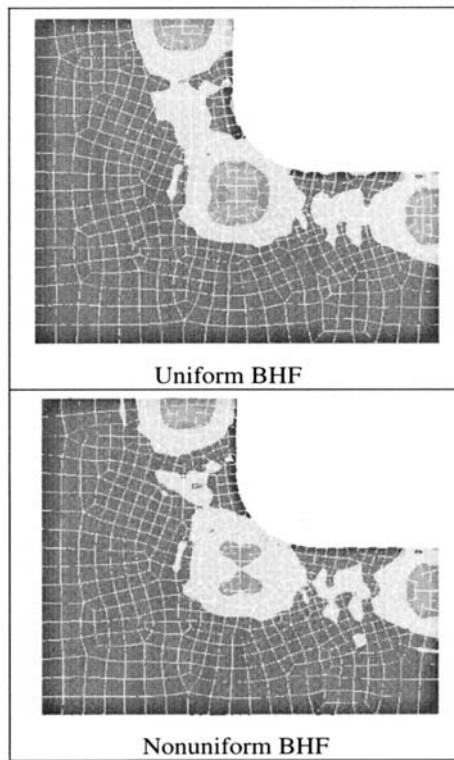
Figure 37 Simulated BHF patterns.
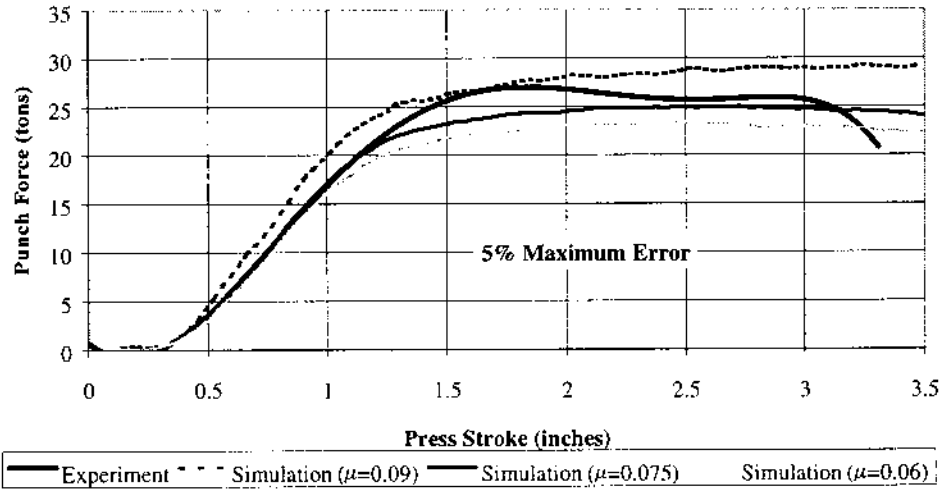
Figure 38 Punch force comparisons.
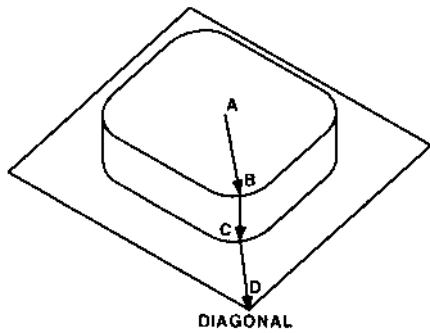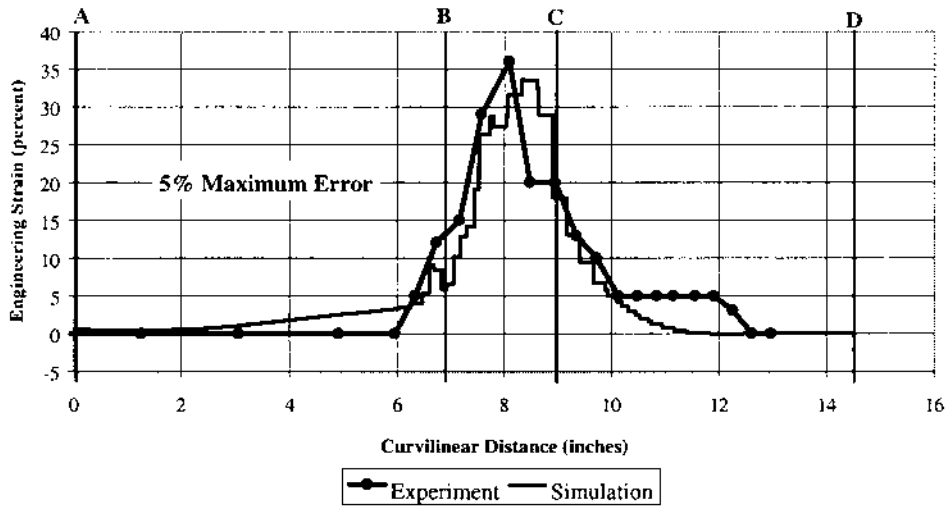
Figure 39 Strain comparisons.

Table 7 Material Properties

	1004 AKDQ Steel	6111-T4 Aluminum
Young's Modulus	200 GPa	70 GPa
	$(29.0 \times 10^6 \text{ psi})$	$(10.2 \times 10^6 \text{ psi})$
Poisson's Ratio	0.300	0.300
Strength Coefficient	0.5365 GPa	0.533 GPa
	(77812 psi)	(77302 psi)
Strain Hardening Exponent	0.227	0.238
Prestrain	0.00442	0.0010
Normal Anisotropy	1.62	0.59
Thickness	0.75 mm	1 mm
	(0.030")	(0.039")

Table 8 Process Conditions

Blank Holder Force	110 tons (100 metric tons)
Contact Model	Coulomb Friction ($\mu = 0.1$)
Forming Depth	5.9" (150 mm)
Punch Velocity	15 mm/ms

of sharp geometry. The meshed surfaces of the die, binder, sheet, and trim line were imported into Pam–Stamp's preprocessor module. The punch surface was created by offsetting the die surface by a sheet thickness. The opposing binder surface was similarly created.

The first step in the forming process was binder wrap. This was simulated by orienting the sheet between the binder surfaces and closing the binders together using a velocity boundary condition. This process formed the initial blank shape shown in Fig. 40(a) into the binder wrap sheet shape shown in Fig. 40(b). The second step was to simulate the stretch-draw operation. The appropriate binder force was applied and the punch was assigned a velocity boundary condition. A typical drawbead restraining force was then applied and the result are shown in Fig. 41 for both materials. Severe wrinkling occurred in the product area for the aluminum blank due to loose material in the die. The steel blank does not exhibit the severe wrinkling but still exhibits less than 1% strain in the same region indicating a similar loose material condition. These predictions were also observed during the soft tool tryouts. The loose material issue was resolved using a drawbar in the addendum region as shown in Fig. 42.

The maximum and minimum thinning in both materials are indicated in Table 9. These numbers show aluminum's tendency to thin and thicken more than steel in this process presumably due to lower normal anisotropy values which increases the tendency to strain in the thickness direction. Both materials exhibit thinning in excess of 24% indicating potential failure. The maximum thinning area occurred in the license plate depression as shown in Fig. 43. The drawbead restraining force in this area was reduced to feed material into this high strain region. Eighty
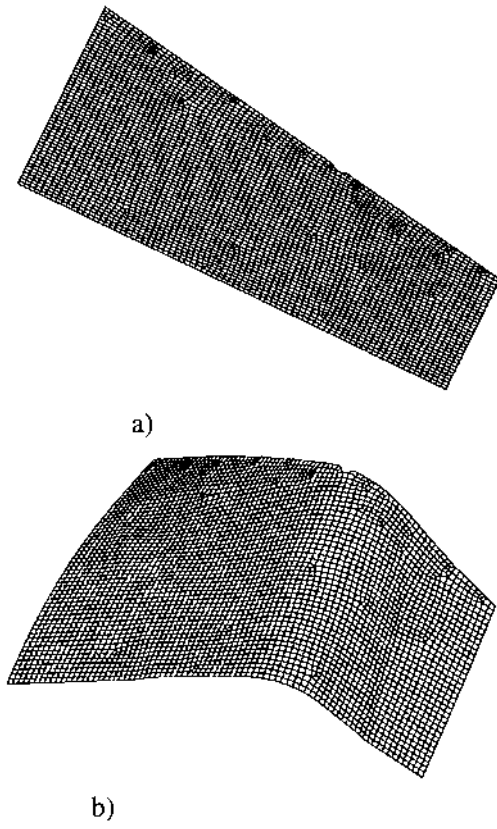
a)

b)

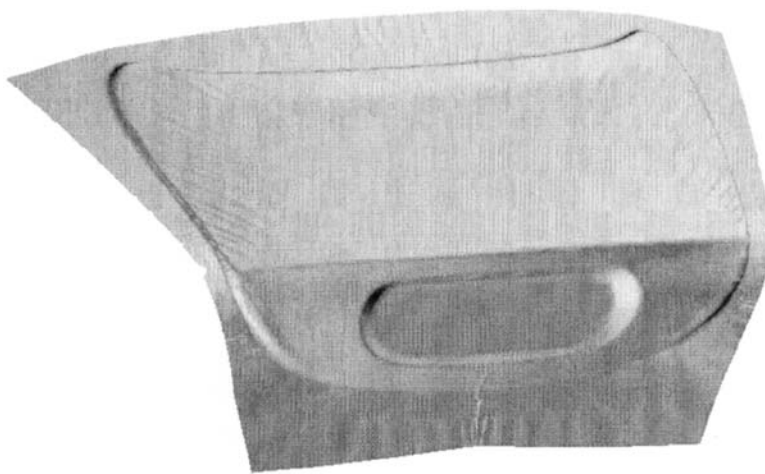**Figure 40** (a) Blank and (b) binder wrap sheet shapes.

Figure 41 Prediction of wrinkling and loose material.

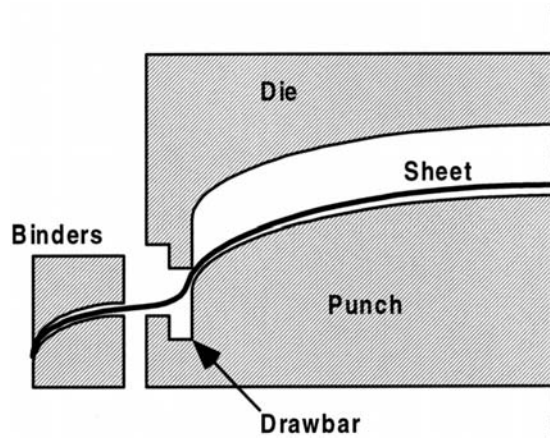**Figure 42** Using a drawbar to eliminate loose material.

Table 9 Thinning and Thickening for Aluminum and Steel Panels

	Thinning	Thickening
AKDQ Steel	24%	7%
6111-T4 Aluminum	27%	13%
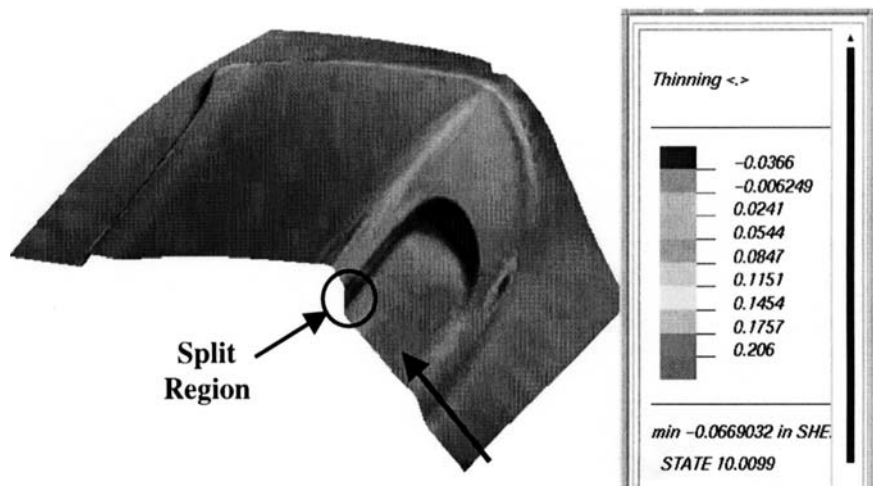
Figure 43 Prediction of splitting and material flow.
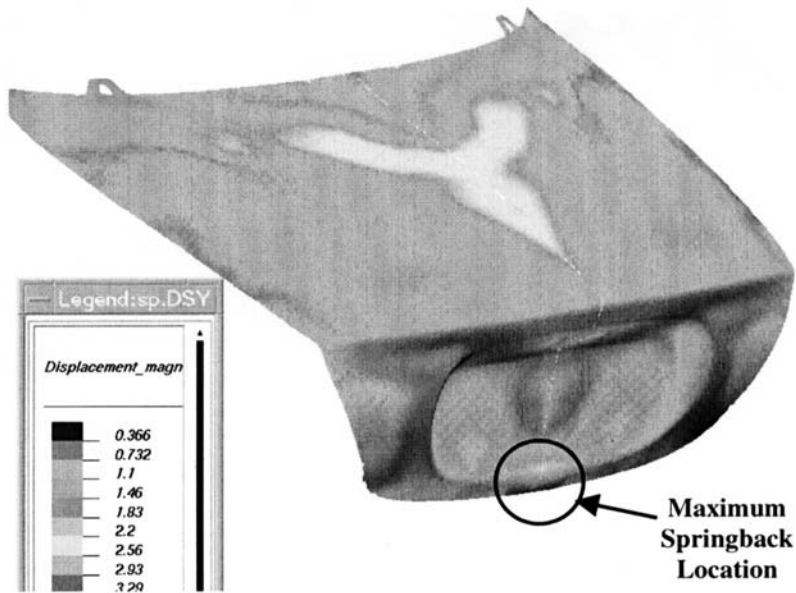
Figure 44 Prediction of trimming and springback.

Figure 45 Prediction of drawbead geometry.

millimeters of material flow was required to relieve this splitting condition as predicted by the simulation. During soft tool tryouts, 70 mm of metal flow was required indicating good correlation between predictions and observations.

Pam-stamp was then used to trim the excess material from the flange. The springback was then calculated and a contour plot of the springback displacement is shown in Fig. 44. The maximum springback was predicted to be 3.7 mm inboard along the edge below the license plate depressions. The soft tool tryouts indicated

that the location was correct and that the deflection was 4.5 mm, again confirming predictions. Once the process was optimized, the predicted drawbead restraining forces were used to predict drawbead geometry using analytical equations as shown in Fig. 45.

REFERENCES

1. M., Ahmetoglu, T. Altan, and G. Kinzel, "Improvement of Part Quality in Stamping by Controlling Blank Holder Force and Pressure," J. Mater. Process. Tech. 1992, 33, pp. 195–214.
2. M., Ahmetoglu, G. Kinzel, and T. Altan, "Advanced Techniques to Improve the Formability of Aluminum Alloys." METALFORM '96 PMA Technical Symposium. March, 1996.
3. *Aida Press Handbook*, 1992, Aida Engineering Ltd.
4. T., Altan, S. Oh, and H. L. Gegel, *Metal Forming: Fundamentals and Applications*, 1983, American Society for Metals.
5. American Society for Testing and Materials (ASTM), 1955.
6. American Society of Metals (ASM), 1988.
7. ASTM E517–81. "Standard Test Method for Plastic Strain Ratio, r, for Sheet Metal," ASTM. 1987, pp. 555–560.
8. D. Blickwede, Metals Progress. 1968, pp. 64–70.
9. T. Burk, "Addendum Design Methodology and Tool Design for Aluminum Sheet Metal Forming" Diploma Thesis. University of Stuttgart, 1994.
10. W. H. Cubberly and R. Bakerjian, *Tool and Manufacturing Engineers Handbook* 1989, Society of Manufacturing Engineers.
11. E., Doege and N. Sommer, "Blank Holder Pressure and Blank Holder Layout in Deep Drawing of Thin Sheet Metal," Advanced Technology of Plasticity, 1987, 2. pp. 1305–1314.
12. J. L. Duncan, "A Tensile Strip Test for Evaluating Friction in Sheet Metal Forming," SAE Paper No: 780391, 1978.
13. D. F. Eary and E. A. Reed, *Techniques of Pressworking Sheet Metal, An Engineering Approach to Die Design*. 2nd Edn. 1974, Prentice-Hall, New Jersey.
14. S. Esche, S. Khamitkar, G. Kinzel, and T. Altan, "Process and Die Design for Multi-Step Forming of Round Parts from Sheet Metal," Special Issue of Journal of Materials Processing Technology, 1996, 59. pp. 24–33.
15. M. P. Groover, *Fundamentals of Modern Manufacturing: Materials, Processes, Systems*, 1996, Prentice-Hall.
16. D. Hardt and R. Fenn, "Real-Time Control of Sheet Stability During Forming," J. Engin. Ind., 1993 115. pp. 299–308.
17. Y. Hayashi and M. Takatani, "New Forming Method for Avoiding Geometrical Defects of Outer Auto-body Panels," IDDRG 13th Beinnal Congress, 1984, pp. 63–72.
18. S. Hecker, *Metallurgical Engineering Quarterly* 1974, 14(4), pp. 30.
19. R. Hobbs, "Section I: Classification of Sheet Metal Operations, Prediction and Analysis of Press Performance for Sheet Steels," BPH Technical Bulletin, 1974, 18. pp. 1–13.
20. R. Holt, "Advances in Forming of Aluminum Sheet for Automotive Applications," 3rd International Conference on Sheet Metal Forming Technology. Fabricators & Manufacturers Association, 1998.
21. W. Hosford and R. Caddell, *Metal Forming: Mechanics and Metallurgy*, 1993, Prentice Hall, New Jersey.

22. T. A. Hylton, C. J. Tyne, and D. K. Matlock, "Frictional Behavior of Electrogalvanized Sheet Steels. SAE Technical Paper Series," Paper No. 930809. International Congress and Exposition March 1993.

23. S. Kalpakjian, *Manufacturing Processes for Engineering Material*, 1991, Addison-Wesley.

24. M., Karima and V. Donatelli, "Understanding Blank Holder Effect on Formability of Sheet Metal Stampings," SAE Annual Congress and Exposition, 1989, pp. 1–10.

25. S. Keeler, "Determination of Forming Limits in Automotive Stampings," Sheet Metal Industries, 1965, pp. 683.

26. R. Kergen, "Computerised control of BHF in deep drawing," Sheet Metal Industries, August 1992, pp. 12–15.

27. K. Lange, *Handbook of Metal Forming (Lehrbuch der Unformtechnik)*, 1985, Springer-Verlag, Berlin.

28. O. D. Lascoe, *Handbook of Fabrication Processes*, 1988, ASM International.

29. E. M. Mielnik, *Metal Working Science and Engineering*, 1991, McGraw-Hill.

30. A. Muderrisoglu, H. Livatyali, M. Ahmetoglu, and T. Altan, "Computer Aided Design for Bending, Flanging and Hemming of Steels and Aluminum Alloys," *Proceedings of the PMA Metalform '97 Symposium*. March 9–12, 1997, Chicago, IL. pp. 151.

31. National Research Council (NRC), "Unit Manufacturing Process Research Committee," *Unit Manufacturing Processes: Issues and Opportunities in Research*, 1995, National Academy Press.

32. B. W. Niebel, A. B. Draper, and R. A. Wysk *Modern Manufacturing Process Engineering*, 1989, McGraw-Hill.

33. H. D. Nine, Proc. of IDDRG WG Meeting Toronto, 1988.

34. K. Roll, "Finite Element Simulation of Internal and External High Pressure Forming." *Proceedings of the Sheet Forming Technology Conference*, 1995, Technical University Stuttgart. pp. 421–434.

35. G. Sachs, *Principles and Methods of Sheet-Metal Fabricating*, 1951, Reinhold Publication.

36. J. Schey, *Friction in Sheet Metalworking*, 1997, SAE International Congress and Exposition, pp. 87–106.

37. Schuler GmbH. *Metal Forming Handbook*, 1998, Springer-Verlag, Berlin.

38. S. Semiatin (Ed.), "Stretch Forming," *Metals Handbook, 14: Forming and Forging*, 1988, American Society of Metals pp. 591–598.

39. S. Semiatin, (Ed.) "Deep Drawing," *Metals Handbook, 14: Forming and Forging*. 1988, American Society of Metals, pp. 575–590.

40. L. Shulkin, D. Rowan, G. Kinzel, and T. Altan, "A New Hydraulic/Nitrogen Blank Holder Force Control System," *Proceedings of the ICTP*. 1996, pp. 813.

41. K. Siegert, Zieheinrichtungen einfachwirkender Pressen fur die Blechformung (Technologies for single action presses in sheet metal forming). Institut fur Umformtechnik Universitat Stuttgart, Germany (excerpts translated), 1991.

42. K. Siegert, "Closed-Loop Control System for Blank Holder Forces In Deep Drawing," Annals of CIRP, 1995, 44(1), pp. 251–254.

43. J. Siekirk, "Process Variable Effects on Sheet Metal Quality," J. Appl. Metal Work, 1986, 4(3). pp. 262–269.

44. W. M. Sing and K. P. Rao "Influence of material properties on sheet metal formability limits," J. Mater. Process. Tech., 1995, 48, pp. 35–41.

45. D. A. Smith, *Fundamentals of Pressworking*, 1994, Society of Manufacturing Engineers (SME) Dearborn, Michigan.

46. B. Taylor, "Formability Testing of Sheet Metals," *Metals Handbook*, 9th Edn., 1988, 14. pp. 878–879.

47. W. Thomas and T. Altan, "Applying Computer Simulation to Automotive Part Stamping," The Fabricator. February 1998,

48. W. Thomas, T. Oenoki, and T. Altan, "Implementing FEM Simulation into the Concept to Product Process." 1999 SAE International Congress. 12th Session on Sheet Metal Stamping (jointly sponsored by the NADDRG). March 1–4, 1999, Detroit, MI.

49. P. Vreede, M. R. Roelofsen, R. Brocking, and W. Kranendonk, *Dent Resistance and Material Properties*, 1996, International Body Engineering Committee, Material and Body Engineering.

50. C. Wick, (Ed.), "Forming," *Tool and Manufacturing Engineer's Handbook*, Vol. 2. Chaps 1 and 4. 1984, Society of Manufacturing Engineers.

51. D. V. Wilson "Friction and Formability in Sheet-Metal Working," Sheet Metal Industries, 1966 43. pp. 929–944.

52. W. Wong, Luders Lines in Cold Worked 5252, 1968.

53. K. Yoshida, (Ed.), *Handbook of Ease or Difficulty in Press Forming*. 1987, The Japan Sheet Metal Forming Research Group. Nikkan Kogyo Shimbun Sha, Japan.

19

Heat Treating Processes and Equipment

ROBERT HOWARD

Consolidated Engineering Company, Kennesaw, Georgia, U.S.A.

NEILS BOGH

International Thermal Systems, Puyallup, Washington, U.S.A.

D. SCOTT MACKENZIE

Houghton International Incorporated, Valley Forge, Pennsylvania, U.S.A.

1   INTRODUCTION

Aluminum in pure form is a relatively soft and ductile metal with a density of approximately 0.096 lb-in^3 of volume as compared to the density of steel at approximately 0.281 lb-in^3 or water at 0.035 lb-in^3. Pure aluminum melts at 1220°F considerably lower than the melting point of most other structural materials. It is an excellent conductor of heat and electricity. It is highly resistant to corrosion once an initial layer of aluminum oxide has formed on its surface. The surface coating of aluminum oxide is extremely thin and tightly adheres to the surface of the aluminum. Aluminum oxide is very hard, transparent, and prevents further oxidation of the base metal. A freshly produced aluminum surface reacts instantly with oxygen in the air, protecting the surface from attacks from other agents and from any further corrosion. Pure aluminum has relatively low strength but high ductility. Its modulus of elasticity is approximately 10,000,000 psi compared to 30,000,000 psi for steel. Thus for a given size and shape under comparable loading, aluminum will elastically deform three times more than steel and will absorb three times more energy. Aluminum can be strengthened by strain hardening or cold working; however, alloying aluminum with other elements provides much greater strengthening. Even further strengthening is achieved by aluminum with heat treatment.

2   ALLOY DESIGNATION SYSTEMS

The principal alloying additions to aluminum are copper, manganese, silicon, magnesium and zinc. Other elements are also added in smaller amounts for grain refinement and to develop special properties. Since there is a variety of aluminum alloys, special designation systems were developed by the Aluminum Association to distinguish the alloys in a meaningful manner and, further, to indicate what metallurgical condition, or temper, has been imparted to the alloy.

Aluminum and its alloys are divided into two classes according to how they are formed: wrought and cast. The wrought category is indeed a broad one, since virtually every known process can form aluminum. Wrought forms include sheet and plate, foil, extrusions, bar and rod, wire, forgings and impacts, drawn and extruded tubing, and others. Cast alloys are those specially formulated to flow into sand or permanent mold, to be die cast, or to be cast by any other process where the casting is the final form.

Each wrought or cast aluminum alloy is designated by a number to distinguish it as a wrought or cast alloy and to broadly describe the alloy. A wrought alloy is given a four-digit number. The first digit classifies the alloy series or principal alloying modification in the basic element. The second digit, if different than 0 (zero), denotes a modification in the basic alloy. The third and fourth digits form an arbitrary number that identifies the specific alloy in the series. A cast alloy is assigned a three-digit number followed by a decimal. Here again the first digit signifies the alloy series or principal addition; the second and third digits identify the specific alloy; the decimal indicates whether the alloy composition is for final casting (.0) or for ingot (.1 or .2). A capital letter prefix (A, B, C, etc.) indicates a modification of the basic alloy. The designation systems for aluminum wrought and cast alloys are shown in Table 1 and Table 2, respectively.

2.1   Temper Designation System

Specification of an aluminum alloy is not complete without designating the metallurgical condition, or temper, of the alloy. A temper designation system, unique for aluminum alloys, was developed by the Aluminum Association and is used for all wrought and cast alloys. The temper designation follows the alloy des-

Table 1   Wrought Alloy Designation System

Alloy Series	Description or Major Alloying Element
1xxx	99.00 Minimum Aluminum
2xxx	Copper
3xxx	Manganese
4xxx	Silicon
5xxx	Magnesium
6xxx	Magnesium and Silicon
7xxx	Zinc
8xxx	Other Element
9xxx	Unused Series

Table 2 Cast Alloy Designation System

Alloy Series	Description or Major Alloying Element
1xx.x	99.00 Minimum Aluminum
2xx.x	Copper
3xx.x	Silicon plus Copper and/or Magnesium
4xx.x	Silicon
5xx.x	Magnesium
6xx.x	Unused Series
7xx.x	Zinc
8xx.x	Tin
9xx.x	Other Element

Table 3 Basic Temper Designations

"F"   *As Fabricated*: Applies to products of forming processes in which no special control over thermal or work hardening conditions is employed. Mechanical property limits are not assigned to wrought alloys in this temper, but are assigned to cast alloys in "as cast," F temper.

"O"   *Annealed*: Applies to wrought products that have been heated to effect re-crystallization, produce the lowest strength condition, and cast products that are annealed to improve ductility and dimensional stability.

"H"   *Strain-Hardened*: Applies to wrought products that are strengthened by strain hardening through cold working. The strain hardening may be followed by supplementary thermal treatment, which produces some reduction in strength. The H is always followed by two or more digits (see Table 4).

"W"   *Solution Heat-Treated*: Applies to an unstable temper applicable only to alloys that spontaneously age at room temperature after solution heat-treatment. This designation is specific only when the period of natural aging is specified. For example, W $\frac{1}{2}$ hour solution heat treatment involves heating the alloy to approximately $1000°F$ to bring the alloying elements into solid solution, followed by rapid quenching to maintain a supersaturated solution to room temperature.

"T"   *Thermally Treated*: Applies to products that are heat-treated, sometimes with supplementary strain-hardening, to produce a stable temper other than F or O. The T is always followed by one or more digits (see Table 5).

ignation, the two being separated by a hyphen. Basic temper designations consist of letters as shown in Tables 4 and 5. Subdivisions, where required, are indicated by one or more digits following the letter. The basic tempers are shown in Table 3.

Wrought alloys are divided into two categories. Non-heat-treatable alloys are those that derive strength from solid solution or dispersion hardening and are further strengthened by strain hardening. They include the 1XXX, 3XXX, 4XXX, and 5XXX series alloys. Heat-treatable alloys are strengthened by solution heat treatment and controlled aging, and include the 2XXX, some 4XXX, 6XXX, and 7XXX series alloys.

Casting alloys cannot be worked-hardened and are either used in the as-cast or heat-treated conditions. Typical mechanical properties for commonly used casting

Table 4   Subdivisions of the H Temper

First digit indicates basic operations:

H1	Strain-hardened only
H2	Strain-hardened and partially annealed
H3	Strain-hardened and stabilized

Second digit indicates degree of strain hardening:

HX2 Quarter-hard
HX4 Half-hard
HX8 Full-hard
HX9 Extra-hard
Third digit indicates variation of two-digit temper.

Table 5   Subdivisions of the T Temper

First digit indicates sequence of treatments:

T1	Naturally aged after cooling from an elevated temperature shaping process
T2	Cold worked after cooling from an elevated temperature shaping process and then naturally aged
T3	Solution heat-treated, cold worked and naturally aged
T4	Solution heat-treated and naturally aged
T5	Artificially aged after cooling from an elevated temperature shaping process
T6	Solution heat-treated and artificially aged
T7	Solution heat-treated and stabilized (over-aged)
T8	Solution heat-treated, cold worked, and artificially aged
T9	Solution heat-treated, artificially aged, and cold worked
T10	Cold worked after cooling from an elevated temperature shaping process and then artificially aged

Second digit indicates variation in basic treatment:
Examples: T42 or T62 Heat-treated to temper by user
Additional digits indicate stress relief:
Examples: TX51 – Stress relieved by stretching
                          TX52 – Stress relieved by compressing
                          TX54 – Stress relieved by stretching and compressing

alloys range from 20–50 ksi for ultimate tensile strength, from 15–40 ksi tensile yield and up to 20% elongation.

Heat-treatable aluminum alloys will naturally age at room temperature following quenching and will be strengthened by precipitation hardening. Natural aging following quenching from a high-temperature forming process, for example casting or extruding, is designated T1. More commonly, natural aging follows solution heat-treatment (T4). Artificial aging is accomplished by heating the product to a temperature of roughly 400F for several hours (time and temperature depend

on the alloy) to accelerate the precipitation process and to further increase the strengthening effect. Here again, artificial aging may follow quenching from a high-temperature forming process (T5) or more commonly following solution heat-treatment (T6). The T7 temper indicates over-aging from a T6 temper of maximum strength to improve characteristics such as resistance to corrosion. The other T tempers indicate that strain hardening has been employed either to supplement the strengths achieved by precipitation or to increase the response to precipitation hardening.

2.2 Effects of Alloy Additions

Table 6 shows the maximum solid solubility of the principal alloying additions in aluminum and the temperature of maximum solubility. These values are for binary systems, and the presence of other elements in the alloy will usually affect the solubility. Additions greater than maximum solubility are often made, especially in the case of silicon, and this results in the presence of element particles in the solid alloy.

Copper is one of the most important additions to aluminum. It has appreciable solubility and a substantial strengthening effect through the age-hardening characteristics it imparts to aluminum. Many alloys contain copper either as the major addition (2XXX or 2xx.x series), or as an additional alloying element, in concentrations of 1–10%.

Manganese has limited solid solubility in aluminum, but in concentrations of about 1% forms an important series of non-heat-treatable wrought aluminum alloys (3XXX series). It is employed widely as a supplementary addition in both heat-treatable and non-heat-treatable alloys and provides substantial strengthening.

Silicon lowers the melting point and increases the fluidity of aluminum. A moderate increase in strength is also provided by silicon additions.

Magnesium provides substantial strengthening and improvement of the work-hardening characteristics of aluminum. It has a relatively high solubility in solid aluminum, but Al-Mg alloys containing less than 7% Mg do not show appreciable heat-treatment characteristics. Magnesium is also added in combination with other elements, notably copper and zinc, for even greater improvements in strength.

Table 6 Maximum Solid Solubility of Principal Alloying Additions in Aluminum

	Maximum Solubility		
Addition	Weight Percent	Atomic Percent	Temp °F
Cu	5.6	2.5	1018
Mg	14.9	16.3	842
Mn	1.8	0.9	1217
Si	1.6	1.6	1071
Zn	82.8	66.4	720
Mg_2Si	1.8	1.9	1103
$MgZn_2$	16.9	9.6	887

Zinc is employed in casting alloys and in conjunction with magnesium in wrought alloys to produce heat-treatable alloys having the highest strength among aluminum alloys.

Magnesium provides substantial strengthening and improvement of the work-hardening characteristics of aluminum. It has a relatively high solubility in solid aluminum, but Al-Mg alloys containing less than 7% Mg do not show appreciable heat-treatment characteristics. Magnesium is also added in combination with other elements, notably copper and zinc, for even greater improvements in strength.

Copper and silicon are used together in the commonly used 3xx.x series casting alloys. Desirable ranges of characteristics and properties are obtained in both heat-treatable and non-heat-treatable alloys.

Magnesium and silicon are added in appropriate proportions to form Mg_2Si, which is a basis for age hardening in both wrought and casting alloys.

Tin improves the anti-friction characteristic of aluminum, and cast Al-Sn alloys are used for bearings.

Lithium is added to some alloys in concentrations approaching 3 wt% to decrease density and increase the elastic modulus.

Copper and silicon are used together in the commonly used 3xx.x series casting alloys. Desirable ranges of characteristics and properties are obtained in both heat-treatable and non-heat-treatable alloys.

Magnesium and silicon are added in appropriate proportions to form Mg_2Si, which is a basis for age-hardening in both wrought and casting alloys.

There are also miscellaneous additions to aluminum wrought and cast alloys. Tin improves the anti-friction characteristic of aluminum, and cast Al-Sn alloys are used for bearings. Lithium is added to some alloys in concentrations approaching 3 wt% to decrease density and increase the elastic modulus.

3   HEAT TREATMENT

Heat-treatable aluminum alloys are currently experiencing a significant rise in demand due to the increasing application in aerospace and automotive applications. Throughput considerations combined with the necessity for quality require the thermal treatment to be very accurate thermally with the most effective heat-up rate possible.

Thermal heat treatments include the following:

- Homogenization
- Annealing
- Solution Heat Treatment
- Quenching
- Natural Aging
- Precipitation Hardening (Aging)

3.1   Preheating and Homogenization

Preheat is used to heat aluminum logs or billets prior to extrusion or forging and involves heating the aluminum to an intermediate uniform temperature. Some applications will tolerate direct flame on the logs or billets in order to expedite the rate of temperature heat-up. Other applications require the aluminum surface

temperature to be tightly controlled in order to avoid surface melting, which may cause tearing of or die sticking during the extrusion process. Generally, preheat applications require the fastest rate of temperature rise consistent with the allowable surface condition of the aluminum.

Reheat is used to heat aluminum slabs prior to rolling. Slabs are generally arranged horizontally with space between individual slabs. Air is directed horizontally across all aluminum surfaces and the aluminum slabs are removed one at a time before rolling. As the slabs are progressively reduced in thickness by the sequential rolling, several reheat applications are required.

Homogenization involves the heating of billets or logs following casting to an elevated temperature at which the alloys form a homogenous solution within the aluminum. Homogenization requires a very long period of thermal soak, generally the 15-20 hour range, in order to allow the alloys to effectively homogenize. Following homogenization, the billets or logs are cooled and formed through rolling or extrusion.

3.2 Annealing

Annealing involves heating the aluminum alloy to an intermediate temperature in order to soften the metal between forming operations in order to soften the aluminum alloy caused by work hardening. Sheet, wire, and coils are annealed several times as intermediate steps following rolling and forming.

Annealing is a thermal heat treatment above the recrystallization temperature. Because of this, the temperature is dependent on the amount of prior strain in the material. In general, in commercial practice, the annealing temperature used is the lowest temperature that yields the softest state in the minimum amount of time.

Non-heat treatable wrought alloys are heated to temperature very quickly to avoid grain growth. It is desired to produce a fine grain size. The rate of cooling from the annealing temperature is unimportant.

For heat treatable wrought alloys, two situations occur. The first situation is where the hardness of the material is primarily from the working or forming operation. In this case, the material is annealed at a lower temperature of approximately 650°F, and cooled in any convenient manner.

The second situation is where the hardness of the material is primarily from prior heat treatments, or hot work. In this case, it is necessary to anneal at a higher temperature, approximately 775F. General practice is to anneal at 775°F for 2–3 hours, then slow cool at approximately 50F/hour to 450F or lower, then cool in any convenient manner. For 7XXX alloys, a two step annealing practice is preferred. The first step consists of 2–3 hours at 775°F, followed by a slow cool at 50F/hour to 450F. The temperature is held at 450°F for 4 hours, then cooled in any convenient manner to room temperature. To achieve proper control of the resulting annealed properties, it is best to resort to trial and error.

For cast aluminum alloys, they are generally annealed at 650°F for 3-4 hours, then slow cooled at approximately 50°F/hour. Annealing of cast alloys does not significantly change the mechanical properties. Generally, a slight decrease in tensile properties and a slight increase in elongation is observed. However, the primary purpose of annealing cast alloys is to relieve the casting residual stresses. Annealing of cast alloys is done to improve dimensional stability.

Table 7   General Annealing Conditions for Wrought and Cast Aluminum and Aluminum Alloys

Alloy	Annealing Temperature, °F	Time at Temperature	Alloy	Annealing Temperature, °F	Time at Temperature
1060	650	/1	5083	650	/1
1100	650	/1	5086	650	/1
1350	650	/1	5154	650	/1
2014	760 /2	2–3	5254	650	/1
2017	760 /2	2–3	5454	650	/1
2024	760 /2	2–3	5456	650	/1
2036	725 /2	2–3	5457	650	/1
2117	760 /2	2–3	5652	650	/1
2219	76760 /2	2–3	6005	760 /2	2–3
3003	775	/1	6053	760 /2	2–3
3004	650	/1	6061	760 /2	2–3
3105	650	/1	6063	760 /2	2–3
5005	650	/1	6066	760 /2	2–3
5050	650	/1	7001	760 /3	2–3
5052	650	/1	7075	760 /3	2–3
5056	650	/1	7178	760 /3	2–3
A140	600	3-4	142	650	3-4
214	600	2–3	319	650	3-4
364	650	4–5	356	600	3-4

/1 Time at temperature should not be any longer than to get the center of the furnace load up to temperature. Rate of cooling from the annealing temperature is not important.

/2 This annealing practice removes the effect of prior solution heat treatment. Material must be cooled at 50°F per hour from the annealing temperature to 500°F. Subsequent cooling rate is not important.

/3 This is a two stage annealing practice that removes the effect of prior solution heat treatment. This is accomplished by air cooling from the annealing temperature to 400°F or less. The second stage requires heating the material to 450°F for 4 hours and cooling to room temperature in any convenient manner.

For alclad materials, shorter annealing times are necessary. This decreases the amount of diffusion of alloying elements into the aluminum cladding. If diffusion of alloying elements occurs, the corrosion protection of the aluminum cladding will be diminished.

Typical annealing practices for wrought and cast alloys is shown in Table 7.

3.3   Solution Heat Treatment

Solution heat treatment involves heating the aluminum and alloys to a temperature slightly below the eutectic melting temperature. Solution heat treatment develops the maximum amount of solute into solid solution. This requires heating the material close to near the eutectic temperature and holding the material at temperature long enough to allow close to complete solid solution. After solution heat treatment, the material is quenched to maintain the solute in supersaturated solid solution.

Table 8 Comparison of Solution Heat Treatment Temperature Range and Initial Eutectic Melting Temperature for Selected 2XXX Alloys

Alloy	Solution Heat Treatment Temperature Range, °C	Initial Eutectic Melting Temperature, °C
2014	496–507	510
2017	496–507	513
2024	488–507	502

Because the solution heat treatment temperature is so close to the eutectic melting temperature, temperature control is critical. This is especially true for 2XXX series alloys. In this alloy group, the initial eutectic melting temperature, is only a few degrees above the maximum recommended solution heat treatment temperature (Table 8).

Non-equilibrium conditions can occur because of localized solute concentrations. Because of the increased concentration of solute, the eutectic temperature could be decreased, causing localized melting. This is often called *incipient melting*. An example is shown in Figure 1. When this occurs, there are significant decreases in properties. Properties most affected include toughness, ductility and tensile properties. Unfortunately, this defect can not be detected visually or by NDT techniques.

Local melting can also occur if the heat-treated load is heated too quickly. This is particularly true of 2XXX alloys. In this alloy system, there are local concentrations of Al_2Cu. At slow heating rates, the Al_2Cu dissolves slowly into the matrix. At high heating rates, there is inadequate time for the Al_2Cu to dissolve. Local concentrations cause the local eutectic temperature to drop, resulting in localized melting. If adequate time is allowed for this metastable liquid to dissolve into the matrix, then in general, there is no decrement in properties. However, this requires long solution heat treatment times. So it is more likely that there will be a component of the liquid present when quenching. Because of surface tension during solidification, small, solidified spheres are formed. This are called rosettes. A rosette formed in a 6XXX series alloy is shown in Figure 2.

Under-heating during solution heat treatment can also cause problems by not allowing enough solute to go into solid solution. This means that less solute is available during subsequent precipitation hardening reactions. As an illustration of this, Figure 3 shows the effect of solution heat treating temperature on the yield strength and ultimate tensile strength. As the temperature is increased for both alloys, the tensile strength is also increased. For the 2024-T4 alloy, it can be seen that there is a change in slope and rapid rise in properties as the temperature is increased past about 488°C.

Typical recommended solution heat treatment temperatures for wrought products (excluding forgings) are shown in Table 9. Recommended solution heat treatment temperatures for forgings are listed in Table 10. Recommended solution heat treatment temperatures for cast alloys are tabulated in Table 11.
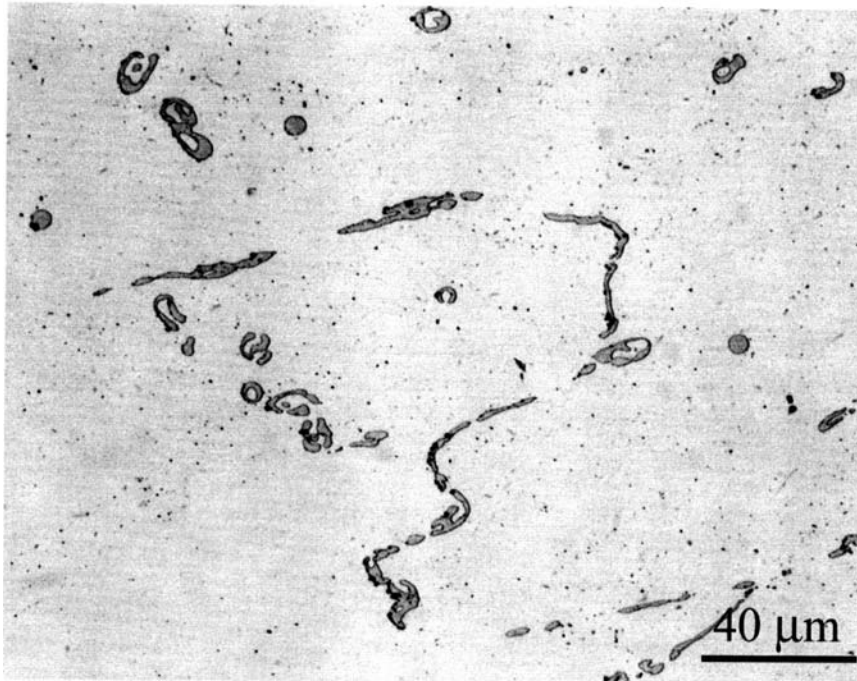
Figure 1   Photomicrograph of incipient melting in a 2XXX series aluminum alloy.
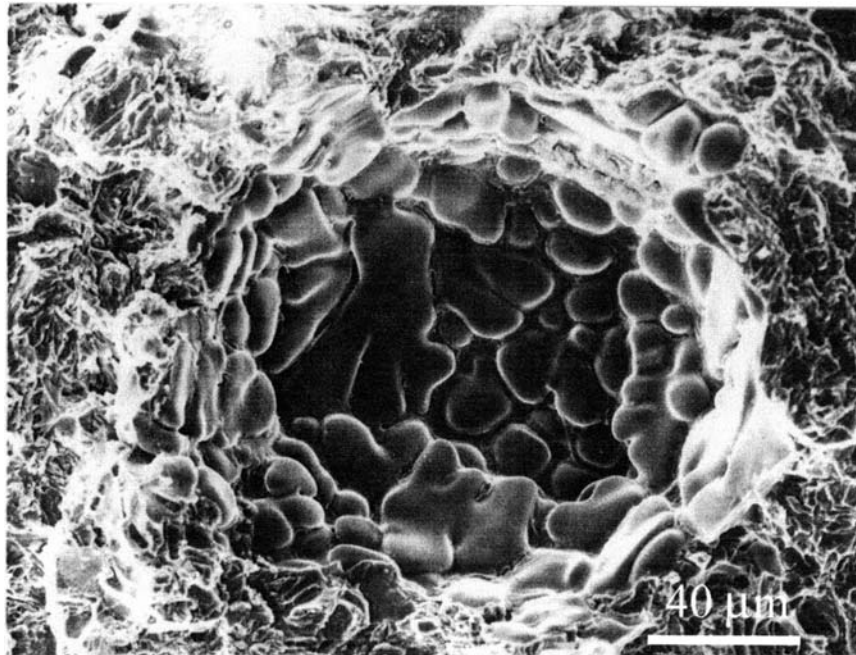
Figure 2   SEM examination of a rosette formed during heat treatment of a 6XXX series alloy.
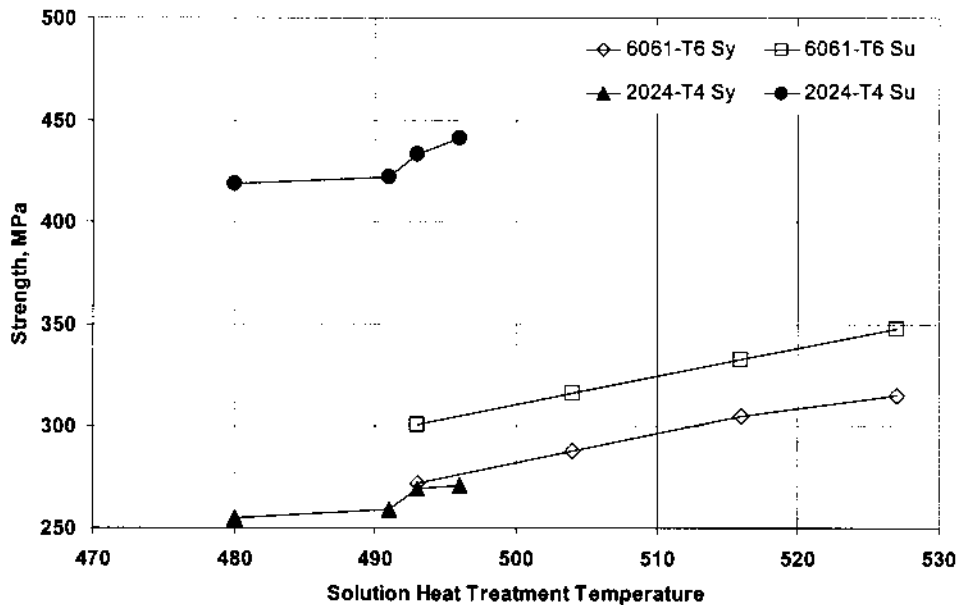
Figure 3 Graph illustrating the effect of solution heat treatment temperature on tensile properties of 2014-T4 and 2014-T6 sheet.

The time at solution heat treating temperature is as important as the temperature. If there is inadequate time at temperature, not all solute will be in solution at time of quench. The time necessary at solution heat treatment is a function of prior microstructure. The more homogeneous the microstructure, the shorter the necessary solution time. For instance, thin sheet requires merely minutes at the solution heat treatment temperature, while thick castings require 20+ hours. A table showing typical solution heat treating times for wrought alloys as a function of thickness is shown in Table 12. A table showing typical solution heat treating times for cast alloys as a function of thickness is shown in Table 13.

When solution heat treating alclad alloys, the shortest possible time at temperature should be used. This prevents solute from diffusing into the alclad. This in turn reduces the corrosion resistance. Because of the risk of solute diffusion, the number of reheat treatments on alclad stock is generally limited to three.

In general, the time during solution heat treatment is counted from the time the process thermocouple or load thermocouple recovers to within $6°C$ of the process temperature. For salt bath furnaces the time is measured at the instant of total immersion, as long as the temperature of the bath does not drop more than $6°C$ from the process temperature.

Because of the lower heat transfer, air furnaces require greater spacing between parts to insure proper heat-up of the parts. Generally a 2″ spacing is used. However, with larger parts, like wing skins, a greater separation may be required. The direction of part stacking is also important. In general, parts should be placed in-line with the flow of air. They should not "hide" the airflow from other parts, preventing proper heat-up of the parts.

Table 9   Solution Heat Treatment Temperatures for Wrought Alloys (Excluding Forgings)

Alloy	Product Type	Solution Heat Treating Temperature, °F
2011	Wire, Rod and Bar	945–985
2014	Sheet, Plate, Extrusions and Tube	925–945
2017	Wire, Rod and Bar	925–950
2020	Sheet, Plate	950–970
2024	Sheet, Plate, Extrusions and Tube	910–930
2048	Sheet, Plate	910–930
2117	Wire, Rod, Bar	925–950
	Rivets	890–950
2124	Plate	910–930
2219	Sheet, Plate, Extrusions and Tube	985–1005
2618	Extrusions	970–990
6061	Sheet, Plate, Extrusions and Tube	960–1075
6066	Extrusions and Tube	960–1010
6262	Sheet, Plate, Extrusions and Tube	960–1050
6951	Sheet	975–995
7001	Extrusions	860–880
7039	Sheet, Plate	840–860
7049	Extrusions	865–885
7050	Sheet, Plate, Extrusions, Wire and Rod	880–900
7075	Sheet, Plate, Wire, Rod and bar	860–930
	Extrusions, Drawn Tube	860–880
7178	Sheet	860–930
	Plate	860–910
	Extrusions	860–880

If parts are exposed to temperature too long, high temperature oxidation could become a problem. The term high temperature oxidation is really a misnomer. The culprit is actually moisture in the air during solution heat treatment. This moisture is a source of hydrogen, which diffuses into the base metal. Voids form at inclusions or other discontinuities. The hydrogen gas gathers, and forms a surface blister on the part. In general, 7XXX alloys are the most susceptible (particularly 7050), followed by the 2XXX alloys. Extrusions are the most prone to blistering, followed by forgings.

Eliminating the moisture will minimize the problem of surface blistering. This is accomplished by sequencing of door over quench tanks, and thoroughly drying and cleaning furnace loads prior to solution heat treatment. It is also important to make sure that the load racks used for solution heat treatment are also dry. However, it is not always possible to eliminate high humidity in the air to prevent surface blistering. Often the ambient relative humidity is high (St. Louis in the summer), so that other measures may have to be taken.

The use of ammonium fluoroborate is typically used to prevent blistering on 7XXX extrusions and forgings. An amount equivalent to 5 g per m^3 of workload space is usually used to prevent surface blistering. This is applied as a powder

Table 10 Solution Heat Treatment Temperatures for Forgings

Alloy	Product Type	Solution Heat Treating Temperature, °F
2014	Die and Hand Forgings	925–945
2018	Die Forgings	940–970
2024	Die and Hand Forgings	910–930
2025	Die Forgings	950–970
2218	Die Forgings	940–960
2219	Die and Hand Forgings	985–1005
2618	Die and Hand Forgings	975–995
4032	Die Forgings	940–970
6053	Die Forgings	960–980
6061	Die and Hand Forgings, including Rolled Rings	960–1075
6151	Die and Hand Forgings, including Rolled Rings	950–980
7049	Die and Hand Forgings	865–885
7050	Die and Hand Forgings	880–900
7075	Die and Hand Forgings, including Rolled Rings	860–890
7076	Die and Hand Forgings	850–910

Table 11 Typical Solution Heat Treatment Temperatures for Castings

Alloy	Casting Type	Solution Heat Treating Temperature, °F
222.0	Sand and Permanent Mold	930-960
242.0	Sand and Permanent Mold	950-980
295.0	Sand	940-970
296.0	Permanent Mold	935-965
319.0	Sand	920-950
A336.0	Permanent Mold	940-970
355.0	Sand and Permanent Mold	960-990
C355.0	Permanent Mold	960-990
356.0	Sand and Permanent Mold	980-1010
A356.0	Sand and Permanent Mold	980-1010
520.0	Sand	800-820

in a shallow pan hanging from the furnace load rack. This material is very corrosive and requires operators to wear the appropriate personal protective safety equipment. Because the material is corrosive at temperature, it is recommended that the inside panels in the furnace be manufactured with stainless steel. This will reduce corrosion and maintenance.

An alternative to the use of ammonium fluoroborate in solution heat treating furnaces, is anodizing the parts prior to solution heat treatment. This is generally practical for larger extrusions and forgings, where the cost of anodizing is small compared to the cost of the part. However, for small parts, the additional added

Table 12   Soaking Time for Solution Heat Treatment of All Wrought Products

| Thickness (inches) | Soaking Time (minutes) | | | |
| | Salt Bath | | Air Furnace | |
	Minimum	Maximum (alclad only)	Minimum	Maximum (alclad only)
0.016 and below	10	15	20	25
0.017–0.020	10	20	20	30
0.021–0.032	15	25	25	35
0.033–0.063	20	30	30	40
0.064–0.090	25	35	35	45
0.091–0.124	30	40	40	50
0.125–0.250	35	45	50	60
0.251–0.500	45	55	60	70
0.501–1.000	60	70	90	100
1.001–1.500	90	100	120	130
1.501–2.000	105	115	150	160
2.001–2.500	120	130	180	190
2.501–3.000	150	160	210	220
3.001–3.500	165	175	240	250
3.501–4.000	180	190	270	280

Table 13   Soaking Times for Solution Heat Treatment of Cast Alloys

Alloy	Casting Type	Time (hours)
222.0	Sand and Permanent Mold	6–18
242.0	Sand and Permanent Mold	2–10
295.0	Sand	6–18
296.0	Permanent Mold	4–12
319.0	Sand	6–18
336.0	Permanent Mold	6–18
355.0	Sand and Permanent Mold	6–18
C355.0	Permanent Mold	6–18
356.0	Sand and Permanent Mold	6–18
A356.0	Sand and Permanent Mold	6–18
520.0	Sand	12–24

cost does not generally justify the possible benefit of anodizing prior to solution heat treatment.

Rapid quenching in water or a water solution with a polymer additive such as poly (alkylene) glycol follows solution heat treatment. The quenching is performed rapidly in order to achieve a supersaturated solid solution. The aluminum in the as-quenched (AQ) condition is soft but is very uniform in mechanical characteristics.
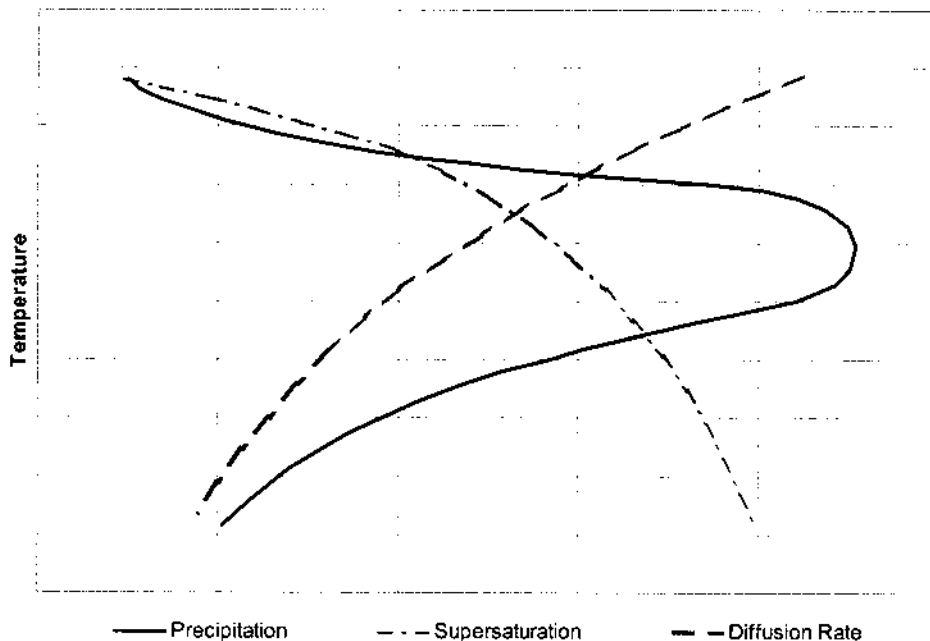
Figure 4 Schematic representation of temperature effects on factors that determine the heterogeneous precipitation rate during quenching (after Hatch [1]).

3.4 Quenching

An understanding of heterogeneous precipitation during quenching can be understood by nucleation theory applied to diffusion controlled solid-state reactions [1]. The kinetics of heterogeneous precipitation occurring during quenching is dependent on the degree of solute supersaturation and the diffusion rate, as a function of temperature. So, as an alloy is quenched, there is greater supersaturation (assuming no solute precipitates). But the diffusion rate increases as a function of temperature. The diffusion rate is greatest at elevated temperature. When either the supersaturation or the diffusion rate is low, the precipitation rate is low. At intermediate temperatures, the amount of supersaturation is relatively high, as is the diffusion rate. Therefore the heterogeneous precipitation rate is the greatest at intermediate temperatures. This is shown schematically in Figure 4. The amount of time spent in this critical temperature range is governed by the quench rate.

The amount of precipitation occurring during quenching reduces the amount of subsequent hardening possible. This is because as solute is precipitated from solution during quenching, it is unavailable for any further precipitation reactions. This results in lower tensile strength, yield strength, ductility and fracture toughness.

Quantifying quenching, and the cooling effect of quenchants has been extensively studied [2–5]. The first systematic attempt to correlate properties to the quench rate in Al-Zn-Mg-Cu alloys was performed by Fink and Wiley [6] for thin (0.064″) sheet. A Time-Temperature-Tensile Property curve was created and was probably the first instance of a TTT diagram for aluminum. It was determined that the critical

temperature range for 75S is 400°C to 290°C. This is similar to the critical temperature range found for Al-Zn-Mg-Cu alloys [7]. At quench rates exceeding 450°C/sec., C/sec., it was determined that maximum strength and corrosion resistance were obtained. At intermediate quench rates of 450°C to 100°C/sec., the strength obtained is lowered (using the same age treatment), but the corrosion resistance was unaffected. Between 100/sec and 20°C/sec, the strength decreased rapidly, and the corrosion resistance is at a minimum. At quench rates below 20°C/sec, the strength decreases rapidly, but the corrosion resistance improved. However, for a given quenching medium, the cooling rate through the critical temperature range was invariant no matter the solution heat treat temperature. An illustration of the effect of average cooling rate from the solution heat treating temperature on tensile strength is shown in Figure 5.

One method that quantifies the quench path and material kinetic properties is called the "Quench Factor" and was originally described by Evancho and Staley [8]. This method is based on the integration of the area between the Time-Temperature-Property Curve and the quench path. Wierszykkowski [9] provided an alternative explanation of the underlying principles of the Quench Factor. However, his discussion is more generally applied to the thermal path prior to isothermal transformation. The procedures for developing the Quench Factor have been well documented [10–15]. This procedure could be used to predict tensile properties [16], hardness [17] and conductivity [11]. It was found that the Quench Factor could not be used to predict elongation because of its strong dependence on grain size [11]. This method tends to overestimate the loss of toughness [15]. This
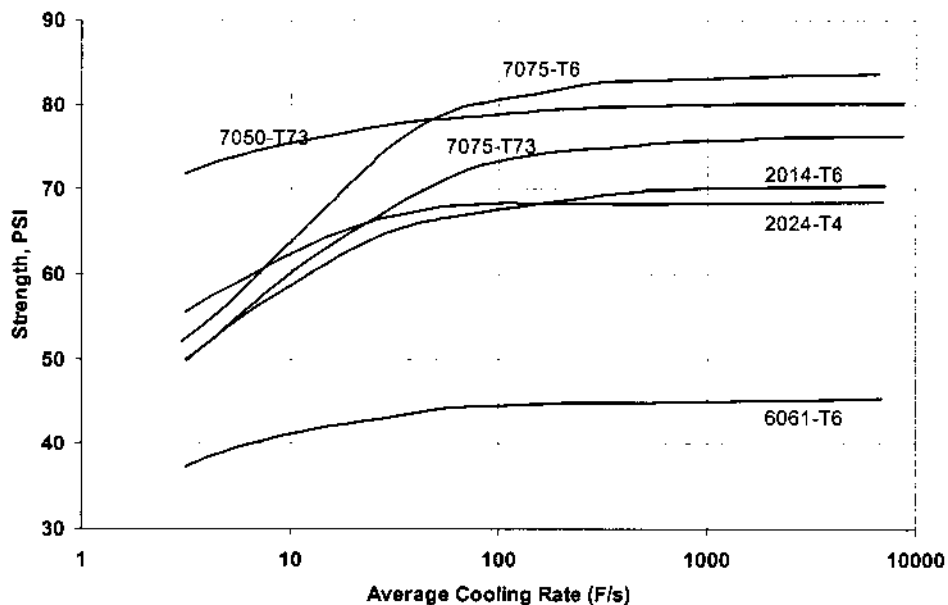
Figure 5   Tensile strengths of six alloys as a function of average cooling rate during quenching.

method also can be used to determine the critical quench rate for property degradation [18].

Historically, the average quench rate has been used to predict properties and microstructure after quenching [2–4]. However average quench rates are not sufficient to provide accurate property data, and serve as a predictive tool [8]. The quench factor [8] was developed to quantitatively predict properties. This quench factor depends on the rate of precipitation during quenching. The rate of precipitation during quenching is based on two competing factors: supersaturation and diffusion. As temperature in decreased during quenching, the amount of supersaturation increases, providing increased driving force for precipitation. In addition, at the beginning of quenching, the temperature is high, increasing the rate of diffusion. The Avrami precipitation kinetics for continuous cooling can be described by [8]:

$$\zeta = 1 - \exp(k\tau)''$$

where ζ is the fraction transformed, k is a constant, and τ is defined as:

$$\tau = \int \frac{dt}{C_t}$$

where τ is the Quench Factor, t is the time (sec) and C_t is the critical time. The collection of the C_t points, also known as the C-Curve, is similar to the Time-Temperature-Transformation curve for continuous cooling.

In general, the C_t function is described by [10]:

$$C_t = K_1 K_2 \left[\exp\left(\frac{K_3 K_4^2}{RT(K_4 - T)^2} \right) \exp\left(\frac{K_5}{RT} \right) \right]$$

where C_t is the critical time required to precipitate a constant amount of solute, K_1 is a constant that equals the natural logarithm of the fraction that was not transformed during quenching, and $K_1 = \ln(0.995)$ or -0.00513. K_1 is chosen that for $\tau > 1$, a decrease in properties is observed. K_2 is a constant related to the reciprocal of the number of nucleation sites, and K_3 is a constant related to the energy required to form a nucleus. K_4 is a constant related to the solvus temperature, K_5 is a constant related to the activation energy for diffusion, R is the universal gas constant and T is the temperature in $^\circ K$.

To determine the parameters K_1, K_2, K_3, K_4, and K_5, it is first necessary to have the C-Curve. C-Curve data is scarce, and of limited availability. Table 14 shows some previously published data.

The Quench factor is determined by integrating the above equation graphically. This is shown schematically in Figure 6. Mathematically, this is shown by:

$$\tau = \frac{\Delta t_1}{C_1} + \frac{\Delta t_2}{C_2} + \frac{\Delta t_3}{C_3} + \ldots + \frac{\Delta t_{nl}}{C_n}$$

where $C_1 \ldots C_n$ are the critical times of the C-Curve, and $\Delta t_1 \ldots \Delta t_n$ are the incremental times described by the quench path. But, to do this integration, the C-curve must be known.

Table 14   Coefficients for Calculating Quench Factors at 99.5% of Attainable Strength

Alloy	K_2 (sec)	K_3 (cal/mol)	K_4 (K)	K_5 (cal/mol)	Reference
7050-T76	2.2×10^{-19}	5190	850	1.8×10^5	[8]
7075-T6	4.1×10^{-13}	1050	780	1.4×10^5	[8]
2024-T851	1.72×10^{-11}	45	750	3.2×10^4	[19]
7075-T73	1.37×10^{-13}	1069	737	1.37×10^5	[13]
2219-T87	0.28×10^{-7}	200	900	2.5×10^4	[20]

Note: Data for 2024-T851 was evaluated using R = 1.987. All others were evaluated with R = 8.3143
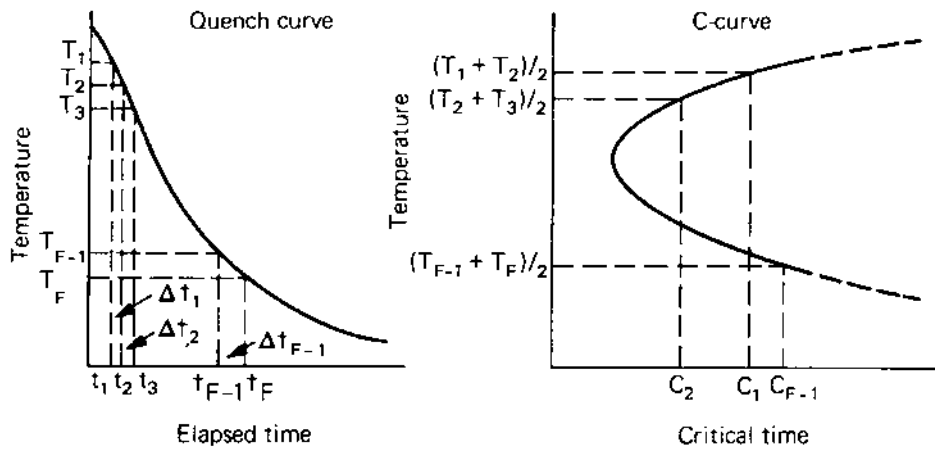
Figure 6   Schematic showing how quench factors are calculated.

Typically, it is necessary to measure the quench path of several sheets of material, and then measure the properties after processing. The quench factor is determined for each quench path and associated with the measured properties. Typically, hardness and tensile properties have been used [13]. Examples of calculated quench factors and their associated quench paths are shown in Table 15. Properties are then related to the quench factor by the equation [10]:

$$p = p_{max} \cdot \exp(K_1 \tau)$$

where p is the property of interest, p_{max} is the maximum property attainable with infinite quench rate, and K_1 is -0.005013 (natural log of 0.995).

There are two difficulties with this method. First, it is necessary to know the specific quench path that the part experienced. This is often difficult to measure, and requires specialized equipment to achieve repeatable results [13]. Secondly, it is also necessary that the C-Curve is known with sufficient precision. As indicated previously, this data is often not available for the specific conditions of interest. The lack of having detailed information regarding the C-Curve has limited the applicability of the use of the quench factor.

Table 15 Quench Factors and Measured Yield Strength for 1.6-mm Thick 7075-T6 Sheet [1]

Quench path	Quench Factor	Measured Yield Strength (MPa)
Cold Water, Strongly Agitated	0.464	73.4
Denatured Alcohol to 290°C, then Cold water	8.539	69.1
Boiling Water to 315°C, then Cold water	15.327	66.4
Still air to 370°C, then Cold Water	21.334	67.9

To avoid excessive precipitation during quenching, three requirements must be met. First the transfer time from the solution heat-treat furnace into the quench tank must be minimized. Second, the quenchant properties must be fast enough to insure that proper supersaturation is achieved, and that desired properties can be achieved. Lastly, the quench tank must have adequate thermal inertia so that the quenchant does not heat excessively, causing an interrupted quench. In addition, the quenching system must extract heat uniformly to minimize property variations.

The quench delay time, or the transfer time from the furnace to the quench tank, for air furnaces, is defined as the time the furnace door first begins to open, until the last corner of the workload is immersed into the quench tank. For salt baths, the quench delay time is defined as the time that the first corner of the workbasket is exposed to the time the last corner of the workload is immersed into the quench tank. In general, it is independent of the alloy, but depends on the solution heat treating temperature, the velocity of movement, and the emmissivity of the workload. Table 16 shows typical allowable quench delay times for various thicknesses.

The quench delay time is based on the amount of cooling of the workload before it enters the quenchant. In general, the maximum quench delay times can be exceeded if it can be demonstrated that the part temperatures do not fall below approximately 413°C before immersion. An exception to this is for AA2219, where the part temperatures can not fall below 482°C before immersion.

It is difficult to directly measure and control the temperature drop during transfer of the workload from the solution heat treating furnace to the quench tank. However, the quench delay time is easily controlled using only a stopwatch. This is augmented with the results from routine tensile testing and intergranular corrosion testing.

Table 16 Typical Maximum Quench Delay Times

Minimum Thickness		Maximum Time (Seconds)
mm	inch	
Up to 0.41	Up to 0.016	5
Over 0.41–0.79	Over 0.016–0.031	7
Over 0.79–2.29	Over 0.031–0.090	10
Over 2.29	Over 0.090	15

There are two types of quenching commonly used for commercially heat treating aluminum: direct immersion and spray quenching. Direct immersion quenching requires that the workbasket is completely immersed into a quenchant bath. Spray quenching is a specialized form of quenching, where a stream of quenchant is directed onto the part.

Immersion quenching is controlled by specifying the quenchant (and concentration if appropriate), and temperature of quenching. There are two types of quenchants used for aluminum heat-treating: water and polyalkylene glycol (polymer) quenchants.

Cold water quenching is the most severe of commonly used quenchants. In an early study using cooling curves [21], it showed that quenching into still water caused rapid heat transfer. This study showed that heat transfer at the surface of the part was very turbulent at the metal/water interface. This study also showed that there was a marked difference between hard water and distilled water. Distilled water showed an extensive vapor blanket that extended to very low temperatures (Figure 7).

The cooling rate of water quenching is independent of material properties like thermal conductivity and specific heat. It is primarily dependent on water temperature and agitation [22]. Water temperature is the largest primary variable controlling the cooling rate. With increasing water temperature, the cooling rate decreases. The maximum cooling rate also decreases as the water temperature is increased. In addition, the temperature of maximum cooling decreases with increasing water quench temperature. The length of time and stability of the vapor barrier increases, with increasing water temperature. This is shown in Table 17.
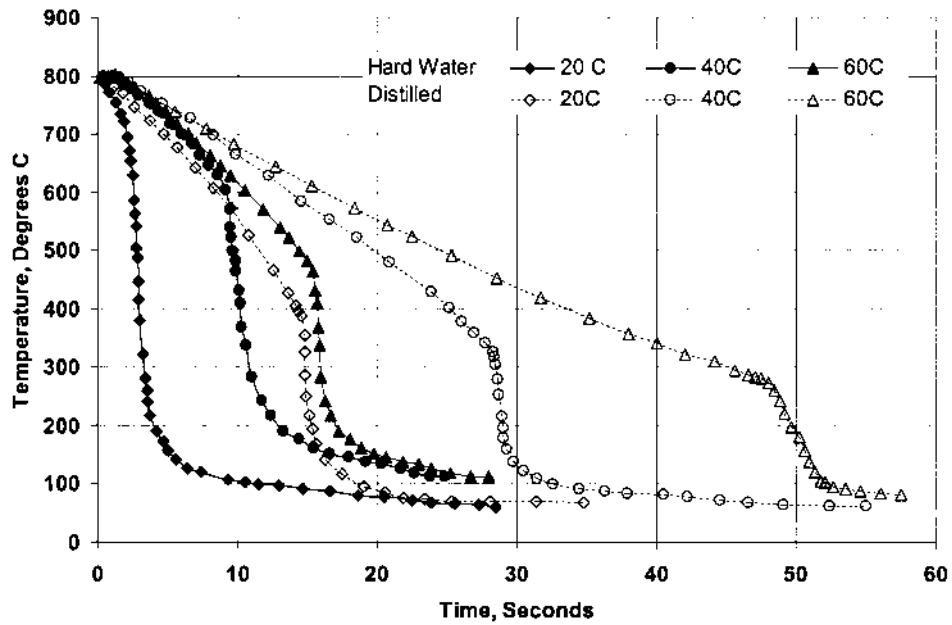
Figure 7   Comparison of the cooling rates of distilled water and normal "hard" water.

Table 17 Effect of Water Temperature on Cooling Rates [23]

Water Temperature (°C)	Maximum Cooling Rate (°C/s)	Maximum Cooling Rate Temperature (°C)	Cooling Rate (°C/s) at T		
			704°C	343°C	232°C
40	153	535	60	97	51
50	137	542	32	94	51
60	115	482	20	87	46
70	99	448	17	84	47
80	79	369	15	77	47
90	48	270	12	26	42

Quenching into water at < 50–$60°C$ often produces non-uniform quenching. This non-uniformity manifests itself as spotty hardness, distortion and cracking. This non-uniformity is caused by relatively unstable vapor blanket formation. Because of this difficulty, it was necessary to develop an alternative to water quenching. Polyalkylene Glycol quenchants (PAG) were developed to provide a quench rate in between that of water and oil. By control of agitation, temperature and concentration quench rates similar to water and thick oil can be achieved.

There are two types of polymer quenchants on the market. The first quenchant is polyvinyl alcohol (PVA). This quenchant is resistant to bacterial attack. However, because of its chemical make-up, it is prone to degrade and change its heat transfer characteristics over time. It also produces a hard plastic type lacquer finish on the parts which is difficult to remove.

The other type of polymenr quenchant is polyalkyene glycol (PAG). For the past 40 years, it has captured the largest market share. It is a copolymer of ethylene oxide and propylene oxide. It exhibits an inverse solubility with water. In other words, as the water temperature is increased, the solubility of PAG quenchants in water is decreased. A two-phase system results, as the temperature of the water is raised. The lighter phase is water, with floats to the top. A second phase, denser than water, sinks to the bottom. Each region contains a bit of the other in solution. In other words, the glycol-rich region contains some water, while the water rich region contains some PAG quenchant. However, as the temperature is increased, the partitioning of PAG and water increases.

The temperature at which separation occurs is called the cloud point. The cloud point is effected by pH, %PAG, and other contaminates in the system. As the pH is increased, the cloud point decreases. As the concentration of PAG increases, the cloud point also decreases.

Water is one of the most severe quench media. Because of the severity of the quench, this quench media presents problems with residual stresses and distortion. Residual stresses in thick sections are caused by differential thermal stresses that occur during quenching. The magnitudes of the stresses also increase as the thickness of the part increases. Since large sections are often machined, a redistribution of the residual stress occurs. This redistribution can cause warpage. Residual stresses can also impact the fatigue of the part.

Slow cooling minimizes temperature differences between the surface and center of a part. This reduces the residual stresses since residual stresses are the result of large differential thermal strains. However, slow cooling also results in heterogeneous precipitation during quenching. This decreases properties by decreasing the amount of supersaturated solute. So a balancing act between residual stresses and acceptable properties occurs. To achieve the best balance, it is necessary to use the slowest possible quench that will still achieve properties, with an appropriate safety factor.

Increasing the PAG concentration decreases the quench rate (Figure 8). Because of a concept called ''zero-delta'', concentrations of PAG quenchants are limited in the aerospace industry to those that only produce equivalent properties to a hot water quench. These typical concentrations are shown in Table 18. This results in products that have a reduced residual stress and warpage, but have properties in excess of those required.

Spray Quenching is the second type of quenching that is used commercially. However, it is generally limited to mill operations. In immersion quenching heat transfer progresses first by an extended vapor blanket, then nucleate boiling, followed by convective heat transfer. Increased agitation reduces the stability of the vapor phase. Increased agitation also increases the temperature at the onset of nucleate boiling. It also increases the heat transfer in the convective region. The same occurs in spray quenching.

Fluid flow impacts the part, and mechanically ruptures the vapor blanket. The extreme agitation rate of the impacting spray accelerates nucleate boiling and enhances convective heat transfer. The droplet size is a critical factor in spray quenching. The mechanical energy of the droplet and the droplet size depend on
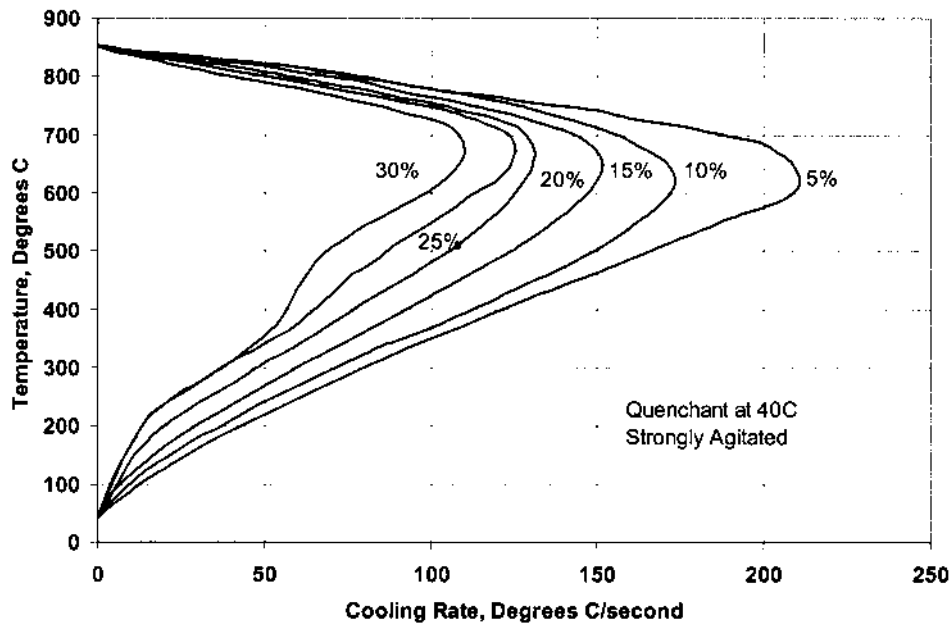
Figure 8   Effect of PAG concentration on cooling rate.

Table 18 Typical Concentration Limits for Quenching in PAG. (From Ref. 107.)

Alloy	Form	Maximum Thickness		Concentration Volume Percent
		Inches	Millimeters	
2024	Sheet	0.040	1.02	34 Max.
		0.063	1.60	28 Max.
		0.080	2.03	16 Max.
2219	Sheet	0.073	1.85	22 Max.
6061	Sheet, Plate	0.040	1.02	34 Max.
7049				
7050				
7075				
		0.190	4.83	28 Max.
		0.250	6.35	22 Max.
6061	Forgings	1.0	25	20–22
7075				
		2.0	50	13–15
		2.5	64	10–12
7049	Forgings	3.0	76	10–12
7149				
7050	Forgings	3.0	76	20–22
6061	Extrusions	0.250	6.35	28 Max.
7049				
7050	Extrusions	0.375	9.52	22 Max.
7075				

the air and water pressures used. This also is affected by the geometry of the nozzle orifice and mixing chamber. The velocity of a droplet, as it is leaving the nozzle is a function of water and air pressures, the tube diameter of the nozzle, water flow rate, and head loss through the tube [24]. The velocity of the droplet hitting the surface is a function of the initial velocity, water and air density, droplet size and the spray distance. The optimum droplet diameter for quenching has been reported to be approximately 0.8 mm [25].

This technique has great flexibility, but has not been adopted on a commercial basis. In general, this technique is only used in plate and sheet mills because of the simple quenching geometry, enabling sprays to be placed on either side of the plate. In addition, aerospace specifications require extensive documentation and testing to insure that the spray quenching system is operating at peak performance at all times. All spray nozzles must be monitored during the quench for any intermittent or faulty operation. A daily log of quench temperatures and pressures are usually maintained. In addition, a detail first article inspection is required, documenting the placement and location of all spray nozzles used. Aerospace forgings and machined parts, because of their complex shape are generally good candidates for spray quenching. However, because of the equipment and documentation cost, most heat treaters opt for more conventional immersion quenching.

3.5   Stretching or Mechanical Deformation after Quenching

Immediately after quenching, AQ Temper alloys are nearly as ductile as the ''O'' or annealed condition. Because of this, as-quenched alloys are often formed after quenching, but before artificial aging.

Stretching of plate materials is generally performed to relieve the stresses induced from quenching. The amount of stretch varies, but is generally in the range of 1 to 5%. Because the stretch plastically deforms the plate, a large number of dislocations are introduced into the material. This plastic deformation causes the elastic stresses resulting from quenching to be redistributed into a less deleterious amount. Applying about 1–3% plastic deformation on the part generally causes this mechanical stress redistribution. This is accomplished by stressing by stretching of extrusion and plate, or by compression striking forgings. This is illustrated in Figure 9, showing the effect of compression striking a 4-inch thick forging that was water quenched.

It is known that the dislocations increase mechanical properties and change the precipitation sequence. This has been found for Al-Mg-Si 26], Al-Li [27–28], Al-Li-Cu [29–30]. In these systems, the dislocations provide nucleation sites for the transitional precipitates. In some alloy systems, such as Al-Cu-Mg-Ag, nucleation of fine, homogeneously distributed precipitates is readily accomplished, and the presence of dislocations may decrease tensile properties [29].

At room temperature, the presence of dislocations slows precipitation kinetics due to the annihilation of quenched-in vacancies [31, 32]. At elevated aging temperatures (120°C–180°C), dislocations increase precipitation kinetics and coarsening because of an enhanced diffusion path [32, 33]. Coarsening of precipitates on
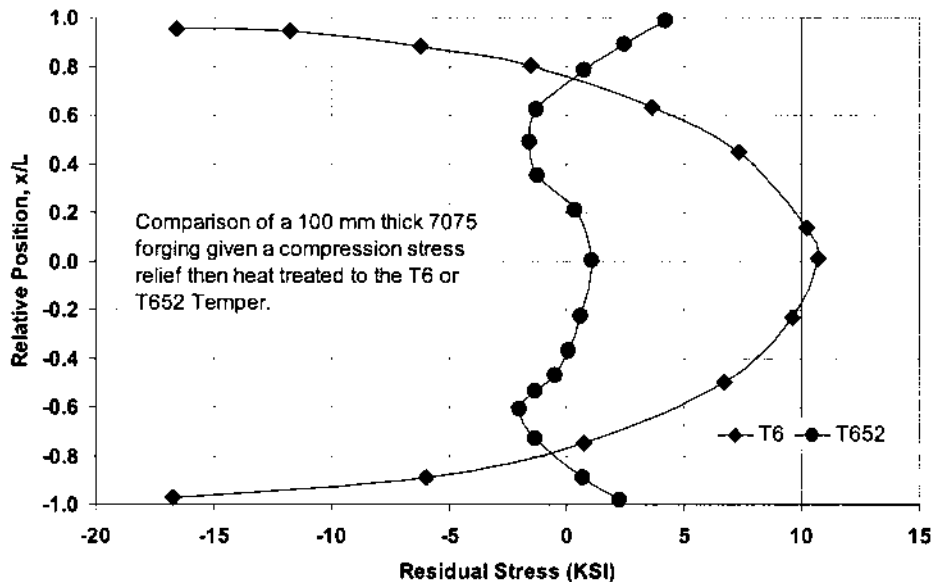
Figure 9   Effect of compression striking a 4-inch thick 7075-T652 forging in the as-quenched condition on the measured residual stresses.

dislocations also cause a decrease in mechanical properties [34]. However, an increase in mechanical properties has been reported [35, 36] if stretching is performed on naturally aged 2XXX and 7XXX material, followed by artificial aging. It was shown that deformation before aging at 120°C improved the stress corrosion resistance, but deformation before aging at 210°C reduced the stress corrosion resistance [1].

In 7XXX series aluminum alloys, the precipitate that forms on the dislocation is η', and grows faster on dislocations than in the base material [37–39]. It was shown by Deschamps *et al* [40, 41], that for short aging times, slow heating to the artificial aging temperature will produce a fine, homogenous distribution of η' and the influence of dislocations is reduced. For short aging times and fast heating rates, the precipitation of η' is more difficult. There is increased precipitation of η at dislocations, with fine precipitates at a distance from the dislocation. There is a decrease in the peak strength as the percent of deformation or stretch is increased. For long aging times, larger precipitates occur with increasing stretch and a decrease in mechanical properties is observed during coarsening, that is independent of heating rate. This is illustrated in Figure 10.

The effects of cold working on toughness after precipitation hardening, are directly opposite for 2XXX and 7XXX alloys. Cold working after quenching improves the combination of strength and toughness in 2024 (Figure 11) and decreases the combination of strength and toughness in the overaged tempers. This is attributed to the precipitation of a fine distribution of S' on dislocations. However, in 7050, cold working after quenching has the opposite effect (Figure 12). This is attributed to the nucleation and preferential growth of coarse η' on dislocations. This decreases the strength, without improving the toughness.
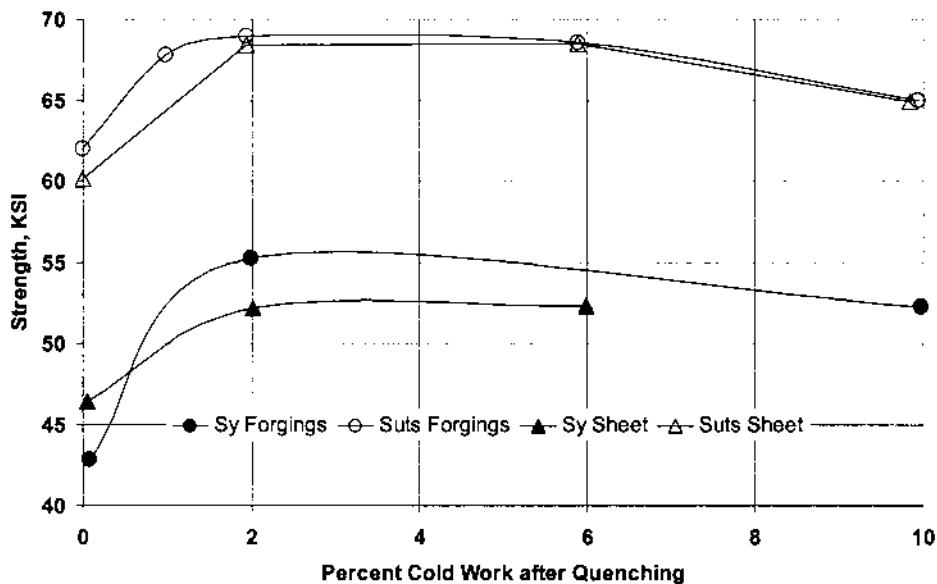
Figure 10   Effect of cold work on the strength of 2219 artificially aged at 375F.
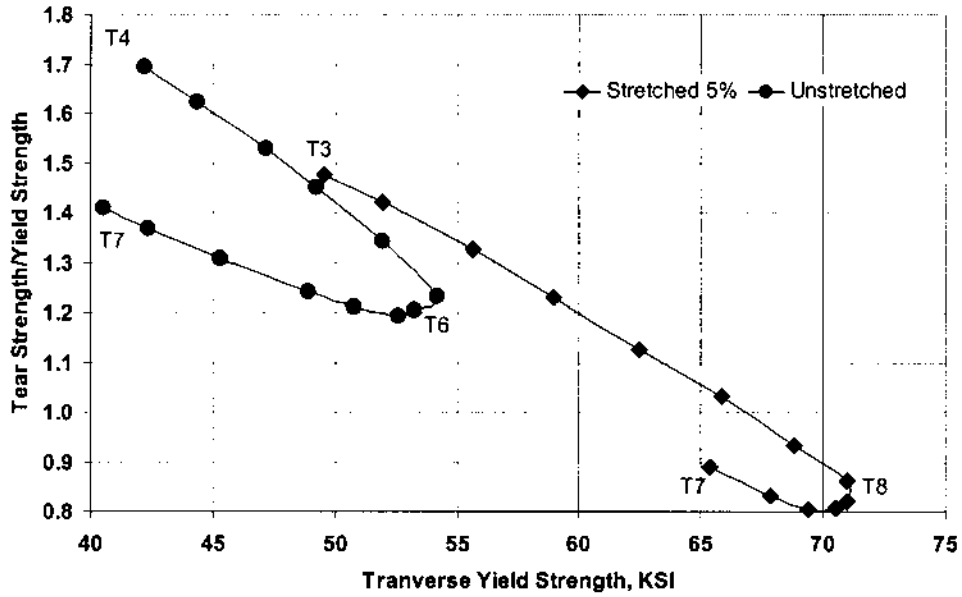
Figure 11 Effect of stretching and aging on the toughness of 2024 sheet [1].
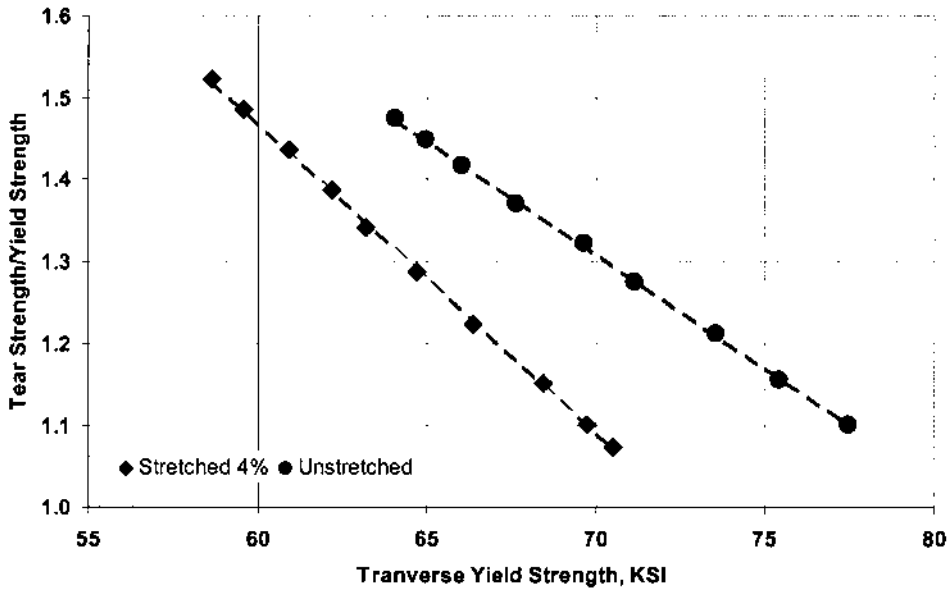
Figure 12 Effect of stretching on the toughness of 7050 plate [1].

Forming of parts in the as-quenched condition is readily performed. There are a variety of methods used to form parts. Typical methods include brake forming, hydro-forming, roll forming and stretching. Other methods include drop hammer forming, and spinning.

Brake forming is inexpensive to perform and requires little or no die cost. Very simple shapes are formed by this method. Examples include clips, and angles. Grain direction affects formability. It is desired to bend perpendicular to the grain direction. This can avoid orange peel or Luders lines.

Hydro-Forming is nearly always performed in either the O (annealed) condition or when the part is as-quenched. In this process part blanks are placed between the die and a large bladder that is filled with hydraulic fluid. When the bladder is pressurized, the bladder expands, and causes the bladder to form into the die. When parts are formed when the part is annealed, the sequence is hydro-form, solution heat treat, quench, reform, then artificial aging to the desired properties. If the parts are formed in the AQ condition, then the sequence is solution heat treat, quench, hydro-form, then age harden. This process has the benefits of low die cost, and can be applied to a large variety of complex parts. However, the equipment is expensive and difficult to maintain. Examples include frames and lightening holes.

Roll forming is a simple process where the work piece is placed between two rolls and formed over a bending roll. There is no die cost. One additional advantage is that this process can roll form parts in any heat treat condition. Typical roll formed parts are single contour skins and nose cones.

Straightening after quenching is used to correct distortion. Usually this is accomplished by placing the part (in the as-quenched condition) on a die, and hitting the part with leather straps or mallets. Generally, it is best to heat treat the parts, then form in the as-quenched condition. However, this is often not practical. In that case, straightening should only be performed in areas of uniform section. Straightening across thickness transitions and areas containing holes or cut-outs. This is because the holes maybe be warped by straightening. In heavy sections, twist is very difficult to remove, and is usually impractical. A good example of twist in a large heat treated forging is shown in Figure 13. Unfortunately, because of the extent of twisting in this forging, it was not possible to salvage this forging.

3.6 Natural Aging

Some heat treatable alloys, especially 2XXX alloys, harden appreciably at room temperature to produce the useful tempers T3 and T4. These alloys that have been naturally aged to the T3 or T4 tempers, exhibit high ratios of ultimate tensile strength/yield strength. These alloys also have excellent fatigue and fracture toughness properties.

Natural aging, and the increase in properties occurs by the rapid formation of GP (Guinier-Preston) Zones from the supersaturated solid solution and from quenched-in vacancies. Strength increases rapidly, with properties becoming stable after approximately 4–5 days. The T3 and T4 tempers are based on natural aging for 4 days. For 2XXX alloys, improvements in properties after 4–5 days are relatively minor, and become stable after one week.
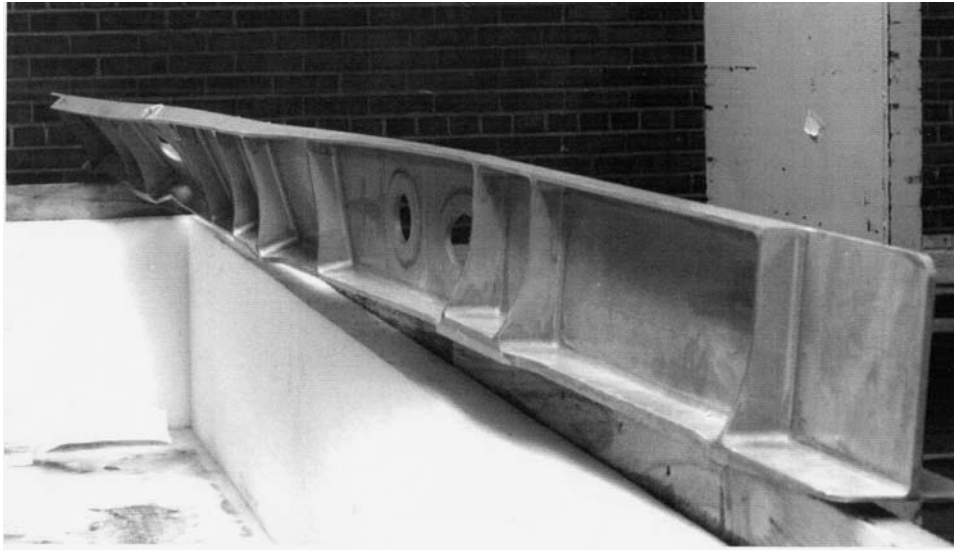
Figure 13 Extreme example of a large aerospace forging exhibiting twisting due to improper racking during solution heat treatment.

The Al-Zn-Mg-Cu and Al-Mg-Cu alloys (7XXX & 6XXX), harden by the same mechanism of GP Zone formation. However, the properties from natural aging are less stable. These alloys still exhibit significant changes in properties even after many years.

The natural aging characteristics change from alloy to alloy. The most notable differences are the initial incubation time for changes in properties to be observed, and the rate of change in properties. Aging effects are suppressed with lower than ambient temperatures. In many alloys, such as 7XXX alloys, natural aging can be nearly completely suppressed by holding at $-40°C$. This is illustrated in Figure 14.

Because of the very ductile and formable nature of as-quenched alloys, retarding natural aging increases scheduling flexibility for forming and straightening operations. It also allows for uniformity of properties during the forming process. This contributes to a quality part. However, refrigeration at normal temperatures does not completely suppress natural aging. Some precipitation still occurs. Table 19 shows typical temperature and time limits for refrigeration.

Often refrigeration systems are inadequate to cool thick gage parts quick enough to rapidly cool parts. In this case several heat-treaters immerse the parts in Stoddard's Solvent at $-40°C$ immediately after quenching. Alternatively, the use of dry ice and methanol has also been used. However, either solution is very flammable and requires special precautions for operating and disposal of organic wastes. Immersion of the parts in very cold liquid insures that the parts will rapidly cool to the desired temperature. The parts are then transferred to the normal refrigeration system.

6061

2024

7075
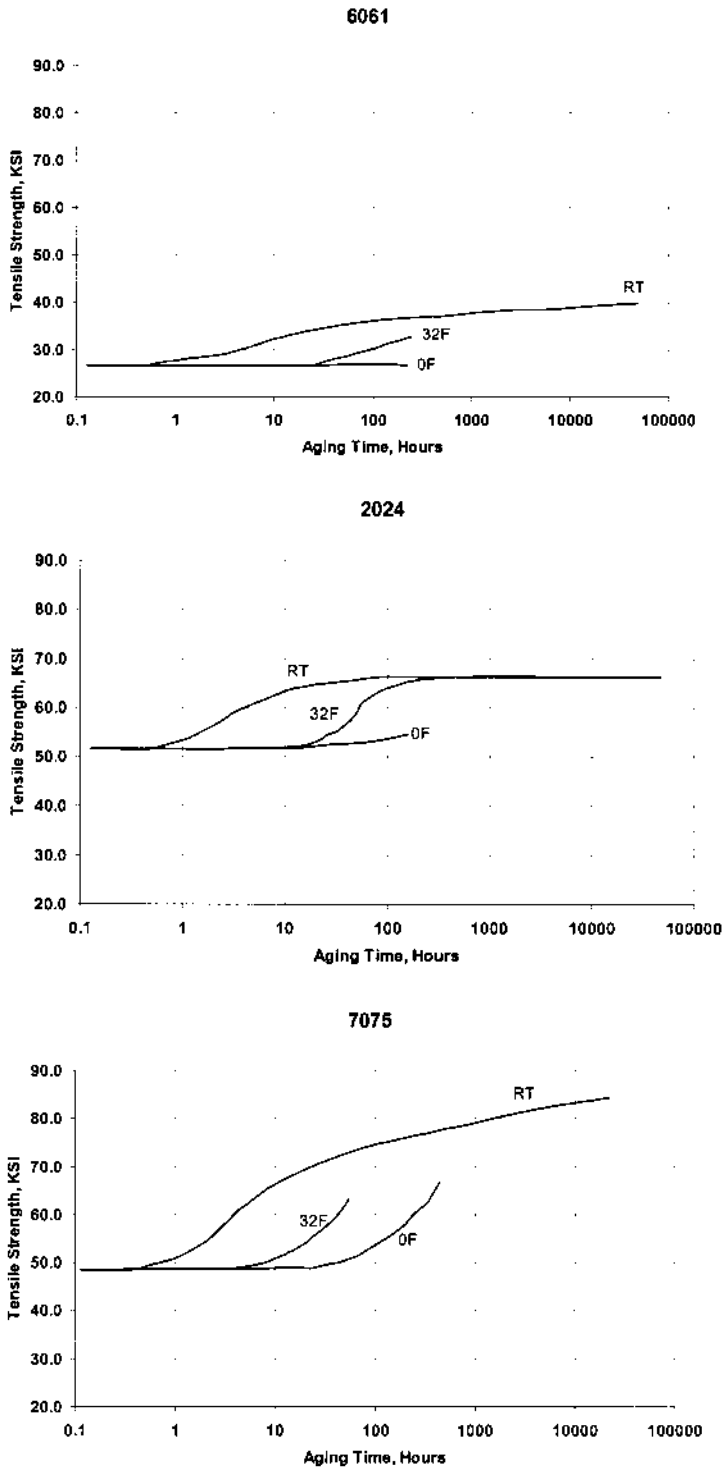
Figure 14 Effects of temperature on the natural aging response of three alloys.

Table 19 Typical Time and Temperature Limits for Refrigerated Parts Stored in the As-Quenched Condition

		Maximum Storage Time for Retention of the AQ Condition		
Alloy	Maximum Delay Time after Quenching	−12°C (10°F) Max.	−18°C (0°F) Max.	−23°C (−10°F) Max.
2014 2024 2219	15 minutes	1 day	30 days	90 days
6061 7075	30 minutes	7 days	30 days	90 days

Interestingly, the electrical conductivity decreases with the progression of natural aging. Generally, the reduction of solid solution content would indicate an increase in the conductivity. This decrease in conductivity indicates that GP Zones are forming, instead of "true" precipitates. This decrease in conductivity is related to the consumption of vacancies by the GP Zones. This decrease in conductivity is illustrated in Figure 15.

Besides conductivity changes, dimensional changes also occur during natural aging. The dimensional change observed is not consistent with a reduction in
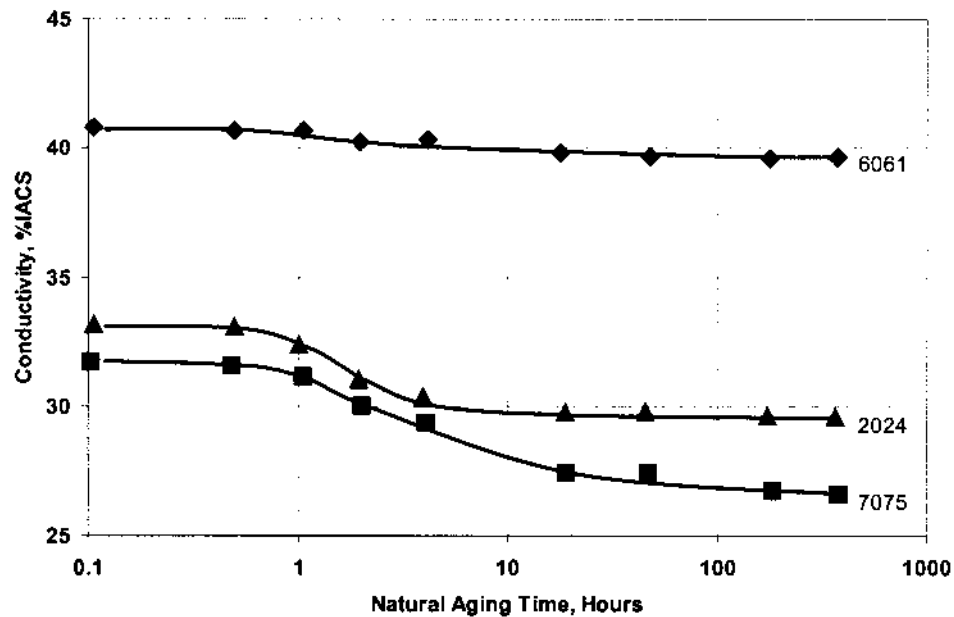
Figure 15 Effect of natural aging on the conductivity of solution heat-treated and quenched sheet.
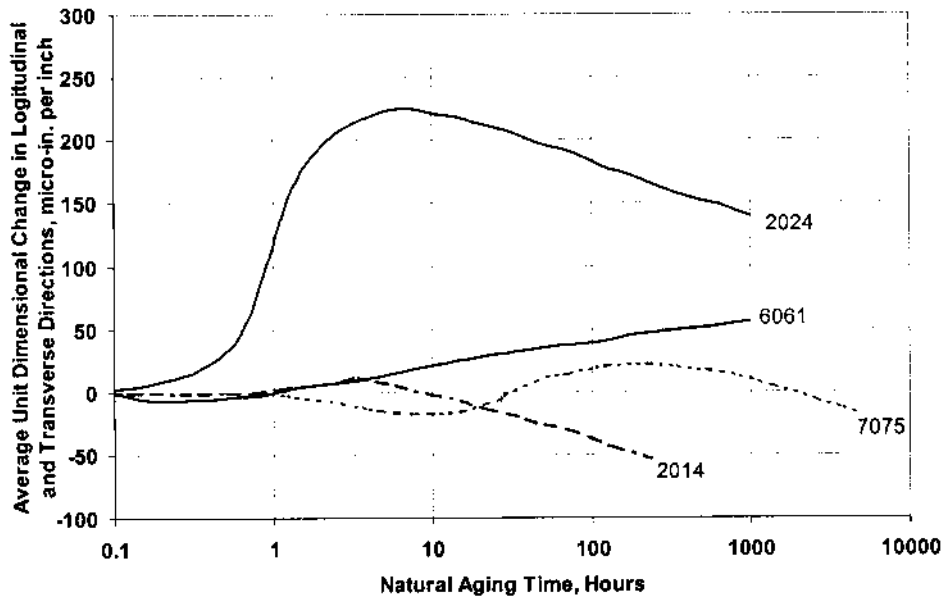
Figure 16   Dimensional changes occurring during natural aging of several alloys.

the amount of solute in solid solution. However, it also suggests the formation of GP Zones, or the formation of a precipitate during natural aging. These dimensional changes occurring natural aging of several alloys is shown in Figure 16.

3.7   Precipitation Heat Treatment (Artificial Aging)

Precipitation hardening (aging) involves heating the alloyed aluminum to a temperature in the 200–450°F range. At this temperature, the supersaturated solid solution created by quenching from the solution heat treating temperature, begins to decompose. Initially there is a clustering of solute atoms near vacancies. Once sufficient atoms have diffused to these initial vacancy clusters, coherent precipitates form. Because the clusters of solute atoms have a mismatch to the aluminum matrix, a strain field surrounds the solute clusters. As more solute diffuses to the clusters, eventually the matrix can no longer accommodate the matrix mismatch. A semi-coherent precipitate forms. Finally, after the semi-coherent precipitate grows to a large enough size, the matrix can no longer support the crystallographic mismatch, and the equilibrium precipitate forms. What follows is a brief description of the precipitates and precipitation sequence of the most common precipitation hardenable aluminum alloys.

Precipitation hardening is the mechanism where the hardness, yield strength, ultimate strength dramatically increase with time at a constant temperature (the aging temperature) after rapidly cooling from a much higher temperature (solution heat treat temperature). This rapid cooling or quenching results in a supersaturated solid solution, providing the driving force for precipitation. This phenomena was

first discovered by Wilm [42], who found that the hardness of aluminum alloys with minute quantities of copper, Magnesium, Silicon, and Iron, increased with time, after quenching from a temperature just below the melting temperature.

The first rational explanation for this effect was by Merica *et al* [43], who explained that the hardening that occurred over time was because since the solid solubility increased at higher temperatures, the lower aging temperature enabled a new phase to occur by precipitation from the initially solid solution.

The concept of precipitation hardening opened up a new field of physical metallurgy, and was the primary focus of research in the 1920's and 1930's. This concept was very difficult to validate because the precipitates during the initial and intermediate stages of aging were too small to be observed with the instruments of that era.

Mehl and Jelten [44] describe the history and progression of thought by the 1930's on the mechanisms of precipitation hardening in the review article. It is interesting to note that in the review article, the concept of dislocations was not mentioned, although dislocations were discovered and discussed in the early 1930's.

The earliest attempt at explaining precipitation hardening by dislocations [45] thought that the strength increases derived from precipitation hardening was from the interaction of dislocations and the internal stresses developed by coherent particles and the resulting misfit.

Orowan [46] developed his famous equation relating the strength of an alloy containing hard particles to the particle shear modulus and the inter-particle spacing. The Orowan equation is a remarkable achievement and is the basis for the theory of dispersion hardening.

Precipitation hardening strengthens alloys by coherent particles sheared by dislocations, with a drastic effect on properties. The mechanisms of precipitation hardening all have in common the method in which dislocations are impeded through the particle and matrix, and the description of that motion.

Six primary mechanisms of precipitation hardening have been described in the literature. They are Chemical Strengthening; Stacking Fault Strengthening; Modulus Hardening; Coherency Strengthening; Order Strengthening; and Spinodial Decomposition. Briefly, Chemical Strengthening provides hardening from the formation of an additional matrix-precipitate interface from the dislocation shearing the particle. Stacking Fault Strengthening hardens from the different stacking fault energies of the matrix and the precipitate. In Modulus Hardening, the increased strength is because the shear modulus of the matrix and precipitate differ. In Coherency Strengthening, there is an elastic interaction between the strain fields of the dislocation and the coherent particle. Order Strengthening is when the precipitate is a superlattice, and the matrix is a relatively disordered solid solution. Spinoidal decomposition is a special case where the lattice changes in solute concentration, yielding a periodic variation in the elastic strength from changes in composition.

Nearly all the above mechanisms are based on dislocation/particle interactions, with the exception of spinoidal decomposition.

Chemical Strengthening is the earliest theory, and explained precipitation hardening by passing a dislocation through a particle. This dislocation creates two new ledges of new precipitate/matrix interface with a specific interfacial energy [47].

Theory predicts that the critical resolved shear stress decreases with decreasing particle size. This is contrary to observed behavior. The large predicted magnitude of the critical resolved shear stress is not supported experimentally, and does not contribute much to the strength of aged alloys. It is not felt to be an important mechanism for aluminum alloys, unless for very small particle sizes.

Stacking Fault Strengthening. When the stacking fault energy between the matrix and the precipitate differ, the motion of the dislocation is impaired. The separation of the dislocation depends on the phase that the dislocation resides. The theory by Hirsch and Kelly [48] indicates that a different situation arises depending on the average radius of the precipitate, $< r >$, the ribbon widths, and the stacking fault energies of the precipitate and the matrix. Gerold and Hartman [49] determined that the maximum force experienced by the split dislocation occurs at the critical breaking condition. Ardell [50] found that the incremental change in the critical resolved shear stress would vary provided that the diameter of the particle was less than the ribbon width of the matrix. Edge dislocations will provide higher values of the critical resolved shear stress because of the greater dislocation line tension.

Gerold and Hartman [49] demonstrated that the critical resolved stress would decrease as the particle size increased.

The resultant behavior depends on the magnitude of the dimensionless critical force exerted by the particle on the dislocation. These theories provide only a rough estimate for the critical resolved shear stress. However, these relationships show that stacking fault energy produces overaging behavior for a wide range of particle sizes when the particle size is much greater than the ribbon width or when the stacking fault energy of the matrix is large.

Modulus Hardening is difficult to deal with theoretically. There are two regimes, depending on whether the dislocation is inside the particle or outside the particle. When a dislocation penetrates the precipitate, the force of interaction increases, and a different calculation is required. The interaction energy between a straight screw dislocation has been calculated by Weeks [51, 52]. This force interaction is obtained by the differentiation of the interaction equation. The interaction forces are greatest when the dislocation has just entered the precipitate, and is the important case for determining the amount of increase in the critical resolved stress.

Several theories regarding the mechanism of Modulus Hardening have been proposed. The theory of Knowles and Kelly [53] is one of overaging. In this theory, particles are increasing in size, while maintaining a constant volume fraction. They assumed a fixed particle spacing along the dislocation to calculate the critical resolved shear stress.

The theory of Weeks [52] used the maximum force the precipitate could withstand before shearing. This force was used for predicting normal age hardening response for small particles. This theory demonstrated that modulus hardening provided an explanation for the experimental data on Al-2% Zn-1.4% Mg, and showed good agreement with the data. They concluded that it was the dominant mechanism in the under aged and the peak aged condition. However, one difficulty is that the shear modulus of the precipitate can not be determined experimentally. The possible agreement may be fortuitous.

There is evidence that modulus hardening may be important in several systems. Further, overaging was found not to be the result of an Orowan mechanism because

of the low work hardening rates in over-aged systems, and no evidence of Orowan Loops were found in over-aged Cu_3Au–1.5%Co [54].

Coherency Hardening is the oldest mechanism for precipitation hardening recognized. In this mechanism, misfitting coherent particles, and the interaction of the stress field of the dislocation and precipitate causes hardening. It is poorly characterized quantitatively. It is most thoroughly modeled if a pure edge dislocation interacts elastically with a spherical coherent precipitate with misfit.

The problem is solved by calculating the interaction force per line length on the slip plane of an edge dislocation. The result is integrated over the length of the dislocation to calculate the force. Base on the result, the interaction force can be negative or positive, attractive or negative. It depends on the nature of the edge dislocation and the degree of misfit. Statistically equal numbers of attractive and repulsive particles are encountered by the dislocation. Normally only repulsive particles are considered in the calculation. Since the force is identical for both repulsive and attractive precipitates, the primary difference is that for repulsive particles, the maximum force occurs before the dislocation passes through the center of the particle; for attractive precipitates, the maximum force occurs after the dislocation passes through the center of the particle. If the coherent spherical precipitate is large, then the bending of the dislocation becomes substantial, and the straight dislocation assumption is no longer valid.

If the interaction is between a screw dislocation and a spherical particle, then the net force is zero. But the maximum force is non-zero because it is calculated by integrating over only one-half of the length. Screw dislocations appear to control flow stress. It has been observed in Al-Zn alloys. However, observations disagree strongly with theory. This theory strongly overestimates the strength in these alloys, with the peak values much smaller than predicted. This theory does not predict the magnitude and the particle size expected by a wide margin.

Based on the above, the theory of coherency strengthening is inadequate to describe or provide rough estimates of the strengthening expected in under-aged, peak aged, or over-aged alloys.

Order Strengthening occurs by an ordered coherent precipitate sheared by a dislocation and creating and antiphase boundary (APB) on the slip plane of the precipitate. The antiphase boundary energy per unit area on the slip plane and the force per unit length of the dislocation oppose the motion of the dislocation as it moves through the precipitate.

In general, the dislocations in this type of strengthening mechanism move in groups. The groups are the numbers of dislocations that are necessary to restore order in the particle. Stainless steels, nickel alloys, and Aluminum-Lithium alloys [55] are commonly strengthened by this mechanism. In these alloys, the dislocations travel in pairs, because a pair of matrix dislocations ($b = a < 11\ 0 > /2$) passing through a $L1_2$ type structure (Cu_3Au) restores perfect order on the {111} slip plane.

The effect of the second dislocation is difficult to quantify. This is because the trailing dislocation is experiencing the strain field of the particles sheared by the first dislocation. If the structure is more complicated than Cu_3Au ($L1_2$) then the number of dislocations can be greatly increased. Brown and Ham [47] discussed the effect of the second dislocation, and they found that the weakly coupled pairs of dislocations were the most important in providing increases in the critical resolved stress.

3.8 Al-Cu Alloys

The Al-Cu system has been reviewed in detail [56]. The equilibrium phase diagram [57] is a eutectic, in equilibrium with $CuAl_2$ (θ) at 548C at approximately 32% Copper. The extent of solution solubility at the aluminum rich end is approximately 5.7% Copper. Comercial alloys of this type are 2219, 2011, and 2025.

The precipitation sequence was originally established by Guiner [58, 59] and Preston [60–61]. Hornbogen further examined the precipitation in Al-Cu and confirmed the results of Guiner and Preston [62]. The precipitation sequence after rapid quenching has been accepted as being Guiner-Preston Zones (GPZ) plates parallel $\{001\}_{Al}$, transforming to the coherent precipitate θ'', followed by semi-coherent θ' plates parallel $\{001\}_{Al}$. The final equilibrium precipitate is θ (Cu_2Al). Silcock, et al [63], examined this progression of precipitates, and showing multiple stages in precipitation, evidenced by changes in hardness and Laue reflections (Figure 17).

The coarsening behavior of θ'' and θ' in Al-Cu alloys was examined by Boyd and Nicholson [64], and found to follow the theory of Lifshitz, Slyozov [65] and Wagner [66]. In this theory, originally applied to the dispersion of spherical particles in a fluid, the rate of coarsening of is controlled by the diffusion of solute through the matrix. The variation of the mean radius, $\bar{r}$, with respect to time, t of spherical particles in a matrix is given by:

$$\bar{r}^3 - \bar{r}_0^3 = \frac{8}{9}\frac{\gamma D c_0 V_m^2}{RT}(t - t_0)$$

where $\bar{r}_0$ is the mean particle radius when coarsening begins at $t-t_0$. D and V_m are the diffusivity and the molar volume of the precipitate, while c_0 is the equilibrium molar
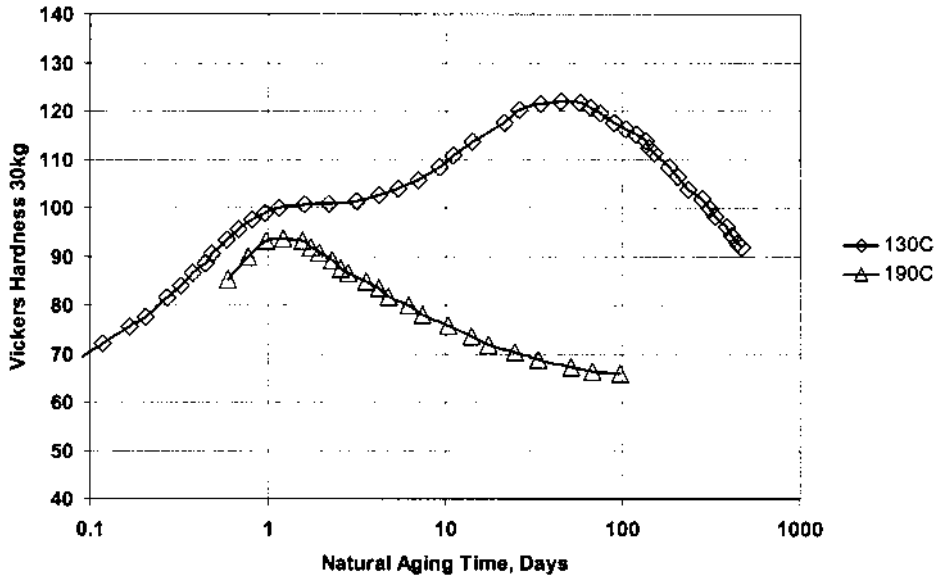
Figure 17 Correlation of structure and hardness of an Al-4%Cu alloy aged at 130°C and 190°C [63].

concentration and ã is the precipitate/matrix interfacial energy. Boyd and Nicholson [64] found that the measured coarsening kinetics of θ'' was in good agreement with the Lifshitz-Wagner theory. However, the coarsening of θ' occurred at a much higher rate than expected, and did not follow the Lifshitz-Wagner theory. They attributed this difference to short circuiting diffusion and particle coalescence.

3.9   Al-Cu-Mg Alloys

Aluminum-Copper-Magnesium alloys were the first precipitation hardenable alloys discovered [67]. The first precipitation hardenable alloy was a precursor to alloy 2017 (4% Cu, 0.6% Mg and 0.7% Mn). A very popular alloy in this group is 2024.

The addition of magnesium greatly accelerates precipitation reactions. In general, the precipitation sequence is:

$$SS \rightarrow GP\ Zones \rightarrow S'(Al_2CuMg) \rightarrow S\,(Al_2CuMg)$$
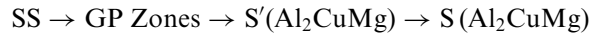
The GP Zones are generally considered to be collections of Cu and Mg atoms collected as disks on the $\{110\}_{Al}$ planes. S' is incoherent, and can be directly observed in the TEM. S' precipitates heterogeneously on dislocations. These precipitates appear as laths on the $\{210\}_{Al}$, oriented in the $<001>$ direction [68]. Since S' precipitates on dislocations, cold working after quenching increases the number density of S' and produces a fine distribution of precipitates in the matrix.

3.10   Al-Mg-Si Alloys

This alloy system forms the basis for the 6XXX series aluminum alloys. In this heat treatable alloy system, magnesium is generally in the range of 0.6–1.2% Mg, and silicon is in the range of 0.4–1.3% Si. The sequence of precipitation is the formation of GP Zones, followed by metastable β' (Mg_2Si), followed by the equilibrium β (Mg_2Si). The GP Zones are needles oriented in the $<001>$ direction, with β' and β showing similar orientations.

3.11   Al-Zn-Mg-Cu Alloys

In 7XXX Al-Zn-Mg-Cu alloys, several phases have been identified that occur in Al-Zn-Mg-Cu alloys as a function of precipitation sequence. Four precipitation sequences have been identified. This is shown schematically below:

$$\alpha_{sss} \Rightarrow S$$
$$\alpha_{sss} \Rightarrow T' \Rightarrow T$$
$$\alpha_{sss} \Rightarrow VRC \Rightarrow GPZ \Rightarrow \eta' \Rightarrow \eta$$
$$\alpha_{sss} \Rightarrow \eta$$
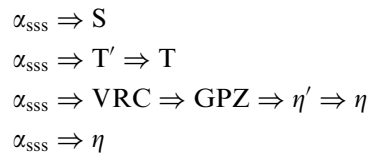
In the first precipitation sequence, the S phase, Al_2CuMg, is precipitated directly from the supersaturated solid solution. It is reported to be orthorhombic [69], with a space group of Cmcm, and 16 atoms to the unit cell. The lattice parameters are [70]: a = 0.401 nm, b = 0.925 nm, and c = 0.715 nm. This phase has been identified [71] as a coarse intermetallic that is insoluble in typical Al-Zn-Mg-Cu

alloys at 465C and as a fine lath precipitate in Al-4.5%Zn-2.7%Cu-2.2%Mg-0.2%Zr alloys. No orientation relationships to the matrix have been identified in the literature.

In the second precipitation sequence, an intermediate phase T' occurs in the decomposition of the supersaturated solid solution. Bernole and Graf first identified this phase [72]. Auld and McCousland [73] suggested that the structure was hexagonal with the reported lattice parameters a = 1.39nm, and c = 2.75nm. It was further suggested that the orientation of the hexagonal cell to the aluminum matrix be:

$$(0001)T'/\!/(111)Al \quad (10\bar{1}0)T'/\!/(11\bar{2})Al$$

Further in the second precipitation sequence, the equilibrium T phase forms. This phase was reported [74] to be cubic, space group Im3, with 162 atoms in the unit cell. It was indicated that the lattice parameter varies from 1.41 to 1.47nm, with this variation due to compositional variations. It has been proposed by Bergman *et al* [75] that the chemical formula $Mg_{32}(Al,Zn)_{49}$ was appropriate. It was found incoherent with the aluminum matrix. Several orientation relationships have been reported [76] between the T phase and the aluminum matrix. These are:

$(100)\ T_1/\!/(112)\ Al\ (001)\ T_1/\!/(1\bar{1}0)\ Al$
$(100)\ T_2/\!/(10)\ Al\ (010)\ T_2/\!/(111)\ Al$
$(100)\ T_3/\!/(110)\ Al\ (01\bar{1})\ T_3/\!/(001)\ Al$
$(100)\ T_4/\!/(110)\ Al\ (0\bar{2}5)\ T_4/\!/(1\bar{1}0)\ Al$

This phase has been rarely reported in substantial quantities, even though commercial heat treatments up to 150°C lay in the $Al + MgZn_2 + Mg_{32}(Al,Zn)_{49}$ phase field. In general, the T phase only precipitates above 200°C [1].

In the third sequence of precipitation, the supersaturated solid solution decomposes to form vacancy-rich clusters, Guinier-Preston Zones, η' and then η. Guinier-Preston Zones have been inferred in Al-Zn-Mg alloys, and is based on small increases in electrical conductivity and an increase in hardness during the initial stages of aging [7].

The η' phase is an intermediate step toward the precipitation of the equilibrium phase η ($MgZn_2$). Direct evidence of η' is rare, and difficult to obtain. It has recently been accepted that the η' phase is hexagonal, however, the reported lattice parameters vary widely (Table 20).

Review of the literature indicates that there is a dispute over the occurrence of η' and its nucleation [77–79]. Investigations with similar compositions have found discrepancies regarding the presence of η'. This leads to the speculation that the formation of η' is path dependant, and subject to local chemical variations. Mondolfo *et al*. [77] and others [80] indicate that nucleation of η' occurs by the segregation of alloying elements to stacking faults, gradually losing coherency until the ordered η phase develops [74]. Others indicate that the formation of η' is the result of vacancy-rich clusters (VRC) [78]. GP zones are also thought to nucleate η' [84] [79].

In a detailed examination by Auld and McCousland, [73] using single crystals, they report that the structure of η' is hexagonal and belongs to the P6m2 space group. The precipitate has the following possible orientation relationships with the matrix:

$$(0001)\ \eta'_1/\!/(1\bar{1}1)\ Al\ (10\bar{1}0)\ \eta'_1/\!/(110)\ Al\ [73]$$

Table 20   Structure of η'

Structure	a	c	Reference
Hexagonal	0.496nm	0.868nm	[80]
Monoclinic	0.497nm	0.554nm	[81] [82] [83]
Hexagonal	0.496nm	1.402nm	[83] [84]
Hexagonal (P6)	0.496nm	1.402nm	[85]

Table 21   Orientation Relationships Between η and the Aluminum

	Orientation relationship between η and the Al lattice [81] [74] [102]		
Type	$\eta//\text{Al}$	$\eta//\text{Al}$	Morphology
η_1	$(0001)//(1\,1\,0)$	$(10\bar{1}0)//(0\,0\,1)$	Plates
η_2	$(0001)//(1\,\bar{1}\,\bar{1})$	$(10\bar{1}0)//(1\,1\,0)$	Plates
η_3	$(0001)//(1\,\bar{1}\,\bar{1})$	$(\bar{1}\,100)//(1\,1\,0)$	Plates [103]
η_4	$(0001)//(1\,1\,0)$	$(\bar{1}\,2\,\bar{1}\,0)//\,(1\,1\,\bar{1})$	Rods
η_5	$(\bar{1}\,2\,\bar{1}\,0)//(1\,\bar{1}\,\bar{1})$	$(30\bar{3}\,2)//(110)$	Rods
η_6	$(12\bar{3}\,0)//(1\,\bar{1}\,\bar{1})$	$(20\bar{2}\,1)//(1\,\bar{2}\,2)$	Rods
η_7	$(\bar{1}\,2\,\bar{1}\,0)//(1\,\bar{1}\,\bar{1})$	$(10\bar{1}\,4)//(110)$	Rods
η_8	$(12\bar{3}\,0)//(1\,\bar{1}\,2)$	$(0001)//(31\,\bar{1})$	Rods
η_9	$(\bar{1}\,2\,\bar{1}\,0)//(0\,0\,1)$	$(0001)//(110)$	Laths [81]
η_{10}	$(0001)//(1\,\bar{1}\,\bar{1})$	$(1100)//(1\,\bar{3}\,4)$	[88]
η_{11}	$(0001)//(1\,1\,0)$	$(10\bar{1}0)//(1\,\bar{1}\,\bar{1})$	[102]
η_{12}	$(0001)//(0\,1\,0)$	$(10\bar{1}0)//(001)$	[104]

$(10\bar{1}0)\ \eta'_2//(100)$ Al $(0001)\ \eta'_2//(01\bar{1})$ Al [86]

The equilibrium precipitate in the third sequence is the hexagonal η (MgZn$_2$) phase with a $= 5.21$Å and c $= 8.60$Å [87]. This phase is the prototype of the hexagonal Laves phase, with 12 atoms to the unit cell and belonging to the space group P6$_3$/mmc. There are twelve orientation relationships between the precipitate and the Aluminum lattice. It has been suggested that the orientation is related to the type of nucleation during or after quenching [88]. These are shown in Table 21.

Bigot, Deniox, Auger, *et al* [89] determined compositions and volume fractions of metastable $\acute{\eta}$ and stable η by 3D atomic probe in 7050 aluminum. They found that $\acute{\eta}$ and η contain approximately 55 and 40 at% aluminum. The Zn:Mg ratio was found equal to one. Results indicated that η contains slightly more solute (Zn and Mg) than $\acute{\eta}$. $\acute{\eta}$ was found to be growing when aged between 24 and 100 hours at 120°C because precipitate concentration remained the same, but solute concentration in solid solution decreased. This analysis is consistent with the suggestion that η' can nucleate directly from GP Zones.

In another examination of Al-Zn-Mg alloys by 3D atomic probe [90], the authors found strong evidence that the composition of η' is not the same as the equi-

librium phase η. They indicate that the composition of η' is more closely related to the composition of GP zones. It was found that the composition of the GP zones and η' varies from Zn:Mg $= 1{:}1$ to 1.5:1. This is good evidence that the intermediate precipitate η' nucleates directly from GP Zones. The ratio of Zn:Mg for the equilibrium phase η was found to be 2:1, consistent with the formula of the Laves phase MgZn$_2$ and the Al-Zn-Mg phase diagram. These results are similar to recent studies [91, 92] of precipitation in 6XXX series Al-Mg-Si alloys. Those studies found that the intermediate precipitate had a Mg:Si ratio of approximately 1:1, while the equilibrium precipitate had a Mg:Si ratio closer to 2:1.

Electron and X-ray diffraction of an Al-Zn-Mg alloy revealed that η', η and T' were present in -T6 condition and only η and T' were present in the -T73 condition [93]. Only the precipitates η and η' were detected in the Al-Zn-Mg-Cu alloy in the -T73 condition. The presence of copper suppresses the formation of T' in favor of η. Copper also stabilizes the η phase resulting in little strength loss during overaging compared to significant strength loss of the ternary alloy during overaging. It was observed that the η phase in the quaternary alloy was multi-layered and interpreted in terms of the MgZn$_2$ Laves Phase. The size, interparticle spacing and volume fraction of the precipitated metastable phase (η') were evaluated [94] on the effect of artificial aging time. It was found that the amount of η' increases with aging time, but that the electron density remained constant. A strong correlation between yield strength and the structure of the fine precipitates was found. If precipitates were less than 2nm in average radius, dislocations cut through the precipitates. When precipitates grew in size to approximately 50–60 Å, the yield stress was governed by the Orowan mechanism. Hirsch and Humpherys' Theory provided a quantitative explanation [95]. The Langer - Schwartz model was accurate for predicting precipitation as long as a time dependant nucleation rate term was added [96]. The elastic strain increases the work of formation of a critical radius, and lowers the nucleation rate.

It was found [6] that rates of precipitation of η and η' were limited by reaction kinetics. Dissolution of η' is dominated by diffusion, while the dissolution of η is dominated by thermodynamic equilibrium between precipitate and the matrix.

Taylor [97] found that the width of precipitate free zones (PFZ) in aluminum alloys vary as a function of the solution heat-treat temperature, and the aging temperature. It was found that the width of the PFZ decreased as the solution heat treat temperature was increased from 410 to 490°C (at a constant age temperature). Hardness remained constant above 440°C, indicating that the solute atoms were completely in solution above 430°C. It was also found that the width of the precipitate free zone increased as the aging temperature was raised from 120 to 200°C. The width of the PFZ is inversely proportional to the quench rate [98].

The decrease in the PFZ width as the solution heat treat temperature was increased, was explained by the increase of vacancies, which in turn expedited diffusion, limiting the width of the PFZ. The decrease in the width of the PFZ at lower aging temperatures was explained by a higher degree of solute supersaturation and a change in the volume free energy. This reduces the critical value of vacancies required for nucleation, and reduces the width of the PFZ.

Al-Zn-Mg-Cu alloys deform mainly by inhomogeneous "planar" slip that applies large stress concentrations at the grain boundaries (the end of the slip bands) [99, 100]. The ductility of the alloy was not influenced by the width of the PFZ up to

full aged hardness. The area fraction of the grain boundary precipitates increased the predominance of intergranular fractures [101]. It was also found that creating narrow PFZ with large grain boundary precipitates could also increase the fracture stress. This was thought to occur because the large grain boundary precipitates impede the shearing of the particles required for crack nucleation.

The kinetics of precipitation during artificial aging, measured by yield strength and conductivity, obey an Arrhenius relationship and indicate that the activation energies of 7075 and 7050 are similar. The higher strength by aging at higher temperatures for 7050 was attributed to the effect of copper increasing the G.P. Zone solvus.

3.12   Artificial Aging

Heating the quenched material in the range of 95–205°C accelerates precipitation in heat treatable alloys. This acceleration is not completely due to changes in reaction rate. As was shown above, structural changes occur that are dependent on time and temperature. In general, the increase in yield strength that occurs during artificial aging increases faster than the ultimate tensile strength. This means that the alloys lose ductility and toughness. T6 properties are higher than T4 properties, but ductility is reduced. Overaging decreases the tensile strength, and increases the resistance to Stress-Corrosion-Cracking. It also enhances the resistance to fatigue crack growth. It also imparts dimensional stability of the part.

Precipitation hardening curves have been developed for all the most common alloys. Figure 18 shows aging curves for 2024 and 6061. Both alloys show evidence of reversion of GP Zones by initial reductions in hardness. This is caused by the destruction of small GP Zones that are below the critical size. Similar aging curves have been developed for 7075 (Figure 19) and for the cast alloy 356 (Figure 20).

The aging curves for the various alloys vary; however, generally the higher the aging temperature, the shorter the time required to attain maximum properties. When high aging temperatures are used, properties are reached very rapidly with time. For this reason, aging temperatures are usually lower to assure that the entire load is brought to the required aging temperature without risk of reduced properties caused by over-aging of the fastest rising aluminum.

It is not necessary to develop aging curves for each alloy and desired temper. The times and temperatures are proscribed in many process specifications. Typical precipitation heat treating sequences are shown in Table 22 (Wrought products), Table 23 (Sand Castings), and Table 24 for permanent mold castings.

4   EQUIPMENT

Aluminum heat treat systems can be continuous or batch types. Continuous heat treat systems include roller hearth, pusher, belt and chain types. The requirements for the various continuous furnaces vary only as to the type of conveyor used with the furnace. Batch solution heat treat types include drop-bottoms, side discharge, fluidized bed, and pit furnaces. Continuous and batch furnaces have many components in common:

- Operating temperatures in the 830°–1080°F range
- ±5°F or ±10°F temperature uniformity requirements

2014-T4

6061-T4
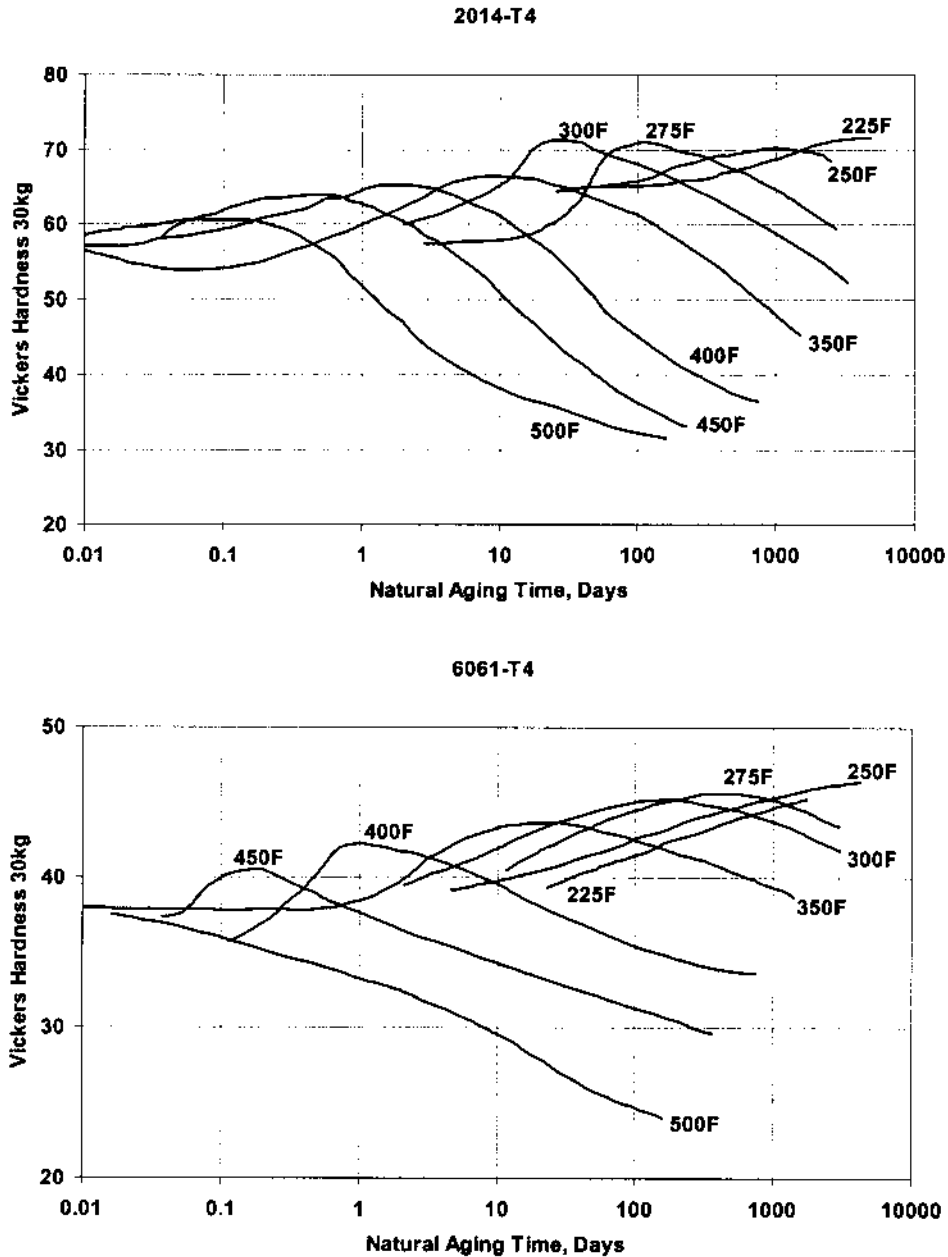
Figure 18 Aging curves for 2014 (top) and 6061 (bottom).

- No temperature overshoot above the upper thermal uniformity limit allowed
- Ceramic fiber insulation up to 8″ thick
- Maximum quench delay in the 5–15 second range beginning when the door begins to open
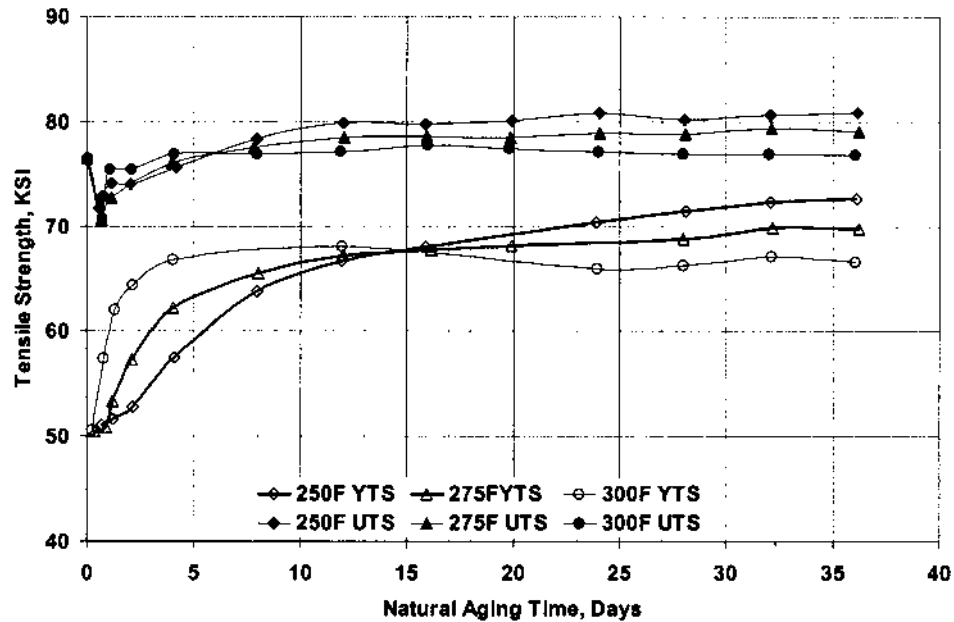
Figure 19 Aging curves for 7075.

- Controls to within 2°F accuracy
- Continuously records both high and low air temperature in each zone
- Electric, indirect radiant tube, or direct-fired natural gas heat source
- Recirculated air directed at relatively high velocities past the aluminum
- Hot air is recirculated using ductwork – usually stainless steel
- Quenchant temperature rise and thermal uniformity are limited.

4.1 Furnace Types

As indicated previously, there are standard types of aluminum heat treating equipment. This includes car-bottom furnaces, vertical tower and pit furnaces, continuous conveyer and batch furnaces.

Car bottom furnaces are useful for annealing large forgings, plates or other product forms. In this type of furnace, the hearth of the furnace is usually an insulated car that rides on rails. The furnace door could either be part of the furnace shell or part of the car. The hearth is sealed to the furnace by using knife edges into sand. This prevents cold air leaking causing cold spots in the furnace. This type of furnace is heated by either radiant tubes (natural gas) or by electric heating elements. An example is shown in Figure 21.

Vertical tower furnaces or pit furnaces are specialized furnaces used for heat treating very long items. Typically, extrusions are heat treated in this type of furnace. Because of the length of the hot zone, it is necessary to break the furnace into several heating zones, controlled by individual temperature controllers. Each zone will have a separate thermocouple and excess temperature controller. Often each zone will have a separate chart recorder. Also, because of the size of the work zone, a large

356-F (Permanent Mold Cast)

356-T4 (Permanent Mold Cast)

356-T4 (Sand Cast)
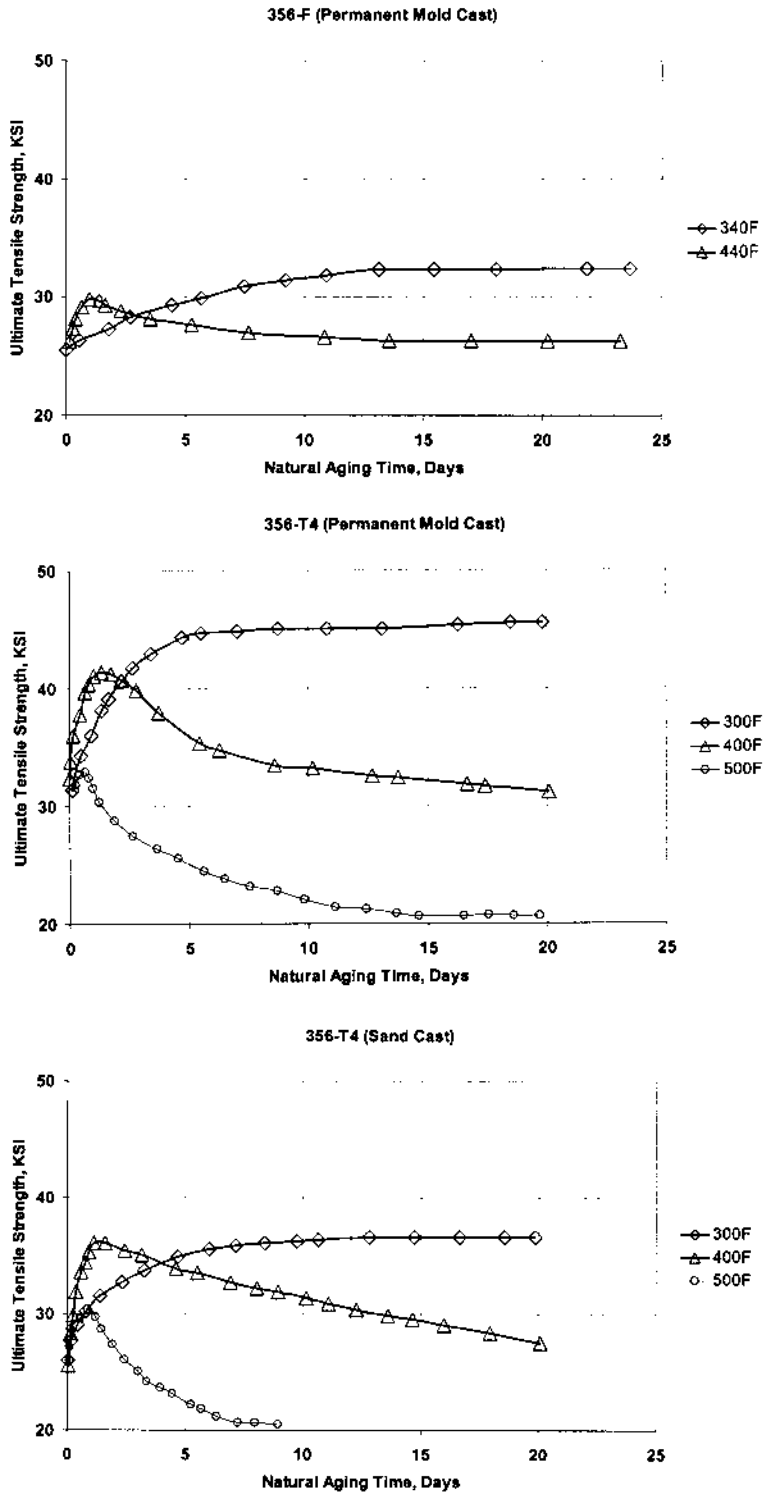
Figure 20 Aging curves for 356 cast alloy.

Table 22 Typical Aging Treatments for Precipitation Hardening Wrought Aluminum Alloys (From Ref. 107)

Alloy	Form	Temper Before Aging	Temper After Aging	Temperature °F	°C	Soaking Time (Hours)
2XXX	Sheet, Other	AQ, W	T4	Ambient	Ambient	96 Min.
2004	Sheet	T4	T6	350	177	10–11
2014	Sheet, Other	T3	T6	320	160	18–20
		T4	T6	350	177	8–9
2024	Sheet, plate, Drawn Tube	T3	T81	375	191	12–13
	Forgings	T361	T861	375	191	8–9
		T4	T6	375	191	9–10
		T4	T7	375	191	16–18
	Wire, Rolled Bar	T4, T352	T6, T852	375	191	12–13
		T351, T351X	T851, T851X	375	191	12–13
	Extruded Bar and Shapes	T4, T42	T6, T62	375	191	12–13
2048	Plate	T351	T851	375	191	12–13
		T42	T62	375	191	9–10
2142	Plate	T351	T851	375	191	12–13
2219	All	T42	T62	375	191	35–37
	Sheet	T31	T81	350	177	17–19
		T37	T87	325	163	23–25
	Forgings	T352	T852	350	177	17–19
		T4	T6	375	191	25–27
	Plate	T351, T37	T851, T87	350	177	17–19
	Rivets	T31	T81	350	177	17–19
	Extruded Bar and Shapes	T31, T351X	T81, T851X	375	191	17–19
6013	Sheet	AQ, W	T4	Ambient	Ambient	336 Min.
		T4	T6	375	191	4–5
6951	Sheet	AQ, W	T4	Ambient	Ambient	48 Min.
		T4	T6	320	160	17–19

Alloy	Product	Temper	Final Temper	Temp, °F	Temp, °C	Time, h
6XXX	All Other	AQ, W	T4	Ambient	Ambient	96 Min.
6061 6063 6066	All	T4	T6	350	177	8–10
7049	Extruded Bar and Shapes	W	T73*	250	121	24–25
				330	166	21–22
7149		W	T76*	250	121	24–25
				330	166	14–15
	Forgings	W	T73	250	121	24–25
				330	166	13–14
7050	Rivets	AQ, W	T73	250	121	4 Min.
				355	179	8 Min.
	Plate, Extruded Bar and Shapes	AQ, W	T73	250	121	6–8
				350	177	12–13
	Plate	AQ, W	T76	250	121	6–8
				350	177	6–7
	All Except Plate	AQ, W	T76	250	121	6–8
				350	177	4–5
	All	AQ, W	T74	250	121	6–8
				350	177	6–8
7075	All	AQ, W	T6	250	121	23–25
	Sheet, Plate	T6+	T73	325	163	26–28
		T6+	T73	350	177	8–9
	Wire, Rolled Bar, Forgings	T6+	T76	325	163	16–18
		T6+	T73	350	177	8–10
	Extruded Bar, Shapes	T6+	T76	325	163	16–18
		T6+	T73	350	177	6–8

Table 22 *Continued.*

Alloy	Form	Temper Before Aging	Temper After Aging	Temperature °F	Temperature °C	Soaking Time (Hours)
7178	All	T6+	T76	320	160	19–21
	Sheet, Plate	AQ, W	T62	250	121	22–26
		T6+	T76	325	163	16–18
	Extruded Bar and Shapes	T6+	T76	320	160	18–21
7475	Sheet	AQ, W	T61	250	121	3–5
				315	157	3–4
		AQ, W	T761	250	121	3–5
				325	163	10–12
	Plate	AQ, W	T6	250	121	24–25
		AQ, W	T76	250	121	3–5
				325	163	12–18
		AQ, W	T73	250	121	3–5
				325	163	24–30

* Requires Two-Step Age
+ An initial age of AQ or W temper parts, consisting of 4–6 hours at 250°F (121°C) may be substituted for the normal T6 age

Table 23 Typical Aging Treatments for Aluminum Sand Castings

Alloy	Temper Before Aging	Temper After Aging	Temperature		Soaking Time (Hours)
			°F	°C	
222.0	T4	T6	380–400	193–204	10–12
242.0	F	T571	320–350	160–177	22–26
395.0	T4	T6	300–320	149–160	12–20
520.0	W	T4	Ambient	Ambient	96 Min.
319.0	T4	T6	300–320	149–160	1–6
355.0	F	T51	430–450	221–232	7–9
	T4	T6	300–320	149–160	1–6
	T4	T7	430–450	221–232	3–5
356.0	T4	T6	300–320	149–160	1–6
	F	T51	430–450	221–232	6–12
A356.0	T4	T6	300–320	149–160	1–6
712.0	F	T5	345–365	174–185	9–11
	F	T1	Ambient	Ambient	21 Days

Table 24 Typical Aging Treatments for Aluminum Permanent Mold Castings

Alloy	Temper Before Aging	Temper After Aging	Temperature		Soaking Time (Hours)
			°F	°C	
222.0	T4	T65	330-350	166–177	7–9
242.0	T4	T61	400-450	204–232	1–3
296.0	T4	T6	300-320	149–160	1–8
336.0	T45	T65	300-350	149–177	14–18
355.0	T4	T6	300-320	149–160	1–6
356.0	T4	T6	300-320	149–160	1–6
A356.0	T4	T61	300-320	149–160	6–10
C355	T4	T61	300-320	149–160	10–12

volume of air is required to maintain temperature uniformity. Vertical tower furnaces may be on rails in a similar fashion to a gantry furnace to enable loading and quenching. Specialized loading mechanisms may also be used. An example of a vertical tower furnace is shown in Figure 22.

Pit furnace are similar to a vertical tower furnace except the furnace work zone is below grade. This type of furnace is typically used for homogenizing or preheating ingots or coils. It is also used for annealing ingots and coils. It is not often used for solution heat treatment because of the difficulties lifting the load and quenching it within the allowable quench delay time. These furnaces are simple to operate and maintain. Excellent temperature uniformity can be obtained. Often in the case of larger pit furnaces, multiple temperature control zones may be used.

Table 25   Typical Hardness and Conductivity Values for Aluminum Alloys Heat Treated to Various Tempers (From Ref. 107)

| Alloy | Temper | Brinnell | Rockwell hardness | | | | | Typical Conductivity |
			B	E	H	15T	
1100	O	–	–	–	50 Max.	–	57.0–62
3003	O	–	–	–	65 Max.	–	44.5–50.5
5052	O	–	–	70 Max.	95 Max.	–	34-37
2014	O	–	22 Max.	70 Max.	95 Max.	–	43.5–51.5
	T3	100	65	95	–	82	31.5–35
	T4	100	65	95	–	82	31.5–34.5
	T6	125	78	102	–	86	35.5–41.5
2024	O	–	22 Max.	70 Max.	95 Max.	–	46–51
	T3	110	69	94	–	82	28.5–32.5
	T4	100	63	94	–	82	28.5–34
	T6	118	72	98	–	84	36.5–40.5
	T8	120	74	99	–	85	35–42.5
2124	T3	110	69	97	–	–	28.5–32.5
	T8	120	74	99	–	–	35.0–42.5
2219	O	–	22 Max.	95			44–49
	T3	98	60	92	–	79	26.0–31.0
	T37	99	62	93	–	81	27.0–31
	T4	96	58	90	–	78	28.0–32
	T6	99	62	93	–	81	32.0–35.0
	T8	116	71	98	–	83	31.0–35
	T87	124	75	100	–	84	31.0–35
6061	O	40 Max.	–	–	75 Max.	–	42.0–49
	T4	50	–	70	–	64	35.5–43.0
	T6	80	42	85	–	78	40.0–47.0
6063	O	–	–	–	70 Max.		57.0–65.0
	T1	–	–	37	–	53	48.0–58.0
	T4	–	–	40	–	54	48.0–58.0
	T5	–	–	44	–	57	50.0–60.0
	T6	60	–	70	–	68	50.0–60.0
6066	O	–	–	40 Max.	–	–	42.0–47.0
	T4	–	–	85	–	76	34.0–41.0
	T6	102	65	95	–	82	38.0–50.0
7049	O	-	22 Max.	70 Max.	95 Max.		44.0–50.0
	T73	134	81	104	–	85	40.0–44.0
	T76	142	84	106	–	87	38.0-44.0
7050	O	–	22 Max.	70 Max.	95 Max.	–	44.0–50.0
	T73	134	81	104	–	85	40.0–44.0
	T736	140	82	105	–	86	40.0–44.0
	T76	142	84	106	–	87	39.0–44.0
7075	O	–	22 Max.	70 Max.	95 Max.	–	44.0–48.0
	T6	142	84	106	–	87	30.5–36.0
	T73	129	78	102	–	85	40.0–43.0
	T76	136	82	104	–	86	38.0–42.0

Table 26 Typical Values of Hardness and Conductivity for Heat Treated Aluminum Alloys (Clad) (From Ref. 107)

Alloy	Temper	Sheet Thickness	Rockwell Hardness, minimum			Typical Conductivity
			B	E	15T	
2014	T6	.062 & Under	76	102	85	35.5–44.0
		.063 & Over	75	101	–	35.5–44.0
2024	T3	.062 & Under	57	91	79	28.5–35.0
		.063 & Over	60	93	–	28.5–35.0
	T4	.062 & Under	57	91	79	28.5–35.0
		.063 & Over	60	93	–	28.5–35.0
	T6	.062 & Under	60	93	81	35.0–45.0
		.063 & Over	62	94	–	35.0–45.0
	T8	All	65	97	82	35.0–45.0
2219	T6	.062 & Under	61	92	80	32.0–37.0
		.063 & Over	60	91	–	32.0–37.0
	T8	.062 & Under	64	96	82	31.0–37.0
		.063& Over	63	95	–	31.0–37.0
6061	T6	All	84	74	–	40.0–53.0
7075	T6	.032 & Under	78	103	86	30.5–36.0
		.033 – .062	76	102	–	30.5–36.0
		.063 & Over	75	101	–	30.5–36.0
	T76	.032 & Under	76	102	84	38.0–42.0
		.033 – .062	75	101	–	38.0–42.0
		.063 & Over	74	100	–	38.0–42.0
7178	T6	.036 & Under	79	104	86	29.0–34.0
		.037 – .062	78	103	–	29.0–37.0
		.063 & Over	76	102	–	29.0–37.0

Continuous furnaces are used in high volume heat treating, where there is little change in the alloy, processing parameters and part configuration. A typical installation is shown in Figure 23.

Batch furnaces used for solution heat treating include pusher-type furnaces, drop-bottom furnaces and other batch type furnaces (fluidized bed and salt-bath furnaces). Drop-bottom and pusher-type furnaces are constructed nearly identically, except they differ in the manner that they quench a workload. In pusher-type, the loads are pushed out of the furnace on to an elevator, and then translated vertically into the quench tank. Drop-bottom furnaces have doors on the bottom of the furnace, and the furnace load is rapidly lowered into the quench tank. The differences are schematically illustrated in Figure 24. Pusher furnaces are generally not used for solution heat treating applications. Because of the dual motions required, it is difficult to meet the required quench delay times. However, this type of furnace is amenable to hand quenching workloads, if the size and weight of the furnace load is small. Drop-bottom furnaces are the most commonly used for solution heat treating applications. Two examples are shown in Figure 25 and in Figure 26.
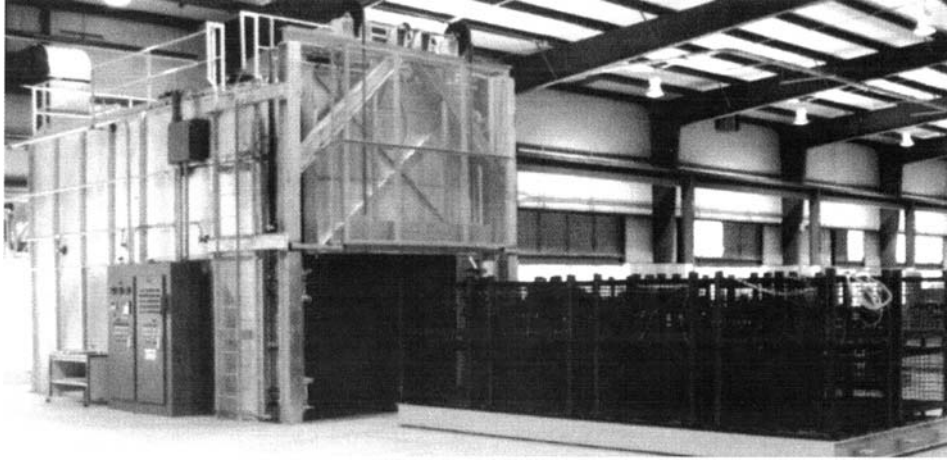
Figure 21 Three-zone car-bottom furnace used for precipitation hardening, annealing and homogenizing 40,000 pound loads at $\pm 5°F$ temperature uniformity.

Figure 22 Vertical tower drop-bottom furnace used for solution heat treating 16-foot long extrusions. A mobile transfer car with quench tank is used to load the furnace.

Figure 23 Two continuous roller hearth solution heat-treating furnaces, with age hardening ovens. Each of the furnaces process 150 aluminum cast aluminum wheels per hour. The system layout requires only a single operator to periodically load/unload furnace work baskets.
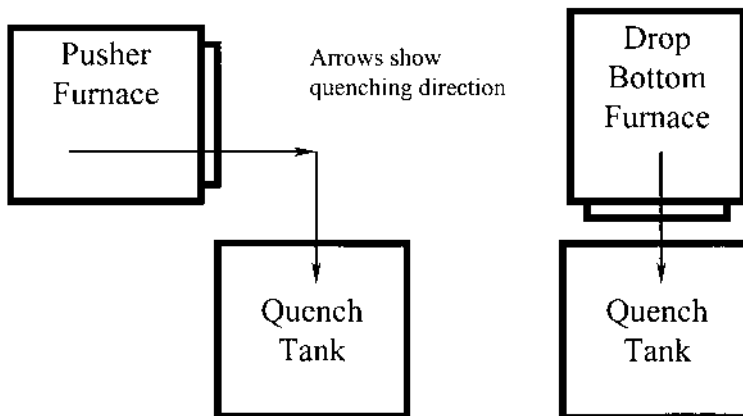
Figure 24 Schematic showing the difference between pusher-type furnaces and drop-bottom furnaces.

Drop-bottom and pusher-type furnaces are designed in a similar fashion, except for the quenching mechanism. Both are indirectly fired using either natural gas in radiant tubes or electric heating elements. The heating sources are shielded from direct radiation on the parts. Air is moved down across the heating elements in a plenum, then past the temperature control thermocouples. Additional thermocouples are used for excess temperature control and process temperature recorders. The heated air is passed up through the workload using a series of adjustable louvers. These louvers are adjustable to allow precise control of the temperature uniformity within the work zone. A minimum of $\pm 10°F$ temperature uniformity is usually required, but better temperature uniformity is preferred and provides more consistent properties.
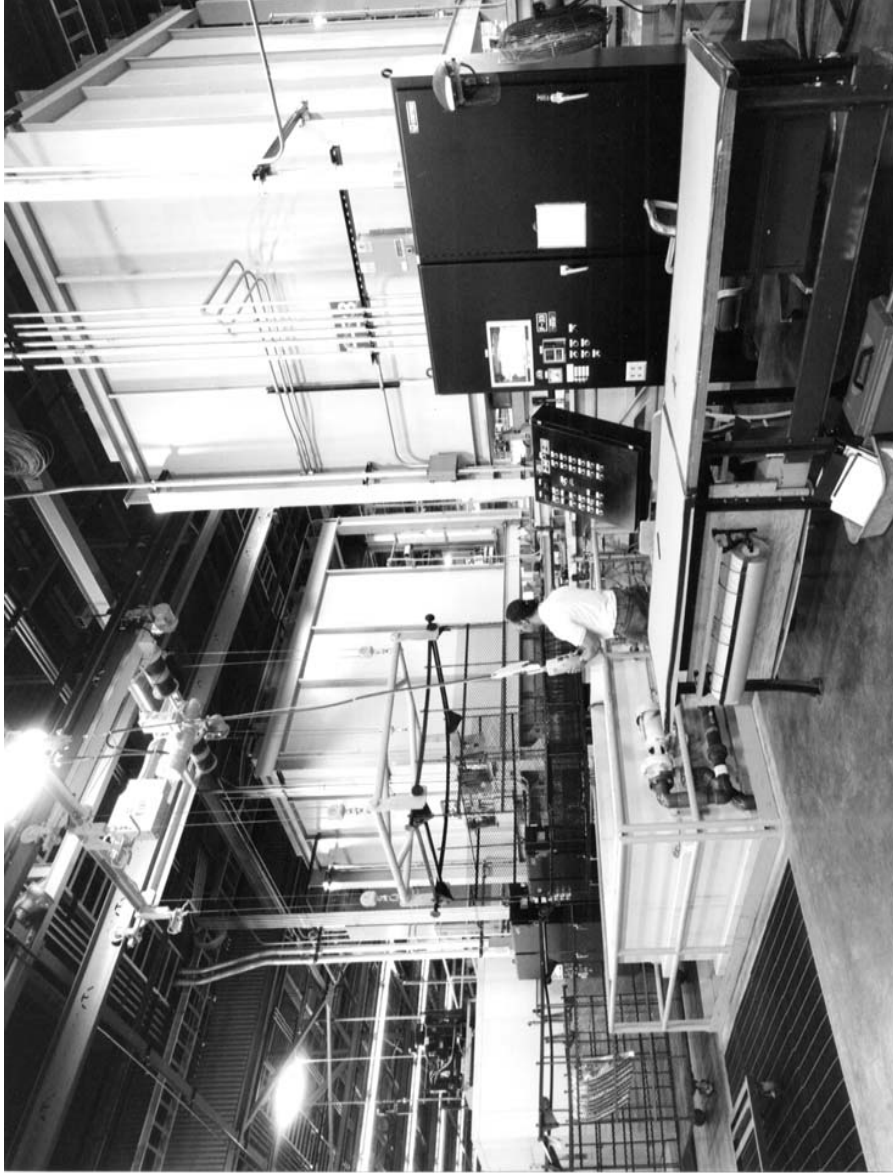
Figure 25 Dual drop-bottom furnace installation utilizing a single quench car. Water and PAG quench tanks are used. The quench car shuttles between the two furnaces. This concept results in a very compact and efficient installation.

Figure 26 Large drop-bottom furnace with a single quench tank. Work rank is in the "LOAD" position, and quench tank is to the left.

Aluminum ovens and furnaces with working zones as large as 10° wide x 12° high x 60' long are now required to certify within ±5°F and to recover within less than 30 minutes following insertion of aluminum loads weighing in excess of 25,000 pounds. Performance must be programmable, verifiable, and repeatable in order to support historical process reporting requirements. Recovery criteria vary, but usually thermocouples are inserted and attached to the aluminum load for certification of temperature uniformity and thermal recovery. It is important for the furnace heating and air recirculation system to be matched with the load characteristics. Aluminum forms that are heat treatable include sheets, plates, extrusions, impacts, castings, forgings and formed shapes.

Solution heat treat racks are configured to accept a variety of forms and shapes in arrangements that allow air and quenchant movement, and that assist in distortion control. Racks are fabricated from stainless steel, mild steel or 4130 aircraft grade tool steel. Generally, stainless steel is preferred because of improved properties at solution heat treating temperatures. Joints are constructed to pivot during expansion/contraction cycles in order to avoid weld breakage or distortion. Racks constructed in this way show minimal visible distortion or oxidation after thousands of cycles. The aluminum throughput to rack weight ratio continues to improve as racking materials and configurations improve. A comparison of two different racks is shown in Figure 27.

Indirect natural gas-fired aluminum solution heat treat furnaces are used extensively in ±5°F applications. Advancements in combustion control techniques allow for very high turndown of gross heat into the radiant tubes. PC/PLC sequencing techniques provide the control scheme necessary to achieve very fast thermal recovery without overshoot, and with the ability to hold a wide range of temperatures (350–1200F). Recuperators are installed in the exhaust legs of the radiant tubes and preheat the combustion air to achieve verifiable efficiency improvements of up to 15%.

Rate of quench speed is infinitely variable over the typical range of 5–15 second quench delay (start of door opening until aluminum load is completely submerged). Variability and speed control are achieved through use of servo controls with microprocessor based feedback loops. Hoist speed profiles can be configured to attain elapsed time delays and optical rate of entry into the quench while contouring acceleration/deceleration to minimize jarring of parts, splashing and excessive distortion on entry into to the quenchant.

The quench portion of the heat treating cycle is increasingly recognized to have equal influence on properties of the metal as the heating phase. Poly (alkylene) glycol (PAG) in water over a range of up to 40% PAG is increasingly used to mediate the rate of heat transfer from hot metal to quenchant to provide a homogenous solution in order to minimize and control distortion in the aluminum. Water is also used as a quenchant and is effectively used over a range of 40–210°F. In many applications, the heat treater can choose between poly (alkylene) glycol in water over a wide range of concentrations (water − 40% PAG); water over a range of 40-190F, water or PAG in water spray with a variable rate of flows and cooling characteristics, and air for a slower rate of cooling. The successful implementation of separation technologies (thermal and membrane) has allowed for concentration changes upon demand. Chillers and tank heaters provide rapid quenchant temperature changes and recovery, and filtration improvements provide very clean quench tanks. Con-

Figure 27 Two different rack designs for heat treating identical parts. The rack on the left is fabricated from 4340 steel and low alloy steel mesh. Note the distortion on the support rack and the amount of rusting that has occurred. The rack on the right is fabricated from RA330 stainless steel and has been processed for twice as many heat treating cycles as the rack on the left. The rack is much lighter and shows significantly less distortion.

centration, dissolved solids, pH, temperature, refractive index and conductivity are all monitored in the quench tank and corrective actions are initiated in order to control the characteristics of the quench.

Quenchant agitation rates are controlled over a defined range to provide variable agitation from still to 2–3 fps velocities. Pump, propeller or eductor agitation devices are all used successfully, depending upon the characteristics of the load. Figure 3 shows agitation devices on a solution heat treat drop-bottom furnace. Tanks are typically mobile for ease of loading/unloading and maintenance. Splash, free board, and movement of mobile tanks are carefully controlled. Liquid is transferred to and from the above ground tanks through hoses mounted in mobile hose carriers. Metallurgical requirements for heat treatable aluminum alloys include a cooling rate of $200°$–$1000°F$ per second in the temperature range of $800°$–$500°F$. These cooling rates are controlled by varying the quenchant temperature, poly (alkylene) glycol concentration, quenchant agitation rate, and speed of entry into the quench.

Aluminum heat treat furnaces are designed so that the temperature rise in the recirculated air as it passes the heat source is the same as the sum of all the temperature losses in the air as it passes the load, walls, openings, and exhaust. Whenever a diagnostic is required regarding a change in basic heat transfer characteristics of a furnace system, the components to this heat transfer equation must be analyzed to see what has changed. Changes in temperature uniformity conditions within a heat treat chamber are generally a result of one or more of the following:

- The volume of recirculated air has changed. Temperature uniformity is directly proportional to recirculated airflow.
- Cold air is being aspirated through an opening.
- Hot air from the heat source is being entrained in the air stream and is not adequately mixed before entering the work chamber.
- The recirculated air is missing the heat source.
- The load has changed.
- The thermocouples sensing the delivered air temperature are out of the air stream or inaccurate.
- The control instrument is inaccurate.
- The insulation has been damaged or deteriorated.

Cold air entrainment is best diagnosed by evaluating door, roller, and conveyor opening seals. Cold spots found in thermal surveys are almost always near doors or in areas within the work zone farthest away from the fan. Drop-bottom solution furnaces are twice as troublesome because the area directly above the seal between the split door halves is also the farthest from the fan. If air is leaking past the seam between the door halves, the negative pressure caused by the fan suction will almost certainly cause a non-uniform condition in the air pathway to the return duct. The best way to repair this problem is to repair the door seal. One diagnostic to find cold air infiltration is to evaluate the thermal surveys and to use smoke or light flags to spot areas of inflow. Another way to correct cold spots is to increase the positive pressure within the chamber by increasing the ratio between fresh air admitted and exhaust air discharged. This change in ratio causes a more positive pressure within the chamber, which tends to force the chamber to fill with hotter air. The resulting hot air blowout can cause other related problems.

Air delivered from the recirculating fan tends to build up at the ends of the supply duct. The middle of the duct is often supplied with less air. Louver adjustment generally involves opening the slots in areas with slower rates of heat-up and closing slots with faster heat-up rates. Many ductwork designs for solution systems target a pressure drop of 1″ (water column) across the louver opening. This equates to an outlet velocity of approximately 4,000-fpm average for the entire opening area. The amperage draw on the recirculation fan motor can reveal much about the airflow path. If the motor is drawing too much amperage, the ductwork is too open, and the dampers or louver adjustments need to be closed some. If the motor is drawing under the rated current, the path is too restricted, limiting the volume of recirculated air. If the fan is controlled by a variable frequency drive (VFD), adjustments can be made to get the most of the power of the recirculation fan motor.

Natural gas-fired furnaces present unique diagnostic problems. The flame relay will not allow the natural gas safety shut-off valve to remain open if certain safety conditions are not met. These safety conditions include:

- Over-temperature condition within the furnace
- High natural gas pressure
- Low natural gas pressure
- Low combustion air pressure
- Absence of flame after the trial for ignition
- Loss of recirculated air flow
- Loss of exhaust flow

Any of these adverse conditions will cause the safety shut-off and the blocking valves to automatically go to the closed position. Check the strength of the flame sensor signal, and check the condition of the lens on ultraviolet detectors. Check the depth and location of flame rods. Check all belts on recirculation, exhaust, and combustion fans. Fan belts need to be checked for tightness at least quarterly. Also, listen for belt squealing, a sure sign of loose fan belts.

Increasing numbers of heat treatable aluminum alloys and the diversity of process parameters required to optimize metallurgical properties have created the need for versatility in aluminum solution heat treatment drop-bottom furnace systems. The broadening need for parts-driven process capabilities has been paralleled with advancements in PC/PLC controls and in adaptations of technologies necessary to achieve the required process versatility.

Salt bath furnaces are often used to solution heat treat aluminum parts. Molten potassium and sodium nitrate/nitrite salts are used as the heat transfer medium. Potassium or sodium chromate salts are often added to the baths to maintain neutrality. Salt-bath furnaces offer the advantages of rapid heat up and short process cycles. However, there are physical and environmental limitations to the use of salt-bath furnaces for heat treating aluminum.

Salt bath furnaces require fast cranes to remove the workload from the salt bath and translate it to the quench tank. This requires three motions: up out of the salt bath furnace, translate over the quench tank, then down to immerse the workload into the quench tank. Because of this complicated movement, monitoring of the quench delay time is important.

Salt bath furnaces are always heated internally. This can be accomplished using natural gas in immersed radiant tubes or directly heated using immersed electric

heating elements. Agitation of the salt bath furnace is usually required to maintain temperature uniformity. However, because of the thermal mass of the molten salt, the temperature uniformity is excellent - usually much better than $\pm 5°F$. Salt bath furnaces are usually best left at a single temperature because of the thermal mass of the salt. If temperature changes are required, long heat-up or cool down periods are required. Figure 28 and Figure 29 show typical salt bath installations for solution heat treating aluminum.

Fluidized bed furnaces are similar in concept to a salt-bath furnace. The motions necessary to quench a furnace load are identical. Heat-up is rapid, and there is little environmental impact. Fluidized bed furnaces include a reservoir filled with a solid heat transfer media such as sand. A gas/air mixture is blown into the sand bed at the bottom by means of a forced air distribution system, which fluidizes the media mass. A pilot burner above the surface of the bed ignites the gas/air mixture. A layer of combustion takes place on top of the fluid bed. The resulting combustion heat is directly absorbed by the sand bed and heats up quickly and evenly due to the constant fluidizing.

Because a fluidized bed behaves as a boiling liquid, the media mass retains a very even temperature throughout the whole reservoir. The operating temperature is adjustable.

For solution heat treatment, the aluminum is lowered into the fluidized bed. The hot media transfers heat into the aluminum very rapidly. The heat transfer coefficient is greatly enhanced by the increased density and viscosity of the heat transfer media. Heat transfer is also more uniform than heat transfer within an air furnace. The operating costs of heating a solid media such as sand must be weighed against the savings from decreased heat-up and cycle times. If the parts being heat-treated are subject to distortion, the rapid heat-up characteristics can shock certain sections; however, generally warping is decreased due to the uniformity of heat transfer around all surfaces of the part.

4.2   Quenching Facilities and Quenchants

Quench tank design is difficult, and not well understood. The fluid used, temperature, flow and parts configuration all interact during the quench cycle. It is very difficult to exactly predict the outcome in the production environment.

Quenching aluminum parts can typically two types: Sheet metal parts and parts up to $\frac{1}{4}''$ thickness, heavy gauge parts which have more than $\frac{1}{4}''$ thick cross sections. The load configuration, the quenchants used for the quench, agitation rate, total load weight and the density of the load on the racks all impact successful design of a quench system.

4.3   Basic Quench Tank Design

The basic quench tank design takes following considerations into account:

- Material selection
- Heat load
- Agitation
- Part Racking and Baskets
- Cooling/Heating

Figure 28 Typical salt-bath installation for solution heat treating small aluminum parts. Note the crane and salt drag-out.

Figure 29   Salt-bath furnace installation for heat treating large aluminum forgings and extrusions. A vapor degreaser is used to clean parts prior to entry into the salt-bath furnace.

- Fluid Maintenance
- Concentration control and separation methods

4.4 Material Selection

Aluminum can be affected by free iron (rust) in the quench bath during the quenching. Surface corrosion is particularly troublesome with sheet metal parts. The corrosion will show up as dark splotches that with closer examination reveal a black spot in the center (iron particle). Free iron is not the only cause for surface corrosion but can be a contributor. Other contributors to surface blemishes or corrosion can be contamination of the parts by oil, cutting fluids and poor material handling before entry to heat treat. This is generally not a problem for castings and forgings, because the surface is generally machined after heat treatment. The main source for the free iron is the tank wall and agitation system if the tank is made from mild steel. Secondary sources can be racks and fixtures. The piping materials used for agitation and pumping can also be a source for iron and rust contamination.

With the above in mind, the tanks for the heavy castings and forgings are normally made from mild steel with stainless baffles, agitators and elevators. The tanks for sheet metal parts are normally made from stainless steel with all internal components made from stainless. Most of the piping will be made from CPVC or stainless for water and hot water quench tanks. For PAG-containing quench tanks, the shell and components can be made from mild steel since these quenchants usually contain a rust inhibitor. The use of a light gage stainless steel insert has also been used successfully in several aerospace companies. This method offers the advantage of inexpensive structural tank construction, with the advantages of corrosion protection provided by the stainless steel insert.

Several coatings on mild steel have been tried over the years with various successes. The most successful is a two component epoxy coating. However, PAG and hot water has a tendency to lift this coating from the metal. This is especially true where mechanical damage has occurred. Coatings are normally used as a cost saving compared to the use of stainless steel. A stainless steel insert is preferred since the cost of replacements and repairs to the coatings will exceed the initial high cost of the stainless steel lining.

The use of PVC and CPVC piping can be used if care is taken to protect the piping from the hot load and direct heat from the open furnace. It must always be remembered that Murphy's Law will ensure that the tank and piping will be exposed to the full heat of the furnace when it is stuck under the furnace during quenching or a hot basket is hung in the furnace.

4.5 Heat load

Per most of the Aluminum specifications, the tank shall be sized so the temperature rise does not exceed $10°F$ for parts processed in accordance with AMS 2750 during quenching. The automotive industry allows a higher temperature rise for castings and forgings; typically, $20°F$. In the following example, the parts are 5000 pounds of Aluminum racked on a 1500 pounds steel rack. The temperature of the water quench is $160°F$. The parts and rack are heated to $1000°F$ in the furnace.

The definition of a BTU (British Thermal Unit) is the amount of heat it takes to heat one pound of water 1°F. The basic formula for finding the amount of water in a quench tank to keep the temperature rise at 10°F is shown below.

$$G = \frac{\Delta H_{parts}}{\Delta T}$$

where ΔH_{parts} is the heat given up by the parts (and rack) during quenching from the solution heat treating temperature, (BTU) and ΔT is the allowed temperature rise (°F). In this instance, the allowable temperature rise is 10°F.

In this example, the parts are at 1000°F hot at the start of the quench and is quenched in 160°F water. The BTU's given to the water is shown below.

Heat load calculation:

Aluminum:	(Start temp-End temp) × specific heat × load weight	= BTU
Steel	(Start temp-End temp) × specific heat × load weight	= BTU
	Total	

Example:

Aluminum:	(1000–160) × .22 × 5000	= 924,000 BTU
Steel	(1000–160) × .15 × 1500	= 189,000 BTU
	Total	1,113,000 BTU

The water volume will now be calculated by dividing the total BTU's with the allowed temperature rise.

Water volume in gallons:
$$\frac{\text{Total BTU}}{\text{Temperature rise} \times 8.34 \text{ pounds}} = \text{Gallons}$$

Example:
$$\frac{1,113,000}{10 \times 8.34 \text{ pounds}} = 13,345 \text{ Gallons}$$

As shown in the example the tank volume must be a minimum of 13,345 gallons of water to ensure that the quench temperature does not rise more than the specified 10°F. Standard practices do not include the heat requirement for heating the tank shell and other components that get in direct contact with the quench. This provides an additional safety factor for temperature rise.

This calculation should always be done to determine the minimum volume of the tank. In addition to the volume, the size of the tank must also accommodate the parts and rack being processed. Sufficient clearance is needed for the instrumentation, agitation and for the maintenance access to components. The next step in the process is to consider the required agitation rate for the type of product processed in the quench facility.

4.5 Agitation design and considerations

Agitation and design of agitation systems has been covered in the literature [105] [10]. Agitation design has over time been specified as changeovers of tank volumes (Gallons per hour), description of surface movement (Babbling brook) or measured flow past the parts in feet/sec. The best way to specify the quench flow is a calculated or measured flow past the parts. The maximum flow that should be specified for aluminum batch quenching with water or PAG (Poly Alkylene Glycol) is in the area of .8–1.2 feet/sec past the parts. Higher flow will not add to the cooling of the parts unless spray quenching is used. However, this amount of quench fluid might be impossible to move. It will in some cases mean the complete tank volume must be changed over every 1–3 minutes. This is not practical in large tanks. Many tanks are successfully producing heavy gage parts with measured flows in the area of 0.25–0.4 feet/sec.

The main difference between sheet metal quenching and the heavy gauge load is the fact that sheet metal will normally be cooled by the time the parts reaches the bottom of the quench bath. The hoist or elevator provides the main means of agitation for the cooling cycle, while the agitator system only need to provide proper mixing and uniformity of the tank before and during the quench. Figure 30 illustrates the different travel distances obtained at different hoist speeds. As a general rule for sheet metal parts, the hoist speed should be as slow as possible to avoid high hydraulic forces on the soft metal. The quench must still be completed within the allowable quench delay for the type of metal and furnace used. The slower speed will reduce distortion of the part. To accommodate this the travel distance from furnace to quench must be as short as possible. New drop bottom furnaces with moveable quench carts are superior designs compared to older pit type drop bottoms in this regard.

Travel 1 ft/sec

Travel at 5 ft/sec

Bath 80⁰F
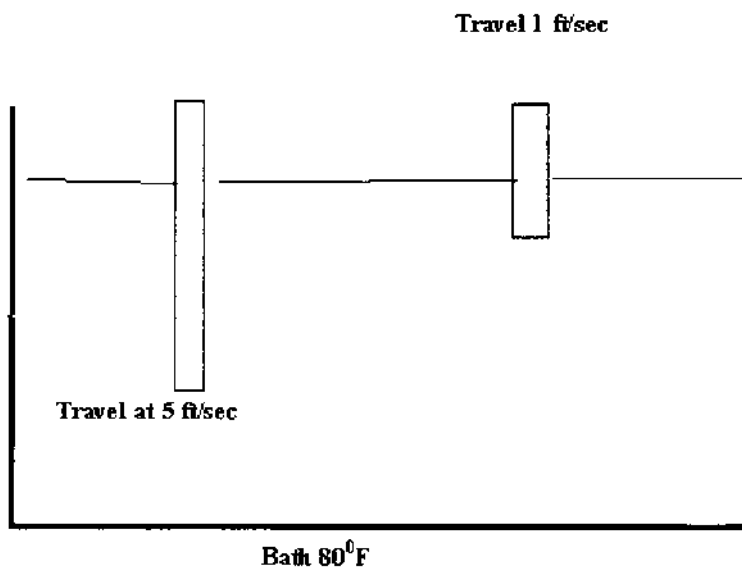
Figure 30 Schematic illustrating the effect of different hoist speeds during quenching.

Modern technology and computer simulation has allowed designers and process engineers to design quench systems without expensive trial and error type approaches. The best flow possible around a part is a linear flow with enough turbulence to get into the nooks and crannies of the part to break up the vapor layer and provide the required cooling. Racking methods and flow design must accommodate this. The bottom to top flow is preferred since it will utilize the mechanical agitation from the agitator and the agitation from steam formation and thus increase the total flow around the parts. The use of finite element analyses gives the designer a good tool to start with. The tools available are mechanical tank modeling and Computational Fluid Dynamics (CFD).

4.7 Mechanical tank modeling

The use of mechanical tank modeling can give very good direction for how to design an agitation system. The simulation of loads and flows will be able to solve almost any questions related to the quench tank. However, the design and building of the models are time consuming and expensive. Secondly, scaling-up the model to the finished tanks size and product might not be a straightforward process. An illustration of mechanical tank simulation is shown in Figure 31.
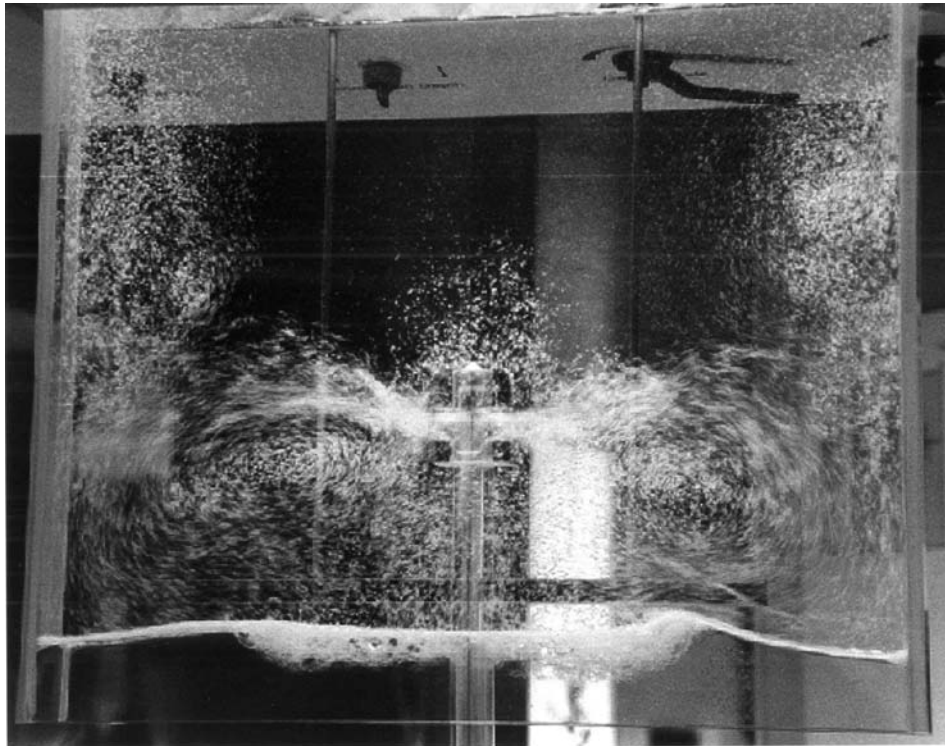
Figure 31 Tank used for flow modeling of a proposed quench tank.
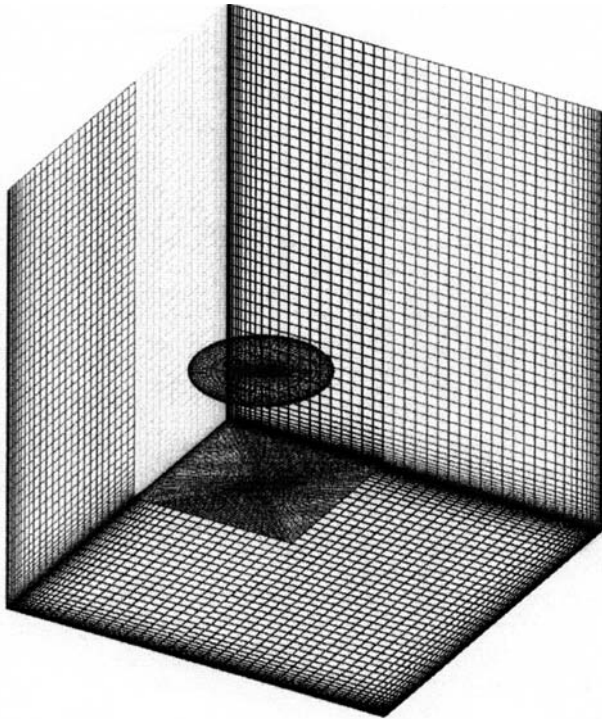
Figure 32 Illustration of boundary conditions used for finite element modeling of flow.

4.8 Finite Element Analyses

The use of computer modeling for quench tank and furnace design has used to verify and predict the mechanical design and process variables. As the capability and sophistication of new computer hardware and software improves, it is very easy to calculate and visualize the fluid flow process. Typically, the whole tank or a section of the tank is modeled as shown in Figure 32. The dotted line shown in Figure 32 depicts the model area used in the program. The velocity vector diagram shows different areas of the tank with different flow. This diagram is shown in Figure 33.

With the initial modeling completed, it is possible to review and change parameters and then observe the calculated results. As shown in Figure 33, it appears that a low flow area exists towards the center of the tank on the bottom. This low flow area had caused several large machined parts to be "soft" after final precipitation hardening due to inadequate quench cooling of the part. The next step was to model different methods of generating more flow in the area where the parts were placed during the quench. Eductors and flow directors were used in addition to inserting a baffle wall to direct the fluid more up through the parts (Figure 34). When dealing with quenchants it must be noted that direct high velocity impingement of the fluid against the part must be avoided to ensure that spot cooling does not occur. Spot cooling can cause severe distortion and uneven properties in the finished product.
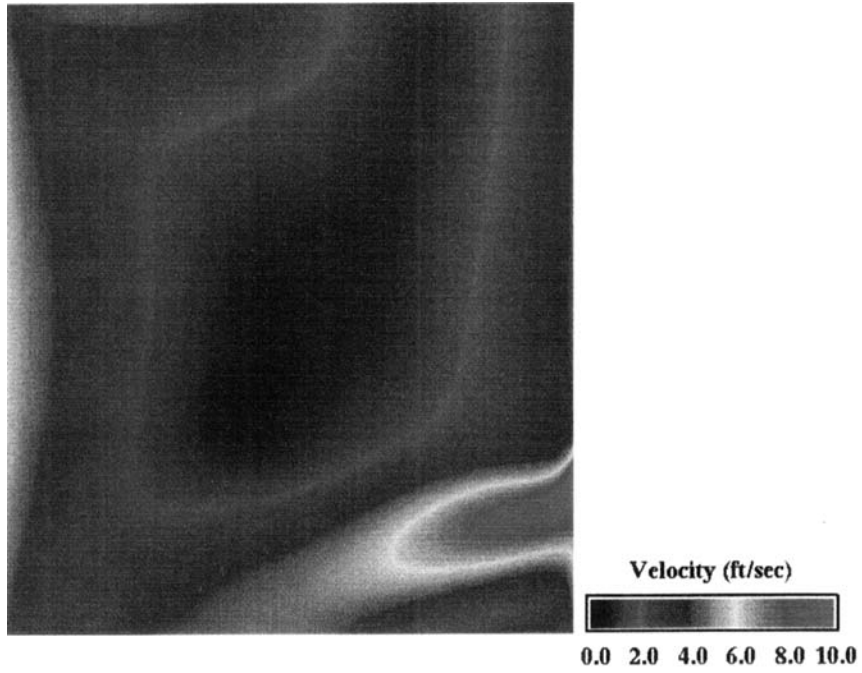
Figure 33 Resultant Computational Fluid Dynamics (CFD) model showing velocity vectors of a quench tank with a single impeller in the corner of the tank.
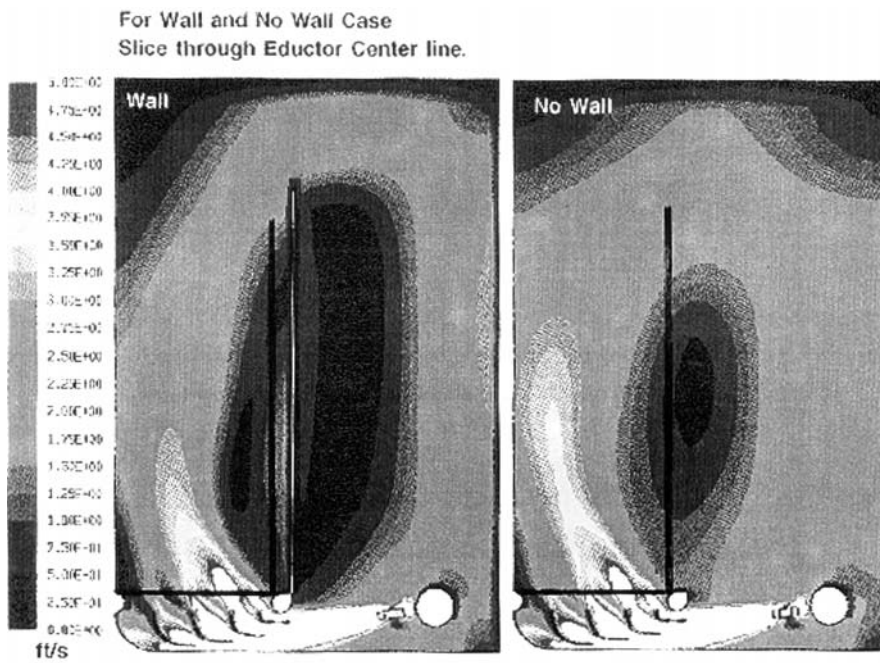
Figure 34 CFD model of two different configurations of a quench tank using an eductor.
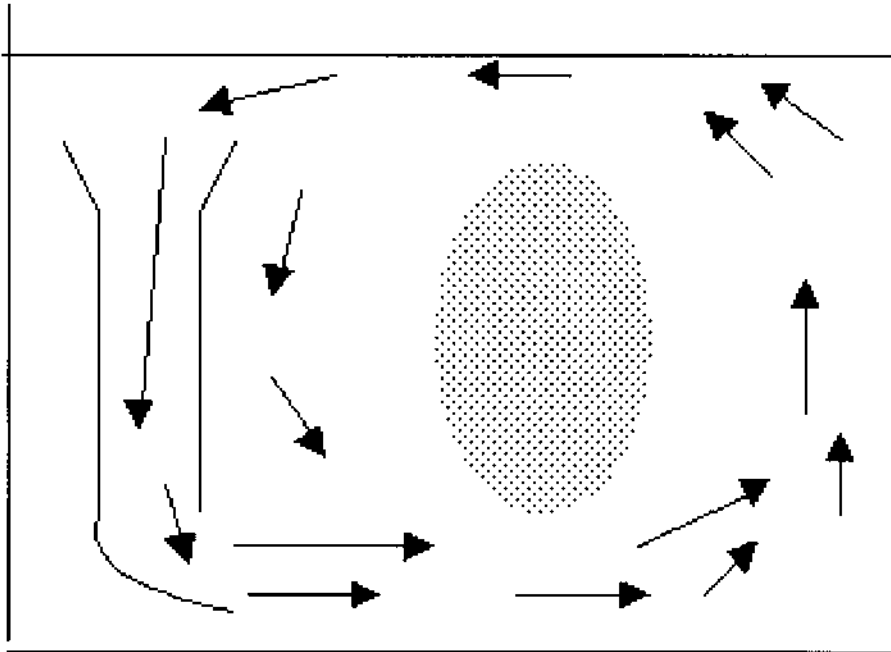
Figure 35 Schematic showing probable flow pattern for a single draft-type tube, with quiet region in the center of the tank.

Flow modeling is a powerful and versatile tool enabling the designer and process engineer to make decisions necessary to design a good quench system. When the modeling is completed, a tank can be built and will most likely produce good quality parts.

The testing and modeling shows that tanks typically has high and low flow areas in the patterns shown on Figure 35, Figure 36, and Figure 37. Flow can be generated from one side, center or both sides and the corresponding flows and low flow areas are shown on Figure 35 through Figure 37. The shaded areas indicate low flow conditions and these areas are natural to the flow conditions. It is very difficult to change this without significant additions for pumping and flow devices. These devices will normally not improve the quench quality significantly to justify the expenditure of modifying the equipment. It is advised to move the parts and rack to areas where the natural flow help improve the flow instead of hindering the quenchants flow around the parts. This is illustrated in Figure 38 where the basket is placed in the highest flow area. The addition of perforated plates and flow vanes can help direct the quenchants [105].

4.9 Parts testing

Parts testing are typically used when existing equipment is used for new products or for improvements of product processes. A proper test plan must be developed that addresses the areas that can affect the part. Placement of the part in the tank,
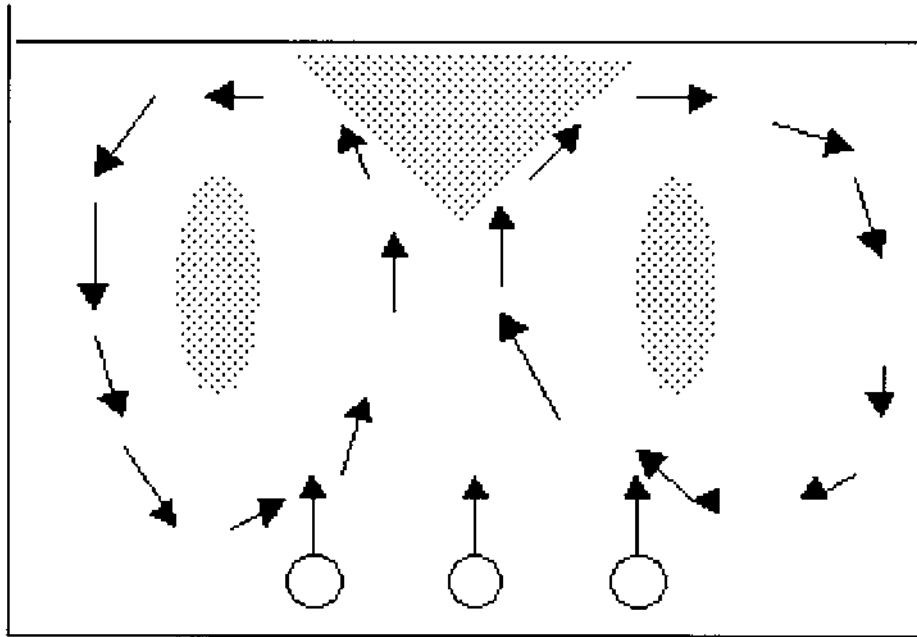
Figure 36 Low flow areas with three draft-tubes.
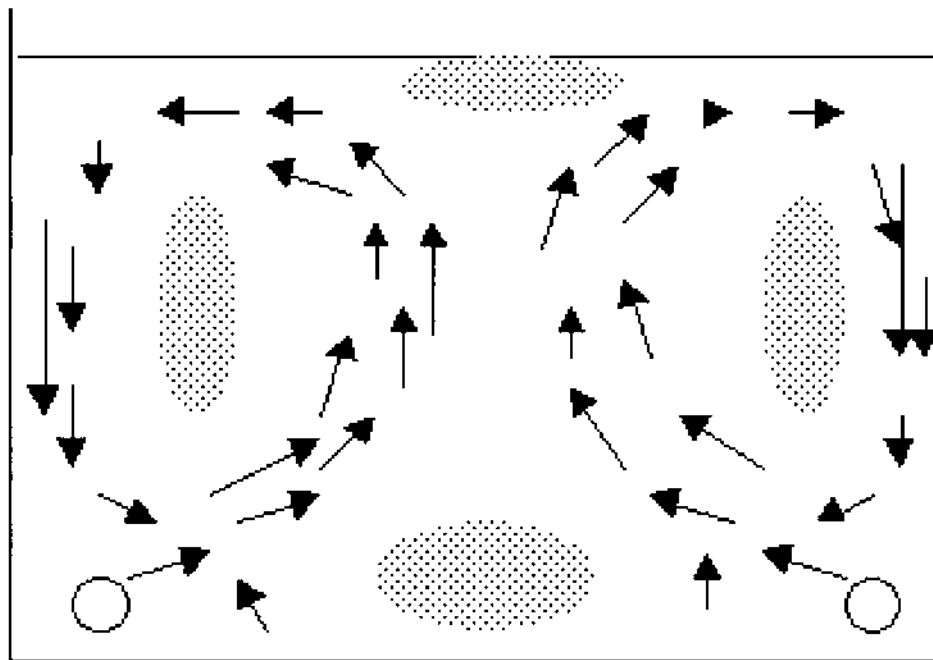
Figure 37 Low flow regions with two draft tubes in different locations.
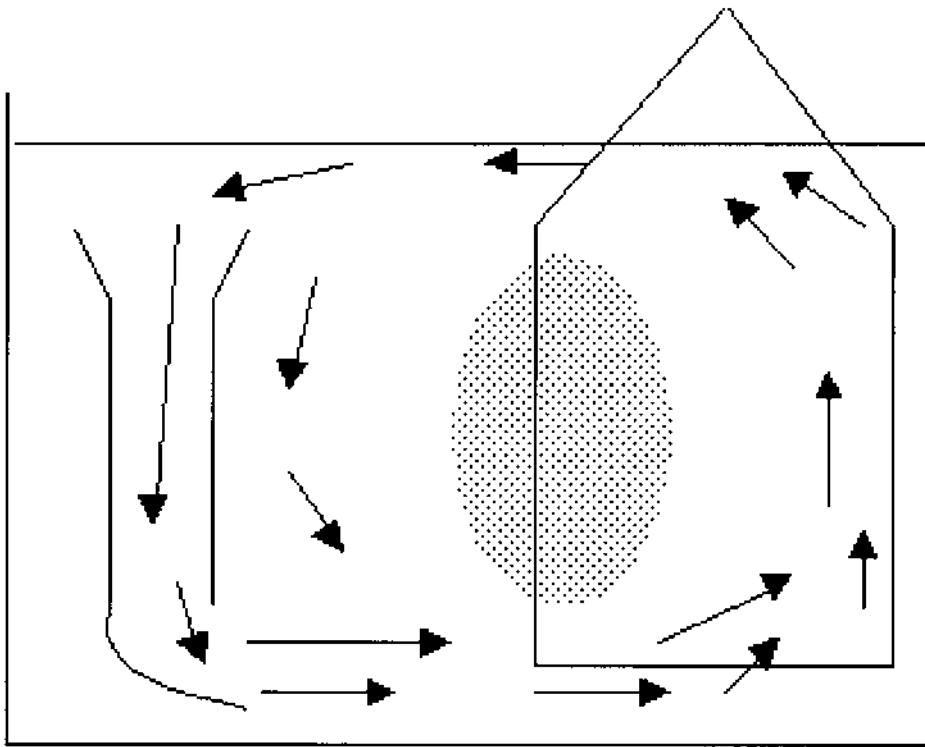
Figure 38   Effect of flow and location of load basket for the best location of quenching.

orientation of the part in the tank and areas of high and low flow in the tank. It is very important to find out where the flow is in the tank by mapping it with a flow meter. An open type flow meter is preferred compared to a closed type flow meter as shown in Figure 39.

The measurements of the flow will normally be taken without parts in the tank. When the parts displace space and volume in the tank the speed of the quench around the parts goes up. In addition to this, the thermal action of the rising heated quench from the contact with the parts will add to the velocity of the quench past the parts. With this in mind it is understandable that tanks with less than desired flows empty as described in this chapter can in fact produce satisfactory parts.

4.10   Flow Generation

Flow is generated utilizing several methods. Pumping and the use of different types of propeller agitation provide the most common method. Part or basket movement is used on rare occasions. It is important to realize that quench agitation is different than mixing of chemicals. Heat-treat facilities are specifically looking for the linear flow with some turbulence past the part that gives the best and most efficient cooling of the part in a predictable manner across the whole section of the product rack or part each time a quench is performed.
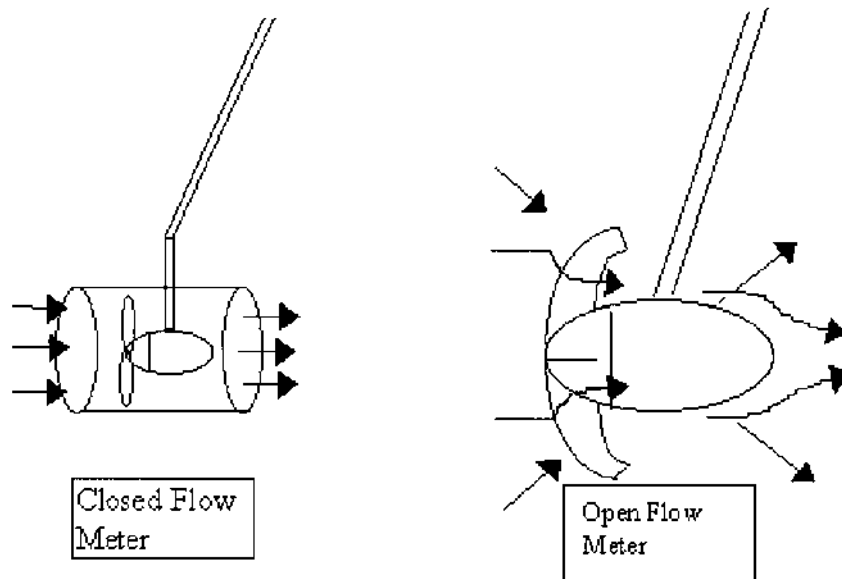
Figure 39   Two different types of flow measurement devices.

4.11   Pumping Agitation

Pumping is versatile and does not take up much space in the tank since sparger pipes; eductors and nozzles can be tucked close to the sidewall or bottom of the tank. Pumping has a low efficiency per gallon of quench moved compared to other types of agitation devices especially draft tube designs. The use of an eductor can significantly increase the amount of quench moved inside the tank. The volume goes up by a factor of four and the velocity goes down with the same factor. However, the overall flow generated will be sufficient to make a good quench. Figure 40 shows a schematic of an eductor and the generated flows. Compared to nozzles the eductor provides a better distributing of the flow and does not generate point cooling of parts by hitting the part with a very high velocity of fluid at a concentrated spot.

4.12   Propeller Agitation

Propeller agitation is divided between open placement and agitation tube placement. In addition there are marine type propellers and airfoil type propellers used for agitation purposes. The following will describe the different steps required to decide which system will work the best. The open type propellers are most commonly used in side mounted systems for example integral quench furnace. These propellers are typically marine type propellers. Marine type propellers are slow spinning compared to airfoil type propellers. The swirling action of the quench when it leaves the propeller tips generates a good non-linear flow. However, the flow is very uneven and can affect properties in the parts. The horsepower requirements are large compared to airfoil type systems, however it is less than pumping. Table 27 shows a comparison of the required horsepower (energy) between pumping and draft-tubes.
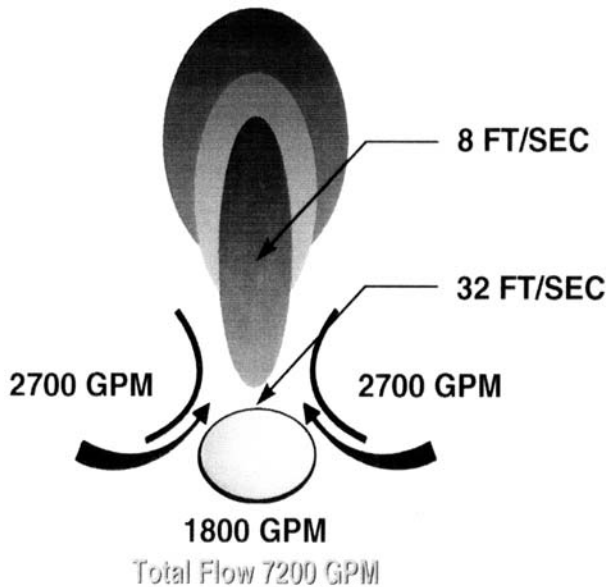
Figure 40   Schematic of an eductor.

Table 27   Comparison Between Airfoil-Type Draft-Tubes and Pumping Horsepower for Different Volumes of Water

Propeller Agitators				Pump Agitators		
Propeller type	HP	RPM	GPM	Pump	PSI	HP
13.5″ airfoil	5.5	810	5600	End suction	20	75.5
13.5″ airfoil	2.0	520	3200	End suction	20	42.6
13.5″ airfoil	1.0	426	2950	End suction	20	39.0

The draft-tube is widely used in the larger open tank systems. The draft tube consists of a propeller (airfoil or marine type) placed inside a tube. The placement of the propeller inside the tube increases the efficiency of the prop in addition to giving the designer the ability to direct the quench flow in a more controlled and predictable manner. Figure 41 shows typical placements of agitation tubes in square tanks. The draft tube design has been covered in detail [106]. Figure 42 shows a typical schematic for a draft tube. The distance from the water to the edge of the flared tube, entrance must be big enough to prevent air from being pulled down into the tube and thus creating bubbles in the quench. The bubbles can create an insulating layer on the parts and must be avoided in the quench tank. Several methods are available to prevent the vortex from being started. One way is to place a flat plate 2 inches under the surface and force the water to enter the agitator in a more horizontal manner. This will create a slight restriction in the inlet but normally this will not reduce the volume significantly. The other method is to place the propeller and the flared cone deep enough to prevent the inlet vortex from
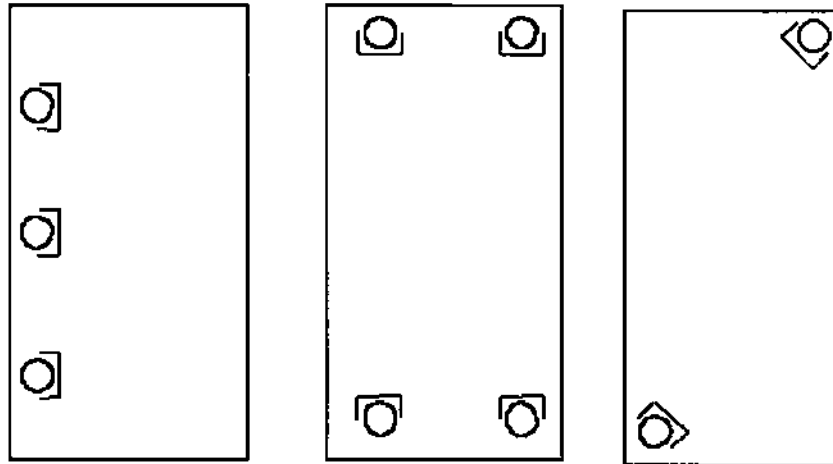
Figure 41 Typical locations of agitation tubes in rectangular tanks.
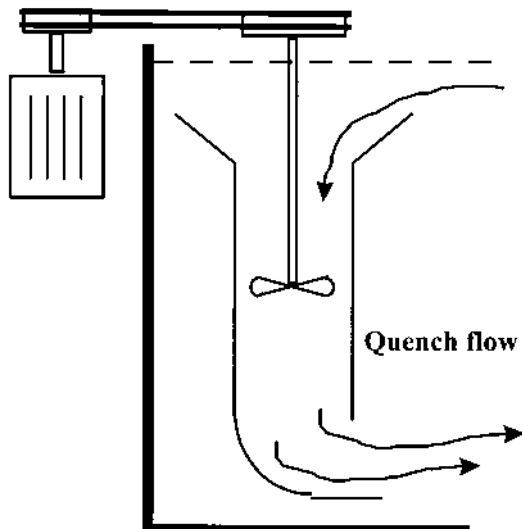
Figure 42 Typical schematic for a draft-tube type agitator.

forming. Flow modeling and field measurements [106] proved that additional flow of up to 20% could be generated in the tank. Placing parts baskets in the maximum natural flow area and using the proper method for generating the flow will ensure the best quenching possible.

For example, a 15,000 Gallon quench tank was agitated by three large side mounted marine type propellers. The quench area for the parts was in the top 16″ ′ of the tank since parts were quenched one at a time every 20–30 seconds. The flow

Figure 43 Flow in a large 15,000 gallon quench tank, agitated by three large side mounted marine propellers.

was very strong but uneven as shown on Figure 43. Several methods were used to solve the problem. Baffling and flow direction vanes did very little to even the flow out. The final fix was to install a perforated plate under the parts. The perforated plate/plenum created a very even and desirable flow. Figure 44 shows the surface of the tank after the installation of the plenum and a 2″ "crown" can be seen in the middle of the tank where the quench is forced up and then returns to each side of the tank. The use of perforated plenums in conjunction with tube or open type agitators is very successful in generating controlled even flows.

The configuration of the rack must not restrict the airflow during the heat treat or the quench flow to the parts during quenching. The racks should be designed and
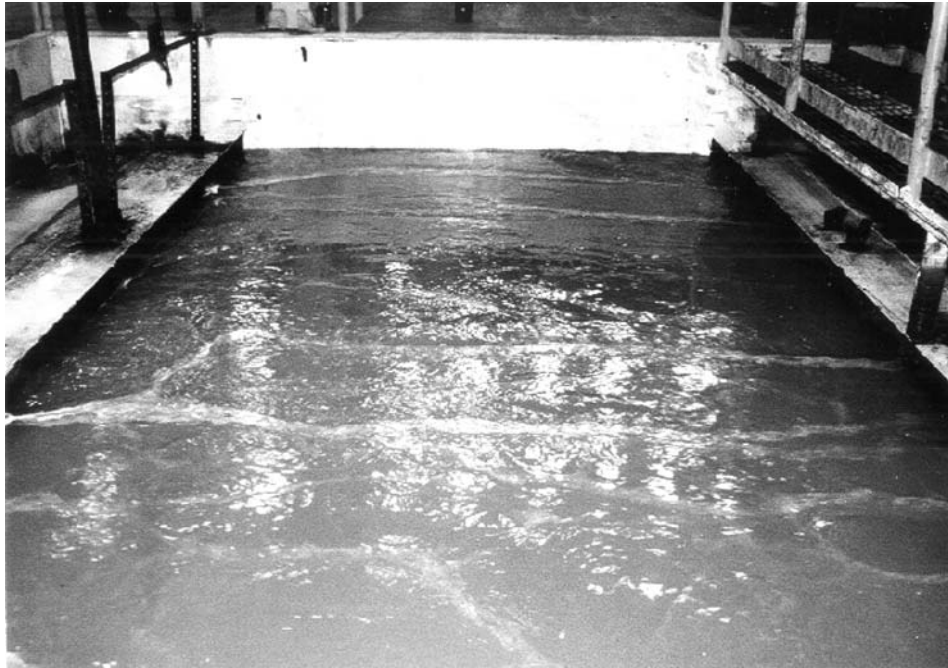
Figure 44 Flow of 15,000 gallon tank after modifications to quench system. These modifications included baffling, and the addition of a perforated plate underneath the load basket.

constructed with the rack weight as low as possible compared to the parts. The continuous heating and cooling of the fixtures/rack is a waste of energy and causes the requirement for additional cooling capacity for removing the heat from the quenchant.

The rack must be fabricated of materials that can endure the repeated heating and cooling cycles without any detrimental effect on the rack. (Distortion or cracking.) The racks must be pinned and bolted together to allow the rack to expand and contract without restriction during the heating and cooling. Welding must be eliminated as much as possible since they have a high tendency to crack. The use of tubing especially 4130 steel tubing has been very successful throughout the aluminum aerospace industry with racks that heat to maximum 1050°F. These production racks have thousands of cycles without any repairs or distortion. For temperatures above 1050°F other material is required. The round tube or rod shape is preferred to structural shapes like I beams or C channels. I beams and C channels will cool not cool evenly during the quench and distort severely after a few quenches

The load configuration is probably the most important aspect of heat-treating any parts. The load must be configured to allow the air to heat the parts during the heat cycle and the parts must be spaced so the quench has access to all surfaces and can remove the heat quickly during the quench cycle. There is a tendency to pack same size and configured parts tightly on the racks and this can have very detrimental effect on the process. The tightly packed parts can have significant dif-
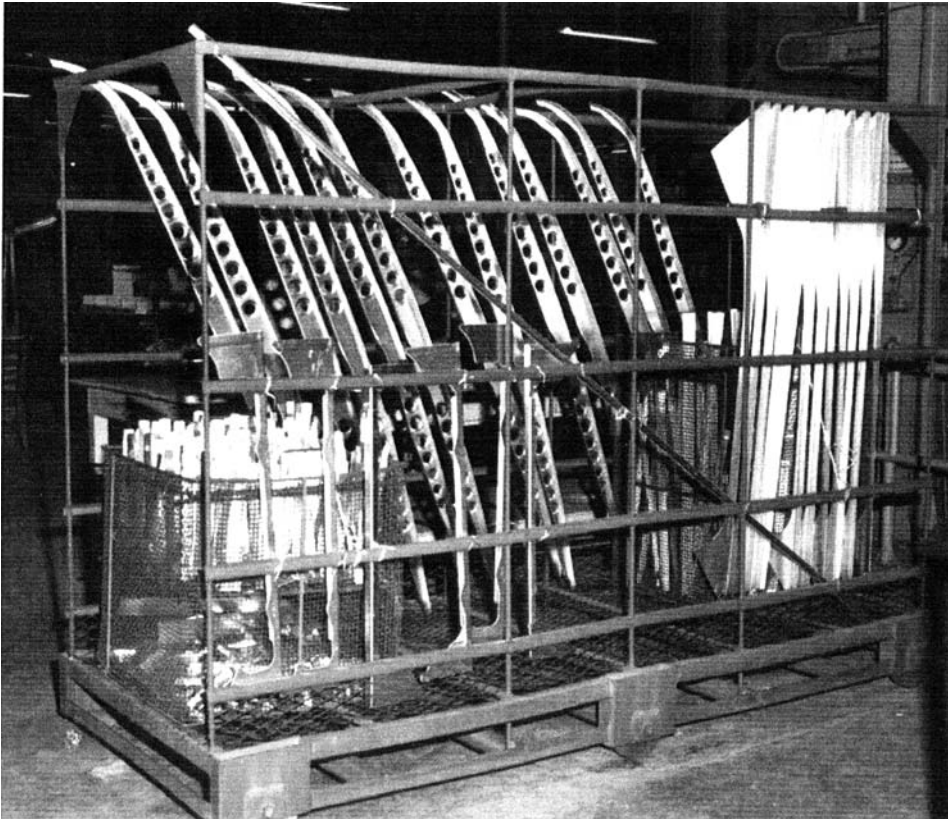
Figure 45 An example of good racking practice allowing adequate space between parts and racked for minimum distortion during quenching.

ferent properties after heat treat than the same parts spaced properly on the fixture. This in fact ties back to the problem with tank modeling and parts testing for design of quench tanks. If single parts or small load are used for this testing, the results can be different than the actual production loads.

The rule of thumb is that there must be a minimum of 1 inch plus the thickest part of the material between each part to achieve good heat transfer. An example of good racking practice is shown in Figure 45.

Care must be taken when racking the parts. As show in Figure 46 it can significantly change the process when different approaches is used for hanging the same part. The main concern in the example shown in Figure 46 is the fact that the steel rod has a different cool down rate than the aluminum and the part might have a "soft" spot where the rod is in contact with the part due to slow cooling and slow heat up during the solution heat treat cycle. The rod is preventing proper access and cooling for the quench. The use of thin wall tubing/pipe for hanging the parts is preferred compared to solid rod.

The size of the rod or tube supporting the part is important. Since the aluminum part at solution heat treating temperatures is weak and very plastic,

Minimum distance =1" +Material gage
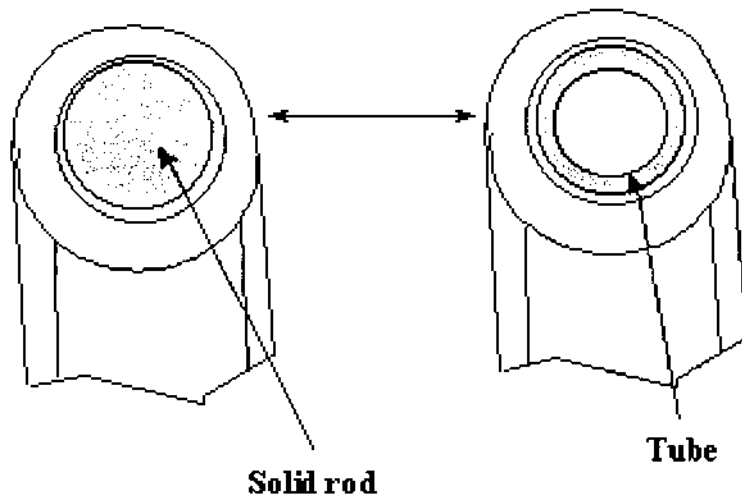
Figure 46 Schematic representation of the use of tubing for par support.

deformation can occur from the support. This is shown in Figure 47. In this instance, a small tube was used to support the part through a hole. However, because the weight of the part, the hole deformed, matching the radius of the rod. The use of a larger diameter tube spread the weight of the part over a greater area, reducing the apparent deformation.

The quench tank must be equipped with a mean of heating if the tank is used for hot water quenching. The heating can be done with steam, natural gas or electric. The most commonly used heating media is a submerged burner tube fired by natural gas or electric heating elements submerged directly in the tank. Flow through electric heaters are also used. A heat up time of 6–8 hours is normally used. During production, the parts that are quenched provide the heat. The control for the heating is generally an on/off system. There are no requirements for PID control due to the very slow response time on the tanks. Agitation is usually interlocked with the heaters to ensure that there is good flow across the heaters and temperature uniformity is achieved in the tank during the heat-up.

For temperatures above 160°F, the quench tanks and piping must be insulated or guarded to protect personnel. In addition, the insulation will cut down on the heat losses during slow production and weekends and in that way save energy for heating the quench. Some areas of the country have very hard water and calcium deposits on heating elements can cause damage.

The cooling of the tanks is done by the use of heat exchangers or chiller. The heat exchangers can be water/water or water/air. Water air exchangers are placed either inside or outside of the buildings. For exchangers placed outside provisions shall be made for freeze protection in the winter and if located inside it is recommended to duct the exhaust to the outside to prevent and significant heat load

Figure 47 Deformation around a hole caused by the use of a small diameter rod for support duriong solution heat treatment.

being added to the factory. Figure 48 shows a typical schematic for a cooling loop on a quench tank.

The sizing of the cooling systems will depend on how fast the tank is required to recover to the start temperature. To find the required size of the cooling system, the removed BTU per hour must be divided by 12000 to obtain the size of the refrigeration system (in tons).

As an example, it was previously determined that the parts transfer 1,113,000 BTU to the water during quenching. If the system is quenching every two hours, the heat load must be removed in two hours. This would indicate that 46.4 tons of cooling capacity are required (1,113,000 BTU/2 hours/12,000 BTU per Ton = 46.4).

Air to air heat exchangers, swamp coolers and cooling towers must be sized according to the geographical area of the equipment, and the desired quench temperature. A 120°F quench temperature cooled with an air-to-air heat exchanger or swamp cooler in Galveston Texas will not provide sufficient cooling during the summer time. The same system placed in Seattle or Denver will have a much better chance of working properly all year round.

The cleanliness of the quench is an important factor in the quench system. A dirty contaminated quench bath can have significantly different quench qualities and cooling capabilities than a clean bath. Contamination can be categorized as particle contamination, chemical contamination and biological contamination.

Particle contamination can come from several sources, tank and rack scale, sand and dirt from the factory environment or from the manufacturing of the part

Exhaust if heat exchanger is placed
inside building.

Flow
switch

Air heat exchanger

A filter can be installed before the heat
exchanger if the environment requires.

Quench solution from quench tank

Cooled quench solution to quench tank
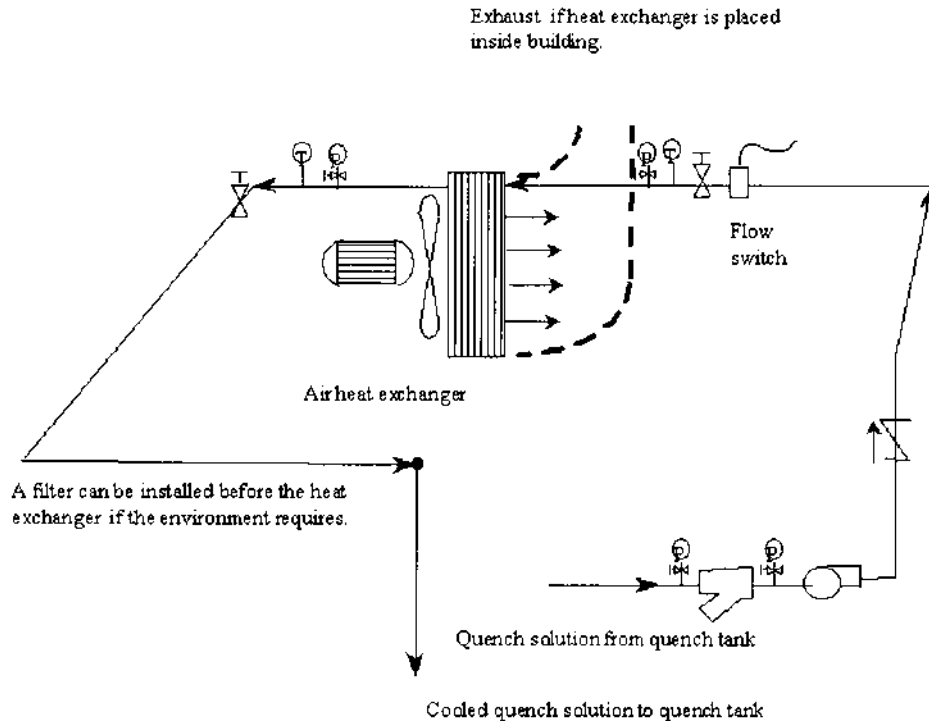
Figure 48 Typical schematic for a quench tank cooling loop.

itself. Casting and forgings often produce contamination to the quench tank. One of
the release agents used in the forging process is graphite. The graphite adheres to the
parts and is removed during quenching. Sand casting may entrain sand from the
casting process. Filters are employed to remove dirt from the tank to maintain a
reasonable clean quench. The filters must be sized to allow for maintenance. If they
are too small, the changing/cleaning will be to big a burden and if they are too big,
the equipment cost will be excessive. It is important to get a good picture of the
dirt loading in the tank before the design is decided for the filtering system. Bag
filters or cartridge filters are the most common used filter types. Typically, the filter
sizes are in the 5–10 micron range. For sand removal, centrifuge type filters is used
and conveyor systems for the heavier loading.

   The use of PAG has added some additional requirements to the heat-treat
operation. The PAG quenchants consists of polymers and several different additives.
The polymer molecule does not change much during the life of the bath, which can be
several years in a properly maintained system. However, some of the components
can disappear over time. The corrosion inhibitor (Sodium Nitrate) can be diluted
and removed with some concentration methods and the pH level can change.
Low pH levels can damage parts by an etching effect. The supplier of the polymers
will be able to assist in testing and replenishments of the chemicals as needed to
maintain the bath. This service will with the larger suppliers be part of the contract
for delivering the quenchant. Any changes that are not detected can be detrimental

to the performance of the quench system. The heat-treating facility must implement a regimented quality assurance program that will detect problems in the quench before they become detrimental to the process.

Aqueous solutions will experience bacteria and algae growth if there are no biocides present. Bacteria growth can cause corrosion of parts (MIC, Micro Induced Corrosion) and can detrimentally affect membranes used for separation in reclamation systems. The bacteria can also reduce the sodium nitrate in the bath if they are anhydrous bacteria. Algae will coat the insides of the tanks and piping and will result in incorrect concentration data. Biocides are used with various successes to control the problem. Biocides with Glutealdehyde are the most commonly used. They last from 10-21 days in the bath and must be replenished periodically to remain effective. The amount varies according to contamination levels however, 150–250 parts per million (ppm) will normally be added every two weeks and can keep the bath in complete control. It is highly recommended to use an automatic injection system to limit the workers exposure to the very toxic materials used in the biocides. Figure 49 and Figure 50 show typical injection systems.) Shop test procedures that check for bacteria and fungi will tell the operators of the need to treat the bath. Small paddle sticks such as those shown in Figure 51 are used for this testing with satisfactory results. An occasional change of biocide will keep the bacteria from becoming resistant to the product.

Concentration measurements for the PAG quench systems are accomplished using densitometers, refractometers, and viscosity meters. The concentration of the polymer in the quench bath is one of the most significant influences on the finished product. The cleanliness of the bath directly influences the accuracy of the
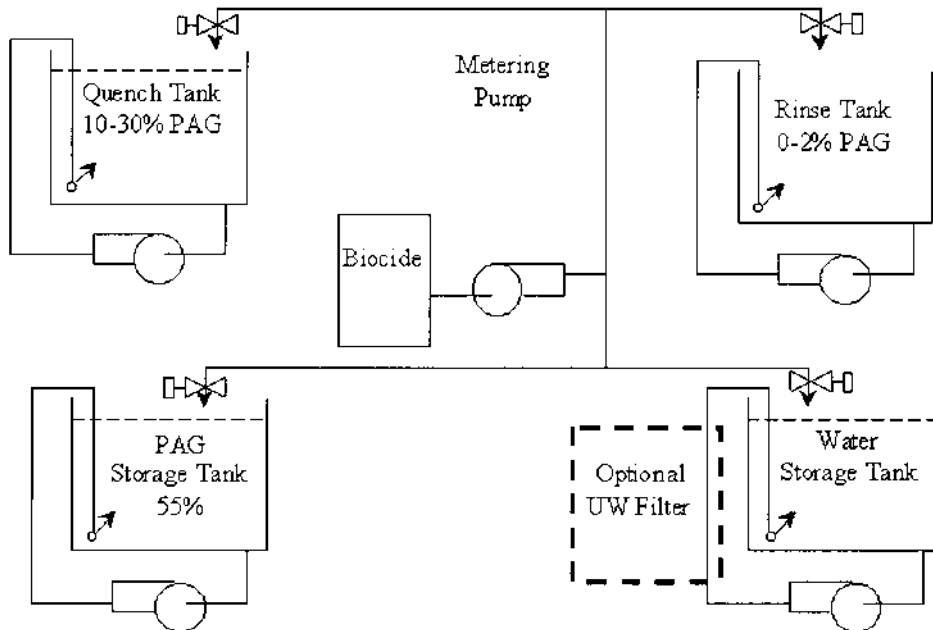
Figure 49   Biocide injection schematic.

Figure 50 Biocide injection tank with distribution manifold. The metering pumps are not shown on the picture.

measurements. Several of the instruments require frequent calibration, which adds to the maintenance burden in the factory. The electronic refractive index monitor with remote sensing and optional connection to a PLC has proven to be very stable if the solution is conditioned and filtered. The accuracy levels are within ±0.5% over time with only very limited maintenance requirements.

With the use of PLC and operator interfaces, concentration changes tailored to the product can be carried out accurately and quickly. The use of fully automatic systems has proven somewhat impractical since troubleshooting becomes difficult. For example, the status of the filling and draining operations are hard to monitor. Startup and commissioning of fully automatic systems are longer and more expensive compared to semiautomatic systems where an operator initiates each. When the operator initiates each phase the system has proven more robust and less troublesome.

The cost of PAG is about $10–$15 a gallon. With the development of fully closed loop systems with variable concentration control and conditioning, the costs of PAG replacement have drastically decreased in comparison to previous practice when rinse water was flushed to a drain causing drag-out from the quench tank
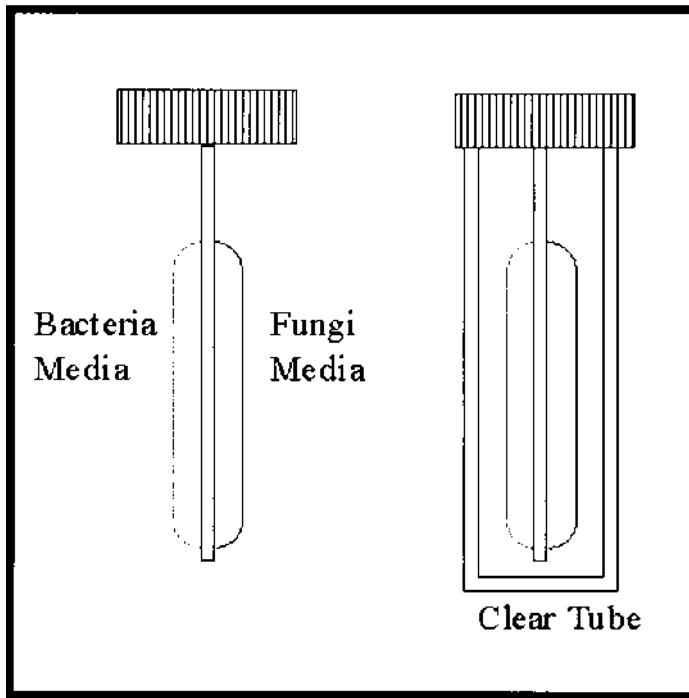
Figure 51   Typical test paddle for quenchants and aqueous cutting fluids.

to be lost. The typical drag out from a 20% PAG solution Type 1 (For example Aqua Quench 260, 251 and 365) is in the range of .001 to .0015 ounces per square inch of material. The capital cost of installing these systems must be compared to the savings in PAG replacement cost. The reduction of fire hazards and environmental concerns in conjunction with the quench process are also items to be considered. Wastewater reduction is also a major factor especially in areas where water is a treasured commodity.

There are two (2) ways of separating PAG from the water: heat separation; and membrane separation.

The oldest and possible most common used separation methods is done by heating a tank, as illustrated in Figure 52, to about 165–185°F. The PAG will settle out to the bottom unless there are considerable amounts of salt present in which case it settles to the top. The water is then siphoned off and a new batch can be mixed.

Membrane separation utilizes a micro-filtration unit to effect separation of the polymer quenchant from water. Essentially, because of the differences in size between the quenchants and water, micro-filtration can be readily accomplished. Figure 53 illustrates a typical closed loop quench system with RO separation. In this method the PAG is separated from the water using membranes that allow the water to pass but reject PAG and salt which stay on the process side of the membranes. The water (Permeate) is stored in a water tank for later use or sent to drain. This technology does not work well in conjunction with salt baths or steel heat treat since the salt concentration in the PAG will increase during the concen-
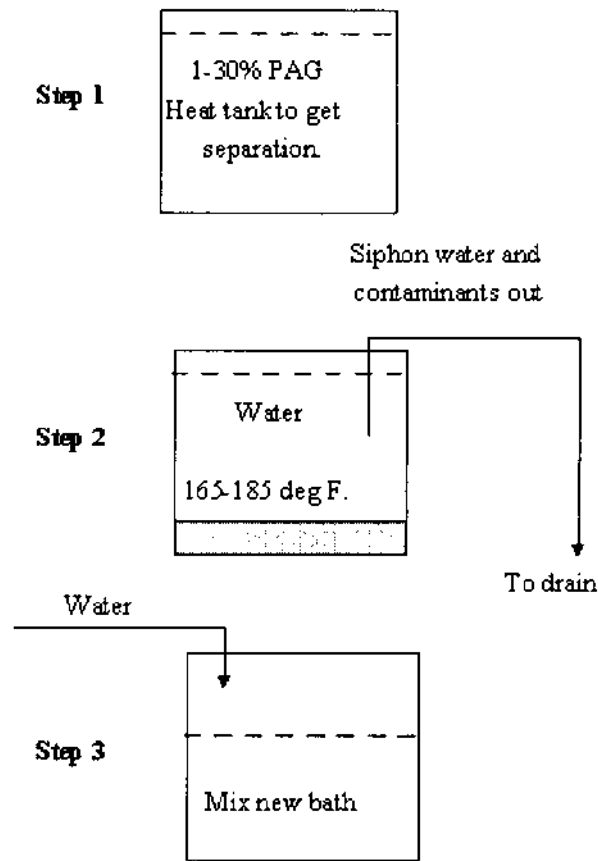
Figure 52 The three steps necessary for re-concentrating PAG by batch heat separation.

tration cycle. Salt is not desired in the quench bath since it can cause corrosion on the parts and significantly change the quenchants-cooling curve. Steel scale and free iron will damage the membranes and must be removed from the solution before it reaches the RO machine.

A new method has been developed and implemented that uses the heat separation. The first design work was done in 1995 and laboratory testing by the author was completed in 1996. Four commercially production systems are currently installed at four different locations in the aerospace industry. These systems were installed in 1998/1999. Figure 54 shows the schematic for this system. Note that the process tank is optional compared to the RO system shown in Figure 53. The heat separation method does not utilize membranes and is not sensitive to salt or iron in the bath. Production testing concentrated a 1% PAG solution into a 60% solution and clean water in one pass at a rate of 1 gallon per minute. Other concentrations included 22% PAG where the recovery rate also generated up to 60% PAG on the product side of the stream and clean water on the other side. The system is very compact, robust and less costly than RO separation. The built-in
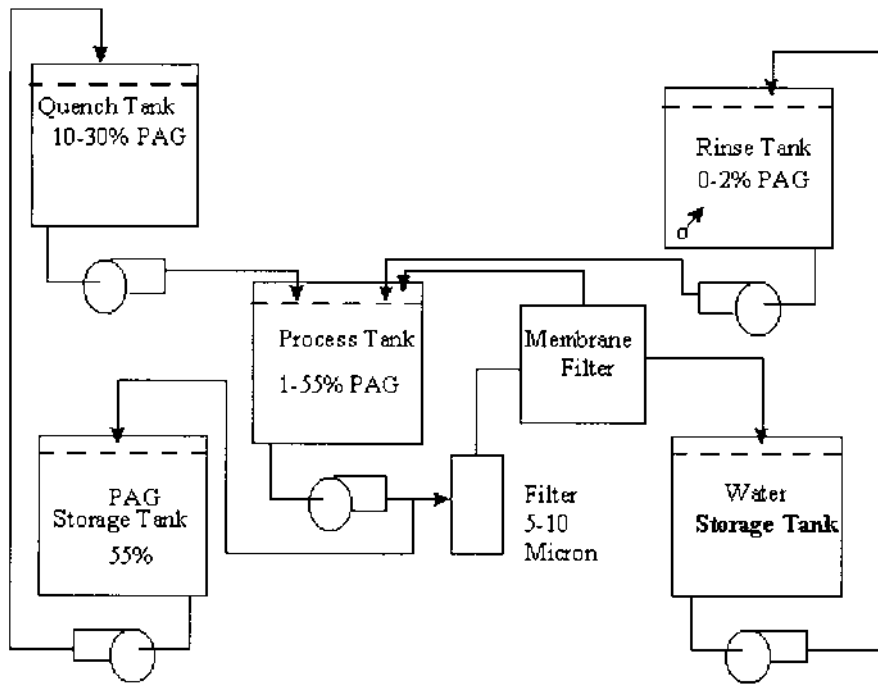
Figure 53 Membrane filter system schematic.
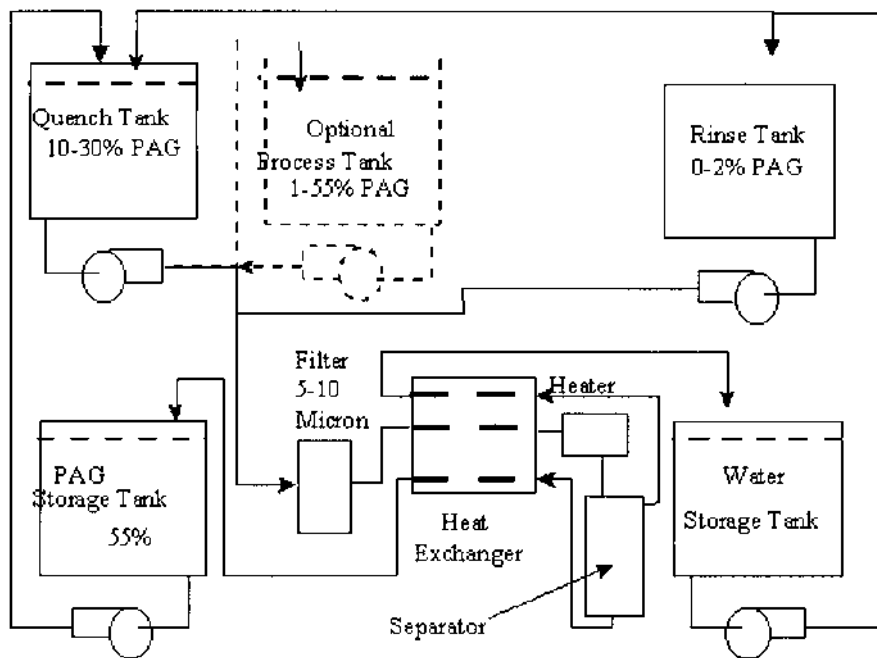
Figure 54 Schematic of flow through heat separation system with heat recovery.

heat recovery by using heat exchangers cut energy cost by up to 50% for re-concentration/reclamation compared to RO or standard heat separation methods. Additional development is in progress to make the system more affordable to the general heat-treat industry.

5 QUALITY CONTROL AND QUALITY ASSURANCE

Heat-treating is critical to the performance of many aluminum parts. Nearly all aerospace aluminum components are heat treated, as well as many automotive components. Failure to properly heat-treat a part could have catastrophic consequences in terms of life, property and liability. Therefore it is critical that the heat treater have the processes and procedures in place that will insure that only a properly heat-treated part will go through the door. It is also critically important that the heat treater have in-place procedures and practices to properly monitor equipment performing heat-treating. In addition, the heat treater must have a methodology for dealing with non-conforming parts, and corrective action to rectify any problems. Properties that are monitored on parts include tensile strength, fatigue, fracture toughness, hardness and conductivity.

In general, the specifications for heat treatment will already have been previously established. This includes record keeping, types of testing required and the frequency. Part-specific testing may also be mandated. However, in lieu of specific specification and quality criteria, good practice dictates that proper documentation of procedures is necessary to insure consistent and reliable heat treatment of aluminum alloys.

In terms of record keeping and documentation of procedures, it is a good idea to be maintained on file for at least four years, unless otherwise specified by contract. These records should include current and past records of process qualifications and process re-qualifications. Calibration records and calibration procedures should also be keep for four years. Calibration records should include the procedure used, results of the calibration and an equipment serial number or property number. This insures the results of calibration are traceable to specific pieces of equipment.

The test results, including hardness, conductivity, tensile, fatigue and fracture toughness records should be maintained. If possible, this should be kept with the part serialization, or if the parts are not serialized, then with the order and heat-treat lot. Temperature records, including temperature charts should also be maintained with the test result records.

In addition, records should be kept to document any changes in the heat treatment or quenching practices. If any new equipment is installed, and it causes a change in the heat treatment or quenching practice, records should be kept that indicate the changes in process. Documentation should also be established if existing equipment utilizing standard practices produce unacceptable product. The corrective action taken should also be documented.

In addition to the record retention, and the measurement of properties, other in-process test must be performed to insure reliable, efficient and consistent heat-treating. One of the most important tests usually required is the temperature uniformity survey. In this test, a series of thermocouples are used to measure how much the temperature changes within the furnace work zone. If the furnace

is used for solution heat treating, the usual temperature variation is $\pm 10°F$, centered about the process temperature. For precipitation hardening, the usual temperature variation is $\pm 5°F$, centered about the process temperature. This test is required as the furnace enters service, and whenever substantial changes are made to the furnace that might change the temperature uniformity. An example is rebuilding the refractory, installing different size recirculating fans, etc.

The initial temperature survey is performed at the upper and lower operating temperatures used for all aluminum product heat-treated in this furnace. At least one test thermocouple for each $25\,\text{ft}^3$ of furnace volume is usually used. Up to 40 thermocouple locations can be used to qualify a furnace, with a minimum of 9 thermocouples in the furnace work zone. The thermocouples are located at each corner of the furnace work zone, and have a thermocouple in the center of the work zone. In the case of a salt bath furnace, because of its greater thermal mass and uniformity, only one thermocouple per each $40\,\text{ft}^3$ of volume is usually used, with a minimum of 9 test locations. If the furnace is small, say less then $9\,\text{ft}^3$ of volume, then only three thermocouples are generally used. These thermocouples are located at the top, center and bottom, or at the front, center and rear of the furnace.

The temperature surveys are performed to reflect the standard operating procedures of the furnace. This means that an effort is made to test the actual temperature uniformity of the furnace during normal operating procedures. For example, this means that if the heat treated parts are introduced into the furnace, after the furnace is stabilized at temperature, then the temperature uniformity test is performed by introducing the thermocouples into a furnace stabilized at the desired temperature. If the parts are introduced into a cold furnace, and allowed to heat to the process temperature, then the thermocouples should be introduced into the cold furnace, and the furnace set to the desired test temperature.

After the thermocouples have been inserted into the furnace, temperature reading should be taken frequently to determine when the temperature of the hottest part of the work zone reaches the bottom of the temperature range.

The temperature of salt bath furnaces can be determined using a thermocouple encased in a protection tube. The furnace is manually probed using the thermocouple probe at each of the required locations (each corner and center). The thermocouple should be allowed to reach thermal equilibrium. Again, the temperature uniformity requirements should be maintained and documented.

Solution heat treating furnaces should be surveyed every month, and precipitation-hardening furnaces should be surveyed every six months after the initial temperature uniformity survey. This assumes that the precipitation hardening furnaces continue to meet temperature uniformity requirements,. Often the six-month interval between temperature uniformity measurements can be reduced if the furnace has a multi-point recorder with load thermocouples.

After insertion of the temperature sensing elements, readings should be taken frequently to determine when the temperature of the hottest region of the furnace or salt bath approaches the bottom of the temperature range being surveyed. After reaching the bottom of the temperature range being surveyed, temperature readings shall be taken at 2-minute intervals to ascertain any overshooting and thermal equilibrium. After thermal equilibrium is reached, readings should be taken at

5-minute intervals and for not less than 15 minutes to determine the recurrent temperature pattern. After thermal equilibrium is reached, the maximum temperature variation of all sensing elements shall not exceed 20°F and shall not vary outside the temperature range being surveyed.

Monthly surveys for batch furnaces are not necessary if the furnace or bath is equipped with thermocouples located permanently in each of the 8 corners of the work zone. This generally allowed, if uniformity surveys show a history of satisfactory performance for a period of at least 6 months. The sensing thermocouples are installed to record the temperature of the heated media (air, salt, etc.) or actual metal temperatures. However, periodic surveys should also be made at 6 month intervals in accordance with the procedures outlined for the monthly survey.

For continuous heat treating furnaces, the type of survey and the procedures for performing the survey should be established for each type of furnace involved. The types of continuous heat treating furnaces may vary considerably depending upon the product and sizes involved. For some types and sizes of furnaces, it is only practical to determine properties from actual parts. Recently new digital data acquisition devices are available that enable an *in-situ* temperature uniformity survey. Generally monthly and periodic surveys are made using load thermocouples.

The accuracy of temperature control systems is generally checked using a separate thermocouple located within three inches of the process thermocouple. If the two thermocouples do not check within ±3°F, then the furnace should be shut down. Any work processed since the last thermocouple check should be impounded and verified for properties. The calibration of the thermocouples should be checked weekly to minimize drifting. This is critical because of the proximity of process temperatures to the liquidus temperature. Calibration of the check instrument and thermocouple should be made against NIST standards.

Additional tests are necessary to insure that the furnace and process system are operating properly. These tests include monthly property testing for tensile properties. Tensile testing is usually required monthly, for the alloys processed the previous month. The testing is usually performed to either ASTM E8 or ASTM B557. A minimum of nine tensile tests is generally required. These test specimens are typically loaded into the furnace to reflect the high and low temperatures within the work-zone, and the fastest and slowest quenched region s in the furnace. If because of size, sampling from large forgings, castings or other large parts is impractical, then samples of similar thickness and alloy can be used to insure properties.

Additional testing is usually required to meet common heat treating specifications. This testing is accomplished using metallography on the heat-treated tensile specimens. These tests include eutectic melting, high temperature oxidation, alclad diffusion and intergranular corrosion testing.

High-temperature oxidation and eutectic melting specimens from at least one of the heat-treated tensile samples are usually sectioned, and prepared metallographically. These specimens are also usually examined for evidence of eutectic melting by etching lightly with Keller's etch. The prepared samples should show no signs of eutectic melting and be substantially free from high-temperature oxidation.

Intergranular corrosion testing is also conducted. In the case of aldad alloys, the alelad shall be removed from both sides of the sample by filing or by other suitable means. Surface preparation of samples is accomplished by etching for 1 minute at 200°F to produce a uniform surface condition. This solution typically contains 50 milliliters of concentrated Nitric acid, 5 milliliters of Hydrofluoric acid (48 percent) and 945 milliliters of distilled or deionized water. Appropriate personal safety equipment should be worn at all times.

After this etching treatment, the sample is rinsed in distilled or deionized water, immersed for 1 minute in concentrated nitric acid (70 percent) at room temperature to remove any metallic copper that may have been plated out on the specimen, rinsed in distilled or deionized water, and allowed to dry. The sample is immersed for 6 hours at room temperature into a solution of 57 grams NaCl, 10ml H_2O_2, then diluted to 1 liter with distilled water. Multiple specimens may be immersed in the solution, if the specimens are electrically isolated from each other, and the quantity of solution is at least 30 milliliters per square inch of surface area of all the specimens.

Once the specimens have been immersed for six hours, the specimens are removed from the solution and washed with distilled water and allowed to dry. Metallographic specimens are prepared and examined at 100X and 500X to determine if any high temperature oxidation or eutectic melting has occurred. Generally the metallographic specimens are examined before and after etching with Keller's etch.

If the material is alclad, then additional tests to determine the extent of alclad diffusion is performed. If the sheet is less than 0.020'' thick, then there is usually no requirement to examine for alclad diffusion. The extent of diffusion is determined by examining the metallographic specimens at 100X–1000X after etching with Keller's etch.

Typical inspection requirements are summarized shown in Table 28. Typical periodic monitoring requirements are shown in Table 29.

Table 28 Typical Inspection Requirements for Aluminum Heat Treating

Requirement	Inspection Provision
Process Qualification	- Inspection records and approval of changes in heat treating and quenching practices - Furnace and salt bath temperature uniformity or batch and continuous furnaces - Calibration procedures and records
Periodic Process Surveys	- New surveys for temperature and bath temperature uniformity - Monthly and Interval surveys on batch furnaces
Periodic Monitoring	- Spray quench equipment - Quench delay times - Monthly property testing of furnace capability (intergranular corrosion, eutectic melting and high temperature oxidation

Table 29 Typical Test Requirements for Periodic Monitoring

Material	Tests				
	Mechanical Properties[1]	High Temperature Oxidation[2]	Intergranular Corrosion[3]	Alclad Diffusion (alclad only)	Eutectic Melting
Plate and Sheet	X	X	X[4]	X	X
Castings	X	–	–	–	X
Bar, Rod, wire and Shapes	X	X	X[4]	–	X
Forgings	X	–	–	–	X
Tubing	X	X	–	X	X
Rivets and other Fastening Components	X	X	X	–	X

[1] Properties requied
[2] Only for air furnaces used for solution heat treatment
[3] Only 2XXX or 7XXX alloys (clad and bare)
[4] Only for product less than 0.250 inches thick.

REFERENCES

1. J. E. Hatch, *Aluminum: Properties and Physical Metallurgy*, ASM (Metals Park:1984) 154.
2. M. A. Grossman, *Metal Progress*, 4 (1938) 373.
3. H. Scott, "*Quenching Mediums*," *Metals Handbook*, ASM (1948) 615.
4. F. Wever, Archiv fur das Eisenhüttenwesen, 5 (1936) 367.
5. M. Dakins, Central Scientific Laboratory, Union Carbide, Report CSL?226A.
6. W. L. Fink and L. A. Wiley, Trans. AIME 175 (1948) 414.
7. H. Suzuki, M. Kanno and H. Saitoh, *Keikinzoku* 33 1 (1983) 29.
8. J. W. Evancho and J. T. Staley, Met. Trans. 5 1 (1974) 43.
9. I. A. Wierszykkowski, Met. Trans. A 22A (1991) 993.
10. C. E. Bates and G. E. Totten, Heat Treatment of Metals 4 (1988) 89.
11. L. Swartzenruber, W. Beottinger, I. Ives, *et al.*, *National Bureau of Standards Report NBSIR 80?2069* (1980).
12. C. E. Bates, T. Landig and G. Seitanakis, *Heat Treat* 12 (1985) 13.
13. C. E. Bates, "*Recommended Practice for Cooling Rate Measurement and Quench Factor Calculation*", *ARP 4051 Aerospace Materials Engineering Committee (SAE)* 1 (1987).
14. J. T. Staley, R. D. Doherty and A. P. Jaworski, *Met. Trans. A.* 24A 11 (1993) 2417.
15. J. T. Staley. *Mat. Sci. Tech.* 3 11 (1987) 923.
16. D. D. Hall, I. Mudawar, J. *Heat Transfer* 117 5 (1995) 479.
17. J. S. Kim, R. C. Hoff and D. R. Gaskell, *Materials Processing in the Computer Age*, Ed. V. R. Vasvev (1991) 203.
18. C. E. Bates, "Quench Factor?Strength Relationships in 7075?T73 Aluminum" *Southern Research Institute* 1 (1987).
19. Processing/Microstructure/Property Relationships in 2024 Aluminum Alloy Plates, US Department of Commerce, National Bureau of Standards Technical Report NBSIR 83-2669, January 1983.

20. Nondestructive Evaluation of Nonuniformities in 2219 Aluminum Alloy Plate - Relationship to Processing, US Department of Commerce, National Bureau of Standards Technical Report NBSIR 80-2069, December 1980.
21. K. Speith and H. Lange, *Mitt. Kaiser Wilhelm Inst. Eisenforssch*, 17 (1935) 175.
22. A. Rose, Arch. *Eisenhullennes*, 13 (1940) 345.
23. C. E. Bates, G. E. Totten and R. J. Brenner, ASM Handbook, V4 Heat Treating, ASM (1991) p. 51.
24. C. Kaijiang, Y. Waixia and C. Kaike, *Acta Metall Sin. (China)* 21 (1985) B297.
25. V. G. Labeish, *Steel USSR*, 19 (1989) 134.
26. K. Matsuda, S. Tada and S. Ikeno, *Proc. 4th ICAA*, Atlanta GA, 1994, p. 605.
27. D. L. Sun, D. Z. Yang, Y. Hong and T. C. Lei, Proc. 8th ICSMA, Tempere Finland, Pergamon Press, Oxford, 1988, p591.
28. M. R. Edwards and M. J. Whiley, *Proc. 4th ICAA*, Atlanta GA, 1994, p. 473.
29. S. P. Ringer, B. C. Muddle and I. J. Polmear, *Met. Trans.* 1995 26A 1659.
30. W. S. Cassada, G. J. Shiflet and E. A. Starke, *Met. Trans.* 1991 22A 299.
31. S. Ceresana, P. Fiorina, *Mat. Sci. Eng.* 1972 10 205
32. S. Komatsu, Y. Nakata, T. Sugimoto and K. Kamei, *J. Jap. Inst. Light Metals*, 1980 30 330.
33. P. Gomiero, A. Reeves, A. Pierre, F. Bley, F. Livet and H. Vichery, *Proc. 4th ICAA, Atlanta Ga, Georgia Institute of Technology, 1994 p.664.*
34. T. Uno and Y. Baba, *Suminoto Light Metals Technical Reports* 20 (1979) 3.
35. E. Di Russo, M. Conserva, F. Gatto and H. Markus, *Met. Trans.* 4 (1973) 1133.
36. R. J. Sinko, T. Ahrens and G. Shiflet, J., *Al?Li V.*, (1992) 89.
37. N. Ryum, *Aluminum* 51 (1975) 595.
38. R. Allen, J. B. VanderSande, *Met. Trans.* A9 (1978) 1251.
39. R. Allen, J. B. VanderSande, *Acta Met.* 28 (1980) 1185.
40. A. Deschamps, F. Livet and Y. Brechet, *Acta Mater.* (1999) 47 281.
41. A. Deschamps, Y. Brechet, *Acta Mater.* (1999) 47 293.
42. A. Wilm, *Metallurgie*, 8 (1911) 225.
43. R. Merica, W. Waltenburg and T. Scott, *Trans AIME*, 64 (1920) 41.
44. R. Mehl and T. Jelten, Age Hardening of Metals (ASM: Cleveland) 1940, p 342.
45. N. Mott and R. Nabarro, Proc. Royal Soc. (*London*) *A*, 145 (1940) 362.
46. Orowan, *Symposium on Internal Stresses in Metals and Alloys – Session II Discussion*, Inst. Metals, London, England, (1948) p.51.
47. Brown, Ham, Strenthening Methods in Crystals, Kelly, Nicholson, eds., (Halsted Press, John Wiley and Sons: New York), 1971, 9.
48. Kelly, Hirsch, Phil. Mag., 12 (1965) 881.
49. Gerold, Hartman, Trans. Jap. Inst. Metals, 9 Supplement (1968) 509.
50. Ardell, *Met. Trans. A*, 16A (1985) 2144.
51. Weeks, Pati, Ashby, Barrand, Acta Met., 7 (1969) 1403.
52. Weeks, Lealand, Persson, Newbach, Phy. Stat. Sol. A, 78 (1983) 571.
53. Knowles, Kelly, Effect of Second Phase Particles on the Mechanical Properties of Steel, (Iron and Steel Inst.: London) 1971 p. 9.
54. Ibrahim, Ardell, Mat. Sci. Eng., 36 (1978) 139.
55. Noble, Harris, Dinsdale, Metal Sci., J., 16 (1982) 425
56. L. Mondolfo, Aluminum Alloys, Structure and Properties, (Butterworths, 1976) London.
57. Metals Handbook, 8th Ed., Vol. 8, ASM (Metals Park:1973) p.259.
58. A. Guinier, Compt. Rend., 204 (1937) 1115.
59. A. Guinier, Nature 142 (1938) 669.
60. G. D. Preston, Proc. Royal Soc. A 166 6 (1934) 572.
61. G. D. Preston, Nature 142 (1938) 570.

62. E. Hornbogen, Aluminum, 43 (1967) 115.
63. J. M. Silcock, T. J. Heal, H. K. Hardy, J. Inst. Met., 82 (1953) 239.
64. J. D. Boyd, R. B. Nicholson, Acta Met., 19 (1971) 1379.
65. I. M. Lifshitz, V. V. Slyozov, Soviet Phys JETP, 35 (1959) 331.
66. Z. Wagner, Electrochem., 65 (1961) 581.
67. A. Wilm, Metallugie 8 (1911) 225.
68. R. Wilson, P. Partridge, Acta Met., 13 (1965) 1321.
69. G. C. Weatherly, *Ph.D. Dissertation*, Cambridge, (1966).
70. C. J. Peel, *RAE Technical Report 75062* (1975).
71. M. V. Hyatt, Proc. Int. Conf. Aluminum Alloys, Torino, Italy, October 1976.
72. M. Bernole, R. Graf, Mem. Sci. Rev. Met., 69 (1972) 123.
73. J. Auld, S. Cousland, Met. Sci. 12 (1971) 445.
74. H. Loffler, I. Kovacs, J. Lendvai, J. Mat. Sci. 18 (1983) 2215.
75. G. Bergman, L. Waugh, L. Pauling, Nature 169 (1952) 1057.
76. N. Ryum, Z. Metallkd. 66 (1975) 377.
77. L. F. Mondolfo, N. A. Gjostein, Lewisson, *TAIMME* 206 (1956) 1378.
78. N. Ryum, Z. Metallkd., 65 (1975) 338.
79. D. W. Pashley, M. H. Jacobs, J. T. Vietz, Phil. Mag. 16 (1967) 51.
80. G. Thomas, J. Nutting, J. Inst. Met. 88 (1959) 81.
81. J. Gjonnes, C. Simensen, Acta Met. 18 (1970) 881.
82. J. H. Auld, S. McCousland, Scripta Met. 5 (1971) 765.
83. J. H. Auld, S. McCousland, J. Aust. Inst. Met. 19 (1974) 194.
84. R. Graf, Compt. Rend. 242 (1956) 1311.
85. X. Li, V. Hansen, J. Gjonnes, L. Wallenberg, Acta Mater. 47 (1999) 2651.
86. A. Chou, Scripta Met. 12 (1978) 421.
87. F. Laves, "*Theory of Alloy Phases*", ASM Symp. Cleveland (1956) p. 124.
88. P. Auger, J. M. Raynal, M. Bernole, R. Graf, Mem. Sci. Rev. Mat. 71 (1974) 557.
89. A. Bigot, F. Denoix, P. Auger, *et al*, Mat. Sci. Forum 217–222 (1996) 695.
90. S. K. Maloney, K. Hono, I. J. Polmear and S. P. Ringer, Scripta Mater. 41 (1999) 1031.
91. M. Takeda, F. Ohkubo, T. Shirai, K. Fukui, J. Mat. Sci. 33 (1998) 2385.
92. K. Matsuda, Y. Uetani, H. Anadi, S. Tada and S. Ikeno, Proc. 3rd Int. Conf. Aluminum Alloys, Trondheim, Norway, Ed. L. Araberg (1992) 272.
93. C. J. Peel, D. Clark, P. Poole, *et al.*, *RAE Technical Report 78110*, 1978.
94. K. Osamura, S. Ochai, T. J. Uehara, Inst. Metals 34 9 1984 p517.
95. P. B. Hirsch and F. J. Humphereys, *Physics of Strength and Plasticity*, (MIT Press, 1969) 189.
96. G. Sundar, J. J. Hoyt, Phys Rev. B 46 12 (1992) 266.
97. J. L. Taylor, J. Inst. Met. 92 (1963) 301.
98. J. W. Newkirk, D. S. MacKenzie, K. Ganapathi, *to be published, TMS San Diego*, 1999.
99. P. N. T. Unwin, G. C. Smith, J. Inst. Met. 97 (1969) 229.
100. A. K. Vasudevan, R. D. Doherty, Acta Metall. 35 6 (1987) 1193.
101. P. C. Varley, M. K. B. Day, A. Sendorek, J. Inst. Met. 86 (1957) 337.
102. H. P. Degischer, W. Lacom, A. Zahra, A. Zahra, *Z. Metallkd.* 71 (1980) 231.
103. L. F. Mondolfo, *Metallography of Aluminum Alloys*, (J. Wiley, New York) 1943.
104. A. Deschamps and Y. Brechet, Scripta Mat. 39 (1998) 1517.
105. N. Bogh ASM Heat treating Conference 18–20 April 1994.
106. G.E. Totten, C.E. Bates and N.A. Clinton, *Handbook of Quenchants and Quenching Technology*, (ASM International:Cleveland) 1989.
107. SAE Specification AMS 2770E, Heat Treatment of Aluminium Alloys, SAE, Warrendale, PA.

20

Quenching

GEORGE E. TOTTEN and GLENN M. WEBSTER

G. E. Totten & Associates, Inc., Seattle, Washington, U.S.A.

CHARLES E. BATES

The University of Alabama at Birmingham, Birmingham, Alabama, U.S.A.

1 INTRODUCTION

When aluminum is solution heat treated at elevated temperatures, generally in the range of 750–1000°F (400–540°C), some alloying elements are re-dissolved to produce a solute rich solid solution. The objective of the solution process is to maximize the concentration of hardening elements including copper, zinc, magnesium, and (or) silicon in the solid solution. The concentration and rate of dissolution of these elements increases with temperature so solution treating temperatures are usually near the liquidus temperature of the alloy.

If an alloy is slowly cooled from an elevated temperature, alloying elements are precipitated and diffuse from the solid solution to concentrate at the grain boundaries, small voids, on undissolved particles, at dislocations, and other "imperfections" in the aluminum lattice. To achieve optimal strength, toughness, and corrosion resistance, it is desirable to retard this diffusion process and keep the elements in solid solution until the alloy is age hardened. Elements are kept in solution by quenching from the solution treating temperature. After quenching, aluminum is aged and during this process, a fine dispersion of elements and compounds are precipitated that significantly increase the strength of the material. These processes are illustrated in Fig. 1 [1].

Diffusion and precipitation kinetics are slower in some alloys than others, permitting lower cooling rates while still allowing high strengths and corrosion resistance to be obtained. Figure 1 illustrates that excessively slow cooling allows excessive concentrations of alloying elements to develop on the grain boundaries. Figure 2 shows that intergranular corrosion for 2024-T4 will be aggravated if cooling
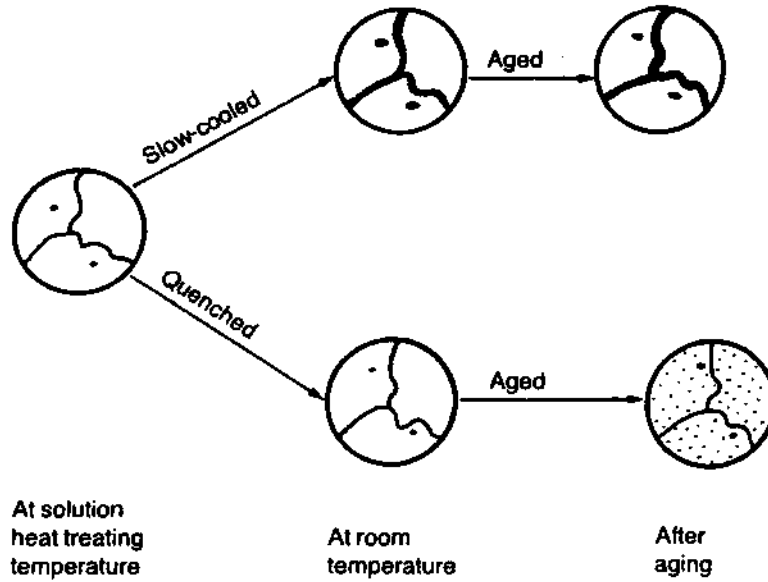
Figure 1 Schematic illustration of the solid diffusion processes that may occur during solution heat treating.
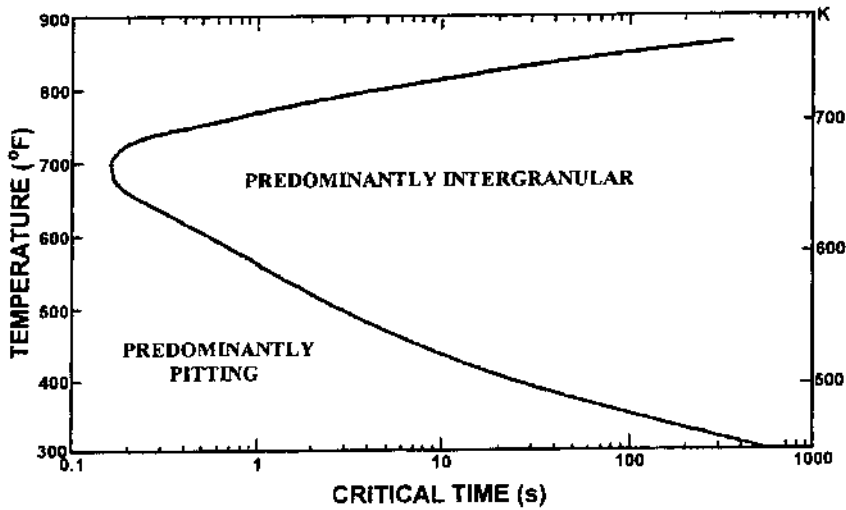
Figure 2 C-Curve indicating type of cooling rate dependent corrosion attack on AA2024-T4 sheet.

rates are excessively slow during quenching. (See Sec. 2.5) Similar behavior has been found for other aluminum alloys [2]. Therefore, it is important that cooling rates during quenching be sufficiently fast to minimize precipitation during cooling.

The cooling process of age-hardenable aluminum alloys affects material

properties such as strength, ductility, and thermal stresses. Thermal stresses are minimized by reducing the cooling rate from the solution heat treatment temperature. However, if the cooling rate is too slow, undesirable precipitation will result. But, if the cooling rate is too fast, there may be an increased tendency for distortion [3,4]. Therefore, one of the primary challenges in quench process design is to select quenching conditions that optimize the desirable quench parameters and minimize the undesirable ones.

Various aspects of aluminum quenching are discussed in this chapter including quenching processes, aluminum hardenability, surface cooling mechanisms and their effect on material properties, effects of quenchants and quench processes, quenchant maintenance, cooling curve analysis, property predictions, importance of racking on distortion minimization, and quenchant media selection to reduce residual stresses and minimize distortion.

2   DISCUSSION

2.1   Quench Sensitivity

The physical properties of age hardenable aluminum alloys are dependent on many factors including alloy composition, structure and temper. The tendency for an alloy to form non-hardenable precipitates during quenching is referred to as ''*quench sensitivity*'' [5]. Quench sensitivity of AA6082 sheet stock (2 mm) containing varying alloy composition using different quench media summarized in Table 1 and Fig. 3 [5]. In general, as-quenched hardness increases with cooling rate as shown in Table 2 [5]. The higher hardness is a result of more solute elements being kept in solution at high cooling rates.

Although little variation in Vickers hardness is observed after furnace cooling and then tempering to the T6 condition, the final hardness does increase with quench cooling rate. Quench sensitivity increases with decreasing cooling rates and lower homogenization temperature. Process models have been developed which successfully predict AA6082 quench sensitivity, and the models are reviewed by Lim and Shercliff [5].

Table 1   Cooling Rates for AA6082 [Al-Mg-Si] in Various Quenching Media

Quench Medium	Quench Temp. (°C)	Cooling Rate (°C/sec @ 450–200°C)[a]
Still Water	19	240
Still Oil	20	34
Molten Salt	170	19
Fluidized Bed	170	9.6
Moving Air	20	40
Moving Hot Air	60	3.4
Still Air	20	1.4

[a]The specimens were $20 \times 20 \times 2$ mm
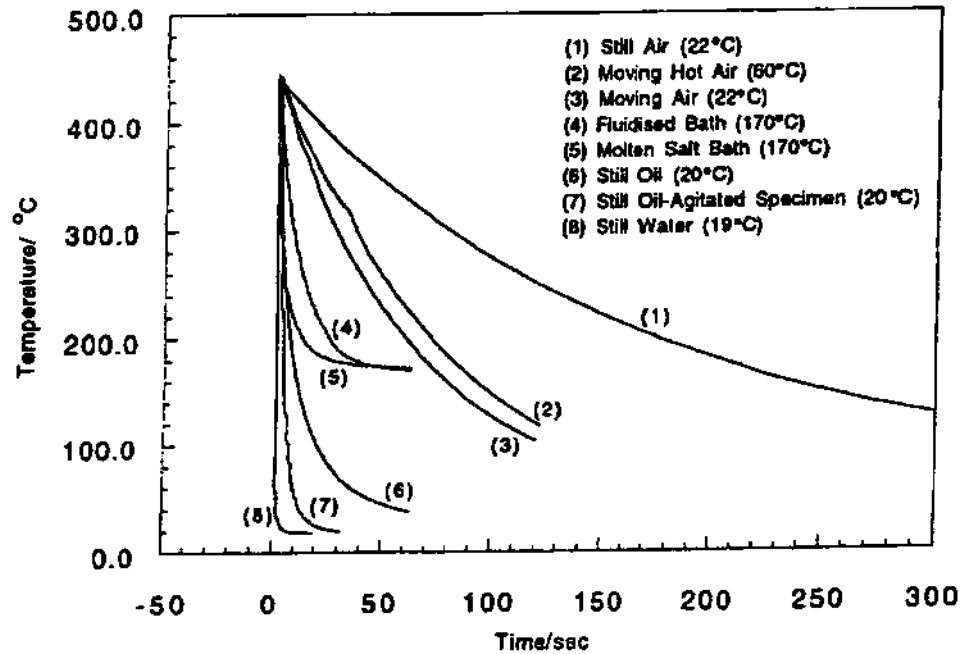
Figure 3 Cooling curves for different type of cooling media for quenching AA6082 aluminum sheet.

Table 2 Effect of Cooling Rate on As-Quenched Hardness of AA6082

| Quenchant | Vickers Hardness After Homogenization (°C) | |
	530	580
Water	52.1	53.1
Moving Air	46.9	49.0
Furnace Cooled	40.6	42.6

Vruggink examined the effect of cooling rate on the variation of yield stress as an indicator of quench sensitivity using various commercially available aluminum alloys [6]. The quench media included cold water, boiling water, and still air. These media produced a range of cooling rates varying from 5000°F/sec to 3°F/sec. Midplane cooling rates (750–550°F/sec) of various 12×12 in. test specimens of 7075-T6 with varying thicknesses are illustrated in Fig. 4 [6]. The data show that the average mid-plane cooling rates of about 5000°F/sec, 40°F/sec and 3°F/sec can be expected if 0.064, 3.0 and 10.0 in. thick test specimens are quenched into water at 70°F. From these data, quench sensitivity of age-hardenable aluminum alloys could be compared by quenching $12 \times 12 \times 0.064$ in. test specimens in cold water, boiling water and still air and aging to the desired temper. It was concluded that quenchants providing lower cooling rates have the same effect as increasing product thickness.
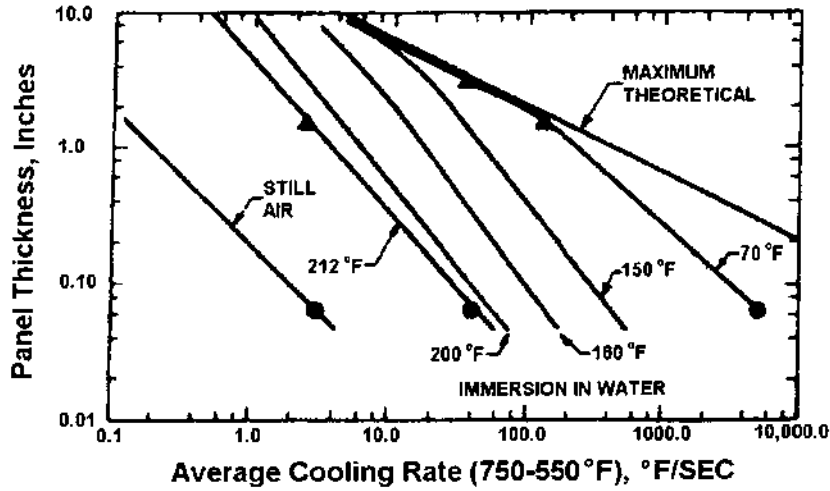
Figure 4 Effect of aluminum alloy panel thickness on the cooling rates in different quench media. (Centerline cooling curves.)
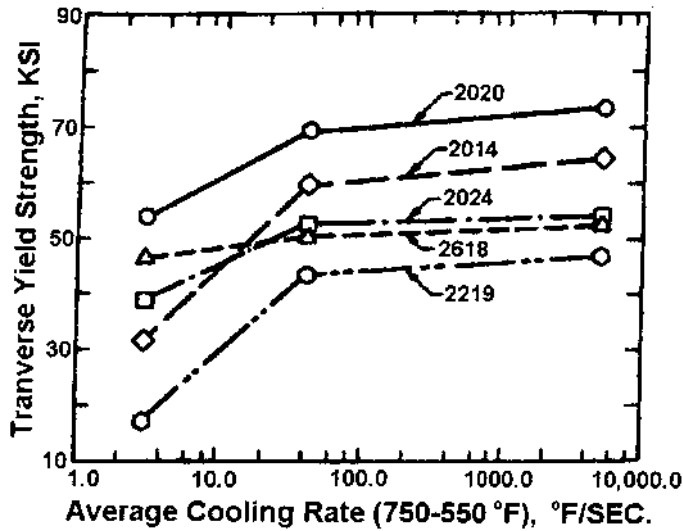
Figure 5 Effect of cooling rate on the properties of 2xxx series of aluminum alloy sheet in T6 temper.

The quench sensitivity of various 2xxx and 7xxx aluminum alloys have been examined using this methodology, and the results are summarized in Fig. 5 and 6, respectively [6]. Although a wide range of strengths are achievable in the 2xxx series when quenched at 5000°F/sec, significant variations in quench sensitivity were observed only when decreasing the cooling rate from 40°F/sec to 3°F/sec (See Fig. 5). Alloy AA2618 exhibited the least quench sensitivity and AA2014 exhibited
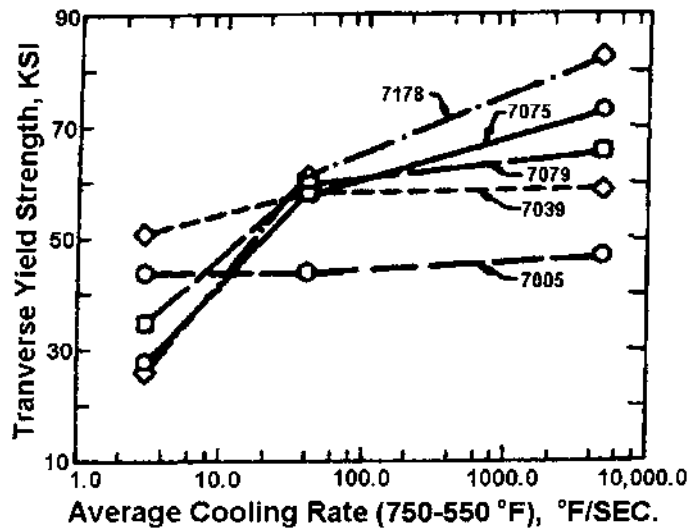
Figure 6   Effect of cooling rate on the properties of 7xxx series of aluminum alloy sheet in T6 temper.

the greatest sensitivity. The results of a similar study conducted on various 7xxx series aluminum alloys are illustrated in Fig. 6. It was found that quench sensitivity increased with increasing concentrations of Cu and Cr.

Vruggink also attempted to quantify quench sensitivity effects for thicker cross-sections using a modified Jominy test commonly used for steel. A 3 in. dia by 13 in. long cylindrical test specimen was used, as illustrated in Fig. 7 [6]. A wedge-shaped specimen, illustrated in Fig. 8, was also used. Test specimens were solution treated and quenched into 70°F water. Vruggink reported a poor correlation between yield strengths in end-quench or wedge tests compared with results from test specimens. The properties in plate were higher than in forged and quenched specimens as illustrated in Fig. 9 [6]. Wedge specimens machined from plate exhibited higher strengths than test specimens cooled at the same rate as illustrated in Fig. 10 [6].

Hart, et al. used the Jominy end-quench test to evaluate the influence of quench rates on corrosion properties of AA2024-T4 and -T6 and 7075-T73 [7]. Their experimental apparatus is illustrated in Fig. 11, and tests were conducted according to ASTM A255-48T. A summary of cooling rates as a function of section thickness is provided in Fig. 12 [7]. Aluminum extrusions were used in this study because the more pronounced grain structure would be expected to provide greater sensitivity to stress corrosion and exfoliation corrosion. The water quenchant temperature was 286K; a metal screen was placed over the orifice; and the transfer time from the furnace to the quench was < 5 sec. Variations in water pressure produced no measurable effect on cooling rate. The hardness and conductivity data obtained from Jominy bars for different aluminum alloys are illustrated in Fig. 13 [7].

Specimens were removed from the Jominy bars for stress corrosion studies using the cutting plan illustrated in Fig. 14. The results of the study are illustrated in Fig. 15 [7], and the conclusions drawn from this study are summarized as follows:
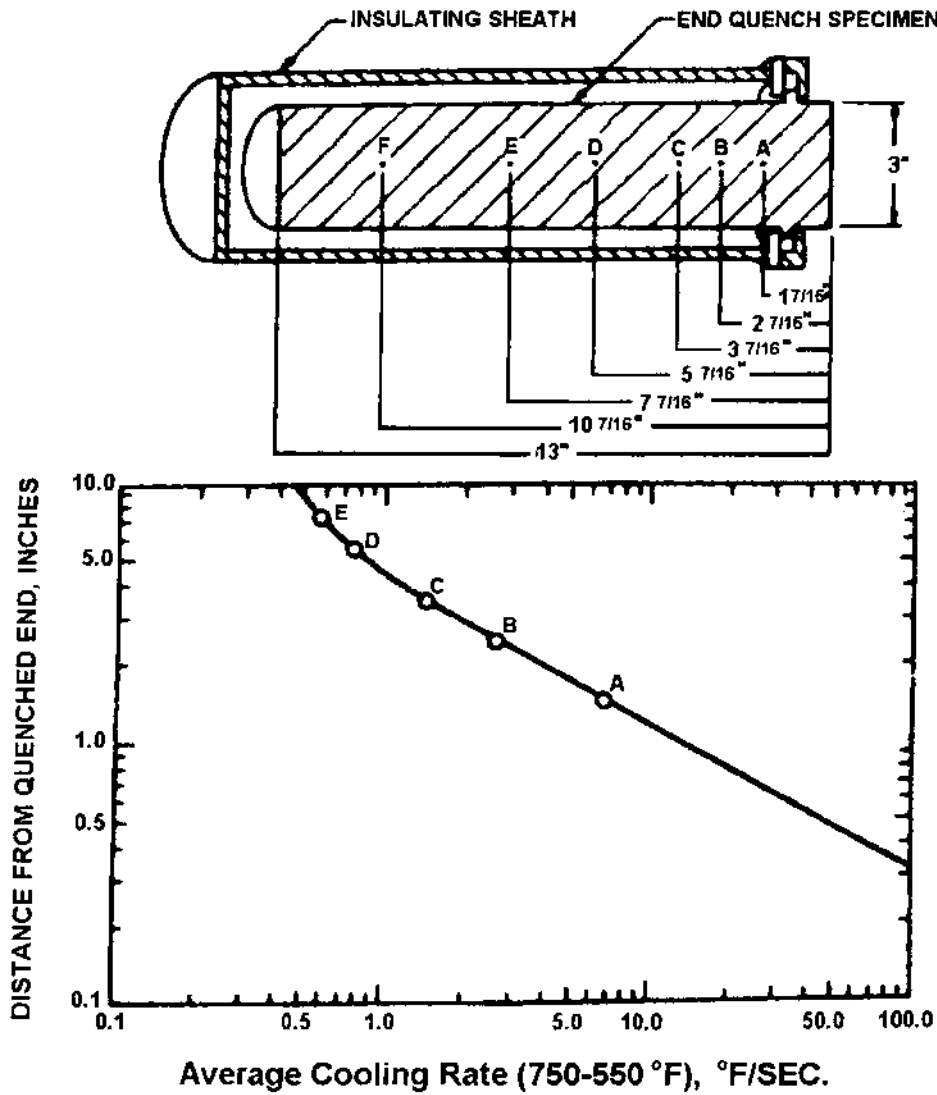
Figure 7   Jominy end quench test specimen and cooling rates at different locations along the specimen.

- Naturally aged AA2024 exhibited the lowest stress corrosion life.
- Alloy AA2024-T6 was slightly superior to AA2024.
- No effect of Jominy bar distance on stress corrosion life was observed in either the T4 or T6 conditions for AA2024.
- Alloy AA7075-T6 was approximately equivalent to AA2024 in its stress corrosion resistance over the first 40 mm of the Jominy bar.
- The overaged alloy AA7075-T73 was quite resistant to stress corrosion.
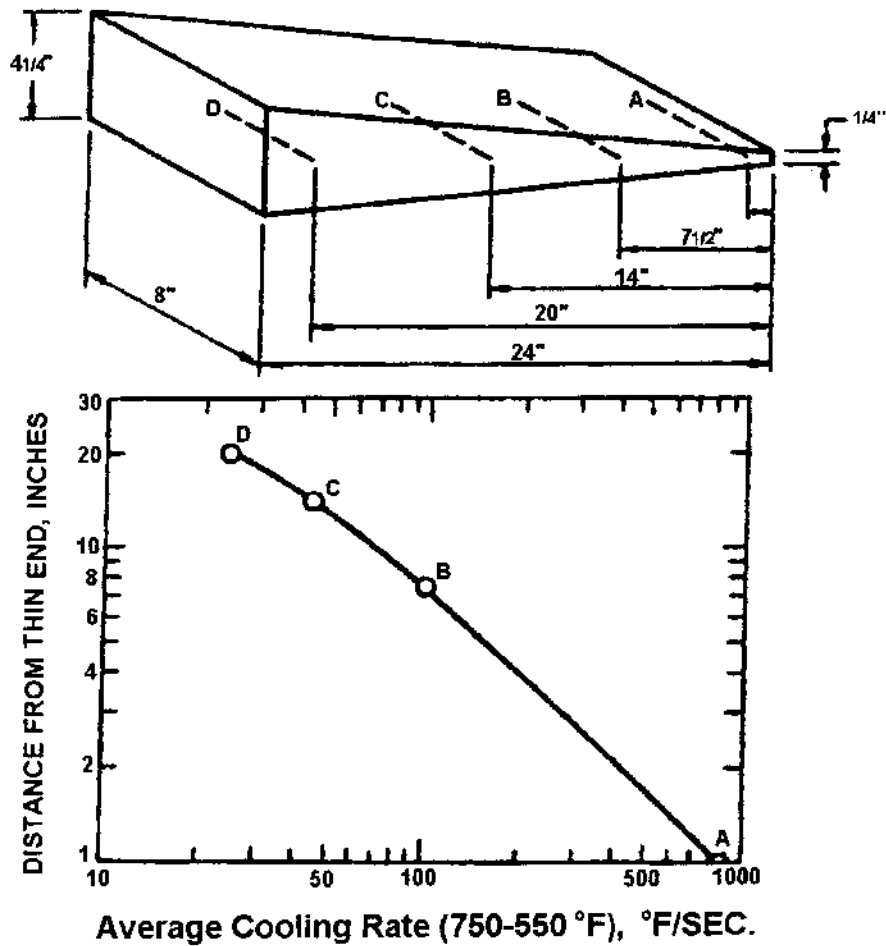
Figure 8   Wedge specimen and cooling rates at various locations in the specimen.

The Jominy end-quench specimen was also used to compare the hardenability of AA7075 and AA7050 using the alloy compositions shown in Table 3 [8,9].

A 13 mm dia. × 100 mm long cylindrical bar of the desired alloy was instrumented with Type K thermocouples at the positions shown in Fig. 16 and quenched according to ASTM A255 [8]. A comparison of the hardness and conductivity data obtained as a function of distance from the quenched end illustrated in Fig. 17 indicate that AA7050 is less sensitive to quench rate than AA7075 [8]. AA7050 was developed for use where thicker cross-section sizes are required [8]. Transmission electron micrographs of AA7075 and AA7050 at positions corresponding to 7 mm, 24 mm, 56 mm, and 79 mm distances on the Jominy bar are shown in Figs. 18 and 19, respectively [9]. These micrographs compare AA7075 and AA7050 specimens that were quenched at different cooling rates but tempered under identical conditions. This work suggests that the Jominy end-quench test may be
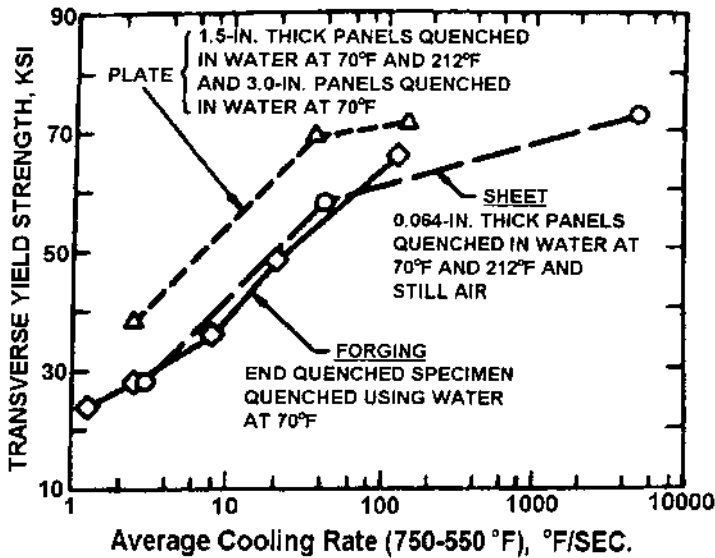
Figure 9 Effect of quenching rate on the properties of 7075-T6 sheet, plate and forging.
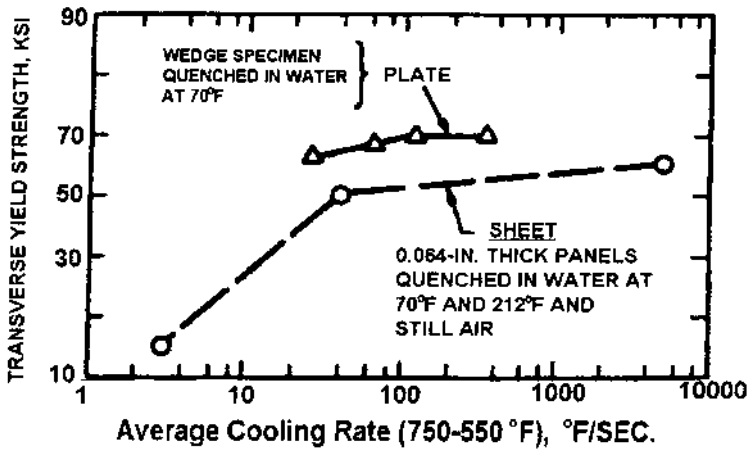
Figure 10 Effect of cooling rate on the properties of 7079 sheet and plate.

quite useful for aluminum alloy design and for determining the impact of quench severity on aluminum properties and microstructure.

2.2 Cooling Curve Analysis

2.2.1 Experimental Apparatus

Sheet and Bar Probe Construction

Two types of aluminum probes, constructed from bar and sheet stock of the aluminum alloys of interest, have been constructed to obtain experimental cooling rate
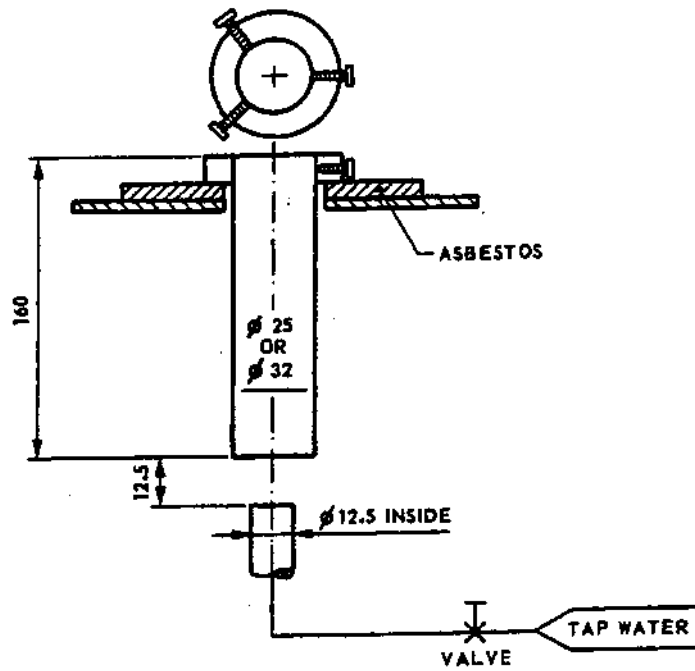
Figure 11   Schematic of Jominy end-quench test speciment and quenching jig.
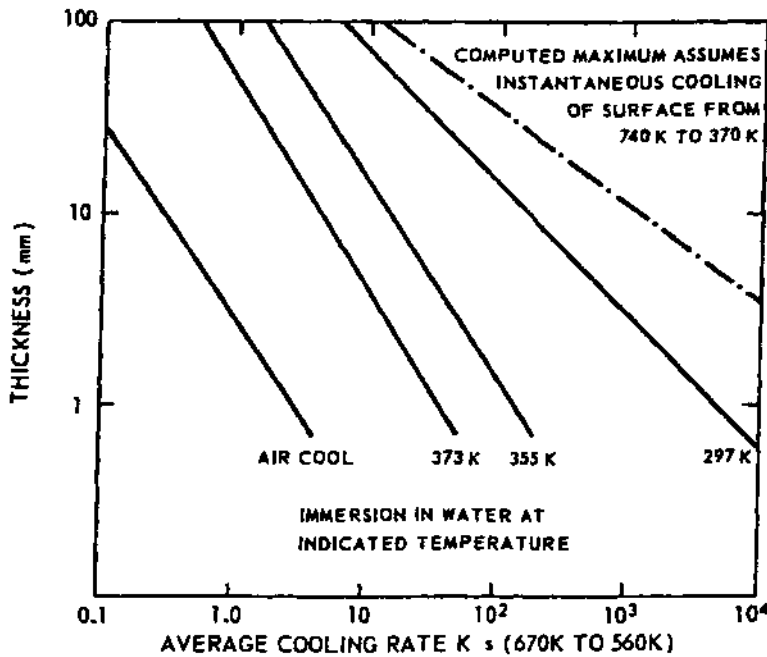
Figure 12   Effect of thickness on average cooling rates at the centerline (mid-plane) of aluminum sheet and plate quenched from solution temperatures.
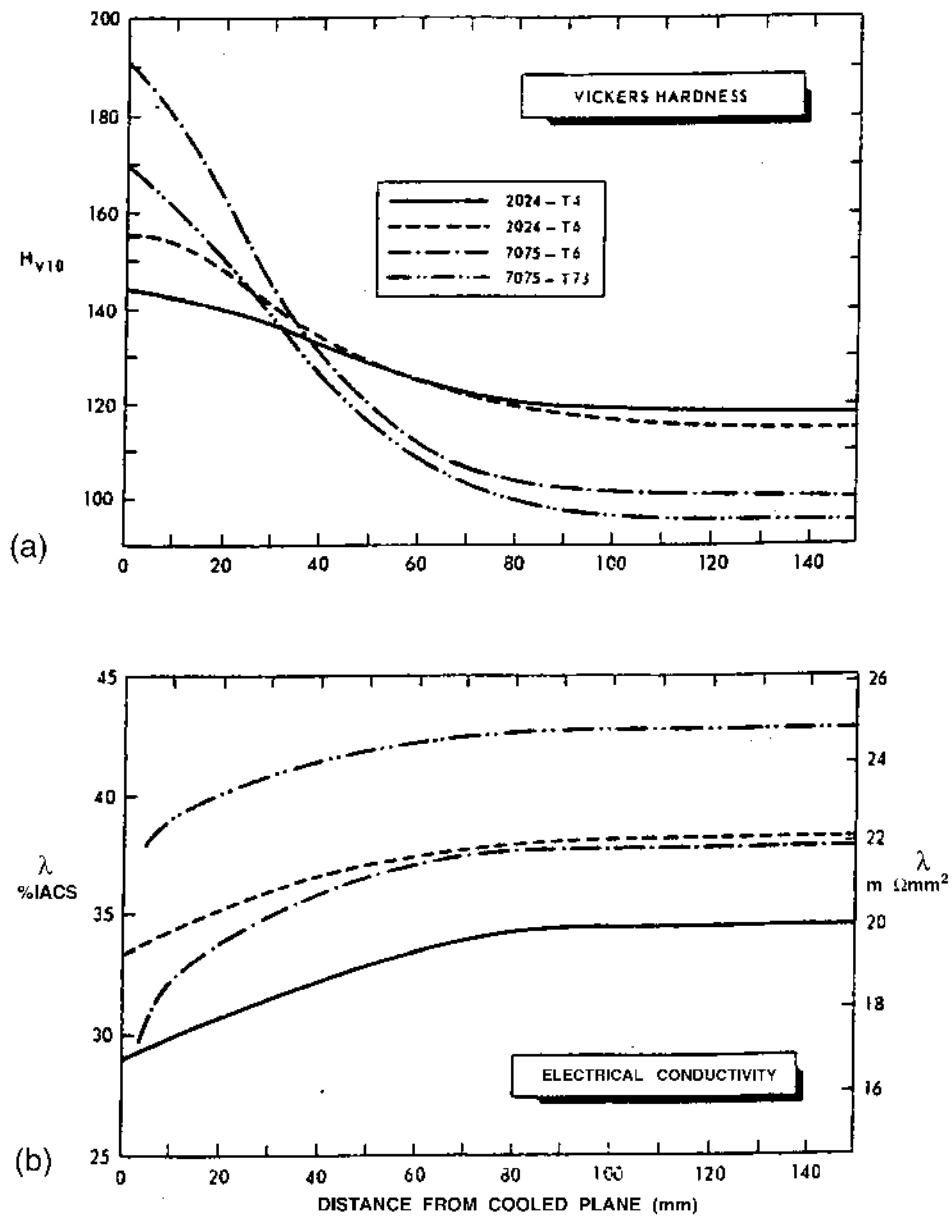
Figure 13   (a) Hardness and (b) conductivity as a function of Jominy distance. (AA).

data [10]. Cylindrical bar probes were prepared as shown in Fig. 20. The bar length was at least 4 times the diameter to approximate an infinite cylinder. A Type K thermocouple was inserted to the geometric center of the bar. Thermocouple contact with the probe material was maintained by using a spring loaded thermocouple or by brazing. An aluminum tube was TIG welded to the bar probe to provide a handle and protect the thermocouple from the quenchant.

FLATTENED AFTER HEAT TREATMENT
TO ENABLE HARDNESS AND
CONDUCTIVITY MEASUREMENTS

TUNING FORK TYPE
STRESS CORROSION
SPECIMEN

STRIP FOR INVESTIGATION OF THE
EXFOLIATION CORROSION RESISTANCE

ALL DIMENSIONS ARE IN mm
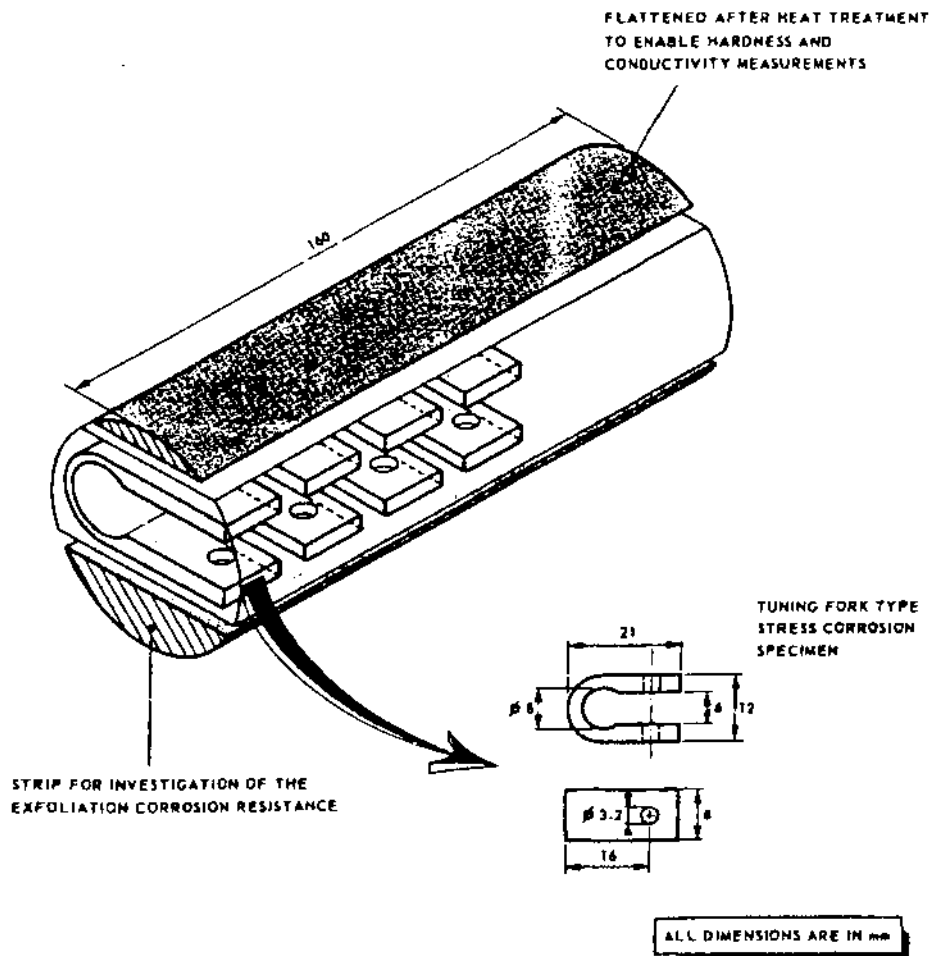
Figure 14   Location of stress corrosion specimens in the Jominy bar.

Probes to measure the cooling rates of aluminum sheet stock were prepared as illustrated in Fig. 21. The probe consisted of two 2×2 in. aluminum sheets with a combined thickness equal to the thickness being simulated. The sheets and handle were cleaned, thoroughly degreased, and the surface deoxidized. An intrinsic thermocouple was prepared using 30 gage chromel-alumel wire by spot welding the wire to the interior of the sheet [10]. A spacer was sandwiched between the sheets to allow the thermocouple wire to exit. The assembly was placed on a notched handle and TIG-welded water tight.

PROBE HEAT TRANSFER.   Several material and quenchant characteristics influence the rate of heat removal from a part during quenching. An infinite quench is one that instantly decreases the skin of the part to the bath temperature. The rate of cooling in the part is then a function of only the thermal diffusivity of the metal, i.e. its ability to diffuse heat from the interior to the surface. In practice, however, quenchants never provide the idealized "infinite" quench.
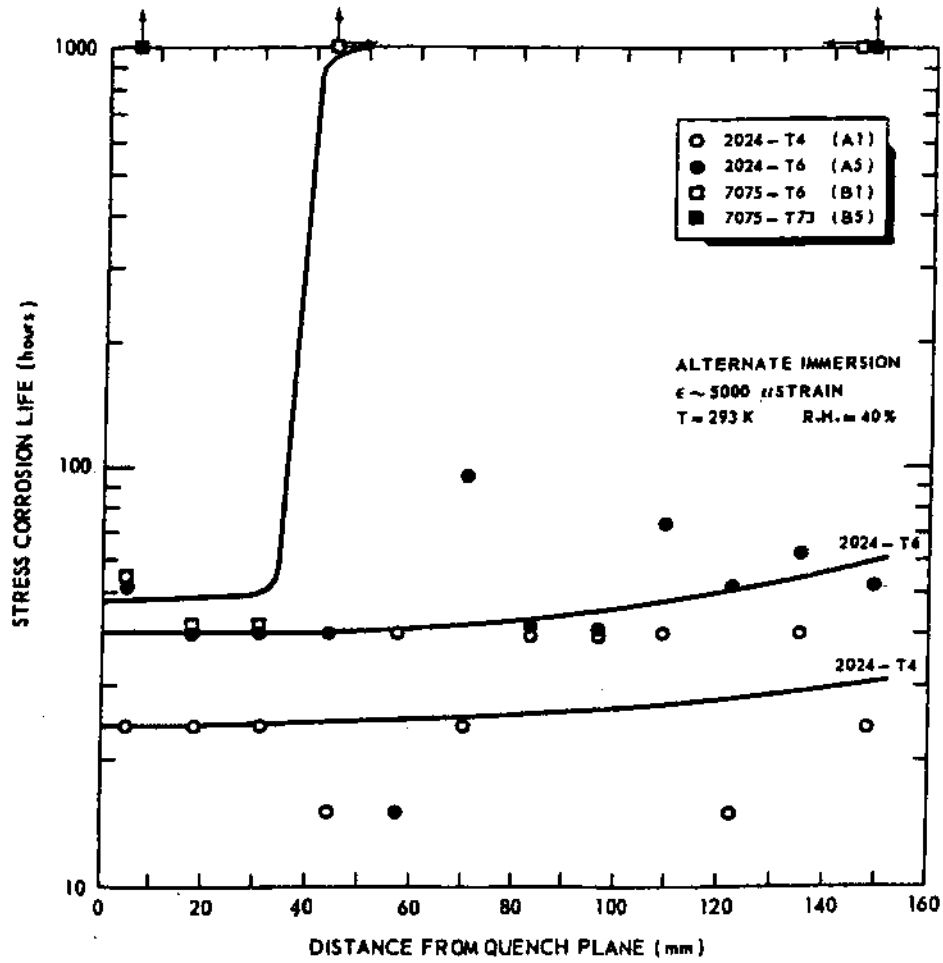
Figure 15 Stress corrosion crack initiation by alternate immersion.

Cooling rates achieved in actual quenching situations are controlled by the vapor blanket formation, boiling characteristics, flow velocity, temperature, specific heat, heat of vaporization, conductivity, density, viscosity, and wetting characteristics of the quenching fluid. Practically, cooling rates are controlled by the quenching medium and its use conditions.

Mathematically, heat transfer from parts can be described using Newton's law of cooling:

$$q = hA\,(T_1 - T_2)$$

where

q = rate of heat transfer
A = surface area of the part in contact with fluid
T_1 = surface temperature

Table 3   Chemical Composition of AA7075 and AA7050

						Elemental Composition (% b.l.)				
Alloy	Cu	Fe	Si	Mn	Mg	Zn	Ni	Cr	Ti	Zr
7075-T6	1.36	0.20	0.10	0.04	2.62	5.77	0.003	0.20	0.0170	0.0115
7050-T7451	2.11	0.12	0.050	0.04	1.98	5.74	< 0.000	0.026	0.031	0.09
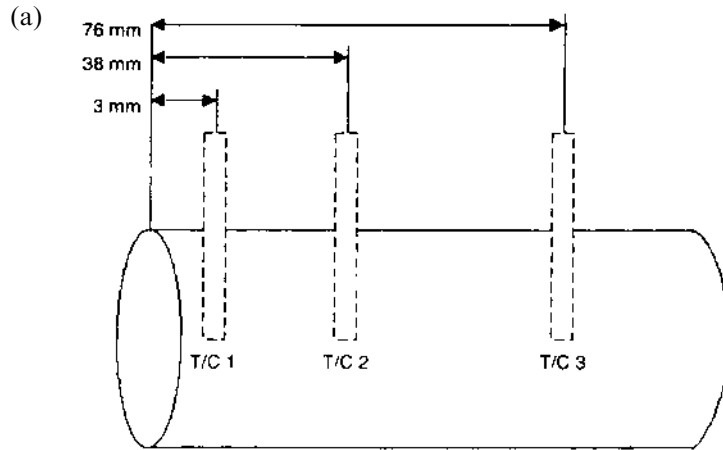
Figure 16   Schematic illustration of Jominy end-quench specimen (a) location of thermocouples (b) photograph of instrumented bar being quenched.
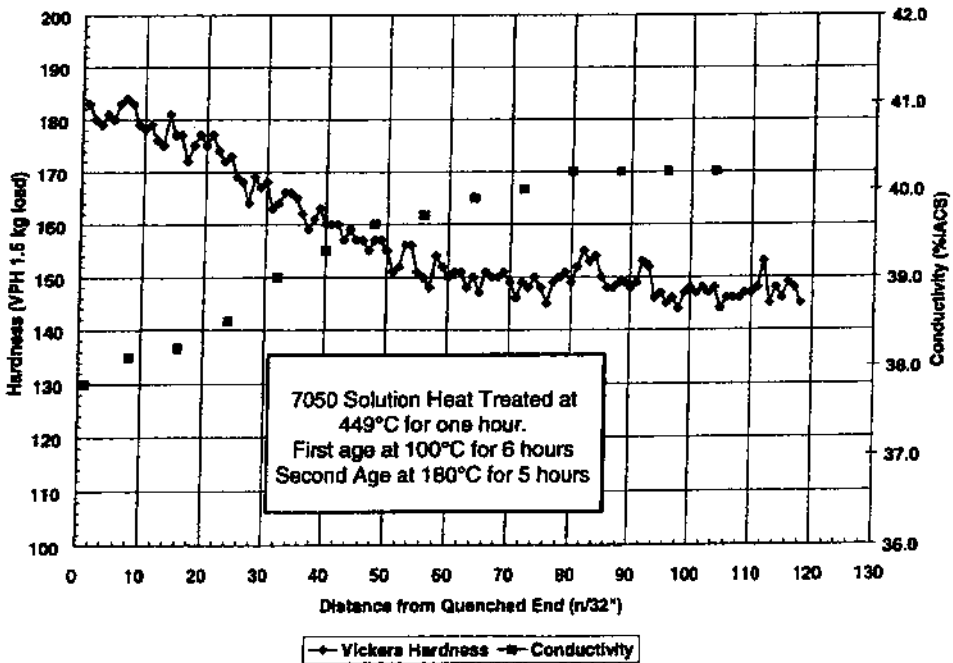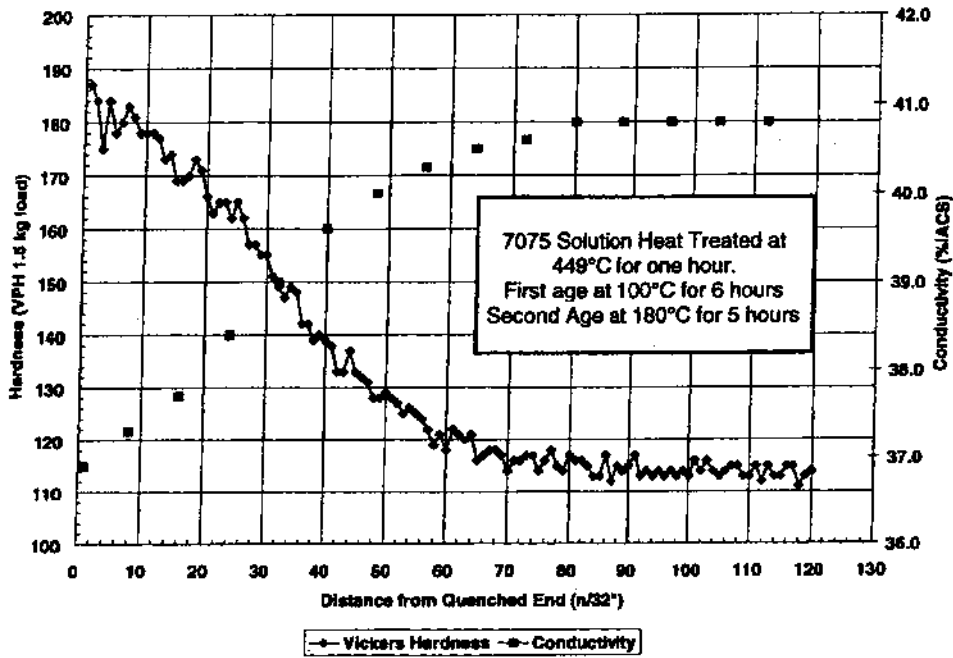
Figure 17 Comparison of hardness and conductivity traverses of AA7075 and AA7050 aluminum Jominy end-quench specimens heat treated and aged identically.
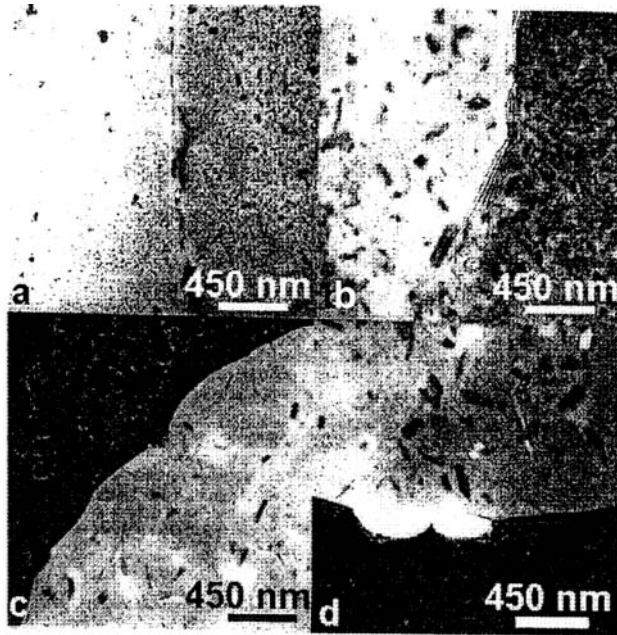
Figure 18 Transmission electron micrographs of 7075 at positions corresponding to (a) 7 mm; (b) 24 mm; (c) 56 mm; (d) 79 mm (110 orientation).
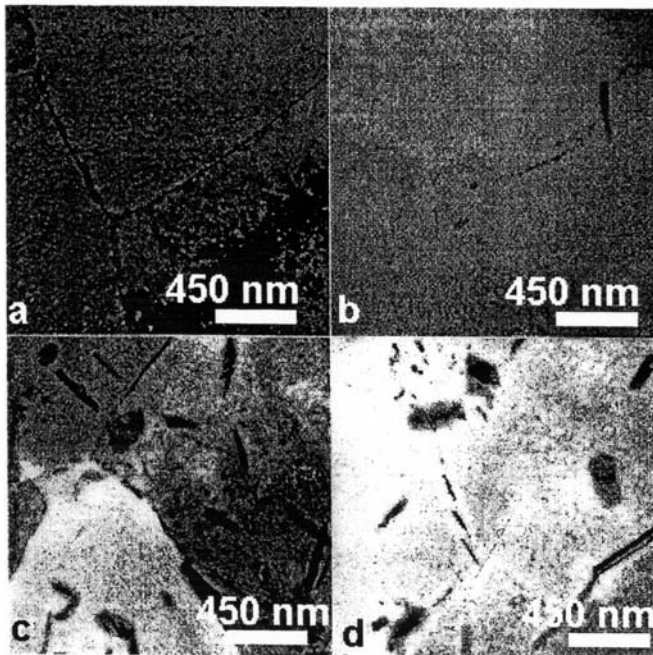
Figure 19 Transmission electron micrographs of 7050 at positions corresponding to (a) 7 mm; (b) 24 mm; (c) 56 mm; and (d) 79 mm (110 orientation).
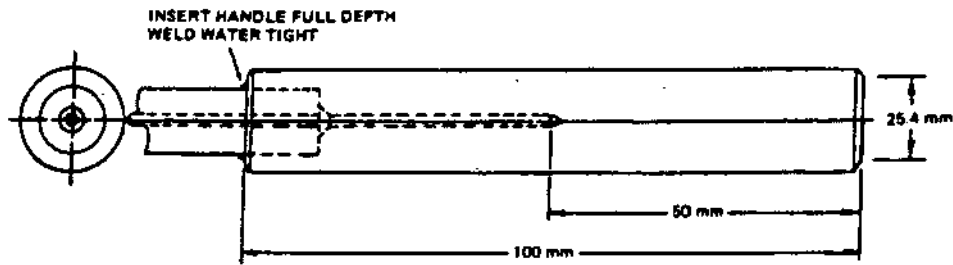
Figure 20 Illustration of an aluminum bar probe.
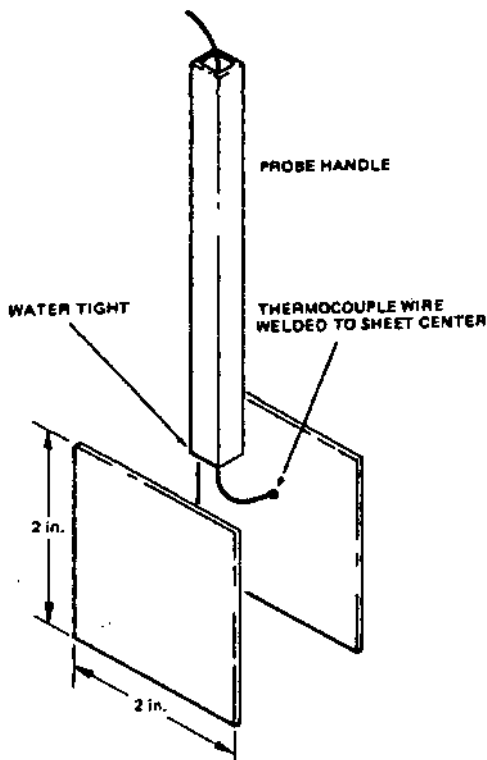
Figure 21 Aluminum sheet probe. Sheet edges must be TIG welded water tight before use.

$T_2 =$ fluid temperature away from surface

$h \ \ =$ interfacial or film coefficient

If this equation is rearranged, h, the film coefficient, can be determined in terms of the area of the part, difference in temperature between the part and the quenchant, and the amount of heat being transferred. An analytical determination of the interfacial heat transfer coefficient, h, requires examination of the properties of the fluid moving past the part, such as boiling temperature, viscosity, density, thermal conductivity, and specific heat. These properties, taken together, combine

to make the quenchant an important, if not the most important, variable affecting quench severity. For example, increases in quenchant velocity generally increase the quench severity. Conversely, increasing the bath temperature reduces the $(T_1 - T_2)$ value, which reduces the rate of heat transfer and decreases the quench severity.

The actual heat flow from the interior of a part being quenched to the surface can be described with Fourier's equation:

$$q = K \bullet A \bullet dT/dx$$

where

q = amount of heat transferred
k = thermal conductivity of the alloy
A = area of the part
dT/dx = thermal gradient in the part

The expression for heat transfer from a bar, neglecting axial heat flow is:

$$\frac{d^2T}{dr^2} + \frac{1}{r} \bullet \frac{dT}{dr} = \frac{1}{\alpha} \bullet \frac{dT}{dt}$$

where

r = bar radius
α = thermal diffusivity
dT/dr = thermal gradient

The Grossman number, defined in the equation below, is also used to describe the rate of heat removal from metal parts and is the ratio of the interfacial heat transfer coefficient divided by twice the metal conductivity:

$$H = h/2K$$

The Grossman number has been reported to equal approximately one for 1 in. sections of steel quenched in water. The film coefficient for various experimental conditions evaluated can be determined by first solving the Fourier equation, using a closed-form heat transfer program which allows specific film coefficients to be employed as input values.

Cooling curves at the center of various-sized bars and plates were calculated and the cooling rate between 425°C and 150°C determined. A polynomial least-squares fit was then obtained to relate the average cooling rate between 425°C and 150°C from the cooling curve, and this value was put into the polynomial expression relating the cooling rate to the imposed film coefficient.

The film coefficient, h, is then determined by recording a cooling curve using a thermocouple located in the center of a test probe, determining the cooling rate between 425°C and 150°C from the cooling curve, putting this value into the polynomial expression relating the cooling rate to the film coefficient and solving for the h value. This procedure provides an average or effective film coefficient over this temperature range. Other investigators have described methods of determining heat flux as a function of time or surface temperature [11–13].

EFFECT OF PROBE SHAPE. Cooling rate variation for round and square bars and flat plates as a function of thickness is shown in Fig. 22 [14]. Croucher and Van Horn have shown that there is no simple direct correlation between round cooling rates obtained in round bars, square bars, and flat plates [14,15]. This conclusion is supported by the data in Table 4 obtained during a still water quench [14]. Similar data for an aqueous polymer quench is not available.

SURFACE OXIDATION. Surface oxidation can substantially retard the cooling rate of aluminum. This is illustrated in Fig. 23(A) and 23(B) for centerline cooling rates obtained from 0.5 in. AA7075 aluminum plates [14]. These data show that to assure reproducible cooling rate results, the surface condition of the aluminum must be specified along with the cleaning process if such data are to be used for predicting mechanical properties in parts.
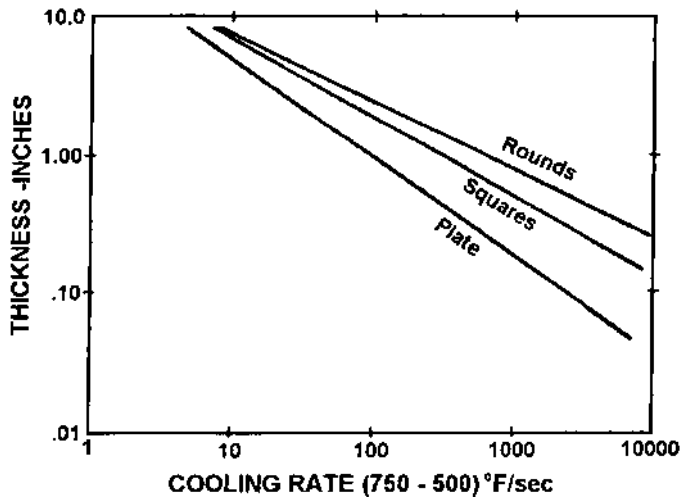
Figure 22 Effect of geometry of the probe shape on cooling rate when quenching into 70°water.

Table 4 Cooling Rate Versus Section Size of Aluminum (75°F, No Agitation)

Section Size	Cooling rate (°F/sec)		
	Plate	Round	Ratio
1	95	1000	10.5
2	23	106	4.6
3	15	41.5	2.8
4	12.5	23.0	1.8
5	10.0	17.4	1.7
6	7.5	13.5	1.8
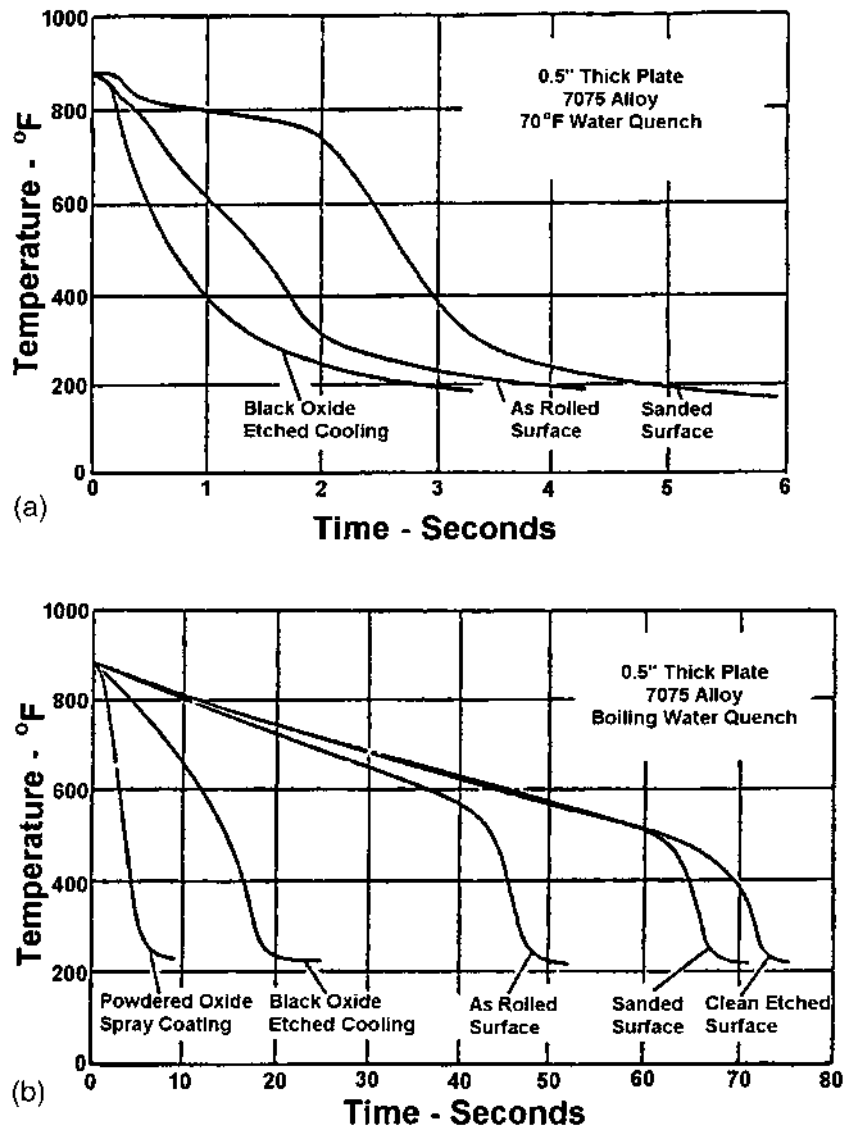
Figure 23 (a) Effect of surface preparation on mid-plane cooling rates of a 0.5 in. thick AA 7075 plate quenched into 70°F water; (b) Effect of surface preparation on mid-plane cooling rates of a 0.5 in. AA7075 plate quenched into boiling water.

2.2.2 Surface Rewetting Measurements

Temperature variation with time during the cooling process can be measured by a thermocouple inserted to the geometric center of a cylindrical probe and the rewetting kinematics studied by measuring the change in conductance between the probe and a counterelectrode during the transition from film boiling to nucleate boiling. Changes in boiling around a probe surface at selected points during quenching in water are illustrated in Fig. 24 [16,17].

(a)   Time (s) ➔

(b)
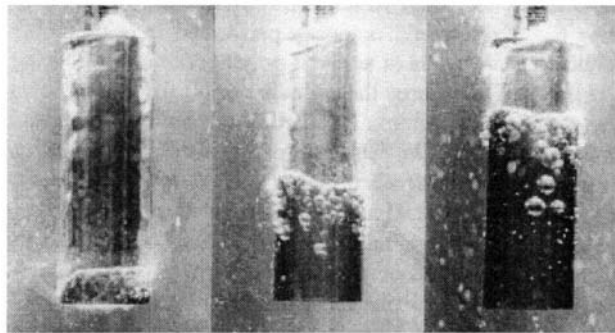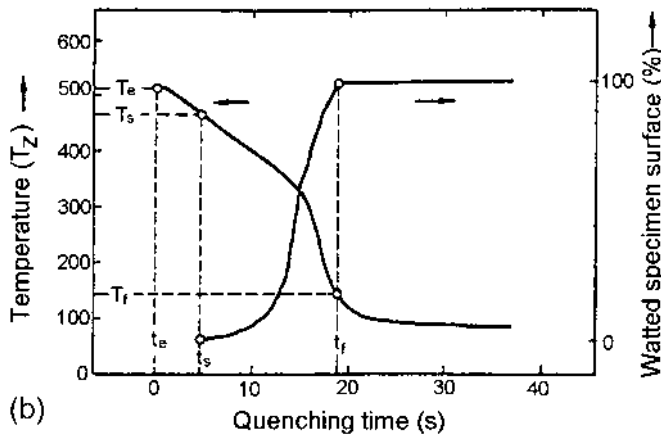
Figure 24 (a) Wetting sequence for a cylindrical specimen quenched in distilled water at 40°C; (b) Temperature T_Z (measured in the center of the specimen) and wetted specimen surface as a function of time during cooling of an AlMg5 sample in distilled water at 80°C T_Z and t_Z: Temperature in the center of the specimen when it is immersed in the quenchant and the time of immersion. T_s and t_s: Temperature in the specimen center and time when wetting starts. T_f and t_f: Temperature in the specimen center and time when the wetting process is concluded.

If the heated probe is completely surrounded by a vapor blanket, the electrical resistance between the probe surface and the counterelectrode is high because of the insulating effect of the vapor blanket. As the vapor blanket collapses, the quenching fluid wets the probe resulting in a reduced resistance and a higher conductance. Using calibration curves, the percentage of the wetted surface area (A) from the conductance (C) and the wetting kinematics (dA/dt) may be determined from the change in conductance with respect to time (dC/dt).

Table 5 Thermal Conductivity and Specific Heat Capacity for Different Materials

Material	Thermal Conductivity (W/M°K)	Specific Heat Capacity (kJ/kg^{-1} K^{-1})
Aluminum 99.5	218@100°C	0.896
Silver 99.5	425@100°C	0.235
Nickel	88.5@100°C	0.448
Cr Ni Steel*	12.6@100°C	0.477
INCONEL 600**	14.8@21°C	0.465

Comparison of Quenching Characteristics of Silver and Aluminum Probes

Silver probes are sometimes used to evaluate the quench severity provided by different quenchants [18,19]. Because of the similarity of the thermal characteristics of silver and aluminum and because of the significantly lower oxidation tendency for silver relative to aluminum, the cooling behavior of AlMgSiCu and a silver (99.5%) probe was compared. Thermal conductivity (λ) and specific heat capacity of various materials is provided in Table 5. Thermal diffusivity (α) is a measure of the "rate of propagation" of a temperature change in a body and is related to the specific heat capacity by:

$$\alpha = \frac{\lambda}{\rho \times C_{\mathrm{p}}}$$

Where: C_{p} is the specific heat capacity, λ is the thermal conductivity and ρ is the density.

Cooling curves recorded during quenching of an aluminum (AlMgSiCu) and a silver specimen (Ag 99.5) in a water-soluble polymer are illustrated in Fig. 25 [16,17]. The aqueous polymer quenchant concentration was 10% by volume and the bath temperature was 25°C. Both probes were cleaned with 600 grit abrasive paper before each test, and the initial probe temperature was 520°C.

The polymer film surrounding the probe surface ruptured simultaneously around the entire surface of both probes (a phenomena called "explosive" rewetting), and the rewetting times ($t_{\mathrm{f}} - t_{\mathrm{s}}$) were extremely short. However, a stable film-boiling stage lasting about 4 sec was observed around the silver probe which was not observed for the aluminum probe. The centerline probe temperature at "rewetting" was about 440°C for silver and 500°C for aluminum. The reason that the rewetting of the silver occurs about 4 sec later for the silver probe is probably due to the higher heat capacity and mass of the silver. This means that it will take longer for the surface temperature to drop to the nucleate boiling stage because more heat must be removed.

When the quenching temperature of the silver probe is increased to 800°C, considerable stabilization of the film-boiling occurs as illustrated in Fig. 26(A) [16]. Wetting now starts at about 260°C after 24 sec compared to the start of wetting of the AlMgSiCu probe after 1 sec at about 500°C. The maximum cooling rate of the silver probe is not reached until a centerline probe temperature of 200°C as shown in Fig. 26(B) [16].
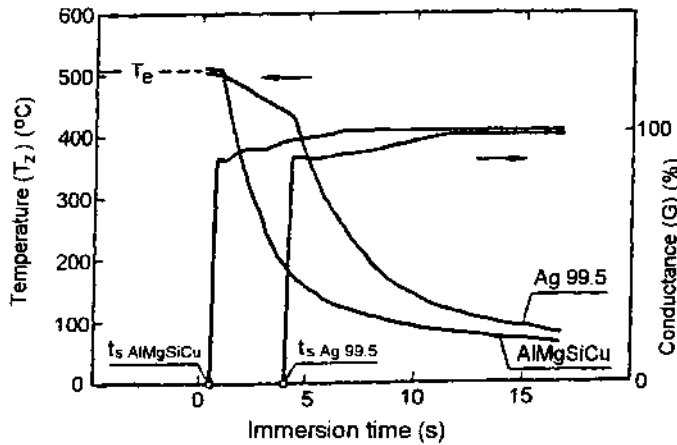
Figure 25 Comparison of the cooling processes of a cylindrical AlMgSiCu probe (dia. 15 × 45 mm) with a silver probe of the same dimensions: probes quenched into a 10% solution of a water-soluble polymer at 25°C (temperatures at the geometric center of the probe); solution treating temperature: 520°C (AlMgSiCu probe); annealing temperature 520°C for the Ag probe.

If distilled water at room temperature is used as the quenchant instead of an aqueous polymer, the silver and the AlMgSiCu probes show almost identical cooling behavior with coinciding rewetting kinematics shown in Fig. 27 [16]. This means that the quenching behavior determined in water with silver probes can be compared with those obtained for aluminum probes. However, when aqueous polymer-quenchant solutions are used, there are clear differences, especially with respect to initial wetting.

Rewetting Kinematics from Quenched Aluminum Probes

Cooling behavior of aluminum during quenching is affected by quenchant composition (type and concentration of a polymer quenchant), bath temperature, temperature of the aluminum being quenched, and surface condition of the aluminum. Aluminum rewetting behavior when quenched into distilled water is strongly affected by bath temperatures above 40°C. The temperatures for the beginning of the rewetting process (T_s) and for the end of the process (T_f) and the elapsed time between t_f and t_s within which the two boiling phases (film boiling and nucleate boiling) are illustrated in Fig. 28, as a function of bath temperature [17]. Up to bath temperatures of 40°C, the probe surface wets very quickly (< 1 sec) and the rewetting process always began at the surface that was geometrically lower in the bath. At temperatures above 60°C (the rewetting time, the time when the entire probe surface is wetted with the quenchant ($t_f - t_s$), increased sharply with increasing bath temperature and the temperature distribution in the probe became extremely uneven. This means that with increasing bath temperature, the precipitation kinetics become increasingly non-uniform in the longitudinal direction. For example, if aluminum castings are quenched in water at ≥60°C to reduce distortion and residual stresses, a stress gradient may be developed from end to end of the part [20,21].
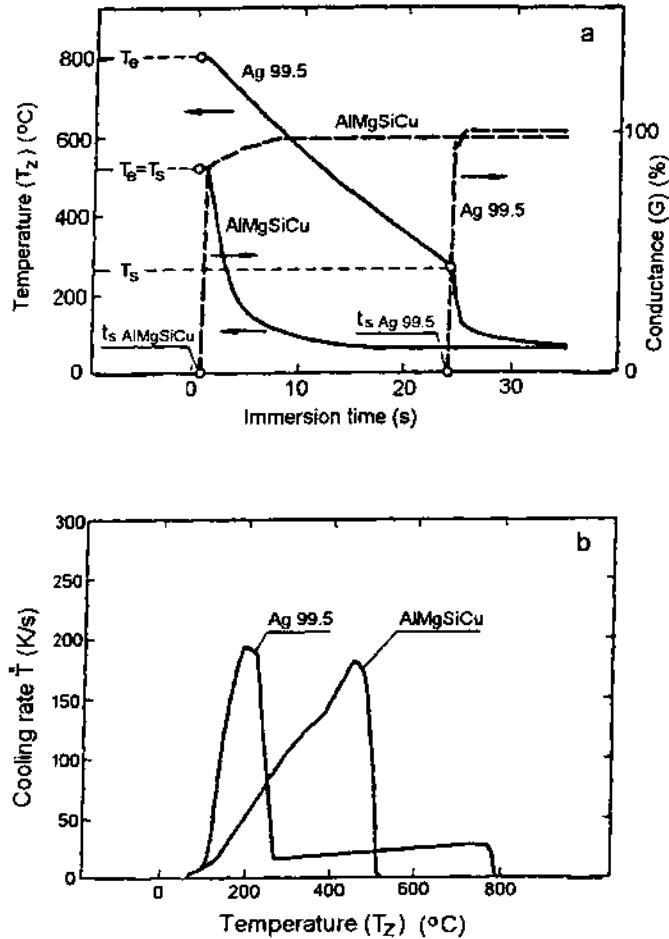
Figure 26 Comparison of the cooling processes of a cylindrical AlMgSiCu probe (dia. 15 × 45 mm) with those of a silver probe; cooled into a 10% solution of a water-soluble polymer at 25°C (temperatures recorded at the geometric center of the probe); solution treating temperature is 520°C for the AlMgSiCu probe; annealing temperature is 800°C for the silver probe; (a) changes in temperature and conductivity as a function of time; and (b) cooling rate as a function of temperature.

These difficulties can be minimized by using water-soluble polymers as aluminum quenchants [22–25]. Aqueous polymer quenchants for aluminum heat treating applications are usually used at bath temperatures of 20–30°C. (See Sec. 2.4.2 for a discussion of polymer quenchants.) The quenching characteristics of polymers in this temperature range are practically independent of bath temperature [25]. Aqueous polymer quenchants provide a less severe quench than cold water and the quench severity can be varied by varying quenchant concentration [24–27].

The effect of polymer concentration on the wetting behavior of a cylindrical AlMgSiCu probe quenched in a commercial polymer quenchant is illustrated in Fig. 29 [16,17]. The time for initial wetting of the probe surface increases with polymer
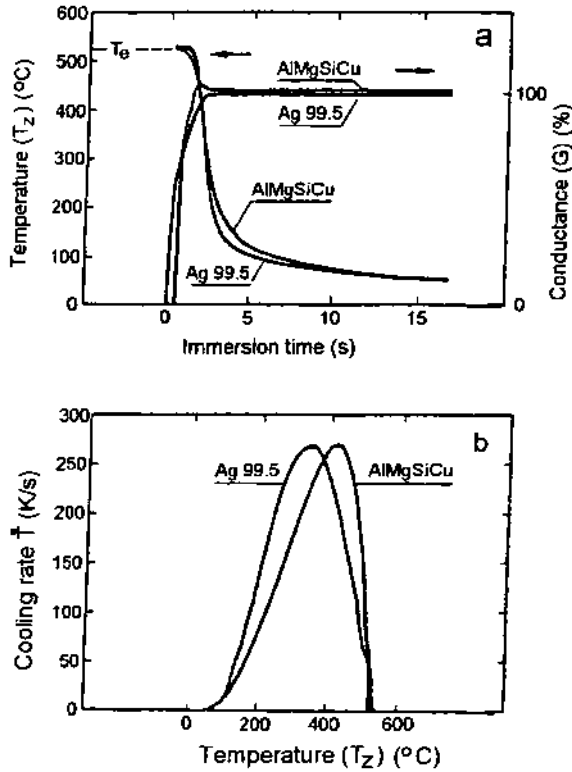
Figure 27 Comparison of cooling processes of a cylinArical AlNIgSiCu, probe (dia. 15 x 45 mn) with those of a silver probe; probes quenched into distilled water at 25°C (probe temperatures recorded at the geometric center); solution treating temperature is 520°C for the AlMgSiCu probe; annealing temperature is 520°C for the silver probe; (a) changes in temperature and conductivity as a function of lime and (b) cooling rate as a function of temperature.

Figure 28 Dependence of temperatures T_s and T_f (measured at the geometric center of the probe) and wetting time ($t_f - t_s$) on bath temperature during immersion cooling of a cylindrical AlMgSiCu probe (dia. 15×45 mm) in distilled water.
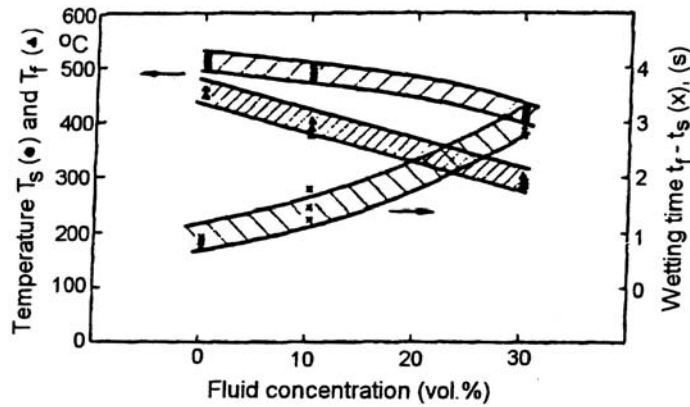
Figure 29 Dependence of temperatures T_s and T_f (measured at the geometric center of the probe) and wetting time ($t_f - t_s$) on polymer quenchant concentration during immersion cooling of a cylindrical AlMgSiCu probe (dia. 15×45 mm) in a water-soluble polymer at $25°C$.
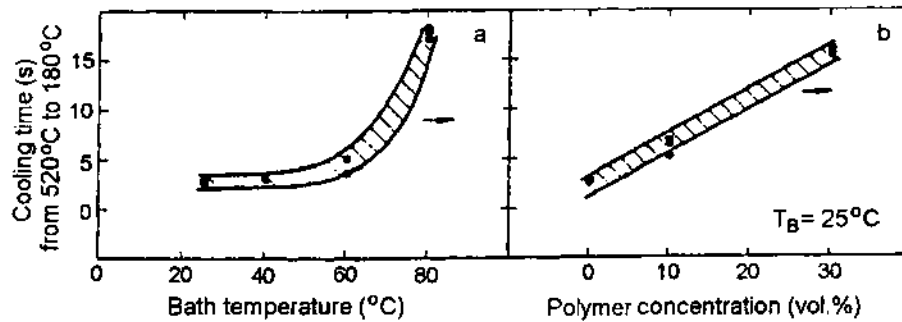
Figure 30 Time required for cooling a cylindrical AlMgSiCu probe (dia. 15×45 mm) from solution treating temperature (temeerature at which the probe was immersed) to $180°C$; (a) Cooling in distilled water at varying bath temperatures; and (b) Cooling in a water-soluble polymer quenchant at varying quenchant concentrations and $25°C$.

concentration which means that film boiling persists for longer periods of time with higher polymer concentrations. This behavior appears in Fig. 29 as a decrease in the starting temperature for wetting (T_s) measured at the geometric center of the probe. The rewetting time increases by only about 2 sec with increased polymer concentrations up to 30%.

   The cooling time from the solution treating temperature where precipitation begins is very important for age-hardenable aluminum alloys [4]. The effect of water temperature and polymer concentration on cooling time has been compared and some results are illustrated in Fig. 30. The cooling time varied between 2 sec and 16 sec but, the effect achieved by varying the polymer concentration in the water was more favorable. (Note: The temperature was measured in the center of the

probe, and this reveals nothing about rewetting behavior on the surface or about the temperature distribution within the probe [16,17]. In addition to bath temperature and polymer concentration, bath agitation is also an important variable [27,28].

Aluminum surface condition during the quenching process has a large effect on quenching rewetting behavior. Surface characteristics can be altered by variations in the duration of solution treatment [29]. The cooling and rewetting behavior of AlMgSiCu cylindrical probes that were solution-treated for various times and then quenched in distilled water ($T_B = 25°C$) are illustrated in Fig. 31. With increasing solution treatment time from 1 min to 180 min, which may increase the depth of the surface oxide layer, the conductance-time curves and temperature-time curves clearly show the retardation of cooling, i.e. a prolonged wetting time with increasing solution treatment time (Fig. 31(A)) [17]. The cooling rate decreased with increasing duration of solution heat treatment as illustrated in Fig. 31(B) [16,17].
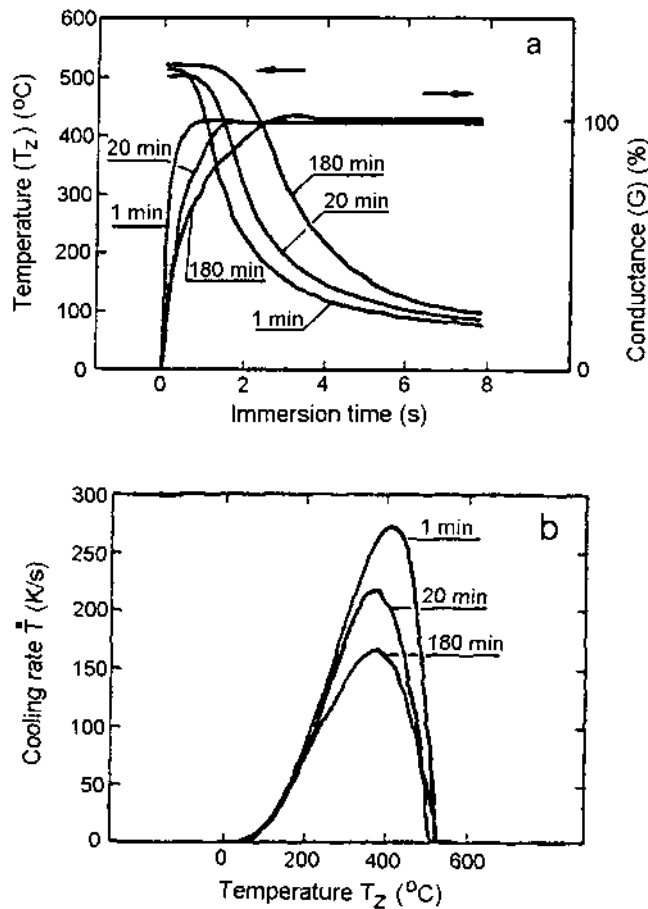
Figure 31 Cooling process of a cylindrical AlMgSiCu probe (dia. 15 × 45 mm) annealed in air for different periods of time: quenchant = distilled water, 25°C, (a) changes in temperatures and conductivity as a function of time; (b) cooling rate as a function of the temperature at the geometric center of the probe.
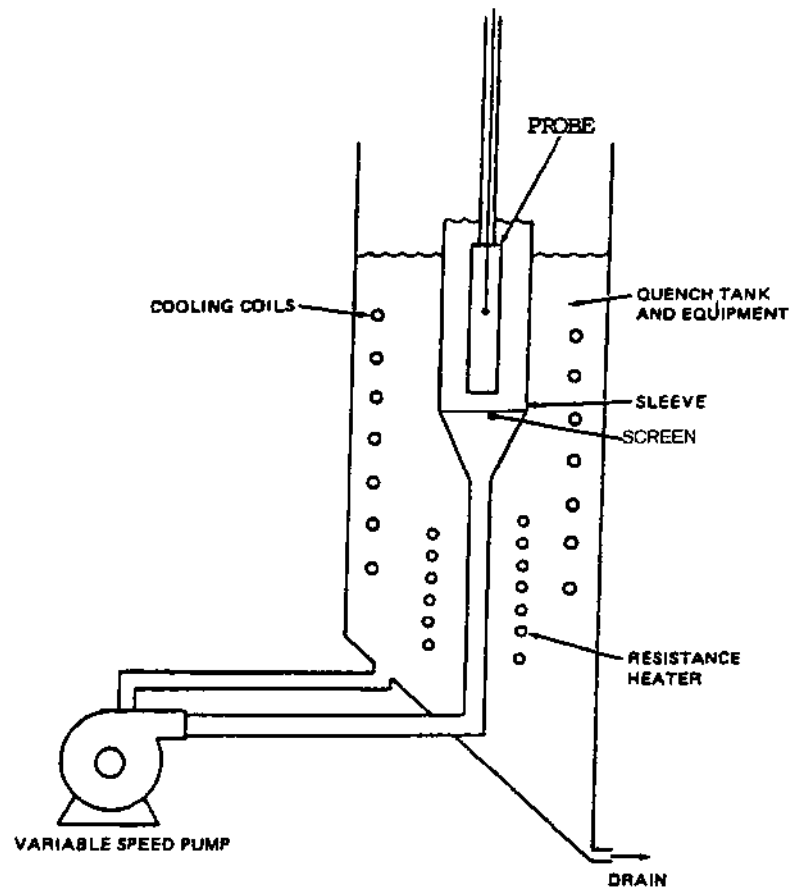
Figure 32   Illustration of the quench tank.

2.2.3   Quench System

Some investigators have proposed instrumented bar and sheet probes that can be preheated in an electrical air furnace or in a fluidized bed and quenched into larger tanks such as illustrated in Fig. 32 [10]. AA7075 bar and sheet probes were solution treated at 870°F and AA2024 alloys were solution treated at 920°F. The quenchant fluid velocity flowing past the probe was controlled with a variable speed pump. The linear flow velocity was calculated using the volume flow from the pump and the cross-sectional area of the sleeve and the probe. The quenchant temperature was controlled to within 2°F and maintained at the correct temperature with resistance heaters and a cooling coil.

Furnace and Racking System
The furnace system utilized for the aluminum sheet distortion is illustrated in Fig. 33. A stainless steel radiation shield was located between the heating elements located on the sides of the furnace and the sheet rack shown in Fig. 34 to protect the panels from
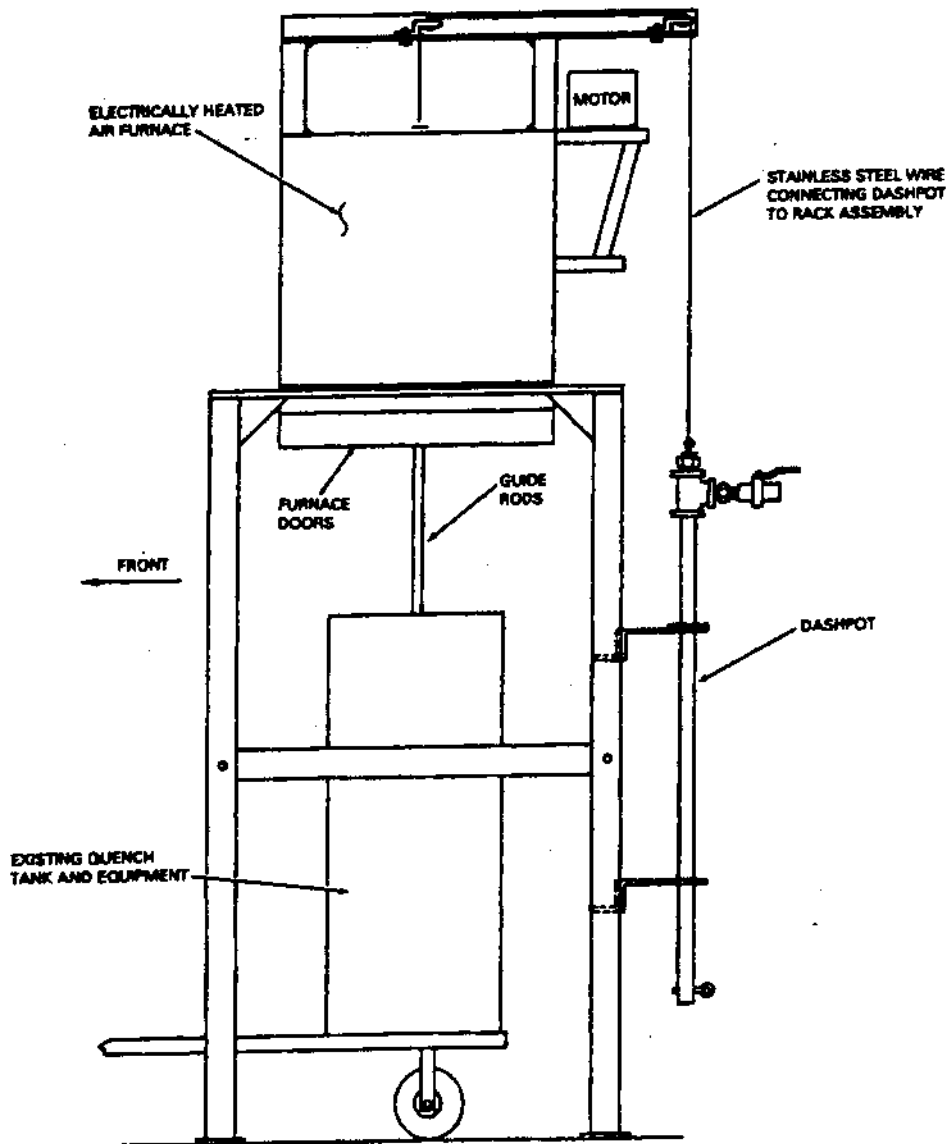
Figure 33 Schematic of the "rapid quench" furnace system and drop mechanism used for sheet distortion studies.

direct radiation. A fan was used to provide brisk air flow for uniform heating. Sliding doors on the furnace bottom provided a seal during soaking and allowed the panels to be dropped at a controlled rate. The furnace was located approximately 5 ft above the floor and the quench system illustrated in Fig. 27 was placed directly underneath the furnace.

(a)

(b)
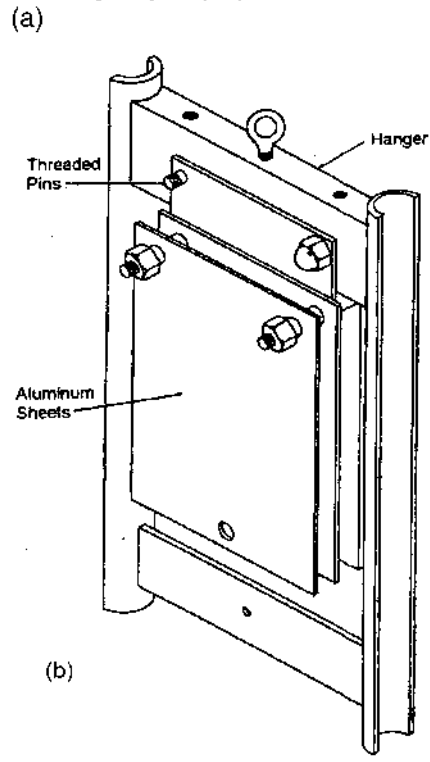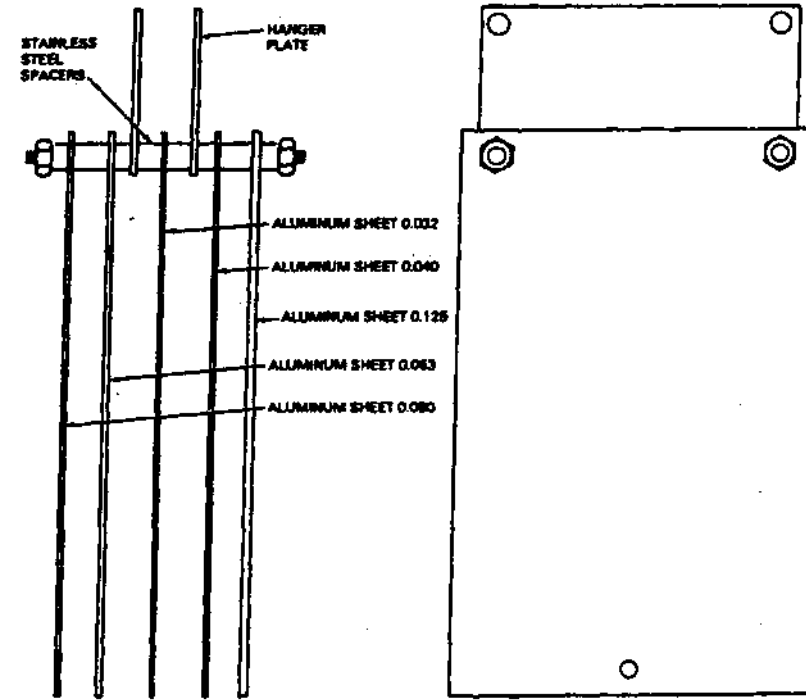
Figure 34 Schematic representation of (a) aluminum sheets, sheet spacing; and (b) rack assembly.

Three 5/16 in. holes were drilled into each aluminum nominal 5×7 in. aluminum panel, as shown in Fig. 34. The sheets were annealed after shearing and machining to remove any mechanically induced residual stress. Two 1/4 in. threaded rods were placed through the top two holes and stainless steel spacers were used to provide at least a 1/2 in. gap between each sheet. Fine gage thermocouple wire was threaded through the bottom hole to secure the lower half of the panels to the hanger. Slack was left in the wire so that any distortion could freely occur. Each rack contained four sheets with thicknesses of 0.032, 0.040, 0.063 and 0.125 in. as shown in Fig. 34(A).

The drop velocity of the rack into the quenchant was controlled using a pneumatic dashpot. The actual drop velocity was determined by measuring the time required for the piston to move a fixed distance. A 20 KHz clock and counter were triggered as the piston moved between the two Hall-effect probes. The distance between the Hall-effect probes divided by the time required for the piston to pass between the probes provided the drop velocity. Total sheet probe distortion was determined photographically. The results are discussed in Sec. 2.7.1.

2.3 Quench Factor Analysis (QFA)

Fink and Willey performed an extensive study of the effects of quenching on the strength of 7075-T6 and corrosion behavior 2024-T4 [30]. This was done by constructing C-curves, which were plots illustrating the times required to precipitate sufficient alloy content to change the strength by a specified amount in AA 7075 (as shown in Figure 35), or change the corrosion from pitting to intergranular (AA 2024). Figure 2 is a C-curve for AA2024 illustrating the critical temperature range for the transition from pitting to intergranular corrosion [31]. Various studies have subsequently determined the relative quench rate sensitivity to different properties for various alloys. Figure 35 illustrates the effect of cooling rate on tensile strength for several aluminum alloys and tempers [2].

The "critical temperature range" is defined as the temperature range that provides the highest precipitation rates [2]. The "average cooling rate", shown in Fig. 37, is determined by dividing the time in seconds to cool from 750°F to 550°F. This technique provides only an approximation of the cooling process for the quenchant and cross-section size of interest since the quenching process may be non-linear, interrupted, or delayed. It is desirable to utilize a process that integrates a cooling curve for the quenching process and cross-section part being used with a C-curve (Time-Temperature-Property) curve for the specific alloy of interest.

Most workers have performed QFA using published C-curves to predict properties. However, it must be remembered that the particular C-curves obtained for an alloy are composition-dependent. This becomes a potential limiting factor in the widespread use of QFA [32,33]. It is essential to validate the properties being predicted.

A numerical process that incorporates all features of the cooling curve in property prediction was developed by Evancho and Staley [2,34]. The principles of the QFA calculation and the experimental procedures used for QFA determination from cooling curve data will be discussed here.
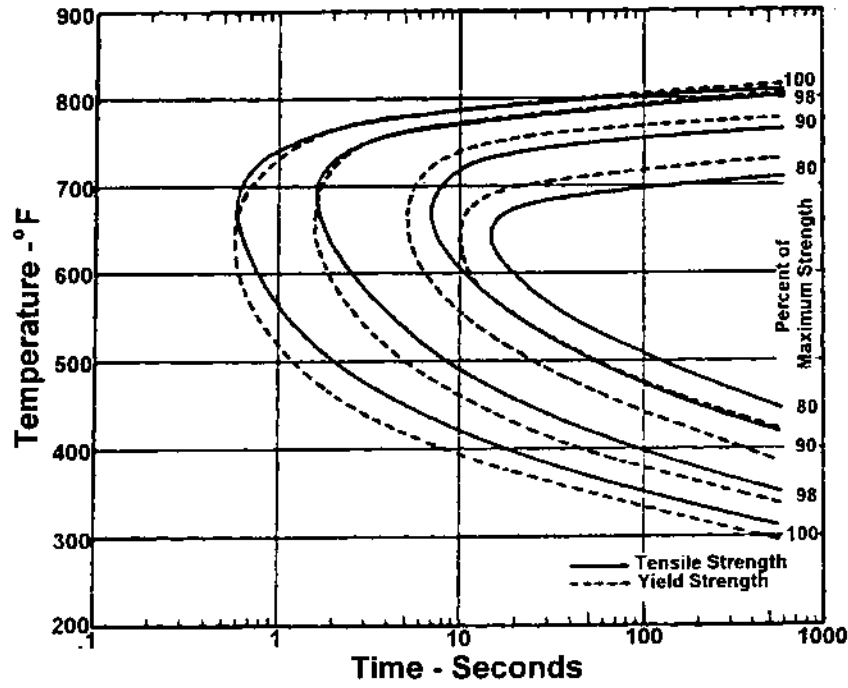
Figure 35 C-Curves illustrating the effect of alloy precipitation on tensile strength for 7075-T6 generated by Fink and Willey. (From Ref. 1.)
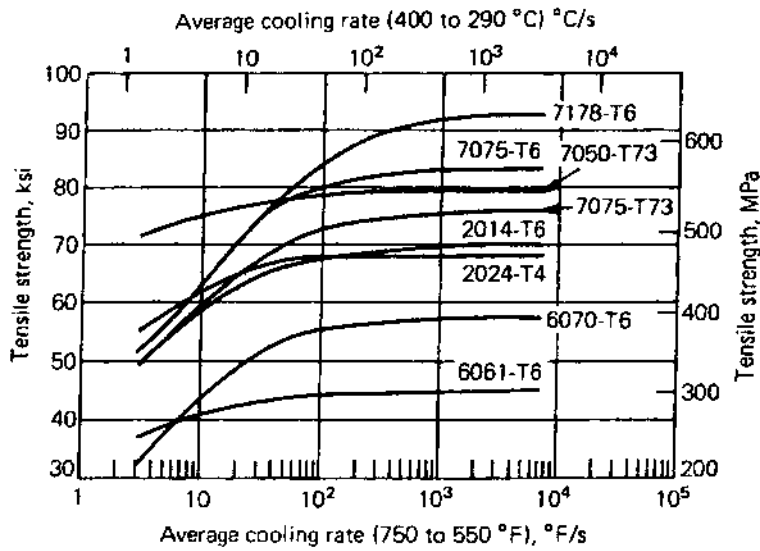
Figure 36 Tensile strength as a function average cooling rate.
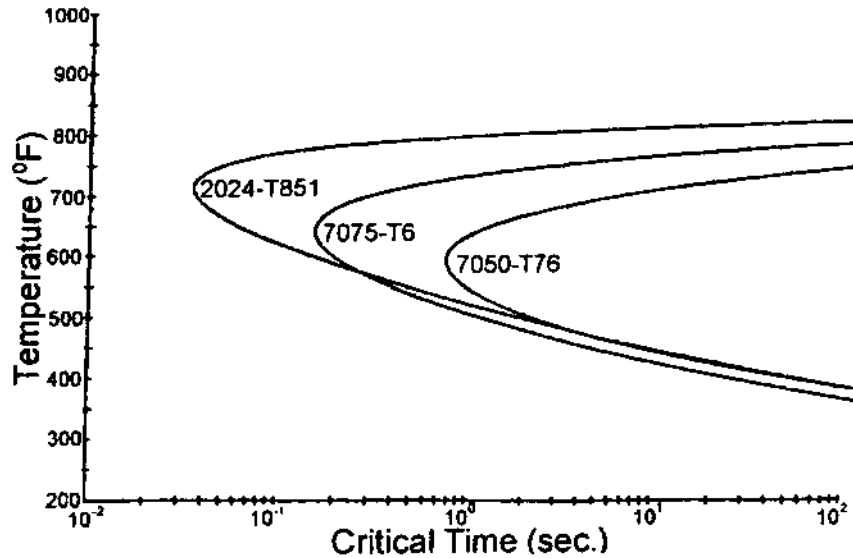
Figure 37 C-curves for 2024-T851, 7075-T6 and 7050–T76 aluminum alloys. (From Ref. 9.)

2.3.1 Calculation of Quench Factors from Precipitation Kinetic Data

The properties of aluminum alloys are dependent on the amount of alloy precipitation that occurs during cooling. The rate law for isothermal precipitation kinetics is [35]:

$$\zeta = 1 - \exp\left[\frac{-t}{k}\right] \tag{1}$$

where: ξ is the fraction of precipitation which has occurred in time (t) and k is a temperature-independent constant. The value of k depends on the degree of supersaturation and the rate of diffusion and is estimated from [36]:

$$k = \frac{C_T}{k_1} = k_2 \exp\left[\frac{k_3 k_4^2}{RT(k_4 - T)^2}\right] \exp\frac{k_5}{RT} \tag{2}$$

where:

C_T = critical time required to precipitate a constant amount (the locus of the critical line is the the C-curves). Coordinates for C_T curves for different aluminum alloys are provided in Table 6 [37,38].

k_1 = constant which equals the natural logarithm of the fraction untransformed (1–fraction defined by the C-curve).

k_2 = constant related to the reciprocal of the number of nucleation sites,

k_3 = constant related to the energy required to form a nucleus,

k_4 = constant related to the solvus temperature,

k_5 = constant related to the activation energy for diffusion,

R = 8.3143 J.K.$^{-1}$ mol^{-1}.

Table 6 Coefficients for Calculating Quench Factors at 99.5% of Attainable Yield Strength

Alloy*	Maximum Strength (σ_m, MPa)	k_1	k_2	k_3	K_4	k_5	Calculated Range (°C)
7050-T76	544	−0.00501	2.2×10^{-19}	5190	850	1.8×10^5	425–150
7075-T6	485	−0.00501	4.1×10^{-13}	1050	780	1.4×10^5	525–150
2024-T851	459	−0.00501	1.72×10^{-11}	45	750	3.2×10^4	425–150
7075-T73	475	−0.00501	1.37×10^{-13}	1069	737	1.37×10^5	525–150

*Alloy heat treatment and temper designations:

7050-T76: Solution treated at 471–482°C, quenched and overaged to obtain exfoliation resistance.

7075-T6: Solution treated at 460–471°C, quenched and aged at 115–125°C, for 22–24 h.

2024-T851: Solution treated at 460–471°C, slack quenched, strained 2.25–2.5%, aged at 190° for 12 h.

7075-T73: Solution treated at 460–471°C, quenched and aged at 100–112°C for 6–8 h and 170–182°C for 8–10 h.
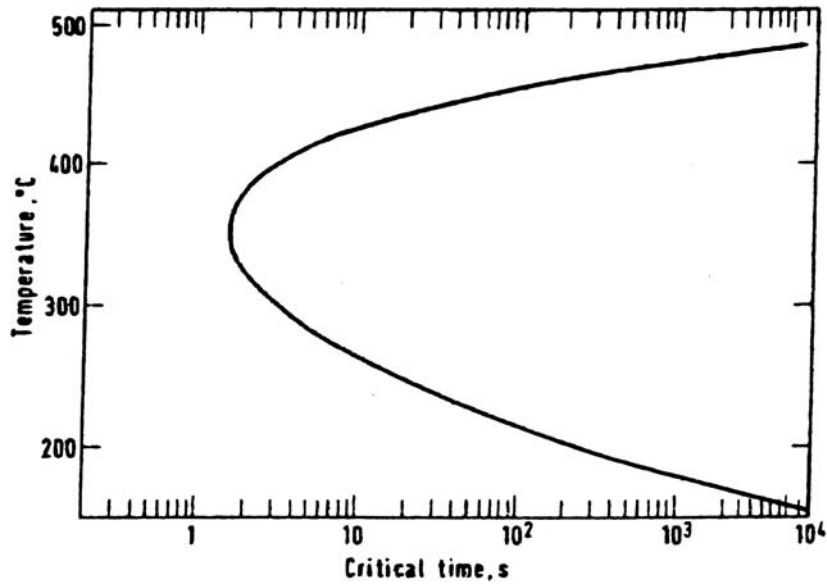
Figure 38 C-Curve for 6351-T6. (From Ref. 7.)

$$T = \text{temperature in } °K.$$

C-curves for different alloys and tempers are illustrated in Fig. 37, 38, 39 and 40.

From these C-curves and the mathematical parameters that describe them, it is possible to redefine the equation for the amount of solute precipitated during the quench (ζ) which can be calculated [2]:

$$\zeta = 1 - \exp\left[\frac{k_1 t}{C_t}\right] \tag{3}$$
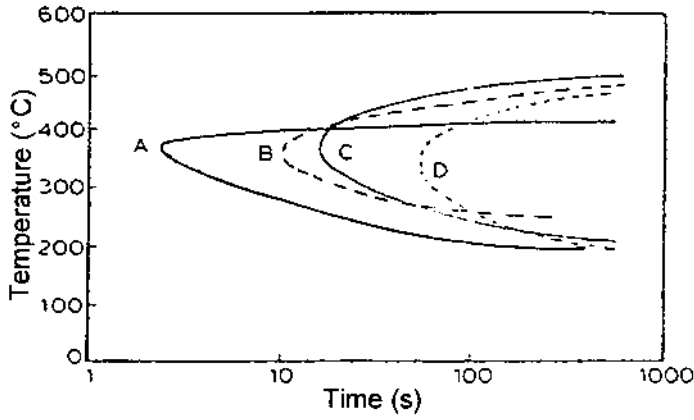
Figure 39 C-Curves for (A) 2017 (B) 7075 (C) 6061 and (D) 6063. (From Ref. 12.)
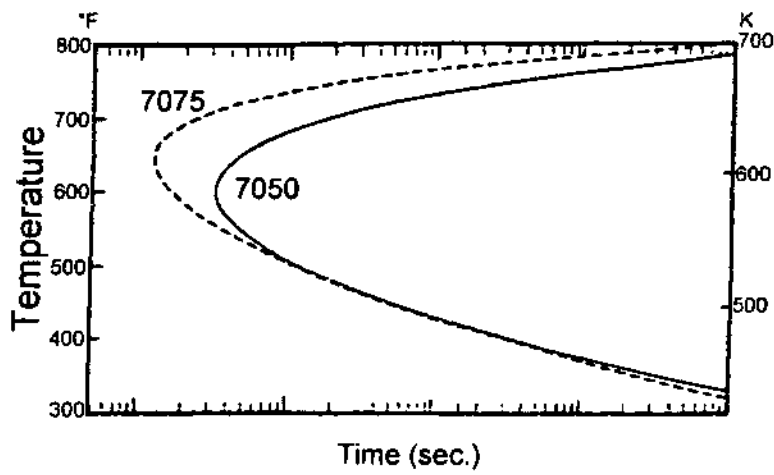
Figure 40 C-Curves for 7075-T6 and 7050-T73. (from Ref. 2.)

Cahn has shown that the transformation kinetics for non-isothermal conditions, such as those that would be present during a typical quenching process, may be described by [36,39]:

$$\tau = \int_{t_0}^{t_f} \frac{1}{C_T} dt \tag{4}$$

where:

C_T = critical time from the C-curve,
t = time from the cooling curve,
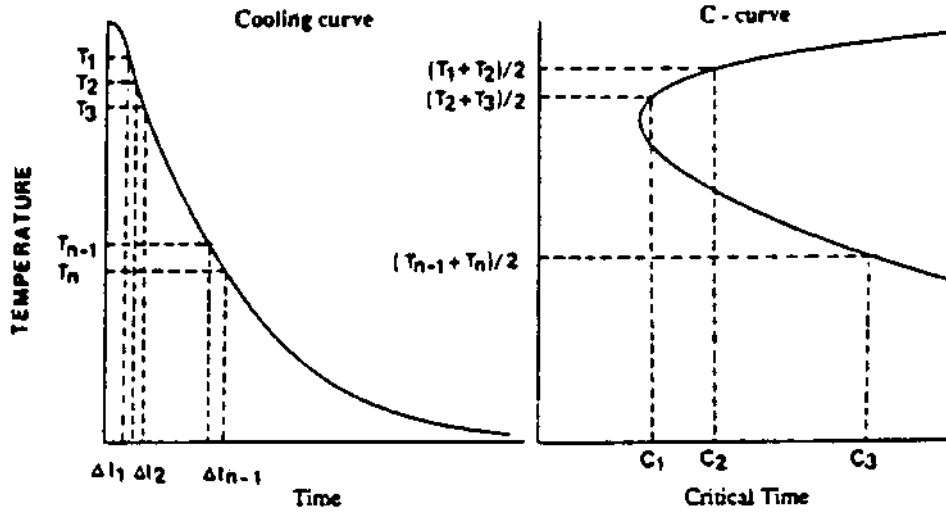
Figure 41 Determination of quench factor ( ) by the combination of a quenchant cooling curve and a C-curve.

t_0 = time at the start of the quench,
t_f = time at the finish of the quench,
τ = measure of the amount transformed (quench factor).

When $\tau = 1$, the fraction transformed equals the fraction represented by the C-curve.

As illustrated in Fig. 38 [35], the quench factor (τ) is obtained by combining the cooling curve for the quenching process with the C-curve and the value for τ is obtained by [2]:

$$\tau = \frac{\Delta t_1}{C_1} + \frac{\Delta t_2}{C_2} + \cdots \frac{\Delta t_{n-1}}{C_{n-1}} = \sum_1^{n-1} \frac{\Delta t_n}{C_n} \tag{5}$$

A graphical representation of a quench factor determined earlier by Kim, Hoff and Gaskell is illustrated in Fig. 41 [35]. The quench factor shown is the area projected on to the ($1/C_T$ - 1) plane.

2.3.2 Experimental Determination of Quench Factors

Figure 43 illustrates the superposition of a cooling curve on a C-curve [37]. Experimentally, cooling curves are obtained by acquiring time-temperature data over finite time steps (Δt_i) which is determined by the data acquisition rate. The average temperature between each time step interval is then calculated. The C_T value is then calculated for each average temperature using the above equation. The ratio of the time step length used for data acquisition, (Δt_i) is divided by the C_T value at that temperature to provide an "incremental quench factor" (q) [37].

$$q = \frac{\Delta t}{C_T} \tag{6}$$
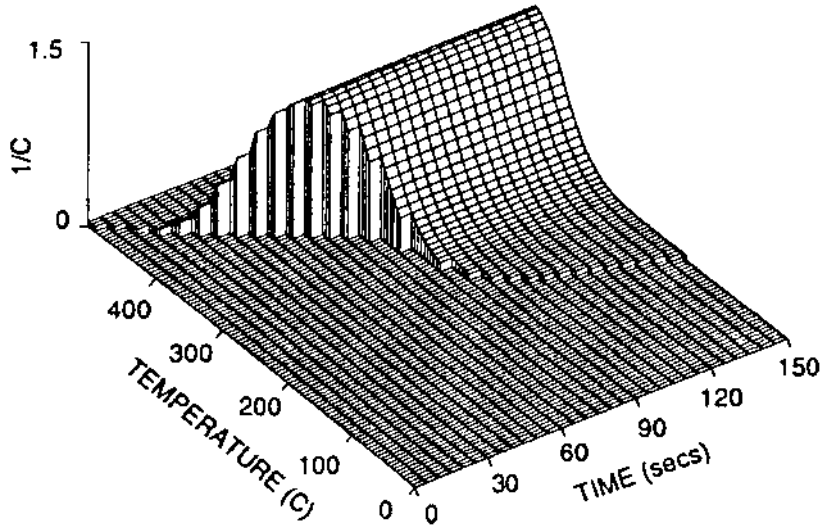
Figure 42 Graphical representation of the quench factor as the area of the "cliff" projected on to the $1/C_T$-t plane [5].
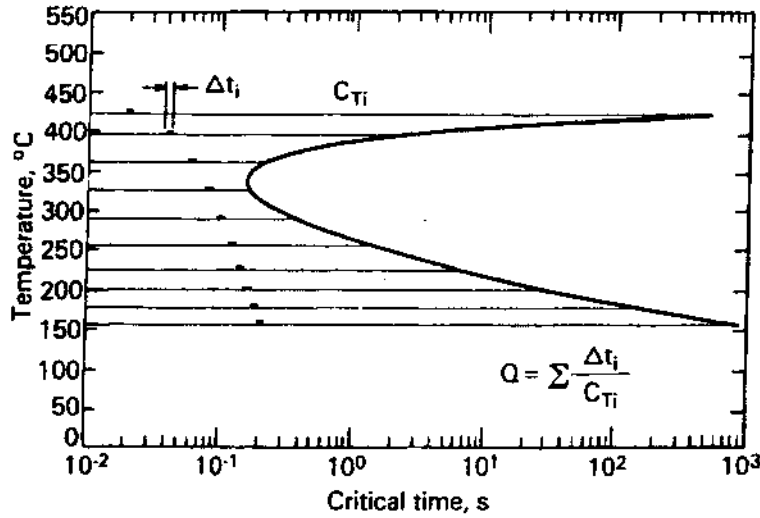
Figure 43 Schematic illustration of the experimental method used for calculating a quench factor.

To obtain the overall quench factor, Q, the incremental quench factor values are summed progressively as the probe or part is cooled through the precipitation range, normally about 800–300°F (425–150°C) as shown in Fig. 43 [37].

$$Q = \sum_{300}^{800} q \qquad (7)$$

Table 7   Effect of Time Step Magnitude on Quench Factor Calculation[a]

Time step, sec	0.1	0.2	0.3	0.4	0.5	0.6	0.7	0.8
Quench factor	1.19	1.19	1.17	1.14	1.30	1.52	1.53	1.33

[a] The values were calculated for a cooling curve obtained by quenching an aluminum probe into 38°C water flowing at 0.25 m/sec.

2.3.3   Effect of Time Step (Δt) Selection

The quench factors for 7075-T73 quenched in 100°F (38°C) water flowing at 50 ft/min (0.25 m/sec) have been studied to determine the effect of the size of the time step on the quench factor calculation. The results of this study are shown in Table 7 [10]. These data show that time step changes in the range of 0.1–0.4 sec caused no appreciable change in the calculated quench factor. However, time step variations between 0.5 and 0.8 sec caused considerable scatter in the calculated quench factor (Q). Excessively long time steps may result in an inadequate number of data points to properly calculate transition in the critical portion (knee) of the C-curve. It is suggested that the time step interval should be selected such that the average temperature drop is not greater than 75°F (25°C) over the critical cooling range for the alloy of interest.

2.3.4   Property Calculation

The tensile strength of the alloy after proper aging can be predicted from the quench factor – Q [2]:

$$\sigma_y = \sigma_{max} e^{K_1 Q} \tag{8}$$

where:

σ_y = predicted yield strength,
σ_{max} = yield strength after an infinite quench (and aging cycle),
e = base of the natural logarithm,
K_1 = In (0.995) = -0.00501
Q = quench factor

The relationship between quench factor and yield strength for 7075-T73 is shown in Fig. 44. [37] Low values of Q are associated with high quench rates, minimum precipitation during cooling and high yield strengths. Conversely, higher Q-values are obtained with slower quench rates and are associated with lower strength values.

An alloy with a low rate of precipitation will produce a lower quench factor (Q) than an alloy with a high precipitation rate at the same cooling rate. Quench factors calculated for different alloys might be different even if similar section sizes are cooled in the same quenchant, because quench factors take into account individual alloy precipitation kinetics by means of the equation describing the C-curve (C_T function) for each alloy.
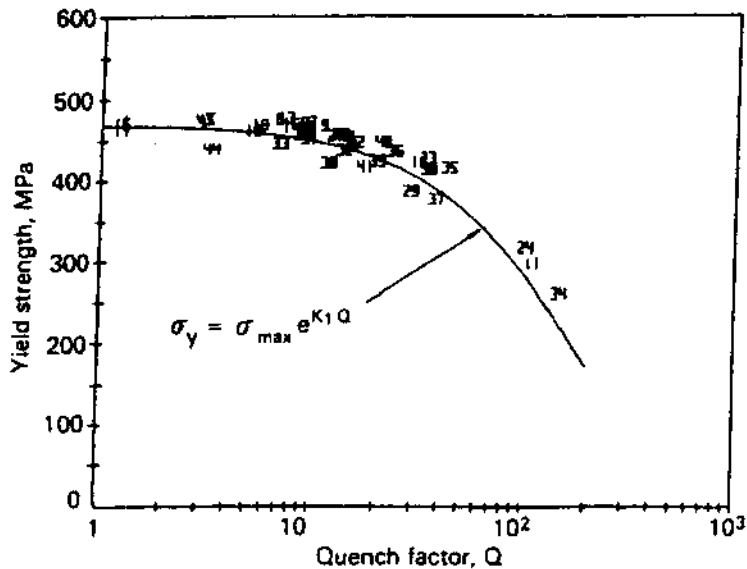
Figure 44 Yield strength of aluminum 7075-T73 as a function of quench factor of the material.

Solute elements are precipitated during cooling from the solution treating temperature at "high" Q-values. As a consequence, an improperly quenched alloy may not properly harden during aging, and it may be susceptible to intergranular corrosion, stress corrosion or exfoliation.

The relationship between quench factor and yield strength for 7075-T73 aluminum extrusions is illustrated in Fig. 44. Forty-five tensile specimens were removed from five lots of bar extrusions ranging in diameter from 12.7 mm to 127 mm (0.5–5.0 in.). Sections of the bar stock were solution treated at 465°C and quenched in water ranging in temperature between 25°C and 100°C. Additional quenching media, including a polymer quenchant, fast oil, and a fluidized bed were also employed.

The standard deviation in yield strength about the regression line was 2.1 MPa and ± 3 standard deviations was 11.0 MPa. This implies that the yield strength in a part can be predicted rather accurately if the $C(T)$ expression for the alloy being quenched is known and if a valid cooling curve is available. The coefficients describing the C-curve for 7075-T73 are given in Table 6. [37]

Since there is a predictable functional relationship between the quench factor and the yield strength of alloys where the C-curve is available, it is possible to select an upper-limit value of Q, above which specified yield strength values can be met statistically. Data relating the quench factor to predicted yield strength in 7075-T73 are given in Table 8 [37].

The minimum allowable properties for aluminum alloys quenched for use in the aerospace industry in the United States are taken from *Military Handbook V* [40]. Table 3.7.3.0 from this source, reproduced in part in Table 9, specifies minimum longitudinal yield strength "A" and "B" design allowable values of 413.7 MPa

Table 8 Relationship Between Quench Factor and Yield Strength in Aluminium Alloy ($\sigma_{max} = 475$ 1Mpa).

Quench Factor (Q)	% Attainable Yield Strength	Predicted Yield Strength (MPa)	Quench Factor (Q)	% Attainable Yield Strength	Predicted Yield Strength (MPa)
0.0	100.0	475.1	26.0	87.8	417.2
2.0	99.0	470.2	28.0	86.9	413.0
4.0	98.0	465.4	30.0	86.0	408.9
6.0	97.0	461.3	32.0	85.2	404.7
8.0	96.1	456.5	34.0	84.3	400.6
10.0	95.1	451.6	36.0	83.5	396.5
12.0	94.2	447.5	38.0	82.7	393.0
14.0	93.2	442.7	40.0	81.8	388.9
16.0	92.3	438.5	42.0	81.0	384.7
18.0	91.4	434.4	44.0	80.2	381.3
20.0	90.5	429.6	46.0	79.4	377.2
22.0	89.6	425.4	48.0	78.6	373.7
24.0	88.7	421.3	50.0	77.8	396.6

Table 9 Design Mechanical and Physical Properties of 7075 Aluminum Alloy. Specification: QQ-A-200/11. Form Extrusion (Rod bars and Shapes) Temper: T73, T73510, T73511

Cross-sectional area, cm²		≤129		≤161								≤129		>129 ≤206	
Thickness, mm		1.57–6.32		6.35–12.67		12.70–19.02		19.05–38.07		38.10–76.17		76.20–114.27		76.20–114.27	
Basis		A	B	A	B	A	B	A	B	A	B	A	B	A	B
Mechanical Properties Mpa	F_tu L	469	496	483	510	483	503	483	503	476	510	469	490	448	483
	F_tu LT	495	483	469	496	462	483	455	476	427	462	400	421	386	414
	F_ty L	400	421	414	434	414	434	414	434	407	448	393	427	379	414
	F_ty LT	386	407	393	414	393	414	386	403	352	386	317	345	303	331

and 434.4 MPa respectively to 19–38 mm thick extruded rods, bars and shapes. The data in Table 8 indicates that, to meet the A allowables, the quench factor for 7075-T73 must not exceed 28.0 and to meet the B allowables, the quench factor must not exceed 18.0. These values represent upper-limit values. To provide an adequate safety margin, and to accommodate other variables in the quench system such as racking differences, a quenchant capable of providing somewhat lower quench factors in the section thicknesses being heat treated must be used.

2.3.6 Quenchant Selection

The upper limit quench-factor value has been defined, above which properties in quenched parts cannot be expected to meet specified minimum values. The question now becomes how to select quenchants that will provide appropriate quench factors in section thickness of interest.

The ability of a particular medium to provide adequate properties can be evaluated by instrumenting a variety of probe sizes, solution treating each one, quenching the probes into quenchant solutions of interest, recording the cooling curves, and calculating film coefficients and quench factors. In one study, 7075 probes were solution treated at 465°C and quenched in a variety of solutions under controlled conditions using a 25.4 mm round probe constructed as shown in Fig. 20 [38].

Table 10 provides experimental data for water under a range of velocity and temperature conditions. The film coefficient, h, provides useful information about the rate of heat removal from the surface of a part. The thermal conductivity of

Table 10 Quench Factors and Film Coefficients Obtained with a 25.4 mm diameter 7075-T73 Alloy Probe Quenched in Water Under Various Conditions

Water Temperature °C	Water Velocity, m/s	Quench Factor, Q	Effective Film Coefficient (h), W/cm^{2}K
27	0.00	2.87	3.89
	0.25	2.72	4.22
	0.50	2.36	5.53
38	0.00	3.12	3.43
	0.25	2.73	4.05
	0.50	2.39	6.05
49	0.00	3.22	2.67
	0.25	2.75	3.53
	0.50	2.23	3.27
60	0.00	3.83	1.83
	0.25	3.02	2.76
	0.50	2.45	2.76
71	0.00	12.53	0.35
	0.25	4.38	1.39
	0.50	3.65	1.31
82	0.00	24.22	0.37
	0.25	13.78	0.70
	0.50	10.38	0.89

Table 11 Quench Factors and Film Coefficients Obtained with Various Diameter 7075-T73 Alloy Probes Quenched in 30°C UCON® Quenchant A Solutions Under Selected Conditions

Quenchant Concentration, %	Probe Diameter, mm	Quenchant Velocity, m/sec	Quench Factor, Q	Effective Film Coefficient (h), W/cm²K
	12.7	0.00	2.7	1.64
		0.25	2.3	1.80
10	25.4	0.00	5.8	1.79
		0.25	5.7	1.79
	38.1	0.00	8.8	1.87
		0.25	8.8	1.82
	12.7	0.12	3.7	1.11
20	15.4	0.12	8.1	1.38
	38.1	0.12	12.1	1.35
	12.7	0.00	5.2	0.66
		0.25	5.0	0.79
30	25.4	0.00	11.2	1.22
		0.25	10.7	0.97
	38.1	0.00	17.1	0.88
		0.25	16.2	0.92

7075 aluminum is about $1.70\,W/cm^2K$. Unagitated water at 25°C has a film coefficient of about $3.9\,W/cm^2K$. The film coefficient increased to 4.22 and $5.53\,W/cm^2K$ at velocities of 0.25 and 0.50 m/sec, respectively. With these high film coefficient values, cold water quenching can create high thermal gradients from surface to center of parts and high temperature differences between thick and thin sections. The film coefficients generally decrease with increasing water temperature until, at temperatures of 70–80°C, they were in the range of $0.35–1.3\,W/cm^2K$. A more extensive listing of water quenching data is provided in the Appendices.

Similar data on polymer solutions under selected conditions are provided in Table 11. Depending on section size, the 20% solution of a polymer quenchant produced quench factors of approximately 4–12 and film coefficients of approximately $1.2–1.4\,W/cm^2K$ when the bath was operated at 30°C and with velocities of about 0.12 m/sec. (A more extensive listing of quenchant data for a polymer quenchant is provided in the Appendices.)

If the effective heat transfer coefficient, **h**, between the part and the quenchant is established, the quench factor in commercial parts can be calculated using finite element or finite difference heat transfer programs. The results of calculations on sheets and plates made using constant film coefficients are shown in Fig. 45 and 46, respectively. These diagrams illustrate the interrelationship between 7075 aluminum sheet or plate thickness, film coefficient and quench factor. The calculations for these graphs were performed using the film coefficients indicated at the ends of the diagonal lines, each of which represent a line of constant film coefficient.
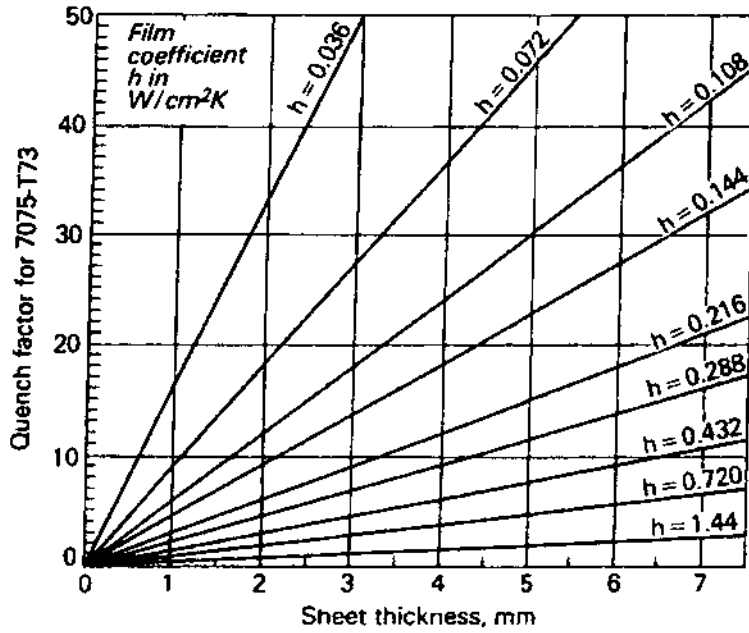
Figure 45 Effect of sheet thickness on film coefficient on the quench factor for AA7075-T73 alloy.
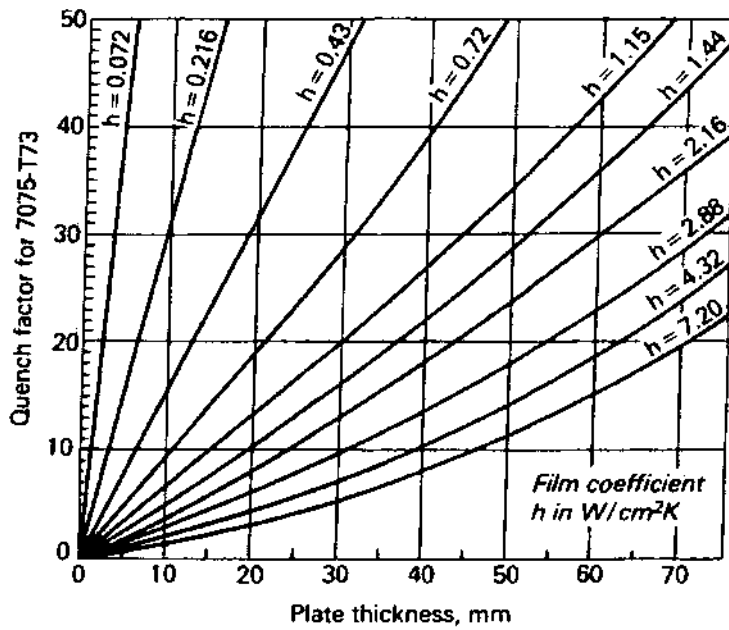
Figure 46 Effect of plate thickness on film coefficient on the quench factor for AA7075-T73 alloy.

The important feature of these figures is that, when used in combination with Table 8, which relates quench factor to predicted yield strength, and data on film coefficient such as that presented in Table 10 and 11, estimates can be made about the ability of specific quenching media and operating conditions to provide cooling rates sufficiently high to meet minimum mechanical properties in parts of various thicknesses. Using a previous example, *Military Handbook V* specifies a ''B'' allowable minimum strength in 7075-T73, in 19–38.1 mm thick extrusions, of 434.4 Mpa [40]. The upper-limit Q-value capable of meeting this strength is 18.0.

Boiling water without agitation has a film coefficient of $0.20 \, \text{W/cm}^2\text{K}$ and could not be expected to provide an acceptable quench factor in a 20–38 mm thick section. This can be determined by locating the upper-limit Q value of 28 on the ordinate of Fig. 46, following this value horizontally until it intersects the diagonal line representing a film coefficient of $0.21 \, \text{W/cm}^2\text{K}$, and the reading the abscissi value for the maximum thickness that can be expected to be properly quenched. In this case, the maximum hardenable thickness is expected to be about 5.5 mm. To produce an acceptable quench factor in a 38 mm thick plate, a quenchant providing a film coefficient of about $2.16 \, \text{W/cm}^2\text{K}$ or higher is required. A film coefficient of $2.88 \, \text{W/cm}^2\text{K}$ provides a higher margin of safety, and will produce a quench factor of about 6 in a 19 mm-thick plate and a quench factor of 113 in a 38.1 mm-thick plate. High film coefficients can be obtained by immersion quenching in agitated cold water, brine, or with high-pressure spray quenching.

2.3.5 C-curve Availability

There are a number of problems that have prevented widespread acceptance of quench factor analysis procedures by the general heat treating industry. One of the most often encountered criticisms of the quench factor calculation is the unavailability of C-curves for performing QFA calculations. Although it is true that there is not extensive data, C-curves for many of the more commonly encountered alloys have been published. See Table 6 and Fig. 37–40.

C-curves have been reported for other alloys but are not shown here. These include: 2219-T87, 2024-T851, and 2024-T351 [34]. Unfortunately, few C-curves for quench hardenable aluminum casting alloys have been published [42].

Bates has summarized the C_{T} constants for a limited number of alloys and tempers which can be used in quench factor calculations [37,38]. These values are summarized in Table 6.

2.4 Quench Media

2.4.1 Water

When water is used to quench age-hardenable aluminum alloys, heat transfer from the workpiece to the quenchant is controlled by events occurring in three stages: film boiling, nucleate boiling and convective heat transfer. Film boiling occurs upon initial immersion. This is a slow cooling process because the hot surface is surrounded by a vapor blanket. As the part cools, the vapor blanket collapses and nucleate boiling begins. The transition temperature between film boiling and nucleate boiling is called the ''Leidenfrost temperature''. Heat transfer is fastest during nucleate boiling, and the heat transfer coefficient, α, for nucleate boiling
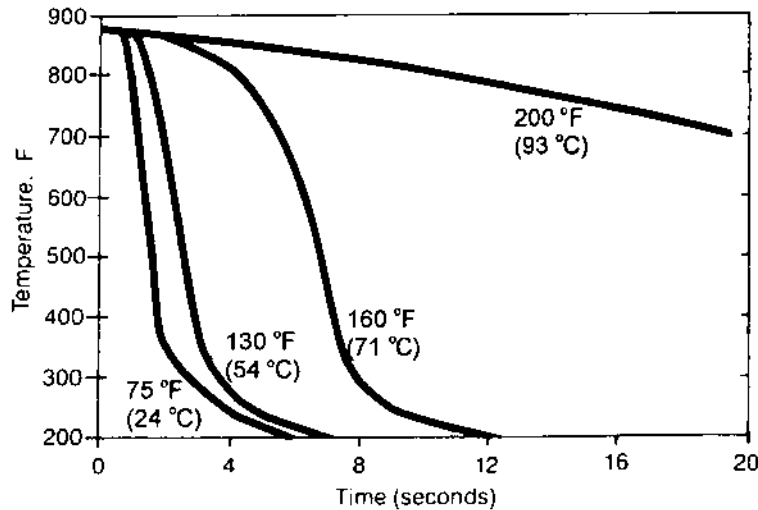
Figure 47 Cooling curves as a function of water temperature for 1/2 in. 7075 aluminum plate.

is about 100 times the value of α during film boiling [43,44]. When the part has cooled below the boiling point of the quenchant, the rate is again reduced during the convective heat transfer stage.

Since aluminum solution heat treatment temperatures are significantly higher than the Leidenfrost temperature, film boiling is to be expected initially when quenching into water [45,46]. If the surface temperature at any point on the workpiece is less than the Leidenfrost temperature, stable wetting and nucleate boiling will occur at that point [47–49]. Figure 24 illustrates a typical wetting sequence during cooling of a cylindrical specimen quenched in distilled water at 40°C. The simultaneous presence of different boiling phases with the heat transfer coefficient of one surface region greater than 100 times the other causes extremely uneven workpiece cooling. This will strongly affect the wetting processes and result in substantial thermal gradients and increased distortion during quenching. The boiling mechanism is stabilized by increasing the water temperature and it is clearly evident above about 55°C as illustrated in Fig. 47 [50,51].

The consequences of uneven cooling include [16,17]:

- Regions where the film boiling persists have more precipitate formation during quenching, than regions of faster cooling (low t_s). During age-hardening, these regions (high t_s) experience a smaller increase in hardness and also exhibit greater potential for intergranular corrosion than neighboring regions where the cooling rate was faster.
- Volume regions where film boiling persists exhibit a much lower yield point during the cooling process than regions with shorter film-boiling phases. The non-uniformity of this process can result in significant plastic deformation and increased distortion due to increased thermal stresses.
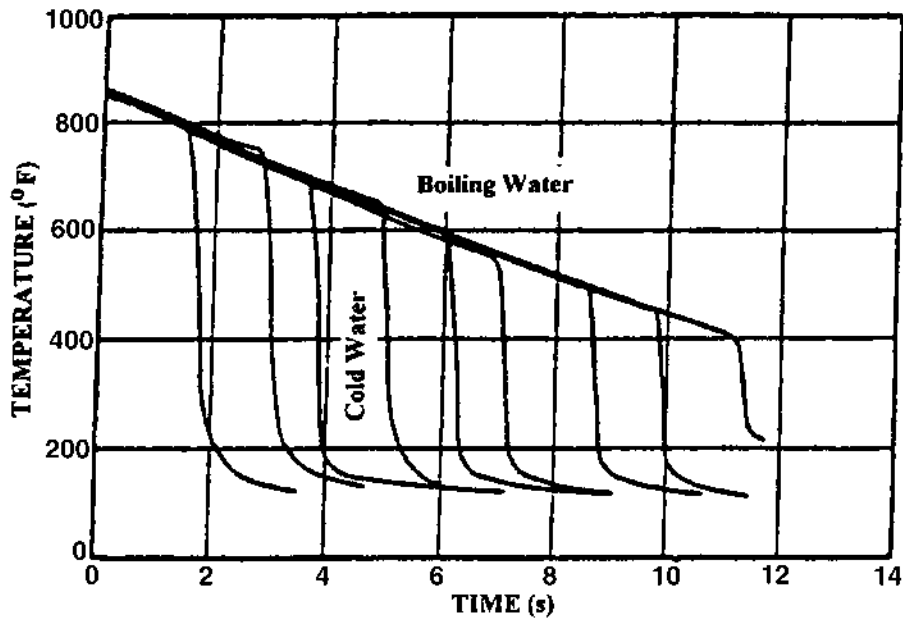
Figure 48 Delayed quenching cooling curves for 0.064 in. thick 7075 aluminum alloy quenched in boiling and cold water.

Therefore, determination and characterization of the cooling processes involved in quenching is critically important, especially with water quenching. To satisfy this need, a process to quantitatively measure the rewetting process of standard quenched aluminum probes was developed [52,53]. (See Sec. 2.2.2. on Rewetting measurements.)

Age hardenable alloys such as 2024, 2219, 7075, 7050 and 6061 are often quenched in cold water. However, cold water quenching may produce unacceptable distortion due to the high thermal gradients produced. One of the earliest alternatives to cold water quenching was ''delayed quenching''. For example, Fink and Willey used a delayed quenching process where the aluminum alloy was initially quenched in boiling water and then transferred to a cold water quench bath at the appropriate time, as illustrated in Fig. 48 [30].

Alternatively, if distortion problems are encountered with cold water (50–90°F, 10–32°C) quenching, then ''hot water'' (140–160°F, 60–71°C) quenching is used [50]. Cooling curves as a function of water temperature are provided in Fig. 47 and properties of AA7075-T73 aluminum plate as a function of water temperature are given in Fig. 49 [50].

Agitation Rate Dependence
Quench factor charcterization of quenching media can provide a valuable insight into the quenching of aluminum alloys with water [54]. Many practices in the United
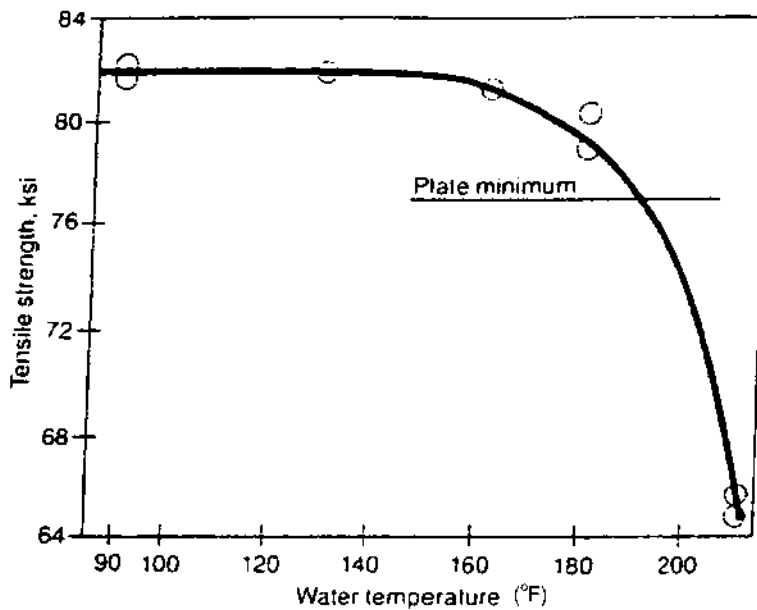
Figure 49 Tensile strength of 1 in. 7075 aluminum plate as a function of water temperature.

States allow a water quenchant temperature range from 49°C to 60°C. The influence of water temperature and velocity on the quench factor obtained for 7075-T73 aluminum alloy is illustrated in Fig. 50(A) and 50(B) for 25.4 mm and 38.1 mm sections. The quench factor is relatively constant in 12.5 mm and 38.1 mm diameter extrusions, irrespective of water velocity, so long as the water temperature is below about 50°C. However, at low velocities when quenching in 70°C water, which is allowed by AMS 2770, the quench factor may vary by 300% depending on the water velocity around the part.

Thus, the attainable properties are highly dependent on both the localized circulation velocity and temperature, especially in the range 0–0.25 m/sec. Many quench tanks use relatively low quenchant velocities and the result may be erratic and uncontrolled aging response. Furthermore, it may also be noted by comparing Fig. 50(A) and 50(B) that the quench factor variation increases as the section size increases. These data show that it is insufficient to specify only water temperature to assure meeting minimum properties. The circulation velocities required must also be specified.

2.4.2 Polymer Quenchants

Although hot water quenching has been used for many years to reduce quench distortion in aluminum, excessive distortion still sometimes occurs. In such cases, an aqueous poly(alkylene glycol)-PAG copolymer solution may be used. The distortion reduction advantages of PAG quenchants relative to both cold and hot water are illustrated in Fig. 51 [55]. PAG polymer quenching media were first reported by Blackwood and Cheesman [56]. Polymer quenchants are solutions of water, a polyalkylene glycol copolymer and additives such as corrosion inhibitors.
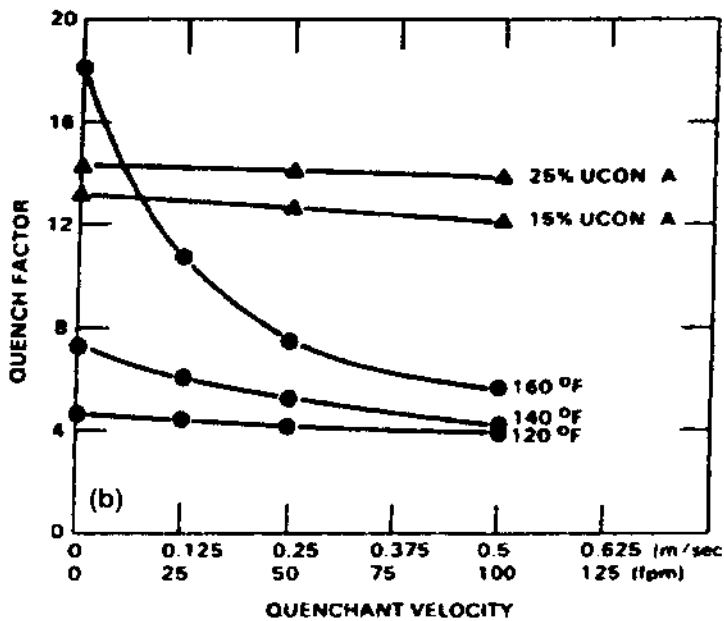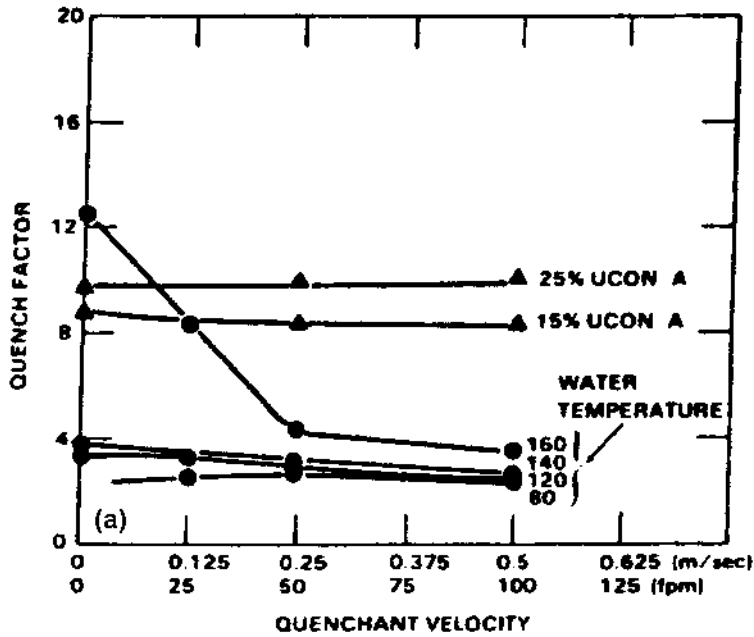
Figure 50 Effect of agitation rate and temperature on quench factor for (a) 1.0 in. (25.4 mm) and (b) 1.5 in. (37.6 mm) diameter round bars of 7075-T73 aluminum.

Water - 85 F
Agitation Rate - 25 FPM
Total Distortion - 1.55 in.

Water - 160 F
Agitation Rate - 25 FPM
Total Distortion   1.385 in.

UCON⁹ Quenchant A 20%
Agitation Rate   25 FPM
Total Distortion - 0.12 in.
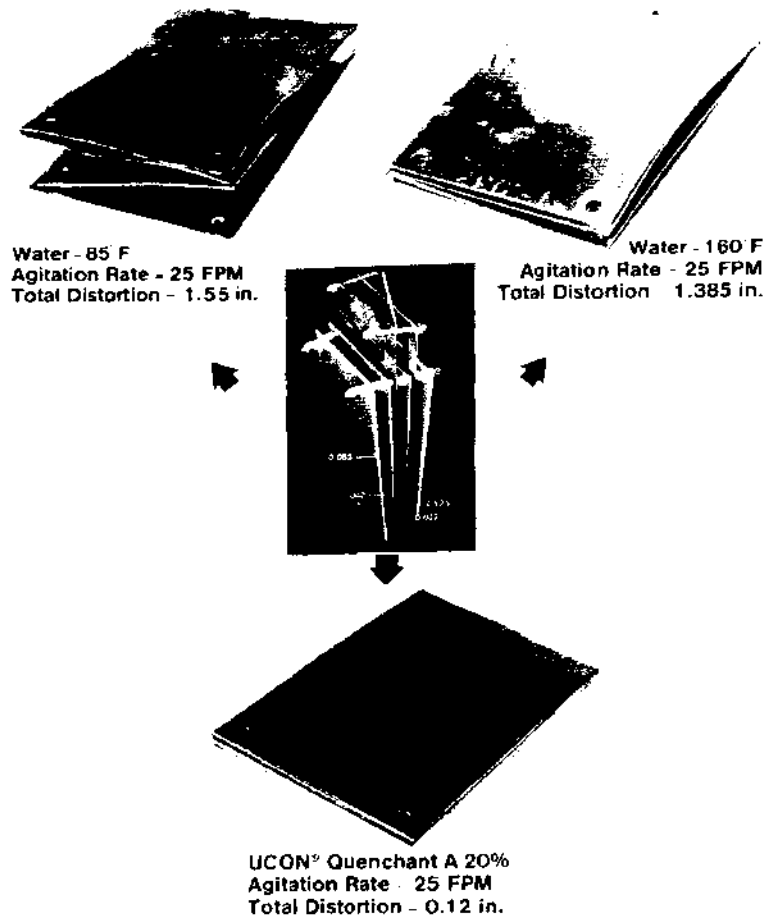
Figure 51 Comparison of distortion reduction achieved with aluminum sheet quenched in cold water, hot water and a 20% solution of a Type 1 quenchant.

It has been shown that water does not effectively wet the surface of aluminum during quenching [16,17]. Figure 24 shows that three distinctly different cooling regimes, with dramatically different heat transfer characteristics, are present on the surface of aluminum simultaneously during the quenching process, these cooling regimes can produce sufficient thermal gradients to increase distortion [17].

PAG copolymer quenchants form a surface film which surrounds the aluminum surface during quenching, as illustrated in Fig. 52 [57]. The film mediates heat transfer and enhances wetting uniformity, thus minimizing distortion. The improved wetting process is evident by comparing "rewetting" times of aluminum quenched in water and a PAG copolymer quenchant solution [8]. Rewetting times (t_f-t_s) are the difference in the time when film boiling begins (t_s) and when nucleate boiling ends (t_f) and data are presented in Figs 28 and 29 for water and polymer quenchant respectively [17].
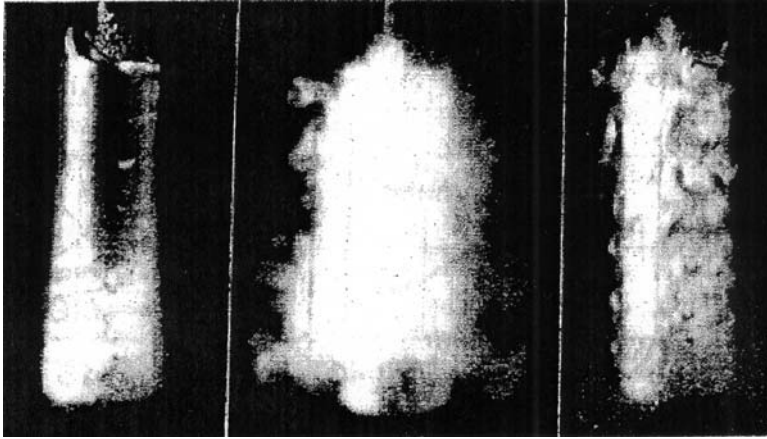
Figure 52 Illustration of the quenching mechanism of an aqueous solution of a PAG copolymer during the cooling of hot metal. (Courtesy of Prof. H. M. Tensi, Technical University of Munich.)

A study conducted on A356-T6 and A357-T6 castings showed that it was possible to achieve similar, but more uniform, mechanical properties with a PAG polymer quenchant than with hot water [58]. The relationship between cooling rate and thickness for A356 aluminum quenched in water and a polymer quenchant is shown in Fig. 53 [58,59].

Heat transfer rates decrease as the thickness of the polymer film increases, and the polymer film thickness is dependent on both agitation and quenchant concentration. Agitation induced film breakage as a function of the polymer structure, concentration, and bath temperature. Cooling curves as a function of polymer concentration are illustrated in Fig. 54 [51]. In general, the duration of the film boiling region increases and cooling rates in the critical region decrease with increasing polymer concentrations.

AMS Specifications

The most common PAG quenchants used in the aerospace industry today are designated as "Type I" quenchants [24]. Type I quenchants are defined by the physical properties that they exhibit in aqueous solution. These physical properties are specified in AMS 3025A and are summarized in Table 12 [60].

There has been some discussion in the industry regarding the meaning of the values in Table 12. Taken together, they do reasonably specify the composition of the quenchant being evaluated. For example:

1. Viscosity, at constant water content, is indicative of the copolymer molecular weight (size).
2. Refractive index, while a very old characterization method, has traditionally been related to the molar refractance values (structure) of chemical compounds and their concentrations.
3. Specific gravity, while not a critical parameter, is often used in chemical engineering processes as an indicator of composition and concentration.
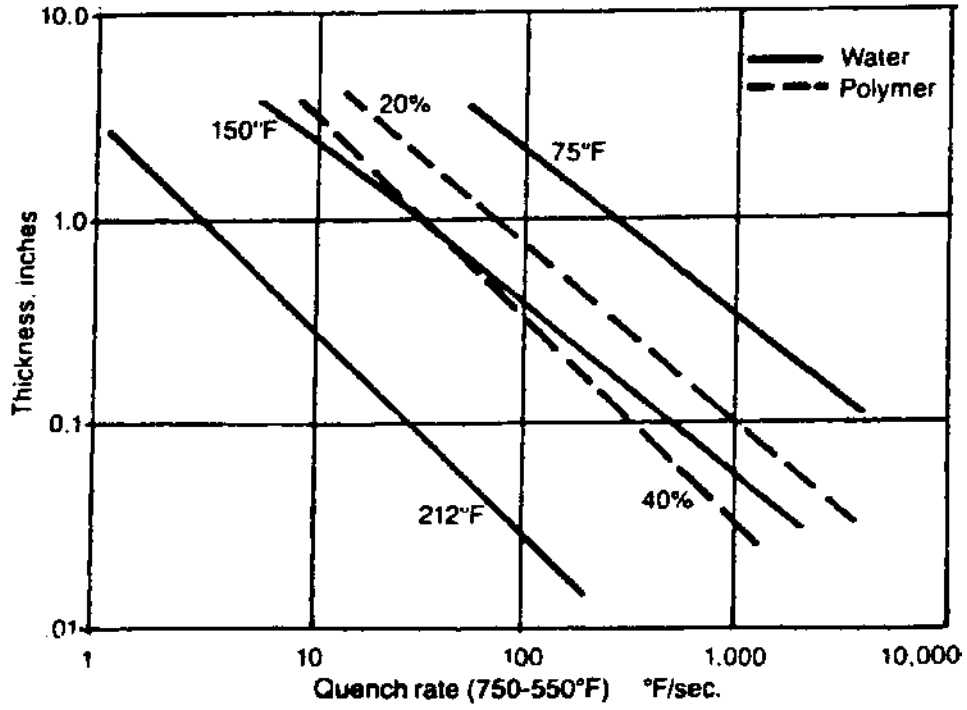
Figure 53   Cooling rate/plate thickness correlation for water and a Type 1 quenchant.
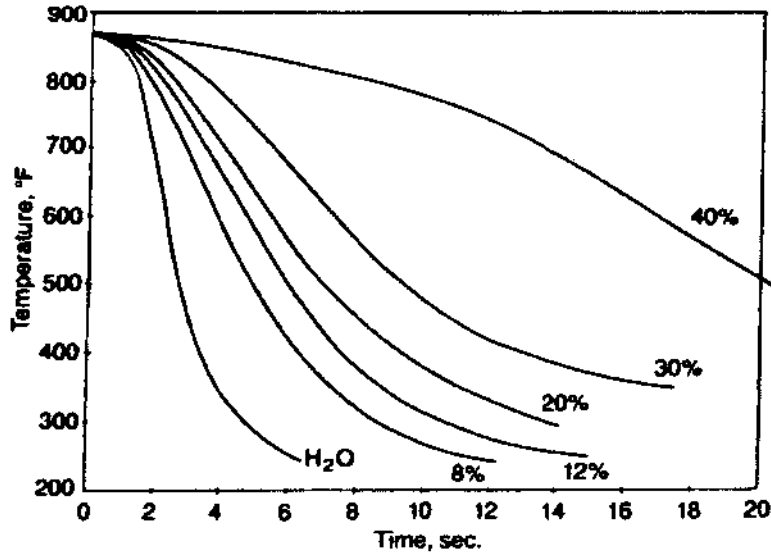
Figure 54   Cooling curves for 1 in. 7075 aluminum alloy plate quenched into different concentrations of a Type I polymer quenchant.

Table 12 Physical Properties of Type I Polymer Quenchants

Property	Specification Limits
Water	45–48%
Specific Gravity (20°C/68°F)	1.094 ± .005%
Refractive Index (20°C/68°F)	1.4140 ± 0.005%
Viscosity (cS @100°F)	535 ± 70
20% Dilution with water (cS @100°F)	5.5 ± 0.5
Separation Temp.	165°F ± 5

Table 13 Selected Military Handbook V Design Minimums

Alloy	Section Size (inches)	Yield Strength (ksi)	Ultimate Tensile Strength (ksi)
2024-T6	0.010–0.249	47	60
2024-T6	0.063–0.249	49	62
2024-T6	0.250–0.499	49	62
7075-T73	0.250–0.499	63	72
7075-T73	< 3.0	56	66
7075-T73	3–4	55	64
7075-T73	4–5	53	62
7075-T6	0.750–1.000	65	75
7050	2.001–3.00	65	74

4. Diluted solution viscosity is a validation that the correct polymer molecular weight and concentration are being used.
5. Separation temperature is indicative of the chemical composition of the PAG copolymer used to formulate the quenchant.

Therefore, these values reflect the chemical composition of the copolymer, molecular weight, concentration, and additive content. While additional tests could be performed, they are probably not necessary. More importantly, the as-quenched physical properties and alloy cooling rates should be determined for proper quenchant certification as already required by ASM 3025A. The physical properties must at least meet the *Military Handbook V* design minimums [40]. Selected design minimum values for 2024, 7075 and 7050 from *Military Handbook V* are provided in Table 13 [24,40].

Recommended heat treating conditions when using Type I quenchants are provided in AMS 2770E [61]. Selected recommended limitations from AMS 2770E are provided in Table 14.

The maximum attainable strength properties are dependent on the cooling rate between 750–550°F (400–290°C). Generally, faster cooling rates provide greater strengths up to a limit, as illustrated by the data in Fig. 55 [62]. However, increasing cooling rates produce increasing thermal gradients which produce increasing

Table 14 Type I Quenchant Limitations By AMS 2770E

Alloy	Form	Maximum Thickness (inches)	Maximum Type I Polymer Concentration (%)
2024-T62	Sheet	0.080	16
7075-T6	Forgings	1.0	20–22
7075-T73	Forgings	2.5	10–12
7050	Forgings	3.0	20–22
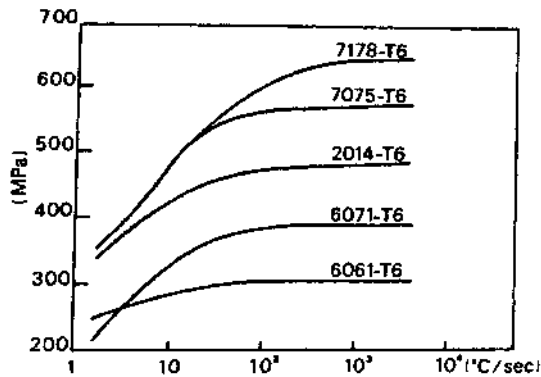
Figure 55 Cooling rate dependence on tensile strength for various alloys.

thermal stresses and the potential for increased distortion. Thermal gradients are reduced by reducing the cooling rate and by increasing the duration of the film boiling region up to, but not past, the "nose" of the C-curve. (This is why "hot" or boiling water is used.)

There is a cooling rate "window" that must be identified to obtain both optimal physical properties and minimum residual stress and distortion. The position and width of the window is a function of the specific hardenability of the alloy and the geometry of the part. This concept is illustrated by Fig. 56 which shows [63]:

1. Curve A is the maximum cooling rate for obtaining specific structural characteristics.
2. Curve B is the cooling rate beyond which the alloy undergoes plastic deformation resulting in residual stresses.
3. Curve 1 does not introduce residual stresses but does not produce the desired mechanical characteristics such as boiling water.
4. Curve 2 produces the desired mechanical properties but also produces unacceptable residual stresses such as cold water.
5. Curve 3 is an optimized cooling process where the cooling rate is controlled to optimize mechanical properties with minimum residual stresses.

Type 1 Quenchant Concentration Limits
The selection of the polymer concentration for specific aluminum alloys is section size dependent. Section size/concentration curves for 6061 [64], 2024-T3 and T4
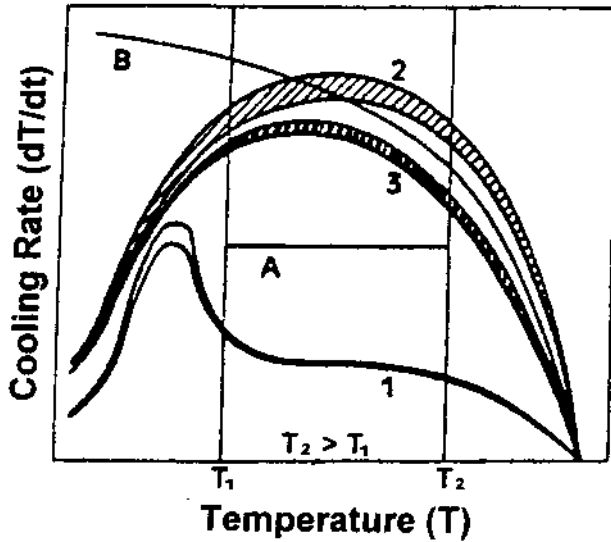
Figure 56 Diagram illustrating the hardenability window (optimum cooling law) for aluminum alloys.

[65], and 7075-T6 and T73 [65] have been reported and are illustrated in Fig. 57 [66]. The recommended concentration range for the Type I polymer quenchants varies significantly with hardenability of the particular alloy.

Effect of Agitation, Section Size, and Quenchant Concentration on Physical Properties

The effects of part section thickness on the necessary polymer quenching conditions have been developed based on various industry studies [24]. The results obtained from a designed experiment conducted to simultaneously evaluate the effects of polymer quenchant concentration, agitation rate and section size on 7075 aluminum sheet and bar stock will be discussed here.

The agitation rate dependence of water at different temperatures is compared with a Type I polymer quenchant in Fig. 50 [24]. These data show that there is relatively little agitation rate dependence for the polymer quenchant. This is one reason why polymer quenchants provide better distortion control than hot water.

Statistically designed experiments were used to examine the effects of polymer concentration, bath agitation (velocity), and cross-section on the quench factor for one sheet thickness for 2024-T851 and a broader range of sheet thickness and bar diameters for 7075-T73 [67]. For each point of the experimental design, a reproducible cooling curve was obtained using a bar or sheet probe as illustrated in Figs. 20 and 21, respectively. Statistical models for quench factor and predicted yield strength were developed using standard multiple linear regression analysis techniques to determine the significant variables relative to the modeled response being examined.
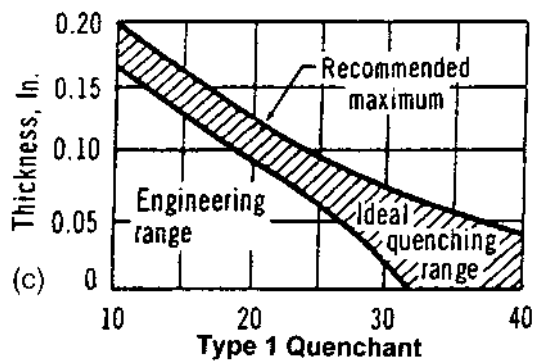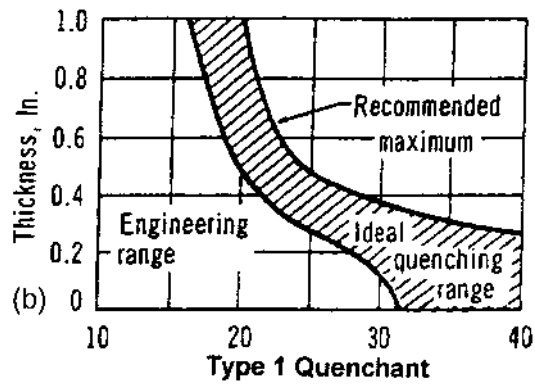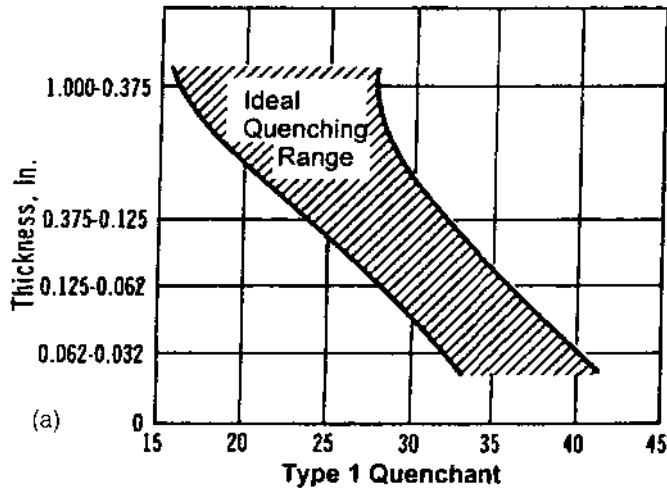
Figure 57 Working curves Type 1 quenchant concentration selection as a function of cross-section size for (a) 6061; (b) 2024-T3 and T-4; and (c) 7075-T6 and T-73.
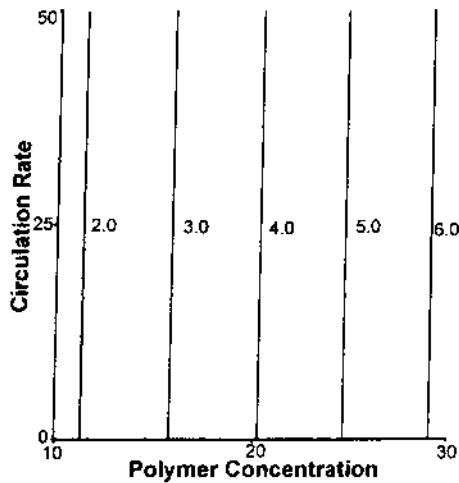
Figure 58 Quench factor dependence on quench process parameters: 2024 aluminum sheet data.

The contour plot shown in Fig. 58 for the 2024-T851 model (0.063 in.) shows that increasing polymer concentration has the expected effect of decreasing the quench factor. Variations in quenchant velocity had no effect on quench factor at this sheet thickness [67]. A similar study was performed on 7075-T73 aluminum sheet except three sheet thicknesses were examined: 0.063, 0.126 and 0.25 in. Contour plots for these quench factors are provided in Fig. 59 [67]. In this case, quenchant velocity had an effect, especially as the sheet thickness increased.

The quenching data for 7075-T73 bar stock with diameters of 0.5, 1.0 and 1.5 in. were also modeled. Contour plots, holding bar diameter and bath temperature constant, are shown in Fig. 60 [67]. These results show that agitation rate had no significant effect on quench factor under these experimental conditions.

The regression equations developed from this work along with standard deviations and R^2 values are shown in Table 15. Since only one sheet thickness of 2024 was evaluated, sheet thickness does not appear in the statistical model. Thickness, agitation rate and bath temperature factors were modeled for both 7075 sheet and bar and these variables do appear in the statistical model. The statistical fit of the data to the model was better for the 7075 than for 2024 which is due to the larger data set used.

Polymer Quench Bath Maintenance
It is suggested that the following analyses be conducted to maintain consistency of the quenchant: concentration by viscosity, concentration by refractive index, determination of "delta" (the difference between concentration determined by refractive index and viscosity), determination of thermal separation temperature, conductance, biological contamination, pH and corrosion inhibitor concentration [68,69]. The following comments will provide some insight into the physical meaning and the reasons for determining these data.
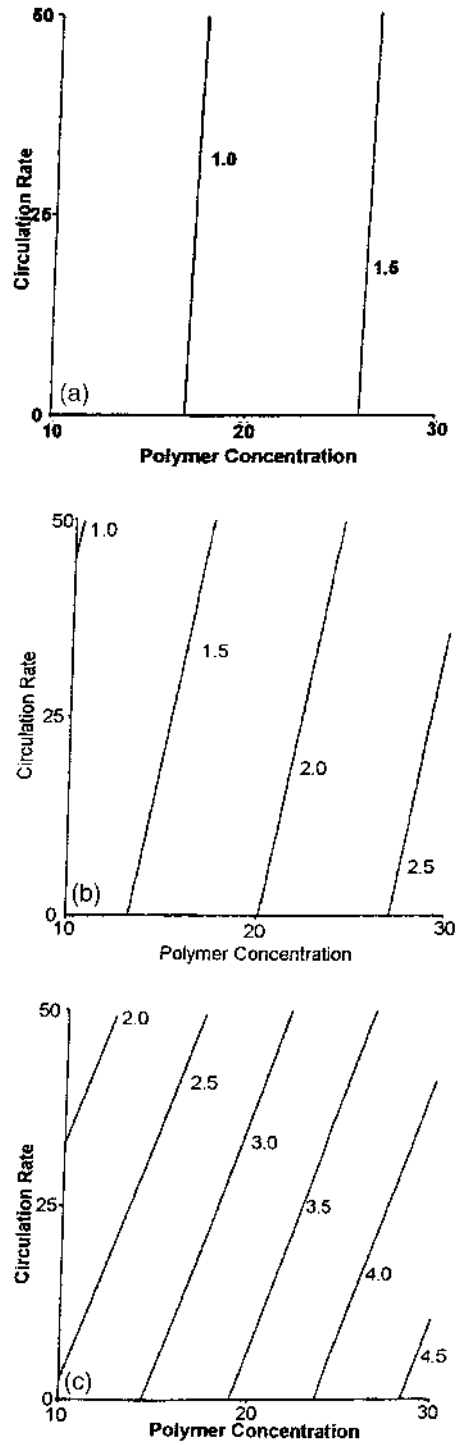
Figure 59 Quench factor dependence on quench process parameter: 7075-T73 sheet data; (a) Sheet thickness = 0.063 in.; (b) Sheet thickness = 0.125 in.; (c) Sheet thickness = 0.250 in.
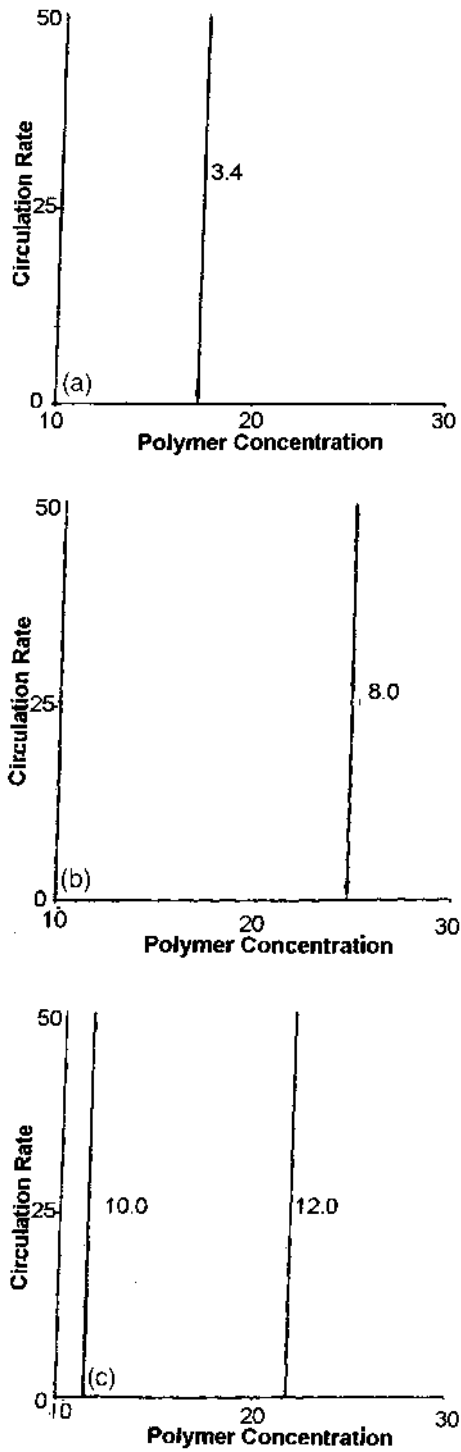
Figure 60 Quench factor dependence on quench process parameters: 7075=T73 bar data; (a) Bar diameter = 0.5 in.; (b) Bar diameter = 1.0 in.; (c) Bar diameter = 1.5 in.

Table 15 Statistical Quenchant Performance Models for Quench Factor and Yield Strength for 2024 Sheet and 7075 Sheet and Bar Data

A. 2024-T851 Sheet Data – 0.063 in.
$Q = -0.552 + 0.225 * C$
$\sigma \pm 0.74,\ R^2 = 90.2$
$YS = 66.78 - 0.0738 * C$
$\sigma \pm 0.2421,\ R^2 = 90.3$

B. 7075-T73 Sheet Data
$Q = 0.399 + 0.004554 * CR + 0.03754 * C + 7.491 * ST - 0.08374 * CR * ST + 0.2765 * C * ST$
$\sigma \pm 0.2007,\ R^2 = 97.6$
$YS = 69.19 - 0.00153 * CR - 0.00866 * C - 1.999 * ST + 0.02638 * CR * ST - 0.07747 * C * ST$
$\sigma \pm 0.06109,\ R^2 = 96.8$

C. Type I 7075-T73 Bar Data
$Q = -39.96 + 2.345 * C + 4.483 * D + 0.4557 * T + 0.1876 * C * D - 0.02703 * C * T$
$\sigma \pm 0.5003,\ R^2 = 98.5$
$YS = 69.41 - 0.00833 * C - 1.17 * D - 0.0525 * C * D$
$\sigma \pm 0.1304,\ R^2 = 98.7$

$T =$ Temperature (°F)
$st =$ Sheet Thickness (in.)
$D =$ Bar Diameter (in.)
$CR =$ Agitation Rate (ft/min)
$C =$ Concentration (%)
$Q =$ Quench Factor
$YS =$ Yield Strength (ksi)
$* =$ Multiply

1. Concentration by Refractive Index—The refractive index of a solution is dependent on its composition. In general, refractive index is most dependent on contamination effects. For example, build-up of metal ions from industrial water sources results in faster cooling rates and sometimes increased distortion. Also, contamination by hydraulic oils, forging lubricants and metalworking fluids may have deleterious effects. Variations in refractive index is one indicator of such contamination affects. Polymer degradation also may affect refractive index but to a lesser extent than contamination.
2. Concentration by Viscosity—Polymer degradation will result in reduced viscosity [69,70]. The viscosity of PAG solutions may be affected by contaminants, but to a lesser extent than if significant degradation has occurred.
3. Delta—It is useful to determine the difference between the concentration obtained from refractive index and that obtained by viscosity. The difference in these two values is called delta. Typically, large changes in the value of delta over time indicate an out of control process and further work must be done to determine the cause of the problem and to take

corrective action. However, the quenchant may undergo slow contamination, such as metal ion build-up, or even a slow molecular weight degradation process. If so, the delta value, after being reasonably stable for some time, will gradually increase. When the delta value exceeds 6–8, corrective action must be taken or the quenchant must be replaced.

4. Thermal Separation—Thermal separation provides a measure of the cloud point of the quenchant [71]. If significant degradation has occurred, the cloud point will increase. Usually, this is accompanied by cooling rate increases.

5. Inhibitor Concentration—Polymer solutions contain water and therefore, not surprisingly, may cause corrosion. The normal remedy is to add a corrosion inhibitor but because the corrosion inhibitor may be lost due to drag-out and other processes, it must be periodically replenished. Therefore, the corrosion inhibitor concentration must be monitored.

6. Conductance—Solution conductance is dependent on ionic content. If substantial ionic contamination has occurred, increases in solution conductance will be observed.

7. Other tests—Additional tests may be conducted to determine causes of physical property variations. For example, size exclusion chromatography – SEC (or gel permeation chromatography) may be performed to determine the degree of polymer degradation. Alternatively, infra-red spectroscopy may be performed to determine if oxidation of the polymer has occurred.

8. Biological Contamination—A common cause of polymer degradation is biological contamination. Contamination can be easily monitored using commercially available patch tests.

All of these measurements should be periodically made, recorded and tracked using a data sheet such as the one shown in Fig. 61 [69].

THERMAL SEPARATION. The cooling rate control provided by an aqueous PAG solution is dependent on an inverse solubility mechanism as illustrated in Fig. 62 [71]. Every PAG quenchant exhibits a characteristic temperature at which thermal separation occurs. The characteristic temperature is called the "cloud point" of the polymer and it is dependent on the polymer structure and composition. At the cloud point, the hydrated PAG polymer becomes insoluble. The thermally separated polymer is significantly more viscous than the homogeneous solution and the viscosity of the hydrated polymer is dependent on both the molecular weight of the polymer and the bath temperature which dictates the degree of hydration of the polymer. Increasing amounts of polymer hydration reduces the viscosity this layer. The thermal separation process is reversible, with the separated layer redissolving as the solution temperature decreases below the cloud point.

Quench baths can become contaminated by salts if the parts are preheated in a salt bath. Salt contamination may also occur from a build up of metal ions if tap water is used to dilute the quenchant. In either case, the presence of salt may produce higher cooling rates (see Table 16) and increase the separation temperature of the PAG copolymer in the Type I quenchants [68]. Salts may be removed by thermal separation as illustrated in Fig. 62 [71] or the quenchant can be replaced if salt contamination becomes excessive.

POLYMER QUENCHANT ANALYSIS

FOR:_____   DATE:_____

_____   REFERENCE:_____

ANALYSIS OF:
****

UCC CODE:					
SAMPLE IDENTIFICATION					
REFRACTOMETER READING* PERCENT QUENCHANT					
VISCOSITY, cSt, 100°F PERCENT QUENCHANT					
DELTA pH					
PERCENT INHIBITOR					
SPECIFIC CONDUCTANCE**					

OTHER COMMENTS:

        DIAGNOSTICA:

        SETTLED APPEARANCE:

*MODEL 10440 / IFT40: FACTORS
JQA, UQC, UQHT: 2.0   **CONDUCTANCE: MICRO-MHOS /CM
JQB, UQRL, UQE: 2.5   FOR 1 TO 100 DILUTION

Figure 61 Illustration of a typical analytical data log sheet. (Courtesy of Tenaxol Inc., Milwaukee, WI)

Although thermal separation may be performed by simply heating the quenchant in the tank until separation occurs, this process is not applicable for larger tanks. For these applications, a "One Pass Through With Heat Recovery" process has been developed and is illustrated schematically in Fig. 63. This process may be applied to quenchant solutions with polymer concentration as low as 1% [72].

MEMBRANE SEPARATION. Reverse osmosis (RO) and ultrafiltration (UF) are two pressure driven separation techniques that may be used to separate polymers and if the system is properly designed, additives can also be separated from aqueous quenchant solutions [73,74]. The primary difference in these two techniques is the system pressures and the size of the molecules which can be effectively separated. Currently RO is the more favored method since better separation of the polymer and additives is possible. This will be the focus of the remainder of this section. Data on the size of the solute separated and the working pressure is given in Table 17.
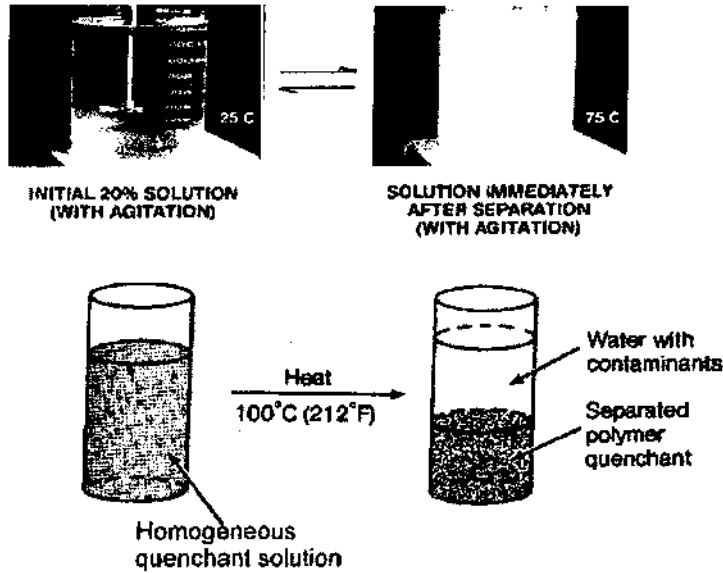
Figure 62 Schematic illustration of thermal separation of a Type 1 polyalkylene glycol polymer quenchant.

Table 16 Effect of Salt Contamination on Cooling Rates Produced by an Aqueous Polymer Quenchant[a]

Salt concentration[b]	Maximum Cooling Rate		Cooling Rates at 343°C (650°F)	
	°C/sec	°F/sec	°C/sec	°F/sec
0	39.0	70.2	25.3	45.5
3.0	54.0	97.2	31.8	57.2
6.0	65.8	118.4	35.0	63.0
Water[c]	61.8	111.2	33.0	59.4

[a]Data obtained using a 25×50 mm (1.4 in.) cylindrical Type 304 stainless steel probe instrumented with a Type K Thermocouple at the geometric center. Agitation was provided by the radial flow by the probe surface at 23 L/min (6 Gal/min) at 40°C (100°F).
[b]The salt was sodium nitrate.
[c]Distilled water containing no polymer quenchant.

The initial quenchant solution is called the "feed solution". This solution is passed through a pressurized membrane as illustrated in Fig. 64. The fluid that passes through the membrane, called the "permeate", is typically pure water. The permeate passes into the core of the membrane assembly where it is either released from the system or delivered to a storage tank for further use. The concentrated solution which does not pass through the membrane is either recycled through the membrane assembly for further concentration or delivered to a storage tank for reuse.
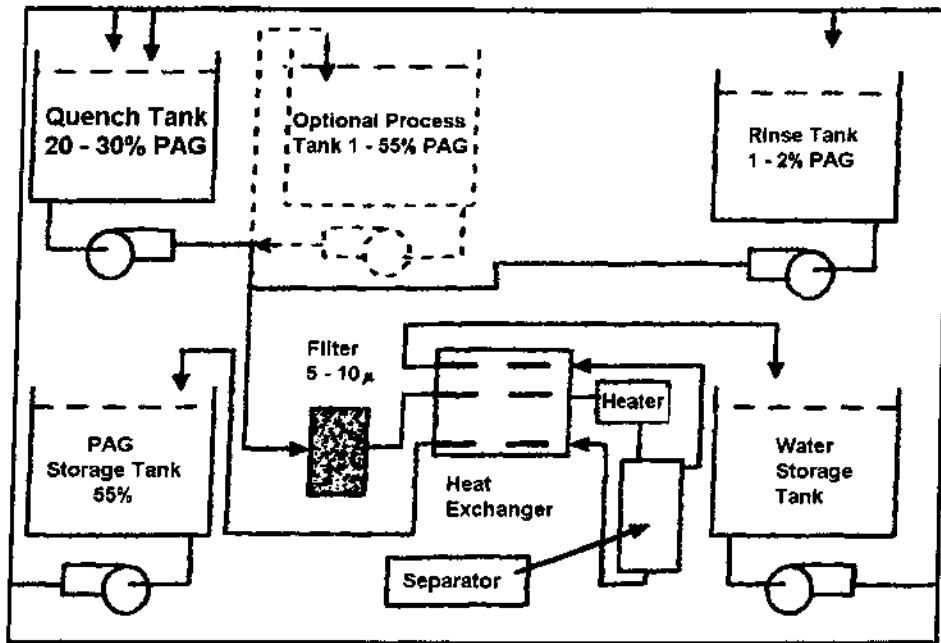
Figure 63 One-pass through heat separation of a Type 1 polyalkylene glycol polymer quenchant.

Table 17 Relationship Between the Membrane Separation Method, System Pressures and Size of Molecules Separated

Membrane Type	Size of Solute Separated	Pressure (psig)
Ultrafiltration	0.001–2 μm, (5000–200000 molecular weight)	10–100
Reverse Osmosis	0.0001–0.001 μm	200–1000

The rate of permeate separation, Q_P, is equal to the rate of purified water passing through the membrane. This is usually expressed as volume/min at 25°C. The flow of the concentrate, Q_C, is equal to the flow of the retained polymer. The flow rate of the feed stream of the incoming quenchant, Q_F, is equal to the permeate rate plus the concentrate rate.

In membrane separation technology, the recovery rate is used to characterize the separation system. Recovery rate (%) is defined as:

$$\text{Recovery} (\%) = Q_p/Q_f \times 100$$

The total concentration, % C, is typically reported as:

C_F = Feed concentration,
C_P = Permeate concentration,
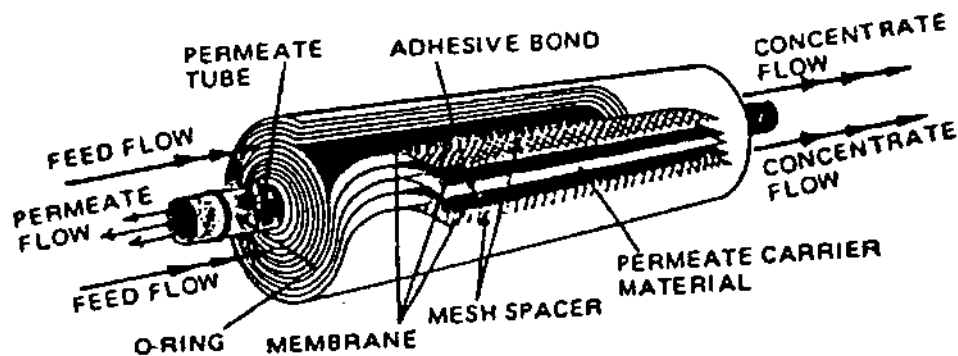
Figure 64 Schematic illustration of a typical membrane filter assembly. (Courtesy of Osmonics, Inc.)

$$C_C \quad = \quad \text{Concentrate concentration,}$$
$$C_{AVE} \quad = \quad \text{Average concentration.}$$

$$C_{ave} = \frac{C_f + C_c}{2}$$

$$\text{Passage } G = \frac{C_c}{C_{ave}}$$

$$\text{Retention} = \frac{C_f}{C_{ave}}$$

All well-formulated polymer quenchants contain corrosion inhibitors. One problem with membrane separation is that corrosion inhibitors will be removed with the permeate stream. One way to minimize this problem is to use "salt rejecting" membranes.

As water is separated from the quenchant during separation, the feed concentration (C_F) increases, the concentrate concentration (C_C) increases, and the permeate concentration (C_P) remains essentially unchanged. The permeate flow rate decreases asymptotically, feed flow rate decreases proportionate to the flow/pressure curve of the pump supplying the solution, salt passage increases, and the pressure required to perform the separation increases. These process changes with time are illustrated in Fig. 65 [73].

The polymer concentration may be automatically monitored by one of three methods: density, viscosity or refractive index. Trouble-free operation requires that the system be properly engineered. For example, the density method is susceptible to bias from contamination and air bubbles. Viscosity-concentration relationships are typically non-linear and require appropriate detector calibration. Refractive index is affected by oil and metallic salts.

In some cases, there may be sludge, oil or oxides present in the quenchant solution which may damage the membrane assembly and therefore must be separated from the quenchant solution before the separation process. The sludge is prefiltered from the feed stream using conventional 50–100 mesh filter cartridges. Such strainers require frequent cleaning.
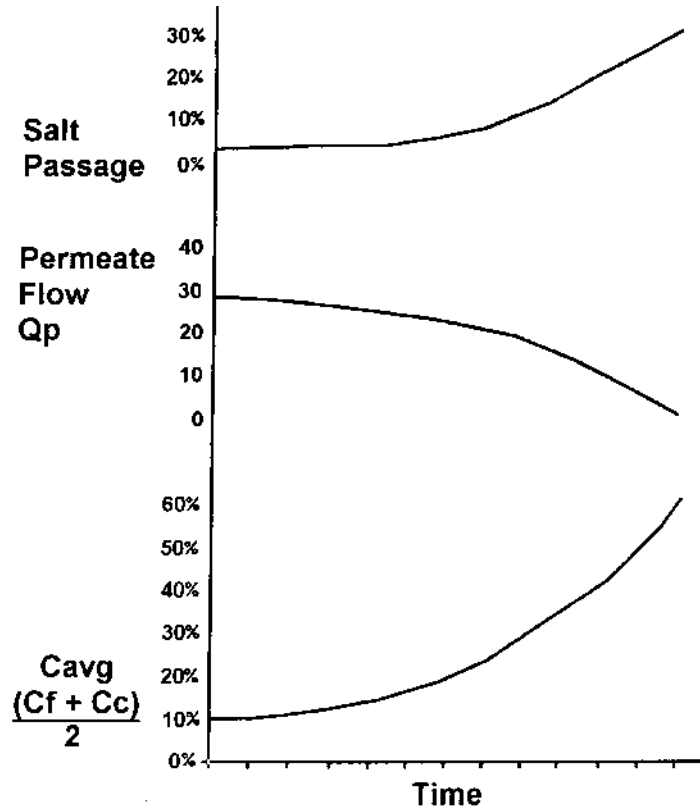
Figure 65 Representative curves for salt passage, permeate flow and average concentration (Cave) as a function of time.

Oil can be separated from the feed stream by coalescing technology which permits the removal of the micron size oil droplets by coalescing them into larger particles which are then separated by density differences. This process is illustrated in Fig. 66 [73]. The primary driving force affecting oil separation by coalescence is the excess free energy at the interface of the dispersed oil droplet caused by unbalanced forces at the droplet surface. The relatively small interfacial tension values are sufficient to permit oil coalescence in a contaminated quenchant solution. Thus, the dispersed oil can be collected in a settling tank where it is separated from the quenchant solution based on specific gravity.

BLISTERING DUE TO LUBRICANT/QUENCHANT POLYMER CONTAMINATION.   Instances have been reported where residual polymer quenchants, die lubricants, and other hydrocarbon materials are present on the surface of the aluminum during tempering. This may lead to the formation of surface blisters and voids after quenching. This effect may be observed metallographically by the presence of "water marks" on AA7075 as illustrated in Fig. 67 [5]. Cleaning the parts with a caustic etch and nitric acid accentuated the appearance of the blisters and produced a "smutty" residue in the area of the blisters. Sectioning showed that the blisters and voids were present to a depth of 0.050 in. with no indications of stringers, laps, etc.
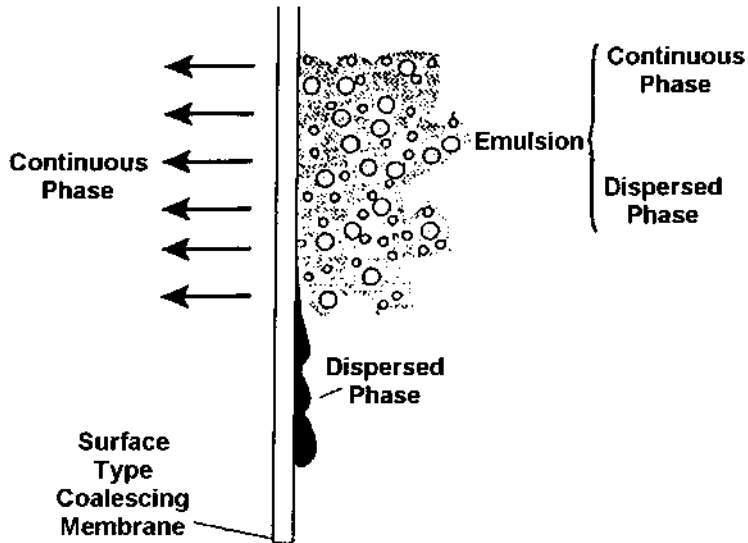
Figure 66 Illustration of the sequence of operation of liquid/liquid surface coalescing.
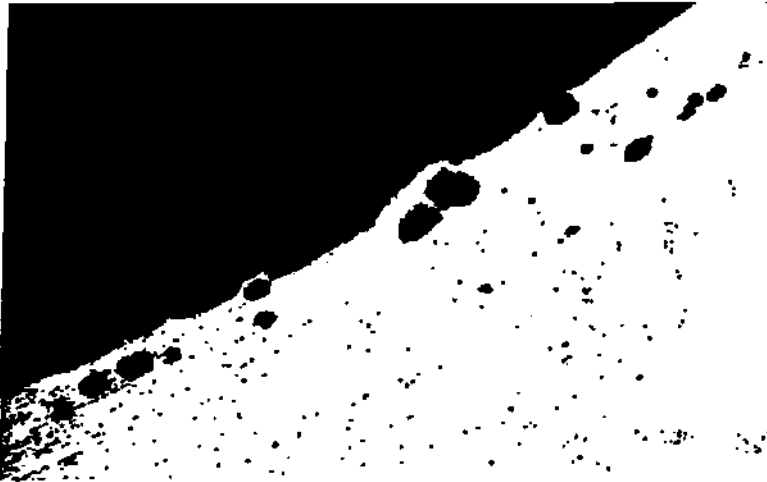
Figure 67 Cross-section of surface blistering (as polished, 50 ×).

Schuler reported that such blisters were due to high temperature oxidation of the residual hydrocarbon material during solution heat treating which produced hydrogen or water vapor which may have migrated into the grain boundaries. Similarly, residual poly(alkylene glycol) polymer after quenching due to incomplete rinsing may produce the same effect during tempering.

High temperature oxidation may be controlled or eliminated by more effective precleaning or rinsing. A volatile fluoride atmosphere, such as that produced by
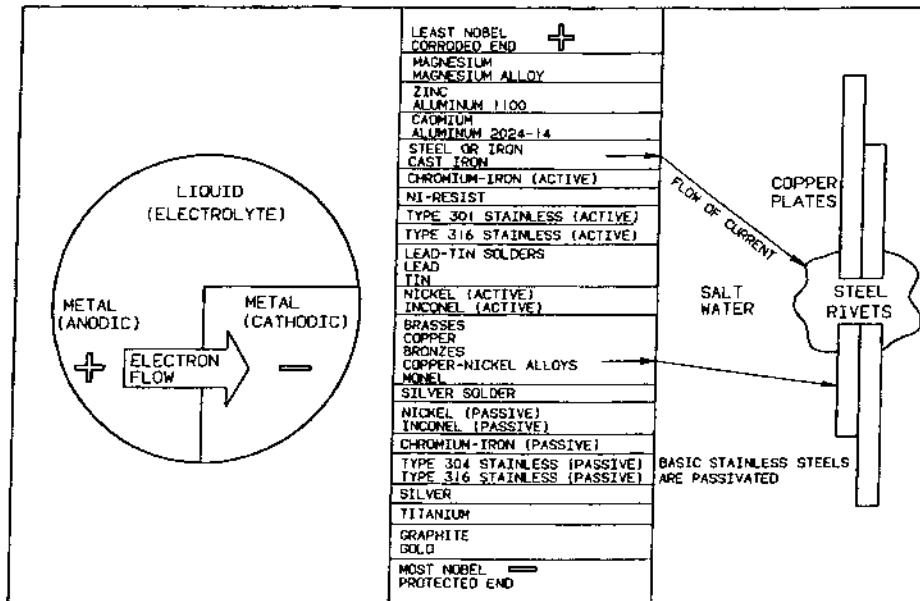
Figure 68   Illustration of galvanic corrosion and the galvanic series.

ammonium perfluoroborate (0.004 oz/ft^3 of furnace volume) may also be used to control the effect of water vapor [75,76].

GALVANIC CORROSION. Galvanic corrosion is caused by the contact of dissimilar metals with an electrochemical potential sufficient to allow current flow between the metals. For galvanic corrosion to occur, an electrolyte (salt solution) must be present as shown in Fig. 68. The galvanic series of metals is presented in Table 18 [77]. Metals close to each other will not undergo galvanic corrosion. Aluminum galvanic corrosion may occur if the parts are in contact with a steel quench tank and exposed to a salt solution. Similar problems may occur if aluminum is joined to copper, such as can occur when copper wire is used to fasten aluminum parts to a rack and the assembly is immersed into a quenchant having salt contamination. Although galvanic corrosion is not commonly encountered, it may occur if these situations are allowed to occur.

2.4.3 Carbonated Water

Cold water is the most commonly used quenching medium for many hardenable aluminum alloys (2xxx, 6xxx and 7xxx). However, the relatively fast cooling rates obtained while cooling through the critical region (750–550°F) shown in Fig. 69 produces high thermal gradients that can produce residual stress, distortion or crack formation [78,79]. Thermal stress due to high thermal gradients may be reduced by raising the water temperature as illustrated in Fig. 70 [79] by comparing t_{cw} (cold water cooling time) with t_{ww} (warm water cooling time). Although the overall thermal gradient was decreased, the cooling rate through the critical region was also

Table 18 The Galvanic Series of Metals

Corroded End (Anode)
Magnesium
Magnesium Alloys
Zinc
Aluminum 2S
Cadmium
Aluminum 17ST
Steel or Iron
Cast Iron
Chromium–iron (active)
Ni–resist
18–8 Chromium–nickel–iron
18–8–3 Chromium–nickel–molybdenum–iron (active)
Lead–tin Solder
Lead
Tin
Nickel (active)
Iconel (active)
Hart alloy C (active)
Brass
Copper
Bronzes
Copper–nickel alloys
Monell
Silver Solder
Nickel (passive)
Iconel (passive)
Chromium (non-passive)
18–8 Chromium–nickel–iron (passive)
Hastelloy C (passive)
Silver
Graphite
Gold
Platinum
Protected end (Cathode)

reduced which may result in undesirable reductions in strength or corrosion resistance. In addition, hot water quenching is known to produce non-uniform cooling which may cause greater distortion than expected [80].

ALCOA has used carbonated water to moderate the rate of heat removal. Carbonated water is prepared by dissolving carbon dioxide (CO_2) at 0.001–0.2 standard cubic feet of gas per gallon of water, depending on the water temperature [79,81,82]. Although other gases that exhibit sufficient solubility in water may be used, such as ammonia and nitrogen, CO_2 is preferred because it is odorless, relatively inexpensive and highly soluble in water. A typical immersion and spray quench system for use with carbonated water quench systems is illustrated in Figs. 71 and 72 respectively [79].
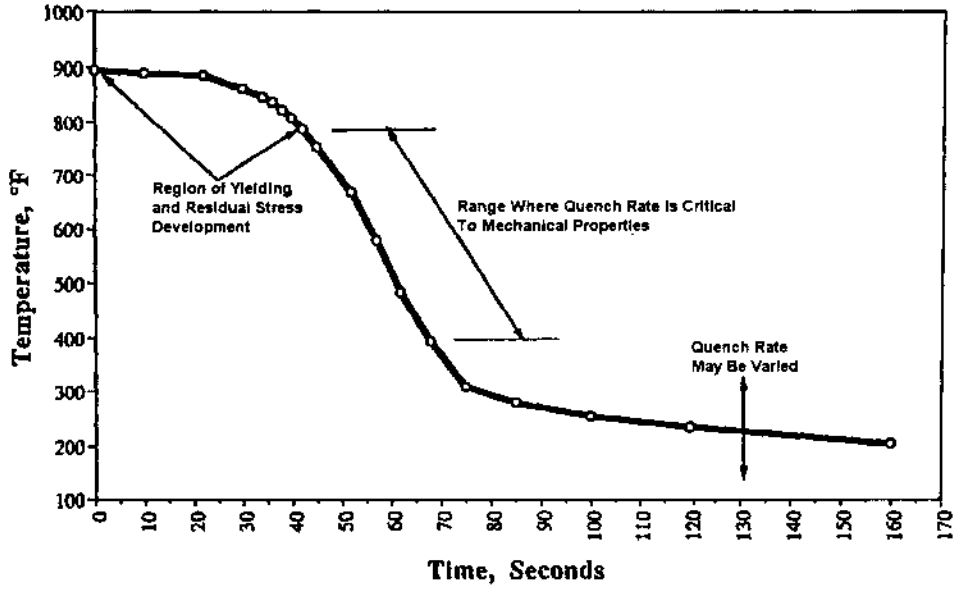
Figure 69 Ideal quench path for high strength aluminum alloys.
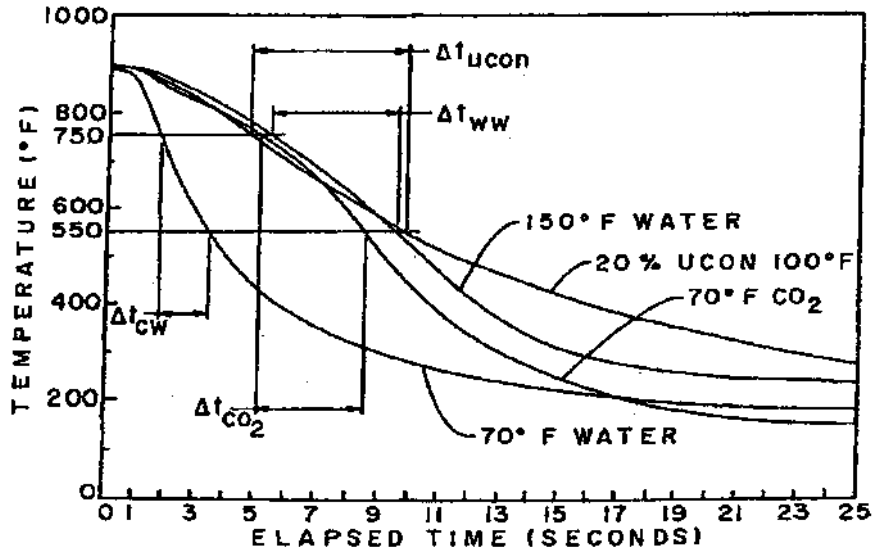
Figure 70 Comparison of the cooling profile of cold water, warm water, a single concentration of a Type 1 polymer quenchant and carbonated water.

NOTE: Industrial processes using these gases must be subjected to careful safety reviews in view of the potential safety hazards associated with high concentrations of these gases in the work area that may lead to asphyxiation. Proper ventilation is essential!
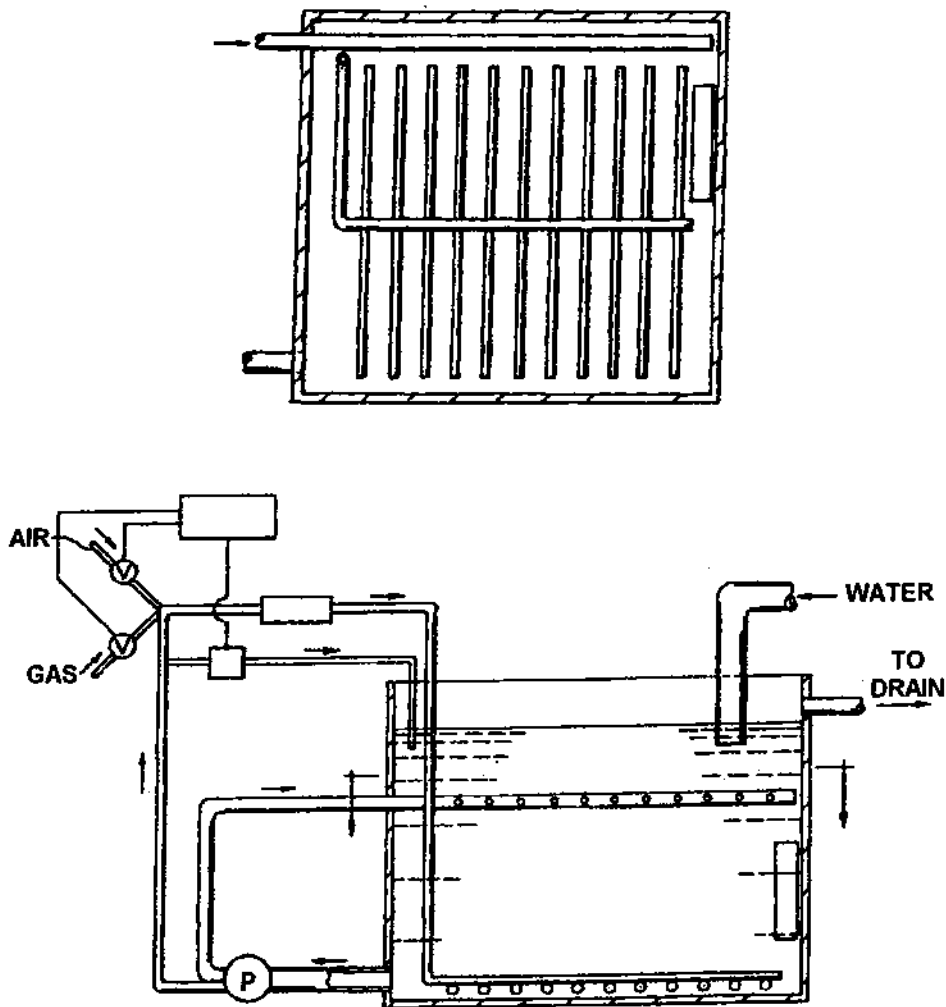
Figure 71 Quench tank design for immersion quench using carbonated water.

It is thought that the mechanism of quenching in carbonated water involves the formation of an insulating gas or vapor barrier around the aluminum surface upon initial immersion. The gas or vapor barrier is formed by the coalescence of water and CO_2 bubbles (varying from 100 to 350 microns in size). Upon further cooling, the CO_2 and water vapor bubbles break away from the surface and are reabsorbed into the water. Very little fluid motion at the water surface is observed during cooling. When vaporization of CO_2 ceases, the cooling capacity of the quench medium approximates that of cold water (if cold water is used).

If cold water quenching is needed, the carbonated water may be pumped to a storage tank or discarded (since CO_2 is environmentally benign) and cold water added to the tank. Alternatively, a pressurized air sparge may be used to remove the CO_2, thus quickly restoring the quenchant to that of a cold water quench.
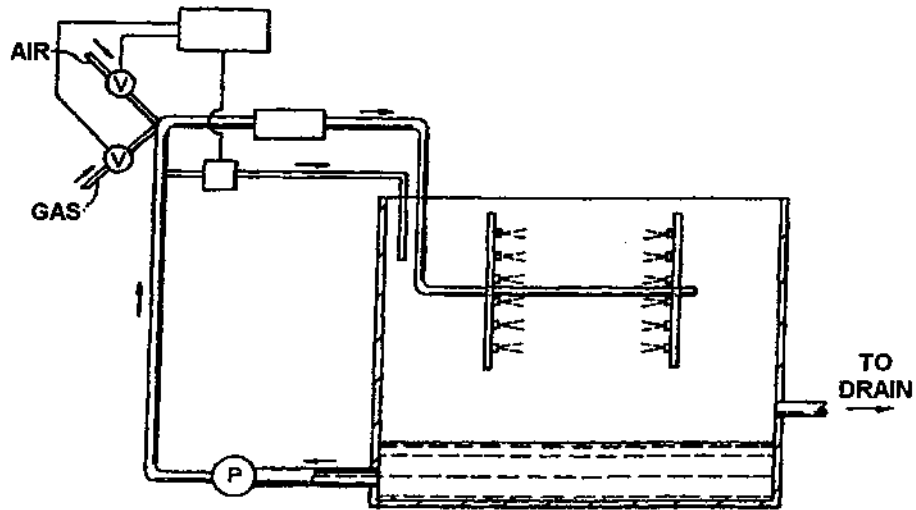
Figure 72 Schematic of a spray quench system for use with carbonated water.

Variations of this technology may be employed to achieve continuously variable cooling rates.

A related process has been patented by Japanese workers where the film boiling region is extended to a sufficiently low temperature and the material strength exceeds the induced thermal stress. At this point, the cooling rate is increased and the metal cooled at a rate equal to or greater than the critical cooling rate [83]. In some cases, sodium chloride or sodium carbonate additives are used to control the stability through the film boiling region.

2.4.4 Other Quenching Media

Other quench media have been reported which include cryogenic liquids such as liquid nitrogen [84], aqueous concentrates of sulfite-yeast media [85], and quenching into "mud" composed of water, clay, an additive of magnetite or ferrosilicon [86]. Other additives may be present to provide corrosion protection, anticoagulation and antifoaming. However, cold water, hot water and aqueous polymer solutions are the most frequently used throughout the world to process aerospace aluminum parts.

2.5   Intergranular Corrosion

If the diffusion process is sufficiently fast during quenching, alloying elements and compounds may precipitate in the grain boundaries. Intergranular corrosion occurs in aluminum-copper alloys; Al-Cu-Mg (2xxx), Al-Zn-Mg-Cu (7xxx) and Al-Mg (5xxx) alloys containing $> 3.5\%$ Mg [87]. Intergranular corrosion in 2xxx and 7xxx series aluminum alloys is caused by the loss of copper or sufficient magnesium in areas near the grain boundaries to create an anodic electrochemical potential. The electrochemical potential of various aluminum alloys, provided in Table 19, shows that the presence of copper in solid solution with aluminum makes it more

Table 19 Electrode Potentials of Aluminum Solid Solutions and Constituents[a]

Solid Solution Composition	Potential, Volts, 0.1N Calomel Scale[b]
α (Ag-Mg) (Mg_5AL_8)	-1.24
$Al+Zn+Mg$ (4% $MgZn_2$ Solid Solution)	-1.07
$Al+Zn$ (4% Zn Solid Solution)	-1.05
β (Zn-Mg) ($mmgZn_2$)	-1.05
$Al+Zn$ (1% Zn Solid Solution)	-0.96
$Al+Mg$ (7% Mg Solid Solution)	-0.89
$Al+Mg$ (5% Mg Solid Solution)	-0.88
$Al+Mg$ (3% Mg Solid Solution)	-0.87
α (Al-Mn) ($MnSi_6$)	-0.85
Aluminum (99.95%)	-0.85
$Al+Mg+Si$ (1% $MgSi_2$)	-0.83
$Al+Si$ (1% Si Solid Solution)	-0.81
$Al+Cu$ (2% Cu Solid Solution)	-0.75
(Al - Cu) ($CuAl_2$)	-0.73
$Al+Cu$ (4% Cu Solid Solution)	-0.69
α (Al-Fe) ($Fe-Al_3$)	-0.56
$NiAl_3$	-0.52
Silicon	-0.26

[a]Data from ALCOA Research Laboratories.
[b]Measured in aqueous solution of 53 g NaCl + 3 g H_2O_2 per liter at 25°C

cathodic [88]. An aluminum alloy containing 4% copper in solid solution will exhibit an electrochemical potential of -0.69 V. However, copper concentrations in grain boundaries may reduce the electrochemical potential to -0.84 V making it more anodic. Grain boundary corrosion may also occur when the grain boundary precipitates are either more anodic than the adjacent solid solution ($Mg_2 Al_3$, $MgZn_2$, and Al_x-Zn_xMg) or more cathodic ($CuAl_2$ and $Al_x Cu_x$ Mg) [89].

The degree of intergranular corrosion may be controlled by selection of the temper and maximizing the cooling rate permissible to still provide distortion control. For example, the T4 and T6 temper conditions are typically selected when optimum resistance to intergranular corrosion is required [90]. Schuler reported that the critical cooling rates (cooling rates between 750–550°F) for the 7xxx series to be <400°F/sec and 1000°F/sec for the 2xxx series for optimal resistance to intergranular corrosion [90]. However, insufficient quench rates are not the only cause of intergranular corrosion. Other factors include transfer rate from the furnace to the quench, air entrainment in the quench tank, and the ratio of section mass/surface area [90]. The data in Table 20 show the effect of cooling rate on increasing intergranular corrosion in AA7075 cylindrical bar [91]. The depth of attack was consistently higher toward the center of quenched bars when the cooling rate was slower.

Table 20   Effect of Cooling Rate on Maximum Intergranular Penetration of 7075 as a Function of Cooling Rate

Sample	Cooling Rate (50 mm Dia Bar) (°C/sec)	Location[a]	Depth of Attack (mm)
A	53	Surface	0.46
		Center	0.56
B	50	Surface	0.30
		Center	0.86
C	30	Surface	0.46
		Center	0.61
D	17	Surface	0.74
		Center	1.09

[a]Surface—within 3.2 mm of cylinder surface
Center—within 3.2 mm of cylinder centerline.

2.6   Residual Stress Reduction

Type I polymer quenchants have been reported to offer significantly greater residual stress reduction than hot water in a number of studies. The results of one of the earliest reported studies which was conducted using the Sach's Bore Out Method on aluminum A 356 castings are shown in Fig. 73 [55,91].

Torgerson and Kropp conducted residual stress and other mechanical property measurements on specimens quenched in hot water and a Type I polymer quenchant at various concentrations using both AA7050-T736 forgings and plate [92]. It was found that Type I quenchants provided minimum distortion while still meeting the design minimums for forgings up to 5 in. thick.

2.6.1   Campbell's Analysis

When an aluminum part, such as a casting, is solution heat treated and quenched into room temperature water, the difference between the initial and final temperature is nearly 500°C. Since the core of the casting cools more slowly than the surface, strains (ε) will be introduced that are proportional to the coefficient of thermal expansion (α) and the temperature difference (ΔT) [93].

$$\varepsilon = \alpha \bullet \Delta T$$

α has a value of approximately $20 \times 10^{-6} \mathrm{K}^{-1}$. The approximate value of quench strain under these conditions is:

$$20 \times 10^{-6} \bullet 500 = 1.0\%$$

The strains are at least ten times the yield strain, as illustrated in Fig. 74 [93], and exceed the elastic limit which may lead to cracking during quenching.

Measured centerline quench rates for a 20 mm bar are illustrated in Fig. 75 [93]. The modulus is determined from its volume/surface area (area/circumference ratio) and is determined to be 5 mm. From this estimation and Fig. 75, it is possible to determine the cooling rate where distortion and cracking problems may occur.
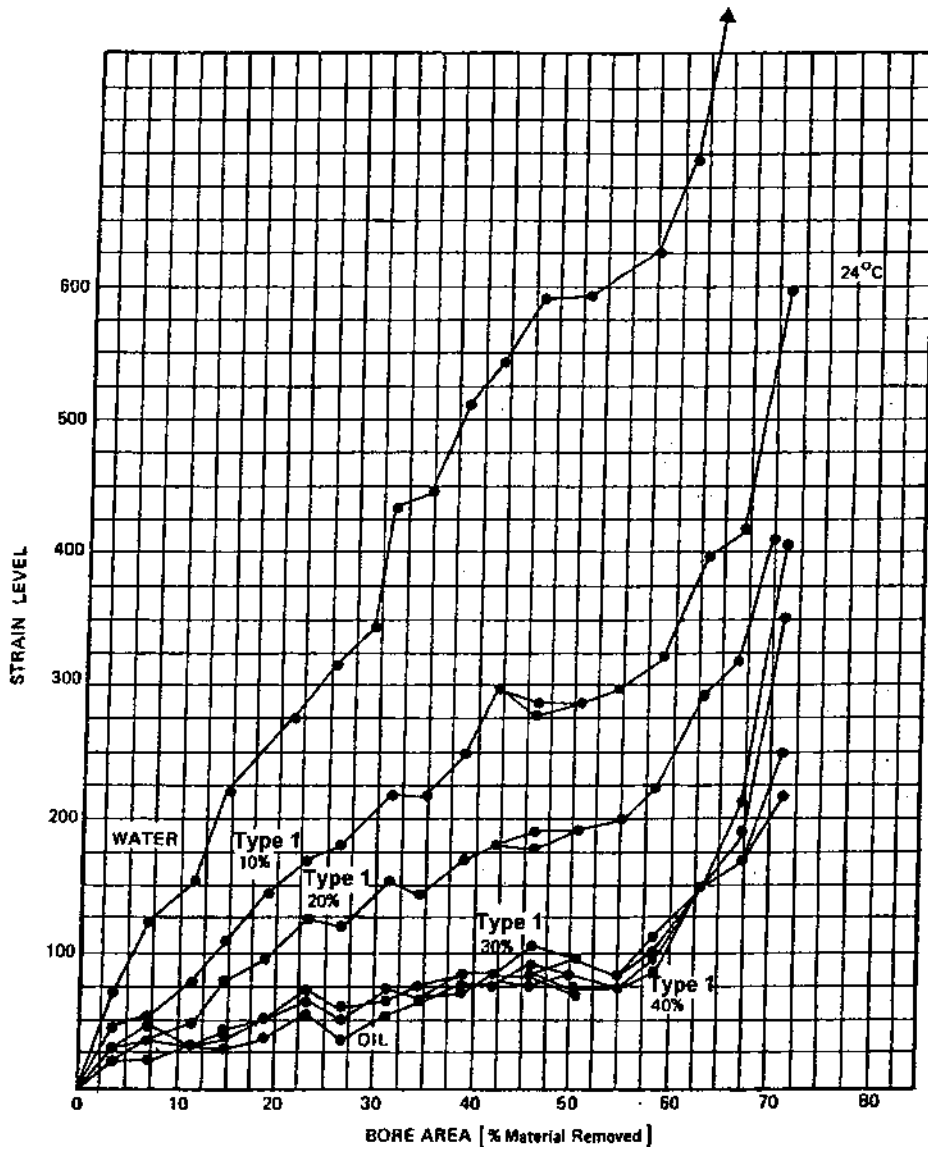
Figure 73   Residual stress comparison of hot water and a Type 1 quenchant as a function of concentration for A356 aluminum castings.

Using the thermal properties from Table 21, which relate to aluminum at approximately 250°C and steel at 500°C, the thermal diffusivity (d) of aluminum is calculated. The diffusivity for different thicknesses (x) where heat can diffuse, may be estimated from:

$$x = (dt)^{-1/2}$$
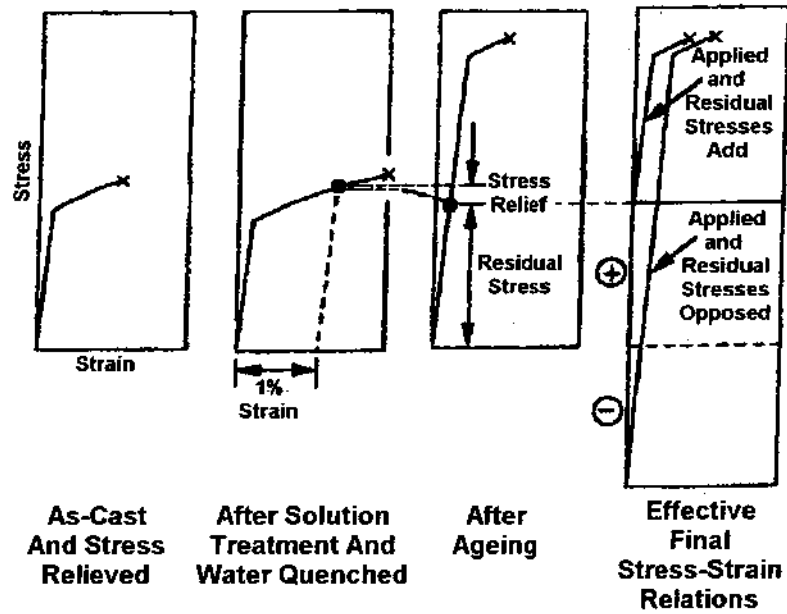
Figure 74   Sequence of steps to illustrate the origin of residual stress in quenching and aging treatments.
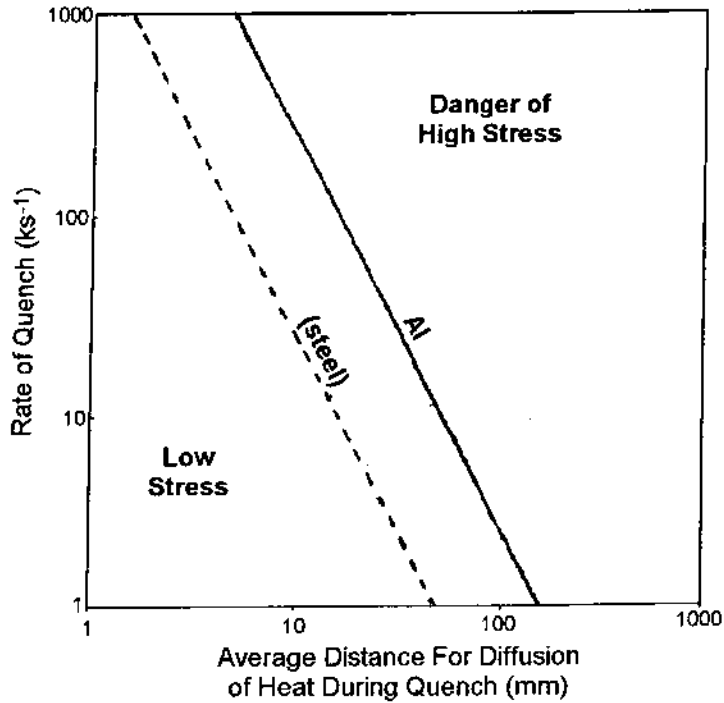
Figure 75   Cooling rate for a 5 mm modulus aluminum plate subjected to various quench severities.

Table 21 Comparison of Physical Properties of Aluminum and Steel

Metal	Thermal Conductivity (W/m/K)	Density (ρkg/m³)	Specific Heat (Cp) J/kg/k	Thermal Diffusivity (d) (m²/k)
Aluminum	200	2700	1000	10^4
Steel	50	7800	500	10^3

If $x = 10$ mm, $t = 1$ sec, the cooling rate upon cooling from 500°C to 250°C is:

$$\text{Cooling Rate (CR)} = \frac{\Delta T}{d} = \frac{250}{1} = 250 \text{ K/sec}$$

Using this process, the relationship between average diffusion distance at different cooling rates may be determined as shown in Fig. 76.

If the following relationship is used [93]:

$$\tau = \frac{\Delta T}{CR}$$
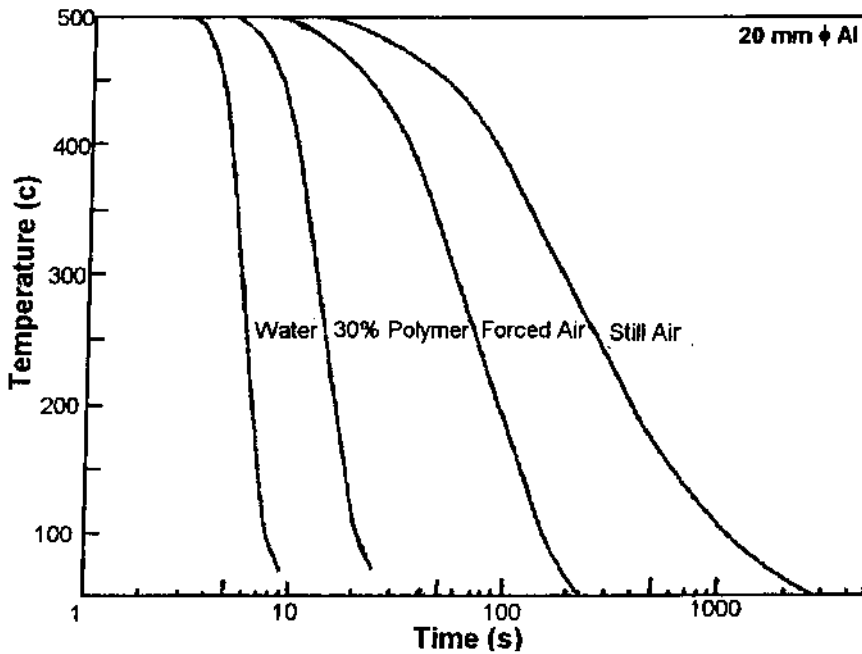
Figure 76 Rate of quench versus diffusion distance for heat during the critical time of the quench showing the extent of safe and dangerous regimes for aluminum castings and test bars. Area 1 was the regime for test bars quenched in water. Area 2 was quenched in 35% of a polymer quench.

Where ΔT is $500 - 250 = 250$ for aluminum and a critical parameter may be calculated:

$$(x^2 \bullet CR)_{\text{CRIT}} = D \bullet T_{\text{CRIT}}$$

Where the critical value of $D\Delta T$ for aluminum alloys is: 2.5×10^{-2} for aluminum alloys and 2.5×10^{-3} for steel. Therefore, if the value for X or Q is sufficient to meet the critical parameter, then there will be a high probability of quench stresses in excess of the yield stress in the casting.

2.6.2 Uphill Quenching

Uphill quenching is also known as ''deep freezing'' or ''tricycle stress relieving''. This process is conducted by immersing quenched aluminum parts into dry ice or liquid nitrogen followed by immersion in boiling water or blasting with high pressure steam [94]. (See Table 22 for comparison of different cooling-heating processes [95].) The objective of uphill quenching is to offset residual stresses formed by rapid cooling by rapid heating thus producing a substantial decrease in residual stresses of the overall process. To be effective, the temperature gradients (T) formed from the uphill quench must be greater than those formed by normal ''deep freezing'' and the subsequent heating must not be sufficient to affect the tensile properties [95].

The uphill quench process, shown schematically in Fig. 77, is conducted in four steps [95]:

1. The quenched part is cooled to a ''sub-zero'' temperature, usually using liquid nitrogen. The effect of delay in conducting the uphill quenching process on stress reduction is shown in Table 23 [5].
2. The parts are held at the sub-zero temperature until they have achieved thermal equilibrium.
3. The parts are immediately transferred to the elevated temperature medium, high-pressure steam.
4. The part is then aged in accordance with the alloy and desired temper.

Although uphill quenching may be effective for some parts, such as those quenched in cold water, the uphill quenching process may not be effective with parts having low residual stresses such as those quenched in hot water or aqueous polymer quenchants.

Table 22 Comparison of the Effectiveness of Various Cooling and Heating Media for Uphill Quenching (AA7049 Aluminum Alloy)[a]

| | METHOD | | |
Cooling Medium	Heating Medium	ΔT	% Stress Relief
Liquid Nitrogen	High-Pressure Steam	371	82
Dry Ice	High-Pressure Steam	219	48
Liquid Nitrogen	Low-Pressure Steam	244	44
Liquid Nitrogen	Boiling Water	110	19
Dry Ice	Boiling Water	110	19

Methods compared

	Method	ΔT	Stress relief
LN_2 ⟶	Steam (high velocity)	371	82%
Dry ice ⟶	Steam (high velocity)	219	48%
LN_2 ⟶	Steam (low velocity)	244	44%
LN_2 ⟶	Boiling water	110	19%
Dry ice ⟶	Boiling water	110	19%

2- x 2- x 12-inch specimens processed within 1½ hours after quench

The uphill quench process

Steps required   **Variables**

1) Cool to required temperature ⟶ LN_2
                                        ⟶ Dry ice (sometimes)

2) Stabilize at temperature

3) Transfer to heating chamber ⟶ Steam recommended
                                ⟶ Boiling water (sometimes)
                                ⟶ Oven (not usually effective)

4) Uphill quench to establish ΔT
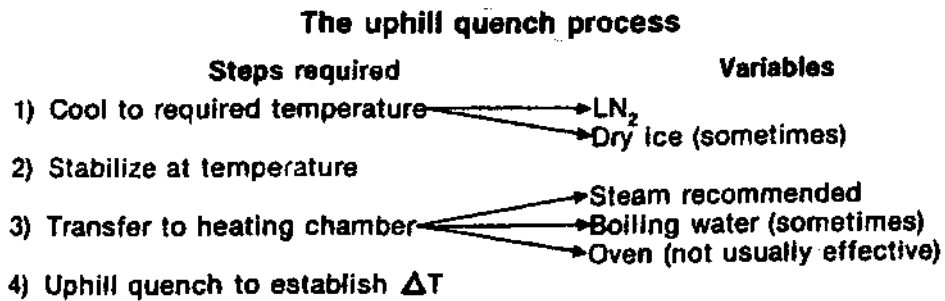
Figure 77 Comparison of different uphill quenching methods.

Table 23 Effect of Delay in Uphill Quenching from the Initial Quench on Stress Reduction (AA7049 Aluminum Alloy)

Delay After Quench (hr)	Measured Residual Stress (psi)	Stress Reduction (%)
1	4000	83
3	7000	71
8	10000	58
24	14000	42

2.7 Distortion Control

One of the most difficult problems in the aluminum heat treating industry is distortion control [95]. Type I polymer quenchants will significantly reduce distortion relative to a water quench as shown in Fig. 51 [55]. Selected examples of parts that have been successfully quenched in a Type I quenchant are shown in Fig. 78 [96], Fig. 79 [96], and Fig. 80 [97]. Suttie reported that a Type I PAG quenchant provided significant distortion reduction for 7075-T6 forgings relative to cold water while producing substantially higher tensile strengths than boiling water [27]. Similar results were reported by Collins and Maduell on the same alloy [98].

2.7.1 Quench Severity and Distortion

Quenching media must be selected to provide film coefficients and quench factors capable of producing acceptable properties in the section thicknesses of interest,
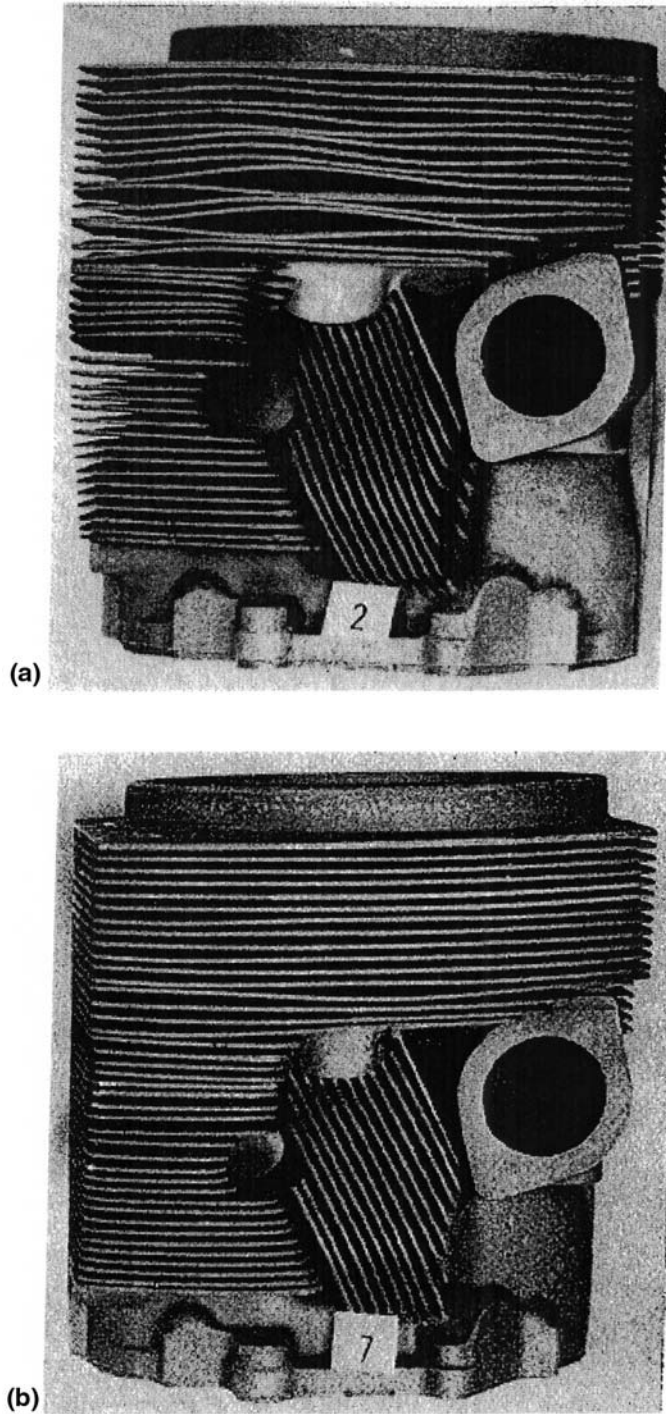
Figure 78 Lycoming engine head (390 alloy) (a) quenched upright in 25% Type 1 quenchant and (b) quenched in 25% Type I quenchant on its side to facilitate more uniform fluid flow to minimize distortion. (This engine cracked in boiling water.)
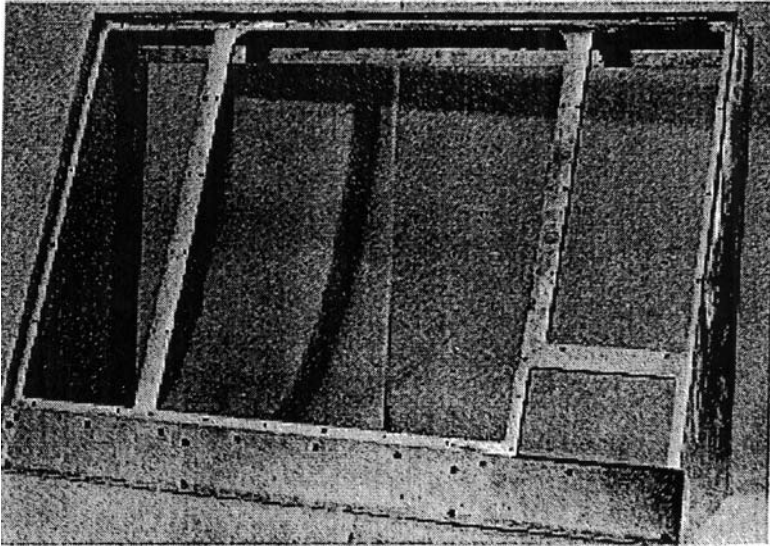
Figure 79   Dip-Brazed 6061 panel section.
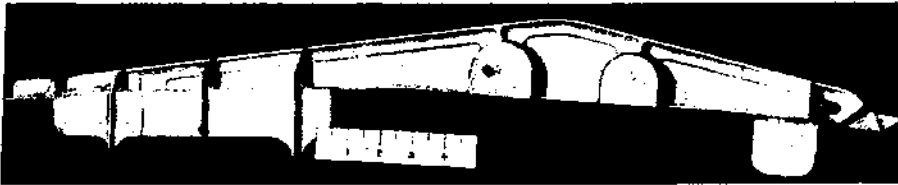
Figure 80   7075-T6 die forging quenched in 20% Type 1 quenchant.

as previously discussed. However, it is desirable not to use a medium which possesses an excessively high film coefficient if distortion is to be minimized consistent with meeting the required properties. Excessively high film coefficients result in higher temperature gradients across thick sections and large temperature differences between thick and thin sections. This in turn aggravates residual stress and distortion problems.

Figure 81 illustrates a 76.2 mm diameter aluminum alloy bar probe instrument with two thermocouples, one in the center and the other 6.35 mm from the surface. Beck has employed dual thermocouples to study thermal gradients in silver probes used in quenchant studies in Europe [99]. The data from properly instrumented probe may also be used to determine residual stresses introduced during quenching [100].

Cooling curves were obtained at these thermocouple positions when this bar was quenched in 32°C water flowing at 0.25 m/sec, and the curves are illustrated in Fig. 82. The temperature difference between the two thermocouples, calculated at the center temperature minus the surface temperature, is also shown plotted
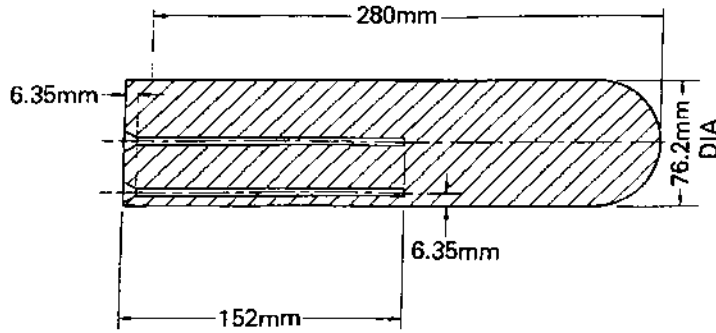
Figure 81 Cross-section of a 76.2 mm AA7075 alloy probe instrumented with center and near surface thermocouples.
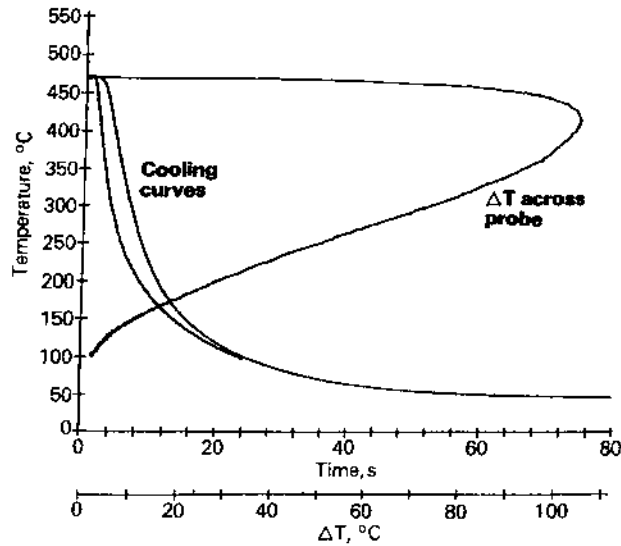
Figure 82 Cooling curves and temperature difference across a 76.3 mm diameter AA7075 probe quenched into 32°C water flowing at 0.25 mm/sec.

as a function of the center temperature (on the ordinate) [4]. It is observed that the maximum temperature difference across the bar was approximately 110°C and the maximum value occurred shortly after the start of quenching while the center temperature was approximately 425°C.

Similar temperature-time histories and the temperature differences across the probe when quenching in 60°C water and 20% Type I Polymer Quenchant flowing at 0.25 m/sec past the probe are illustrated in Figs. 83 and 84 respectively. The data in both cases are superimposed on the 32°C water data previously shown in Fig. 82. The higher water temperature of 60°C reduced the maximum temperature difference to 60°C and the 20% solution of Type I Polymer Quenchant reduced the difference to a value of 69°C. The film coefficients associated with these quenchants
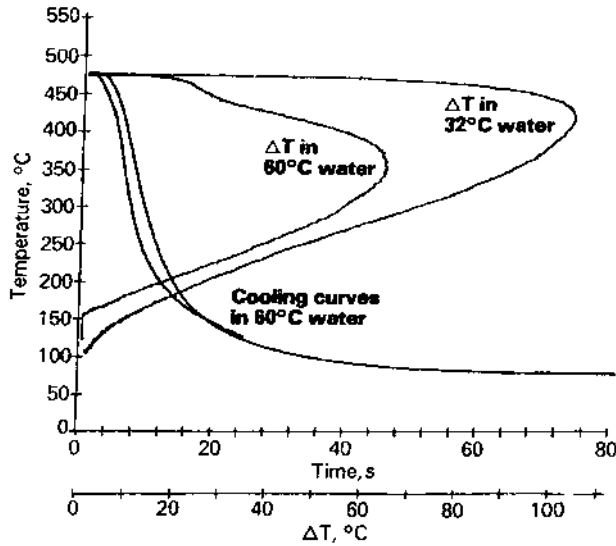
Figure 83 Cooling curves and temperature difference across a 76.3 mm diameter AA7075 probe quenched into 32 and 60°C water flowing at 0.25 mm/sec.
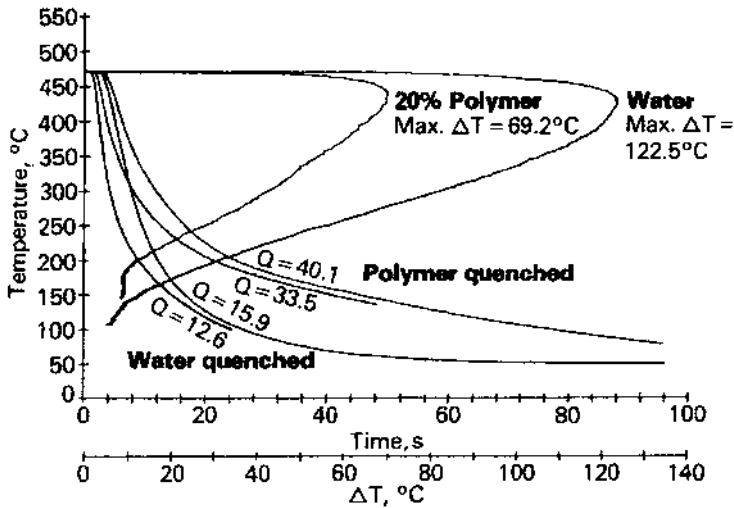
Figure 84 Cooling curves and temperature difference across a 76.3 mm diameter AA7075 probe quenched into water and a 20% solution of a Type 1 polymer quenchant solution at 32°C flowing at 0.25 mm/sec.

were presented in Tables 10 and 11. The temperature difference across the section decreased as the film coefficient decreased.

High film coefficients can produce even larger differences in temperature between thick and thin sections of a part. Cooling curves associated with a 76.2 mm
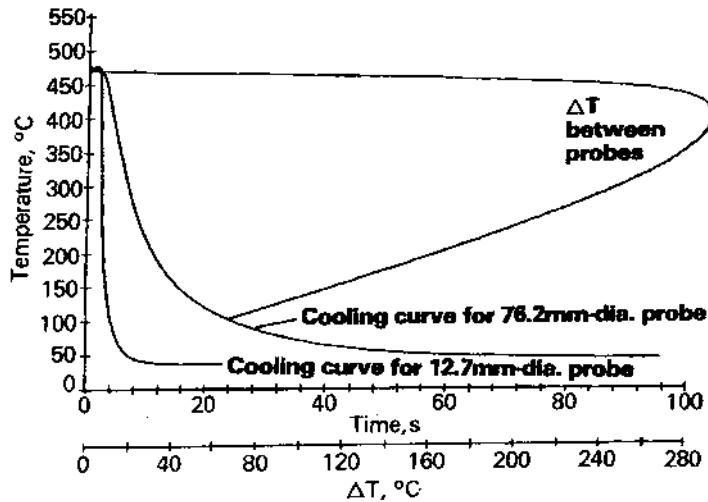
Figure 85   Cooling curves and temperature difference across a 12.7 and a 76.3 mm diameter AA7075 probe quenched into 32°C water flowing at 0.25 mm/sec.

section and a 12.7 mm section quenched in 32°C water flowing over the part at a velocity of 0.25 m/sec are illustrated in Fig. 85. Water at this temperature and velocity had a film coefficient of about 4.78 W/cm^{2}K and produced a maximum temperature difference between the two sections of approximately 290°C.

The thermal stress in a part, which causes distortion during quenching, is a function of the alloy thermal expansion coefficient, elastic modulus and temperature difference within the part. Minimizing the thermal stress requires that the temperature difference be minimized since no control can be exercised over either of the physical properties.

The temperature differences across plates up to 76 mm thick were calculated using a finite difference heat transfer program in which the film coefficient was used as an input value. The results are illustrated in Fig. 86 where the temperature difference is the maximum calculated value between the plate center and a location 1.60 mm beneath the surface. The temperature difference across a given section thickness increased progressively as the film coefficients increased. In order to minimize the temperature across a part to reduce the thermal stress, the film coefficient must be minimized while cooling fast enough to guarantee the minimum yield strength can be met. This can be done by selecting and using the most appropriate quenchant and operating conditions.

Archambault et al. have suggested an alternative technique involving computer control of quenchant spray heads aimed at different areas of a part [101]. This approach can be used to control cooling rates and minimize thermal gradients. Additional control can be exercised, as a function of time, on the heat transfer coefficient by these means [4,102,103]. More precision in the calculated results can undoubtedly be obtained using film coefficients that vary with the probe temperature. Several investigators have shown how a functional relationship can
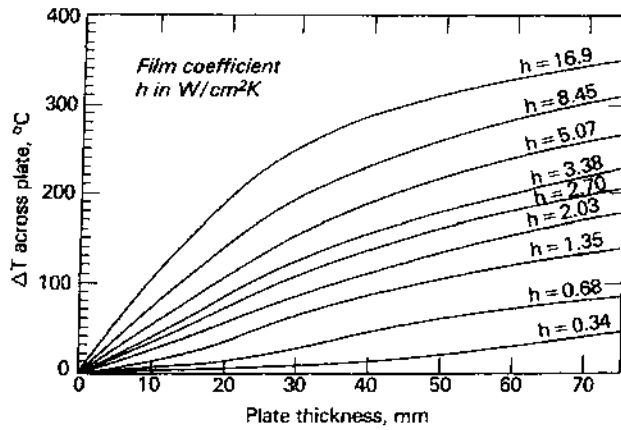
Figure 86 The effect of film coefficient on the temperature difference between the surface and center of AA7075 aluminum alloy plates.
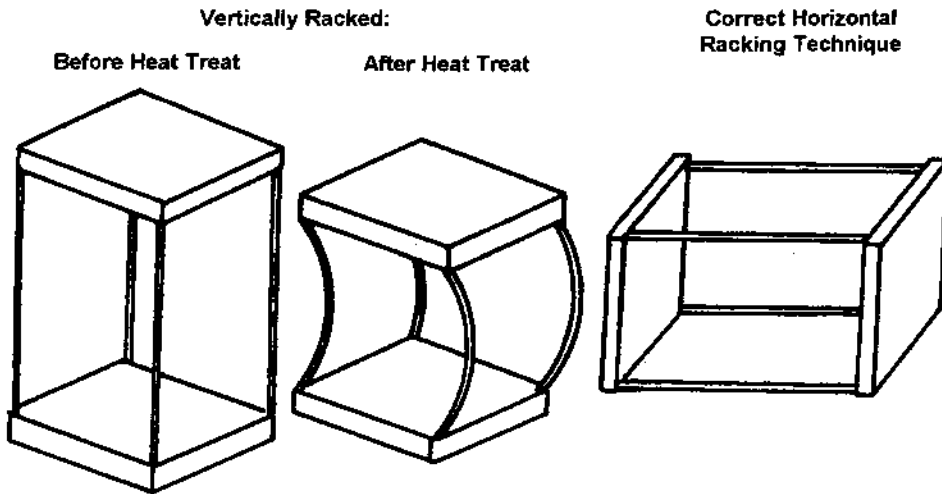
Figure 87 AA6061 assembly showing effects of different racking methods on distortion.

be established between film coefficient or heat flux and the probe temperature [104–107], but these methods were not used in the current study which assumed a constant effective film coefficient.

Quenching real parts is usually more complicated than quenching sheets, bars and plates because most real parts do not have a uniform cross-section. Many aircraft structural members consist of flanges reinforced by thin web sections. When such a part is quenched in water, the web section temperature drops far more quickly than the temperature in the heavier flange. The large temperature difference creates a high thermal stress which often causes plastic deformation in the web. When the heavy flange cools, it contracts onto the thin web and often causes buckling or

the "oil-can" effect. Efforts to reduce web thicknesses in order to remove weight from structural members aggravates the buckling problem by producing thinner sections that cool even faster than the flanges. The only feasible approach to reducing plastic flow in web sections with conventional quenching technology is to reduce the heat transfer coefficient at the web-quenchant interface, while not reducing the film coefficient so much that the quench factor in the flange is too high to allow properties to be met.

2.7.2 Racking

One of the major causes of distortion is non-uniform heat removal from the parts being quenched. To minimize distortion, the placement of the parts, commonly known as "racking", in the quench tray is critical. The most important factors to be considered in this regard are [108–111].

1. Part Spacing.
2. Part Configuration.
3. Agitation.
4. Immersion Rate.
5. Thickness Variation within the Part.
6. Quench Medium.
7. Part Spacing—Perhaps the most important consideration is part spacing. It is essential that sufficient space be provided around the part to optimize quenchant—surface area contact. This enhances heat extraction from the hot surface while minimizing the formation of hot spots or localized temperature increases within the quenchant due to poor fluid flow (agitation) [109].
8. To achieve optimal flow, parts must be properly "racked" with the use of "fixtures" [97]. Fixtures may be a basket or a rack with places to hang or place small parts so that they will not move when immersed in the quenchant. Larger parts, although relatively heavy, must be racked properly to assure uniform heat removal during the quench. Such parts should not be indiscriminately dumped into a basket and quenched. Instead, the parts must be placed in the tank so that adequate fluid flow around all of the surfaces is assured.
9. The amount of space between the parts must be increased with increasing mass. For water quenching, the distance between part surfaces must increase with with higher quenchant temperatures. Water temperatures greater than $160°F$ should not be used for larger cross-sections [110].
10. Part Configuration – Croucher's rule of thumb is to place parts in a basket so that they will offer least resistance to fluid flow [111].
11. Agitation—Figure 87 shows that the directional placement of a complex part in the quenchant is often important if distortion and cracking are to be prevented. A simple analysis is often sufficient to assure that reasonable fluid flow around the part is obtained. For example, situations where the part would be placed to block fluid flow may create hot spots leading to more distortion [110]. An illustration of such a part is provided

in Fig. 80. (Note: Similar distortion problems may be observed during heating where the mechanical load on a part may be sufficiently high to cause plastic deformation [111].)

12. Immersion (Dropping) Rate—Immersion rate is defined as the rate that the part is immersed into the quenchant [109]. Distortion is generally reduced by increasing immersion rates. Immersion rates are usually in the range of 0.5–8 ft/sec but, in some cases, it is not possible to rack the part in a way that promotes fluid flow around the surface. In such cases, lower immersion rates are recommended.

13. Thickness Variations—Since large cross-sections cool more slowly than thinner cross-sections, complex shapes may be inherently prone to distortion. When this occurs, racking configuration may be used to help offset cross-section size variations.

14. Quench Media Selection—Although certain quench media may provide lower propensity for distortion, proper racking procedure cannot be ignored. Generally, the same racking considerations are recommended for aqueous polymer quenchants as for water.

REFERENCES

1. T. Croucher, "Quenching of Aluminum Alloys: What This Key Step Accomplishes", Heat Treating, 1982, pp. 20–21.
2. J. W. Evancho and J. T. Staley, "Kinetics of Precipitation in Aluminum Alloys During Continuous Cooling", Metall. Trans., 1974, 5, pp. 43–47.
3. W. Köster and G. Hofmann, "The Effect of Quenching Rate on the Kinetics of Cold Age Hardening of an Aluminum-Zinc Alloy with 10% Zinc", Z. Metallknd., 1963, 54, pp. 570–575.
4. C. E. Bates, "Selecting Quenchants to Maximize Tensile Properties and Minimize Distortion in Aluminum Parts", J. Heat Treating, 1987, 5, pp. 27–40.
5. C-Y. Lim and H. R. Shercliff, "Quench Sensitivity of Aluminum Alloy 6082", University of Cambridge, Department of Engineering, Technical Report No. CUED/C-MATS/TR205, April, 1993.
6. J. E. Vruggink, "Quench Rate Effects on the Mechanical Properties of Heat Treatable Aluminum Alloys", Presented at Fall Meeting of TMS, October 13–15, 1968, Detroit, MI.
7. W. G. G.'t Hart, H. J. Kolkman, and L. Shra, "Jominy End-Quench Investigation of Corrosion Properties and Microstructures of High Strength Aluminum Alloys", Report No. NLR TR 80102 U, National Aerospace Laboratory, Amsterdam, The Netherlands, November 1980.
8. J. W. Newkirk, K. Ganapati, and D. S. MacKenzie, "Faster Methods of Studying Quenching Aluminum Through Jominy End-Quench", *Heat Treating Including the Liu Dai Memorial Symposium–Proceedings of the 18th Conference*, (R. A. Wallis and H. W. Walton, eds.), October 12–15, 1998, ASM International, Materials Park, OH, pp. 143–150.
9. J. W. Newkirk, D. S. MacKenzie, and Y. Wei, "The Study of Quench Sensitivity in Aluminum Alloys using Accelerated Methods", in *Heat Treatment and Surface Engineering of Light Alloys, Proceedings of the 7th International Seminar of IFHT*, September 15, 1999, Budapest, Hungary, Hungarian Scientific Society of Mechanical Engineering, Budapest, Hungary, pp. 229–238.

10. G. E. Totten, C. E. Bates, and L. M. Jarvis, "Cooling Curve and Quench Factor Characterization of 2024 and 7075 Aluminum Bar Stock Quenched in Type I Polymer Quenchants", in *Heat Treating–Proceedings of the 16th Conference*, (J. L. Dossett and R. E. Luetje, eds.), 1996, ASM International, Materials Park, OH, pp. 221–229.

11. B. Liscic and T. Filetin, "Computer-Aided Evaluation of Quenching Intensity and Prediction of Hardness Distribution", J. of Heat Treating, 1988, 5(12), pp. 115–124.

12. Beck and J. Chevrier, "Comparison des donnees de trempe, determinees a l'aid d'une methode numerique, a celles du regime permantent", Int. J. Heat Mass Transfer, 1971, 14, pp. 1731–1751.

13. M. Bamberger and B. Prinz, "Determination of Heat Transfer Coefficients of Water Cooling of Metals," Mat. Sci. and Tech., 1986, 2(4), pp. 410–415.

14. T. Croucher, "Critical Parameters for Evaluating Polymer Quenching of Aluminum", Heat Treating, 1987, 19(12), pp. 21–25.

15. *Aluminum, Volume 1: Properties, Physical Metallurgy and Phase Diagrams*, (Dent R. Van Horn, ed.), 1967, ASM International, Materials Park, OH, p. 135.

16. H. M. Tensi and P. Stitzelberger-Jacob, "Effects of Rewetting on the Cooling of Quenched Aluminum Specimens", HTM, 1988, 43(3), pp. 148–155.

17. H. M. Tensi, P. Stitzelberger-Jacob, and G. E. Totten, "Quenching Fundamentals: Surface Rewetting of Aluminum", Adv. Mat. and Proc., 1999, 156(5), pp. H15–H20.

18. J. Wüning and D. Leidtke, "Tests for Determining Heat Flux Density During Steel Quenching in Liquid Quenchants by the QTA Method", Härterei-Tech. Mitt., 1983, 38(4), pp. 149–155.

19. M. Tagaya and I. Tamura, "Studies on Quenchants. Part 8: Effects of the Dimensions of the Silver Sample on the Quenching Process", Härterei-Tech. Mitt., 1963, 18(4), pp. 63–76.

20. H. Bomas, "Quenching Rate of AlMgSi Alloys Affects the Strength Values", Maschinemarkt, 1982, 88, pp. 1220–1222.

21. T. Croucher, "Water Quenching Procedure for Aluminum Alloys", Heat Treating, 1982, 14 (9), pp. 18–19.

22. E. H. Burgdorf, "Properties and Uses of Synthetic Quenching Solutions", Z. Wirtsch. Fertig., 1979, 74, pp. 431–436.

23. H. Beitz, "Uses and Limitations of Synthetic Aqueous Quenching Liquids in Hardening Technology", Härterei-Tech. Mitt., 1979, 34(4), pp. 180–188.

24. G. E. Totten, C. E. Bates, and L. M. Jarvis, "Type I Quenchants for Aluminum Heat Treating", Heat Treat., December 1991, pp. 16–19.

25. C. E. Bates and G. E. Totten, "Procedure for Quenching Media Selection to Maximize Tensile Properties and Minimize Distortion in Aluminum–Alloy Parts", Heat Treat. of Metals, 1988, 4, pp. 89–98.

26. H. M. Tensi and E. Steffen, "Measuring the Quenching Effect of Liquid Hardening Agents on the Basis of Synthetics", Steel Research, 1985, 56(9), pp. 489–495.

27. H. M. Tensi and P. Stitzelberger-Jacob, "Convection in Quenching Baths–Different Ways of Determining the Effects of Convection", Eingereicht bei Materials Science and Technology, October 1987.

28. H. M. Tensi, P. Stitzelberger-Jacob, and Th. Künzel, "Laboratory Test for Assessing the Cooling Characteristic of Polymer Quenchants", Draft International Standard, Technical University of Munich, Munich, Germany, Inst. of Material and Processing Sciences, 1987, 28 pages.

29. K. Wefers, "Properties and Characteristics of Surface Oxides on Aluminum Alloys", Aluminum, 1987, 57, pp. 722–726.

30. W. L. Fink and L. A. Willey, "Quenching of 75S Aluminum Alloy", Trans. AIME, 1948, 175, pp. 414–427.

31. "Quench Factor Analysis" in *Aluminum Properties and Physical Metallurgy*, (J. E. Hatch, ed.), 1984, ASM International, Materials Park, OH, pp. 159–164.
32. V. G. Davydov, I. I. Novikov, and Ye. D. Zakharov, "C-Curves of the Decomposition of a Supersaturated Solid Solution in Duralumin-Type Alloys", Izv. Vyssh. Ucheb. Zaved. Tsvet. Met., 1968, 11(4), pp. 117–123.
33. G. L. Schneyder, "Effect of Chemical Composition on the Hardenability of Aluminum Alloys", Tsvetn. Met., 1993, 2, pp. 55–58.
34. J. T. Staley, "Modeling Quenching of Precipitation Strengthened Alloys: Application to an Aluminum-Copper-Lithium Alloy", Ph.D. Thesis, Drexel University, 1989.
35. J-S. Kim, R. C. Hoff and D. R. Gaskell, "A Quench Factor Analysis of the Influence of Water Spray Quenching on the Age-Hardenability of Aluminum Alloys", in *Materials Processing in the Computer Age*, (R. Voller, M. S. Stachowicz, and B. G. Thomas, eds.), 1991, The Minerals, Metals and Materials Society, pp. 203–221.
36. J. W. Cahn, "The Kinetics of Grain Boundary Nucleated Reactions", Acta Met., 1956, 4, pp. 449–459.
37. C. E. Bates and G. E. Totten, "Procedure for Quenching Media Selection to Maximize Tensile Properties and Minimize Distortion in Aluminum-Alloy Parts", Heat Treat. of Metals, 1988, 4, pp. 89–97.
38. C. E. Bates, "Quench Optimization for Aluminum Alloys", AFS Transactions, 1994, 93–25, pp. 1045–1054.
39. J. T. Staley, "Quench Factor Analysis of Aluminum Alloys", Mater. Sci. Tech., November 1987, 3, pp. 923–935.
40. "Metallic Materials and Elements for Aerospace Vehicle Structures", *Military Standardization Handbook* 5D, June 1983.
41. T. Sheppard, "Press Quenching of Aluminum Alloys", Mater. Sci. Tech., July 1988, 4, pp. 635–643.
42. P. A. Rometsch, G. B. Schaffer, J-Y. Yao, and M. J. Cooper, "Application of Quench Factor Analysis to A356.0 and A357.0 Foundry Alloys", Aluminum Alloys: Their Physical and Mechanical Properties Vol. 2, July 1998; pp. 727–732.
43. D. Hein, "Model Concepts on Rewetting by Flooding", Ph.D. Thesis, Technical University of Hanover, Hanover, Germany, 1980, 182 pages.
44. R. Jeschar and R. Maass, "Determination of Heat Transfer During Quench Hardening of Metals in Water", Gas Wärme Intern., 1985, 34(9), pp. 348–354.
45. O. Zach, "Experimental Investigation of the Cause of the Variation of the Leidenfrost Point", Institute of Nuclear Energetics, IKE 2–34, Stuttgart, 1976, 78 pages.
46. Y. Kikuchi, T. Hori, and J. Michiyoshi, "Minimium Film Boiling Temperature for Cooldown of Insulated Metals in a Saturated Liquid", Int. J. Heat Mass Transfer, 1985, 28(6), pp. 1105–1114.
47. Th. Künzel, "Effect of Rewetting on Allotropic Modification of Quenched Metal Bodies", Ph.D. Thesis, Technical University of Munich, Munich, Germany, 138 pages.
48. K. J. Baumeister and F. F. Simon, "Leidenfrost Temperature – Its Correlation for Liquid Metals, Cryogens, Hydrocarbons and Water", J. Heat Transfer, 1973, pp. 166–173.
49. R. E. Henry, "A Generalized Correlation for the Minimum Point in Film Boiling", 14th National Heat Transfer Conference, AICHE-ASME, August, 1973, Atlanta, Georgia.
50. T. Croucher, "Water Quenching Procedures for Aluminum Alloys", Heat Treating, September 1982, pp. 18–19.
51. T. R. Croucher, "Applying Synthetic Quenchants to High-Strength-Alloy Heat Treatment", Metals Engineering Quarterly, May 1971, pp. 6–11.
52. H. M. Tensi, Th. Künzel, and P. Stitzelberger, "Wetting Kinetics as an Important Hardening Characteristic in Quenching:, Häterei-Tech. Mitt., 1987, 42(3), pp. 125–132.

53. Th. Künzel, H. M. Tensi, and G. Welzel, "Rewetting Rate – The Decisive Characteristic of a Quenchant", Tagungsband 5th Intern. Congress on Heat Treatment of Materials, Budapest, October 20–24, 1986, pp. 1806–1813.

54. G. E. Totten, C. E. Bates, and L. M. Jarvis, "Quench Factor Analysis: Polymers vs. Hot Water", Heat Treating, May 1989, pp. 38–40.

55. R. R. Blackwood, L. M. Jarvis, G. E. Totten, G. M. Webster, and T. Narumi, "Reducing Aluminum Distortion With Type I Quenchants", Metal Heat Treating, May/June 1996, pp. 28–31.

56. R. R. Blackwood and W. D. Cheesman, "Metal Quenching Medium", U.S. Patent 3,220,893, November 30, 1965.

57. H. M. Tensi, A. Stich, and G. E. Totten, "Fundamentals of Quenching", Metal Heat Treating, Mar./Apr. 1995, pp. 20–28.

58. T. Croucher and D. Butler, "Polymer Quenching of Top Quality, High-Strength Aluminum Castings", Heat Treating, October 1982, pp. 28–31.

59. T. Croucher and D. Butler, "Polymer Quenching of Aluminum Castings", 26th National SAMPE Symposium, April 26–28, 1981, pp. 527–534.

60. "Polyalkylene Glycol Heat Treat Quenchant", Aerospace Material Specification AMS 3025A, Society of Automotive Engineers Inc., April 15, 1990.

61. "Heat Treatment of Wrought Aluminum Alloy Parts", Aerospace Material Specification AMS 2770E, Society of Automotive Engineers Inc., January 1, 1989.

62. J. C. Chevrier, A. Simon, and G. Beck, "Optimal Cooling Rate and Process Control in Metallic Parts Heat Treatment", *Heat Mass Transfer Metall. Syst.*, Seminar. Int. Cent. Heat Mass Transfer, 1981, Hemisphere Press, Washington, D.C., pp. 535–544.

63. J. M. Naud, F. Moreaux, G. Beck, B. Dubost, and J. Olivier, "New Aqueous Solutions that Minimize Strains and Residual Stresses When Quenching Products of High Strength Aluminum", Mém. Etud. Rev. Métall., 1985, 82(11), pp. 603–608.

64. J. K. Scott, "Organic Quenchant Aids—Heat Treatment of Dip-Brazed Aluminum Parts", Metal Progress, March 1969, pp. 80–82.

65. T. Croucher, "Synthetic Quenchants Eliminate Distortion", Metal Progress, 1973, pp. 52–55.

66. E. Meckelburg, "Synthetic Quenching Media to Supress Distortion", Seifen, Öle, Fette, Wachse, 1977, 103(4), pp. 105–107.

67. G. E. Totten, G. M. Webster, L. M. Jarvis, and C. E. Bates, "Effect of Section Size, Quenchant Concentration and Agitation on the Physical Properties of Type I Polymer Quenched Aluminum Alloys", in *Proc. of the 1st Int. Non-Ferrous Processing and Technology Conference*, March 10–12, 1997, St. Louis, MO, (T. Bains and D. S. MacKenzie, eds.), ASM International, Materials Park, OH, pp. 7–16.

68. G. E. Totten, C. E. Bates, and N. A. Clinton, *Handbook of Quenchants and Quenching Technology*, ASM International, 1993.

69. G. E. Totten and G. M. Webster, "Quenching Fundamentals: Maintaining Polymer Quenchants", Adv. Mat. & Proc., June 1996, pp. 64AA–64DD.

70. G. E. Totten and G. M. Webster, "Quenching Fundamentals: Stability and Drag-Out of Polymers" Adv. Mat. & Proc., 1999, 155(6), pp. H63–H66.

71. L. M. Jarvis, R. R. Blackwood, and G. E. Totten, "Thermal Separation of Polymer Quenchants for More Efficient Heat Treatments", Ind. Heat., November 1989, pp. 23–24.

72. N. Bogh, "Aqueous Based Quench Fluid Control", in *18th Heat Treating Society Conference Proceedings*, (H. Walton and R. Wallis, eds.), ASM International, Materials Park, OH, 1998, pp. 594–597.]

73. R. D. Howard and G. E. Totten, ''Expansion of Application Potential of Polymer Quenchants Using Membrane Separation'', *Environmental and Energy Efficient Heat Treatment Technologies: Proceedings of the 4th International Seminar of International Federation for Heat Treatment and Surface Engineering*, (S. Zhoujun and W. Yingsi, eds), Int. Academic Publishers, Sept. 15–17, 1993, Beijing China; pp. 298–306.]

74. D. N. Herival, ''The Theory and Operation of Reverse Osmosis Systems in Quenchant Management Applications'', *Heat Treating: Equipment and Processes – 1994 Conference Proceedings*, (G. E. Totten and R. A. Wallis, eds.), ASM International, Materials Park, OH, Schaumberg, IL, April 1994, pp. 377–382.

75. M. D. Schuler, ''Forging Blister Evaluation for Newton Heat Treating'', Hughs Aircraft Company, Fullerton, CA, letter to R. R. Blackwood, August 14, 1972.

76. T. Croucher, ''Part 2: Solution Heat Treating of Aluminum'', Heat Treating, 1982, 13(3), pp. 18–19.

77. D. M. Berger, ''Electrochemical Corrosion of Coated Steel Surfaces'', Chemical Engineering, June 28 1982, pp. 109–112.

78. J. A. Nicol, E. D. Seaton, H. Yu, R. Pishko, and G. W. Kuhlman, ''Advanced Aluminum Alloy Quenchants'', Aeromat '95, ASM International, 6th Conference on Aerospace Materials and Processes, Anaheim, CA, May 8, 1995.

79. H. Yu, J. A. Nicol, R. A. Ramser, and D. E. Hunter, ''Method of Heat Treating Metal with Liquid Coolant Containing Dissolved Gas'', U. S. Patent 5, 681, 407, October 28, 1997.

80. O. G. Senatorova, S. A. Vigdforchik, N. I. Kolobnev, V. V. Lak'yanenko, A. V. Sverdlin, I. A. Nabatova, and T. M. Yaroslavyseva, ''Possibility of Quenching Aluminum Alloys D16 and V95 in an Aqueous Polymer Solution'', Doklady Akademii Naa\uk USSR, 1978, 1, pp. 50–51.

81. G. W. Kuhlman and E. D. Seaton, ''Enhancing Machining Performance of Aluminum Forged Products'', Metal Heat Treating, Jan/Feb 1996, pp. 33–40.

82. J. A. Nicol, E. D. Seaton, G. W. Kuhlman, H. Yu, and R. Pishko, ''New Quenchant for Aluminum'', Adv. Mat. and Proc., 1996, 4, pp. 4OS–4OV.

83. K. Yoshimoto, R. Abe, Y. Sugimoto, F. Ishimura, Y. Yamamoto, N. Oda, I. Fukuda, T. Miyatani, H. Kodama, and N. Nakano, ''Light-Alloy Casting, Heat Treatment Method'', EP 897995A1, February 24, 1999.

84. A. S. Bedarev, G. P. Konyukhov, E. G. Il'yushko, and G. I. Beloborodov, ''Use of Water Soluble Polymers for Quenching Aluminum Alloys'', Metal Science and Heat Treatment, 1978, 20(1–2), pp. 48–52,

85. G. Yu Krotov, D. Kh. Khamidullin, and S. N. Anan'in, ''Selection of a Quenching Medium for Aluminum Alloys'', Metalloved. Term. Obrab. Met., 1989, 3, pp. 5–7.

86. J. Rauche, ''Process of Quenching Metal Pieces and Product Produced'', U.S. Patent 4,243,439, January 6, 1981.

87. D. G. Altenpohl, *Aluminum: Technology, Applications and Environment—A Profile of a Modern Metal, 6th Edn*, 1998, The Aluminum Association, Inc., Washington, D. C., p. 234.

88. E. H. Dix, ''The Resistance of Aluminum Alloys to Corrosion'', in *Metals Handbook, 8th Edn. Vol. 1 – Properties and Selection of Metals*, (T. Lyman ed.), 1961, ASM International, Materials Park, OH, pp. 916–935.

89. J. E. Hatch, *Aluminum: Properties and Physical Metallurgy*, 1984, ASM International, Materials Park, OH, pp. 260–272.

90. M. D. Schuler, ''Intergranular Corrosion'', Univ. of California, May 18, 1998, unpublished report.

91. ''UCON Quenchant A—Quenching Aluminum for Minimal Distortion and Low Residual Stresses'', brochure published by Tenaxol Inc., 5801 W. National Ave, Milwaukee, WI, 53214.

92. R. L. Torgerson and C. J. Kropp, "Improved Heat Treat Processing of 7050 Aluminum Alloy Forgings Using Synthetic Quenchants", *22nd National SAMPE Symposium*, 1977, pp. 111–132.

93. J. Campbell, "The Heat Treatment of Castings", Foundry Trade Journal, May 1996, pp. 212–214.

94. R. H. Rein, "Cryogenic Cooling", Canadian Patent, 841903, May 19, 1970.

95. T. Croucher, "Uphill Quenching of Aluminum: Rebirth of a Little-Known Process", Heat Treating, October 1983, pp. 30–34.

96. R. Creal, "Distortion is the Enemy in Heat Treating Aluminum", Heat Treating, December 1996, pp. 27–29.

97. O. R. Singleton, "An Analysis of New Quenchants for Aluminum", J. of Metals, November 1968, pp. 1–8.

98. T. R. Croucher and M. D. Schuler, "Distortion Control of Aluminum Products Using Quenchants", Metals Engineering Quarterly, August 1970, pp. 14–18.

99. G. Beck, "Determination of the Cooling Process of a Metallic Specimen Quenched in Water at $100°C$, in Terms of the Temperature of the Initial Metal Liquid Contact and the Limiting Temperatueres of Film Vaporization and Bubble Nucleation in the Liquid", C. R. Acad. Sci., 1967, 265(15), pp. 793–796.

100. J. Jeanmart and J. Bouvaist, "Filter Element Calculation and Measurement of Thermal Stresses in Quenched Plates of High-Strenght Alumiumun Alloy", Mat. Sci. and Tech., 1985, 1(10), pp. 765–769.

101. P. Archambault, J. Bouvailst, J. C. Chevrier and G. Beck, *A contribution to the 7075 Heat Treatment*, Materials Science and Engineering, 1980, 43, pp. 1–6.

102. J. S. Kirkaldy, D. Venugopalan, and M. McGirr, "Keeping the Heat On", First National Heat Treatment Conference, Sydney, Australia, August 1984.

103. J. C. Chevrier, A. Siman, and G. Beck, "Optimal Cooling Rate and Process Control in Metallic Parts Heat Treatment", Heat and Diffusion Treatment, 1979, pp. 535–544.

104. P. Archambault, J. C. Chevrier, G. Beck, and J. Bouvaist, "Optimum Quenching Conditions for Aluminium Alloy Castings". Heat Treatment '76, Book No. 181, The Metals Society, 1976, pp. 105–109.

105. B. Liscic, "The Temperature Gradient at the Surface as a Criterion for the Actual Quenching Effect During Hardening", Harterei-Technische Mitteilungen, 1978, 33(4), pp. 1789–191 (In German).

106. H. M. Tensi and E. Steffen, "Neue Methode zur Quantitiven Bestimmung der Abschreckwirking Flussing Hartemetter, Hier Speziell Wassrige Kinstsoffloslungen", Wärme-und-Stpffibertragimg, 1985, 19, pp. 279–286.

107. N. Lamber and M. Economopoulos, "Measurement of the Heat Transfer Coefficients in Metallurgical Processes, Mathematical Models in Metallurgical Process Deveopment., Publication 123, The Iron and Steel Institute, 1970, pp. 133–146.

108. J. F. Collins and C. E. Maduell, "Polyalkylene Glycol Quenching of Aluminum Alloys", Materials Performance, July 1977, pp. 20–23.

109. T. Croucher and D. Butler, "Racking for the Quench: Critical Factors for Controlling Distortion", Heat Treating, 1983, 15(5), pp. 16–17.

110. T. Croucher and D. Butler, "Additional Factors to Consider", Heat Treating, 1983, 15(7), pp. 7–8.

111. T. Croucher and D. Butler, "Proper Racking—The Key to Distortion Control for Aluminum Alloys", Heat Treating, 1983, 15(3), pp. 19–20.

21

Machining

I. S. JAWAHIR

University of Kentucky, Lexington, Kentucky, U.S.A.

A. K. BALAJI

The University of Utah, Salt Lake City, Utah, U.S.A

1 INTRODUCTION

Machining constitutes one of the major and most important manufacturing processes. Typically, a machining operation is one of the final requirements in the production of a component used in the industrial sector including the automotive and aerospace industries. In these industries, aluminum and its alloys continue to play a critical role in the manufacture of components. Of particular importance to designers is the high strength to weight ratios which aluminum enables and good appearance characteristics. The addition of alloying elements and subsequent tempering processes have made aluminum and its alloys into viable alternatives for traditional steels in many applications. However, with this newfound thrust towards using aluminum and aluminum alloys, considerable confusion and apprehension has been caused due to the corresponding inability to predict the machining performance when using a particular aluminum alloy.

This chapter is aimed at providing professionals involved in machining of aluminum an up-to-date perspective on the current state-of-art and the future directions in aluminum machining. Initial emphasis is placed on the classification of the aluminum alloys, since a major portion of process planning decisions are dependent on the properties of the material being machined. The chapter then focuses on the topic of machining performance, the different machining performance measures such as cutting forces, tool-life, chip-form/chip breakability, etc. and their impact when machining aluminum and its alloys. The increased challenges in machining aluminum alloys has resulted in innovative approaches towards the design of cutting tools, especially diamond-based cutting tools. This issue is addressed with corre-

lation to the effects on the machining performance. Finally, three current challenging areas which provide much future scope are studied, namely: (i) high speed machining of aluminum alloys; (ii) dry machining of aluminum alloys; and (iii) machining of aluminum-based metal matrix composites (MMCs).

2   CLASSIFICATION OF ALUMINUM AND ITS ALLOYS FROM A MACHINING STANDPOINT

A detailed classification of aluminum and its alloys based on the work material properties, temper grades, individual effects of alloying constituents, etc., has been provided in many handbooks and research literature (e.g. *ASM Specialty Handbook: Aluminum and Aluminum Alloys* [1].) In this section we deal with the classification only from a machining standpoint and the effect of such a classification on the selection of the tooling (from the cutting tool geometry such as inclination angles, rake angles, etc. for the corresponding cutting conditions such as feed, cutting speed and depth of cut.) A broad general classification of aluminum alloys can be made on the basis of the primary mode of fabrication of the alloy and its properties and capabilities as follows:

- Cast alloys
- Wrought alloys
- Strain-hardenable alloys
- Heat-treatable alloys

A more specific of classification of aluminum alloys can be made on the basis of the quantity of the silicon content in the material; namely, low-silicon content and free-machining aluminum alloys; and high-silicon content aluminum alloys.

2.1   Low-Silicon Content and Free-Machining Aluminum Alloys

These alloys are classified on the basis of their low silicon content which is typically less than 12%. They are also termed as hypoeutectic alloys. Typical examples of alloys falling under this classification are: 2024-T4, 6061-T6, 2011-T3, Duraluminum, etc. These materials are generally rather soft and gummy and have a tendency to stick to the cutting tool when machining. They are also characterized by low melting temperatures. Built-up edge problems may occur during machining due to the tendency to stick to the cutting tool. They can be machined by carbides as well as diamond-based tools (PCD or diamond coated tools).

2.2   High-Silicon Content Aluminum Alloys

These alloys are based on their comparatively higher silicon content which is usually greater than 12%. They are also commonly termed as hypereutectic alloys. Typical examples of such alloys are: A390, A390-1, etc. These materials are more abrasive to machine and the degree of abrasiveness increases with an increase in the silicon content. This abrasiveness is usually caused by the hard particles of free silicon which are dispersed throughout the material. The constitution of such alloys results in tearing of the material when machining rather than the usual shearing mechanism. Cutting forces are comparatively higher when compared with low-silicon content

alloys. Carbide tools cannot be used for machining these alloys and the most effective cutting tool materials are the diamond-based cutting tools. These alloys are now finding wide application in the automobile industry.

3 MACHINING PERFORMANCE

The assessment of machining performance is a much sought-after goal of manufacturers keen on achieving excellent quality at reasonable costs. However, there have been very few attempts at a comprehensive definition for indicating the machining performance. The term "machinability" has been traditionally used to indicate some level of the machining performance, however, it has been largely restricted to the work material alone. Machinability ratings for aluminum alloys span into 5 groups, with ratings: A, B, C, D and E; and are ordered in increasing order of chip length and decreasing order of surface quality. In many cases changing the temper grade on an alloy will improve the chip breakability, thereby improving the machinability. A case in this regard is the application of a T6 temper to the 2024 and 7075 alloys; this results in an improvement in the machinability rating from D (continuous, unbroken chips) to B (curled and easily broken chips). Table 1 shows the machinability ratings for wrought aluminum alloys whereas Table 2 shows the machinability ratings for cast aluminum [1]. However, it must be noted that the ratings in these tables must need constant updating due to the tremendous advances in cutting tool materials, coatings and chip breaker geometries.

3.1 Machining Performance Measures

In order to shift the traditional focus of machinability on the work material to a more comprehensive level involving the technological machining performance which includes the other two major components of the machining system (namely the cutting tool and the machine tool in addition to the work material), a comprehensive consideration of important measures which indicate the machining performance needs to be taken into account. These performance measures typically include the following:

- Cutting force/power/torque: This provides important diagnostic information on the energy required to machine the work material, thereby indicating the level of machining performance and the ease or machinability of cutting the material. This measure also gives important interrelated insights into the other performance measures such as tool-wear and chip-form.
- Tool-wear/tool-life: The tool-wear and ensuing tool-life indicate the level of performance attainable for that particular work material–cutting tool–machine tool combination under a given set of cutting conditions. The progressive tool-wear significantly affects the other machining performance measures. The rate of tool-wear is a most frequently used performance measure.
- Chip-form/chip breakability: The chip-form and chip breakability are immediate and easily recognizable performance measures for assessing machinability. In fact, in order to quickly assess the machining performance, the chip form is an invaluable indicator of the level of

Table 1   Machinability Ratings of Wrought Aluminum Alloys

Alloy designation	Temper	Product form	Hardness, HB (500 kg load, 10 mm ball)	Machinability rating(a)
1060	O	Extruded rod, bar, extruded and drawn tube, pipe	19	E
	H12		23	E
	H14		26	D
	H16		30	D
	H18		35	D
1100	O	Sheet, plate; rolled and extruded rod, bar; extruded and drawn tube, pipe; other	23	E
	H12		28	E
	H14		32	D
	H16		38	D
	H18		44	D
2011	T3	Rod, bar, tube, pipe	95	A
	T8		100	A
2014	O	Plate, rod, bar, tube, pipe; other	45	D
	T4		105	B
	T6		135	B
2017	O	Rolled rod, bar; other	45	C
	T4		105	B
2018	T61	Forging stock	120	B
2024	O	Sheet, plate, rod, pipe; other	47	D
	T3		120	B
	T4		120	B
	T61		130	B
2025	T6	Forging stock	110	B
2117	T4	Rivet wire, rod	70	C
2218	T72	Forging stock	95	B
2219	O	Sheet, plate; extruded rod, bar; extruded and drawn tube, pipe; forging stock	...	...
	T42		...	...
	T351		100	B
	T37		117	B
	T62		115	B

Alloy designation	Temper	Product form	Hardness, HB (500 kg load, 10 mm ball)	Machinability rating[a]
	T851		130	B
	T87		130	B
2618	T61	Forgings	115	B
3002	O	Sheet	25	...
	H25		...	...
3003	O	Sheet, plate; rolled and extruded rod, bar; extruded and drawn tube, pipe; other	28	E
	H12		35	E
	H14		40	D
	H16		47	D
	H18		55	D
3004	O	Sheet, plate; drawn tube pipe	45	D
	H32		52	D
	H34		63	C
	H36		70	C
	H38		77	C
4032	T6	Forging stock	120	B
5005	O	Sheet, plate; rolled rod and bar; other	28	E
	H12		36	E
	H14		41	D
	H16		46	D
	H18		51	D
	H32		36	E
	H34		41	D
	H36		46	D
	H38		51	D
5050	O	Sheet, plate; drawn tube, pipe	36	E
	H32		46	D
	H34		53	D
	H36		58	C
	H38		63	C

Alloy / Temper	Form	Rating	Class
5052 . . . . O	Sheet, plate; rolled	47	D
H32	rod, bar; drawn	60	D
H34	tube, pipe; other	68	C
H36		73	C
H38		77	C
5056 . . . . O	Rivet rod, wire	65	D
H18		105	C
H38		100	C
5083 . . . . O	Sheet, plate, rod, bar,	67	D
H321	tube, pipe, forgings	82	D
5086 . . . . O	Sheet, plate; extruded	60	D
H32	rod, bar; extruded	72	D
H34	and drawn tube,	82	C
H112	pipe	64	D
5154 . . . . O	Sheet, plate; welding	58	D
H32	wire and rod	67	D
H34		73	C
H36		78	C
H38		80	C
H112		63	D
5252 . . . . H25	Sheet	68	C
H38		75	C
5254 . . . . O	Sheet, plate	58	D
H32		67	D
H34		73	C
H36		78	C
H38		80	C
H112		63	D
5257 . . . . H25	Sheet	32	C
H28		43	C
5357 . . . . O	Sheet, plate	32	D
H25		50	C
H28		55	C
5454 . . . . O	Sheet, plate; other	62	D
H32		73	D
H34		81	C
H111		70	D
H112		62	D
5456 . . . . O	Sheet, plate; extruded	70	D
H111	rod bar; extruded	75	D
H112	tube, pipe; forgings	70	D
H116		90	D
5457 . . . . O	Sheet	32	E
H25		48	C
H28		55	C
5557 . . . . O	Sheet	27	E
H25		46	D
H28		55	D
5652 . . . . O	Sheet, plate	47	D
H32		60	D
H34		68	C
H36		73	C
H38		77	C
5657 . . . . H25	Sheet	40	D
H28		50	D
6005 . . . . T5	Extruded rod, bar	95	C
6061 . . . . O	Sheet, plate, rod,	30	D
T4	bar, tube, pipe;	65	C
T6	forging; other	95	C

Table 1 *Continued.*

Alloy designation	Temper	Product form	Hardness, HB (500 kg load, 10 mm ball)	Machinability rating(a)	Alloy designation	Temper	Product form	Hardness, HB (500 kg load, 10 mm ball)	Machinability rating[a]
6063 . . . . . .O	O	Extruded rod, bar;	25	D	6951 . . . . . .O	O	Sheet	28	. . .
	T1	extruded and drawn	42	D		T6		82	. . .
	T4	tube, pipe	60	D	7001 . . . . . .O	O	Extruded rod, bar	60	B
	T5		60	C		T6		160	B
	T6		73	C	7005 . . . . . .T53	T53	Rod, bar, tube, pipe	. . .	. . .
	T83		82	C	7075 . . . . . .O	O	Sheet, plate, rod, bar,	60	D
	T831		70	C		T6	tube, pipe; forging stock	150	B
	T832		95	C	7079 . . . . . .O	O	Sheet, plate, rod, bar,	. . .	. . .
6066 . . . . . .O	O	Extruded rod, bar;	43	D		T6	tube, pipe; forging stock	145	B
	T4	forging stock	90	C	7178 . . . . . .O	O	Sheet, plate, rod, bar,	60	. . .
	T6		120	B		T6	tube, pipe	160	B
6070 . . . . . .T6	T6	Rod, bar, tube, pipe	120	C		T76		. . .	. . .
6151 . . . . . .T6	T6	Forging stock	100	. . .	8280 . . . . . .O	O	Sheet, plate	. . .	B
6262 . . . . . .T9	T9	Rod, bar, tube, pipe	120	B		H12		. . .	A
6463 . . . . . .T1	T1	Extruded rod, bar;	42	D					
	T5	extruded and drawn	60	C					
	T6	tube, pipe	74	C					

(a) A, B, C, D, and E are relative ratings in increasing order of chip length (see Fig. 1) and decreasing order of quality of finish. A, free cutting, very small broken chips and excellent finish; B, curled or easily broken chips and good-to-excellent finish; C, continuous chips and good finish; D, continuous chips and satisfactory finish; E, optimum tool design and machine settings required to obtain satisfactory control of chip and finish. *Source:* Ref. 1.

Table 2 Machinability Ratings of Cast Aluminum Alloys

Alloy designation	Temper	Casting form	Hardness, BH (500 kg load, 10 mm ball)	Machinability rating(a)
208 . . . . .F	F	Sand	55	B
213 . . . . .F	F	Permanent mold	85	. . .
222 . . . . .T52	T52	Permanent mold	100	. . .
	T551	Permanent mold	115	. . .
	T65	Permanent mold	140	. . .
238 . . . . .F	F	Permanent mold	100	B
A240 . . . . . . .F	F	Sand	90	A
242 . . . . .F	F	Sand	. .	. . .
	T21	Sand	70	B
	T571	Sand	85	B
	T571	Permanent mold	105	B
	T61	Permanent mold	110	B
	T77	Sand	75	B
A242 . . . . . .T77	T77	Sand	70	. . .
295 . . . . .T4	T4	Sand	60	B
	T6	Sand	75	B
	T62	Sand	90	B
B295 . . . . . .T4	T4	Permanent mold	75	B
	T6	Permanent mold	90	B
	T7	Permanent mold	80	B
308 . . . . .F	F	Permanent mold	70	B
319 . . . . .F	F	Sand, permanent mold	70	C
	T5	Sand	80	B
	T6	Sand	80	B
	T6	Permanent mold	95	B
A332	T551	Permanent mold	105	C
	T65	Permanent mold	125	C
F332	T5	Permanent mold	105	C
333	F	Permanent mold	90	C
	T5	Permanent mold	100	B
	T6	Permanent mold	105	B
	T7	Permanent mold	90	B
354	T61	Permanent mold	100	B
	T62	Permanent mold	110	B
355	F	Sand	. .	. . .
	T51	Sand	65	'B
	T51	Permanent mold	75	B
	T6	Sand	80	B
	T6	Permanent mold	90	B
	T61	Sand	90	B
	T62	Permanent mold	105	B
	T7	Sand	85	B
	T7	Permanent mold	85	B
	T71	Sand	75	B
	T71	Permanent mold	85	B
C355	T6	Sand	85	. . .
319	T6	Permanent mld	90	. . .
	T61	Permanent mold	100	B
356	F	Sand	. .	. . .
	F	Permanent mold	. .	. . .

Table 2 *Continued.*

Alloy designation	Temper	Casting form	Hardness, BH (500 kg load, 10 mm ball)	Machinability rating(a)	Alloy designation	Temper	Casting form	Hardness, HB (500 kg load, 10 mm ball)	Machinability rating[a]
	T51	Sand	60	C	360	F	Die	75	C
	T51	Permanent mold	...	C	364	F	Die	...	C
	T6	Sand	70	C	380	F	Die	80	B
	T6	Permanent mold	90	C	A380	F	Die	80	B
	T7	Sand	75	C	384	F	Die	...	C
	T7	Permanent mold	70	C	390	F	Die	120	...
	T71	Sand	60	C	A390	F	Sand	100	...
A356	F	Sand	...	...		F	Permanent mold	110	...
	T51	Sand	...	...		T5	Sand	100	...
	T6	Sand	75	...		T5	Permanent mold	110	...
A356	T6	Permanent mold	80	...		T6	Sand	140	...
	T61	Permanent mold	80	B		T6	Permanent mold	145	...
357	F	Permanent mold	...	...		T7	Sand	115	...
	T51	Permanent mold	...	...		T7	Permanent mold	120	...
	T6	Sand	90	B	413	F	Die	80	E
	T6	Permanent mold	84	B	A413	F	Die	80	...
	T7	Sand	60	...	443	F	Sand	40	E
	T7	Permanent mold	70	...		F	Permanent mold	45	E
A357	T6	Sand	85	...	A444	F	Die	50	E
	T6	Permanent mold	85	...		F	Sand	...	...
B358	T6	Permanent mold	90	B		F	Permanent mold	44	...
	T62	Permanent mold	...	...		T4	Sand	...	...

Alloy	Temper	Casting process	Rating	Finish	Alloy	Temper	Casting process	Rating	Finish
359	T61	Permanent mold	90	. . .		T4	Permanent mold	45	. . .
	T62	Permanent mold	100	B	514	F	Sand	50	B
360	F	Die	75	C	A514	F	Permanent mold	60	B
	F	Die	. . .	B	707	F	Sand	85	B
B514	F	Sand	50	. . .	A712	F	Sand	75	B
F514	F	Sand	50	B	C712	F	Permanent mold	70	B
L514	F	Die	. . .	. . .	D712	F	Sand	75	B
518	F	Die	80	B	713	F	Sand	75	B
520	T4	Sand	75	B	850	T5	Sand	45	A
535	F	Sand	70	. . .		T5	Permanent mold	45	A
A535	F	Sand	65	B	A850	T5	Sand, permanent mold	45	A
B535	F	Sand	65	A	B850	T5	Sand	65	A
705	F	Sand	65	B		T5	Permanent mold	70	A

[a]A, B, C, D, and E are relative ratings in increasing order of chip length (see Fig. 1) and decreasing order of quality of finish; A. free cutting, very small broken chips and excellent finish; B, curied or easily broken chips and good-to-excellent finish; C. continous chips and good finish; D, continous chips and satisfactory finish: E, optimum tool design and machine settings required to obtain satisfactory control of chip and finish. *Source*: Ref. 1.

machining performance. The direct reference to machinability of the work material (in this case, aluminum alloy) in general however needs to be counter-balanced by an appropriate consideration of the cutting tool (the tool material – substrate and coating; and the chip-breaker configuration).

- Surface roughness/surface integrity: The surface quality, as indicated by the surface roughness, and to a lesser extent, the surface integrity (in terms of direct visual observation as well as a simple test of the surface roughness) provide immediate information regarding the level of machining performance.
- Part accuracy: The part accuracy is one of the least modeled of machining performance measures, despite its significance in product specification. It has very close interrelationships with the other performance measures. The accuracy achieved during the machining process provides valuable information about the performance attained and possible indicators for rectification.

3.1.1 Cutting Force/Power/Torque

The cutting force or power required to machine aluminum alloys is generally much lower than that for conventional steels and irons. From a productivity viewpoint, the low cutting forces generated when machining aluminum alloys are thus an advantage when selecting aluminum alloys as the work material. Figure 1 shows the effect of cutting speed on five different aluminum alloys [2]. In a very direct reference to the machining performance, it is clear that the 2011-T3 alloy provides the best results of the surveyed materials from general machining knowledge; the lower cutting forces exhibited in this plot confirm the good machinability of 2011-T3 alloy.

The use of flat-faced and grooved cutting tool inserts result in variation in cutting forces. Also, changes in the cutting parameters such as feed and depth of cut will cause changes in the cutting forces. One of the more complex operations involved in machining is the contour turning operation. From a research point of view, the contour turning operation provides an opportunity to study the effect of continuous variation of effective tool geometry (due to the varying side-cutting edge angles and effective rake and inclination angles) and the cutting parameters such as depth of cut on the machining performance. Figures 2(a) and 2(b) show the variation of cutting forces along the contour (in terms of effective side-cutting edge angle) for a flat-faced (PCD) tool and a grooved (CVD diamond-coated) tool respectively [3], when machining 2011-T3 aluminum alloy. One can notice the negative radial forces arising due to the changes in the effective geometry of the cutting tool. The large changes in the cutting forces along the contour profile result in varying chip flow and consequently varying chip-form. This is discussed in greater detail in the section on chip-form/chip breakability (Sec. 3.1.3).

The variation in cutting forces when machining with carbide tools and PCD tools has been investigated by Konig [4]. Figure 3 shows a plot of this comparison; it is observed that the forces in machining with PCD tools are much lower and that the machining is done at much higher cutting speeds.

One of the recent technological advances in machining methods has been the use of ultrasonic vibration machining [5]. This research work investigated the high silicon content A390 alloy which is typically hard to machine due to the widespread
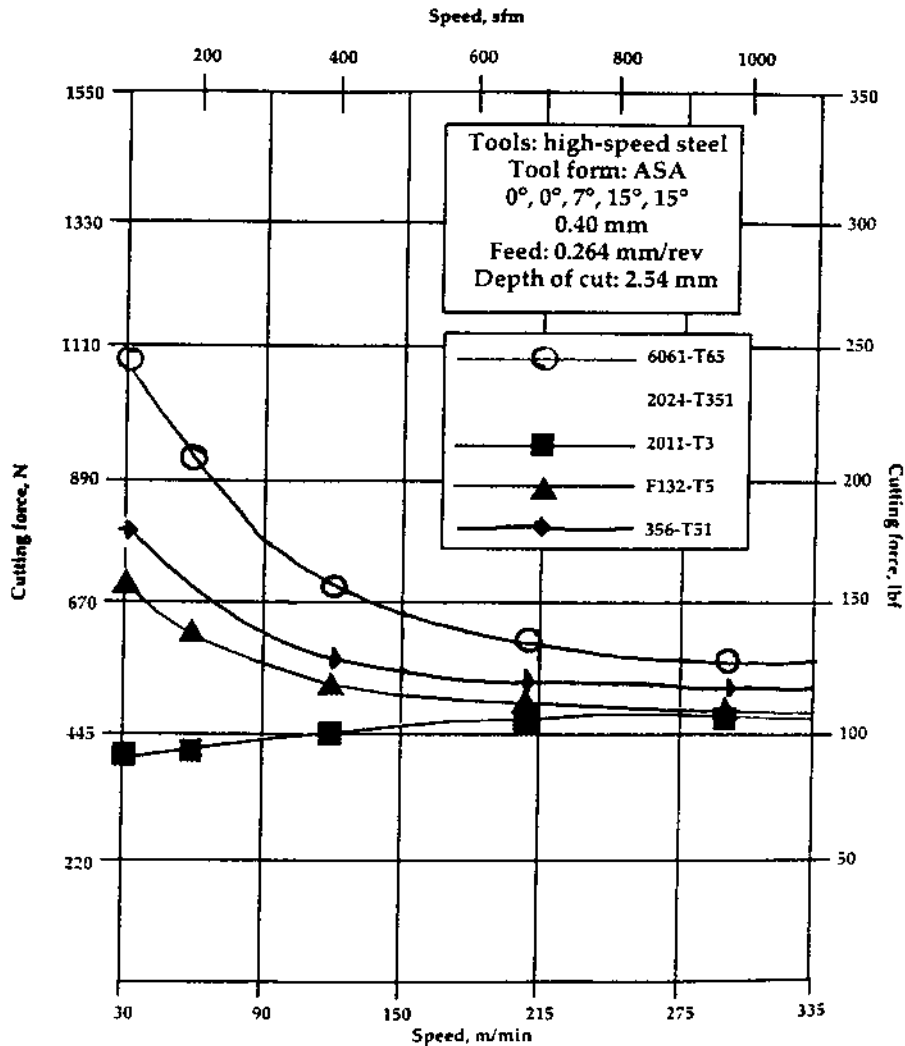
Figure 1 Effect of cutting speed on cutting force for five aluminum alloys. (From Ref. 2.)

content of abrasive silicon. This alloy is generally used in the manufacture of engine blocks and air compressor cylinders due to their high wear resistance, low density and high strength at elevated temperatures. Figure 4 shows the variation of cutting forces as functions of (a) cutting speed; (b) depth of cut; and (c) feed rate when using conventional and ultrasonic vibration methods.

3.1.2 Tool-Life/Tool-Wear

Tool-life and tool-wear are very important criteria for assessing the machining performance when machining aluminum with carbides and HSS tools. However, with the widespread use of diamond-based tools, the tool-life problem has been alleviated to a great deal. Konig [4] in his work on machinability of cast aluminum alloys has
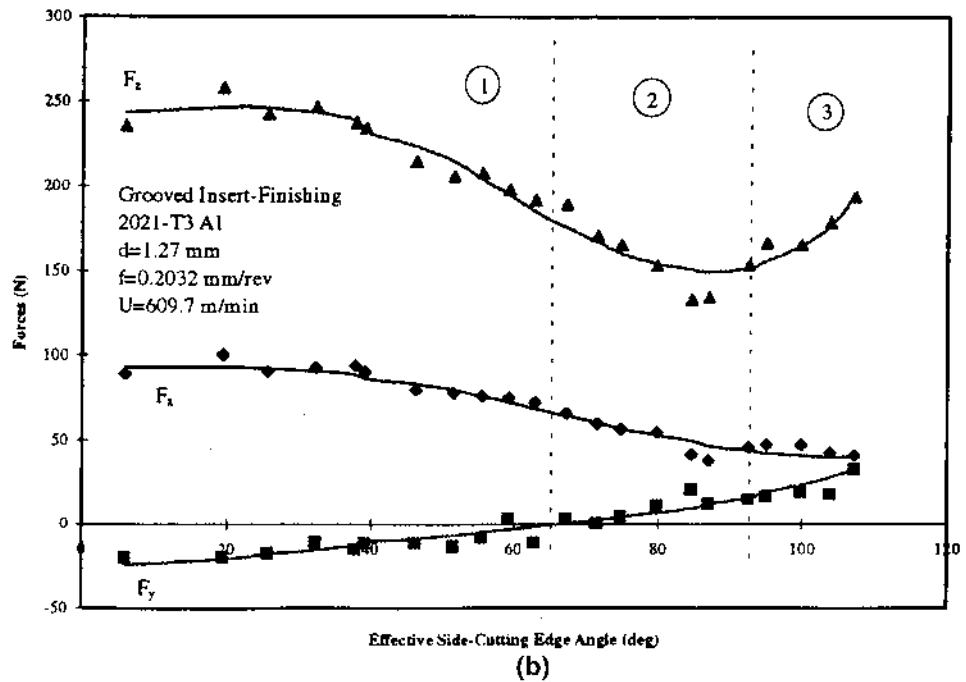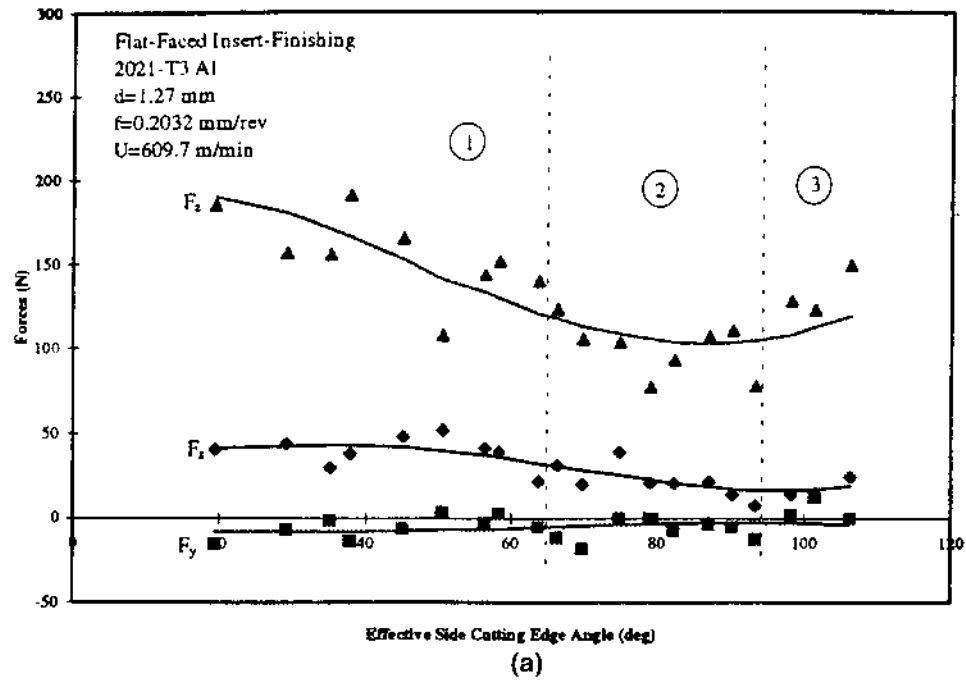
Figure 2 Variation of cutting forces with effective side cutting edge angle during a contour turning Operation using (a) flat-faced tools; and (b) grooved tools. (From Ref. 3.)
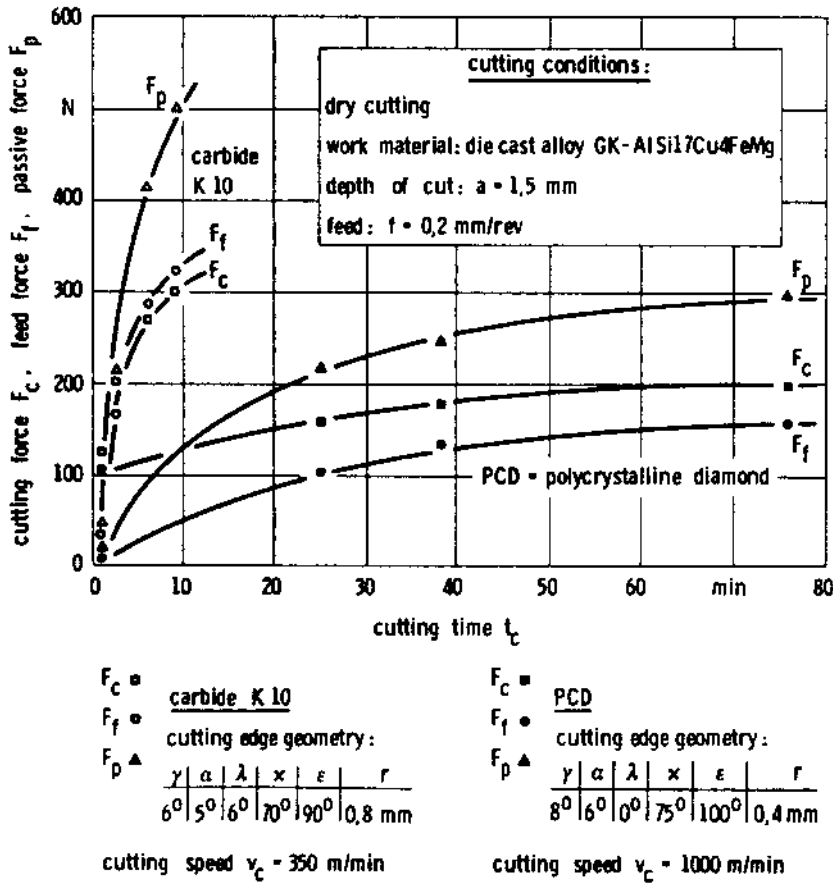
Figure 3 Variation of cutting forces in turning of aluminum alloy (GK-AlSi17Cu4FeMg) with carbide and PCD tools. (From Ref. 4.)

clearly shown the quantitative advantages of using diamond-based tools (in this case, PCD tools) as compared with conventional carbide tools (Fig. 5). There is also strong evidence of the negligible role of the machining operation on the tool-life when machining aluminum alloys; the tool-life was very similar for turning and face milling operations [Fig. 6(a) and 6(b)]. Typically, tool-life is very much dependent on the silicon content in the work material. This corresponds very well with the higher cutting forces that are necessary for the machining of hypereutectic alloys. Also, the sticky nature of aluminum alloys tends to cause a build-up of material on the cutting tool thereby reducing the tool-life although without considerable wear of the tool.

A comparative study of dry machining of aluminum alloys by using uncoated carbide tools, PCD tools and CVD diamond tools has revealed the importance of selecting the suitable tool material in order to attain the "best" tool-life and consequently a high level of machining performance [6]. In order to compare the wear characteristics between the uncoated cemented carbide tool and the CVD
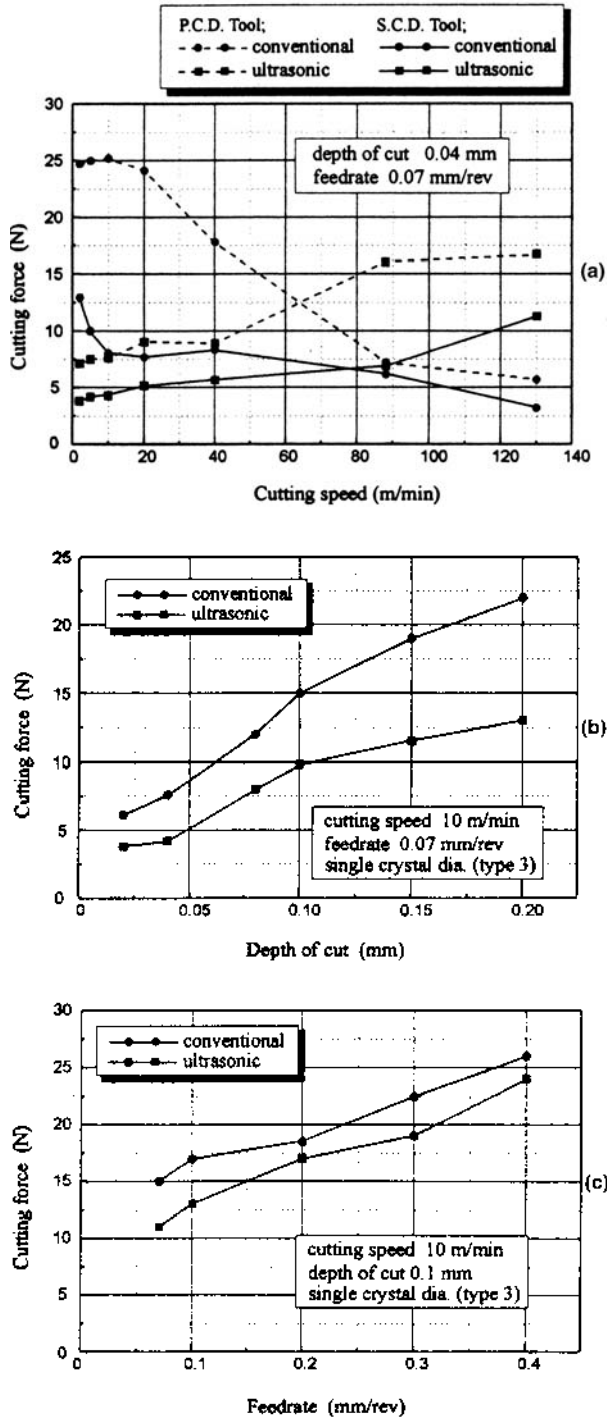
Figure 4 Variation of cutting forces with (a) cutting speed; (b) depth of cut; and (c) feed, when machining A390 alloy using conventional and ultrasonic vibration methods. (From Ref. 5.)
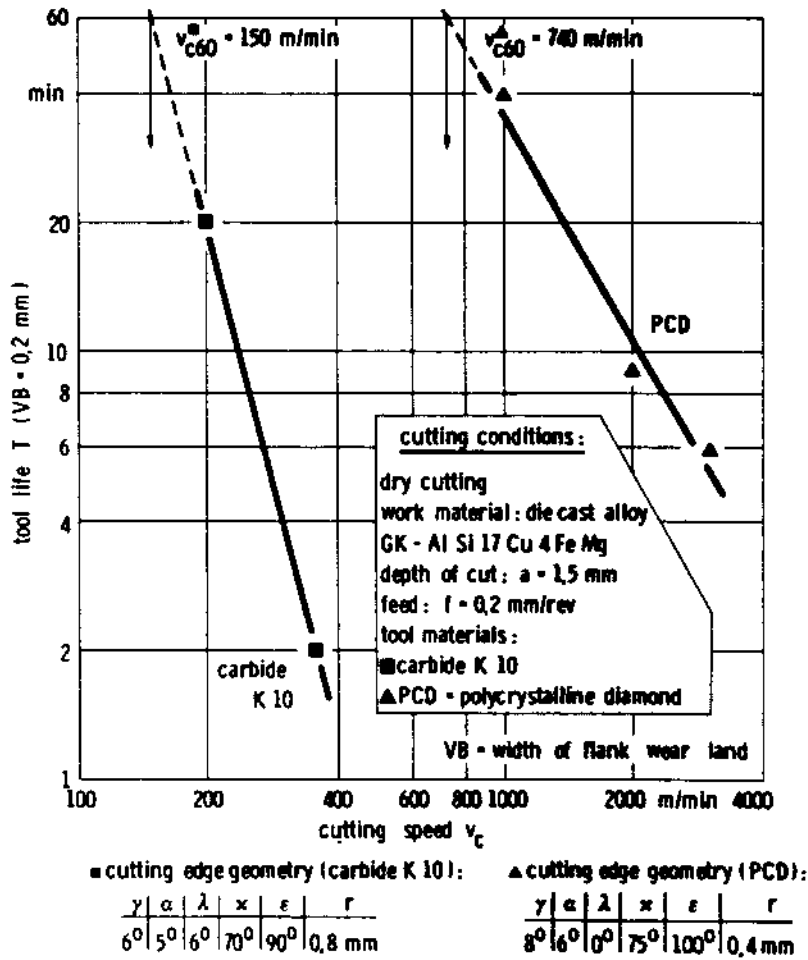
Figure 5 Comparison of tool-life in turning of aluminum alloy (GK-AlSi17Cu4FeMg) with carbide and PCD tools. (From Ref. 4.)

diamond-coated tool, the machining was performed on a low silicon content aluminum alloy (A380 with 8.5% Si). However, to compare the PCD tool's performance with the CVD diamond tool, the machining was carried out on a high silicon content aluminum alloy (A390 with 17% Si) since carbide tools cannot be used when machining high silicon content aluminum alloys. The plots showing the flank wear over the cutting time for the machining of A380 and A390 alloy are shown in Fig. 7(a) and 7(b) respectively. It can be seen that the CVD diamond-coated tool performed exceptionally well when compared with the uncoated carbide tool. The excellent performance of the CVD diamond-coated tool was attributed to the outstanding mechanical properties of the diamond coating and the strong adhesion to the carbide substrate. Since the A380 alloy has comparatively low silicon content, the abrasive action of silicon is not present and the CVD diamond tool suffered hardly any tool-wear. It can be seen that the CVD diamond tool also
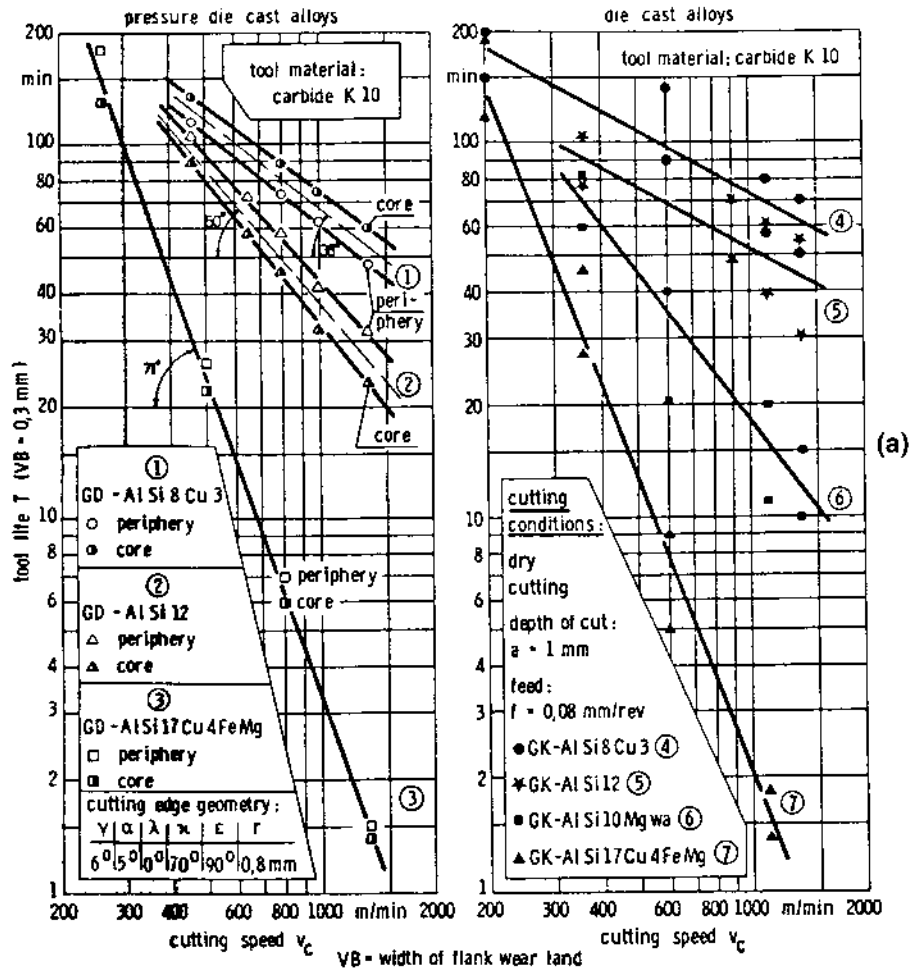
Figure 6   (a) Comparison of tool-life in turning. (From Ref. 4.)

performed very well when compared to the PCD tool when machining the more abrasive and tough-to-machine A390 alloy. The failure of both tools was attributed to abrasive wear mechanisms. However, the PCD tool provided a much better degree of surface finish when compared to the CVD diamond-coated tool.

3.1.3   Chip Form/Chip Breakability

Chip form and chip breakability are very strong indicators of the degree of machining performance that is achieved. A thorough, state-of-art research work which explains the role of chip control in machining has been recently produced under the sponsorship of CIRP [7]. A very effective method of observing the effect of machining parameters, depth of cut and feed, is in the form of a chip chart. Figure 8(a) and 8(b) shows representative chip charts for the machining of Aluminum alloy
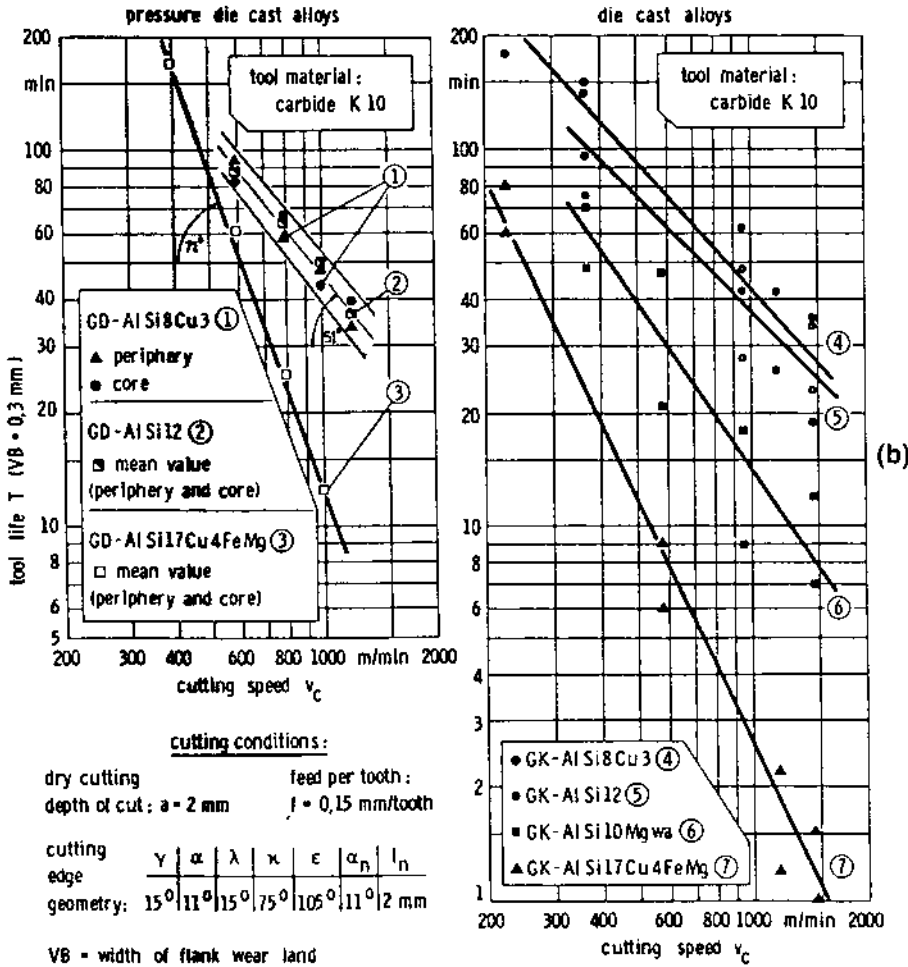
Figure 6 (b) Comparison of tool-life in face milling of aluminum alloy (GK-AlSi17Cu4FeMg) with carbide tools. (From Ref. 4.)

6061 with two different nose radii of 0.4 mm and 0.8 mm [8]. Specifically related to aluminum and its alloys, chip control has been a vexing issue, especially due to the typical snarled and stringy chips that aluminum machining produces.

The final chip-form results from the direction of chip flow, the chip curl radius and the bending moment caused by the free-end of the chip anchoring on the tool flank or the rotating workpiece, thereby causing the chip to break. The chip-groove configurations on tools force the chip to curl tightly and enable it to effectively break into a small size. Typical areas wherein chip control can be a problem are in finish machining of components with complex contours, e.g. the wheel rims of auto-mobiles. The finish cut during such operations involves machining along a contour. This results in a continuously varying depth of cut and a relative continuously chang-ing tool geometry. In order to obtain a better understanding of the complex chip flow mechanism in contour turning of aluminum alloys, Blasius [3] performed exper-
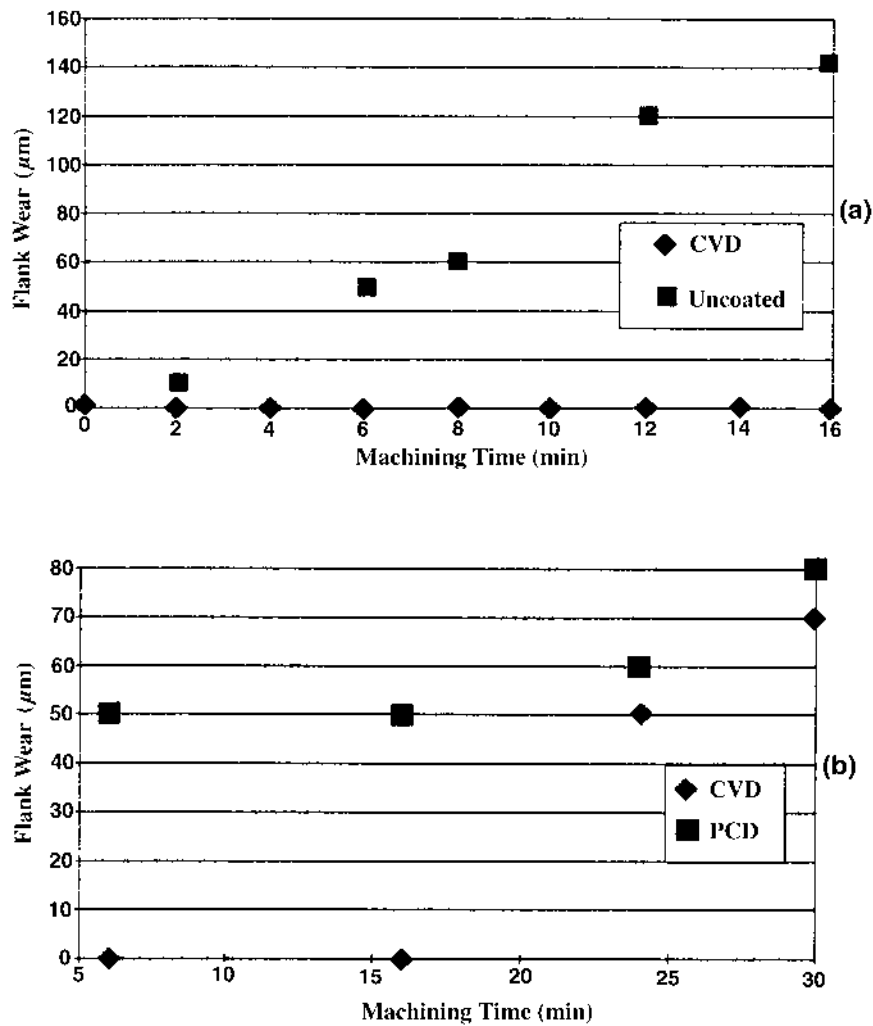
Figure 7 Variation of flank wear with time using (a) uncoated carbide inserts; and (b) PCD brazed carbide inserts during machining of A390 alloy. (From Ref. 6.)

iments with 2011-T3 aluminum alloy with a PCD flat-faced tool and a CVD diamond coated grooved tool. The work contour was experimentally designed to provide continuously varying machining parameters and tool geometry. The chip side-flow angle was measured by using a high speed filming system which operated at 1000 p.p.s. [Fig. 9(a) and 9(b)]. The surface roughness obtained from machining using the two different cutting tool inserts was also measured.

Chip-form and chip breakability are greatly influenced by the type of aluminum alloy used and its material properties. The aluminum alloy 2011 is a high strength and free cutting alloy which exhibits excellent machinability. It provides excellently broken chips thereby exhibiting a strong degree of chip control, in addition to excellent surface quality and low tool-wear rates. Alloys such as 2024-T4
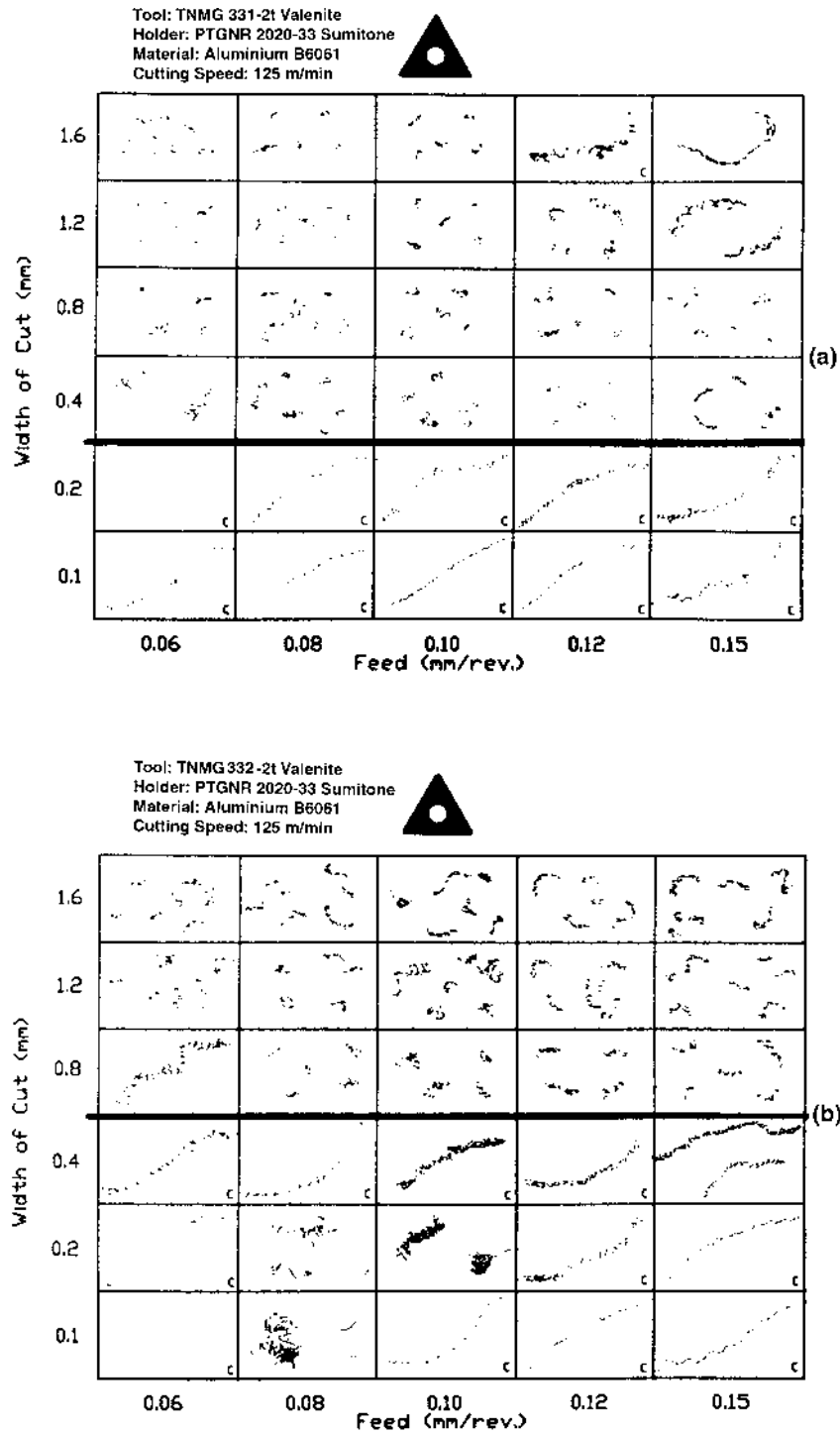
Figure 8 Chip charts showing effect of varying nose radius (a) $r_\varepsilon = 0.4$ mm and (b) $r_\varepsilon = 0.8$ mm on resulting chip-form when machining of Aluminum B6061 alloy. (From Ref. 8.)
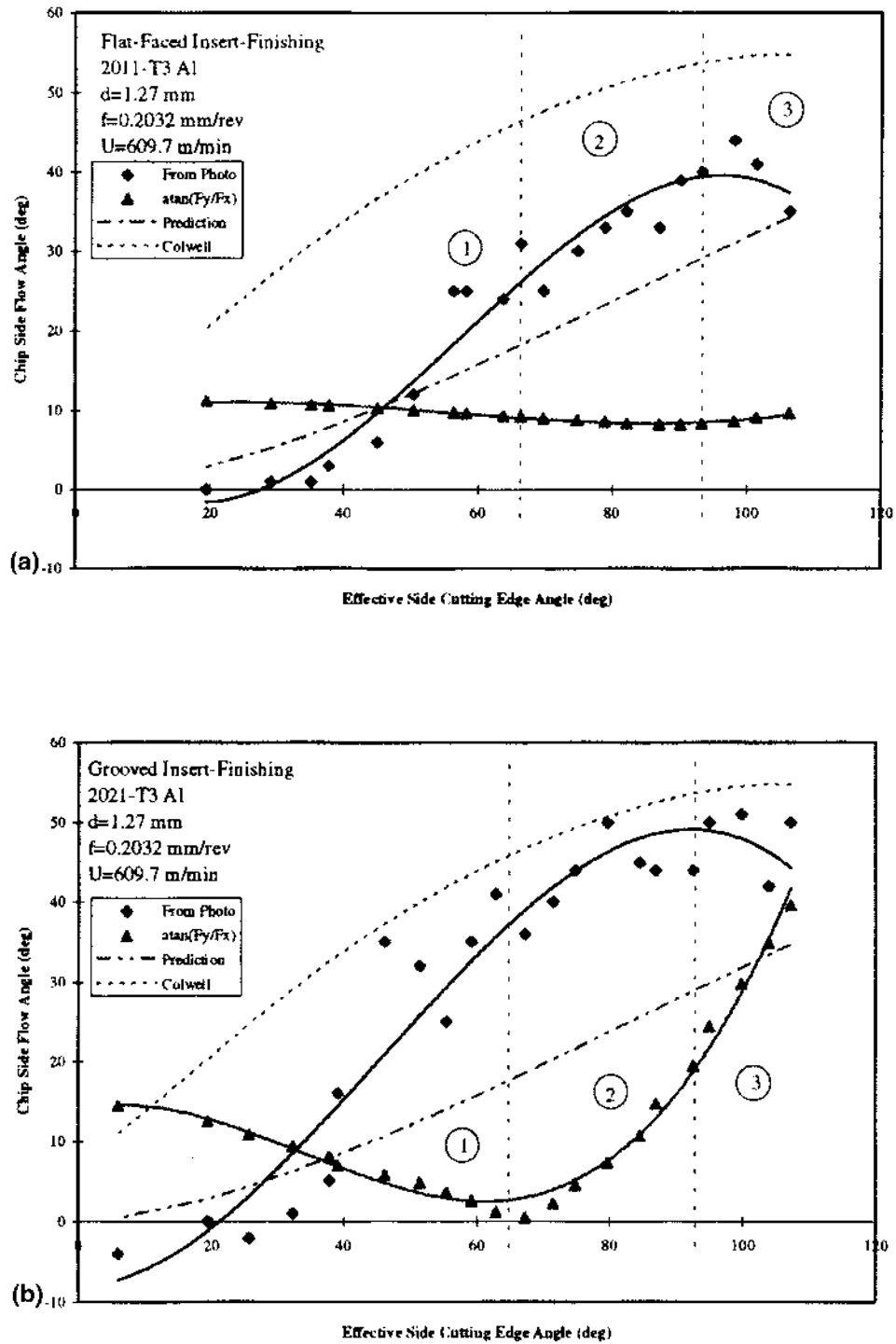
Figure 9 Variation of chip side-flow angle with the effective side cutting edge angle in contour turning of Al6061 with (a) flat-faced inserts; and (b) grooved inserts. (From Ref. 3.)

and 2017-T4 tend to produce continuous chips, thereby necessitating the use of a chip-breaker geometry on the cutting tool insert. The CVD diamond-coated tool inserts with chip-breaker geometry are ideally suited for ensuring a high degree of chip control with these materials. Alloys such as 6061-T6 and 5056-H38 are comparatively more difficult to machine and produce sharp and stringy chips which are difficult to break. Soft alloys such as 5052, 3003 and 1100 tend to produce more soft and gummy chips, thereby necessitating careful selection of chip-breaker geometries and tool coatings [1].

In an investigative case study on trouble shooting of uncontrollable chips, Maekawa et al. [9], studied the machining of aluminum heat rollers. The cutting conditions used are shown in Table 3. Six different types of tool inserts and tool geometry were used in the analysis. The details of these tool inserts and geometry are provided in Table 4. The resulting chip morphology at the various combinations of cutting conditions and tool geometry are provided in the form of a chip chart in Fig. 10. It can be seen that the tool geometry of Cases 5 and 6 and the cutting conditions corresponding to Case (c) (see Table 3) provided the best degree of chip control for the machining operation. This case study shows the importance of selecting the right tool geometry (especially the chip-groove geometry and the tool angles).

Case Study: Change in Material Improved Chip Breakability Performance

The hydraulic division of Parker Hannifin improved machining performance by obtaining better chip control when they replaced the conventional Al 6061-T6511 extruded aluminum alloy with the cold finished A1 6013-T8 aluminum alloy for production of hydraulic valve blocks [10]. The 6013-T8 alloy produced small, well broken chips, thereby negating continuous monitoring for chip control problems. In addition to better chip control, the new material possessed 50% higher strength than the extruded 6061 alloy and provided anodizing and corrosion resistance comparable to the 6061 alloy. The excellent degree of chip control provided by this material also improved other performance measures such as surface quality and resulted in the capability to machine to finer tolerances. The overall machining productivity improved by 15–25% due to the selection of the 6013 alloy with great reductions on the deburring required for the finished part.

3.1.4 Surface Roughness/Surface Integrity
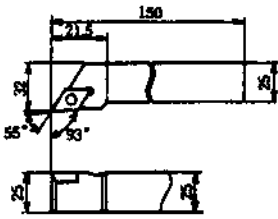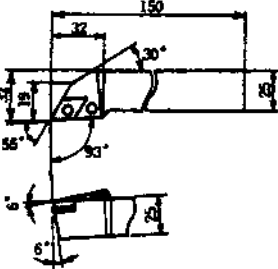
Surface roughness and surface integrity are important performance measures which indicate the performance level attained by using the particular work material-tool material combination and the corresponding suitable feeds, speeds and depth of cut. The importance of considering surface roughness/surface integrity when machining Aluminum and its alloys arises due to the high thermal conductivity and low melting temperatures. This can result in considerable deformation to the generated surface. The residual stress induced in the machined work material has been used as a significant measure of the surface integrity. Considerable work has been done by researchers on the generation of residual stresses when machining aluminum alloys [11–13]. The effects of the cutting speed on the residual stresses at various nose radii, feeds and depths of cut respectively, when machining aluminum alloy 2014 are shown in Fig. 11(a), 11(b) and 11(c) [14]. One can see that in all three cases the

Table 3   Cutting Conditions for Machining of Aluminum Heat Rollers

	Case (a)	Case (b)	Case (c)
Cutting speed (m/min)	375	375	375
Feed (mm/rev)	0.5	0.25	0.35
Depth of cut (mm)	0.5	1.0	1.0

Source: Ref. 9.

Table 4   Tool Geometry Used in Machining of Aluminum Heat Rollers

	Insert	Shank
Case #1		
Case #2		
Case #3		
Case #4		
Case #5		
Case #6		

Source: Ref. 9.

least peak residual stress occurs at the middle of the tested range, indicating the need for considering this type of a non-linear optimum when selecting the tool geometry and cutting conditions in order to minimize the effect of the residual stresses. It can also be seen that the depth of cut plays a very minor role in influencing the residual stresses induced in the surface of the machined material. The microstructure

	Case #1	Case #2	Case #3	Case #4	Case #5	Case #6
Case (a)						
Case (b)						
Case (c)						50mm
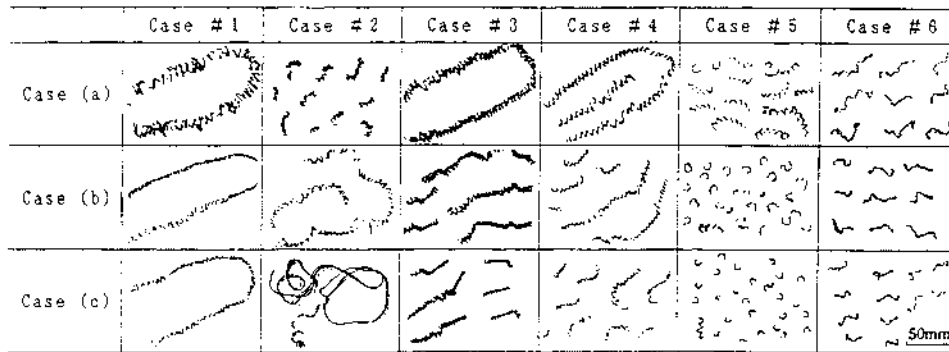
Figure 10 Chip morphology at various combinations of cutting conditions and tool geometry. (From Ref. 9.)

of the machined surface for the 3014 aluminum alloy at a feed rate of 0.1 mm/rev and 0.2 mm/rev is shown in Fig. 12(a) and 12(b) [14].

The relationship between the surface roughness and the cutting parameters such as cutting speed, axial and radial depth of cuts and the feed rate was investigated in high-speed machining of aluminum with a diamond and a sintered carbide end-mill [15]. The results of this study are shown in the plots in Fig. 13. It can be seen that the diamond end-mill far outperformed the carbide end-mill as far as performance in terms of surface roughness. The relative quality of the surfaces produced by the carbide end-mill and the diamond end-mill can be seen in Fig. 14, where the diamond end-mill provides almost near perfect reflective surface quality.

The role of advanced technology such as ultrasonic vibration cutting was discussed earlier in Sec. 3.1.1. The comparison of surface roughness as a function of cutting speed is provided in Fig. 15(a). The conventional and ultrasonic methods were compared with both a PCD tool and a SCD (single crystal diamond) tool when machining A390 alloy. The SCD tool far outperformed the PCD tool but is not an economic alternative. The variation of the surface roughness with respect to the depth of cut and the feed rate is shown in Fig. 15(b) and 15(c) respectively. The ultrasonic method tended to provide better results in terms of surface roughness just as it did in the case of cutting forces. However, this technology is yet to be tested at a major level on industrial platforms to see its true benefits for large scale production.

General Case Study: Machining Performance Evaluation of Hypereutectic Al-Si Alloys

As mentioned earlier in Sec. 2, hypereutectic aluminum alloys are finding niche applications in the automotive industry due to their high resistance to deformation at high temperatures, resistance to wear and the advantageous strength–weight ratio. However, the excellent resistive properties of this material also make it very difficult to machine. The high content of hard silicon crystals contributes a great deal making it difficult to machine. Weinert et al. [16] in a recent study have examined the machining performance of hypereutectic aluminum alloys in a heat treated (T6) and a non-heat treated condition with varying cutting materials and cutting conditions. The machining performance measures used for assessing the machining
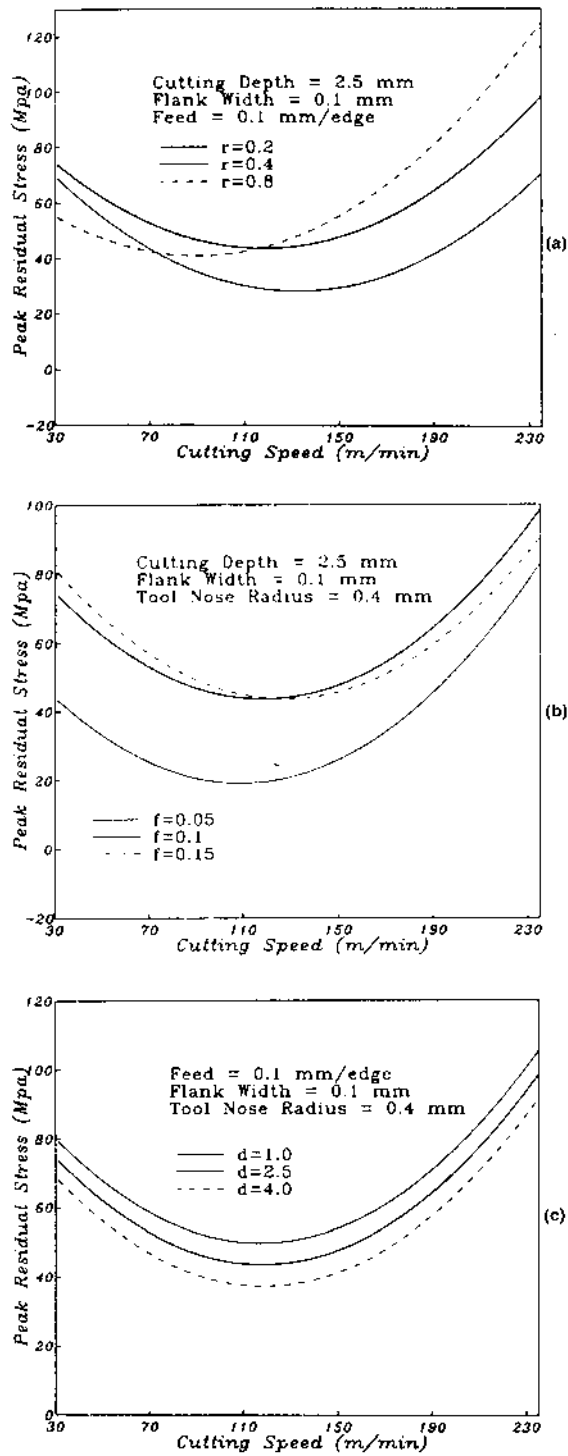
Figure 11 Variation of the residual stress with cutting speed at varying (a) tool nose radii; (b) feeds; and (c) depths of cut when machining Aluminum 2014 alloy. (From Ref. 13.)
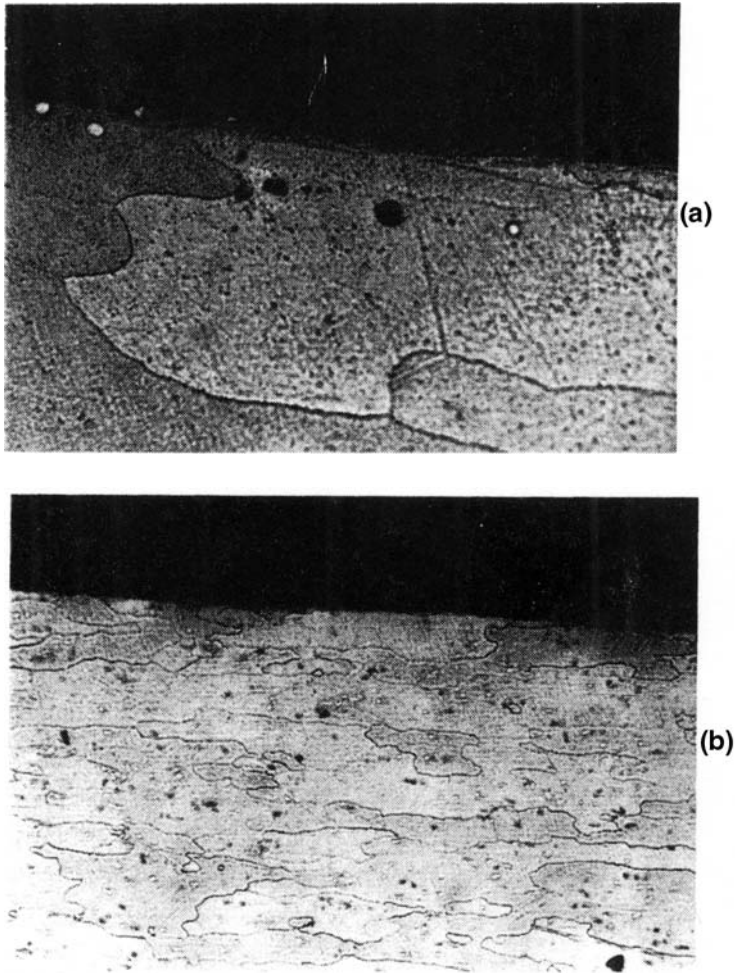
Figure 12 Microstructure of the machined surface of Aluminum 2014 alloy at (a) feed = 0.1 mm/rev. (magnification = 400×); and (b) feed = 0.2 mm/rev. (magnification = 100 ×) (depth of cut = 3 mm, flank wear = 0.1 mm, cutting speed = 125.7 m/min. and tool nose radius = 0.4 mm). (From Ref. 14.)

performance were tool-wear and surface quality. The range of cutting speeds used in the study varied from 200 to 400 m/min. This study concluded that the CVD diamond-coated tools and the PCD tools exhibited excellent wear resistance, whereas carbide tools coated with titanium nitride performed very poorly due to high wear-rates. Figure 16 shows the SEM pictures of four cutting tools after 750 sec of cutting time: (a) uncoated carbide; (b) coated carbide (titanium nitride coating); (c) diamond-coated onto carbide substrate; and (d) polycrystalline diamond (PCD) tool. Figure 17 shows the different widths of the wear land VB for the different cutting tools and their dependence on cutting time t_c. A comparative analysis of cemented carbide tools and the different grain sizes showed that the larger grain size improved resistance to tool-wear. The performance study on the surface
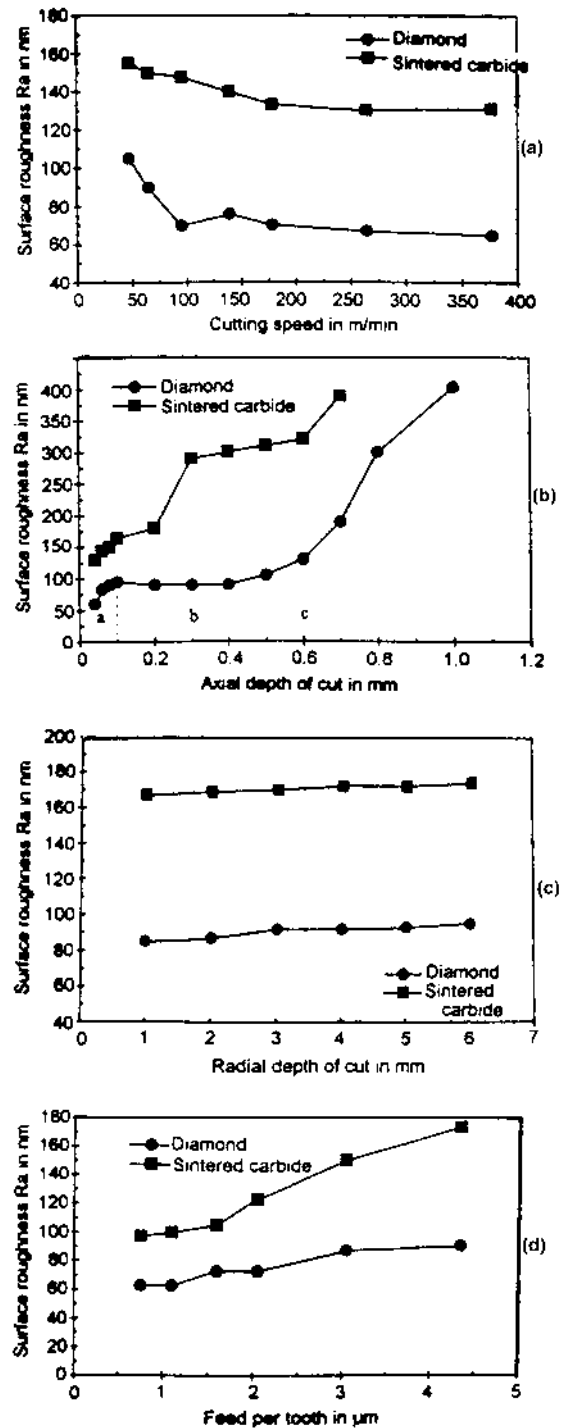
Figure 13 Variation of surface roughness with (a) cutting speed; (b) axial depth of cut; (c) radial depth of cut; and (d) feed per tooth during high-speed machining of Aluminum 2024 alloy with a diamond and sintered carbide end-mill. (From Ref. 15.)
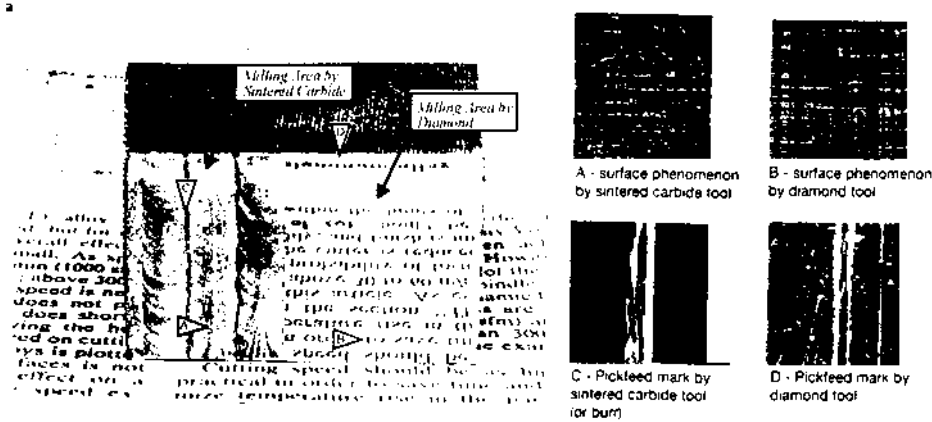
Figure 14 Relative surface quality obtained by using a diamond end-mill and a sintered carbide end-mill during milling of Aluminum 2024 alloy (cutting speed $= 377$ m/min., feed/tooth $= 0.00038$ mm/tooth, radial depth of cut $= 6$ mm, axial depth of cut $= 0.04$ mm). 0.04 mm). (From Ref. 15.)

roughness showed that surface quality depended primarily on the cutting tool composition and the wear conditions of the tool. The PCD tool gave the best surface quality ($R_z = 2–3 \,\mu$m) and the coated and uncoated carbide tools gave R_z of around $3–6 \,\mu$m. An investigative analysis of the surface integrity of the heat-treated alloys (machined material) with a SEM showed no metallurgical changes in the material. The analysis of the non heat treated alloy showed that severe plastic deformation, cracks and breaks in the hard phases were observed when machining with the carbide tools. The analysis with a PCD tool showed minimal damage to the surface microstructure. The representative SEM micrographs showing the sub-surface microstructure when machining with carbide tools and PCD tools are shown in Fig. 18 [16].

4 THE CUTTING TOOL

The selection of the most appropriate cutting tool is a major selection decision for a process planner when planning for the machining of an aluminum alloy. Additionally, there has to be a decision on the necessity of a coating (especially for carbides) as well as the presence of a chip-groove for breaking the "stringy" chips typical of finish machining of aluminum alloys. The use of carbides for machining of aluminum alloys is slowly fading out. Even with a tool coating, the tool-wear rates compare very inferiorly with that of the more effective diamond-based tools. Unless the machine tool cannot operate at the recommended high speeds for diamond-based tools, the usage of carbide tools is not recommended. Diamond tools and coatings exhibit ideal properties for the machining of non-ferrous alloys. The most suitable of these properties are:

- high hardness
- low coefficient of friction
- high thermal conductivity.
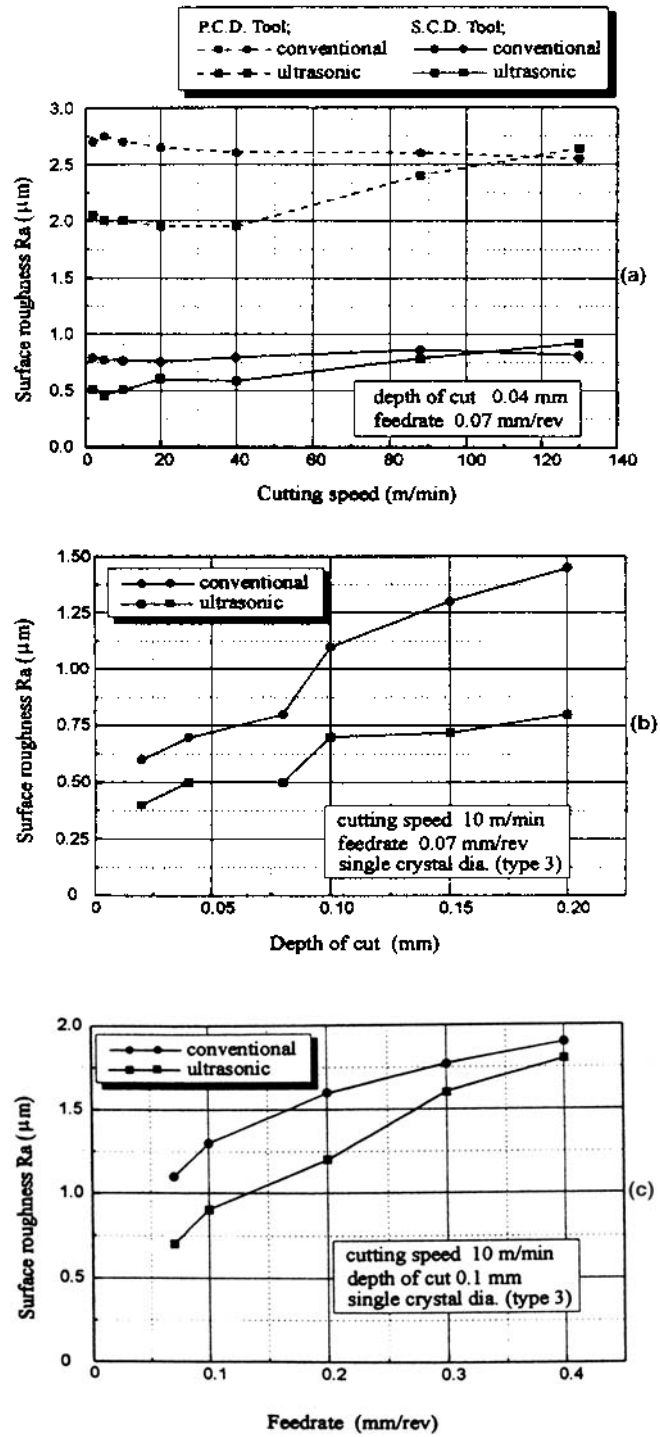
Figure 15   Variation of surface roughness with (a) cutting speed; (b) depth of cut; and (c) feed when machining A390 alloy with conventional and ultrasonic methods. (From Ref. 5.)
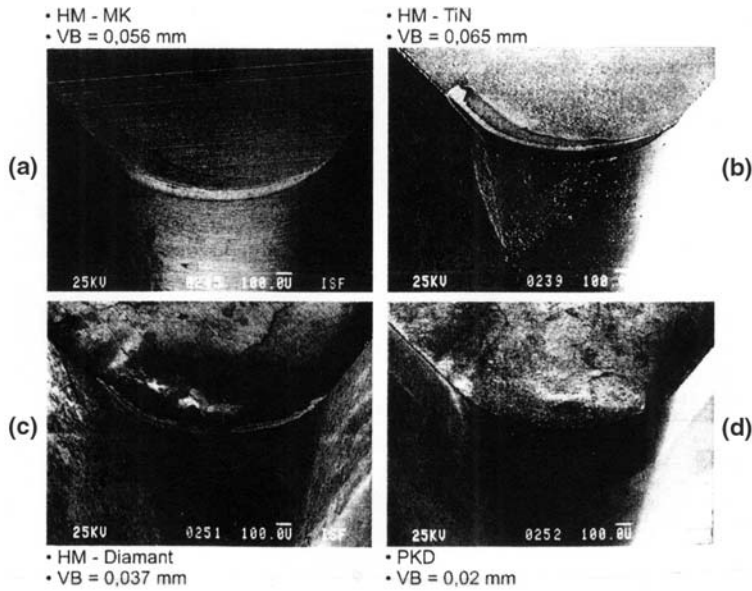
Figure 16 SEM photographs of four cutting tools after 750 sec of cutting of hypereutectic Al-Si alloys: (a) uncoated carbide (VB = 0.056 mm); (b) titanium nitride coated carbide (VB = 0.065 mm); (c) diamond coated carbide (VB = 0.037 mm); and (d) polycrystalline diamond PCD (VB = 0.02 mm); (Work material = AlSi25X, cutting speed = 400 m/min., feed = 0.1 mm/rev., depth of cut = 1.0 mm, tool nose radius = 0.8 mm). (From Ref. 16.)
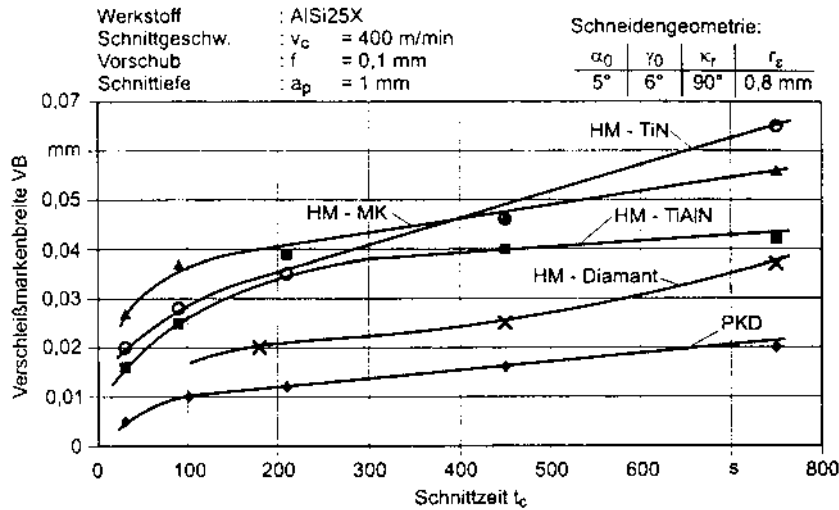
Figure 17 Variation of flank wear land VB with cutting time t_c for different cutting tools (Notation: HM-TiN = TiN coated carbide, HM-MK = uncoated carbide, HM-TiAlN = TiAlN coated carbide, HM-Diamant = diamond coated carbide, HM-PKD = PCD.) (From Ref. 16.)
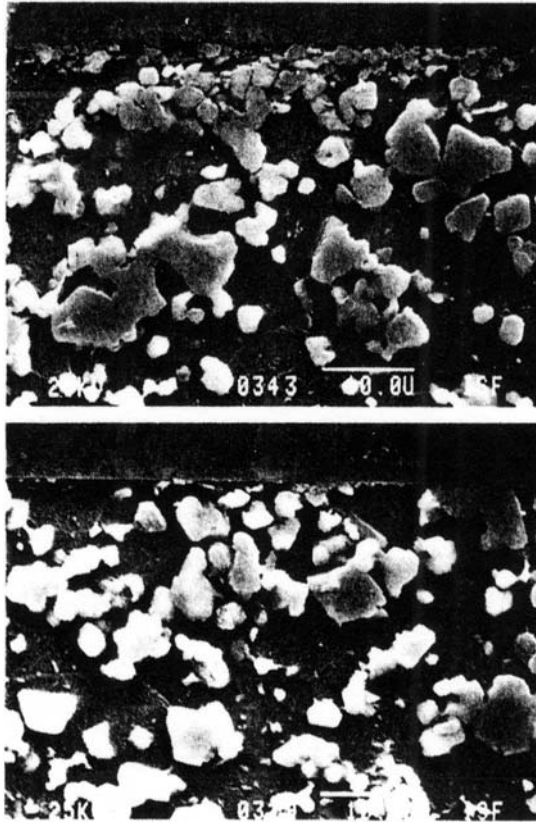
Figure 18 Representative SEM micrographs showing the sub-surface microstructure after machining of hypereutectic Al-Si alloy (AlSi25X) with (a) uncoated carbide; and (b) PCD tools. (From Ref. 16.)

There exist two major classes of diamond-based tools:

1. Polycrystalline diamond (PCD) tools
2. CVD diamond coated tools

Polycrystalline diamond tools have been in use for almost 40 years. These tools are manufactured by brazing a PCD tip onto a substrate such as carbide. However, this type of tool manufacture restricts the usage to just one cutting edge per insert. The CVD diamond coated tools are available typically in two sub-classes; with thick and thin coatings. The thin film diamond coating is applied directly to the substrate material whereas the thick film diamond coating is grown, polished and then brazed onto the substrate material.

Recent tests by a prominent toolmaker (Kennametal, Inc.) have shown that tools with a CVD coating (approximately $30\,\mu$m thick) equaled or exceeded the tool-life of comparable PCD tools, depending on composition and microstructure of the work material [17]. However, the PCD tool provided a better surface finish. In terms of tool-life, the PCD and thick CVD diamond coated tools provided excellent tool-life but a poor degree of chip control. The thin CVD diamond-based tools

offer the advantage of easy applicability on to a tool with an effective chip-breaker design, thereby providing added chip control benefits.

The higher cost of diamond-based tools is offset by the higher productivity due to operation at high cutting speeds (ranging from 500 to 2500 m/min) and the better quality of the machined surface. However, when machining hypoeutectic alloys with a solid PCD tool, chip control is a big problem. In these cases the use of a CVD diamond-coated tool with a chip breaking groove is highly recommended. This type of cutting tool insert provides the advantage of a diamond tool with the effectiveness of good chip breaking. In the case of hypereutectic alloys, the abrasive particles of silicon embedded in the work material serve as a natural chip breaker, and in many cases a solid PCD tool can be used for effective machining of such alloys.

5   HIGH SPEED MACHINING OF ALUMINUM ALLOYS

High speed machining is one of the fast growing technological areas closely related with the machining of light metal alloys. High speed machining has several advantages apart from the obvious increase in machining productivity and these include [18]:

- increased machining accuracy, especially in the manufacture of parts containing thin webs
- better surface finish and reduction in the damaged layer
- reduced burr formation
- better chip disposal
- possibility of higher stability due to superposition of stability lobes against chatter vibration.

Since the typically used diamond tools have excellent tool-life characteristics, tool-life is not a limiting factor in the high speed machining of aluminum alloys. Advances in machine tool structural technology and control systems have enabled the production of dedicated machine tools capable of effectively using high speed machining. Chip removal rates can be increased by five times in high-speed roughing and finishing of aluminum alloys. The recommended machining parameters for wrought aluminum alloys are a cutting speed of 4700 m/min. For cast hypoeutectic alloys (< 12% Si), CVD diamond coated chip-breaker tools are highly suitable at cutting speed of 1300 m/min. The high speed machining of cast hypereutectic alloys (> 12% Si) requires the use of PCD tools with cutting speeds of 1200 m/min.

Recent research work [15] has shown the remarkable improvement of surface quality and the reduction in built-up edge and burr formation when performing high speed milling with diamond end mills. Figure 19 shows the advantages of using high speed machining with diamond end mills as compared to conventional milling methods. Also, previously shown in Fig. 14 are the contrasting results obtained in surface quality by high speed machining with diamond tools as compared with conventional carbide tools. The excellent surface quality obtained from such high speed machining negated the necessity of using a finishing process such as lapping or polishing. They also determined that the most critical parameter affecting the surface quality was the axial depth of cut.
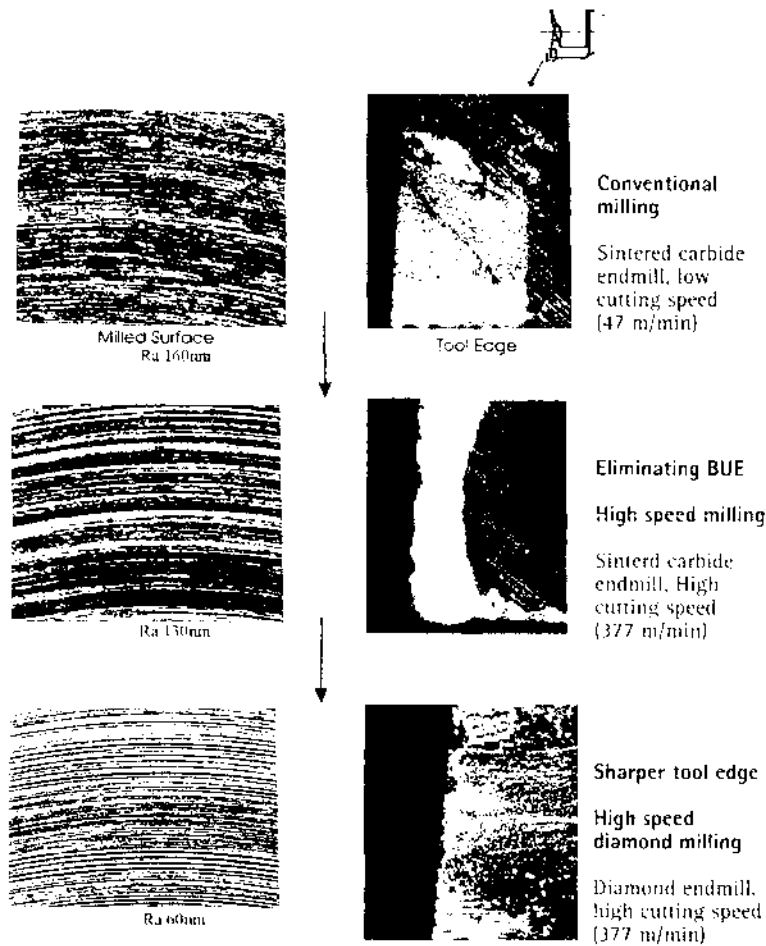
Figure 19 Advantages of using high-speed diamond milling over conventional milling and plain high-speed milling. (From Ref. 15.)

Case Study: Machining of Thin Web Structures for Boeing's 737 Aircraft

High speed machining has been used very effectively in the production of thin web aluminum alloys stringers which assemble onto the Boeing 737 aircraft. Stringers are long, horizontal members to which the aircraft's aluminum skin is riveted. Spindle speeds upto 25000 rpm were used in the drilling of the holes for the stringers. A dedicated fixturing system had to be designed for performing the high speed machining [19].

6 DRY MACHINING

Dry machining of advanced materials is being widely promoted in the manufacturing industry. The major reasons for shifting towards dry machining are:

1. environmental concerns over disposal of cutting fluids and the damage they cause to the environment
2. economic factors
3. health hazards to operators due to wet machining.

A recent study by Daimler Benz showed that up to 16% of the total production cost is coolant related [20]. There has been a renewed initiative in German industries to aim for dry or ''nearly dry'' machining. The U.S. Council for Automotive Research's Partnership for a New Generation of Vehicles (PNGV) has targeted dry machining of aluminum as one of the major focus areas for further research leading to development of new tools and materials, and development of innovative systems for optimal chip formation, ejection and disposal [21].

Aluminum alloys are extremely critical to the subject of dry machining. Typically, the problems associated with dry machining of aluminum alloys arise from the high level of thermal conductivity of the work material thereby leading to surface deformation. The other very significant problem arises from the adhesion of the work material onto the cutting tool, which resulted in ending of the tool-life. In a recent CIRP keynote paper, the most critical aspects to be considered in the dry machining of aluminum alloys are discussed [22]. It is suggested to use MQL (minimum quantity of lubricant) to offset the problems in pure dry machining of aluminum alloys. The positive effect of using MQL when machining aluminum alloys is shown in Fig. 20. It is also recommended that PCD inserts or more preferably diamond-coated inserts with a chip-groove be used for effective machining of aluminum alloys. The use of a chip-groove causes considerable difference in the level of chip control that is attainable, especially for breaking the stringy chips which are very typical of aluminum machining.

In a recent study of industrial perspectives on dry machining, it was suggested that for machining aluminum, near-dry machining with minimal coolant consumption is a promising approach [23]. A metered supply of biodegradable oil drops at the cutting edge through a nozzle in the tool aids in effective machining of aluminum with large savings in lubricant consumption and environmental damage.

However, in terms of tool-life, wet machining still provides better tool-life. This can be seen in Fig. 21 [1] wherein there is a comparison of dry turning with wet turning when using diamond and carbide tools. Table 5 provides a list of common cutting fluids used for machining aluminum. The cutting fluids used however need to be reduced scientifically to attain MQL in order to provide better machining performance without undergoing the hazards of truly wet machining.

7 MACHINING OF ALUMINUM-BASED METAL MATRIX COMPOSITES (MMCS)

One of the major developments which has provoked the necessity of a revised material selection process by designers and manufacturers has been the introduction of metal matrix composites (MMCs). These MMCs are finding niche areas for application wherein they are replacing traditional materials. MMCs have advantages over other fiber-based composites and their wear resistance and lightness make them very
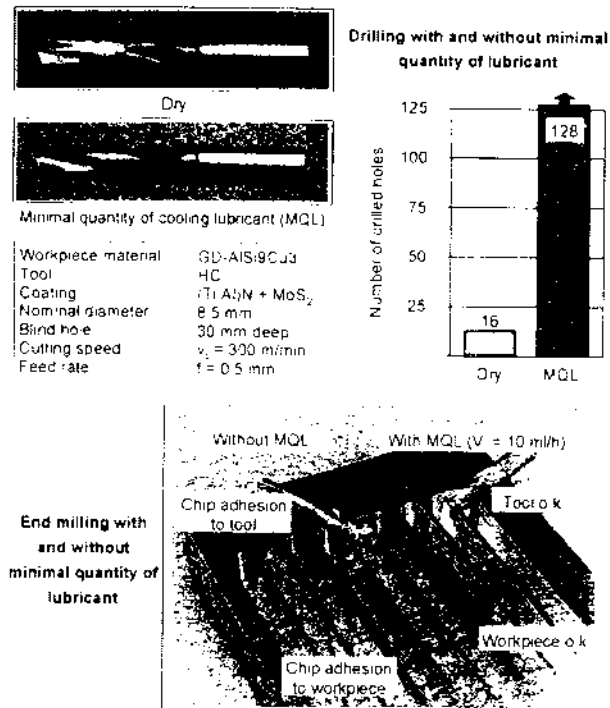
Source Daimler Benz, wbk, WZL

Figure 20 Comparative effects of using pure dry machining and MQL (minimum quantity of lubricant) machining on aluminum workpieces. (From Ref. 22.)

suitable in automobile body parts such as brake drums and rotors. The MMCs typically comprise of aluminum matrix composites reinforced by either of the following:

- continuous fibers (boron, silicon carbide, alumina, graphite)
- discontinuous fibers (alumina, alumina-silica)
- whiskers (silicon carbide)
- particulates (silicon carbide, boron carbide, alumina, etc.).

MMCs are renowned for their high specific strength, high wear resistance but poor machinability. The major problem associated with MMCs containing silicon carbide is the difficulty in machining due to the presence of the hard and abrasive silicon carbide or other reinforcement materials. Correspondingly, the major focus of research on the application of MMCs has been directed towards the following two areas:

1. Establishment of machinability parameters and scientific selection procedure for tool inserts and cutting conditions for the MMCs; and
2. Assessing the effect of reinforcement directions on the machining performance of such MMCs.
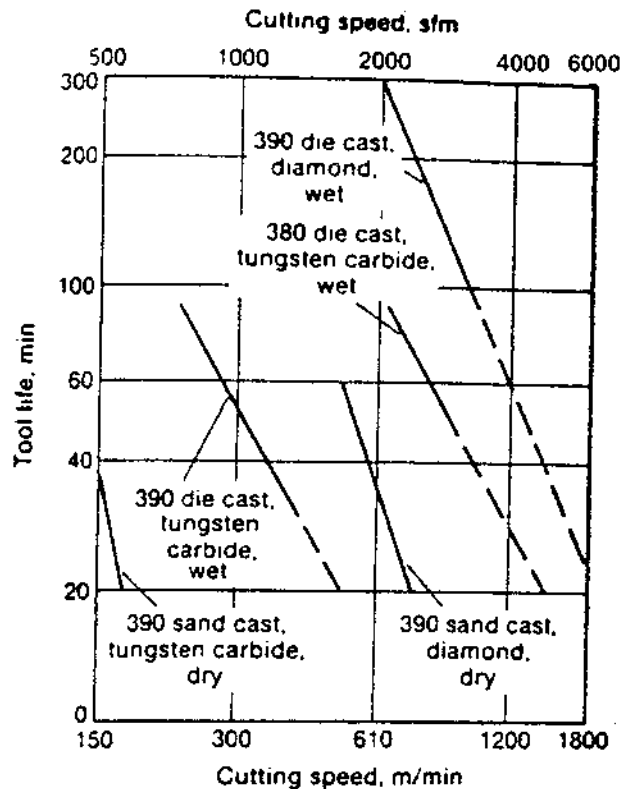
Figure 21 Comparison of tool-life when dry turning and wet turning of sand cast alloy 390 with carbide and diamond tools. (From Ref. 1.)

The literature on machinability of the MMCs is very limited in content. Machining performance measures such as the cutting force, torque and tool-wear were studied during the drilling and reaming of aluminum alloys and MMCs by using a PCD tipped tool [24]. The MMC (containing silicon carbide particulates) produced the largest tool-wear whereas the hypoeutectic alloy (with low silicon-content) produced the lowest tool-wear (Fig. 22). It can also be seen that the MMC produced the larger cutting force [Fig. 23(a)] and the largest torque [Fig. 23(b)] when using the PCD tipped drill. Hung et al. [25] have researched the machining performance of silicon carbide-based MMCs by using tool-wear as a machining performance indicator. They tested a variety of tool materials (ranging from high speed steel to polycrystalline diamond (PCD)) and concluded that cubic boron nitride (CBN) and PCD tools fractured the silicon carbide particles along their crystallographic planes and thereby induced little damage on the MMC matrix, whereas the other tools delaminated the particles from the matrix, further roughened the particles and also significantly deformed the MMC matrix. Figure 24 shows the comparative tool-life given by the different tool materials when facing Al-Li SiC_p MMC. The comparative pictures showing the sub-surface deformation undergone by the machined material when using the carbide tool and the diamond tool is clearly shown in Figure 25 (a) and (b).

Table 5 List of Cutting Fluids for Machining of Aluminum and its Alloys

Type of lubricant	Principal ingredients	Viscosity range	Application; maintenance	Relative effectiveness	Necessary precautions
Mineral oils (fatty-additive type preferred)	Mineral oil, lard, or neats-foot oil; oleic acid or butyl stearate	40 SUS at 40°C (100°F) for high-speed machining to 300 SUS for low speeds	Generous flow at all cutting edges; keep recirculating fluid clean and cool.	Good lubricity and chip flushing; fair cooling; excellent finish as built-up edge is minimized	Control air above oil where mis application endangers shop air; remove oil from finished parts (also from chips to reclaim and reduce fire hazard).
Soluble oils (emulsions) (3–5% soluble oil in water)	Soluble oil, petroleum sulfonate emulsifying agents, water (oil is added); rust inhibitor, germicide, stain inhibitor	Generally low	Generous flow at all cutting edges: keep recirculating fluid clean; cool when necessary.	Good chip flushing; lubrication adjustable by varying concentration; excellent cooling; good finish	For high-speed machining cooling is more import than lubrication; where emulsion is applied as mist, keep oil content as low as possible to reduce air and shop contamination.
Aqueous chemical solutions	Water; soluble synthetics (usually clear); sometimes, fatty materials; rust inhibitors; germicides	Generally low	Generous flow at all cutting edges; keep recirculating fluid clean; cool as required.	Good chip flushing; excellent visibility of cut; excellent cooling; adjustable lubrication; good finish	Keep oil conten low; control mist; consider cost (significantly higher than soluble-oil emulsions).
Stick lubricants	Mineral compounds, animal fats, waxes, synthetics	Various hardnesses	Applied as required to blades, wheels, disks, or files or to workpiece	Prevents the loading of abrasive surfaces or of teeth of saws and files	Applied is intermittent, but should be monitored and made as required throughout run.

Source: Ref. 1.
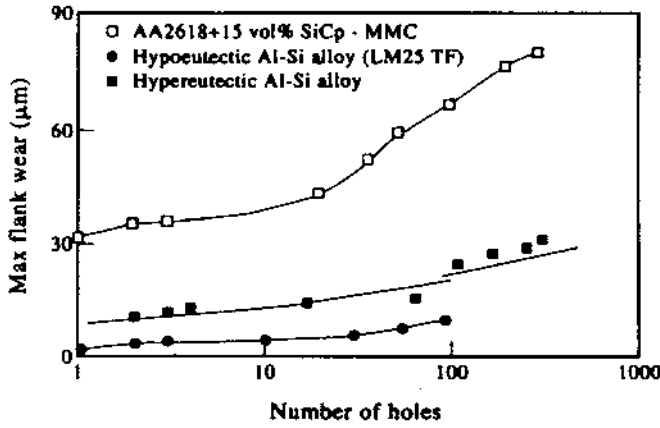
Figure 22 Flank wear results from drilling experiments on Al-Si alloys and MMC using PCD tipped drills. (From Ref. 24.)
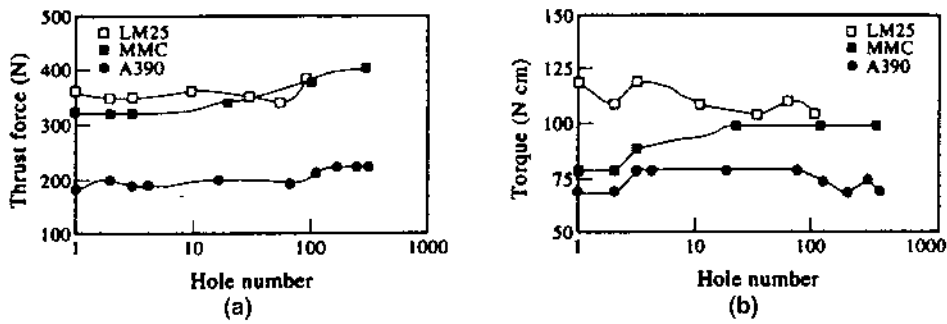
Figure 23 Experimental results from drilling of Al-Si alloys and MMCs with PCD tipped drills showing the variation of (a) thrust force, and (b) torque with number of holes drilled. (From Ref. 24.)
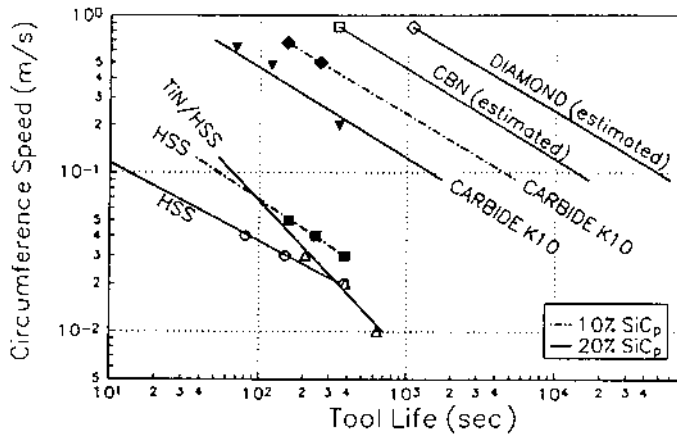
Figure 24 Comparative tool-life produced by different tool materials when facing Al-Li SiC$_p$ MMC (depth of cut $= 0.5$ mm, feed $= 0.07$ mm/rev., dry machining), (From Ref. 25.)
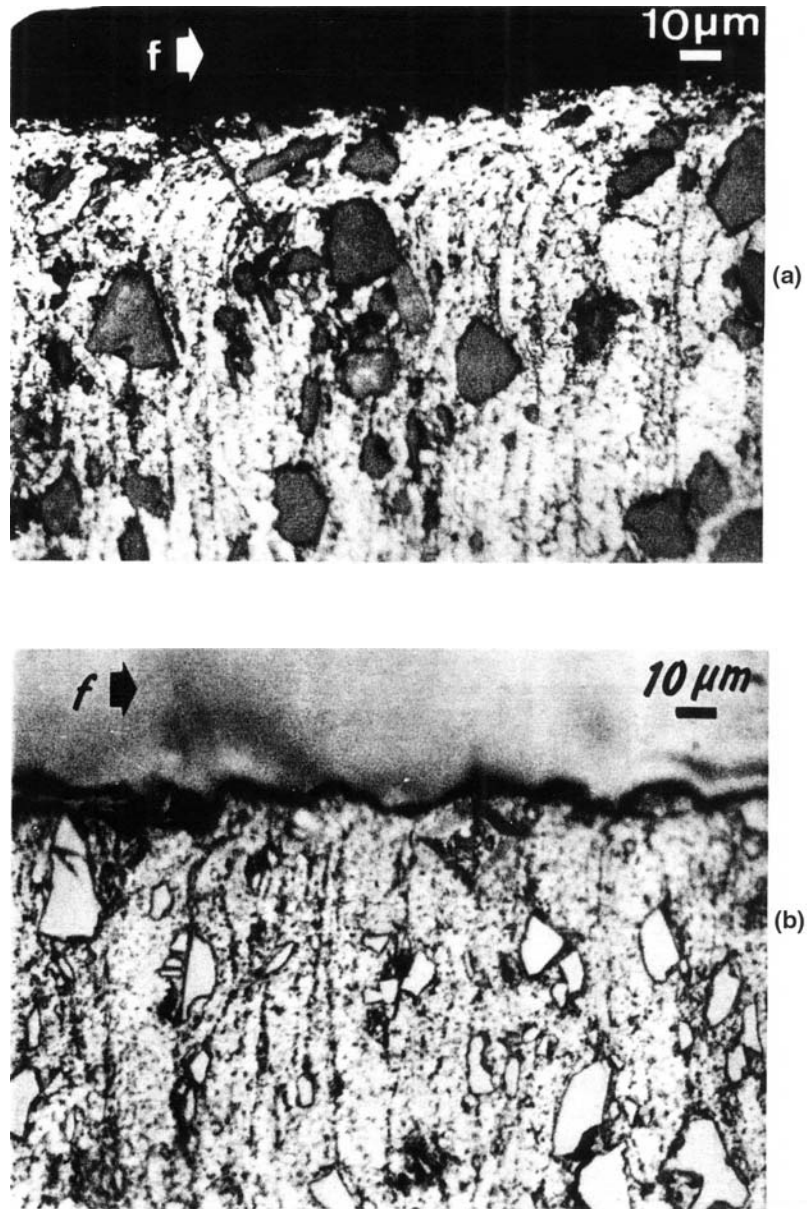
Figure 25 Sub-surface plastic deformation of 20% Al-Li SiC$_p$ MMC due to facing with (a) a carbide tool; and (b) a diamond tool. (From Ref. 25.)

The critical role of tool-wear in the machining of MMC's has been discussed already. The reinforcement materials which are very hard, cause severe g abrasive wear of the tool materials. The higher the hardness of the reinforcement material, the higher the tool-wear. Figure 26 shows the tool-wear (flank wear VB) when machining (a) silicon carbide and (b) boron carbide reinforced aluminum MMC's
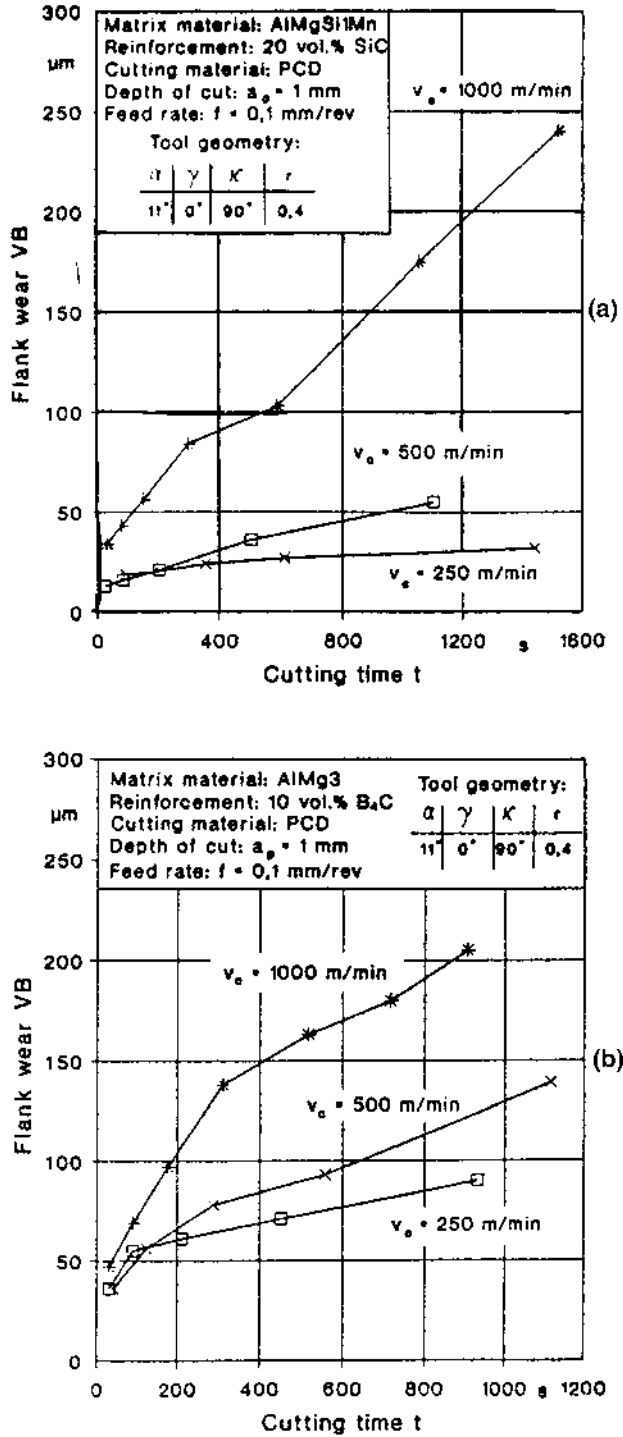
Figure 26 Tool-wear when turning (a) 20% SiC reinforced aluminum; and (b) 10% B_4C reinforced aluminum with a PCD tool. (From Ref. 26.)

with PCD tools [26]. It can be seen that just 10% of boron carbide (B_4C) induces higher tool wear at a cutting speed of 250 and 500 m/min. Until the severe problems of abrasive tool-wear during the machining of MMCs is not solved, the overall machining performance cannot improve. Considering the many advantages of MMCs, the research community needs to address the issue of higher cutting forces (to a lesser extent) and the high degree of abrasive tool-wear in order for promoting more widespread use of MMCs in industrial practices.

8 SUMMARY

The review and analysis presented in this chapter on machining of aluminum and its alloys indicates the growing industrial trend in the application of machined parts and the associated technological challenges involved in achieving "optimum" machining performance. The role of new cutting tool development and the related machining applications are also presented in this chapter. Emerging areas of research and applications are identified, and this includes high speed machining, dry machining and machining of aluminum-based MMCs. The advantages of pursuing high speed machining have been highlighted with experimental results and a case study. Currently, the use of MQL (minimum quantity of lubricant) machining has found to be more favorable over purely dry machining of aluminum from the machining performance standpoint. Further research is necessary for approaching effective pure dry machining of aluminum alloys. The advantages of using aluminum-based MMCs has been counterbalanced by the poor machinability exhibited by them. The issue of high cutting forces and accelerated tool-wear during machining of aluminum-based MMC's needs to be researched more thoroughly before they can be used on a large scale. Automotive and aerospace applications of aluminum alloys have in recent years strengthened the need for future research and partnership among the various industry groups and universities/research institutions.

REFERENCES

1. *ASM Specialty Handbook*, Machining, (J. R. Davis, ed.), pp. 328–375.
2. Anon, Machinable Wrought Aluminum Alloy. Adv. Materials & Processes, April 1998, pp. 37–38.
3. J. Blasius, "A Machining Performance Study in Contour Turning of Aluminum 2011-T3 Using Diamond-Coated Tools," M.S. Thesis, University of Kentucky, 1996.
4. W. Konig and D. Erinski, "Machining and Machinability of Cast Aluminum Alloys," Annals of the CIRP, 1983, 32(2) pp. 535–540.
5. J-D. Kim and E-S. Lee. "Ultrasonic Vibration Cutting of a Hypereutectic Al-Si Alloy. Aluminium," 1997 73(9), pp. 624–629.
6. A. P. Malshe, M. A. Taher, A. Muyshondt, W. F. Schmidt, H. Mohammed, and H. Mohammed, "A Comparative Study of Dry Machining of A390 Alloy Using PCD and CVD Diamond Tools," Trans, NAMRI/SME, 1998, 26, pp. 267–272.
7. I. S. Jawahir and C. A. van Luttervelt, "Recent Developments in Chip Control Research and Applications," Keynote paper, Annals of the CIRP, 1993, 42(2), pp. 659–691.
8. D. Grant, "An Experimental Study of the Effects of Tool Geometry on Thin Chip Control in Machining," B. E. Thesis, University of Wollongong, 1989.
9. K. Maekawa, I. Ohsima, and Y. Nakano. "Case Studies of Troubleshooting in Connection with Uncontrollable Chips," J. Mat. Proc. Tech., 1996, 62, pp. 352–357.

10. Anon, "Alloy Improves Machining Productivity," Design News, 1995, 50(51), p. 47.
11. M. M. Elkhabeery and J. A. Bailey, "Surface Integrity in Machining Solution-Treated and Aged 2024-Aluminum Alloy, Using Natural and Controlled Contact Length Tools," Part 1 – Unlubricated Conditions," ASME J. Engg. Ind., 1984, 106, pp. 152–160.
12. R. Natarajan, S. Biswas, and S. Jeelani, "Residual Stress Distribution in 2024-T351 Aluminum Alloy Due to Machining," Computers in Engineering. *Proc. Int. ASME Computers in Eng. Conference*, 1985, 2, pp. 59–63.
13. K-H. Fu and C-F. Wu, "A Proposed Statistical Model for Surface Quality Prediction in End-Milling of A1 Alloy," Int. J. Mach. Tools Manufact., 1995, 35(8), pp. 1187–1200.
14. K-H. Fu and C-F. Wu, "A Residual Stress Model for the Milling of Aluminum Alloy (2014-T6)," J. Mat. Proc. Tech., 1995, 51, pp. 87–105.
15. J. D. Kim and Y. H. Kang, "High Speed Machining of Aluminium Using Diamond Endmills," Int. J. Mach. Tools Manufact., 1997, 17(8), pp. 1155–1165.
16. K. Weinert, D. Biermann, and M. Buschka, "Turning of Spray Deposited Hypereutectic Al-Si Alloys," Aluminium, 1998, 74(5), pp. 352–359.
17. Kubel, "Coatings Crank Up Tool Performance," Manufacturing Engineering, 1998, 120(1), pp. 40–46.
18. H. Schulz and T. Moriwaki. "High-Speed Machining. Keynote Paper," Annals of the CIRP, 1992, 41(2), pp. 637–643.
19. "Machining of Thin Web Structures—Boeing Case Study," Manufacturing Engineering, 1996.
20. Daimler-Benz Umwalt Magazine, "Trend: Drying out the Machines," (Internet: www.daimler-benz.com/um welt/magazin/magazin3/umwelt1 _e.html)
21. "Dry Machining of Aluminum," U.S. Council for Automotive Research – PNGV, (Internet: www.uscar.org/pngv/technical/machining.html)
22. F. Klocke and G. Eisenblatter, "Dry Cutting," Keynote Paper, Annals of the CIRP, 1997, 47(2), pp. 519–526.
23. Industry Executive Perspectives, 1998, American Machinist, (Internet: www.penton.com/am/exec_perspective/perspective 11.html)
24. R. T. Coelho, S. Yamada, D. K. Aspinwall, and M. L. H. Wise. "The Application of Polycrystalline Diamond (PCD) Tool Materials when Drilling and Reaming Aluminium Based Alloys Including MMC," Int. J. Mach. Tools Manufact., 1995, 35(5), pp. 761–774.
25. N. P. Hung, F. Y. C. Boey, K. A. Khor, Y. S. Phua, and H. F. Lee, "Machinability of Aluminum Alloys Reinforced with Silicon Carbide Particulates," J. Mat. Proc. Tech., 1996, 56, pp. 966–977.
26. L. Cronjager and D. Biermann. "Turning of Metal Matrix Composites," *EUROMAT'91—Proceedings of the 2nd European Conference on Advanced Materials and Processes*, Cambridge, UK, 1991, pp. 73–80.

22

Superplastic Forming

NORMAN RIDLEY

University of Manchester, Manchester, England

1 INTRODUCTION

An inherent limitation of conventional aluminum (Al) alloys, like many metals and alloys, is that they are unstable when plastically deformed by stretching. This is responsible for the catastrophic necking observed on tensile testing and also for the limited extent of uniform deformation possible during processes such as stretch forming which involve mainly tensile stresses [1].

In recent years attention has turned to superplastic (SP) materials which are relatively stable when deformed in tension. This behavior is related to the observation that the flow stress of a superplastic material is very sensitive to the rate of deformation. The characteristic equation which describes superplastic behaviour is usually written:

$$\sigma = k \, \dot{\varepsilon}^m \tag{1}$$

where σ is the flow stress, k is a constant, $\dot{\varepsilon}$ is strain rate and m is the strain rate sensitivity of flow stress. If superplasticity is regarded as a type of creep behavior then Eq. (1) may be re-written as:

$$\dot{\varepsilon} = k_1 \, \sigma^n \tag{2}$$

where n, the stress exponent for deformation is equal to $1/m$.

A material is usually considered to be superplastic under conditions where it displays an m value > 0.3. An important feature of SP alloys is that their flow stresses are low compared with those of conventional materials. During tensile deformation the effect of high m is to inhibit catastrophic necking. Necks which tend to develop lead to a localized rise in $\dot{\varepsilon}$ and to strain rate hardening which inhibits

neck propagation. Hence, differences in cross-sectional area propagate very slowly so that necking is diffuse and relatively uniform. The m values of commercial SP alloys lie in the range 0.4–0.8. The consequences of these high m values is that SP materials are capable of undergoing abnormally high tensile strains prior to failure with elongations of 500–1000% not being uncommon, although an alloy which exhibited an elongation in excess of 200% could be considered to be superplastic. The highest elongation recorded to date is $\sim 8000\%$ for a commercial aluminum bronze [2].

The combination of low flow stresses, usually $< 10\,\mathrm{MNm^{-2}}$, and relatively high uniformity of plastic flow has led to commercial interest in the superplastic forming (SPF) of components, often of complex shape, from sheet materials using techniques similar to those developed for the gas pressure bulge forming of thermoplastics. SPF can lead to considerable savings in materials and manufacturing costs, particularly if a component can be redesigned to take advantage of the benefits of the process or where a component of complex shape which is normally built up from several pieces can be formed as a single part. Other advantages are that SPF is a near net-shape forming process, multiple parts can be produced in one operation, there is little or no spring-back, only one major tool is required rather than an accurately matched pair of tools or multiple tools, and for Al alloys the die sets are relatively inexpensive because of the moderate temperatures associated with the process ($\sim 500^{\circ}\mathrm{C}$), and they can be produced quickly.

While it is clear that SP alloys have numerous attractions for use in tensile sheet forming processes, there are also some limitations. Firstly, superplasticity is confined to relatively few Al alloys and is a characteristic of materials which can be thermomechanically processed to develop fine stable grains, of size preferably $< 10\,\mu\mathrm{m}$. Superplasticity is associated with slow strain rates, usually in the range $10^{-4}\,\mathrm{sec^{-1}} - 5 \times 10^{-3}\,\mathrm{sec^{-1}}$, that can lead to relatively long forming times involving several minutes, or even up to 2 h for critical parts, rather than seconds, and with a limited range of temperatures, $> 0.5\,T_{\mathrm{m}}$, where T_{m} is the melting point in degrees Kelvin. For Al alloys the forming temperatures are likely to lie in the range 460–530°C, which is $\sim 0.9\,T_{\mathrm{m}}$, so the problem of maintaining small grain sizes requires special attention. Further, Al alloys are prone to cavitation during superplastic flow.

Superplastic forming is not a high volume production process and it caters for what have been termed niche markets involving low to medium volume production (10s to 1000s) of medium sized parts (0.1–4 m^2), often of complex shape and high

---

There are two main types of superplastic behavior: fine grain or micrograin superplasticity, and internal stress superplasticity. In the latter case, internal stresses of magnitude similar to the flow stress of the material can be developed by thermal cycling of a polycrystalline metal or solid solution exhibiting a phase change, or having anisotropic thermal expansion coefficients, or of a composite with constituents of different thermal expansion coefficients, e.g. Al alloy/SiC. Under these conditions the material exhibits $m \sim 1$. Hence, the application of a small external stress leads to an increment of tensile plastic flow during each cycle, while repeated cycling can give substantial tensile strains. The potential for bulge forming of metal matrix composites (MMCs) by thermal cycling has been demonstrated for AA6061-10% volSiC$_{\mathrm{p}}$ sheet material [3]. However, an internal stress superplasticity has not so far been exploited as the basis of a commercial process, the present Chapter will be concerned only with fine grain superplasticity. Internal stress superplasticity has been reviewed by Nieh et al. [4].

added value. However, it is an important sheet metal forming process for a number of Al alloys and is used to produce a wide range of products for structural and non-structural applications in fields as diverse as aerospace, architecture, medical equipment, telecommunications and transport.

2 MECHANICAL ASPECTS OF SUPERPLASTICITY; CHARACTERIZATION OF SUPERPLASTIC ALLOYS

2.1 Mechanical Aspects of Superplasticity

The most important mechanical characteristic of a SP material is its high strain rate sensitivity of flow stress, m, as defined in Eq. (1). It can be seen from this equation that if the relationship between σ and $\dot{\varepsilon}$ is plotted logarithmically, then the slope of the plot is m where:

$$m = \frac{\partial(\log \sigma)}{\partial(\log \dot{\varepsilon})} \tag{3}$$

Data for AA7475 for several temperatures are shown plotted in Fig. 1(a) [5]. It is seen that where the stress-strain rate curve is fully developed it has a sigmoidal shape and that m (~ 0.85) is observed at passes through a maximum (Fig. 1(b)). For this material, maximum m (~ 0.85) is observed at 516°C at a strain rate of $\sim 3 \times 10^{-4}\text{sec}^{-1}$. A value of $m > 0.3$ delineates the superplastic regime (Region II). The high (Region III) and low (Region I) strain rate regions exhibit values of m in the range 0.1–0.3, although for Region I the slope of the curve can vary.

At high strain rates (Region III) $m \sim 0.2$, deformation is by recovery controlled dislocation creep (power law creep). Strain is accumulated by the glide of dislocations within the grains but is dependent on the rate at which obstacles such as other dislocations, solutes and precipitates, can be by-passed. It is generally assumed that dislocation climb is the rate controlling process. The observed activation energy for flow in Region III is similar to that for lattice diffusion and the strain rate is relatively insensitive to grain size. Other features of this region are the observation of slip lines and the development of high dislocation densities within the grains. Crystallographic texture increases and significant grain elongation occurs.

At intermediate strain rates in Region II where high relatively uniform strains are observed, i.e. the SP regime, the flow process is less well understood, although there is substantial agreement on the microstructural features associated with it. Equiaxed grains tend to remain equiaxed throughout deformation, regions which initially show microstructural banding tend to develop a more uniformly equiaxed structure, and crystallographic texture may be reduced. The activation energy for flow in Region II is similar to that for grain boundary diffusion. Strain is accumulated in the SP regime by the motion of individual grains, or groups of grains, relative to each other by sliding and rotation.

If grain boundary sliding occurred in a completely rigid assembly of grains then holes or cavities would develop in the microstructure. However, as several SP materials do not cavitate, grain boundary sliding must be accommodated. The most probable accommodation processes involve diffusion and/or glide and climb of dislocations. Many attempts have been made to develop theories capable of predicting
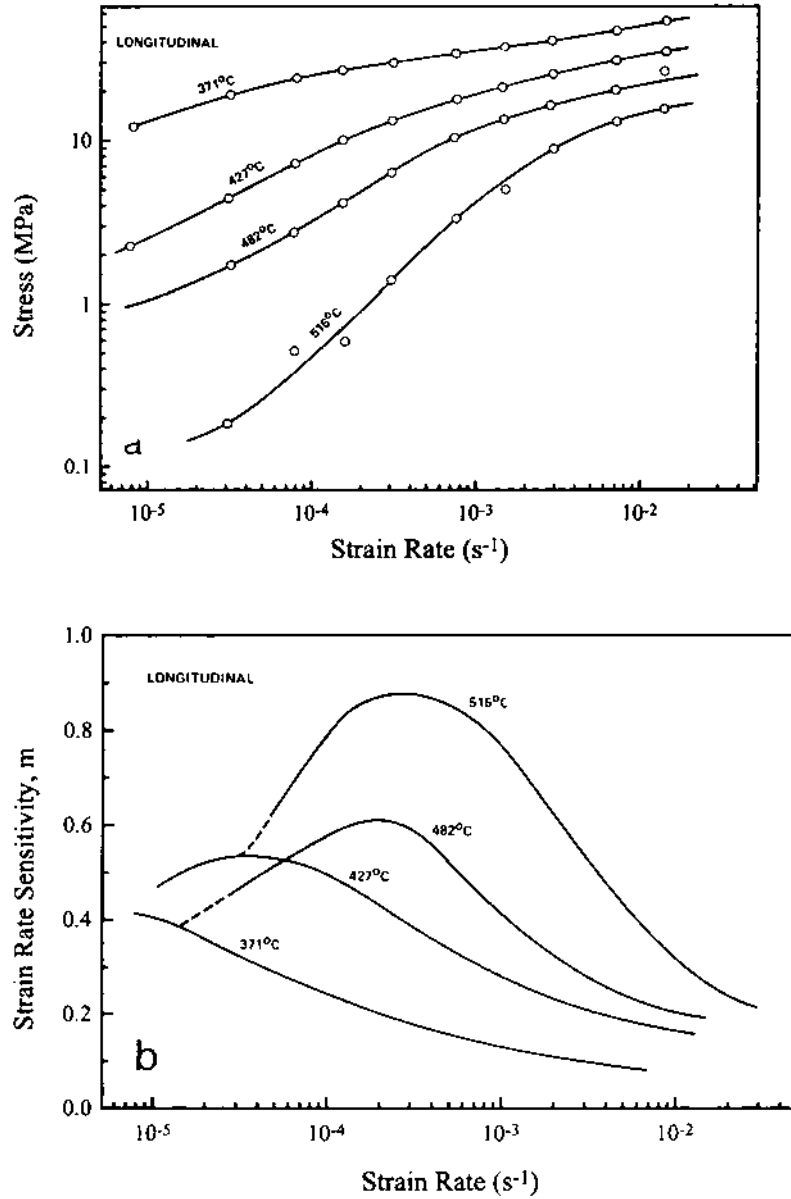
Figure 1 (a) Stress versus strain rate; (b) *m* versus strain rate, for AA7475. (From Ref. 5.)

both mechanical and microstructural features of SP deformation but none has been completely successful. The various models proposed are outside the scope of the present text but some have been subject to review [6–8].

At low strain rates (Region I) the slope of the stress versus strain rate plot can vary. In many alloys *m* is low and this has been interpreted as evidence for some form of threshold stress for SP flow, although grain growth hardening at low strain rates can complicate the interpretation of this region.

The mechanical behavior of superplastic materials is very sensitive to temperature and grain size. In general, increasing temperature or decreasing grain size have similar effects on the variation of flow stress with strain rate. Increasing the temperature decreases the flow stress, particularly for Regions I and II [Fig. 1(a)]. Maximum m has been found to increase with increasing temperature and decreasing grain size, and the strain rate for maximum m moves to higher values [Fig. 1(b)].

While the strain rates at which superplasticity is normally observed in aluminum alloys, $10^{-4} sec^{-1} - 5 \times 10^{-3} sec^{-1}$, are considerably less than those often associated with conventional hot and cold shaping processes, there has recently been a substantial interest in high strain rate superplasticity ($> 10^{-2} s^{-1}$). Aspects of this phenomenon will be outlined in a later section.

2.2 Characterization of Superplastic Alloys

To determine whether a given material is superplastic it is necessary to characterize its flow behavior as a function of strain rate and temperature. As noted above, the most important mechanical characteristic of a superplastic alloy is its high strain sensitivity of flow stress, or m value, and the optimum conditions of strain rate and temperature would be those which led to a maximum value of m. However, alternatively, or additionally, characterization could involve measurement of tensile elongation for a range of constant strain rates, including that for optimum m if this was known, since during SPF a part being shaped can experience significant variations in strain rate. In addition these tests could be used to gain metallogaphic information about cavitation and the effect that this has on fracture behavior.

Constant strain rate tensile tests also give useful information about flow stress levels and hence, the pressures required for SPF. They frequently provide evidence of significant hardening which may occur during SP flow (Fig. 2) [9]. This is primarily related to grain growth. At higher strain rates approaching Region III of the stress-strain rate curve, hardening is associated with dislocation creep in the material.
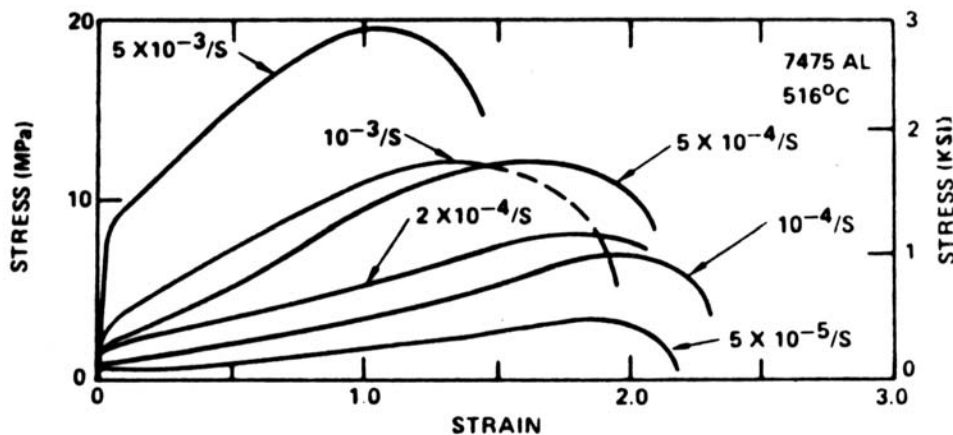
Figure 2 Stress versus strain curves at various constant strain rates for 7475. (From Ref. 9.)

The above tests would normally be carried out under laboratory conditions using uniaxial testing, but it has been shown that the information gained can reflect behavior during biaxial forming [10,11]. Grimes and Butler used a drape forming tool devised by Superform Aluminium, which had corner radii of progressively increasing severity, for the qualitative evaluation of SP formability [10]. Only material showing high tensile ductility was capable of being formed without failure at the sharpest radii.

Attempts to produce a standard test for SP formability led to the development of the biaxial cone test [12] (Fig. 3). Sheet is bulged into a conical die of constant angle ($\sim 57°$), designed to give a constant average strain rate by maintaining constant pressure conditions after the expanding sheet had just made contact with the side of the die. The geometry was subsequently modified by Goforth et al. to a variable angle to give a more constant strain rate throughout the test [11].

The cone test can be carried out with an imposed hydrostatic pressure (back pressure). The parameters measured from the test include the radius of curvature and sheet thickness at the pole, and the height of the cone. Material flow stress, strain and strain rate, obtained from the cone test provides useful data for the modeling of SPF. Metallography can be used to detect cavitation in the cone. The cone test is also used as an acceptance test for SP sheet material in that the cone is required to rise to a predetermined height when subjected to a given pressure-time cycle.

An essential component of any process model of SPF is the constitutive relationship for the material, that is the relationship between stress, strain, strain rate, temperature and microstructure. The strain rate, $\dot{\varepsilon}$, at which a SP material will

Figure 3   Cone test carried out on 1.5 mm thick 7475 SP sheet.

deform has been defined by the simple relationship given in Eq. (2). This can be restated in an expanded temperature dependent form given by:

$$\dot{\varepsilon} = \frac{AGbD}{kT} \left(\frac{b}{d}\right)^p \left(\frac{\sigma_{\text{eff}}}{G}\right)^n \tag{4}$$

where G is shear modulus, b is the burgers vector, k is Boltzmann's constant, T is absolute temperature, d is grain size and p is the exponent of inverse grain size (usually 2 or 3 in Region II); D is a diffusion coefficient ($= D_o \exp(-Q_s/RT)$), where D_o is a frequency factor, Q_s is the activation energy for the appropriate diffusion process and R is the gas constant. Deformation is driven by the deviatoric (shear) component of the effective stress field characterized by σ_{eff}, equal to $\sigma - \sigma_0$, where σ is the applied stress and σ_0 is a threshold stress. A is a dimensionless constant.

For constant stress and temperature it can be seen from the above equation that:

$$\dot{\varepsilon} \propto \frac{1}{d^p} \tag{5}$$

Since the value of p lies between 2 and 3 for SP flow, the dramatic effect that a reduction in grain size could have on strain rate is clearly apparent, e.g. an order of magnitude reduction in grain size could lead to an increase of 10^2–10^3 in SP strain rate. Alternatively, for a given strain rate, a reduction in grain size could enable SPF to be carried out at a lower temperature, although this would be accompanied by an increase in flow stress. Procedures used to develop ultra-fine grain sizes and the effect that these have on SP behavior will be considered in the final section.

To establish a constitutive relationship such as Eq. (4) it is necessary to determine values for the materials parameters m, p, Q_s and σ_o. Procedures for obtaining these values are outlined. Since the effective stress, σ_{eff}, rather than the applied stress, σ, should be used in the determination of the first three parameters, unless σ and σ_{eff} are little different, then the principles involved in the measurement of σ_o will be considered first.

2.3 Determination of σ_o

It can be seen from Eq. (4) that the threshold stress, σ_o, for a given T and grain size, can be obtained by plotting the applied stress, σ, against $\dot{\varepsilon}^m$ and extrapolating to zero strain rate. Although the value of this parameter may be relatively small compared with stress levels in the middle of the SP range (Region II) its existence can have a significant effect on the magnitude of σ_{eff} at lower strain rates.

2.4 Determination of m

In an ideal material where the microstructure remains constant, true flow stresses can be obtained by carrying out tensile tests at a range of constant strain rates and measuring the steady state loads. As indicated above, most engineering materials are microstructurally unstable at elevated temperatures and the flow stress will continue to increase with increasing strain due to the effects of grain growth

(Fig. 2). It is therefore important to determine the flow stress at constant structure and this can be done by carrying out step strain rate or strain rate jump tests, originally developed by Backofen et al. [13].

To measure m over a range of strain rates a tensile specimen is deformed at a velocity which will produce a strain rate in the middle of the range until a steady state is attained. The crosshead speed is reduced to a low value and allowed to stabilize before being measured. A repeated incremental increase in crosshead velocity allows the load to be measured at a range of strain rates. A typical load-time plot is shown in Fig. 4. The true stresses are calculated from the maximum loads, crosshead velocities and instantaneous lengths of the sample, and corrected for threshold stress. The derivative of the best fit curve to a logarithmic plot of true effective stress against true strain rate then gives m and its variation with strain rate in the range of interest [Fig. 5(a) and (b)]. It should be noted that the data shown in these figures have not been corrected for σ_o, which is relatively small for 8090.

2.5 Determination of p

To obtain the grain size exponent, p, for a given temperature, it is necessary to obtain logarithmic plots of σ_{eff} versus $\dot{\varepsilon}$, as outlined above, for material with a range of grain sizes. It then follows from Eq. (4) that p can be obtained from plots of log σ_{eff} versus log d for constant $\dot{\varepsilon}$ and T, or log $\dot{\varepsilon}$ versus log d for constant σ_{eff} and T.

2.6 Determination of Activation Energy, Q_s

To determine the activation energy for SP flow, Q_s, the temperature dependence of the relationship between flow stress, σ, and strain rate, $\dot{\varepsilon}$, for a constant microstructure must be determined as described above. To a first approximation
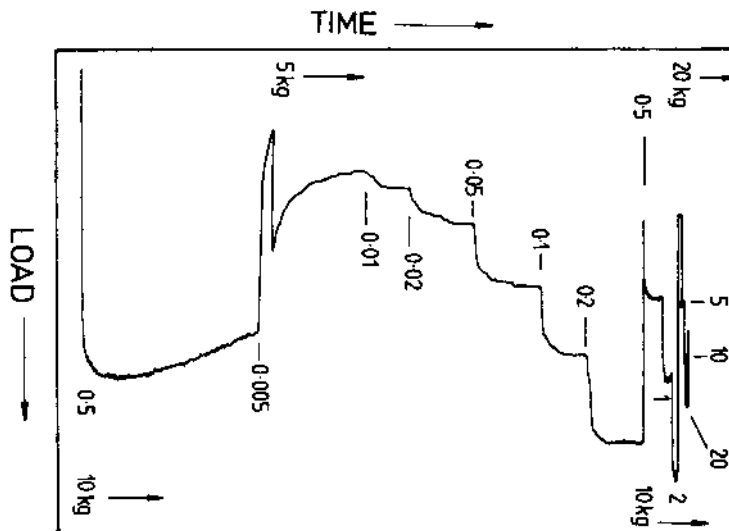
Figure 4   Load versus time record for a repeated velocity jump test on AA8090 at 500°C. Crosshead speed in mm/min is given on graph.
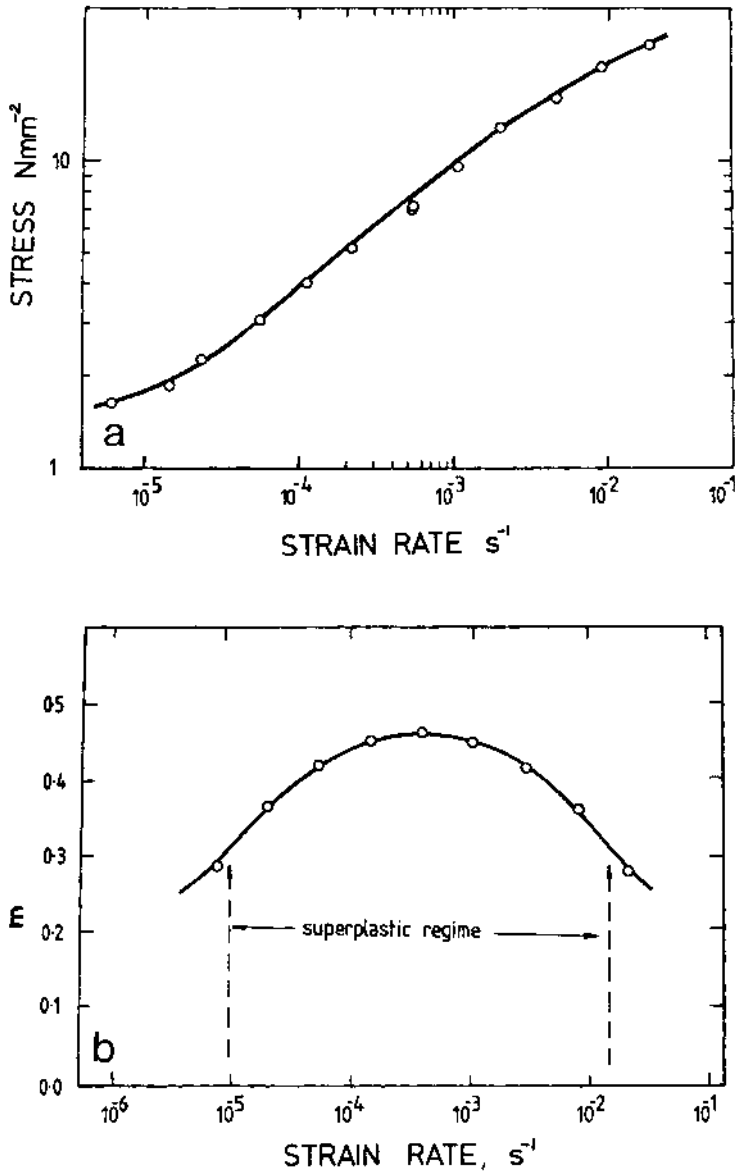
Figure 5 (a) True stress versus true strain rate derived from data in Fig. 4; (b) m versus strain rate calculated from the best fit curve to Fig. 5(a).

Eq. (4) may be written:

$$\dot{\varepsilon} = B \exp\left(-Q_s/RT\right)/kT \cdot \sigma_{\text{eff}}^{1/m} \tag{6}$$

which for a narrow range of temperature gives:

$$\ln(\dot{\varepsilon}) = C + 1/m \ln(\sigma_{\text{eff}}) - Q_s/RT \tag{7}$$

where B and C are material constants. Provided m remains constant over this range of temperatures, then Q_s may be obtained from an Arrhenius plot of ln $\dot{\varepsilon}$ versus reciprocal of absolute temperature at constant stress (slope $= -Q_s/R$). In practice the temperature range used may not be insignificant, m may vary with T at a given stress, and measurements should be made for a modulus compensated stress rather that the actual stress. For these reasons it may be difficult to relate the measured Q_s value to a particular physical process. The significance of constitutive equations in relation to SPF will be considered later.

3   TYPES OF SUPERPLASTIC MATERIALS: ALUMINIUM ALLOYS FOR SPF

For superplastic behavior a material must be capable of being processed into a fine grain equiaxed structure which will remain stable at the forming temperature. It is important also that processing leads to a predominance of high angle boundaries (lattice misorientation $> 15°$), in order that grain boundary sliding and grain rotation, characteristic of superplasticity, can occur. There are two main types of SP alloys: microduplex and pseudo-single phase. The former materials are thermomechanically processed to give a fine grain/phase size and grain growth is limited by having a microstructure containing roughly equal proportions of two or more chemically and structurally different phases. Materials of commercial interest in this group include the α/βTi alloys, particularly Ti-6Al-4V, and to a lesser extent α/γ stainless steels, while Zn-22A1 alloy finds a limited number of non-load bearing applications at ambient temperature. Eutectic alloys based on Al-33Cu, Al-5Ca-5Zn and Pb-Sn, have been processed to develop superplasticity, and along with Zn-22Al, are used as model systems to investigate fundamental aspects of superplastic flow.

Pseudo-single phase alloys, which include the SP aluminum alloys of commercial interest, would normally contain $< 10\%$ by volume of second phase. They are processed to develop a distribution of fine precipitates (dispersoids) so that on recrystallization the alloy will have a fine grain size. This is due to the pinning effect of the dispersoids which will also inhibit grain growth during SPF. The conditions for the pinning of high angle grain boundaries by dispersoids (Zener pinning) [14] is given by:

$$P_g = \frac{3F_v\gamma}{2r} \tag{8}$$

where P_g is the restraining pressure of a group of particles of radius, r, and volume fraction, F_v, and γ is the grain boundary energy. For the boundary to move away from the particles, P_g must be exceeded. The pinning effect of closely spaced, small particles, may also inhibit recrystallization and restrict subgrain growth. It has been proposed for a group of fine particles that Zener pinning will occur when $F_v/r \geq 2$ [15].

While numerous aluminum alloys have been shown to exhibit superplasticity, those of commercial interest are included in Table 1 with typical room temperature mechanical properties and include SUPRAL 100 (AA2004; unclad), SUPRAL 150 (AA2004; clad), AA7475 and AA5083. The alloys can be subdivided into 2

Table 1 Compositions (wt%) and Typical Room Temperature Properties of Superplastic Aluminum Alloys

Alloy	Composition, wt%	Temper	0.2% PS MNm^{-2}	UTS MNm^{-2}	El %	Modulus GPa	Density Mgm^{-3}
2004	Al-6 Cu-0.4 Zr (UNCLAD)	T6	315	420	9	74	2.84
2004	Al-6 Cu-0.4 Zr (UNCLAD)	0	150	250	10	74	2.84
2004	Al-6 Cu-0.4 Zr (CLAD)	T6	290	390	9	74	2.84
2004	Al-6 Cu-0.4 Zr (CLAD)	0	140	230	7	74	2.84
5083	Al-4.5 Mg-0.7 Mn	0	140	290	23	72	2.67
7475	Al-5.7 Zn-2.3 Mg-1.5 Cu-0.2 Cr	T76	500	550	10	70	2.80
8090	Al-2.4 Li-1.2 Cu-0.7 Mg-0.12 Zr	T6	350	460	5	78	2.55
2090	Al-2.3 Li-2.5 Cu-0.12 Zr	T6	340	450	5	79	2.57

groups: those which are recrystallized prior to SPF, and those which develop a super-plastic microstructure during the early stages of hot forming. The former group includes the 7000 series alloys, e.g. AA7475 and AA5083, while the latter includes AA2004. The Al-Li alloys, AA8090/AA2090, are also listed in Table 1 because of their interesting SP properties, even though they are currently not of great commercial interest as will be discussed below. These alloys can be processed by either route to develop superplasticity [16].

The SUPRAL alloys based on Al-Cu-Zr are unique in that they were designed so that they could be readily processed to develop superplastic microstructures, while having useful ambient temperature properties typical of existing medium strength alloys [17,18]. However, because of the resistance to the adoption of new alloys, attention was subsequently turned to existing qualified alloys which were capable of developing SP microstructures by thermomechanical processing, and hence to be shaped by SPF. These included 7000 and 5000 series alloys.

4   PROCESSING OF ALLOYS FOR SPF

The procedures used to develop superplastic microstructures in 7000 series alloys by static recrystallization, using AA7475 as an example, and in AA2004 by dynamic recrystallization, will be outlined. Consideration will also be given to the increasingly important AA5083 and also to Al-Li-based alloys.

4.1   AA7475 (Al-Zn-Mg-Cu-Cr)

Several variants of the processing route exist but they all involve the production of microstructures with mean grain sizes of $10-15\,\mu m$, by rapid heating of heavily warm- or cold-worked material containing a bimodal distribution of precipitates. The most well documented of these is the "Rockwell" route shown schematically in Fig. 6 [5,19]. After initial processing, the material is solution treated at $480°C$ to dissolve all the precipitates except the Cr-rich dispersoids, which are typically $0.1-0.2\,\mu m$ in diameter. The alloy is quenched to retain the solute in solution, and then held at $400°C$ for 8 h to produce an overaged distribution of large M-phase and T-phase precipitates.

On heavy warm working ($\sim 80\%$) at $\sim 200°C$, these particles lead to intense localized deformation and lattice rotation which provide sites for discontinuous recrystallization (i.e. particle stimulated nucleation, PSN)[20]. Rapid heating to $480°C$ results in a large number of recrystallization nuclei in the locally deformed regions adjacent to the coarse precipitates, and thus to the development of a small grain size. At this temperature the large precipitates dissolve, but the small Cr-rich precipitates inhibit grain growth following recrystallization and during subsequent SPF by exerting a drag effect on grain boundaries (Zener pinning). After processing the grains tend to have a "pancake" shape, i.e. the grain dimensions in the transverse and longitudinal directions are equal, but greater than for the short transverse grain direction [5]. However, the material would normally be capable of sustaining large tensile strains, e.g. 500–1000% elongation under optimum deformation conditions ($515°C$; $2 \times 10^{-4}\,sec^{-1}$). This processing route can be applied to 7000 series alloys produced by the ingot route or by powder metallurgy.
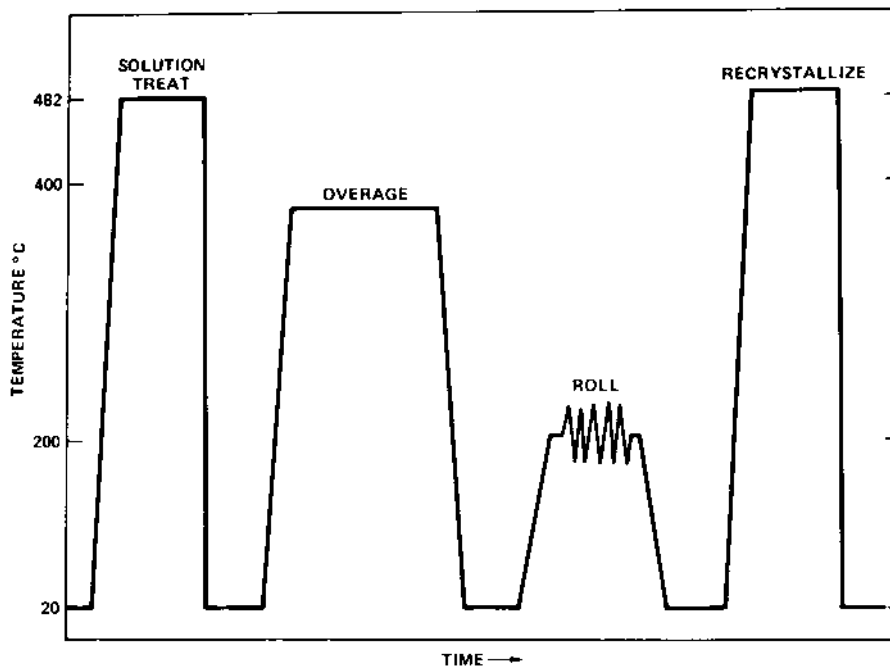
Figure 6 Schematic of processing route to develop fine grain sizes in AA7475.

4.2 AA2004 (Al-Cu-Zr)

The processing route for AA2004 (Al-6 Cu-0.4 Zr) has been described by Watts et al. [17,18]. The alloy is rapidly solidified from a high superheat ($\sim 780°$C) to avoid the formation of coarse primary $ZrAl_3$ precipitates and to retain the Zr in solid solution. Fine $ZrAl_3$ particles (< 10 nm) are precipitated on aging at $360°$C. They have a volume fraction of ~ 0.003 and are homogeneously distributed. The alloy is solution treated at $500°$C and hot rolled to break down the as-cast structure. The material is subsequently heavily warm/cold worked to $\sim 80\%$ reduction, when recovery and recrystallization are prevented by the pinning action of the $ZrAl_3$. The alloy can be formed at $460°$C at a strain rate of $\sim 10^{-3}\ \text{sec}^{-1}$, and is capable of giving very substantial tensile strains to failure, $\sim 1000\%$. To improve corrosion resistance the alloy may be roll-clad with pure aluminum.

During forming, continuous dynamic recrystallization of the heavily dislocated alloy occurs and a fine grain SP microstructure evolves [(Fig. 7(a)]. The mechanism by which this occurs is uncertain, although it has been the subject of much investigation and discussion [21]. One view is that it involves a progressive increase in grain boundary misorientation as a result of sub-grain boundary coalescence and the incorporation of dislocations into the evolving boundaries. An alternative proposal is that if the initial grain size is not too great and the amount of warm/cold work is large then the high angle boundaries may be sufficiently closely spaced for geometrical dynamic recrystallization (GDRX) to occur on subsequent hot (SP) forming [22,23].
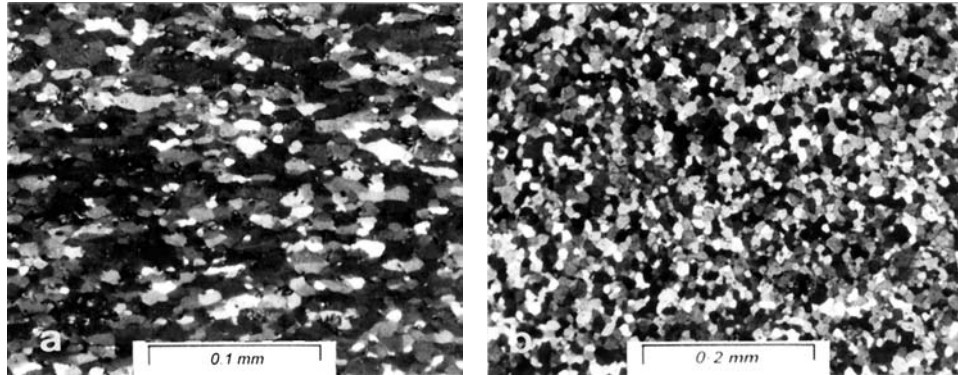
Figure 7 Fine grain SP microstructures developed in (a) AA2004 by dynamic recrystallization; 450°C, $\varepsilon = 1.39$ (300%); and (b) AA5083 by static recrystallization; 520°C.

A schematic of GDRX is seen in Fig. 8. During the initial stages of hot deformation, dynamic recovery results in the formation of sub-boundaries and the serration of the original grain boundaries. As the reduction in cross-section increases with further straining, the impingement of serrations gives rise to small equiaxed grains and hence, to favorable conditions for grain boundary sliding and grain rotation.

4.3 AA5083 (Al-Mg-Mn)

AA5083 is essentially a non-heat treatable alloy which contains 4–4.9 wt% Mg and 0.4–1.0 wt% Mn. A typical composition would be Al-4.7 Mg-0.8 Mn-0.1 Cr, with residual levels of Fe and Si. It is a relatively inexpensive alloy with medium strength, excellent cold forming, welding and spot welding behavior, and good corrosion resistance. The alloy can be processed to give a moderate degree of superplasticity. This attractive combination of characteristics has led to its increasing use for the SPF of a range of parts for non-structural applications which do not involve substantial forming strains.
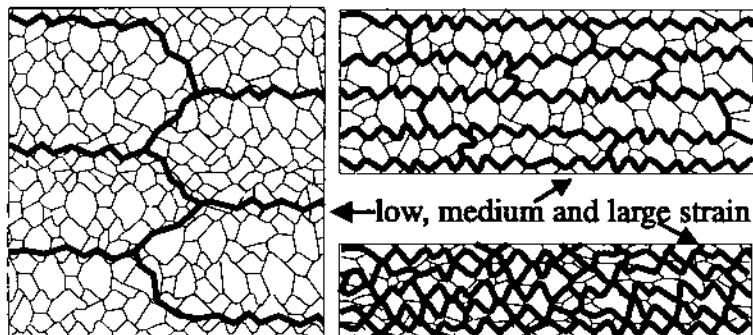
Figure 8 Schematic illustration of GDRX.

After casting and thermomechanically processing to sheet the alloy contains two types of particles: constitutive particles of size 1–5 m which typically contain Al, Mn, Fe and Si, and Al_6Mn particles of size 0.2–0.8 μm, with a mean size near the lower end of the range. Following heavy cold work (70–80% reduction), the larger particles act as nuclei for recrystallization, although at lower temperatures nucleation at shear bands has been reported, while the smaller Al_6Mn precipitates pin grain boundaries and stabilize a small grain size [24]. The cold worked material statically recrystallizes very rapidly at temperatures of 350–570°C to give a grain size of 10–15 μm [Fig. 7(b)]. For SP deformation at 525°C at a strain rate of 10^{-4} sec^{-1}, tensile elongations of about 600% may be obtained, while elongations of 300–350% are observed for grain sizes of about 10 μm, at the commercially more attractive forming rate of 10^{-3} sec^{-1} (when $m \sim 0.5$) [25].

AA5083 is now the dominant alloy used for the production of non-structural parts by SPF and, as a consequence, numerous attempts are being made to improve its SP formability. Matsuo [26] has shown for the basic 5083 alloy (coded ALNOVI-1) that reducing the levels of Fe and Si leads to a reduction in the number and size of constitutive particles at grain boundaries, and to lower levels of cavitation and higher tensile strains during SP deformation

Matsuo also noted that AA5083 showed significant strain hardening during SP flow, which increased with increasing strain rate and reduced deformation temperature. These observations were not consistent with grain growth hardening, and were attributed to the simultaneous occurrence of slip and grain boundary sliding. While SP deformation is usually assumed to involve a unique mechanism consisting of accommodated grain boundary sliding, there is strong evidence for this material that strain is also accumulated by intragranular dislocation creep which occurs independently of grain boundary sliding [27]. The dislocation creep leads to significant grain elongation in the straining direction.

4.4 Al-Li-based Alloys

Although the history of Al-Li-based alloys goes back some 70 years, the sharp increase in fuel prices in the late 1970s led to a dramatic growth of interest in these materials for aerospace applications [16,28]. Most Li-bearing alloys were developed to substitute for established airframe alloys of the 2000 and 7000 series, with an expected reduction of density of about 10% and a stiffness increase of at least 10% while matching the service properties of existing alloys (Table 1). Considerable efforts were devoted to the investigation of a wide range of alloy combinations by major aluminum companies, aerospace constructors, universities and research institutions. These materials were the exclusive subject of 6 major international conferences held between 1981 and 1991.

It was shown that several alloys produced by ingot or powder routes could be processed to develop excellent SP formability and numerous studies were made of their potential for diffusion bonding. Fine grain microstructures were produced by processes which involved static recrystallization prior to SPF, or dynamic recrystallization in the early stages of deformation [16,28]. For AA8090 (Lital A) sheet material processed by the SUPRAL route, tensile elongations > 1000%

have been reported for temperatures of 520–530°C and a strain rate of $\sim 5 \times 10^{-4}\text{sec}^{-1}$. Optimization of the strain rate path can lead to further enhancement of SP strain to failure [29].

An interesting feature of alloys such as 8090 (and SUPRAL), when processed to develop fine grain microstructures by dynamic recrystallization, is that they show a high resistance to necking in the early stages of deformation before superplasticity has developed. Measurement of m, and the strain hardening exponent, N, has shown that while m is low initially, < 0.3, it rises with strain, and while N is high at the start it decreases [30] (Fig. 9). Thus the stability of the material is initially dependent on strain hardening for its necking resistance. A relationship appropriate to this behavior would be:

$$\sigma = k'' \dot{\varepsilon}^m \varepsilon^N \qquad (9)$$

As the value of N falls, $\varepsilon^N \rightarrow 1$ when $\sigma = k\dot{\varepsilon}^m$ [Eq. (1)].

In 1982 Superform Aluminium exhibited a superplastically formed component in Lital A at the Farnborough International Air Show. By 1986 demonstrator parts made from AA8090, including parts produced by SPF, had been introduced into prototype models of military aircraft being test flown in the USA and Europe. In the late 1980s it was predicted by the Boeing Company that Al-Li based alloys would make up 7% and 10% of the structural weights of civil and military aircraft, respectively, by 1990, rising to 35% and 25%, respectively by 1995 [31].

Despite these optimistic forecasts, the development of Al-Li alloys had slowed dramatically by the early 1990s because of their slow take-up by the aerospace companies. The main reasons for this were the high costs of the alloys, and the high projected costs, combined with some concern about mechanical properties, with the result that these interesting materials at present find relatively few commercial applications.
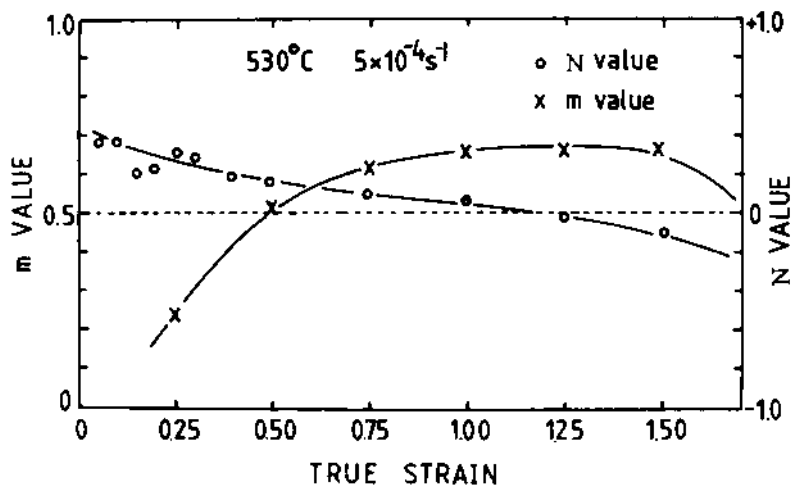
Figure 9 Variation of m and strain hardening exponent, N, with strain at 520°C, AA8090.

5 CAVITATION AND FAILURE OF SUPERPLASTIC ALLOYS

5.1 Failure of Superplastic Alloys

When a superplastic material fails during tensile flow it is either the result of unstable plastic flow or a consequence of the growth and interlinkage of internally nucleated cavities. In the former process, inhomogeneities in the cross-sectional area of a test piece lead to a localized increase in strain rate and the difference in cross-sectional area increases at a rate which depends on the extent of work hardening and the value of m [32]. In SP materials, where true strain hardening is usually minimal (but not always), any neck which is present will always grow, although the rate of growth decreases with increasing m. Unstable plastic flow normally results in the material pulling down to a fine point at failure.

On the other hand, when failure occurs as a result of the nucleation, growth, coalescence and transverse interlinkage, of internal cavities the fracture surface is much more abrupt. The value of m is important in determining the rate at which cavities grow and thus to some extent controls the strain to failure, which can be substantial, in systems which exhibit cavitation. Such systems include Al alloys. In general, the higher the m value, the greater the elongation to failure, as seen in the well known Woodford plot, although the scatter shown by the data can be considerable (Fig. 10) [33]. This is due to factors such as cavitation, and to microstructural evolution during SP flow causing significant changes to the m value. Even so, m is a first order effect.

5.2 Cavitation

Not all SP alloys pull to a fine point at failure. Two different modes of failure seen in tensile test pieces are shown in Fig. 11. Both specimens have the same strain at failure, but the flat fracture surface of the lower specimen, termed pseudo-brittle, arises from tearing of tiny ligaments between regions of internal cavitation. In
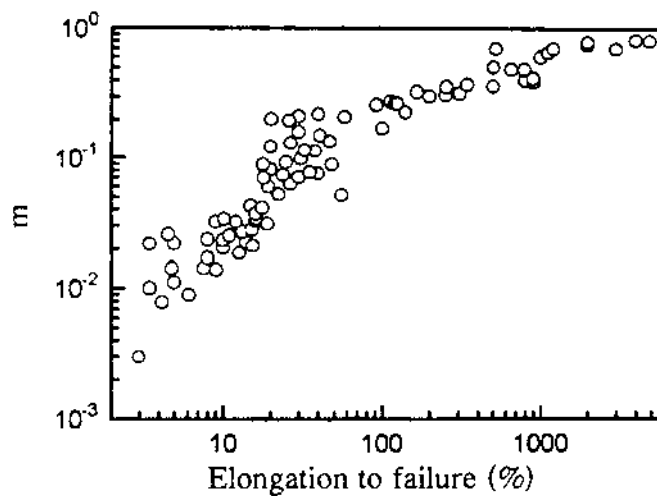
Figure 10 Elongation to failure versus m for a range of alloys (after Woodford).
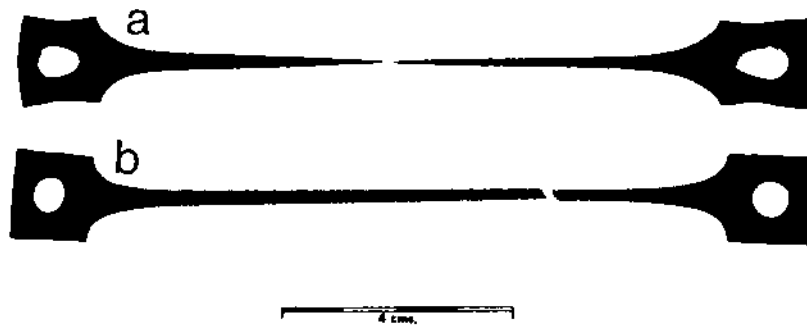
Figure 11 Shadowgraphs of fracture in two SP alloys at 900% elongation showing (a) unstable plastic flow in Ti-6A1-4V alloy; (b) pseudo-brittle fracture in AA2004.

addition to its effect on fracture behavior, cavitation may also have an adverse effect on the mechanical properties of commercially formed parts. All Al alloys are prone to cavitation during SP flow. It can be seen from Fig. 12 for AA2004 that the level of cavitation can be substantial, although the highest strain illustrated is well in excess of that used for SPF [34]. There is a substantial interest in cavitation and reviews of the subject have been given [35,36]. Consideration will be given to some aspects of cavity nucleation, cavity growth and coalescence, during deformation and to procedures for controlling cavitation.

5.2.1 Cavity Nucleation

For most SP materials, it is widely accepted that strain is accumulated primarily by grain boundary sliding. However, the relative displacements of boundaries need to be accompanied by a redistribution of matter and this may be achieved by diffusion or dislocation processes. When the accommodation processes fail to meet the requirements imposed by the deformation rate, then the stress concentrations which develop at various grain boundary features are not relaxed sufficiently quickly and cavities may nucleate.

Metallographic observations suggest that in Al alloys cavities are most likely to develop at grain boundary particles [37]. Relationships have been developed for the critical strain below which cavity nucleation at a grain boundary particle is likely to be inhibited by diffusive stress relaxation. These predict that to minimize cavity nucleation both grain and particle sizes should be small, and that SPF should be carried out at as high a temperature (high diffusivity) or as slow a strain rate as possible, commensurate with microstuctural stability and sensible commercial practice [38].

Factors which influence cavity nucleation include those which relate to microstructure such as grain size, the type, size, volume fraction, interfacial energy and distribution of second phase particles, and those associated with deformation conditions such as strain, strain rate, temperature and stress state. The role of grain size on cavity nucleation has been clearly demonstrated for Al alloys [7]. The higher flow stress associated with the larger grain size reduces the critical size of a cavity which constitutes a nucleus, making nucleation easier. In addition to nucleation at grain boundary particles, the observation of intersecting rows of cavities in 7475
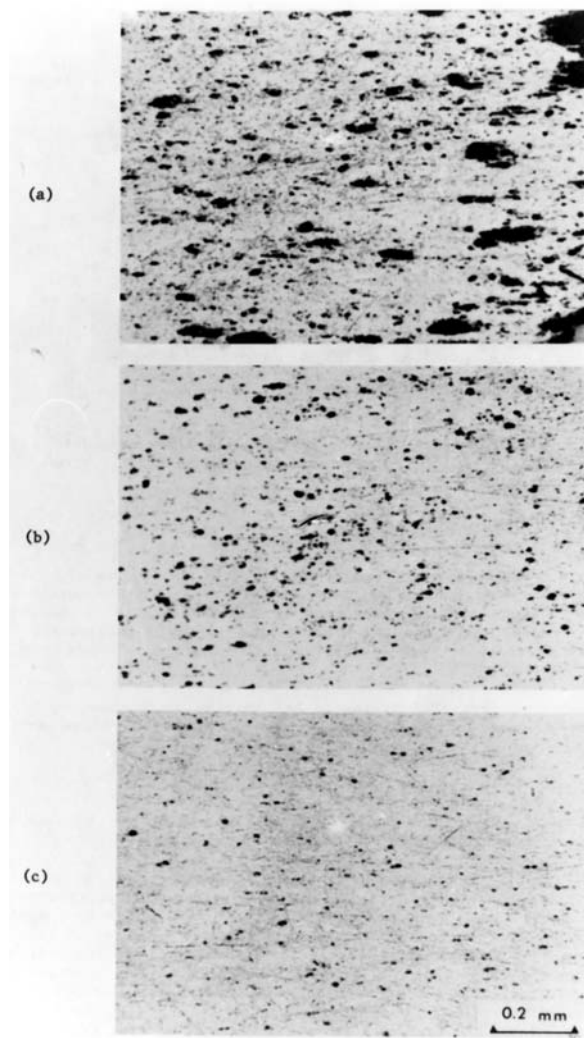
Figure 12 Effect of increasing SP strain on cavitation in AA2004, (a) 2.26 (860%); (b) 1.31 (270%); (c) 0.69 (100%). (From Ref. 34.)

Al alloy deformed by biaxial bulging and in uniaxial tension have been attributed to cavity nucleation at intersecting surfaces of grain boundary sliding. However, it is not clear how general a phenomenon this might be in SP materials [39].

5.2.2 Growth of Cavities

A cavity located at a grain boundary, whether nucleated or pre-existing, may grow during SP deformation by diffusion processes and/or plastic deformation of the surrounding matrix. Relationships have been developed which describe the change of cavity radius and the change of cavity volume with strain, for different growth mechanisms [35,36]. These relationships have been tested experimentally using

metallography and or precision density measurements and it has been shown that while diffusion may be important in the early stages of cavity growth, strain controlled growth is dominant for cavity radii above about $1\,\mu$m.

For strain control, the rate of cavity growth increases linearly with cavity size and is independent of strain rate within the SP regime [40]. This leads to the relationship:

$$C_v = C_o \exp(\eta\varepsilon) \tag{10}$$

where C_v is the volume fraction of voids at strain ε, and C_o is a constant; η is the cavity growth rate parameter and is given by the expression:

$$\eta = \frac{3}{2}\left(\frac{m+1}{m}\right)\sin h\left(2\left(\frac{2-m}{2+m}\right)\right)\left(\frac{K}{3} - \frac{P}{\sigma_e}\right) \tag{11}$$

and

$$\left(\frac{K}{3} - \frac{P}{\sigma_e}\right) = \frac{\sigma_m}{\sigma_e} \tag{12}$$

where K is a constant whose value depends on the deformation geometry and the extent of grain boundary sliding, P is the imposed pressure, σ_m the mean stress and σ_e is equal to the uniaxial flow stress. Plasticity dominated growth is controlled by the mean stress whereas it is the principal stress which is important in diffusive growth. If 50% of SP strain is attributed to grain boundary sliding, then it can be shown that $K = 1.5$ and 2.25 for uniaxial and biaxial straining, respectively, and 2.7 for plane strain [7,41].

It can be seen from Eqs. (10–12), that the application of an imposed pressure will reduce η, the cavity growth rate parameter, and hence the level of cavitation for a given strain. For the same strain, cavitation will be higher for biaxial and plane strain deformation than for uniaxial flow. This is an important prediction since most studies of cavitation are made for uniaxial deformation, whereas SPF processes will involve biaxial and plane strain stress states which will be more damaging in terms of cavitation than a uniaxial tensile stress. Figure 13 shows the effect of back pressure on cavitation for AA7475 deformed in equi-biaxial tension to different strains [42], while Fig. 14 shows the beneficial effect of imposed pressure on the level of cavitation seen in the microstructure of AA2004 deformed to a strain of 1.7 (450%) [41].

5.2.3 Cavity Coalescence

It has been noted that once plasticity controlled growth has become dominant, the predicted size to which cavities grow may be significantly less than is observed experimentally [43]. These differences are attributed to cavity coalescence for which there is much metallographic evidence [Fig. 12(a) and (b)]. Large elongated cavities lying parallel to the rolling direction, which may be observed, are almost certainly the result of the coalescence of cavities nucleated on closely spaced inclusions. These cavities are likely to be particularly damaging in their effect on post-forming pro-
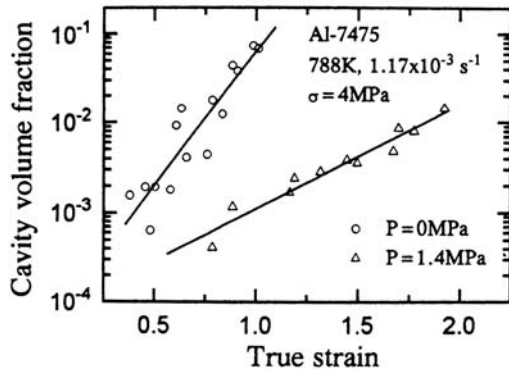
Figure 13   Effect of imposed pressure on cavitation in 7475 Al alloy. Biaxial.
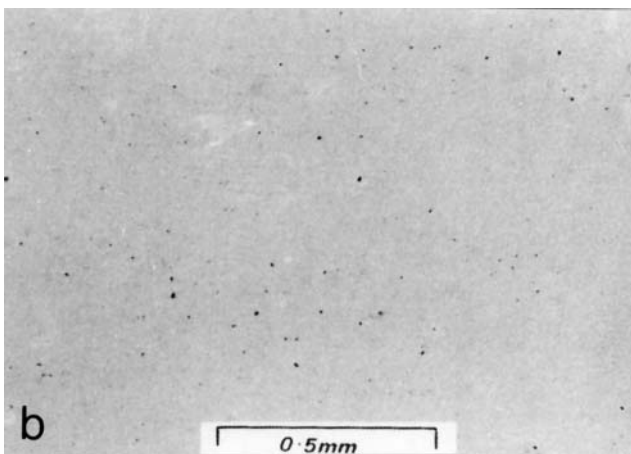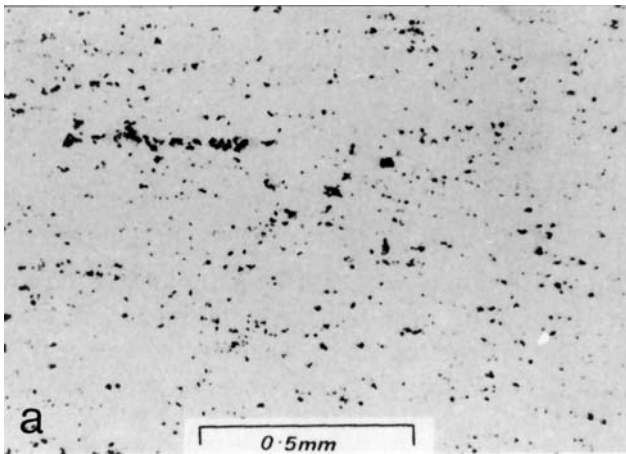
Figure 14   Effect of imposed pressure on the level of cavitation seen in the microstructure of AA2004 deformed to a strain of 1.7 (450%), (a) 0.1 MPa; (b) 4.75 MPa.

perties. Some cavities which develop in Al alloys may be associated with outgassing of hydrogen. This leads to fine localized porosity which provides pre-existing sites for cavity growth.

5.2.4 Control of Cavitation

To minimize cavitation in Al alloys during SPF, the first requirement is to have a material with a stable fine uniform grain size comprised predominantly of high angle grain boundaries. Dispersoids should be small and uniformly dispersed. It is, therefore, essential that there is sound control of the processing required to produce the SP microstructure. An important requirement for cavitation is the presence of a local tensile stress. Under conditions of homogeneous compression cavitation is not observed and cavities which have been produced by SP tensile flow are removed by subsequent compressive flow.

Cavitation can be controlled by various procedures including annealing and/or the application of hydrostatic pressure either prior to, during, or after SPF [44]. Annealing before deformation can lead to sintering of pre-existing cavities by vacancy diffusion, and if a hydrostatic pressure is also applied this will accelerate cavity closure. Annealing can also lead to hydrogen outgassing and can be particularly effective if carried out in a vacuum. However, consideration must be given to detrimental effects of grain growth and solute loss by volatilization.

The most effective and practical way of controlling cavitation is to superimpose a hydrostatic pressure during SPF. Work carried out on Al alloys deformed in uniaxial and balanced biaxial tension, and plane strain has shown that increasing imposed pressure:

(i) decreases the rate at which the volume of cavities increases with increasing strain (Fig. 13),
(ii) decreases the level of cavitation for a given strain (Fig. 13),
(iii) displaces to a higher level the strain at which cavities are first detected, and
(iv) increases to a limiting value the strain to failure (Fig. 13).

Since cavity growth is plasticity dominated then it can be seen from Eqs. (11) and (12) that to prevent cavity growth during SPF it is necessary for the imposed pressure, $P > K\sigma_e/3$ (or $\sigma_m/\sigma_e < 0$), i.e. $P > 0.5\sigma_e$ for uniaxial deformation (although $P > \sigma_e/3$ is also quoted in the literature), $P > 0.75\sigma_e$ for equibiaxial straining and $P > 0.9\sigma_e$ for plane strain deformation. These predictions are broadly in accord with observation. It can be seen from Eq. (12) that the ratio P/σ_e is important in determining the level of cavitation. In commercial forming, it is unlikely that P would exceed ~ 4 MPa (600 psi) for technical reasons, so that the value of σ_e (dependent on grain size and strain rate for a given SPF temperature) should not be too high if cavitation is to be prevented. However, even if the criterion $P > K_e/3$ is not met, any level of imposed pressure is likely to be beneficial in its effect on cavitation, as is seen in Fig. 13.

Other methods which have been proposed include annealing after SPF. This can be effective in removing small cavities, but the larger cavities which have the most deleterious effect on properties are little effected. Post-forming HIPping also has the potential to remove cavities but is likely to be limited in application because of cost and its restriction on component size. It has also been noted for an Al alloy that some cavities may reappear on subsequent heat treatment, probably

due to the presence of hydrogen. Conrad and co-workers have reported that the application of an external electric field during SPF reduced the level of cavitation for 7475 alloy, and so improved its post-forming properties [45].

6   SUPERPLASTIC FORMING OF AL ALLOY SHEET MATERIALS

6.1   Bulge Forming of a Dome

Prior to discussion of various forming procedures, important features of SP sheet forming can be illustrated by considering the bulge forming of a dome, a procedure which is frequently involved in the early stages of commercial SPF. To form the sheet, the periphery of a heated blank is rigidly clamped to provide a gas tight seal. On application of gas pressure to cause the material to stretch into the die cavity, the constraint provided by the clamped edge results in a stress system which varies across the sheet. For a circular blank, plane strain conditions exist in regions adjacent to the clamped edge while an equibiaxial strain state occurs at the pole. The differential stress system leads to thickness strains across the sheet with maximum thinning occurring at the pole. Although a thickness variation would occur if $m = 1$, 1, the differential thinning is smallest for alloys possessing the highest m value, and increases with increasing dome height. Predictions of thickness variation in a free blown hemisphere for a range of m values, taken from the early work of Cornfield and Johnson [46], are shown in Fig. 15.

6.2   Simple Female Forming

This simple forming procedure involves the use of gas pressure to blow a sheet which is rigidly clamped around its periphery into a female die, as illustrated in Fig. 16(a). During forming both the sheet and the die are maintained at the optimum forming temperature and the rate of application of pressure is such that the strain rates induced in the sheet are maintained in the SP range. The first stage of the process involves free stretch forming, leading to thickness variations as described above. Once the pole of the bulged sheet contacts the die surface it is locked against
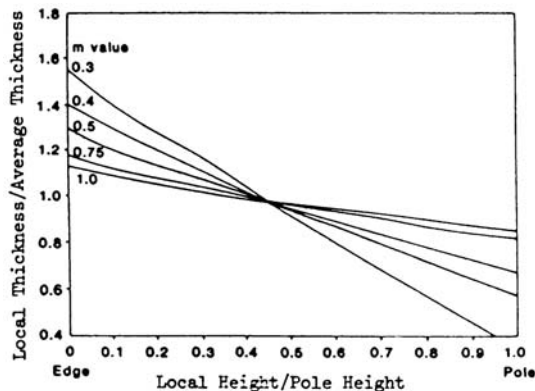
Figure 15   Predicted variation in thickness in a free blown hemisphere for different m values. (From Ref. 46.)
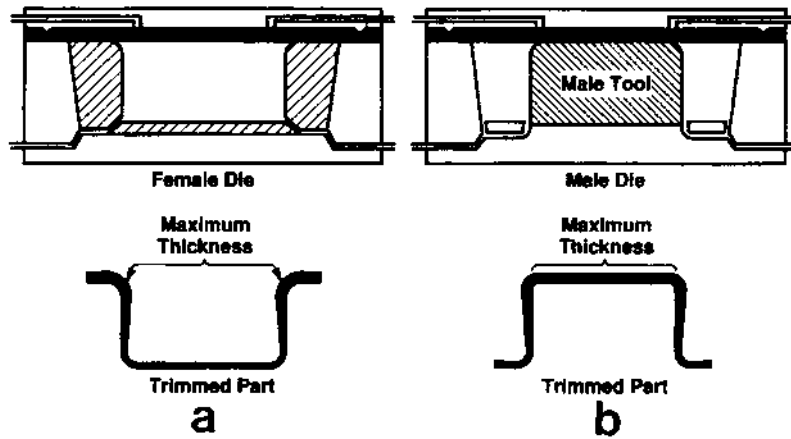
Figure 16 Illustration of (a) simple female forming; (b) drape forming. (From Ref. 47.)

the tool by friction and forming pressure, and this inhibits further thinning in this region. Continuing deformation leads to progressively more of the unsupported regions making contact with the die. Since the corners of the die are the last to fill, the greatest strain occurs in these regions as seen in Fig. 16(a).

Simple female forming is preferred when the height to diameter ratio is low and the corner radii are large, and when the *m* values are towards the lower end of the useful range. In this way, wide variations in material thickness can be avoided. Stiffening features such as deep pockets or grooves can also be incorporated into the design of the part.

6.3 Drape Forming

This process consists of bulge forming a sheet into a female die in which one or more male tools are located [Fig. 16(b)] [47] When gas pressure is applied, the polar region of the bulging sheet will make early contact with the male tool. Continued application of pressure will drape the sheet over the male tool as it bulges into the female annular regions. The process can yield a more uniform material thickness particularly if the height of the annular space is small with respect to the dimensions of the blank.

The choice of either female forming or drape forming could be influenced by whether the internal or external dimensions of the part were the most critical. As seen in Fig. 16, if the outside shape is specified as the critical dimension, then female forming will be used. When the inside shape is critical, then drape forming will be used. If a number of male tools are placed within the female forming tool several similar parts, or different parts of a given component, can be produced at the same time.

6.4 Back-Pressure Forming

Aluminum alloys are susceptible to cavitation during SPF and in high strength alloys such as AA7475 for important structural components it is essential that the number,

size and/or volume fraction, of cavities be held below critical levels to avoid degradation of service properties. Fortunately, cavitation can be controlled by the application of back pressure during forming, as was discussed previously. In back-pressure forming both sides of the sheet are pressurized, as shown schematically in Fig. 17. This produces a hydrostatic pressure capable of suppressing cavitation. Gas control creates a positive pressure differential enabling forming to be carried out. Back pressure can be applied to both female and drape forming to keep cavitation to a minimal level.

The total die separating force in back pressure forming can be quite considerable. For example, if 1 MPa (~ 144 psi) is required to form 7475 sheet at 2×10^{-4} sec^{-1} and 515°C, into a part with sharp final detail, then back pressure of 4 MPa might be needed to suppress cavitation. If the projected size of the die is 1 m $\times$ 1 m then it can be readily calculated that the clamping force must be 7.8 GPa (560 tons US). The capacity of the press must be sufficient to contain this separating force and provide sealing round the periphery of the die.

6.5 Male Forming (Bubble Forming)

This involves the combined use of gas pressure and tool movement to enable deeper parts of more uniform thickness to be made. Male forming is carried out on presses designed by the Superform companies and the stages in the process are illustrated in Fig. 18 [1]. Male forming is applied mainly to 2004 and 5083 alloys and is a commonly used forming technique.

In the technique illustrated, the sheet to be formed is first blown into a bubble away from the sheet. The tool is then moved into the bubble and the pressure is reversed forcing the bubble to collapse onto the plug. A combination of friction and forming pressure lock the sheet in contact with the tool and effectively prevent any further deformation. As the tool continues to move, deformation switches
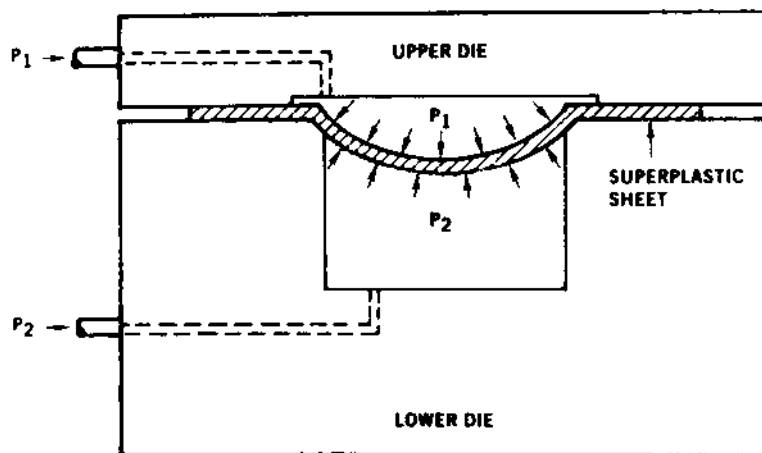
Figure 17   Illustration of back-pressure forming during SPF. (From Ref. 47.)
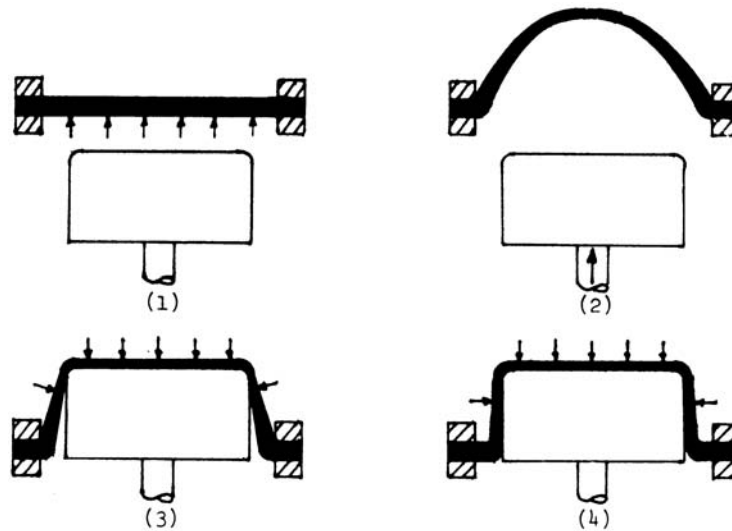
Figure 18 Male forming (schematic). (From Ref. 1.)

to the relatively underformed material adjacent to the flange (Fig. 18). Parts with a depth to width ratio of 0.7 or more, with a relatively uniform wall thickness, can be formed in this way.

Other forming procedures which can be carried out include reverse billowing, in which a sheet is bulged away from a female die to a predetermined height, and the pressure is reversed to blow the sheet into the die to produce the required shape. This procedure increases the thickness at the corners at the expense of greater thinning at the pole (base). Barnes [48] has pointed out that, if the various forming procedures outlined are available, the choice of which forming method to use to produce a component for a specific application is a complex one.

6.6 Diaphragm Forming

Diaphragm or membrane forming uses a rigidly clamped sheet of SP alloy to deform an unclamped smaller sheet into a die (Fig. 19) [47]. The SP diaphragm deforms by stretching, while the smaller sheet is free to slide down the die and is drawn into shape by the membrane until it conforms exactly with the die. The drawing action
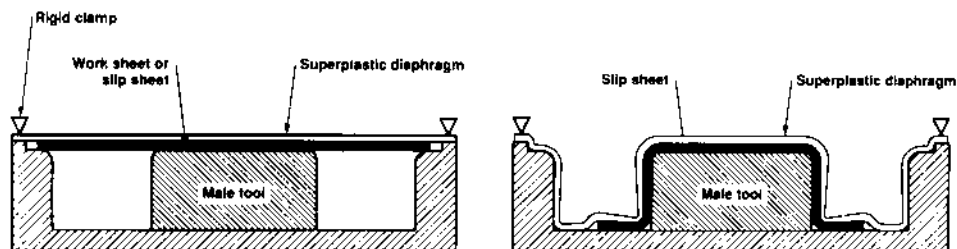
Figure 19 Schematic of diaphragm forming. (From Ref. 47.)

in the part being shaped causes much less thinning than would occur by SP stretching. The process can shape non-SP alloys having limited room temperature formability, provided the material has adequate ductility at the forming temperature. Superplastic alloys can be also be shaped in this way when limited thickness variations are required.

The membrane must be SP at the forming temperature and should have a low flow stress so that it carries the sheet being formed into all of the die corners. It should have low initial cost and should have adequate stretchability over a wide range of strain rates. Providing the membrane does not burst there is no need to use low forming rates. The strain in the formed part is low, 0.1–0.2. In addition to the benefits associated with low thinning, diaphragm forming avoids the expense of using back pressure to prevent cavitation associated with SPF. Properties of 7000 alloys which have been membrane formed have been shown to be comparable with those produced by SPF using back pressure [49].

6.7 Forming Equipment

The two main types of sheet forming equipment include the presses developed by Superform, which are currently used to form alloys 5083 and 2004, and the platen type presses used in the SPF of 7475 and 8090, which would include back pressure facilities. The generalized configuration of a Superform pressure chamber set up for male forming is seen in Fig. 20 and this would be located in a hydraulic press framework [1]. The configuration could be changed so that simple female forming or drape forming could be carried out. Important characteristics of the equipment include: the ability to control pressure either side of the sheet, controlled tool
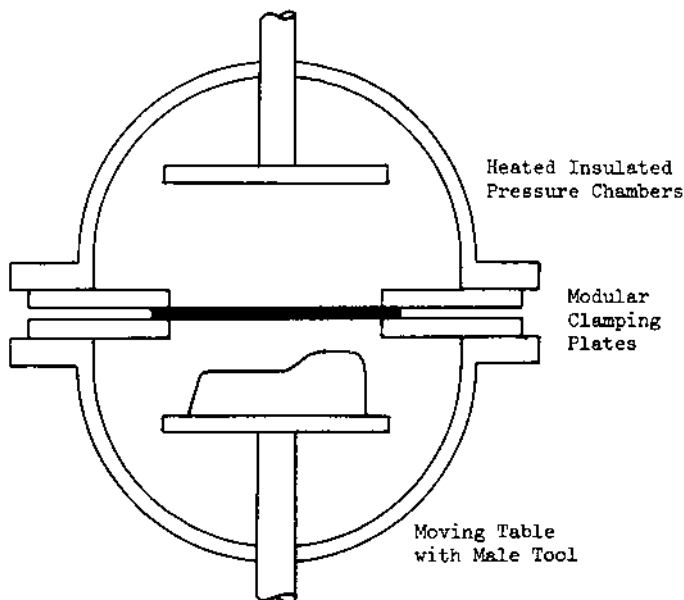
Figure 20   Configuration of a Superform pressure chamber set up for male forming. (From Ref. 1.)

movement, accommodation of blanks of different sizes, ability to sense bubble height, heating elements within the chambers, pressure chambers that can be moved rapidly with respect to each other by the hydraulic system which also provides the clamping force.

For female and drape forming, particularly of 7475 with back pressure, and diaphragm forming, the tooling package is located between the platens of a hydraulic press (or a mechanical clamping system) (Fig. 21). As above, the main function of the press is to keep the dies closed during forming by applying a clamping pressure, although the hydraulic system can also perform other functions. Hydraulic presses can be rapidly loaded and unloaded, but they represent a significant capital investment. The main features of a 4-column hydraulic press are seen in Fig. 22, while both the design and manufacture of presses for SPF have been described by Whittingham [50].

Heating of the tools can be achieved by conduction from heated platens, which may be metal or ceramic, or by the use of cartridge resistance heaters inserted into holes drilled in the tooling chamber. Care is taken to minimize thermal gradients during SPF as these can lead to excessive thinning or failure. A microprocessor controls all functions of the press including platen and tool temperatures, press movements, gas management systems and control of the forming pressure-time cycle.

For either type of press, machined Al alloy tools can be used for the forming of low strength alloys, whereas ferrous alloy tools, machined or cast, perform well with higher strength alloys. Forming gases can be air, nitrogen or argon. The choice is product dependent, with air being cheapest but most reactive, while argon would be preferred but has cost and safety implications. The tool/blank face is lubricated with graphite or boron nitride. Graphite is easiest to use and least expensive but can cause post-forming surface corrosion problems if not completely removed. Boron nitride is non-reactive, expensive, and must be carefully applied and monitored in order to avoid build up on the tool. The method of trimming of parts formed
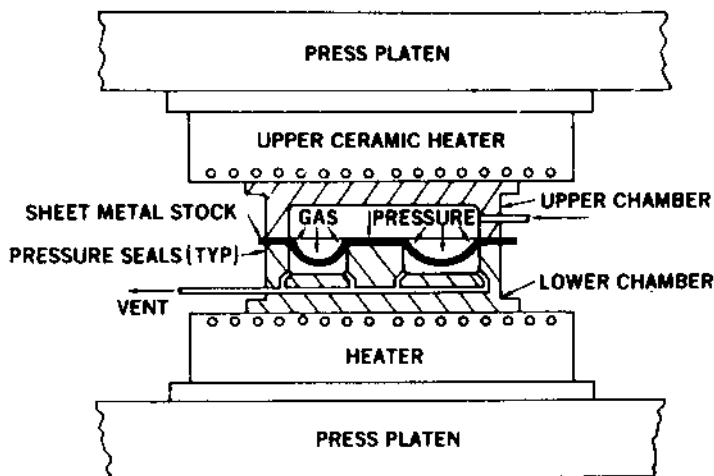
Figure 21 SPF Tooling package for SPF. (From Ref. 47.)
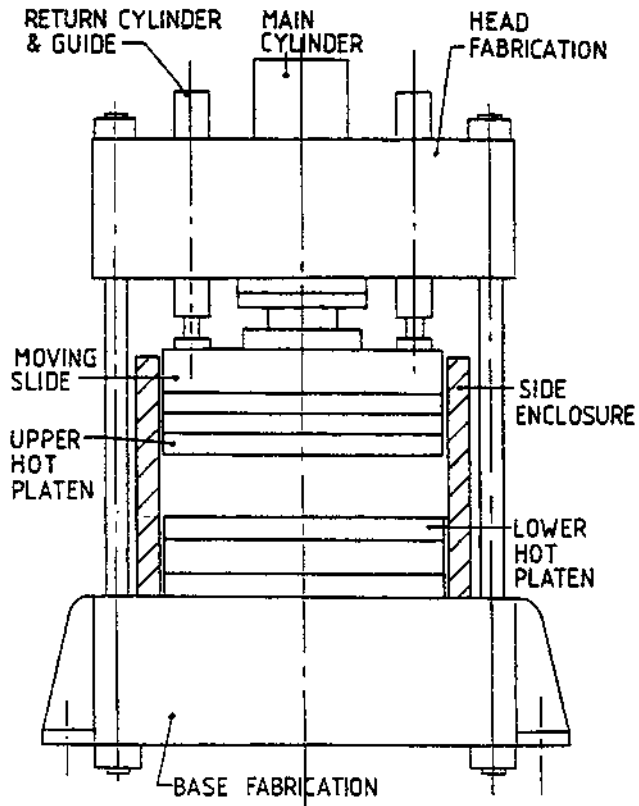
Figure 22 Main features of a 4-column hydraulic press. (From Ref. 50.)

by SPF depends on quantity and the quality requirement. For smaller quantities items may be hand trimmed, whereas larger numbers may be mechanically, laser or water jet, cut by numerically controlled machines.

6.8 Simulation and Control of SPF

SP sheet forming processes have usually been designed on a trial and error basis coupled with considerable experience and some simple calculations. However, if maximum benefit is to be gained from SPF then some form of numerical simulation of the process is desirable. A number of numerical analyses have been developed but the finite element (FE) method has emerged as the most potent technique for SPF.

Wood and Bonet [51] have reviewed the numerical analysis of SPF. It was pointed out that non-FE analyses are usually confined to two special cases involving bulge-forming of a circular sheet and plane strain forming of long rectangular box sections. In the majority of cases the simple constitutive equation: $\sigma = k\dot{\varepsilon}^m$ is used. These techniques are valuable as they enable insight to be gained into SPF processes as a result of changing process parameters. They are computationally inexpensive and in many cases are entirely appropriate for practical purposes.

The use of FE analysis to simulate SPF is a relatively complex topic and will only be considered in outline. However, to be successful FE analysis requires an accurate constitutive equation. Kannan et al. [52] in their investigation of SP ductility in an Al-Mg-Mn alloy used a constitutive equation based on the relationship proposed by Ashby and Verrall [53], which includes a transition from SP flow to power law creep, as well as a threshold stress. The form of the equation is:

$$\dot{\varepsilon} = \left(\frac{K_{II}\,(\sigma - \sigma_o)\exp(-Q_s/RT)}{d^p} + K_{III}\,\sigma^{n'}\,(\exp - Q_c/RT) \right) \tag{13}$$

The first part of this expression is essentially identical to Eq. (4) and procedures for determining σ_0, m $(=1/n)$, Q_s and p, have been outlined; Q_s and Q_c are the activation energies for SP flow and creep, respectively; n' is the stress exponent for creep, and K_{II} and K_{III} are constants. By a combination of constant strain rate tensile tests, as described previously, and least squares fitting the constitutive model parameters for Eq. (13) can be determined.

It is well established that microstructural evolution occurs during SPF and the value of d in Eq. (13) will change. This affects only the first term and not the creep term. By incorporating microstructural evolution, the material flow properties should be more representative of local mechanical conditions, and provide for the variation of strain, strain rate and microstructure, throughout the material which can effect strain localization. The grain size, d, at any strain, (or time for constant $\dot{\varepsilon}$) is given by:

$$d = d_0 + \int_0^t \dot{d}\, dt \tag{14}$$

where

$$\dot{d} = \frac{D}{qd^{q-1}} + \lambda\dot{\varepsilon} \tag{15}$$

The first term in Eq. (15) represents static grain growth rate and the second represents the rate of dynamic enhanced grain growth. These are considered to be separate mechanisms. D, q and λ are empirical constants that can be determined by least squares fit of experimental data, and $\dot{d}$ is the overall rate of grain growth. Equation (14) can be incorporated into Eq. (13) to give a relationship which accounts for the grain growth processes.

Once the constitutive equations have been established they can be introduced into a FE simulation package that essentially solves the quasi-static equilibrium equations in order to determine, as forming progresses, the variation of the shape of the part with time, the stress and the strain rate, and the evolution of grain size. The FE simulation can also predict the final thickness distribution in the formed part and the pressure-time forming cycle. It is also possible to introduce into the FE simulation, factors such as friction and cavitation which can affect the thickness distribution. The advantage of FE simulation is that it can enable many numerical

''experiments'' to be carried out before a real production run. For complex components involving chemi-etched blanks that need to form into specific locations, the simulations can substantially reduce the cost of trial runs.

7   SOME APPLICATIONS OF PARTS/COMPONENTS PRODUCED BY SPF

The present section will deal with products produced by the SPF of sheet material although there is some interest in the SP bulk forging of Al alloys and composites. Much of the success of the SPF of Al alloy sheet is the result of the pioneering and innovative work undertaken by Superform Aluminium, which started production in Worcester, UK, in 1974, and Superform USA opened later at Riverside, California. The Superform plants produce many thousands of parts per annum from the Al alloys 5083, 2004, 7475 and 8090, with other alloys being shaped by diaphragm forming [48]. The bulk of manufacture is from AA5083 and AA2004, with most parts being produced from the former material.

Many aerospace companies in the USA, Europe, Russia and China, have dedicated forming equipment, particularly for the production of parts in AA7475 (and Ti-6A1-4V alloy), while various subcontractors also have SPF manufacturing facilities. Aluminum alloy components produced by SPF are found in civil and military aircraft, helicopters, unmanned reconnaissance vehicles, air weaponry and space craft. The SP alloys 7475, 8090, 2004 clad and unclad, and 5083 are used to produce a wide range of parts, while the non-SP alloys 2014 and 2024 (Al-Cu-Mg-Si-Mn) and 6061 (Al-Mg-Si), find applications after diaphragm forming. AA 5083 can be used as a diaphragm because of its relatively low cost. All parts are subjected to heat treatment where appropriate.

On military aircraft parts range from leading edge components capable of withstanding bird strikes, access and inspection doors, and fairings (aerodynamic covers). For primary structures, AA7475 is used to produce two basic configurations. One is a waffle pan type structure where a built-up framework of extrusions and/or beams is replaced by a single piece superplastically formed pan. The pan is joined to an outer skin but the costly riveting involved in assembling the pan frame is eliminated. The pan would be produced by drape forming using back pressure. The second type of structure is the sine wave beam or spar (Fig. 23). This type of channel is used to construct a frame of high torsional rigidity and replaces built-up channels.

Applications of the waffle pan structure are found in many military aircraft and include the avionics and gun doors on the British Aerospace Hawk (Fig. 24) and the engine bay doors on the Typhoon (Eurofighter 2000). In the latter aircraft, sine wave spars of lengths up to 1.5 m are used in the construction of the tail fin. Chemical milling of formed parts is frequently used to reduce weight. In civil aircraft, the Lear Jet baggage bay door is a waffle pan structure produced in 7475 and the outer skin is joined to this by adhesive bonding. Other parts produced by SPF which find applications on civil and/or military aircraft include avionics enclosures, access door frames, air intake skins, ejector seat panels, engine cowling and engine cowling stiffeners, window surrounds, hydraulic and mechanical equipment housings, wing and tail leading edge panels. Interior parts include ceiling lighting panels, cabin surfaces, floor panels and door frames.
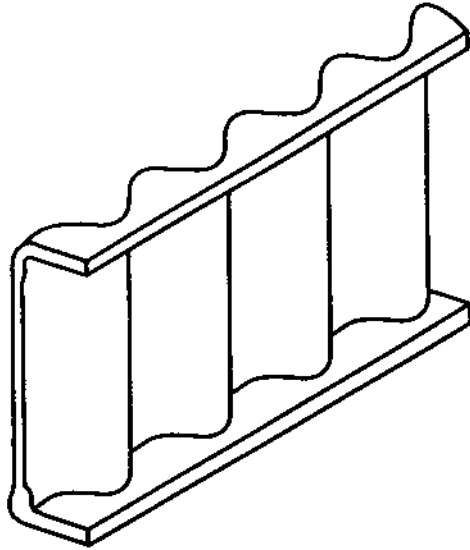
Figure 23   Illustration of sine wave spar. (From Ref. 47.)
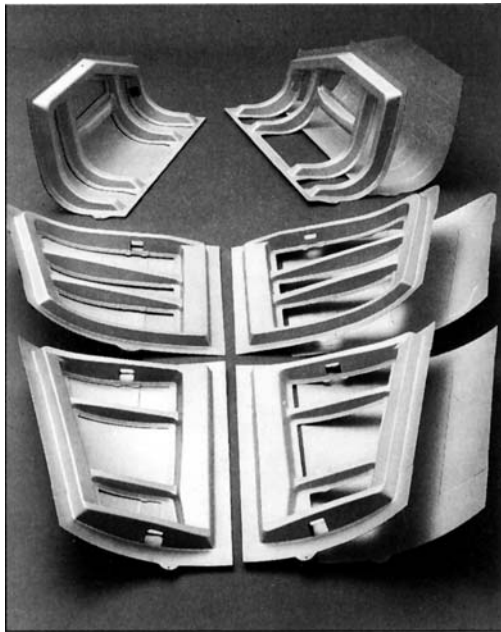
Figure 24   Access door components for British Aerospace Hawk aircraft; 7475. Courtesy of Superform Aluminium.

The rail market is important, particularly in Europe, where large numbers of parts produced from SP 5083 find external and internal applications on commuter trains. The interior fittings often replace plastics so reducing fire hazards. Examples of external parts include end panels fitted to more than 700 Underground trains

(Fig. 25), roof canopies and double curvature transition panels, while internal fittings include window surrounds, door pillar panels, and ventilation, roof and door panels. More than 2500 seats comprising one piece seat shells produced by SPF and covered with fire resistant fabrics have been fitted to the Heathrow Express to Central London, one piece pillars (2 m × 0.25 m) and window surrounds (1.6 m × 1.3 m) are used on the Stockholm Metro, and equipment covers on the Bern Tram (Switzerland).

Architecture and building is a market which uses mainly 5083 and where products are used for external and internal cladding. The most frequent use is on external cladding systems where ribbed panels can enhance both the aesthetic and structural performance, and also be designed to function as a rain screen. Examples of clad buildings include the Financial Times print works in London, Gatwick Airport N. Terminal, and the roof of the Charlety Stadium, Paris, which makes use of around 4000 SP panels in 14 different sizes. Panels can be coated/colored using polymer-based paints. SPF components have been used successfully in applications such as ceiling panels, e.g. 2000 sq. m in the British Library, London, logo panels, display and shelving systems, and complex column cladding. Figure 26 shows applications of decorative and double curvature panels.

Numerous parts are formed from SP 5083 for specialist and prototype automobiles. These include the entire bodies of the Roadster and Esperante models produced for the American sports car maker Panoz. The UK sports car manufacturer Morgan has the wings on all of its models produced by SPF, and has replaced a 3-piece steel fabrication with a single component formed from a 3.2 m × 1.5 m 5083 sheet (Fig. 27). Other components are the rear valance for the Aston Martin Vantage, and the radiator grill and the boot finisher for the Bentley Arnage. There is interest in the mass production automobile industries in SPF as a production tool and if this is maintained it could have an enormous impact on the field.
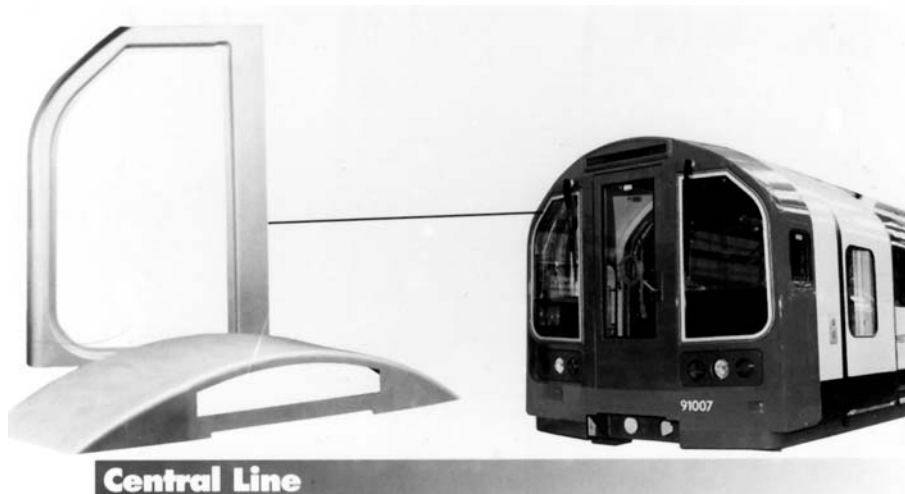
Figure 25 End panels for London Underground trains; 5083. Courtesy of Superform Aluminium.
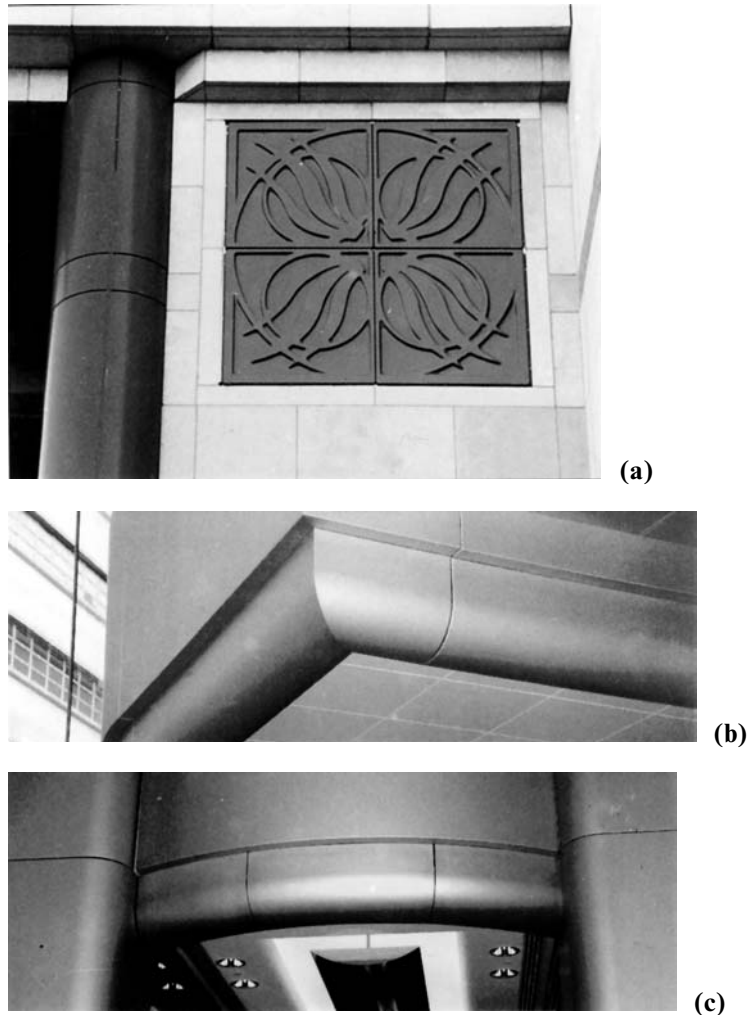
Figure 26 (a) Decorative panel, Grady Hospital, Atlanta, USA; double curvature panels, Dorset House, Hong Kong (b) and Victoria Station Shopping Mall, London (c). Courtesy of Superform Aluminium.

Other parts produced by SPF are used in medical diagnostic and test equipment and range from large diameter end plates for body scanners, to covers and finishing items with an aesthetic bias, and in communications include radar and satellite receiver dishes up to 2 m diameter. Deep formed parts are produced from 2004, and others with a lower forming strain from 5083. Figure 28(a) shows a defence computer housing produced from 2004 and 5083, and Fig. 28(b) a 2.6 m (8 ft 6 in.) dingy formed from a single sheet of 5083.

8. POST-SPF MECHANICAL PROPERTIES

SPF of Al alloys leads to two effects which can degrade mechanical properties. Firstly, and potentially the most serious, is that all Al alloys undergo cavitation

Figure 27   Morgan sports car with wings produced by SPF; 5083. Courtesy of Superform Aluminium.

during SP flow, and secondly, a combination of elevated temperature and SP strain can lead to an increase in grain size. This section will examine the effect of SPF, particularly strain and post-forming heat treatment, on tensile, fatigue, fatigue crack growth and corrosion data, where available, for 7475, 2004 and 5083 alloys, while noting that for some applications data on a wider range of properties may be required. A considerable amount of post-SPF property data was generated for Al-Li alloys during their development era. The subject has been reviewed by Partridge et al. and includes data on 8090 [54].

Aluminum alloy 7475 sheet is used for the manufacture of primary structures for aerospace applications and it is essential to prevent cavitation, or to hold it at a low level, so as to avoid property degradation. This is achieved both by back pressure forming and not exceeding an equivalent SP elongation of 150%. The optimum forming rate for 7475 is low, $\sim 2 \times 10^{-4}\,\mathrm{sec}^{-1}$, and, as a consequence, forming times can be up to 2 h. To prevent cavitation during forming the condition $P > K\sigma_e/3$ [Eq. (11)] must be fulfilled, where σ_e is dependent on strain rate and grain size. Static and strain enhanced grain growth will cause an increase in σ_e because of the low forming rate, so it is important that an increase in back pressure, or an decrease in strain rate within the optimum strain rate range, compensates for this.

A detailed study has been made of post-SPF material properties for back pressure formed material [55]. Data shown in Fig. 29(a) is for room temperature tensile properties of 7475-T6 for test pieces lying parallel and transverse to the sheet rolling direction. It can be seen that neither YS nor UTS are affected by equivalent SP elongations up to 150%, although elongation shows a drop beyond 100%. Fatigue behavior shown in Fig. 29(b) for two orientations lies within the cross-hatched band obtained for the non-SP formed parent sheet. For fatigue crack growth rate in air, no measurable effect was reported for equivalent SP elongations up to 150%. Resistance to stress corrosion cracking and exfoliation corrosion showed no deleterious effect of SP strain. However, the T76 temper provides for improved exfoliation and corrosion resistance over the T6 temper, although with some decrease in strength. Overall, it is seen that provided cavitation can be minimized then post-SPF properties should be similar to those for the parent metal sheet.
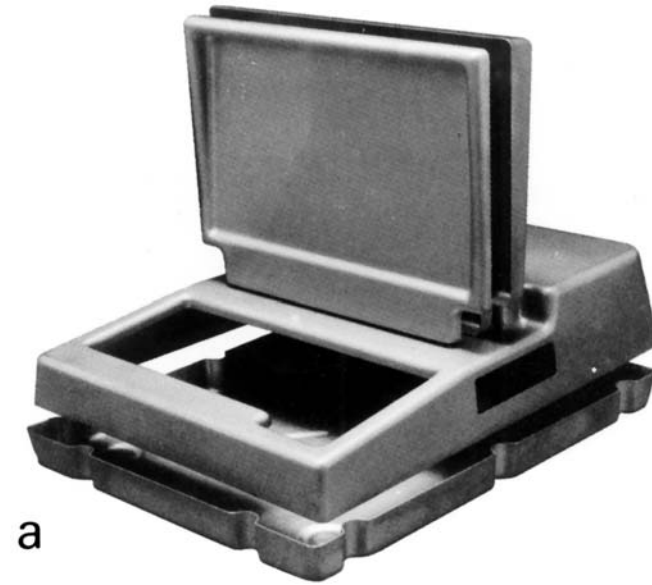
Figure 28   (a) Defense computer housing; 5083 and 2004; (b) sailing dingy; 5083. Courtesy of Superform Aluminium.
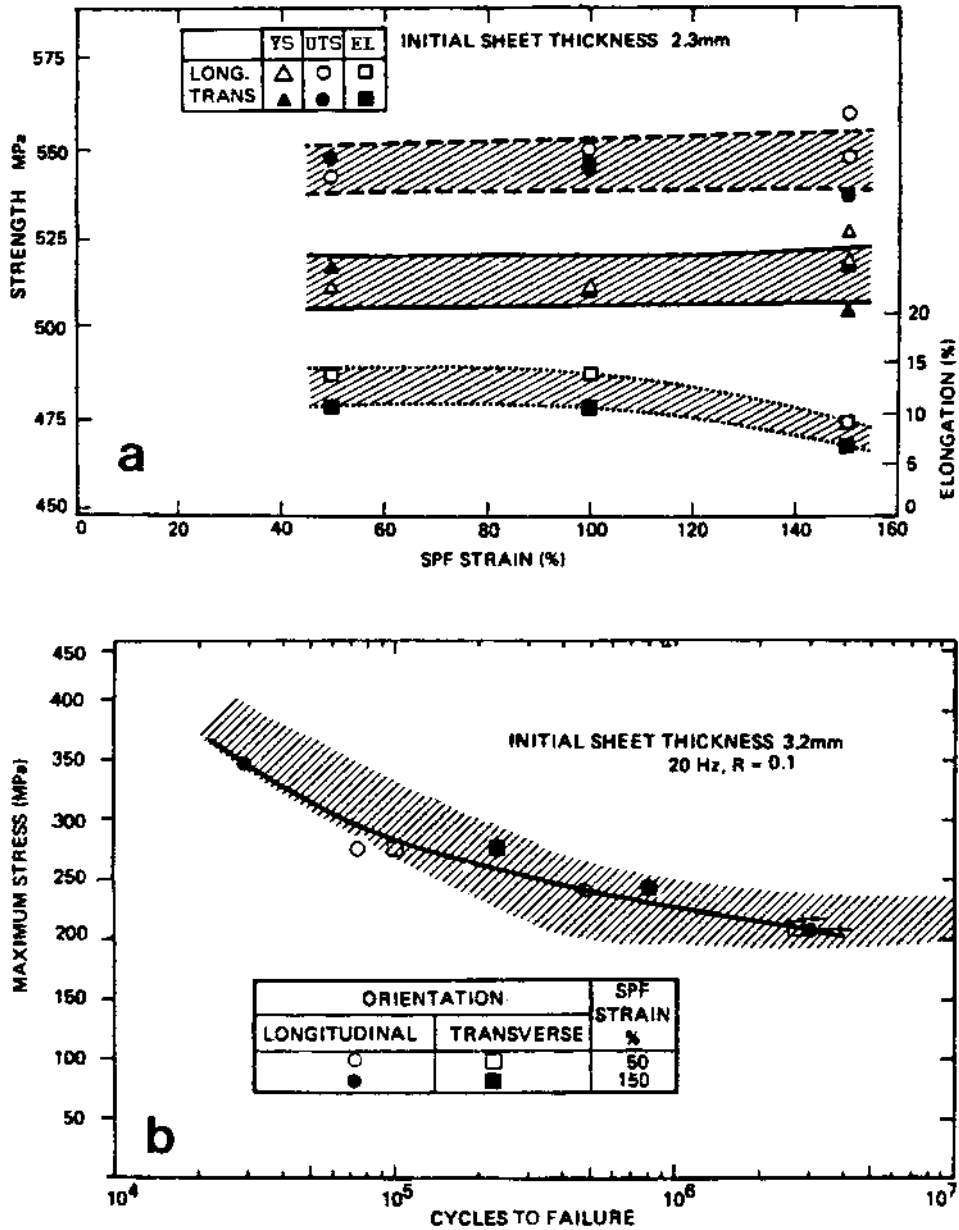
Figure 29 Post-SPF properties of AA7475 at room temperature. Back pressure formed. T6 condition. (a) tensile properties; (b) fatigue strength. (From Ref. 55.)

AA2004 is available in the form of sheet of thickness ranging from 1 mm to 6 mm, and is supplied in the unclad condition (SUPRAL 100), or is roll clad with a layer of commercially pure aluminum (SUPRAL 150) for use in aggressive environments. Clad alloys are weaker than unclad material because of the pure Al layer, and show enhanced levels of cavitation. The alloy is highly superplastic
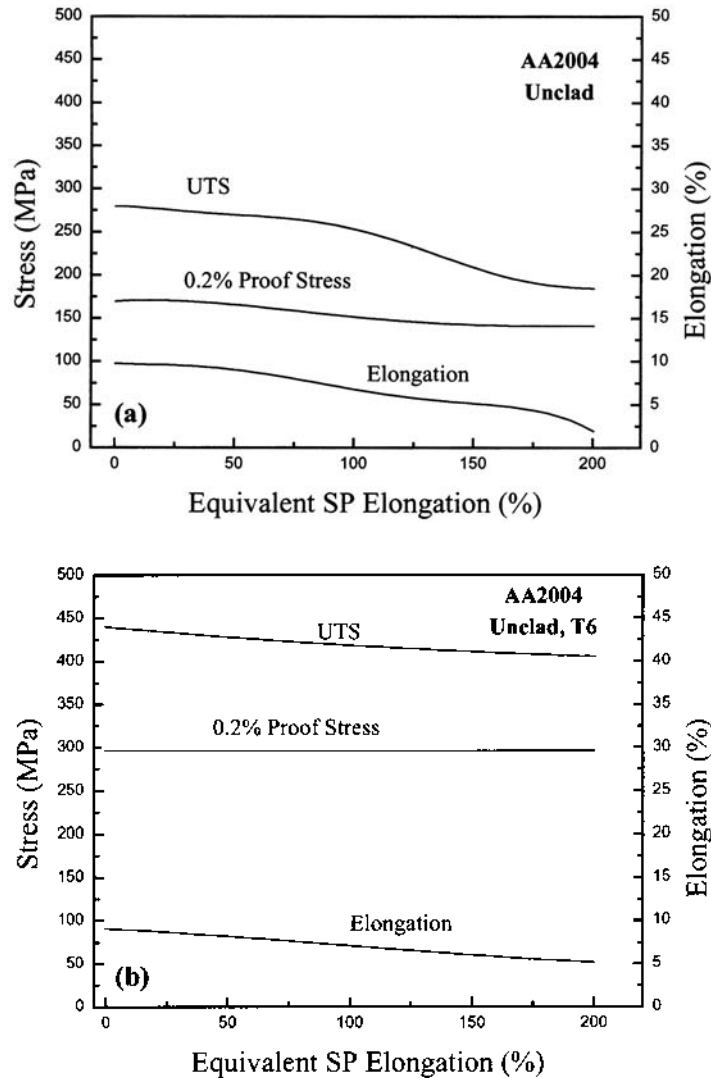
Figure 30 Post-SPF properties of unclad AA2004 at room temperature. Tensile properties (a) as-formed; (b) T6 condition.

but forming strains are generally limited to an equivalent SP elongation of $\sim 250\%$. It is not usually back pressure formed as it is not used for primary structures. However, the flow stress of the alloy is relatively high, ~ 10 MPa at $460°$C, at normal forming rates, $\sim 10^{-3}$ sec^{-1}, so this would require a high back pressure to eliminate cavitation. Both the unclad and clad materials may be used in the as-formed or fully heat-treated condition T6 condition.

Shakesheff [56] has examined the effect of SPF on tensile properties, fatigue, and fatigue crack growth rates, of formed and fully heat treated 2004 alloys for equivalent strains up to 200%, and has related this data to the cavitation behavior of the materials. Further post-SPF mechanical property data is found on materials
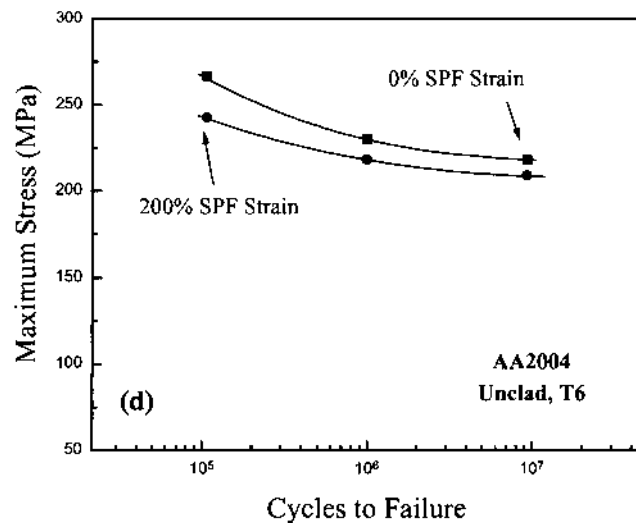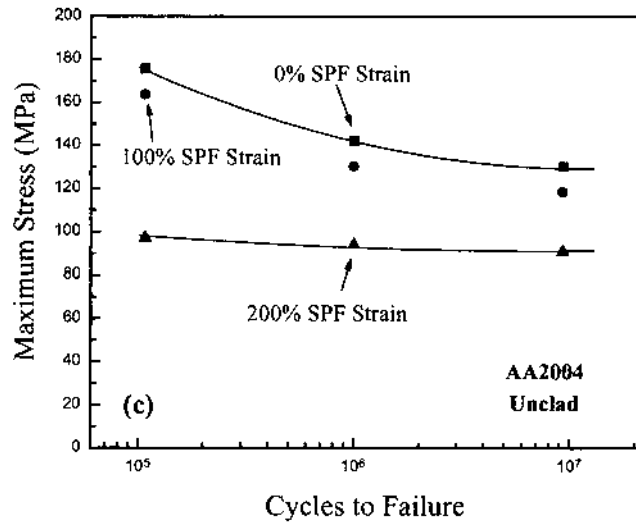
Figure 30 Post-SPF properties of unclad AA2004 at room temperature. Fatigue strength (c) as-formed; (d) T6 condition.

data sheets produced by Superform Aluminium. The room temperature tensile and fatigue properties for unclad material in the as-formed and fully heat treated T6 conditions are shown in Fig. 30. At low equivalent SP elongations ($\sim 100\%$), the ductilities of the unclad (0.7 vol% cavities) and the clad (1.5% cavities) are similar but the PS and UTS are both ~ 30–40 MPa lower for the clad alloy. A reduction in strength and ductility is observed with increasing SP strain up to 200% and, hence, increasing cavitation, with the effect being greater for the clad alloy (5/6 vol% cavities) than the unclad (~ 3 vol% cavities).

The fatigue performance of unclad and clad alloys is little affected by SP strain provided the material is fully heat treated after forming [Fig. 30(d)]. However,

fatigue crack growth rates are adversely affected by both strain and heat treatment. This is attributed to the influence of cavitation and to the increased strength from heat treatment which reduces fracture toughness. The corrosion resistance of unclad 2004 is similar to that of other copper containing aluminum alloys such as 2014 and 2024. Clad 2004 is designed to give good corrosion resistance. Environmental exposure tests at industrial and marine sites have shown that the material has a corrosion resistance equal to that of 99.8% pure Al sheet. In salt spray tests and acetic acid + salt spray tests clad 2004 performs as well as 99.8% pure aluminum.

AA5083 is available in the form of sheet of thickness ranging from 0.5 mm to 6 mm and is formed at $\sim 500°$C. The forming strain is limited to about 100% equivalent SP elongation because the material does not have large reserves of superplasticity. However, the post-SPF properties shown in Fig. 31 cover a wider range of forming strains [26,57]. For normal forming strains, the loss in strength and tensile ductility is relatively small although as the SP strain increases towards 200% elongation it can be seen that falls in these properties become quite significant [Fig. 31(a)]. The alloy does not show appreciable cavitation at small strains.

The fatigue strength of post-formed sheet is reduced but the fall is not catastrophic for an equivalent SP elongation of 100% [Fig. 31(b)]. The alloy is particularly resistant to corrosion in sea water and tests have shown that weight losses after 4000 h of salt spray exposure (3.5% NaCl) for parts formed by SPF are similar to those for non-formed sheet.

9 DIFFUSION BONDING OF SUPERPLASTIC ALLOYS

9.1 Introduction

Diffusion bonding (DB) is a joining process which involves minimal macroscopic distortion of the parts being bonded. Joining may occur entirely within the solid state or may involve isothermal melting and re-solidification of a thin interfacial region of transient liquid phase [58]. The applied pressures tend to be relatively low so as to avoid macroscopic flow. To ensure reasonably short process times, bonding takes place at high homologous temperatures which usually correspond with those for optimum SP flow. It is important that grain growth is minimized during bonding so that the potential for subsequent SPF is not lost.

In solid state diffusion bonding two suitably prepared surfaces are brought into intimate contact at an appropriate temperature. Since the surfaces are not atomically flat there will be a finite number of contacting asperities which will undergo instantaneous plastic collapse on the application of pressure to give a planar array of interfacial voids. Diffusion and creep processes transport atoms to the void surfaces from adjacent areas so reducing the volume of interfacial voids until, with time, they are completely removed, and an atom to atom bond is formed across the original interface. In the absence of local melting, the microstructure of the bond is identical to that of regions remote from the bond and, as a consequence, has parent metal properties.

There have been several attempts, of varying refinement, to predict the time required to obtain 100% contact between surfaces of measured roughness, including models which assume DB to be analogous to pressure sintering [59]. The actual bond is assumed to form instantaneously on contact. Several models assume that bonding
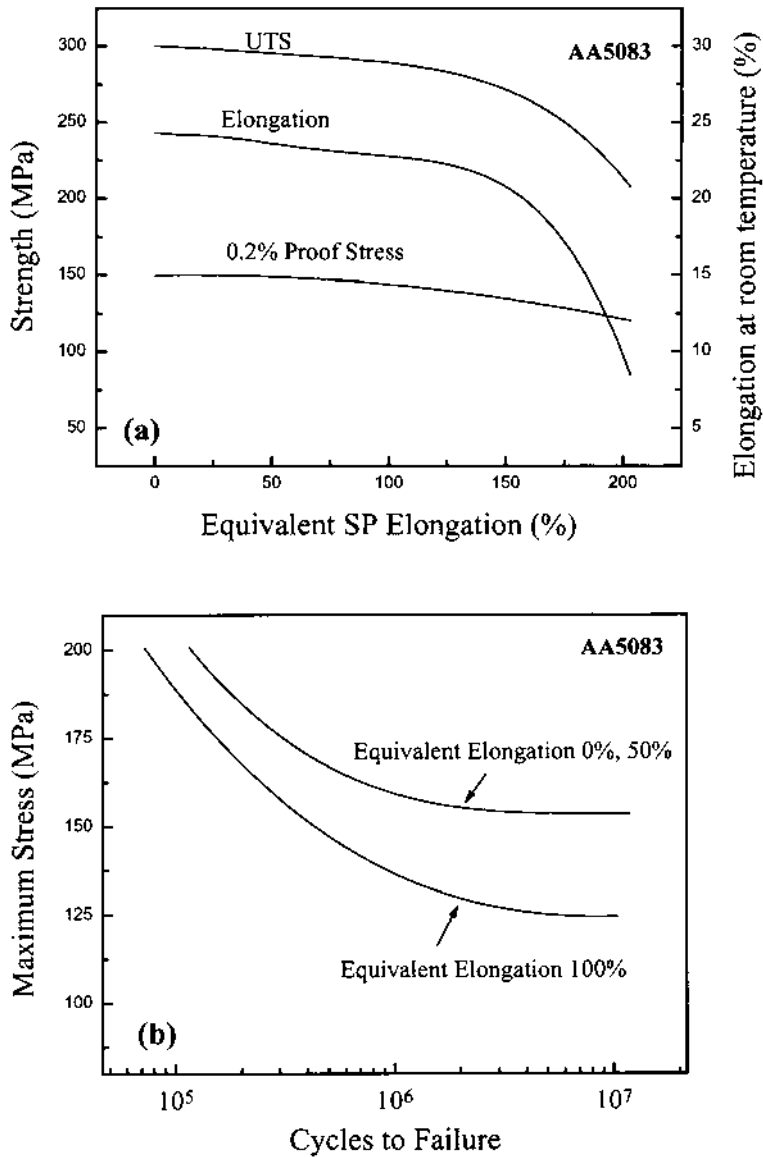
Figure 31   Post-SPF properties of AA5083 at room temperature, (a) tensile properties; and (b) fatigue strength. (From Refs. 26 and 57.)

occurs under plane strain conditions, although there is current interest in isostatic bonding. While the same physical processes will be involved in both cases, it has been predicted that the kinetics of the processes will differ such that the rate of void closure during isostatic bonding will be 2–3 times faster than for plane strain bonding [60].

9.2   DB/SPF Technology

In the context of superplasticity, DB can be used for the selective bonding of sheet materials into sandwich-like constructions. These can then be expanded by gas pressure to form cellular structures. The shape of a cellular structure depends on the number of sheets which make up the initial sandwich and the pattern of the bonded and non-bonded areas. These cellular structures have low overall densities and, if formed from high strength alloys, have extremely high torsional rigidity and high strength-to weight ratios.

DB/SPF technology is readily applicable to titanium alloys, e.g. Ti-6A1-4V, since the Ti lattice is capable of taking into solution the surface oxide and other contaminants which would normally prevent the formation of a metal–metal bond. It has been used for a number of years to manufacture a range of complex components, particularly for aerospace applications, and more recently for the construction of large heat exchangers. Figure 32 shows a 4-sheet cellular structure which has been produced by DB/SPF of Ti-A1-4V. There is considerable interest in extending the technology to other SP materials, particularly aluminum alloys.

However, Al alloys are difficult to bond because of their stable and tenacious surface oxide films which both inhibit the formation of a metal to metal contact and interfacial diffusion. Oxide films inevitably form on the surface of Al alloys when they are exposed to the atmosphere. The films are mainly composed of Al_2O_3, which with a melting point of $> 2000°C$, neither passes into solid solution, decomposes, nor evaporates at bonding temperatures. To achieve a sound DB joint it is necessary to remove the oxide films at least partially, or to disrupt their continuity. The DB of Al alloys has been extensively investigated.

Procedures used to produce diffusion bonds in SP aluminum alloys have been outlined by Partridge [58] and Huang et al. [61]. Methods have included solid state bonding of uncoated surfaces using static compression or gas pressure; the use of a range of interlayers; the deposition of protective coatings on, or implantation in, sputter cleaned surfaces; the application of an organic solution to give a protective layer on an oxide-free surface obtained by mechanical cleaning, or roll cladding of transient liquid layers to the surfaces to be bonded. All of these procedures have been shown to be capable of developing high quality bonds on a laboratory scale, although in a number of cases a variability in bond strength was noted. However, several of the procedures outlined would be difficult to scale up to produce demonstrator or production parts
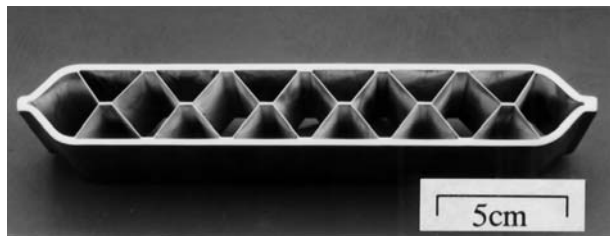
Figure 32   A 4-sheet cellular structure produced by DB/SPF of Ti-6A1-4V.

9.3   Testing of Diffusion Bonds

The quality of a diffusion bond can only be reliably assessed by comparing its mechanical properties/fracture characteristics with that of the parent metal subjected to the same heat treatment. Direct observation of the bond region using optical metallography and SEM is a useful procedure for identifying incomplete bonds, defects in the bond line and the extent of migration of grain boundaries across the original interface. Non-destructive evaluation using ultrasonics is useful for the detection of large disbonds. However, this procedure would not be able to resolve bond line microvoids ($< 5\,\mu$m) since the wavelength used ($\sim 200\,\mu$m) is much greater than the defect size, and in thin sheets the transit times are very short.

For bonds produced in thick sections conventional tensile, rotating bend fatigue and impact test pieces can be readily produced and tested. In practice, parent metal tensile strengths are often achieved with more than 85% interfacial contact, while parent metal fatigue endurance normally requires a complete absence of interfacial voids. The most discriminating measure of bond quality is obtained by impact testing, when poor bonds which show complete interfacial contact may exhibit low impact strengths (58). Impact testing is not widely applicable because the majority of bonds are formed between sheet materials. In such cases, the room temperature fracture strength of the bond is measured using a constrained lap shear test.

In addition to good room temperature strength, it is particularly important that the bond should be capable of resisting peel during SPF after DB. For a 2-sheet structure it would be possible to constrain the bond during SPF by appropriate tool design. However, for producing 3-sheet structures, or a 4-sheet structure of the type illustrated in Fig. 32, the hot peel strength becomes critical, and the bond region must be able to withstand the pressures encountered during SPF. This is dependent on sheet thickness and SP flow stress. It is important to develop a high hot peel strength during bonding but at the same time taking care not to increase the grain size and hence the flow stress of the SP alloy.

9.4   Selected Bonding Procedures

Two examples of industrially-based projects illustrate the position with regard to DB/SPF of aluminum alloys. Firstly, one of the most successful attempts to produce high strength joints in AA7475 sheet is seen in the work of Kennedy [62]. Bonding was carried out at the SPF temperature of 516°C, without the use of interlayers. The material was prepared for bonding by a proprietary technique and bonding was carried out using a relatively low pressure of argon [Fig. 33(a)]. The microstructure of a bond region is seen in Fig. 33(b) and, although there has been some boundary migration across the original interface, the bond line is clearly visible in places and is probably outlined by small amounts of the original surface oxide. Both tensile shear strength and peel strength at room temperature, and cyclic shear behavior of bonds given a T6 heat treatment were similar to those of the AA7475 base material (Fig. 34). It was also demonstrated that DB and SPF could be used to produce a two-sheet stiffened compression panel which exhibited superior buckling resistance compared with riveted built-up panels, although the bond was constrained during forming.
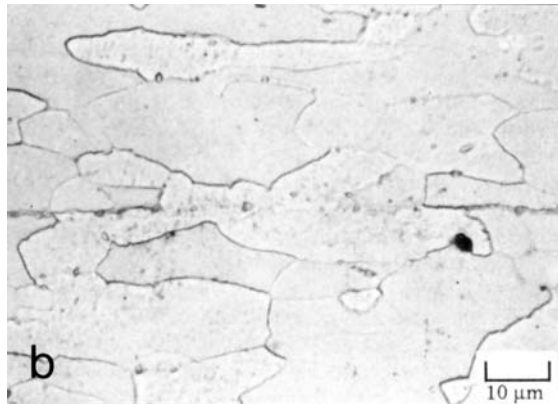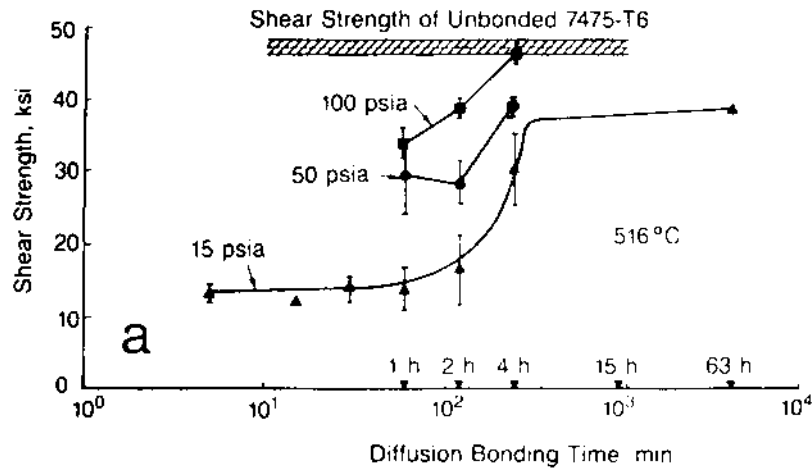
Figure 33 AA7475. (a) Effect of pressure and time on bond shear strength (144 psi = 1 MPa); (b) microstructure of bond interface, T6 condition. (From Ref. 62.)

Bonding of AA8090 has been carried out using a transient liquid phase based on the invariant reaction [63]:

$$Al + CuAl_2 + Si \rightarrow Liquid$$
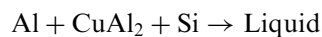
at a temperature of $\sim 524°C$. This was achieved by cladding 8090 with an Al alloy containing 7% Si (AA4343) and then electroplating with a thin layer of copper. Bonding was carried out at 540°C using 1 MPa for 0.5 h, which gave sufficient time for the solute atoms to diffuse away from the bond line. Hot peel strengths of 5/6 MPa at 520°C were developed with room temperature bond shear strengths > 150 MPa. The former were considered to be high enough to prevent peeling during SPF. The procedures were used to produce a 2-sheet demonstrator part, 220 mm × 220 mm, by subsequent SPF but the bond was constrained during forming.
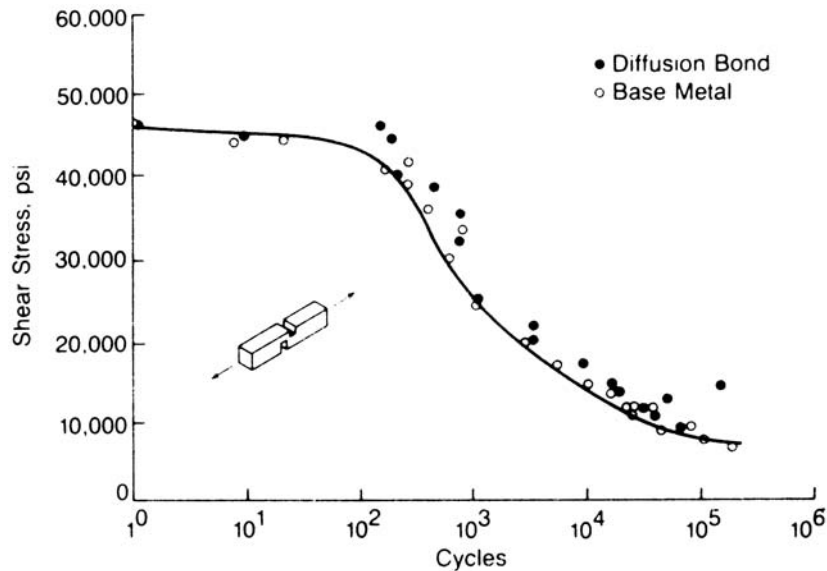
Figure 34 Cyclic shear strength of bonds in 7475; T6 condition (144 psi = 1 MPa). (From Ref. 62.)

It is clear from the literature that while procedures for producing bonds with good ambient mechanical properties and good hot peel strength appear to have been established, their suitability for producing 3-sheet structures by subsequent SPF remains to be tested.

10 CURRENT AND FUTURE DEVELOPMENTS

10.1 Introduction

A simplified view of the economics of sheet forming is shown schematically in Fig. 35 where relatively high materials costs and slow forming rates offset the benefit of relatively low tooling costs [48]. This diagram indicates that the cost effective niche for SPF would involve the production of between 50 and 5000 parts of a given product. For a lower annual output a manufacturing route involving substantial hand fabrication could be more cost effective while at the higher end matched dies could be a less expensive option. For SPF to become a high volume production process would require a reduction in materials costs and/or forming times. This points to the benefits of lower cost, faster forming alloys.

The market for products continues to grow but there are a number of factors which may limit this growth and need to be addressed. These have been outlined by Barnes [48], and include the existence of only a restricted range of qualified alloys, the relatively high cost of these alloys, the high cost of developing and qualifying new alloys, limited awareness by designers of the potential of SPF, need for an accurate thickness prediction modeling technique accessible to designers, and the integration of SPF parts into existing joining, assembly and finishing systems.
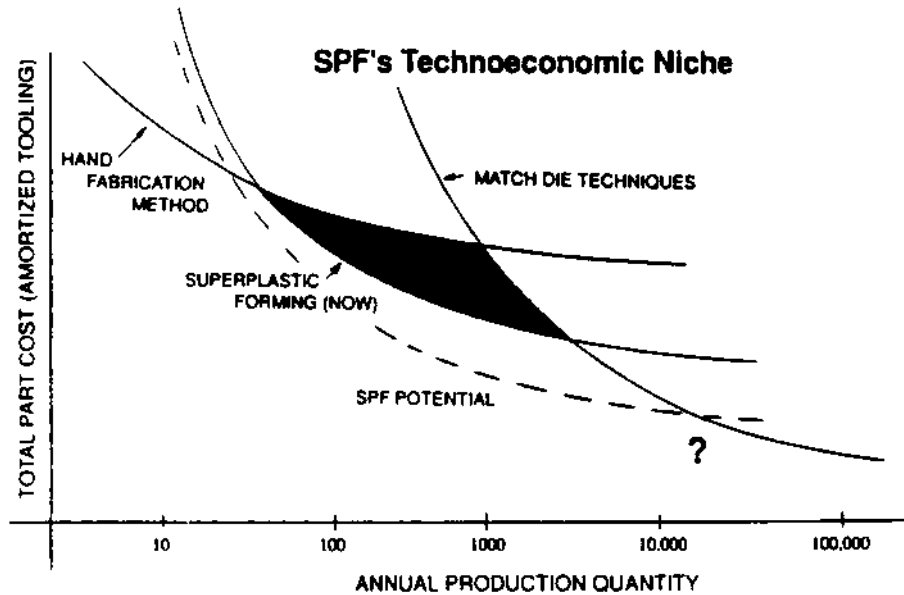
Figure 35 Economics of SP sheet forming. Schematic. (From Ref. 48.)

Research and development activity has largely concentrated on materials rather than the SPF process. It was noted by Sanders [64] that while the number of research publications relating to superplasticity had been growing rapidly for several years, the number of parts produced by SPF had been increasing at a much slower rate.

10.1.1 Materials

Much effort has been devoted to the development of new and faster forming SP materials. This has led to the observation of high strain rate superplasticity (HSRS) which is defined in JISH7007 by the Japanese Standards Association as SP observed at strain rates $> 10^{-2} \sec^{-1}$ [65]. Most high strain rate SP materials are Al-based, either alloys or Al alloy composites containing ceramic or particulate reinforcement. Although HSRS was initially reported in the mid-1980s [66], it has been intensively studied in Al-base materials since about 1990. The subject has been reviewed by Mabuchi and Higashi [67].

It is recognized that HSRS is associated with an ultra-fine grain size and this is consistent with the predictions of Eq. (5). A combination of thermomechanical processing and powder metallurgy has been used to produce alloys with grain sizes of $< 3\,\mu$m. In addition the techniques of physical vapour deposition, mechanical alloying or consolidation of amorphous and nanocrystalline powders result in increasingly small sub-micron grain sizes, capable of giving SP strains to failure at increasingly high strain rates (up to $10^3 \sec^{-1}$). Data for Al alloys is summarized in Figs. 36 and 37 [68,69].
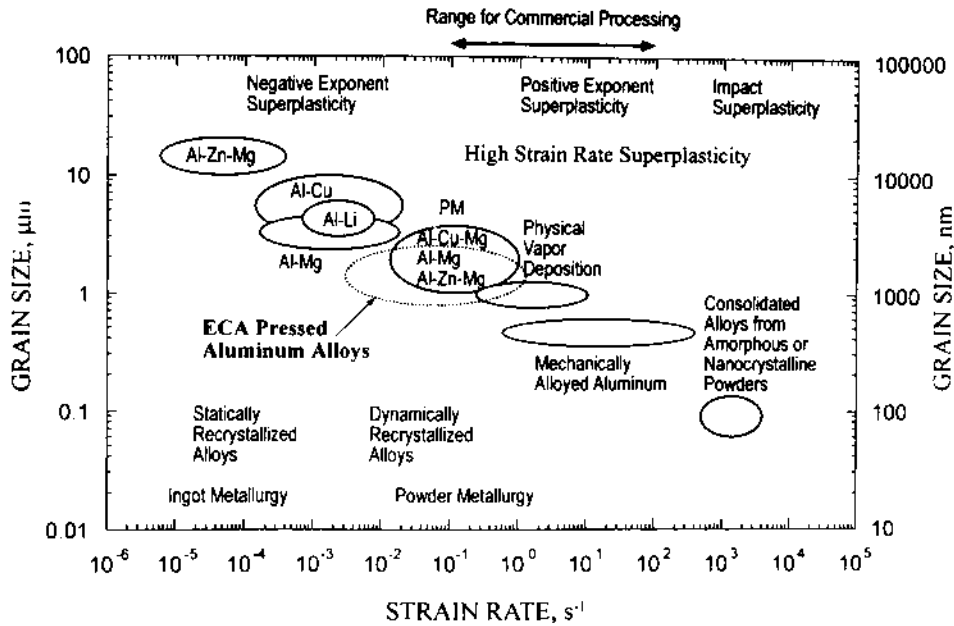
Figure 36   Variation of optimum strain rate for several Al alloys with different grain sizes produced by different processing routes. (From Refs. 68 and 69.)
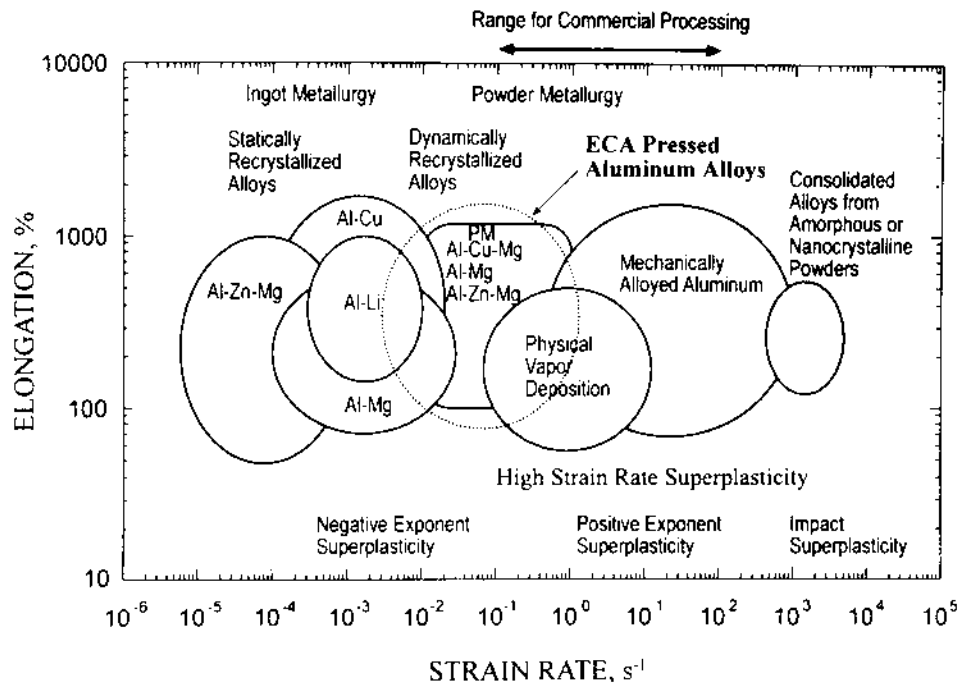
Figure 37   Relation between elongation to failure and strain rate for several Al alloys produced by various processing routes. (From Ref. 68 and 69.)

While some nano-phase microstructures show poor thermal stability, those produced by mechanical alloying such as IN9021 (wt% composition: Al-4.0 Cu-1.5 Mg-1.1 C-0.8 O_2) are stable at elevated temperatures because of the presence of about 5% volume of fine (~ 30 nm) dispersed carbides (Al_4C_3) and oxides (Al_2O_3 and MgO). For this alloy, and for many other HSRS materials, the optimum temperature for maximum SP elongation is above the solidus temperature, or above a temperature at which partial melting has occurred. It is believed that the liquid phase helps with the accommodation of grain boundary sliding, but a liquid phase is not always necessary for a material to exhibit HSRS [68].

Although the above materials are interesting and illustrate the importance of grain size on SP behavior, they have only been produced in relatively small amounts by expensive processing and are unlikely to be of significance in a commercial SPF context, at least in the near future.

A further procedure for producing very small grain sizes ($\sim 1 \mu$m or less) involves equal-channel angular extrusion (ECAE) [68,69]. The principle of this process is illustrated in Fig. 38. A die is used which contains 2 channels of equal cross-section which intersect near the centre of the die. A bar of material which fits the channels is pressed through the die to undergo straining by shear. By control of the rotation of the bar between successive passes, the deformation temperature and the number of passes, considerable strains can be developed leading to fine equiaxed recrystallized microstructures.

This redundant work procedure has been applied to several materials including SUPRAL 100 and a Russian SP Al-Mg-Li-Zr alloy (01420), giving grain sizes in the range 1/2–1 μm [70]. Although the resulting microstructures lacked thermal stability on heating to their normal SPF temperatures, they did exhibit HSRS at appreciably lower temperatures, e.g. 300°C for SUPRAL, with elongations of 500–1000%. However, at these lower temperatures flow stresses could be appreciably higher than conventional levels (Fig. 39). Grain refinement by ECAE has so far been applied to material of relatively small cross-section, ~ 10 mm diameter, but it may be possible for the technique to be scaled-up to process larger sections which could be rolled to produce ultra-fine grained sheet for subsequent SPF.
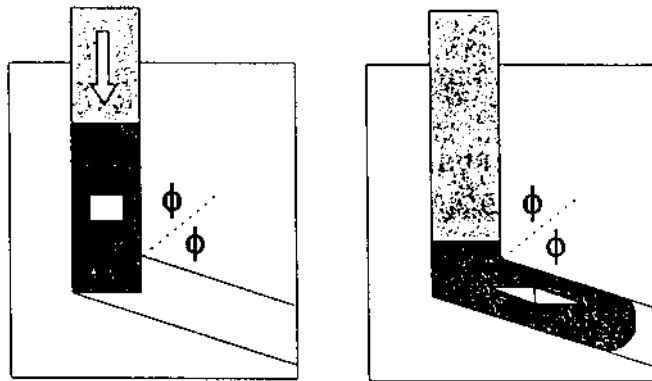
Figure 38   Principle of ECAE.
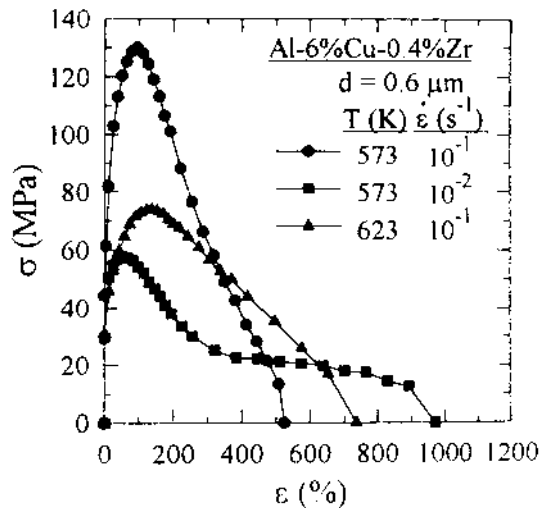
Figure 39 True stress versus strain for tensile tests on SUPRAL processed by ECAE. (From Ref. 70.)

It has been noted that materials such as SUPRAL and Al-Li 8090, which develop SP microstructures by dynamic recrystallization during the early stages of hot forming, have smaller grain sizes, $\sim 5\,\mu$m, than those processed by the static recrystallization route such as AA7475 and AA5083 (10–15 μm) and, as a consequence, have higher optimum strain rates for SP flow. To induce dynamic recrystallization it is necessary to prevent recovery and recrystallization during thermomechanical processing of the sheet material by the pinning action of very fine precipitates, e.g. $ZrAl_3$. It has been demonstrated that AA7475–0.7Zr produced by powder metallurgy can be processed to develop a fine grain ($\sim 2\,\mu$m) microstructure by dynamic recrystallization during hot (SP) forming, and elongations of 500–1000% could be obtained at strain rates of 10^{-3}–$10^{-2}\,\mathrm{sec}^{-1}$ [71].

Various attempts have been made to improve the SPF properties of AA5083 because of it commercial significance, and these have been summarized by Vetrano et al. [24]. It was shown that by applying a range of thermal treatments to Mn, Sc and Zr-containing Al-Mg alloys, the recrystallization behavior could be modified to create either fine, stable grains or a microstructure that was resistant to static recrystallization (i.e. dynamically recrystallizing). However, apart from the costs of producing and qualifying new or modified alloys, it should be noted that sheet producing industries are volume sensitive businesses and there are viable tonnages below which production is not worth while.

10.1.2 SPF Process

The production of a part by SPF initially requires the manufacture of a tool. The manufacturing process then involves several stages. These include the application of lubricant to the sheet blank/tool interface, the loading of the sheet into the press, clamping around the edge to ensure a gas tight seal, heating of the sheet to forming temperature, the forming of the part, opening of the press to allow the part to cool

sufficiently to enable it to be removed without distortion, and finally trimming. It is important to optimize all of these steps to ensure that overall costs are minimized.

Tooling is vital to the success of SPF as it has to operate at elevated temperatures without being degraded, contain the gas pressure and withstand the mechanical force applied. It must produce parts of high dimensional accuracy and good surface finish, which should be manufactured at minimum cost. The use of non-planar split clampline tooling can be utilized in female and drape forming to bend the sheet into a near-net shape before starting SPF in order to minimize SP strain levels and thickness variations [48]. Where CAD data for a part is available, this can be used to produce tools of high quality from solid blocks in commercially competitive times by Computational Numerical Control (CNC) machining. Multiaxial CNC milling can be used to trim parts.

Continual refinement of currently available materials, tooling and forming equipment, will help to expand the cost-effective niche. However, a breakthrough in the development of an Al alloy of ultra-fine grain size and fast forming rate produced at low cost would help to transform SPF from its expanding niche into main stream manufacturing. The evidence so far is that lower cost and faster forming are mutually exclusive objectives.

ACKNOWLEDGMENTS

REFERENCES

1. D. B. Laycock, "Superplastic Forming of Sheet Material," in *Superplastic Forming of Structural Alloys*, (N. E. Paton and C. H. Hamilton, eds.), 1982, TMS-AIME, Warrendale, PA, pp. 257–271.
2. K. Higashi, unpublished work, University of Osaka Prefecture, Japan, 1988.
3. Y. C. Chen, G. S. Daehn, and R. H. Wagoner, "The Potential for Forming Metal Matrix Composites via Thermal Cycling," Scr. Metall. Mater., 1990, 24, pp. 2157–2162.
4. T. G. Nieh, J. Wadsworth, and O. D. Sherby, *Superplasticity in Metals and Ceramics*, 1997, Cambridge University Press, pp. 208–218.
5. C. H. Hamilton, C. C. Bampton, and N. E Paton, "Superplasticity in High Strength Aluminum Alloys," in *Superplastic Forming of Structural Alloys*, (N. E. Paton and C. H. Hamilton, eds.), 1982, TMS-AIME, Warrendale, PA, pp. 173–189.
6. B. P. Kashyap and A. K. Mukherjee, "On the Models for Superplastic Deformation," in *Superplasticity*, (B. Baudelet and M. Suery, eds.), 1985, CNRS, Paris, pp. 4.1–4.27.
7. J. Pilling and N. Ridley, *Superplasticity in Crystalline Solids*, The Institute of Materials, London, 1989.
8. T. G. Langdon, "Mechanisms of Superplastic Flow," in *Superplasticity: 60 Years after Pearson*, (N. Ridley, ed.), 1995, The Institute of Materials, London, pp. 9–24.
9. A. K. Ghosh, "Characterization of Superplastic Behavior of Metals," in *Superplastic Forming of Structural Alloys*, (N. E. Paton and C. H. Hamilton ed.), 1982, TMS-AIME, Warrendale, PA, pp. 85–103.
10. R. Grimes and R. G. Butler, "The Forming Behavior of Commercially Available Superplastic Aluminum Alloys," *Superplasticity in Aerospace* (H. C. Heikkenen and T. R. McNelley, eds.), 1988, TMS-AIME, Warrendale, PA, pp. 97–113.

11. R. E. Goforth, N. A. Chandra, and D. George, "Analysis of the Cone Test to Evaluate Superplastic Forming Characteristics of Sheet Metal," *Superplasticity in Aerospace* (H. C. Heikkenen and T. R. McNelley eds.), 1988, TMS, Warrendale, PA, pp. 149–166.

12. T. L. Mackay, S. M. L. Sastry, and C. F. Yalton, *Metallurgical Characteristics of Superplastic Forming*, ARWAL-tr-80–4038, 1980.

13. W. A. Backofen, I. R. Turner, and D. H. Avery, "Superplasticity in an Al-Zn Alloy," Trans. ASM, 1964, 57, pp. 980–990.

14. C. Zener, quoted by C. S. Smith, "Grains, Phases, Interfaces: An Interpretation of Microstructure," Trans. AIME, 1948, 175, pp. 15–51.

15. F. J. Humphreys and M. Hatherly, *Recrystallisation and Related Annealing Phenomena*, Pergamon, Oxford, 1995.

16. R. Grimes, "Superplasticity in Aluminum-Lithium Based Alloys," in *Superplasticity*, (B. Baudelet and M. Suery, eds.), 1985, CNRS, Paris, pp. 13.1–13.12.

17. R. Grimes, C. Baker, M. J. Stowell, and B. M. Watts, "Development of Superplastic Aluminum Alloys," Aluminum, 1975, 51, pp. 720–723.

18. B. M. Watts, M. J. Stowell, B. L. Baikie, and D. G. E. Owen, "Superplasticity in Al-Cu-Zr Alloys, Part 1: Material Preparation and Properties," Metal Sci., 1976, 10, pp. 189–197.

19. C. C. Bampton, J. A. Wert, and M. W. Mahoney, "Heating Rate Effects on Recrystallised Grain Size in Two Al-Zn-Mg-Cu Alloys," Metall. Trans., 1982, 13A, pp. 193–198.

20. F. J. Humphreys, "The Nucleation of Recrystallisation at Second Phase Particles in Aluminum," Acta Metall., 1977, 25, pp. 1323–1344.

21. T. R. McNelley and M. E. McMahon, "Recrystallisation and Superplasticity in Aluminum Alloys," in *Superplasticity and Superplastic Forming* (A. K. Ghosh and T. R. Bieler, eds.), 1998, TMS-AIME, Warrendale, PA, pp. 75–87.

22. F. J. Humphreys, "Inhomogeneous Deformation of some Aluminum Alloys at Elevated Temperatures," in *ICSMA-6*, (R. C. Gifkins, ed.), 1982, Pergamon, Sydney, pp. 625–630.

23. N. Ridley, E. Cullen, and F. J. Humphreys, "Effect of Thermomechanical Processing on Evolution of Superplastic Microstructures in Al-Cu-Zr alloys," Mater. Sci. Technol., 2000, 16, pp. 117–124.

24. J. S. Ventrano, C. H. Henager, S. M. Bruemmer, Y. Ge, and C. H. Hamilton, "Use of Sc, Zr and Mn for Grain Size Control in Al-Mg Alloys," in *Superplasticity and Superplastic Forming*, (A. K. Ghosh and T. R. Bieler, eds.), 1998, TMS, Warrendale, PA, pp. 89–98.

25. H. Imamura and N. Ridley, "Superplastic and Recrystallisation Behavior of a Commercial Al-Mg Alloy 5083," *Superplasticity in Advanced Materials*, S. Hori, M. Tokizane and N. Furushiro, eds.), 1991, JSRS, Osaka, pp. 453–458.

26. M. Matsuo, "Properties of Superplastic 5083 Alloy and its Applications," in *Superplasticity: 60 Years after Pearson* (N. Ridley, ed.), 1995, Institute of Materials, London, pp. 277–283.

27. F. Li, W. T. Roberts, and P. S. Bate, "Superplasticity and the Development of Dislocation Structures in an Al-4.5% Mg Alloy," Acta Mater., 1996, 44, pp. 217–233.

28. R. Grimes, "The Manufacture of Superplastic Alloys," in *Superplasticity*, (AGARD-LS-168), AGARD, Neuilly-sur-Seine, France, 1989, pp. 8.1–8.16.

29. R. Amichi and N. Ridley, "Superplastic Behavior And Microstructural Evolution in Al-Li Alloy 8090 (LitalA)," in *Aluminum-Lithium 5*, (T. H. Sanders and E. A. Starke, eds.), 1989, MCPE, Birmingham, UK, pp. 159–167.

30. B. A. Ash and C. H. Hamilton, "Strain and Strain Rate Hardening Characteristics of a Superplastic Al-Li-Cu-Zr Alloy," Scripta Metall., 1988, 22, pp. 277–282.

31. I. J. Polmear, *Light Alloys*, 1989, Edward Arnold, London, pp. 104–109.

32. C. H. Hamilton, "Simulation of Static and Deformation-Enhanced Grain Growth Effects on Superplastic Ductility," Metall. Trans., 1989, 20A, pp. 2783–2792.
33. D. A. Woodford, "Strain-Rate Sensitivity as a Measure of Ductility," Trans. ASM, 1969, 62, pp. 291–293.
34. Y. Ma, X.Zhao, and T. G. Langdon, "Cavity Evolution in Superplastic Aluminum-Based Alloys," in *Hot Deformation of Superplastic Aluminum-Based Alloys*, (T. G. Langdon, H. D. Merchant et al., eds.) 1991, TMS, Warrendale, PA, pp. 331–341.
35. N. Ridley and Z. C. Wang, "The Effect of Microstructure and Deformation Conditions on Cavitation in Superplastic Materials," Mater. Sci. Forum, 1997, 233–234, pp. 63–80.
36. A. H. Chokshi, "The Influence of Grain Size on Cavitation in Superplasticity," Mater. Sci. Forum, 1997, 233–234, pp. 89–108.
37. A. K. Ghosh, D-H. Bae, and S. L. Semiatin, "Initiation and Early Stages of Cavity Growth During Superplastic and Hot Deformation," Mater. Sci. Forum, 1999, 304–306, pp. 609–616.
38. M. J. Stowell, "Cavitation in Superplasticity," in *Superplastic Forming of Structural Alloys*, (N. E. Paton and C. H. Hamilton, eds.), 1982, TMS-AIME, Warrendale, PA, pp. 321–336.
39. M. G. Zelin, H. S. Yang, R. Z. Valiev, and A. K. Mukherjee, "Cavity Distribution Pattern in a Superplastically Deformed Aluminum Alloy," Metall. Trans., 1993, 24A, pp. 417–424.
40. J. W. Hancock, "Creep Cavitation without a Vacancy Flux," Metal Sci., 1976, 10, pp. 319–325.
41. J. Pilling and N. Ridley, "Cavitation in Superplastic Alloys and the Effect of Hydrostatic Pressure," Res. Mechanica, 1988, 23, pp. 31–63.
42. J. Pilling and N. Ridley, "Effect of Hydrostatic Pressure on Cavitation in Aluminum Alloys," Acta Metall., 1986, pp. 669–679.
43. M. J. Stowell, D. W. Livesey, and N. Ridley, "Cavity Coalescence in Superplastic Deformation," Acta Metall, 1984, 32, pp. 35–42.
44. A. Varloteaux, J. J. Blandin, and M. Suery, "Control of Cavitation during Superplastic Forming of High Strength Aluminum Alloys," Mater. Sci. Technol., 1989, 5, pp. 1109–1117.
45. H. Conrad, W. D. Cao, X. P. Lu, and A. F. Sprecher, "Effect of Electric Field on Cavitation in Superplastic Aluminum Alloy," Mater. Sci. Eng., 1991, A138, 247–258.
46. G. C. Cornfield and R. H. Johnson, "The Forming of Superplastic Sheet Material," Intl. J. Mech. Sci., 1970, 12, pp. 479–490.
47. J. M. Story, "Part Selection Criteria and Design Considerations for the Use of Superplastically Formed Aluminum for Aerospace Structures," in *Superplasticity in Aerospace II*, (T. R. McNelley and H. C. Heikkenen, eds.), 1990, TMS-AIME, Warrendale, PA, pp. 151–166.
48. A. J. Barnes, "Superplastic Aluminum Forming – Expanding The Techno-Economic Niche," Mater. Sci. Forum, 1999, 304–306, pp. 785–796.
49. D. M. Ward, "Forming Non-Superplastic Materials with Superplastic Membranes," in *Superplasticity and Superplastic Forming*, (C. H. Hamilton and N. E. Paton, eds.), 1988, TMS, Warrendale, PA, pp. 595–599.
50. R. Whittingham, "Design and Manufacture of Hydraulic Presses for Superplastic Forming," in *Superplasticity: 60 Years after Pearson*, (N. Ridley, ed.), 1995, Institute of Materials, London, pp. 253–259.
51. R. Wood and J. Bonet, "A Review of the Numerical Analysis of Superplastic Forming," J. Mater. Process. Technol., 1996, 60, pp. 45–53.
52. K. Kannan, C. H. Johnson, and C. H. Hamilton, "The Role of Flow Properties and Damage Accumulation in Superplastic Ductility of Al-Mg-Mn Alloys," Mater. Sci. Forum, 1997, 243–245, pp. 125–130.

53. M. F. Ashby and R. A. Verrall, ''Diffusion-Accommodated Flow and Superplasticity,'' Acta Metall., 1973, 21, pp. 149–163.
54. P. G. Partridge, D. S. McDarmaid, I. Bottomley, and D. Common, ''The Mechanical Properties of Superplastically Formed Ti and Al Alloys,'' in *Superplasticity*, (AGARD-LS-168), 1989, AGARD, Neuilly-sur-Seine, France, pp. 6.1–6.33.
55. S. P. Agrawal and J. M. Tuss, ''Superplastic Forming and Post-SPF Mechanical Behavior of an Al Alloy for Airframe Applications,'' in *Superplasticity in Aerospace–Aluminum*, (R. Pearce and L. Kelly, eds.), 1985, SIS, Cranfield, England, pp. 296–325.
56. A. J. Shakesheff, ''Effect of Superplastic Deformation on the Post-Formed Mechanical Properties of Commercially Produced Supral Alloys,'' in *Superplasticity in Aerospace—Aluminium*, (R. Pearce and L. Kelly, eds.), 1985, SIS, Cranfield, England, pp. 36–54.
57. B. J. Dunwoody, R. J. Stracey, and A. J. Barnes, ''Mechanical Properties of 5083 SPF after Superplastic Deformation,'' in *Superplasticity in Metals, Ceramics and Intermetallics*, (M. J. Mayo, M. Kobayashi and J. Wadsworth, eds.), 1990, MRS, Pittsburgh, PA, pp. 161–166.
58. P. G. Partridge, ''Diffusion Bonding of Metals,'' in *Superplasticity* (AGARD-LS-168), 1989, AGARD, Neuilly-sur-Seine, France, pp. 5.1–5.29.
59. B. Derby and E. R. Wallach, ''Theoretical Model for Diffusion Bonding,'' Metal. Sci., 1982, 16, pp. 49–56.
60. J. Pilling, ''The Kinetics of Isostatic Diffusion Bonding in Superplastic Materials,'' Mater. Sci. Engin., 1988, 100, pp. 137–144.
61. Y. Huang, N. Ridley, F. J. Humphreys, and J.-Z. Cui, ''Diffusion Bonding of Superplastic 7075 Aluminum Alloy,'' Mater. Sci. Eng. 1999, A266, pp. 295–302.
62. J. Kennedy, ''Diffusion Bonding and SPF of AA7475,'' in *Superplasticity and Superplastic Forming*, (C. H. Hamilton and N. E. Paton, eds.), 1988, TMS-AIME, Warrendale, PA, pp. 523–527.
63. P-J. Winkler, T. Heinrich, R. Keyte, G. J. Mahon, and R. A. Ricks, ''Bonding and Superplastic Forming of Al-Li Alloy AA8090 for Commercial Applications,'' in *6th Al-Li Conf.*, (M. J. Peters and P-J. Winkler, eds.), 1992, DGM, Oberursel, pp. 1069–1074.
64. D. G. Sanders, ''Superplastic Forming Manufacturing Technology Moves Towards the Twenty-First Century,'' Mater. Sci. Forum, 1999, 304–306, pp. 805–812.
65. Japanese Standards Association, Tokyo, JIS H 7007, *Glossary of Terms used in Metallic Superplastic Materials*, 1995, p. 3.
66. T. G. Nieh, P. S. Gilman, and J. Wadsworth, ''Extended Ductility at High Strain Rates in a Mechanically Alloyed Aluminum Alloy,'' Scripta Metall., 1985, 19, pp. 1375–1378.
67. M. Mabuchi and K Higashi, ''The Processing, Properties, and Applications of High Strain-Rate Superplastic Materials,'' JOM, June 1998, pp. 34–39.
68. K. Higashi, ''Positive Exponent Superplasticity in Metallic Alloys and Composites,'' in *Superplasticity: 60 Years after Pearson*, (N. Ridley, ed.), The Institute of Materials, London, 1995, pp. 93–102.
69. T. G. Langdon, ''An Examination of Flow Processes in High Strain Rate Superplasticity,'' Mater. Sci. Forum, 1999, 304–306, pp. 13–20.
70. P. B. Berbon, N. K. Tsenev, R. Z. Valiev et al. ''Superplasticity in Alloys Processed by Equal-Channel Angular Pressing,'' in *Superplasticity and Superplastic Forming*, (A. K. Ghosh and T. R. Bieler, eds.), 1998, TMS, Warrendale, PA, pp. 127–134.
71. K. Matsuki, G. Stanick, H. Natagawa, and M. Tokizawa, ''Superplasticity of Rapidly Solidified 7475 Al Alloys with 0.7 wt% Zr,'' Z. Metallkunde, 1988, 79, pp. 231–236.

23

Aluminum Chemical Milling

BRUCE M. GRIFFIN

The Boeing Company, St. Louis, Missouri, U.S.A.

1 INTRODUCTION

Perhaps the hallmark of any useful manufacturing process is its longevity. The origins of the chemical milling process can be traced back to the discovery of organic acid, followed by the discovery that the acids could be used to encourage corrosion [1]. Once maskants were developed that allowed selective exposure to the corrosive liquids, the chemical milling process was essentially defined.

The earliest written evidence of deliberate use of etching on iron appears in a fifteenth-century English manuscript [1]. The manuscript describes an etchant consisting of salt, charcoal and vinegar and a ''maskant'' of linseed oil paint. The paint was brush applied in the required pattern, and later the etchant was applied to all unprotected areas. The use of chemical etching as a technique for engraving weapons and body armor became more widespread in the early fifteenth-century. Weapons and body armor were forged as hard as a craftsman's engraving tools, hence the old engraving technique was quickly replaced chemical etching process.

Craftsman employing chemical etching techniques were faced the same problems experienced in modern day chemical milling operations. Maskants developed by the sixteenth-century were an amalgam of wax, resins and asphalt [1]. After applying the maskant by brush the craftsman would work the maskant with scribing tools consisting of needles and scrapers [1]. Once the masking work was completed the etchant would be applied drop by drop and perhaps moved about with a brush to move the etchant to the precise locations necessary. Just as today, the craftsman pondered problems such as poor maskant adhesion, or

complete maskant failure. Corrections for such problems included hand polishing to blend-in chemical burns, or pits, and perhaps adjusting a design to cover areas damaged by maskant failure.

The chemical etching technique as developed for armor etching also found use in the early printing industry and had profound affect on graphic printing [1]. The primary advantage of an etched line over that of an engraved line is that the etched line is produced without an upstanding burr.

In more recent times the chemical milling process has been employed to manufacture filter elements for internal combustion engines, cut hard or thin materials that challenged conventional mechanical techniques, cut recesses in bearing journal to facilitate bearing lubrication, create printed circuits, and facilitate the manufacture of large metal structures for the aerospace industry. Variants of the chemical milling are used primarily in the electronics industry and the aerospace industry [1]. One important spin-off of chemical milling technology is its use to manufacture intricate replacement parts for the human body.

In 1953 application of the chemical milling technique for aluminum was developed by Manuel C. Sanz and a group of manufacturing process investigators at North American Aviation in California, USA [1]. The team developed maskants and etchants that could be used to produce consistent surface finishes on formed aluminum sheets. The use of a closely adhering maskant and etchants to create exact pocket dimensions and structurally useful ribs was essentially the first time the process had been used as a structure forming technique for aerospace applications. Before the chemical milling process, sheet metal structures for aerospace applications were created by forming two or more identical parts; routing one or more parts to create lightening holes, then joined all parts with rivets or threaded fasteners. With chemical milling one part is formed from a thicker substrate, then selected areas are removed by etching to create a lighter and stronger part without the concerns of sandwich or crevice corrosion.

Modern applications and uses of aluminum chemical milling include:

- Stock reductions to create material dimensions not available from metal suppliers or rolling mills.
- Stock reductions to reduce web thickness on machined components.
- Selective metal dissolution from sheet material to reduce part weight.
- Selective metal dissolution from sheet material to accurately locate structural features such as land or boss areas for mating parts or a pass-through.
- Tapering to create special part features or shim stock.

Covered in this chapter are:

- Five process steps of aluminum chemical milling.
- A review of maskant technology and solvent emission limits from masking operations.
- Discussion of tooling requirements, i.e. how to calculate removals and tooling offsets.
- A review of etchants used for aluminum chemical milling and appropriate waste disposal techniques.
- A review of materials best suited for tank and work rack construction.

2 CHEMICAL MILLING PROCESS STEPS

2.1 Pre-mask Cleaning

Aluminum must be cleaned to remove forming lubricants and soils before maskant application. Cleaning solutions must be capable of removing soils and preventing re-deposition of the soils. Techniques for pre-mask cleaning vary from a simple degreasing step by solvent wiping to elaborate processes that include aqueous degreasing, alkaline clean, acid pickle (etch), acid desmutting and application of a colorless conversion coat.

The minimum requirement for pre-mask cleaning is a solvent wipe. The preferred solvents have long been Toluene and Xylene, however emissions of both solvents are now regulated in the USA by the 1998 Aerospace NESHAP segment of the 1990 Clean Air Act [2]. Other solvents such as Acetone or a new compliant solvent, Oxsol-100, are candidates for a pre-mask cleaning solvent.

Aqueous degreasing followed by alkaline or acid etching and an acid based desmutting solution represents a more consistent pre-mask cleaning process. Typically parts are degreased and alkaline cleaned before masking. A variety of proprietary aqueous degreasing and alkaline cleaning solutions are available. Most employ sodium hydroxide, sodium or potassium carbonate or bicarbonate, sodium metasilicate or trisodium phosphate. The user should select an aqueous degreaser and alkaline cleaner that effectively removes the soils encountered, and then develop the cleaning process around the selected cleaner(s). Pre-mask cleaning will influence maskant adhesion, therefore, the cleaning process must be designed to make bare and claded aluminum surfaces appear the same to the maskant. To simplify basket loading, the cleaning process should accept mixed loads of bare and clad aluminum. Failure to properly condition the substrate for masking will result in large maskant adhesion variations, which will impact the quality of the finished chem-mill product. A pre-mask cleaning process should include aqueous degreasing, alkaline cleaning and deoxidize (Fig. 1). A more elaborate pre-mask cleaning process would include alkaline or acid etch following alkaline cleaning followed with an acid desmut or deoxidize step (Fig. 1).

Colorless conversion coat is recommended if the masking process is located at a remote site and shipping by truck is required. The conversion coat will impede surface corrosion if the parts should get wet due to rain or other mechanism during transfer. If a conversion coat for part protection is necessary the cleaning process should be extended by increasing the process time in the Deoxidizing solution, or adding a Nitric/Hydrofluoric acid, or alkaline etch before deoxidizing.

2.2 Maskant Application

Chemical milling maskants may be applied by a variety of techniques. Brushes or paint rollers may be used for small parts, or to cover small surface areas (1–2 ft^2) on large parts. Sophisticated immersion coating or spray coating systems, that include solvent flash-off and drying ovens are used for large-scale operations. Depending upon the type of maskant selected, an attendant solvent emission control system may also be necessary. The maskant film must provide chemical resistance, abrasion resistance, tear resistance and reasonable adhesion to the aluminum substrate. The maskant film must maintain adhesion at the scribe line and prevent
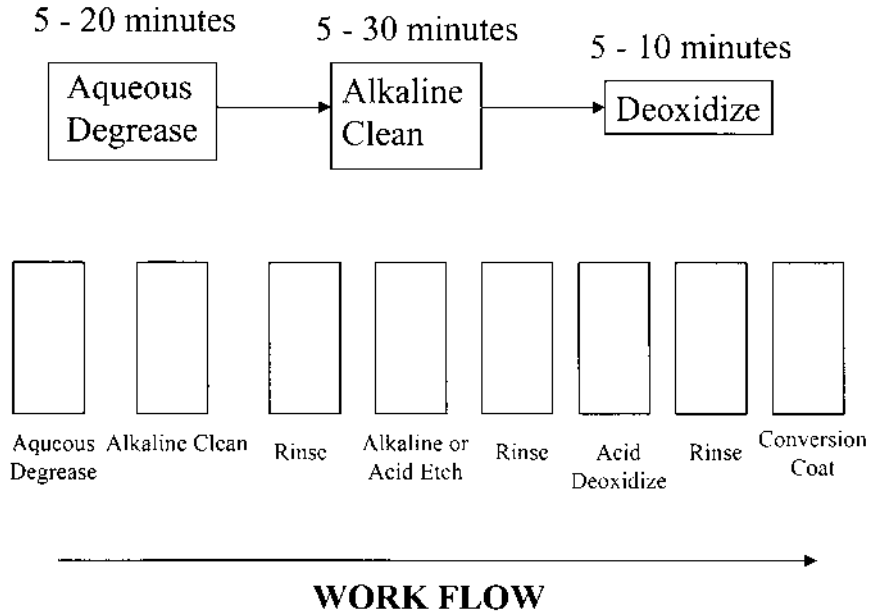
Figure 1 Pre-mask cleaning.

etchant leakage beneath the maskant. The maskant film must be uniform over the entire part surface, easy to scribe, provide contrast to highlight scribed areas such that operators can see the scribe lines, and must retain ink or graphite markings. An ideal maskant film thickness for most chemical milling is 0.014 to 0.02 in. Solvent-based maskants perform well with 0.012–0.016 in. of maskant film; waterborne maskants perform best in the 0.016–0.02 in. maskant film thickness range.

The techniques most often used for maskant application are flow coating, immersion coating and spray coating. Maskant application by brush or roller is discouraged because this technique imparts coating defects such as bubbles and pinholes that must be repaired before chemical milling.

2.2.1 Flow Coating

The Flow Coating apparatus (Fig. 2) consists of a shallow tank, a low volume pump with flexible hoses and part racking devices. The parts are positioned over the tank and operators manually direct the maskant flow over the surface of the part from the top edge to the bottom. The maskant film is dried, then the parts are typically rotated and coated a second and third time to achieve a somewhat uniform film of proper thickness. The flow coating technique is most effective on medium sized parts (i.e. 3 ft wide × 10 ft long). Small parts and extrusions are usually dipped in the shallow tank. Flow coating large parts (10 ft wide × 30 ft long) is near impossible as it is difficult maintaining an even flow over large part surfaces. The frequency of maskant film defects such as bubbles and pinholes is greater with flow coating than either immersion coating or spray coating.
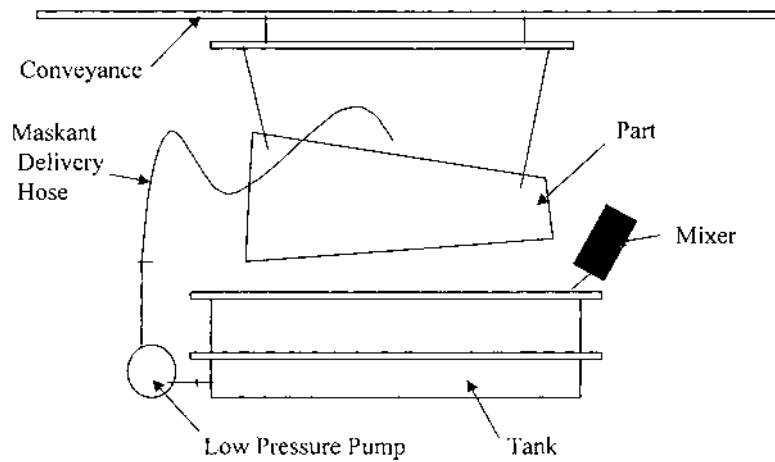
Figure 2 Flow coat apparatus for maskant application.
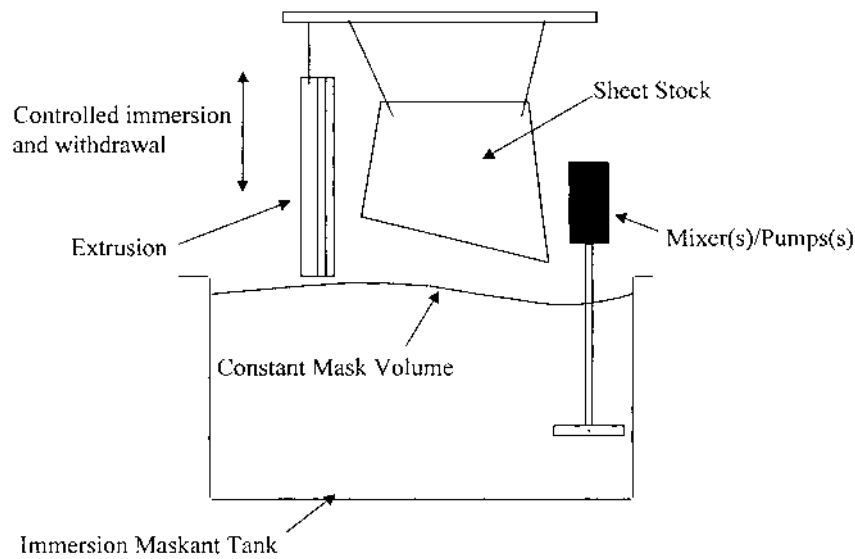
Figure 3 Immersion tank coat apparatus for maskant application.

2.2.2 Immersion Coating

Immersion coating is ideal for small to large parts, particularly if the parts have complex contours. Immersion coating provides the best quality maskant films for the broadest range of applications. Immersion coating is accomplished with a hoist, or lowering device located directly above a maskant tank. The parts are lowered into the maskant at a controlled rate, then are withdrawn from the maskant at a controlled rate (Fig. 3).

Flash-off Area

Cure Oven

Mask Tank
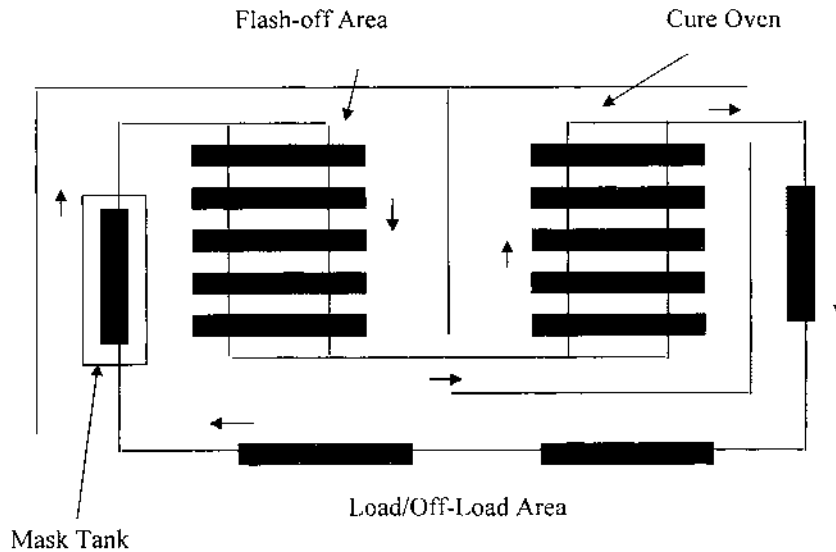
Load/Off-Load Area

Figure 4 Conveyance scheme for automated maskant application.

Immersion coating is easily linked to conveyance systems that can shuttle the coated parts through a drying oven and out to a load/offload work area where parts are rotated for additional maskant coats or removed for scribing (Fig. 4).

Immersion coating systems offer exceptional transfer efficiency as virtually all the maskant applied remains on the part, or is reclaimed as it drips back into the maskant tank. Immersion coating systems have been constructed with a drip pan included to catch and reclaim maskant that drips from parts. Including a drip pan should decrease coating cycle-time as parts do not have to remain over the maskant tank. In practice however, drip pans and the attendant pump(s) and piping require frequent maintenance. The more practical approach is to plan for mask line capacity such that sufficient drip time over the maskant tank (10–15 min can be accommodated.

The primary disadvantage of immersion coat systems is the initial cost of filling the maskant tank. Project planners must plan for either a large increase in overhead costs in the year that the tank is filled, or include the maskant cost as an expensive item in the project cost. A secondary disadvantage of immersion coating systems is the somewhat greater complexity of immersion coat tanks versus a flow coat tank. The immersion tank design must include means for maskant circulation by either pumps or a mixer apparatus to insure consistency of the maskant, and to sweep bubbles from the maskant surface between part immersion cycles. Tank design schemes successful for immersion coating systems are discussed in Sec. 3.

2.2.3 Spray Coating

Spray application of maskant is a good maskant application technique for large flat parts and large parts with a mild contour (200 in. radius), (Fig. 5).
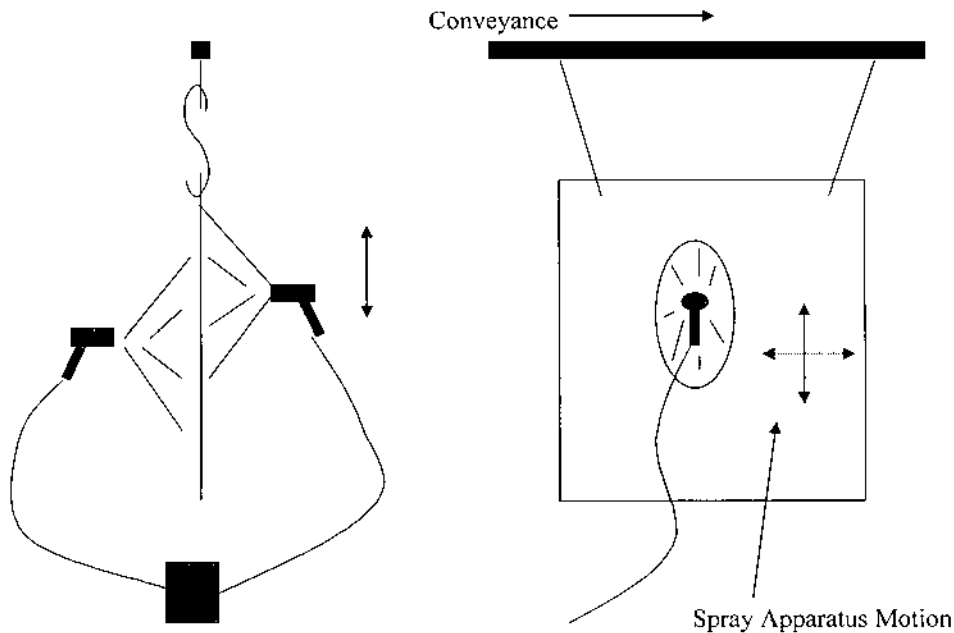
Figure 5 Spray apparatus for maskant application.

Spray coating of large parts with airless spray equipment can be accomplished with transfer efficiencies approaching 70–80%. Large, relatively flat surfaces limit excessive losses due to coating over-spray. An equally important aspect of spray masking is that maskant may be purchased and used in convenient quantities, thus there is less maskant inventory.

Preferred equipment for the spray application is airless or airless/air assisted. Spray gun and spray tip requirements are based on the application conditions and can be determined by the maskant supplier.

Spray application of chemical milling maskant is easily automated. A typical approach is for the part to pass between opposing spray guns. Conveyance equipment designs can be identical to immersion coat systems, except a maskant spray apparatus is constructed instead of an immersion tank, (Fig. 5).

The primary disadvantage of spray application is that generally 4–5 coats are required to build the same maskant film thickness that can be applied in 2–3 immersion coats. Each additional coat requires a cure step as well, so actual cycle time for a completed spray applied maskant coating could be 67% longer than required for flow or immersion coating.

2.3 Maskant Scribing

Scribing for the general aluminum chemical milling application is accomplished with a standard X-Acto® Knife, (e.g. #2 Handle with the #11 Stainless Steel Blade). Knife orientation relative to the tool is important. Poor scribing technique can result in mis-located chem-mill lines and substantial rework effort, (Fig. 6).
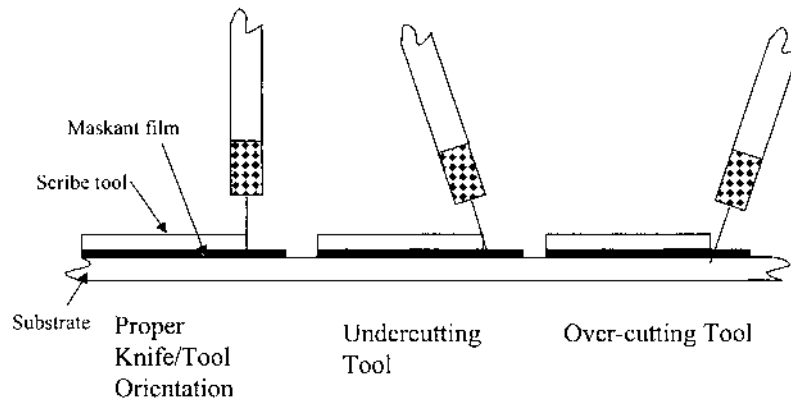
Figure 6 Scribe knife orientation.
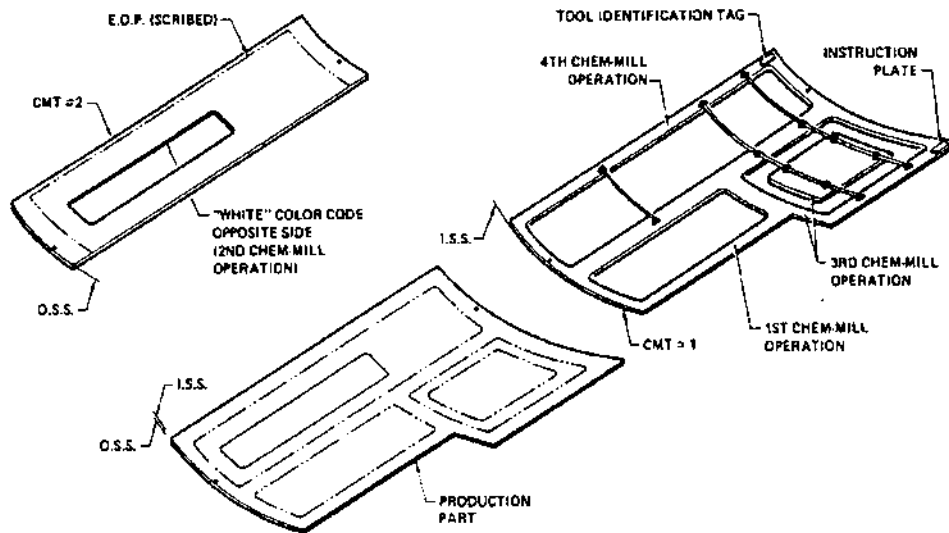
Figure 7 Chem-mill scribe tool application.

Chem-mill tools are constructed of sheet aluminum, sheet steel, or fiberglass [3]. Scribe tools are typically located on the blank parts by pinning through pre-punched tooling holes. The tool is used as a guide for the scribe knife. Tools are generally color-coded to indicate multi-cut parts. Each airframe manufacture, and perhaps each chemical milling subcontractor has a color code to indicate cut number. The color is painted around the perimeter of each pocket. Operators mark the order of cut with a pencil or ink pen according to the color-code that appears on the tool (Fig. 7).

Brush apply scribe line sealer product
to protect scribe lines while pocket 1, then
pocket 2 are etched.

Scribe all pockets with one
tool set-up, and pull maskant
from Pocket, or Cut 1
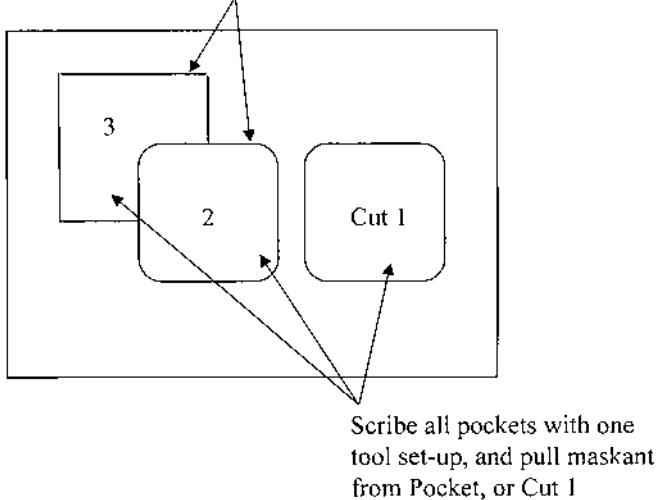
Figure 8 Scribe line sealer advantage.

Parts with multiple chem-mill cuts may be processed by scribing and milling Cut 1, and then scribing and milling Cut 2 etc., or by scribing all pockets/lines with one tool set-up then sealing all lines for Cuts 2 and greater. To successfully complete the latter process a line sealer is applied by brush over all scribe lines that define preceding cuts such as 2, 3, 4, ... (Fig. 8). Scribe line sealers must prevent etchant leakage into scribe lines during the chemical milling process, but pull away cleanly as each pocket is pulled for further chemical milling. In addition line sealers must apply rapidly without foaming. Just as with chem-mill maskants line sealer choices are solvent-based or waterborne. Without question, recently introduced waterborne line sealer products are superior to their solvent-based predecessors.

2.3.1 Laser Scribing

The scribing process was automated with the introduction of a Laser Scribing Machine in the early 1980s at McDonnell-Douglas in St. Louis, Missouri. The machine was designed and constructed to scribe flat aluminum sheet stock only. More sophisticated multi-axis laser scribing machines were developed at the Douglas Aircraft Division of McDonnell-Douglas in the mid 1980s. Laser Scribing machines are now available from virtually any manufacturer of laser machine tools. CO_2 lasers are typically used for maskant scribing applications, and when possible the number of optics in the beam path should be minimized (Fig. 9).

Locating the laser close to the work surface, and moving the work surface instead of the laser, allows for a short beam path and should allow use of fewer optics and a low power laser.

Laser Scribing Technique
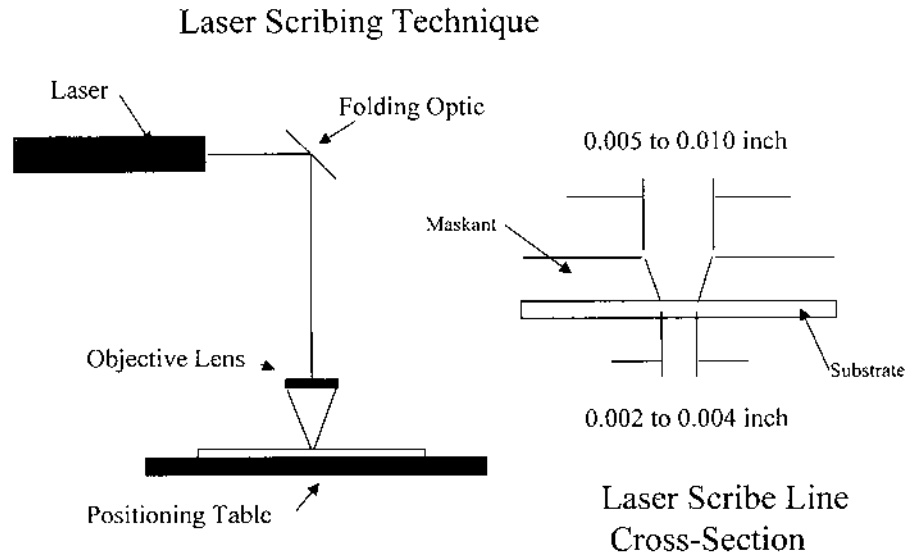
Figure 9   Laser scribing chem-mill maskant.

Laser power requirements for maskant scribing are determined by the number of optics in the beam path, and the desired feedrates for laser scribing. For example, with one folding optic and an objective lens in the beam path, and a 400 in./min. (ipm) on axis feedrate a minimum of 200 W of laser power at the work surface is necessary. Less laser power will cut the maskant, however with a minimum of 200 W at the cutting surface, the laser scribing process can easily accommodate variations in maskant film thickness, and variations on work-piece flatness. Such variations move the cut area in and out of the depth of field of the objective lens. Having adequate laser power is the most practical way of correcting for focus variations.

The light energy emitted from lasers in the 200–500 W range will reflect from the aluminum substrate, thus there is no damage to the substrate, but an enclosure should be constructed around the scribing machine. Since the laser vaporizes the maskant, there is an effluent generated by the process. Silica and quartz dust are possible by-products as is small amounts of styrene (from the styrene butadiene rubber typically used in maskants), CO and CO_2. Therefore, the process must be ventilated and emissions may be regulated by local air quality authorities.

Once the scribing machine is installed the supplier and user of the laser must work out an acceptable scheme for laser power control. As the machine slows for corners or splines in the part geometry, laser power must be reduced to prevent overheating of the maskant. A typical scheme is to run the laser in continuous wave mode while operating at feedrates greater than 100 ipm, then converting to laser pulse mode for lower feedrates as the machine negotiates corners.

Laser scribed lines are more difficult to line seal than knife scribed lines. Laser scribe line kerf width is 0.002–0.01 in. compared to 0.001–0.002 in. for a knife scribed line (assuming that a sharp knife is used) (Fig. 9). Waterborne scribe line sealers recently formulated for laser scribed lines have provided excellent performance.

As with knife scribed lines the line sealer products should be flowed over the scribe lines with unidirectional brush or applicator strokes. Multi-directional brush strokes, or "painting" the scribing lines can draw the line sealer out of the scribe line, which will allow leaks at the scribe line during the etching process.

The primary advantage of laser scribing is the elimination of scribing tools – reduction in scribing time is significant for large parts only. Once part data has been digitized, scribing automation can be easily expanded to include tooling hole location and final routing. Integrating chem-mill scribing with pre- and post chem-mill processes will eliminate requirements for all tools and sample parts. Hence, the manufacture and administration of many tools can be eliminated, plus part design changes can be incorporated in minutes instead of months.

For large part scribing, the expansion coefficient for metal or fiberglass scribing templates is sufficient to cause significant dimensional problems for long parts (20–40 ft long) when scribing is performed manually. Material used for scribing templates and work surfaces or holding devices must be selected to mitigate dimension changes that may occur due to differences in morning and mid-day temperature. Laser scribing allows for simple correction by using machine control unit functions for temperature compensation. Temperature compensation can easily be programmed into laser scribing machines to correct for problems with part/tool expansion or contraction.

2.4 Etching

Once scribing and line sealing are complete, parts are ready for etching. Parts are loaded into simple baskets or onto load bars. The preferred load position is diagonal, (e.g. 45°), but parts are frequently loaded in a vertical, or 90° position (Fig. 10). Parts horizontally (flat) in work baskets will carry larger amounts of etchant into the first rinse.

Parts are held in position by simply wiring the part to the basket structure, or by weighing the parts down with heavy screens. Small parts are generally placed in special dividers and held in place with heavy screens. If the chem-milled cut depth exceeds 50 mm, then good practice dictates stopping the process half way through the cut, and rotating the part

Two etchant types are used for aluminum chemical milling, Type I and Type II (Table 1). A preferred practice in some chemical milling operations is to mill 80% of the cut in Type I Etchant, and finish the cut in Type II Etchant to improve surface finish.

Agitation of the etchant while parts are in process is good practice. Depending upon etch rate, some chem-mill operators refer to aluminum etchants as self-agitating, but agitation by mechanical means is necessary. Etchant agitation by air sparging is discouraged as injecting oxygen into the etchant will produce thiosulfate [4, 5], which will in turn cause rough surface finish. Use of mixers, or pump(s) and fluid eductors is a preferred choice for etchant agitation.

2.5 Demasking

Demasking consists of removing all chem-mill maskant after all chem-mill cuts have been completed to the proper depth. Demasking is generally accomplished by simply pulling the maskant away from the substrate by hand. Specialized demasking tools
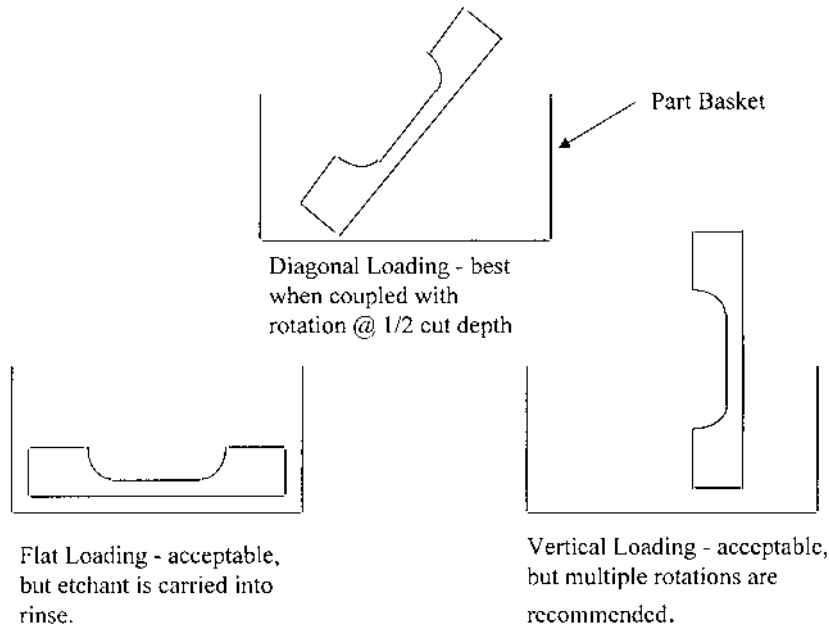
Figure 10 Basket loading.

have been developed for removing maskant from those substrates that exhibit excessive maskant adhesion (Fig. 11). The demasking tools are also valuable for expediting the demasking process. Other techniques such as dissolution of solvent based maskants (by immersing the part in the original maskant diluent) require long cycles times and expensive clean-up. Demasking by hand is the best compromise.

3 MASKANTS FOR ALUMINUM CHEMICAL MILLING

Masking for chemical milling is the most critical of the five basic process steps. The maskant type and application technique selected influence all aspects of the process. The pre-mask cleaning technique employed is dependent upon the maskant type

Table 1 Aluminum Etchants

Aluminum Etchant	Constituents	Operating Temperature, °F	Etch Rate mm/m/sec	Surface Finish, Ra
Type I	sodium hydroxide sodium gluconate sulfur	180–205	0.5–1.2	120–250
Advantage: low cost				
Type II	sodium hydroxide sodium sulfide triethanolamine	180–225	0.8–3	40–70
Advantage: fast etch; excellent surface finish.				
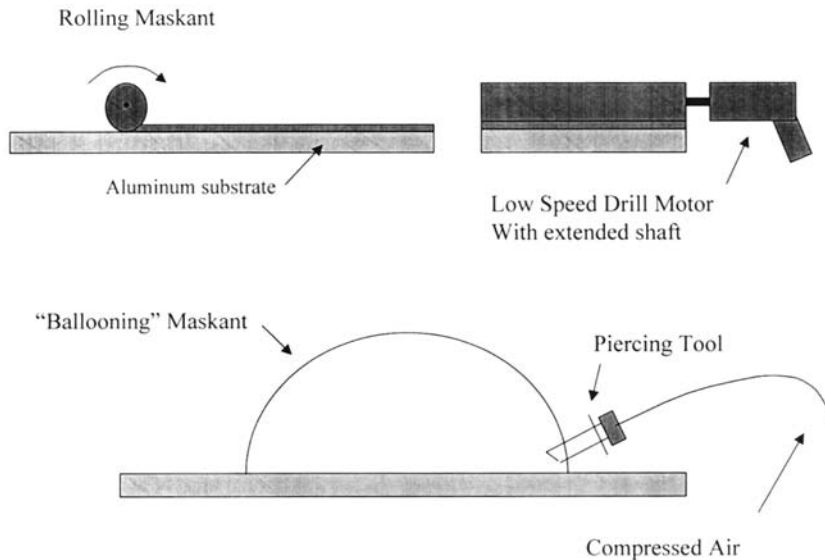
Figure 11 Demasking techniques.

selected. Overall process cycle-time is influenced by masking dry and curing time requirements and the maskant adhesion to the aluminum substrate. High maskant adhesion (adhesion in excess of 40–45 oz/in.) extends scribe and patch times and the time required final desmasking efforts. High maskant adhesion contributes to employee discomfort and medical costs in the form of muscle strains and injury. High maskant adhesion contributes to increased scrap as thin gage material may yield and deform as large areas of maskant are pulled away during the demasking operation.

For aluminum chemical milling there are two maskant types, waterborne or organic solvent systems. The Environmental Protection Agency (EPA) established limits for control of emissions from chemical milling maskant application based on the etchant type used. If Type I aluminum etchant is used emissions may be 622 g/l (grams solvent per liter of liquid maskant applied). If Type II aluminum etchant is used and compliant maskants (waterborne or compliant solvent) are selected then solvent emissions are limited to 160 g/l. If Type II aluminum etchant is used and solvent-based maskant with solvent abatement equipment is selected, the abatement equipment must demonstrate a minimum 81% capture efficiency [6]. The use of etchant types as a determinator for allowed solvent emission is based on performance failures of waterborne maskants in the Type I aluminum etchant.

Solvent-based chemical milling maskants are based on synthetic rubbers and one or a combination of organic solvent diluents. Filler materials and other additives are also included to enhance certain performance characteristics such as tensile strength, abrasion resistance or chemical resistance.

Development of organic solvent-based maskants began with Dr. Sanz and development of chemical milling as a modern manufacturing process. Solvent-based masking systems experienced some development pains, but the products evolved and improved and solvent-based maskants have remained essentially the same since the

early 1980s. The lingering attraction to solvent-based maskants is that they are a known entity. Chemical milling operators can purchased solvent-based maskants from suppliers, or make solvent-based maskant. Formulas for solvent-based chemical milling maskants are available from resin suppliers. Solvent-based maskant formulae are mature and in terms of potential variations in pre-mask cleaning and aluminum etchants, solvent-based maskants are robust.

Early waterborne maskants employed natural rubbers emulsified in water. Chemical resistance was excellent, but the emulsion proved unstable and early waterborne maskants tended to fail in the mask tank in the form of uncontrollable viscosity or conglomerated rubber particles. Early arguments against waterborne maskant centered on the instability of the emulsions. Waterborne maskants that were mixed violently, or not properly maintained in the correct pH range, etc. could set-up into viscous lumps of rubber.

3.1 Equipment Designs

Strategies for use of such unstable maskants included improved equipment designs and different maskant chemistry. Early offerings of waterborne maskant were piloted in 500–1000 gal capacity tanks. The tank size selected for pilot operations allowed for reasonable evaluation and development cost, and allowed sufficient space for processing some production parts. Initial tank designs centered on simple rectangular tanks with circulation pump(s) connected to chambers located at opposing ends of the tank. Maskant was pumped from one chamber to the opposing chamber, hence maskant flowed across the tank surface (Fig. 12). Maskant flow
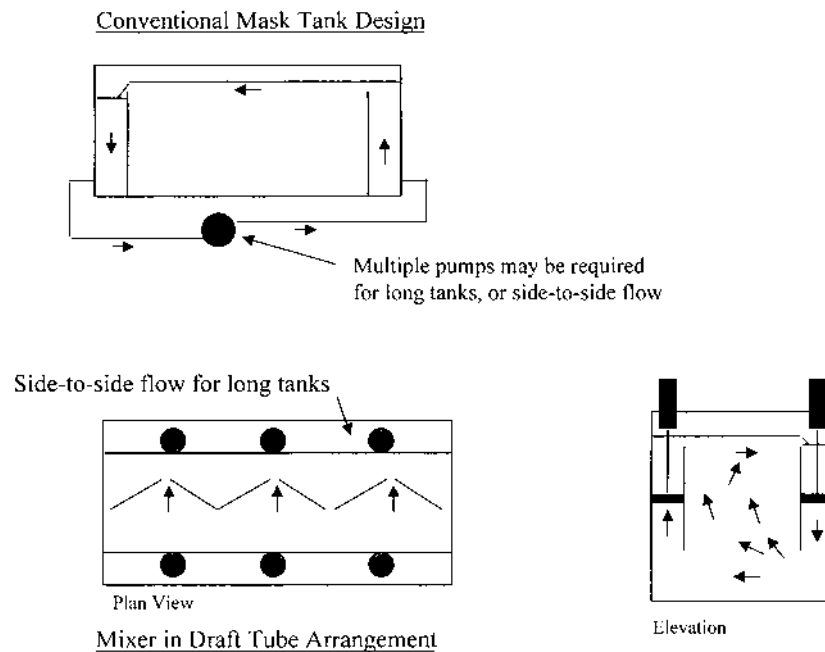
Figure 12 Mask tank designs for immersion coating.

problems are a potential problem with conventional tank designs. Maskant "skins"[1] may appear in surface areas where there was insufficient fluid flow. Valves installed to allow some control of pump will produce little improvement.

In addition to the flow problems, pump selections can produce disastrous results. High shear pumps, such as gear or vein pump designs will destroy waterborne maskant. Within a short time high shear pumps will likely seize due to large amounts of conglomerated maskant collecting on pump internals. Diaphragm pumps are considered low shear pumps and they provide considerable improvement over the high shear designs. Diaphragm pumps do not correct flow problems in the tank, and they create their own maintenance problem. Diaphragm pumps are marginal for continuous duty service. This fact has been demonstrated in production facilities where diaphragms fail with regularity and fillers in the maskant quickly erode valve seats. Generally, complete pump rebuilds will be required at intervals ranging from 100–500 hr of pump operation. Attempts to extend the service interval increases the risk of catastrophic diaphragm failure, which will immediately contaminate the maskant with small air bubbles. Repairing pumps and "de-airing" maskant typically entails 16–24 hr downtime.

An alternate tank design for waterborne maskants as developed in the 1980s [7] (Ref. Fig. 12). Mixers in a draft tube were selected to correct maskant flow problems, and the mixer and draft tube arrangement created weir flow at the down-flow mixer, a desirable attribute of the pump driven circulation design. Mixers are capable of moving large volumes of fluid at low pressure [8], hence the maskant surface could be quickly displaced and all bubbles and drippings from a previous part are quickly swept away. A successful waterborne maskant installation at the Boeing facility in St. Louis, Missouri (formerly McDonnell-Douglas) employs the mixer design (Ref. Fig. 12). A diaphragm pump is used for maskant transfer to the immersion tank, and a progressive cavity pump is used to circulate maskant through a bag filter.

Construction costs for either design are similar, however designs that use mixers will incur lower maintenance costs and less downtime. Design elements outlined in reference [7] have been greatly simplified to reduce costs, while retaining all claimed attributes of the tank design.

Less complicated tank designs may be used. Designs that employ mixers for localized maskant blending have been used with limited success. For example, marine type impellers may be used and are least expensive, but are best used in draft tubes and with impeller tip speed limited to 11 ft/sec. Low shear impellers may also be used, but are less effective than marine type impellers in draft tube applications. Any mask tank design that will provide the following performance attributes will provide trouble free operation:

- Mix maskant volume to maintain viscosity and pH consistency.
- Sweep bubbles and drippings from the maskant surface between part immersion cycles.
- Create weir flow to break entrained bubbles and provide opportunity for maskant filtering.

---

[1] Dried maskant that forms on the maskant surface in the immersion tank. Always occurs in areas of low or no fluid flow.

- Create surface flow velocities sufficient to prevent the formation of large maskant skins.

3.1.1 Long Term Mixing Studies for Waterborne Maskants

Due to stability problems experienced with early waterborne maskants testing was conducted to determine the tank life of maskant products. Mathematical formulas were derived to estimate the service life of waterborne maskant such that suppliers and users could perform adequate testing to evaluate long term performance of waterborne chem-mill maskant.

Historic records indicate waterborne chem-mill maskants were evaluated, developed, and considered for implementation at a few chemical milling operations in the late 1970s, however, a perchloroethylene based maskant and solvent collection system was selected as the best process for compliance with the regulations enacted by some states. The primary concern with waterborne maskants during those initial evaluations was in-tank stability. Early waterborne maskant systems demonstrated sensitivity to mechanical forces exerted by the pumps used for material transfer and tank circulation.

In the late 1980s there was a renewed effort to develop and implement waterborne chem-mill maskants. The initial maskant formulations offered in the late 1980s were essentially the same products that did not work when evaluated ten years earlier. Hence the maskant stability question was again foremost in the minds of those considering implementation of waterborne maskants. The need for techniques for estimating the tank life of a maskant was apparent.

Immersion, or dip application of chem-mill maskant is the preferred coating technique for sheet metal parts with severe contours and extrusions. Immersion coating reduces maskant coating defects, eliminates difficulties with spray or flow coating equipment and spray booth maintenance. Along with equipment development activities [7], a series of equations was derived to describe the service life of maskant in an immersion coating system. Mixing studies were conducted to determine the tank life of waterborne maskants. Tank designs, maskant operating temperatures, pH and impeller configurations were tested (Table 2). The time base for each test run was determined with Eqs. (1)–(4). Mixing study research demonstrated that waterborne maskant stability concerns are essentially unfounded, provided process control recommendations for maskant maintenance are adopted as standard practice.

Maskant tank life calculations are based the observation that new, or fresh maskant is added to an immersion coating system, then thoroughly mixed with maskant resident in the tank (Fig. 13). Assume a 200 gal/day mask usage, and a total tank volume of 6000 gal. This relation can be modified and written in the form of the "Law of Natural Decay" [9]. The new expression is:

$$G_r = C_{e^{kt}} = 6000\, e^{kt} \tag{1}$$

where

G_r = Gallons of original mask remaining
C = Constant tank volume, 6000 gallons for current tank
t = time, days
k = Coefficient of mask usage = -3.39×10^{-2} day^{-1}, for 200 gal/day mask usage.

Table 2   Mixing Study Test Plan Example

Factors	(−)	Levels Units	(+)
A Impeller Tip Speed	4	ft/sec	15
B Impeller Type	100	Model #	310
C Maskant pH	low		high
D Maskant Temperature.	80	°F	150
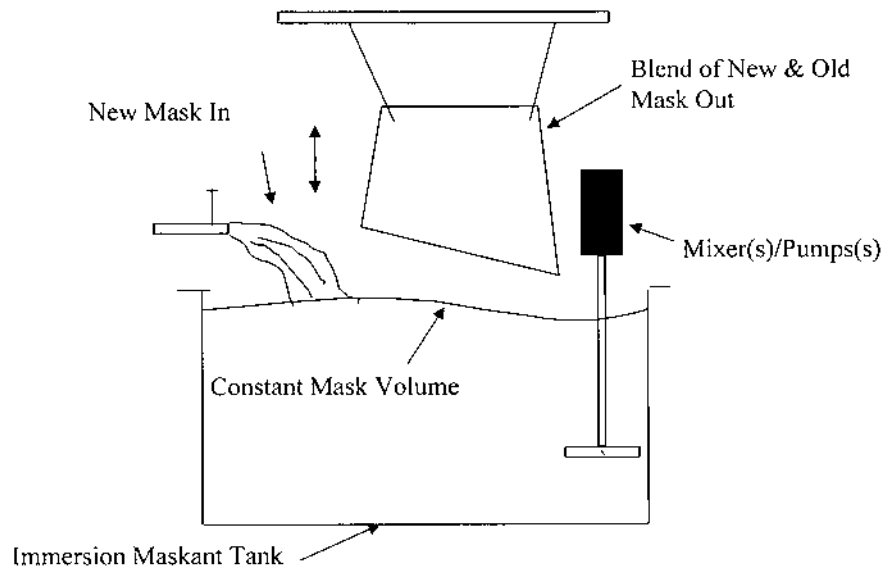
Figure 13   Immersion tank operating schematic.

The linear plot of $G_r = 6000\ e^{kt}$- for $k = -3.39 \times 10^{-2}$ (Fig. 14).

The new expression provides an accurate estimate of the volume of the original tank charge of maskant remaining in the tank at any time (t). However, values for G_r are valid only if maskant added to maintain tank volume is sufficiently mixed with resident maskant to produce a homogeneous mixture.

Impeller (or propeller) type mixing apparatus may be used to promote homogeneity of newly added and resident maskant. When placed in a draft tube apparatus mixers become inefficient pumps capable of moving large volumes at low pressure. Mechanical pumps are more effective for moving low volumes at high pressure. Hence, mechanical pumps are less effective for mixing/blending large tank volumes. Also, proper placement of mixing impellers produce tank surface flow conditions conducive to good quality mask coatings. Therefore, a new unit is introduced, Impeller Cycles (C_1). Impeller Cycles shall be defined as the number of times the tank volume passes through a mixing impeller per unit time. Impeller Cycles can be simply defined as the quotient of the total pumping capacity of the mixing impellers used in the tank, and the tank volume.
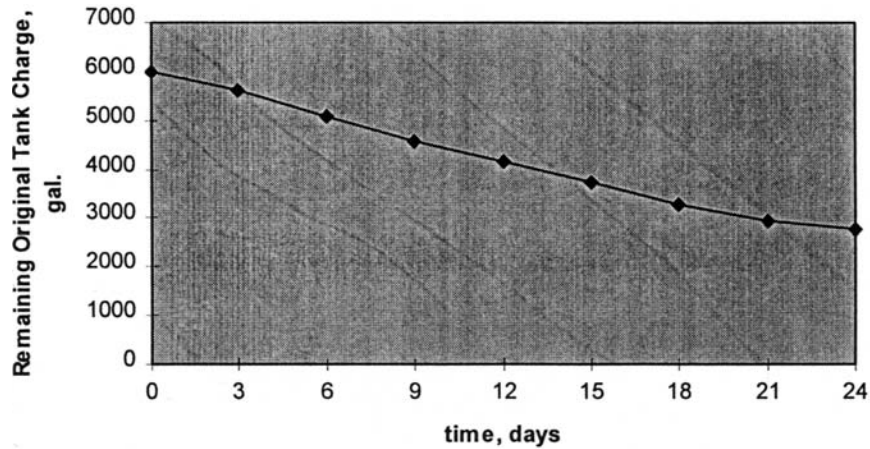
Figure 14 Mask tank original charge versus time.

$$C_1 = \text{Average number of impeller cycles occurring each day}$$

where

$$C_1 = \text{total pumping capacity (gal/day)/tank volume (gal/cycle)}$$
$$C_1 = \text{Cycles/day}$$

C_1 describes the rate at which the tank contents passes through the mixing impellers. However, as described per Eq. (1), the volume of the original tank charge diminishes relative to time. The original tank charge is blended with new mask and the mixture is applied to parts immersed in the maskant. Therefore, the impeller cycles experienced by the original tank charge also diminish relative to time. The diminishing impeller cycle rate is (I_c), and is defined as

$$I_c = C_1 e^{kt} \tag{2}$$

where

I_c = Impeller Cycles, rate for original tank charge at any time (t), cycles/day.
C_1 = Average number of impeller cycles occurring each day, for the entire tank volume, cycles/day
t = time, days
k = coefficient of mask usage, day^{-1}

Perhaps more useful information would be an estimate of the total number of impeller cycles to which a maskant is subjected from the time of mixer activation, ($t = 0$), to any time (t). The following equation provides a numerical estimate of the total number of impeller cycles (I_{ct}), at any time (t):

$$I_{ct} = C_1(e^{kt} - 1)/k \tag{3}$$

where I_{ct} = Impeller Cycles, total

Equation (3) is derived from Eq. (2), reference Appendix A.

The total number of impeller cycles to which a maskant will be subjected to during its entire tank life is:

$$I_{cm} = -C_1/k \tag{4}$$

where I_{cm} = Impeller Cycles, maximum

Reference Appendix A.

Substitution of different constants and mask usage coefficient allows the equations to be used to model mask tank operations of any magnitude. For example, a manufacturer uses a particular maskant product that covers $650\,\text{ft}^2$ at 1.0 mils (1 mil = 0.001 in.) coating thickness. Parts immersed in the maskant actually receive a nominal coating thickness of 6.5 mils. The manufacturer has a 2000 gal capacity maskant tank and coats $500{,}000\,\text{ft}^2$ of substrate each year.

Maskant usage per year:

$(650\,\text{ft}^2/\text{gal})/6.5\,\text{mils} = 100\,\text{ft}^2/\text{gal}$ actually surface coverage.
$(500{,}000\,\text{ft}^2)/100\,\text{ft}^2/\text{gal} = \textbf{5000 gal of maskant per year}$, minimum usage.

Maskant time in tank: the manufacturer operates a 2000 gal tank, 16 hr per day, 250 days per year. The average maskant usage per day is:

$(5000\text{ gal mask}/\text{yr})/250\text{ mfg. days}/\text{yr} = 20$ gal mask/day.

Equation (1) can be rearranged was follows:

$$G_r = 2000\,e^{kt}$$
$$k = 1\text{n}[(2000 - 20)/2000] = -1.005 \times 10^{-2}$$

The mask tank used by the manufacturer has six (6) mixing impellers with a pumping capacity of 2500 gal/min. The mixers are operated intermittently. Total mixer operation time is 8 min each hr, or 128 min each day. Impeller Cycles per day (average):

$(2500)(8)(16)[\text{gal*min*hr}/\text{min*hr*day}] = 320{,}000$ gal/day
$\Rightarrow C_1 = (320{,}000)/2000\,[\text{gal*cycle}/\text{day*gal}] = \textbf{160 Impeller Cycles/day}$.

Thus, Eq. (4) becomes:

$$I_{ct} = 160(e^{kt} - 1)/k.$$

Providing the total number of impeller cycles at any time (t).
The maximum number of impeller cycles experienced by the original tank charge of maskant during time in tank is:

$$I_{cm} = -160/(-1.005) \times 10^{-2} = \textbf{15, 920 Impeller Cycles}.$$

The test apparatus for such a system would consist of a small scale tank (10 gal with mixer(s) and draft tube(s). A pump could also be used if such a tank design is desired. Assuming that mixers are selected a test plan is developed to compare the additive effects of impeller selection, impeller tip speed, maskant pH control and maskant operating temperature (Ref. Table 2). Based on the estimations from Eq. (1)–(4), each test run should last 15,160 Impeller Cycles.

The advantage provided by the equations allowed for rapid evaluations of equipment designs and maskant formulae while modeling the expected tank life of waterborne maskant products. Derivation of the equations appears in the Appendix A as they are also applicable for other processes that employ emulsions and immersion tanks, e.g. electroprime painting.

3.2 Waterborne Maskant Chemistry

In addition to the stability issue, some waterborne maskant product offerings in the 1980s consisted of multiple coatings and cure cycles. A maskant product promoted by the DeSoto Aerospace Coatings Co., consisted of three separate coatings, (applied by immersion or spray), with a cure cycle for each. Although complicated, the products produced very good results. Unfortunately, the product was considered too complicated by most potential users for practical use.

Competition among maskant suppliers resulted in much improved masking systems with stable chemistry and simple control techniques. Actual waterborne maskant chemistries are proprietary formulas protected by the maskant suppliers. Waterborne maskant offerings now provide performance attributes equal to, and in some categories, exceeding the present capabilities of solvent based maskants. Waterborne maskants as applied have higher volume solids, which equates to covering more surface area per gallon of maskant.

3.3 Waterborne Maskant Limitations

Waterborne maskants may not be used in process lines that serve to prepare parts for bonding. Surfactants inherent in waterborne maskant systems will leach into processing solutions, and influence the surface tension of anodize solutions. However, no bond adhesion test specimens processed with a surfactant ''contaminated'' anodize solution are reported to have failed acceptance testing

Waterborne maskants currently available will not perform well following autoclave cycles. In metal bonding applications a bond cycle of 8–10 hr at 250–350°F exceeds the capabilities of waterborne maskants. The long cure time at high temperature over-cures maskant resulting in excessive adhesion. A waterborne maskant could be developed for such an application, but there have been no development attempts to date.

3.4 Regulatory Requirements

The viable compliance approaches are reduced to use of a waterborne maskant, use of a maskant with a compliant solvent diluent, or use of standard solvent-based maskant with solvent emission abatement equipment. In some regulatory environments, emissions compliance with abatement equipment triggers additional record keeping requirements to insure verification of meeting a required emission capture efficiency[2].

---

[2] In the USA Aerospace NESHAP (National Emissions Standard for Hazardous Air Pollutants) derived from the 1990 Clean Air Act require 81% capture efficiency for solvent emission abatement equipment.

There are essentially three options for use of solvent-based masking systems while remaining compliant with most solvent emission limits.

- Use solvent-based maskant in conjunction with solvent abatement equipment.
- Use a compliant solvent such as Oxsol-100.
- Purchase the maskant as a concentrate such that the solvent content is 622 g/l, then cut the maskant to operating viscosity with a compliant solvent (applicable for Type I etchant users only).

In all cases the user must insure that the compliance technique and application process does not exceed the worker exposure limits (i.e. OSHA Personal Exposure Limit (PEL) in USA) for the solvent(s) selected. In addition the user must be certain that solvents selected comply with all local regulations and that all equipment used near masking areas where flammable solvents are used comply with local fire codes[3].

Solvent-based maskants with abatement equipment allows two options.

- Use a flammable solvent diluent such as toluene, actone, xylene or Oxsol-100 with thermal oxidation equipment. Solvent emissions are burned and the heat of combustion can be captured for use elsewhere in the facility. All equipment near the masking operation must be explosion proof and when the solvent load from the masking operation drops before a prescribed minimum, natural gas or other fuel must be used maintain proper combustion temperature.
- Use a chlorinated solvent such as perchloroethylene and Carbon Bed Solvent Collection.

Perchloroethylene with carbon bed solvent collection is perhaps the best choice if solvent-based masking operations are preferred. Carbon beds can tolerate low solvent loading and remain relatively efficient. Properly designed carbon bed systems can maintain 95–98% collection efficiency of all solvent that enters the inlet plenum, (Fig. 15 and 16).

Once a collection bed is completely loaded, steam is injected into the bed to strip the solvent. The mixture of solvent and steam is piped to a condensing section. From the condenser the mixture is piped to a water separation tank. Solvent is piped to a storage tank for reuse, and water is routed to an industrial sewer, or water-solvent stripping device to assure that no solvent enters the sewer system. The collected solvent may be returned to the maskant supplier and used in new maskant, and used to dilute incoming maskant concentrate. For abatement equipment 81% capture efficiency is required per the Aerospace NESHAP[4]. A capture efficiency of 81% equates to a solvent emission of approximately 236 g/l (grams of solvent emitted/liter of maskant applied) depending on the solvent-based maskant used. To operate within prescribed emission limits solvent emissions must be prevented before the solvent laden reaches the abatement equipment (Ref. Fig. 16).

A gross comparison of three frequently used compliance techniques appears in Table 3.

---

[3] Oxsol-100 is a flammable solvent as is Toluene. Perchloroethylene is not flammable and can be used with solvent emission abatement equipment.
[4] Applicable in the USA.
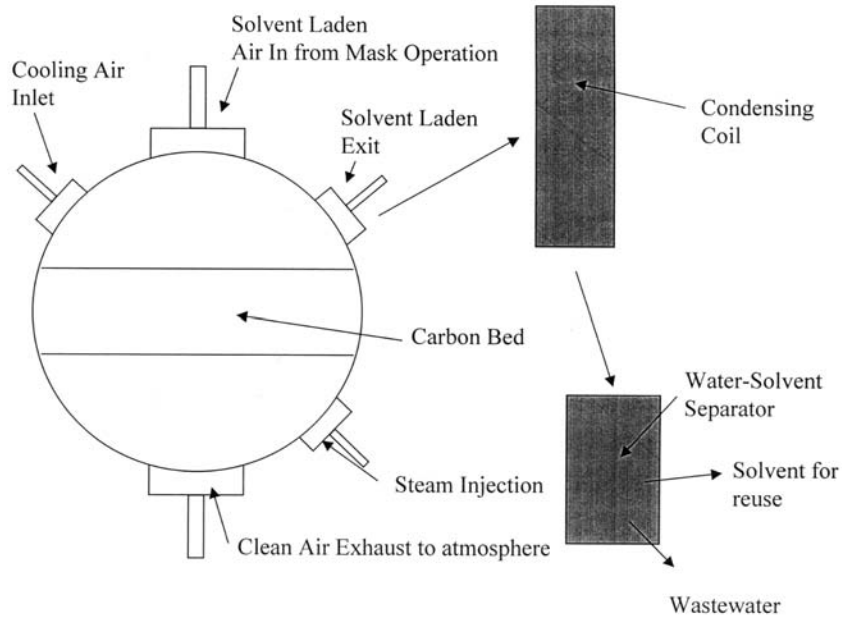
Figure 15 Primary elements of carbon bed solvent collection.
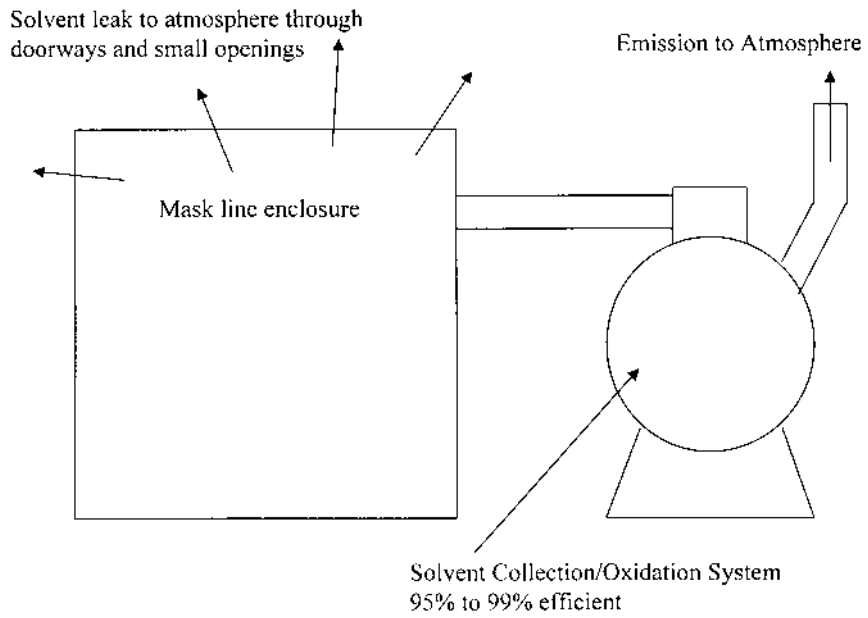
Figure 16 Operation schematic for solvent emission abatement.

Table 3 Maskant Compliance Approach

Flammable Solvent Diluent with Thermal Oxidation	Chlorinated Solvent with Carbon Bed Solvent Collection Equipment	Waterborne Chem-Mill Maskant
Allowed Emission: 81% Capture	Allowed Emission: 81% Capture	Allowed Emission: 160 g/l
Reporting Frequency: 7–30 day	Reporting Frequency: 7–30 day	Report Frequency: none
Rolling Average (Site Specific).	Rolling Average (Site Specific).	
Advantages:	Advantages:	Advantages:
Low cost maskant	Low cost maskant relative to water-borne maskants or compliant solvent alternatives.	Compliant – no record keeping requirements
Low cost abatement equipment	Non-flammable	Improved abrasion and pull-up resistance.
Waste heat from combustion can be reclaimed for use	Collected solvent can be reused for cutting mask concentrate or making new maskant	
Disadvantages:	Disadvantages:	Disadvantages:
24 hr/day stack emissions and equipment monitoring. Ongoing record keeping requirements for local and federal regulatory agencies	Daily material balance	Higher maskant adhesion to substrate, (if solvent-based maskant adhesion is 12–14 oz/in., waterborne maskant adhesion will be 20–25 oz/in.
	Ongoing recording keeping requirements for local and federal regulatory agencies	
Equipment maintenance	Equipment maintenance	
Mask line downtime during equipment maintenance and emergency repairs	Mask line downtime during equipment maintenance and emergency repairs	
Introduction of any chlorinated solvent carries the risk of severe corrosion potential	Corrosion – chlorinated solvents will evolve small amounts of hydrochloric acid, which will corrode equipment components and eventually the carbon bed vessels.	
Flammable solvent use increases insurance premiums and necessitates use of explosion proof equipment.	Limited service life—10–15 years.	
Limited service life.		

Table 3 *Continued*

Cost Estimate:
Asymptotic to both *X* and *Y* Axes as abatement equipment costs remain fixed, i.e.
y ($/sq ft) = Fixed $/Area Coated.

Plan for equipment replacement at or about the end of the capital equipment depreciation periods

Cost Estimate:
Asymptotic to both *X* and *Y* Axes as abatement equipment costs remain fixed, i.e.
y ($/sq ft) = Fixed $/Area Coated.

Plan for equipment replacement at or about the end of the capital equipment depreciation periods

Cost Estimate:
Asymptotic to both *X* and *Y* Axes as abatement equipment costs remain fixed, i.e.
y ($/sq ft) = Fixed $/Area Coated.
Cost estimate function is essentially linear beyond capital equipment depreciation period as maskant and operating costs track with usage
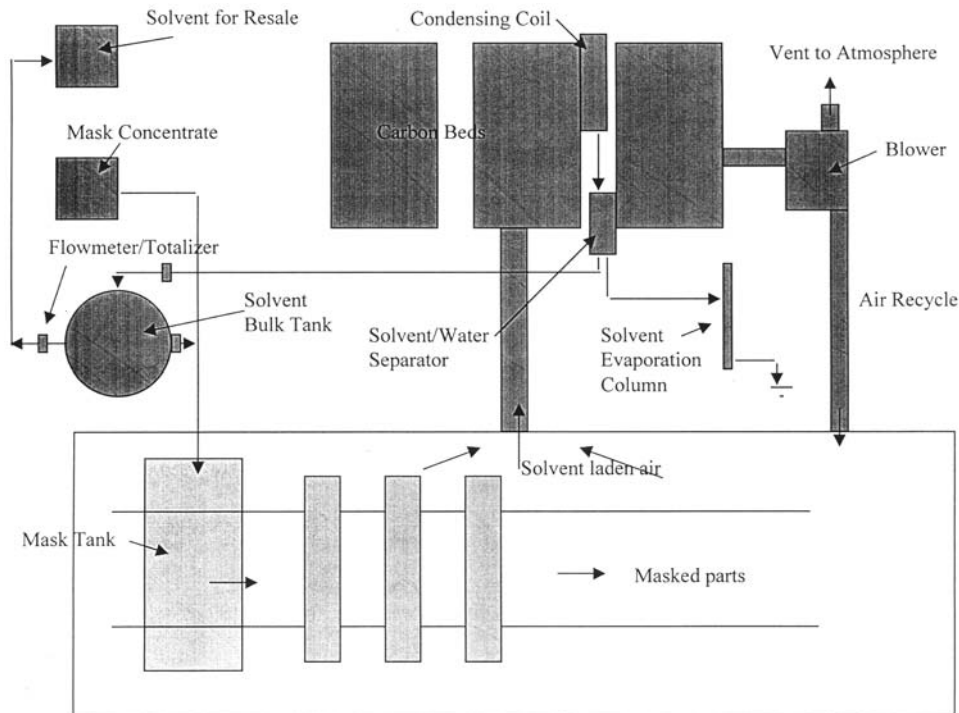
Figure 17 Solvent abatement material balance.

3.4.1 Record Keeping Requirements [7]

Following initial compliance demonstration/verification, operators of thermal oxidation systems must retain daily records of exhaust stack emissions and equipment operation parameters. All instrumentation must be operational while the oxidation equipment is operating.

Operators of carbon bed solvent collection equipment must maintain a daily material balance to and report emissions for a 7–30 day rolling average to demonstrate 81% capture. The material balance is an accounting of all solvent that entered the maskant system with all solvent collected by the solvent collection system. The difference is the solvent emission. The material balance is based on information from flow totalizers that measure the volume of solvent transferred from the solvent bulk storage tank to the maskant tank, and solvent collected and transferred to the bulk storage tank (Fig. 17). An example of a material balance performed on an operation carbon bed solvent collection system appears in Table 4.

Material Balance Summary, reference Table 4:

- Maskant Inventory: Maskant is conveniently received in totes of 250–400 gal capacity. Drums (55 gal) may be used also, but increased handling labor is incurred. A flow meter or flow totalizer could be used, however maskant concentrate viscosity of 22–24 Poise as received, compounded with higher viscosity in cold weather and entrained air (from tote changes), etc. make accurate flow measure difficult.

Table 4 Solvent Emission Material Balance

Maskant Inventory		
Full totes last report:	13	Maskant tote volume: 350 gal
Full totes this report:	8	Mask concentration solvent content: 69%
Deliveries:	9 3150 gallons	Incoming maskant is diluted with solvent to operating viscosity.
		Dilution ratio is 1 gal solv: 5.8 gal mask concentrate.

I. Maskant Use (gallons) = Deliveries + [(Full totes last report—full totes this report) (tote volume)]

			Uncertainty
[1] Mask use this report:	4900	gallons	350 gal
[2] Solvent content:	3381	Mask use × 69%	245 gal

Maskant in a tote that is connected to the system is assumed to be maskant added to the system. Since the tote may full, the uncertainty of maskant use is +/− measurement applies to both the maskant and the solvent content of the maskant.

Measurement Error: Measurement of solvent transfers or the volume of solvent in a bulk storage tank are made with flow totalizers, or by sight glass. Measurement resolution for each instrument is defined for each measurement activity. Error propagation is calculated for the material balance.

Maskant Viscosity Control		Solvent for Resale	
Meter total this report:	23,025	Meter total this report:	14,485
Meter total last report:	17,000	Meter total last report:	7,000
[3] total added:	6,025	[6] total removed:	7,485
Uncertainty, 1.5% of total added		Uncertainty, 1.5% of total added	
Viscosity Control		Solvent for Resale	
Total uncertainty ± =	45.1875	Total uncertainty ± =	56.1375
Solvent in Bulk Storage		Solvent Removals	
Meter total this report:	500	Meter total this report:	70
Meter total last report:	350	Meter total last report:	40
[4] total added:	150	[7] total removed:	30
Uncertainty, 1.5% of total added		Uncertainty, 1.5% of total added	
Bulk Storage		Solvent Removals	
Total uncertainty ± =		Total uncertainty ± =	0.225

If Site Glass Used:
Error Present Reading: 10
Error Past Reading: 10
    Total uncertainty ± = 20

Solvent Added for Replenishment
Added this report [5]: 0

II. Total mask and solvent applied: $[1]+[3]=[8]=$ 11,734 gal
    Uncertainty ± = 350 gal
III. Total solvent added: $[2]+[3]+[5]=[9]=$ 9,406 gal
    Uncertainty ± = 290 gal
    $[9] \times 13.47$ lb/gal $=[10]=$ 126,699 lbs.
    Uncertainty ± = 3,909 lbs.
IV. Total solvent recovered: $[4]+[6]+[7]=[11]$ 7,665 gal
    Uncertainty ± = 60 gal
    $[11] \times 13.47$ lb/gal $=[12]=$ 103,248 lbs.
    Uncertainty ± = 803 lbs.
V. Recovery Efficiency $=([11]/[9])(100)=$ 81%
    Uncertainty ± (for this report) = 3.15%
VI. Weight of solvent emitted/volume of maskant applied $=([10]-[12])/[8]=$ 2.0 lb/gal
    240 g/1
    Uncertainty ± = 0.20 lb/gal
    24 g/1

1185Maskant may be purchased as a concentrate to reduce shipping costs. Recovered solvent is used to dilute the maskant to operating viscosity (18–20 Poise). The volume of solvent can be metered from the bulk tank (Fig. 17). An alternate arrangement would be to pump mask concentrate directly to the mask tank, then increase solvent additions for viscosity control.

- Maskant Viscosity is controlled with solvent pumped directly into the maskant tank.
- Solvent in bulk storage is solvent collected and stored for reuse in the maskant system, or pumped to empty maskant totes for resale to the maskant supplier.
- Solvent added for system replenishment is any solvent added to the system from an outside source. For example, if the bulk storage tank is low, new solvent may be purchased in 55-gal drums and the contents of said drums pumped directly into the mask tank. If no new solvent is added to the bulk storage tank then the entry for Solvent Added is zero (0).
- Solvent for Resale is recovered solvent excess to system needs. The solvent is pumped to empty maskant totes and returned to the maskant supplier where it is used in the manufacture of new maskant.
- Solvent Removals are quantities of solvent workers remove from the system for other purposes. For example, the solvent may be used to dissolve maskant from mask line hang hooks. Solvent used for such purposes, i.e. recovered solvent now containing a small amount of maskant solids should be added directly to the maskant tank, and an entry made for Solvent Added to System.
- Recovery efficiency is the quotient of Total Solvent Recovered and Total Solvent Added. The Uncertainty associated with Recovery Efficiency results from measure error propagation. Error propagation is additive and for solvent emissions, which is the quotient of Solvent Recovered and Solvent Added to System error is:

$$\delta \text{Emission}/\text{Emission} = (\delta \text{Solv. Recovery}/\text{Solv. Recovered}) \\ + (\delta \text{Solv. Add}/\text{Solv. Added}). \tag{5}$$

As indicated by the Material Balance, solvent collection efficiency must be a minimum of 81% to meet regulatory requirements. To assure compliance, collection efficiency must be maintained at 83%. Pitfalls with solvent collection and the material balance is equipment maintenance and control of solvent removals and additions. A valve failure on a carbon bed, if not repaired in a timely manner, will result in non-compliance. Workers removing or adding solvent without recording the activity, and volumes of solvent transferred, will greatly skew the material balance. To be successful as a compliance approach, carbon bed solvent collection and material balance reporting requires timely equipment maintenance and careful material control.

3.4.2 Estimating Costs for Masking Systems

The cost estimating technique presented for all compliance approaches are based on an exhaustive accounting of solvent-based and waterborne masking systems. The cost estimate were developed by aerospace airframe manufacturer as a means of comparing the relative costs of three techniques for complying with Aerospace NESHAP emission limits in the USA. The cost estimate results are presented here

to demonstrate the unit cost of coating aluminum with chem-mill maskant and how solvent abatement equipment can be prohibitively expense of work load falls below the economic threshold. Cost estimates are based on 1997 dollars and include equipment costs, maintenance and operating costs for the particular control device and support costs for safety and environmental issues. Items not included are equipment installation costs, or costs for material handling and automated conveyance equipment as such costs are site specific.

Calculating Maskant Surface Coverage and Estimating Maskant Use
Maskant suppliers will report the solids content of a maskant as % by weight, and sometimes they will include solids content as % by volume. To determine the area that a maskant will cover, solids as % by weight must be converted to solids as % by volume. The unit used to describe coating coverage is ft^2–mil/gall, i.e. the area covered by 1 gall of maskant, with a dry coating thickness of 1 mil (0.001 in.). Calculating the actual coverage for a particular maskant is important as suppliers offering a lower price may simply be diluting their product and selling more water or solvent, whatever the situation may be. See Appendix B for surface coverage calculation technique.

Thermal Oxidation
Thermal oxidation equipment for flammable solvent is generally the least expensive abatement equipment. The function describing the unit cost of operating thermal oxidation equipment is the quotient of capital cost of the abatement equipment (depreciated over 13 years), plus recurring costs for maskant and abatement equipment, and the total area of aluminum to be coated at an idea maskant film thickness. It is reasonable to assume a service life for thermal oxidation equipment is equal to the depreciation period. Hence, once the depreciation period ends, the equipment will be replaced with like equipment (Fig. 18).

$$\$/ft^2 = (\$63,000 + Recurring\,Costs)/Surface\,Area. \tag{6}$$

Where Recurring costs are all maintenance and equipment utility costs and maskant costs. Solvent-based maskants will cover approximately $28\,ft^2$ with a dry mask film, 14–15 mil thickness.

Carbon Bed Solvent Collection
Carbon Bed Solvent Collection of non-flammable solvent such as perchloroethylene is a good compliance choice for varying solvent loads. The function describing the unit cost of operating carbon bed solvent collection equipment is the quotient of capital cost of the abatement equipment (depreciated over 13 years), plus recurring costs for maskant and abatement equipment, and the total area of aluminum to be coated at an idea maskant film thickness. It has been demonstrated that service life of carbon bed solvent collection equipment is equal to the depreciation period. Hence, once the depreciation period ends, the equipment will be replaced with like equipment (Fig. 19).

$$\$/ft^2 = (\$53,000 + Recurring\,Costs)/Surface\,Area \tag{7}$$
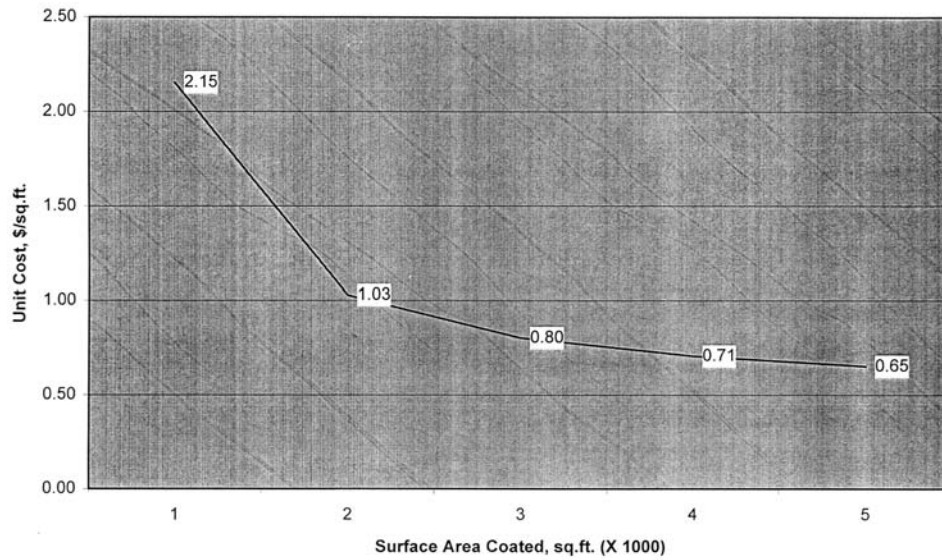
Figure 18 Thermal oxidation, $/sq ft versus area coated.
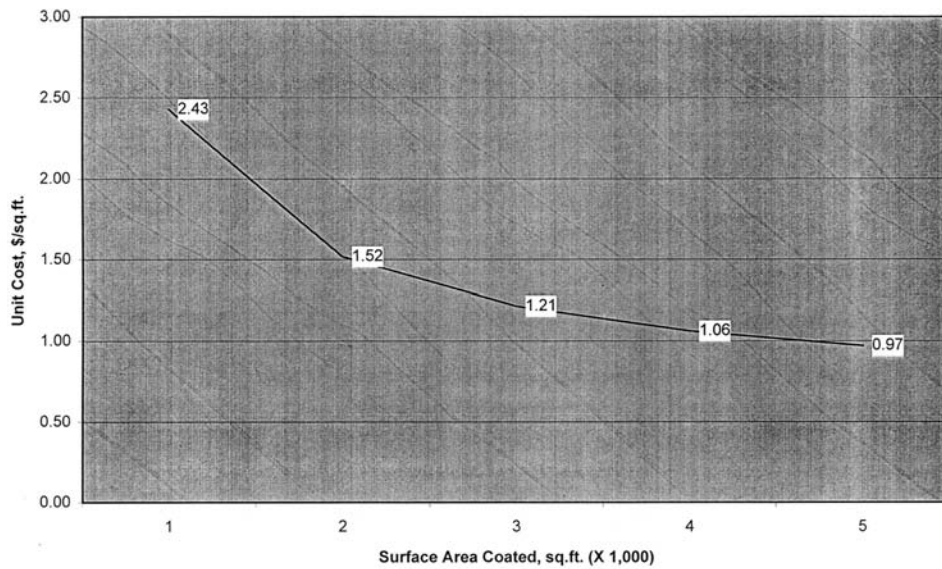
Figure 19 Carbon bed solvent collection, $/sq ft versus area coated.

Waterborne Maskant

Waterborne maskant requires the lowest capital expenditure and the lowest costs for maintenance. Unlike abatement equipment, waterborne maskant will become less expensive when the depreciation period ends (Fig. 20).

$$\$/ft^2 = (\$45,000 + \text{Recurring Costs})/\text{Surface Area} \tag{8}$$
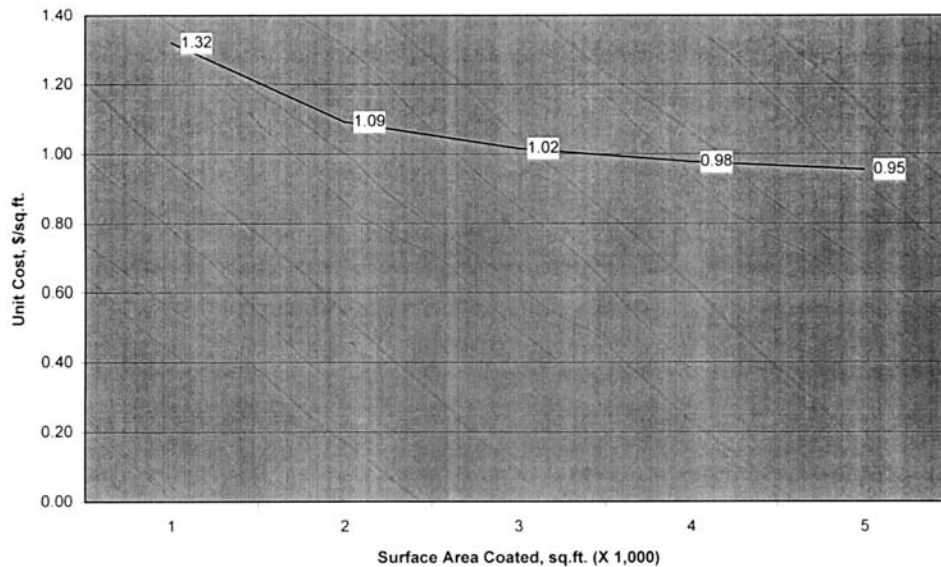
Figure 20 Waterborne maskant, $/sq ft versus area coated.

Waterborne maskants will cover approximately $29\,ft^2$ with a dry mask film, 18–20 mil thickness. Waterborne maskants will cover more surface area with greater film thickness due to higher volume solids content of the liquid maskant. Typical weight solids for solvent-based maskant is 20 wt% and 25 vol% and the product is used at viscosity of 18–22 Poise. Waterborne maskant are typically 42–45 wt% and 30–40 vol% and are applied at viscosity of 25–40 Poise. In the out-years following the capital equipment depreciation period the unit cost function is (Fig. 21).

$$\$/ft^2 = (\$700 + Recurring\,Costs)/Surface\,Area \tag{9}$$

Taguchi Loss Function as Cost Estimating Technique

An unconventional cost estimating technique that is valuable for all projects with an environmental impact, i.e. any manufacturing process regulated by a government agency, is the Taguchi Loss Function [10]. The traditional view of environmental compliance is simply reducing emissions to fall within compliance bounds. Hence, if an emission limit is 160 g/l, then compliance is achieved if emissions are controlled to 159 g/l.

The Taguchi Loss Function ranks processes, or a compliance approach by the overall impact on society. By Taguchi's logic a violator starts paying a debt to society when emission limits are exceeded, however society still pays for health disorders even at emission levels somewhat lower than the limit defined by law. Hence, emitting 159 g/l, though legal, really is not any better in terms of environmental improvement than emitting 161 g/l, which would trigger a fine.
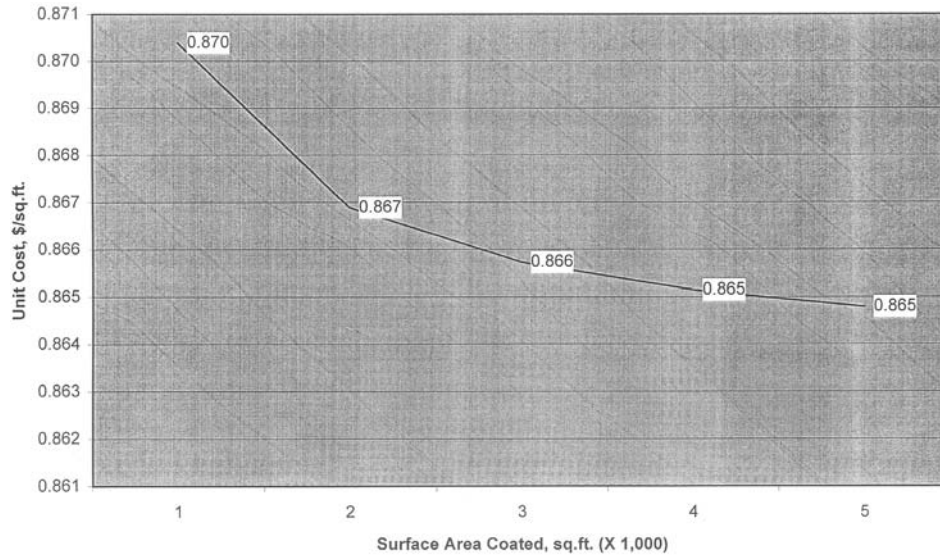
Figure 21   Waterborne maskant, $/sq ft versus area coated.

    In the case of environmental issues the loss to society is the cost paid to treat cancer, respiratory disorders, and other health issues. The loss to a company is in the form of fines paid to regulatory agencies, and increased health and operating insurance premiums. Taguchi's Loss Function

$$\text{\$ Loss} = kx^2 \tag{10}$$

where

        $ Loss is the loss to society due to poor air quality, e.g. ozone alert days.

        x is solvent emissions from a chem-mill masking operation

            let $x = \sigma + \mu$

where

        σ is the Standard Deviation of solvent emissions from abatement equipment, and μ is the average emission from solvent abatement equipment.

$$\Rightarrow \text{\$Loss} = k[\sigma^2 + \mu^2] \tag{11}$$

    Industry example—a "Case Study" of statistical methods for cost comparison. First calculate probabilities of exceeded allowed emission limits, then compare Taguchi Loss Function.

    Solvent Abatement—a 10,000 CFM Carbon Bed Solvent Collection system operated for 13 years capturing solvent emission from a chem-mill masking operation at a large aerospace company. Operating history indicated average emission (μ) to atmosphere from the system was 120 grams solvent per liter of maskant applied, with Standard Deviation $\sigma = 74$ g/l. Emission limits allowed per the Aero-

space NESHAP, effective September 1998, are 160 g/l for Type II etching (for compliant maskants), 236 g/l for Type II etching (for solvent abatement equipment), and 622 g/l for Type I etching.

The probability of exceeded the mandated emission limits can be estimated based on the long-term performance of the system described. It should be noted that maintenance of the system described was not a priority. This fact is evident in the standard deviation of solvent emissions for the system.

With the solvent collection system operating as described, the probability of a compliance failure based on the equipment operating history and the 236 g/l limit may be calculated [11]. It is assumed that solvent emissions from the described system are normally distributed with mean emissions of $\mu = 120$ g/l and standard deviation $\sigma = 74$ g/l., i.e. $x \sim N(\mu, \sigma^2)$, or $x \sim N(120, 74^2)$. A process drift of 1.5σ is included [12], i.e. $(1.5)(74) = 111$ g/l.

$$P\{x \geq a\} = 1 - P\{z \leq (a - \mu)/\sigma\} = 1 - \Phi[(a - \mu)/\sigma] \tag{12}$$

Where $\Phi(\bullet)$ is the cumulative distribution function of the standard normal distribution (mean $= 0$, standard deviation $= 1$) [11].
Then, from Eq. (11)

$$
\begin{aligned}
P\{x \geq 236\} &= 1 - P\{z \leq (236 - 120)/111\} \equiv 1 - \Phi[(a - \mu)/\sigma] \\
&= 1 - P\{z \geq 1.0450\} \\
&= 1 - \Phi(1.0450) \\
&= 1 - 0.85199 \text{ (table value)} = 0.15, \text{ or } 15\%
\end{aligned}
$$

Based on the historical data, that particular solvent collection system would be out of compliance 15 days out of 100.

Assume that the latest in solvent collection equipment, plus careful maintenance, can reduce both average solvent emissions and emissions variance such that $\mu = 110$ g/l and $\sigma = 40$ g/l; $1.5\sigma = 60$ g/l. The probability of compliance failure and fines becomes

$$
\begin{aligned}
P\{x \geq 236\} &= 1 - P\{z \leq (236 - 110)/60\} \\
&= 1 - P\{z \leq 2.1\} \\
&= 1 - \Phi(2.4) \\
&= 1 - 0.98422 \text{ (table value)} = 0.016, \text{ or } 1.6\%
\end{aligned}
$$

Thus, unless equipment maintenance remains a high priority, the solvent collection system could slip out of compliance 15 days for every 100 days. At \$22,000/day the potential annual fine is approximately \$818,400 (Fig. 22).
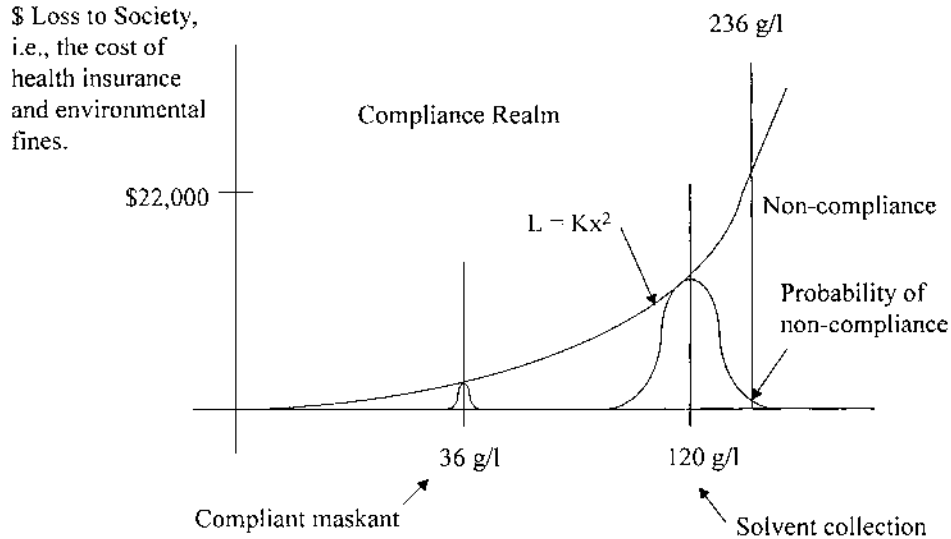
Figure 22 Taguchi loss function.

In contrast, a waterborne system is available at lower capital cost that contains 36 g/l of a VOC and solvent content standard deviation is $\sigma = 3$ g/l. The probability of non-compliance with the 1.5σ process drift is

$$P\{x \geq 160\} = 1 - P\{z \leq (160 - 36)/4.5\}$$
$$= 1 - P\{z \leq 27.556\}$$
$$= 1 - \Phi(27.556)$$
$$= 1 - 1.0 \text{ (table value)} = 0.0, \text{ or no chance.}$$

Thus, the potential annual fine for a waterborne masking system is $0. Assume that the maskant supplier, or the resin supplier mistakenly creates a batch of maskant with 50 g/l VOC or HAP

$$P\{x \geq 160\} = 1 - P\{z \leq (160 - 50)/4.5\}$$
$$= 1 - P\{z \leq 24.4444\}$$
$$= 1 - \Phi(24.4444)$$
$$= 1 - 1.0 \text{ (table value)} = 0.0, \text{ or no chance.}$$

A Taguchi Loss Function example can be developed from the information provided. The federal fine for exceeding emission limits is $22,000/day for each day of non-compliance. Then rearrange Eq. (11)

$$k = \$22,000/[(74)^2 + (120)^2] = 1.11$$

The theoretical loss to society, for the best solvent collection system is

$$\$\text{Loss} = 1.11[(60)^2 + (110)^2] = \$17,427/\text{day}$$

The theoretical loss to society for a competing waterborne maskant, relative to the solvent collection system becomes

$$\$Loss = 1.11[(4.5)^2 + (36)^2] = \$1,461/\text{day}.$$

Where possible, the compliant maskant system is a better choice. New zero VOC waterborne maskants will enter the market in 1999, reducing the loss to society to $0.

4 TOOLING

Tools for chemical milling may consist of a simple scribing template, or may be a group of tools and sample pieces consisting of a Drill Template, Chem-Mill Template, Router Block, Sample Part #1 and Sample Part #2.

A typical sheet metal fabrication process includes forming, heat treat and age followed by chemical milling, chemical processing and paint. A Drill Template is applied to the formed part after heat treat and age. The Drill Template locates the reference holes (tooling holes) necessary for proper location of the Chem-Mill Template and the Router Block[5]. The Chem-Mill Template is located on the part contour with tooling pins that are inserted into the holes located by the Drill Template. After Chemical Milling, the Router Block is located on the part contour by pinning the Router Block into the holes located by the Drill Template. Sample Part #1 is a reference part that is formed to contour and has notations of all final part features engraved in the part surface. Sample Part #2 is a reference part that has been produced with the Drill Template, Chem-Mill Template and Router Block and inspected to confirm that part produced by the tools conform to blueprint requirements.

Tooling materials are dictated by part fabrication requirements. Flat parts can be produced with tools fabricated from fiberglass or sheet metal (aluminum or steel). Sheet metal tools are typically used when the part to be fabricated is flat. The tools can be cut on a laser or water-jet machine at minimal labor cost. Flat tool fabrication is a relatively simple matter if the chem-mill geometry is available in electronic form. Fiberglass tools may also be used for flat parts, but tool fabrication cost is somewhat higher. The advantage of fiberglass as a tool material is that the tool can be easily modified. Metal tools are typically scrapped and replaced. In general, sheet metal is used as fabrication tools for flat parts, and fiberglass is used as fabrication tools for parts with contour.

The location and geometry for chemically milled features are generally transferred from a master model of the part in a lofting[6] operation, however loft data in electronic form will greatly accelerate the process.

---

[5] When possible the Drill Template and Routing Functions are combined into one tool.
[6] In ship building a loft is constructed above the keel and hull surface points are scaled off a model of the hull and transferred via plumb lines and levels and measuring instruments to define points on the hull surface.

Etching Action

Fillet

Substrate

Chem-Mill Template Line (CMTL)   Undercut

Maskant

Depth of Cut

Chem-Mill Line (CML)

$$\text{Undercut Ratio} = \frac{\text{Undercut}}{\text{Depth of Cut}} \qquad (13)$$
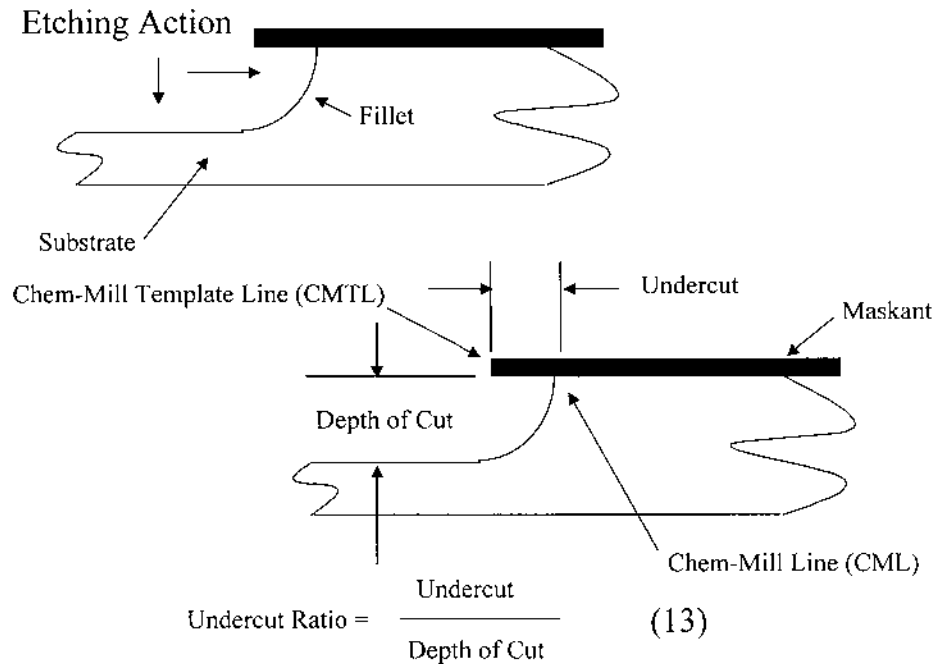
Figure 23   Chem-mill undercut ratio, or etch factor.

    Chem-mill Templates are used to locate the scribe line relative to some reference point. An important distinction here is that the scribe tool defines the Chem-Mill Scribe Line, or Chem-Mill Template Line (CMTL). After etching, the Chem-Mill Line (CML) remains. It is the chem-mill line that must be located correctly relative to a reference point (Fig. 23).

    Tool-makers must accommodate two phenomenon know as Chem-Mill Undercut, and Chem-Mill Set-Back (Fig. 24). Undercut is analogous to the cutter offsets employed by programmers of numerical control machines. Set-Back is unique to chemical milling.

4.1 Chem-Mill Undercut and Undercut Ratio

Chemical etchants etch beneath the maskant, parallel to the substrate surface simultaneously with the etching action normal to the substrate surface. The rate of simultaneous etching parallel and normal to the substrate surface usually is note equivalent (Ref. Fig. 23). Chem-Mill Undercut is typical defined as a ratio such that the tool-maker need only multiply the undercut ratio by the depth of cut to calculate the necessary tool offset.

    Design Engineers may require that some chemically milled features are located accurately. For example, chemical milling may be used to create a recessed area for an overlapping part (Figs. 25–27), or to create boss areas for fasteners or bulkhead pass-through holes (Fig. 28). Land areas located between chemically milled pockets must be very close to the target dimension to insure proper edge distance for rivet
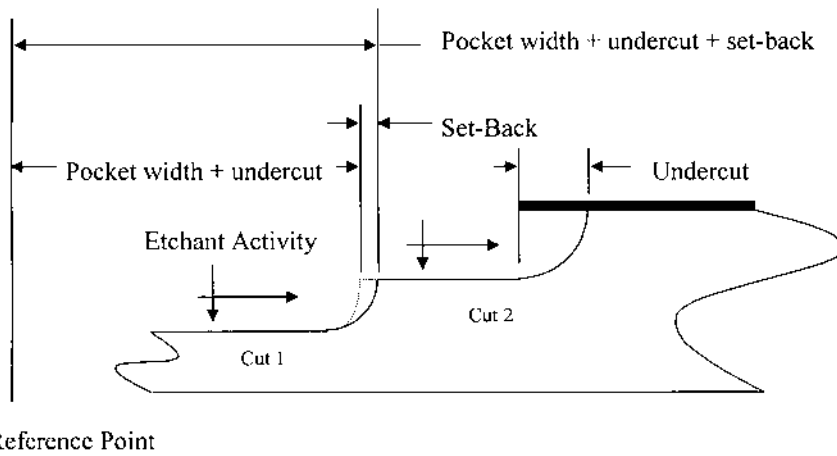
Reference Point

Figure 24 Chem-mill set-back.

$$\text{Undercut Ratio} = \frac{\left| \text{CMTL - CML} \right|}{\text{Initial Thickness (T1) - Final Thickness (T2)}} \quad (14)$$
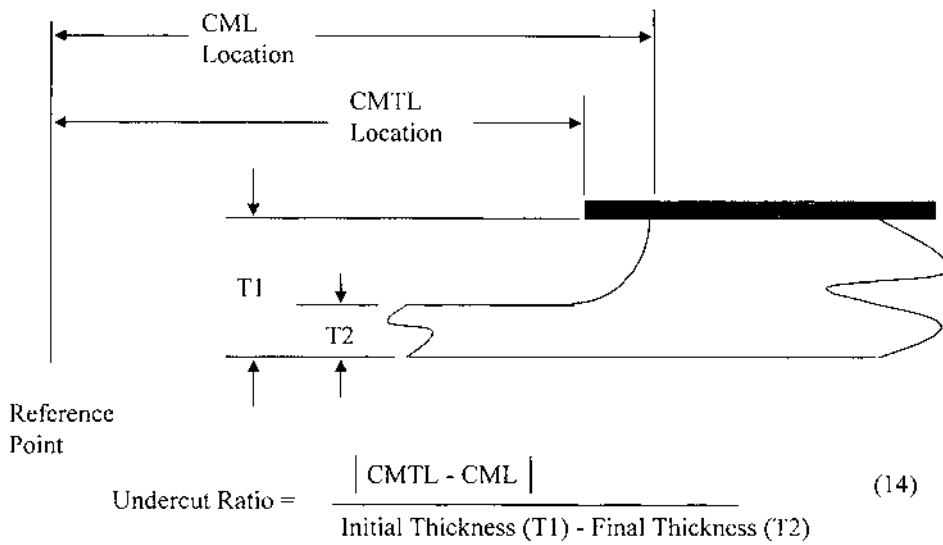
Figure 25 Chem-mill pocket recess.

holes. For example, a tool-maker must construct a chem-mill template that will produce a chem-mill line located 1 in. from two reference points (Figs. 25 and 26); chem-mill pocket (Fig. 27) 2.0 in. wide, and in an adjacent part area a 2.0 in. wide chem-mill land (Fig. 28). The Undercut Ratio, or Etch Factor for the material is 1.5, and the depth of cut is 0.070 in.

- Tool Dimension for Line, Left Ref. Point (Fig. 25):
  $1 - (0.070)(1.5) = 0.9$ in. from reference point, i.e. CMTL must be 0.9 in. from reference to produce CML 1.0 in. from reference.
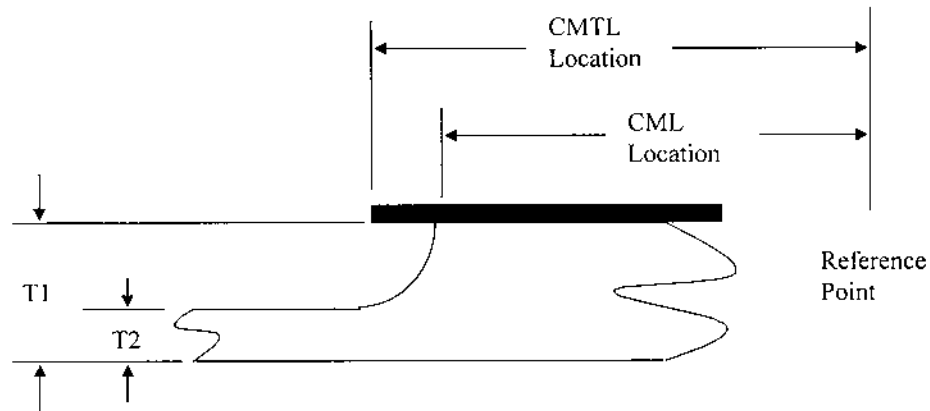
Figure 26 Chem-mill pocket recess, right reference point.

$$\text{Undercut Ratio} = \frac{(W1 - W2)}{2(T1 - T2)} \qquad (15)$$
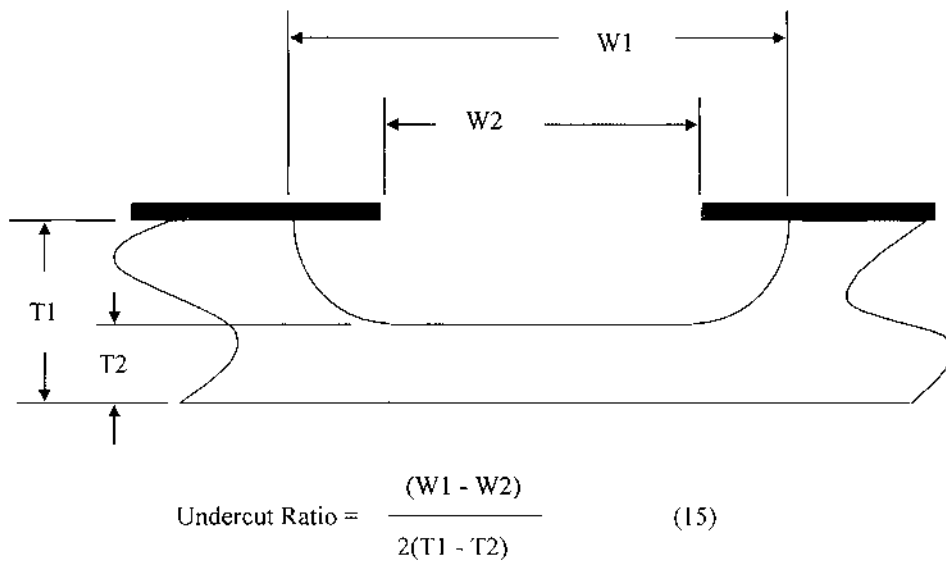
Figure 27 Chem-mill pocket.

- Tool Dimension for Line, Right Ref. Point (Fig. 26):
  $1 + (0.070)(1.5) = 1.11$ in.
- Tool Dimension for the Pocket:
  $2 - (2)(0.070)(1.5) = 1.79$ in.
- Tool Dimension for the Land:
  $2 + (2)(0.070)(1.5) = 2.21$ in.

Chemically milled features that do not meet the target, or nominal, blueprint dimensions could make the part heavier than necessary, and could perhaps create a geometrical stress riser that could cause premature fatigue failure.
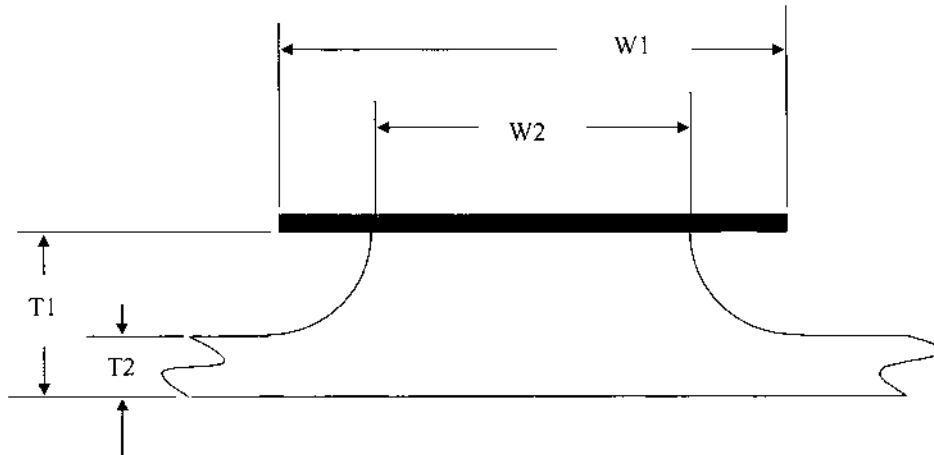
Figure 28 Chem-mill land.

4.2 Chem-Mill Set-Back

Chem-Mill Set-Back applies to multi-cut parts only. Chem-Mill Set-Back occurs between joining pockets of different cut depths. Once maskant is removed from an area adjacent to a previous cut, etching occurs on all surfaces (Fig. 24). The initial chem-mill line will move relative to a fixed reference point, but not as far as undercut. The accepted rule of thumb is that set-back is 1/3 of the depth of cut for the remaining pocket, however this heuristic is not entirely correct. Chemical milling is area sensitive. If the initial or previous cut is shallow (20 mils or less), there will be little or no set-back. If the initial cut depth is 50% of the joining cut, set-back is the multiple of 0.8 and the depth of the joining cut. If the initial cut depth is 100% of the joining cut the set-back is the multiple of 1.2 and the depth of the joining cut. Assume a tool-maker must construct a tool that will locate the first cut CML 1 in. from the reference point, and the Cut 2 CML 2 in. from the reference point (Fig. 24). The undercut ratio for the material is 1.0; Cut 1 depth is 60 mm, Cut 2 depth is 70 mm, and the ratio is $\sim$ 1.0. Then the CMTLs must be located accordingly:

- CMTL Cut 2: 2 - (0.07)(1.0) = 1.93 in. from reference
- CMTL Cut 1: 1 - (0.06)(1.0) - (0.07)(1.2) = 0.86 in. from reference.

4.3 Area Rules in Chemical Milling

Chemical milling is a convenient manufacturing technique for reducing the weight of complex sheet metal forms. Without chemical milling, aircraft such as the North American XB-70 Valkyrie or Boeing's 747 would have been more difficult to fabricate, and perhaps hopelessly overweight. As a weight reduction technique, designers tend to position chem-mill pockets in every available space without regard to pocket size. Unfortunately, large variations in pocket sizes will result in large variations in finished pocket depth (Fig. 29).
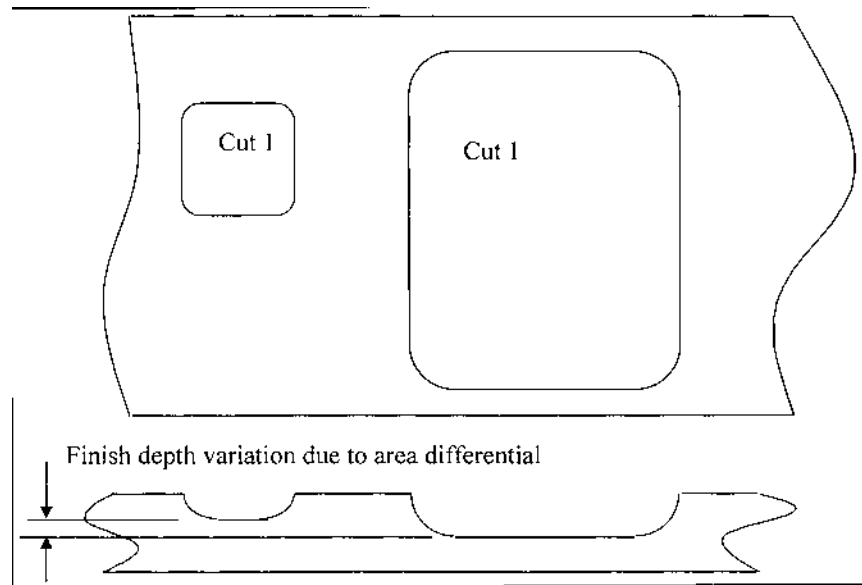
Figure 29 Chem-mill pocket differential.

For example, if a pocket of approximately 2 in^2 area is adjacent to a 48 in^2 pocket and both pockets are the same cut, the finished dimensions will differ by as much as 10 mils. Therefore, a relevant design heuristic is to minimize variation of pocket size for a particular cut, e.g. no pocket within a particular cut number should have area twice as great as any other pocket. Also, part designers should minimize the number of cuts while maximizing the cut depths. This heuristic will serve to limit finished dimension variations to approximately 4 mils, reduce finished part weight and simplify all tooling (Fig. 30).

4.4 Calculating Cut Removals

In addition to calculating undercut offsets, set-backs and sizing scribing templates according, tool-makers must also determine the actual removals for each chem-mill cuts Part blueprints will show the finished dimension for each pocket, i.e. the final thickness of each chemically milled pocket for a complete part. The finish dimensions must be converted into removals for the chem-mill operator (Fig. 31). Finish dimensions are converted to removals for a simple multi-cut part (Table 5).

Chemical milling simultaneously from multiple surfaces, or Double Cut, requires special considerations (Fig. 32). Finish dimensions are converted to removals for a simple multi-cut part with removals from opposing surfaces (Table 6).

Double cut areas will eventually confuse both tool-makers and chem-mill operators. The problem is inconsistency in part dimensioning practice. Part dimensions on the blueprint may appear relative to either the substrate stock thickness, or relative to the finish dimension in the double cut area. The tool-maker must pay close attention to the finish dimensions and their locations relative to other
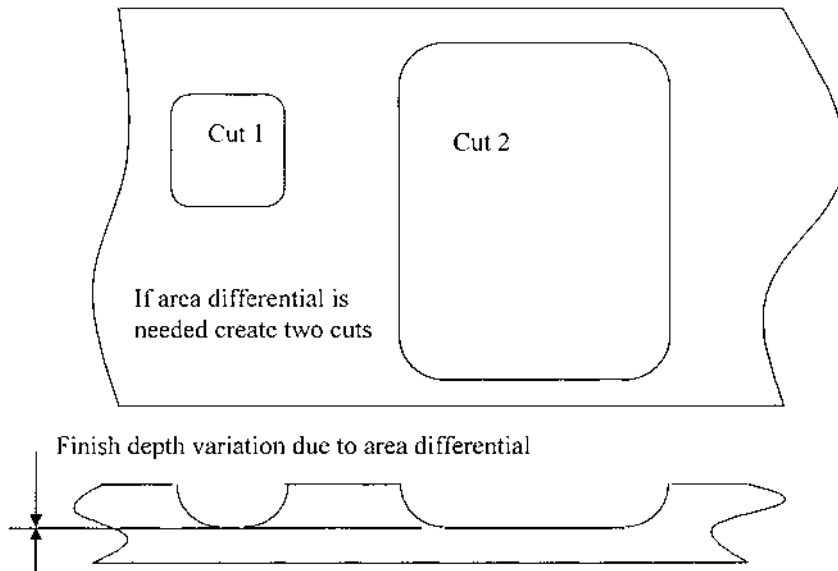
Figure 30 Pocket change order to correct pocket depth differential.
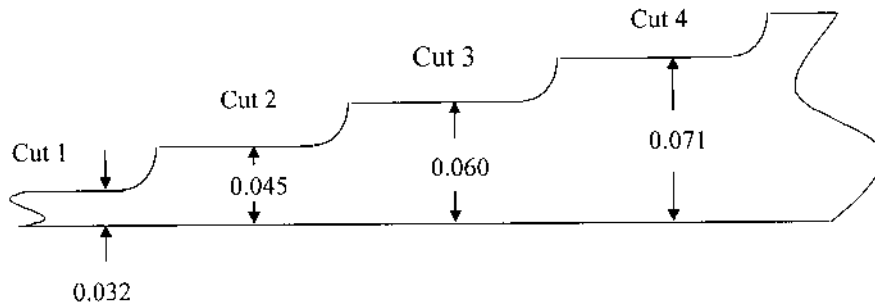
Figure 31 Cut removal calculations, 4-Cut part.

cuts on the opposite side of the part. For example, if the part designer had instead indicated a finish dimension of 105 mils for Cut # 6, and a finish dimension of 140 for Cut # 5, (Fig. 33) then all cuts are be calculated (Table 7 and 8).

5 ETCHANTS FOR ALUMINUM CHEMICAL MILLING

Aluminum is amphoteric, i.e. it is soluble in both acids and bases. Acid based aluminum etchants are used for aluminum cleaning operations, but seldom used for chemical milling operations. Acid etchants produce slow etch rates and leave a rough surface (Table 9).

The most widely used aluminum etchants are alkaline based with sodium hydroxide as the most popular alkali [1].

Table 5 Removal Calculation, 4-Cut Part (Fig. 31)

Cut	Stock Thickness (mil)	Finish Dimension (mil)	Delta	Double Cut	Delta— Previous Cuts	Removal (mil)
4	100	71	29			29
3		60	40		40 − 29	11
2		45	55		55 − 29 − 11	15
1		32	68		68 − 29 − 11 − 15	13

Check Cut	Stock Thickness (mil)	Removals	Finish Dimension (mil)
1	100	13 + 15 + 11 + 29	32
2		15 + 11 + 29	45
3		11 + 29	60
4		29	71
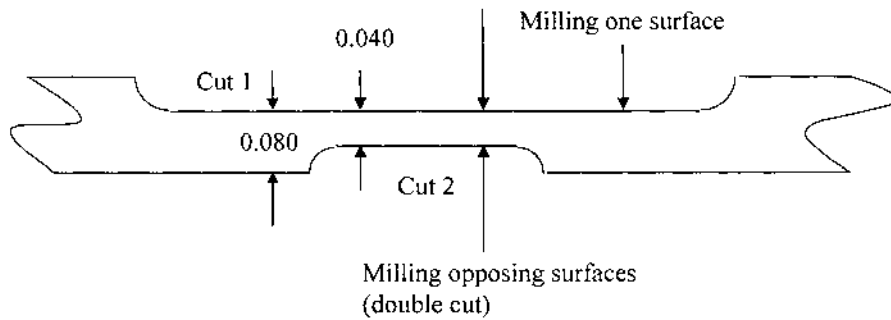
Figure 32 Double cut.

Table 6 Removal Calculation, Double Cut (Fig. 32)

Cut	Stock Thickness (mil)	Finish Dimension (mil)	Delta	Double Cut	Delta— Previous Cuts	Removal (mil)
2	160	40	120	yes	120 − 2(40)	40
1		80	80		80 − 40	40

Check Cut	Stock Thickness (mil)	Removals	Finish Dimension (mil)
1	160	40 + 40	80
2		40 + 40	40
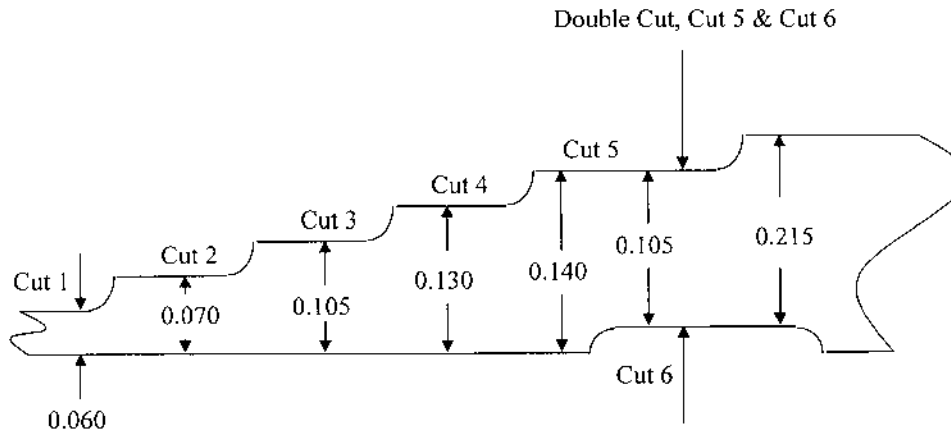
Figure 33 Double cuts and dimensioning practice.

Aluminum etchant may consist of only sodium hydroxide and water, but most always include additives for improvement of surface finish, chem-mill radius, or fillet and other process attributes. There have been no extensive studies to define the chemical mechanisms of etching, or metal dissolution, however the process is thought to be a electrochemical reaction similar to the accepted description of general corrosion [13]. Hence, aluminum goes into solution at cathodic areas while anodic areas of the part emit electrons and reduce water to hydrogen and hydroxides. Current densities of 10×10^{-10} A/cm^2 have been measured [13]. The cathodic and anodic surfaces must be approximately equal and moving rapidly about the part surface to produce an even etch. The generally accepted reaction in aluminum chemical milling is [1]

$$2H_2O + 2NaOH + 2Al \rightarrow 2NaAlO_2 + 3H_2 \uparrow \qquad (16)$$
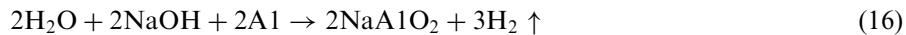
As the aerospace industry began wide use of the chemical milling process there were a variety of solution formulae developed for various aluminum alloys (Table 10). As the process evolved the number of etchant formulae have been reduced to two general etchant formulas. For special applications and/or alloys various etchant constituents have been used [14] (Table 11).

There are chemical milling operations that use only sodium hydroxide and water as an aluminum etchant. Such etchants produce a rough surface finish and may therefore be followed by a shot peening operation. It is left to the user to determine if savings in chemical costs justifies additional post-etch processing, and if their customer base would agree to such a process. Additions of scrap aluminum and additives such as sodium polysulfide will improve process output. In general the industry has moved to create etchants that produce fine surface finishes, thus eliminating post-etch processes such as shot peening.

The wide variety of solutions has been reduced to two basic solution formulas that are applicable to virtually all aluminum alloys with little modification required. (Ref. Table 10)

Table 7 Removal Calculation, Multi-Cuts with Double Cut (Fig. 33)

Cut	Stock Thickness (mil)	Finish Dimension (mil)	Delta	Double Cut	Delta— Previous Cuts	Removal (mil)
6	250	215	35			35
5		105	145	yes	145 − 2(35)	75
4		130	120		120 − 35 − 75	10
3		105	145		145 − 35 − 75 − 10	25
2		70	180		180 − 35 − 75 − 10 − 25	35
1		60	190		190 − 35 − 75 − 10 − 25 − 35	10

Check Cut	Stock Thickness (mil)	Finish Dimension (mil)	Removals
1	250	60	10 + 35 + 25 + 10 + 75 + 35
2		70	35 + 25 + 10 + 75 + 35
3		105	25 + 10 + 75 + 35
4		130	10 + 75 + 35
5		105	75 + 2(35)
6		215	35

Table 8 Removal Calculation, Multi-Cuts with Double Cut (Fig. 33)

Cut	Stock Thickness (mil)	Finish Dimension (mil)	Delta	Double Cut	Delta— Previous Cuts	Removal (mil)
6	250	105	145	yes	145 − (70/2)	35
5		140	110		110 − 35	75
4		130	120		120 − 35 − 75	10
3		105	145		145 − 35 − 75 − 10	25
2		70	180		180 − 35 − 75 − 10 − 25	35
1		60	190		190 − 35 − 75 − 10 − 25 − 35	10

Check Cut	Stock Thickness (mil)	Removals	Finish Dimension (mil)
1	250	10 + 35 + 25 + 10 + 75 + 35	60
2		35 + 25 + 10 + 75 + 35	70
3		25 + 10 + 75 + 35	105
4		10 + 75 + 35	130
5		75 + 35	140
6		75 + 2(35)	105

Table 9 Aluminum Chemical Milling Solutions, Acid Based

Constituent	Range	Temperature (°F)
Hydrochloric Acid	2–3 N	7045, 85
Aluminum Chloride	50–80 g/l	2024, 115
Hydrofluoric Acid	22–75 g/l	
Hydrochloric Acid	26–42 g/l	
Nitric Acid	111–300 g/l	85–120
Acetic Acid	as required	
Oxalic Acid	0–0.8 g/l	
Chromic Acid	30–53 g/l	
Sulfuric Acid	165–225 g/l	90–175

Table 10 Alkaline Aluminum Chemical Milling Solutions

| Etchant Constituents | Aluminum Alloy, Series | | |
	2000	6000	7000
Sodium Hydroxide, g/l	136–280	136–280	136–280
Sodium Gluconate, g/l	0.3–3	0.3–3	0.3–3
Sulfur, g/l	7–8	7–8	7–8
*Sodium Sulfide, g/l	8–9	8–9	8–9
*Triethanolamine, g/l	20–60	20–60	20–60
*Sodium Polysulfide (Turco #3)	51–77	51–77	51–77
Temperature, °F	160–225	160–225	160–225
Etch Rate, mils/min/surface	Range for all: 0.5–3.0		

*Type II Etchants

Table 11 Special Application Alkaline Etchant Additives

Constituent	Range
Sodium Sulfide, g/l	4–190
Sodium Meta-aluminate, g/l	120–240
Potassium Chromate, g/l	30
Sulfur, g/l	4–11
Sorbitol, g/l	2
Tributyl phosphate, g/l	0.8–1
Carboxymethyl cellulose, g/l	4
Wyandotte Ferlon, g/l	0.8–1
Thiourea, g/l	1–2

Type I aluminum etchants have a cost advantage over the Type II etchant. Both etchant types are available as propriety formulas from chemical suppliers such as Turco Products, Inc. The etchant supplier will provide general operating parameters to insure good process results (Fig. 34).
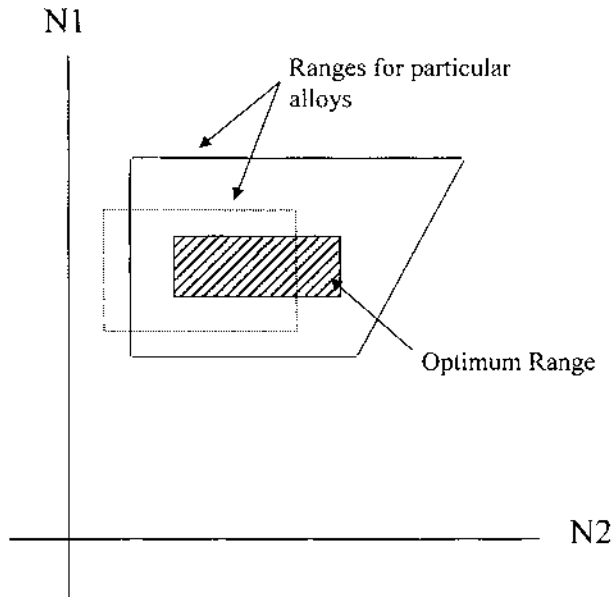
Figure 34 Typical graph of optimum etchant chemistry ranges.

Additives such as sulfur, or sodium sulfide are included in the etchant formula to improve on chemical milling characteristics. Characteristics such as undercut, chem-mill fillet smoothness, surface finish and pocket dishing are all attributes directly related to the etchant. Sulfur, or a form of sulfur is added to both Type I and Type II etchant to promote good surface finish. The sulfur precipitates zinc and copper alloying elements from solution and prevents the metals from plating back onto the substrate aluminum substrate surface, a phenomenon known as secondary masking. Triethanolamine, added to Type II etchants, is present to promote smooth fillets and to reduce/control chem-mill undercut. Ethylenediamine-tetraacetic acid (EDTA) is also a useful chelating agent that can influence chem-mill fillet quality.

Etchant operation typically proceeds from etchant make-up to eventual disposal of spent etchant. Aluminum etchants begin to produce poor surface finish and fillet quality as dissolved metal content reaches 60–70 g/l.

Control of the etchant is accomplished by simple titration. A sample of etchant is prepared and titrated with 1 Normal sulfuric acid. The first titration end-point is pH 11.3 (Fig. 35). The volume of titer represents that amount of free sodium hydroxide in solution, or N_1. The second titration end-point is pH 8.2. The volume of titer needed to go from pH 11.3 to pH 8.2 represents the dissolved metal in solution, or N_2.

Additions of sodium hydroxide, and decisions regarding the dump point of aluminum etchant is based on the titration results. Etchant N_1 and N_2 should be maintained as prescribed in the technical bulletin provided by the etchant supplier.
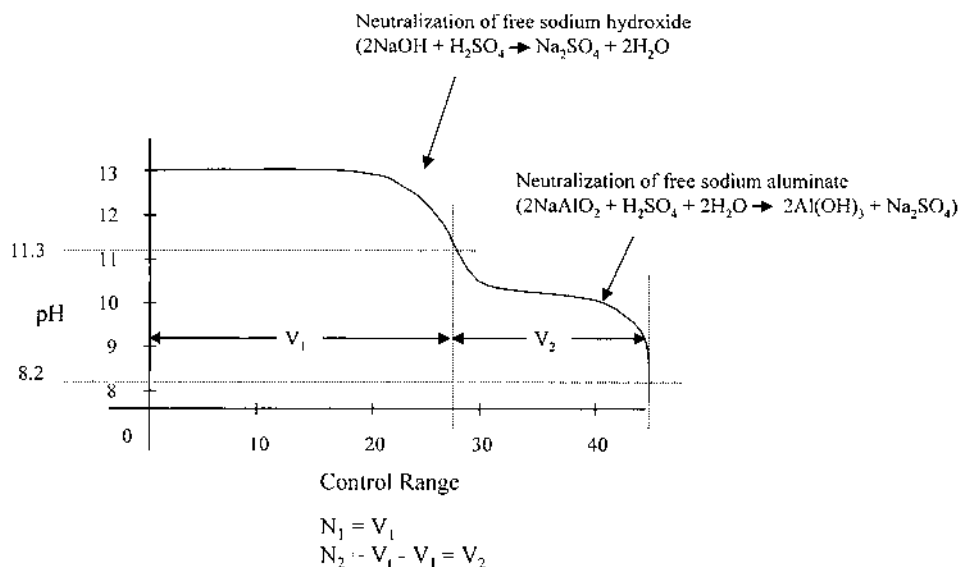
Figure 35 Etchant control.

Addition of other etchant constituents is dependent upon how the etchant is operated. The traditional technique for Type II etchant, for example, is to operate the etchant until N_2 is in the range of 14–17, (or 60–75 g/l of dissolved aluminum), then dump the etchant and replace. All additives are added at etchant makeup and only water and sodium hydroxide are added thereafter. Other techniques include saving a portion of the spent etchant for the next etchant makeup to increase dissolved metal content in the new etchant. Regeneration of spent etchant to remove metals and recovery of sodium hydroxide and additives. In the latter techniques the user will follow analytical techniques supplied by the etchant supplier, or etchant regeneration equipment supplier to determine the timing and quantity if additive additions.

Spent etchant may convert from sodium aluminate to sodium hydroxide plus a mixture of aluminum hydroxide and aluminum oxide [1]

$$NaAlO_2 + 2H_2O \rightarrow Al(OH)_3 + NaOH \tag{17}$$

$$NaAlO_2 + 4H_2O \rightarrow Al_2O_3 \bullet 3H_2O + 2NaOH \tag{18}$$
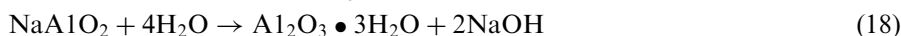
These reactions describe the mechanism by which sodium hydroxide can be recovered while separating the aluminum in solution. The process described by Eqs. (17) and (18) is used by aluminum manufacturers to purify bauxite.

There are undesirable effects of the chemical milling etchant chemistry (Fig. 36).

- Channeling is most often observed in titanium chemical milling, however if it occurs in aluminum chemical milling it is caused by part/pocket position during etching; low etchant temperature, or low N_1.
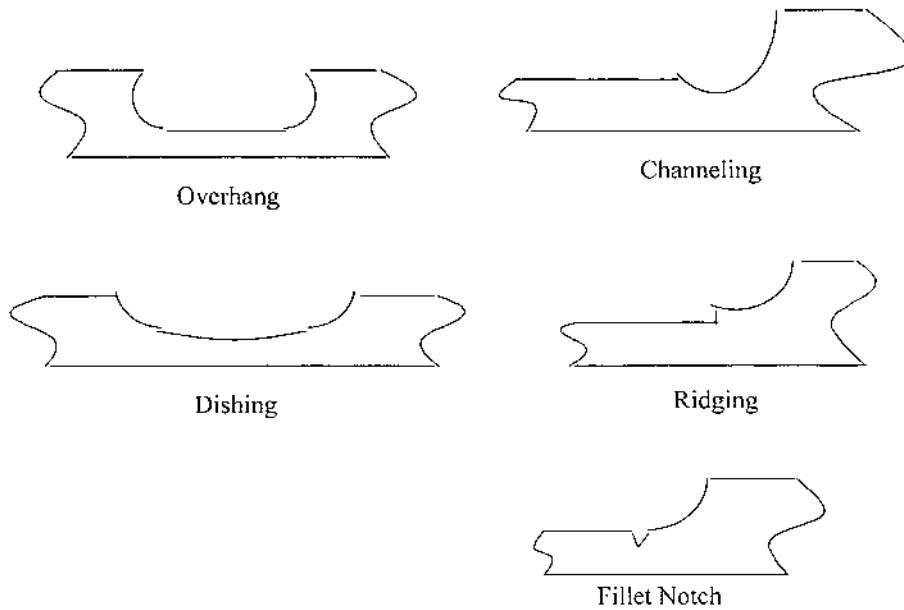
Figure 36 Pocket defects.

- Overhang is caused by excessive triethanolamine concentration, or in come cases excessive dissolved metal in solution.
- Dishing results from excessive metal in solution, and excessive sodium hydroxide.
- Ridging in the fillet is caused in part by the orientation of the part during milling; hydrogen gas entrapment which can create flow-lines; poor desmutting practice[7], or low N_1.
- Rough, mottled, or "orange peel" surface is caused by "secondary masking", or redeposition of zinc and copper alloying elements back onto the aluminum surface. Secondary masking occurs at low sulfur levels, and/or when N_2 reaches a range of 14–17 (in the absence of etchant regeneration).
- Fillet Notch is the result of excessive scribe knife pressure.

Complete reformulation of either Type I or Type II is seldom necessary. For a particular manufacturing situation, revision, or modification of an etchant may be necessary. Factorial design of experiment represents the best and quickest method for etchant development. Factorial designs are the correct choice by definition [15]:

- "A factorial design experiment is arranged to study the effect on some observable quantity (the response) of varying two or more factors, such as process temperature and source of raw material. A series of values or levels of each factor is selected and certain combinations of the levels of all factors is tested. The objective of a factorial experiment is to measure the change in response when changing

---

[7] For deep cuts (< 50 mm), and for all 7000 Series Aluminium etch and ddesmutting after 10 mm and desmutting for a few minutes will prevent ridging and pitting in the fillet.

Factors				(-)	Levels Units	(+)
A. Sodium Hydroxide.				10	g/l	30
B. Sodium Sulfide				18	g/l	40
C. Triethanolamine				9	ml/l	25
D. Etch Temperature				190	F	210

				Measured Response		
A.	B.	C.	D.	Surface Finish, Ra	Undercut Ratio	Line Quality
-	-	-	-			
+	-	-	+			
-	+	-	+			
+	+	-	-			
-	-	+	+			
+	-	+	-			
-	+	+	-			
+	+	+	+			

Figure 37 Etchant development test plan.

the level of some process factors while hold all other process factors constant. Such changes in the response are called the main effects of the factors and interaction effects between the factors.''

- "Definition of a Mixture Experiment—An experiment in which the response is assumed to depend only on the relative proportions of the ingredients present in the mixture, not the amount of the mixture. In a mixture experiment if the total amount is held constant and the value of the response changes when changes are made in the relative proportions of those ingredients that make up the mixture, then the behavior of the response is said to be a measure of the joint blending property of the ingredients of the mixture.''

In general etching operations, a volume of etchant is prepared, but is operated at varying volumes until analysis indicates an addition of sodium hydroxide or water is necessary. Therefore, a Factorial experiment design is appropriate for etchant formulation. Development of chem-mill maskants is a good example of a situation where a mixture experiment will provide the best experiment test plan. A typical test plant outline for etchant development (Fig. 37).

5.1 Waste Disposal

As the total dissolved metal content (N_2) reaches 14–17, or approximately 70 g/l, the quality of surface and fillet produced by the etchant will diminish rapidly (in the absence of etchant regeneration). Spent aluminum etchants can be handled in a variety of ways depending on the resources available.

5.1.1 Neutralization/Waste Haul Out

If an industrial waste-water treatment facility is on site, spent aluminum etchant can be neutralized and the resulting sludge de-watered and hauled to landfill. This option is not entirely practical because mixing aluminum etchant with acid results in an extreme exothermic reaction, and hydrogen sulfide (H_2S) gas is a noticeable by-product. Use of neutralization as an on-site disposal technique would require dilution of the etchant with a large volume of water and a fume scrubbing system to remove hydrogen sulfide gas.

Licensed waste handlers with disposal facilities will accept spent aluminum etchant. The waste disposal facility may neutralize and de-water the resulting sludge, or use the spent etchant to treat acidic wastes. Paying someone else for complete waste disposal is probably a more expensive option, plus shipping costs are still incurred, and the risk of transporting a hazardous solution over public highways remains. For a short term operation, such etching a short run of parts then terminating a chemical milling operation, sending spent etchant to a waste handler is the more convenient option.

5.1.2 Etchant Regeneration or Point Source Recovery

Spent aluminum etchants may be regenerated, i.e. spent etchant rich in sodium aluminate may be converted to sodium hydroxide (for reuse) and high quality aluminum trihydroxide that can be sold as a feedstock for other processes.

Advantages of etchant regeneration include [16]:

- Resource recovery
- Waste minimization
- Pollution control
- Consistent Dissolved Metal Content (N_2)
- Chemical use reduction (NaOH recovered and reused).

Etchant regeneration is attractive for chemical milling operations that use large volumes of etchant, or where local restrictions on hazardous waste disposal/transport make hazardous waste reductions imperative. One important advantage of etchant regeneration is that consistent etchant chemistry is maintained, thus promoting consistent product quality. Etchants that are operated from low to high N_2 and then dumped when N_2 exceeds a value of 14–17 produce large variations in chem-mill undercut.

Before selecting a regeneration process it is imperative that all systems and techniques are reviewed. Where possible, on-site reviews of operating systems should be pursued. Manufacturers of regeneration system should able provide a list of customers and assist with visitation arrangements. Virtually all etchant regeneration technologies are Patent protected in some form – they may use a unique membrane material or use the optimum water dilution ratio, etc.

Etchant Regeneration by Dilution
Diluting spent aluminum etchant with water will precipitate aluminum trihydroxide and regenerate sodium hydroxide for reuse in the etchant [17].

$$NaAlO_2 + 2H_2O \rightarrow NaOH + Al(OH)_3 \downarrow \tag{19}$$
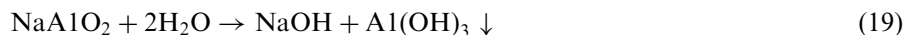
Traditional Recovery Process Scheme
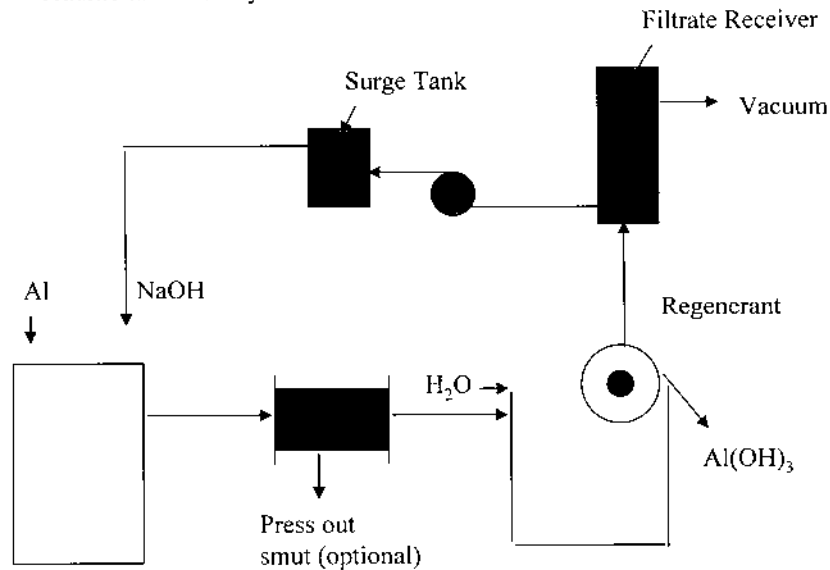
Figure 38   Etchant regeneration—dilution process.

Variants of the dilution regeneration process employ a filter press or centrifuge to remove smut; special settling tanks and "seeding" compounds (flocculants) to facilitate solutions removal or Al(OH$_3$) quality. Dilution based regeneration processes (Fig. 38) work best with Type I aluminum etchant, however there are two proprietary dilution systems that are operating with Type II etchants are and producing acceptable results.

Membrane Based (Diffusion Dialysis) Etchant Regeneration

When two solutions of different concentrations are separated by the right kind of membrane, their concentrations change in the direction of becoming equal. Once the solution concentration everywhere within the diffusion chamber is same, the process stops [18]. The Diffusion Dialysis process employs a unique membrane material to separate sodium hydroxide from spent etchant. Purified etchant consisting of sodium hydroxide, dissolved aluminum and the etchant additives is transferred to a crystallization process where aluminum trihydroxide and aluminum metal is extracted. The remainder, or "regenerant," consisting of sodium hydroxide, etchant additives and a small amount of dissolved aluminum is transported back to the aluminum etchant (Fig. 39) [17].

The engineering details of etchant regeneration by diffusion dialysis have been worked out by Malek, Incorporated. Malek's performance claims regarding the diffusion dialysis process is that pretreatment of spent etchant by membrane simplifies aluminum trihydroxide precipitation and increases yield, i.e. with membrane pretreatment 50% of available aluminum is recovered, verses 10% by the dilution process. In addition, a large portion of etchant additives such as
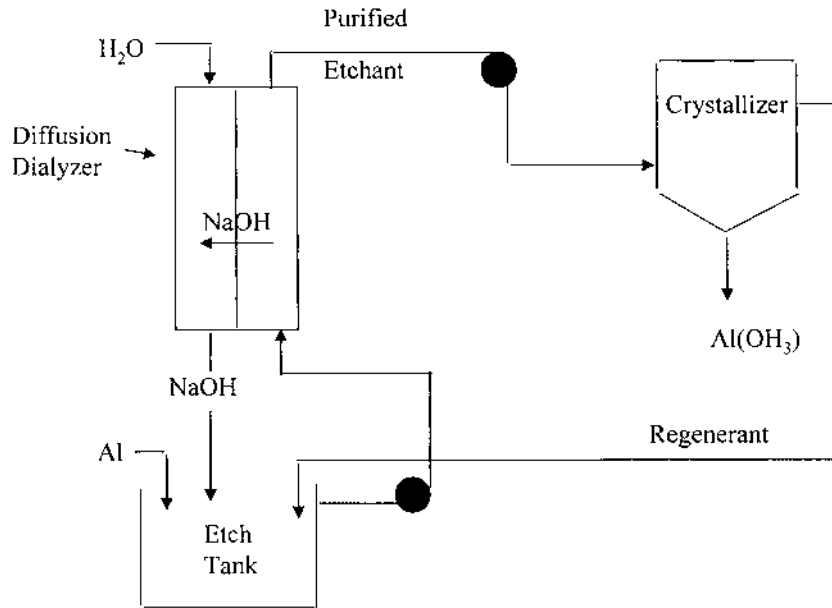
Figure 39 Etchant regeneration—diffusion dialysis.

triethanolamine and sodium sulfide are captured in the regenerant and returned to the etchant, hence use of additive chemical necessary for chemical milling are decreases also.

Electrodialysis Etchant Regeneration

Electrodialysis is an electrochemical process that also employs a cation permeable membrane. As with diffusion dialysis, electrodialysis involves transport of ions through an ion permeable membrane, however electrodialysis includes a motive force to speed ion transport through the membrane. The electromotive force is the electrical potential between an anode and cathode (Fig. 40) [19].

As with diffusion dialysis the etchant is pretreated to remove sodium hydroxide. The purified etchant is then treated to remove aluminum hydroxide and the regenerant consisting of remaining sodium hydroxide, a small amount of dissolved aluminum and etchant additives is returned to the process.

Aluminum etchant regeneration by the electrodialysis process was jointly developed by Martin-Marietta and Ionsep Corporation and employs an Ionsep® electrochemical cell with proprietary Ionsep™ anolyte additives (Fig. 41). Spent etchant is introduced into the anolyte compartment where aluminate hydrolyzes to form insoluable aluminum hydroxide. Formation of aluminum hydroxide is enhanced by electrolysis and by pH control. The free sodium cation crosses the membrane to the catholyte where it combines with hydroxide to form sodium hydroxide. Other metals such as copper and zinc remain as insoluable metal hydroxides in the anolyte compartment. Most of the etchant additives remain in the anolyte and are reclaimed in the regenerant that is eventually returned to the process. As with diffusion dialysis, small additions of additives to the process
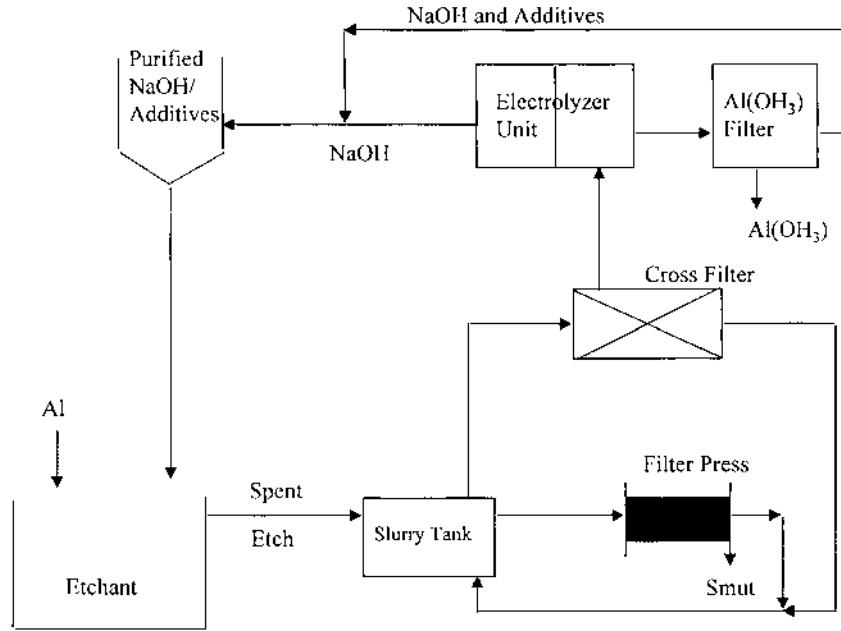
Figure 40 Etchant regeneration—electrodialysis.
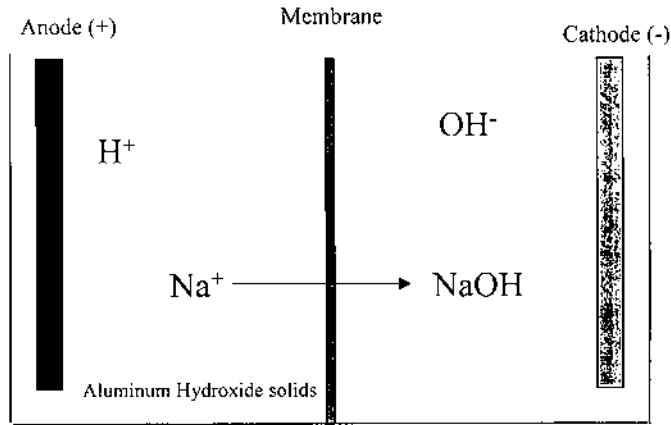
Figure 41 Ionsep electrochemical cell.

will be necessary as some of the additives are lost with the solids removed by the regeneration process. Concentration of sodium hydroxide in the catholyte is controlled by etchant feedrate into the anolyte, and the potential across the electrodes [19].

The yields of sodium hydroxide and aluminum trihydroxide are highest with electrodialysis, however pH control in the anolyte solution is critical to prevent for-

mation of hydrogen sulfide. In practice a fume scrubber would likely be necessary at the electrolyzer station (Ref. Fig. 40).

Etchant Regeneration Summary

The dilution process requires more floor space and yields less, but uses inexpensive components, in relative terms. Diffusion dialysis is a passive form of etchant regeneration relative to Electrodialysis. Electrodialysis is faster and yields more, but requires greater energy input. Diffusion dialysis and Electrodialysis systems are modular and comprised primarily of plastic components, hence maintenance is simplified.

A complete analysis of all regeneration processes by the end user is necessary to insure that all issues of factory floor space requirements, energy use, capacity and process yields are carefully evaluated.

5.1.3   Aluminum Etchant as Feedstock

An attractive alternative to etchant regeneration is use of spent aluminum chem-mill etchant as a feedstock for other processes. For example, if an aluminum chemical milling operation is within reasonable distance of an aluminum reduction operation, spent aluminum etchant can be used as feedstock for purification of bauxite. Bauxite is purified with sodium hydroxide before electrolysis and reduction of aluminum. Spent aluminum etchant is rich in sodium hydroxide and can therefore be used in the bauxite purification process. Aluminum etchant additives do not influence the bauxite purification process, but companies receiving spent etchant will require analysis of spent etchant to insure that no undesirable elements reach their process.

Disposing of spent aluminum etchant as a feedstock eliminates a hazardous waste, but shipping costs are still incurred, and the risk of transporting a hazardous solution over public highways remains.

5.2   Quality Issues

Chem-mill quality issues by Cause and Effect Diagrams (Fig. 42):

The majority of quality issues in chemical milling center on the etchant and its influence on process attributes. Undercut ratio and set-back factors used by tool-makers are influenced by etchant constituents, dissolved metal in solution, etch temperature and part loading techniques employed by operators. Static tools coupled with a dynamic process will cause significant quality problems. In aerospace this situation translates into expensive rework in assembly, and parts that may be within dimensional tolerance, but heavier than the expected nominal weight. Both situations cost the customer in terms of higher product costs, and higher fuel expenditures.

Aerospace Example

A chemical milling department received a commercial air transport part for processing (Fig. 43).

The chem-mill tool was constructed by the original equipment manufacturer and was used directly, however, the undercut ratio used to determine the tool offset was sufficiently different from the average process undercut ratio that all chem-mill
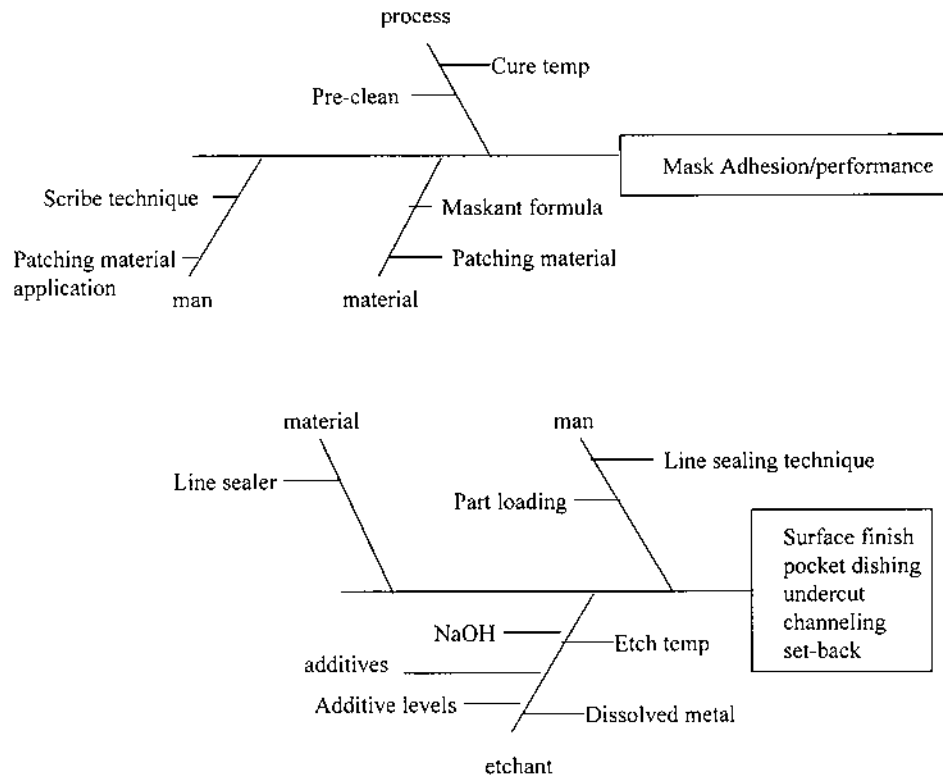
Figure 42 Quality issues in chemical milling.

Part Section with Integral Stiffeners by Chemical Milling
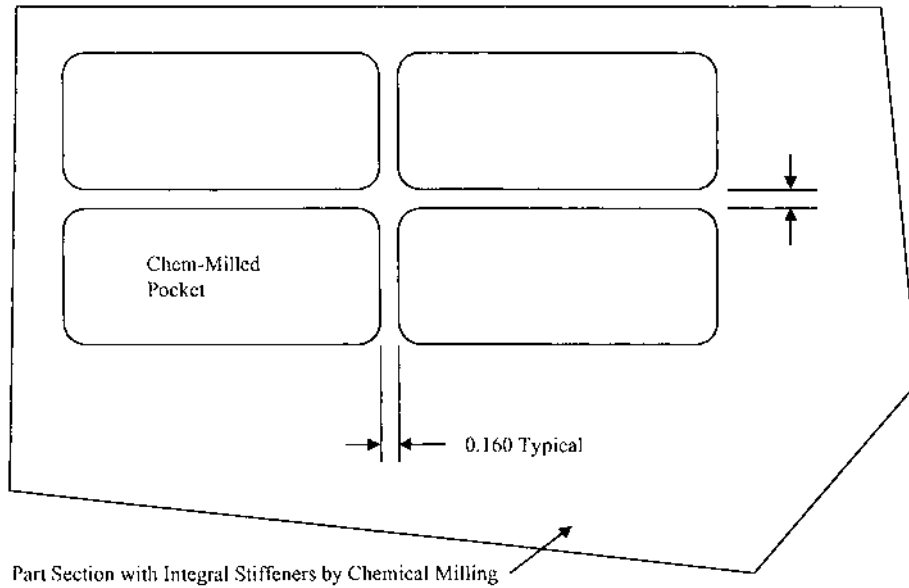
Figure 43 Critical dimension produced by chemical milling.

land areas were undersized. Thus, the entire order of parts was rejected and scrapped. Approximate value of the parts at the time the order was scrapped: $11,000 Taguchi Loss Function for the Chem-Mill Example.

Design of Experiment/Taguchi techniques are important tools for improving process quality [20].

5.2.1 Application of Quality Tools in Chemical Milling

All parts are inspected following the chemical milling process as required by contract. Quality measures are: (1) depth of chem-mill cut; (2) absence of burn marks or pits caused by etchant leaking through thin spots in the maskant coating; (3) surface finish in the chem-mill cut area; (4) location and dimensions of chem-mill lines and land areas (Fig. 25–28). Allowable tolerances are established for each parameter by the engineering drawing. If all measures fall within the allowed tolerance the parts are considered to be acceptable for use and are forwarded to the next process for painting and eventual assembly.

5.2.2 Problems/Quality Deficiencies

Often, when new scribe tools are released for use in manufacturing, the parts produced do not meet allowable tolerances. To correct the problem a tool maker modifies the scribe tool, effectively changing the undercut ratio, or etch factor. Two to four iterations of tool modifications are typically necessary. Holding parts in queue while scribe tool modifications are completed and tested causes production schedule delays.

Parts that are within allowable tolerance still cause assembly interference (Fig. 44).

To correct the interference problem assembly workers must manually grind excess material from the chem-mill pocket. After grinding is complete, the corrosion preventive coatings, (conversion coating and paint), must be repaired and the parts
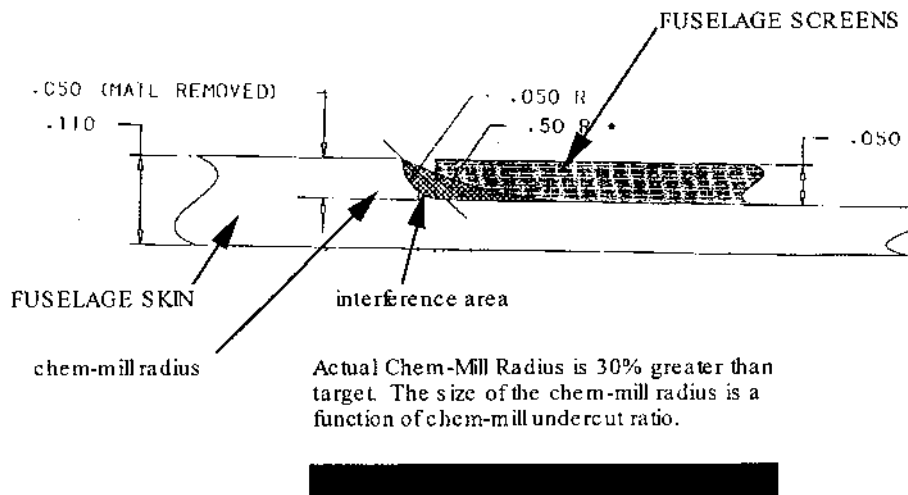
Figure 44 Part to part interference in chem-mill fillet.

reassembled. Part rework that occurs during the aircraft assembly phase is most expensive, and has the greatest impact on production and delivery schedules. The study efforts for undercut ratio may be organized by the following seven guidelines [21]:

- Recognition and statement of problem
- Choice of control factors and levels
- Selection of the response variable
- Choice of experimental design
- Experiment execution
- Data analysis
- Conclusions and recommendations.

5.2.3 Recognition and Statement of Problem

Chem-mill tank operators will explain that the actual undercut ratio changes as metal is dissolved by the etchant. For some alloys, many iterations of tool modifications are performed to find an undercut ratio that will produce acceptable parts throughout the process. The situation forces operating personnel to:

- Obtain material and test new chem-mill tools. The point estimate of undercut ratio generated by the test was not applicable throughout the process.
- Scrap and replace parts when the target value for undercut ratio is not achieved and a chem-mill land width or line location is out of tolerance.

The following 8 control factors are judged to have an important influence on the chem-mill undercut ratio:

- metal alloy
- heat treat, or age condition
- clad coating or bare metal
- etchant temperature
- triethanolamine concentration
- amount of dissolved metal in solution, N_2
- amount of free sodium hydroxide in solution N_1
- depth of chem-mill cut
- part load position

   Note that the amount of dissolved metal in solution, N_2, and the amount of free sodium hydroxide in solution, N_1, are continuous variables.

5.2.4 Control Factor Level Selection

Levels for the respective control factors are defined on engineering drawings and in process specifications. However, the operators may often run the process inside, or outside of specified levels to improve process efficiency. Therefore, operating levels indicated by the process operators should be used (Table 12).

Table 12 Process Control Parameters, Process versus Specification

	Actual Levels		Process Spec.	
Control Factors	(−)	(+)	(−)	(+)
Depth of Cut	40	140	15	200
Etch Temperature	195–205	210–220	190	220
Free Caustic	24	34	21	34
Dissolved Metal	2	14	0	14
Load Position	45	90	none	none

5.2.5 Quality Tools Application

Once execution of the experiment is complete, data can be used to develop regression models that describe undercut ratio, or any other measured response, in terms of the process (Table 13)

$$
\begin{aligned}
\text{Predicted Undercut Ratio} = {}& 8.3429 - 0.04342(\text{DOC}) - 0.02062(\text{TEMP}) \\
& - 0.0186(\text{N1}) - 0.0589(\text{N2}) + 0.002948(\text{POS}) + 0.00008816(\text{DOC})^2 \\
& + 0.000101(\text{DOC} \times \text{TEMP})
\end{aligned}
$$

(20)

The process regression model is most important as the model can be used by chem-mill operators to predict undercut ratio results and control the chem-mill process to achieve a desired outcome.

Before relying on the regression quality tools such as Residual Plots and regression model confirmation via Hypothesis Testing or other quality tool is recommended.

In Sec. 5.1, etchant regeneration is described as a way of controlling etchant chemistry such that consistent surface finish, fillet quality and undercut ratio are always produced. Certainly, etchant regeneration holds such an advantage, however Design of Experiment techniques coupled with development of process regression models allows operators to predict undercut ratio and schedule jobs accordingly. Hence, aluminum etchant can be operated without etchant regeneration and still produce consistent part quality.

Taguchi Loss Function, Nominal-is-Best—general case for Chemical Milling [10,22].
Taguchi's Loss function can be used to estimate cost reductions realized by using quality tools for better process control (Fig. 45).

$$
\text{Loss to Society, or Enterprise} = k[S^2 + (y - m)^2]
$$

(21)

$$
\begin{aligned}
\text{where}: \quad & k = \text{coefficient} \\
& S = \text{Standard Deviation} \\
& y = \text{Target Value} \\
& m = \text{Actual, or Measured Value}.
\end{aligned}
$$

Table 13 Regression Model for Undercut Ratio

Regression Analysis of Chem Mill Process
6061 Aluminum
Quadratic Model

Dependent Variable: Undercut Ratio

Source	DF	Sum of Squares	Mean Square	F Value	Prob > F
Model	7	7.25882	1.03697	78.351	0.0001
Error	26	0.34411	0.01324		
C Total	33	7.60293			

	Root MSE	0.11504		R-Square	0.9547
	Dep Mean	2.24926		Adj R-Sq	0.9426
	C. V.	5.11473			

Parameter Estimates

Variable	DF	Parameter Estimate	Standard Error	T for HO Parameter=0	Pro b. > |T|
INTERCEP	1	8.342934	0.96028592	8.688	0.0001
DOC	1	-0.043424	0.00934707	-4.646	0.0001
TEMP	1	-0.020624	0.00459128	-4.492	0.0001
N1	1	-0.018601	0.005502391	-3.702	0.001
N2	1	-0.058901	0.003411193	-17.263	0.0001
POS	1	0.002948	0.00089549	3.292	0.0029
DOC × DOC	1	8.8158E-05	0.00002326	3.79	0.0008
DOC × TEMP	1	0.000101	0.0000392	2.574	0.0161

Source: Table 5. SAS Regression Analysis, Quadratic Model from 6061 DOE.
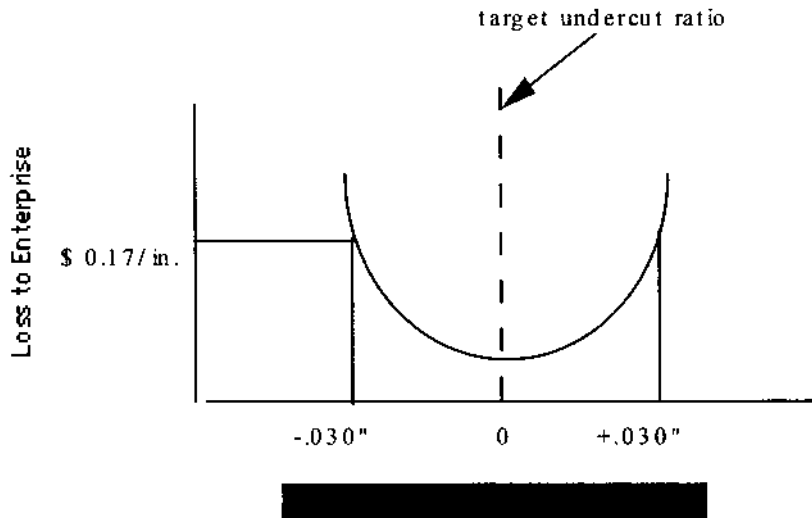
Figure 45 Taguchi loss function—costs incurred for failure.

Some loss is incurred whenever a target undercut ratio is not achieved. Equation (21) defines undercut ratio as the quotient of undercut and chem-mill depth of cut. Hence when a target undercut ratio is not achieved, labor hours must be expended to correct the chem-mill undercut. Therefore, for the Loss Function example, the cost to repair chem-mill undercut is estimated. Undercut is calculated by rearranging Eq. (13), (Ref. Fig. 23).

$$UC = UCR \times DOC \tag{22}$$

Assembly interference can result when the target undercut ratio value is not achieved (Ref. Fig. 44). Parts such as the one depicted are not generally scrapped because the chem-mill line location is within the allowed $\pm$ 0.03 in. tolerance. Instead, the parts are reworked to eliminate the interference.

For the general case of the Taguchi Loss Function, only the rework cost be considered, i.e. the loss function estimates the cost of rework per part if the problem is corrected in the chemical milling department. In reality, if the part is reworked during assembly operations there would be additional costs to cover rework of conversion coatings and paint repair.

The Taguchi Loss Function for the Chemical Milling example:

- From Eq. (21), the coefficient k:

$$k = (\text{Loss})/\text{tolerance}^2 \tag{23}$$

- Assume the cost to move a chem-mill line is approximately \$0.17/linear in. (Ref. Fig. 45).

- An undercut that causes parts to be rejected would be the result of an undercut ratio that produces a chem-mill line mislocation of $\pm\,0.03$ in. Substituting into Eq. (20), the loss (L) incurred if the chem-mill undercut must be reworked: Calculate k

$$k = [(\$0.17/\text{in.})/(0.03\,\text{in.})^2] = \$189/\text{in.}^3$$

- The Mean Square Error estimate of Variance ($S_{\text{UCR}}{}^2$) of undercut ratio from the quadratic model for undercut ratio [20] (Ref. Table 12). $S_{\text{UCR}}{}^2$ includes the effects of systematic and instrument error observed in the gage repeatability and reproducibility study. Note that undercut ratio is without units, therefore, S_{UCR} and (y - m) are also without units. Substituting into Eq. (21), the loss/part is:

$$\text{Loss/part} = k[S_{\text{UCR}^2} + (y - m)^2]$$

from Eq. (23), $k = \$189/\text{in}^3$, therefore

$$= \$189/\text{in}^3[S_{\text{UCR}^2} + (y - m)^2]$$
$$- \$/\text{in}^3$$

- The Loss/part is expressed as a volume (in^3). As defined in Eq. (23), undercut is directly proportional to undercut ratio. Chem-mill undercut defines the location of the chem-mill line, if the line is mislocated the chemical milling operator or its customer must incur the cost to manually grind away a volume of metal to correct the chem-mill line location and pocket radius (Ref. Fig. 4).

The total cost, or loss/part is directly proportional to the volume of metal that must be removed, which, is the multiple of the target undercut less the actual undercut (ΔUC); the depth of cut, and the length of chem-mill line, or the perimeter of all chem-mill pockets on the part. An expression for the volume of metal that must be removed due to incorrect undercut ratio is

$$VM = (\Delta\text{UC})(\text{DOC})(\text{Pocket Perimeter})$$
$$= \text{in}^3 \tag{24}$$

For the aircraft part (Ref. Fig. 44) $\Delta\text{UC} = 0.03$ in.; $\text{DOC} = 0.05$ in., and the part has 731 linear in. of chem-mill lines. Then, substituting into Eq. (24)

$$VM = (0.03\,\text{in.})(0.05\,\text{in.})(731\,\text{in.}) = 1.1\,\text{in}^3$$

- Modifying the Taguchi Loss Function, Eq. (21), by multiplying by Eq. (24) produces a new expression for the loss/part:

$$\text{Loss/part} = (VM)k[S_{\text{UCR}^2} + (y - m)^2] \tag{25}$$

- For the aircraft part (Ref. Fig. 44) the actual undercut ratio achieved (y) was 1.8, the target value (m) was 1.2. $S_{\text{UCR}}{}^2 = 0.01324$ (Ref. Table 12). The coefficient k from Eq. (25), $k = \$189/\text{in}^3$, and from Eq. (23), $VM = 1.1$ in^3. Substituting

Chem-Mill Undercut Ratio

Clad, Vertical Load Position
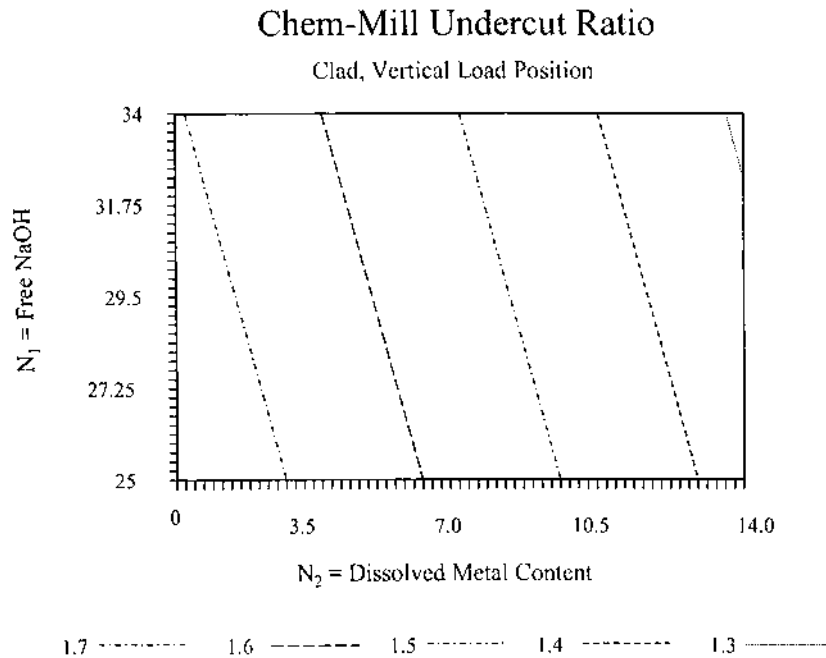
Figure 46 Response surface chart—chem-mill undercut ratio.

all values into Eq. (25) produces an estimate of the loss/part due to incorrect undercut ratio.

$$\text{Loss/part} = (1.1\,in^3)(\$189/in^3)[0.01324) + (1.8 - 1.2)^2]$$
$$= \$77.60/\text{part}$$

- If the target value for undercut ratio is achieved within 1.5 sigma (Motorola uses this factor as a rule of thumb to account for typical shifts and drifts of process averages), [12], then the loss per part due to process shifts is:

$$\text{Loss/part} = (VM)k[(2.385)(S_{UCR})^2]$$
$$\text{Loss/part} = (1.1\,in^3)(\$189/in^3)[(2.385)(0.01324)]$$
$$= \$6.56/\text{part}$$

$$\text{Net savings} = \$77.60 - \$6.56 = \$71.04/\text{part}.$$

Use of quality tools in chemical milling can generate substantial savings. Process Data could by presented to operators by Response Surface Charts (Fig. 46), or perhaps process procedure cards. Process Procedure Cards could be created by part number and a program written to use operator input to determine and display ideal operating conditions for parts with critical pocket, line, or land dimensions (Fig. 47).

Operator Input:

- critical chem-mill land width, or line location
- alloy type & age condition
- material thickness
- finished thickness requirement
- scribe tool width
- nominal land width or line location (from engineering drawing)
- part surface coating
- dissolved metal content of etchant
- preferred part load position
- selected etch tank for processing
- etchant temperature
- Will Modified Al-Li Etchant be Used?
- Are parts Laser Scribed?
- Re-Run Parameters?

Calculate:

- depth of cut
- target undercut ratio
- process tolerance limits
- test target relative to tolerance

Flag:
Check chem-mill tool, modification may be necessary, scribe tool is too narrow.

Calculate Process Parameters for Target:

- free caustic
- etchant temperature
- part load position

Message: For Target Undercut Ratio
N1 = ____; N2 = ____; Load Position = ____;
Etchant Temperature = ____.

Flag:
Check chem-mill tool, modification may be necessary, scribe tool is too wide.

Figure 47   Reference card system schematic.

6 MATERIAL SELECTION FOR TANKS AND PART RACKING

Type II aluminum etchants are popular due to surface finish and etch rate improvements. The typical scenario for introduction of Type II etchant in the aerospace industry was to drain the Type I etchant, and then prepare and use the Type II etchant in existing process tanks. Some time later, failure of the process tank occurred. Large cracks appeared at the weld seams. The tanks could not be repaired and severe schedule delays were incurred.

The materials selected must resist the corrosive effects of specific solution used for aluminum chemical milling. Chemical milling operation typically employ Type I or Type II Aluminum Etchants, a Desmutter or Deoxidizer and rinse water. The materials selected for tanks and work racks are acceptable for both etchant types, but requirements for Type II aluminum etchants will be studied in detail.

Type II aluminum etchants consist of sodium hydroxide triethanolamine, sodium polysulfide and the remainder is water, (chlorine content varies by location). Operating temperatures are 190°F to 225°F. Normal etch rate on aluminum is 0.001–0.003 in/min. Occasional splashing that occurs during solution preparation may expose the tank material to 50% sodium hydroxide at ambient temperature.

Desmut or deoxidize solutions may consist of nitric acid and sodium dichromate, or a mix of nitric and hydrofluoric acid. Small amounts of sodium dichromate or hydrofluoric acid may produce brighter parts, due to environmental and safety concerns, both compounds are generally avoided where possible. A typical desmutting solution for aluminum chemical milling is equal volumes of water and 42°Be′ Nitric Acid. Desmutting solutions are used at ambient temperature.

Process tanks are welded structures specified with water-tight welds. Process tanks are normally constructed at small fabrication shops that possess limited fabrication and welding capability. Therefore, the materials selected must be compatible with conventional welding techniques, i.e. electric arc "stick" welding, or inert gas arc welding. The process tank must support and contain chemical processing solutions. Loads will be uniform, increasing from tank rim to tank bottom. Impact loading may occur should an operator drop a process basket. The material selected must resist abrasion as operators frequently scrape the tank walls with process baskets.

Candidate materials for tanks and work racks frequently exposed to the aluminum etchant are those low in carbon, manganese, and sulfur, but higher in chromium, copper, nickel and molybdenum. Sodium hydroxide is considered as the primary corrosive constituent. As noted, Type II etchant also contain triethanolamine and sodium sodium polysulfide (some etchant formulas substitute sodium sulfide for sodium polysulfide). In low concentrations neither the amine or the sulfide appear as important as sodium hydroxide in the corrosion mechanism [23]. It is possible that at least two and perhaps all etchant constituents interact to produce higher corrosion rates. For example, corrosion resistance tables suggest a uniform corrosion rate of stainless steel in a 15% hot caustic solution of less than 0.02 in. per year [24]. Actual uniform corrosion rates measured in an aluminum etch tank are greater than 0.04 in./yr, but did not exceed 0.05 in./yr. Determining the relative affects of the etchant constituents on tank and work rack materials could be accomplished by design of experiment techniques. Such efforts are better expended on improving quality of aluminum chemical milling. Instead, a formula

for determination of tank lining degradation can be derived and maintenance or tank replacement schedules can be developed around tank degradation predictions.

6.1 Etch Tank Service Life Estimation

Calculation example: 316 stainless steel plate, removed from tank lining material is tested in Type II aluminum etchant. The etchant is 20–30% sodium hydroxide and is operated at 215°F. The apparent density of the sample is 0.287 lb/in³. Test specimen dimensions (Fig. 48) are $l = 5.906$ in.; $w = 1.505$ in.; $t = 0.251$ in. Initial sample mass is 284.2297 g, and final sample mass (after etching) = 269.6042 g.

$$dM = 284.2297 - 269.6042 = 14.6255 g.$$

$$ds = dM/[2\rho(yz + xz + xy)]$$

$$ds = 14.6255/[2(0.2872)(1.505)(0.251) + (5.906)(0.251) + (5.906)(1.505)]$$

$$ds = 0.005203\,\text{in.}[(\text{Kg}/1000\text{g})(2.204)\,1\text{b/Kg})/1\text{b/in.}]$$

$$\Delta t = 31\,\text{days}/278\,\text{manufacturing days (days is in use)} = 0.112\,\text{yrs.}$$

$$\therefore \text{etch rate} = 0.047\,\text{in.yr.}$$

Error estimation : $\delta ds/ds = \delta dM/dM + \delta A/A$

$\delta dM/dM = (0.005\,\text{g}/14.6255\,\text{g}) = 0.000319$

$\delta A1/A1 = (0.05\,\text{in.}/1.505\,\text{in.}) + (0.002\,\text{in.}/0.251\,\text{in.}) = 0.0411$

$\delta A2/A2 = (0.05/5.906) + (0.002/0.251) = 0.0164$

$\delta A3/A3 = (0.05/5.906) + (0.05/1.505) = 0.0416$

$\therefore \delta A/A = 0.0991$

$\delta ds/ds = 0.000319 + 0.0991 = 0.09942$

$\delta ds = (0.09942)ds = (0.09942)(0.005203\,\text{in.}) = 0.0005173\,\text{in.}$

$\therefore \delta\text{etch rate} = (0.0005173\,\text{in.})/0.112\,\text{yr.} \cong 0.005\,\text{in./yr.}$
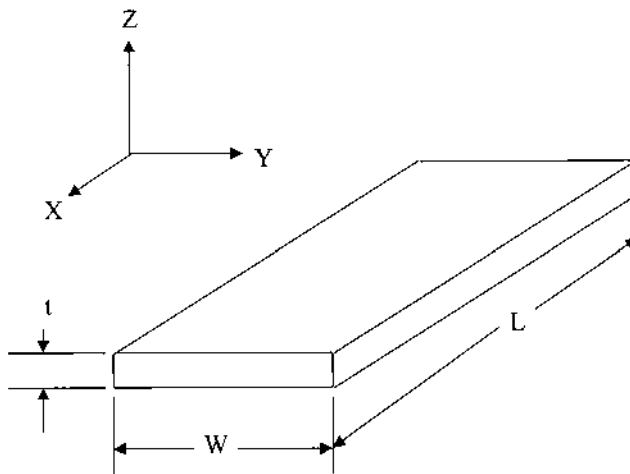
Figure 48   Tank lining test specimen—plate stock.
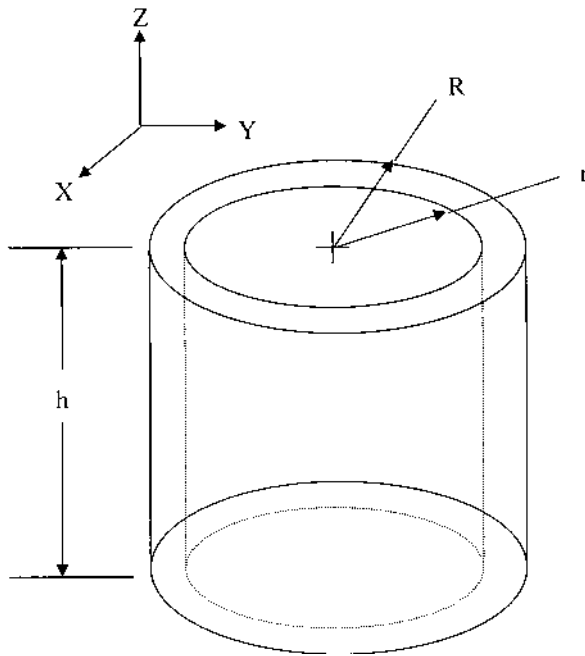
Figure 49 Tank lining test specimen—tubing.

The estimated etch rate of tank lining material is 0.047 in. $\pm$ 0.005 in. If 3/8 in. 316 stainless steel plate stock is used for tank construction then operators should plan for relining or lining repair in 6th or 7th year of operation. Annual measurement of tank lining thickness by ultrasonic techniques is recommended, particularly near heat exchange devices.

Tubing may also be used as sample material (Fig. 49). Equations for tubing are as follows:

$$ds = dM/[\rho(2\pi h(R + r) + 2\pi(R^2 + r^2)]\tag{28}$$

Error is again, from Eq. (23):

$$\delta ds/ds = \delta dM/dM + \delta A/A$$
$$\delta dM/dM = \delta M1 + \delta M2 \tag{29}$$
$$\delta A/A = [\delta h/h + ((\delta R + \delta r)/R + r)] + (2\delta R/R + 2\delta r/r)$$

Although tubing may be used as sample material, experience in the aerospace industry indicates that the apparent etch rate is approximately 72% greater. It could be that tubing samples were of welded tubing, hence the heat effected zone caused an etch rate greater than that observed on plate stock. Hence, tubing is not a good test specimen material for the tank lining, but is a good choice if tubing is used for any in-tank piping. The best specimen for tank linings is material cut directly from the material used for tank construction, lining or repair.

The affects of the etchant constituents are considered separately. For Type II aluminum etchants the candidate materials for tank and work rack fabrication are plain carbon steels, high strength low alloy steels, and chrome/nickel based alloys.

6.2 Materials for Etch Tank Construction

6.2.1 Plain Carbon Steels

Corrosion resistance is sufficient in low temperatures, as demonstrated by years of reliable service with Type I etchants. As temperature and sodium hydroxide concentrations increase mild steel structures are subject to stress corrosion cracking (SCC) in the weld joint heat effected zone (HAZ) [25]. This phenomenon has been observed in mild steel process tanks used in the aerospace industry. Post weld stress relief of the tank may alleviate SCC in weld joints, but stress relief of most large tank structures is impractical. Vibratory stress relief techniques may be useful for large tanks.

Stress relief coupled with a reduction in etchant operating temperature to less than 200°F could make carbon steel an acceptable choice, however reducing etchant temperature will also reduce etch rate and process output. Therefore, mild steels are not a good choice for this process application.

6.2.2 Low Alloy, or Weathering Steels

Weathering steels provide improved atmospheric corrosion resistance, but show no significant improvement in corrosion resistance in immersion service [25].

6.2.3 Ferritic Stainless Steels

Ferritic stainless steels should not be considered due to carbon content. Chromium carbides that precipitate in weld HAZ can result in SCC when the material is exposed to hot sodium hydroxide solutions [26].

6.2.4 Austenitic Stainless Steels

Types 304 and 316 are acceptable for use in hot sodium hydroxide solutions to temperatures of 250°F. SCC remains a concern with austenitic stainless steels. Type 304 tanks used in the aerospace industry exhibited evidence of SCC in the weld HAZ, and intergranular corrosion in the weld fill area. Rapid corrosion occurs in the HAZ adjacent to the weld deposit due to chromium carbide precipitates. Corrosion of Type 304 can be minimized by using 304L (low carbon, 0.03–0.08%), and use of preferential carbide formers such as Tantalum or Columbium. Tantalum or Columbium will prevent formation of chromium carbides at the grain boundries, thus the chrome content in the HAZ is not depleted and intergranular corrosion is prevented.

6.2.5 High Nickel Alloys and Super Alloys

Nickel 200 and 201, Hastelloy™ grades and Inconels are excellent choices. The nickel based alloys provide unsurpassed resistance to corrosion by hot sodium hydroxide solutions [27]. Unfortunately, when the cost of Inconel 625 is compared to Type

304L Stainless Steel the high nickel steels are approximately 5–6 times more expensive that austenitic stainless steels. Use of the high nickel alloys is considered cost prohibitive.

Use of Type 304L Stainless Steel is considered the best material choice for tank construction. Use of Columbium stabilized welding rods, or wire, (e.g. Type 308 or 347 stainless steel) [28] will minimize the possibility of SCC and intergranular corrosion. Plain carbon steel, AISI grades 1005–1008 can be used for exterior tank structure. To prevent galvanic corrosion or crevice crack corrosion all carbon steel must be covered with a stainless steel drip shields. The shields should be attached by continuous weldment, or tack welded and caulked as appropriate for a water-tight barrier.

An often selected alternative is to construct the tank of low carbon steel and then insert a 304L stainless steel "drop-in" liner. A liner is undesirable because

- Should water leak between the liner and tank shell a galvanic cell will exist. Stainless steels are cathodic and mild steel is anodic when coupled by a corrosion media [29], thus the tank shell will eventually sustain corrosion damage.
- Fabricating liners within a tank is difficult, particularly around tank outlets. Material distortion of thin gage liners is a problem, which will likely result in liner failure, and the beginning of a corrosion problem.

6.3 Materials for Desmutting Tank

6.3.1 Austenitic Stainless Steels

Austenitic Stainless Steels provide excellent corrosion protection from nitric acid solutions. Austenitic grades such as 304 are not recommended for hydrofluoric acid service when hydrofluoric acid concentration is less than 70%. Therefore, direct and continuous contact of austenitic stainless steels with the desmut solution is not recommended.

6.3.2 Hastelloy™

Hatelloy™ C-276 provides acceptable corrosion resistance to both nitric and hydrofluoric acids, and it can be fabricated by common welding techniques. Hastelloy™ resists formation of grain boundary precipitates in the weld HAZ, however the high cost of high nickel alloys is prohibitive for large tank structures.

6.4 Tank Lining Materials

Tank lining material are used in many chemical processing applications. Liner types range from "bag" to drop-in liners. Bag liners are identical in form to the rubber liners used in swimming pools, and drop-in liners are fabricated from rigid plastic sheet materials and dropped into the tank shell. Bag liners are a poor choice as they are easily punctured and abraded. Drop-in liners provide more reliable service if the liner fits correctly. For all tank liner types, failure means extended process line down-time while tank contents are removed and linings and tank shells are repaired.

6.4.1 Polyvinyl Chlorides

Rigid PVC sheets or Koroseal™ are acceptable materials. Both materials may be used to fabricate drop-in liners. Operating experience in the aerospace industry has demonstrated that both materials, rigid PVC in particular, fail frequently (approximately once per year) resulting in tank shell damage. Koroseal is flexible and can be bonded to a metal tank shell [30]. Bonded liners conform to surface undulations. Koroseal liners have excellent abrasion resistance, which will limit damage caused by a wayward process basket. When damage to the tank shell does occur, the bonded lining will flex with the steel tank shell and retain the process solution. Tank shell damage incurred due to pinholes leaks, lining abrasions, etc. will be localized as process solutions cannot easily propagate behind a bonded liner as it could if the liner type were a drop-in or bag liner.

6.4.2 Elastomers

Elastomeric lining material can also be bonded directly to the steel tank shell. Elastomers must be vulcanized after bonding; steam is used to vulcanize the elastomer. Butyl Rubber is a candidate elastomeric material for Nitric/HF desmutting solutions used at ambient temperatures.

6.4.3 Polyvinyl Choride (Kynar): Polyvinylidene Fluoride (Kynar™)

Kynar™, or PVDF provides excellent chemical resistance to both nitric and hydrofluoric acids. Kynar is the best choice for temperatures up to 284°F, however Kynar is 6 times more expensive than Koroseal. For desmutting, which is performed at ambient temperature, Kynar is cost prohibitive.

6.4.4 Fiberglass Reinforced Plastic (FRP)

FRP structures are excellent alternatives to rubber lined steel tanks [31] for special applications such as high etch temperatures or high concentrations of nitric/hydrofluoric acid. For tank volumes about 3000 gal FRP structures become difficult to fabricate. The relative costs of FRP tanks are twice that of mild steel and 1.3 times that of stainless steel.

Conclusions: Best choice is a 304L stainless steel tank shell with carbon steel exterior support structure. Do not use hydrofluoric acid as a constituent in the desmutting solution. Hydrofluoric acid in an aluminum desmutting solution will make part "brighter". But aside from value, use of hydrofluoric acid will add nothing to the overall process.

6.5 Fume Scrubbers

Fume scrubbers for aluminum chemical milling with acid desmutting can be conventional packed or cross-flow water wash scrubbers with pH control. Stainless steel, PVC or polypropylene are ideal materials for fume scrubber construction. Slot ventilation at the tank rim is adequate for fume control, provided tank width does not exceed 4–5 ft. For wider tanks the user must consider additional adjacent ventilation, passive surface cover such as floating plastic balls, or active tank covers. For large etch tanks (10 ft wide or greater) slot ventilation at the tank rim in con-

junction with active tank covers a vented hood that surrounds the crane. The combination of ventilation techniques allows for minimal ventilation while the tank cover is closed and maximum ventilation when the tank is in use.

6.6 Maskant Tank Materials

6.6.1 Solvent-Based Maskants

Carbon steel is sufficient for tank construction.

6.6.2 Waterborne Maskants

Stainless steel, 304L, is an excellent material for mask tank construction. Plain carbon steels cannot be used for direct continuous contact with waterborne maskants due to oxidation problems.

Plain carbon steel lined with polypropylene (bonded to the steel tank wall) is an acceptable alternative to stainless steel. Plain carbon steel structure supporting a polypropylene tank is also acceptable for large tanks. If the required tank volume is only 1000 gal or less, then a tank constructed completely of polypropylene should be considered. Tank suppliers can provide assistence with proper material selection.

7 PROCESS ORGANIZATION

Chemical milling includes 5 distinct steps that naturally migrate to clean, mask, scribe, etch and demask, which are generally located in one facility. Process flow may be straight line, or be arranged in a ''U'' shape depending upon the building configuration, number of shipping docks, etc.

Queuing for the process should be arranged such that one part queue is maintained in the scribing area. In reality, there will also be a queue area in masking and etching. The masking and etching queues should be considered as secondary and minimized to the greatest extent possible. Assuming the masking operation is an automated immersion or spray system, the scribing operation will be the most labor intensive. Second most labor intensive is part basket loading and etching.

Automation of the etching operation has been attempted at many facilities with varying degrees of success. Automated etch lines tend to maximize output of simple chem-mill part configurations while complicating the process for parts that include chemically milled tapers. A typical etch line automation plan arranges etch, rinse, desmut and final rinse in order. Producing a chemically milled taper requires a hoist remain stationary over the etch tank as it is used to raise and lower the part. Automation plans (Fig. 50) would stop all etch line work while a taper is produced[8].

The etch line configuration (Fig. 51) allows for automation and for special work to be processed at one end of the etch line while general work is completed at the other end.

---

[8] Alternative schemes such as using high volume pumps and a holding tank to pump etchant to and from the tank, or using a lift to raise and lower the tank are feasible, but many times more complicated and costly.
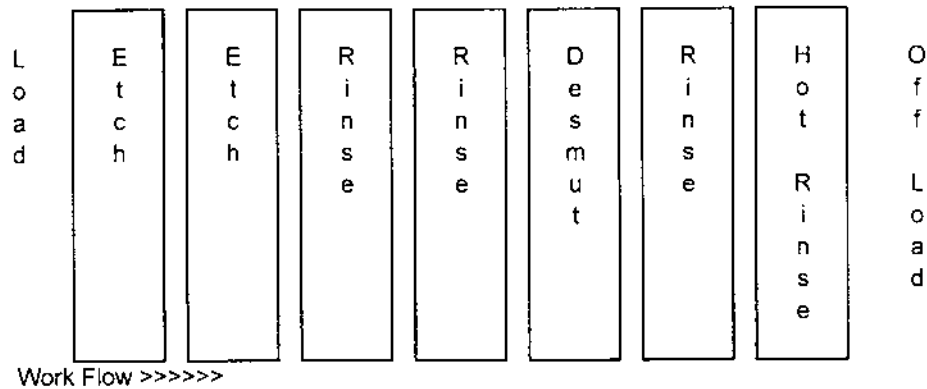
Figure 50   Typical etch line automation planning.
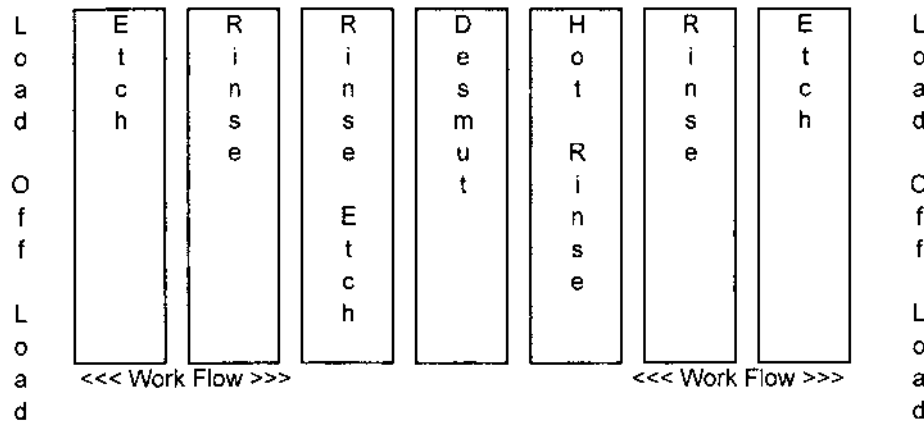
Figure 51   Flexible etch line automation.

8   PROCESS POTENTIAL

The primary use of chemical milling in the aerospace industry is for removing unneeded material from sheet metal parts. The same condition exists with machined parts. The thickness of machined webs is limited by cutter deflection and machine tool vibration, hence webs must remain heavier than is actually necessary. The aerospace industry has invested enormous amounts of money in new high speed machining technologies that allow fast machine feedrates without machine tool vibration, and allow production of thinner machined webs. Development of high speed machining has continued while the industry has essentially ignored the achievements of British Aerospace [1] while fabricating machined parts for the Concorde supersonic passenger jet. Machine tools of the time were not capable of producing the thin web sections necessary, so the parts were machined as far as practical, then immersed in chemical milling etchant for an overall stock

reduction. Parts produced by this process exhibit improved surface finish after etching, and they are ready for non-destructive testing (penetrant inspection) without further processing.

Large removals by etching will generally produce an etch rate differential between thin and thick web sections, but this problem can be addressed by designing for chemical stock reduction and sizing the web sections accordingly.

The chemical milling process may eventually find use in the automotive industry as automobile designers use lighter materials such as aluminum and weight savings techniques to reduce automobile weight and fuel consumption. Chemical milling, once and perhaps still, popular with race teams, was a technique for stock reducing metal car bodies to provide a weight advantage over other race cars [1].

As used in aerospace, chemical milling does not fit the requirements of mass production. Cycle times for liquid maskant application and manual scribing are prohibitive in mass production settings. Developing maskant products that apply in a fashion similar to that of adhesive tapes, with pre-cut pockets or other features would speed maskant application and eliminate scribing. Parts could remain on original conveyance through masking, etching and demasking. A "mass production" chemical milling process would be analogous to automotive painting operations. For now, chemical milling is used primarily for aerospace applications.

APPENDIX A

Derivation of Equations (1) and (2)

1. The relation used to generate Appendix A, Fig. 52 is derived from Table 14:
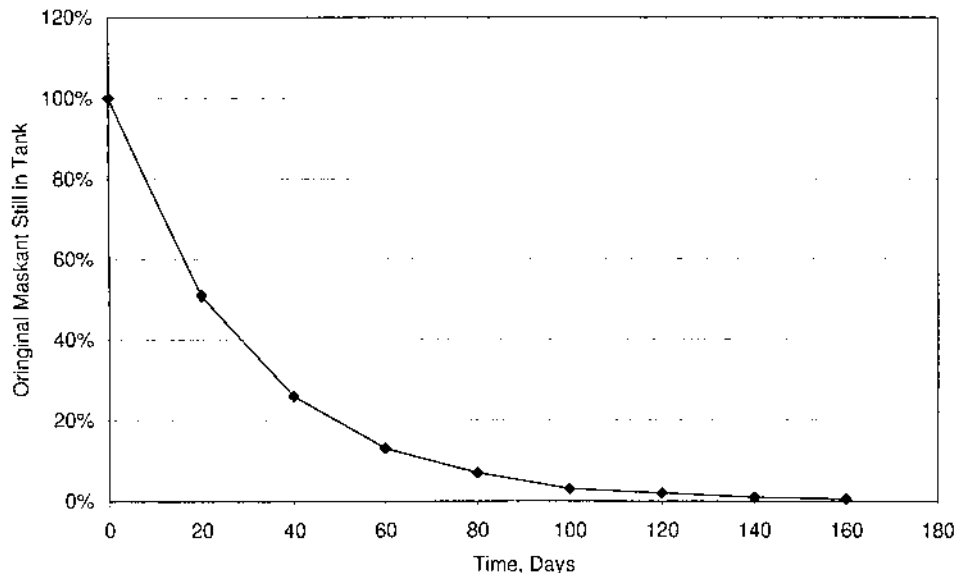
Figure 52 Mask age versus time (hrs) reconstruction of maskant versus time relationship. (Courtesy of R. G. Werkema.)

Table 14 Reconstruction of Maskant – Time Relationship

Basis of Calculations: 6000 gal Mask Tank, 200 gal Withdrawal and Addition per day.

Legend:
- Volume of original mask remaining, day 2
- Volume of original mask removed, day 2
- Running total of new maskant added.

Day	Volume of original mask remaining	Volume of original mask removed	Running total of new maskant added	% Remain
1	6000.0	200.0	200.0	100
2	5800.0	193.3	400.0	97
3	5606.7	186.8	600.0	93
4	5419.8	180.6	800.0	90
5	5239.1	174.6	1000.0	87
6	5064.5	168.8	1200.0	84
7	4895.7	163.1	1400.0	82
8	4732.5	157.7	1600.0	79
9	4574.7	152.5	1800.0	76
10	4422.2	147.4	2000.0	74
11	4274.8	142.5	2200.0	71
12	4132.3	137.7	2400.0	69
13	3994.6	133.1	2600.0	67
14	3861.4	128.7	2800.0	64
15	3732.6	124.4	3000.0	62
16	3608.2	120.2	3200.0	60
17	3487.9	116.2	3400.0	58
18	3371.7	112.3	3600.0	56
19	3259.3	108.6	3800.0	54
20	3150.6	105.0	4000.0	53
21	3045.7	101.5	4200.0	51
22	2944.1	98.1	4400	49
23	2846.0	94.8		47
24	2751.1			46

(Column headers in original appear as numbered day columns 1–24 along a diagonal layout; the three values per day correspond to the legend above.)

Source: R. G. Werkema.

$f(n) = 5800n/6000$.The relation is used as follows:

$f(6000) = 5800(6000)/6000 = 5800,$

$f(5800) = 5800(5800)/6000 = 5606.7,$

$f(5606.7) = 5800(5606.7)/6000 = 5419.8,$ etc.

The relation cannot be defined as a numerical sequence as (n) is not an integer value in most cases. However, suppose $f(n)$ were a numerical sequence. The graph of Appendix I, Fig. 1 depicts a function that approaches infinity while converging on zero (0). Taking the limit of $f(n)$ as (n) goes to infinity:

$$\lim_{n\to\infty} f(n) = \lim_{n\to\infty} 5800n/6000 \neq 0$$

Thus, the original relation, when defined as a sequence describes a function that is divergent, i.e. the function does not converge on any real number value. Therefore, the relation is not a correct description of Appendix A, Fig. 52.

2. The relation $f(n)$ can be rearranged to fit the definition of a numerical sequence.

   2.1 $f(n)$:

   $f(6000) = 5800(6000)/6000 = 5800,$

   $f(5800) = 5800(5800)/6000 = 5606.7,$

   $f(5606.7) = 5800(5800)/6000 = 5419.8,$ etc.

   2.2 $f(n)$ redefined as $f(t)$:

   let $f(t) = [6000(5800/6000)^t]$

   where (t) equals time (days) and all positive integers greater than zero (0), i.e. $(t = 0,1,2,3,4,5, \ldots n)$.

   $f(t)/for = 6000/t = 0, 5800/t = 1, 5606.7/t = 2, 5419.6/t = 3, \ldots$

   A limit test demonstrates that $f(t)$ is convergent, and converges on zero (0).

   $$\lim_{t\to\infty} 6000(5800/6000) = 0$$

   Therefore, the function $f(t)$ converges to zero as (t) approaches infinity. Thus, the function $f(t)$ adequately describes the graph of Appendix A, Fig. 52.

3. A plot of function $f(t)$ is (Fig. 53):

   Careful substitution for $f(t)$ reveals a common form of a frequently used differential equation.
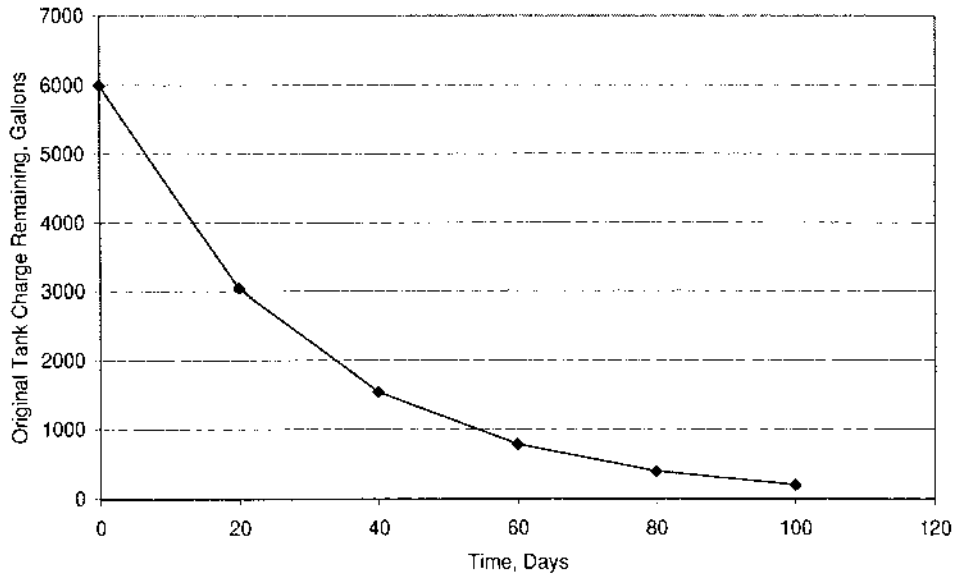
Figure 53   Mask volume versus time (days).

3.1 Let $f(t) = G_r$, gallons remaining

Constant, $C = 6000$ gallon constant tank volume
$a = 5800/6000$, ratio of maskant usage
$G_r = 6000(29/30)^t = C(a)^t$

by definition of the natural exponential function

$$Ce^x = G_r = C(a)^t$$
$$\text{let } x = \text{In } G_r = \text{In } (a)^t$$

then $e^x = (a)^t$ (constants eliminated)
because by definition

$$\ln e^x = x$$
$$e^{\ln x} = x; \text{ then substituting for } x,$$
$$e^{\ln(a)t} = (a)^t, \text{and}$$
$$e^{t\ln(a)} = (a)^t$$

substituting the new expression for $(a)^t$ into G_r produces

$$G_r = Ce^{t\text{In}(a)}$$

which is

$$G_r = 6000e^{t\ln(5800/6000)}$$

where $\ln(5800/6000) = -3.39 \times 10^{-2}$ day^{-1}
$G_r = 6000\ e^{(-3.39\ E-2)t}$
let $k = -3.39 \times 10^{-2}$ day^{-1}

$$\Rightarrow G_r = 6000e^{kt}.$$

3.2 Application of the definition of the natural exponential function provides a new expression for the mask versus time relation. The new expression for G_r is continuous for all (t) greater than or equal to zero (0), and it converges to zero as (t) approaches infinity. The expression is a common form of the, "Law of Natural Decay" [9].

3.3 A much easier approach is direct application of the Law of Natural Decay:

3.3.1 The rate at which the original maskant is removed from the tank with respect to time is proportional to the quantity of the original maskant present in the tank at a given instant, i.e.

$$dG_r/dt = kH_r$$

where: dG_r = rate at which the original tank volume diminishes.

dt = change, or rate of change of time (days)
k = coefficient of mask usage
G_r = gallons of original mask remaining
$dG_r/G_r = kdt$
$\int dG_r/G_r = \int k\ dt$
In $|G_r| = kt + C$
$G_r = e^{kt}e^C = e^{(kt+C)}$

when $t = 0$, $G_r = 6000$, $e^{kt} = 1$
then $6000 = e^C$
therefore $G_r = 6000\ e^{kt}$.

If maskant is used at a rate of 200 gal per day, then when $t = 1$, G_r must equal 5800 gal:

$$6000 - 200 = 6000e^{(1)}$$
$$5800/6000 = e^k$$
$$\text{In}(5800/6000) = k$$
$$-3.39 \times 10^{-2} = k$$

which is the same coefficient derived in paragraph 3.1.

3.4   As demonstrated, direct application of the Law of Natural Decay produces an expression for mask time in tank. However, the technique fails to demonstrate that logic used to generate Appendix A, Fig. 52 and 53 is in fact correct.

Continuity and Asymptote Testing of Equation 1

1. Test the expression $G_r = 6000\,e^{kt}$ for continuity and asymptotes. A convergence test of the expression was completed in Appendix A, paragraph 2.2.

    1.1   Continuity Test: A function is said to be continuous at the number (t) if and only if the following three conditions are satisfied.

    (a) $f(t)$ exists
    (b) $\lim_{x \to t} f(x)$ exists
    (c) $\lim_{x \to t} f(x) = f(t)$

    Let $f(t) = G_r$, when $t = 0$, the volume of the original tank charge must equal the constant tank volume, i.e. at $t = 0$, the entire tank must be filled with new maskant.

    (a) $f(t) = f(0) = 6000\,e^{k(0)} = 6000$, thus $f(t)$ does exist.
    (b)   Let $f(t) = f(x)$

    $\lim_{x \to t} f(x) = \lim_{x \to t} 6000\,e^{kx}$; $t = 0$
    $\lim_{x \to 0} 6000\,e^{k(0)} = 6000$, thus the limit does exist.

    (c)   Summary, from parts 1.1(a) and 1.1(b): (1) $f(t)$ exists and equals 6000; (2) the limit of $f(x)$ as x approaches zero (0) exists and is equal to $f(t)$. Therefore, the expression for gallons remaining, G_r, is continuous for all (t).

2. The line $y = b$ is said to be a horizontal asymptote of the graph of the function (G_r) if at least one of the following statements is true.

    Let $G_r = f(t)$

    (a) $\lim_{x \to +\infty} f(t) = b$, and for some number N,
             if (t) is greater than N, then $f(t)$ does not equal (b).
    (b) $\lim_{x \to -\infty} f(t) = b$, and for some number N,
             if (t) is greater than N, then $f(t)$ does not equal (b).

    Therefore:

    (a) $\lim_{x \to +\infty} f(t) = \lim_{x \to +\infty} 6000\,e^{kt}$; for $k = -3.39 \times 10^{-2}$ day^{-1}
             $\lim_{x \to +\infty} 6000\,e^{-kt} = \lim_{x \to +\infty} 6000/e^{kt} = 0$
    As (t) becomes large, the ratio of (G_r) $6000/e^{kt}$ converges to zero (Fig. 54).

Since the limit of $f(t)$ is zero as (t) approaches infinity $(+\infty)$, $f(t) = G_r = 0$ is a horizontal asymptote. Thus, as (t) becomes large, G_r converges on zero, but never actually equals zero.
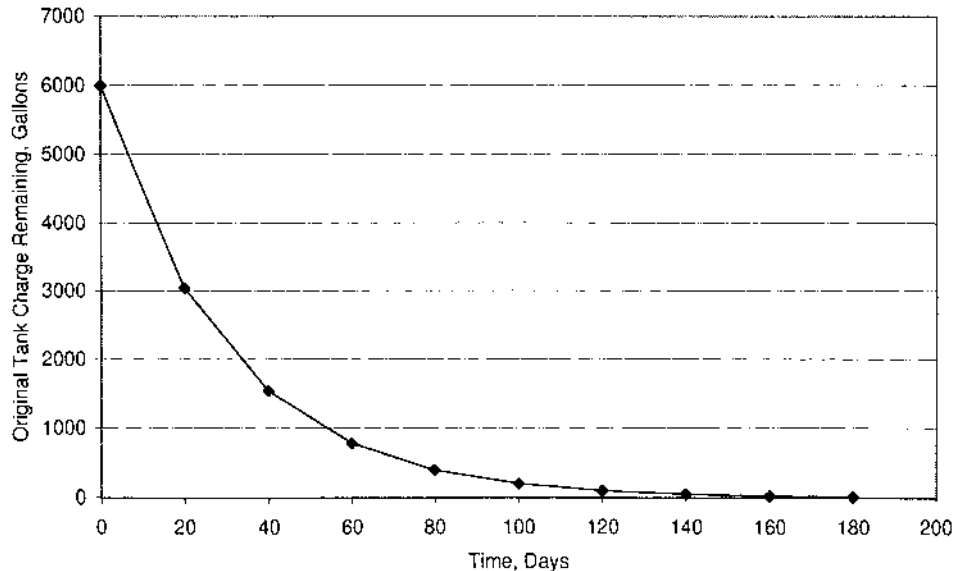
Figure 54 Mask volume versus time (days), continuous function.

Derivations of Equations (2), (3) and (4)

Definition, Impeller Cycles: The number of times the original tank charge of maskant, or some remnant thereof, passes through a mixing impeller.

1. A production mask tank contains 6000 gal of maskant. To simplify equation derivation, assume that a single large impeller is used to mix and circulate the maskant. The unit of time considered is one 24-hour day, manipulated as necessary.

   1.1 Assume the pumping rate of the mixing impeller is 6000 gal/min. The impeller must be stopped for each part immersion cycle to prevent loss of parts from part racks. Assume that immersion cycles occur every 9.5 min and the transfer time of part racks into the lowering device, or hoist, is 1 min. Thus, six immersion cycles occur each hour, and the entire tank volume is mixed six time each hour, or 36,000 gallons of mask is pumped per hour.

   $$(36{,}000)(16)[\text{gal*hr/hr*day}] = 5.76 \times 10^5 \text{ gal/day}$$

   $$C_1 = (5.76 \times 10^5 / 6000)\{\text{gal*cycles/day*gal}] = 96 \text{ cycles/day}$$

   Therefore, the entire mask tank volume will be cycled through the mixing impeller 96 times each day. Since the volume of the original mask declines relative to time, the number of impeller cycles to which the original mask is subjected will decline at the same rate.

   1.2 The number of impeller cycles may be expressed as the ratio of original mask remaining to the total volume of mask, multiplied by

the number of impeller cycles occurring each day, e.g. after day one of operation, 5800 gallons of original mask remain:

$$(5800/6000)(96 \text{ cycles/day}) = 92.8 \text{ cycles/day}.$$

Thus, at the end of day one, the original mask is cycled approximately 93 times/day.

$$I_c = C_1 e^{kt} = 96\, e^{kt}[\text{cycle/day}] \tag{2}$$

where I_c = Impeller Cycles, rate for original tank charge at any time (t), cycles/day.

C_1 = Average number of impeller cycles occurring each day, for the entire tank volume, cycles/day. Impeller Cycles per unit time

t = time, days
k = coefficient of mask usage, day^{-1}.

for I_c = 92.8 cycles/day
$k = \ln(92.8/96) = \text{-}3.39 \times 10^{-2}$

1.3 An equation for estimation of the number of impeller cycles which will have occurred at any time is obtained by integration of Eq. (2).

$$dI_c/dt = C_1\, e^{kt}$$
$$\int dI_c = \int C_1 e^{kt} dt$$
$$= C_1 \int_0^t e^{kt} dt$$
$$= C_1 (e^{kt}/K)|_0^t \tag{3}$$
$$= C_1 (e^{kt}/k - e^{k(0)}/k)$$
$$= C_1 (e^{kt}/K - 1/k)$$
$$= C_1/K(e^{kt} - 1)$$
$$= C_1 (e^{kt} - 1)/k$$

Equation (3) is an expression for the number of impeller cycles to which the original mask will be subjected at any time (t).

1.4 The maximum number of impeller cycles experienced by the original mask during its tank life may be estimated by integration of Eq. (4) with limits zero to infinity (∞).

$$I_{cm} = \int_\infty^0 C_1 e^{kt} dt, \text{ improper integral}$$

let $b =$ the upper limit of the integral, as b approaches infinity (∞).

$$\lim_{b\to\infty} \int_0^b C_1 e^{kt} dt = \lim_{b\to\infty} C_1 \int_0^b e^{kt} - dt$$

$$I_{cm} = C_1 \lim_{b\to\infty} (e^{kt}/k)|_0^b$$

$$= C_1 \lim_{b\to\infty} (e^{kb}/k - e^{k(0)}/k)$$

$$= C_1 \lim_{b\to\infty} (e^{kb}/k - 1/k)$$

$$= C_1 \lim_{b\to\infty} (e^{kb}/k) - C_1 \lim_{b\to\infty} (1/k)$$

where $C_1 \lim_{b\to\infty}(e^{kb}/k) = 0$, by L'Hopital's Rule.
then $I_{cm} = 0 - C_1 \lim_{b\to\infty}(1/k) = -C_1/k$
therefore,

$$I_{cm} = -C_1/k [\text{cycles} * \text{day/day}]$$

1.4.1 Application of L'Hopital's Rule [9]:

$$\lim_{b\to\infty} C_1 e^{kb}/k = 0$$

since the limit converges to zero as (b) increases to infinity, apply L'Hopital's Rule, i.e. take the derivative of e^{kb}/k.

$$\Rightarrow C_1 \lim_{b\to\infty} ke^{kb}/k = C_1 \lim_{b\to\infty} e^{kb} = 0,$$

for

$$k = -3.39 \times 10^{-2} \text{day}^{-1}.$$

Since the subject limit equals zero, all that remains in the derivation of Eq. (4) is $(-1/k)$, multiplied by the constant number of impeller cycles per day, as is shown in para. 1.4.

Assumptions:

- The use of mixers will promote a homogeneous mixture of maskant. Mixers, capable of moving large volumes at low pressure, can thoroughly mix/blend maskant from the initial tank charge with new maskant added to maintain a constant fluid level in the tank.
- By estimating the total number of impeller cycles to which maskant will be subjected, one can estimate the length of time the original tank charge of maskant will be resident in the maskant tank. These estimates can then be used to establish an appropriate mask stability test period/apparatus by the maskant vendor.

Test Apparatus (Fig. 55):
Experiment Set Up:

- Place a 3.5 l Griffin beaker in a black colored laboratory sink (for color contrast).
- Fill the beaker to over flow (4.95 l capacity when completely full), then insert mixer.
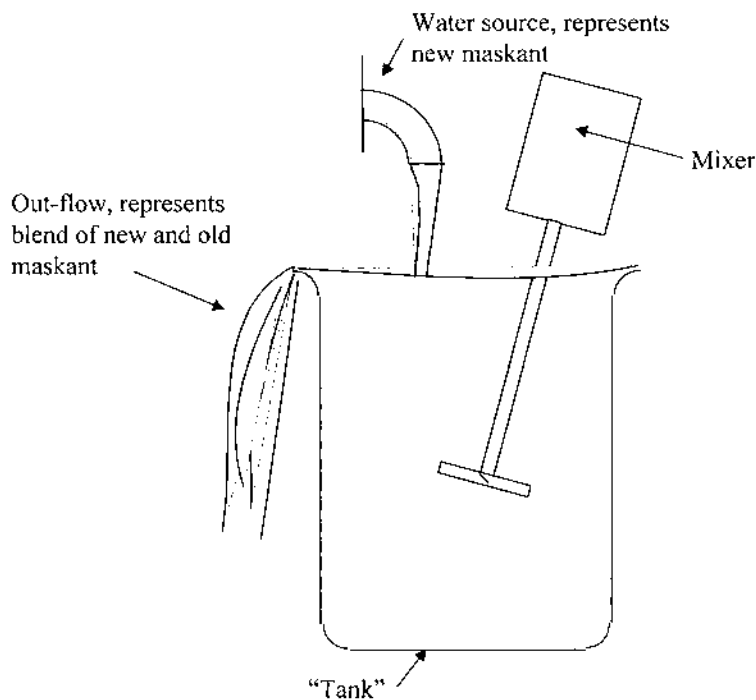
Figure 55 Test apparatus.

- Set mixer speed at 300 RPM for minimal vortex. Mixer rotational speed selection is dependent upon impeller diameter and type. For this experiment apparatus a Lightnin' Labmaster mixer with a 3.4 in. diameter A310 impeller was selected. The 3.4 in. A310 has a pumping capacity of 28 gal/min (gpm) at 300 RPM.
- Add 50 ml of AC JW4–87 waterborne scribe line sealer, or other colorant, to create opaque white color, (AC JW4–87 Line Sealer was selected because it was within reach—white colored latex paint would have been a good choice too—select any colorant that provides good contrast with the background color).
- Measure flow rate from faucet at beginning and end of test run and used the average flow rate for calculations.

Execution:

1. The experiment apparatus was assembled and water flow rate from the faucet determined. The faucet flow was directed into the full beaker of opaque white colored solution. A timer was started as water from the faucet entered the beaker. As time elapsed the following observations were noted: (a) the color of the solution remained uniform, no stratification occurred as is typical when cold water runs into a container and the intent is to displaced whatever is in the container; (b) condensate formed on the sides of the beaker, which complicates determination of when the original solution is completely displaced from the beaker.

2. Results:

- Water flow rate from the faucet was 0.366 gpm.
- At 26 min elapsed time distortion created by the beaker glass and condensate on the glass surface began to obscure the contrast between the black colored lab sink and the solution in the beaker. Therefore the viewing position was changed to directly over the beaker, such that one could view the sink bottom. Distortion was minimal in the new viewing position.
- At 31 min the solution appeared completely clear and the run was stopped. A replicate experiment was set up and executed.
- In the replicate experiment the opaque white color seemed to dissipate between 30 and 34 min Allowing the water to run through 41 min elapsed time did not seem to make the solution in the beaker any clearer, therefore the experiment run was terminated. The experiment data indicates that with a 0.366 gpm flow rate into the beaker, virtually all of the original solution resident in the beaker had been displaced in approximately **28–34** min.

3. Calculations/Estimates:

   3.1   System Information:

          Flow Rate (Usage Rate) from Faucet: 1.385 l/min
          Volume of container/tank: 4.95 l
          Pumping Capacity of Mixer: 28 gpm (106 l/min)

       Coefficient of Use: $k = \text{In}[(4.95\ l - 1.385\ l/min)/4.95\ l]$
                          $= -0.328\ min^{-1}$

   3.2   Mixing Cycles: $C_1 =$ total pumping capacity (gal/day)/tank volume (gal/cycle)

$$C_1 = cycles/day$$
$$\Rightarrow C_1 = 106/4.95\ [\text{litres*cycle/litres*min}]$$
$$= 21.41\ cycles/min$$

$$I_{cm} = -C_l k \tag{4}$$

     where $I_{cm} =$ Impeller Cycles, maximum
$$\Rightarrow I_{cm} = -(21.41)/-0.328\ [\text{cycles*min/min}]$$
$$= 65.27\ total\ cycles.$$

   3.3   Estimate of maskant time in tank (*Note*: time base converted to minutes):

$$I_{ct} = C_l(e^{kt} - 1)/k \tag{3}$$

     where $I_c =$ Impeller Cycles, rate for original tank charge at any time (*t*), cycles/minute.
          $C_1 =$ Average number of impeller cycles occurring each day, for the entire tank volume, cycles/minute.
          $t =$ time, minutes
          $k =$ coefficient of mask usage, min^{-1}

To estimate time in tank, substitute I_{cm} for I_{ct} in Eq. (3), and solve for (t).

$$65.27 = 21.41(ekt - 1)/k$$
$$65.27(k)/21.41 = ekt - 1$$
$$(65.27(k)/21.41) + 1 = ekt$$
$$\ln[(65.27(k)/21.41) + 1] = kt$$
$$t = (\ln[(65.27(k)/21.41) + 1])/k$$
$$t = (\ln[(65.27(-0.328)/21.41) + 1]/ - 0.328)$$
$$[\text{cycles} * \min * \min/\text{cycles} * \min]$$
$$t = \mathbf{29.3} \text{ min}$$

The estimate for maskant "time in tank", and the results from the experiment, given the stated opportunities for experiment error, are virtually the same. Therefore, it is concluded that the underlying assumptions, or hypothesis about the mixer based tank design are correct.

4. Discussion regarding the mathematical estimate of Impeller Cycles (I_{cm} and I_{ct}) and Time in Tank, (t).

4.1 Equation (3) is asymptotic like Eq (2) from which Eq. (3) is derived. A proof will not be attempted here, but a chart of Eq. (3) with the parameters outlined in para. 3 demonstrates the situation sufficiently:

Impeller Cycles where $k = -0.328$, $C1 = 21.41$ (Fig. 56)

The chart demonstrates that possible solutions for Eq. (3) fall between 21 min elapsed time and infinity (∞). However, a review of I_{ct} calculations, which are the basis for the chart indicate the best estimate, or at least and adequate estimate, for (t) is between 25 and 30 min.

elapsed time (t)	I_{ct}, Impeller Cycles
5	52.61
10	62.82
15	64.8
20	65.18
25	65.256
30	65.271
35	65.274
40	65.2743
45	65.2744
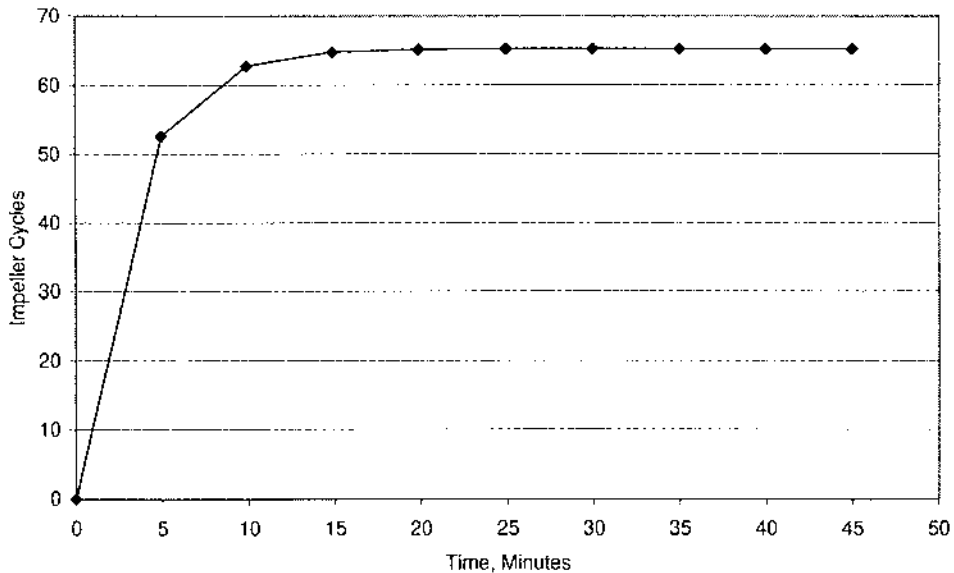
Figure 56   Impeller cycles versus time (min).

4.2   In para. 3, note that estimates for C_1 and I_{cm} are carried to 2 decimal places. The estimate for (k) is carried to three decimal places. The convention for significant digits was ignored for C_1 and I_{cm} estimates. However, the estimate for (t) is rounded to the least number of significant digits found in the information defining system parameters.

4.3   The SOLVE algorithms available with most any scientific calculators may also be used to find and estimate for (t), as outlined in para. 3. SOLVE algorithms require that the equation be re-arranged as follows:

$$I_{ct} = C_l(e^{kt} - 1)/k$$
$$0 = [C_l(e^{kt} - 1)/k]/I_{ct} \tag{3}$$

The SOLVE algorithm must then find a value for (t) that makes the mathematical statement true. Since computing devices such as a scientific calculator carry calculations to 8–16 decimal places the solution derived by a SOLVE algorithm could be significantly different, i.e. larger than the result calculated in para. 3. Based on the chart, the answer derived by a SOLVE algorithm would be correct such that it makes the mathematical statement, $0 = [C_l(e^{kt} - 1)/k]/I_{ct}$ true. However, in a practical sense, the solution for (t) derived by the SOLVE algorithm is not the answer. For example, the observations described in para. 2, and the calculation outlined in para. 3 provide the same answer in practical terms. The SOLVE algorithm available

on the authors Hewlett–Packard 15C Scientific Calculator found that
(t) must equal 71.075 min for the statement $0 = [C_1(e^{kt} - 1)/k]/I_{ct}$ to
be true.

4.4   A suggested practice for those testing maskant stability would be to
estimate (t) as outlined in para. 3, then apply a safety factor of 3.
Hence, the stability test would run approximately three times longer
than would be expected for maskant resident in the production tank.

APPENDIX B

Maskant Surface Coverage Calculation and Maskant use Estimation.

Surface Coverage, Chem-mill Maskants

Suppliers always report the solids content of a coating as % by weight, and some-
times they will include solids content as % by volume. To determine the area that
a particular coating will cover, solids by % weight must be converted to a % by
volume. Calculation of coating coverage is included as reference for those instances
when the supplier does not include solids content as % by volume. *Note*: the unit
for coating coverage is sq ft – mil/gal i.e. the area covered by 1 gal of material,
dry coating thickness 1 mil, (0.001 in.).

     Solvent maskant may be purchased as a concentrate. As per the supplier's tech
data sheet the density is 12.4 lb/gal. However, as per the suppliers technical data
sheet, 55 gal of maskant must be thinned with 14 gal of perchloroethylene, hence
the weight of the perchloroethylene must be added; then the new total weight divided
by the total gallons, mask concentrate plus thinner.

$$
\begin{array}{cc}
12.4 \text{ lb/gal mask} & 13.47 \text{ lb/gal perc} \\
\times \quad \underline{55 \text{ gal}} & \underline{14 \text{ gal}} \\
682 \text{ lb mask} & 188.58 \text{ lb perc}
\end{array}
$$

$$
\begin{array}{cc}
682 \text{ lb mask} & 55 \text{ gal mask} \\
+ \quad \underline{188.58 \text{ lb perc}} & \underline{14 \text{ gal perc}} \\
870.58 \text{ lb total} & 69 \text{ gal total}
\end{array}
$$

$$
\begin{array}{l}
870.58 \text{ lb mask and perc} \\
/ \quad \underline{\quad\quad 9 \text{ gal mask and perc}} \\
12.62 \text{ lb gal.}
\end{array}
$$

Adding perc to thin the mask concentrate effects the weight solids. Therefore, the
weight solids must be recalculated. The MSDS sheet reports weight solids of 20%.
The suppliers technical data sheet reports a weight solids of 25% before thinning.
Check:

$$
\begin{array}{l}
55 \text{ gal mask con.} \\
12.4 \text{ lb/gal} \\
\times \quad \underline{0.25 \text{ wt\% solids}} \\
170.5 \text{ lb solids}
\end{array}
$$

$$
\begin{array}{r}
170.5 \text{ lb solids} \\
/ \underline{\quad 870.58 \text{ lb mask and perc}} \\
0.2 \text{ wt\% solids}
\end{array}
$$

Coverage: Coating capability of 1 gal of solvent mask.

$$
\begin{array}{r}
12.62 \text{ lb mask} \\
\times \underline{\quad 0.2 \text{ wt\% solids}} \\
2.471 \text{ lb solids}
\end{array}
$$

$$
\begin{array}{r}
12.62 \text{ lb mask} \\
- \underline{\quad 2.471 \text{ lb solids}} \\
10.1461 \text{ lb solvent} \\
/ \underline{\quad 13.47 \text{ lb perc}} \\
\times \underline{\quad 100} \\
75.32 \text{ vol \% perc. (gal)}
\end{array}
$$

$$
\begin{array}{r}
1\% \\
- \underline{\quad 0.7532 \text{ vol. perc solvent}} \\
\times \underline{\quad 100} \\
24.68 \text{ vol \% solids}
\end{array}
$$

$$
\begin{array}{r}
231 \text{ in(3)/gal} \\
\times \underline{\quad 0.2468 \text{ vol. solids}} \\
57 \text{ in(3)/gal.}
\end{array}
$$

$$
\begin{array}{r}
0.001 \text{ in.} = 1 \text{ mil} \\
\times \underline{\quad 144 \text{ in(2)/ft(2)}} \\
0.144 \text{ in (3)/ft(2)}
\end{array}
$$

$$
\begin{array}{r}
57 \text{ in(3)/gal.} \\
/ \underline{\quad 0.144 \text{ in (3)/ft(2)}} \\
396 \text{ ft(2)-mil/gallon}
\end{array}
$$

Thus, the solvent mask covers 396 sq ft—mil gal as used. Note, the technical data sheet lists coverage as 500 sq ft/gal, which, is correct for the concentrate form, however, the maskant is thinned before use and therefore covers less area.

Metal Surface Coated Per Year

(a) Volume of maskant purchased = 4091 gal
(b) Volume of perc added to dilute maskant = 1043 gal
(c) Area, (sq) ft, that 1 gal of solvent mask can cover with a 1 mil thick coating = 391 sq ft
(d) Average film thickness = 15 mil
(e) Area covered by 1 gal of solvent mask @ 15 mil:

$$
\begin{array}{r}
396 \text{ sq ft} - \text{mil/gal} \\
/ \underline{\quad 15 \text{ mil}} \\
26.39 \text{ sq ft/gal, actual coverage}
\end{array}
$$

$$
4091 \text{ gal mask purchased}
$$

$+\underline{\quad 1043\quad}$ gal perc added
 5135 total mask and perc used
$\times\underline{\quad 26.39\quad}$ sq ft/gal, atual coverage
 135,500 sq ft metal coated.

Surface Coverage and Volume Estimate, Waterborne Maskant

The maskant technical data sheet reports density of 10.1 lb/gal and 615 sq ft—mil gal coverage, which, is correct if the maskant is maintained at 49.1 wt% solids.

 10 lb/gal mask
$\times\underline{\quad 0.45\quad}$ wt% solids
 4.5 lb solids

 10.1 lb/gal mask
$-\underline{\quad 4.5\quad}$ lb solids
 5.6 lb water/gal mask
$/\underline{\quad 8.34\quad}$ lb/gal water
 0.6715 vol% water, (gal)

 1%
$-\underline{\quad 0.6715\quad}$ % water
 0.3285 vol % solids

 231 in(3)/gal
$\times\underline{\quad 0.3285\quad}$ vol % solids
 75.89 in(3)/gal

 0.001 in. $=$ 1 mil
$\times\underline{\quad 144\quad}$ in(2)/ft(2)
 0.144 in(3)/ft(2)

 75.89 in(3)/gal
$/\underline{\quad 0.144\quad}$ in(3)/ft(2)
 527 ft(2) mil/gal

Cost of Waterborne Maskant

(a) Metal surface area coated = 135,500 sq ft
(b) Optimum coating thickness = 18 mil
(c) Waterborne maskant coverage = 527 sq ft – mil/gal

 527 sq ft mil/gal
 18 mil coating
$/\underline{\quad 29.28\quad}$ sq ft covered by each gallon of maskant with a 18 mil
 thick dry film
 135,500 sq ft surface coated
$/\underline{\quad 29.28\quad}$ sq ft/gal @ 18 mil
 4628 gal of waterborne maskant required.

APPENDIX C

Derivation of tank lining erosion equation.

1. Derivation of etch rate formula for plate or sheet stock samples. Assume that equal amounts of material are removed from all surfaces. The density of sample material must be known. The apparent density may be used, or an accepted value for the particular alloy may also be used.

2. The volume of the plate of sheet stock is defined as follows (Ref. Fig. 48)

$$V = (x)(y)(z)$$

A partial derivative may be used to determine the change in sample volume relative to the changes in the samples physical measurements. Thus, the change in the sample volume (dV) is defined by

$$dV = (\partial V/\partial x)dx + (\partial V/)dy + (\partial V/\partial z)dz; \ \partial V/\partial x = yz, \text{ etc.}$$

As stated, equal amounts of material are assumed to be removed from all surfaces. Thus, a total of six surfaces, two xy, two xz and two yz, are reduced by chemical etching.
Therefore, the equation defining the change in volume becomes

$$dV = 2yzdx + 2xzdy + 2xydz$$

The change in volume (dV) can also be defined as the quotient of the change in sample mass (dM) and the material density (ρ), or

$$dV = dM/\rho$$

Since all sample dimensions are changing by an equal distance, let that distance be defined as (ds). Thus,

$$ds = dx = dy = dz.$$

With appropriate substitutions the change in sample volume becomes

$$dM/\rho = 2yzdx + 2xzdy + 2xydz$$

Therefore,

$$ds = dM/[2\rho(yz + xz + xy)].$$

The new expression for (ds) describes the change in sample dimensions for each surface for a change in sample mass. Elapsed time for the test is Δt (years), then the apparent etch rate is $ds/\Delta t$.

3. Error estimation: error in etch rate calculation is estimated by adding all error associated with sample dimension measurement and mass measurement. Balance scale accuracy is ± 1.0 mg for 0–10 g, ± 1.5 mg for 10–100 g and ± 2.5 mg for 100–1000 g. Caliper accuracy is ± 0.002 in. and dial indicator accuracy is ± 0.002 in. The unitless ratio of error in etch distance (δds) and the distance

calculated (ds) is

$$\delta ds/ds = \delta dM/dM + \delta A/A$$

where

$dM/dM =$ error in mass measurement
$\delta A/A =$ cumulative error in measurements for determination of surface area

$$\delta dM = \delta M_1 + \delta M_2$$
$$= (0.0025 + 0.0025)\text{g}$$
$$\delta dM = 0.005\text{g}$$
$$\delta A/A = \delta A_1/A_1 + \delta A_2/A_2 + \delta A_3/A_3$$

where,

$$\delta A_1/A_1 = (0.05)/w + (0.002)/t^*$$
$$\delta A_2/A_2 = \delta 1/1 + \delta t/t = (0.05)/1 + (0.002)/t$$
$$\delta A_3/A_3 = \delta 1/1 + \delta w/w = (0.05)/1 + (0.05)/w.$$

REFERENCES

1. W. T. Harris, *Chemical Milling, The Technology of Cutting Materials by Etching*, Oxford Unifversity Press, 1976.
2. T. W. Smith and P. E. *Clean Air Act: Overview and Strategies for Industry*, MAC Equipment, Inc., 1992.
3. R. G. Werkema, "Fabrication of Parts by Chemical Techniques," *ASME Design Engineering Conference*, Chicago IL, 1974.
4. T. D. Brown and L. E. Bruce, "High Thiosulfate – An Unwelcome Member in Aluminum Chemical Milling Baths," McDonnell-Douglas, Long Beach CA. Presented at SUR/FIN™ '97, Detroit MI, American Electroplaters and Surface Finishers, 1997.
5. T. C. Foulds, "Effect of Sulfur Compounds on Surface Roughness from Aluminum Chemical Mill Etch Tanks," Boeing Commercial Airplane Group, Seattle WA. Presented at SUR/FIN™ '97, Detroit MI, American Electroplaters and Surface Finishers, 1997.
6. B. M. Griffin, et al., "Tank Arrangement Particularly Designed for Chemical Milling Operations," US Patent 5,015,322, May 14, 1991.
7. Aerospace NESHAP Segment of the 1990 Clean Air Act.
8. J. Y. Oldshue, *Fluid Mixing Technology*, Chemical Engineering McGraw-Hill Publishing Co., 1983.
9. L. Leithold, *The Calculus*, 5th Edn, Harper and Row Publishers, New York, NY.
10. P. J. Ross, *Taguchi Techiques for Quality Engineering*, McGraw-Hill, Inc., 1988.
11. D. C. Montgomery, *Introduction to Statistical Quality Control*, 2nd Edn, John Wiley and Sons, Inc., 1991.
12. M. J. Harry, *The Nature of Six Sigma Quality*, Government Electronics Group, Motorola, Inc.

---

* Measurements of sample width and length are considered accurate to 0.05 in. due to rough cut surfaces.

13. B. Chatterjee and R. W. Thomas, "The Chemical Etching of Aluminum in Caustic Soda Solutions", Trans. Inst. Metal Finishing, 1976, 54.

14. "Fundamentals of Chemical Milling," *American Machinist*, American Machinist Resource Center, New York, NY July 1984.

15. J. A. Cornell, *Experiments with Mixtures, Designs, Models, and the Analysis of Mixture Data*, 2nd Edn, John Wiley & Sons, Inc., 1990.

16. G. F. Bennett and C. T. Philipp, "Industrial Wastewater Pretreatment – Water Conservation, Product Recovery, Pollution Abatement, Waste Minimzation," Sponsored by The University of Toledo, Division of Continuing Education, Toldeo OH.

17. M. Jaffari, "Membrane Systems for Recycling of Sodium Hydroxide and Recovery of all from Aluminum Milling Baths," Malek, Inc., San Diego CA. Presented at SUR/FIN® '97, Detroit MI, American Electroplaters and Surface Finishers, 1997.

18. J. E. Brady and J. R. Holum, *Fundamentals of Chemistry*, John Wiley and Sons Inc., 1981, 1984.

19. M. G. Barth-Jr. and G. M. Wortham, "A Novel Caustic Aluminum Etchant Recycle System," Martin-Marietta Astronautics Group, Denver CO and Ionsep Corporation, Inc., Broken Arrow OK, respectively.

20. D. C. Montgomery, *Design and Analysis of Experiments*, 3rd Edn, John Wiley and Sons Inc., 1991.

21. D. E. Coleman and D. C. Montgomery, "A Systematic Approach to Planning for a Designed Industrial Experiment", Technometrics, February 1993, 35(1).

22. G. Taguchi, *Taguchi on Robust Technology Development*, ASME Press, 1983.

23. *ASM Metals Handbook*, 9th Edn, Vol. 13.

24. P. A. Schweitzer, *Corrosion Resistance Tables*, Marcel-Dekker, Inc.

25. Ibert, Mellan, *Corrosion Resistant Materials Handbook*, 3rd Edn, Noyes Data Corp.

26. H. P. Leckie, *Iron, Carbon Steel and Low Alloy Steel in the Process Industries*, National Association of Corrosion Engineers, 1975.

27. H. H. Lavson, *Stainless Steels and Their Application*, National Association of Corrosion Engineers, 1975.

28. D. L. Graver, *Nickel and High Nickel Alloys*, National Association of Corrosion Engineers, 1975.

29. M. G. Fontana, *The Eight Forms of Corrosion*, National Association of Corrosion Engineers, 1975. Originally from Corrosion Engineering by Fontana and Greene, 1967, McGraw-Hill Book Co.

30. T. H. Harris, *Elastomeric Linings – Advantages Over Other Materials of Construction for Corrosion and Other Abrasion Sources*, National Association of Corrosion Engineers, 1975.

31. O. H. Fenner, *Fiberglass-Reinforced Plastic Structures*, National Association of Corrosion Engineers, 1975.

24

Powder Metallurgy

JOSEPH W. NEWKIRKN

University of Missouri–Rolla, Rolla, Missouri, U.S.A.

1 INTRODUCTION

One of the main driving forces for the use of conventional powder metallurgy (P/M) in many materials, such as iron, is to reduce fabrication costs through near net shape processing. Aluminum P/M is typically driven by different forces, since alternative low cost fabrication techniques are available and result in P/M being more expensive [1]. Often with aluminum other attributes are being exploited, such as the good properties that can be achieved through rapid solidification or adding dispersoids to form composites.

Aluminum powder is readily available, due to its uses in other areas than powder metallurgy. Conventional press and sinter processes can be used to make parts with all of the advantages and disadvantages of powder metallurgy. A selection of these parts is shown in Fig. 1. Elemental powders are used for these materials, leading to relatively low costs of material and fabrication. However, properties are considerable lower than for wrought or even for cast aluminum alloys.

Advanced aluminum alloys are designed to incorporate the advantages of rapid solidification or mechanical alloying in increasing the alloying elements that can be used to form new aluminum alloys. These alloys extend the use of aluminum alloys, offering a lighter weight alternative to existing materials in the areas of high strength, wear resistance, and high temperature applications. For example, high temperature aluminum alloys have been developed that can replace titanium alloys in moderate temperature applications in aerospace. Along with the promise of greater properties, advanced aluminum alloys are usually more difficult to fabricate than conventional alloys.

Figure 1 Various aluminum parts produced using conventional press and sinter metallurgy techniques. (Photo courtesy of Alcoa.)

Particulate metal matrix composites based on aluminum are also a significant application for aluminum P/M. Aluminum P/M produces near net shape composites with greater uniformity in the reinforcement distribution and finer microstructure size than for other fabrication techniques, leading to significant improvements in properties.

Aluminum P/M has traditionally been a small part of the total P/M market, and indeed, a small part of the total aluminum market as well. However, recently the automotive and aerospace markets have given aluminum P/M a large boost. Aluminum P/M is expected to see a large growth in the next decade. Research initiatives are looking at developing improved aluminum P/M alloys and reducing the cost and complexity of fabrication. It is an exciting time for aluminum P/M.

2   APPLICATIONS

Over 48,000 tons of aluminum powder was shipped in North America in 1998 [2]. This tonnage is second only to iron as the largest amount of powder shipped. However, of the total tonnage of aluminum shipped, most is unalloyed aluminum powders for use in other applications than the production of P/M parts. The amount of alloyed aluminum powder used for P/M is rising, but still constitutes only a few percent of the total aluminum production.

In 1998, 1200 tons of aluminum powder was consumed in P/M applications [2]. This represents a 82% increase over the previous year. The market is expected to grow by more than 20% annually. The market is expected to eventually reach 25,000 tons per year. Japan has been a leader in the commercialization of aluminum P/M [3].

2.1 Direct Use of Powder

The majority of aluminum powder is used for the special properties of the powder, rather than the final properties of a finished part. The uses are important and diverse, but include pyrotechnic uses, pharmaceuticals, chemical processes, and as additives to concrete, paint and inks, etc. Aluminum powders are used in steelmaking, as well. Aluminum powders are also sometimes used for cladding steel parts and wires [4].

The pyrotechnic properties of aluminum are exploited in explosives, rocket fuels, fireworks, thermite welding, etc. They significantly increase the heat of the explosive transformation of materials and improve their performance [4]. This useful property of aluminum powders comes with a concomitant safety concern, which is discussed later.

2.2 Transportation

Parts made from aluminum alloy powders have the properties associated with aluminum alloys. Some of these properties are low density, corrosion resistance, high thermal and electrical conductivity, good machinability and compatibility with a number of important finishing treatments [5].

This combination of properties is well suited to applications in aerospace. The somewhat lower properties of aluminum P/M parts is offset by the ability to produce complex net or near net shapes that need minimal or no machining. This makes P/M aluminum parts competitive with other fabrication techniques in many applications, particularly those that are not the most critical. The current push in aerospace for cost reduction favors the increased use of P/M for fabricating aluminum parts.

There is a strong need for higher temperature aluminum alloys that can challenge titanium in moderate temperature aerospace applications. High temperature aluminum alloys are being developed that can be rolled into fine gage sheet for the construction of honeycomb and sandwich structures [6]. In addition the sheet can be formed into shapes for inlet ducts and ducts.

While aluminum P/M alloys look promising for aerospace applications, the problem of cost is still an issue [7]. For short run applications where performance is the major driver, such as military applications, aluminum P/M may do well. However, in the commercial sector, the lower cost of wrought aluminum will be a challenge to overcome. High temperature applications are still a major advantage for aluminum P/M.

One of the areas in which aluminum P/M is expected to grow significantly is automotive. The need for light-weight, high performance parts is increasing in new car designs. The potential number of parts that would need to be fabricated to use in automobile manufacture would dramatically increase the amount of aluminum powder shipped for P/M applications. This is a significant component of the expected market increase in the next few years.

The need for lighter weight parts is leading to the increased use of aluminum P/M to replace ferrous parts made by P/M. These parts are those for which cast properties are insufficient, but the cost of wrought parts is prohibitive. Intricate moving parts, where mass is most critical and fabrication by other means is expensive, are prime components for aluminum P/M.

An aluminum RSP alloy has been used to replace iron P/M parts in a oil pump [8]. The housing is made of an aluminum casting, while the rotor is made from an aluminum silicon alloy. The alloy is designed for good wear and seizure resistance. A very high hardness alloy must be used in order to provide the necessary properties for the part. Vanes and rotors for automotive air conditioner compressors have also been developed [9]. Inlet valves and turbocharger compressors are currrently being developed [3].

General Motors and Chrysler are currently producing aluminum alloy camshaft bearing caps for several of their top-of-the-line engines using powder metallurgy processing [10]. Other applications are either being developed or talked about.

Another area where aluminum is making in-roads is in replacing forged parts. Powder metallurgy preforms for forging give lower waste and higher part properties. P/M forgings are finding uses in gears, connecting rods and pistons.

Composites based on aluminum and fabricated by powder metallurgy represent a new and expanding field in aluminum P/M. New composites provide the possibility for new areas of aluminum P/M use and higher performance alloys.

2.3 Other Uses

Some small room air conditioners use a Al-25Si-Cu-Mg alloy for the rotor of a spiral pump [3]. The low thermal expansion, good wear resistance and high bending strength of the alloy are put to good use. The rotor is shaped by a direct powder forging process.

Other areas in which aluminum P/M parts may find application include business machines, appliances, electrical and electronic applications, and in military ordinance [11]. The combination of near net shape, good corrosion resistance and light weight is attractive. However, the acceptance of aluminum P/M in these areas is slow.

3 POWDER PRODUCTION

3.1 Commercial Atomization

Nearly all aluminum powder used for the production of light-weight parts is produced by inert gas atomization. This technique uses a high-velocity inert gas stream to break molten aluminum into very fine particles. The molten particles solidify during free fall, typically giving them a spherical shape. The small size of the molten droplets combine with the cooling ability of the inert gas to create a very high solidification rate. The resultant powders have a high degree of homogenization and a fine microstructure.

The break up of the molten aluminum is accomplished by injecting the molten metal into a stream of inert gas that has been confined in a nozzle. A region of low pressure in the nozzle pulls the molten metal into the gas stream, and the molten aluminum is broken up in a series of events.

The powders that are produced in this manner will have a distribution of particle sizes that are dependent on a number of processing parameters. Some of the most important parameters are the nozzle configuration, gas pressure, gas temperature, gas velocity, and temperature of the molten aluminum. The actual alloy composition also has an effect on the resultant particle sizes. A small amount of oxygen is usually added to the inert gas to passivate the surface of the aluminum particles. This adds to the surface oxide layer that is produced during cooling.

In ordering aluminum alloy powders from a powder supplier, the particle size distribution will be important to the processing of the P/M parts. In addition to the particle size distribution, other factors, such as particle shape and the thickness of the surface oxide will also be important. Most powder suppliers will supply a complete characterization of the powder upon request.

Water atomization is receiving some attention as a method for producing aluminum alloy powders [12]. In water atomization the impinging water stream cools the molten aluminum and breaks it into small pieces. The result is a rapidly cooled (faster than gas atomization) powder of irregular shape. One of the concerns with water atomization is oxygen contamination of the powder and the formation of hydrated layers by reaction with water. Therefore degassing and drying procedures will be necessary to utilize this powder for P/M. Good properties are reported for compacts made from these powders [12].

Commercial air atomization is a technique for producing low cost aluminum powders that are passivated. As implied by the name, air is used as the carrier gas. The exposure of the molten aluminum droplets to air results in significant oxygen pickup and oxide formation. However, one study has determined that the resulting oxide is similar to that produced by inert gas atomization [13]. Commercial air atomization produces a shape that is more ligamental than the nearly spherical shape of the inert gas atomized powders.

Gas atomization reaction synthesis (GARS) is a modification of the inert gas atomizer [13]. The atomization chamber is evacuated prior to use, and the working gas is ultra-pure nitrogen. This results in a spherical powder with a thinner oxide film. The oxide film also is cleaner and contains less adsorbed water. The thinner oxide layer did not result in an increased safety hazard. It is suggested that this powder will allow for simpler processing routes to forming final parts, which would greatly reduce the cost of aluminum P/M parts.

3.2 Rapid Solidification

The very high cooling rates that a powder particle undergoes during atomization can be used to create powders with unique microstructures and compositions. The area of rapid solidification processing (RSP) has the potential to produce a large number of new alloys for use in aluminum P/M.

Table 1 Techniques for Producing RSP Aluminum Powders

Technique	Typical Diameter (μm)	Typical Cooling Rate (°C/sec)
Gas Atomization	50–100	10^2–10^3
Water Atomization	75–200	10^2–10^4
Ultrasonic Atomization	10–50	Up to 10^6
Rotating Electrode Process (REP)	125–200	10^2
Rapid Solidification Rate (RSR)	25–80	10^5

Source: Ref. 16.

The effect of RSP on the microstructure is to either refine the structure or to produce unique structures, such as amorphous alloys. The secondary dendrite arm spacing (SDAS) is drastically reduced by RSP, depending on the actual cooling rate [14]. For example, a cooling rate of 1°C/sec gives approximately a 70 μm SDAS, while a cooling rate of 1×10^{6}°C/sec should result in a SDAS of 0.7 μm.

The solid solubility of various alloying elements in aluminum can be dramatically increased by RSP [14]. Elements such as Fe, Si, and Cr can be dissolved at levels that are up to ten times the equilibrium amount that can be dissolved at high temperatures. This allows the design of dispersion strengthened alloys with many times the normal amount of strengthening phase. Some of these alloys will be discussed later.

Several methods exist to rapidly solidify aluminum and aluminum alloy powders. As mentioned, conventional atomization can be used, but if higher cooling rates are desired, then alternate methods must be used. Ultrasonic gas atomization is one method that can be used which uses much of the same technology as gas atomization [15]. Other techniques for producing RSP aluminum powders are listed in Table 1 along with the typical dimensions of the powder particles and the cooling rates.

3.3   Mechanical Alloying

Once a laboratory curiosity, mechanical alloying (MA) has now become a viable method for producing aluminum powders with attributes similar to those discussed for RSP. In addition to extended solid solubility and microstructural refinement, MA also is very well suited to the production of composite powders.

Mechanical alloying uses techniques such as ball milling or attritor milling to mechanically mix the elemental constituents at temperatures well below their melting temperature. Usually a very fine powder is produced with an irregular shape and a high degree of chemical homogeneity. Large amounts of alloying elements can be solutionized, similar to RSP [17]. Additionally, MA can also produce nanocrystalline or amorphous powders [18,19]. One study of Al-Fe-Si-B, found that if one of the starting powders was amorphous, then the resulting powder was more likely to be amorphous [20]. The formation of a supersaturated solution has been attributed to the formation of defects by the mechanical deformation [21].

Table 2 Process Control Agents Reported Used in Mechanical Alloying

Agent	Amount	Comments	Reference
Ethanol	0.05 ml/g[26]	Prevents sticking	26, 17
Wax	1.5%	Micropowder C	27
Sodium Stearate	1.5%	Carbides and oxides	28
Stearic Acid	N/A	Carbides and oxides	25

One advantage of MA over RSP is in alloying elements with widely different melting temperatures. Titanium and other refractory metals can be alloyed by MA. However, one study found that MA did not produce as fine a dispersion of intermetallics as RSP [22]. Another study indicates that although there are similarities in the results of the two processes, they achieve similar results through different mechanisms [19].

Mechanical alloying can be used to alloy aluminum with Ti and dramatically reduce the size of the Al_3Ti particles [23]. Mechanical alloying reduced the particles to sub-micron sizes. This is not possible with conventional casting techniques.

Several specialty alloys have been developed that use the ability of MA to produce powder of unique compositions [24,25]. Some of these alloys are non-heat treatable dispersion strengthened alloys, while others contain Li to lower density. The alloys offer some advantages over existing materials and even were in commercial production for a time. Market conditions forced the cessation of production, however, the viability of the technique was shown.

A process control agent is often added to reduce sticking of the powder during milling, and also to refine the particle size. One study of Al-Fe indicated that using ethanol as a process control agent reduces the diffusion rate of the two elements into each other [26]. Another study used the same agent, wax, for a die wall lubricant [27]. Table 2 lists several process control agents that have been reported in the literature.

3.4 Reaction Milling

The addition of oxygen or carbon to MA powders can result in an in situ reaction with reactive elements leading to the formation of fine dispersoids [28]. A double MA process has been utilized to produce very fine uniform dispersions of reinforcing phases [29]. The elemental powder mix is mechanically alloyed, followed by a heat treatment to form the dispersoid. Then it is mechanically alloyed a second time to produce the fine dispersion in the aluminum matrix. This resulted in an improvement in properties over the single MA method.

In another technique, an exothermic reaction during ball milling between aluminum and Fe_2O_3 resulted in the formation of AlFe and Al_2O_3 [30]. The milling time necessary to produce the reaction was a function of the energy input. The reaction resulted in nearly 100% conversion of the material.

Composites of aluminum alloys and aluminum nitride can be produced in situ by cryomilling the alloy powders [31]. Cryomilling is mechanical alloying carried out with liquid nitrogen added to the milling chamber. The liquid nitrogen cools the powder and increases the fracturing of the alloys, typically decreasing particle

size. Some of the nitrogen also is incorporated into the aluminum powder as a nitride, typically AlN. The AlN appears to stabilize the fine structure of the powder during subsequent thermal processing.

4   HANDLING OF ALUMINUM POWDERS

When considering whether to become involved in aluminum powder metallurgy, one major consideration is the safety and handling procedures that must be adopted. Aluminum powders can be handled safely. However, without attention to proper safety and handling procedures, aluminum can be very dangerous. After all, the solid fuel rocket boosters on the space shuttle are powered with aluminum. This section describes several aspects of the safe handling of aluminum powders. It should not be treated as a complete manual for those involved in the business of aluminum powder metallurgy, but rather as a primer. Aluminum powder suppliers have a great deal of experience with the safe handling of these materials, and are a good source for information pertaining to a particular application.

While aluminum powders can be dangerous, historically, the powder producer assumes the greatest risk. There are relatively few reported explosions from companies which use aluminum powders in their process [32]. Someone considering whether to become involved with aluminum powders should be cautious and informed about safe handling procedures, but should not be afraid to become involved.

4.1   Safety

Any powdered material which can react or combine with oxygen will have the potential to ignite. If the powder particles are fine enough and are dispersed into a dust cloud then an explosion could result. The sensitivity to ignition will be dictated by many factors, one of which is the ease with which the material combines with oxygen. Since aluminum is very reactive in this respect, the powder is generally regarded as highly dangerous.

Data for the degree of explosion hazard is available. Elemental aluminum powder and a prealloyed aluminum powder are compared to several other commercially important metal powders in Table 3.

Table 3   Data for Various Metal Powders

Metal Powder	Min. Ignition Energy (mJ)	Min. Explosive Concentration (g/m^3)	Max. Rate of Pressure Rise (bar/sec)	Min. Ignition Temperature (°C)
6 μm Al	13	30	1331	420
Al-Ni alloy	80	190	690	950
Zinc	200	400	125	630
Tin	80	190	117	630
Titanium	15	45	759	375
Iron	150	200	145	510

Source: Ref. 32.

The minimum ignition energy, MIE, is an indication of the sensitivity of the powder to ignition. The lower the value of MIE, the more precautions must be taken to avoid ignition. Values of MIE below 25 mJ indicate a high degree of sensitivity and can be ignited by electrostatic charges [33]. Note that both elemental aluminum and titanium are below this level. However, the prealloyed aluminum powder is above this level, indicating the lower sensitivity to explosion of powders of aluminum alloys.

The minimum explosive concentration determines how much powder needs to be in a dust cloud to allow an explosion to occur, if ignited. The maximum rate of pressure rise is used for the design of explosion venting. Venting is used to prevent the buildup of pressure to the explosive level.

The minimum ignition temperature is the temperature at which metal dust will ignite when laying in a pile. This measure should have little relevance to actual practice, since properly handled metal powders should not be allowed to accumulate.

In addition to these values, the minimum amount of oxygen must be present for an explosion to occur. The amount changes with the atmosphere present. In nitrogen, at least 9% oxygen must be present [34]. In helium, the number is 10%, while in carbon dioxide only 3% is needed to support an explosion.

Of course, for an explosion to occur, the powder needs to be suspended. In other words, a dust cloud needs to be formed. Dust clouds are easy to form with small, light-weight powders such as used in aluminum powder metallurgy processing. The finer the particle size of the powder, the greater the chance of creating a dust cloud and the longer that it will stay suspended. In addition, the finer particles require less energy to ignite and create a more powerful explosion. In general, aluminum powders greater than 450 microns in diameter pose no hazard, while powders greater than 75 microns are difficult to ignite [32,34]. Finally, powders below 10 microns are very sensitive and great care must be taken in handling them.

4.2 Storage and Handling

Aluminum powder should be stored and handled in such a way as to avoid prolonged contact with water. This requirement is due to the reaction between water and aluminum, which produces hydrogen gas. This, of course, adds to the hazard of using aluminum powder. Other practices which should be adopted for handling aluminum powders are similar for any flammable material. Store in appropriate containers, keep away from oxidizers and combustible materials.

There are two areas specific to powder metallurgy operations that need to be considered when discussing the safe handling of aluminum powders [34]. First, metal powders are typically transferred during processing from one container to another. There are several opportunities to create dust clouds during this powder handling. Care should be taken to ensure that powder transfers are slow and deliberate. Non-sparking implements should be used and the two containers should be attached to ground and to each other.

Second, during mixing of the aluminum powder a dust cloud is created in the mixer. It is recommended that inert atmospheres be used for this operation [34]. A mixer that reduces the creation of frictional heat is also recommended.

Good housekeeping practices are highly recommended for any plant that will be using metal powders, especially aluminum powders. Specific methods for cleaning up metal powders should be researched and adopted. Guidelines for handling aluminum powders are available from the Aluminum Association [35].

5   CONVENTIONAL TECHNOLOGIES

5.1   Tailoring Powders

Blending aluminum with other alloying elements, elemental blends, and then consolidating and sintering has many advantages in ease of simplicity of processing and lowered cost. The elemental powders typically have a higher compressibility than alloyed powders, therefore reducing tool wear, increasing green strength, and green density. The alloy would form upon sintering. Using blended master alloys similarly offers many cost advantages. While costs may be significantly lower, the properties are also lower than that found in other processing routes. Most conventional aluminum P/M alloys are elemental blends.

In order to produce an alloy by this technique, it is required that the alloying elements have certain important characteristics [36]. Specifically, the elements to be alloyed must have a significant solubility in aluminum at the sintering temperature, and the diffusion rate in aluminum must be rapid enough that the elements can be homogeneously distributed in a reasonable period of time. Many common alloying elements in aluminum meet these criteria. Cu, Mg, Zn, and Si all have extended solubility and rapid diffusion rates.

The prealloyed powder route is a way to get higher properties than achievable by blending elemental powders. An alloy of the desired composition is melted and then typically atomized, although mechanical alloying is another way to produce a prealloyed powder. In addition to producing a part that has properties closer to wrought, certain aspects of the process can be used to create new alloys with distinctly different compositions and properties than wrought. These aspects are the extended solid solubility and microstructural refinement that occurs during the atomization or mechanical alloying process.

Elements which do not meet the requirements for blending, can have significant solubility during atomization. Elements, such as Fe, Cr, Mn, and Ni have limited solubility in aluminum, less than 1%. However solubility levels of 4–6% can be achieved during atomization, leading to the use of these alloying elements as strengthening agents in alloys which cannot be produced by ingot metallurgy or by powder blending. The wear resistant Al-Si and the high temperature alloys based on intermetallic dispersoids of Fe are examples of these types of alloys.

While prealloyed powders offer significant improvements in properties, they are more difficult to fabricate due to the higher strengths of the powders. Retaining the fine microstructure and the dispersion of hard phases also is complicated by the sintering temperatures used for densification.

Aluminum metal matrix composites can be produced by powder metallurgy. Incorporation of reinforcing phases can be accomplished with good uniformity and good densities. However, the fabrication becomes more difficult and a large number of steps may be required to produce the best properties. This leads to relatively high costs.

The size ratio between the reinforcement particles and the matrix particles can significantly effect the sintered strengths of an aluminum matrix composite compact [37]. If the reinforcing particles are smaller than the aluminum particles, then they will occupy interstitial sites in the aluminum particle structure before pressing. The final structure has the reinforcement particles distributed at the prior aluminum particles boundaries, which reduces strength considerably. If the particle volume is large enough, then the aluminum particles can be kept from making good contact and the sintered density can be poor. When the reinforcement size is equal or greater than the matrix powder size, then the reinforcements particles will be well dispersed, giving the greatest increase in strength.

Degassing of aluminum prior to consolidation can be performed to improve the final properties of the sintered compact. The degassing should be carried out at elevated temperatures, in order to fully desorb the water vapor and decompose the hydride that forms on the surface [38]. Degassing times and temperature are dependent on the desired amount of degassing achieved and the economics of the treatment. Complete degassing is very difficult to achieve, even at high temperatures (550°C) and long times.

The degassing is carried out in a partial vacuum. Temperatures vary, but a range of 200–400°C is effective. Many techniques have been developed to perform the degassing. A good discussion of several of these, is contained in reference [39].

Degassing has been shown to convert the ductile aluminum hydroxide into a brittle form of alumina [40]. Once the hydroxide has been converted, it is stable for several days in air, possibly allowing batch degassing to be included in a production process. The brittle alumina is broken during pressing, allowing for a much larger number of metal-to-metal contact areas. This results in improved compressibility and improved strengths after sintering. Green densities and green strengths are also improved dramatically by prior degassing, with strength improving by greater than 100% [41].

5.2 Press and Sinter

Low cost P/M components are routinely produced with press and sinter processing. The low cost is usually offset with lower densities, and hence lower properties. Near net shapes can be easily fabricated with the design limitations of the press and sinter process. These limitations include a simple shape in the direction of pressing, while the part can have a complex shape in the other dimensions. For general information on the limitations in the design of press and sintered parts, the reader if referred to the Powder Metallurgy Design Manual, published by MPIF [42]. Tolerances that can be achieved in press and sintering of aluminum are quite good. As-sintered dimensional tolerance is 0.051 mm, while the as-sized tolerance is 0.013 mm [42].

As in most P/M materials the higher the compaction pressure and resulting green density, the higher the final density. Aluminum alloys can be cold compacted to higher green densities than the more commonly used ferrous powders. The compaction pressures used are also considerably lower than those used for ferrous P/M. This can be seen by looking at Fig. 2 [39]. Compaction presses used for aluminum can be considerably smaller, while still achieving excellent green densities. Table 4 shows
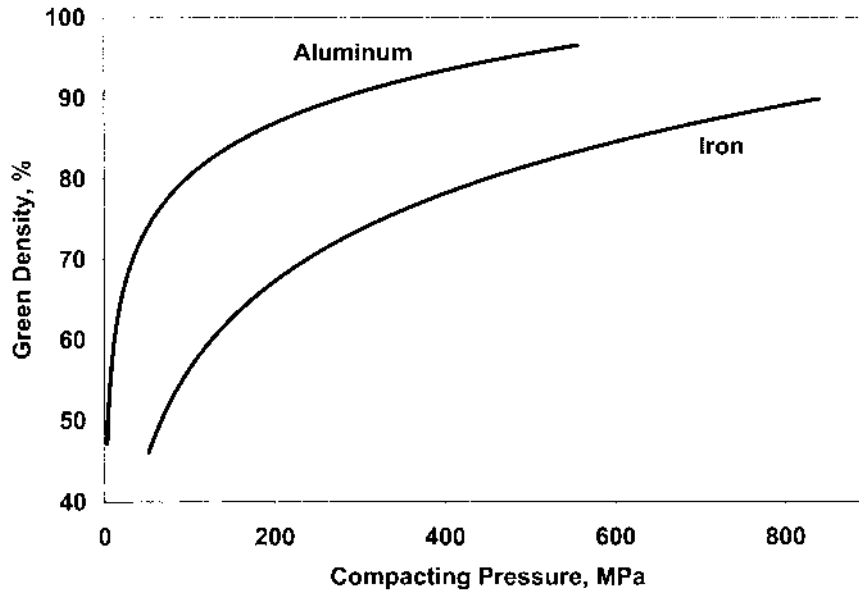
Figure 2 The effect of compacting pressure on the green density of aluminum and iron powders. Note the much lower pressures needed to compact aluminum compared to iron. (From Ref. 39.)

Table 4 Green Density as a Function of Compaction Pressure

Compaction Pressure (MPa)	201AB	601AB	Water atomized Fe
110	85	83	61
180	90	88	71
410	95	93	85

Source: Ref. 39.

a comparison of several commercial aluminum P/M alloys and water atomized iron powder. The higher relative density that can be achieved with the aluminum alloys is clearly shown.

One study has shown that aluminum alloy powders can be cold compacted to full density at sufficiently high pressures [43]. Unalloyed atomized aluminum powders (< 20 μm) were consolidated to 100% density at pressure of 1 GPa. Atomized alloy powders containing various amounts of Fe and Ni were consolidated to full density at a pressure of 3 GPa. Strength values were not reported.

Aluminum alloys are usually sintered at least 90% of their melting temperature. Many times a transient liquid phase is involved when sintering elemental blends. A typical sintering cycle contains three stages, a lubrication burn-off stage, the high temperature sintering stage, and a furnace cool-down stage. Good properties require the proper selection of dew point, atmosphere, and temperature.

Furnaces for aluminum sintering include both batch and continuous conveyor types. Batch furnaces have lower investment costs, moderate atmosphere requirements, and greater control than continuous furnaces. Continuous conveyor furnaces have the distinct advantage of higher production rates. A humpback furnace can lead to lower atmosphere usage.

A vacuum furnace, which is a special type of batch furnace, can also be used to achieve high densities after sintering. If a lubricant is used, then it must be removed prior to vacuum sintering. Parts are cooled before the vacuum is released and the furnace is opened.

The choice of atmosphere has a significant effect on final properties and dimensional accuracy [44]. Aluminum can be sintered in nitrogen, dissociated ammonia, inert gas, or in vacuum. Hydrogen has been used, but is not recommended for aluminum due to lower properties in the sintered part. Humidity should be low during sintering. A dew point of $-40°C$ or lower is recommended.

Nitrogen is a particularly good atmosphere for aluminum due to the combination of low cost and ready availability, with excellent sintered properties. The highest sintered strengths of several commercial aluminum alloys is achieved in nitrogen atmospheres. For example, 601AB, starting with a 95% green density, has a 12% higher yield strength when sintered in nitrogen compared to dissociated ammonia. The ductility is also slightly improved in this example. One study of the sintering of a 2014 (MD-24) PM composite reinforced with various hard phases showed at least a 50% decrease in ultimate tensile strength with a nitrogen atmosphere compared to the same composites sintered in argon and vacuum [45]. However, the nitrogen used had a dew point of greater than -20°C, which may account for some of the difference.

Dissociated ammonia is an available atmosphere used for sintering non-ferrous P/M materials, and can be used with aluminum. Properties of parts sintered in Dissociated ammonia are usually lower than those sintered in nitrogen. The lower properties have been associated with the hydrogen in the dissociated ammonia. The heat treatment in ammonia of 2024 sheet is known to cause a 29% reduction in strength and an 82% reduction in elongation [46].

Dimensional changes during sintering of aluminum parts is effected by the usual P/M factors such as green density and sintering temperature, but also by choice of sintering atmosphere and dew point. The change in dimensions can be either positive or negative depending on a combination of the green density and the atmosphere.

Using vacuum, both 201AB and 601AB can either shrink, remain unchanged or swell depending on green density. By the right choice of atmosphere and green density, good dimensional control can be achieved. If maximum properties are needed, sintering in nitrogen gives little or no shrinkage in both alloys.

The decrease in density that can occur during sintering has been associated with entrapped gases from the atomization process [41]. Swelling can increase with higher compaction pressures and also higher sintering temperatures.

5.3 Advanced Sintering

Aluminum alloys can be liquid phase sintered by blending aluminum powders with powders that form a eutectic with aluminum [47]. Melting occurs at the contact

points between the aluminum and the blended eutectic powder forming a liquid phase. The oxide on the powder particle surface is dispersed and disseminated, leading to metallic contact and an improvement in sintering.

A study of RSP A1-5% Cu powders, alloyed to create a composition with a large freezing range, shows that they can be consolidated by sintering [47]. During sintering in the solid–liquid temperature region, the particles melted along grain boundaries and dispersed the surface oxides leading to good bonding.

Dynamic compaction has also been tried to retain the RSP microstructure and create high density compacts [48]. While high densities were reached and the nanostructure was preserved, bonding between the particles was hampered by a lack of oxide breakup.

Trace elements can also enhance sintering of aluminum [49]. Additions of Mg in a concentration of $\sim 0.15\%$ promotes sintering. The Mg reduces the oxide film on the powder particles, exposing the underlying aluminum. Additions of 0.1% Pb or Sn can promote densification of alloys based on 7xxx wrought alloys, in contrast to the expansion that sometimes occurs during sintering. This leads to significant strength improvements. The elements Sn, Pb, Sb, In, and Bi have been found to activate the liquid phase sintering of alloys based on 2xxx series alloys. Only a small amount of each element, typically 0.1%, is necessary to get the full effect on the sintering. While improving densification, the liquid phase sintering results in a slight decrease in strength, with a significant increase in ductility in the as-sintered condition.

5.4 Lubrication

In order to improve powder compaction in the die, and to reduce problems in ejecting green parts from the mold, lubricants are used. Admixed lubricants are preferred for ease of use and uniformity from batch-to-batch, however, properties usually are effected by the residue of the lubricant that is not removed prior to sintering. The same is true in aluminum P/M.

Most conventional aluminum powders come with an admixed lubricant. Usually this takes the form of Ethylene Bis-stearamide (EBS) in quantities of 1–2%. Liquid polypropylene glycol and polyethylene wax have also been used [50,51]. The lubricant must be removed prior to sintering. Effective removal of the lubricant is important to the final properties, therefore a delubrication step is usually incorporated into the sintering cycle.

A recent study has shown good results with substituting polyethylene wax for EBS in Al-6061 [51]. Adding quantities that were identical to that used commercially with EBS, higher green properties were achieved and sintered transverse rupture strengths were increased approximately 15%. A 420°C delubrication treatment was used.

Another recent study has proposed the use of die wall lubrication instead of admixed lubricants [50]. Higher sintered strengths were produced by a mixture of die wall lubrication with Acrawax C and an admixed 0.2% EBS, instead of the more typical 1.2%. No ejection problems were noted and green strengths improved.

5.5 Repressing

Pressed and sintered aluminum parts can be repressed to increase the density further. In addition to increasing the density, repressing can be used to improve the dimensional accuracy of the part. When the primary purpose of the repressing is dimensional accuracy, then it may be termed "sizing".

Repressing can be followed by resintering, which may relieve residual stresses caused by repressing, and also may further increase the density. Any additional density increase will depend on the repressed density of the part. Parts with very high density will have little driving force for further densification.

A study of repressing of press and sintered ring and disk preforms showed that the use of a lubricant can have an effect on the strain induced in the part, and the effect is dependent on the height to diameter ratio of the compact [52]. Admixed powders in the composition of Al-4% Cu were pressed and sintered into either rings or disks, and then cold pressed to different strains and densities. The use of graphite as a lubricant reduced the change in the internal diameter during repressing. It also induced a larger height strain for a given densification.

A study of mechanically alloyed Al-Fe powders demonstrated that a double cold pressing and sintering process can produce final properties similar to vacuum hot pressed and DISPAL [27]. The recommended process is to mechanically alloy, degas, press at 850 MPa, sinter at 650°C, repress at 1300 MPa, and finish by sintering at 650°C. Sintering in each step was for 1 hr in vacuum.

5.6 Vacuum Hot Pressing

Aluminum alloy powders can be vacuum hot pressed to high densities. This is often necessary for prealloyed powders that are difficult to fabricate by more conventional means. For example, fully dense samples of 2014 and a 2014 based composite were produced by hot pressing at temperatures up to 540°C for 1–2 h [53]. Pressing loads of 4–11 MPa were used for both monolithic alloys and SiC composites. Densification rates decreased with increasing volume of the reinforcing phase. The temperature used indicated that supersolidus conditions existed during pressing.

Powders which are loosely loaded into the hot press, require longer heat up times than precompacted powders. Measured lag times for the center of a 75 mm cylindrical compact varied from 30 min for loose powder to 5 min for powder precompacted at 11 MPa. A longer soak time should be used if loose powders are being compacted.

The distribution of pressure during compaction may differ for blended composite powders than for the matrix powder alone [53]. Measurements of the pressure transferred to the die during pressing show that greater pressure is transferred as the amount of reinforcing phase is increased.

A method for pressing powders to nearly full density, that has an extremely fast rate of densification is bidimensional compression [54]. A more complicated pressing die than for conventional hot pressing allows for compaction pressures to be applied from two perpendicular directions simultaneously. In addition to the high strain rate produced, the technique also allows lower pressing temperatures to be used. A MB85 powder was pressed to better than 97% density at 300°C using a pressure of 172 kPa for only 15 sec.

5.7 Forging of PM Alloys

Forging of aluminum PM alloys leads to good bonding, low porosity, and good dimensional tolerances. The properties of conventional PM alloys can approach those of wrought. Not only can strength and elongation comparable to wrought be achieved by this processing route, but also fatigue resistance [55]. Forging also results in a lower cost than extrusion due to the higher material yield and near net shape capability [56].

Aluminum is will suited for making P/M preforms for forging. Preforms are typically coated with a graphite lubricant to help metal flow during forging. Forging can be performed hot or cold. Hot forging is typically done at 300–450°C. Forging pressure usually does not exceed 345 MPa. A confined die is often used so that no flash is produced. Scrap loss is $< 10\%$ compared to conventional forging, which can be as high as 50%. Forged aluminum P/M parts have very high densities, usually $> 99.5\%$ of theoretical density.

An example of a forging process developed for automotive parts made from high silicon aluminum alloys, starts with the powder, which is mixed prior to compaction to a preform [57]. The preform is preheated to 480°C in a high frequency furnace, both to reduce the forging pressures, but also to degass the powder, which is critical for good forged properties. After forging the compacts are heat treated to meet properties, and then machined to final shape. Care must be taken in the compaction of the preform not to introduce any defects that will be carried over into the final part.

Aluminum alloys have been shown to be able to be forged to very large reductions by using the superplastic properties of fine grained compacts [58]. A 7475 alloy powder and a IN90211 alloy powder were each prepared by ball milling for 80 h in argon with zinc stearate as a process control agent. The powders were subsequently cold compacted with 770 MPa of pressure and then sintered at 500°C for 1 h. Hot extrusion was carried out at 350°C using a 16:1 extrusion ratio. The compacts were solutionized and quenched before forging. An elongation of greater than 200% was achieved at a strain rate of 1 sec^{-1} when heated to 475°C. A forging limit of better than 70% was measured.

5.8 Extrusion of P/M Alloys

Extrusion is used to produce extruded shapes of conventional P/M alloys, and also to consolidate RSP powders for high strength and high temperature applications. The method of extrusion, and degassing process effect the resulting mechanical properties of the extruded material [59].

Difficulties with dimensional tolerance during extrusion have been overcome with die design and process parameter optimization [9]. Control of the temperature during hot extrusion was critical for dimensional control and retention of the RSP microstructure. The gas atomized powders were consolidated by cold isostatic pressing prior to hot extrusion.

Atomized Al-5Cr-2Zr powders were extruded to study the effect of extrusion parameters on the extrusion pressure [60]. The powders were canned in 6063 and extruded at different ratios and speed. Powder size and temperature were also examined. Powder particle size and temperature were dominant factors for control-

ling extrusion pressure. Large particle size and high extrusion temperatures both dramatically lower extrusion pressure. Decreased reduction ratio and extrusion speed slightly lowered extrusion pressures.

5.9 Heat Treatment of Aluminum P/M Alloys

Many aluminum P/M alloys respond to aging treatments, like their wrought counterparts. The temper designations for aluminum P/M parts are somewhat different from those used for wrought alloys [61]. The following designations are often used for conventional aluminum alloys.

- T1: As-sintered.
- T2: As cold formed (after sintering).
- T4: Solution heat treated and at least four days at room temperature.
- T6: Solution heat treated and artificially aged.

Other designations are used and mean various processing steps. Some indicate repressing was applied. Some are overaged or a cold deformation step is included in the heat treatment, similar to T7 and T8.

6 EMERGING TECHNOLOGIES

6.1 Spray Forming

Spray forming is emerging as a production process for new advanced aluminum alloys. The process takes the concept of an atomizer and instead of producing powder that then has to be consolidated, deposits the atomized droplets onto a substrate. The deposit is built up until the final thickness is achieved. Usually secondary operations, such as machining, are necessary to turn the deposit into the final product. Spray forming has an advantage over ingot techniques in that the final microstructure is uniform and homogeneous, like those produced by conventional P/M. This gives the material produced by this technique excellent properties.

The as-sprayed billet typically has densities of greater than 97% [3]. This high density allows for easier forging and extrusion. The extrusion ratios are not as high, and there are less steps in the process. Also the lower gas contents allow fusion welding processes like laser or electron beam welding [3].

One commercial form of this technique is the Osprey process [62,63]. The Osprey process atomizes the aluminum alloy in an argon atmosphere to reduce oxygen contamination of the deposit. The substrate is rotated to produce an even deposit, and as the deposit thickness increases the substrate is lowered. The deposit thickness is limited only by the supply of molten metal. The resulting billet has 1–3% porosity, which can be eliminated by a subsequent extrusion step. Other shaping operations, such as machining or forging, are necessary to produce the final shape.

The Osprey process has been used to make a variety of parts for automotive applications. These include, wear resistant Al-Si cylinder liners [63], and dispersion strengthened Al-Si alloys for forged connecting rods and pistons [64]. The properties of the alloys produced by this process exceeds those of the alloy that it replaces.

Other techniques for spray forming have been described. These include liquid dynamic compaction (LDC) and variable co-deposition of multiphase materials (VCM) [65]. In one study a 2024-T4 alloy was produced by LDC, with a 40% increase

in yield strength with a 25% reduction in elongation [66]. The same process combined with small addition of Ni and Zr, resulted in more than a 20% increase in the yield strength of an extruded 7075-T6 with no loss in ductility. A fine dispersion of $A_{13}Ni$ and $A_{13}Zr$ were achieved through the rapid solidification that occurred during formation.

6.2 Ceracon

The Ceracon process utilizes a solid powder, known as a pressure transmitting medium, as the working fluid to pseudo-isostatically press a green compact. The short exposure time to the high temperatures leads to a retention of a small grain size in aluminum alloys [67]. In aluminum alloy 6061, an increase in the tensile strength, yield strength, and elongation compared to wrought can be realized using the ceracon process. For example, the ductility can be increased by 25% over wrought, and 500% over P/M 6061. The fine grain size that can be achieved should also result in higher fracture toughness, cracking resistance, and corrosion resistance.

Compacts consolidated using the Ceracon process have also been used as starting material for extrusion. Compacts were extruded in the solution treated state at lower extrusion pressures and greater extruded lengths. It has been reported that the pressure can be reduced by 15% and the length increased by 20% during extrusion.

6.3 Vapor Deposition

In the process of physical vapor deposition, material is deposited on a substrate after being vaporized by some means. PVD has similar benefits to RSP in that non-equilibrium compositions can be produced with very fine microstructures. Deposition rate is a problem for this process, and one method of producing a sizable deposit in a practical period of time is by electron beam evaporation.

Electron beam evaporation has been used to produce RAE 72 [69]. The alloy was deposited at a rate of 6 mm/hr to a thickness of 44 mm and then warm rolled to sheet. RAE 72 contains 7.5% Cr and 1.2% Fe, and has a higher tensile strength than 7075 at both room temperature and 300°C. It also has a higher specific strength than Ti6Al-4V from room temperature up to 300°C. The Young's modulus is 20% higher than for 7075.

7 ALUMINUM PM ALLOYS

Aluminum P/M alloys fall into two major groups, conventional alloys and advanced alloys. The conventional alloys are often based on existing wrought aluminum alloy compositions, with little or no changes to optimize them for powder metallurgical processing. These alloys currently represent the bulk of aluminum alloys used to produce parts. Advanced alloys have been developed, and continue to be developed, to take advantage of many of the special aspects of powder metallurgy. Metal matrix composites, high temperature aluminum alloys and high wear resistant aluminum alloys are among those that are seeing increased development. These alloys are slowly beginning to be used in commercial applications, but will eventually command a considerable slice of the available market.

Table 5 Compositions of Conventional P/M Alloys

	Cu	Mg	Zn	Si
601AB	0.25	1.0		0.6
602AB		0.6		0.4
201AB	4.4	0.5		0.8
202AB	4.0			
MD-22	2.0	1.0		0.3
MD-24	4.4	0.5		0.9
MD-69	0.25	1.0		0.6
MD-76	1.6	2.5	5.6	

7.1 Conventional Aluminum Alloys

Conventional alloys consist of blends of elemental powders, often containing lubricants, which are consolidated by press and sinter processing. Table 5 lists a number of alloy powders which are based on either 6xxx or 2xxx wrought alloys. Alloys 201AB and MD-24 are similar alloys that are related to alloy 2014. These alloys can have relatively high strength, and moderate corrosion resistance. Alloy 202AB is designed for forging, and is especially suited to cold forging [68]. Alloys 601AB and MD-69 are similar to each other and are related to alloy 6061. These alloys offer good strength, ductility, and corrosion resistance, and can be anodized. For a higher conductivity, alloy 602AB can be used. Depending on heat treatment, conductivity can be as high as 49% IACS. Alloy 601AB is also available for processes in which an admixed lubricant is not desirable. Die wall lubrication would be used for compaction. MD-76 is an alloy based on 7075, and similarly offers good strengths in the T6 condition.

The mechanical properties of some of these alloys are shown in Table 6 in various conditions. The sintered density and the heat treatment applied has a major

Table 6 Mechanical Properties of Conventional P/M Alloys

Alloy	Green Density	Sintered Density	YS	UTS	%El	Hardness HRE
6061-T6			283	335	7	
601AB-T6	85	91.1	176	176	1	70–75
	90	93.7	224	232	2	75–80
	95	96.0	230	238	2	80–85
201AB-T6	85	91.0	248	248	0	80–85
	90	92.9	322	323	0.5	85–90
	95	97.0	327	332	2	90–95
202 AB-T6	90	92.4	147	227	7.3	45–50
202 AB Cold Formed 19%-T6	90	92.4	173	274	8.7	85

Source: Ref. 39.

effect on the expected properties. Increased density will increase strength, hardness, and ductility. The highest densities are achieved by using higher compaction pressures which lead to higher green strengths. Aging treatments can also be applied, and will result in increased strength and hardness, but a lower ductility. The effect of cold forming on the properties of alloy 202AB is also shown for comparison. Significant strengths can be achieved with very good ductilities.

7.2 Advanced Aluminum Alloys

Advanced aluminum alloys are typically prealloyed powders that are designed to make use of the extended solubility range that can be achieved with rapid solidification or mechanical alloying. These alloys are generally grouped according to the purpose that they are intended to serve.

RSP is being used to develop new alloys that fall into four basic groups [69,70]. The groups are; high-strength corrosion-resistant alloys based on traditional 7000-series aluminum, lower density Al-Li alloys having higher Li levels than possible by conventional means, high temperature alloys containing normally low solubility elements such as Fe, Mo, Ni, and rare earth elements, and finally Al-Si alloys with improved wear, modulus and decreased thermal expansion coefficients.

Alloys based on 7xxx series alloys include alloys 7064, 7090, 7091 and 7093. Typically these alloys have better stress corrosion cracking resistance than 7075, or similar SCC and slightly higher strengths. Alloys 7064, 7090, and 7091 all contain cobalt which forms an intermetallic compound, Co_2Al_9. The cobalt acts as a grain size stabilizer, helping to preserve the fine grains of the RSP powder [71]. In 7093, Ni and Zr are substituted for Co to form intermetallic dispersoids. The compositions of these alloys are shown in Table 7.

7090 is an alloy that has been developed for P/M which is very similar to 7075. The composition of 7090 is shown in Table 7. When compared to ingot metallurgy 7090, P/M 7090 made from RSP powder has improved fatigue strengths and stress corrosion cracking resistance [1]. The SCC improvement is attributed to refinement

Table 7 Compositions of Advanced Al P/M Alloys

	Zn	Mg	Cu	Ni	Zr	O
7064	7.1	2.3	2.0		0.2 Co, 0.1 Cr	
X7093	8.3–9.7	2.0–3.0	1.1–1.9	0.04–0.16	1.2 Zr	0.20–0.50
7090	8.0	2.5	1.0		1.5 Co	0.35
7091	6.5	2.5	1.5		0.4 Co	
X8091	7.3–9.3 Fe	3.5–4.5 Ce				0.2–0.5
Al-9021		1.5	4.0		1.2 C	0.75
Al-9051		4.0			0.7 C	0.6
Al-9052		4.0			1.1 C	0.75
8090		1.0	1.3	2.4 Li	0.25 Zr	
Al-905XL		4.0		1.3 Li	1.1 C	0.4

Source: Ref. 73.

Table 8 Mechanical Properties of Advanced Al P/M Alloys

Alloy	Form	YS	UTS	% El.	R_B	K_{IC}
7090-T7E71	Forged	579	614	10		22
7091-T7E69	Forged	531	579	13		30
X7093	Extruded	582	612	11		49
X8019	Forged	390				
Al-905XL	Forged	448	517	9		30
X7064-T76	Forged	572	607	15		30
8090	Spray Cast	310	450	10		
IN 9021-T4	Forged	469	538	13		
IN 9052	Forged	379	448	13		44

Source: Refs. 73 and 75.

of the intermetallic phases, while the fatigue resistance has been attributed to both the refinement of the intermetallics and grain size refinement. Alloy 7091 has slightly lower strengths and SCC resistance, but higher ductility and toughness.

X7093 is a P/M analog of 7075, which in its extruded condition shows up to a 30% improvement in strength and a 40% improvement in toughness over 7075 [69]. The composition of X7093 is shown in Table 7. X7093 was developed to provide a high strength, high toughness alloy superior to 7075. The mechanical properties of X7093 are shown in Table 8.

X7093 is fabricated by a process that consolidates RSP powder by cold isostatic pressing, followed by a degassing step, and then vacuum hot pressed [72]. The resulting billet is then extruded to break up the oxide surfaces and then is followed by either rolling, extrusion, or forging. Hand forging has also been tried with success without the extrusion step.

Alloys Al-9021, 9051, 9052, and 905XL can be either rapidly solidified or mechanically alloyed. Usually they are produced by mechanical alloying and are not typically heat treated. They were developed to achieve higher tensile fatigue and corrosion properties. The composition of each alloy is given in Table 7. Al-9021 (MA) has very good properties with the fracture toughness and fatigue properties comparable to wrought 7075 [74].

The strength properties are developed through microstructure refinement, solid solution hardening, and dispersion hardening. Carbides and oxides are produced by the mechanical alloying. Table 8 gives the properties of these alloys. It shows the good balance between strength, ductility and fracture toughness.

Al-905XL is a higher stiffness alloy containing Li. Its combination of high stiffness and good strength, corrosion and SCC resistance offers many advantages over conventional aluminum alloys. It can be P/M forged to high strengths with good toughness and ductility.

7.3 High Temperature Alloys

In order to achieve higher elevated temperature strength, stable dispersoids need to be incorporated into the aluminum alloys, and grain growth must be controlled.

Table 9   Properties of Extruded P/M-RS Al Alloys at 315°C

Alloy	UTS (MPa)	YS (MPa)	El. (%)
Al-Fe5-Cu2-Ti2-Ce1-Zr1	357	281	3.2
Al-Fe4-Cu2-Ti1-W1-Ce1-Zr1	356	287	3.7
Al-8 Fe-7 Ce	270	225	7
Al-8 Fe-2 Mo	235	210	10
Al-12 Fe-1.2 V-2.2 Sn	310	300	7
Al-4.5 Cr-1.5 Zr-1.2 Mn	235	215	—
7075-T6 Wrought	70	55	60
2024-T81 Wrought	140	115	20

Source: Refs. 69 and 77.

The elevated temperature properties receive a boost by creating large numbers of dispersoids from RSP supersaturated solutions of elements such as Zr, Ti, Fe, Ce, Mo, etc. These elements not only readily form intermetallics with aluminum, but they also have low diffusivities in aluminum, helping to control coarsening [22]. Some examples of the elevated temperature properties of some of these alloys are shown in Table 9.

As shown in Table 9, iron is often the first alloying addition to aluminum used to form intermetallic dispersoids. In aluminum-iron binary alloys the intermetallic $Al_{13}Fe_4$ forms. Often the ternary alloying element modifies the intermetallic or creates multiple intermetallic phases from the RSP powders.

X8019 is an alloy based on Fe and Ce [72]. The composition of X8019 is Al-8.3Fe-4Ce. X8019 was designed to replace titanium alloys in applications that are exposed to temperatures up to 315°C. Not only is aluminum lighter than the titanium it replaces, but it is also more machinable. This alloy has better properties than the 2xxx alloys, particularly after high temperature exposure, and also has better corrosion resistance than 7xxx. This alloy is processed similar to the X7093 described above.

The elevated temperature strength of several P/M high temperature alloys are shown in Table 9. When compared to Al 7075-T6 and 2024-T8, the dispersoid containing alloys have two to five times higher strengths at 315°C. The specific strength of these alloys clearly challenges the strength of titanium at temperatures up to 315°C.

Extrusion temperature has been found to effect the combination of tensile strength and fracture toughness in a RSP alloy with a composition of Al-7Mg-1Zr [76]. When extruded at different temperatures between 350°C and 550°C, the strength began to drop off at the highest extrusion temperature, while the fracture toughness began to rise. The extrusion temperature of 500°C gave the best combination of tensile strength and fracture toughness. The effect of extrusion temperature could be quantitatively modeled using standard models for solid solution, dispersoid, and substructural strengthening mechanisms.

The creep resistance of conventional aluminum alloys has been studied. Extruded PM 6061 was tested at different stresses and temperatures and found to have a threshold stress, similar to dispersion strengthened aluminum PM com-

Table 10 Creep Data for High Temperature Aluminum P/M Alloys

Alloy	% vol Dispersoid	Stress Exponent	Activation Energy (kJ/mol)
Al-Ti	8	7–8	240
Al-Fe-Ce	25	1–8	84–142
Al-Fe-Ni	19–32	10–13	310–329
Al-Fe-V-Si	36	13–32	360
Wrought 6061	—	3	—

Source: Ref. 11.

posites [78,79]. The origin of the threshold stress is believed to be aluminum oxides that are incorporated into the structure of the compact during processing. The creep behavior of aluminum RSP P/M alloys depends on the dispersoids in two manners [80,81]. Dislocation creep is controlled by the ratio of the interparticle spacing to the grain or subgrain size. Diffusion creep is controlled by interphase interfaces.

The creep behavior of some high temperature P/M alloys is shown in Table 10. When compared to wrought aluminum alloy 6061 the high temperature P/M alloys have a much higher stress exponent. The activation energy is also relatively high.

Heat treatment of RSP aluminum P/M alloys can significantly improve the creep rate [82]. An Al-20% TiC composite was studied in the as-extruded condition, and after being heat treated at 620°C for various lengths of time. The steady state creep rate decreased two orders of magnitude after heat treatment at 620°C for 24 hr. Further decreases were measured with longer heat treating times. XRD results showed that the major cause of the heat treating response was the formation of Al_3Ti and Al_4C_3 from a reaction between the TiC and the aluminum matrix. The greater number of dispersoids, as well as their finer size was suggested as the reason for the increase in creep strength.

The effect of both RSP and MA on the creep resistance of Al-5Fe-5Ni and Al-8Fe-4Ce (X8019) alloys has been investigated [83]. It was felt that the dispersoids produced by RSP were still too large to effectively prevent microstructural evolution at elevated temperatures. The combination of RSP with MA reduced the dispersoid size slightly, but also added a fine dispersion of oxides and carbides. The sources of the oxygen and carbon were the atmosphere inside the milling chamber and the added process control agent respectively.

After elevated temperature exposure the alloys that were RSP, but not MA coarsened considerably [83]. In comparison, the RSP and MA alloys retained their structure and were only 10% less hard after two weeks at 450°C. The creep rate of both the Al-Fe-Ni and Al-Fe-Ce alloys was found to have decreased by several orders of magnitude with the combined treatment. Further improvements in properties are expected with optimization of the process.

7.4 Al-Si Wear Resistant Alloys

Light-weight alloys with high wear resistance are important for a number of critical applications in automotive applications as described above. It has been found that

high silicon alloys have improved wear over conventional aluminum P/M alloys. The distribution of silicon particles and transition metal intermetallics have been both shown to make an important contribution to the wear properties [8].

P/M Al-Si alloys typically achieve higher room temperature strength, 290–390 MPa, than cast Al-Si, 117 to 160 MPa [84]. In addition, elongation is slightly improved and hardness is raised considerably, from about 40–65 R_B. In particular, the wear and high temperature stability also are increased over cast alloys. Higher silicon levels typically increase the properties, but begin to plateau for some properties around 18% Si.

RSP is important to high performance of Al-Si P/M alloys, due to the low solubility of silicon in aluminum (1.65%) and the ensuing difficulty in producing a numerous fine dispersion of silicon particles. An alloy designed for good wear resistance employs both of the above microstructural features, fine silicon particles and even finer dispersions of transition metal intermetallics [8]. The alloy Al-12 Si-5 Fe-6 Ni has a higher hardness, higher Young's Modulus, and better elevated temperature strength than conventional alloys. This resulted in improved wear performance of a rotor for an automotive oil pump. An Al-20 Si-5 Fe was chosen for an automotive air compressor application [9].

Forging of an Al-25Si alloy based on 2024, showed a marked increase in properties over the same alloy which had been extruded [56]. Small improvements were made in the UTS, % elongation, and hardness, while the fatigue strength increased a dramatic 13%. These improvements were attributed to the greater break-up of the oxide at prior particle boundaries and shorter exposure to high temperatures. The latter helped to preserve some of the properties of the RSP powders.

Al-Si alloys that had been hot pressed and extruded were compared to the same compositions that had been extruded only [85]. The hot pressed and extruded alloys showed a significant increase in the ductility, up to 50%, at various elevated temperatures. Apparently the precompaction by hot pressing altered the final microstructure and effected the properties. These alloys showed superplastic properties.

7.5 Low Density/High Stiffness Alloys

The beneficial effect of Li additions on the density and stiffness of aluminum alloys is well known. Alloy Al-905XL has already been discussed. The addition of Li to this alloy results in good strength properties with a higher stiffness. The alloy system that could benefit the most from P/M is Al-Be-Li.

Beryllium has a solubility of only 0.3% in aluminum. RSP can dramatically extend the solid solubility of Be. Alloy compositions of Al-20.5 Be-2.4 Li and Al-29.6 Be-1.3 Li have been reported [86]. Al-20.5 Be-2.4 Li has a density of about 2.3 g/cc, or a better than 15% reduction over most Al alloys. The mechanical properties of Al-20.5 Be-2.4 Li are a yield strength of 451 MPa, a tensile strength of 531 MPa, with an elongation of 3.3%, and a modulus of 123 GPa. The Al-29.6 Be-1.3 Li alloy has a yield strength of 497 MPa, a tensile strength of 536 MPa, with an elongation of 2.6%, and a modulus of 142 GPa. These values are representative of both alloys in their peak aged condition. This combination of properties results in a high specific strength and specific stiffness.

7.6 MMCs

Powder metallurgy is an excellent fabrication method for aluminum matrix composites. It offers a method of adding large percentages of hard reinforcing phases in a uniform distribution, and producing a near net shape. This results in the potential for significant property improvements. One major drawback to the use of P/M to produce aluminum MMCs is a potentially higher cost over other methods [87].

Specific advantages of P/M in the fabrication of aluminum MMCs include a much higher volume percent of reinforcing phase possible when compared to casting or spray forming techniques [87]. The ability to produce a more uniform dispersion of the hard particles leads to both higher fracture toughness values and higher ductilities. In a 15% SiC reinforced 6061 composite, a 50% improvement in K_{IC} occurred through producing a more uniform dispersion. A 20% SiC reinforced CP Al alloy also had a 50% improvement in the percent elongation with a more uniform distribution.

One of the first commercial aluminum matrix composites is called sintered aluminum powders (SAP) [88]. SAP uses aluminum powder which contains a large quantity of oxygen. The oxygen forms Al_2O_3, which acts as a dispersoid, providing significant elevated temperature strength. Parts from SAP are thermally stable at temperatures up to 500°C, and exhibit good corrosion resistance, thermal and electrical conductivity, and erosion resistance [4]. Semifinished parts in the form of sheet, tube, forgings, etc., are available commercially [89].

Aluminum can also be dispersion strengthened by reaction milling with carbon black. An Al_4C dispersoid is formed which gives excellent high temperature stability. Dispal can be heated to 260°C for 100 h without significant loss of strength [90].

Nitrogen can also be incorporated into the structure of aluminum by reaction milling. Cryomilling involves using liquid nitrogen in the milling chamber while mechanically alloying an aluminum powder. AlN particles are formed, which improve the properties of the resulting compacts. The refined microstructure of the MA powders can be retained after sintering through cryomilling. The AlN particles formed appear to stabilize the grain structure during the elevated temperature exposure during sintering. A 5083 alloy treated by cryomilling was sintered to 99.6% density, while retaining most of its refined grain size during either extrusion or hot isostatic pressing [31]. A 30% increase in both the yield strength and ultimate tensile strength were observed when compared to wrought 5083-H343. Surprisingly, there was no decrease in ductility accompanying this increased strength. The grain size of the resulting compact was approximately 30 nm.

A P/M 6061/20% SiC particulate composite showed a 47% increase in stiffness and a 35% increase in tensile strength over wrought AA 6061 [91]. Ductility and fracture toughness are often lower in the composite materials, when compared to the monolithic wrought alloy. One study of layered particulate composites showed that fracture toughness values equivalent to wrought can be achieved [92]. SiC and aluminum 6061 were codeposited by spray atomization into layers of higher and lower SiC volume percent. A layer spacing of 700 μm produced the highest ductility and ultimate tensile strength. The fracture toughness was similar to the wrought alloys toughness. The codeposited layers were effectively graded, unlike similar composites produced by P/M, diffusion bonding and coextrusion.

Table 11   Properties of some Al MMCs

Composite	Form	YS (MPa)	UTS (MPa)	%El	KIC	E (GPa)
2124/SiC/20p-T8	Extruded	550	620	7		
6061/SiC/20p-T6	Extruded	340	420			103
6091/SiC/20p-T6	N/A	396	448	4.1		103
6091/SiC/30p-T6	N/A	407	496	3.0		121
6091/SiC/40p-T6	N/A	431	538	1.9		138

Source: Ref. 90.

Table 12   Effect of Volume Percent of SiC on Properties of 6061

Volume Percent	Stiffness (GPa)	CTE (10^{-6}/K)
0	70	21.5
15	97	18.5
20	103	16.8
25	114	
30	121	15.7
35	135	
40	145	13.2
50		12.0
55		10.5
60		9.7

Source: Ref. 87.

The effect of the volume percent of the reinforcing phase, as well as the choice of matrix is shown in Table 11. Composites based on the higher strength 2124-T8 are stronger when produced with the same volume percent of SiC. Also, the strength and modulus increase with the amount of reinforcing phase can also be seen. Ductility decreases with the increasing strength.

The effect of volume fraction on the stiffness and thermal coefficient of expansion (CTE) can be seen in Table 12 for a 6061 alloy reinforced with SiC. The CTE decrease with increasing volume fraction of SiC. This effect is being used to develop aluminum alloys with controlled CTE for use in the electronics industry. Substrates with CTE that closely match silicon reduce the problems of thermal fatigue in integrated circuit applications.

The route used to fabricate a P/M aluminum MMC is critical to the cost of the final product [93]. Typical processing sequences would include atomization of the aluminum alloy, followed by blending of the reinforcement particles with the matrix powder, then cold pressing or cold isostatic pressing, followed by canning, degassing, and then a forming technique which produces a high degree of deformation such as extrusion, forging, or hot pressing. The blending of the aluminum alloy powder and the reinforcing phase is critical to producing a uniform distribution in the final part [93]. Alternate routes that have less steps and less cost have been proposed. Each of these routes typically trades off properties for reduced expense.

Compressibility of aluminum MMCs decreases with increasing particle volume [94]. As particle volume increases, the green density will typically decrease. A limit may be reached where additional particle volume may prevent sufficient densification to get an additional increase in properties.

7.7 Porous Al

Porous P/M products have many uses for filters and self-lubricating bearings. Work has shown that porous aluminum materials can be produced by ball milling, followed by gravity sintering [95]. No compaction is used in the processing. Since compaction is not performed the oxide surfaces must be broken by other means, therefore ball milling is performed prior to sintering to obtain good sintered strengths. Additives, such as Cu, promote sintering. Strengths were good, 30–70 Mpa, and good permeability can be achieved. Porosities of 30–45% resulted from the different processing parameters.

Aluminum foams can also be produced by powder metallurgy [96]. A foaming agent in incorporated into a P/M compact by blending with the aluminum alloy powder. After compaction, the foaming agent is activated by heating close to the melting point of the aluminum alloy. Gases evolved from the foaming agent expand the cells of the foam and create a light weight structure. Prior to foaming the compact can be mechanically deformed to shape. Application for the aluminum foam is in higher stiffness body parts for automotive use, and increasing energy absorption during collisions.

REFERENCES

1. R. F. Singer, "Recent Developments And Trends in High Strength PM Materials." Powder Metallurgy International, 1986, 18(2), pp. 79–82.
2. D. G. White, "State-of-the-P/M Industry in North America – 1999" International J. Powder Metall., 1999, 35(5), pp. 25–29.
3. R. Schattevoy, and K. Hummert, "High Performance Aluminum for Applications in IC Engines," ISATA International Symposium on Automotive Technology and Automation, 1993, pp. 277–283.
4. V. G. Gopienko, Val. G. Gopienko, and Y. G. Olesov, "Aluminum Alloy Powders for the Production of Sintered Materials (Review)," All-Union Aluminum and Magnesium Institute, Translated from Poroshkovaya Metallurgiya, 1985, 4(268), pp. 24–28.
5. *Powder Metallurgy Design Manual*, 2nd Edn, MPIF, 1995, pp. 61–62.
6. P. S. Gilman, "Light High Temperature Aluminum Alloys for Aerospace Applications," International Conference on PM Aerospace Materials, 1991, pp. 16-1–16-11.
7. H. E. Chandler, "Emerging Trends in Aerospace Materials and Processes." Metal Progress, 1984, pp. 21–29.
8. K. Kondoh, T. Kosuge, and Y. Takeda, "Lubrication Pump Made of Rapidly Solidified Aluminum Alloy for High Performance Engine," SAE Technical Paper Series, SAE International Congress and Exposition, 1990, Paper 960281.
9. T. Hayashi, Y. Takeda, K. Akechi and T. Fujiwara, "Rotary Car Air Conditioner Made with P/M Al-Si Wrought Alloys," SAE Technical Paper Series, SAE International Congress and Exposition, 1990, Paper 900407.
10. A. Wrigley, "Aluminum in Family Vehicles; The Recent History and a Forecast," Powder Metallurgy Aluminum and Light Alloys for Automotive Applications Conference, 1998, pp. 135–145.

11. R. B. Baghat, "Advanced Aluminum Powder Metallurgy Alloys and Composites," *ASM Metals Handbook*, Vol. 7, 10th Edn, 1998, ASM/I, pp. 840–858.

12. O. D. Neikov, and A. V. Krajnikov, "Water Atomized Powders of Aluminum and Its Alloys." Materials Science Forum, 1996, 217–222, pp. 1649–1654.

13. I. E. Anderson, J. C. Foley, and J. F. Flumerfelt, "Simplified Aluminum Powder Metal Processing Routes for Automotive Applications," Powder Metallurgy Aluminum and Light Alloys for Automotive Applications Conference, 1998, pp. 75–82.

14. J. E. Hatch, (Ed.), *Aluminum: Properties and Physical Metallurgy*, 1984, ASM, pp. 35–38.

15. T. W. Clyne, R. A. Ricks, and P. J. Goodhew, "The Production Of Rapidly-Solidified Aluminum Powder By Ultrasonic Gas Atomization Part I: Heat And Fluid Flow." Int. J. Rapid Solidification. 1984–85, 1, pp. 59–80.

16. J. M. Sater, S. C. Jha, and T. H. Sanders Jr., "Microstructure And Properties Of Rapidly Solidified Aluminum-Transition Metal Alloys," *Treatise on Materials Science and Technologies*, 1989, 31, pp. 409–444.

17. K. Uenishi, K. H. Yong, and K. F. Kobayashi, "Mechanical Alloying in the Al-Bi Alloy System." J. Mater. Sci., 1996, 31, pp. 3605–3611.

18. K. F. Kobayashi, and H. Kawaguchi, "Amorphization of Al-Cr Atomized Powder by Mechanical Grinding," Mater. Sci. Engin., 1994, A181/A182, pp. 1253–1257.

19. Y. He, G. J. Shiflet, and S. J. Poon, "Ball Milling-Induced Nanocrystal Formation in Aluminum-Based Metallic Glasses." Acta Metallurgica Materialia. 1995, 43(1), pp. 83–91.

20. K. Y. Wang, A. Q. He, T. D. Shen, M. X. Quan, and J. T. Wang, "Synthesis of Al-Based Metastable Alloys by Mechanical Milling Al and Amorphous $Fe_{78}Si_{12}B_{10}$ Powders," J. Mater. Res., 1994, 9(4), pp. 866–874.

21. G. J. Fan, M. X. Quan, and Z. Q. Hu, "Evidence of Kinetically Controlled Process in Preparing Supersaturated Al-Ti Solid Solutions," J. Mater. Sci. Lett., 1995, 14, pp. 523–525.

22. W. E. Frazer, "The Elevated Temperature Capabilities of Dispersion-Strengthened PM Aluminum Alloys Rival Those of Titanium in Advanced Aerospace Structures." Metal Progress, 1988, 11, pp. 42–46.

23. M. Hunt, "Powder Metallurgy Elevates Performance." Mater. Engin., Sep. 1990, pp. 16–19.

24. J. H. Weber, and D. J. Chellman, "Mechanically Alloyed Aluminum Alloys for Aircraft Applications." Structural Application of Mechanical Alloying, ASM International Conference. March 1990, pp. 147–154.

25. M. J. Fleetwood, "Mechanical Alloying – The Development Of Strong Alloys." Mater. Sci. Techn., Dec. 1986, 2, pp. 1176–1182.

26. E. Bonetti, S. Enzo, G. Principi and L. Schiffini, "Structural and Elastic Properties of Al-Fe Alloys Prepared by Mechanical Alloying." *Processing and Properties of Nanocrystalline Materials*, 1996, TMS, pp. 153–164.

27. J. A. Rodriguez, J. M. Gallardo, and E. J. Herrera, "Consolidation of Mechanically Alloyed Aluminum by Double Cold-Pressing and Sintering." J. Mater. Process. Techn., 1996, 56, pp. 254–262.

28. D. C. Jia, Y. Zhou and T. C. Lei, "Microstructure and Mechanical Properties of Al-12Ti-6Nb Prepared by Mechanical Alloying". Mater. Sci. Engin., 1997, A232, pp. 183–190.

29. X. P. Niu, L. Froyen, L. Delaey and C. Peytour, "Effect of Fe Content on the Mechanical Alloying and Mechanical Properties of Al-Fe Alloys." J. Mater. Sci., 1994, 29, pp. 3724–3732.

30. M. T. Stawovy, A. O. Aning, and S. L. Kampe, "Processing of Aluminum Powder Metallurgy Alloys Containing Self-Propagating Reaction Products." Mater. Sci. Forum, 1996, 217–222, pp. 913–918.

31. V. Tellkamp, M. Ice, and E. Lavernia, "Consolidation and Mechanical Properties of Nanostructured Al-Alloys," *Proceedings of the Powder Metallurgy Aluminum and Light Alloys for Automotive Applications Conference*, MPIF, 1998, pp. 59–65.

32. J. W. White, "Handling aluminum powders: safety issues." JWW/ALPOSAF/12/98, The Aluminum Powder Company Limited, Dec. 1998.

33. S. S. Grossel, "Fire and explosion hazards in powder handling and processing." *Handbook of Powder Science*, pp. 854–868.

34. Aluminum Association, "Recommendations for storage and handling of aluminum powder and paste." Brochure TR-2.

35. Aluminum Association, "Guidelines for handling aluminum fines generated during various aluminum fabricating operations." Brochure F-1.

36. W. H. Hunt, Jr., "Metallurgical Considerations on the Design and Processing of Aluminum Powder Metallurgy Parts, "*Proceedings of the Powder Metallurgy Aluminum and Light Alloys for Automotive Applications Conference*, MPIF, 1998, pp. 1–9.

37. G. T. Campbell, R. Raman and R. Fields, "Optimum Press and Sinter Processing for Aluminum/SiC Composites," *Proceedings of the Powder Metallurgy Aluminum and Light Alloys for Automotive Applications Conference*, MPIF, 1998, pp. 35–42.

38. J. L. Estrada, J. Duszczyk and B. M. Korevaar, "Heating Sequences and Hydrogen Evolution in Alloyed Aluminum Powders," J. Mater. Sci. 1991, 26, pp. 1631–1634.

39. "Conventional Aluminum Powder Metallurgy Alloys," *ASM Handbook*, Vol. 7, 1998, Powder Metal Technologies and Applications, ASM International, pp. 834–839.

40. A. Ziani, and S. Pelletier, "Supersolidus Liquid-Phase Sintering Behavior of Degassed 6061 Al Powder," Int. J. Powder Metall., 1999, 35(8) pp. 49–58.

41. A. Ziani and S. Pelletier, "Sintered 6061 Al Prealloyed Powder: Processing and Mechanical Behavior," Int. J. Powder Metall., 1999, 35(8), pp. 66.

42. *Powder Metallurgy Design Manual*, 3rd Edn, 1998, MPIF, p. 24.

43. M. Djuricic, M. Dragojlovic and R. Novakovic, "Cold Sintering of Aluminum and Its Alloys." Science of Sintering, 1986, 18, pp. 87–89.

44. "Sintering of Aluminum and Aluminum Alloys," *ASM Handbook*, Vol. 7, 1998, Powder Metal Technologies and Applications, ASM International, pp. 381–385.

45. A. K. Jha and G. S. Upadhyaya, "Effect of Atmosphere on Sintering of Age-Hardenable 2014 Al-Alloy and Its Composites." Light Metal Age, Oct. 1983, pp. 42–43.

46. K. R. Van Horn, *Aluminum*, Vol. 3, 1967, ASM, pp. 313–314.

47. V. A. Vasil'ev, B. S. Mitin and M. M. Serov, "Liquid-Phase Sintering of High-Density Compacts from Atomized Aluminum Alloy Powders." Moscow Aviation Technology Institute. Translated from Poroshkovaya Metallurgiya. 1987, 1(289), pp. 29–34.

48. T. G. Nieh, P. Luo, W. Nellis, D. Lesuer and D. Benson, "Dynamic Compaction of Aluminum Nanocrystals," Acta Materialia, 1996, 44(9), pp. 3781–3788.

49. G. B. Schaffer, T. B. Sercombe, R. N. Lumley and S. H. Huo, "Trace Element Effects in the Sintering of Aluminum Alloys," *Proceedings of the Powder Metallurgy Aluminum and Light Alloys for Automotive Applications Conference*, MPIF, 1998, pp. 11–18.

50. W. G. Ball, R. R. Phillips and J. T. Webster, "Die wall lubrication of aluminum." *Proceedings of the Powder Metallurgy Aluminum and Light Alloys for Automotive Applications Conference*, MPIF, 1998, pp. 27–34.

51. L. P. Lefebvre and Y. Thomas, "Evaluation of a Polyethylene Lubricant for Aluminum P/M Applications," Int. J. Powder Metallurgy, 1999, 35(5) pp. 45–53.

52. T. S. Rao and K. S. Pandey, "Axial Cold Compression of Sintered Al-4Cu Disc- and Ring-Preforms." J. Mater. Process. Techn., 1993, 39, pp. 319–326.

53. J. H. Tweed, R. M. K. Young, I. W. Pearson, and C. M. Jones, ''Manufacture of 2014/SiC and 8090/SiC Metal Matrix Composites by Vacuum Hot Pressing,'' International Conference on PM Aerospace Materials, 1991, Paper 35.

54. S. M. Joslin and K. H. G. Ashbee, ''Powder Metallurgy by Bidimensional Compression.'' Metall. Mater. Trans. May 1995, 26A, pp. 1087–1091.

55. T. B. Gurganus, ''Aluminum Powder Applications.'' Adv. Mater. Process, 1995, 8, pp. 57–59.

56. T. Kaji, T. Hayashi and Y. Takeda, ''Mechanical Properties of Powder Forged RS Aluminum Alloys,'' RASELM, 1991, 0, p. 709.

57. Metal Powder Report, ''Powder Forged Al Alloy to Challenge Ferrous Metals,'' PM Special Feature, April, 1994, pp. 36–41.

58. T. Ishikawa, N. Yukawa, K. Suzuki, Y. Suzuki and T. Jimma, ''Formability of Superplastic Aluminum Alloy Processed by Mechanical Alloying.'' J. Mater. Process. Techn. 1997, 68, pp. 236–240.

59. N. J. E. Adkins and P. Tsakiropoulos, ''Design of Powder Metallurgy Aluminum Alloys for Applications at Elevated Temperatures. Part 2: Tensile Properties of Extruded and Conformed Gas Atomised Powders.'' Mater. Sci. Techn. May 1991, 7, pp. 419–426.

60. M. Lieblich, G. Caruana, M. Torralba and H. Jones, ''Inert Gas Atomised Al-Cr-Zr Alloy Powders Consolidated by Extrusion: Effect of Powder Variables and Extrusion Parameters on Extrusion Pressure,'' Powder Metallurgy, 1996, 39(2), pp. 143–149.

61. J. E. Hatch, ''Aluminum Powder and Powder Metallurgy Products,'' *Aluminum: Properties and Physical Metallurgy*, 1984, ASM/I, pp. 379–397.

62. L. G. Elias, A. J. W. Ogilvy, A. G. Leatham and W. Kahl, ''Production of Light Alloys and Composites by Means of the Osprey Preform Process,'' International Conference on PM Aerospace Materials, 1991, Paper 41.

63. K. Hummert, B. Commandeur, A. G. Leatham, A. J. W. Ogilvy and W. Hunt, ''High Performance, Low Cost Aluminum Alloys Manufactured by Spray Forming,'' *Proceedings of the Powder Metallurgy Aluminum and Light Alloys for Automotive Applications Conference*, MPIF, 1998, pp. 107–114.

64. K. Hummert, R. Schattevoy and D. Ringhand, ''Forming P/M Aluminum Alloys into Con-Rods, Pistons, Liners and Other Automotive Components,'' *Proceedings of the Powder Metallurgy Aluminum and Light Alloys for Automotive Applications Conference*, MPIF, 1998, pp. 115–126.

65. E. J. Lavernia, J. D. Ayers and T. S. Srivatsan, ''Rapid Solidification Processing with Specific Application to Aluminum Alloys.'' International Materials Reviews. 1992, 37(1), pp. 1–44.

66. E. J. Lavernia and N. J. Grant, Mater. Sci. Engin. 1988, 98, pp. 381–394.

67. H. W. Chan, ''The Ceracon Process for P/M Technology.'' Materials and Design. Nov/Dec. 1988, 9(6), pp. 355–357.

68. ''Conventional Aluminum Powder Metallurgy Alloys,'' *ASM Metals Handbook*, Vol. 7, 10th Edn, 1998, ASM/I, pp. 834–839.

69. C. M. Ward-Close and F. H. Froes, ''Developments in the Synthesis of Lightweight Metals.'' J. Metals, 1994, 46(1), pp. 28–31.

70. F. H. Froes, C. M. Ward-Close and M. L. Ovecoglu, ''Synthesis of Light Metals for Demanding Applications,'' *Eighth International Metallurgy and Materials Congress* 1995, pp. 533–538.

71. E. J. Lavernia, G. Rai and N. J. Grant, ''Rapid Solidification Processing of 7XXX Aluminum Alloys: A Review.'' Mater. Sci. Engin. 1986, 79, pp. 211–221.

72. A. D. Jatkar and R. R. Sawtell, ''Aluminum PM Alloys for Aerospace Applications,'' International Conference on PM Aerospace Materials, 1991, pp. 15–1–15–14.

73. G. J. Hildeman and M. J. Koczak, ''Powder Metallurgy Aluminum Alloys.'' Treatise on Materials Science and Technology. 1989, 31, pp. 323–364.

74. M. J. Couper, R. Schafer and G. R. D. Shrimpton, ''Fatigue And Fracture of Advanced PM-Al Alloys,'' pp. 1311–1318.

75. ''Powder Systems and Applications,'' *ASM Handbook*, 9th Edn, Vol. 7, 1984, ASM International, pp. 652–656.

76. R. J. Dashwood and T. Sheppard, ''Effect of Consolidation Temperature on Mechanical Properties of Rapidly Solidified Al-7Mg-1Zr Alloy.'' Mater. Sci. Techn., 1993, 9, pp. 678–685.

77. J. Q. Guo and N. S. Kazama, ''Mechanical Properties of Rapidly Solidified Al-Ti-Fe, Al-Cu-Fe and Al-Fe-Cu-Ti Based Alloys Extruded from Their Atomized Powders,'' Mater. Sci. Engin., 1997, A232, pp. 177–182.

78. K-T. Park, E. J. Lavernia and F. A. Mohamed, ''High-Temperature Deformation of 6061 Al,'' Acta Metallurgica Materialia, 1994, 42(3), pp. 667–678.

79. F. A. Mohamed, ''On creep behavior in powder metallurgy 6061 Al.'' Scripta Materialia, 1998, 38(5), pp. 457–463.

80. R. S. Mishra and A. K. Mukherjee, ''Creep Behavior of rapidly Solidified and Processed Aluminum Alloys,'' *Light Weight Alloys for Aerospace Application III*, 1995, TMS, pp. 319–331.

81. A. K. Mukherjee and R. S. Mishra, ''Creep Mechanisms in Dispersion Strengthened Materials,'' *The Johannes Weertman Symposium*, 1996, TMS, pp. 119–126.

82. A. B. Pandey, R. S. Mishra and Y. R. Mahajan, ''Effect of Isothermal Heat Treatment on the Creep Behavior of an Al-TiCp Composite,'' Mater. Sci. Engin. A, A206, 1996, pp. 270–278.

83. A. Lawley, Case study 6. ''Elevated Temperature Aluminum Alloys''. *Powder Metallurgy – Selected Case Studies*, MPIF, pp. 66–75.

84. S. S. Cho, et al. ''Rapidly Solidified Aluminum Alloy Powder.'' Adv. Mater. Process, 1997, 1(97), pp. 29–31.

85. T. Satoh, K. Okimoto and S. Nishida, ''High Temperature Deformation Behavior of Aluminum Alloys Produced from Centrifugally-Atomized Powders,'' J. Mater. Process. Techn., 1997, 68, pp. 221–228.

86. J. R. Pickens, ''High-Strength Aluminum P/M Alloys,'' *ASM Metals Handbook*, Vol. 2, 10th Edn, 1990, ASM/I, pp. 200–215.

87. A. R. Begg, ''Development, Manufacture and Properties of PM Aluminum-Based Metal Matrix Composites,'' International Conference on PM Aerospace Materials 1991, Paper 40.

88. R. Irmann, Tech. Rund., 1949, 41(36), p. 19.

89. V. G. Gopienko, V. P. Kiselev and N. S. Zobnina, ''Methods of Manufacture of Aluminum Powders and Their Fields of Application.'' All-Union Scientific-Research and Design Institute of the Aluminum, Magnesium, and Electrode Industry. Translated from Poroshkovaya Meallurgiya, 1984, 12(264), pp. 32–37.

90. F. H. Froes, et al., SAMPE Quarterly, 1991, 22(4), p. 11.

91. A. R. Begg, ''Metal-Matrix Composites by Powder Metallurgy,'' Powder Metallurgy, 1993, 36(2), pp. 107–110.

92. Q. Xu, R. W. Hayes, W. H. Hunt and E. J. Lavernia, ''Mechanical Properties and Fracture Behavior of Layered 6061/SiCp Composites Produced by Spray Atomization and Co-Deposition,'' Acta Materialia, 1999, 47(1), pp. 43–53.

93. W. H. Hunt Jr., ''Cost-Effective High Performance P/M Aluminum Matrix Composites for Aerospace Applications''. International Conference on PM Aerospace Materials, 1991, Paper 32.

94. M. H. Carvalho, T. Marcelo, M. Varella de Oliviera and H. Carvalhinhos, ''Al 6061/SiCp MMCs Production by Sintering and Forging'', International Conference on PM Aerospace Materials, 1991, Paper 34.

95. J. A. Vivas and G. Jangg, *Production of Sintered Porous Aluminum Materials*, pp. 1319–1324.
96. H. Eifert, C. J. Yu, J. Banhart, J. Baumeister and W. Seeliger, "Weight Savings by Aluminum Metal Foams: Production, Properties and Applications in Automotive," *Proceedings of the Powder Metallurgy Aluminum and Light Alloys for Automotive Applications Conference*, 1998, MPIF, pp. 127–134.

Appendixes

APPENDIX 1 Water Quenching Data: 7075-T73 Aluminum Bar Probes

Probe diameter (in)	Quenchant temp (deg F)	Velocity (FPM)	Cooling rate (°F/sec)	H (h/2K)	Film coefficient (BTU/Hr.FT∧2.°F)	Q
0.5	80	25	450.05	0.63		2.0
0.5	80	50	787.8	1.06	2449	1.1
0.5	80	100	926.1	1.14	2633	1
1	80	25	373.25	1.28	2948	2.15
1	80	50	386.6	1.34	3078	2.2
1	80	100	456.5	1.62	3733	1.9
1.5	80	25	221.6	1.38	3177	3.55
1.5	80	50	255.6	1.64	3775	3.5
1.5	80	100	282.9	1.9	4361	3.3
2	85	25	163.5	—	4332	6.9
3	85	25	75	—	3137	8.1
0.5	100	25	427.8	0.58		2.1
0.5	100	50	721.8	0.96	2207	1.1
0.5	100	100	815.4	0.1	2523	1
1	100	25	312.1	1.055	2427	2.6
1	100	50	376.8	1.25	2874	2.2
1	100	100	483.3	1.56	3660	2
1.5	100	25	205.8	1.345	3093	3.7
1.5	100	50	225.2	1.42	3256	3.7
1.5	100	100	269.3	1.75	4029	3.4
0.5	120	0	675.9	1.07	2460	1
0.5	120	25	559.8	1.07	2460	1
0.5	120	50	654.3	1.23	2834	0.9
0.5	120	100	723.6	1.25	2865	0.9
1	120	0	298.2	1.13	2597	2.5
1	120	25	370.4	1.21	2790	2.2
1	120	50	370.4	1.33	3059	2.2
1	120	100	392.9	1.73	3976	1.7
1.5	120	0	188.2	1.3	3001	3.6

Appendix 1   Continued

Probe diameter (in)	Quenchant temp (deg F)	Velocity (FPM)	Cooling rate (°F/sec)	H (h/2K)	Film coefficient (BTU/Hr.FT∧2.°F)	Q
1.5	120	25	203.6	1.21	2790	3.6
1.5	120	50	222.8	1.48	3415	3.3
1.5	120	100	266.6	1.83	4207	3.2
0.5	140	0	522.9	0.74	1706	1.2
0.5	140	25	485.1	0.82	1877	1.1
0.5	140	50	567.6	1.06	2437	1
0.5	140	100	665.1	1.1	2520	1
1	140	0	223.7	0.89	2058	2.9
1	140	25	282.9	0.97	2225	2.4
1	140	50	334.2	1.1	2539	2.4
1	140	100	348.3	1.35	3097	1.9
1.5	140	0	128	0.95	2180	5.4
1.5	140	25	163.7	0.95	2180	4.8
1.5	140	50	170.7	1.1	2528	4
1.5	140	100	242.8	1.55	3565	3.4
2	140	25	122	—	2266	8.1
3	140	25	63	—	2011	15.8
0.5	160	0	83.3	0.19	439	2.5
0.5	160	25	88.5	0.22	511	2.3
0.5	160	50	196.2	0.46	1048	1.4
0.5	160	100	276.9	0.62	1423	1.4
1	160	0	48	0.25	567	8
1	160	25	75.5	0.3	691	5.6
1	160	50	217.8	0.66	1515	3.4
1	160	100	174.4	0.75	1718	2.7
1.5	160	0	30.3	0.2	455	12.7
1.5	160	25	64	0.37	859	8
1.5	160	50	106.7	0.6	1384	5.7
1.5	160	100	150.9	0.99	2285	4.4
0.5	180	0	39.7	0.11	262	6.7
0.5	180	25	59.8	0.17	384	5
0.5	180	50	72.4	0.23	526	4
0.5	180	100	113.2	0.28	653	3.8
1	180	0	19.2	0.12	272	14
1	180	25	31.5	0.16	376	9.1
1	180	50	39.2	0.18	410	9.2
1	180	100	60.2	0.26	606	7.3
1.5	180	0	11.4	0.11	247	29.5
1.5	180	25	21.8	0.17	382	13.4
1.5	180	50	37.4	0.23	540	10.4
1.5	180	100	39.6	0.26	609	12
0.5	200	0	13.6	0.04	89	44.3
0.5	200	25	15.9	0.05	114	28.9
0.5	200	50	26.5	0.08	178	13.8
0.5	200	100	31	0.09	198	12.4
1	200	0	11.6	0.08	184	33.8

Appendix 1   Continued

Probe diameter (in)	Quenchant temp (deg F)	Velocity (FPM)	Cooling rate (°F/sec)	H (h/2K)	Film coefficient (BTU/Hr.FT∧2.°F)	Q
1	200	25	15.5	0.09	214	22.6
1	200	50	12.8	0.09	202	26.7
1	200	100	14.5	0.09	217	24.5
1.5	200	0	5.5	0.07	160	86.9
1.5	200	25	6	0.07	171	73
1.5	200	50	6.9	0.08	183	62.9
1.5	200	100	14.5	0.13	291	24.5
0.5	212	0	9.6	0.02	52	76.3
0.5	212	25	9.2	0.02	52	78.1
0.5	212	50	9.6	0.03	60	68.5
0.5	212	100	9.4	0.02	52	74.8
1	212	0	5.7	0.06	137	94.6
1	212	25	6.9	0.06	146	75.1
1	212	50	5.1	0.06	133	116.7
1	212	100	5	0.06	132	118.7

Quenched into water at various temperatures (Solution temperature $= 870°F$)

APPENDIX 2   Type I Polymer Quench Data: 2024–T851 Aluminum Sheet Probes

Polymer concentration %	Circulation rate (ft/min)	Cooling rate (°F/sec)	Film coefficient (BTU/Hr.ft.°F)	Quench factor	Predicted yield strength (KSI)
10	0	2038.5	3747.5	1.9	65.9
10	50	2100.6	3807.5	1.8	66
20	25	1165.8	2827.5	3.2	65.5
30	0	542.35	1922.5	7.2	64.2
30	50	682.2	2160	5.6	64.7

Solution temperature $= 870°F$, Quenchant bath temperature 85°F.

APPENDIX 3   Type I Polymer Quench Data: 7075-T73 Aluminum Sheet Probes

Polymer concentration %	Sheet thickness (in)	Circulation rate (ft/min)	Cooling rate (°F/sec)	Film coefficient (BTU/ Hr.ft.°F)	Quench factor	Predicted yield strength (KSI)
10	0.063	0	1277.20	2995.00	0.7	68.9
10	0.063	50	1546.90	3305.00	0.7	68.9
10	0.126	0	1019.25	2832.50	1.0	68.8
10	0.126	50	1107.60	2962.50	0.99	68.9
10	0.25	0	408.90	1832.50	2.7	68.4
10	0.25	50	638.70	2357.50	1.7	68.7
20	0.063	25	667.60	2190.00	2.0	68.6
30	0.063	0	501.20	1865.00	1.8	68.7
30	0.063	50	582.45	2015.00	1.8	68.7
30	0.126	0	355.35	1622.50	2.7	68.4
30	0.126	50	450.60	1835.00	2.2	68.5
30	0.25	0	205.85	1272.50	4.7	67.9
30	0.25	50	270.75	1470.00	4.0	68.1

Solution temperature = 870°F, Quenchant bath temperature 85°F.

APPENDIX 4 Type I Polymer Quenchant Data: 7075-T73 Aluminum Bar Probes

Polymer concentration %	Bar diameter (in)	Bath temperature (F)	Circulation rate (ft/min)	Cooling rate (°F/sec)	Film coefficient (BTU/Hr.ft.°F)	Quench factor	Predicted yield strength (KSI)
10	0.5	85	0	433.5	1210.0	2.6	68.5
10	0.5	85	50	458.1	1250.0	2.3	68.5
10	1	85	0	190.1	1232.5	5.8	67.6
10	1	85	50	195.2	1252.5	5.6	67.7
10	1.5	85	0	133.2	1275.0	8.9	66.8
10	1.5	85	50	129.7	1235.0	8.9	66.8
15	0.5	90	0	292.1	785.0	3.1	—
15	0.5	90	50	286.5	738.0	3.4	—
15	0.5	90	100	317.1	856.0	3.0	—
15	1	90	0	135.1	559.0	7.5	—
15	1	90	50	143.2	681.0	7.0	—
15	1	90	100	143.4	681.0	7.1	—
15	1.5	90	0	92.1	597.0	11.1	—
15	1.5	90	50	98.7	621.0	10.8	—
15	1.5	90	100	104.5	689.0	10.3	—
20	0.5	85	25	276.2	770.0	3.7	68.1
20	0.5	85	25	296.5	805.0	3.6	68.2
20	1	85	25	140.0	930.0	8.0	67.0
20	1.5	85	25	109.1	980.0	11.5	66.1
20	2	85	25	65.5	858.9	18.4	64.7
20	3	85	25	36.5	793.0	31.9	61.6
25	0.5	90	0	215.5	611.0	3.7	—
25	0.5	90	50	217.8	539.0	4.0	—
25	0.5	90	100	232.4	643.0	3.6	—
25	1	90	0	116.7	404.0	8.2	—
25	1	90	50	118.1	436.0	8.5	—

APPENDIX 4 Continued

Polymer concentration %	Bar diameter (in)	Bath temperature (F)	Circulation rate (ft/min)	Cooling rate (°F/sec)	Film coefficient (BTU/Hr.ft.°F)	Quench factor	Predicted yield strength (KSI)
25	1	90	100	121.8	500.0	8.5	—
25	1.5	90	0	78.0	507.0	11.9	—
25	1.5	90	50	86.3	460.0	12.0	—
25	1.5	90	100	91.0	497.0	11.9	—
30	0.5	85	0	178.3	457.5	5.1	67.8
30	0.5	85	50	217.7	615.0	4.8	67.9
30	1	85	0	112.8	775.0	10.6	66.4
30	1	85	50	107.3	750.0	10.3	66.4
30	1.5	85	0	68.3	647.5	16.0	65.0
30	1.5	85	50	73.0	329.8	15.4	65.1

Solution temperature = 870°F, Quenchant bath temperature 85°F.

Index